IMMC 2014

17th International Metallurgy and Materials Congress

17. Uluslararası Metalurji ve Malzeme Kongresi

UCTEA CHAMBER OF METALLURGICAL ENGINEERS

TMMOB METALURJİ MÜHENDİSLERİ ODASI

11-13 September / Eylül 2014

TÜYAP Fair, Convention & Congress Center, ISTANBUL-TURKEY

PROCEEDINGS BOOK
BİLDİRİLER KİTABI

www.facebook.com/IMMC2014 | www.metalurji.org.tr/IMMC2014

DEMİSAŞ

GEÇMİŞTEN GELECEĞE TAŞINAN KALİTE VE GÜVEN...
FOR THOSE SEEKING QUALITY AND RELIABLE PARTNERSHIP...

Talaşlı imalat yatırımıyla gücüne güç katan Demisaş, müşterilerinin özgün ihtiyaçlarına en üst düzeyde cevap verebilecek sistemleri oluşturarak katma değeri artıran en uygun çözümleri tek elden sunuyor.

With the edge gained by the addition of machining investment, Demisaş turned into a single point solution company, who possesses the flexibility to provide innovative solutions to its customers' unique needs.

www.demisas.com.tr

IMMC 2014

17th International Metallurgy and Materials Congress

17. Uluslararası Metalurji ve Malzeme Kongresi

11 - 13 Eylül 2014

TÜYAP Fuar ve Kogre Merkezi
İSTANBUL

11 - 13 September 2014

TÜYAP Fair Convention & Congress Center
ISTANBUL-TURKEY

PROCEEDINGS BOOK
BİLDİRİLER KİTABI

TMMOB METALURJİ MÜHENDİSLERİ ODASI
UCTEA CHAMBER OF METALLURGICAL ENGINEERS

IMMC 2014

CONGRESS SPONSORS
KONGRE SPONSORLARI

PLATINUM SPONSORS / PLATİN SPONSORLAR

AVEKS

ÇUKUROVA KİMYA

DEMİSAŞ

İDDMİB
İSTANBUL DEMİR ve DEMİR DIŞI METALLER İHRACATÇILARI BİRLİĞİ
ISTANBUL FERROUS AND NON-FERROUS METALS EXPORTERS' ASSOCIATION

UNIKON

The Editorial Board / Editörler

Prof.Dr. Macit ÖZENBAŞ

Hüseyin SAVAŞ

ISBN No : 978 - 605 - 01 - 0634 - 3

ISBN No : 978 - 605 - 01 - 0634 - 3

ORGANIZATION COMMITTEE
KONGRE YÜRÜTME KURULU

Chairman / Başkan

Prof.Dr. Macit ÖZENBAŞ	Middle East Technical University

Members / Üyeler

Assoc.Prof.Dr. Arcan F. DERİCİOĞLU	Middle East Technical University
Assoc.Prof.Dr. Derya DIŞPINAR	Istanbul University
Assoc.Prof.Dr. Caner DURUCAN	Middle East Technical University
Assist.Prof.Dr. Yunus Eren KALAY	Middle East Technical University
Prof.Dr. Bülent ÖNAY	Dokuz Eylül University
Hüseyin SAVAŞ	UCTEA Chamber of Metallurgical Engineers
Assist.Prof.Dr. Nuri SOLAK	Istanbul Technical University
Akif TUNABOYLU	CVS Technologies
Ahmet İrfan TÜRKKOLU	UCTEA Chamber of Metallurgical Engineers
Gürolhan YAŞAR	Demisaş Döküm Emaye Mamülleri Sanayi A.Ş

SESSION COORDINATORS

Biomaterials / Biyomalzemeler
Prof.Dr. Gültekin Göller
Assoc.Prof.Dr. Caner Durucan

Casting / Döküm
Gürolhan Yaşar
Assoc.Prof.Dr. Derya Dışpınar

Ceramic, Glasses and Refractory Materials / Seramik, Cam ve Refrakter Malzemeler
Prof.Dr. Abdullah Öztürk
Prof.Dr. Ali Aydın Göktaş

Composite Materials / Kompozit Malzemeler
Prof.Dr. Can Kurnaz
Prof.Dr. Cevdet Kaynak

Energy Materials / Enerji Malzemeleri
Prof.Dr. Macit Özenbaş
Assoc.Prof.Dr. Caner Durucan

Heat Treatment / Isıl İşlem
Prof.Dr. M. Vedat Akdeniz
Assist.Prof.Dr. Ziya Esen

Iron and Steel Metallurgy / Demir Çelik Metalurjisi
Akif Tunaboylu
Assist.Prof.Dr. Nuri Solak

Materials Characterization / Malzeme Karakterizasyonu
Assist.Prof.Dr. İlkay Kalay
Assist.Prof.Dr. Yunus Eren Kalay

OTURUM KOORDİNATÖRLERİ

Modelling and Simulation / Modelleme ve Simülasyon
Prof.Dr. C. Hakan Gür
Assist.Prof.Dr. Caner Şimşir

Nanomaterials / Nanomalzemeler
Prof.Dr. Macit Özenbaş
Assoc.Prof.Dr. Caner Durucan

Non-Ferrous Metallurgy / Demir Dışı Metaller Metalurjisi
Prof.Dr. Onuralp Yücel
Prof.Dr. Sebahattin Gürmen

Powder Metallurgy / Toz Metalurjisi
Assoc.Prof.Dr. Burak Özkal
Assist.Prof.Dr. Ziya Esen

Recyling and Sustainability / Geri Dönüşüm ve Sürdürülebilirlik
Prof.Dr. Servet Timur
Prof.Dr. Gökhan Orhan

Surface Treatment and Coatings / Yüzey İşlemler ve Kaplamalar
Prof.Dr. Mustafa Ürgen
Prof.Dr. Bülent Önay

Welding Metallurgy / Kaynak Metalurjisi
Prof.Dr. C. Hakan Gür

ADVISORY BOARD

Prof.Dr. Hatem AKBULUT	Sakarya University
Prof.Dr. Bünyamin AKSAKAL	Yıldız Technical University
Prof.Dr. Cüneyt ARSLAN	Istanbul Technical University
Prof.Dr. Süheyla AYDIN	Istanbul Technical University
Abdi AYDOĞDU	Maden Tetkik Arama Enstitüsü
Assist Prof.Dr. Tahsin BOYRAZ	Cumhuriyet University
Prof.Dr. Ümit CÖCEN	Dokuz Eylül University
Hayrettin ÇAYCI	Sarkuysan A.Ş.
Feyzi DEMİR	Teknometalurji Ltd. Şti.
Prof.Dr. Erdem DEMİRKESEN	Istanbul Technical University
Prof.Dr. İsmail DUMAN	Istanbul Technical University
Prof.Dr. Nuri DURLU	TOBB University
Prof.Dr. Mehmet DURMAN	Sakarya University
Serdar Ali EROL	Aveks İç ve Dış Ticaret A.Ş.
Prof.Dr. Niyazi ERUSLU	Yalova University
Assist Prof.Dr. Kadri Vefa EZİRMİK	Atatürk University
Atamer GİYİCİ	Kroman Çelik Sanayi A.Ş.
Prof.Dr. Mustafa GÜDEN	Izmir Institute of Technology
Assoc.Prof.Dr. Mehmet Ali GÜLGÜN	Sabancı University
Yaylalı GÜNAY	Günay Danışmanlık
Hüseyin Alper HIZLI	UCTEA Chamber of Metallurgy Engineers
M.Erhan İŞKOL	UCTEA Chamber of Metallurgy Engineers
Prof.Dr. Ali KALKANLI	Middle East Technical University
Prof.Dr. İshak KARAKAYA	Middle East Technical University
Prof.Dr. Eyüp Sabri KAYALI	Istanbul Technical University

KONGRE DANIŞMA KURULU

Mahmut KİPER	UCTEA Chamber of Metallurgy Engineers
Mustafa KOÇAK	Gedik Holding
Prof.Dr. Orhan Şerif KOMAÇ	Eskişehir Osmangazi University
Prof.Dr. Nilgün KUŞKONMAZ	Yıldız Technical University
Tunçay ŞULAN	UCTEA Chamber of Metallurgy Engineers
Prof.Dr. Bilgehen ÖGEL	Middle East Technical University
Hüseyin ÖNER	Marmara Metal
Prof.Dr. Lütfi ÖVEÇOĞLU	Istanbul Technical University
Alp Eren Sinan ÖZHAN	Aselsan
Prof.Dr. Tayfur ÖZTÜRK	Middle East Technical University
Alaattin Ayfer ÖZYURT	Çukurova Kimya Endüstrisi
Prof.Dr. Naci SEVİNÇ	Atılım University
Prof.Dr. Ender SUVACI	Anadolu University
Prof.Dr. Yılmaz TAPTIK	Istanbul Technical University
Barış TELSEREN	Bodycote Istaş
Prof.Dr. Muharrem TİMUÇİN	Middle East Technical University
Assist.Prof.Dr. Kazım TUR	Atılım University
Prof.Dr. Mehmet TÜRKER	Gazi University
Prof.Dr. Narin ÜNAL	Akdeniz University
Prof.Dr. Fatih ÜSTEL	Sakarya University
Assist.Prof.Dr. Çekdar VAKIFAHMETOĞLU	İstanbul Kemerburgaz University
Hakan YAŞAR	Demisaş Döküm Emaye Mam. San. A.Ş.
M.Uğur YILMAZ	İskenderun Demir Çelik
Prof.Dr. İbrahim YUSUFOĞLU	İstanbul University
M. Önder YÜCEL	Böhler Uddeholm Çelik

INTERNATIONAL SCIENTIFIC COMMITTEE
ULUSLARARASI BİLİM KURULU

Prof.Dr. Igor ALEXANDROV	Ufa State Aviation Technical University, Russia
Prof. Dr. S. Pamir ALPAY	University of Connecticut, USA
Prof. Dr. İlhan A. AKSAY	Princeton University, USA
Prof.Dr. Leandru G. BUJOREANU	Gheorghe Asachi Technical Univ. of IASI, Romania
Dr. Matthew J. KRAMER	Ames Laboratory, DOE, USA
Dr. Ali ERDEMIR	Argonne National Laboratories, USA
Prof.Dr. Zoltan GACSI	Miskolc University, Hungary
Prof.Dr. Janez GRUM	University of Ljubljana, Slovenia
Prof.Dr. Yutaka KAGAWA	University of Tokyo, Japan
Dr. Amine KHALİL	Argonne National Laboratories, USA
Prof.Dr. Hyoung Seop KIM	POSTECH, South Korea
Prof.Dr. M. Reza TOROGHINEJAD	Isfahan University of Technology, Iran

UCTEA CHAMBER OF METALLURGICAL ENGINEERS

The Chamber of Metallurgical Engineers (CME) is a non-profit public organization founded in 1970 and is one of twenty-three Chambers, which constitute the Union of Chambers of Turkish Engineers and Architects. The CME membership is currently 4500 and increasing each year with new graduates from national and foreign universities.

The main functions of CME are to organize required and necessary activities and conduct studies in broad fields of production, shaping, improving properties, destructive and non-destructive testing of metallic and nonmetallic materials, and also introducing the new technologies and the knowledges for the use and benefits of the members of CME and the country.

Within this context CME publishes a bimonthly journal entitled "METALURJI" and a bulletin called "BULTEN" in which news related to metallurgy and materials science appear. CME also organizes seminars, symposiums, panels, forums, congresses and fairs.

The supreme governing body of CME is the General Assembly which consists of the Chamber members and is elected biannually. Board of Directors elected at the General Assembly is responsible from the execution of the functions mentioned above. Additionally, detailed studies on certain specific subjects are conducted by "work groups" that consist of specialists from universities, research institutions and the industry and established by the Board of Directors.

TMMOB METALURJİ MÜHENDİSLERİ ODASI

Mühendis ve Mimar Odaları Birliği'ne bağlı olarak ilgili yasa hükümlerine uygun şekilde 1970 yılında kurulan Metalurji Mühendisleri Odası, kamu kurumu niteliğinde bir meslek kuruluşudur. Halen 4500 olan Metalurji Mühendisleri Odası üye sayısı, her yıl metalurji dalında mühendislik eğitimi veren yurtiçi ve yurtdışı üniversitelerinden mezun olanlarla artmaktadır.

Ülke ve Oda üyelerinin hak ve yararları gözetilerek, metal ve metal dışı malzemelerin üretimi, şekillendirilmesi, özelliklerinin geliştirilmesi, hasarlı ve hasarsız kontrolleri vb. alanlarda, ihtiyaç duyulan ve gerek görülen etkinliklerin organizasyonu ve çalışmaların yapılması, sektörümüzde yapılan çalışmaların, yeni teknolojilerin ve bilgi birikiminin çeşitli araçlarla meslektaşlarımıza ve sektör mensuplarına duyurulması, üyelerin durumlarının iyileştirilmesi, oda amaçlarının temelini oluşturmaktadır.

Bu amaçlar doğrultusunda Metalurji Mühendisleri Odası iki ayda bir "METALURJİ" dergisini ve Oda faaliyetlerinin, sektörel haberlerin güncel şekilde aktarıldığı "BÜLTEN"i yayınlamakta ve seminer, sempozyum, panel, forum, kongre, fuar gibi etkinlikler organize etmektedir.

İki yılda bir yapılan ve Odaya kayıtlı üyelerin katılımıyla gerçekleştirilen Genel Kurullarda oluşan Oda Yönetim Kurulu yukarıda bahsedilen çalışmaların yürütülmesinden sorumludur. Ayrıca, Oda Yönetim Kurulunca oluşturulan ve üniversite, araştırma kuruluşları ve sanayiden uzmanların yer aldığı çalışma gruplarınca belli konularda ayrıntılı çalışmalar yapılmaktadır.

17th International Metallurgy & Materials Congress IMMC'17, 2014 Istanbul

17th International Metallurgy & Materials Congress (IMMC 2014), organized by UCTEA Chamber of Metallurgical Engineers, is going to be held in the TUYAP Exhibition and Convention Center - İstanbul between 11-13 September 2014.

Starting from the first congress held in 1975, "IMMC" has been the leading activity covering all the related metallurgy-materials industry of Turkey.

During this activities, the participants will have the opportunity to follow the latest developments in the industry and academic researches of universities and institutions. Novel designs and products will also be presented by the national and international companies.

IMMC 2014 will be held at the same time and place with;

- 7th International Ankiros Foundry Congress, organized by **Turkish Foundrymen Association**,

and the following exhibitions organized by **Hannover-Messe Ankiros Fair Organization**:

- ANKIROS 2014, ANNOFER 2014 and TURKCAST 2014.

These congresses and fairs organized simultaneously by UCTEA Chamber of Metallurgical Engineers, Turkish Foundrymen Association, and Hannover-Messe Ankiros Fair Organization are the largest events of metallurgy-materials sector of Turkey. This organization awaited for a long time will cover all the expectations of the sector, and will contribute to its development.

There are165 papers from 18 different countries. These papers will be presented in 25 sessions namely; Recovery and Environment, Biomaterials, Energy Materials, Composite Materials, Nanomaterials, Powder Metallurgy, Iron and Steel Metallurgy, Non-Ferrous Metallurgy, Heat Treatment, Surface Treatment and Modification, Welding Metallurgy, R&D and Innovation, and Education.

Young Researcher Awards, which were started at the first time in IMMC'06, will be granted. The candidates who are participating to the congress with poster or oral presentation will prepare a poster for the award. Participants could be undergraduate, graduate, post-graduate students or engineers under 35 years old. Three participants will be awarded with equivalently.

During this congress, **"Microstructure Contest"** will be held under the technical and artistic categories. The best photo microstructure will be awarded in these two categories.

During the 17th International Metallurgy & Materials Congress (IMMC 2014) , **invited papers** will be presented by the following experts:
Bernd Friedrich, RWTH Aachen University, Germany; **Matthew J. Kramer**, Iowa State University, USA; **Toshio Maruyama**, Tokyo Institute of Technology, Japan; **Cenk Aktaş**, Leibniz Institute for New Materials, Germany; **Maria Pau Ginebra,** Universitat Politecnica de Catalunya, Spain; **Pance Naumov**, New York University Abu Dhabi, United Arab Emirates.
the following experts are invited contibutions from the industry;
Yaylalı Günay, Günay Danışmanlık, Türkiye; **Nihat Ali Işıtman**, Goodyear Innovation Center Luxembourg, Luxembourg; **Akın Malaş**, Linde Gaz, Germany; **Ziya Can Aksakal**, İnci Akü, Türkiye; **Başak Bengü**, Arçelik, Türkiye; **Mesut Güney**, Borçelik, Türkiye.

We expect and wish success on this greatest meeting of the metalurgy sector with it's congresses and fairs.

17. Uluslararası Metalurji ve Malzeme Kongresi
IMMC'17, 2014 İstanbul

17.Uluslararası Metalurji ve Malzeme Kongresi, 11-13 Eylül 2014 tarihlerinde TÜYAP Fuar ve Kongre Merkezi-Beylikdüzü / İstanbul'da, TMMOB Metalurji Mühendisleri Odası tarafından düzenlenecektir.

1975 yılından bu yana gerçekleştirilen kongremiz, sürekli gelişme göstererek tüm sektörü kucaklayan ve bu alanda ülkemizde yapılan en kapsamlı etkinliktir.

Bu etkinlik sayesinde, katılımcılar, mesleğimizle ilgili dünyadaki gelişmelerden, üniversiteler ve diğer kuruluşlarda yapılan araştırmalardan, teknolojik ilerlemelerden, yeni ürünler ve tasarımlardan haberdar olmaktadır.
Bu kongre ile eş zamanlı olarak;

Hannover-Messe Ankiros Fuarcılık A.Ş. tarafından;
- ANKIROS 2014, ANNOFER 2014 ve TURKCAST 2014

Türkiye Döküm Sanayicileri Derneği tarafından;
- 7.Uluslararası Ankiros Döküm Kongresi, düzenlenecektir.

TMMOB Metalurji Mühendisleri Odası, Türkiye Döküm Sanayicileri Derneği ve Hannover-Messe Ankiros Fuarcılık A.Ş. tarafından eş zamanlı olarak yapılan kongreler ve fuarlar ile metalurji sektörünün en büyük birlikteliği bir araya gelmektedir. Bu birliktelik metalurji sektörünün gelişmesine büyük katkılar sağlamaktadır.

17.Uluslararası Metalurji ve Malzeme Kongresi'nde yurt içinden ve yurt dışında 18 ülkeden toplam 165 bildiri sunulacaktır.

Biyomalzemeler, Döküm, Seramik-Cam-Refrakter Malzemeler, Kompozit Malzemeler, Enerji Malzemeleri, Isıl İşlem, Demir Çelik Metalurjisi, Malzeme Karakterizasyonu, Nanomalzemeler, Demir Dışı Metaller Metalurjisi, Toz Metalurjisi, Geri Dönüşüm ve Sürdürülebilirlik, Yüzey İşlemler ve Kaplamalar, Kaynak Metalurjisi, Ar-Ge ve İnovasyon ve Eğitim konu başlıklarında toplam 25 oturum gerçekleştirilecektir.

13.Uluslararası Metalurji ve Malzeme Kongresi'nde verilmeye başlanan **"Genç Araştırmacı Ödülü"** bu kongre'de de verilecektir. Kongreye sözlü yada poster olarak bildiri sunan ve bu bildirinin posterini hazırlayan lisans öğrencileri, yüksek lisans, doktora çalışmalarına devam eden mühendisler veya 35 yaş altı mühendislerden 3 kişiye oylama sonucunda eş değer ödül verilecektir.

Bu kongremizde **"Mikroyapı Yarışması"** kapsamında teknik ve artistik olmak üzere 2 kategori de en iyi mikroyapı fotoğrafına ödül verilecektir.

17.Uluslararası Metalurji ve Malzeme Kongresinde;
Bernd Friedrich, RWTH Aachen University, Germany; **Matthew J. Kramer**, Iowa State University, USA; **Toshio Maruyama**, Tokyo Institute of Technology, Japan; **Cenk Aktaş**, Leibniz Institute for New Materials, Germany; **Maria Pau Ginebra**, Universitat Politecnica de Catalunya, Spain; **Pance Naumov**, New York University Abu Dhabi, United Arab Emirates **davetli konuşmacı** olarak,

Yaylalı Günay, Günay Danışmanlık, Türkiye; **Nihat Ali Işıtman**, Goodyear Innovation Center Luxembourg, Luxembourg; **Akın Malaş**, Linde Gaz, Germany; **Ziya Can Aksakal**, İnci Akü, Türkiye; **Başak Bengü**, Arçelik, Türkiye; **Mesut Güney**, Borçelik, Türkiye, **endüstriden davetli konuşmacı** olarak katılacaklardır.

Kongreleri ve fuarları ile metalurji sektörünün bu en büyük buluşmasının başarılı geçmesini beklemekteyiz.

INVITED LECTURERS
DAVETLİ KONUŞMACILAR

11 September Thursday / 11 Eylül Perşembe 2014

Hall Marmara / Salon Marmara

13.30 - 14.10 **Mechanical Properties of Organic Molecular Crystals**
Organik Moleküler Kristallerin Mekanik Özellikleri

Pance Naumov
New York University Abu Dhabi
United Arab Emirates

11 September Thursday / 11 Eylül Perşembe 2014

Hall Marmara / Salon Marmara

17.00 - 17.40 **Recent Advances in Bioceramics Design: Key Biomaterial Properties for Bone Regeneration**
Biyoseramik Alanındaki Güncel Gelişmeler: Kemik Dokusu Oluşumu İçin Gerekli Önemli Biyomalzeme Özellikleri

Maria Pau Ginebra
Universitat Politecnica de Catalunya
Spain

12 September Friday / 12 Eylül Cuma 2014

Hall Marmara / Salon Marmara

11.20 - 12.00 **Techniques for Characterizing Complex Chemistries at the Nanoscale**
Kompleks Yapıların Nanoboyutlarda Karakterizasyon Teknikleri

Matthew J. Kramer
Iowa State University
USA

12 September Friday / 12 Eylül Cuma 2014

Hall Marmara / Salon Marmara

13.30 - 14.10 **Chemical Potential Distribution and Microstructure Evolution in Oxide Scales during High Temperature Oxidation of Metals**
Metallerin Yüksek Sıcaklık Korozyonuyla Oluşan Oksit Kabuklarında İçyapı Gelişimi ve Kimyasal Potansiyel Dağılımı

Toshio Maruyama
Tokyo Institute of Technology
Japan

INVITED LECTURERS
DAVETLİ KONUŞMACILAR

12 September Friday / 12 Eylül Cuma 2014

Hall Karadeniz / Salon Karadeniz

15.10 - 15.50 **Recycling of Metals from Electronic Scrap – Finding the Optimum Between Pretreatment and Metallurgy**
Elektronik Hurdadan Metallerin Geri Kazanımı-Önişlem Süreçleri ve Metalurji Arasında Optimumun Belirlenmesi

Bernd Friedrich
RWTH Aachen University
Germany

13 September Saturday / 13 Eylül Cumartesi 2014

Hall Marmara / Salon Marmara

11.20 - 12.00 **Selective Laser Sintering (SLS)/Selective Laser Melting (SLM) for Functional Applications**
İşlevsel Uygulamalar için Seçmeli Lazer Sinterleme / Seçmeli Lazer Eritme

Cenk Aktaş
Leibniz Institute for New Materials
Germany

THE CONTRIBUTIONS FROM THE INDUSTRY INVITED
ENDÜSTRIDEN KATKILAR

11 September Thursday / 11 Eylül Perşembe 2014
Hall Marmara / Salon Marmara

15.10 - 15.40 **Re-Inventing the Wheel With Materials Nanotechnology?**
Malzeme Nanoteknolojisi ile Tekerlek Yeniden mi İcat Ediliyor ?
Nihat Ali Işıtman
Goodyear Innovation Center Luxembourg
Luxembourg

11 September Thursday / 11 Eylül Perşembe 2014
Hall Karadeniz / Salon Karadeniz

15.10 - 15.40 **Easy to Clean and Antibacterial Coatings for White Good Applications**
Beyaz Eşya Uygulamalarında Kolay Temizlenebilir ve Antibakteriyel Kaplamalar
Başak Bengü
Arçelik A.Ş.
Türkiye

12 September Friday / 12 Eylül Cuma 2014
Hall Marmara / Salon Marmara

15.10 - 15.40 **High Energy and Power Density Battery Production Process in Turkey**
Türkiye'de Yüksek Enerji ve Güç Yoğunluklu Pil Üretimi Yöntemleri
Ziya Can Aksakal
İnci Akü
Türkiye

12 September Friday / 12 Eylül Cuma 2014
Hall Marmara / Salon Marmara

17.00 - 17.30 **Furnace Atmospheres and Troubleshooting in Heat Treatment**
Isıl İşlem Fırın Atmosferleri ve Problem Çözüm Yöntemleri
Akın Malaş
Linde Gaz
Germany

THE CONTRIBUTIONS FROM THE INDUSTRY INVITED
ENDÜSTRIDEN KATKILAR

12 September Friday / 12 Eylül Cuma 2014

Hall Karadeniz / Salon Karadeniz

11.20 - 11.50 **An Overview of Flat Steel Sector in Turkey**
Türkiye'de Yassı Çelik Sektörüne Genel Bir Bakış

Mesut Güney
Borçelik
Türkiye

13 September Saturday / 13 Eylül Cumartesi 2014

Hall Karadeniz / Salon Karadeniz

11.20 - 11.50 **New World, New Trends, Technologies and the Turkish Foundry Industry**
Yeni Dünya, Yeni Eğilimler, Teknolojiler ve Türk Döküm Sektörü

Yaylalı Günay
Günay Danışmanlık
Türkiye

SPECIAL SESSION LECTURERS
ÖZEL OTURUM KONUŞMACILARI

13 September Saturday / 13 Eylül Cumartesi 2014

Hall Marmara / Salon Marmara

13.30 - 13.55 **Ar-Ge - İnovasyon ve Teknoloji Yönetimi**
R&D - Innovation and Technology Management

Tayfun Sığırtmaç
Coşkunöz Metal Form A.Ş.
Türkiye

13 September Saturday / 13 Eylül Cumartesi 2014

Hall Marmara / Salon Marmara

13.55 - 14.20 **Endüstriyel Ar-Ge Çalışmalarında İşbirliği Mekanizmalarının Rolü**
Role of Strategic Cooperations in Industrial Research and Development Activities

Altan Yıldırım
Farplas A.Ş.
Türkiye

13 September Saturday / 13 Eylül Cumartesi 2014

Hall Marmara / Salon Marmara

14.20 - 14.45 **Sanayi Kurumlarında Ar-Ge ve İnovasyon ile Katma Değerin Arttırılması**
Increasing the Added Value by R&D and Innovation in Industry

Koray Mert Yılmaz
Cengiz Makine Sanayi
Türkiye

13 September Saturday / 13 Eylül Cumartesi 2014

Hall Marmara / Salon Marmara

15.00 - 15.25 **Trends in University Education and Engineering Education**
Universite Eğitiminde Trendler ve Mühendislik Eğitimi

Yılmaz Taptık
İstanbul Technical University
Türkiye

SPECIAL SESSION LECTURERS
ÖZEL OTURUM KONUŞMACILARI

13 September Saturday / 13 Eylül Cumartesi 2014

Hall Marmara / Salon Marmara

15.25 - 15.50 **Redefining Core Curriculum for Materials and Metallurgical Engineering**
Malzeme ve Metalurji Mühendisliğinde Eğitim Programı Nasıl Olmalı?

Tayfur Öztürk
Middle East Technical University
Türkiye

13 September Saturday / 13 Eylül Cumartesi 2014

Hall Marmara / Salon Marmara

15.50 - 16.15 **Adoption of E-learning Tools in Metallurgical and Materials Engineering Education**
Çevrimiçi Eğitim Araçlarının Metalurji ve Malzeme Mühendisliği Eğitimine Uyarlanması

Arda Çetin
Mühendishane
Türkiye

13 September Saturday / 13 Eylül Cumartesi 2014

Hall Marmara / Salon Marmara

16.15 - 16.40 **Introducing Metallurgical and Materials Engineering to Prospective College Students**
Lise Öğrencilerine Yönelik Metalurji ve Malzeme Mühendisliği Tanıtımları

Yunus Eren Kalay
Middle East Technical University
Türkiye

CONGRESS PROGRAMME
KONGRE PROGRAMI

NANOMATERIALS
NANOMALZEMELER

Session Chairman / Oturum Başkanı: **ARCAN F. DERİCİOĞLU**

13.30 - 14.10

Mechanical Properties of Organic Molecular Crystals

Organik Moleküler Kristallerin Mekanik Özellikleri

Pance Naumov
New York University Abu Dhabi
United Arab Emirates
(Invited Lecturer)

14.10 - 14.30

Thermal Plasma Synthesis of Metallic Nanoparticles

Metalik Nanoparçacıkların Termal Plazma Yöntemiyle Sentezlenmesi

Burak Aktekin, Tayfur Öztürk
Middle East Technical University
Türkiye

14.30 - 14.50

Production of NiO/Al_2O_3 Nanosized Catalysts by Ultrasonic Spray Pyrolysis (USP) Process

Nikel Alüminat Nano Katalizörlerinin Ultrasonik Sprey Piroliz (USP) Yöntemi ile Üretimi

Tunçağ Cihangir Şen[1], Burçak Ebin[2], Sebahattin Gürmen[1]
[1]İstanbul Technical University, [2]Nanokomp Advanced Materials R&D Consulting Co. Ltd.
Türkiye

NANOMATERIALS
NANOMALZEMELER

Session Chairman / Oturum Başkanı: **ÇEKDAR VAKIFAHMETOĞLU**

15.10 - 15.40

Re-Inventing the Wheel with Materials Nanotechnology?

Malzeme Nanoteknolojisi ile Tekerlek Yeniden mi İcat Ediliyor?

Nihat Ali Işıtman
Goodyear Innovation Center Luxembourg
Luxembourg

(Invited Contribution from the Industry)

15.40 - 16.00

Synthesis of Nano- Manganese Oxide (Mn_2O_3) Particles by Using High Frequency-Induction System

Nano Mangan Oksit (Mn_2O_3) Partiküllerinin Yüksek Frekanslı İndüktif Sistem ile Sentezi

Levent Kartal, Yasin Kılıç, Servet Timur
İstanbul Technical University
Türkiye

16.00 - 16.20

Synthesis and Applications of Anti-Microbial Hematite Nanorods (α-Fe_2O_3) and Their Coatings on 3-D Filters

Anti-Mikrobiyal Özellik Kazandırmak İçin Filtrelere Kaplanılan Hematit Nanorodların Sentezi ve Uygulaması

Ahmet Özkan, Cansu Noberi, Figen Kaya, Cengiz Kaya
Yıldız Technical University
Türkiye

16.20 - 16.40

Al-Re Amorphous-Nanocrystal Composite Alloys

Al-Re Bazlı Amorf-Nanokristal Kompozit Yapılı Alaşımlar

Mustafacan Kutsal, Can Yıldırım, Tuba Demirtaş, Fatih Sıkan, Yunus Eren Kalay
Middle East Technical University
Türkiye

BIOMATERIALS
BİYOMALZEMELER

Session Chairman / Oturum Başkanı: **CANER DURUCAN**

17.00 - 17.40

Recent Advances in Bioceramics Design: Key Biomaterial Properties for Bone Regeneration

Biyoseramik Alanındaki Güncel Gelişmeler: Kemik Dokusu Oluşumu İçin Gerekli Önemli Biyomalzeme Özellikleri

Maria Pau Ginebra
Universitat Politecnica de Catalunya
Spain
(Invited Lecturer)

17.40 - 18.00

Cement-Type Reactivity and Setting Efficiency of Calcium-Phosphate Based Composite Bone Filler

Kalsiyum Fosfat Esaslı Kompozit Kemik Çimentolarının Reaksiyon Kinetiği ve Mekanik Özellikleri

Gözde Alkan, Caner Durucan
Middle East Technical University
Türkiye

18.00 - 18.20

Characterization of Apatite Formation Ability of Alkali Treated Bulk Ti6Al7Nb Alloy by in Vitro Studies

Alkali Muamele Edilmiş olan Ti6Al7Nb Alaşım Kütlelerinin in Vitro Çalışmalarla Apatit Oluşturma Potansiyelinin Belirlenmesi

Ezgi Bütev[1,2], Elif Eda Yeni[3], Emre Yılmaz[1], Ziya Esen[1], Şakir Bor[2]
[1]Çankaya University, [2]Middle East Technical University, [3]Anadolu University
Türkiye

SURFACE TREATMENT and COATINGS
YÜZEY İŞLEMLERİ ve KAPLAMALAR

Session Chairman / Oturum Başkanı: **KÜRŞAT KAZMANLI**

13.30 - 13.50

Synthesis of TiB_2 From Molten Salts on Different Substrates

Ergimiş Tuzlardan Farklı Taban Malzemeler Üzerinde TiB_2 Biriktirilmesi

Perim Özkalafat, Güldem Kartal Şireli, Servet Timur
İstanbul Technical University
Türkiye

13.50 - 14.10

An Innovative Silver Lines Embedded Substrate Design for Dye Sensitized Solar Modules

Boya Uyarımlı Güneş Modülleri İçin Gümüş Yolluk Gömülü İnovatif bir Altlık Tasarımı

Kerem Çağatay İçli, Ahmet Macit Özenbaş
Middle East Technical University
Türkiye

14.10 - 14.30

Gaseous Nitriding of 31CrMoV9 Steel: Modelling Residual Stress – Depth Profile Relation Using Indentation Method

31CrMoV9 Çeliğinin Gaz Nitrürlenmesi: Kalıntı Gerilmeleri-Derinlik İlişkisinin Batırma Yöntemiyle Modellenmesi

Rıdvan Gecü[1], Ahmet Fatih Yayla[2], Nuri Solak[2], Kürşat Kazmanlı[2], Mustafa Ürgen[2]
[1]Yıldız Technical University, [2]İstanbul Technical University
Türkiye

14.30 - 14.50

Accelerated Electrochemical Corrosion Testing of Powder Painted Carbon Steel Surfaces via AC DC AC Technique and Its Potential for Industrial Use

AC DC AC Tekniği ile Toz Boya Uygulanmış Karbon Çeliği Yüzeylere Elektrokimyasal Hızlandırılmış Korozyon Testi Uygulanması ve Yöntemin Endüstriyel Olarak Kullanım Potansiyeli

Aslı Özel[1,2]
[1]Arçelik A.Ş., [2]İstanbul Technical University
Türkiye

SURFACE TREATMENT and COATINGS
YÜZEY İŞLEMLERİ ve KAPLAMALAR

Session Chairman / Oturum Başkanı: **MUSTAFA ÜRGEN**

15.10 - 15.40

Easy to Clean and Antibacterial Coatings for White Good Applications

Beyaz Eşya Uygulamalarında Kolay Temizlenebilir ve Antibakteriyel Kaplamalar

Başak Bengü
Arçelik A.Ş.
Türkiye

(Invited Contribution from the Industry)

15.40 - 16.00

Conical Shaped Surface Features Formation on Different Aluminum Alloys

Farklı Alüminyum Alaşımlarının Yüzeylerinde Konik Şekilli Yapıların Oluşumu

B. Deniz Polat, Özgül Keleş, Mustafa Ürgen
İstanbul Technical University
Türkiye

16.00 - 16.20

Surface Treatment and Characterization of the Ti6Al4V Alloy Powders for Biomedical Applications

Biyomedikal Uygulamalar İçin Ti6Al4V Alaşım Tozlarının Yüzey İşlemi ve Karakterizasyonu

Elif Eda Yeni[1], Ezgi Bütev[2,3], Emre Yılmaz[2], Ziya Esen[2], Servet Turan[1]
[1]Anadolu University, [2]Çankaya University, [3]Middle East Technical University
Türkiye

16.20 - 16.40

The Effect of Annealing Parameter on Anodizing Performance of the AA5005 Aluminum Alloy Produced by Twin Roll Casting

Çift Merdaneli Döküm Yöntemiyle Üretilen AA5005 Alüminyum Alaşımının Anotlama Davranışına Tavlamanın Etkisi

Beyza Yeşilbağ[1], Nuri Solak[2]
[1]Teknik Alüminyum, [2]İstanbul Technical University
Türkiye

COMPOSITE MATERIALS
KOMPOZİT MALZEMELER

Session Chairman / Oturum Başkanı: **CEVDET KAYNAK**

17.00 - 17.20

Production and Characterization of Bronze-Cr-Ni Composites Produced by Powder Metallurgy

Toz Metalurjisi Yöntemiyle Bronz-Cr-Ni Kompozitlerinin Üretimi ve Karakterizasyonu

Aykut Çanakçı, Temel Varol, Hamdullah Çuvalcı, Fatih Erdemir, Serdar Özkaya
Karadeniz Technical University
Türkiye

17.20 - 17.40

Processing and Characterization of Carbon Fiber-Reinforced Silicon Carbide (C/SiC) Matrix Composites

Karbon Fiber Takviyeli Silisyum Karbür Matrisli Kompozitlerin Üretimi ve Karakterizasyonu

Simge Tülbez, Arcan F. Dericioğlu
Middle East Technical University
Türkiye

17.40 - 18.00

Incorporation of Fly Ash Into PVC Based Plastic Composites

PVC Esaslı Plastik Kompozitlere Uçucu Kül Eklenmesi

Raman Aliti, Anita Grozdanov, Perica Paunović
University Ss Cyril and Methodius in Skopje
Macedonia

CERAMICS, GLASSES and REFRACTORY MATERIALS
SERAMİK, CAM ve REFRAKTER MALZEMELER

Session Chairman / Oturum Başkanı: **ABDULLAH ÖZTÜRK**

13.30 - 13.50

Synthesis and Sintering of TiB_2

TiB_2'ün Sentezi ve Sinterlenmesi

Ahmet Turan[1,2], Filiz Çınar Şahin[1], Gültekin Göller[1], Onuralp Yücel[1]

[1]İstanbul Technical University, [2]Yalova University

Türkiye

13.50 - 14.10

UO_2-Gd_2O_3 Burnable Absorber Nuclear Fuel Production and Characterization at TAEK-CNRTC

TAEK-CNRTC Merkezinde UO_2-Gd_2O_3 Yanabilir Soğurucu Nükleer Yakıt Üretimi ve Karakterizasyonu

Ahmet Yaylı, İlker Özdemir, Elvan Başçetin, Sevgi Akbal, Ecem Altınok, Ferhan Can, A. Sibel Sökücü

Cekmece Nuclear Research and Training

Türkiye

14.10 - 14.30

Microstructural Development and Adherence Ability of Thin Silica Sol Gel Films on Al Alloy; Effect of Additives and Substrate Pretreatment

İnce Silika Sol-Jel Filmlerin Al Alaşımları Üzerindeki Mikroyapı Gelişimleri ve Yapışma Özellikleri; Katkı Maddelerinin ve Altlık Önişleminin Etkisi

Ali Aydın Göktaş

Dokuz Eylül University

Türkiye

14.30 - 14.50

A Response Surface Analysis of the Process of Biosorption of Cd(II) Ions by Using Rice Husk

Pirinç Kabukları Kullanılarak Cd(II) İyonlarının Biyosoğurma İşleminin Yüzey Analizi

Kiril Lisichkov, Mahi Ljatifi, Stefan Kuvendziev, Mirko Marinkovski

University Ss Cyril and Methodius in Skopje

Macedonia

CERAMICS, GLASSES and REFRACTORY MATERIALS
SERAMİK, CAM ve REFRAKTER MALZEMELER

Session Chairman / Oturum Başkanı: **ALİ AYDIN GÖKTAŞ**

15.10 - 15.30

Effect of Molten Salt Synthesis Parameters on the Morphology and Magnetic Properties of Barium Hexaferrite Ceramics Synthesized in x wt% NaCl-(100–X) wt% KCl Fluxes

Eriyik Tuz Yöntemi Parametrelerinin Ağırlıkça X % NaCl-(100–X) % KCl Eriyik Tuzlarında Sentezlenen Baryum Hekzaferrit Seramiklerinin Morfoloji ve Manyetik Özelliklerine Etkileri

Seray Kaya, Eda Aydoğan, Arcan F. Dericioğlu
Middle East Technical University
Türkiye

15.30 - 15.50

Production of ZrB_2-TiB_2 Ceramic Powders by SHS

Kendiliğinden İlerleyen Yüksek Sıcaklık Sentezi Yöntemi ile ZrB_2-TiB_2 Kompozit Seramik Tozlarının Üretilmesi

Ayşe Ece Yıldızçelik[1], Mehmet Buğdaycı[1,2], Onuralp Yücel[1]
[1]İstanbul Technical University, [2]Yalova University
Türkiye

15.50 - 16.10

Thermal and Structural Characterization of Quaternary Antimonite Glasses

Antimon Oksit Esaslı Camların Isıl ve Yapısal İncelenmesi

Ali Erçin Ersundu[1], Miray Çelikbilek[2], Mohamed Toufik Soltani[3], Süheyla Aydın[2]
[1]Nişantaşı University, [2]İstanbul Technical University, [3]University of Biskra
Türkiye, Algeria

16.10 - 16.30

Thermal and Environmental Characteristics of Glass Produced from Metalurgical Wastes

Metalurjik Artıklardan Üretilen Camın Termal ve Çevresel Karakteristikleri

Ejup Ljatifi[1], Alexandra Kamusheva[2], Alexander Karamanov[2], Perica Paunović[1]
[1]University Ss Cyril and Methodius in Skopje, [2]Bulgarian Academy of Sciences
Macedonia, Bulgaria

WELDING METALLURGY and NON-DESTRUCTIVE TESTING
KAYNAK METALURJİSİ ve TAHRİBATSIZ MUAYENE

Session Chairman / Oturum Başkanı: **AHMET TOPUZ**

16.50 - 17.10

Estimation of Residual Stresses in Steel Components by Magnetic Barkhausen Noise Technique: Welding and Shot-Peening

Çelik Parçalarda Manyetik Barkhausen Gürültü Tekniği Yöntemiyle Kalıntı Gerilimi Tayini

C. Hakan Gür
Middle East Technical University
Türkiye

17.10 - 17.30

Development of New Lead-Free Solder Alloys

Kurşun İçermeyen Yeni Lehim Malzemelerinin Geliştirilmesi

Serkan Yılmaz, Anıl Kantarcıoğlu, Yunus Eren Kalay
Middle East Technical University
Türkiye

17.30 - 17.50

Metallurgical Changes in the Forge Weld Area During Post Weld Local Heat Treatment

Kaynak Sonrası Bölgesel Isıl İşlemi Sırasında Dövme Kaynağı Bölgesinde Oluşan Metalurjik Değişimler

Rrahim Maksuti[1], Hamit Mehmeti[2], Nexhat Çerkini[1]
[1]Newco IMK Pipe Factory, [2]State University of Tetova
Kosovo, Macedonia

MATERIALS CHARACTERIZATION
MALZEME KARAKTERİZASYONU

Session Chairman / Oturum Başkanı: **TAYFUR ÖZTÜRK**

10.00 - 10.20

Synthesis of TiO_2 and Titanate Nanopowders in Various Morphologies via Hydrothermal Method

Hidrotermal Yöntemle Farklı Morfolojilerde TiO_2 ve Titanat Nanotoz Sentezi

Nursev Bilgin[1], Abdullah Öztürk[1], Jongee Park[2]
[1]Middle East Technical University, [2]Atılım University
Türkiye

10.20 - 10.40

The Effect of the Contact Cycles Microstructure and Performance of Electrical Contact Materials

Elektrik Kontak Malzemelerinin Mikroyapısı ve Performansı Üzerine Kontak Çevriminin Etkisi

Aykut Çanakçı, Temel Varol, Hüseyin İpek, Sinan Amran
Karadeniz Technical University
Türkiye

10.40 - 11.00

Production and Development of Dye-Sensitized Solar Cells on Flexible Polymeric Substrates by Binder-Free Electrophoretic Deposition Method with a Subsequent Cold Isostatic Pressing Treatment

Boya Duyarlı Güneş Gözelerinin Esnek Polimer Tabanlıklar Üzerine Elektroforetik Kaplama ve Soğuk İzostatik Presleme Yöntemi ile Üretimi ve Geliştirilmesi

Bahadır Can Kocaoğlu, Ahmet Macit Özenbaş
Middle East Technical University
Türkiye

MATERIALS CHARACTERIZATION
MALZEME KARAKTERİZASYONU

Session Chairman / Oturum Başkanı: **İLKAY KALAY**

11.20 - 12.00

Techniques for Characterizing Complex Chemistries at the Nanoscale

Kompleks Yapıların Nanoboyutlarda Karakterizasyon Teknikleri

Matthew J. Kramer
Iowa State University
USA
(Invited Lecturer)

12.00 - 12.20

Transmission Electron Microscopy and Atom Probe Tomography Studies of Laves Phase Nucleation in Creep of a 12% Cr Tempered Martensite Ferritic Steel

Sürünme Testlerinde Laves Fazı Çekirdeklenmesinin Menevişlenmiş %12Cr Martensit Ferrit Çeliklerinde Geçirimli Elektron Mikroskobu ve Atom Probu Tomografi Yöntemleri ile İncelenmesi

Mehmet İkbal Işık, Aleksander Kostka, Gunther Eggeler
Max Planck Institut, Ruhr-Universitat Bochum
Germany

12.20 - 12.40

Electron Microscopy Analysis of Heat-Treated CN3MN Grade Super Austenitic Stainless Steels

Isıl İşlem Görmüş CN3MN Süper Östenitli Paslanmaz Çeliklerin Elektron Mikroskobu ile İncelenmesi

Mertcan Başkan[1], Scott L. Chumbley[2], Yunus Eren Kalay[1]
[1]Middle East Technical University, [2]Iowa State University
Türkiye, USA

MATERIALS CHARACTERIZATION
MALZEME KARAKTERİZASYONU

Session Chairman / Oturum Başkanı: **BÜLENT ÖNAY**

13.30 - 14.10

Chemical Potential Distribution and Microstructure Evolution in Oxide Scales during High Temperature Oxidation of Metals

Metallerin Yüksek Sıcaklık Korozyonuyla Oluşan Oksit Kabuklarında İçyapı Gelişimi ve Kimyasal Potansiyel Dağılımı

Toshio Maruyama
Tokyo Institute of Technology
Japan
Invited Lecturer)

14.10 - 14.30

Particular Aspects of Constrained Recovery Shape Memory Effect in a Severely Plastic Deformed Fe-Mn-Si-Cr Alloy

Yoğun Plastik Deforme Olmuş Fe-Mn-Si-Cr Alaşımlara Özel Kısıtlı Geri Kazanımlı Şekil Bellek Etkisi

Leandru-Gheorghe Bujoreanu[1], Gheorghe Gurau[2], Radu-Ioachim Comaneci[1], Burak Özkal[3], Elena Mihalache[3]
[1]Gheorghe Asachi Technical University of Iaşi,
[2]Dunarea de Jos University of Galati, [3]İstanbul Technical University
Romania, Türkiye

14.30 - 14.50

Characterization of Multi Walled Carbon Nanotube (MWCNT)-Maleic Anhydride-Octene1 / Copper Sulfide Nanocomposite with Instrumental Methods

Çok Cidarlı Karbon Nanotüp (ÇCKNT) -Maleik Anhidrit Okten 1 / Bakır Sülfür Nano Kompozitlerin Enstrümental Yöntemlerle Karakterizasyonu

Melek Cumbul Altay[1], Elvin Y. Malikov[2], Goncha M. Eyvazova[2], Mustafa B. Muradov[2], Oktay H. Akperov[2], Robert Puskas[3], Daniel Madarasz[3], Zoltan Konya[3], Akos Kukovecz[3]
[1]İstanbul University, [2]Baku State University, [3]University of Szeged
Türkiye, Azerbaijan, Hungary

ENERGY MATERIALS
ENERJİ MALZEMELERİ

Session Chairman / Oturum Başkanı: **ÖZGÜL KELEŞ**

15.10 - 15.40

High Energy and Power Density Battery Production Process in Turkey
Türkiye'de Yüksek Enerji ve Güç Yoğunluklu Pil Üretimi Yöntemleri

Ziya Can Aksakal
İnci Akü
Türkiye

(Invited Contribution from the Industry)

15.40 - 16.00

ZrO_2 Blocking Layer Application on Dye Sensitized Solar Cells
ZrO_2 Bloklama Tabakasının Boya Uyarımlı Güneş Hücrelerinde Kullanımı

Halil İbrahim Yavuz, Kerem Çağatay İçli, Ahmet Macit Özenbaş
Middle East Technical University
Türkiye

16.00 - 16.20

Combinatorial Thin Film Membranes for Hydrogen Separation
Hidrojen Ayırmaya Yönelik İnce Film Membranların Kombinatoryal Yöntemle Geliştirilmesi

Fatih Pişkin, Tayfur Öztürk
Middle East Technical University
Türkiye

16.20 - 16.40

Thermal Stability Tests of Uranium Dioxide and Thorium Dioxide
Uranyum Dioksit ve Toryum Dioksit Nükleer Yakıtların Termal Kararlılık Testleri

Ahmet Yaylı, İlker Özdemir, Şinasi Ekinci, Mücahit Çetin, Sebahahattin Güvendik, A. Sibel Sökücü, Sevgi Akbal, Ferhan Can, Esra Keşaf
Cekmece Nuclear Research and Training
Türkiye

HEAT TREATMENT
ISIL İŞLEM

Session Chairman / Oturum Başkanı: **M. VEDAT AKDENİZ**

17.00 - 17.30

Furnace Atmospheres and Troubleshooting in Heat Treatment

Isıl İşlem Fırın Atmosferleri ve Problem Çözüm Yöntemleri

Akın Malaş
Linde Gaz
Germany
(Invited Contribution from the Industry)

17.30 - 17.50

Effect of Prior Heat Treatment on the Microstructure and Mechanical Properties of Austempered AISI 4340 Steel

Ön Isıl İşlemin Östemperlenmiş AISI 4340 Çeliğinin Mikroyapısı ve Mekanik Özelliklerine Olan Etkisi

Erkan Konca[1], Kazım Tur[1], Mustafa Elmadağlı[2], Fatih Güner[2]
[1]Atılım University, [2]Roketsan Missile Industries Inc.
Türkiye

17.50 - 18.10

The Effect of Hydrogen Content Over the Aging Characteristics of Al-Cu Alloy

Al-Cu Alaşımında Hidrojen İçeriği ve Su Verme Ortamlarının Yaşlandırma Üzerine Etkisi

Muhammed Raşit Eryılmaz[1], Muhammet Uludağ[1], Derya Dışpınar[2]
[1]Selçuk University, [2]İstanbul University
Türkiye

18.10 - 18.30

Investigation of Recrystallization Conditions in 2205 Duplex Stainless Stell

2205 Dubleks Paslanmaz Çelikte Rekristalizasyon Koşullarının İncelenmesi

Sevilay Akpınar, Alptekin Kısasöz, Ahmet Karaaslan
Yıldız Technical University
Türkiye

IRON and STEEL METALLURGY
DEMİR ÇELİK METALURJİSİ

Session Chairman / Oturum Başkanı: **NURİ SOLAK**

10.00 - 10.20

Is World Iron and Steel Production Sustainable?
Dünya Demir Çelik Üretimi Sürdürülebilir mi?

Yusuf Ziya Kayır
KOSGEB Sincan Merkezi
Türkiye

10.20 - 10.40

New Challenge in Preheating Technology for EAF Steelmaking Furnace Energy Saving and Continuous Charging (FESCON) Systems
EAF Çelik Fırınları Enerji Tasarrufu ve Sürekli Besleme (FESCON) Sistemleri İçin Önısıtma Teknolojisinde Yeni Bir Bakış

Doğan Ertaş
CVS Makine Sanayi
Türkiye

10.40 - 11.00

Sıcak Haddehanelerde Enerji Tasarrufu İçin Sıcak ve Direkt Şarj Uygulaması
Hot Charge and Direct Charge Application for Energy Saving at Hot Strip Mill

Nazmi Sarıkaya, Özgür Bilgin
İSDEMİR A.Ş.
Türkiye

IRON and STEEL METALLURGY
DEMİR ÇELİK METALURJİSİ

Session Chairman / Oturum Başkanı: **AKİF TUNABOYLU**

11.20 - 11.50

An Overview of Flat Steel Sector in Turkey

Türkiye'de Yassı Çelik Sektörüne Genel Bir Bakış

Mesut Güney
Borçelik
Türkiye

(Invited Contribution from the Industry)

11.50 - 12.10

The Use of Eti Krom Concentrate Through SHS Process in the Production of Low Carbon Ferrochromium

Eti Krom Konsantrelerinden SHS Yöntemiyle Düşük Karbonlu Ferrokrom Üretilmesi

Meryem Niş Güngör, Murat Alkan, Onuralp Yücel
Istanbul Technical University
Türkiye

12.10 - 12.30

Iron Ore of Concentrate Used at İSDEMİR Sinter Plants

İsdemir Sinter Fabrikalarında Konsantre Demir Cevheri Kullanımı

Ömer Saltuk Bölükbaşı[1], Ali Uçar[2], Uğur Demir[2]
[1]Mustafa Kemal University, [2]İSDEMİR A.Ş.
Türkiye

NON-FERROUS METALLURGY
DEMİR DIŞI METALLER METALURJİSİ

Session Chairman / Oturum Başkanı: **ONURALP YÜCEL**

13.30 - 13.50

Carbothermic Reduction of Lead-Oxide at Low-Temperature
Kurşun Oksitin Düşük Sıcaklıkta Karbotermik Redüksiyonu

Bengisu Yolcu, Cevahir Durmaz, Yasin Kılıç, Güldem Kartal Şireli, Servet Timur
Istanbul Technical University
Türkiye

13.50 - 14.10

Next Generation of High Temperature Materials
Yeni Jenerasyon Yüksek Sıcaklık Malzemeleri

Bo Jönsson, Thomas Helander, Erik Ström
Sandvik WHT
Sweden

14.10 - 14.30

Heat Treatment of a CuNiSiCr-Fe Alloy As an Alternative of Hard Beryllium Alloys
Sert Bakır Berilyum Alaşımlarına Alternatif bir CuNiSiCr-xFe Alaşımının Isıl İşlemi

Turhan Ürün Koçak, Feriha Birol
Sağlam Metal A.Ş.
Türkiye

14.30 - 14.50

The Use of Cu, Cu-Mg and Cu-Ag Alloys in Overhead Catenary Systems and Inspection of Characteristic Properties
Cu, Cu-Mg ve Cu-Ag Alaşımlarının Havai Hat Katener İletkeni Olarak Kullanımı ve Karakteristik Özellikleri

A. Gamze Onuk
Sarkuysan Elektrolitik Bakır Sanayi
Türkiye

NON-FERROUS METALLURGY
DEMİR DIŞI METALLER METALURJİSİ

Session Chairman / Oturum Başkanı: **SEBAHATTİN GÜRMEN**

15.10 - 15.50

Recycling of Metals from Electronic Scrap – Finding the Optimum Between Pretreatment and Metallurgy

Elektronik Hurdadan Metallerin Geri Kazanımı-Önişlem Süreçleri ve Metalurji Arasında Optimumun Belirlenmesi

Bernd Friedrich
RWTH Aachen University
Germany
(Invited Lecturer)

15.50 - 16.10

Bath Movement Effect on Agglomeration of Inclusions in Aluminium Melts

Alüminyum Eriyiklerinde Banyo Hareketinin İnklüzyonların Topaklanmasına Olan Etkisi

Mertol Gökelma, Bernd Friedrich
RWTH Aachen University
Germany

16.10 - 16.30

The Behavior of Celestite in Oxalic Acid Solutions

Selestitin Okzalik Asit Çözeltilerindeki Davranışı

Mert Zorağa, Cem Kahruman, İbrahim Yusufoğlu
İstanbul University
Türkiye

RECYCLING and SUSTAINABILITY
GERİ DÖNÜŞÜM ve SÜRDÜRÜLEBİLİRLİK

Session Chairman / Oturum Başkanı: **GÖKHAN ORHAN**

16.50 - 17.10

An Overview of Non-Ferrous Metals Recycling
Demir Dışı Metallerin Geri Dönüşümüne Genel Bakış

Mehmet Şeref Sönmez
İstanbul Technical University
Türkiye

17.10 - 17.30

Eco Audit in Materials Selection
Malzeme Seçiminde Eko Denetim

Kazım Tur, Ozan Özkan
Atılım University
Türkiye

17.30 - 17.50

Recovery of Gold From Jewellery Based Slags by Flotation
Kuyumculuk Kökenli Curuflardan Flotasyonla Altın Geri Kazanımı

Cevahir Durmaz, Yasin Kılıç, Servet Timur
İstanbul Technical University
Türkiye

POWDER METALLURGY
TOZ METALURJİSİ

Session Chairman / Oturum Başkanı: **NURİ DURLU**

10.00 - 10.20

Fabrication and Characterization of Ti-Ni/SiCp Shape Memory Composites
Ti-Ni/SiCp Şekil Bellekli Kompozitlerin Üretimi ve Karakterizasyonu

Kerim Emre Öksüz, Mehmet Şimşir, Hülya Akkan
Cumhuriyet University
Türkiye

10.20 - 10.40

Effects of Borax on the Wear Behavior of Organic Brake Lining Materials
Organik Fren Balata Malzemelerinin Aşınma Davranışına Boraksın Etkisi

İrem Burcu Algan, Adem Kurt
Gazi University
Türkiye

10.40 - 11.00

The Effect of Nickel/Copper Ratio on the Mechanical Properties For Tungsten Based Heavy Alloys
Nikel/Bakır Oranının Tungsten Esaslı Ağır Alaşımların Mekanik Özellikleri Üzerindeki Etkisi

Necmettin Kaan Çalışkan[1], Nuri Durlu[2]
[1]TÜBİTAK SAGE, [2]TOBB University of Economics and Technology
Türkiye

POWDER METALLURGY
TOZ METALURJİSİ

Session Chairman / Oturum Başkanı: **ZİYA ESEN**

11.20 - 12.00

Selective Laser Sintering (SLS)/Selective Laser Melting (SLM) for Functional Applications

İşlevsel Uygulamalar için Seçmeli Lazer Sinterleme / Seçmeli Lazer Eritme

Cenk Aktaş
Leibniz Institute for New Materials
Germany
(Invited Lecturer)

12.00 - 12.20

The Effect of Sintering Temperature and Tungsten Content on the Microstructural Characteristics of W-rich W-Ni-Co Heavy Alloys

Sinterleme Sıcaklığı ve Tungsten Miktarının Tungstence Zengin W-Ni-Co Ağır Alaşımlarının Mikroyapı Karakteristiği Üzerindeki Etkisi

Onur Dinçer[1], Ali Kalkanlı[2], İshak Karakaya[2], M. Kaan Pehlivanoğlu[1]
[1]TÜBİTAK SAGE, [2]Middle East Technical University
Türkiye

12.20 - 12.40

Sinter-Hardening of Ferrous Astaloy Mo and Distaloy Dh Alloys Powders

Astaloy Mo ve Distaloy Dh Tozlarının Sinter-Sertleştirilmesi

Ahmet Murat Öge, Hakan Hafızoğlu, Nuri Durlu
TOBB University of Economics and Technology
Türkiye

R&D and INNOVATION
AR-GE ve İNOVASYON

Session Chairman / Oturum Başkanı: **TUNÇAY ŞULAN**

13.30 - 13.55

Ar-Ge - İnovasyon ve Teknoloji Yönetimi
R&D - Innovation and Technology Management

Tayfun Sığırtmaç
Coşkunöz Metal Form A.Ş.
Türkiye

13.55 - 14.20

Endüstriyel Ar-Ge Çalışmalarında İşbirliği Mekanizmalarının Rolü
Role of Strategic Cooperations in Industrial Research and Development Activities

Altan Yıldırım
Farplas A.Ş.
Türkiye

14.20 - 14.45

Sanayi Kurumlarında Ar-Ge ve İnovasyon ile Katma Değerin Arttırılması
Increasing the Added Value by R&D and Innovation in Industry

Koray Mert Yılmaz
Cengiz Makine Sanayi
Türkiye

EDUCATION
EĞİTİM

Session Chairman / Oturum Başkanı: **MACİT ÖZENBAŞ**

15.00 - 15.25

Trends in University Education and Engineering Education
Üniversite Eğitiminde Trendler ve Mühendislik Eğitimi

Yılmaz Taptık
İstanbul Technical University
Türkiye

15.25 - 15.50

Redefining Core Curriculum for Materials and Metallurgical Engineering
Malzeme ve Metalurji Mühendisliğinde Eğitim Programı Nasıl Olmalı?

Tayfur Öztürk
Middle East Technical University
Türkiye

15.50 - 16.15

Adoption of E-learning Tools in Metallurgical and Materials Engineering Education
Çevrimiçi Eğitim Araçlarının Metalurji ve Malzeme Mühendisliği Eğitimine Uyarlanması

Arda Çetin
Mühendishane
Türkiye

16.15 - 16.40

Introducing Metallurgical and Materials Engineering to Prospective College Students
Lise Öğrencilerine Yönelik Metalurji ve Malzeme Mühendisliği Tanıtımları

Yunus Eren Kalay
Middle East Technical University
Türkiye

CASTING
DÖKÜM

Session Chairman / Oturum Başkanı: **GÜROLHAN YAŞAR**

10.00 - 10.20

Semi-Solid Forming and Pressure Die Casting of 7075-T6 Aluminum Alloy with Thermal Analysis Method

7075-T6 Alaşımının Termal Analiz Desteği ile Yarı Katı Şekillendirme ve Sıkıştırma Döküm Yöntemleri ile Üretilmesi

Ahmet Umur Güngör, Ali Kalkanlı
Middle East Technical University
Türkiye

10.20 - 10.40

Effect of Grain Reining on Microstructure of A357 Alloy

A357 Alaşımında Tane İncelticilerin Mikroyapıya Etkisi

Muhammet Uludağ[1], Remzi Çetin[1], Derya Dışpınar[2]
[1]Selçuk University, [2]İstanbul University
Türkiye

10.40 - 11.00

Verification of the Function of Feeders by Casting Simulation

Dökümlerde Besleyici İşlevinin Süreç Benzeşimi ile Kontrolü

Haydar Kahraman[1], Mithat Kemal Tozan[2], Ümit Cöcen[1]
[1]Dokuz Eylül University, [2]Cukurova Chemical Industry Company
Türkiye

CASTING
DÖKÜM

Session Chairman / Oturum Başkanı: **DERYA DIŞPINAR**

11.20 - 11.50

New World, New Trends, Technologies and the Turkish Foundry Industry
Yeni Dünya, Yeni Eğilimler, Teknolojiler ve Türk Döküm Sektörü

Yaylalı Günay
Günay Danışmanlık
Türkiye

(Invited Contribution from the Industry)

11.50 - 12.10

Microstructural Characterization of Rapidly Solidified 8% Chromium Cold Work Tool Steel
Hızlı Katılaşmış %8 Kromlu Soğuk İş Takım Çeliğinin Mikroyapısal Karakterizasyonu

İsmail Seçkin Çardaklı, Ali Kalkanlı
Middle East Technical University
Türkiye

12.10 - 12.30

The Investigation of the Relationship Between Grain Refiners and Hot Tearing in A357 Alloy
A357 Alaşımında Tane İnceltme ve Sıcak Yırtılma Arası İlişki

Muhammet Uludağ[1], Remzi Çetin[1], Derya Dışpınar[2]
[1]Selçuk University, [2]İstanbul University
Türkiye

12.30 - 12.50

The Effect of Dendrite Arm Coarsening on Microsegregation Without Back-Diffusion in Solid
Katıda Difüzyon Olmaksızın İkinci Dendrit Kolları Kabalaşmasının Mikrosegregasyona Etkisi

Altan Türkeli
Marmara University
Türkiye

CONGRESS POSTERS
KONGRE POSTERLERİ

POSTER PRESENTATIONS
POSTER SUNUMLAR

BIOMATERIALS / BİYOMALZEMELER

BM-01

Effect of Grinding on the Properties of Alumina-Bovine Hydroxyapatite Composite Powders

Öğütmenin Alümina-Bovine Hidroksiapatit Kompozit Tozlarının Özellikleri Üzerine Etkisi

Azade Yelten, Suat Yılmaz
İstanbul University
Türkiye

BM-02

Bioactivity of Electrodeposited CaP Coatings with Different PVA Addition

Farklı PVA Katkıları ile Elektroçöktürülmüş CaP Kaplamaların Biyoaktivite Özellikleri

Tülay Koç Delice, Güler Ungan, Funda Ak Azem, Ahmet Çakır
Dokuz Eylül University
Türkiye

BM-03

Effect of Surfacebo Modification on Electrochemically Deposited CaP Coatings on Ti6Al4V Substrates for Bioactive Properties

Ti6Al4V Altlıklar Üzerine CaP Kaplamaların Biyoaktivite Özelliklerine Yüzey Modifikasyonunun Etkisi

Bensu Bakın, Tülay Koç Delice, Utku Tiriç, Funda Ak Azem, Işıl Birlik, Erdal Çelik, Mustafa Toparlı
Dokuz Eylül University
Türkiye

BM-04

Effect of Dispersant on the Electrophoretic Deposited of CaP on Titanium and Ti6Al4V Alloy Substrates

Elektroforetik Biriktirme Yöntemiyle Titanyum ve Ti6Al4V Alaşımı Altlıklar Üzerinde Üretilen CaP Kaplamalarda Dispersantın Etkisi

Utku Tiriç, Bensu Bakın, Tülay Koç Delice, Funda Ak Azem, Işıl Birlik, Erdal Çelik,Mustafa Toparlı
Dokuz Eylül University
Türkiye

BM-05

Chemical and Structural Characterization of Selenium-Incorporated Hydroxyapatite

Tedavi Amaçlı Kemik Analogu Olarak Selenyum Katkılanmış Hidroksiapatit Tozlarının Sentez ve Karakterizasyonu

Barış Alkan, Caner Durucan
Middle East Technical University
Türkiye

POSTER PRESENTATIONS
POSTER SUNUMLAR

IRON and STEEL METALLURGY / DEMİR ÇELİK METALURJİSİ

IS-01

New Generation Microalloyed Steel, AMÇ 1200®
Yeni Nesil Mikro Alaşımlı Çelik, AMÇ 1200®

Mehmet Çakıcı
Asil Çelik Sanayi ve Ticaret A.Ş.
Türkiye

IS-02

Quality Design in Iskenderun Iron and Steel Works (İSDEMİR)
İskenderun Demir ve Çelik Fabrikaları'nda (İsdemir) Kalite Tasarımı

Muhammet Bilen
İSDEMİR A.Ş.
Türkiye

IS-03

The Solution of Problems due to the Weight of Cold Pig
Külçe Pik Ağırlığından Kaynaklanan Problemlerin Çözümü

Mehmet Gökoğlu, Kamil Eken
İSDEMİR A.Ş.
Türkiye

IS-04

Problems Encountered During Welding of Austenitic Cr-Ni Stainless Steels and Possible Solutions
Östenitik Krom-Nikelli Paslanmaz Çeliklerin Kaynağında Karşılaşılan Problemler ve Giderilmesi

Yüksel Bilir
İSDEMİR A.Ş.
Türkiye

IS-05

Blast Furnace Heat Exchanger System
Yüksek Fırın Heat Exchanger Sistemi

Ümit Gebenli, Ahmet Serter Karabıyık
İSDEMİR A.Ş.
Türkiye

IS-06

Vacuum Plants (VD/VOD) with Dry Mechanical Pumps for Steel Making Process
Çelik Üretim Prosesleri İçin Kuru Mekanik Pompalı Vakum Tesisleri (VD/VOD)

Doğan Ertaş
CVS Makine Sanayi
Türkiye

IS-07

Synthesis of Bulk Amorphous Steels Having Extreme High Hardness
Çok Yüksek Sertlikteki Amorf Çeliklerin Sentezlenmesi

Bengi Yağmurlu, M.Vedat Akdeniz, Amdulla O. Mekhrabov
Middle East Technical University
Türkiye

CASTING / DÖKÜM

CS-01

Solidification Modeling of an Axial Steel Cast Impeller by Using Finite Volume Method
Sonlu Hacimler Yöntemini Kullanarak Tek Eksenli Çelik Döküm Parçaların Katılaşmasının Modellenmesi

Murat Çopur[1,2], Ahmet Turan[1,3], Mehmet Niyazi Eruslu[1,3]
[1]Istanbul Technical University, [2]Alarko Carrier Sanayi, [3]Yalova University
Türkiye

CS-02

A Modification for The Ohnaka Back Diffusion Equation
Ohnaka Geri Difüzyon Denklemi için Bir Modifikasyon

Altan Türkeli
Marmara University
Türkiye

CS-03

The Effect of Holding Time on Porosity of A357
A357 Alaşımında Tutma Süresinin Porozite Üzerine Etkisi

Muhammet Uludağ[1], Remzi Çetin[1], Lokman Gemi[1], Osman Aydoğuş[1], Kerim Çam[1], Derya Dışpınar[2]
[1]Selçuk University, [2]İstanbul University
Türkiye

CS-04

Effect of Holding Time on The Efficiency of Sr Modification in Al-Si Alloys
Al-Si Alaşımlarında Sr Modifikasyonu Sonrasında Tutma Süresinin Mikroyapıya Etkisi

Muhammet Uludağ[1], Remzi Çetin[1], Lokman Gemi[1], Merve Bingöl[1], Özgür Ortaç[1], Ahmet İrbey Arslan[1], Derya Dışpınar[2]
[1]Selçuk University, [2]İstanbul University
Türkiye

CS-05

The Microstructural Change of Hypereutectic Al-Si Alloy by Addition of Sr and B
Ötektik Üstü Al-Si Alaşımlarında B ve Sr Modifikasyonunun Mikroyapısal Dönüşüm Mekanizması

Muhammet Uludağ[1], Lokman Gemi[1], Zafer Yavaş[1], Ümmühan Öztürk[1], Nesibe Sevde Ülvan[1], Derya Dışpınar[2]
[1]Selçuk University, [2]İstanbul University
Türkiye

POSTER PRESENTATIONS
POSTER SUNUMLAR

CS-06

The Effect of Sr Modification and Holding Time on Microstructure in Hypereutectic Al-Si Alloys

Ötektik Üstü Al-Si Alaşımlarında Modifikasyon ve Bekletme Sürelerinin Mikroyapı Üzerine Etkisi

Muhammet Uludağ[1], Lokman Gemi[1], Muhammed Raşit Eryılmaz[1], Derya Dışpınar[2]
[1]Selçuk University, [2]İstanbul University
Türkiye

CS-07

Assessment of Mechanism of Pore Formation in Directionally Solidified Al-Si Alloy

Yönlendirerek Katılaştırılan Al-Si Alaşımlarında Porozite Oluşum Mekanizmasının İncelenmesi

Muhammet Uludağ[1], Derya Dışpınar[2]
[1]Selçuk University, [2]İstanbul University
Türkiye

ENERGY MATERIALS / ENERJİ MALZEMELERİ

EM-01

Improving the Reversible Cyclability of the Si Based Composite Thin Film Anode

Si Esaslı Kompozit İnce Film Anotun Çevrilebilirliğinin Geliştirilmesi

B. Deniz Polat, Özgül Keleş
Istanbul Technical University
Türkiye

EM-02

Low Cost Preparation of VO_2-Based Thermochromic Thin Films

VO_2 Esaslı Termokromik İnce Filmlerin Düşük Maliyetli Bir Yöntem İle Hazırlanması

Melis Can Özdemir[1], Miray Çelikbilek[1], Ali Erçin Ersundu[2], Süheyla Aydın[1]
[1]İstanbul Technical University, [2]Nişantası University
Türkiye

EM-03

Development and Characterization of New Layered Cathode Materials for Lithium Ion Batteries

Lityum İyon Bataryaları İçin Yeni Tabakalı Katot Malzemelerinin Geliştirilmesi ve Karakterizasyonu

Berke Pişkin, M. Kadri Aydınol
Middle East Technical University
Türkiye

EM-04

Recycled Lead Acid Paste as an Anode Material for Li-Ion Batteries
Li-iyon Piller İçin Geri Dönüşümle Kazanılmış Kurşun Asit Pastadan Anot Malzemesi

Mehmet Şeref Sönmez, Bora Derin, Özgül Keleş, Sebahattin Gürmen
İstanbul Technical University
Türkiye

RECYCLING and SUSTAINABILITY / GERİ DÖNÜŞÜM ve SÜRDÜRÜLEBİLİRLİK

RES-01

Pretreatment of Jewelry Wastes by Pyrolysis Technology
Kuyumculuk Atıklarının Piroliz Teknolojisi İle İyileştirilmesi

Hasret Ağırcan, Levent Kartal, Yasin Kılıç, Servet Timur
İstanbul Technical University
Türkiye

RES-02

Bioleaching of Metals From Printed Circuit Boards by Acidithiobacillus Thiooxidans
Acidithiobacillus Thiooxidans Kullanılarak Baskı Devre Plakalarından Metallerin Biyoarındırılması

Mehmet Şeref Sönmez, Cansu Demirel, Nurgül Balcı
İstanbul Technical University
Türkiye

HEAT TREATMENT / ISIL İŞLEM

HT-01

The Effect of Cu Addition and Austempering Heat Treatment on Mechanical Properties of GGG 50
GGG 50 Dökme Demire Cu İlavesinin ve Östemperleme Isıl İşleminin Mekanik Özelliklere Etkisi

Sebahattin Kırtay, Berkin Kılınç
İstanbul University
Türkiye

HT-02

The Effects of Nitration Conditions on the Wear Properties of Powder Metallurgical Steels Consisting of Different Vanadium
Farklı Vanadyum İçeren Toz Metalurjik Çeliklerin Aşınma Özelliklerine Nitrasyon Şartlarının Etkisi

Aydın Şelte[1], Burak Özkal[1], Koray Arslan[2], Sakine Ülker[2], Aziz Hatman[2]
[1]İstanbul Technical University, [2]Böhler Uddeholm Türkiye
Türkiye

HT-03

Evaluation of the Relation Between Internal Stress and Mechanical Properties of Al-Cu Alloy

Etial 221 Alaşımında İç Gerilimler ile Mekanik Özellikler Arasındaki İlişki

Muhammet Uludağ[1], Muhammed Raşit Eryılmaz[1], Lokman Gemi[1], Serdar Çelebi[1], Derya Dışpınar[2]
[1]Selçuk University, [2]İstanbul University
Türkiye

HT-04

Determination and Calculation of Secondary Phase Formation in Saf 2205 Duplex Stainless Steel

Saf 2205 Dubleks Paslanmaz Çeliklerde İkincil Faz Oluşumunun İncelenmesi ve Hesaplanması

Sezin Gürel, Alptekin Kısasöz, Ahmet Karaaslan
Yıldız Technical University
Türkiye

HT-05

Microstructural Behaviour of Saf 2205 Duplex Stainless Steel Under Isothermal Conditions

Eşsıcaklıklı Isıl İşlem Koşullarında Saf 2205 Paslanmaz Çeliklerin Mikroyapısal Davranışı

Alptekin Kısasöz, Ahmet Karaaslan
Yıldız Technical University
Türkiye

WELDING METALLURGY and NON-DESTRUCTIVE TESTING
KAYNAK METALURJİSİ ve TAHRİBATSIZ MUAYENE

WND-01

Effect of Heat Treatment on the Welding Zone of Martensitic-Austenitic Steels Welded by Friction Welding

Sürtünme Kaynağı İle Birleştirilmiş Martensitik-Östenitik Çeliklerin Kaynak Bölgesine Isıl İşlemin Etkisi

Nuray Beköz
İstanbul University
Türkiye

WND-02

Microstructure Investigation of Micro Alloy Boron Added 205 Austenitic Manganese Steel Joined by Gas-Metal Arc Welding Technique

MİG MAG Tekniği ile Birleştirilen Bor Katkılı 205 Manganlı Çeliğin Mikroyapı Özelliklerinin Araştırılması

Cemal Çarboğa, Bülent Kurt, Serkan Dal
Nevşehir University, Türkiye

WND-03 **Determination of Residual Stress Field on a Multipass Welded Steel Butt-Joint by Finite Element Modeling**

Sonlu Elemanlar Modellemesi Kullanılarak Çok Pasolu Kaynak Ek Bölgelerinde Kalıntı Gerilim Tayini

Nuriya Garipova, Caner Batıgün, C. Hakan Gür
Middle East Technical University, Türkiye

WND-04 **Determination of the Optimum Magnetic Barkhausen Noise Measurement Parameters for Evaluating the Microstructure of Quenched and Tempered AISI-4140 Steels**

Su Verilmiş ve Temperlenmiş AISI-4140 Çeliğinin Mikroyapısal Değerlendirilmesi İçin Optimum Manyetik Barkhausen Gürültü Ölçümü Parametrelerinin Belirlenmesi

Kemal Davut, Tuba Demirtaş, Caner Şimşir
Atılım University, Türkiye

COMPOSITE MATERIALS / KOMPOZİT MALZEMELER

CM-01 **A Comparison of the Effects of Modified and Unmodified Halloysite Nanotubes on the Mechanical Behaviour of Polyamide-6**

Modifiye Edilmiş ve Edilmemiş Haloysit Nanotüplerin Poliamid-6'nın Mekanik Davranışı Üzerine Etkilerinin Karşılaştırılması

Ali Rıza Erdoğan, İlker Kaygusuz, Cevdet Kaynak
Middle East Technical University, Türkiye

CM-02 **Processing and Characterization of Glass Flake-Reinforced Thermoplastic Polymer Matrix Bio-Inspired Bulk Lamellar Composites**

Cam Pulu Takviyeli Termoplastik Polimer Matrisli Biyo-Esinli Lamellar Kompozitlerin Üretimi ve Karakterizasyonu

Aylin Güneş, Simge Tülbez, Arcan F. Dericioğlu
Middle East Technical University, Türkiye

CM-03 **Processing and Characterization of the Electromagnetic Wave Absorption Potential of Glass Fiber-Reinforced Thermoplastic Polymer Matrix Composites**

Cam Fiber Takviyeli Termoplastik Polimer Matrisli Kompozitlerin Elektromanyetik Dalga Soğurumu Potansiyelinin Karakterizasyonu

Aylin Güneş, Özgür Hamat, Tuğçe Altuntop, Esma Avil, Arcan F. Dericioğlu
Middle East Technical University, Türkiye

CM-04 **Analysis of the Structural Defects in Glass Fiber Fabric/Epoxy Resin Laminate**

Cam Fiber/Epoksi Reçine Laminatlardaki Yapısal Hataların Analizi

Abdelghani Naceri
M'Sila University
Algeria

CM-05

The Effect of Mg Addition on the Microstructure and Mechanical Properties of Al/SiCp Composite Subjected to ECAP

Mg Katkısının, EKAP ile yapılan Al/SiCP Kompozit Malzemelerin Mikroyapı ve Mekanik Özelliklerine Etkisinin İncelenmesi

Saman Ahmadzadeh[1], Necip Camuşçu[2], Ömer Keleş[1]
[1]Gazi University, [2]TOBB University of Economics and Technology
Türkiye

CORROSION / KOROZYON

CR-01

Corrosion Resistance of Hybrid Silica Sol Gel Coatings on Mild Steel

Düşük Karbonlu Çeliğe Yapılan Hibrid Silika Sol Jel Kaplamaların Korozyon Direnci

Sebahattin Kırtay
İstanbul University
Türkiye

CR-02

Preparation and Electrochemical Evaluation of Hybrid SiO_2-TiO_2 Sol Gel Thin Film

Hibrid SiO_2-TiO_2 Sol Jel İnce Film Hazırlanması ve Elektrokimyasal Ölçümü

Sebahattin Kırtay
İstanbul University
Türkiye

CR-03

Evaluation of the Effectiveness of Coatings on Reinforcement Corrosion Applied to the External Surface of Reinforcement Steel

Betonarme Çeliğinin Dış Yüzeyine Uygulanan Kaplamaların Betonarme Korozyonu Üzerine Etkinliğinin Değerlendirilmesi

Özlem Aydın[1], Zeki Çizmecioğlu[2]
[1]Gedik University, [2]İstanbul Ticaret University
Türkiye

MATERIALS CHARACTERIZATION / MALZEME KARAKTERİZASYONU

MC-01

Development of Mn-Al Magnets

Al-Mn Mıknatısların Geliştirilmesi

Özgün Acar[1], Yunus Eren Kalay[1], İlkay Kalay[2]
[1]Middle East Technical University, [2]Çankaya University
Türkiye

POSTER PRESENTATIONS
POSTER SUNUMLAR

MC-02

The Prediction of Properties of B_4C Particle Reinforced Metal Matrix Composites Using Artificial Neural Networks

Yapay Sinir Ağı Yöntemi Kullanılarak B_4C Partikül Takviyeli Metal Matrisli Kompozitlerin Özelliklerinin Tahmini

Temel Varol, Aykut Çanakçı, Şükrü Özşahin
Karadeniz Technical University
Türkiye

MC-03

Synthesis and Characterization of B_4C Particles Reinforced Al-Cu-Mg Alloy Matrix Nanocomposite Powders by High Energy Mechanical Milling

B_4C Partikül Takviyeli Al-Cu-Mg Alaşım Matrisli Nanokompozit Tozların Yüksek Enerjili Mekanik Öğütme ile Sentezi ve Karakterizasyonu

Serdar Özkaya, Aykut Çanakçı, Temel Varol
Karadeniz Technical University
Türkiye

MC-04

Determination of Flow Curves of Metastable Austenite

Yarı-Kararlı Östenitin Akma Eğrilerinin Belirlenmesi

Ozan Müştak[1,2], Kemal Davut[3], Caner Şimşir[3], C. Hakan Gür[2]
[1]ORS Bearings Company, [2]Middle East Technical University,
[3]Atılım University
Türkiye

MC-05

Investigation of Parameters that Affect Formability of Steel Sheets

Çelik Sacların Biçimlendirme Özelliklerini Etkileyen Parametrelerin Araştırılması

Elvin Özcan Işıklıgil[1], Adem Bakkaloğlu[2]
[1]Erdemir A.Ş., [2]Yıldız Technical University
Türkiye

MC-06

Photocatalytic Properties of TiO_2 Powders Synthesised by Sol-Gel Process using Different Water/Ti-Precursor Ratio

Farklı Su/Ti-Prekürsor Oranları Kullanılarak Sol-Jel Tekniğiyle Üretilmiş TiO_2 Tozlarının Fotokatalitik Özellikleri

Lütfi Agartan[1], Derya Kapusuz[1], Jongee Park[2], Abdullah Öztürk[1]
[1]Middle East Technical University, [2]Atılım University
Türkiye

POSTER PRESENTATIONS
POSTER SUNUMLAR

MODELLING and SIMULATION / MODELLEME ve SİMÜLASYON

MS-01

Production of Metallic Parts by Additive Manufacturing

Metalik Parçaların Eklemeli İmalatla Üretimi

Fevzi Yılmaz[1], Ebubekir Koç[1], Mustafa Tekkeşin[2]
[1]Fatih Sultan Mehmet Vakıf University, [2]Medistate Kavacık Hospital
Türkiye

MS-02

Artificial Neural Network Approach for the Prediction of Coating Thickness in Fe-Al Coatings Fabricated by Mechanical Milling

Mekanik Öğütme ile Üretilen Fe-Al Kaplamalarında Kaplama Kalınlığı İçin Yapay Sinir Ağı Yaklaşımı

Aykut Çanakçı, Fatih Erdemir, Temel Varol, Şükrü Özşahin, Serdar Özkaya
Karadeniz Technical University
Türkiye

MS-03

Longer Range Correlations in Liquid and Amorphous $Al_{91}Tb_9$ Alloy

Amorf ve Sıvı $Al_{91}Tb_9$ Alaşımında Uzun Erim Atomik Korelasyonların İncelenmesi

Mert Övün[1], Tuba Demirtaş[1], Matthew J. Kramer[2], Yunus Eren Kalay[1]
[1]Middle East Technical University, [2]Ames Laboratory US DOE
Türkiye, USA

MS-04

Molecular Dynamic Simulation Study of Mechanical Behavior of Fe-B Amorphous Nanowires

Amorf Fe-B Nano Tellerin Mekanik Davranışlarının Moleküler Dinamik Davranışları

Mahsuni Yalçın, Amdulla O. Mekhrabov, M. Vedat Akdeniz
Middle East Technical University
Türkiye

MS-05

Determining Graphene Layers Number and N-Layer Region Coverage by XRD Data Distribution Model

XRD Veri Dağıtım Modeli ile Grafen Tabaka Sayısının ve N-tabaka Bölge Kapsamasının Belirlenmesi

Beti Andonovic, Anita Grozdanov, Perica Paunović, Aleksandar Dimitrov, Abdulakim Ademi
SS Cyril and Methodius University
Macedonia

POSTER PRESENTATIONS
POSTER SUNUMLAR

NANOMATERIALS / NANOMALZEMELER

NM-01

Production of Copper Tin (CuSn) Alloy Nanoparticles by Aerosol Process

Bakır Kalay (CuSn) Alaşım Nanopartiküllerinin Aerosol Yöntemi ile Üretimi

Burçak Ebin[1], Sebahattin Gürmen[2]
[1]Nanokomp Advanced Materials R&D Consulting Co. Ltd.,
[2]İstanbul Technical University
Türkiye

NM-02

Syntesis of Nano-Boric Acid and Nano-Titanium Dioxide Particles with Different Thermal Decomposition Systems

Farklı Termal Dekompozisyon Sistemleri ile Nano Borik Asit ve Titanyum Dioksit Partikül Üretimi

Levent Kartal, Yasin Kılıç, Mehmet İkbal Işık, Güldem Kartal Şireli, Servet Timur
İstanbul Technical University
Türkiye

NM-03

Synthesis and Characterization of Transition Metal Oxide Doped $SrAl_2O_4$ Based Nanocrystalline Phosphors

Geçiş Metal Oksitleri Katkılı $SrAl_2O_4$ Temelli Nanokristalın Fosforesan Malzeme Sentezi ve Karakterizasyonu

Mehmet Durmuş Çalışır, Nuri Solak
İstanbul Technical University
Türkiye

NM-04

Photocatalytic Properties of Potassium Titanate Whiskers Synthesized by Sol-Gel Process

Sol-Jel Süreciyle Sentezlenmiş Potasyum Titanat Viskerlerin Fotokatalitik Özellikleri

Derya Kapusuz[1], Jongee Park[2], Abdullah Öztürk[1]
[1]Middle East Technical University, [2]Atılım University
Türkiye

CERAMICS, GLASSES and REFRACTORY MATERIALS
SERAMİK, CAM ve REFRAKTER MALZEMELER

CGRM-01

Color Change in Transition Metal Oxide Doped Tellurite Glasses

Geçiş Metal Oksit Katkılı Tellürit Camların Renk Değişimi

M. Kazım Saygılı[1], Cihan Sipahioğlu[1], Zeynep Yurdakul[1], Mustafa Kerem Yücetürk[1], Miray Çelikbilek[1], Ali Erçin Ersundu[2], Süheyla Aydın[1]
[1]İstanbul Technical University, [2]Nişantaşı University
Türkiye

POSTER PRESENTATIONS
POSTER SUNUMLAR

CGRM-02

Temperature Dependent Optical and Electrical Investigation of Alkali-Tungsten-Tellurite Glasses

Alkalı-Tungsten-Tellürit Camların Sıcaklığa Bağlı Optik ve Elekriksel İncelenmesi

Miray Çelikbilek[1], Ali Erçin Ersundu[2], Süheyla Aydın[1]
[1]İstanbul Technical University, [2]Nişantaşı University
Türkiye

CGRM-03

Preparation and Characterization of Silver Containing Soda-Lime Glasses

Gümüş İçeren Soda-Kireç Camların Hazırlanması ve Karakterizasyonu

Duygu Güldiren[1], Miray Çelikbilek[1], Ali Erçin Ersundu[2], Süheyla Aydın[1]
[1]İstanbul Technical University, [2]Nişantaşı University
Türkiye

CGRM-04

Chemically Strengthened Soda-Lime Glasses Via Ion Exchange Process

İyon Değişim Prosesi ile Kimyasal Olarak Güçlendirilmiş Soda Kireç Camlar

İpek Erdem[1], Duygu Güldiren[1], Miray Çelikbilek[1], Ali Erçin Ersundu[2], Süheyla Aydın[1]
[1]İstanbul Technical University, [2]Nişantaşı University
Türkiye

CGRM-05

Characterization and Sintering Behavior of the UO_2 Pellets Made by Internal Gelation Technique

İç Jelleşme Tekniği ile Hazırlanan UO_2 Peletlerinin Karakterizasyonu ve Sinterleme Davranışı

Ayşe Sibel Sökücü, Metin Bedir, M. Timuçin Aybers
Cekmece Nuclear Research and Training
Türkiye

CGRM-06

Preparation and Characterization of Uranium Oxide Pellets by Sol-Gel Process

Uranyum Oksit Peletlerinin Sol-Jel Prosesi ile Hazırlanması ve Karakterizasyonu

Ecem Altınok[1], Hayati Sarı[2]
[1]Turkish Atomic Energy Authority, [2]Gaziosmanpaşa University
Türkiye

CGRM-07

Preparation and Characterization of 20 mol % Samarium-Doped Ceria (SDC20) Electrolyte Materials for Solid Oxide Fuel Cells

Katı Oksit Yakıt Hücresi İçin % 20 Mol Samaryum-Katkılı Seryum Oksit (SDC20) Elektrolit Malzemesinin Hazırlanması ve Karakterizasyonu

Özgün Serin, Aliye Arabacı
İstanbul University
Türkiye

CGRM-08

Effect of Sintering Temperature and Pressure on Properties of SPSed ZrC-TiB_2 Composites

Sinterleme Sıcaklığı ve Basıncının SPSed ZrC-TiB_2 Kompozitlerinin Özellikleri Üzerindeki Etkiler

Özden Ormancı, İpek Akın, Filiz Çınar Şahin, Onuralp Yücel, Gültekin Göller
İstanbul Technical University
Türkiye

CGRM-09

The Influence of Pozzolanic Admixture on the Mechanical Strength of Mortar

Pozolanik Katkının Harcın Mekanik Özellikleri Üzerindeki Etkisi

Chikouche Hamina Makhloufi
M'Sila University
Algeria

CGRM-10

Effect of Copper Content on Glass Forming Ability of Ni-Cu-W-B Metallic Glasses

Bakır İçeriğinin Ni-Cu-W-B Metalik Cam Sisteminin Camlaşma Kabiliyetine Olan Etkisi

Aytekin Hitit, Hakan Şahin, Pelin Öztürk, A. Malik Aşgın
Afyon Kocatepe University
Türkiye

POWDER METALLURGY / TOZ METALURJİSİ

PM-01

Characterization of Al-Al_2O_3P Composites Produced by Using Different Mixing Media

Farklı Karıştırma Ortamı Kullanılarak Üretilen Al-Al_2O_3P Kompozitlerin Karakterizasyonu

Hanife Kurt[1], Halil Arık[1], Cengiz Bağcı[2]
[1]Hitit University, [2]Gazi University
Türkiye

PM-02

Mechanical Properties of Sinter-Hardened and Heat Treated Astaloy CrA Alloys

Sinterleme ile Sertleştirilmiş ve Isıl İşlem Uygulanmış Astaloy CrA Alaşımlarının Mekanik Özellikleri

Hakan Hafızoğlu, Ahmet Murat Öge, Nuri Durlu
TOBB University of Economics and Technology
Türkiye

PM-03

Sintering Studies on W-rich W-Ni-Co Heavy Alloys with High Cobalt/Nickel Ratio

Yüksek Kobalt/Nikel Oranı İçeren Tungstence Zengin W-Ni-Co Ağır Alaşımlarda Sinterleme Çalışmaları

Onur Dinçer[1], Ali Kalkanlı[2], İshak Karakaya[2], M. Kaan Pehlivanoğlu[1], Necmettin Kaan Çalışkan[1]
[1]TÜBİTAK SAGE, [2]Middle East Technical University
Türkiye

POSTER PRESENTATIONS
POSTER SUNUMLAR

PM-04

Variation of Microstructure and Hardness with Composition in W-Rich Ternary W-Ni-Co Alloys

Tungstence Zengin W-Ni-Co Alaşımlarında Mikroyapı ve Sertliğin Kompozisyon ile Değişimi

Onur Dinçer[1], Ali Kalkanlı[2], İshak Karakaya[2], M. Kaan Pehlivanoğlu[1]
[1]TÜBİTAK SAGE, [2]Middle East Technical University
Türkiye

PM-05

Microstructural Investigation of Sinter-Hardened Distaloy DH Powder Alloys

Sinterleme ile Sertleştirilmiş Distaloy DH Tozlarının İç Yapı İncelemeleri

Gülten Kılıç[1], Bilgehan Ögel[1], Nuri Durlu[2]
[1]Middle East Technical University,
[2]TOBB University of Economics and Technology
Türkiye

PM-06

Macro and Micro Porosity Contents of Low Alloy Steel Foams

Düşük Alaşımlı Çelik Köpüklerin Makro ve Mikro Gözenek Oranları

Nuray Beköz, Enver Oktay
İstanbul University
Türkiye

PM-07

Characterization Investigations of Mechanochemically Synthesized VB_2, VB and V_3B_4 Powders

Mekanokimyasal Yolla Sentezlenmiş VB_2, VB ve $V3B_4$ Tozlarının Karakterizasyon Çalışmaları

Özge Balcı, Duygu Ağaoğulları, İsmail Duman, M. Lütfi Öveçoğlu
İstanbul Technical University
Türkiye

PM-08

The Effect of Reaction Temperature on the Synthesis of Elemental Boron Powders

Reaksiyon Sıcaklığının Elementel Bor Tozu Sentezine Etkisi

Duygu Ağaoğulları, Özge Balcı, Nazlı Akçamlı, İsmail Duman, M. Lütfi Öveçoğlu
İstanbul Technical University
Türkiye

SURFACE TREATMENT and COATINGS / YÜZEY İŞLEMLERİ ve KAPLAMALAR

ST-01

Effect of Alkali Treatment Parameters on Surface Structures and Mechanical Properties of Porous Ti6Al7Nb Scaffolds

Alkali İşlem Parametrelerinin Gözenekli Ti6Al7Nb İskelelerin Yüzey Yapıları ve Mekanik Özelliklerine Etkisi

Ezgi Bütev[1,2], Elif Eda Yeni[3], Emre Yılmaz[1], Ziya Esen[1], Şakir Bor[2]
[1]Çankaya University, [2]Middle East Technical University, [3]Anadolu University
Türkiye

ST-02

Investigation of Coatability of NiAl Powder to AISI 304 Stainless Steel Using SHS Process

SHS Yöntemi Kullanılarak AISI 304 Paslanmaz Çeliğine NiAl Tozunun Kaplanabilirliğinin Araştırılması

Mehmet Akkaş[1], Sermin Ozan[2], Serkan Islak[1], Uğur Çalıgülü[2]
[1]Kastamonu University, [2]Fırat University
Türkiye

ST-03

Effect of Air Plasma Spray Parameters on the Properties of YSZ and C-YSZ Thermal Barrier Coatings

Atmosferik Plazma Sprey Parametrelerinin YSZ ve C-YSZ Termal Bariyer Kaplama Özelliklerine Etkisi

Muhammet Karabaş, Ahmet Durmaz, Ayşe Kılıç, Yılmaz Taptık
İstanbul Technical University
Türkiye

ST-04

Substrate - Enamel Interface Relation and Impact on Quality of Enamel

Taban Malzeme Emaye Arayüz İlişkilerinin Emaye Kalitesine Etkisi

Özge Işıksaçan[1], Ezgi Yılmaz[1,2], Onuralp Yücel[1], Alper Yeşilçubuk[2]
[1]İstanbul Technical University, [2]Arçelik A.Ş.
Türkiye

ST-05

Gaseous Nitriding of Diesel Injector Components

Dizel Enjektör Parçalarının Gaz Nitrürlenmesi

Ahmet Fatih Yayla[1], Rıdvan Gecü[1,2], Nuri Solak[1], Kürşat Kazmanlı[1], Mustafa Ürgen[1]
[1]İstanbul Technical University, [2] Yıldız Technical University
Türkiye

ST-06

Boriding Kinetics of Ferritic GGG40.3 Ductile Iron

Ferritik GGG40.3 Küresel Grafitli Dökme Demirin (KGDD) Borlama Kinetiği

Fatma Ünal, Ahmet Topuz
Yıldız Technical University
Türkiye


IMMC
2014

TABLE of CONTENTS / İÇİNDEKİLER

Nanomaterials // Nanomalzemeler

Biomaterials // Biyomalzemeler

Surface Modification // Yüzey İşlemleri ve Kaplamalar

Composite Materials // Kompozit Malzemeler

Ceramics, Glasses and Refractory Materials // Seramik, Cam ve Refrakter Malzemeler

Welding Metallurgy and Non-Destructive Testing
Kaynak Metalurjisi ve Tahribatsız Muayene

Materials Characterization // Malzeme Karakterizasyonu

Energy Materials // Enerji Malzemeleri

Heat Treatment // Isıl İşlem

Iron and Steel Metallurgy // Demir Çelik Metalurjisi

Non-Ferrous Metallurgy // Demir Dışı Metaller Metalurjisi

Recycling and Sustainability // Geri Dönüşüm ve Sürdürülebilirlik

Powder Metallurgy // Toz Metalurjisi

R&D and Innovation // Ar-Ge ve İnovasyon

Education // Eğitim

Casting // Döküm

Corrosion // Korozyon

Modelling and Simulation // Modelleme ve Simülasyon

Mechanical Properties of Organic Molecular Crystals

•

Organik Moleküler Kristallerin Mekanik Özellikleri

Pance Naumov

New York University Abu Dhabi - United Arab Emirates

ABSTRACT

The classical perception of single crystals of molecular materials as rigid and brittle entities has downsized the research interest in mechanical effects that was initiated and was active during the 1980s. More recently, the modern analytical techniques for mechanical, electron-microscopic, structural, spectroscopic and kinematic characterization have contributed to accumulate compelling evidence that under certain circumstances, even some seemingly rigid molecular single crystals can deform, bend, twist, hop, wiggle or perform other 'acrobatics' that are atypical for non-soft matter. These examples contribute to a paradigm shift in our understanding of the elasticity of molecular crystals and also provide direct mechanistic insight into the structural perturbations at the limits of the susceptibility of ordered matter to internal and external mechanical force. As the relevance of motility and reshaping of molecular crystals is being recognized by the crystal research community as a demonstration of a very basic concept—conversion of thermal or light energy into work—a new and exciting crystal chemistry around mechanically responsive single crystals rapidly unfolds. The characterization of the extraordinary mechanical properties of molecular crystals could benefit greatly from the achievements in the methods for mechanical characterization of metals and alloys. In this lecture, I will elaborate on the possibilities to bring these two worlds together.

Keywords: Organic molecular crystals, mechanical properties, crystal chemistry.

THERMAL PLASMA SYNTHESIS OF METALLIC NANOPARTICLES

Burak AKTEKİN, Tayfur ÖZTÜRK

Middle East Technical University, Ankara, Turkey
ozturk@metu.edu.tr

ABSTRACT

Nanoparticles are of great interest for a wide range of applications. A variety of techniques are available for their synthesis and among these methods, thermal plasma approach offers continuous production of high purity nanoparticles in large scale where the particle size is usually less than 100 nm. In this technique, precursors, which are normally powders, are fed to the thermal plasma where they are evaporated and nanoparticles are derived from condensation of this vapor in the quenching zone. In this study, a 30 kW RF thermal plasma system was used. This system has currently a nanopowder reactor but when needed could be replaced by a coating chamber or a spheroidization unit. The system was configured with injection probes which were located axially in the reactor, one from the top and the other from the bottom. This allowed injection of precursor powders into different temperature zones of the plasma. In the current study, nanoparticles in Mg-Ni binary system were produced. This involved Ni, Mg and Mg_2Ni. Ni nanoparticles can be produced at ease yielding particles less than 100 nm in size. Moreover, when Ni was fed together with methane, Ni particles could be encapsulated with 6-10 layers of graphite yielding a core-shell structure. Mg_2Ni intermetallic nanoparticles could be synthesized from elemental powders when Ni was fed from the top injector and Mg was fed through the bottom injector which was positioned just below the quenching zone in the reactor. The weight fraction of Mg_2Ni could be as high as 55 wt%. The use of thermal plasma in the synthesis of metallic nanoparticles was discussed especially with regard to intermetallic alloys.

Keywords: Thermal Plasma, Nickel, Magnesium, Mg_2Ni, Core-shell.

1. INTRODUCTION

There is a considerable interest in sub-micron sized metallic powders as they may offer some specific size dependent properties mostly resulting from their high surface to volume ratio. One approach to producing sub-micron metallic powders is to use thermal plasma torches. Although D.C. plasma could also be used for this purpose, RF inductively coupled plasma (RF-ICP) is more common in the synthesis of nanopowders [1]. Here, the torch is electrodeless and it provides continuous production ability forming contamination free nanoparticles. Properties such as high heat capacity, high chemical reactivity and large plasma volume as well as ability of central injection and long residence time for precursors in the plasma make RF-ICP torches advantageous

for the synthesis of sub-micron powders [2,3]. In this technique, plasma is basically formed by the coupling of the energy provided by an RF power to the streaming plasma gas via electromagnetic fields [4]. Initial powders are melted and evaporated in the high temperature region and condense into fine particles at the exit of the plasma. Induction thermal plasma torches have been used for the synthesis of nanoparticles of a variety of materials. These materials can be listed as mainly pure metals, carbides, nitrides, oxides, borides, nanostructured carbon-based materials and metallic alloys [5,6,7,8,9,10,11]. Metal nanoparticles include Al, Cu, Ag, Ni, Fe, Co, Mo, W, etc. [3]. Differing from pure metals, the synthesis of alloys and intermetallics which involve more than one component has its difficulties [12]. In such a system, nucleation usually starts with one of the component and other component(s) may nucleate with the existing particles, or they may form new particles [13].

The present work was undertaken to produce metallic nanoparticles in Mg-Ni binary system. Here the interest is Ni as well as Mg to produce them in sizes less than 100 nm as well as the intermetallic nanoparticles namely Mg_2Ni again in sizes smaller than 100 nm. The nanopowders reactor in use has two injectors located axially in the torch one from above and the other from the bottom. This provides flexibility in the synthesis of compounds such as Mg_2Ni as well as producing nanoparticles encapsulated with carbon.

2. EXPERIMENTAL

The apparatus used for the nanoparticle synthesis is a 30 kW thermal induction plasma system (Tekna Plasma Systems Inc.). The system consists of a high RF power terminal with a nominal frequency of 2-5 MHz and the inlet power of 50 kVA, Figure 1.

Induction plasma system was operated at 25 kW under 0.97 bar pressure. Central gas (plasma forming gas) used in the experiments was pure argon (Linde, 99.995% purity) and provided at a rate of 15 standard liters per minute (slpm). Sheath gas was a mixture of pure argon (60 slpm, Linde, 99.995% purity) and pure hydrogen (6 slpm, Linde, 99.995% purity). As quenching gas, nitrogen gas was used with flow rate of 150 slpm.

Materials used as precursors included methane (CH_4, 99.5% pure, Linde), nickel (99.9% pure, -325 mesh, Höganäs), magnesium (99.8% pure, -300 mesh, Alfa Aesar) and pre-alloyed Mg_2Ni (induction melted, -300 mesh). Typical duration of the production runs lasted 10-15 minutes. The torch incorporated two probes for feeding of these precursors, Figure 1(b). They were fed into the plasma using either the top or the bottom injection probe, or both of them. Carrier gas was Ar (Linde, 99.995% purity) and flow rate was kept at 5 slpm.

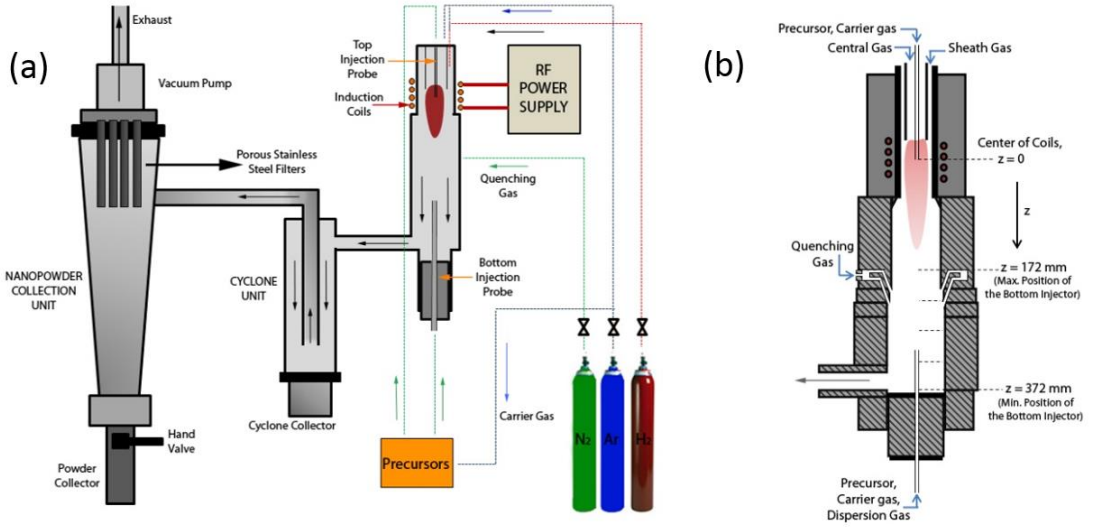

Figure 1. A general view of the thermal plasma system (a) and the schematic view of the reactor incorporating two injection probes (b).

3. RESULTS & DISCUSSION

Preliminary experiments with thermal plasma synthesis were carried out with Ni. This is one of the constituent in Mg_2Ni. Ni was preferred over Mg since it has a higher melting - boiling point and also it is less reactive. The unit was operated for 15 minutes with Ni powder at a feed rate of 3 g/min. Powders collected from bottom, cyclone and powder collector were removed and examined with SEM. Powders collected from the bottom collector are given in Figure 2(b). These powders are quite comparable to the starting powder given in Figure 2(a) except for their shape. Powders collected from the cyclone unit were also spherical in shape but much smaller (around several microns) in size and were decorated with nanoparticles, Figure 2(c). These have probably originated from incompletely vaporized liquid droplets, or highly coagulated nanoparticles. Another reason could be the relatively high exposure of some nuclei to moderate temperatures so that more time was available for the particle growth. Large agglomerates of fine particles were also present in the cyclone. SEM image of powders collected from the powder collector are shown in Figure 2(d). Here the particles are quite fine and they are again spherical in shape. Mean particle size was 80 nm with a standard deviation of 15 nm (determined over nearly 50 particles analyzed from SEM images). These were obviously derived from the evaporation-condensation process.

While metallic nanopowders may have desired properties, there are also some important drawbacks related to their size such as agglomeration and higher sensitivity to oxidation. These drawbacks usually limit their application and necessitate protective measures to be taken during their handling. One solution to this problem is seen as the stabilization of metallic nanoparticles by covering them by an inert material. For this purpose, we also fed methane (as carbon source) together with nickel to encapsulate nanopowders with graphitic layers.

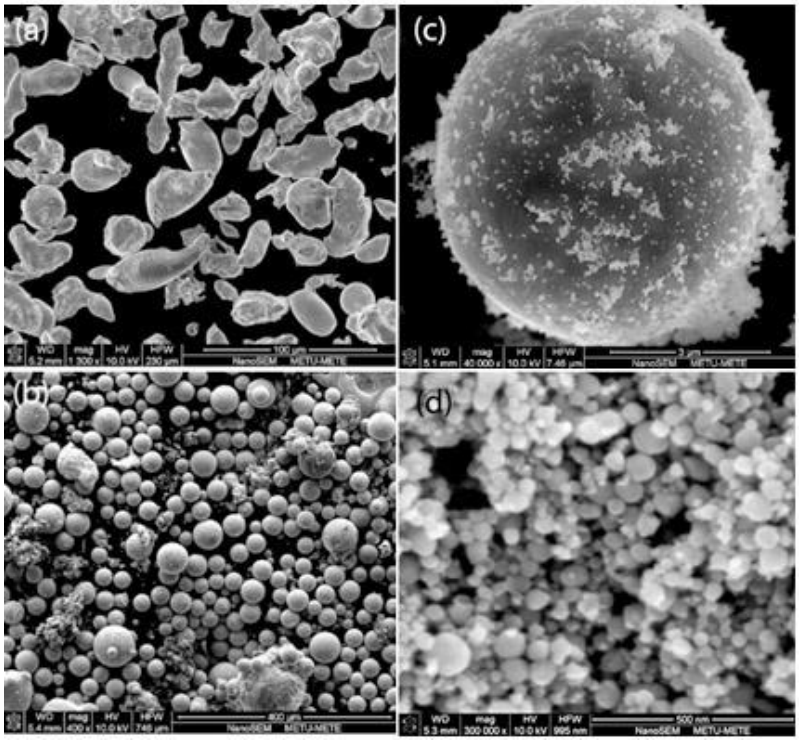

Figure 2. SEM images of initial powders (a) and synthesized powders collected from bottom collector (b), cyclone (c), powder collector (d).

Upon feeding Ni and methane to the plasma reactor, the product collected from the powder collector was mostly carbonaceous as they were black in color. In TEM images obtained from these powders, structures were mostly graphitic, but Ni particles could easily be located. Figure 3(a) and 3(b) show typical TEM images of such particles. As seen in these images, nickel nanoparticles were encapsulated by several outer layers. Interplanar spacing measured between these layers derived from the digital diffractogram (FFT image obtained with ImageJ software) was 0.33 nm which is in well agreement with the value reported for graphite in the literature (0.3347 nm, ICSD #031829). Also, lattice fringe separation inside the core yielded a value of 0.204 nm. This value is in agreement with the reported interplanar distance for (111) plane of Ni, which is 0.2041 nm (NIST #23929). Thus carbon encapsulated Ni particles were successfully synthesized where Ni particles of 5-200 nm in size were covered by 3-9 graphitic layers.

The diameter of particles was 56 nm with a standard deviation of 35 nm (measured over 35 particles). It can be concluded that carbon encapsulation also hinders the further particle growth by confining the particles within carbon layers resulting in finer particle size. These values together with TEM images (Figure 3) refer to the case where Ni was fed from the top and methane was fed from the bottom injector. Similar observations were made for the case of reverse feeding.

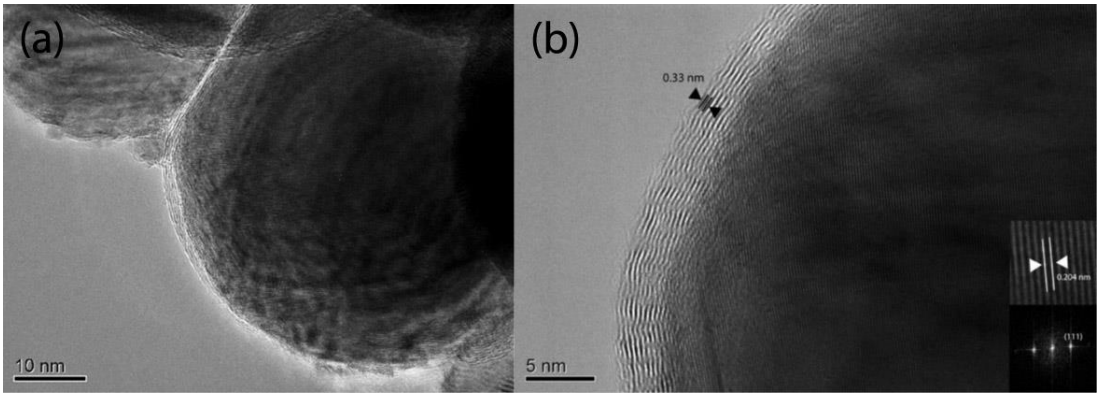

Figure 3. TEM images of carbon encapsulated nickel nanoparticles.

Following the preliminary experiments with nickel, two additional experiments were conducted with the pre-alloyed Mg_2Ni powders. They were either injected using the top injection probe or injected from the bottom probe. Samples collected were characterized with X-ray diffraction. Phases present in this sample were mainly Ni (ICDD# 4-0850) and MgO (ICDD# 45-0946). No significant Mg_2Ni was present in this sample. This implies that Mg_2Ni disintegrated within the plasma into its elements. Moreover, Mg formed in this way was oxidized to MgO. When the bottom probe was used (located 372 mm below induction coils, z=372 mm), similarly, no Mg_2Ni formation was observed. These results indicate that when Mg and Ni follow similar pathways in the reactor, they prefer to nucleate separately, which is probably due to the large differences in their nucleation temperatures.

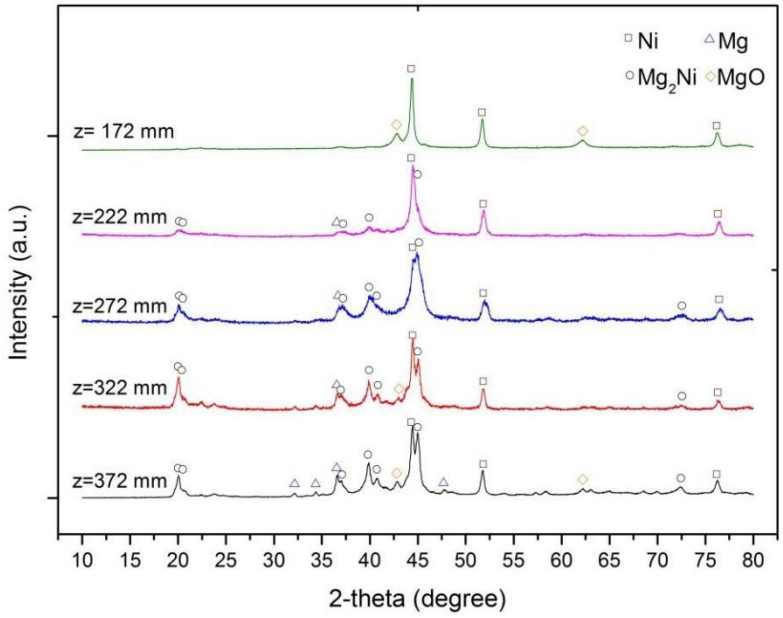

Figure 4. XRD patterns of powders when Mg was fed via bottom and Ni via top injector.

As an alternative approach, Mg and Ni were sent into the plasma separately. Since boiling and melting temperatures of Mg are lower than those of Ni, it was decided that Ni could be fed through the top probe as it provides a more effective heat transfer between the plasma and the particles, while Mg could be fed through the bottom probe (positioned at z = 372 mm). XRD pattern of nanopowders obtained in this geometry is given in Figure 4. Considerable fraction of the sample was Mg_2Ni (ICDD# 35-1225). The other phases present were Ni (ICDD# 4-0850), Mg (ICDD# 35-0821) and MgO (ICDD# 45-0946). The amount of Ni in the sample was quite comparable to that of Mg_2Ni. As done in an additional test, when excessive Mg was fed, there was only a slight increase in the Mg_2Ni content.

So as to further increase Mg_2Ni yield, an approach was adopted in which the position of Mg probe was changed in the reactor. It was anticipated that, moving the injector towards the plasma torch would affect the precursor penetration into the different regions of the plasma and could lead to alterations in the volume fractions of the phases formed. Experiments involved the use of five locations; z= 372, 322, 272, 222, 172 mm. When the bottom injector was positioned at z = 272 mm, an increase in the Mg_2Ni yield was observed; but still there was a significant amount of Ni (ICDD# 4-0850). When injector tip was moved further towards the plasma (z = 222 mm), the same trend did not continue. The fraction of Mg_2Ni was now decreased while MgO peaks became comparable to those observed in the earlier positions. It might be worth mentioning that at z = 272 mm, the tip of the injector is located just below the inlet of the quenching gas.

The resulting nanopowders gave maximum Mg_2Ni yield at z=272 mm, these powders were analyzed with SEM-EDS and also Rietveld analysis was made on XRD pattern. Mg_2Ni amount was determined as 53.9 wt% while other phases were Ni (11.6 wt%), $MgNi_2$ (11.1 wt%), MgO (17.6 wt%) and Mg (5.8 wt%). Elemental analysis result was in accordance with the Mg/Ni ratio calculated from these phase fractions.

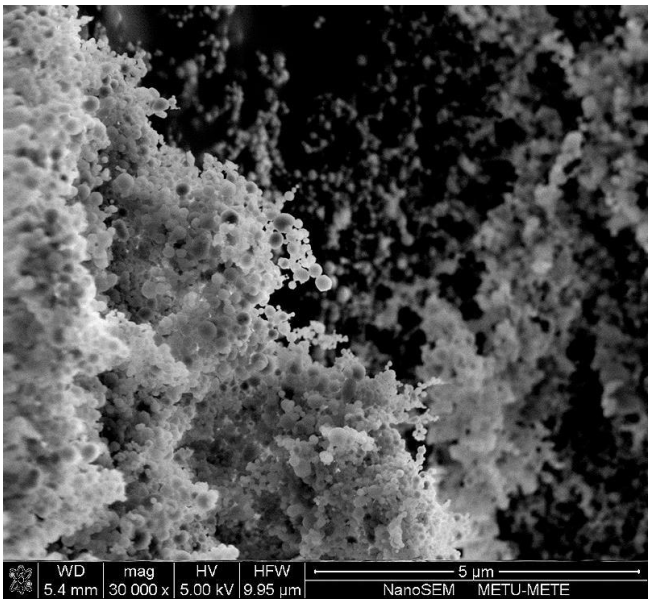

Figure 5. SEM image of powders obtained when bottom probe was located at z=272 mm.

This sample with maximum Mg_2Ni content was further analyzed with regard to its particle size. BET analysis yielded a specific surface area of 16 m^2/g. This has yielded a value of 98 nm particle size assuming spherical shape. This value was quite close to values obtained with SEM measurements which yielded an average particle size of 89 nm (with a standard deviation of 39 nm) determined over 110 particles, Figure 5.

4. CONCLUSIONS

In this study, it was shown that the induction plasma method is an effective way of synthesizing nanoparticles in large-scale. Particles were generally spherical in shape and less than 100 nm in size. Ni nanoparticles were successfully synthesized in one-step without being oxidized. Additionally, the method of induction plasma by feeding Ni together with methane can be used successfully for the synthesis of carbon encapsulated nickel nanoparticles. Feeding methane with precursors also reduces the size of the resulting particles. Secondly, it is also possible to synthesize multicomponent materials via induction plasma method. Intermetallic Mg_2Ni compound with a significant yield was synthesized; but it was seen that the injector configuration of the precursors was quite decisive for the relative content of products. Feeding Ni from the top of the plasma and Mg from the bottom of the plasma was found to be the most effective feeding configuration.

It can be concluded that the synthesis of pure metals can be achieved easily with thermal plasma as shown for nickel in this study and as can be seen for other metals in the literature. In the case of multicomponent materials, synthesis of more stable phases such as oxides, carbides, borides with thermal plasma seems more convenient compared to metallic alloys or intermetallics. As we show in this study for Mg_2Ni, even melting and evaporation points of components are quite different from each other, significant yields of desired multicomponent materials can be achieved with a careful control of precursor feeding into the plasma.

REFERENCES

1. Boulos, M. I. (1985). The inductively coupled RF (radio frequency) plasma. Pure&Appl. Chem., Vol. 57, No. 9, pp. 1321—1352.
2. Cheng, Y., Shigeta, M., Choi, S., & Watanabe, T. (2012). Formation mechanism of titanium boride nanoparticles by RF induction thermal plasma. *Chemical Engineering Journal, 183*, 483-491.
3. Jiayin, G., Xiaobao, F., Dolbec, R., Siwen, X., Jurewicz, J., & Boulos, M. (2010). Development of nanopowder synthesis using induction plasma. *Plasma Science and Technology, 12*(2), 188.
4. Hopwood, J. (1992). Review of inductively coupled plasmas for plasma processing. *Plasma Sources Science and Technology, 1*(2), 109.
5. Yoshida, T., & Akashi, K. (1981). Preparation of ultrafine iron particles using an rf plasma. *Trans.Jpn.Inst.Met.,22*(6), 371-378.
6. Károly, Z., Mohai, I., Klébert, S., Keszler, A., Sajó, I., & Szépvölgyi, J. (2011). Synthesis of SiC powder by RF plasma technique. *Powder Technology, 214*(3), 300-305.

7. Baba, K., Shohata, N., & Yonezawa, M. (1989). Synthesis and properties of ultrafine AlN powder by rf plasma. *Applied Physics Letters, 54*(23), 2309-2311.

8. Wang, X., Li, J., Kamiyama, H., & Ishigaki, T. (2006). Fe-doped TiO2 nanopowders by oxidative pyrolysis of organometallic precursors in induction thermal plasma: Synthesis and structural characterization. *Thin Solid Films, 506*, 278-282.

9. Szépvölgyi, J., Mohai, I., Károly, Z., & Gál, L. (2008). Synthesis of nanosized ceramic powders in a radiofrequency thermal plasma reactor. *Journal of the European Ceramic Society, 28*(5), 895-899.

10. Cota-Sanchez, G., Soucy, G., Huczko, A., & Lange, H. (2005). Induction plasma synthesis of fullerenes and nanotubes using carbon black–nickel particles. *Carbon, 43*(15), 3153-3166.

11. Çakmak, G., Károly, Z., Mohai, I., Öztürk, T., & Szépvölgyi, J. (2010). The processing of Mg–Ti for hydrogen storage; mechanical milling and plasma synthesis. *International Journal of Hydrogen Energy, 35*(19), 10412-10418.

12. Aktekin, B, Çakmak G, and Öztürk, T. "Induction thermal plasma synthesis of Mg2Ni nanoparticles." International Journal of Hydrogen Energy 39.18 (2014): 9859-9864.

13. Gurav, A., Kodas, T., Pluym, T., & Xiong, Y. (1993). Aerosol processing of materials. *Aerosol Science and Technology, 19*(4), 411-452.

Production of NiO/Al_2O_3 Nanosized Catalysts by Ultrasonic Spray Pyrolysis (USP) Process

Tunçağ Cihangir ŞEN*, Burçak EBİN and Sebahattin GÜRMEN***

*Istanbul Technical University, Department of Metallurgical & Materials Eng., Istanbul, Turkey
tuncagsen@gmail.com, gurmen@itu.edu.tr
**Nanokomp Advanced Materials R&D Consulting Co. Ltd., Istanbul, Turkey
burcak.ebin@gmail.com

Abstract

Nanosized catalysts are increasingly required for specific applications in the energy conversion area. Production of hydrocarbons from the mix of CO_2 and H_2 over a multifunctional catalyst is aimed as a function of large applications of the hydrocarbons such as combustible fuel sources and chemicals. Although several methods have been considering for production of nanoparticles, USP is a 4 step production technique that allows producing different kinds of nanomaterials such as metallic, intermetallic, ceramic, composit nanomaterials at high purity, spherical and non-agglomerated morphology, homogeneous composition and narrow size distribution. In this study, production of NiO/Al_2O_3 nanoparticles was investigated by USP process from an aqueous solution including nickel nitrate and aluminium nitrate. NiO/Al_2O_3 nanoparticles obtained by thermal decomposition of ultrasonically formed aerosol droplets from corresponding solution at 800°C and concentration of 0,1M with the molar ratio of 1:1. SEM, EDS and XRD characterization studies shows that the optimum morphology and conditions of NiO/Al_2O_3 nanoparticles are successfully obtained at 800°C. Results demonstrate that USP process is an effective technique to produce NiO/Al_2O_3 nanoparticles.

Keywords: Nickel aluminate, USP technique, Nanosized catalysts, Energy conversion

Nikel Alüminat Nano Katalizörlerinin Ultrasonik Sprey Piroliz (USP) Yöntemi ile Üretimi

Enerji dönüşüm alanında özel uygulamalar için kullanılan nano boyutlu katalizörlere olan ihtiyaç günden güne artmaktadır. Özellikle CO_2 ve H_2 karışımı olan sentez gazından multi fonksiyonel katalizörler üzerinden sentetik yakıt üretimi konusunda birçok çalışma yapılmaktadır. Nanopartiküllerin üretimi için birçok yöntem bulunmasına rağmen, Ultrasonik Sprey Piroliz (USP) prosesi metalik, intermetalik, seramik ve kompozit nano partiküllerin yüksek saflıkta, küresel morfolojide, dar boyut dağılımında ve homojen kompozisyonda üretiminde öne çıkan bir yöntemdir. Bu çalışmada, USP tekniği ile 1:1 molar oranında 0,1M nikel nitrat ve alüminyum nitrat başlangıç çözeltisi kullanılarak NiO/Al_2O_3 nanopartiküllerinin üretimi araştırılmıştır. NiO/Al_2O_3 nanopartikülleri, ultrasonik kaynakla sulu çözeltiden oluşturulmuş aerosol damlacıklarının 800°C sıcaklıkta termal dekompozisyonu ile elde edilmiştir. SEM, EDS ve XRD karakterizasyon çalışmaları NiO/Al_2O_3 nano partiküllerinin USP tekniği ile 800^0C'de optimum morfolojide ve koşullarda üretimi için efektif bir yöntem olduğu tespit edilmiştir.

1. INTRODUCTION

The most important usage area of NiO/Al_2O_3 nano sized catalysts is in syngas production, which is a mixture of H_2 ve CO, from methane (Eq.1). Syngas is the raw material of many fuels (fuel gas, LPG, benzine, naphtha, diesel) which are produced by the raffination of crude oil. In recent years, many researches and big investmens have been made on this field. Moreover, the conversion of natural gas (methane) and liquid hydrocarbons to syngas exists in entire fuel processing systems and it is seen as the key step of the hydrogen economy in the future. The most promising syngas production method is partial oxidation reforming of methane (POM):

$$CH_4 + 1/2\ O_2 = CO + 2H_2\ \Delta H = -35.9\ kJ/mole \qquad (1)$$

This process can be operated at low temperature and it is more efficient. It has been considered to be the most promise CH_4 reforming process in the future. A number of catalysts have proven to be active in POM, mainly platinum group metals on various supports, such as Rh, Ru, Pd, Pt and Ir. However, because of the high cost of noble metal-based catalysts, from the industrial standpoint, the development of cheaper and alternative metal-based catalysts is very important. In particular, alumina supported Ni catalysts have been widely investigated because of their lower cost and relatively high activity in the partial oxidation of methane [1,5]. Furthermore, NiO/Al_2O_3 nanocomposite is an important candidate as anode material in aluminium electrolysis due to its high termal stability and high resistance to alkaline and melt aluminium attacks and it is being investigated as anode coating material in solid oxide fuel cells (SOFCs) [6,7].

NiO/Al_2O_3 nanoparticles can be produced by sol-gel, wet impregnation, combustion, ultrasonic spray pyrolysis (USP) and many other methods [8,12]. Among them, Ultrasonic Spray Pyrolysis (USP) method is one of the rarely used methods to produce NiO/Al_2O_3 nano particles. This method is suitable to obtain particles in a single step. Metals and metal oxides in various morphologies can be obtained by USP. Comparing to solution based synthesis methods; USP allows better secondary phase dispersion, spherical and non-agglomerated morphology, homogenous composition and narrow size distribution. Thermal decomposition of aerosol droplets of the precursor solution created by ultrasound source is basic phenomena for the USP method [13,16].

In this work, NiO/Al_2O_3 nano particles were produced by thermal decomposition of aerosol droplets of nickel nitrate and aluminium nitrate solution obtained by ultrasonic atomization. Particle properties such as size, morphology, crystal structure were characterized by scanning electron microscopy (SEM), energy dispersive spectroscopy (EDS), X-ray diffraction (XRD).

2. EXPERIMENTAL

NiO/Al_2O_3 nanoparticles were produced with ultrasonic spray pyrolysis method by thermal decomposition. The precursor solution was prepared by dissolving a stoichiometric amount of $Ni(NO_3)_2.6H_2O$ and $Al(NO_3)_3.9H_2O$ (all from Merck^{TM}) in distilled water at the molar ratio of 1:1. The precursor solution was atomized using an ultrasonic nebulizer with a resonant frequency of 1.7 MHz. The aerosol stream was introduced into the horizontal quartz reactor at 800°C by air flow. The quartz reactor was placed inside the tube furnace (Nabertherm, R 50/250/12) with a temperature control of ±1 ◦C. The heated length and diameter of the quartz reactor are 250 and 20

mm, respectively. The air flow rate was fixed at 500 ml/min. The particles obtained by the thermal decomposition of aerosol droplets were collected in the washing bottles connected to outlet of the quartz reactor.

X-ray diffraction (XRD, Phillips PW 1700) using Cu Kα radiation was used to examine the crystalline phase and size of the prepared particles. The conditions for the data collection were continuous scanning of a detector covering an angular range from 10° to 80° with a step size of 0.0167 and wavelengths 1.541874 Å. The chemical compositions of particles were analyzed by the energy dispersive spectroscopy (EDS) instrument. Particle size and morphology of the samples were investigated by field emission scanning electron microscopy (FE-SEM, JEOL JSM 700F).

3. RESULTS AND DISCUSSION

The thermodynamic analysis was done using HSC Software in temperature range between 0 and 1000°C (Fig. 1). The thermal decomposition of nickel and aluminium nitrate for the formation of NiO/Al_2O_3 nano particles can be described in Eq.2-3.

$$2Al(NO_3)_{3(ia)} \rightarrow Al_2O_3 + 6NO_2\,(g) + 3/2O_2\,(g) \qquad (2)$$

$$Ni(NO_3)_2 \rightarrow NiO + 2NO_2\,(g) + 1/2O_2\,(g) \qquad (3)$$

The values of Gibbs free energy (ΔG) for the reactions (3 and 4) in the temperature range up to 1000°C confirm the probability for the formation of NiO and Al_2O_3 by thermal decomposition of nickel and aluminium nitrates. The Gibbs free energy values for thermal decomposition of aluminium nitrate to aluminium oxide (Al_2O_3) becomes negative approximately after 250°C and it decreases through the negative values at elevated temperatures. Free energy values for thermal decomposition of nickel nitrate to nickel oxide (NiO) becomes negative after 260°C temperature. Formation of NiO/Al_2O_3 nano particles by thermal decomposition of their nitrates is thermodynamically possible at desired temperature, 800°C.

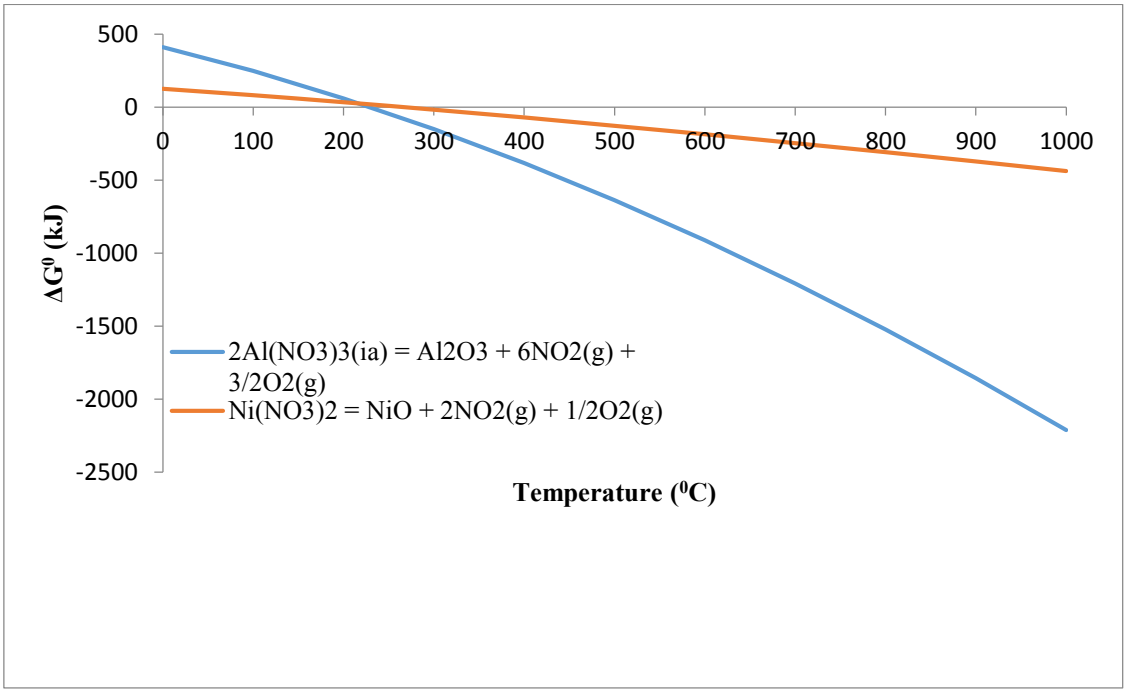

Figure 1. Change of the Gibbs free energy for thermal decomposition of nickel and aluminium nitrates.

The composition of the products prepared by thermal decomposition of the nickel and aluminium nitrates precursor was further studied by EDS. Fig. 2 displays the EDS analysis of the particles produced at 800°C. Al, Ni and O peaks can easily detected and any impurities was not observed. Amount of aluminium, nickel and oxygen in weight % is (Al:Ni:O) is %19.76, %37.88 and %42.36.

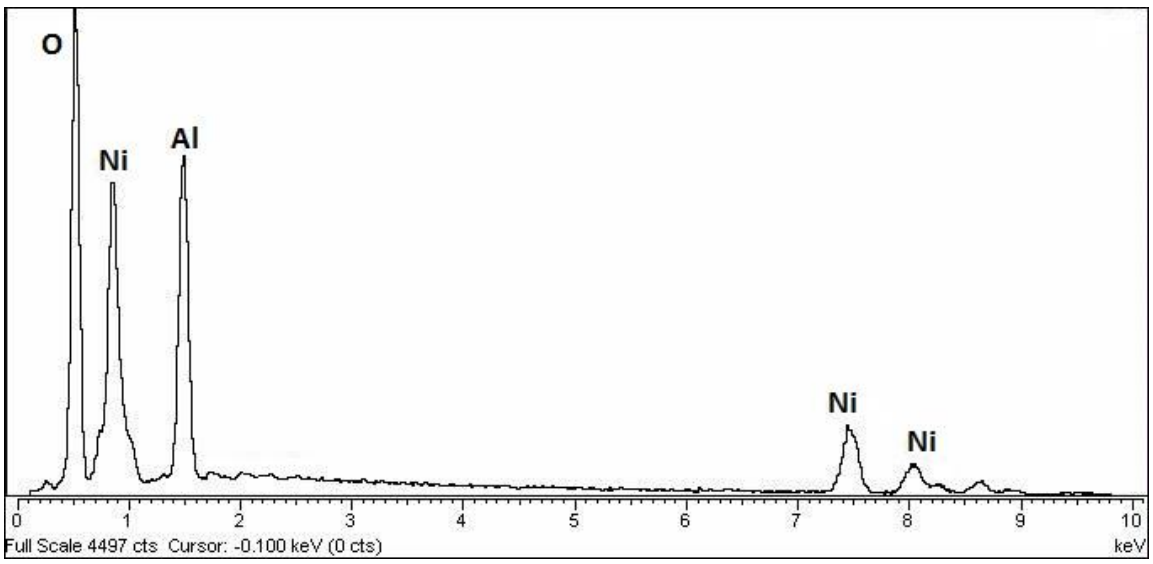

Figure 2. EDS analysis of NiO/Al_2O_3 nano particles.

Figure 3 shows the XRD pattern of NiO/Al_2O_3 nano particles produced at 800°C by thermal decomposition of nickel and aluminium nitrate. The observed XRD peak at 37,2° belongs to cubic crystal structured NiO/Al_2O_3 (311) and the next peak at 43,3° belongs to cubic crystal structured NiO/Al_2O_3 (400) and cubic crystal structured NiO (111). The third peak at 58,8° belongs to cubic crystal structured NiO/Al_2O_3 (440) and cubic crystal structured NiO (200).

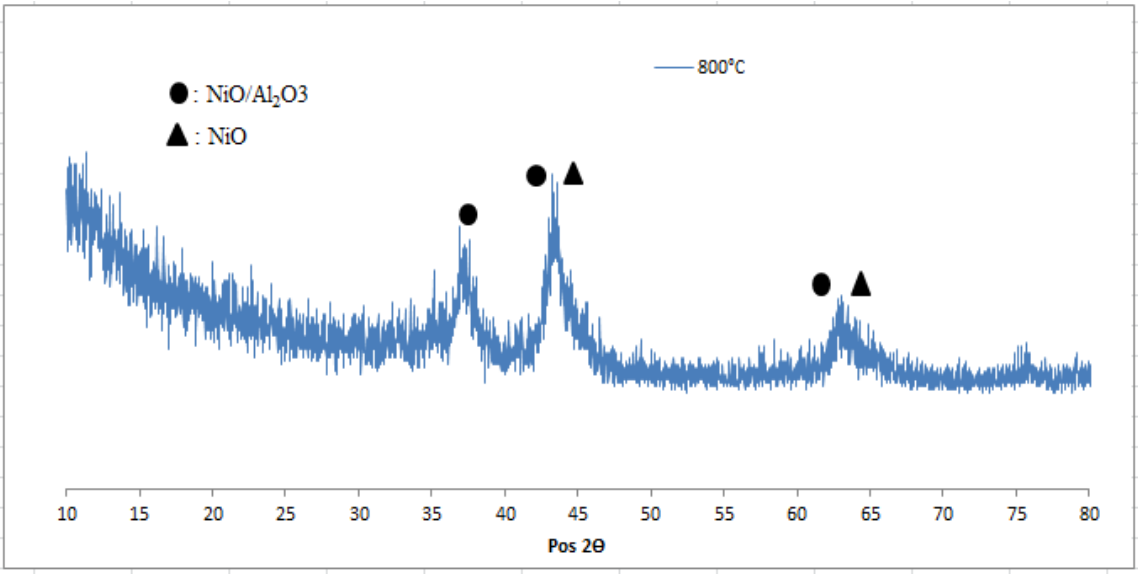

Figure 3. XRD pattern of NiO/Al_2O_3 nano particles.

SEM images of NiO/Al_2O_3 nano particles is given in Fig. 4. Particles exhibit spherical shape morphology and average particle size is around 570 nm. In Ultrasonic Spray Pyrolysis (USP) process, precursor reduces/decomposes to nanosized (primary) particles, and then nanoparticles aggregate to form secondary (submicron) particles. In SEM results, partly aggregated particles can be observed on Fig. 4b.

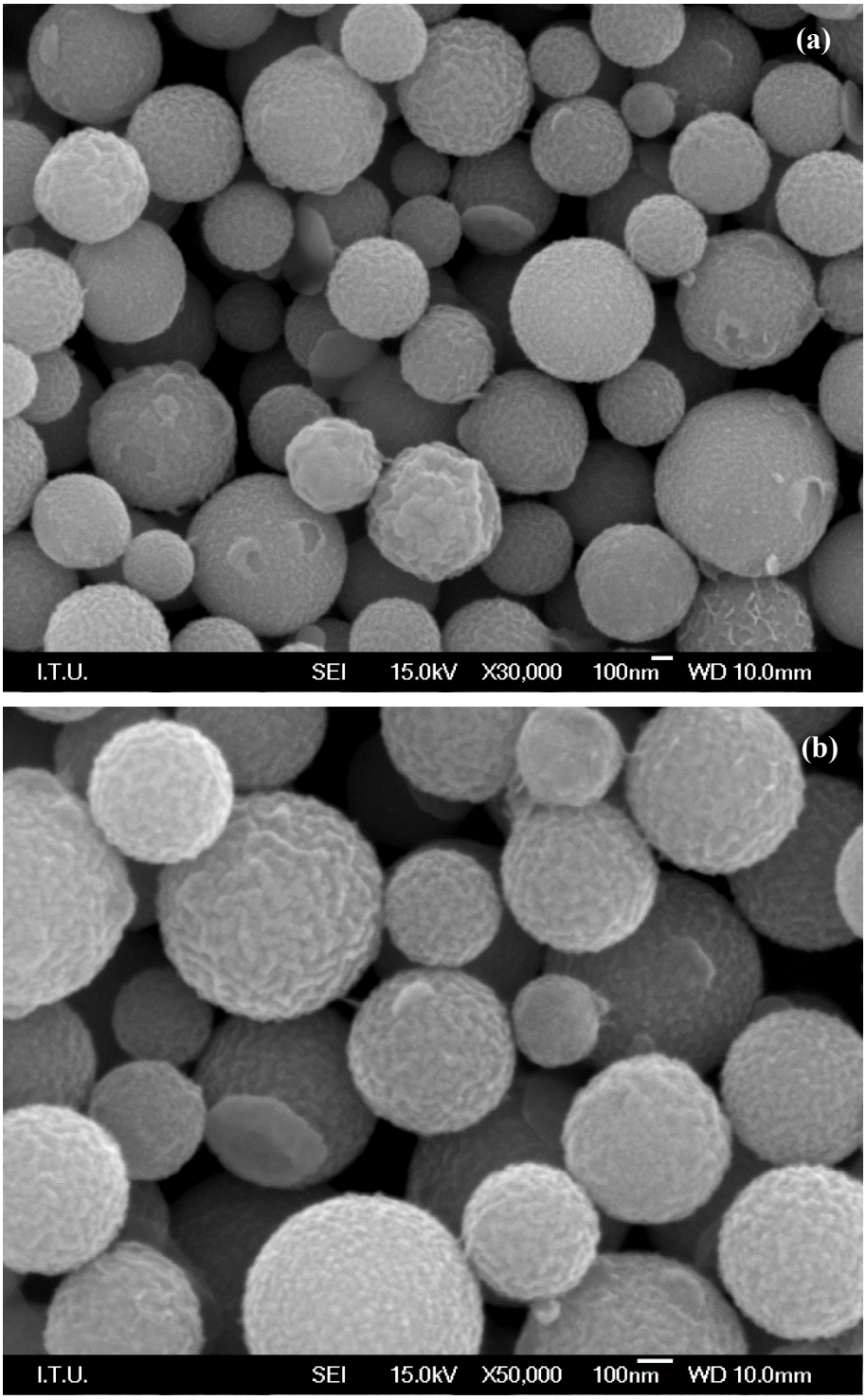

Figure 4. SEM images of NiO/Al_2O_3 nano particles (a) x30K and (b) x50K.

4. CONCLUSION

NiO/Al_2O_3 nano particles were successfully produced by USP process from nickel and aluminium nitrate precursor by thermal decomposition at 800°C. As a result, USP process is a suitable method to produce NiO/Al_2O_3 nanoparticles.

REFERENCES

1. S. Chokkaram, R. Srinivasan, D. R. Milburn and B. H. Davis, J. Mol. Catal. A-Chem. 121, 169, 1997.
2. T. Osaki, T. Mori, J. Non-Cryst. Solids, 335, 1596, 2009.
3. L. Maxim, R. Subir and L. P. Rene, Catal. Lett., 99, 4, 2005.
4. C. J. Gonzalez, Z. Boukha, B. D. Rivas, J. J. Delgado, M. A. Velasco and R. L. Fonseca, Appl. Catal. A-Gen. 466, 20, 2013.
5. M. Nazemi, S. Sheibani, F. Rashchi, V. C. Gonzalez and A. Caballero, Advances in Powder Technology, 23, 838, 2012.
6. Y. S. Han, J. B. Li, X. S. Ning and B. Chi, J. Am. Ceram. Soc., 88, 3455, 2005.
7. B. H. Kwak, H. K. Youn and J. S. Chung, J. Power Sources, 185, 633, 2008.
8. C. Dueso, A. Abad, F. G. Labiano, L. F. Diego, P. Gayan, J. Adanez and A. Lyngfelt, Fuel, 89, 3409, 2010.
9. N. F. Ribeiro, R. C. Neto, S. F. Moya, M. M. Souza and M. Schmal, Int. J. Hydrogen Energy, 35, 11732, 2010.
10. N. Bayal and P. Jeevanandam, J. Alloy Compd, 516, 32, 2012.
11. N. Deraz, Int. J. Electrochem. Sci., 8, 5212, 2013.
12. R. L. Fonseca, C. J. Gonzalez, B. D. Rivas and J. I. Ortiz, Appl. Catal. A-Gen. 437-438, 62, 2012.
13. S. Gürmen, B. Ebin, S. Stopic and B. Friedrich, J. Alloy Compd., 480, 529, 2009.
14. B. Ebin, E. Yazıcı and S. Gürmen, T. of Nonferr. Metal. Soc., 23 841, 2013, 841.
15. B. Ebin, Ö. Gençer and S. Gürmen, Int. J. Mater. Res., 104, 206, 2013.
16. S. C. Tsai, Y. L. Song, C. S. Tsai, C. C. Yang, W. Y.Chiu and H. M. Lin, J. Mater. Sci. 39, 3647, 2004.

Re-Inventing the Wheel with Materials Nanotechnology?

•

Malzeme Nanoteknolojisi ile Tekerlek Yeniden mi İcat Ediliyor?

Nihat Ali Işıtman

Goodyear Innovation Center Luxembourg - Luxembourg

ABSTRACT

The "magic triangle" represents three major technological requirements; rolling resistance – wet traction – wear resistance, that a modern tyre should deliver to meet ever-growing needs of the automotive industry. In this context, the new European Union tyre label is a legislative step taken to address the increasing awareness of consumers in road safety and environment. The current EU tyre label covers wet stopping distance, rolling resistance and noise level. However, today's tyre performance is more suitably identified by "3/15/50" where the EU label measures 3 tyre performances, European car and tyre magazines measure and publish approx. 15 attributes while Goodyear in its tyre development process measures and monitors at least 50 tyre performance criteria before the tyres are released for sale on the European market.

This contribution will give an overview of the journey from raw materials to public roads describing the key steps in tyre evolution. Particular emphasis will be placed on precipitated nanosilica as well as non-silica nanotechnologies like exfoliated graphite, carbon nanotubes, nanoclay, nanocellulose and nano-aluminium hydrate used in combination with state-of-the-art coupling agents and chemical functionalization to provide adequate bonding to the cross-linked elastomeric network. The talk will provide filler structure – mixing – viscoelasticity relationships in rubber compounds containing nanoscopic reinforcing fillers, aiming to describe the impact of materials nanotechnology on tyre road performances.

Located in the heart of Europe in Luxembourg, Goodyear Innovation Center is a major tire research and development center, hosting a large group of dedicated associates with talented educational and cultural backgrounds from more than 40 nationalities. Goodyear Tire & Rubber Co. is recognized among the top 100 Global Innovators by Thomson Reuters. The contribution of the Innovation Center in Luxembourg manifests itself as submission of numerous patents/trade secrets each year.

Keywords: Tyre evolution, precipitated nanosilica, non-silica nanotechnologies.

SYNTHESIS OF NANO-MANGANESE OXIDE (Mn_2O_3) PARTICLES BY USING HIGH FREQUENCY-INDUCTION SYSTEM

Levent KARTAL*, Yasin KILIÇ, Servet TİMUR

Istanbul Technical University, Metallurgical and Materials Eng. Dept., Istanbul-Turkey
*kartall@itu.edu.tr

1. ABSTRACT

The aim of this study is to synthesize manganese-oxide particles with a high purity as well as a controlled morphology and size distribution. The continuous production of nano-Mn_2O_3 particles was achieved by a designed system consisting of three major units: (1) a high frequency ultrasonic spray for generating aerosol, (2) a high frequency induction reactor for thermally decomposing aerosols and (3) particle collection bottles for accumulating powders. Initial concentration of $Mn(NO_3)_2$ solutions was investigated as a main process parameter to optimize the nano-scale particle fabrication. Synthesized Mn_2O_3 powders were characterized via scanning electron microscopy (SEM) and X-ray diffraction (XRD) techniques. It was found that 90 – 200 nm Mn_2O_3 particles was possibly producible after 15 minutes of process at 1073 K with the initial $Mn(NO_3)_2$ concentrations of 0.01 M, and the carrier gas flow rate of 1.0 L/min.

Keywords: Manganese oxide, Nanoparticle, Ultrasonic spray, High frequency inductive system

NANO MANGAN OKSİT (Mn_2O_3) PARTİKÜLLERİNİN YÜKSEK FREKANSLI İNDÜKTİF SİSTEM İLE SENTEZİ

ÖZET

Bu çalışmanın amacı dar ve homojen boyut dağılımına sahip, yüksek saflıkta mangan oksit nanopartiküllerinin üretilmesidir. Mangan oksit partikülleri 3 ana üniteden oluşan; (1) Yüksek frekans ultrasonik atomizer, (2) yüksek frekans indüksiyon reaktörü ve (3) toz toplama şişelerinden oluşan deney sistemi kullanılarak başarıyla üretilebilmiştir. Ana parametre olarak partikül boyutu üzerinde büyük etkisi olan çözelti konsantrasyonu seçilmiş ve üretilen Mn_2O_3 partikülleri SEM ve XRD teknikleri kullanılarak karakterize edilmiştir. Yaklaşık 90 ile 200 nm arasında değişen boyutlarda Mn_2O_3 partikülleri 1073 K reaksiyon sıcaklığında, 0,01 M' lık $Mn(NO_3)_2$ başlangıç çözeltisi kullanılarak ve 1,0 L/dk. taşıyıcı gaz debisinde üretimleri gerçekleştirilmiştir.

***Anahtar kelimeler*:** Mangan oksit, Nanopartikül, Ultrasonic Spray, Yüksek Frekans İndüktif Sistem

2. INTRODUCTION

Metal oxide nanoparticles have a significantly big portion in nano-science applications, especially in sensors. Among oxide forms of transition metals, manganese has many different oxide states, namely; MnO, Mn_2O_3, Mn_3O_4, Mn_5O_8, and MnO_2. Alpha manganese sesquioxide (α-Mn_2O_3) is a cubic bixbyite-type oxide, and considered as the most popular transition metal oxide [1]. Some studies reported that mesoporous α-Mn_2O_3 particularly

exhibits higher catalytic performance and lithium storage properties compared to the corresponding bulk Mn_2O_3 due to its high surface area as well as the number of active sites [2,3,4]. Moreover, non-toxic manganese oxide nanoparticles have a wide range of applications such as an oxygen storage component (OSC) for a 3-way catalyst systems [5], catalyst for removing carbon monoxide and nitrogen oxide from waste gases [6], high density magnetic storage media [7], molecular adsorption [8], ion exchange [9], electrochemical supercapacitor [10], biosensors [11] and as an adsorbent in water treatment [12].

Manganese oxide nanoparticle can be producible via thermal decomposition [13,14], thermochemical [15], hydrothermal [16], arc evaporation [17] techniques. Nanoparticle production from all soluble or organometallic compounds by using aerosol-based systems is more flexible and easier compared to the others. For this reason, we designed our nanoparticle fabrication according to this production technique. Basically a combined system was developed which composed of a powerful source of ultrasound for aerosol generation with uniform droplet size and a medium frequency induction furnace for thermal decomposition of formed aerosols. During thermal decomposition, the evaporation/drying and thermolysis of transported aerosols occurred in a single-step process. The aerosols and hence samples was heated by induction method never come into direct contact with a flame or other heating elements. Consequently, spherical, solid, either submicron or nano-scaled particles are obtained with a continuous process (Fig.2).

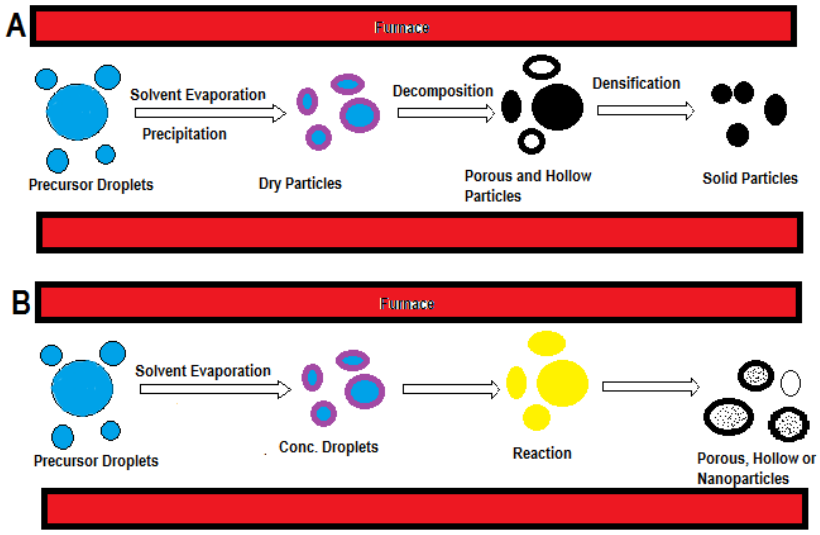

Fig. 1. **A)** and **B)** simplified gas-solid and gas-liquid chemical aerosol flow synthesis reaction processes, respectively [18].

The goal of this study is to investigate the effect of precursor concentration on Mn_2O_3 nanoparticle production via a medium frequency induction system. Mn_2O_3 nanoparticles were produced by using two different solutions concentrations (0.1 and 0.01M) at constant process conditions; 15 min. of running time, 1073 K of reduction temperature, and 1.0 L/min. of air volumetric flow rate. XRD and SEM analyses were carried out to inspect the purity, size as well as morphology of produced nanoparticles.

3. MATERIALS AND METHODS

All the reagents were analytical grade and used without further purification. A solution of $Mn(NO_3)_2$ compound was utilized as a starting material for Mn_2O_3 production.

The nano-structured manganese oxide particles were synthesized by using a system which facilitated to produce nano metal/metal oxide within a medium frequency inductive power supply. A well-designed ultrasonic nebulizer with the frequency of 1.7 MHz was used in the ultrasonic spray part and hence very fine droplets of the aerosol were observed in the transportation of the aerosol where air was utilized as a carrier gas though the quartz tube (0.7 m length and 0.025 m diameter). Nanoparticle trapping system consisted of three interconnected identical glass tubes that filled up with alcohol.

The schematic depiction of the nanoparticle production system setup was given in Fig.2. The developed design consisted of three major units: (1) a high frequency ultrasonic spray for the aerosol generation of particles from their solutions, (2) a medium frequency induction reactor for the thermal decomposition of relevant aerosol and (3) collection bottles for the accumulation of the nanoparticles.

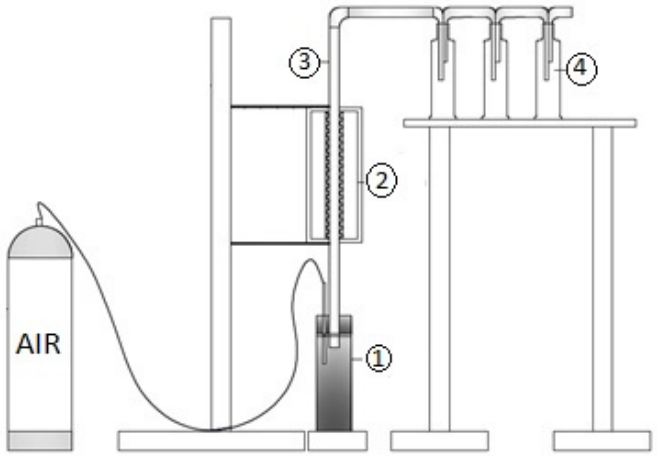

Fig. 2. Schematic drawing of the experimental set-up. (1-Ultrasonic generator, 2-Inductive reactor, 3- Quartz tube, 4- Powder collectors)

The crystal structures of synthesized particles were identified by a X-ray diffraction (XRD, Philips 1700 diffractometer) using Cu Kα radiation (λ=1.54187 Å, 2θ range 10°−90°). For XRD analysis, the particles were placed on a glass substrate and allowed to dry in air at room temperature. The morphology and size of produced samples were studied using a field emission scanning electron microscopy (FE-SEM, Jeol JSM 700F).

The effect of precursor concentration on Mn_2O_3 nanoparticle was studied in two different solutions concentrations (0.1 and 0.01 M) at constant process conditions; 15 min. of running time, 1073 K of reduction temperature, and 1.0 L/min. of air volumetric flow rate.

4. RESULTS AND DISCUSSION

4.1. Thermodynamic analysis of precursor materials

The possible decomposition reactions were proposed with the change of Gibbs free energy calculations carried out by HSC Software program.

The possible formation of Mn_2O_3 metal could be as in Eq.1.

$$2Mn(NO_3)_{2(aq)} = Mn_2O_{3(s)} + 4NO_{2(g)} + 1/2O_{2(g)} \quad \textbf{(1)}$$

The values of Gibbs free energy (ΔG^o) for the reaction (1) in the temperature up to 1273 K confirm the possibility for the formation of manganese oxide by the thermal decomposition of manganese nitrate (see Fig 3). It could be deduced that manganese formation by thermal decomposition of manganese nitrate was thermodynamically possible at the desired temperatures between 393 K and 1273 K.

The large difference between the decomposition temperature determined with thermodynamic calculations and the experimentally applied temperature (1073 K) would possibly enable the manganese oxide nanoparticle production with higher oxidation states in the inductive conditions.

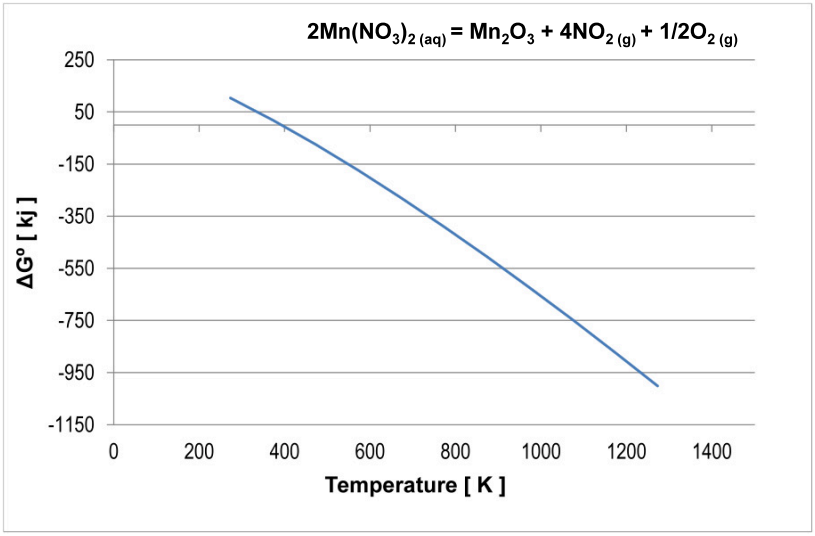

Fig. 3. Change of Gibbs free energy for thermal decomposition of manganese nitrate

4.2. The effect of precursor concentration on the synthesis of Mn_2O_3 nanoparticles

The effects of precursor $Mn(NO_3)_2$ concentration were investigated in two different solutions concentrations (0.1 and 0.01 M) at constant process parameters; 15 min. of process duration, 1073 K of reaction temperature and 1 L/min. of air volumetric flow rate.

Morphological SEM examinations of synthesized Mn_2O_3 powders reveal that Mn_2O_3 particles generated at both 0.1 and 0.01 M were composed of a large number of particles (Fig. 4 and Fig. 5). As seen higher magnified SEM image (Fig. 4), there were considerable amount of pore and spherical nano particle formations on big globular submicron particles formed at the

initial solution concentration of 0.01 M. However, Mn_2O_3 particles became less porous and more solid at higher initial solution concentration (see Fig.5)

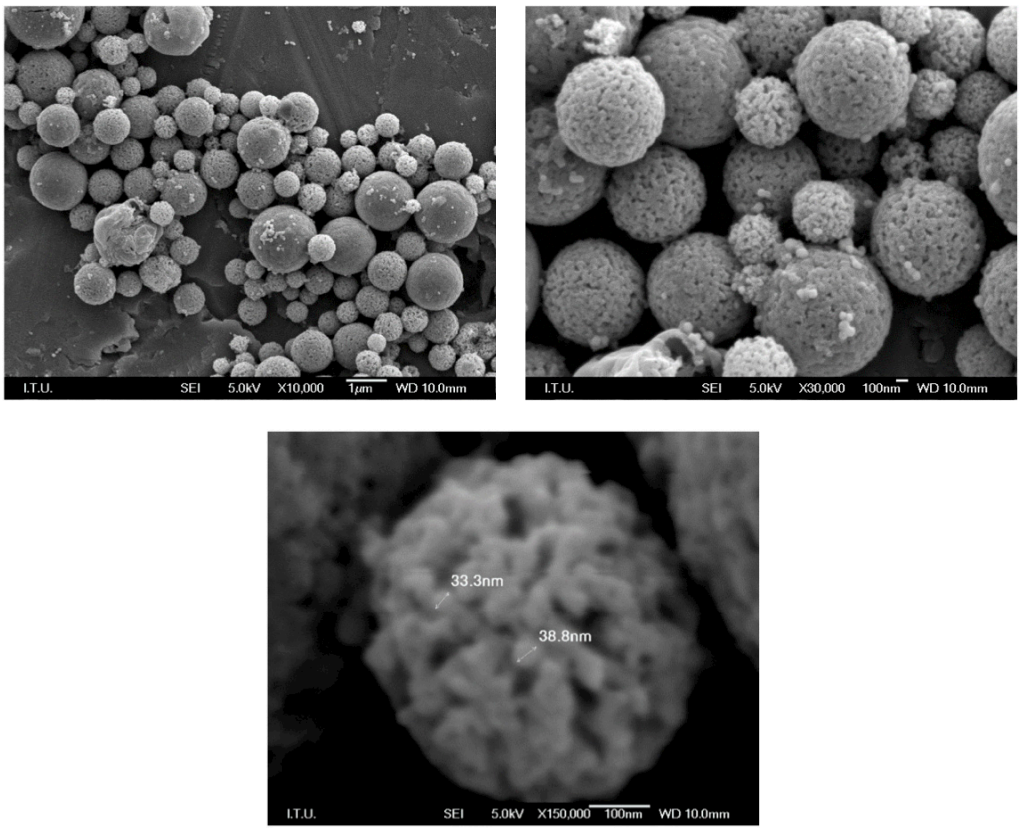

Fig. 4. SEM images of Mn_2O_3 particles produced using 0.1 mol/L. $Mn(NO_3)_2$ solution [1073K, 1 L/min.]

As clearly seen in Fig. 4-5, the decrease in the concentration of precursor solution caused a dramatic decline in the average diameter of the particles. Apparently, the variation in concentration had a significant effect on the particle size; moreover very fine less than 100 nm of particles was producible at relatively low concentration of precursor solution; i.e. 0.01 M.

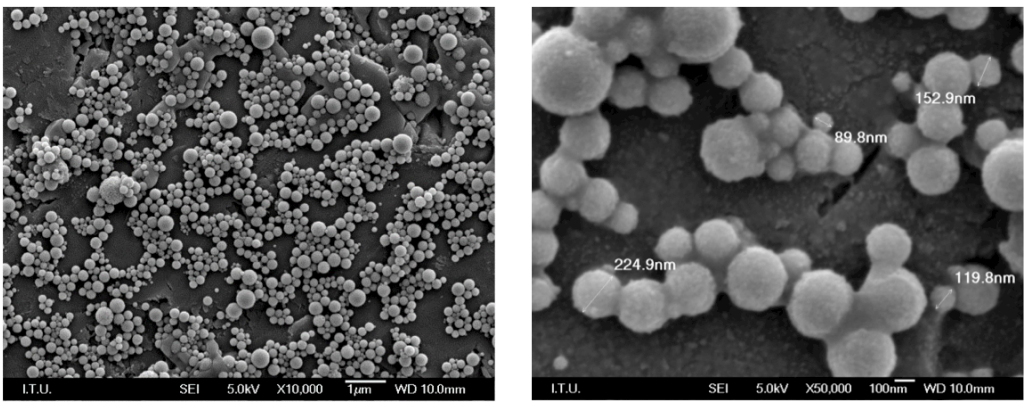

Fig. 5. SEM images of Mn_2O_3 particles produced using 0.01 mol/L $Mn(NO_3)_2$ solution [1073K, 1 L/min.]

The XRD analysis of synthesized mesoporous nanoparticles confirmed cubic Mn_2O_3 phase formation without the presence of any impurities. (Manganese oxide, JCPDS no. 089-4836) (Fig. 6).

Crystalline size of particles was calculated from XRD patterns according to Scherrer Equation (Eq. 2) that defines a simple relationship between crystalline size, and peak width.

$$L = \frac{K\lambda}{B(2\theta)\cos\theta} \quad \textbf{(2)}$$

where K is constant whose value is between 0.85 and 0.9, ƛ is the wavelength of the X-ray (Cu K_1 = 1.5418 Å), B is the full width high maximum (FWHM -in radians) of the peak due to size effect), θ is the Bragg angle, and L is the particle size.

The peak belonging to the (222) crystal orientation was used for the determination of crystalline size (see Fig. 5). The full width high maximum (FWHM) of (222) peak located at 32.9° was 0.57° and hence the size of Mn_2O_3 crystallites was calculated as 17.4 nm based on FWHM value and equation 2.

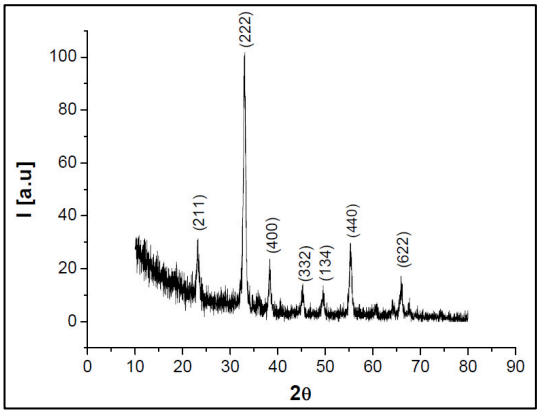

Fig. 6. XRD diffraction spectra of Mn_2O_3 particles (JCPDS: 089-4836) [0.1 M, 1073K, 1 L/min.]

5. CONCLUSIONS

In this study, manganese-oxide particles with a high purity as well as a controlled morphology produced by developed continuous nano particle synthesis method. The design fabrication technique was combined two separate systems: (1) Ultrasonic spray that allowed using basic soluble chemical compounds instead of expensive volatile organometallic compounds, and (2) induction technology, which is one of the most efficient and economic heating technology. The influences of the most critical process parameter, initial solution concentration of $Mn(NO_3)_2$, were investigated to idealize the nano-scale manganese oxide particle production. Based on the results reported, the following conclusions could be drawn:

- This research proved that the necessary energy for the decomposition of precursor material could be easily derivable with an induction system.
- Mn_2O_3 nanoparticles production was probable from the initial solution of $Mn(NO_3)_2$ by sequence reactions of thermal decomposition and oxidation.
- The decrease in the solution concentration from 0.1 M to 0.01 M leaded to decrease in the average particle size.
- The formations of second phase(s) or any impurities were not observed in Mn_2O_3 nanoparticles production.

Acknowledgement

This work was supported by TUBITAK with project number of 110M687. The authors would like to thank SEM laboratory personnel under the management of Prof. Dr. Gultekin Goller for their contributions on SEM analyses.

6. REFERENCES

[1] K. Byrappa T. Adschiri , 2007. Progress in Crystal Growth and Characterization of Materials *Hydrothermal technology for nanotechnology* Volume 53, Issue 2, June, Pages 117–166

[2] Y. Ren, Z. Ma, L. Qian, S. Dai, H. He, P.G. Bruce, 2009. Ordered crystalline mesoporous oxides as catalysts for CO oxidation, *Catalysis Letters* 131 146–154.

[3] J.N. Park, J.K. Shon, M. Jin, S.H. Hwang, G.O. Park, J.-H. Boo, T.H. Han, J.M. Kim, 2010. Highly ordered mesoporous α-Mn2O3 for catalytic decomposition of H_2O_2 at low temperature, *Chemistry Letters* 39 493–495.

[4] Hu, L. et al., 2013. Facile synthesis of porous Mn_2O_3 hierarchical microspheres for lithium battery anode with improved lithium storage properties. *Journal of Alloys and Compounds*, 576, pp.86–92.

[**5]** Salavati-Niasari, M., Esmaeili-Zare, M. & Gholami-Daghian, M., 2014. Synthesis and characterization of Mn2O3 nanorods using a novel manganese precursor. *Advanced Powder Technology*, pp.3–8.

[**6]** Pugazhvadivu, K.S., Ramachandran, K. & Tamilarasan, K., 2013. Synthesis and Characterization of Cobalt doped Manganese Oxide Nanoparticles by Chemical Route. *Physics Procedia*, 49, pp.205–216.

[7] Han, Y.-F. et al., 2006. Synthesis and characterization of Mn_3O_4 and Mn_2O_3 nanocrystals on SBA-15: Novel combustion catalysts at low reaction temperatures. *Catalysis Communications*, 7(10), pp.739–744.

[8] Gnanam, S. & Rajendran, V., 2013. Facile hydrothermal synthesis of alpha manganese sesquioxide (α-Mn_2O_3) nanodumb-bells: Structural, magnetic, optical and photocatalytic properties. *Journal of Alloys and Compounds*, 550, pp.463–470.

[9] Liu L, Liang H, Yang H, Wei J, Yang Y., 2011.The size-controlled synthesis of uniform Mn_2O_3 octahedra assembled from nanoparticles and their catalytic properties *Nanotechnology.* 22(1) 015603.

[10] Zhao, D., Tan, J. S., Ji, Q. Q., Zhang, J. T., Zhao, X. S. and Guo, P. Z., 2010. Mn_2O_3 Nanomaterials Facile synthesis and electrochemical properties, *Chinese Journal of Inorganic Chemistry,* Vol 26 No 5

[11] Soundappan Thiagarajan, Tsung Hsuan Tsai, Shen-Ming Chen, 2011. Electrochemical Fabrication of Nano Manganese Oxide Modified Electrode for the Detection of H_2O_2, *Int. J. Electrochem. Sci.*, 6 2235 – 2245

[12] Jie Cao QingheMaoa, Yitai Qian, 2012. Synthesis of Mn_2O_3 homogeneous core/hollow-shell structures with excellent adsorption performance, *Journal of Solid State Chemistry* 191 10–14

[13] Yang, Z. et al., 2006. Synthesis of porous and hollow microspheres of nanocrystalline Mn2O3. *Chemical Physics Letters*, 418(1-3), pp.46–49.

[14] Tokeer A., Kandalam V. R., Samuel E. L., Ashok K. G., 2004. Nanorods of manganese oxalate: a single source precursor to different manganese oxide nanoparticles (MnO, Mn_2O_3, Mn3O4) *J. Mater. Chem.*, ,14, 3406-341

[15] Francis, T.M., Lichty, P.R. & Weimer, A.W., 2010. Manganese oxide dissociation kinetics for the Mn_2O_3 thermochemical water-splitting cycle. Part 1: Experimental. *Chemical Engineering Science*, 65(12), pp.3709–3717.

[16] M. Shamshi Hassan, Touseef Amna, Dipendra Raj Pandeya, A. M. Hamza, Yang You Bing, Hyun-Chel Kim, Myung-Seob Khil, 2012. Controlled synthesis of Mn_2O_3 nanowires by hydrothermal method and their bactericidal and cytotoxic impact: a promising future material, *Applied Microbiology and Biotechnology,* Volume 95, pp 213-222

[17] Jie Cao, QingheMao, YitaiQian, 2007. Large coercivity and small exchange bias in Mn_3O_4/MnO nanoparticles, *Solid State Communications* 142 723–726

[18] Jin Ho Bang, Yuri T. Didenko, Richard J. Helmich, and Kenneth S. Suslick, Nanostructured Materials Through Ultrasonic Spray Pyrolysis, *Material Matters,* Volume 7, Number 2, 15–20

Al-RE AMORPHOUS-NANOCRYSTAL COMPOSITE ALLOYS

Mustafacan KUTSAL*, Can YILDIRIM, Tuba DEMIRTAŞ***,**
Fatih SIKAN**, Y.Eren KALAY*****

* Middle East Technical University, Turkey
mkutsal@metu.edu.tr
** Middle East Technical University, Turkey
ycan@metu.edu.tr
*** Middle East Technical University, Turkey
demirtas.t@gmail.com
**** Middle East Technical University, Turkey
e173927@metu.edu.tr
***** Middle East Technical University, Turkey
ekalay@metu.edu.tr

ABSTRACT

Al-RE (RE: Rare-earth element) metallic glasses have recently attracted much attention due to their superior properties such as mechanical and corrosion resistance as well as having low density. The controlled devitrification of such alloys results in extraordinary nucleation number density of fcc-Al nanocrystals, values reaching up to 10^{24} m^{-3}. The predicted tensile strength of amorphous-nanocrystalline composites Al alloys are within the 1200-1500 MPa ranges. The unusual nucleation and growth behavior of fcc-Al in Al-RE based metallic glasses was investigated using complementary experimental methods such as differential scanning calorimetry (DSC), X-ray diffraction (XRD) and transmission electron microscopy (TEM). Our recent results confirmed the controlled nanoscale ordering in amorphous matrix which gives rise to superior mechanical properties, i.e. hardness values reaching up to 280 HV. The formation of nanocrystals within the amorphous matrix will be discussed.

Keywords: Nanocrystals, metallic glasses, mechanical properties

ÖZ

Al-RE BAZLI AMORF-NANOKRİSTAL KOMPOZİT YAPILI ALAŞIMLAR

Alüminyum-Nadir Toprak elementi (Al-NTE) bazlı metalik camlar düşük öz kütlelerinin yanında sahip oldukları üstün mekanik özelliklerinden dolayı araştırmacıların ilgisini çekmektedir. Söz konusu alaşımlar, kontrollü olarak kristallendirildiklerinde klasik çekirdeklenme kuramı ile açıklanamayacak sayıda, metreküpte 10^{24} nanokristal olacak şekilde kristallenmektedir. Bu

alaşımların çekme dayanımları 1200-1500 MPa arasında olarak tahmin edilmektedir. Eriyik savurma yöntemi ile üretilmiş $Al_{90}Tb_{10}$ kompozisyonlu Al-NTE metalik camlarının sıra dışı çekirdeklenme ve büyüme davranışı ayrımsal taramalı ısıölçer (DSC), geleneksel ve sinkrotron bazlı X-ışını kırınımı (XRD) ve geçirimli elektron mikroskobu (TEM) ile incelenmiştir. Yapılan çalışmalar, fcc-Al fazının kontrollü olarak nano düzeyde kristallendirilmesi halinde 280 HV sertliğe ulaşılacak kadar üstün mekanik özelliklere sebep olduğu gözlemlenmiştir. Amorf faz içinde nanokristal oluşumu detaylı biçimde incelenmiştir.

Anahtar kelimeler: Nanokristaller, metalik camlar, mekanik özellikler

1. INTRODUCTION

Aluminum based metallic glasses have gathered much attention due to their extremely high number density nucleation capability upon devitrification which improves its mechanical properties (i.e. strength and hardness) as compared to conventional aluminum alloys [1]. Upon devitrification, fcc-Al nanocrystals having a nucleation density of 10^{21} to 10^{24} m^{-3} form in amorphous matrix, which cannot be explained by applying the classical nucleation theory [2]. There are two main hypotheses for this enigmatic behavior, namely as "quenched-in nuclei" [3] and phase separation in amorphous state theories [4]. The former suggests that fcc-like medium-range-ordered (MRO) Al have already existed in the amorphous matrix upon rapid solidification. This has been shown by series fluctuation electron microscopy (FEM) studies [5], which indicated the growth of already existed MRO Al clusters. On the other hand, "phase separation" theory states that upon devitrification, the amorphous matrix decomposes into aluminum-rich and aluminum-depleted regions in nano scale, creating high density of phase boundaries for fcc-Al nanocrystals to nucleate heterogeneously. Our previous studies on $Al_{90}Tb_{10}$ and $Al_{91}Tb_9$ amorphous melt spun ribbons using reverse Monte Carlo simulations constrained by high energy X-ray diffraction (HEXRD) and atom probe tomography (APT) supports the idea of having nano-scale phase separation within the amorphous matrix [6]. The high temperature HEXRD experiments from the molten Al-RE alloys [7] also indicated a heterogeneous liquid structure within the range of metallic glass formation.

In this study, the devitrification of melt-spun $Al_{90}Tb_{10}$ alloy was investigated using transmission electron microscopy (TEM) and X-ray diffraction (XRD). The mechanical behavior of the amorphous and partially crystalline melt-spun ribbons was studied by tensile tests and micro hardness tests.

2. EXPERIMENTAL PROCEDURE

Ingots of $Al_{90}Tb_{10}$ alloy were prepared by using high purity precursors of Al (99.99 wt. %) and Tb (99.9 wt. %) by electric arc-melting under protective argon atmosphere. Amorphous ribbons of 30 μm thickness were produced using a Cu block single melt-spinner at a tangential speed of

30 m/s. XRD experiments were conducted using Cu Kα radiation at Bragg-Brentano geometry. TEM analyses were conducted by a JEOL JEM2100F scanning/transmission electron microscope. Samples for electron microscopy were prepared by dimpling and electropolishing with a solution of 25 vol.% HNO3 and 75 vol.% methanol. The indentations for hardness testing were held with a Shimadzu HMV MicroHardness Tester under a load of 980.7 mN (HV 0.1) for 10 s of dwell time. An aluminum plate was used as a substrate for ribbons, having a hardness value of 154 HV. To eliminate the errors that can be due to aluminum substrate, hardness tests were repeated using a steel plate having a hardness value of 354 HV. Tensile tests were performed using Instron 5565 Universal Testing Machine by clamping melt-spun ribbons to the device. A strain rate of 0.1 mm/min was used for tensile test experiments.

3. RESULTS AND DISCUSSION

Figure 1 shows scanning electron microscopy (SEM) images of chill cast $Al_{90}Tb_{10}$ ingots. Due to the low glass forming ability (i.e. requiring higher cooling rates to have fully amorphous structure upon casting) of Al-RE alloys, the cooling rate (~10^3 K/s) supplied from the nature of the chill casting was not enough to bypass the crystallization curve in the time-temperature-transformation diagram (Fig.2); hence, relatively large fcc-aluminum dendrites and Al-Tb intermetallics were present after chill casting.

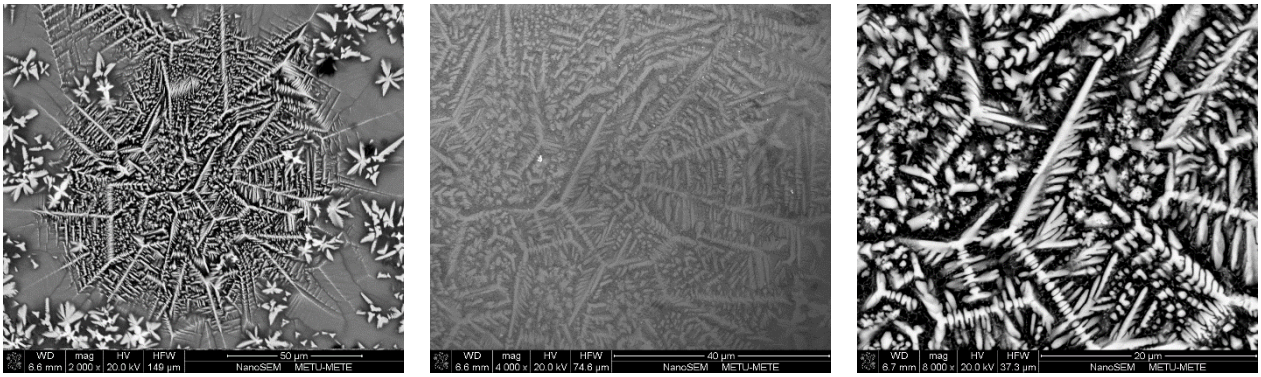

Figure 1. SEM images of chill cast samples at different magnifications.

Upon increasing the cooling rate by changing the production pathways from chill cast to melt-spinning (~10^6 K/s), amorphous $Al_{90}Tb_{10}$ could be produced. Figure 3 shows TEM micrographs indicating melt-spun $Al_{90}Tb_{10}$ ribbons of amorphous state and different annealing times; namely A,B, and C stands for annealing times of 298, 469, and 1270 seconds, respectively. The same notation will be used thought this manuscript. The annealing temperatures were selected according to a previous study [6] in which the isothermal devitrification of the same alloy composition was studied at 220 °C. The annealing times correspond to the on-set of the initial crystallization, peak of the initial crystallization and the peak of the second crystallization event, respectively. Figure 3(a) shows the amorphous state with no crystalline feature, which is confirmed by the selected area electron diffraction (SAED) pattern having a diffuse halo. As it can be seen from Figure 3(b) and 3(c), with annealing of the amorphous ribbon, dendritic fcc-Al

nanocrystals were formed and grew within the amorphous matrix. From Figure 3(d), it can be seen that large plate like Al-Tb intermetallic phase appears by the end of fcc-Al crystallization event. This indicates the existence of a second phase transformation after fcc-Al nanocrystallization.

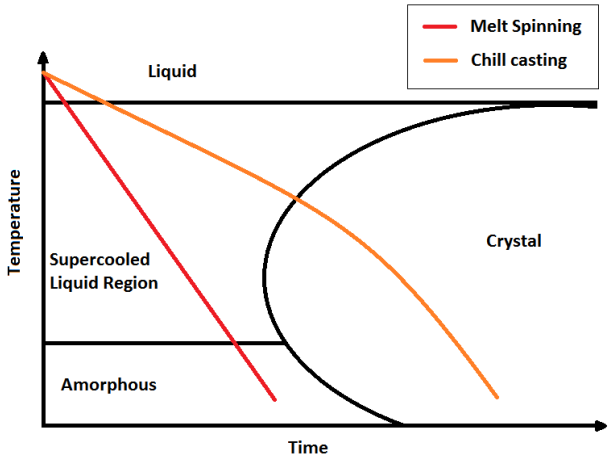

Figure 2. Schematic TTT diagram representing melt-spinning (red line) and chill casting (orange line)

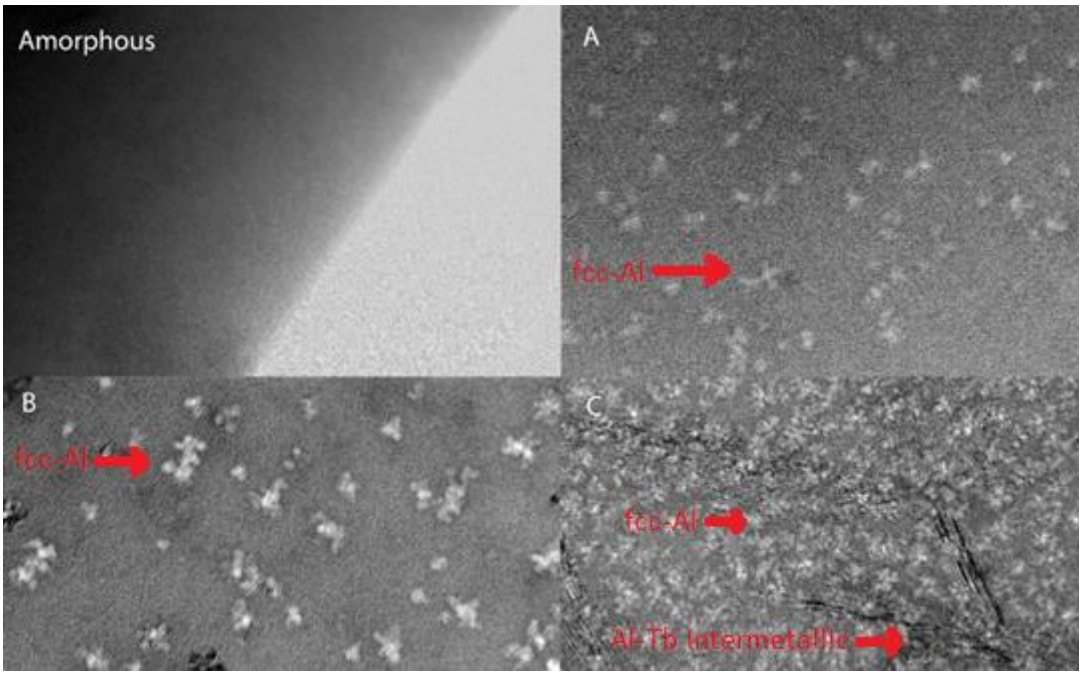

Figure 3. TEM micrographs of amorphous and 298 (A), 469 (B), and 1270 (C) seconds annealled specimens.

Figure 4 shows the XRD results for as-quenched and isothermally annealed (at 220 °C) $Al_{90}Tb_{10}$ ribbons. The XRD from the as-quenched specimens confirms the amorphous nature of the ribbons by making a diffuse scattering peak around 38 degrees 2theta.. Furthermore, there also exists a pre-peak before the main amorphous hump and a side peak after the main hump which is a characteristic of marginal glass forming alloys. From previous studies, the presence of these pre & side peaks were attributed to the strong RE-Al and Al-Al interactions that could be correlated to the medium range ordering [6]. The evolution of fcc-Al crystals can be clearly seen from the patterns denoted as A and B. In that sense, the XRD results are in good agreement with the TEM analyses

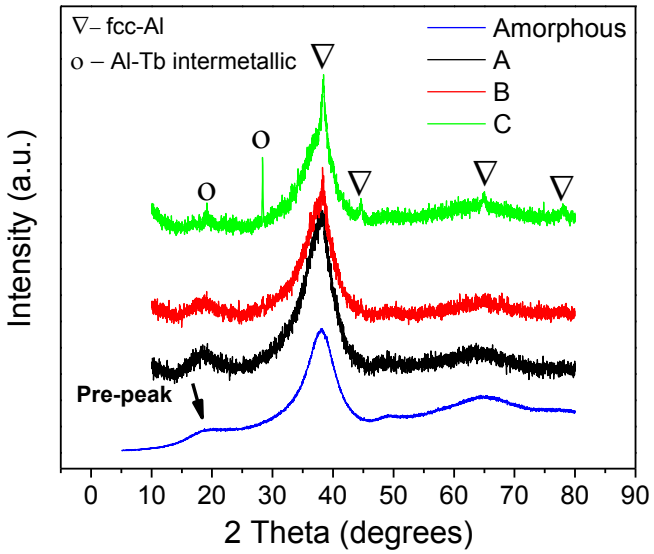

Figure 4. XRD patterns of as-quenched (amorphous) and isothermally annealed (A: 298; B: 469; C: 1270 seconds) $Al_{90}Tb_{10}$ ribbons.

The hardness values and the measured tensile strengths for the amorphous and partially devitrified ribbons were given in Table 1. It can be seen from the table that with increasing annealing times, the hardness increases and reaches its maximum value after the precipitation of the product of the second transformation. Under partially (B) and fully nanocrystalline (C) condition, hardness is almost increased to its 1.5 of original value. It is interesting to note that the critical aerospace material AA2024 has an ultimate hardness values of $150H_v$ and $195H_v$ after peak-aged and equal channel angular pressing (ECAP) process [8]. In our case, nanocrystalline ribbons show a much higher hardness values indicating the potential strength of these materials. In line with the previous studies in literature, the tensile test results are quite chaotic because of the ribbon geometry used in measurements. All of the specimens fractured before considerable plastic deformation, so very little ductility was observed. As it is expected, the specimen having intermetallics (C) showed the weakest strength and ductility. The as-quenced and B-coded specimens (having approximately 37% of nanocrystal according to DSC [9]) have considerable amount of strength at fracture point. A potential ground for having relatively high strength might be related to MRO present in the amorphous matrix. Rather than having a fully disorder

configuration, MRO structure may trigger the mobility of relatively long range ordered clusters (1-3nm) which results in an increase in strain. Upon isothermal annealing, defect free fcc-Al nanocrystals with extraordinarily high nucleation density are formed from these MRO region resulting higher stress requirement for yielding. It should be noted that further critical mechanical testing and corresponding microstructural investigations should be performed by using relatively thicker specimens before drawing a solid conclusion.

Table 1. Mechanical Test Results

Annealing State	Percent Nanocrystalline fcc-Al [9]	Stress at Fracture (MPa)	Hardness on Aluminum (HV)	Hardness on Steel (HV)
AMORPHOUS	0	345.6	187.7	187.4
B	37	312.1	254.7	258.6
C	Second phase formed	167.5	281.6	278.3

Fracture analysis was performed on the tensile test specimens of as-quenched and partially devitrified melt-spun ribbons by using scanning electron microscope (SEM) in order to probe any microstructural change that would have produced upon deformation. It is known from the literature that the deformation is accepted in certain zones as shear (namely shear bands [10],) where the strain is accommodated, and it is customary to observe shear bands after plastic deformation took place or even after manually bending elastically. It is also well known that the number of the shear bands produced is directly proportional to the fracture strain; meaning that the fracture surfaces of materials which shows high plastic strain possesses high number of shear bands [10]. Further, it is said that presence of nanocrystals inside an amorphous matrix increases the plastic strain due to the fact that the nanocrystal-matrix interface acts as shear band nucleation site and during deformation nanocrystals tend to force shear bands to branch out, by which material creates more zones to accommodate further strain [10].

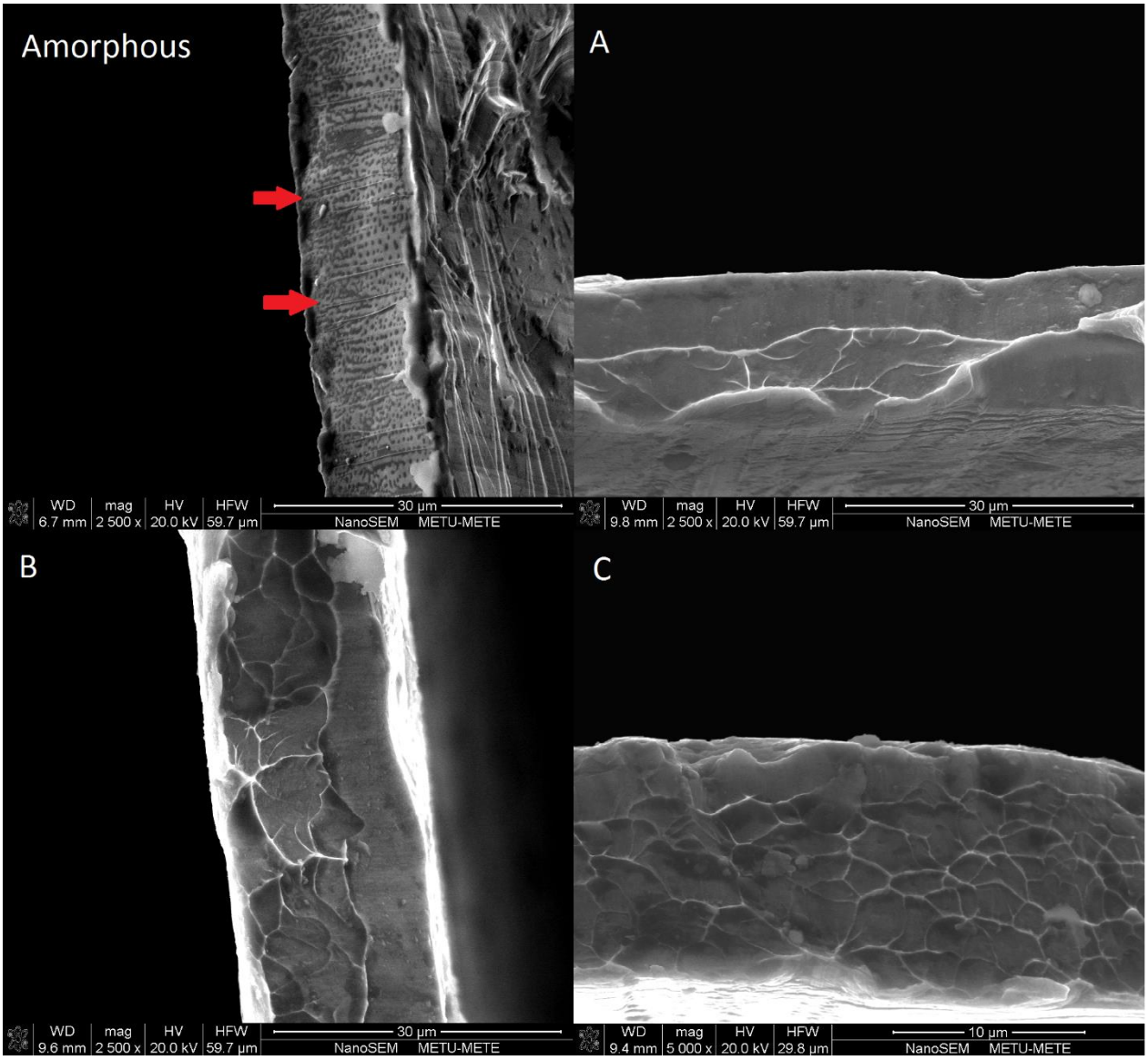

Figure 5. SEM fractrographs of the amorphous and partially devitrified states of melt-spun ribbons. The shear bands in amorphous state are indicated by red arrows.

Figure 5 shows the SEM fractographs of the as-quenched and partially devitrified melt-spun ribbons after tensile testing. In the light of the information that was stated above, all samples show shear band like zones in their fracture surfaces, and it can be inferred from the figure that the population of these zones increases with increasing annealing times. However, it can be seen that in amorphous state shear bands were in more regular fashion; they were aligned parallel to each other and could be said to be high in number, further no branching was present. As nanocrystals appear, i.e. A and B states, shear bands become branched. Comparing the amorphous and B states, it can be seen that B state, shear bands were much more populated per fracture surface area and branching was more prominent than amorphous states. Therefore, by

considering the branching observed, it is expected that higher tensile strength would be reached in case of B which is contradicting with the measured tensile strength. However, as it was noted previously the ribbon geometry of the specimens makes difficult to collect representative tensile strengths. On the other hand, the micro hardness data clearly indicated the clues for better mechanical properties of amorphous-nanocrystalline composites. State C shows high number of shear bands and branching as expected, since fcc-Al nanocrystallization was completed after this state. However, the reason behind the low tensile strain is the presence of the brittle secondary devitrification product. As it can be seen in the TEM micrographs in Figure 3, the secondary crystallization product is a needle-like sharp edges Al-Tb bearing intermetallic phase, which could act as stress riser upon deformation rather than creating an amorphous/nanocrystalline composite effect.

In conclusion, it can be summarized that fcc-Al precipitation in amorphous matrix enhances mechanical properties if the nanocrystal density is optimized. On the other hand, introducing further devitrification products (i.e. Al-Tb intermetallics) deteriorates the favorable effects of the fcc-Al nucleation.

4. CONCLUSION

The solidification behavior of $Al_{90}Tb_{10}$ alloy was studied using different cooling rate possessing techniques. The fully amorphous $Al_{90}Tb_{10}$ metallic glass alloy was produced using melt-spinning which corresponds to a cooling rate of 10^6K/s. The metallic glassy structures were devitrified to from highly populated fcc-Al nanocrystals embedded in amorphous matrix. The mechanical properties of the as-quenched amorphous alloy; partially crystalline specimen with and without the formation of Al-Tb intermetallic were investigated using microhardness and tensile tests. The specimens with Al-Tb intermetallic formation showed the lowest tensile strength with the highest hardness. Despite their high hardness, the material becomes brittle due to the needle like Al-Tb forming within the matrix. The as-quenched amorphous specimens showed the highest tensile strength whereas its average hardness value is quite low. The partially crystalline alloy with 37% of fcc-Al nanocrystals embedded within the amorphous matrix exhibited the relatively high hardness and tensile test values with reasonable amount of ductility.

ACKNOWLEDGEMENT

The assistance of Materials Preparation Center of the Ames Laboratory is acknowledged for supplying the samples.

5. REFERENCES

1. Inoue, Akihisa. "Amorphous, nanoquasicrystalline and nanocrystalline alloys in Al-based systems."Progress in Materials Science, 1998,43: 365-520.
2. Schroers J, Busch R, Masuhr A, Johnson, W. L.. "Continuous refinement of the microstructure during crystallization of supercooled $Zr_{41}Ti_{14}Cu_{12}Ni_{10}Be_{23}$ melts." Applied Physics Letters 1999,74: 2806.
3. Wilde G., Sieber H.,Perepezko, J.H.. "Glass formation versus nanocrystallization in an Al92Sm8 alloy." Scripta Materialia 40: 779-783.
4. Gangopadhyay A.K., Croat T.K.,Kelton, K.F.. "The effect of phase separation on subsequent crystallization in Al88Gd6La2Ni4." Acta Materialia 48: 4035-4043.
5. Stratton W.G., Hamann J., Perepezko J.H., Voyles P.M., Aluminum nanoscale order in amorphous Al92Sm8 measured by fluctuation electron microcopy, Appl. Phys. Lett. 86 (2005) pp. 1419101 – 1419103.
6. Kalay, Y.E., Kalay, I., Hwang, J., Voyles, P.M., Kramer, M.J.. "Local chemical and topological order in Al–Tb and its role in controlling nanocrystal formation." Acta Materialia 2012,60: 994-1003.
7. Kalay Y.E., Chumbley L.S., Kramer M.J., Anderson I.E., Local structure in marginal glass forming Al-Sm alloy, Intermetallics 18 (2010) pp. 1676 – 1682.
8. Kotan G., Tan E., Kalay Y.E., Gür C.H., Homogenization of ECAPed Al 2024 alloy through age-hardening, Mater. Sci. Eng. A 559 (2013) pp. 601 – 606.
9. Demirtaş, T., and Y.E. Kalay. "Kinetics of fcc-Al nanocrystallization in Al90Tb10 metallic glass." Journal of Non-Crystalline Solids 378: 71-78.
10. Schuh, C.A., T.C. Hufnagel, and U. Ramamurty. "Mechanical behavior of amorphous alloys." Acta Materialia 55: 4067-4109.

Production of Copper Tin (CuSn) Alloy Nanoparticles by Aerosol Process

Burçak EBİN[*] and Sebahattin GÜRMEN[**]

*Nanokomp Advanced Materials R&D Consulting Co. Ltd., Istanbul, Turkey
burcak.ebin@gmail.com
**Istanbul Technical University, Department of Metallurgical & Materials Eng., Istanbul, Turkey
gurmen@itu.edu.tr

Abstract

Nanosized metallic and alloys particles of high purity are increasingly required for specific applications in many technological areas. Although several methods have been considering for production of nanoparticles, aerosol process is a suitable and simple method for the preparation of submicron or nano-scale particles in a wide range of composition and phase content. It is a single-step production technique leading to low cost, narrow particle size distribution and homogeneous chemical composition. In this study, production of copper tin (CuSn) alloy nanoparticles was investigated by aerosol process from an aqueous solution including copper sulfate and tin sulfate. CuSn alloy nanoparticles obtained by hydrogen reduction of ultrasonically formed aerosol droplets from corresponding solution at 800°C. Characterization studies shows that alloy nanoparticles have around 20 nm size with orthorhombic and face centered cubic crystal structures. Energy dispersive spectroscopy analysis indicates Cu:Sn ratio in the alloy structure is 3.55:1. Results demonstrate that aerosol process is an effective technique to produce CuSn alloy nanoparticles.

Keywords: Alloy, Copper-tin, Nanoparticles, Aerosol process

Bakır Kalay (CuSn) Alaşım Nanopartiküllerinin Aerosol Yöntemi ile Üretimi

İleri teknoloji alanlarında özel uygulamalar için kullanılan nano boyutlu yüksek safiyetli metalik ve alaşım partiküllerine olan ihtiyaç günden güne artmaktadır. Nanopartiküllerin üretimi için birçok yöntem bulunmasına rağmen, aerosol prosesi mikronaltı ve nano boyutlu partiküllerin geniş kompozisyon ve faz aralığında üretimi için uygun ve kolay bir yöntemdir. Tek adımlı bir üretim yöntemi olan aerosol prosesinin düşük maliyet, ürünlerinin dar boyut dağılımı ve homojen kimyasal kompozisyonu yöntemi ön plana çıkaran avantajları olarak sıralanmaktadır. Bu çalışmada aerosol prosesi ile bakır sülfat ve kalay sülfat içeren sulu çözelti kullanılarak bakır kalay (CuSn) ikili alaşım nanopartiküllerinin üretimi araştırılmıştır. CuSn alaşım nanopartikülleri, ultrasonik kaynakla sulu çözeltiden oluşturulmuş aerosol damlacıklarının 800°C hidrojen redüksiyonu ile elde edilmiştir. Karakterizasyon çalışmaları 20 nm boyuta sahip alaşım nanopartiküllerinin boyuta sahip olduğunu ortorombik ve yüzey merkezli kübik kristal yapılarından oluştuğunu göstermektedir. Enerji dağılım spektroskopisi incelemelerinden nanopartiküllerin yapısında Cu:Sn oranının 3,55:1 değerinde olduğu belirlenmiştir. Sonuç olarak aerosol prosesinin CuSn nanopartiküllerinin üretimi için efektif bir yöntem olduğu tespit edilmiştir.

1. INTRODUCTION

Nanosized alloy particles have drawn increasing interest due to their unique mechanical electrical, magnetic, optical, chemical and electrochemical properties. They have already been used in industrial applications such as electronic devices, biosensor, medical diagnosis and treatments, catalyzer in automobiles, fuel cells, and chemical reactions. Also scientific studies daily introduce various potential applications for them [1,2]. Cu-Sn alloy particles are lead free solder alternative for electronic applications due to their low melting point, good wettability, thermal and electrical conductivity [3].

Recently, nanosized alloy particles became a promising candidate as an anode material to increase the energy density of Li-ion batteries [4,5]. Cu-Sn alloy particles attracts attentions as an anode material because of not only good retention of capacity, but also high conductivity and low cost. Cu-Sn alloy anode capacity can be as high as 950 $mAh.g^{-1}$ in the first cycle depending on composition and particle properties [6,7]. On the other side, researches go on to control size and shape of the electrode particle as well as alloying for better electrochemical features. Studies show that nanostructured and spherical particle morphology provide larger electrode/electrolyte contact area and reduce diffusion pathway for Li^+ leading to improved C-rate performance, higher power density and longer cycle life [8,9,10].

Cu-Sn alloy particles can produce various methods such as high energy ball milling, chemical reduction techniques and solid state reactions [11,12]. Among them, aerosol process, which is also known as spray pyrolysis, is used for preparation of spherical non-agglomerated ultrafine particles in controlled chemical composition, size and crystallinity, which are suitable for direct application or fabrication of high technology materials. It is a versatile method to produce metallic, alloy and metal oxide particles in various size and morphology in short production time. In ultrasonic spray pyrolysis (USP) method, spraying is performed by applying high frequency ultrasound to the precursor solution that forms aerosols with constant droplet size, which depends on the characteristic of the liquid and the frequency of the atomizer. Particle formation occurs from the reduction or thermal decomposition of the aerosol droplets [13,18]. Among studies on metallic and alloy particles, the production of Cu-Sn alloy particles by ultrasonic spray pyrolysis were not well investigated.

In this work, Cu-Sn binary alloy nanoparticles were produced by hydrogen reduction of aerosol droplets of copper sulfate and tin sulfate solution obtained by ultrasonic atomization. Particle properties such as size, morphology, crystal structure were characterized by scanning electron microscopy (SEM), energy dispersive spectroscopy (EDS), X-ray diffraction (XRD).

2. EXPERIMENTAL

Cu-Sn alloy nanoparticles were produced by ultrasonic spray pyrolysis method under reducing hydrogen atmosphere. The precursor solution was prepared by dissolving a stoichiometric amount of $CuSO_4.5H_2O$ and $SnSO_4$ (all from MerckTM) in distilled water. The ion concentrations of the precursor solution were 0.1M Cu^{2+} and 0.1 M Sn^{2+}. Tartaric acid solution was added to control the pH of the precursor solution and as an organic agent. The precursor solution was atomized using an ultrasonic nebulizer with a resonant frequency of 1.3 MHz (RBI-Instrumentation). Due to the safety regulations, and to create an inert atmosphere, nitrogen with a flow rate of 500 ml/min was

used prior to the reduction process. The aerosol stream was introduced into the horizontal quartz reactor at 800°C by hydrogen flow. The quartz reactor was placed inside the tube furnace (Nabertherm, R 50/250/12) with a temperature control of ±1 ◦C. The heated length and diameter of the quartz reactor are 250 and 20 mm, respectively. The flow rate of hydrogen used as a carrier gas and reducing agent was fixed at 500 ml/min. The particles obtained by the reduction of the metal sulfates aerosol droplets were collected in the washing bottles connected to outlet of the quartz reactor. The residence time, calculated from geometry of the reactor and the carried gas flow rate, was about 9.4 sec with the assumption that the rate of droplets and the carrier gas are equal. However, the real residence time can be obtained when the correction for gas flow rate due to temperature caused gas expansion. The real residence time taking into account the gas expansion for 800 °C is nearly 2.6 sec. Thermodynamic of the reactions were investigated by HSC software.

X-ray diffraction (XRD, Phillips PW 1700) using Cu Kα radiation was used to examine the crystalline phase and size of the prepared particles. The conditions for the data collection were continuous scanning of a detector covering an angular range from 10° to 90° with a step size of 0.0167 and wavelengths 1.541874 Å. The chemical compositions of particles were analyzed by the energy dispersive spectroscopy (EDS) instrument. Particle size and morphology of the samples were investigated by field emission scanning electron microscopy (FE-SEM, JEOL JSM 700F).

3. RESULTS AND DISCUSSION

The thermodynamic analysis was done using HSC Software in temperature range between 0 and 1000°C (Fig. 1). The hydrogen reduction of copper and tin sulfate for the formation of metallic Cu-Sn can be described in Eq.1.

$$SnSO_4 + 2H_2\,(g) \rightarrow Sn + 2H_2O + SO_2\,(g) \quad (1)$$

$$SnSO_4 + C\,(g) \rightarrow Sn + CO_2\,(g) + SO_2\,(g) \quad (2)$$

$$SnSO_4 + 2C\,(g) \rightarrow Sn + 2CO\,(g) + SO_2\,(g) \quad (3)$$

$$CuSO_4 + 2H_2\,(g) \rightarrow Cu + 2H_2O + SO_2\,(g) \quad (4)$$

The values of Gibbs free energy (ΔG) for the reactions (2, 3 and 4) in the temperature range up to 1000°C confirm the probability for the formation of Cu and Sn by reduction of copper and tin sulfates. The Gibbs free energy values for reduction of copper sulfate to copper are always negative between 0 and 1000°C temperature range and it decreases through the negative values at elevated temperatures. However the Gibbs free energy values for hydrogen reduction of tin sulfate to tin are positive between 0 and 1000°C temperature, which indicates thermodynamically impossible reaction. Thus, we added organic reducing agent into the precursor solution to assist the hydrogen reduction of tin sulfate. Cu-Sn alloy formation by reduction of their sulfates is thermodynamically possible at desired temperature, 800°C. We assume that short reaction time (2.6 sec) are sufficient for the reduction of aerosol droplets to alloy particle in the air atmosphere.

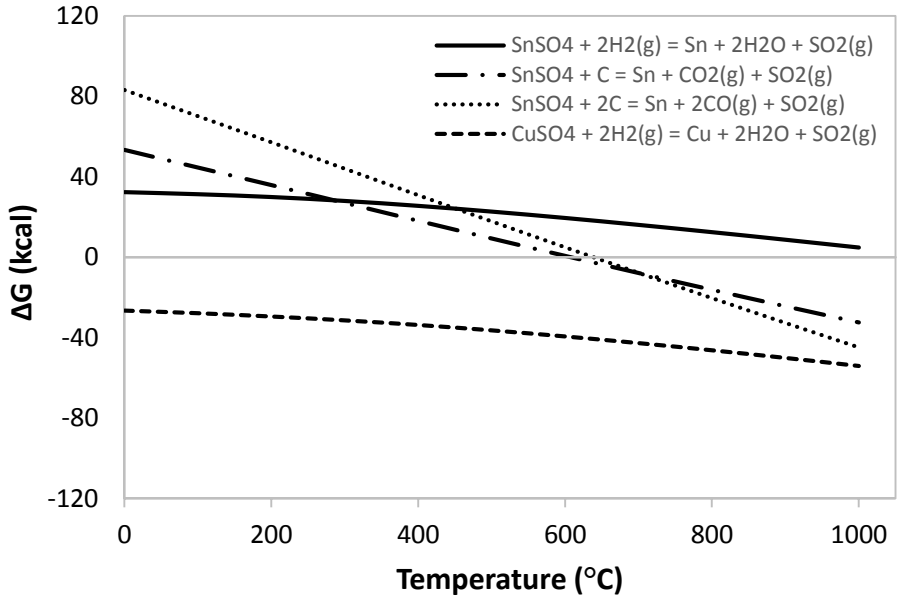

Figure 1. Change of the Gibbs free energy for hydrogen reduction of copper and tin sulfates.

The composition of the products prepared by hydrogen reduction of the copper and tin sulfates precursor was further studied by EDS. Fig. 2 displays the EDS analysis of the particles produced at 800°C. The peak observed at 1.5 keV arises due to Al substrate. Cu and Sn peaks can easily detected and any impurities such as sulfur or oxygen was not observed. Atomically amount of copper and tin (Cu:Sn) is 3.55:1, which shows lower amount of Sn in the structure than desired concentration (1:1) in the precursor solution.

Figure 2. EDS analysis of CuSn alloy nanoparticles.

Binary phase diagram of Cu-Sn (Fig. 3) is plotted by FactSage software to investigate stable phases for the CuSn nanoparticles. Mole amount of Cu:Sn is 78:22 in the nanoparticles. In detected mole amount, Cu_3Sn intermetallic compound and FCC Cu should exist in the nanoparticle structure.

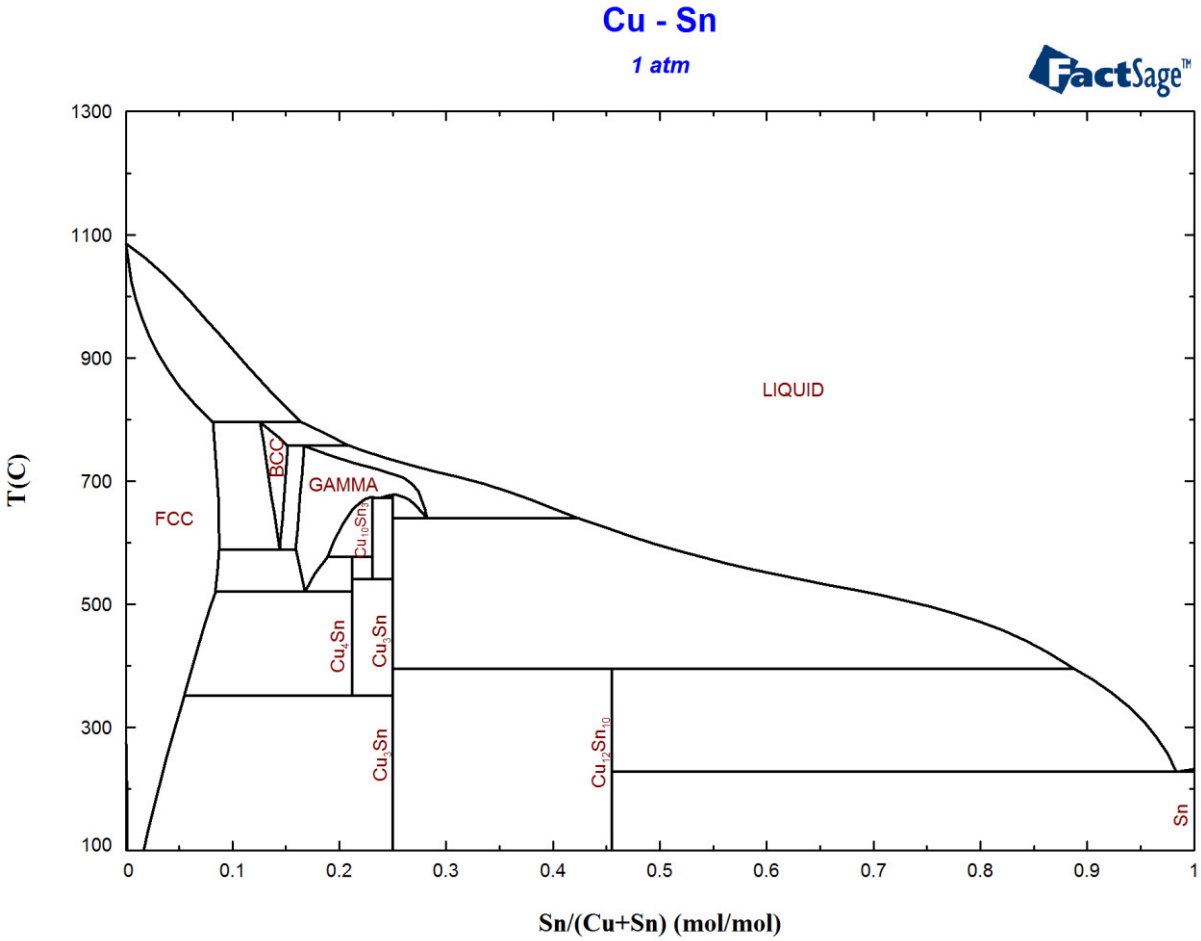

Figure 3. Binary phase diagram of Cu-Sn.

Figure 4 shows the XRD pattern of CuSn nanoparticles produced at 800°C by hydrogen reduction of copper and tin sulfate. The observed XRD peaks are belongs to orthorhombic crystal structured Cu_3Sn and face centered cubic crystal structured Cu. The strongest peak of Cu_3Sn (211) and Cu (111) overlap at 43.2°.

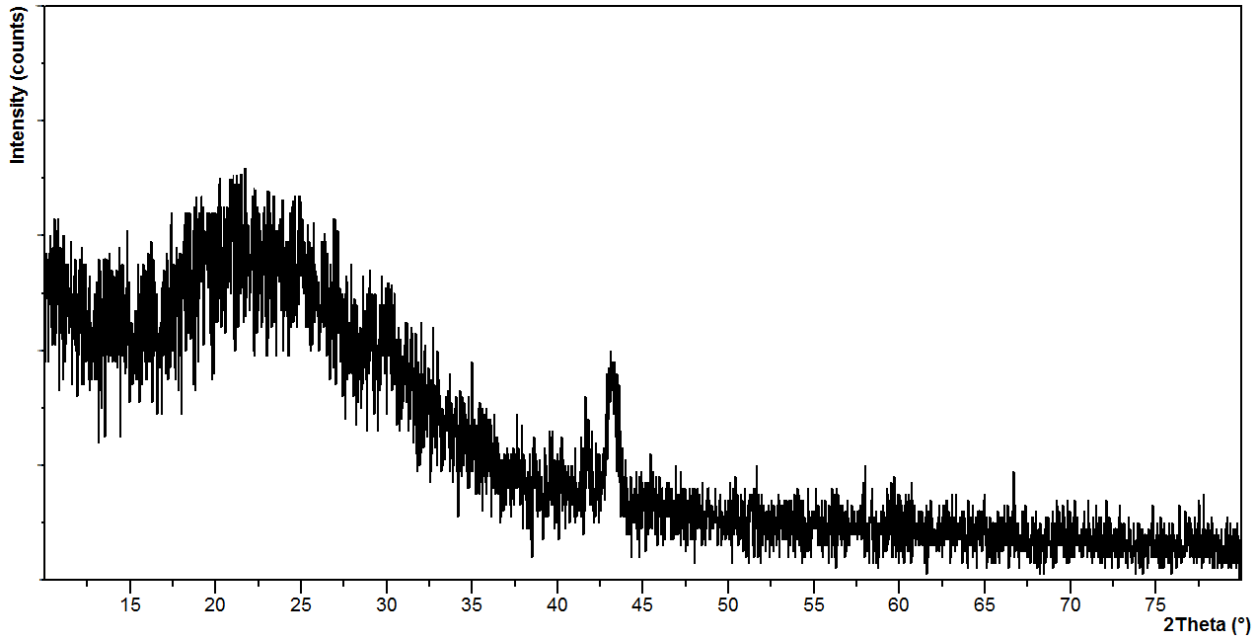

Figure 4. XRD pattern of CuSn alloy nanoparticles.

SEM images of CuSn alloy nanoparticles is given in Fig. 5. Particles exhibit spherical shape morphology and average particle size is around 20 nm. In conventional aerosol process, precursor reduces/decomposes to nanosized (primary) particles, and then nanoparticles aggregate to form secondary (submicron) particles. In this study, SEM results show that aggregation of nanoparticles prevented using organic agent. However, partly aggregated particles still can be observed on Fig. 5a.

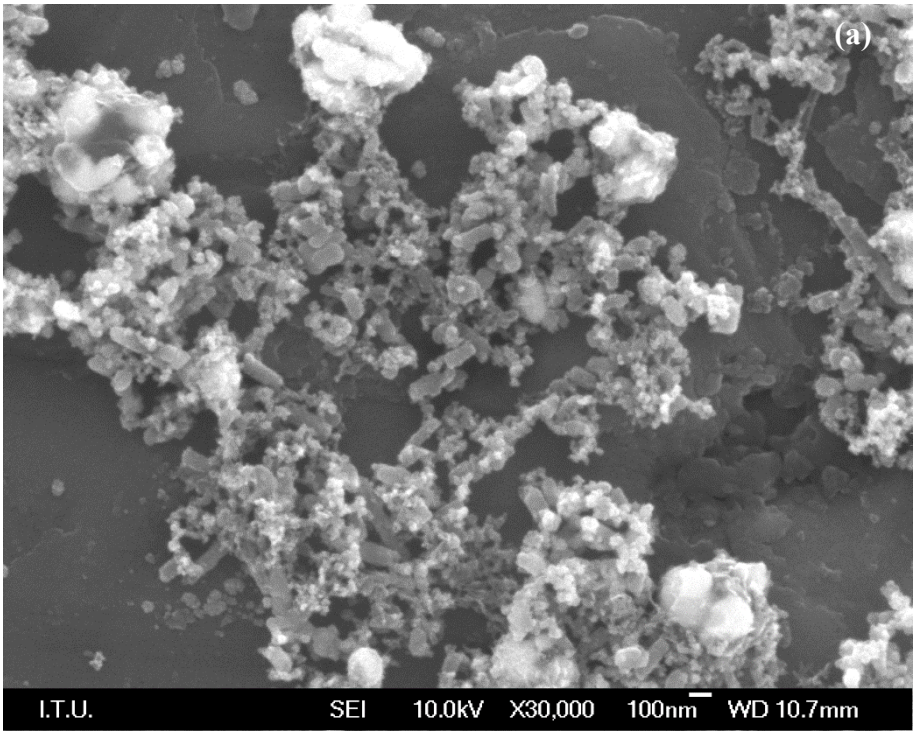

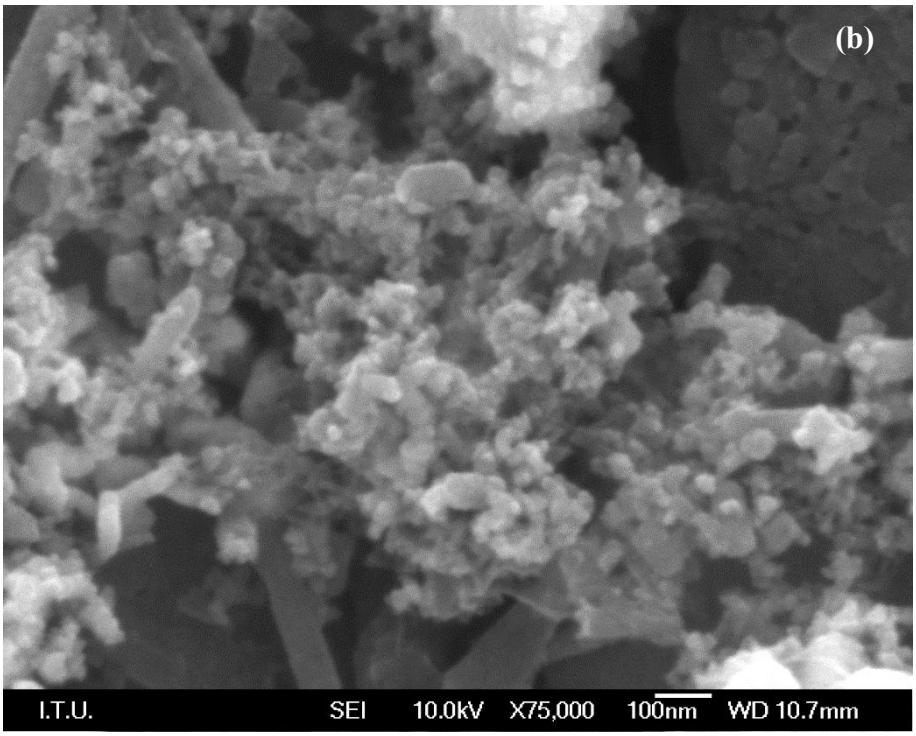

Figure 5. SEM images of CuSn alloy nanoparticles (a) x30K and (b) x75K.

CuSn alloy nanoparticles were successfully produced by aerosol process from copper and tin sulfate precursor under hydrogen atmosphere at 800°C. Lower amount of Sn than the desired value in Cu-Sn alloy nanoparticles indicates that reaction rate for reduction of tin sulfate to tin is slower than copper sulfate's. As a result, aerosol process is a suitable method to produce CuSn binary alloy nanoparticles.

REFERENCES

1. K. E. Gonsalves, H. Li, R. Perez, P. Santiago and M. Jose-Yacaman, Coordination Chemistry Reviews, 206-207, 607, 2000.
2. R. Ferrando, J. Jellinek and R. L. Johnston, Chemical Reviews, 108, 845, 2008.
3. W. R. Osorio, E. S. Freitas, J. S. Spinelli and A. Garcia, Corrosion Science, 80, 71, 2014.
4. H. Li, L. Shi, Q. Wang, L. Chen and X. Huang, Solid State Ionics, 148, 247, 2002.
5. H. Mukaibo, T. Osaka, P. Reale, S. Panero, B. Scrosati and M. Wachtler, J. Power Sources, 132, 225, 2004.
6. S. H. Ju, M. Q. Zeng and M. Zhu, Electrochemica Acta, 54, 2843, 2009.
7. A. R. Kamali and D. J. Fray, Rev. Adv. Mater. Sci. 27, 14, 2011.
8. C. Jiang, E. Hosono and H. Zhou, Nanotoday, 1, 28, 2006.
9. A. Manthiram, A. V. Murugan, A. Sarkar and T. Muraliganth, Energy Environ. Sci., 1, 621, 2008.
10. I. Taniguchi, D. Song and M. Wakihara, J. Power Sources, 109, 333, 2002.
11. F. Wang, M. Zhao and X. Song, J. of Alloy. Compd., 439, 249, 2007.
12. S. H. Ju, H. C. Jang, Y. C. Kang, J. Power Sources, 189, 163, 2009.

13. B. Ebin and S. Gürmen, KONA Powder Part. J., 29, 134, 2011.
14. S. C. Tsai, Y. L. Song, C. S. Tsai, C. C. Yang, W. Y.Chiu and H. M. Lin, J. Mater. Sci. 39, 3647, 2004.
15. H. Xu, B. W. Zeiger and K. S. Suslick, Chem. Soc. Rev., 42, 2555, 2013.
16. B. Ebin, E. Yazıcı and S. Gürmen, T. of Nonferr. Metal. Soc., 23 841, 2013, 841.
17. R. O. Apaydın, B. Ebin and S. Gürmen, Metall, 67/10, 397, 2013.
18. S. Gürmen, B. Ebin, S. Stopic and B. Friedrich, J. Alloy Compd., 480, 529, 2009.

SYNTHESIS OF NANO-BORIC ACID and NANO-TITANIUM DIOXIDE PARTICLES WITH DIFFERENT THERMAL DECOMPOSITON SYSTEMS

Levent KARTAL*, Yasin KILIC, Mehmet Ikbal ISIK, Güldem KARTAL SIRELI, Servet TİMUR

Istanbul Technical University, Metallurgical and Materials Eng. Dept., Istanbul-Turkey
*kartall@itu.edu.tr

1. ABSTRACT

The synthesis of nanoparticles is an active area of academic and, more significantly, in applied sciences. This study is an attempt to present nano-boric acid and nano-titanium dioxide particle synthesising by using three different methods which are high frequency induction, flame pyrolysis and RF plasma method. Producibility of nano-boric acid by via flame synthesis and nano-titanium dioxide particles by using medium frequency induction and RF plasma method were investigated. Organic boron and titanium compounds as precursor were used in this study. In flame pyrolysis process parameters like distance from flame and in high frequency induction system initial concentrations of solutions were investigated. Synthesized boric acid and titanium dioxide particles were characterized via scanning electron microscopy (SEM) investigations and X-ray diffraction (XRD) techniques in order to explore the effects of these process parameters.

Keywords: Nano-titanium dioxide powder, Nano-boric acid, Nanoparticles, Flame pyrolysis, High frequency inductive system, RF Plasma

FARKLI TERMAL DEKOMPOZİSYON SİSTEMLERİ İLE NANO BORİK ASİT VE TİTANYUM DİOKSİT PARTİKÜL ÜRETİMİ

ÖZET

Bu çalışmanın amacı nano borik asit ve nano titanium dioksit partiküllerinin 3 farklı; alev piroliz, yüksek frekanslı indüktif ve RF plazma sistemleri ile üretilmesi ve partikül özellikleri açısından karşılaştırılmasıdır. Başlangıç çözelti kaynağı olarak organik bor ve titanyum bileşikleri(Trimetil Borat ve Titanyum Tetra izoproporoksit(TTIP)) kullanılmıştır. Alev pirolizi ile nano borik asit partikülleri üretiminde değişken parametre olarak partikül oluşumunun alevden uzaklığı, orta frekanslı indüktif sistemde ise çözelti konsantrasyonu incelenmiştir.

Üretilen borik asit ve titanyum dioksit partikülleri SEM ve XRD analiz teknikleri kullanılarak incelenmiştir.

***Anahtar kelimeler*:** Nano borik asit, Titanyum dioksit, Nanopartikül, Yüksek Frekans İndüktif Sistem, Alev piroliz, RF plazma

2. INTRODUCTION

Boric acid and titanium dioxide nanoparticles are critical importance in nanoparticles research. Boric acid is an effective solid lubricant providing friction coefficients of 0.02 to 0.1 to the sliding surfaces of metallic & ceramic materials. Its lubricity, self-lubrication and self-replenishment mechanisms and its potential importance for tribological applications demand serious consideration [1]. Moreover, like other solid lubricants, such as graphite, molybdenum disulfide (MoS_2), titanium dioxide (TiO_2), tungsten disulfide (WS_2), boron nitride (BN) and silicon nitride (Si_3N_4). Boric acid has lamellar structure which provides good lubrication capabilities [2]. In such compositions boric acid is about 0.1-1.0 weight percent and has a crystal dimension of about 0.1-40 microns [3]. Recently, it is shown that nano-boric acid improves the lubricity of low-sulfur diesel and gasoline fuels [4].

Titanium dioxide is typically used as a pigment because of its high refractive index. Although this is one of the most common demands of titanium dioxide, interest for other implementations has increased tremendously; especially in waste water treatment, air purification, self-cleaning paints and solar cells [5, 6, 7, 8].

The purpose of this study is to introduce nanoparticle production systems that settled up by us, with producing two different nanoparticles. For this reason, two different nanoparticles were produced at three different nanoparticle production system and results are compared. XRD and SEM analyses were carried out to inspect the purity, size as well as morphology of produced nanoparticles.

3. MATERIALS AND METHODS

Three methods; flame pyrolysis, high frequency induction and RF plasma method were investigated while using volatile organic boron and titanium compounds (trimethylborate, titanium tetra isopropoxide).

3.1 Flame pyrolysis

Flame pyrolysis was investigated while using volatile organic boron compound (trimethylborate) used as precursor. The experimental set-up used in flame pyrolysis is schematically shown in Figure 1. It consists of precursor transporting, burning reactor and particle collection section connected to vacuum pump. In flame pyrolysis precursor solution was carried into the burner by using hydrogen gas. Nitrogen used as auxillary gas was fed into the burning reactor for cooling burning gases. Also auxillary gas can be used to control flow velocity and stay time of flame made nanoparticles in hot zone.

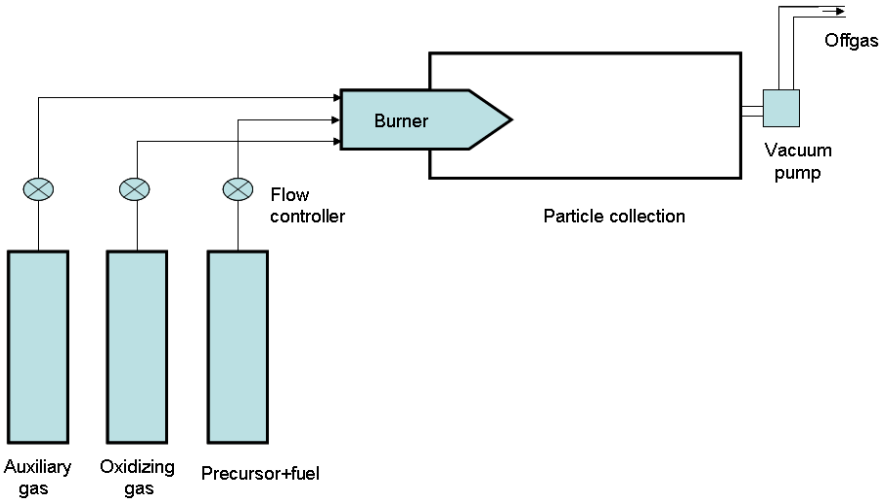

Fig. 1. Schematic drawing of the experimental set-up for boric acid synthesize by flame synthesis process.

3.2 Medium Frequency Induction

The schematic depiction of the medium frequency induction system setup was given in Fig. 2. The developed design consisted of three major units: (1) a high frequency ultrasonic spray for the aerosol generation of particles from their solutions, (2) a high frequency induction reactor for the thermal decomposition of relevant aerosol and (3) particle collection bottles for the accumulation of the produced nanoparticles.

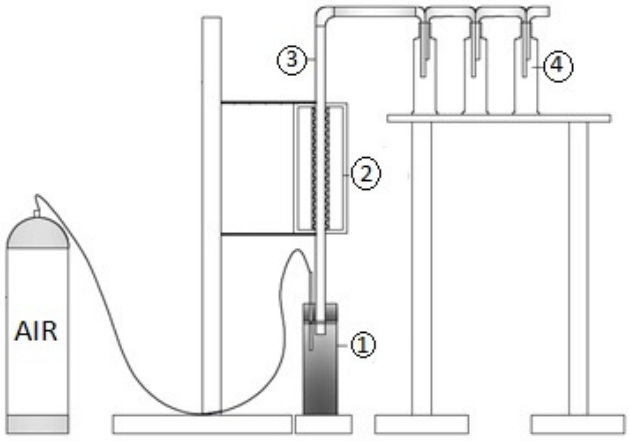

Fig. 2. Schematic drawing of the experimental set-up.(1-Ultrasonic generator, 2-Inductive reactor, 3- Quartz tube, 4- Powder collectors)

3.3 Nanoparticles synthesize in RF plasma method

Schematic drawing of the experimental set-up for nanoparticle production in RF plasma was given in Fig. 3. The developed design consisted of four major units: a high frequency ultrasonic spray for the aerosol generation of particles from their solutions, RF generator and induction system for the thermal decomposition of relevant aerosol, particle collection on + and - electrostatic filters and particle collection system for escaped nanoparticles from electrostatic filter.

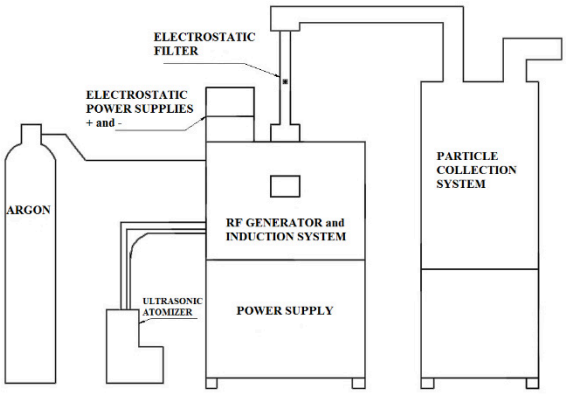

Fig. 3. Schematic drawing of the experimental set-up.(Ultrasonic atomizer, RF generator, Electrostatic power supplies, electrostatic filter and particle collection system)

The crystal structures of synthesized particles were identified by a X-ray diffraction (XRD, Philips 1700 diffractometer) using Cu Kα radiation (λ=1.54187 Å, 2θ range 10°−90°). For XRD analysis, the particles were placed on a glass substrate and allowed to dry in air at room temperature. The morphology and size of produced samples were studied using a field emission scanning electron microscopy (FE-SEM, Jeol JSM 700F).

4. RESULTS AND DISCUSSION

4.1 Flame pyrolysis

In all series of experiments the $(H_2+precursor)/O_2$ ratio was kept constant at 1.61. The reaction for the formation of boric acid from trimethyl borate vapour can be described as in Eq. (1).

$$2B(OCH_3)_3 + 9.5O_2 + H_2 + N_2 = B_2O_3 + 10H_2O + 6CO_2 + N_2 \quad (1)$$

$$B_2O_3 + 3H_2O = 2H_3BO_3 \quad (2)$$

Nitrogen gas decreases temperature and causes second reaction (Eq. 2) to occur. Gibbs free energy versus temperature diagram is seen in Figure 4a.

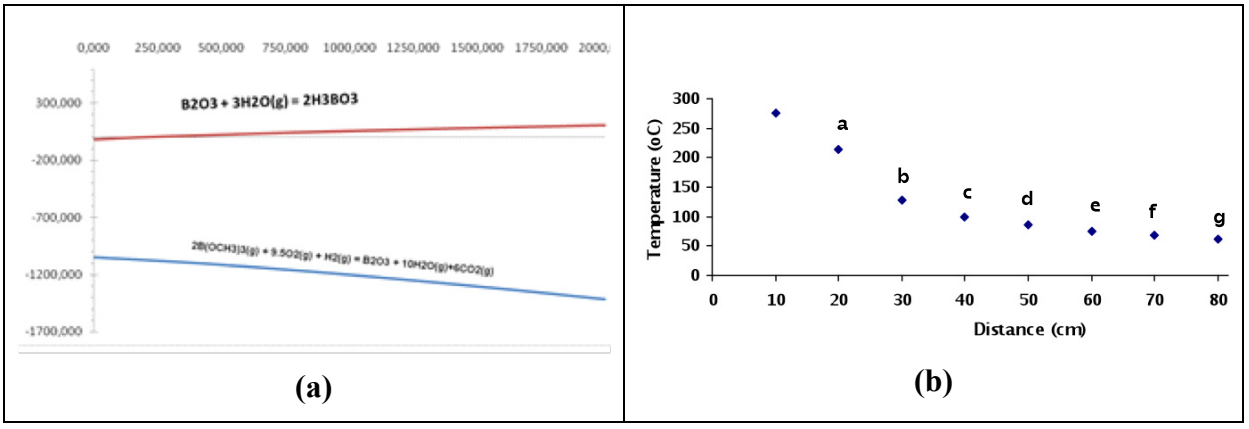

Fig. 4 : (a) Delta G – Temperature graph. **(b)**Temperature variation measured from surface of glass pipe in flame synthesis.

Particle collection section is an important parameter effecting shape, morphology and crystal structure. In Figure 4b, temperature variation depending on distance from flame is shown.

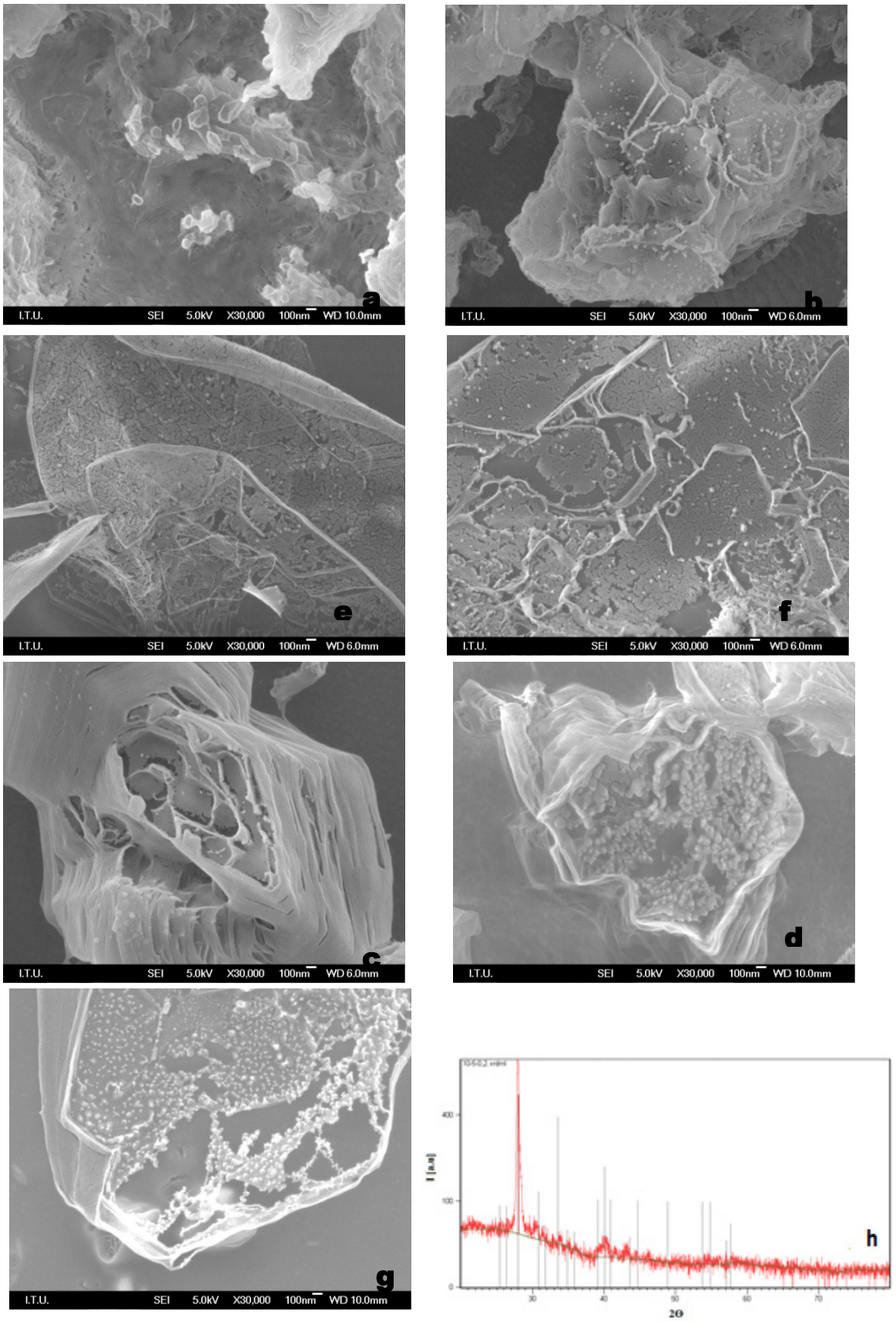

Fig. 5 : (a,b,c,d,e,f,g) Scanning electron images of flame-made boric acid structures showing morphological changes due to substrate collection distance from the burner **, (h)** X-ray diffraction results of flame pyrolysis made particles (JCPDS: 10043-35-3).

Figure 5 shows morphological changes of flame-made boric acid structures due to substrate collection distance from the burner. As it is seen, particles collected from 20 cm and 30 cm (Fig.6a and b) are fully dense. However, nanostructures were observed at 40 cm, 50 cm, 60 cm and 70 cm (Fig. 5c, d, e, f) distances. Wall thicknesses of structures in Fig. 6d approximately 25 nm with a diameter of 1-2 µm. Moreover, it is easily seen from Fig.5 that lamellar structure is obtained. Boric acid provides good lubrication in the case where structure is lamellar.

Also, XRD results proved that flame-made boric acid particles are lamellar, orthorombic metaboric acid (Fig. 5h). Since all forms of boric acid are not providing good lubrication properties, it is crucial to know which form they have. XRD results showed that flame-made boric structures were α-metaboric acid which has orthorhombic and lamellar structure that provides better lubrication.

4.1 Nanoparticles Synthesize in Medium Frequency Induction System

The thermogravimetric (TG) curve of TTIP at the temperature ranging from 25 to 1000°C was shown in Fig. 6. Apparently, the decomposition of TTIP was completed at around 250 °C.

The stoichiometric reaction for the decomposition of TTIP could be suggested as in Eq.3 **[9]**

$$(Ti[OCH(CH_3)_2]_4)_{(l)} \rightarrow TiO_{2(s)} + 4C_3H_{6(g)} + 2H_2O_{(g)} \qquad \textbf{(3)}$$

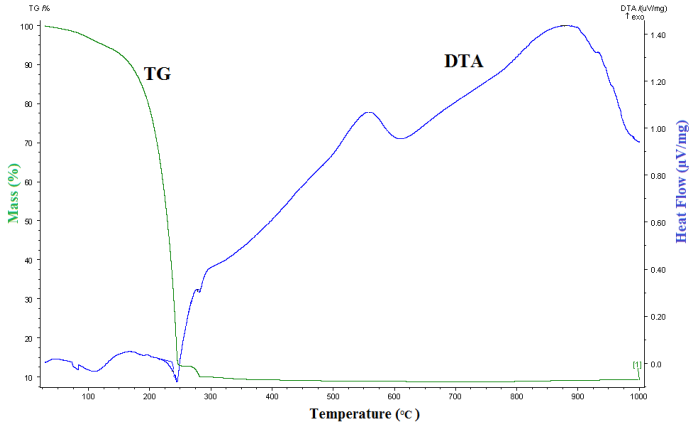

Fig. 6: TG/DSC thermograms of TTIP.

Since the initial feed solution concentration determinates the amount of metals into generated aerosols, hence the transferring quantity to the induction heating zone for nanoparticle production, it is the most critical parameters to be investigated first.

The optimization study of precursor concentrations was carried out at two different concentrations (0.01 and 0.1M) under the constant conditions of 15 min. running time, 800 ºC decomposition temperature, and 1.0 L/min. air volumetric flow rate.

Typical SEM images of the TiO_2 spheres synthesized using 0.1 and 0.01 mol/L TTIP precursor concentrations were shown in Fig. 7. Generally, TiO_2 particles have perfect spherical morphology with smooth surfaces. Ultrafine particle formations on the surface of submicron TiO_2 particles were also observed on this particle synthesis (see Fig 7d).

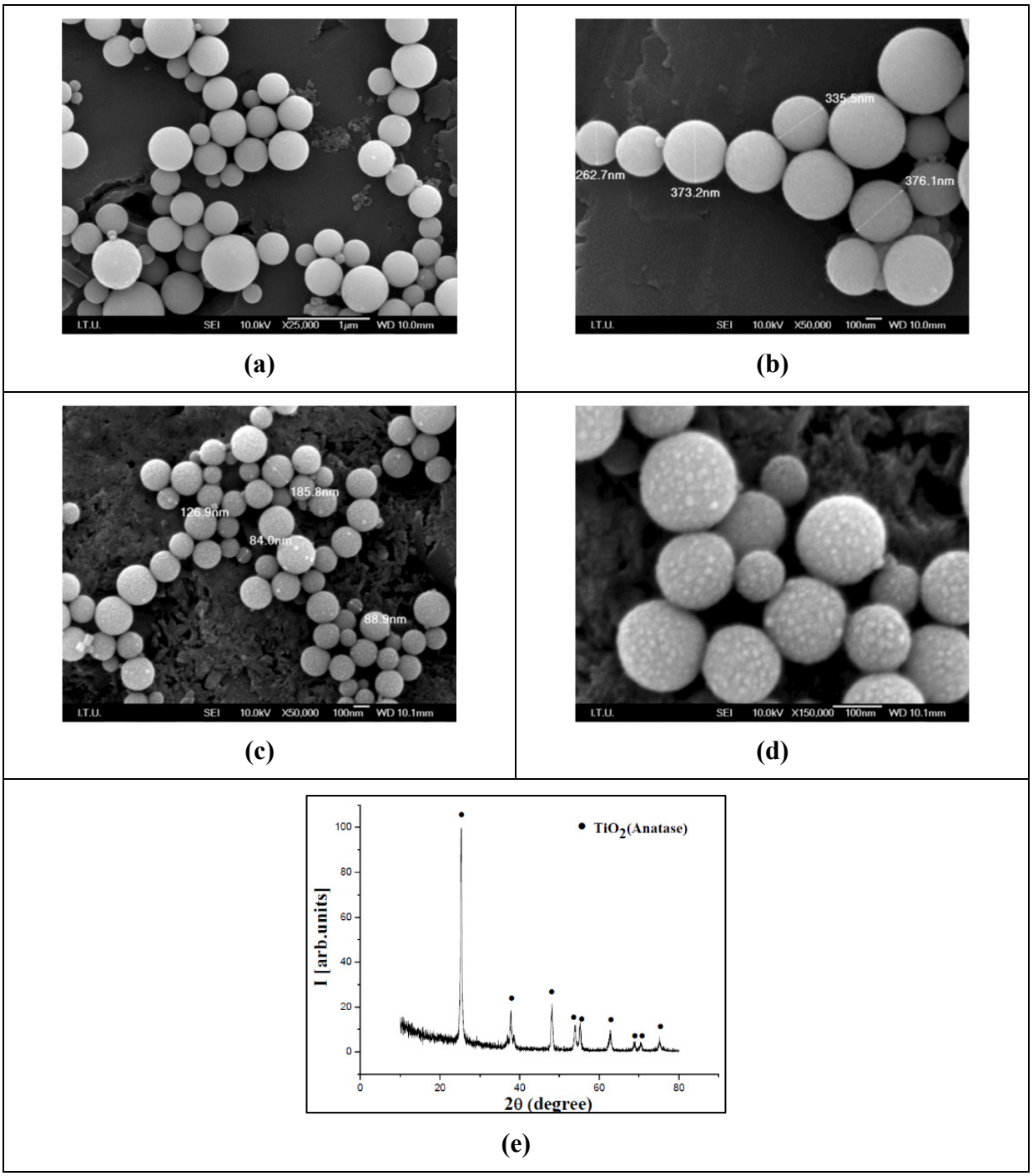

Fig. 7. SEM images of titanium dioxide particles produced at 800 °C using 0.1 mol/L(a,b) 0.01 mol/L(c, d) TTIP solution, (e) XRD diffraction spectra of TiO_2 particles [0,1 M Ti^{4+}, 800 ºC, 1 L/dk.](JCPDS:084-1286)

XRD study of generated TiO_2 particles revealed the pure TiO_2 formation with an anatase structure. (JCPDS card no. 084-1286) (Fig. 7e).

4.2 Nanoparticles synthesize in RF plasma method

In RF plasma experiment 0.1 M TTIP used as precursor concentration and 15 L/min. argon used as carrying gas. SEM images of the TiO_2 particles produced were given in Fig.8. All secondary TiO_2 particles that made up of highly agglomerated primary particles are under 100 nm and exhibited a perfect spherical morphology with smooth surfaces. Moreover, the

primary nanoparticles were also detected on the surface of substrate and pointed with arrows on the high magnification micrograph in Fig 8c.

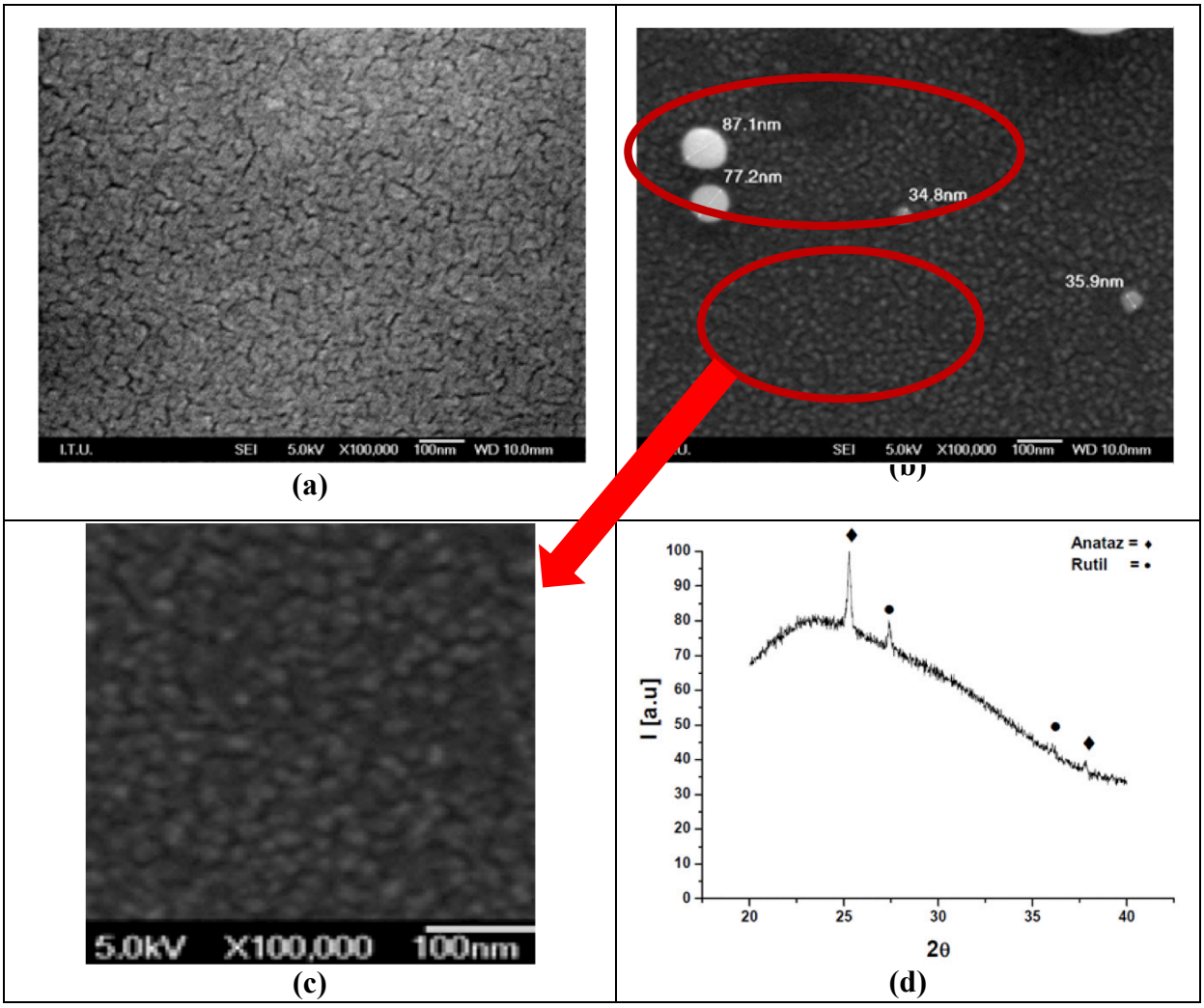

Fig. 8. SEM images of titanium dioxide particles produced by RF plasma method **(a)** Pt plated glass substrate **(b)** primary and secondary nanoparticles **(c)** primary nanoparticles **(d)** XRD diffraction spectra of TiO_2 particles [0,1 M Ti^{4+}] (JCPDS: Anatase 00-001-0562, Rutile 01-076-0318)

XRD study of generated TiO_2 particles revealed the pure TiO_2 formation with an anatase and rutile structure. (JCPDS: Anatase 00-001-0562, Rutile 01-076-0318) (Fig. 11d).

5. CONCLUSIONS

In this study, Boric acid and titanium dioxide nanoparticles synthesing were investigated by using three different nanoparticle production systems which were settled up by our group.

Ultrasonic spray technique used in high frequency induction system, that allowed us to use basic soluble chemical compounds instead of expensive volatile organometallic compounds, and induction technology, which is one of the most efficient and economic technology, were combined. This system was configured with a temperature and a gas flow controller.

- In high frequency induction system the size of synthesized TiO_2 particles could be possibly decreased by reducing the molarity of precursor solutions.

- Flame pyrolysis provides lamellar, metaboric acid structures having wall thickness approximately 25 nm. Less consistence and less wall thickness were observed when substrate place become distant from burner.
- The size of TiO_2 nanoparticles produced by the RF plasma method were compared with those produced by using high frequency induction system and flame pyrolysis. The diameters of the nanoparticles synthesized by RF plasma method were smaller than those produced by both high frequency induction system and flame pyrolysis methods.
- Finally, the formations of second phase(s) or impurities were not observed in the production of three different nanoparticles.

Acknowledgement

This work was supported by TUBITAK with project number of 110M687. The authors would like to thank Prof. Dr. Gultekin Goller and Talat Alpak for their contributions on SEM analysis.

6. REFERENCES

[1] Seyed Mirmiran, "Tribological Behavior Of Boric Acid Solid Lubricant", (Paper presented at the Oakland University Mechanical Engineering Department Graduate Student Seminar Series, 2004).

[2] E. Y. A. Wornyoh, V. K. Jasti, C.F. Higgs,"A Review of Dry Particualate Lubrication: Powder and Granular Materials," *Journal of Tribology*, 129 (2007), 438-449.

[3] Ali Erdemir,"Lubrication with boric acid additives," USPTO Patent number 6,025,306, (2000).

[4] Ali Erdemir,"Method to improve lubricity of low-sulfur diesel and gasoline fuels," USPTO 6,783,561 B2, (2004).

[5] Y. Lan, Y. Lu, and Z. Ren, Mini review on photocatalysis of titanium dioxide nanoparticles and their solar applications, Nano Energy, vol. 2, (2013) 1031–1045.

[6] J. Yang, X. Zhang, C. Wang, P. Sun, L. Wang, B. Xia, and Y. Liu, Solar photocatalytic activities of porous Nb-doped TiO2 microspheres prepared by ultrasonic spray pyrolysis, Solid State Sci., 14, (2012) 139–144.

[7] M. V Liga, E. L. Bryant, V. L. Colvin, and Q. Li, Virus inactivation by silver doped titanium dioxide nanoparticles for drinking water treatment, Water Res., 45, (2011) 535–44.

[8] H. Shi, R. Magaye, V. Castranova, and J. Zhao, Titanium dioxide nanoparticles: a review of current toxicological data, Part. Fibre Toxicol 10 2013 15.

[9] P. Moravec, J. Smolík, and V. V. Levdansky, Preparation of TiO_2 fine particles by thermal decomposition of titanium tetraisopropoxide vapor, J. Mater. Sci. Lett., (2001) 2033–2037.

SYNTHESIS AND CHARACTERIZATION OF TRANSITION METAL OXIDE DOPED $SrAl_2O_4$ BASED NANOCRYSTALLINE PHOSPHORS

Mehmet D. CALISIR*, Nuri SOLAK**

*Nano-Science & Nano-Engineering Department, Istanbul Technical University, Maslak, 34469, Turkey

** Chemical & Metallurgical Engineering Faculty, Istanbul Technical University, Maslak, 34469, Turkey

ABSTRACT

$SrAl_2O_4$: Eu^{2+}, Dy^{3+} based phosphors have been used in several application areas such as emergency signs, paints, ceramic products, LEDs, PDPs, textile, and accessorize materials due to their high luminescence intensity, pure color, long lasting time, chemical, and thermal stability. The Eu^{2+} ions serves as the luminescence center in the structure and its emission is due to 4f→5d electronic transition. The emission characteristics are significantly affected by the composition of the matrix material. The present study aims to investigate the effects of different compositions of transition metal oxides on morphology and luminescent properties of these phosphorescent particles. Samples were prepared by sol-gel method using the $Sr_{0,92-X}M_XAl_2O_4$: $Eu^{+2}{}_{0,02}$, $Dy^{+3}{}_{0,06}$ (M = Fe, Co, Ni) chemical formula.. All samples were sintered at 1300C in %5 H_2-N_2 reductive atmosphere for 3 hours to reduce Eu^{3+} to Eu^{2+}. It is observed that the monoclinic $SrAl_2O_4$ is the main phase in the XRD patterns of all samples. According to SEM micrographs, all samples have highly sintered microstructure. Emission at about 510 nm and excitation by wide wavelength range (generally 300-450 nm) was observed from fluorescence spectrophotometric analysis.

Keywords: Nanocrystalline Phosphors, $SrAl_2O_4$, Luminescence

GEÇİŞ METAL OKSİTLERİ KATKILI $SrAl_2O_4$ TEMELLİ NANOKRİSTALIN FOSFORESAN MALZEME SENTEZİ VE KARAKTERİZASYONU

ÖZET

$SrAl_2O_4$: Eu^{2+}, Dy^{3+} temelli fosforesan malzemeler yüksek ışıma şiddeti, uzun ışıma süresi ve kimyasal ve termal kararlığı özelliklerinden dolayı acil durum işaretlerinde, boyalarda, seramik ürünlerde, aksesuarlarda, LED'lerde ve plazma görüntü panellerinde kullanılmaktadır. Yapı içerisinde Eu^{2+} lüminesans merkezi, Dy^{3+} ise tuzaklama merkezi olarak görev yapmaktadır. Evropiyumun emisyonu 4f 5d elektronik geçişlerinden kaynaklanmakta olup matris malzemenin kompozisyonundan çok etkilenmektedir. Bu çalışmada farklı geçiş metallerinin farklı kompozisyonlardaki katkılarının morfoloji ve optik özelliklere etkisi incelenmiştir. Deneysel çalışmada, $Sr_{0,92-X}M_XAl_2O_4$: $Eu^{+2}{}_{0,02}$, $Dy^{+3}{}_{0,06}$ (M = Fe, Co, Ni; X=0,005 ve 0,01) birleşiminde numuneler sol-jel metodu ile sentezlenmiştir. Bütün numuneler 1300^0C de %5 H_2-N_2 indirgeyici atmosferde 3 saat ısıl işleme tutularak Eu^{3+}'ün Eu^{2+}'ye indirgenmesi sağlanmıştır. XRD sonuçlarına göre bütün numuneler monoklinik $SrAl_2O_4$ yapısında olup ortalama kristal çapı 25 nm'dir. SEM mikrograflarına bakıldığında yapının kuvvetlice sinterlenmiş morfolojide olduğu görülmektedir. Optik analiz sonuçlarına göre bütün numuneleri 510- 515 nm dalga boyunda ışıma yaptığı ve numunelerin elektromanyetik spektrumun UV ve görünür aralığında uyarıldığı görülmüştür.

Anahtar kelimeler: Nanokristalin Fosfor, $SrAl_2O_4$, Lüminesans

1. INTRODUCTION

The first phosphor material known as ‘’bologna stone’’ was discovered in the early seventeenth century but the potential of the phosphorescent materials still excites modern researchers. [1]. A number of studies have been done to find new phosphor materials with persistent luminescence. In 1996, Matsuzawa et al. [2] reported a new type of long persistent phosphor, $SrAl_2O_4:Eu^{2+}$, Dy^{3+} which has color purity, longer afterglow time, higher radiation intensity, and chemical, thermal, and radiation stability than conventional sulfide based phosphors. [1, 2, 3]. They have a large application areas such as luminous paints on highways, airports, buildings, and ceramic products as well as textiles, the dial plates of luminous watches, warning, and escape route signs. [3, 4].

Emission of these type phosphors is due to 4f 5d electronic transition of Eu^{2+} and peak position in the emission spectra strongly depends on host material and the environment of the Eu^{2+} ions in the structure [5]. Different emission color of Eu^{2+} ion is reported in different matrix such as green emission in $SrAl_2O_4:Eu^{2+}$, Dy^{3+} [2], blue emission in $Sr_2MgSi_2O_7$: Eu^{2+}, Dy^{3+} [6] and red emission in $Y_2O_3:Eu^{2+}$ [7] The monoclinic $SrAl_2O_4$ has been proven an efficient host material, which is formed by a three-dimensional framework of corner-sharing AlO_4 tetrahedron. The each oxygen is shared with two aluminum ions so that each tetrahedron has one net negative charge that balanced by the large divalent cations that occupy two different interstitial sites within the tetrahedron framework [8].

Long persistent of this type phosphor is thought a result of excited electron trapped–detrapped process. As a recent purposed model, excited electrons of Eu^{2+} luminescent centers can easily escape into the conduction band of matrix material. Both oxygen vacancies and trivalent co-dopant ions introduce trap levels in forbidden band gap of matrix. The excited electrons in the conduction band are then captured from these trap levels. When enough thermal energy is available, the captured electrons can slowly escape again into the conduction band and recombine in a luminescent center which results emission at about 515 nm in $SrAl_2O_4$ matrix [9].

In this study we aim to sensitize $SrAl_2O_4:Eu^{2+}$, Dy^{3+} nanocrystalline phosphors with sol-gel method and characterize with XRD, SEM and fluorescence spectrophotometer. Besides, we also investigated the effect of co-doping with Fe, Ni and Co on the structure and luminescence characteristics..

2. EXPERIMENTAL

2.1. Materials

In the experimental study, $Sr(NO_3)_2$, $Al(NO_3)_3.9H_2O$, $Co(NO_3)_2.6H_2O$, $Fe(NO_3)_3.9H_2O$, $Ni(NO_3)_2.6H_2O$, Eu_2O_3, Dy_2O_3, $C_6H_8O_7.H_2O$ and H_3BO_3 were used as starting materials with high purity (99,99). Samples were prepared with different co-doping composition of transition metals in strontium aluminate host matrix material ($Sr_{0.92-X}M_XAl_2O_4$: $Eu_{0.02}$, $Dy_{0.06}$; M: Fe, Ni and Co; X=0.005 and 0.01).

2.2. Methods

Firstly, required amounts of starting materials were calculated and weighed in order to produce 0,025 mol sample. After that, nitrate based compounds and boric acid were dissolved with deionized distilled water in a beaker. On the other hand, in order to obtain nitrate forms of oxide based compounds, they were dissolved with concentrated nitric acid. All solution stirred with magnetic stirrer at 100°C until the solutions became homogeneous and transparent and then two solutions were combined in a 100 ml beaker. After complete mixing, citric acid was added to the solution as chelating agent to achieve a 2:1 ratio of CA to total metal ions in the solution. By keeping the solution at 100°C for 2-3 hours under constant stirring, the solution became viscous. After that, the viscous solution was dried at 200°C for 12 h, brown dried-gels were obtained. The dried-gels were calcined at 800°C in air atmosphere for 6 h to remove the residual carbon. Finally, the calcined powders were sintered at 1300°C for 1 h in 5% H_2-N_2 reducing atmosphere.

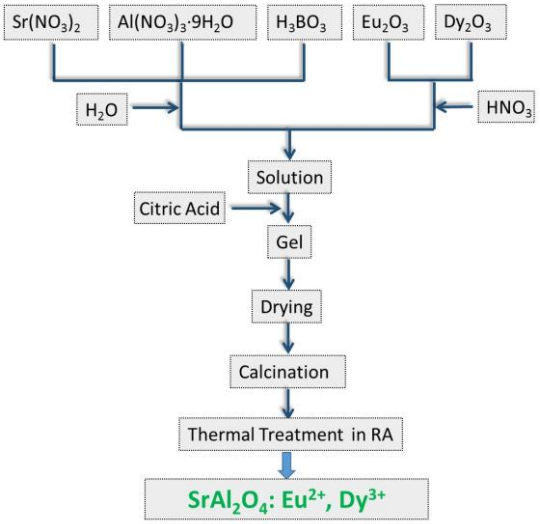

Figure 1: **Flow Chart of the sol-gel process**

2.3. Characterization

X-ray diffraction (XRD) studies of the samples was carried out using a Philips™ PW 3710 X-Ray diffractometer with Cu-K_α radiation (λ=0.15418 nm), V=40 kV and I=40 mA in the 2θ range of 10- 90°. Crystalline sizes of the sample were calculated using Scherrer formula

$$\tau = \frac{K\lambda}{\beta \cos\theta} \quad \textbf{(1)}$$

where τ is the mean size of the ordered (crystalline) domains, K is a dimensionless shape factor (0.9), λ is the X-ray wavelength (0.15418 nm), θ is the Bragg angle and β is the line broadening at half the maximum intensity. The morphology and the size of phosphors powders were observed using scanning electron microscope (JEOL™ JSM 5410 SEM). Measurements of emission and excitation intensity and phosphorescence decay time of the samples were carried out using Varian Fluorescence Spectrometer. Samples were excited in the wavelength range 300 to 500 nm and emission behaviors were investigated in the wavelength range 400 to 650 nm. Decay lifetime analyses were made in 5 millisecond time interval after excitation 0.1 millisecond for all samples. Additionally, in order to analyze the

afterglow decay time characteristics of the samples, decay time curves are fitted to equation 2.

$$y = y0 + A1 * e^{-\frac{x}{\tau_1}} + A2 * e^{-\frac{x}{\tau_2}} \quad \textbf{(2)}$$

where, y is luminescence intensity at the time of any x, A_1 and A_2 is constants, τ_1 and τ_2 are the exponential afterglow times.

3. RESULTS AND DISCUSSION

3.1. Phase Analysis

XRD patterns of samples which were sintered at 1300C are shown in Figure 2. It can be seen, from Figure 2, that monoclinic $SrAl_2O_4$ (JCPDS card no-34-0379) phase were detected in the doped and un-doped samples. Additionally, dopant concentration (up to 1%) has almost no effect on the crystal structure**.** Crystalline sizes of the samples were calculated using Scherrer formula according to 220 peak of the $SrAl_2O_4$ and found in 17-42 nm range. In table 1, calculated grain sizes of the samples are given.

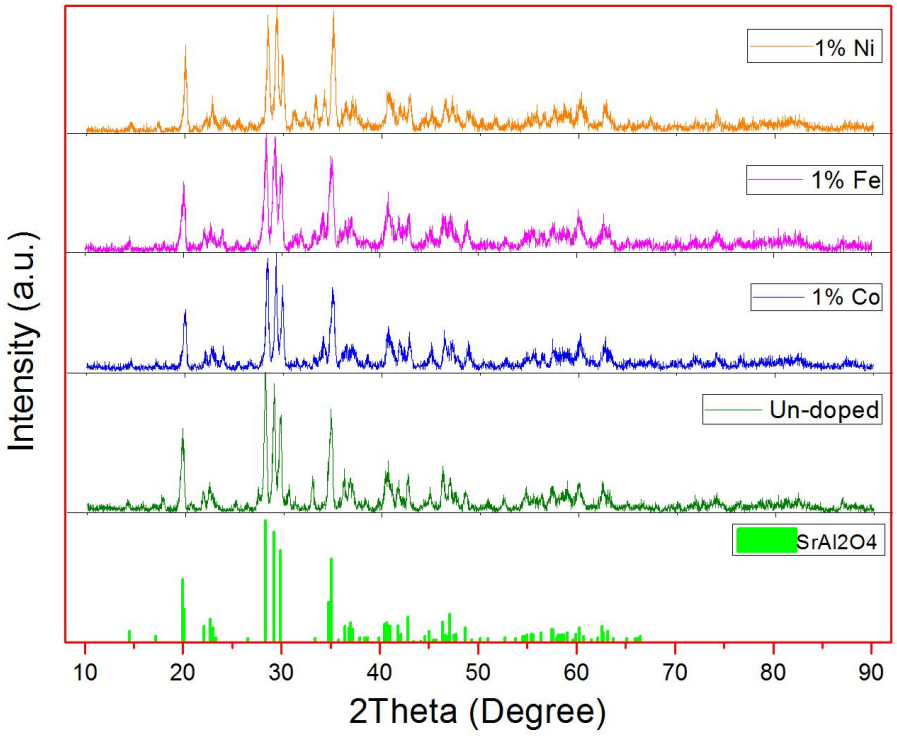

Figure 2 : **XRD patterns of 1% Co, Fe and Ni doped $SrAl_2O_4:Eu^{2+}, Dy^{3+}$.**

Table 1 : **Calculated crystallite size for doped samples.**

Samples	**1% doped $SrAl_2O_4:Eu^{2+}, Dy^{3+}$**			
Dopant	Co	Fe	Ni	Un-doped
Crystalline size (nm)	28,52	17,11	42,79	34.26

3.2. Morphological Analysis

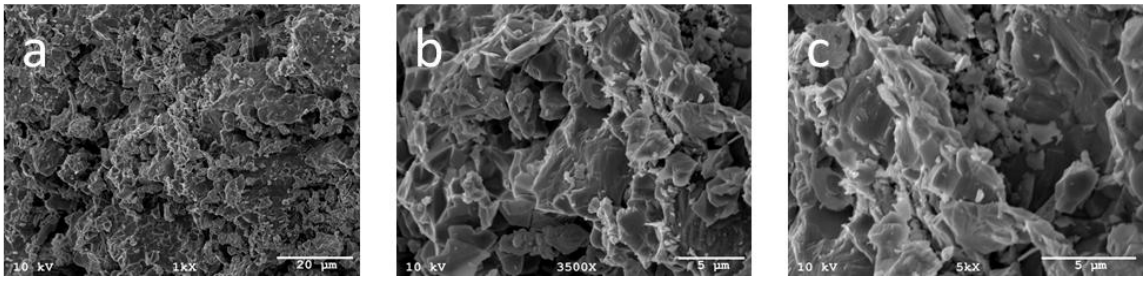

Figure 3 : **a) 1 kx and b) 3,5 kx and c) 5 kx magnified SEM micrographs of $SrAl_2O_4:Eu^{2+}$, Dy^{3+} phosphor samples.**

SEM analysis was carried out to view the sintered powder morphologies. In figure 3, SEM micrographs of phosphor sample synthesized with sol-gel method (which are annealed in RA at 1300°C for 1 h) are shown. It can be seen that the whole of them consists of highly sintered structure. Sharp edges are the result of grinding process after sintering.

3.3. Optical Analysis

The effect of dopant types and concentration on luminescence properties of phosphor samples is shown in figure 4 and 5. Optical characteristics of Eu^{2+} in $SrAl_2O_4$ matrix, which are Emission at about 515 nm and excitation between 300 and nearly 430, can be seen in both figures. This emission pattern is attributed to $4f^65d^1 \rightarrow 4f^7$ electronic transitions of Eu^{2+}. In the case of doping transition metal ions, except Fe, all 0,5% doped samples shows lower emission and excitation performance than reference sample, which is un-doped one. Moreover, increasing in dopant concentration affects the performance negatively for all samples.

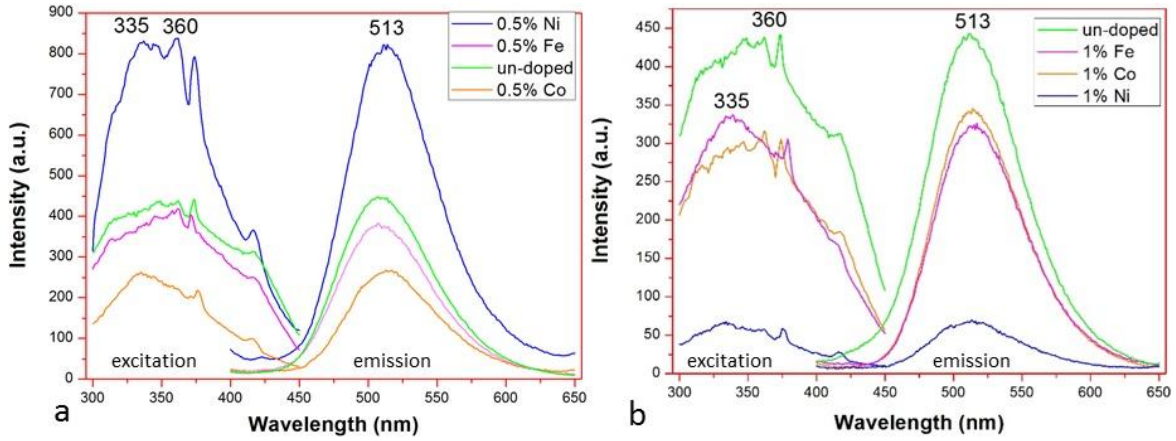

Figure 4 : **Emission and excitation spectrums of $^+$ a) x= 0,5 % and b) 1 % Co, Fe and Ni doped $SrAl_2O_4$: Eu^{2+}, Dy^3 phosphors annealed in H_2/N_2 RA for 3 h.**

Although all samples show similar shape of emission spectrum and can be excited between 300-450 nm, they have different excitation spectrum in shape. It can be said that different type and/or amounts of dopant elements may cause different lattice defects and create different trap levels in the structure. So, excited electrons of Eu^{2+} may be trapped these defects and give excitation spectrums peaked at different wavelength.

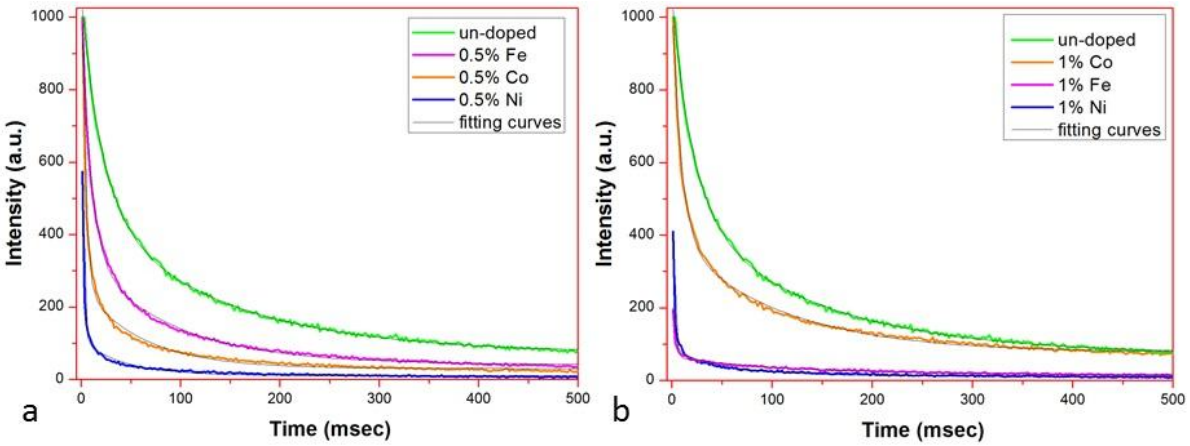

Figure 5 : **Afterglow decay curves of a) % 0,5 and b) 1% Co, Ni and Fe doped $SrAl_2O_4$: Eu^{2+}, Dy^{3+} phosphors annealed in H_2/N_2 RA for 3 h.**

It can be seen from afterglow decay curves (figure 5a and 5b) that $SrAl_2O_4$: Eu based phosphors show two component decay characteristics: the first is initial rapid and the second is relative slow decay. Therefore, decay curves were fitted using equation 2 to rationalize the decay behaviors. In table 2, afterglow decay parameters all of samples are given. In the case of doping transition metals, all doped samples without depending on amount of concentration, show worse lifetime than un-doped one. Additionally, increasing dopant concentrations causes decreasing in lifetime, except Co doped sample, which improve lifetime. But all samples have lowest lifetime and initial intensity than un-doped one. This effect can be clearly seen in figure 6, which include presentation of decay parameters with comparing each others.

Table 2 : **Afterglow decay parameters of 0,5 and 1% of Co, Fe, Ni doped $SrAl_2O_4$: Eu^{2+}, Dy^{3+} phosphor samples.**

Pechini Samples		y_0	A_1	A_2	τ_1	τ_2
Un-doped		31,51	265,57	851,81	275,00	38,54
0.5 %	Ni	15,65	1014,04	131,29	1,86	49,95
	Co	27,66	924,35	233,79	4,42	61,14
	Fe	35,43	876,79	250,62	28,01	186,75
1 %	Ni	16,41	1064,31	120,65	1,61	47,88
	Co	66,72	756,99	301,66	10,36	110,00
	Fe	21,88	315,88	71,15	2,26	103,75

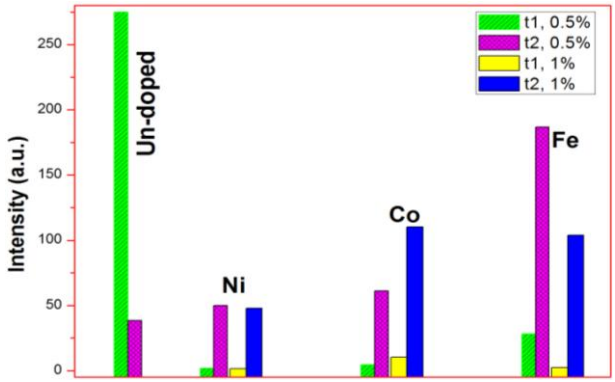

Figure 6 : **Columnar presentation of afterglow parameters.**

REFERENCES

1. Yen, W. M., Shionoya, S., Yamamoto, H., "Phosphor Handbook,". 2nd ed. New York: CRC Press, , 2007
2. T. Matsuzawa, Y. Aoki, N. Takeuchi, and Y. Murayama, J. Electrochem. Soc., 143, 8, 1996
3. H. Song and D. Chen, Luminescence, 22, 554-558, 2007
4. M. Yoshihiko, T. Nobuyoshi, A. Yasumitsu, M. Takashi, Phosphorescent Phosphor, Euro. Patent Off., 0622440A1, 1994
5. B. Faridnia and M.K. Motlagh, Pigment & Resin Tech., 36, 4, 216–223, 2007
6. Y. Xu, D. Chen, Ceramics International, 34, 2117–2120, 2008
7. Yen-Pei Fu**,** J Mater Sci, 42, 5165–5169, 2007
8. T. Peng, L. Huajun, H. Yang and C. Yan, Materials Chemistry and Physics, 85, 68–72, 2003
9. K. Van den Eeckhout, P.F. Smet and D. Poelman, Materials, 3, 2536-2566, 2010

PHOTOCATALYTIC PROPERTIES OF POTASSIUM TITANATE WHISKERS SYNTHESIZED BY SOL-GEL PROCESS

Derya KAPUSUZ[*1], Jongee PARK[2], Abdullah OZTURK[*3]**

* Middle East Technical University, Turkey

[1]dkapusuz@metu.edu.tr, [3]abdullah@metu.edu.tr

** Atilim University, Turkey

jpark@atilim.edu.tr

ABSTRACT

Photocatalytic activity and band gap energy of potassium titanate whiskers synthesized by sol-gel process were determined with respect to Ti/K (molar) ratio and calcination time. Four gels for Ti/K of 1, 1.5, 3, and 3.5 were produced. Powders were obtained after drying xerogels at 100 °C for 6 h. The powders then were calcined at 600 °C for 1 and 3 h. The X-ray diffraction analysis identified that potassium hollandite and hexa- titanate phases (KTi_8O_{16}, $K_2Ti_6O_{13}$) were formed during calcination. Morphology of the phases was in nonowires as determined by using scanning electron microscopy. The photocatalytic activity was evaluated by methylene blue degradation tests in UV-light irradiation. A diffuse reflector was employed for the band gap measurements. Results revealed that both the photocatalytic activity and band gap energy were dependent on Ti/K ratio. Highest MB degradation rate was obtained for the product synthesized in Ti/K ratio of 3.5 and calcined at 600 °C for 3 h. The energy band gap of powders decreased with increasing the Ti/K ratio.

Keywords: Photocatalysis, Potassium titanate, Whisker, Synthesis, Sol-Gel process.

SOL-JEL SÜRECİYLE SENTEZLENMİŞ POTASYUM TİTANAT VİSKERLERİN FOTOKATALİTİK ÖZELLİKLERİ

ÖZET

Sol-jel süreciyle sentezlenmiş potasyum titanat viskerlerin fotokatalitik aktivite ve bant aralığı enerjisi Ti/K molar oranı ve kalsinasyon süresine bağlı olarak değişimi belirlenmiştir. Ti/K oranı 1, 1,5, 3, ve 3,5 olan dört farklı jel hazırlanmıştır. Jellerin 100 °C'de 6 saat kurutulmasından sonra edilen tozlar 600 °C'de 1 ve 3 saat kalsine edilmiştir. X-ışını kırınım analizi potasyum hollandit ve hexa-titanat (KTi_8O_{16}, $K_2Ti_6O_{13}$) fazların oluştuğunu açığa çıkarmıştır. Taramalı electron mikroskobu fazların morfolojilerinin nanotel şeklinde olduğunu göstermiştir. Fotokatalitik aktivite metilen mavisi bozunum deneyiyle UV-ışık altında değerlendirilmiştir. Bant aralığı enerjisi difuse reflektör kullanılarak belirlenmiştir. Sonuçlar hem fotokatalitik aktivitenin hemde bant aralığı enerjisinin Ti/K oranına bağlı olarak değiştiğini ortaya koymuştur. En yüksek MB bozunum hızı Ti/K oranı 3,5 olan ve 600 °C'de 3 saat kalsine edilen üründe elde edilmiştir. Bant aralığı enerjisi Ti/K oranı arttıkça azalmıştır.

Anahtar Kelimeler: Fotokataliz, Potasyum titanat, Visker, Sentez, Sol-Jel süreç.

1. INTRODUCTION

Low dimensional structures such as nanowires (1D) and nanoplatelets or nanosheets (2D) have been attractive structures for many applications. Researches have focused on alkali titanate nanostructures in the past decades due to their superior specific surface area and photocatalytic capabilities [1]. Among the alkali titanates, potassium titanates ($K_2O.nTiO_2$, where n=2,4,6,8) are of importance since they possess photoresponsive properties similar to TiO_2 and comparably lower costs then their alternatives [2-5]. Photoresponsive properties mainly depend on the crystallite size and morphology of final nano-structures. Xu et al mentioned absorption edge differences of TiO_2 nanotubes, nanofiber/nanoparticle mixtures and nanoparticles as 441 nm, 411 nm, and 416 nm, respectively [6].

Size and morphology of the products depend directly on the technique used for the production. Several methods including hydrothermal [7,8], ion exchange [9], molten salt [10,11], and sol-gel process [5,12] have been tried for the synthesis of potassium titanate nanostructures. Among these methods, calcination technique has been used for the production of high aspect ratio fibers. However, the method was limited to synthesis of high aspect ratio fibers in microscale. Hydrothermal synthesis provides the synthesis of nanostructures by precipitation inside a solvent liquid at its saturated vapor pressure at lower temperatures. By changing hydrothermal reaction parameters like solvent type/amount and the temperature, it is possible to obtain potassium titanate nanowires or sheets at temperatures lower than 200 °C. But, the required reaction durations are rather high, usually around 24 h. Alternatively, sol-gel process has the advantages like ease of preparation and handling at ambient temperatures. It also provides various morphologies in nanoscale. Kang et al [12] reported the sol-gel synthesis of $K_2Ti_4O_9$ and $K_2Ti_6O_{13}$ after calcination at 800 °C for 3 h. They concluded that, $K_2Ti_4O_9$ formation dominates and the sizes get bigger as the calcination temperature increased up to 1000 °C. Sol-gel followed by calcination method becomes more advantageous than hydrothermal synthesis if the calcination temperature after sol-gel reaction is decreased.

The purpose of the present study was twofold; to determine whether potassium titanate nanostructures could be produced by sol-gel technique followed by calcination at temperatures lower than 800°C, and to determine the change in band gap energy by changing the Ti/K ratio for bridging the nanostructure to energy band gap features.

2. EXPERIMENTAL

2.1. Materials and method

Non-hydrous sol-gel technique followed by calcination treatment was used to synthesize potassium titanate ($K_2O.nTiO_2$) nanostructures as described previously in the literature [12,13]. In a typical synthesis, certain amounts of titanium ethoxide (TEOT; $Ti(OC_2H_5)_4$) were dissolved in 20 ml of ethanol. After complete dissolution, potassium methylate (PM; CH_3OK) was added to the mixture. The reaction was catalyzed by 0.1 M of HCl^{aq} solution. All additions were made during continuous magnetic stirring at room temperature.

Four gels for Ti/K molar ratio of 1, 1.5, 3, and 3.5 were produced. Powders were obtained after drying xerogels at 100 °C for 6 h. The powders were then calcined at 600 °C for 1 and 3 h. TEOT amount was arranged to provide a stoichiometric balance for Ti/K ratios of 1 to 3.5. PM amount was kept constant at 30 mmol. After calcination, chunks of powders were crushed using alumina mortar with pestle.

2.2. Characterization and testing

The phase compositions of the calcined powders were identified using X-ray diffractometer (Rigaku D/MAK/B). Cu Kα (λ=1.54056 nm) radiation with a constant rate of 0.02°/min was used to detect phases present at 2θ between 5 and 75°. XRD patterns were indexed using Rigaku 4.2 software. The morphology of the powders was analyzed using scanning electron microscopy (SEM, Nova NANOSEM 430). Crushed powders were collected on carbon and then coated with 10 nm of gold before SEM analysis.

Photodegradation kinetics and band gap energy of the powders were determined using UV-Vis Spectrometer (Scinco S-3100). For a typical photodegradation test, 300 ml of Methylene Blue (MB) solution (10 mg/l) was prepared by dissolving MB powder in deionized water and 0.2 g of powders was added to this solution. After keeping 30 min in dark to establish absorption-desorption equilibrium, 3 ml of MB solution sample was taken from the solution by using a syringe filter unit (Millipore, 0.22μm) and measurement was done. Then, the powder containing MB solution was exposed to UV-light. A 100W UV lamp (UVP Co., South Korea) was used as the UV-light source. For the MB degradation, 3 ml of MB solution was taken from the solution after each 30 min and measurements were done. The UV–vis absorption spectrum of the powders was detected between 200 and 800 nm. The MB degradation amount was monitored by the variation in light absorbance at 664 nm of the MB chromophore, as it was degraded by time.

Reflectance of the powders was measured by using the diffuse reflectance sphere that was integrated to the same UV-Vis Spectrophotometer. Direct and indirect band gaps were determined by plotting and extrapolating $F(R)^{1/2}$ and $F(R)^2$ versus energy (eV) curves, respectively, to the zero energy level.

3. RESULTS AND DISCUSSION

3.1. XRD Analysis

The XRD patterns of the sol-gel derived powders composed of different Ti/K ratio and calcined at 600 °C for 1 and 3 h are shown in Figures 1 and 2, respectively. Four different phases namely; potassium chloride (KCl, ICDD: 41-1276), anatase (TiO_2, ICDD: 21-1272), potassium hollandite (KTi_8O_{16}, ICDD: 41-1097) and potassium hexa-titanate ($K_2Ti_6O_{13}$, ICDD: 40-0403) were identified after calcination regimes.

XRD analysis revealed that it is possible to form potassium hexa-titanates at lower calcination temperature and times than those previously mentioned by Kang et. al [5] by following the same experimental procedure if the Ti/K ratio of the initial solution is changed. In addition, KCl crystals acting as an intermediate phase during the formation of potassium titanates were detected in the XRD patterns.

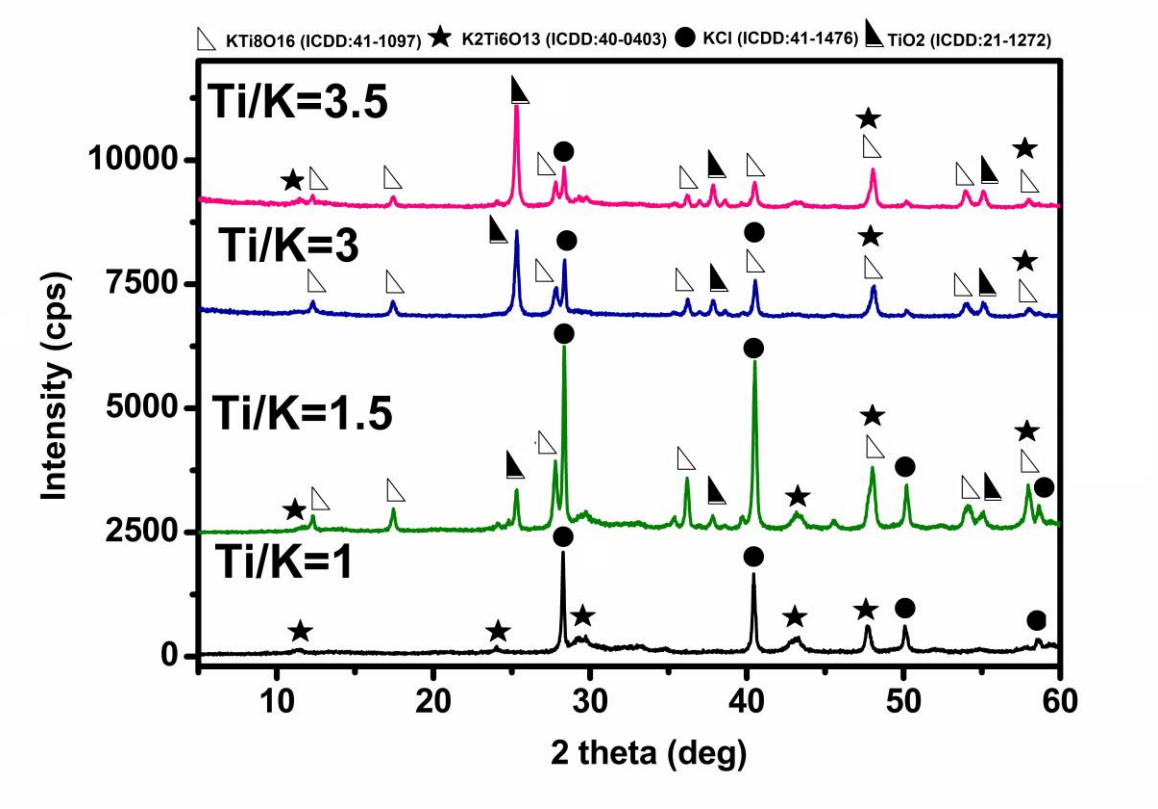

Figure 1. XRD patterns of sol-gel derived powders calcined at 600 °C for 1 h.

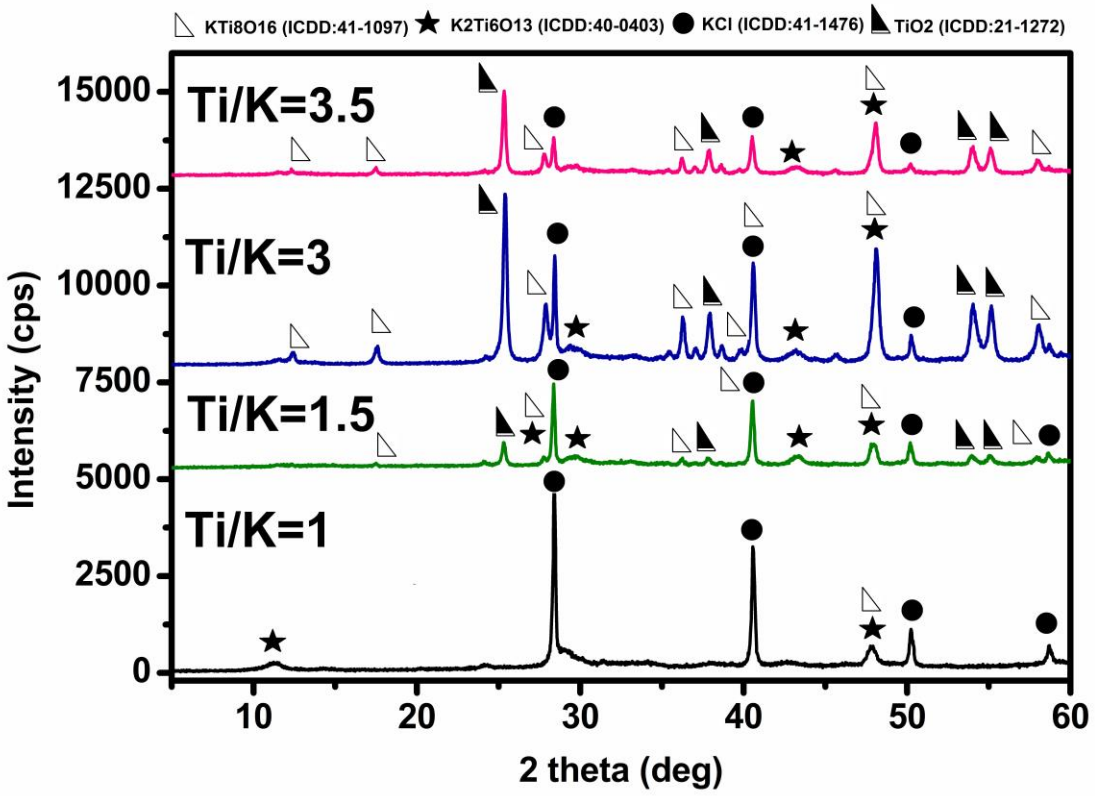

Figure 2. XRD patterns of sol-gel derived powders calcined at 600 °C for 3 h.

XRD results suggest that the Ti/K ratio has a profound effect on the phases formed during calcination due to the stoichiometric balance desired for the formation of potassium titanate structures as previously mentioned for the solid state methods [14]. Some KCl remained unreacted and some anatase was formed at almost all experimental conditions. XRD analysis of the xerogels before calcination was pure KCl for the powders synthesized for all Ti/K ratios. It was foreseen that there is an amorphous Ti-O network and KCl crystals dispersed in this network. However, a detailed XRD analysis of xerogels is necessary to get the assurance of this envision.

The XRD peaks belonging to two potassium titanate phases were noticeable in the XRD patterns of the powders synthesized at all conditions. The XRD peaks corresponding to KTi_8O_{16} phase were sharper and at relatively at higher intensity than those to $K_2Ti_6O_{13}$ phase. The broadening of peaks implies that $K_2Ti_6O_{13}$ crystals are in nano-scale in dimensions.

3.2. SEM Analysis

The morphology of the sol-gel derived powders calcined after 1 and 3 h at 600°C are shown in Figures 3 and 4, respectively.

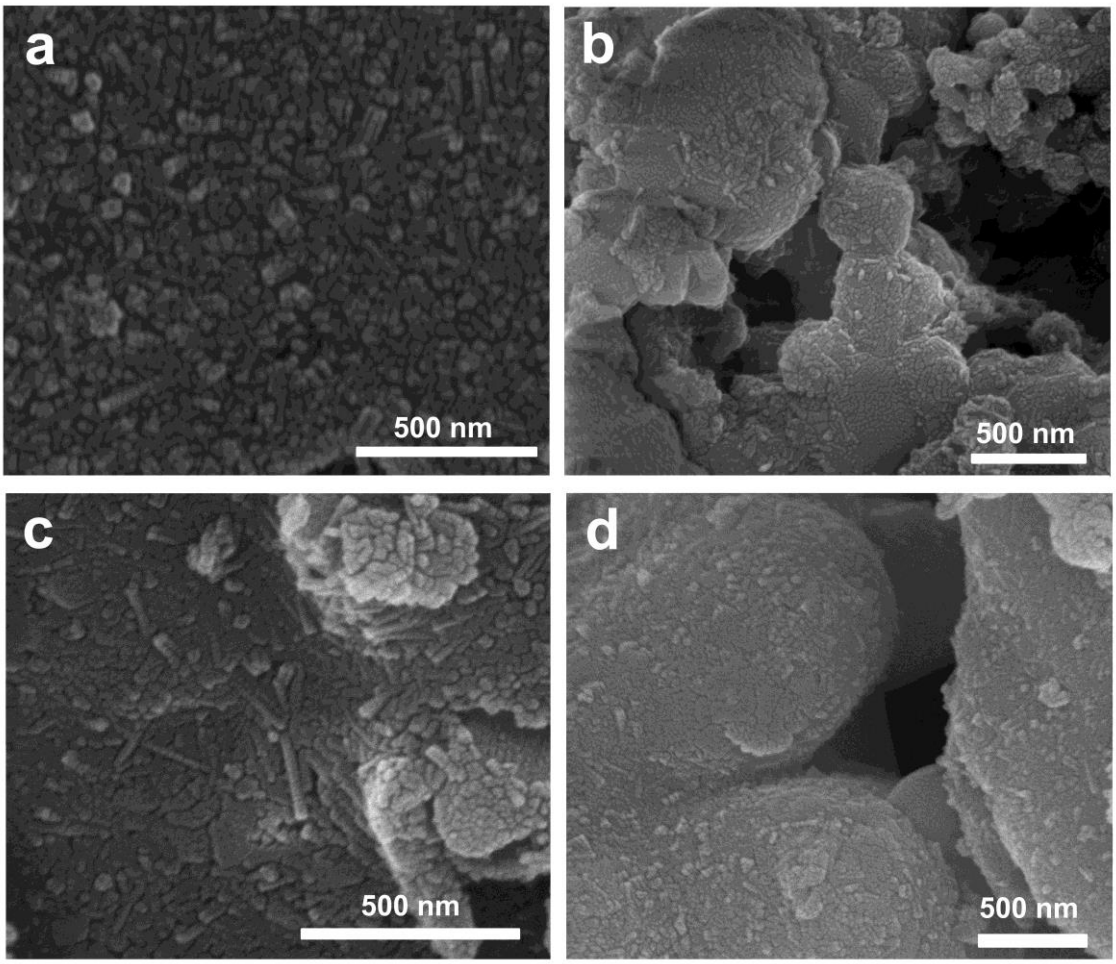

Figure 3. SEM images of sol-gel derived powders calcined at 600 °C for 1 h for Ti/K ratio of a) 1, b) 1.5, c) 3, and d) 3.5.

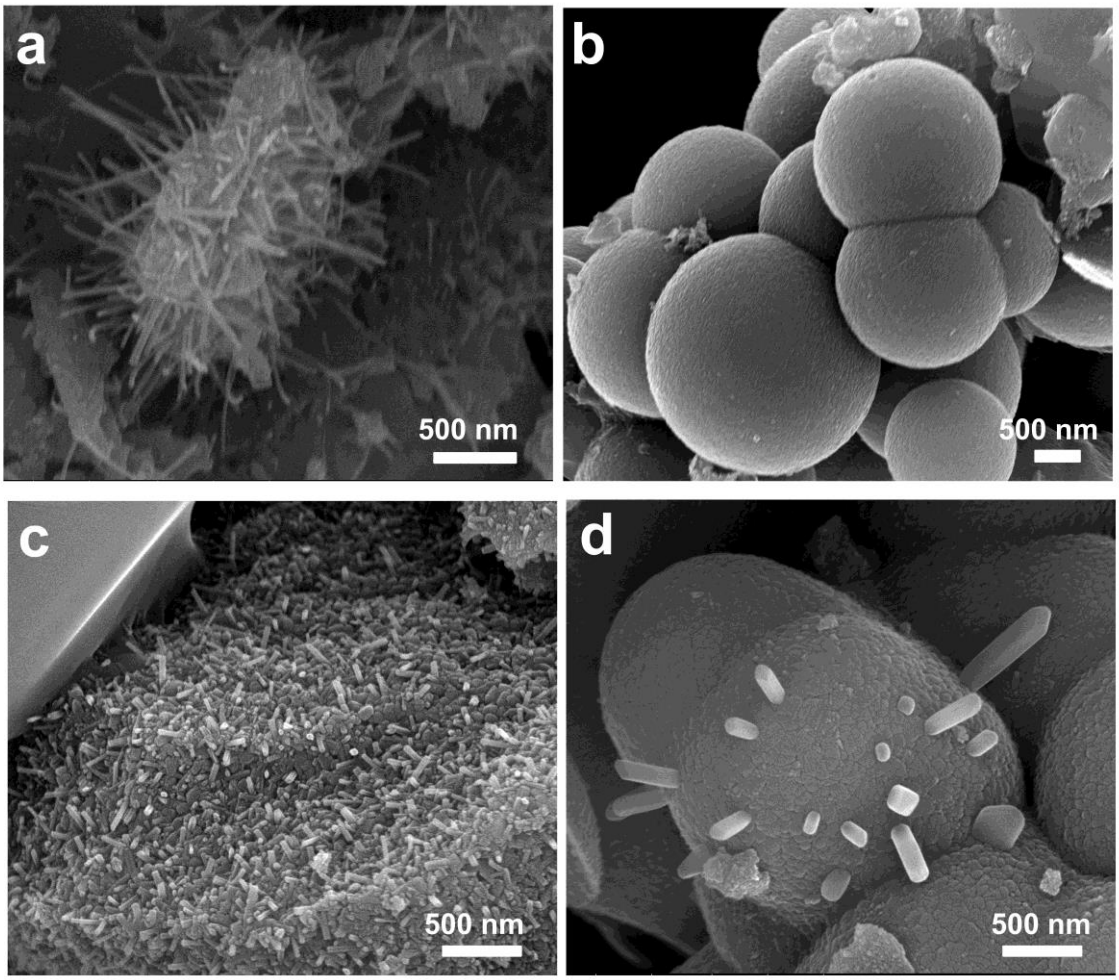

Figure 4. SEM images of sol-gel derived powders calcined at 600 °C for 3 h for Ti/K ratio of a) 1, b) 1.5, c) 3, and d) 3.5.

SEM images verify that potassium titanates were in nanowire and whisker form, in concomitant with the broadened peaks in XRD patterns. A severe degree of agglomeration which increases with increasing Ti/K ratio for both calcination times is seen in all powders. Turaif [15] stated that van der waals forces are intensified in high aspect ratio fibers, wires or nano-sheets forming agglomerated particles. This is rather obvious in Figure 4, showing the images taken from the powders calcined at 600 °C for 3 h. It is not possible to differentiate KTi_8O_{16} and $K_2Ti_6O_{13}$ phases just by examining the SEM images. However, with the combination of XRD results, it is meaningful to propose that agglomeration intensifies by the formation and growth of KTi_8O_{16} nanowires with relatively thicker cross sections than $K_2Ti_6O_{13}$ nanowires, as the calcination time and Ti/K ratio are increased.

3.3. Methylene Blue (MB) Degradation

In Figure 5, UV-vis scans of the MB solutions containing calcined powders for different Ti/K ratios are shown with respect to time of UV-light irrediation. Since MB chromophore absorbs light specifically around 664 nm, the UV-vis curves are shown in 400-800 nm ranges. The black lines in all graphs show the absorption of untreated MB solution and MB concentration can be related to the light absorption at 664 nm (C_0). As the MB adsorbed by or intercalated into the pores on surface of powders, the absorption of UV-light, thus the concentration of

MB decreases by irradiation of UV-light by time (C_{30} to C_{150}). This provides a comparison of photo activity between the powder samples. As the total amount of MB is adsorbed, the adsorption peak disappears. As seen in Figure 5, all powders showed some degree of photocatalytic activity, some of them even without exposing to UV-light irradiation. That is, red lines, after 30 min in dark.

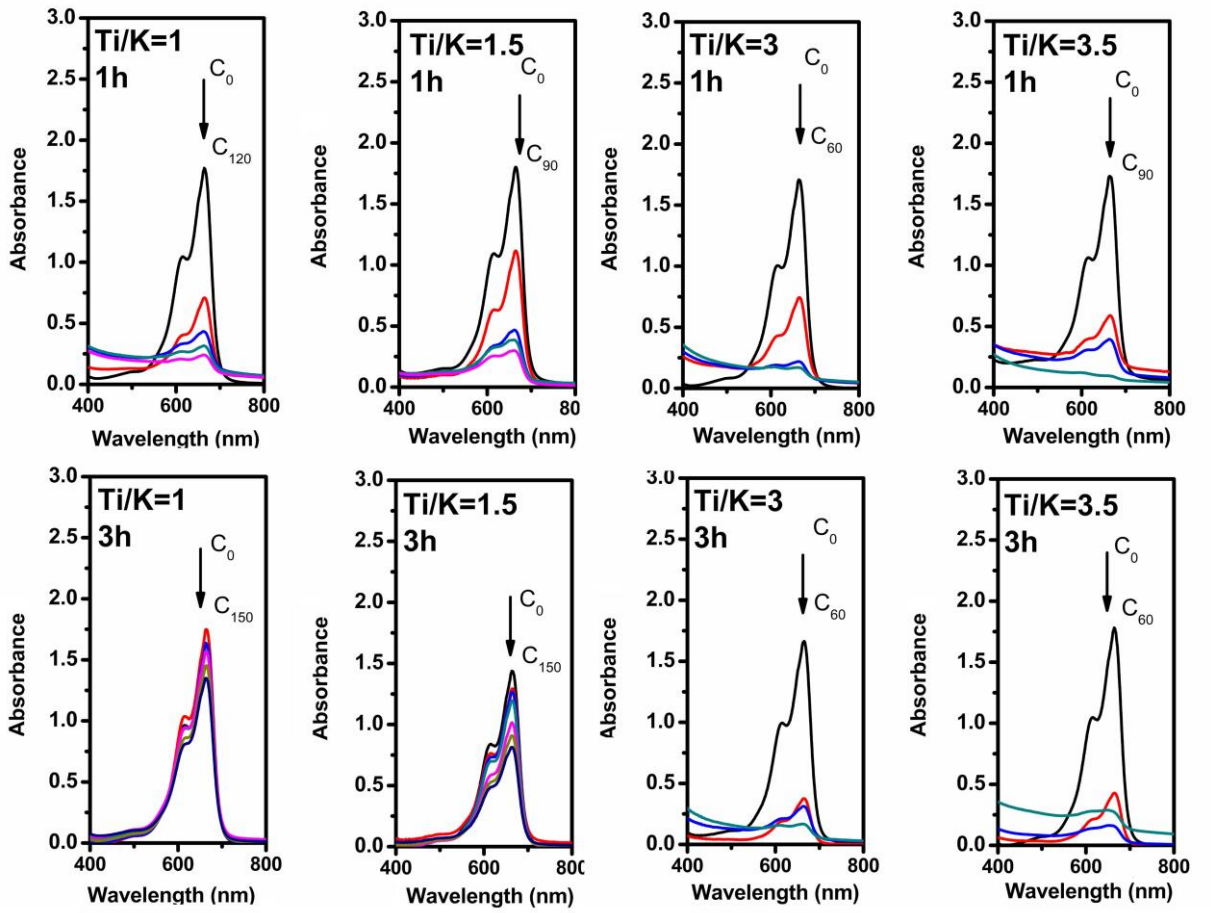

Figure 5. MB degradation curves of sol-gel derived powders calcined at 600 °C for 1 and 3 h.

The remarkable degradation rate of MB by the powders without UV-light irradiation for Ti/K ratio of 3 and 3.5 could be related to the surface pores in the structure. There is not a systematic study reported for KTi_8O_{16} with capability of photocatalytic activity. The increased degradation of MB by powders for Ti/K ratio of 3 and 3.5 is attributed directly to the increased surface area and the presence of photocatalytic TiO_2 and $K_2Ti_6O_{13}$ phases present in the structure.

3.4. Diffuse Reflectance Spectroscopy

The changes in direct and indirect band gap energy of the sol-gel derived powders composed of different Ti/K ratio and calcined at 600 °C for 1 and 3 h are shown in Figure 6. Both for the direct and indirect band gaps of powders, there was a decreasing trend as the Ti/K ratio

increased. In addition, the lowest indirect band gap was 3.08 eV for the powder composed of Ti/K ratio of 3 calcined for 1 h, which was lower than 3.10 eV reported for rutile phase [16]. The direct band gap energies for TiO_2 and $K_2Ti_6O_{13}$ are 3.29 and 3.47 eV, respectively. The formation of KTi_8O_{16} might cause a decrease in the band gap energy of the powders.

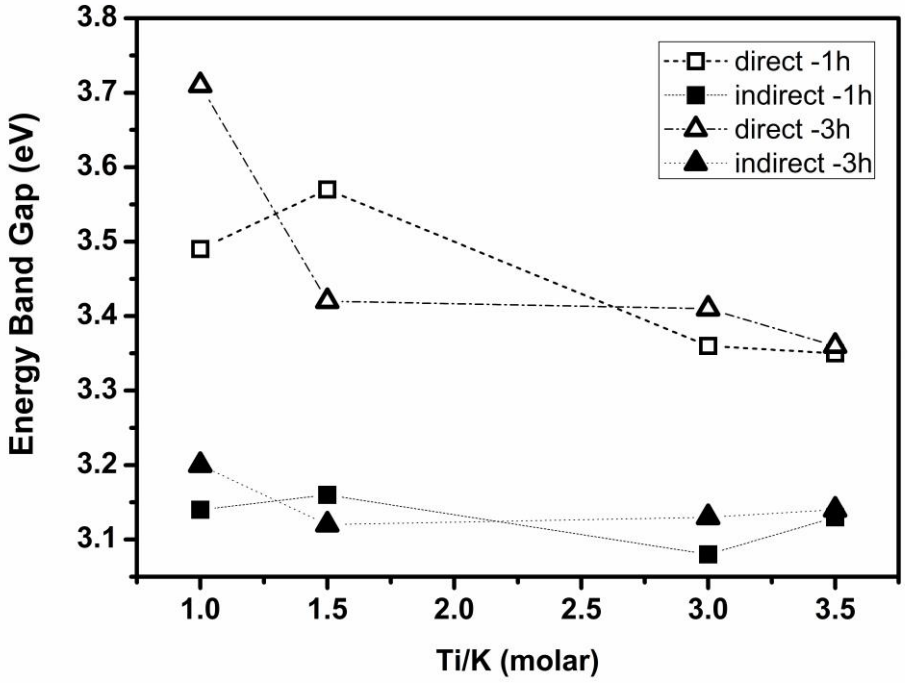

Figure 6. The change in band gap energy with Ti/K ratio for the powders calcined at 600 °C for 1 and 3 h.

4. CONCLUSIONS

The present study involves the results obtained about the structure-property relationships of sol-gel derived potassium titanate nanowires. The results showed that sol-gel synthesis could be an alternative method for the production of low band gap titanate crystals. It is possible to obtain potassium titanate nanowires and whiskers by sol-gel technique after calcination at temperatures lower than 800 °C. It has been shown that the band gap energy of potassium titanate obtained for Ti/K ratio of 3 is lower than the band gap energy of rutile phase. Studies involving the examination of phase composition and morphology of potassium titanates could provide the desired information for the production of materials that are visible light responsive.

ACKNOWLEDGEMENT

The authors would like to thank Middle East Technical University for the partial financial support to perform the experiments through Project No: BAP-03-08-2013-004.

REFERENCES

1. Y. Zhou, C. Liu, M. He, X. Lu, X. Feng and Z. Yang, J Mater. Sci., 43, 155, 2008

2. J.H. Choy and Y.S. Han, Mater. Lett., 34, 111, 1998

3. J. Zhang, Y. Wang, J. Yang, J. Chen and Z. Zhang, Mater. Lett., 60, 3015, 2006

4. L.M. Sikwivhilu, S.S. Ray and N.J. Coville, Appl. Phys. A, 94, 963, 2009

5. S.O. Kang, H. S. Jang, Y. Kim, K.B. Kim and M. J. Jung, Mater. Lett., 61, 473, 2007.

6. G.R. Xu, J. N. Wang and C.J. Li, Appl. Surf. Sci., 279, 103, 2013

7. G.H. Du, Q. Chen, P. D. Han, Y.Yu and L. M. Peng, Phys. Rev. B, 67, 035323, 2003

8. B. Wang, Y. Shi and D. Xue, J Solid State Chem., 180, 1028, 2007

9. Y. Liu, T. Qi and Y. Zhang, Mater. Res. Bull., 42, 40, 2007.

10. X. Zhang, S. Tang, L. Zhai, J. Yu, Y. Shi andY. Du, Mater. Lett., 63, 887, 2009

11. T. Sanchez-Monjaras, A. Gorokhovsky, J. I. Escalente-Garcia, J Am. Ceram. Soc., 91(9), 3058, 2008.

12. K.T. Jung and Y. G. Shul,J. Sol Gel Sci. Tech., 6, 227, 1996

13. D. Kapusuz, J. Park and A. Ozturk. Adv. Bioceram. Porous Ceram. VI, 35, 2014

14. C. Li, M. He, X. Lu, Q. Zhang and Z. Xu, Cryst. Growth Des., 5, 1399, 2005

15. H. A. Turaif, Progress in Organic Coatings, 69, 241, 2010.

16. F. Amano, T. Yasumodo, T. Shibayama, S. Uchida and B. Ohtani, Appl. Catal. B Environ., 89, 583, 2009.

Recent Advances in Bioceramics Design: Key Biomaterial Properties for Bone Regeneration

•

Biyoseramik Alanındaki Güncel Gelişmeler: Kemik Dokusu Oluşumu İçin Gerekli Önemli Biyomalzeme Özellikleri

Maria Pau Ginebra

Universitat Politecnica de Catalunya - Spain

ABSTRACT

Bone is a self-repairing material. However, the defect healing capacity is limited to a few millimetres in humans. Large bone defects pose a great clinical and socioeconomic challenge. In these situations it is necessary to induce bone formation beyond the capacity of the host tissue. The development of synthetic materials, including calcium phosphates, is an alternative strategy that overcomes the limitations associated with bone grafts.Calcium Phosphate materials are bioactive, this meaning that they develop a direct, adherent, and strong bonding with the bone tissue. Since the 1970's, a wide range of calcium phosphates are used in the clinic, from high-temperature sintered calcium phosphates, to biomimetic nanoapatites. Research and clinical evidence have provided considerable insight into the role of different material properties in the bone regeneration process. In the light of this knowledge, the most recent developments in the field of bioceramics as synthetic bone substitutes will be presented.

Keywords: Bioceramics design, bone regeneration, calcium phosphate, defect healing capacity.

CEMENT-TYPE REACTIVITY AND SETTING BEHAVIOUR OF CALCIUM-PHOSPHATE BASED COMPOSITE BONE FILLER

Gözde ALKAN[1,2], Caner DURUCAN[1,2]

[1]Department of Metallurgical and Materials Engineering,
[2]BIOMATEN Center of Excellence in Biomaterials and Tissue Engineering,
Middle East Technical University, 06800 Ankara, TURKEY
agozde@metu.edu.tr, cdurucan@metu.edu.tr

ABSTRACT

Bone fillers of self-setting nature can be used in irregularly shaped bone defect filling operations. Calcium phosphate based composite cements blended with polymers are promising due to their structural and chemical similarity with bone tissue. In this study, preparation of self-setting α-TCP:polycaprolactone (PCL) composite cements have been reported. A comparative and parametric study was carried out in determining hydraulic reactivity of α-TCP in forming CDHAp with various amounts of PCL addition by isothermal calorimetry studies at 37° C. Furthermore, fracture strength of cement end product was evaluated by diametral compression test to elucidate the effect of PCL on mechanical properties of final hardened mass. It was found that PCL addition retards α-TCP to CDHAp conversion. However, it improves mechanical strength/integrity of pre-hydrated compacts and CDHAp-based cement products by providing physical interlocking between the inorganic granules without any chemical interaction.

Keywords: bioceramics, cement reaction, α-tricalcium phosphate (α-TCP)

KALSİYUM FOSFAT ESASLI KOMPOZİT KEMİK ÇİMENTOLARININ REAKSİYON KİNETİĞİ VE MEKANİK ÖZELLİKLERİ

ÖZET

Kemikte oluşabilecek boşlukları doldurmak için kemik dolgu ve çimentoları kullanılmaktadır. Kalsiyum fosfat esaslı ve polimer eklenmiş sistemler, doğal kemiğe yapısal ve kimyasal açıdan benzerlikleri nedeniyle bu kullanımda öne çıkmaktadır. α-trikalsiyum fosfat (α-TCP) su ile reaksiyona girip sertleşerek kalsiyumca eksik hidroksiapatite (CDHAp)dönüşebilmektedir. Bu çalışmada α-TCP : polikaprolakton (PCL) hibritleri hazırlanmış ve α-TCP'nin çimento tipi reaksiyonuyla CDHAP:PCL kompozit çimentoları elde edilmiştir. Farklı miktarlardaki PCL eklentisinin α-TCP'nin hidrolik reaktivitesi üzerindeki etkisi izotermal kalorimetre ile karşılaştırmalı olarak araştırılmıştır. Ayrıca, PCL eklentisinin son çimento-benzeri yapıların mekanik özelliklerine etkisi belirlenmiştir. PCL'un α-TCP'nin reaksiyon kinetiğini yavaşlattığı fakat kırılım dayanımını iyileştirdiği saptanmıştır.

Anahtar Kelimeler: biyoseramikler, çimento tipi reaksiyon, α-trikalsiyum fosfat

1. INTRODUCTION

A variety of synthetic materials have been used as bone grafts for filling bone defects and fixation of severe bone fractures. The need for materials in irregularly shaped bone defect filling operations has induced the development of self-setting bone cements that can be applied as injectable or moldable defect filler. In this respect; calcium phosphates have been commonly preferred as bone cements due to their chemical similarity to mineral part of natural bone, superior bioactivity and osteoconductivity [1-4]. There are quite a large number of binary combinations of calcium phosphates resulting into two major cement end products; apatite ($Ca_{10}(PO_4)_6(OH)_2$) or brushite ($CaHPO_4 \cdot 2H_2O$) [5,6]. From those, apatitic ones are more promising as the inorganic part of natural bone is an apatite-like mineral. There are two variations for apatitic cement reactions. In the first one, an acidic calcium phosphate reacts with a relatively basic calcium phosphate in aqueous environment to produce a solid and hardened compound . However; different chemical characteristics of two precursors such as solubility may result in additional end products or deviations from physiological pH during setting reaction [7]. Another cement-type reaction is hydration of a metastable calcium phosphate to form more stable calcium phosphate with same Ca/P ratio. One example to this group is, α-tricalcium phosphate ($Ca_3(PO_4)_2$) or α-TCP) which in fact is the only calcium phosphate compound that hydrolyzes to hardened calcium-deficient hydroxyapatite (CDHAp) from a "single" solid precursor [8-12]. Hardened CDHAp resembles the natural bone mineral more than stochiometric HAp; both structurally and chemically [13]. In addition, solubility of CDHAp is higher than that of stochiometric HAp; it degrades with time and provide new tissue generation with the same processes during the remodeling of healthy bone [4, 9]. However, α-TCP has still limited utilization due to relatively poor mechanical properties, tensile strength, and fracture toughness and also due to poor setting reaction kinetics [4]. In this study, a composite system has been introduced to enhance functional properties of α-TCP. For mechanical strength improvement biodegradable polymer polycaprolactone (PCL), which can also change the reaction kinetics and mechanism, has been added to pre-hydrated α-TCP powders. The effects of PCL addition on hydration kinetics, microstructure and mechanical properties of cement type HAp products have been investigated in comparative parametric approach.

2. MATERIALS AND METHODS

2.1 Materials

The major calcium source was calcium carbonate ($CaCO_3$, reagent grade Merck, Germany) and phosphoric acid H_3PO_4 (85% wt. Merck, Germany) was used as phosphorous source. The solid state synthesis of α-TCP (hereafter will be referred as TCP) was accomplished by firing proper amount of $CaCO_3$ and chemically synthesized monetite ($CaHPO_4$) at 1200 °C for 2 hs. The details of synthesis method can be found elsewhere [14, 15]. Hydration and calcium deficient hydroxyapatite (CDHAp) formation was achieved by cement-type reaction of TCP at near physiological temperature (37°C) according to the following reaction,

$$3\ Ca_3(PO_4)_2 + H_2O \rightarrow\ Ca_9(HPO_4)(PO_4)_5(OH) \quad (1)$$

PCL and chloroform (commercial grade) used in composite cement processing were obtained from Sigma-Aldrich (Germany).

2.2 Experimental Methods

The kinetics of cement-type conversion and mechanical properties of cement-end products were investigated for four different cement compositions. Cement conversion was performed on pre-consolidated forms of disc shaped pellets for obtaining proper shapes for mechanical testing. The first group is pure (plain) TCP compacts which were prepared by pressing 1 g of solid state synthesized TCP powders (average particle size of 10 μm) using in a cylindrical die at a uniaxial pressure of 4MPa at ambient temperature. These coin shaped pellets were typically 3mm thick with a diameter of 15 mm. In addition, hybrid pellets containing 3 wt. %, 6 wt. %, and 9 wt. % polycaprolactone (PCL) addition to the same TCP powder were prepared. These TCP:PCL hybrid cements will be referred as T3CP, T6CP, T9CP; respectively. In preparing the hybrid pellets; initially, PCL was dissolved in chloroform and mechanically mixed with TCP powders by Turbula T2F mixer (System Schatz, Switzerland) for 0.5 h at room temperature. Pre-cement mixtures were kept in vacuum furnace for 12 h to remove solvent and achieve complete drying. After that, mixtures were ground to fine powders using mortal and pestle and 1 g of mixture powder were pressed in a cylindrical die at a pressure of 4 MPa at ambient temperature. The size of hybrid compacts was comparable to that of plain TCP. All pellets were inserted into polypropylene vials and closed with equal amount of deionized (DI) water and kept in a water bath at a constant temperature of 37 °C to allow cement-type TCP→CDHAp setting reaction.

2.3 Material Characterization

Phase identification was performed by x-ray diffraction analyses using a Rigaku D/Max-2000 PC model diffractometer. The diffraction tests were performed for diffraction angle (2θ) range of 20°-40°, at a scanning rate of 2°/min using Cu-Kα radiation and an operation voltage of 40 kV and a current of 30 mA.

The morphologies of samples before and after hydration were examined by a FEI Quanta 400F model field emission scanning electron microscope (SEM). SEM examinations were performed on conductive metal thin film coated representative samples.
Cement-type reactivity of TCP was determined by isothermal microcalorimetry (TAM-Air). Plain TCP and three TCP:PCL pellets were examined to observe PCL effect on hydraulic reactivity of TCP. Details of isothermal calorimetry can be found elsewhere [16]. In a typical experiment, first a glass cup containing 1 g of dry pre-cement pellet and a syringe containing 2 mL liquid reactant (DI-water) were placed into the closed calorimetry chamber. Meanwhile, equivalent amount of dry calcium sulfate ($(CaSO_4)\cdot\frac{1}{2}H_2O$) filled glass cup was placed into the reference chamber. After achieving thermal equilibrium, the cement reaction was started by injecting the DI-water into the sample-containing calorimetry cup that initiates hydration and heat evolution. Heat flow rate were recorded to investigate reaction kinetics.
Mechanical properties were evaluated by diametral compression testing [17]. To investigate the effect of cement-type reaction and PCL effect on mechanical properties of cement-end product, five pellets of each pure CDHAp and CDHAp:PCL pellets with various PCL amounts were prepared and be subjected to diametrical compression test, before and after hydration by an automated Instron machine at a crosshead speed of 0.05 cm/min. Maximum compressive loads that they can sustain were recorded. The tensile strengths of samples at fracture were calculated by following formula;

$$\sigma = 2P/\pi Dt \quad (2)$$

where *P, D, t* are maximum load, diameter of sample and thickness of sample, respectively. Porosities of pellets before and after hydration were determined by Archimedes method. Densities of samples were measured and by comparing them with their theoretical values, total porosity amount was calculated using following formula;

$$\% \text{ Porosity} = (1 - \text{bulk density/theoretical density}) \times 100 \quad (3)$$

Theoretical density values of non-hydrated pellets (TCP:PCL) and hydrated pellets (CDHAp:PCL) were calculated by rule of mixture. The theoretical density values for the CDHAp and TCP are 2.79 g/cm^3 and 2.863 g/cm^3, respectively [18]. The theoretical density of organic constituent PCL is 1.145 g/cm^3 [19].

3. RESULTS AND DISCUSSION

The rates of heat evolution (dQ/dt vs. time) during hydration of plain TCP and TCP:PCL hybrid pellets are illustrated in **Figure 1**.

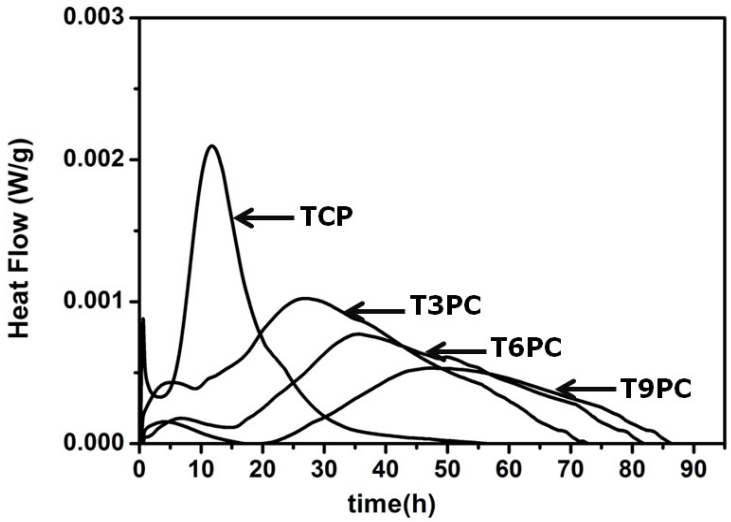

Figure 1. The heat flow curves for hydration of pure TCP, T3PC, T6PC, T9PC at 37 °C.

The isothermal calorimetry analyses were performed at 37 °C for all samples. These curves indicate that hydration reactions of all samples are exothermic. The complete conversion was determined and evidenced by the time span after no further heat was evolved, i.e. heat flow becomes steady at around zero. Although the time for complete conversion are different for four different cement systems, the general apperance of heat evolution rate curves is same for all samples including one short low heat intensity peak at the early times of reaction and one broad highly intense peak expanding to longer times saturating at the end of conversion. These two peaks correspond to nucleation and growth of CDHAp crystals, respectively [9]. Heat evolution rate during hydration of TCP indicates that pure TCP compacts were completely converted into CDHAp after 42 h. The time for complete conversion was retarded from 42 h to 72 h, 82 h and 85 h by addition of 3, 6 and 9 wt.% PCL additions; respectively. Comparison of these plots implies that the presence of PCL affects the hydraulic reactivity of TCP with significantly hampering growth of HAp crystals and extends the time for completion. Isothermal calorimetry findings indicate that increase in PCL content supresseses TCP to CDHAp cement-type conversion.

In order to have more precise conclusion on effect of PCL on hydraulic reactivity of TCP, phase evaluation behavior for pure TCP and a hybrid TCP-PCL blend (here T3PC) as a function of reaction time are shown by the XRD diffractograms in **Figure 2.** This figure provides additional analytical information for direct comparison.

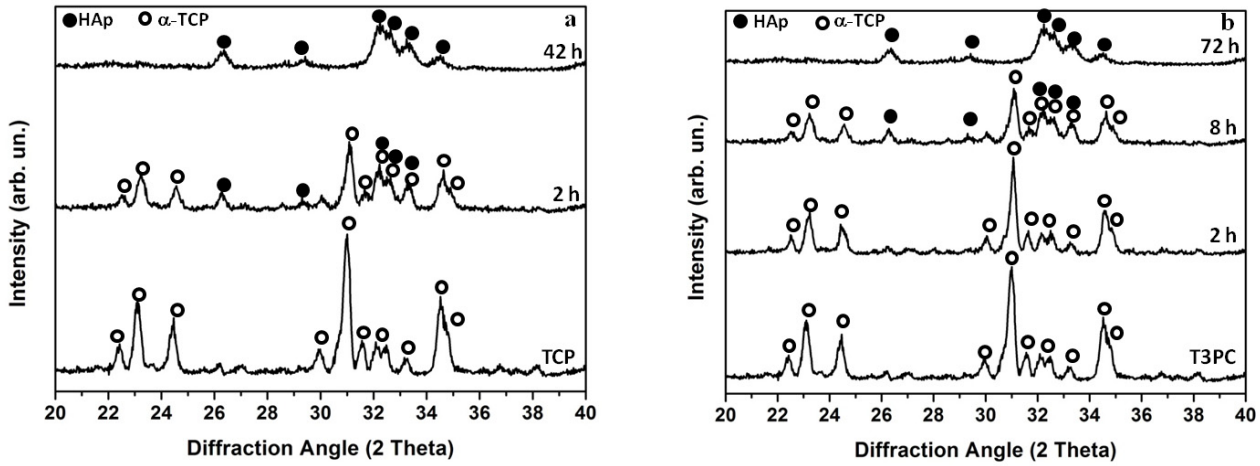

Figure 2. The XRD diffractograms as a function of reaction time for **(a)** pure TCP **(b)** TCP-PCL blend (T3PC).

The XRD diffractograms given in **Figure 2 a and b** illustrate phase evaluations during cement-type reaction of TCP and T3PC as a function of reaction time, respectively. Regardless of PCL addition, initial XRD diffractograms of both systems exhibited the characteristic peaks of TCP (JCPDS card no 9-348). First apperance of HAp evidenced by low intensity peaks at around 2θ≈ 26.5 and 2θ≈31-33 matching with characteristic peak positions of HAp (JCPDS card no 9-342) upon 2 h and 8 h hydration of TCP and T3PC, respectively. XRD findings show that by addition of 3 wt. % PCL addition, first appearance of HAp during hydration of TCP retarded by 6 h. Ultimately, there is not any peak for TCP and XRD diffractograms suggest a complete conversion to HAp at the end of 42 h for TCP and 72 h for T3PC, respectively. Comparison of phase evaluations as a function of reaction time for two selected systems shows that PCL delays both first apperance of and complete conversion to HAp. In parallel to isothermal calorimetry findings, XRD results also suggest retarding effect of PCL on cement-type conversion of TCP to HAp. This may be due to the fact that, PCL is a biodegradable polymer with low glass transtion (-60° C) and melting temperature (60° C) [19]. Hydration temperature (37 °C) of samples is significantly higher and slightly lower than glass transition temperature and melting temperatures of PCL, respectively. Therefore, PCL may impede and retard access of water to inorganic constituent of hybrid cements by covering the free surfaces of TCP powders.

Even though PCL slows down the cement-type reaction of TCP, it was found that all TCP in hybrid cements complete converts to CDHAp when at extended times of hydration, which was determined by isothermal calorimetry as 42 h, 72 h, 82 h and 85 h for TCP, T3PC, T6PC, T9PC; respectively. **Figure 3** illustrates XRD diffractograms of cement end products of pure TCP and three hybrid cements at the end of reaction.

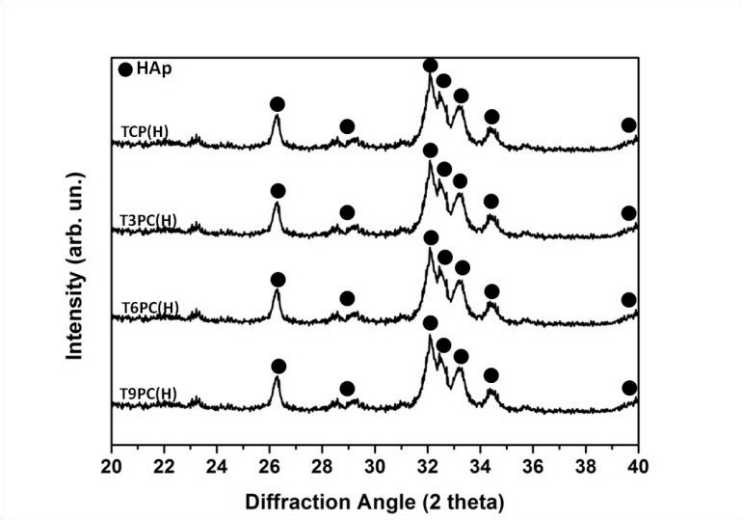

Figure 3. The XRD diffractograms of hydration products of pure TCP and hybrid blends of TCP-PCL of different compositions; T3PC, T6PC and T9PC.

In all cement systems, regardless of PCL amount, diffractograms match with characteristic peaks of HAp without any unreacted TCP. Detailed kinetic analyses highlight that PCL addition resulted in poor hydraulic reactivities of cement systems. However, poor reactivity of T3PC, T6PC and T9PC were still accompanied by complete conversion to HAp at the end. SEM micrographs of three hybrid system before and after hydration illustrated in **Figure 4.**

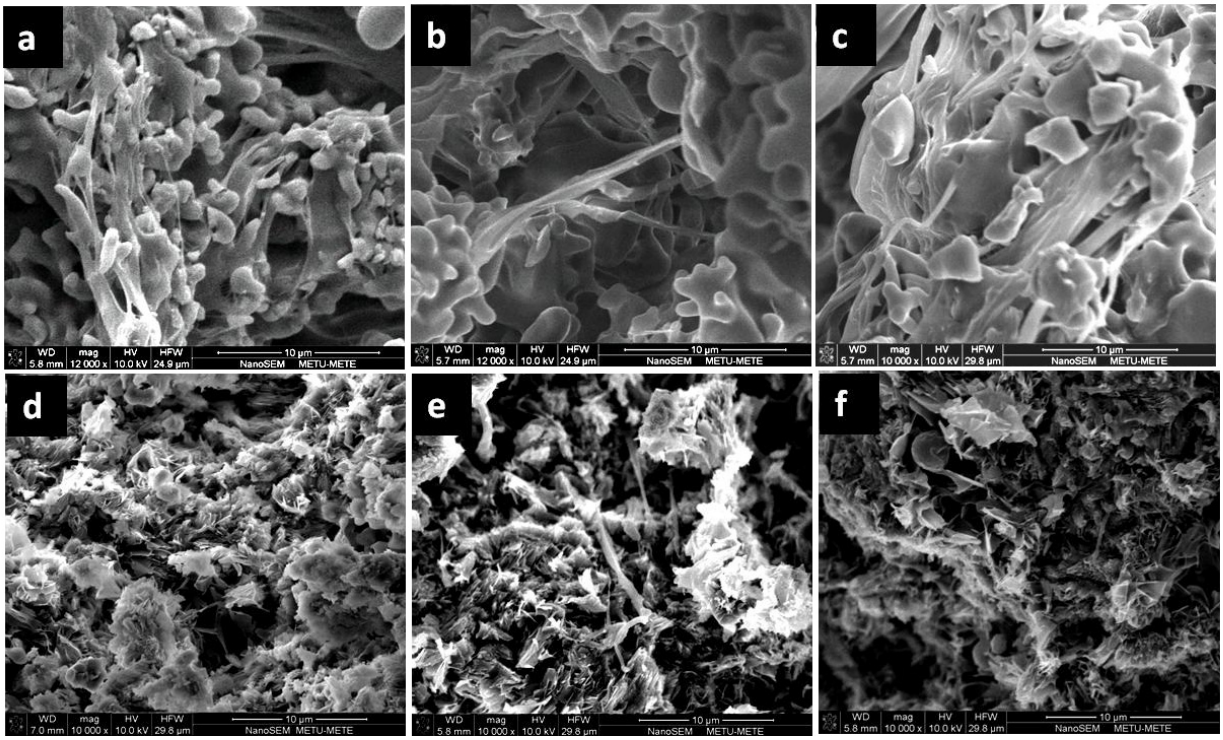

Figure 4. SEM micrographs of pre-cement hybrids **(a)**T3PC **(b)** T6PC **(c)**T9PC and their hydration products **(d)**T3PC **(e)** T6PC **(f)** T9PC.

For all systems, initial equiaxed-like inorganic constituent granules connected via polymer network completely converted into entangled needles of HAp crystals. SEM micrographs correlate with XRD findings emphasize that all three hybrid systems with different reaction kinetics are rective and completely converted into HAp at the end.

Fracture strengths of TCP and TCP:PCL hybrid systems prior to hydration containing 3 wt.%, 6 wt. % and 9 wt. % PCL are listed in **Table 1.** The strength values were obtained by averaging five measurements. The average tensile strength of pure TCP compacts was determined as 0.169±0.05 MPa. This value increased to 0.181 ± 0.05 MPa, 0.325 ± 0.05 MPa and 0.337 ± 0.05 MPa by addition of 3 wt.%, 6 wt.% and 9 wt.% PCL, respectively. Additionally, it is worth to emphasize that the average porosity amounts of non-hydrated TCP, T3PC, T6PC and T9PC compacts consolidated by 4 MPa pressure were determined to be 60 vol.%, 58 vol.%, 56 vol.% and 55 vol.%; respectively. Porosity measurement of non-hydrated compacts coherent with fracture strength values indicates that PCL behaves as a binder by acting like bridges and filling the pores between TCP particles during pressing as also evidenced in SEM micrographs in **Figure 4** and improves mechanical integrity. All hydrated samples subjected to diametral compression test completely converted to HAp as evidenced by XRD analyses. A significant increase in mechanical properties and densities at the end of cement-type reaction was observed. Porosity amount changing between 54-59 vol.% for non-hydrated samples decreased to 40-45 vol% after hydration. Further, hydrated TCP, T3PC, T6PC and T9PC exhibited average tensile strength of 4.46±0.1MPa, 6.54±0.1MPa, 6.25±0.1MPa and 4.86±0.1MPa, respectively.

Table 1. Fracture strengths of cement systems before and after hydration.

Fracture Strengths	Before Hydration	After Hydration
TCP	0.169 ± 0.05 MPa	4.46 ± 0.1 MPa
T3PC	0.181 ± 0.05 MPa	6.54 ± 0.1 MPa
T6PC	0.325 ± 0.05 MPa	6.25 ± 0.1 MPa
T9PC	0.337 ± 0.05 MPa	4.86 ± 0.1 MPa

From microstructural point of view, increase in mechanical properties and density based on conversion of sphere-like TCP granules into entangled CDHAp flakes. Moreover, in hybrid cements, PCL enhances mechanical properties by behaving as reinforcing agent. T3PC exhibits the highest tensile strength of 6.54 MPa±0.1MPa, which is relatively lower than that of cortical bone which is about 70-150 MPa [4,20]. However, it is comparable with that of cancellous bone which is around 10 MPa [20]. Mechanical test results with density measurements suggest that cement-type reaction results in hardening and PCL improves mechanical integrity/strength and fracture toughness of the HAp-based product by providing a mechanical interlocking effect between the hard/stiff inorganic cement particles.

4. CONCLUSIONS

CDHAp:PCL composites were produced by hydration of TCP:PCL hybrid pre-cements at around physiological temperature (37 °C). The effect of PCL on reaction kinetics of cement-type reaction of TCP and mechanical properties of HAp based cement-end products were examined. It was found that as PCL content of cements increases, the time for complete conversion of TCP into CDHAp prolonged to later times of reaction. However, PCL addition improves mechanical integrity/strength of the HAp-based products by providing a mechanical interlocking effect between the hard/stiff inorganic cement granules/particles. Among hybrid

cements, the one with 3 wt. % PCL exhibited highest tensile strength of 6.54±0.1MPa which is comparable with that of cancellous bone. The results obtained from present study imply that an optimum amount of PCL addition (3 wt. %) is required for effective fracture strength improvement with minimum adverse effect on hydration kinetics.

ACKNOWLEDGEMENTS

The authors thank METU-BAP 03-08-2013-006 for financial support.

REFERENCES

1. Damien CJ, Parsons JR. Bone graft and bone graft substitutes: a review of current technology and applications. J Appl Biomater. 199; 3: 187-208.
2. Ginebra MP, Espanol M, Montufar EB, Perez RA, Mestres G. New processing approaches in calcium phosphate cements and their applications in regenerative medicine. Acta Biomaterialia. 2010;6: 2863–2873.
3. Bohner M. Resorbable biomaterials as bone graft substitutes. Materials Today. 2010;13:24-30.
4. Dorozhkin SV. Bioceramics of calcium orthophosphates. Biomaterials. 2010;31:1465-1485.
5. Bohner M. Calcium orthophosphates in medicine: from ceramics to calcium phosphate cements. Injury. 2000;31:37-47.
6. Bohner M. Reactivity of calcium phosphate cements. J Mater Chem, 2007; 17: 3980-3986.
7. Tamimi F, Sheikh Z, Barralet J. Dicalcium phosphate cements: brushite and monetite. Acta Biomaterialia .2012; 8: 474–487.
8. Brunner TJ, Grass RN, Bohner M, Stark WJ. Effect of particle size, crystal phase and crystallinity on the reactivity of tricalcium phosphate cements for bone reconstruction. J Mater Chem , 2007; 17: 4072–4078.
9. Brown PW, Durucan C, Greish Y. Formation of hydroxyapatite and hydroxyapatite-based composites. Bioceramics. 1998;11.
10. Durucan C, Brown PW. Reactivity of α-tricalcium phosphate. Journal of Materıals Scıence. 2002; 37: 963–969.
11. Dorozhkin SV. Self-setting calcium orthophosphate formulations cements concretes pastes and putties. International Journal of Materials and Chemistry. 2011; 1: 1-48.
12. Carrodeguas RG, Aza SD. α-Tricalcium phosphate: Synthesis, properties and biomedical applications. Acta Biomaterialia. 2011; 7: 3536–3546.
13. Kasten P, Luginbuhl R, Griensven MV, Barkhausen T, Krettek C, Bohner M, Bosch U. Comparison of human bone marrow stromal cells seeded on calcium-deficient hydroxyapatite, b-tricalcium phosphate and demineralised bone matrix. Biomaterials. 2003; 24 : 2593–2603.
14. Cicek G, Aksoy EA, Durucan C, Hasirci N. Alpha-tricalcium phosphate (alpha-TCP): Solid state synthesis from different calcium precursors and the hydraulic reactivity. Journal of Materials Science:Materials in Medicine. 2011; 22(4): 809-817.
15. Durucan C, Brown PW, Alpha-Tricalcium phosphate hydrolysis to hydroxyapatite at and near physiological temperature. Journal of Materials Science-Materials in Medicine. 2000; 11 (6): 365-371.
16. Zimehl R, Drews J, Fischer-Brandies H. Thermometric monitoring of setting biomaterials. Thermochimica Acta. 2002; 382: 161–168.
17. Thomas MB, Doremus RH, Jarcho M, Salsbury RL. Dense hydroxylapatite: Fatigue and fracture strength after various treatments from diametral tests. J Mater Sci. 1980;15:891–894.
18. Monma H, Ueno S, Kanazawa T. Properties of hydroxyapatite prepared by the hydrolysis of tricalcium phosphate. J Chem Technol Biotech 1981;31:15–24.
19. Labet M , Thielemans W. Synthesis of polycaprolactone: a review. Chem Soc Rev. 2009; 38, 3484–3504.
20. Meyers MA, Chen PY, Lin AYM, Seki Y. Biological materials: structure and mechanical properties. Prog Mater Sci 2008; 53, 1-206.

CHARACTERIZATION OF APATITE FORMATION ABILITY OF ALKALI TREATED BULK Ti6Al7Nb ALLOY BY IN-VITRO STUDIES

Ezgi BUTEV[*,], Elif Eda YENI[***], Emre YILMAZ[*], Ziya ESEN[*], Şakir BOR[**]**

[*]Çankaya University Ankara/Turkey
ebutev@cankaya.edu.tr, emreyilmaz.com@gmail.com, ziyaesen@cankaya.edu.tr
[**]Middle East Technical University, , Ankara/Turkey
bor@metu.edu.tr
[***]Anadolu University, Eskisehir/Turkey
elifedayeni@gmail.com

ABSTRACT

Bulk Ti6Al7Nb alloys were exposed to alkali and heat treatment in order to enhance osseointegration ability of the surface by formation of sodium based titanate layers suitable for biomedical applications. Thin slices of Ti6Al7Nb alloys were immersed in 5 M NaOH solutions at 60ºC for 24 h followed by heat treatments carried out at 600°C temperature. Bioactivity of Ti6Al7Nb surfaces was evaluated by immersing the treated and untreated samples in simulated body fluid (SBF) for 1 and 5 days at 36.5ºC and pH 7.4. Composition and morphology of titanate layers formed as a result of alkali treatment and apatite layers nucleated during immersion in SBF were investigated using scanning electron microscope (SEM), energy dispersive spectroscopy (EDS) and thin film X-Ray Diffraction technique (TF-XRD). X-Ray Photoelectron Spectroscopy (XPS) was also used to investigate the chemical composition and the elemental state at the surface of the samples before and after alkali-heat treatment.

Keywords: Biomaterials, hydrothermal treatment, apatite formation, surface activation, Ti6Al7Nb alloy.

1. INTRODUCTION

There is a growing interest for titanium and titanium alloy in biomedical application due to their desirable properties such as low density, low corrosion resistance, good biocompatibility and better mechanical properties compared to other metallic implant materials used especially in load bearing applications [1]. However, by considering the long term success of the implant material, functional properties of surfaces are becoming crucial in addition to structural properties to have stable direct connection between surfaces of implant and bone tissues [2].

Several surface modification techniques pertaining to titanium and titanium alloy have been introduced which are plasma spray, sol-gel coating, H_2O_2 oxidation and alkali treatment [3-8] to enhance bone tissue attachment on the surface. However, high cost of processing, existence of weak bonding with substrate or disintegration of coating material makes the mentioned techniques unsuitable for the modification of surfaces [2]. By considering these drawbacks, alternative technique can be applied in order to improve the bonding strength of the coating material. Alkali treatment is simple technique which ensure to control the process parameters

easily and homogeneous coating layer is obtained [9]. In alkali treatment, samples were soaked at lower temperature in NaOH solution with different concentration. During the alkali treatment processing, the structural change of titanium surface is described that native TiO_2 layer existed on the surface partially dissolved in NaOH solution and result in formation of hydrated gel titanate layer by replacing of Ti-OH hydroxyl groups with Na^+ ions on the surface [1,2, 9]. The technique is generally finalized by a final heat treatment in air subsequent to alkali treatment with the aim of crystallization of sodium titanate layer [1, 2, 4]. There are various studies which make use of alkali treatment for modification of pure titanium and titanium alloys like Ti6Al4V alloys. As it is known, vanadium is toxic element and its release may be observed in long term application so that new vanadium free titanium alloys have been developed. Niobium, for example, is non-toxic element and replaced by vanadium to obtain Ti6Al7Nb alloy having mechanical properties similar to that of Ti6Al4V alloy.

The biocompatibility of surface treated materials and suitability of their surfaces for bone tissue attachment may be controlled by in-vivo and in-vitro studies. Among the techniques utilized, in-vitro studies, which make use of simulated body (SBF) and give information about bone formation, is practical way of checking the material's surface suitability for biomedical applications. Apatite is known to be a kind of precursor for new bone formation on implants' surfaces so that surface of the material which induces apatite nucleation during immersing in SBF is classified as bioactive. Studies have shown that during the immersion of the samples in SBF, Na^+ ions are released from sodium titanate layer and hydronium ions enters into surface layer, causing the formation of titanium oxide hydrogel layer that is the potential nucleation sites for the precipitation of hydroxyapatite on the titanium surfaces [10,11].

Although the alkali treatment technique is extensively used for the surface modification of pure titanium, there is not enough information and detailed study about the surface modification of Ti6Al7Nb alloys. Thus, in the present study, the attempt was made to get bioactive surfaces by creating sodium titanate layers on Ti6Al7Nb substrates with the help of alkali and heat treatment. Simulated body fluid (SBF) was used in order to check the apatite formation abilities of alkali-heat treated surfaces.

2. EXPERIMENTAL

3 mm thick, round Ti6Al7Nb alloy samples confirming to ASTM F1295-05 standard were used as substrate material. Prior to surface processing, the alloy samples were ground with SiC paper up to 2000 grit and washed with acetone, ethanol and finally with distilled water in an ultrasonic cleaner. Samples were then alkali treated by immersing in 5 M NaOH (aq.) solutions at 60°C for 24 h. Subsequent to alkali treatment, they were gently rinsed in distilled water and dried in an oven at 40°C for 24 h under vacuum. After alkali treatment, crystallization heat treatments were conducted at 600°C in air in order to obtain crystalline sodium titanate layer on the surfaces.

To examine the apatite formation abilities of as-received and alkali treated Ti6Al7Nb alloys, specimens were immersed in stimulated body fluid (SBF) (pH 7.4) at 36.5°C for one day and 5 days. The Ti6Al7Nb samples were placed on the bottom of polypropylene container with 30 ml of SBF which was renewed every 2 days in order to maintain the ion concentration stable.

SBF solution was prepared according to recipient of Kokubo [12] by dissolving following chemicals in the sequence of NaCl, $NaHCO_3$, KCl, $K_2HPO_4 \cdot 3H_2O$, $MgCl_2 \cdot 6H_2O$, 1.0m-HCl, $CaCl_2$, Na_2SO_4 into deionized water. The solution was buffered at pH 7.4 with tris-hydroxymethyl aminomethane (TRIS) and 1.0M HCl at 37°C. Ion concentration of SBF is (Na^+ 142.0, K^- 5.0, Mg^{2+} 1.5, Ca^{2+} 2.5, Cl^- 103.0, HCO^-_3 4.2, HPO^{2-}_4 1.0, SO^{2-}_4 0.5) (nearly equal to that of human blood plasma [12]. After being immersed for one day and 5 days, the alloys were taken from SBF, washed with distilled water gently and dried in oven at 30°C for 15 h.

Variation in surface morphology of Ti6Al7Nb alloy surfaces after alkali treatment and immersion in SBF were examined by FEI 430 Nano Scanning Electron Microscope SEM. Specimens were coated with platinum prior to SEM observation. The crystalline phases present on the surfaces were identified by thin film XRD (TF-XRD) with grazing incident angle of 0.5°. Surface chemical composition of the samples evaluated by X-ray photoelectron spectrometer (XPS) and Energy Dispersion Spectroscopy (EDS).

3. RESULTS AND DISCUSSION

3.1. Microstructure and Chemical Composition

Figure 1 shows the underlying microstructure of Ti6Al7Nb alloy which was used as substrate material for surface processing. The lamellar microstructure consisting of dark alpha phase and bright beta phase. The alpha was rich inα-stabilizer elements like aluminium (7.58% Al, 5.69% Nb), β-phase was depleted aluminium and relatively higher niobium content (22.03%Nb, 4.69% Al) was detected.

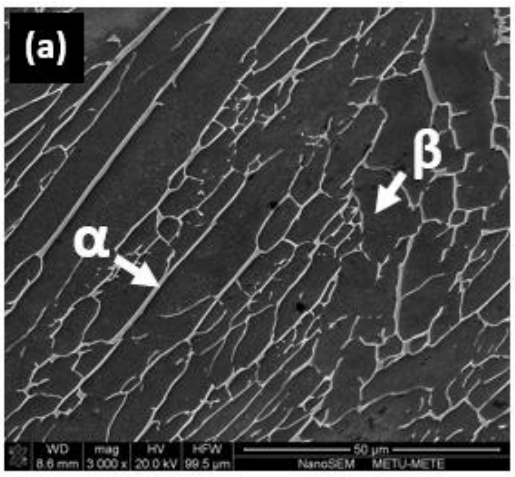

Figure 1: Microstructure of starting Ti6Al7Nb alloy having lamellar microstructure.

Surface processing using hydrothermal alkali method changed the starting surface morphology entirely. The surface of as-received Ti6Al7Nb alloy was relatively smooth with rarely observed grinding scratches, Figure 2(a). Immersion the samples in NaOH solution and subsequent heat treatment resulted in formation of very fine nano-porous network structure, Figure 2(b), 2(c). The network structure obtained after heat treatment at 600ºC was relatively

coarser compared to as-alkali treated samples mainly due to excessive oxidation during heat treatment in air, Figure 2(c),(d).

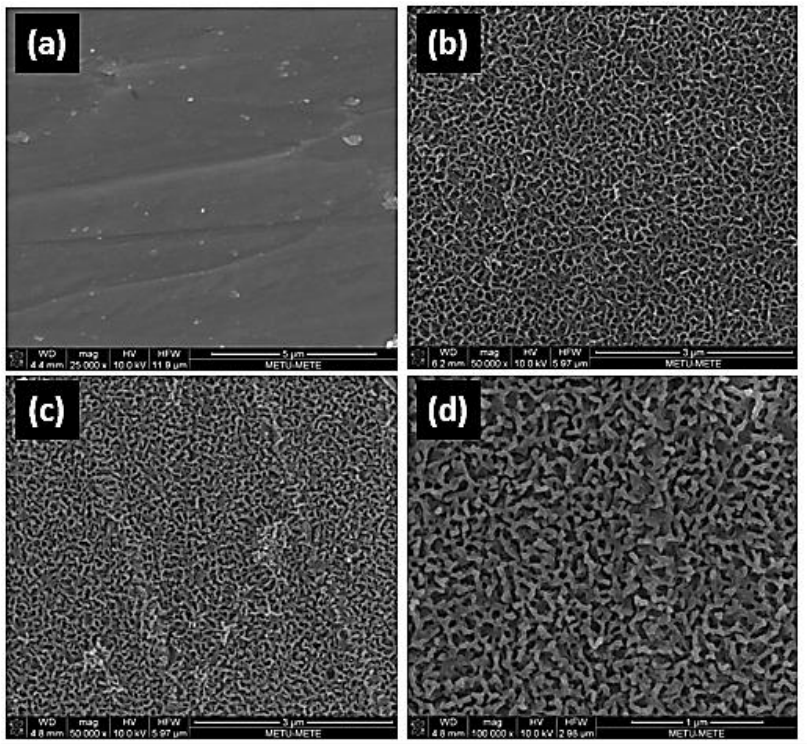

Figure 2: Scanning electron microscope (SEM) images of bulk Ti6Al7Nb surfaces, (a) as received sample, (b) 5M NaOH-treated at 60°C, and then (c) heat treated at 600°C, (d) enlarged image of (c).

As it can be seen in Figure 3 and Table 1, although as-received samples contained mainly titanium, aluminium and niobium around 83.92, 7.80 and 8.28 wt., respectively, an element with high concentration of oxygen was found to occur on alkali and alkali-heat treated samples' surfaces which was attributed to formation of Na-rich phase on the surfaces. However, depending on the applied heat treatment, the ratio of oxygen and sodium elements (O/Na) was different such that in as-alkali treated samples the ratio was around 3, while the ratio was higher in subsequently heat treated samples and calculated as around 5 probably due to formation of oxygen rich sodium compound in the samples. Although O/Na ratio was observed to be high in heat treated samples, relative quantity of oxygen was lower compared to as-alkali treated samples. It is known that alkali treatment applied to titanium induces formation of sodium titanate hydrogel ($Na_2Ti_3O_7.nH_2O$) on the surfaces which has relatively high oxygen content. The hydrogel layer then is converted to sodium titanate phases ($Na_2Ti_6O_{13}$, $NaTiO_2$, Na_2TiO_3) by removal of physically bound water, which have comparatively low oxygen content. Therefore, the difference in the relative oxygen contents of as-alkali treated and heat treated specimens was attributed to such transformation which occurs during subsequent heat treatment.

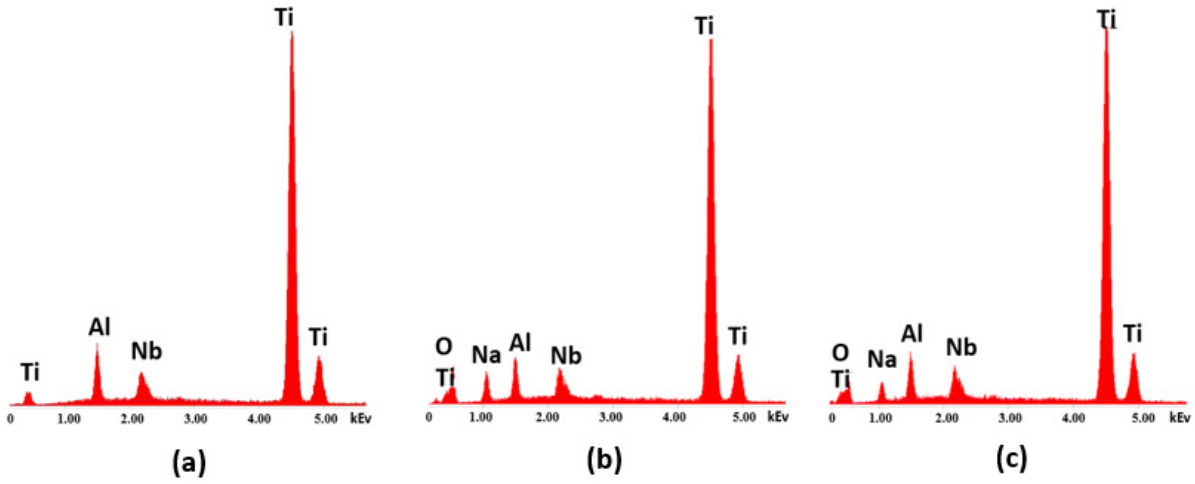

Figure 3: EDS results of Ti6Al7Nb alloy surface (a) as-received, (b) 5M NaOH treated at 60°C, and then (c) heat treated at 600°C

Table1. EDS results showing chemical composition of the alkali treated and untreated specimens

SPECIMEN	Wt.%				
	Ti	Al	Nb	O	Na
As-Received	83.92	7.80	8.28	-	-
NaOH Treated	63.19	4.42	6.60	19.59	6.20
NaOH+Heat Treatment	69.30	5.06	7.07	15.34	3.23

In addition to EDS studies, X-ray photoelectron spectroscopy (XPS) analysis were performed in order to determine the composition of the samples just at the surfaces. In Figure 4(a) XPS results of as-received sample has been presented. The starting material's surface was rich in mainly C, O and Ti elements and the concentration of Al was relatively low and no Nb element was detected. Titanium and titanium alloys generally form a very thin stable titanium oxide layer on their surface when exposed to open atmospheres and the observed titanium oxide layer in Ti6Al7Nb alloys is deficient in Al and Nb elements. The relatively high concentrations of oxygen and titanium elements were supposed to be due to formation of natural TiO_2 phase. In addition to this, high concentration of C element (35.5 at. %)on the surfaces is mainly due to organic molecules since it is reported that C always exists on the oxide surface due to adsorption of organic molecules [13].

As it can be seen in Figure 4(b) and 4(c), Al disappeared and Na element observed at the surfaces upon alkali and heat treatment processing. Additionally, Na element adsorb to surface reacts and thus, results in increasing the oxygen concentration of surface. Moreover, the subsequent heat treatment at 600°C caused to increase Na concentration from 14.7% to 16.4% seen in Figure 4(c) which could be due to the formation of stable sodium titanate layer, thereby, oxygen element diffuse into inner surface and TiO_2 oxide layer in starting as-received specimens completely dissolves.

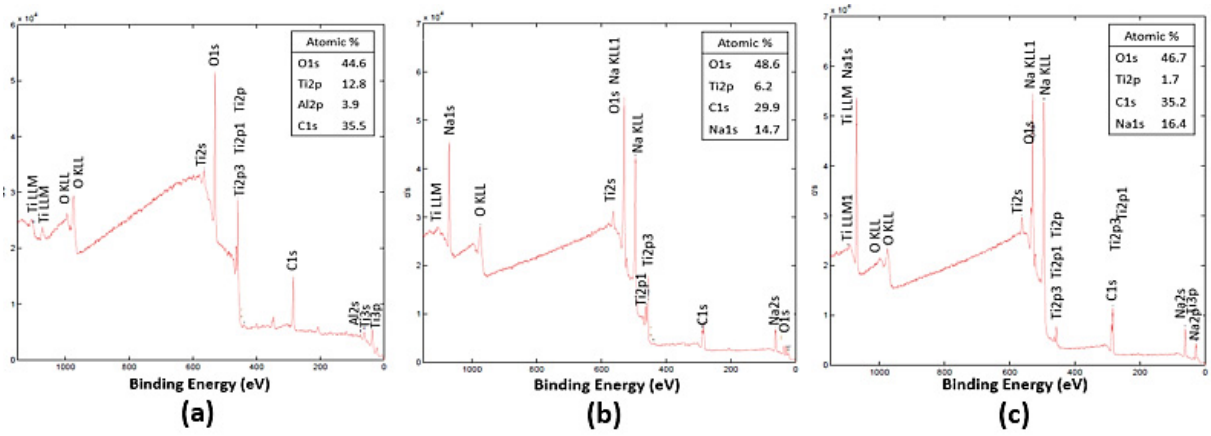

Figure 4: XPS results of bulk Ti6Al7Nb surfaces (a) as received, (b) 5M NaOH treated at 60°C, and then (c) heat treated at 600°C.

The formation of stable sodium titanate layers subsequent to heat treatment was detected during XRD studies, Figure 5. The titanate layer was observed to be $Na_2Ti_6O_{13}$ type crystalline layer and hardly observed at low diffraction angles mainly due to thickness of the layer which is supposed to be very thin. On the other hand, formation of sodium titanate hydrogel ($Na_2Ti_3O_7.nH_2O$) in alkali treated samples couldn't be detected mainly due to amorphous nature of the hydrogel layer. Instead, very low amount of titanium oxide phase was observed in addition to α-Ti (HCP-structure) and β-Ti (BCC-structure) phases.

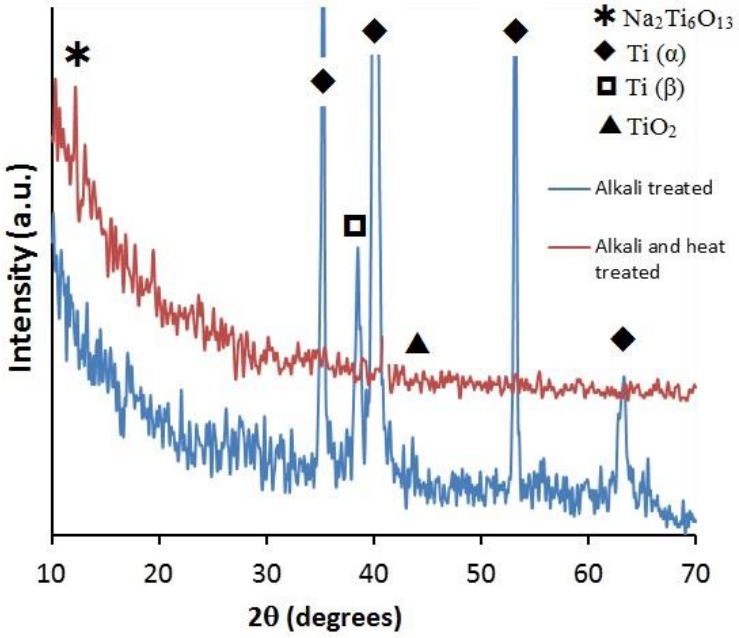

Figure 5. XRD patterns of alkali and, alkali and heat treated samples

3.2. SBF Tests

Figure 6 shows the SEM images of as-received and surface treated Ti6Al7Nb alloy surfaces immersed in SBF solutions for 5 days. After immersion the samples in SBF for 5 days, nucleation of small bright particles was observed throughout surface of the samples, Figure 6 (a)-(c). Closer examination of these particles revealed that the particles were basically NaCl (22.41% Na, 37.45% Cl) compound in the shape of faceted crystals, Figure 6d, and neither Ca and P elements (Figure 7(a), Table 2) nor Ca-P based apatite formation was detected on as received Ti6Al7Nb surfaces.

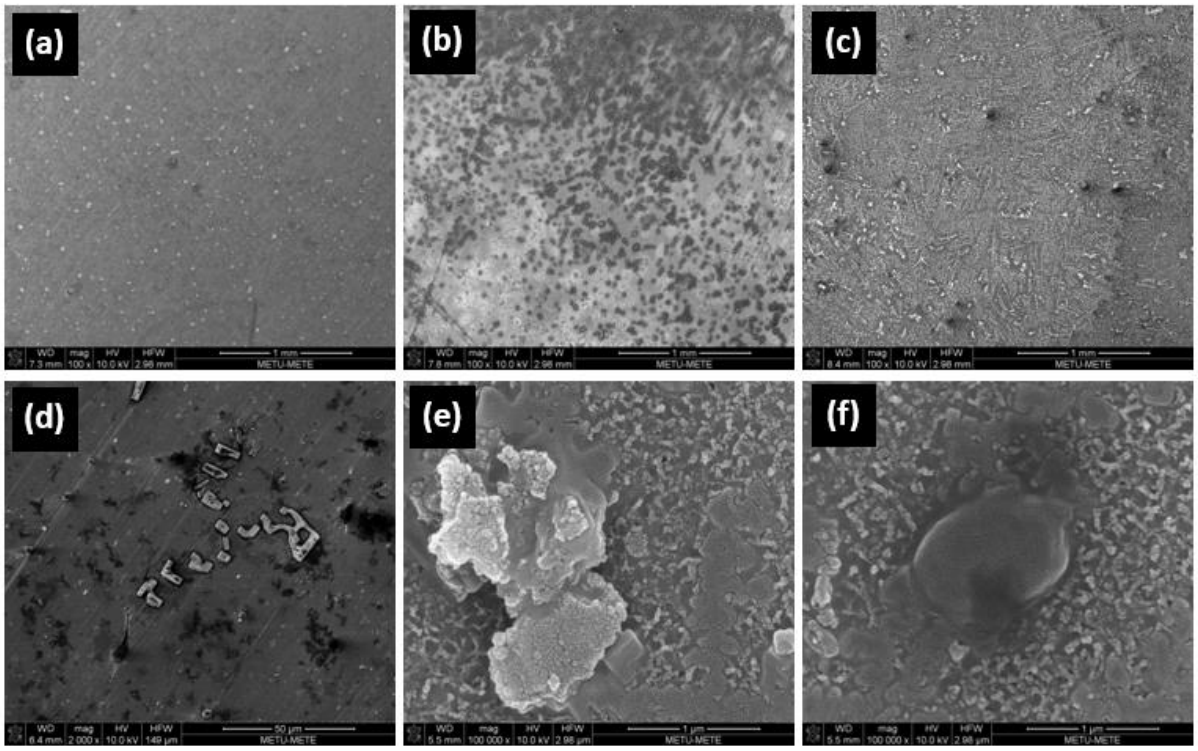

Figure 6: SEM images of bulk Ti6Al7Nb alloy surfaces immersed in SBF for 5 days, (a) as received, (b) 5M NaOH treated at 60°C,(c)5M NaOH treated at 60°C and heat treated at 600°C. (d), (e), (f): enlarged images of (a), (b) and (c), respectively.

After immersion the surface treated samples in SBF for 5 days, the interconnected porous surface structures seen in Figures 2 (b)-(d) have been observed to be covered with dark phases with some white hemi-spherical particles, Figures 6 (e) and (f). The main components of the layer formed in as-alkali treated, and alkali and heat treated samples were Ca, P , O and Cl elements and some Na probably coming from Na-rich coating layer and NaCl present in SBF, Table 2. The hemi-spherical particles formed in addition to thin coating layer was in the form of white globular form in alkali treated samples, Figure 6(e), which had similar morphology to apatite formed in different surfaces upon keeping in SBF. On the other hand, the shape of the particles formed on the surfaces of alkali and heat treatment samples were completely different and rather smooth surface was detected, Figure 6(f).

EDS analysis have shown that there was a clear difference in relative amounts of oxygen and calcium elements between the particles formed on alkali treated, and alkali and heat treated

samples. The main component of the both particles were Ca, P and O elements and their relative amounts (5.31% Ca, 6.98% P, and 23.69% O) were higher in alkali treated samples compared to that of alkali and heat treated samples'. Thus, the globular particles formed on the surfaces is thought to be an apatite layer, however, detailed XRD studies have to be conducted for identification of phases. Simply, it can be concluded from these results that alkali treated surfaces are more prone to form a compound rich in Ca, P and O elements similar to apatite.

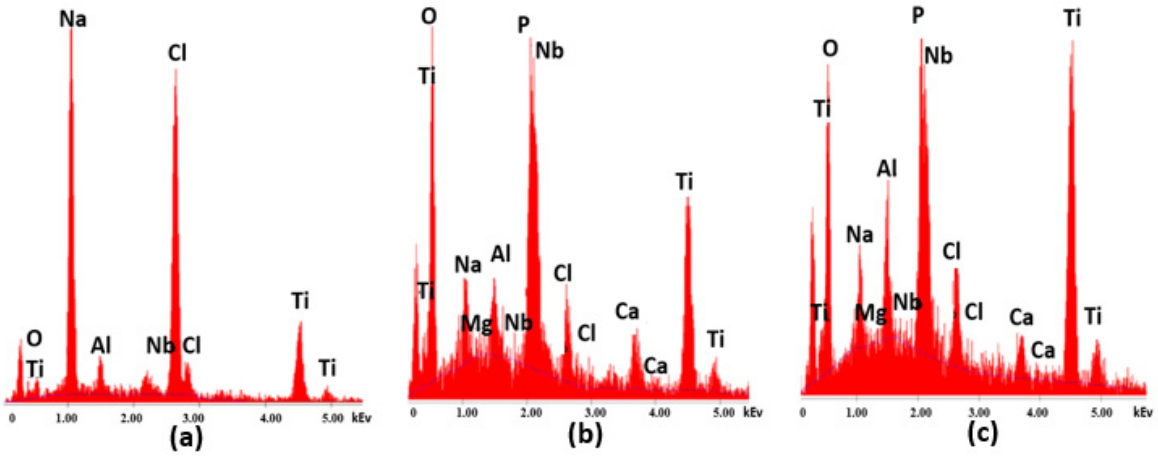

Figure 7: EDS result of bulk Ti6Al7Nb alloy surfaces; as received (a), 5M NaOH treated at 60°C (b) and then heat treated at 600°C (c) after immersion in SBF solution for 5 days

Table 2. EDS results showing chemical composition of the samples immersed in SBF.

SPECIMEN	WT.%								
	Ti	Al	Nb	O	P	Ca	Na	Cl	Mg
As received	31.09	2.43	3.93	2.69	-	-	22.41	37.45	-
NaOH-treated	35.84	2.21	18.63	23.69	6.98	5.31	2.79	4.39	0.17
NaOH-heat treated	47.16	2.99	15.08	18.13	5.94	3.13	2.21	5.19	0.18

4. CONCLUSION

The surfaces of Ti6Al7Nb alloys were successfully modified by alkali and heat treatment surface processing. Homogenous porous network structure formed on alkali treated samples was observed to coarsen after subsequent heat treatment and sodium titanate hydrogel layer transformed into more stable crystalline titanate phase ($Na_2Ti_6O_{13}$). After immersion of untreated and treated surfaces in SBF solutions for 5 days, results showed that alkali treated surfaces have higher potential to form Ca and P rich compound layers than untreated, and alkali and heat treated Ti6Al7Nb surfaces so that the attachment of apatite layer consisting of Ca, P and O elements is easier. In addition to this, it is clearly seen that 5 days immersion period is not sufficient for complete apatite formation on the entire surfaces of as-received and surface treated Ti6Al7Nb alloys.

Acknowledgement

This work was supported by The Scientific and Technological Research Council of Turkey, TUBITAK, Project # 112M341.

REFERENCES

1. X. Liu, P. Chu, C. Ding, "Surface modification of titanium, titanium alloys, and related materials for biomedical applications". Materials Science and Engineering: R: Reports, 47(3-4), pp.49–121, 2004
2. S. Tamilselvi, et al. "In vitro and in vivo studies of alkali- and heat-treated Ti-6Al-7Nb and Ti-5Al 2Nb-1Ta alloys for orthopedic implants". Journal of biomedical materials research, Part A, 90(2), pp.380–6, 2009.
3. S. Nishiguchi, H. Kato, M. Neo, M. Oka, H.M. Kim, T. Kokubo, T. Nakamura, "Alkali- and heat-treated porous titanium for orthopedic implants". J. Biomed. Mater. Res., vol. 54, no. 2, pp. 198–208, 2001..
4. H.M. Kim, F. Miyaji, T. Kokubo, T. Nakamura. "Effect of heat treatment on apatite-forming ability of Ti metal induced by alkali treatment". Journal of Materials Science: Materials in Medicine, 8(6): 341−347, 1997.
5. A. Nouri, P.D. Hodgson, C. Wen. "Biomimetic Porous Titanium Scaffolds for Orthopedic and Dental Applications". Biomimetics Learning from Nature, Amitava Mukherjee (Ed.), InTech 2010.
6. C.E. Wen, Y. Yamada, A. Nouri, P.D. Hodgson. "Porous titanium with porosity gradients for biomedical applications". Materials Science Forum, Vol. 539-543, 720-725, 2007.
7. I.C. De Lavos-Valereto, M.C. Deboni, N. Azambuja. "Evaluation ofthe titanium Ti-6Al-7Nb alloy with and without plasma-sprayedhydroxyapatite coating on growth and viability of culturedosteoblast-like cells". J Periodontol; 73(8):900–5, 2002
8. D. Martini, M. Fini, M. Franchi, V. DePasquale, B. Bacchelli, M. Gamberini, et al. "Detachment of titanium and fluorohydroxyapatiteparticles in unloaded endosseous implants". Biomaterials, 24:1309–16. 200.,
9. M. Geetha, A.K. Singh, R. Asokamani, A.K. Gogia. "Ti based biomaterials, the ultimate choice for orthopaedic implants – A review," Prog. Mater. Sci., vol. 54, no. 3, pp. 397–425, 2009
10. A. Rakngarm, Y. Miyashita, Y. Mutoh. "Formation of hydroxyapatite layer on bioactive Ti and Ti-6Al-4V by simple chemical technique". J. Mater. Sci. Mater. Med., vol. 19, no. 5, pp. 1953–61, 2008
11. L. Jonášová, F.A. Müller, A. Helebrant, J. Strnad, J. Greil." Biomimetic apatite formation on chemically treated titanium". Biomaterials. 2004, vol. 25, no. 7, pp. 1187-1194, 2004
12. T. Kokubo, H. Takadama. "How useful is SBF in predicting in vivo bone bioactivity?" Biomaterials, 27(15), 2907–15, 2006.
13. C. Sittig, M. Textor, N. D. Spencer, M. Wieland, and P. H. Vallotton. "Surface characterization of implant materials c.p. Ti, Ti-6Al-7Nb and Ti-6Al-4V with different pretreatments." J. Mater. Sci. Mater. Med., 10(1), 35–46, 1999.

EFFECT OF GRINDING ON THE PROPERTIES OF ALUMINA-BOVINE HYDROXYAPATITE COMPOSITE POWDERS

Azade YELTEN, Suat YILMAZ

Istanbul University, Department of Metallurgical and Materials Engineering, Istanbul, Turkey
azade.yelten@istanbul.edu.tr, syilmaz@istanbul.edu.tr

ABSTRACT
Alumina becomes the focus of attention with its good mechanical strength and hydroxyapatite with its superior bioactivity. The idea of combining these bioceramic materials is thought to be a promising way to achieve a biocomposite material with great properties. Sol-gel technique is well-known for enabling the production of high-technology materials such as alumina and in this study aluminum iso-propoxide (AIP, $Al(OC_3H_7)_3$) was the starting material of the sol-gel process to obtain alumina powders. Boehmite (AlOOH) sol was prepared by hydrolyzing AIP. Peptization and condensation continued during the hydrolysis step. Different amounts of (wt.%) bovine hydroxyapatite (BHA) powders were added to the boehmite sol. Following the mixing process of the boehmite sol and BHA powders, boehmite-BHA mixtures were gelated at 110 °C for 3 hours and heat treatments were applied to the boehmite-BHA gels at 1300 °C for 2 hours. At the end of the experimental study, irregular shaped alumina-HA-tricalcium phosphate composite powders were obtained. Apparent density values of the composite powders before and after grinding were determined by using an Arnold meter. These experimental results were discussed by considering the parameters such as the amount (wt.%) of BHA addition to the boehmite sol and particle shape.

Keywords: sol-gel technique, alumina, hydroxyapatite, grinding, Arnold meter

ÖĞÜTMENİN ALÜMİNA-BOVINE HİDROKSİAPATİT KOMPOZİT TOZLARININ ÖZELLİKLERİ ÜZERİNE ETKİSİ

ÖZET
Alümina, iyi mekanik mukavemeti; hidroksiapatit ise üstün biyoaktivite özelliğinden ötürü dikkat çekmektedir. Söz konusu bu biyoseramik malzemeleri bir araya getirme fikri, yüksek özellikler gösteren bir biyokompozit malzemesinin elde edilmesi için umut verici bir yol olarak düşünülmektedir. Sol-jel tekniği ile alümina gibi ileri teknoloji malzemelerini üretmek mümkündür ve bu çalışmada, alümina tozlarının sol-jel metodu ile elde edilebilmesi için alüminyum izopropoksit (AIP, $Al(OC_3H_7)_3$) başlangıç malzemesi kullanılmıştır. Böhmit solü, AIP hidroliz edilerek hazırlanmıştır. Peptizasyon ve kondenzasyon, hidroliz adımı boyunca devam etmiştir. Üretilen böhmit solüne farklı miktarlarda (%ağ.) bovine hidroksiapatit (BHA) tozları ilave edilmiştir. Böhmit-BHA karışımları, 110 °C'de 3 saat jelleştirilmiştir. Daha sonra böhmit-BHA jellerine 1300 °C'de 2 saat ısıl işlem uygulanmıştır. Deneysel sürecin sonucunda; düzensiz şekilli alümina-HA-trikalsiyum fosfat kompozit tozları elde edilmiştir. Kompozit tozlarının öğütme işlemi öncesi ve sonrasına ait görünür yoğunluk değerleri Arnold metre kullanılarak belirlenmiştir. Tüm bu deneysel veriler, böhmit solüne ilave edilen BHA (%ağ.) miktarı ve partikül şekli gibi parametreler göz önünde bulundurularak tartışılmıştır.

***Anahtar kelimeler*:** sol-jel tekniği, alümina, hidroksiapatit, öğütme, Arnold metre

1. INTRODUCTION

Bioceramics is an important class of biomaterials and can be labeled as bioinert, bioactive, and bioresorbable according to the implant-host tissue reactions. Alumina (Al_2O_3) and hydroxyapatite (HA, $Ca_{10}(PO_4)_6(OH)_2$) are very promising bioceramic materials in clinical trials that stand out in many applications, e.g., dental and orthopedic applications. Hydroxyapatite (HA) which is the main constituent of the bone structure is a bioactive ceramic material. HA can be defined as mechanically weak due to its' low load-bearing capacity but excellent in terms of bioactivity because of forming biochemical bonds with the living tissues. Conversely, alumina is well-known for its high compression strength, hardness, wear resistance and chemical stability, i.e. corrosion resistance, and bioinert character [1, 2]. In this research, it is aimed to obtain biocomposite powders composed of alumina and HA bioceramic components. For the production of alumina powders, sol-gel method which is an effective way for the synthesis of inorganic and/or organic/inorganic composite solid materials was chosen. Some of the advantages of the sol-gel process can be expressed as obtaining high-purity powders to be used for high technology applications, enabling a homogeneous mixture at molecular level, working at relatively low temperatures, being environmentally friendly and economical [3-5]. Derivation of the HA powders used in this research was realized from natural sources, i.e. bovine bones, by Oktar et al [6]. Preparation procedures of both of the powders are presented in the "Materials and Method" part in detail.

Physical properties of the powders such as particle size distribution, mean particle size, specific surface area, etc. are essential in terms of identifying the apparent density, flow and compacting characteristics of the powders. Particle morphology directly affects the apparent density of the powders, i.e. the density of the powders in a loose mode, owing to the friction issue. As the particle shape yields to spherical, the apparent density of the powders tends to increase. The reason for this situation is the decrease of the potential surface area for friction. Interparticle friction is the main factor for the resistance to the flow and compacting of the powders. By this way flow of the powders is enhanced and therefore higher apparent density values are obtained. When irregular and spherical shaped powders of the same material are compared, higher apparent densities will be acquired from the latter. Irregularity of the powders can be remarked as a sign of a porous structure hence a decrease in the apparent density. Particle size is also related to the apparent density of the powder while particle size distribution has a great influence on the flow behavior of the powders. Generally, as the particle size of the powder decreases, surface area per unit mass of the powder increases and this situation leads to an increase in the interparticle friction and less effective flow and compacting properties as well [7-10].

2. MATERIALS AND METHOD

Pure α-alumina (α-Al_2O_3) powders were obtained by the sol-gel method. Boehmite (AlOOH) sol was derived by using aluminium isopropoxide (AIP, $Al(OC_3H_7)_3$), Aldrich ~98%) as the starting material. According to the Yoldas principle [11] distilled water/AIP molar ratio was determined as 100, i.e. 40 moles of distilled water/0.4 moles of AIP. Sol-gel technique has 4 main stages and hydrolysis is the first one where 0.4 moles of AIP was reacted with water which was heated up to 90 °C with a heater equipped magnetic stirrer. Peptization, the second stage of the sol-gel process, was carried out during the hydrolysis reactions by adding 30 ml of HCl (Merck, 37% diluted up to 10%) periodically to the solution. pH (usually ~ 2.5) and temperature values of the solution were continuously kept under control while hydrolysis and peptization reactions were occurring. HCl played a role of acid catalyst in the system since it

accelerated the hydrolysis reactions and enabled the homogeneous dispersion of the particles throughout the solution. Following the last 10 ml of HCl addition and 1 more hour stirring, boehmite (AlOOH) sol was obtained which can be also realized from the gel-like appearance of the solution [3, 12-14].

In order to prepare alumina-HA composite powders, bovine hydroxyapatite (BHA) powders were added in proportions of 10, 20, 30 and 50% weight of AIP to each boehmite solution and mixed for 1 hour with a mechanical stirrer. BHA powders were derived from natural sources, i.e. bovine bones, by applying the procedure composed of deproteinization of the bovine bones in NaOH, washing the deproteinized bovine bones, calcination of the washed bones and grinding the calcined bones, respectively. Also, sodium alginate (Na-alg, $NaC_6H_7O_6$, Aldrich) was added as 1, 2, 3 and 5% weight of its own molecular weight to the boehmite-BHA mixture to overcome the precipitation tendency of the BHA powders and help for the homogeneous dispersion of the BHA particles in the boehmite sol. The third stage of the sol-gel process defined as gelation and it was done by keeping the boehmite-BHA mixtures at 110 °C for 3 hours. Gelation was a pre-heat treatment step, i.e. drying, to make the boehmite phase lose the residual water and alcohol groups in its structure and form a more rigid mixture. Finally, heat treatments of the boehmite-BHA gels were applied at 1300 °C for 2 h with 10 °C/min heating speed by using a high temperature laboratory furnace, Nabertherm LHT 08/17. The powders obtained after the heat treatments were irregularly shaped [12-14]. Aim of this study was to investigate the effect of grinding on the properties of the produced composite powders. Therefore an amount of the composite powders were manually ground for five minutes with a mortar and pestle. Different properties such as particle size distribution, particle morphology, apparent density, etc. of the powders before and after grinding were investigated and compared.

Various characterization studies were performed to analyze these two groups of powder products. Particle size distribution analyses of the powders were done by using a Brookhaven Instruments Corporation branded 90 Plus model particle size analyzer. Apparent densities of the powders were determined by using an Arnold meter (Figure 1). The principle of this technique consists of filling the cylindrical center hole on the test block with the sample powders by slowly sliding the bushing towards the hole, removing the excess powder and the steel block then weighing the powders that collected from the cavity. Apparent densities were calculated by dividing the weight of measured powders that filled the hole by making free fall motion to the volume of the filled center hole on the steel test block [10, 15].

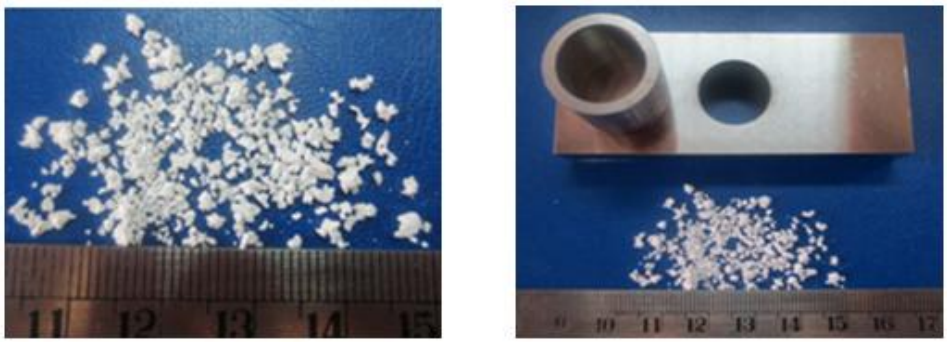

Figure 1. Photographs of the irregularly shaped powders produced and the Arnold meter.

X-Ray Diffraction (XRD) analyses were applied through monochromatic Cu-Kα radiation (λ = 0.154 nm) at Rigaku D/Max-2200/PC branded device to find out the phases that the

powders comprise. Microstructure observations of the composite powders were done by using a Jeol branded JSM 6335F (field emission) model Scanning Electron Microscope (SEM) and Inca and Oxford Instruments (AZtec) branded Energy Dispersive Spectroscopy (EDS) semi-quantitative elemental analysis systems. Results of all these characterization tests are displayed in the "Results and Discussion" part and hereafter powder samples will be defined with codes as 1300AH10, 1300AH20, 1300AH30 and 1300AH50 where 1300 (500, 800 and 1000 can be seen in the XRD graph) stands for the heat treatment temperature; 10, 20, 30 and 50 represent the amount (%) of BHA added to the boehmite sol and A stands for the alumina phase while H indicates the BHA phase.

3. RESULTS AND DISCUSSION

Stereo microscope images (Figure 2a, b) show that the powders produced have an irregular, rough morphology which is a sign of a porous structure. But these powders also have a tendency to separate into smaller particles. This was clearly observed during the grinding process. From the XRD results (Figure 3), it can be seen that three main phases exist in the obtained composite powders. These phases are α-alumina, HA and tricalcium phosphate (TCP) which are all biocompatible ceramic materials. TCP is a bioresorbable ceramic and can be used for biomedical studies in terms of prosthesis and implant applications [16-18]. The particle size of the powders decreased after grinding and this can be easily recognized from the stereo microscope images of the powders. Particle size distribution analyses (Figure 4) demonstrated the decrease in the particle size of the powders after grinding. Median diameter of the powders before grinding was measured as ~ 0,181 μm while it was determined as ~ 0,169 μm after grinding. The decrease in the median diameter was found to be slightly low.

When the SEM images (Figure 5a, b, c) of the powders before grinding were examined, it was observed that the morphology of the powders can be described as flake-like and needle-like. Thickness of these flake-like powders is very low and the particles extend horizontally. SEM images (Figure 5d, e, f) of the powders which were ground for 5 minutes exhibited that the particles have smaller sizes however this difference is not obvious enough to realize. It is thought that longer grinding times or using a more efficient grinding system such as planetary ball milling would have a more prominent effect on decreasing the particle size of the powders. In order to understand the agglomeration characteristics of the composite powders testing different grinding times may be helpful.

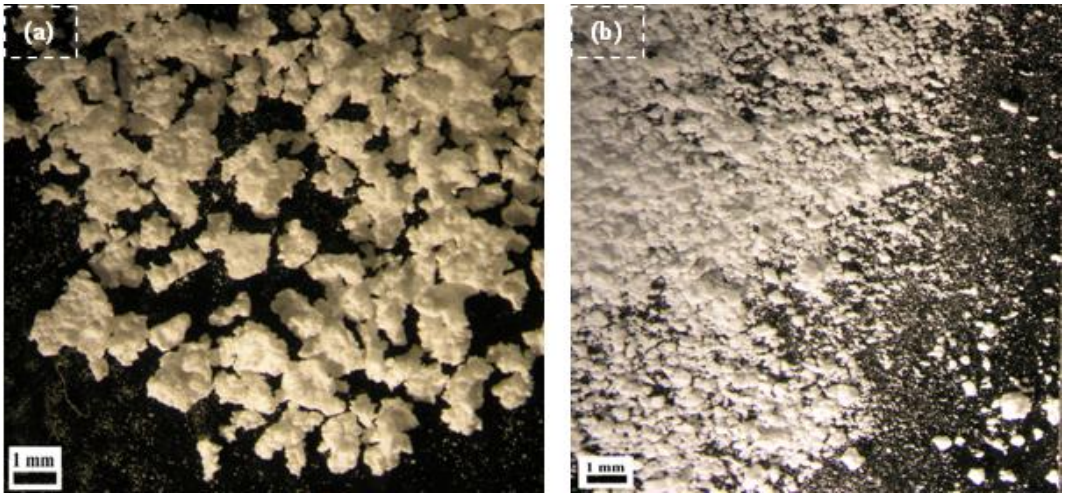

Figure 2. Stereo microscope images of the produced powders **a)** before and **b)** after grinding.

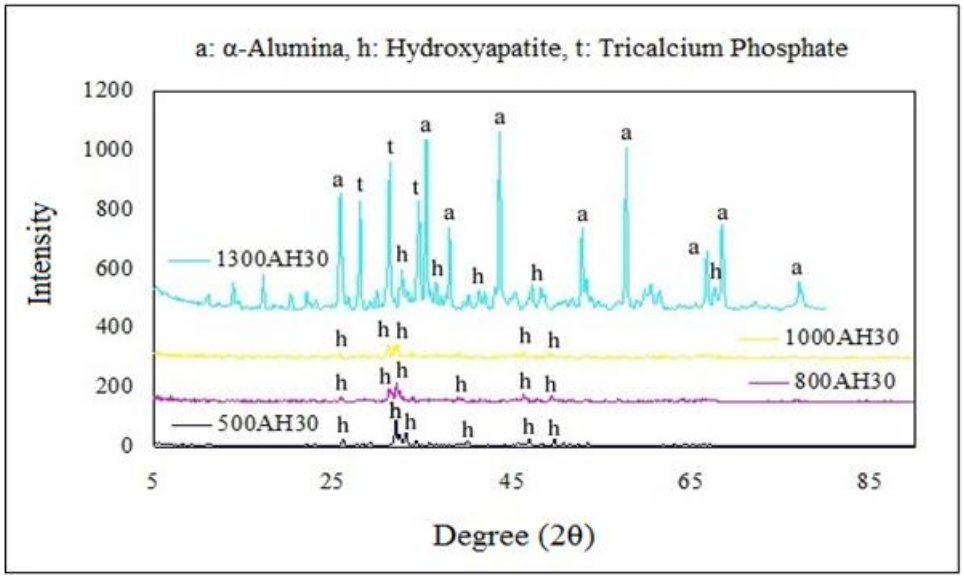

Figure 3. XRD graph of the 1300AH30 powder sample.
(a: PDF 74-1081, h: PDF 76-0694 and 89-6438, t: PDF 09-0169 and 70-2065)

Apparent densities of the powders before and after grinding are presented with a graph in Figure 6. Theoretical density is 3,156 g/cm^3 for the HA phase and ≥3,90 g/cm^3 for the α-alumina phase [1]. Therefore as the amount of HA added to the boehmite sol increased, the apparent density of the composite powders decreased which is an expected result. Generally, as the particle size decreases, the apparent density of the powders also decreases. Since the friction enhances due to greater surface area of the smaller particles, it becomes more difficult for the powders to fill the center hole of the Arnold meter and this situation results with a lower apparent density. However, it is seen from the graph that the apparent densities of the powders after grinding are higher than the apparent densities of the irregular powders. The reason for the increase in the apparent density of the powders after grinding may be interpreted as the little changes occurred in the particles 'morphology such as deformation of the edges and sharp corners of the structure and reduction of the height to diameter ratio of the needle-like particles. Thereby friction somewhat reduced and induced the increase of apparent density. So that effect of grinding appeared as an influence on the morphology of the powders. However, grinding the pure BHA powders resulted in lower apparent density values which can be observed during grinding due to the agglomeration behavior of BHA particles and adhering tendency of them to the mortar-pestle.

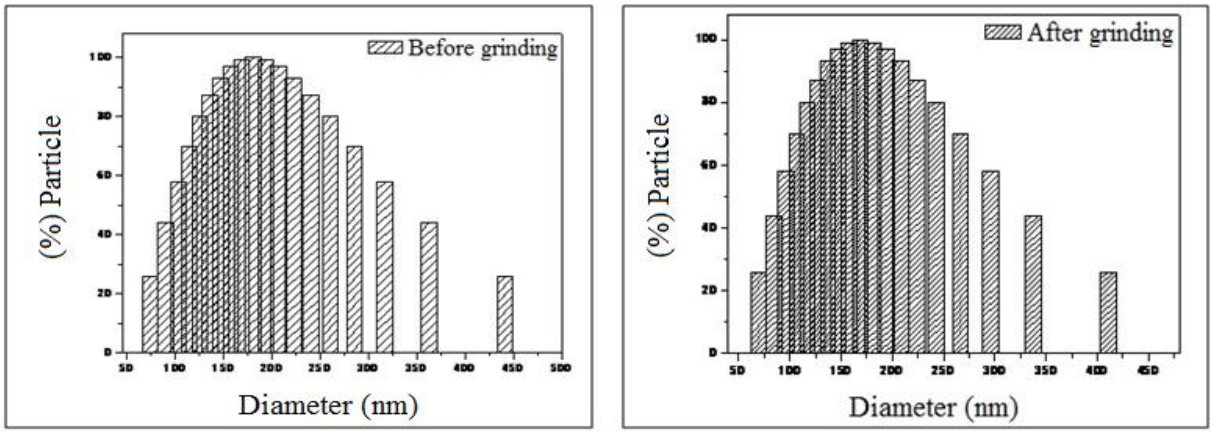

Figure 4. Particle size distribution of the 1300AH30 powders before and after grinding.

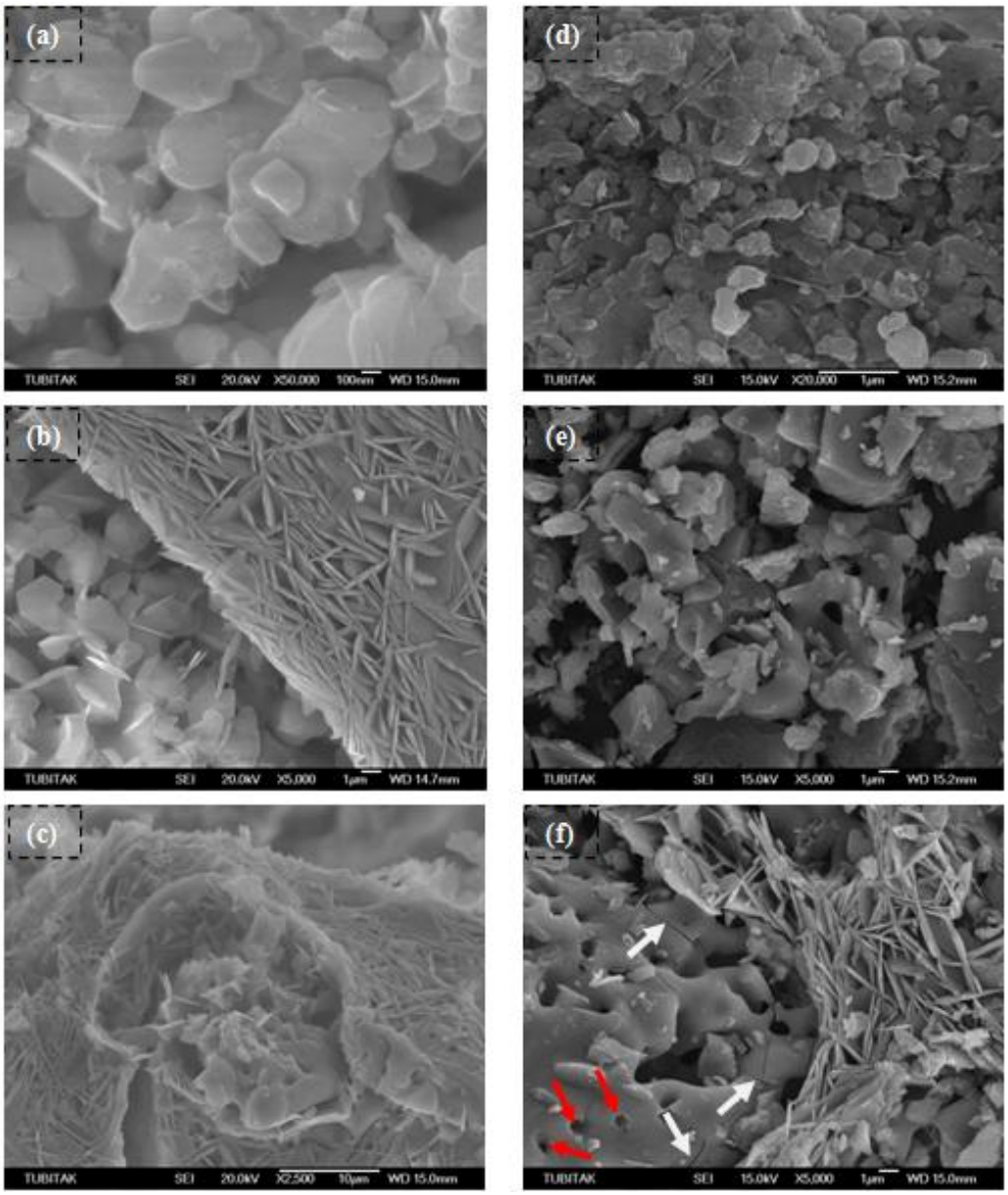

Figure 5. SEM images of **a)** BHA, **b)** 1300AH10 and **c)** 1300AH50 powders before grinding; **d)** BHA, **e)** 1300AH10 and **f)** 1300AH50 powders after grinding.

SEM images (Figure 5d, e, f) indicated that powders were deformed by the mechanical effect of grinding but this case did not result with the decrease of apparent density and increase of friction. Contrarily there was an increase in the apparent densities of the composite powders after grinding where the morphology of the alumina phase plays an important role for this fact. Alumina powders produced by using the sol-gel technique have a needle-like morphology and cannot meet the expected mechanical strength. Hence deformation of the alumina particles occurred even after grinding with a mortar and pestle. Moreover, needle-like particle morphology cannot support the sintering phenomenon due to insufficient contact surface area for sintering and this situation leads to lower mechanical properties. Therefore applying grinding to the composite powders may enable the better sintering of the powders by providing smaller particles and hence more potential contact surface area. According to the SEM images, α-alumina and BHA phases are not fused into each other well and look like two separate phases which could not form neck bonds through the sintering process. EDS analyses also chemically demonstrated that α-alumina and BHA particles were not fully mixed with

each other, and Ca-P rich and Al-O rich regions were determined distinctly. BHA particles also showed deformation where cracks pointed with white arrows can be noticed clearly from Figure 5f. Since HA is a brittle bioceramic material [1], these cracks formed in the particle structures were found to be a normal outcome. In addition to the intergranular cracks occurred, also small pores which were displayed with red arrows can be seen in the BHA structure. These pores were attributed to the decomposition of the BHA phase because of the heat treatment process at 1300 °C which caused the formation of the bioresorbable TCP phase. Although tetracalcium phosphate ($Ca_4(PO_4)_2O$, TTCP) phase was not detected from the XRD analysis, TCP phase presented in the composite powders. It is interpreted that decomposition process was not entirely completed and the pores were created depending on the removal procedure of the (OH) groups from the BHA structure. The small pores on the BHA powders and insufficient integration of the calcium phosphate-based phases and the alumina phase after sintering can be described as the reasons for the porous structure of the composite powders and thus slightly low mechanical properties which did not meet the expectations. In this regard, mechanical deformation in terms of cracks took place even after manually grinding. However, obtaining smaller particles may be effective for ~~a~~ better sintering between the α-alumina and BHA phases by enabling more potential contact surface area, a higher density, lower porosity and greater mechanical properties.

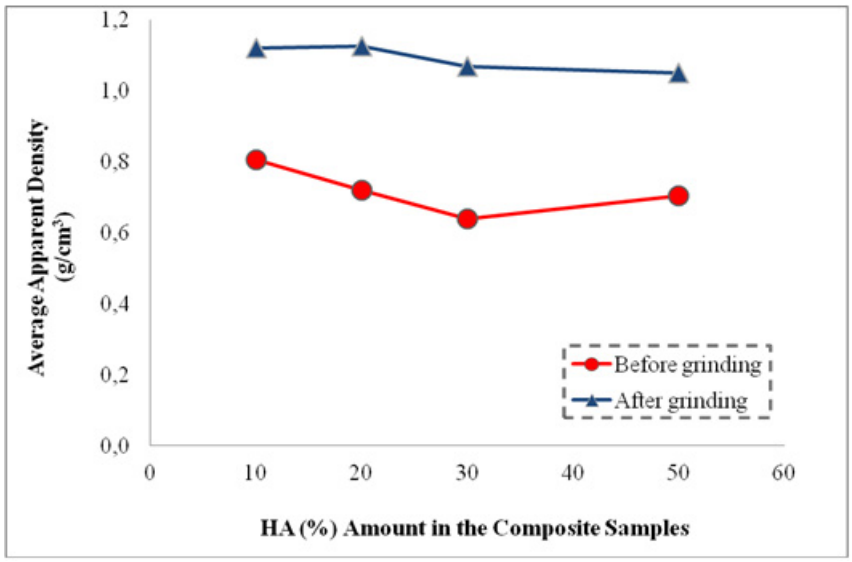

Figure 6. Average apparent density values of the composite powders before and after grinding.

4. CONCLUSION

Some important points of this study were summarized below:

- ✓ Composite powders composed of sol-gel derived α-alumina and BHA of natural sources were produced. TCP phase was also detected in the composite powders depending on the decomposition of the BHA phase.
- ✓ The composite powders obtained have an irregular, rough morphology which is a sign of a porous structure. But these powders also have a tendency to break into smaller particles and thus the particle size of the powders decreased after manually grinding with a mortar and pestle.
- ✓ The apparent densities of the powders after grinding are higher than the apparent densities of the irregular powders. It is considered that the reasons for the increase in

the apparent density of the powders after grinding may be interpreted as the little changes occurred in the particles' morphology.

- ✓ α-alumina powders produced by using the sol-gel technique have a needle-like morphology and cannot meet the expected mechanical strength. So that deformation of the alumina particles occurred even after grinding with a mortar and pestle.
- ✓ HA particles also showed deformation such as cracks and small pores on its structure due to the brittle character of itself and decomposition of the phase during the heat treatment process at 1300 °C.
- ✓ Studies are planned to continue by applying longer grinding times and/or using a more efficient grinding system such as planetary ball milling in order to have a more prominent effect on decreasing the particle size of the powders. Hence more potential contact surface area, a higher density, lower porosity and greater mechanical properties may be enabled by obtaining a more efficient sintering integration between the α-alumina and BHA phases.

Acknowledgment

This work was financially supported by the Research Fund of Istanbul University with Project No: 4201. The authors would like to thank Prof. Dr. Şerafettin Eroğlu for useful discussions.

REFERENCES

1. B.D.Ratner, A.S.Hoffman, F.J.Schoen and J.E.Lemons, "Biomaterials Science An Introduction to Materials in Medicine (2. Edition)", Elsevier Academic Press, San Diego, London, 2004
2. S.Ramakrishna, Z.M.Huang, G.V.Kumar, A.W.Batchelor and J.Mayer, "An Introduction to Biocomposites Series on Biomaterials and Bioengineering Vol.1", Imperial College Press, London, 2004
3. J.D.Wright and N.A.J.M.Sommerdijk, "Sol-Gel Materials Chemistry and Applications", CRC Press Taylor&Francis Group, Boca Raton-Florida, 2001
4. J.Zarzycki, J Sol-Gel Sci Techn, 8, 17-22, 1997
5. D.R.Uhlmann and G.Teowee, J Sol-Gel Sci Techn, 13, 153-162, 1998
6. F.N.Oktar, S.Agathopoulos, L.S.Ozyegin, O.Gunduz, N.Demirkol, Y.Bozkurt and S.Salman, J Mater Sci-Mater M, 18, 2137-2143, 2007
7. A.O.Kurt, "Toz Üretim Yöntemleri ve Sinterleme", Lecture Notes, Sakarya University, http://web.sakarya.edu.tr/~aokurt/dersler/toz/dersnotu.pdf, [Visiting Date: 21 April 2014]
8. A.Dikicioglu, "Toz Metalurjisi", Lecture Notes, Istanbul Technical University, http://web.itu.edu.tr/~dikicioglu/Toz%20metalurjisi.pdf, [Visiting Date: 21 April 2014]
9. E.Al-Hassani, "Powder Metallurgy", Lecture Note 1, University of Technology, http://uotechnology.edu.iq/dep-materials/lecture%202012-2013/therd/Powder%20Technology%20lecture%201-4.pdf, [Visiting Date: 22 April 2014]
10. R.M.German, "Toz Metalurjisi ve Parçacıklı Malzeme İşlemleri", Turkish Powder Metallurgy Association Publications (No: 05), Ankara, 2007
11. B.E.Yoldas, Am Ceram Soc Bull, 54(3), 289-290, 1975
12. A.Yelten, "Properties and Characterization of Alumina-Bovine Hydroxyapatite (BHA) Composites Produced by Sol-Gel Method", M.Sc. Thesis, Istanbul University, Istanbul, 2010
13. A.Yelten, S.Yilmaz and F.N.Oktar, Ceram Int, 38(4), 2659-2665, 2012
14. A.Yelten, S.Yilmaz and F.N.Oktar, Key Eng Mat, 493-494, 551-555, 2012
15. ASTM B703-94(1999)e1 Standard Test Method for Apparent Density of Powders Using Arnold Meter
16. R.B.Heimann, CMU. Journal, 1(1), 23-46, 2002
17. P.N.De Aza, A.H.De Aza, S.De Aza, Bol. Soc. Esp. Ceram. V., 44(3), 135-145, 2005
18. S.M.Best, A.E.Porter, E.S.Thian, J.Huang, J Eur Ceram Soc, 28, 1319-1327, 2008

BIOACTIVITY OF ELECTRODEPOSITED CaP COATINGS WITH DIFFERENT PVA ADDITION

Tulay KOC*, Guler UNGAN*, Funda AK AZEM, Ahmet CAKIR****

*Dokuz Eylul University, The Graduate School of Natural and Applied Sciences, 35390, Buca-Izmir, Turkey
tulaykocdelice@gmail.com; gulerungan@hotmail.com
**Dokuz Eylul University, Department of Metallurgical and Materials Engineering, 35390, Buca-Izmir, Turkey
funda.ak@deu.edu.tr; ahmet.cakir@deu.edu.tr

ABSTRACT

Calcium phosphate (CaP) coating of metallic prostheses has received much attention due to their affirmative effect on accelerating bone fixation. In this study, electrochemical deposition of CaP coatings on titanium substrates was performed galvanostatically at different constant current densities (-2.5, -5 and - 7.5 mA/cm^{-2}) for 60 min in an aqueous solution of $Ca(NO_3)_2.4H_2O$ and $NH_4H_2PO_4$ with some additional amounts of polyvinyl alcohol (PVA) at 80°C. The objective of this study was to investigate bioactivity of the so produced CaP coatings in simulated body fluid (SBF). X-Ray Diffraction (XRD), Fourier Transform Infrared Spectroscopy (FTIR) and Scanning Electron Microscopy (SEM) were used to identify the chemical and morphological properties of coatings. Results obtained so far indicated that chemical and morphological properties of coatings have changed with immersion in simulated body fluid (SBF). It was also shown that phase structure of the coatings was converted into hydroxyapatite (HAP) which was confirmed by XRD analysis.

Keywords: Hydroxyapatite, Ti alloy, electrochemical deposition, PVA.

FARKLI PVA KATKILARI ILE ELEKTROÇÖKTÜRÜLMÜŞ CaP KAPLAMALARIN BİYOAKTİVİTE ÖZELLİKLERİ

ÖZET

Metalik protezlerin kalsiyum fosfat (CaP) ile kaplanması kemik sabitlenmesini hızlandırmaya olumlu etkisi nedeniyle oldukça dikkat çekmiştir. Bu çalışmada, CaP esaslı seramik kaplamalar elektrokimyasal çöktürme yöntemiyle titanyum altlık üzerine değişik polivinil alkol ilaveli $Ca(NO_3)_2.4H_2O$ ve $NH_4H_2PO_4$ sulu çözeltisi içinde, 80°C de 60 dakika süreyle galvanostatik yöntemle, farklı sabit akım yoğunluklarında (-2.5, -5 ve -7.5 mA/cm^{-2}) kaplanmıştır. Çalışmanın amacı üretilen CaP kaplamaların yapay vücut sıvısında (SBF) biyoaktivite özelliklerini araştırmaktır. Kaplamaların kimyasal ve morfolojik özelliklerinin araştırılmasında X-Işını Difraksiyonu (XRD), Fourier Dönüşümlü Kızılötesi Spektroskopisi

(FTIR) ve Taramalı Elektron Mikroskobu (SEM) kullanılmıştır. Elde edilen sonuçlar kaplamaların kimyasal ve morfolojik yapılarının SBF içinde bekletme ile değiştiğini, XRD analiz sonuçları da kaplamaların faz yapısının hidroksiapatit'e (HAP) dönüştüğünü göstermiştir.

Anahtar kelimeler: Hidroksiapatit, Ti alaşım, Elektrokimyasal Çöktürme, PVA

1. INTRODUCTION

Calcium phosphate (CaP) ceramic coatings are nowadays used to improve the success of titanium alloy prostheses in some orthopedic and special dental cases. Indeed, CaP coatings are recognized as biocompatible and able to accelerate bone ingrowth and attachment to the surface of implant during the early stage after implantation [1]. Hydroxyapatite [(HAP); $Ca_{10}(PO_4)_6(OH)_2$] has been widely used as an implant material, in forms of coating in particular, for many years due to its close similarity in chemical composition and high biocompatibility with natural bone tissue. A significant difference between HAP and biocompatible surgical metal alloys such as Ti6A14V lies in the ability of HAP to form a strong chemical bond with natural bone**.** Owing to the inferior mechanical properties of bulk HAP, such as brittleness, low tensile strength and difficulties in fabrication, significant research activities have been associated with the development of HAP coatings. Much effort has been made in recent years to develop processing technologies to coat HAP onto metallic substrate surfaces [2].

Additionally, it is reported that growth and dissolution of Brushite (DCPD) play an important role in the biological mineralization process as well as the setting of a variety of calcium phosphate cements for orthopedic and dental uses [3]. The reports indicated that DCPD is one of the precursors of HAP, which has similar mineral components of the human bone. Initially formed DCPD coatings can be transformed into HAP through chemical methods [4, 5]. Ducheyne and his colleagues reported that the phenomena of bioactivity, especially improvement of bone formation and bonding rates, is associated with dissolution of Ca^{+2} and PO_4^{-3} ions to implant-bone interface from the implant surface coatings [6, 7]. In this case DCPD which is one of the soluble CaP phase can enhance the HAP phase formation at implant-bone interface by increasing Ca^{+2} and PO_4^{-3} ion concentrations at the interface necessary for bone formation [8]. However, mechanical properties of HAP are poor and their inadequate property restricts usage of HAP in clinical applications. The addition of the polymeric components to HAP-based materials is one of the most preferred methods to improve mechanical properties of HAP and to–form an organic–inorganic nano-composite. Polyvinyl alcohol (PVA), a biodegradable and biocompatible polymer, has been widely used in biomedical applications. PVA has a hydroxyl pendant group on every second carbon atom on its backbone. The high concentration of hydroxyl pendant groups of PVA makes it unique as it is a physically cross-linked property without any chemical additive [9].

There are several methods including magnetron sputtering, laser ablation, sol-gel processes and diverse electrochemical methods for producing CaP based ceramic coatings on metallic implant materials. Electrodeposition methods have been used due to the advantages compared to other techniques including cost-effective deposition technology, energy economies, and the ability to cover complex shapes and a variety of materials. Additionally, the compositional and structural control of coating by easy manipulation of process parameters, such as time and current density, made this process a plausible method among others, due in part to the relatively low processing temperature [10, 11].

In present study CaP coatings were produced by electrochemical deposition technique aiming to improve the adhesive strength of deposited coatings on substrate by some additional amount of polyvinyl alcohol (PVA) into $Ca(NO_3)_2.4H_2O + NH_4H_2PO_4$ electrolyte during the deposition process. In-vitro degradation and bioactivity behavior of the coatings were investigated in simulated body fluid (SBF) for different time periods.

2. EXPERIMENTAL PROCEDURE

Galvanostatic deposition of coatings was performed in an aqueous solution consisting of 1.05 mM $Ca(NO_3)_2.4H_2O$ + 0.625 mM $NH_4H_2PO_4$, without and with PVA addition. Details for electrolyte preparation and deposition process were given in our previous study [12]. Nomenclatures of the produced samples are given in Table 1 in association with process parameters of current density and amount of the PVA addition.

Table 1. Abbreviation of the produced coatings.

PVA Addition (vol. %) \ Current density (mA/cm^2)	-2.5	-5	-7.5
No addition	S1	S2	S3
0.0125	S4	S5	S6
0.05	S7	S8	S9

In order to evaluate bioactivity of the coatings, the coated substrates were immersed in SBF solution with ion concentrations similar to that of human blood plasma. The SBF solution was prepared according to the procedure described by Kokubo and Takadama [13]. The coated samples were immersed in the SBF at 37±1 °C for 7, 14 and 28 days and the SBF solution was kept refreshed in every other day. After the predetermined time of incubation samples were taken out from the SBF and gently washed with distilled water and then dried.

After SBF immersion, the coatings were characterized in order to determine the changes in terms of their composition and morphology. The phase structure of the coatings was examined by using an X-Ray Diffractometer (XRD, Rigaku/Dmax 2200/PC model) with a Cu anode (40 kV, 36 mA). The functional groups present in the produced coatings were identified by Fourier Transform Infrared Spectroscopy (FTIR) measurements by using Perkin Elmer FTIR spectrometer in transmission mode. The measurements were performed in a range of 4000-650 cm^{-1} with the resolution of 4 cm^{-1} and a scanning speed of 0.2 cm/sec. The morphological observation and elemental analysis of the coatings were examined using a scanning electron microscope (SEM, JEOL JSM-6060) and energy dispersive spectrometer (EDS) coupled with SEM were utilized to determine the Ca/P ratio of the coatings.

3. RESULTS AND DISCUSSION

Figure 1 shows XRD patterns of the deposited coatings at constant current density without and with different PVA addition (0.0125 and 0.05 % vol.) before and after immersion in SBF for 7, 14 and 28 days. Coatings deposited at all conditions consist of major HAP ($Ca_{10}(PO_4)_6(OH)_2$) (JCPDS 09-432) and minor DCPD ($CaHPO_4.2H_2O$) (JCPDS 72-0713) phases. In general, there was no the effect of PVA addition and applied current density on phase structure of the coating with the immersion time in SBF. This result is consisted with the study of Zuo et al. which showed that the addition of PVA had no any effect on the phase composition of the structure [14].

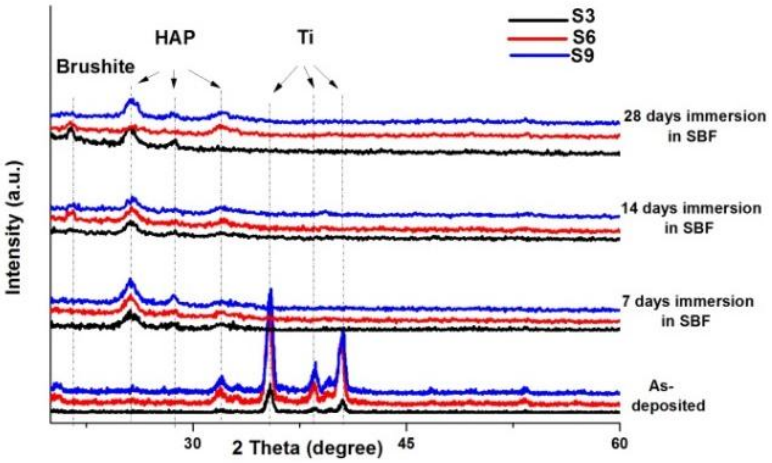

Figure 1. XRD patterns of S3, S6, and S9 coatings before and after immersion in SBF.

The XRD patterns of the coating after immersion in SBF show that DCPD was converted into HAP with immersion in SBF solution. There is no significant change of the XRD patterns of the coatings with immersion in SBF solution. Besides, broad peaks between 31° and 33°, mainly the (112), (211) and (300) reflection, showed that the apatite layer formed in SBF was of lower crystallinity [15]. For all of the coatings, the diffraction peaks associated with titanium substrate disappeared after samples were immersed in the SBF.
FTIR spectra of the samples before and after immersed in SBF solution for 7, 14 and 28 days coatings are shown in Figure 2. The chemical structures of the coatings were similar as can be seen from Figure 2. Phosphate bands overlapped and give a broad-strong peak in the wavenumber interval of 1100 cm^{-1} to 960 cm^{-1} [16, 17]. The band at 2360 cm^{-1} was the characteristic peak due to the HPO_4^{2-} in the DCPD [18]. The bands observed at 3400 cm^{-1} and

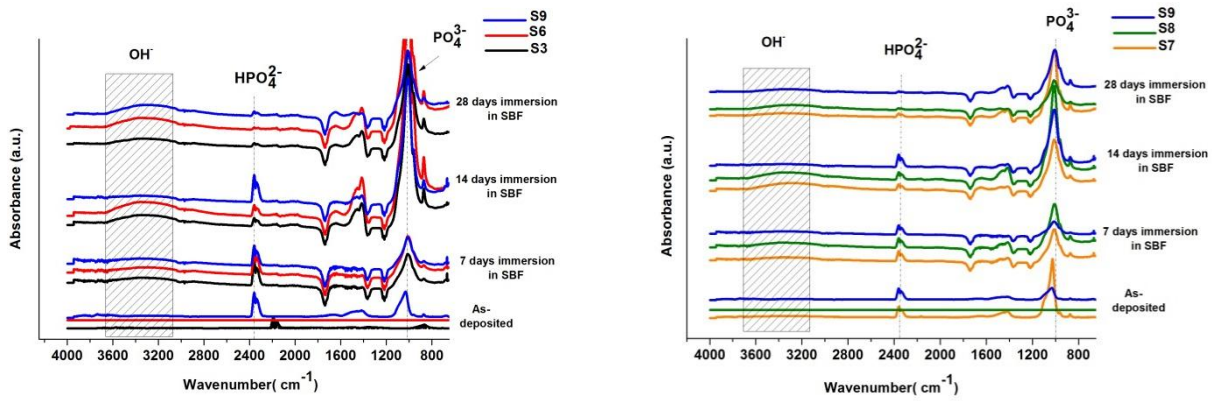

Figure 2. FTIR spectra of S3, S6, S7, S8, S9 coatings before and after immersion in SBF

1647 cm^{-1} were assigned to O-H stretching and bending of H_2O. Absorbed water was showed by the broad bands from 3700 to 3100 cm^{-1} this may be explained because of the lower crystallinity structure of the coating with increasing immersion in SBF. Bands at 1456 cm^{-1} , 1423 cm^{-1} and 876 cm^{-1} were ascribed to CO_3^{2-}groups [19, 20]. Observed vibration mode of carbonate in the FTIR is attributed to the evidence of the precipitated apatite. Also, carbonate ions are part of apatite structures and not as different phase [21]. As can be seen from the FTIR spectra of the coatings intensity of PO_4^{3-}bands gradually increases with increasing immersion time in SBF. On the other hand, prolonged immersion time have an adverse effect on intensity of HPO_4^{2-} bands. This alteration could be interpreted to the phase transformation

from DCPD into HAP structure with increasing immersion time in SBF. This result is also in agreement with the XRD findings.

Figure 3 and 5 show the SEM images of the CaP coatings electrodeposited on Ti6Al4V substrate as-deposited and after 7, 14 and 28 days of immersion in the SBF solution. It could be seen clearly from figures, the surface of the CaP coatings after 7 days of immersion in SBF solution slightly changed as compared to as-deposited CaP coating. After 7 days of immersion, samples were fully covered newly grown apatite layer. The morphology of the coating surface transformed to spherical shapes and these spheres covered the entire surface as shown in Fig. 3 and 5. After 14 days of immersion, newly formed crystals on the coatings surface had similar morphology with transformed structures reported in Park's study as can be seen in higher magnification of S3 in Figure 4 [22]. According to the XRD results, the broadening of these apatite peaks with increasing immersion time in SBF show that the apatite crystal are relatively small as can be seen in Figure 4. Although similar spherical shape obtained 7 days of immersion were observed after 28 days of immersion, the coatings were more compact and denser indicating higher degree of uniformed distribution all over the coating area as shown in Figure 4. This morphology was similar to that reported by Kokubo [13].

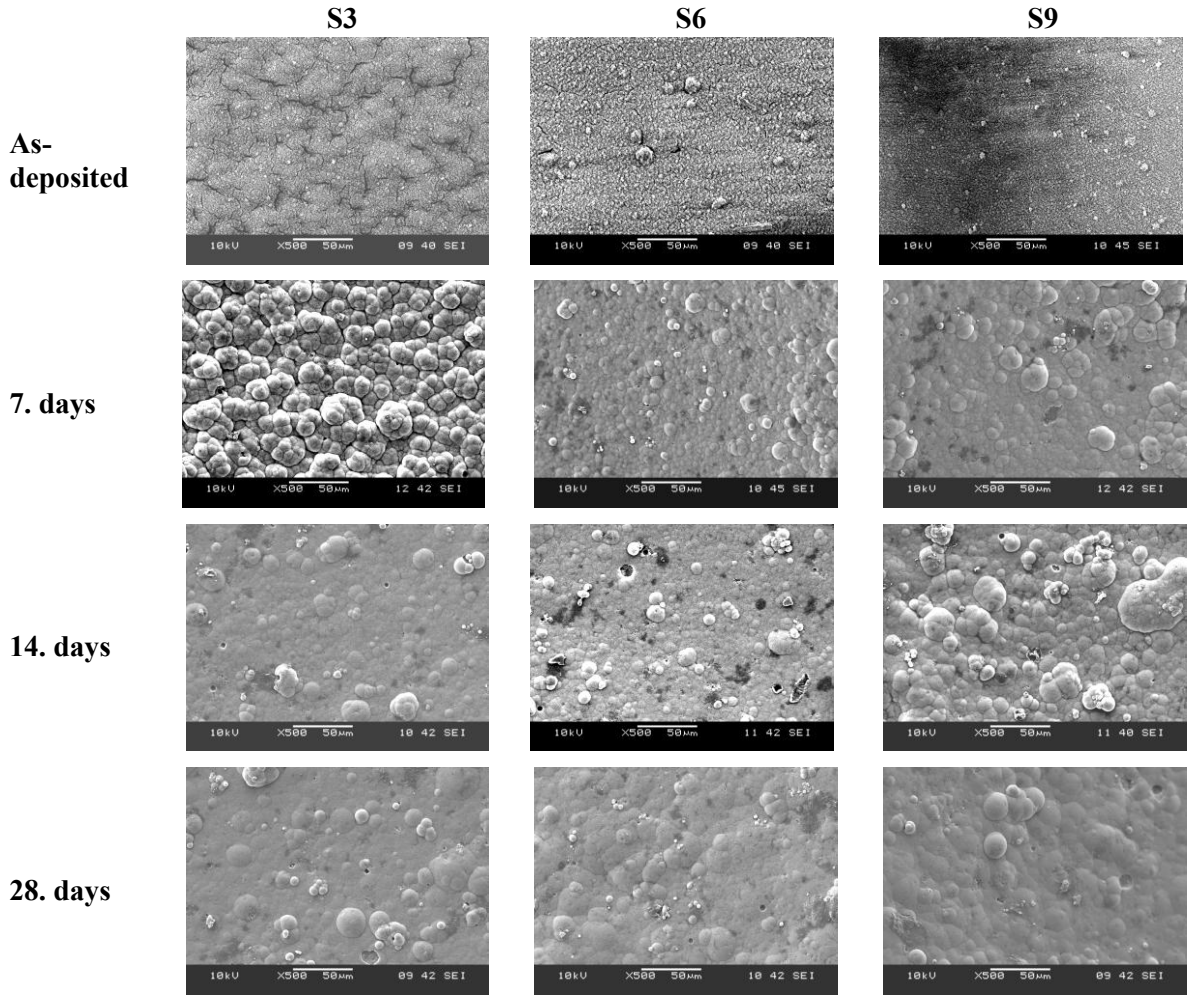

Figure 3. SEM images of coatings S3, S6, S9 as-deposited and after immersion in SBF

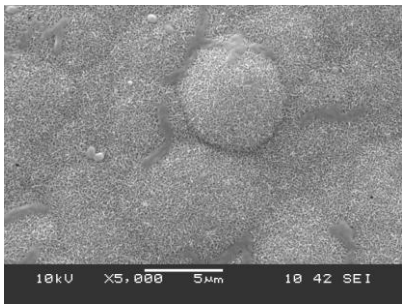

Figure 4. SEM images of coating S3 higher magnification after 14 days immersion in SBF

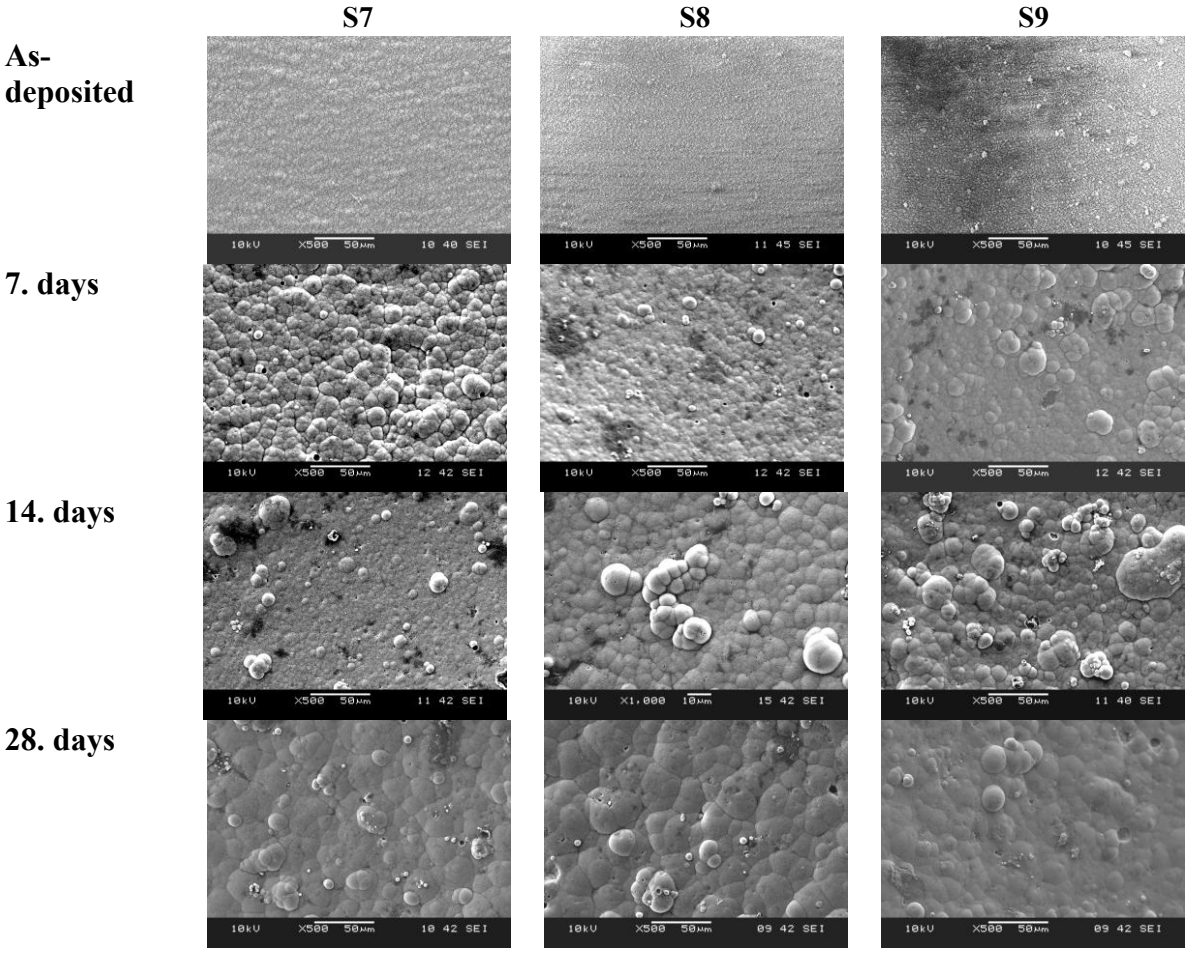

Figure 5. SEM images of coatings S7, S8, S9 as-deposited and after immersion in SBF

3. CONCLUSION

CaP coatings were successfully deposited on Ti6Al4V substrates by electrochemical deposition technique. The effect of PVA addition and applied current density was investigated on bioactivity behavior of produced coating in SBF solution. XRD patterns and FTIR spectrum confirmed that the coatings consist of brushite and HAP phases. The surface morphology of the CaP coatings has significantly changed as function of immersion time in SBF solution as observed by SEM. It can be concluded that the bioactivity of synthesized CaP coatings are improved by forming new apatite crystals when immersed in SBF solution. On the other hand, it could not be detected any considerable differences with addition of PVA in terms of morphological structure after immersion in SBF for 14 days. FTIR results showed

that newly formed layer is composed of carbonate-containing apatite which has wide applications from laboratories to clinical medicine.

REFERENCES

1. N. Dumelie´, H. Benhayoune, C. Rousse-Bertrand, S. Bouthors, A. Perchet, L. Wortham, J. Douglade, D. Laurent-Maquin, G. Balossier, Thin Solid Films, 492, 131, 2005.
2. L. Huang, K. Xu and J. Lu, J. Mater. Sci. – Mater. Med., 11, 667, 2000.
3. R.R. Kumar, M. Wang, Mater. Lett., 49, 15, 2001.
4. X. Lu, Z. Zhao, Y. Leng, J. Cryst. Growth, 284, 506, 2005.
5. T. M. Sridhar, T. K. Arumugam, S. Rajeswari, M. Subbaiyan, J. Mater. Sci. Lett., 16, 1964, 1997.
6. P. Ducheyne, J. Beight, J. Cuckler, B. Evans, S. Radin, Biomater., 11, 531, 1990.
7. P. Ducheyne, J. Cuckler, Clin. Orthop. Relat. Res., 276, 102, 1992.
8. X. Lu, Z. Zhao, Y.Leng, J. Cryst. Growth, 284, 506, 2005.
9. O. Kaygili, S. Keser, R. H. Al Orainy, T. Ates, F. Yakuphanoglu, Mater. Sci. Eng., C, 35, 239-244, 2014.
10. M. Manso, C. Jimehnez, C. Morant, P. Herrero, J.M. Martmhnez-Duart, Biomater. , 21, 1755-1761, 2000.
11. S.K. Yen and C.M. Lin, Mater. Chem. Phys., 77, 70, 2002.
12. G. Ungan, F. Ak Azem, A. Cakir, 25th Southern Biomedical Engineering Conference, Miami, USA, 156, May 2009
13. T. Kokubo, H. Takadama, Biomater., 27, 2907, 2006.
14. A. Stoch, W. Jastrzebski, A. Brozek, J. Stoch, J. Szaraniec, B. Trybalska, G. Kmita, J. Mol. Struct., 555, 375, 2000.
15 J. Weng , Q. Liu , J.G. Wolke , X. Zhang ,K. de Groot, 18, 15,1027, 1997.
16. R.A. Surmenev, M.A. Surmeneva, K. E. Evdokimov, V. F. Pichugin, T.Peitsch, M. Epple, Surf. Coat. Technol., 205, 3600, 2011.
17 N. Pleshko, A. Boskey, R. Mendelsohn, Biophys. J., 60, 786, 1991.
18. H. M. Han, G.J. Phillips, S.V. Mikhalovsky, S. FitzGerald, A.W. Lloyd, J. Mater. Sci.: Mater. Med., 19, 4, 1787, 2008.
19. J. Zhang, C. Dai, J. Wei, Z. Wen, S. Zhang, L. Lin, Appl. Surf. Sci., 280, 256, 2013.
20. H.K Varma, S.S. Babu, Ceram. Int. 31, 109, 2005.
21. Y. Shucong, P. H. Kithva, K. Rajendra,C. Philip ,K. A. Khor, Biomater. , 26, 2343, 2005.
22. J-H Park, D-Y Lee, K-T Oh, Y-K Lee, K-M Kim, K-N Kim, Mater. Lett., 60, 2573, 2006.

EFFECT OF SURFACE MODIFICATION ON ELECTROCHEMICALLY DEPOSITED CaP COATINGS ON Ti6Al4V SUBSTRATES FOR BIOACTIVE PROPERTIES

Bensu BAKIN[*], Tulay KOC DELICE[*], Utku TIRIC[*], Funda AK AZEM[**], Isil BIRLIK[**], Erdal CELIK[,***,****], Mustafa TOPARLI[**,***,****]**

[*]Dokuz Eylul University, The Graduate School of Natural and Applied Sciences, 35390, Buca, Izmir, Turkey
bensubakin@hotmail.com
[**]Dokuz Eylul University, Department of Metallurgical and Materials Engineering, 35390, Buca, Izmir, Turkey
[***]Dokuz Eylul University, Center for Fabrication and Applications of Electronic Materials (EMUM), Buca 35390, Izmir, Turkey
[****]Dokuz Eylul University, Department of Nanoscience and Nanoengineering, Buca 35390, Izmir, Turkey

ABSTRACT

CaP coatings on metallic substrates have been widely used in dental and medical applications to combine the excellent mechanical properties of metal alloys with the bioactive properties of bioceramics. However, calcium phosphates are brittle, this impairing their use for load-bearing applications. Coating bioactive ceramics onto Ti6Al4V substrate is therefore a popular method to provide metals with bone bonding ability. Several mechanical and chemical treatments have been used to modify the surface morphology and properties of titanium implants. In the present work, surface of Ti6Al4V substrates were modified by grinding, polishing and etching. Morphological characterizations of these substrates were examined by using Atomic Force Microscope (AFM). CaP coatings were deposited on these substrates by using electrochemical deposition technique. Bioactivity properties of CaP coatings investigated in simulated body fluid (SBF), chemical and morphological characterizations of the coatings were examined by using X-Ray Diffraction (XRD), Fourier Transform Infrared Spectroscopy (FTIR) and Scanning Electron Microscopy (SEM).

Keywords: electrodeposition, hydroxyapatite, surface modification, Ti6Al4V, bioactivity

Ti6Al4V ALTLIKLAR ÜZERİNE CaP KAPLAMALARIN BİYOAKTİVİTE ÖZELLİKLERİNE YÜZEY MODİFİKASYONUNUN ETKİSİ

ÖZET

Metalik altlıklar üzerine CaP kaplamalar, metal alaşımlarının mükemmel mekanik özellikleri ve biyoseramiklerin biyoaktivite özelliklerini birleştirmesi nedeniyle dental ve medikal uygulamalarda yaygın bir şekilde kullanılmaktadır. Bununla birlikte, kalsiyum fosfatların gevrek yapıda olması yük taşıyıcı uygulamalarda kullanımını engeller. Ti6Al4V altlık üzerine seramik kaplamalar, metalin kemiğe bağlanma özelliğini sağlamak için yaygın bir metottur. Titanyum implantların yüzey morfolojilerini ve özelliklerini değiştirmek için birçok mekanik ve kimyasal işlem kullanılmaktadır. Bu çalışmada, Ti6Al4V altlıkların yüzeyleri zımparalama, parlatma ve dağlama işlemleri ile modifiye edilmiştir. Altlıkların morfolojik karakterizasyonu Atomik Kuvvet Mikroskobu (AFM) ile incelenmiştir. CaP kaplamalar altlıklar üzerine elektrokimyasal çöktürme ile biriktirilmiştir. CaP kaplamaların biyoaktivite özellikleri vücut benzeri sıvı (SBF) içerisinde, kimyasal ve morfolojik karakteristikleri X-ışını Difraksiyonu (XRD), Fourier Dönüşümlü Kızılötesi Spektroskopisi (FTIR) ve Taramalı Elektron Mikroskobu (SEM) ile incelenmiştir.

Anahtar kelimeler: elektrokimyasal çöktürme, hidroksiapatit, yüzey modifikasyonu, Ti6Al4V, biyoaktivite

1. INTRODUCTION

Ti and alloys have been widely used in orthopedics and dental surgery as implant material because of their strong mechanical properties and good chemical stability and biocompatibility [1]. Surface characteristics of the implant play an important role for the evolution of bone tissue of the recipient site, after implantation [2]. The success and loading resistance of implants is determined by their physical and chemical surface properties. To support cell attachment, spread and growth, and to improve cell function, a number of reports have been published concerning roughened implant surface treatment as well as controlled microtopography. Application of surface treatment facilitates to change the surface features of the titanium implant, such as chemical composition, energy level, morphology, topography and roughness. Sandblasting and acid etching treatment can change the surface topography and energy [3]. Surface topography can be modified by plasma-sprayed coatings, by grit blasting with various types and sizes of abrasives, by acid etching and electrochemical processes with different solutions, or by a combination of some of them.

In this study to investigate effect of surface modification on bioactivity properties, different surface modification have been introduced to the surface by grinding, polishing and etching processes. Grinded, polished and etched Ti6Al4V substrates were coated CaP by using electrochemical deposition technique. Bioactivitity tests of the coatings were conducted in SBF.

2. EXPERIMENTAL

Ti6Al4V substrate was cut into discs with a diameter of 16 mm. Three different surfaces were prepared by grinding, polishing and etching of substrates in order to obtain different surface properties. Grinded surface prepared by grinding with SiC abrasive papers (80, 240, 400, 800 grit). Polished surface was prepared by polishing with 3µm diamond paste and 3 µm colloidal

silica. Etched surface prepared by etching in 30 second in etching solution (%15 HNO_3, %5 HF and %80 distilled water).

Surface profiles were measured with a surface roughness tester and roughness profiles were calculated by filtering the surface profiles with a Gaussian filter. A 0.8 mm "cut-off" value was applied for filtering. R_a (arithmetic average of peak-valley height) was calculated from the roughness profiles with appropriate software (Surfpack-SJ, Mitutoyo, Japan), according to international standards (JIS:1994). Surface morphology of grinded, etched and polished substrates was investigated by Atomic Force Microscopy (AFM, Nanosurf Easyscan 2).

The electrochemical deposition of CaP coatings on Ti6Al4V substrates was conducted in the mixed solution of calcium nitrate tetrahydrate ($Ca(NO_3)_2.4H_2O$, Merck), ammonium dihydrogen phosphate ($NH_4H_2PO_4$, Merck) and distilled water. Deposition of CaP was carried out by galvanostatic method in a three-electrode cell using Gamry Reference 600 potentiostat–galvanostat. The CaP coating was successfully deposited on Ti6Al4V substrates under -1 mA/cm^2 current density for 1 h.

Bioactivity test was performed in simulated body fluid (SBF). The SBF recipe was prepared according to the Kokubo's formulation and buffering at pH 7.4 with Trisehydroxymethyl amino methane and 1.0 M HCl at 37 $^{\circ}C$ [4]. Each sample was placed in a polypropylene beaker with 15 ml SBF and kept in 36±1 °C for 1, 7 and 14 days. To keep the ion concentration stable, the SBF solution was refreshed every 2 days. After immersion samples were taken out from the SBF and gently washed with distilled water, and then samples were dried. pH measurements of solution were carried out by using WTW-pH 3110 pH meter.

The phase analysis of the deposited films were analyzed by X-ray diffractometer (XRD, Rigaku D/max-2200/PC) with grazing incident of 1° at 40 kV and 36 mA using CuK_{α} radiation. The chemical composition of the deposited coatings was analyzed by Fourier Transform Infrared Spectroscopy (FTIR, Perkin Elmer Spectrum BX) with a spectral range of 650-4000 cm^{-1}. Surface morphology investigation and the element analysis of the films were carried out by using a Scanning Electron Microscope coupled with Energy Dispersive Spectroscopy (SEM/EDS, JEOL JSM 6060).

3. RESULTS

The results of the surface roughness parameter R_a is 0.246±0.005 for grinding sample, 0.186±0.020 for polishing sample and 0.193±0.025 for etching sample. Surface roughness measurements did not show significant differences between the roughness values of the samples.

Figure 1 shows the AFM images of the grinded, polished and etched Ti6Al4V substrates. The morphologies are consistent with the obtained surface roughness results. Polished surface is the smoothest surface in comparison to grinded and etched surfaces.

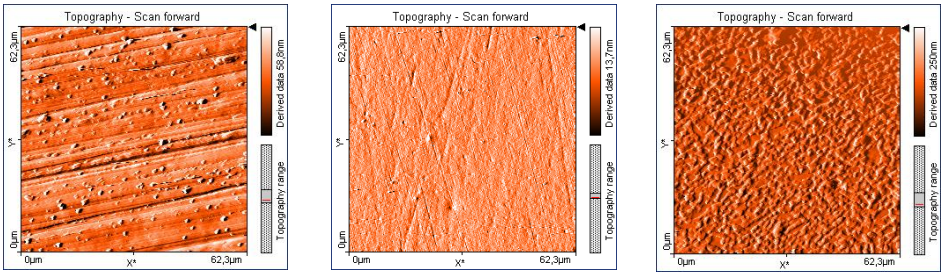

Figure 1. AFM 2D images of (a) grinded, (b) polished and (c) etched Ti6Al4V substrates.

Figure 2 shows the XRD patterns of the coatings after immersion in SBF. For as-deposited coatings the main phase was identified as brushite ($CaHPO_4.2H_2O$, dicalcium phosphate dihydrate) according to JCPDS 072-124. With immersion in SBF the main characteristic peaks transformed to hydroxyapatite according to JCPDS 009-0432. It was observed that there was no significant change in coating phase structure with varying surface roughness.

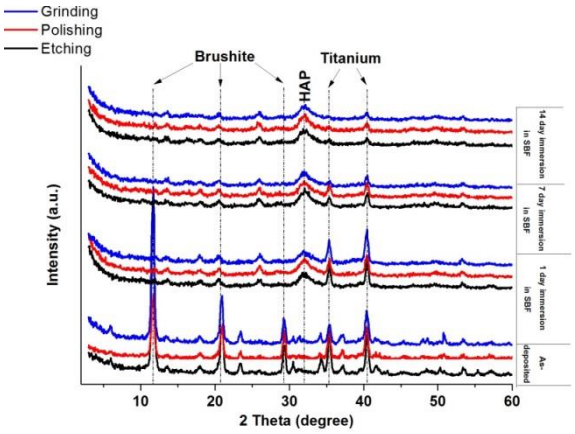

Figure 2. XRD patterns of grinded, polished and etched samples.

Figure 3 shows the FTIR spectra of the coatings with various surface modifications. According to the data in the literature, for as-deposited coatings all bands are attributed to DCPD. In literature, the four sharp distinct bands between 870 cm^{-1} and 1150 cm^{-1} are attributed to the P-O/P-O(H) stretching in DCPD [5]. The band at 2360 cm^{-1} was the characteristic peak due to the HPO_4^{2-} in the DCPD [6]**.** The characteristic bands of DCPD (786 and 1651 cm^{-1}), HPO_4^{2-}, have completely disappeared and transformed to HAP after immersed in SBF. It could be seen from Figure 3 that PO_4^{3-} absorption peaks at 1036 cm^{-1} and 963 cm^{-1} roughly combines and becomes broaden as one peak with increasing immersion time in SBF.

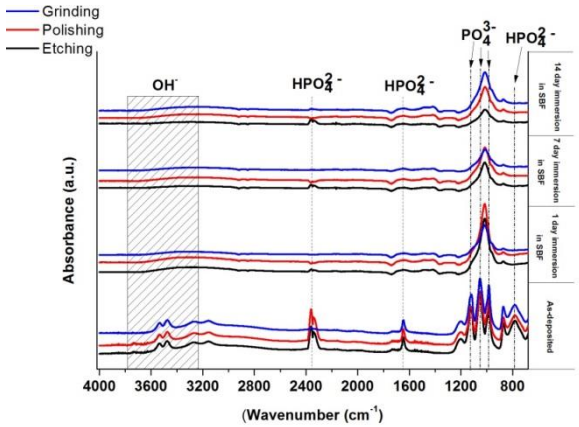

Figure 3. FTIR spectra of grinded, polished and etched samples before and after immersion in SBF.

Surface morphologies of coatings before and after immersion process is presented in Figure 4. For as-deposited samples the morphologies are consisted of plate like structure with varying dimensions. A significant change was observed with immersion in SBF. Plate like structures gradually covered with porous layer afterwards surface morphology transformed to spherical structures and these spherical structures gradually increased with increasing immersion time. Similar results were reported by M.S. Djo˘si ´c et. Al. [7].

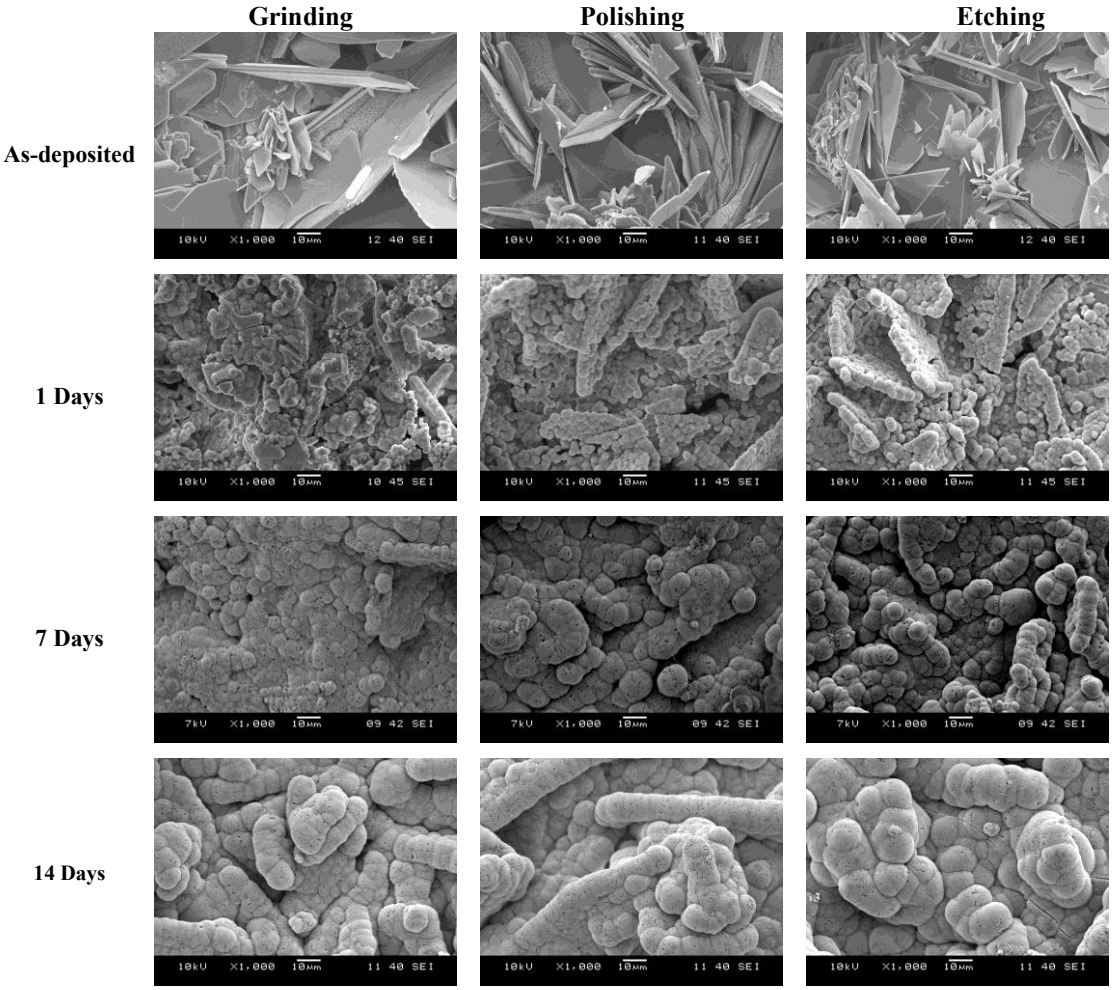

Figure 4. SEM images of grinded, polished and etched samples before and after immersion in SBF.

The Ca/P molar ratios of the samples calculated from the EDS analyses are listed in Table 1. The Ca/P molar ratios of the as-deposited samples were changed in range of 1.04-1.10. This ratio is similar to the brushite's Ca/P ratio [8]. The Ca/P ratios increased with soaking in SBF and changed in range of 1.56-1.67 and these values are close to the ratio of hydroxyapatite [8]. This results also confirmed by XRD and FTIR.

Table 1. Ca/P ratios of the coatings before and after immersion in SBF.

	Grinding	**Polishing**	**Etching**
As-deposited	1.10	1.07	1.04
1 Days	1.67	1.64	1.56
7 Days	1.58	1.64	1.66
14 Days	1.65	1.60	1.55

4. CONCLUSION

Three different surfaces properties were prepared by grinding, polishing and etching of substrates. CaP coatings were successfully produced by the electrochemical deposition method on surface modified Ti6Al4V substrates. Surface morphology of substrates was investigated by AFM. The properties of coatings were characterized by XRD, FTIR, SEM coupled with EDS, and bioactivity properties examined by bioactivity test in SBF. The following experimental results were obtained:

- According to XRD analyses all as-deposited coatings are composed of brushite phase, and brushite transformed to hydroxyapatite with immersion in SBF.
- Obtained FTIR results are consistent with the XRD findings.
- Surface morphology of the as-deposited coatings are composed of plate-like structures with varying dimensions.
- The morphology of the coatings shows an alteration from plate like structure to spherical like structure.

REFERENCES

[1] L. Lin, H. Wang, M. Ni, Y. Rui, T.Y. Cheng, C. K. Cheng, X. Pan, G. Li, C. Lin, Journal of Orthopaedic Translation, 2, 35, 2014.
[2] J. I. Rosales-Leal, M. A. Rodríguez-Valverde , G. Mazzaglia, P. J. Ramón-Torregrosa, L. Díaz-Rodríguez, O. García-Martínez, M. Vallecillo-Capilla, C. Ruiz, M. A. Cabrerizo-Vílchez, Colloids and Surfaces A: Physicochemical and Engineering Aspects, 365, 222, 2010.
[3] C. N. Elias, Y. Oshida, J. H. C. Lima, C. A. Muller, Journal of the Mechanical Behavior of Biomedical Materials, 1, 234, 2008.
[4] T. Kokubo, J. Non-Cryst. Solids, 120, 138, 1990.
[5] S. Singh, V. Singh, S. Aggarwal, U.K. Mandal, Chem. Papers, 64, 491, 2010.
[6] H. M. Han, G. J. Phillips, S.V. Mikhalovsky, Journal of Materials Science: Materials in Medicine, 19, 1787, 2008.
[7] M.S. Djoˇsi ´c, V. Pani´c, J. Stojanovi´c, M. Mitri´c, V.B. Miˇskovi´c-Stankovi´c , Colloids and Surfaces A: Physicochem. Eng. Aspects, 400, 36, 2012.
[8] S. Shadanbaz, G. J. Dias, Acta Biomaterialia, 8, 20, 2012.

EFFECT OF DISPERSANT ON THE ELECTROPHORETIC DEPOSITION OF CaP ON TITANIUM AND Ti6Al4V ALLOY SUBSTRATES

Utku TIRIC[*],Bensu BAKIN[*], Tulay KOC DELICE[*], Funda AK AZEM[**], Isil BIRLIK[**], Erdal CELIK[,***], Mustafa TOPARLI[**,***]**

[*]Dokuz Eylul University, The Graduate School of Natural and Applied Sciences, 35390, Buca, Izmir, Turkey
utkutiric@gmail.com
[**]Dokuz Eylul University, Department of Metallurgical and Materials Engineering, 35390, Buca, Izmir, Turkey
[***]Dokuz Eylul University, Center for Fabrication and Applications of Electronic Materials (EMUM), Buca 35390, Izmir, Turkey

ABSTRACT

Titanium and titanium based alloys are preferred materials for load bearing implants and the properties of titanium surface are important variable in implant design. Surface modifications are widely used to adjust the properties of titanium surface to the specific needs of the medical applications. In this study surface modification was performed on Ti6Al4V alloy and pure Titanium substrates by electrophoretic deposition (EPD) method. The purpose of the study is to investigate the effect of type of dispersant on structure and morphology of produced CaP coatings. Chemical and morphological characterizations of the produced samples were examined X-ray Diffraction (XRD), Fourier Transform Infrared Spectroscopy (FTIR) and Scanning Electron Microscope (SEM).

Keywords: Calcium phosphate coatings; electrophoretic deposition; Triethanolamine; Diethanolamine; Titanium; Ti6Al4V alloy

ELEKTROFORETİK BİRİKTİRME YÖNTEMİYLE TİTANYUM VE Ti6Al4V ALAŞIMI ALTLIKLAR ÜZERİNDE ÜRETİLEN CaP KAPLAMALARDA DİSPERSANTIN ETKİSİ

ÖZET

Titanyum ve Titanyum esaslı alaşımlar yük taşıyıcı implant uygulamalarında tercih edilmektedir ve titanyumun yüzey özellikleri implant tasarımında kullanılan önemli değişkenlerdendir. Titanyumun yüzey modifikasyonu, medikal uygulamalarda spesifik ihtiyaçları karşılamak amacıyla yaygın bir şekilde kullanılmaktadır. Bu çalışmada saf Titanyum ve Ti6Al4V alaşımı altlıklara yüzey modifikasyon işlemi elektroforetik biriktirme yöntemi ile uygulanmıştır. Çalışmanın amacı dispersant türüne bağlı olarak üretilmiş olan CaP kaplamaların yapısal ve morfolojik özelliklerinin incelenmesidir. Üretilen numunelerin kimyasal ve morfolojik karakteristikleri X-ışını Difraksiyonu (XRD), Fourier Dönüşümlü Kızılötesi Spektroskopisi (FTIR) ve Taramalı Elektron Mikroskobu (SEM) ile incelenmiştir.

Anahtar Kelimeler: Kalsiyum fosfat kaplamalar; Elektroforetik biriktirme; Trietanolamin; Dietanolamin; Titanyum; Ti6Al4V alaşım

1. INTRODUCTION

Titanium and its alloys are widely used as implant materials because of their excellent mechanical properties and chemical stability in physiological environment. However, the difficultly is to bond with living tissue. [1]. Deposition of calcium phosphate on titanium implants has been investigated for many years. Several researches have demonstrated that thin calcium phosphate layers can effectively establish bonding between the implants and host bone tissue [2]. Titanium implants are commonly coated with hydroxyapatite ($Ca_{10}(PO_4)_6(OH)_2$), a bioceramic which resembles the mineral constituents of human bones and teeth [3]. But the mechanical strength of HAP is too poor to be used in load-bearing applications. Therefore, HAP coating was deposited on the surface of metallic implants to improve the biocompatibility property [4, 5].

There are many techniques that have been used to obtain hydroxyapatite coatings on metallic implant materials such as sol-gel processing [6], plasma spray [7], electrophoretic deposition (EPD) [8], pulsed laser deposition (PLD) [9], biomimetic coating [10], dip coating [11] and magnetron sputtering [12]. EPD is commonly employed in processing of ceramics, coatings and composite materials. It is a high-level efficient process for production of films or coatings from colloidal suspensions: electrophoretically deposited materials exhibit good microstructure homogeneity and high packing density. The interest in the EPD technique is driven not only by its applicability to a great variety of materials but also by its simplicity; EPD is a cost-effective method usually requiring simple equipment as well as being amenable to scaling-up to large dimensions. Additionally, this method is capable of rapid deposition rates (seconds to minutes) with a high degree of control over deposition thickness and morphology, and the ability to produce coatings on metal implants with a broad range of thicknesses from 1μm to 500μm. Electrophoresis involves the migration of charged colloidal-sized particles towards the counter-charged electrode at which deposition occurs. Positively charged particles deposit on the cathode (cataphoresis), and negatively charged particles deposit on the anode (anophoresis) [13, 14].

Also performance of EPD technique depends on parameters of the suspension such as particle size, dielectric constant of liquid, conductivity of suspension, viscosity of suspension, zeta potential [15]. There are many solvents for EPD technique such as methanol, ethanol, *n*-propanol, iso-propanol, ethylene glycol, acetone, acetylacetone. Among these solvents *n*-butanol has the lowest dielectric constant [16]. On the other hand it provides sufficient stability for HAP suspension during the EPD process. Butanol was preferred over ethanol in order to lower the evaporation rate which subsequently reduces cracking during drying of HAP deposits [17].The zeta potential of the electrolyte and the colloidal stability of particles in the electrolyte can be enhanced by the addition of an efficient dispersant. Triethanolamine (TEA) and diethanolamine (DEA) are organic bases which can be used as the dispersant to increase the zeta potential and colloidal stability of particles in non-aqueous suspensions [18].

Suspensions of hydroxyapatite (HAP) particles were prepared in *n*-butanol and triethanolamine (TEA) and diethanolamine (DEA) were used as the dispersant. The aim of this study is to investigate of different dispersant effect (diethanolamine and triethanolamine) on morphological properties of CaP coatings prepared by electrophoretic deposition in the CaP based suspension.

1. EXPERIMENTAL

The sheets of Titanium and Ti6Al4V alloy with the dimensions of 12 mm x 25 mm x 1.5 mm were used as the substrate. The sheets were abraded with 600-grit silicon carbide paper. After abrading, substrates were etched with a solution containing 15% nitric acid (HNO_3), 5% hydrofluoric acid (HF) followed by washing with acetone in an ultrasonic bath for 10 min, then washing with distilled water and then dried at room temperature. Two different suspensions were prepared containing 20 g/L of HAP powders to *n*-butanol with 0.7% triethanolamine (TEA) and 0.7% diethanolamine (DEA). The suspension were dispersed for 24 hour with magnetic stirrer and 30 min with ultrasonically bath before EPD process. To deposit CaP coating on titanium substrates, an electrophoretic cell using pure titanium and Ti6Al4V alloy sheets as cathode and 316L plate as anode was connected to an electrophoresis apparatus. The distance between cathode and anode was 1 cm. The deposition process was conducted at a constant voltage of 30 V for 13 min at room temperature. Abbreviation of the produced coatings was shown at **Table 1.** After EPD process, coated samples were dried at room temperature and then sintered in a tubular furnace at 800 °C for 2 h in argon atmosphere with a heating rate of 1 °C/min until 200 °C and 5 °C/min from 200 °C to 800 °C. Finally cooling rate to room temperature was 1 °C/min.

The electric conductivity and pH measurements of the suspension was determined by a conductivity meter (Mettler Toledo S47-K SevenMulti dual meter pH/conductivity). The size distribution and zeta potential of the HAP particles was determined by a zeta-sizer (Malvern-nano).The phase analysis of the coatings were examined by X-Ray Diffractometer (XRD, Rigaku/Dmax 2200/PC model) with grazing incident of 1° at 40 kV and 36 mA using CuKα radiation. The analyses by Fourier transform infrared spectroscopy (FTIR) were performed with (FTIR, Perkin Elmer Spectrum BX) with a spectral range of 4000 -650 cm^{-1}. Surface morphology and elemental analysis of the coatings were investigated by a Scanning Electron Microscope (SEM, JEOL JSM-6060) equipped with Energy Dispersive Spectrometer (EDS).

Table 1. Abbreviation of the produced coatings.

HAP solution / Substrate	No additive	Additive of Diethanolamine	Additive of Triethanolamine
Pure Titanium	E-0	E-0-D	E-0-T
Ti-alloy (Ti6Al4V)	E-1	E-1-D	E-1-T

2. RESULTS

The electrical conductivities, pH, zeta potentials and average size of the suspensions are shown in **Table 2.** Results show that addition of dispersant results in decrement of average size of particles. This is probably due to the increment of pH value of suspension with usage of dispersant. The increment of the pH causes a great amount of positive ion to increase, which also causes the increment of the thickness of the double layer. Thus, the particles start to repulse each other; and this decrease the amount of agglomerated particles. Accordingly, the size distribution of particles in suspension decreases. Consequently, with the formation of homogeneous suspension, electrical conductivity increases. This results were similiar to that reported by Besra et. al. and Shahrabi et. al. [15, 18].

Table 2. pH, conductivity values, zeta potential and average size values of suspensions.

Suspension	pH	Conductivity Value (µS/cm)	Zeta Potential (mV)	Avarage Size (nm)
HAP	6.95	0.07	4.73	733.5
HAP+TEA	8.86	0.205	16.1	502.6
HAP+DEA	11.12	0.330	16.9	433.9

The XRD patterns of coated samples on pure titanium and Ti6Al4V alloys substrates after heat treatment process are shown in **Figure 2.** all coatings are composed of HAP phase according to JCPDS 09-0432. Besides, diffraction peaks of Ti (JCPDS 044-1294) arise from substrate. It was observed that there was no significant change in coating phase structure with varying dispersant type.

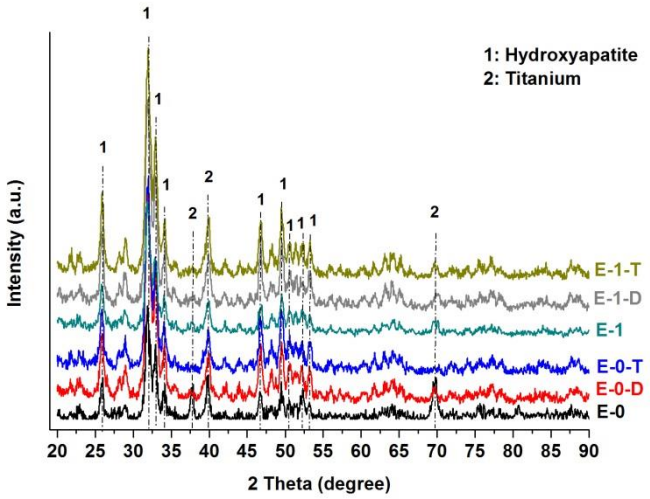

Figure 2. XRD patterns for samples E-0, E-0-D, E-0-T, E-1, E-1-D and E-1-T.

Figure 3. shows the FTIR spectra of the coatings with different dispersants. According to the FTIR spectra, all bands between 960 and 1100 cm^{-1} (1100,1030 and 960 cm^{-1}) are attributed to characteristic peak due to the PO_4^{3-} in HAP [19]. The band at 3400 cm^{-1} is assigned to O-H stretching of H_2O [20].

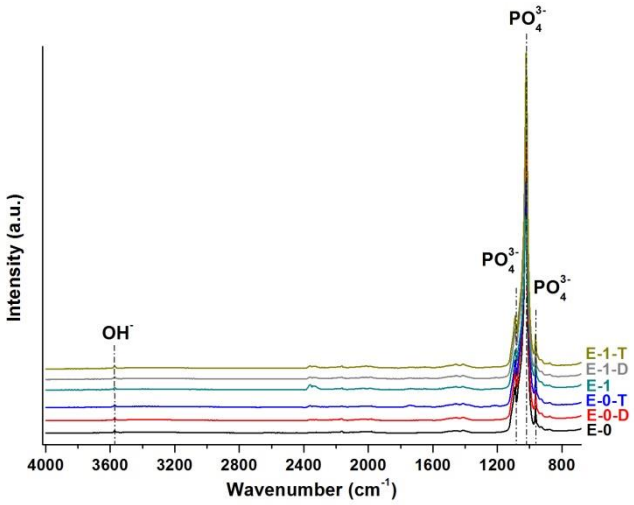

Figure 3. FTIR spectra for samples E-0, E-0-D, E-0-T, E-1, E-1-D and E-1-T.

Surface morphologies of coatings are presented in **Figure 4.** In general, morphology of coatings produced by using HAP suspension with DEA addition are crack-free and more homogenous in comparison to coatings produced by using HAP suspension with TEA addition.

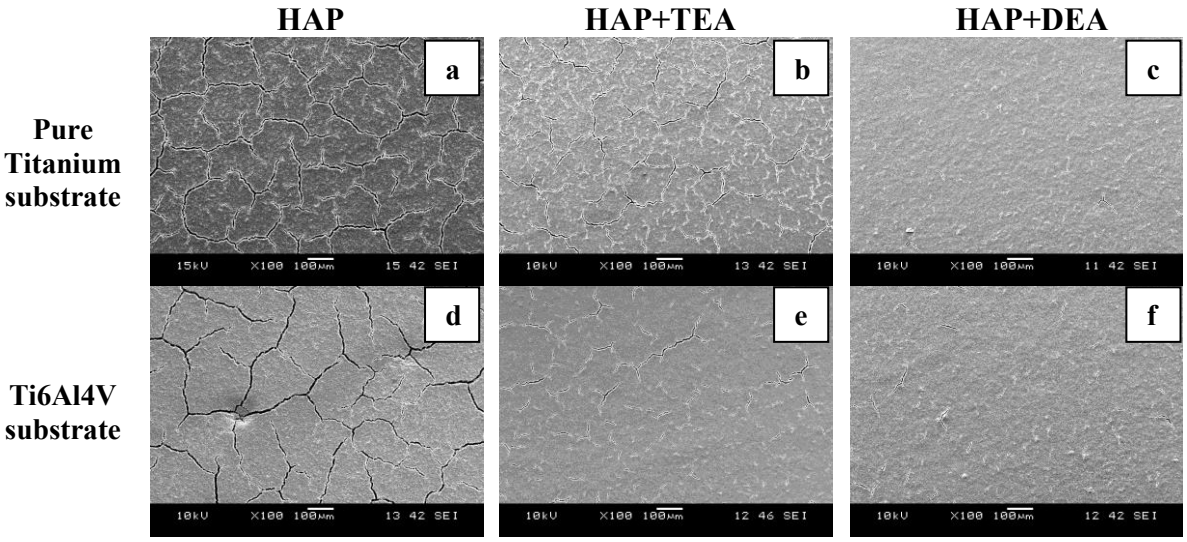

Figure 4. SEM micrographs of the samples at 100x magnification; (a) E-0, (b) E-0-D, (c) E-0-T, (d) E-1, (e) E-1-D, (f) E-1-T.

SEM images of the coatings at higher magnification presented in **Figure 5.** Coating produced by using HAP suspension with DEA addition has microstructure with fine particles and small number of agglomerates. However in the coatings especially produced without the use of dispersant have rough microstructure with coarse agglomerated particles. HAP suspension

with DEA addition has the highest zeta potential, so the particles agglomeration is small in it due to the large repulsion electrostatic between them. Shahrabi et al. found the similar results in their study [18].

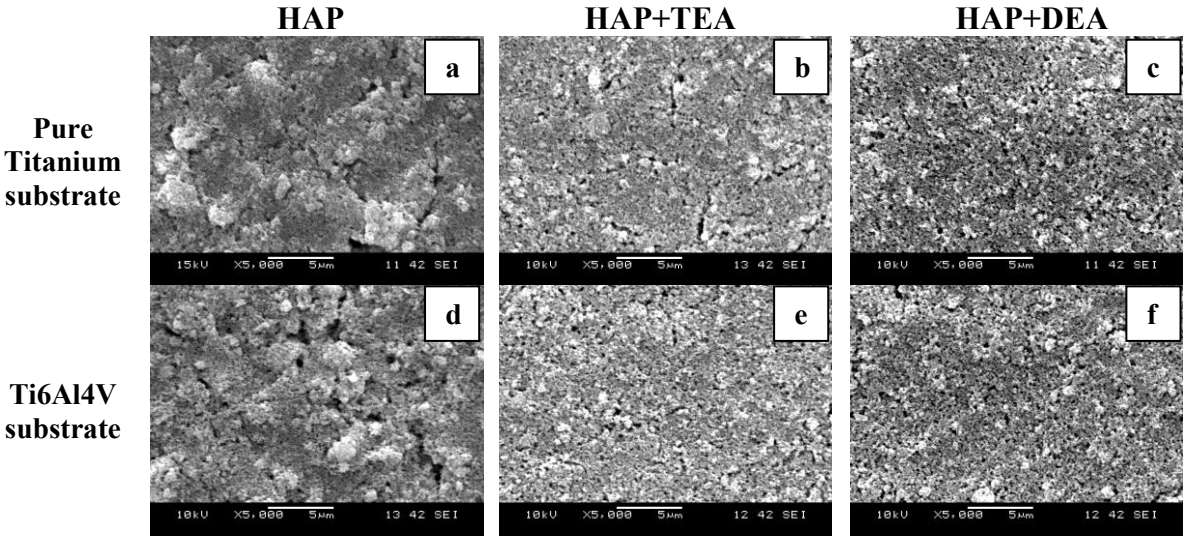

Figure 5. SEM micrographs of the samples at 5000x magnification; (a) E-0, (b) E-0-D, (c) E-0-T, (d) E-1, (e) E-1-D, (f) E-1-T.

The Ca/P molar ratios of the samples calculated from the EDS analyses and for all samples were changed in range from 1.72 to 1.78 and these values are close to the ratio of hydroxyapatite [21]. This results also confirmed by XRD and FTIR analyses.

3. CONCLUSION

CaP coatings were successfully deposited on pure Titanium and Ti6Al4V alloy substrates by electrophoretic deposition technique. The effect of diethanolamine and triethanolamine dispersants was investigated on structural properties of coatings. The properties of coatings were characterized by XRD, SEM coupled with EDS and FTIR.

According to XRD and FTIR analyses all coatings are composed of HAP and a significant change was not observed with using dispersant.

TEA and DEA dispersants has made a distinct change at surface morphology of the coatings due to the pH, zeta potential and conductivity increment of the suspension. As result, particles was repulsed each other, agglomeration of particles were decreased and the stability of suspension changed.

In conclusion it was found that HAP-DEA suspension leads to homogeneous and crack-free microstructure due to the highest zeta potential and better colloidal stability in comparison to the HAP and HAP-TEA suspensions.

REFERENCES

[1] S. Huang, K. Zhou, B. Huang B., Z. Li, S. Zhu, G. Wang, Journal of Materials Science: Materials in Medicine, 19, 437–442, 2008.
[2] K. Cheng K., T. Wang, W. Weng, M. Yu, J. Lin, H. Wang, P. Du, G. Han, Thin Solid Films, 544, 206-211, 2013.
[3] C.T. Kwok, P.K Wong, F.T. Cheng, H.C. Man, Applied Surface Science, 255, 6736-6744, 2009.
[4] S.K Yen, C.M. Lin, Materials Chemistry and Physics, 77, 70–76, 2002.
[5] Y.W. Song, D.Y. Shan, E.H. Han, Materials Letters, 62, 3276-3279, 2008.
[6] F. Ak Azem, E. Ovgu Eroglu, A. Çakir, Journal of Biomechanics, 44, 13, 2011.
[7] Y.C. Yung, C.Y. Yang, Ceramics International, 39, 6509-6516, 2013.
[8] P. Mondragon-Cortez, G. Vargas-Gutiérrez, Materials Letters, 58, 1336-1339, 2004.
[9] H. Zeng, W.R. Lacefield, Journal of Biomedical Materials Research, 50, 239, 2000.
[10] P. Habibovic, F. Barrére, C.A. van Blitterswijk, K. de Groot, P. Layrolle, Journal of the American Ceramic Society, 85, 517-522, 2002.
[11] A. Abrishamchian, T. Hooshmand, M. Mohammadi, F. Najafi., Materials Science and Engineering C, 33, 2002-2010, 2013.
[12] J.D. Long, S. Xu, J.W. Cai, N. Jiang, J.H. Lu, K.N. Ostrikov, C.H. Diong, Materials Science and Engineering C, 20, 175-180, 2002.
[13] M. Wei M., A.J. Ruys, B.K. Milthorpe, C.C. Sorrell, Journal of Materials Science: Materials in Medicine, 16, 319-324, 2005.
[14] A.R. Boccaccini, J. Cho, J.A. Roether, B.J.C. Thomas, E.J. Minay, M.S.P. Shaffer, Carbon, 44, 3149-3160, 2006.
[15] L. Besra, M. Liu, Progress in Materials Science, 52, 1-61, 2007.
[16] H. Negishi, K. Yamaji, N. Sakai, T. Horita, H. Yanagishita, Journal of Materials Science, 39, 833-838, 2004.
[17] V. Ozhukil Kollath, Q. Chen, R. Closset, J. Luyten, K. Traine, S. Mullens, A.R. Boccaccini, R. Cloots, Journal of the European Ceramic Society, 33, 2715-2721, 2013.
[18] M. Farrokhi-Rad, T. Shahrabi, Ceramics International, 39, 7007-7013, 2013.
[19] C.M. Botelho, M.A. Lopes, I.R. Gibson, S.M. Best, J.D. Santos, Journal of Materials Science: Materials in Medicine, 13, 1123-1127, 2002.
[20] F. Barrere, C.A. van Blitterswijk, K. de Groot, P. Layrolle, Biomaterials, 23 1921-1930, 2002.
[21] S. Shadanbaz, G.J. Dias, Acta Biomaterialia, 8, 20-30, 2012.

CHEMICAL AND STRUCTURAL CHARACTERIZATION OF SELENIUM-INCORPORATED HYDROXYAPATITE

Barış ALKAN[1,2] and Caner DURUCAN[1,2]

[1]Department of Metallurgical and Materials Engineering
[2]BIOMATEN Center of Excellence in Biomaterials and Tissue Engineering,
Middle East Technical University, 06800 Ankara, TURKEY
abaris@metu.edu.tr, cdurucan@metu.edu.tr

ABSTRACT

In case of severe bone damage or fracture, synthetic bone grafts such as hydroxyapatite (HAp) and related materials have long been applied for replacing natural bone tissue. Recent advances in this area have led to development of dual-functional synthetic hard tissue analogs exhibiting high biocompability/osteoconductivity together with therapeutic effect. Metallic ions are promising therapeutic agents in treatment of bone tumors due to their high physiological stability and availability compared to other alternative therapeutic agents such as recombinant proteins, therapeutic nucleic acids and anti-cancer drugs. Selenium, in that respect, is effective therapeutic agent with promising anti-oxidant and anti-carcinogenic effect when used in proper doses. In this study, selenium-doped HAp (HAp:Se) particles have been synthesized by modified aqueous precipitation method using calcium ($Ca(NO_3)_2 \bullet 4H_2O$) and phosphate ($(NH_4)_2HPO_4$) salts with sodium selenite (Na_2SeO_3). The effect of Se dopant in different amounts on the physical, chemical and crystal structure of resultant HAp powders have been investigated. Complete chemical identification was performed with spectroscopical analyses including fourier transform infrared (FTIR) and X-ray photoelectron spectroscopy (XPS) to elucidate the mechanism and chemical nature of Se doping in HAp. Meanwhile, x-ray diffraction (XRD) studies by Rietveld refinement have conducted to explain changes in the HAp crystal structure upon Se doping.

Key words: Bone graft, Therapeutic agent, Metallic ion, Selenium

TEDAVİ AMAÇLI KEMİK ANALOGU OLARAK SELENYUM KATKILANMIŞ HİDROKSİAPATİT TOZLARININ SENTEZ VE KARAKTERİZASYONU

ÖZET

Kemikte meydana gelen büyük ölçekli hasar ve kırılmalarda doğal kemik dokusunun yerini alması için hidroksiapatit ve benzeri seramik yapılı malzemeler sentetik kemik grefti olarak uzun süredir kullanılmaktadır. Son yıllardaki gelişmeler sentetik kemik greft malzemelerinin yalnızca vücuda uyumlu ve doğal kemik dokusunun üzerinde büyüyebilmesine elverişli ortama sahip olması dışında, tedavi ve hasarlı dokuların iyileştirilmesinde kullanılabileceğini göstermektedir. Bu anlamda, yüksek fizyolojik dengesi ve elverişli olmasından dolayı metalik iyonların kemik tümörü tedavisi ve iyileştirilmesinde kullanımı yaygınlaşmaktadır. Özellikle günlük alım miktarından fazla dozlarda kullanıldığında selenyum iyonu antioksidan ve antikarsinojenik etki göstermekte ve kanserli kemik hücrelerinin tedavisinde kullanılabilecek bir ajan olarak öngörülmektedir. Bu çalışmada, saf ve artan oranlarda selenyum dahil edilmiş hidroksiapatit tozları belirli kalsiyum ($Ca(NO_3)_2 \bullet 4H_2O$), fosfat ($(NH_4)_2HPO_4$) ve selenyum

(Na_2SeO_3) tuzlarının kullanımıyla sulu çökeltme yöntemiyle sentezlenmiş ve farklı selenyum miktarlarının hidroksiapatit tozlarının kimyasal, fiziksel ve yapısal özelliklerinin değişimine etkisi araştırılmıştır. Tozların kimyasal doğasında meydana gelen değişiklikler enerji yayılım spektroskopisi, kızılötesi spektroskopisi ve x-ışını fotoelektron spektroskopisiyle belirlenmiş ve selenyum iyonunun değerliliği tespit edilmiştir. Ayrıca, x-ışını difraksiyonu analiziyle hidroksiapatit tozunun kristal yapısı incelenmiş, iyon transfer mekanizması ve yapısal parametreler detaylı olarak araştırılmıştır.

Anahtar kelimeler: Kemik Grefti, Tedavi edici ajanlar, Metalik iyonlar, Selenyum

1. INTRODUCTION

Calcium phosphates such as hydroxyapatite ($Ca_{10}(PO_4)_6(OH)_2$ or HAp) and Ca-deficient hydroxyapatite ($(Ca_{(10-x)}(HPO_4)_x(PO_4)_{(6-x)}(OH)_{(2-x)}$ or CDHAp) have been widely used as ceramic components of bone graft materials due to their similarity with natural bone mineral in terms of chemical and structural properties as well as due to their superior bioactivity and osteoconductivity [1]. Natural bone mineral is also an ion reservoir and contains various kinds of ionic species in its structure mostly including strontium, magnesium, zinc, fluorine, sodium, carbonates and different metallic ion incorporates alter cell regulation and cell-cell signaling implying that interaction of ion species with body fluids have been a complex phenomenon. Yet, metallic ions substituted systems are able to exhibit therapeutic effects depending on the proper doses not leading to any toxicity to surrounding cells. Particularly, copper and cobalt ions trigger blood vessel formation with induction of pro-angiogenic factor such as VEGF while gallium and silver ions have been incorporated into bone tissue engineering scaffolds to prevent bacterial infections by release of the ions [2]. The ionic species of selenium , in this sense, are fundamentally important since they are the constitutes of selenoproteins which are essential to human immune systems with their antioxidant function, catalyst role in producing active thyroid hormone and cell proliferation [3,4]. Supranutritional levels of selenium (200 μg/day) exhibits chemopreventive effect due to their maximal expression of selenoproteins and are influential in initiation and progression of tumor [5, 6]. Indeed, supranutritional levels of selenium is protective against colon, skin, breast and cervical cancers as confirmed by the laboratory studies [7].

Different forms of selenium species have been recently employed in anticancer orthopedic applications including the coating of elemental selenium on titanium surfaces, use of nanostructured selenium compacts, selenite substituted hydroxyapatite powders [8, 9, 10, 11]. Structural modifications during the processing of selenium coatings and the synthesis of Se incorporated powders appreciably affect biological response of monoculture, co-culture and in vivo experiments, thereby emphasizing detailed analysis of structural properties of bone analogs [12]. Motivated by this relationship, selenium incorporated hydroxyapatite particles have been synthesized by the aqueous precipitation method with the addition of sodium selenite salt during the synthesis. Although there are several studies including determination of ion exchange mechanism in hydroxyapatite surface and modified structural parameters in hydroxyapatite lattice due to selenium substitution, full chemical and structural analyses are needed for detailed explanation of possible changes in HAp crystal structure and were completed in this study using advanced analytical tools and structural refinement software [13]. By means of that the relationship between anti-cancerous cell response and structural changes in HAp structure were established depending on the selenium content employed through the synthesis process.

2. EXPERIMENTAL STUDIES

2.1 Materials and Methods

Calcium nitrate tetrahydrate ($Ca(NO_3)_2 \cdot 4H_2O$), ammonium hydrogenphosphate ($(NH_4)_2HPO_4$) and sodium selenite (Na_2SeO_3) powders were purchased from Sigma (St Louis, MO, USA) and used as calcium, phosphate and selenium precursors respectively. Stoichiometric hydroxyapatite (HAp) and selenium-doped hydroxyapatite (HAp:Se) powders were synthesized by conventional precipitation method and atomic ratios of the elements (Ca/P and Ca/(P+Se)) were kept at 1.667. Also, atomic ratio percent of elements (Se/P) was selected as 1, 2 and 3 % and selenium-incorporated powders labeled as HAp:Se(α) where α is corresponding molar ratio percent of Se/P.

All reagents were initially dissolved in deionized water (100 ml) under constant stirring and pH of phosphate solution was kept at 10 to initiate HAp precipitates. Afterwards, drop-wise addition of calcium solution to phosphate solution was performed while keeping pH of the precipitated solution at roughly 10 with the addition of ammonium hydroxide solution ($NH_4(OH)$). After the precipitation process the mixed solution was heated to 60ºC and aged at this temperature overnight. All experiments were carried out open to atmosphere. Following that, HAp and HAp:Se powders were centrifuged and ultrasonically treated in DI water for removing excess NO_3^- and subsequently treated in ethanol solution for removing excess water from the surface of the precipitate and controlling the agglomeration state of powders. After the powders were filtered and dried at 105ºC overnight, they were mechanically ground by zirconia balls in acetone solution to reduce their particle sizes. Finally, certain amount of ground powders were sintered at varying calcination temperatures from 900ºC to 1000ºC while some are kept in as-synthesized form.

2.2 Characterization

Elemental analysis of synthesized HAp and HAp:Se powders were examined by energy dispersive x-ray spectroscopy (EDS, Nova Nano430-FEI) and x-ray photoelectron spectroscopy (XPS, PHI-5000 Versaprobe). As for EDS, elemental analysis was carried out in at least eight different regions of each sample and average atomic percent of each element was obtained. Furthermore, fourier transform infrared radiation (FTIR, Frontier-Perkin Elmer) was employed in order to reveal modifications in hydroxyl ion occupancy, incorporation of carbonate ion as regards to their corresponding absorption band regions and specifically determine selenium- related absorption bands as well as other chemical structure alterations due to the effect of selenium incorporate. To confirm the results of FTIR, XPS was utilized for determining the presence of carbonate ions in HAp lattice and chemical state of selenium in HAp:Se powders were investigated after adjusting the resultant XPS data with respect to the adventitious carbon (C1s) binding energy as 284.8 eV.

As for morphology determination, HAp and HAp:Se powders were coated with gold coater and morphological analyses of the powders were achieved using scanning electron microscopy (SEM-Nova Nano430-FEI) and crystallite sizes of individual sample were estimated at high magnifications. In addition, the powders were exposed to ultrasonic treatment for 2 min. and average particle size of each sample was obtained using particle size analyzer (Master Sizer). Secondary phase formation, crystallinity degree and crystallite size of each sample were specifically examined in as-synthesized and calcined form of the powders by x-ray diffraction analyses (XRD- A Rigaku D/Max-2000 PC diffractometer). Cu-Kα radiation (λ: 1.5418 Å) was used as x-ray source and the x-ray machine was operated at 36 mA, 40 kV in the 2Θ range from 20-80º with a step size of $0.02^{o}\ s^{-1}$ and scanning rate of 2º/min. For detailed analysis of

structural parameters the samples were exposed to x-ray diffraction with the same input except the scanning rate that was selected as 0.1°/min. With the aid of the slowly scanned x-ray results, Rietveld refinement was executed using GSAS sofware for background and peak fitting and the results was examined for each sample to reveal doping nature, charge compensation mechanism and modifications in HAp lattice and crystal structure due to the effect of selenium incorporate.

3. RESULTS AND DISCUSSION

Pure and selenium-incorporated HAp powders were morphologically examined using SEM analysis and the results indicate equiaxed, sphere-like morphology for HAp crystallites with similar forms while exhibiting a tendency to anisotropic shape as selenium content increases within the particles demonstrated in Figure 1. The powders also had analogous particle sizes regardless the selenium content shown in Table 1. Particle size range was close to the ideal particle size for full profile structural analysis as well (1-5 μm) implying that equal representation of crystallite anisotropy can be likely and satisfy the randomness within the particles [14].

The elemental compositions of pure and selenium-incorporated HAp powders and their corresponding atomic ratios were computed through EDS analysis and oxygen atomic percent in each powder was excluded in the calculation due to its instability owing to low-atomic weight. Increasing ratios of Se/P in as-synthesized powders were suited with initial molar percent Se/P ratios and the atomic percent of each atom was appreciably close to initial atomic percent meaning that selenium was well incorporated into HAp structure. Table 1 revealed that measured Ca/P and Ca/(P+Se) atomic ratios tended to decrease within the powders and were not equal to 1.667 and the result can be attributed to either the atomic extinction in HAp lattice for charge neutrality due to selenium ion incorporation or low crystallinity degree with increasing Se content.

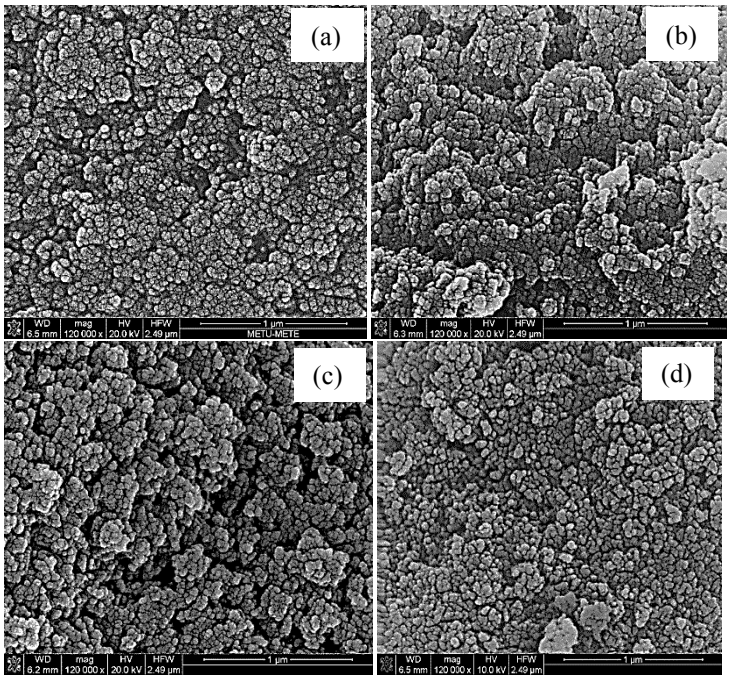

Figure 1: SEM micrographs of pure HAp (a), HAp:Se1 (b), HAp:Se2 (c) and HAp:Se3 (d) in as-synthesized condition.

Table 1: Comparison of the inital and resultant atomic ratios among Se, P and Ca and distinct atomic percent values of each atom as well as the particles size distribution of pure and selenium-incorporated HAp powders.

Atomic Ratios	Pure HAp	HAp:Se1	HAp:Se2	HAp:Se3
Se/P % (nominal)	0.00	1.00	2.00	3.00
Se/P % (measured)	0.00	0.97 ± 0.05	1.79 ± 0.13	2.67 ± 0.27
Ca/P & Ca/(P+Se)	1.50 ± 0.09	1.46 ± 0.08	1.43 ± 0.03	1.41 ± 0.02
Se %	0	0.39 ± 0.02	0.73 ± 0.06	0.99 ± 0.07
P %	40.76 ± 1.78	40.02 ± 1.24	40.50 ± 0.52	40.41 ± 1.03
Ca %	59.24 ± 1.78	59.59 ± 1.24	58.78 ± 0.56	58.60 ± 1.00
Particle Size (μm)	7.31	7.71	6.95	8.80

Chemical structure of pure and Se-incorporated HAp powders was determined using infrared spectra of the absorption bands of the functional groups within HAp lattice with the aid of FTIR analysis. In Figure 2 (i) stretching vibration of hydroxyl ions (OH^-) with their corresponding absorption band at around 3571 cm^{-1} was observed and magnitude of the absorption band exhibited a decreasing tendency with increasing Se content implying the substitution of OH^- with other ions. Wide absorption band of physically adsorbed water was also observed in the range of 2600-3600 cm^{-1}. Figure 2 (ii) show A-type carbonation in the absorption band at around 1540 cm^{-1} and increase in the magnitude of the absorption band with increasing selenium content suggest that OH^- ions were substituted with carbonate ions (CO_3^{2-}). In addition B-type carbonation was noticed at around 1420 cm^{-1} and 1455 cm^{-1} with no explicit change in the absorption band in question.

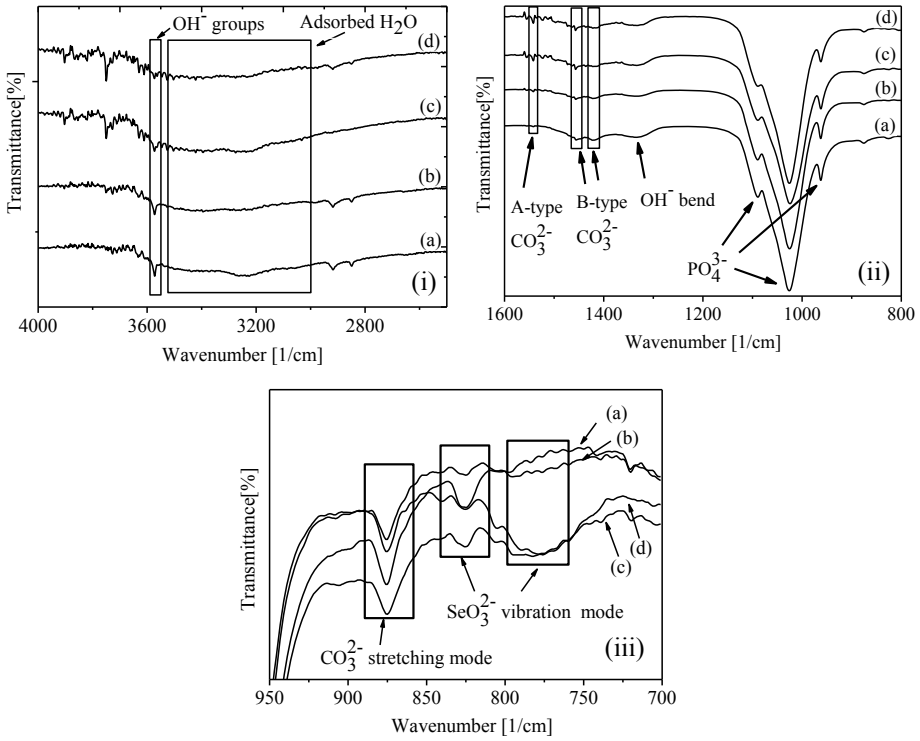

Figure 2: FTIR absorption spectra of the functional groups within pure and selenium-incorporated HAp mainly showing the modification in OH^- groups (i), carbonation within HAp to different ionic sites(ii), selenium-related functional groups in HAp lattice(iii). Pure HAp (a), HAp:Se1 (b), HAp:Se2 (c) and HAp:Se3 (d) listed in as-synthesized condition.

According to Figure 2 (iii) the absorption bands at 775 cm^{-1} and 824 cm^{-1} were attributed to selenite (SeO_3^{2-}) vibration mode and the absorption band at 824 cm^{-1} particularly enlarges with increasing content of selenium in HAp. No selenate ion (SeO_4^{2-}) was present within selenium-incorporated HAp due to extinction of the absorption band at 872 cm^{-1} and CO_3^{2-} stretching mode was noticed to match with the absorption band at 875 cm^{-1} while exhibiting no apparent difference in magnitude. The results suggest that selenium incorporated into HAp crystal structure in the form of SeO_3^{2-}. Also, CO_3^{2-} initially set to phosphate site in HAp lattice while tended to place into OH^- site with increasing Se contents.

Chemical state of Se was determined using XPS survey scans to confirm the implications remarked in FTIR results. Binding energies between 75-50 eV was scanned for Se*3d* and the obtained data was calibrated in accordance with C*1s* peak at 284.8 eV. Figure 3 shows Se*3d* belonged to peaks at 60.24 eV, 59.67 eV and 59.56 eV respectively with increasing Se content. As the binding energies of Se$3d_{5/2}$ and Se$3d_{3/2}$ were at around 54.6 eV and 55.5 eV, Se was expected to be in ionic form and oxidized state. Indeed, chemical state of SeO_3^{2-} and SeO_4^{2-} were demonstrated as approximately 59.5 eV and 61.0 eV in XPS database. Therefore, XPS survey analyses pointed out the existence of SeO_3^{2-} group in HAp crystal structure as its average values in literature were appreciably comparable with the binding energy of indicated peaks in Figure 3 [15]. Also, XPS peaks at 288.76 eV were noticed to enhance with increasing content of Se and related to CO_3^{2-} as the binding energy of CO_3^{2-} is expected to be near 4.5 eV above C*1s* at 284.8 eV.

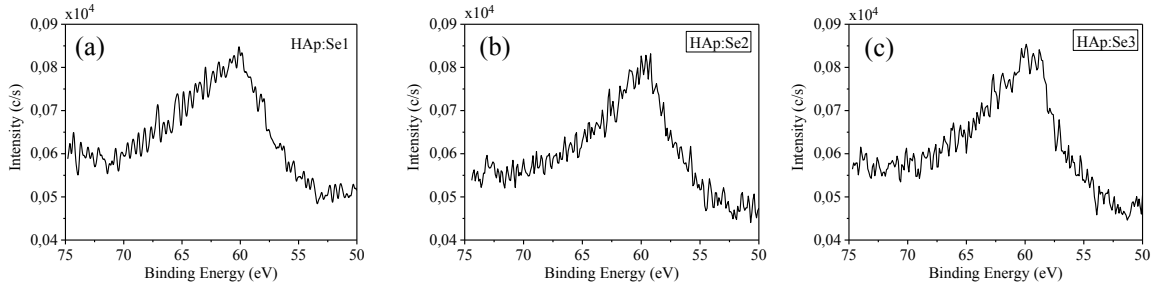

Figure 3: XPS survey scans of HAp:Se1 (a), HAp:Se2 (b) and HAp:Se3 (c) for chemical state analysis of Se3d.

Structural modifications and incorporation mechanism/nature in HAp lattice depending on Se content was revealed by XRD analysis and full Rietveld refinement through GSAS software. Figure 4 demonstrates the slowly-scanned XRD data of pure and Se-incorporated HAp powders as well as the result of the refined powder patterns through GSAS software. As to XRD patterns, reduction in diffracted intensity of the samples and destruction of the sharpness for the diffraction peaks suggest that crystallinity percent diminished as Se content increased within HAp lattice. Qualitative phase analysis revealed that there was no secondary phase formation in all powder diffractograms. Moreover, diffraction peaks having wider peak widths in higher Se content emphasized that crystallite size of the samples decrease as regard to increasing content of Se.

To supplement the qualitative information obtained from XRD patterns, full profile refinement was carried out and the refined structural parameters were demonstrated in Table 2. According to the results, the lattice parameters of pure and Se incorporated HAp did not exhibit any systematic changes as regard to Se content and were almost alike to one another. In addition, the reduction in crystallite sizes of the samples with increasing Se content was confirmed

quantitatively by the computations of crystallite size broadening in GSAS software. Table 2 also noted that atomic occupancies of phosphor and oxygen in OH^- bond diminished while that of selenium increased within HAp lattice. Summation of phosphor and selenium occupancies were not completed to 1 implying that the mechanism that CO_3^{2-} incorporated into PO_4^{3-} site or OH^- site was suited to the remarks in FTIR analysis. Likewise, enhancement in the deficiency of oxygen in OH^- site suggest that CO_3^{2-} favoured to place into the position of OH^- group at high Se contents. Thus, the charge compensation mechanism was clarified in that extra positive charge owing to exchange of SeO_3^{2-} with PO_4^{3-}at different Se contents was compensated by the exchange of CO_3^{2-} with OH^- .

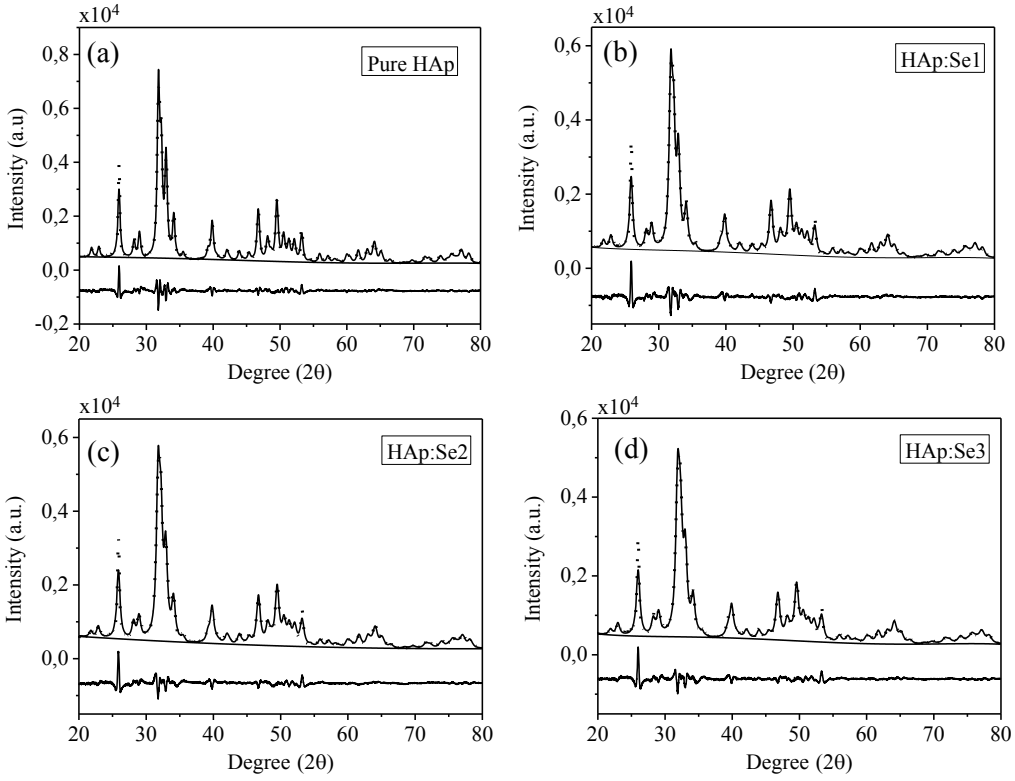

Figure 4: Rietveld refinement plots of pure HAp(a), HAp:Se1 (b), HAp:Se2 (c) and HAp:Se3 (d) in as-synthesized for revealing structural parameters of HAp lattice.

Table 2: Structural parameters of pure and selenium-incorporated HAp obtained with aid of full rietveld refinement analysis.

Structural Parameters	**Pure HAp**	**HAp:Se1**	**HAp:Se2**	**HAp:Se3**
Lattice Parameters (Å)	a= 9.4225 c= 6.8842	a= 9.4231 c= 6.8831	a= 9.4218 c= 6.8844	a= 9.4229 c= 6.8828
Crystallite Size (nm)	25.95	18.91	17.91	16.19
F_{Se}	0	0.0132	0.0146	0.0265
F_P	0.9775	0.9632	0.9594	0.9584
F(O in (OH))	0.5820	0.5635	0.5545	0.5486
Chi^2	3.105	3.102	2.778	2.502
R_{wp}	0.064	0.063	0.060	0.058
R_p	0.048	0.045	0.043	0.040

References

1. Dorozhkin S.V., "Calcium Orthophosphates in Nature, Biology and Medicine", Materials, 2, 399-498, 2009.
2. Mouriño, V.,Cattalini, J. P., Boccaccini, A. R., Metallic ions as therapeutic agents in tissue engineering scaffolds. Journal of the Royal Society, 2011.
3. Brozmanova, J., Manikova, D., Vlckova, V., Chovanec, M. Selenium: a double-edged sword for defense and offence in cancer. Arch Toxicol 84:919–938, 2010.
4. Rayman, M. P. The importance of selenium to human health. THE LANCET 356, 2000.
5. Zheng, H., Cao, J. J., Combs G. F. Selenium in bone health: Roles in antioxidant protection and cell Proliferation. Nutrients 5, 2013.
6. Spallholz, J. E., Selenium and the prevention of cancer. The bulletin of Selenium-Tellurium development association, 2011.
7. Moss, R., Antioxidants against cancer PhD, page 79, 1999.
8. Rodriguez-Valencia, C., Alvarez, M. L., Cochon-cores, B., Pereiro, I., Serra, J., Gonzalez, P., Novel selenium-doped hydroxyapatite coatings for biomedical applications. Journal of Biomedical Materials Research Part A, 2012.
9. Tran, P. A., Sarin L., Hurt R. H., Webster T .J. Titanium surfaces with adherent selenium nanoclusters as a novel anticancer orthopedic material. Journal of Biomedical Materials Research Part A, 2009.
10. Wang, Y., Ma, J., Zhou, L., Chen, J., Liu, Y., Qiu, Y., Zhang, S., Dual functional selenium-substituted hydroxyapatite. Journal of the Royal Society, 2012.
11. Ma, J., Wang, Y., Zhou, L., Zhang, S., Preparation and characterization of selenite substituted hydroxyapatite. Material Science and Engineering C 33, 2012.
12. Tran, P. A., Sarin, L., Hurt, R. H., Webster, T. J. Differential effects of nanoselenium doping on healthy and cancerous osteoblasts in coculture on titanium. International Journal of Nanomedicine 5352, 2010.
13. Monteil-Rivera, F., Fedoroff, M., Jeanjean, J., Minel, L., Barthes, M. G., Dumonceau, J., Sorption of selenite (SeO_2^{-3}) on hydroxyapatite: An exchange process. Journal of Colloid and Interface Science 221, 291–300, 2000.
14. McCusker, L. B., Von Dreele, R.B., Cox, D.E., Louer, D. Scardi, P., Rietveld refinement guidelines. J. Appl. Cryst. (1999). 32, 36-50.
15. Moulder, J.F., Stickle, W.F., Sobol, P.E., Bomben, K.D., Handbook of x-ray photoelectron spectroscopy, Perkin-Elmer corporation, Physcal electronics division, Eden Praire, Minn., 1992.

SYNTHESIS OF TiB_2 FROM MOLTEN SALTS ON DIFFERENT SUBSTRATES

Perim OZKALAFAT*, Guldem KARTAL SIRELI, Servet TİMUR

* Istanbul Technical University, Turkey
ozkalafat@itu.edu.tr

ABSTRACT

In this study, continuously dense and hard TiB_2 coating was investigated on different substrate materials, namely nickel, low carbon steel, tungsten and WC-Co cutting tool. The deposition of TiB_2 was carried out by using molten salt electrolysis where substrate materials were polarized as a cathode and graphite crucible acted as an anode. During TiB_2 electrodeposition researches, a unique and environmentally-friendly electrolyte composition was formulated which composes of borax, sodium titanate and calcium fluoride. Thin film X-Ray diffraction (XRD) analysis confirmed TiB_2 layer formation on different substrates. The thickness, morphology as well as chemistry of the coating were determined with scanning electron microscopy (SEM) and energy-dispersive X-ray spectroscopy (EDS) examinations. Cross sectional Vickers micro-indentation test revealed that the deposited TiB_2 layer had a hardness value up to 3000±200 HV.

Keywords: Titanium diboride, Electrochemical Deposition, Molten salt, Surface Treatment

ERGİMİŞ TUZLARDAN FARKLI TABAN MALZEMELER ÜZERİNDE TiB_2 BİRİKTİRİLMESİ

ÖZET

Bu çalışmada, TiB_2'nin nikel, düşük karbonlu çelik, tungsten ve WC-Co kesici uç üzerinde düzgün ve sürekli olarak kaplanması araştırılmıştır. Biriktirme işlemi, ergimiş tuz elektrolizi yöntemi ile gerçekleştirilmiş olup, taban malzeme katot olarak polarize edilmiş ve grafit pota anot olarak kullanılmıştır. Elektrokimyasal biriktirme sırasında özgün ve çevre dostu bir elektrolit bileşimi kullanması amaçlanarak boraks, sodyum titanat ve kalsiyum florür karışımı tercih edilmiştir. Elde edilen TiB_2 kaplamalar ince film X-ışınları yöntemi ile karakterize edilmiştir. Kaplama kalınlığı ve morfolojisi taramalı elektron mikroskobu (SEM) ile analiz edilirken, kaplamanın kompozisyonu enerji dağılım X-ray spektrometresi (EDS) ile tespit edilmiştir. Kesit alan mikro sertlik analizi ile biriktirilmiş TiB_2 tabakasının 3000±200 HV kadar yüksek bir sertlik değerine sahip olduğu belirlenmiştir.

***Anahtar kelimeler*:** Titanyum diborür, Elektrokimyasal Biriktirme, Ergimiş Tuz, Yüzey İşlemleri

1. INTRODUCTION

Titanium diboride (TiB_2) is known as an advanced structural ceramic material due to its high strength and excellent durability to corrosion and wear, as well as high electric and thermal conductivity. Currently, TiB_2 find many demanding applications including cutting tools, automotive and aircraft industry because of its promising properties [1-3].

The common production of TiB_2 is to implement as a thin-film coating by chemical vapor deposition (CVD) and physical vapor deposition (PVD) in which expensive and complicated equipment are required with additional precautions for highly toxic gas emissions [4-7]. Compared to the vapor deposition techniques, high temperature electrochemical synthesis from molten salts can be considered as one of the most favorable methods owing to its simplicity and the usage of cheap raw materials [8-10].

Basically, electrochemical synthesis of titanium diboride is based on the co-deposition of boron and titanium from molten salt electrolytes on the surface of any conductive materials which have not necessarily had a chemically stabile boride phase. By changing the electrolysis parameters such as current density, temperature as well as electrolyte composition, it is possible to obtain a desirable coating morphology and thickness [8-10]. In the open literature, electrodeposition of TiB_2 is generally performed in a halide-based molten electrolyte systems, namely FLINAK melts (LiF-NaF-KF), and the addition of fluoride compounds of boron and titanium [9-20]. Because of highly corrosive nature of fluoride gas and chemicals, the electrolysis set-up and handling of electrolyte during and after the TiB_2 synthesis is extremely difficult. The novel part of present research is to elimination of toxic gaseous emissions by uniquely formulated simple and stable oxide-based electrolytes; hereby, TiB_2 coating electrolysis is able to be conducted in an open atmosphere without taking any extreme precautions for the corrosion prevention of fluoride or gas leakages.

2. MATERIAL AND METHODS

2.1. Coating Process

All cathode materials, namely nickel, tungsten, 7114 low carbon steel (DIN EN 10130-99 DC 04) and WC-%6Co cutting tool were mirror-polished and ultrasonically cleaned before the coating process in order to obtain oxide or dirt-free surfaces.

Electrodeposition of TiB_2 was carried out in a borax-based electrolyte with the addition of sodium titanate (3-10 wt.%) and small amount of calcium fluoride (1-3 wt.%) serving as a titanium source and an activator, respectively. The electrolyte was dehydrated at 110 °C for 24 h. During electrolysis, graphite crucible acted as an anode whereas substrate material was polarized as a cathode. The system was externally heated by high frequency induction furnace in while electrolyte temperature was controlled both by a Pt-PtRh13 thermocouple and a laser thermometer. Electrodeposition experiments were conducted under galvanostatic condition and all cell potential values were recorded by a data acquisition system. The coating of TiB_2 on different substrate materials was performed at idealized process parameters; 70 mA/cm^2 of current density, 850°C of electrolyte temperature and 120 minutes of electrolysis duration. After the electrodeposition experiments, TiB_2 coated samples were cooled down in air and the solidified electrolyte was washed away with hot water.

2.1. Boride Layer Characterization

TiB_2 coated samples were sectioned and metallographically polished for further characterizations. Phase compositions of grown TiB_2 layer were determined by thin film X-Ray diffraction (XRD-Philips Model PW3710) with a glancing angle of 1° using CuKα radiation. The thickness, morphology and chemical analysis of TiB_2 coating were analyzed with the scanning electron microscopy (SEM-JEOL JSM 7000F) and energy-dispersive X-ray spectroscopy (EDS) investigations. Cross-sectional micro hardness of TiB_2 deposited samples were measured by Vickers micro hardness indenter (Leica) by applying 50 gf.

3. RESULTS AND DISCUSSION

Different substrate materials were selected by considering the linear thermal expansion coefficient values to prevent the possible stresses and cracks formations between the grown TiB_2 layer and substrate materials (given in Table 1).

Table 1. Linear expansion coefficient of different materials at 25 °C; ppm/°C [21].

Material	Linear expansion coefficient [at 25 °C; ppm/°C]
TiB_2	8.1
Fe_2B	7.65 (200-600 °C)
Nickel	13.3
Tungsten	4.6
WC	4-7
Low carbon steel	10.1-11.7

Thin film XRD analysis results revealed that after 120 minutes electrolysis, TiB_2 layer was successfully deposited on different substrate materials (Fig.1). Although a survey of titanium-boron binary phase diagram [1] showed the intermetallics of the Ti-B systems ranking in the order of TiB, Ti_3B_4, and TiB_2 with respect to increasing boron content, only TiB_2 phase was distinguished**.** Therefore with the developed environmentally-friendly electrodeposition technique it is possible to be grown the exact stoichiometric TiB_2 layer**.** Depending on the thickness of grown TiB_2 layers, peaks from below matrix material was also detected (see both TiB_2 and nickel/steel matrix peaks in Fig. 1).

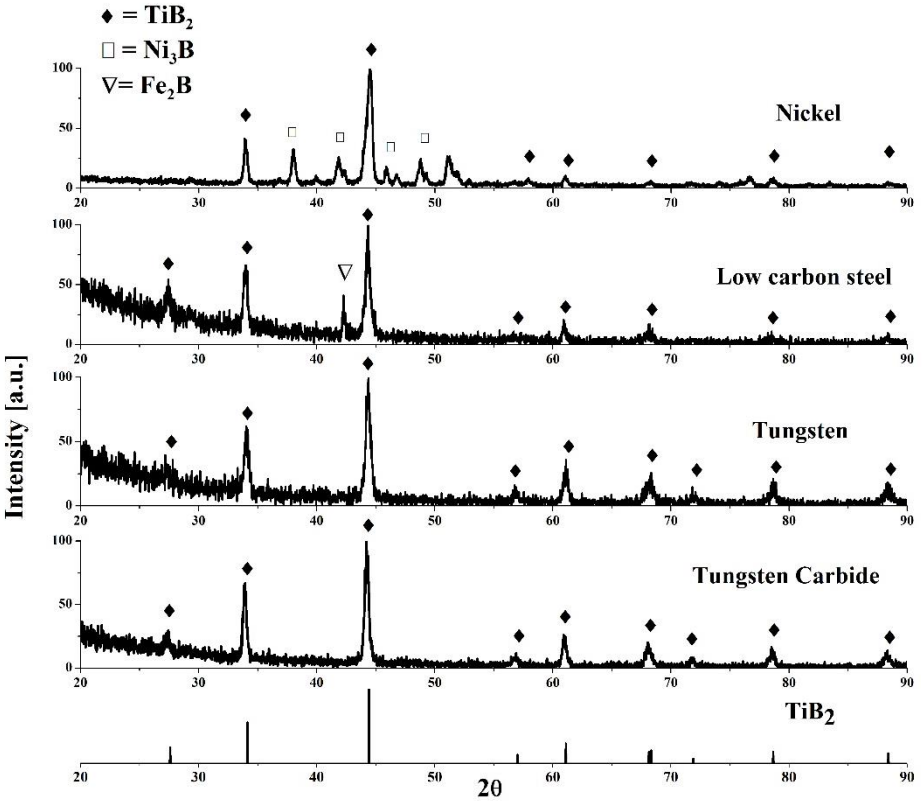

Figure 1. XRD pattern of TiB_2 deposited on different substrate materials.

The cross-sectional SEM inspections exhibited that TiB_2 layers were dense and homogeneous with a band type structure (Fig. 2). Apparently, the same experimental conditions leaded different TiB_2 coating thicknesses on different substrate materials (Fig. 3). The maximum TiB_2 coating thickness was obtained on low carbon steel with the value of approximately 32 µm, while the minimum TiB_2 coating was seen on nickel with 2.3 µm. The adhesion of TiB_2 on the substrates was rather good; since there was no cracking/cleavage between the deposition and the matrixes. EDS analysis taken from TiB_2 layers revealed that the TiB_2 top layer compositions varies between 68-70 at.%B and 29-32 at.%Ti which is very similar to intermetallic TiB_2 (~66 at.%B) [1,22]. Additional EDS measurements were performed on 1 µm below the TiB_2 deposition to examine any either boron or titanium diffusion zone formations (DZF). Interestingly, no DZF was observed on W and WC-%6Co substrates, whereas $(Ti_xNi_y)B_z$ diffusion/transition zone (57 at.%B, 16.34 at.%Ti, 26.09 at.%Ni) was detected on nickel substrates. Moreover, on steel substrates, there were also boron DZF right underneath TiB_2 deposition with 39.60 at.%B and 55.19 at.%B composition which is very close to Fe_2B intermetallic. Since the solubility of titanium and boron in nickel plus boron in iron are considerably high according to the binary phase diagrams of them [22], it is very likely to form such stable chemical compounds or intermetallic at elevated process temperature, 850°C.

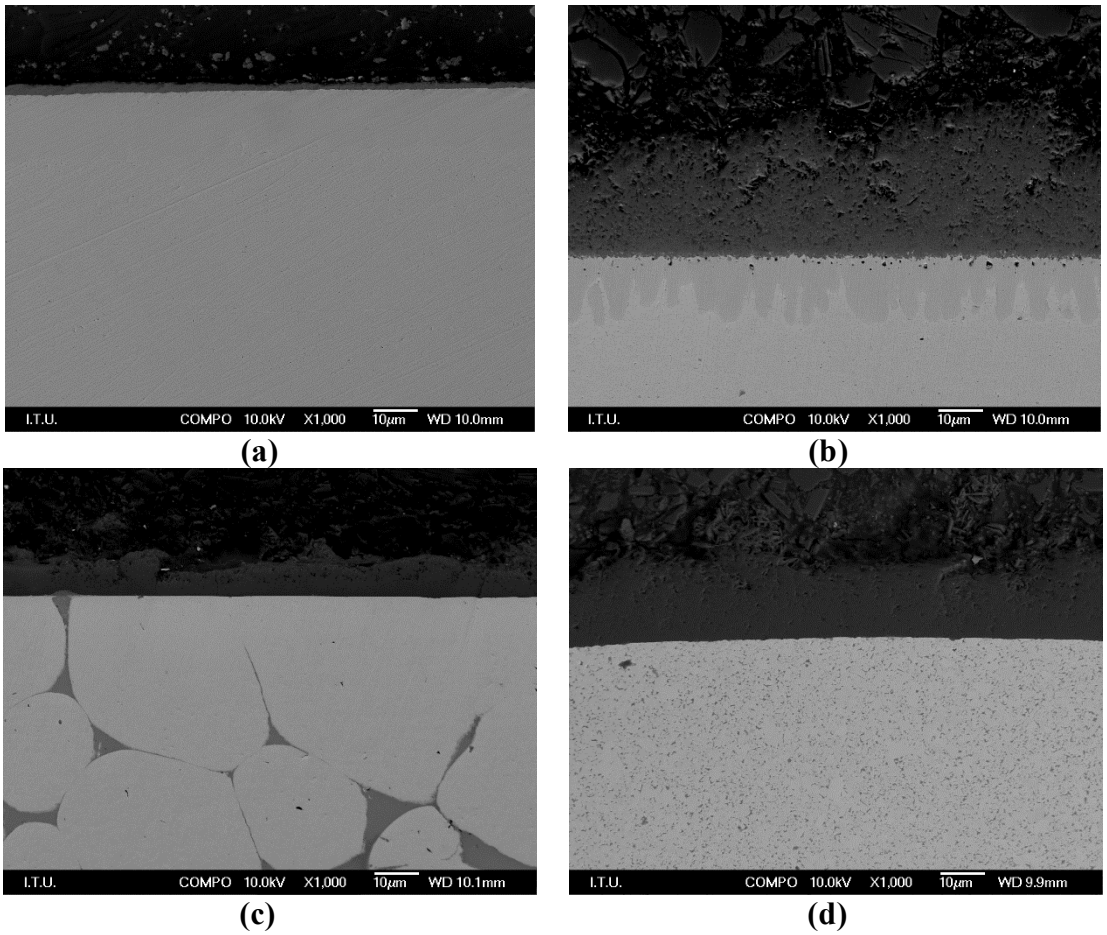

Figure 2. Cross-sectional SEM images of TiB_2 layers deposited on different substrates (a) Nickel, (b) Low carbon steel, (c) Tungsten, (d) WC-Co cutting tool.

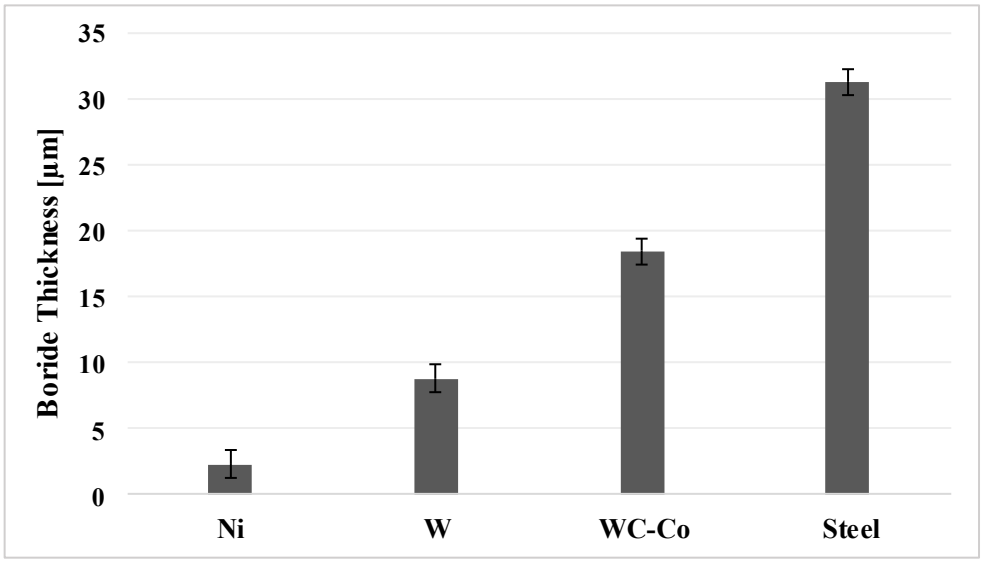

Figure 3. Coating thicknesses of TiB_2 layers on different substrates.

Vickers micro hardness test of cross-sectioned TiB_2 coated samples showed that the formed TiB_2 layer was hard as 3000±200 HV (Fig. 4). Obtained hardness value is consistent with the values determined both in experimentally measurements [18-20,23] and in theoretical calculations [1,2,24]. It is noteworthy that 10 µm below the TiB_2 deposition the hardness was around 1000±100 HV due to $(Ti_xNi_y)B_z$ diffusion/transition zone formation. It could be deduced that after electrochemical synthesis of TiB_2, around 40 µm thick-hard modified layer was additionally formed between the TiB_2 layer and the nickel matrix.

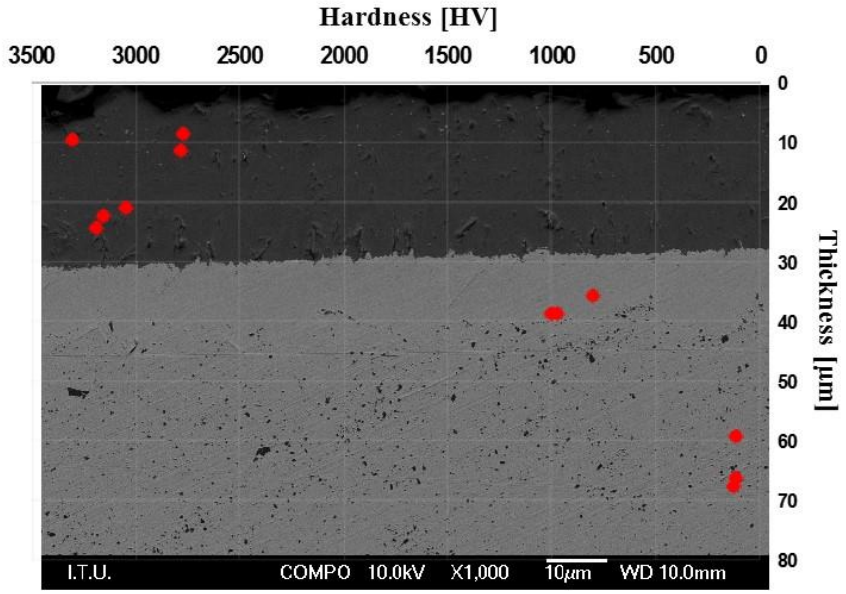

Figure 4. Cross-sectional hardness profile of TiB_2 grown after 120 min of electrodeposition.

4. CONCLUSION

In this study, electrochemical coating of TiB_2 from molten salts was introduced as an alternative way to vacuum based coating techniques and classical electrochemical metal boride synthesis methods. In addition to its simplicity and cost effectiveness of electrolysis system, the usage of environmentally friendly chemicals makes this newly developed coating process more

promising compared to currently available TiB_2 coating methods.

The deposition thickness of TiB_2 varied in a wide range between approximately 2.5 to 31 μm depending on the nature of substrate materials. The grown TiB_2 layer demonstrated the hardness value as high as 3000±200 HV.

With this novel green TiB_2 coating technique, it is possible to grow dense, homogenously thick and hard TiB_2 layer on any conductive material to improve its oxidation, corrosion and wear resistance with considerably less investment cost. We believe that this presented metal boride coating method will potentially get more attention from industry and consequently find many implementations in near future.

REFERENCES

1. R. Riedel, Handbook of Ceramic Hard Materials, WILEY-VCH, Germany, 2000.
2. R.G. Munro, J. Res. Natl. Stand. Technol. 105 (2000) 709.
3. Y. Han, Y. Dai, D. Shu, J. Wang, B. Sun, J. Alloys Comp. (2007) 327.
4. P. M. Martin, Handbook of Deposition Technologies for Films and Coatings Science, Applications and Technology, 3rd Ed., 2010.
5. K. Holmberg, A. Matthews, Coating Tribology Properties, Mechanism, Techniques and Applications in Surface Engineering, Elsevier, 2nd Ed., 2009.
6. K. Seshan, Handbook of Thin-Film Deposition Processes and Techniques Principles, Methods, Equipment and Applications, Noyes Publications, 2nd Edition, USA, 2002.
7. H. O. Pierson, E. Randich, Thin Solid Films 54 (1978) 119.
8. R. S. Sethi,. J. Appl. Electrochem. 9 (1979) 411.
9. G. Kaptay, S. A. Kuznetsov, Plasmas Ions 2 (1999) 45.
10. V.I. Shavopal, V.V. Malyshev, I.A. Novoselova, K.B. Kushkhov, Russ. Chem. Rev. 64 (1995) 125.
11. J. D. Kellner, US 3880729 (1975).
12. M. Makyta, K. Matiašovský, V.I. Taranenko, Electrochim. Acta 34 (1989) 861.
13. Wendt, H., Reuhl, K., Schwarz, V., Electrochim. Acta 37 (1992) 237.
14. M. Makyta, V. Danék, J. Appl. Electrochem. 26 (1996) 319.
15. S.V. Devyatkin, G. Kaptay, Refractory Metals in Molten Salts, Kluwer Academic Publishers, 73-80, 1998.
16. G. Ett, E.J. Pessine, Electrochem. Acta 44 (1999) 2859.
17. J. Li, B. Li, Mater. Lett. 61 (2007) 1274.
18. U. Fastner, T. Steck, A. Pascual, G. Fafilek, G. E. Nauer, J. Alloys Comp. 452 (2008) 32.
19. N. Rybakova, Production of titanium diboride coatings by electrolysis of high-temperature molten salts, Ph.D Thesis, Wien Universität, 2011.
20. J. R. A., Godinho, Optimization of TiB2 coatings electrodeposited from halide melts, Master's Thesis, Universidade Técnica de Lisboa, 2008.
21. W. F. Gale, T. C. Totemeier, T.C., General Physical Properties, Smithells Metal Reference Book, 8th Edition, USA, 2004.
22. Massalski, T.B., Okamoto, H., Subramanian, P.R, Kacprzak, L, Binary Alloy Phase Diagrams, 2nd Ed., ASM International The Materials Information Society, USA, 1990.
23. G. Kartal, S. Timur, M. Urgen, A. Erdemir, Surf. Coat. Technol. 204 (2010) 3935.
24. F. Habashi, Handbook of Extractive Metallurgy, Wiley-WCH, 1997.

AN INNOVATIVE SILVER LINES EMBEDDED SUBSTRATE DESIGN FOR DYE SENSITIZED SOLAR MODULES

Kerem Çağatay İÇLİ[a] , A. Macit ÖZENBAŞ[b]

[a] Micro and Nanotechnology Graduate Program, Middle East Technical University, Dumlupınar Bulvarı, 06800 Ankara, Turkey, cagatayicli@yahoo.com
[b] Department of Metallurgical and Materials Engineering, Middle East Technical University, Dumlupınar Bulvarı, 06800 Ankara, Turkey, ozenbas@metu.edu.tr

ABSTRACT
We employed ultrasonic spray deposition method for production of high quality FTO and ITO thin film TCOs to be employed in a novel silver embedded grid type dye sensitized solar module. Produced films exhibited dense and crytalline structure with homogeneous coverage on solar glass substrates. Obtained resistivity and light transmission values of FTO are almost same with commercially available FTO coated glasses used widely in the industry. After optimization of the chemistry and deposition conditions, 10x10 cm sized glass substrates could be produced for large area photovoltaic modules. Produced FTO films were used to construct dye sensitized solar cells and modules in comparison with commercial coating. Efficiency value of 3% on active area could be achieved which is slightly higher than commercial substrate. In order to enhance active area, silver grid lines were embedded in glass substrate and FTO coating was deposited on the lines. Due to this novel design, we achieved 2.42% efficiency on the total area of the 5x5 cm sized module, proving that this design is suitable for enhancing efficiency values of parallel type dye sensitized solar modules.

Keywords: Ultrasonic spray pyrolysis, FTO, DSSC module

BOYA UYARIMLI GÜNEŞ MODÜLLERİ İÇİN GÜMÜŞ YOLLUK GÖMÜLÜ İNOVATİF BİR ALTLIK TASARIMI

ÖZET
Bu çalışmada, özgün bir gümüş gömülü ızgara içeren boya uyarımlı güneş modüllerinde kullanılmak üzere, ultrasonik sprey kaplama metodu ile yüksek kalitede FTO ve ITO ince filmler üretilmiştir. Üretilen filmler kristal yapıda, yoğun ve yüzeyi kaplayacak biçimde cam altlıklar üzerine kaplanmıştır. Elde edilen FTO filmlerin özdirenç ve ışık geçirgenliği değerleri endüstride kullanılan ticari kaplamalarla aynı mertebededir. Kaplama koşullarının optimize edilmesinin ardından, 10x10 cm boyutlarındaki altlıklar fotovoltaik modül üretimi amacıyla hazırlanmıştır. Elde edilen FTO kaplamalar ticari kaplamalarla kıyaslamalı olarak boya uyarımlı güneş modüllerinin üretiminde kullanılmıştır. Ticari kaplamadan çok az farkla aktif alanda %3 civarında modül verimi elde edilmiştir. Aktif alanı arttırmak amacıyla, gümüş ızgaralar cam altlığa gömülmüş ve üzerine FTO kaplama yapılmıştır. Bu özgün tasarım sayesinde, 5x5 cm boyutundaki modülden toplam alan üzerinde %2.42 verim elde edilmiştir ve bu durum bu tasarımın paralel tipteki boya uyarmlı güneş hücrelerinin verimini arttırmak için uygun bir yol olduğunu ispatlamaktadır.

***Anahtar kelimeler*:** Ultrasonik sprey kaplama, FTO, BUGH modül

1. INTRODUCTION

Fluorine doped tin dioxide (FTO) thin films are emerging as the choice of transparent conducting oxide (TCO) material in most opto electronic applications like lasers, electrochromic devices, light emitting diodes, LCDs, heat resisting windows, thick film gas sensors and solar cell applications. High electronic conductivity, low cost, chemical and mechanical strength and moderate visible light transmission are the major advantages of FTO thin films compared to In_2O_3, ZnO etc [1]. Tin dioxide has a wide band gap of around 3.2 eV and in addition to visible light transmissivity, shows limited conductivity in intrinsic form, however upon doping with cations like antimony or anions like fluorine, carrier concentration values can be extended and n-type electrical conductivity is achieved [2]. Fluorine has an ionic radii of 1.17 A^o in comparison to oxygen ion having 1.22 A^o and easily substitutes in tin dioxide lattice [3]. This donor effect leads to electron density increase in tin dioxide conduction band similar to oxygen vacancies present in the structure. As a result of high mobility observed in SnO_2, FTO is a common TCO material. In contrast to indium tin oxide (ITO) which is known to be the highest performance TCO material, FTO can withstand most reactive chemicals and especially high temperatures in which ITO films face degradation due to oxidation of oxygen vacancies and lose most of their performance by means of electrical conductivity [4]. FTO is the choice of TCO material for applications requiring high temperature treatment like DSSCs, OLEDs or organic solar cells.

Several methods for growth of FTO thin films have been proposed including sol-gel methods like spin and dip coating [5-6], chemical vapour deposition [7], reactive sputtering [8] and spray deposition [9-14]. Among all, spray pyrolysis method is the most widely preferred technique for growing homogeneous and dense thin films, especially the oxides because deposition can be carried out in athmospheric conditions and eliminates the necessity of expensive vacuum chambers and complicated metallorganic precursors required in CVD method. Spray pyrolysis can also be referred as atmospheric CVD because atomization of the precursor is achieved by compressed gas introduction. Precursors are firstly dissolved in solvents like water or alcohols and broken into fine droplets under compressed gas. Degradation of precursor and chemical reactions take place on the heated substrate surfaces simultaneously [15]. Ultrasonic spray pyrolysis (USP) method uses high frequency ultrasonic vibrations to create a fine mist of precursor solvents including the fine droplets instead of compressed air. The droplet sizes vary between 30-100 microns depending on the frequency of piezo crystal. USP method has the advantage of fine and homogeneous droplet size distribution where conventional spraying contains fine droplets mixed with coarser ones. The mist is transported to the heated substrates with a carrying gas like air or nitrogen. Deposition of various metal oxides have been achieved using USP method on different substrates from simple precursors, mainly nitrates or chlorides of selected metals. Deposition of FTO layers using USP have been reported using aqueous solutions of dimethyltindichloride or tin dichloride as precursors on glass substrates [16,17].

Dye sensitized solar cells attract attention due to their low cost and simple production techniques. For commercialization of DSSCs, large area module production is essential. There are several types of module architectures including parallel type, serial Z type, serial W-type and monolithic structures [18]. Parallel type connection of dye sensitized solar cells requires addition of current collecting silver grids due to limited conductivity of the large FTO substrate. However, these lines are strongly corroded by the redox electrolyte and unprotected silver grid containing modules fail [19]. In order to protect silver lines, additional protecting

layers are used and stripe type modules are produced. This situation leads to reduction of active working area of the module and efficiency values are decreased compared to cells.

In this paper, we report an innovative module design for dye sensitized modules. A silver line embedded FTO coated glass substrate is introduced where silver grids are embedded to the glass substrate and FTO layers are deposited over the silver lines in order to protect corrosive electrolyte form the silver line without decreasing the active working area of the module. Deposition of FTO and ITO layers on glass substrates were conducted by USP method from methanolic solutions. Effect of fluorine and tin concentration in precursor solution on electrical, optical and morphological properties have been investigated. As a demonstration for mass production with USP method, a 10x10 cm sized glass substrate was also coated using our laboratory made coating system equipped with an x-y scanner stepper motor and piezoelectric transducer. Parallel type dye sensitized solar modules were constructed using the produced glass substrates in comparison to commercial FTO glass. A 5x5 cm sized parallel type silver line embedded module was demonstrated.

2. EXPERIMENTAL

For deposition of FTO layers, firstly precursor solutions were prepared using $SnCl_4.5H_2O$ as tin source and NH_4F as the fluorine source. Concentration of $SnCl_4.5H_2O$ was kept constant at 0.2 M for all depositions and ammonium fluoride was added to the solution according to F/Sn atomic ratios from 0 to 3. In the preliminary experiments, water was used as the solvent, however, it was observed that using water based solutions yielded poor sheet resistance values. In literature ethanol is the mainly employed solvent, but in our work, 1.63 MHz nebulizer frequency is not sufficient to break the bonds of ethanolic solution and no mist formation occurred. Due to this reason, methanol was chosen as the solvent and $SnCl_4.5H_2O$ was dissolved in this solution. Saturated aqueous solutions of NH_4F were prepared and added to the main solution and subjected to ultrasonic treatment in an ultrasonic bath until a completely clear solution was obtained. 50 ml of each deposition solution was enough for small samples; for 10x10 cm sample, 100 ml solution was consumed. Depositions were carried out on clear solar glass substrates (having a 90% visible light transmission) at a hot plate programmed to 500^oC and temperature was kept constant for all depositions. ITO layers were deposited in the same way as the FTO layers using $InCl_3.4H_2O$ as indium source and $SnCl_2.2H_2O$ as tin source for Sn/In atomic ratios ranging from 0 to 0.125. The deposition setup is made of two components, the nebulizer where precursor solutions are converted to fine mist under ultrasonic vibrations derived from the piezocrystal and the x-y scanner stepper motor which scans the surface of the substrate and delivers the mist through a nozzle which is carried by air. Factors like the scan speed, nozzle height, mist flow rate and scanning area were all optimized in order to achieve the best homogeneity. Films were characterized by XRD, four point electrical measurements, UV-Visible light transmission and scanning electron microscopy studies.

Parallel type dye sensitized solar module was constructed using the 10x10 cm sized FTO coated substrate and for comparison, with a commercial FTO coated solar glass (Solaronix 22-7). Both substrates had a sheet resistance value of 7 ohm/sq and similar visible light transmission. For preparation of the solar modules, TiO_2 layers were deposited on the precleaned substrates using screen printing method. The screen paste including 20 nm TiO_2 nanoparticles was prepared by acidic hydrolysis and peptization of titanium isopropoxide and obtained particles were dispersed in terpineol and ethyl cellulose according to a previously published procedure [20]. For deposition of 200 nm scattering layer, Dyesol WER2-O

commercial paste was used. The module is consisted of 7x92 mm sized 8 stripes which corresponds to an active area of 51.5 cm^2 and fired at 500°C. Silver grids were deposited by screen printing a commercial silver paste between and around each stripe. The thick fims were immersed in a 0.5mM N719 (Solaronix) acetonitrile solution for 24 hours. Counter electrodes were prepared using a commercial platinium paste (Dyesol) and electrolyte was injected through the holes pre-drilled on each stripe. Working and counter electrodes were laminated by hot pressing at 100°C using a hot melt thermoplastic Surlyn film. I-V characterization of the modules were conducted under 1.5 AM conditions.

Silver line embedded substrate was prepared by firstly scribing grid lines on the 5.5x5.5 mm sized uncoated solar glass separated by 1 cm distance between each line. A silver paste was used to fill the grids and the glass was fired at 450°C. FTO layer was deposited by USP method until 15 ohm/sq sheet resistance value was reached. The parallel module was constructed by depositing 5x5 cm sized titania layer diretly on the FTO covered grids and modules were prepared by laminating the counter electrode similar to the parallel type modules. The active area of the module was 25 cm^2 .

3. RESULTS AND DISCUSSION

XRD spectra of the FTO and ITO films are given in Figure 1. Here, sample name FT0 1.62 and ITO 5 refer to F/Sn ratio and Sn/In ratio inside the precursor solutions, respectively. It is seen that FTO films were formed in cassiterite crystal structure of tin dioxide (ICDD Card No 41-1445) without any secondary phase and preferential orientation of (200) plane can be seen. ITO films similarly are formed in bixbyte structure of indium oxide (ICDD Card No 6-0416) without any secondary phase.

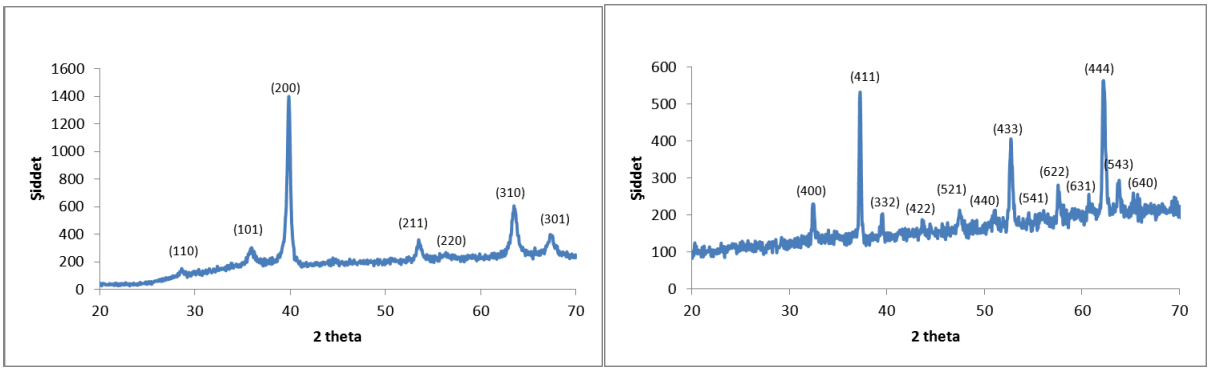

a) **b)**

Figure 1. XRD spectra of the samples **a)** FTO 1.62 **b)** ITO 5

For both FTO and ITO films, absence of secondary phases like tin fluoride or residual ammonium fluoride for FTO and tin dioxide or tin oxide for ITO films show that both fluorine and tin are succesfully doped into the lattice which is the main reason of the enhancement of electrical properties. It is known that substitutional replacement of the dopant atoms into the lattice leads to increased electron concentration in conduction band of semiconductors. Films are well crystallized and show dense structure as there is no significant peak broadening in the XRD spectra and revealed by the cross sectional and surface SEM images of the films given in Fig. 2.

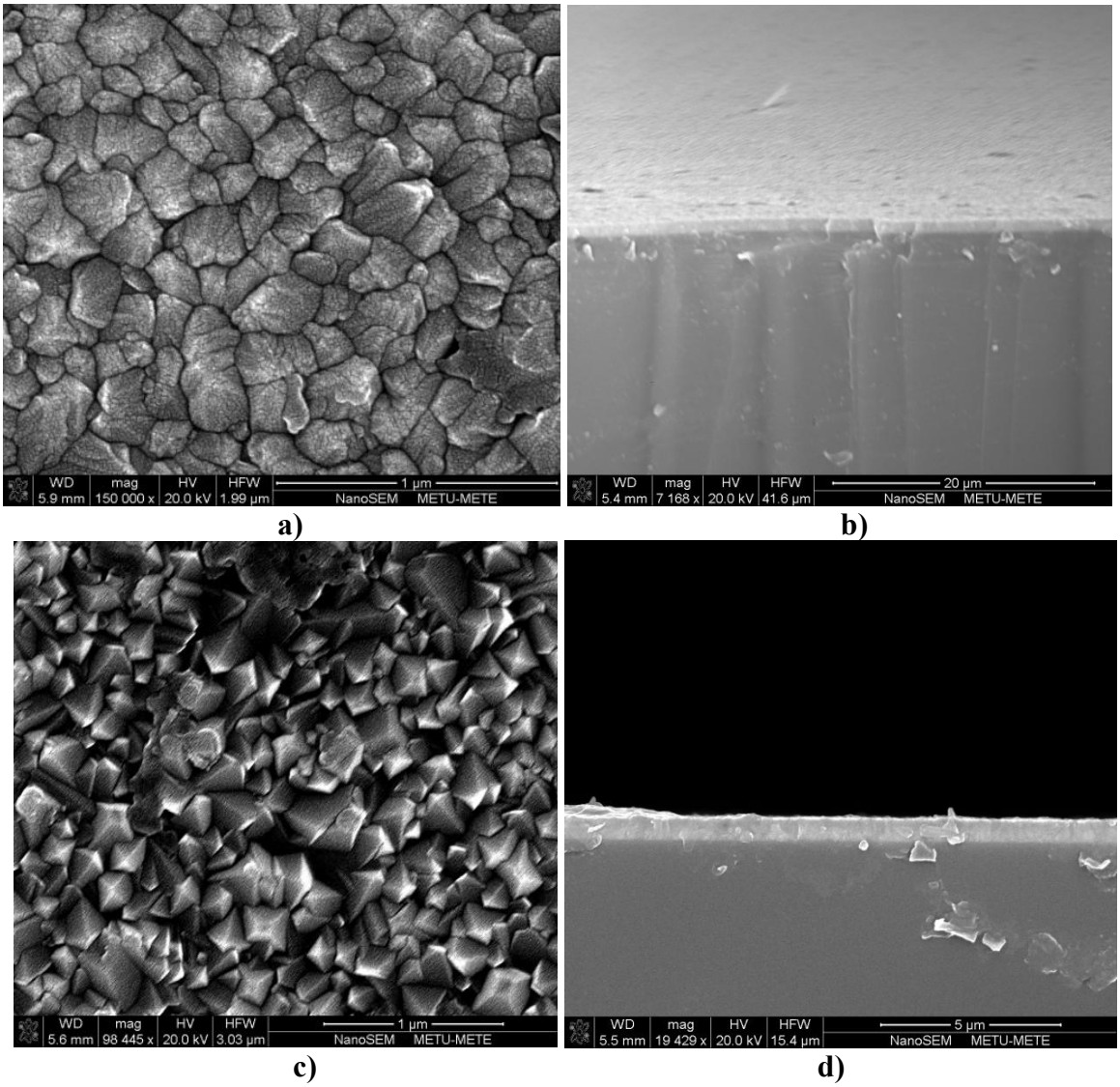

Figure 2. SEM images of the surface **(a)** and cross section **(b)** of FTO and surface **(c)** and cross section **(d)** of ITO thin films

In Table 1 and Table 2 sheet resistance and resistivity values of FTO and ITO films measured with four point probe method related to different dopant concentration in the starting solution are given.

Table 1. Variation of sheet resistance, measured thickness and resistivity values of FTO films

Sample	Fto 0	Fto 0.25	Fto 0.5	Fto 0.75	Fto 1	Fto 1.25	Fto 1.62	Fto 2	Fto 2.5	Fto 3
Sheet resistance (Ohm/sq)	25.0	20.6	6.7	7.3	6.2	7.2	6.5	7.1	9.2	7.4
Thickness (nm)	510.0	600.0	1200.0	910.0	875.0	890.0	750.0	1500.0	680.0	870.0
Resistivity (Ohm.cm) x10^4)	12.76	12.38	8.08	6.61	5.43	6.43	4.9	10.65	6.25	6.40

Table 2. Variation of sheet resistance, measured thickness and resistivity values of ITO films

Sample	Ito 0	Ito 2.5	Ito 5	Ito 7.5	Ito 10	Ito 12.5
Sheet resistance (Ohm/sq)	20.6	8.8	7.4	7.7	18.9	21.9
Thickness (nm)	670	690	740	715	580	660
Resistivity (Ohm.cm) x10^4)	13.84	6.11	5.52	5.55	11.0	14.45

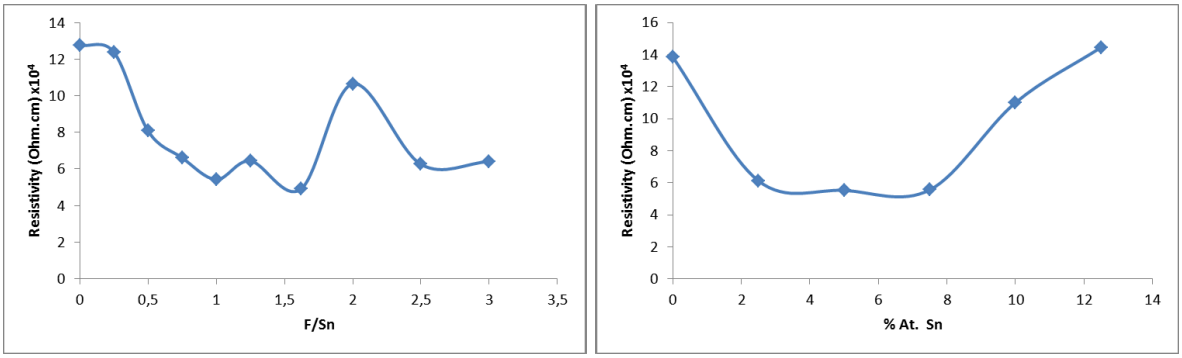

a) **b)**

Figure 3. Dependence of resistivity values of **(a)** FTO and **(b)** ITO thin films on dopant concentration

From Fig. 3, it is seen that resistivity of films decreases upon doping and an optimum doping concentration is achieved while after this value, resistivity starts to increase again. This trend has been reported by many authors and it is explained with the supression of electronic conduction [21,22]. Although doping increases the electron concentration of the films, after a critical value electron scattering due to ionized impurities becomes the dominant factor which retards the electron motion through the crystal [23]. For FTO films, highest resistivity value belongs to 1.62 F/Sn (20% weight ratio) ratio value in the starting solution which is the most common recipe employed in other works [24]. Similarly, for ITO films highest resistivity is obtained for 5% Sn atomic ratio which is also consistent with early reports.

For solar cell applications, window layers not only should provide a low resistivity, but also should have high light transmission values for maximum light harvesting. In Fig.4 visible light transmission values of the FTO coatings and ITO for two different sheet resistance values are given. It is seen that upon coating, visible light transmissions are decreased compared to that of uncoated glass (Fig.4c) and lower sheet resistance leads to lower transmission at the same time. This is due to both thicker coatings required for lower resistance and free electron absorption event in the conduction band. ITO films produced in this work yield poor light transmission compared to FTO films for similar sheet resistance values. Although ITO is known to be high performance material, most ITO films used in the market are produced under reducing or oxygen deficient atmospheres which results in enhanced electron concentrations for thinner films.

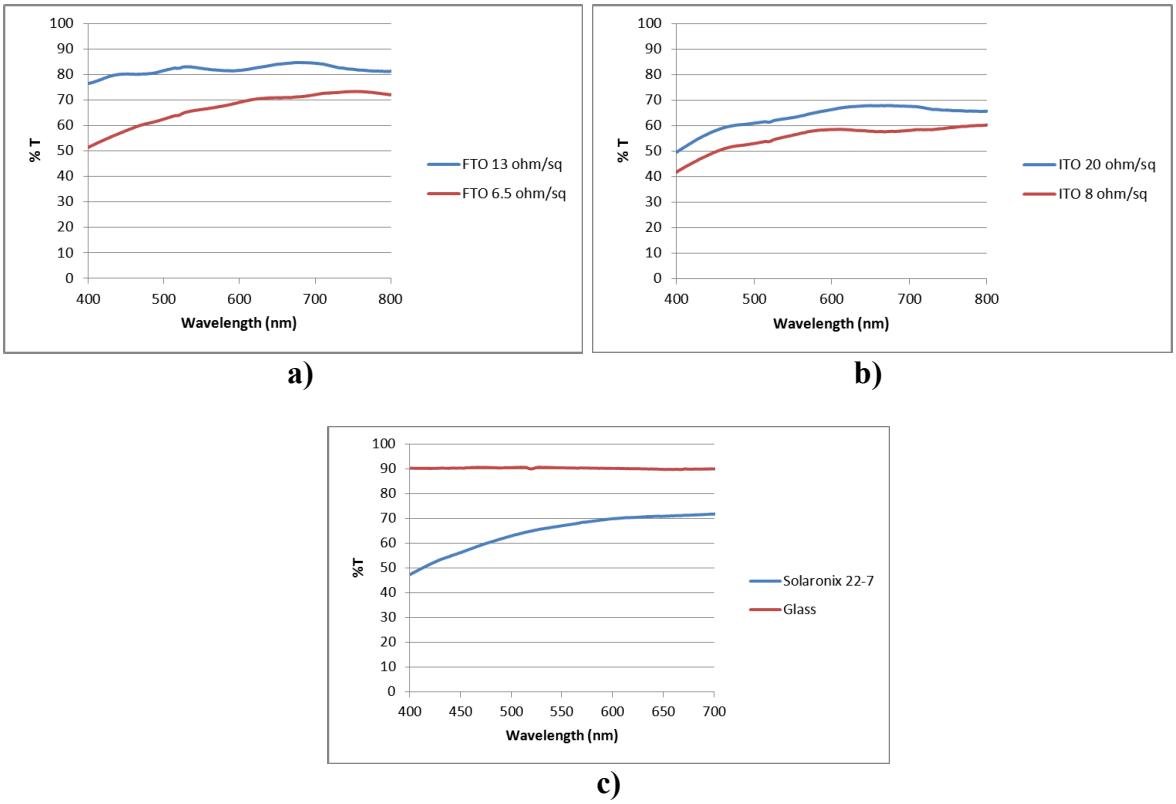

Figure 4. UV-Vis spectra of **(a)** FTO thin films **(b)** ITO thin films with different sheet resistance values and **(c)** uncoated solar glass and commercial FTO substrate

For production of dye sensitized cells and modules, FTO thin films having sheet resistance of 6.5 ohm/sq and for comparison commercial FTO film with 7 ohm/sq were used. These two films have similar resistance and visible light transmission as can be seen from Fig.4. 10x10 cm sized glass substrates were deposited and used to construct parallel type modules and I-V characteristics of the small scale cells (0.20 cm^2) and modules are given in Figure 5 and Table 3.

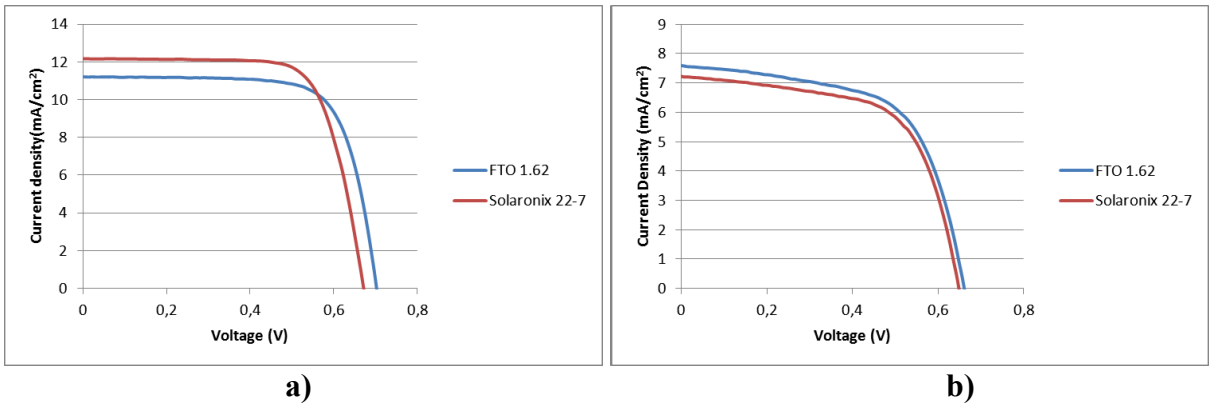

Figure 5 J-V curves of **(a)** cells and **(b)** modules

Table 3. Cell characteristics of cells and modules constructed in this work measured under AM1.5

Sample	V_{oc} (V)	J_{sc} (mA/cm^2)	FF	% Eff.	Power (Wp) (mW)
FTO 1.62 (Cell)	0.69	11.2	0.73	5.64	-
Solaronix 22-7 (Cell)	0.67	12	0.72	5.78	-
FTO 1.62 (Module)	0.66	7.57	0.61	3.04	156.5
Solaronix 22-7 (Module)	0.64	7.2	0.62	2.85	146.7

Dye sensitized solar cells produced using the commercial substrates and substrates deposited by USP method in this work have similar performances as expected from the sheet resistance and light transmission values which are close to each other for two substrates. Small deviations in the open circuit voltage, current density and fill factors are attributed to cell preparation conditions. Modules of 10x10 cm size have efficiency values lower close to 2 fold than cells. This situation is a common property of all types of solar cells and is related to high surface resistance of large area substrates. Although silver lines deposited on the coated glasses, fill factors around 0.72 are not possible for modules which have around 0.61. This low fill factor and related decreased photo current values are the main reason of the reduction in the overall efficiency values. Best efficiency value obtained in this work is 3.04% for the USP deposited substrate and is slightly higher than the commercial substrate which again can be related to module preparation conditions.

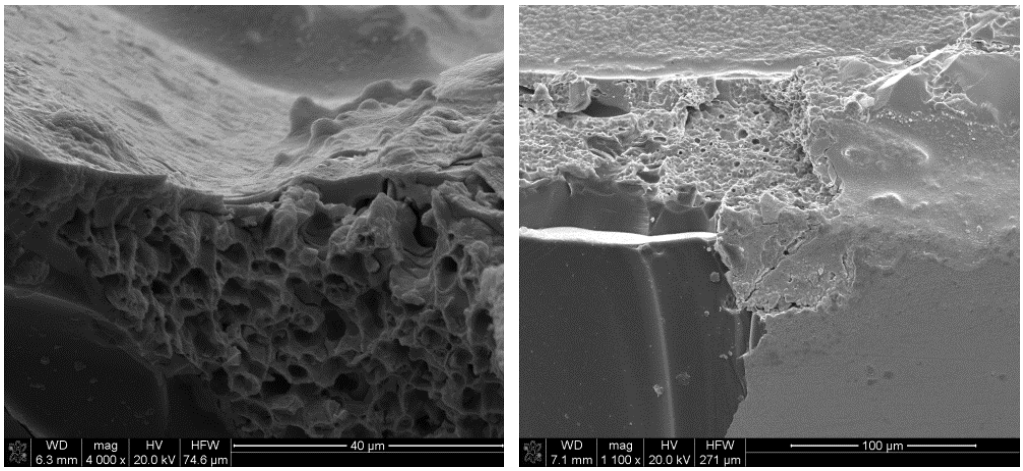

a) **b)**

Figure 6. SEM images of a silver grid from **a)** cross section and **b)** top view

For constructing silver embedded substrates, silver lines were scribed and silver was deposited using a silver paste. USP method was chosen as the deposition method for FTO layer because of the fact that USP method yields higher coverage compared to conventional spray. USP method employs vapourized form of the precursor solution and its ability to penetrate into hole and pores is higher. From Fig. 6, it can be seen that surface of the silver

grid is completely covered by FTO layer and although the silver lines are porous, coverage can be achieved.

The silver line embedded and FTO covered substrate was used to construct parallel dye sensitized solar modules. J-V curve of the 55x55 mm sized module is given in Fig. 7.

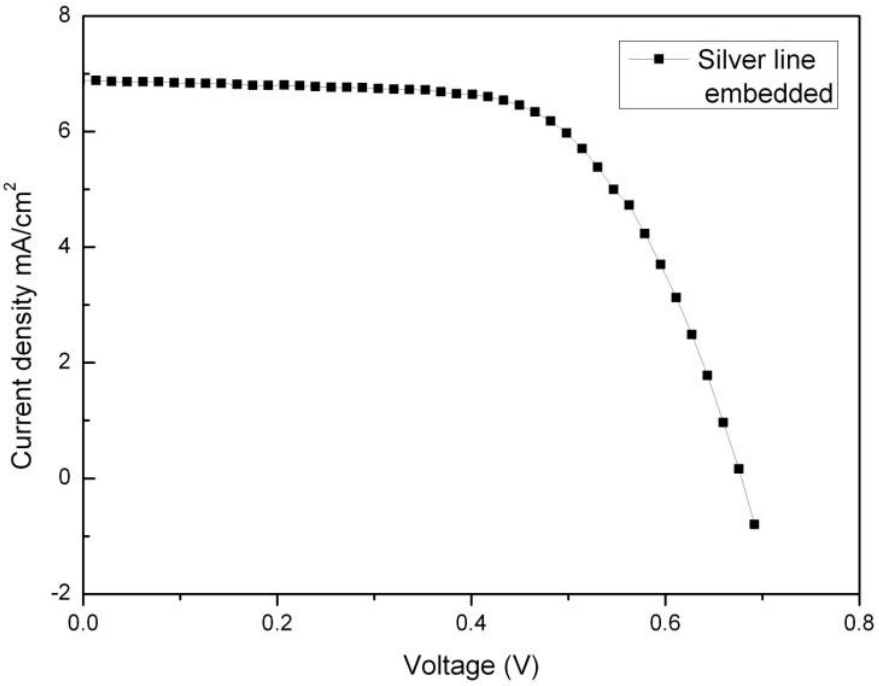

Figure 7. J-V curve of the silver line embedded parallel module

Silver line embedded parallel module gives an efficiency value of 2.9% from active area which is 25 cm^2 in this work where total area is 30 cm^2 and corresponding total area efficiency is 2.42%. This small difference in efficiency values of total and active area is directly related to the design employed in this work. The efficiency of the parallel module given in Table 3 is 3.04% calculated from active area, however this value is 1.56% calculated from total area. As long as silver lines are buried in the glass and covered with a dense non-porous FTO layer as can be seen from SEM images, the whole silver line no more needs additional protection and titania layer can be deposited on these lines to which in turn leads to enhanced active area of the module. Such a high active area cannot be achieved for the parallel type conventional modules where lines are protected by surlyn film and totally inactive.

In summary, ultrasonic spray deposition method is a versatile and low cost alternative method to deposit high quality and homogeneous oxide layers on glass substrates used in dye sensitized solar cells and thin film photovoltaics. Enlargement of the coating to commercial sizes is possible and seems to be an efficient way of mass production. Laboratory scale cells as well as modules prepared from USP deposited substrates show no significant difference in performance compared with commercial substrates prepared under identical conditions. An embedded silver line substrate was introduced and showed higher active total area efficiency value compared to conventional parallel type module. USP is a convenient method for formation of FTO layers on the grids and full coverage of the grid was achieved. For future

directions, deposition of hole and crack free lines is the critical parameter to achieve full active area paralel type modules.

REFERENCES

1. J. Robertson, J. Phys. C, Solid State Phys., 12, 4767, 1979.
2. Z.M. Jarzebski, J.P. Marton, J. Electrochem. Soc. 123, 2, 2000
3. A. Vincent, J. Electrochem. Soc. 119, 515, 1972
4. M. Gross, A. Winnacker, P. J. Wellmann, Thin Solid Films 515, 8567–8572, 2007
5. Y. Takahashi, Y. Wade, J. Electrochem. Soc. 127, 267, 1990
6. S. Rani, N.K. Puri, S.C. Roy, M.C. Bhatnagar, D. Kanjilal, Nucl. Instrum. Methods Phys. Res. B 266, 1987, 2008
7. J.R. Brown, P.W. Haycock, L.M. Smith, A.C. Jones, E.W. Williams, Sens. Actuators B 63, 109, 2000
8. S. Boycheva, A.K. Sytchkova, M.L. Grilli, A. Piegari, Thin Solid Films 515, 8469, 2007
9. T. Fukano ,T. Motohiro, Solar Energy Materials & Solar Cells 82, 567–575, 2004
10. M. Abd-Lefdil, R. Diaz, H. Bihri, M. A. Aouaj, F. Rueda, Eur. Phys. J. Appl. Phys. 38, 217–219, 2007
11. C. Agashe , J.Hupkes, G.Schope, M.Berginski, Solar Energy Materials&SolarCells 93 (2009) 1256–1262
12. B. Thangaraju, Thin Solid Films 402, 71–78, 2002
13. K. S. Ramaiah, V. S. Raja, Applied Surface Science 253, 1451–1458, 2006
14. A.V. Moholkar, S.M. Pawar, K.Y. Rajpure, C.H. Bhosale, J.H. Kim, Applied Surface Science 255, 9358–9364, 2009
15. D. Perednis, L. J. Gauckler, Journal of Electroceramics, 14, 103–111, 2005
16. K.Omura, P. Veluchamy, M. Tsuji, T. Nishio, M. Murozono, Journal of The Electrochemical Society, 146 (6), 2113-2116, 1999
17. V. Bilgin, I. Akyuz, E. Ketenci, S. Kose, F. Atay, Applied Surface Science 256, 6586–6591, 2010
18. A. Hinsch et al. Prog. Photovolt: Res. Appl. 16, 489–501, 2008
19. R. Sastrawan, J. Renza, C. Prahl, J. Beier, A. Hinsch, R. Kern, Journal of Photochemistry and Photobiology A: Chemistry, 178, 33–40, 2006
20. M. Gratzel et al.,. Prog. Photovolt: Res. Appl, 15 , 603–612, 2007
21. T. Kawashima, H. Matsui, N. Tanabe, Thin Solid Films 445, 241, 2003
22. E. Elangovan , K. Ramamurthi, Applied Surface Science 249, 183–196, 2005
23. A. I. Martınez, L. Huerta, J. M. O-Rueda de Leon, D. Acosta, O. Malik, M. Aguilar, J. Phys. D: Appl. Phys. 39, 5091–5096, 2006
24. Y. Sawada, C. Kobayashi, S. Seki, H. Funakubo, Thin Solid Films 409, 46–50, 2002

Gaseous Nitriding of 31CrMoV9 Steel: Modelling Residual Stress – Depth Profile Relation Using Indentation Method

•

31CrMoV9 Çeliğinin Gaz Nitrürlenmesi: Kalıntı Gerilmeleri-Derinlik İlişkisinin Batırma Yöntemiyle Modellenmesi

Rıdvan Gecü[1], Ahmet Fatih Yayla[2], Nuri Solak[2], Kürşat Kazmanlı[2], Mustafa Ürgen[2]

[1]Yıldız Technical University, [2]İstanbul Technical University - Türkiye

ABSTRACT

This study aims to investigate the effects of gaseous nitriding parameters on microstructure and residual stress behavior of 31CrMoV9 nitriding steel. Nitriding experiments were done in a gas mixture of ammonia and hydrogen at 525°C for 2 hours at different nitriding potentials. The microstructure of the nitrided specimens was analyzed by employing hardness measurements, optical microscopy and X-ray diffraction. The thickness of compound layer was determined by glow discharge optical emission spectroscopy (GDOES). Indentation method was performed for calculating depth dependent residual stress profile and results were also verified by XRD using sin2Ψ technique. Results of indentation showed that compressive residual stress developed in all specimens and compressive residual stress values decreased by approaching deeper regions into the specimen. Multiplication of the calculated stress values of indentation tests with a correction coefficient (K) resulted in a very good correlation between the stresses measured with the XRD.

Keywords: Gaseous nitriding, indentation, residual stress, GDOES, XRD.

ACCELERATED ELECTROCHEMICAL CORROSION TESTING OF POWDER PAINTED CARBON STEEL SURFACES VIA AC-DC-AC TECHNIQUE AND ITS POTENTIAL FOR INDUSTRIAL USE

Aslı ÖZEL*,**

*Arcelik A.S, Istanbul, Turkey

asli.ozel@arcelik.com

** Istanbul Technical University, Istanbul, Turkey

ABSTRACT

The corrosion test methods for powder painted materials need very long time periods and may not always present an objective data. In contrast to these existing methods, Electrochemical Impedance Spectroscopy (EIS) allows the evaluation of corrosion behaviour of materials quantitatively in a shorter period of time. With EIS, accelerated cyclic methods using AC-DC-AC techniques can be developped according to corrosion mechanism and the corrosion resistance of the system that is being studied.

In this study, a cyclic test method with 5 substeps is generated focussing on the corrosion failure mechanism of painted surfaces. DC 03 quality low-carbon steel sheets with 100cm^2 surface area are used as substrate material. 3.5% NaCl solution is used as electrolyte. Effects of different surface preparation techniques on the corrosion behaviour is also investigated. Final electrochemical impedance values of the paint systems are used as the indicative criteria. Results showed that using this method; the test periods can be shortened up to 20 times for powder painted steel surfaces. Using this method as a quality control tool in industry helps to save time and allows an efficient investigation of both paint adhesion strength and corrosion resistance.

Keywords: EIS, AC DC AC, corrosion, powder paint

AC-DC-AC TEKNİĞİ İLE TOZ BOYA UYGULANMIŞ KARBON ÇELİĞİ YÜZEYLERE ELEKTROKİMYASAL HIZLANDIRILMIŞ KOROZYON TESTİ UYGULAMASI VE YÖNTEMİN ENDÜSTRİYEL OLARAK KULLANIM POTANSİYELİ

ÖZET

Toz boya sanayide yaygın olarak kullanılmakta olup, farklı yüzey hazırlama sistemleri ile oldukça yüksek korozyon dayanımları elde edilebilmektedir. Ancak, özellikle sanayide sıklıkla kullanılmakta olan korozyon test yöntemleri tercih edildiğinde bu sistemlerin korozyon test süreleri oldukça uzun olmaktadır. Test süresinin uzun olmasının yanı sıra, düşük numune adetleri ile elde edilen sonuçlar da her zaman sağlıklı olamamaktadır. Daha kısa sürelerde daha etkin şekilde korozyon performansının değerlendirilebilmesi elektrokimyasal empedans spektroskopisi (EIS) ile mümkündür. EIS ile hızlı bir şekilde kantitatif olarak korozyon dayanımları belirlenebilmektedir.

Bu çalışmada; toz boya uygulanmış karbon çeliği yüzeylerin korozyon dayanımları 5 alt adımdan oluşan çevrimsel bir hızlandırılmış test yöntemi ile belirlenerek, sonuçlar ASTM B117 tuzlu su sisi deneyi sonuçları ile karşılaştırmalı olarak incelenmiştir. Çalışmada elektrolit olarak ağ. %3,5'luk tuzlu su çözeltisi ve taban malzeme olarak da DC03 kalite düşük karbonlu çelik sac malzeme kullanılmıştır. Test plakaları 10cm x 10cm ebatlarında olup, EIS ile incelenen yüzey alanı 14,6cm^2'dir. Farklı yüzey hazırlama yöntemlerinin korozyon dayanımına etkileri de aynı yöntem ile incelenmiştir. Sonuçlar; AC-DC-AC tekniklerinin endüstride kullanımlarının boyalı sistemlerin korozyon dayanımlarının belirlenmesinde zaman kazandıran ve etkin bir araç olduğunu göstermiştir.

Anahtar Kelimeler: EIS, AC-DC-AC, korozyon, toz boya

1. INTRODUCTION

Improved methods for assessing the corrosion controlling performance properties of powder painted steel surfaces are needed in many industries such as aerospace, automotive and appliance. Difficulties with widely used and accepted test procedures like ASTM B117 (salt spray test) have been well documented by many researchers worldwide.[1-3] There is a great need for reliable short-term testing procedures since paint formulators are working on stronger protection systems which need longer testing periods. A useful test must be reproducible and fast.

Measuring electrical impedance of a coating across its thickness gives very useful information about the corrosion protection properties of the system being studied. The paint system is a multilayer system that is placed inbetween the conductive electrolyte on top and the metallic substrate underneath. It is known that intact coatings have very high impedance (both resistance and capacitance) Low frequency impedance deteriorates upon weathering until it drops to the value of a bare metallic substrate.

Stated simply EIS is the measurement of impedance over a range of frequencies. Using an electrolyte solution, a voltage (electrical potential) is applied to a coating and the resulting

impedance of the coating is measured. Impedance is defined as the ability of a circuit to resist the flow of alternating electrical current.

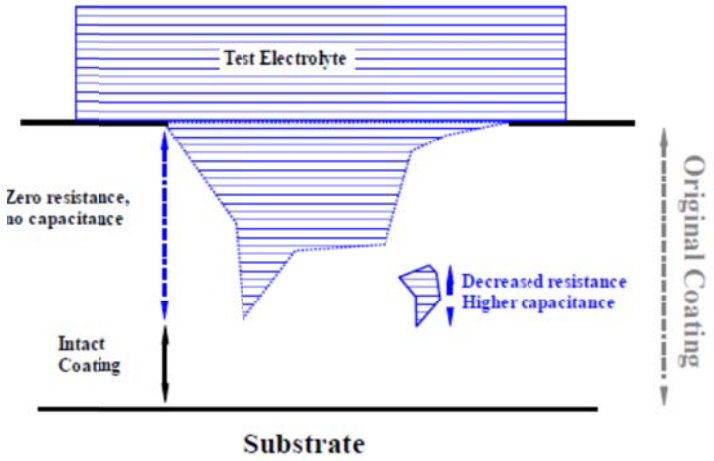

Figure 1. Coating deteriotion during electrochemical testing [4]

A plot is generated of the impedance values over a range of frequencies and the impedance at 100 mHz is used as a measure of the corrosion resistance of the sample. Higher impedance values mean better corrosion resistance.

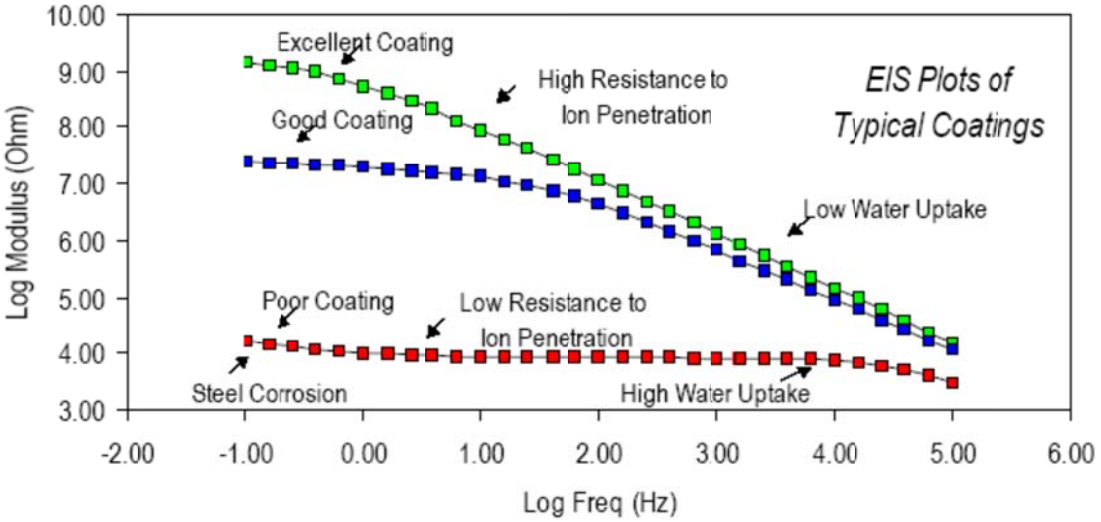

Figure 2. EIS Plot of typical coatings [5]

Many studies are made for investigating corrosion resistance performance of coated metals by using different techniques; many of which involve dipping in different agressive (usually 0.1N NaCl or 3.5 wt. % NaCl solution) electrolyte solutions for long time periods and measuring impedance values at low frequencies both in the beginning and at the end of the dipping periods. This type of testing protocols are mainly used for the ranking of different paint systems. On the other hand, there also limited number of works focussing on lifetime prediction of painted surfaces as well. Hollaender et al. developed a rapid method for testing coated metals in food packaging consisting in a combination of DC and AC measurements (AC-DC-AC procedure) which has been successfully adapted and used by Suay et al. in wet paints applied to steel substrates. [6-8] Also, Kendig et al. made studies about lifetime prediction of solvent based automotive paints.[9] More recent works of J. J. Gracenea, J.J. Suay and M. J. Gimeno on the characterization of organic coating systems by accelerated cyclic electrochemical tests develeoped by their group is an improved method which

Hollaender et al used. Technique is based on a AC-DC-AC method which is very similar to the approach used in this study. [10-14]

In this study four different powder painted systems which differ in their surface preparation techniques are investigated using both ASTM B117 protocol and AC-DC-AC method. Both techniques are used to compare the efficiencies of the surface preparation techniques. Also, more importantly the two testing methods are analyzed for further correlation studies.

2. EXPERIMENTAL

2.1. Materials

Test panels are cut from DC03 quality steel sheets. Their dimensions are 10cm x 10cm. Powder paint used is a 60% epoxy-40% polyester system. As surface pretreatment; four different cases are studied. Corrosion resistance of zinc phosphate, zinc phosphate + cataphoresis, silane based pretreatment, silane based pretreatment + cataphoresis systems are evaluated using two different test methods. Powder coating thickness is 40 µm. Synonyms used for the samples are summarized in Table 1.

Table 1. Synonyms used in representation of materials

ZP	zinc
C	cataphoresis
PP	powder paint
SBP	silane based pretreatment

2.2. Testing Methods & Equipment

2.2.1.AC-DC-AC Method:

The paint testing cell design is given in Figure 3. Three electrode principle is used where a graphite rod is used as the counter, saturated calomel is used a the reference electrolyte. The potentiostat used is Gamry Interface 1000 and the data is analyzed using EIS300 software. Tests are repeated until reproducible results are achieved.

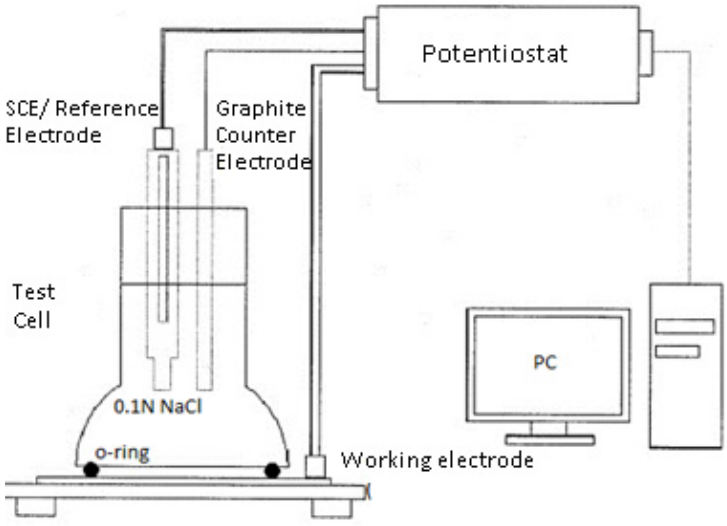

Figure 3. Test cell design

The substeps of the testing is as follows:
AC Step: Initial impedance measurement of intact painted surface.
DC Step: Constant cathodic voltage (-4mV, at 23°C) is applied forcing H_2 formation and paint delamination is triggered. Electrolyte-substrate contact and corrosive ion migration is also forced to occur.
Open Circuit Potential Step: After the cathodic disbonding step a new level of balance is reached in this relaxation period.
AC Step: Final impedance measurement of the system after the relaxation.

Each cycle consists of four substeps defined above. For the systems tested, six cycles of testing is required.

2.2.2. Salt Spray Test:

Salt spray tests were made by using Weiss SC450 cabin in accordance with ASTM B117 standard. The plates placed in the cabin with 15 to 30˚ angle from vertical. The testing solution is 5% by weight of pure sodium chloride and the solvent is pure water used in salt spray test. Spraying is done with water saturated air. Spray pressure is 0,9-1 bar. Condensing solution have the range of 6,5-7,2 pH and testing temperature is 35±2˚C. In this test a cross is drawn in the center of the test panel on the painted side. The depth of the cross ensures to reach the bare metal substrate surface. The cutting sides of the test panels are protected by lacquer application as stated in the standard procedure. The samples are then introduced in a salt fog spray chamber where a brine fog is created with a 5 wt. % NaCl water solution. The samples are collected at the end of 240 – 360 – 500 hours and evaluated after 24h of ambient exposure. The length of the rusted region from the cross is measured in mm and recorded.

3. RESULTS

Cyclic electrochemical test and salt spray test results of all the systems tested are given in Table 1.

Table 2. Summary of test results for all tested systems

	SBP + PP	**ZP + C + PP**	**ZP + PP**	**SBP + C + PP**
F= 1Hz Z initial	1.73 x 10^8	1.86 x 10^10	2.79 x 10^7	1.84 x 10^8
F= 1Hz Z final	2.73 x 10^7	2.67 x 10^8	1.707 x 10^6	8.30 x 10^5
Salt spray test result (mm)	2.0-2.5	1.0	1.0	2.0-3.0
Adhesion at the end of salt spray test (%)	80 - 85	95	90	90 - 95

The Bode graphs of the impedance measurements for all the systems are given in Figure 4. The curves further apart from each other on the same graph indicate a poorer resistance of corrosion where there is a sign of significant impedance drop inbetween the inital intact impedance and the final impedance values. On the other hand, curves closer to each other mean a smaller difference among impedance values of a system that can also be followed from Table 1.

Cathodic disbonding depends on transport of some reactants through the coating film. Thicker film slows the permeation of reactive species and the cathodic disbondment rate, therefore in

this study panels with similar powder paint thicknesses have been investigated in order to compare the differences between surface preparation techniques. Additionally, cathodic disbondment increases with test time. Cathodic disbonding test step duration and the applied voltage is fixed; in order to make sensiible comparisons.

For ranking of the paint systems one should also consider making adhesion tests after salt spray, since cathodic disbonding step triggers delamination in electrochemical testing. When taken into consideration the adhesion strength after the salt spray; the strongest system is zinc phosphate + cataphoresis system where we see both higher impedance values both initially and finally. This is also confirmed with the salt spray test results as well in terms of creepage and adhesion strength. On the other hand; the lowest corrosion resistance is seen in the silane based pretreatment + cataphoresis + powder paint system. Same result is also achieved with the salt spray test results.

Table 3. Overview of samples after salt spray test and Bode plots for all systems

ZP + C + PP	
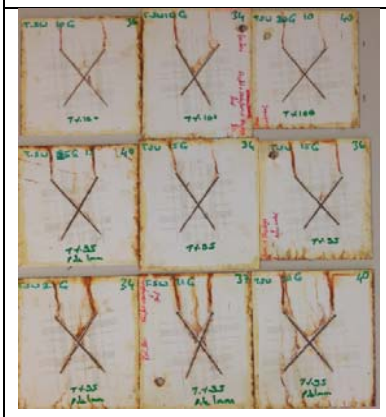	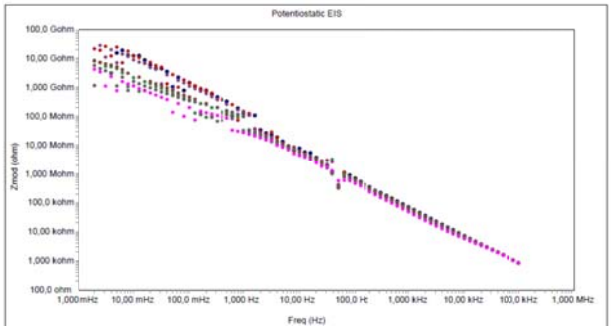
SBP + C + PP	
	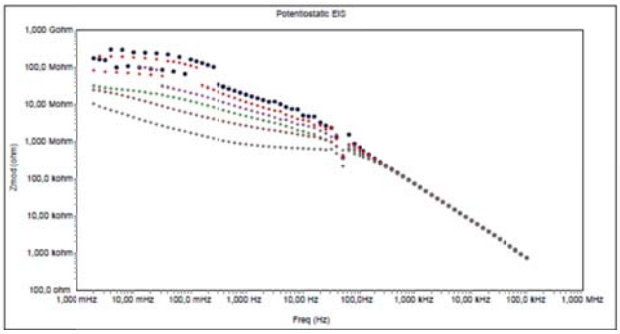
ZP + PP	
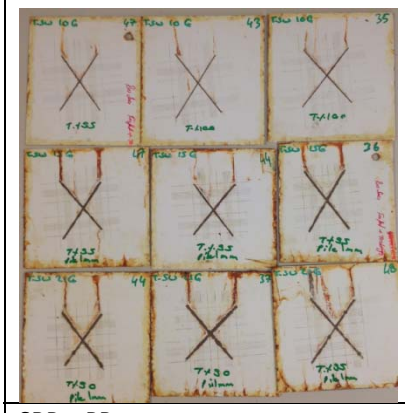	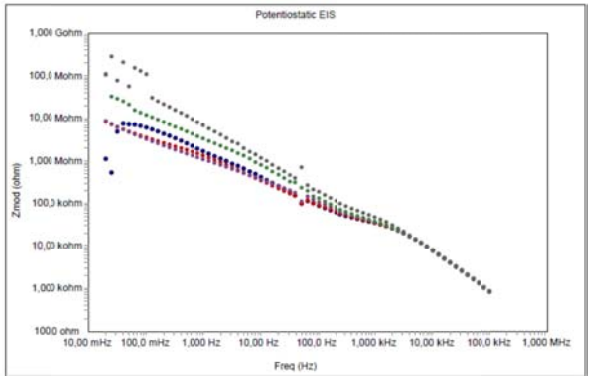
SBP + PP	
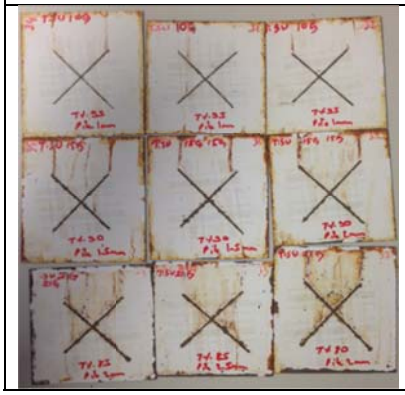	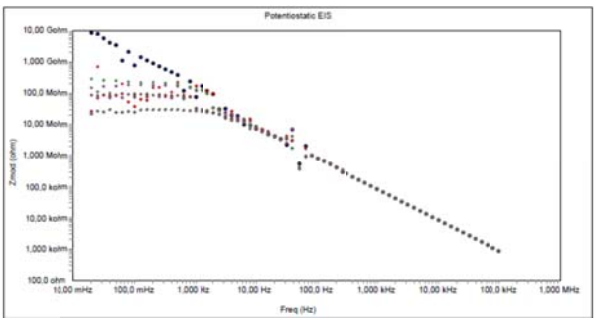

4. CONCLUSIONS

- Electrochemical methods are very advantageous over accelerated test procedures widely used in industry, in terms of quantative results and very short testing time periods.
- Among electrochemical techniques, AC-DC-AC technique seems to be effective for evaluating of the powder painted systems in industry giving reproducible and reliable results. This method can be altered procedurally in a specific way which suits the system to be tested the best in terms of testing electrolyte decision, cathodic disbonding conditions and the number of testing cycles.
- Zinc phosphate + cataphoresis + powder paint system is determined to be the strongest in terms of corrosion resistance with both of the testing techniques.
- Correlation studies of AC-DC-AC technique with ASTM B 117 salt spray test is promising and can be the next step forward for this study since results obtained are very consistent.
- Additionally, correlation of methods of testing delamination characteristics of paints with cathodic disbonding can also be a further research.

REFERENCES

1. J.B. Harrison and T.C.K. Tickle, "New Aspects of the Atmospheric Corrosion of Steel and their Implications," JOCCA, Vol. 45, No. 8, 1962, p. 571.
2. W. Funke, "Corrosion Tests for Organic Coatings-A Review of their Usefulness and Limitations," JOCCA, Vol. 62, No. 2, 1979, p. 63.
3. B.R. Appleman and Campbell, "Salt Spray Testing for Short Term Evaluation of Coatings, Part 1-Reactions of Coatings in Salt Spray," Journal of Coatings Technology, Vol. 54, No. 3, 1982, p. 17.
4. Stuart Croll, Brian Hinderliter "Simulation of Electrochemical Impedance Spectroscopy Response to Coating Flaws, Or A step towards predicting corrosion" Department of Coatings and Polymeric Materials North Dakota State University, 2010.
5. David Dubowik & Greg Ross –Air Products, "Employing Electrochemical Impedance In Predictig Corrosion Events", 2011.
6. J. Hollaender, E. Ludwig, S. Hillebrand, Proc. 5th International Tinplate Conference, London, 1992.
7. J. Hollaender, C.A. Schiller, W. Strunz, Proc. EIS 2001, Marilleva-Italy, 2001.
8. J. Hollaender, C.A. Schiller, W. Strunz, Food additives and contaminants 14, 6-7 (1999) 617.
9. Kendig,M., Jeanjaquet, S., Brown, R., and Thomas, F., "Rapid Electrochemical Assessment of Paint," JOURNAL OF COATINGS TECHNOLOGY, 68, No. 863, 39 (1996).
10. S.J. García, J. Suay. Prog. Org. Coat., XX (2009)
11. S. J. García, J. Suay. Prog. Org. Coat., 59 (2007) 251-258.
12. J. García, M. Rodríguez, R. Izquierdo, J. Suay. Prog. Org. Coat., 60, 4, 303-311 (2007).
13. S.J. García, J. Suay. Prog. Org. Coat., 57 (3) (2006) 273–281.
14. Rodriguez, M.T., Gracenea, J.J., García, S.J., Saura, J.J., Suay, J.J. Progress Prog. Org. Coat., 50 (2004) 123-131.

Easy to Clean and Antibacterial Coatings for White Good Applications

•

Beyaz Eşya Uygulamalarında Kolay Temizlenebilir ve Antibakteriyel Kaplamalar

Başak Bengü

Arçelik A.Ş. - Türkiye

ABSTRACT

The technology of easy to clean coatings has developed rapidly in recent years. As commercial products, their potential is huge and their market truly global. Because of the wide range of possible applications, from window glass and cement to textiles, easy to cleaning (ETC) coatings may become an important labor-saving device. Antimicrobial surfaces and bacteria-resistant coatings are also important technological breakthrough in household products. Health and hygiene are the primary requirements for human beings to live comfortably. To protect people from pathogens and to avoid cross infection, a special finish like antimicrobial finish has become a necessity in living areas. Food storage areas such as refrigerators are also considered to be healthy ambiance by consumers. Lots of leading appliances industries are focusing on value added applications such as bacteria resistant (antibacterial) products. With the aim of providing antibacterial goods, in refrigerators some antibacterial additives are used in finishes (such as coatings). Those antibacterial additives can disrupt the cell membrane integrity of the bacteria. In this way microbial growths are prevented in refrigerator atmosphere. In this study, several formulations of multifunctional coatings that offer both easy-to-cleanability and antibacterial efficiency were developed for glass substrates. Both hydrophobicity and oleophobicity provided at the same time in order to develop easy-to-clean coatings. For this purpose, tetraethylorthosilicate (TEOS), methyltriethoxysilane (MTES) and two types of fluorosilanes were used in sol-gel system in order to obtain easy-to-clean effect. ZnO nanoparticles suspension was also used in coating formulation to obtain antibacterial effect. Surface free energy calculations were performed in order to measure the degree of hydrophobicity and oleophobicity. In addition physical (scratch, haze, abrasion resistance and contact angle measurements), chemical (humidity and detergent resistance test) and functional (easy to clean and antibacterial efficiency) tests were performed on coated substrates for choosing the optimum formulation.

Keywords: Easy to clean, antibacterial coatings, hydrophobicity, oleophobicity, fluorosilanes.

Conical Shaped Surface Features Formation on Different Aluminum Alloys

B.Deniz POLAT*, Ozgul KELES*, Mustafa ÜRGEN*

*Department of Metallurgical and Materials Engineering, Istanbul Technical University, 34469, Maslak, Istanbul, Turkey

ABSTRACT

Anodic polarization is an electrochemical process which aims to get oxide film on anode materials. In our previous study, mechanically grounded pure aluminum specimens were anodically polarized in order to get unique conical shaped surface in the anodic oxide film. The mechanism of formation and growth of these structures and the correlation between its structure and the polarization process parameters were discussed previously. This study is aimed to investigate the effect of substrate composition on the conical shaped surface features formation mechanism. Four different substrate with different compositions (1xxx, 5xxx, 6xxx) have been used in this this study. They are all polarized in a stagnant electrolyte of 60ºC containing 350ml phosphoric acid and 150ml sulfuric acid. Anode-cathode surface ratio is 1/9, their interdistance is 15mm. SEM micrographs show that barnacle like structures form on each sample however some alteration in their morphology is observed. The results are qualitatively in agreement with our predictions and highlight the stability of conical structures on different aluminum alloys.

Keywords: Anodic Oxide Film, Pattern Formation, Anodic Polarization

1. INTRODUCTION

Using self assembly structures of nanometer scale, it is possible to fabricate various nanostructures for magnetic [1-4], electronic [4-6] and optoelectronic [4-7] devices [8] by either direct metal deposition or replication process [9-13]. Today the research on self assembly structures has been mostly based production via electrochemical processes. Particularly aluminum anodic oxide film formation (AAO) by electrochemical process has seen to be promising for future investigations because of its advantages: being cheap, practical and short processing time.

Aluminum anodic oxide (AAO) film has served over a wide range of applications related to its high resistivity at high temperature, high capability of pore size controlling (5-100nm), as well as it leads to get high aspect ratio in final product [14] and makes the template not easily being ruined by subsequent step [15]. Thereby, there have been many different investigations, where the production of self assembly AAO template based on electropolishing [17] or anodization processes have been highly investigated [18].

In our previous study, our research group also produced a conical shaped surface feature on AAO film by anodic polarization of pure aluminum [16]. The formation mechanism of these features is different than the electropolishing and anodization process. Since electropolishing process relies on the formation of a viscous surface layer, which controls the anodic dissolution behavior of aluminum depending on the shape induced electrical field. However, the conical surface features formation mechanism is controlled by the polar molecules adsorption on the high electric field regions, to prevent the dissolution related to "field enhanced dissolution" mechanism (Figure 1). Thereby, the presence of any polar molecules (water, phosphate molecules) is not the only condition for the formation of conics, but a relatively rough surface is also required.

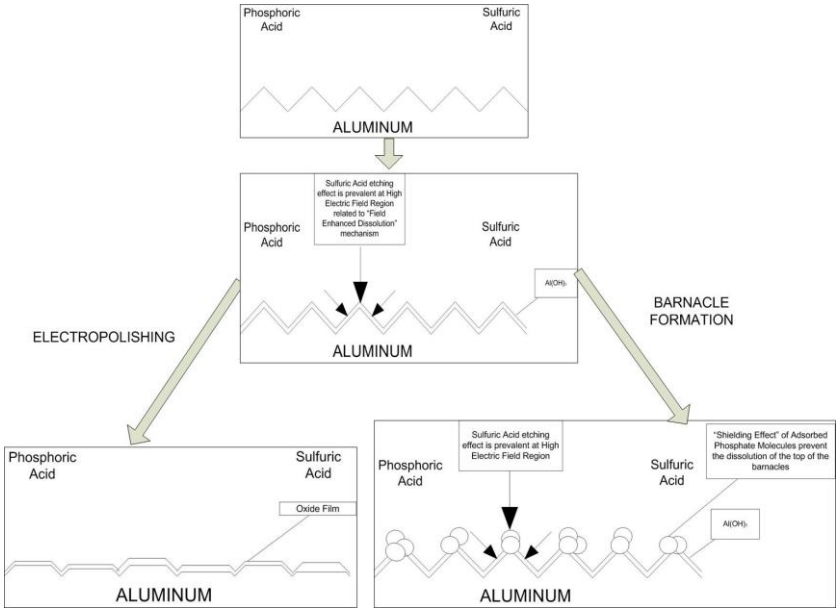

Figure 1. Schematic representation of barnacle formation mechanims compared to conventional electropolishing process.

Recently, research groups have focused their work on understanding the effect of various alloying elements (Si, Fe, Mg, Cu, Mn, Ni, Ti, V, B, Be, Pb, Zr, Cr, Zn) on pattern formation process [19], to make the AAO pattern formation process valid for industrial applications. They have found that the alloying elements which are present in aluminum as solid solutions, or second phases of various shapes, sizes and compositions may result changes in the ionic transport mechanism within the oxide film, the ejection of ionic species to the electrolyte and the solubility of the film material (both in the presence and in the absence of the electric field) due to the differentiation in surface energy. Moreover, they have shown that the quantity of alloying elements is also critical because depending on their relative concentration, they cause modifications in oxide film growth and film composition during anodization process [20-26].

So far, there have been many different studies in literature investigating the behavior of several intermetallic during anodization process in detail. In 1953, Keller et al [27] have made a research on aluminum anodization process parameters then about 30 years ago Spooner, Brace and other researchers (Alcan Laboratories) tried to establish the electrochemical reactivity of several alloying elements and the behavior of several intermetallic compounds in aluminum alloys during sulfuric acid anodization under constant voltage [19]. As a result of extensive researches it has been seen that the oxidation of alloying elements start at the alloy/film interface during the formation of barrier type anodic film.

This work is aimed to investigate the effect of substrate material composition on the conical shaped surface features formation mechanism to form a solid prove for the previously proposed model of the conic's formation mechanism, stated in our previous study [16].

The composition of the alloys has been determined by Optical Emission Spectroscopy (OES). The qualitative characterization and surface morphology of the forming oxide film has been investigated via Field Emission Scanning Electron Microscopy (FE-SEM) as well as Energy Dispersive Spectroscopic (EDS) analyses.

2. EXPERIMENTAL

2.1. Production of conical shaped surface features by anodic polarization

Four substrates having three different aluminum alloys (1xxx, 5xxx, 6xxx) were used as substrate material, beside the pure Al. The specimens were 1mm in thickness sheets with dimension of 20x100 mm^2. The specimens grounded with sand papers of 600, 1200 and 2400 before the polarization process, then rinsed in deionized water and dried in a stream of air at room temperature.

To have conical surface features on different aluminum alloys, each sample was polarized in a stagnant electrolyte containing 350ml phosphoric and 150ml sulfuric acid of 60°C. AISI 316 stainless steel sheet was used as a cathode. The distance between anode and cathode was 15mm. The anode to cathode surface ratio was 1/9, and process duration was 12s. During the anodic polarization, a cell voltage of 32 +/- 5 V was applied by an unregulated DC power supply (Ruhstrat 72/12). After polarization process, the specimens were rinsed thoroughly with deionized water for 1 min and dried in a stream of air at room temperature.

2.2. Characterization

The conical surface feautures formed on pure Al was characterized by Atomic force microscopy (AFM) and Auger electron spectroscopy (AES). Atomic force microscopy (AFM) (Ntegra Prima) under Tapping Mode was used to determine the morphology of the cones. A Digital Instrument nanoprobe SPM standard silicon nitride tip B was used. All images were taken in height mode at 0° scan angle and using sample dependent Z ranges.

The surface composition of a conic pattern formed on pure Al was determined using scanning Auger electron microscopy (SAM, Jeol FEG SAM, 9500F). The spectra were acquired by using a probe beam current of 10 nA and a primary acceleration voltage of 10 keV. Tilt angle was fixed at 30□. Charging that may arise from the sample was corrected in reference to C KLL (270.958 eV). The base pressure during analysis was 1-1.5 x10^{-7} Pa.

The composition of alloys was determined by Optical Emission Spectroscopy (OES). The relative standard deviation (%) for this method using three experimental measurements was less than 5%. The specimens' surfaces and cross sections were examined by Field emission gun scanning electron microscope (FEG -SEM) (Jeol 7000F FEGSEM). The film was made conductive by deposition with sputtering of an extremely thin layer of platinum (200 A°) on its surface.

3. RESULTS and DISCUSSIONS

3.1. Composition of Aluminum Alloys

OES analyses of four different aluminum alloys were given in Table 1. It is worth to note that high Si and Fe content in the first sample made it a member of 1xxx series aluminum alloys. On the other hand, high Si and Mg content made the second sample as a member of 6xxx series, in addition to the third and fourth sample containing high amount of Mg which make them being member of 5xxx series aluminum alloys.

Table 1. OES analysis of four different aluminum alloys (wt. %)

	Si	Fe	Cu	Mn	Mg	Cr	Ni	Zn	Ti	P	Pb	Sb	Sn	V	Al
1	0.121	0.262	<0.0004	0.0019	0.0012	0.0012	0.00048	0.0027	0.0049	0.0119	0.001	0.0052	0.0001	0.0104	99.6
2	1.22	0.221	0.0686	0.0566	0.410	0.0023	0.00098	0.0056	0.0147	0.0011	0.0011	<0.0001	0.00029	0.0076	98.0
3	0.0944	0.220	0.00047	0.0057	2.59	0.0016	0.0016	0.0057	0.0179	<0.0002	<0.0002	<0.0001	<0.0001	0.00703	97.1
4	0.156	0.272	0.0089	0.179	3.00	0.1	0.0025	0.0029	0.0327	0.00075	<0.003	<0.0001	0.0001	0.0087	96.2

3.2. Conical shaped surface formation on pure Aluminum

Since a grounded pure Al was used as a substrate, we assumed that aluminum surface has asperities left from the grinding process. These asperities on the surface do not prefentially dissolve as in electropolishing due to the screening - blocking effects of the insoluble phosphates/precipitates formed due to the electrolyte. Hence, these precipitates do not cover the whole aluminum surface as in phosphating due to the etching effect of sulfuric acid. Thereby, the preferential precipitation occurs on the asperities due to the initial higher dissolution rate induced by the electrical field. On the peripheries, the dissolution action induced by the sulfuric acid is expected to continue. And, with the help of decreasing electrical field, cone shape features may form (Figure 2).

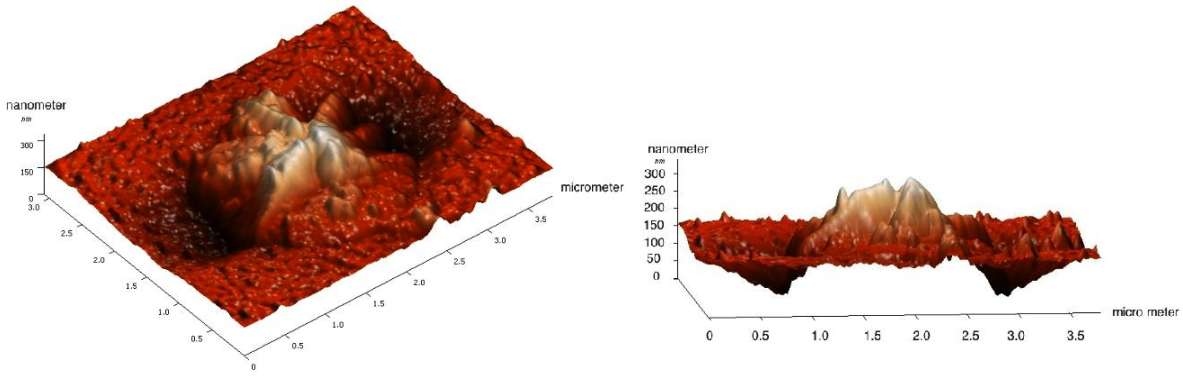

Figure 2. AFM analyses of the conical shaped surface features formed as a result of anodic polarization of pure aluminum

The AES analyses show that the aluminum surface is covered by a thin phosphate based film supporting our proposal (Figure 3) about the conical shaped surface features formation mechanism.

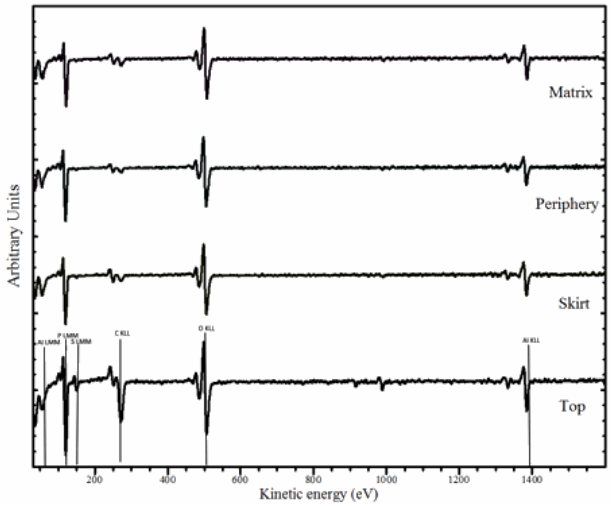

Figure 3. AES analysis of the conical shaped surface features formed formed as a result of anodic polarization of pure aluminum

3.3. Conical shaped surface formation on different Aluminum Alloys

The studies for investigating the effect of aluminum composition on the surface pattern formation were conducted on mechanically ground aluminum surfaces possessing asperities in the form of scratches, as in the case of pure Al.

SEM analyses show that after the electrochemical treatment process, conical structures were seen in the anodic oxide film of 1xxx alloy (Figure 4a). Even no appreciable conics formed on the surface, some distinguished conic like features were clearly observable in anodic oxide film. When the anodic oxide film morphology of the sample of 6xxx alloy was investigated, it was seen that conics were formed in it (Figure 4b). It is worth to note that the stripes were remarkably

present on the periphery of the barnacles, as in the case of pure Al. Moreover Figure 4c-d demonstrate that numerous conics were formed in the anodic oxide film of the sample of 5xxx alloy, and conics were approximately covered the entire anode material of 5xxx surface having higher amount of alloying elements in it.

The differentiation in the morphology might be explained considering the composition of the substrates. According to literature it is seen that [28-32] alloys containing Si and Fe form different oxide film than that of pure aluminum substrate since these foreign species form Al-Fe-Si intermetallic which block the growth of the oxide film. Infact, changes in the conventional oxide film formation mechanism in aluminum alloys can be explained by differentiation of current distribution within the forming film. This fact represents the reason why no appreciable barnacle forms in the anodic oxide film of the first sample [30,33]. The incorporated silicon particles in the growing layers lead to a non-uniformity in the AAO film. On the other hand, the presence of iron impurities influences also the polarization process. Additionally, particles made of Al–Fe and Al–Fe–Si present in the aluminum substrate, are either inert or undergo oxidation in lower rate compared with the adjacent aluminum [32]. Considering that iron rich phases locally inhibited the nucleation and growth of the anodic oxide film [34] contrary to the rest of the anode material, these asperities may be act as active sides where polar molecules can be adsorbed related to the "surfactant adsorption principle" (Figure 4a) [16]. EDS analyses prove low oxidation rate of 1xxx series aluminum substrate since high amount of aluminum with low oxygen amount is detected from the AAO film (Table 2).

However, in case of aluminum of 6xxx series, which contains high amount silicon and magnesium, the barnacle structure becomes remarkable because under standard anodizing conditions, aluminum of 6xxx alloy has an oxide growth rate similar to that of pure aluminum [19]. Yet, high amount of siliocon and iron with other transition metal (Cr,Ni,Cu) traces changes in the oxidation kinetic, the presence of magnesium enhances the oxidation process. The latter balances the electric field distribution within the oxide film leads to form conical surfce structures in AAO film (Figure 4b). EDS analyses display that aluminum of 6xxx series has a thick oxide since oxygen amount is relatively high in the composition (Table 2).

The results of the third and fourth specimens are consistent with what has mentioned in literature (Figure 4c-d). High amount of magnesium substantially increases the rate of aluminum oxidation at a given anodizing voltage, at least initially, so the kinetic of pattern formation mechanism advances. This fact may be explained by referring to the higher Gibbs energy value of the magnesium oxidation reaction than that of pure aluminum; hence the initial and preferential oxidation of aluminum takes place at the beginning of anodizing. This results in the formation of thin layers (1–5 nm into the substrate) enriched with the respective alloying element in the anodic oxide film [36]. EDS analyses of AAO film show that the oxide film do not only made of alumina but some amount of magnesium and iron present in the anodic oxide film (Table 2). Magnesium is present in AAO film because its migration is very fast within the film so that Mg is

easily incorporated into the oxide film, which results in a slight decrease in ionic resistivity of the AAO film. This fact forms a non-uniform flow of ionic current due to different ionic resistivity of alumina and magnesia. Besides, iron still exists in AAO film since the compound containing iron act as inert whereas the rest is anodically polarized.
Knowing that the presence of oxidizing agent promotes the conical shaped surface features formation process the top of the barnacles is dissolved in 12 seconds when aluminum of 5xxx series is used as substrate. However, in the same operation condition, the top of the pattern is stable when pure aluminum is used as anode material (Figure 4e).
The particular case which differs Figures 4c from 4d is that anodically polarized hot rolled aluminum of 5xxx series (Figure 4d) contains incorporated magnesium oxides besides other impurities, which increase the defect density in the barrier layer so that the channeling of the current and the roughness of the substrate material is changed resulting in the coalescence of the barnacles in shorter polarization time [37].

When the SEM views of 5 samples are compared (Figure 4a-e), the results show that the oxidation process of the intermetallics differs from that of pure aluminum related to different migration rates of the oxidized species within the films. Because these intermetallics having different potential compared to matrix, act as active/inert side, hence they represent the point on which high electrical field can be localized, This, results in the formation of complex compete reactions between the local film formation over particular particles and the general film formation over the surrounding matrix regions which results in changes of the conical structures in AAO film.

Table 2. EDS analyses of the AAO film formed on different Al alloys

(at%)	O	Mg	Al	Si	P	S	Fe
1xxx	24.72	-	71.55	-	2.65	1.08	-
6xxx	44.48	2.11	17.12	33.62	0.68	0.97	1.02
5xxx	11.48	2.17	75.45	-	2.3	0.6	7.99
5xxx	11.52	2.21	77.48	-	2.0	0.5	6.29

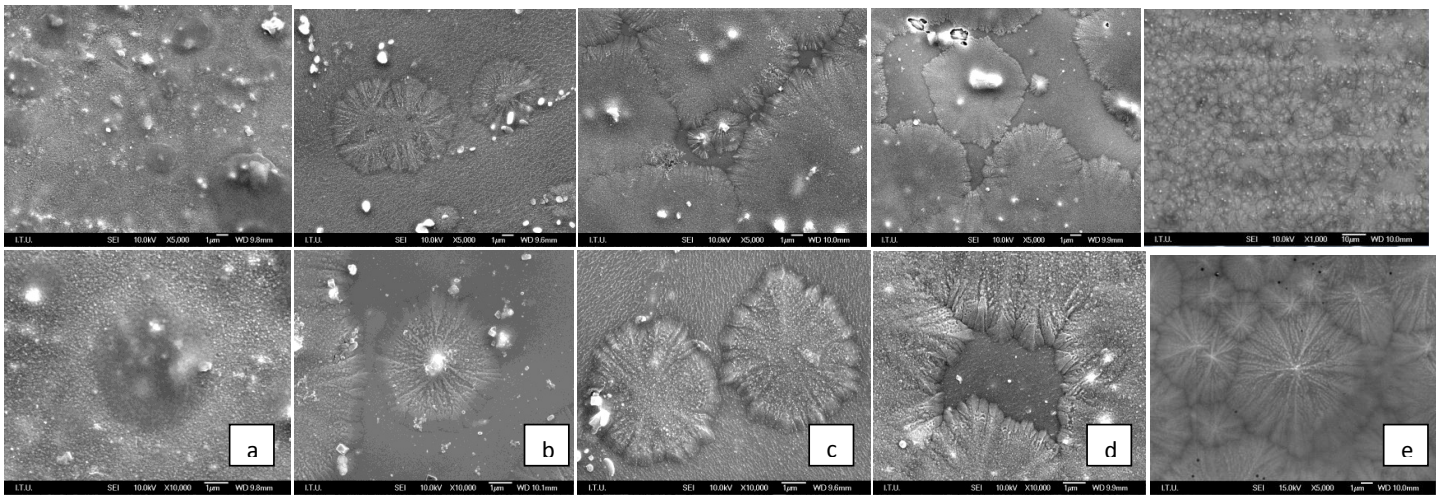

Figure 4. Barnacle formation on different aluminum alloys a) 1xxx b) 6xxx c) 5xxx d) 5xxx e) pure Al

4. CONCLUSIONS

Aluminum alloys of 1xxx, 5xxx and 6xxx were anodized in a mixture of phosphoric and sulfuric acid baths. They are all polarized in a stagnant electrolyte of 60°C containing 350ml phosphoric acid and 150ml sulfuric acid. The FEG-SEM micrographs were compared with those of pure aluminum. The following were concluded:

- The conical shaped surface features form in anodic oxide film of 5xxx and 6xxx alloys. High amount of magnesium favors the oxidation process. The conics formation mechanism progress at shorter time.
- Silicon content and iron content of the alloy is very important for the formation of conical shaped surface features, since they inhibit the oxide growth process and slows down the oxide film formation.
- This study proves that the purpose model of the conical shaped surface fatures formation mechanism stated in our previous study is well established and shows that conics are formed in different aluminum alloys but their morphology has to be optimized depending on the alloy composition.

5. REFERENCES

[1] A.P.Li, F.Müller, A.Birner, K.Nielsch and U.Gösele, J. Adv. Mater., 11, 483-487, 1999.
[2] V. V. Konovalov, G. Zangari and R. M. Metzger, Chem of Mat, 11, 1949-1951, 1999.
[3] P. Takhistov, Biosensors and Bioelectronics, 11, 1445–1456, 2004.
[4] L.Zhang, H.S.Cho, F.Li, R.M.Metzger and W.D.Doyle, Journal of Materials Science Letters, 17, 291-294, 1998.
[5] G.D.Sulka and G.P.Parkola, J. Thin Solid Films, 515, .338-345, 2006.
[6] Z.Su and W.Zhou, Science Foundation in China, 16,11-30, 2008.
[7] G.D.Sulka and K.G.Parkola, Electrochimica Acta, 52, 1880–1888, 2007.
[8] V.V.Yuzhakov, H.C.Chang and A.Miller, The American Physical Society, 56, 12608-12624, 1999.
[9] V.V.Konovalov, G.Zangari and R.M.Metzger, Chemistry of Materials, 11, 1949-1951, 1999.
[10] C.U.Yu, C.C.Hu, A.Bai and Y.F.Yang, Surface & Coatings Technology, 201, 7259-7265, 2007.
[11] W.Guo and D.T.Johnson, Journal of Crystal Growth, 268, 258-271, 2004.
[12] P.Takhistov, Biosensors and Bioelectronics, 19, 1445-1456, 2004.
[13] A.Belwalkar, E.Grasing, W.V.Geertruyden, Z.Huang and W.Z.Misiolek, J Memb. Sci., 319, 192-198, 2008.
[14] X.Wang and G.R.Han, Microelectronic Engineering, 66, 166-170, 2003.
[15] O.Jessensky, F. Muller and U. Gosele, Applied Physics Letters, 72, 1173-1175, 1998.
[16] M.Urgen, O.Keles, B.D.Polat and F. Bayata, J. Electrochem. Soc, 159, C411-C415, 2012.

[17] V.V.Yuzhakov, P.V.Takhisov, A.E.Miller and H.Chang, American Institute of Physics, 9, .62-73, 1998.
[18] H.Masuda and K.Fukuda, Mat Science, 268, 1466-8, 1995 .
[19] I.Tsangaraki-Kaplanoglou, S. Dimogerontakis, Y. Wang, H. Kuo and S. Kia, Surface&Coatings Technology, 200, 2634–2641, 2006.
[20] K.Shimizu, G.M.Brown, K.Kobayashi, P.Skeldon, G.E.Thompson and G.C.Wood, Corros. Sci., 40, 1049, 1998.
[21] K.Shimizu, G.M.Brown, H.Habazaki, K.Kobayashi, P.Skeldon, G.E.Thompson and G.C.Wood, Corros. Sci., 42, 831, 2000.
[22] A.C.Crossland, G.E.Thompson, C.J.E.Smith, H.Habazaki, K.Shimizu and P.Skeldon, Corros. Sci., 41, 2053, 1999.
[23] H.Habazaki, X.Zhou, K.Shimizu, P.Skeldon, G.E.Thompson and G.C.Wood, Electrochim. Acta, 42, 2627-2635, 1997.
[24] J.Cote, E.E.Howlett, M.J.Wkeeler and H.J.Lamb, Plating Surf. Finish, 386, 1969.
[25] H.Habazaki, K.Shimizu, P.Skeldon, G.Thompson and G.C.Wood, Corros. Sci., 39, 2, 339, 1997.
[26] X.Zhou, G.E.Thompson, P.Skeldon, G.C.Wood, K.Shimizu and H.Habazaki, Corros. Sci., 41, 1599-1613, 1999.
[27] F.Keller, M.S.Hunter and D.L.Robinson, J. Electrochem. Soc., 100, 411-419, 1953.
[28] G.E.Thompson, H.Habazaki, K.Shimizu, M.Sakaizi, P.Skeldon, X.Zhou and G.C.Wood, Aircr. Eng. Aerosp. Technol., 71, 228, 1999.
[29] L.E.Fratila-Apachitei, F.D.Tichelaar, G.E.Thompson, H.Terryn, P.Skeldon, J.Duszczyk and L.Katgerman, Electrochim. Acta, 49, 3169-3177, 2004.
[30] L.E.Fratila-Apachitei, H.Terryn, P.Skeldon, G.E.Thompson, J.Duszczyk and L.Katgerman, Electrochim. Acta, 49, 1127-1140, 2004.
[31] X.Zhou, G.E.Thompson, H.Habazaki, K.Shimizu, P.Skeldon and G.C.Wood, Thin Solid Films, 293, 327-332, 1996.
[32] L.E.Fratila-Apachitei, J.Duszczyk and L.Katgerman, Surf. Coat. Technol., 157, 80-94, 2002.
[33] H.Habazaki, K.Shimitzu, P.Skeldon, G.E.Thompson and G.C.Wood, Thin Solid Films, 300, 131-137, 1997.
[34] K.Mukhopadhyay and A.K.Sharma, Surf. Coat. Technol., 92, 212-,220, 1997.
[35] K.Shimizu, K.Kobayashi, G.E.Thompson, P.Skeldon and G.C.Wood, Corros. Sci., 39, 281-284,1997.
[36] Y.Liu, P.Skeldon, G.E.Thompson, H.Habazaki and K.Shimitzu, Corros. Sci. 44, 1133-1142, 2002.
[37] SK. Wang, H. W. Pickering and K. G. Weil, , Plating Surf. Finish. 91, 34-37, 20.

SURFACE TREATMENT AND CHARACTERIZATION OF THE Ti6Al4V ALLOY POWDERS FOR BIOMEDICAL APPLICATIONS

Elif Eda YENI*[a1], Ezgi BUTEV [b,c,2], Emre YILMAZ[b,3], Ziya ESEN[b,4], Servet TURAN[a,5]

[a] Anadolu University, Eskişehir, Turkey
[1]eeyeni@anadolu.edu.tr, [5]sturan@anadolu.edu.tr
[b] Cankaya University, Ankara, Turkey
[2]ebutev@cankaya.edu.tr, [4]ziyaesen@cankaya.edu.tr, [3]emreyilmaz.e@gmail.com
[c] Middle East Technical University, Ankara, Turkey

ABSTRACT

Titanium and its alloys are widely used in production of bone implants due to their excellent biocompatibility, corrosion resistance, low modulus of elasticity and high strength. However, various surface treatment techniques such as etching, sand blasting, oxidation and alkali treatment are being applied to enhance the osseointegration properties of the alloys. In the present study, formation and characterization of biocompatible sodium titanate layers was investigated using hydrothermal treatment in which the samples were soaked in 5M NaOH aqueous solution for 24 hours kept at 60 ^{o}C. Subsequent to crystallization heat treatment of powders at 600 ^{o}C in a muffle furnace for one hour, the apatite forming abilities of surfaces were checked via immersing the powders in simulated body fluid (SBF) (36.5 ±0.5^{o}C) for 1 and 5 days. Structure and chemical composition of the resultant titanate layers and apatite layers were characterized using scanning electron microscopy (SEM), energy dispersive X-ray spectroscopy (EDS), and X-ray diffraction (XRD) techniques.

Keywords: Ti6Al4V, biomaterials, apatite formation, surface activation

1. INTRODUCTION

Nowadays, research and the development of new surgical materials improve individual's life quality and lifetime expectancy [1]. Due to the low mechanical strength of polymeric materials and low fracture toughness of ceramic materials; metallic materials such as titanium and titanium alloys are preferred for load-bearing bone repairing applications especially because of their high specific strength, biocompatibility and resistance to corrosion [2]. Nonetheless, osseointegration related problems are the main limitations for titanium and its alloys in terms of the direct connection of bone tissues to the implant surface. Due to the long duration of postoperative recovery, surface of titanium and titanium alloy implants need to be improved for rapid bone regeneration [3]. Acid, hydrogen peroxide, sol-gel, anodic oxidation and alkali treatment are the most accepted utilized surface processing techniques for titanium and titanium alloys [4]. These surface improvement techniques, enhance the bioactivity of the implant materials and induce active apatite layer formation, thus result in rapid osseo-integration [5]. Because of its simplicity and possibility of applying at relatively lower

temperatures (<100^{o}C) for getting homogenous coating on irregular surfaces alkali treatment is one of the most popular technique among the surface processing methods listed literature [6].

Firstly, Kokubo et all (1996) [1] formed sodium titanate hydrogel ($HTiO_3^-nH_2O$) layer on titanium, approximately 1 μm in thickness, by alkali treatment method using different concentrations of NaOH aqueous solutions. The layer was too thin to detect or to form desired apatite layers in SBF [1]. Then, the need for additional heat treatment for improvement bioactivity of alkali treated samples and coating strength was discovered by Kim et all [4]. Hydrogel titanate layers formed in NaOH treated samples were converted crystalized stable sodium titanate ($Na_2Ti_nO_{2n+1}$, n=3, 4, 9) layers by subsequent heat treatment at around 600^{o}C [2]. Such surfaces are known to be highly active in terms bone tissue attachment by inducing bone-like apatite formation when implanted into body. In vitro tests conducted using simulated body fluid (SBF) have shown that Na^+ ions on the surface are exchanged with H_3O^+ which results in Ti-OH ions formation and subsequent reaction of Ti-OH with Ca^{2+} and P, and apatite formation on the surface [5, 7].

Alkali treatment technique has been extensively used especially for surface processing of pure titanium and some of the titanium alloys. However, there is limited information about the alkali treatment of Ti6Al4V alloys' and their response to SBF. In the present study, Ti6Al4V alloy powders were surface treated in 5M NaOH solution at 60^{o}C for 24 hours and heat treated at 600^{o}C. Eventually, the biocompatibility of the samples was characterized by checking apatite formation on the surfaces via immersing the surface treated powders in SBF for different periods of time.

2. MATERIALS AND METHODS

Ti6Al4V alloy powders with an average particle size of 107 μm, conforming to ASTM F136 standart, were used as starting materials.

The powders were alkali treated by immersing in 5 M NaOH solution at 60^{o}C in a pressure vessel (Parr 5500 Series Compact Reactor) for 24 hours. Subsequently, the surface activated Ti6Al4V powders were washed with distilled water gently and dried in an oven (EVO) for 24 hour at 40^{o}C under vacuum. To enhance the bonding strength of the coating and to get crystalline titanate layers the alkali treated Ti6Al4V powders were subsequently heat treated in air at 600 ^{o}C for 1 hour and then allowed to cool slowly in furnace.

Ti6Al4V alloy powders' in vitro bioactivities were examined by investigating the apetite formation on powder surfaces via soaking the powders in cellular simulated body fluid (SBF), recommended by Kokubo & Takadama [8] (pH=7.4, 36.5±0.5^{o}C), for one and 5 days.

The crystalline titanate layers formed during alkali and heat treatment, and apatite formation during SBF soaking tests were examined using X-ray diffraction (XRD, RIGAKU) by continuous scanning with CuKα at a scan speed of 1^{o}/min. Surface morpoholgy of powders were investigated with scanning electron microscopy (SEM, SUPRA 500, 20 kV), and energy dispersive spectrometry (EDX, INCA) was used to get information about chemical composition.

3. RESULTS AND DISCUSSION

Figure 1 shows the surface structure of alkali treated (5M NaOH at 60°C for 24 hours), alkali and subsequently heat treated (at 600°C) powders. As can be seen, non-continuous porous network structure was formed on the surfaces as a result of hydrothermal treatment in NaOH solution, Figure 1(a)-(c). Heat treatment in air conducted subsequent to hydrothermal treatment changed the surface morphology and interconnected porous structure transformed into relatively dense layers. Additionally, depending on the heat treatment temperature, rod like and cubical structures have been observed on the dense coating layers. Heat treatment at 600°C in air induced the formation of nano-fibers perpendicular to surface (Figure 1 (d)-(f)),

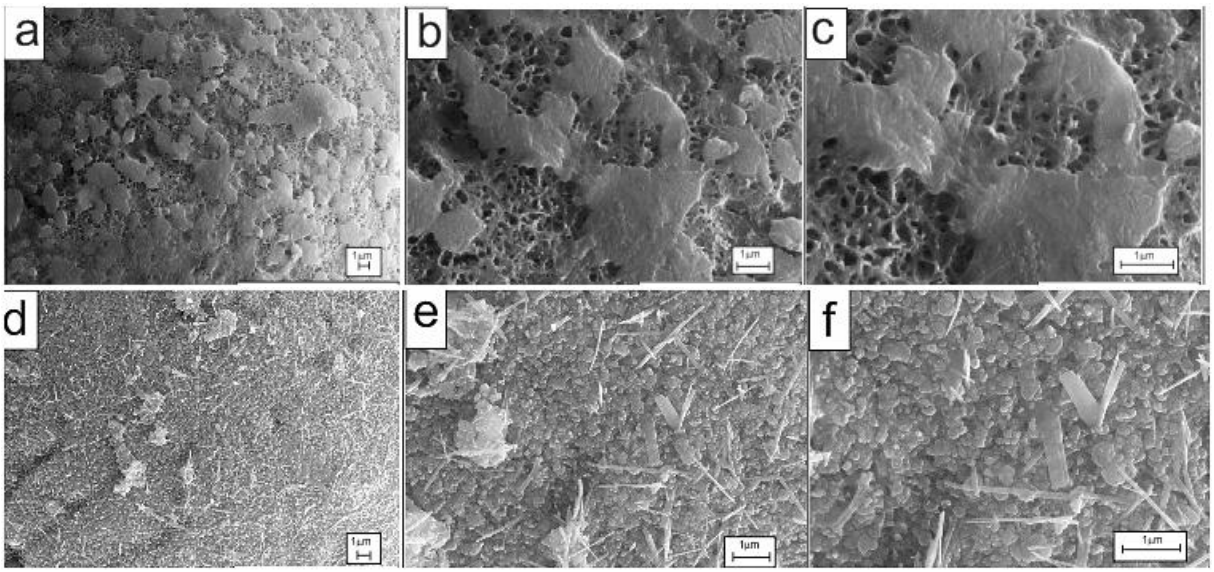

Figure 1: Surface structures of; alkali treated Ti6Al4V powders at different magnifications: a) mag 10 kx, b) mag 30kx, c) mag 50kx, alkali and heat treated (600 °C) Ti6Al4V powders at different magnifications:, d) mag 10 kx, e) mag 30 kx, f) mag 50 kx

Figure 2 is the closer examination of alkali and heat treated powders surface which shows acicular morphology on the surfaces. According to general EDX results 38.86% O and 7.63% Na (in wt. %) exist on the processed surfaces. However, EDX analysis taken from rod like acicular structures shown in Figure 2 exhibited higher amount of oxygen and sodium elements around 40.1wt.% and 13.4 wt.%, respectively, which indicates the Na-rich phase formation that is indicated as essential phase for apatite nucleation and forming [7].

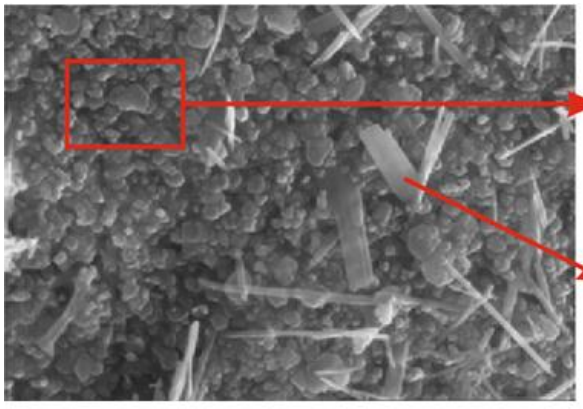

Element	Weight%	Atomic%
Na K	7.63	8.53
Al K	1.00	0.95
Ti K	50.54	27.11
V K	1.98	1.00
O	38.86	62.41
Totals	100.00	

Element	Weight%	Atomic%
Na K	13.04	14.17
Al K	0.19	1.03
Ti K	36.94	18.41
V K	0,85	0.86
O	40.01	59.39
Totals	100.00	

Figure 2: EDX results surface of the alkali and heat treated Ti6Al4V powder at 600 °C

As it is known, titanium and titanium alloys are prone to oxidation above 500°C and formation of excessive amount of rutile becomes possible. Although, titanium oxides are known to be highly biocompatible, they may degrade the mechanical properties and in some cases lead to removal of coating layer due to mismatch of thermal expansion coefficients of titanium base and ceramic oxide. Therefore, alkali treatment and subsequent heat treatment at 600°C is seen to be optimum surface processing technique to get active coating layer which enhances apatite forming.

The XRD patterns of as-received and surface processed powders are given in Figure 3. As can be seen in the chart, both as-received and alkali treated samples exhibited main peaks, namely, alpha and beta phases, of the titanium alloy. Although alkali treated powders' surfaces composed of interconnected porous structure, Figure 1 (a)-(c), containing sodium element (according to EDS analysis wt % of Na : 10.97), it was not seen in XRD patterns mainly due to amorphous nature of formed Na-rich phase, which is generally classified as sodium titanate hydrogel layer. After heat treatment, this layer was dehydrated and fairly and densified at 600 °C and as a result Na-rich phases appeared in the form of crystalline phases in the XRD patterns. The observed sodium titanate phase was not only the one type, on the contrary, two different sodium titanate phases were observed ($Na_2Ti_3O_8$, $Na_2Ti_3O_7$), all of which is known as bioactive phases. Kim et al, identified the coating layer as sodium pentatitanate ($Na_2Ti_5O_{11}$), while the other studies recognized formation of the compounds of sodium titanate as $Na_2Ti_3O_7$ and $Na_4Ti_3O_8$ as instead of $Na_2Ti_5O_{11}$ [9].

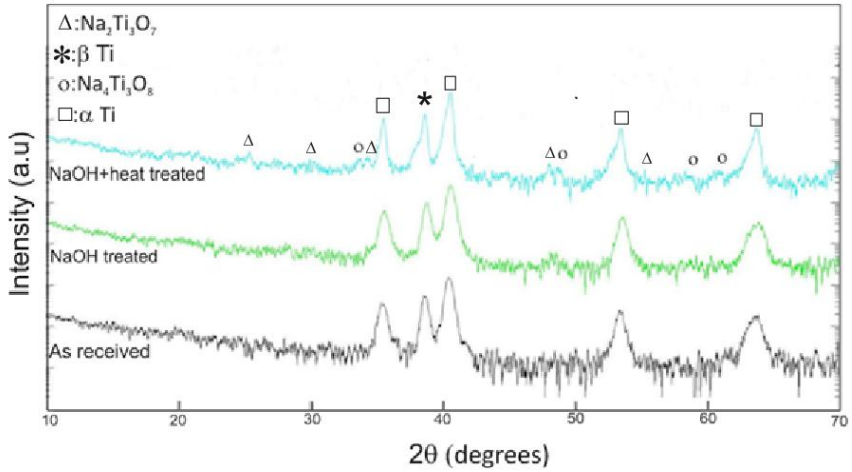

Figure 3: XRD patterns of the as-received, alkali treated, alkali and heat treated(600°C) Ti6Al4V powders.

The bone forming ability of various biomaterials is checked by the apatite formation on the surfaces which is usually investigated by immersion the samples into SBF having ion concentration similar to human blood plasma. In this way, prior to implantation, by in-vitro studies using SBF tests the surface is classified as highly biocompatible and prone to form bone tissue on its surface if the apatite formation is possible. Generally, when the alkali and heat treated Ti6Al4V alloys are immersed in SBF, negatively charged Ti-OH groups are formed initially, which are fundamental for apatite nucleation and formation. The negatively charged Ti-OH groups then, reacts with Ca^{2+} in the SBF and surface of the alloy begins to the meet the demands and apatite nuclei grows with tightly bonded to surface [10, 11].

The surface structures of the powders soaked in SBF for one and 5 days in as-received and alkali and heat treated conditions are shown in Figure 4. The as-received powders' surfaces

were fairly smooth and no apatite formation was detected after soaking for one day and 5 days (Figure 4.a and b). On the other hand, alkali and heat treated powders' surfaces exhibited apatite formation on their surfaces. Initially, the apatite particles were rarely observed after one day of soaking (bright regions, Figure 4(c)), while the entire surface of the powders were coated with Ca-rich phases after 5 days of immersion, Figure 4(d).

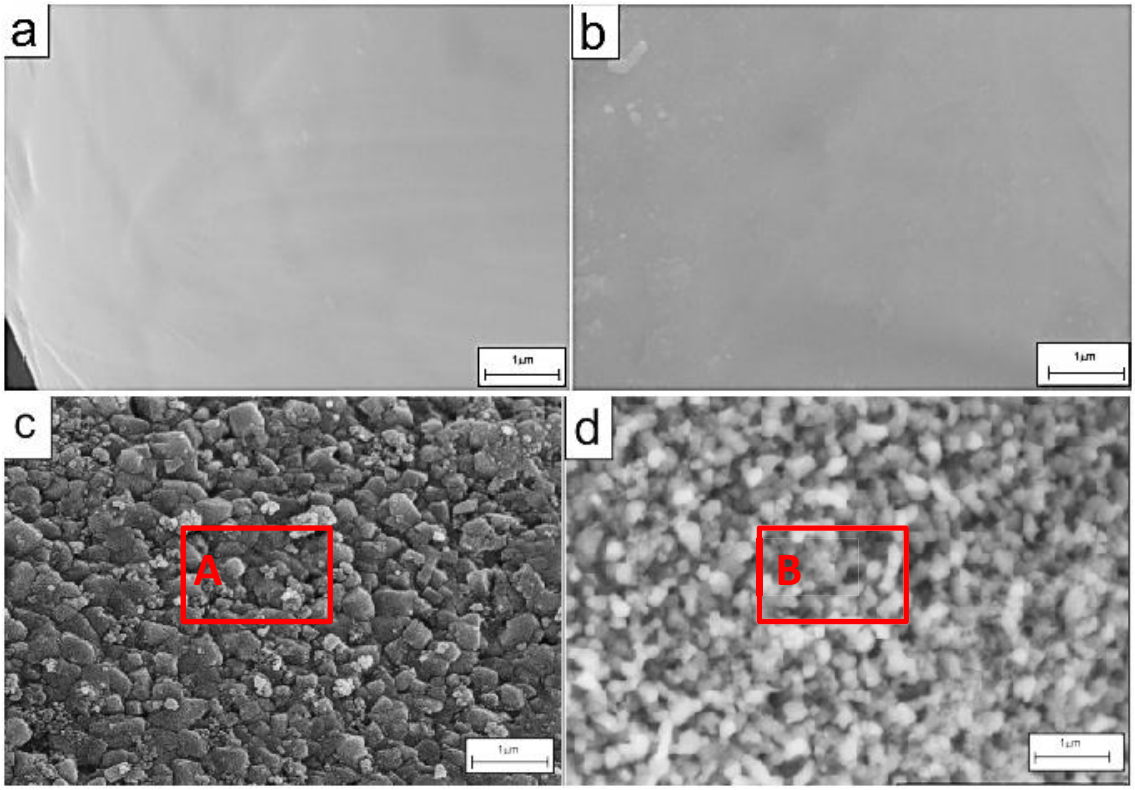

Figure 4: Microphotographs of as-received Ti6Al4V powders immersed in SBF for (a) one day and (b) 5 days; alkali and heat treated Ti6Al4V powder immersed in SBF for (c) one day, (d) 5 days.

In human bone Ca/P ratio is known to be around 1.61 [11] and this ratio is similar to that of synthetic hydroxyapatite (1.7). Table 1 shows EDX results of region A for one day immersion and region B for 5 day immersion into SBF. In the present study, as shown in EDX results (Table 1), Ca/P ratio was initially low after one day of immersion, while Ca/P ratio reached to 1.79, which is similar to human bone and synthetic hydroxyapatite.

Table 1: EDX analysis of the alkali and heat treated powders kept in SBF for one and 5 days.

Ti64, one day SBF			**Ti64, 5 day SBF**		
Element	**Weight %**	**Atomic %**	**Element**	**Weight %**	**Atomic %**
Na	9.56	11.56	Na	9.07	9.08
Al	2.24	2.31	Al	1.01	0.86
Ti	47.99	27.91	Ti	38.69	18.6
V	2.58	1.41	V	0.88	0.41
O	27.8	48.42	O	48.3	69.5
Ca	1.85	1.29	Ca	1.54	0.88
P	7.14	6.42	P	0.86	0.64
Cl	0.86	0.68	Cl	0.48	0.31
Ca/P	**0.259104**	**0.200935**	**Ca/P**	**1.790698**	**1.375**

The formation of apetite via immersing the samples in SBF was verified by XRD studies. The well defined peaks at around 40.6, 35.25, 38.47 and 53.20 2θ values are due to (001), (010), (002) and (012) planes of Ti and rutile TiO_2 phases. It can be also observed from the XRD patterns that alkali and heat treated Ti6Al4V powders' sodium titanate layers started to turn into apetite phase after one day of immersion and excessive apetite formation was observed throughout the powders' surfaces, Figure 4(d) and 5.

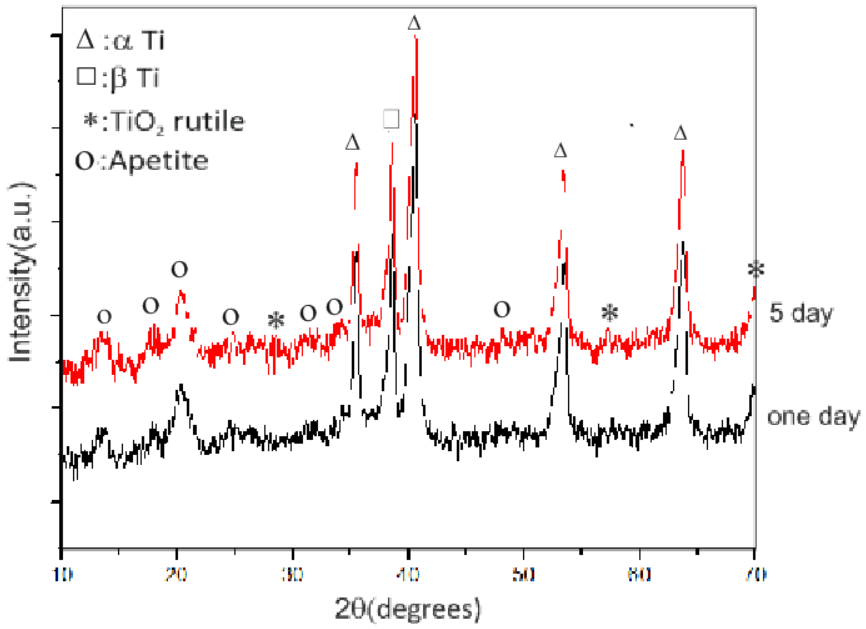

Figure 5: XRD patterns of the alkali and heat treated Ti6Al4V powders kept in SBF for one day and 5 days.

4. CONCLUSIONS

The surface activation of Ti6Al4V alloy powders was successfully applied to and crystalline sodium titanate layers were obtained. During alkali treatment, the bioactive sodium titanate hydrogel layer was formed as a result of hydrothermal treatment in NaOH solution and it was densified due to heat treatment and transformed to crystalline sodium titanate It has been also concluded that alkali and heat treated surfaces were relatively more active compared to as-received powders's surfaces such that in 5 days of immersion in SBF fluid they induced apatite formation on their surfaces, while formation of apatite, which is the fundamental for ingrowth of bone, couldn't be observed on the surfaces of untreated powders.

Acknowledgment

This research has been supported by TUBITAK #112M341.

REFERENCES

1. Luana Marotta Reis de Vasconcellos et all Porous titanium by powder metallurgy for biomedical application: characterization cell citotoxity and in vivo tests of osseonintegration. (2012)
2. Alireza Nouri et al. Biomimetic porous titanium scaffolds for orthopedic and dental application (2010)
3. K Anselme Biomaterials 21667-681 Osteoblast adhesion on biomaterials review (2000)
4. Liu et all Materials Science and Engineering R, Vol. 47, 49-121Surface modification of titanium, titanium alloys, and related materials for biomedical applications. (2004).
5. Chen X, Nouri A, Li Y, Lin J, Hodgson PD et all Biotecnical Bioceng 101:378-387 Effect of surface roughness of Ti, Zr, TiZr an apetite precipitation from simulated body fluid. (2008)
6. Zhao C.Y, Fan HS, Zhang XD et all. Advance in biomimetic apetite coating on metal implants.(2011)
7. Tadashi Kokubo and Seiji Yamaguchi Materials *3*(1), 48-63 Novel bioactive titanate layers formed on Ti metal and its alloys by chemical treatments (2010)
8. Kokubo, T, Takadama, H Biomaterials 27How useful is SBF in predicting in vivo bone bioactivity? (2006)
9. Masaki Uchida et all J Biomed Mater Res A. 64(1):164-70. Structural dependence of apetite formation on Titania gels in a SBF (2002).
10. Matthieu Ravelingien et all J Dent Res 83: 465-469, Characterization of alkali- and heat-treated titanium surfaces for apatite deposition (2004)
11. Medeiros, W.S et all XIX Congress of the Brazilian Society of Microscopy and Microanalysis Microstructural analysis of porous Ti (2010)
12. Fanghui Liang, Lian Zhou Surface and coating Technology 165 133-139 Apetite formation on porous titanium by alkali and heat treatment (2003)

The Effect of Annealing Parameter on Anodizing Performance of the AA5005 Aluminum Alloy Produced by Twin Roll Casting

•

Çift Merdaneli Döküm Yöntemiyle Üretilen AA5005 Alüminyum Alaşımının Anotlama Davranışına Tavlamanın Etkisi

Beyza Yeşilbağ[1], Nuri Solak[2]

[1]Teknik Alüminyum, [2]İstanbul Technical University - Türkiye

ABSTRACT

Anodization is an electrochemical surface modification technique that has been used for improving material properties such as wear, corrosion and chemical resistance; providing a decorative appearance. Anodized aluminum is favored for applications specially for architecture and construction. Aluminum alloys have different anodization behavior due to their alloying elements and microstructure. AA5005 is a suitable alloy for anodizing because of its main alloying element magnesium, also it has an ease of coloring. The sheets produced by twin roll continuous casting (TRC) have a characteristic microstructure and to perform a high quality anodizing, casting and subsequent processes like rolling and annealing must be controlled. In this paper, the effect of annealing conditions on microstructure as well as anodizing behavior is investigated.

Keywords: Twin roll casting, anodizing, annealing, AA5005.

EFFECT OF ALKALI TREATMENT PARAMETERS ON SURFACE STRUCTURES AND MECHANICAL PROPERTIES OF POROUS Ti6Al7Nb SCAFFOLDS

Ezgi BUTEV[*,], Elif Eda YENI[***], Emre YILMAZ[*], Ziya ESEN[*], Şakir BOR[**]**

[*]Çankaya University Ankara/Turkey
ebutev@cankaya.edu.tr, emreyilmaz.com@gmail.com, ziyaesen@cankaya.edu.tr
[**]Middle East Technical University, Ankara/Turkey
bor@metu.edu.tr
[***]Anadolu University, Eskisehir/Turkey
elifedayeni@gmail.com

ABSTRACT

In the present study, highly porous Ti6Al7Nb alloy scaffolds having 70% pore contents with 200-250 μm average pore size were produced through the spacer holder technique as a result of evaporation of Mg powder from the Ti6Al7Nb-Mg powder mixtures. In order to make the manufactured Ti6Al7Nb foam surfaces more suitable for biomedical applications they were exposed to alkali and heat treatment. Porous samples were immersed in 5M NaOH (aq.) solutions at 60°C for 24 hours then subsequent heat treatment was carried out to obtain crystalline sodium titanate layer. Crystallization heat treatments were also conducted in muffle furnaces to investigate the effect of heat treatment environment on titanate formation. Then, the morphology, structure and chemical composition of the formed titanate layers were characterized by using scanning electron microscopy (SEM) and TF-XRD techniques. According to mechanical testing, produced Ti6Al7Nb alloy foams had elastic moduli and yield strength very close to that of bone which makes them suitable for biomedical application because of the lessened stress shielding problem.

Keywords: Porous materials, Biomaterials, Hydrothermal treatment, Ti6Al7Nb alloy

1. INTRODUCTION

Porous metallic materials are increasingly gaining importance as a method of reducing mechanical mismatch due to their low elastic moduli that simulate mechanical properties of bone. Also, open porosities present in scaffolds structure enable ingrowth of bone tissues through the implant via transfer of body fluids through the pores.

Liquid state and solid state processing are the two major techniques for producing porous materials [1]. Some of foams like those of aluminum and aluminum alloys are produced with liquid state techniques owing to their low relativities and melting points [2]. However, because of their high melting temperate and high chemical affinity the method is not suitable for titanium and titanium alloys. [1]. By considering the such drawbacks of titanium, space holder method which is one of the solid state sintering method arises as the most convenient method for the production of titanium foams. In the method, pores are obtained by removal of

different types of space holder materials like carbamide, ammonium hydrogen carbonate, polymeric granules or magnesium powder [3] from the powder mixture compacts at relatively high temperatures. Researches on metallic materials have focused mainly on reducing the stress-shielding problem and enhancing the biocompatibility by avoiding possible adverse body reaction. As stated, the stress-shielding problem is alleviated by manufacturing foams of metals having similar elastic moduli to that of bone. On the other hand, biocompatibility is directly related to chemical composition of the implant material.

Thereby, titanium and its alloys are preferred metallic materials due to their good biocompatibilities. Ti6Al4V alloys are widely used as implant materials; however, some studies show that vanadium element has potential cytotoxicity and long term usage of such alloy causes vanadium ion release in the body environment [4][5]. Because of this reason, new titanium alloys including non-toxic elements like Nb, Zr, Ta have been developed. Ti-6Al-7Nb is a real alternative to the well-known Ti-6Al4V alloys which has been used for decades as an implant material [6].

Providing better mechanical properties and enough space for ingrowth of bone in foam materials are generally insufficient for the direct bonding of bone tissues to titanium alloy surface. Therefore, additional remediation is necessary for processing of porous surfaces to make them more active for bone tissue attachment [7-9]. Chemical treatment, anodic oxidation, sol-gel and plasma spray methods are the major surface modification techniques to enhance osseointegration properties of titanium and titanium alloys by modifying the surface structure [10-13]. Hydrothermal methods one of the chemical treatment technique, which enable formation of a uniform bioactive titanate coating layer on porous surface, is a relatively simple technique and controlling the process parameters is rather easier. In the technique, samples are immersed in NaOH solutions at lower temperature with changing solution concentration and temperature in the range of 2-10 M and 60°C-100°C, respectively. In order to obtain stable sodium titanate layers heat treatment at various temperature such as 600-800°C [14, 15] is applied subsequent to NaOH treatment. In the previous studies, porous titanium alloy was subject to chemical treatment in order to obtain sodium titanate layer [14-16]; however, there is no detailed study about the surface processing of Ti6Al7Nb alloy foams.

In the present study, porous Ti6Al7Nb structures having 70% porosity content was manufactured by space holder methods by evaporating magnesium powder. Then, alkali treatment (NaOH and heat treatment) was applied to make the foams' surfaces more active for bone attachment. Mechanical behaviors of as-received and surface treated porous samples were characterized by a series of compression tests. Resultant activated surfaces were examined by Scanning electron microscope (SEM), Energy dispersive analyses (EDS) and phases present were investigated by Thin Film X-ray (TF-XRD).

2. EXPERIMENTAL

In the present study, Ti6Al7Nb alloy powders with 20μm average particle size were used as the raw material and spherical magnesium powders (99.8%purity) with particle size in the range 250-355 μm were used as space holder materials to generate porosity.

Porous Ti6Al7Nb alloy structures were manufactured by space-holder method in which Ti6Al7Nb alloy powders were mixed with spherical magnesium by adding polyvinyl alcohol

(PVA) as binder and then, the mixture was mixed around 15 minutes in order to obtain homogeneous distribution of powders. After cold compaction of Ti6Al7Nb-Mg mixtures at around 500 MPa the powder mixtures were heated to 1200°C and held for 1 h for evaporation of magnesium and sintering the titanium alloy powders. In addition to foam production, to simulate the cell wall structure of manufactured Ti6Al7Nb foams, Ti6Al7Nb disc shape pellets, with no magnesium in them, were also produced using the same processing variables defined for manufacturing of foams using prealloyed Ti6Al7Nb alloy powders alone.

Preliminary studies were performed on disc shape Ti6Al7Nb alloy in order to determine the optimum process parameters for surface activation of porous Ti6Al7Nb scaffolds. Sintered Ti6Al7Nb disc samples of 10mm diameter and approximately 2 mm in thickness were immersed in 5M NaOH (aq.) solution at different solution temperatures of 60°C and 80°C. After holding the samples for 24 h in NaOH solutions, the samples were washed with distilled water in ultrasonic cleaner and dried in oven at 40°C. After alkali treatment, sintered Ti6Al7Nb discs were heated at 600°C for 1 h and cooled to room temperature by furnace cooling.

Considering the homogeneity of sodium titanate formation over disc shaped Ti67Al7Nb surfaces, optimum process parameters were chosen as 5 M NaOH (aq.) solution at 60°C for 24 h and heat treatment at 600°C for 1 h to achieve better surface activation for porous Ti6Al7Nb scaffolds. Porous and discs Ti6Al7Nb samples without any treatment were also used as reference samples for the comparison of sodium titanate layer created on the surfaces.

Physical properties of porous Ti6Al7Nb scaffolds as of density and total porosity content were identified with Archimedes' methods with the help of Xylol solutions ($CH_3C_6H_4CH_3$) by Sartorius CP224S-OCE balance. Surface morphology and elemental composition analysis of surface activated alloy discs and porous Ti6Al7Nb alloys were examined by FEI 430 Nano Scanning Electron Microscope SEM and EDS analysis. Phase constituents of sintered Ti6Al7Nb alloy were analysis by using thin film X-Ray diffractometer (TF-XRD). Compression tests were performed using 100 kN capacity Instron 5582 Universal Testing Machine equipped with extensometer at a crosshead-speed of 0.5 mm/min to analyze mechanical properties cylindrical samples having height to diameter ratio (H/D) of one.

3. RESULTS AND DISCUSSION

Figure 1 shows the change in surface morphologies of disc shape Ti6Al7Nb specimens subject to various surface processing. As it can be seen from Figure 1a, as-sintered Ti6Al7Nb alloy's surface is relatively rough and initially free of any layer. It is known that, during immersion of the titanium alloys in NaOH solutions, native TiO_2 layer partially react with Ti-OH hydroxyl group ions and form negatively charged $HTiO_3^-$ hydrates which combine with alkali ions in aqueous solution. As a result, unstable sodium titanate hydrogel layer was formed on the surfaces [17].

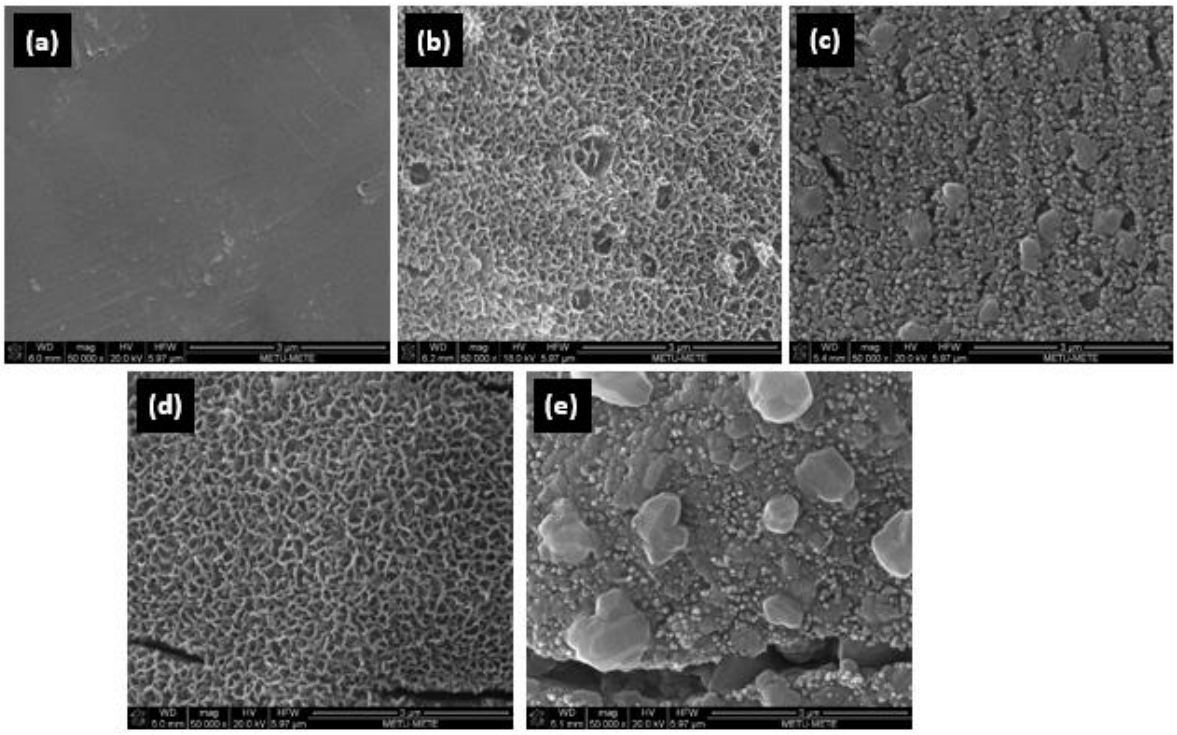

Figure 1: Disc shape Ti6Al7Nb surfaces; (a) as sintered, (b) alkali treated with 5M NaOH at 60°C then, (c) heat treated at 600°C, (d) alkali treated with 5M NaOH at 80°C then (e) heat treated 600°C.

In the present study, disc shape Ti6Al7Nb specimens were immersed in 5M NaOH solutions at 60°C and 80°C, and then heat treated at 600°C in air to get relatively high strength coating. Figure 1b reveals that 5M NaOH at 60°C alkali treated surfaces covered with porous network structure which is defined as hydrogel titanate layer consisting of Na and O elements, 6.29 % and 22.71 %, respectively, (Table 1). Subsequent heat treatment at 600°C resulted in the formation of relatively dense coating layer Figure 1c, which is explained as the transformation of hydrogel layer to dense dehydrated stable sodium titanate layer. During the transformation, porous network structure disappeared and rod-like sodium titanate with around 100 nm diameter were formed.

As the NaOH alkali solution temperature increased from 60°C to 80°C, resulted sodium titanate network structure with 5.42 % sodium and 14.18 % oxygen, was observed to contain deep cracks, Figure 1d. Similar to alkali treated samples at 60°C, heat treatment at around 600°C, resulted in the formation of dense and non-homogenous coating layer for the samples alkali treated at 80°C. As shown in Figure 1e globular and rod-like (100 nm diameter) sodium and oxygen rich (7.93%.Na and 11.02% O) regions have formed. It is expected that relative content of the sodium increases with additional heat treatment process at 600°C, Table 1.

Table 1: EDS results of disc shape Ti6Al7Nb surfaces after various treatments.

Specimen		Wt. %				
		Ti	Al	Nb	Na	O
Untreated Ti6Al7Nb alloy		80.36	4.96	14.96	-	-
5M NaOH at 60°C	No heat treatment	59.5	4.52	6.99	**6.29**	22.71
	600°C	58.86	3.11	4.64	**7.84**	15.46
5M NaOH at 80°C	No Heat Treatment	70.24	1.49	8.67	**5.42**	14.18
	600°C	63.74	1.04	2.89	**7.93**	11.02

Figure 2 shows the Thin Film X-Ray analysis results of disc shape Ti6Al7Nb surfaces activated with NaOH solutions at 60°C and 80°C and then heat treated at 600°C. Results show that Ti6Al7Nb surface layers, which were fully densified by subsequent heat treatment, were observed to consist of crystalline sodium titanate and rutile phases. Porous network structure seen in Figure1c and rod like structure in Figure 1e are crystalline sodium titanate phases with different crystal structures which are labelled as $Na_2Ti_6O_{13}$ and $Na_2Ti_4O_9$ in X-Ray Diffractogrammes. Also, Rutile phase was observed in the surface layers mainly due to the oxidation of Ti6Al7Nb alloy surfaces during heat treatment conducted at 600°C in air. .

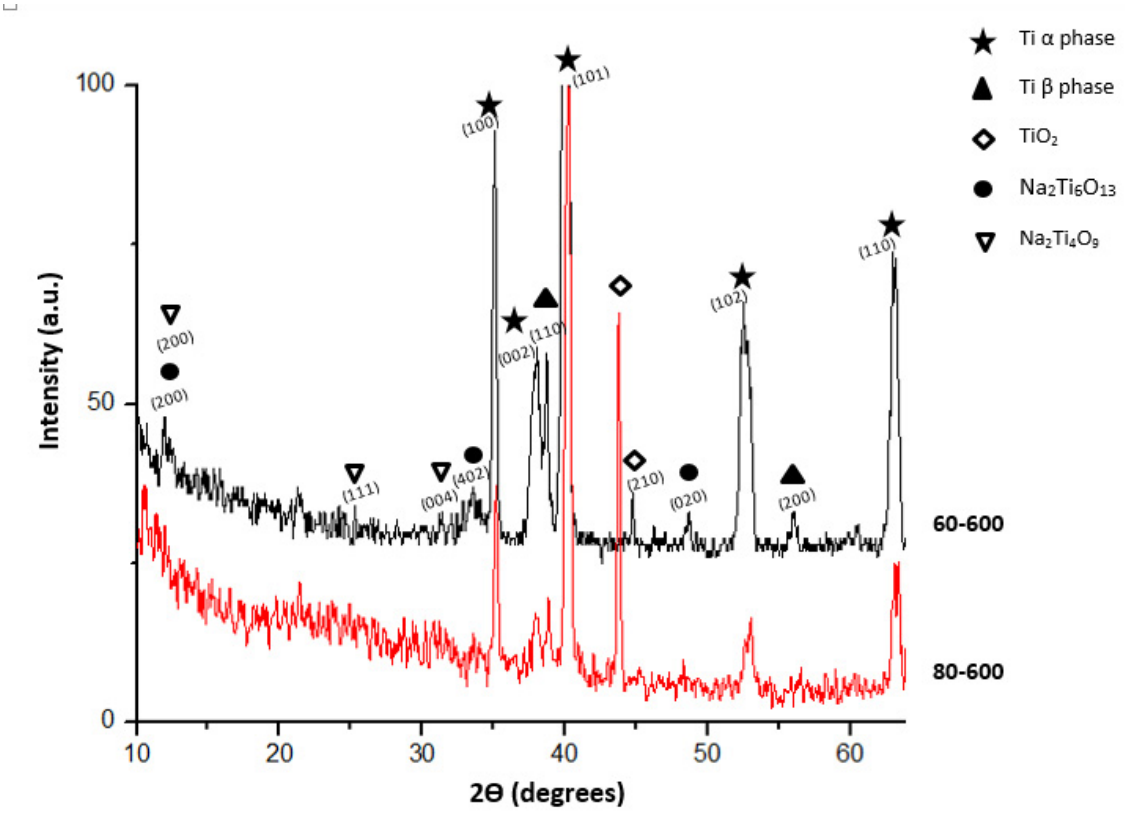

Figure 2: Thin Film X-Ray (TF-XRD) results of disc shape Ti6Al7Nb alloy surfaces. Black line: alkali treated with 5M NaOH at 60°C then heat treated at 600°C, Red line: alkali treated with 5M NaOH at 80°C then heat treated 600°C.

In the second part of the study, surface processing similar to those of disc shape sintered Ti6Al7Nb powders were applied to porous Ti6Al7Nb samples. Figure 3a shows the open porous structure of Ti6Al7Nb foams with the pore size in the range of 190-230 μm, which is specified as suitable size for bone ingrowth and transport of body fluid. Two types of pore structure can be examined, namely; macro pores formed due to evaporation of magnesium particles and rarely observed micro pores due to inadequate sintering, Figure 3b. After sintering the porous Ti6Al7Nb alloys at 1200°C for 1 hour, equilibrium cooling in furnace resulted in formation of lamellar microstructure, composed of aluminum rich (8.60%Al, 6.49%Nb) α phase and niobium rich (5.60% Al, 18.45% Nb) β phases as shown in Figure 3c.

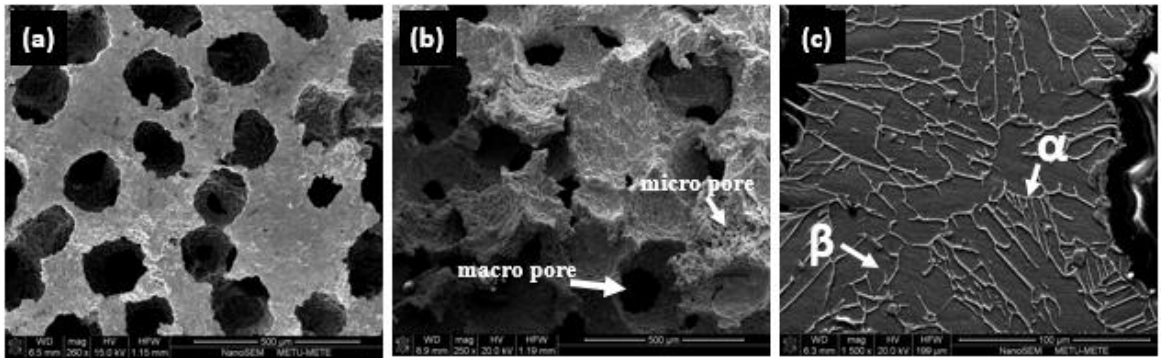

Figure 3: SEM images showing, (a) macro porous structures of Ti6Al7Nb foams, (b) fracture surface of sintered Ti6Al7Nb foam (c) underlying microstructure of foams containing lamellar microstructure with α-β phases.

Similar to disc shape Ti6Al7Nb specimens, porous Ti6Al7Nb alloys samples with 70% porosity were immersed in 5M NaOH solutions at 60°C for 24 h and subsequently heat treated at 600°C for 1h followed by equilibrium furnace cooling. The hydrothermal treatment at 80ºC followed by 600ºC heat treatment was not preferred due to excessive rutile phase formation which may leads brittleness in foams. Figure 4a shows that the surface of as-manufactured porous Ti6Al7Nb samples was relatively rough surface and contained around 4.22%Al, 7.28%Nb and 88.51%Ti as shown in Table 2.

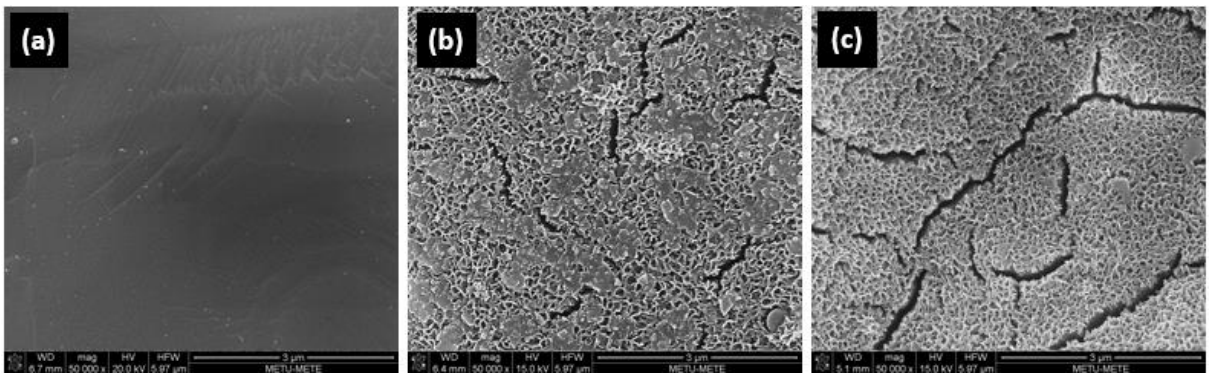

Figure 4: The surface structure of Ti6Al7Nb foams(a) as manufactured, (b) 5M NaOH-treated at 60°C, 24 h then (c) heat treated at 600°C, 1h.

Similar to disc shape specimens, nano-porous sodium reach layer was formed on the surfaces of porous samples after immersion in NaOH solution. Not all the surface contained network structure, however, relatively smooth and continuous sodium rich regions were also observed, Figure 4b. Upon heating the samples to heat treatment temperature of 600^{o}C, entire surface turned into porous network structure with some cracks, Figure 4c. Presence of cracks on the surfaces of alkali, and alkali heat treated samples seen in Figure 4b-c, was attributed to relative fast drying process applied at 40°C subsequent to alkali treatment.

EDS results taken from the porous Ti6Al7Nb samples processed in various conditions are given in Table 2. The existence of Na and O elements for both alkali, and alkali and heat-treated samples gives clue about formation of sodium titanate layer. Although sodium content is around 5.59% for the alkali treated samples, its relative content has risen to 8.58 % as a result of subsequent heat treatment process, which may be attributed to formation of sodium rich compounds including titanium and oxygen near the surface region.

Table 2: EDS results of porous Ti6Al7Nb surfaces after various treatments

Porous Ti6Al7Nb Alloy	***Wt. %***				
	Ti	**Al**	**Nb**	**Na**	**O**
As manufactured	84.91	8.6	6.49	-	-
Alkali Treated	70.41	2.61	4.77	**5.59**	16.63
Alkali and Heat Treated	55.28	3.75	8.21	**8.58**	24.19

Mechanical properties of surface treated samples' are also crucial in terms of avoiding the 'stress-shielding' problem by obtaining similar mechanical properties to that of bone. In Figure 5, compression stress-strain curves of as-manufactured porous Ti6Al7Nb alloys are given in addition to alkali treated, and alkali and heat treated samples for comparison. Untreated porous samples exhibit a typical behavior of metallic foams, which consists of linear elasticity region, plateau region and densification region, Figure 5(curve a). Compressive strength of as-manufactured specimen with 70% porosity is around 69 MPa and elastic modulus is 6.7 GPa. By considering compression test results, elastic modulus of bulk alloys, which is around 110 GPa, is lessened by introducing pore to the structure so that porous samples with elastic moduli similar to that of cancellous bone is obtained.

It is expected that alkali heat treatment improves the biocompatibility of porous titanium alloy foams while decreasing the mechanical properties [18]. However, 5M NaOH-treated specimen exhibit similar mechanical properties to that of as-manufactured specimen shown in Figure 5 (curve b). Compressive strength and elastic modulus of the alkali treated porous samples were measured as 73 MPa and 9 GPa, respectively. On the other hand, additional heat treatment in air at 600^{o}C, resulted in a sharp decrease in compressive strength probably due to excessive oxidation, while the elastic modulus remained relatively the same, Figure 5c.

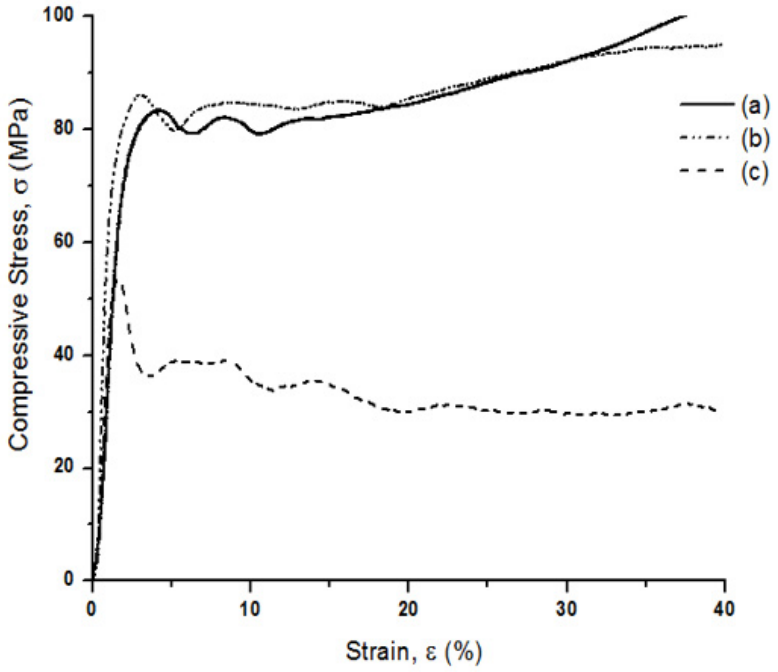

Figure 5 : Mechanical behavior of porous Ti6Al7Nb scaffolds under different conditions (curve a) untreated porous Ti6Al7Nb foam, (curve b) 5M NaOH-treated at 60°C, 24 h then (curve c) heat treated at 600°C, 1h

4. CONCLUSION

Porous Ti6Al7Nb foams with 70% porosity content and pore size in the range 165-230 μm were manufactured through the use of space holder technique. The pore size and content were suitable for bone ingrowth of bone tissues and body fluid transportation. The porous Ti6Al7Nb samples had compressive strength of 69 MPa and elastic modulus of 6.7 GPa similar to that of cancellous bone. As a result of alkali treatment in NaOH solution Ti6Al7Nb surfaces covered with partially sodium rich porous network structure. The structure became more uniform and continuous after additional heat treatment conducted at 600ºC, which also caused transformation of unstable hydrogen sodium titanate phases to crystalline sodium phases ($Na_2Ti_6O_{13}$ and $Na_2Ti_4O_9$). However, NaOH-treated foams had better mechanical properties than that of NaOH and heat treated foams due to oxidation of porous samples during additional heat treatment.

Acknowledgement

This work was supported by The Scientific and Technological Research Council of Turkey, TUBITAK, Project # 112M341.

REFERENCES

1. D.C. Dunand. "Processing of Titanium Foams". Advanced Engineering Materials, 6(6), 369-76, 2004.
2. A. Laptev, M. Bram, H.P. Buchkremer, D. Stöver. "Study of production route for titanium parts combining very high porosity and complex shape". Powder Metallurgy, 47, 85-92, 2004.
3. Z. Esen, Ş. Bor, E. Tarhan. "Characterization of loose powder sintered porous titanium and Ti6Al4V alloy". Turkish J. Eng.Env.Sci. 33, 207-19, 2009.
4. S. Fujibayashi, T. Nakamura, S. Nishiguchi, J. Tamura, M. Uchida, H.M. Kim, T. Kokubo. "Bioactive Titanium: Effect of Sodium Removal on the Bone-Bonding Ability of Bioactive Titanium Prepared by Alkali and Heat Treatment". In: J. Biomed. Mater Research, 56, No. 4, p. 562-570, 2001.
5. M.E.G. Doreste, D.G. Martin. "Preliminary Studies For In Vivo Application of Surface Treated Ti-6 Al-7Nb Prostheses". Bulletin of the Transilvania University of Braşov, 2 (51), 2009.
6. M. Semlitsch, H.Weber, R. Steger. "15 Years Esperience with the Ti-6Al- 7Nb Alloy for Joint Prostheses". In: Biomed. Technik, 40, 347- 55, 1995.
7. Z. Esen, Ş. Bor. Characterization of Ti–6Al–4V alloy foams synthesized by space holder technique. Mat Sci Eng A-Struct, 528(7-8):3200–09, 2011
8. Y. Chen, B. Feng, Y. Zhu, J. Weng, J. Wang, X. Lu. "Preparation and characterization of a novel porous titanium scaffold with 3D hierarchical porous structures". J Mater Sci-Mater M, 22(4): 839–44, 2011
9. X. Liu, P.K. Chu, C. Ding. "Surface nano-functionalization of biomaterials". Mater Sci Eng R, 70(3-6): 275–302, 2010.
10. S. Izman, M.R. Abdul-Kadir, M. Anwar, E.M. Nazim, R. Rosliza, A. Shah et al. "Surface Modification Techniques for Biomedical Grade of Titanium Alloys: Oxidation, Carburization and Ion Implantation Processes". In: Nurul Amin AKM, editor. "Titanium Alloys-Towards Achieving Enhanced Properties for Diversified Applications". In tech, 201, 2012
11. C.E. Wen, Y. Yamada, A. Nouri, P.D. Hodgson. "Porous titanium with porosity gradients for biomedical applications". Mater Sci Forum, 539-543: 720-725, 2007.
12. I.C. De Lavos-Valereto, M.C. Deboni, N. Azambuja. "Evaluation of the titanium Ti-6Al-7Nb alloy with and without plasma-sprayedhydroxyapatite coating on growth and viability of cultured osteoblast-like cells". J Periodontol 73(8):900–5, 2002.
13. D. Martini, M. Fini, M. Franchi, V. DePasquale, B. Bacchelli, M. Gamberini, et al. "Detachment of titanium and fluorohydroxyapatite particles in unloaded endosseous implants". Biomaterials, 24:1309–16, 2003.
14. X. Liu, P. Chu, C. Ding. "Surface modification of titanium, titanium alloys, and related materials for biomedical applications". Mater Sci Eng R 2004; 47(3-4): 49–121, 2004.
15. H.M. Kim, F. Miyaji, T. Kokubo, T. Nakamura. "Preparation of bioactive Ti and its alloy via simple chemical surface treatment". J Biomed Mater Res 32:409-417, 1996.
16. J. Xiong, Y. Li, X. Wang, P. Hodgson, C. Wen." Mechanical properties and bioactive surface modification via alkali-heat treatment of a porous Ti-18Nb-4Sn alloy for biomedical applications". Acta Biomater, 4(6):1963–8, 2008.
17. W. A. N. Xiao, "Effects of alkali and heat treatment on strength of porous Ti35Nb". Trans. Nonferrous Met. Soc. China 21: 1335-39, 2011.
18. X. Wang, Y. Li, P. D. Hodgson, and C. Wen. "Biomimetic modification of porous TiNbZr alloy scaffold for bone tissue engineering". Tissue Eng. Part A, 16(1); 309–16, 2010.

INVESTIGATION OF COATABILITY OF NiAl POWDER TO AISI 304 STAINLESS STEEL USING SHS PROCESS

Mehmet AKKAŞ*, Sermin OZAN, Serkan ISLAK*, Uğur ÇALIGÜLÜ****

* Kastamonu University, Turkey
mehmetakkas@kastamonu.edu.tr; serkan@kastamonu.edu.tr
** Fırat University, Turkey
serozan@firat.edu.tr; ucaligulu@firat.edu.tr

ABSTRACT
This study relates to the coatability of the Ni-Al powder to surface of AISI 304 stainless steel substrate using self-propagating high temperature synthesis (SHS) method. Effects of different pressing pressure and sintering after igniting on the microstructure and microhardness of the coating was investigated experimentally. Scanning electron microscope (SEM), X-ray diffraction (XRD) techniques were used to characterize the coatings. The microhardness was measured by microhardness device. Along the depth from the surface towards the substrate coating has been found microhardness variations. Micro hardness of the coating layer increased with increasing of the pressing pressure and the sintering temperature.

Keywords: SHS, Ni-Al, microstructure, micro hardness

SHS YÖNTEMİ KULLANILARAK AISI 304 PASLANMAZ ÇELİĞİNE NiAl TOZUNUN KAPLANABİLİRLİĞİNİN ARAŞTIRILMASI

ÖZET
Bu çalışma, kendi kendine ilerleyen yüksek sıcaklık sentezlemesi (SHS) yöntemi kullanılarak AISI 304 paslanmaz çelik yüzeyine Ni-Al tozunun kaplanabilirliği ile ilgilidir. Farklı presleme basıncının ve ateşleme sonrası sinterlemenin kaplamanın mikro yapısına ve mikro sertlik değerlerine etkileri deneysel olarak araştırılmıştır. Taramalı elektron mikroskobu (SEM) ve X-ışın difraktogramı (XRD), kaplama tabakasını incelemek için kullanılmıştır. Mikrosertlik, mikrosertlik test cihazı ile ölçülmüştür. Kaplama yüzeyinden alt tabakaya doğru kaplama derinliği boyunca mikrosertlik değişimleri tespit edilmiştir. Kaplama tabasının mikrosertliği, presleme basıncının ve sinterleme sıcaklığının artması ile artmıştır.

***Anahtar kelimeler*:** SHS, Ni-Al, mikroyapı, mikrosertlik

1. INTRODUCTION

Recently, SHS (Self Propogating High Temperature Synthesis) has been used as a new method. SHS is an advanced technology to produce ceramics, cermets and intermetallic materials. Materials prepared by SHS are reported to be purer and require less energy than conventional methods, which are generally energy-and time-intensive processes **[1-3]**. Austenitic stainless steels are used in the areas such as the medical, kitchen supplies, food, energy and shipping industry. Increasing the wear and corrosion resistance of these steels will expand the application fields. For this purpose, so far paint, polymer coating and ceramic coating and surface modification processes have been used in studies. A potential application to improve high

temperature wear and corrosion resistance is to coat the surfaces of this materials with an intermetallic compounds **[4-7]**. In this study, coatability of Ni-Al powder to AISI 304 stainless steel using SHS was investigated method. The microstructure and phase compositions of the coatings were determined via scanning electron microscope (SEM), energy dispersive spectrometer (EDS) and X-ray diffraction (XRD) analyses.

2. EXPERİMENTAL STUDIES

Commercially available Ni (99.9 wt% purity, -325 mesh), Al (99.9 wt% purity, -325 mesh), and B (95-97 wt% purity, diameter <1 μm), powders (purchased from SavKim Chemical Co., Ltd. and Alfa Easer Company) were selected as starting materials. Powders were prepared as 25 wt. % Al and 75 wt.% Ni. 1 wt.% B was added to NiAl mixture, and then mixed. Powder mixture was pressed into cylindrical compacts of 12 mm in diameter using a hydraulic press at a cold compaction pressure of 50 and 100 MPa. Then green compacts were sintered at 700 and 800 °C. The compacted samples were placed in a furnace with the protection of high purity argon gas. Then specimens were ignited. Microhardness was measured using a LEICA MHF-10 tester with a load of 100 g and a loading time of 10 s. The microstructure was examined with a scanning electron microscope (SEM) (LEO Evo-40VP) equipped with energy dispersive X-ray spectrometer (EDS). The phase constituents were characterized on an X-ray diffractometer XRD (Rigako Rad-B D-Max 2000 XRD).

3. RESULTS AND DISCUSSION

3.1. Microstructure

Figure 1 show SEM images of NiAl coatings produced by SHS. When the microstructure is examined, two different structures draw the attention. Coating layer and the substrate material can't be clearly distinguished by the difference, which at the specimen produced at 700 °C and 50 MPa (Figure 1a). Any crack or separation was not observed at the interface. As the sintering temperature and pressure increased, in the amount of pores in the coating layers decreased (Figure 1b and d) **[8, 9]**. Moreover, chromium carbide precipitates occurred at the grain boundaries of the material cooled on the air. This situation is because carbides formed in the grain boundaries of austenitic stainless steel a high temperature. It is observed that interface completely disappeared with increasing of pressure (from 50 MPa to 100 MPa) (Figure 1c and d).

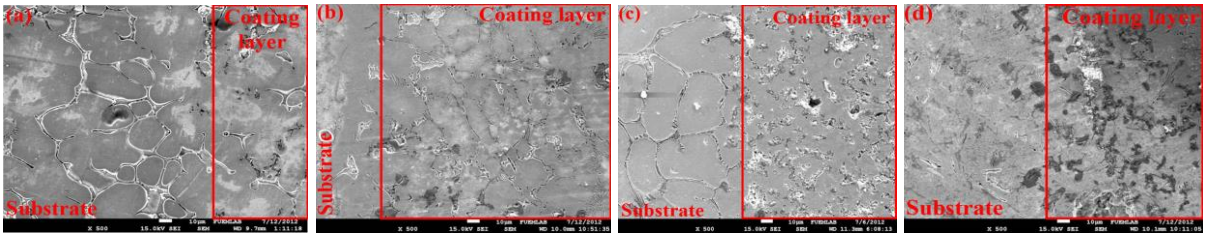

Figure 1. SEM images of NiAl coating, (a) 50 MPa, 700 °C, (b) 50 MPa, 800 °C, (c) 100 MPa, 700 °C and (d) 100 MPa, 800 °C

Figure 2 illustrates EDS analysis of coating produced at 50 MPa and 700 °C. According to EDS analysis, in the microstructure was identified C, Si, Cr, Fe, Ni, O, Al, and Mn elements. Boron was identified in none of the samples because the EDS analysis was

carried out in a very small area. As a small amount of Cr and Fe elements transferred to coating layer from AISI 304L stainless steel, a small amount of Ni and Al elements transferred to AISI 304L stainless steel from coating layer.

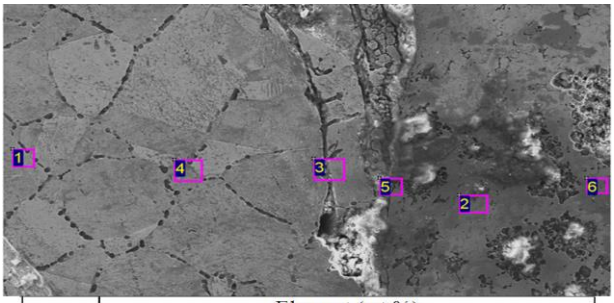

Points	Element (wt.%)								
	C	Si	Cr	Fe	Ni	O	Al	Mn	B
1	4	0.61	18	66.3	8.6	-	-	1.6	-
2	4	-	0.43	1.27	64	12	16.5	-	-
3	4	0.59	17.3	63.9	9.34	2.9	0.48	-	-
4	3	0.57	17.4	65.5	8.21	-	-	1.61	-
5	4	-	0.71	2.91	50	28	14	-	-
6	3	-	0.35	0.9	76.5	3.4	14.5	-	-

Figure 2. EDS analysis of coating produced at 50 MPa and 700 °C

The XRD pattern of coating produced at 50 MPa and 700 °C is shown in Figure 3. The products such as Fe and Ni are the predominant phases. In addition, several second phases, such as Fe_3Ni_2, Cr_2Ni_3, and $Fe_{0.64}Ni_{0.36}$ formed. Finally, a ternary phase, such as $B_2Fe_3Ni_3$. Boron not detected in the EDS analysis was determined by XRD analysis.

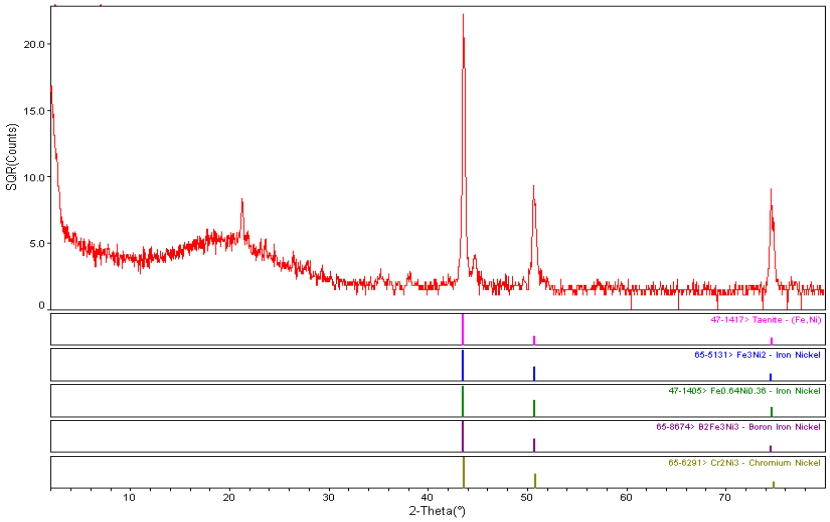

Figure 3. XRD pattern of coating produced at 50 MPa and 700 °C

3.2. Microhardness

Microhardness measurements were conducted throughout a line from the uppermost region of the coating through AISI 304L stainless steel substrate at intervals of 0.5 mm (Figure 4a). Figure 4b shows microhardness change between coating layer and substrates.

Microhardness varied as depending on pressure and sintering temperature. It decreased towards substrate from coating layer. While the highest hardness value taking from S_4 sample that was produced at 100 MPa and 800 °C was 280 $HV_{0.1}$, the lowest hardness value taking from S_1 sample that was produced at 50 MPa and 700 °C was 245 $HV_{0.1}$. Microhardness of substrate was 195 $HV_{0.1}$. Microhardness of the coating layer to the substrate material are increased by 45%.

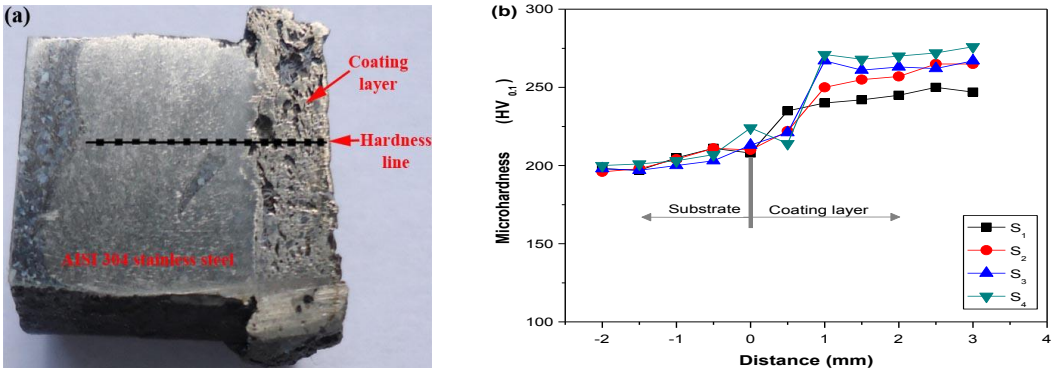

Figure 4. (a) Microhardness taking representative and (b) Microhardness graph (S_1: 50 MPa, 700 °C; S_2: 50 MPa, 800 °C; S_3: 100 MPa, 700 °C; S_4: 100 MPa, 800 °C)

4. CONCLUSIONS

The NiAl coatings on the surface of AISI 304L stainless steel substrate were produced successfully using self-propagating high temperature synthesis (SHS) method. SEM images showed that any crack or separation was not observed at the interface coating layer and substrate. The amount of pores in the coating layers decreased with increasing sintering temperature and pressure. According to XRD pattern, binary and ternary phases formed in the microstructure. Microhardness of coating layer increased markedly as depending on increasing of pressure and sintering temperature, which it is 45% higher than substrate.

Acknowledgment

The research was supported by the Firat University Scientific Research Projects Unit (Project no: TEF.11.12).

REFERENCES

[1] J. Subrahmanyam, M. Vijayakumar, J. Mater. Sci., 27, 6249, 1992.
[2] P. La, M. Bai, Q. Xue, W. Liu, Surf. Coat. Tech., 113, 44, 1999.
[3] X. Yuan, G. Liu, H. Jin, K. Chen, J. Alloys and Comp., 509, L301, 2011.
[4] J.H. Jin. D.J. Stephenson, Wear, 217, 200, 1998.
[5] J.A. Jımenez, S. K1aus, M. Carsı, O.A. Ruano ye G. Frammeyer, Acta Mater, 174, 3655, 1999.
[6] B.J. Johnson, F.E. Kennedy ye I. Baker, Wear, 192, 241, 1996.
[7] P. J. B1au, C. E. DeVore, Tribo1. Inter., 23, 226, 1990.
[8] G. Tosun, L. Ozler, M. Kaya, N. Orhan, J. Alloys and Comp., 487, 605, 2009.
[9] C.L. Yeh, W.Y. Sung, J. Alloys and Comp., 376, 79, 2004.

EFFECT OF AIR PLASMA SPRAY PARAMETERS ON THE PROPERTIES OF YSZ AND C-YSZ THERMAL BARRIER COATINGS

Muhammet KARABAŞ*, Ahmet DURMAZ, Ayşe KILIÇ, Yılmaz TAPTIK

Istanbul Technical University, Metallurgical and Materials Eng. Dept., Istanbul- Turkey

ABSTRACT

Thermal Barrier Coatings (TBC) find a wide application area as a protection shield against high temperature for the structural components in stationary and aerospace gas turbines. The Thermal Barrier Coating (TBC) concept is based on placing a thermally insulating layer between a cooled metallic component and the hot working gas with the aim of reducing the heat transfer to the component. Ceramic layer, known as thermal insulating layer, is applied in order to improve adhesive strength, oxidation and corrosion resistance and also to reduce the thermal expansion differences and on the other hand a metallic layer as a bond coat, MCrAlY (M = Co, Ni), is coated between ceramic layer and substrate.

YSZ and C-YSZ are known as the most commonly used coating materials due to their low thermal conductivity and having close characteristics like metals in terms of thermal expansion coefficient, good corrosion resistance. Plasma spray process parameters, such as spray distance and gas mixture ratio have vital impact on thermal barrier coating properties.

In this study; metallic bond coat and ceramic thermal insulating layer are conducted by HVOF (High Velocity Oxy Fuel) and APS (Atmospheric Plasma Spray) processes, respectively. Effects of plasma spray distance and Ar/H_2 gas mixture ratio on YSZ and Z-YSZ thermal barrier coating properties are investigated with the experiments and characterization studies. Within the scope of characterization studies; SEM analysis, porosity analysis with ASTM 2109 standard, and also adhesion strength tests compliance with ASTM C633 are performed.

Keywords: Thermal Barrier Coatings, air plasma spray, YSZ, C-YSZ

ATMOSFERİK PLAZMA SPREY PARAMETRELERİNİN YSZ VE C-YSZ TERMAL BARİYER KAPLAMA ÖZELLİKLERİNE ETKİSİ

ÖZET

Termal bariyer kaplamalar; uçak ve uzay araçlarındaki gaz türbin bileşenlerinin yüksek sıcaklık etkisinden korunmasında geniş bir uygulama alanına sahiptir. Termal bariyer kaplama kavramı; havayla soğutulan metalik malzeme ile sıcak gaz katmanı arasına, ısı transferini yavaşlatacak termal yalıtım yeteneği yüksek malzeme katmanının kaplanması esasına dayanmaktadır. Isıl yalıtım katmanı olarak da bilinen seramik esaslı kaplama; yapışma, oksidasyon ve korozyon direncini arttırmak, taban malzeme ile ısıl genleşme farklılığını gidermek için uygulanmakta olup; seramik kaplama ile taban malzeme arasına da bağlanma katmanı olarak bilinen metalik katman, MCrAlY (M=Co,Ni) kaplanmaktadır.

YSZ ve C-YSZ; düşük termal iletkenliğin yanı sıra metalik malzemelere yakın termal genleşme katsayısı, yüksek korozyon direnci gibi özellikleri sebebiyle endüstride en çok kullanılan kaplama malzemeleri olarak bilinmektedir. Sprey mesafesi ve gaz karışım oranı

gibi plazma sprey parametreleri termal bariyer kaplamaların özelliklerine önemli derecede etki etmektedir.
Bu çalışmada, HVOF (Yüksek Hızlı Oksi-Yakıt) sistemi ile metalik bağlanma katmanı ve APS (Atmosferik Plazma Sprey) sistemi ile seramik ısıl yalıtım katmanı uygulaması yapılmıştır. Sprey mesafesi ve Ar/H_2 gaz karışım oranı gibi proses parametrelerin YSZ ve C-YSZ termal bariyer kaplamaların karakteristik özellikleri üzerine etkisi yapılan deneyler ve karakterizasyon çalışmaları ile ortaya konmuştur. Gerçekleştirilen karakterizasyon çalışmaları kapsamında; SEM analizleri, , ASTM 2109 standardına göre porozite analizi ve ASTM C633 standardına göre yapışma mukavemeti testleri gerçekleştirilmiştir.

Anahtar Kelimeler: Termal bariyer kaplama, atmosferik plazma sprey, YSZ, C-YSZ

1. INTRODUCTION

Thermal Barrier Coatings (TBC) find a wide application area as a protection shield against high temperature for the structural components in stationary and aerospace gas turbines. The Thermal Barrier Coating (TBC) concept is based on placing a thermally insulating layer between a cooled metallic component and the hot working gas with the aim of reducing the heat transfer to the component. Ceramic layer, known as thermal insulating layer, is applied in order to improve adhesive strength, oxidation and corrosion resistance and also to reduce the thermal expansion differences and on the other hand a metallic layer as a bond coat, MCrAlY (M = Co, Ni), is coated between ceramic layer and substrate. Plasma spray process parameters have vital impact on the quality of thermal barrier coatings due to the powder particles and plasma flame interactions [1-3].

Ar/H_2 gas mixture ratio (known as plasma power) and also plasma spray distance play a key role on the quality of TBCs. Taking into account the effect of spray distance on the particle properties, it is indicated that the particle velocity and particle temperature decreases because of the increase in spray distance. This means that spray distance determines cooling rate of in-flight particles and accordingly long spray distance causes more cooling. On the other hand, due to the heating of the substrate surface by plasma flame, much more melting particles and low density TBCs occur resulting from short spray distance. Spray distance also affects adhesion strength of the TBCs on account of both fast cooling at long spray distance and also the overheating of substrate material at short spray distance. Therefore determination of the optimum spray distance is very important in terms of TBCs quality [4-6].

Based upon the high thermal conductivity and specific heat capacity of the H_2 gas, the ratio of H_2 in the Ar/H_2 gas mixture is more influential on plasma power than Ar. As the flow rate of H_2 gas increases, plasma power and in-flight particle temperature also increase [7-9]. From the point of ascent in Ar flow rate; despite the increase in kinetic energy of plasma, plasma temperature decreases depending on particle velocity acceleration. Particles move at a very fast speed in the plasma jet areas and in parallel with this, the heat transfer between particles and plasma flame may not be sufficient. Poor heat transfer causes poor adhesion of the splats and in the microstructure more porosity and more melted particles are observed [8,9].

In this study, we investigated the effect of spray distance and Ar/H_2 ratio on microstructure, thickness, porosity and adhesion strength of YSZ and C-YSZ TBCs.

2. EXPERIMENTAL PROCEDURE

Disc shaped 316L stainless steel samples with a diameter of 25.4 mm and thicknesses of 2mm were used as a substrate material. Prior to bond coat production, the substrate was grit blasted with using 50-80 grain mesh alumina. Commercial Sulzer Metco Amdry 997 (Ni- 23Co-20Cr-8 .5Al-4Ta-0.6Y) powders were used for the the bond coats. The spray torches (APS and DJ2700 HVOF gun) were fastened on a three-axis CNC robot and gun speed is 600 mm/min. Grit blasted samples were clamped on the turntable and the number of passes was 12. HVOF process parameters were given at Table 1.

Table 1: Process parameters of HVOF

Material	Pressure (bar)			Flow rate (SCFH)			Process	
AMDRY 997	Oxygen	Propane	Air	Oxygen	Propane	Air	Spray distance (mm)	Powder feed rate (g/min)
	10.3	6.2	7.2	24	40	50	250	75

Commercial Sulzer Metco 204NS (ZrO_2–8 wt.%Y_2O_3) and Sulzer Metco 205NS (C-YSZ) powders were used for top coats.
Two types of coatings were produced by air plasma spray (APS) method with the usage of Sulzer Metco 9MB plasma spray gun. Sulzer Metco Commercial 730C was used as the Gun nozzle. Powder injection angle was placed perpendicularly to plasma flame. Process parameters of plasma spraying were given in Table 2.

Table 2: Process parameters of plasma spray

Materials	Current (A)	Primary gas, Ar (scfh)	Secondary gas, H_2 (scfh)	Carrier gas flow rate, Ar (scfh)	Number of passes	Spray distance (mm)	Gun speed (mm/min)	Turntable speed (rpm)
C-YSZ	500	80	20	13.5	12	65	200	200
	500	90	15	13.5	12	75	200	200
	500	80	10	13.5	12	100	200	200
	500	80	20	13.5	12	75	200	200
	500	90	15	13.5	12	65	200	200
	500	80	10	13.5	12	75	200	200
	500	80	20	13.5	12	100	200	200
	500	90	15	13.5	12	100	200	200
	500	80	10	13.5	12	65	200	200
YSZ	500	80	20	13.5	12	65	200	200
	500	90	15	13.5	12	75	200	200
	500	80	10	13.5	12	100	200	200
	500	80	20	13.5	12	75	200	200
	500	90	15	13.5	12	65	200	200
	500	80	10	13.5	12	75	200	200
	500	80	20	13.5	12	100	200	200
	500	90	15	13.5	12	100	200	200
	500	80	10	13.5	12	65	200	200

The cross section microstructure and thickness of the coatings were inspected with Scanning Electron Microscopy (SEM) investigations (JSM-7000F Model Field Emission SEM).
Porosity analysis was carried out by cross section SEM micrographs of the coatings according to ASTM 2109 standard. Adhesion tests of the coatings were performed in compliance with ASTM C633 standard.

3. RESULTS AND DISCUSSION

3.1 Microstructure, Thickness and Porosity of TBCs

The cross-sections of the YSZ and C-YSZ TBCs including bond coats and top coats were given in Figure 1. Bond Coat thicknesses were achieved between 80 and 110 µ. As the characteristic feature of the TBCs, porosity and cracks in the top coat were observed clearly.

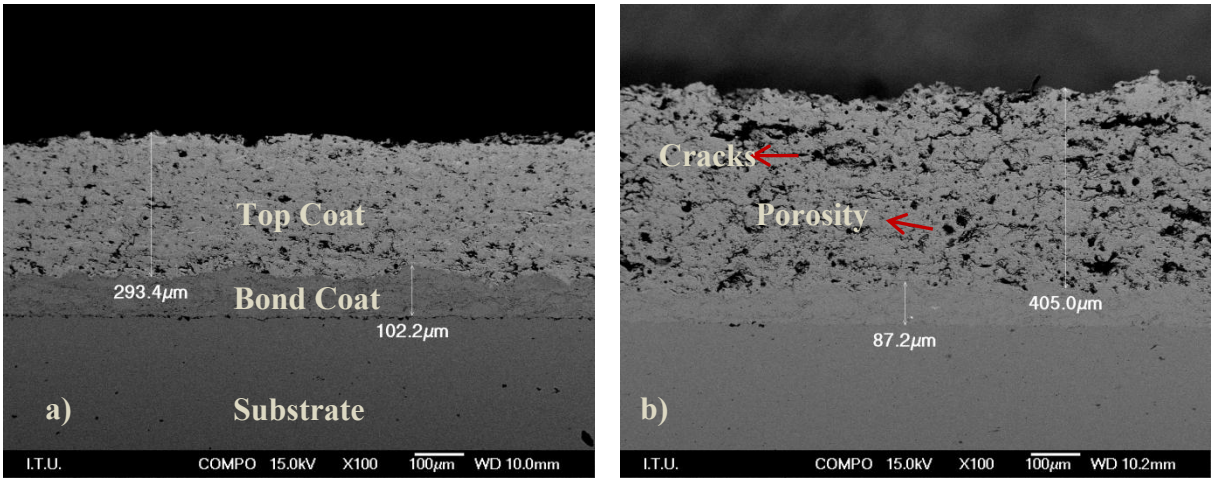

Figure 1: SEM images of C-YSZ TBC (a) and YSZ TBC (b)

The effect of spray distance on coating thicknesses (Figure 2-a) showed that the highest thickness values of TBCs were obtained at the spraying distance of 65 mm. Increasing spray distance from 65mm to 100mm resulted in coating thickness decrease. C-YSZ coatings have higher thickness values than YSZ coatings at a spray distance of 65 mm. However, different Ar/H_2 ratio cause great changes on the TBCs thickness due to the effects of plasma spray parameters on deposition efficiency, porosity percentage and density of the TBCs (Figure 2-b). Maximum coating thickness was achieved at the spray distance of 65 mm and at the Ar and H_2 flow rates of 80 scfh and 20 scfh, respectively.

Figure 3 shows the effect of spray distance and Ar/H_2 ratio on the coating porosity percentage. The increase in Ar/H_2 ratio reduces the porosity % of C-YSZ TBCs. However, porosity % of TBCs declines at the Ar/H_2 ratio of 8 and for the YSZ, there is no regular change in the porosity % of TBCs (Figure 3-a). At all spray distances, as the Ar and H_2 flow rate increases, porosity % decreases. Low porosity TBCs occurs in the consequence of the increase in plasma temperature, particle velocity and also Ar and H_2 flow rates.

At Ar/H_2 flow rate of 4 and 8, increasing of H_2 flow rate, porosity % of C-YSZ TBCs decreases at all spray distances. Nevertheless, the similar case cannot be observed for YSZ TBCs. Porosity % declines with the rise in H_2 flow rate at the spray distance of 75 mm. On the other hand, 65 and 100mm spray distances cause an increment in the porosity % of YSZ TBCs.
The porosity % of C-YSZ TBCs decreases with the increasing spray distance (Figure 3-b). At short spray distances, the sample surface temperature rises with the effect of plasma flame and this leads to the formation of higher porosity % in TBCs. Also long spray distance causes a long flight time in the plasma flame for the particles. In contrast with C-YSZ TBCs, YSZ TBCs does not demonstrate regular differences.

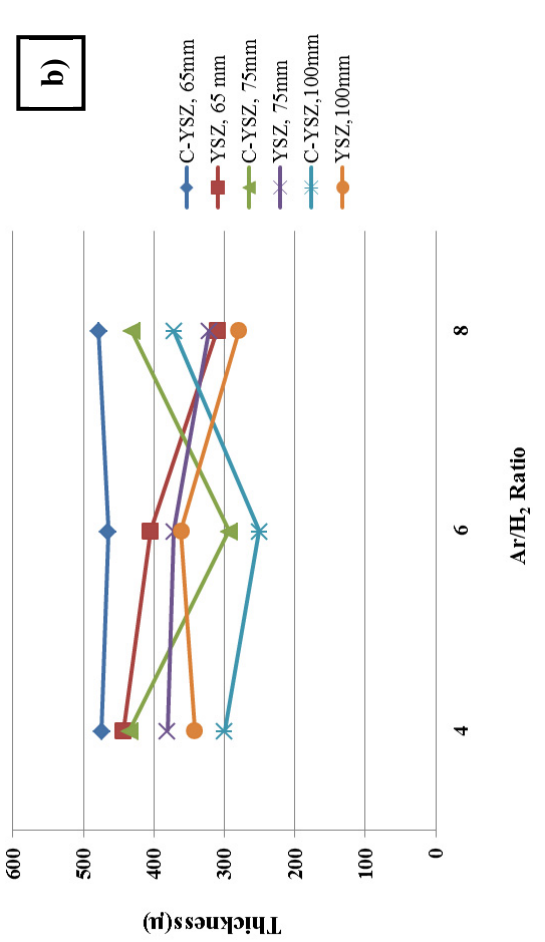

Figure 2: Effect of spray distance (a) and Ar/H_2 ratio (b) on TBCs thickness.

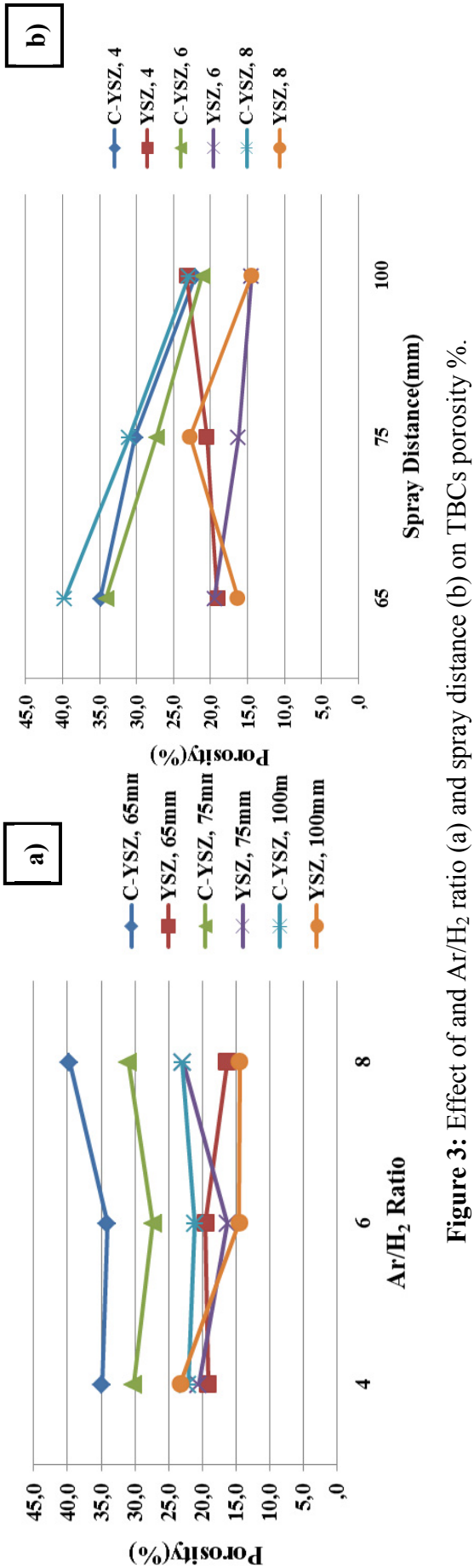

Figure 3: Effect of and Ar/H_2 ratio (a) and spray distance (b) on TBCs porosity %.

3.2 Adhesion strength of TBCs

There are many factors that affect the adhesion strength of the TBCs. Coating thickness and % porosity of TBCs are the factors that have the vital importance. As the top coating becomes thicker, the internal stress in the structure arises. Also mechanical properties of the TBCs are getting worse due to the increasing porosity of the coating.
Cohesive rupture occurred within the top coat at result of adhesion tests for all samples.
Figure 4 shows the effect of spray distance and Ar/H_2 ratio on the adhesion strength of the coatings. Highest adhesion strength is reached at the Ar/H_2 ratio of 6 (Figure 4-a). Heat transfer between particles and plasma flame becomes excessive and particles accelerate tremendously at the flow rates of primary gas Ar and secondary gas H_2, 90 scfh and 15 scfh, respectively. It was observed that adhesion strength of TBCs decreases drastically at the Ar and H_2 flow rates in order of 80 scfh and 10 scfh.

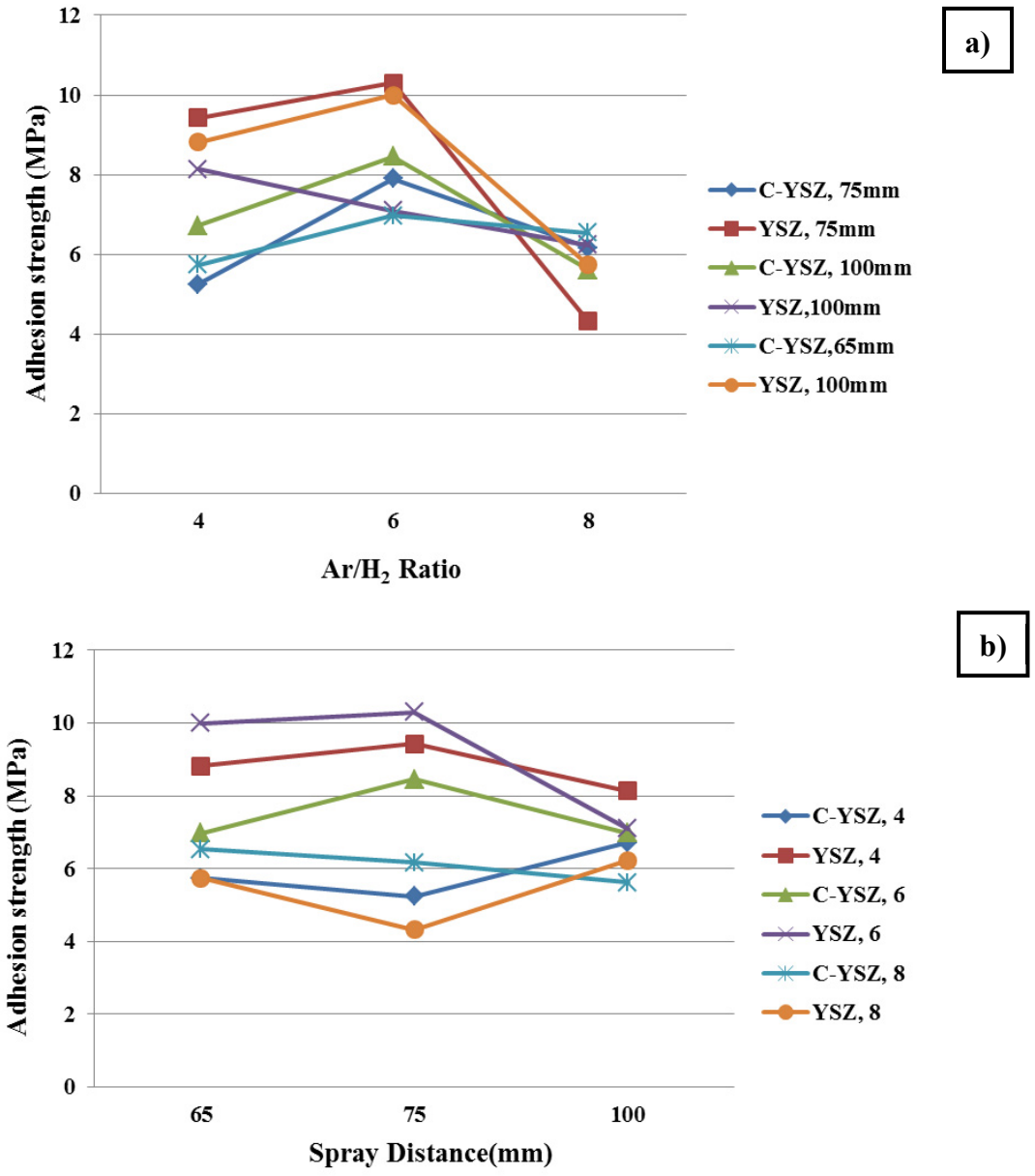

Figure 4: Effect of Ar/H_2 ratio (a) and spray distance (b) on TBCs adhesion strength

Spray distance has much more influence on the adhesion strength of TBCs than Ar/H_2 ratio. Highest adhesion strength results at the spray distance of 75 mm and Ar/H_2 ratio of 6. For these mentioned parameters; adhesion strength of YSZ TBCs which have Ar/H_2 ratio of 4 and 6, is greater than C-YSZ TBCs.

4. CONCLUSION

As a result of this study, following important conclusions can be drawn:

- Ar/H_2 ratio and spray distance have a great influence on some properties of zirconia based TBCs.
- Increasing the spray distance from 65 mm to 100 mm, both the thickness of TBCs and also the deposition efficiency decrease.
- Porosity level of C-YSZ TBCs decreases as the spray distance ascends. On the other hand, YSZ TBCs does not exhibit a similar behavior. Increasing Ar/H_2 ratio value from 4 to 6 brings out a decrease in the porosity level of C-YSZ TBCs. Besides porosity level of C-YSZ TBCs. YSZ TBCs did not show an alteration at spray distance and Ar/H_2 ratio differences when Ar/H_2 ratio value increases from 6 to 8.
- Highest adhesion strength was determined at the Ar/H_2 ratio of 6 and 75 mm spray distance for two types of TBCs except YSZ. Spray distance has not significant effect on adhesion strength of TBCs.

REFERENCES

1. HERMAN, R. B., Plasma Spray Coating, Principles and Applications, VCH, USA, 1-100, 1996.

2. MATEJKA, D., BENKO B., Plasma spraying of metallic and ceramic materials, John Wiley and Sons, UK, 11-51, 1989.

3. DAVIS, J.R.(ed.), Introduction to thermal spray technology and surface science, Handbook of Thermal Spray Technology, ASM International: Materials Park, OH, 06994G, 1-14, 2004.

4. KUCUK, A., LIMA, R.S., BERNDT C.C., Influence of plasma spray parameters on formation and morphology of ZrO2-8 wt% Y2O3 deposits, J. Am. Ceram. Soc. 84/4, 693-700,.2001.

5. VAIDYA, A., SRINIVASAN V., STREIBL T., FRIIS M., CHI W., SAMPATH S., Process maps for plasma spraying of yttria-stabilized zirconia: An integrated approach to design, optimization and reliability, Mater. Sci. Eng. A 497, 239-253, 2008.

6. ZHAO, Y.Y.,GRANT P.S., and CANTOR B., Modeling and experimental analysis of vacuum plasma spraying part I: prediction of initial plasma properties at plasma gun exit, Modelling Simul. Mater. Sci. Eng. 8, 497-513, 2000.

7. [182] FANG, J.C., XU W.J., ZHAO Z.Y., ZENG H.P., In-flight behaviors of ZrO_2 particle in plasma spraying, Surf. Coat. Tech., 201, 5671-5675, 2007.

8. XIONG, H.B., ZHENG L.L., SAMPATH S., WILLIAMSON R.L., FINCKE J. R. , Three-dimensional simulation of plasma spray: effects of carrier gas flow and particle injection on plasma jet and entrained particle behavior, Int. J. of Heat and Mass Transfer 47, 5189–5200, 2004.

9. LEBLANC, L., MOREAU C., LEGOUX J.-G., ARSENAUL B., Characterization of plasma spray processes by monitoring the state of the sprayed particles, Uni. Ther. Spray Conf., Edited by E. Lugscheider P.A. Kammer. German Weld.Soc., Dusseldorf, Germany,329–334, 1999.

SUBSTRATE – ENAMEL INTERFACE RELATION AND IMPACT ON QUALITY OF ENAMEL

Özge IŞIKSAÇAN*, Ezgi YILMAZ*,, Onuralp YÜCEL*, Alper YEŞİLÇUBUK****

* Metallurgical and Materials Engineering Department, Faculty of Chemical and Metallurgical Engineering, Istanbul Technical University, 34469, Maslak, Istanbul, Turkey
ozdemiro@itu.edu.tr
ezgiyilmaz02@gmail.com
yücel@itu.edu.tr
** Arçelik A.Ş., 34950, Tuzla, İstanbul, Turkey
alper.yesilcubuk@arcelik.com

ABSTRACT
The aim of this study is to discover the enamel substrate adhesion mechanism. Enamel is composed of organics in oxide forms, applied on a metal substrate with a firing temperature range of 800-870°C. Most important factors that affect adhesion of the enamel to the substrate are; enamel composition, firing time, substrate-enamel compatibility and surface roughness of the substrate. Adhesion mechanisms can be explained by 3 base theories; chemical, mechanical and diffusion. This study focuses on examining adhesion mechanisms between enamel coatings and substrates. During laboratory studies, enamel composition variations were investigated for explaining chemical theory; different samples with different surface roughness values were observed via different characterization techniques in order to explain mechanical theory. Adhesion of enamel to the substrate was scaled via SEM and impact tests. It is concluded that; cobalt oxide presence in enamel composition affects adhesion positively, adhesion ability deteriorates with lowering cobalt oxide content. It is proved that; the increment in surface roughness also increases adhesion ability. It is established via SEM analysis that; the dendritic formations along the enamel substrate interface are oxidation of metal substrate surface fuses through enamel.

Keywords: *Enamel, adhesion mechanism, enamel substrate interface.*

TABAN MALZEME EMAYE ARAYÜZ İLİŞKİLERİNİN EMAYE KALİTESİNE ETKİSİ

ÖZET
Emaye oksit yapıdaki organik bileşenlerden oluşan, metal taban üzerine uygulanarak 800-870° pişirme sıcaklıklarında ergitme yolu ile kaplanan camsı görünüme sahip bir malzemedir. Kaplamanın emaye üzerine yapışma performansı emaye kalitesini etkilemektedir. Emayenin taban malzeme üzerine yapışmasını etkileyen en önemli faktörler; emaye bileşimi, pişirme süresi, pişirme sıcaklığı, taban malzeme emaye uyumu ve taban malzeme yüzey pürüzlülüğüdür. Emaye taban malzeme tutunma mekanizması kimyasal, mekanik ve difüzyon teoremi olmak üzere 3 temel mekanizma ile açıklanmaktadır. Bu çalışma, emaye kaplanmış yüzeylerin taban malzemeye tutunma mekanizmalarının incelenmesi amacıyla yapılmıştır. Çalışmada kimyasal teoriyi incelemek için emaye bileşimi, mekanik teoriyi incelemek için taban malzeme yüzey pürüzlülüğü farklı numuneler üzerinde karakterizasyon çalışmaları yapılmıştır. Emayenin taban malzemeye tutunması; darbe testi ve SEM analizleri ile ölçülendirilmiştir. Yapılan çalışmalar sonucunda emaye bileşiminde bulunan kobalt oksit

bileşiğinin tutunmayı olumlu etkilediği, emaye bileşimindeki kobalt oksit oranı azaldıkça tutunma kabiliyetinin düştüğü görülmüştür. Farklı yüzey pürüzlülüğüne sahip taban malzemelere yapılan kaplamalara uygulanan tutunma testi sonucunda; yüzey pürüzlülüğünün artmasıyla emayenin taban malzemeye tutunmasının iyileştiği görülmektedir. Yapılan SEM analizleri sonucunda taban malzemenin oksitlenerek emaye içerisine doğru viskozlaşarak oluşturduğu dentritik yapıların da emaye tutunması için gerekli arayüz oluşumları olduğu tespit edilmiştir.

***Anahtar kelimeler*:** Emaye, emaye taban malzeme arayüz yapışma mekanizması.

1. INTRODUCTION

Enamel consist inorganic metal oxide components and can be applied one or more coat on the metal substrate by melting from 800 to 870°C at the heating temperatures of the adhesion is provided a coating material having a glassy appearance. Adhesion of the coating to the substrate determines the quality of the coating performance [1-3].

Vitreous enamel play a very important role in the coating production process of steel in accordance with the technical and esthetic properties induces by the enamel to the final material. Vitreous enamel coatings show excellent resistance to chemical degradation processes as well as a good resistance to tribological phenomena such as abrasive wear. Enamel coatings are generally defined as a substantially vitreous glassy inorganic layer bonded to various metal substrates by fusion at the defined temperature [4-7].

Vitreous enamel has been used for many centruies in artistic field for manufacturing jewels, art objects, religious items and other pieces of work, owing to its attractive appearance with brillant colours. With the advent of the industrial recolution since 18th century, the use of enamel began to spread over several products on industrial scale, such as household goods, furnishing, and interior decoration items [8-10].

The key factor affecting the functionality of the final material is the achievement of a good bond between the enamel and the metal substrate during the enameling process. Several factors could affect interface reactions and the adhesion mechanism between the glass coatings and the metal substrate such as chemical composition of enamel, the type of steel, the roughness of the metal surface, the heating process and the temperature of glazing, the atmosphere of the oven and so on [11-15].

The enamelling procedure on a steel surface has been studied by many researches from various points of view. To ensure good adherence of the enamel, different methods of pre-treatment of the steel sheets plates have been tested including pickling using dilute sulfiric acid, high power diode laser surface treatment and electrochemicalprocessing. With the aim of modifying structure and composition of the steel-enamel interface, doping of enamels with selected transition metal elements or pre-treatment of the steel surfaces with such elements has also been used. Most commonly used elements include Ni, Co and Ti. Doping of enamel with Co or pre-treatment of the steel surface with Co was observed to be more effective than procedures with Ni, Ti or taht without any transition elements. Transition metal pre-treatment leads more complex oxidation of the steel surface [16-22].

Adhesion mechanism of the enamel coating explained with three basic adhesion mechanism; chemical theory, mechanical theory and diffüsion theory. Chemical theory indicate that; a continuous shift of the type of bond must be achived in the region of the phase boundary from the metallic bond of the base metal via an oxide adherence layer to the ionic bond of the enamel layer. Mechanical theory is defined by; the prerequisite for good adherence is

roughning of the interface surface leading to a tight mechanical clinging of the enamel to the steel surface. Such roughning of surface is obtained when the attack on the iron in microscopic ranges is not uniform, but occurs as concantrated localized attack [22-26].

Additionaly, there are other theories such as electrolytic theory and dentritic theory which are used to analyze the adherence of the enamel and metallic matrix. However, none of the theories can adequately describe adhesion for all systems. In electroytic theory the adhesion oxides, mainly cobalt and nickel oxides (CoO and NiO) play an important role which is complicated and diffucult to explain. According to this theory the base metal reduces the oxides in the enamel to the metallic state during firing process.These adherence promoting metals are believed to form shorted galvanic cells that strongly corrode the base metal.Respect to the dentritic theory; the dentrites with tooth like apperance have the essential role in the adherence in the interface. The dentrites are form in which metal normally crystalizes from the melt, aqueous solutions or any nonmetalic liquid in which compounds of the metal to the enamel tending to attach the enamel mechanically to the metal base after cooling [24-26].

2. EXPERIMENTAL STUDIES

2.1. Materials

Experimental studies made by 100x100x8 mm sized DC 04 ED steel which obtained from Arçelik Bolu Cooking Appliances Factory, white enamel powder which has poor adhesion obtained from Ferro Company, black enamel powder which has good adherence obtained from Gizem Frit Company. Samples coated with electrostatic powder spray device and baked 830°C for 4 minutes.

2.2. Experimental Methodology

During laboratory studies, two different coating methods were used; electrostatic powder coating and wet spray enameling.

Figure 1. Electrostatic Powder and Wet Spray Coating

2.2.1. Preparation of Substrate

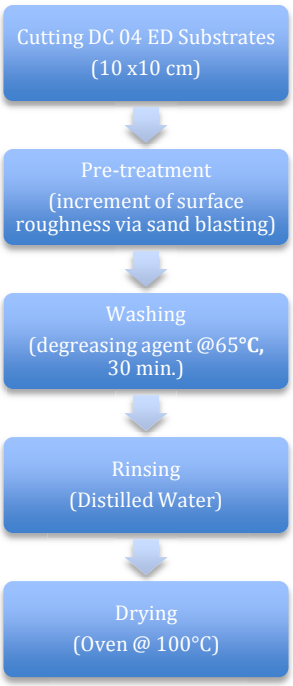

Figure 2. Flow Chart of Preparation of Substrates

2.2.2. Preparation of Enamel and Coating

White enamel powder consists of 0.01 % cobalt oxide and black enamel powder consists of 0.8% were mixed via ball mixer in percentages shown in Table 1 with 200 spin/min. for 6 hours.

Table 1. Enamel Composition Percentages

Sample Code	*White Powder wt %*	*Black Powder wt %*
K-1	**100**	**0**
K-2	**90**	**10**
K-3	**80**	**20**
K-4	**70**	**30**
K-5	**60**	**40**
K-6	**50**	**50**
K-7	**40**	**60**
K-8	**30**	**70**

K-9	**20**	**80**
K-10	**10**	**90**
K-11	**0**	**100**

2.2.3. Firing Enamel

Coated samples were fired in the oven at 830 and 840°C for 1-10 min. Samples coated by wet spraying were dried at 100°C for an hour before firing.

2.2.4. Characterization

SEM Analysis was utilized for enamel coating interface examination. Samples were placed in bakelite for cross-sectional examination. Then, bakelites were subjected to abrasion and polishing before examination.

After SEM analysis, coatings were examined for colour, thickness, scratching and impact tests.

3. RESULTS AND DISCUSSION

3.1. Determination of Optimum Firing Period and Temperature

By using SEM analysis interface dendritic formation was observed with respect to firing period. After several trials firing period was fixed to 4 minutes. Interface examinations were shown in Figure 3.

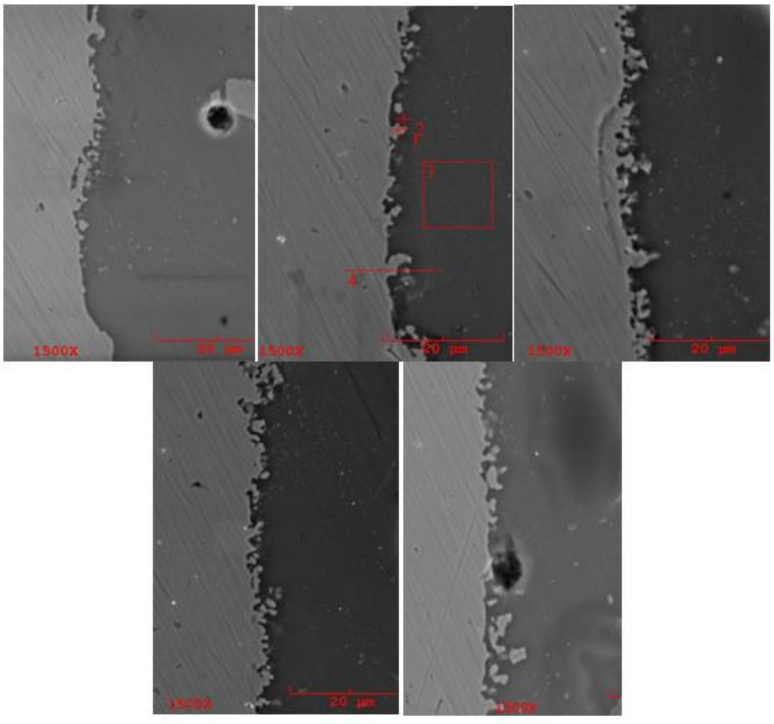

Figure 3. Influence of Firing Period on Dendritic Formation a) 3 min. b) 3.5 min. c) 4 min. d) 4.5 min. e) 5 min.

Impact test results of coatings exposed to different firing periods are shown in Figure 4. With respect to adherance quality, it was clearly seen that, optimum firing period should be 4 minutes.

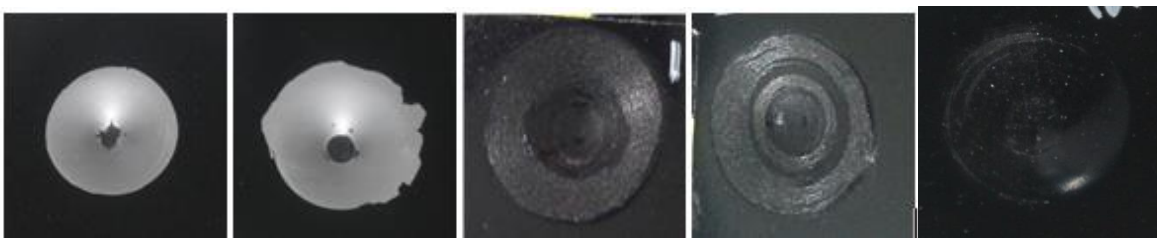

Figure 4. 1-2-3-3.5 and 4 Minutes Firing Period Adherence Results

Trials were performed at 830 and 840°C and 4 minutes in order to determine the optimum firing temperature. Dendritic formation is shown in Figure 5. With respect to better formation of dendrites optimum firing temperature is fixed to 830°C.

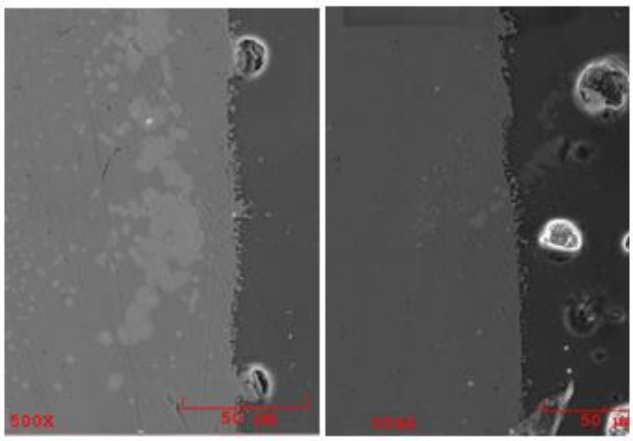

Figure 5. a)830°C b)840°C

3.2. Results of White Enamel Powder with Low Cobalt Oxide Percentage

Coatings using trace amount of cobalt oxide containing white enamel powder didn't show high quality adherance. Coatings are shown in Figure 6.

Figure 6. Coatings with Different Firing Periods

3.3. Results of White and Black Powder Mixtures with Various Percentages

Figure 7 shows various enamel trials and thickness values prepared with respect to compositions given in Table 1. Coating thicknesses vary between 110-390 μm due to density difference of white and black powders.

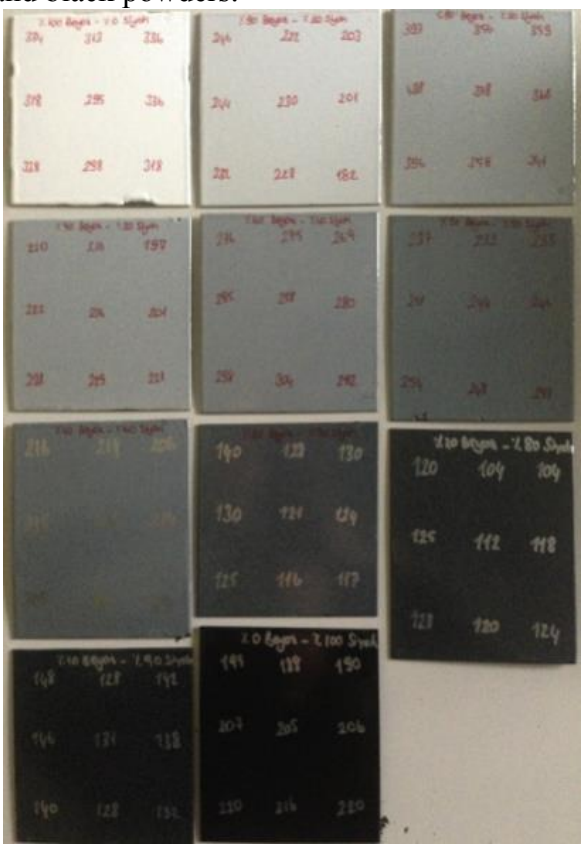

Figure 7. Enamel Trials with Different Compositions

Impact resistance performances of enamel samples are shown in Figure 8. It was observed that, with decreasing the white powder quantity, adhesion quality decreases as well.

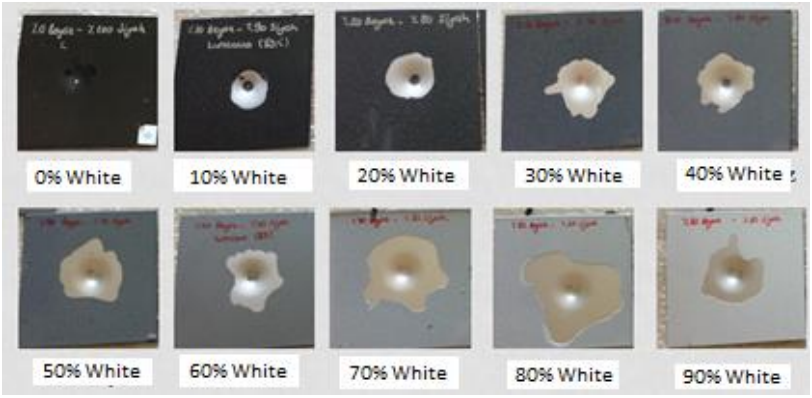

Figure 8. Impact Test Results of Enamels

20% white, 80% black enamel line scanning from interface shows element diffusion from metal substrate to enamel (Figure 9). From substrate towards enamel, it was detected that Fe concentration decreases where Si concentration increases in return.

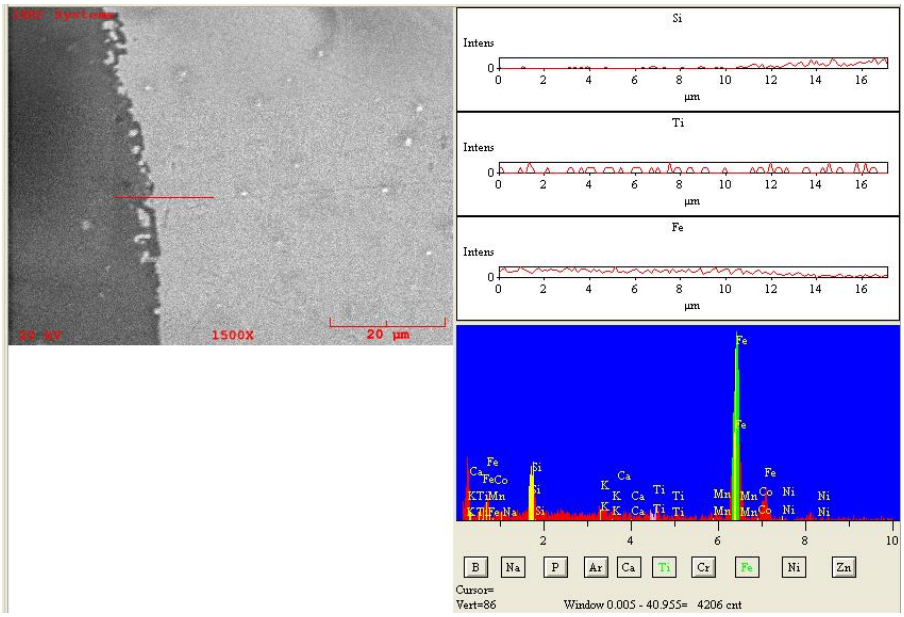

Figure 9. 20% White Enamel Line Scaning

3.4. Enamel Coating After Pre-treatment of Sand Blasting

3 different sand blasted substrates were utilized during the study. The correlation between the surface roughness and impact resistance is detected after the standardized tests.

It was observed that increment of roughness results lower adhesion in return. Figure 10 and Figure 11 shows the results of this correlation.

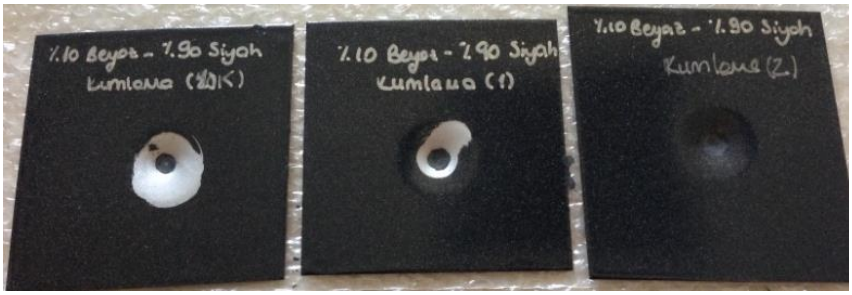

Figure 10. Adhesion Test Results of 90% Black Enamel Content

Figure 11. Adhesion Test Results of 70% Black Enamel Content

Nevertheless, manipulating surface roughness in low cobalt bearing samples does not alter adherence.

3. RESULTS AND DISCUSSION

As a result of the experimental studies; optimum firing temperature is decided 830°C and optimum firing time 4 and 4.5 minutes. To explain enamel adhesion mechanism the impact test made to various ratio of the cobalt oxide coating enamel.

Experimental studies shows that; increasing ratio of the cobalt oxide in the enamel increases the adhesion of the enamel. These data for the adhesion of the enamel with the enamel chemical reaction between iron and nickel oxide, cobalt oxide proves that carried out via and is illustrated by the chemical theory. In enamel firing temperature; iron oxidized to the FeO, cobalt oxide and nickel oxide into the enamel become metallic cobalt and nickel. For this reason; decreasing in the proportion of nickel and cobalt within the enamel, the adhesion of the enamel decreases.

İnterface analysis with the SEM and linear change rate of the element shows that; iron concentration in the region close to the substrate is higher than the other parts of enamel. Iron concentration in the region close to the substrate in other parts of the enamel are seen to be more than the percentage of the iron in enamel. As mentioned in the chemical theory, the iron from base element in the firing temperature oxidizes to the Fe^{+2} and diffuse in to the enamel. In literature, this is described in diffusion theorem.

Enamel coated on the surface which have different surface roughness. The experimental studies shows that with the increasing surface roughness, the adhesion of the enamel increases. In literature this phenomenon is explained by the theory of mechanics.

During experimental work were used to kinds of coating methods. Adhesion properties of the coated samples of the two methods compared with the age of the sample coated with the adhesion of the spray gun by the electrostatic spray gun is more effective.

REFERENCES

[1] Akdağ, F. (2011). Emaye okulu ders notları, *II. International Ceramic, Glass, Porcelain Enamel, Glaze and Pigment Congress*, 11, 236-244.

[2] Barcova, K., Mashlan M., Zboril R., Filip J., Podjuklova, J., Hrabovska, K. ve SChaaf, P. (2006). Phase composition of steel-enamel interfaces: Effects of chemical pre-treatment, *Surface&Coatings Technology*, 201, 1836-1844.

[3] Çavuşoğlu, A. (2011). Emaye okulu ders notları, *II. International Ceramic, Glass, Porcelain Enamel, Glaze and Pigment Congress*, 11, 13-36.

[4] Pemco International (2008). Pemco enamel manual, *Brugge, Belgium.*

[5] Edige, E. (2011). Emaye okulu ders notları, II. *International Ceramic, Glass, Porcelain Enamel, Glaze and Pigment Congress*, 11, 225-235.

[6] Dietzel, A. H. (1981). Emaillierung wissencahftliche grundlagen und grundzüge der technologie, *Springer-Verlag, Berlin Heidelberg, Newyork.*

[7] Evcimen, N. (2007). Emaye üretiminde kaplama ve özelliklerinin araştırılması (Yüksek Lisans Tezi), *Yıldız Teknik Üniversitesi Fen Bilimleri Enstitüsü, İstanbul.*

[8] Pagliuca, S. (2011). Emaye okulu ders notları, *II. International Ceramic, Glass, Porcelain Enamel, Glaze and Pigment Congress*, 11, 38-45.

[9] Fırat, D. (2011). Emaye okulu ders notları, *II. International Ceramic, Glass, Porcelain Enamel, Glaze and Pigment Congress,* 11, 125-132.

[10] Paytuncu, S. (2011). Emaye Okulu Ders Notları, *II. International Ceramic, Glass, Porcelain Enamel, Glaze and Pigment Congress*, 11, 145-149.

[11] Sezer, A. S. (2009). Emaye kaplamaları uygulamaları için gerekli sac özelliklerini ve sacdan kaynaklanan emaye hataları tespiti (Yüksek Lisans Tezi), *İstanbul Teknik Üniversitesi Fen Bilimleri Enstitüsü, İstanbul.*

[12] Hoeke, J. V. (2011)). Emaye okulu ders notları, *II. International Ceramic, Glass, Porcelain Enamel, Glaze and Pigment Congress,* 11, 186-191.

[13] Ege Ferro Kimya Sanayi ve Ticaret A.Ş., Emaye el kitabı, İstanbul.

[14] Honig, S. (2005). Laboratory notes, *TU Bergakademic Freiberg, Almanya,*

[15] Bodaghi, M. ve Davarpanah, A. (2011). The influence of cobalt on the microstructure and adherence characteristicsof enamel on steel sheet, *Processing and Application of Ceramics*, 5, 215-222.

[16] Eppler, R. A. ve Eppler, D. (2000). Glazes and glass coatings, *The American Ceramic Society Westerville, Ohio.*

[17] Ünlükal, F. F. (2006). Çelik ve dökme demirlerin emayelenmesi (Yüksek Lisans Tezi), *Eskişehir Osmangazi Üniversitesi Fen Bilimleri Enstitüsü*, *Eskişehir*,.

[18] Liu, H., Shueh, Y., Yang, F. S. ve Shen, P. (1991). Microstructure of the enamel-steel interface: cross-sectional TEM and metallographic studies, *Materials Science and Engineering*, A149, 217-224.

[19] Wendel, J.C. and Hellmold, P., (1956), Vitreous enamel a highly effective material compound, Wendel Email, Dillenburg and Univ. Clausthal-Zellerfeld, Almanya.

[20] Collins, M. A. (1995). Atlas of enamel defects, *The Institute of Vitreous Enamellers.*

[21] King (1959). Grenzflachennahe Bereiche einer emaillierung nach der Haftheorine, *UA.*

[22] Lupescu, M. B., Zaharescu, M. Ve Andrei A., (1997), Material Science Engineering,

A232, 73-79.
[23] Muda, I., Manaf, A. ve Fergus, J. W. (2003) Development of low carbon cold rolled steel sheets for enamelling application, *Materials Science Forum*, 437, 321-32.
[24] Pask, J. A. (1971). Chemical reactions and adherence of glass-metal interfaces, *PEI Technology*, 33, 1-6.
[25] Porcelain Enamel Institute (1995). Manual for selection of porcelain enamelling steels, *PEI Technology*, 201.
[26] Samiee, L., Sarpoolaky, H. ve Mirhabibi, A. (2006). Microstructure and adherence of cobalt containing and cobalt free enamels to low carbon steel, *Material Science and Engineering*, A 458, 88-95.

Gaseous Nitriding of Diesel Injector Components

•

Dizel Enjektör Parçalarının Gaz Nitrürlenmesi

Ahmet Fatih Yayla[1], Rıdvan Gecü[1,2], Nuri Solak[1], Kürşat Kazmanlı[1], Mustafa Ürgen[1]

[1]İstanbul Technical University, [2]Yıldız Technical University - Türkiye

ABSTRACT

Gaseous nitriding is a well-known method which improves fatigue life and serviceability of engineering components; such as gears, crankshafts, springs and injectors. In this study, microstructure and depth dependent behavior of residual stress profile of gaseous nitrided 50CrMo4 steel was investigated by performing gaseous nitriding experiments at 525°C. Phase analysis before and after nitriding were performed by means of X-ray diffraction (XRD). Light optical microscopy and microhardness tests conducted for microstructural characterization of the nitrided zone. Depth dependent residual stress analyses were determined by performing indentation tests on cross-sections of nitrided specimens, starting from the surface across the cross-section towards the unnitrided core. X-ray diffraction "$\sin^2\Psi$ method" is also used for residual stress analyses and indentation results are verified by this technique. According to results, compressive stresses formed in all nitrided specimens and compressive stress values decreases from the surface towards the unnitrided core.

Keywords: Gaseous nitriding, 50CrMo4 steel, indentation, residual stress, XRD.

BORIDING KINETIC OF FERRITIC GGG40.3 DUCTILE IRON

Fatma ÜNAL, Ahmet TOPUZ

Yildiz Technical University, Faculty of Chemical and Metallurgical Engineering, Department of Metallurgical and Materials Engineering, 34220 Istanbul, Turkey

fatmau@yildiz.edu.tr, topuz@yildiz.edu.tr

ABSTRACT

In this study, kinetics of boride layers formed on the surface of ferritic GGG40.3 ductile iron were investigated by conducting a series of experiments in Ekabor I powder at 850, 900 and 950 ℃ treatment temperature for 1, 2 and 4 h. Obtained FeB and Fe_2B phases were confirmed by X-ray diffraction, optical microscopy and scanning electron microscopy. Saw tooth-shape morphology of boride layers was examined in optical microscopy and scanning electron microscopy. The hardness of boride layer was measured by Vickers method. For the process, the calculated activation energy(Q) and k_o values were 110.562 kJ/mol and $4{,}48x10^{-7}$ cm^2/sn, respectively.

Keywords: activation energy, boride layer, ductile iron, kinetics

FERRİTİK GGG40.3 KÜRESEL GRAFİTLİ DÖKME DEMİRİN (KGDD) BORLAMA KİNETİĞİ

ÖZET

Bu çalışmada, ferritik GGG40.3 küresel grafitli dökme demir numunesinin üzerinde oluşan borür tabakalarının kinetiği; 1, 2 ve 4 saat sürelerde 850, 900 ve 950 ℃ ısıl işlem sıcaklıklarında Ekabor I tozuyla bir seri deney yapılarak, incelenmiştir. Elde edilen FeB ve Fe_2B fazları, X-ışınları difraksiyonu, optik mikroskop ve taramalı elektron mikroskobu ile doğrulanmıştır. Borür tabakalarının testere dişi morfolojisi optik mikroskop ve taramalı elektron mikroskobunda incelenmiştir. Borür tabakasının sertliği Vickers metodu kullanılarak ölçüldü. Proses için, hesaplanan aktivasyon enerjisi ve k_o değerleri sırasıyla 110.562 kJ/mol ve $4{,}48x10^{-7}$ cm^2/sn' dir.

Anahtar kelimeler: aktivasyon enerjisi, borür tabakası, küresel grafitli dökme demir, kinetik

1. INTRODUCTION

Boronizing is one of the thermochemical surface coating techniques, which is done, in order to improve surface hardness, wear resistance and corrosion resistance of ferrous, non-ferrous metals and cermet materials. The boriding treatment enables to produce the boride layers on various metallic materials by a thermodiffusion of boron atoms into their substrates in the temperature between 700 and 1000°C for 1–12 h. [1].

For boronizing process, it is applied to various technical such as solid, paste, liquid and gaseous state according to the state of boron source and in addition to these, physical and chemical vapor deposition (PVD and CVD), plasma spraying, and ion implantation are alternative nonthermo-chemical surface-coating processes[1,2] and fluidized bed technique[1,3].

2. EXPERIMENTAL PROCEDURES

2.1 CHEMICAL COMPOSITION OF EXPERIMENTAL MATERIAL AND PACK-BORIDING METHOD

Ferritic GGG40.3 ductile iron was used as a substrate material in this paper. An optical Emission Spectrometer was used for determining the chemical composition which is listed in Table 1.

Table1. Chemical composition of GGG40.3

%Fe	%C	%Si	%P	%Mg	%S
93.6	3.69	2.46	0.029	0.026	0.011

Prepared samples were embedded in the powder mixture and subjected to pack-boriding by using commercial Ekabor I powder at the process temperature of 850, 900 and 950 °C for 1, 2 and 4 h.

2.2 MICROSTRUCTURE AND CHARACTERIZATION

Borided samples were cut and metallographically prepared, then etched in a 2% Nital solution. Morphology and thickness of layers was investigated by using optical microscopy. Cross-sectioned borided samples were analyzed by optical microscopy, the thickness of formed boride layers was measured by an optical micrometer attached to a Leica optical microscope The hardness of borided samples were measured by Vickers method under the load of 50g.

2.3 KINETICS

Provided that boron diffuses and grows parabolically, the squared thickness of boride layer as a function of process time can be described by the following equation:

$$x^2=k.t \quad (1)$$

with x: the depth of boride layer (cm), t: the process time (s), k: the growth rate constant (cm^2/s). k value depends on process temperature and is calculated from slopes of the x^2 versus the process time graph. The relationship between growth rate constant, k, activation energy, Q, and the temperature, T (°K), can be expressed by the Arrhenius equation as follows:

$$k = k_o \exp(-Q/RT) \quad (2)$$

with k_o: pre-exponential constant, Q:the activation energy (J/mol), T: the absolute temperature (°K) and R: the gas constant (J/mol°K) [2,4].

3. RESULTS AND DISCUSSION

3.1 MICROSTRUCTURE AND CHARACTERIZATION

Microstructure images and SEM images of borided ductile iron are shown in Figure 1 and Figure 2, respectively.

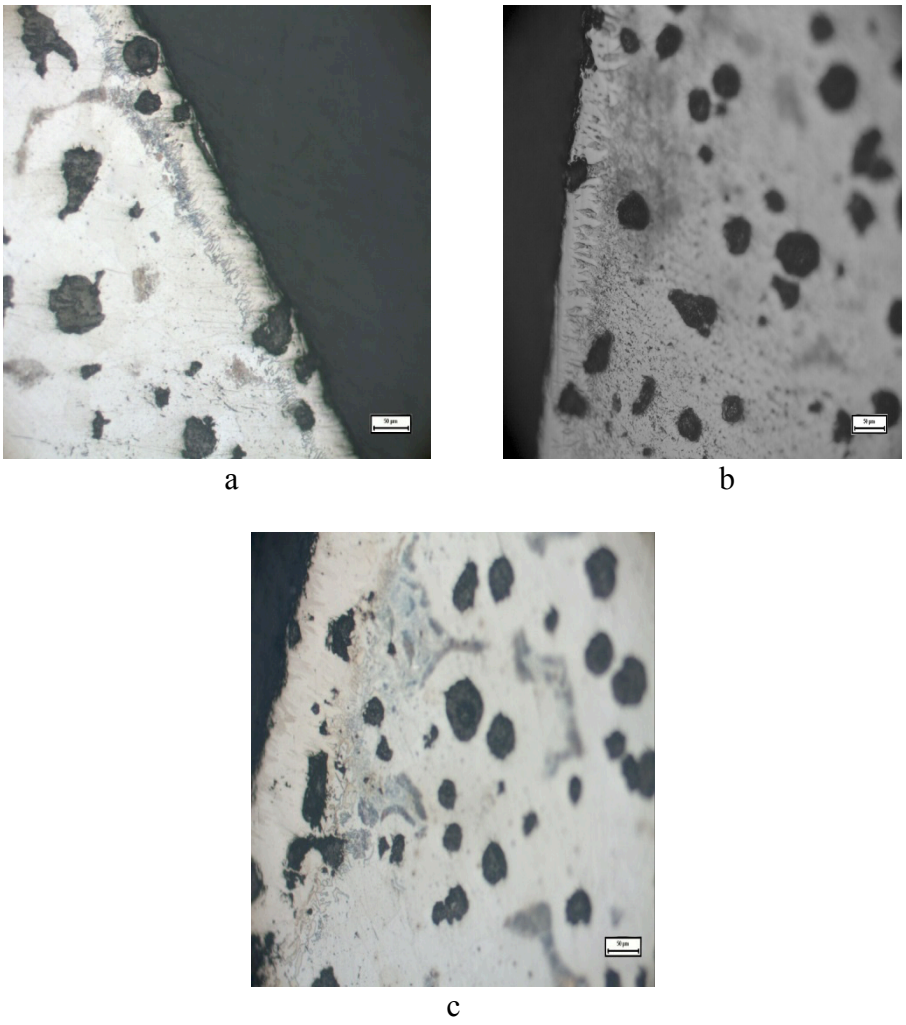

a b c

Figure 1. Microstructure images of borided GGG40.3 ductile iron (200x)

Ekabor I for 2 h; *a)* at 850^{0}C *b)* at 900^{0}C *c)* at 950^{0}C

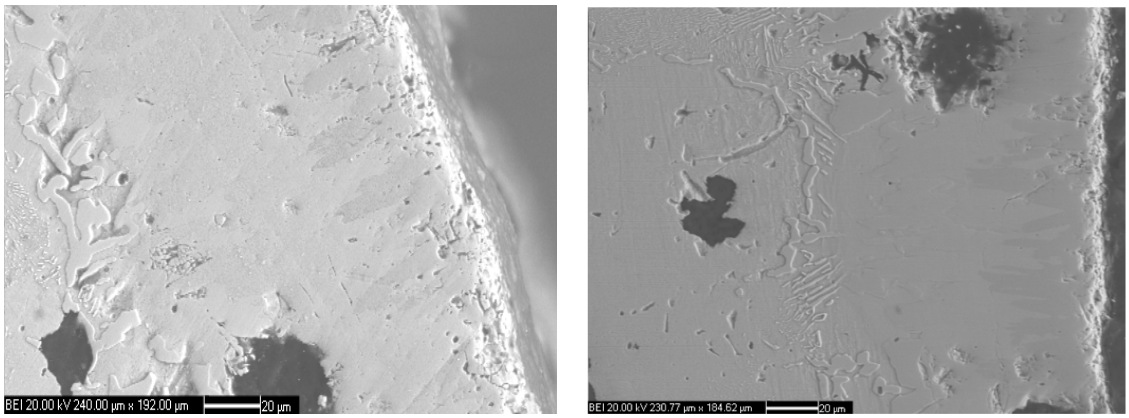

a b

Figure 2. SEM images of borided GGG40.3 ductile iron

Ekabor I *a)* at 950^{0}C for 2 h (x500) *b)* at 950^{0}C for 1 h (x520)

It shows SEM images of borides having saw tooth-shape morphology in Figure 2. This morphology is a characteristic property of the boride layers and depends on treatment temperature and time as well as the concentration of alloying elements.

Boride layer thickness values depending on process time and temperatures are listed in Table 2.

Table 2. Average thickness of the boride layer

Boriding temperature (^{0}C)	**Boriding time (hour)**	**Average thickness of the boride layer (µm)**
850	1	38
	2	46
	4	60
900	1	53
	2	68
	4	81
950	1	92
	2	145
	4	198

X-ray diffraction patterns of samples borided at 950 ^{0}C for 1 h and 2 h are given in Figure 3.

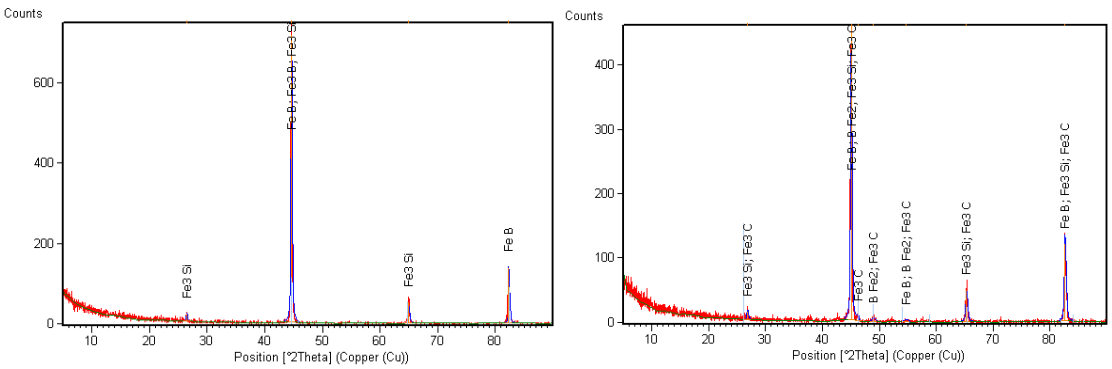

a b

Figure 3. X-ray diffraction patterns of borided GGG40.3

a) Ekabor I 950^{0}C 1 h b) Ekabor I 950^{0}C 4 h

3.2 MICROHARDNESS OF BORIDE LAYER

Measured microhardness values by Vickers method are listed in Table 3. Hardness of the boride layers was affected by boronizing time and temperature. The higher the process temperature and the longer the process time, the harder the boride layer became as shown in Table 3.

Table 3. Microhardness values of borided samples

Boriding temperature (^{0}C)	Boriding time (hour)	Microhardness values ($HV_{0.05}$)
850	1	1173
	2	1271
	4	1503
900	1	1210
	2	1297
	4	1792
950	1	1392
	2	1560
	4	1820

3.3 KINETIC STUDIES

The effects of the process time and temperature on the growth kinetics of the boriding layer were investigated in this paper. Firstly, from boride layer thickness of borided GGG40.3 ductile iron, the growth rate constant values were calculated by using equation 1 (Fig. 4). The calculated growth rate constant values are listed in Table 4.

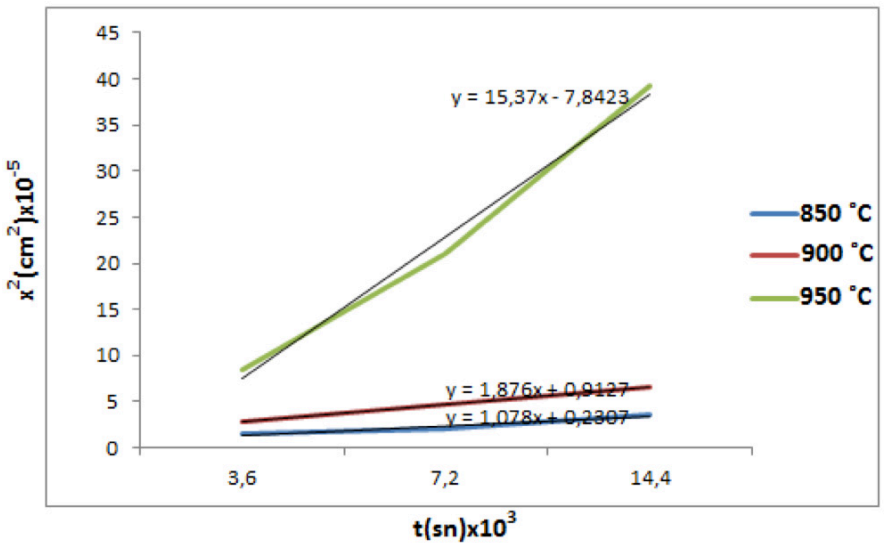

Figure 4. Square of the boride layer thickness versus process time in GGG40.3 ductile iron

We profited by equation 2. The plot of ln k versus 1/T reveals a linear relationship (Fig. 5) and activation energy of 110.562 kJ/mol was measured from the slope of the line for GGG40.3 ductile iron.

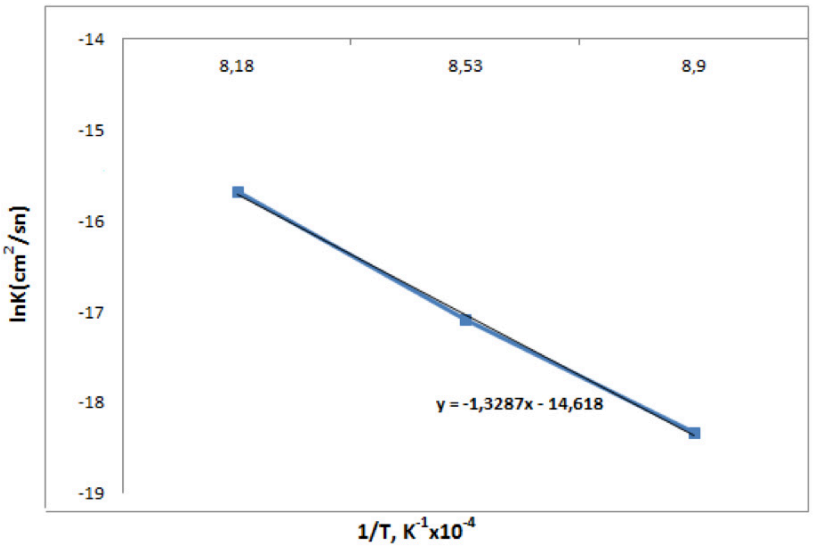

Figure 5. The growth rate constant versus process temperature in GGG40.3 ductile iron

Table 4. The growth rate constant values of borided samples at different temperatures

Boriding temperature (^{0}C)	The growth rate constant values (cm^2/s)
850	1,078x10^{-8}
900	1,876x10^{-8}
950	1,537x10^{-7}

4. CONCLUSION

It was used pack-boriding method in this study. It was determined FeB and Fe_2B phases. In addition to them, it was detected presence of Fe_3B phase which is not appear in the Fe-B equilibrium diagram. This can be explained: Carbon does not dissolve significantly in the boride layer and does not diffuse through the boride layer and during boriding, carbon is diffused away from the boride layer to the substrate and forms, together with boron, borocementite $Fe_3(B,C)$ (in the case of Fe-0,08%C steel) as a separate layer between Fe_2B and the substrate [1].

The thickness boride layer ranged from 38 to 198 μm depending on boronizing time and temperature. Longer boronizing time and higher boronizing temperature result in the thicker boride layer.

As expected, the hardness of borides was much higher than substrate. The hardness values of untreated ductile iron substrate and of borided ductile iron were 196 HV and 1173- 1820HV, respectively.

Activation energy (Q) of 110.562 kJ/mol and pre-exponential constant value (k_o) of 4,48x10^{-7} cm^2/sn were determined.

.

REFERENCES

[1] A.K. Sinha. Boriding (boronizing). ASM Int Handbook, vol. 4. Mater. Park (OH, USA): The Mater. International Society. (1991) 437–447 [CrossRef]

[2] M. Ipek, G. Celebi Efe, I. Ozbek, S. Zeytin and C. Bindal, Investigation of boronizing kinetics of AISI 51100 steel, Journal of Materials Engineering and Performance, 21 (2012) 733-738 DOI:[CrossRef]

[3] K.G. Anthymidis, N. Maragoudakis, G. Stergioudis, O. Haidar, D.N. Tsipas, A comparative study of boride coatings obtained by pack cementation method and by fluidized bed technology, Materials Letters, 57 (2003) 2399– 2403 DOI:[CrossRef]

[4] S. Sen, U. Sen, and C. Bindal, An approach to kinetic study of borided steels, Surface and Coatings Technology, 21 (2005) 274–285 DOI:[CrossRef]

Production and characterization of bronze-Cr-Ni composites produced by powder metallurgy

Aykut Canakci[a*], Temel Varol[a], Hamdullah Cuvalci[a], Fatih Erdemir[a], Serdar Ozkaya[a]

[a]Department of Metallurgical and Materials Engineering, Engineering Faculty,
Karadeniz Technical University, Trabzon, Turkey
aykut@ktu.edu.tr

Abstract
In this paper, the bronze-Cr-Ni composites were fabricated by means of powder metallurgical method. The effect of the composition and compact pressure on microstructure, density, hardness and electrical conductivity was examined. The results showed that density of the bronze-Cr-Ni composites decreased with increasing Ni content. Increasing compact pressure led to lower porosity and consequently improved the density of bronze-Cr-Ni composites. The relative green density increased from 78 to 95% with the increase in the compact pressure from 200 to 800 MPa. The hardness values showed a decrease from 95.1 to 71.6 BHN by the addition of Ni from 1 to 5 wt.% at 800 MPa. It was found that addition of Ni at 1 wt% was required to achieve high hardness and sufficient conductivity for bronze-Cr-Ni composites.

Keywords: Composite; electrical contact materials; powder metallurgy

Toz metalurjisi yöntemiyle bronz-Cr-Ni kompozitlerinin üretimi ve karakterizasyonu

Aykut Çanakçı[a*], Temel Varol[a], Hamdullah Çuvalcı[a], Fatih Erdemir[a], Serdar Ozkaya[a]

[a]Metalurji ve Malzeme Mühendisliği Bölümü, Mühendislik Fakültesi,
Karadeniz Teknik Üniversitesi, Trabzon, Türkiye
aykut@ktu.edu.tr

Özet
Bu çalışmada bronz-Cr-Ni kompozitleri toz metalurjisi yöntemiyle üretilmiştir. Microyapı, yoğunluk, sertlik ve elektriksel iletkenlik üzerine bileşim ve sıkıştırma basıncının etkisi araştırılmıştır. Sonuçlar artan Nikel miktarı ile bronz-Cr-Ni kompozitlerinin yoğunluğunun azaldığını göstermiştir. Artan sıkıştırma basıncı gözenek miktarını azaltmış ve dolayısıyla yoğunluğu artırmıştır. Bağıl yoğunluk değerleri 200 MPa sıkıştırma basıncının 800 MPa yükselmesi ile %78 değerinden %95 değerine yükselmiştir. Sertlik değerleri 800 MPa sıkıştırma basıncında Nikel ilavesinin %1'den %5'e kadar artışı ile 95.1 Brinell sertlik değerinden 17.6 Brinell sertlik değerine yükselmiştir. Çalışma sonucunda ağırlıkça %1 Ni ilavesinin bronz-Cr-Ni kompozitlerinde yeterli iletkenlik ve yüksek sertlik için yeterli olduğu bulunmuştur.

Anahtar Kelimeler: Kompozit; elektrik kontak malzemeleri; toz metalurjisi

1. INTRODUCTION

Bronze electrical contacts are usually used in small and medium-pitch signal, moderate-power connectors and connector contacts. Their main advantages are excellent long-term spring properties, resistance to high temperature conditions, electrical conductivity, temperature conductivity, melting point as well as low cost. On contrast, they have also some disadvantages including low resistance to corrosion, oxidation, wear, arc erosion and self-lubricating ability and welding. In order to eliminate these shortcomings, bronze-Cr-Ni composites can be replaced with bronze contact materials. Bronze alloys have self-lubricating ability and so the adverse effect of welding process between contact materials during operation can be reduced. The addition of chromium to copper facilitates formation of chromium oxide layers on the contact surface and provides a good voltage withstand and anti-corrosion property of arcing. Furthermore, the additions of nickel to bronze improve the mechanical properties and resistance to oxidation and wear [1-5]. The P/M method has several advantages over other manufacturing processes. Compared with melting methods, powder metallurgy requires the low manufacturing temperature. That is why undesired phases between the matrix phase and the reinforcement phase are eliminated. Moreover, reinforcement particles are also well-distributed in the matrix. Another significant feature is the ability to produce near net shape parts, which is cost effective [5-10]. The aim of this paper was to produce bronze-Cr-Ni composites by the powder metallurgy and to study the effect of material composition and compression pressure on the properties of novel bronze-Cr-Ni composites.

2. EXPERIMENTAL

As-atomized bronze powders (CuSn10, Alfa Aesar, Karlsruhe, Germany) with an average powder particle size of 28μm and a theoretical density of 8.7 g/cm^3, chromium powders (99.9%, Alfa Aesar, Karlsruhe, Germany) with an average powder particle size of 40 μm and a theoretical density of 7.19 g/cm^3 and nickel powders (99.9%, Alfa Aesar, Karlsruhe, Germany) with an average powder particle size of 58 μm and a theoretical density of 8.91 g/cm^3 were used to produce bronze-Cr-Ni electrical contact materials. Bronze-Cr-Ni powders were mixed together in a laboratory mixer as presented in Table 1. Then, all powder mixtures were uniaxially cold pressed at 200MPa, 300 MPa, 500 MPa and 800 MPa to form a series of cylindrical specimens. The compacted green bulk specimens were sintered at 900 °C for 3h under protective pure argon gas in a tube furnace.

Table 1. The properties of as-received materials and milling parameters

Material composition (wt.%)			Code	Compact Pressure (MPa)	Sintering Temp. (°C)	Sintering Time (h)
CuSn10	Cr	Ni				
89	10	1	C1	200-300-500-800	900	3
87	10	3	C3	200-300-500-800	900	3
85	10	5	C5	200-300-500-800	900	3

Zeiss Evo LS10 scanning electron microscope (SEM) equipped with an energy dispersive spectroscopy (EDX) was used to characterize the microstructure of the contact samples. Brinell hardness values of the samples were measured on the polished samples using a ball with 2.5 mm diameter at a load of 60 kg. The electrical conductivity of contact materials was carried out on Sigmascope SMP10 HF electrical conductivity measurement device.

3. RESULTS AND DISCUSSION

3.1 Microstructure

Fig. 1 shows the microstructures of the samples compacted at 500 MPa for C3 composite. From SEM image, it was observed that the size and amount of porosities decreased with increasing compact pressure. This can be explained by the good packing or densification of powders due to rearrangement, elastic deformation, and plastic deformation. As it can be seen in Fig. 1, Cr particles showed semi-homogeneous distribution in the bronze matrix. Also there were some black points representing porosities which were formed during powder metallurgy process. It should be noted that Cr particles were usually placed between the bronze matrix powders. With increasing compression pressure, two major events were took place during rearrangement and elastic deformation. The first event was the settlement of Cr powders (which was more than Ni powders) between matrix powders due to rearrangement of ductile bronze powders. The second event was that hard Cr powders could be embedded into ductile bronze powders.

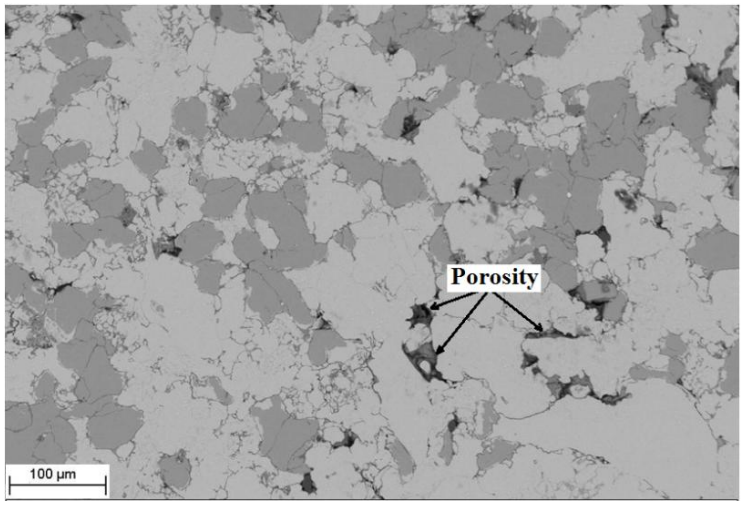

Figure 1. SEM image of C3 electrical contact materials at 500 MPa

With increasing the amount of Ni, both the amount of porosities and size of porosities increased due to highly resistant to plastic deformation of Ni powders. In other words, the packing ability of mixture powders decreased with increasing the Ni content. Higher Ni content did not allow for contact of ductile bronze powders, while lower Ni have supported the contact of ductile bronze powders. The chemical compositions of the marked points on the image were measured by EDX techniques (Fig. 2). These three regions were marked as A, B and C, and the magnified pictures were shown in Fig 2. EDX results showed that more Cu and Sn elements were found in region A, compared to that of regions B and C. However, more Ni element was found in region C, than in A and B. B region contained only the element chromium.

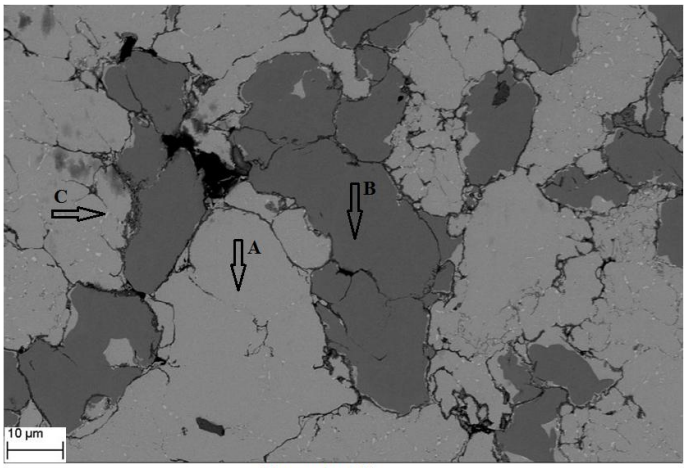

Figure 2 SEM images of C3 electrical contact materials at 800 MPa

EBSD (electron backscatter diffraction) map were obtained for C3 composite (Fig. 3). As shown in Fig. 3, Cu-Ni solid solution formed during the sintering process (at 900 °C). It should be noted that Cu and Ni are completely soluble in each other in solid state. However, Cu-rich region did not contain the Cr element due to the fact that maximum solubility of Cu in body-centred cubic (bcc) Cr is less than 0.2 at.% (the limit of solid solubility).

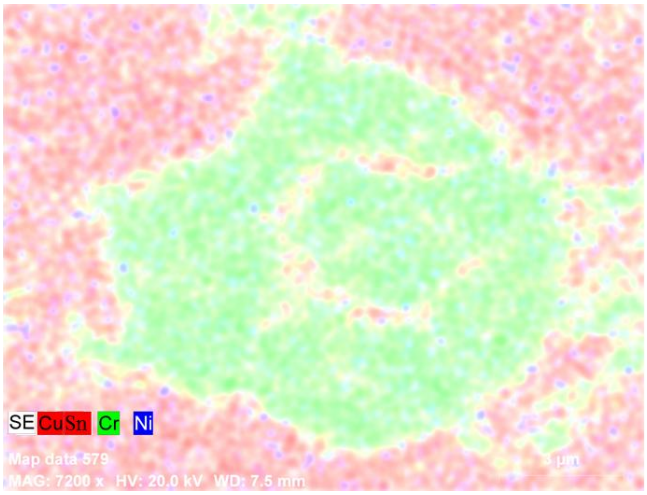

Figure 3. electron backscatter diffraction (EBSD) image map for C3 electrical contact material

3.2 Density

Fig. 4 shows the measured relative sintered densities of the compacted samples at different pressures and Ni content. The relative sintered densities of samples significantly decreased with decreasing the compact pressure and increasing Ni content. The relative sintered densities of the three compositions pressed at 800 MPa, which were 98.7% (C1), 94.8% (C3) and 91.6% (C5). Pressing for 800 MPa in C1 samples obtained a relative sintered density of 98.7 % of theoretical value while 300 MPa only increased to 85 %. As shown in Fig. 4, relative sintered density increased from 79.5% to 84% when compact pressure was extended from 200 MPa to 800 MPa for C3 samples.

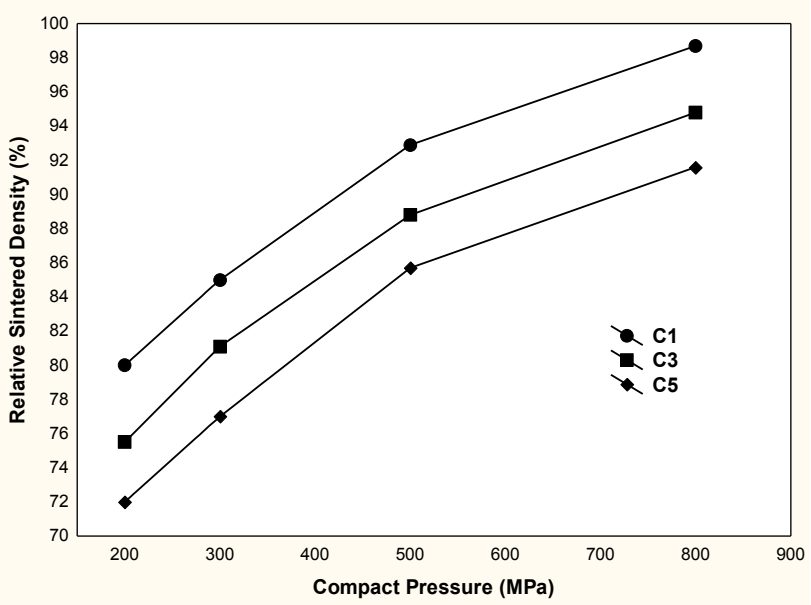

Figure 4. The change of relative sintered density as a fuction of compact pressure for different samples

3.3 Hardness

The hardness values for each of the three material compositions consolidated at 800 MPa were very high and much above the values obtained at 200 MPa (Fig. 5). Brinell hardness values increased from 50.7 to 95.1% with increasing the compact pressure from 200 to 800 MPa for the C1, from 40.5 to 82.21 for the C2, and from 34.53 to 74.6 for the C3 compositions. The hardness was found to decrease with Ni particles additions. The sample containing 1 wt. Ni showed higher hardness compared to that of containing 3 and 5 wt. %Ni. The difference between hardness of the C1, C2 and C3 samples stemmed from the increase in Ni content. These results can be attributed to the effect of Ni on the densification or compressibility behavior of the powder metallurgy bronze-Cr-Ni electrical contact materials.

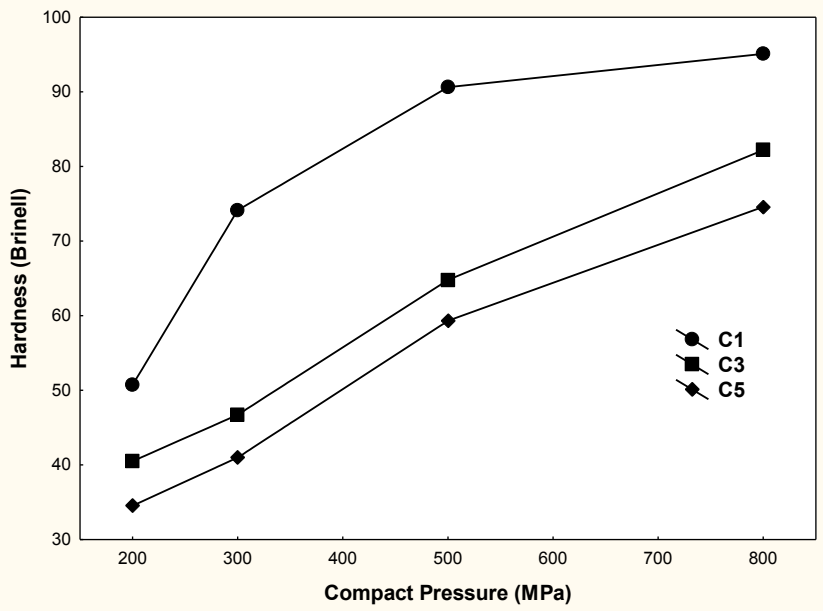

Figure 5. Effect of compact pressure and Ni content on hardness of bronze-Cr-Ni electrical contact materials

3.4 Electrical Conductivity

It is well known that the electrical properties of the contact materials are significantly influenced by material composition, production method and their microstructure, such as the amount of porosities, distribution of porosities. In this study, the Ni content in the bronze-Cr-Ni composites varied from 1 wt.% to 5 wt. %. It can be seen from Fig. 6 that the electrical conductivity of bronze matrix decreased with the addition of alloying elements. The electrical conductivity decreased with increasing Ni content because the compressibility ability of powders decreased due to increasing Ni content. It is also worth mentioning that comparing the electrical conductivities of contact materials revealed that C1 composites showed higher electrical conductivity. The porosity present in the bronze-Cr-Ni electrical contact materials reduced the electrical conductivity as shown in Fig. 6. The electrical conductivity of all the contact materials compacted at 800 MPa were higher than that acquired at 200 MPa. Moreover, the electrical conductivity of the bronze-Cr-Ni contact material compacted at 800 MPa decreased with the increase in Ni content, and reached the lowest conductivity for C5 composites.

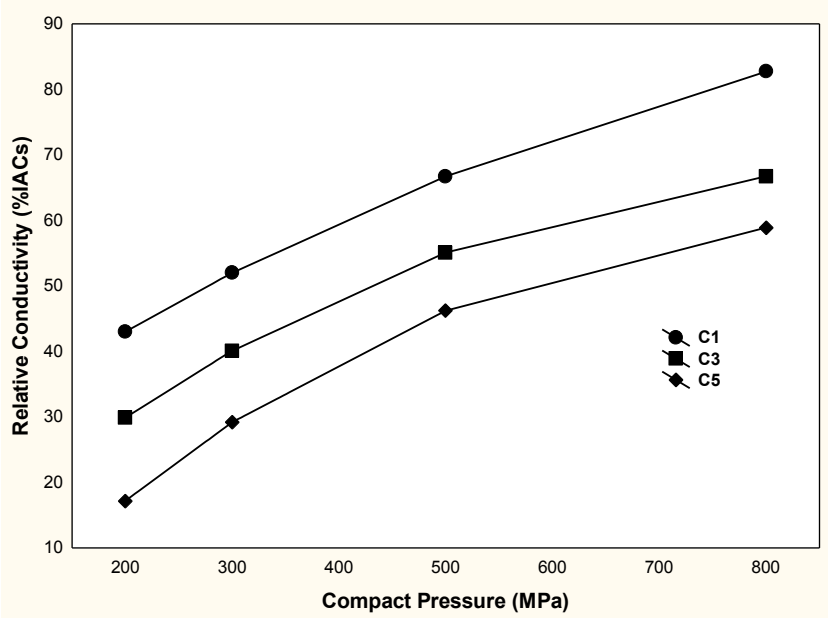

Figure 6. The change of relative conductivity with compact pressure and Ni content

4. CONCLUSIONS

The microstructure of the bronze-Cr-Ni composites revealed that the Ni particles were distributed uniformly in the matrix phase, while Cr particles were distributed semi-homogeneous in the bronze matrix. The Ni content in the bronze considerably decreased the density and increased the porosity. The hardness values decreased from 95.1 to 71.6 BHN by the Ni addition from 1 to 5 wt.% at 800 MPa. The Brinell hardness of the C1 composites fabricated at 800 MPa was about 1.36 fold higher than that of the bronze matrix (70 BHN). The electrical conductivity, density and hardness of C1 electrical contact materials were larger than those of C3 and C5 composites. For 800 MPa in C1 samples obtained a relative conductivity of 82.73 % of bronze matrix (11 IACs) while 200 MPa only increased to 43 %. The new bronze-Cr-Ni composites can be used as contactors, switch gear, low-voltage regulators due to their sufficient conductivity and high hardness.

Acknowledgement

The authors are grateful to the Karadeniz Technical University Research Foundation for financially supporting this research (No: 2010.112.0105).

REFERENCES

[1] O. Guler and E. Evin, J. Mater. Process Technol., 209, 1286, 2009
[2] V.V. Bukhanovsky, N.I. Grechanyuk, R.V. Minakova, I. Mamuzich, V.V. Kharchenko and N.P.Rudnitsky, Int. J. Refract. Met. Hard. Mater., 29, 573, 2011
[3] X. Shi-xin, Y. Ren, X. Jun and W. Jin-xing, Properties of vacuum cast CuCr25Te contact material. Trans. Nonferrous Met. Soc. China 19, 444, 2009
[4] S. Mula, P. Sahani, S.K. Pratihar, S. Mal and C.C. Koch, Mater. Sci. Eng. A, 328, 4348, 2011
[5] I. Lahiri and S. Bhargava, Powder Technol. 189, 433, 2008
[6] A. Gokçe, F. Fındık and A.O. Kurt, Mater. Charact., 62, 730, 2011
[7] I. Pokorska, J. Mater. Process Technol. 196, 15, 2008
[8] L.A. Dobrzanski, A. Weodarczyk and M. Adamiak, J. Mater. Process Technol. 175, 186, 2006
[9] M. Rahimian, N. Parvin and N. Ehsani, Mater. Sci. Eng. A, 527, 1031, 2010
[10] C. Xu, D. Yi, C. Wu, H. Liu and W. Li, Mater. Sci. Eng. A, 538, 202, 2012

PROCESSING AND CHRACTERIZATION OF CARBON FIBER REINFORCED SILICON CARBIDE (C/SiC) MATRIX COMPOSITES

Simge TÜLBEZ, Arcan F. DERİCİOĞLU

Middle East Technical University, Dept. of Metallurgical and Materials Eng., Ankara-Turkey
stulbez@metu.edu.tr, arcan@metu.edu.tr

1.ABSTRACT

Processing of carbon fiber-reinforced silicon carbide (C/SiC) matrix ceramic composites starts with the production of carbon fiber-reinforced polymer (CFRP) composite part. This part is pyrolyzed in a high temperature furnace under nitrogen flow to burn out their polymeric binder and to achieve a carbon rich porous carbon/carbon composite preform. In the following stage, silicon (Si) is infiltrated into the preform to react with the free carbon. Most frequent technique used during this stage is liquid silicon infiltration (LSI). In the scope of this study, the evolution of microstructure and properties of CFRP during pyrolysis at different temperatures has been investigated along with the effects of different pyrolysis temperatures on the efficiency of the liquid silicon infiltration process.

Keywords: Carbon/Carbon Composite, Ceramic Matrix Composite, Microstructure, Pyrolysis, Silicon Infiltration.

1.ÖZET

Karbon fiber takviyeli silisyum karbür (C/SiC) seramik matris kompozit malzemelerin üretim prosesi karbon elyaf takviyeli polimer matrisli kompozit (CFRP) parça üretimi ile başlar. Parçalar daha sonra yüksek sıcaklık fırınında nitrojen atmosferinde piroliz işlemine tabi tutularak polimerik bağlayıcıları uzaklaştırılır. Piroliz işlemi sonrasında gözenekli, karbonca zengin preform elde edilir. Bir sonraki aşamada, preform içindeki serbest karbon ile reaksiyona girecek silisyum preforma emdirilir. Bu işlem için yaygın olarak kullanılan yöntem, sıvı silisyum (Si) emdirme yöntemidir. Bu çalışma kapsamında farklı sıcaklıklarda piroliz edilen karbon elyaf takviyeli polimer matrisli kompozitin (CFRP) mikroyapı ve özelliklerinin sıvı silisyum emdirme işleminin verimliliği üzerine etkileri incelenmiştir.

Anahtar Kelimeler: Karbon/Karbon Kompozit, Seramik Matris Kompozit, Mikroyapı, Piroliz, Silisyum İnfiltrasyonu.

2. INTRODUCTION

In recent years, usage of carbon fiber-reinforced silicon carbide (C/SiC) matrix ceramic composites has increased considerably because of their high temperature mechanical properties in additon to their erosion and thermal shock resistance along with low weight compared to their counterparts. Carbon fibers used in these types of composites provide the material a wide range of physical properties. As a result of these properties, C/SiC ceramic composites are being used as high temperature structural materials in applications such as components in thrust providing parts of rocket/missile systems, thermal protection systems of

the nose cap of the reentering spacecrafts and high performance brake pads and clutches Due to high temperature and erosive environment operation conditions, these composites must have superior thermal-mechanical properties, where they retain their high strength at elevated temperatures along with good oxidation and erosion resistance.

One major manufacturing process of these materials is the liquid silicon infiltration which is an attractive method considering the processing time and cost efficiency [1]. Processing of C-SiC composites via liquid silicon infiltration (LSI) or reactive melt infiltration (RMI) can be divided into three separate process steps [2,3]:

i) Manufacturing of carbon fiber reinforced polymer matrix (CFRP) preform by common methods like resin transfer molding or autoclave technology,
ii) Conversion of the polymeric matrix into carbon by pyrolysis (900 °C, inert atmosphere) thus forming a porous carbon/carbon preform,
iii) Converting carbon matrix into SiC matrix by melt infiltration of liquid silicon (1650 °C, vacuum) and formation of the ceramic end product termed C-SiC.

In the third step, liquid silicon infiltrates into the preform via capillary forces, therefore microstructures and properties of CFRP have an important effect on infiltration process. As a result, the aim of this study is to investigate the effects of different pyrolysis temperatures on the microstructure and resulting properties of CFRP.

3. EXPERIMENTAL PROCEDURE

3.1 Fabrication of CFRP

Carbon fiber reinforced polymer (CFRP) composites were fabricated using autoclave. As the matrix material resol type phenol formaldehyde resin which is in oligomer condition was used along with PAN based 2D plain woven carbon fiber fabrics of (60 vol%) as the reinforcement. The composites were fabricated in the autoclave at 175 °C temperature under 3-5 bar pressure with the holding time of 4 h.

3.2 Pyrolysis of CFRP

CFRP composites were pyrolyzed to obtain C/C composite preforms. Carbonization of CFRP composites was performed at different temperatures with a constant heating rate of 10°C / min under flowing nitrogen atmosphere. The holding time at each temperature was 3 h. In order to investigate the effect of the pyrolysis temperature on the microstructure and properties of CFRP composites, 5 different pyrolysis temperatures of 500, 600, 700, 800 and 900 °C were used throughout this study.

3.3 Liquid Silicon Infiltration (LSI) of C/C Preforms

In this stage, silicon (Si) is infiltrated into the C/C preforms that were pyrolyzed at different temperatures. Infiltration of the porous C/C preform with liquid silicon was achieved beyond the melting point of pure Si (1411 °C). Elemental Si was infiltrated to allow its reaction with the free carbon in the C/C preform emerging from the phenolic matrix of the initial CFRP. Si reacts with the free carbon to form SiC, and this yields a dense material with C/C segments separated from each other by SiC.

3.4 Characterization

Microstructural characterization of the pyrolyzed CFRP composites was conducted using scanning electron microscope (SEM) (FEI Nova Nano SEM 430). All of the studied materials were observed directly without metallographic preparation and conductive coating. Observations

were done at accelerating voltages between 5 and 10 kV. Flexural strength and strain of the composites were determined by three-point bending tests. Length, width and thickness of the three-point bending test specimens were 15, 3 and 3 mm, respectively. Fracture surfaces of the three-point bending tested specimens were examined using SEM. Density and open porosity content of C/C preforms were measured by the Archimedes' principle according to ASTM D792. X-ray diffraction (XRD) was used to analyze the structural evolution of phenolic resins and C/C preforms after pyrolysis at different temperatures using Rigaku D/MAX2200/PC. The source was Cu K_α containing both wavelengths $K_{\alpha1}$ = 1.54056 Å and $K_{\alpha2}$=1.5444 Å. Scans were done in the 2θ range of 5-90° with a rate of 2°/min.

4. RESULTS AND DISCUSSION

4.1 Microstructural Evolution of the C/C Preform

The aim of the pyrolysis step is converting the phenolic polymer matrix into free carbon. In order to monitor the occurrence of this conversion, X-ray diffraction analysis results of as-received phenolic resin and phenolic resin which was pyrolyzed at 900 °C were compared. As shown in Fig. 1, the diffraction patterns points out to the presence of an amorphous structure with a broad peak at 2θ≈18.5° which is due to adjacent chains of the linear polymer [4]. This diffraction profile became broader in the pyrolyzed condition. Pyrolysis of the phenolic resin resulted in glassy carbon formation. Its diffraction pattern shows two broad peaks corresponding to the (002) and (101) planes of turbostratic carbon structure [5].

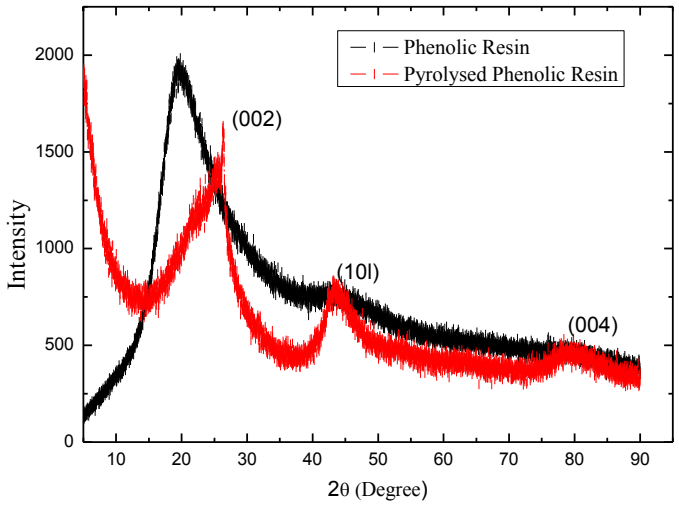

Figure 1. XRD patterns of the as-received phenolic resin and phenolic resin that was pyrolyzed at 900 °C.

In order to investigate the effect of the pyrolysis temperature on the microstructure and properties of CFRP composites, different pyrolysis temperatures were used throughout this study. When the SEM micrographs of the pyrolyzed preforms are compared, it is seen that non-pyrolyzed condition does not contain any crack and pore initially. After pyrolysis at 500 °C, some pores started to be observed in the matrix. Formation of these pores can be attributed to the evolution of different gases (solvent, monomer, steam etc) during extended curing, which are trapped in the matrix. Furthermore, at the beginning of pyrolysis huge amount gases also evolve from the converting matrix which are also trapped in the structure. This may cause the formation of new pores and enlarge existing ones. It is seen that, pyrolysis at 600 °C results in debonding at the fiber and matrix interface. Weak fiber-matrix interface due to Wan-der-Waals interactions along

with the pores and pore channels frequently existing at the interface may have caused debonding at this temperature. At 700 °C some partial at the interface between warp and weft fibers, was observed. Transversal cracks started to appear at 800 °C and crack opening displacement of these cracks increased in size at 800 °C.

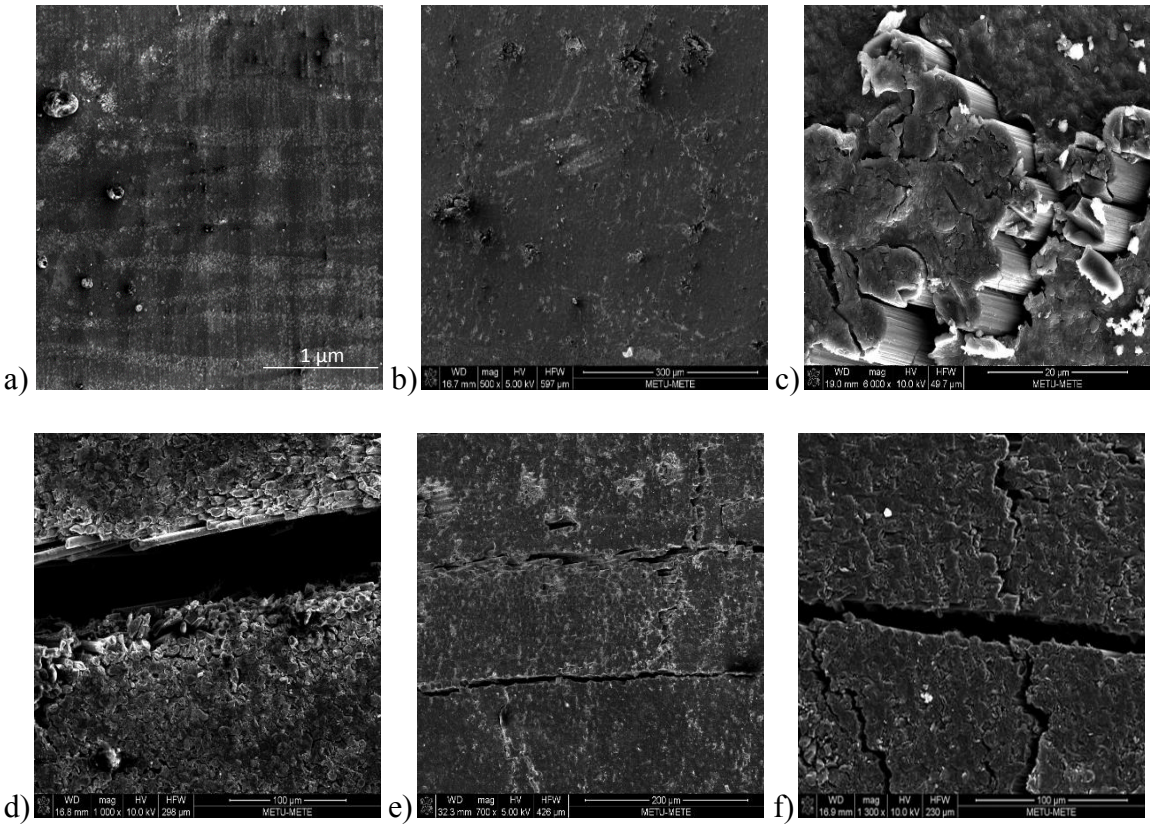

Figure 2. SEM micrographs of phenolic resin-based C/C composites preforms pyrolyzed at different temperatures: (a) Non-pyrolyzed CFRP, (b) 500 °C, (c) 600 °C, (d) 700 °C, (e) 800 °C, (f) 900 °C.

4.2. Open Porosity and Density of the C/C Preform

Open porosity and density are important control parameters for the C/C preform which were measured after every process step. They were used for fundamental material classification serving as a quantitative parameter to assurance quality. Morphology, size, type and content of the pores are critical parameters strongly affecting the densification behavior during the LSI process.

As it is clearly seen in Figs. 3 and 4, respectively, with the increasing pyrolysis temperature, density of the C/C preform decreases while its open porosity is vice versa. At this point, it is important to note that the higher the density of the C/C preforms the more difficult is following Si infiltration process. In the lower density condition, content of the pores is higher leading to a higher probability of having available interface between the free carbon and the infiltrated Si. Therefore, the fraction of SiC formation, i.e. density of the resulting C/ SiC composite, increases with decreasing density of C/C preform.

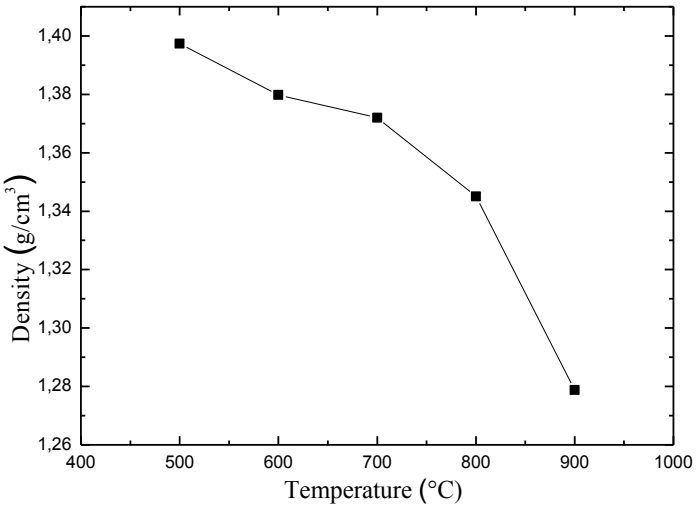

Figure 3. Density of the phenolic resin-based C/C preforms after pyrolysis at different temperatures.

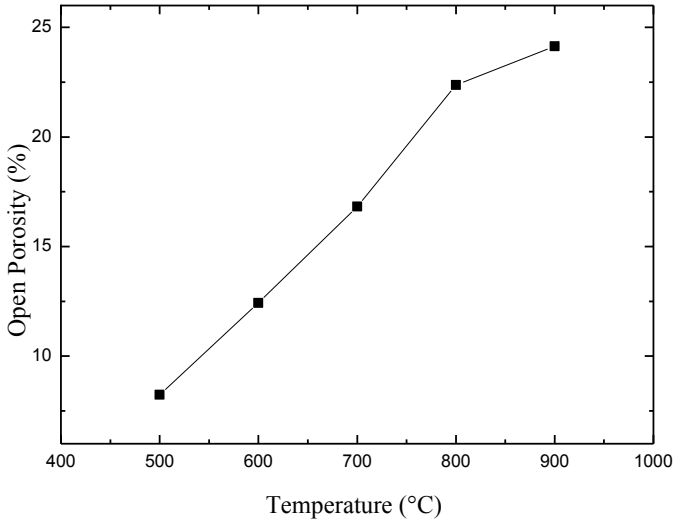

Figure 4. Open porosity of the phenolic resin-based C/C preforms after pyrolysis at different temperatures.

4.3. Effect of Pyrolysis on the Mechanical Behavior of the C/C Preforms

Mechanical properties and fracture behavior of the C/C preforms that pyrolyzed at different temperatures were studied using three point bending test. As it is seen in Fig. 5, pyrolysis affects the mechanical properties of the initial CFRP composite and the C/C preforms which change significantly with the pyrolysis temperatures. Expectedly, with increasing pyrolysis temperature, mechanical properties of the CFRP composite and the C/C preforms degrade. While converting the phenolic polymer matrix into free carbon via pyrolysis, the composite behavior of the CFRP diminishes. This is caused by the lack of load transfer from the matrix to the fiber which lose their contact at the vanishing interface. Consequently, fracture in the C/C preforms occurs at lower strains.

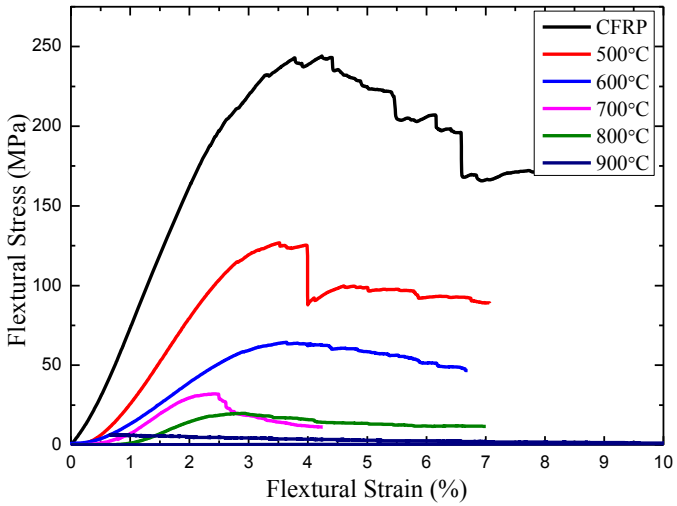

Figure 5. Flextural stress - Flextural strain curves of the CFRP composite and the C/C preforms pyrolyzed at different temperatures.

4. CONCLUSION

The evolution of microstructure and changes in the properties of the CFRP during pyrolysis at different temperatures has been investigated. It was shown that by pyrolysis phenolic resin converts to glassy carbon. According to SEM micrographs, different pyrolysis temperatures give rise to different pore sizes and cracking behavior. Correspondingly, it is expected that efficiency of consequent liquid silicon infiltration process will be affected by these differences. According to three point bending test results it has been shown that mechanical properties and fracture behavior of the C/C preforms is dependent on the pyrolysis temperature. Consequently, morphology, size, type and content of the pores and density of the C/C preforms resulting from the pyrolysis process are critical parameters strongly affecting the densification behavior during the LSI process.

5. REFERENCES

1. Fitzer, E. and Gadow, R., Fiber-reinforced silicon carbide. *Am. Ceram. Soc.Bull.*, 1986, 65, 326–335.
2. Kochendorfer, R., Liquid silicon infiltration - A fast and low cost CMC manufacturing process. In Proceedings of the Eighth International Conference on Composite Materials, ICCM-8, Vol. 3, Woodhead Publishing Limited, Abington, Cambridge, UK, 1991, pp. 23-F-1-23-F-9.
3. Schanz, P. and Krenkel, W., Description of the mechanical and thermal behaviour of liquid siliconized C/C. In Proceedings of the Sixth European Conference on Composite Materials, ECCM-6 and HT-CMC 1, Woodhead Publishing Limited, Abington, Cambridge, UK, 1993, pp. 715-724.
4. Z. Lausevic, S. Marinkovic, Carbon 24 (1986) 575.
5. G.M. Jenkins, K. Kawamura, Polymeric Carbons—Carbon Fibre, Glass and Char, Cambridge University Press, Cambridge, 1976.

INCORPORATION OF FLAY ASH INTO PVC BASED PLASTIC COMPOSITES

Raman ALITI*, Anita GROZDANOV*, Perica PAUNOVIC*

Faculty of Technology and Metallurgy, University Ss Cyril and Methodius in Skopje, R.Macedonia

anita@tmf.ukim.edu.mk

ABSTRACT

Fly Ash (FA) waste particles, obtained as a combustion by-product from the fero-nickel production process as well as from the coal mine, were used like reinforcements of plastic matrices. In this work, FA was chemically modified and used in Poly Vinyl Chloride (PVC) composites aimed for geomembranes. Plasticized PVC was used as a matrix. Concentration of the fly ash was varied in the range of 5, 10 and 20 %. FA/PVC composite samples were prepared using two different types of FA. The FA surface was modified by NaOH and HCl treatment. The obtained samples were analyzed by TGA/DTA, FTIR, SEM and swelling test. Uniform reinforcement dispersion in the polymer matrix is very important in order to ensure that there was a good interactions between both constituents that will result in good composite's properties. SEM microphotographs of the obtained FA/PVC composites have shown region of well dispersed FA particles, but also and FA agglomerations in the composites. Thermal parameters of the PVC composites decreased in the presence of both types of FA. Lower values were obtained due the HCL treatement of FA particles compared to NaOH treated FA. Generally, all the FA/PVC composites have shown higher swelling degree than PVC.

Keywords: flyash, polymer composites

1. INTRODUCTION

Fly ash is a pozzolanic material generated from the fero-nickel production process as well as coal-burning thermal power plants. Though a significant fraction of coal fly ash is used as a cement and concrete additive in the world, only a very small portion of the million tons of fly ash generated is re-utilized in Macedonia. Fly ash contains a range of heavy metals of different mobilities in its structure [1]. Since it is usually disposed of in the form of a slurry in the vicinity of the power plant, fly ash possesses significant environmental risk due to the possibility of leaching of these metals into environment [1,2]. This risk has led to extensive studies on the physical-chemical properties and leaching behavior of fly ash [3,4]. There is a large body of work on the use of fly ash in cement and brick

production [5,6]. In one study, the Derjaguin–Landau–Verway–Overbeek (DLVO) theory for dispersion–flocculation of heterogeneous particles with different surface potentials was applied to explain the effect of fly ash on the rheology of cement paste containing naphthalene sulfonate superplasticizer. The fly ash and ordinary porland cement were compared. The fly ash–cement paste without superplasticizer resulted the sign of zeta potential of fly ash was different from ordinary Portland cement. So, the extent of the potential energy barrier between particles was small or showed negative value, and the change in the rheology of the fly ash–cement paste was mainly dependent on the bulk solid volume of fly ash. The fly ash–cement paste with naphthalene sulfonate superplasticizer, fly ash and cement had the same sign and dispersed well due to higher potential barrier. The extent of potential energy barrier depended on the absolute value of surface potential, which was represented by a function of the amount of adsorbed superplasticizer. The bulk solid volume of fly ash also affected the change in flow ability [7].
The purpose of this study was to investigate the application of fly ash as an alternative filler material in PVC pastisols aimed for geomembrane.

2. EXPERIMENTAL

Composite films based on PVC and Fly ash were prepared by solvent-casting method in 1,4-Dioxin with the total mixing time of 30 min. Plasticized PVC was used as a matrix. Concentration of the fly ash was varied in the range of 5, 10 and 20 %. FA/PVC composite film-samples were prepared using two different types of FA (FA from fero-nickel production and FA from coal mine). The FA surface was modified by 2M NaOH and 1M HCl treatment. The obtained samples were analyzed by TGA/DTA, SEM and swelling test. TGA/DTA measurements were performed using a Perkin Elmer PYRIS Diamond Thermogravimetric/Differential Thermal Analyzer. The studied material was heated in the temperature interval of $25^{o}C \div 1100^{o}C$ by heating rate of $20^{o}C \cdot min^{-1}$ air atmosphere. SEM analysis were performed using FEI Quanta 200 FEG system. FTIR spectra were recorded using PARAGON Perkin Elmer System.

3. RESULTS AND DISCUSSION

Chemical composition of both types of Fly ash used in the preparation of the PVC based composite films is shown in Table 1.

Table 1. Chemical composition of Fly Ash samples

Elements	FA-Oslomej [%]	FA-FENI [%]
SiO_2	50	37,5
Al_2O_3	30	1,8
Fe_2O_3	13	22,5
MgO	1,5	14,5
CaO	3,0	2,3
TiO_2	1,0	/

Uniform reinforcement dispersion in the matrix materials is very important in order to ensure that there was a good interactions between both constituents that will result in good composite's properties. Scanning electron microscope (SEM) was used to take pictures of the powder materials to determine the general look of particles such as shape. Characteristic SEM picture of FA is shown in Figure 1. As it is seen from Figure 1, the shape of fly ash is not regular and uniform. There are large and small particles. This is expected due to the mixed compositon of ash content.

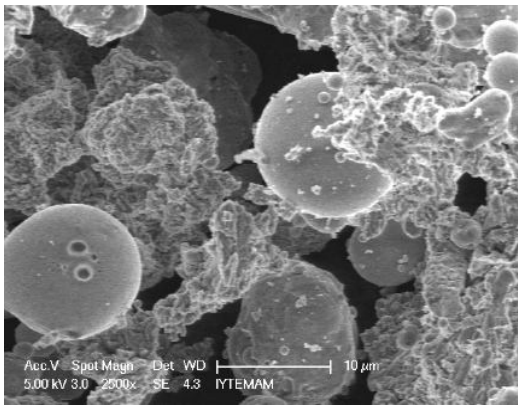

Figure 1. SEM photos of Fly ash (x2500)

SEM microphotographs of the obtained FA/PVC composites are shown in Figure 2 and Figure 3. They have shown region of well dispersed FA particles, but also and FA agglomerations in the composites. Besides information for the FA dispersion in the polymer matrix, SEM photos have shown that voids and micro pores were present in the obtained composites.

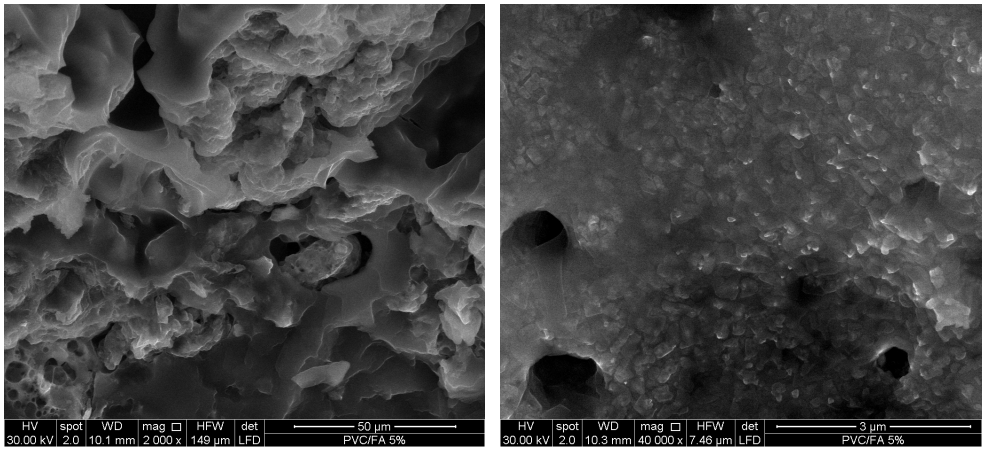

(a)(x2000) (b) (x40000)

Figure 2. SEM photos of 5% FA/PVC

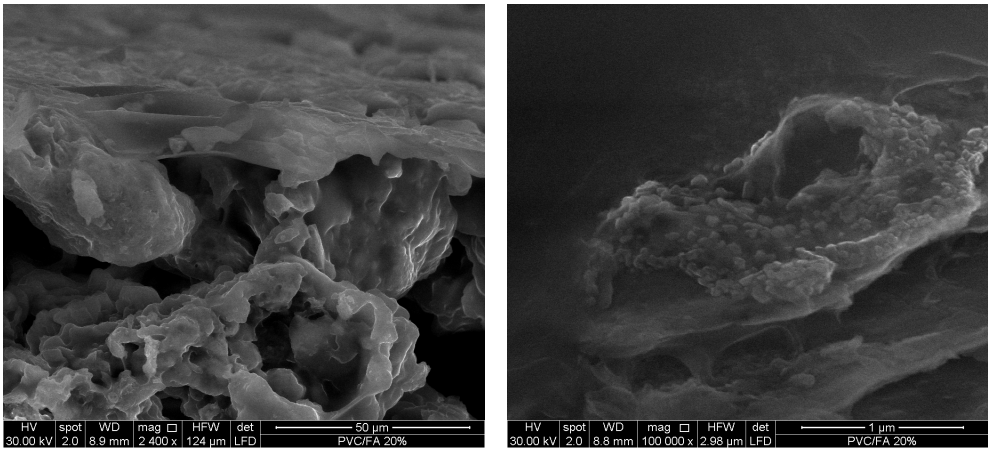

(a) (x2400) (b) (x100000)

Figure 3. SEM photos of 20% FA/PVC

Thermal stability and all the other characteristic thermal parameters of the PVC composites decreased in the presence of both types of FA. Lower values were obtained due the HCL treatment of FA particles compared to NaOH treated FA. Characteristic TGA/DTA thermogram for FA/PVC is shown in Figure 4.

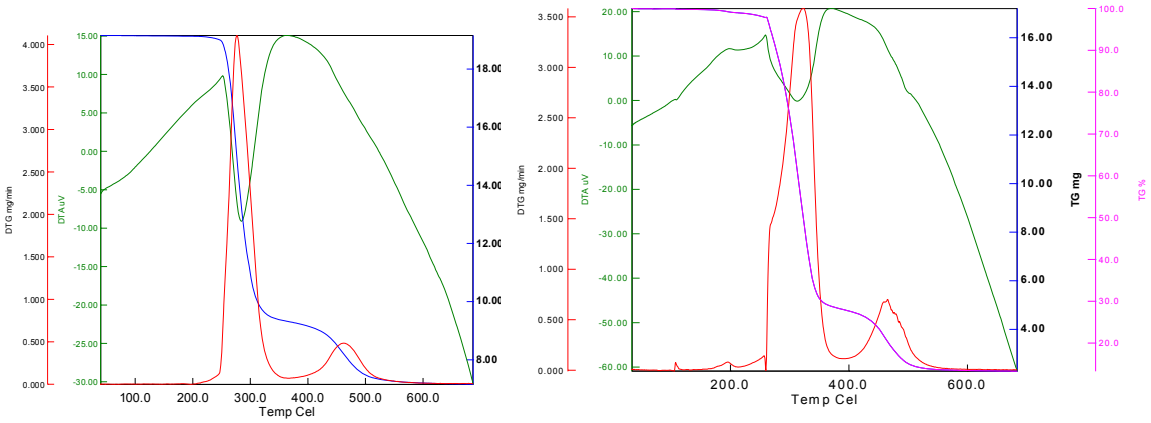

(a) 10% FA/PVC (b) 20%FA/PVC

Figure 4. Characteristic TGA/DTA for FA/PVC composites

Generally, all the FA/PVC composites have shown higher swelling degree than PVC. Swelling degree increase by increasing the flay ash content. Higher values were obtained for composites with NaOH treated FA particles. Swelling behavior was studied for both types of FA used. Characteristic curves are shown in Figure 5 and Figure 6.

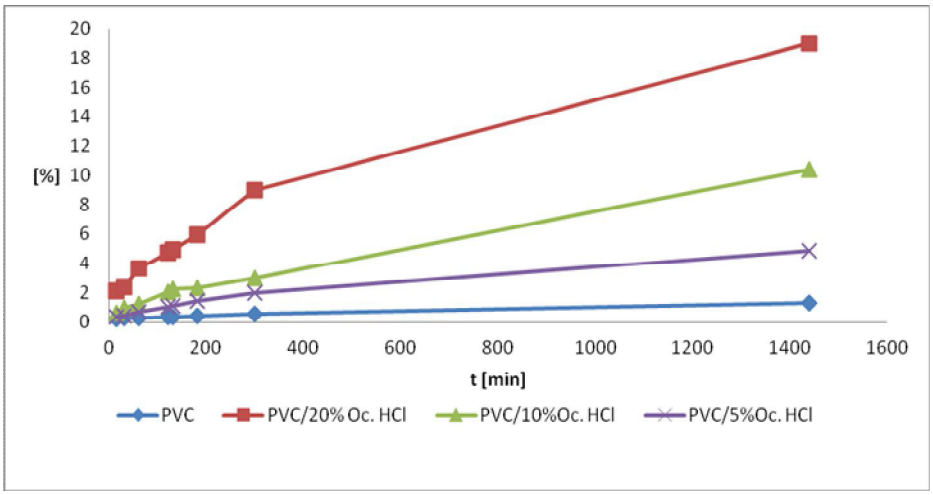

Figure 5. Swelling behavior of PVC/FA Os-HCl treated

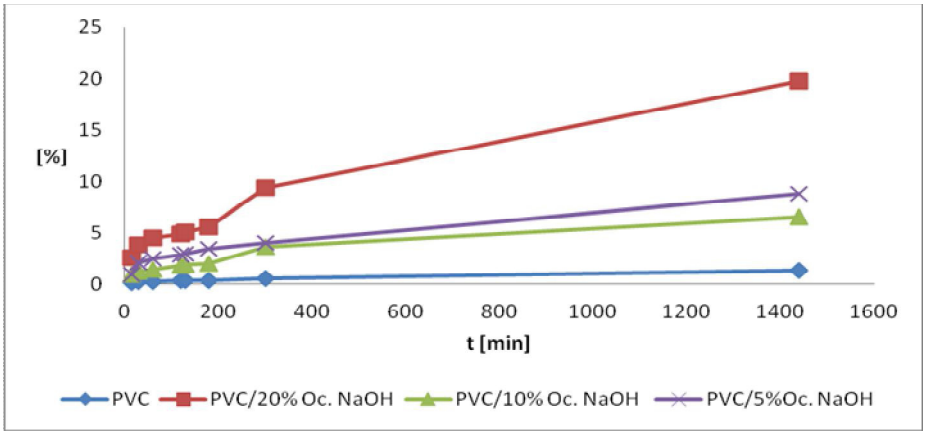

Figure 6. Swelling behavior of PVC/FA Os-NaOH treated

Acknowledgment: This research was performed within the Project "Environment protection of industrial waste through valorisation of metallurgical dust and slags in new environmental friendly polymer mortars and concretes" founded by Ministry of environment and physical planning of R. Macedonia.

4. REFERENCES

1. M. Polat, E. Guler, G. Akar, H. Morogan, U.Ipekoglu, H.J.Cohen, J. Chem. Technol. Biotechnol., 77, 372 (2002)
2. A. Baba, 19th World Energy Congres, Sydney, Australia (2004)
3. S. V. Vassilev, C.G, . Vassieva, Energy Fuels, 19, 1084 (2005)
4. N. Singh, R.D. Ramachandran, A.K. Sarkar, Int.J.Environ.Anal.Chem., 83,891 (2003)
5. A. Demirbas, Cement and Concrete Res., 26, 1737 (1996)
6. F. Canpolat, K.Yilmaz, M.M. Kose, M.Sumer, M.A. Yurdusev, Cement and Concrete Res., 34, 731 (2004)
7. P. Termkhajorkit, T. Nawa, Cement and Concrete Res., 34 (6) 1017, (2003)

A COMPARISON OF THE EFFECTS OF MODIFIED AND UNMODIFIED HALLOYSITE NANOTUBES ON THE MECHANICAL BEHAVIOUR OF POLYAMIDE-6

Ali Riza ERDOGAN[a] , Ilker KAYGUSUZ[b] , Cevdet KAYNAK [a,b,c*]

[a] Polymer Science and Technology Department, Middle East Technical University, Turkey
[b] Micro and Nanotechnology Department, Middle East Technical University, Turkey
[c] Materials and Metallurgical Eng. Department, Middle East Technical University, Turkey
*ckaynak@metu.edu.tr

ABSTRACT

The main purpose of this study was to explore effects of silane-modified and unmodified halloysite nanotubes (HNT) on the mechanical properties of polyamide-6 (PA6). Nanocomposites were compounded via melt mixing method in a twin-screw extruder, while specimens were shaped by injection molding. Scanning electron microscopy and mechanical tests indicated that even the use of unmodified HNTs could be homogenously distributed in the matrix leading to increased mechanical properties as much as more than 30%. Aminosilanization of HNTs resulted in effective amounts of Al-O-Si bridging bonds between the matrix and reinforcement, making composite strengthening mechanisms more operative. In this condition, increases in the mechanical properties were as much as more than 50%.

Keywords: Halloysite nanotubes, polyamide-6, aminopropyltriethoxysilane (APTES), nanocomposites

MODİFİYE EDİLMİŞ VE EDİLMEMİŞ HALOYSİT NANOTÜPLERİN POLİAMİD-6'NIN MEKANİK DAVRANIŞI ÜZERİNE ETKİLERİNİN KARŞILAŞTIRILMASI

ÖZET

Bu çalışmanın amacı silan modifiye edilmiş ve modifiye edilmemiş haloysit nanotüplerin (HNT) poliamid-6 (PA6) matrisinin mekanik özelliklerine olan etkisini incelemektir. Nanokompozitler çift vidalı ekstrüderde eriyik halde karıştırılarak elde edilmiş ve enjeksiyon kalıplama ile şekillendirilmiştir. Taramalı elektron mikroskobu ve mekanik test sonuçları modifiye edilmemiş nanotüplerin bile matris içinde düzgün dağılabildiğini ve mekanik özellikleri %30'a kadar artırabildiğini göstermiştir. HNT'nin aminosilanlanması matris ve nanotüpler arasındaki köprüleyici bağların artmasına ve güçlendirme mekanizmalarının daha etkili olmasını sağlamıştır. Bu durumda mekanik özelliklerde %50'ye kadar daha fazla artış gözlenmiştir.

Anahtar Kelimeler : Haloysit nanotüpler, poliamid-6, aminopropiltrietoksisilan (APTES), nanokompozitler

1. INTRODUCTION

Polymeric nanocomposites are one of the important landmarks in conventional composite perception. Having the reinforcement material at nano-size allows interaction between polymer matrix and reinforcement at molecular (atomic) scale, thus polymer matrix and nano-reinforcement materials bond to each other at a higher degree compared to micro/macro reinforcements, which leads to more effective load transfer mechanism from the matrix to reinforcements. Apart from the well-established nano-reinforcements of carbon nanotubes (CNT), montmorillonite (MMT), nano-SiO_2, nano-TiO_2, nano-$CaCO_3$ etc, "halloysite nanotubes" (HNT) are becoming an alternative one.

Halloysite nanotubes (HNTs) are 1:1 type (silica tetrahedral and gibbsitic octahedral) naturally occurring clay minerals generally having tubular shape. Normally there is weakly bonded monolayer of water molecules between their rolled walls which may easily dehydrate at room conditions. Chemical formula of HNTs can be expressed as $Al_2Si_2O_5(OH)_4.nH_20$, where n is equal to 2 or 0 for hydrated and dehydrated states, respectively. Hydrated HNTs have interlayer spacing of 10 Å, whereas it is 7 Å for completely dehydrated ones. Other typical properties of HNTs are; inner diameter 10-30 nm, outer diameter 50-100 nm, length 150-3000 nm, and cation exchange capacity (CEC) of 8 to 58 meq/100g.

Just like for the other nano-reinforcements, one of the main problem for HNTs is the formation of bundles or agglomerates leading to difficulty in obtaining homogeneous distribution in the matrix causing insufficient load transfer mechanism from the matrix. These problems could be overcome by an effective surface modification of HNTs, such as silanization.

γ-aminopropyltriethoxysilane (γ-APTES) is a widely used aminosilane which has an amine (-NH_2) group as the organo-functional group, a propyl linkage (-$CH_2CH_2CH_2$-) between amine group and Si atom, and three ethoxy groups (- OCH_2CH_3) attached to the Si atom as silicon functional group. It is a unique silane type compatible with many polymer matrices that could catalyze both hydrolysis and condensation reactions via its polar amine group. On the other hand, this situation may leads to increased level of self-oligomerization. Today, APTES is used to improve interfacial interactions between many polymer matrices and many macro-, micro-, and nano-reinforcements.

To the best of our knowledge, there seems to be only one work studying the effects of silanization of HNTs on the properties of PA6 matrix. In that work, Guo et al. [1] used 3-(trimethoxysilyl) propyl methacrylate (MAPTS) for the silanization of HNTs. They indicated that use of 5 wt% silanized HNTs in PA6 matrix increased flexural and tensile strength values by 21% and 15% respectively; while heat distortion temperature (HDT) increased from 65° to 108°C. They also revealed that silanized HNTs acted as nucleating agents increasing the level of crystallinity of PA6 matrix.

Since silanization related literature on PA6/HNT nanocomposites are very scarce, i.e. only one, the main purpose of this study was to investigate effects of APTES type silanization on the mechanical properties of PA6/HNT nanocomposites.

2. EXPERIMENTAL

In this study, the polymer used as the matrix material was polyamide-6 (PA6) (EMS Griltex D1894A) having a melting range of 220-225°C and density of 1.14 g/cm^3, while the reinforcement was halloysite nanotubes (HNT) (Sigma-Aldrich). General view of HNTs (Figure 2) taken by using TEM (Jeol JEM 2100F) in this study shows that nanotubes are longer than 500 nm, while as stated by the supplier they have average inner diameter of 30-70 nm and surface area of 64 m^2/g. During silanization procedures of HNTs, γ-aminopropyltriethoxysilane (APTES) (99%, Sigma–Aldrich), ethanol (99.5%, Sigma–Aldrich) and acetic acid (%100 Sigma-Aldrich) were used.

PA6 nanocomposites were prepared with 5 wt% HNT and designated by using the format "PA/s-HNT". For the specimens having unmodified HNTs, no prefix was used.

PA6 granules and all types of HNTs (95:5) (w:w) in powder form were first pre-mixed by shaking in a plastic bag for several minutes, then for compounding fed into a laboratory scale co-rotating twin screw extruder (Rondol Microlab 400) having a screw diameter of 10 mm and L/D ratio of 20. The temperature profile of the extrusion process was 185–220–230–225–205°C (from feeder to die, respectively) and the screw speed was 75 rpm.

Compounded materials were dried in a vacuum oven for 18 hours at 80°C before shaping. Test specimens were shaped by a laboratory scale injection molder (DSM Xplore Micro 10 cc). The barrel and mold temperatures were 240°C and 70°C respectively, while the holding time in the barrel was 4 minutes.

3. RESULTS AND DISCUSSION

SEM analysis, as shown in Figure 1, was conducted to evaluate dispersion state and pull-out morphology of HNTs in PA6 matrix under a magnification of 40000X. Figure 1 indicates that unmodified HNTs and aminosilanized HNTs were rather randomly and homogenously dispersed in PA6 matrix. There seems to be no significant differences except for the slightly better distribution of silanized HNTs. It is believed that chemical groups (e.g. –OH) present on the surfaces of unmodified HNTs and silanized HNTs might act as effective surfactants, leading to sufficient degree of distribution via secondary chemical attraction of these groups to the amide groups of polyamide matrix.

In order to characterize mechanical behavior of the specimens tension and three-point bending tests, and dynamic mechanical analysis were conducted. Figures 2 and 3 gives tensile and flexural stress-strain curves, while storage modulus and tan δ curves are given in Figures 4 and 5. Mechanical properties determined from these tests and analyses for all specimens are tabulated in Tables 1, and 2.

All these figures and tables show that incorporation of only 5 wt% HNTs into PA6 matrix improved all mechanical properties. Even the use of unmodified HNTs resulted in certain level of increases. For example, increases in the yield and tensile strength values of PA/HNT, were 8%, while it was 24% in flexural strength. Similarly, increases in the tensile and flexural modulus values were 32%, while it was 38% in storage modulus at 25^{0}C. Peak of tan δ values

(T_g) also increased by 2^0C, while due to the strengthening and stiffening effects, % strain at break values decreased, which was expected.

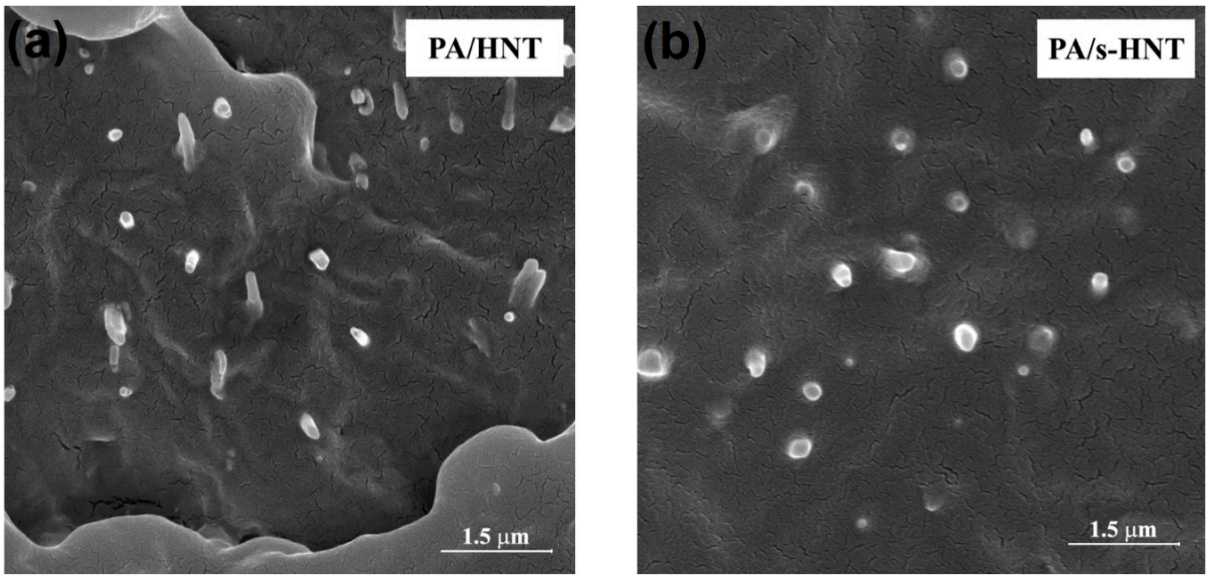

Figure 1. SEM micrographs showing dispersion state and pull-out morphology of unmodified and aminosilanized HNTs in PA6 matrix

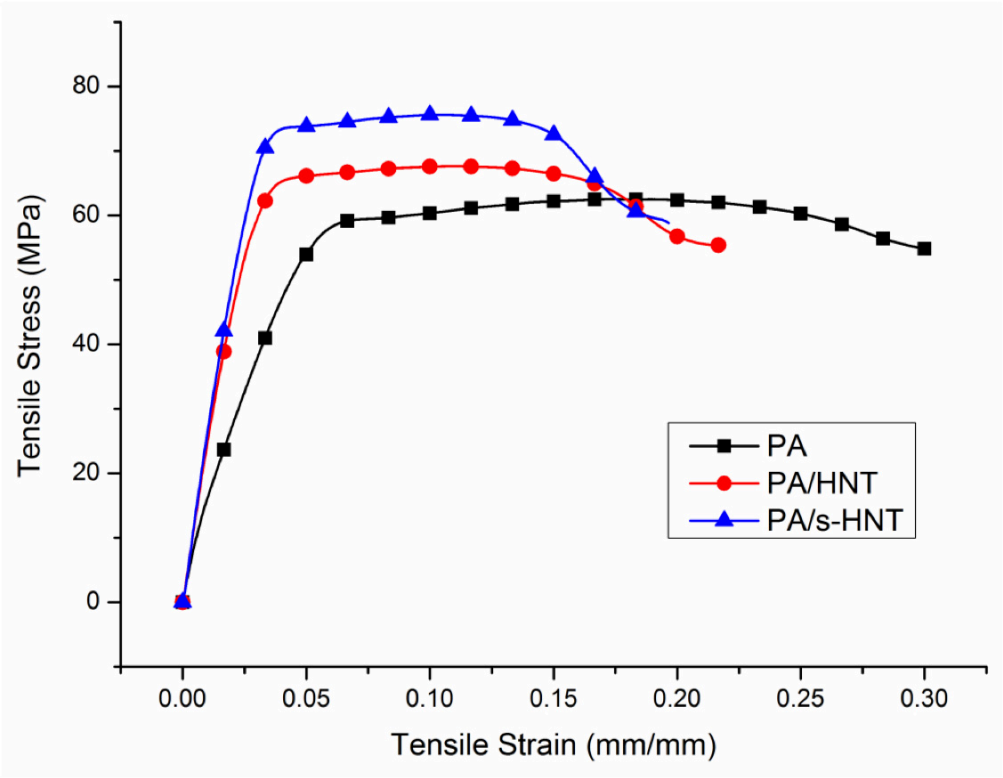

Figure 2. Tensile stress-strain curves of the PA6 matrix and its nanocomposites with HNTs

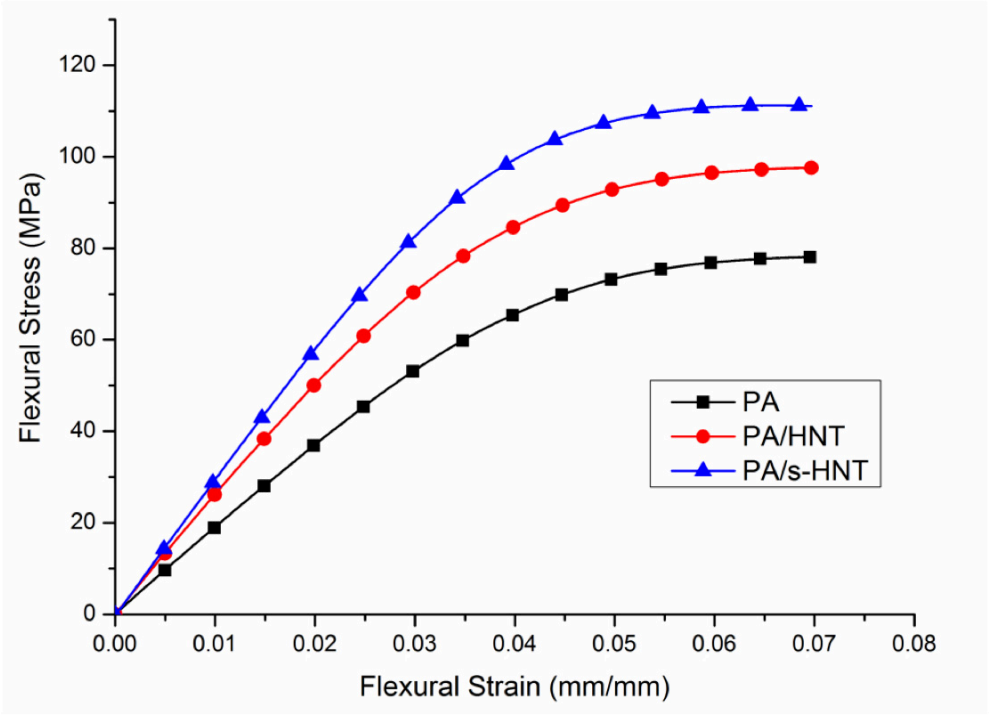

Figure 3. Flexural stress-strain curves of the PA6 matrix and its nanocomposites with HNTs

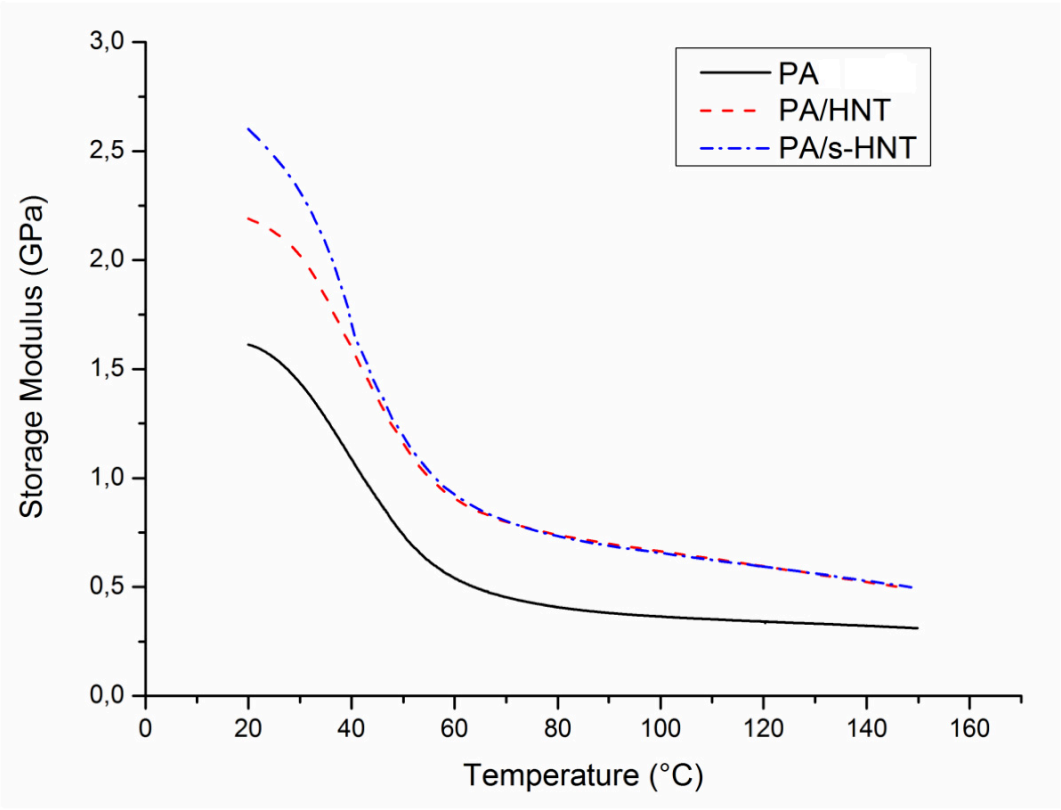

Figure 4. Storage modulus curves of the PA6 matrix and its nanocomposites with HNTs

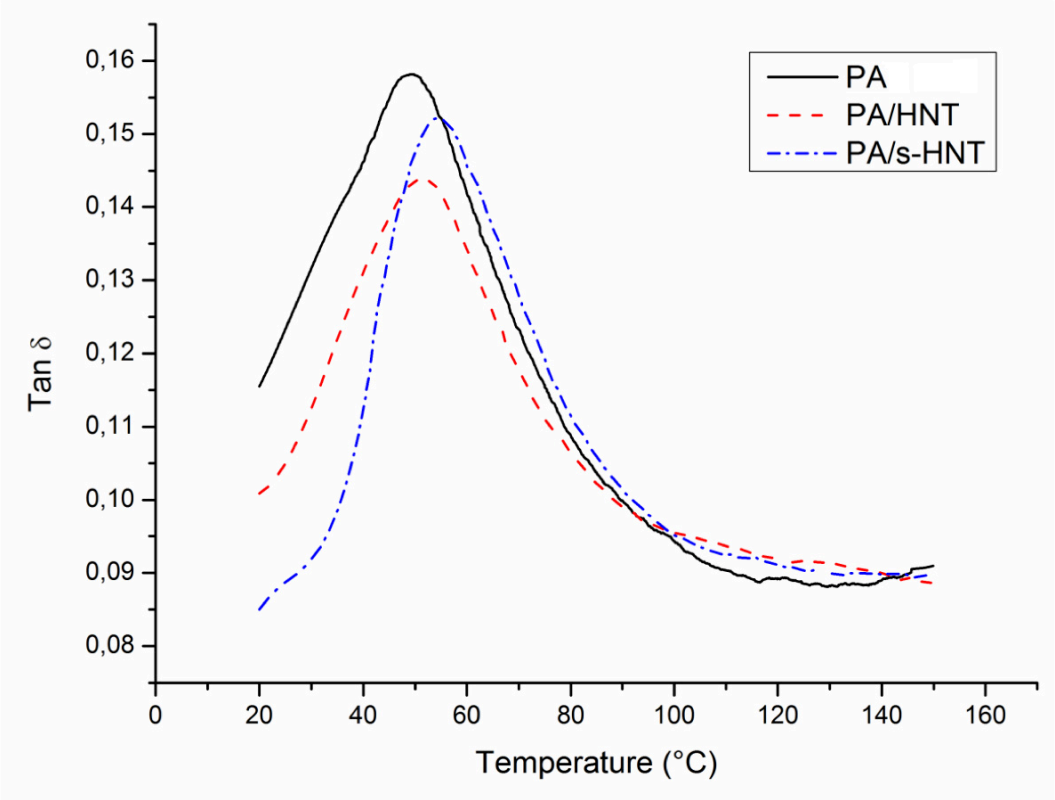

Figure 5. Tan δ curves of the PA6 matrix and its nanocomposites with HNTs

Table 1. Tensile and flexural properties of PA6 matrix and its nanocomposites with HNTs

Specimens	Yield Strength (MPa)	Tensile Strength (MPa)	Tensile Modulus (GPa)	Strain at Break (%)	Flexural Strength (MPa)	Flexural Modulus (MPa)
PA	60 ± 1.9	62 ± 0.5	1.96 ± 0.31	30 ± 0.2	79 ± 1.2	1.97 ± 0.09
PA/HNT	65 ± 0.2	67 ± 0.3	2.59 ± 0.04	22 ± 0.1	97 ± 0.3	2.59 ± 0.04
PA/s-HNT	73 ± 0.8	75 ± 0.5	2.84 ± 0.02	19 ± 0.2	79 ± 1.2	1.97 ± 0.09

Table 2. DMA results of PA6 matrix and its nanocomposites with HNTs

Specimen	Storage Modulus at 25˚C (GPa)	Tan δ peak (T_g) (˚C)
PA	1.55	49
PA/HNT	2.13	51
PA/s-HNT	2.48	55

Aminosilanized HNTs resulted in much higher mechanical properties compared to unmodified HNTs. For example, compared to neat PA6, increases in the strength values of PA/s-HNT nanocomposites, i.e. yield strength, tensile strength and flexural strength were as much as 22%, 21%, and 41% respectively. Similarly, increases in the modulus values, i.e. tensile modulus, flexural modulus and storage modulus at 20^0C were as much as 45%, 51% and 52%, respectively. Peak of tan δ also increased by 6^0C.

It is known that increases in the strength and modulus values are basically due to the two strengthening mechanisms in composite materials; i.e. "load transfer from the matrix to the reinforcements" and "decreased chain mobility of the matrix by the reinforcements". Since nano-sized HNTs have excellent mechanical properties, relatively high aspect ratios, and very high volume to surface area ratios, these two basic mechanisms were operative even for the PA nanocomposites with unmodified HNTs.

Of course, for these two basic mechanisms to be significantly operative there are two requirements; these are "uniform distribution of reinforcements in the matrix", and "chemical bonding between the matrix and reinforcements". It was supposed that these two requirements were partially fulfilled by the reactive hydroxyl site of Al-OH groups present at the edges and defected surfaces of unmodified HNTs, leading to certain level of interfacial chemical interaction, such as hydrogen bonding. In order to have higher improvements in the properties, higher interfacial chemical interactions, such as covalent bonding, would be necessary. It is discussed in the literature such as Laura et al. [18] that amine edges of APTES are capable of reacting with the carboxylic acid end groups of the polyamide chains forming covalent bonds.

4. CONCLUSIONS

Main conclusions drawn from this study, investigating the effects of aminosilanization of HNTs on the mechanical properties of PA6/HNT nanocomposites are as follows:

- SEM studies showed that even unmodified HNTs could be homogenously distributed in the matrix due to hydroxyl groups present on the surfaces of the HNTs acting as surfactants. Aminosilanization further improved interfacial bonding, leading to shorter pulled-out lengths of HNTs.
- Mechanical tests revealed that use of only 5 wt% HNTs resulted in significant improvements in the mechanical properties of PA6. For instance, the increases in the flexural strength and modulus values with unmodified HNTs were 24% and 38%, respectively. For the aminosilanized HNTs, these values were increased as much as 41% and 51%, respectively.

REFERENCES

1. B. Guo, Q. Zou, Y. Lei, D. Jia, *Polym. J.*, **41**, 835 (2009)
2. D.M. Laura, H. Keskkula, J.W. Barlow, D.R. Paul, *Polym*. **43**, 4673 (2002)

Processing and Characterization of Glass Flake-Reinforced Thermoplastic Polymer Matrix Bio-Inspired Bulk Lamellar Composites

Aylin Gunes, Simge Tulbez and Arcan F. Dericioglu

Middle East Technical University, Dept. of Metallurgical and Materials Eng., Ankara-Turkey
aylin.gunes@metu.edu.tr, s.tulbez@metu.edu.tr, arcan@metu.edu.tr

1. ABSTRACT

Natural materials/composites reveal superior specific properties compared to their artificial counterparts because of their unique microstructural architectures and high volume fraction of inorganic components. Because of these outstanding characteristics scientists and engineers have been using natural materials as a source of inspiration in order to achieve mechanically more reliable materials with higher specific strength, stiffness, fracture toughness etc. for lightweight structural designs. Among the natural materials, nacre has a highly special and regular brick-and-mortar arrangement of organic and inorganic constituents in which the inorganic volume fraction is about 95%. The key behind such a high volume fraction seems to be the well-alignment of the non-equiaxed inorganic phase involved.

In the scope of the present study, a slip casting-based hybrid conventional process called Hot Press Assisted Slip Casting (HASC) has been utilized through which glass flake-reinforced polystyrene and acrylonitrile butadiene styrene bulk nacre-like lamellar composites with brick and mortar structure could have been achieved. Tape casting preceded HASC process to improve flake alignment in the bio-inspired composites. Correlation between flake alignment, content and orientation as well as enhancement in the mechanical properties was investigated. Microstructural characterization of the fabricated bulk lamellar polymer matrix composites was performed by means of scanning electron microscopy (SEM) and mechanical characteristics were examined by three point bending test along with hardness measurement. In order to further enhance the mechanical properties an initial organofunctional silane treatment was applied on glass flakes where the efficiency of surface functionalization was monitored by X-ray photoelectron spectroscopy (XPS). Enhancement in the mechanical properties of the bio-inspired bulk lamellar composites with the applied surface modification was demonstrated.

Keywords: Bio-inspired composites, Hot-press assisted slip casting, Artificial nacre, Silane coupling.

1. ÖZET

Doğada bulunan malzemeler/kompozitler benzersiz mikroyapıları ve hacimce yüksek oranda inorganik bileşen içermelerinden dolayı yapay olarak üretilenlere göre üstün özellikler göstermektedir. Bu emsalsiz özelliklerinden dolayı bilim adamları ve mühendisler yüksek dayanım, sertlik ve mukavemet özellikleri içeren mekanik açıdan daha kullanışlı hafif yapısal malzemeler oluşturmak için doğal malzemeleri ilham kaynağı olarak kullanmaktadır. Doğada bulunan malzemeler arasında sedef hacimce %95 inorganik bileşene sahip, çok özel ve düzenli organik ve inorganik kısımlardan oluşan tuğla ve harç mimarisine sahiptir. Hacimce yüksek orana sahip olmasının ana nedeni yapıda bulunan ve eş eksenli olmayan inorganik fazın iyi dizilimidir.

Mevcut çalışma kapsamında, alçı kalıba döküm bazlı, sıcak pres destekli asıltı döküm (HASC) olarak adlandırılan bir hibrid konvansiyonel yöntem vasıtasıyla ince cam plakalarla zenginleştirilmiş,

polistiren ve akrilonitril butadien stiren termoplastik polimer matrisli tuğla ve harç mikroyapısına sahip sedef yapısına benzer hacimli lamelar kompozit üretimi gerçekleştirilmiştir. HASC yönteminden önce şerit döküm yöntemi ile ince cam plakaların dizilmleri gerçekleştirilmiştir. Tabakaların dizilimi, içeriği ve yönelimleri arasındaki ilişkinin yanı sıra mekanik özelliklerdeki gelişme de incelenmiştir. Üretilen hacimli lamelar polimer matrisli kompozitlerin mikroyapısal karakterizasyonu taramalı elektron mikroskobu (SEM) kullanılarak, mekanik özelliklerinin belirlenmesi ise üç noktadan eğme ve sertlik testleri yapılarak gerçekleştirilmiştir. Mekanik özelliklerini ilerletmek amacıyla bir organofonksiyonal silan ince cam plakaların yüzeyine uygulanmış ve yüzeyin değişimi XPS yöntemiyle incelenmiştir. İnorganik takviye malzemesinin yüzey değişimiyle sedef yapısına benzer hacimli lamelar kompozitlerin mekanik özelliklerinde ilerleme sağlandığı gösterilmiştir.

Anahtar Kelimeler: Doğadan esinlenilen kompozitler, Sıcak pres destekli asıltı döküm,Yapay sedef, Silanlama.

2. INTRODUCTION

Nature has incredible materials in terms of their mechanical, chemical and structural properties because of the excellent combination of different compounds and their magnificent geometric arrangement in such structures. As a result, the intriguing property-structure relationship make natural materials worth inspiring. Taking inspiration from nature and designing artificial materials mimicking the microstructural architecture of the natural ones has created a scientific area called "bio-inspired materials."

One of the inspiring natural materials is nacre-mother of pearl- i.e. inner layer of mollusc shells. Nacre has exceptional structural properties. This splendid seashell comprises 95 vol% inorganic phase (aragonite) and 5 vol% organic biopolymer (proteins such as β-chitin and lustrins) as its matrix revealing enhanced mechanical characteristics including unique toughness and mechanical strength combination [1, 2]. Its exceptional properties result from the fact that it has brick and mortar arrangement of its constituent phases. Generally there are two main methods to produce nacre-like artificial composites which are formation of a layered nanostructure by self-assembly [3, 4, 7, 9, 11, 12–13] and a brick-and-mortar nanostructure by sequential deposition of the inorganic and organic phases [3, 5, 6, 8, 10]. In addition to these studies chemical vapor deposition, dip coating, physical vapor deposition could be alternative methods to generate nacre-like nanocomposite materials [14-17]. However, although there are various studies about synthesizing nacre-like structures, materials resulting from these approaches are generally in the form of thin nanocomposite structures which is not in the bulk form. Consequently, the efforts on producing bulk composites with brick and mortar architecture are quite scarce, as they are usually time inefficient.

Recently, some useful techniques have been proposed for the fabrication of nacre-like bulk lamellar composite materials. One of these techniques is based on Pulsed Current Sintering (PCS) of metal-coated inorganic platelets [14]. Although achieved composites were inorganic platelet reinforced metal matrix composites rather than being a polymer matrix one, this conceptual study has shown the possibility of aligning inorganic platelets in an elastic-plastic matrix by the assistance of pressure. Following this study, "Hot press Assisted Slip Casting'' (HASC) was attempted to fabricate bulk lamellar composites composed of inorganic platelets aligned in a thermoset polymeric matrix [3]. In this technique applied pressure forces the liquid resin to flow out through a porous filter in a mold during which the alignment of platelets with their basal surfaces perpendicular to the hot-pressing direction is achieved. This newly proposed technique has provided well alignment of the inorganic platelets in the polymeric matrix in brick-and-mortar architecture leading to improved mechanical properties compared to the neat polymer matrix and the composite with irregular inorganic distribution. Investigations on the composites formed by HASC methods have shown that optimization of the mechanical properties with the help of a coupling agent applied on the organic-inorganic interface is

possible. Following the coupling agent application, work of fracture of this 2D alumina or glass platelet reinforced nacre-like bulk lamellar thermoset matrix composites has reached to about 178 J/ m^2 [18].

The aim of this study is to achieve glass flake reinforced nacre-like bulk lamellar thermoplastic matrix composites using HASC and/or Tape Casting (TC) method which is scraping an organic-inorganic dispersion on a glass surface via a moving blade that is commonly used in fine ceramic processing. In the scope of this study, these methods were used both consecutively or individually to observe and compare differences between these two techniques in resulting glass flake alignment. As Reference specimens, composites were fabricated by HASC combined with Simple Mixing (SM) and also by TC combined with Hot Press (HP).These specimens are shown the effect of HASC and TC processes on the alignment of glass flakes separately. Glass flake surfaces were functionalized by applying silane treatment to create an optimized interfacial bonding between thermoplastic polymer matrix and the inorganic reinforcement, and hence to improve the mechanical properties. Silane is known to be an effective coupling agent supplying good adhesion and contributing to the stabilization of the composite material. The main effort was to determine the suitable treatment with silane for optimum surface functionalization. In this study, aminopropyltriethoxy silane (APS) was used. It has been observed that functionalization with silane improves adhesion between glass flakes and thermoplastic polymer matrices behaving like a chemical bridge between them resulting in further enhancement of the mechanical properties of nacre-like bulk lamellar thermoplastic polymer matrix composites.

3. EXPERIMENTAL STUDIES

3.1 Materials and Methods

Nacre-like bulk lamellar thermoplastic polymer matrix composites are composed of glass flake as inorganic reinforcement and polystyrene and acrylonitrile butadiene styrene as thermoplastic polymer matrices**.** Two types of glass flakes designated as GF 003 and GF 750 were used as reinforcement. Their basal plane diameters are <50 μm and 150-1700 μm and theır thickness are 2.3-3.3 μm and 5.5-9.5 μm, respectively (Glass Flake Ltd., Leeds, UK). Thermoplastic polymers matrices were supplied in granular form. Average molecular weight of polystyrene is 64946 g/mole and average molecular weight of acrylonitrile butadiene styrene is 28309 g/mole while their solvents were chloroform and dimethyl form amide, respectively.

The scope of this study is to apply different processing method combinations composed of two different primary processes which are Tape Casting (TC) and Simple Mixing (SM) methods followed by two different secondary processes which are Hot Press Assisted Slip Casting (HASC) and Hot Pressing (HP) to achieve brick and mortar architecture. Consequently, there are four types of variations, namely SM+HASC, SM+HP, TC+HASC, TC+HP. For all variations, same amount glass flake and polymer solutions were used initially.

Glass flakes were mixed with polystyrene and acrylonitrile butadiene styrene polymer solutions separately. For the preparation of each polymer solution, 80 ml solvent and 10 g polymer granules were used. Glass flakes were added into these polymer solutions as a mixture of two different glass flakes, namely 3 g glass flake mixture containing 80 wt% GF 750 and 20 wt% GF 003 was prepared. Later, glass flake mixture was added to the polymer solution while stirring it on a magnetic stirrer. In the case of the first primary process namely SM process, final glass flake-polymer suspension was poured on a glass surface and kept approximately one day to dry. Dried film like structures were removed from the glass surface with the help of a fresh knife by cutting them as square shaped specimens.

The second primary process used in this study is TC. This process is based on scraping a suspension on a glass surface via a blade (doctor blade). The equipment used for this process is composed of a solution chamber and a blade the height of which from the glass surface is adjusted by a caliper. Calipers are controlling the height of the blade to control the final thickness of tapes. In this study, polymer- glass flake mixture was poured into the solution chamber after adjusting the blade height to 50 μm. Following this, equipment moved the solution chamber with a speed of 20 cm/s to scrape. Later on, scraped tapes were kept on the glass surface approximately one day to dry, and dried tapes were removed from the surface by cutting as described before.

After cutting, film-like structures were put into a steel die that was used for one of the secondary processes, namely HASC. In this technique, plaster is cast in the square cross sectioned steel die to form a porous filter which will drain the excess polymer from the suspension in order to increase the reinforcement content in the composite structure. Die assembly was then placed in a conventional hydraulic hot-press, and pressure was adjust to a distinct value. Following the melting of the polymer, it started to flow through the porous plaster from underneath the steel die. Temperature of the system was also increased simultaneously with the increase in pressure. Finally, heating was interrupted at 160 °C for polystyrene under the applied pressure and at 155 °C for acrylonitrile butadiene styrene. In this particular process, the flow of the draining liquid polymer from the suspension has provided the alignment of flakes. Detailed information about HASC procedure has been presented elsewhere [3].

The other secondary process used in this study is HP. This process includes the same procedure with that of the HASC, yet in the case of HP there was no pressure increment. In this process the die assembly was placed in a conventional hydraulic hot press, and an initial pressure was applied while heating the system. Heating was stopped at 200 °C for polystyrene and at 170 °C for acrylonitrile butadiene styrene while the die assembly was under the action of the applied initial pressure.

Consequently, in the scope of this study efficiency of the four processing routes applied on the alignment of the inorganic phase in the composite, and hence achievement of the brick and mortar structure has been investigated. To reveal the effect of flake alignment and volume fraction on the improvement of the mechanical properties, simple mixed and then hot pressed (SM+HP) specimens were prepared as control samples.

3.2 Surface Modification of Glass Flakes with Silane Coupling Agent

To improve compatibility and interfacial bonding between inorganic and organic phases, surfaces of the glass flakes were treated with a silane coupling agent. Aminopropylytiethoxy silane (APS, Silquest A-1100) used as the coupling agent in this study was supplied by Momentive Performance Materials Inc., Ohio, USA. Chemical structure of the organofunctional silane coupling agent is demonstrated in Fig. 1. Surface functionalization procedure was applied using reagent grade acetic acid and ethanol in basal solution preparation.

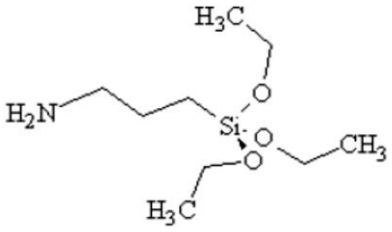

(b)

Aminopropyltriethoxysilane

(Silquest A-1100)

Figure 1. Chemical structure of organofunctional silane coupling agent used in this study (Aminopropyltriethoxysilane-APS)

Basal solution was prepared by using ethanol-water mixture (95 vol%-5 vol%). Followed by adjusting the pH of solution with acetic acid addition in trace amount, amino-functional silane was added drop by drop to the solution. Solution was left for 1.5 h to allow complete hydrolysis and silanol formation. Glass flakes were then added to the silane solution during magnetic stirring. After 30 minutes mixing, flakes were filtered off to remove the excess amount of solvent and dried at 120 °C for 1 h under ambient conditions.

3.3 Fabrication of Surface Functionalized Glass Flake Reinforced Nacre-Like Bulk Lamellar Thermoplastic Polymer Matrix Composites

Composite fabrication using surface modified glass flakes was conducted using one of the procedures described in Section 3.1. According to the mechanical properties of the composites fabricated by the four procedure combinations described, the most efficient method was determined to be SM+HASC. Consequently, only this procedure was used to fabricate composites containing surface modified glass flakes. Identical SM+HASC procedure described in Section 3.1 was applied to fabricate nacre-like composites containing surface functionalized glass flakes for both thermoplastic polymer matrices.

3.4 Characterization

Specimens from composites fabricated by four different process combinations were cut both parallel and perpendicular to hot-pressing direction, and their surfaces were ground and polished down to 0.3 μm diamond suspension. Microstructural characterization of the as-processed composites was conducted using scanning electron microscope (FEI Nova Nano SEM 430). Vickers hardness measurements were carried out using micro hardness tester (Shimadzu HMV 0.2) with an applied maximum load of 1.92 N for 10 seconds. Flexural strength, strain to fracture and modulus of the composites were determined by three-point bending tests. Length, width and thickness of the three-point bending specimens were 20, 5 and 1 mm, respectively. Tests were conducted with a span length of 16 mm and cross-head speed of 0.4 mm/min. For both Vickers hardness measurements and three-point bending tests applied loading direction was parallel to the hot-pressing direction (perpendicular to flake basal surfaces). Fracture surfaces of the three-point bending tested specimens were examined using SEM. Volume fractions of the flakes in the resulting composites were determined applying the "rule of mixtures" using the densities of composite samples and thermoplastic polymer matrices measured by the Archimedes' principle.

Surface functionalization of the glass flakes with silane coupling agent was characterized by X-ray photoelectron spectroscopy (XPS, PHI 5000 Versa Probe). XPS analysis of both as-received and silane-treated flakes was carried out using monochromatic Al K_α radiation source. XPS spectra were collected with pass energy of 187.85 eV at a photoelectron take-off angle of 45°.

4. RESULTS AND DISCUSSIONS

4.1 As Received Glass Flake Reinforced Nacre-Like Thermoplastic Polymer Matrix Composites

Four different processing combinations namely SM+HP, SM+HASC, TC+HASC, TC+HP were applied to achieve brick and mortar architecture similar to that of nacre, and hence to obtain improvement in the mechanical properties of the composites. Mechanical properties of the composites fabricated by HASC process was expected to be superior to those of the others fabricated by other methods owing to the high inorganic reinforcement content along with the alignment of flakes achieved using HASC. Flexural strength and strain to fracture of the composites fabricated by varying process combinations is presented in Table 1.

Table 1. Three point bending test results of the composites fabricated by varying process combinations.

Processing Method	Matrix	Flexural Strength (MPa)	Strain to Fracture%
SM+HASC	ABS	14.88 ± 1.45	3.28 ± 0.56
SM+HEAT	ABS	5.15 ± 0.95	3.01 ± 0.45
TC +HASC	ABS	14.11 ± 0.49	3.12 ± 0.67
TC+HEAT	ABS	6.68 ± 0.95	3.52 ± 0.73
SM+HASC	PS	19.59 ± 1.63	2.09 ± 0.40
SM+HEAT	PS	8.70 ± 1.01	2.98 ± 0.85
TC +HASC	PS	16.19 ± 2.78	3.12 ± 0.61
TC+HEAT	PS	11.57 ± 2.10	1.69 ± 0.24

Three point bending test results showed that HASC is a more effective secondary process in achieving nacre-like composite structures compared to HP. Results showed that SM+HASC combination is the most effective pathway, as the alignment of flakes was achieved by draining excess polymer with the help of the porous plaster filter as a result of which the amount of polymer remaining between flakes is optimum. In addition to these according to the mechanical results polystyrene was a more appropriate matrix material due to its better interfacial compatibility with glass flakes compared to that of ABS.

Investigation of the cross sectional microstructures of the composites under SEM (Fig. 1) revealed that all of the applied processing combinations were effective in the alignment of the glass flakes in the composite structure with the only difference being the amount of polymer remaining in the composite. As it is clear from Fig. 1, nearly all processing combinations were successful in revealing brick and mortar arrangement. The amount of polymer remaining in the structure seems to be dependent on the processing procedure applied, where it seems to be larger amount in SM+HEAT processed composites (Fig. 1.b and f).

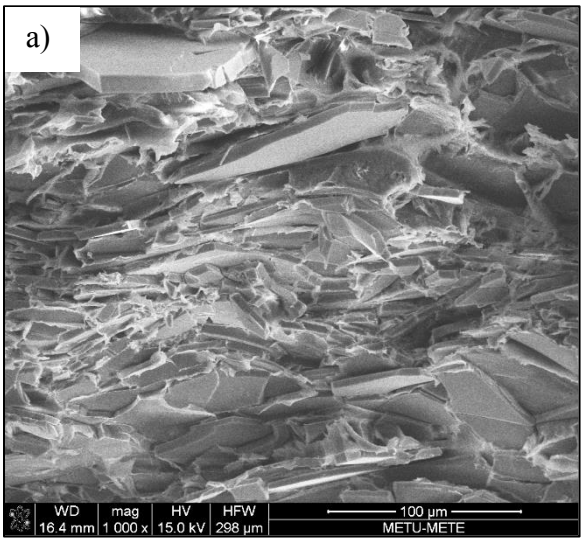
a)
WD 16.4 mm
mag 1 000 x
HV 15.0 kV
HFW 298 µm
100 µm
METU-METE

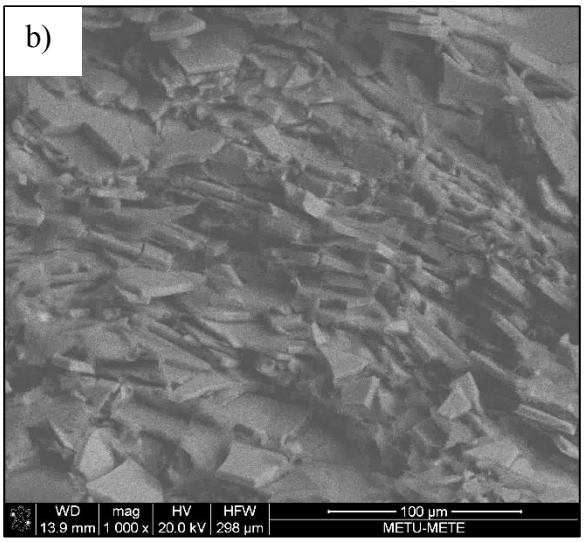
b)
WD 13.9 mm
mag 1 000 x
HV 20.0 kV
HFW 298 µm
100 µm
METU-METE

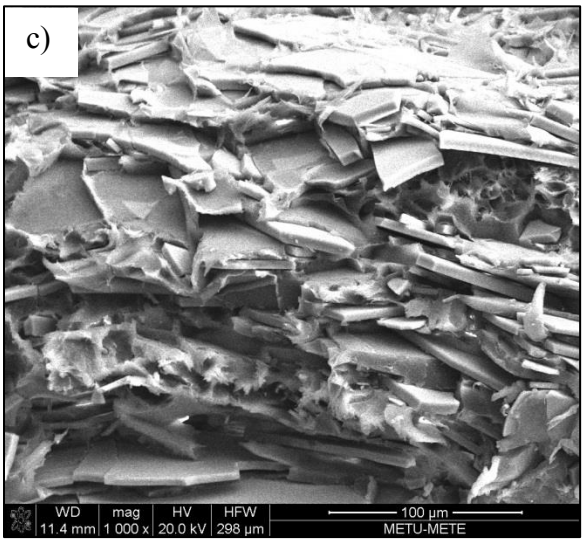
c)
WD 11.4 mm
mag 1 000 x
HV 20.0 kV
HFW 298 µm
100 µm
METU-METE

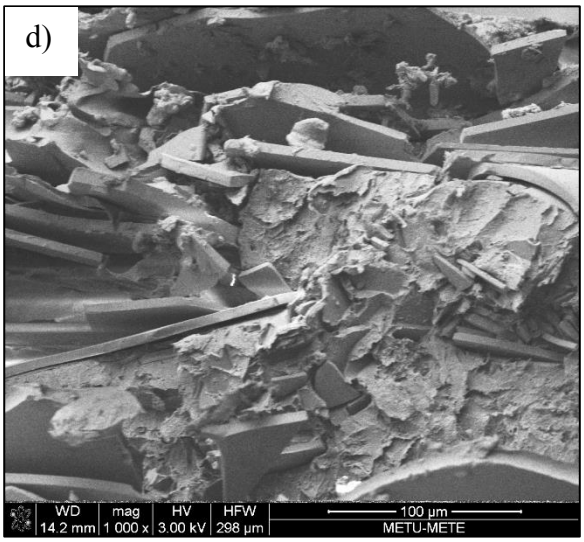
d)
WD 14.2 mm
mag 1 000 x
HV 3.00 kV
HFW 298 µm
100 µm
METU-METE

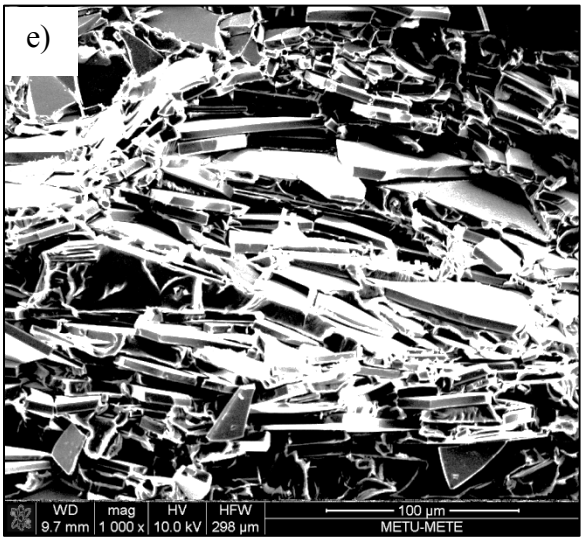
e)
WD 9.7 mm
mag 1 000 x
HV 10.0 kV
HFW 298 µm
100 µm
METU-METE

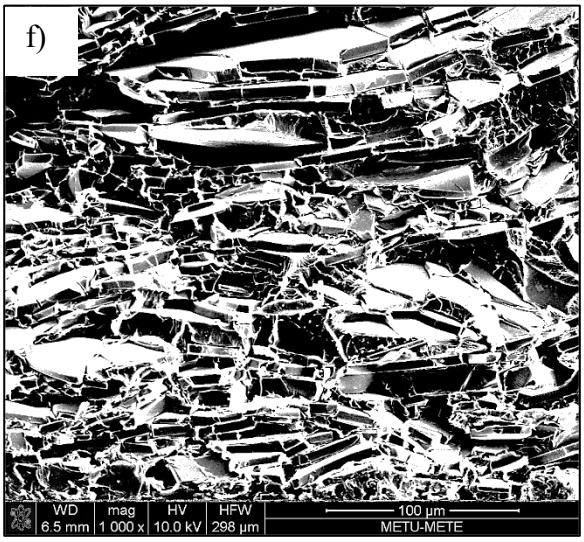
f)
WD 6.5 mm
mag 1 000 x
HV 10.0 kV
HFW 298 µm
100 µm
METU-METE

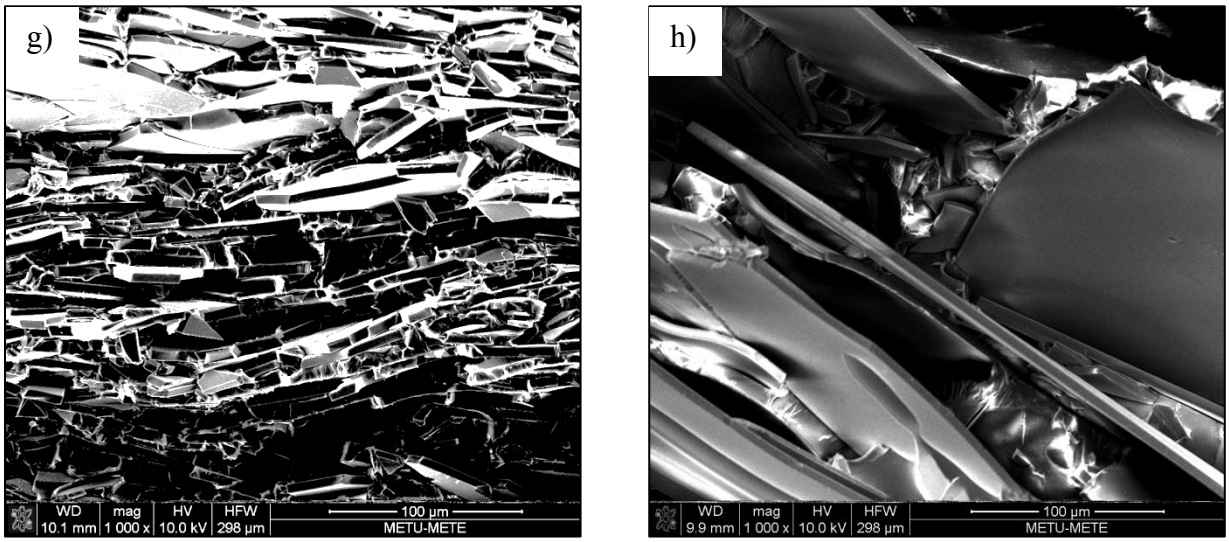

Figure 1. Cross sectional microstructures of the composites fabricated by varying process combinations; a) SM+HASC (ABS), b) TC+HASC (ABS), c) TC+HP (ABS), , d) SM+HP (ABS) e) SM+HASC (PS), f) TC+HASC (PS) ,g) TC+HP (PS), h) SM+HP (PS)

Two different thermoplastic polymers were used in all cases, and the polymer type was determined to be affecting the resulting mechanical behavior of the composites directly. Significant points related to the polymeric material effective on its final properties are the monomer type and the structure of polymer. Crystalline polystyrene used in this study and its structure could be important for its interfacial interaction with the glass flake surface. Therefore, steric effect of the polymer structure plays a crucial role in this interaction. ABS which is a terpolymer consisting of three different monomers. The interaction at the polymer-glass flake interface in ABS matrix seems to be relatively deficient compared to that of polystyrene matrix. Both of the thermoplastic polymers were useful in terms of the process combinations applied as their working temperatures are suitably low. However, according to the main chemical structure differences in their monomers and the polymer solutions they form, nacre-like bulk lamellar composites fabricated using these two thermoplastic polymer matrices demonstrated different mechanical and microstructural characteristics. Fig. 1 d clearly shows that in TC+HP process of ABS, polymer content remaining between flakes is insufficient which leads to deficiency in energy distribution and results in fracture preference. The same situation is also valid for TC+HP process of PS (Fig.1 g).

4.2 Surface Functionalization of Glass Flakes

Figure 2 illustrates the XPS spectra of as received glass flakes and APS treated glass flakes for comparison. Peaks at 102 eV, 153eV, 284 eV-293 eV, 540 eV and 1071eV correspond to Si2p,Si2s, C1s, O1s, Na1s, respectively, where peaks at 978 eV, 999 eV and 496 eV correspond to OKL1,OKL2 and NaKL1 Auger peaks (Fig. 2 a). Peaks at 102 eV, 285 eV, 400 eV and 532 eV observed in Fig. 2 b correspond to Si2p, C1s, N1s and O1s, respectively. Presence of N1s peak in the case of the silane treated glass flakes proves the silane attachment to the surface by the applied procedure. The intensity difference in C1s and Si2p peaks points out to the difference in the chemical bonding and the interaction between organic and inorganic phases resulting from the applied surface functionalization.

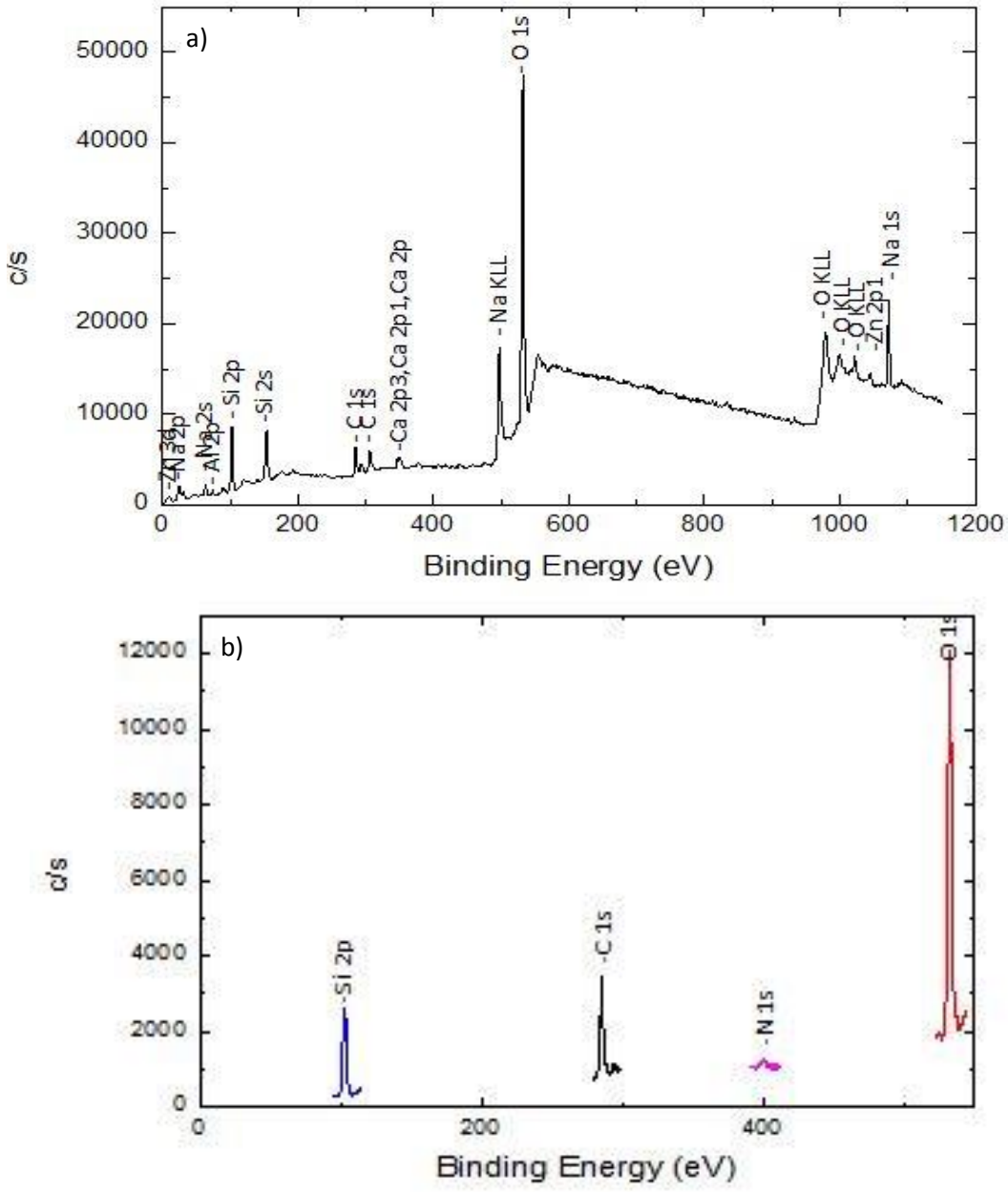

Figure 2. a) XPS spectra of a) as received and b) silane treated glass flakes.

4.3 Surface Functionalized Glass Flake Reinforced Thermoplastic Polymer Matrix Composites

Interaction at the interface of the inorganic and organic phases directly controls the mechanical behavior of the composites. Mother of pearl i.e. mollusc shell reveals efficient inorganic-organic surface interaction. Despite its relatively high inorganic content (95 vol %), toughness of mollusc shell is remarkably high due to superior compatibility between the surface of its inorganic constituent and the organic matrix.

In artificial composites to provide inorganic-organic constituent interaction, organofunctional coupling agent could be effective. It behaves like a chemical bridge attaching the organic phase to the inorganic surface. In the scope of this study the interaction of the thermoplastic polymer namely polystyrene and acrylonitrile butadiene styrene with glass flake has been studied. In case of monomer chemical structure and sequencing of monomer in polymerization reaction, polystyrene matrix composite

materials demonstrate better result than acrylonitrile butadiene styrene. However, for both of these thermoplastic polymers APS could be one of the useful coupling agents.

Among four different techniques SM+HASC process combination resulted in the highest improvement in the mechanical behavior of the composites compared to other combinations. Therefore, without changing the parameters, the same procedure applied on the as-received glass flake reinforced composites has been applied on the surface functionalized glass flakes. Table 2 presents the mechanical properties of surface functionalized glass flake reinforced nacre-like polystyrene and acrylonitrile butadiene styrene matrix composites.

Table 2. Mechanical properties of composites fabricated by SM+HASC using surface modified and as-received glass flakes.

Processing Method	Matrix	Flexural Strength (MPa)	Strain to Fracture%
SM + HASC (ST)	ABS	18.90 ± 4.74	1.80 ± 1.20
SM + HASC	ABS	14.87 ± 0.47	3.27 ± 0.67
SM + HASC (ST)	PS	26.22 ± 3.03	1.09 ± 0.24
SM + HASC	PS	19.59 ± 1.63	2.08 ± 0.40

Mechanical results show that silane treatment is a useful way to increase flexural strength while lowering the strain to fracture because of the enhanced interaction between inorganic and organic phases. Mechanical properties of polystyrene matrix composites are better than those of acrylonitrile butadiene styrene matrix composites, since PS reacts more effectively with the coupling agent compared to ABS.

Figure 3 shows the fracture surfaces of three point bending tested composites reinforced with silane treated flakes in two different thermoplastic polymer matrices. Figure 3 clearly illustrates the presence of chemical bonding between the flakes and the matrix for the SM+HASC processed composites reinforced with silane functionalized glass flakes. It is clear that for these composites main fracture mechanism is not flake-matrix debonding, yet rather it is through the propagation of cracking through the matrix.

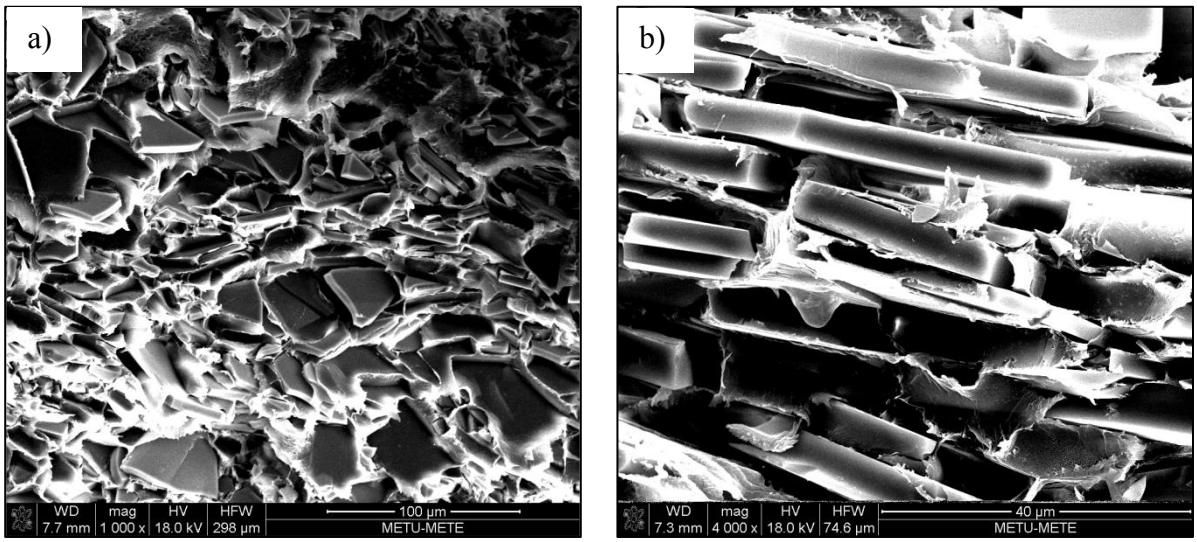

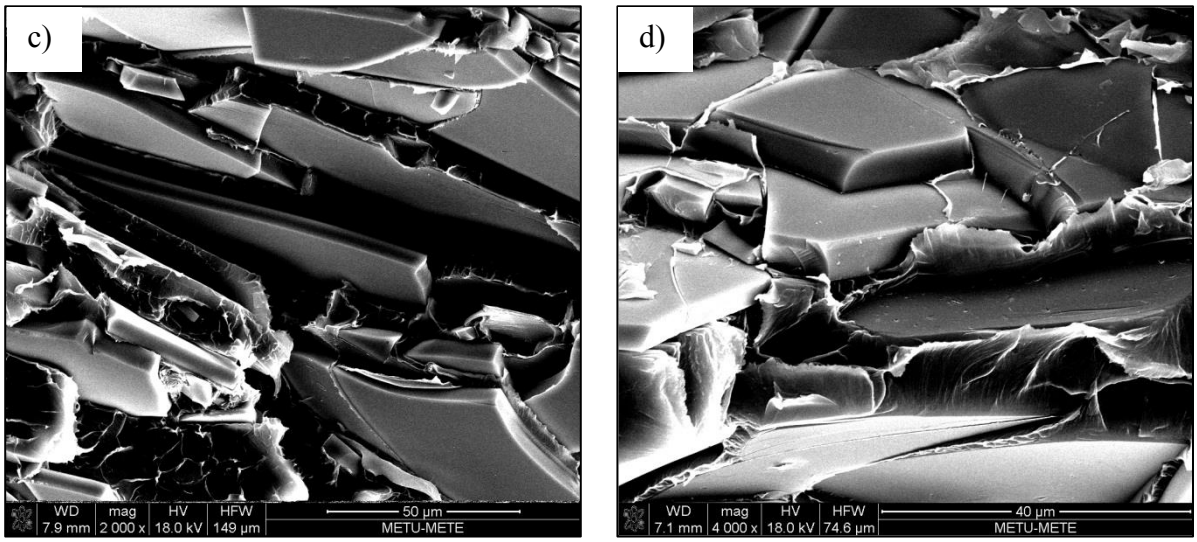

Figure 3. a, b) ABS matrix composite reinforced by silane treated glass flakes and c, d) PS matrix composite reinforced by silane treated glass flakes.

5. CONCLUSION

Hot-Press Assisted Slip Casting process is a newly proposed technique combining two easy and conventional material processing methods; hot-pressing and slip casting. This technique enables the fabrication of organic matrix bulk composites reinforced with preferentially oriented high aspect ratio fillers leading to a lamellar architecture resembling to "brick and mortar" structure. In this study, to improve its effect on alignment of glass flakes, HASC process was combined with other techniques namely tape casting and simple mixing. Mechanical results demonstrated that HASC process was really an efficient technique to achieve brick and mortar structure when combined by simple mixing method. Although there are various studies to fabricate nacre-like composites, one of the main points in this study was to fabricate nacre-like bulk lamellar thermoplastic matrix composites reinforced by glass flakes. Two types of different polymer solutions were used and investigated as organic component in composite structures which are acrylonitrile butadiene styrene and polystyrene. To investigate the effect of interfacial bonding between the matrix and the reinforcement on the resulting mechanical properties, surfaces of the flakes were functionalized with organofunctional silane, APS. The results indicated that together with reinforcement content enhanced by HASC process (~45-60%), nacre-like lamellar architecture of the HASC processed composites results in substantial increase in strength, modulus and stiffness. Functionalization of flake surfaces with amino-functional silane also improves the compatibility and interfacial bonding between the flakes and the matrix leading to further enhancement of the mechanical properties of bulk lamellar composites fabricated by SM+HASC.

REFERENCES

1.H. Wei, N. Ma, F. Shi, Z. Wang, X. Zhang, Chemistry of Materials., 2007, 19 (8), 1974-1978
2.A.P.Jackson, J.F.V.Vincent, R.M.Turner, Journal of Material Science 25 (1990) 3173-3178
3.O. O. Ekiz, A.F. Dericioglu, H. Kakisawa, Materials Science and Engineering C 29 (2009) 2050–2054
4.I.A. Aksay, M. Trau, S. Manne, I. Honma, N. Yao, L. Zhou, P. Fenter, P.M. Eisenberger, S.M. Gruner, Science 273 (1996) 892.
5. F. Bennadji-Gridi, A. Smith, J.-P. Bonnet, Materials Science & Engineering B: Solid- State Materials for Advanced Technology 130 (2006) 132.
6. R. Chen, C.-a.Wang, Y. Huang, H. Le, Materials Science and Engineering C 28 (2008) 218.
7. Z.-W. Du, J.-L. Hao, H.-R. Li, Acta Chimica Sinica 63 (2005) 587.
8. N. Gehrke, N. Nassif, N. Pinna, M. Antonietti, H.S. Gupta, H. Colfen, Chemistry of Materials 17 (2005) 6514.
9. J. Lahiri, G. Xu,T.Lee,D.M.Dabbs, N. Yao, I.A.Aksay, J.T. Groves,Proceedings of SPIE-The International Society for Optical Engineering, vol. 2716, 1996, p. 317.
10. Z. Tang, N.A. Kotov, S. Magonov, B. Ozturk, Nature Materials 2 (2003) 413.
11. C. Tamerler, S. Dincer, D. Heidel, M.H. Zareie, M. Sarikaya, Progress in Organic Coatings 47 (2003) 267.
12. G. Xu, I.A. Aksay, J.T. Groves, Journal of the American Chemical Society 123 (2001) 2196.
13. A. Sellinger, P.M.Weiss, A. Nguyen, Y. Lu, R.A. Assink,W. Gong, C.J. Brinker, Nature 394 (1998) 256.
14. H. Kakisawa, K. Minagawa, S. Takamori, Y. Osawa, Journal of the Ceramic Society of Japan 113 (2005) 808.
15.X.Li et al, Journal of Material Society (2007) 71-74
16.Z. R. Tian,J. A. Voight, J. Liu, B. Mckenzie, M. J. Mcdermott, M. A. Rodriguez, H. Konishi, H. ,Xu, Nature 2(2003) 821-826
17. Y.Lu, Y. Yang, A. Sellinger, M. Lu, J. Huang, H. Fan, R. Haddad, G. Lopez, A. R. Burns, D. Y. Sasaki, J. Shelnutt, C. J. Brinker,Nature 410(2001) 913-917
18.S.N.Gürbüz, A.F.Dericioglu ,Materials Science and Engineering C 33 (2013) 2011-2019
19. M. Xanthos, Modification of Polymer Properties with Functional Fillers, in: M. Xanthos (Ed.), Functional Fillers for Plastics, 2nd Edition, Willey-VCH Verlag GmbH & Co KGaA, Weinheim, 2010.

PROCESSING AND CHARACTERIZATION OF THE ELECTROMAGNETIC WAVE ABSORPTION POTENTIAL OF GLASS FIBER-REINFORCED THERMOPLASTIC POLYMER MATRIX COMPOSITES

Aylin GÜNEŞ, Özgür HAMAT, Tuğçe ALTUNTOP, Esma AVİL and Arcan F. DERİCİOĞLU

Middle East Technical University Department of Metallurgical & Materials Engineering
aylin.gunes@metu.edu.tr, ozgur.hamat@metu.edu.tr, tugce.altuntop@metu.edu.tr,
esma.avil@metu.edu.tr, arcan@metu.edu.tr

1. ABSTRACT

In the scope of this study processing and electromagnetic properties of glass woven fiber reinforced thermoplastic polymer matrix composites has been studied. Fabrication of metallic coating surface modified glass fiber reinforced thermoplastic polymer matrix composites was achieved by using polystyrene and acrylonitrile butadiene styrene as thermoplastic polymer matrices and quadriaxial glass fiber as reinforcement. Electromagnetic wave absorption and electromagnetic interference shielding (EMI) potential of the fabricated composites in 18-40 GHz frequency range was determined using free space method. Microstructural investigation of the composites has been conducted through scanning electron microscope examinations. Furthermore, by the application of three point bending tests, the effect of surface modification applied on the glass fibers on the mechanical properties of the glass fiber reinforced thermoplastic polymer matrix composites has been studied.

Keywords: *EMI shielding, Thermoplastic-matrix composites, Three point bending test, Electromagnetic characteristic*

1. ÖZET

Bu çalışma kapsamında cam fiber takviyeli termoplastik polimer matrisli kompozitlerin yapımı ve elektromanyetik ölçümlerinin belirlenmensi gerçekleştirilmiştir. Cam fiber yüzeylere metal kaplanarak fiber yüzeylerinde yapılan değişimin ardından termoplastik polimer matrisine gömülerek üretilen kompozitlerde termoplastik polimer matrisi olarak polistiren ve akrilonitril butadien stiren, takviye malzemesi olarak ise quadriaksial cam fiber kullanılmıştır. Free space yöntemiyle, yapılan kompozitlerin 18-40 (Ghz) frekans aralığında elektormanyetik geçirgenlikleri ve perdelemeleri belirlenmiştir. Mikroyapısal incelemeler taramalı elektron mikroskobu kullanılarak gerçekleştirilmiştir. Mekanik özelliklerin belirlenmesi ise cam fiber takviyeli termoplastik kompozitlere üç nokta eğme testi uygulanmasıyla sağlanmıştır.

Anahtar kelimeler: *Termoplastik kompozitler, Elektromanyetik kalkanlama, Üç nokta eğme testi*

2. INTRODUCTION

Composite material is a combination of two or more different materials which is formed to compensate the negative properties of the constituent phases while reinforcing the positive ones [1]. Production of composite materials has strict limitations. Depending on their application areas, the production method and their constituent materials can be arranged so that the desired structural properties or required mechanical properties can be obtained.

Polymer matrix composite materials are classified according to their fiber and matrix types [1, 6]. For the matrix, most commonly used polymers are thermosets. However, recently there is an increasing trend to use thermoplastics as the matrix materials due to the relatively high elasticity and toughness they provide along with their reusability. This reusability is driven from the chemical property of thermoplastics. They can be remelted and recycled. Moreover, since they can be remelted, they have a thermal shaping possibility which makes them favorable in commercial areas. Although they have no curing temperature, which can be considered as an advantage, thermoplastics generally have high processing temperatures which requires more energy during production [1, 3, 6].

Besides their recyclability, thermoplastic resins provide unique mechanical characteristics. Thermoplastic polymers have high viscosity which results in longer time requirement for polymer resin to interact with the glass fiber so processing time interval of their composites is longer than that of thermosets [1, 4]. To take precautions for this aspect, stiff and dry prepregs, which are polymer absorbed glass fibers woven fabrics, can be prepared beforehand and processing time interval can be shortened. In addition, thermoplastic matrix polymer composites are expected to reveal high toughness and environmental resistance due to structural and bonding morphologies.

The aim of this study is to understand the mechanical and electromagnetic behaviors of matrix glass fiber woven fabric reinforced thermoplastic polymer composites and to compare obtained data with the previous studies on the thermoset polymer matrix composites. In this scope, glass fiber woven fabric surfaces were modified by Ni coating with thickness below 50 nm before embedding them in the thermoplastic matrices. To understand the behaviors of thermoplastic composites in a broader range two different polymers , namely polystyrene (PS) and acrylonitrile butadiene styrene (ABS), have been used in this study. PS is a single monomer polymer that contains one repeating chain, while ABS is a terpolymer composed of three different monomers. Differences in the electromagnetic characteristics and mechanical behavior of the resulting composites based on this chemical structure difference has been demonstrated.

3. EXPERIMENTAL PROCEDURE

3.1. Materials Used

Polystyrene and acrylonitrile butadiene styrene were both supplied in granular form. Solutions of polystyrene and acrylonitrile butadiene styrene were achieved by dissolving them in chloroform and dimethylformamide, respectively. Polymer solutions for both type of the polymers were prepared using 10 g polymer granules and 80 ml solvent. Prepared solutions were mixed with a magnetic mixer, and they were kept mixing for 30 min.

3.2. Composite Fabrication

To observe the interaction between polymer solution and glass fiber woven fabrics and to determine the optimum polymer amount to be used, three layered glass fiber woven fabrics of dimensions 7 x 7 cm were treated with PS. Glass fiber woven fabrics were dipped into the polymer solution and kept in open atmosphere for a day to reduce the solvent in them. When they were fully dry, they were put on top of each other with a 90° differing orientation and compacted in a conventional hydraulic hot press applying heat and pressure. Maximum temperature to be reached was set to 200 °C for polystyrene and 170 °C for ABS. After the application of a constant pressure initially, the temperature was increased to the desired level where it was kept for 10 min. After cooling down the composites to room temperature, obtained composites were cut with a micro cutter at 6.6 mm/min feeding speed and 3000 rpm.

Polymer amount per unit glass fiber woven fabric area has been calculated empirically by experiments, and the optimum amount of PS solution was found to be 0.18 ml/cm^2. Using the same procedure the optimum amount of ABS solution to be applied on the glass fiber woven fabrics has been found to be 0.11 ml/cm^2. To achieve a uniform polymer solution distribution on the glass fiber woven fabric surfaces, injection technique has been used in this study.

3.2. Mechanical Charcterization

Mechanical behavior of composites has been studied in two main parts. First part involves the investigation of the effect of the polymer type on the mechanical properties of the resulting composites. In the second part the effect of metallic surface coating applied on the glass fiber woven fabrics on the mechanical properties of the resulting composites has been studied. In the first part, two specimens were prepared. They both contained five layers of glass fiber woven fabrics of dimensions 7.5 x 7.5 cm where in both cases optimum polymer resin per unit area has been used. 6 ml of ABS solution was applied on each woven fabric while it was 10 ml in the case of the PS solution. Since the main object of this part was to observe the difference in the mechanical property due to varying types of polymer, other parameters were kept constant in both specimens.

PS resin composite was prepared in the same way with the three layered PS composite. Woven fabrics were placed on top of each other with 90° orientation difference and hot pressed at 200 °C. ABS resin composite was also prepared with the same procedure with the only difference being the hot pressing temperature which was 170 °C. Three point bending test was applied to characterize the mechanical properties of glass fiber woven fabric reinforced thermoplastic polymer matrix composites. Sizes of specimens used in the test were arranged according to ASTM D-790.

3.3 Characterization of the Electromagnetic Properties

In order to investigate the electromagnetic behavior of the thermoplastic polymer matrix composite materials, two composite specimens were prepared using the aforementioned fabrication procedure. PS matrix composite reinforced by as-received glass fiber woven fabrics was fabricated as the control sample, while the other one contained Ni coated glass fiber woven fabrics. Glass fiber woven fabric surfaces were coated by Ni using thermal evaporation method, where three different Ni coating thicknesses namely 15, 20 and 25 nm were applied in this study based on the result of our previous study on thermosetting polymer matrix composites [2]. Electromagnetic wave absorption and EMI shielding characteristics of

the two composites were investigated using free–space method in 18-40 GHZ frequency range. Free–space method is a technique used to characterize complex electromagnetic properties and EM wave reflection–transmission behavior of a medium with certain thickness. Main advantage of free–space method is its applicability to inhomogeneous and/or anisotropic media [2, 5].

4. RESULTS AND DISCUSSION

4.1. Microstructural Characteristics of the Fabricated Composites

Fabricated PS and ABS matrix glass fiber woven fabric reinforced composites are shown in Fig. 1. While determining the optimum amount of polymer resin per unit area of glass fiber woven fabric, it was observed that polymer and glass fiber did not interact with each other adequately so to understand the reason behind this, microstructural investigation using scanning electron microscope (SEM) was conducted. Using SEM, microstructure of glass fiber composite and the lack of interaction between the resin and the fiber could be observed. The main reason behind this inadequate interaction and bonding was attributed to the usage of insufficient amount of polymer resin (Fig. 2). In this context, if the amount of polymer is not enough, some porosity seemed to remain in the composite that causes the composite specimen to get weak even for cutting. Consequently, usage of sufficient amount of polymer resin has been determined to have a significant importance in polymer matrix glass fiber composite production.

By checking the microstructure of composite using SEM, optimum amount of polymer solution was determined. This amount was found as 0.18 ml/cm^2 for PS and 0.11 ml/cm^2 for ABS. The reason of the difference between these amounts is that ABS is a denser polymer forming a solution with higher viscosity. Therefore, it attaches to the fiber surface more tightly, and even though it has a higher viscosity, uniform ABS distribution can be obtained with the use of the injection technique.

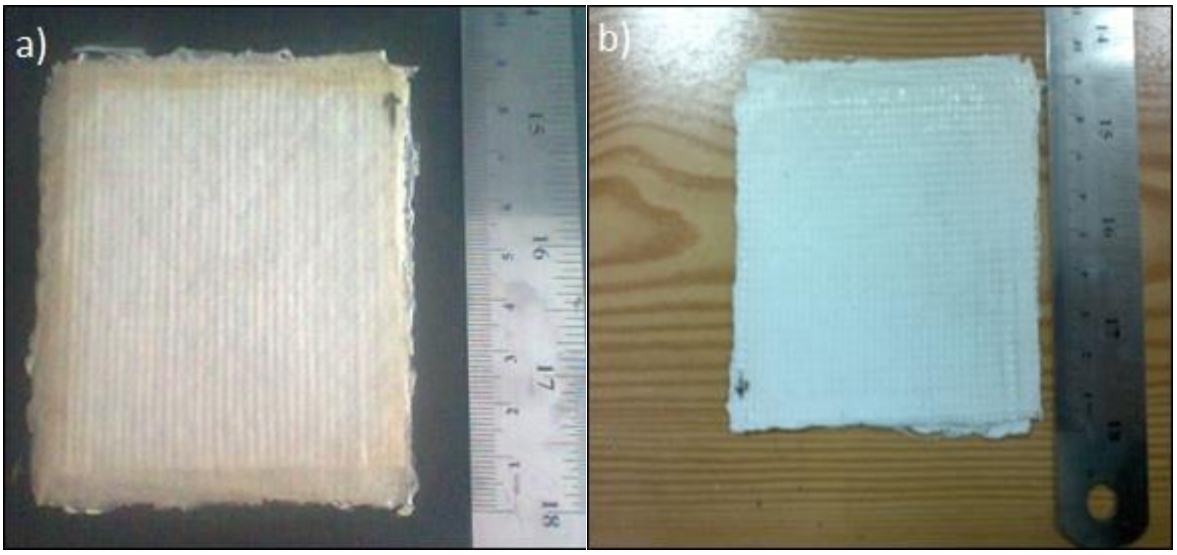

Figure 1. a) Glass fiber composite with PS matrix, b) Glass fiber composite with ABS matrix.

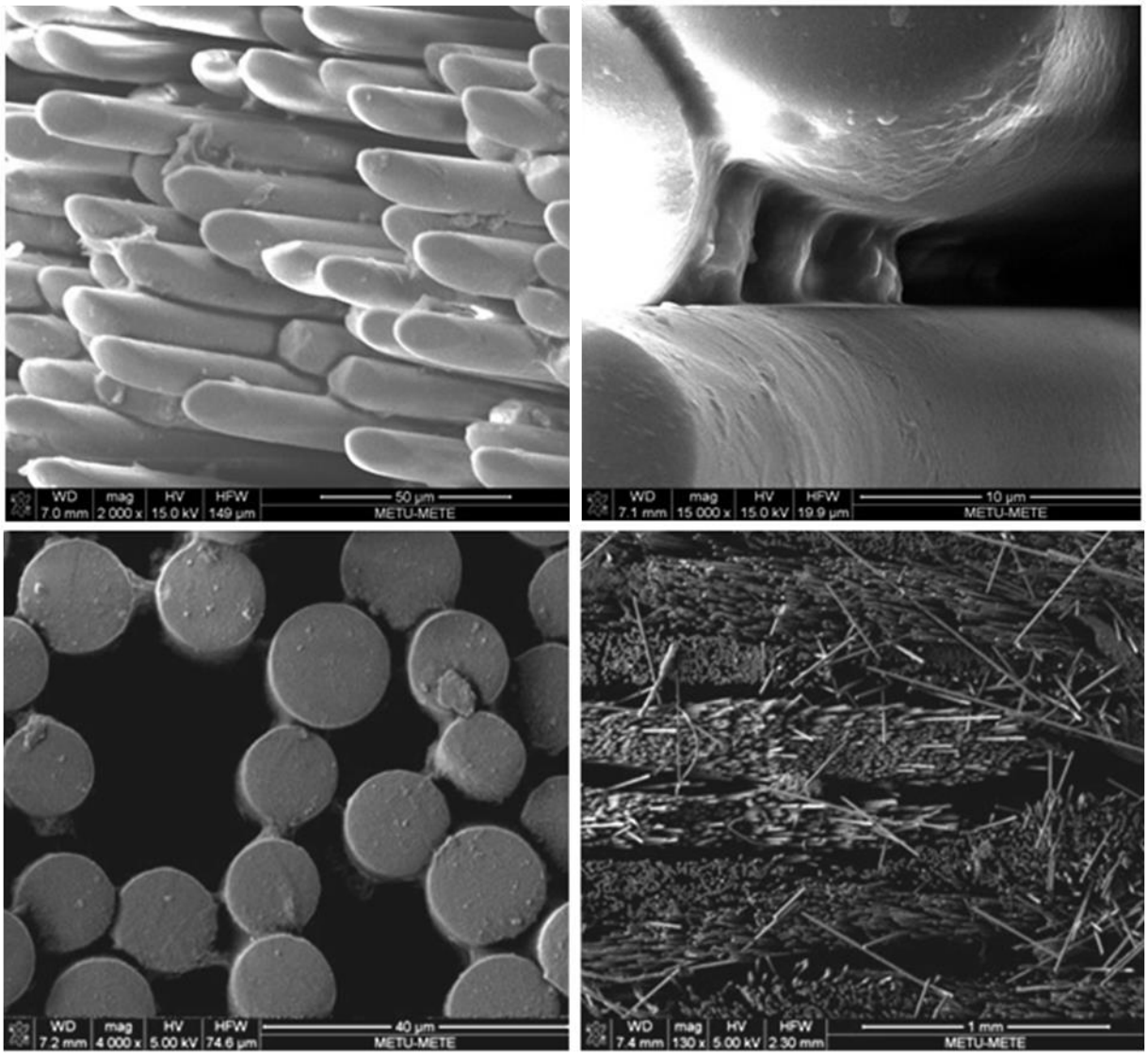

Figure 2. SEM images showing the insufficient amount of PS matrix in the fabricated composites.

4.2. Mechanical Characteristics of the Fabricated Composites

Flexural stress vs. flexural strain data of glass fiber woven fabric reinforced PS and ABS matrix composites obtained by three point bending tests are shown in Fig. 3. It is obvious that flexural strength is strongly dependent on the type of polymer matrix used in the composite. ABS matrix composite has lower flexural strength than PS matrix composite. Mechanical behavior of ABS matrix mainly depends on the its chemical properties. ABS is a terpolymer composed of three different monomers. According to the chemical structure of ABS, it is an amorphous polymer, and its interaction with glass fiber surfaces is expected to be lower than that of the polystyrene, as some chemical groups in ABS could have steric effect creating deficiency in interacting with inorganic surfaces. However, PS used in this study is crystalline. This leads to a stronger interaction with the glass fiber surface, and accordingly it reveals superior mechanical behavior as a thermoplastic polymer matrix compared to ABS.

Three point bending test results revealed that PS matrix composite has higher flexural strength than ABS matrix one with higher flexural strain to failure as well. Simultaneously higher strength and toughness in the case of PS matrix composite can be attributed to the optimum fiber-matrix interfacial bonding leading to more effective stress transfer from the matrix to the fibers which also allows stress redistribution at the tip of an advancing crack. Consequently, two different polymer matrices reveal distinct mechanical characteristics based on their chemical and structural differences. Results demonstrated that polystyrene is a more effective thermoplastic polymer matrix to fabricate glass fiber woven fabric reinforced thermoplastic polymer matrix composites.

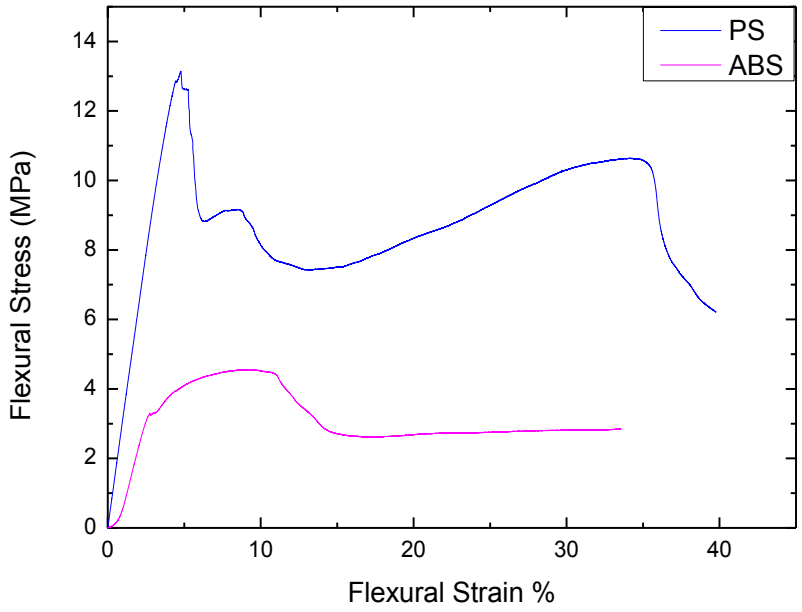

Figure 3. Three point bending test data of thermoplastic polymer matrix composites.

4.3. Electromagnetic Characteristics of the Fabricated Composites

Electromagnetic (EM) wave absorption potential of surface-modified glass fiber woven fabrics to be used as reinforcement materials in thermoplastic polymer matrix composites was investigated in this part of the study. Electromagnetic properties of as-received glass fiber woven fabrics were improved by surface modification with nickel coatings in nanometer thickness levels. Using these surface-modified reinforcement materials and polystyrene as the matrix, composite structure that has a high EM wave absorption potential was obtained. Electromagnetic reflection and transmission behavior of these surface modified multilayered woven fabric structures, which are ordered with respect to increasing intrinsic impedance of single layered ones, were measured with free-space method in the frequency range of 18-40 GHz. These EM characteristics of the modified glass woven fabric reinforcements and composite structure were correlated with the applied coating thickness and the number of layers used in multilayered structure as it can be seen in Fig. 4-6. Multilayered woven fabric structure containing 5 layers and the composite reinforced by this structure reached to 85%

and 90% EM wave absorption, respectively, with their reflection and transmission losses being below -5 dB throughout the whole frequency range measured.

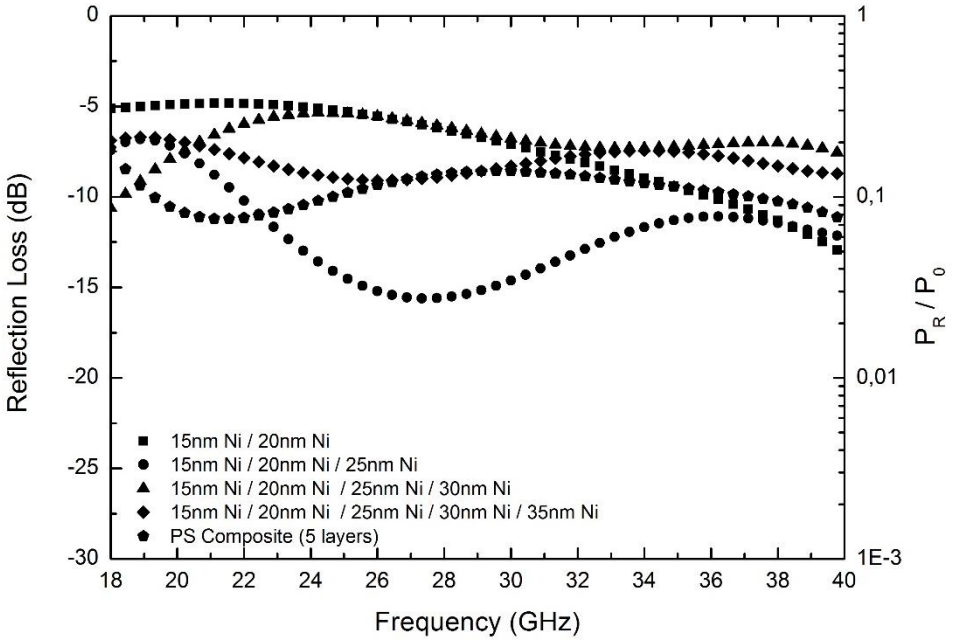

Figure 4. Reflection loss vs frequency graph for Ni surface-modified glass fiber woven fabrics and PS matrix composite reinforced by 5 layers of these surface-modified glass fiber woven fabrics.

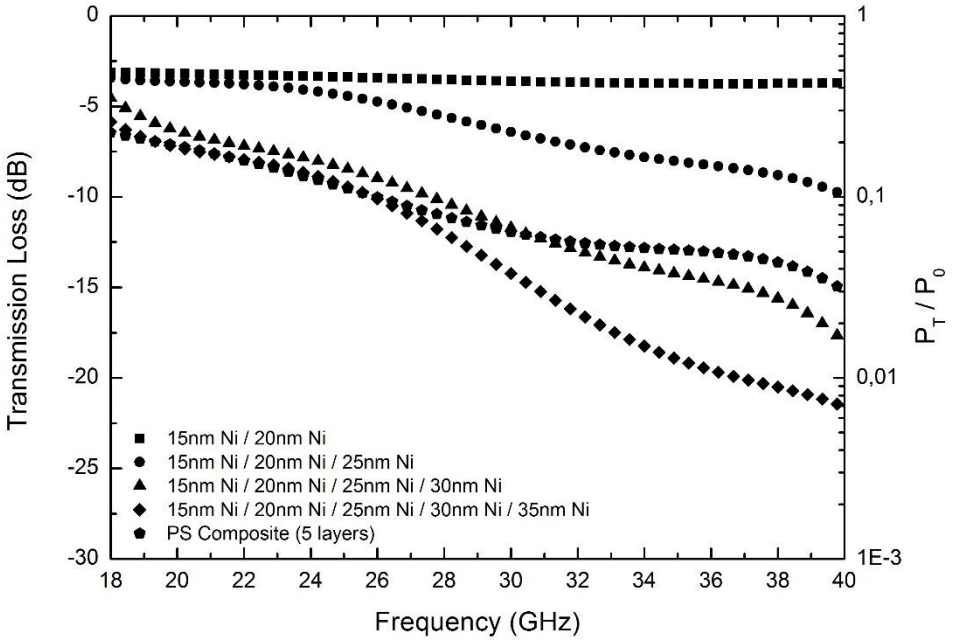

Figure 5. Transmission loss vs frequency graph for Ni surface-modified glass fiber woven fabrics and PS matrix composite reinforced by 5 layers of these surface-modified glass fiber woven fabrics.

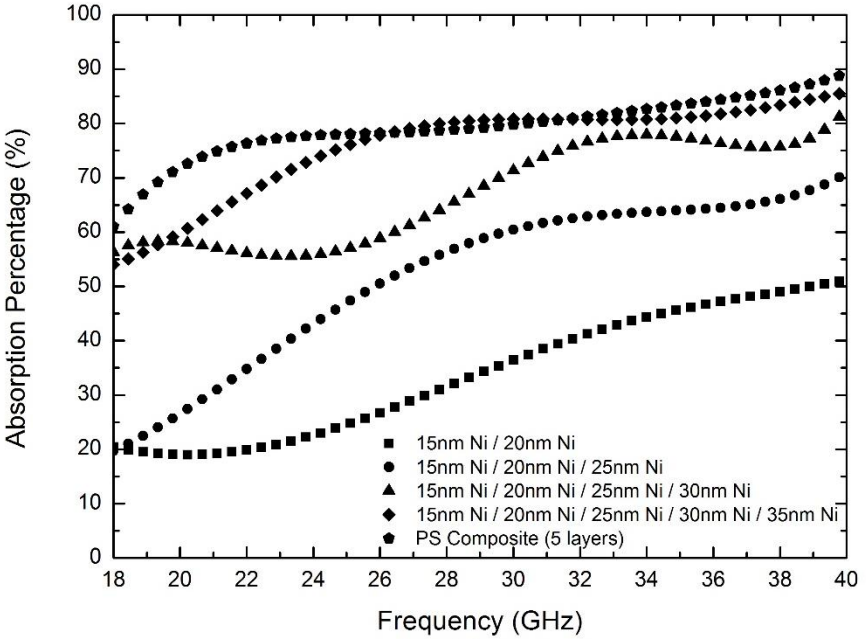

Figure 6. Absorption percentage vs frequency graph for Ni surface-modified glass fiber woven fabrics and PS matrix composite reinforced by 5 layers of these surface-modified glass fiber woven fabrics.

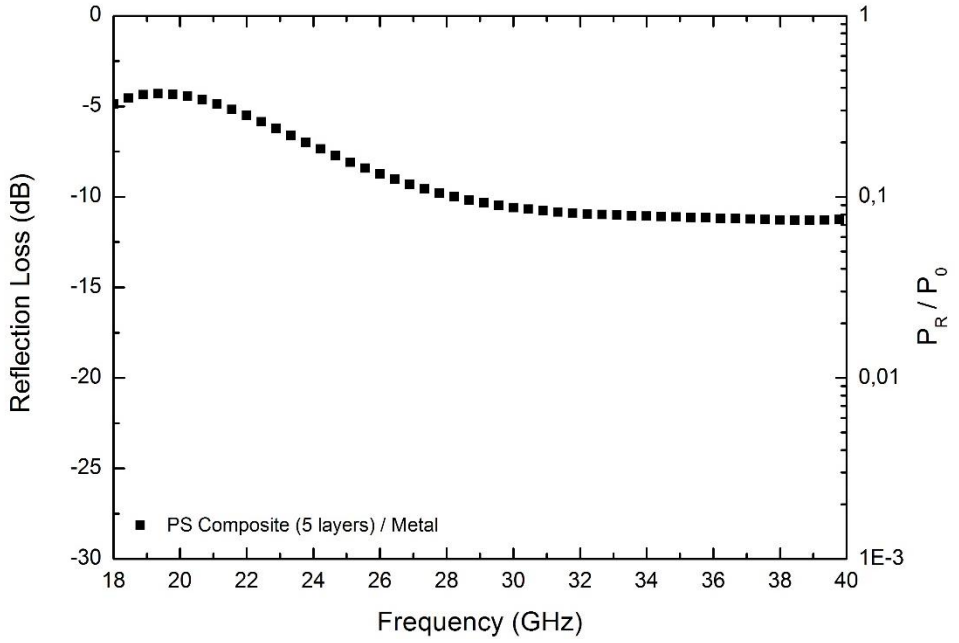

Figure 7. Reflection loss vs frequency graph for PS matrix composite reinforced by 5 layers of Ni surface-modified glass fiber woven fabrics backed by a completely reflective metallic plate.

Reflection behavior of the PS matrix composite that resulted in 90% EM wave absorption was also observed with a completely reflective metallic backing plate in order to investigate its EMI shielding potential. For this purpose, the composite material was placed in the free-space measurement setup with a fully reflective metal plate backing it. Obtained EM wave

reflection loss results can be seen in Fig. 7. According to this result, PS matrix composite material reinforced by 5 layers of Ni surface-modified glass fiber woven fabrics reflects only 7-10% of the incident EM waves.

EM wave absorption potential of 5 layers of as-received glass fiber woven fabrics, PS and ABS matrix composites containing 5 layers of as-received glass fiber woven fabrics along with PS matrix composite containing 5 layers of Ni surface-modified glass fiber woven fabrics can be seen in Fig. 8. Without surface modification 5 layered glass fiber woven fabrics and PS and ABS matrix composites containing this as-received reinforcement structure showed only under 10% EM wave absorption. However, PS matrix composite reinforced by 5 layers of Ni surface modified glass fiber woven fabrics resulted in EM wave absorption changing between 60 and 90% in the same frequency.

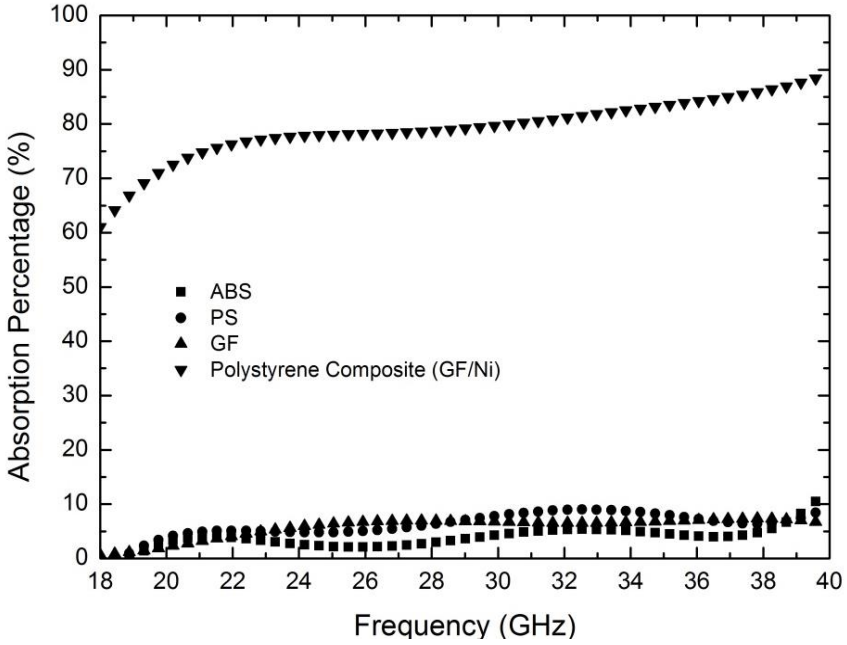

Figure 8. Absorption percentage vs frequency graphs for 5 layers of as-received glass fiber woven fabrics, PS and ABS matrix composites containing 5 layers of as-received glass fiber woven fabrics along with PS matrix composite containing 5 layers of Ni surface-modified glass fiber woven fabrics.

5. CONCLUSION

This report includes microstructural, mechanical and electromagnetic behaviors glass fiber woven fabric reinforced PS and ABS thermoplastic polymer matrix composites. In terms of the processing of thermoplastic polymer matrix composites it was observed that there exists an optimum amount of polymer resin required per unit area of glass fiber woven fabrics to obtain an optimum interaction between the polymer and the fiber. Moreover, it was observed that the mechanical properties of the composites strongly depend on the type, and hence, chemical and structural characteristics of the polymer used as the matrix material. In addition, it was observed that the electromagnetic characteristics of thermoplastic polymer matrix composites can be tuned by reinforcing them with glass fiber woven fabrics having their surfaces modified my metallic coatings. Consequently, it can stated that the absorption capability of the polymer composite depends on the surface condition of the fiber woven

fabrics along with their number and order in the composite structure. Effect of surface modification on EM reflection, transmission and absorption characteristics could easily be seen on both reinforcement materials and composite structures. 90% EM wave absorption at high frequencies has been achieved in PS matrix composites reinforced by surface modified glass fiber woven fabrics. Mechanical and electromagnetic properties of this composite material showed that there is a huge potential of using surface-modified glass fiber woven fabric reinforced thermoplastic matrix composites as structural materials also providing an extra function namely EM wave absorption and EMI shielding.

REFERENCES

1. Chung, D.D.L.,Composite Materials Science and Applications, Springer-Verlag London (Second Edition), 2010.
2. Ö.Hamat, A.Güneş, A.F. Dericioğlu, Electromagnetic shielding effect of surface gold-modified single and multilayered glass and aramid fiber woven fabrics on microwave frequency, Metallurgical and Materials Engineering Department, METU, 2013.
3. A.T. DiBenedetto, Tailoring of Interfaces in Glass Fiber Reinforced Polymer Composites: a Review. Department of Chemical Engineering and Institute of Materials Science, University of Connecticut, USA, 2001.
4. J.L. Thomason, The Interface Region in Glass Fibre-Reinforced Epoxy Resin Composites:1.Sample Preparation, Void content and Interfacial Strength. Shell Research B.V.(Koninklijke/Shell Laboratorium, Amsterdam), 1995.
5. Gurer, G., Çivi, Ö.A., Dericioğlu, F.A. (2010). Characterization of Surface-Modified Fiber Glass Woven Fabrics for Electromagnetic Wave Absorption in K-Band. Middle East Technical University Department of Metallurgical and Materials Engineering, METU, 2010.
6. F.T. Wallenberger, P.A. Bingham, Fiberglass and Glass Technology, Energy-Friendly Compositions and Applications. Springer New York Dordrecht Heidelberg London, 2010.
7. Department of Defence Handbook. Composite Materials Handbook, Volume 2. Polymer Matrix Composites Materials Properties, 2002.

ANALYSIS OF THE STRUCTURAL DEFECTS IN GLASS FIBER FABRIC/EPOXY RESIN LAMINATE

Abdelghani Naceri*
* Department of Civil Engineering, Faculty of Technology, University of M'sila, Algeria
abdelghani_naceri@yahoo.fr

ABSTERACT
We present the experimental methods proposed for the identification of structural defects of the laminate constituted of 12 layers of glass fiber fabric/epoxy resin. Two techniques of control were used to analyze the principal structural defects(local or global disorientation). The first technique provides a superficial observation (macroscopic analysis) of the superior and lower surfaces of each layer, while the second one ensures internal observation (microscopic analysis) of the different layers after pyrolysis of the matrix (delamination of the laminate).

Keywords: Structural defects, laminate, glass fiber, composite material.

1. INTRODUCTION

The greatest advantage of composite materials is strength and stiffness combined with lightness. Generally, a composite material is composed of reinforcement (fibers, particles and/or fillers) embedded in a matrix (polymers, metals or ceramics). The matrix holds the reinforcement to form the desired shape while the reinforcement improves the overall mechanical properties of the matrix [1]. According to the form of reinforcement, composite materials can be classified as follows: a) fibers as reinforcement (fibrous composites): random fiber- (short fiber-) reinforced composites and continuous fiber- (long fiber-) reinforced composites, b) particles as reinforcement (particulate composites) and c) fillers as reinforcement (filler composites).
The microstructural analysis describes the composition and structure (including defects) of the material that are significant for study of its properties. The analysis of manufacturing defects of a composite is necessary for the control of the material quality. Among widely used methods are: optical microscope (OM), transmission electron microscope (TEM) or scanning electron microscope (SEM). The nondestructive testing methods used to verify voids, delaminations and density are acoustic emission, radiography and ultrason. The investigations of the microstructure of fiber-reinforced polymer composite laminates can be visualized by means of optical or acoustic techniques [2,3].
The structural strength of laminate is dependent on filament strength, matrix or resin strength and fiber orientation. The mechanical strength of a composite is based on the interaction of fiber and matrix in a process that depends upon ply or layer thicknesses and percent of fiber volume. In the manufacturing process, filaments should be tested for tensile strength, elastic modulus, density, diameter and stiffness [4]. Matrix rheology must be characterized through chemical and physical testing. The preimpregnated material should be tested as to its satisfaction of chemical and thermal requirements. The laminate composites should be tested for mechanical strengths (compression, flexion and shear).
The two principal parameters which guarantee the quality of the system of weaving are [5]:
- surface density (size of yarns and type of armour),
- and counts (number of chain yarns and fill yarns).

This study, presents the identification approach used for analysis of manufacture defects of laminate (glass fabric fiber/resin epoxy). The results obtained show the good detection of defects of composite studied. The structural properties of laminate depend strongly of fabrication process and the material microstructure.

2. EXPERIMENTAL DETAILS

2.1. Material used

The material used was a laminate constituted of 12 layers of glass fiber fabric at taffeta weave (the warp yarn and weft weaving alternatively) drowned in an epoxy resin. It is delivered in the form of plane plates (five plates) of average size: 350 (weft direction) x 340 (warp direction) x 3.2 mm^3 (thickness). The fiber volume fraction of the woven fabric composite (glass fiber fabric/epoxy resin) was approximately 55% and the density was about 1.94 g/cm^3. The volume fraction of fibers was given according to the method of calcination and found equal to V_f = 30 %. The five studied plates carried numbers 1, 2, 3, 4 and 5 and have 12 layers each.

2.2. Analysis of structural defects

Initially, the visual observation of external surfaces was used to make a sketch of the orientation of the rovings of the chain (warp) and weft of the two external layers of the sheet (plate) on a tracing (Fig. 1).
The control method of the orientation defects of rovings used consisted in measuring the four representative angles of the defects observed in ten points distributed in each plate, then the average of the values obtained was assessed, whereas the following angles were measured:
- α_{warp}: angle measured between the warps of the layers (superior/lower),
- α_{weft}: angle measured between the wefts of the layers (superior/lower),
- α_{1warp}/weft: angle measured between the rovings of the warp (chain) and the weft for the superior layer (1),
- $\alpha_{12warp/weft}$: angle measured between the rovings of the warp and the weft for the lower layer (12).

3. RESULTS AND DISCUSSION

From the results of the visual observations (Table 1) one can see that the variation of the angles α_{warp}, α_{weft}, $\alpha_{1warp/weft}$, and $\alpha_{12warp/weft}$ of the layers (superior/lower) is very low for the most plates (Nos.1 to 4), except for plate 5 for which the variation is very significant. In particular, the angles α_{warp} (angle measured between the warps of the layers: superior/lower) and α_{weft} (angle measured between the wefts of the layers: superior/lower) are definitely larger for plate 5 than for the other plates.
The variation of the weaving in the weft direction is, in general, much more significant than that observed in the warp direction. This variation is more reduced for plate 4.
The second phase of the study implied the analysis and identification with precision and a certain degree of confidence of the local orientation defects in the structure of the layers of each plate. This requires the pyrolysis of the matrix (epoxy resin). Two samples of 20 mm were studied in each plate in the left (small white square) and right (small black square) sides.

The study of visual observation of the various layers after pyrolysis of the matrix required the following steps:
- to carbonize the resin, in order to preserve only the separated layers of the laminate (taffeta of glass),
- to photograph each layer on slide,
- to project these slides, in order to obtain a schematic of the orientation of rovings of the warp and weft of each layer,
- to superimpose the schematics obtained for the same sample of the layers in order to analyze the local orientation defects possibly observed.
For each layer one defines the following angles:
- α'_{warp}: maximum angle between the rovings of the warp relative to a reference,
- α'_{weft}: maximum angle between the rovings of the weft relative to a reference,
- $\alpha'_{warp/weft}$: angle between the rovings of the warp and the weft of the layer.
Table 2 shows for each plate the maximum values (α'_{warp}, α'_{weft} and $\alpha'_{warp/weft}$) of the three defined angles, those clearly confirm notable confusions of plate 5 and a good quality of plates 1 and 2.

4. CONCLUSION

The above visual observation method (macroscopic and microscopic analysis) has permitted us to identify and classify the studied plates, starting from the results obtained, in three categories which are:
- plates 1 and 2 are *a priori* acceptable to realize tests (light variation of the undulation defects with a dispersion about 2°),
- plates 3 and 4 are of average quality but can be used,
- plate 5 is of poor quality.

REFERENCES

1. H.A.K. Hamed and K.S.H. Sadek, Mechanical properties of woven fabrics, Inst, Mech Engrs, 2004.
2. W. Bai and B.S. Wong, Evaluation of defects in composite plates under convective environments using lock-in thermography, Meas. Sci. Technol., 12, 142-150, 2001.
3. M. Abu-Khousa, W. Saleh, and N. Qaddoumi, Defect imaging and characterization in composite structures using near-field microwave nondestructive testing techniques, Composites Structures., 62, No. 3-4, 255-259, 2003.
4. G. Giorleo and C. Meola, Location and geometry of defects in composite laminates from infrared images, Journal of Materials Engineering and Performance., 7, No. 3, 367-374, 1998.
5. R. Leurt, Tissus pour de nouveaux champs d'application, Revue Technique, 1997.

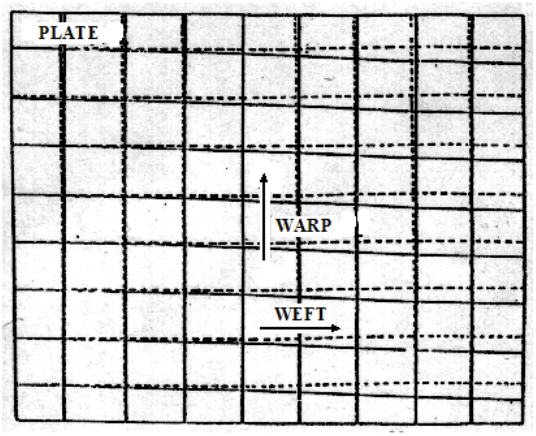

Figure 1. Orientation defects of layers of the plate.
———— warp and weft directions of the superior layer,
---------- warp and weft directions of the lower layer.

Table 1. Results of the representative angles of the defects observed

Plates	α_{warp}	α_{weft}	$\alpha_{1warp/weft}$	$\alpha_{12warp/weft}$
1	0.6°	1.5°	91.5°	89.0°
2	0.0°	1.5°	90.5°	89.5°
3	0.0°	1.6°	90.5°	89.5°
4	0.0°	1.0°	91.5°	88.5°
5	1.0°	4.0°	93.5°	88.5°

Table 2. Results of the principal orientation defects of the plates

Samples	α'_{warp}	α'_{weft}	$\alpha'_{warp/weft}$
1 Left side	0.0°	0.0°	90°
1 Right side	2.0°	2.0°	88° to 90°
2 Left side	0.0°	2.0°	88° to 90°
2 Right side	0.0°	0.0°	88,5° to 90°
3 Left side	0.0°	0.0°	90° to 91°
3 Right side	3.5°	4.0°	86° to 91°
4 Left side	0.0°	2.0°	88° to 90°
4 Right side	0.0°	2.0°	88° to 90°
5 Left side	2.0°	1.5°	87° to 89°
5 Right side	4.0°	1.5°	84° to 86°

SYNTHESIS AND SINTERING OF TiB_2

Ahmet TURAN*,, Mehmet BUĞDAYCI*,***, Filiz ÇINAR ŞAHİN*, Gültekin GÖLLER*, Onuralp YÜCEL***

* Metallurgical and Materials Engineering Department, Faculty of Chemical and Metallurgical Engineering, Istanbul Technical University, 34469, Maslak, Istanbul, Turkey
** Yalova Community College, Yalova University, 77100, Yalova, Turkey
*** Chemical and Process Engineering Department, Faculty of Engineering, Yalova University, 77100, Yalova, Turkey
aturan@yalova.edu.tr, mehmetbug@gmail.com, sahin@itu.edu.tr, goller@itu.edu.tr, yucel@itu.edu.tr

ABSTRACT
TiB_2 is a significant boride based ceramic material with remarkable properties such as high melting point, wear resistance and chemical durability. Its main application areas are impact armors, coating materials and aluminum evaporation boats according to its unique properties. In the present study, the optimum parameters were tried to determine on the Self-propagating High Temperature Synthesis (SHS), Spark Plasma Sintering (SPS) and Pressureless Sintering of TiB_2. In the first set of the experiments, SHS parameters of TiB_2 were studied. Investigated parameters were reaction atmosphere, reductant stoichiometry and functional additives. In the second set, synthesized by SHS and commercial grade (carbothermically synthesized) TiB_2 powders were sintered by using pressureless sintering method. After characterization stage (SEM, density measurement, microhardness, etc.), the results were compared with each other. Furthermore, pressureless sintering results were compared with the SPS results of compacts which were sintered from carbothermically synthesized TiB_2 powders.

Keywords: *Pressureless Sintering, Self-propagating High-temperature Synthesis, Spark Plasma Sintering, TiB_2*

TiB_2'NİN SENTEZİ VE SİNTERLENMESİ

ÖZET
TiB_2, yüksek ergime sıcaklığı, aşınma direnci ve çeşitli kimyasallara dayanım gibi dikkate değer özelliklere sahip önemli bir borür esaslı seramiktir. Eşsiz özelliklerine uygun olarak zırh plakaları, kaplama malzemeleri ve alüminyum buharlaştırma kayıkçıkları başlıca kullanım alanlarıdır. Bu çalışmada, TiB_2'nin Kendiliğinden-ilerleyen Yüksek-sıcaklık Sentezi (SHS), Spark Plazma Sinterleme (SPS) ve basınçsız sinterleme şartları belirlenmeye çalışılmıştır. İlk deney setinde, TiB_2'nin SHS şartları araştırılmıştır. Araştırılan parametreler, reaksiyon atmosferi, redüktan stokiyometrisi ve fonksiyonel ilavelerin etkileridir. İkinci deney setinde, SHS ile sentezlenen ve karbotermik olarak sentezlenen (ticari kalite) TiB_2 tozlarının basınçsız sinterleme koşulları irdelenmiştir. Basınçsız sinterlenmiş TiB_2 tozlarının karakterizasyonlarından (SEM, yoğunluk, mikrosertlik v.b.) sonra, elde edilen sonuçlar birbirleri ile ve ticari kalite TiB_2 tozlarının SPS ile sinterlenmesinden elde edilen numunelerin karakterizasyon sonuçları ile karşılaştırılmıştır.

Anahtar kelimeler: *Basınçsız Sinterleme, Kendiliğinden-ilerleyen Yüksek-sıcaklık Sentezi, Spark Plazma Sinterleme, TiB_2*

1. INTRODUCTION

TiB_2 (titanium diboride) is characterized with its unique properties such as high hardness, strength, melting point, wear resistance, thermal and electrical conductivity and it also has high durability against chemical substances and molten metals. It is a transition metal boride and it has hexagonal crystal structure with space group of P6/mmm. The melting point of TiB_2 is about 3225 °C. Its covalently bonded atomic structure provides the hardness values as high as 45 GPa [1-5]. Impact resistant armors, cutting tools, aluminum evaporation crucibles, wear resistant coatings and aluminum electrolysis cathodes are between the main applications areas of TiB_2 [1, 2].

Synthesis of TiB_2 is conducted via several methods in laboratory or in industrial scale. Carbothermic synthesis of TiB_2 from the oxides of titanium and boron by a reducing agent such as carbon or B_4C at high temperatures, metallothermic reduction of oxides of titanium and boron by a reducing agent such as magnesium or aluminum, mechanical alloying of titanium and boron oxides by using metallothermic route or mechanical alloying of elemental forms of titanium and boron, sol-gel method and aluminum melt reaction process of titanium and boron oxides following leaching of aluminum matrix to recover synthesized TiB_2 powders are among the most important techniques to synthesize TiB_2 [6-15].

Self-propagating high temperature synthesis (SHS) is one of the important methods to synthesize advanced materials such as ceramics (e.g. TiB_2, B_4C, Si_3N_4); abrasives, cutting tools and polishing powders (e.g. TiC, cemented carbides); resistive heating elements (e.g. $MoSi_2$), shape-memory alloys (e.g. TiNi); high-temperature structural alloys (e.g. nickel aluminides); master alloys (e.g. AlTiB); neutron attenuators (e.g. refractory metal hydrides) as well as conventional metals and their alloys. Although the discovery of metallothermic reactions (Beketov 1865; Goldschmidt 1895) is earlier, combining with flame propagation theories and the first gasless metallothermic combustion experiments were conducted by Merzhanov et al. in the middle of 1960s. SHS reactions are highly exothermic. Thus, the propagation of reactions and the yield of reaction products continue in self-sustaining mode without requiring additional heat or energy [16-19].

SPS is one of the newest approaches for the sintering of ceramics and metallic powders. It provides an internal heating by the formation of spark plasma, which is generated from direct current electricity discharge, between powders. Shorter sintering times at relatively lower temperatures are the most important features of the process. An SPS system is roughly the combination of graphite die system, electrodes, pressure mechanism, chamber to work under vacuum or gas atmosphere, pyrometers, water cooling unit, DC generator and a control unit [20, 21].

2. EXPERIMENTAL STUDIES

In the SHS stage, TiO_2 and B_2O_3 powders were mixed with 90%, 100% and 110% of stoichiometrically required amount of Mg powders. SHS experiments were conducted under both air and argon atmospheres to determine the optimum process atmosphere. The effects of some functional additives (NaCl and $MgSO_4 \cdot 7H_2O$) were also carried out with the various addition ratios. SHS products were leached in HCl media to purify their TiB_2 contents.

In the first set of SPS stage, TiB_2 powders were sintered at various temperatures between 1600 – 1800 °C under vacuum atmosphere and under 50 MPa pressure which was applied before the beginning of heating stage. In the second SPS experimental set, 50 MPa sintering pressure was applied after the die reached to 1500 °C and maximum sintering temperature was achieved to be 1780 °C. It was proposed that removing the glassy boron film (formed around the grains) by sparks

was possible up to 1500 °C without applying pressure. Furthermore, because of 20 °C lower sintering temperature is that at 1800 °C sintering temperature melting started to occur under these experimental conditions as it was already experienced. In the third SPS experimental set, powders were sintered between 1600 °C and 1780 °C under vacuum atmosphere and under an initial sintering pressure of 70 MPa.

3. RESULTS AND DISCUSSION

The optimum SHS parameters were determined as stoichiometrically 100% Mg addition and Ar process atmosphere. Mg content of the experiment which was conducted with the optimum parameters was measured as 0.81%. Besides, its specific surface area was measured as 6.42 m^2/g and its average grain size is about 200 nm. The experiment, which was conducted with 90% Mg addition under atmospheric conditions, also provided the purest TiB_2 powders having a Mg content as 0.77%. But this experiment had lower leaching cake weight as 3.9 g and lower specific surface area value as 5.77 m^2/g than the experiment which was conducted with stoichiometrically 100% Mg addition and under Ar process atmosphere.

Addition of NaCl and $MgSO_4 \cdot 7H_2O$ increased the amounts of impurities in the synthesized powders and in the leached TiB_2 powders. The mentioned impurities were TiO_2 for NaCl addition and Mg based oxides for $MgSO_4 \cdot 7H_2O$. But, specific surface area values of the leached powders were remarkably increased with the addition of NaCl. Measured values were 11.50 m^2/g for 2.5% NaCl addition ratio and 11.78 m^2/g for 5.0% NaCl addition ratio. It showed that if leaching step is modified to remove remaining TiO_2 phase, NaCl addition can be utilized to synthesize TiB_2 powders with superior specific surface area values. On the contrary, $MgSO_4 \cdot 7H_2O$ addition dropped the specific surface area values (Table 1, Figure 1).

Table 1. Filter cake weights, specific surface area values and Mg contents of leached TiB_2 SHS products

Mg Stoichiometry, %	Reaction Atmosphere	Additive Addition Ratio	Filter Cake Weight, g	Specific Surface Area, m^2/g	Mg Content in Filter Cake, mass%
110	Air	-	7.4	6.20	22.31
100	Air	-	6.5	6.05	9.90
90	Air	-	3.9	5.77	0.77
110	Ar	-	4.0	7.83	3.26
100	Ar	-	4.0	6.42	0.81
90	Ar	-	5.2	4.25	1.77
100	Ar	5.0% NaCl	5.0	11.78	2.30
100	Ar	2.5% NaCl	3.8	11.50	4.15
100	Ar	5.0% $MgSO_4 \cdot 7H_2O$	8.3	3.72	13.01
100	Ar	2.5% $MgSO_4 \cdot 7H_2O$	8.4	3.74	13.05

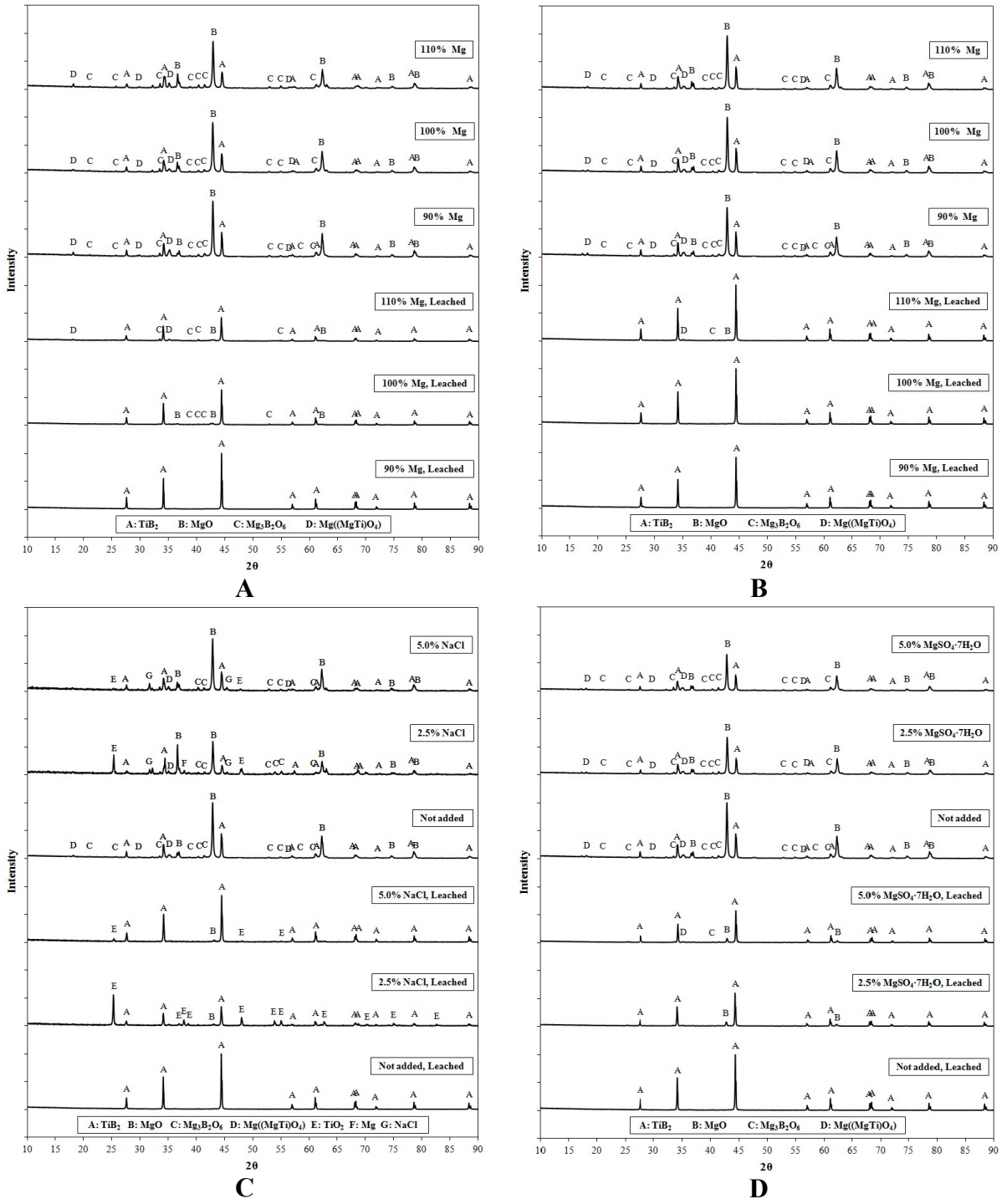

Figure 1. XRD patterns of unleached and leached SHS products synthesized under **(A)** atmospheric conditions, **(B)** argon atmosphere, **(C)** %100 Mg addition, argon atmosphere and NaCl addition, **(D)** %100 Mg addition, argon atmosphere and $MgSO_4 \cdot 7H_2O$ addition

In the SPS stage, determination of the optimum SPS sintering parameters of commercial grade monolithic TiB_2 was the first objective of the present study. TiB_2 powders were sintered at various temperatures both under vacuum and argon atmospheres with different pressure values for this purpose. XRD, SEM, micro hardness and Archimedes density measurement techniques were applied to the sintered compacts for the characterization.

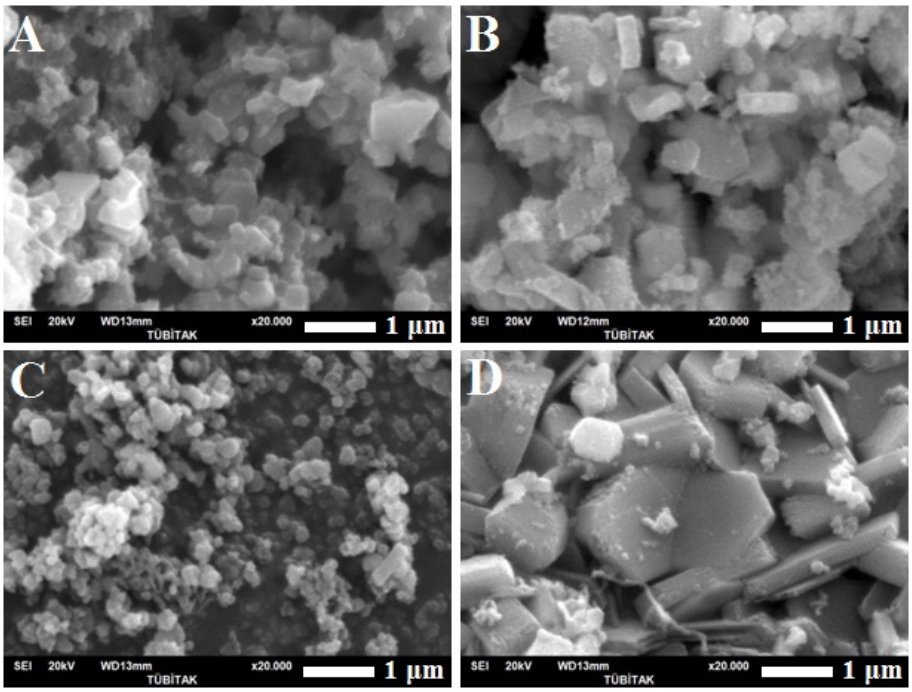

Figure 2. SEM micrographs of self-propagating high temperature synthesized and leached TiB_2 powders (**A:** Atmospheric conditions and 100% Mg; **B:** Ar atmosphere and 100% Mg; **C:** 2.5% NaCl addition, Ar atmosphere and 100% Mg; **D:** 2.5% $MgSO_4 \cdot 7H_2O$ addition, Ar atmosphere and 100% Mg)

Sintering parameters of monolithic TiB_2 ceramics which have an average grain size of 6.240 µm were investigated by using SPS. Effects of sintering temperature between 1600 °C and 1800 °C, sintering pressure of 50 MPa and 70 MPa and sintering pressure mode as initial and after 1500 °C were among the parameters to be investigated. The constant parameters of SPS were heating rate of 150 °C·min^{-1} and 5 minutes of soaking time.

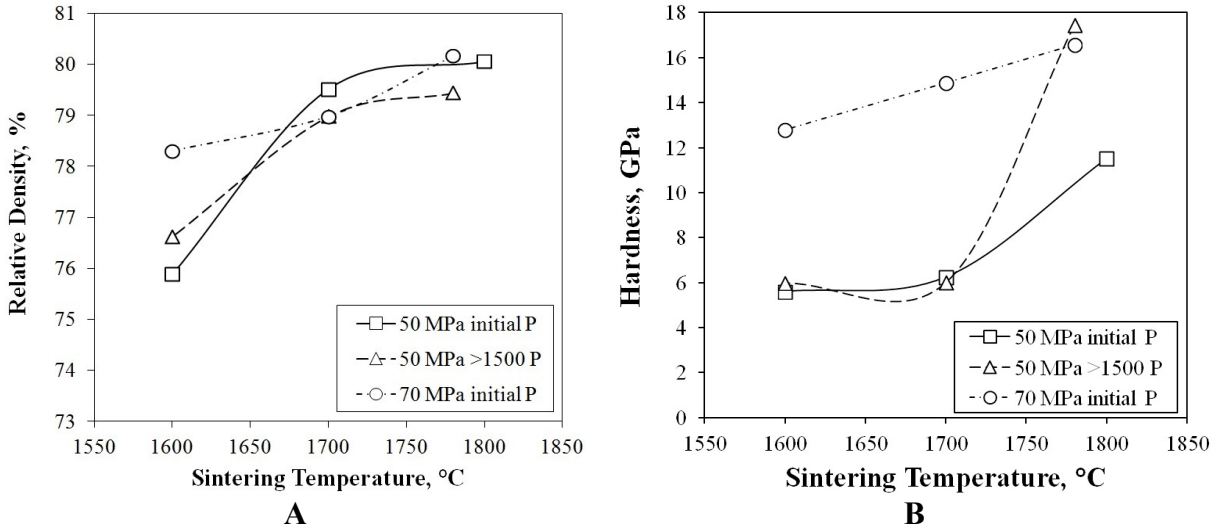

Figure 3. Relative density and hardness values of the TiB_2 ceramics which were sintered by using SPS with increasing sintering temperature

It was clearly observed that increase in sintering pressure from 50 MPa to 70 MPa, the application of sintering pressure after 1500 °C (to prevent the negative effects of the oxide films surrounding ceramic grains) and the use of argon sintering atmosphere beneficially influenced the density and

hardness values. The highest hardness values were obtained in the experiments as 17.46 GPa at 1780 °C under 50 MPa pressure applied after 1500 °C and as 16.59 GPa at 1780 °C under initially applied pressure of 70 MPa under both vacuum atmosphere. Relative density values of the compacts which were produced in these experiments were 79.44% and 80.17% respectively. The highest relative density value was achieved as 94.22% from the sample which was sintered under argon atmosphere with an initial pressure of 50 MPa at 1800 °C. Also the increase in the average grain sizes of sintered samples was determined in accordance with higher hardness and relative density values due to the increase in diffusion between the grains (Figure 3).

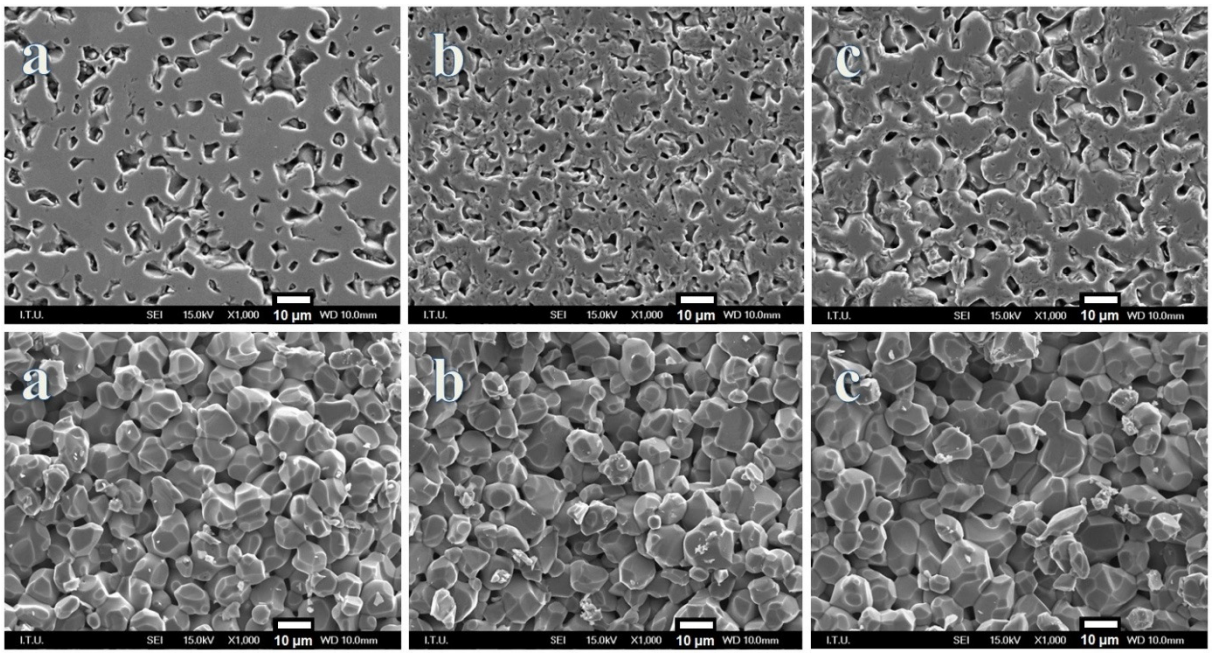

Figure 4. SEM micrographs of polished (above) and fractured (below) TiB_2 samples (a: 50 MPa initial pressure at 1800 °C, b: 50 MPa pressure applied after 1500 °C at 1780 °C, c: 70 MPa initial pressure at 1780 °C)

TiB_2 powders which synthesized by SHS were also sintered by pressureless sintering and SPS. Pressureless sintering was conducted under argon atmosphere for 60 minutes at 1500 °C. The relative density and hardness values of pressureless sintered SHS synthesized and commercial grade TiB_2 powders were 69.67%, 70.86% and 7.26 GPa, 10.01 GPa, respectively. SPS experiment of SHS synthesized powders was conducted under argon atmosphere with an initial pressure of 35 MPa at 1600 °C. The measured relative density and hardness values were 94.64% and 17.51 GPa. These values are higher than measured results from the sintered samples of commercial grade TiB_2 powders. It is clear to understand that TiB_2 powders synthesized by SHS are more suitable to monolithically sinter by using SPS.

Table 2. Relative density and hardness values of the pressureless sintered compacts which were sintered from the powders synthesized by using self-propagating high temperature synthesis and carbothermic synthesis

Synthesis Method of Sintered Compact	SHS	Carbothermic
Relative Density, %	69.67	70.68
Hardness, GPa	7.26	10.01

4. CONCLUSION

In this study, SHS of TiB_2, pressureless sintering and SPS of SHS synthesized and carbothermically synthesized TiB_2 powders were investigated. The optimum SHS parameters of TiB_2 were determined as %100 Mg stoichiometry under Ar atmosphere. Under these conditions, synthesized powders had a average grain size of 200 nm, 6.42 m^2/g specific surface area and Mg content of %0.81.

In the SPS experiments of carbothermically synthesized (commercial grade) TiB_2 powders, it was clearly observed that increase in sintering pressure from 50 MPa to 70 MPa and the application of sintering pressure after 1500 °C beneficially influenced the hardness values. The highest hardness values were obtained in the experiments as 17.46 GPa at 1780 °C under 50 MPa pressure applied after 1500 °C and as 16.59 GPa at 1780 °C under initially applied pressure of 70 MPa. Relative density values of the compacts which were produced in these experiments were 79.44% and 80.17% respectively.

Also SHS synthesized TiB_2 powders were sintered by using pressureless sintering and SPS respectively. In the experiment conducted under 35 MPa sintering pressure at 1600 °C and under Ar atmosphere, the measured relative density and hardness values were 94.64% and 17.51 GPa. It was the highest values in the SPS experiments and it was understood that the TiB_2 powders which synthesized by using SHS are more suitable for sintering operations than carbothermically synthesized.

REFERENCES

1. R. G. Munro, J. Res. Natl. Inst. Stand. Technol., 105 (2) (2000) 709-720.
2. Y. Han, Y. Dai, D. Shu, J. Wang and B. Sun, J. Alloys Compd., 438 (2007) 327-331.
3. G. Will, J. Solid State Chem., 177 (2004) 628-631.
4. R. Telle, L. S. Sigl and K. Takagi, Chapter 7 in Handbook of Ceramic Hard Materials edited by R. Riedel, Wiley-VCH, Weinheim, (2000), p.879.
5. H. O. Pierson, Handbook of Refractory Carbides and Nitrides, Noyes Publications, Westwood, New Jersey, (1996), p.65.
6. C. Subramanian, T. S. R. Ch. Murthy and A. K. Suri, Int. J. Refract. Met. Hard Mater., 25 (2007) 345-350.
7. S. H. Kang and D. J. Kim, J. Eur. Ceram. Soc., 27 (2007) 715-718.
8. B. Derin, K. Kurtoglu, F. Sahin and O. Yucel, Proceedings of the Extraction and Processing Division (EPD) Congress, The Minerals, Metals & Materials Society (TMS) 2008 Annual Meeting, March 9-13, 2008, New Orleans, USA, pp. 379-383.
9. U. Demircan, M.Sc. Thesis (ITU), 2004.
10. E. Bilgi, H. E. Çamurlu, B. Akgün, Y. Topkaya and N. Sevinç, Mater. Res. Bull., 43 (2008) 873-881.
11. Wen-ming Tang, Zhi-xiang Zheng, Yu-cheng Wu, Jian-min Wang, Jun Lü and Jun-wu Liu, Trans. Nonferrous Met. Soc. China, 16 (2006) 613-617.
12. Y. Hwang and J. K. Lee, Mater. Lett., 54 (2002) 1-7.
13. J. Schmidt, M. Boehling, U. Burkhardt and Y. Grin, Sci. Technol. Adv. Mater., 8 (2007) 376-382.
14. L. Baca and N. Stelzer, J. Eur. Ceram. Soc., 28 (2008) 907-911.
15. P. Li, Y. Wu and X. Liu, Mater. Res. Bull., 48 (2013) 2044-2048.
16. Z. A. Munir and U. Anselmi-Tamburini, Mater. Sci. Rep., 3 (1989) 277-365.
17. O. Yücel and F. Ç. Şahin, High Temp. Mater. Processes (Berlin, Ger.), 20 (2) (2011) 137-142.
18. A. G. Merzhanov, Ceram. Int., 21 (1995) 371-379.
19. A. Varma and J. P. Lebrat, Chem. Eng. Sci., 47 (1992) 2179-2194.
20. M. Tokita, J. Soc. Powder Tech. Jpn., 30 [11] (1993) 790-804.
21. M. Omori, Mater. Sci. Eng., A 287 [2] (2000) 183-188.

Microstructural development and adherence ability of thin silica sol gel films on Al alloy ; Effect of additives and substrate pretreatment

Ali Aydın Göktaş

Department of Metallurgical and Materials Engineering, Dokuz Eylül Üniversity, İzmir, TURKEY

Tel : +90 232 301 74 62, Fax : +90 232 301 74 52 , email : aydin.goktas@deu.edu.tr

Abstract

Sol gel solutions containing alkoxides of silicium have been prepared with and without addition of boric acid and ormosils. The Al substrates were undergone to various pretreatment as polishing and Plasma Electrolitic Oxidations - PEO treatment and dipcoated in the sol gel solutions. The samples were heattreated at 220^{o}C and 350 ^{o}C. A film thickness of 2-3 micron could be reached by multilayers coatings for 3 times. Microstructures of coatings were analysed by SEM. According to SEM results ormosil added samples showed increased adherence ability of the coatings but with some microhole defects at higher temperatures, whereas boron additives showed better adherence of solutions. On the other hand PEO pretreated substrates showed better adherence and coverage of the coatings. These findings were confirmed with corrosion resistance test results. The crystallisation and thermal behaviour of bulk samples were studied with the aid of XRD and DTA, respectively.

Keywords: Sol-gel, coatings, corrosion, surface morphology, Al-alloy

Introduction

Aluminum light metal alloys have excellent physical and mechanical properties and find wide range of uses for automotive and aircraft applications with their high strength: weight ratio [1,2,3]. But susceptibility to corrosion limits their useful applications [4,5]. The traditional coatings with chromate solutions have excellent corrosion resistance but due to the causes of serious health problems one need to find an alternative method [1,2,4,6].

Sol gel technology is economic and environmentally friendly coating techniques but there are adherence weaknesses of the coatings to the substrate, microcracks occurring by the heat treatment specially with multilayer coatings which cause decreasing the corrosion resistance [7-10]. The cause of these se problems need to be studied to make it a reliable method.

The use of metal alkoxide M(OR)n precursor, where M represents the metal and R the alkyl group is the most common in sol-gel processing. When alkoxides react with water a hydroxyl part becomes attached to the metal atom. Surfaces bearing hydroxyl groups create amorphous film growth. Condensation occur when two partially hydrolyzed molecules or a partially hydrolyzed molecules with an OR group react each other. In this work, it is targeted to develop multilayer sol gel coatings with special attention to improve the adherence ability of sol gel solutions to the substrate and to study the microstructural development of the coatings process. For this purpose two kinds of additives as of boric acid and glymo are used as additives in the sol gel solutions prepared with Tetraethylorthosilicate (TEOS) - silicon alkoxide precursor.

Experimental

The substrates of aluminum 7075 alloy in the size of 15 × 15 mm were subjected to various pretreatment as polishing and PEO, degreased in nitric acid and ethanol and

then washed with distilled water, and dried in dry air.

As starting compounds Tetraethylorthosilicate, glymo, and H_3BO_3 are used. To prepare sol gel solutions different amount of ingredients were used, distilled H_2O for hydrolysis, HCl as a catalyst and C_2H_5OH as solvent. HCl was used with 0.01 of concentration. In general it was started with 50ml TEOS and 50 ml ethanol and finaly 100 ml ethanol were used in total. The molar ratio of water to TEOS varied from 2 to 3. All solutions were prepared at room temperature under continuous stirring. Water needed to be added drop by drop in order to avoid precipitation.

The gels subjected to X-ray diffraction analysis appeared to be amorphous. DTA analyses(ShimadzuModel) made in air atmosphere at 10 ^oC/ min, showed transformation of the gel upon heating with regard to releasing temperature of organic solvents and water in the dried sample. The thickness of coatings after heat treatment were measured with profilometer (Ambios XP Series). SEM analyses were used to investigate the microstructure development of heat treated films.

The electrochemical tests of coated samples were performed by using potentiodynamic polarization module of Gamry Reference 600 Potentiostat at room temperature in 3.5 wt.% NaCl solution. All of the electrochemical tests were performed in a PVC cell

Three different sol gel solutions were prepared to make multilayer coatings on the substrates and to study the adherence ability of the coating to the substrate.

For obtaining a clear solution following procedures were made; For the first starting solution TEOS mixed with ethanol and then a part of H_2O-HCl solution (20 % volume in total) was added drop by drop into the solution in order to prevent precipitation. The solution was stirred for two hours. At the end, the remaining amount of ethanol and H_2O-HCl solution were added to the solution with continued stirring for another 1hour. A clear solution was obtained. The other solutions were prepared by adding glymo and

H_3BO_3 in to the first solution, and stirred further for another 1hour.

The second solutions containing H_3BO_3, was firstly dissolved in warm H_2O and then added into the first solution. The amount of H_3BO_3 was was approximately 2-5 wt %. dependent upon the condition of the solution.When the solution started to become cloudy the addition were stopped.

The third solution contains 10 % volume glymo ratio to the existing TEOS.

To prepare sol gel coatings on substrates the cleaned substrates were dipped into the solutions and withdrawn slowly with a speed of 30 sec./ cm. The films prepared in this way were firstly dried overnight and then heat treated at two different temperatures of 220 ^{o}C, and 350 ^{o}C. In order to prepare multilayer thin films, heat treatments were repeated after each coating step.

Results and Discussion

The dried and heat treated gels of all three compositions were subjected to XRD analyses. According to XRD results the composition containing ormosil remained amorphous up to 1200 ^{o}C while the composition containing B_2O_3 showed an early crystalline structure starting at 900 ^{o}C. Later crystallization of the composition containing ormosil may be explained with slow down of reactions caused by ormosil in the structure. Early crystallization of the composition with boric acid may be indicated that boron oxide incorporate into silica structure. Figure 1 shows XRD patterns of both composition heat treated at 1000 ^{o}C.

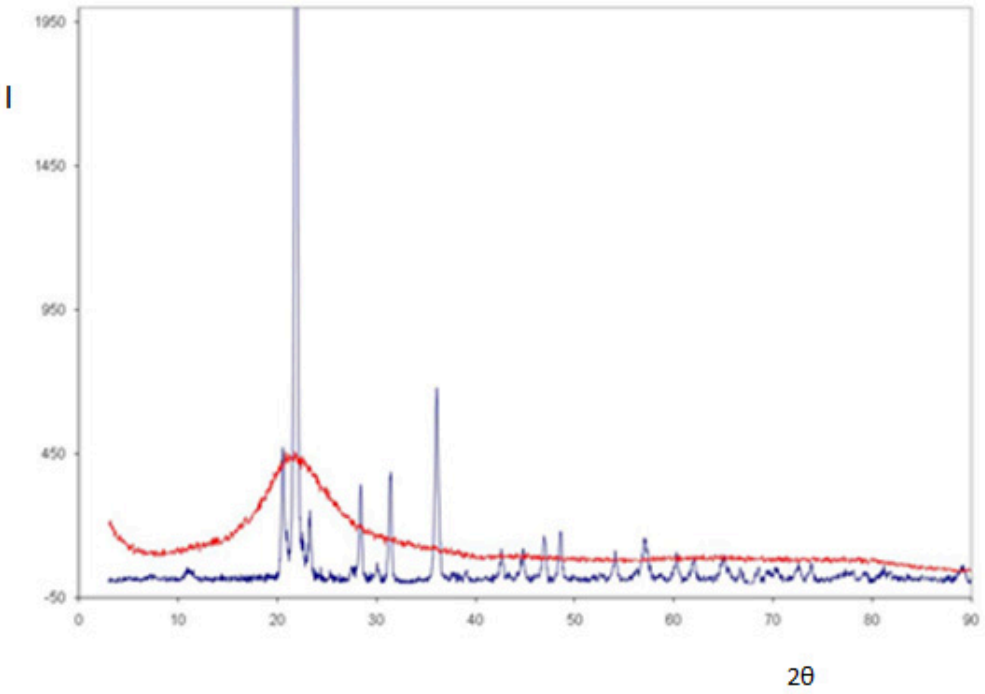

Figure 1. XRD patterns of the compositions 3 with ormosil and 2 with boric acid at 1000 ^{o}C

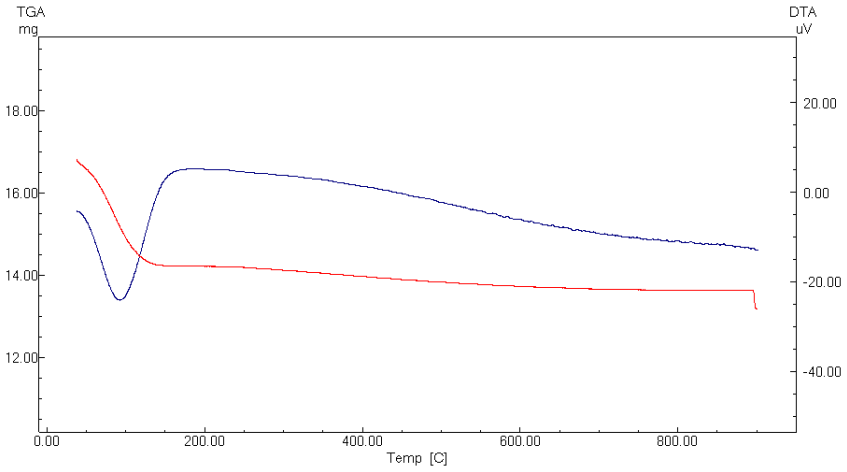

(a)

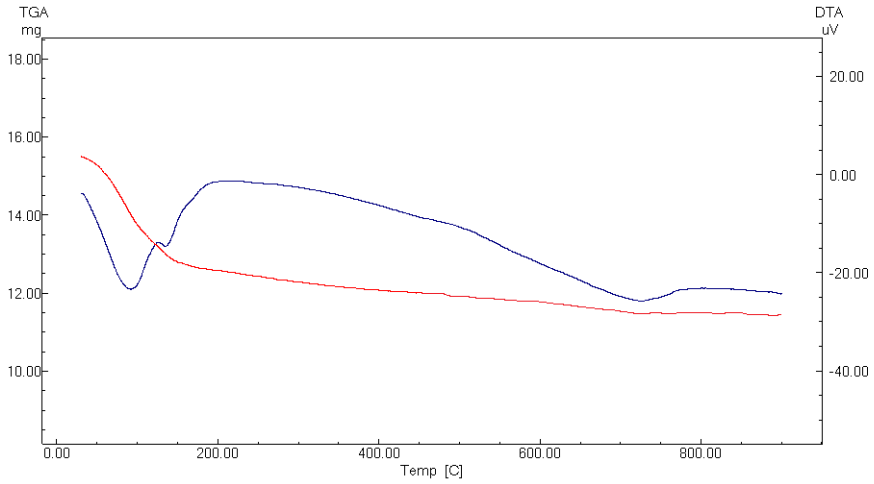

(b)

Figure 2. DTA analysis of coatings (a) composition 1, (b) composition 3

DTA results of compositions 1 and 3 without and with ormosil are shown in Figure 2 The curves exhibit low temperature endoterms at about 100 ^{o}C. These endoterms may be associated with the loss of organic solvent and and water. At about 200 ^{o}C, one observes exoterms which are attributed to the oxidation of residual organic matter of the precursor. The peak position shift to higher temperature with the composite 3 containing ormosil. These findings are in accord with those of Ref. 11 and may be interpreted as an exoterm due to combustion of high content of organics. For the heat treatments of coatings there are two different temperatures as of 220 ^{o}C and 350 ^{o}C chosen since according to DTA results at about 220 ^{o}C residual organics are released from the samples, and 350 ^{o}C is about the temperature where Al samples may withstand any deformation .

The measurements of surface tension were made by Wilhelmy plate method.

Surface tension of the prepared Sol-gel solution with only TEOS solution was measured with 170 mN/m, while with the addition of glymo or boric acid were are measured with

about 100 mN/M and 90 mN/m respectively

As can be understand from the results that both boric acid and ormosil addition lower the surface tension. These finding might be an indication for the explanation of better adherence ability of solutions with boric acid and ormosil additions.

SEM micrographs of single and multilayer coatings on two different pretreated substrates heat treated at two different temperatures are shown in Figures 3-6 Morphologies observed in these Figures are different from each other.

Figure 5 shows the single layered surface morphologies of the coatings on polished Al substrates heat treated at 220 ^{o}C. Comparing their surface morphologies we realize their adherence ability to the substrate. Figure 3a represents composition 1 which prepared with only TEOS shows a seperated island forms of coatings instead of a full coverage, whereby Figure 3c shows a full covered coating without any serious defects. Figure 5c represents the composition 3 containing ormosil additive. The morphology of the coatings of the composition 2 containing boric acid shown by Figure 3b indicates a better covering capability compared to the morphology of Figure 3a. These findings explain the effects of boric acid and ormosil on the adherence ability of coatings to the substrate, whereby boric acid play a roll of chemical etching and ormosil a binding effect to the substrate.

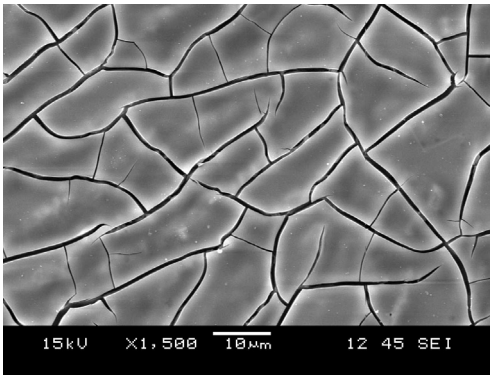

(a)

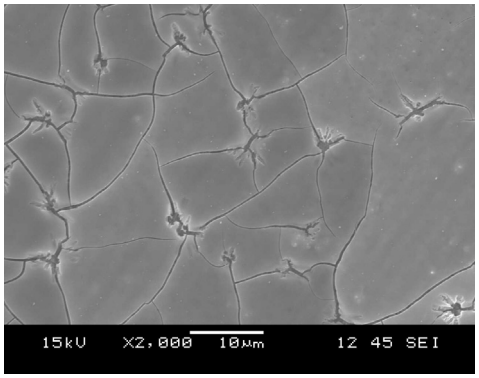

(b)

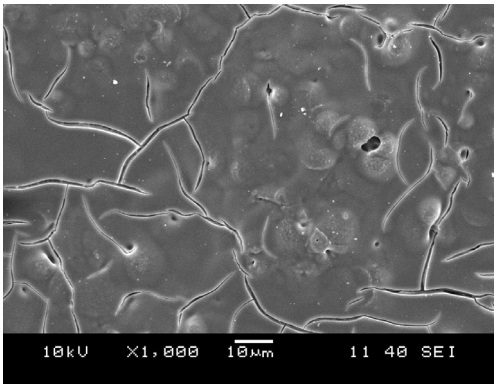

(c)

Figure 3 SEM images of Sol-gel coatings on polished Al-substrates with a) composition 1, b) composition 2, c) composition 3

Morphologies of the same coatings but on PEO treated substrates were also observed. (Figure 4)

Morphologies in this figure 4 shows an homogeneous and full coverage of coatings with only some defects of micro holes which may be associated with the combustion of high residual content of organics in the created holes of PEO treated substrates.

Figure 4a represents composition 2 with boric acid and Figure 4b composition 3 with ormosil. One can see on micrographs much better coverage with the composition 3

containing ormosil.

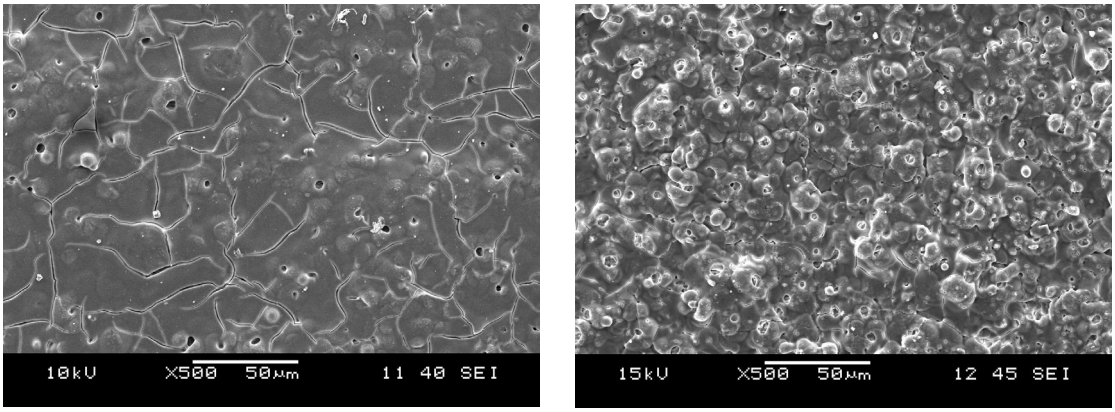

a) b)

Figure 4. SEM image of the coating on PEO treated substrate with a) composition 2, b) composition 3

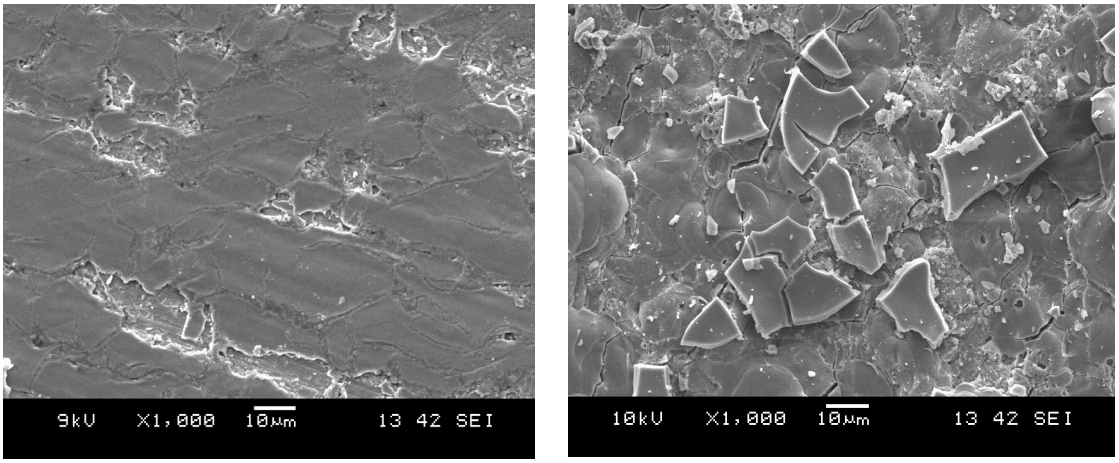

a) b)

Figure 5. SEM images of multilayer coatings on polished sample heat treated at 350^{o}C with a) composition 2, b) composition 3

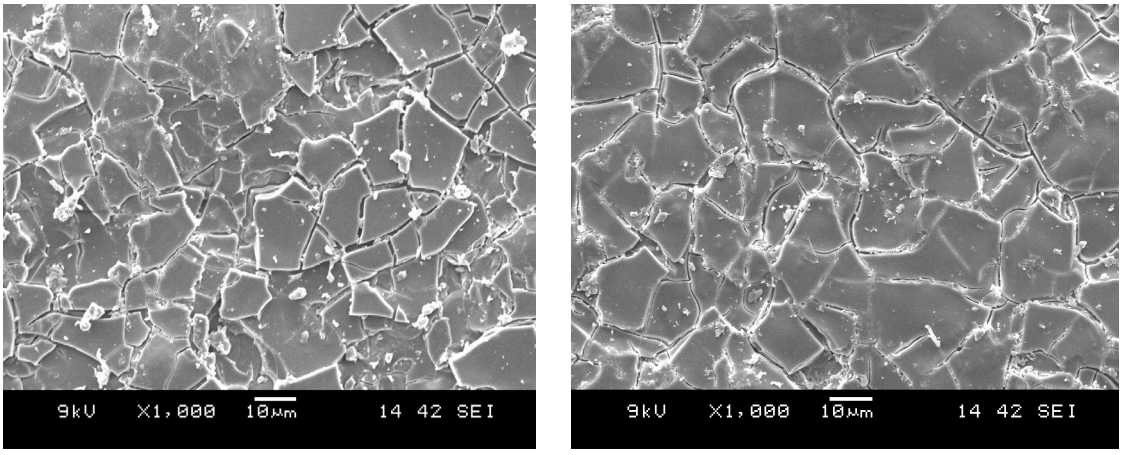

a) b)

Figure 6. SEM images of multilayer coatings on PEO treated sample heat treated at 350^{o}C with a) composition 2, b) composition 3

Figure 5 and 6 demonstrate the morphologies of multilayer films heat treated at 350 ^{o}C and coated 3 times.

While Fig.5 represent the coatings on Polished samples, Fig.6 represent the coatings on PEO treated samples, where a) indicate again the composition 2 with boric acid, and b) indicate the composition 3 with ormosil.

Fig5a shows a good coverage of coatings with only some broken parts on top coatings covering the underlayer. Fig 5b shows the morphology of composition 3 with ormosil additives. Compared to Fig.5a one see a better coverage of coatings with only some microcracks, better coverage can be explained with binding effects of ormosil.

Morphologies of multilayer coatings on PEO treated substrates are shown on Fig.6 a) and b). Comparing 6a) and 6b), one see similar morphology results with an homogeneous and full coverage of coatings without any serious defects. One can see only some microcracks which might be interpreted due to the stress occurring upon

deposition of films in the pores of PEO treated substrates, and so certain thickness of coatings.

By Heattreatment at 220°C, with single layer coatings we could obtain a film thickness of max.1 micron only, while multilayer coatings with 3 times enabled us to obtain a film thickness of 2-3 micron.

The electrochemical behavior of sol-gel coatings is influenced by many factors including surface roughness, coating thickness and porosity level.

The potentiodynamic polarization curves of uncoated and coated samples are given in Figure 7.

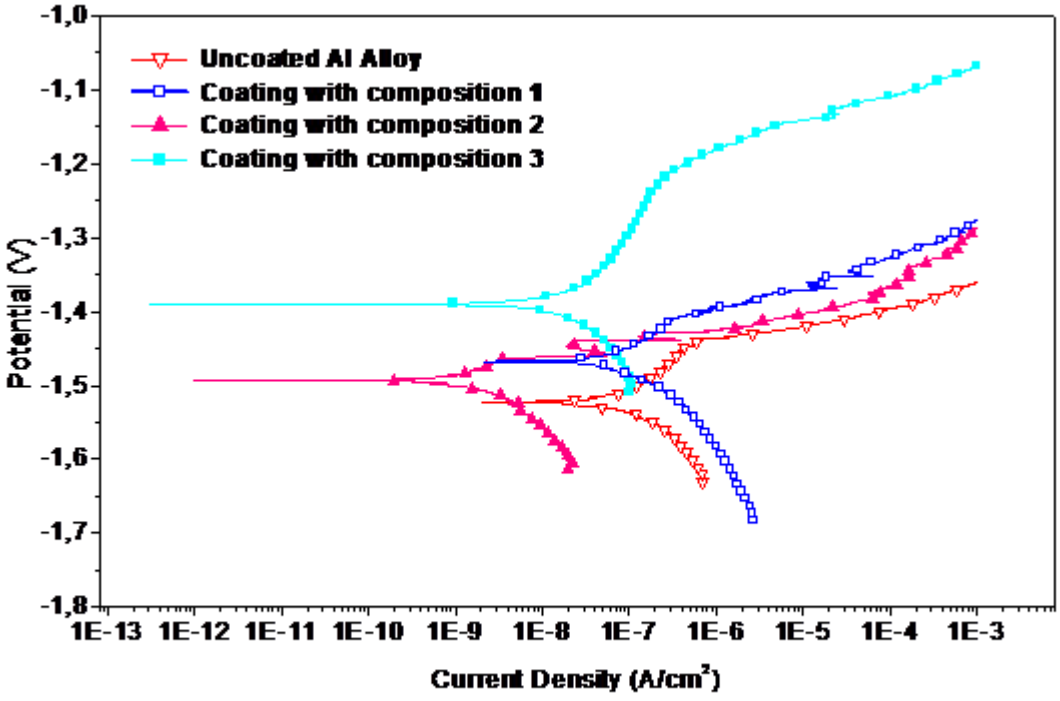

Figure 7 Potentiodynamic polarization curves of uncoated and coated Al alloy

Uncoated Al alloy corroded at 3.5% NaCl solution during the test potential reach to steady state at stabilization period. Moreover, several active pitting site on the surface were seen prior to starting of the polarization tests. In the anodic branch of potentiodynamic polarization curve of bare Al Alloy, slightly pseudo passive zone was observed due to an active corrosion first and a subsequent coverage of the working electrode surface with the corrosion products. This is related to the high reactivity of Al alloys in Cl^- containing environments. As potential increased from open circuit potential in the noble direction rapid dissolution of bare metal took place.

All of the coated specimens reveal lower corrosion current density which decreases by approximately two orders of magnitude as compared to bare Al alloy.

Conclusions

A multi-layer sol–gel coatings on7075 Al alloy were obtained using TEOS, TEOS/ Ormosil, or TEOS/ Boric acid with the aim of obtaining coatings with improving the corrosion resistance of 7075 Al alloy. Coatings were made by using dipcoating method and heat treatments repeated after each coating.

It is found that the addition of boric acid or ormosil in to sol gel solution increased the adherence ability of coating promoting the corrosion protection of 7075 Al alloy. The low surface tensions of the solutions with additives were also related to better adherence of solutions to the substrate.

Our results demonstrated that with sol gel coatings using TEOS/ Ormosil or boric acid better corrosion resistance of coating could be obtained

XRD patterns revealed a completely amorphous structure of the samples heat treated up

to 800 ^{o}C. The composition containing B_2O_3 started to crystallize at 800 ^{o}C, whereby the other compositions remained amorphous up to 1000 ^{o}C. Early crystallization of the composition with boric acid may indicate incorporation of boron oxide into silica structure.

The thermal degradation process of gel powder was characterized by TGA/DTA. The results showed that organic solvent and water are released at about 100 ^{o}C and residual organic compounds in the film decomposed in the temperature range from 200 ^{o}C to 250 ^{o}C. Based on the DTA and SEM results, two different temperatures as of 220 ^{o}C and 350 ^{o}C are chosen for the heat treatment of coatings since according to DTA results at about 220 ^{o}C residual organics are released from the samples, and 350 ^{o}C is about the temperature where Al samples may withstand any deformation .

For multilayer coatings heat treated at 220 ^{o}C and repeteadly coated for 3 times, a film thickness of 2-3 micron were obtained, while for single layer coatings a maximum film thickness of 1 micron could be obtained.

Surface morphologies of single layered coatings on Aluminum 7075 are demonstrated by SEM micrographs. On polished Al substrate composition containing ormosil additives heat treated at 220 ^{o}C demonstrate a good coverage of coatings .while other compositions show a weak adherence of coatings even though composition with boron additives represent a better coverage.

On PEO treated substrates comparing to the polished substrates one could obtain on both boric acid and ormosil added solutions a full covered coatings with much better

adherence ability. These findings may be explained with increased surface area and roughness of surfaces.

Multilayer coatings were made both on polished and PEO treated substrates heat treated at 350 ^{o}C and coated 3 times using composition of 2 and 3. Comparing micrographs of coatings one see clearly an homogeneous and full covered coatings on PEO treated surfaces with only some microcracks due to the stress occurring upon deposition of films in the pores of PEO treated substrates. In case of polished samples a good coverage of coatings but with less homogeneity were obtained.

Composition containing ormosil and boron additives gave better corrosion resistance.

Acknowledgment

The author would like to thank Assoc. Prof. Dr.U.Malayoglu for performing PEO treatment.

References

1. A.R. Phani, F.J. Gammel, T. Hack and H. Haefke, *Mater. Corros.*, **56**, 2, (2005).
2. D. Raps, T. Hack, J. Wehr, M. Zheludkevich, A.C. Bastos, M.G.S. Ferreira and O. Nuyken, *Corros. Sci.*, **51**, 1012, (2009).
3. N.C. Rosero-Navarro, L. Paussa, F. Andreatta, Y. Castro, A. Durán, M. Aparicio and L. Fedrizzi, *Prog. Org. Coat.*, **69,** 167, (2010).
4. H. Wang and R. Akid, *Corros. Sci.*, **49**, 4491, (2007).
5. P. Álvarez, A. Collazo, A. Covelo, X.R. Nóvoa, C. Pérez, *Prog. Org. Coat.,* **69**, 175, (2010).
6. Y. Liu, D. Sun, H. You and J.S. Chung, *Appl. Surf. Sci.*, **246**, 82, (2005).
7. D. Wang and G.P. Bierwagen, *Prog. Org. Coat.*, **64**, 327, (2009).
8. T.L. Metroke, R.L. Parkhill and E.T. Knobbe, *Prog. Org. Coat.*, **41**, 233, (2001).
9. D.A. López, N.C. Rosero-Navarro, J. Ballarre, A. Durán, M. Aparicio and S. Ceré, *Surf. Coat. Tech.*, **202**, 2194, (2008).

10. M.L. Zheludkevich, R. Serra, M.F. Montemor, K.A. Yasakau, I.M. Miranda Salvado and M.G.S. Ferreira, *Electrochim. Acta*, **51**, 208, (2005).
11. H. Moller, *Corros. Sci.*, **49**, 1992, (2007).

A RESPONSE SURFACE ANALYSIS OF THE PROCESS OF BIOSORPTION OF Cd(II) IONS BY USING RICE HUSK

Kiril Lisichkov, Mahi Ljatifi, Stefan Kuvendziev, Mirko Marinkovski

Faculty of Technology and Metallurgy,Univ. Ss. Cyril and Methodius, Skopje, Republic of Macedonia
klisickov@yahoo.com

ABSTRACT

Republic of Macedonia is considered to be an agricultural region and one of the most produced cultures is rice. In the production process, rice husk is considered to be a by-product. As a low-cost agricultural by-product, rice husk can be used in various purposes - as biomass fuel (bulk or pellets), kettle food, or as a biosorbent to be used in heavy metal removal. The application of this material as a biosorbent for toxic heavy metals such as Ni, Cr, Cu, Pb, Zn, Cd, Hg has gained a lot of attention in recent scientific studies.

In the frame of this work, rice husk was used as a biosorbent for removal of heavy metal-Cd(II) from its aqueous solutions in batch conditions. Rice husk was obtained from the Kocani region in Macedonia. During the process of preparation of the biosorbent, a basic chemical composition of the rice husk was determined through chemical analysis. After establishing the risk husk as an effective and low-cost biosorbent for removal of above mentioned heavy metals, the influence of operating conditions on the amount of absorbed metal ions was determined. In the frame of this work, a surface response analysis of the process of biosorption of Cd(II) ions by using rice husk was performed.

***Keywords*:** biosorption, rice husk, biosorbent, heavy metals removal

1. INTRODUCTION

Water is an important article and was poor for many countries of the world. Drinking water, urban wastewater, industrial wastewater, process waste water and groundwater are vulnerable to different types of treatment for removal of substances contained in them.
In recent years the interest for purification of industrial wastewater containing heavy metals that jeopardize human health, animals and nature is growing up.
Heavy metals industry (heavy metallurgy) are characterized by large water consumption which comes from the washing process during production, and many other indirect application, which leads to the fact that the resulting waste water has a different composition. Therefore, the resulting wastewater during washing processes of cadmium, zinc and lead has a huge concentration of these metals which should be reduced to a value prescribed by standards. The metals can accumulate in toxic concentrations and can cause environmental damage. In aquatic systems, the metals are present as complex ions, suspended and colloidal ions and solid components in sediments. The concentrations of these metal ions are highly dependent on biological processes, redox potential, ionic strength, pH of organic and inorganic solvents and cleaning processes.
The biggest source of metals pollution comes from municipal water (especially As, Cr, Cu, Mn and Ni), plants that burn coal (As, Hg and Se), smelters that melt Cd, Ni, Pb and Se, iron and steel plants (Cr, Mo, Sb and Zn) and waste removal (As, Mn and Pb), ceramics, electro

polishing, metallurgy, glass industry, mining, coating industry etc. There are different methods for wastewater purification: flotation, flocculation, filtration, ultrafiltration, precipitation, chlorination, reverse osmosis, aeration and adsorption [1-8].
Using of adsorption as a method for control of water pollution has several advantages: smaller investments in terms of initial costs and costs for land, simple project, ease in working by plant, , no side effects from toxic substances, as superior extraction of organic waste materials and heavy metals. As adsorbents in the waste water purification process from heavy metals different adsorbents can be used, including: granular activated carbon, silica gel, activated alumina, bauxite, zeolites and ion exchange resin, peat, clay, chitosan, different microorganisms, chimney rice and peanut shell, metal oxides, peat, ash and agricultural wastes.
Natural rice husk are materials with big surface area due to their big porosity. Rice husk is one of the byoproducts of rice production which could be used in biosorption processes for removal of toxic heavy metals from synthetic wastewaters [9-11]

2. EXPERIMENTAL PART

Rice hush as agricultural waste is obtained from Kocani region in R. Macedonia. Prior of the experiment, rice husk was naturally dried to 7.70 % mas humidity. After granulation, 0.63-0.8 mm working biosorbent was obtained . A cadmium solution with the concentration of 15 mg/dm^3 and initial pH=6.5 was prepared. The stock solution was made by dissolving calculated amount of $CdCl_2 \cdot H_2O$ (Merck,Germany) in distilled water. Experiments are made in batch conditions in laboratory glass reactor. During the experiments temperature (from 20-40^oC), contact time (from 20-160 min) and sorbent concentration (from 2-6 g/dm^3) were changed. The influence of temperature, contact time and sorbent concentration on amount of removed metal per adsorbent mass unit were monitoring.

3. RESULTS AND DISCUSSION

To determine the objective function of amount of removed metal per adsorbent mass unit from temperature, contact time and sorbent concentration Statgraphic Centurion was used.
In order to initiate the 3D optimization of the investigated system within Statgraphics Centurion, it is essential to define the initial temperature levels, contact time and sorbent concentration. The Statgraphic Centurion analysis produced the regression coefficients, Pareto chart of the influence of inlet values and their interactions on the output amount of removed metal per adsorbent mass unit.
The regression coefficients from Statgraphic Centurion analysis are given in table 1.

Table 1. Regression coefficients from Statgraphic Centurion analysis (R = 0.999747).

Coefficient	***Estimate***
constant	0.230357
A:T	0.0191429
B:time	-0.00410714
C:C	-0.00794643
AB	0.000405357
AC	0.0009375
BC	0.000366071

The overall model is:

$$Q = 0.230357 + 0.0191429*T - 0.00410714*time - 0.00794643*C + 0.000405357*T*time + 0.0009375*T*C + 0.000366071*time*C$$

where: Q- amount of removed metal per adsorbent mass unit (mg/g); C- biosorbent concentration (mg/dm^3), time- contact time (min) and T- temperature (^{o}C).

The Pareto chart represents the influence of operating parameters and their interaction on the output values of the amount of removed metal per adsorbent mass unit which is given on figure 1.

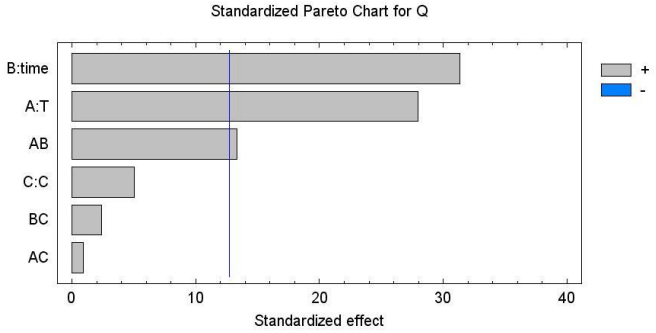

Figure 1. Pareto chart for the influence of operating parameters and their interaction on the output values of the amount of removed metal per adsorbent mass unit

From Pareto chart (figure 1) it can be seen which coefficients are influential. The most influential coefficients are: A-temperature, B-contact time, AB-interaction of contact time and temperature. This means that the resulting model will be reduced and will be in the following form:

$$Q = 0.230357 + 0.0191429*T - 0.00410714*time + 0.000405357*T*time$$

The 3D response surface for constant biosorbent concentration is given on figure 2 which provides the dependence of output amount of removed metal per adsorbent mass unit from contact time and temperature.

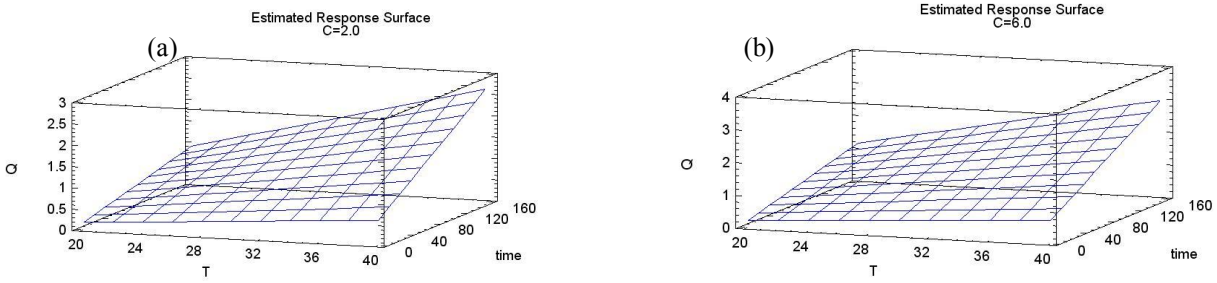

Figure 2. 3D response surface for the dependence of output amount of removed metal per adsorbent mass unit from the contact time and temperature (constant biosorbent concentration: (a)-C=2 and (b)-C=6 g/dm^3).

The contours of estimated response surface for constant biosorbent concentration is given on figure 3.

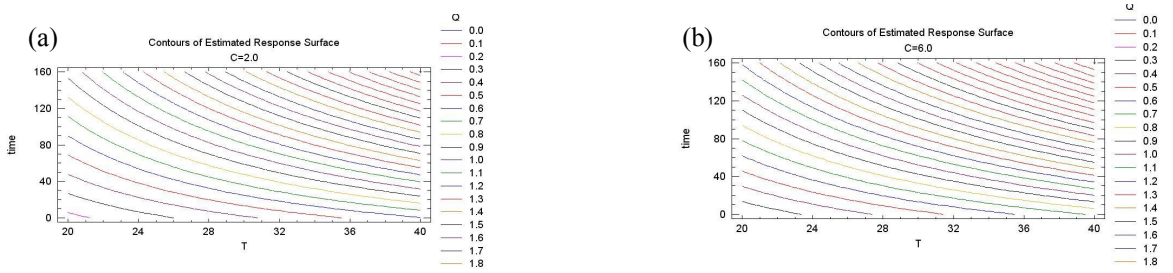

Figure 3. Contours of estimated response surface for amount of removed metal per adsorbent mass unit from the contact time and temperature (constant biosorbent concentration: (a)-C=2 and (b)-C=6 g/dm^3).

For biosorption operating temperature (T=33^{o}C) and contact time 140 min from the 3D surface optimization (figure 2) it can be seen that the biosorption efficiency is Q=1.51 mg/g and Q=1.73 mg/g for constant biosorbent concentration C=2 g/dm^3 and C=6 g/dm^3 respectively. The used biosorbent was shown that its biosorption capacity depend on temperature and contact time and their interaction. This type of natural by-product can use as a friendly ecological adsorbent for removal of Cd(II) ions from wastewater.

4. CONCLUSIONS

The natural rice husk used as an adsorbent showed a good adsorption performance for removal of Cd(II) ions from aqueous solutions. The effect of different operational parameters on the adsorption of Cd(II) ions onto natural raw material (rice husk) was investigated and optimized.
Obtained model correlated the output amount of removed metal per adsorbent mass unit as a function of the contact time and temperature as well as their interactions.
As a general conclusion the performed simulation based on the Statgraphic Centurion model can provide a further contribution to the knowledge development regarding the dynamic behavior of the biosorption process.

Acknowledgment: This research was performed within the Project "Realization of projects in the field of clean technologies for education of master and PhD students and workshops for increase public awareness" founded by Ministry of environment and physical planning of R. Macedonia.

5. REFERENCES

1. M. Singanan, *Removal of lead(II) and cadmium(II) ions from wastewater using activated biocarbon*, ScienceAsia 37 (2011): 115–119

2. S.Khaoya, U. Pancharoen, *Removal of Lead (II) from Battery Industry Wastewater by HFSLM*, International Journal of Chemical Engineering and Applications, Vol. 3, No. 2, April 2012
3. L. Tofan, C. Paduraru, *Sorption Studies of Ag^{I}, Cd^{II} and Pb^{II} Ions on Sulphydryl Hemp Fibers*, Croatica Chemica Acta CCACAA 77 (4) 581-586 (2004)
4. Z. K. Sarkar, F. K. Sarkar, *Selective Removal of Lead (II) Ion from Wastewater Using Superparamagnetic Monodispersed Iron Oxide (Fe_3O_4) Nanoparticles as a Effective Adsorbent*, Int. J. Nanosci. Nanotechnol., Vol. 9, No. 2, June 2013, pp. 109-114
5. M. Moyo, L. Chikazaza, *Bioremediation of Lead(II) from Polluted Wastewaters Employing Sulphuric Acid Treated Maize Tassel Biomass*, American Journal of Analytical Chemistry, 2013, 4, 689-695
6. F.A. Pavan, A.C. Mazzocato, R.A. Jacques, S.L.P. Dias, *Ponkan peel: A potential biosorbent for removal of Pb(II) ions from aqueous solution*, Biochemical Engineering Journal 40 (2008) 357–362
7. J. Acharya, U. Kumar, B.C. Meikap, *Thermodynamic characterization of adsorption of lead(II) ions on activated carbon developed from tamarind wood from aqueous solution*, South African Journal of Chemical Engineering,vol.18, no. 1, pp70-76
8. J.K. Mbadcam, S.G. Anagho, J.N. Nsami, A.M. Kammegne, *Kinetic and equilibrium studies of the adsorption of lead (II) ions from aqueous solution onto two Cameroon clays: Kaolinite and smectit*e, Journal of Environmental Chemistry and Ecotoxicology Vol. 3(11), pp. 290-297, October 2011
9. M. Saidi, *Experimental studies on effect of Heavy Metals presence in Industrial Wastewater on Biological Treatment*, International Journal of Environmental Sciences Volume 1, No 4, 2010, pp. 666-676
10. I. Mobasherpour, E.Salahi,A. Asjodi, *Research on the Batch and Fixed-Bed Column Performance of Red Mud Adsorbents for Lead Removal*, Canadian Chemical Transactions, Vol. 2 (1), (2014) pp 83-96
11. I.J. Vassilis, *Ion Exchange and Adsorption Fixed Bed Operations for Wastewater Treatment- PART I: Modeling Fundamentals and Hydraulics Analysis*, Journal of Engineering Studies and Research, Vol. 16 (3) (2010) pp 29-41

EFFECT OF MOLTEN SALT SYNTHESIS PARAMETERS ON THE MORPHOLOGY AND MAGNETIC PROPERTIES OF BARIUM HEXAFERRITE CERAMICS SYNTHESIZED IN X WT% NACL-(100−X) WT% KCL FLUXES

Seray KAYA, Eda AYDOĞAN, Arcan F. DERİCİOĞLU

Middle East Technical University, Dept. of Metallurgical and Materials Eng., Ankara-Turkey
moonseray@hotmail.com, arcan@metu.edu.tr

1. ABSTRACT

Micron size barium hexaferrite ($BaFe_{12}O_{19}$, BaHF) platelets were prepared by the molten-salt synthesis method in various weight proportions of NaCl–KCl salt mixtures as the liquid medium. The effect of molten salt composition—x wt% NaCl and (100−x) wt% KCl—on the amount of barium hexaferrite phase formation, as well as, on the morphology and magnetic properties of the final products were discussed. X-ray diffraction analysis (XRD), scanning electron microscopy (SEM) and vibrating sample magnetometer (VSM) were used to identify the characteristics of the synthesized barium hexaferrite platelets. Quantitative XRD results showed that calcination in the molten salt containing 100 wt% NaCl at 900 °C (for 2 h) resulted in the highest amount of barium hexaferrite formation from the initial hematite and barium carbonate phases. Furthermore, SEM results showed that calcination in KCl-rich molten salts have led to the formation of sharper faceted platelet morphology, whereas calcination in NaCl-rich ones resulted in more round platelets. Data from magnetic measurements showed that as the content of NaCl in the molten salt increases, hysteresis losses became higher. This points out to the achievement of a stronger hard magnetic behavior in the synthesized barium hexaferrite ceramics. The composition of the KCl/NaCl molten salts was shown to play an important role on the extent of barium hexaferrite formation, resulting platelet morphology and the magnetic properties.

Keywords: Molten salt synthesis (MSS), Morphology, Platelets, Magnetic properties, Ferrites

ERİYİK TUZ YÖNTEMİ PARAMETRELERİNİN AĞIRLIKÇA X % NACL-(100−X) % KCL ERİYİK TUZLARINDA SENTEZLENEN BARYUM HEKZAFERRİT SERAMİKLERİNİN MORFOLOJİ VE MANYETİK ÖZELLİKLERİNE ETKİLERİ

Seray KAYA, Eda AYDOĞAN, Arcan F. DERİCİOĞLU

Orta Doğu Teknik Üniversitesi, Metalurji ve Malzeme Mühendisliği Bölümü, Ankara-Türkiye
moonseray@hotmail.com, arcan@metu.edu.tr

1. ÖZET

Sıvı ortamı ağırlıkça farklı oranlarda NaCl–KCl tuz karışımlarının olduğu eriyik tuz yönteminde mikrometre boyutlu baryum hekzaferrit ($BaFe_{12}O_{19}$, BaHF) plakaları üretilmiştir. Eriyik tuz kompozisyonun (ağırlıkça x % NaCl ve (100−x) % KCl) baryum hekzaferrit fazı oluşumu ve aynı zamanda da son ürünlerin morfoloji ve manyetik özellikleri üzerine etkileri tartışılmıştır. Sentezlenen baryum hekzaferrit plakalarını karakterize etmek için X-Işınları Kırınımı (XRD), Taramalı Elektron Mikroskobu (SEM) ve Titreşimli Numune Manyetometresi (VSM) kullanılmıştır. Sayısal XRD sonuçları, ağırlıkça yüzde 100% NaCl içeren eriyik tuz içerisinde, 900 °C ve 2 saatte yapılan sentezin en yüksek oranda baryum hekzaferrit oluşturduğunu göstermiştir. Ek olarak, SEM sonuçları, KCl oranı yüksek olan eriyik tuzlarda yapılan kalsinasyonların keskin köşeli plaka morfolojisi oluşturduğunu göstermiştir. Buna karşın, NaCl tuzunun zengin olduğu kompozisyonlarda yapılan kalsinasyonlarda ise, daha yumuşak köşeli plakalar oluşmuştur. Manyetik ölçüm verilerine göre, eriyik tuz içerisindeki NaCl oranı arttıkça, histeresis kayıpları artmıştır. Bu da, sentezlenen baryum hekzaferrit seramiklerinde daha sert manyetik özelliğin oluşumunu göstermiştir. Eriyik KCl/NaCl tuz kompozisyonunun, baryum hekzaferrit oluşum miktarında, son plaka morfolojisinde ve manyetik özelliklerde önemli bir role sahip olduğu vurgulanmıştır.

Anahtar Sözcükler: Eriyik Tuz Sentezi (MSS), Morfoloji, Plakalar, Manyetik özellikler, Ferritler

2. INTRODUCTION

Technological developments and innovations have promoted widespread usage of electromagnetic waves with a broad band frequency range. The electromagnetic waves are used in various civilian and military application areas such as radars, telecommunication systems, wireless information transfer along with medical diagnostic and research systems [1]. These applications operate at high frequencies and wide frequency bands and need to meet both high performance and operational security requirements with acceptable stability. These requirements boosted the development of electromagnetic wave absorbing material, as the interaction of emitted waves with the environment and with each other has become a growing social and industrial problem. In this context, research studies have been focused on the development of electromagnetic (EM) wave absorbing and interference shielding materials made of ferrites.

Ferrites having certain magnetic and dielectric properties have been used extensively for various purposes, such as permanent magnets, chip inductors [1, 2], microwave absorbers, etc. Polycrystalline barium hexaferrite ($BaFe_{12}O_{19}$) is a hexagonal ferrimagnetic ceramic commonly used in permanent magnets [3]. It has a large saturation magnetization, high Curie temperature, excellent chemical stability and high corrosion resistance, and it is relatively easily processed [4].

Various chemical methods such as the sol–gel process [5], hydrothermal synthesis [6],chemical co-precipitation [7], crystallization from a glass precursor [7], spray-pyrolysis [8],and molten salt method [9] have been used for the production of barium hexaferrite ceramics. These methods result in varying particle sizes, morphologies and magnetic properties. In a former study on the composition and morphology of the ferrite ceramics, it has been shown that their magnetic properties are related to the anisotropy in the shape of the particles [8].

Molten salt synthesis (MSS) is a technique by which large (up to millimeter-size) seed crystals used in textured barium hexaferrite processing can be synthesized. This method allows for the low temperature synthesis starting from mixed oxides [10]. Reactions can be completed in a relatively short time interval because of the short diffusion distances and highmobility of raw materials in molten salts in addition to the high reactivity of the salts [11].

In the present study, barium hexaferrite platelets with micron sizes were synthesized by molten salt synthesis method using barium carbonate and iron(III) oxide as the raw materials. This specific synthesis method was shown to allow the preparation of complex oxide ceramics with anisometric morphologies [12, 13] which will further facilitate fabrication of bulk materials with crystallographically textured microstructures [14-16]. The effect of synthesis time and temperature, as well as, flux type and concentration on the formation, morphology and magnetic behavior of the barium hexaferrite ceramics has been investigated.

3. EXPERIMENTAL PROCEDURE

In this process, reagent grade powders of $Fe2O_3$ (Sigma-Aldrich, 99.999%), $BaCO_3$ (Sigma-Aldrich, 99%), KCl (Sigma-Aldrich, 99%) and NaCl (Sigma-Aldrich, 99.5%) were used as the raw materials. Fe_2O_3 and $BaCO_3$ were mixed in a molar ratio of $Fe_2O_3/BaCO_3$=5.3 based on a former report [16, 19].

To investigate the effects of time and temperature, as well as, flux type on the formation and morphology of barium hexaferrite ceramics, $Fe_2O_3/BaCO_3$ mixtures were added to the salt mixture with the following compositions; 100 wt% NaCl, 90 wt% NaCl–10 wt% KCl, 44 wt% NaCl–56 wt% KCl (1:1 mol), 90 wt% KCl–10 wt% NaCl and 100 wt% KCl (Fig. 1). The initial mixtures comprised of 50 wt% flux and 50 wt% oxide/carbonate mixture (Fe_2O_3:$BaCO_3$, 5.3:1 mol) were calcined at 850, 900 and 950 °C for 1, 2, 2.5 and 3.5 h.

Additionally, the average platelet radius was measured by applying quantitative metallographic analysis on the scanning electron microscope (FE-SEM, FEI 430 NanoSEM, Oregon-USA) images of the solid residues. X-Ray diffraction (XRD) technique was used to determine the phase content of the obtained powders and platelets. Rigaku D/MAX2200/ PC with Cu K_α source having $K_{\alpha1}$=1.54056 Å and $K_{\alpha2}$=1.5444 Å wavelengths was utilized in the 2θ range of 15º to 80º with a scanning rate of 2º/min. Quantitative XRD analyses were applied to the solid residues obtained from the flux compositions of 100 wt% NaCl, 90 wt% NaCl–10 wt% KCl, 44 wt% NaCl–56 wt% KCl (1:1 mol), 90 wt% KCl–10 wt% NaCl and 100 wt% KCl by using the software of Rigaku D/MAX2200/ PC . Rietveld refinement was applied to the XRD analyses using General Structure Analysis System (GSAS) which is based on the non-linear least squares approach. Before starting the GSAS refinement, Configuration Management Process(CMPR) software was utilized to convert the raw data to GSAS format. The resulting data was then run through GSAS and after several cycles of refinement, structures for all compositions investigated were obtained.

Magnetic behavior of the synthesized barium hexaferrite ceramics was investigated via magnetic hysteresis curves recorded by vibrating sample magnetometer (VSM) (Cryogenic Limited PPMS, London-UK) at 300 K.

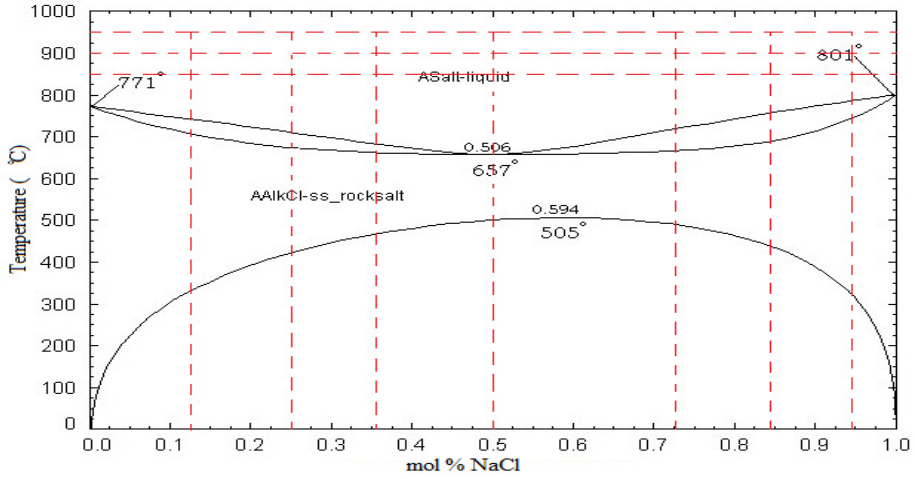

Figure 1. Binary phase diagram of NaCl and KCl on which the studied compositions and temperatures are labeled.

4. RESULTS

The platelets were synthesized in order to be used in a further study for the fabrication of textured bulk barium hexaferrite ceramics utilizing tape casting technique. Thus, the largest possible platelet radius with high aspect ratio is desired. Calcination time, temperature and flux type were investigated systematically in order to determine the optimum condition to achieve maximum possible platelet size.

Fig. 2 shows the platelet size distribution as a function of flux composition for varying calcination durations and temperatures. In Fig. 2, it is observed that under all conditions platelet size in KCl flux is the smallest. With the increase in the NaCl flux content, platelet size increases. However, after a certain concentration approaching to the equi-molar flux composition, platelet size starts to decrease. It should be noted that platelet size in NaCl flux was larger than that in KCl for all of the calcination temperatures and durations applied. This demonstrates the lower apparent activation energy for platelet growth in NaCl rich fluxes. As a result, for the same calcination temperatures and durations, platelet growth is more pronounced in NaCl flux compared to that in the KCl flux. Compared to other temperatures, platelet size at 900 °C was the largest for most of the compositions, especially for 2 h calcination duration. For this reason, morphology studies using SEM were concentrated on the barium hexaferrite ceramics calcined at 900 °C for 2 h.

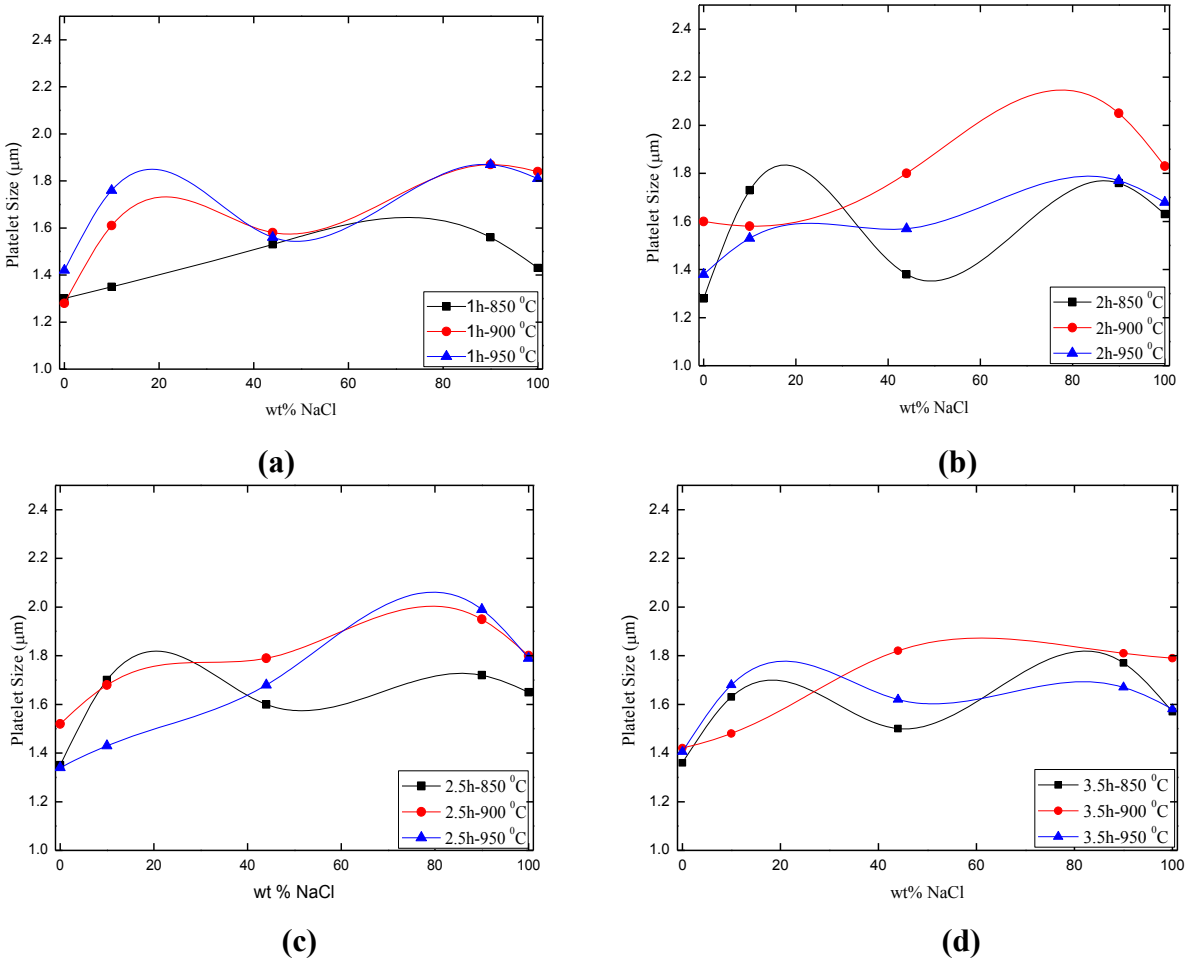

Figure 2. Particle size as a function of flux composition at 850, 900 and 950 °C for (a) 1 h, (b) 2 h, (c) 2.5 h and (d) 3.5 h of calcination.

As for the morphology of the barium hexaferrite platelets, in the case of the synthesis at 900 °C in NaCl flux, corners of the platelets became rounder (Fig. 3(e)). This is speculated to be caused by the selective desorption from the corners as a result of the chemical potential change around the sharp corners of the platelets in the molten NaCl flux. In the case of platelet synthesis in KCl flux, either no desorption occurred or desorption occurred homogenously on all of the surfaces and corners of the platelets so that platelet shape with sharp corners was preserved (Fig. 3(a)).

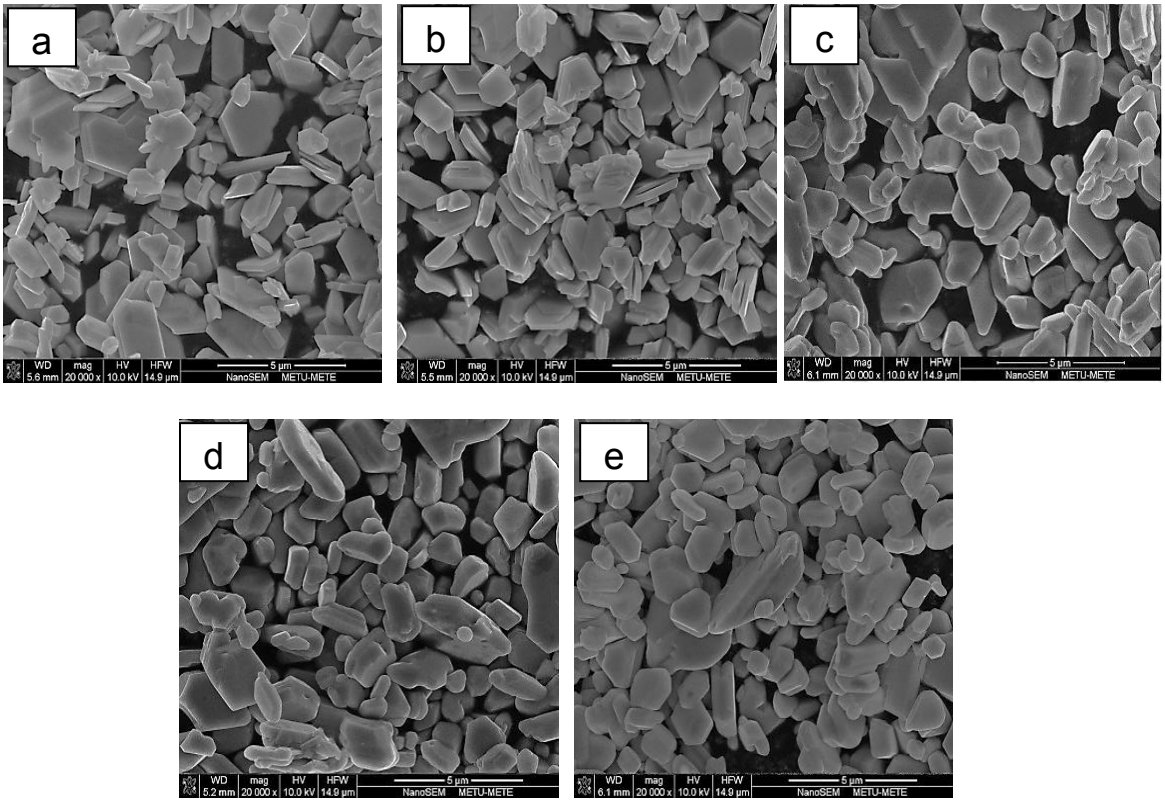

Figure 3. SEM images of barium hexaferrite platelets calcined in (a) 100 wt% KCl, (b) 90 wt% KCl–10 wt% NaCl, (c) 44 wt% NaCl–56 wt% KCl (1:1 mol), (d) 90 wt% NaCl–10 wt% KCl, and (e) 100 wt% NaCl at 900 °C for 2 h.

The aspect ratios of the platelets were approximately 3 to 4 for all calcination conditions (Fig 3 a-e). In addition to the platelet size and morphology, yield (mass of products/mass of raw materials) and amount of barium hexaferrite formation in the structure are crucial. Since the amount of flux evaporation during calcinations is unknown, yield of the barium hexaferrite ceramic production was calculated by ignoring the flux as raw material and product. A typical batch of 1.32 g containing equal amounts of salt and oxide/carbonate mixture gives 0.53 g barium hexaferrite resulting in a yield of ~80%. Furthermore, Fig. 4 shows the amount of barium hexaferrite formed during calcination at 900 °C for 2 h as a function of flux composition which was determined using quantitative XRD analysis. It is obvious that formation of barium hexaferrite phase within the system was the lowest when synthesis was done in 100 wt% KCl flux. With the increase in the NaCl content, the amount of barium hexaferrite phase increased gradually up to 97.8% at 100 wt% NaCl flux composition.

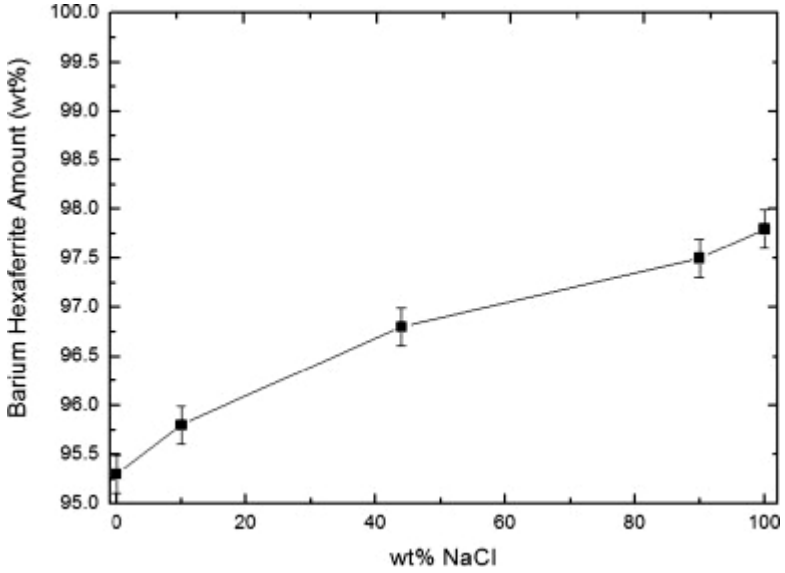

Figure 4. Quantitative XRD analysis of platelets calcined in varying flux compositions at 900 °C for 2 h.

Magnetization curves were taken at 300 K for the barium hexaferrite platelets synthesized at 900 °C for 2 h in 100 wt% KCl, 10 wt% NaCl, 44 wt% NaCl, 90 wt% NaCl and 100 wt% NaCl. In Fig. 5, M–H curves of synthesized barium hexaferrite ceramics exhibit a clear hysteresis behavior for the magnetization under applied magnetic field. When the applied magnetic field is around 10 kOe, the magnetization saturates.

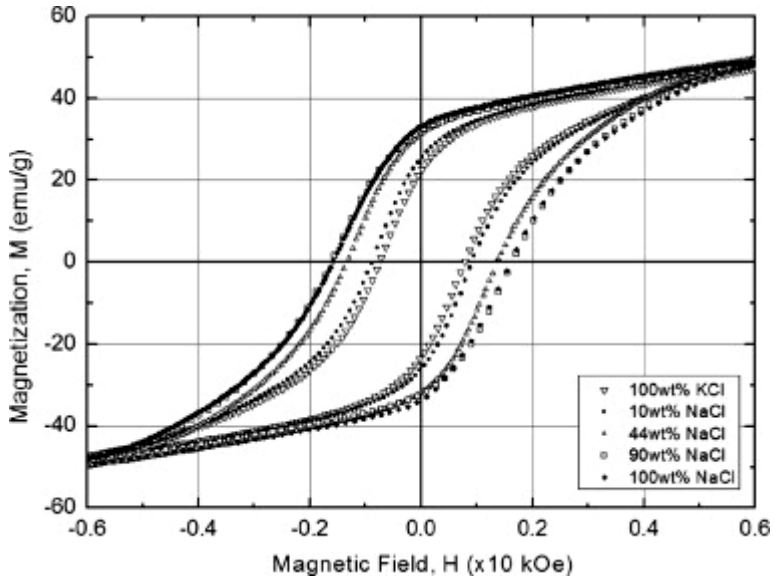

Figure 5. 300 K hysteresis curves of barium hexaferrite ceramics synthesized in 100 wt% KCl, 10 wt% NaCl, 44 wt% NaCl, 90 wt% NaCl and 100 wt% NaCl.

As the NaCl content in the molten flux increases, the area under the hysteresis curve increases, and the ceramic reveals a stronger hard magnetic behavior (Fig.5). The saturation magnetization (Ms), remanent magnetization (Mr), squareness ratio (Mr/Ms) and the coercive field (Hc) of the barium hexaferrite platelets obtained from Fig. 5 are given in Table 1.
As the NaCl content increases, there is an increase in barium hexaferrite amount that improves the hard magnetic behavior of the synthesized ceramics. Although magnetic saturation values change around 55 emu/g for all flux compositions, the highest saturation value of 56.5 emu/g was obtained in the case of 44 wt% NaCl composition. On the other hand, the highest coercivity of 1600 Oe was obtained for 90 and 100 wt% NaCl flux compositions. It is clear that NaCl content increase in the flux improves the barium hexaferrite conversion which in turn results in higher coercivity and remanent magnetization. High coercivity and remanent magnetization indicate the augmentation in the hard magnetic behavior of the synthesized ceramics.

Table 1. Magnetic properties of barium hexaferrite ceramics synthesized by molten salt synthesis method using five different molten flux compositions.

Flux Composition (wt %)	Barium Hexaferrite Amount (wt%)	H_c(Oe)	M_r(emu/g)	M_s(emu/g)	M_r/ M_s
100 wt % KCl	95.3	753	21.9	55.0	0.40
90 wt % KCl-10 wt % NaCl	95.8	838	25	54.3	0.45
44 wt % NaCl	96.8	1380	31.4	56.5	0.55
90 wt % NaCl	97.5	1600	32.0	55.2	0.58
100 wt % NaCl	97.8	1600	33.2	55.6	0.59

5. CONCLUSIONS

Micron size barium hexaferrite ($BaFe_{12}O_{19}$) platelets were prepared by molten-salt synthesis method in various weight proportions of NaCl–KCl salt mixtures. It was observed that NaCl plays a prominent role on the formation of barium hexaferrite phase. As the content of NaCl in the flux increases, barium hexaferrite formation is enhanced. The highest conversion which is 97.8% is obtained in the case of 100 wt% NaCl flux. The morphology of the barium hexaferrite platelets is also influenced by the NaCl–KCl flux composition. Platelets synthesized in NaCl flux are rounded which can be attributed to the selective desorption at the sharp corners of the barium hexaferrite platelets in NaCl rich fluxes.

However, either no desorption or homogenous desorption on all of the platelet surfaces occurs in the case of barium hexaferrite platelets synthesized in KCl leading to the preservation of cornered platelet morphology. The platelets synthesized in NaCl have higher average sizes than those synthesized in KCl.

Flux composition has clear impact on the magnetic properties of barium hexaferrite ceramics mainly based on the efficiency of transformation. Increasing NaCl content in the flux improves the coercivity and remanent magnetization of barium hexaferrite along with the area under the hysteresis curve leading to a more pronounced hard magnetic behavior in the synthesized ceramics. In conclusion, presented results demonstrate that the composition of the NaCl–KCl flux as the synthesis medium plays an important role on the extent of barium hexaferrite formation, resulting platelet morphology and the magnetic properties.

REFERENCES

[1]: Retrieved on 5th of May 2012, from http://www.wisegeek.com/what-is-an-electromagnetic-wave.htm
[2]: A. Ghasemi, X. Liu, A. Morisak, Magnetic and microwave absorption properties of BaFe12_x(Mn0.5Cu0.5Zr)x/2O19 synthesized by sol–gel processing, Journal of Magnetism and Magnetic Materials 316 (2007) e105–e108
[3]: K. Miura, K. Masuda, M. Itoh, T. Horikawa, K. Machida, J. Alloys Compds, in press
[4]: H. Cho, S. Kim, IEEE Trans. Magn. 35 (1999) 3151.
[5]: I. Nedkov, A. Petkov, IEEE 26 (1990) 1483.
[6]: M.R. Meshram, N.K. Agrawal, B. Shina, P.S. Misra, J. Magn. Magn. Mater. 271 (2004) 420.
[7]: A. Ghasemi, A. Hossienpour, A. Morisako, A. Saatchi, M. Salehi, Electromagnetic properties and microwave absorbing characteristics of doped barium hexaferrite, Journal of Magnetism and Magnetic Materials 302 (2006) 429–435
[8]: 1. T. Carisey, I. Levin, and D. G. Brandon, J. Eur. Ceram. Soc. 15, 283 (1995).
[9]: 3. E. Suvaci, M. M. Seabaugh, and G. L. Messing, J. Eur. Ceram. Soc. 19, 2465 (1999).
[10]: 4. T. Carisey, A. Laugierwerth, and D. G. Brandon, J. Eur. Ceram. Soc. **15**, 1 (1995).
[11]: D. B. Hovis and K.T. Faber, Textured Microstructures In Barium Hexaferrite By Magnetic Field Assisted Gelcasting And Templated Grain Growth, Scripta mater. 44 (2001) 2525–2529
[12]: Y. Du, H. Gao, X. Liu et al."Solvent-Free Synthesis Of Hexagonal Barium Ferrite ($BaFe_{12}O_{19}$) Particles'', J. Mater Sci, **45**, 2442–2448 (2010)
[13]: E. K. Akdogan, R. E. Brennan et al., ''Effects of Molten Salt Synthesis (MSS) Parameters on the Morphology of $Sr_3Ti_2O_7$ and $SrTiO_3$ Seed Crystals'', *J. Electroceram.* **16** 159–165 (2006).
[14]: R.H. Arendt, "The molten salt synthesis of single magnetic domain BaFe12O19 and SrFe12O19 crystals", Journal of Solid State Chemistry, 8 (4) pp. 339–347 (1973).
[15]: C. Duran, G.L. Messing, S. Trolier-McKinstry, "Molten salt synthesis of anisometric particles in the SrO–Nb2O5–BaO system", Materials Research Bulletin, **39** (11) pp. 1679–1689, (2004).
[16]: S. Dursun, R. Topkaya, N. Akdoan, S. Alkoy, "Comparison of the structural and magnetic properties of submicron barium hexaferrite powders prepared by molten salt and solid state calcination routes", Ceramics International, **38** (5) pp. 3801–3806, (2012).

PRODUCTION OF ZRB_2-$TİB_2$ CERAMIC POWDERS BY SHS

Ayşe Ece Yıldızcelik[1], Mehmet Buğdaycı[1, 2], Onuralp Yücel[1]

yildizcelik@itu.edu.tr, mbugdayci@itu.edu.tr, yucel@itu.edu.tr

[1]İstanbul Technical University, Metallurgy and Materials Engineering, Maslak, Istanbul, 34469, Turkey

[2]Yalova University, Chemical and Process Engineering Department, Yalova, 77100, Turkey

ABSTRACT

ZrB_2 and TiB_2 are one of the most significant metal borides. They are being used in various industrial areas from space technology to nuclear industry owing to their physical properties such as high melting point, high thermal/electrical conductivity and low density. Present study was conducted in two main stages: Self-propagating high-temperature synthesis (SHS) reactions and leaching. ZrO_2, TiO_2, B_2O_3 were used as starting material to produce ZrB_2-TiB_2 powders via SHS. Therefore, it was aimed to determine production parameters, leaching conditions and comprehensive examination of final product features.

INTRODUCTION

Nowadays, consumption of high-tech ceramics in industry have been increasing depending on advancing technology. High-tech ceramics are divided into sub-groups: carbides, borides,nitrites and silicates.

Borides is the remarkable part of high-tech ceramics. Compound between a metal and a nonmetal is called as "boride". ZrB_2 and TiB_2 have specific properties of IVB group such as: high hardness, high melting point, high thermal conductivity, high electrical conductivity and low density [1]. Owing to these properties, they are being used in various industrial areas such as metallurgy, aeronautical industry and nuclear industry. IVB group metals can be produced by carbothermic reduction, metallothermic reduction, fused salt electrolysis or powder metallurgy [1].

Most important sources of zirconium are Zircon ($ZrSiO_4$) ve baddeleyit (ZrO_2) minerals. The ore deposits are located in USA, Bu maden yatakları ABD,Australia, Brazil, India, and Russia [2]. Well known sources of titanium are rutile (TiO_2) and ilmenite (Fe-TiO_3). Bu maden yatakları These ore deposites are located in USA, Australia, Sri Lanka, New Zealand, Uruguay and Mozambique [3]. %80 of boride reserve of World is found at Turkey.

Furthermore, Dünya bor rezervlerinin %80'i ülkemizde bulunmaktadır. Colemanite (%50,8 B_2O_3), ulexite (%43 B_2O_3), and borax (%36,5 B_2O_3) having highest grade are found at Turkey. Reserves at Turkey are generally compoused of colemanite, and it is approximately 1.4 gigaton [4]. Experiments were carried out in two main stages. One of them is self-propagating high-temperature synthesis (SHS) reactions, and other one is leaching. ZrO_2, TiO_2, B_2O_3 were used as starting material to produce ZrB_2-TiB_2 powders by SHS. Therefore, it was aimed to determine production parameters, leaching conditions and comprehensive examination of final product features.

EXPERIMENTAL STUDIES

Producing of zirconium diboride- titanium diboride powders by SHS was aimed with experiments. Experimantal studies were carried out in two main stages. At first stage: TiO_2, ZrO_2, B_2O_3 were used as starting material and Mg was used as reductant to produce ZrB_2-TiB_2 powders. Purifying of SHS product by acid leaching was aimed at the second stage of experimantal studies.

SHS EXPERIMENTS

Before SHS experiments, ZrO_2, TiO_2, B_2O_3 ve Mg powders prepeared in various ratio and weighed. Prepared blends were mixed in turbula mixer during 15 minutes. After that, starting blend was put in copper curicible, and tungsten wire was inserted in the blend owing to this electric connection was provided. After cooling, SHS product was grinded to prepare leaching process. Weight ratio and amount of raw materials which was used at starting blend are shown at Table.1.

Table 1. SHS starting blend parameters and final product

Number	Ratio Zr/Ti	ZrO2	TiO2	B2O3	Mg	Amount of SHS final product
1	90/10	23,202 g	2,964 g	41,9 g	31,92 g	90 g
2	80/20	20,642 g	5,928 g	40,12 g	33,33 g	90,3 g
3	70/30	18,046 g	8,892 g	38,324 g	34,371 g	71,9 g
4	60/40	15,468 g	11,856 g	36,53 g	36,14 g	71,8 g
5	50/50	12,89 g	14,82 g	34,74 g	37,54 g	91,2 g
6	40/60	10,312 g	17,784 g	32,94 g	38,95 g	94,9 g
7	30/70	7,734 g	20,748 g	31,2 g	40,4 g	57 g
8	20/80	5,156 g	23,712 g	29,3 g	41,7 g	97,5 g
9	10/90	2,578 g	26,676 g	27,572 g	43,16 g	60,3 g

LEACHING EXPERIMENTS

Merck quality 37% HCl acid was used at leaching experiments. Distilled water was used when solution was preparing. 100 ml solution was prepared for leaching experiments. Leaching experiments were carried out for 20 g specimen using magnetic stirrer at 80 °C .The solutions obtained by leaching were prepared for chemical analysis. Leaching cakes were dried at drying owen during 24 hours. After that XRD analysis of the leaching cakes was made. Leaching parameters and amount of final product are shown at Table 2.

Table 2. Leaching parameters

Number	%37- HCl (ml)	Filter Paper (g)	Final Product (g)
1	52,48	1,043	7,27
2	46,02	1,03	6,65
3	47,9	1,04	7,18
4	49,9	1,03	4,4
5	51,87	1,03	8,99
6	53,82	1,02	8,36
7	55,82	1,06	8,91
8	57,59	1,01	8,92
9	59,61	1,03	8,8

RESULTS

TiB_2, ZrB_2, MgO and $Mg_3B_2O_6$ phases were detected at SHS product. XRD analysis of specimen-5 is shown at Figure 1.

Figure 1. XRD analysis of specimen-5 (After SHS)

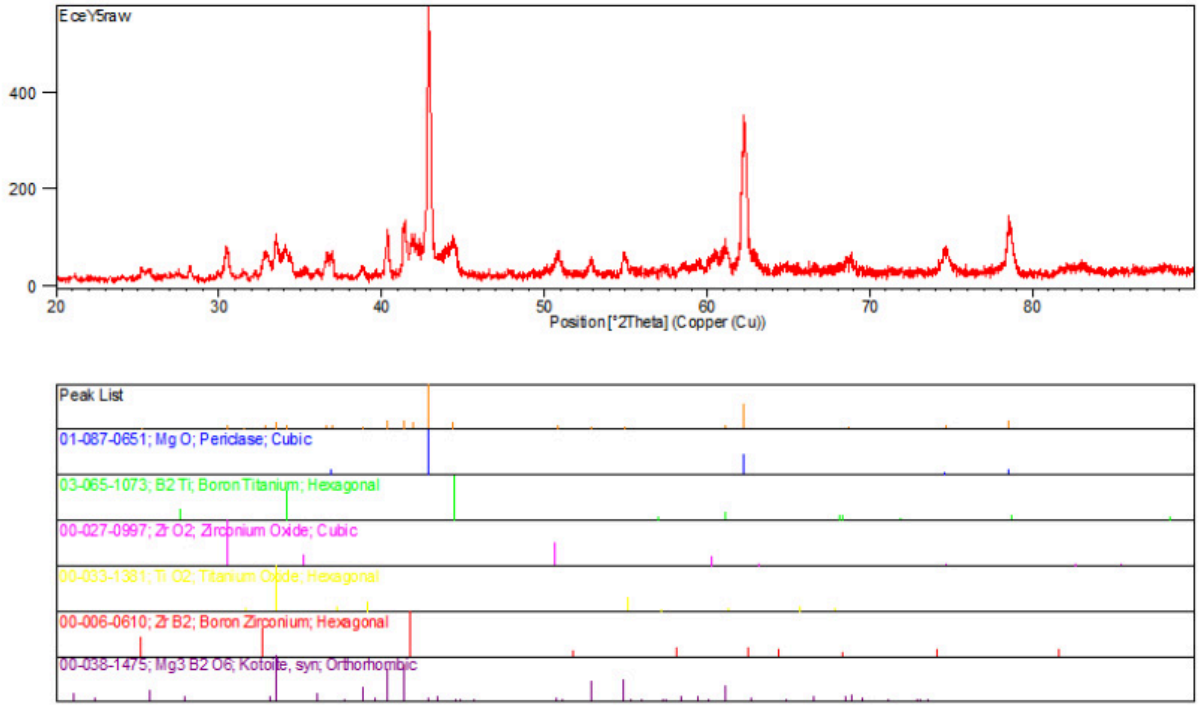

At the result of leaching experiments, MgO phases could not be eliminated. Also, a far amount of ZrB_2 dissolved. XRD analysis of specimen-5 is shown at Figure 2.

Figure 2. XRD analysis of specimen-5 (After Leaching)

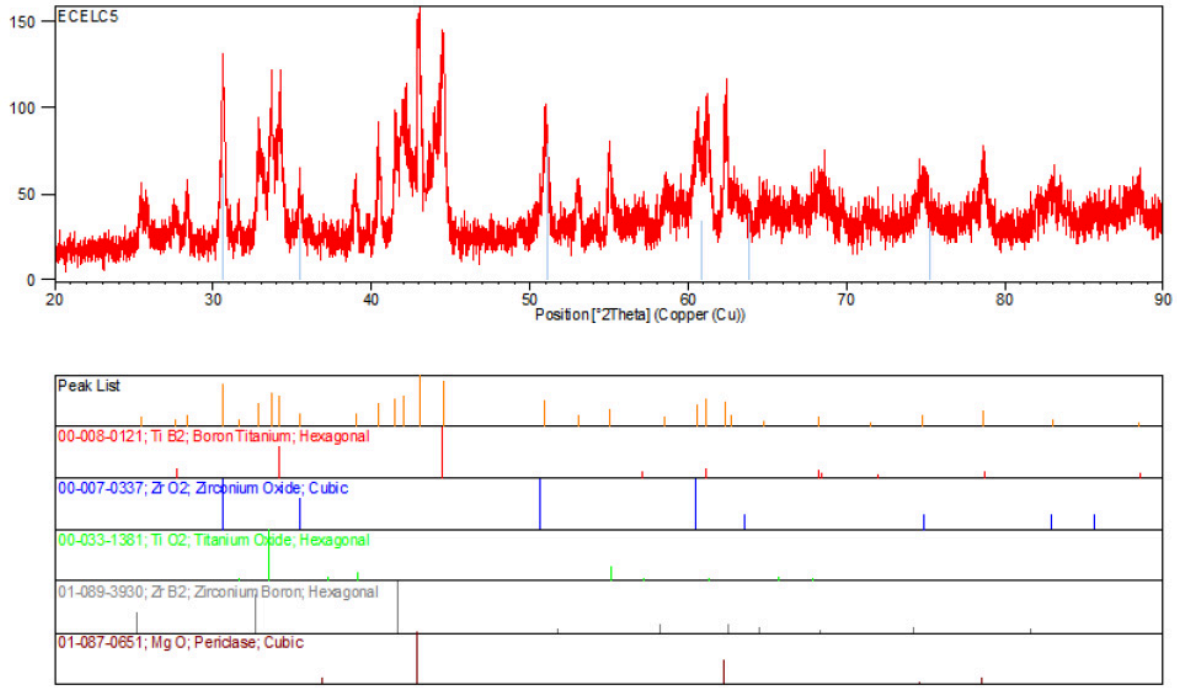

CONCLUSION

Present study have not yet completed. Optimization of leaching parameters will be completed. After that, effect of different reductants and catalyst will be examined.

REFERENCES

[1] Riedel, R, 2000 Handbook of ceramic hardmetals Vol. 1, sf.875-876,WILEY-VCH Verlag GMBH, Weinheim

[2] Habashi, F., 1997: Boron in Handbook of Extractive Metallurgy, Vol. 4, pp. 1431-1458, Wiley-VCH, New York.

[3] Clarke, G., Titanium Minerals, Industrial Minerals, (1986)

[4] TMMOB Chamber of Metallurgical Engineers, 2003, Boron Report

THERMAL AND STRUCTURAL CHARACTERIZATION OF QUATERNARY ANTIMONITE GLASSES

Ali Erçin ERSUNDU[*], Miray ÇELİKBİLEK[**], Mohamed Toufik SOLTANI[***], Süheyla AYDIN[**]

*Nişantaşı University, Istanbul, Turkey
aliercin.ersundu@nisantasi.edu.tr
**Istanbul Technical University, Istanbul, Turkey
miraycelikbilek@gmail.com, saydin@itu.edu.tr
*** University of Biskra, Biskra, Algeria
mt.soltani@univ-biskra.dz

ABSTRACT

Antimonite glasses in the quaternary system Sb_2O_3–Na_2O-WO_3-PbO were prepared by using melt-quenching technique. Glass formation behavior, thermal, physical and structural features of these quaternary glasses were investigated by X-ray diffraction (XRD), differential scanning calorimetry (DSC) and FTIR analysis according to the increasing PbO content in the expense of Sb_2O_3 and WO_3 at constant Na_2O. Thermal behavior of the glasses was studied in terms of glass transition temperature (T_g), crystallization temperature (T_c/T_p) and glass stability against crystallization (ΔT). Density (ρ), molar volume (V_M), oxygen molar volume (V_O), oxygen packing density (OPD) and related structural parameters such as average cross-link density (n_c), Poisson's ratio (μ_{cal}) and number of bonds per unit volume (n_b) values were calculated for the physical investigation of the glasses. FTIR spectra of the glasses were interpreted in terms of the structural transformations on the glass network by the changing composition.

Keywords: Sb_2O_3 glasses, FTIR, thermal properties, physical parameters

ANTİMON OKSİT ESASLI CAMLARIN ISIL VE YAPISAL İNCELENMESİ

ÖZET

Antimon oksit esaslı camlar, Sb_2O_3–Na_2O-WO_3-PbO dörtlü sisteminde ergitme-döküm tekniği ile hazırlanmıştır. Bu camların cam oluşturma davranışları, ısıl, fiziksel ve yapısal özellikleri sabit Na_2O bileşiminde artan PbO ve azalan Sb_2O_3 ve WO_3 bileşimine bağlı olarak X ışınları difraksiyonu (XRD), diferansiyel taramalı kalorimetre (DSC) ve FTIR analizleri ile incelenmiştir. Camların ısıl davranışları cam geçiş (T_g) ve kristalizasyon (T_c/T_p) sıcaklıkları ve cam kararlılık (ΔT) değerleri açısından incelenmiştir. Yoğunluk (ρ), molar hacim (V_M), oksijen molar hacim (V_O), oksijen paketleme yoğunluğu (OPD) değerleri ve ortalama çapraz bağlanma yoğunluğu (n_c), Poisson oranı (μ_{cal}) ve birim hacim başına düşen bağ sayısı (n_b) değerleri camların fiziksel açıdan incelenmeleri amacıyla hesaplanmıştır. FTIR analizleri ile değişen bileşimle cam şebekesinde meydana gelen yapısal dönüşümler incelenmiştir.

Anahtar Kelimeler: Antimon oksit camlar, FTIR, ısıl özellikler, fiziksel parametreler

1. INTRODUCTION

Heavy metal oxide glasses have attracted great attention of researchers for their potential use in opto-electronic applications due to their broad transparency from visible to infrared region, high solubility of rare-earth ions and good non-linear optical properties [1-6]. Among all heavy metal oxide glasses, antimony oxide-based glasses have appeared promising since they possess low phonon energy and large optical non-linearity that is correlated to high refractive index, good mechanical properties, and better chemical durability than that of fluoride or tellurite glasses [1-5,7,8]. These advantageous properties make them potential candidates for non-linear optical devices like ultra-fast optical switches and power limiters [9]. They also have potential for broad band optical amplifiers operating around 1.5 mm as antimony-silicate glass fibers and in the field of optical amplification in telecommunication C-band (1530 - 1560 nm) [1,10].

Numerous Sb_2O_3-based binary and multi-component glasses including conventional glass formers have been reported in the literature [1-4,7,8,11-14]. In this paper we aim to present new quaternary antimonite glasses in the Sb_2O_3-Na_2O-WO_3-PbO system.

In order to develop new glasses for opto-electronic applications, the knowledge of the physical properties of glasses together with their thermal and structural properties seems to be a useful tool for understanding the structure of glass. Therefore, in the present study the authors aim to investigate the thermal, physical and structural properties of Sb_2O_3-Na_2O-WO_3-PbO glasses by applying XRD, DSC and FTIR techniques.

2. EXPERIMENTAL

In the experimental studies, to prepare and characterize antimony oxide-based multicomponent glasses, high purity chemicals of Sb_2O_3 (Acros, 99.99%), PbO (Aldrich, 99.9%), WO_3 (Aldrich, 99.995%) and Na_2CO_3 (Aldrich, 99.99%) were used as starting materials in the quaternary glassy system: Sb_2O_3-Na_2O-WO_3-PbO. The glass synthesis was realized with a conventional melt-quenching method in open silica glass crucibles. After weighing and thoroughly mixing, powder batches of 5 g in weight were flame heated at a temperature close to 900 °C for 15 minutes in air. Vitreous samples were obtained by pouring the melts onto brass molds. The samples were annealed near the glass transition temperature for 6 hours in order to remove their thermal history. For different physical measurements, a set of samples were prepared according to the following composition rule: $x$$Sb_2O_3-10Na_2O$-$y$$WO_3$-$z$PbO, z varying between 10 and 40 (mol %), the ratio x/y=6 is maintained constant and $x+y+z$=90. Compositions of the prepared glasses are given in Table 1 with their sample ID's.

X-ray diffraction (XRD) investigations were carried out to check the amorphous nature of the samples in a Bruker^{TM} D8 Advanced Series powder diffractometer using Cu K_α radiation in the 2θ range from 10° to 90°.

Differential scanning calorimetry (DSC) analyses were realized to investigate the thermal behavior of the glass samples in a Netzsch DSC 204 F1 (limit of detection: <0.1 μW, with an

error estimate of ± 1 °C) using a constant sample weight of 25 ± 1 mg in aluminum pans, under flowing (25 ml/min) argon gas with a heating rate of 10 °C/min. The glass transition onset (T_g), first crystallization onset and peak (T_c/T_p) temperatures were determined from the DSC scans. The glass transition onset temperatures (T_g) were determined as the inflection point of the endothermic change of the calorimetric signal. Crystallization onset temperatures were specified as the beginning of the reaction where the crystallization first starts and peak temperatures represent the maximum value of the exotherm. The temperature difference between the glass transition (T_g) and the first exothermic peak onset (T_{c1}), $\Delta T = T_{c1} - T_g$, representing the value of glass stability was calculated for all glass samples.

Densities, ρ, of the glasses were determined at room temperature by the Archimedes' principle with an error of ± 0.1 % using ethanol as the immersion liquid and a digital balance of sensitivity 10^{-4} g. Density values obtained by three repeated measurements showed an error of ± 0.1 %.

The molar volume, V_M, oxygen molar volume, V_O, oxygen packing density, OPD, average cross-link density, $\overline{n_c}$, number of bonds per unit volume, n_b and Poisson's ratio, μ_{cal} values were calculated to investigate the physical properties of Sb_2O_3-Na_2O-WO_3-PbO glasses.

The molar volume, V_M was calculated as a function of the molar fraction of each of the four components and the oxygen molar volume, V_O, was calculated by using the following expression [15,16]:

$$V_O = \left(\Sigma \frac{x_i M_i}{\rho} \right) \left(\frac{1}{\Sigma x_i n_i} \right) \quad (1)$$

where x_i is the molar fraction of each component i; M_i is the molecular weight; ρ is the glass density and n_i is the number of oxygen atoms in each oxide.

Oxygen packing density of the glasses, OPD, was calculated using the density and composition values by applying the following formula:

$$OPD = 1000C(\rho / M) \quad (2)$$

where C is the number of oxygen atoms per each composition, ρ is the density and M is the molecular weight of the glass sample [15,16].

Average cross-link density, $\overline{n_c}$, of the glasses was calculated using the following relation:

$$\overline{n_c} = \frac{\sum_i x_i (n_c)_i (N_c)_i}{\sum_i x_i (N_c)_i} \quad (3)$$

where x_i is the molar fraction of each component, n_c is the cross-link per cation and N_c is the number of cations per glass formula unit [15,17].

Number of bonds per unit volume of the glasses, n_b, was calculated by applying the following

formula:

$$n_b = \frac{N_A}{V_M}\sum_i (n_f x)_i \quad (4)$$

where N_A is the Avogadro's number, V_M molar volume of the glass sample, n_f coordination number of the cations, x molar fraction of each component oxide and i represents the component oxide [15,17].

Poisson's ratio of the glasses, μ_{cal}, was calculated theoretically according to the following expressions:

$$\mu_{cal} = 0.5 - \frac{1}{7.2V_t} \quad (5)$$

$$V_t = \frac{\rho}{M}\sum_i x_i V_i \quad (6)$$

$$V_i = \frac{4\pi N_A}{3}(nr_A^3 + mr_O^3) \quad (7)$$

where V_t is the packing density, ρ density and M molecular weight of the glass sample, V_i packing factor of the oxide A_nO_m, N_A Avogadro's number, r_A and r_O are the ionic radius of cation A and anion O, respectively [15,17].

Fourier transform infrared (FTIR) spectroscopy analyses were realized to investigate the structural transformations on the glass network at room temperature, using the CsI pellet technique, in the wave number range from 1200 to 400 cm^{-1} with a resolution of 1 cm^{-1} using a Perkin Elmer Frontier spectrometer. For FTIR experiments 0.005 g of glass samples were weighed, mixed and ground with 0.5 g CsI. After which the mixture was pressed at 10 tons, to yield transparent disks suitable for mounting in the spectrometer.

3. RESULTS AND DISCUSSION

XRD analysis was carried out to identify the amorphous nature of the samples and as seen from Figure 1 the XRD patterns revealed no detectable peaks proving their vitreous structure.

DSC analysis was performed to investigate the thermal properties of Sb_2O_3-Na_2O-WO_3-PbO glasses. DSC curves of the glass samples are shown in Figure 2 and thermal analysis details are given in Table 1.

A shallow endothermic change between 287 and 289 °C corresponding to the glass transition temperature (T_g) was observed for the glasses and the glass transition temperatures showed a slight increase with increasing PbO content. Similar to the change observed in T_g, first crystallization onset temperatures showed an increase with increasing lead oxide content. As reported in the literature, the increase in both glass transition and crystallization temperatures with increasing modifier (PbO) content is due to the increase in number of bonds per unit volume [18,19].

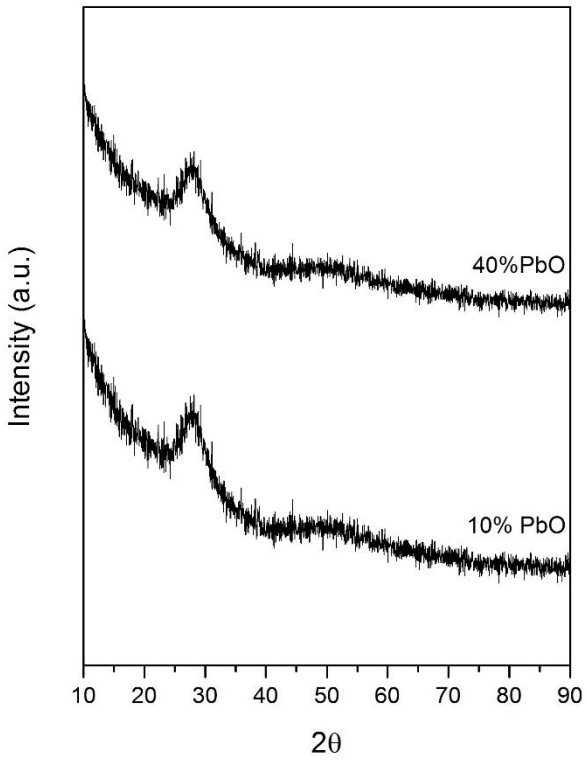

Figure 1: X-ray diffraction patterns of Sb_2O_3-Na_2O-WO_3-PbO glasses

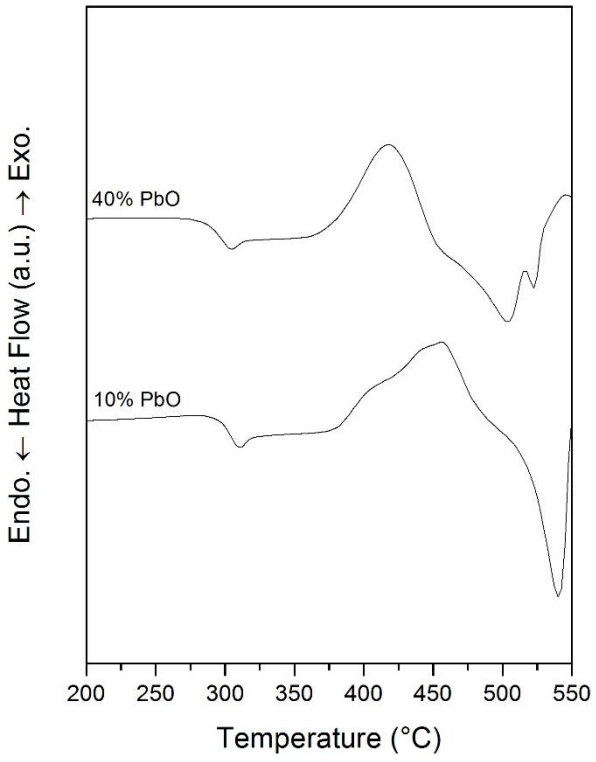

Figure 2: DSC curves of Sb_2O_3-Na_2O-WO_3-PbO glasses

The temperature difference between T_g and the first exothermic peak onset T_{c1}, ΔT, indicating the glass stability against crystallization varied between 86 and 89 °C and it was found that the ΔT values showed a slight increase with increasing PbO content. The glass stability value of the glasses should usually be larger than 100 °C to obtain thick glass samples for their

possible use in opto-electronic applications [18]. Therefore, the ΔT values obtained for Sb_2O_3–Na_2O-WO_3-PbO glasses might not be sufficient to obtain thick samples.

Table 1. Glass transition (T_g) and first crystallization onset and peak (T_{c1}/T_{p1}) temperatures and glass stability (ΔT) values of Sb_2O_3–Na_2O-WO_3-PbO glasses.

Sample ID	Sb_2O_3	Na_2O	WO_3	PbO	T_g	T_{c1} / T_{p1}	ΔT
	mol%				(°C)	(°C)	(°C)
SNWP1	68.57	10	11.4	10	287	373 / -	86
SNWP2	42.86	10	7.14	40	289	378 / 412	89

- : undetermined values

Physical properties of Sb_2O_3–Na_2O-WO_3-PbO glasses were investigated by measuring the density, ρ, molar volume, V_M, oxygen molar volume, V_O and oxygen packing density, OPD values and the obtained values are given in Table 2.

Table 2. Values of density (ρ), molar volume (V_M), oxygen molar volume (V_O), oxygen packing density (OPD), average cross-link density ($\overline{n_c}$), number of bonds per unit volume (n_b) and Poisson's ratio (μ_{cal}) of Sb_2O_3–Na_2O-WO_3-PbO glasses.

Sample ID	ρ 25 °C (g/cm^3)	ρ theoretical (g/cm^3)	V_M (cm^3/mol)	V_O (cm^3/mol)	OPD (mol/l)	$\overline{n_c}$	n_b (x10^{21} cm^{-3})	μ_{cal}
SNWP1	5.31	5.56	48.01	31.55	54.16	2.21	75.24	0.174
SNWP2	5.68	6.78	41.72	31.92	47.94	2.13	77.92	0.158

The density values of the glasses changes between 5.31 and 5.68 g/cm^3 and they showed an increase with increasing PbO content. Densities of glasses were found to be consistent with their theoretical values. The increase in the density with increasing PbO content is due to the higher density of PbO among other constituent oxides.

The molar volume values were calculated by taking the measured densities into account. Calculated molar volume values exhibited a decrease with increasing PbO content from 48.01 to 41.72 cm^3/mol. The decrease in molar volume values with increasing PbO content is due to the decrease in the percentage of oxygen atoms which have the highest ionic radius in the glass structure (O^{2-}: 0.14nm, Sb^{3+}: 0.076nm, W^{6+}: 0.065nm, Pb^{2+}: 0.119nm) [15,20].

Oxygen molar volume and oxygen packing density values exhibited opposite behavior to each other. The oxygen molar volume values showed an increase from 31.55 to 31.92 cm^3/mol with increasing PbO content. On the other hand, oxygen packing density values showed a decrease from 54.16 to 47.94 mol/l with increasing PbO concentration. It can be said that in Sb_2O_3-Na_2O-WO_3-PbO glasses due to the substitution of higher field intensity constituent ions (Sb^{3+}: 0.73, W^{6+}: 1.47 with lower field intensity Pb^{2+} ions (0.27) a slight increase in oxygen molar volume and a decrease in oxygen packing density values were observed which results a less dense glass structure [15,21].

In order to interpret thermal and physical properties of Sb_2O_3-Na_2O-WO_3-PbO glasses deeply,

structural parameters such as average cross-link density, $\overline{n_c}$, number of bonds per unit volume, n_b, and Poisson's ratio, μ_{cal}, were calculated and the results are given in Table 2.

Average cross-link density values decreased from 2.21 to 2.13 with increasing PbO concentration which implies a decrease in the network connectivity. Number of bonds per unit volume increased from 75.24 to 77.92 x 10^{21} cm^{-3} with the increase in PbO content. Oppositely, the theoretically calculated Poisson's ratio values decreased from 0.174 to0.158 and decreased with increasing PbO content. The increase in number of bonds per unit volume and decrease in calculated Poisson's ratio with the increase in PbO concentration yields a rigid glass network.

FTIR spectra of Sb_2O_3–Na_2O-WO_3-PbO glasses in the spectral range of 1200-400 cm^{-1} are given in Figure 3. FTIR spectra of the glasses showed broad peaks and shoulders due to the disorder of the glass structure.

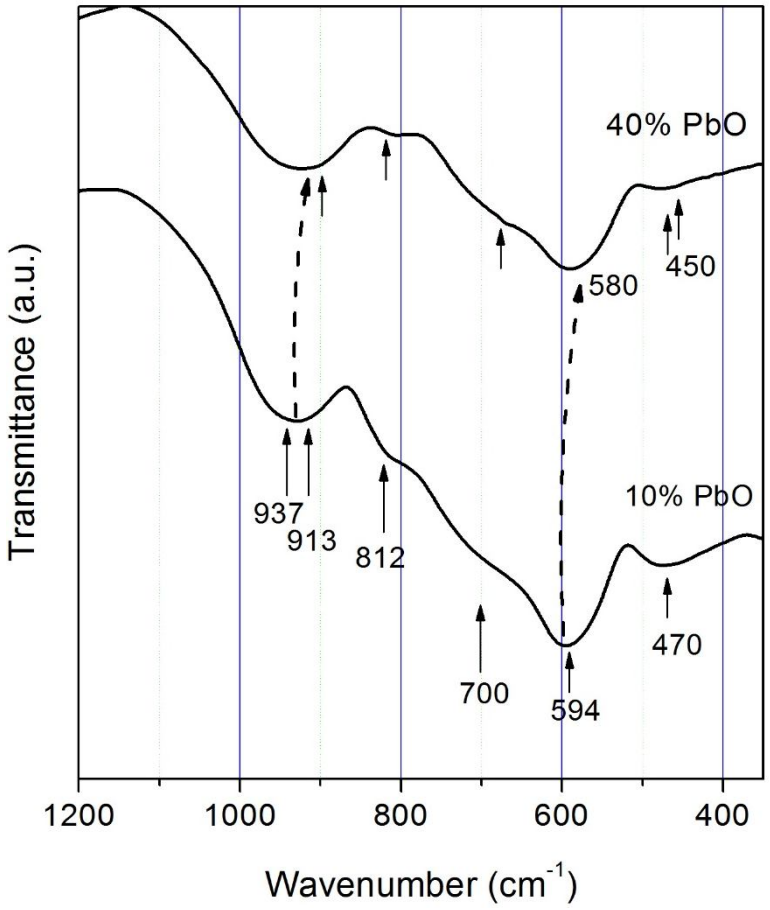

Figure 3: FTIR spectra of Sb_2O_3-Na_2O-WO_3-PbO glasses

The spectra for Sb_2O_3-Na_2O-WO_3-PbO glasses are dominated by four main bands centered at around 937, 700, 594 and 470 cm^{-1}. The band at 700 cm^{-1} corresponds to the v1 (sym. stretching) vibration mode and the band at 937 cm^{-1} is assigned to the Si–O stretching vibration of SiO_4 tetrahedra. It is thought that these bands are resulted from the contamination from the silica crucible used for glass synthesis. The bands at 594 and 470 cm^{-1} are related to

the ν4 (asym. bending) and ν3 (asym. stretching) vibration modes of SbO_3 of the valentinite form of Sb_2O_3 as reported by Terashima et al. [22]. With increasing PbO concentration, for 40 mol% PbO containing glass a new band appears at 450 cm^{-1} which can be assigned to the vibrational mode of covalent bonds in [PbO_4] or [PbO_3] units. In the literature it was observed that the equimolar substitution of Sb_2O_3 with PbO creates weak Sb–O–Pb bonds [23]. These weak bonds are thought to be the consequence of the presence of the band at 812 cm^{-1}. Similarly, the shift of [SbO_3] units from 594 to 580 cm^{-1} can be caused by the presence of weak bonds corresponding to Sb–O–Pb linkages. The intensity of this band increases with increasing PbO content therefore it excludes the possibility of assigning this band to W–O vibrations. In the FTIR spectra given in Figure 3, a weak shoulder at 913 cm^{-1} is found to be related to the tungstate units in Sb_2O_3-Na_2O-WO_3-PbO glasses. The decrease of WO_3 concentration with increasing PbO content results a shift of this band from 913 to 893 cm^{-1}. According to the literature, this shift is due to the change of tungsten coordination from [WO_6] to [WO_4] units [24].

4. CONCLUSIONS

In this work, thermal, physical and structural properties of glasses in the Sb_2O_3-Na_2O-WO_3-PbO system were investigated. Thermal investigations revealed that the glass transition and first crystallization onset temperatures showed a slight increase with increasing PbO content. Physical and structural investigations revealed that increasing PbO concentration in glass structure results a decrease in molar volume, oxygen packing density, average cross-link density and calculated Poisson's ratio values and on the contrary results an increase in the density, refractive index, oxygen molar volume and number of bonds per unit volume. By taking these changes into account, it can be concluded that increasing PbO content decrease the network connectivity of quaternary antimonite glasses which results less tightly packing of the glass network.

REFERENCES

1. K. Ouannes, M.T. Soltani, M. Poulain, G. Boulon, G. Alombert-Goget, Y. Guyot, A. Pillonnet, K. Lebbou, J. Alloy. Compd., 63, 132, 2014
2. M.T. Soltani, M. Hamzaoui, S. Houhou, H. Touiri, L. Bediar, A.M. Ghemri, P. Petkova Acta Phys. Pol. A, 123, 227, 2013
3. M. Hamzaoui, S. Azri, M.T.Soltani, R.Lebullenger, M. Poulain, Phys. Scr.,T157, 014029, 2013
4. M. Baazouzi, M.T. Soltani, M. Hamzaoui, M. Poulain, J. Troles, Opt. Mater, 36, 500, 2013
5. M.T. Soltani, A. Boutarfaia, R. Makhloufi, M. Poulain, J. Phys. Chem. Solids, 64, 2307, 2003
6. M. Çelikbilek, A.E. Ersundu, S. Aydin, J. Am. Ceram. Soc., 96, 1470, 2013
7. M. Hamzaoui, M.T. Soltani, M. Baazouzi, B. Tioua, Z.G. Ivanova, R. Lebullenger, M. Poulain, J. Zavadil, Phys. Status Solidi B, 249, 2213, 2012
8. P. Petkova, H. Touiri, M.T. Soltani, Acta Phys. Pol. A, 123, 2005, 2013
9. R.E. de Araujo, C.B. de Araujo, G. Poirier, M. Poulain, Y. Messaddeq, Appl. Phys. Lett,. 81, 4694, 2002
10. J. Minelly, A. Ellison, Opt. Fiber Tech., 8, 123, 2002
11. G. Poirier, M. Poulain, J. Non-Cryst. Solids, 284, 117, 2001
12. B.V. Raghavaiah, C. Laxmikanth, N. Veeraiah, Opt .Commun, 235, 341, 2004
13. M. Nouadji, A. Attaf, R. El Abdi, M. Poulain, J. Alloy. Compd., 511, 209, 2012
14. B. Dubois, H. Aomi, J.J. Videau, J. Portier, P. Hagenmuller, Mater. Res. Bull., 19, 1317, 1984
15. M. Çelikbilek, A.E. Ersundu, S. Aydin, J. Non-Cryst. Solids, 378, 247, 2013

16. A.E. Ersundu, M. Çelikbilek, N. Solak, S. Aydin, J. Eur. Ceram. Soc., 31, 2775, 2011
17. I.Z. Hager, R.A.H. El-Mallawany, J. Mater. Sci., 45, 897, 2010
18. R. El-Mallawany, I. Abbas Ahmed, J. Mater. Sci., 43, 5131, 2008
19. A.E. Ersundu, G. Karaduman, M. Çelikbilek, N. Solak, S. Aydin J. Alloys Compd., 508, 266, 2010
20. R.D. Shannon, Acta Crystall. A-Crys. 32, 751, 1976
21. D. Munoz-Martín, M.A. Villegas, J. Gonzalo, J.M. Fernández-Navarro, J. Eur. Ceram. Soc., 29, 2903, 2009
22. K. Terashima, T. Hashimoto, T. Uchnio, S. Kim, T. Yoko, J. Ceram. Soc. Jpn., 104, 1008, 1996
23. M.T. Soltani, T. Djouama, A. Boutarfaia, M. Poulain, J. Optoelectron. Adv. M., 1, 339, 2009
24. S. Al-Ani, C.A. Hogarth, R.A.H. El-Mallawany, J. Mater. Sci., 20, 661, 1985

THERMAL AND ENVIRONMENTAL CHARACTERISTICS OF GLASS PRODUCED FROM METALURGICAL WASTES

Ejup LJATIFI[*], Alexandra KAMUSHEVA[**], Alexander KARAMANOV[**], Perica PAUNOVIĆ[*]

Faculty of Technology and Metallurgy, University "SS Cyril and Methodius", Skopje, R. Macedonia
pericap@tmf.ukim.edu.mk
Institute of Physical Chemistry, Bulgarian Academy of Sciences, Sofia, Bulgaria
karama@ipc.bas.bg

ABSTRACT

The subject of this study is glass produced by mixed metallurgical waste from ferronickel production, aimed for further production of glass-ceramic. Characterization of waste materials includes determination of chemical and mineralogical composition and standard leaching test. The waste materials contain several heavy metals (Fe, Ni, Mn, Zn, Cr) which exceed the applied limits and can be potential hazard to the soils. On the other hand, the waste mixture contains sufficient amount of glass-forming component - SiO_2. The components in the waste mixture aimed for glass production were in the ratio as they are produced in the Fe-Ni smelter (flay ash:electro-furnace slag:converter slag = 1:10:1). Thermal characterization of the glass was performed by means of hot stage microscopy (HSM) and DTA analysis, where the temperatures of sintering, softening, smelting and crystallization were determined. The results highlight that fine-crystalline glass-ceramic with high crystallinity can be obtained. Standard leaching test has shown that the concentration of all heavy metals is bellow applied limits for 5 to 400 times. Thus, the produced glass is environmental safety product.

***Keywords*:** fly ash, electric furnace slag, converter slag, glass, glass-ceramic

1. INTRODUCTION

Disposal or stabilization of waste materials from metallurgical industry such as slags, dust, hydrometallurgical by-products etc., is not an easy task because of the complex composition and high content of regulated heavy metals as well as different local circumstances. Often, recovery of some metal can not be economic efficient or the recovery procedure produce new waste. Disposal of waste containing heavy metals can be hazardous to environment. Vitrification of hazardous wastes, i.e. transformation of waste materials to glass can be considered as an environmentally compatible stabilization process. It is considered as an ultimate method for immobilization hazardous wastes, because during glass melting, the harmful elements are chemically bonded in a durable amorphous network [1-3]. This significantly reduces their solubility and, in addition, drastically decreases waste in volume. On the other hand, depending on the composition, with or without any additives, the waste-based glass can be transformed to glass-ceramic with properties comparable or better than commercial ones. This is illustrated by numerous researches focused on using slags originated from iron and steel production for production of glass or glass-ceramic [4-10]. The research of Karamanov and co-workers was directed on production of glass and glass ceramic from by-products originated from zinc and copper hydrometallurgical production [11-15]. All these studies highlight good chemical, physical and mechanical properties of the produced glass or glass-ceramic, close or even better than those produced from virgin raw materials. Besides

technical and economic effects, this route of processing metallurgical waste materials was shown as environmental efficient. According to various standard leaching tests [16], the glass and glass-ceramic products based on metallurgical waste, are environmental friendly materials.
The aim of this study is vitrification of solid waste from ferronickel smelting plant, such as dust, slag from electro-furnace and converter slag. Characterization of waste materials and produced glass is directed to estimate their possibility for further production of glass-ceramic as well as to determine their environmental impact.

2. EXPERIMENTAL

Dust (D), electro-furnace slag (EFS) and converter slag (CS) from ferronickel smelting plant in R. Macedonia, were used as a raw material for glass production. Their annual production is in ratio D:EFS:CS = 1:10:1. The content of different type of waste was in this ratio within the waste mixture aimed for vitrification.
Chemical composition of the waste materials was determined by X-ray fluorescence (XRF) spectrometer (Model XRF ARL 9900). Mineralogical analysis was carried out by X-ray diffraction method using Philips APD 15 diffractometer, operating at CuKα-radiation. Diffraction data were collected at a constant rate of $0.02^{o}\cdot s^{-1}$ over an angle range of $2\theta = 5–90^{o}$.
To determine environmental impact of the waste materials, standard leaching test – TCLP (Toxicity Characteristic Leaching Procedure) was performed. Shown in Table 1 are the leaching test conditions. Concentrations of heavy metals after testing were measured by atomic absorption spectroscopy (AAS) using the instrumentation Perkin Elmer AA400.

Table 1. Leaching conditions according to TCLP test

Solvent	CH_3COOH
pH	5
Volume of the solution	2 L
Weight of solid phase	100 g
s:*l* ratio	1: 20
Intensity	30 rpm
Duration	24 h

To correct the content of MgO and Cr_2O_3 in the waste mixture (WM), standard glass (SG) powder was added in ratio WM:SG = 7:3. Waste materials and the standard glass were homogenized and melted in chamber furnace at $1450^{o}C$ for 1 h.
Thermal characteristics of the produced glass were studied by means of hot stage microscopy (HSM) and differential thermal analysis (DTA). A glass sample was observed in heating microscope MISURA HSML. The sample was heated from ambient to $1300^{o}C$ with heating rate of $1^{o}C\cdot min^{-1}$. During the heating reduction of dimensions and characteristic temperatures were recorded. DTA measurements were performed using a Perkin Elmer PYRIS Diamond Thermogravimetric/Differential Thermal Analyzer. The studied material was heated in the temperature interval of $25^{o}C \div 1100^{o}C$ by heating rate of $20^{o}C\cdot min^{-1}$ air atmosphere.
The glass sample was undergoing on standard TCLP leaching test. The test conditions are the same as in previous case shown in Table 1.

3. RESULTS AND DISCUSSION

Chemical composition of the waste materials is shown in Table 2. All waste materials have high amount of Fe, especially converter slag (CS). So, these wastes could be used for Fe extraction, but, there is not smelter for iron production in R, Macedonia. Only in the dust Ni content is appropriate to be returned in the Fe-Ni production process. Annual production of these waste materials is 102.000 t dust, 1.135.000 t slag from electro-furnace and 109.000 t converter slag. The ratio of their production is approximately D:EFS:CS = 1:10:1. On the other hand, the dust and slag from electro-furnace contain high enough SiO_2 - glass forming component. Also, the waste mixture has appropriate content of SiO_2 (47.8%) for glass forming. But, MgO and Cr_2O_3 is high in the waste mixture (15.9 and 2.2 % respectively) and can cause spontaneous uncontrolled crystallization. Cr_2O_3 is not soluble in the glass, while in lower amount can improve the nucleation during transformation of glass to glass-ceramic. Thus, the composition of the waste mixture should be corrected in order to reduce the content of MgO and Cr_2O_3. For this purpose standard glass (SG) was added in the waste mixture in ratio WM:SG = 7:3.

Table 2. Composition of dust (D), slag from electro-furnace (EFS), converter slag (CS), waste mixture (WM) in ratio D:EFS:CS = 1:10:1, standard glass and overall glass mixture in ratio WM:SG = 7:3

Item	D	EFS	CS	WM	SG	GM
SiO_2	37.5	53	1.9	47.8	71.4	55
MgO	14.5	16.9	6.2	15.9	3.3	12.1
CaO	2.3	2.4	15.9	3.5	9.8	5.4
Al_2O_3	1.8	2	0.3	1.9	0.6	1.5
Cr_2O_3	1	2.5	0.7	2.2		1.5
CoO	0.1	0.1	0.1	0.1		0.1
NiO	2.7	0.1	0.45	0.3		0.2
Fe_2O_3	30	14	60	19		13.3
FeO		9	19	9		6.5
Na_2O					13.3	4
K_2O					1.3	0.4

The waste mixture as well as the overall glass mixture is iron-rich. It is similar to a typical natural petrurgical raw material - basalt rock [17,18], containing typically 10–15 wt% iron oxides and it is characterized by high chemical durability and good resistance to abrasion and corrosion. Fe rich phases in glass-ceramic, also typical for waste-derived glasses, have been shown to impart functional properties to the final products [7]. As magnetic, electrical and thermal properties of glass–ceramics can be altered by controlling the crystalline phase concentrations, crystallisation kinetic studies of iron rich silicate waste derived glass-ceramic are important for optimising functional properties [7, 12].

According to XRD analysis (Fig. 1), iron is present as hematite (Fe_2O_3, i.e. Fe^{3+} form) and as non-stoichiometric mixed oxide with Cu, Zn and Cr ($Cu_{0.5}Zn_{0.5}Cr_{1.1}Fe_{0.9}O_4$) in the dust. The similar appearance of iron is in slag of electro-furnace – non-stoichiometric mixed silicate (forsterite) and non-stoichiometric Fe^{3+} oxide – maghemite. Converter slag contains Fe^{3+} as hematite and calcium iron oxide ($CaFe_2O_4$), Fe^{2+} as wuestite and mixed Fe^{3+} and Fe^{2+} oxide – hagnetite (Fe_3O_4). The glass forming component – SiO_2 is present as pure oxide quartz and silicates with other metals, mainly with Mg and Ca. According to the Fe content and appearance, it is expected to produce glass similar to basalt based one [17].

The results of the TCLP test, carried out on the waste materials and produced glass are summarized in Table 3. There are several metals which exceed the applied limits and can be potential hazard to environment if the waste materials would be disposed at landfill. Ni, Mn, Zn, As and Cu are hazardous components in the dust, in the electric-furnace slag are Fe, Ni and Mn, while in converter slag are Fe, Ni and Cr. Concentration of Fe and Ni are to far from the applied limits.

One of possible and effective options to immobilize heavy metals is to capture them in glass matrix after vitrification of waste materials. So, next step in this research was vitrification of mixture of waste materials and standard glass. To ensure transformation of the mixture in liquid state, vitrification was performed at 1450°C for 1 hour. After cooling at ambient temperature, the produced glass was undergone to thermal investigations.

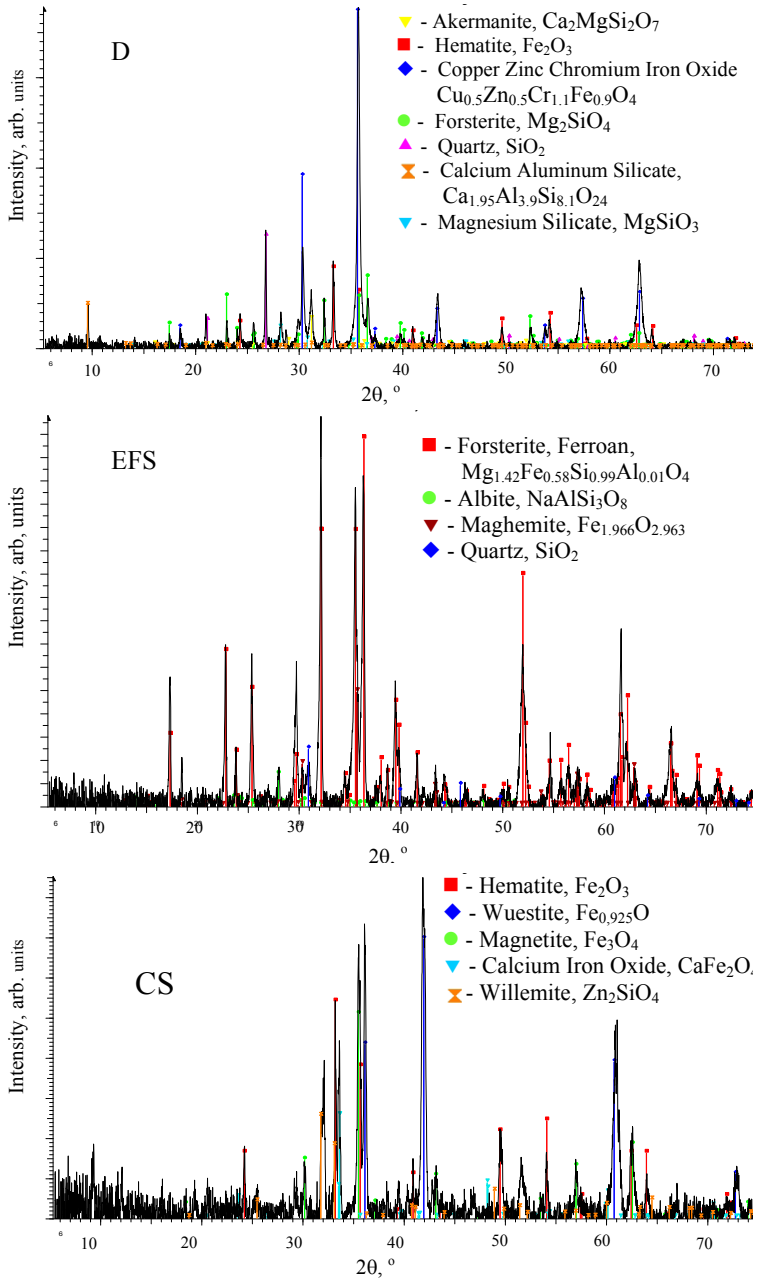

Figure 1. XRD spectra of the waste materials

Hot-stage microscopy is an analytical technique which combines the best properties of microscopy and thermal analysis to enable the characterization of the physical properties of materials as a function of temperature. During the measurements, video and pictures of the sample were recorded with registered reduction of dimensions. Also, a diagram temperature – change of dimensions (%) was constructed and determined temperatures of sintering, softening and melting were determined (Fig. 2). Produced glass shows high stability of dimensions and shape during the heating. The sintering occurs at high temperature (1167°C) at very short interval and practically this material does not sinter. At sintering temperature reduction of dimension is very low. Lowering of dimensions to 78.25% of starting ones reaches at softening temperature at 1222°C, but the shape is still stable. Forming of half-sphere occurs at 1245°C and melting point is 1251°C. This is relatively low melting point, which contributes to more economically efficient process of vitrification of waste based glass. The HSM results, obtained by pressed glass powders, highlight that the sintering method is not appropriated for the investigated glass, because the traditional low-temperature densification is totally inhibited by intensive crystallization.

Table 3. Concentration of heavy metals in the solution after TCLP test

	D, $mg \cdot dm^{-3}$	EFS, $mg \cdot dm^{-3}$	CS, $mg \cdot dm^{-3}$	Glass, $mg \cdot dm^{-3}$	Applied limits, $mg \cdot dm^{-3}$
Fe	1	202	1155	0.416	2
Ni	6,1	2.7	19.2	0.311	2
Co	0.4	0.14	1.1	< 0.005	2
Cd	< 0.005	< 0.005	< 0.005	< 0.005	0.02
Cu	0.15	0.093	0.07	0.011	0.1
Mn	4.7	14.6	1.5	< 0.005	2
Pb	0.026	0.031	0.086	0.017	0.2
Zn	3.6	0.29	0.42	< 0.005	2
Cr	0.22	1.1	2.9	< 0.005	2
Sb	0.020	0.038	0.023	0.023	
As	1.2	0.011	0.18	0.009	5

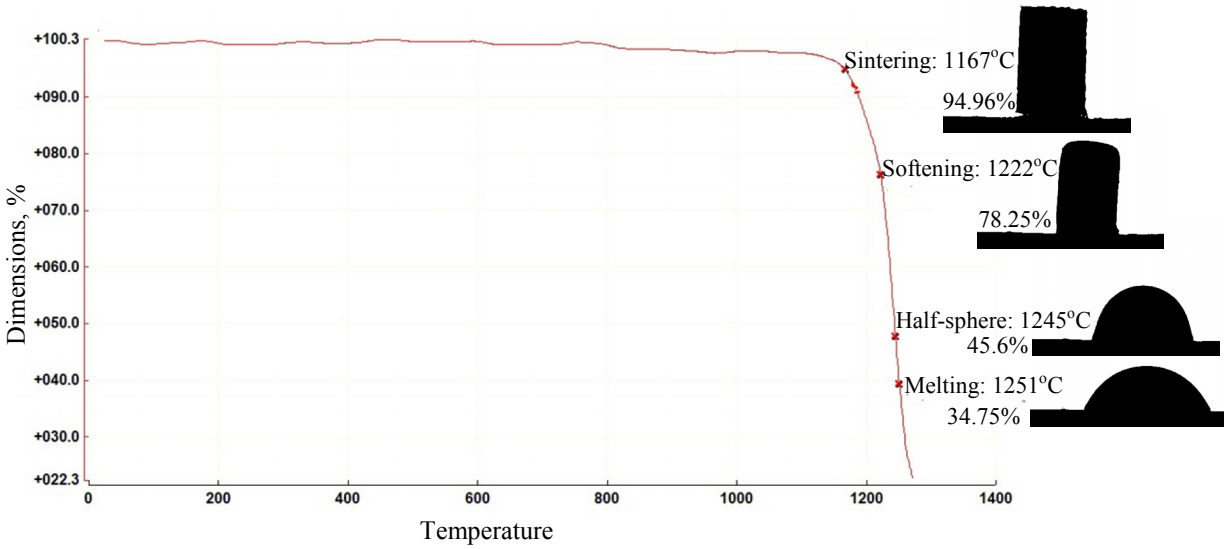

Figure 2. Change of dimensions as function of heating temperature registered by HSM

In order to determine how and at which temperature the studied glass crystallize, DTA analysis was performed at temperature region from ambient to 1100°C by heating rate of 20°C·min^{-1}. Crystallization of the waste based glass occurs at 800°C. The shape and the intensity of peak indicate intensive bulk crystallization. If we previously perform nucleation of glass with retention of heating at 650°C for 1 hour, the temperature of crystallization shifts to lower temperature of 785°C, while the intensity of the bulk crystallization increases. This points out that the waste based glass is appropriate for production of glass-ceramic and can be performed by two-stage process: firstly heating at 650°C to perform nucleation and crystal growth at 785°C. At the same time, the preliminary DTA and density results demonstrate that this composition have good trend for bulk nucleation, giving possibility to obtain material with fine crystalline structure at low temperatures and short times.

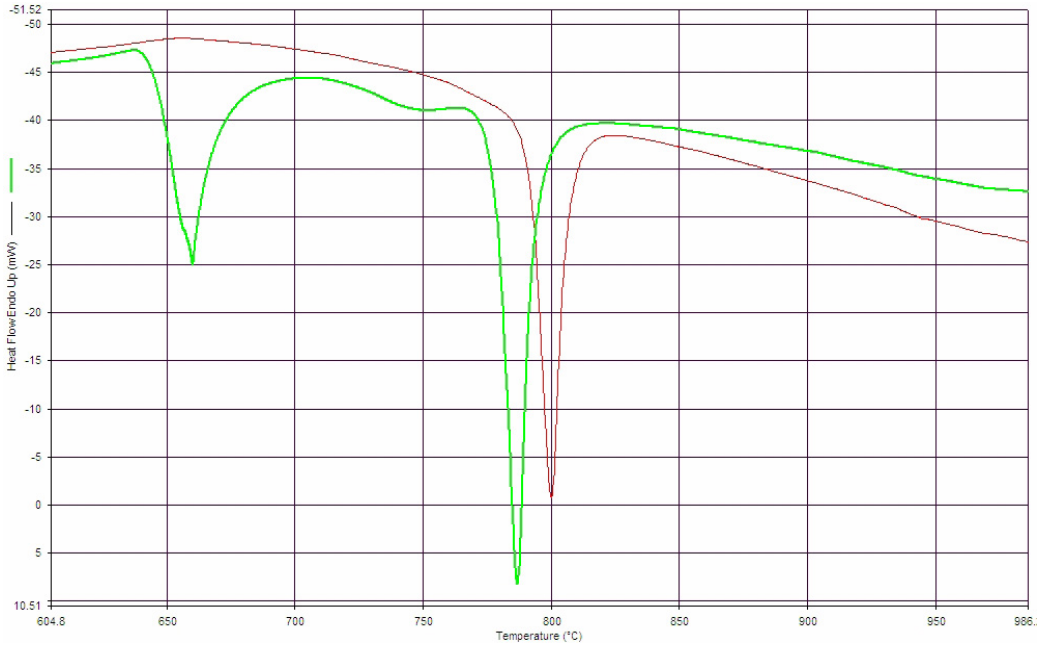

Figure 3. DTA curves of the studied waste based glass: non-nucleated (red line) and nucleated at 650°C (green line)

TCLP test of the produced glass was performed, in order to evaluate the environmental impact. The results of TCLP test are given in Table 3. The results show the vitrification procedure is successful and that the obtained glass demonstrates high chemical durability, corresponding to an inert material.

CONCLUSION

According to the obtained results from this study, we can draw several conclusions:
Waste materials from ferronickel production process contain components which are potential hazard to environment.
Waste materials contain glass-forming components enough, so they are appropriate for vitrification and further transformation of the produced glass to glass ceramic.
TCLP test of the produced waste based glass has shown that it is environmental friendly, i.e. the amount of all heavy metals in the leachate is far below the applied limits.
The produced waste based glass has shown very short interval of sintering at high temperature (1167°C) and low melting point, which point out on its economical efficient production at lower temperatures.

The produced glass showed intensive bulk crystallization at 800°C without previous nucleation. Nucleation at 650°C for 1 hour decreased the crystallization temperature to 785°C, as well as increased the intensity of the bulk crystallization. This offers possibility for efficient two-stage production of glass-ceramic from the studied glass: 1st stage of nucleation at 650°C and 2nd step crystallization at 785°C.

Acknowledgment: This research was performed within the Project "Environment protection of industrial waste through valorisation of metallurgical dust and slags in new environmental friendly polymer mortars and concretes" founded by Ministry of environment and physical planning of R. Macedonia.

REFERENCES

1. W. Vogel, "Glass Chemistry", Springer-Verlag, Berlin, Heidelberg 1994
2. D. Festa and M. Gudagnino, Rivista della Stazione Sperimentale del Vetro, 5, 189, 1995
3. P. Pisciella, S. Crisucci, A. Karamanov and M. Pelino, Waste Management, 21, 1, 2001
4. R. D. Rawlings, J. P. Wu and A. R. Boccaccini, J. Mater. Sci., 41, 733, 2006
5. H. Isa, Int. J. Phys. Sci., 6, 6781, 2011
6. P. Colombo, G. Brusatin, E. Bernardo and G. Scarinci, Current Opinion in Solid State and Materials Science, 7, 225, 2003
7. R.K. Chinnam, A.A. Francis, J. Will, E. Bernardo and A.R. Boccaccini, J. Non-Crystalline Solids, 365, 63, 2013
8. C. Fredericci, E. D. Zanotto and E. C. Ziemath, J. Non-Crystalline Solids, 273, 64, 2000
9. N. A. El-Alaily, Glass Technology**,** 44, 30, 2003
10. E. B. Ferreira, E. D. Zanotto and L. A. M. Scudeller, Glass Science and Technology, 75, 75, 2002
11. A. Karamanov, M. Aloisi, M. Pelino, J. Hazar. Mater., 140, 333, 2007
12. A. Karamanov, G. Taglieri and M. Pelino, J. Am. Ceram. Soc., 82, 3012, 1999
13. A. Karamanov, R. Di Gioacchino, P. Pisciella and M. Pelino, Glass Technol., 43, 34, 2002
14. A. Karamanov, P. Pisciella and M. Pelino, J. Europ. Ceram. Soc., 20, 2233, 2000
15. A. Karamanov and M. Pelino, J. Non-Cryst. Solids, 281, 139, 2001
16. H. A. Van der Sloot, L. Heasman and Ph. Quevauviller, "Harmonization of leaching/extraction tests", Elsevier, Amsterdam 1997
17. H. Beall and H.L. Rittler, Ceram. Bull. 55, 579, 1976
18. J. Hlavac, "The Technology of Glass and Ceramics: An Introduction", Elsevier, Amsterdam, 1983.

COLOR CHANGE IN TRANSITION METAL OXIDE DOPED TELLURITE GLASSES

M. Kazım SAYGILI*, Cihan SİPAHİOĞLU*, Zeynep YURDAKUL*, M. Kerem YÜCETÜRK*, Miray ÇELİKBİLEK*, Ali Erçin ERSUNDU, Süheyla AYDIN***

*Istanbul Technical University, Istanbul, Turkey
saydin@itu.edu.tr
**Nişantaşı University, Istanbul, Turkey

ABSTRACT

Tellurite glasses have the ability to change their color with addition of transition metal oxides and therefore they are promising materials for high-end applications, such as optical sensors and filters. In the present study, different tellurite glasses were prepared with the addition of 2 and 4 mole% TiO_2, Fe_2O_3 and CuO transition metal oxides. For this purpose, $0.90TeO_2$-$0.10K_2O$ glass composition was selected due to its favorable thermal and chemical stability. Thermal investigation of glass samples was realized by DSC analysis to determine the glass transition (T_g), crystallization (T_c/T_p) temperatures and value of thermal stability (ΔT). Optical properties of transition metal oxide doped tellurite glasses were studied in the visible region by UV-Vis spectrophotometer and effect of TiO_2, Fe_2O_3 and CuO addition and their changing composition on the color change of glasses were investigated.

Keywords: Potassium-Tellurite Glasses, Spectroscopic Analysis, Thermal Analysis, Transition Metal Oxides

GEÇİŞ METAL OKSİT KATKILI TELLÜRİT CAMLARIN RENK DEĞİŞİMİ

ÖZET

Geçiş metal oksit katkısı tellürit camlarda renk değişimine sebep olmaktadır. Bu özellikleri sayesinde geçiş metal oksit katkılı tellürit camlar; optik ölçüm cihazları ve optik filtreler gibi katma değeri yüksek ileri teknoloji uygulamalarda kullanım potansiyeline sahiptir. Bu çalışmada, % 2 ve % 4 oranında TiO_2, Fe_2O_3 ve CuO geçiş metal oksitleri katkılı farklı tellürit camlar hazırlanmıştır. Bu amaçla, yüksek termal ve kimyasal kararlılığından dolayı $0.90TeO_2$-$0.10K_2O$ bileşimindeki potasyum-tellürit camı seçilmiştir. Cam numunelerin cam geçiş (T_g) ve kristalizasyon sıcaklıklarını (T_c/T_p) ve cam kararlılık değerlerini (ΔT) belirlemek için DSC ısıl karakterizasyon tekniği kullanılmıştır. TiO_2, Fe_2O_3 ve CuO geçiş metal oksit katkılarının ve değişen bileşimlerinin cam numunelerin görünür bölgedeki optik özelliklerine etkisi UV-Vis spektrofotometresi ile incelenmiştir.

Anahtar Kelimeler: Geçiş Metal Oksitler, Isıl Analiz, Potasyum-Tellürit Camlar, Spektroskopik Analiz

1.INTRODUCTION

Tellurite glasses are outstanding materials due to their low glass transition and melting temperature, thermal and chemical stability, relatively low phonon energy, high refractive index, high corrosion resistance, high dielectric constant and wide transmission range [1-4]. Therefore, tellurite glasses have been used in many fields like optical data storage, lasers, sensors and spectroscopic devices [1-7].

Tellurium dioxide (TeO_2) has no ability to form glass without the addition of a secondary component such as alkalis, heavy metal oxides or halogens [1-7]. Addition of K_2O, an alkali oxide, to tellurite glasses provide many advantageous properties such as low-melting temperature and good homogeneity. Furthermore, comparing to other tellurite glasses, potassium-tellurite glasses show high transparency [8]. According to TeO_2-K_2O binary phase diagram, the $0.90TeO_2$-$0.10K_2O$ glass composition have the lowest melting temperature and the highest glass stability among the other compositions of the glass forming region of the system. Also, this composition show high thermal stability and moisture resistance [9].

Therefore, in this study $0.90TeO_2$-$0.10K_2O$ glass composition was selected as the reference glass matrix and TiO_2, Fe_2O_3 and CuO are selected as add-on transition metal oxides to generate an appropriate glass composition for optical sensors and filters. The present work aims to investigate the color change of transition metal oxides doped potassium-tellurite glasses in terms of thermal and optical properties by thermal and spectroscopic analysis.

2.EXPERIMENTAL

In the experimental studies, different samples were prepared by applying conventional melt-quenching technique. $0.90TeO_2$-$0.10K_2O$ glass composition (now hereafter referred to as TK10) was prepared as reference sample. All other samples were prepared with the addition of transition metal oxides (TiO_2, Fe_2O_3 and CuO) in 2 and 4 mole% to $0.90TeO_2$-$0.10K_2O$ composition (now hereafter referred to as TK10-2Ti, TK10-4Ti, TK10-2Fe, TK10-4Fe, TK10-2Cu and TK10-4Cu samples, respectively). High purity powders of TeO_2 (99.99% purity, Alfa Aesar Company), K_2CO_3 (99.0% purity, Alfa Aesar Company), TiO_2 (99.8% purity, Alfa Aesar Company), Fe_2O_3 (99.5% purity, Alfa Aesar Company) and CuO (98.0% purity, Riedel-De Haen) were thoroughly mixed in an agate mortar. The powder batches of 8 g in weight were melted in a platinum crucible with a closed lid at 750 ^oC for 30 minutes in an electrical furnace and they were casted onto pre-heated stainless steel molds. Finally, glass samples were annealed at 250 ^oC for 1 hour to remove the internal stresses.

Thermal behavior of the glass samples were investigated using differential scanning calorimetry (DSC) technique in a Netzsch DSC 204 F1 (limit of detection: <0.1 μW, with an error estimate of ± 1 °C) using a constant sample weight of 25 ± 1 mg in aluminum pans, under flowing (25 ml/min) argon gas with a heating rate of 10 °C/min. The glass transition onset (T_g), first crystallization onset and peak (T_{c1}/T_{p1}) temperatures were determined from the DSC curves. The glass stability ($\Delta T = T_c - T_g$) value, which is the temperature difference

between the glass transition (T_g) and the first crystallization onset (T_c) temperatures was calculated.

UV-Vis spectroscopy analyses were carried out at room temperature by using PG T 80+ Model Spectrophotometer in the visible range to determine the transmittance values of glass samples.

3.RESULTS AND DISCUSSION

Samples prepared by the addition of 2-4 moles% TiO_2, Fe_2O_3 and CuO to $0.90TeO_2$-$0.10K_2O$ glass composition were obtained as transparent glasses under the applied preparation conditions. Glass samples showed a color change depending on the type and composition of transition metal oxides. Addition of CuO and Fe_2O_3 changed the color of glasses from yellow to green and brown, respectively, while TiO_2 doped glasses were obtained as yellow.

DSC analyses were performed to investigate the thermal behavior of the glasses. DSC thermograms of TeO_2-K_2O glass and CuO, Fe_2O_3, TiO_2 doped glasses are shown in Figure 1, Figure 2, Figure 3 and Figure 4, respectively and the detailed thermal analysis results are given in Table 1. According to the DSC results, a shallow endothermic change between 279 and 323 °C corresponding to the glass transition temperature (T_g) was observed for all glasses.

As it can be seen from Figure 1, TK10 shows a glass transition temperature reaction at 279 °C, two crystallization reaction. The value of thermal stability for TK10 sample was calculated as 89 °C. The sample also shows an endothermic peak corresponding to the melting reaction.

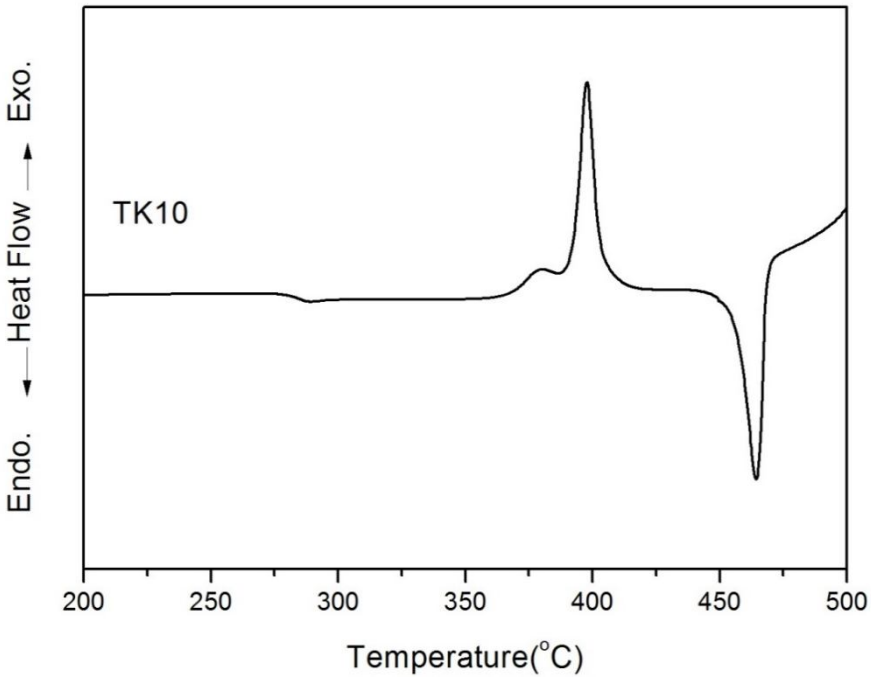

Figure 1. DSC thermogram of $0.90TeO_2$-$0.10K_2O$ glass

As can be seen in Figure 2, TK10-2Cu and TK10-4Cu glasses show a glass transition temperature reaction at 281 °C and two crystallization reactions with onset temperatures 369 °C and 357 °C, respectively. It can be said that addition of CuO to tellurite glasses increase the glass transition temperature and decrease the glass stability.

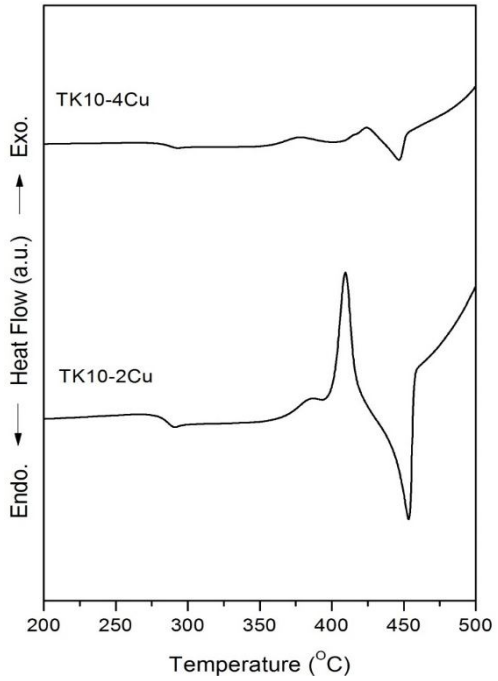

Figure 2. DSC thermograms of CuO doped $0.90TeO_2$-$0.10K_2O$ glasses

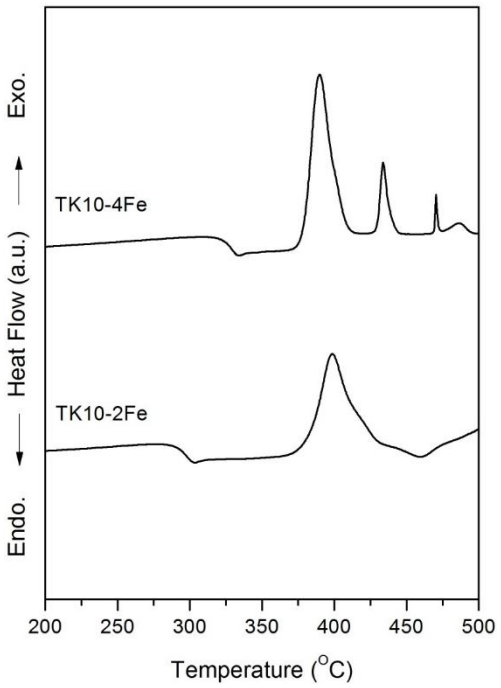

Figure 3. DSC thermograms of Fe_2O_3 doped $0.90TeO_2$-$0.10K_2O$ glasses

As it can be seen from Figure 3, TK10-2Fe glass shows a glass transition reaction at 290 °C and a crystallization reaction with a broad exothermic peak. TK10-4Fe glass show a glass transition reaction at 323 °C and four exothermic peaks. It was observed that addition of

Fe_2O_3 to $0.90TeO_2$-$0.10K_2O$ glass cause a significant increase in the glass transition temperature while decreasing the glass stability value. Fe_2O_3 doped $0.90TeO_2$-$0.10K_2O$ glasses did not show any endothermic peak between 200-500 °C, which means that the addition of Fe_2O_3 shifted the melting reaction to higher temperatures.

As seen in Figure 4, TK10-2Ti glass sample shows a glass transition reaction, two exothermic peaks corresponding to crystallization reaction and one endothermic peak referring to melting reaction, however TK10-4Ti glass show a glass transition and only one crystallization reaction in the same temperature range. It is concluded that addition of TiO_2 to $0.90TeO_2$-$0.10K_2O$ glass causes an increase in the glass transition temperature and a decrease in glass stability. Also addition of TiO_2 shifted the melting reaction to higher temperatures.

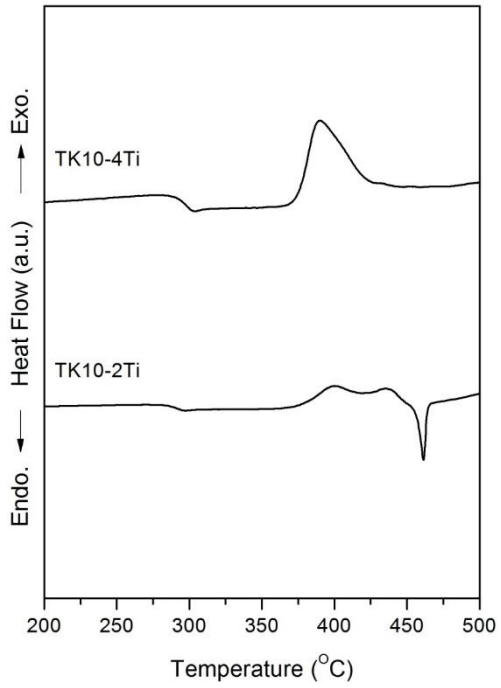

Figure 4. DSC thermograms of TiO_2 doped $0.90TeO_2$-$0.10K_2O$ glasses

Table 1. Values of glass transition onset (T_g) temperature, first crystallization onset and peak (T_c/T_p) temperatures, glass stability (ΔT) of potassium-tellurite glasses

Sample ID	Composition (mole%)	T_g (°C)	T_{c1} / T_{p1} (°C)	ΔT (°C)
TK10	$0.90TeO_2$-$0.10K_2O$	279	368 / 397	89
TK10-2Cu	$0.90TeO_2$-$0.10K_2O$-$0.02CuO$	281	369 / 387	88
TK10-4Cu	$0.90TeO_2$-$0.10K_2O$-$0.04CuO$	281	357 / 378	76
TK10-2Fe	$0.90TeO_2$-$0.10K_2O$-$0.02Fe_2O_3$	290	382 / 398	92
TK10-4Fe	$0.90TeO_2$-$0.10K_2O$-$0.04Fe_2O_3$	323	380 / 391	57
TK10-2Ti	$0.90TeO_2$-$0.10K_2O$-$0.02TiO_2$	284	377 / 400	93
TK10-4Ti	$0.90TeO_2$-$0.10K_2O$-$0.04TiO_2$	291	376 / 391	85

UV-Vis spectroscopy analyses were performed to determine the optical properties of the glasses in the visible region at the room temperature. Figure 5, Figure 6 and Figure 7 show UV-Vis spectra of CuO, Fe_2O_3 and TiO_2 doped TK10 glasses, respectively and the optical analysis details are given in Table 2.

Table 2. Values of the measured cut-off wavelength of the tellurite glasses

Sample ID	Composition (mole%)	Cut-off Wavelength (nm)
TK10	$0.90TeO_2$-$0.10K_2O$	388
TK10-2Cu	$0.90TeO_2$-$0.10K_2O$-$0.02CuO$	460
TK10-4Cu	$0.90TeO_2$-$0.10K_2O$-$0.04CuO$	483
TK10-2Fe	$0.90TeO_2$-$0.10K_2O$-$0.02Fe_2O_3$	495
TK10-4Fe	$0.90TeO_2$-$0.10K_2O$-$0.04Fe_2O_3$	523
TK10-2Ti	$0.90TeO_2$-$0.10K_2O$-$0.02TiO_2$	410
TK10-4Ti	$0.90TeO_2$-$0.10K_2O$-$0.04TiO_2$	415

As seen in Figure 5, cut-off wavelength of TK10 glass obtained at 388 nm shifted to higher values with the increasing CuO content and the transmittance % of TK10 glass shows a significant decrease with CuO addition. It was also obtained that CuO doped potassium-tellurite glasses which were obtained as dark green are transparent only in 460-575 nm range of the visible region and their transmittance % values are lower than 15%.

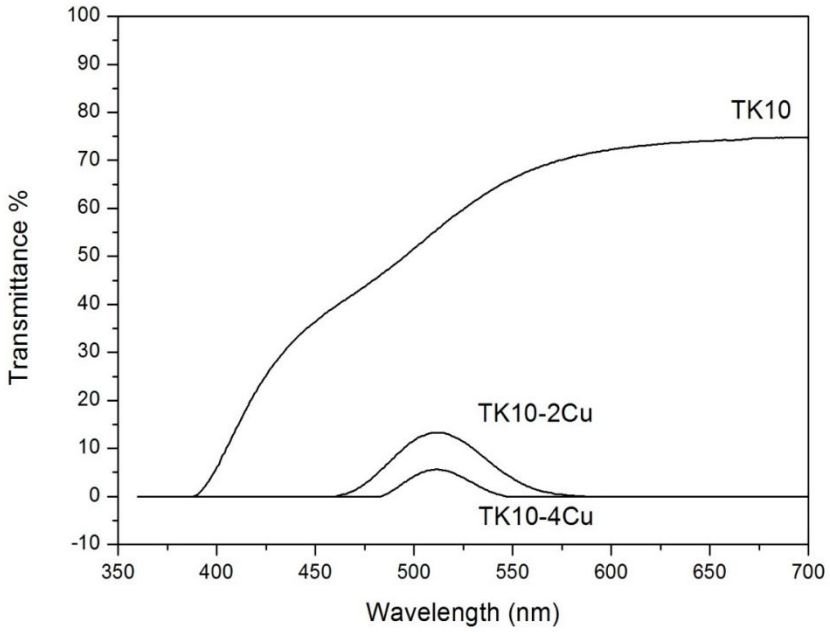

Figure 5. UV-Vis spectra of CuO doped $0.90TeO_2$-$0.10K_2O$ glasses in comparison with $0.90TeO_2$-$0.10K_2O$ glass

As can be seen in Figure 6, the cut-off wavelength of TK10 glass (388 nm) shifted to higher values and the tranmittance % showed a decrease with increasing of Fe_2O_3 content. The cut-off wavelength of TK10-2Fe glasss which was obtained as brown was obtained as 495 nm and show a shift to 523 nm with increasing and Fe_2O_3 content.

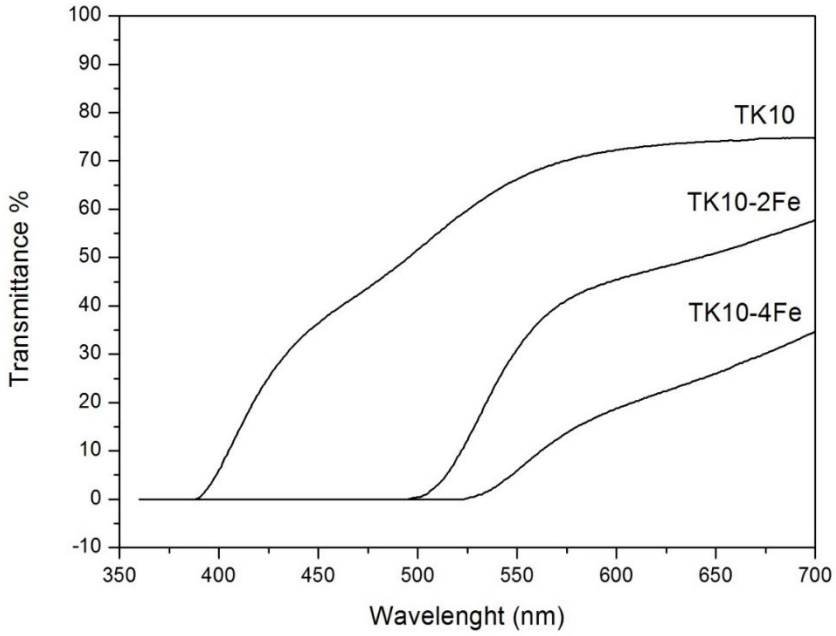

Figure 6. UV-Vis spectra of Fe_2O_3 doped $0.90TeO_2$-$0.10K_2O$ glasses in comparison with $0.90TeO_2$-$0.10K_2O$ glass

As seen from Figure 7, the transmittance % values of TiO_2 doped glasses are higher than other doped glasses. The cut-off wavelengths of $0.90TeO_2$-$0.10K_2O$ glass was shifted higher values and obtained as 410 and 415 nm for TK10-2Ti and TK10-4Ti glasses, respectively. Also, it was obtained that addition of TiO_2 to potassium-tellurite glasses causes a decrease in transmittance.

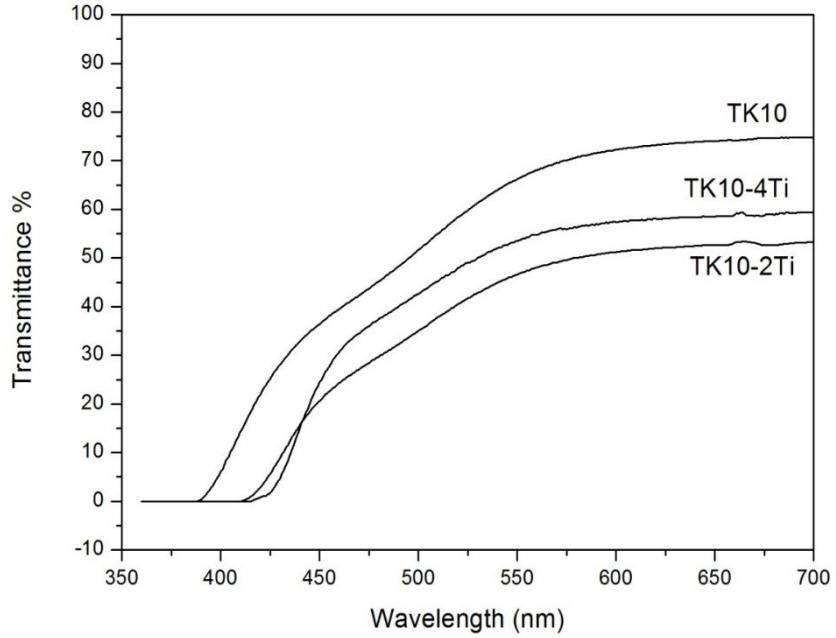

Figure 7. UV-Vis spectra of TiO_2 doped $0.90TeO_2$-$0.10K_2O$ glasses in comparison with $0.90TeO_2$-$0.10K_2O$ glass

4.CONCLUSIONS

In this work, investigation of thermal and optical behavior of 2 and 4 mole % CuO, Fe_2O_3, TiO_2 doped $0.90TeO_2$-$0.10K_2O$ glasses was realized through DSC and UV-Vis analysis. Thermal analysis results showed that the glass transition temperatures shifted to higher values by the addition of transition metal oxide to potassium-tellurite glasses. Spectroscopic analysis showed that cut-off wavelengths of $0.90TeO_2$-$0.10K_2O$ glass shifted higher values and the tranmisttance % values decrease with addition transition metal oxides. According to the obtained cut-off wavelength values, it can be said that CuO doped potassium-tellurite glasses are favourable materials for green optical filters, while Fe_2O_3 and TiO_2 doped glasses are convenient for blue and violet optical filters, respectively.

Acknowledgment

The authors of this study gratefully acknowledge The Scientific & Technological Research Council of Turkey (TUBITAK) for the financial support under the project numbered 111M236.

REFERENCES

1. R. A. H. El-Mallawany, "Tellurite Glasses Handbook Physical Properties and Data", Boca Raton: CRC Press 2002
2. A. E. Ersundu, M. Çelikbilek, S. Aydın, Journal of Non-Crystalline Solids, 358, 641, 2012
3. A. E. Ersundu, M. Çelikbilek, S. Aydın, Materials Science and Technology Conference and Exhibition (MS&T'12), Pittsburgh, Pennsylvania, U.S.A., 257, 2012
4. A. E. Ersundu, M. Çelikbilek, N. Solak, S. Aydın, Journal of the European Ceramic Society, 31, 2775, 2011.
5. D. Yardimci, M. Çelikbilek, A. E. Ersundu, S. Aydın, Materials Science and Technology Conference and Exhibition (MS&T'12), Pittsburgh, Pennsylvania, U.S.A., 243, 2012
6. M. Çelikbilek, A. E. Ersundu, S. Aydın, Materials Science and Technology Conference and Exhibition (MS&T'12), Pittsburgh, Pennsylvania, U.S.A., 229, 2012
7. M. Çelikbilek, A. E. Ersundu, N. Solak, S. Aydın, Journal of Alloys and Compounds, 509, 5646, 2011
8. B. Öz, I. Kabalcı, M. L. Öveçoğlu, G. Özen, Journal of the European Ceramic Society, 27, 1823, 2007
9. B. Öz, "Thermal, Microstructural and Optical Characterization of TeO_2-K_2O Glasses", M.Sc. Thesis, Istanbul Technical University, İstanbul, 2006

TEMPERATURE DEPENDENT OPTICAL AND ELECTRICAL INVESTIGATION OF ALKALI-TUNGSTEN-TELLURITE GLASSES

Miray ÇELİKBİLEK[*], Ali Erçin ERSUNDU[**], Süheyla AYDIN[*]

**Istanbul Technical University, Istanbul, Turkey
miraycelikbilek@gmail.com, saydin@itu.edu.tr
*Nişantaşı University, Istanbul, Turkey
aliercin.ersundu@nisantasi.edu.tr

ABSTRACT

Semiconductor oxide glasses are promising materials due to their potential use in thermistors, channel-type photo amplifiers, switches and chromogenic applications. Tellurite glasses show semiconducting behavior due to their medium band gap energy which lies within the visible spectrum photon energy range. Comparing to other glass systems, besides their advantageous optical properties such as high refractive index and good infrared transmissivity, tellurite-based glasses also have high dielectric constant and electrical conductivity owing to their unshared pair of electrons of TeO_4 groups. In the present study, temperature dependence of transmission spectra, optical band gap energy and electrical properties of alkali-tungsten-tellurite glasses was investigated with in-situ UV-Vis spectroscopy and electrical conductivity analyses.

Keywords: Alkali-tungsten-tellurite glasses, Transmission spectra, Band gap energy, Electrical properties

ALKALI-TUNGSTEN-TELLÜRİT CAMLARIN SICAKLIĞA BAĞLI OPTİK VE ELEKRİKSEL İNCELENMESİ

ÖZET

Yarı iletken oksit camlar, termistörler, kanal tipi fotoyükselticiler, ince film anahtarlar ve kromik uygulamalarda kullanım potansiyeline sahip gelecek vaadeden malzemelerdir. Tellürt camlar, görünür bölgenin foton enerjisi civarında olan bant aralığı enerjisi değerleri ile amorf yarı iletkenler olarak adlandırılabilir. Tellürit camlar, yüksek kırılma indisi ve yüksek kızıl ötesi geçirgenlik gibi diğer cam sistemlerle karşılaştırıldığında sahip oldukları avantajlı optik özelliklerin yanı sıra, bağ yapılarına katılmayan TeO_4 gruplarının eşleşmemiş elektron çiftleri sayesinde yüksek elektriksel iletkenlik ve yüksek dielektrik sabiti değerlerine sahiptir. Bu çalışmada, alkali-tungsten-tellürit camların sıcaklığa bağlı gerçigenlik özellikleri, optik bant aralığı enerjisi değerleri ve elektriksel özellikleri özel olarak tasarlanmış dahili sıcaklık üniteli UV-Vis spektrofotometre ve elektriksel iletkenlik ölçüm cihazları ile incelenmiştir.

Anahtar Kelimeler: Alkali-tungsten-tellürit camlar, bant aralığı enerjisi, elektiksel özellikler, geçirgenlik

1.INTRODUCTION

Comparing with silicate, borate and phosphate glasses, tellurite glasses have advantageous properties, such as high refractive index, relatively low-phonon energy, good visible and infrared transmissivity, suitability for doping with rare earth elements in a wide range, high dielectric constant, thermal and chemical stability, high devitrification resistance, low glass transition and melting temperature [1]. These outstanding features make tellurite glasses promising materials for opto-electronic applications, such as fiber optics, lasers, sensors, spectroscopic devices, host materials for some infrared and infrared to visible up-conversion applications in optical data storage and non-linear optical materials. TeO_2 does not have glass forming ability under normal quenching conditions without addition of a secondary component. Therefore, addition of secondary components such as alkalis, heavy metal oxides and halogens are required to obtain tellurite glasses [1]. Combination of TeO_2 with two or more secondary components yields stable glasses and provides control of the desired properties [2,3].

Tellurite glasses are also promising candidates for thermochromic applications due to their good electrical properties owing to the unshared pair of electrons of the TeO_4 groups that do not take part in bonding and due to their potential semiconductor behavior. It is known that the nature, concentration and field strength of the modifier oxides in multi-component tellurite systems substantially determine the electrical properties of glasses. Due to their semiconductive properties, transition metal oxide containing tellurite glasses are convenient materials for chromic applications, thin-film switches, thin-film memory elements, thermistors and channel-type photo amplifiers [1]. Addition of WO_3 to the tellurite glass network enhances chemical stability and devitrification resistance, gives possibility to modify the composition by a third, fourth, and even fifth component and as being a transition metal oxide it makes the electronic transitions possible in the glass network [4-7]. Addition of alkali oxides (A_2O, A= Li, Na, K) to the tellurite glass network improve thermal stability, generates non-bridging oxygen sites in the glass network and makes the ion-exchange process suitable [1,2,8,9]. Due to this favorable properties in this work, WO_3 and alkali oxides were selected as secondary components to obtain tellurite glasses. In this study, investigation of the thermochromic behavior of alkali-tungsten-tellurite glasses was realized by optical and electrical analysis via temperature.

2.EXPERIMENTAL

In the experimental studies, different compositions of the TeO_2-WO_3-A_2O system (A_2O, A= Li, Na, K) were prepared with a conventional melt-quenching technique. High purity powders of TeO_2 (99.99% purity, Alfa Aesar Company), WO_3 (99.8% purity, Alfa Aesar Company) Li_2CO_3 (99.5% purity, Alfa Aesar Company), Na_2CO_3 (99.0% purity, Alfa Aesar Company) and K_2CO_3 (99% purity, Alfa Aesar Company) were thoroughly mixed, 7g size powder batches were melted in a platinum crucible with a closed lid at 750 °C for 30 minutes and quenched in a pre-heated stainless steel mold. In this paper, the sample with the composition of $0.80TeO_2$-$0.10WO_3$-$0.10Na_2O$ was selected in order to represent alkali-tungsten-tellurite glasses.

The amorphous nature of the as-cast samples was checked by X-ray diffraction analyses (XRD) analyses, which were carried out with powdered glass samples in a Bruker™ D8 Advanced Series powder diffractometer using Cu K_α radiation in the 2θ range from 10^o to 90^o.

Optical analysis of the glasses was realized using a PG T 80+ Model UV-Vis spectrophotometer with a spectral bandwidth 0.1 nm in the wavelength range 360 - 700 nm. For temperature dependent measurements a custom made sample holder which is heated by cartridge type heaters made of NiCr was used to heat the samples from room temperature to 240 °C and the cooling of the holder was obtained by using a suction air pump. The temperature of the holder was controlled and monitored with PtRh-Pt thermocouples. To test the reversibility, heating and cooling measurements were repeated several times. The wavelength at which the absorbance value reaches 0 was taken as the absorption edge for the glasses.

In amorphous materials, the variation of optical absorption with photon energy needs to be assumed to match to the experimental data. Tauc was presented the shape and position of the absorption edge for high absorption region by the following equation:

$$\alpha(\omega) = \frac{A\left(\hbar\omega - E_{opt}\right)^{p}}{\hbar\omega}$$

where, A is constant, α is absorption coefficient, ω is angular frequency, $\hbar\omega$ is photon energy, E_{opt} optical band gap energy and p is an exponent depending on the mechanism of interband transitions [10-12]. For amorphous materials, p is selected as 2 by taking into account that indirect transitions are valid and the band gap energy of the glasses was determined by the intersection point of $(\alpha h\omega)^{(1/2)}$ - hω change with the photon energy according to Tauc equation.

The electrical conductivity of the glasses was measured by using electrode guard technique. Before the electrical measurements both surfaces of the glass samples were plated with silver paint (SPI Supplies). To prevent the environmental effects such as light and moisture, the measurements were carried out in a dark cladding vacuum bell jar. To measure the volumetric conductivity, two electrodes are placed on the center of the opposite faces of glass samples and a third electrode, named guard electrode was surrounded one of them on one face only. This guard electrode was short circuit with the central electrode placed at the opposite face and connected to a potential voltage used as reference during all experiments. Current-voltage characteristics of the glasses were investigated up to 400 V at different temperatures. A Keithley 6514 System Electrometer was used to measure the current across the sample. The resistivity values, ρ, of glasses were determined following the Ohm's law by measuring the resulting current at 400 V. Keithley 2410-C 1100V Sourcemeter allowing the measurement of currents in pA range was used and the temperature control was provided with two thermocouples placed on the upper surfaces of the glass samples.

3.RESULTS AND DISCUSSION

Samples in the TeO_2-WO_3-Li_2O, TeO_2-WO_3-Na_2O and TeO_2-WO_3-K_2O systems were prepared with different compositions. Amorphous nature of the glass samples which were visually obtained as homogenous glasses was checked by XRD analysis.

To investigate the change in tranmittance of glasses with changing temperature UV-Vis spectroscopy analyses were realized via temperature. Figure 1 shows the transmittance spectrum of $0.80TeO_2$-$0.10WO_3$-$0.10Na_2O$ glass in the visible region for different temperatures. It was observed that with changing temperature alkali-tungsten-tellurite glass sample show a significant transmittance change and there is a shift in their absorption edges.

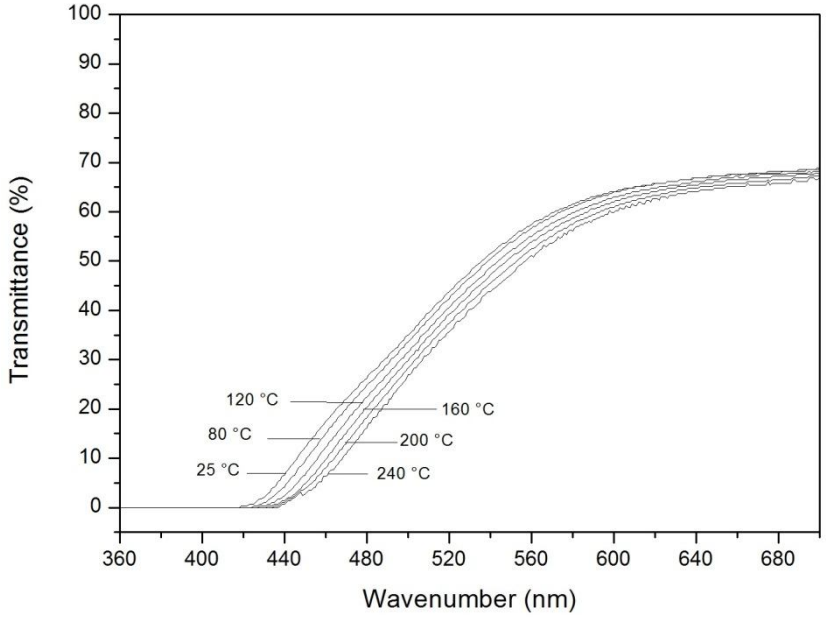

Figure 1. Visible transmittance of $0.80TeO_2$-$0.10WO_3$-$0.10Na_2O$ glass for different temperatures.

Considering on that the temperature dependent change of the absorption edge originates from the change of the band gap energy, to examine the change of band gap energy via temperature the absorption edge values for different temperatures are compared and the results are given in Figure 2 and Table 1. Table 1 also shows the shift of the absorption rate. It was observed that the absorption edge of the alkali-tungsten-tellurite glasses moves toward the long wavelength with increasing temperature and the shift rate of the absorption of the alkali-tungsten-tellurite glasses is close to the thermal rate of change of the band gap energy in semiconductors [13].

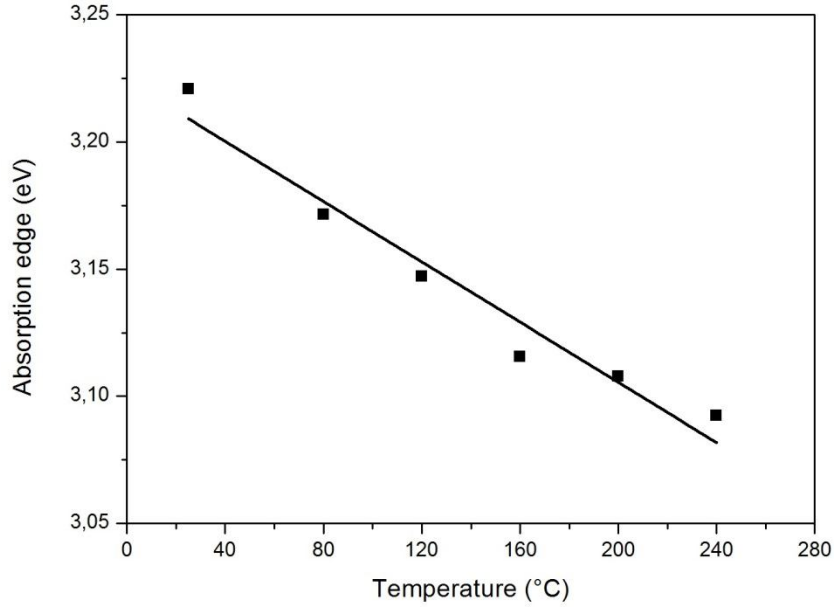

Figure 3. Variation of the absorption edge values of $0.80TeO_2$-$0.10WO_3$-$0.10Na_2O$ glass with changing temperature.

Table 1. Shift rate of the absorption, values of band gap energy and conductivity of $0.80TeO_2$-$0.10WO_3$-$0.10Na_2O$ glass.

Sample ID	Shift rate of the absorption	Band gap energy (eV)		σ $(ohm.cm)^{-1}$	
	(10^{-4} eV/K)	25 °C	240 °C	25 °C	100 °C
T80W10N10	-5.95	2.46	2.41	$1.2\ 10^{-16}$	$6.7\ 10^{-13}$

The optical band gap energy values of the glasses were calculated using the Tauc equation by the relation between the absorption coefficient and photon energy. The Tauc plots of the glasses and the values of the band gap energy are given in Figure 3 and Table 1, respectively. It was found that the band gap energy value of $0.80TeO_2$-$0.10WO_3$-$0.10Na_2O$ glass showed a decrease from 2.46 eV to 2.41 eV with increasing temperature.

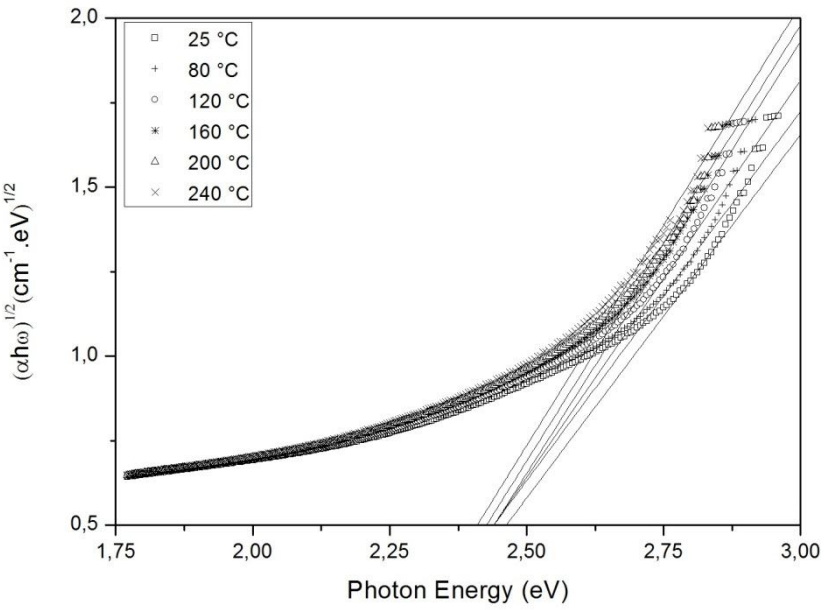

Figure 4. Plots of $(\alpha\hbar\omega)^{½}$ as a function of photon energy for $0.80TeO_2$-$0.10WO_3$-$0.10Na_2O$ glass.

The electrical measurements via temperature show that the conductivity values of alkali-tungsten-tellurite glasses change with changing temperature. As shown in Table 1, with increasing temperature conductivity of $0.80TeO_2$-$0.10WO_3$-$0.10Na_2O$ glass show an increase from $1.2\ 10^{-16}$ to $6.7\ 10^{-13}$ $(ohm.cm)^{-1}$. It can be concluded that alkali-tungsten-tellurite glasses show a semiconductor behavior.

4.CONCLUSIONS

In this work, temperature dependent investigation of optical and electrical properties of alkali-tungsten-tellurite glasses was realized through spectroscopic and electrical analyses. It was found that tranmittance % in the visible region, absorption edge values, shift rate of the absorption, band gap energy, photon energy and conductivity values of alkali-tungsten-tellurite glasses were changed with changing temperature and alkali-tungsten-tellurite glasses show semiconductor behavior.

Acknowledgment

The authors of this study gratefully acknowledge The Scientific & Technological Research Council of Turkey (TUBITAK) for the financial support under the project numbered 111M236.

REFERENCES

1. R. A. H. El-Mallawany, "Tellurite Glasses Handbook Physical Properties and Data", Boca Raton: CRC Press 2002
2. M. Çelikbilek, A. E. Ersundu, S. Aydın, Journal of the American Ceramic Society, 96, 1470, 2013
3. R. Stepien, R. Buczynski, D. Pysz, I. Kujawa, A. Filipkowski, M. Mirkowska, R. Diduszko, Journal of Non-Crystalline Solids, 357, 873, 2011
4. M. Çelikbilek, A. E. Ersundu, N. Solak, S. Aydın, Journal of Alloys and Compounds, 509, 5646, 2011
5. M. Çelikbilek, A. E. Ersundu, N. Solak, S. Aydın, Journal of Non-Crystalline Solids, 357, 88, 2011
6. A. E. Ersundu, M. Çelikbilek, N. Solak, S. Aydın, Journal of the European Ceramic Society, 31, 2775, 2011.
7. A. E. Ersundu, M. Çelikbilek, S. Aydın, Journal of Non-Crystalline Solids, 358, 641, 2012
8. M. Çelikbilek, A. E. Ersundu, S. Aydın, Journal of Non-Crystalline Solids, 378, 247, 2013
9. P. Thomas, K.B.R. Varma, Journal of Advanced Dielectrics, 02, 1250020, 2012
10. M. H. Cohen, H. Fritzsche, S. R. Ovshinsky, Physical Review Letters, 22, 1065, 1969.
11. E. A. Davis, N. F. Mott, Philosophical Magazine, 22, 0903, 1970
12. M. Y. Nadeem, T. B. Sadhana, M. Altaf, M. A. Chaudhry, Journal of Research (Science), 15, 245, 2004
13. S., Inoue, Y., Shimizugawa, A.Nukui, T. Maeseto, Journal of Non-Crystalline Solids, 189, 36, 1995

PREPARATION AND CHARACTERIZATION OF SILVER CONTAINING SODA-LIME GLASSES

Duygu GÜLDİREN*, Miray ÇELİKBİLEK*, Ali Erçin ERSUNDU, Süheyla AYDIN***

*Istanbul Technical University, Turkey
yardimcid@gmail.com, miraycelikbilek@gmail.com, saydin@itu.edu.tr
**Nişantaşı University, Turkey
aliercin.ersundu@nisantasi.edu.tr

ABSTRACT

Owing to their antibacterial behavior and nontoxicity, silver containing glasses are promising to be widely used in many applications, such as touch screens, glassware, architectural applications, cosmetics, textiles, dental and orthopedic implants and biomaterials. In the present study, which is a preliminary work of a project on the investigation of glasses showing antibacterial property, it is aimed to prepare silver doped soda-lime glasses by ion exchange treatment. Silver ions were incorporated into the glass via ionic exchange reactions in an ionic medium containing different concentrations of $AgNO_3$. After ion exchange treatment, glasses were submitted to atomic absorption spectroscopy (AAS) analysis in order to determine the amount of silver ions incorporated into the glass. The ion exchanged glasses were further characterized by using scanning electron microscopy (SEM), energy dispersive X-ray spectroscopy (EDS) and UV-Vis spectroscopy techniques.

Keywords: Antibacterial, glass, ion exchange, silver ions

GÜMÜŞ İÇEREN SODA-KİREÇ CAMLARIN HAZIRLANMASI VE KARAKTERİZASYONU

ÖZET

Gümüş içeren camlar antibakteriyel özellikleri ve toksik olmamaları sebebiyle dokunmatik ekranlar, cam eşyalar, mimari uygulamalar, kozmetik ürünler, tekstil ürünleri, diş implantları, ortopedik uygulamalar ve biyomalzemeler gibi pek çok alanda yaygın olarak kullanılmaktadır. Antibakteriyel özellik gösteren camların geliştirilmesi konusunda bir ön çalışma niteliğinde olan bu çalışma kapsamında, gümüş içeren soda-kireç camların iyon değişim prosesi kullanılarak hazırlanması amaçlanmıştır. Gümüş iyonları iyon değişim prosesi ile farklı konsantrasyonda $AgNO_3$ içeren iyon banyoları kullanılarak cam yapıya kazandırılmıştır. Cam yapıya geçen gümüş iyonu miktarının tespiti için iyon değişim prosesi sonrası elde edilen camlar atomik absorpsiyon spektroskopi (AAS) tekniği kullanılarak analiz edilmiştir. Ayrıca, iyon değiştirmiş camlar taramalı elektron mikroskobu (SEM), enerji dispersif X-ışınları spektroskopi (EDS) ve UV-görünür spektroskopi tekniği kullanılarak incelenmiştir.

Anahtar Kelimeler: Antibakteriyel, cam, iyon değişim, gümüş iyonu

1. INTRODUCTION

Glasses have become widely used in all aspects of our lives especially with the new developments in technology. In accordance with the need for developing high quality glasses for different uses, the interest in glassy materials showed a rapid increase. Owing to their high chemical durability, hardness, transparency and forming ability glasses have become essential materials in many applications, such as screens and panels, architectural and residential use, glassware and optical applications [1]. Glasses showing antibacterial property have become highly important in recent years especially for their use in textiles, cosmetics, touch screens, wall and floor coverings, hospital applications, biomaterials etc. [2-5]. Antibacterial property can be gained to the glasses either by doping metal ions to the glass network or coating metal oxides or nitrides to the glass surface [4, 6]. Ion exchange process which modifies only the glass surface can also be used for this purpose [1, 7-11].

Ion exchange process was studied for many years for the production of optical waveguides, chemical strengthening of glass surfaces and coloration of glasses. It is based on dipping the glass into a molten salt bath containing metal ions that will be exchanged with the ions within the glass [1, 11]. In order to impart antibacterial property to glasses, ion exchange process is a preferable technique since it offers several advantageous properties, such as ease of application without the need of expensive equipment, ability of controlling the amount of ions incorporated into the glass and released to the environment, applicability only on the surface properties without changing the bulk glass [1, 10, 12].

Metal ions such as silver, zinc and copper have a positive influence on avoiding bacterial growth and their colonization. Silver is the most widely known and used antibacterial metal ion due to its high antibacterial activity against a broad range of bacteria and low toxicity to human health [2-6, 9-13]. Silver ions are ideal for ion exchange process with their high mobility which lets them to be incorporated to the glass surface using different silver salts ($AgNO_3$, AgCl, Ag_2SO_4 etc.) as the ionic medium [10,14].

In the present study, due to its potential antibacterial behavior, it was aimed to prepare silver containing soda-lime glasses using ion exchange process and to investigate the effect of ionic exchange time and ionic medium concentration on the amount of silver ions incorporated to the glass.

2. EXPERIMENTAL

Soda-lime glasses were prepared by conventional melt-quenching technique according to the following composition in molar ratio; $70SiO_2$-$15Na_2O$-$10CaO$-$5Al_2O_3$. High purity powders of SiO_2 (99.5% purity, Alfa Aesar Company), Na_2CO_3 (99.5% purity, Alfa Aesar Company), $CaCO_3$ (99.0% purity, Alfa Aesar Company) and Al_2O_3 (99.0% purity, Alfa Aesar Company) were homogenously mixed in an agate mortar. 100 g size powder batch was melted in a platinum crucible with a closed lid at 1500 ^oC for 3 hours. Afterwards the molten samples were removed from the furnace and poured on a preheated stainless steel molds.

Thermal analysis of the as-cast samples was carried out using a PerkinElmer^{TM} Diamond TG/DTA, with a constant sample weight of 25 mg, in platinum pans, from room temperature to 800 °C under a flowing (100 ml/min) argon gas. The glass transition onset temperature (T_g) was determined from the DTA curve as the inflection point of the endothermic change of the

calorimetric signal. As-cast samples were annealed below the glass transition temperature at 550 ^{o}C for 3 hours to remove residual internal stresses.

In order to increase the efficiency of the ionic exchange process, firstly glass surfaces were cleaned and prepared using distilled water and ethanol in an ultrasonic cleaner. For the ion exchange process, the ionic medium was prepared using $AgNO_3$ (99.9% purity, Alfa Aesar Company) and KNO_3 (99.0% purity, Alfa Aesar Company). Pre-cleaned glasses were immersed into the ionic medium, containing 1 and 2 wt % $AgNO_3$, at 420 ^{o}C for 2 and 4 hours in an electrical furnace. The temperature of the ion exchange process was determined according to the glass transition temperature (T_g) values obtained from thermal analysis. After the process, glasses were kept in distilled water in an ultrasonic cleaner to remove any residues from their surfaces.

The amount of silver ions incorporated into the glass were calculated according to the following formula:

$$W_{Ag} = [(Wg_{after} - Wg_{before}) / (aW_{Ag} - aW_{Na})] * aW_{Ag} \quad (1)$$

where W_{Ag} is the amount of incorporated silver ion, Wg_{before} is the sample weight before the process, Wg_{after} is the sample weight after the process and aW_{Ag} and aW_{Na} atomic weight of silver and sodium, respectively.

After the ion exchange process silver ions introduced into the glass were determined by atomic absorption spectroscopy (AAS) analysis using a Perkin Elmer Analyst 800 atomic absorption spectrometer with an error estimate of ±2%.

Scanning electron microscopy (SEM) and energy dispersive X-ray spectroscopy (EDS) techniques were used to characterize the ion exchanged glasses. SEM/EDS investigations were carried out with the platinum-coated bulk samples at 15 kV in JEOL^{TM} JSM 5410 microscope connected to Noran 2100 Freedom energy dispersive X-ray spectrometry.

UV-Vis spectroscopy technique was used to investigate the effect of incorporated silver ions on the optical properties of the glasses. Transmission spectra of the ion exchanged glasses in the range of 360-700 nm wavelength with a spectral bandwidth 0.1 nm were examined by PG Instruments T80+ UV-Vis spectrophotometer at room temperature.

3. RESULTS AND DISCUSSION

In the present study, colorless glass samples were obtained under the applied preparation conditions having the $70SiO_2$-$15Na_2O$-$10CaO$-$5Al_2O_3$ composition in molar ratio. DTA analysis was performed to investigate the thermal behavior of the glasses. DTA thermogram of the $70SiO_2$-$15Na_2O$-$10CaO$-$5Al_2O_3$ glass sample in the temperature range of 200-800 ^{o}C is shown in Figure 1.

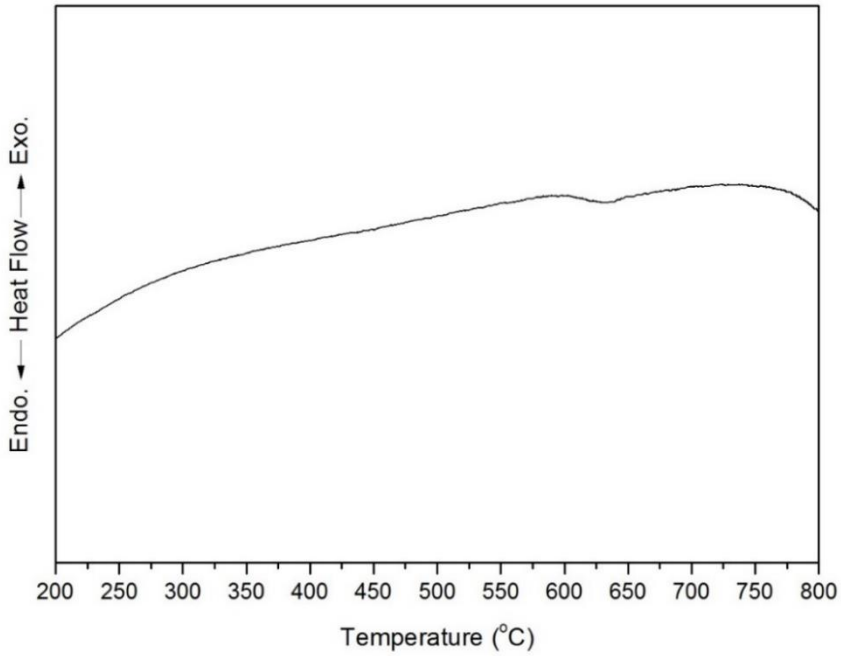

Figure 1. DTA curve of the $70SiO_2$-$15Na_2O$-$10CaO$-$5Al_2O_3$ glass.

A broad endothermic change corresponding to the glass transition reaction was detected at 582 °C. According to the DTA result, as-cast glass samples were annealed below the glass transition temperature at 550 °C for 3 hours which.

Glass samples prepared for the ion exchange process were kept in distilled water and ethanol in an ultrasonic cleaner for 1 hour. The ionic exchange treatment was carried out below the glass transition temperature of glasses at 420 °C for 2 and 4 hours in an electrical furnace. Glass samples were dipped into different ionic media containing 1 wt % $AgNO_3$ – 99 wt % KNO_3 and 2 wt % $AgNO_3$ – 98 wt % KNO_3. After the ion exchange process, glass samples were cleaned in an ultrasonic cleaner using distilled water to dissolve any residues that can be remained on the glass surface during the ion exchange process. Glass samples showed pale yellow color after the ion exchange process and they became darker with the increase in ion exchange time.

Silver ion concentration introduced into the glass was calculated using the sample weight before and after the ion exchange process and the atomic weight of silver and sodium from the Eq. 1. Also, chemical analysis of the samples were realized by atomic absorption spectroscopy (AAS) analysis. Table 1 represents the amount of silver ions incorporated into the glass and chemical analysis results with the sample ID's specified as to the ion exchange process parameters.

Table 1. The amount of silver ions introduced into the glass and chemical analysis results of the ion exchanged glass samples.

Sample ID	$AgNO_3$ in the ionic medium (wt %)	Ion exchange time (hour)	Glass weight (mg)		Amount of silver (mg)	Ag/glass (wt %)
			Before	After		
1Ag-2h	1	2	3754.4	3764.6	12.963	0.12
1Ag-4h	1	4	3780.4	3793.2	16.267	0.15
2Ag-2h	2	2	4240.7	4259.7	24.146	0.21
2Ag-4h	2	4	4601.9	4624.3	28.467	0.28

Chemical analysis results showed that the silver concentration in the glasses, which is concentrated on the glass surface, vary between 0.12 to 0.28 wt %. As can be seen in Table 1, the amount of silver introduced into the glass showed an increase with increasing ionic exchange time and $AgNO_3$ concentration in the ionic medium.

SEM analysis was carried out with the ion exchanged glasses showed that no microstructural change occur after the ionic exchange treatment. EDS analysis was performed to investigate the compositional changes from the surface to the bulk of the glass samples, hence the analysis were applied to the cross-section of the glasses. EDS analysis results revealed that the silver concentration on the surface of the glasses increase with increasing ionic exchange time and $AgNO_3$ concentration in the ionic medium which is in a good agreement with the chemical analysis results. Also according to the EDS analysis results, it is revealed that the silver concentration gradually decreased from the surface to the bulk of the glass samples.

Transmission spectra of the $70SiO_2$-$15Na_2O$-$10CaO$-$5Al_2O_3$ glass (glass before the ion exchange process), 1Ag-2h and 1Ag-4h glass samples are shown in Figure 2 in the range of 360-700 nm wavelength. As can be seen in Figure 2, transmittance of the glasses shifted to lower values with the increase in ion exchange time.

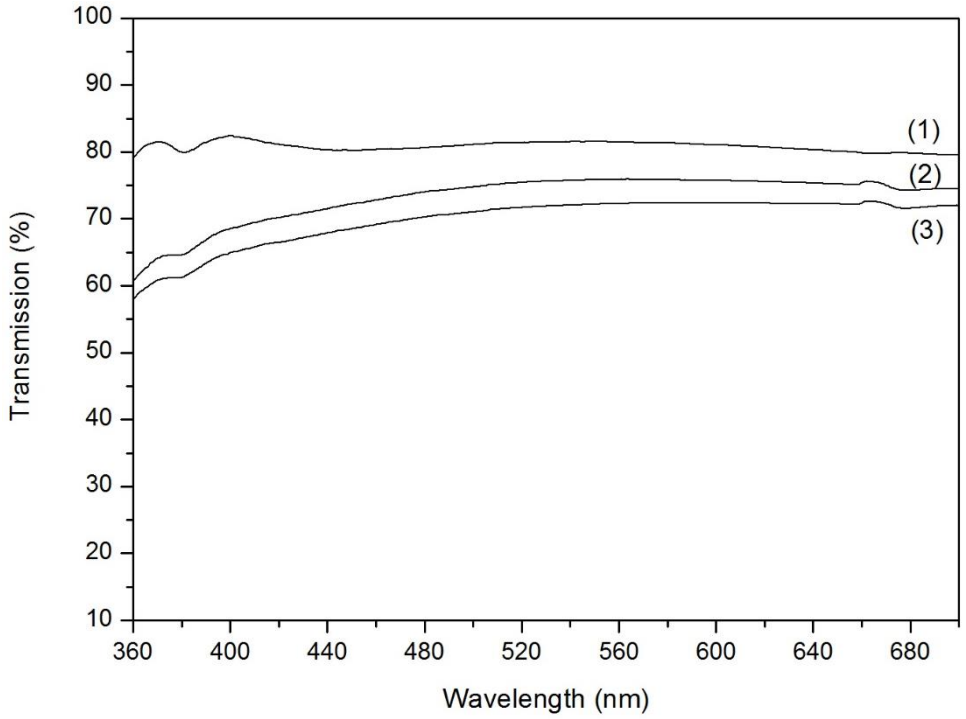

Figure 2. Transmission spectra of the glass samples, (1) $70SiO_2$-$15Na_2O$-$10CaO$-$5Al_2O_3$ glass, (2) 1Ag-2h, (3) 1Ag-4h.

4. CONCLUSIONS

In the present study, preparation of silver containing soda-lime glasses by using ion exchange process was realized for the development of antibacterial glasses. According to the SEM/EDS and chemical analysis results, the amount of silver introduced into the glass surface increase with increasing ionic exchange time and $AgNO_3$ concentration in the ionic medium. Also it was revealed that the transmittance of the ion exchanged glasses shifted to lower values increasing ion exchange time.

Acknowledgements

The authors of this study gratefully acknowledge The Scientific & Technological Research Council of Turkey (TUBITAK) for the financial support under the project numbered 113M145.

REFERENCES

1. S.Karlsson "Modification of Float Glass Surfaces by Ion Exchange", Ph.D. Thesis, School Of Engineering, Linnaeus University, İsveç, 2012
2. M.A.Fiori, M.M.S.Paula, A.M.Bernardin, H.G.Riella, E.Angioletto, Materials Science and Engineering C, 29, 1569, 2009
3. C.Özgür, F.Çolak, O.Şan, Journal of Non-Crystalline Solids, 357, 116, 2011
4. A.A.Ahmed, A.A.Ali, D.A.R.Mahmoud, A.M.El-Fiqi, Journal of Biomedical Materials Research Part A, 98, 132, 2011
5. I.Ahmed, D.Ready, D.Wilson, J.C.Knowles, Journal of Biomedical Materials Research Part A, 79, 618, 2006
6. A.A.Ahmed, A.A.Ali, D.A.R.Mahmoud, A.M.El-Fiqi, Solid State Sciences, 13, 981, 2011
7. A.Quaranta, E.Cattaruzza, F.Gonella, Materials Science and Engineering B, 149, 133, 2008
8. R.Gy, Science and Engineering B, 149, 159, 2008
9. N.F.Borrelli, D.L.Morse, W.Senaratne, F.Verrier, Y.Wei, Coated, Antimicrobial, Chemically Strengthened Glass and Method of Making, US 2012/0034435 A1, 2012
10. E.Verne, M.Miola, C.V. Brovarone, M.Cannas, S.Gatti, G.Fucale, G.Maina, A.Masse, S.Di Nunzio, Journal of Material Science, 20, 733, 2009
11. S.Di.Nunzio, C.V.Brovarone, S.Spriano, D.Milanese, E.Verne, V.Bergo, G.Maina, P.Spinelli, Journal of The European Ceramic Society, 24, 2935, 2004
12. A.Razzaghi, M.Maleki, Y.Azizian-Kalandaragh, Applied Surface Science, 270, 604, 2013
13. E.Mendes, R.Piletti, T.Barichello, C.M.Oliveira, C.T.Kniess, E.Angioletto, H.G.Riella, M.A.Fiori, Material Science and Engineering, 32, 1518, 2012
14. R.A.Eberhard, Antimicrobial Glass and Glass-Like Products and Method of Preparing Some, EP 1 449 816 A1, 2004

CHEMICALLY STRENGTHENED SODA-LIME GLASSES VIA ION EXCHANGE PROCESS

İpek ERDEM*, Duygu GÜLDİREN*, Miray ÇELİKBİLEK*, Ali Erçin ERSUNDU, Süheyla AYDIN***

*Istanbul Technical University, Turkey
erdemi@itu.edu.tr, yardimcid@gmail.com, miraycelikbilek@gmail.com, saydin@itu.edu.tr
**Nişantaşı University, Turkey
aliercin.ersundu@nisantasi.edu.tr

ABSTRACT

In the late half century, chemically strengthened glasses have proven to become highly advantageous in several applications for both daily and extreme conditions, such as touch screens, glassware, hurricane resistant architectural applications and aircraft windshields. Chemical strengthening is based on ionic exchange between ions from the original glass surface and invading ions from the salt melt it is in contact with. The disparity between the ion diameters results in a compressive stress on the surface of the glass that leads to the improvement of mechanical properties such as hardness, fracture toughness, scratch resistance etc.. In the present study, Corning® 2947 soda-lime glass slides were submitted to ion exchange process using KNO_3 salt bath at temperatures below the glass transition temperature. Mechanical properties of the ion exchanged glasses were studied in terms of the Vickers hardness. Investigation of the concentration profile of potassium ions incorporated into the ion exchanged glasses and microstructural characterization of the samples were performed by using energy dispersive X-ray spectroscopy (EDS) and scanning electron microscopy (SEM) techniques, respectively.

Keywords: Chemical strengthening, ion exchange, soda-lime glass, mechanical properties

İYON DEĞİŞİM PROSESİ İLE KİMYASAL OLARAK GÜÇLENDİRİLMİŞ SODA KİREÇ CAMLAR

ÖZET

Kimyasal güçlendirme işlemi ile mekanik özellikleri geliştirilen camlar, avantajlı özellikleri sayesinde, son yıllarda dokunmatik ekranlar, züccaciye amaçlı cam eşyaları, kasırgaya dayanıklı binalar, kokpit camları gibi günlük hayattan zorlu koşullara kadar geniş bir yelpazede kullanım bulmaya başlamıştır. Kimyasal güçlendirme işlemi, cam içerisindeki iyonlar ile camın temas halinde olduğu bir tuz banyosundaki iyonlar arasında gerçekleşen bir iyon değişim prosesi temeline dayanır. Banyodan cam yüzeyine geçen iyonların cam yüzeyinden ayrılan iyonlardan daha büyük iyonik çapta olması difüzyon bölgesi boyunca bir basma gerilim profili oluşturmaktadır. Bu gerilim profili; sertlik, kırılma tokluğu, aşınma dayanımı, vb. gibi camın çeşitli mekanik özelliklerinin iyileştirilmesini sağlamaktadır. Bu çalışmada, Corning® 2947 soda-kireç camı cam geçiş sıcaklığının altındaki bir sıcaklıkta KNO_3 içeren bir banyo kullanılarak iyon değişim işlemine tabi tutulmuştur. İşlem sonrası camların mekanik

özelliklerinin incelenmesi amacıyla Vickers sertlik ölçümleri gerçekleştirilmiştir. Taramalı elektron mikroskobu (SEM) ve enerji dispersif X-ışınları spektroskopi (EDS) teknikleri kullanılarak cam yapıya katılan potasyum miktarı ve konsantrasyon profili tespit edilmiştir.

Anahtar Kelimeler: Kimyasal güçlendirme, iyon değişimi, soda-kireç camı, mekanik özellikler.

1. INTRODUCTION

In more recent years, increasing concerns on product safety and environment have prompted researchers to improve mechanical properties of glasses using different techniques, most involving the introduction of compression stress to the glass surface. Thermal tempering, chemical strengthening and surface crystallization are the few of the common methods of introducing surface compression to the materials. Among these, chemical strengthening has become widely applied for its advantages as being a technique generating comparatively higher compressive stress on the surface, creating no measurable optical distortion, applicability to even 1mm thin samples and complex shaped products. Years of accelerating studies on chemical strengthening enabled new applications of glass materials such as cockpit windows for aircrafts, high speed train windshields, copy machines, drug delivery, display windows of electronic devices, transparent armors, hurricane resistant architectural windows, solar energy conversion tubular etc. [1-6].

Chemical strengthening is an ionic exchange process performed with an alkali containing glass immersed into a molten alkali salt bath at a temperature below the glass transition, resulting in the strengthening of glass. Alkali ions in the glass that are close enough to the surface and having a smaller diameter are exchanged with larger ions from the salt bath. The strengthening effect is due to the residual compressive stress generated by this disparity that expand the original glass structure and limiting crack propagation under tensile stresses. The concentration of invading ions decrease from surface to the bulk of glass, generating a concentration profile. Diffusion depth, surface compression stress and compression stress profile are identifying factors on the amount of strengthening and depend precisely on temperature and time. The process requires high alkali content in the original glass in order to provide for the ions to exchange, so a glass with appropriate composition must be selected [1-3,6-8].

The effect of stress present on materials has been studied by many authors from the perspective of mechanical properties such as hardness, fracture toughness and scratch resistance. A common outcome of these studies revealed that indentation hardness was dependent on residual stress present in materials, including glass systems [5,7,9-13].

In this study, it was aimed to prepare chemically strengthened glasses by applying ion exchange process on Corning® 2947 soda-lime glasses. Soda lime glasses were selected due to their availability and reasonable price making them accessible to everyone thus preferable in applications. The effect of the process time on hardness was investigated on 5 different samples immersed in KNO_3 bath for 0.5, 1, 2, 4, and 8 hours. The concentration profile of potassium ions incorporated into the ion exchanged glasses was characterized by using energy dispersive X-ray spectroscopy (EDS) technique.

2. EXPERIMENTAL

Experimental studies were conducted using Corning® 2947 soda-lime glass slides. Glass slides were cut to obtain samples with dimensions 25x25x0.9 mm. Thermal analysis of the

unprocessed glass samples was performed using a PerkinElmer™ Diamond TG/DTA, in platinum pans, from room temperature to 600 °C with a heating rate of 10°C/min under flowing (100 ml/min) argon gas. Ion exchange process temperature was determined according to the glass transition onset temperature (T_g) obtained from the thermal analysis results.

Glass samples were cleaned in an ultrasonic cleaner using distilled water and ethanol prior to ionic exchange process to maintain the quality of the surface and improve the efficiency of the process. The process was performed using a ProthermPLF 120/7 furnace by immersing the samples into the melted KNO_3 bath (99.0% purity, Alfa AesarCompany) as ionic medium in stainless steel tanks. Immersion was realized at 475°C for 0.5, 1, 2, 4 and 8 hours and the samples were named according to the process time as 0.5h, 1h, 2h, 4h and 8h, respectively. It was assured that the sample surface to be completely in contact with KNO_3 bath. After the ion exchange process, the samples were cleaned again to remove bath residues from the surface.

The atomic weight of potassium ion is higher than sodium ion, therefore an increase in sample weight is expected after the ion exchange process. Following formula shows how to calculate the amount of potassium ions incorporated into the glass via ion exchange:

$$W_K = [(Wg_{after} - Wg_{before}) / (aW_K - aW_{Na})] * aW_K \quad (1)$$

where W_K is the amount of incorporated potassium ion, Wg_{before} and Wg_{after} are the sample weights before and after the process and aW_K and aW_{Na} are atomic weights of potassium and sodium ions, respectively. A digital balance of 10^{-4} precision was used to calculate the amount of the potassium ions incorporated into the glass.

Vickers hardness (HV) measurements of the unprocessed and ion exchanged samples were performed using Schimadzu HMV-G21D microhardness tester under 50g load for 10 seconds.

Scanning electron microscopy (SEM) and energy dispersive X-ray spectroscopy (EDS) techniques were used to characterize the ion exchanged glasses in terms of the diffusion depth and concentration profile from the surface to the bulk of the samples. SEM/EDS investigations were carried out with platinum-coated bulk samples at 15 kV in JEOL™ JSM 5410 microscope connected to Noran 2100 Freedom energy dispersive X-ray spectroscopy.

3. RESULTS

DTA analysis was performed to determine the glass transition onset temperature of the unprocessed samples. DTA thermogram of the Corning® 2947 glass sample in the temperature range of 300-600 °C is given in Figure 1.

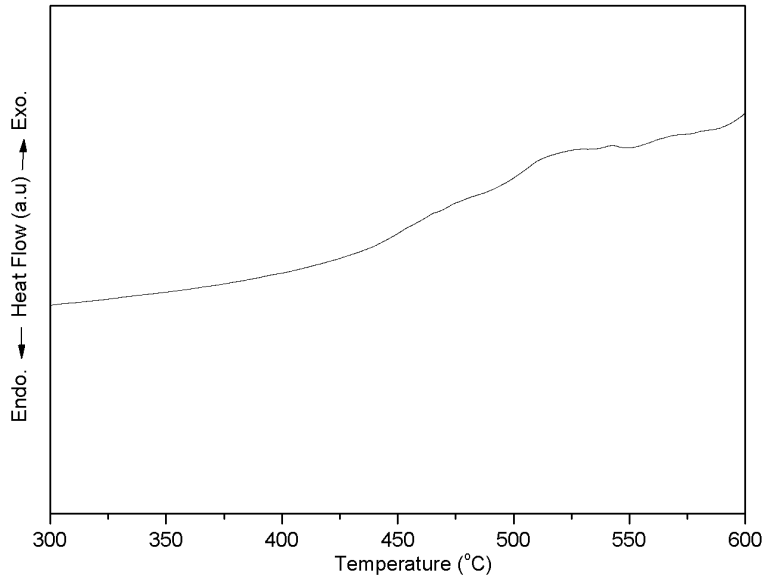

Figure 1. DTA curve of Corning® 2947glass.

The endothermic change corresponding to the glass transition reaction was detected at 544 °C.

After the ion exchange process, no color change was observed at any time duration.

The amount of potassium ions introduced into the glass via ion exchange was calculated using Equation 1. The weight of glass samples before and after the process, the increase in weight and the amount of potassium ions incorporated into the glass for different time periods are given in Table1.

Table 1. The weight values of the samples and amount of potassium ions introduced in the glass.

Sample ID	Glass weight (mg)		Weight increase (mg)	Amount of potassium (mg)
	Before	After		
0.5h	1562.2	1563.2	1.0	2.427
1h	1562.6	1563.8	1.2	2.912
2h	1544.2	1545.9	1.7	4.126
4h	1549.3	1551.9	2.6	6.311
8h	1423.5	1427.2	3.7	8.982

As can be seen in Table 1, the amount of potassium ions introduced into the glass surface increased with increasing ion exchange time.

The results of Vickers hardness measurements of the glass samples are given in Table 2. Measurements were performed under 50 g load for 10 seconds and the hardness values were obtained from the average of the four indentations performed on each sample in order to minimize experimental errors.

Table 2. Vickers hardness values of the ion exchanged glass samples.

Sample ID	Vickers hardness (HV) (50g load, 10 seconds)
Unprocessed glass	505.59
0.5h	606.15
1h	592.32
2h	591.05
4h	574.57
8h	568.11

Hardness measurements indicated that 0.5 hours of ion exchange time resulted a dramatic increase in Vickers hardness values. In further measurements, a continuous decrease with increasing ion exchange time was observed in Vickers hardness values of the ion exchanged glass samples. These results pointed out that increasing the ion exchange time and hence increasing the amount of potassium ions incorporated to the surface reduced the hardness of the samples.

As can be seen in Figure 2, SEM analysis carried out with the ion exchanged samples showed no microstructural change comparing with the unprocessed sample proving the amorphous structure. EDS analysis results revealed that the potassium concentration on the surface of the glasses increased with increasing ion exchange time and potassium concentration gradually decreased from the surface to the bulk of the glass samples.

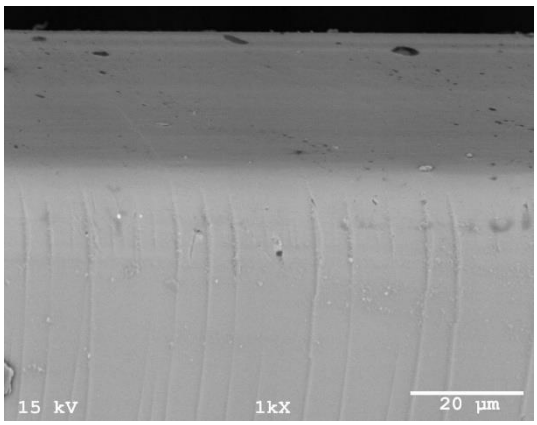

Figure 2. Cross-sectional SEM image of an ion exchanged glass sample.

4. CONCLUSIONS

In the present study, potassium was used to perform ion exchange process on Corning® 2947 soda lime glass in order to obtain chemically strengthened glasses. The effect of the ionic exchange time was investigated by performing weight measurements before and after the process and energy dispersive spectroscopy analysis. EDS results showed that concentration of potassium ions decreases from surface to the bulk of the samples and potassium concentration on the surface increases with increasing process time. Hardness measurements were performed to investigate the effects of ion exchange process time on mechanical properties of glasses and it was found that hardness values first showed a dramatic increase from 505.59 HV to 606.15 HV and then regularly decreased to 568.11 HV with increasing ion exchange time.

Acknowledgement

The authors of this study gratefully acknowledge The Scientific & Technological Research Council of Turkey (TUBITAK) for the financial support under the project numbered 113M145.

REFERENCES

1. A.K.Varshneya, Int. J. Appl. Glass Sci., 1[2], 131, 2010.
2. A.I.Fu and J.C.Mauro, J. Non-Cryst. Solids, 363, 199, 2013
3. R. Gy, Mater. Sci. Eng., B 149, 159, 2008
4. V. M. Sglavo, "Influence of KNO_3 Bath Composition on Ion Exchange Process of Commercial Soda Lime Silicate Float Glass", A.Kilislioğlu, Ed., "Ion Exchange Technologies", DOI: 10.5772/52064
5. P.Jannotti, G.Subhash, P.Ifj, P.K.Kreski and A.K.Varshneya, Int. J. Appl. Glass Sci., 2 [4], 275, 2011
6. V.M.Sglavo, A.Quaranta, V.Allodi, G.Mariotto, J. Non-Cryst. Solids, DOI:10.1016/j.jnoncrysol.2014.01.026
7. S.Karlsson, B.Jonson and C.Stalhanske, Eur. J. Glass Sci. Technol., 51(2), 41, 2010
8. V.Tyagi and A.K.Varshneya, J. Non-Cryst. Solids, 238, 186, 1998
9. K.O.Kese, Z.C.Li and B.Bergman, J. Mater. Res., 19, 3109, 2004
10. Z.Tóth, A.Nagy, G.Steinbach and A.Juhász, Mater. Sci. Eng., A387–389, 542, 2004
11. K.Kese and D. J. Rowcliffe, J. Am. Ceram. Soc., 86[5], 811, 2003
12. S.Carlsson and P.L.Larsson**,** Acta mater. 49, 2193, 2001
13. N.Huber, and J.Heerens, Acta Mater., 56, 6205, 2008

PREPARATION AND CHARACTERIZATION OF 20 MOL % SAMARIUM-DOPED CERIA (SDC20) ELECTROLYTE MATERIAL FOR SOLİD OXİDE FUEL CELLS

Özgün SERİN, Aliye ARABACI

İstanbul University, Turkey

aliye@istanbul.edu.tr,

ABSTRACT

Oxides such as, ceria (CeO_2) with the cubic fluorite structure are known to be good solid electrolytes when they are doped with cations of lower valence than the host cations. The high ionic conductivity of doped ceria makes it an attractive electrolyte for solid oxide fuel cells, whose prospects as an environmentally friendly power source are very promising. In this study, samarium-doped ceria materials were synthesized by Pechini method using citric acid as chelating agent and the fundamental properties of the samarium-doped ceria electrolyte material is characterized by a variety of experimental methods such as XRD, SEM, FTIR and TGA-DTA. Furthermore, it is confirmed by XRD analysis that the fluorite structure of ceria is maintained in samarium-doped ceria material. The crystallite size was calculated using Scherrer equation.

Keyword: Fuel cells, Doped-CeO_2, SEM, FT-IR

KATI OKSİT YAKIT HÜCRESİ İÇİN % 20 MOL SAMARYUM-KATKILI SERYUM OKSİT (SDC20) ELEKTROLİT MALZEMESİNİN HAZIRLANMASI VE KARAKTERİZASYONU

ÖZET

Seriya (CeO_2) gibi kübik florit yapılı oksitler, kendilerinden daha düşük değerlikli katyonlarla katkılandırıldıklarında, iyi katı elektrolitler olarak bilinirler. Katkılı seryum oksidin yüksek iyonik iletkenliği, onu katı oksit yakıt hücresi için çekici bir elektrolit malzemesi yapmaktadır, ayrıca çevre dostu bir güç kaynağı olarak da umut vaat etmektedir. Bu çalışmada, samaryum katkılı seryum oksit malzemeleri Pechini metoduyla şelatlama ajanı olarak sitrik asit kullanılarak sentezlenmiştir. Samaryum katkılı seryum oksit elektrolit malzemesi XRD, SEM, FTIR ve TGA-DTA gibi farklı deneysel metodlar kullanarak karakterize edilmiştir. Ayrıca, seryum dioksit florit yapısının, samaryum katkılı seryum oksit malzemesi içinde muhafaza edildiği XRD analizi ile teyit edilmiştir. Kristal boyutu, Scherrer denklemi kullanılarak hesaplanmıştır.

Keyword: Yakıt hücreleri, Katkılı-CeO_2, SEM, FT-IR

1. INTRODUCTION

Increase in the industrialization has led to development of new energy sources. Coal, petrol and fossil based fuels are still the high portions of energy sources in the world. Natural gas, fossil fuels and coal lead to the cause of climate change and greenhouse gases such as methane and CO_2 released during combustion which heats the earth. Nowadays the need to protect the ecosystem, clean and renewable energy sources such as wind energy, solar energy alternatives are being developed. Clean, efficient and environmentally friendly methods of energy production is one of the most important research topics for engineers and scientists. Solid oxide fuel cells (SOFCs) are the most efficient devices that convert the chemical energy of a fuel into electrical energy in a clean and cost-effective route.

In general, traditional SOFC systems that use yttria-stabilized zirconia (YSZ) as an electrolyte for their high conversion efficiency are operated at around 1000 ^oC [1,2]. However, operation at high temperatures yields some problems, including interfacial reaction between the components, mechanical and thermal degradation, thermal expansion mismatch, and high cost materials. To overcome these problems, electrolytes which have high ionic conductivity at intermediate temperatures are needed.

Researchers in recent years have concantreted to lower (<800 ^oC) the operating temperature of the SOFCs. It is known that the replacement of YSZ electrolyte by the doped CeO_2 (ceria), which has high oxide-ionic conductivity at intermediate temperature, is one of the most promising methods for lowering the operating temperature [3]. The ionic conductivity of ceria increases significantly with the oxygen vacancies created by the doping of rare earth cations (such as, Gd^{3+},Sm^{3+}, Nd^{3+}) into the ceria lattice. The ionic conductivity value at 750 ^oC of doped ceria is similar to that of YSZ at 1000 ^oC[4]. Among the various dopants used, Sm^{3+}, Dy^{3+}, and Gd^{3+} are favorable for increasing the ionic conductivity of doped ceria[4,5].

To synthesize ceria-based electrolytes with the desired properties,various methods such as hydrothermal synthesis [6,7], homogenous precipitation [8,9], the sol-gel process [10], the glycine nitrate process [11], combustion [12], the polyol method [13] and avariant of the sol-gel process known as cation complexation [14] have been employed.

Compared with many chemical routes, pechini method is a simple, feasible and less time consuming technique for preparing various oxide ceramics with the ability of direct and precise control of stoichiometry, homogeneity and purity. The aim of present work is to investigate the effect of calcination temperature on the crystal structure of samarium doped ceria. The thermal decomposition behavior of the samples was evaluated by using thermal gravimetric analysis. The microstructural features of the samples were also characterized by scanning electron microscopy (SEM) studies.

2. EXPERIMENTAL ANALYSIS

2.1. Preparation of SDC Powders

The starting materials were cerium (III) nitrate hexahydrate ($Ce(NO_3)_3.6H_2O$, 99.9% purity) and samarium (III) nitrate hexahydrate ($Sm(NO_3)_3.6H_2O$, (99.99 % purity), purchased from Aldrich. Ethylene glycol and citric acid were obtained from R.P.Normopur, Boehringer Ingelheim, respectively. All chemicals were used as provided. Nitrate salts were dissolved in de-ionized water individually and then the solutions were mixed in a beaker. An hydrous citric acid was dissolved in de-ionized water and then was added to the cation solution. The

molar ratio of total oxide (TO): citric acid (CA) and ethyleneglycol: citric acid was selected as 2:1, 4:1, respectively. After homogenization of this solution, temperature was raised to 80 ^{o}C and the solution was kept for 3 h at this temperature with magnetic stirring to remove excess water. During this time, the color of the liquid turned from white to orange and then dark brown. Then the obtained dark brown gel was cooled down to room temperature.The initial thermal decomposition of the precursor was dried 110 ^{o}C for 24 h.

The thermal behavior of $Sm_{0.2}Ce_{0.8}O_{1.95}$ (SDC20) powders was carried out with SII Exstar 6000 TG/DTA 6300 from room temperature to 850 ^{o}C at a heating rate of 5 ^{o}C min^{-1} in air atmosphere.

The XRD technique was used to examine the crystalline structure and phase purity. Calcined powder was studied by XRD using a Rigaku D/max-2200 Ultima X-ray diffractometer with CuKα radiation. Data in an angular region of 2θ =20–90^{o} were collected. From the X-ray diffractograms, phases and average crystallite sizes, D, of the $Ce_{1-x}Sm_xO_{2-x/2}$ samples were calculated from X-ray line broadening of the reflections of (111) by using the well-known Scherrer equation:

$$D = 0.9\,\lambda/\beta\cos\theta \qquad (1)$$

where λ is the wave length of the X-rays (1,5418 Å), θ is the scattering angle of the main reflection (111) and β is the corrected peak at full width at half maximum (FWHM) intensity.

3. RESULTS AND DISCUSSION

3.1. DTA–TG Results

Simultaneous differential thermal analysis and thermogravimetry (DTA–TG) were carried out on the dried gel (at 110^{o}C). The samples were heated from room temperature to 850 ^{o}C at a heating rate of 5 ^{o}C /min under air atmosphere. Fig. 1 displays the DTA–TG results of the dried gels. As seen in the figure,weight loss occurred in three steps. In the first step, a weight loss of 3.1% occurred due to the dehydration in the temperature range of 40–135 ^{o}C. In the second step, a weight loss of 25.5% occurred in the temperature range of 135-253 ^{o}C. The next step which is shown in Fig. 1 at 253 ^{o}C, an abrupt weight loss of about 47.4 % is accompanied by a strong exothermic DTA peak, which indicates the removal of the combustion of organic materials and the thermal decomposition of the dried gels. No apparent mass loss occurs at temperatures T >400 ^{o}C, suggesting the formation of crystalline $Ce_{0.8}Sm_{0.2}O_{1.90}$ as a decomposed product. The XRD results also verify this finding.

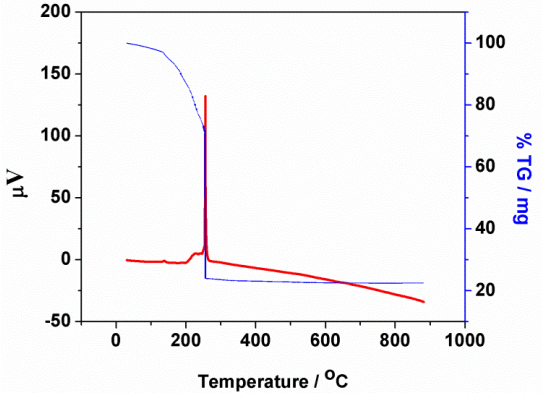

Figure 1. Differential thermal analysis (DTA) and thermogravimetry (TG) curves for the dried gels.

3.2. Phase Analysis

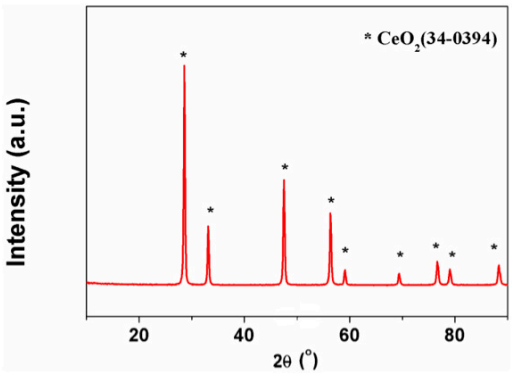

Figure 2. XRD patterns of 20 mol% Sm doped ceria powders calcined in air for 2 h at 500 °C.

X-ray diffraction is a versatile, non-destructive technique that reveals detailed information about the crystallographic structure of natural and manufactured materials. The phase evolution of the precursors upon calcination was determined by the method of XRD.

To ensure the complete dissolution of dopant in CeO_2, XRD patterns were measured for samarium doped ceria samples calcined at 500 °C. XRD patterns of the calcined powders are shown in Fig. 2. In accordance with the results of DTA/TG, crystallization of the powder occurred by calcination at 500 °C, and almost all the characteristic diffraction peaks corresponding to the fluorite structure of ceria (JCPDS Powder Diffraction File No. 34-0394). Crystallite size of $Ce_{0.8}Sm_{0.2}O_{1.90}$ powders was found as 11.7 nm for the calcination temperature of 500°C. No crystalline phases corresponding to Sm_2O_3 could be found at calcination temperature of 500 °C for the Sm-doped ceria. The results indicate that the dopant ion was fully substituted in the CeO_2 lattice.

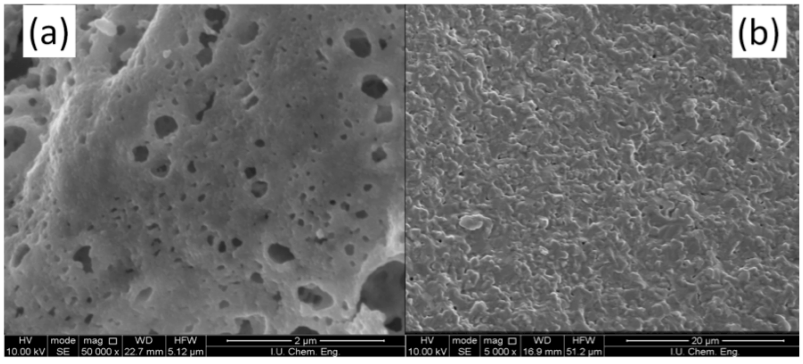

Figure 4. SEM images (a) of SDC20 powders calcined at 400°C/4 h (b) cross-sectional fracture surfaces of SDC20 samples sintered at 1400 °C/6 h

Fig.4 (a and b) displays the SEM images of SDC20 powders at selected calcinating temperature and the sintered SDC20 pellets. As can be seen from in Fig.4 (a) The powders

showed a foam-like morphology at 400°C. This is probably due to the fact that the decomposition products of the organic residues in the complexes, such as CO, CO_2, H_2O, NO_x and volatile hydrocarbon, did not escape easily from the obtained powders. The sintered pellets at 1400 °C/6 h had dense structures.

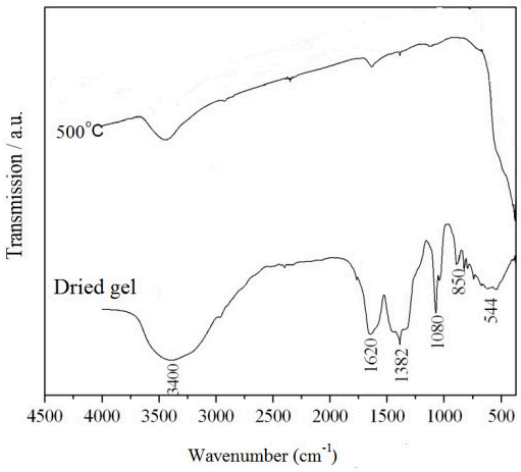

Figure 5. FTIR spectroscopy analysis of $Ce_{0.8}Sm_{0.2}O_{1.95}$ gel precursors (dried at 110 °C) and calcined at 500°C in air atmosphere.

Fig.5 displays FTIR spectroscopy analysis of dried $Ce_{0.8}Sm_{0.2}O_{1.95}$ gel at 110 °C in air atmosphere and calcined $Ce_{0.8}Sm_{0.2}O_{1.95}$ at 500 °C. All FTIR measurements were done using the KBr method at room temperature. The intense bands detected in the range of 3000–3700 cm^{-1} are attributed to O–H stretching of physically absorbed H_2O or surface –OH group. The spectra of SDC sample displays the band at about 1382 cm^{-1} which is the characteristic of ionic nitrate (ν (N=O))[15]. The $\nu_s(NO_2)$ is detected at about 1080 cm^{-1}. After heat treatment of 500°C, the bands of nitrate group almost disappeared. After heat treatment at 500°C, the hydroxyl groups of absorbed water were disappeared significantly. At 500°C, the high intensity bands in the range of 400 and 700 cm^{-1} are attributed to the metal-oxygen stretching vibrations, indicating the formation of the samarium doped ceria solid solutions.

4. CONCLUSIONS

$Ce_{0.8}Sm_{0.2}O_{1.95}$ solid solutions having a fluorite structure were prepared by pechini method. The TG-DTA curve indicated that almost no weight loss is observed at above 400°C, indicating the formation of the SDC20 oxide products. The XRD result also verify this finding. It indicate that the dopant ion was fully substituted in the CeO_2 lattice. The small particle size of the doped ceria powders allowed the sintering of dense ceramic pellets at 1400 °C/6 h, which was smaller than 1600 °C, the temperature required to sinter the corresponding materials prepared by the conventional solid state method. The formation of the samarium doped ceria solid solutions occurred at 500°C, which was confirmed with TG-DTA, XRD and FTIR analyses.

REFERNCES

1. J. P. P. Huijsmans, F. P. F. van Berkel and G. M. Christie, J. Power Sources, 71, 107, 1998
2. H.Yoshida, K.Miura, T. Fukui, S.Ohara and T.Inagaki, J. Power Sources,106, 136, 2002
3. X.Guan, H. Zhou, Y.Wang, and J. Zhang, J. Alloys Compd., 464, 310 ,2008

4. S. Kuharuangrong, J. Power Sources, 171,506, 2007
5. D. H. Prasad, J. W. Son, B. K. Kim, H. W. Lee, and J. H. Lee, J. Eur. Ceram. Soc., 28, 3107, 2008
6. M. Hirano, E. Kato, Journal of the American Ceramic Society, 79 (3), 777, 1996
7. Y.C. Zhou, M.N. Rahman, Journal of Materials Research 8, 1680, 1993
8. N. Uekewa, M. Ueta, Y.J. Wu, K. Kakewa, Chemistry Letters, 8, 854, 2002
9. H.I. Chen, H.Y. Chang, Colloids Surface A242, 61, 2004
10. G.S. Wu, T. Xie, X.Y. Yuan, B.C. Cheng, L.D. Zhang, Materials Research Bulletin, 39, 1023, 2004
11. C.R. Xia, M.L. Liu, Solid State Ionics, 152–153, 423, 2002
12. M.M.A. Sekar, S.S.Manoharan, K.C. Patil, Journal of Materials Science Letters, 9, 1205, 1990
13. M.A. Faruk Öksüzömer, Göknur Dönmez, Vedat Sariboğa, Tuba Gürkaynak Altinçekiç, Ceramics International, 39, 7305, 2013
14. R.A. Rocha, E.N.S. Muccillo, Materials Research Bulletin, 38, 1979, 2003
15. M. Gaye, F.B. Tamboura, A.S. Sall, Bull. Chem. Soc. Ethiop.,17(1), 27, 2003

Effect of Sintering Temperature and Pressure on Properties of SPSed ZrC-TiB_2 Composites

•

Sinterleme Sıcaklığı ve Basıncının SPSed ZrC-TiB_2 Kompozitlerinin Özellikleri Üzerindeki Etkiler

Özden Ormancı, İpek Akın, Filiz Çınar Şahin, Onuralp Yücel, Gültekin Göller

İstanbul Technical University - Türkiye

ABSTRACT

ZrC-TiB_2 composites containing 10 vol. % TiB_2 were prepared by spark plasma sintering (SPS) at 1685 and 1700°C for 300 s under 40 MPa, 50 MPa and 60 MPa sintering pressure. Densification behavior, microstructure and mechanical properties of the composites were investigated. ZrC-TiB_2 composites with a relative density of more than 94% were obtained without using sintering aids. Sintering time and pressure did not have a significant effect on Vickers hardness of ZrC-TiB_2composites. ZrC-TiB_2 composite sintered at 1700°C under a pressure of 50 MPa showed the highest hardness, 18.11 GPa. Fracture toughness and oxidation resistance of the composites will also be investigated.

Keywords: ZrC-TiB_2 composite, spark plasma sintering, fracture toughness, oxidation resistance.

THE INFLUENCE OF POZZOLANIC ADMIXTURE ON THE MECHANICAL STRENGTH OF MORTAR

Makhloufi Chikouche Hamina*
* Institute of G.T.U, University of M'sila, 28000, M'sila/Algeria
chikmak@yahoo.fr

ABSTRACT
The mineral addition substituted to various percentages (0%, 5%, 10%, 15% and 20%) is the waste fired bricks (from the clay subjected to 900 °C) collected of a manufacturing unit (factory of manufacture of bricks). In this experimental work, we varied the percentage of the pouzzolanic admixture (waste bricks) in cement by the substitution method (partial replacement of the clinker by the calcined clay) to study its effect on the physico-chemical properties of cement manufactured with mineral addition and mortar mechanical behaviour. The physico-chemical properties of cement at anhydrous state and the hydrated state (chemical composition, specific weight, fineness, consistency of the cement paste, setting times and shrinkage), thus the characteristics of the mortars made at their bases, such as, the mechanical behaviour (flexural and compressive strengths) for the mortar were studied. According to the experimental results obtained, it comes that the quantity of mineral additive (calcined clay) and the chemical composition of cement manufactured are the principal parameters who influence on the variation of the mechanical strengths (flexural and compressive) of the mortars tested.

Keywords*:* Pozzolanic admixture, cement, mortar, and mechanical strength.

1. INTRODUCTION

The research of the economic binder by using the industrial by products (blast furnace slag, silica fume, fly-ashes) and the natural resources (natural pozzolan, limestone) is a major concern to reduce the deficit recorded during the manufacture of Portland cement [1]. These last years, a large effort of research was provided on the use of the supplementary cementitious materials as a partial replacement to Portland cement [2].
A partial replacement of cement by mineral admixture such as, fly ash, silica fume or blast furnace slag in cementing materials (mortar or concrete) mixes would help to overcome these problems and lead to improvement in the workability, strength and durability of cementing materials [3]. This would also lead additional benefits in terms of reduction on cost, energy savings, promoting ecological balance and conservation of natural resources etc. The Portland cement with pozzolanic admixture is low in C_3S (tricalcium silicate), low in C_3A (tricalcium aluminate) and low heat of hydration and high long term strength. The continuing search for partial cement replacement materials has led the authors to investigate the utlisation of waste fired clay bricks as a pozzolan for mortar and concrete.
Clay is a widespread natural material on all the continents and in particular in the countries of North Africa (Algeria). It consists of a variety of phyllosilicate minerals rich in silicon and aluminium oxides and hydroxides, which include variable amounts of structural water. Clay is distinguished by its small size, layered shape, affinity for water and tendency toward high plasticity [4]. The Algerian clay industry (bricks, tiles,

ceramics, etc.) has particular problems (mineral wastes) with its very high level of mineral waste who remains without being to exploit until now. Calcined clay (waste bricks) is an artificial pozzolana and it can hydrated in the presence of $Ca(OH)_2$. The formation of cementitious material by the reaction of free lime (CaO) with the pozzolan admixture (AlO_3, SiO_2, Fe_2O_3) in the presence of water is known as hydration. The hydrated calcium silicate gel or calcium aluminate gel (cementitious material) can bind inert material together. Since the lime content of calcined clay is relatively low, addition of lime is necessary for hydration reaction with the pozzolan of the calcined clay [5]. This paper presents an investigation of various blended cements produced by replacing 0%, 5%, 10%, 15% and 20% of these cements with a calcined clay (pozzolanic additive). The objective of this present experimental work is to evaluate the influence of pozzolanic admixture (waste bricks) on the physico-chemical properties of cement manufactured with mineral addition (latent hydraulicity) and the mechanical behavior (flexural and compressive strengths) for the mortar.

2. CHARACTERISTICS OF USED MATERIALS

2.1. Natural sand (fine aggregates)

The fine aggregate used was dune sand with a maximum diameter of 3 mm. The fineness modulus calculated was $M_f = 1,76$. The information on the physical properties of the natural sand used is given in Table 1. The fine aggregate (dune sand) contained 94,13% SiO_2; 2,96% CaO; 0,88% Al_20_3; 0,37% Fe_2O_3 and 0,11% MgO.

Table 1. Characteristics of dune sand used in the tests

Materials	Absolute density (Kg/dm^3)	Apparent density (Kg/dm^3)	Compactness (%)	Porosity (%)	Sand equivalent value (sight/test)
Dune sand	02,56	01,64	64,06	35,94	76/78

2.2. Pozzolanic admixture (waste bricks), gypsum and clinker

The substitution of a part of clinker with the mineral addition to various percentages (0%, 5%, 10%, 15% and 20%) is the waste fired bricks collected of a manufacturing unit (factory of manufacture of bricks). In this experimental work, we varied the percentage of the pouzzolanic admixture (waste bricks) in cement by the substitution method (partial replacement of the clinker by the calcined clay). The clay used in the present investigation was heated to 900 °C with a heating ramp pf 100 °C per hour. The chemical compositions (Oxide compositions) of gypsum and clay (raw and calcined) are shown in Table 2.

Table 2. Chemical composition (%, by weight) of gypsum and clay (raw and calcined)

Oxides, %	SiO_2	Al_2O_3	Fe_2O_3	CaO	MgO	K_2O	Na_2O	SO_3
Gypsum	07.70	03.20	01.44	26.82	01.40	-	-	27.83
Raw clay	52,03	16,22	06,30	06,68	02,71	02,38	00,96	00,68
Calcined clay	66,52	14,20	05,45	06,06	02,35	02,09	00,67	00,75

The Table 3 presents the chemical analysis of the clinker and the Bogue composition.

Table 3. Chemical analysis of the clinker and the Bogue composition

SiO_2	Al_2O_3	Fe_2O_3	CaO	MgO	CaO_{free}	SO_3	C_3S	C_2S	C_3A	C_4AF
22.10	04.57	03.95	66.34	01.60	00.02	00.54	65.70	14.15	5.42	12.03

The investigation was performed using the mixes composition for the preparation of the five types of cements containing clinker, gypsum and calcined clay (mineral admixture). Table 4 presents the mixes composition used in this experimental work as well as their finenesses.

Table 4. Mixes composition and finenesses of the five cements prepared

Cements	Clinker (%)	Calcined clay (%)	Gypsum (%)	Finenesses S.S.A (cm^2/g)
CEM I	95	0	5	3310
CEM II-1	80	5	5	3328
CEM II-2	75	10	5	3346
CEM II-3	70	15	5	3332
CEM II-4	65	20	5	3368

In this experimental work, we varied, the percentage of the calcined clay (waste bricks) in cement prepared (chemical effect) by the method of substitution (partial replacement of the clinker by the calcined clay). We used five types of cements manufactured with mineral admixture (waste bricks), this in the aim of analyzing the influence of a partial replacement of the clinker by the calcined clay (0%, 5%, 10%, 15% and 20%) prepared on the physical and chemical characteristics of hydraulic cements prepared at the anhydrous state and the state hydrated and also on the mechanical behaviour (flexural and compressive strengths) for the mortar studied.

3. MECHANICAL TESTS (Flexural and compressive strengths)

The mortar mixtures had proportions of 1:3:0,5 (binder:sand:xwater). Five different mixtures compositions were examined in the present study. The clinker was partially replaced by 0%, 5%, 10%, 15% and 20% of pozzolan (calcined clay).
The mortars samples were subjected to flexural and compressive mechanical tests. Mechanical strength was determined at 7, 28 and 90 days on 4 x 4 x 16 cm^3 prisms specimens with 50% water-binder ratio and 1:3 binder/sand (By mass). The moulds with fresh mortar test specimens were cured for 24 h at relative humidity of 95% RH. Three specimens were tested per specimen age.

4. RESULTS AND DISCUSSION

4.1 Effect of the quantity of calcined clay added on the cement paste studied

The experimental results obtained (Figures 1 and 2) presents the effect of the content of calcined clay (waste bricks) on the normal consistency of cement paste. The water demand of cements pastes prepared with different percentage of calcined clay (replacement level : 0%, 5%, 10%, 15% and 20%) is measured using the Vicat needle test (standart Vicat test). The influence of the quantity of pozzolanic admixture (calcined clay) added on the cement paste is expressed by the changes in normal consistency (water demand ratio). According to the results obtained (Figures 1 and 2), one notices that the increase of the quantity or percentage of the calcined clay (waste bricks) incorporated in the cement has a double effect : increase of the quantity of water required to have a normal consistency of the cement paste and decrease of the setting times. One also notices that the progressive addition of the pozzolanic addition (calcined clay) influences appreciably the water demand, this results in an increase in the quantity of water as a function of the percentage of mineral addition used. That can be due to the porosity of the added calcined clay. In the same way, it is noticed that setting times (initial and final set times) decrease proportionally with the increase the quantity of calcined clay.

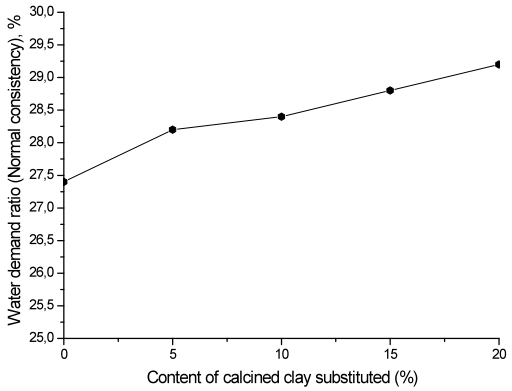

Figure 1. Variation of the normal consistency cement paste as a function of the content of calcined clay.

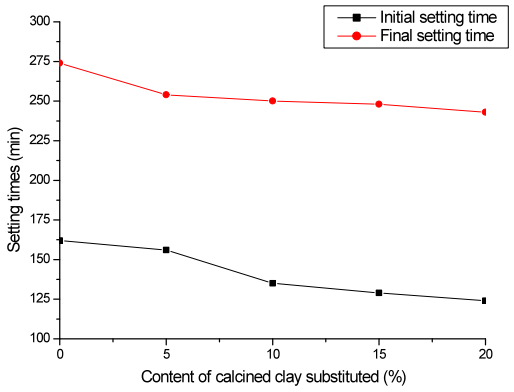

Figure 2. Variation of the setting times as a function of the content of calcined clay.

4.2 Effect of the quantity of pozzolanic admixture added (chemical effect) on the mechanical behaviour (flexural and compressive strengths)

The development of mechanical response (compressive and flexural strengths) of the mortar tested is shown in Figures 3 and 4. In this experimental work, we varied the percentage of the calcined clay (mineral addition) in cement (chemical effect) by the method of substitution (partial replacement of the clinker by the waste bricks). The increase of the pozzolanic admixture (calcined clay) gives an decrease of the mechanical strength at 7 and 28 days (at short and medium-term). That is explained by the decrease of the fast kinetics of hydration of the mineral C_3S (tricalcium silicate) and C_2S (dicalcium silicate). These latter are the two principal minerals which ensure the development of the resistances to short and medium-term. At 90 days (3 months) the mortars containing up to 10% of the calcined clay will reach resistance comparable to those of a witness without calcined clay. Thus, the weakness of strengths to short term can be compensated by the pozzolanic activity of the calcined clay.

The pozzolanic admixture (calcined clay) added in cement clearly improves the mechanical strength of the mortar at long term (90 days). This confirms the role of the pozzolanic reaction of the waste bricks in the fast and complete hydration of the cement (pozzolanic activity) by the formation of the $Ca(OH)_2$ released during the hydration of the cement.

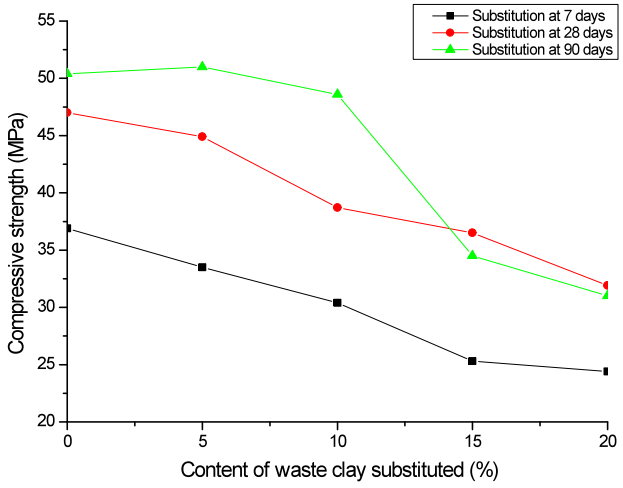

Figure 3. Evolution of compressive strength of mortar a function of the content of calcined clay.

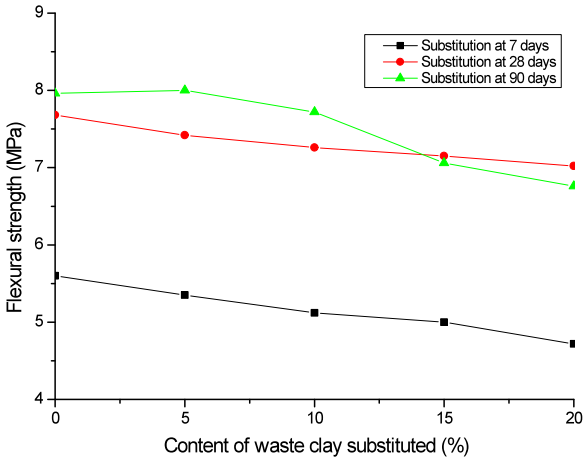

Figure 4. Evolution of flexural strength of mortar a function of the content of calcined clay.

5. CONCLUSION

The pozzolanic activity of calcined clay has mainly been pointed out as well as the possibility to use this mineral addition with a content of 10% for the manufacture of cement. The main conclusions of this study are summarized as follows:

* The increase of the quantity or percentage of the calcined clay (waste bricks) incorporated in the cement has a double effect : increase of the quantity of water required to have a normal consistency of the cement paste and decrease of the setting times.

* The increase of the pozzolanic admixture (calcined clay) gives an decrease of the mechanical strength at 7 and 28 days (at short and medium-term).

* At 90 days (3 months) the mortars containing up to 10% of the calcined clay will reach resistance comparable to those of a witness without calcined clay.

REFERENCES

1. KAMINSKAS, R., MITUZAS, J. and KAMINSKAS, A., The effect of pozzolona on the properties of the finest fraction of separated Portland cement, Ceramics,Vol. 50, (2006), 15-21.
2. Tikalsky, P. and Freeman, RL., The effect of pouzzolan and slag on the resistance of concrete, Master's Thesis, University of Texas, (1998).
3. Schindler, A.K. and Folliard, K.G., Influence of supplementary cementing materials on the heat of hydration of concrete, Avanced in Cement and Concrete IX Conference, Colorado, (2003), 10-14.
4. Baronio, G. and Binda, L., Study of the pozzolanicity of some bricks and clays, Construction and Building Materials, Vol. 11, (1997), 70-78.
7. He, C., Makovicky, E. and Osaeck, B., Thermal stability and pozzolanic activity of calcined kaolin, Applied Clay Science, Vol. 9, (1994), 165-187.

ESTIMATION OF RESIDUAL STRESSES IN STEEL COMPONENTS BY MAGNETIC BARKHAUSEN NOISE TECHNIQUE: WELDING AND SHOT-PEENING

C. Hakan GÜR

Middle East Technical University, Ankara, Turkey
chgur@metu.edu.tr

ABSTRACT

Global competition requires continual improvement in the performance and service life of the steel components and structures. Since manufacturing processes cause considerable amount of residual stress, any design ignoring the residual stress state may lead to early failure or distortion of the products. Thus, development of non-destructive techniques for determination of residual stresses in a rapid, reliable and cost-effective manner has been a challenging task in recent years. Magnetic Barkhausen Noise (MBN) method has been considered as an alternative technique for non-destructive determination of residual stresses in ferromagnetic steels. This paper presents the studies on the determination of residual stresses in the welded plates and shot-peened components by MBN.

Keywords: Residual stress, Steels, Welding, Shot-peening

1 INTRODUCTION

Residual stresses are self-equilibrating elastic stresses that remain in the material after removal of the external causes. Since residual stresses are added to the applied stresses, ignorance of them may cause distortion or early failure either in the subsequent processes or in their use under service conditions. Therefore, determination of residual stresses is important for quality, integrity and service performance of the engineering components and structures. On the other hand, high production rates and strict quality requirements force the industry to use fast and non-destructive methods for controlling and characterization of the products.

Welding is widely used in almost all industrial applications. It may generate residual stresses at a remarkable level due to non-uniformities in heating/cooling, plastic deformation and phase transformations during welding. Shot-peening is also a critical process for manufacturing of mechanical parts. A remarkable increase in fatigue life obtained by shot-peening is due to the effects of the residual compressive stresses and the cold work. Under the effect of peening media, local plastic deformation locally stretches the surface whereas the core shows resistance to stretching; and thus, it results in a compressive stress region at the surface.

Magnetic Barkhausen Noise (MBN) method has become an alternative to the conventional residual stress measurement methods for ferromagnetic materials. Ferromagnetic materials consist of very small magnetic regions called domain which is magnetized along a certain crystallographic direction of easy magnetization. Domains are separated from one another by domain walls to minimize the magnetic energy due to oppositely magnetized domains. When a variable external field is applied, irreversible jumps of domain walls occur due to discontinuous domain wall motion, domain rotation, nucleation and annihilation of domains. On removing the field, the magnetization declines to zero if there is no barrier to domain wall motion. When the

strength of externally applied magnetic field reaches the critical level, motion of the domain wall continues by Barkhausen jumps which can be detected as the voltage pulses induced in a pick-up coil positioned close to the surface. Microstructural features such as dislocations, inclusions and grain boundaries hinder and local stress regions affect the domain wall motion. Since MBN signals are sensitive to changes in both microstructure and residual stresses for characterization of microstructure or stresses, one of those parameters should be known.

Changes in microstructure affect the pinning sites for domain walls whereas residual stresses affect the area of the domain walls which were specified as 180^o and 90^o domain walls for steels (Figure 1). It has been proposed that main motion capability of the domains coming from 180^o. MBN technique can detect the residual stress differences on the basis of the changing area in these domain walls. While tensile type of stresses increases the area of 180^o domain wall by causing an increase in the MBN emission, compressive residual stress has a reverse effect [1].

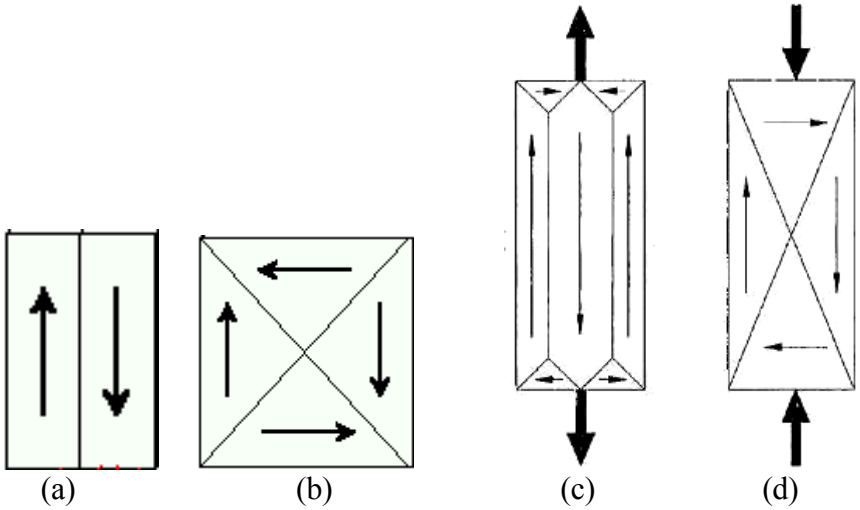

Figure 1. a) 180^o domain walls, b) 90^o domain walls,
c) the effect of tensile stress, d) the effect of compressive stress

Residual stresses can be measured by destructive methods (sectioning, hole-drilling, etc.) or by non-destructive methods (X-ray diffraction, ultrasonic and magnetic methods, etc.) [2]. X-ray measurement method is reliable for residual stress characterization, but it is slow and proper for the laboratory conditions; on the other hand, the MBN technique is fast, qualitative but with a calibration it can make measurement quantitatively and proper measurement technique after production in the industry and service conditions of the components [3]. The comparison of the results of MBN and hole drilling techniques on the shot peened components showed a difference up to 150 MPa [4]. Few studies exist on evaluation of residual stresses in welded steels by MBN [5-7].

The aim of this paper is to present the non-destructive monitoring of the effect of surface residual stresses on the welded and shot peened samples by MBN. Residual stresses on welded plates were measured by an automated MBN measurement system after performing the calibration procedure. Various sets of samples having different surface residual stress states were prepared by changing the important shot peening parameters, and surface residual stresses were measured by MBN. The efficiency and effectiveness of MBN measurements as a fast and non-destructive evaluation tool for controlling these operations was investigated.

2. EXPERIMENTAL PROCEDURE

2.1 Preparation of the samples

Welded plates: API5LX70 plates (0.04%C, 0.39%Si, 1.48%Mn, 0.08%Ni, 0.031%Al, 0.16%Cu, 0.03%Cr, 0.02%Ti, 0.05%Nb) were cut into the samples with dimensions of 300x80x15 mm. After abrasive machining, a V-shaped groove was opened with 10mm-width and 10mm-depth. Plates were tack welded to the table in order to avoid distortion, and then, they were welded by MAG welding (22 V, 140 A) using G3Si1 electrodes.

Shot-peened samples: The samples having the dimensions of 15 mm x 120 mm x 19 mm were prepared from a low-C steel (0.08%C, 0.24%Si, 0.6%Mn, 0.02%S, 0.33%Cu, 0.13%Cr, 0.04%Mo, 0.15%Ni, <0.003%P). The microstructures of all samples consist of mainly ferrite and some pearlite with an average hardness of 215 HV. For the sample groups, four intensities (7, 8, 9.8 and 12.3Almen) and three coverage values (50%, 100%, and 300%) were specified. Intensity values were obtained for 45^{o} peening angle by applying different shot mass flow and air pressures. The coverage values were obtained for 2,5 bar air pressure, 7 kg/minute shot mass flow rate, and 45^{o} peening angle. All parameters were specified by means of the saturation curves, Almen strips, and time calculation for coverage. The curvatures of the shot-peened Almen strips were measured with a gauge in order to quantify the peening intensity.

2.3 Investigations and measurements

For metallographic investigations each specimen was finely ground, polished and etched with %2 Nital.

In the MBN measurements, two channels of the Stresstech 500-2 equipment, namely Rollscan and µscan, and S1–138–13-01 sensor were used. Rollscan channel is capable of taking real time measurements and gives a single value namely magneto-elastic parameter whereas µscan channel has offline measurement capability and it gives pulse height distribution and representative hysteresis curve. The magnetic excitation frequency was 125 Hz and received Barkhausen signals were filtered in the range of 70-200 kHz. Before measurements, all samples were demagnetized to eliminate the effects of remanent magnetization on the results.

In the welded plate, the MBN probe was attached to a motor driven platform, and carefully aligned to get a full contact with the surface. The plate was put on this platform which was driven at a constant speed of 0.2 cm/sec along the x-direction. Three measurement lines seperated 20 mm from each other were defined for MBN measurements. About 1500 data points were recorded during MBN measurements along the measurement line. MBN values were converted to the residual stress by using the calibration curves. In order to investigate the effect of microstructure on the residual stress measurement by MBN, one calibration specimen was prepared from the heat affected zone (HAZ), and the other one was prepared from the parent metal. After adhering a single element strain gauge to the calibration samples, tensile and compressive stresses in the elastic deformation range were applied to the specimens in a step-wise manner by a loading equipment. Then, the strain values changed to stress values by using elasticity equations. Parallel to the strain-gauge measurements corresponding MBN values were measured, and the calibration curves for elastic stress versus MBN parameter were prepared (Figure 2). For the MBN values outside the calibration curve, extrapolation method was applied to determine the corresponding stress values, which might be an error source.

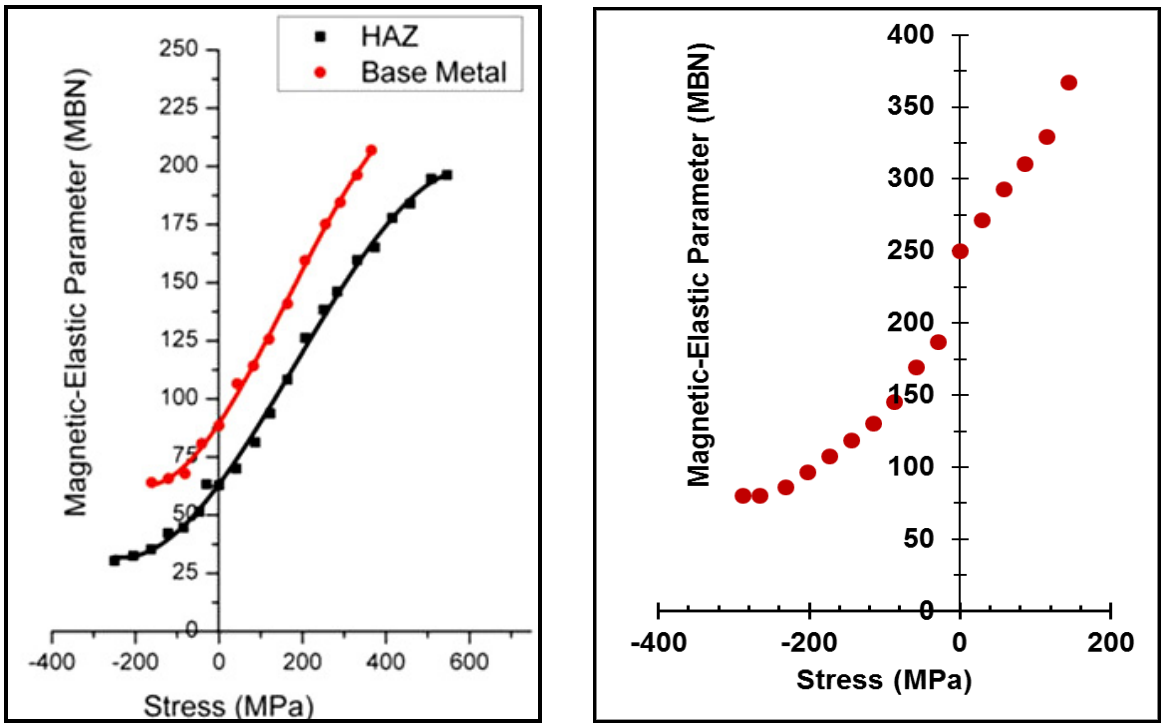

(a) (b)

Figure 2. Calibration curves: a) welded sample [7], b) shot-peened sample [8]

3. RESULTS AND DISCUSSION

The results are given in different forms because there is a combined effect of microstructure and residual stress in the welded samples. However, this is not the case for the shot-peened samples that have the identical microstructure, i.e. there is only the effect of residual stresses on the MBN emission.

3.1 Welded samples

Metallographic examinations showed that parent metal consists of ferritic-pearlitic structure with an average grain size of about 15 µm; weld metal has a microstructure of acicular ferrite with the average grain size of 5 µm; in the coarse grained HAZ region the average grain size is about 30 µm; a very fine grain size (5 µm) was observed in the fine grained HAZ region.

The variation of the longitudinal component of the surface residual stresses is given in Figure 3. The decline of stress values near the weld line can be explained by grain coarsening since MBN value decreases with increasing grain size. Two different results were obtained using calibration based on the parent metal and HAZ. The results based on HAZ-calibration gave higher residual stress values.

It is known that microstructure has a significant effect on MBN activity. If practical, all zones having remarkably different microstructure should be separately considered in the calibration procedure. Otherwise, depending on the severity level of the microstructure effect on MBN emission, the residual stress values determined by MBN measurements may show deviations from the exact values.

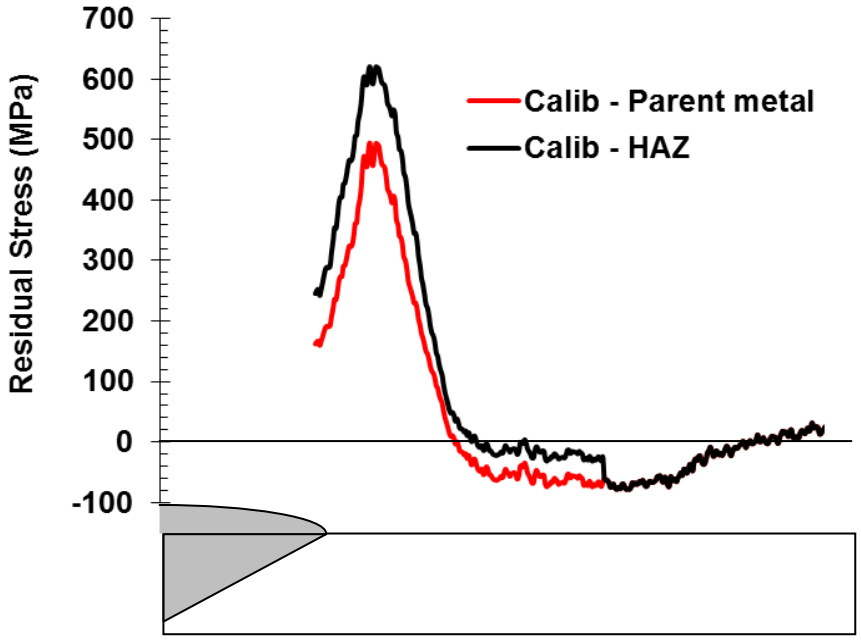

Figure 3. Variation of the longitudinal residual stress on the surface of the weldment

3.2 Shot-peened samples

The microstructures of the shot-peened samples are identical. Therefore, the changes in the MBN emission are directly related to the changes in the residual stress state. Figure 4 gives the variation of the MBN profile with intensity of shot peening. MBN emission reduces as peening intensity increases, which is the sign of increasing the magnitude of compressive residual stress. Moreover, peak positions of the MBN r.m.s. profiles shift to the higher magnetic strength values. It can be explained by reduction of the total 180^{o} domain wall area due to the presence of compressive residual stresses. The loss in the motion capability of domain walls leads to an increase in the critical level of external magnetic field, so the components start to be magnetized harder.

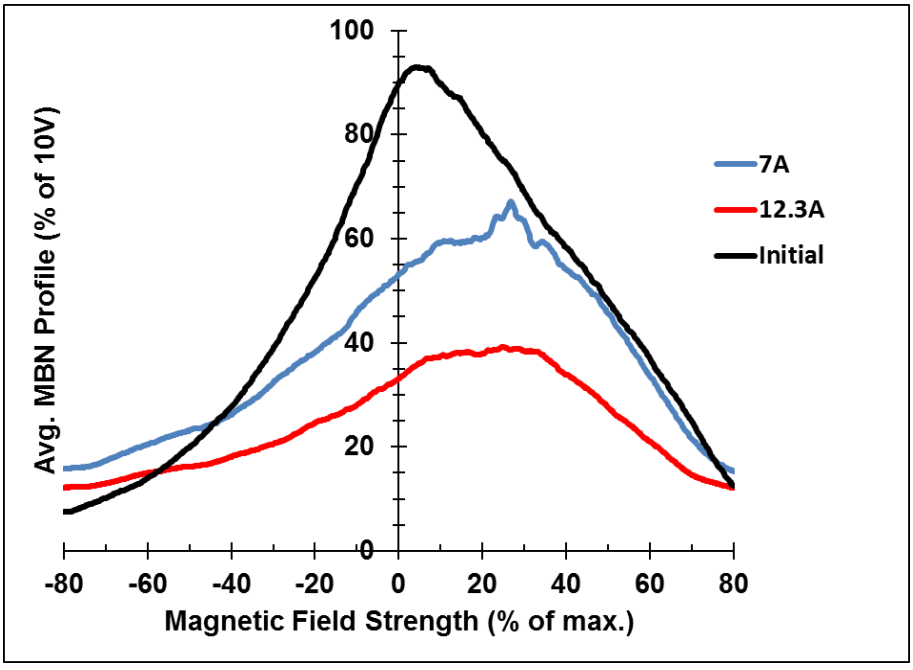

Figure 4. Effect of shot peening intensity on MBN emission (A: Almen value)

Figure 5 shows the effect of shot peening coverage on the MBN profile. An increase in the peening coverage causes higher magnitude of compressive residual stress on the surface, and therefore, MBN activity decreases.

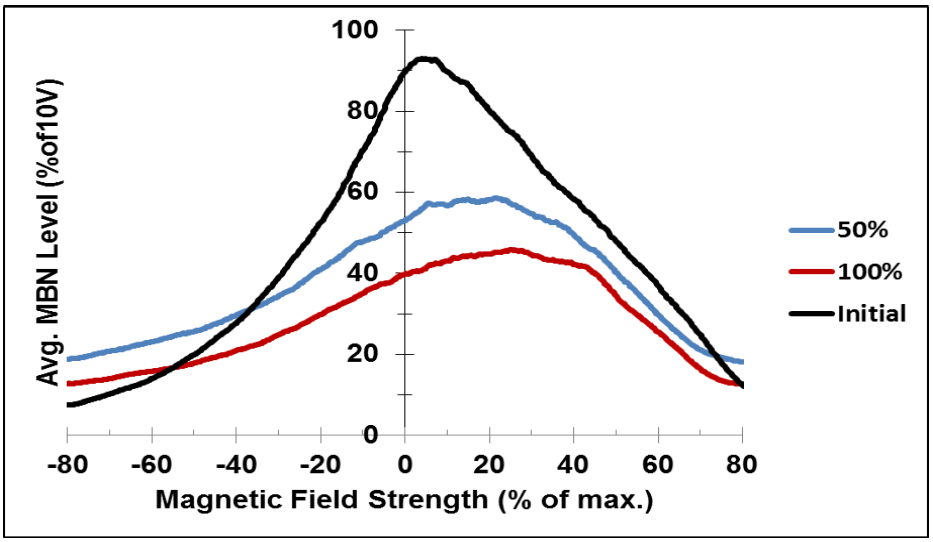

Figure 5. Effect of shot peening coverage on MBN emission

MBN measurements by the Rollscan module were performed real-time on the samples (10 random data from each sample). The results show significant changes in MBN with different shot-peening parameters. The variation in the results is taken as ±5 MBN amplitude change which is calculated from the random collected data maximum variation from the average. By using the calibration curve the MBN values, obtained from the shot-peened samples with different intensity and coverage, the variations of surface residual stresses were determined (Figure 6 and Figure 7). Maximum compressive residual stress, 270 MPa, was obtained at 300% coverage. These values can be taken as a reasonable residual stress values for a low alloy steel material.

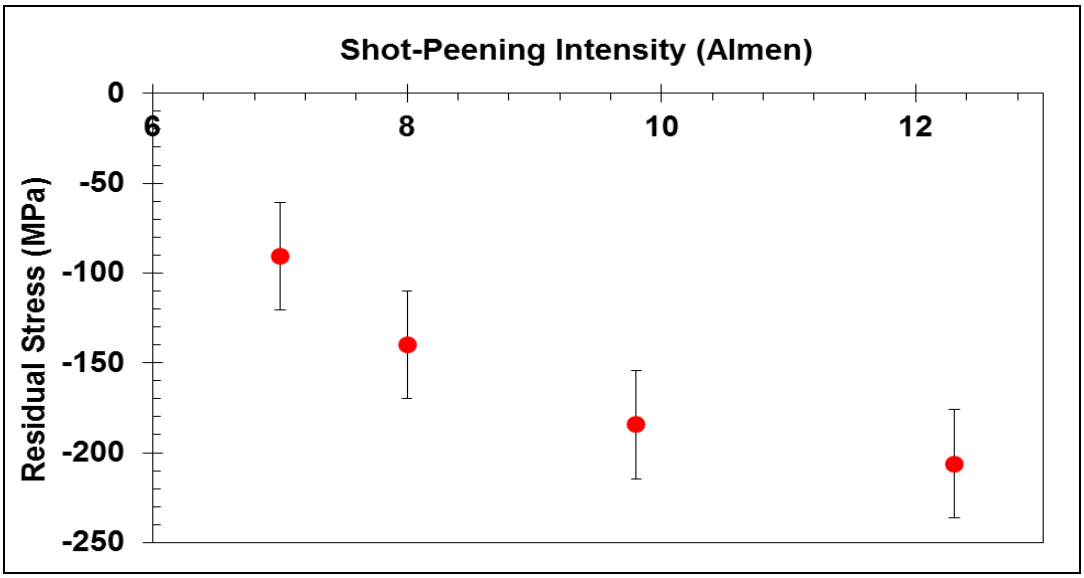

Figure 6. Effect of shot-peening intensity on the surface residual stress

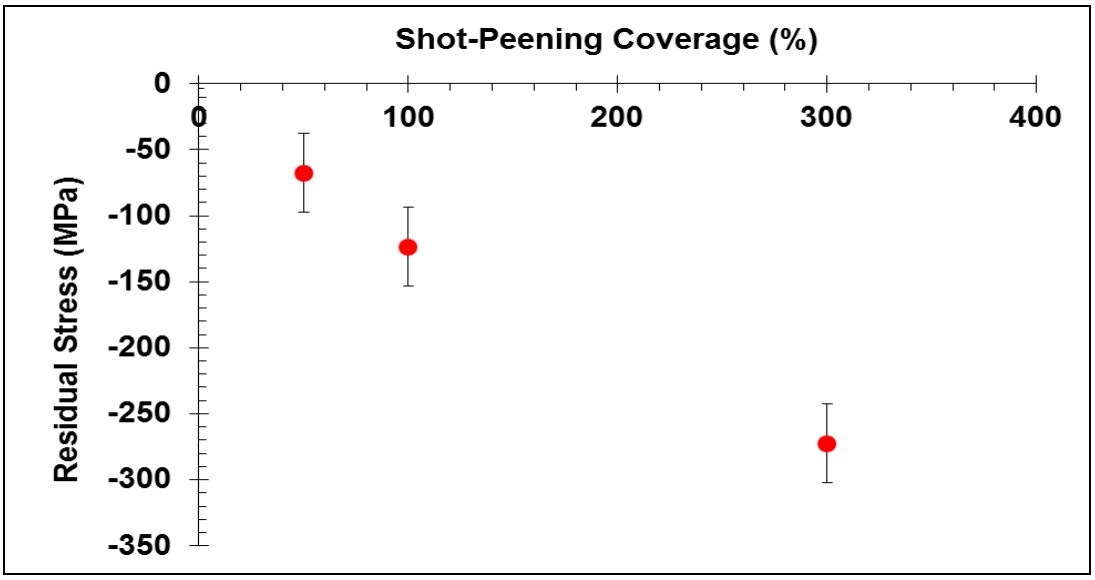

Figure 7. Effect of shot-peening coverage on the surface residual stress

4. CONCLUSIONS

Surface residual stresses on the welded API5LX70 steel plates, and on the shot-peened low-C steel plates were determined non-destructively by Magnetic Barkhasuen Noise (MBN) method. The following conclusions can be drawn from the results.

- MBN technique is a promising nondestructive technique for automated measurement of surface residual stresses on ferromagnetic steel components. At the process design stage and the production stages, MBN measurements may provide critical information about the residual stress state. From the differences in the MBN emission, the residual stress state at the surface of the welded and shot-peened can be monitored just in seconds.
- Calibration procedure is vital for reliable results. Any difference in the microstructure also affects the MBN signal. The phases in the shot-peened samples are the same; therefore, the changes in the MBN emission are directly related to the changes in the residual stress state. However, in the case of welded samples the parent metal and HAZ region may have significantly different microstructures. It results in a combined influence of microstructure and residual stress on the MBN emission, which requires a complex calibration procedure.

Acknowledgement

The author wishes to acknowledge Dr. Ibrahim Cam, Ilker Yelbay and Serdar Savas for their support in the experiments. The author also wishes to acknowledge his appreciation to Turkish Aerospace Industry for permission to use the NADCAP certified shot peening equipment.

References

1. J.Gauthier, "Magnetic Barkhausen Noise and Acoustoelasticity: A Comparasion of two NDT Methods of Measuring Residual Stress", MSc Thesis, Queen's University, Kingston, 1994
2. J.Lu, "Handbook of Measurement of Residual Stresses", Society for Experimental Mechanics, Prentice-Hall Inc., 1996
3. A.Wojtas, Metal Finishing News, 5, Enquiry No 012-09, 2004
4. S.Zagar, P.Zerovnik, J.Grum, 10th Int. Conf. of the Slovenian Society for NDT: Application of Contemporary NDT in Engineering - Ljubljana, 539, September 2009
5. J.B.Ju, S.K.Lee, J.Jang, W.S.Kim, D.Kwon, Int. J. Pressure Vessels & Piping, 80, 641, 2003
6. K.Kesavan, K.Ravisankar, S.Parivallal, P.Sreeshylam, Experimental Techniques, 29, 17, 2005
7. İ.Yelbay, İ.Çam, C.H.Gür, NDT&E International, 43, 29, 2010
8. S.Savaş, C.H.Gür, INSIGHT – J British Inst of NDT, 52, 672, 2010

DEVELOPMENT OF NEW LEAD-FREE SOLDER ALLOYS

Serkan YILMAZ*, Anil KANTARCIOĞLU, Y.Eren KALAY*****

* Middle East Technical University, Turkey
yserkan@metu.edu.tr
** Middle East Technical University, Turkey
kanil@metu.edu.tr
*** Middle East Technical University, Turkey
ekalay@metu.edu.tr

ABSTRACT

In this study, modification of traditional Sn-3.5Ag-0.9Cu (wt%) lead-free solder (SAC) alloy was studied by two approaches. In the first approach, the nominal composition of the SAC was modified by microalloying of this alloy using Fe element. In the second approach, the problematic Ag element was totally replaced with Al which was chosen according to Darken and Gurry criterion and Hume Rothery rules. In this manner, Sn-0.7Cu composition were alloyed by 0.1 to 0.5 Al (wt%). The thermal, microstructural and mechanical behaviors after and before compositional modifications were investigated by a combined study of differential scanning calorimetry (DSC), scanning electron microscopy (SEM), energy dispersive spectroscopy (EDS), universal testing machine (for shear strength tests) and a thermal shock set-up. Addition of 0.07 Fe (wt%) gave the best thermal shock properties to modified SAC alloy. In terms of replacing the Ag element, Al addition gives the ideal eutectic microstructure on the other hand, almost all compositions suffered from poor wetting. For Sn-0.7Cu-(0.4-0.5)Al, needle-like Sn-Cu-Al intermetallic formation was observed.

Keywords: Lead-free solders, electronics industry, microstructure

KURŞUN İÇERMEYEN YENİ LEHİM MALZEMELERİNİN GELİŞTİRİLMESİ

ÖZET

Bu çalışmada, geleneksel kurşunsuz Sn-3.5Ag-0.9Cu (wt%) lehimi (SAC) iki ayrı yaklaşımla modifiye edilmiştir. İlk yaklaşımda, SAC alaşımı içine demir elementi eklenerek mikro alaşımlama yapılmıştır. İkinci yaklaşımda, SAC alaşımı içindeki problem yaratan gümüş elementi tamamen sistemden çıkartılmış, yerine Darken ve Gurry kriterleri ve Hume Rothery kuralları doğrultusunda seçilen alüminyum konulmuştur. Bu yaklaşım doğrultusunda, Sn-0.7Cu alaşımının içine 0.1(ağ%)'den 0.5(ağ%)'e kadar Al eklenmiştir. Kompozisyon değişikliğinden önce ve sonra elde edilen kompozisyonların termal, mekanik ve mikroyapısal özelliklerinin incelenmesi ayrımsal taramalı kalorimetre (DSC), taramalı elektron mikroskobu (SEM), enerji ayrımlı spektroskopi (EDS), evrensel test cihazı (kesme testleri için) ve termal

şok test cihazları kullanılarak yapılmıştır. SAC alaşımları içinde en iyi termal şok özelliğini, içerisine 0.7(ağ%) Fe eklenmiş kompozisyon göstermiştir. Ag yerine Al eklendiğinde ideal ötektik bir yapı elde edilmesine rağmen, neredeyse bütün kompozisyonlar düşük ıslatma özelliği göstermişlerdir. Sn-0.7Cu-(0.4-0.5)Al kompozisyonlarında iğnemsi yapıda intermetalikler gözlenmiştir.

Anahtar kelimeler: Kurşunsuz lehim, elektronik endüstrisi, mikroyapı

1. INTRODUCTION

Soldering has been widely used in various industrial applications, particularly in electronics industry. A successful solder joint should be electrically conductive, mechanically strong and thermally stable against thermal deviations [1]. In this respect, Sn-Pb solder alloys had been used successfully because of their low melting temperature, good workability, excellent wetting and ductility. However, restrictions and regulations towards to reducing hazardous Pb in consumer electronics drive the soldering technology to design new solder alloys [2, 3]. Among these alloy systems, Sn-Ag-Cu (SAC) has been found to be the most promising and it has been already commercialized in consumer's electronics industry. On the other hand, there are still unsolved problems, such as the relatively high melting temperature and brittle intermetallics (IMCs) formation (i.e. Ag_3Sn)[4]. Particularly, the formation of IMCs upon solidification causes a sharp drop in thermal shock and fatigue resistance of the solder alloy during its service. This issue has become more and more important due to miniaturization trend of electronic circuits [1]. The common practices of eliminating the unwanted brittle IMCs are (i) the addition of a fourth element by microalloying and (ii) replacement of Ag element within SAC alloy [4, 5]. Elimination of Ag has another advantage of decreasing the price of the lead-free solder (see the increasing silver price in last two decades) [6]. Replacement element was chosen according to Darken and Gurry criterion and Hume-Rothery rules [7-8].

In this study, we applied both strategies of adding a fourth element and replacing the problematic Ag element. In this respect, Sn–3.5Ag–0.9Cu (wt%) solder was modified with iron (Fe) additions. Fe was chosen according to its ability to substitute into Cu_6Sn_5 in place of Cu atoms [9]. In the second approach, Sn-0.7Cu composition were alloyed with 0.1 to 0.5 Al (wt%). Al was choosen according to Darken and Gurry criterion and Hume-Rothery rules with its ability to substitute into alloy in place of Ag atoms.

2. EXPERIMENTAL PROCEDURE

Solder alloys were produced in a quartz tube under argon atmosphere. High purity raw materials Sn (99.99%), Ag(99.9%), Cu (99.9%), Fe (99.99%) and Al (99.999%) were weighed, placed into the quartz and melted three times in order to achieve an homogenous alloy. Final compositions of the produced alloys were verified using energy dispersive spectrometer (EDS) attached to a scanning electron microscope (SEM). Nominal compositions of the prepared samples are shown in Table 1.

Table 1. The nominal solder alloy compositions used in this study.

Solder Alloy	**Composition (wt.%)**
SAC (Eutectic)	Sn–3.5Ag–0.9Cu
SAC+0.01Fe	Sn–3.5Ag–0.9Cu–0.01Fe
SAC+0.03Fe	Sn–3.5Ag–0.9Cu–0.03Fe

SAC+0.05Fe	Sn–3.5Ag–0.9Cu–0.05Fe
SAC+0.07Fe	Sn–3.5Ag–0.9Cu–0.07Fe
SAC+0.1Fe	Sn–3.5Ag–0.9Cu–0.1Fe
Sn-0.7Cu	Sn–0.7Cu
Sn-0.7Cu+0.1Al	(Sn–0.7Cu)+0.1Al
Sn-0.7Cu+0.2Al	(Sn–0.7Cu)+0.2Al
Sn-0.7Cu+0.3Al	(Sn–0.7Cu)+0.3Al
Sn-0.7Cu+0.4Al	(Sn–0.7Cu)+0.4Al
Sn-0.7Cu+0.5Al	(Sn–0.7Cu)+0.5Al

A thermal shock set-up, illustrated in Figure 1, was designed and built for this study. The set-up mainly consists of a cold chamber, a hot chamber, a motor and an electronic control unit. The cold chamber contains liquid ethanol at -30 °C. The hot chamber is a tube furnace, which was held at ~140 °C. Specimens continuously move between the cold and hot chamber for a pre-determined time and speed. All the specimens were tested together so that they would be exposed to the same thermal conditions. Each thermal cycle took 3 minutes with the temperature profile shown in Figure 2. The specimens were taken out at every 500 cycles for detailed investigation with SEM.

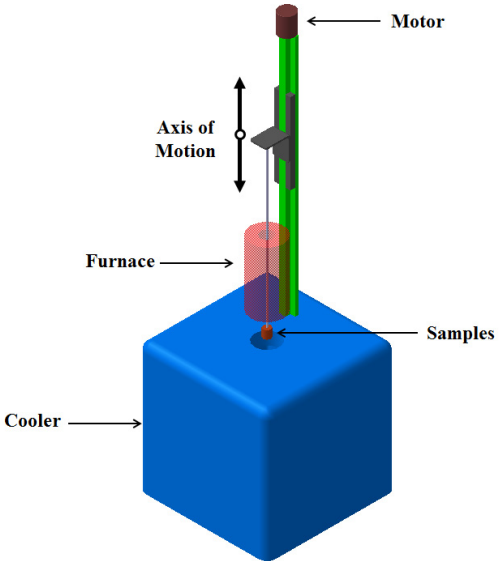

Figure 1. Thermal shock set-up.

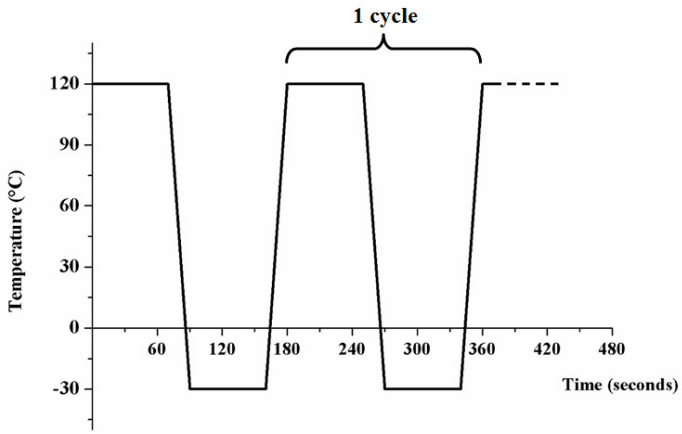

Figure 2. Temperature profile of samples during thermal shock test.

Thermal properties of the samples were determined using differential scanning calorimeter (DSC-Perkin Elmer Diamond). DSC pans made of Cu were applied to solder flux and filled with 10 mg of solder alloys. All analyses were performed between 30 °C and 260 °C under N_2 atmosphere. The melting and solidification temperatures were determined compared to reference sample. Cu pans were chosen on purpose to mimic the real service conditions of the solder alloy.

Micro hardness tests of the sample were performed using SHIMADZU® Micro-Vickers Tester, 980.7 mN for 15 seconds were applied for indentation ($HV_{0.1}$). 10 separate measurements were collected for each sample and average value of these measurements was taken as the hardness of the sample.

50x12x1.5 mm copper plates were used for shear strength tests. Solder alloys were reflowed between 2 copper plates forming a 12x12 mm^2 soldered area. Soldering flux was applied prior to all reflowing operations. Shear test was conducted on a universal testing machine at an extension rate of 0.1mm/min at room temperature.

Samples were prepared for metallography and etched using a solution of 60 ml HCl, 15 ml H_2O, 15 ml HNO_3, 15 ml CH_3COOH for10 s. Microstructures of the samples were analyzed using FEI Nova NanoSEM 430 scanning electron microscope.

3. RESULTS AND DISCUSSION

Microalloying of SAC:

Our previous study [9] has shown that addition of 0.05wt% Fe to traditional SAC alloy remarkably enhanced the microstructural and mechanical properties of the host solder alloy. In this respect, we analyzed the effects of microalloying with Fe in more details. SAC alloys were microalloyed with 0.01 to 0.1 wt% pure Fe. For determination of melting (T_m) and solidification (T_s) temperatures, thermal measurements were performed using a differential scanning calorimeter (DSC). 0.17 °C/sec was chosen as heating and cooling rate of the experiment. The corresponding DSC curves of the samples are shown in Figure 3.

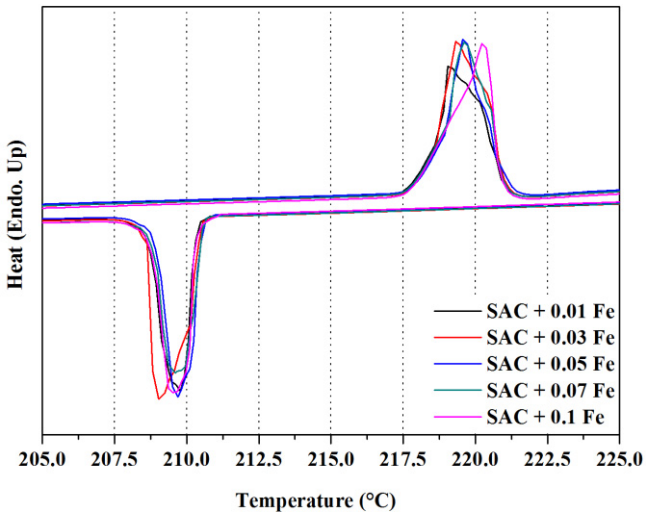

Figure 3. DSC curves of alloys.

The melting temperatures of the alloys are within the range of 217.1 - 217.9 °C; which shows that melting temperature of the iron added alloys just slightly differ from the SAC eutectic alloy. Table 2 and Figure 4 show the undercooling ($\Delta T = T_m - T_s$) values measured for eutectic SAC and Fe microalloyed specimens. The addition of Fe greatly decreased the undercooling.

Table 2. Melting(T_m), solidification (T_s) temperatures and undercoolings for solders cooled at 0.17 °C/sec.

Alloy	Tm (°C)	Ts (°C)	ΔT (°C)
SAC (Eutectic)	217.9	198.9	19
SAC + 0.01 Fe	217.7	210.5	7.2
SAC + 0.03Fe	217.8	210.6	7.2
SAC + 0.05 Fe	217.7	210.3	7.4
SAC + 0.07 Fe	217.8	210.6	7.2
SAC + 0.1 Fe	217.6	210.6	7.0

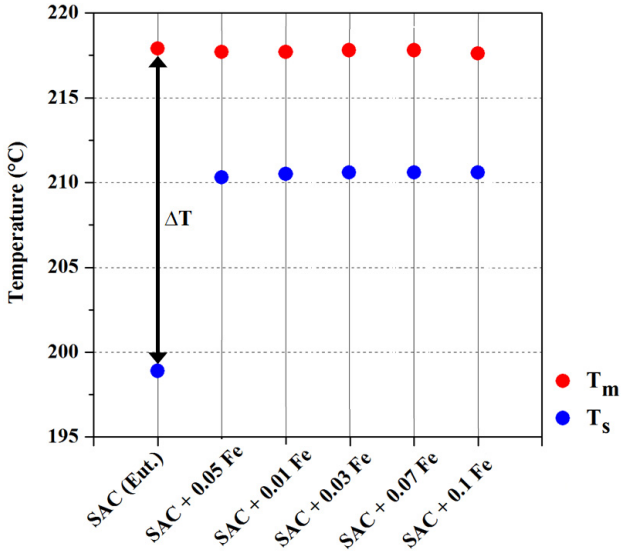

Figure 4. Melting (Tm) and solidification (Ts) temperatures of the alloys. Their difference is undercooling, shown with ΔT.

The major effect of Fe addition is the refinement of microstructure. This is most due to the decrease in the undercooling during solidification of solder alloy. The bare eutectic composition contains large pro-eutectic Cu_6Sn_5 and Ag_3Sn phases. For the formation of large Cu_6Sn_5, large amount of Cu atoms must diffuse near the Cu_6Sn_5 nuclei since matrix is originally poor in Cu. If the added fourth element acts as a barrier to the diffusion of Cu to large distances, then Cu_6Sn_5 crystals can no longer grow into large particles but many Cu_6Sn_5 crystals form in many sites and grows less with small amount of Cu that diffuse only in small distance. Similarly, for the formation of large Ag_3Sn, Ag must diffuse large distances since matrix is poor in Ag. If diffusion of Ag is hindered and it undergoes into eutectic reaction, it forms many nano-sized Ag_3Sn crystals. Our previous study has shown that the additional Fe prefer to go into the Cu_6Sn_5solder/copper joints [9]. This slows-down the growing solid/liquid Cu_6Sn_5 interface which results in a lower undercooling and formation of β-Sn dendrites instead of brittle proeutectic Ag_3Sn blades. It seems that within the range of 0.01 and 0.1 wt. %Fe a similar mechanism is active which results in a finer microstructure. Figure 5 shows the resultant microstructures after fourth element additions. Fewer Cu_6Sn_5 and Ag_3Sn on the matrix have

been resolved after Fe modification.

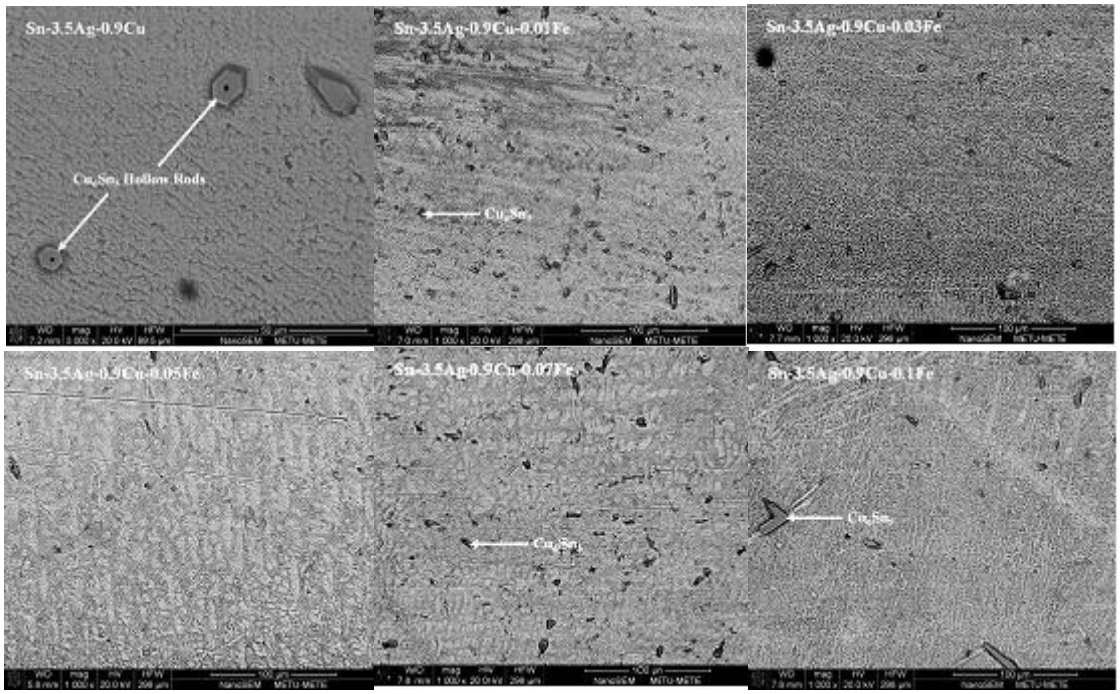

Figure 5. Back-scattered SEM images of produced solders.

For thermal shock tests, solders alloys were applied onto copper pieces and their surfaces are polished for electron microscopy analysis prior to the test. Thermal shock resistance was analyzed from each specimen after every 500 cycles.

SAC (Eutectic)

Figure 6.a shows the images taken after 500 cycles and it reveals that the dissociation between interface and matrix was started. The cracking was not observed after 1000 cycles, however as shown on Figure 6.b, the cracks are visible after 1500 cycles. The intermetallic at interface was almost detached.

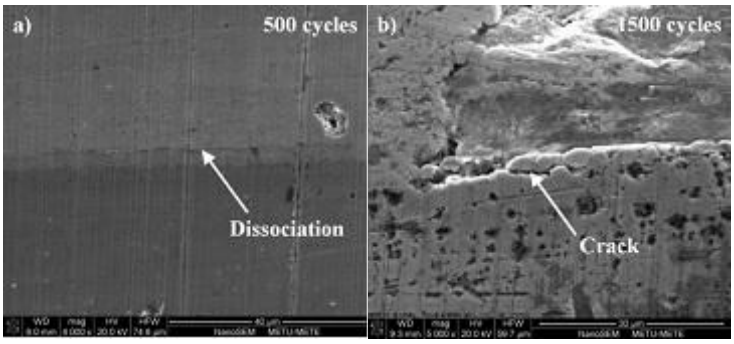

Figure 6. Eutectic SAC alloy after 500 and 1500 thermal shock cycles.

SAC + 0.01Fe

Figure 7.a, shows the image taken before thermal shock. Figure 7.b shows the same region and the cracking at the interface is visible after 500 cycles. No further propagation of the crack was observed.

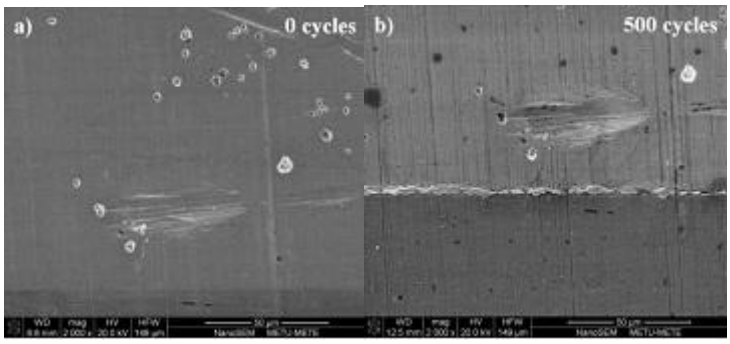

Figure 7. SAC+0.01Fe alloy before test and after 500 thermal shock cycles.

SAC + 0.03Fe

Figure 8.a shows the visible cracks formed after 500 cycles at the tip of the solder. The cracks were determined to be propagated when Figure 8.b, taken after 1000 cycles were investigated. No further propagation was observed after 1500 cycles.

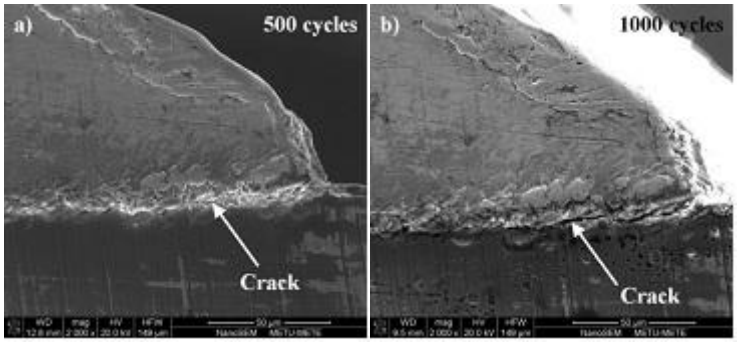

Figure 8. SAC+0.03Fe alloy after 500 and 1000 thermal shock cycles.

SAC + 0.05Fe

Figure 9.a, shows the image taken before thermal shock. No initiation of micro-cracks was observed after 500 cycles. However, as seen on Figure 9.b, after 1000 cycles, the detachment of interface scallop was observed.

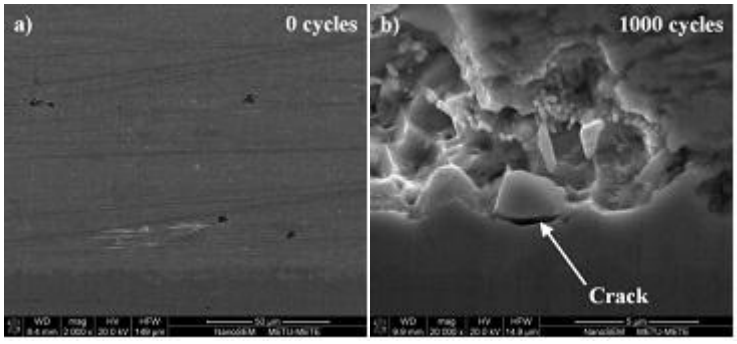

Figure 9. SAC+0.05Fe alloy before test and after 1000 thermal shock cycles.

SAC + 0.07Fe

Figure 10.a shows the image taken before thermal shock. No crack initiation was observed at 500 cycles. However, micro-cracking of the matrix was observed at 1500 cycles as seen in Figure 10.b.

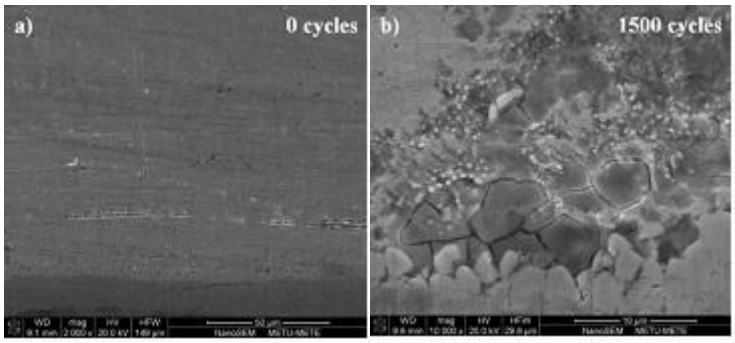

Figure 10. SAC+0.07Fe alloy before test and after 1500 thermal shock cycles.

SAC + 0.1Fe

Figure 11.a shows the visible cracks formed after 500 cycles at the interface and the matrix. There may be a critical iron concentration which, further iron addition may be causing the cracking of matrix, since this observed only in SAC+0.07Fe and SAC+0.1Fe alloys. The crack were observed to further propagate after 1000 cycles of thermal shock and shown in Figure 11.b, but no further propagation was determined after 1500 cycles.

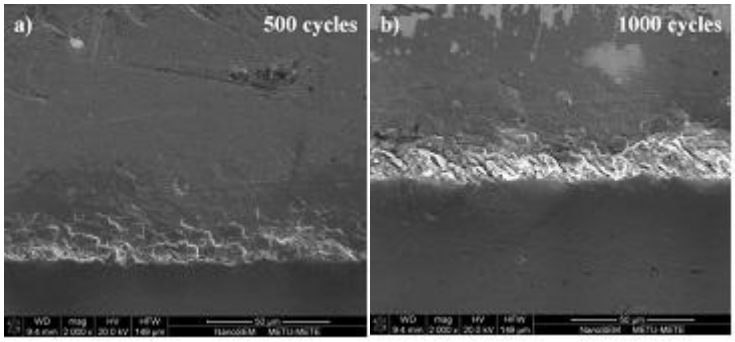

Figure 11. SAC+0.1Fe alloy after 500 and 1000 thermal shock cycles.

Thermal shock test behavior of the alloys is summarized in Table 3. As shown, except 0.1 wt.%Fe, addition of Fe seems to impede the initiation of the crack. In the eutectic composition, crack was initiated after 500 cycles only. On the other hand, for 0.07 wt.% Fe, solder/copper joint resisted up to 1500 cycles. Since the crack is almost always initiated on solder/copper joint, the interface structure Cu_6Sn_5 should play an important role on the stability of the boundary during the thermal shock cycles. From the previous detailed spectroscopic analysis[9], we know that the Fe accumulate inhomogeneously on the Cu_6Sn_5 solder/copper joint. Therefore, 0.07 wt.% Fe may be the threshold for a solid solution strengthening of this structure. Further analysis will be surely carried out to establish the relationship between the Fe content and thermal shock properties.

Table 3. Thermal shock test behavior of the samples

Alloy	0 cycles	500 cycles	1000 cycles	1500 cycles	Result
SAC (Eutectic)	No Cracks	Initiation	-	Propagation	Failed
SAC+0.01Fe	No Cracks	Initiation	-	-	Failed
SAC+0.03Fe	No Cracks	Initiation	Propagation	-	Failed
SAC+0.05Fe	No Cracks	-	Initiation	Propagation	Failed
SAC+0.07Fe	No Cracks	-	-	Initiation	Failed
SAC+0.1Fe	No Cracks	Initiation	Propagation	-	Failed

Replacement of Ag with Al:

In the first part of the study, the unwanted Ag_3Sn phase was inhibited by microalloying. In the second part, Ag was completely removed and the remaining Sn-0.7Cu base alloy was microalloyed with Al. By applying Darken-Gurry approach [7], Al was found suitable to replace the Ag exists in original SAC alloy. The melting temperatures of the produced alloys are in the range of 227-228 °C which is nearly the same with eutectic Sn-0.7Cu composition. Melting points of the alloys are given in Table 4.

Table 4. Melting points of the Al added Sn-Cu solder alloys.

Alloy	Melting Point (T_m)
Sn-0.7Cu	227
Sn-0.7Cu+0.1Al	**227.9**
Sn-0.7Cu+0.2Al	**228**
Sn-0.7Cu+0.3Al	**228**
Sn-0.7Cu+0.4Al	**227.9**
Sn-0.7Cu+0.5Al	**228**

In all the Al replaced samples, Sn-Cu-Al intermetallics were seen in microstructure of the alloys. The amount of the Sn-Cu-Al IMC seems to be increased with increasing amount of Al added into the alloy. Particularly in 0.4 and 0.5 wt% Al added specimens, considerable amount of Sn-Cu-Al IMC was observed. Considering the needle like morphology of these IMC, we believe that they may cause a similar lousy effect as Ag_3Sn structure. Specimens with Al addition up to 0.3wt% Al show almost a perfect eutectic structure. This is a highly desirable microstructure for a solder alloys and it reminds the traditional Pb-Sn eutectic structure. Figure 12 shows the representative microstructures.

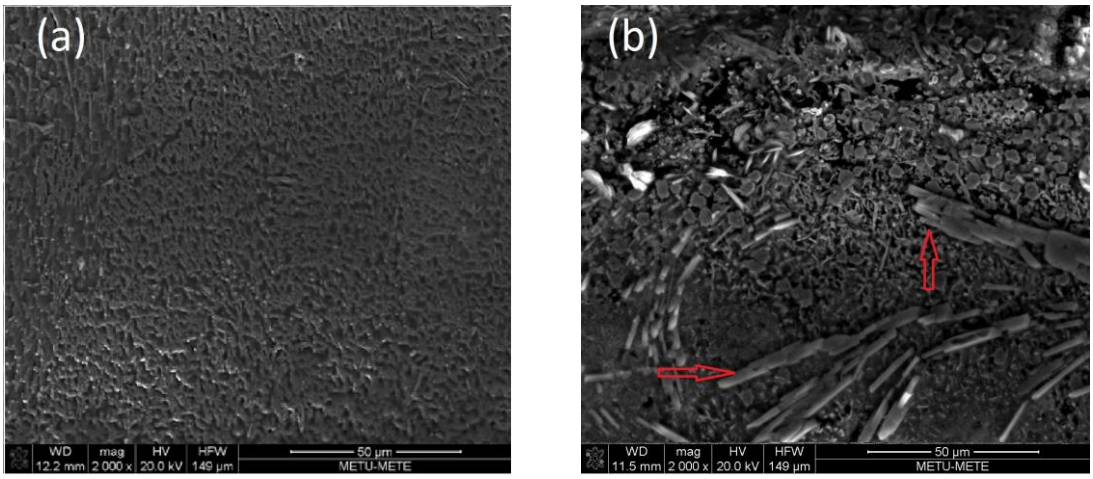

Figure 12. SEM images showing microstructures of samples (a) Sn-0.7Cu+0.3Al (b) Sn-0.7Cu+0.5Al

Shear strength results obtained from single-lap shear tests are shown in Figure 13. As seen from the figure, Sn-0.7Cu alloy gives similar shear strength values as SAC alloys. Al addition seems to decrease the shear strength slightly. The decrease for the 0.4 wt% and 0.5 wt% Al should be related to the formation of needle like Sn-Cu-Al IMC that creates stress concentration points in the alloy. On the other hand, the slight decrease in low Al containing specimens, this is a little surprising because, particularly for 0.1 wt% Al addition, a perfect eutectic like microstructure was observed. The reason of this unexpected result is related to the wetting ability of the alloy after Al addition. Figure 14 shows the visual examination of solders after shear tests. Almost all specimens show a poor wetting ability. Particularly, high Al containing solder joints even show some unsoldered copper regions. Therefore, even though Al addition helps to create an ideal microstructure for soldering application, the wetting problem prevent these alloys to be an effective solder materials. Further studies towards to a better bonding the Ag free solders effectively to copper substrates are in progress.

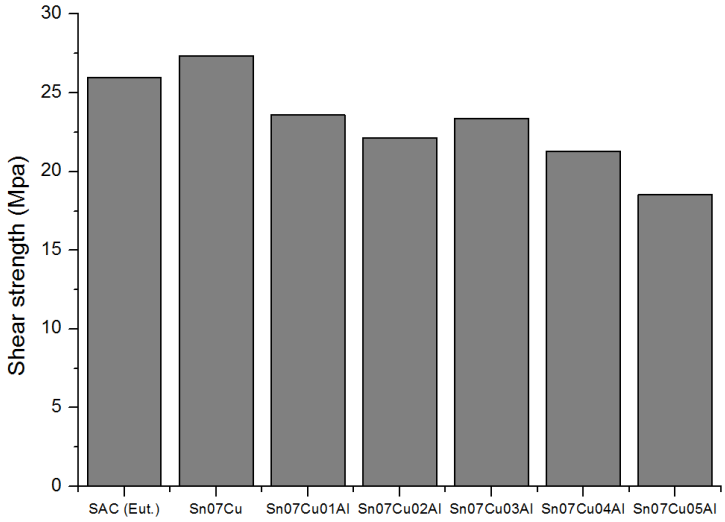

Figure 13. Shear strength values of SAC eutectic, Sn-0.7Cu and Al modified Sn-0.7Cu alloys.

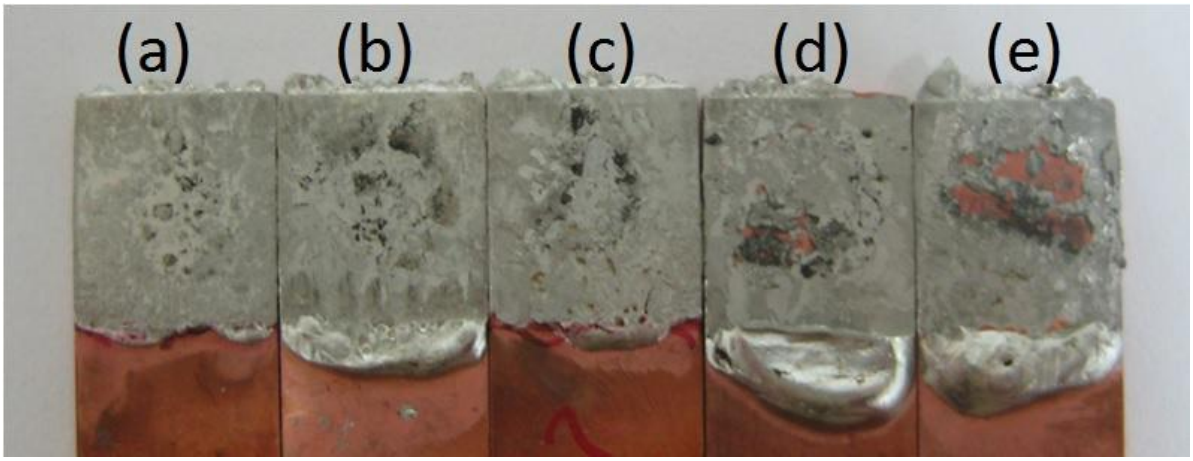

Figure 14. Images of the samples after shear strength test (a) Sn-0.7Cu+0.1Al (b) Sn-0.7Cu+0.2Al (c) Sn-0.7Cu+0.3Al (d) Sn-0.7Cu+0.4Al (e) Sn-0.7Cu+0.5Al

4. CONCLUSION

In this study, the efforts to create an effective lead-free solder alloy were summarized. In the first approach, the effect of Fe addition into traditional eutectic SAC alloy was investigated. It was seen that the addition of Fe leads to a reasonable decrease in undercooling which forms a finer microstructure. Additionally, IMC amount of the samples with iron addition was found to be suppressed. Results of the thermal shock tests showed that SAC with 0.07 Fe (wt%) has the best thermal shock resistance among other SAC and micro alloyed SAC alloys. In the second approach, a completely new solder alloy was designed using the principles of Darken-Gurry approach. In this alloy, Ag was totally replaced with Al element. The low Al containing solder alloys seem to be promising in terms of creating an ideal solder microstructure. On the other hand, all solder alloys suffered from poor wetting within the range of 0.1 to 0.5 wt% Al. The poor wetting also affected the shear strength to reach reasonable values.

5. REFERENCES

1. M. Abtew, G.Selvaduray, Mater.Sci.Eng.R27,95–141, 2000.
2. I.E. Anderson, J.Mater.Sci.:Mater.Electron.18, 55–76, 2007.
3. K. Suganuma, Current Opinion in Solid State&Material Science 5, 55-64, 2001.
4. K.S. Kim,S.H.Huh,K.Suganuma,J.AlloysCompd.352, 226–236, 2003.
5. P.G.Harris, K.S.Chaggar, Soldering Surf. Mt. Technol.10/3, 38–52, 1998.
6. http://www.infomine.com/investment/metal-prices/silver/all/
7. Darken L.S., Gurry R.W., Physical Chemistry of Metals, McGraw-Hill, New York, 1953.
8. Hume-Rothery W., Powell H.M., Z. Kristallographie , 91, 23, 1935.
9. A. Kantarcioglu, Y.E.Kalay, Mater.Sci.& Eng. A , 593, 79-84, 2014.

EFFECT OF HEAT TREATMENT ON THE WELDING ZONE OF MARTENSITIC-AUSTENITIC STEELS WELDED BY FRICTION WELDING

Nuray BEKÖZ

Metallurgical and Materials Engineering Department, Istanbul University, Istanbul, Turkey
nbekoz@istanbul.edu.tr

ABSTRACT

Friction welding method is a highly important and recently developed joining technology that produces a solid state bonding methods. The most important advantages of friction welding are high material saving, low production time and possibility of welding dissimilar metal combinations. One of the widely application fields of friction welding is the production of exhaust valves manufactured by joining two different materials. In this study, the effect of heat treatment on the mechanical and metallurgical properties of high alloyed X45CrSi9-3 and X53CrMnNiN21-9 steel couple joining with friction welding (known as martensitic and austenitic valve steels, respectively) was investigated. For this purpose, tensile and hardness tests were carried out before and after heat treatment of the welding samples, and the results were discussed in accordance with the microstructure of the welding zone. The results indicate that heat treatment process applied after welding is required to be made to improve the microhardness distribution of welded joints, and achieve a suitable microstructure.

Keywords: Friction welding, heat treatment, welding zone, martensitic-austenitic steels.

SÜRTÜNME KAYNAĞI İLE BİRLEŞTİRİLMİŞ MARTENZİTİK-ÖSTENİTİK ÇELİKLERİN KAYNAK BÖLGESİNE ISIL İŞLEMİN ETKİSİ

ÖZET

Sürtünme kaynak yöntemi, katı hal kaynaklı birleştirmelerin son yıllarda geliştirilen en önemlilerinden biridir. Sürtünme kaynağının en önemli avantajları; yüksek malzeme tasarrufu, düşük üretim zamanı ve farklı metal alaşımların kaynak edilebilirliğinin mümkün olmasıdır. Sürtünme kaynağının yaygın uygulama alanlarından biri, iki farklı malzemenin kaynağı ile üretilen egzost supaplarının üretimidir. Bu çalışmada; sürtünme kaynağı ile birleştirilmiş yüksek alaşımlı X45CrSi9-3 ve X53CrMnNiN21-9 çelik çiftinin (sırasıyla martezitik ve östenitik supap çeliği olarak bilinen) mekanik ve metalurjik özellikleri üzerine ısıl işlemin etkisi araştırılmıştır. Bu amaç için; kaynaklı parçaların ısıl işlemden önce ve sonra çekme ve sertlik testleri yapılmış ve sonuçlar kaynaklı bölgenin mikroyapısına bağlı olarak tartışılmıştır. Sonuçlar, kaynak sonrası uygulanan ısıl işlem prosesinin malzemelerin sertlik dağılımını iyileştirmek ve uygun mikroyapı elde etmek için gerekli olduğunu göstermiştir.

***Anahtar kelimeler*:** Sürtünme kaynağı, ısıl işlem, kaynak bölgesi, martenzitik-östenitik çelikler.

1. INTRODUCTION

Friction welding is a method of manufacturing which is being used extensively in recent times due to its advantages such as low heat input, production time, ease of manufacture and

environment friendliness [1]. Welding of different composition steel parts has been necessary due to the increasing need in the manufacturing area. Various ferrous and nonferrous alloys having different thermal and mechanical properties can easily be joined by friction welding method. Friction welding is classified as a solid-state welding process where metallic bonding is produced at temperatures lower than the melting point of the base metals [2]. Nowadays, valves, bandix gears, axle shafts, gearshaft components, turbocharged fan shafts, fork-shaft connections etc. in automotive industry are manufactured by the consolidation of high and low alloy steels by friction welding process [3].

Austenitic steels have in most cases good weldability. However, martensitic steel has inherently poor weldability, and its weldments are susceptible to cracking, primarily due to high alloy content and hardness. Austenitic steels are welded with consumables with a similar or over-alloyed chemical composition with respect to the parent metal. The toughness of martensitic steel is limited and decreases with increasing carbon content. Furthermore, the presence of residual stress could obviously deteriorate the mechanical properties [4-5]. However, martensitic-austenitic steels, alloyed with significant amounts of nickel, have improved toughness and weldability [6]. The joining of dissimilar materials is generally more challenging than that of similar materials because of differences in the physical, chemical and mechanical properties of the base metals welded. These differences may be removed with the selection of solid state welding processes, such as friction welding [7]. With the technological development in the valve manufacturing industry, the exhaust valves of normal and diesel engines are manufactured from two different types of steels. The 'handling' parts of exhaust valves are manufactured from 1.4718 steel (martensitic valve steel) which is tough, ductile and resistant against wearing due to friction while the 'head' parts are manufactured from 1.4871 steel (austenitic valve steel) which shows a very good resistance to oxidation and corrosion caused by combustion products [3]. The exhaust valves temperature is between 700°C and 800°C and, in some more severe cases, 900°C is achieved. Thermal failures can occur at the head area of valves causing radial cracks due to stresses generated by temperature gradients near to seat face due to mechanical bending stress, and these failures can be improved by heat treatment [8]. Uzkurt et al. [3] carried out studies on the effects of the parameters that were friction time, friction pressure and forging pressure of these steel couple welded by friction welding. A lot of studies [9-12] investigated the effect of heat treatment on the properties of friction welded different alloys; however, there is no study on the above mentioned steel couple in the literature. Song and Nakata [13] reported that the applying heat treatment after friction welding led to the improvement of mechanical properties of the Ni-base superalloy welds such as hardness, strength and creep rupture life. Normally the friction welding is used in the as-welded condition; there maybe some advantages in carrying out the welding with base material in a soft condition and the heat treatment process applied after welding would restore the properties [14]. Although a wide range of mentioned valve steels have recently become available, the investigation of the effect of heat treatment process applied after welding on the mechanical properties is still lacking. In this study, the effect of heat treatment on the mechanical and metallurgical properties of high alloyed 1.4871 and 1.4718 steels joining with friction welding was investigated.

2. EXPERIMENTAL PROCEDURES

The test materials used in this study were commercial available 1.4718 (X45CrSi9-3) and 1.4871 (X53CrMnNiN21-9) high alloyed steels couple. The chemical composition and mechanical properties of the starting parent metals are listed in Table 1 and Table 2, respectively (BS EN 10090).

Table 1. Chemical compositions of test materials (wt.%)

Material	C	Si	Mn	Cr	Ni	N	P	S
1.4718	0.4-0.5	2.7-3.3	<0.8	8-10	<0.5	-	<0.04	<0.03
1.4871	0.48-0.58	<0.25	8-10	20-22	3.25-4.5	3.25-4.5	<0.045	<0.03

Table 2. Mechanical properties of test materials

Material	Tensile strength (MPa)	Elongation (%)	Hardness (HRC)
1.4718	850-950	20.0	35-40
1.4871	950-1150	22.5	25-38

For friction welding studies, the material employed was in the form of rods of 8 mm diameter obtained from of cold drawn bars, and faced to prepare the weld surfaces. The surfaces of the parts were ground with SiC paper and cleaned with acetone before welding. The 1.4871 high alloyed steel was rotated, while the 1.4718 high alloyed steel was held and exerted the force. Friction welding was carried out using a brake type friction welding machine. At the beginning of the study, pilot tests were conducted to determine the optimum parameters for a successful joint, and described in Ref. [15]. Friction welding parameters are rotation speed (N), friction time (t_1), upset time (t_2), friction pressure (P_1) and upset pressure (P_2) when welding with this machine. All welding parameters were kept constant in this study; N, t_1, t_2, P_1 and P_2 were fixed at 3000 rev/min, 3.5 s, 2.2 s, 200 MPa and 180 MPa, respectively. Suitable size specimens, approximately 10 mm, were cut along longitudinal direction for the heat treatment experiments. The as-welded specimens were heat treated by austenitizing at 1050 °C for 30 min and then quenched in water at room temperature and tempered at 750 °C for 60 min in air. This operation was carried out within 8 hours of welding.

The quality and integrity of the as-welded and heat treated specimens were examined by carrying out tensile and hardness tests. The Vickers hardness distribution of each group in the vicinity of the weld interface was measured with a load of 100 g, for 10 s using microhardness tester, at least five indents were made at each location and the average values were taken. Tensile tests were conducted at room temperature using an Instron type machine with strain rate of 1 mm min^{-1}. The tensile properties of each joint were evaluated using four tensile specimens cut from the same joint. Figure 1 shows the dimension and shape of tensile test specimen. Optical microscopy of the joints was done to observe changes in microstructure of the welding zones. The resultant welds were sliced using a diamond cutting wheel to provide cross-sections, avoiding thermal degradation. They were then ground with SiC paper, and finally polished using Al_2O_3 powder. The 1.4871 steels were etched with %4 nital for 8 s and the 1.4718 steels with %4 nital solution for 4 s, before metallurgical examination.

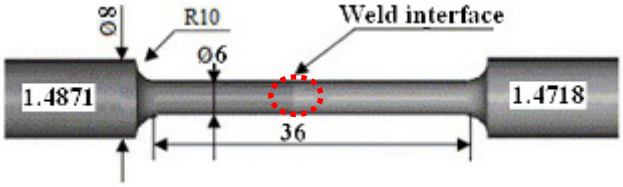

Figure 1. Dimension and shape of the tensile test specimen

3. RESULTS AND DISCUSSION

3.1. Macro and Microstructure Examinations

The macro-view of as-welded and heat treated specimens shown in Figure 2. Figure 3 shows the cross sections of the joints welded before and after the heat treatment. Visual examination of the welded specimens showed uniform and good welded joints. Additionally, no visible porosity or defect was observed on the weldment. Differences in thermal and physical properties of the materials generally result in asymmetric deformation in welding of dissimilar metals [16]. Formation of the flash indicates plastic deformation on both austenitic and martensitic steel side, and depends on the mechanical properties of these materials. The weld flash and the contact zone can easily be observed in Figure 2. Austenitic steel (1.4871 steel) sides was less deformed because this steel has lower thermal conductivity and greater hardness at higher temperatures compared to martensitic steel (1.4718 steel) and is thus more resistant to deformation [17].

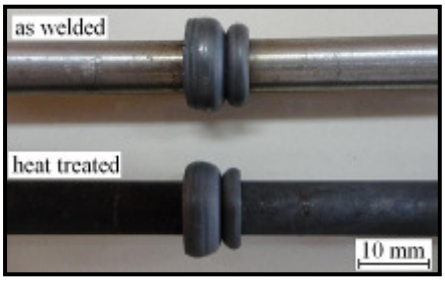

Figure 2. Visual view of as-welded and heat treated specimens

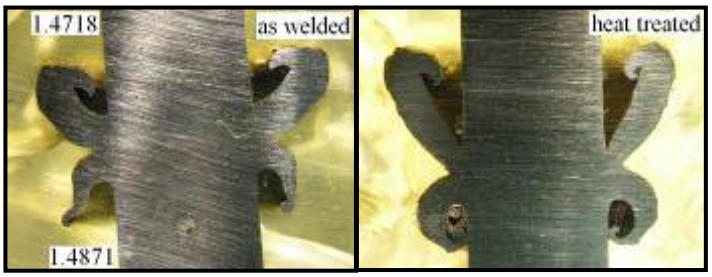

Figure 3. Cross-sectional macrophotographs of as-welded and heat treated joints

Kırık et al. [7] reported that microstructural evaluation of friction welded joints revealed four distinct zones across the specimens which were identified as parent metal, partial deformed zone, deformed zone, and transformed and recrystallized fully plasticized deformed zone. The microstructural transition from weld interface to base metal along the central axis in the as-welded condition is shown in Figure 4. The microstructural transition of the weld region in the heat treated joint is also shown in Figure 5. In this study, three distinct zones can be seen across the specimens, namely the 1.4871 steel base metal, the plastically deformed interface and the 1.4718 steel base metal. Apparent thickness and obvious heat affected zone were observed on as-welded joint. It was observed that the heat treatment influenced the weld region width. The microstructural changes took place in the 1.4718 parts and deformed zone region. Microstructure of the 1.4871 steel did not a remarkable change, relative to the base metal. However, grain orientation appears to be a natural consequence of heat treatment. The directionality of the grains is also a very important factor. The heat treatment, in general, produced regular and orientation grain structure, observed to be close the welding line which is normal to the deformation direction due to welding [10].

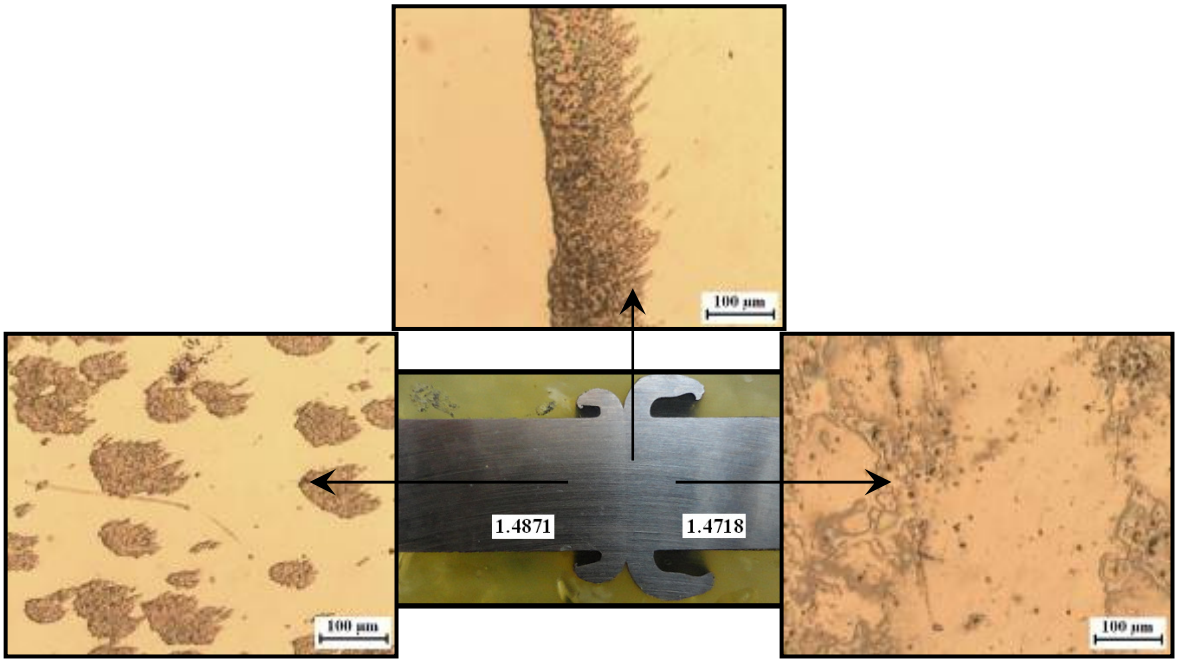

Figure 4. Micrographs of the weld zones of as-welded joint

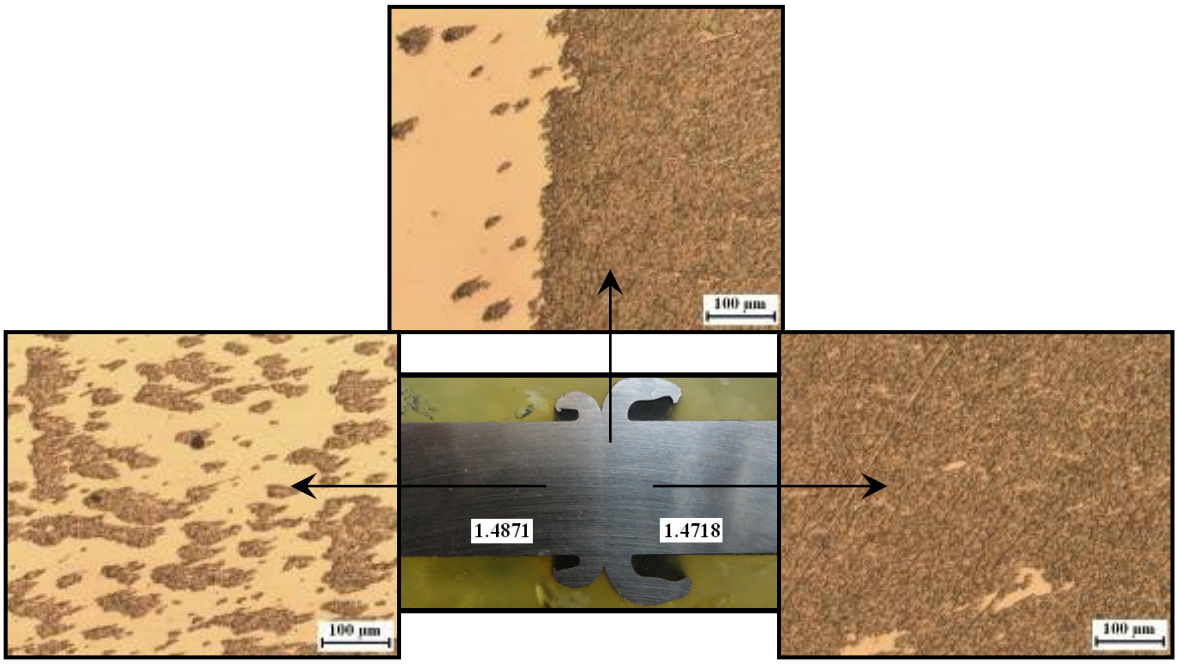

Figure 5. Micrographs of the weld zones of heat treated joint

The mechanical deformation and the frictional heat at the interface that dissipated through the parent materials had resulted in a temperature gradient causing zones of materials with different microstructure. Heat treatment condition causes wider heat affected zone. It is well known that when pressure is used to bring joint pair together by plastic deformation results in dynamic recrystallization leading to a grain refinement in the central region of the weld [7]. The 1.4718 steel was more deformed by the severe plastic deformation and frictional heat near the weld zone. This because in solid state bonding, especially in friction welding, due to the deformation, the refined grain structure is observed at the weld zone which results in improvement in properties [1]. As a result of the heat treatment, the microstructure of 1.4718

steel consists of tempered martensite with fine precipitated carbide throughout the matrix. The austenite microstructure was changed to the other phases due to the diffusion of carbon to the grain boundary. The heat affected zone experienced a martensite transformational the surface in contact with the 1.4718. Other researchers [4,7,8] also found similar structure in the weld region of martensitic steel joining with friction welding. Microstructure of heat treated 1.4871 steel contains uniformly distributed second phase stable precipitates. Heat affected zone can not be seen in the microstructures and carbide formation is in parallel with the mechanical orientation. In addition, typical austenitic structure is found away from the welding zone for 1.4871. On the other hand, martensitic structure is found for 1.4718 in the same region. In 1.4871, grain orientation is significantly observed in the regions closer to the welding zone. Grain orientation is normal to the deformation direction due to welding. Many researches observed grain orientation on HAZ in medium carbon steels and stainless steels [2,3,7,18]. Kaçar and Baylan [5] reported that the grain orientation to the direction of martensitic base metal was observed in both joints due to heat transformation coefficient of the martensitic stainless steel base metal higher than that of austenitic base metal. In our study, similar microstructure results were obtained.

3.2. Mechanical Properties

Tensile properties of defect free friction stir welding joint are only dependent on the micro hardness distributions across the different weld zones [12]. The measured microhardness values are presented in Figure 6 for as-welded and heat treated joints. The welded joints had a higher hardness than the base metal, and maximum hardness was obtained at the center of welding. Singh et al. [12] reported that the hardness at weld centre of as-welded joints is higher than base metal because hardness in nugget zone recovers slightly due to recrystallization to very fine equiaxed grain structure. The hardness curve is asymmetrical with respect to the weld centre line because of nonuniform field of plastic flow.

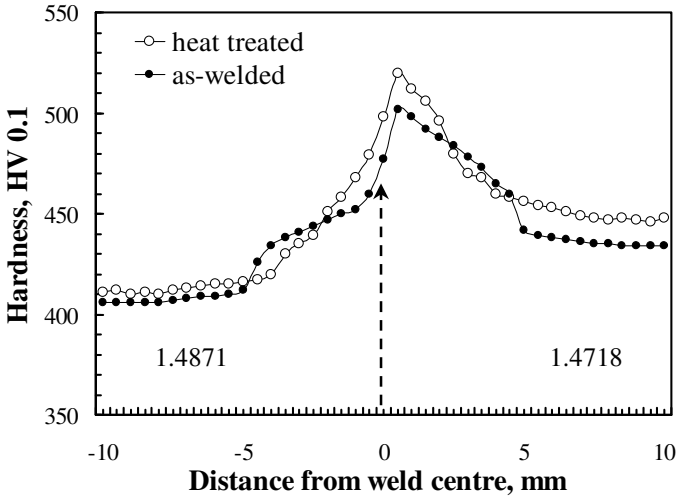

Figure 6. Microhardness distribution across the welding interfaces at central region of as-welded and heat treated joints

The similar trend is observed in the microhardness profiles of as-welded and heat treatment joints. The hardness profile of the weld zone showed roughly homogeneous values. The microhardness values of as-welded joint for 1.4871 and 1.4718 steels were 412 HV and 442 HV in outer cross section; 477 HV and 498 HV at the centre, respectively. The corresponding values for heat treated joint were 416 HV and 456 HV in outer cross section; 498 HV and 512 HV at the centre, respectively. These comparisons show that there is a slight increase in the

hardness in the heat affected zone. It was seen from microhardness results that hardness after heat treatment increased in the deformed region. The hardness is higher on martensitic steel side of the interface. The increasing hardness in the welding interface can be related directly to the microstructure formed in the welding interface as a result of the increasing heat input and severe plastic deformation. The material removed at the interface increased and the width of the deformed region decreased. The increase in the hardness values in the 1.4718 side could be attributed to the work hardening of the steel due to the presence of carbide. It is widely accepted that work hardening of steel is due to a martensite formation [8]. This infers that Fe-Cr-C intermetalics formation is more important when considering friction welding of high alloyed steel to carbon steel. This explanation is also corroborated by microscopic studies which revealed a plastically deformed zone at the weld interface. Hardness values in the weld zone of 1.4871 steel are not too high. Studies on austenitic steel joints using friction welding have reported a decrease in hardness at the interface zone of the joint. This has been attributed to the fact that austenitic steel is not hardenable by heat-treatment [1].

Many researches conducted tensile tests studies on welding zone to determine HAZ and metallurgical variations on dissimilar materials using different parameters of friction welding. They reported that heat treatment significantly affected mechanical properties of heat affected zone near the joining [9-12]. Table 3 represents the mechanical properties of friction stir welds in as welded and heat treated condition of martensitic-austenitic alloy couple.

Table 3. Mechanical properties of as-welded and heat treated joints

Material condition	Tensile strength (MPa)	Yield strength (MPa)	Elongation (%)	Fracture location
As-welded	1143	862	13.0	Base metal
Heat treated	1128	851	12.2	Base metal

The tensile strength slightly decreased after applying heat treatment. The formation of the intermetallics at the welding interface is responsible for higher hardness and lower tensile strength of friction welded joints. These hard intermetallics will have a detrimental effect on the mechanical strength. Heat treatment promotes the growth of brittle intermetallic which in turn affects the bond strength adversely. Therefore, the low values of elongation and strength can be attributed to presence of aligned chromium precipitation which reduces these properties [7]. Singh et al. [12] reported that reduction was observed in yield strength and tensile strength after heat treatment and same may be attributed to the coarsening of second phase precipitates. The elongation values of the un-welded 1.4871 and 1.4718 parent metals were 22.5% and 20.0%, respectively. However, the as-welded and heat treated joints exhibited elongation values of 13.0% and 12.2%, respectively. Kou and Lee [19] reported that applying heat treatment after the friction welding process decreased the tensile strength and elongation, and increased the ductility of the material. The decrease in tensile strength may be attributed to the reduction of preexisting dislocations and elimination of strengthening precipitates. Fracture of defect free weld tensile specimens occurs in the minimum hardness zone. As-welded joints have minimum hardness in base material and joints were fractured in the base material while heat treated joints were fractured in weld nugget because of minimum hardness in weld nugget [12]. The heat treatment procedures examined in this investigation have no significant effect on the fracture locations of the joints. Break-out did not occur in welding zones of as-welded and heat treated joints. The joint strength was found acceptable because all test samples was broken from 1.4871 steel base metals.

4. CONCLUSIONS

The effect of heat treatment on the mechanical and metallurgical properties of high alloyed X45CrSi9-3 and X53CrMnNiN21-9 steel couple joining with friction welding are listed below:

- Heat treatment of the steels used for welding play an important role in deciding the properties of the weld.
- The microstructure of the joints in the heat treatment state contains uniformly distributed hardening precipitates. This is the main reason for the enhanced hardness and improved microstructure properties of the joint in heat treatment state.
- Heat treatment applied after welding cause an increase in hardness and a decrease tensile strength values. The low values of elongation and strength can be attributed to presence of aligned chromium precipitation which reduces these properties.
- It was observed that the difference of hardness between zones unchanged by heat treatment. The highest hardness value was obtained at the center of welding on martensitic steel side of the interface.
- Rupture zones did not change at the end of the heat treatment applied after welding. The fracture mainly occurred at the austenitic steel side.

Acknowledgements
The author is grateful to Elzem Automotive Industry and Trade Limited Company, and especially to Mustafa Taşdemir, for their support.

REFERENCES

1. D.Ananthapadmanaban, V.S.Rao, N.Abraham and K.P.Rao, Mater. Design, 30, 2642, 2009
2. M.Şahin and H.E.Akata, Industrial Lubrication and Tribology, 56(2), 122, 2004
3. M.Uzkurt, B.S.Ünlü and M.Akdağ, Bull. Mater. Sci., 34, 815, 2011
4. W.Wu, L.Y.Hwu, D.Y.Lin and J.L.Lee, Scripta Mater. 42, 1071, 2000
5. R.Kaçar and O.Baylan, Mater. Design, 25, 317, 2004
6. Technical Handbook, "Welding Consumables for Joining and Cladding Stainless Steels and Nickel-Base Alloys" ESAB AB, Göteborg, Sweden, 2008
7. İ.Kırık, N.Özdemir and T.Teker, 1st International Iron&Steel Symposium, Karabük University, Karabük, Türkiye, 826, April 2012
8. H.J.C.Voorwald, R.C.Coisse and M.O.H.Cioffi, Procedia Engineering, 10, 1256, 2011
9. Y.C.Chen, H.J.Liu and J.C.Feng, J. Mater. Sci., 41, 297, 2006
10. H.Aydın, A.Bayram and İ.Durgun, Mater. Design, 31, 2568, 2010
11. A.G.Olabi and M.S.J.Hashmi, J. Mater. Process. Technol., 55, 117, 1995
12. R.K.R. Singh, C. Sharma, D.K.Dwivedi, N.K.Mehta and P.Kumar, Mater. Design, 32, 682, 2011
13. K.H.Song and K.Nakata, Mater. Design, 31, 2942, 2010
14. K.N.Krishnan, J. Mater. Sci., 37, 473, 2002
15. N.Bekoz, 16th International Metallurgy&Materials Congress, Convention&Congress Center, Istanbul, Turkey, 1276, September 2012
16. M.Sahin, E.Çıl, and C. Misirli, J. Mater. Eng. Perfor., 22, 840, 2013
17. R.Y.Tylecote, "The Solid Phase Welding of Metals", Edward Arnold Ltd., London, 1968
18. V.V.Satyanarayana, G.M.Reddy and T.Mohandas, J. Mater. Process. Technol., 160, 128, 2005
19. S.Kou and Y.Le, Weld J., 65(4), 65, 1986

DETERMINATION OF RESIDUAL STRESS FIELD ON A MULTIPASS WELDED STEEL BUTT-JOINT BY FINITE ELEMENT MODELING

Nuriya GARIPOVA[1], Caner BATIGÜN[2], C.Hakan GÜR[1,2]

[1] Middle East Technical University, Ankara, Turkey
e170638@metu.edu.tr chgur@metu.edu.tr
[2] Welding Technology & NDT Center, Ankara, Turkey
bgun@metu.edu.tr

ABSTRACT

Arc welding of a steel component brings in various thermally induced changes around the welded zone. The extent of these changes is mostly affected by the welding process parameters, and also the geometrical construction of the weld sequence. This study presents a finite element computational approach for evolution and distribution of residual stress field around the multi-pass welded steel butt-joint. At first, temperature fields were calculated for each welding pass. In continuation, progressed residual stress fields were numerically simulated for every pass and the final state. Microstructural changes in connection with heat input and weld passes were considered as well. The results were compared with those of the Magnetic Barkhausen Noise measurements.

Keywords: Multipass Welding, Residual Stress, Finite Element Analysis, Magnetic Barkhausen Noise

ALIN FORMATINDA BİRLEŞTİRİLMİŞ ÇOK PASOLU ÇELİK KAYNAKLARI ÜZERİNDEKİ GERİLME DAĞILIMININ SONLU ELEMAN MODELLEME TEKNİĞİ İLE BELİRLENMESİ

ÖZET

Bir çelik parça üzerinde uygulanan ark kaynağı işlemi, kaynak bölgesi çevresinde ısıyla bağlantılı çeşitli değişikliklere yol açmaktadır. Bu değişikliklerin miktarı büyük ölçüde uygulanan kaynak prosesine bağlı parametreler ve kaynak sıralamasına bağlı geometrik yapıdan etkilenmektedir. Bu çalışma, alın formunda birleştirilmiş çok pasolu çelik kaynakları üzerindeki iç gerilme dağılımı oluşumunu belirlemek üzere kullanılan bir sonlu eleman modelleme yaklaşımı sunmaktadır. İlk önce, her bir paso için sıcaklık dağılımı hesaplanmıştır. Takiben, her bir paso için meydana gelen iç gerilme dağılımları nümerik olarak simule edilmiştir. Isı girdisi ve kaynak pasolarına bağlı mikro yapı değişimleri dikkate alınmıştır. Sonuçlar, "Manyetik Barkhausen Gürültüsü" ölçüm sonuçları ile kıyaslanmıştır.

***Anahtar kelimeler*:** Çok Pasolu Kaynak, İç Gerilme, Sonlu Eleman Analizi, Manyetik Barkhausen Gürültüsü

1. INTRODUCTION

Multi-pass welds are widely used in industrial joining applications, such as construction, pressure equipment, cranes, oil- and gas lines, shipbuilding, etc. During the formation of the multipass weld joints, complex microstructural and mechanical changes that influence the loading capacity occur. The root reasons can be summarized as phase transformations during each pass, heat and mass transfer between weld passes, subsequent or repeated heat inputs, which have diverse influences on microstructure, contribution of every pass to the mechanical properties of the entire joint, residual stress state of the weldment, distortions of the construction, final geometry characteristics of the obtained weld and many others.

The studies of Okerblom and Vinokurov are one of the first works on the analysis of welded structures including multi-pass welds [1]. Among the authors of the fundamental books on the welding residual stress formation the names of J.Goldak, D.Radaj, L.E.Lindgren have to be mentioned [1,2]. Due to the development of computer hardware, numerical simulation investigations have become much more easier even than ten years ago. Also, such complex processes as welding appear to be routine already. P.Duranton et al. [3] via 3-D modeling have investigated residual stresses and distortions of a 316L stainless steel pipe after multipass welding. C.D.Elcoate et al. [4] have performed three-dimensional multi-pass repair simulations of 19.6 mm thick pipes. There are a number of works by D.Deng et al. [5-7] on finite element method (FEM) prediction of temperature field, microstructure, residual stresses in welded pipes and welding distortion in large structures, as well as considering phase transformation effects. Katsina tried to understand the effect of thermal cycles on the metallurgical and microstructural characteristics of the heat affected zone of a multi-pass pipeline weld of API 5L grades X65, X70 and X100 steels [8]. Ponomareva revealed residual stresses evolution and distribution in the multi-pass welds of API 5L-X80 steel [9].

In order to get deeper insight into interaction of weld passes, their final effect on the welded joint and the formed residual stress state, numerical calculations have been carried out on the SYSWELD software. The results were compared with the Barkhausen noise measurements on the equivalent steel samples.

2. COMPUTATIONAL APPROACH

In presented approach finite element method (FEM) has been applied. A moving heat source was used to imitate the heat input. Numerical model consists of finite elements mesh; the quantity of elements in locations close to the weld lines has higher density because of higher temperature, stress and deformation gradients (Fig.1).

Heat transfer problem during arc welding process can be described by governing equation:

$$\lambda\left(\frac{\partial^2 T}{\partial x^2}\right)+\lambda\left(\frac{\partial^2 T}{\partial y^2}\right)+\lambda\left(\frac{\partial^2 T}{\partial z^2}\right)+Q_{arc}=\rho C_p\frac{\partial T}{\partial t}$$

where λ, T, Q_{arc}, ρ and C_p are thermal conductivity, temperature, rate of internal heat generation by welding arc, density and specific heat capacity, respectively.

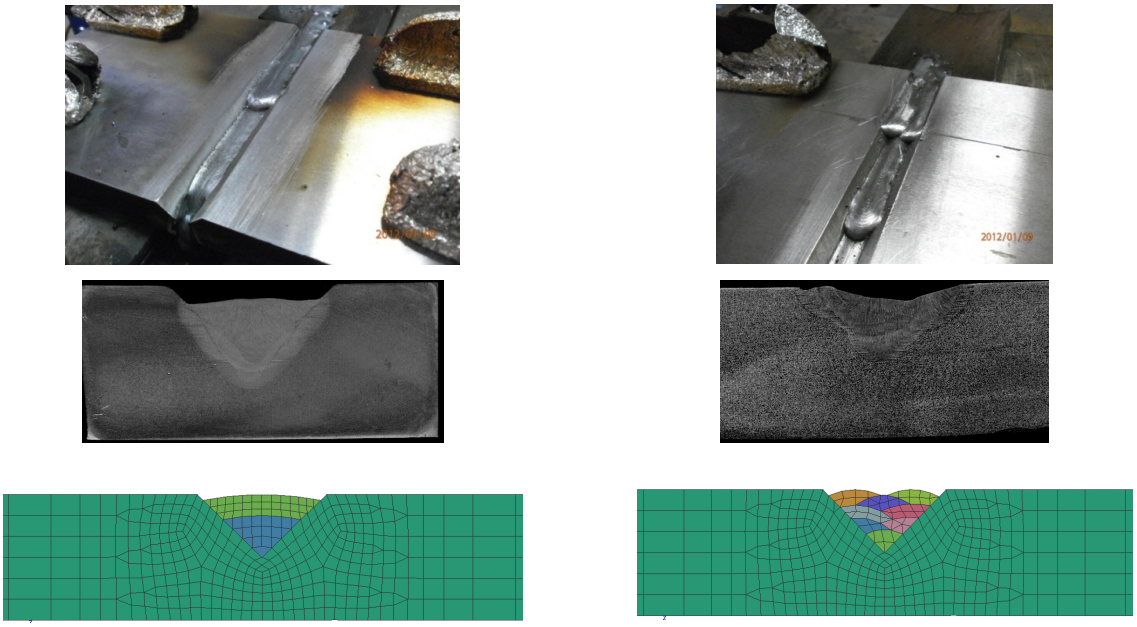

Figure 1. Two- and eight-pass weld joints: experiments, macro-sections and its FEM meshes.

For diffusion controlled phase transformations Leblond's model was applied:

$$\frac{dP}{dt} = f(\dot{T}) \cdot \frac{P_{eq}(T) - P}{\tau(T)}$$

where P, P_{eq}, T, τ and $\dot{T}$ are phase proportion, proportion at phase equilibrium, temperature, time and heating/cooling rate, respectively.

For martensitic transformations Koistinen-Marburger law has been used:

$$P(T) = 1 - exp\left(-b(M_s - T)\right)$$

where b and M_s are law coefficient and martensite start temperature. In all the calculations temperature-dependent thermo-physical and mechanical properties were taken into account.

3. EXPERIMENTS

Following surface grinding two sets of steel samples were austenitized (960°C/1,5 h), and then, cooled in a furnace under controlled atmosphere. The yield strength and UTS were measured as 279 MPa and 427 MPa, respectively. Plates had fixed ends during metal active gas welding (MAG) process. No preheat was applied. Shielding gas for welding procedure consisted of 20% CO_2 and 80% Ar. Two- and eight-passes weldings were performed. After the full-scale experiment, two sets of multi-pass welding 3-D FEM models were computed. All the samples had a V-groove of 18 mm width and 19 mm depth in the middle of each plate with dimensions of 280 x 150 x 18 mm, as on the real test samples. In the thermal analysis, the arc efficiency was assumed to be 0.8. The entire numerical calculations consisted of two stages: thermal and mechanical. The output results of the first thermal computation with all applied thermal boundary conditions and loads become the input data for the second mechanical computations with mechanical boundary conditions and loads respectively.

Table 1. Welding process parameters used in the experiments

Number of passes	Wire feed speed, m/min	U, V	I, A	Linear weld speed, m/min	Line energy/pass, kJ/mm	Effective line energy, kJ/mm
2	11,5	29	290	4	1,26	2,02
8	6,5	21	170	8	0,27	1,71

3. RESULTS AND DISCUSSION

3.1. Computations of the temperature history and metallurgical transformations

After finishing numerical computations, it was possible to observe the temperature history at any point of the 3-D model of the weldment. Below, results for the point 15 mm far from the weld centerline are presented (Fig.2).

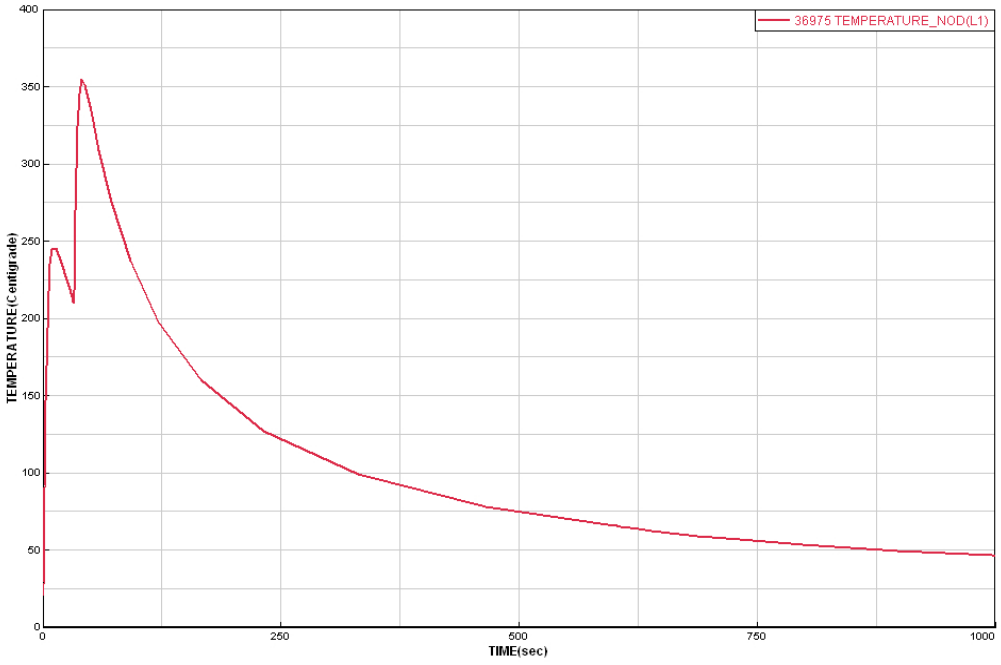

Figure 2. Temperature profile at the point 15 mm far from weld center line for two-pass weld

The distribution of main phases can be investigated in details. Below formed martensite phase was chosen to be shown, as one of the critical phases for weldment (Fig.3). For eight-pass weldment, temperature profile during the process is shown in Fig.4. On side of the applied heat, as getting closer to the bead, the height of the peaks were found as higher. In eight pass sample, applied heat input levels were less as compared with two-pass welds due to thinner weld beads which demand less energy for melting and fusion, and higher linear speed of the process. The sequence of the passes could be noticed as well. From the resultant phases evolution the martensite growth was observed on weld beads. For eight-pass welding, its proportion is much pronounced approaching to 99.5% (Fig.5) due to higher cooling rate due to higher linear welding speed and less filler material deposition on thinner weld beads.

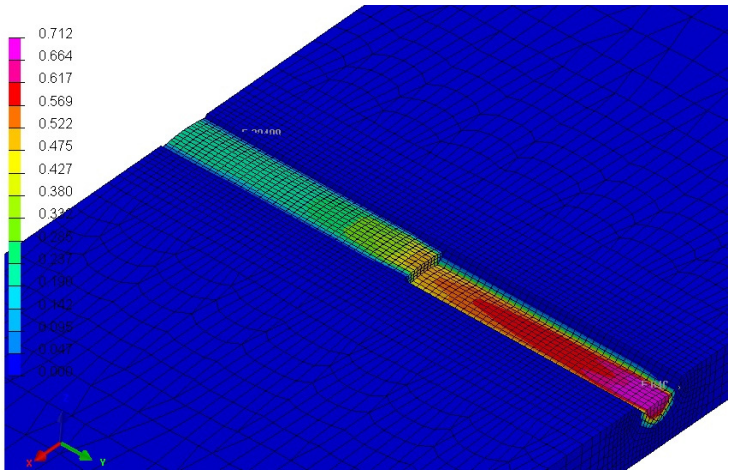

Figure 3. Martensite distribution after 1 hour for two-pass weld

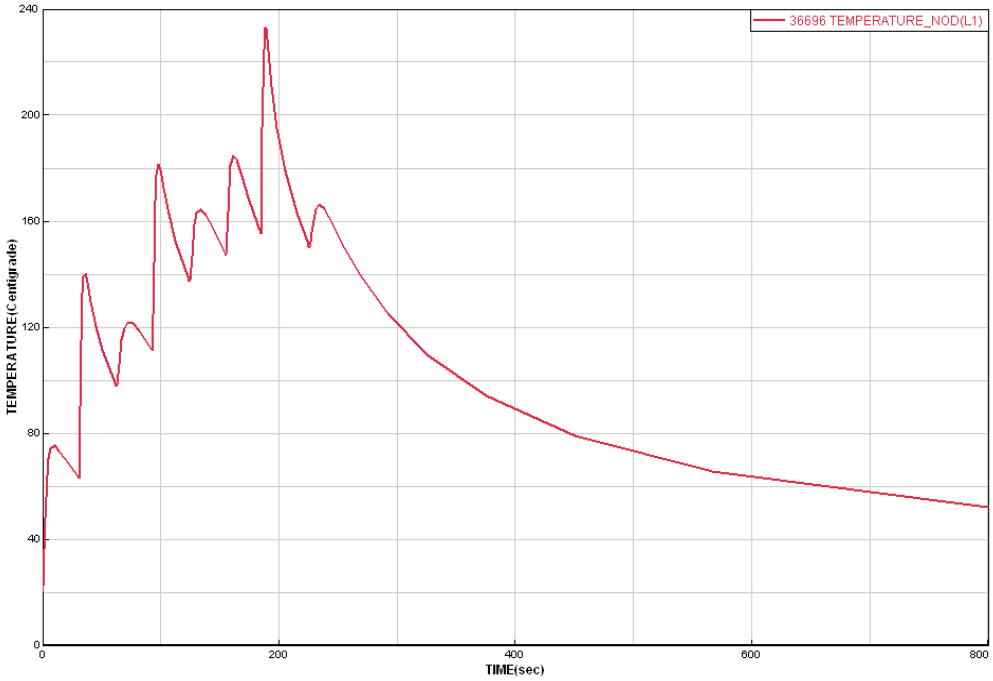

Figure 4. Temperature profile at the point 15 mm far from weld center line for eight-pass weld

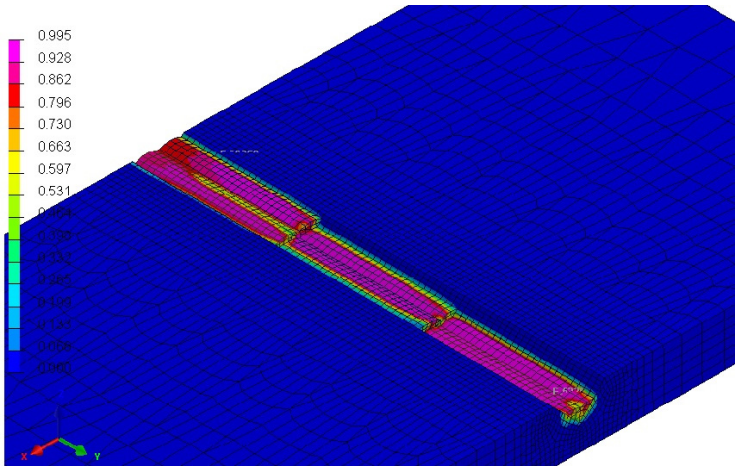

Figure 5. Martensite distribution after 15 minutes for eight-pass weld

3.2. Computations of the mechanical properties

Consequent mechanical calculations enabled to show service characteristics of the multi-pass weldments. One of the important exploitation parameter such as yield strength reveals the zones which can withstand with permanent deformation. For the two-pass joint, maximum level of yield strength reached at a level of 872 MPa locating on weld beads (Fig.6). Weld joint was in total harder than the base metal. Also, there were apparent zones that were got weakened to deformation operations. Especially along the borders of the welds the boundary zone was found as critical due to the potential possibility of crack initiation. The von Mises criterion gives a reasonable estimation of failure, including fatigue damage. From the stress pattern it is obvious that welding and heat affected zone are potentially critical damage regions.

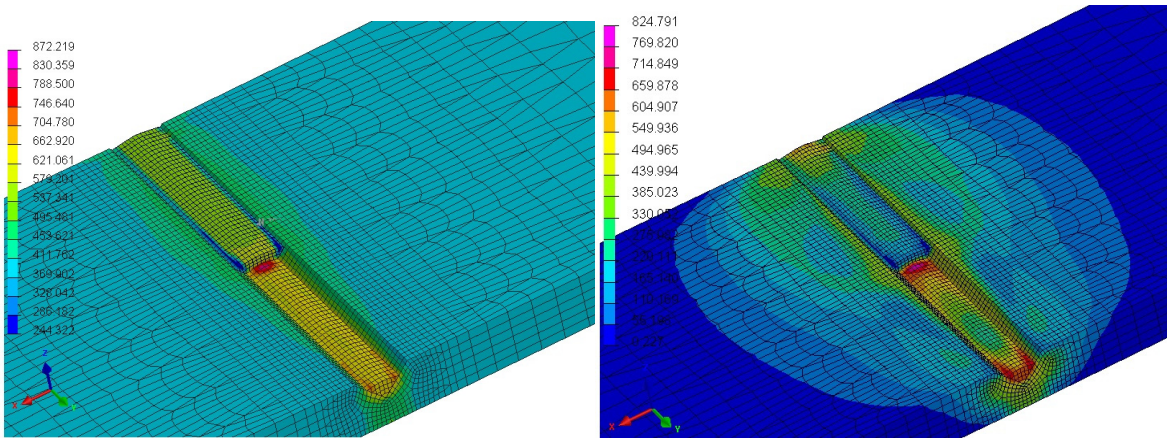

Figure 6. Yield strength and von Mises stress distribution after 1 hour for two-pass weld

For the eight-pass joint, maximum level of yield strength reached at a level of 1098 MPa (Fig.7) that was owing to the raised amount of martensite compared to that in two-pass weldment. Again, the zones subjected to the melting had higher values of yield strength comparatively with the base metal. And similarly, weakened fusion boundary along the border of the welds indicates the probable damage start locations.

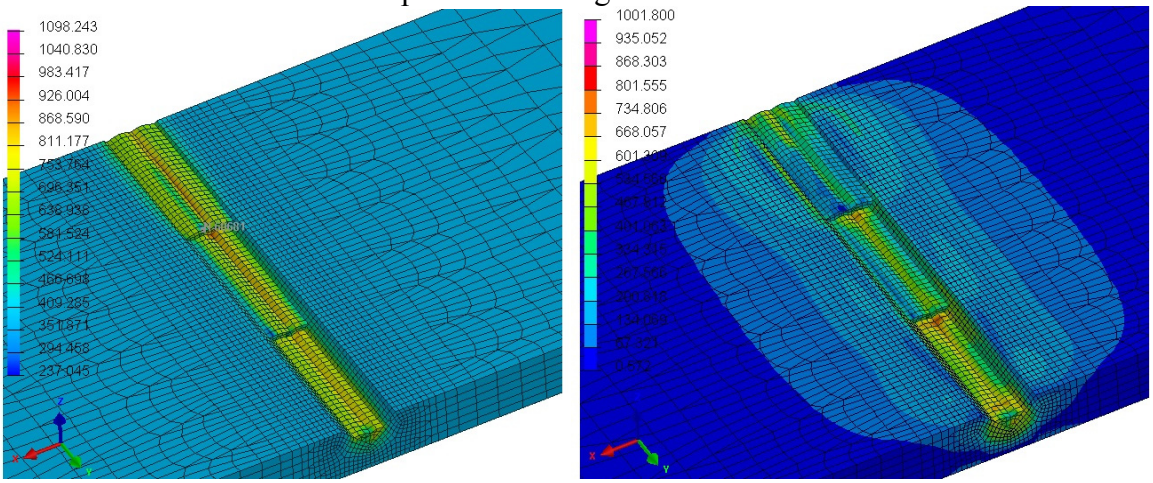

Figure 7. Yield strength after 15 minutes for eight-pass weld

The von Mises stress state for eight-pass joint looks to be more localised than in case of two-pass, though areas with elevated values are present as well. However, in both cases last passes seem to be safer than the first passes. This may be explained by favourable slow cooling rate in the last passes. The von Mises stress spreading from the backside of the sample displays safe state as does the heat affected zone due to lower temperature influence through the bulk of base metal (Fig. 8).

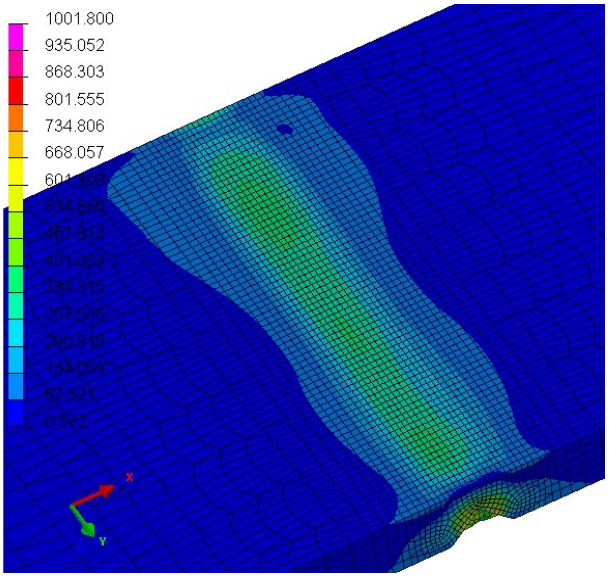

Figure 8. Von Mises stress distribution from backside after 15 minutes for eight-pass weld

Three-dimensional surface contour plot of residual stress state demonstrates peaks on the starts and ends of welding as it was presented in the study of D.Deng et al. [7]. The maximum peak specifies the start location of first and second welding passes (Fig.9).

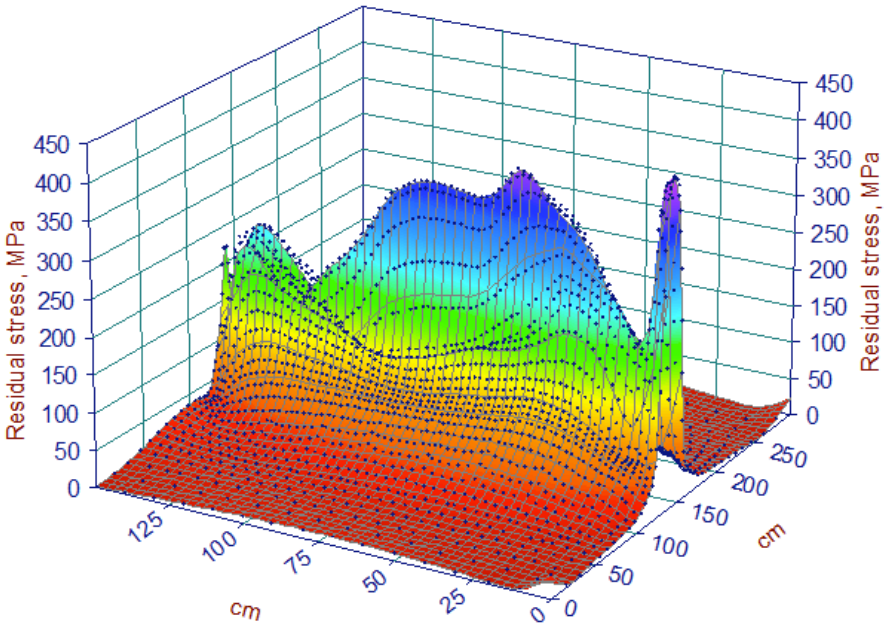

Figure 9. Three-dimensional stress state for two-pass weld

4. VERIFICATION USING BARKHAUSEN NOISE TECHNIQUE

With verification purposes, Barkhausen noise technique measurement results have been confronted with numerical results of residual stresses (Fig.10). Since penetration capacity of the Barkhausen noise technique was insufficient comparatively with calculated bulk stresses, some mismatch was observed in results. In spite of the presence of dicrepancies between the predictions and measurements, however, the computational approach has basically captured the general trends of residual stress distributioin.

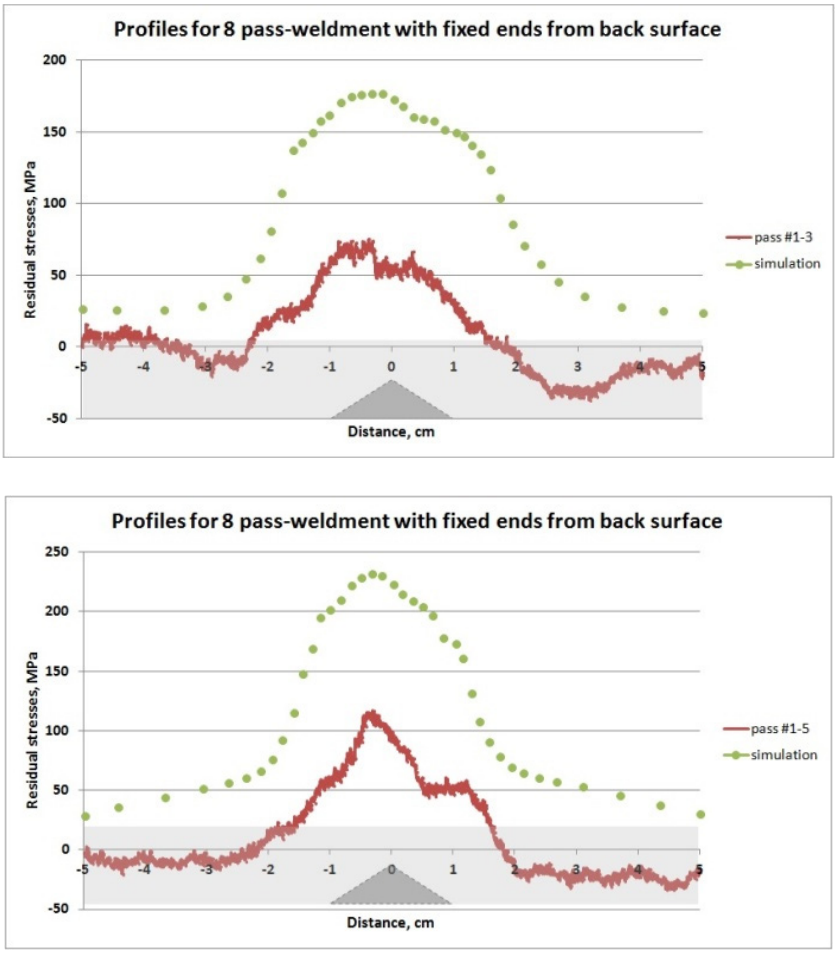

Figure 10. Measured and calculated residual stress distributions

5. CONCLUSION

The computer welding simulation becomes a safe instrument for investigating important technological processes. In multi-pass welding modeling, inter-pass temperature appear to be one of the essential technological parameters affecting the final residual stress state. Due to pre-heat effect of previous weld passes, it is recommended to minimize the time between pass welding in order to impede the martensite phase formation on the joint and to prevent reaching the critical values of post-weld residual stresses. The variation of welding residual stress changing with weld pass is examined numerically. Results of the Magnetic Barkhausen Noise method validate calculated stress distribution states.

REFERENCES

1. J.A.Goldak, M.Akhlaghi, "Computational welding mechanics", Springer, 2005.
2. D.Radaj, "Heat Effects of Welding Temperature Fields, Residual Stress, Distortion", Springer-Verlag, 1992.
3. P.Duranton, J.Devaux, V.Robin, P.Gilles, J.M.Bergheau, "3D modelling of multipass welding of a 316L stainless steel pipe", Journal of Materials Processing Technology, 153–154 (2004) 457–463
4. C.D.Elcoatea, R.J.Dennisa, P.J.Bouchardb, M.C.Smithb, "Three dimensional multi-pass repair weld simulations", International Journal of Pressure Vessels and Piping, 82 (2005) 244–257
5. D.Dean, M.Hidekazu, "Prediction of welding residual stress in multi-pass butt-welded modified 9Cr–1Mo steel pipe considering phase transformation effects", Computational Materials Science 37 (2006) 209–219
6. D.Dean, M.Hidekazu, "Finite element analysis of temperature field, microstructure and residual stress in multi-pass butt-welded 2.25Cr–1Mo steel pipes", Computational Materials Science 43 (2008) 681–695
7. D.Dean, Sh.Kiyoshima, "FEM prediction of welding residual stresses in a SUS304 girth-welded pipe with emphasis on stress distribution near weld start/end location", Computational Materials Science 50 (2010) 612–621
8. I.N.Katsina "Effect of welding thermal cycles on the heat affected zone microstructure and toughness of multi-pass welded pipeline steels", Ph.D. Thesis, Cranfield University, England, 2012
9. I.N.Ponomareva, "Development of the procedure for design assessment of residual weld stresses in pipeline welds" (in russian), Ph.D. Thesis, Bauman Moscow State Technical University, 2013

Determination of the Optimum Magnetic Barkhausen Noise Measurement Parameters for Evaluating the Microstructure of Quenched and Tempered AISI-4140 Steels

Kemal DAVUT*,, Tuba DEMİRTAŞ*, Caner ŞİMŞİR*,*****

* Metal Forming Center of Excellence, Atılım University, Turkey
kemal.davut@atilim.edu.tr
** Department of Metallurgical and Materials Engineering, Atılım University, Turkey
t.demirtas@atilim.edu.tr
*** Department of Manufacturing Engineering, Atılım University, Turkey
caner.simsir@atilim.edu.tr

ABSTRACT

Magnetic Barkhausen noise technique offers fast and non-destructive inspection of parts against grinding burns. Moreover, the applicability of the technique to evaluate residual stresses, microstructure heterogeneity, hardness, and heat treatment faults has been subject of intense research for the past 10 years. However, the influence of measurement parameters on the results has not been studied in detail. The present work aims at comparing the MBN response of quenched and tempered steels for different magnetizing frequency and voltages. For that purpose identical specimens from an AISI 4140 steel bar were quenched and the tempered at various temperatures between 200ºC and 600ºC. The microstructures were characterized by metallographic examinations and hardness measurements. The results show that as the tempering temperature increases, the Barkhausen activity increases due to the enhancement of domain wall displacement with softening of the martensite. Due to the linear relation between magnetic coercive force and hardness a linear relation is expected between mechanical hardness and MBN activity. In the present work the degree of linear dependence between hardness and MBN response was evaluated using Pearson's correlation coefficient. The optimum MBN measurement parameters was determined based on bringing the correlation coefficient closer to -1. This optimization work showed that the reliability, repeatability and sensitivity of Barkhausen noise technique strongly depends on the selection of measurement parameters.

Keywords: Magnetic Barkhausen Noise, quenching, tempering, measurement parameters, optimization, Pearson's correlation coefficient

1. INTRODUCTION

Steels are widely utilized in different industries, and one the most common form is quenched and tempered condition. Tempering in the range of 200 ºC to 700 ºC relieves residual stresses and improves toughness and ductility by modifying the microstructure of the quenched steel. For consistency, quenched steel components are generally tempered for 1 to 2 hours. If the principal desired property is hardness or wear resistance, the part is tempered at about 200ºC; if the primary requirement is toughness, the part is then tempered above 400 ºC. Residual stresses are relieved almost completely when the tempering temperature reaches 500 ºC [1].

In order to provide longer service life with higher performance of steel components, quality control is essential. There is a growing need for non-destructive characterization of steel components. Magnetic Barkhausen Noise (MBN) measurement provides a good alternative to the traditional methods in terms of fastness and accuracy.

Ferromagnetic materials below their Curie temperature retain a large spontaneous magnetic moment due to the cooperative alignment of unpaired electron spins along a common direction. Oppositely magnetized domains divided by domain (Bloch) walls form to minimize the magnetic energy. The change in magnetization, caused by the application of external magnetic field, takes place by movement of the boundaries between domains in weak fields or by rotation of the direction of magnetization in strong fields. On removing the field, the magnetization again declines to zero if there is no hindrance to Bloch wall motion [2-4].

When a variable external field influences a ferromagnetic material, irreversible jumps of domain walls cause the formation of Barkhausen noise. High resolution examination of hysteresis cycles of ferromagnetic materials reveals discontinuous flux changes due to discontinuous domain wall motion as magnetic field strength is increased. Microstructural features such as dislocations, inclusions and grain boundaries pin the domain walls. When the strength of externally applied magnetic field reaches the critical level, motion of the domain wall continues by Barkhausen jumps. These jumps can be detected as the voltage pulses induced in a pick-up coil positioned close to the surface. These signals are amplified, filtered and then processed in order to characterize the microstructures.

Changes in microstructure and/or residual stresses effect the Barkhausen signals. Various studies have been published on characterization of steel microstructures by MBN method. MBN in low carbon steel was found to be strongly dependent on the grain size [5]. Grain boundary misorientation effects MBN response as well [6]. Important changes have been observed in the MBN response during martensite decomposition due to tempering of steels [7-9]. The effect of tempering was also studied for case carburized steel, and a correlation between hardness depth profile and MBN was found [10]. Although the effect of tempering on MBN response have been studied intensively [7-13], the influence of selection of measurement parameters; such as magnetizing frequency and voltage; have yet to be studied. The present work aims at closing this gap, by comparing the MBN response of quenched and tempered steels at different magnetizing frequency and voltages. For that purpose identical specimens from an AISI 4140 steel bar were quenched and the tempered at various temperatures between 200 ºC and 600 ºC.

2. EXPERIMANTAL

The specimens of 5 mm-thick and 22 mm diameter were prepared from a hot formed SAE 4140 bar. Table 1 gives the chemical composition of the steel used. All the cutting and grinding operations were done prior to the heat treatments in order to avoid surface machining residual stresses. All specimens were quenched in water after austenitization at 860 ºC for 45 minutes. Then, specimens were separately tempered at 200 ºC, 300 ºC, 400 ºC, 500 ºC and 600ºC for 60 minutes. One specimen was left as-quenched.

Table 1 – Chemical Composition of the SAE 4140 Steel (wt%)

C	Cr	Mo	Mn	Ni	Si	P	S	Fe
0.375	1.04	0.158	0.782	0.0624	0.225	<0.0005	0.0304	Bal.

Before metallographic investigation, the samples were finely ground, polished with diamond paste and etched with 2% Nital. The surface sections of the specimens were examined using Nikon LV150N optical microscope and Zeiss EVO LS 15 scanning electron microscope. For each specimen an average hardness value was determined by measuring Vickers hardness at 10 different locations with the Zwick / Roell ZHV 10 instrument using a load of 19.61 N.

MBN measurements were performed using a commercial system (Rollscan, µscan 600). The general purpose sensor S1-18-13-01 was used for the MBN measurements. A sinusoidal cyclic magnetic field was induced in a small volume of the specimen via a ferrite core C-coil. The Barkhausen signals were collected at a sampling rate of 2.5 MHz and then filtered with a wide band-pass filter (10-1000 kHz). The MBN signals were analyzed using the Rollscan-software. A total of 30 signal bursts, each of which represent one half of the magnetization cycle, were used to analyses the Barkhausen signal of each specimen. The peak magnetizing voltage was varied between 1-16V and the magnetizing frequency between 50 – 250 Hz. Table 2 summarizes the variation of those measurement parameters. For each set of those parameters, 3 MBN measurements were performed in order to ensure repeatability.

Table 2 – The MBN measurement parameters of the experiments

Measurement Number	Magnetizing Frequency (Hz)	Magnetizing Voltage (mV)	Sampling Rate	Waveform
1	50	1	2.5 MHz	Sine
2	100	1	2.5 MHz	Sine
3	150	1	2.5 MHz	Sine
4	200	1	2.5 MHz	Sine
5	250	1	2.5 MHz	Sine
6	50	6	2.5 MHz	Sine
7	100	6	2.5 MHz	Sine
8	150	6	2.5 MHz	Sine
9	200	6	2.5 MHz	Sine
10	250	6	2.5 MHz	Sine
11	50	11	2.5 MHz	Sine
12	100	11	2.5 MHz	Sine
13	150	11	2.5 MHz	Sine
14	200	11	2.5 MHz	Sine
15	250	11	2.5 MHz	Sine
16	50	16	2.5 MHz	Sine
17	100	16	2.5 MHz	Sine
18	150	16	2.5 MHz	Sine
19	200	16	2.5 MHz	Sine
20	250	16	2.5 MHz	Sine

3. RESULTS AND DISCUSSION

Representative micrographs (Figure 1) and hardness values (Table 3) of the samples show that typical martensitic structure (Figure 1. a) and tempered structures (Figure 1. b-d) were successfully obtained. Martensite has a tetragonal lattice with interstitial carbon in solid

solution and high dislocation density formed by shear; all of which make it the hardest of all specimens. A transition carbide (ε-carbide) and low-carbon martensite occur during tempering at temperatures lower that 250 ºC. At higher tempering temperatures (up to 400 ºC) cementite precipitates start to nucleate and the dislocation density reduces. In addition, martensite loses its tetragonality and low-carbon martensite becomes body-centered-cubic (BCC) ferrite. When the tempering temperature is above 400 ºC, carbide precipitates coarsen and spheroidise and ferrite starts to recrystallize. Moreover, residual stresses are reduced remarkably [14]. As tempering temperature increases martensite softens as indicated by the hardness values shown in Table 3, via the mechanisms explained here.

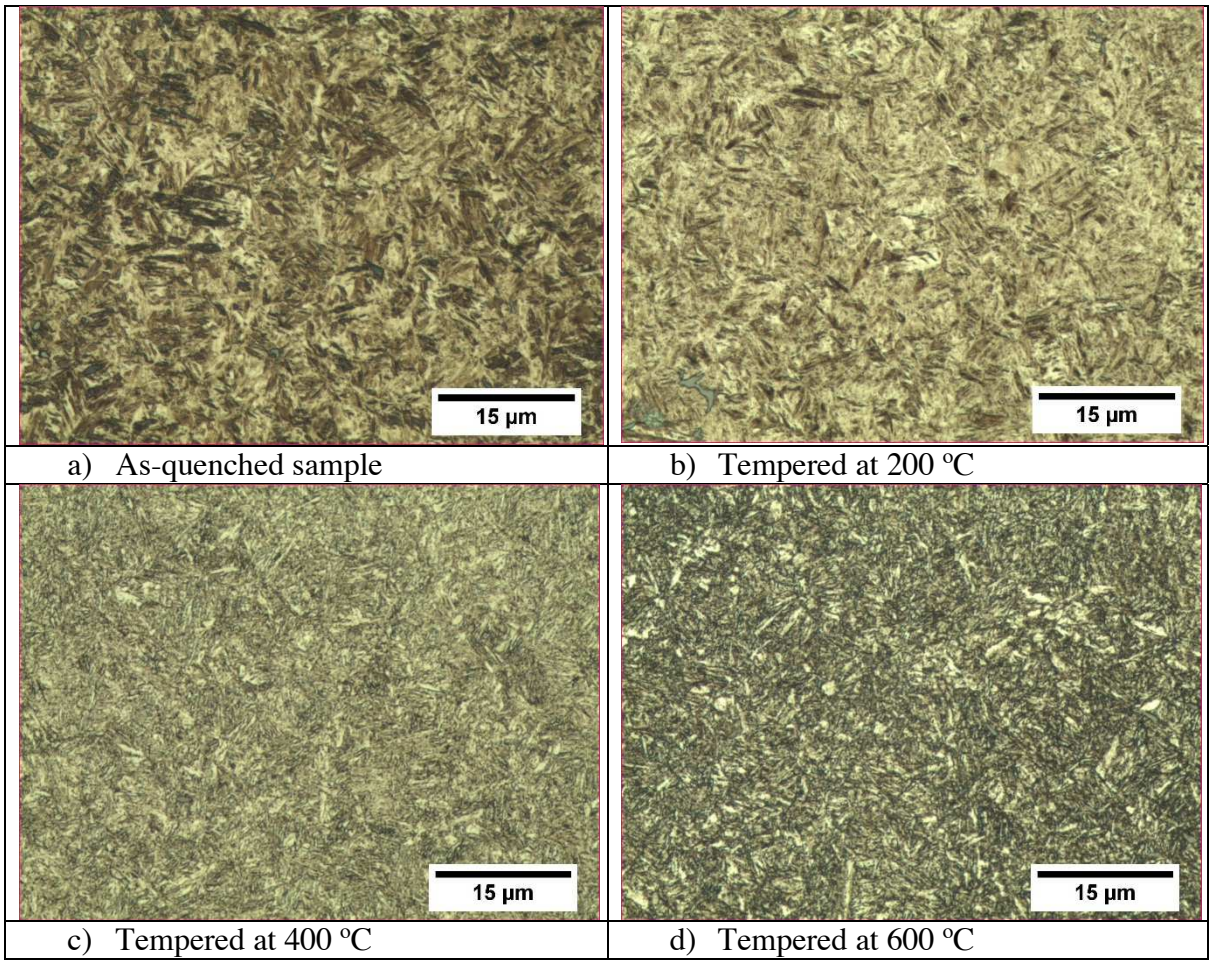

a) As-quenched sample b) Tempered at 200 ºC

c) Tempered at 400 ºC d) Tempered at 600 ºC

Figure – 1 Representative micrographs of the samples

Table 3 – Vickers hardness values (HV) of the specimens

As quenched	Tempered at				
	200ºC	300ºC	400ºC	500ºC	600ºC
701 ± 52	590 ± 7	521 ± 6	447 ± 5	396 ± 3	324 ± 7

MBN measurements were performed under the effect of an alternating magnetic field, which induces a representative magnetic hysteresis loop in a small volume of the specimen. The hysteresis loop is due the energy loss, associated with the irreversible process of magnetization.

This irreversible process is strongly related to the dynamic behavior of domains; i.e. nucleation, annihilation and growth of domains. Grain/lathe boundaries, dislocations and precipitates affect this dynamic behavior. Consequently, the number of domain walls moving at a given instant and the mean free path of the domain wall displacement would determine the strength of the MBN signal.

The raw magnetic noise data consists of series of voltage pulses and associated magnetic field values. The strength of the MBN signal is quantified with the root-mean-square (RMS) value which is calculated according to the following formula:

$$RMS = \sqrt{\frac{1}{n}\sum_{i=0}^{n-1} x_i^2} \qquad (1)$$

where x_i represents the MBN signal amplitudes that passed through the wide band-pass filter specified in the experimental section.

Figure 2 shows the correlation graph between RMS values of the MBN signal and hardness of the quenched and tempered specimens for the measurement number 20. These results show that MBN is influenced by the tempering which, as a function of temperature, causes changes in dislocation density, lattice straining (i.e. micro-residual stresses) as well as morphology and size of cementite. All those changes cause a change in the hardness and those results are in agreement with previous studies [7-13].

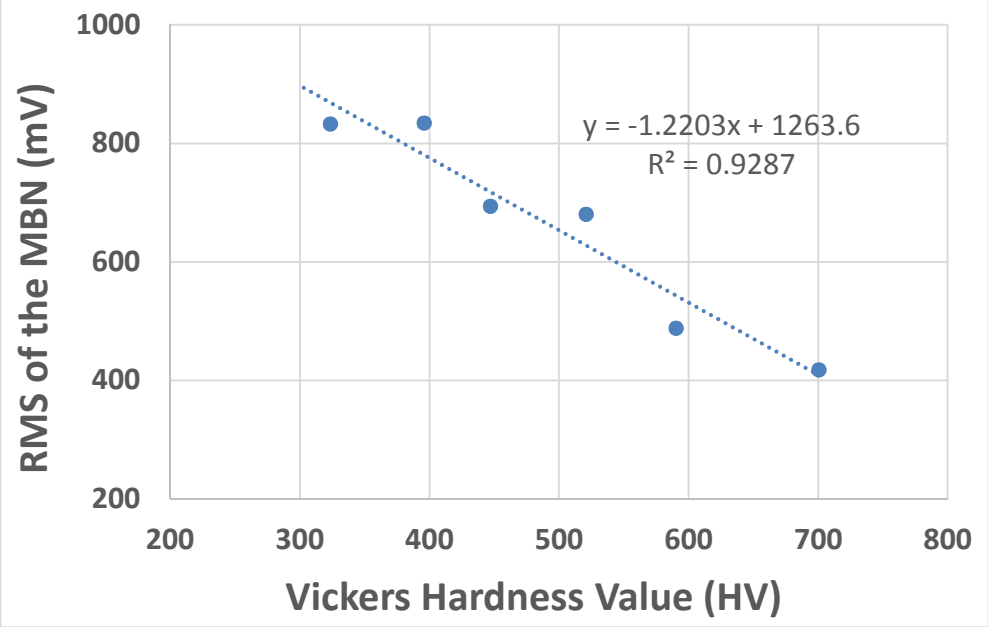

Figure 2 – Correlation between hardness and RMS for measurement number 16

It is seen in Figure 2 that the as-quenched specimen, which is the hardest specimen, produces the weakest MBN signal as indicated by the lowest RMS value. Pinned domain walls due to high dislocation density and restricted domain wall motion due to small martensite needles cause lower RMS values for the as-quenched specimen. As tempering temperature increases, dislocation density decreases, micro-residual stresses diminish and the magnetic structure comes close to those of a ferrite. Thus, RMS values increases due to the enhancement of domain wall displacement with the softening of martensite.

Figure 2 was obtained via a simple linear regression analysis using least squares method. The goodness of fit was quantified by the "coefficient of determination" and it is denoted as R^2. The R^2 value is obtained from Pearson's correlation coefficient (denoted as R), which is defined as the covariance of the two variable (i.e. hardness and RMS) divided by the product of their standard deviations [15]. Here R^2 value estimates the fraction of variance in hardness that can be explained by RMS in a simple linear regression.

The previous studies [7-13, 16] has showed that a linear relation is found between mechanical hardness and peak position or RMS of the Barkhausen noise. The linear relation between magnetic coercive force and hardness explains such behavior. The microstructural features that impede dislocation movement, also inhibit the motion of domain walls. In addition, presence of residual stresses effect the motion of dislocations and domain walls in the same manner. Regarding these, a very good correlation between hardness and RMS is expected.

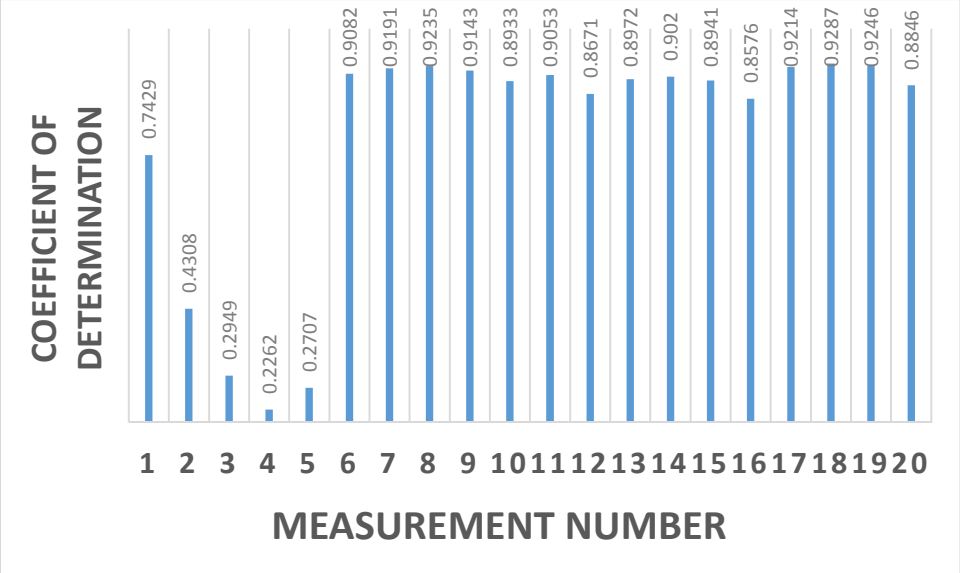

Figure 3 – The coefficient of determination (R^2) values of 20 different measurements having different magnetizing frequencies and voltages as tabulated in Table 2.

Figure 3 shows the results of the linear regression analysis performed for 20 different measurements tabulated in Table 2. The first 5 measurements, for which the magnetizing voltage was 1V, the coefficient of determination is very low. For the other measurements, for which the magnetizing voltage is higher up to 16 V, the R^2 value varies between 0.86 – 0.92; which indicates that the expected good correlation between hardness and RMS is observed. At those higher magnetizing voltages, the magnetizing frequency does not influence the R^2 value significantly. Nevertheless, the highest R^2 values are observed at magnetizing frequencies of 150 – 200 Hz (i.e. measurement numbers 8-9, 13-14 and 18-19).

Apart from the goodness of fit, the selection of optimum magnetization parameters can also be evaluated via sensitivity of the MBN. In the present study, the sensitivity index (SI) given by the following equation is used:

$$SI = 100 \times \frac{\left(RMS_{T600} - RMS_{As-Q}\right)}{RMS_{As-Q}} \qquad (2)$$

In this equation, RMS_{T600} and $RMS_{As\text{-}Q}$ denote the root mean square values of the sample tempered at 600 °C and the as quenched specimen. Here the optimum measurement parameters should maximize the SI of the RMS values.

Figure shows the SI values of the 20 different measurements, tabulated in Table 2. The highest SI is observed for 6 V of magnetizing voltage (i.e. measurement numbers 6-10), and among those the maximum SI is observed of 250 Hz of magnetizing frequency.

Changing the magnetizing frequency and voltage allows varying the strength of the magnetizing field. Increasing the magnetizing voltage increases the level of magnetization. When the magnetizing frequency is increased while keeping the voltage constant, the magnetizing level will decrease. On the other hand the MBN level and RMS values will increase due to the fact that much more domain walls are participated. Moreover, the frequency also influences the depth from which the MBN comes.

In this study, the best correlation with hardness and the best sensitivity levels are observed at intermediate magnetizing voltages. When the voltage is too low (i.e. measurement numbers 1-5) the Barkhausen noise is too low; it is actually at the same level as background noise. Increasing the voltage and the corresponding magnetic field strength improves both the hardness correlation and sensitivity index. This improvement can be attributed to the fact that the domain walls have a greater capacity to overcome the pinning obstacles in the microstructure when the magnetic field strength is increases. However, saturation magnetization is reached in the pick-up coil when the magnetizing voltage is higher than 11V, and this reduces the sensitivity of the MBN. On the other hand, the hardness correlation is not influenced significantly from this effect.

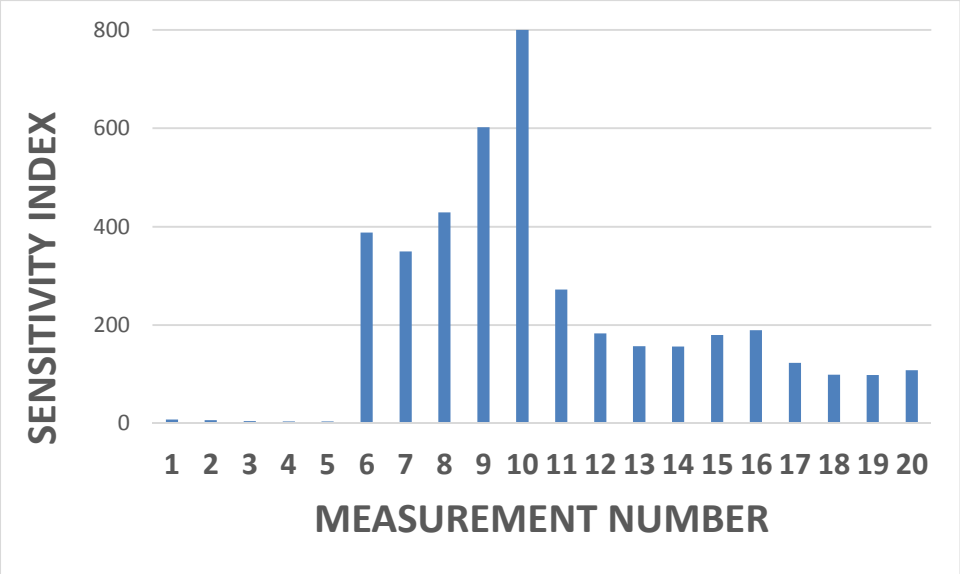

Figure 4 – The sensitivity index values of 16 different measurements having different magnetizing frequencies and voltages as tabulated in Table 2.

It should be noted that the here presented optimization of measurement parameters is only applicable to characterization of quenched and tempered AISI 4140 steels by using the standard general purpose probe of a commercial MBN system. When the design and/or magnetic properties of the probe, pick-up coil as well as the microstructure of the sample material change

another set of optimized measurement parameters should be determined. Nevertheless, the concepts and methods explained here would still be valid.

4. CONCLUSIONS

The influence of MBN measurement parameters on the validity of results were investigated on a set of quenched and tempered AISI 4140 specimens. The following points should be highlighted:

- In the as-quenched sample, pinned domain walls due to high dislocation density and small martensite needles cause low MBN activity. As tempering temperature increases dislocation density decreases, micro residual stresses diminish and the magnetic structure comes close to those of a ferrite. Thus, MBN activity gets higher due to the enhancement of domain wall displacement with softening of martensite.
- The microstructural features that impede the domain wall motion, influence the motion of dislocations in the same manner. Therefore; a linear relation between RMS of MBN signal and hardness is found; which is also used to evaluate the reliability of each set of measurement parameters.
- A too low magnetizing voltage causes the MBN signal to be indistinguishable from background noise. Increasing the magnetizing voltage, increases the sensitivity of the MBN. However; saturation magnetization is exceeded in the pick-up coil when too high magnetizing voltages are used. Therefore the most sensitive response of MBN is obtained at an intermediate magnetizing voltage which is 6V.
- The best correlation with hardness and the best sensitivity levels are reached in the range of 150 – 250 Hz magnetizing frequency. Within this range, changing the magnetizing frequency does not influence the results significantly.

This optimization work has showed that the reliability and sensitivity of Barkhausen noise technique strongly depends on the selection of measurement parameters.

REFERENCES

1. S.H. Avner, "Introduction to Physical Metallurgy", McGraw Hill, 1974
2. G. Montalenti, Zeitschrift für angewandte Physik, 28, 295, 1970
3. P. Gaunt, Can. J. Phys., 65, 1194, 1987
4. H.J. Williams, R.M. Bozorth, W. Shockley, Phys. Rev., 75, 155, 1949
5. J. Anglada-Rivera, L.R. Padovese, J. Capo Sanchez, Jnl. Magnetism and Magnetic Mater., 231, 299, 2001
6. S. Yamaura, Y. Furuya, T. Watanabe, Acta Mater, 49, 3019, 2001
7. O. Saquet, J. Chicois, A. Vincent, Mater. Sci. Eng. A, 31A, 1053, 1999
8. M. Blaow, J.T. Evans, B.A. Shaw, Acta Mater, 53, 279, 2005
9. V. Moorthy, S. Vaidyanathan, T. Jayakumar, B. Raj, Jnl. Magnetism and Magnetic Mater., 171, 179, 1997
10. V. Moorthy, B.A. Shaw, J.T. Evans, NDT&E Int., 36, 43, 2003a,
11. V. Moorthy, S. Vaidyanathan, T. Jayakumar, K.B.S. Rao B. Raj, Mater. Sci. Eng. A, 231A, 98, 1997
12. D.H.L. Ng, M.L. Wong, S.L.I. Chan, X.-Y. Ma, Mater. Sci. Eng. A, 358A, 98, 2003
13. M. Blaow, J.T. Evans, B.A. Shaw, Mater. Sci. Eng. A, 386A, 74, 2004
14. R.W.K. Bhadeshia and H.K.D.H. Bhadeshia, "Steels – Microstructure and Properties", Arnold Sevenoaksi 2005
15. Wikipedia: Pearson product-moment correlation coefficient, http://en.wikipedia.org/wiki/Pearson_product-moment_correlation_coefficient, last access: 10/07/2014
16. K. Davut, C.H. Gur, Jnl. Nondestruct. Eval., 26, 107, 2007

SYNTHESIS of TiO_2 AND TITANATE NANOPOWDERS IN VARIOUS MORPHOLOGIES VIA HYDROTHERMAL METHOD

Nursev BİLGİN[*], Jongee PARK[**], Abdullah ÖZTÜRK [*]
[*] Middle East Technical University, Ankara, Turkey
nbilgin@metu.edu.tr
abdullah@metu.edu.tr
[**] Atılım University, Ankara, Turkey
jpark@atilim.edu.tr

ABSTRACT

Titania (TiO_2) and titanate nanopowders in various morphologies were synthesized via hydrothermal method using P25 powder and 10 M NaOH-H_2O solution at temperatures of 110 and 150 ^oC for 18 h. The hydrothermal reactions were allowed to execute at autogeneous pressure at a stirring rate of 250 rpm. Products yielded from hydrothermal process were acidic treated for different times. X-ray diffraction, scanning electron microscopy, and energy dispersive spectroscopy analyses were conducted to characterize the TiO_2 and titanate products synthesized. Experimental results revealed that tubular structure or nanorods formed during the hydrothermal synthesis. Morphology of the products changed with increasing hydrothermal temperature and time. HCl acidic treatment disrupted the morphology of elongated titanates. Upon calcination of the products at 450 ^oC for 1 h, recrystallization occurred and pure anatase crystals with a spherical morphology were obtained. The photocatalytic activity of the products was evaluated in terms of the degradation of aqueous methylene blue solution under UV-light illumination for 30, 60, and 90 min.

Keywords: Synthesis, TiO_2, Titanates, Nanopowder, Morphology, hydrothermal process.

HİDROTERMAL YÖNTEMLE FARKLI MORFOLOJİLERDE TiO_2 VE TİTANAT NANOTOZ SENTEZİ

ÖZET

Değişik morfolojilerde titanya (TiO_2) ve titanat nanotozları hidrotermal yöntemle P25 tozu ve 10 M NaOH-H_2O solüsyonu kullanılarak 110 ^oC ve 150 ^oC de 18 saatte sentezlenmiştir. Hidrotermal reaksiyonların kendiliğinden oluşan basınç altında 250 rpm hızla karıştırılarak oluşması sağlanmıştır. Hidrotermal süreçte elde edilen ürünler değişik sayıda tekrar edilen asidik işleme maruz bırakılmıştır. Sentezlen TiO_2 ve titanat ürünleri X-ışını kırınımı, taramalı electron mikroskobu, ve elektron saçınım spektroskopi analizleriyle karakterize edilmişlerdir. Deney sonuçları hidrotermal sentez sırasında tabular yapıda nanotel ve nanoboru şeklinde titanatların oluştuğunu ortaya çıkmıştır. Ürünlerin morfolojisi artan hidrotermal sıcaklığı ve süresiyle değişmişir. HCl asitle yapılan işlem tek boyutlu titanatların morfolojisini bozmuştur. Ürünlerin 450 ^oC'de 1 saat süreyle yapılan ısıl işlemi yeniden kristallenmeye neden olmuş ve küresel morfolojide saf anataz kristalleri elde edilmiştir. Ürünlerin fotokatalitik aktivitesi metilen mavisi çözeltisinin UV ışık altında 30, 60, ve 90 dakika bozunumuna göre değerlendirilmiştir.

Anahtar kelimeler: Sentez, TiO_2, Titanatlar, Nanatoz, Morfoloji, hidrotermal yöntem.

1. INTRODUCTION

In modern societies ecological friendship of materials plays an important role and thus emerging ecological concerns are invariably ensuing [1]. Titania (TiO_2) is a well-researched photocatalyst due to its chemical stability, biocompatibility, physical, optical, and electrical properties [2]. These desirable engineering properties enable TiO_2 to be used in various environmental, medical, optical, cosmetic and energy related applications such as paint pigments, sunscreen lotions, capacitors, solar cells, tooth pastes and food coloring agents [2,3]. It is possible to synthesize TiO_2 nanostructures in various morphologies via sol-gel, precipitation, solvothermal and hydrothermal methods [4-6]. TiO_2 nanotubes are synthesized also using anodizing and assisted template method [7,8].
The discovery of carbon nanotubes intrigued the researches of one-dimensional nanostructures, such as nanotube, nanorod, nanowire, and nanobelts. TiO_2-based nanotubes, therefore, attracted extensive interest due to its high specific surface area, ion-exchange ability, and photocatalytic ability [9,10]. Apart from TiO_2, some titanate structures such as $M_2Ti_2O_5.H_2O$, $M_2Ti_3O_7$, and $M_2Ti_4O_9$ (M=H or Na) have been confirmed as nanotube components [11-13].
Tubular nanotube (TNT) structures could be synthesized through the treatment in acidic or basic solutions [14]. The treatment in basic solution is conducted either chemically or hydrothermally under significant pressures and generally followed by other post treatments such as washing and calcination. TNT structure is formed during hydrothermal treatment and post treatments are critical for nanotube formation [15,16]. The post treatments enhance the morphology, remove the impurities, and stabilize the pure phase [17,18]. It is possible to synthesize TiO_2 or titanate nanotubes intelligently using a catalyzing media via hydrothermal method.
The purpose of this study was to investigate the influence of acid treatments on the morphology of the elongated titanate structures synthesized via hydrothermal process and to characterize the products using SEM and XRD characterization techniques.

2. EXPERIMENTAL

2.1. Powder Synthesis

Na- and H- titanates were synthesized through hydrothermal method at temperatures of 110 and 150 ^oC for 18 h in concomitant with the procedure followed by Ou and Lo [5]. Hydrothermal synthesis began by mixing 2 g of commercially available TiO_2 powder (P25, Degussa) with 10 M NaOH aqua solution under ultrasonic stirring for 10 min. The mixture was then placed into the pressure vessel of the reactor and heated to predetermined synthesis temperature at a rate of 5 ^oC/min. It was kept at this temperature for 18 h while continuous stirring at a rate of 250 rpm. The autogeneous pressure formed in the vessel was about 10 bars. Then, the mixture was cooled down to room temperature at a rate of 5^o C/min. The resultant product was taken out of the vessel, filtered, and washed with distilled water several times. After that, it was dehydrated to evaporate free H_2O at 60 ^oC for 6 h. After dehydration, the product was mixed with 0.1 M HCl acidic solution in a glass beaker while magnetic stirring for 10 h. This process was repeated 2 and 4 times to see the influence of the number of acid treatments on the morphology of the product synthesized. After each treatment, the product was washed with distilled water, filtered again, and dried in an oven at 60 ^oC. Finally, the products were calcined at 450 ^oC for 1 h at a rate of 5^o/min.

2.2. Characterization

The crystalline phases present and amount of crystallinity in the products were determined by using an X-ray diffractometer (Rigaku, D/MAK/B, Japan). X-ray diffraction (XRD) analysis was conducted using CuKα radiation (λ=1.5406 ^{o}A) at a rate of 2^{o}/min from 20^{o} to 80^{o}. Morphologies of the products were examined by using scanning electron microscopy (FE-SEM, Nova Nanosem 430, USA) at 20 kV operating voltage. The size of the products was measured also by using SEM.

2.3. Photocatalytic activity

The photocatalytic activity of the products was evaluated in terms of the degradation of aqueous methylene blue (MB) solution under UV-light illumination using a 100-W UV lamp (UVP Co, Canada.) for 30, 60, and 90 min of illumination. UV-vis spectrophotometer (Scinco S-3100, Korea) was employed to measure the photocatalytic activity at the wavelength of 664 nm. UV-vis absorption was measured between 200 and 800 nm. The changes in absorption and absorption percentage were calculated with respect to illumination time.

3. RESULTS AND DISCUSSION

Hydrothermally synthesized products were coded regarding to the hydrothermal temperature, applied number of acidic treatment repetition, and calcination temperature. The codes of the products are listed in Table 1.

Table 1. Product code list and their production conditions.

Code	Hydothermal Temperature (^{o}C)	Acidic Treatment Repetition	Calcination Temperature (^{o}C)
HB	110	No	No
HB1	150	No	No
HB2	150	2	No
HB3	150	4	No
HB4	150	4	450

3.1. X-Ray Diffraction (XRD)

X-ray diffraction analysis revealed that the products hydrothermally synthesized at temperatures of 110 and 150 ^{o}C consisted of different Na-titanates. $Na_2Ti_3O_7$, $Na_2TiO_4.H_2O$, and $Na_2Ti_6O_{13}$ phases were identified in the XRD patterns. Besides Na-titanates, different salts were also detected because of ineffective washing of the products. No significant change was observed in the SEM images of the products hydrothermally synthesized at 110 and 150 ^{o}C, implying that an increase in hydrothermal synthesis temperature from 110 ^{o}C to 150 ^{o}C is inconsequential in terms of the phases formed during hydrothermal reactions. However, crystallinity increased at 150 ^{o}C. Therefore the product hydrothermally synthesized at 150 ^{o}C for 18 h (HB1) has been selected for the determination of the effects of acid treatments on the morphology of the crystalline phases.

XRD patterns of the products in the form of untreated, acid treated, and calcined after acid treatment are shown in Figure 2. After twice acidic treatment with 0.1 M HCl aquaus solution, $H_2Ti_2O_4(OH)_2$ and $Ti_4H_2O_9.1.9H_2O$ phases formed by exchanging Na^+ ions with H^+ ions though Na-titanates remained. Further acidic treatments caused diminishment of Na-titanates although some Na- and H- titanates and NaCl existed.. XRD peaks corresponded well to the $H_2Ti_2O_4(OH)_2$ phase When the product is calcined at 450 ^oC for 1 h, recrystallization occurred and only anatase phase (tetragonal, $I4_1/amd$, JCPDS 21-1272) was detected in the XRD pattern.

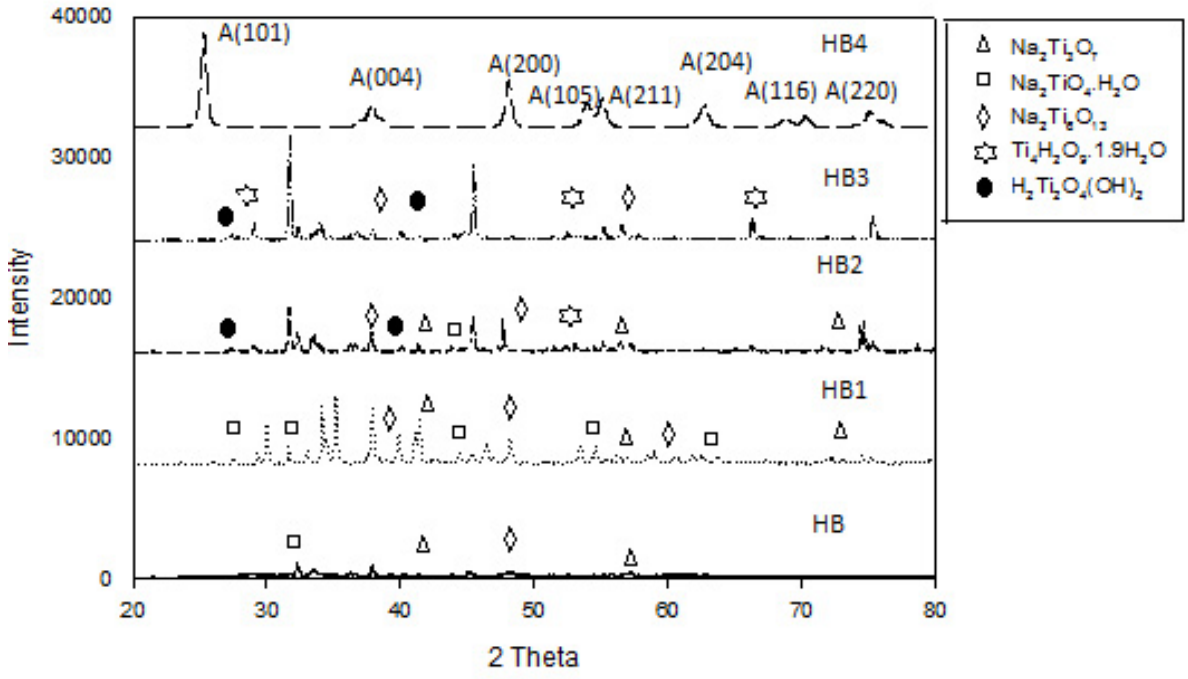

Figure 1. X-ray diffraction patterns of the products.

3.2. Scanning Electron Microscopy (SEM) and Energy Dispersive Spectroscopy (EDS)

Figure 2 shows the longitudinal SEM images of the products. The structure could be both tubular or rod-like which is not very clear in the SEM images. Tubular or nanorod morphology was seen in the product HB1 as seen in Figure 2.b. Product HB2 which was acidic treated twice did not show any significant change in shape and size as compared to the product HB1. The mean diameter and length of Na-titanate nanotubes are about 60 nm and 50 μm, respectively. The EDS spectrum of the product HB1 shows a large peak of Na as seen in Figure 3.a. After acidic treatment twice Na content decreased considerably as seen in Figure 3.b without causing a significant change in the product morphology, see Figure 2.c. However after the 4^{th} acidic treatment, structure of the product turned into needle like arrays as seen in Figure 2.d and no Na peak was observed in the EDS spectrum, see Figure 3.c. SEM image of the product calcined after 4^{th} acidic treatment shows sphere like morphology implying that whole structure was recrystallized as seen in Figure 2.e. Also as seen in Fig 2.c, there are some salts adsorbed on the surface of the nanotubes or nanorods.

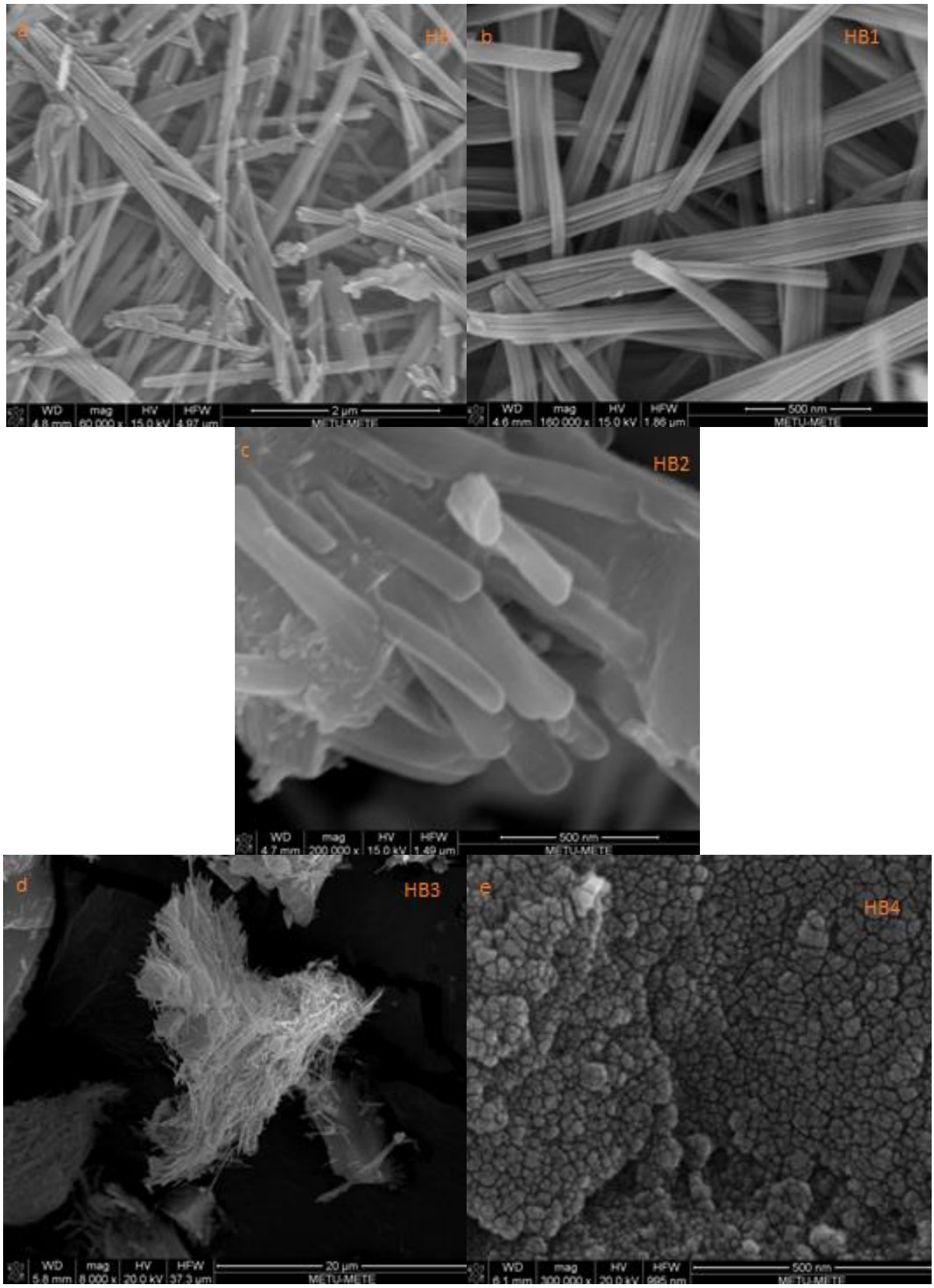

Figure 2. SEM images of the products a) HB, b) HB1, c) HB2, d)HB3, and e) HB4.

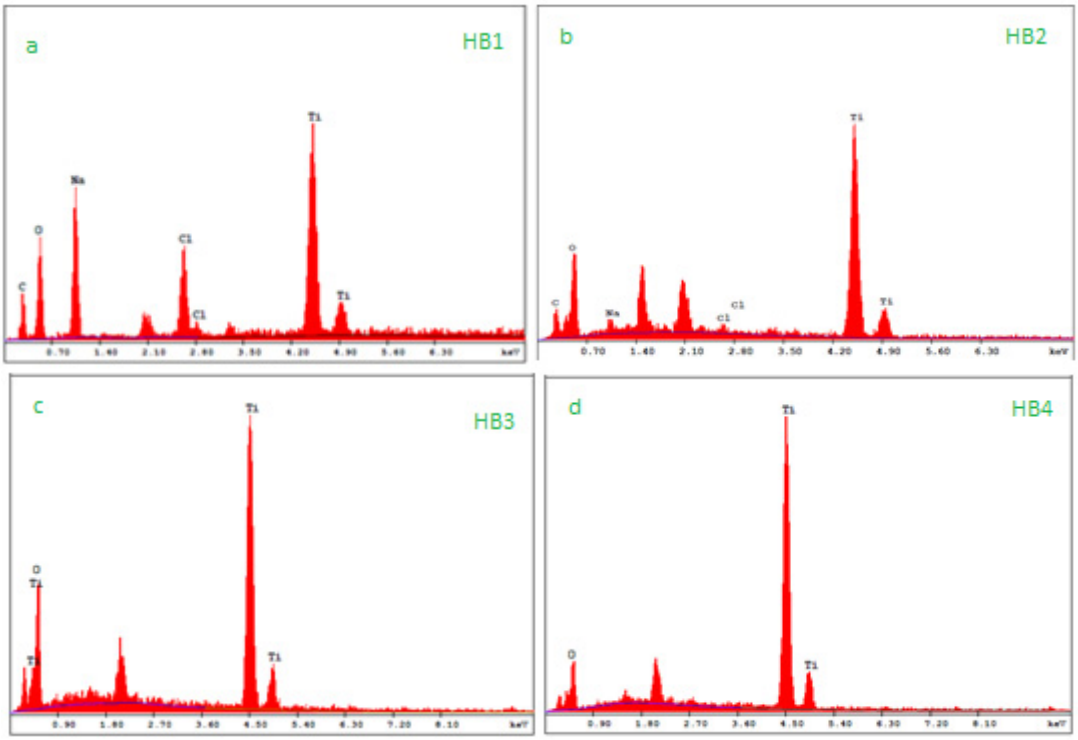

Figure 3. EDS spectra for a) HB1 and b) HB2 c) HB3 d) HB4

As seen in SEM images tubular structure present right after the hydrothermal synthesis in the Na-titanate tubes formed by scrolling of the sheets. Kasuga et al.[16] suggested that TNTs formed after acidic treatment while Peng et al.[17] reported that TNTs form during the reaction of TiO_2 with NaOH at some stage in the hydrothermal synthesis. Peng et al.[17] also noted that nanosheets formed by the reaction between TiO_2 and NaOH grow with an increasing tendency of curling, causing the formation of nanotubes. In another study the mechanism where the hydrogen deficiency on the surface of $(Ti_3O_7)^{2-}$ plates forces them to curl up was emphasized [5]. In the present study it is observed that TNTs are formed during the hydrothermal treatment in the formula of $Na_xTi_2O_x$. Right after hydrothermal synthesis nanotubes are already present in the structure. Even if they are formed during washing process by de-ionized water, it is proven that they have great tendency to curl up since a simple water treatment makes them curled up.

3.3. Photocatalytic Activity Measurement

The photocatalytic activity (MB degradation) test results are given in Figures 4 and 5. MB degradation test results are highly depend on molarity of the MB solution. In order to get over that complication Langmuir-Hinselwood kinetic model (Equation 1) was taken into consideration to calculate rate constant (k) of degradation kinetics.

$$-\ln(C/C_o) = kt \quad (1)$$

Where, C_0 is initial concentration of MB, C_t is MB concentration at a given time, k is apparent rate constant, t is time.

Photocatalytic activity is related with the crystallinity which inhibits electron-hole (e^-/h^+) recombination. Surface area, effective absorbance of dye, crystal structure, morphology, porosity and particle size have also effects indirectly in a similar way [19,20]. The highest degradation of MB was obtained with the product HB4 due to the highest crystallinity in this product as compared to the Na- and H- titanates. It is composed of only anatase phase and anatase phase offers the best photocatalytic performance among the other TiO_2 phases due to its longer e^-/h^+ pair life [21-23]. Other than the product HB4, in the first 60 min of UV illumination the products HB1, HB2 and HB3 exhibited almost the same performance. However after 60 min of UV illumination, MB degradation performance of the product HB1 and HB2 were better than that of the product HB3. This result may rise due to the decrease of surface area of the tubes as seen in Figure 2. The product HB3 which contains H-titanate phases had the less photocatalytic performance as expected because the morphology was destroyed and surface area was decreased in this product. Linear fitting in figure 5 suggests that data follow a linear path and are in a good agreement with each other.

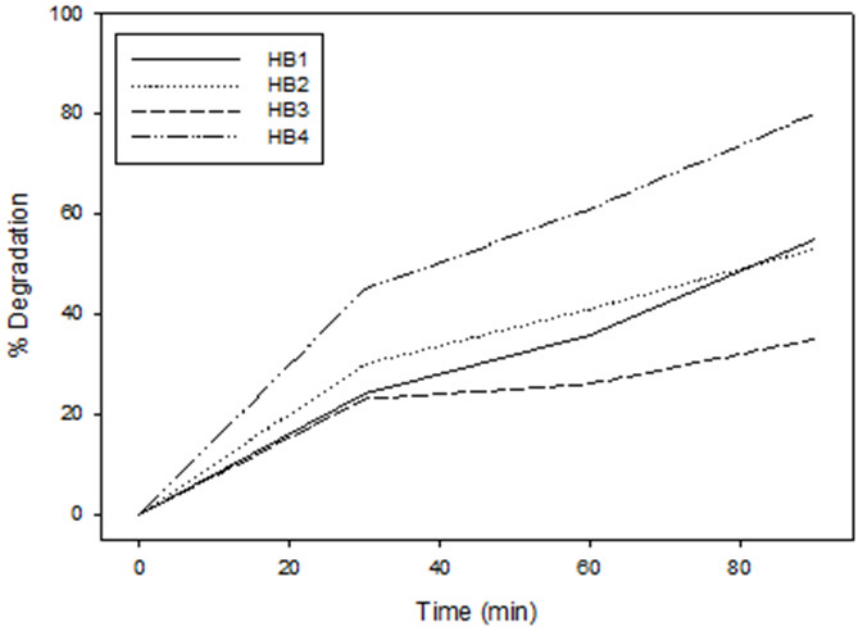

Figure 4. Methylene blue degradation of the products with respect to UV irradiation time.

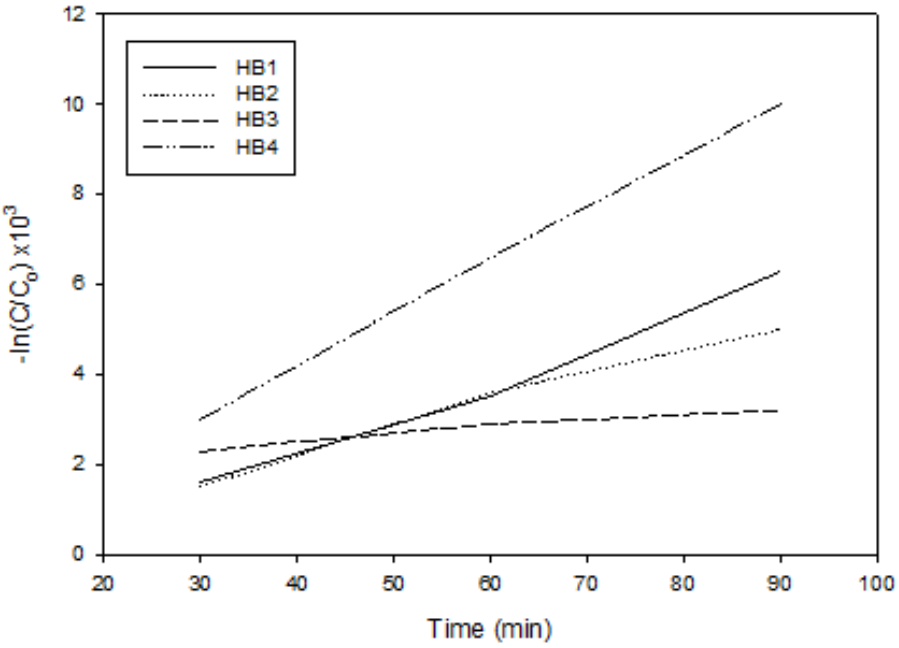

Figure 5. Rate constant of the products with respect to UV irradiation time.

4. CONCLUSIONS

Upon hydrothermal treatment of TiO_2 powder (P25) with 10 M NaOH aqua solution a disordered phase with elongated structure is formed. The exact form of the hydrothermal products could not be determined from SEM analysis. XRD analysis suggested that this disordered structure is composed of a mixture of $Na_2Ti_6O_{13}$, $Na_2Ti_3O_7$, and $Na_2Ti_2O_5$ phases. After washing with HCl, the Na-titanate phases could be converted to $H_2T_2O_5H_2O$ by exchanging ions H^+ and Na^+. Phase pure TiO_2 could not be obtained by ion exchanging because the structure started to be destroyed with repitation of the ion exchange process. A simple calcination process at 450 ^oC for 1 h causes recrystallization and results in formation of phase pure, spherical anatase TiO_2 nano-particles. TNT structures have weaker photocatalytic activity as compared to anatase particles. Changing process variables or modifying the structure may lead to the formation of different types of titanates with better photocatalytic activity than anatase phase.

ACKNOWLEDGEMENT

The authors would like to thank Middle East Technical University for the partial financial support to carry out the experiments through OYP Project.

REFERENCES

1. M. Gratzel, Nature, 414, 338-344, 2011.
2. A. D. Paola, M. Bellardita, L. Palmisano, Catalysts, 3, 36-73, 2013.
3. W. Yuanhao, Novel Structure Dye Sensitized Solar Cells Based on Highly Ordered Titania Nanotube arrays, PhD Thesis, The Honkonk Polytechnic University, 2011.
4. C.-H. Lee, S.-W. Rhee, H.-W. Choi, Nanoscale Res. Lett., 7-48, 2012.
5. H. H. Ou, S. L. Lo, Sep. Purif.n Technol., 58, 179-191, 2007.
6. P. Hoyer, Langmuir, 12, 1445-1447, 2002.
7. C. C. Tsai, H. Teng, Chem Mater., 18, 367-373, 2005.
8. T. Sekino, App. Phys., 117, 17-32, 2010.
9. J. H. Lee, I. C. Leu, M. C. Hsu, Y. W. Chung, M. H. Hon, J. Phys. Chem.B, 109, 13056-13059, 2005.
10. M. Zhang, Z. Jin, J. Zhang, X. Guo, J. Yang, W. Li, X. Wang, Z. Zhang, j. Mol. Catal. A: Chem., 217, 203, 2004.
11. M. Myahkostupov, M. Zamkov, F. N. Castellano, Energy Environ., Sci., 4, 998, 2011.
12. D. S. Seo, J. K. Kim, H. Kim, J. Crystal. Growth, 229, 428-432, 2001.
13. R. Ma, Y. Bando, T. Sasaki, Chem. Phys. Lett., 380, 577, 2003.
14. H. Zhu, X. Gao, Y. Lan, D. Song, Y. Xi, J. Zhao, J. Am. Chem. Soc., 125, 14539, 2003.
15. Luttrell, S. Halpegamage, J. Tao, A. Kramer, E. Sutter, M. Batzill, Sci. Rep., 4, 4043, 2013.
16. T. Kasuga, M. Hiramatsu, A. Hoson, T. Sekino, K. Niihara, Adv. Mater., 11, 1307-1311, 1999.
17. G. H. Du, Q. Chen, R. C. Che, Z. Y. Yuan, L. M. Peng, Appl. Phys Lett., 79, 3702-30704, 2001.
18. M. M. Byranvanda, A. N. Kharata, L. Fatholahib, Z. M. Beiranvand, JNS, 3, 1-9, 2013.
19. W. Q Wu, H. S. Rao, Y. F. Xu, Y. F. Wang, C. Y. Su, D. B. Kuang, Sci. Rep.. 3, 1892, 2013.
20. H. Huang, L. Pan, C. K. Lim, H. Gong, J. Gu, M. S. Tse, O. K. Tan, small, 18, 3153-3160, 2013.
21. O. K. Varghese, D. Gong, M. Poulose, C. A. Grimes, E. C. Dickey, J. Mat. Res., 18, 156-165, 2003.
22. O. Sheikhnejad-Bishe, F. Zhao, A. Rajabtabar-Darvishi, E. Khodadad, Y. Huang, Int. J. Electrochem. Sci., 9, 3068 – 3077, 2014.
23. Luttrell, S. Halpegamage, J. Tao, A. Kramer, E. Sutter, M. Batzill, Sci. Rep., 4, 4043, 2013.

The effect of the contact cycles on the microstructure and performance of electrical contact materials

Aykut Canakci[a*], Temel Varol[a], Hüseyin İpek[a], Sinan Amran[b]

[a]Department of Metallurgical and Materials Engineering, Engineering Faculty,
[b]
Karadeniz Technical University, Trabzon, Turkey.
aykut@ktu.edu.tr

Abstract
Electrical arc erosion plays a crucial role in the reliability and life of electrical contact materials. Moreover, the arc erosion resistance of the contact materials is a very important parameter for the long lifetime of electrical contacts. In this study, the effect of the contact cycles on the microstructure and performance of electrical contact materials was studied. Contact performance of electrical contact materials was investigated for determining contact performance for different contact cycles. The results showed that the weight loss of electrical contact material increased with increasing the number of contact cycles. Moreover, surface image showed that the arc erosion resistance of electrical contact material decreased with increasing contact cycles.

Keywords: Electrical contact materials; arc erosion; contact performance; microstructure

Elektrik kontak malzemelerinin mikroyapısı ve performansı üzerine kontak çevriminin etkisi

Aykut Çanakçı[a*], Temel Varol[a], Hüseyin İpek[a], Sinan Amran[b]
[a]Metalurji ve Malzeme Mühendisliği Bölümü, Mühendislik Fakültesi,
Karadeniz Teknik Üniversitesi, Trabzon, Türkiye
aykut@ktu.edu.tr

Özet
Ark erozyonu elektrik kontaklarının verimli çalışması ömrü üzerinde kritik bir öneme sahiptir. Ayrıca ark erozyon direnci elektrik kontak malzemelerinin çalışma ömrünü etkileyen çok önemli bir parametredir. Bu çalışmada elektrik kontak malzemelerinin mikroyapısı ve performansı üzerine kontak çevrim sayısının etkisi araştırılmıştır. Sonuçlar artan açma kapama sayısı yani çevrim sayısı ile kontak malzemelerindeki ağırlık kaybının arttığını göstermiştir. Ayrıca artan çevrim sayısı ile ark erozyon direncinin azaldığı gözlemlenmiştir.

Anahtar Kelimeler: Elektrik kontak malzemeleri, ark erozyonu, kontak performansı, mikroyapı

I. INTRODUCTION

Electrical contact materials are used in a variety of applications, such as electrical switches, contactors, circuit breakers, voltage regulators, arcing tips, switch gears and relays. Materails used as electrical contacts in these applications must have a good combination of electrical conductivity, wearing qualities and resistance to erosion and welding. Otherwise, the contacts will erode, causing poor contact and arcing. Arcing takes place when contacts are in the process of establishing a current flow or interrupting the flow of current. Arc is characterized by high temperature and a high current density in the arc column. Because of the high temperature and mass flow, the contact material surface is severely corroded and eroded, which results in erratic contact resistance and material loss. Therefore a contact material should have high electrical and thermal conductivity, high melting point, and high resistance to enviromental reaction, as well as high arc erosion to maintain contact integrity [1-2]. Silver-Nickel contact materials produced by powder metallurgy are used extensively as contact materials due to their high conductivity, good resistance to welding and low contact resistance and low arc erosion and good formability. Electrical arc erosion has a critical effect for reliability and life of electrical contact materials. Therefore, the objective of this research is to investigate the arc erosion behavior of Ag-Ni electrical contact materials. Contact count experiments were employed for determining contact performance for counts of 3000, 8000, 18000, 30000, 50000 and 100000.

2. EXPERIMENTAL

In this study, commercial Ag-Ni materials (Siemens) were used as electrical contact materials (Fig. 1). Experimental setup used for contact count experiments in this work is shown in Fig. 2. Zeiss Evo LS10 scanning electron microscope (SEM) equipped with an energy dispersive spectroscopy (EDS) was used to characterize the microstructure of the contact samples. SEM images were focused on the study of the evolution of the contact surface with the number of electrical arcs under the contact cycles. The electrical contacts were subjected to turn on/off counts with 3000, 8000, 18000, 30000, 50000 and 100000 cycles. Weight loss of the samples was measured by a precision (10^{-5} g) weighing scale.

Figure 1. Ag-Ni electrical contact materials

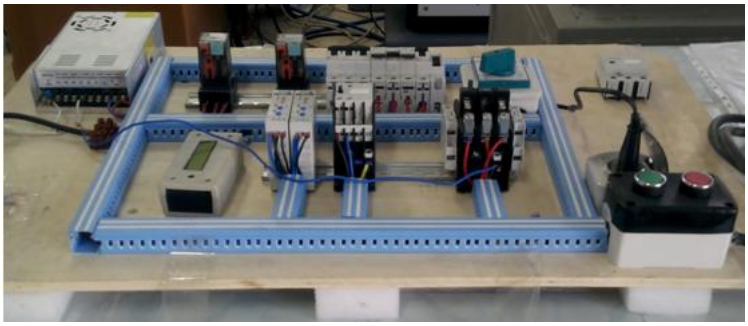

Figure 2. Experimental setup for contact cycles

3. RESULTS AND DISCUSSION

3.1. Surface Morphology

Fig. 3 shows the surface morphology of Ag-Ni electrical contact materials after different contact cycles. As can be seen in Fig. 3, the region of deformation, melting and porosity occurred with increasing cycle number. In other words, it can be seen that the most serious arc erosion was formed in the central or contact region. It should be noted that the amount of deformation during turn on/off of contact increased and deformation region expanded. Compared Fig. 3a-c it can be found that the arc erosion and deformation areas in the initial of contact cycles (3000 turn on/off) were smaller than that of the longer contact cycles (100000 tun on/off). The temperature in the contact zone constantly increased due to arc and contact resistance and so local melting and materials loss were observed in the contact materials.

Low Magnification **High Magnification**

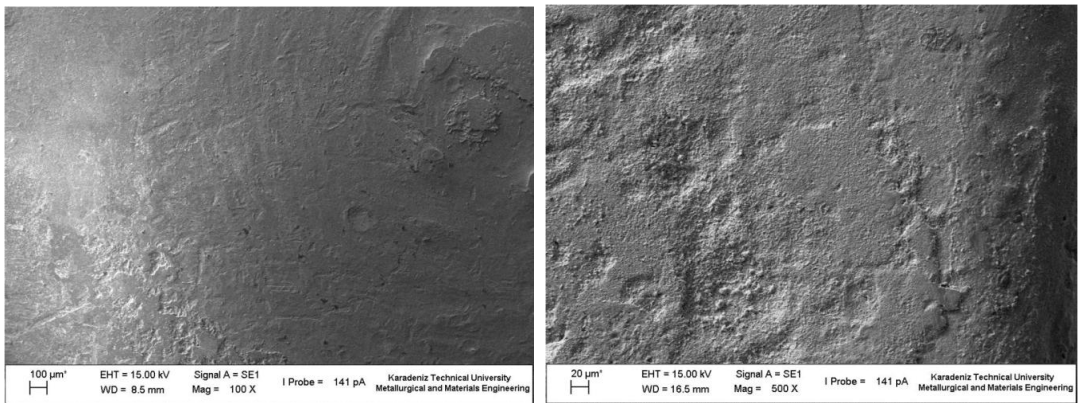

(a)

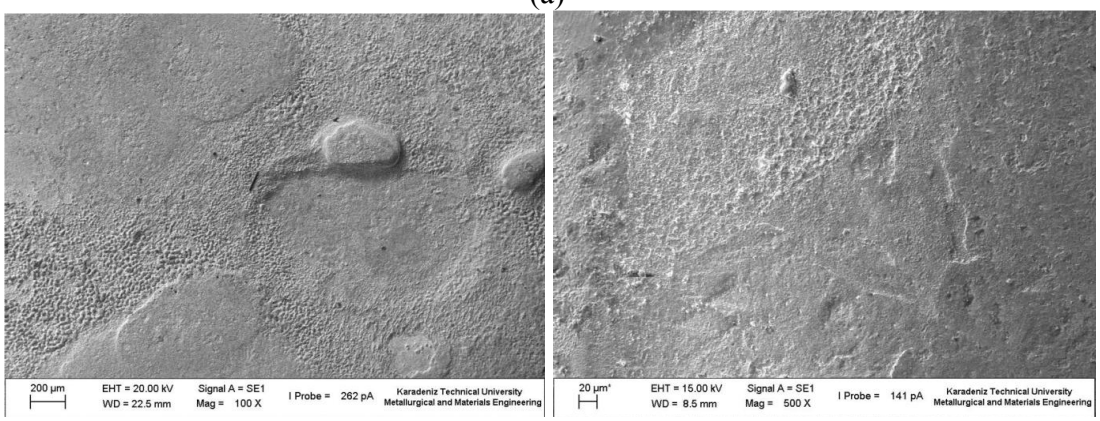

(b)

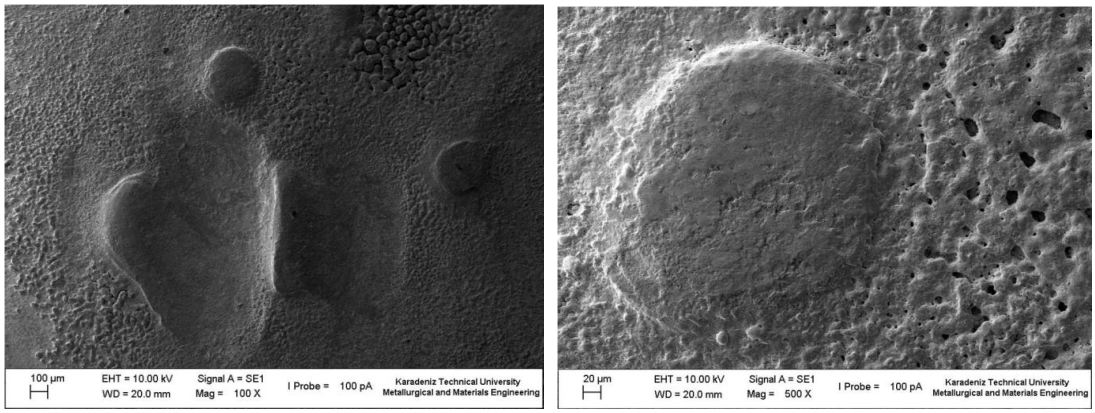

(c)

Figure 3. SEM image of Ag-Ni electrical contact after counts of (a) 3000 turn on/off, (b) 50000 turn on/off, (c) 100000 turn on/off.

3.2. Weight Loss

Fig. 4 shows the change of weight loss of Ag-Ni contacts with increasing contact cycle. As can be seen in Fig. 4, weight loss increased with increasing contact cycle. It was suggested that the increasing contact count adversely affected the arc erosion behavior of contact samples. However, the weight loss of upper and lower contact samples is different. The difference of weight loss between contact samples can be attributed to the effect of local melting and contact welding. With the increase of the temperature during turn on/off process, less continuous lubricating film was formed, therefore the weight loss increased. Moreover, material transfer from upper contact to lower contact or from lower contact to upper contact has previously been observed in opening and closing electrical contacts [3-5].

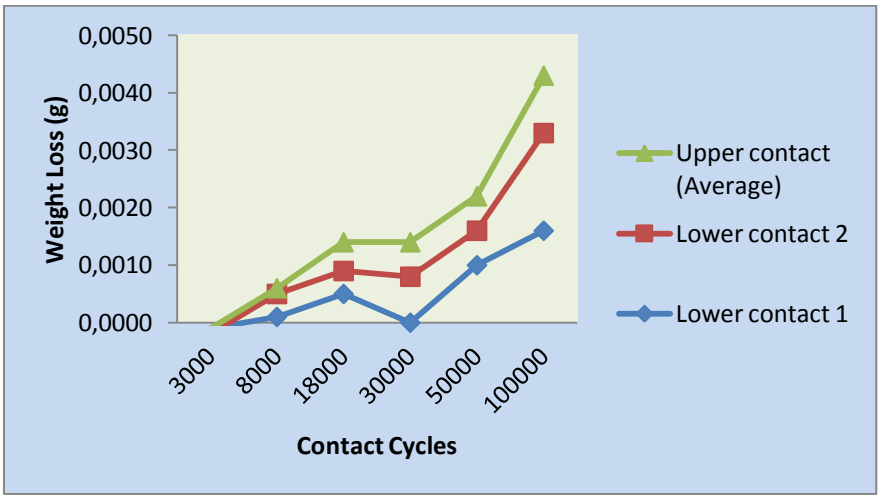

Figure 4. The change of weight loss with increasing contact cycle

Fig. 5 shows EDS spot analysis results after counts of 100000 turn on/off, which was composed by elements of Ag, Ni and O. The reason of oxygen element in the EDS spot analysis was surface oxidation during opening and closing operations.

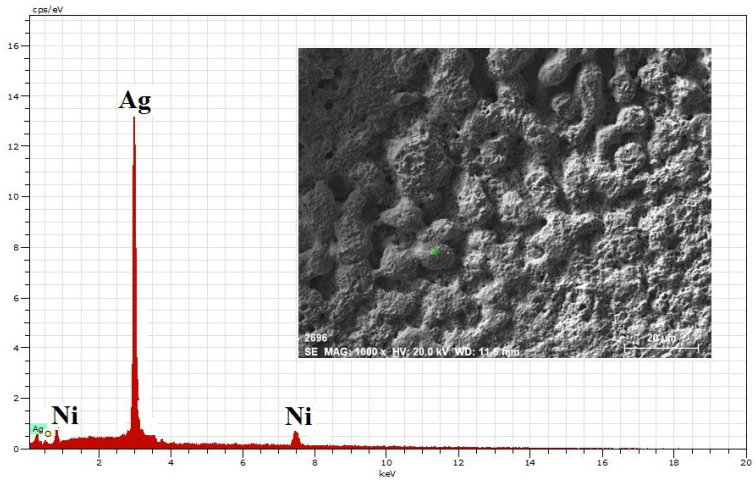

Figure 5. EDS spot analysis of the surface of contact samples after counts of 100000 turn on/off

4. CONCLUSIONS

The commercial Ag-Ni materials (Siemens) were employed to turn on/off experiments from 3000 to 100000 counts. The microstructure of the Ag-Ni electrical contact revealed that there is a good correlation between the number of counts and lifetime of electrical contacts. With increasing the number of count increased arc erosion and deformation and therefore weight loss of Ag-Ni electrical contacts increased. It should be noted that a combination of condition of working and materials has to be met in order to reach the desired contact performance. Oxygen content was observed by surface oxidation during opening and closing operations.

REFERENCES

[1] O. Güler and Ertan Evin, J. of Mater. Process. Technol. 209, 1286, 2009
[2] C.P. Wu, D.Q. Yi, J. Li, L.R. Xiao, B. Wang and F. Zheng, J. of Alloys and Compd. 457, 565, 2008
[3] F. Findik and H. Uzun, Mater. Des. 24, 489, 2003
[4] V.V. Bukhanovsky, N.I. Grechanyuk, R.V. Minakova, I. Mamuzich, V.V. Kharchenko and N.P. Rudnitsky, Int. J. Refract. Met. Hard. Mater., 29, 573, 2011
[5] Q. Li, W. Jie, L. Fu, X. Zhang, X. Wang, X. Bai and G. Zha, Mater. Sci. and Eng. B 135, 15, 2006

PRODUCTION AND DEVELOPMENT OF DYE-SENSITIZED SOLAR CELLS ON FLEXIBLE POLYMERIC SUBSTRATES BY BINDER-FREE ELECTROPHORETIC DEPOSITION METHOD WITH A SUBSEQUENT COLD ISOSTATIC PRESSING TREATMENT

Bahadır Can KOCAOĞLU*,[a], Ahmet Macit ÖZENBAŞ*,[a]

* Middle East Technical University, Metallurgical and Materials Eng. Dept., Ankara, Turkey
[a]Center for Solar Energy Research and Applications (GÜNAM), Middle East Technical University, Ankara, Turkey
kocaoglu@metu.edu.tr , ozenbas@metu.edu.tr

ABSTRACT
Electrophoretic Deposition (EPD) of titania nanoparticles have been utilized in order to form the nanoporous photoanodes of dye-sensitized solar cells (DSSCs) on flexible polymeric (PEN/PET) substrates. Highly uniform, adherent nanoporous thick films were produced by uniformly dispersing the titania nanoparticles in alcoholic suspensions without any binders. Suspension performances of each type of alcohols and mixtures of which have been examined. Additionally, the effect of acetylacetone addition in suspensions on zeta potential and effective particle size of the colloids are investigated. EPD process has been conducted in single step while the uniformity of the morphology and the thickness of the films were maintained preventing the damage on ITO layer due to excessive voltage exposure. Subsequently, the mechanical compression is applied via Cold Isostatic Pressing (CIP) with a pressure profile in order to obtain 12-14 μm film thickness and photon to current conversion efficiency of 3.0 % under AM1.5.

Keywords: Flexible dye sensitized solar cell, Electrophoretic deposition, EPD, Cold isostatic pressing, CIP

BOYA DUYARLI GÜNEŞ GÖZELERİNİN ESNEK POLİMER TABANLIKLAR ÜZERİNE ELEKTROFORETİK KAPLAMA VE SOĞUK İZOSTATİK PRESLEME YÖNTEMİ İLE ÜRETİMİ VE GELİŞTİRİLMESİ

ÖZET
Elektroforetik kaplama, titanyum diyoksit nano parçacıklarının, esnek tabanlıklar (ITO/PEN) üzerine biriktirilerek, boya duyarlı güneş gözelerinin fotoanotlarını üretmek amacıyla kullanılmıştır. Oldukça homojen ve kaliteli kaplamalar, hiç bir yüzey ajanı kullanmaksızın alkol bazlı kolloid süspansiyonlarından elde edilmiştir. Ayrıca, genel olarak en çok kullanılan yüzey ajanı olan asetilasetonun etkisi de zeta potansiyel ve efektif parçacık boyutu ölçülerek incelenmiş ve katkısız süspansiyonlarla karşılaştırılmıştır. Son olarak, soğuk izostatik presleme işlemi alternatif baskılama profili ile gerçekleştirilmiş ve filmlerin hem tabanlıkla hem de parçacıkların birbirleriyle olan bağı kuvvetlendirilmiştir. Son ürün olarak ortaya çıkan fotoanotların kaplama kalınlıkları 12-14 μm olarak ayarlanmıştır. Üretilen foto anotlar, boya duyarlı "esnek" güneş gözeleri olarak birleştirilmiş ve % 3,0 verimliliğe sahip gözeler AM1.5 koşulları altında elde edilmiştir.

Anahtar kelimeler: Esnek boya duyarlı güneş gözeleri, Elektroforetik kaplama, Soğuk izostatik presleme

INTRODUCTION

Dye-sensitized solar cells (DSSC) are one of the most cost effective and versatile alternative for common p-n junction solar cells. Unlike p-n junction photovoltaics, its unique working principle provides efficient low radiation light harvesting properties [1]. Remarkable efficiency values of 10.1 % [2], 11 % [2], 12 % [3] have been reported during the past few years. The fabrication of DSSC on flexible polymeric substrates is possible and relatively efficient such that some commercial application were introduced [4-6]. The most challenging part of such fabrication is the deposition and formation of titania mesoporous thick film on polymeric substrates. Alternatively, several different methods such as low temperature volatile paste deposition by screen printing, doctor blade and deposition of titania nanoparticles by using electrophoretic deposition were used to fabricate dye sensitized solar cells on flexible substrates.

Deposition of titania layer using low temperature volatile paste via doctor blade method had been conducted by Shao et al [7] with subsequent Cold Isostatic Pressing giving an efficiency of 2.87 % at 300 MPa with the final titania layer thickness of 3.2 μm. Weerasinghe et al. [8] also used doctor blade method with subsequent CIP technique and reported 6.3 % efficiency value with 12.3 μm thickness; while, Peiris et al. [9] reported 4.39 % efficiency with subsequent static mechanical compression. Similarly, Ke et al. [10] reported 4.92 % efficiency using doctor blade and mechanical compression techniques applied on titania beads.

Utilization of electrophoretic deposition technique was reported to have highly promising results. Chen et al. [11] reported 4.57 % efficiency using anhydrous ethanol and acetylacetone colloid solution for EPD technique with subsequent mechanical compression. Prepared colloid solution contained 3 g/L solid to liquid ratio with 1:3 ST-41 to P-25 weight ratio. Applied voltage values were in the range of 5 to 25 V. Similarly, Yin et al [12] conducted EPD applying 1.6 V/cm electric field with a mixture of ethanol/isopropanol/butanol as colloid medium with subsequent mechanical compression of 1 ton/cm^2. Assembled cells exhibit 5.76 % efficiency, pointing the remarkable effect of compression on coated electrodes.Chiu et al. [13] reported 6.63 % efficiency values using P-90 for EPD colloids with titania to isopropanol ratio of 0.25 g/100 mL.

There are also studies on not only titania nanoparticles but also titania nanotubes coated by EPD method. Kim et al. [14] synthesized titania nanotubes from commerical P-25 titania nanoparticles suspending 1 ml of nanotube precipitates in 30:70 methanol and distilled water solution at 40 V of applied voltage for 60 min. The coating is conducted on FTO-glass substrates, resulting in 6.71 % efficiency. Another study suggests EPD coating of titania nanoribbons which are synthesized from commercial anatase particles treated with NaOH in autoclave resulting in 0.87 % efficiency [15]. The titania nanoribbons are reported to have pH 5.5 isoelectric point [16,17]. Another nanoribbon EPD process was carried out by mixing 1.5 g of nanoribbons with 30:70 ethanol:distilled water solution with an adjusted pH value of 9 by tetra-metyl ammonium hydroxide [18].

The most important limiting factor of fabrication of DSSC on polymeric substrates is the impossibility of heat treatment of the photoanodes. Therefore, as a pseudo sintering process in order to form solid, mechanically stable films, compression of the substrates take place. Compression has been used as a completing process for the formation of the films as mentioned previously. Apart from uniaxial compression processes [19,20], cold isostatic

process (CIP) has been introduced. Peng et al. [21] reported 4.0 % efficiency using doctor blade method for coating and CIP as subsequent process applying 50, 100 and 200 MPa of compression at different durations. As mentioned before, Weerasinghe et al. [8] and J. Shao [7] applied CIP process in order to provide mechanical stability and increased titania nanoparticle interaction.

In this study, binder-free EPD coating with simplest colloid solutions was applied in order to obtain a rapid and stable production of titania coatings for flexible DSSC photoanodes. Furthermore, subsequent CIP process is applied on the substrates to increase the nanoparticle interaction and mechanical stability by optimizing a pressure profile.

EXPERIMENTAL METHOD

In order to determine the simplest binder-free EPD solution, 2 different types of solutions which are solutions of bare ethanol and ethanol with acetylacetone additive solutions were prepared. Non-acetylacetone additive solutions were prepared by the mixture of 100 mL of ethanol with 0.50 gr of P-25 particles with addition of 2 – 3 mL of deionized water in order to trigger the ionizing and selective effects of the alcohol media. The solution with acetlyacetone addition were prepared by adding ~1 mL of acetylacetone. After stirring the solutions on magnetic stirrer for 24 hours, each solution was homogenized by using ultrasonic solution homogenizer for 90 min. at 20 kHz, 70 W. EPD process was conducted under constant voltage conditions with applied potential differences of 5 V for each solution and current vs time characteristics during coating were in-situ plotted.

Dried specimens were vacuum sealed in 2 layers of polyethylene bags for compression of P-25 particles. Compression is applied for 10 minutes of effective pressure duration at 150, 225 and 300 MPa. The compressed films, then dried at 100° C. Indium tin oxide (ITO) coated PEN substrates (~15 Ω/□, Peccell Technologies, Inc., Japan) were washed with mild soap, rinsed with deionized water, ethanol and isopropanol 3 times and dried with nitrogen.

Coated and compressed specimens were sensitized by N719 dissolved (0.3 mM) in acetonitrile free ethanol solvent for 72 h in order to prevent the degradation of polymeric substrates. Afterwards, the sensitized electrodes were rinsed with ethanol a few times and dried with dry nitrogen. Simultaneously, Pt-coated counter electrodes were prepared by using sputtering with a coating thickness of 25-30 nm. The electrodes were assembled by sandwich closure of the two electrodes, sealed with surylene tape (~25 μm). Then, the acetonitrile deficient electrolyte was injected. The cells were prepared to have 6x6 mm effective surface area, IPCE and photocurrent-voltage characteristics were examined under 1 SUN (AM1.5) by using high sensitivity xenon lamp of 300W Solar Simulator, Newport 91192.

RESULTS AND DISCUSSION

The zeta potential measurements of each ethanol based suspensions prepared by using these particles revealed the effect of acetylacetone addition. The pH values of the ethanol based suspensions, with/out acetylacetone addition, exhibit very small deviations amongst. The bare ethanol based solutions have 5.2 pH value while acetylacetone additive solutions have 5.3 pH value. Therefore, in Fig.1 the zeta potential measurement have been conducted under constant pH conditions (pH=5) in order to observe the electrophoretic performances under low applied voltages. It is observed that the number of ionized particles remarkably increases with the

addition of acetylacetone; on the other hand, there is only a slight increase in the zeta potential values as shown in Table 1.

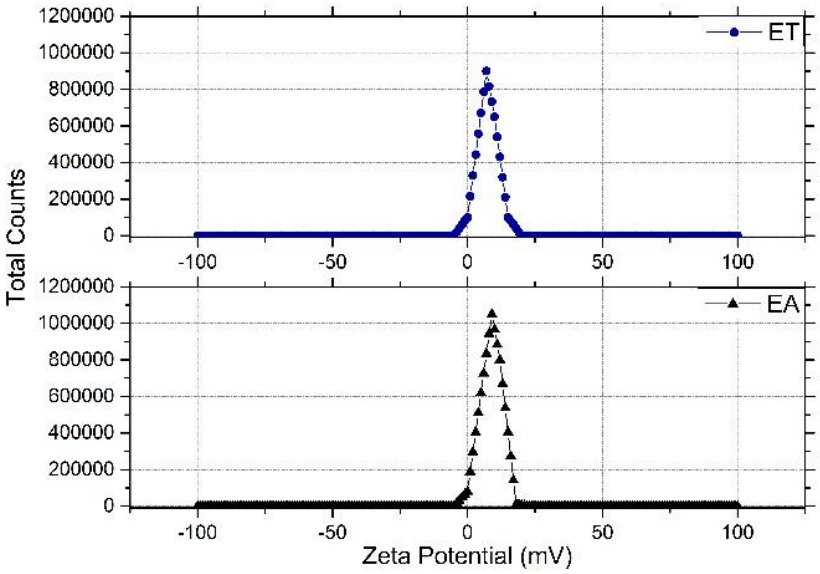

Figure 1. Zeta potential measurements

Table 1. Zeta potential and mean agglomerate size measurements

Sample	Ethanol	Ethanol + AA
Zeta Potential (mV)	7.06	8.88
Mean Agglomerate Size (nm)	150.6	161.4

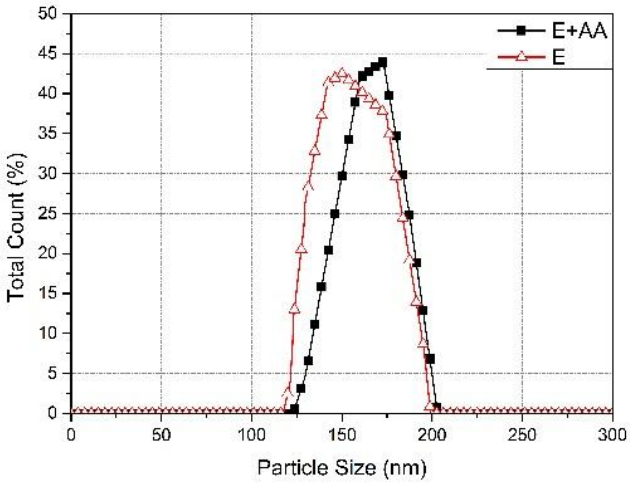

Figure 2. Mean particle size distribution

The threshold voltage values are inversely proportional to the square of the particle radius [22]. However, for low binder content or binder-free suspensions, it is crucial to consider the agglomerates as the effective electrophoretic colloids such that mean agglomerate size is determined as the effective particle size. In Fig. 2, the overall agglomerate size distributions

for suspensions exhibit an adverse effect of acetlyacetone addition on the mean agglomerate/particle sizes. Although, the particle size distribution homogenizes with the acetylacetone addition, the mean agglomerate size increases as modelled in Fig.3. The δ indicates the difference in initial zeta potential to acetylacetone adsorbed agglomerate size such that the mean agglomerate size was increased. This is due to lack of proton (H^+) donor and/or electron (halides) donor in order to create an optimum repulsion force among the particles to obtain smaller particle sizes. Therefore, despite water addition, the effect of acetlyacetone results in a conflict to optimize and stabilize the colloid suspensions.

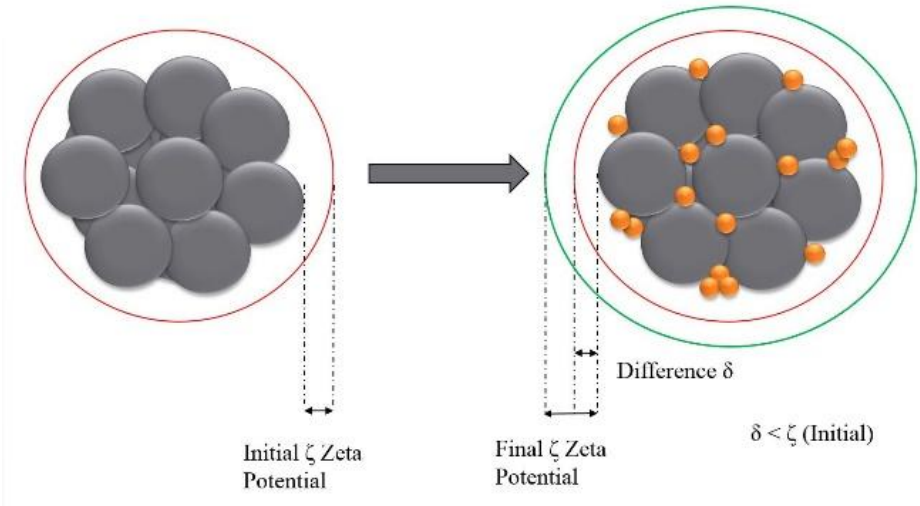

Figure 3. Modelling of acetylacetone (AA) addition and its effect on mean particle size

The specimens were coated via EPD by using each distinct colloidal solutions wherein coating characteristics such as coating rate, thickness and morphology of each type of colloid solutions have been investigated by SEM images. The coating duration was adjusted for 1 min of coating time, initially, while applied voltage is kept at the minimum (threshold+) values for each colloidal solution.

EPD coating conducted for 1 min with an applied voltage of 5 V exhibits extraordinary coating thickness homogeneity. However, as the coating duration extended to 2 min, the homogeneity is dramatically decreased, as shown in Table 2, such that the expected suspension stability and homogeneity performance of acetlyacetone are observed to be limited to coating thicknesses at around 7-8 μm.

Table 2. Coating thicknesses obtained at 5 V for 1 min and 2 min of EPD with observed deviations

Sample	Ethanol + AA (5 V – 1 min)	Ethanol + AA (5 V – 2 min)
Mean Coating Thickness (μm)	7.38	10.48
Deviation (μm)	0.73	4.68
% Deviation	9.9	44.7

On the other hand, the coatings conducted using the non-acetylacetone treated colloid suspension suggested a highly reliable coating homogeneity, density and thickness as shown in Fig. 4. The coatings were conducted under an applied voltage of 5 V with 4 different

durations. The coating thickness values have maintained their homogeneity in thickness upto around 20 μm of coating where the desired coating thickness for DSSC application is 15 μm.

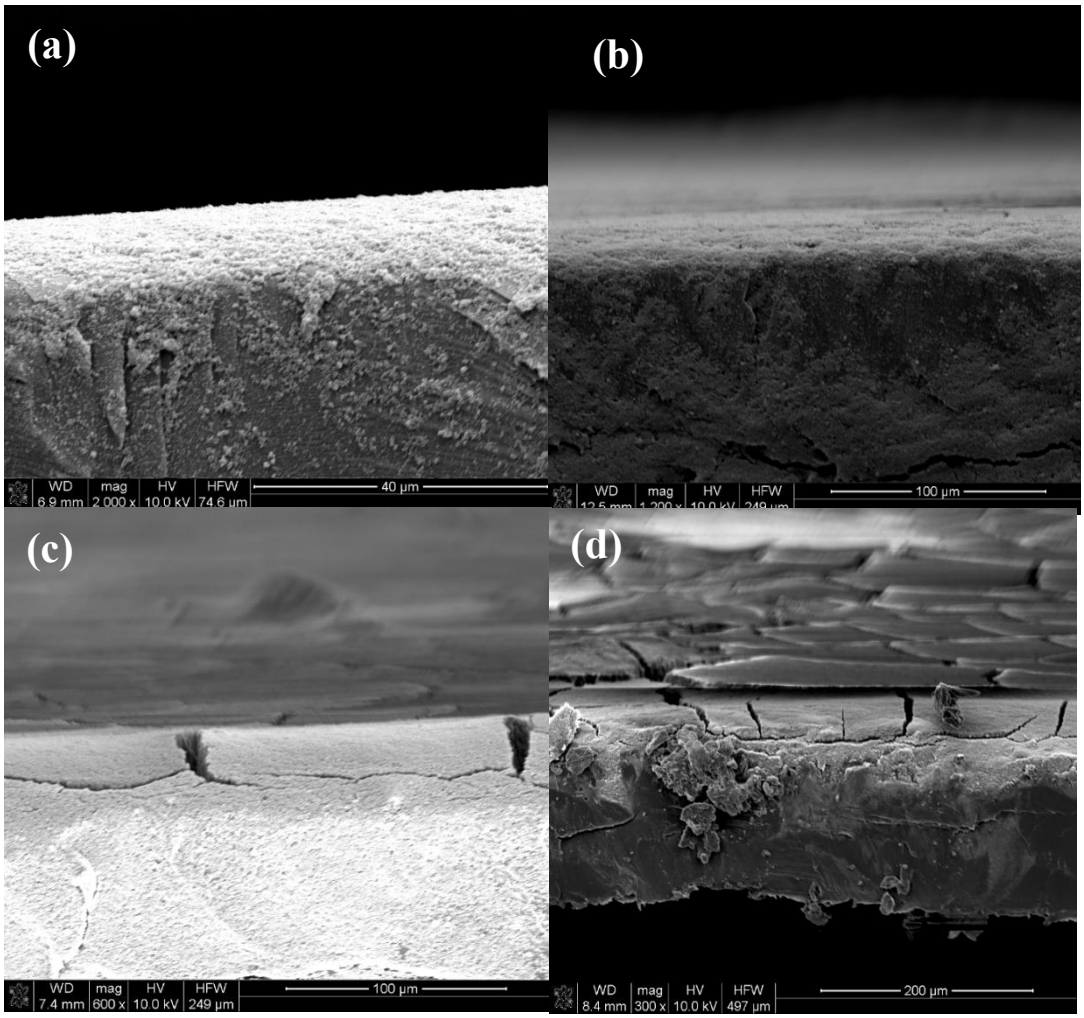

Figure 4. SEM images of colloid suspension of ethanol at 5 V (a) 1 min of coating, (b) 2 min of coating, (c) 3 min of coating and (d) 4 min of coating

Table 3. Coating thicknesses obtained at 5 V for 1, 2, 3 and 4 min of EPD with observed deviations

Sample	Ethanol (5 V – 1 min)	Ethanol (5 V – 2 min)	Ethanol (5 V – 3 min)	Ethanol (5 V – 4 min)
Mean Coating Thickness (μm)	9.76	20.11	28.33	41.17
Deviation (μm)	0.51	0.91	2.93	5.26
% Deviation	5.2	4.5	10.3	12.8

Additionally, the change in the mean coating thickness versus coating duration is plotted and tabulated on Table 3, while the thickness deviations of all suspensions are tabulated in Table 2 and Table 3. In Fig. 5, it is clearly observed that the current decrease rate of acetyacetone additive solutions is higher than the non-additive ones, resulting in decreased coating rate. As

indicated previously by Fig. 2, the acetylacetone addition resulted in homogenization of the colloid agglomerates while the mean agglomerate size increased. Although the measured mean agglomerate size difference were not perceived as a severe fact at first glance, it is proved that considering the low applied voltage values, a few nm change in the mean agglomerate size prevents homogeneous coatings with extended coating durations for ethanol based solutions. Additionally, the acetylacetone addition by itself for colloidal suspensions effects negatively such that it necessitates to be added with relatively strong ionizing agents [14,15,18,23].

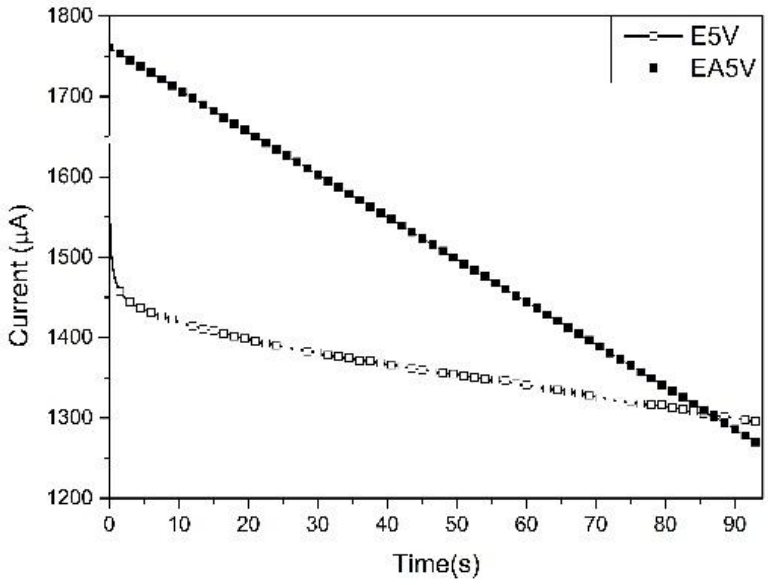

Figure 5. Current vs time plot for solutions with applied voltage values

As a subsidiary process in order to provide electrophoretically coated specimens mechanical stability and the pseudo-sintering effect among the titania nanoparticles, Cold Isostatic Processing (CIP) has been conducted. Although EPD process, generally, is a remarkable method in order to form a highly dense and homogeneous films, in this study, the lack of ionizing agents and surfactants, fortunately, promotes porosity and unfortunately, the adherence of the films are not stable enough, especially while bending the coated substrates. Therefore, the CIP process is expected to perform increased adherence in between titania and ITO layer and adherence among titania nanoparticles. Formation of mesoporous titania layer was completed by using CIP with different pressure intervals of 150 MPa, 225 MPa and 300 MPa.

The as-coated specimens have been dried at 100° C for 2 h, vacuum sealed first with polyethlene, then latex and pressure was applied. The first obtained pressurized specimens were investigated by SEM, in order to observe the changes in morphology of the films. Fig. 6 shows the SEM images of titania layer pressed under 225 MPa. As shown in Fig. 6.a, by applying 225 MPa of isostatic pressure, the majority of the cracks are either eliminated of partially filled, leaving small scale bumpers and voids. In Figure 6.b, the magnified images of reliably homogeneous mesoporous structure can be seen.

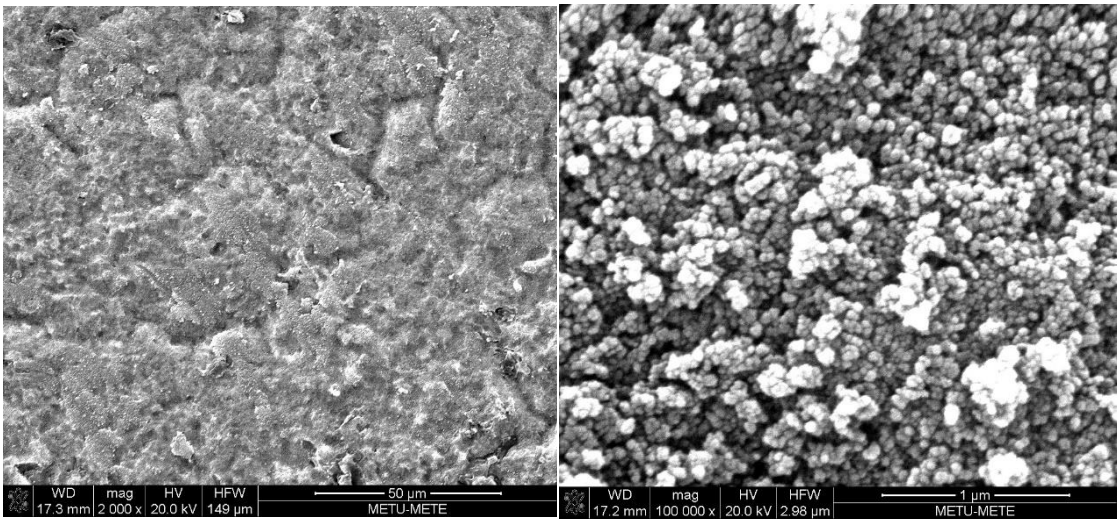

Figure 6. SEM images of specimens compressed with 225 MPa (a) 2000X and (b) 100 000X

However, considering the samples produced by applied pressure of 300 MPa, the titania layer is mostly peeled of leaving remenant titania layers and potential ITO cracks are formed. The sheet resistance of the substrate has been measured to have about 30 times larger than the as received substrates and, alternatively, non-peeled off coatings have been assembled into a DSSC such that the case of ITO cracking will definitely decrease the overall cell efficiency.

Cells are assembled as indicated in the previous section and the overall cell properties are investigated by solar simulator. Commercial liquid electrolyte has been used with some modification in its composition such as acetonitrile content has been totally eliminated while it is balanced with volatonitrile in order to prevent possible degradation of polymeric substrates. Additionally, acetonitrile and/or volatonitrile free dye (N719) solution has been prepared and those solvents have been replaced by ethanol and dye adsorption duration is extended to 72 h from 24 h.

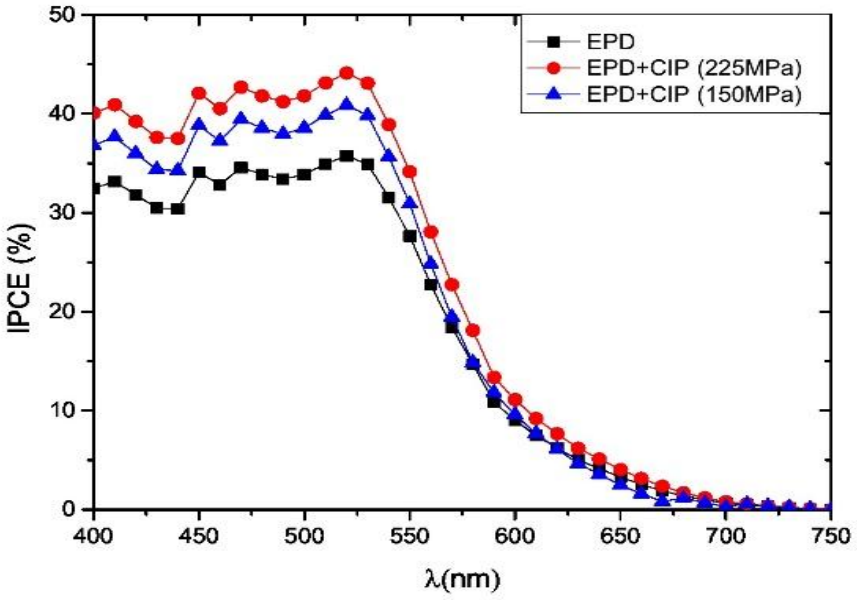

Figure 7. % IPCE performance of the assembled cells

Figure 7 and 8 show the I-V characteristics and the IPCE performance of the assembled cells. It is obvious that the efficiency value of the sample compressed with 300 MPa is even lower than the only electrophoretically coated sample with slightly lower open circuit voltage; however, dramatic decrease in the short circuit current proves that ITO layer is definitely cracked due to excessive pressure. The other two compressed samples have shown expected performance profiles such that as mentioned earlier due to better crack filling and macro scale homogeneity of the titania layer the sample compressed with 225 MPa have shown the best cell efficiency of 3.0 %. Table 4 shows the overall performance parameters of cells assembled.

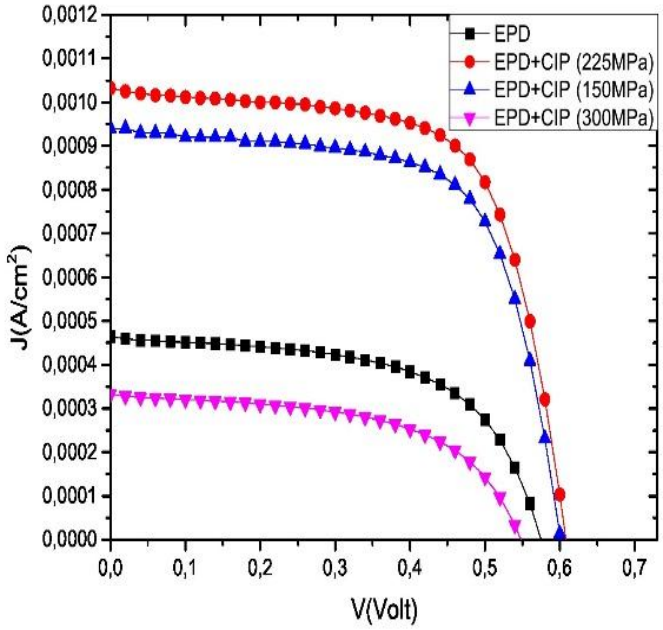

Figure 8. The I-V curve of the assembled cells

Table 4. The photoelectric performances of the assembled cells

Cell	V_{OC} (V)	J_{SC} (A/cm^2)	Fill Factor	Efficiency (%)
EPD	0.57	0.00046	59.0593	1.10988
EPD + CIP-150 MPa	0.60	0.00094	62.8957	2.54404
EPD + CIP-225 MPa	0.61	0.00103	67.2478	2.99843
EPD + CIP-300 MPa	0.55	0.00034	39.2502	0.45936

Considering the purpose of the CIP process, it is found that 225 MPa of applied pressure is the optimum compression value with provided adherence among titania nanoparticles while adherence of ITO layer and titania layer is ensured without the ITO layer cracking as observed for 300 MPa compression sample. The FF value of 225 MPa sample is 67.25 % as well as 62.9 % for 150 MPa and 59.1 % for only EPD samples is another proof of the increased adherence and bridging among titania nano particles and the ITO-titania interface. Additionally, comparing Jsc values, the quality of interfaces are increased remarkably.

CONCLUSION

It is important to have a cost and time effective process in order to manufacture flexible dye sensitized solar cells. Using and optimizing a binder-free EPD process is developed by employing commercially available P-25 titania nanoparticles with a subsequent CIP processes. Prepared EPD solutions were highly dense titania – alcohol based colloid suspensions to obtain a stable close electrode distance process with only additive of deionized water to trigger characteristic zeta potential values for electrophoretic mobility. Completing the photoanode production by CIP process, forming coatings with 12-14 μm thickness, the cells are assembled with modified liquid electrolyte and N719 dye solution by eliminating acetonitrile content. Although observed efficiency values seem to be satisfying with 3.0 %, comparing with commercial DSSCs with its sintering process, ITO coated polymeric substrates have a limited compression strength, limiting the maximum efficiency which can be obtained by using CIP process. However, the flexible DSSCs produced by EPD – CIP technique is a reliable time and cost effective method and versatile enough to manufacture flexible modules.

REFERENCES

1. S. Kambe, 3rd Int. Conference on Industrialisation of DSC, Japan, April 2009
2. S. Ito, T.N. Murakami, P. Comte, P. Liska, C. Grätzel, M.K. Nazeeruddin, M. Grätzel, Thin Solid Films, 516, 4613, 2008
3. M. Grätzel, Acc. Chem. Res., 42, 1788, 2009
4. N. Ikeda and T. Miyasaka, Chem. Lett. 36, 466, 2007
5. C. Kothandaraman, T. Tonon, C. Huang, A. Delahoy, Mater. Res. Soc. Symp. Proc. 219, 475, 1991
6. A. Hedler et al., Proc. 34th IEEE Photovoltaic Specialists Conference, 1102, 2009
7. J. Shao, F. Liu, W. Dong, R. Tao, Z. Deng, X. Fang, S. Dai, Materials Letters, 68, 493 2012
8. H.C. Weerasinghe, P.M. Sirimanne, G.P. Simon and Y.-B. Cheng, Prog. Photovolt: Res. Appl., 20, 321, 2012
9. T.A.N Peiris, S. Senthilarasu, K.G. Upul Wijayantha, J. Phys. Chem. C, 116, 1211, 2012
10. C.-R. Ke, J.-M. Ting, J. of Power Sources, 208, 316, 2012
11. L.-C. Chen, J.-M. Ting, Y.-L. Leed, M.-H. Hon, J. Mater. Chem., 22, 5596, 2012
12. X. Yin, Z. Xue, L. Wang, Y. Cheng, B. Liu, ACS Appl. Mater. Interfaces, 4, 1709, 2012
13. W.-H. Chiu, K.-M. Lee, W.-F. Hsieh, J. of Power Sources, 196, 3683, 2011
14. G.S. Kim, H.-S. Shin, Electrochemistry Communications, 8, 961, 2006
15. C.-C. Tsai, Y.-Y. Chu, H. Teng, Thin Solid Films 519, 662, 2010
16. H. Tokudome and M. Miyauchi, Angewandte Chemie, 44, 1974, 2005
17. H. Tokudome and M.Miyauchi, Chemical Communications, 10, 958, 2004
18. L. Zhao, S. Wang, International Journal of Photoenergy, 2012, 472958, 2012.
19. H. Lindstrom, A. Holmberg, E. Magnusson, S-E. Lindquist, L. Malmqvist, A. Hagfeldt, Nano Letters, 1, 97, 2001
20. G. Boschloo, H. Lindstrom, E. Magnusson, A. Holmberg, A. Hagfeldt, Journal of Photochemistry and Photobiology, A: Chemistry, 148, 11, 2002
21. Y. Peng, J. Z. Liu, K. Wang, Y.-B. Cheng, International Journal of Photoenergy, 2011, 410352.
22. J.H. Dickerson, A.R. Boccaccini, P.J. Sides, "Fundamentals of Electrophoretic Deposition. Electrophoretic deposition of nanomaterials", Springer, New York 2012
23. L. Grinis, S. Dor, A. Ofir, A. Zaban, Journal of Photochemistry and Photobiology A: Chemistry, 198, 52, 2008

Techniques for Characterizing Complex Chemistries at the Nanoscale

•

Kompleks Yapıların Nanoboyutlarda Karakterizasyon Teknikleri

Matthew J. Kramer

Iowa State University - USA

ABSTRACT

Many advanced functional materials are exploiting unique properties of matter at the nano-scale. In order to fully characterize the composition, chemistry and atomic structure of these complex materials the full complement of tools of the modern TEM are brought to bear: Scanning Transmission Electron Microscopy (STEM) and coupled with a High Angle Annular Dark Field (HAADF) detector can help to easily distinguish the high atomic mass compounds from compounds containing lighter elements. Simultaneous energy dispersive spectroscopy (EDS) and electron energy loss spectroscopy (EELS) are complimentary methods where the former is more sensitive to heavy elements while the latter is more sensitive to light elements. Their combined use is crucial to analyzing complex compounds that contain mixtures of light and heavy elements. In addition, EELS has better energy resolution allowing for better separation of neighboring elements on the periodic table. Energy Filtered Transmission Electron Microscopy (EFTEM) allow for rapid elemental mapping. Lessons learned from studies of a number of applied and fundamental studies on transition metal alloys will be used to highlight the strength and weakness of a number of nano-characterization methods in the modern TEM.

Keywords: Advanced functional materials, complex chemistry, nano- characterization methods.

TRANSMISSION ELECTRON MICROSCOPY AND ATOM PROBE TOMOGRAPHY STUDIES OF LAVES PHASE NUCLEATION DURING CREEP OF A 12% CR TEMPERED MARTENSITE FERRITIC STEEL

Mehmet İkbal IŞIK*, Aleksander KOSTKA*, Gunther EGGELER**

* Max Planck Institut für Eisenforschung, Germany
m.isik@mpie.de, a.kostka@mpie.de
**Ruhr-Universität Bochum, Germany
gunther.eggeler@rub.de

ABSTRACT

Tempered martensite ferritic steels (TMFS) are important engineering materials that are used for critical components in fossil fired power plants where they have to withstand mechanical loads at high temperatures. The objective of the present study is to reveal dominant processes governing nucleation and growth of Laves phase (Fe_2Mo) particles during creep of a TMFS with 12 wt. % Cr and 1 wt. % Mo. Prior to creep test, steel was subjected a two-step heat treatment; austenitizing at 1050^o C for 0.5 h and tempering at 770^o C for 2 h both followed by air cooling. Microstructure at this state consists of an ultrafine grained, ferritic matrix with high density of dislocations and present precipitates of type $M_{23}C_6$ and V-rich MX (no Laves phase found at this stage). Interrupted long term creep tests were performed at 550^o C and 120 MPa with a rupture time of 139971 h. Analytical transmission electron microscopy and atom probe tomography techniques were applied to study the combination of elementary processes that lead to the formation of Laves phase. Laves phase particles were detected after 864 h of high temperature exposure with a chemical composition of at.%: 33 Mo, 40 Fe, 13 Cr, 10 Si. Laves phase particles were located on grain boundaries next to $M_{23}C_6$ carbides.

Keywords: Tempered martensite ferritic steels, Creep, Laves phase Nucleation, Transmission Electron Microscopy, Atom Probe Tomography

1. INTRODUCTION

9-12 %Cr steels, also known as tempered martensite ferritic steels, are used in fossil fired power plants as critical components operating at temperature range of 500 – 650°. Creep mechanisms of these steels have been in focus in the last three decades [1-6]. Researchers have studied the creep behavior [7-9], the role of alloy chemistry [10-13], the influence of heat treatment conditions on creep properties [14-15] and the evolution of microstructure during creep of tempered martensite ferritic steels [16-19]. Laves phase particles were detected in the microstructure during service conditions which require high temperature and stress. To the best of our knowledge, processes that lead Laves phase formation are not clearly identified in the literature and there is a need to understand the Laves phase nucleation phenomena for a better control on the microstructure, and hence, for safer operation. In the present work interrupted creep tests were performed at 550°C, 120 MPa in a time range of up to 139971 h. The results obtained by scanning electron microscopy (SEM), transmission electron microscopy (TEM) and three dimensional atom probe tomography (3D-APT) were evaluated on a thermodynamic and kinetic basis to clarify nucleation of Laves phase particles.

2. MATERIALS AND METHODS

The composition of tempered martensite ferritic steel, investigated in the present study, is shown in Table 1. The Salzgitter Mannesmann Research Center (SMRC) provided the materials.

Table 1. Chemical composition of investigated alloy X20CrMoV12-1

	C	Si	Mn	P	S	Cr	Mo	V	Ni
X20 steel	0.2	0.15	0.61	0.01	0.01	11.7	0.8-1.1	0.25	0.65

A typical two stage heat treatment was applied to materials. Austenitizing at 1050 °C for 0.5 h and tempering at 770 °C for 2 h, both followed by air cooling. Long term creep tests were performed in at Salzgitter Mannesmann Research Center and short term creep tests were performed at Max Planck Institut für Eisenforschung.

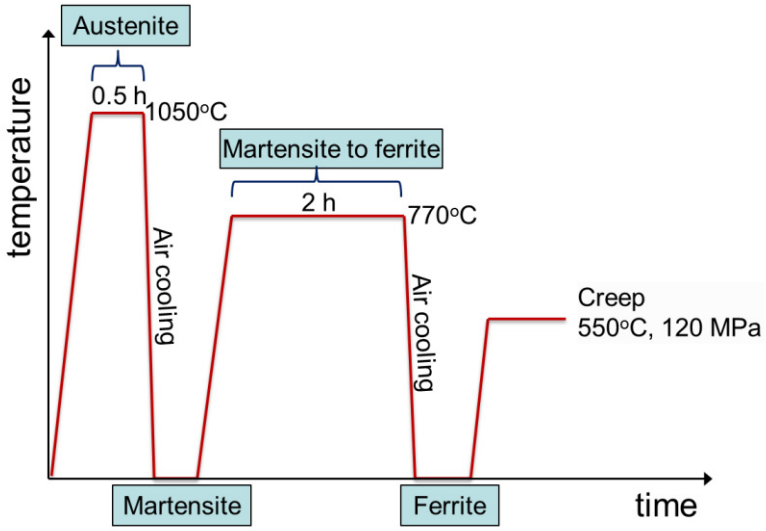

Figure 1. Schema of heat treatment history and creep testing of X20 steel.

Jeol JSM-6450 was used for scanning electron microscope (SEM) studies. Transmission electron microscope (TEM) investigations were carried out using a Jeol JEM-2200FS operating at 200 kV equipped with an energy dispersive analysis system (EDX). 3 mm discs were cut out by wire erosion, mechanically ground and polished to a thickness of 0.1 mm. Electron transparent foils were obtained by electrochemical thinning, using double-jet system (Struers Tenupol 5). An electrolyte of 95 % acetic acid and 5 % perchloric acid was used at 15 °C, 41-58 V. Electropolished 3 mm TEM discs were also used to prepare tips for APT using focused-ion-beam (FIB, FEI Helios NanoLab 600) micromachining in combination with a lift-out method. APT investigations were carried out using a local electrode atom probe (LEAP 3000X HR, Cameca Instr.). LEAP measurements were performed in voltage mode (15 % pulse fraction, 200 kHz, 0.5 % target evaporation rate) at a specimen temperature of 60 K.

3. RESULTS AND DISCUSSION

Prior to creep testing, the microstructure of X20 specimen consists of a high density of interfaces, such as grain/micro grain boundaries, dislocations, carbides ($M_{23}C_6$) and carbonitrides (V-rich MX). Laves phase particles were not detected in initial state microstructure. Formation of Laves phase particles was observed only after high temperature exposure.

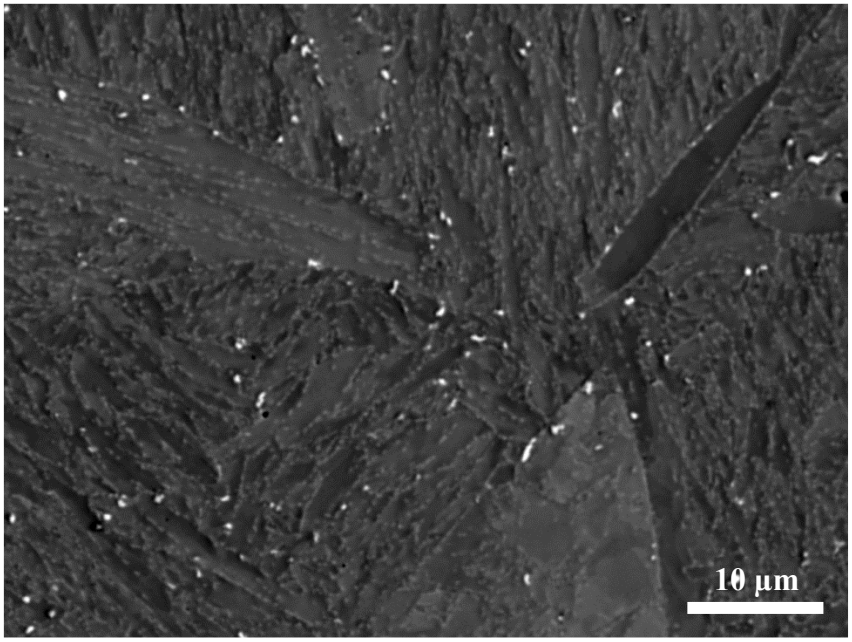

Figure 2. SEM back scatter electron image of specimen after 81984 h of creep.

Figure 2 shows a general overview of microstructure after 81984 h of creep. Laves phase particles appear bright in the BSE mode since they contain high amount of Mo compared to other phases. $M_{23}C_6$ carbides decorate the grain boundaries (grey particles). Usually Laves phase particles are found on µ-grain boundaries next to $M_{23}C_6$ carbides.

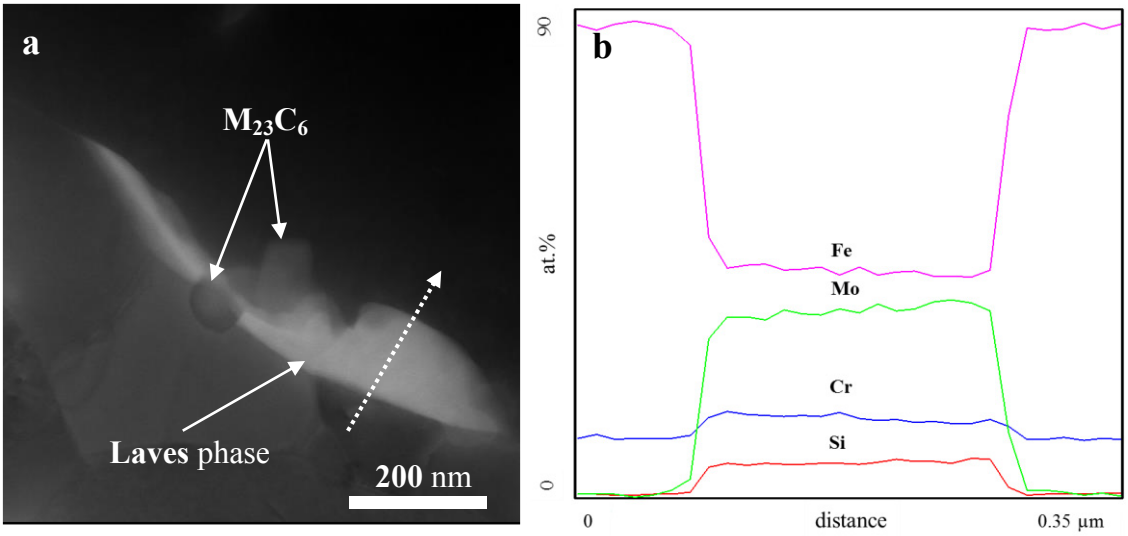

Figure 3. Scanning TEM image of Laves phase particle after 51072 h of creep (head section). (a) HAADF image (b) EDX analysis along the dashed line.

Results of TEM investigation on Laves phase particle is shown in Figure 3. On the left (Figure 3b) a Laves particle is seen which is surrounded by $M_{23}C_6$ carbides. EDX analysis showed that the particle has a composition close to at.%: 32 Mo, 41 Fe, 14 Cr, 9 Si with some minor amount of Ni and P. After confirming the crystal structure with selected area diffraction (not shown here) the particle was identified as C-14 type hexagonal Laves phase (Fe_2Mo).

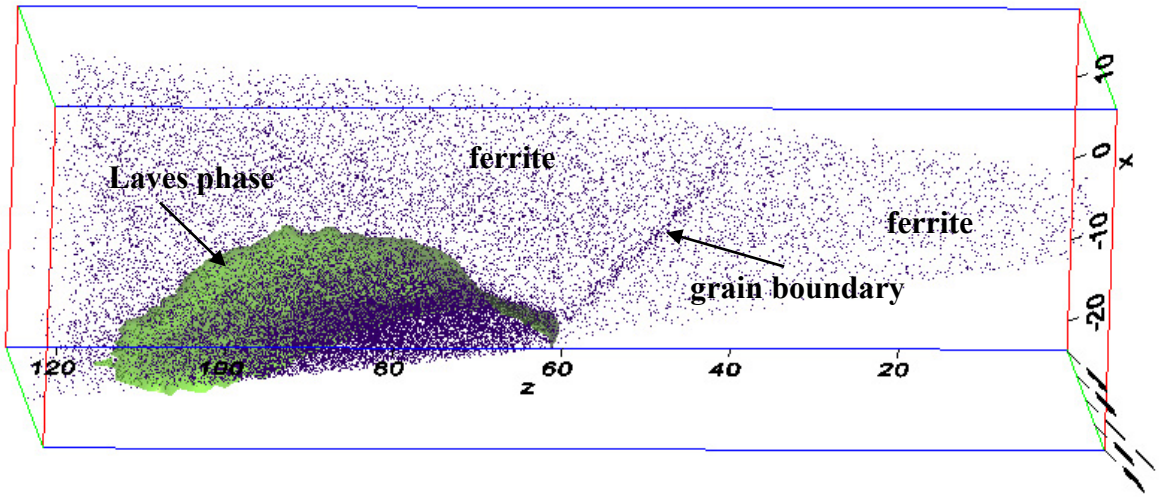

Figure 4. Three dimensional distributions of Si atoms (blue) in 12456 h crept specimen (units are in nm). Isoconcentration surface of 25 at.% Mo (green) is plotted to highlight Laves phase particle.

In figure 4 distributions of Si atoms (blue colored dots) in a crept specimen is shown in three dimensional space. For visualization purposes, Laves phase particle was highlighted by plotting at.% 25 Mo isoconcentration surface, shown in green color. A grain boundary is seen roughly in the center of the figure 4, where an enrichment of Si atoms is visible. Also, it is clearly seen that Laves phase (green region) is rich in Si.

4. CONCLUSIONS

In the present work we investigate the formation of Laves phase particles during creep of a 12% Cr tempered martensite ferritic steel. For microstructural characterizations SEM, analytical TEM and 3D-APT were used. From the results obtained in the present study, the following conclusions can be drawn:

(1) In tempered martensite ferritic steels, Laves phase particles nucleate at micrograin boundaries close to carbides.

(2) Composition of Laves phase particles is close to at.%: 32 Mo, 41 Fe, 14 Cr, 9 Si.

(3) Si enrichment in grain boundary and in Laves particles is observed by 3D APT.

(4) Further work is required to explain the role of carbides in assisting the nucleation of Laves phase.

REFERENCES

[1] Abe F, Kern TU, Viswanathan R. Creep-resistant steels. Cambridge: Woodhead Publishing, CRC Press; 2008.

[2] Bürgel R, Maier HJ, Niendorf T. Handbuch Hochtemperatur-Werkstofftechnik. Wiesbaden: Vieweg Teubner Verlag Springer Fachmedien Wiesbaden GmbH; 2011.

[3] Cadek J. Creep in metallic materials. Amsterdam: Elsevier; 1988.

[4] Evans RW, Wilshire B. Creep of metals and alloys. London: Institute of Metals; 1985.

[5] Robson JD, Bhadeshia HKDH. Mater Sci Technol 1997;13:631.

[6] Robson JD, Bhadeshia HKDH. Mater Sci Technol 1997;13:640.

[7] Eggeler G, Nilsvang N, Ilschner B. Steel Res 1987;2:97.

[8] Eggeler G. Acta Metall 1989;37:3225.

[9] Wiesner C, Earthman JC, Eggeler G, Ilschner B. Acta Metall 1989;37:2733.

[10] Maruyama K, Sawada K, Koike J. ISIJ Int 2001;41:641.

[11] Fujita T, Takahashi N. ISIJ Trans 1978;18:703.

[12] Lundin LM. Scr Mater 1996;34:741.

[13] Tsuchida Y, Okamoto K, Tokunaga Y. ISIJ Int 1995;35:317.

[14] Dronhofer A, Pesicka J, Eggeler G. J. Phys. IV France 2001;11:Pr8-235.

[15] Foldyna V, Kuboň Z, Jokobová A, Vodárek V. Development of advanced high chromium ferritic steels, in: Strang A, Gooch DJ (Eds.). Microstructural development and stability in high chromium ferritic power plant steels. London: The Institute of Materials; 1997.

[16] Tak KG, Schulz U, Eggeler G. Mater Sci Eng A 2009;510–511:121.

[17] Eggeler G, Earthman JC, Nilsvang N, Ilschner B. Acta Metall 1989;37:49.

[18] Cui H, Sun F, Chen K, Zhang L, Wan R, Shan A, Wu J. Mater Sci Eng A 2010;527:7505.

[19] Kipelova A, Belyakov A, Kaibyshev R. Mater Sci Eng A 2012;532:71.

ELECTRON MICROSCOPY ANALYSIS OF HEAT-TREATED CN3MN GRADE SUPER AUSTENITIC STAINLESS STEELS

Mertcan BAŞKAN*, Scott L. CHUMBLEY, Yunus Eren KALAY*****

* Middle East Technical University, Turkey
mbaskan@metu.edu.tr
** Iowa State University, USA
chumbley@iastate.edu
*** Middle East Technical University, Turkey
ekalay@metu.edu.tr

ABSTRACT

Attributed to extreme toughness and corrosion resistance, cast super austenitic steels are widely used in extreme environments such as off-shore oil wells, seawater systems, heat exchangers and piping in purification systems. These steels lose their toughness upon incorrect annealing even at very short times yet keeping their hardness values. In this study, CN3MN grade cast super austenitic stainless steel keel bars were annealed for different times and compared with the as-cast microstructures in order to explain the underlying reasons for the unexpected embrittlement observed after short term heat-treatment procedures. Grain boundary precipitation was investigated using SEM and TEM analyses. The precipitates were found to be the major reason for the brittle fracture in intergranular mode; on the other hand, their sizes are relatively small to cause an abrupt decrease in the toughness. Detailed TEM analysis revealed the formation of stacking-faults and twin-like crystallographic defects with respect to annealing time which appear to be the origin of the embrittlement observed in CN3MN grade steel.

Keywords: CN3MN stainless steel, crystal defects, electron microscopy

ISIL İŞLEM GÖRMÜŞ CN3MN SÜPER ÖSTENİTLİ PASLANMAZ ÇELİKLERİN ELEKTRON MİKROSKOBU İLE İNCELENMESİ

ÖZET

CN3MN süper östenitli paslanmaz çelikleri, sahip oldukları üstün tokluk ve korozyon dayancı sayesinde deniz altı petrol çıkarma rafinerileri, arıtma sistemleri gibi zorlu sistemlerde kullanılmaktadır. Ancak, eğer bu çelikler kısa süreli bile olsa yanlış bir ısıl işleme tabi tutulurlarsa, sertliklerini korurken tokluk dayançlarını kaybetmektedirler. Bu çalışmada, döküm yoluyla üretilmiş CN3MN paslanmaz çelikleri farklı sürelerde tavlanmış ve tavlama sonrası kırılganlaşma mekanizmasını tespit etmek için döküm sonrası tavlanmamış mikroyapılar ile karşılaştırılmıştır. Tane sınırları boyunca oluşan çökeltiler taramalı elektron mikroskobu ve geçirimli elektron mikroskobu ile incelenmiştir ve bunların tane sınırları boyunca oluşan kırılmanın sebebi olarak belirlenmiştir. Ancak tane sınırlarının kapladığı alan çok az olduğundan tokluktaki bu düşmenin tek sebebinin bu olmayacağı öngörülmüştür. Geçirimli elektron mikroskobu analizleri ile, özellikle uzun süre tavlanmış numunelerde ikiz oluşumu benzeri yapılar gözlemlenmiştir ve bu hataların CN3MN çeliklerinde kırılganlaşmaya yol açtıkları düşünülmektedir.

Anahtar kelimeler: CN3MN Paslanmaz Çeliği, kristal hataları, elektron mikroskobu

1. INTRODUCTION

CN3MN grade Super Austenitic Stainless Steel (SSS) is a special kind of steel which exhibits exceptional corrosion performance even at elevated temperatures. Unlike other steels, this grade has also resistance to pitting corrosion at chlorine environments [1-3]. In order to compare pitting corrosion of the steels, an empirical index is often used. This index is known as $PREN_{30}$ (Pitting Resistance Equivalent Number) and it is commonly formulated as:

$$PREN_{30} = \%Cr + 3.3x(\%Mo) + 30x(\%N) \quad (1)$$

It is commonly accepted that , the austenitic stainless steels having $PREN_{30}$ greater than 45 are called as super austenitic stainless steel (SSS). CN3MN satisfies this condition as shown in Table 1 .[4]

Table 1. The composition of the CN3MN steel according to the ASTM Standards (wt %)

Element	C	Si	Mn	P	S	Cr	Ni	Mo	Cu	N	Fe
Concent. (ASTM)	≤ 0.03	≤1.0	≤2.0	≤0.04	≤0.04	20.0-22.0	23.5-25.5	6.0 - 7.0	≤0.75	0.18-0.26	Balanced

Although the relatively high alloying content enhances the corrosion resistance and mechanical properties, steel becomes more prone to precipitation. Precipitation on the austenitic stainless steels is very common and it has widely investigated by many studies [5-7]. For instance, sigma phase, which is an Mo and Cr enriched intermetallic, prefers to form along the triple junctions and grain boundaries and the transformation temperature is estimated to be 950°C based on the kinetical related details [5]. Muller et al. revealed that impact toughness severely drops upon ten minutes annealing after grain boundary segregation [6]. Koutsoukis et al. stated that laves phase, which prefers grain boundaries to form, transforms to sigma phase after 240hr annealing at 950°C [7].There are several studies investigating the crystallographic defects observed in austenitic stainless steels, as well. Lee et al. proved that the twinning partials were confirmed to be Shockley dislocations with Burgers vector 1/6 (121) glissile on the (111) twinning plane based on the visibility criteria in TEM [8]. Koutsoukis observed that twins are formed mainly just next to the precipitates [7]. Although there are studies regarding to defect analysis in SSS, just a few are touching their relationship with mode of fracture. Within this respect, in this study we examined the crystallographic defects in relationship with embrittlement type in CN3MN superaustenitic stainless steel.

2. EXPERIMENTAL PROCEDURE

Test specimens were produced in collaboration with SFSA (Steel Founders` Society of America) foundries in the form of 3x3x35 cm keel bars. These bars were solution heat-treated at 1204°C for 2 hours in order to obtain homogeneous austenite phase, then quenched to room temperature. The Charpy test samples were prepared by electrical discharge machining according to ASTM-E23 standards to compare the impact toughness of the specimens with different annealing times. These samples were encapsulated in a quartz tube and the annealing heat treatments were conducted in vertical tube furnace for changing times 0 to 16 minutes at 927ºC as summarized below in Table 2.

Table 2. The specimen codes and annealing times for specimens heat-treated at 927ºC

Samples	**S0**	**S0.5**	**S1**	**S2**	**S4**	**S8**	**S16**
Annealing Times	0 min	30 sec	1 min	2 min	4 min	8 min	16 min

Charpy impact and hardness tests were applied to all heat-treated samples using a Tinius Olsen Charpy Impact Tester and EmcoTest M4U-025 Hardness Tester with Rockwell B Scale, respectively at room temperatures. The microstructure and fracture surfaces were examined under FEI Nova NanoSEM 430 model field emission scanning electron microscope with EDS attachment. Marble's reagent (10 g $CuSO_4$ in 50 mL HCl and 50 mL water.) was used for metallographic specimen preparation. TEM analyses were conducted by a JEOL JEM2100F field emission gun scanning/transmission electron microscope. Specimens for electron microscopy were mechanically ground then electropolished with 33% nitric acid and 67% methanol solution at -35°C.

3. RESULTS AND DISCUSSION

The fracture surfaces after the Charpy impact tests were examined under SEM. The behavior of ductile to brittle transition upon annealing is clearly seen from these fractographs. The samples denoted as S0 and S1 show the characteristics of ductile fracture. Their surfaces are dull and full of dimples as seen in Fig.1(a) and (b). However, in Fig.1(c), (d) and (e) (from the samples S4 and S8), the fracture surface exhibit both ductile and brittle fracture characteristics, therefore, they can be thought as intermediate state of ductile to brittle transition. The Fig.1(f) from the S16, on the other hand, indicates a fully brittle fracture having a smooth fracture with no dimples.

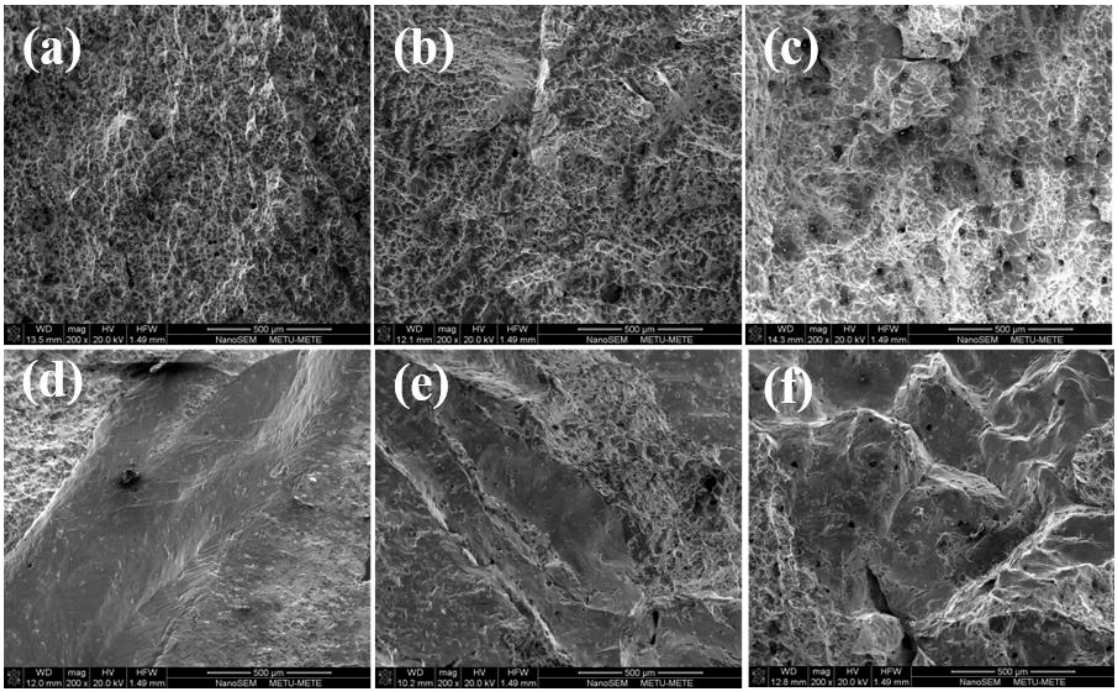

Figure 1. The fracture surfaces from (a) S0, (b) S1 , (c) S2 , (d) S4, (e) S8, (f) S16

Taking the chemical composition of the steel into consideration and the previous studies

[6,9,10], it is reasonable to offer that one of the mechanisms for the embrittlement is the formation of brittle precipitate network on the grain boundaries. To prove this, the samples were examined under SEM. In Fig.2, the microstructures reveal that S0 has no grain boundary precipitation which explains the complete ductile behavior. However, as the annealing time increases, the precipitation on the grain boundaries becomes more and more significant. In Fig.2(b), there are small precipitates in large quantities nucleated along the grain boundary. The precipitates are coarsened and make a continuous brittle network with further annealing as shown in Fig.2(c). This grain boundary precipitation should be the primary reason of intergranular embrittlement.

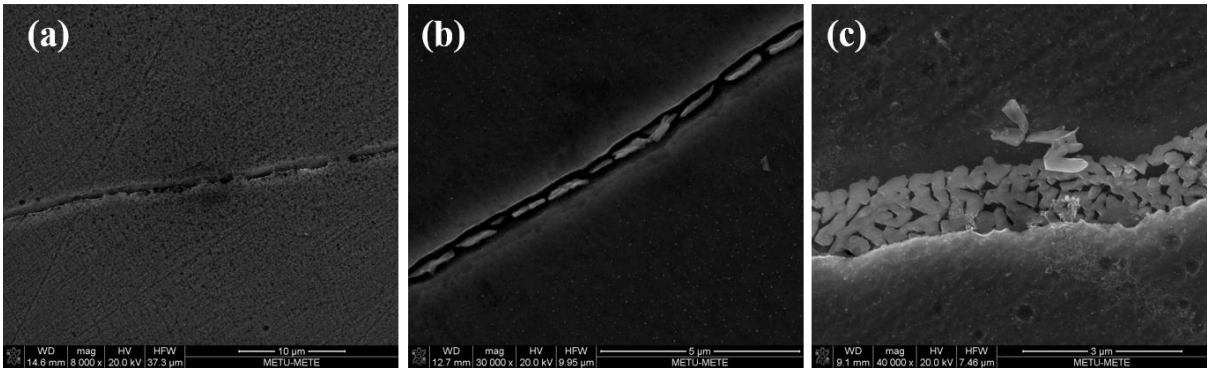

Figure 2. The grain boundaries from the (a) S0 (b) S4 (c) S16

In order to get the chemical composition of these precipitates, we used EDS analysis in scanning transmission electron microscopy (STEM) due to its enhanced spatial resolution as compared to SEM. Figure 3 shows the EDS mapping of selected elements along with the overall chemical composition from a single grain boundary precipitate.EDS showed that the precipitates are highly enriched by Mo and Si.

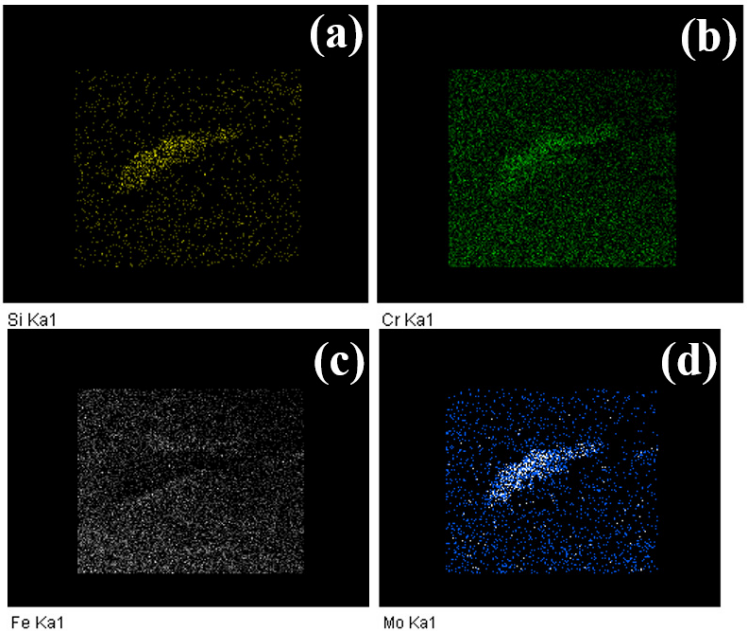

At %	Precipitate	Grain (f)
Cr	24.77 ± 0.55	22.43 ± 0.22
Ni	22.88 ± 0.31	23.30 ± 0.1
Mo	**20.02 ± 0.36**	**4.01 ± 0.14**
Fe	**14.75 ± 0.19**	**47.16 ± 0.22**
Si	**13.13 ± 0.52**	**1.97 ± 0.09**
Mn	0.56 ± 0.07	1.14 ± 0.07

Figure 3. EDS mapping obtained in STEM mode. The corresponding elements are (a) Si, (b) Cr, (c) Fe, (d) Mo. Fig.3(f) shows the chemical composition of precipitate and austenite matrix Although intermetallics precipitated on the grain boundaries seemed to be the primary reason for

the embrittlement, this doesn't fully explain the underlying reason behind the decrease in toughness with respect to annealing time. According to line intercept method, the average grain size of the sample is 900±100 μm independent of annealing time. Since the grains are too large, the total area of the grain boundaries must be small. Moreover, as can be seen on Fig.4(a), X-ray diffraction analysis revealed that all the peaks belong to the austenite phase and there are no secondary phase observed on the pattern. This implies that the amount of the secondary phases is too small to be detected by XRD analysis. Taking into account of these reasons, it is reasonable to offer that there may be other mechanisms other than intergranular fracture due to the brittle precipitates on the grain boundaries.

Figure4. (a) XRD Patterns from the sample S0 and S16. (b) The transgranularly propagated cracks observed on the sample S8. (c) Step-like crystallographic defects from the sample S0.

When the samples were investigated under TEM, crack development making fix angles initiated from the hole to the inside of the specimen were detected. Since there is no grain boundary involvement, the fracture type must be transgranular type. Fig.4(b) is one of the examples for such cracks. The origin of these cracks can be seen in Fig.4(c). Particularly, in the short annealed samples like S0, S0.5, some step like white bands were discovered. These white bands (Fig.4 (b)) and the cracks observed under TEM have common feature in terms of morphology. Another interesting point is that the white bands transform into the twin-like patterns. S16 has almost no white band formation; however, it has many defects, especially just near the cracks where the initial state of which were probably the white band. Fig.5 shows examples for such transformation. In Fig. 5(a), a large crack which was formed in a similar way with the cracks above on the sample S16. Upon annealing they transform into the twin like pattern with the steps, but step like structure was conserved after annealing. While these cracks definitely resulted during specimen preparation they were only observed in brittle specimens around the defected regions and the edges of the cracks were the boundary of the twin-like defects. We believe that these defects indicate a major weakening of the matrix structure, which contributes to the brittleness of the material as a whole. Further analysis are in progress to reveal the mechanism of twin-like defect formation from white band structure.

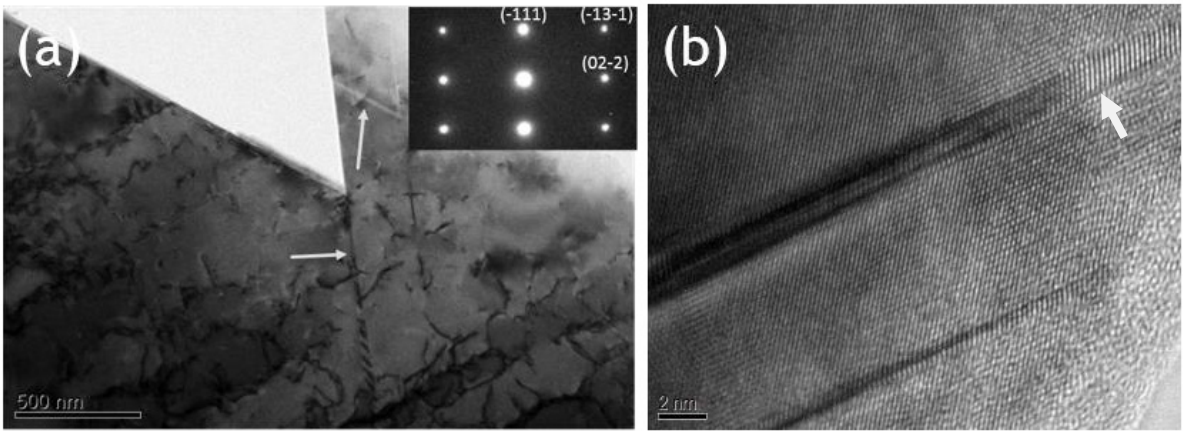

Figure 5. (a) A large crack and defects from the sample S0.5. Arrows indicate the white bands and defects. (b) HRTEM image showing the twin-like crystallographic defects within the austenitic matrix.

4. CONCLUSION

In this study, the unexpected embrittlement behavior of CN3MN grade super austenitic stainless steel was investigated. Two hypotheses were offered regarding to the sudden decrease in toughness with respect to annealing. The first one is the formation of grain boundary precipitation along the grain boundary. The second one is the development of twin-like crystallographic defects within the austenitic matrix. TEM analysis indicated that these defects originated from a white band structure already existed in pre-annealed specimens. Precipitates were observed both in ductile and brittle fractured specimens. Twin-like defects were only seen for brittle specimens. Further studies are needed to reveal the formation of the white band.

REFERENCES

1. A. H. Asli and A. Z. Hanzaki, J. Mater. Sci. Technol., 25, 3, 2009
2. G. R. Ebrahimi, H. Keshmiri and H. Arabshahi, Mater. Sci. Appl., 1, 323, 2010
3. M. Ritoni, M. Martins, F.C. Nascimento and P.R. Mei, Defect Diffus. Forum, 56, 312, 2011
4. J. Anburaj, S.S.M. Nazirudeen, R. Narayanan, B. Anandavel and A. Chandrasekar, Mat. Sci. Eng. A, 535, 99, 2012
5. T. Koutsoukis, A. Redjaima and G. Fourlais, Solid State Phenom., 172, 493, 2011
6. C. Muller and L.S. Chumbley, J. Mater. Eng. Perform., 19, 714, 2010
7. T. Koutsoukis, A. Redjaima and G. Fourlais, Mater. Sci. Eng. A, 561, 477, 2013
8. T.H. Lee, C.S. Oh, S,J. Kim and S. Takaki, Acta Mater., 56, 3649, 2007
9. M. Baskan, L.S. Chumbley and Y.E. Kalay, Metall. Mater. Trans. A, 45, 2405, 2014
10. N.S.L. Phillips, L.S. Chumbley and B. Gleeson, J. Mater. Eng. Perform., 18(9), 1285, 2009

Chemical Potential Distribution and Microstructure Evolution in Oxide Scales during High Temperature Oxidation of Metals

•

Metallerin Yüksek Sıcaklık Korozyonuyla Oluşan Oksit Kabuklarında İçyapı Gelişimi ve Kimyasal Potansiyel Dağılımı

Toshio Maruyama

Tokyo Institute of Technology - Japan

ABSTRACT

In the high temperature oxidation of metals, transport of metallic and oxide ions contributes the growth of oxide scales. The movement of ions is driven by chemical potential gradients so that the quantitative evaluation of chemical potential distribution is important to understand the oxidation process. The divergence of ion fluxes gives the microstructure evolution such as void formation, which voids may affect the mechanical strength of the scales. The quantitative evaluation is compared to the experimental evidence.

Keywords: High temperature oxidation, oxide scales, chemical potential distribution, microstructure evolution.

PARTICULAR ASPECTS OF CONSTRAINED RECOVERY SHAPE MEMORY EFFECT IN A SEVERELY PLASTIC DEFORMED Fe-Mn-Si-Cr ALLOY

Leandru-Gheorghe BUJOREANU*, Gheorghe GURĂU, Radu-Ioachim COMĂNECI*, Burak ÖZKAL***, Elena MIHALACHE***

* Faculty of Materials Science and Engineering, "Gheorghe Asachi" Technical University of Iaşi, Bd. D. Mangeron 61A, 700050 Iaşi, Romania
lgbujor@tuiasi.ro; amvric@yahoo.com; mihalache.elena@yahoo.com
** Faculty of Metallurgy, Materials Science and Environment, "Dunărea de Jos" University of Galati, Str. Domnească 111, 800201, Galați, Romania
gheorghe.gurau@ugal.ro
*** Particulate Materials Laboratory, Metallurgical and Materials Engineering Department, Istanbul Technical University, 34469 Maslak, Istanbul, Turkey
ozkal@itu.edu.tr

ABSTRACT

Coned-disk spring shape modules were processed, by high-speed high pressure torsion (HS-HPT), from an as cast Fe-28Mn-6Si-5Cr (mass %) shape memory alloy (SMA). Scanning electron microscopy (SEM) and X-ray diffraction (XRD) studies revealed that the modules became nanostructured as an effect of HS-HPT processing, which is a variant of severe plastic deformation. When subjected to compression loading-unloading cycles, between flat surfaces, the modules developed a superelastic-like force-displacement response characterized by force plateaus both on loading and unloading. After being compressed beyond the loading force plateau, the modules were subjected to constrained recovery heating and they developed recovery forces larger than those applied during compression cycles. In order to emphasize constrained recovery behavior of the HS-HPT modules, they were tested both by compression between flat surfaces and by surface inversion, which interchanged internal and external surfaces. Based on the variations of recovery force *vs.* temperature the critical temperatures for martensite reversion to austenite were determined, considering that this has been the phase transition that governs shape memory effect in SMAs.

Keywords: Shape memory alloy, High speed high pressure torsion, Constrained recovery, Nanostructure, Stress induced martensite

1. INTRODUCTION

Fe-Mn-Si base Shape Memory Alloys (SMAs) have been developed in the last three decades [1] as cheap substitutes of Ti-Ni base SMAs [2]. The main commercial applications are processed from Fe-28Mn-6Si-5Cr [3] (mass. %, as all chemical compositions will be listed hereinafter) and Fe-14Mn-6Si-9Cr-5Ni [4] and are based on constrained recovery Shape Memory Effect (SME) [5]. This means that, the SMA element is fixed into its final position, within an assembly, and develops recovery forces during heating because it is impeded to recover its initial shape [6]. This working principle was successfully employed for the development of constrained recovery applications such as pipe couplings [7], fishplates for crane rail fastening [8] and concrete pre-straining rods [9].

In previous reports, a part of present authors analyzed the reproducible development of recovery stress at an experimental Fe-23.3 Mn-2.8 Si SMA subjected to heating-cooling cycles at constant strain [10] and other part obtained active modules under the form of coned disk springs [11] by means of a modified procedure of high speed high pressure torsion (HS-HPT), a variant of severe plastic deformation (SPD) [12].

The present paper aims to further investigate the response of HS-HPT modules during compression cycles, without lubrication, and to reveal their constrained behavior, during heating in compressed state, with consideration of accompanying microstructural changes.

2. MATERIALS AND METHODS

Ingots of Fe-28Mn-6Si-5Cr SMA were cast through cold crucible induction melting. Some ingots were axially cut and resulting billets were hot rolled into 1-mm thick lamellas, according to a previously detailed procedure [13].

The first series of experiments had the goal to characterize the material in as-cast and hot-rolled state and to reveal its constrained recovery behavior. For this purpose, tensile specimens were obtained, by electrical discharge wire cutting, and subjected to failure tests, with a deformation rate of 0.5 mm/ min, by means of an INSTRON 3382 testing machine with thermal chamber. The resulting tensile failure curves are shown in Fig.1

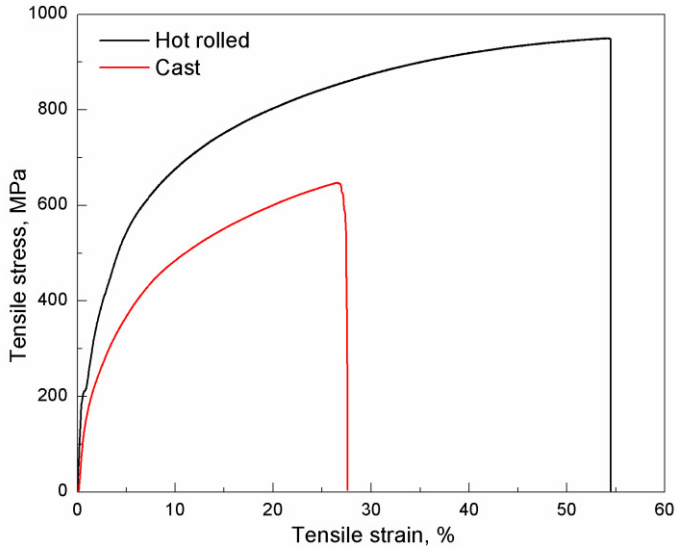

Figure 1. Tensile failure curves of Fe-28Mn-6Si-5Cr SMA specimens

In as-cast state the specimens experienced static failure at ultimate stress and strain of approximately 644 MPa and 27 %, respectively, while in hot rolled state these tensile failure parameters reached approx. 950 MPa and 54 %, respectively. In order to test constrained recovery behavior of hot rolled material, a tensile specimen was subjected to three series of heating cooling cycles, performed at increasingly higher strains, namely $\varepsilon_1 = 0{,}5$ %; $\varepsilon_2 = 1$ % and $\varepsilon_3 = 1{,}5$ %. During the cycle i ($i = 1$ 3), the specimen was subjected to : a_i-b_i – room temperature elongation; b_i-c_i – stress relation at constant strain; c_i-d_i – stress decrease during first heating; d_i-e_i – stress increase during first cooling; e_i-f_i – stress decrease during second heating; f_i-g_i – stress increase during second cooling. The results are summarized in Fig.2

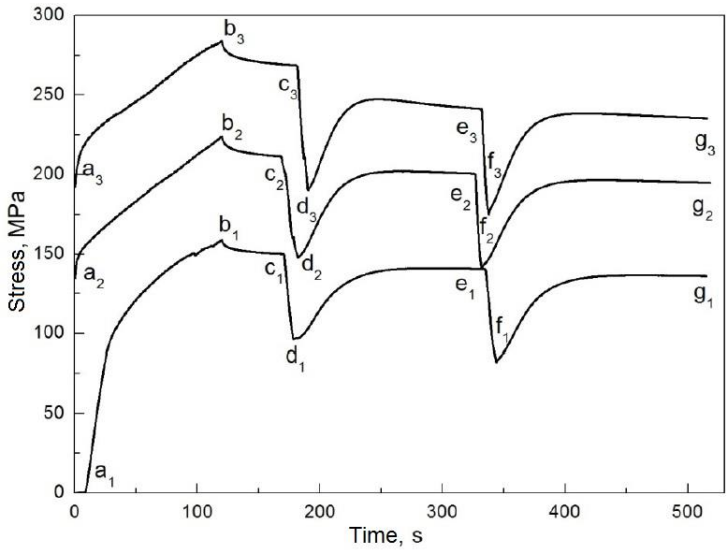

Figure 2. Tensile stress variation during three constrained recovery cycles (i=1-3) at ε_1 = 0.5 %, ε_2 = 1 % and ε_3 = 1.5 % applied to hot rolled Fe-28Mn-6Si-5Cr SMA specimens: a_i-b_i – room temperature elongation; b_i-c_i – stress relation at constant strain; c_i-d_i – stress decrease during first heating; d_i-e_i – stress increase during first cooling; e_i-f_i – stress decrease during second heating; f_i-g_i – stress increase during second cooling.

Summarizing the above results it follows that hot rolled Fe-28Mn-6Si-5Cr SMA specimens are ductile and able to develop reproducible responses by constrained recovery SME.

The next line of experiments comprised the processing of coned disk spring shape modules by severe plastic deformation. In this purpose, the ingots were machined and sectioned into circular crown slices which were deformed by HS-HPT on a special machine equipped with complimentary conical shape anvils. During HS-HPT processing a truncated cone shell was obtained from circular crown billets which kept their inner diameter almost constant, while their thickness decreased, up to 75 % and outer diameter increasing up to 55 %. This non-uniform severe plastic deformation caused a hardness gradient increasing along cone's generator, from the area of inner diameter to that of outer diameter [12].

The modules were further subjected to loading-unloading compression tests, performed on an INSTRON 3382 testing machine with thermal chamber. Compression was applied, without any lubrication, by means of two types of deformation devices: (i) with flat surfaces and (ii) with centered taper reversion, schematized in Fig.3

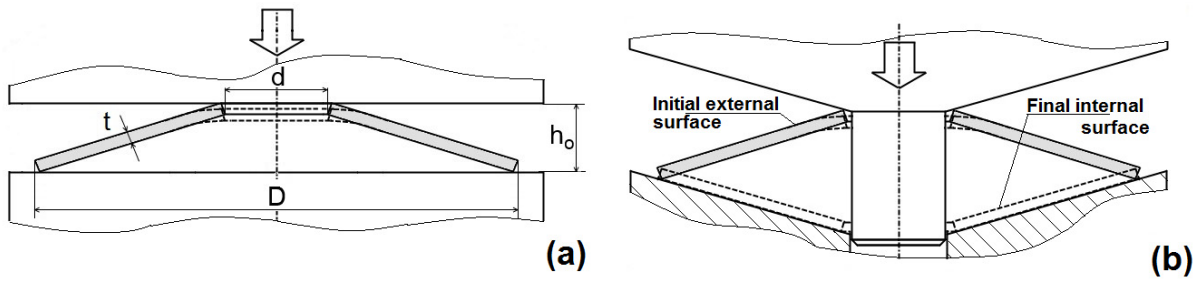

Figure 3. Illustration of compression loading mode and expected deformation predicted by FEM modeling of HS-HPT coned-disk spring shape modules between two types of deformation devices with: (a) flat surfaces and (b) centered taper reversing.

Three modules, in (i) initial, (ii) compressed between flat surfaces, without lubrication and (iii) compressed and heated (up to 480 K) states, were diametrically cut with low rate saw and embedded into cold mounting resin, before being metallographically prepared by grinding, polishing and etching [12].

Structural analyses were performed by scanning electron microscopy (SEM) observations, conducted on a FEI Quanta SEM 200 3D and by dual-beam microscope X-ray diffraction (XRD) on a BRUKER AXS D8 Advance diffractometer with Cu K_α, within the representative region of $2\theta = 40\text{-}85^0$.

The constrained recovery responses of compressed HS-HPT modules were monitored in the thermal chamber of INSTRON testing machine, by recording room temperature (RT) force-deflection evolution and then subsequent force increase during heating in constrained compressed state.

3. **RESULTS AND DISCUSSION**

Classical coned disk springs can be described by the so-called ‘‘shape characteristic ratio’’ [14], determined as $(h_0\text{-}t)/t$, according to geometrical parameters shown in Fig. 3. The results of two successive compression cycles, applied by means of the two deformation devices schematized in Fig.3, are shown in Fig.4.

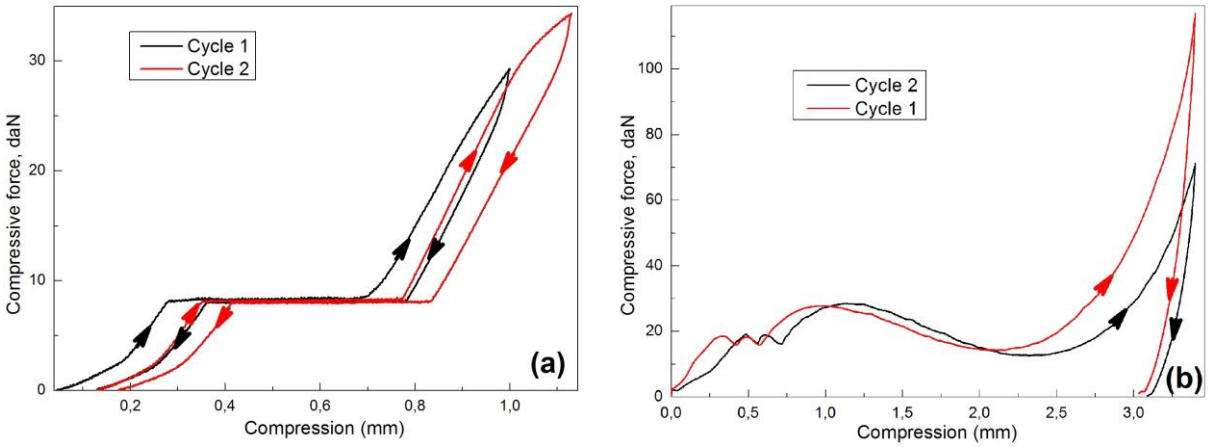

Figure 4. Force-displacement variations recorded during the compression, without lubrication, between different types of deformation devices: (a) HS-HPT module with shape characteristic ratio of 2.8, deformed between flat surfaces and (b) HS-HPT module with shape characteristic ratio of 0.9 deformed between devices with centered taper reversion.

Disregarding the difference in shape characteristic ratios, compression force varied with displacement very differently for the two modules. In Fig.4(a) there is a superelastic-like response, characterized by force plateaus both on loading and unloading portions of the curves. These reproducible load plateaus were not directly connected to ε (hcp) martensite stress-induced formation, but to the occurrence of a hardness gradient along modules generator, which enabled the gradual elastic bending of truncated shells, from inner to outer diameter areas [12]. On the other hand, when deformed with taper reversion devices illustrated in Fig.3(b), force-displacement variation acquired a typical form, characterized by three force maxima, in Fig.4(b). During one deformation cycle of taper reversion, the initial external surface became final internal surface. It is worth noticing that after two such cycles,

the respective surface became external again, each deformation cycle being accompanied by reproducible force-displacement variations. The exact succession of deformation phenomena that caused the occurrence of three force maxima will be analyzed in subsequent work. For present discussion, only the effects of compression between flat surfaces, followed by heating, will be analyzed.

The structural changes, caused by HS-HPT processing and by compression and heating were analyzed by SEM and XRD. Fig.5 shows the representative SEM micrographs of the modules in initial state and after compression and heating.

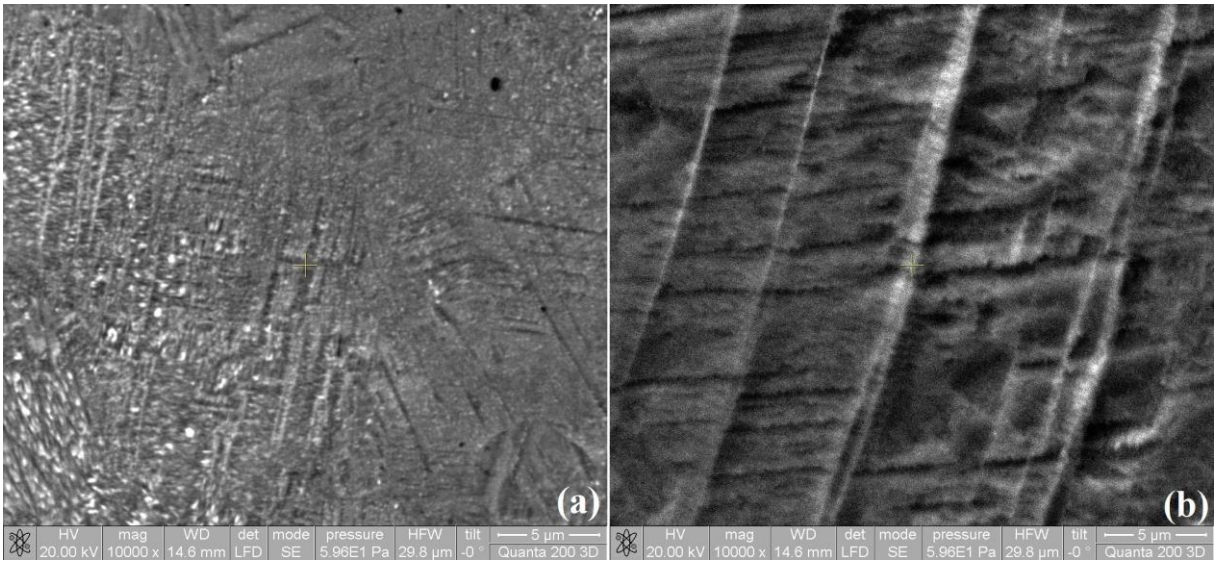

Figure 5. Representative SEM micrographs of HS-HPT modules: (a) in initial state; (b) after compression and heating.

Since HS-HPT is a procedure of severe plastic deformation, (ultra)fine distorted structure is expected to be observed in initial state. Thus, Fig.5(a) does not display the typical triangular morphology of ε (hcp) martensite, caused by plate variant growth along close-packed {111} habit planes of austenite [15]. Instead, a heavily distorted structure is observed with fine interlocking martensite plates. After heating to 480 K, evenly spaced intersecting martensite plates are noticeable in Fig. 5(b), suggesting the existence of at least two parallel-banded relieves along two particular directions, which originate from ε (hcp) stress induced martensite habit planes [16].

The presence of ε (hcp) martensite, which is a pre-requisite for SME occurrence in Fe-Mn-Si-based SMAs, was investigated by X-ray diffraction in the structure of the three HPT'd modules and the results are shown in Fig.6. Within the significant region of 2θ angle between $40^{\mathbf{0}}$ and $85^{\mathbf{0}}$, two non-overlapping γ (fcc) austenite crystallographic planes and four ε (hcp) martensite plate variants of are noticeable. Two of them, ε(100) and ε(101), are clearly distinguishable, while the other two, ε(102) and ε(103) are broader peaks that correspond to rounded diffraction maxima. These distortions of XRD peaks could be indicative for either small crystallite size along the direction normal to the specified planes or strong distortions (microstrains) altering the crystal structure, as an effect of HS-HPT processing. Semi-quantitative analysis [17] was performed by evaluating the ratios determined by the relative intensities of non-overlapping diffraction maxima ε(100), γ(111), ε(101), γ(200), ε(102) and ε(102). The results are summarized in Table 1.

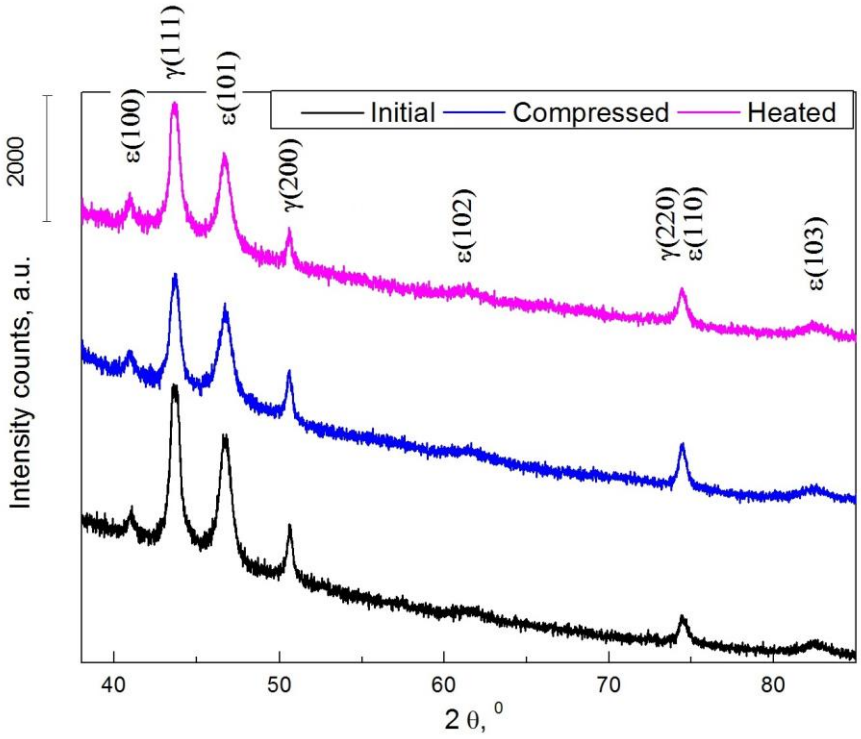

Figure 6. Typical XRD patterns recorded on three HS-HPT modules in initial, compressed and heated states, respectively.

Table 1. Semi-quantitative analysis of relative phase amounts from XRD patterns

Specimen's state	Intensity counts per crystallographic phase						Relative amounts	
	ε(100)	γ(111)	ε(101)	γ(200)	ε(102)	ε(103)	γ, %	ε, %
Initial	963	5222	4099	1840	444	444	54.3	45.7
Compressed	852	3741	3309	1778	568	457	51.6	48.4
Heated	1259	4457	3173	1383	605	580	51.0	49.0

It is obvious that the amount of ε (hcp) martensite increased both after compression and after subsequent heating. These results suggest that, as an effect of compression, ε (hcp) martensite was stress-induced after the loading-unloading cycle. During heating, alongside with martensite reversion to austenite, a part of the highly distorted structure, resulting after HS-HPT processing recrystallized.

After ascertaining the presence of ε (hcp) martensite in the structure of HS-HPT modules, next line of experiments aimed to emphasize the thermally induced reversion of martensite into γ (fcc) austenite and the accompanying SME. In order to be able to display a measurable variation, two different HS-HPT modules were compressed by means of the deformation devices illustrated in Fig.3. In the case of the device with flat surfaces, after one loading-unloading cycle, the module was pre-deformed with about 0.7 mm and heated in compressed state. In the case of the device with centered tapered reversion, after one reversal cycle, the module was removed, rotated with 180^0, compressed again with about 2.7 mm and heated in compressed state. The resulting variations of force-deformation-temperature, in the two cases, are illustrated in Fig.7. In both figures, ABC designates room-temperature compression. After reaching the compression deformation of point C, the devices were blocked and heating was on. Force increase occurred on CD portion, illustrating constrained recovery SME [18].

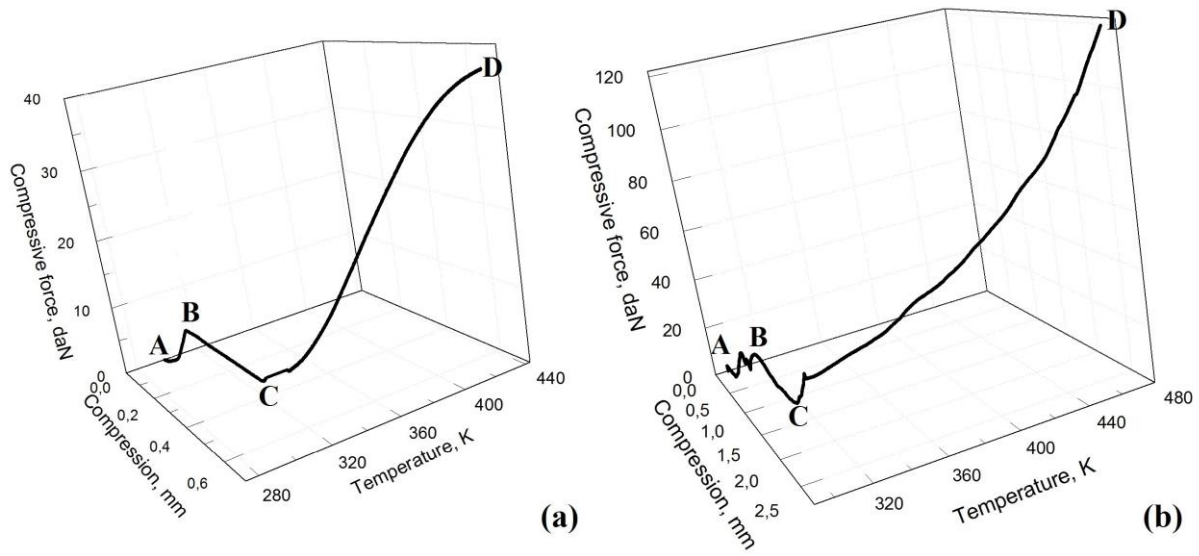

Figure 7. Force-displacement-temperature variations recorded during the compression, without lubrication, between different types of deformation devices and subsequent constrained recovery heating: (a) HS-HPT module with shape characteristic ratio of 2.8, deformed between flat surfaces and (b) HS-HPT module with shape characteristic ratio of 0.9 deformed between devices with centered taper reversion.

Force increase, during constrained recovery heating, represents the best proof that martensite reversion to austenite occurred. Moreover, the final force values are, in both cases, obviously larger than those reached during compression test, according to Fig.4.

In the case of flat surfaces device, the critical temperatures for martensite reversion were determined by tangent method as A_s' = 301 K and A_f' = 407 K. In the case of centered tapered reversion device, the critical transformation temperatures cannot be determined neither by tangent nor by other graphical methods.

4. SUMMARY AND CONCLUSIONS

A Fe-28Mn-6Si-5Cr SMA was tested in as cast and hot rolled conditions, experiencing tensile strengths of 644 MPa and 950 MPa, at ultimate strains of 27 % and 54 %, respectively.

From circular crowns, machined from as cast ingots, coned disk spring-shape modules were processed by HS-HPT routine, with different shape characteristic ratios.

When subjected to compression tests, applied by means of devices with flat surfaces and with centered taper reversion, the modules developed specific reproducible force-displacement responses characterized by "superelastic-like" aspect and by three force maxima, respectively.

In the case of the modules compressed between flat surfaces the presence of ε (hcp) martensite was revealed by SEM observations and XRD patterns, experiencing an obvious increasing tendency after compressing and subsequent heating to 480 K.

By constrained recovery tests, comprising compression and heating under constant deformation, the development of recovery forces, larger than those reached during room temperature compression, was obtained both with the devices with flat surfaces and with those with centered taper reversion.

Acknowledgment:

This work was supported by UEFISCDI, through the research project code PN-II-PT-PCCA-2011-3.1-0174, contract no. 144/ 2.07.2012

REFERENCES

1 A. Sato, E. Chishima, K. Soma and T. Mori, Acta Metall., 30(6), 1177, 1982
2 R.D. James and Hane, K.F., Acta Mater., 48, 197, 2000.
3 H.Otsuka, H.Yamada, T.Maruyama, H.Tanahashi, S.Matsuda, M.Murakami, ISIJ Int., 30, 674, 1990
4 Y.Moriya, H.Kimura, S.Ishizaki, S.Hashizume, S.Suzuki, H.Suzuki, ,T.Sampei, J Phys IV. 01C4, 433, 1991
5 J.L Proft and T.W.Duerig,. The mechanical aspects of constraint recovery, , in: Engineering Aspects of Shape Memory Alloys (Eds. T.W.Duerig, K.N.Melton, D.Stöckel, C.M. Wayman), Butterworth-Heinemann, London, pp 115–129, 1990
6 N.Van Caenegem, L.Duprez, K.Verbeken, Y.Houbaert, D.Segers, J.Van Humbeeck, Eur. Phys. J. Special Topics 158, 27, 2008
7 S.Kajiwara, A.Baruj, T.Kikuchi, N.Shinya, Proc SPIE 5053, 250, 2003
8 T.Maruyama, T.Kurita, S.Kozaki, K.Andou, S.Farjami, H.Kubo, Mater. Sci. Technol. 24, 908, 2008
9 T.Sawaguchi, T.Kikuchi, K.Ogawa, S.Kajiwara, Y.Ikeo, M.Kojima, T.Ogawa, Mater Trans, 47(3), 580, 2006
10 L.G. Bujoreanu, V. Dia, S. Stanciu, M. Susan, and C. Baciu, Eur. Phys. J. Special Topics 158, 15, 2008
11 G.Gurău, C.Gurău, O.Potecaşu, P.Alexandru, Proc of the International Conference on Shape Memory and Superelastic Technologies, Prague, 67, May 2013
12 G.Gurău, C.Gurău., O.Potecaşu, P.Alexandru, L. G.Bujoreanu, J. Mater. Eng. Perform, DOI: 10.1007/s11665-014-1060-2, 2014
13 M-G. Suru, N.M. Lohan, B. Pricop, I.P. Spiridon, E. Mihalache, R.I. Comaneci and L-G. Bujoreanu, Int. J. Mater. Prod. Tec., in press, 2014
14 S. Ozaki, K. Tsuda, J. Tominaga, Thin Walled Struct., 59, 132, 2012
15 S. Kajiwara, Mater. Sci. Eng. A, 273–275, 67, 1999
16 M. Koyama, M. Murakami, K. Ogawa, T. Kikuchi, T. Sawaguchi, Mater. Trans., 48(10), 2729, 2007
17 T.Sawaguchi, L.G.Bujoreanu, T.Kikuchi, K.Ogawa, F.Yin, ISIJ Int. 48(1), 99, 2008
18 L.G.Bujoreanu, V.Dia, S.Stanciu, M.Susan, C.Baciu Eur. Phys. J. Special Topics 158, 15, 2008

CHARACTERIZATION OF MULTİ WALLED CARBON NANOTUBE (MWCNT) -MALEIC ANHYDRIDE –OCTENE 1 / COPPER SULFIDE NANOCOMPOSITE WITH INSTRUMENTAL METHODS

Melek CUMBUL ALTAY*, Elvin Y. MALIKOV, Goncha M. EYVAZOVA**, Mustafa B. MURADOV**, Oktay H. AKPEROV** Robert PUSKÁS***, Dániel MADARÁSZ***, Zoltán KÓNYA***, Ákos KUKOVECZ*****

* Istanbul University, Turkey
mcumbul@istanbul.edu.tr
** Baku State University, Azerbaijan
bsuc@hotmail.com, eygoncha@gmail.com, mbmuradov@gmail.com, oakperov@mail.ru
*** University of Szeged, Hungary
rpuskas@chem.u-szeged.hu, maddani@chem.u-szeged.hu, konya@chem.u-szeged.hu, kakos@chem.u-szeged.hu

ABSTRACT
CuS nano particles deposited onto the oxidized MWCNT in the maleic anhydride octane 1 (MAO) copolymer matrix were synthesized by sonication process. MWCNTs were manufactured by Chemical Vapor Deposition (CVD) technique using $Fe(NO_3)_3.9\ H_2O$, $Co(NO_3)_2.\ 6\ H_2O$ and $Al(OH)_3$ powder mixture and ethylene gas (%99.9) at 923 K for 2 hours. The acid treatment procedure was utilized for functionalization of CNTs. MAO was grafted with oxidized MWCNT under sonication at 353 K for 3 hours. The synthesis of copper sulfide using copper acetate dihydrate and thiocarbamide as initial substances was performed on the basis of initial polymer matrix under same condition with heating excess 2 hours. The side wall defects of MWCNT were achieved by oxidation treatment. Transmission Electron Microscopy (TEM) analysis was revealed that MWCNTs covered with nanoparticles which are agglomerated around of the carbon nanotubes. It was found that nanoparticles (diameter of 3.18 nm) were consisted of CuS phase (Cu:S=1:1) by X- Ray Diffraction pattern.
Keywords: Carbon nanotube (CNT), Characterization techniques, Polymer-matrix composite (PMC), Sonication process.

ÇOK CİDARLI KARBON NANOTÜP (ÇCKNT) -MALEİK ANHİDRİT OKTEN 1 / BAKIR SÜLFÜR NANO KOMPOZİTLERİN ENSTRÜMENTAL YÖNTEMLERLE KARAKTERİZASYONU

ÖZET
CuS nanopartiküllerin, Maleik Anhidrit Okten-1 (MAO) kopolimer matriks içinde oksitlenmiş ÇCKNT üzerindeki sentezi sonikasyon yöntemiyle gerçekleştirilmiştir. ÇCCNT' ler $Fe(NO_3)_3.9\ H_2O$, $Co(NO_3)_2.6\ H_2O$ ve $Al(OH)_3$ toz karışımı ve etilen gazı (%99,9) kullanılarak 923 K' de 2 saat süreyle Kimyasal Buhar Biriktirme (KBB) yöntemiyle üretilmiştir. KNT' lerin fonksiyonlaştırılmasında asit çözelti işlem prosedürü kullanılmıştır. MAO sonikasyon altında 353 K' de 3 saat süreyle oksitlenmiş ÇCKNT' ler ile grafitleştirilmiştir. Bakır sülfür sentezi aynı koşullarda, bakır asetat ve tiokarbamid başlangıç malzemesi kullanılarak aynı polimer matriks üzerinde 2 saat daha fazla süreyle gerçekleştirilmiştir. ÇCKNT' ün yan duvar hataları oksidasyon işlemiyleelde edilmiştir. Geçirimli Elektron Mikroskobu (TEM) analizi,

karbon nanotüplerin etrafında aglomere olmuş nanopartiküllerin ÇCKNT' lerin etrafını kapladığını ortaya koymuştur. X Işınları Difraksiyon paterninden, nano partiküllerin (çap: 3.18 nm) CuS fazından (Cu:S=1:1) ibaret olduğu bulunmuştur.
***Anahtar kelimeler*:** Karbon nanotüp (KNT), Karakterizasyon teknikleri, Polimer matriks kompozit (PMK), Sonikasyon prosesi.

1. INTRODUCTION

Carbon nanotubes (CNTs) were discovered in 1991, by Sumio Iijima [1]. CNTs is best described as a rolled-up tubular shell of graphene sheet on a nanoscopic level which is made of a hexagonal lattice of carbon atoms. CNTs can be classified as single-walled carbon nanotubes (SWCNTs), double walled carbon nanotubes (DWCNTs) and multi-walled carbon nanotubes (MWCNTs). CNTs have been synthesized generally by laser ablation, arc discharge techniques and chemical vapor deposition (CVD) [2, 3].

CNTs can be used as ideal reinforcing agents for advanced polymer composites owing to their unique properties like high surface area, high mechanical strength, good electrical and thermal conductivity [4-6]. A key challenge in reinforcing polymers is to achieve an effective dispersion of carbon nanotubes in the matrix. The CNT surface can be modified by polar functional groups that improve the dispersion characteristics and also ensure good cross-linking abilities with chemical interactions during the polymerization. The main methods used to improve the dispersion of CNTs in polymer matrix are solution blending, melt blending, in situ polymerization and surface functionalization [7-14]. There are two main strategies for the surface functionalization of CNTs. The first one involves the covalent attachment of functional groups to the sidewall and the ends of CNTs. The second one is based on supramolecular chemistry as it involves the non-covalent attachments of molecules through weak interactions [15]. The use of ultrasonic irradiation has recently been extended from the CNT dispersion phase to the enhancement of polymerization stage [16-20].

The reinforcement of polymers with carbon nanotubes has been studied extensively already [7-13, 21-23]. However, literature results about nanoparticle deposition in the reinforced nanocomposites are limited. The present report gives a new perspective in terms of experimental diversity by combining several characterization techniques to study the deposition of CuS nanoparticles in MWCNT reinforced maleic anhydride copolymer synthesized by a sonication process. CuS nanoparticles exhibit very unusual physical and chemical properties compared to their bulk phases. Additionally, TEM, SEM, XRD and FTIR spectroscopy were used to investigate the material properties of the nanocomposite. It should be noted that sonication process is very simple and attractive method especially for synthesizing deposited nanoparticle on polymer nanocomposites.

2. MATERIAL AND METHODS

CNTs were synthesized in a horizontal tubular CVD reactor. The catalyst was prepared by depositing $Fe(NO_3)_3.9\ H_2O$ and $Co(NO_3)_{2.6}\ H_2O$ onto $Al(OH)_3$. The catalyst powder was placed in a quartz boat and allowed to react with 30 ml/min ethylene gas (99.9 % purity) at 923 K for 2 hours. Nitrogen was used during heating and cooling of the samples at a rate of 300 ml/min. Figure 1 summarizes the synthesis steps involved. The synthesized CNTs were purified in HCl (36 % aqueous solution) at boiling temperature for 16 h. Purified CNTs were washed with distilled water, dried for 48 hours in ambient air, refluxed in 10M aqueous NaOH solution for an additional 16 hours and dried again in air to obtain a sufficiently pure

starting material. The purified CNTs were then added to 0.01 M $KMnO_4$ solution and stirred at 353 K for 2 h for oxidative treatment. The oxidized CNTs (denoted as c-MWCNT because of their carboxyl functional groups) were washed with distilled water and dried in air. Maleic anhydride-octene-1 (MAO) was dissolved in 50 ml dimethylformamide. The purified and oxidized CNTs were added to this solution at a weight ratio of m(MAO)/m(oxidized CNTs)= 0.54. Azobisisobutyronitrile was used as a polymerization initiator. MAO was grafted to c-MWCNTs under sonication (sonics vibro cell at 26 kHz) at 353 K for 3 hours. The sonicated mixture is referred to as MAO/c-MWCNT. Copper acetate dihydrate ($Cu(CH_3COO)_2.2H_2O$) and thiocarbamide were added to the MAO/c-MWCNT solution in stoichiometric ratio. The mixture was sonicated (sonics vibro cell at 26kHz) at 353 K for 2 hours. The final product (denoted as MAO/c-MWCNT/CuS) was washed with distilled water several times and dried in air at room temperature.

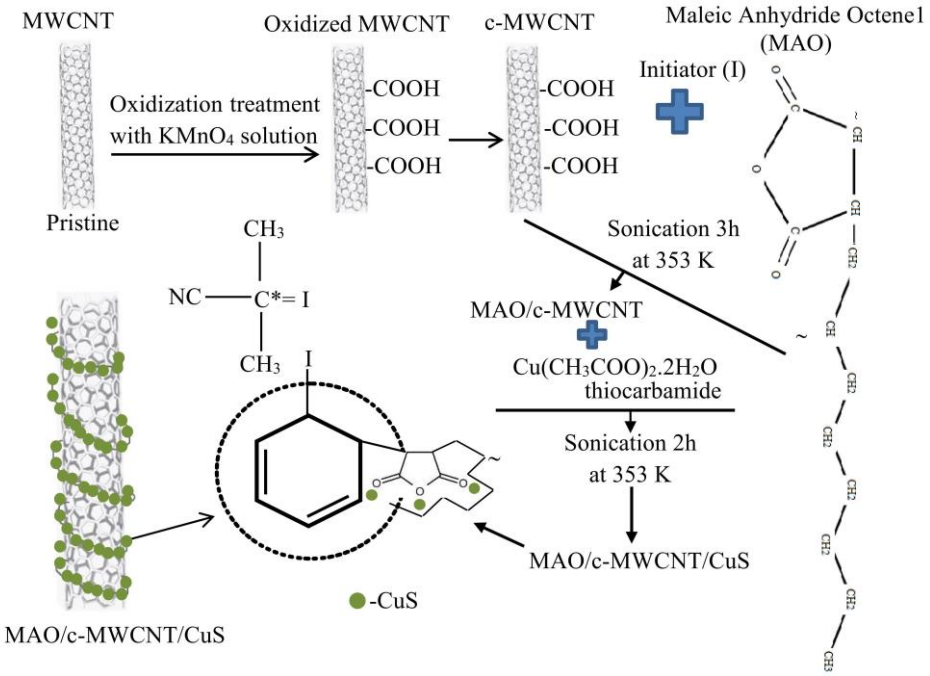

Figure 1. Schematic illustration of synthesis steps.

The microstructures of the samples were examined by a FEI TECNAİ G2 20 X–TWIN Transmission Electron Microscope. Samples for TEM were prepared by dropping the sample suspension (in acetone) onto a carbon coated copper grid. The samples were also characterized by X-ray diffractometry (XRD, Rigaku MiniFlex Desktop X–ray Diffractometer) using Cu Kα radiation (λ=0.15418 nm). The XRD patterns were obtained in the 15-80° 2θ range at a scanning rate 2◦/min. XRD phase identification was assisted by the International Centre for Diffraction Data (ICDD) database. FTIR spectra were recorded on a BRUKER Vertex 70 IR spectrometer. The specimens were prepared in pellet form by mixing the material with KBr.

3. RESULTS AND DISCUSSION

Figure 2 (a-c) shows TEM images of pristine CNTs grown from ethylene atmosphere at 923 K for 2 hours, c-MWCNTs and MAO/c-MWCNTs/CuS. As seen from Fig. 2a, synthesized pristine are hollow multi tubes with an outer diameter of 18 ± 8 nm. There is also a component of catalyst particles inside of tubes. The sidewall defects (marked by an

arrow) of c-MWCNTs are observed with TEM (Fig 2b.) as compared with pristine (Fig. 2a). The diameter of c-MWCNT is 19 ± 9 nm. It is indicated that organic functional groups attached to CNT as result of CNT oxidation and most of graphitic layers become distorted. Fig 2c illustrates that MAO has surrounded the side wall of MWCNTs (mean diameter of 12 ± 7 nm). In additionally deposited nanoparticles on side wall of MWCNTs are existed in microstructure. The nanoparticles with a mean diameter of 3.21 ± 0.2 nm are dispersed homogeneously in polymer matrix. XRD analysis is carried out to determine the nanoparticles composition as explained below. Furthermore, there has been a reduction in tube diameter of CNTs as a result of sonication process.

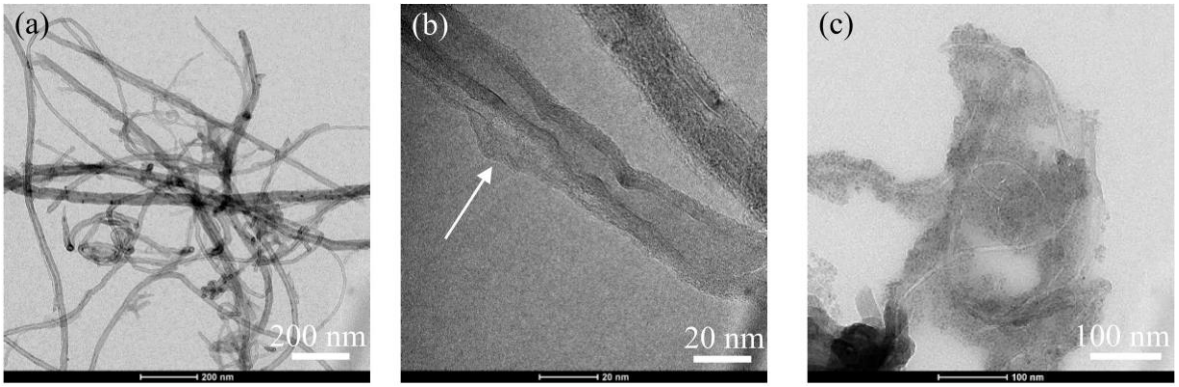

Figure 2. TEM images of the samples: (a) pristine; (b) c- MWCNTs and (c) MAO/c-MWCNTs/CuS nano composites.

XRD pattern of samples was indexed as shown in Figure 3. Standard powder diffraction file numbers of the matched materials and the (hkl) Miller indices are also stated in the patterns. As can be seen from pattern a, major diffraction peaks marked as solid circles at 26.34°, 44.82° and 77.58° are attributed to the (002), (101) and (110) crystallographic planes of carbon phase, respectively. The interplanar (d) spacing of these planes were calculated to be 0.3383, 0.20221, 0.12305 nm, which were in good agreement with the standard d spacings (0.338, 0.202 and 0.123 nm) of carbon of the standard powder diffraction file (PDF No: 00-001-0640) respectively. Oxidized MWCNTs main peaks (26.24°, 44.80° and 77.50°) are similar to carbon structure (pattern b). Comparing with the XRD pattern of pristine MWCNTs, the width of main peaks becomes larger and their intensities come to be lower as clearly shown pattern b. It is known that XRD peaks broadening shows the poor crystallinity. Thus, C (002) peak which has a wider FWHM implies that the oxidation of MWCNTs is actually disrupted the degree of crystallinity. In addition, the peak for (002) plane in oxidation MWCNTs is shifted to a lower 2θ angle of 26.24° in association with that of the pristine MWCNTs which correspond to a d spacing of 0.3396 nm (pattern b). The expansion of the d spacing revealed that intercalation of oxygen contained chains into interlayer spaces of MWCNTs. It indicates that the graphite structure of MWCNTs was oxidized with significant damage. The characteristic peaks of MWCNT can be identified from pattern c. There is no difference among the first three patterns. The MAO/c-MWCNTs exhibits similar type of XRD pattern defining that likely due to oxidation. The MWCNT became incorporated into the polymer chain during polymerization forming a sort of chemically bonded short-term branched copolymer. The peaks observed at 26.26° (0.3393 nm), 44.78° (0.2023 nm) and 77.52° (0.1231 nm) were attributed to the (002), (101) and (110) reflections from C, which were the three most intense peaks, respectively. The intensities of peaks solely decrease in polymer matrix. The amount of the MWCNTs can affect to intensity of peaks as well. The pattern d clearly

reveals that the sample consists of two main phases. One of these phases is CuS and other one is carbon. The peaks (marked as solid circle) observed at 26.36° (0.3380 nm), 44.86° (0.2020 nm), 54.22° (0,1691) and 77.52° (0.1231 nm) were attributed to the (002), (101), (004) and (110) reflections from carbon, which were the most intense peaks with standard d spacings of 0.338, 0.202, 0.169 and 0.123 nm, respectively. CuS phase was marked as a hollow circle in the pattern d. The diffraction peaks at 22.36°, 27.32°, 29.44°, 31.80°, 48.10°, 52.86°, 59.18° and 73.98° can be indexed to hexagonal phase of CuS (covellite) (PDF No: 00-001-1281). The experimental d spacings (0.3975, 0.3033, 0.2813, 0.1891, 0.1731, 0.1561 and 0.1281 nm) were found to be in good agreement with the standard ones (0.397, 0.303, 0.281, 0.189, 0.173, 0.156 and 0.128 nm) of the (004), (102), (103), (110), (114), (116) and (208) crystal planes of covellite, respectively. The average crystallite size of CuS (D) was calculated by using the Scherrer formula (1)

$$D = (0.9\lambda)/(\beta.\cos\theta) \quad (1)$$

where λ is the wavelength of Cu-$K_{\alpha 1}$ radiation (0.15418 nm), β is the broadening of diffraction line measured at half maximum intensity (in radians) and θ is the diffraction angle. The calculated CuS crystalline size is 3.18 nm and it is good agreement with average particle size obtained by TEM analysis.

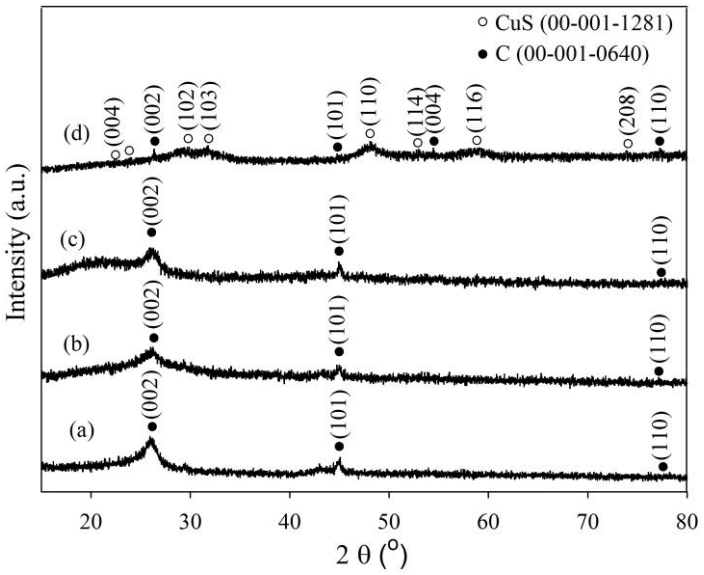

Figure 3. Characteristic XRD patterns of (a) pristine MWNTs, (b) c-MWNTs, (c) MAO/c-MWCNTs and (d) MAO/c-MWCNT/CuS.

FTIR is mainly used as qualitative technique for estimation of functional group. Figure 4 presents far infrared spectra of pristine MWNTs, c-MWNTs, MAO/c-MWCNTs and MAO/c-MWCNT/CuS from 500 to 4500 cm^{-1}. For MWCNTs, the peak at around 1540 cm^{-1}, which can be assigned to the stretching mode of -C=C- groups (spectrum a). Hexagonal structure on the pristine MWCNT is verified with appearance of peak at 1532 - 1560 cm^{-1} elucidating existence of carbon double bonding (C=C) [24]. As seen from spectrum a, the hydroxyl stretching band exists at 3750 cm^{-1} owing to ambient atmospheric moisture. Comparing with pristine MWCNT spectrum, the successful functionalized MWCNT is confirmed by remarkably presence of new bands at around 3400, 2850, 1750, 1170 and 1050 cm^{-1} introduced on the carbon nanotubes during the grafting process in spectrum b. It is pointed that decreased in absorbance of the peak at around 3700 cm^{-1} which is assigned

to the O-H stretching mode suggests some structural change in the side wall of the tube. A broad band was centered at 3400 cm^{-1} which is attributed to O-H stretching bands of carboxylic acids from the surface of MWCNTs. The free oxygen atoms, emerged from strong acid surface treatments, react with unstable carbon atoms to generate COOH groups on the surface of MWCNTs [25]. However, decreasing at C=C stretching bond region are described as a result of acid solution attack to double bonding of carbon [24]. Minor peak at 2800-2900 cm^{-1} appears after functionalization corresponding to the C-H asymmetric and symmetric stretching vibration [26]. Weak absorption bands at 1750 and 1050 cm^{-1} were defined to the stretching of C=O and C-O groups indicating the expansion of carboxylation on the surfaces of purified and functionalized MWCNTs, respectively [27]. In addition to, a peak at 1170 cm^{-1} is corresponding to the stretching vibrations of the COOH groups [25]. As can be seen from spectrum c, O-H stretching band features at around 3450 cm^{-1} were observed in the MAO/c-MWCNT. The strong absorption bands were existed at 2954 and 2856 cm^{-1} which is identified to the symmetric and asymmetric stretching of C–H bonds (C–H stretching in CH, CH_2 and CH_3 groups) [28, 29]. Furthermore, the peaks at around 1440 and 1390 cm^{-1} are associated with CH_2 and CH_3 deformations and the peak at 1180 cm^{-1} is assigned as various vibrations of CH–CH_3 group conformation [29]. The characteristic double peaks of an anhydride symmetric and asymmetric C=O stretching were appeared at 1720 and 1650cm^{-1} while features at 1590 and 1560 cm^{-1} denote the asymmetric –COO-(as) and symmetric –COO-(s) stretches of the carboxylic acids [24, 26, 30, 31]. Other characteristic peaks of MA are corroborated with peaks at 1260, 1100 and 1025 cm^{-1} which are related to vibrations of C-O-C [32, 33]. The band at 680 cm^{-1} is identified with the out-of-plane bending of C-H bond in the aromatic ring. From spectrum c, the broad transmittance band appears at around 3280 cm^{-1} associated with the formation of C-H bonds. Also, the C=C double bond of MA (at 3170 cm^{-1}) disappeared at the same time [34]. The peaks at 1180 and 618 cm^{-1} were assigned to C-C stretching and C-H bond, respectively [35]. It should be noted that peaks were shaper as distinct from spectrum b. Moreover, C–S stretching vibration is observed at around 686 cm^{-1} [36, 37].

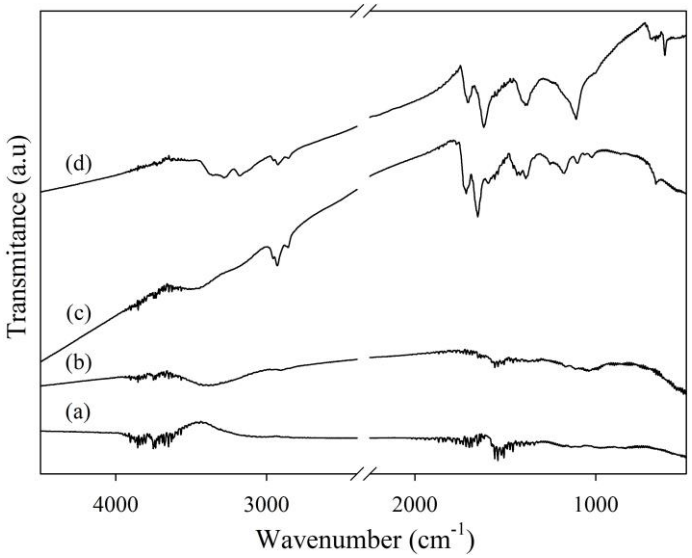

Figure 4. FTIR analysis spectrums,(a) pristine MWNTs, (b) c-MWNTs, (c) MAO/c-MWCNTs and (d) MAO/c-MWCNT/CuS.

The main formation reactions of CuS nanoparticles on CNT reinforced polymer nanocomposites can be described by following equations:

$$(NH_2)_2CS + 2OH^- \leftrightarrow S^{2-} + 2H_2O + H_2CN_2 \quad (3)$$
$$Cu^{2+} + S^{2-} \rightarrow CuS_{(s)} \quad (4)$$

As seen the equation 3, thiocarbamide behaviors as a source of sulfur atoms as well as a reducing agent [38]. Acetate groups of copper acetate and Carboxyl group with MWCNTs such as carboxylic acids can effect reactions given in equations 5 and 6. Acetate ions are generated by the dissociation of the acetic acid (equation 7). The acetate ions will react with thiocarbamide (equation 9). CuS formation will occur according to equation 10 [39].

$$Cu(CH_3COO)_2 + H_2 \leftrightarrow Cu + 2CH_3COOH \quad (5)$$
$$CH_3COOH \rightarrow CH_3CO_2^- + H^+ \quad (6)$$
$$CH_3COOH + H_2O \leftrightarrow H_3O^+ + CH_3COO^- \quad (7)$$

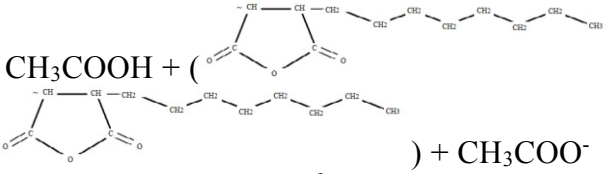

$$CH_3COOH + (\quad) \rightarrow (\text{protonated} \quad) + CH_3COO^- \quad (8)$$

$$(NH_2)_2CS + 2CH_3COO^- \leftrightarrow S^{2-} + 2CH_3COOH + H_2CN_2 \quad (9)$$
$$Cu^{2+} + S^{2-} \rightarrow CuS \quad (10)$$

MAO/c-MWCNTs/CuS formation mechanism could be explained as follows: first MAO copolymers are adsorbed onto the surface of the c- MWCNTs then polymer chains are constrained to grow around the tubes as a result of deposition on the surface of c-MWCNTs. Moreover, addition of copper acetate and thiocarbamide to MAO/c-MWCNT are responsible to CuS formation reaction.

4. CONCLUSION

In this study, CuS nano particles deposited onto the functionalized MWCNT in the copolymer matrix were synthesized by sonication process. Sonication method is very attractive method for synthesizing nanostructured materials compared with the other methods in terms of uniform particle-size distributions, better thermal stability, slightly higher surface area and also inexpensive technique. The samples were characterized by TEM, XRD and FTIR techniques. The side wall defects of MWCNT were achieved by oxidation treatment and most of graphitic layers have distorted as seen TEM images. The ultrasonic technique overcomes the van der waals interactions in the MWCNTs bundles and leads to great dispersion of CuS nanoparticles in polymer matrix. TEM analysis was revealed that only individual MWCNTs covered with nanoparticles which are agglomerated around of the carbon nanotubes. It was found that nanoparticles (diameter of 3.18 nm) were consisted of CuS phase (Cu:S=1:1) by XRD pattern. FTIR spectroscopy confirmed that functionalized MWCNTs and CuS nanoparticles have covalent interaction with maleic anhydride-Octene 1 to formation nanocomposite.

Acknowledgements

This work was supported by the EC FP7 program (NAPEP Grant agreement number: 266600). The financial support of the OTKA NN 110676, TÁMOP-4.2.2.A-11/1/KONV-2012-0047 and TÁMOP-4.2.2.A-11/1/KONV-2012-0060 projects is acknowledged. M. C. Altay also wishes to thank for sabbatical support to Rectorate of Istanbul University.

REFERENCES

1. S.Iijima, Nature, 354, 56, 1991
2. M.Paradise, T.Goswami Mater Des, 28, 1477, 2007
3. B.Bhushan, "Springer handbook of nanotechnology", Springer-Verlag, Berlin, 2004
4. M.Cumbul Altay, S.Eroglu, J Cryst Growth, 364, 40, 2013
5. X.L.Xie, Y.W.Mai, X.Ping, Mater Sci Eng Rep, 49, 89, 2005
6. R.Andrews, M.C.Weisenberger, Curr Opin Solid St M, 8, 31, 2004
7. H.Chen, O.Jacobs, W.Wu, G.Rüdiger, B.Schädel, Polym Test, 26, 351, 2007
8. S.C.Mun, M.Kim, K.Prakashan, H.J.Jung, Y.Son, O.Park, Carbon, 67, 64, 2014
9. D.Kolacyak, J.Ihde, C.Merten, A.Hartwig, U.Lommatzsch, J Colloid Interf Sci, 359, 311, 2011
10. L.Vanyorek, R.Meszaros, S.Barany, Colloid Surface A, 48, 140, 2014
11. C.-C.Hu, C.-C.Wang, J Power Source, 125, 299, 2004
12. C.Yin, J.Dong, Z.Li, Z.Zhang, Q.Zhang, Compos Part B Eng, 58, 430, 2014
13. A. Hirsch, Angew Chem Int Ed, 41, 1853, 2002
14. P.-C.Ma, N.A.Siddiqui, G.Marom, J.-K.Kim, Compos Part A – Appl S, 41, 1345, 2010
15. J.M.Lehn, Science, 227, 849, 1985
16. S.V.Ahir, Y.Y.Huang, E.M.Terentjev, Polymer, 49, 3841, 2008
17. J.Sandler, M.S.P.Shaffer, T.Prasse, W.Bauhofer, K.Schulte, A.H.Windle. Polymer, 40, 5967, 1999
18. K.Lau, M.Lu, C.Lam, H.Cheung, F.Sheng, H.Li, Compos Sci Technol, 65, 719, 2005
19. S.G.Prolongo, M.Burón, M.R.Gude, R.Chaos-Morán, M.Campo, A.Ureña, Compos Sci Technol, 68, 2722, 2008
20. W.S.Chow, P.L.Tan, J Reinf Plast Comp, 29, 2331, 2010
21. S.Bal, S.S.Samal, B Mater Sci, 30, 379, 2007
22. P.M.Ajayan, O.Stephan, C.Colliex, D.Trauth, Science, 265, 1212, 1994
23. L.S.Schadler, S.C.Giannaris, P.M.Ajayan, Appl Phys Lett, 73, 3842, 1998
24. R.Yudianti, H.Onggo, Sudirman, Y.Saito, T.Iwata, J.Azuma, Open Mater Sci J, 5, 242, 2011
25. P.Kar, A.Choudhury, Sensor Actuat B – Chem, 183, 25, 2013.
26. S.Mallakpoura, A.Zadehnazari, Synthetic Met, 169, 1, 2013;
27. V.Ambrogi, G.Gentile, C.Ducati, M.C.Oliva, C.Carfagna, Polymer, 53, 291, 2012
28. C.-C.Chu, K.L.White, P.Liu, X.Zhang, H.-J.Sue, Carbon, 50, 4711, 2012
29. Z.M.O.Rzayev, Int Rev Chem Eng, 3, 153, 2011
30. G.M.O.Barra, J.S.Crespo, J.R.Bertolino, V.Soldi, A.T.N.Pires, J Braz Chem Soc, 10, 31, 1999
31. M.R.McPhail, J.A.Sells, Z.He, C.C.Chusuei, J Phys Chem C, 113, 14102, 2009
32. E.O.Akperov, A.M.Maharramov, O.G.Akperov, J Appl Polym Sci, 118, 3570, 2010
33. G.C.Chitanu, I.Popescu, I.M.Peli, M.I.Avadanei. Rev Roum Chim, 53, 577, 2008
34. C.-F.Kuana, H.-C.Kuana, C.-C.M.Mab, C.-H.Chena, J Phys Chem Solids, 69, 1395, 2008
35. C.-C.Lia, J.-L.Lin, S.-J.Huang, J.-T.Lee, C.-H.Chen, Colloid Surfaces A, 297, 275, 2007
36. M.Reichenbächer, J.Popp, "Challenges in Molecular Structure Determination" Heidelberg, Springer-Verlag Berlin, 2012
37. A.S.Ethiraj, D.J.Kang, Nanoscale Res Lett, 7, 70, 2012
38. S.G.Dixit, A.R.Mahadeshwar, S.K.Haram, Colloid Surfaces A, 133, 69, 1998
39. H.T.Boey, W.L.Tan, N.H.H.Abu Bakar, M.Abu Bakar, J.Ismail, J Phys Sci, 18, 87, 2007

Development of Mn-Al Magnets

•

Al-Mn Mıknatısların Geliştirilmesi

Özgün Acar[1], Yunus Eren Kalay[1], İlkay Kalay[2]

[1]Middle East Technical University, [2]Çankaya University - Türkiye

ABSTRACT

Magnets have been widely used in electric motors, hard drives and many other energy related technological applications. Most of the powerful magnets are based on rare-earth (RE) elements such as Sm and Nd. Recently, scientists have focused on the development of new RE-free magnets mainly because of the current geo-political concerns of RE elements. Manganese-Aluminum (MnAl) alloy system has recently attracted much attention as a potential candidate for magnetic applications. In this study, Mn-Al magnetic alloys were developed and investigated in details. Alloy production methods such as arc melting and suction casting were applied. The as-quenched and heat-treated alloys were investigated using vibrating sample magnetometer (VSM), scanning electron microscopy (SEM), energy-dispersive X-ray spectroscopy (EDS), optical microscopy, differential thermal analysis (DTA) and X-ray diffraction analysis (XRD). The effects of alloy composition and solidification rate on magnetic properties will be discussed in details.

Keywords: Mn-Al magnets, magnetic properties, microstructure.

The prediction of properties of B_4C particle reinforced metal matrix composites using artificial neural networks

Temel Varol[a], Aykut Canakci[a*], Sükrü Ozsahin[b]

[a*]Department of Metallurgical and Materials Engineering, Engineering Faculty,
[b]Department of Industry Engineering, Of Technology Faculty
Karadeniz Technical University, Trabzon, Turkey.
aykut@ktu.edu.tr

Abstract
In this work, artificial neural network (ANN) approach was used for the prediction of physical and mechanical properties of B_4C reinforced Al2024 matrix composites produced by powder metallurgy. Effects of reinforcement size and content (wt.%) on the physical and mechanical properties of composites were determined by measuring the density, hardness and tensile strength values. Density, hardness and tensile values strength of the composites were the outputs obtained from the proposed ANN. The results showed that the effect of reinforcement size and content on the homogeneous distribution of B_4C particles is as important as the effect of milling time. By comparing the predicted values with the experimental data, it was demonstrated that the well-trained feed forward back propagation ANN model is a powerful tool for prediction of physical and mechanical properties of composites.

Keywords: Powder metallurgy; metal matrix composites; mechanical properties; ANN

Yapay sinir ağı yöntemi kullanılarak B_4C partikül takviyeli metal matrisli kompozitlerin özelliklerinin tahmini

Temel Varol[a], Aykut Çanakçı[a*], Sükrü Özsahin[b]

[a]Metalurji ve Malzeme Mühendisliği Bölümü, Mühendislik Fakültesi,
Karadeniz Teknik Üniversitesi, Trabzon, Türkiye
aykut@ktu.edu.tr

Özet
Bu çalışmada toz metalurjisi yöntemi ile üretilen B_4C takviyeli Al2024 matrisli kompozitlerin fiziksel ve mekanik özelliklerinin tahmini için yapay sinir ağı yaklaşımı kullanılmıştır. Takviye boyutu ve miktarının kompozitlerin fiziksel ve mekanik özellikleri üzerine etkisi yoğunluk, sertlik ve çekme mukavemeti değerlerinin ölçümü ile belirlenmiştir. Aynı zamanda yoğunluk, sertlik ve çekme mukavemeti önerilen tahmin modelinden elde edilen çıktı değerleridir. Sonuçlar takviye boyutu ve miktarının B_4C partiküllerinin homojen dağılımı üzerinde öğütme zamanı kadar önemli etkisi olduğunu göstermiştir. Deneysel verilerle tahmin değerleri karşılaştırıldığında iyi bir şekilde eğitilmiş ileri-geri beslemeli yapay sinir ağı modelinin kompozitlerin fiziksel ve mekanik özelliklerinin tahmini için güçlü bir araç olduğu kanıtlanmıştır.

Anahtar Kelimeler: Toz metalurjisi, metal matrisli kompozitler, mekanik özellikler, ANN

1. INTRODUCTİON

MMCs can be synthesized by such methods as conventional casting techniques [1, 2] powder metallurgy [3], spray deposition [4] and diffusion bonding [5] approach. Powder metallurgy method is the most suitable method for making MMCs. Compared with melting methods, the most important advantage of powder metallurgy method is the low processing temperature. That is why undesired phases between the matrix phase and the reinforcement phase are eliminated. Moreover, reinforcement particles are also well-distributed in the matrix [6]. The use of artificial neural networks (ANNs) has recently been used in modeling the manufacturing, physical and mechanical properties of engineering materials. It is a promising field of research in predicting experimental trends and has become increasingly popular in the last few years as they can often solve problems much faster compared to other approaches with the additional ability to learn from small experimental data. The purpose of the present work, therefore, was to: (a) investigate the effect of content (wt.%), size of reinforcing particle and milling time on the physical and mechanical properties of Al2024-B_4C MMCs; (b) develop an ANN model for the prediction the role of reinforcement properties on the physical and mechanical properties of Al2024-B_4C composites produced by powder metallurgy with the use of ANN.

2. EXPERIMENTAL

2.1. Materials

The weight percentages of B_4C particle in the composites are 5, 10 and 20 (wt.%), respectively. To produce Al2024-B_4C composites, Al2024 powders with average particle size of about 75μm and B_4C powders with particle size of 49μm and 5μm were used. The mixtures were milled using a planetary ball mill (Fritsch "Pulverisette 7, Premium line") at different milling times (0.5, 1, 2, 5, 7 and 10h). A ball to powder weight ratio of 10:1 was kept constant in the tungsten carbide vials. Methanol (2 wt.%) was used as a process control agent. The rotational speed was controlled at 400rpm. The composite powder mixtures milled by mechanical milling were loaded into a steel die and cold pressed at 200MPa and then hot-pressed at 400 °C at a pressure of 200MPa. The theoretical density of compacts was calculated from the simple rule of mixtures taking the fully dense values for Al2024 (2.8g/cm^3) and B_4C (2.52g/cm^3). The hardness of all samples was measured by the Brinell hardness method and mean of at least five readings was taken at a load of 31.25kgf. Tensile test was performed using an MTS model 45 electromechanical test instrument at room temperature on plate specimens with a cross-head speed of 0.5mm min^{-1}. At least three samples were tested for each material.

2.2. Artificial neural networks

The addition function (threshold function, Eq.1) (net_j) calculates the net input on a neural cell. The sigmoid function (Eq.2) is the most common activation function in the ANN because it combines nearly linear behavior, curvilinear behavior, and nearly constant behavior [7, 8].

$$net_j = \sum_{i=1}^{n} x_i w_{ij} - \theta_i \quad (1)$$

where x_i indicates the i. input, w_{ij} is the connection weight from j. element to i. element, θ_j is the polarization value (negative of the threshold value), and n indicates the sent input signal of the artificial neuron number in the previous layer. The produced output is sent via the network connections between different cells, as explained by:

$$y_j = f(netj) = 1/(1+e^{-netj}) \quad (2)$$

When more than one parallel processing artificial neuron is necessary, a multi-layered network structure is used. In this study, the alteration of density, hardness, and tensile strength of composites produced by powder metallurgy method were modeled by the ANN. To examine the effect of the reinforcement content (wt.%), size and milling time on the density, hardness and tensile strength, the experimental data were grouped into training and test data. The training data were used in the forecast model, as shown in Table 2.

Table 2. Experimental data and predicted output from the ANN network for training set.

Sample ID	Reinforcement Ratio (%)	Reinforcement Size (μm)	Milling Time (h)	Density (gr/cm^3)			Hardness (BHN)			Tensile Strength (MPa)		
				Measured	Predicted	% Error	Measured	Predicted	% Error	Measured	Predicted	% Error
1	0	0	0	2.675	2.670	0.20	86	85.1	1.06	187	189.7	-1.46
3	0	0	0.5	2.659	2.665	-0.24	90	89.6	0.49	195	188.5	3.32
4	0	0	2	2.634	2.641	-0.28	97	97.7	-0.71	231	230.7	0.12
6	0	0	5	2.621	2.616	0.20	120	118.4	1.32	234	234.5	-0.21
7	0	0	10	2.603	2.605	-0.06	156	157.3	-0.81	144	144.6	-0.41
9	5	49	0.5	2.645	2.640	0.20	113	112.3	0.60	184	181.1	1.59
10	5	49	1	2.630	2.632	-0.09	118	119.0	-0.88	181	182.3	-0.71
12	5	49	5	2.594	2.592	0.09	156	154.3	1.10	255	254.5	0.21
13	5	49	7	2.571	2.571	0.00	206	204.2	0.86	175	176.8	-1.05
15	5	49	10	2.566	2.561	0.19	219	213.7	2.42	167	165.6	0.82
16	10	49	0	2.615	2.604	0.42	113	114.3	-1.18	165	173.6	-5.24
17	10	49	1	2.587	2.585	0.08	129	129.2	-0.12	169	174.3	-3.13
19	10	49	2	2.572	2.569	0.12	135	133.0	1.47	261	260.0	0.39
20	10	49	7	2.465	2.469	-0.16	248	253.4	-2.18	184	184.1	-0.08
22	20	49	0.5	2.551	2.553	-0.07	136	136.0	-0.01	160	161.7	-1.08
23	20	49	2	2.530	2.527	0.13	164	163.0	0.63	220	219.9	0.04
25	20	49	5	2.511	2.509	0.08	245	241.9	1.27	217	216.7	0.13
26	20	49	7	2.420	2.422	-0.06	290	291.9	-0.67	141	141.2	-0.14
28	5	5	0	2.652	2.646	0.23	110	107.5	2.30	182	182.4	-0.23
29	5	5	1	2.624	2.631	-0.27	119	121.2	-1.82	184	183.7	0.17
31	5	5	2	2.613	2.612	0.03	122	121.1	0.71	260	261.0	-0.39
32	5	5	5	2.585	2.586	-0.05	157	160.3	-2.11	264	261.8	0.82
34	5	5	10	2.554	2.559	-0.18	225	229.7	-2.09	172	171.7	0.18
35	10	5	0	2.598	2.599	-0.03	115	117.6	-2.23	170	172.3	-1.35
37	10	5	0.5	2.580	2.589	-0.33	123	125.4	-1.95	178	170.4	4.28
38	10	5	2	2.560	2.560	0.01	136	137.9	-1.40	274	273.7	0.10
40	10	5	5	2.533	2.536	-0.13	222	221.7	0.16	280	281.8	-0.64
41	10	5	7	2.455	2.450	0.20	288	281.0	2.43	191	190.3	0.35
43	20	5	0.5	2.539	2.542	-0.13	146	139.8	4.23	162	159.5	1.52
44	20	5	1	2.532	2.529	0.14	150	150.3	-0.21	165	162.0	1.80
46	20	5	2	2.510	2.515	-0.19	166	170.3	-2.62	225	226.1	-0.50
47	20	5	7	2.402	2.400	0.09	320	322.5	-0.79	144	143.8	0.17
49	20	5	10	2.385	2.386	-0.05	336	333.2	0.84	136	136.1	-0.05
	MAPE			**0.143**			**1.323**			**0.991**		
	RMSE			**0.004**			**2.870**			**2.818**		

From the well known and widespread identification tools, the root mean squared error (RMSE) and the mean absolute percentage error (MAPE) values are calculated from Eqs.3 and 4 [9]. Models that produce the best estimated values were selected as the forecasting models.

$$RMSE = \sqrt{\frac{1}{N}\sum_{i=1}^{N}\left(t_i - td_i\right)^2} \qquad (3)$$

$$\mathrm{MAPE}=\frac{1}{N}\left(\sum_{i=1}^{N}\left[\left|\frac{t_i-td_i}{t_i}\right|\right]\right)\times 100 \quad (4)$$

where t_i is the real value, td_i is the model prediction value and N is the number of testing data. Table 2 shows the actual values, degrees of deviation, percentage error rates, RMSE and MAPE calculated using the estimated models.

2.3. Neural network architecture

Fig. 1 shows the ANN models containing one input layer, two hidden layers and one output layer. The minimum error was obtained at 5 nodes at the first hidden layer and 5 nodes at the second hidden layer for the prediction model of the density, hardness and tensile strength. The reinforcement content (wt.%), size (μm) and milling time were used as the input variables, while the density, hardness and tensile strength values were used as the output variables in the ANN models.

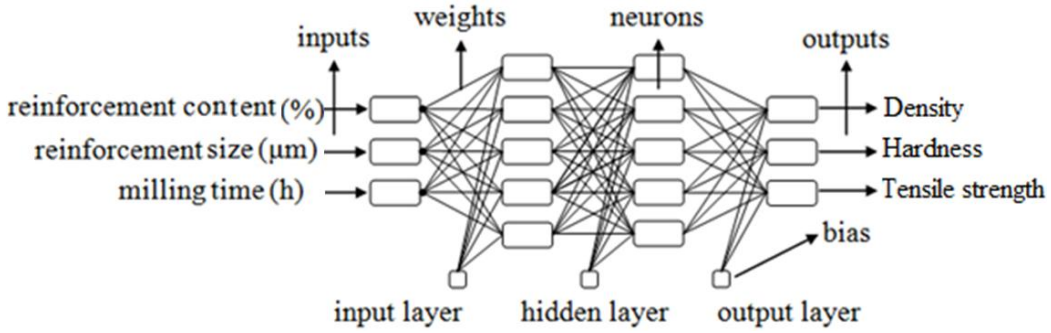

Figure 1. The ANN architecture selected as the prediction model for the density, hardness and tensile strength.

2.4 Network training and testing

The normalization (scaling) operations were carried out using Eq. 5:

$$X_{norm}=2\times\frac{X-X_{\min}}{X_{\max}-X_{\min}}-1 \quad (5)$$

where X_{norm} is the normalized value, X is the true value of the variable, X_{min} is minimum value of the data set and X_{max} is the maximum value of the data set.

3. RESULTS AND DISCUSSION

3.1. The effect of reinforcement properties on the relative density

SEM image of Al2024-5wt.% B_4C_{coarse} composites were given in Fig. 2. As is expected at initial milling time (Fig. 2a), the particle distribution was not uniform and the distance between B_4C particles was too high. But increasing milling time caused the big and brittle B_4C particles to break. Also, with increasing milling time the distance between B_4C particles decreased gradually (Fig. 2b). After 10h milling time, B_4C particles were dispersed throughout the Al2024 alloy matrix with a better homogeneity (Fig. 2c).

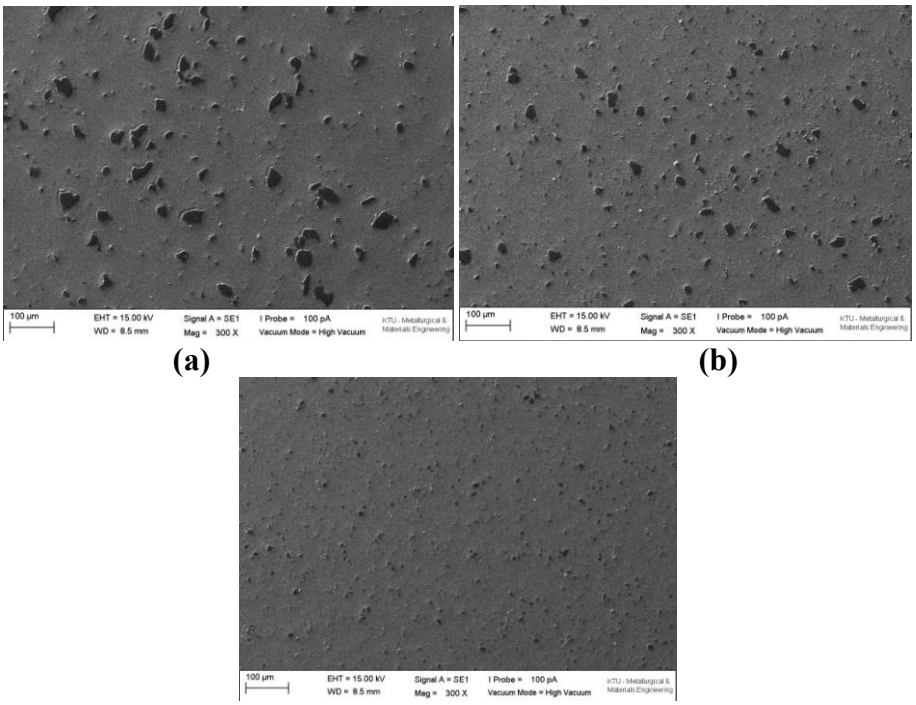

Figure 2. SEM micrograph of Al2024-5wt.% B4C$_{coarse}$ composites: (a) 0.5h, (b) 2h, (c) 10h

3.2. The effect of reinforcement properties on the hardness

The hardness of Al2024 samples and Al2024-B_4C_{coarse} and Al2024-B_4C_{fine} composites versus milling time is plotted in Figs. 3a and 3b. Since the density of samples was around 95% up to 5h of milling, it was possible to characterize their hardness. It can be seen that the produced samples have higher hardness. The increase in hardness is attributed to the milling time as shown in Figs. 3a and 3b. It should be note that the particle size of B_4C powders affects the number of particles within surface area of indentation. The number of reinforcement particles per unit impression area in fine B_4C reinforced composite is greater than that in coarse B_4C reinforced composite due to the embedded process of hard B_4C particles. Therefore, impression diameter decreases with increasing number of hard ceramic particles.

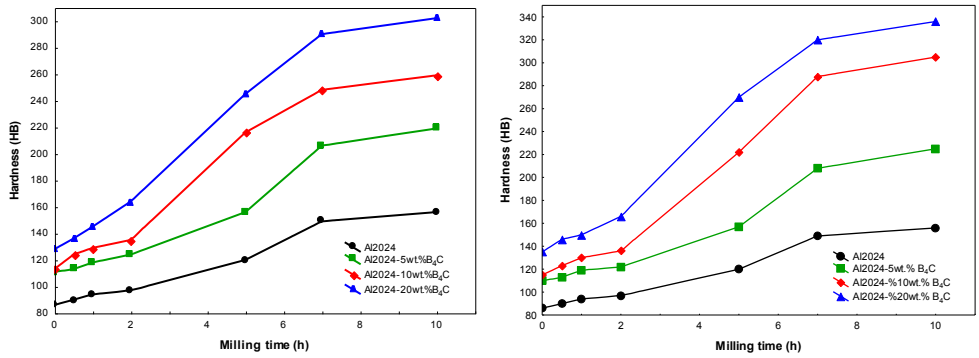

Figure 3. The HB hardness evolution of the composites as a function of milling time and amount of B_4C particles; (a) coarse B_4C reinforced composites and (b) fine B_4C reinforced composites.

3.3 Modeling results

The predicted values, deviation and % error for the density, hardness and tensile strength are provided in Tables 2 and 3. The ANN was tested for accuracy using the test values (Table 3) selected from the experimental results that were not used during the learning processes. In

most cases, the neural network prediction is very close to the actual value. However, several values are not as close as others, which is due to the errors caused by the material, the measurements and process parameters. However, these errors could be neglected given that the learning level of the artificial neural network is 98%. This study revealed that the predictions made using the ANN produced more accurate results.

Table 3. Experiment data and predicted output from the ANN network for testing test.

Sample ID	Reinforcement Ratio (%)	Reinforcement Size (μm)	Milling Time (h)	Density (gr/cm^3)			Hardness (BHN)			Tensile Strength (MPa)		
				Measured	Predicted	% Error	Measured	Predicted	% Error	Measured	Predicted	% Error
1	0	0	0	2.645	2.660	-0.56	94	94.9	-0.93	190	188.5	0.79
3	0	0	0.5	2.612	2.606	0.21	149	151.0	-1.36	152	155.1	-2.03
4	0	0	2	2.658	2.646	0.46	111	106.5	4.09	178	182.5	-2.53
6	0	0	5	2.622	2.615	0.25	124	120.2	3.10	252	248.2	1.50
7	0	0	10	2.595	2.595	-0.01	124	121.4	2.12	173	171.8	0.70
9	5	49	0.5	2.540	2.549	-0.35	216	201.0	6.97	263	272.9	-3.75
10	5	49	1	2.450	2.451	-0.04	259	261.9	-1.14	174	170.0	2.30
12	5	49	5	2.583	2.564	0.73	128	127.2	0.60	153	164.4	-7.48
13	5	49	7	2.542	2.540	0.06	145	145.9	-0.61	157	162.8	-3.68
15	5	49	10	2.415	2.409	0.26	302	298.4	1.21	133	134.1	-0.81
16	10	49	0	2.633	2.639	-0.24	113	114.1	-0.93	190	181.0	4.75
17	10	49	1	2.562	2.568	-0.23	208	216.7	-4.17	181	183.5	-1.38
19	10	49	2	2.572	2.577	-0.19	130	133.6	-2.77	172	175.1	-1.79
20	10	49	7	2.438	2.431	0.27	305	292.7	4.04	182	175.0	3.83
22	20	49	0.5	2.565	2.555	0.37	135	130.3	3.47	158	162.4	-2.79
23	20	49	2	2.473	2.492	-0.75	270	264.8	1.92	221	221.3	-0.13
	MAPE			**0.312**			**2.463**			**2.515**		
	RMSE			**0.010**			**6.054**			**5.543**		

The mean absolute percentage error (MAPE) was used to evaluate the performance of the proposed ANN as a prediction technique. The mean absolute percentage errors (MAPE) were 0.312% for density, 2.463% for hardness and 2.515% for tensile strength. With respect to the results obtained from the plots of the ANN prediction, the highest MAPE value of 2.515% demonstrates that the network effectively generates sensitive results. Fig. 4 shows the regression analysis of the ANN model for the density, hardness and tensile strength. The correlation coefficient was obtained to be 0.99, indicating good agreement between the experimental results and the model predication ($R_{density}$ =0.99138, $R_{hardness}$= 0.99693, $R_{tensile\ strength}$= 0.98746). The statistical results namely, the root-mean squared error (RMSE) and the mean absolute percentage error (MAPE), are within an acceptable range and meet the integrity of the ANN learning and testing stages. Thus, reasonable agreement between the predicted and experimental data supports the accuracy of the model.

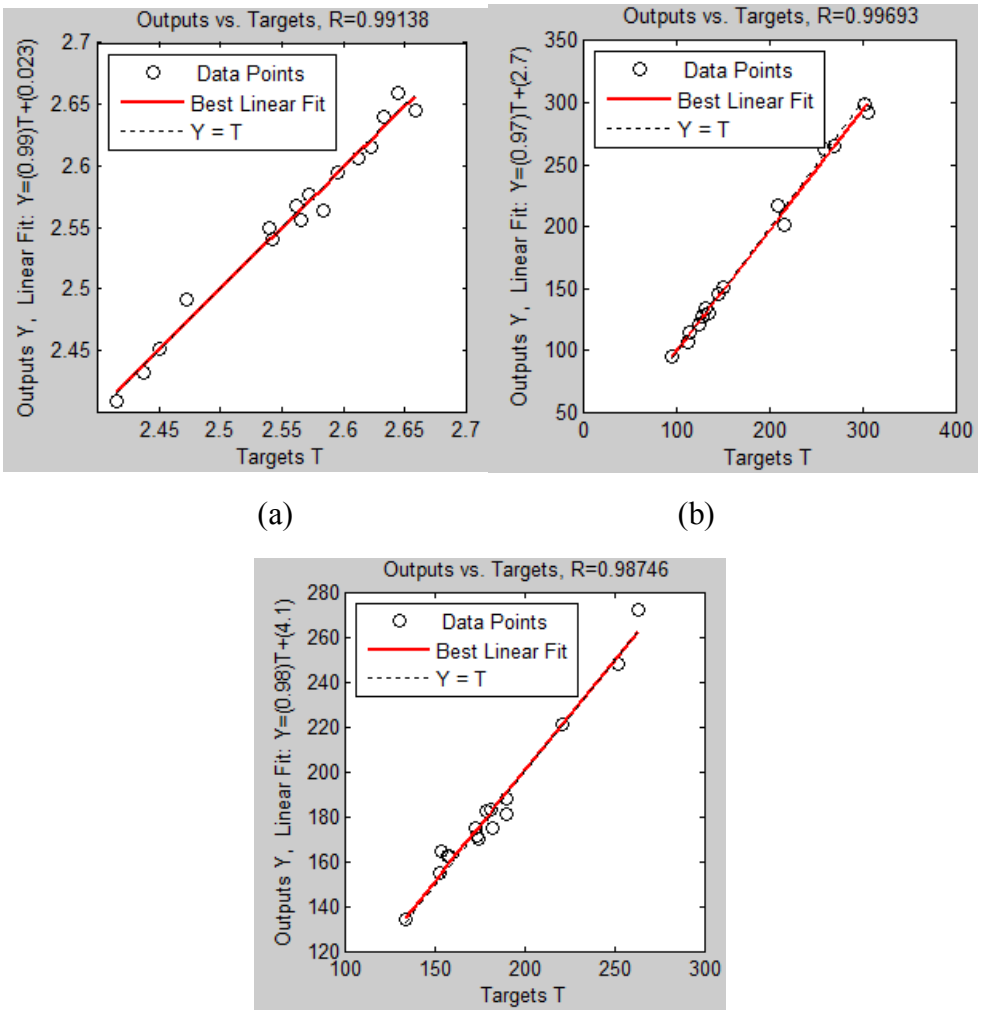

Fig.4. Regression analysis for the neural network responses and the target for all data set: (a) ANN for the density, (b) ANN for the hardness, (c) ANN for the tensile strength

From these comparison charts, it can be clearly observed that the ANN is properly trained and shows consistency in predicting the properties of the powder. A comparison of the measured and predicted density, hardness and tensile strength, at the testing stage is provided in Fig. 5. A comparison between the measured and predicted composite powder properties at the testing stage indicates a high correlation.

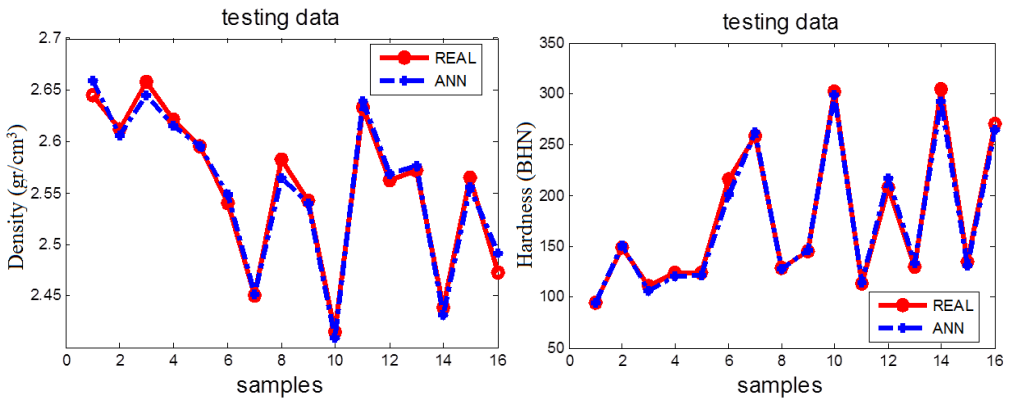

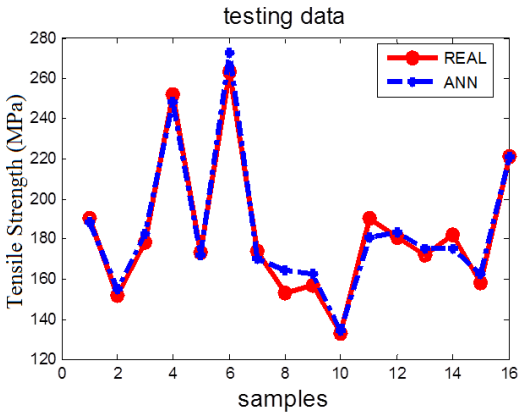

(c)

Fig. 5. The comparison of measured values and ANN values for the (a) density (b) hardness and (c) tensile strength

4. CONCLUSIONS

The relative density decreased with increasing the content of B_4C particles in the consolidated samples. The compressibility of the composite with reinforced coarse B_4C particles was increased as compared to the composite powder with reinforced fine B_4C particles at the same milling time. The lowest relative density is 88.81% in the composite containing 20 wt.% B_4C_{fine} particles and produced after 10h of milling. The strengthening of composites was improved with the increasing milling time (from 1h to 5h), and then decreased with further increasing the milling time. The results of tensile strength measurements showed that after 5h milling process the steady state was achieved at 10wt.% B_4C. The tensile strength of composites with reinforced fine B_4C particles increased by 20 % compared to the unreinforced Al2024 alloy for 5h of milling. The ANN model generates satisfactory results when compared to the experimental measurements. The mean absolute percentage error (MAPE) for predicted values does not exceed 2.15%.

Acknowledgements

The authors are grateful to the Karadeniz Technical University Research Fund for financially supporting this research (No: 2010.112.010.4). The researchers would also like to thank the Gundogdu Exotherm Service for providing the Al2024 powders.

REFERENCES

[1] S. Gopalakrishnan and N. Murugan, Composite Part B: Eng. 43, 302, 2012
[2] K. Sukumaran, K.K. Ravikumar, S.G.K. Pillai, T.P.D. Rajan, M. Ravi, R.M. Pillai and B.C. Pa, Mater Sci Eng A, 490, 235, 2008
[3] N.P. Chenga, S.M. Zenga and Z.Y. Liu, J. Mater. Process Technol., 202, 27, 2008
[4] B. Yang, F. Wang, J.S. Zhang, Acta Mater 51, 4977, 2003
[5] M. Taskin and U. Caligulu, Math. Comput. Appl., 11, 163, 2006
[6] A. Canakci, S. Ozsahin and T. Varol, Powder Technol.. 228, 26, 2012.
[7] M. Hayajneh, A.D. Hassan, A. Alrashdan and A.T. Mayyas, J Alloys Compd., 470, 584, 2009
[8] H.K. Durmus, E. Ozkaya, C. Meric, Mater Des., 27, 156, 2006
[9] M. Taskin, H. Dikbas, U. Caligulu, Math. Comput. Appl., 13, 183, 2008

Synthesis and characterization of B_4C particles reinforced Al-Cu-Mg alloy matrix nanocomposite powders by high energy mechanical milling

Serdar Ozkaya[a], Aykut Canakci[a*], Temel Varol[a]

[a*]Department of Metallurgical and Materials Engineering, Engineering Faculty,
Karadeniz Technical University, Trabzon, Turkey.
aykut@ktu.edu.tr

Abstract
In this study, AlCuMg-B_4C nanocomposite powders with homogeneously distributed B_4C particles were produced by high energy mechanical milling. AlCuMg alloy powders with an average size of 22µm were milled with B_4C particles (5µm average size) at different weight percentages (up to 15 wt.%). Initial mixtures of each composition were milled in a planetary ball mill using tungsten carbide vials, balls with a ball to powder ratio of 10:1 and at a rotation speed of 400 rpm. Results showed that addition of hard ceramic particles provide to achieve a higher level of particle size refinement as compared with monolithic alloy powders, under the same milling conditions. It was found that after 25h of milling the nanocomposite powders with a mean particle size of ~98 nm was obtained. The AlCuMg-15 wt %B_4C nanocomposite powders showed the hardness value of 611 Hv which is significantly higher than 325 Hv obtained for AlCuMg alloy powders after 25h of milling.

Keywords: Nanocomposite powders; high energy mechanical milling; microhardness

B_4C partikük takviyeli Al-Cu-Mg alaşım matrisli nanokompozit tozların yüksek enerjili mekanik öğütme ile sentezi ve karakterizasyonu

Serdar Ozkaya[a], Aykut Çanakçı[a*], Temel Varol[a]

[a]Metalurji ve Malzeme Mühendisliği Bölümü, Mühendislik Fakültesi,
Karadeniz Teknik Üniversitesi, Trabzon, Türkiye
aykut@ktu.edu.tr

Özet
Bu çalışmada homojen B_4C partikül dağılımına sahip AlCuMg-B_4C nanokompozit tozları yüksek enerjili mekanik öğütme ile üretildi. Ortalama toz boyutu 22µm olan AlCuMg alaşım tozları farklı oranlarda (ağırlıkça %15'e kadar) ortalama toz boyutu 5µm olan B_4C partikülleriyle mekanik olarak öğütülmüştür. Herbir bileşimin başlangıç karışımları tungsten karbür öğütücü değirmen ve bilyeleri kullanılarak toz bilye ağırlık oranı 10:1 ve öğütme hızı 400 rpm şartlarında gezegen tip öğütücüde öğütülmüştür. Sonuçlar katkısız alaşım tozları ile karşılaştırıldığında gevrek seramik toz ilavesinin partikül boyutu azalmasına önemli bir oranda katkı yaptığını göstermiştir. 25 saatlik yüksek enerjili mekanik öğütme işlemi sonunda 98nm ortalama toz boyutuna sahip nanokompozit tozlar elde edilmiştir. 25 saat sonunda ağırlıkça %15 B_4C takviyeli nanokompozit tozların sertliği (611 Hv) katkısız alaşım tozlarının sertliğinden 325Hv oldukça yüksektir.

Anahtar Kelimeler: Nanokompozit tozlar, yüksek enerjili mekanik öğütme, mikrosertlik

1. INTRODUCTİON

Metal matrix nanocomposites (MMNCs) are a new research and technology area due to their excellent physical and mechanical properties and their superior features provide significant advantages in advanced industries such as military, aeroscope and automobile. Aluminum based alloys are widely used as aerospace and automotive components, because of their high specific strength, stiffness and formability. However, both pure Al and Al alloys possess poor wear resistance. On the other hand, Al alloy matrix composites are known to offer better wear ressistance and mechanical properties [1]. To improve the mechanical properties and wear performance of Al matrix composites Al_2O_3, SiC, B4C, MgO, and TiC were used as reinforcement within the aluminum matrix [2, 3]. High energy ball milling employs the high energy impacts between ball-powder-ball and ball-powder-vial surface which results both homogenously mixing and decrease in powder size with increasing milling time [4, 5]. It has been observed that there is a plenty of literatures available on the production and characterization studies of alloy powders, intermetallic powders, nanocrystalline powders, metal matrix composite powders. However, there is no study on the morphology, particle size and microhardness of B_4C particle reinforced AlCuMg alloy matrix nanocomposite powders. Therefore, the present study aims to investigate the effect of milling time on the particle size, morphology and microhardness of B_4C particle reinforced AlCuMg alloy matrix nanocomposite powders.

2. EXPERIMENTAL

AlCuMg alloy powders (Gündoğdu Exotherm Company, Turkey) with a mean particle size of 25 µm were used as the matrix. The particles were ligamental in shape (Fig 1a). The chemical composition of the Al 2024 alloy (in wt.%) was 4.85 Cu, 1.78 Mg, 0.385 Si, 0.374 Fe, 0.312 Mn, 0.138 Zn, 0.042 Cr, 0.005 Ti and Al (balance). B_4C particles (density: 2.52 g/cm3, purity >99%, Alfa Aesar) with a mean particle size of 5 µm were used as reinforcement particles (Fig. 1b). B_4C particles were dispersed into aluminum matrix to form nanocomposites by a milling procces. The initial AlCuMg alloy powders as well as different mixtures of composite powders were milled for different milling time. AlCuMg powders were mixed with B4C particles to prepare composite powder mixture of 5, 10 and 15 wt.% of B_4C. For the milling process, gradual process control agent process developed by Canakci and Varol [Canakci 2012] was used like this; 0,5 (wt %) of methanol was added when starting to mill for all milling stage, then 0.25(%wt) of methanol was added to the bowls after all 1h milling. Mechanical milling was carried out at the durations of 0.5, 1, 3, 6, 10, 15, 20 and 25h, respectively. The size distribution of as received and milled powders was obtained using a laser particle size analyzer (Malvern, MasterSizer Hydro 2000e). Scanning electron microscope (SEM) (Zeiss Evo LS10) was used to investigate the morphological and microstructural evolution of milled powders. The microhardness measurements were done on as received and milled powders by using a microhardness tester at a 25g load.

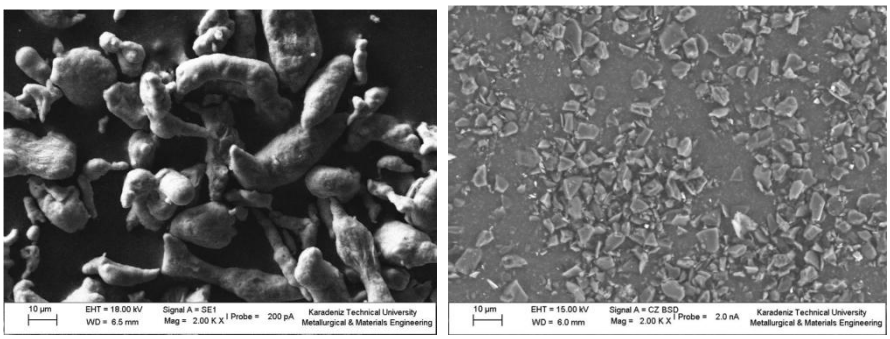

Figure 1. The morphology of as-received (a) Al-Cu-Mg alloy powders and (b) B_4C particles

3. RESULTS AND DISCUSSION

3.1. Powder Morphology Evolution

As it can be seen from the Figure 1a, the initial morphology of AlCuMg alloy was ligamental and irregular in shape, while B_4C particle was angular. In Fig.2, the morphological alteration of milled powders as a function of milling time and B_4C is shown. When examine the figures, it can be seen that, the as-received Al-Cu-Mg alloy powders were irregular and ligamental in shape. In the early stages of milling procees, these powders were deformed and turned into flake morphology as shown in Fig. 2a. By continuing milling process these changes followed by fracture and rewelding (Fig. 2b). For longer milling time, work hardening causes powders to become brittle, and the fracturing process becomes significant, resulting in the observed change in particle morphology. Fig. 2c shows the powder morphologies after 15h of MA. The particle morphologies the end of 15h of milling are semi-equiaxial morphology. As can be seen in Fig. 2d, nano-sized composite powders were obtained at the end of 25h of milling.

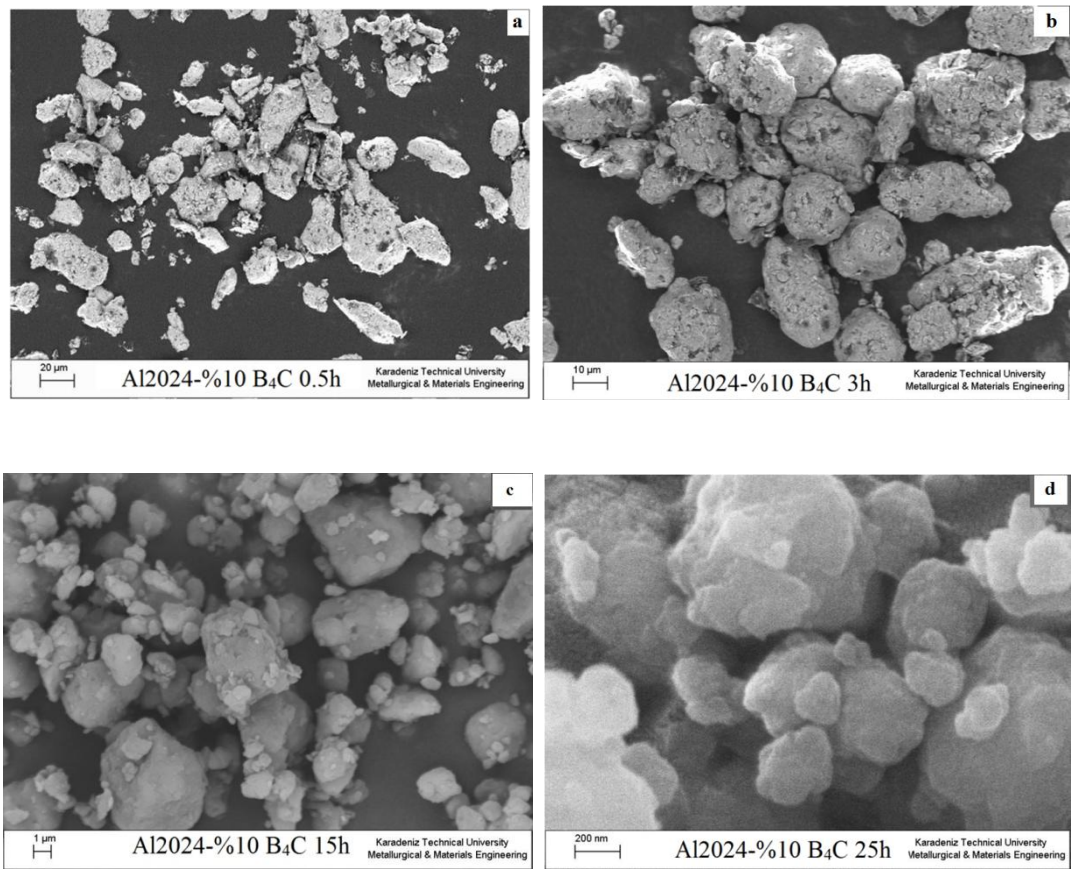

Figure 2. The morphology of Al2024-10wt.% B_4Ccomposite powders: (a) 0.5h, (b) 3h, (c) 15h and (d) 20h

3.2. Particle size

Fig.3 shows the measurement of the particle sizes of milled powders for different B4C contents and different MM duration. The measurements after 0,5h of milling show that the powder sizes decrease rapidly. This decrease can be explained by the morphology of as-received matrix powders which dominates fracturing mechanism. Between 0.5-1h milling time, as can be seen from Fig. 3, the powders sizes increase. This increase is related to the powder morphology because during this milling period, powder morphologies turn into flake morphology. When examine the powder sizes after 1 hour milling, it's shown that for all

compositions the particle sizes were decreased rapidly. As shown in Fig.6, the average particle size of different compositions is changing. In other words, the mean particle size is depends on B_4C content. At the same milling times for different B_4C contents of composite powders, the particle size decrease which was explained by Varol and Canakci [3] as "cutting effect of ceramic particles". The average particle size of 25h milled Al-Cu-Mg-%15(wt) was 98 nm.

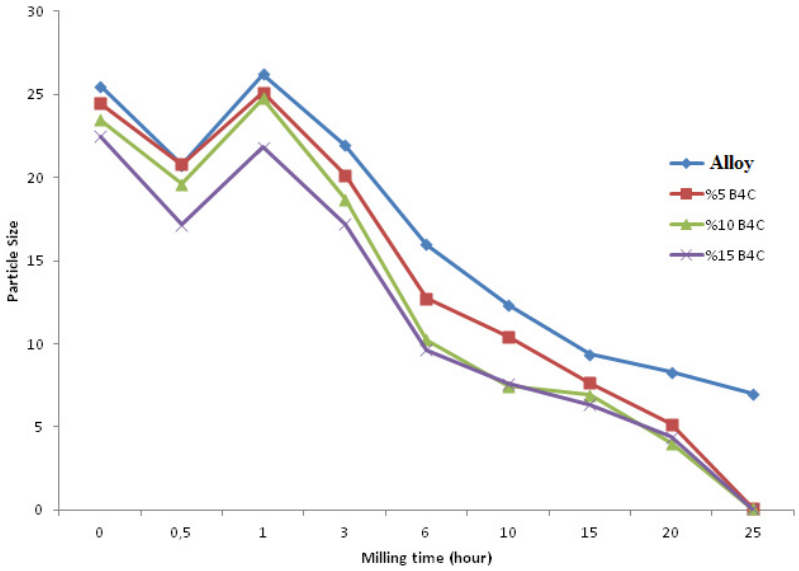

(a)

Figure 3. The change of particle size with milling time and B_4C content

3.3 Microhardness

The change of microhardness of milled particles as a function of milling time is shown in Fig.4. In general, increasing the milling time increases the deformation and work hardening of milled powders. As can be seen from Fig.7., there is a continuous increase in hardness of milled powders with increasing milling time. Moreover increasing B_4C content increases microhardness of powders due to increasing in volume of hard particles and deformation hardening.

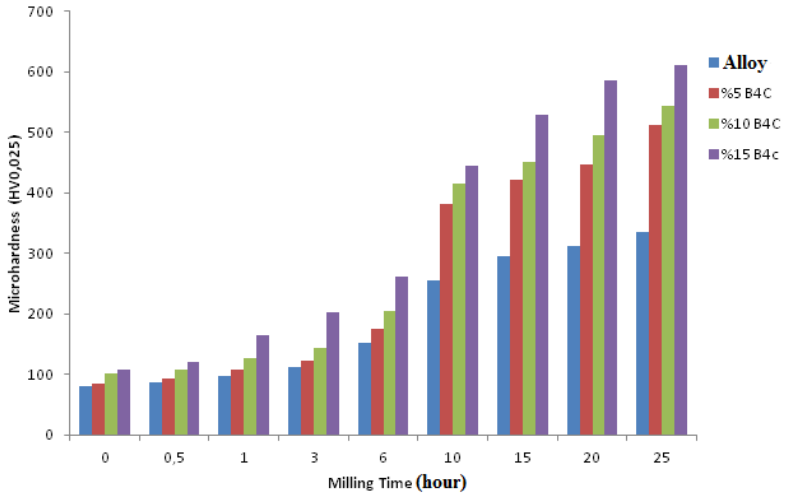

Fig.4. The change of microhardness with milling milling time and B_4C content

4. CONCLUSIONS

The powder sizes decreased with increasing milling time and increasing in content of B_4C for the same milling times. The microhardness values with increasing milling time are increased. The microhardness values for increasing B_4C contents are increased. The results indicate that B_4C content and milling time has considerable effects on final powder's size and powder properties. It was seen that by mechanical alloying technique it's possible to produce Al-B_4C nanocomposites.

Acknowledgements

The authors are grateful to the Karadeniz Technical University Research Fund for financially supporting this research (No: 2010.112.010.4). The researchers would also like to thank the Gundogdu Exotherm Service for providing the Al-Cu-Mg alloy powders.

REFERENCES

[1] R. Pérez-Bustamante, F. Pérez-Bustamante, I. Estrada-Guel, L. Licea-Jiménezc, M. Miki-Yoshida and R. Martínez-Sánchez, Mater. Charact. 75, 13, 2013
[2] A. Canakci, T. Varol and S. Ozsahin, Met. Mater. Int., 19, 519, 2013
[3] T. Varol and A. Canakci, Powder Technol. 246, 462, 2013
[4] C. Tatar and N. Ozdemir, Physica B 405, 896, 2010
[5] H. Abdizadeh, R. Ebrahimifard, M.A. Baghchesara, Composites: Part B 56, 217, 2014

DETERMINATION OF FLOW CURVES OF METASTABLE AUSTENITE

Ozan MÜŞTAK[1,2], Kemal DAVUT[3,4], Caner ŞİMŞİR[3,5], C. Hakan GÜR[2]

(1) ORS Bearings Company, Ankara, Turkey,
ozan.mustak@ors.com.tr
(2) Department of Metallurgical and Materials Engineering, METU, Ankara, Turkey,
chgur@metu.edu.tr
(3) Metal Forming Center of Excellence, Atilim University, Ankara, Turkey,
kemal.davut@atilim.edu.tr
(4) Department of Metallurgical and Materials Engineering, Atilim University, Ankara, Turkey,
(5) Department of Manufacturing Engineering, Atilim University, Ankara, Turkey,
csimsir@atilim.edu.tr

ABSTRACT

Thermo-mechanical properties of metastable austenite are significant parameters for the prediction of distortion and residual stresses by heat treatment simulations. Unfortunately, acquisition of thermo-mechanical properties of a metastable phase in the complete process temperature range requires special techniques and instrumentation. In this study, flow curves of metastable austenite of SAE 52100 (EN 100Cr6) steel were characterized by special compression tests conducted on a deformation dilatometer in 300-850°C range. Since it is not possible to measure the flow curves of metastable austenite below martensite start (M_s) temperature by this method, the obtained data was extrapolated to room temperature in different ways. The validity of extrapolation scheme was justified by comparing of the extrapolated results with the results of a physically based material property calculation software.

Keywords: *Heat Treatment, Simulation, Flow curve, metastable Austenite, SAE 52100.*

YARI-KARARLI ÖSTENİTİN AKMA EĞRİLERİNİN BELİRLENMESİ

ÖZET

Yarı-kararlı östenit fazının termo-mekanik özellikleri, ısıl işlem simülasyonlarında çarpılma ve kalıntı gerilimlerin tahmini açısından önemli parametrelerdir. Maalesef yarı-kararlı fazın termo-mekanik özelliklerinin çıkarılması için özel teknikler ve cihazlara ihtiyaç duyulmaktadır. Bu çalışmada, SAE 52100 (EN 100Cr6) çeliği için yarı-kararlı östenit fazının akma eğrileri deformasyon dilatometresinde yapılan özel basma testleri ile 300-850°C sıcaklık aralığı için belirlenmiştir. Yarı-kararlı östenit fazının martensit başlangıç (Ms) sıcaklığı altındaki akma eğrilerini bu yöntemle elde etmek mümkün olmadığı için elde edilen veriler değişik yollarla oda sıcaklığına ekstrapole edilmiştir. Ekstrapole edilen değerler fiziksel tabanlı malzeme özelliği hesaplama programı kullanılarak hesaplanan değerlerle karşılaştırılmıştır.

Anahtar Kelimeler: *Isıl İşlem, Simülasyon, Thermo-mekanik özellikler, yarı-kararlı östenit, SAE 52100*

1. INTRODUCTION

Heat treatment simulation can be used for optimization of product performance, understanding of heat treatment process and design of innovative heat treatment processes. Residual stresses, distortions, final properties of component might be predicted during the process and at the end of the heat treatment process by simulations. During the last decade, heat treatment simulations have become mature enough for the prediction of final properties of heat treated products with the aid of developments in software packages, computer hardware and accumulation of knowledge in the international heat treatment society. Despite all those improvements, one of the major drawback limiting the industrial use of heat treatment simulations is the availability of reliable material data [1].

The yield strength and the flow curves of metastable austenite are important parameters for the prediction of residual stresses and distortion of heat treated and welded components. In the past, the flow curve data for metastable austenite for heat treatment and welding simulations were obtained by static tension-compression tests on austenitic stainless steel grades. However, more recent results using more advanced equipment demonstrated that the flow curves of the metastable austenite are significantly different from the stable austenite of austenitic stainless steels [2-5].

Flow curves of metastable austenite as a function of temperature can be obtained by using a specialized deformation dilatometer. During the tests, the specimens are heated and austenitized in the test chamber if the system under vacuum and then quenched to the testing temperature. Then, a strain rate controlled uniaxial tension or compression test can be conducted before the phase transformation begins if the steel has a sufficient hardenability. The time-temperature-transformation (TTT) diagram of 100Cr6 steel has already been determined in a preliminary study [6] and from that the time needed for applying the load before transformation is obtained. On the other hand, it is also known that application of uniaxial stress or plastic deformation can change the transformation times [7], thus, the actual test time should be smaller than the time indicated by the TTT diagram.

Heat treatment and welding simulation studies require flow curves of metastable austenite in the complete process range including M_s – RT range. On the other hand, deformation dilatometry technique explained earlier cannot be used below Ms temperature since the martensitic transformation is too fast to perform a mechanical tests before the transformation begins. Mechanical testing of austenite-martensite mixture is possible but it requires additional assumptions and stress induced transformation can cause problems in parameter determination. In order to solve this problem in a simpler way, the flow curves obtained in 300-850°C range is regularized and extrapolated to the room temperature as explained in Section 2. The validity of the flow stress model has been justified by comparing the results with the flow curves from the literature and physically based material property calculation technique.

2. THEORY

Dilatometry can be defined as a technique for the measurement of dimension change of a material as functions of both temperature and time when subjected to pre-defined temperature-time cycles. Obtained data can be converted into strains as functions of both time and temperature, which can later be used for determination of flow curves. Deformation dilatometry is generally used to investigate the effects of stress and deformation on phase transformations such as transformation plasticity, stress/strain induced or assisted phase transformations. Moreover, it can also be used for obtaining the flow curves at elevated temperatures as a plastometer.

In this study, flow curves of austenite phase was determined as a function of temperature using the deformation dilatometry. Acquired stress-strain data was regularized by fitting the data on Ramberg Osgood model as shown in equation (1):

$$\sigma_{true} = K_{RO}\left(\varepsilon_i^{pl}\right)^{n_{RO}} \quad (1)$$

where, σ_{true} is the true stress, ε_i^{pl} is the plastic strain, K_{RO} and n_{RO} values represent material parameter and strain hardening exponent of Ramberg-Osgood model respectively.

Since the deformation measurement system (LVDT) of the deformation dilatometer measures total strain one must calculate ε_i^{pl} from total strain and elastic modulus before fitting the parameters to the model. Assuming an additive decomposition, total strain can be described as the sum of elastic (ε_i^{el}) and plastic (ε_i^{pl}) strains as in Equation (2). Moreover, thermal, transformation and transformation plasticity strains are not involved in the total strain given in Equation (2) since the dilatometry tests were conducted isothermally and they were all finished before the initialization of phase transformation.

$$\varepsilon_i^{total} = \varepsilon_i^{el} + \varepsilon_i^{pl} \quad (2)$$

Equation (1) can be rearranged by using Equation (2), as follows:

$$\varepsilon_i^{total} = \frac{\sigma_{true}}{E_i} + K_{RO}\left[\frac{\sigma_{true}}{E_i}\right]^{n_{RO}} \quad (3)$$

where, ε_i^{total} represents total strain measured by the deformation dilatometer for sample i, and E_i is the elastic modulus of sample i.

Total strain value was obtained from the dilatometric tests and elastic strain component was calculated by dividing total stress to elastic modulus value at a given temperature.

Elastic moduli were obtained using thermodynamically based material property calculation software JMatPro® [8-11]. Calculated values for elastic modulus for austenite phase of 100Cr6 steel as a function of temperature is given in Figure 1.

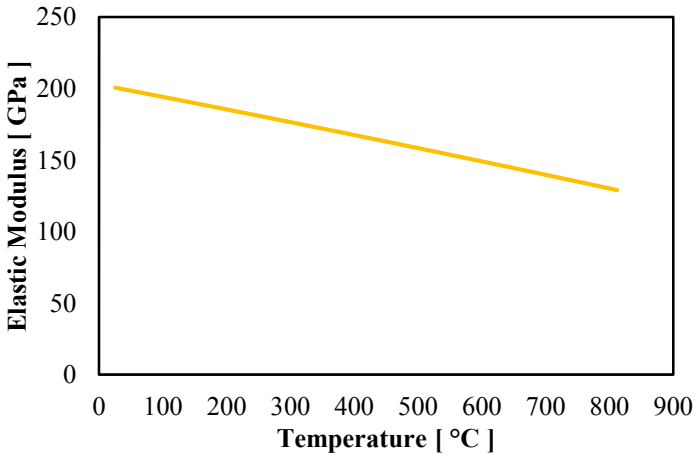

Figure 1: Elastic modulus for 100Cr6 steel calculated with JMatPro®

After calculating plastic strain component, Ramberg-Osgood model parameters K_{RO} and n_{RO} were fitted iteratively by reducing total root-mean-square (RMS) error between plastic strain component of the test and calculated value from the model.

After determining the Ramberg-Osgood parameters for each temperature, second regularization was done in order to determine thermo-mechanical properties below martensite start temperature since, tests could not be performed below the martensite start temperature due to austenite to martensite phase transformation. In the second regularization part, temperature dependency of the parameters K_{RO} and n_{RO} were determined by fitting the calculated values onto linear or polynomial regression lines with a suitable order as a function of temperature. Both first order and second order polynomial regression lines were tested in this study. However, the first order linear regression lines were fitted on the determined Ramberg-Osgood parameters better, as discussed in the results section.

It must be noted that, one of the most important point for determination of flow curves of meta-stable austenite is to perform the test and obtain true stress-true strain data before the decomposition of austenite begins. It is known that, phase transformation might be affected from the applied stress field [12, 13] thus, time needed for obtaining the flow curve might be decreased during the test, which is not desired. During the dilatometry tests, only linear dilation of the sample can be measured. Small amount of transformation might be introduced with the effect of stress; however, it could not be detected since dilation of the sample cannot be measured by dilatometer system used. Since the time needed for the mechanical tests is always shorter than the incubation time of phase transformations at a given temperature, the phase transformation is not expected to take place during the here presented dilatometry tests.

3. EXPERIMENTAL PROCEDURE

The material used in this study was 100Cr6 bearing steel and the chemical composition of this steel is given in Table 1.

Table 1. Chemical Composition of 100Cr6 used in the study.

	C	Cr	Si	Mn	Al	Cu	Mo	Ni	O	P
Wt. (%)	0.99	1.43	0.24	0.36	0.017	0.1	0.02	0.06	$5e^{-5}$	0.016

In this study, thermo-mechanical testing unit (DIL-805 A/D Baehr-Thermoanalysis GmbH) was used as a deformation dilatometer. It employs inductive heating, He/N_2 gas nozzle quenching and it is also capable of applying a uniaxial force simultaneously up to 20 kN in order to obtain flow curves of the specimen at a given temperature. The dilatometer is located in Metal Forming Center of Excellence at Atılım University.

Dilatometry experiments was performed under a vacuum of $5x10^{-5}$ bar in order to avoid oxidation during thermal cycles. Solid specimen with length of 10 mm and diameter of 5 mm was used in tests and they were extracted from length of 6000 mm and diameter of 37 mm as-cast and rolled 100Cr6 steel rods.

For the specimen preparation, 100Cr6 steel rods were sliced down to the slices in length of 10 mm. Then, each slice was spheroidized in an atmosphere controlled spheroidization furnace at 790 °C for 14 hours in order to obtain same and homogenous microstructure in each specimen. After the heat treatment process of slices, specimens were extracted from r/2 of spheroidized sliced rods in order to eliminate the effect of core segregation by electrical discharge machining.

During the tests, specimens were heated with a rate of 4.7 °C/s and austenitized at 850°C for 30 minutes. Then, they were immediately quenched to the testing temperature with a cooling rate of 100 °C/s at which compressive load is subsequently applied. A strain controlled compression test conducted at a strain rate of 0.01 s^{-1} up to %2 strain. The temperature of the specimens was maintained at ±1 °C of hold temperature by closed loop temperature control system of the deformation dilatometer. Both stress and strain values were recorded until %2 strain was achieved. Representative temperature program is shown in Figure 2. Tests were performed at isothermal testing temperatures of 300°C, 400°C, 500°C, 600°C, 700°C and 850°C.

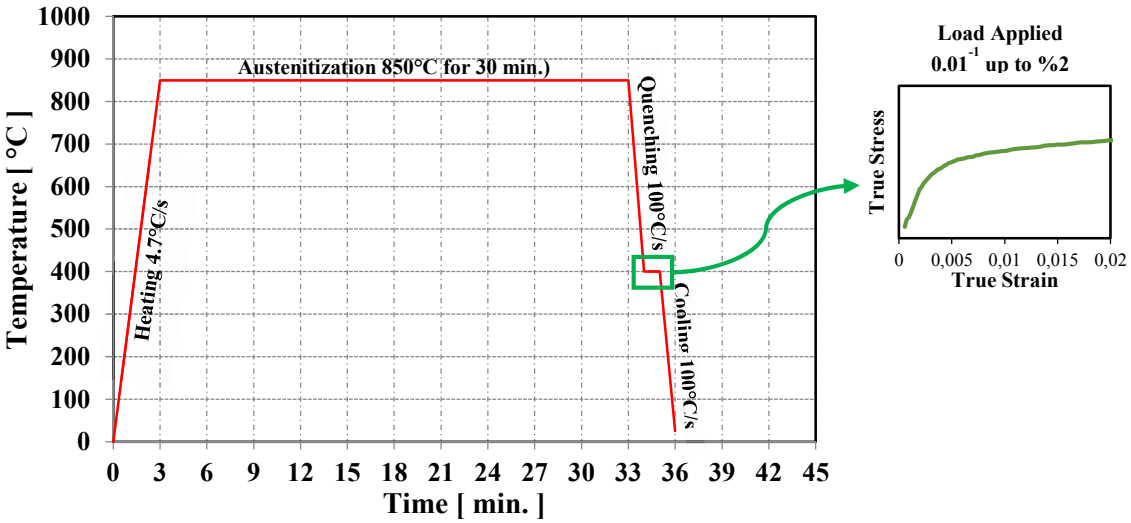

Figure 2: Representative temperature program for mechanical tests of austenite.

4. RESULTS AND DISCUSSION

The test results and fitted regression lines for material parameter K_{RO} are given in Figure 3. Furthermore, temperature dependency of hardening exponent n_{RO} and regression line fitted for it are given in Figure 4. Dashed lines shown on the figures are referred as the extrapolated regions in order to discuss and investigate the tendency of the regression lines below the martensite start temperature.

As it can be seen from the Figure 3, calculated values for material parameter K_{RO} show a linear relationship with temperature. On the other hand, hardening exponent n_{RO} values do not have clear relationship with temperature as it can be seen in Figure 4. Therefore, the value for n_{RO} can be taken as constant as 0,15.

It must be noted that as mentioned in the theory section, another function might be fitted on the curves. However, thermo-mechanical properties of meta-stable austenite cannot be measured below martensite start temperature since it transforms to martensite below the martensite start temperature. Thus, linear fittings are applied and assumed to be applicable since the values below martensite start temperature could not be tested and validated. Furthermore, during quenching it is difficult to reach yield strength value of austenitic phase below martensite start temperature so that minor differences obtained from different functional fittings might be assumed as negligible. Fitting function would be gained importance for different applications depending upon the severity of quenching condition.

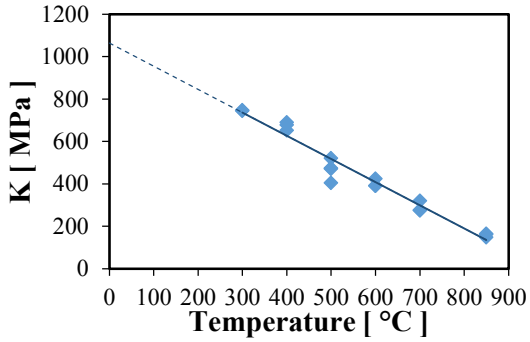

Figure 3: Results of calculations and regression line fitted for material parameter K_{RO} w.r.t. temperature.

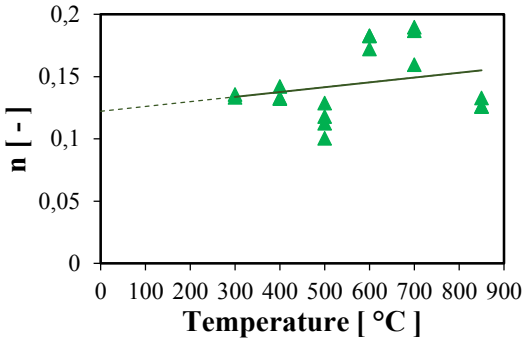

Figure 4: Temperature dependency of hardening exponent n_{RO} and regression line fitted onto calculated values.

Calculated flow curves were given as a function of temperature in Figure 5. Literature data [2, 3] is also indicated in Figure 5 for validation and for comparison with the extracted data. As shown in Figure 5, the flow curves for meta-stable austenite phase obtained in this study are in good agreement with the ones available in the literature [2, 3].

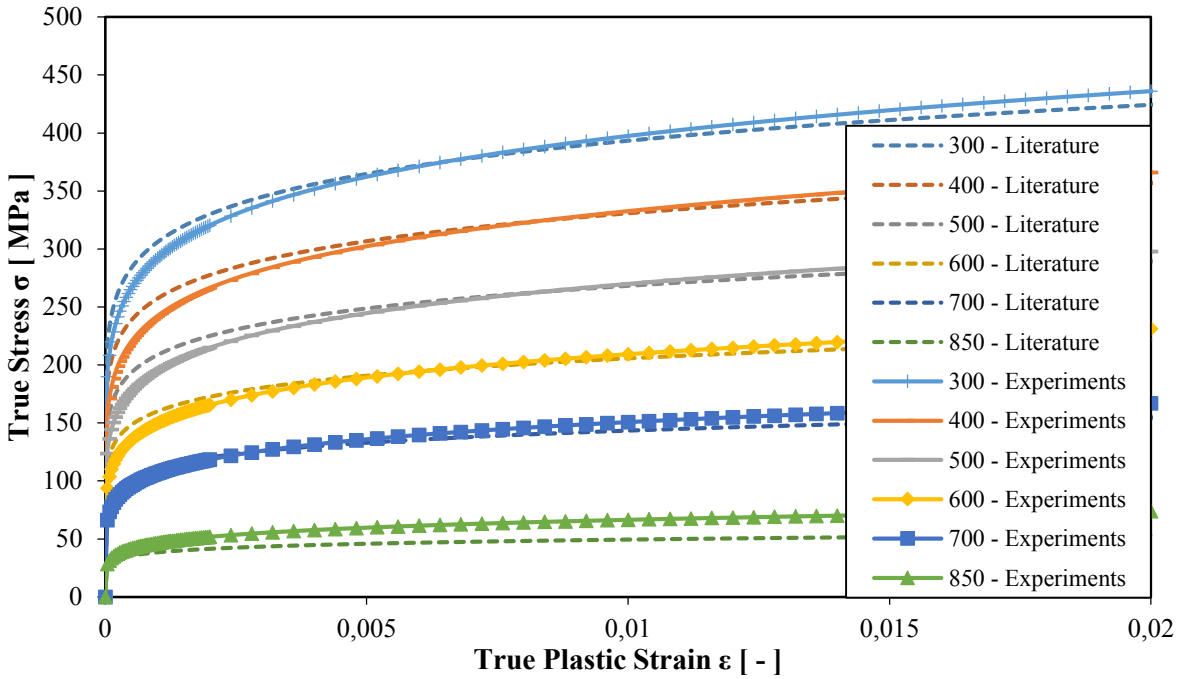

Figure 5: True Stress vs. True Plastic Strain plots for meta-stable austenitic phase with respect to temperature. Literature data also indicated.

Yield strength values of austenitic phase for a temperature range of 300-850°C were calculated in accordance with Ramberg-Osgood equation (4) at 0.005% proof stress. Results are given in Figure 7. Fitting linear regression lines were taken into consideration since they provide physically reasonable values when they extrapolated to room temperature. In addition, several higher order polynomial fits are also indicated on the same figure.

$$\sigma_{yield} = K_{RO}(0.00005)^{n_{RO}} \quad (4)$$

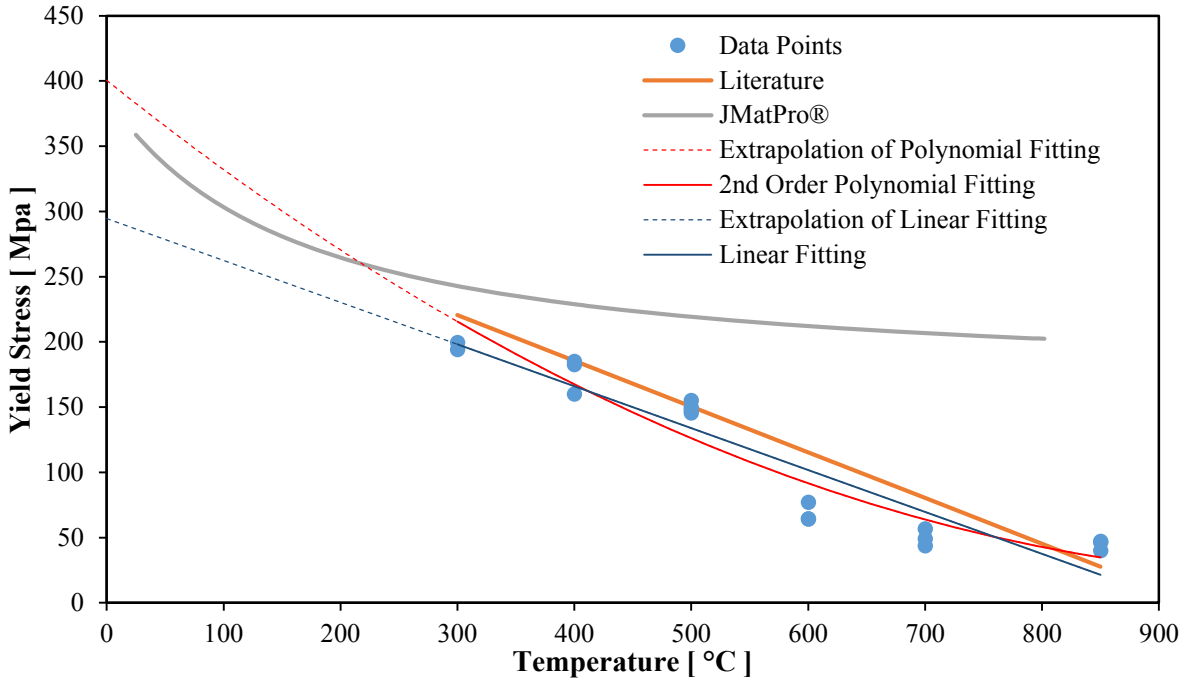

Figure 6: Yield stress of austenitic phase as a function of temperature.

The minor differences between the results of this study and the literature [2,3] might be due to differences in:

i. austenitization conditions
ii. starting materials (i.e. initial microstructure, composition, segregations etc.)
iii. instruments (deformation dilatometers) used (DIL 805 A/D vs. Gleeble 3500)
iv. Strain rates applied on the specimens (0,01 s^{-1} vs. 0,004 s^{-1})
v. Numerical techniques used for calculations and fittings

The common difference of experimentally determined values from the theoretically calculated results of JMatPro software is probably due to usage of a different strain offset (0.2%) in the software for the calculation of yield strength. Moreover, the software is based on thermodynamic equilibrium and the metastable austenite might contain larger number of point defects than the equilibrium fractions [5]. This might also be the reason for the observed behavior.

5. CONCLUSION

In this study, flow curves of meta-stable austenite were determined via deformation dilatometry technique. Flow curves obtained in between 300-850°C were regularized with Ramberg-Osgood model. In order to determine thermo-mechanical properties of metastable austenite below M_s temperature, a second regularization was done on K_{RO} and n_{RO} parameters of Ramberg-Osgood model. Elastic modulus of austenite phase of 100Cr6 steel is computed using the thermodynamically based thermo-physical property calculation method using commercial JMatPro® software. Results of this work were compared and validated with the available literature data and a good agreement is established between the two. The probable reasons for the minor differences between the results of this work and literature were also discussed.

INVESTIGATON OF PARAMETERS THAT AFFECT FORMABILITY OF STEEL SHEETS

Elvin ÖZCAN IŞIKLIGİL, Adem BAKKALOĞLU

Yıldız Technical University, Turkey
elvin.ozcan@erdemir.com.tr
abakkal@yildiz.edu.tr

ABSTRACT

Sheet metals are used in industry for manufacturing the most varied components and products. During forming operations, especially when subjected to combinations of stretching and drawing, they may fail due to localized necking and/or cracking or deviate in shape from the required part geometry. Scrapping caused by such failures affect the economy, continuity and quality of the production in a negative way. Analyzing these operations is very important to reduce wastes and optimize the processes. Formability is the ability of the sheet metal to be formed without developing any failure, and it depends on several interacting factors such as material flow properties, ductility, die geometry, die material, lubrication, press speed, etc. Evaluation of formability is mostly made according to the results of tensile tests and simulation tests. First estimation about the formability of sheet metals is possible on the basis of tensile and drawing test results. However, mechanical and chemical features of sheet metals such as yield strength, tensile strength, or microstructure are not alone sufficient to account for their formability. Therefore new techniques are needed to use the sheet metals effectively in production processes. A useful technique for overall consideration of sheet metal formability is the Forming Limit Diagram (FLD), which represents all combinations of deformations during forming processes for complex parts. With the FLD, the behaviours of sheet metal materials which are subjected to two-dimensional tensile and compression tests can be analyzed. So, the use of FLD allows estimation of sheet metal formability and serves to choose suitable process solutions. This study was carried out for understanding of the formability of steel sheets, which are formed in the shapes from various in industrial applications and that's why in this study, parameters that affect formability were investigated primarily. Formability of ten qualities has been characterized by FLDs and the effects of material properties on FLDs were evaluated.

Keywords: Forming limit diagram, FLD, Formability, Deep drawing,

ÇELİK SACLARIN BİÇİMLENDİRME ÖZELLİKLERİNİ ETKİLEYEN PARAMETRELERİN ARAŞTIRILMASI

ÖZET

Metalik saclar endüstride çok çeşitli parça ve ürün yapımında kullanılmaktadır. Bu sacların biçimlendirilmesinde, özellikle de germe ve derin çekmenin birlikte uygulandığı durumlarda parçanın gerekli geometriye ulaşamaması, boyun verme veya yırtılma söz konusu olabilmektedir. Ortaya çıkan hurda miktarı ekonomiklik, yapılan işin sürekliliği ve kalitesini olumsuz etkilemektedir. Prosesleri optimize etmek ve malzeme kayıplarını azaltmak için bu işlemleri analiz edebilmek oldukça önemlidir. Biçimlenebilirlik malzemenin herhangi bir hasara

uğramadan biçim alma yeteneği olup malzemenin akış özellikleri, sünekliği, kalıp geometrisi, yağlama, pres hızı gibi birden çok parametreye bağlıdır. Genellikle metalik sacların biçimlenebilme özellikleri çekme testleri veya biçimlendirme yöntemine benzer deneyler ile değerlendirilmektedir. Çekme ve derin çekme testleri ile ilk etapta fikir sahibi olmak mümkündür ancak akma mukavemeti, çekme dayanımı veya mikroyapı gibi mekanik ve kimyasal özellikler tek başlarına sac malzemelerin şekillendirilebilirliğini ifade etmeye yetmemektedir. Bu sebepten üretim proseslerinde sac malzemeleri etkin olarak kullanabilmek için, şekillendirilebilirlik sınırlarının belirlendiği yeni tekniklere ihtiyaç duyulmaktadır. Bütün bunlar düşünüldüğünde kompleks parçaların şekillendirilmesinde deformasyonun bütün kombinasyonlarını temsil eden Şekillendirme Sınır Diyagramları(ŞSD) kullanışlı bir teknik olmaktadır. ŞSD ile, iki boyutta çekme ve basma testleri uygulanan sac malzemelerin davranışları analiz edilebilir. Böylece ŞSD malzemenin şekillendirilebilirlik sınırlarını göstererek prosese uygun çözümler bulunmasını sağlamaktadır. Bu çalışmada, öncelikle celik sacların biçimlendirilebilirliğini etkileyen faktörler incelenmiştir ve çeşitli endüstriyel uygulamalarda kullanılan on farklı kalitedeki sacın şekillendirme sınır diyagramları değerlendirilmiştir.

Anahtar kelimeler: Şekillendirme Sınır Diyagramı, ŞSD, Şekillendirilebilirlik, Derin çekme

1. INTRODUCTION

Metallic sheets are widely used in the production of many parts with the help of different forming processes for various sectors. During forming operations, sometimes the amount of scrap is more than acceptable levels because of failures in sheets due to localized necking or cracking or etc. This is observed especially in automotive applications and causes many problems in terms of economy, continuity and quality of the production.[1] The main factors affecting formability of all metallic materials are material properties and manufacturing process properties. At the same time, many variables are involved in the production process each independently. All these parameters are analyzed, formability of the material should be known primarily and material selection must be made according to this.[2] While the choice of materials, low carbon steels are used mostly for sheets to be formed. Such steels generally have content of carbon which is less than 0.15% and a content of alloying elements which are less than 1% in combination with trace elements.[3] Formability of fully killed steels is higher than rimmed steels. While all of properties show a homogeneous distribution on the coil and sheet for killed steels, mechanical properties and chemical composition are not uniform for rimmed steels. On the other hand, rimmed steel sheets are exposed to hardening and aging with in time but killed steel sheets are resistant to aging. In order to be eligible for the forming of hot rolled steel sheet surface has to be cleaned. Cold rolled sheets in terms of both size and features are more reliable. Sheets can be supplied as commercial quality sheets, deep drawing sheets and extra deep drawing sheets in various surface conditions.[4] When the effect of microstructure examined, it is observed that the reduction of grain size affects deep drawability in a negative way in low carbon steels. Setting the grain size depends on the hot-rolling conditions.[5] In addition, low carbon steels have some inclusions such as iron carbides and non-metallic sulfides, silicates and oxides. Carbide particles which occurs with the alloying elements dissolved in ferrite and pearlite phase reduce the formability by increasing the strength. Non-metallic particles are generally more rigid than structure and reduce the formability by increasing the stress.[11] Especially fine particles is harmful in terms of deep drawing because they further increase the strength. Determination of occurrence and size of these particles depend on production parameters such as the chemical composition, slab reheating temperature, rolling, coiling temperature.[5] When the effect of chemical composition examined, an increase in strength and a reduction in the ability to

forming occurs with the increase of carbon content in steels. The manganese content generally is maintained between from 0.15% to 0.35% in order to increase its hot forming ability. Nitrogen content greatly increases the strength of the low carbon steel, causes strain aging and affects the formability in a negative way. The amount of nitrogen is reduced by the addition of aluminum. Titanium provides obtaining high anisotropy coefficient values, prevents discontinuous yielding events and increase the formability by eliminating aging in cold rolled and annealed steels.[6] The presence of silicon leads to the occurrence of silicate inclusions that increases the risk of cracking during bending and also since the increase in the amount of silicon increases the strength, decreases the ability to forming. Sulfur and phosphorus increase the risk of cracks and breaks.[7] Aluminum in the cold rolled and annealed steels provides high anisotropy coefficient values by providing preferably grain arrangement. Furthermore, it prevents the occurrence of strain aging because it binds nitrojen and improves the ability of forming. When the effect of material properties examined, it is observed that the increase in yield strength reduces forming capability. Average vertical anisotropy coefficient (r value) increases, the deep drawability of steel is also increased. Higher strain hardening coefficient (n value) indicates that amount of hardening of the material and sheet formability is increased with the increasing value of strain hardening exponent [6] Higher strain-rate sensitivity index (m value) shows that the stress distribution is uniform and this increases formability of material.[3] When the effect of mechanical properties examined, the increase in slab reheating temperature, rolling temperature and finishing temperature decreases r value and formability. The effect of rapid cooling in the low-carbon steels creates small grain size and provides a better deep drawing properties. If the coiling temperature increases, deep drawability in batch annealed ultra low carbon steels decreases but this ability in continuous annealed steels increases due to the difference in grain structure. Increasing amounts of cold deformation in the steel up to a certain value increases the r value and then acts in the opposite direction. Annealing treatment at high temperatures causes grain growth and increases r value in Al-killed steels. Batch annealed low carbon steels have higher r value than continuous annealed steels.[5] Due to a large number of variables mentioned above participate in the production process independently one of another, the search for a parameter has occurred that describes the behavior of materials in real production conditions and detection of material formability limit has been come into question. A useful technique for overall consideration of sheet metal formability is the Forming Limit Diagram (FLD), which represents all combinations of deformations during forming processes for complex parts. Therefore, the use of FLD allows estimation of sheet metal formability and serves to choose suitable process solutions.[13]

1.1. Basic Understandings Concerning The Forming Limit Diagrams

Partial success has been achieved in the estimation of formability with the base mechanical properties which determined the tensile test. Simulation experiments that similar to the actual forming process such as deep drawing and buckling are unable to characterize forming properties of sheets enough. They only provide a comparison between the sheets and do not give any information about what measures should be taken for process to be successful.[6] These experiments performed under laboratory conditions are different from industrial conditions and there is a need to analyze the plastic deformation to examine the behavior of the material in industrial production conditions.[8] Both the mechanical properties of material as well as simulation experiments are insufficient about formability, therefore "Forming Limit Diagrams" (FLD) are derived.[9] In general the limits of the formability of the sheet metal materials are defined according to the starting point of necking. Although not break immediately in the material after necking, behaviors can not be predicted after this point and so strain values at the necking point are considered as limit values.[10] If situations of

elongation which may occure in sheet material under different loads with different test methods are shown on a diagram, a FLD will be obtained as shown in figure 1.[8] Forming limit diagram (FLD) is defined as a graph of the major strain at the onset of localized necking for all values of the minor strain.[10] When the FLD analyzed, it is observed that changes in shape are among of deep drawing and stretching zones.[8] During forming, the two-axis press, deep drawing, uniaxial tensile, plane elongation and biaxial tensile conditions are comprised. It is accepted that there is no deformation on the sheet in the third dimension. There is no forming identification on the diagram in the painted area since deformation in two axes and direction of elongation from consisting of the starting circle is not important. (Without considering the direction of elongation, elongation which is obtained from the larger diameter of deformed circle is major elongation (vertical diagram axis "φ_1") and which is obtained from the smaller diameter of deformed circle is minor elongation (horizontal diagram axis "φ_2").)[8]

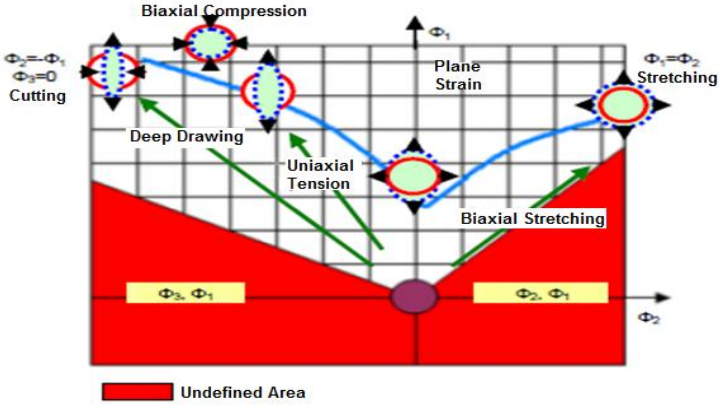

Figure 1. Forming limit diagram for various strain paths [8]

Forming limit diagram shows on diagram two areas of inadmissible (up the curve) and admissible (under curve) deformations in term of acceptable definition about limit state. FLD shows limit of this two areas and determines critical deformations for given limit state. Safe drawing zone-area under limit deformations curve correspond to the area of admissible deformations and area up the curve shows a zone of inadmissible deformations in drawing process.[15] Diagram also divided into two regions including tension – tension (stretching) or tension – compression (drawing) areas. The negative minor strain (φ_2) side indicates strain conditions applying in drawing operations, and the positive minor strain (φ_2) indicates conditions occurring during stretching. The zero point on the diagram of φ_2 is the point which determines the planar deformation. The values of this point are used for comparison of different materials with each other. [8]

2. EXPERIMENTAL DETERMINATION OF FORMING LIMIT DIAGRAMS

2.1. Material

In this study, forming ability of ten different steel grades with different properties and produced in EREĞLİ DEMİR ÇELİK FABRİKALARI was investigated. These qualities are called ERDEMİR 1522, 380, 326, 327, 328, 7114, 6224, 1335, 3937 and 7513. Six of them are ultra low carbon (IF) steels and the others are middle and low carbon steels. Values of chemical composition is given in table 1. Mechanical values are also given in table 2. This value are determined by the tensile test according to EN ISO 6892-1 with the Zwick drawing device (10 tons).

Table 1. Chemical values

No	Erdemir steel grade	Thickness	C %	Mn %	P %	S %	Si %	Al %	Nb %	Ti %	Cu %	Cr %	Ni %
1	326	0,786	0,002	0,13	0,007	0,01	0,009	0,04		0,041			
2	7114	1,230	0,003	0,135	0,009	0,011	0,009	0,036		0,059			
3	327	0,786	0,002	0,116	0,009	0,007	0,006	0,031		0,037			
4	3937	2,060	0,073	0,429	0,014	0,004	0,039	0,025		0,002	0,024	0,024	0,047
5	6224	3,000	0,04	0,287	0,015	0,006	0,01	0,048			0,002		
6	328	0,685	0,003	0,115	0,005	0,006	0,005	0,028		0,03			
7	380	1,098	0,003	0,484	0,038	0,005	0,009	0,033					
8	7513	0,813	0,033	0,137	0,006	0,008	0,007	0,049					
9	1335	0,820	0,074	0,802	0,01	0,01	0,006	0,037					
10	1522	0,773	0,002	0,473	0,039	0,01	0,01	0,034	0,01	0,02			

Table 2. Mechanical values

No	Erdemir steel grade	Thickness	Yield (kg/mm^2)	Tensile (kg/mm^2)	Elongation (A%)	r		n	
						r_{90}	r_m	n_{90}	n_m
1	326	0,79	17,4	31,8	42	1,6	2,98	0,18	0,21
2	7114	1,23	17,4	30,5	45	1,6	2,92	0,18	0,23
3	327	0,79	15,3	30,1	41	1,9	3,56	0,20	0,22
4	3937	2,06	33,3	42,1	35	-	-	-	-
5	6224	3,00	19,9	34,3	47	-	-	-	-
6	328	0,69	16	30,6	42	1,9	3,53	0,20	0,22
7	380	1,10	23,4	35,6	36	1,6	2,62	0,15	0,19
8	7513	0,81	20,1	32,7	38	-	2,02	-	0,21
9	1335	0,82	39,4	49,6	24	-	-	-	-
10	1522	0,77	23,8	35,4	37	1,5	2,82	0,17	0,19

2.2. Forming Tests

Test samples used in the study were cut to the dimensions of 200x200mm by ERDEMİR TAŞ and were prepared as rolling direction marked. The other details of the samples are given in table 3.

Tablo 3. Details of the samples

No	Corresponding		Erdemir Steel Grade	Thickness (mm)	Pieces
	Standard	Grade			
1	52806/9.52873	FEP04-ZNT/F/2S	326	0,78	50
2	DIN EN 10130:2006	DC04	7114	1,2	50
3	52806/9.52873	FEP05-ZNT/F/2S	327	0,78	50
4	DIN EN 10025-2:2004	S235JRC	3937	2	50
5	DIN EN 10111:2008	DD13	6224	3	50
6	52806/9.52873	FEP04/FEP05-ZNT/F/2S	328	0,68	50
7	52814/9.52873	FEE 220 BH-ZNT/F/2S	380	1,09	50
8	DIN EN 10209:1996	DC04 EK	7513	0,81	50
9	DIN EN 10346:2009	S350GD+Z	1335	0,82	50
10	DIN EN 10346:2009	HX220YD+Z	1522	0,77	50

Nakajima method was used to create forming limit diagrams in the study and test coupons were prepared at different sizes are shown in figure 2 and different geometries are shown in figure 3 from each steel plate of size 200x200mm as vertical to the rolling direction. Samples were cut in wire erosion machines.

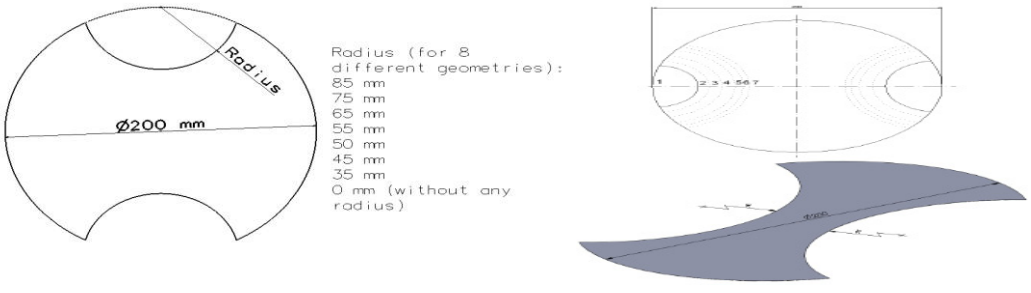

Figure 2. Dimensions and geometries of Nakajima test coupons used in tests

Figure 3. Examples of the paint-coated test coupons and modified Nakajima specimens

By changing the sheet geometries, major and minor strains were measured following varied deformation paths. This variety includes changes of all strain that may occur in forming operations. To improve reliability, tests were repeated for 5 times in each geometry. A total of 400 samples in 8 geometries for 10 grades were prepared in a precise manner with wire erosion device. At first, all test coupons were uniformly coated with white paint and then black colored dots as randomly distributed were coated with spray according to Aramis optical strain measurement system documents. Preparation time and costs are significantly reduced due to randomly generated patterns with using spray. Also the reasons that may occur which negatively affect the forming limits are eliminated with using the conventional method is creating circular patterns on the sample. In addition, the number of points on the surface are more than the number of circular pattern and more measuring points provide an increase for reliability. To determine the FLD, ZWICK-BUP-600 model of the test machine was used. Machine is connected to an Aramis optical strain measurement system and a computer which includes data collection and data processing software.[9] The experiments were carried out at the room temperature (20°C) according to standard ISO 12004-2:2008. At the ZWICK-BUP-600 machine, punch speed was kept constant at 2.5mm/sec during experiments. A suitable lubrication was provided between the test sample and the punch. 4M-ARAMIS-3D system was used for optical strain measurement. 10 photos are taken automatically in seconds (this corresponds to an average of 260 photos for each deformation process) and this photos was processed and transferred to software that calculates the strain.

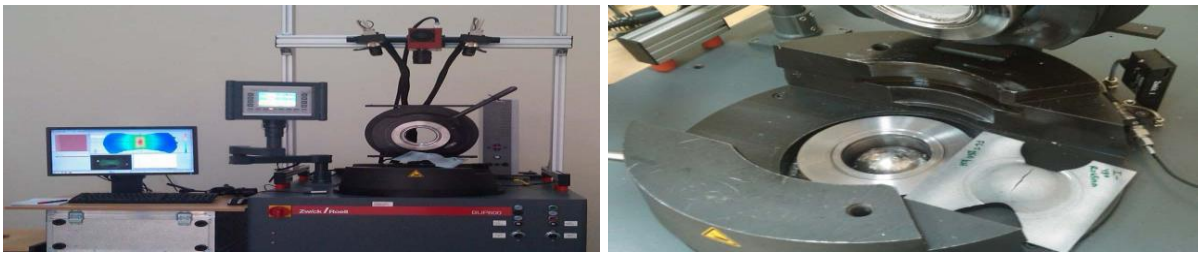

Figure 4. Universal sheet metal formability testing system with optical strain measurement

All stages of deformation until the rupture initiation is recorded in this analysis method. Each stage of deformation can be investigated by getting lots of pictures according to the frequency of the cameras. The principal strains on the sample were traced in a region that includes the first rupture with optical strain measurement system. Their values before rupture occurred a point on FLD curve as critical major and minor strain values. The photo frames before rupture were used in the creation of diagrams. When the algorithm developed by International Deep Drawing Research Group (IDDRG is applied which one of the last three pictures before rupture is used, it was observed that the same results obtained.

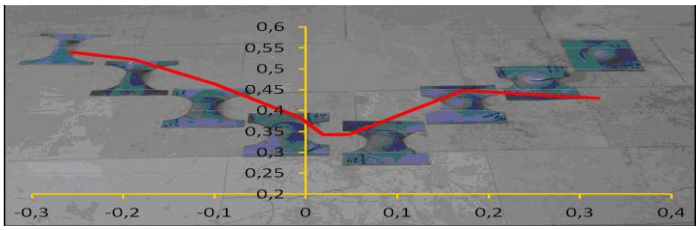

Figure 5. Nakajima sample geometries corresponding to a point on the FLD curve

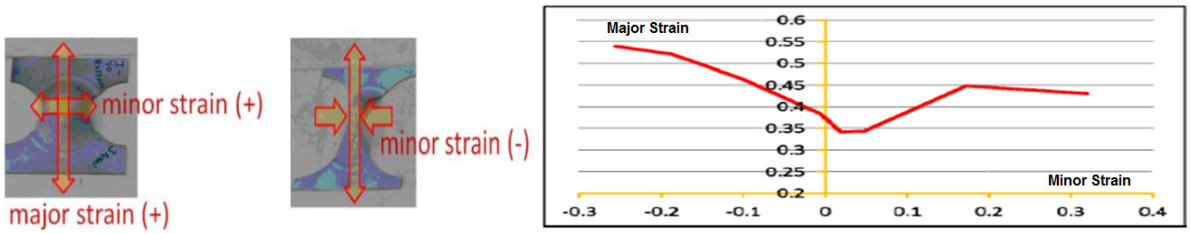

Figure 6. Description of strain on the forming limit diagram

The five parallel sections (the distance between them is 2mm) are taken perpendicular in the previous picture from the rupture for each geometry. From this section data, an FLD curve point with its measuring deviation is calculated automatically according to the currently valid guidelines. For customized FLD calculations, this section data can be exported and processed using proprietary evaluation algorithms. A pair of major-minor strain was found for each dimension in every repetition. Thus, 25 pair of major-minor strain were found for every Nakajima geometries in the repeated tests for 5 times. A point on the curve was calculated by taking the average of these as suggested by IDDRG. The FLD curve was obtained with combining 8 points obtained in this way. Ruptures appeared on test coupons are rolling direction.

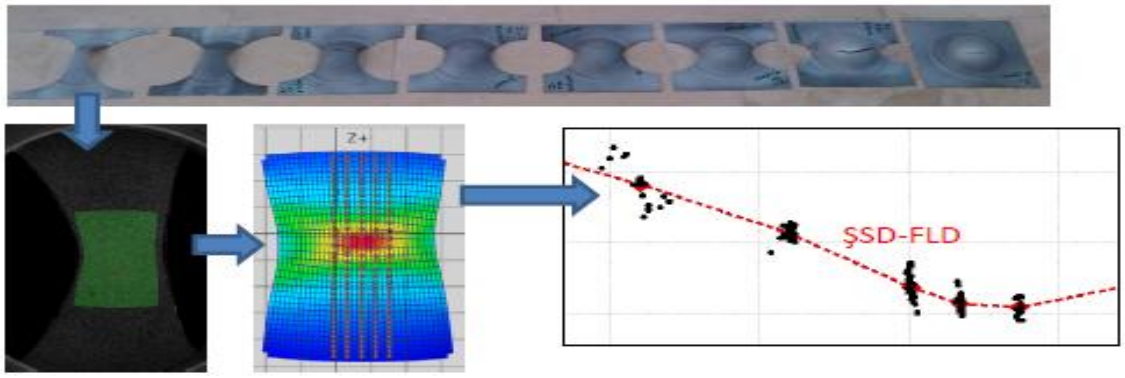

Figure 7. Black dots are the strain values taken from sections and red dots are the average strain values

The calculation is based on the displacement of the point defined. The purpose of determining displacement is to calculate the coordinates of the object for each point P which is one of the black dots created with spray as random pattern at all stages of deformation. The important point is that the coordinates (X,Y,Z) of point P in the undeformed state and the new coordinates (X,Y,Z) of point P after deformation can be found. Thus, displacement and strain values can be calculated. For this, a reference image of sample is created that can be used for comparison before starting the deformation process. Rupture is determined using photographs taken after deformation and the previous image of rupture is used to create FLD. In the general method used in the preparation of the FLD, some errors are caused by people occur

due to the use of mylar tapes, microscopes, flexible measuring tapes, etc. to measure the amount of elongation after deformation. FLD is obtained more reliably with this method because the measurement of spot patterns generated is performed using computer.

3. RESULTS AND DISCUSSION

8 strain pairs obtained were transferred to MS-Excel and graphs were plotted for each steel grades. These graphs are FLDs that illustrate the forming limits for the thicknesses of steels used in the experiments.

1	
Material Designation	
Erdemir Quality	326
Thickness	0.78 mm
8 strain pair values for forming limits	
Minor	Major
-0,291	0,598
-0,2	0,577
-0,0722	0,479
-0,00061	0,387
0,0315	0,358
0,0502	0,342
0,156	0,395
0,312	0,478

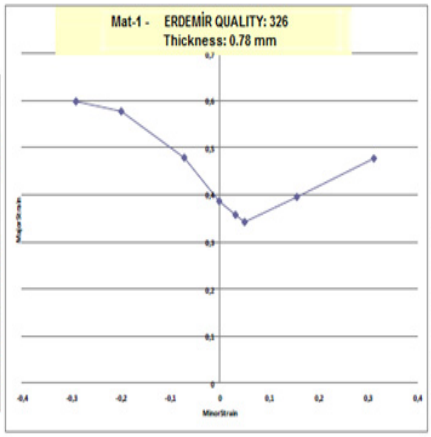

2	
Material Designation	
Erdemir Quality	7114
Thickness	1.2 mm
8 strain pair values for forming limits	
Minor	Major
-0,285	0,645
-0,178	0,581
-0,079	0,513
0,00233	0,436
0,035	0,414
0,0744	0,408
0,36	0,51
0,381	0,5

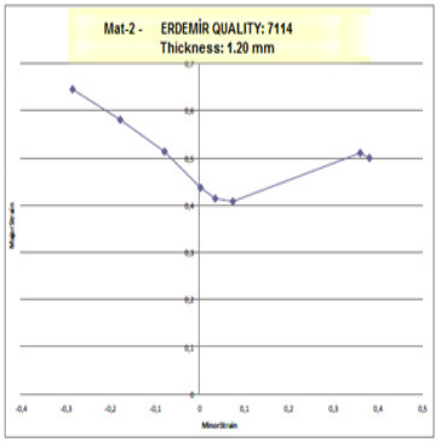

3	
Material Designation	
Erdemir Quality	327
Thickness	0.78 mm
8 strain pair values for forming limits	
Minor	Major
-0,234	0,557
-0,156	0,539
-0,0678	0,471
0,00171	0,415
0,034	0,401
0,0724	0,38
0,174	0,434
0,334	0,477

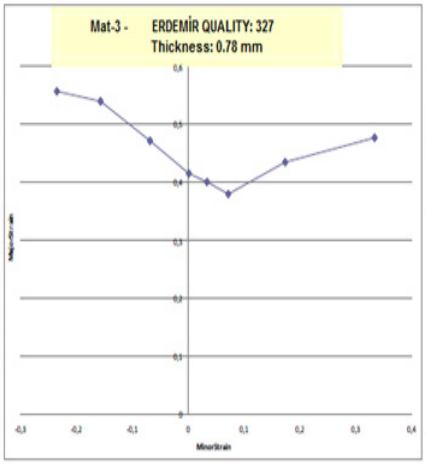

4	
Material Designation	
Erdemir Quality	3937
Thickness	2.00 mm
8 strain pair values for forming limits	
Minor	Major
-0,104	0,43
-0,0524	0,415
-0,00608	0,373
0,0389	0,347
0,0675	0,322
0,103	0,33
0,393	0,439
0,41	0,437

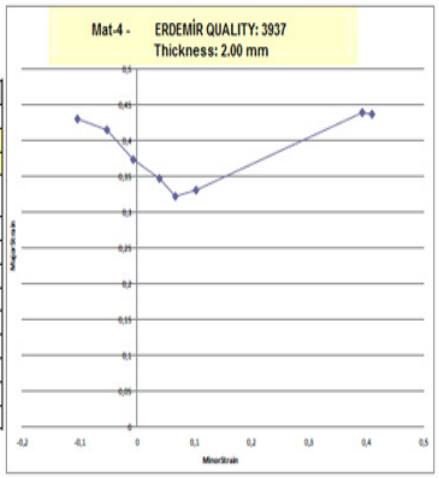

5	
Material Designation	
Erdemir Quality	6224
Thickness	3.00 mm
8 strain pair values for forming limits	
Minor	Major
-0,13	0,537
-0,0772	0,515
-0,0519	0,496
0,042	0,382
0,0662	0,359
0,108	0,378
0,27	0,46
0,3	0,44

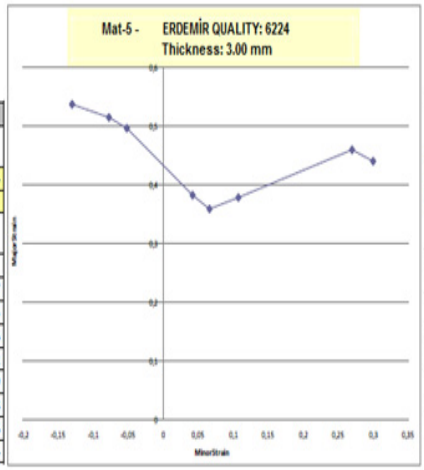

6	
Material Designation	
Erdemir Quality	328
Thickness	0.68 mm
8 strain pair values for forming limits	
Minor	Major
-0,306	0,619
-0,192	0,547
-0,0836	0,476
0,000639	0,372
0,0336	0,351
0,0791	0,337
0,318	0,47
0,33	0,473

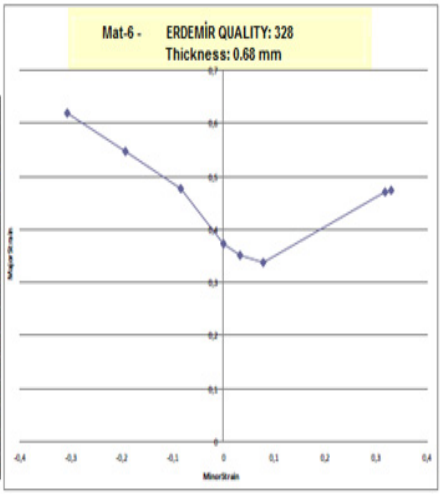

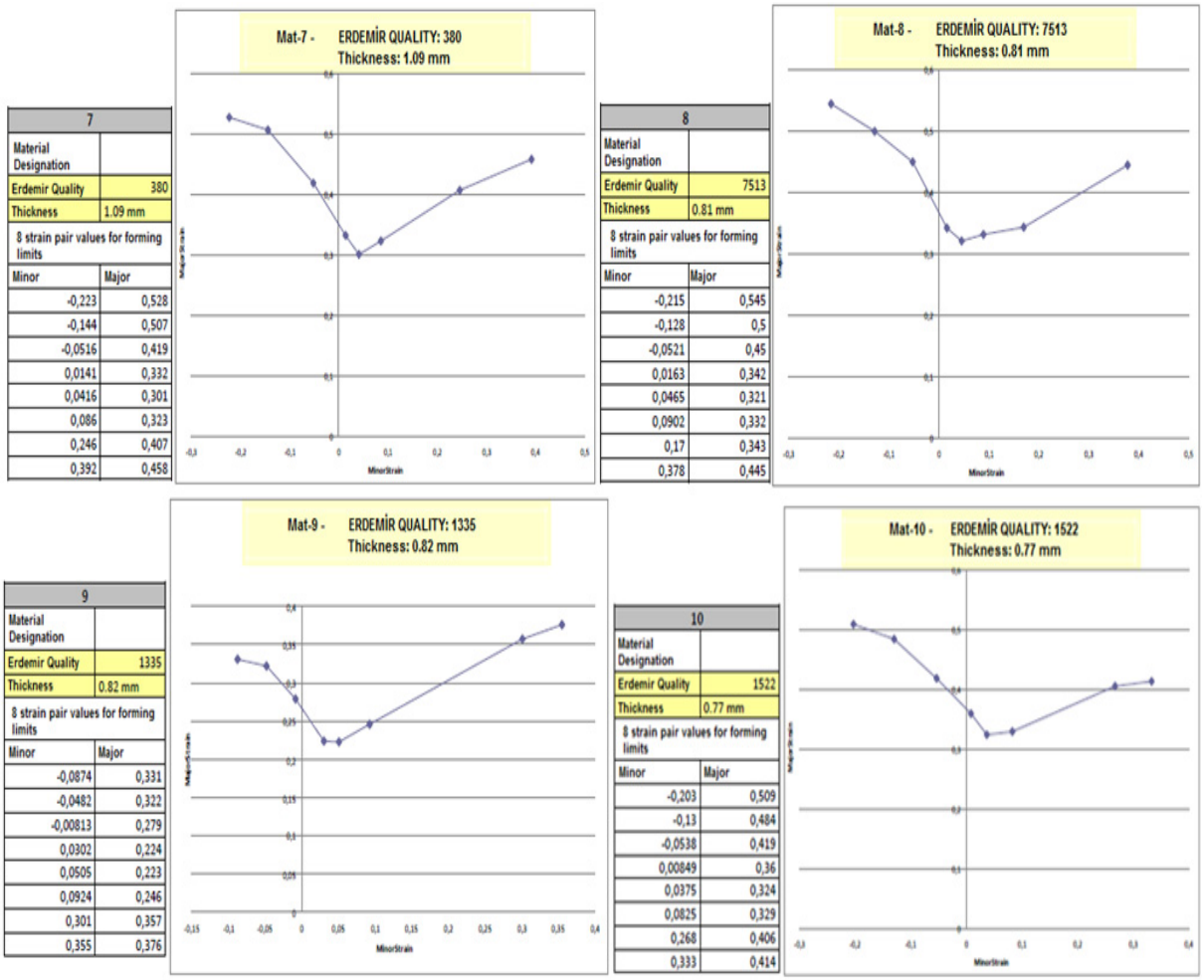

7	
Material Designation	
Erdemir Quality	380
Thickness	1.09 mm
8 strain pair values for forming limits	
Minor	Major
-0,223	0,528
-0,144	0,507
-0,0516	0,419
0,0141	0,332
0,0416	0,301
0,086	0,323
0,246	0,407
0,392	0,458

8	
Material Designation	
Erdemir Quality	7513
Thickness	0.81 mm
8 strain pair values for forming limits	
Minor	Major
-0,215	0,545
-0,128	0,5
-0,0521	0,45
0,0163	0,342
0,0465	0,321
0,0902	0,332
0,17	0,343
0,378	0,445

9	
Material Designation	
Erdemir Quality	1335
Thickness	0.82 mm
8 strain pair values for forming limits	
Minor	Major
-0,0874	0,331
-0,0482	0,322
-0,00813	0,279
0,0302	0,224
0,0505	0,223
0,0924	0,246
0,301	0,357
0,355	0,376

10	
Material Designation	
Erdemir Quality	1522
Thickness	0.77 mm
8 strain pair values for forming limits	
Minor	Major
-0,203	0,509
-0,13	0,484
-0,0538	0,419
0,00849	0,36
0,0375	0,324
0,0825	0,329
0,268	0,406
0,333	0,414

Figure 8. FLDs of the 10 steel grades

In this study, forming limit diagrams were obtained with deep drawing tests for very low carbon (IF), medium and low carbon steel that especially used in the automotive industry. As a result of experiments, measurements were performed in 8 different geometries for each grades in the repeated tests for 5 times and forming limit diagrams were created. The results of this study are as follows.

The paper deals with the theoretical and experimental investigation of forming limit diagrams as a special field of the formability of sheet metallic materials. As a result of research for determining the forming limits of sheet metal in the industry was found to have an important place in terms of economy, continuity, quality and using forming limit diagrams was found to be most common method for determination of these limits. When the forming limit diagrams of grades 326 and 327 that have the same thickness and chemical composition are compared, it was found that higher r and n values have favourable effect on the limit strain values as indicated in the literatüre. The limit curve of grade 327 which have a higher r and n value was determined to be higher than the other quality's curve, so more safe region to work was found for grade 327. Comparing the effect of sheet thickness on the forming limit diagrams for the two different steel grades 7114 and 326 which have close chemical and mechanical properties with different thickness, it can be concluded that the forming limit curves are shifted towards higher limit strains with the increase of the sheet thickness. It was seen from the diagrams that the thicker grade 7114 (1.2mm) has the higher limit curve than the other grade 326 (0,78mm). When analyzing the effect of the increased amount of carbon and increased yield and tensile

strength with increased carbon on the forming limit diagrams, the limit curve of the grade 1335 which have higher carbon manganese ratio and mechanical properties was found to be lower than the grade 7513. So it was proved that increasing of carbon ratio and mechanical properties are negatively impact the ability to forming.

REFERENCES

1. N.S.Köksal, M.Uzkut, "Determination of Formability Parameters of Erdemir 6114 Sheets Tempered at Dual Phase Regions", Journal of Engineering Sciences, Vol. 7, No. 3, pp. 337-341, 2001
2. A.Ç.Çöplü, T.Öztürk, "Using the Forming Maps for Sheet Material", Journal of Metallurgy, Vol. 40, October 1985
3. T.Gündü, "Determination of Deep Drawing Properties for Deep Drawing Steel", MSc Thesis, Istanbul Technical University, Istanbul, June 2000
4. T.Öztürk, "Forming Features of Steel Sheets(Deep-Drawing)", Engineer and Machine, Vol. 25, No. 292, March-April 1984
5. M.A.Akoy, H.Çimenoğlu, E.S.Kayalı, "Improving Ability to Deep Drawing of Low Carbon Steel Sheets", I. Iron and Steel Symposium, October 2001
6. M.A.Akoy, "Determination of Forming Limit Diagrams of Low Carbon Steel Sheets", MSc Thesis, Istanbul Technical University, Istanbul, June 2001
7. A.Bakkaloğlu, "Influence of Process Parameters on Properties of IF Steels", 1. Steel Symposium, pp. 695-703, October 2001
8. O.Anket, T.Koruvatan, İ.Ay, "The Use of Forming Limit Diagrams in Forming Sheet Metal Materials", Politeknik, Vol. 14, No. 1, pp. 39-47, 2011
9. O.Temeltaş, M.A.Akoy, M.Koz, E.S.Kayalı, "Forming Limit Diagrams of 304 Quality Austenitic and 430 Quality Ferritic Stainless Steel Sheets", 9. Denizli Materials Symposium, May 2002
10. E.Uysal, F.Öztürk, "Obtaining Forming Limit Diagram for High Strength Steels with a Sample Application", 2. National Design Analysis and Manufacturing Congress, Balıkesir, November 2010
11. M.K.Yaşar, "The Investigation of Process Parameters for Improving the Formability Properties of Metals, MSc Thesis, Technical University, Istanbul 2006
12. www.gom.com, "Application Example: Material Testing", 2009
13. M.A.Akoy, E.S.Kayalı, H.Çimenoğlu, "The Influence of Microstructural Features and Mechanical Properties on the Cold Formability of Ferritic Steel Sheets", ISIJ International, Vol. 44, No. 2, pp. 422–428, 2004
14. BlueScope Steel Limited, "Press-forming Steel Sheet and Strip", Technical Bulletin TB-F0, TB-F7, Rev 2, November 2003
15. S.Nementh, A. Sunova, E. Evin, "Forming Limit Diagrams as an Important Indıcator of Progressive High-Strength Steel Sheets Forming", Technical University of Košice, 2013
16. M.Tisza, Z.P.Kovacs, "New Methods for Predicting the Formability of Sheet Metals", Production Processes and Systems, Vol. 5, No. 1, pp. 45-54, 2012

PHOTOCATALYTIC PROPERTIES OF TiO_2 POWDERS SYNTHESIZED BY SOL-GEL PROCESS USING DIFFERENT WATER/Ti-PRECURSOR RATIO

Lutfi AGARTAN*, Derya KAPUSUZ*, Jongee PARK, Abdullah OZTURK***

* Middle East Technical University, Ankara, TURKEY
** Atilim University, Ankara, TURKEY

ABSTRACT

The morphology and photocatalytic properties of sol-gel derived TiO_2 powder has been studied with respect to water/Ti-precursor ratio (R). Solutions for R of 1, 3, 5, 10, 30, and 50 have been prepared for the synthesis of TiO_2 powders. Dried xerogels were calcined at temperatures of 300, 400, and 500 °C for 1, 2, and 3 h to obtain TiO_2 powders. The morphology and crystal parameters of the TiO_2 powders were investigated using X-ray diffractometer and scanning electron microscope. Nanosize TiO_2 particles -in the range of 15-40 nm- were obtained after calcination. The photocatalytic performance of the powders was evaluated by methylene blue degradation test for 90 min in UV illumination. A diffuse reflector was employed for the band gap measurements. Results have shown that R had a profound effect on the crystal structure, crystallite size, morphology, band gap energy, and photocatalytic activity of sol-gel derived TiO_2 powders. The best photocatalytic activity was achieved with R30 powder calcined at 400 ^oC for 2 h.

Keywords: *Sol-Gel, TiO_2, Nanopowder, Characterization, Photocatalysis*

FARKLI SU/Ti-PREKÜRSOR ORANLARI KULLANILARAK SOL-JEL TEKNİĞİYLE ÜRETİLMİŞ TiO_2 TOZLARININ FOTOKATALİTİK ÖZELLİKLERİ

ÖZET

Su/Ti-prekürsor oranını (R) değiştirerek sol-jel tekniğiyle üretilen TiO_2 tozlarının morfoloji ve fotokatalitik özellikleri çalışılmıştır. TiO_2 tozlarının sentezi için R değeri 1, 3, 5, 10, 30, ve 50 olan çözeltiler hazırlanmıştır. Kurutulmuş zerojeller 300, 400 ve 500 ^oC'de 1, 2, ve 3 saat kalsine edilerek TiO_2 tozları elde edilmiştir. TiO_2 tozlarının morfolojileri ve kristal parametreleri X-ışını kırınımı ve taramalı elektron mikroskobuyla incelenmiştir. Üretilen TiO_2 tozlarının kalsinasyon sonrası boyutlarının 15-40 nm arasında olduğu tespit edilmiştir. Tozların fotokatalitik performansları metilen mavisi çözeltisinin UV-ışık altında 90 dakikada bozunumu deneyiyle değerlendirilmiştir. Enerji kuşak aralığı ölçümleri için difuze reflektör kullanılmıştır. Sonuçlar olarak, sol-jel tekniğiyle üretilen TiO_2 tozlarının R değerinin kristal yapı, kristal boyutu, morfoloji, enerji kuşak aralığı ve fotokatalitik performansı üzerinde önemli bir etkisinin olduğunu göstermiştir. En iyi fotokatalitik aktivite 400 ^oC'de 2 saat kalsine edilen R30 tozundan elde edilmiştir.

Anahtar kelimeler: Sol-Jel, TiO_2, Nanotoz, Karakterizasyon, Fotokataliz

1. INTRODUCTION

The industrial wastes and pollutants are among the biggest problems in today's world. Pollutants emitted from various sources result in severe ecological problems such as pollution of air, water, or soil [1]. Several methods have been tried to recycle or to make the wastes and pollutants less hazardous for the living environment. Conventional methods such as adsorption [2], biodegradation [3], chlorination and ozonation [4] are not efficient enough in solving hazardous issues. Also, they have formed secondary pollutants [5]. The photocatalysis concept, introduced by Fujishima and Honda [6] in 1972, is more effective than the conventional chemical oxidation methods for the decomposition of toxic wastes to non-hazardous products. In addition, final products of photocatalysis are CO_2 and H_2O [7,8].

Titania (TiO_2) is one of the most commonly used photocatalysts in heterogeneous photocatalysis applications due to its superior properties such as high oxidizing capability, chemical inertness, low price, nontoxicity, and high availability in the market [9-11]. The properties of TiO_2 enable it to be used in a wide range of energy related (solar cell, water splitting, etc.) and environmental (air, water purification, self-cleaning glass, etc.) applications [8]. However, high band gap energy (e.i. 3.2 eV for anatase), limit the applications of TiO_2 photocatalyst since it is not activated by visible-light. It is activated only by UV-light irradiation that accounts for about 5% of the solar spectrum [12, 13]. Studies related to TiO_2 photocatalyst are mainly focused on the improvement of its photocatalytic efficiency in daylight. The photocatalytic properties are affected by particle size, crystallite size, electron/hole (e^-/h^+) recombination rate, type and amount of dopant, powder morphology, degree of crystallinity, specific surface area, calcination time and temperature, band gap energy, phases present and their amount [11-16]. Different strategies i.e., semi-conductor coupling, dye sensitization doping, and physical (particle and crystallite size reduction) have been developed for the improvement of the photocatalytic efficiency of TiO_2 [14, 15].

Various chemical and physical production techniques including ball milling [17], solvothermal [18], and sol-gel [19] were applied for the synthesis of TiO_2 nanopowders. Among these techniques sol-gel is one of the most widely used process since it offers the advantages like high purity, low temperature processing, high control over morphology, crystalline phases, nucleation and growth kinetics, and homogeneity [20, 21]. In sol-gel processing, the pH and viscosity of the initial solution, solvent, type or concentration of precursor, water/Ti-precursor ratio, solvent, aging conditions, and drying and calcination temperatures are among the parameters affecting the powder morphology and properties [22]. Although several studies were conducted on the synthesis of TiO_2 powders by sol-gel process, there are only a few publications related to the effect of water/Ti-precursor ratio on the morphology and photocatalytical properties of the TiO_2 powders synthesized by sol-gel process. Therefore, a good understanding of the role of water/Ti-precursor ratio is important for both scientific and technological point of view.

The purpose of this study is to elucidate the effect of water content of initial solution and calcination regime (time and temperature) on the morphology and photocatalytic properties of sol-gel derived TiO_2 powder. The ultimate aim was to improve photocatalytic properties of TiO_2 up to a point that better efficiency in daylight could be attained. The synthesized TiO_2 powders were characterized by using X-ray diffraction, scanning electron microscopy, and diffuse reflectance spectroscopy. Photocatalytic performance was evaluated by the degradation of methylene blue solution under UV-light irradiation.

2. EXPERIMENTAL PROCEDURE

2.1. Synthesis of TiO_2 nanoparticles

Various solutions with mole of water/mole of TEOT (R) ratio of 1, 3, 5, 10, 30, and 50 were prepared for the sol-gel synthesis of TiO_2 nanoparticles. Initially, 0.1 mole TEOT ($Ti(OC_2H_5)_4$; Merck) was dissolved in 30-ml ethanol (C_2H_5OH; Fluka) by continuous magnetic stirring. Next, 0.1 mole of water was added for preparation of the solution R1. Necessary amount of water was added for the preparation of the solutions having greater R values. Then, 10 ml of glacial acetic acid was added to the solution under magnetic stirring. Upon addition of all ingredients the solution was magnetically stirred at 500 rpm continuously for 15 min in order to obtain a homogeneous mother solution. Obtained mother solutions were aged at room temperature until complete gelation is achieved. Xerogels were dried in an oven at 80 ^oC for 24 h. After drying TiO_2 powders were acquired. The dried powders were calcined at 400 and 500 ^oC for 2 h for crystallization process to take place. The calcination was performed at heating rate of 5 °C/min up to maximum temperature.

2.2. Characterization of TiO_2 nanoparticles

An X-ray diffractometer (Rigaku, D/MAK/B) was employed to identify the crystalline phases formed during aging of the solutions and during heat-treatment of the TiO_2 powders. Cu K_α radiation with a wavelength of 1.54056 Å was used for the X-ray source. Each powder was scanned in a 2θ range from 15^o to 75^o with 2 ^{o}/min rate continuously with an accelerating voltage of 40 kV and applied current of 40 mA. X-ray diffraction data was analyzed by using Rigaku 4.2 Qualitative Analyses program. Rietveld refinement was performed to the powders to determine the lattice parameters and crystallite size using General Structure Analyses System (GSAS) program. A scanning electron microscope (FE-SEM, Nova Nanosem 430) was occupied for morphological analyses of the powders. A 15 kV accelerating voltage was applied during imaging of the powder samples. Diffuse reflector apparatus (Scinco S-3100) of UV-Vis Spectrophotometer was used for the diffuse reflectance measurements. White blank measurement was done according to USRS-99-010 standard. The percentage reflection versus wavelength graph was transformed by Kubelka-Munk method to $[eV]^{(1/2)}$ vs [eV] graph.

2.3. Photocatalytic activity measurements

The photocatalytic activity of the TiO_2 powders was evaluated in terms of the degradation of aqueous methylene blue (MB) solution under ultraviolet (UV) light illumination. Test was conducted in a vessel preventing the passage of light through the sample. Initial concentration of the MB solution was 10 mg/l. A 50 ml of MB aqueous solution was mixed with 50 mg of TiO_2 powder to prepare the suspension that was stirred magnetically at 500 rpm at dark for 30 min until adsorption/desorption equilibrium is formed. At the end of first 30 min, a sample of 4 ml was taken from suspension by means of syringe filters (Millex Millipore, 0.22 μm). Then, the sample was put into the quartz cuvette and transferred to UV-vis spectrophotometer (Scinco S-3100) for measurement of the photocatalytic activity at the wavelength of 664 nm. After the first measurement, UV lamp (UVP Co.) was turned on and the changes taking place upon UV light irradiation via degradation of MB molecules were measured. UV light source was a 100-W UV lamp with a wavelength of 365 nm. The procedure was repeated after 30, 60, and 90 min of UV-irradiation. The degradation percentage was calculated with respect to illumination time using equation 1.

$$\text{Degradation ratio (\%)} = [(I_{dark}-I)*100]/I_{dark} \quad (1)$$

Where;

I= Intensity at 664 nm at 30, 60, and 90 min UV radiation time.
I_{dark}= Intensity at 664 nm after adsorption/desorption equilibrium (30 min in dark).

3. RESULTS and DISCUSSION

3.1. Powder Synthesis

Six different mother solutions were prepared to synthesize TiO_2 powders. The mother solutions prepared for R ratio of 1, 3, 5, and 10 turned into sols that were kept standing in the room temperature until they set to gels. The mother solutions prepared for R ratio of 30 and 50 did not form gels when they were kept standing in the room temperature for a few days. They formed colloidal suspensions form which particles precipitated and collected at the bottom of the beaker. A total of 60 different TiO_2 powders regarding the R ratio, calcination temperature, and calcination time were synthesized. The synthesized TiO_2 powders were named regarding the R ratio, calcination temperature, and calcination time as Rx T0t. Where x is for the numerical value of R ratio, T is for the first integer of the calcination temperature in degree celcius, and t is the calcination time in hour. For instance, the powder synthesized for R ratio of 1 and calcined at 400 ^oC for 2 h was labelled R1 402.

Only the TiO_2 powders synthesized for R ratios of 1 and 30 calcined at 400 and 500 ^oC for 2 h were taken into consideration in this manuscript since the total number of the powders synthesized quite a lot which makes the evaluation and understanding of the data difficult. Details of the experimental results are given in Reference 14. The powders synthesized for R ratios of 1 and 30 were chosen since they represent both synthesis routes encountered. Powder R1 showed a synthesis route of polymeric sol-gel, and its total gelation took place in 3 h. On the contrary, powder R30 showed a colloidal sol-gel route at which no observable polymeric gel formation happens [23].

3.2. Characterization

X-ray diffraction (XRD) analysis revealed that all powders composed of anatase phase (JCPDS #21-1272) in as-dried form, except powders R1 and R3 which did not show any crystallinity. The characteristic anatase peak of (101) plane at 2θ of ~25.3^o was detected in the XRD patterns of the powders R5, R10, R30, and R50 in as-dried form. Increasing water content resulted in better crystallinity in the as-dried powders.

The change in synthesis route as a result of increasing water content caused crystallinity differences in the as dried powders. That is, powder R1 showed a fully amorphous structure while powder R30 showed partial crystallization as suggested by the XRD patterns as shown in Figure 1. Full crystallization took place upon calcination of the powders for both R ratios. Moreover, upon calcination at 400 ^oC anatase crystals were formed in both powders. However, upon calcination at 500 ^oC, powder R1 showed 26.20% rutile phase (JCPDS card no. 12-1276) whereas powder R30 contained only anatase phase.

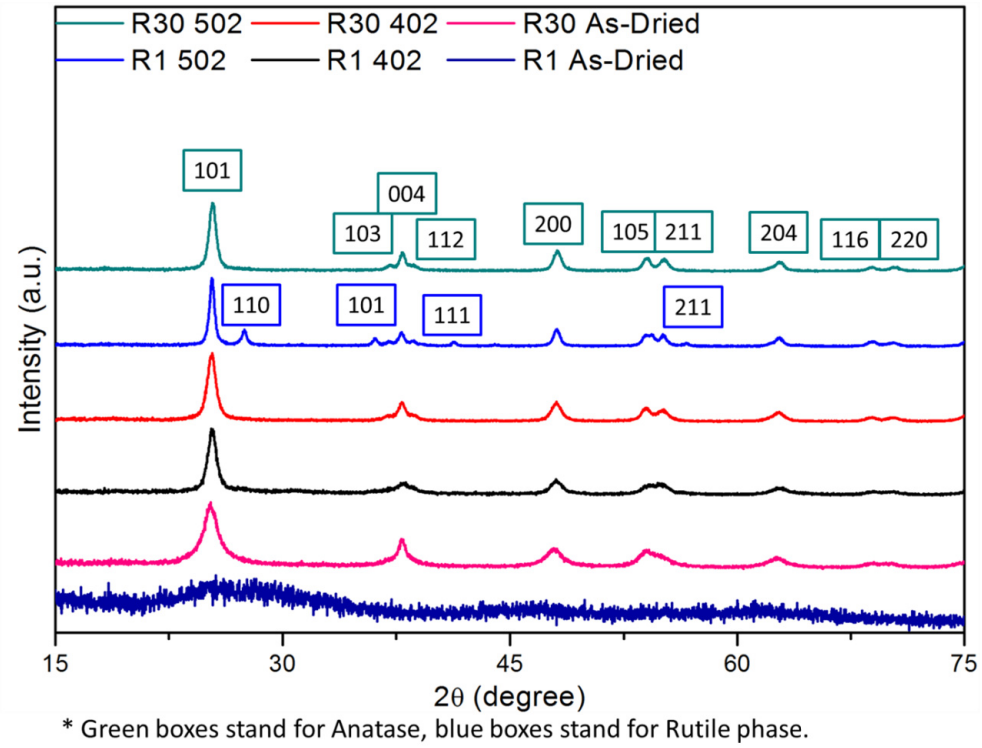

Figure 1. XRD patterns of the powders.

Rietveld fittings of the powders were given in Figure 2. Fittings were done with the following parameters: space group: $I4_1/amd$; atomic positions: Ti (0, 0.75, 0.125), O (0, 0.75, 0.333); instrumental broadening: GU=33.54, GV=-17.8 and GW=11.41. After refinement was done, χ^2, Rp, wRp fitting parameters and lattice parameters were calculated. The calculated values were presented in Table 1. The crystallite sizes, calculated from lorentzian parameters (LX), were given also in Table 1.

Rietveld refinement fitting parameters showed that all four fittings have almost the same quality of fitting. Moreover, both lattice parameters and cell volumes did not show any significant variance neither upon change of water content of mother solution nor by change of calcination temperature. However, crystallite sizes showed significant variation depending upon R ratio and calcination temperature. Since powder R1 was totally amorphous while R30 was partially crystallized in as-dried condition, powder R1 had more driving force than R30 for the nucleation and growth of the crystalline phases. However, temperature of 400 ^{o}C was not high enough for high atomic mobility. Since the energy required for atoms to leave the matrix and attach itself to a growing phase is high, these mechanisms are not too active below 500 ^{o}C [24]. On the other hand at 500 ^{o}C, driving force and mobility were very high so that the crystalline phases could nucleate and grow. Powder R1 had higher crystallite size than powder R30. Also, rutile formation was observed in powder R1. For rutile formation to happen atoms must leave anatase matrix and form rutile matrix [24].

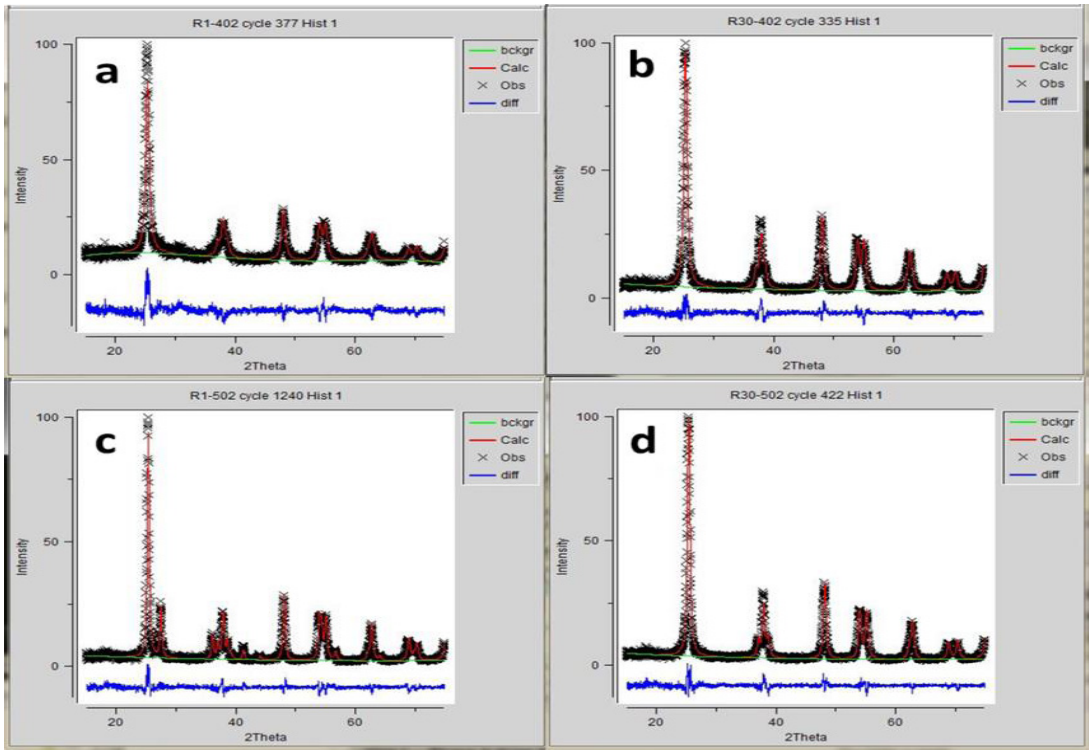

Figure 2. Rietveld fittings of the powders **a.** R1 402, **b.** R30 402, **c.** R1 502, and **d.** R30 502. (Red line is values calculated via Rietveld refinement, black points are experimental data and blue line is the difference between them).

Table 1. Lattice parameters and unit cell volume of crystal phases in the powders.

Lattice Parameters	Powders				
	R1 402	R30 402	R1 502 (A)	R1 502 (R)	R30 502
χ^2	0.1295	0.0897	0.0776		0.0766
Rp	0.0888	0.0873	0.0901		0.0888
wRp	0.1132	0.1144	0.1189		0.1149
a (Å)	3.78	3.79	3.79	4.59	3.79
c (Å)	9.47	9.51	9.52	2.95	9.52
Vol (Å^3)	135.31	136.60	136.75	61.31	136.75
Crystallite Size (nm)	12.37	14.24	23.60	20.92	18.81
% Degradation	43.00	99.35	20.49		94.89
Rate Constant [k_t] (1/Min)	0.0062	0.0560	0.0025		0.0330
Energy Band Gap (eV)	2.83	3.13	2.92		3.14

A: Anatase, R: Rutile

SEM images of the powders are shown in Figure 3. All particles are in nanosize (smaller than 40 nm). However, all powders are highly agglomerated. Shapes of the agglomerates are affected from R ratio of the mother solution. At low water content, agglomerates have monolithic structure with sharp edges. Meanwhile at high water content, agglomerates have both monolithic and porous structure with more spherical shapes and edges. Results are consistent with those reported earlier by the authors [25]. No significant effect of calcination temperature was observed over morphology of the powders. The smallest particle size was obtained in as-dried form whereas in 502 regimes the largest particle size was obtained.

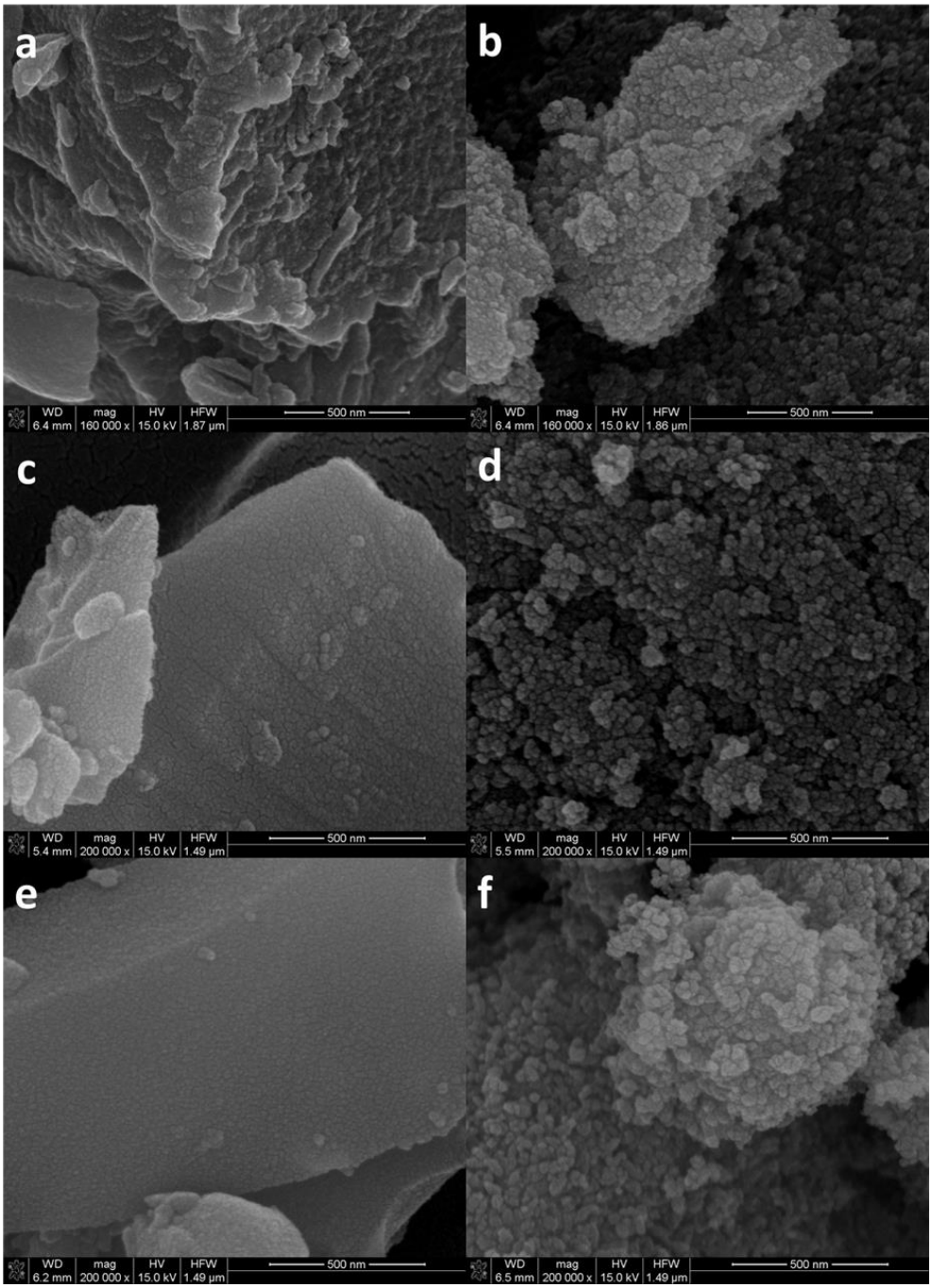

Figure 3. SEM images of the powders **a.** R1 as-dried, **b.** R30 as-dried, **c.** R1 402, **d.** R30 402, **e**. R1 502, and **f.** R30 502.

Diffuse reflectance spectra of the powders are seen in Figure 4. No significant redshift or blueshift was observed in powder R30 upon calcination. On the other hand, powder R1 showed blueshift upon calcination at higher temperature. Water content is found to increase the band gap energy to higher values as noted in Table 1. Nevertheless, the band gap energy of powder R30 is below 3.2 eV after calcination at both temperatures.

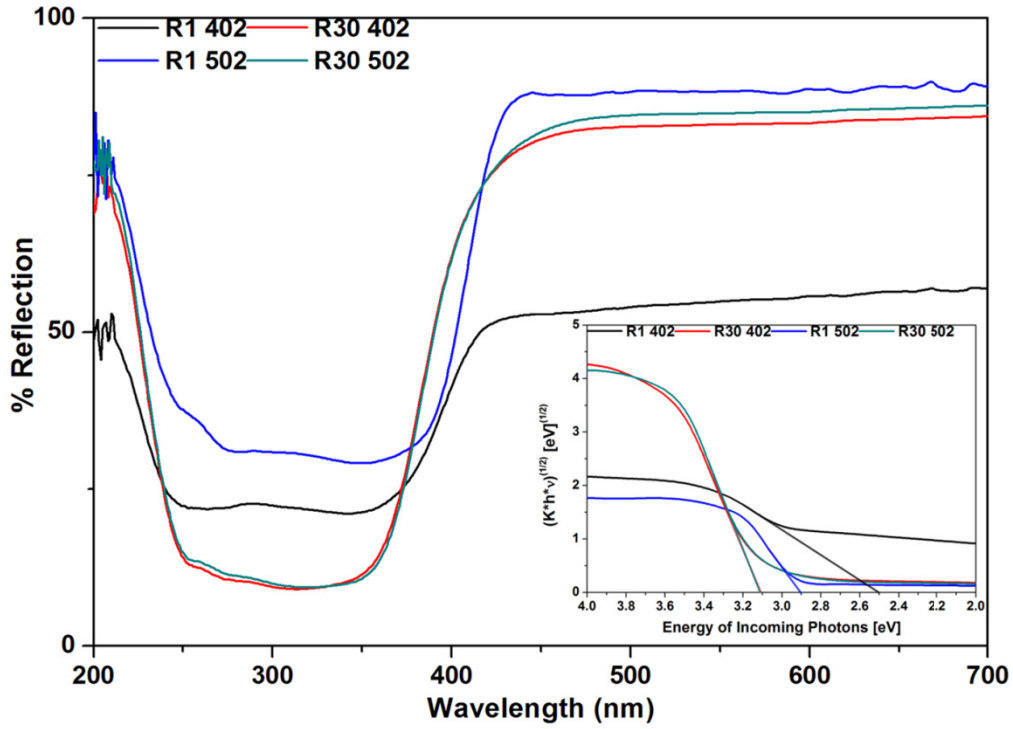

Figure 4. Diffuse reflectance spectra and Kubelka-Munk transform of the powders.

3.3. Photocatalytic activity

MB degradation test results are given in Figure 5. It is seen that photocatalytic activity increases with increasing water content in mother solution. Increasing calcination temperature from 400 to 500 ^{o}C resulted in decreasing photocatalytic performance for both powders. Coexistence of anatase and rutile phases shows synergetic effect due to increased charge separation (e^{-}/h^{+}) [26, 27]. However, the experimental results of powder R1 are not in concomitant with those given in literature. The reason is attributed to the decrease in specific surface area, change of pore size distribution, and increase in crystallite and particle size (see Figure 3). Powder R30 showed a decrease because of the increasing crystallite size, too. Since photocatalytic reactions take place at the surface of the photocatalyst, an increase in crystallite size results in a decrease in the photocatalytic performance and efficiency.

MB degradation test results are highly depend on molarity of the MB solution. In order to get over that complication Langmuir-Hinselwood kinetic model (Equation 2) was taken into consideration to calculate rate constant (k_t) of degradation kinetics. Calculated results were plotted with respect to 90 min of UV-irradiation of the powders as shown in Figure 6.

$$\ln[C_0/C] = k_t * t \quad (2)$$

Where,
C_0= Initial concentration of MB
C_t= MB concentration at a given time
k_t= Apparent rate constant
t= Time

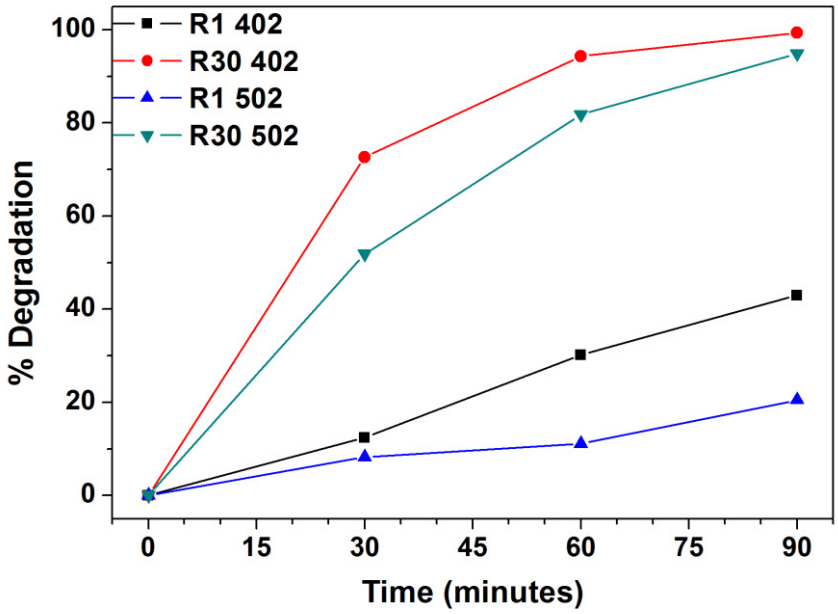

Figure 5. a. Methylene blue degradation of the powders with respect to UV irradiation time.

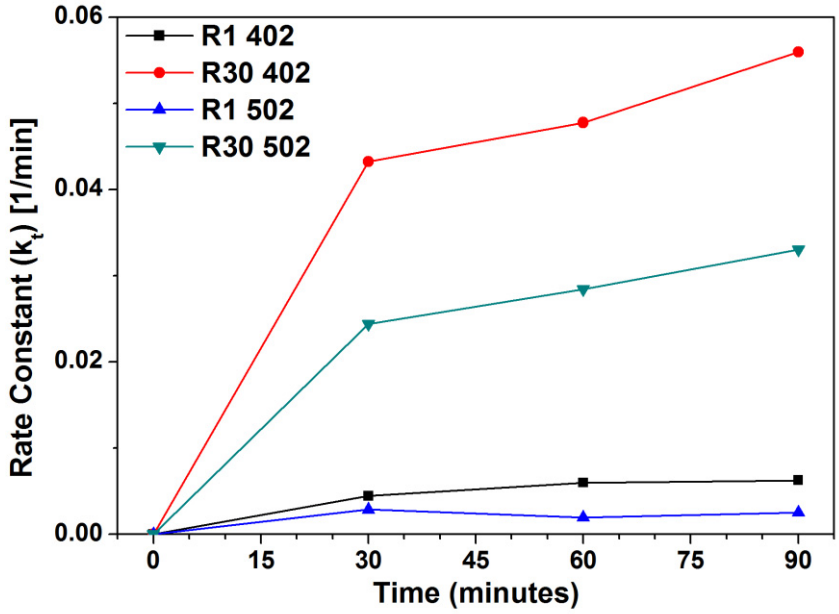

Figure 6. Variation in rate constant of the powders with UV irradiation time.

High photocatalytic performance of powder R30 with respect to powder R1 is attributed to better MB degradation capability of its agglomerates and surface properties [28]. Also, when calcination temperature is increased to 500 ^{o}C, crystallite size of the present phases in powder R1 502 increased much more than that of anatase phase in powder R30 502. Conclusively, smaller calcination temperature with higher water content results in better photocatalytic degradation performance.

4. CONCLUSIONS

Water/TEOT ratio has a profound effect on the formation mechanism, morphology, structure, photocatalytic performance, and band gap energy of the sol-gel derived TiO_2 powders. Increasing water content in the mother solution caused the formation of different phases in the powders at high calcination temperatures and increased the crystallite size. However, water/TEOT ratio has no significant effect on particle size and shape, but influences shape of agglomerates. Increasing water/TEOT ratio resulted in better photocatalytic degradation of methylene blue, whereas increasing calcination temperature caused a decrease in photocatalytic degradation of methylene blue under UV light irradiation.

ACKNOWLEDGEMENT

The authors would like to thank Middle East Technical University for the partial financial support to perform the experiments through Project No: BAP-03-08-2013-001.

REFERENCES

[1] D.Chatterjee and S.Dasgupta, Journal of Photochemistry and Photobiology C: Photochemistry Reviews, 6, 186-205, 2005
[2] P.Dejohn, and R.Hutchins, Journal Textile Chemist and Colorist, 8, 34-38, 1976
[3] S.Patil, and V.Shinde, Environmental Science and Technology, 22, 1160-1165, 1988
[4] Y.Slokar, and A.Le Marechal, Dyes and Pigments, 37, 335-356, 1998
[5] J.Yao, and C.Wang, *International Journal of Photoenergy*, 1-6, 2010
[6] A.Fujishima and K.Honda, Nature, 238, 37-38, 1972
[7] P.Innocenzi, Y.Zub, and V.Kessler, "Sol-Gel Methods for Materials Processing", Springer, Derdrecht, 2008
[8] K.Nakata, and A.Fujishima, *Journal of Photochemistry and Photobiology C: Photochemistry Reviews*, 169-189, 2012
[9] Y.Ichihashi, H.Yamashita, M.Anpo, Supplement au Journal de Physique III d'avril, 2, 883-885, 1997
[10] S.M.Gupta, and M.Tripathi, Chinese Science Bulletin, *56*, 1639-1657, 2011
[11] M.P.Seabra, I.M.Miranda Salvado, and J.A.Labrincha, J. A., Ceramics International, 37, 3317-3322, 2011
[12] V.Etacheri, M.Seery, S.Hinder, and S.Pillai, Advanced Functional Materials, 1-9, 2011
[13] M.Pelaez, N.T.Nolan, S.C.Pillai, M.K.Seery, P.Falaars, A.G.Kontos, et al., Application Catalysis B: Environmental , 125, 331-349, 2012
[14] L.Agartan "Production and Photocatalytic Properties of B and/or Zr Doped Titania Powders by Sol-Gel", M.Sc. Thesis, Middle East Technical University, Ankara, 2014
[15] S.Rehman, R.Ullah, A.M.Butt, and N.D.Gohar, Journal of Hazardous Materials, 170, 560-569, 2009
[16] K.Y.Jung, S.B.Park, and M.Anpo, Journal of Photochemistry and Photobiology A: Chemistry, 170, 247-252, 2005
[17] T.Tokmakci, A.Ozturk, and J.Park, Ceramics International, 39, 5893-5899, 2013
[18] K.Byrappa, and T.Adschiri, Progress in Crystal Growth and Characterization of Materials, 53, 117-166, 2007
[19] D.Kapusuz, J.Park, and A.Ozturk, Journal of Physics and Chemistry of Solids , 74, 1026-1031, 2013
[20] J.D.Wright,and A.J.Sommerdijk, "Sol-Gel Materials Chemistry and Applications", Taylor & Francis Books Ltd., London, 2001
[21] A.C.Pierre, "Introduction to Sol-Gel Processing", Kluwer Academic Publishers, USA, 1998
[22] M.A.Aegerter, and M.Prassas, "Advances in Sol-Gel Derived Materials and Technologies", Springer, New York, 2012
[23] C.Brinker, G.Scherrer, "Sol-Gel Science: The Physics and Chemistry of Sol-Gel Processing", Academic Press, San Diego, 1990
[24] Y.Li, T.J.White, S.H.Lim, Journal of Solid State Chemistry, 177, 1372-1381, 2004
[25] L.Agartan, D.Kapusuz, J.Park, A.Ozturk, Nanomaterials and Energy, 2, 280-287, 2013
[26] O.Carp, C.L.Huisman, and A.Reller, Progress in Solid State Chemistry, 32, 33-117, 2004
[27] S.Nahar, J.Zhang, K. Hasegawa, S.Kagaya, and S.Kuroda, Materials Science in Semiconductor Processing, 12, 168-174, 2009
[28] N.Xu, Z.Shi, Y.Fan, J.Dong, J.Shi, and M.-C.Hu Industrial & Engineering Chemistry Research, 38, 373-379, 1999

In the future, if one can develop a mathematical model based-on inverse analysis of the thermo-mechanical tests conducted below M_s, the results of this study, specifically the ones that are extrapolated in order to calculate properties below the Ms, might also be justified.

Acknowledgement

This study is supported by Republic of Turkey Ministry of Science, Industry and Technology and ORS Bearings Inc. (Project code: 01295.STZ.2012–1). The authors would like to thank for their support.

6. REFERENCES

1. Şimşir, C., *Modeling and Simulation of Steel Heat Treatment: Prediction of Microstructure, Distortion, Residual Stresses and Cracking*, in *ASM Metals Handbook Volume 4B "Steel Heat Treating Technologies"*. To be published in October 2014, ASM International.
2. Acht, C., et al., *Determination of the material properties for the simulation of through hardening of components made from SAE 52100. - Part 1.* Journal of Heat Treatment and Materials (HTM), 2008. **63**(5): p. 234-244.
3. Acht, C., et al., *Determination of the material properties for the simulation of through hardening of components made from SAE 52100. - Part 2.* Journal of Heat Treatment and Materials (HTM), 2008. **63**(6): p. 362-371.
4. Ahrens, U., G. Besserdich, and H. Maier, *Modelling phase transformations in steels-have complex experiments become obsolete?* Harterei-Technische Mitteilungen(Germany), 2002. **57**(2): p. 99-105.
5. Simsir, C., et al., *The Bauschinger effect in the supercooled austenite of SAE 52100 steel.* Acta Materialia, 2010. **58**(13): p. 4478-4491.
6. Müştak, O., *Characterization of SAE 52100 Bearing Steel for Finite Element Simulation of Through-Hardening Process*, in *Metallurgical and Materials Engineering Department*. 2014, Middle East Technical University: Ankara, Turkey.
7. Bhadeshia, H. and J.W. Christian, *Bainite in steels.* Metallurgical Transactions a-Physical Metallurgy and Materials Science, 1990. **21**(4): p. 767-797.
8. Saunders, N., et al., *Using JMatPro to model materials properties and behavior.* JOM, 2003. **55**(12): p. 60-65.
9. Guo, Z., et al., *Material properties for process simulation.* Materials Science and Engineering: A, 2009. **499**(1–2): p. 7-13.
10. Guo, Z., N. Saunders, and J.P. Schillé, *Modelling Phase Transformations and Material Properties Critical to the Prediction of Distortion during the Heat Treatment of Steels.* International Journal of Microstructure and Materials Properties, 2009. **4**(2): p. 187-195.
11. Guo, Z., et al., *Introduction of Materials Modelling into Processing Simulation - Towards True Virtual Design and Simulation.* International Journal of Metallurgical Engineering, 2013. **2**(2): p. 198-202.
12. Patel, J.R. and M. Cohen, *Criterion for the action of applied stress in the martensitic transformation.* Acta Metallurgica, 1953. **1**(5): p. 531-538.
13. Olson, G.B. and M. Cohen, *Kinetics of strain-induced martensitic nucleation.* Metall Trans A, 1975. **6 A**(4): p. 791-795.

High Energy and Power Density Battery Production Process in Turkey

Türkiye'de Yüksek Enerji ve Güç Yoğunluklu Pil Üretimi Yöntemleri

Ziya Can Aksakal

İnci Akü - Türkiye

ABSTRACT

Li-ion batteries are one of the main import items of Turkey. According to import statistics of the ministry, Turkey is importing up to 100 million dollar worth Li-ion batteries. The aim of the project is to produce Li-ion batteries here in Turkey. The feasibility analysis that we setup shows that up to 50% localization can be achievable. The aim of this project is to design, and produce prototype scale lithium ion batteries for handheld electronic devices such as smartphones, tablet or laptops. For the design and production specification of the first prototype units, Fatih project requirements are taken as reference. In addition to prototype scale cell production, improving the energy density of the cell is the other objective of the project. To do that, rather than using standard anode active materials some surface modification techniques and doping materials such as Sn, Si, B have been used. By this manner, stability and capacity changes of anode electrode have been investigated.
To design the cell of the battery, specification of battery will be taken from the tablet producers and according to this data; density of anode and cathode will be determined. Due to specialty, number of anode and cathode, thickness of terminal, electrolyte volume and other needed parameters will be specified. By means of modelling, every parameter of battery will be modeled using COMSOL program.
After modeling and design, batteries were manufactured in TÜBİTAK MAM facilities. Different formation process steps were evaluated with experimental design methods to optimize the formation time and cell life. UL1642 Li-ion standards had applied to batteries after the formation process.

Keywords: Li-ion battery, high energy, power density, modeling, cell life.

ZrO_2 BLOCKING LAYER APPLICATION ON DYE SENSITIZED SOLAR CELLS

Halil İbrahim YAVUZ[a,c] , Kerem Çağatay İÇLİ[b,c] , A. Macit ÖZENBAŞ[a,c]

[a] Department of Metallurgical and Materials Engineering, Middle East Technical University, Dumlupınar Bulvarı, 06800 Ankara, Turkey, yavuz@metu.edu.tr
[b] Micro and Nanotechnology Graduate Program, Middle East Technical University, Dumlupınar Bulvarı, 06800 Ankara, Turkey, cagatayicli@yahoo.com
[c] Center for Solar Energy Research and Applications (GÜNAM), Middle East Technical University, Dumlupınar Bulvarı, 06800 Ankara, Turkey, ozenbas@metu.edu.tr

ABSTRACT

In this study, ZrO_2 thin film was deposited on a fluorine-doped tin oxide (FTO) electrode by hydrothermal treatment and its application as a new blocking layer material for dye-sensitized solar cells (DSSCs) was investigated. According to current-voltage (*I-V*) characteristics and electrochemical impedance spectra (EIS), it was found that ZrO_2 layer functioned as both a blocking layer and a heat treatment protector for transparent conducting oxide (TCO) layer. The ZrO_2 layer as blocking layer increases the electron lifetime and decreases the recombination from TCO to the electrolyte. Finally, this study demonstrated that ZrO_2 could be a promising alternative blocking layer for high efficient DSSCs.

Keywords: ZrO_2, Blocking layer, Dye sensitized solar cell

ZrO_2 BLOKLAMA TABAKASININ BOYA UYARIMLI GÜNEŞ HÜCRELERİNDE KULLANIMI

ÖZET

Bu çalışmada flor katkılanmış kalay oksit film kaplı cam altlıklar (FTO) üzerine hidrotermal yöntem ile ZrO_2 ince filmler kaplanmış ve bu kompozit yapı boya ile duyarlı hale getirilmiş güneş pillerinde (DSSC) elektrot olarak kullanılmıştır. Akım–voltaj eğrileri ve elektro empedans analizleri gibi fotovoltaik karakterizasyonları sonucunda, ZrO_2 katmanının hem pilin fotovoltaik özelliklerini iyileştirmekte hemde FTO nun ısıl işlem sonundaki elektriksel iletkenliğini korumasında yardımcı olduğu görülmüştür. ZrO_2 bloklama tabakasının, fotovoltaik olarak üretilen elektronun yaşam zamanının artmasında ve FTO-elektrolit arasında oluşan geri reaksiyonların azalmasında pozitif etkileri olmuştur. Sonuç olarak bu çalışmada kullanılan ZrO_2 bloklama tabakası yüksek verimli DSSC elde etmekte iyi bir alternatif olarak ön plana çıkmaktadır.

Anahtar kelimeler: ZrO_2, Bloklama tabakası, Boya uyarımlı güneş hücresi

1. INTRODUCTION

Dye sensitized solar cells (DSSC) have been a potential alternative to silicon based solar cells compared to other excitonic solar cells [1-3]. The DSSC have the following advantages: its production is relatively easy and its low cost. In addition, DSSCs also exhibit interesting

optical properties like high transparency, which adds to their architectural application that make them suitable in architecture, and for work under low interior lighting [4]. Increase in the efficiency of DSSCs is strongly related with the dye adsorption, photon absorption, charge injection, charge transport, lower recombination, dye regeneration efficiencies, open circuit voltage, fill factor and indecent photon to current ability of the cell [5, 6].

In the conventional DSSCs, the charge carrier recombination takes place at TiO_2/dye/electrolyte and transparent-conducting oxide (TCO)/electrolyte interfaces [7, 8]. The interface between the TiO_2 nanoparticles and the TCO is exposed to the electrolyte due to the porous structure of the TiO_2 layer. The electron leakage by backward transfer takes place from the TCO layer to the electrolyte. Thus, limiting the backward electrons at these interfaces is one of the most important ways to improve the power-conversion efficiency of DSSC [9, 10]. Electron Blocking Layer (EBL), which is typically composed of a thin film coating on TCO, is significant for reducing undesirable charge carrier recombination, and optimizing the thickness and quality of EBL. Generally, a TiO_2 thin layer is coated with $TiCl_4$ treatment of TCO. Nevertheless, TiO_2 layer deposited on TCO causes lower transmittance spectra resulting in reduced interior light inside the cell. Therefore, several metal oxides, such as Al_2O_3, ZnO, CuO and Nb_2O_5 which have larger band gaps than TiO_2, have been employed as EBL on TCO layer [11-12]. According to our best knowledge, no report related to ZrO_2 as EBL has been published. The present study is the premier example of investigation into EBL performance of ZrO_2. The work also highlighted the need for highly transparent, the lowest charge carrier resistance experimental condition for ZrO_2 – EBL, thus, DSSC efficiency loss could be minimized. In addition, optical properties at the interfacial region between mesoporous TiO_2 and ZrO_2 EBL have been investigated using UV-Vis. Current-density–voltage characteristics (J–V), electrochemical impedance spectroscopy (EIS) and incident photon-to-current efficiency (IPCE) have been studied for better understanding of the kinetics governing the photovoltaic properties.

2. EXPERIMENTAL

In this study, hydrothermal process has been applied in the following stages. First of all, each of commercial FTO substrates (TEC15, Pilkington) was ultrasonically cleaned in a sequence of detergent solution, deionized water, acetone, and isopropanol for 15 min under sonication and subsequently dried with nitrogen gas. Blocking layer deposition on FTO surface was conducted before the preparation of the TiO_2 photo anode. The TiO_2 blocking layer was coated on the conductive side of the FTO glass applying $TiCl_4$ hydrothermal treatment [13]. The ZrO_2 blocking layer was coated on conductive side of FTO glass with hydrothermal treatment in the following steps. FTO glass immersed in 5 mM zirconium (IV) n-propoxide (sigma-Aldrich) dissolved in ethanol (sigma-Aldrich) at 80 °C in a Teflon lined autoclave and annealed at 500 °C for 2 h.

3. RESULTS AND DISCUSSION

In order to determine the thicknesses and surface morphologies of the coated and uncoated FTO films, FE-SEM analyses were investigated and the results were illustrated in Fig. 1. It is seen that ZrO_2 was more successfully coated than TiO_2 on the FTO surface. However, $TiCl_4$ treatment causes the sedimentation of TiO_2 particular film on the FTO. According to FE-SEM analysis, ZrO_2 provides better blocking layer properties than $TiCl_4$ treatment [14].

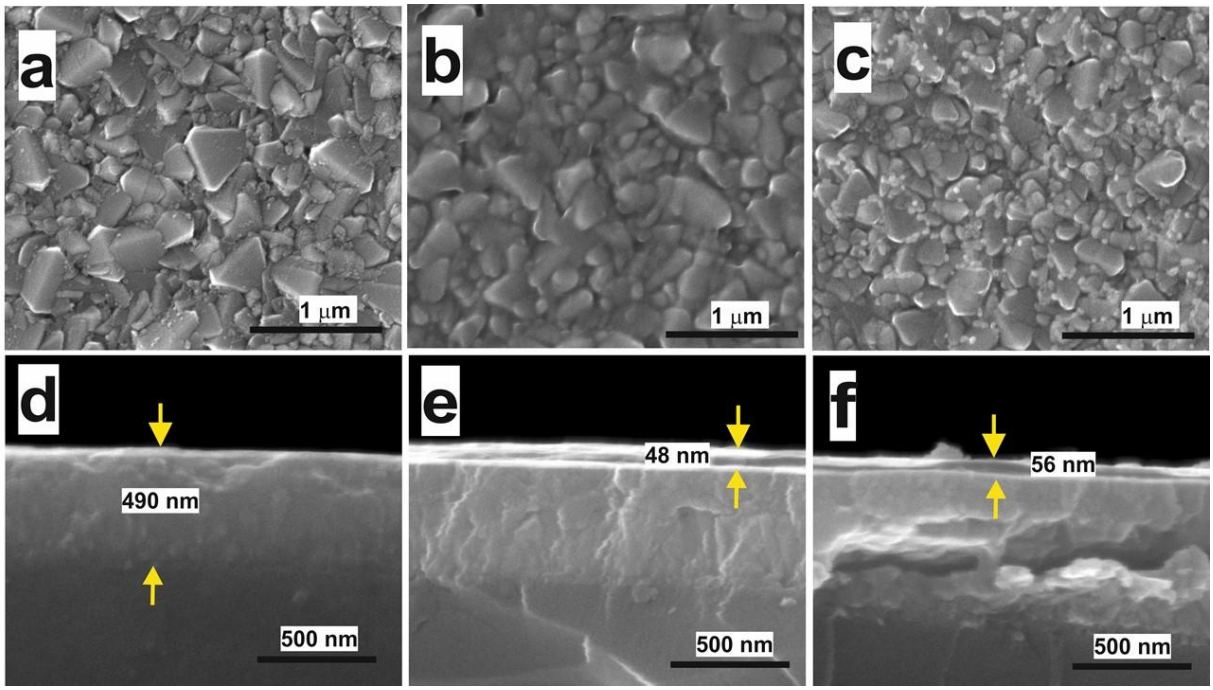

Figure 1. Top view FE-SEM images of bare FTO (a), ZrO_2/ FTO (b) and TiO_2/ FTO (c); cross-sectional FE-SEM images of bare FTO (d), ZrO_2/ FTO (e), and TiO_2/ FTO (f).

X-ray photoelectron spectroscopy (XPS or ESCA) has high surface sensitivity and it is used to gain knowledge on the type of interaction and stoichiometry involved between ZrO_2 film and different substrates [15, 16]. The survey XPS analysis of ZrO_2/FTO sample is shown in Fig. 2a. In addition, Fig. 2b presents the Zr 3d XPS spectrum from 48 nm thick ZrO_2 deposited on FTO. The 3d doublet splitting is observed at 2.4 eV and Zr 3d 5/2 appears at binding energy (BE) of 182.9 eV, which corresponds to ZrO_2 [17] and confirms the presence of ZrO_2 on FTO.

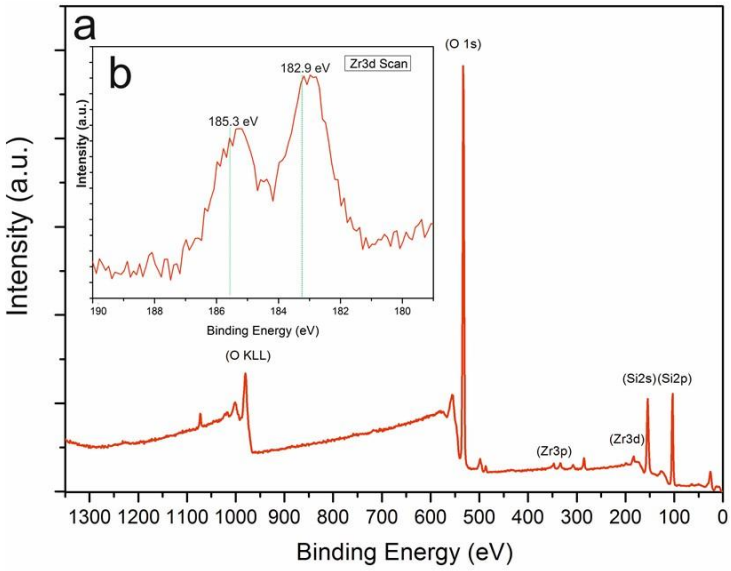

Figure 2. XPS survey spectrum with surface composition of ZrO_2/FTO sample (a) and Zr 3d XPS spectra of ZrO_2/FTO sample (b).

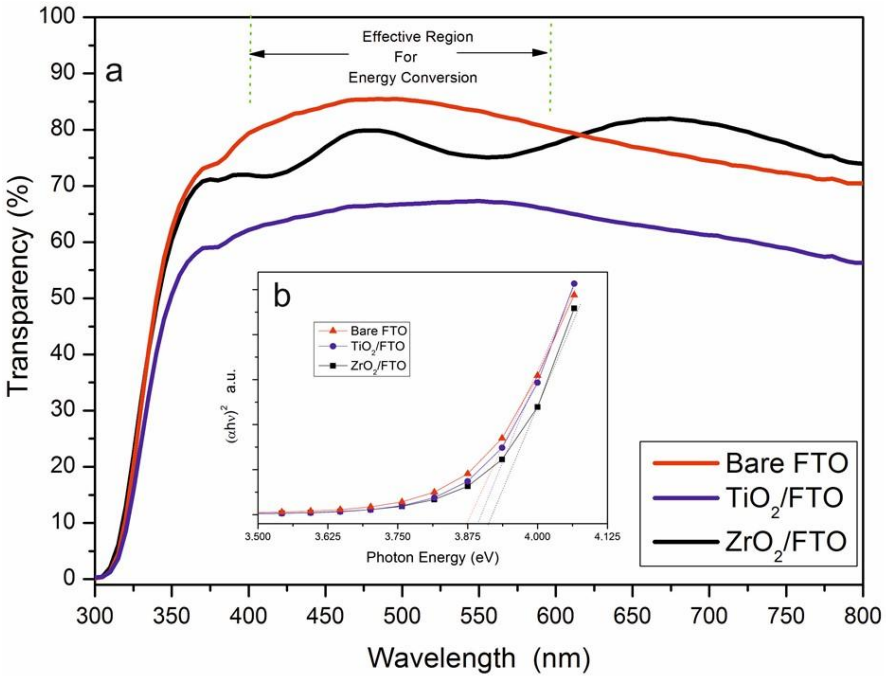

Figure 3. Transmittance spectra for bare FTO, 120 nm ZrO_2/FTO and 105 nm TiO_2/FTO layers in visible region from 300 to 800 nm (a) and linear portion of the $(\alpha hv)^2$ vs photon energy E(eV) graph of bare FTO, 120 nm ZrO_2/FTO and 105 nm TiO_2/FTO layers (b).

UV-Visible measurements were conducted to measure visible light transmission of the samples in visible region from 300 to 800 nm using UV-1900 UV-Vis Spectrometer. Fig. 3.a shows the UV-Vis spectra of bare FTO, 120 nm ZrO_2/FTO and 105 nm TiO_2/FTO layers. Coated FTOs have lower transparency than bare FTO in the range of 300-620 nm. Therefore, the transparency of ZrO_2/FTO is sufficient to be used for the application in DSSCs. The band gap of coated and uncoated FTO films can be calculated from the transmission data in the lower wavelength region. The optical band gap is 3.885 eV for ZrO_2/FTO, while it is 3.875 eV for bare and 3.880 eV for TiO_2/FTO which are presented in Fig.3.b. This positive effect can be seen on the electrical properties of ZrO_2/FTO as it is provided in Table 1. After annealing process, the resistivity of ZrO_2/FTO becomes lower than annealed TiO_2/FTO. That is to say, ZrO_2 preserved conductivity of FTO during the annealing process.

Table 1. Resistivity analysis of bare FTO, ZrO_2/FTO and TiO_2/FTO layer electrodes before and after heat treatment

Sample	Surface Resistance (Ohm/cm^2)	
	Before Annealing	After Annealing
ZrO_2/FTO	16.65	17.45
TiO_2/FTO	17.88	22.12
Bare FTO	14.08	14.88

Fig. 4.a. shows the voltage - photocurrent density curves of the DSSCs employing the bare-FTO, TiO_2/FTO, and ZrO_2/FTO substrates with backside and front illumination, Table 2

summarizes their photovoltaic properties. In this study, the remarkable improvement in the overall efficiency of 43.86 % was ascribed on the front side illumination. The increase in the *J*sc, *V*oc and photovoltaic efficiency (η) of the DSSCs incorporating the TiO_2/FTO and ZrO_2/FTO samples can be linked to decrease in charge recombination by the blocking layer. Cell conversion efficiency (η) of 6.77 % was obtained for the DSSC with the ZrO_2 blocking layer, whereas TiO_2 blocking layer reached 5.72 % efficiency and the DSSC without a compact layer only attained efficiency of 4.71 %. Surprisingly, ZrO_2 compact layer does not only improve the photovoltaic properties of DSSCs but also enhances the properties of backside illumination which is given in Fig.4.b. On the backside illumination, the short current density (Jsc) of ZrO_2/FTO decreases by 8.79 %. The Voc of DSSC improved from 640 mV to 680 mV after ZrO_2 blocking layer treatment.

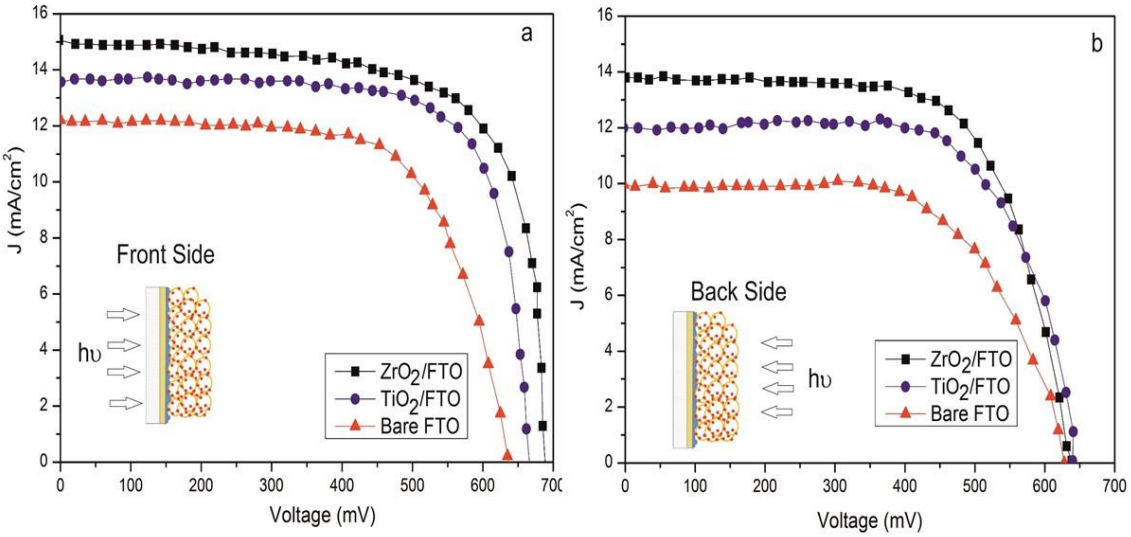

Figure 4. J-V curves of DSSCs employing bare FTO, ZrO_2/FTO and TiO_2/FTO layers electrodes with front (a) and backside (b) illumination (AM 1.5, 100 mW/cm^2).

Table 2. Efficiency analysis of DSSCs employing bare FTO, ZrO_2/FTO and TiO_2/FTO layer electrodes with front and backside illumination

Sample	Backside illumination				Front illumination			
	Voc (mV)	Jsc (mA/cm^2)	FF (%)	Ƞ (%)	Voc (mV)	Jsc (mA/cm^2)	FF (%)	Ƞ (%)
ZrO_2/FTO	630	13.80	59.02	5.13	680	15.13	65.86	6.77
TiO_2/FTO	640	12.01	55.01	4.22	660	13.57	63.88	5.72
Bare FTO	630	10.09	51.22	3.25	640	12.08	60.97	4.71

The IPCE is defined as the ratio of the number of electrons in the external circuit produced by an incident photon at a given wavelength. The IPCE measurements were performed on DSSC cells and the results are given in Fig. 5.

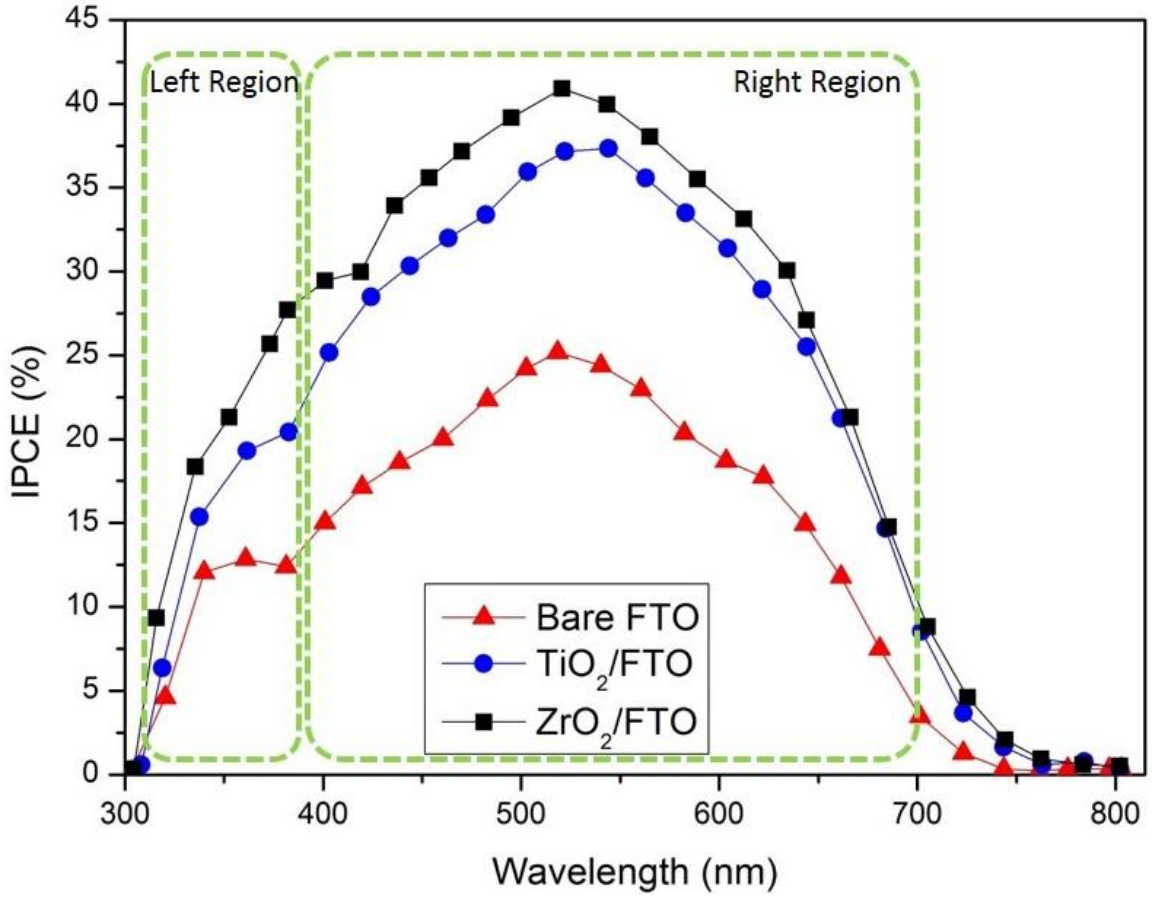

Figure 5. IPCE spectra for the DSSCs with and without blocking layers.

The IPCE spectra can be illustrated with transmittance behavior of samples given in Fig. 5. The IPCE spectra can be analyzed in two regions. First region (left region) is below 390 nm in the IPCE spectra has a small peak at 370 nm wavelength. The peak at first region is directly associated with the absorption from the band-gap of the TiO_2 nanoparticles [18]. The second peak, which is accepted as N719 main peak in the literature, was observed at 550 nm on the right region [19]. DSSC with ZrO_2 blocking layer gave rise to IPCE efficiency of 39 % while bare FTO gives 23 % efficiency. After ZrO_2 blocking layer, DSSC shows 69 % total IPCE improvement when it is compared with bare FTO.

The electrochemical impedance spectroscopy (EIS) has been used as an investigation tool for the electron transport resistance and recombination in DSSCs [20, 21]. The Nyquist plots of the DSSCs with and without blocking layers have been given under one sun illumination with the open-circuit conditions. In the Fig. 6a, two semicircles were observed. Fig. 6b represents equivalent circuit of DSSC used for fitting impedance data which is calculated according to literature [17]. The resistance element Rs in the high-frequency region is related to the sheet resistance of the FTO layer [18]. The first semicircle, which is the resistance of the Z1 component (R1), varies significantly with addition of blocking layer. Due to an identical Pt counter electrode employed for each sample, the difference in the TiO_2/FTO interface is fully responsible for the difference in Z_1 component (R_1).

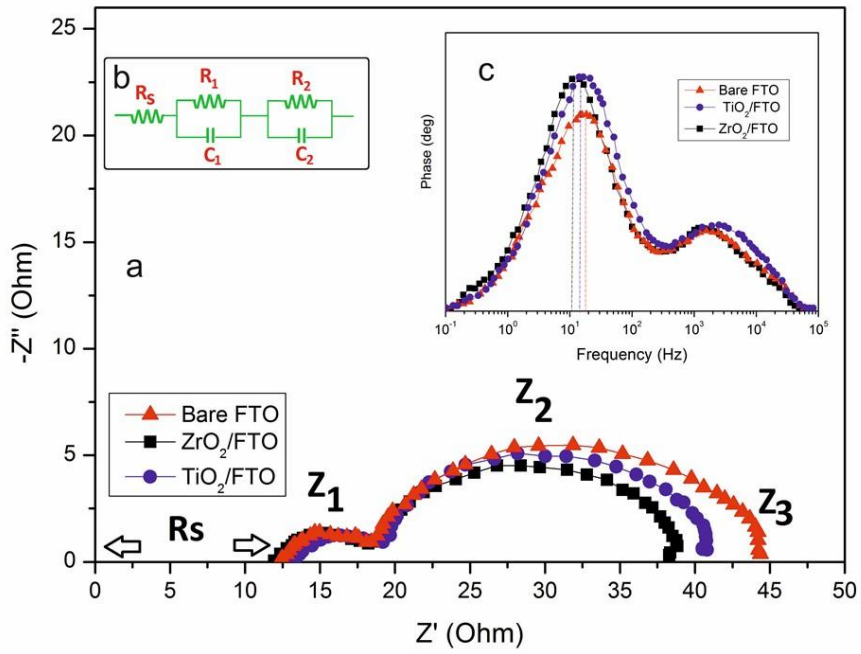

Figure 6. Representative Nyquist plots displaying impedance data taken at open circuit potential (a), equivalent circuit of DSSC used for fitting impedance data (b), and Bode plots displaying impedance data (c).

The second semicircle represents the electron lifetime, τ is obtained from the frequency of maximum Z″ at the Z_2 semicircle. τ can be calculated on Bode plot. The Bode phase plot of EIS spectra is shown Fig. 6.c, which represents the frequency of charge transfer process at different blocking layer interfaces. The characteristic low frequency peaks (f_{max}) are located at 18.49 Hz for bare FTO, 16.43 Hz for TiO_2/FTO and 10.92 Hz for ZrO_2/FTO. Table 3 summarizes the results of the EIS analysis fitted by using an equivalent circuit shown in the inset of Fig. 6.

Table 3. Kinetic parameters of the DSSCs with and without blocking layers

Sample	R_s (Ω)	R_1 (Ω)	R_2 (Ω)	τ (s)
ZrO_2/FTO	11.9	5.01	16.03	0.0146
TiO_2/FTO	12.3	5.24	22.96	0.0097
Bare FTO	12.5	6.02	26.44	0.0086

4. CONCLUSION

In conclusion, the recombination reactions at FTO/electrolyte and TiO_2/electrolyte interfaces were investigated using two surface passivation approaches of ZrO_2 and TiO_2 layers using hydrothermal deposition method in DSSCs. The photovoltaic current characteristics and open-circuit voltage behavior are investigated for coated and uncoated FTO surfaces. The recombination can be prevented using both TiO_2 and ZrO_2 blocking layers. On the other hand, ZrO_2 showed better performance than TiO_2 layer on reducing total recombination. ZrO_2 affects the electrical properties of FTO positively. Because ZrO_2 shows higher transparency

than TiO_2 blocking layer, ZrO_2/FTO photo anode exhibited superior IPCE, probably due to the improvement of photon harvesting and electron collection efficiency caused by electron back transfer blocking effect. These results indicate that the blocking layer of the FTO surfaces using ZrO_2 treatment blocks the recombination substantially in the dye-sensitized solar cells.

REFERENCES

1. B. O'Regan, M.G., Nature, 353, 737, 1991
2. Gratzel, M., Inorganic Chem., 44, 6841, 2005
3. Gratzel, M., Nature, 414, 338, 2001
4. Pettersson, H., et al., Solar Energy Materials and Solar Cells, 77, 405, 2003
5. Nazeeruddin, M.K., et al., Journal of Physical Chemistry B, 107, 8981, 2003
6. Snaith, H.J. and L. Schmidt-Mende, Advanced Materials, 19, 3187, 2007
7. Cameron, P.J., L.M. Peter, and S. Hore, Journal of Physical Chemistry B, 109, 930, 2005
8. Bisquert, J., et al., Journal of Physical Chemistry B, 108, 8106, 2004
9. Lee, S., et al., Solar Energy Materials and Solar Cells, 90, 2405, 2006
10. Ruhle, S. and D. Cahen, Journal of Physical Chemistry B, 108, 17946, 2004
11. Choi, H., et al., Current Applied Physics, 12, 737, 2012
12. Palomares, E., et al., Journal of the American Chemical Society, 125, 475, 2003
13. Zaban, A., et al.,in Chemical Communications, 2231, 2000
14. Xia, J.B., et al., Journal of Physical Chemistry C, 111, 8092, 2007
15. Xia, J.B., et al., Journal of Photochemistry and Photobiology A: Chemistry, 188, 120, 2007
16. Xia, J.B., et al., Chemical Communications, 2, 138, 2007
17. Sahay, R., et al., Journal of Solid State Chemistry, 186, 261, 2012
18. Lee, S., et al., Journal of Physical Chemistry C,. 113, 6878, 2009
19. Gratzel, M., Journal of Photochemistry and Photobiology C: Photochemistry Reviews, 4, 145, 2003
20. Abdullah, M.H. and M. Rusop, Ceramics International, 40, 967, 2014
21. Boschloo, G. and A. Hagfeldt, Journal of Physical Chemistry B, 109, 12093, 2005

COMBINATORIAL THIN FILM MEMBRANES FOR HYDROGEN SEPARATION

Fatih Pişkin and Tayfur Öztürk

Middle East Technical University, Ankara, Turkey
fatih.piskin@metu.edu.tr, ozturk@metu.edu.tr

ABSTRACT
Hydrogen separation membranes allow filtration of hydrogen from mixed gases. Such mixtures may be produced via steam reforming of natural gas/coal/lignite or though gasification of municipal wastes. Hydrogen separated in this way may be used in fuel cells to generate electricity or may be fed directly to the natural gas grid. It is likely that the current network of natural gas will soon be transformed into a "gas" grid where hydrogen would be an essential ingredient. All these require the use of efficient separation membranes, which when made possible would lead to an easy availability of hydrogen as is currently the case for natural gas. Thus the separation membranes have a much wider application scope than normally anticipated and therefore there would be a need for separation membranes that are more efficient and in particular of low cost. In the current work a method is described which can be used to identify material compositions suitable as separation membranes. The method allows the production of multiple material compositions in a single experiment, which are then screened through using a suitable method to identify composition(s) best suited for the purpose. The material library, i.e. multiple material compositions, in question was produced through a purpose built sputter deposition unit incorporating a 6 inch diameter substrate holder. The system incorporates three targets arranged in triangular fashion positioned vertically and axially to yield a uniform film thickness over an extended area in the substrate. The substrate holder was in the form of a magazine comprising a total of 21 disc shape substrates each 18 mm in diameter arranged in triangular form aligned with the sputter targets underneath. This allows the deposition of 21 thin film membranes in a single experiment each with a different composition. The use of this method is illustrated for Pd-Ag-Ti.

Keywords: Hydrogen separation membranes, Sputter deposition, Thin film membranes, Combinatorial approach, Resistivity measurement.

INTRODUCTION
Hydrogen is often produced together with other gases such as CO and CO_2. A separation process is therefore required so as to purify hydrogen from the gas mixture produced by steam reforming of natural gas or methane, or by gasification of coal/lignite (DOE, 2014) or though gasification of municipal wastes (ITC, 2014). Hydrogen separated in this way may be used in fuel cells to generate electricity or (even without separation) the generated gas may be fed directly to the natural gas grid. It is expected that the current natural gas network would probably be transformed into a "gas" grid where hydrogen together with carbon monoxide would be ingredients, together with methane (NaturalHy, 2004).With natural gas grid transforming into a more general form, hydrogen would be available everywhere as it is currently the case with natural gas. For a variety of hydrogen applications, then it is necessary to have separation membranes which would allow the filtration of hydrogen from the grid.

Although there are a variety of methods of hydrogen separation, all metallic membranes are particularly suitable for widespread hydrogen filtration from the gas grid. Of these, Pd is the

most essential element due not only its high permeability and oxidation resistance but also because of its ability to split hydrogen molecule into atomic form, a step that is essential for the permeation of hydrogen through the membrane (Zhang *et al.* 2009). However, membranes based on Pd are extremely expensive and therefore efforts have focused on minimizing or eliminating Pd from the memebranes. Studies have concentrated either on alloying the membrane to reduce Pd content (Keltte and R. Bredesen 2005, Pizzi *et al.* 2008 and Mejdell *et al.* 2009) or to develop non-Pd membranes (Zhang *et al.* 2003). An alternative approach is to reduce the cost via reductions in the membrane thickness through the use of thin film membranes.

It is worth emphasizing that even pure palladium has its problems as a separation membrane. As could be verified from Pd-H phase diagram, when the Pd-H is cooled form an elevated temperature, initially a single phase f.c.c. alloy is converted into a two phase structure which results in a considerable volume expansion. This phenomenon leads to the formation of microcracks which severely affects the durability of the Pd membrane. There are two approaches in handling this embrittlement problem. One method is to control the operating conditions i.e. temperature and pressure, so that the membrane is always in one phase region. The other method is to alloy Pd so that the transition to two-phase structure occur at much lower temperatures or is avoided altogether. This is most commonly achieved by alloying Pd with Ag. An addition of 20-30 at. % Ag is quite common which not only reduces the critical temperature for two-phase transition but also yields the permeability values which are up to 1.7-2.0 times of that of the pure Pd (Gryaznov 2000). A typical commercial separation membrane has a composition of Pd- 23 at% Ag.

In addition to Ag, elements such as Cu could also be used as alloying elements in Pd (Gryaznov 2000). The addition of 40 wt. % Cu can reduce the critical transformation temperature below the room temperature (Howard *et al.* 2004). Cu addition also result in 10% increase in hydrogen permeability which arises mainly from an increase in hydrogen diffusivity (Sholl 2003). Other alloying elements have also been investigated; Pd-Y by Fort *et al.* (1975), Pd-Fe by Bryden and Ying (2002).

All these membranes were developed via the traditional approach of synthesizing one membrane composition at a time and testing it for permeability. This is quite time consuming and not always successful. In the current work, a method is described; the so-called combinatorial approach, that would allow the synthesis of multiple material compositions in a single experiment. The membranes were then screened via resistivity measurement by exposing them to hydrogen atmosphere under controlled heating/cooling conditions. The method was applied to Ag-Pd-Ti ternary system so as to identify possible candidates as separation membrane, with the aim of identifying compositions that are leaner in their Pd content, taking the commercial composition Ag-76%Pd as the reference point.

EXPERIMENTAL

Thin film membranes were deposited in a purpose- built sputter deposition unit incorporating three sputter targets arranged in triangular fashion, Figure 1. Distance between each target were approximately 100 mm. The unit accommodates a 6 inch diameter substrate holder, placed again approximately 100 mm above the targets, in the form of a magazine comprising a total of 21 disc substrates arranged in triangular form aligned with the sputter targets underneath. The disc substrates were soda-lime glass ~0.15 mm thick each 18 mm in diameter. This allows the deposition of 21 thin film membranes in a single experiment each with a different composition

Figure 1. *a) Thin film deposition system and b) viewgraph showing three targets and the magazine older incorporating 21 glass substrates.*

Target to substrate holder distance as well as angular positions of the targets were carefully aligned so that deposited film has the same thickness in the triangular area just above the targets. This has been achieved by carefully aligning each target separately using a 6 inch diameter glass substrate. To obtain a uniform thickness, a given sputter target has to yield a deposition rate which is in the ratio of 1:3, the rates referring to the middle and the corner of the triangular region close to the target. Depositions were carried out for 250 min to obtain approximately 3 µm thick membranes.

Reaction of the thin film membranes with hydrogen was followed in a purpose built reaction chamber with in-situ four-probe resistance measurement. Prior to each resistance measurements thin film membranes were annealed under argon atmosphere at 450 ˚C for 3 hours in order to stabilize their microstructure, Figure 2. Following this treatment, membranes were subjected to two isochronal measurements; one was carried out under argon where the membrane was heated up to 450 ˚C and then cooled down to room temperature. . The other was carried out under hydrogen with a 1 bar pressure. Heating/cooling rate in both measurement was 6 K/sec. The reactivity of thin film with hydrogen was expressed in terms of resistivity ratio $\rho H_2/\rho Ar$ at selected temperatures. Here ρ refers to the resistance values obtained from the membrane under hydrogen and under argon respectively, Figure 3.

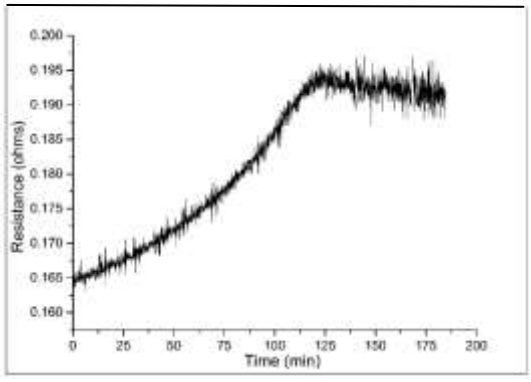

Figure 2. *Resistivity chance as a function of temperature in a typical membrane annealing at 450 ˚C.*

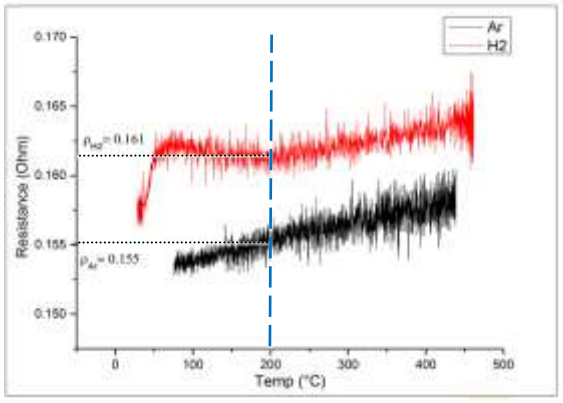

Figure 3. *Illustration of reactivity index used to in screening of membranes. Index for this example refers to 200°C and has a value of* ρ_{H2}/ρ_{Ar} *= 1.038.*

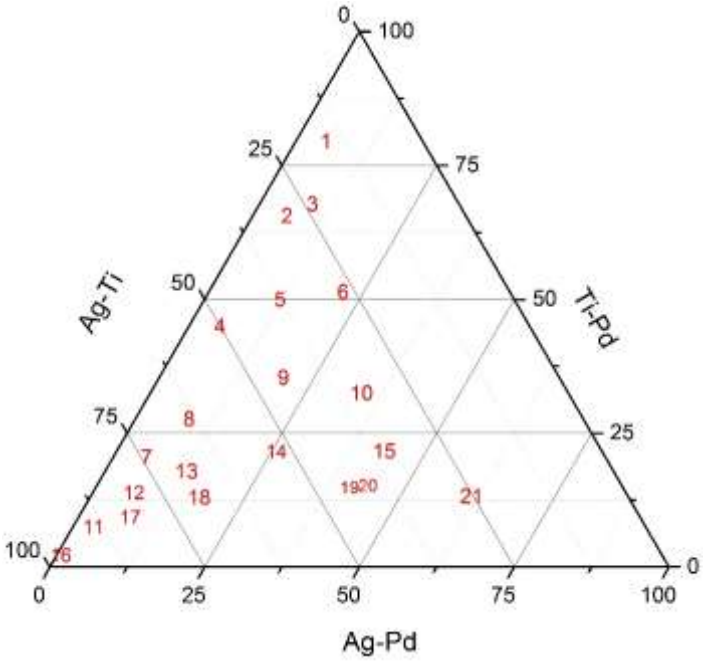

Figure 4. *Position of thin film membranes in the ternary diagram as determined with EDS analysis.*

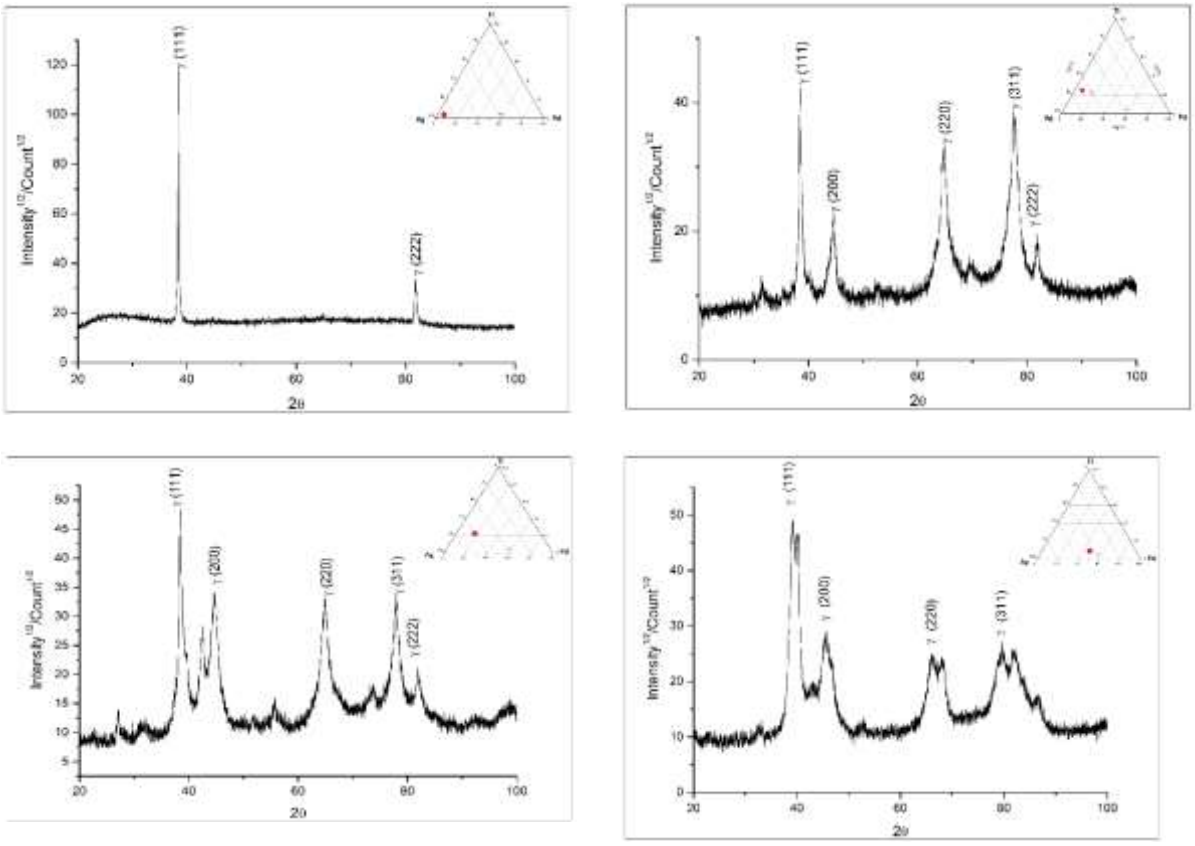

Figure 5. XRD pattern of membranes delineating the area in the ternary field where the structure is predominantly f.c.c. The membrane compositions are indicated in the inset.

RESULTS AND DISCUSSION

Since the interest in the current work was in Pd lean composition, deposition was carried out in such a manner as to cover compositions away from Pd rich corner. Having deposited the films, the resulting chemical composition of each membrane was determined with EDS analysis. The distribution of membrane compositions in the ternary diagram is given in Figure 4.

Subsequent to annealing, all thin film membranes were structurally characterized with X-ray diffraction. One of the aim in the current work was to synthesize membranes with f.c.c. structure, thus structural characterization concentrated on to delineate the area in the ternary diagram which has this particular structure. Representative XRD patterns given in Figure 5 exhibit the main phase is f.c.c.. This pattern delineates quite a large compositional field in the ternary diagram.

Considering the resistivity measurement, most of the deposited thin films exhibited the resistivity versus temperature curve which were identical under argon and hydrogen. This imply that the films did not react with hydrogen. Here, the resistivity ratio has a value of $\rho_{H2}/\rho_{Ar} = 1$. Figure 6 shows an example of a membrane that did react with hydrogen. Here the curves are quite different. The resistivity ratio ρ_{H2}/ρ_{Ar} was calculated for various temperatures. The values are shown mapped in Figure 7. This shows in many compositions $\rho_{H2}/\rho_{Ar}=1$, i.e. membranes do not react with hydrogen. However Ag25Ti13Pd62 and its near compositions do react with hydrogen. This implies that the membranes Ag25Ti13Pd62 and Ag44Ti12Pd44 and their near compositions which are positioned in the red area in the contour mapping could be considered as candidates for separation membrane.

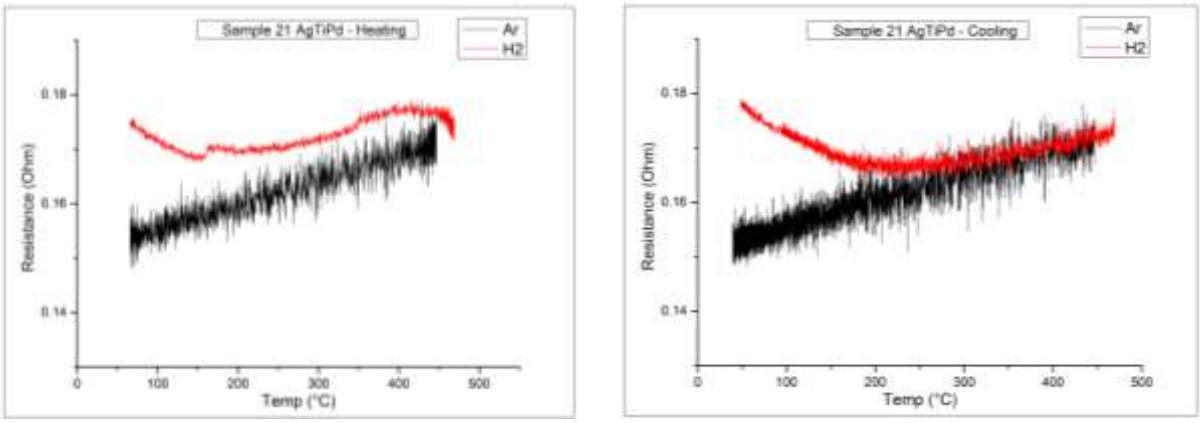

Figure 6. *Resistance measurements of Ag25Ti13Pd62 under argon and hydrogen a) during heating up to 450 ˚C and b) during cooling to room temperature.*

There are two aspects which may be worth emphasizing with regard to the relevance of resistivity mapping to permeability. The fact that there is a resistance change in the thin film is an indication that the membrane do react with hydrogen. This might be in the form of forming a solid solution or a new hydride phase. The higher solubility would be desirable for improved permeability since the permeability is the product of solubility and diffusivity of hydrogen in the membrane. This could be correlated with the compositions in the mapping where the resistivity change is high. On the other hand, in the case of a formation of a new hydride phase, the resistance change is also expected to be high. Normally the formation of a

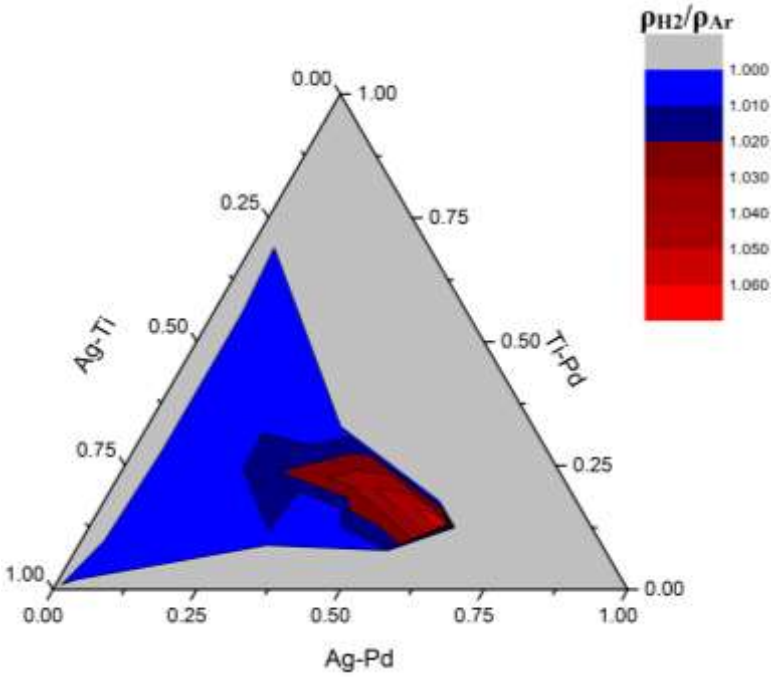

Figure 7. Contour mapping of resistivity ratio in Ag-Ti-Pd system at 400 ˚C.

hydride phase is associated with a large volume change which, as discussed above, leads to embrittlement problem. So what is desirable is normally the reaction with hydrogen to form solid solution. Thus perhaps in resistivity mapping more attention should be concentrated on those compositions which are at the tails of resistivity peak rather than the peaks themselves.

CONCLUSIONS

In this study, a magnetron sputtering system was constructed which would yield multiple thin film membranes in a single experiment covering a wide compositional field. Thin film membranes were then screened with regard to their tendency to react with hydrogen using an in-situ four probe resistivity measurement. The approach was applied to a portion of Ag-Ti-Pd ternary system. This has shown that Ag25Ti13Pd62 and its near compositions are candidates for hydrogen separation membranes. This implies that Pd content in commercial membranes (Ag-77% Pd) might be reduced to a lower value by a Ti substitution.

ACKNOWLEDGEMENT

Support for this work was provided by TUBITAK (project Number MAG 109M580), which the authors gratefully acknowledge.

REFERENCES

Bryden K.J., Ying J.Y., "Nanostructured palladium-iron membranes for hydrogen separation and membrane hydrogenation reactions", Journal of Membrane Science, 203, 29-42, 2002

DOE "Hydrogen from Coal Multi-Year RD&D Plan" http://www.netl.doe.gov/ File%20Library/ Research/Coal/ ccbtl/20100908_Draft_H2fromCoal-RDD_final.pdf Accessed on January 15 2014

Fort D., Farr J.P.G., Harris I.R., "A comparison of palladium-silver and palladium-yttrium alloys as hydrogen separation membranes", Journal of the Less Common Metals, 39, 293-308, 1975

Gryaznov V., "Metal Containing Membranes for the Production of Ultrapure Hydrogen and the Recovery of Hydrogen Isotopes", Separation & Purification Reviews, 29, 171-187, 2000.

Howard B.H., Killmeyer R.P., Rothenberger K.S., Cugini A.V., Morreale B.D., Enick R.M., Bustamante F., "Hydrogen permeance of palladium-copper alloy membranes over a wide range of temperatures and pressures", Journal of Membrane Science, 241, 207-218, 2004.

ITC www.itcturkiye.com . Accessed on January 15 2014.

Keltte H. and Bredesen R., Membrane Technology, 75, 7, 2005.

Mejdell A.L., Jondahl M., Peters T.A., Bredesen R., Venvik H.J., "Experimental investigation of a microchannel membrane configuration with a 1.4 μm Pd/Ag23 wt.% membrane-Effects of flow and pressure", Journal of Membrane Science, 327, 6-10, 2009.

NaturalHy ftp://ftp.cordis.europa.eu/pub/sustdev/docs/energy/sustdev_eu-russia_h2-fc_florisson.pdf Accessed on January 15 2014.

Pizzi D., Worth R., Baschetti M.G., Sarti G.C., Noda K., "Hydrogen permeability of 2.5 μm palladium-silver membranes deposited on ceramic supports", Journal of Membrane Science, 325, 446-453, 2008.

Piskin F. and Ozturk T. "Thin film Ag-Ti-Pd membranes for hydrogen separation", 13th International Conference on Clean Energy 2014. Ed. Dincer et al 8-12 June 2014 Istanbul.

Sholl D.S. and Kamakoti P., "A comparison of hydrogen diffusivities in Pd and CuPd alloys using density functional theory", Journal of Membrane Science, 225, 145-154, 2003.

U.S. Energy Department. "Hydrogen from Coal Multi-Year RD&D Plan". http://fossil.energy.gov/programs/fuels/hydrogen/2010_Draft_H2fromCoal_RDD_final.pdf

Zhang K., Gao H., Rui Z., Liu P., Li Y., Lin Y.S., "High-Temperature Stability of Palladium Membranes on Porous Metal Supports with Different Intermediate Layers", Industrial & Engineering Chemistry Research, 48, 1880-1886, 2009

Zhang Y., Ozaki T., Komaki M., Nishimura C., "Hydrogen permeation of Pd-Ag alloy coated V-15Ni composite membrane: effects of overlayer composition", Journal of Membrane Science, 224, 81-91, 2003

IMPROVING THE REVERSIBLE CYCLABILITY OF THE Si BASED COMPOSITE THIN FILM ANODE

B.Deniz POLAT, Ozgul KELES
Department of Metallurgical and Materials Engineering, Istanbul Technical University, 34469, Maslak, Istanbul, Turkey

Abstract
The reversible cyclability of Si based composite anodes is greatly improved by optimizing the atomic ratio of Cu/Si, the thickness and the evaporation rates of films fabricated by electron beam deposition method. The galvanostatic test results show that the best result is achieved when the composite thin film having of 10%at. Cu-90%at. Si is used as anode in half cell. It is possible to explain this remarkable performance by the amorphous structure of the thin film and its enhanced physical and mechanical properties due to the Cu content of the film. This study proves that electron beam evaporation can be an alternative method to fabricate electrodes used in lithium ion batteries, because this environmentally friendly process enables one to make production in one step without using any binders or conductive additives.

Keywords: CuSi thin film; Anode; Cycling performance; electron beam deposition

1. INTRODUCTION

Nowadays, lithium ion batteries (LIB) are widely used in portable devices, and recently they have received much attention as power sources for hybrid and pure electric vehicles. In present day carbonaceous materials, having around 372 mAh/g theoretical capacity are used as anodes commercially, which increase the requirement of new electrode materials' usage, in the near feature. So far, different research groups have been working to replace carbon with other active elements from the third, fourth, and fifth row of groups. Among alternatives Si becomes remarkable because of its high theoretical capacity (3579mAh/g) and high abundance on earth [1]. However, Si performs large volume changes in its lithiated state, which is followed by cracks and delaminations. Therefore, such Si electrodes deteriorate easily in just a few cycles. To overcome this problem Yang et al. proposed to use active materials (Si) with small grain size as anode materials [2]. Then Kim et al [3] suggested to uniformly distribute the small sized active metal (Si) within an inactive matrix (like Cu, TiN etc.). Herein Cu becomes prominent as an inactive material, because it increases the adhesion of the anode to the current collector, plus its electrical conductive and ductile behavior improve the electrical and mechanical properties of the anode [4]. Additonally, previous works demosntrate that by the addition of Cu, the cycle life of the Si electrode is also improved since the formation of Cu_3Si intermetallics enhances the reversibility of the lithiation reactions during the cycle test [5]. However, deciding the amount of Cu in the electrode is a challenging task because not only the film morphology changes but also it leads to a considerable decrease in the energy density of the electrode.

So far, to produce anodes made of nano-sized Si and Cu particles, variety of methods have been used [6-8]. Among them, electron beam evaporation method becomes remarkable since it has no risk from handling flammable, explosive or cancerogen metal nanoparticles, plus the

deposition of the evaporated particles forms a film with good adhesion, without using binder or conductive additive [9]. Previosuly published studies about this process show that the electrical properties of thin film electrodes are affected by a few factors such as the type and the temperature of the substrate during deposition [10-13]. The composition and the thickness of the film [14-17], the deposition rate [12,13,15-18] the annealing conditions [17,19] and the background gas composition [20].

Data on the rate, composition, and thickness dependent properties of thin CuSi films deposited on Cu discs are lacking so far in literature. In the present paper, first we investigate the structure and the morphology of composite thin films produced by electron beam evaporation, as a function of deposition rate, composition and thickness; then we evaluate their electrochemical performances when used as anodes in lithium ion batteries.

2. EXPERIMENTS

In the experiemnetal setup, two separate electron-beam evaporation sources, containing Si pellets and Cu pellets, were located approximately 31 cm below the center of the substrate holder unit, with the separation of the two sources approximately 9 cm (see Figure 1). Two quartz-crystal microbalances (QCM) were present in the vacuum chamber to monitor and control the deposition rate of each evaporation source independently during the coating process. A shield ("source shutter") is used for each source to assure correct stoichiometry.

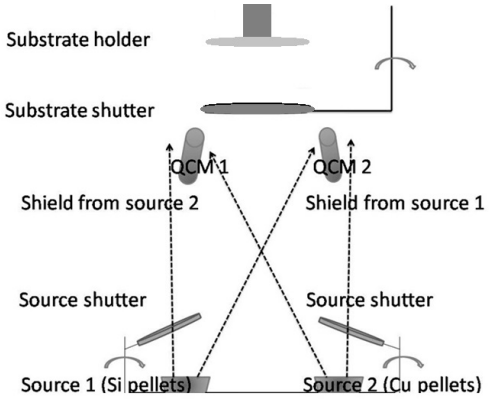

Figure 1. Experimental setup used in this study

The deposition was done on three types of substrates: a Si wafer for X-ray diffraction (XRD) analysis, a stainless steel disc (15.5-mm diameter and 1.5-mm thickness) for compositional analysis, and copper discs (15.5-mm diameter and 1.5-mm thickness) for electrochemical experiments with half cells. The source materials were placed in graphite crucibles. The substrates were initially cleaned by presputtering them for 5 minutes with Ar^+ ions prior to opening the shutters and starting the deposition. For this cleaning, an 8-cm Kaufman ion source was used to produce a beam of Ar^+ ions. The source parameters were 1 kV at 30 mA, 40V discharge, 100V accelerator and 8 sccm Ar feed gas. The incident angle to the substrate's normal was about 35°, and the pressure in the chamber was 0.01. During the evaporation, the deposition rates were constant for Cu and Si, respectively using QCM feedback. The rates were controlled by the power of the electron gun. The oxygen pressure was fixed around 8 x 10^{-5} Pa throughout the deposition process. Different experimental conditions used for the production of samples were summarized in Table 1.

Table 1. Experimental conditions used for the production of samples

Sample No	Evaporation rates of Cu (Å /s)	Evaporation rates of Si (Å/s)	Evaporation duration
1	0.9	10	16
2	1.8	10	16
3	2.7	10	16
4	1.8	20	16
5	0.4	4	16
6	0.9	10	8
7	0.9	10	32

The surface roughnesses of the samples were measured by using a Profilometer (WYKO NT 1100 Optical ProfilingSystem).The composition of the film was determined by energy dispersive X-ray spectroscopy (Oxford, EDS) analysis (Table 2). The weight of the thin film was measured by using (My weight i101) microbalance before and after the coating process. Moreover, the active material weight in the thin films was found by multiplying the total weight of the coating with the weight percentage of the active material determined through EDS analyses (Table 2). This value was then used to calculate the specific capacity delivered by anode materials.

On the other hand, the surface morphologies and the thicknesses of the films were looked at by utilizing a field-emission scanning electron microscopy (FE-SEM, JEOL JSM 7000F and JEOL 5410). The phases exist in the pristine were determined using Philips PW3710 System with a 2θ range of 10–100 in steps of 0.05(with CuKα at 40 kV and 30 mA).

Furthermore, to evaluate the electrochemical performance of the electrodes during Li^+ insertion and extractions, half cells were examined. All half cells were assembled as described and tested in the earlier study [21].

3. RESULTS and DISCUSSIONS

For all films, a grainy surface structure is observed (Figures 2a-g). Knowing that the film formation is a dynamic process, beside the composition, the deposition rate and the process duration change the film morphology as expected. The cross sectional images prove that all samples except samples 6 and 7 have a thickness around 1micron, where samples 6 and 7 have 0.5 and 2 microns thicknesses respectively (Figures 2h-m). The SEM surface images of Samples 1-3 (Figures 2a-c) demonstrate that, higher amount of Cu leads agglomeration. and inhomogeneous thin film morphology with larger grain sizes. Additionally, the comparison in Figure 1e demonstrates that the films produced at the lowest deposition rate (Si and Cu have 4 and 0.4 Å/s, respectively) display smooth grainy surface where the grains have mostly spherical shape and are almost uniform in size. The size of these grains is proportional to the evaporation rate (see Fig 2a). At the highest deposition rate (Si and Cu have 20 and 1.8 Å/s, respectively) leads the formation of few hillocks protruding (Figure 2d). Thicker film that is resulted from the prolonged evaporation duration has inhomogeneous morphology with larger grains and numerious hillocks (see Figures 2a,f,g.)

In Table 2, Ra and Rms surface roughness for CuSi thin films produced on Cu discs are summarized.

These results might be explained considering the "structure zone model" proposed by Thornton first in 1977 [22]. In the present study, the CuSi thin films were deposited at room

temperature (20^{o}C, T_S/T_M<0.3), which corresponds in zone 1. Herein, it is worth to mention that even if there is a slight heating of the substrate by radiation from the evaporation source, this should not lead to any significant changes in the film structures, according to the "zone model". Thereby, the differences in the morphology of the films are most probably caused by the Cu/Si atom ratio, film thicknesses and deposition rate. As explained previously, higher Cu amount and larger evaporation duration enhance agglomeration, which result in higher Ra and Rms values. The evaporate effect on surface morphology is more complicated.

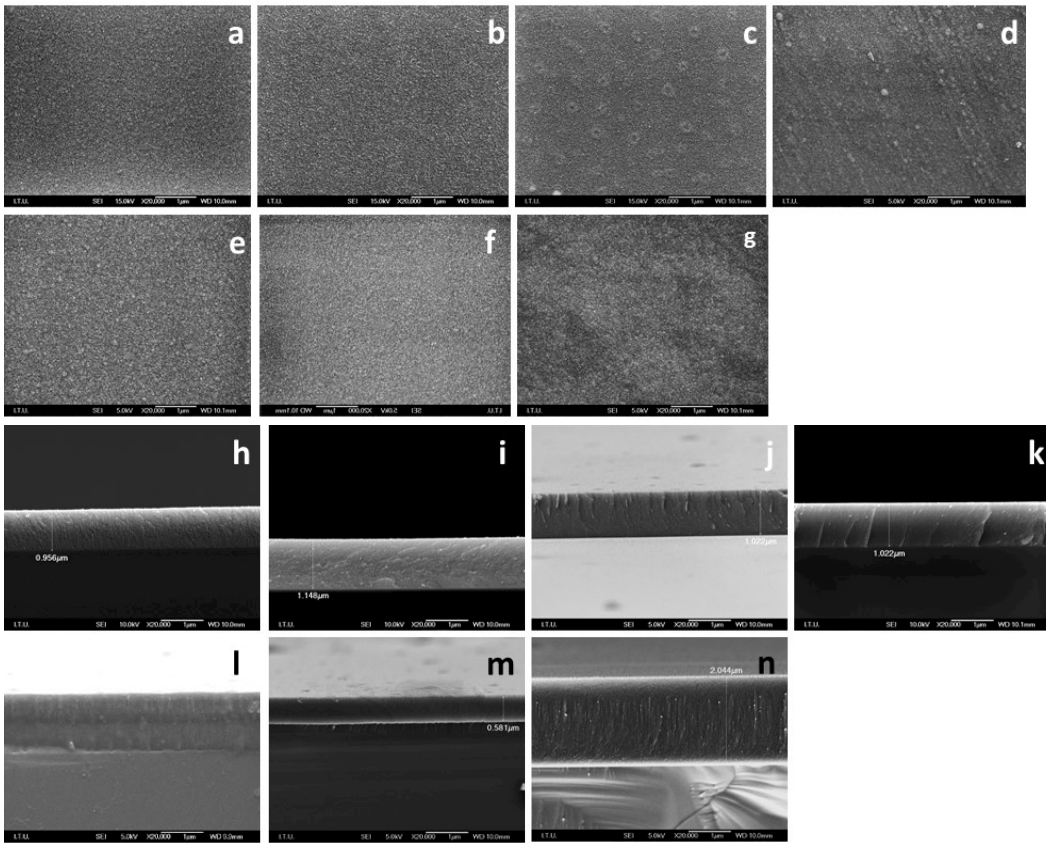

Figure 2. SEM surface (a-g) and cross sectional (h-n) views of samples 1-7

Table 2. Ra and Rms surface roughnesses of thin CuSi films evaporated on Cu discs (as a function of Cu/Si atomic ratio, deposition rate and film thickness). The mean values are obtained from 3 scans on each sample.

Sample number	Substrate	
	Cu discs	
	Ra	Rms
0 (baresubstrate)	1.1±0.07	1.22±0.20
1	2.2±0.04	1.28±0.09
2	5.79±0.02	1.52±0.12
3	17.29+0.04	1.99±0.50
4	36.3 ± 0.20	10.72±0.20
5	14.99 ± 0.08	1.93±0.10
6	1.97± 0.05	1.03±0.11
7	4.02 ±0.3	58.92±0.42

During electron beam method, the evaporated particles originated from the crucibles, are adsorbed on the substrate surface where they can diffuse and form nuclei, which leads to the formation of crystallites (grains) in the thin film. In our case, since the subtrate temperature is always at the room temperature, difference in the atomic mobility of the Si and Cu particles affects the film morphology. Besides, at the low evaporation rates, since the surface diffusion of Cu and Si particles are not strong they adsorbed on the active sites of the substrate surface, thus the density of nuclei forming grains, remains slow, resulting in small sized grains in the composite thin film. On the other hand, at the higher deposition rate, since the number of evaporated atoms arriving on the substrate surface per unit time is higher, the number and the size of nuclei are bigger. Plus, knowing that self shadowing is one of the main factor, contributing the roughening of the film, an increase of the film thickness causes an increase in the surface roughness of the film as explained by Bordo et al [23]. Because due to the limited ad-atoms surface diffusion, the incoming evaporated particles are deposited preferentially on the highly active sides of the film enhancing the columnar film growth in the thin film hence enhances the surface roughness.

In Table 3, EDS analyses reveal that except samples 2 and 3, other samples contain similar amount of silicon, approximately (90% at.) independent from the variations in the experimental conditions.

Table 3. EDS analyses of the films produced in this study

Sampleno	Atomic %		Weight %	
	Cu	Si	Cu	Si
1	11.12	88.88	22.07	77.93
2	20.34	79.66	30.70	69.30
3	28.51	71.49	46.35	53.65
4	11.47	88.93	23.37	76.63
5	11.42	88.58	23.28	76.72
6	11.04	88.96	23.32	76.68
7	11.22	88.78	22.23	77.77

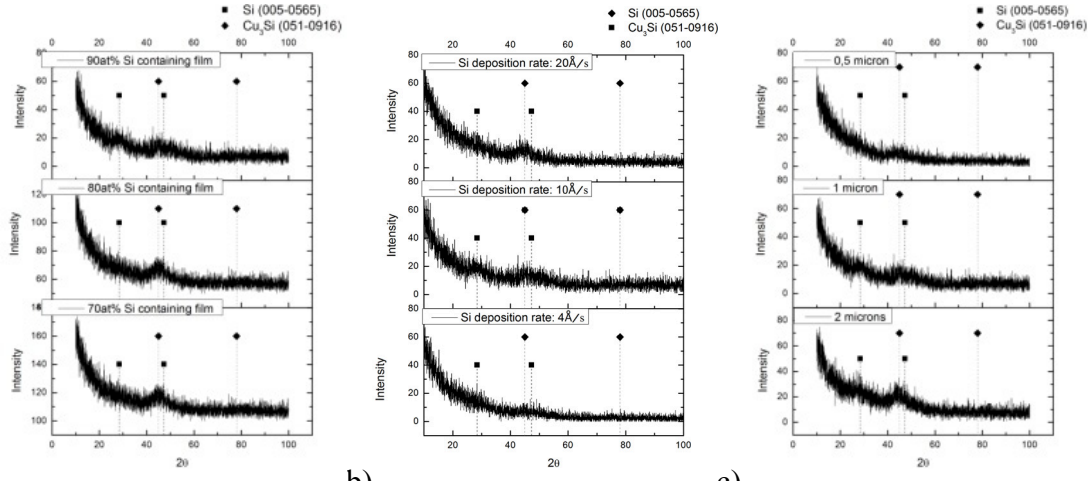

a) b) c)

Figure 2. Comparison of XRD data of samples a) composition effect, b) deposition rate effect, c) thickness effect

The structural analysis results (Figures 3a-c) are in well agreement with that of the SEM and profilometric analyses. The sharp slope seen in the low diffraction angles demonstrate that all samples are mostly made of amorphous particles. Moreover, the bumps noted around 27^0 and 44^0 reveal that in addition to amorphous particles, the samples contain Si (JCPDS: 00-051-0565) and Cu_3Si (JCPDS: 00-051-0916) crystallites, as well. Figure 1a shows the effect of the composition on the thin film structure: an increase in Cu content forms larger sized particles since the FWHM of the peaks are decreased and the intensities of the peaks are augmented. Furthermore, Figure 3b demonstrates that a decrase in the deposition rate enhances the amorphous particles and small grained thin film formation. Additionally, Figure 1c displays that a decrease in the film thickness promotes the amorphisation.

Infact, the existence of the nanocystalline (α-Si) and amorphous (a-Si) Si particles is very critical for the electrochemical performances of the electrodes since their reactions with Li^+ differentiate, depending on the cell potential [24-27]. Using α-Si results Li^+ trapping since a phase transiton occurs during lithiation. Whilst, for a-Si Li^+ diffusion paths are developed in the thin film, leading to a higher electrochemical performance during the cycling test.

Moreover, the comparison of the characteristic peak of the Cu_3Si phase (around 44^o) proves the size of the particles increases when the deposition rateor film thickness orthe amount of Cu in the thin film is increased. Herein, the nano sized Cu_3Si presence on thin films is very important since it is believed that the high electronic conductivity of the Cu_3Si alloy promotes a good interparticles electronic conduction, which in turn suppresses the Si volume changes effectively. In Equation 1, the reaction mechanism of the Cu_3Si with Li^+ is shown: the elemental Cu formed during initial lithiation reaction would act as a buffering matrix to minimize the destroying effect of the volume changes due to LixSi formation (Equation 1). This lithiated Si product surrounded in the conductive Cu matrix enhances the reversibility of the charge/discharge reactions, which intensifies the cycle stability of the electrode, eventually [28].

$$x\,Li^+ + xe^- + Cu_3Si \rightarrow Li_xSi + 3Cu \rightarrow 3Cu + Si + xLi^+ + xe^- \qquad (1)$$

The comparison of CV tests (Figure 4a-c) reveals that samples 1,6,7 demonstrate very similar current-potential characteristics, even differences are noted in their curvature shapes. This proves that the film thickness does not affect the electrochemical behaviour of the anode material. However the fact that the amount of Cu is higher for samples 2 and 3, a capacitive effect is noted, which result in changes in the peak morpholgogy. Plus, the difference in the thin film morphology resulted from the different evaporation rates causes differentiation in the CV curvatures of Samples 1,4,5. Herein, the fact that all samples's CV curves have similar anodic and cathodic peak positions to that of the pure Si anodes, this study justifies that Cu is electrochemically inactive versus Li, and the current intensities on Cv curves are sensitive to the surface morphology of the samples. To summarize the peaks noted on Figures 3a-c, we found that the cathodic peak (around 0.2V) is attributed to the lithiation of amorphous and crystalline Si particles. Then, on the anodic side, a broad peak around 0.6V is noted which demonstrate recovery of Si particles form the Li_xSi [29].

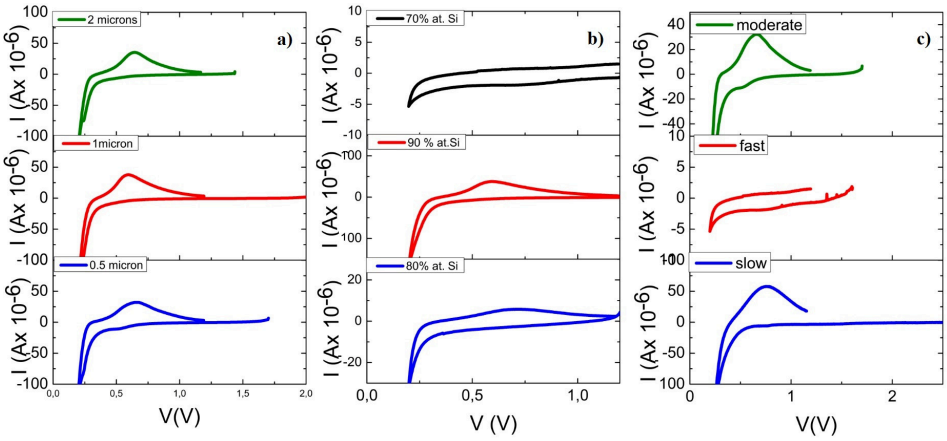

Figure 3. CV of the samples with a) different thicknesses (Samples 7,1,6), b) compositions (Samples 3.1.2), c) evaporation rates (Samples 1,4,5).

The EIS data (Figures 4a-c) of the as-deposited samples 1-3 show that Cu amount of the thin film decreases the charge transfer resistance of the films due to its conductive behaviour. Plus, Samples 1-3 display that after the first cycle another semi-circle forms on the high frequency region demonstrating SEI (solid electrolyte interface) formation on the three electrodes. Moreover the comparison among Figs 4a,d-e display that due to the changes in film morphology resulted from different evaporation rates, Samples 1,4 and 5 have different EIS data. Sample 1 and 4 shows that the "electrochemical grinding" might be occurred during cycling, leading to a decrease in particle size [30]. However, Fig4e shows that the charge transfer resistance of the sample 5 increases after 1st cycle. "Electrochemical agglomeration" might be the reason for this behavior [31]. Furthermore, Figures 4f-g reveal that thick film demonstrates two semi-circles at high frequency region, different than that of the thin film. The inhomogeneous morphology and multiple contacts of the thick film electrode surface with Li might explain the presence of the second semi-circle. After the first cycle, a remarkable change in EIS data is noted for the thick film electrode. Delamination of the film followed by the untolerated volume changes occured as a result of lithiation of si particles, can be a reason for it. On the other hand, for the thin film, as deposited electrode reveals only one semi-circle, but another semi-circle forms on the thin film electrode surface after the 1st cycle. The formation of SEI layer can elucidate this change.

For samples 3,4 and 7in low frequency regions a low Li^+ diffusion is noted since the capacitive behavior or inhomogeneous morphology of the electrodes limit Li^+ reaction with the active particles present in the anode, thus the slope at low frequency region deviates far away from 45^0 or disappears.

Figures 5a-g display the cycle number dependence of the insertion and extraction capacities of the samples respectively. The capacity values are calculated based on the active material present in the thin films. Table 4 gives the first cycle coulombic efficiency and the capacity retention of the samples after 20 cycles, beside the theoretical capacities of the films calculated based on EDS quantification (3579 mAh $g^{-1}$is the theoretical capacity of Si assuming the formation of $Li_{3.75}Si$ and the fractions are those provided in Table 2).

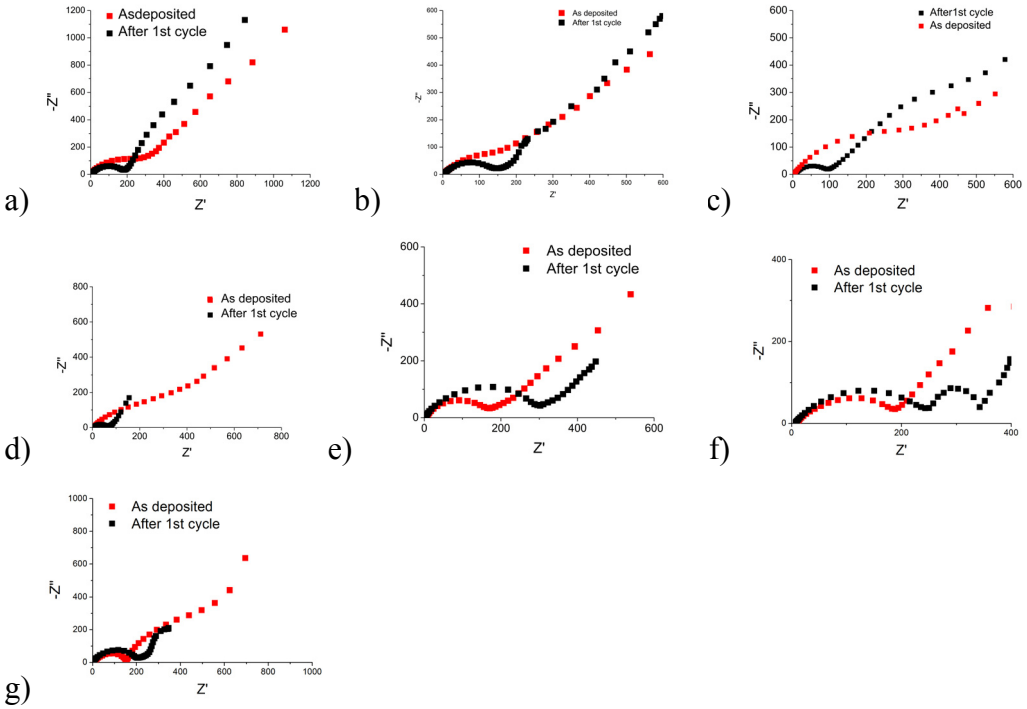

Figure 4. (a-g) EIS analyses of samples (1-7) as deposited and after 1st cycles.

Table 4. The comparison of the electrochemical performances of samples 1-8

Samples number	Theoretical first discharge capacity (mAh g^{-1})	First cycle discharge capacity (mAh g^{-1})	First cycle coulombic efficiency (%)	Discharge Capacity retention after 20th cycles (%)
1	2755.83	922.32	91	30
2	2469.51	1640.26	75	10
3	1896.87	2448.04	3	5
4	2720.04	2556.83	3	4
5	2720.04	2376.03	7	27
6	2720.04	2642.37	76	99
7	2755.83	1876.82	2	2

The low initial discharge capacity value (1896.87mAhg^{-1}) of the sample 3 is related to the high Cu content of the film, of which inactive behaviour restricts reaction of Li with Si in the thin film. Moreover, the ductile properties of the Cu enhance the first cycle coulombic efficiency as expected. Figure 5a shows that by decreasing the Cu content of the film the initial discharge capacity value gets closer to its theoretical value, but the coulombic efficiencies decrease abruptly, due to the untolerated volume changes occurred during cycles. When the deposition rate effect on the electrochemical performance of the CuSi thin film anode is observed, Figure 5b shows that the films formed at higher deposition rate fails very fast since big particle present in the thin film are more prone to pulverization and delamination, as explained previously [21]. Thereby the films formed under the lowest evaporation rates performs a higher coulombic efficiency even a continuous decay in capacity

is stil valid, due to the delamination and pulverization occuring in the anode. Finally, by depositing different thicknesses composite films having 10%at. Cu, with moderate evaporation rate (Si and Cu have 10 and 0.9Å/s, respectively) the thickness effect on the electrochemical performance of the anode is analyzed in Figure 5c. The results reveal that 0.5 micron thin film with 90%at. Si, deposited at 10 Å/s, performs the best performance since the stress between the electrode and the substrate is minimized and the internal electrical resistance is decreased when the film thickness decreaess. Moreover, since the deposition of the thin film doesnot require long process duration when a moderate evaporation rate is used, the generation of any agglomerates or inhomogeneities in the morphology are highly prevented, which enables longer cycle life with a moderate capacity retention.

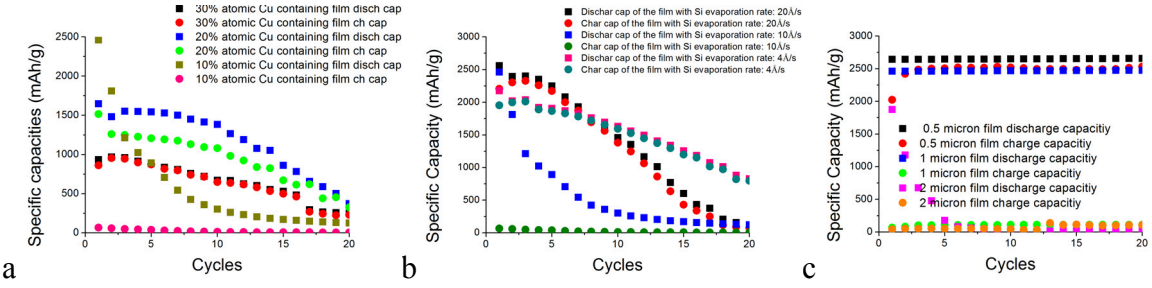

Figures 5. The galvanostatic test results of the samples: a) composition(Cu/Si atomic ratio), b) evaporation rate, c) film thickness effects on the electrochemical performance of the electrodes

Here in, it is worth to note that eventhough the capacity retention of the electrode is improved, still some amount of capacity delivered by the electrode is decreased during the cycle test. The Li^+ trapping in the thin film electrode, the SEI covering the anode surface or the Li^+deficient intermetallics formation after the first lithiation causing irreversible reactions with Si could explain this decrease in the Coulombic efficiency.

4. CONCLUSIONS

The galvanostatic test results show that using a 0.5 micron thin film having 90 %at. Si formed with a moderate evaporation rate (Si and Cu have 10 and 0.9Å/s, respectively) gives the best electrochemical performance among the others.

The analyses show that copper presence plays an important role in the improving of the cycling performance of the material. Cu acts as a mechanical and electrochemical buffer in the anode, thereby reducing the electrochemical sintering of silicon particles during cycling. Moreover the presence of Cu increases significantly the electrical conductivity of the electrode, which allows working at 50 mA/g. Additionaly, film thickness and the evaporation rate are also important because they affect the thin film morphology. Thereby, optimizations in the evaporation rate and the thickness of the electrode are highly required to further improve the performance of the anode.

5. ACKNOWLEDGEMENT

The authors thank Dr O. Levent Eryilmaz, Dr Bob Erck and Dr Ali Erdemir for their helps. This work is a part of the research project 213M511 approved by The Scientific and Technological Research Council of Turkey (TUBİTAK).

REFERENCES

1. J. Tani, H. Kido, Intermetallics, 32, 72-80, 2013.
2. J. Yang, M. Watchler, M. Winter, J.O. Besenhard Electrochem. Solid State Lett., 2, 161, 1999.
3. I.-S. Kim, P. Kumta, G.E. Blomgren, Electrochem. Solid State Lett., 3, 493, 2000.
4. V. A. Sethuraman, K. Kowolik, and V. Srinivasan, J. Power Sources, 196, 393, 2011.
5. A.A. Istratovand, E.R. Weber, Appl. Phys., 66, 123, 1998.
6. B.D. Polat, O.R. Eryilmaz, O. Keles, ECS Electrochem. Lett., 3, A45-49, 2014.
7. X. Zhou, A.M. Cao, L.J. Wan, Y.G. Guo, Nano Research, 5, 845-853, 2012.
8. P. Wang , Y.N.Li, J. Yang, Y. Zheng, Int. J. Electrochem Soc., 1, 122-129, 2006.
9. J. P. Maranchi, A. F. Hepp, and P. N. Kumta, Electrochem. Solid-State Lett., 9, A198, 2003.
10. M.Higo, K.Fujita, M.Mitsushio, T.Yoshidome, T.Kakoi, Thin Solid Films, 516, 17-24, 2007.
11. J.Podbrdsky, V.Drahos, Czechoslovak Journal of Physics B, 19, 217-221, 1969.
12. M.Higo, K.Fujita, Y.Tanaka, M.Mitsushio, T.Yoshidome, Applied Surface Science, 52, 2066-2072, 2006.
13. D.J.Semin, K.L. Rowlen, Analytical Chemistry, 66, 4324-4331, 1994.
14. P. Quintana, A.I.Oliva, O.Ceh, J.E.Corona, Superficies y Vacio, 280-282, 1999.
15. N.G.Semaltianos, Applied Surface Sciene, 183, 223-229, 2001.
16. M.Aguilar, P.Quintana, A.I. Oliva, Materials and Manufacturing Process, 17, 57-65, 2002.
17. S.-J.Hwang, J.-H.Lee, C.-O. Jeong, Y.-C.Joo, Scripta Materialia, 56, 17-20, 2007.
18. K.Cai, M.Müller, J.Bossert, A.Rechtenbach, K.D.Jandt, Applied Surface Science, 250, 252-267, 2005.
19. P.A.Flinn, D.S.Gardner, W.D.Nix, IEEE Transaction on Electron Devices, Vol. Ed-34, 3, 1987.
20. H.Qui, F.wang, P.Wu, L.Pan, L.Li, L.Xiong, Y.Tian, Thin Solid films, 414, 150-153, 2002.
21. B.D.Polat, A.Abouimrane, N.Sezgin, O.Keles, K.Amine, Electrochim Acta, 2014 (accepted).
22. J.A.Thornton Review of MaterialScience, 7, 239-260, 1977.
23. K. Bordo, H.-G. Rubahn, Material Science, 18, 4,313-317, 2012.
24. U. Kasavajjula, C. Wang, A.J., Appleby, J. Power Sources, 163, 1003-1039, 2007.
25. H. Li, X. Huang, L. Chen, H. Zhou, Z. Zhang, D. Yu, Y.J. Mo, N. Pei, Solid state Ionics, 135, 181-191, 2000.
26. P. Limothongkul, Y.-I. Jang, N. J. Dudney, Y.-M. Chiang, J. Power Soruces, 119-121, 604-609, 2003.
27. P. Limothongkul, Y.-I. Jang, N.J. Dudney, Y.-M. Chiang, Acta Mater., 51, 1103-1113, 2003.
28. R.D. Thomson, K.N. Tu, Phys.Lett., 41, 440-443, 1982.
29. T.D. Hatchard, J.R. Dahn, J. Electrochem. Soc., 151, A838-842, 2004.
30. D. Andre, M. Meiler, K. Steiner, H.Walz, R. S. Guth, D. U.Sauer, J.Power Sources, 196, 5349, 2011.
31. H. Li, L. Shi, Q. Wang, L. Chen, X. Huang, Solid state Ionics, 148, 247-248, 2002.

LOW COST PREPARATION OF VO_2-BASED THERMOCHROMIC THIN FILMS

Melis Can ÖZDEMİR*, Miray ÇELİKBİLEK*, Ali Erçin ERSUNDU, Süheyla AYDIN***

*Istanbul Technical University, Istanbul, Turkey
meliscanozdemir@gmail.com, miraycelikbilek@gmail.com, saydin@itu.edu.tr
** Nişantaşı University, Istanbul, Turkey
aliercin.ersundu@nisantasi.edu.tr

ABSTRACT
Thermochromic thin film coated glasses showing spectrally selective properties have emerged as an innovative solution for energy losses through windows since thermochromic thin films have the ability to change their optical properties in response to the change in temperature. Recently, VO_2-based thin films have been the focus of attention for energy-efficient windows due to their relatively low thermochromic transition temperature which is close to room temperature. In the present study, sol-gel method was applied to obtain VO_2-based thin films by using vanadium pentoxide (V_2O_5) and oxalic acid ($C_2H_2O_4.2H_2O$) precursors. All glass slides were primarily coated with SiO_2 interlayer to prevent the possible alkali attack. Thin films were coated on soda lime glass slides by dip coating technique. Coated samples were annealed under nitrogen atmosphere to obtain four-valence VO_2 films. Thermochromic behavior of VO_2-based thin films was investigated by a custom made in-situ temperature controlled UV-Vis spectrophotometer.

Keywords: Thermochromic, Thin films, VO_2, Energy Efficiency

VO_2 - ESASLI TERMOKROMİK İNCE FİLMLERİN DÜŞÜK MALİYETLİ BİR YÖNTEM İLE HAZIRLANMASI

ÖZET
Termokromik ince filmlerin sıcaklık değişimi ile optik özelliklerini değiştirebilmeleri sayesinde, seçimli spektral özellikler gösterebilen termokromik ince film kaplamalı camlar, pencerelerden kaybedilen enerji için yenilikçi bir çözüm olarak ortaya çıkmıştır. VO_2 esaslı ince filmler, diğer malzemelere kıyasla gösterdikleri oda sıcaklığına yakın termokromik dönüşüm sıcaklıkları ile son zamanlarda enerji tasarrufu sağlayan pencereler için ilgi odağı olmuştur. Bu çalışmada, VO_2 esaslı ince film elde etmek için sol-jel yöntemi uygulanmış ve başlangıç malzemesi olarak V_2O_5 ve $C_2H_2O_4.2H_2O$ kullanılmıştır. Altlık olarak kullanılan camlar olası alkali atağını engellemek amacı ile önceden SiO_2 ara katmanı ile kaplanmıştır. Termokromik ince filmler soda-kireç camlar üzerine, daldırmalı kaplama yöntemi ile kaplanmıştır. Dört değerlikli VO_2 film elde etmek amacı ile, numuneler azot atmosferi altında ısıl işleme tabi tutulmuştur. Hazırlanan VO_2 esaslı ince filmlerin termokromik davranışı özel tasarım sıcaklık kontrollü UV-Vis spektrofotometre ile incelenmiştir.

Anahtar Kelimeler: Termokromik, İnce filmler, VO_2, Enerji tasarufu

1.INTRODUCTION

A significant amount of energy is used for heating and cooling systems in buildings, while a large portion of this energy (about 20-40%) is lost through windows. Therefore, today's growing glass market has focused on new glasses that can provide energy saving, heat and light control [1,2].

Smart windows have become a popular topic for researchers to respond energy efficiency problems. Smart windows are defined as windows that can block the unwanted solar radiation by switching radiative and thermal properties and they provide reduced HVAC (Heating, Ventilation and Air Conditioning) size, energy consumption and hence energy requirement of building. There is a wide range of smart windows, such as Low-E coatings, micro blinds, dielectric/metal/dielectric (D/M/D) films and switchable reflective devices like electrochromic, gasocromic, liquid crystal glazing and thermochromic windows. Owing to their low price, simple structure, no wiring necessity and good ability to visible transmission thermochromic windows are today's cutting-edge products [2].

Thermochromism, is a reversible/irreversible change in optical properties of a material which occurs with color change. Among a large number of transition metal-oxides showing metal-semiconductor phase transformation characteristics, monoclinic/rutile phase transformation of vanadium dioxide (VO_2) emerges as one of the most important functional properties with its thermochromic transition at approximately 68˚C which is close to room temperature. The phase transformation temperature of VO_2 can be named as metal-semiconductor transition temperature (MST), critical transition temperature or thermochromic transition temperature. This structural transition of VO_2 leads to significant changes on electrical conductivity and near infrared (NIR) optical transmittance. All of these distinctive properties allow the use of VO_2 for different applications, such as optical switching devices, temperature sensors, data storage medias, optical modulators, smart windows applications for energy saving buildings etc. [2,3-7].

VO_2 can be applied on glass surfaces as a thin film via different methods: chemical/physical vapor deposition, laser deposition, sputtering and sol-gel. Sol-gel method is usually preferred due to its low cost equipment, simple application and high transmittance performance in the visible region [2,8-14].

VO_2 has a narrow stoichiometric range in all of the vanadium oxidation states and it is quite difficult to obtain pure VO_2 . In the literature four-valence and five-valence vanadium oxide precursors are used to prepare the sols, and different atmospheric conditions (inert or reductive) are used for the reduction [2,8-14].

The aim of the present study is to prepare VO_2 thin film coated soda-lime glasses using five-valence vanadium oxide precursors under N_2 atmosphere without the necessity of any flammable reduction gases to obtain four-valence VO_2 thin films and to investigate their thermochromic behavior using in-situ temperature controlled UV-Vis spectroscopy analysis.

2.EXPERIMENTAL

In the experimental studies, vanadium pentoxide (V_2O_5) (%99.9 purity, Alfa Aesar Company) was used as vanadium precursor and oxalic acid dihydrate ($C_2H_2O_4.2H_2O$) (Merck Company) was used as catalyst, in the molar ratio 1:3. A chemical reaction was carried out between

vanadium precursor and catalyst under ethanol reflux at 120 °C, for 24 hours by magnetic stirring and a transparent bluish-green solution was obtained.

To prevent a possible alkali attack from soda-lime glass to vanadium oxide based thin film layer, an interlayer coating was done on glass slides. For this purpose, SiO_2 solution was prepared using tetraethylorthoslicate (TEOS) (Sigma Aldrich Company), ethanol, hydrochloric acid (HCI) and distillated water in the molar ratio 1:4:0.3:4, respectively by magnetic stirring for 2 hours.

Soda-lime glass slides (Corning 2947) were used as substrate for thin film coating. Glass slides were cleaned ultrasonically in acetone, ethanol, methanol and distillated water, respectively for 10 minutes to remove the organic residues.

SiO_2 solution was deposited on glass substrates by spin coating at 1800 rpm/min. Afterwards, the slides were dried at 80 °C for 10 min to remove excess ethanol solvent and finally coated slides were annealed at 300 °C for 1 hour. Vanadium oxide based solution was coated on with/without SiO_2 interlayered soda-lime glass substrates by dip coating method at 100 mm/min rate, then the slides were dried at 80 °C for 10 min to remove excess ethanol solvent. This process was repeated four times by applying the drying step for each layer. All coatings were applied on one side of the slides.

Finally coated samples were reduced under N_2 flow at 500 °C in a tube furnace for 2 hours to obtain VO_2 thin films. Thermochromic behavior of the vanadium oxide based thin films was characterized by a custom made in-situ temperature controlled UV-Vis Spectrometer (PG, T 80+ Model) from 360 to 1100 nm at 25 °C and 100 °C.

3.RESULTS AND DISCUSSION

Vanadium oxide based thin film samples reduced at 500 °C with and without SiO_2 interlayer were investigated by an in-situ UV-Vis Spectrometer (PG, T 80+ Model) from 360 to 1100 nm at 25 °C and 100 °C.

Firstly, vanadium oxide based thin film without SiO_2 interlayer attached on the light path of the UV-Vis Spectrometer and spectrum was obtained from 360-1100 nm at 25 °C, then temperature was increased to 100 °C and the measurement was repeated. Transmission spectra of vanadium oxide based thin film without SiO_2 interlayer are shown in Figure 1.

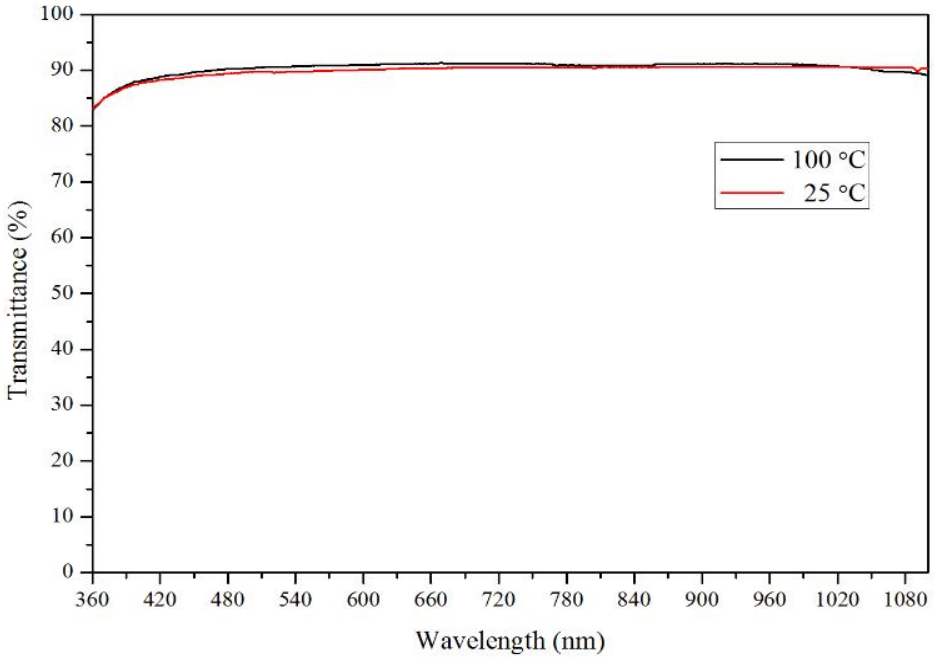

Figure 1. UV-Vis spectra of vanadium oxide based thin film without SiO_2 interlayer at 25°C and 100° C.

The same measurements were applied on vanadium oxide based thin film with SiO_2 interlayer and the transmission spectra obtained at 25 °C and 100 °C are shown in Figure 2.

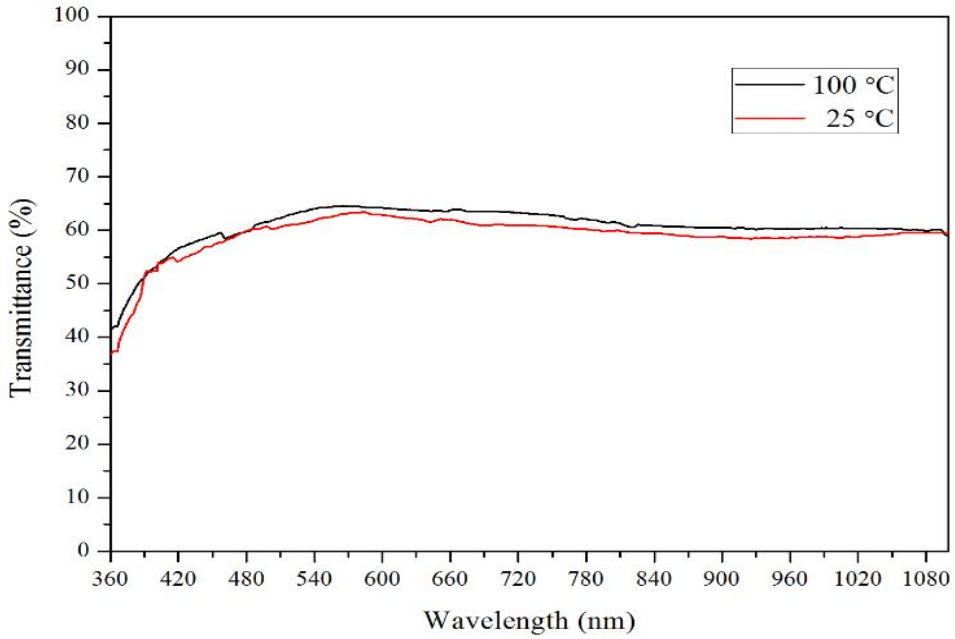

Figure 2. UV-Vis spectra of vanadium oxide based thin film with SiO_2 interlayer at 25 °C and 100 ° C.

It was observed that SiO_2 interlayer decreases the tranmittance values from 87 % to 57 % and samples reduced under N_2 flow at 500 °C did not show any change in transmittance with changing temperature which means there was no phase transformation resulting a thermochromic change.

In their study carried out using V_2O_5 as precursor under the same annealing conditions Zhao et al. observed a decrease in transmittance with increasing temperature due to a metal-semiconductor phase transformation [9]. However, according to Guzman, there is no need for a reductive gas atmosphere and an inert atmosphere is convenient when using four-valence vanadium oxide precursors while it is necessary to use reductive atmosphere to obtain VO_2 phase from five-valence vanadium oxide precursors [11]. This approach proves the transmittance results via temperature obtained in this study and explains the unrealized metal-semiconductor phase transformation.

4.CONCLUSION

In this study vanadium oxide based thin films were synthesized on plain and SiO_2 interlayer coated soda lime glasses with a low cost sol-gel method using V_2O_5 as precursor. Annealed samples under N_2 atmosphere at 500 °C for 2 hours were characterized by a custom made in-situ temperature controlled UV-Vis Spectrometer from 360 to 1100 nm at 25 °C and 100 °C. Samples did not show any transmittance change with changing temperature proving that four-valence VO_2 thin films were not obtained. It can be concluded that under the experimental reduction conditions, the samples did not show a metal-semiconductor phase transformation resulting a thermochromic change. This result proves the literature approach on the necessity of reduction of the five-valence vanadium oxide precursor under a reductive atmosphere instead of an inert atmosphere.

REFERENCES

1. Saeli, M., Piccirillo, C., Warwick, M.E.A., Binions, R., "Thermochromic ThinFilms: Synthesis, Properties and Energy Consumption Modelling", Materials and Progress for Energy, A. Méndez-Vilas, Ed., 2013
2. Kamalisarvestani, M., Saidur R., S.Mekhilef , F.S.Javadi, Renewable and Sustainable Energy Reviews, 26,353,2013
3. Kiri, P., Hyett,G., Binions, R. , Advanced Materials Letters, 1(2),86,2010
4. Zhang, Z., Gao, Y., Chen, Z., Du, J., Cao,C., Kang, L., Luo, H., Langmuir Article, 26 (13), 10738, 2010
5. Beteille, F., Livage, J., Journal of Sol-Gel Science and Technology, 13, 915, 1998
6. Parkin, I.P., Binions, R., Piccirillo,C., Blackman, S.,C., Manning, T.D., J. of Nanoresearch, 2,1,2008
7. Morin, F.J., Physical Review Letters, 3, 34, 1959
8. Kang, L., Gao, Y., Luo, H., App.Mater.&Inter., 1, 2211, 2009
9. Zhao, L., Miao, L., Tanemura, S., Zhou, J., Chen, L., Xiao, X., Xu, G., Thin Solid Films, 543,157, 2013
10. Warwick, E.,A., J. of Materials Chemistry A, 2, 3275, 2014
11. Url-1 < http://www.solgel.com/articles/august00/thermo/guzman.htm >, downloaded on 17.11.2013
12. Pan, M., Zhong, H., Wang, S., Liu, J., Li, Z., Chen, X., Lu, W., J. of Cryst. Growth, 265, 121, 2003
13. Hanlon, T.J., Coath, J.A., Richardson, M.A., Thin Solid Films, 436, 269,2003
14. Wang, N., Magdassi, S., Mandler, D., Long, Y., Thin Solid Films, 534, 594, 2013

RECYCLED LEAD ACID PASTE AS AN ANODE MATERIALS FOR Li-Ion BATTERIES

M. Seref Sonmez; Bora Derin; Ozgul Keles; Sebahattin Gurmen

Istanbul Technical University, Faculty of Chemistry & Metallurgy, Department of Metallurgical & Materials Engineering, Maslak, 34469, Istanbul, Turkey;

ABSTRACT

In this study, lead acid battery paste was recycled to be used as anode for lithium ion batteries (LIB). First, lead-acid battery paste was leached with citrus acids to transform into lead citrate following calcination-combustion reaction. Then, the product was used as an electrode material for lithium ion batteries. Used lead acid battery pastes contain typically 55-60 % $PbSO_4$, 20-25 % PbO and 1-5 % PbO_2. The reaction among PbO and $C_6H_8O_7.H_2O$, PbO_2, the mixture of $C_6H_8O_7.H_2O$ and H_2O_2, $PbSO_4$ and the mixture of $C_6H_5Na_3O_7.H_2O$ and $C_6H_8O_7.H_2O$ caused lead citrate to form. Reaction time, temperature and concentration were important parameters. In leaching step, the effects of poly-hydroxyl alcohol addition as grain refiner was investigated to synthesize lead based powder having submicron particles after the combustion-calcination process. Chemical and morphological characterization of battery paste and products were made. Galvanostatic half-cell electrochemical measurements conducted between 0.2-1.2V using lithium counter electrode was realized to understand the electrochemical behaviour of the anodes produced.

Keywords: Lead acid battery paste recycling, Li ion batteries, lead citrate, combustion-calcination synthesis.

Li-İYON PİLLERİ İÇİN KURŞUN ASİT PASTASINDAN GERİ KAZANILMIŞ ANOT MALZEMESİ

ÖZET

Bu çalışmada, lityum iyon pilleri (LIB) için anot malzemesi olarak kullanılmak üzere kurşun asit pastasının geri kazanımı gerçekleştirilmiştir. Öncelikle, kurşun asit pastası kurşun sitrata dönüştürülmek üzere sitrik esaslı asitlerle çözümlendirilmiş ve ardından yanma-kalsinasyon reaksiyonuna tabi tutulmuştur. Daha sonra, elde edilen ürün lityum iyon pilleri için anot malzemesi olarak kullanılmıştır. Kullanılmış kurşun akü pastası % 55-60 $PbSO_4$, % 20-25 PbO, ve % 1-5 PbO_2 içermektedir. Çözümlendirme sırasında PbO ile $C_6H_8O_7.H_2O$, PbO_2 ile $C_6H_8O_7.H_2O$ ve H_2O_2 karışımı, $PbSO_4$ ile $C_6H_5Na_3O_7.H_2O$ ve $C_6H_8O_7.H_2O$ karışımı arasındaki reaksiyonlar sonucunda kurşun sitrat oluşmaktadır. Bu işlemde reaksyon süresi, sıcaklık ve konsantrasyon önemli parametrelerdir. Çözümlendirme aşamasında tane inceltici olarak poli-hidroksi alkol ilavesiyle sonraki yanma-kalsinasyon prosesiyle mikron altı boyutta kurşun esaslı tozun sentezlenmesine etkisi incelenmiştir. Akümülatör pastasının ve ürünlerin kimyasal ve morfolojik karakterizasyonu yapılmıştır. Üretilen anot malzemesinin elektrokimyasal davranışını anlamak amacıyla lityum karşı elektrodu kullanılarak 0.2-1.2V arasında galvanostatik yarım hücre ölçümleri gerçekleştirilmiştir.

Anahtar Kelimeler: kurşun asit akümülatör pastası geri kazanımı, Li iyon pilleri, kurşun sitrat, yanma-kalsinasyon sentezi.

1. INTRODUCTION

Lithium-ion (Li-ion) batteries consist of cells that employ lithium intercalation compounds as the positive and negative materials. Li-ion batteries have quickly evolved from research and development interest to a significant and growing fraction of the worldwide battery market. The acceptance of the technology has been driven by its unique ability to offer a high level of performance in many aspects, including energy density, specific energy, rate capability, cycle life, and storage life, with a rather safe, low cost product. Further improvements in cell performance will be made possible through both more efficient mechanical designs and improved materials. Improved positive electrode materials that offer higher capacity and improved safety properties are in development, as are new negative electrode materials offer the potential for further improvement in specific energy, energy density, rate capability, and longevity [1].

Lithium based alloys are taken into account as alternative anode materials to lithium and graphite anodes. These new anode materials build alloy compositions during discharge operation and exhibit high capacities without safety issues. Li, C, $Li_4Ti_5O_{12}$ (LTO), Si, Sn, Sb, Al, Mg, Bi are very promising metals to satisfy this expectation due to their unique properties. The theoretical specific capacities of alloy anodes are 2-10 times higher than that of graphite, and 4-20 times higher than that of LTO. Even if the full volume expansion of lithiated product is considered, the charge densities of alloy anodes are still 2-5 times higher than those of graphite and LTO. The second merit of alloy anodes is their moderate operation potential versus lithium. For example, both Si and Al anodes have an onset voltage potential of 0.3-0.4 V above Li/Li^+. This moderate potential averts the safety concern of lithium deposition as with graphite anodes (~0.05 V vs. Li), meanwhile, avoids the energy penalty of battery cells assembled with the LTO anodes (1.5 V vs. Li/Li^+). The high capacities causes extensive volume changes (up to 300%) within the negative electrode. Even if high capacities are obtained during first cycles, large volume changes make anode fracture and lead low cycle life to occur. To obtain both high capacity and long cycle life, the researchers develop different methods that tolerate abrupt volume changes and keep anode uniform. [2].

Chae et al. synthesised MnO_x/C nanocomposite materials as an anode for Li-ion batteries (LIB) having theoretical capacity of MnO_x (700-750 $m.Ahg^{-1}$ at 100 $m.Ag^{-1}$) with excellent rate capability. The $LiMn_2O_4$ (LMO)-MnO_x/C cell exhibits reversible capacity of the LMO cathode, with the cycling stability and rate capability dependent upon those of the MnO_x/C anode. An LMO-MnO_x/C cell with anode loading in slight excess delivers reversible capacity of LMO without capacity fading for up to 245 cycles [3].

Nano sized oxides as anode materials for lithium ion batteries have been investigated intensively recently. Nuli et al. fabricated tin oxides and oxide thin film anodes by vacuum thermal evaporation of metallic tin or nickel and subsequent thermal oxidation in air or oxygen ambient. The reversible capacities of SnO and SnO_2 film electrodes reached 825 and 760 $m.Ahg^{-1}$, respectively at the current density of 10 μAcm^{-2} between 0.10 and 1.30 V. Nanocrystalline NiO thin film prepared at a temperature of 600°C can deliver a reversible capacity of 680 $m.Ahg^{-1}$ in the voltage range of 0.10 and 1.30 V and good cyclability up to 100 cycles [4].

Martos et al. produced PbO material via spray pyrolysis process. They prepared and characterized both bulk oxide and PbO film electrodes. Electrochemical test results proved that bulk oxide electrodes showed poor performance due to ohmic cell resistance. On the other hand, PbO film electrodes show satisfactory capacity values which were attributed to the LixPb phase that helps particles to attach to the electrode surface thus improve ionic and electronic conductivity [5]. Martos et al., then, formed three lead-based materials by PbO_2, PbO and Pb as main phases were prepared by following different synthetic procedures and tested as anodic materials in Li-ion

batteries by using potentiostatic and galvanostatic methods. While the reduction of Pb(IV) to Pb(II) takes place in a single step, that of Pb(II) to Pb is a complex process involving several steps. Both reduction reactions are irreversible. Lead, whether electrochemically or chemically formed, undergoes an electrochemical reaction with lithium that over the 1.0-0.0 V potential range yields Li_xPb alloys ($0 \leq x \leq 4.4$). Electrochemical tests indicate that the presence of irreversible Li_2O phase acts as a dispersion agent thus improves cycling performances of the electrodes. Furthermore, this phase inhibits the formation of large Pb aggregates which increase the reversibility of alloying/de-alloying processes [6].

Konstantinov et al. produced PbO powders by spray pyrolysis. Different spray pyrolysis parameters were investigated to determine the effects on grain size of the product. Test results showed that materials with crystal sizes between 100-120 nm exhibited better cycle life compared to the powders with small particle size. Nonetheless, it is admitted that cycle life and capacity depend on many factors [7]. In 2009, Pan et al. studied the electrochemical performance of PbO@C core–shell nano-composites as an anode material of lithium-ion batteries. The PbO@C nano-composites were prepared via the pyrolysis of lead benzoate precursor. Compared to the reported Pb-based anodes, the PbO@C nano-composites exhibited higher reversible capacity and longer cycling life. A reversible capacity of 170 $m.Ahg^{-1}$ could be maintained after discharging/charging for 50 cycles, which was at least 1.5 times than the previously reported values. The enhanced electrochemical performance was attributed to the presence of carbon shells that could alleviate the large volume-change of Pb particles during the alloying / de-alloying process [[8]].

In this work, a waste lead-acid battery paste was converted into submicron powders by new leaching and calcination method to examine the behaviour as an electrode material for Li-ion batteries.

2. EXPERIMENTAL

Lead based anode materials were synthesised from waste lead-acid battery paste which was obtained from used lead-acid battery subjected to preliminary acid removal, grinding and elimination process. Homogeneous paste has obtained in particle size under 125 µm. Chemical composition and X-ray diffraction pattern of battery paste were given in Table 1 and Figure 1, respectively.

Table 1: Chemical composition of spent battery paste used for processing.

Spent battery paste components	Amount (%)
PbO	10.27
PbO_2	8.18
$PbSO_4$	58.85
Pb	negligible
Total Pb	56.83

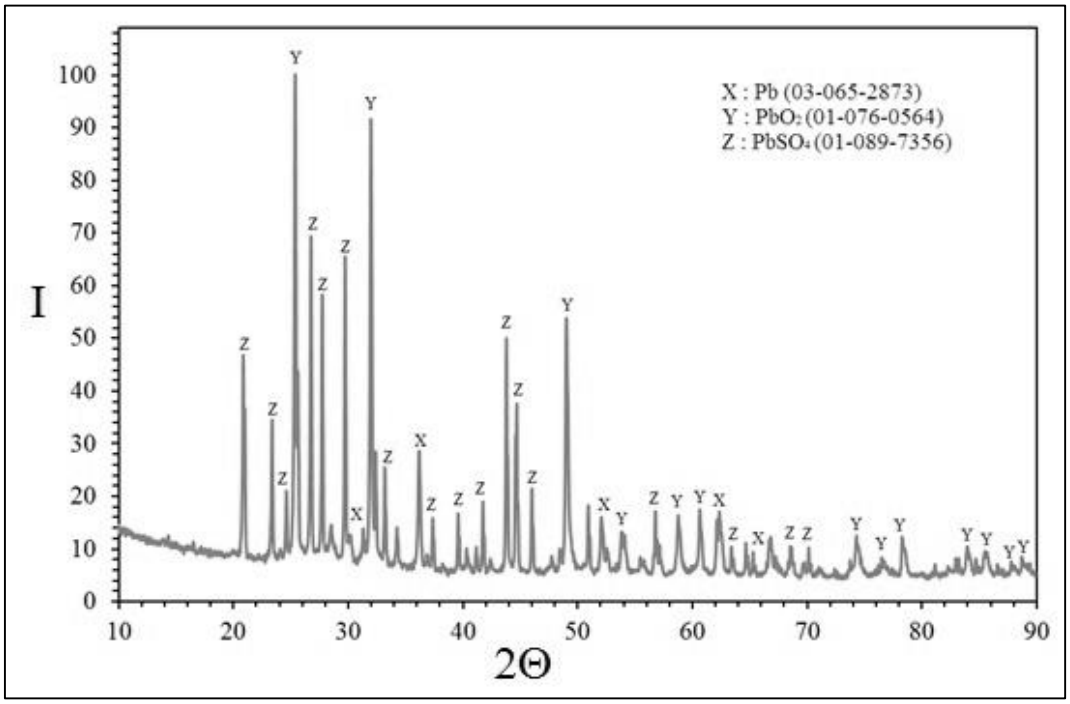

Figure 1: XRD analysis of spent battery paste

Battery paste was leached using reactants such as hydrogen peroxide, sodium citrate, citric acid and diethylene glycol. During leaching processes, solid/liquid ratio, leaching duration, temperature and stirring rate were taken into consideration.

Obtained lead compound was transformed into submicron lead-based powders in ceramic crucibles via calcination-combustion method in the furnace. Reaction time and temperature were investigated parameters to obtain fully transformed powders.

Submicron lead-based powders were subjected to mixing for anode preparation. Mixing step was done in argon filled glove box (MBRAUN Labmaster). 70% lead-based powder (active material), %20 carbon black (added to improve electronic conductivity), %10 PVDF (binder) and 2mg NMP were used to obtain homogeneous slurry. To increase homogeneity and strength of the mixture, mechanical attrition was carried out for 2 hours in Turbula. Two different coatings were fulfilled with doctor blade equipment. Coatings were made on copper (50 µm thickness) and aluminium substrate (50 µm thickness) with thickness of 15 µm. In order to evaporate the binder, the coatings were put into oven at 120°C for 1 day.

CR2032 coin cell was fabricated to test the electrochemical properties of the thin-film electrode. The cell was assembled in argon filled glove-box (MBRAUN Labmaster). The testing cell was prepared based on following sequence: i) a working electrode, ii) a 1M LiPF6 in ethylene carbonate-dimethyl carbonate, EC:DMC 1:1 (Merck Battery Grade) electrolyte solution iii) separator (Celgrad 2400) and iv) a lithium metal foil counter electrode.

The cell was tested at room temperature in between 0.2–1.2 V versus Li/Li+ with a rate of 75 $mA.g^{-1}$.

The phase analysis was performed by X-ray diffractometer (Bruker D8 Advance) (CuKα, 40kV, 25mA), Atomic absorption spectroscopy (Perkin Elmer Analyst 800). Sulphate analysis of battery paste and lead citrate were performed by Carbon/Sulphate Analyser (ELTRA CS 800). Particle

size distribution of products was measured by laser particle measurement device (Malvern Mastersizer).

3. RESULTS

Leaching of 5g of waste battery paste was carried out by using the solution mixture of 5.87g of citric acid, 11.41g of sodium citrate, 1.32g of hydrogen peroxide, and 10g of diethylene glycol. Leaching and crystallization behaviour of lead-based powder was optimized by considering initial solid/solution ratio, leaching duration, temperature and mixing rate. The best leaching conditions were obtained at 1/20 solid/solution ratio for 60 minutes leaching duration at room temperature while the stirring rate was kept at 400 rpm. Increase in solid/solution ratio prevented reactants not to dissolve homogeneously in aqueous solution. In addition, decrease in time inhibited full conversion of battery paste into lead citrate precursor. Change in temperature and leaching duration had not dramatic effects on leaching behaviour.

Conversion reactions occur in leaching process were represented by the following equations.

$$\mathrm{PbO} + \mathrm{C_6H_8O_7.H_2O} \rightarrow \mathrm{Pb(C_6H_6O_7).H_2O} + \mathrm{O_2} + 2\mathrm{H_2O} \quad (1)$$

$$\mathrm{PbO_2} + \mathrm{C_6H_8O_7.H_2O} + H_2O_2 \rightarrow \mathrm{Pb(C_6H_6O_7).H_2O} + \mathrm{O_2} + 2\mathrm{H_2O} \quad (2)$$

$$3\mathrm{PbSO_4} + 2[Na_3\mathrm{C_6H_5O_7.2H_2O}] \rightarrow [3\mathrm{Pb.2(C_6H_5O_7)}].3\mathrm{H_2O} + 3Na_2\mathrm{SO_4} + \mathrm{H_2O} \quad (3)$$

Lead based components in spent battery paste were converted into citreous salt compounds by using citric acid solution while hydrogen peroxide acted as reducing agent for the complete removal of PbO_2 in paste. On the other hand sulphur removal from the spent battery paste was achieved by the addition of sodium citrate together with citric acid to the solution mixture. Depending on the composition of spent battery paste pre-leaching process might be added to the process for increased efficiency. Sulphate content of the obtained product was analysed as 0.006 % after the complete transformation to lead citrate based salts. Ethylene glycol was also added to the leaching mixture to reduce particle size of obtained lead citrate according to the procedure described elsewhere [9].

Calcination-combustion process was applied to the obtained lead citrate powders after leaching. The submicron sized lead based powders were obtained in short reaction time and with low energy requirements via this novel method which is described elsewhere [10, 11, 12]. This process was carried out by simple heating of the powder under normal atmosphere in the furnace. XRD data for the powders obtained after calcinations at 350, 370 and 400°C for 60 minutes were given in Figure 2, Figure 3, and Figure 4, respectively. It was clear that best results were obtained after the calcination at 400°C for 60 minutes. The convenient weight loss of powders after the calcination was observed after 400°C as seen in Figure *5*. Fewer calcination periods were insufficient for the decomposition of citrate based lead compound, while even with the best calcination conditions, formation of lead carbonate was detected in the lead based powder. This situation demonstrated that calcination of lead citrate achieved by the series of decomposition reactions including the formation of lead carbonate. Calcination process was carried out without the addition of any reagents as carbon and hydrogen itself in lead citrate structure was removed from the system during the decomposition.

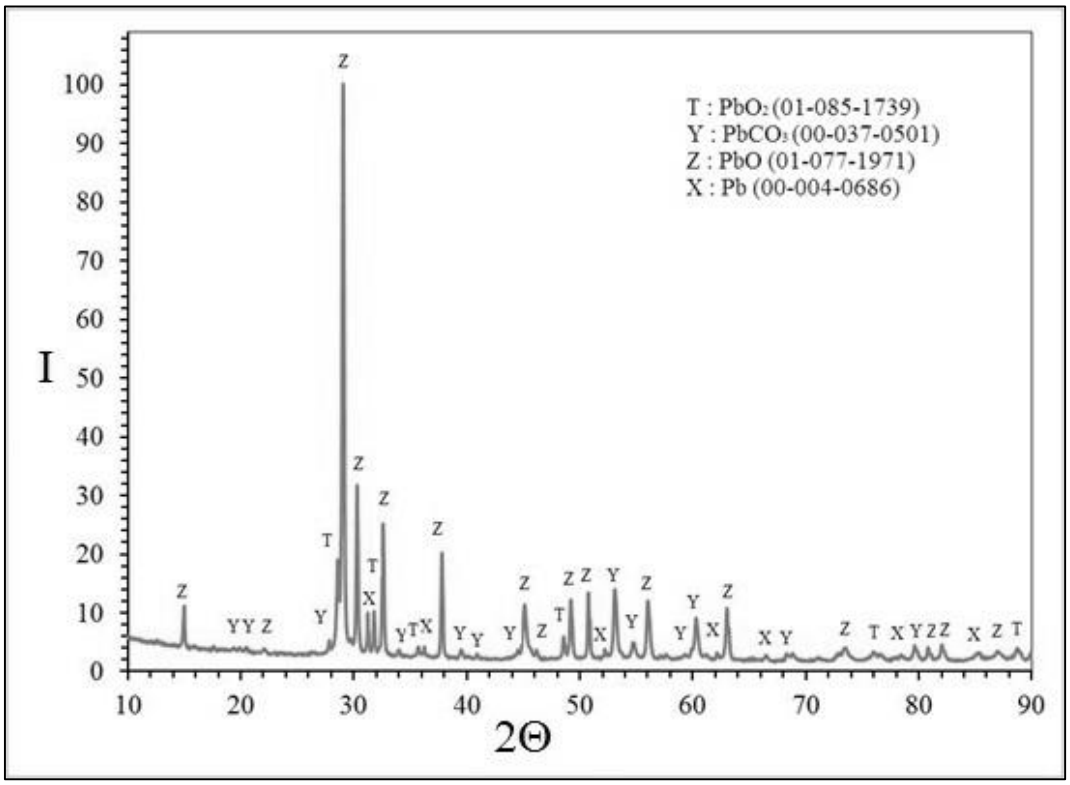

Figure 2: XRD analysis of Pb based powder obtained after the calcination at 350°C for 60 min.

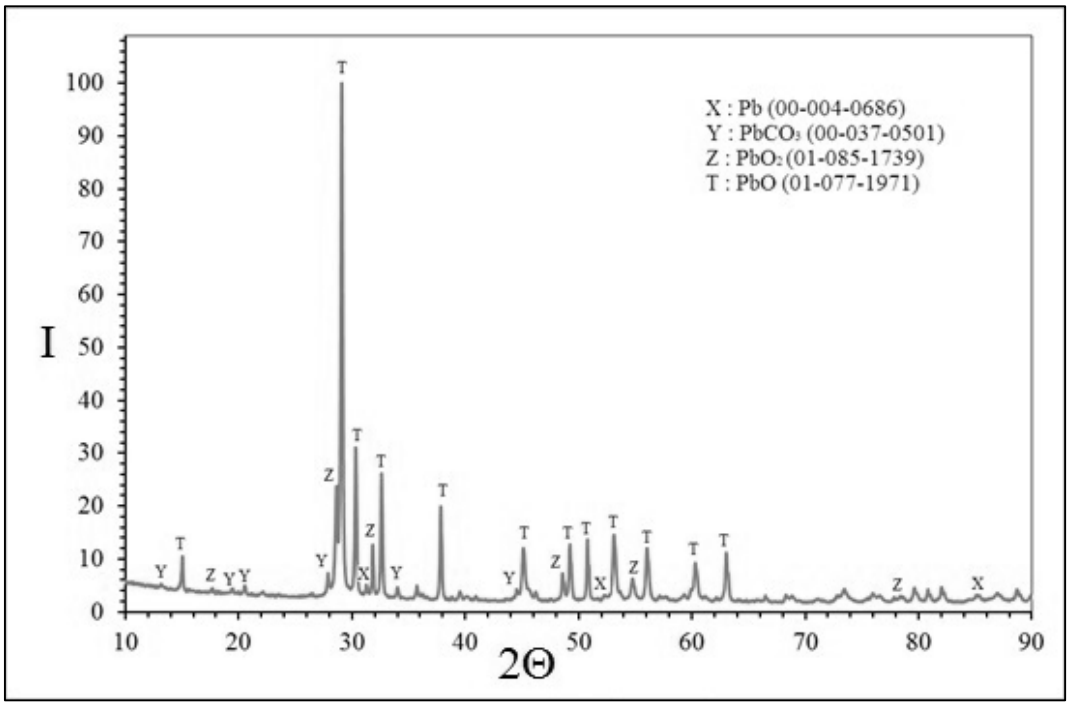

Figure 3: XRD analysis of Pb based powder obtained after the calcination at 370°C for 60 min.

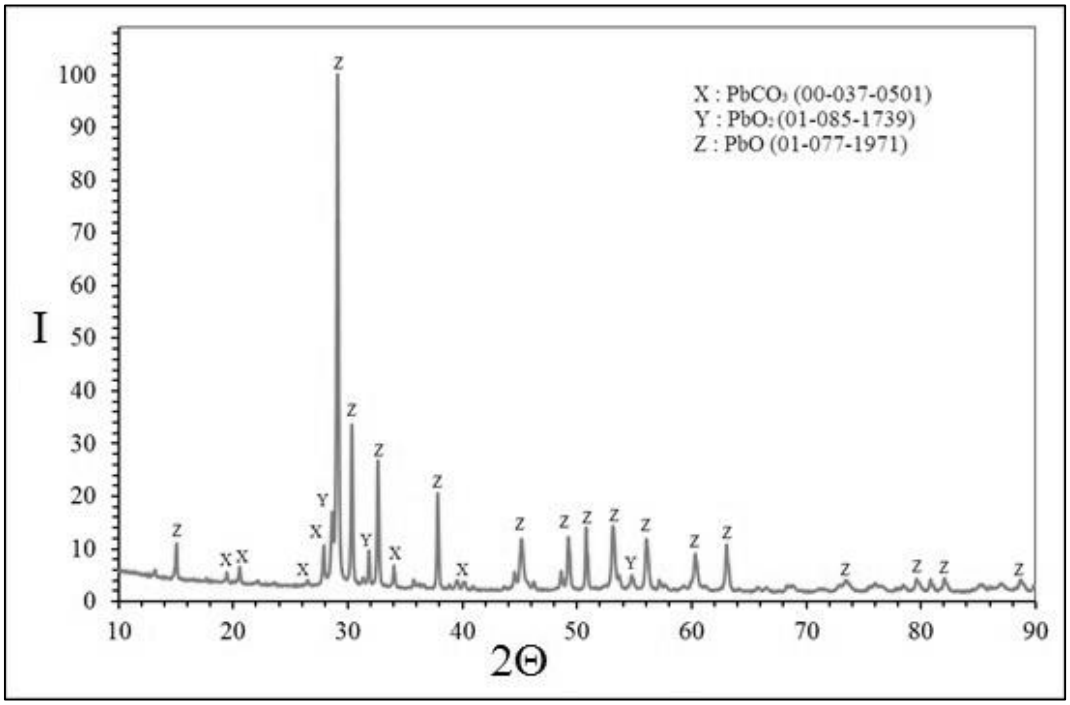

Figure 4: XRD analysis of Pb based powder obtained after the calcination at 400°C for 60 min.

The particle size distribution of product was determined to be around 0.1 and 0.3 μm with the average of 167 nm. Such a uniform submicron sized particles were obtained by the addition of diethylene glycol during the leaching step. Diethylene glycol, as known as polyhydroxyl alcohol, is commonly used in leaching processes due to its grain refining property. When detrimental volume changes in anode material during charge and discharge reactions was considered, submicron sized negative electrodes had great opportunity to avoid structural fractures.

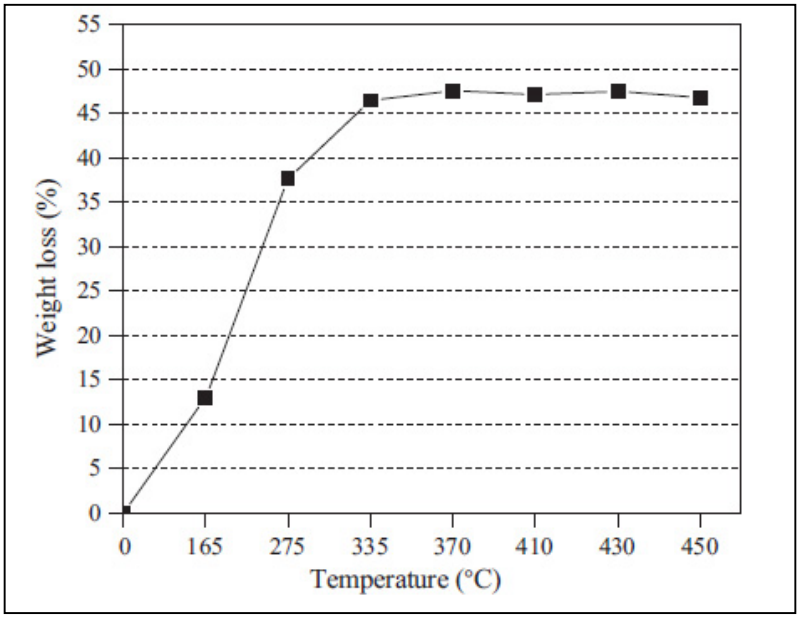

Figure 5: Weight loss of the powder during the calcination at different temperatures.

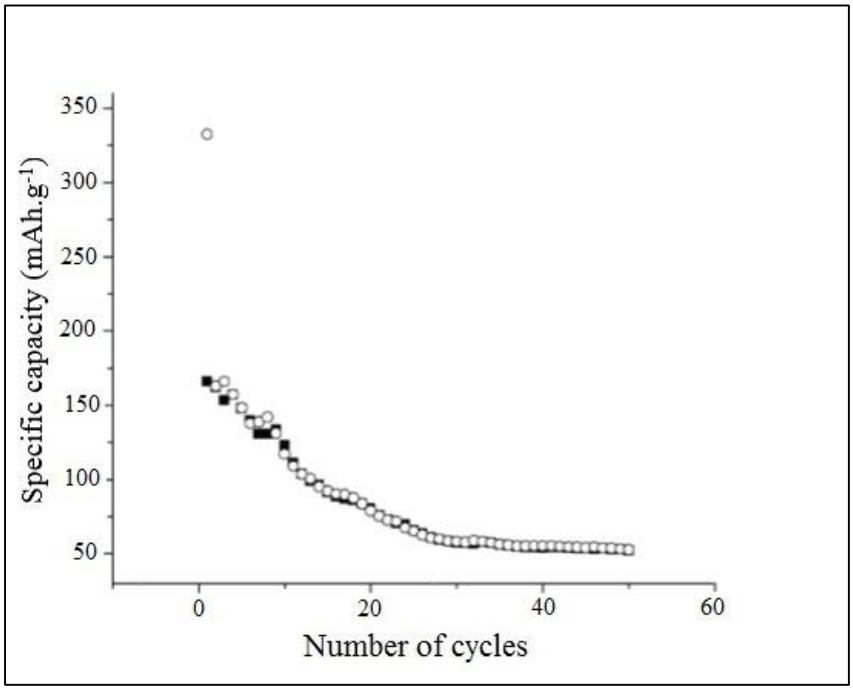

Figure 6: Charge-cycle curve of anode material coated on aluminium substrate

In Figure 6 and Figure 7, typical charge-discharge capacities of (approx. 80 mAh/g- 125 mAh/g) different coatings made on aluminium and copper substrates were shown respectively. High initial discharge capacity (appr.350 mAh.g-1) with low coulombic efficiency becomes 99.5% in following 25 cycles. Sudden decrease in the first cycle is likely due to the SEI formation. After the first cycle capacity degrades gradually with following cycles. As it is known that the cycle life and capacity depend on many factors and detailed experiments are needed before making any definitive conclusions, coating on copper substrate showed better performance compared to aluminium substrate. Obviously this diversity depends on the high conductive property of copper substrate.

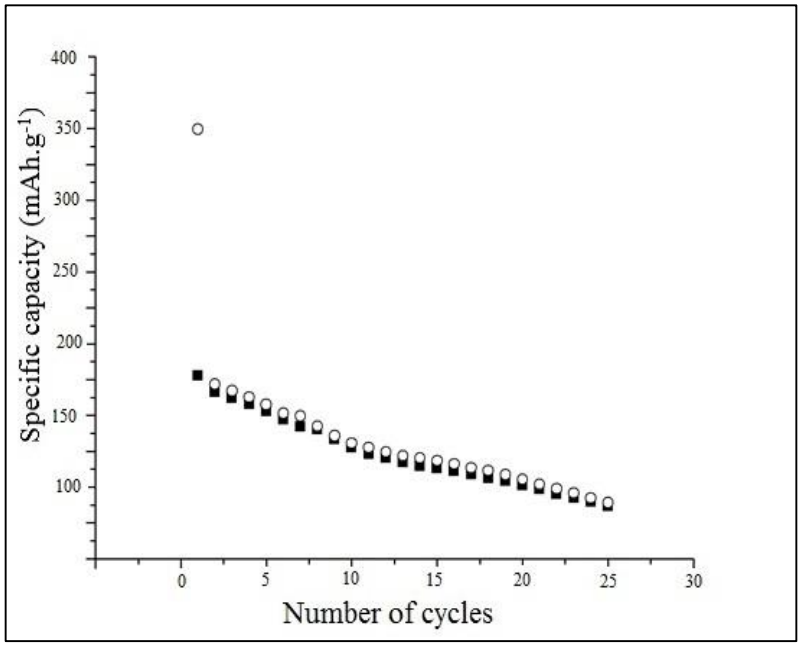

Figure 7: Charge-cycle curve of coating made on copper substrate

4. CONCLUSION

In this study lead based material as an anode for Li-ion batteries was experimented. A prediction about the possible use of recycled leady compound showed promising outcomes after the preliminary investigations. A waste lead-acid battery paste was converted into submicron lead-based powders to produce negative electrode for lithium-ion batteries by using new leaching and calcination methods. 80 $mAhg^{-1}$ average capacity was obtained on aluminium substrate, while 125 $mAhg^{-1}$ average capacity was achieved on copper substrate. The results may showed that conductive property of copper affects the capacity of anode.

Acknowledgements

This work was done by the contribution of BA. Ozkaya, M. Yigili, MB. Yenici, D. Ozbek, G. Koken, and M. Kocer as their graduation project under the supervision of authors.

REFERENCES

[1] D. Linden, TB. Reddy. LITHIUM-ION BATTERIES, *Handbook Of Batteries*, The Mc Graw Hill, 2001, McGraw Hill, chapter 35.
[2] WJ. Zhang. A Review Of The Electrochemical Performance Of Alloy Anodes For Lithium-İon Batteries, *Journal of Power Sources*, 196 (2011), 13-24.
[3] C. Chae, H. Park, D. Kim, J. Kim, ES. Oh, JK. Lee. A Li-ion Battery Using $LiMn_2O_4$ Cathode And MnO_x/C Anode, *Journal Of Power Sources*, 244 (2013), 214-221.
[4] YN. Nuli, SL. Zhao, QZ. Qin. Nanocrystalline Tin Oxides and Nickel Oxide Film Anodes for Li-ion Batteries, *Journal Of Power Sources*, 114 (2003), 113-120.
[5] M. Martos, J. Morales, L. Sanchez, R. Ayouchi, D. Leinen, F. Martin, JR. Barrado. Electrochemical properties of lead oxide films obtained by spray pyrolysis as negative electrodes for lithium secondary batteries, *Electrochimica Acta*, 46 (2001), 2939-2948.
[6] M. Martos, J. Morales, L. Sanchez. Lead-based systems as suitable anode materials for Li-ion batteries, *Electrochim. Acta,* 48 (2003), 615–621.
[7] K. Konstantinov, SH. Ng, JZ. Wang, GX. Wang, D. Wexler, HK. Liu, Nanostructured PbO materials obtained in situ by spray solution technique for Li-ion batteries, *Journal of Power Sources*, 159 (2006), 241-244.
[8] Q. Pan, Z. Wang, J. Liu, G. Yin, M. Gu. PbO@C core–shell nanocomposites as an anode material of lithium-ion batteries, *Electrochemistry Communications*, 11, 4 (2009), 917-920.
[9] J. Yang, X. Zhu, RV. Kumar, Ethylene glycol-mediated synthesis of PbO nanocrystal from $PbSO_4$: A major component of lead paste in spent lead acid battery, *Materials Chemistry and Physics*, 131 (2011), 336-342.
[10] MS. Sonmez, RV. Kumar. "Leaching of waste battery paste components. Part 1: Lead citrate synthesis from PbO and PbO_2", *Hydrometallurgy*, 95 (2009), 53-60.
[11] MS. Sonmez, RV. Kumar. "Leaching of waste battery paste components. Part 2: Leaching and desulphurisation of $PbSO_4$ by citric acid and sodium citrate solution", *Hydrometallurgy*, 95 (2009), 82-86.
[12] RV. Kumar, J. Yang, MS. Sonmez. Relevance of Reaction of Lead Compounds with Carboxylic acid in Lead Recovery from Secondary Sources, J. Powder Metall. Min., 2 (2013), 107.

Furnace Atmospheres and Troubleshooting in Heat Treatment

•

Isıl İşlem Fırın Atmosferleri ve Problem Çözüm Yöntemleri

Akın Malaş

Linde Gaz - Germany

ABSTRACT

There are generally two types of surface change commonly encountered when metals are heated in furnaces. One is oxidation/reduction; the second one is carburisation/decarburisation that relates to the reaction of the gases with the metal surface in such a way as to add or remove carbon to and from the substrate. The latter is known as decarburisation which is generally an undesirable material characteristic. The oxidation / reduction however determine the surface appearance of the metals in the manufacturing industry. When components are hardened, decarburisation will reduce the surface hardness of the material and hence decrease its operational life under conditions of wear. Oxidation in the furnace however is also an undesirable consequence when furnaces and atmospheres are not optimised in terms of gas interactions within. There is also a correlation between these two undesirable conditions. This speech will address these issues as well as the furnace atmosphere reactions and gases used to create conditions for optimised furnace conditions. The speech will also comprise of actual case studies for the trouble shooting of the furnaces and their atmospheres for the most optimised heat treatment process.

Keywords: Furnace atmosphere, troubleshooting, optimised heat treatment.

EFFECT OF PRIOR HEAT TREATMENT ON THE MICROSTRUCTURE AND MECHANICAL PROPERTIES OF AUSTEMPERED AISI 4340 STEEL

Erkan KONCA*, Kazım TUR*, Mustafa ELMADAĞLIand Fatih GÜNER****

*Atılım University, Department of Metallurgical and Materials Engineering, Ankara, TURKEY
**Roketsan Missile Industries Inc., Department of Materials and Ballistic Protection Technologies, Ankara, TURKEY

ABSTRACT
Bainitic steels with specifically designed compositions are coming into use as armor materials due to their remarkable combination of mechanical properties resulting in much higher ballistic performance as compared to the current armor steels (MIL-A 12560). Besides these special steels, it is also of interest to see if the mechanical properties of commercial steels, which are typically used in tempered martensite microstructure, can be increased through bainitic microstructure that would in turn improve their ballistic performance.

In an attempt to answer this question, AISI 4340 steel, which is one of the most widely used commercial low alloy steels, was selected. 100x100x12.7 mm AISI 4340 samples were austempered using a specially designed setup that ensures isothermal treatment conditions. Various combinations of austenitizing (840-900°C) and tempering (290-360°C) temperatures were used as the austempering conditions with the aim of obtaining lower bainite containing microstructures. Different pre-heat treatments were applied on the samples before austempering. In addition to Brinell hardness measurements and microstructural examinations, impact tests were performed on v-notch Charpy samples at -40°C. It was found that the microstructures and mechanical properties of the samples austempered under the same conditions but with different pre-austempering treatment significantly varied. Therefore; it is suggested that in addition to the austempering conditions, pre-austempering thermal history of the steel also needs to be engineered in order to reach the desired combination of mechanical properties after austempering.

Keywords: Austempering, 4340, Bainite, Austenite, Toughness, Armor,

ÖN ISIL İŞLEMİN OSMENEVİŞLENMİŞ AISI 4340 ÇELİĞİNİN İÇYAPI VE MEKANİK ÖZELLİKLERİNE ETKİSİ

ÖZET
Kompozisyonları özel olarak tasarımlanmış beynitli çelikler, mevcut zırh çeliklerine göre çok daha yüksek balistik performansa yol açan mekanik özellikleri nedeniyle, zırh çeliği olarak kullanılmaya başlanmaktadır. Bu özel çeliklerin yanısıra, tipik olarak menevişli martensitli içyapıda kullanılan ticari çeliklerde mekanik özelliklerin, daha yüksek balistik performans vermek üzere, beynitli içyapıyla arttırılıp arttırılamayacağı konusu ilgi çekmektedir. Bu soruya cevap verebilmek amacıyla bu çalışmada yaygın olarak kullanılan ticari alaşım çeliklerinden biri olan AISI 4340 çeliği seçilmiştir. 100x100x12.7 mm boyutlarındaki AISI 4340 numuneler, izotermal ısıl işlem koşullarını sağlamak üzere özel olarak dizayn edilen bir

düzenek kullanılarak osmenevişlendi. Alt beynit içeren içyapılar elde etmek amacıyla osmenişleme koşulları olarak farklı ostenitleme (840-900°C) ve meneviş (290-360°C) sıcaklık kominasyonları kullanıldı. Numunelere osmenevişleme işlemi öncesi farklı sıcaklıklarda ön ısıl işlemler uygulandı. İçyapı incelemeleri ve Brinell sertlik ölçümlerine ek olarak v-çentikli Charpy numunelere -40°C'de darbe deneyleri yapıldı. Önce farklı ön ısıl işlemlere tabi tutulup sonrasında aynı şartlarda osmenevişlenen numunelerin içyapı ve mekanik özellikleri arasında ciddi farklılıklar gözlendi. Bu nedenle, osmenevişleme sonrası istenen mekanik özellikler kombinasyonuna ulaşabilmek için osmenevişleme koşullarına ek olarak çeliğin osmenevişleme öncesi ısıl işlem geçmişinin de ele alınıp dizayn edilmesi gerektiği öne sürülmektedir.

***Anahtar kelimeler*:** Osmenevişleme, 4340, Beynit, Ostenit, Tokluk, Zırh

1. INTRODUCTION

1.1. Motivation

Although there are many ballistic protection applications where non-ferrous even non-metallic armors are being used there are still other applications, such as heavy armored vehicles, where steel is the main material of choice as armor and it seems to stay as such.

Ballistic performance of steel is essentially dependent on its dynamic behavior under very high rate of deformation. Unfortunately, experimentally studying the dynamic behavior of steels at ballistics speeds in a laboratory is very difficult.

Therefore, the results of hardness and impact tests, although they remain very "static" as compared to the ballistic conditions, remain as the only conventional indicators of ballistic performance. Harder and tougher steel is expected to have a higher ballistic performance which means better overall protection.

In addition to some ballistic performance requirements, armor steel standards such as MIL-A 12560H (now MIL-DTL-12560J) also specify certain hardness and impact toughness values [1]. Current armor steels meet these requirements through their tempered martensite microstructures.

Bainite is one of the most investigated types of microstructures in steels. It is basically the partial or full decomposition of high temperature austenite into other transformation products that is ferrite + cementite or ferrite + retained carbon rich austenite at lower temperatures. Although bainite is grouped into two as upper and lower types in classical physical metallurgy textbooks there are also other forms such as carbide-free bainite [2].

Carbide-free bainitic steels developed by Bhadesia and his team have remarkable combination of high hardness and high toughness values [3]. These steels are now being implemented as armor steels due to their much higher ballistic performance as compared to the current armor steels used in British Army [4].

These developments generate the question of whether an alloy steel like AISI 4340, which is typically used in a tempered martensite microstructure, can have better a combination of hardness and toughness values in a bainite containing microstructure, which in turn could improve its ballistic performance.

AISI 4340 is a well established Cr-Ni alloy steel and it has been the subject of numerous experimental investigations. While most of the studies about AISI 4340 focused on its mechanical properties in a quenched and tempered state, there are also several studies which produced and characterized the properties of AISI 4340 steel with bainitic microstructure [5].

Carbide-free bainitic steels can be produced only when there is sufficient amount of silicon or a few certain other elements present in solution to prevent or retard the formation of cementite. This usually correspond to a silicon content of 1.5 wt.% or higher [6]. The fact that AISI 4340 has about 0.15-0.30 wt.% Si basically eliminates the possibility of obtaining carbide-free bainitic microstructure in AISI 4340 and leaves upper or lower bainite containing microstructures as the two options.

Upper bainitic microstructure is considered as poor in terms of mechanical properties. Most of the studies on bainitic microstructures focused on a lower bainitic or lower bainite containing mixed structures as this structure promises higher combination of hardness and toughness values [7-9].

A look at the time-temperature-transformation (TTT) diagram of AISI 4340 steel (**Figure 1**) reveals that a fully lower bainitic microstructure can be obtained within the temperature range of 290-380°C through an isothermal treatment which requires a medium such as a salt bath.

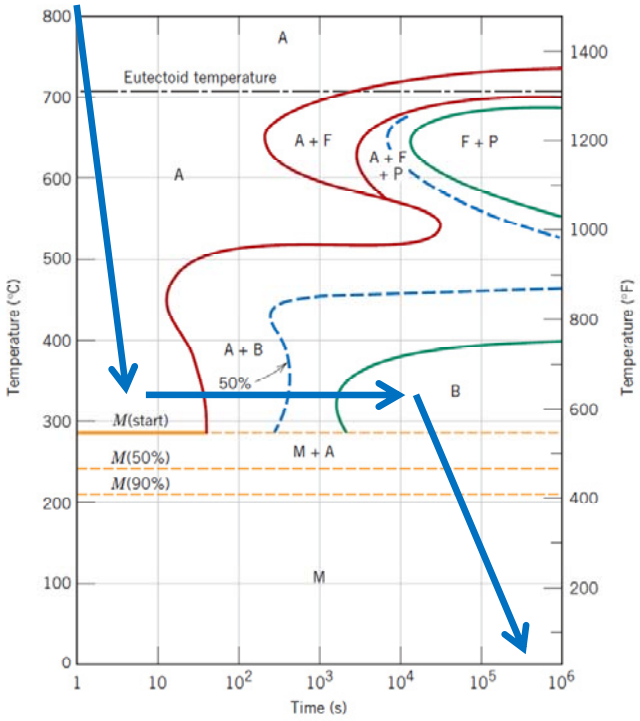

Figure 1. TTT diagram [10] of AISI 4340 steel with a superimposed austempering process to yield a lower bainitic microstructure.

Use of an agitated salt bath is a very effective method to quickly remove heat from a steel sample bringing its temperature from an austenitizing temperature (> 800°C) down to the isothermal treatment temperature (< 400°C) within seconds, obviously depending on the size of the sample, size of the salt bath, severity of agitation and the thermal properties of the salt used. Salt bath also provides a suitable medium for isothermal transformation.

1.2. Objective of This Work

This work is a part of a larger project which aims to investigate the ballistic performance of isothermally heat treated alloy steels. The objectives of this work in particular were

1) To obtain lower bainite containing microstructures in AISI 4340 steel by austempering under different conditions and perform their characterization.
2) To find out if a prior heat treatment can be used to improve the properties of austempered AISI 4340 steel.
3) To assess the suitability of austempered AISI 4340 as armor steel based on its mechanical properties.

2. EXPERIMENTAL

The chemical composition of the AISI 4340 steel used in this study is given in **Table 1**. 100x100x12.7mm heat treatment samples were cut from a 1000x1500x12.7 mm hot rolled plate using a flame torch. Then the samples were subjected to normalizing treatments (i.e. prior heat treatments) followed by austempering under different conditions.

The prior heat treatment and austempering conditions of the samples are summarized in **Table 2**. As an example, heat treatment conditions for sample C is graphically represented in **Figure 2**.

Table 1. Chemical composition (wt.%) of the AISI 4340 steel used in this work.

Element	C	Mn	P	S	Si	Ni	Cr	Mo	V	Fe
wt.%	0,42	0,68	< 0,005	< 0,0006	0,28	1,75	0,73	0,26	0,05	rest

Table 2. Prior heat treatment and austempering conditions of the samples.

Sample	Prior Treatment Temperature (°C)	Austenitizing Temperature (°C)	Austenitizing Time (min.)	Austempering Temperature (°C)	Austempering Time (min.)
C	1050	900	30	360	30
D	1050	900	30	320	30
G	1050	900	30	290	30
J	1050	840	30	320	30
U	840	840	30	320	30
N	1050	840	60	320	60
O	1050	840	60	290	60
T	840	840	60	320	60
Y	840	840	60	290	60
Z2	840	840	60	Quenched to 165°C followed by tempering at 550°C for 120 min.	

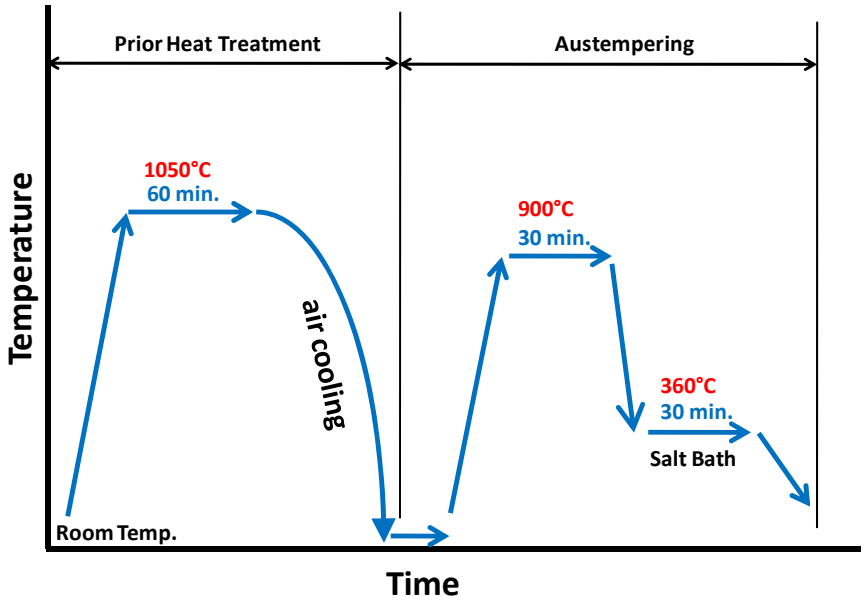

Figure 2. Graphical representation of the heat treatment conditions for sample C.

A Protherm PLF 110/6 muffle furnace was used for the prior heat treatments. A custom design heat treatment setup, shown in **Figure 3.a**, was used for the austempering treatments. This setup contains two units where the top unit serves for austenitizing while the bottom unit serves for isothermal treatment. The top unit is placed on a motorized tilting stage that allows quick transfer of the samples to the bottom unit through the guides (**Figure 3.b**). The bottom unit is a 200 liter capacity temperature controlled salt bath filled with Petrofer AS135 heat treatment salt. The salt bath is continuously stirred during operation using a motorized mixer which ensures both efficient heat removal from the sample at the time of quenching and uniform temperature in the bath during the isothermal treatment (**Figure 3.c**). A PC connected to the setup records the furnace temperatures of the top and bottom units and those of the thermocouples immersed into the salt bath. The salt used allows heat treatments from 140°C to 500°C.

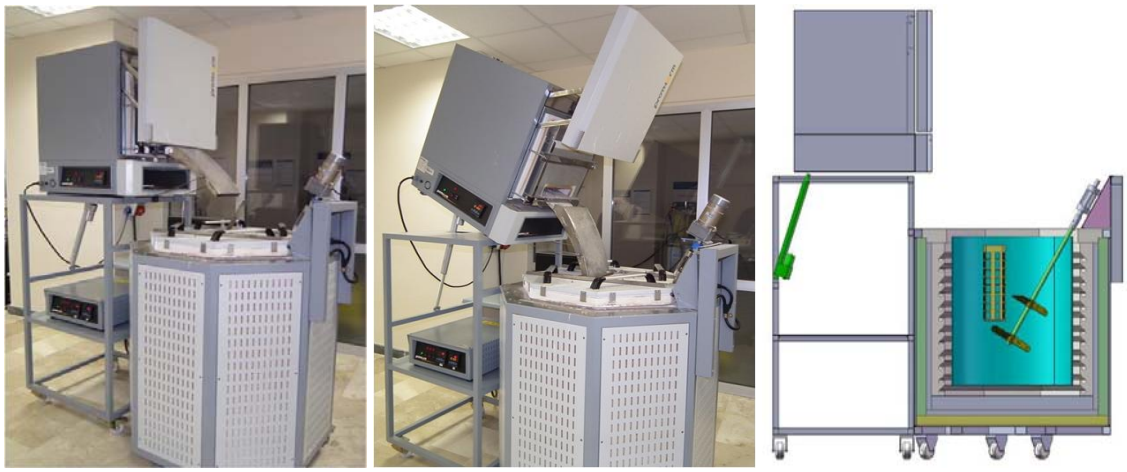

a) **b)** **c)**

Figure 3. a) Custom design heat treatment setup used in this study, **b)** Top unit (austenitizing) is tilted for quick transfer of the samples to the bottom unit (salt bath – isothermal treatment) through the guides, and **c)** Computer drawing of the setup showing the impeller and the sample basket in the salt bath.

After austempering, three standard v-notched Charpy impact test specimens (10x10x55 mm in size) were prepared from each sample parallel to the rolling direction in compliance with the related standard ASTM E23. Impacts tests were performed at -40°C using an Instron SI pendulum impact testing machine. Metallographic examinations were performed on 2% nital etched sample surfaces normal to the rolling direction using a Nikon LV 150 optical microscope and a Zeiss Evo LS 15 scanning electron microscope. Brinell hardness measurements (HBW 2.5/187.5) were taken using an EMCO M4U 025 G3 universal hardness testing machine.

3. RESULTS AND DISCUSSION

3.1. Performance of the Salt Bath

Figure 4 shows two examples of the temperature variation of the salt bath as the samples were dropped in it. It is seen that the salt bath efficiently removes the heat from the samples in about 20 seconds bringing down their temperature from 840°C to 320°C. The temperature of the salt bath increases by only 0.5°C during this process.

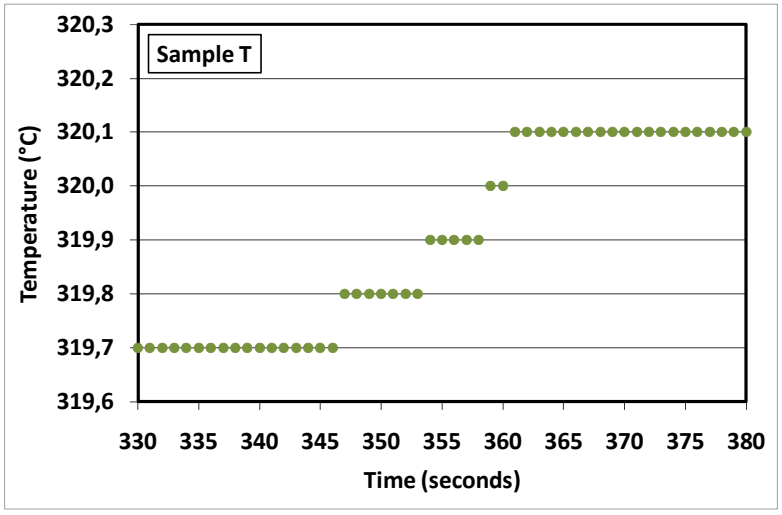

a)

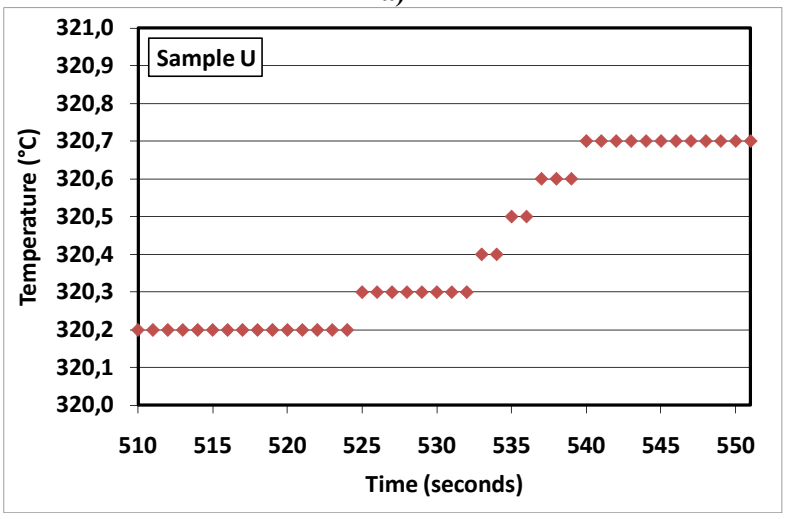

b)

Figure 4. Temperature variations of the salt bath as the 100x100x12.7 mm AISI 4340 steel samples at 840°C were dropped in it; **a)** Sample T and **b)** Sample U

3.2. Hardness Measurements and Impact Test Values of the Samples

Average hardness and -40°C impact toughness values of the tested samples are given in **Table 3**. The highest hardness measured was 502.7 HB and it belonged to the sample Y with an austempering temperature of 290°C. Among the austempered samples, the sample with the highest impact toughness value of 21.8 Joules was sample J and it was austempered at 320°C. The lowest hardness value of 362.7 HB was measured on sample C which had the highest austempering temperature of 360°C. The -40°C impact toughness of this sample was also second lowest with 14.0 Joules. The hardness of the quenched and tempered sample (Z2) was 394.3 HB and it had the highest impact toughness value of 22.7 Joules among all samples.

Table 3. Average hardness and -40°C impact toughness values of the tested samples

Sample	Hardness (Brinell)	Impact Toughness (J)
C	362,7	14,0
D	390,7	14,8
G	404,3	18,8
J	380,0	21,8
U	465,0	15,3
N	458,3	14,5
O	499,0	13,5
T	461,0	17,2
Y	502,7	16,7
Z2	394,3	22,7

3.3. Discussion of the Results

Effect of Prior Heat Treatment: Comparison of the results for samples O and Y which had identical austempering conditions but different prior treatment temperatures (1050°C vs 840°C) shows that both samples have practically the same hardness (499.0 vs. 502.7 HB) whereas the impact toughness of sample Y is higher (13.5 J vs. 16.7 J).

In a similar manner, comparison of the results for samples N and T which had identical austempering conditions but different prior treatment temperatures (1050°C vs 840°C) shows that both samples have almost the same hardness (458.3 vs. 461.0 HB) whereas the impact toughness of sample T is higher (14.5 J vs. 17.2 J). It is clear that lower prior treatment temperature results in higher impact toughness values after austempering. Examination of the microstructures of these two samples (**Figure 5**) reveals that sample T, with a lower prior treatment temperature, has a finer microstructure.

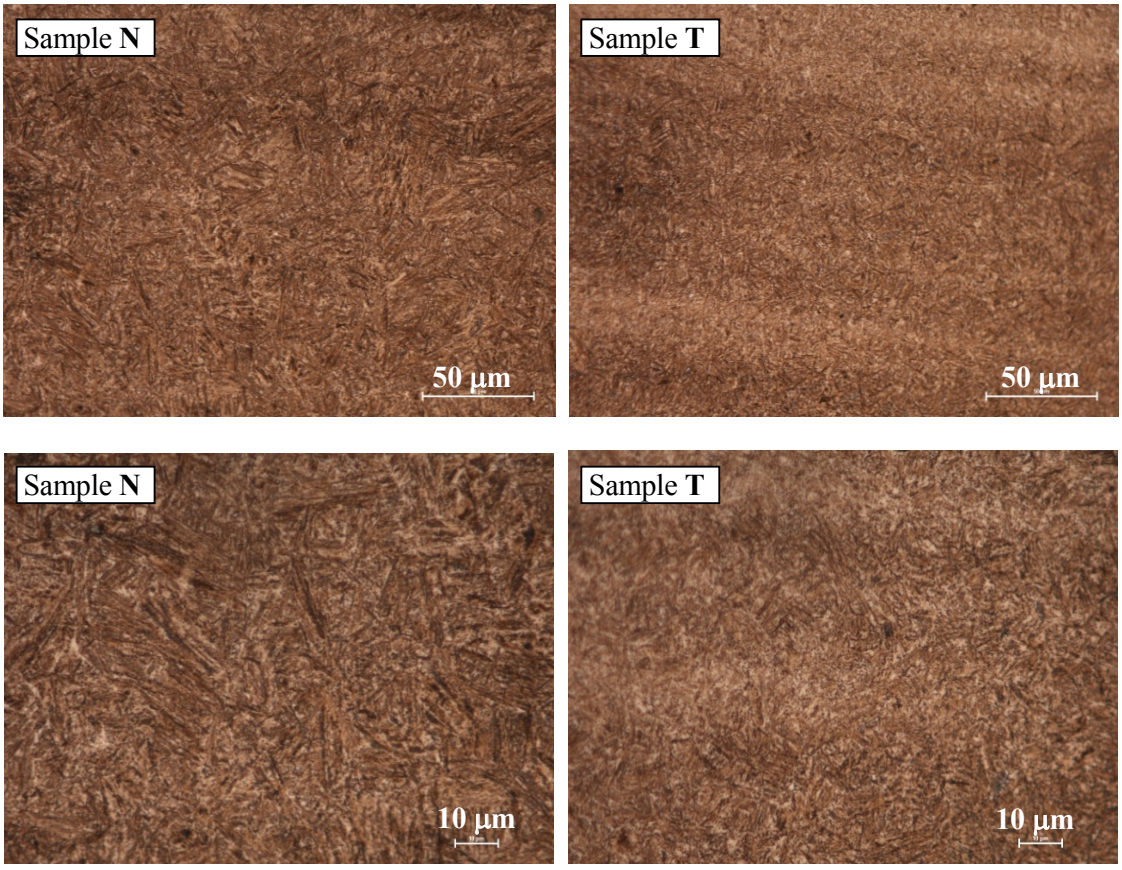

Figure 5. Optical images of the microstructures of sample N (left) and sample T (right). These two samples have identical austempering conditions but different prior treatment temperatures (1050°C vs 840°C) resulting in a difference in the microstructure.

Effect of Austempering Conditions: Within the conditions tested in this study the hardness of the austempered samples increases as the austempering temperature gets closer to the martensite start temperature (M_s) of the AISI 4340 steel (M_s = 290°C).

Comparison of the sample G and sample O shows that for the same prior treatment and austempering temperatures, differences in the austenitizing temperature and duration cause great differences in mechanical properties (404.3 HB vs. 499.0 HB and 18.8 J vs. 13.5 J). Examination of the microstructures of these samples reveals that the higher austenitizing temperature of 900°C (vs. 840°C) and the shorter treatment duration of 30 minutes (vs. 60 min) for sample G created a coarser and non-homogeneous microstructure as seen in **Figure 6**.

Austempered AISI 4340 as a Candidate Armor Steel: MIL-A 12560 is an US army standard for rolled homogeneous armor steel plates [1]. In addition to some ballistic performance criteria this standard also specifies certain hardness and corresponding minimum toughness values to be met by a steel plate. These required hardness-minimum impact toughness values are plotted in **Figure 7** together with the results obtained in this work. **Figure 7** clearly demonstrates that while almost all of the isothermally treated AISI 4340 samples have exceedingly high hardness values only one of them (sample J) barely meets the toughness requirement of the standard. It is suggested that an additional tempering treatment should be performed on these samples in order to increase their impact toughness [7, 11].

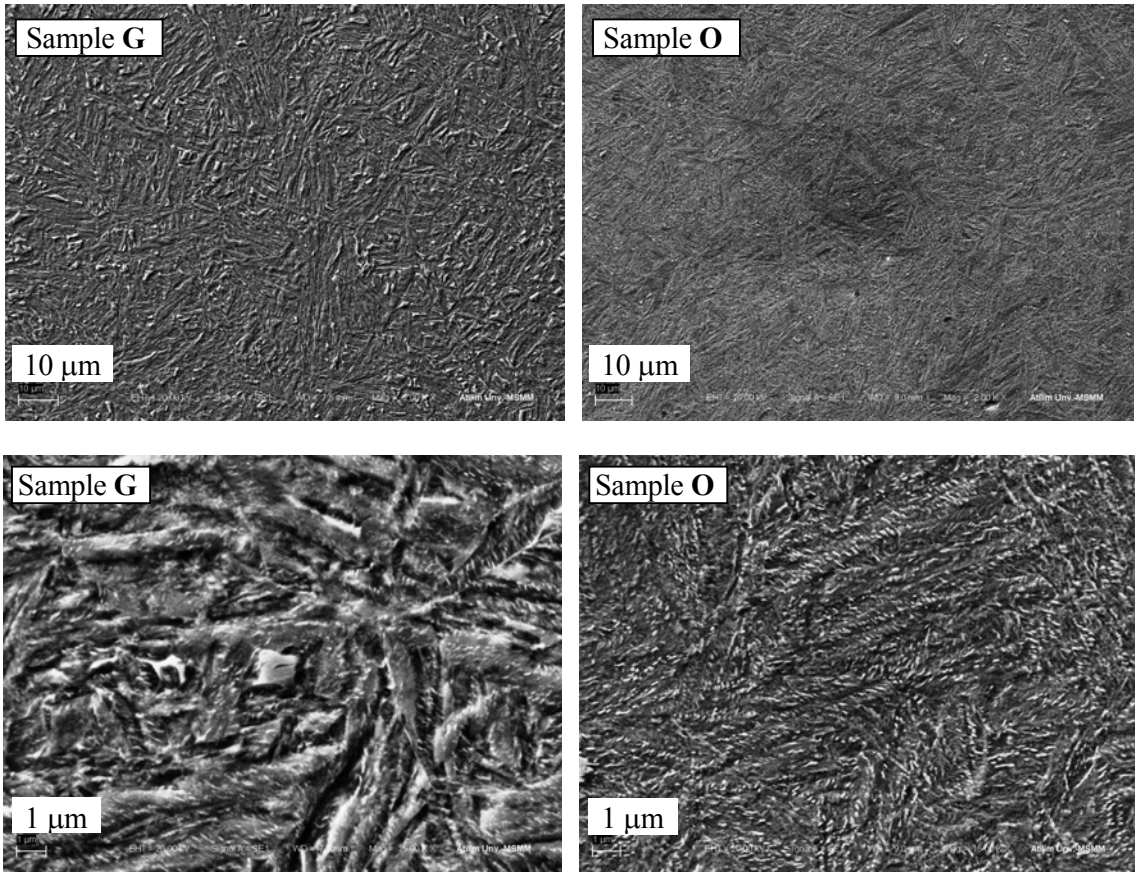

Figure 6. SEM images of the microstructures of sample G (left) and sample O (right). These two samples have identical prior treatment and austempering temperatures but different austenitizing temperatures (900°C vs 840°C) and treatment durations resulting in a clear difference in the microstructure and mechanical properties.

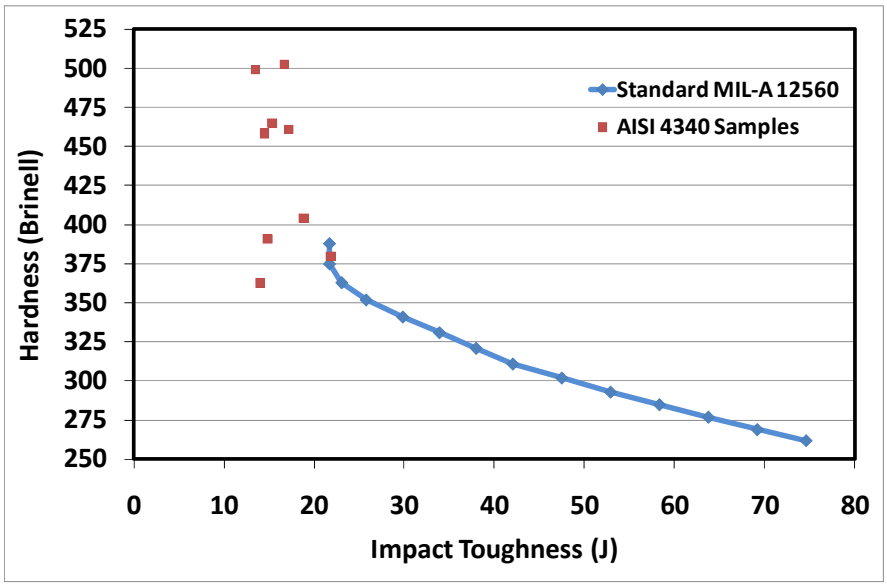

Figure 7. Plot of -40°C impact toughness versus hardness values of the austempered AISI 4340 samples and their comparison with the minimum values required by the military standard MIL-A 12560. Only one of the samples (Sample J) meets the requirements.

4. CONCLUSION

- AISI 4340 steel samples with bainitic microstructures were obtained by austempering under different conditions and using different prior heat treatment temperatures.
- For the same austempering conditions, AISI 4340 steel with a lower prior treatment temperature had finer microstructure resulting in a higher impact toughness value.
- The hardness of the austempered AISI 4340 steel samples increased as the austempering temperature was lowered from 360°C to 290°C.
- -40°C impact toughness values of the austempered AISI 4340 steel samples are short of the minimum values required by the related armor steel standard. An additional tempering treatment is suggested to help the impact toughness values increase.

Acknowledgments

The work presented here is a part of the project RS-ATILIM-76201-01N-R and it is released under the permission of ROKETSAN Missile Industries Inc. The authors are thankful to Extra Metal Ltd. for their help with the preparation of the impact test samples.

REFERENCES

1. Military Specification, MIL-DTL-12560J (MR), Armor Plate, Steel, Wrought, Homogeneous, (For Use in Combat-Vehicles and for Ammunition Testing) 24 July 2009
2. F.G.Caballero ve H.K.D.H. Bhadesia, High-Strength Bainitic Steels, International Journal of ISSI, v1, no 1, 15-23, 2004
3. H. K. D. H. Bhadeshia, Large chunks of very strong steel, Materials Science and Technology, v 21, no 11 1293-1302, 2005
4. TATA PAVISE™ SBS 600P data sheet, downloaded from http://www.tatasteeleurope.com/en/markets/end-markets/manufactured/defence_and_security/ on 17 April 2014
5. Y. Tomita, Effect of Microstructure on Plane-Strain Fracture Toughness of AISI 4340 Steel, Metallurgical Transactions A, Volume 19A, 2513-2521, 1998
6. H. K. D. H. Bhadeshia, C. Garcia-Mateo, P. Brown, Super Bainite Steels and Manufacture Thereof, World Intellectual Property Organisation (WIPO), International Publication Number WO 2010/013054 A2, 04.02.2010
7. M. Barranco, P. J. Cote, J.A. Kapp., Tempering Effects For Lower Bainite, Martensite and Mixed Microstructures on Impact, Fracture and Related Mechanical Properties of ASTM A723 Steel, Technical Report ARCCB-TR-92024, US Army Armament Research Development and Engineering Center, 1992
8. Y. Hong-Seok, Design of Low-Carbon Low-Temperature Bainite, PhD Thesis, Graduate Institute of Ferrous Technology, Pohang University of Science and Technology, 2011
9. E.H. Niccols, Literature Review: Impact Toughness of Bainite vs Martensite, Technical Report, WVT-TR-70012, 1976
10. W.D. Callister, Materials Science and Engineering: An Introduction, 7th ed., Wiley, 2006
11. D. R. Johnson and W. T. Becker, Toughness of tempered upper and lower bainitic microstructures in a 4150 steel, Journal of Materials Engineering and Performance, Volume 2, Issue 2, pp 255-263, 1993

THE EFFECT OF HYDROGEN CONTENT OVER THE AGING CHARACTERISTICS OF AL-CU ALLOY

Muhammed Raşit ERYILMAZ*, Muhammet ULUDAĞ*, Derya DIŞPINAR**

* Selcuk University, Faculty of Engineering, Metallurgical and Materials Eng. Dept., Konya-Turkey, rasit.eryilmaz@gmail.com, uludag@selcuk.edu.tr
** Istanbul University, Faculty of Engineering, Metallurgical and Materials Eng. Dept., Istanbul-Turkey, deryad@istanbul.edu.tr

ABSTRACT
Solution heat treatment is carried out by a series of process such as solutionizing, quenching and aging in order to increase the strength of many aluminum alloys. During quenching, the most important parameter is to be able to achieve high concentration of voids which will eventually aid the nucleation of secondary phases during aging. In this work, a series of tests were carried with Al-5Cu alloy where the alloy was melted and the hydrogen content of the melt was measured by AlSPEK. Cylindrical parts were produced and they were subjected to solution heat treatment where different quenching medium was selected. In this way, the effect of hydrogen content over the size and distribution of the secondary phases were investigated. Microstructural investigation was carried and image analysis software was used for phase characterisation.

Keywords: casting, T6 heat treatment, Al-Cu alloys, Hydrogen content, casting quality, mechanical properties

Al-Cu ALAŞIMINDA HİDROJEN İÇERİĞİ VE SU VERME ORTAMLARININ YAŞLANDIRMA ÜZERİNE ETKİSİ

ÖZET
Yaşlandırma ısıl işleminin alüminyum döküm alaşımlarında mekanik özellikler üzerine önemli etkisi olduğu bilinmektedir. Yaşlandırma ısıl işlem yöntemlerinden T6 ısıl işlem rejimi Al-Cu alaşımlarında en çok tercih edilen metoddur. Bu çalışmada, Al-Cu alaşımlarında hidrojen miktarının yaşlandırma ısıl işleminde etkinliği araştırılmıştır. Sıvı metalde hidrojen çözünürlüğü ölçümleri Alspek cihazı ile yapılmıştır. Su verme işlemi ise oda sıcaklığındaki suda, yağda ve kaynayan suda olmak üzere üç farklı ortamda uygulanmıştır. Elde edilecek numuneler mikroyapısal ve mekaniksel incelemelere tabi tutulmuştur. Çalışmamızda, hidrojen içeriğinin ve farklı su verme ortamlarının boşluk konsantrasyonu miktarı ve mikroyapısal dönüşümler üzerine etkisi incelenmiştir. Ayrıca azaltılmış basınç test numuneleri incelemelerinden elde edilen verilerle, döküm kalitesi ve yaşlandırma ilişkisi ortaya çıkartılmıştır.

Anahtar kelimeler: Döküm, T6 ısıl işlemi, Al-Cu alaşımları, Hidrojen içeriği, Döküm kalitesi, Mekanik özellikler

1. INTRODUCTION

Aluminium alloys have been used in several engineering applications for years [1]. Heat treatment is one of the well-known processes for increasing mechanical properties of aluminium alloys. Al-Cu alloys can be listed on top of the aluminium alloys as showing the highest improvement in properties [2-4].

Solution heat treatment which is also known as T6 is the most common method [5]. The steps of this process are as follows: solutionizing, quenching and aging [6]. Solutionizing temperature and duration is important, because at higher temperatures partial remelting can occur and higher holding times, grain growth can be observed. Therefore it has to be optimised. Quenching is another critical step. The higher the cooling rate, the more the voids form which help secondary phases to nucleate on [7]. However, as the quenching rate is increased, the quantity of internal stress increases. The final step is the aging where secondary phases are precipitated [8].

Since the quenching rate is a function of void formation, therefore in this work, the effect of hydrogen content of Al-Cu alloy over the aging characteristics has been studied. In addition, reduced pressure test (RPT) was used to quantify the melt quality by measuring bifilm index [9-10]. In this way, a correlation between melt quality, hydrogen content and quench rate was investigated.

2. EXPERIMENTAL WORK

Primary Al-Cu was provided from Eti Aluminum A.S. and the chemical composition is given in Table 1.

Table 1. Chemical composition of Etial 221

Si	Fe	Cu	Mn	Mg	Zn	Ti	Ni	Pb	Al
0,30	0,30	4,00-5,00	0,10	0,05	0,10	0,15-0,30	0,10	0,05	Rem.

The melting procedure was carried out in a 20 kg capacity resistance furnace. To pouring temperatures were selected: 700°C and 775°C. Degassing was carried out for 25 minutes with Ar. Hydrogen content of the melt was measured by AlSPEK. RPT samples were collected during all the casting experiments. Samples were sectioned and subjected to image analysis for bifilm index measurement.

As-cast microstructure was analysed and hardness values were recorded and then T6 heat treatment was applied to the samples. Solutionizing temperature was selected as 537°C and aging temperature was set to 195°C. Three different quenching mediums were used: water at room temperature, boiling water and oil.

Microstructural analysis was carried on an optical microscope (Nikon) and hardness values were measured by Brinell method.

3. RESULTS and DISCUSSION

Some of the selected microstructures of samples quenched in water at room temperature, boiling water and oil are given in Figure 1.

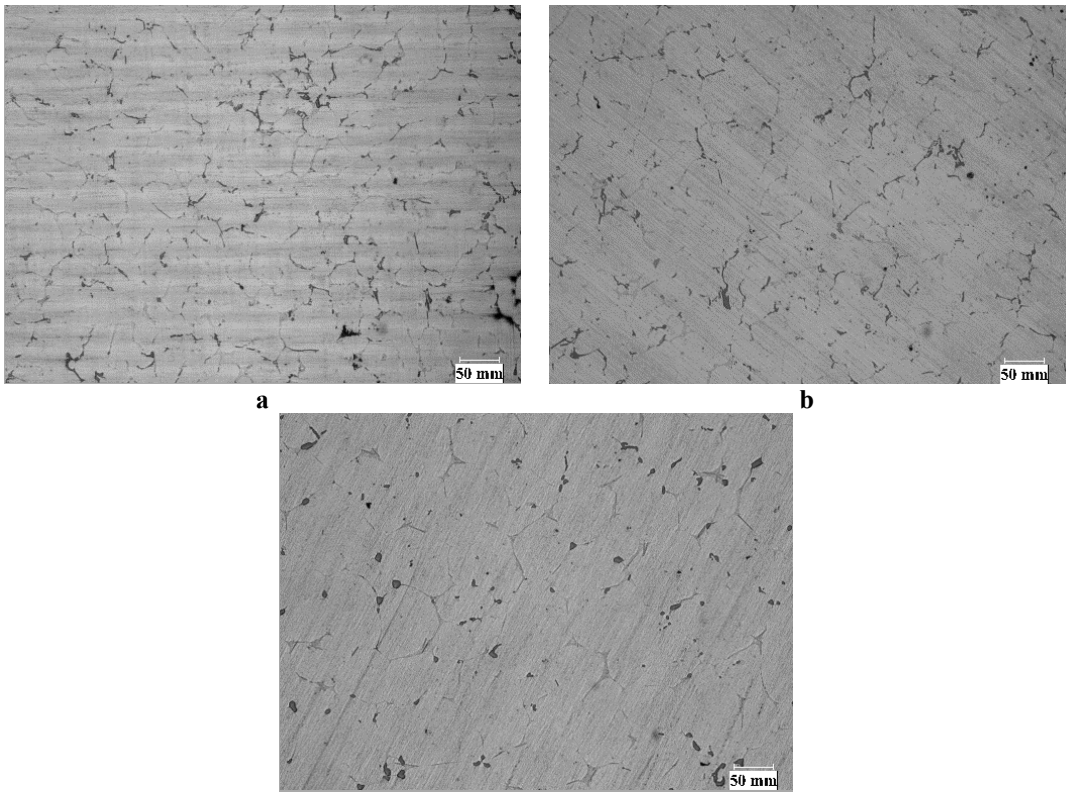

Figure 1. Microstructures of samples quenched at different mediums
a) water, b) oil, c) boiling water

The optimum duration for solutionizing was found to be 30 minutes for water quenching and 60 minutes for oil and boiling water mediums.

The hydrogen levels of the melts before and after degassing at the pouring temperatures were given in Figure 2.

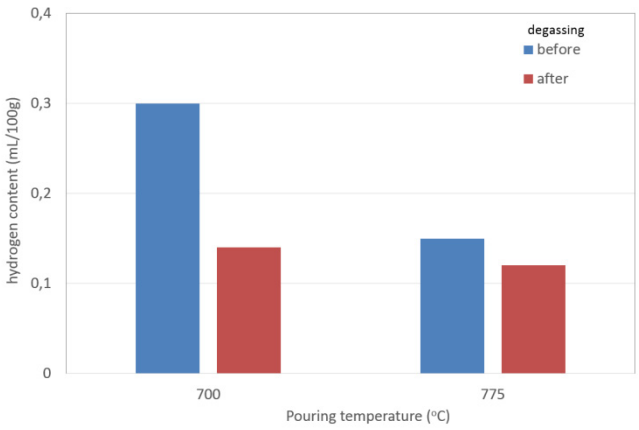

Figure 2. Hydrogen contents of the melts prior to casting

As seen in Figure 2, the hydrogen content of the melts prior to degassing is high and after degassing it is lowered. However, it is interesting to note that for the castings at 775°C, although the temperature is higher, higher hydrogen levels were not recorded compare to the castings at 700°C.

The change in the hardness with various quenching mediums are given in Figure 3.

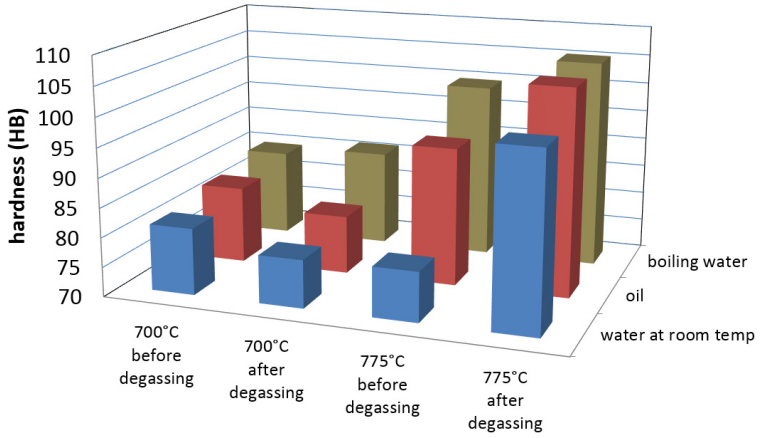

Figure 3. Hardness change with casting temperature and quenching medium

Figure 3 can be discussed in several way. For example, if quenching mediums are considered, room temperature water has the lowest hardness followed by oil quenched samples and the highest hardness was achieved when samples were quenched in boiling water. When the effect of pouring temperature is considered; it can be clearly seen that when the castings were carried out at 775°C, the hardness was highest. One final comparison can be made with regard to the effect of degassing. For each of the pouring temperatures, after degassing was carried out, the hardness was increased.

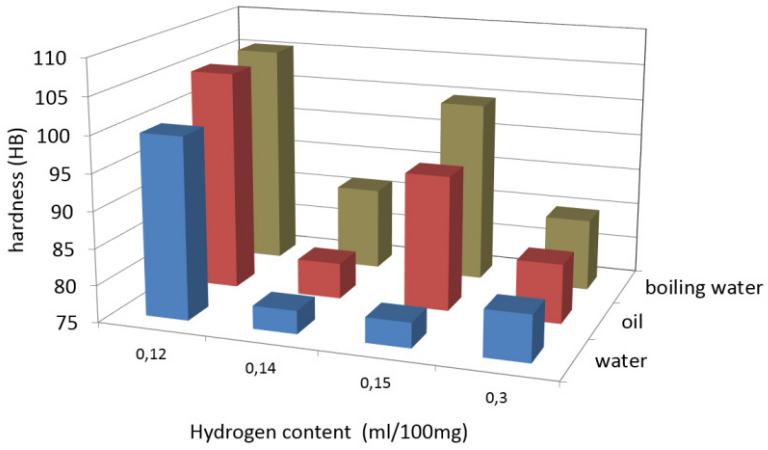

Figure 4. Hardness-hydrogen content-quenching medium relationship

Figure 4 shows the relationship between hardness-hydrogen content and quenching medium. As can be seen from the figure, one cannot make a solid statement as to whether hydrogen content is dominant, or quenching medium is significant. The only conclusion was the achievement of highest hardness at 0.12 mL/100g hydrogen levels. There is also almost no effect of quenching medium. In all hydrogen levels, there is not much clear trend but it is clear that the highest hardness was achieved at boiling water. During quenching, as the concentration of void formation is increased, it is expected that the distribution of secondary phases would increase; and thus, mechanical properties would increase. As the hydrogen content of the melt is increased, the void concentration would increase. However, the highest hardness was not achieved at the highest hydrogen levels, on contrary, it was found at the lowest hydrogen level.

Therefore, the bifilm index measurements were made in all the casting trials and the effect of melt quality was also incorporated into the discussion. The change of bifilm index with the hydrogen level is given in Figure 5.

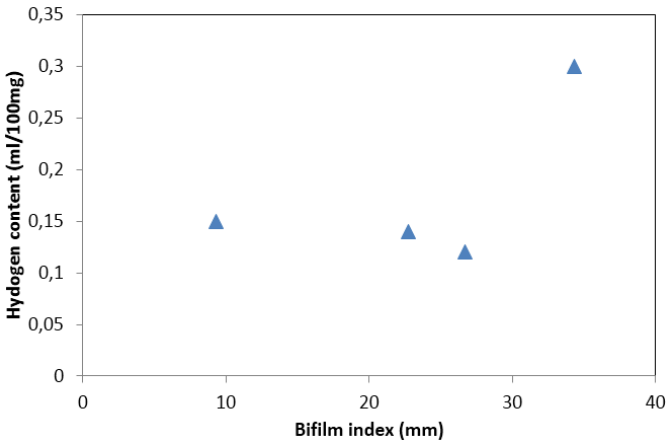

Figure 5. Bifilm index-hydrogen content of the melt

As seen from Figure 5, there is no relationship between bifilm index and hydrogen content. As the bifilm index was increased from 10 to 20 to 30, the hydrogen level was remained unchanged. It is also important to note that as Dispinar proposed, according to the bifilm index classification, index values between 10 mm and 50 mm would indicate good quality castings. This is probably the reason why there was no correlation between bifilm index and hardness. These results were summarised in Figure 6.

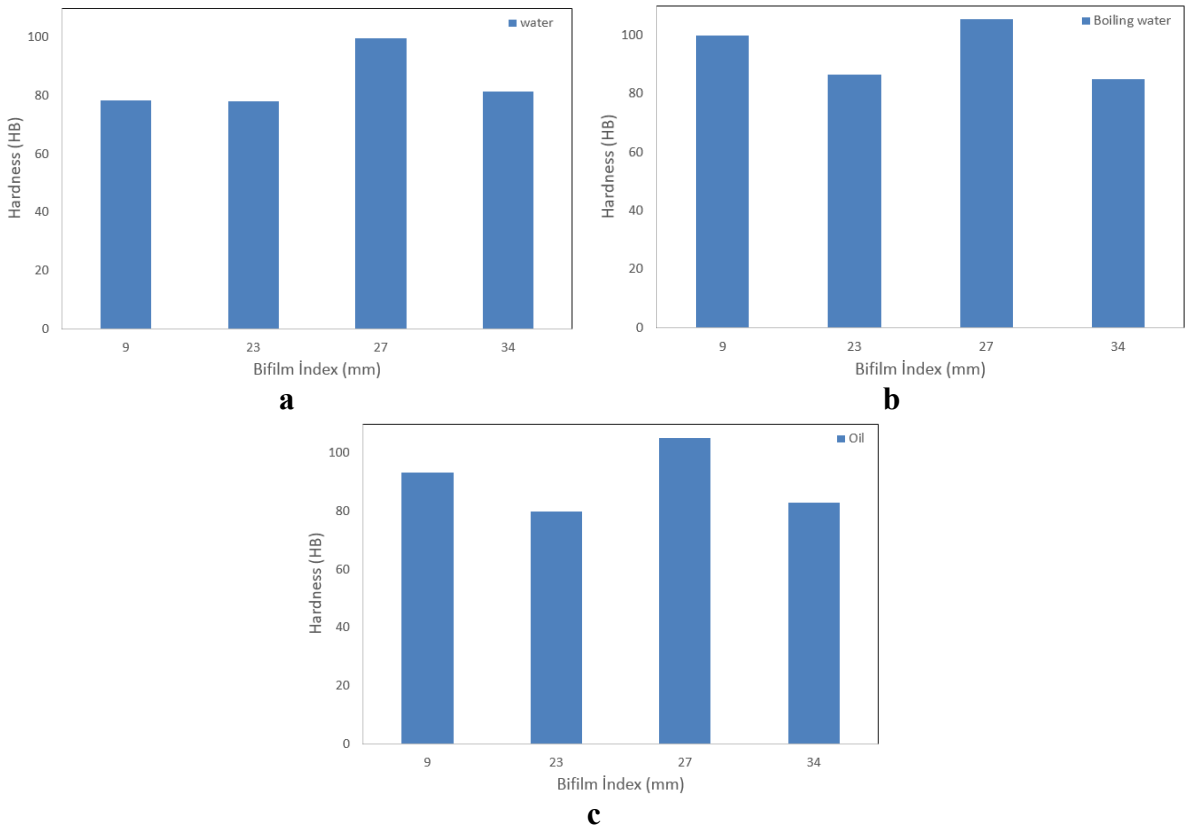

Figure 6. Bifilm index and hardness relationship with quenching mediums
a) water b) boiling water c) oil

4. CONCLUSIONS

There is no linear relationship between hydrogen content and melting temperature.

The quality of the primary alloy is high as measured by the very low bifilm index.

There is no correlation between bifilm index and hardness, simply because when the bifilm index is too low, it indicates that there are not much bifilms to be effective enough to change the hardness.

The hardness of Al4Cu alloys can be maximised as the melting temperature is increased to 775ºC from 700ºC.

The hardness of Al-4Cu-T6 can be highest when boiling water is used as the quenching medium. Room temperature water reveals the lowest and oil quenching lies in between.

Acknowledgment

This work has been supported by the Scientific Research Projects Coordination Unit of Selcuk University (Project number: 14201038). The authors would like to thank Metal Market Metalurji San. Tic. Ltd. Şti. for their support in this study.

REFERENCES

1. Zolotorevsky, V.S., N.A. Belov, and M.V. Glazoff, *Chapter one - Alloying Elements and Dopants: Phase Diagrams*, in *Casting Aluminum Alloys*, V.S. Zolotorevsky, N.A. Belov, and M.V. Glazoff, Editors. 2007, Elsevier: Amsterdam. p. 1-93.
2. Kovarik, L., et al., *GPB zones and composite GPB/GPBII zones in Al–Cu–Mg alloys.* Acta Materialia, 2008. 56(17): p. 4804-4815.
3. Liu, X.Y., et al., *Effects of solution treatment on the microstructure and mechanical properties of Al–Cu–Mg–Ag alloy.* Materials & Design, 2010. 31(9): p. 4392-4397.
4. Sjölander, E. and S. Seifeddine, *The heat treatment of Al–Si–Cu–Mg casting alloys.* Journal of Materials Processing Technology, 2010. 210(10): p. 1249-1259.
5. Wang, S.C., M.J. Starink, and N. Gao, *Precipitation hardening in Al–Cu–Mg alloys revisited.* Scripta Materialia, 2006. 54(2): p. 287-291.
6. Callister Jr, W.D., *Materials science and engineering: An introduction (2nd edition).* Materials & Design, 1991. 12(1): p. 59.
7. Jang, J.-H., et al., *Effect of solution treatment and artificial aging on microstructure and mechanical properties of Al–Cu alloy.* Transactions of Nonferrous Metals Society of China, 2013. 23(3): p. 631-635.
8. MacKenzie, D.S.T.G.E., *Handbook of aluminum. Vol. 2, Vol. 2*. 2003, New York: Dekker.
9. Dispinar, D. and J. Campbell, *Effect of casting conditions on aluminium metal quality.* Journal of Materials Processing Technology, 2007. 182(1–3): p. 405-410.
10. Dispinar, D. and J. Campbell, *Porosity, hydrogen and bifilm content in Al alloy castings.* Materials Science and Engineering: A, 2011. 528(10–11): p. 3860-3865.

THE EFFECT OF Cu ADDITION AND AUSTEMPERING HEAT TREATMENT ON MECHANICAL PROPERTIES OF GGG 50

Sebahattin KIRTAY, Berkin KILINÇ

Istanbul University, Turkey
kirtay@istanbul.edu.tr

ABSTRACT

The effect of austempering on the microstructure and mechanical properties of nodular cast iron (designated as GGG 50) alloyed with 1,1.5 and 2 wt% copper were studied. Optical microscopy analyses were performed for microstructural characterization, whereas hardness and tensile strength tests were applied. Specimens were austenitised at 900 °C for an hour, then austempered for an hour at 330 °C in salt bath and cooled at room temperature in air.

The results of the study indicated that the addition of Cu into GGG 50 encouraged pearlite formation in the matrix structure. After austempering heat treatment, the structure was transformed from ferrite + pearlite into ausferrite and retain austenite. Furthermore, with the addition of 2 wt% Cu, it was noted that the graphide nodules diverged from sphericity and the added Cu was concentrated around the spheroidal graphide.

Mechanical properties were significantly improved when the samples were austempered compared to the as-cast condition. In both cases, whether as-cast or austempered, the highest mechanical properties were found at 1.5 wt% Cu.

Keywords: Austempering, Cast iron, Mechanical properties, Microstructure

GGG 50 DÖKME DEMİRE Cu İLAVESİNİN VE ÖSTEMPERLEME ISIL İŞLEMİNİN MEKANİK ÖZELLİKLERE ETKİSİ

ÖZET

Bu çalışmada ağırlıkça % 1, 1.5 ve 2 Cu ile alaşımlandırılmış GGG 50 küresel grafitli dökme demirin östemperleme ve mekanik özellikleri incelenmiştir. Mikroyapı karakterizasyonu optik mikroskopta yapılmış, ayrıca sertlik ve çekme testleri uygulanmıştır. Numuneler 900 °C'de 1 saat ostenitlenmiş ve 330 °C'de tuz banyosunda 1 saat bekletilerek östemperleme işlemi yapılmıştır.

Çalışma sonucunda GGG 50'ye Cu ilavesi yapıda perlit oluşumunu desteklemiştir. Ostemperleme ısıl işleminden sonra yapı ferrit + perlitten osferrit ve kalıntı ostenite dönüşmüştür. Ayrıca, % 2 Cu ilavesi ile yapıdaki grafit nodüllerinin küresellikleri bozulmuş ve Cu grafit nodüllerinin etrafında yoğunlaşmıştır.

Döküm hali ile ostemperlenmiş numuneler kıyaslandığında mekanik özelliklerde artışlar sağlanmıştır. Her iki durumda da en yüksek mekanik özellikler % 1.5 Cu ilavesinde gerçekleşmiştir.

Anahtar kelimeler: Ostemperleme, Dökme demir, Mekanik özellikler, Mikroyapı

1. INTRODUCTION

Spheroidal graphide cast irons contain 3.4 – 3.9 % C and 1.8 – 3.1 % Si. Also, these are obtained from melted cast iron mixed with small amount of Mg or Ce. Their mechanical properties are better than those of other cast irons. The mechanical properties of austempered spheroidal graphide cast iron and steel are very similar.

Austempered spheroidal graphide cast irons constitute high carbon austenite+ferrite (often referred to as an ausferrite microstructure) as a matrix. Such a dual phase microstructure confers a high strength with favorable toughness [1]. Ductile cast iron can possess ausferrite structure by alloying addition such as Ni, Mo and Cu together with heat treatment. A two-stage heat treatment is employed for spheroidal graphide cast irons, austenitization and austempering [2].

Austempered spheroidal graphide cast irons combine the high strength, elastisity [3-5], fracture toughness [6], impact resistant [7,8] and wear resistance [9] of steel with the castability and low production cost. This, in turn, has enabled manufacturers to produce low cost machine parts. It is widely used in manufacturing components as diverse as gears, crankshafts, locomotive wheels, connecting rods, brake shoes, among others [10,11].

The chemical composition of austempered ductile iron (ADI) is similar to that of conventional ductile cast iron. However, some alloying elements, such as nickel, copper and molybdenum, are usually added to increase its heat treatability, which impedes austenite decomposition to pearlite and ferrite upon cooling [12]. When discussing the microstructure of ADI, it is necessary, according to some authors, to distinguish the residual austenite that exists at the isothermal transformation temperature from the retained austenite that remains untransformed at ambient temperature [13].

In this study, the effects of copper and austempering heat treatment on the microstructural changes and mechanical properties have been studied by adding different amount of Cu (1 wt%, 1.5 wt% and 2 wt%) into GGG 50 grade cast iron.

2. EXPERIMENTAL PROCEDURE

GGG 50 grade ductile iron was prepared in a commercial foundry using induction melting furnace (Inductotherm) of 1500 kg capacity and sand cast in the cylindrical shape with 20 mm diameter and 190 mm length. The charge was consisted of pig iron (500 kg), steel sheet (900 kg), nodular iron scrap (100 kg), sphero carbon (34 kg) and FeSi (30 kg). After heating 1580 °C, the melt was treated with FeSiMg alloy (45 % Si) for nodularization process. Then, it was treated with Fe-Si alloy to promote a higher nodule count and nodularity during the flow. Following this step, Cu addition was carried out in a 20 kg capacity crucible. Then the parts were cast. The spectral analyses of the cast parts are given in Table 1.

Table 1. Spectral analyses results of samples

Sample	C%	Si %	Mn %	P %	S %	Mg %	Cu %
No added	3.68	2.75	0.165	0.027	0.020	0.038	**0.044**
1% Cu added	3.80	2.78	0.121	0.033	0.013	0.041	**0.958**
1,5% Cu added	3.72	2.83	0.134	0.029	0.017	0.047	**1.57**
2% Cu added	3.75	2.62	0.161	0.012	0.011	0.033	**2.09**

Samples were austenitized at 900°C for 60 min and transferred rapidly to a salt bath containing 50 % KNO_3 and 50 % $NaNO_3$ and then held at 330°C for 60 min and air-cooled to room temperature.

For optical properties invesitigation, both as-cast and austempered samples were polished, etched with 2 % Nital solution for 4 sec, and examined using standart metallographic techniques. Microstructure investigations were carried out by Nikon optical microscope.

Rockwell C and Vickers hardness was measured by using Zwick / Roell ZHU under a load of 150 kg and 10 kg respectively (determined as the average value of four readings).

Both as-cast and austempered tensile test specimens were prepared as ASTM standard E 8M [14]. Tensile tests were conducted to failure on specimens by using a 10 kN hydraulic testing machine (model : Losenhausen) at room temperature and ambient atmosphere with a cross-head speed of 6 mm/min. Three samples of each condition were subjected to tensile testing. The conditions were 0, 1, 1.5 and 2 % Cu addition with and without austempering. Thus, there were total of 24 tensile testings. Load and displacement plots were obtained on a X-Y recorder and from these load displacement diagrams yield strength and ultimate tensile strength values were calculated. The average values from three test samples are reported in this paper.

3- RESULTS AND DISCUSSION

Microstructural analyses of samples cast into sand mould is given in Fig 1.

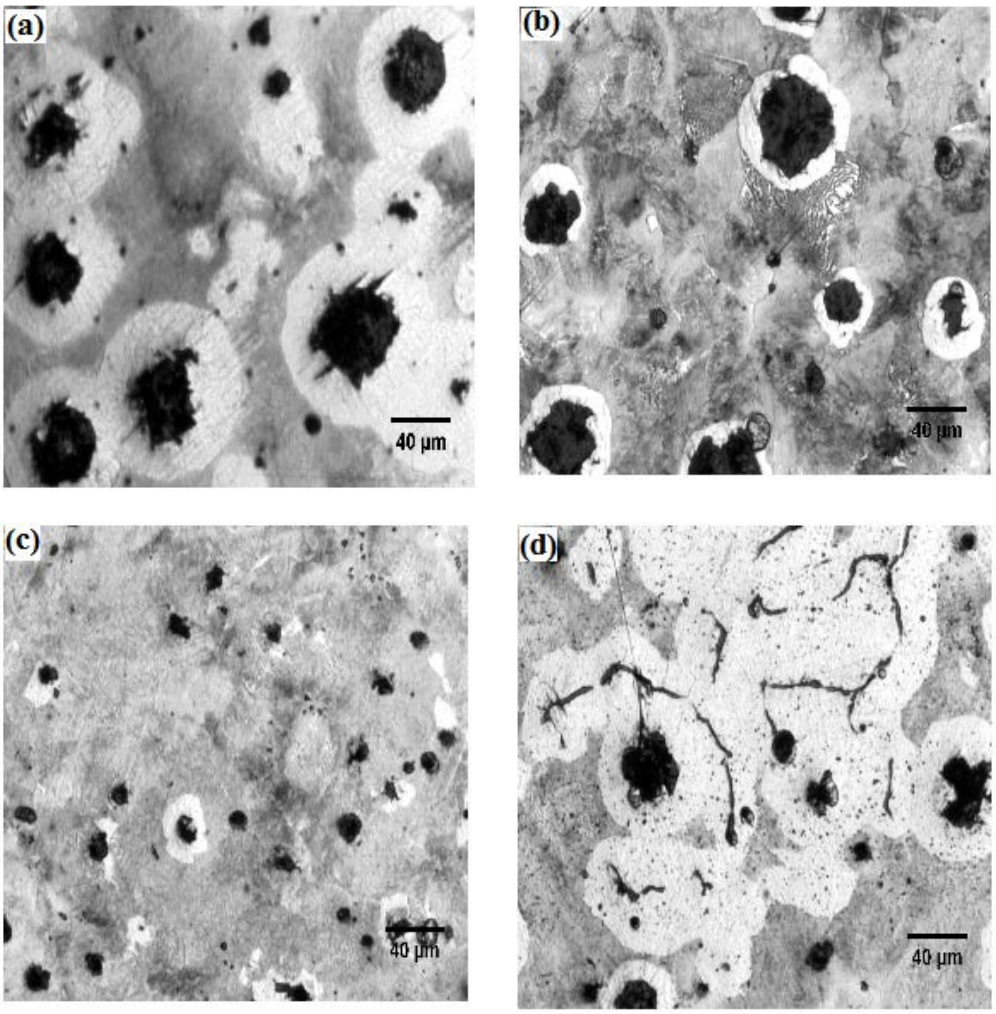

Figure 1. As-cast microstructures
a) unalloyed with Cu b) 1 % Cu alloyed c) 1.5 % Cu alloyed d) 2 % Cu alloyed

As it was shown in Fig 1a the as-cast structure showed a typical bull's eye structure with ferrite surrounding the graphite nodules in a pearlitic matrix. The nodule count of the specimen was about 200-220 nodule / mm^2.

As seen in Fig 1b, the matrix consists of ferrite and pearlite for the alloy containing 1 % Cu. It can be seen that as the copper content was increased, pearlitic phase formation was promoted, and ferrite was transformed to pearlite. The matrix still contains a small ratio of ferrite where the spherical graphites are formed within. Hasırcı [15] concluded that Cu promoted the formation of pearlite up to 4.9 % when the alloy contained Sn, Mo, P, Ti, Mn, Ni and Cr.

Pearlite phase ratio was significantly increased and ferrite was decreased in Fig 1c. Thus, it can be concluded that with the addition of Cu to GGG 50, the microstructure was transformed from ferrite+pearlite to pearlitic. It can easily be seen that the microstructure of 1.5 % Cu added alloy was almost completely pearlitic. Similar findings have been reported in the literature [15, 16].

By the addition of 2 % Cu, it can be seen in Fig 1d that the spherical geometry of graphite was converted to flake-like structure. Some studies in the literature also reported that excess addition of Cu could break down spherical structure to flake graphite [17].

The microstructure of the samples austenised at 900°C for 1 hour and austempered at 330°C for 1 hour is given in Fig 2.

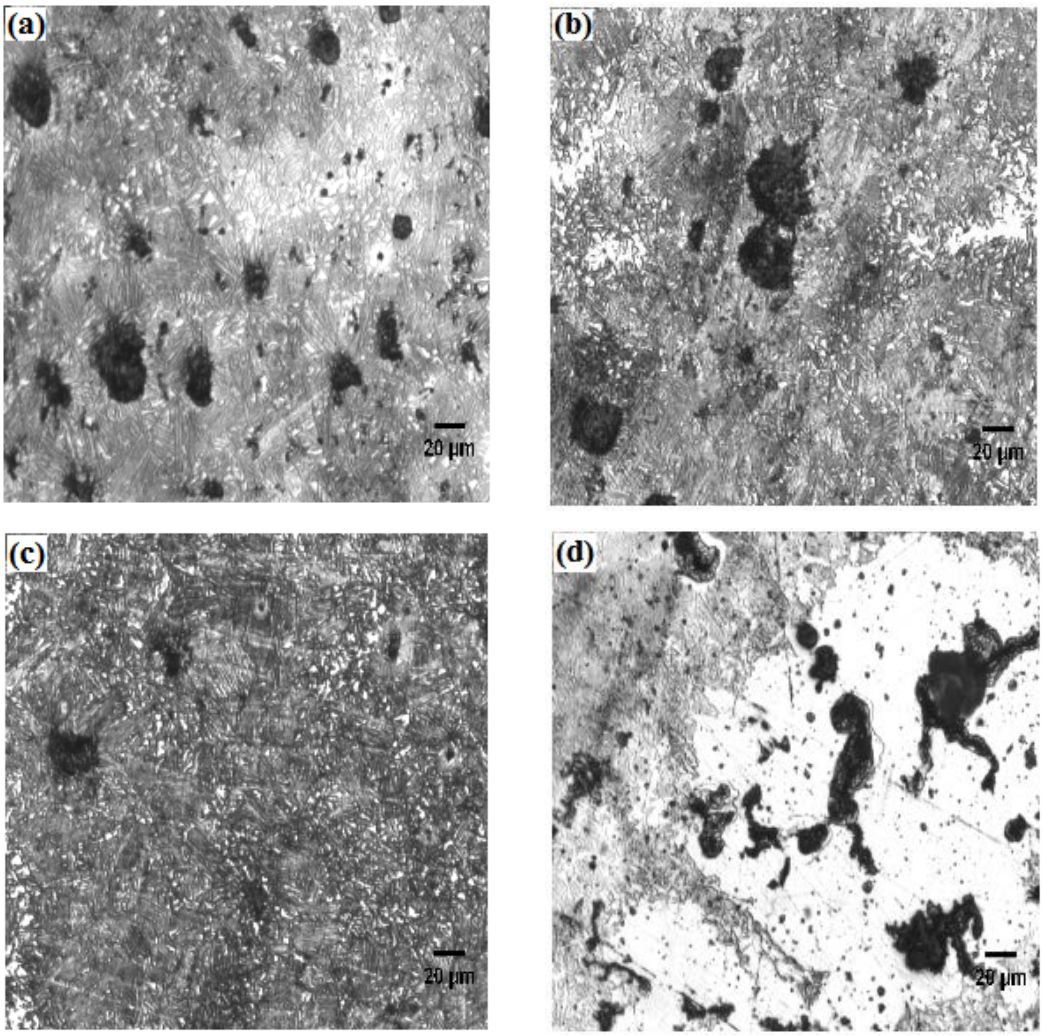

Figure 2. Microstructures after austempering at 330 °C an hour
a) unalloyed with Cu b) 1 % Cu alloyed c) 1.5 % Cu alloyed d) 2 % Cu alloyed

When closely examined, it can be seen in Fig 2 a-c that instead of ferrite and pearlite, the microstructure consists of retained austenite and ausferrite. Ausferrite is formed from bainitic ferrite + high carbon austenite. The light regions in the microstructure represents retained austenite, dark regions are bainitic ferrite and light gray regions are high carbon austenite. As well known, C, Ni, Mn, Co and Cu are austenite stabilizing elements in steels. Therefore, the addition of Cu to cast iron would lead to the formation of retained austenite.

The microstructure of austempered 1 % Cu added alloy contains retained austenite. Similar findings have been reported in the literature [15,18] about the formation of retained austenite by the copper addition.

In Fig 2d, flake graphite can be seen in the microstructure of austempered 2 % Cu added alloy. In addition, wide spread-densely distributed retained austenite can be observed in the microstructure. It is important to note that the spherical graphite was transformed to flake-like structure; and this phase is seen in the center of retained austenite.

It can be concluded that four of the austempered microstructures look similar to each other. The matrix of the austempered sample consists of high carbon austenite and ferrite plates with retained austenite. This forms due to the high carbon austenite and bainitic ferrite where it mainly consists of upper bainite. Literature survey results indicate similar findings where upper bainite was formed at these working temperatures [18-20].

Hardness measurements of as-cast and austempered GGG 50 samples were carried out by HRC and HV. These results are given as a function of Cu content in Fig 3.

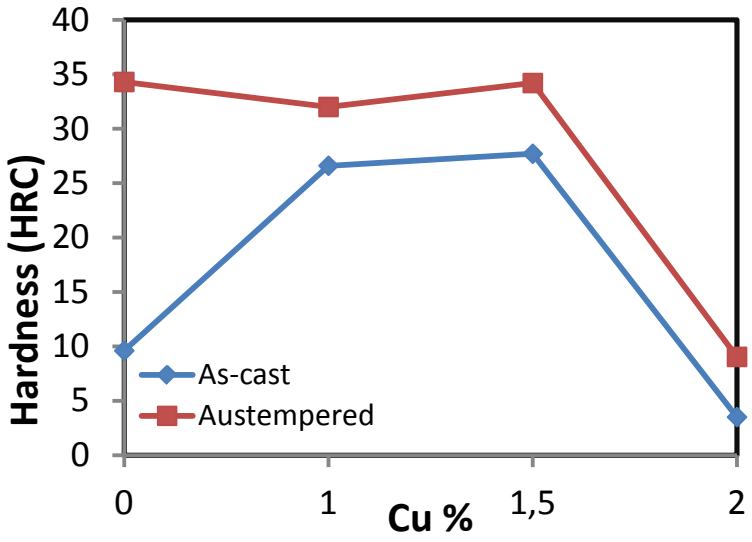

Figure 3. Hardness change as a function of copper content for as cast and austempered samples

HRC values of 2 % Cu added alloy for as-cast and austempered are 3,5 and 9,03 respectively. As known, readings below HRC 20 are generally considered unreliable. In accordance with this information, Vickers hardness test was conducted instead of HRC in order to obtain more reliable results. These are given in Table 2.

Table 2. Vickers hardness test results of the samples

Sample	Hardness (HRV) As-cast	Hardness (HRV) Austempered
As-cast	182,7	332
1 % Cu added	267	316,1
1.5 % Cu added	290,7	329
2 % Cu added	166	187

It can be clearly seen from Fig 3 and Table 2 that the hardness of the austempered samples are higher than the as-cast samples. When comparing the effect of Cu addition on the hardness of as-cast samples, it can be seen that hardness increases up to 1.5 % Cu addition and drops after 2 % Cu addition. For the hardness of austempered samples, although the hardness seems to decrease slightly at 1 % Cu, yet the trend of hardness appears to be unchanged regardless of the copper content.

As seen in Fig 3 and Table 2, the hardness of non-copper added samples are always the lowest. The change in the hardness is 9.6, 26.6, 27.4 and 3,5 HRC for 0, 1, 1.5 and 2 % Cu additions respectively. This can be easily explained by the deformation of graphite structure in the microstructure. Austempered samples have 72% higher hardness than the as-cast samples. The same comparison was found to be 17 and 19 % for 1 and 1.5 % Cu additions. Since there was a decrease in hardness for 2 % Cu added samples, no comparison was made for those samples. The findings also show that for 1 and 1.5 % Cu added GGG 50 alloy, the hardness of the as-cast and austempered samples can be found to be similar. Kırcalı [21] shows that Cu addition to spheroidal graphide cast iron promotes pearlite formation and since pearlite is harder than ferrite, the strength and hardness of Cu added spheroidal graphide cast iron increases. In addition, Hafız [22] also found that as the pearlite phase ratio was increased in spheroidal graphide cast iron alloys, the hardness was increased. Yazman [16] reported that hardness was increased with increased ausferrite phase in spheroidal graphide cast iron alloys. Hasırcı [15] studied the change of hardness in spheroidal graphide cast iron alloys. Non-alloyed as-cast samples had hardness values of as low as 9.2 HRC. By the addition of Cu and Ni, this value was increased to 21-26 HRC. By additional austempering heat treatment, 32-33 HRC values were obtained. Akca [24] concluded that addition of alloying elements had no effect on hardness or tensile properties of spheroidal graphide cast iron alloy. On the other hand, Seyfi [25] obtained 33.5 HRC value when spheroidal graphide cast iron alloy was austempered at 360^{o}C for 1 hours. These findings are in good agreement with results found in this work.

In order to determine the effect of copper addition and austempering heat treatment, three samples were collected and subjected to tensile testing. The average values were given in Table 3. As seen in Table 3, for the as-cast alloy that was not austempered, the yield and tensile strength is increased up to 1.5 % Cu addition. However, for 2 % Cu addition, these values decreased significantly. Similarly, for the austempered alloy, the mechanical test results were increased up to 1.5 % Cu and decreased for 2 % Cu. It is important to note that this decrease was not as sharp as the as-cast condition. The graphical representation of these results are given in Fig 4 and 5.

Table 3. Tensile test results of specimens

	As-cast		Austempered	
Sample	Yield Strength (MPa)	Tensile Strength (MPa)	Yield Strength (MPa)	Tensile Strength (MPa)
As-cast	411	497	810	859
1 % Cu added	547	624	791	842
1.5 % Cu added	719	820	823	880
2 % Cu added	365	415	648	728

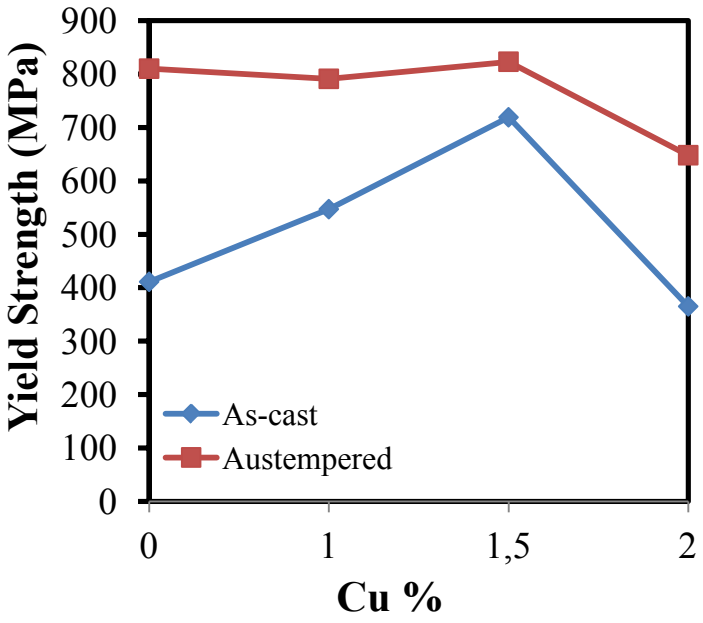

Figure 4. Yield strength change with Cu %

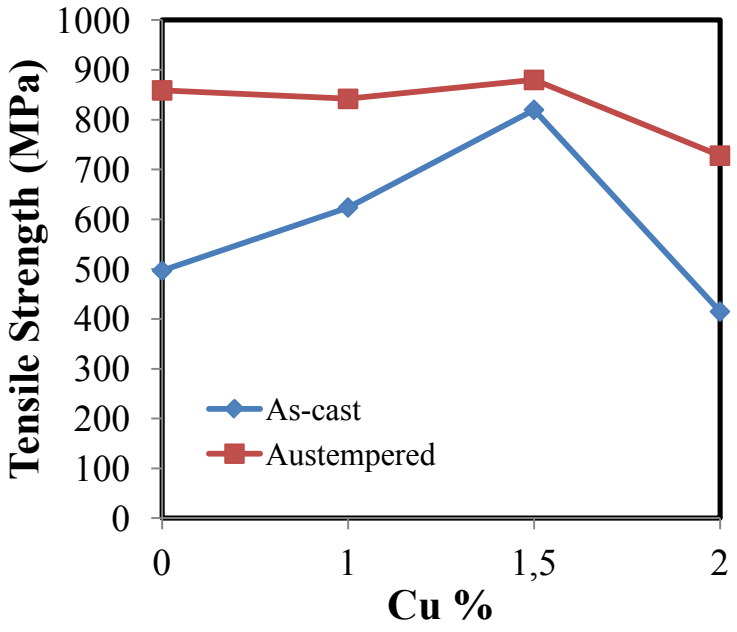

Figure 5. Tensile strength change with Cu %

In accordance with the tensile test results obtained in this study, as the copper content was increased, both yield and tensile strength was increased but it was decreased after 2 % Cu addition. These results were expected regarding the hardness and microstructural analysis. It is interesting to note that for the as-cast alloy with 1.5 % Cu addition, the mechanical test results were similar to the ones that was austempered. For the unalloyed samples, the difference between the yield and tensile strength of as-cast and austempered samples was nearly two-folds. On the other hand, when copper was added, the difference was not so high. Literature survey results [21, 25] show that as the copper content was increased, pearlitic structure was promoted and thus, the tensile strength was increased. In addition, Seyfi [25] reported that 850 MPa tensile strength was achieved for 1 hour austempering at 360^{o}C for

spheroidal graphide cast iron alloy. Akca [24] found out that tensile strength was increased to 900 MPa for Cu added spheroidal graphide cast iron. These reported results are in good agreement with the findings in this work. Akca [24] also concluded that austempering had no significant effect over the tensile properties for Cu added alloys. Ovalı [20] found that tensile strength was doubled for the austempered samples in comparison to the as-cast conditions due to the ausferritic structure.

4. CONCLUSIONS

- Cu addition to GGG 50 promotes pearlite formation in the matrix.
- After austempering heat treatment, the microstructure was transformed from ferrite + pearlite to ausferrite and retained austenite.
- Cu addition to GGG alloy is in two-folds: up to 1.5 % Cu addition, the mechanical properties increase and after 2 % Cu addition, this effect is reversed. This can be explained by the destruction of spherical graphite to flake-like structure.
- Due to the promotion of pearlitic phase, the highest hardness, yield and ultimate tensile strength values were obtained in the 1.5 % Cu added alloy in the as-cast condition.
- Cu addition has no effect on hardness, yield and ultimate tensile strength of austempered spheroidal graphide cast iron samples.
- Up to 1.5 % Cu addition have increased on hardness, yield and ultimate tensile strength of spheroidal graphide cast iron samples compared to as-cast specimen.

REFERENCES

1. W.F. Smith, "Structure and Properties of Engineering Alloys", second ed. McGraw-Hill, New York, 1993.
2. K. Yoon-Jun, S. Hocheol, P. Hyounsoo, J. Dae, Mater. Lett., 62, 357, 2008
3. J. Dodd, Mod. Cast., 68, 60, 1978
4. R.B. Gundlach, J.F. Janowak, AFS Trans., 94, 377, 1983
5. R.A. Harding, G.N.J. Gilbert, The British Foundryman, 79, 489, 1986
6. G. Wilkinson, C. Grupke, 2nd International Conference on Ductile Iron, Ann Arbor, Michigan, 349, March1986
7. O. Eric, L. Sidjanin, Z. Miskovic, S. Zec, M. Jovanovic, Mater. Lett., 58, 2707, 2004
8. C. Hsu, S. Lee, Y. Shy, W. Chiou, Mater. Sci. Eng. A, 282, 115, 2000
9. I. Schmidt, A. Schuchert, Z.Metal Kunde, 78, 871, 1987
10. J. Panasiewicz, C. Grupke, J. Huth, World Conference on Austempered Ductile Iron, Bloomingdale, IL, 176, March 1991
11. K. Okazaki, H. Asai, M. Tokuyoshi, H. Kusonoki, H. Sakahara, ProceedingWorld Conference on Austempered Ductile Iron, Bloomingdale, IL, 288, March 1991
12. S.K. Putatunda, A. V. Singar, R. Tackett, G. Lawes, Mat. Sci. Eng. A, 513-515, 329, 2009
13. M.A. Yescas, H.K.D.H. Bhadhesia., Mater. Sci. Eng. A, 333, 60, 2002
14. ASTM E8 M. (1990) : "Standart Test Methods for Tension Testing of Metallic Materials [Metric]", Annual Book of ASTM Standards, Vol. 01.02
15. H. Hasırcı, "Effects of Alloying elements(Cu and Ni) and Austempering Time on Microstrucuture and Mechanical Properties in Austempered Spheroidal Graphide Cas Irons", M.Sc. Thesis, Gazi University, Ankara, 2000
16. Ş. Yazman, " The Effects of Cutting Parameters on Machining for Austempered Ferritic Ductile Iron", M.Sc. Thesis, Selçuk University, Konya, 2006
17. P.W. Shelton, A.A. Bonner, J. of Mater. Process. Technol., 173, 269, 2003
18. U. Batra, S. Ray, S.B. Prabhakar, J. of Mater. Eng. and Perfomance, 12, 426, 2003

19. Y. Kayalı, "Investigation of Mechanical Properties and Wear Behaviour of Borontempered Ductile Iron", M.Sc. Thesis, Afyon Kocatepe University, Afyon, 2006
20. I. Ovalı, "The Fatigue Properties of Ductile Irons with Dual Matrix Structure Austempered from Intercritical Annealing Temperatures", M.Sc. Thesis, Gazi University, Ankara, 2006
21. K. Kırcalı, "Investigation of Mechanical and Machinability Properties of Ductile Irons Which Have Different Matrix Structure", M.Sc. Thesis, Uludag University, Bursa, 2006
22. M. Hafız, J. of Mater.Sci., 36, 1293, 2001
23. C. Akca, " The Effect of Alloying Elements to Austenite-Martensite Transformation on Austempered Spheroidal Graphite Cast Iron", Ph.D Thesis, Yıldız Technical University, Istanbul, 2005
25. A. Seyfi, "An Evaluation of Austempered GGG 60 Grade Ductile Irons' Machinability in Terms of Cutting Forced and surface Quality", M.Sc. Thesis, Gazi University, Ankara, 2006

Nitrasyon Isıl İşlem Koşullarının Farklı Vanadyum ve Krom İçeriğine Sahip Toz Metalurjik Çeliklerin Aşınma Davranışlarına Etkileri

The Effects of Nitriding Conditions on the Wear Properties of Powder Metallurgical Steels Consisting of Different Vanadium and Chromium

Aydın Şelte, Burak Özkal[1], Koray Arslan, İsmail Gezici, Sakine Ülker, Aziz Hatman[2]

[1] İstanbul Teknik Üniversitesi [2] Böhler Uddeholm Türkiye

ÖZET

Bu çalışmanın amacı nitrasyon işlemi sırasında uygulanan farklı nitrasyon potansiyeli (K_N değeri) neticesinde elde edilen farklı V ve Cr içeriğindeki toz metalurjik çeliklerin yüzey mikroyapısı ile aşınma davranışının ilişkilendirilmesidir. Bu kapsamda toz metalurjik yöntemlerle üretilmiş Uddeholm Vanadis 4E (3.7 % V, 4.7 % Cr) Uddeholm Vanadis 6 (5.4 % V, 6.8 % Cr) ve Uddeholm Vanadis 10 (9.8 % V, 8.0 % Cr) toz metalurjik çelikleri seçilmiştir.

Nitrasyon sıcaklığı her iki malzeme için de 450^{o}C olarak seçilmiştir. K_N değerleri değiştirilerek elde edilen nitrasyon tabakasının kalınlığı ve derinliği ölçülmüştür. Sertlik değeri mikro Vickers yöntemi ile ölçülmüştür. Karakterizasyon işlemleri olarak X ışınları difraksiyonu (XRD), optik mikroskop (OM) kullanılmıştır. ASTM standartlarına uygun olarak aşınma testi yapılmış ve her iki toz çeliğin de aşınma dirençleri karşılaştırılmıştır.

SUMMARY

The purpose of this study is to associate surface microstructures and wear properties by including different V and Cr content P/M steels which were nitrided by various nitration potential values (K_N). In this manner, powder metallurgically produced Uddeholm Vanadis 4E (3.7 % V, 4.7 % Cr), Uddeholm Vanadis 6 (5.4 % V, 6.8 % Cr) and Uddeholm Vanadis 10 (9.8 % V, 8.0 % Cr) P/M steels were chosen.

Nitriding temperature was chosen 450^{o}C for both of the steels. The hardness depth and thickness of nitriding layer were measured depending on the K_N values. The characterization investigations were performed by X-Ray diffraction (XRD) and optical microscopy (OM). Wear properties of the materials were carried out by wear testing due to ASTM standards.

EVALUATION OF THE RELATION BETWEEN INTERNAL STRESS AND MECHANICAL PROPERTIES OF AL-CU ALLOY

Muhammet ULUDAĞ[*], Muhammed Raşit ERYILMAZ[*], Lokman GEMİ[**], Serdar ÇELEBİ[*], Derya DIŞPINAR[***]

* Selcuk University, Faculty of Engineering, Metallurgical and Materials Eng. Dept., Konya-Turkey, uludag@selcuk.edu.tr, rasit.eryilmaz@gmail.com, serdarcelebi@windowslive.com
** Selcuk University, Institute of Science, Konya-Turkey, lgemi@selcuk.edu.tr
*** Istanbul University, Faculty of Engineering, Metallurgical and Materials Eng. Dept., Istanbul-Turkey, deryad@istanbul.edu.tr

ABSTRACT
Heat treatable aluminum alloys contain elements such as Cu, Mg and Zn. Typically, age hardening method is used to increase the hardness, yield stress and ultimate tensile stress. In this work, ETIAL 221 (Al-5Cu) alloy was solution heat treated and quenched at different mediums in order to achieve various levels of internal stress (i.e. residual stress). The quenching medium was selected to be water at room temperature, boiling water and oil. The solutionizing temperature and aging temperature were selected to be 537^{o}C and 195^{o}C, respectively. In order to optimise the solutionizing duration, samples were collected at certain time intervals and microstructural investigation was carried out by using image analysis software. The alloy was melt at 775^{o}C and cast into a cylindrical shape (Ø15 x 150) into two different moulds (sand and permanent) in order to achieve different dendrite arm spacing. One of the castings were used for microstructural characterisations, and the remaining castings were used for hardness testing. DSC (differential scanning calorimetry) method was used to measure the residual stress in the castings.

Keywords: artificial aging, quenching atmosphere, casting, Al-Cu alloys, mechanical properties,

ETİAL 221 ALAŞIMINDA İÇ GERİLİMLER İLE MEKANİK ÖZELLİKLER ARASINDAKİ İLİŞKİ

ÖZET
Alaşım elemanı olarak Cu, Zn ve Mg gibi elementler kullanılan alüminyum alaşımlarında; sertlik, akma ve çekme mukavemeti gibi mekanik özellikleri iyileştirmek amaçlı yaşlandırma işlemi uygulanmaktadır. Bu çalışmada, Al-Cu alaşımlarından biri olan ETİAL 221 için farklı su verme ortamlarının iç gerilimler ve yaşlandırmaya etkisi incelenmiştir. Su verme ortamı olarak oda sıcaklığındaki suda, yağda ve kaynayan suda su verme çalışmaları yapılmıştır. Çözeltiye alma sıcaklığı 537^{0}C ve yaşlandırma sıcaklığı da 195^{0}C olarak alınmıştır. Optimum sürenin hesaplanması için hem çözeltiye alma ve hem yaşlandırma için farklı sürelerde numune alımı yapılmıştır. Bu çalışmada, altı adet 15 mm çapında ve 150 mm boyunda silindir numune üretmek üzere tasarlanmış kum ve kokil kalıplar kullanılmıştır. Döküm sıcaklığı 775^{0}C olarak alınmış ve her bir döküm öncesi gaz giderme işlemi uygulanmıştır. Çalışma sonrası mikro yapı analizi, sertlik ölçümü yapılmıştır. DSC (Differential Scanning Calorimetry) yöntemi ile iç gerilimler hesaplanmıştır. Aynı zamanda, döküm kalitesini

belirlemek için azaltılmış basınç test numuneleri alınarak bifilm indeks hesaplanmış ve alaşımın mekanik özellikler ile döküm kalitesi arasındaki ilişki incelenmiştir.

Anahtar Kelimeler: Yapay yaşlandırma, Su verme ortamları, Döküm, Al-Cu alaşımları, Mekanik özellikler

1. INTRODUCTION

One of most important features of some of the aluminium alloys is the improvement of mechanical properties by heat treatment [1-3]. Solution hardening is one these method that is typically used. During this process, alloy is heated to the single phase region under eutectic temperature and solutionized; followed by quenching to room temperature to produce voids where secondary phase is nucleated. This method allows fine and homogeneously distributed secondary phase formation which acts as stress risers and barriers to dislocation motion and thus mechanical properties are improved. In order to do so, depending on the alloys composition, alloy is either held in room temperature or to an elevated temperature what is called natural aging or artificial aging respectively [4].

Solution hardening is applied to Cu, Mg or Zn containing Al alloys and these alloys exhibit good properties such that they find application areas in aerospace and defence industry. In Al-Cu alloys, Al_2Cu (θ) intermetallic is the secondary phase that increases mechanical properties [5-6]. This phase forms transition phases until stable θ phase is formed; namely θ', θ" which is known as the GP zones.

During the heat treatment process, quenching step plays an important role. It is required to be as high as possible in order to obtain more homogeneous and fine distribution of θ phases. However, when quenched rapidly, internal stress arises. Thus, solution heat treated alloys are typically subjected to DSC (differential scanning calorimetry), XRD or TEM analysis in order to measure the internal stress [7]. Either the area under the curve in DSC, or 2θ phase shift from XRD or TEM is used to quantify the amount of stress [8].

In this work, Etial 221 alloy was used and three different quenching rates were selected to measure the internal stress by means of DSC analysis.

2. EXPERIMENTAL WORK

The chemical composition of Etial 221 is given in Table 1. The charge was melted in a resistance furnace, SiC crucible at 775ºC.

Table 1. Composition of Etial 221

Si	Fe	Cu	Mn	Mg	Zn	Ti	Ni	Pb	Al
0,30	0,30	4,00-5,00	0,10	0,05	0,10	0,15-0,30	0,10	0,05	Rem.

Reduced Pressure Test (RPT) samples were collected to check the melt quality by measuring bifilm index. Samples were cast into sand moulds that were prepared from 40/45 and 60/65 AFS sands. The dimension of the mould is given in Figure 1.

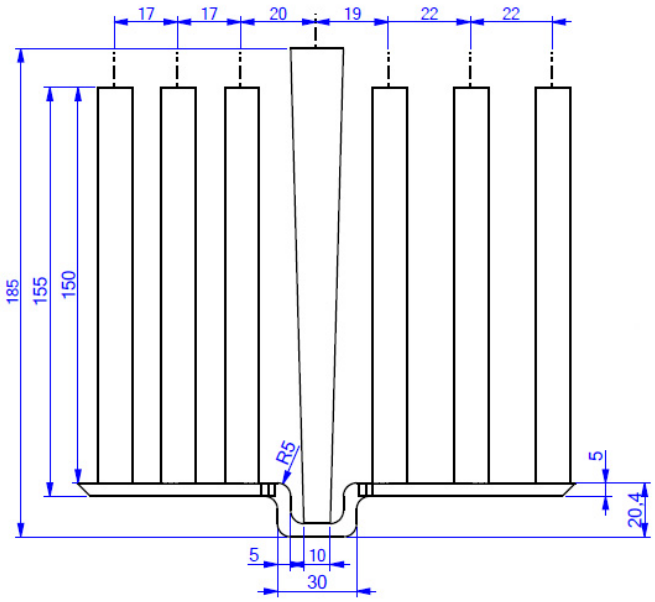

Figure 1. The dimension of the mould

The bars produced by the casting into the mould (Fig 1) was cut into slices and the samples were subjected to solution heat treatment. For the quenching step, room temperature, boiling water and oil mediums were used. Solutionizing temperature was selected to be 537ºC and artificial aging temperature was chosen to be 195ºC. Samples were collected at every 15th minutes in order to check the optimum conditions. Samples were subjected to metallographical examination.

For the aging, samples were held in the furnace for 48 and 96 hours and hardness values were measured every hour.

All the samples were then subjected to DSC analysis to compare the internal stress.

3. RESULTS and DISCUSSION

The optimum condition determination was determined with regard to the metallographical analysis. As seen in Figure 2, 30 minutes was selected for water quenched samples and 60 minutes was selected for the boiling water and oil quenched samples to be the optimum solutionizing duration.

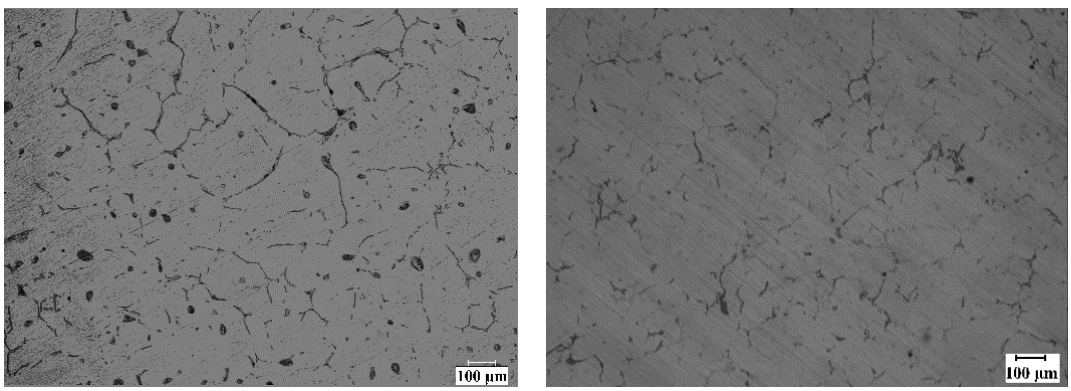

a b

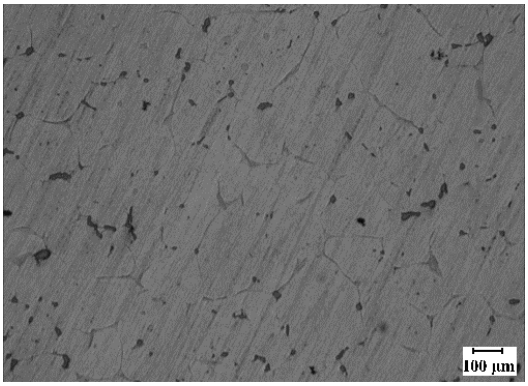

c

Figure 2. Solutionized samples in
a) Room temperature water, b) Oil, c) Boiling water

The hardness measurements were made at every hour for the samples and the results are given in Figure 3.

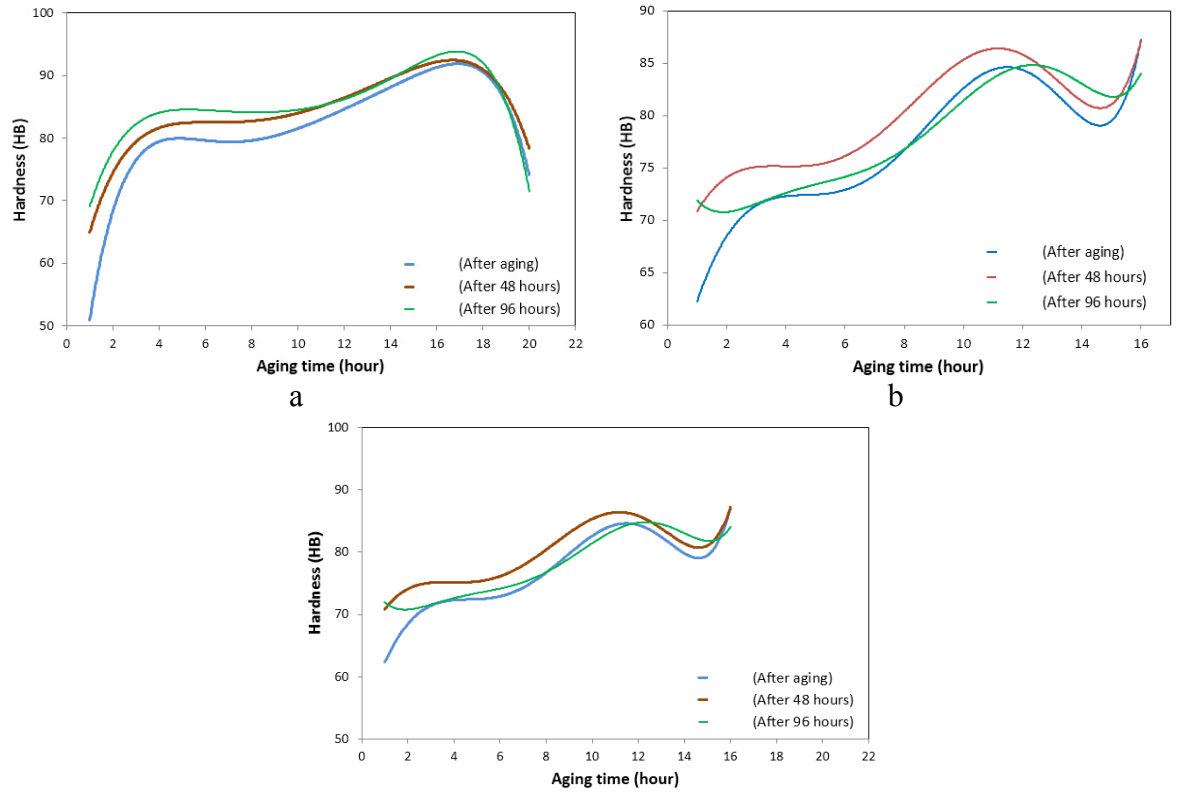

a b

c

Figure 3. Hardness change with quenching medium
a) quenched in boiling water, b) quenched in oil, c) quenched in water at room temperature

As seen in Figure 3, after artificial aging at 195ºC, the maximum hardness was obtained at 12 hour for water quenched samples and 16 hour for boiling water and oil quenched samples.

DSC analysis results for the samples after they were solutinized are given in Figure 4. It is important to note that the heating rate was selected to be 20ºC/min for these tests.

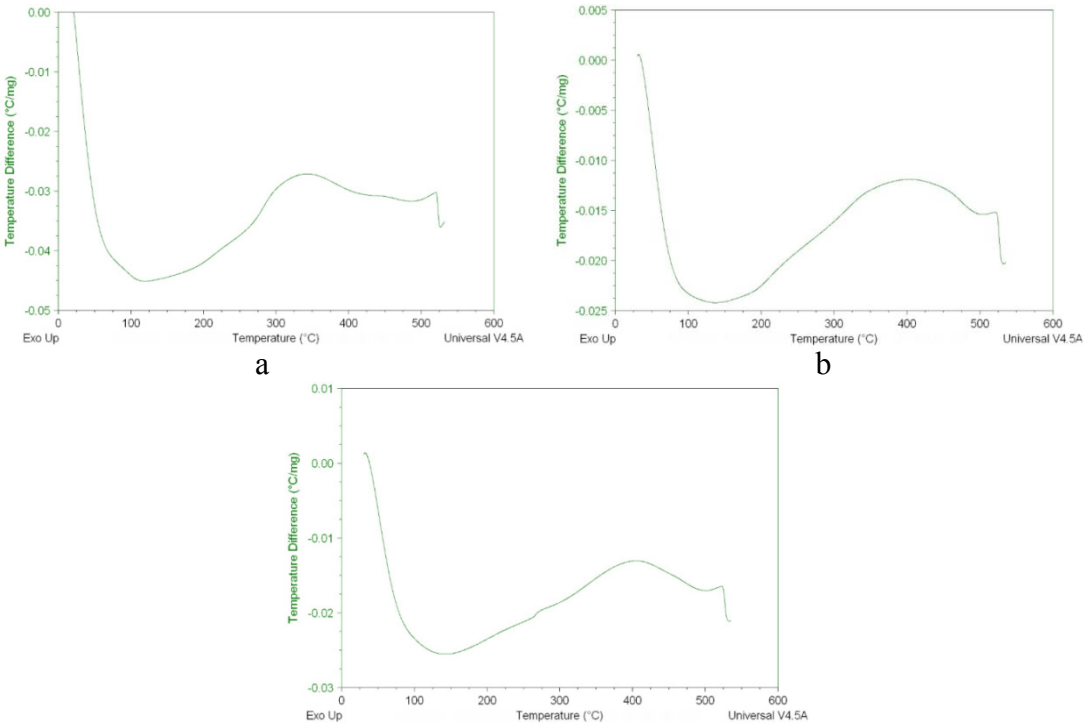

Figure 4. DSC analysis results after solutinizing
a) water quenched, b) boiling water quenched, c) oil quenched

DSC analysis results for the samples after they were aged are given in Figure 5. It is important to note that the heating rate was selected to be 20°C/min for these tests.

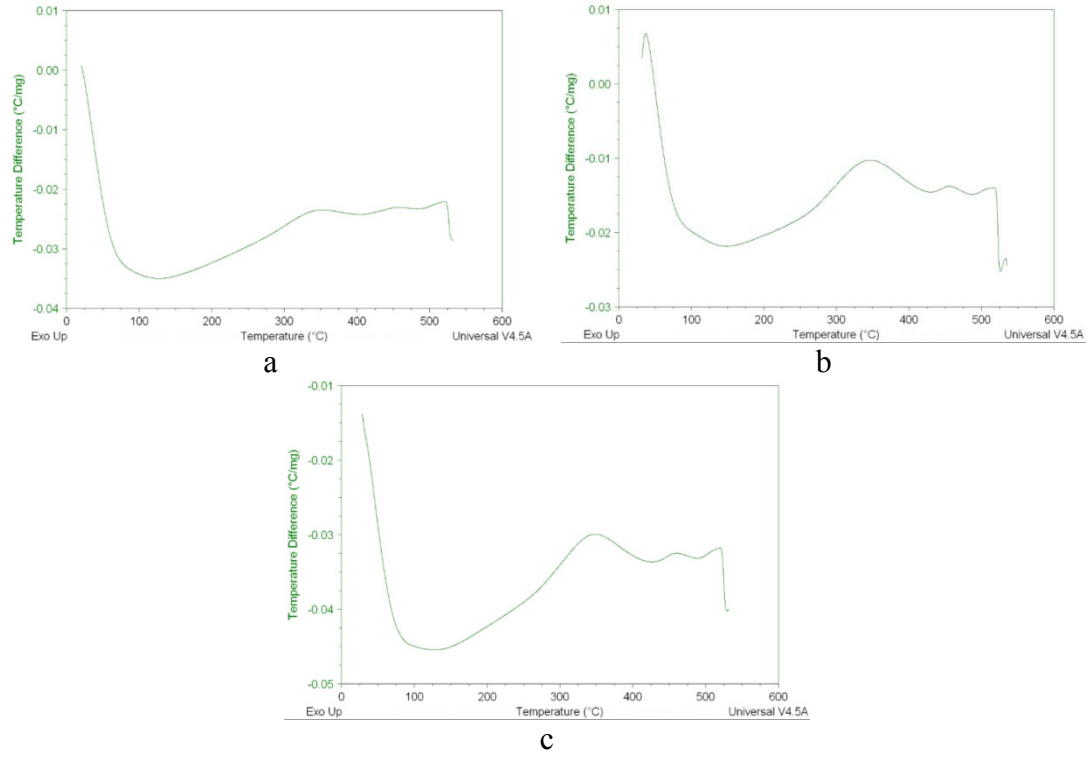

Figure 5. DSC analysis results after aging
a) water quenched, b) boiling water quenched, c) oil quenched

As seen from Figure 4, after the solutinizing step, the water quenched samples has the highest internal stress compare to the boiling water and oil quenched samples. This is understood from the height and area of the peaks. It is important to note that the peak heights for oil quenched and boiling water quenched are similar and very close to each other. In addition, for the water quenched samples, the peak correspond to 320ºC whereas boiling water and oil quenched samples, peaks correspond to around 400ºC.

Figure 3 shows the hardness values of the samples quenched in room temperature water, boiling water and oil and the results were 86, 85 and 92 HB respectively. It is important to note that for the samples quenched in boiling water, the increase in the hardness by every hour is the smoothest amongst the more complex increase in water and oil quenching mediums. DSC results show that boiling water quenched samples have the lowest internal stress. Thus, these results make the boiling water quenching to be the optimum choice of medium for solution heat treatment process.

DSC analysis were carried out at two different heating rates: 20ºC/min and 5ºC/min. Figure 4 and 5 show the results for 20ºC/min and Figure 6 shows the effect of 5ºC/min. When both heating rates are compared, it can be seen that the intensity of the peaks at 5ºC/min are smaller and weaker. This suggests that when the heating rate is low, it is most likely that recovery process becomes active and slowly reduces the internal stress.

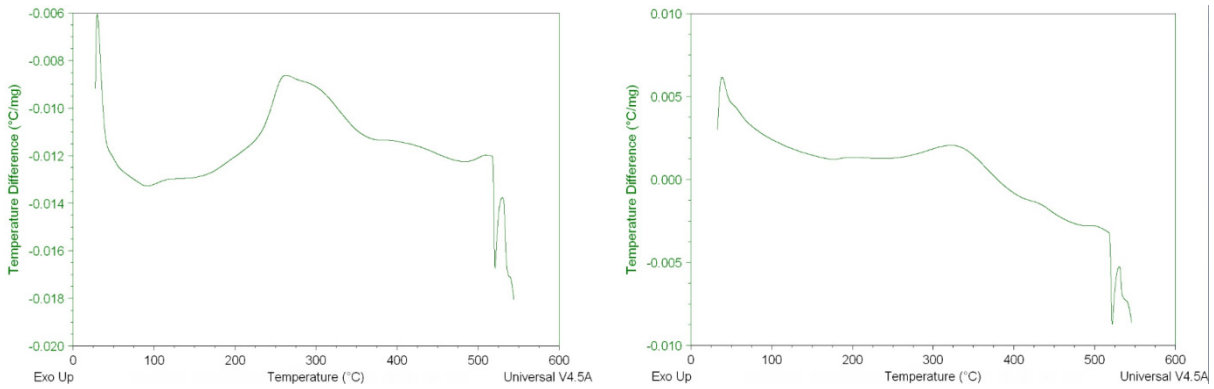

Figure 6. DSC carried out at a heating rate 5^{0}C/min.
a) room temperature water b) boiling water

4. CONCLUSIONS

Quenching Al-4Cu alloy in boiling water has the highest hardness and lowest internal stress.

DSC analysis can be used to quantify the internal stress and higher the heating rate sharper the peaks. At low heating rates, recovery process takes in place causes the peaks to be lower and makes the determination of internal stress harder.

Acknowledgment

The authors would like to thank Metal Market Metalurji San.Tic.Ltd.Şti for their support in this study.

REFERENCES

1. Gupta, A.K., D.J. Lloyd, and S.A. Court, "*Precipitation hardening processes in an Al–0.4%Mg–1.3%Si–0.25%Fe aluminum alloy"*. Materials Science and Engineering: A, 2001. **301**(2): p. 140-146.
2. Li, R.X., et al., "*Age-hardening behavior of cast Al–Si base alloy*. "Materials Letters, 2004. **58**(15): p. 2096-2101.
3. Wang, S.C., M.J. Starink, and N. Gao, "*Precipitation hardening in Al–Cu–Mg alloys" revisited*. Scripta Materialia, 2006. **54**(2): p. 287-291.
4. Committee, A.I.H., *ASM handbook: Heat treating*. 1991: ASM International.
5. Samuel, A.M., J. Gauthier, and F.H. Samuel, "*Microstructural aspects of the dissolution and melting of Al2Cu phase in Al-Si alloys during solution heat treatment"*. Metallurgical and Materials Transactions A, 1996. **27**(7): p. 1785-1798.
6. Starink, M.J. and P. van Mourik, "*Cooling and heating rate dependence of precipitation in an Al-Cu alloy"*. Materials Science and Engineering: A, 1992. **156**(2): p. 183-194.
7. Starink, M.J. and A. Dion," *DSC study of precipitation in an Al–Mg–Mn alloy microalloyed with Cu"*. Thermochimica Acta, 2004. **417**(1): p. 5-11.
8. Hersent, E., J.H. Driver, and D. Piot, "*Modelling differential scanning calorimetry curves of precipitation in Al–Cu–Mg"*. Scripta Materialia, 2010. **62**(7): p. 455-457.

IS WORLD IRON AND STEEL PRODUCTION SUSTAINABLE?

Yusuf Ziya KAYIR*

*KOSGEB Ankara Sincan Hizmet Merkezi, Ankara/Turkey
ziya.kayir@kosgeb.gov.tr

ABSTRACT

In this present study, the effect of the iron and steel production on climate change was investigated. Recent changes and developments in the iron and steel production were evaluated. While a production-weary world is being rocked by a series of crises and the top players are changing places with unprecedented speed. International successes are the result not merely of joining the ranks of those who can recognize the world's steadily growing environmental problems early, but having the courage to propose solutions.

According to World Steel Association, crude steel production in the world was achieved in quantity of 1.5 billion tons in 2012. Major steel-producing countries were China, Japan, United States, India, Russia, South Korea, Germany, Turkey, Brazil and Ukraine. Rising at the same ratio as that of world production figures compared to the previous year, crude steel production of Turkey has increased up to 35.9 million tons. Our country has retained its position at the 8th rank in world ranking, while taking the 3rd rank in Europe and the 2nd rank in EU-27, following Germany. This was equal to 2.3% of crude steel production in the world. The per capita consumption of steel of Turkey was 303kg which exceeds 294kg of the European Union. Turkey, as a rapidly growing and steadily developing country, has the 16th largest economy in the world. The center of gravity for the steel industry has shifted from the developed economies towards the developing and emerging economies. Overall, the developing and emerging world will account for 72% of the global steel demand in 2011. Steel is essential for a low-carbon world in transport, construction, housing and power generation. Demand for steel will significantly increase in the period up to 2050, to support ongoing global development.

Human influence on the climate system is clear. This is evident in most regions of the globe. Assessment of the science finds that the atmosphere and ocean have warmed, the amount of snow and ice has diminished, the global mean sea level has risen and the concentrations of greenhouse gases have increased. Warming in the climate system is unequivocal and since 1950.

As one of the major energy-consuming industries in the world the iron and steel industry has a great influence on global warming. It is committed to making a positive contribution to the climate change issue. In the various countries, new projects and researches have started to decrease CO2 emissions. New iron making processes such as top gas recycling, hydrogen reduction and biomass utilization have been proposed.

Keywords: Iron and steel, development, technology, climate change, environment

DÜNYA DEMİR ÇELİK ÜRETİMİ SÜRDÜRÜLEBİLİR MİDİR?

ÖZET

Bu çalışmada demir çelik üretiminin iklim değişimi üzerine etkisi incelendi. Yakın zamanda demir çelik üretimindeki değişim ve gelişmeler değerlendirildi. Üretim yorgunu dünyamız peş peşe krizleri yaşarken, baş oyuncular öngörülemeyen bir hızla yer değiştiriyorlar. Uluslar arası başarılar, yalnızca ön sıralarda olmakla değil, dünyanın giderek büyüyen çevresel sorunlarının önemini erken anlamak ve çözüm önerme cesaretine sahip olmakla mümkün olmalıdır.

Dünya çelik derneğinin verilerine göre, 2012 yılında dünya ham çelik üretimi 1 milyar 500 milyon tona ulaştı. Başta gelen çelik üretecisi ülkeler Çin, Japonya, ABD, Hindistan, Rusya, Güney Kore, Almanya, Türkiye, Brezilya ve Ukrayna'dır.

Çelik üretiminde bir önceki yıla göre dünya rakamlarıyla ayni artışı gerçekleştiren Türkiye'nin ham çelik üretimi, 2012 yılında 35,9 milyon tona ulaştı. Ülkemiz dünya sıralamasında 8.nci, Avrupa'da 3.ncü, EU-27 içinde Almanya'nın peşinden 2.nci oldu. Türkiye'nin ham çelik üretimi, dünya üretiminin yüzde 2,3'üdür. Ülkemizin kişi başına çelik üretimi 303 kilogram, Avrupa'nın 294 kilogramdır. Hızlı ve kararlı büyüyen Türkiye ekonomisi dünyanın 16.ncı büyük ekonomisidir. Çelik üretiminin ağırlık merkezi gelişmiş ülkelerden gelişen ve yükselen ekonomilere doğru kaydı. Genel olarak 2011 yılında çelik talebinin yüzde 72'si gelişen ve yükselen ekonomilerde oluştu. Çelik, düşük karbon dünyası için taşıma, ulaşım, inşaat, iskan ve elektrik üretiminde zaruridir. Devam eden küresel gelişmeyi desteklemek için çelik talebi 2050 yılına kadar ciddi miktarda artacaktır.

İnsanoğlunun iklim sistemine etkisi kesindir. Bu yerkürenin bir çok bölgesinde bellidir. Bilimsel bulguların değerlendirmesi, atmosferin ve okyanusların ısındığını, kar ve buz miktarının azaldığını, küresel anlamda deniz düzeyinin yükseldiğini, sera gazı yoğunluğunun arttığını göstermiştir. 1950 yılından beri iklim sistemindeki ısınma şüphe götürmemektedir.

Dünyada en çok enerji tüketen sanayilerden biri olan demir çelik sanayinin küresel ısınmaya etkisi büyüktür. Iklim değişimi konusuna olumlu bir katkı yapmayı önemsemek gerekir. Birçok ülkede karbondioksit (CO_2) çıkışını azaltmak için yeni proje ve araştırmalar başlatılmış, tepe gazı geri dönüşümü, hidrojen indirgemesi ve biyokütle kullanımı gibi yeni demir yapım süreçleri önerilmiştir.

Anahtar sözcükler: demir çelik, kalkınma, teknoloji, iklim değişimi, çevre

1. GİRİŞ

Çelik metalik demirin, karbon, manganez, silisyum, fosfor, kükürt ve bir çok elementlerle bileşim, alaşım, ve karışımı ile oluşan bir malzemedir.[1] Dünya metal üretiminin yaklaşık yüzde 95'i demir olup demirin karbon ile yaptığı alaşımlar en yaygın kullanılan mühendislik malzemelerini oluşturmaktadır. Bunun başlıca nedeni, demirin kristal yapısının sıcaklığa bağlı olarak değişen (allotropik) bir metal olması ve demir-karbon alaşımlarına ısıl işlemler ve / veya alaşımlama yoluyla çok farklı özellikler kazandırılabilmesidir.[2]

Çelik, düşük karbon dünyası için taşıma, ulaşım, inşaat, iskan ve elektrik üretiminde zaruridir.

[1] Selahaddin Şanbaşoğlu, Metalurji Yüksek Mühendisi, Standart Çeliklerin Uluslararası Eşdeğerleri,1985,Sayfa3
[2] Prof. Dr. H. Çimenoğlu, Prof. Dr. E. Geçkinli, Y. Müh. S. Yıldırım, Y. Müh. M. Baydoğan, TMMOB Metalurji Mühendisleri Odası, Çelik ve Dökme Demirlerin Metalografisi ve Mekanik Muayenesi, 16-18.05.2001 Sayfa 1.1

İklim bilimcilerin yüzde 97'si ve dünya çapındaki bilimsel kuruluşların çoğu, geçen yüzyıldan itibaren insan faaliyetleri kaynaklı iklimsel ısınma artışı ve eğilimleri konusunda ayni görüşü paylaşmaktadır. [3] İklim değişikliğinin ekosistemlere olan etkisi nedeniyle her canlı yaşamı olumsuz etkilenme riski taşımaktadır. İnsanlık varoluşunu tehdit eden ve dünya tarihinin en önemli sorununa çözüm aramalıdır.

2. DÜNYADA DEMİR ÇELİK

20. yüzyılın başında 28 milyon ton olan dünya demir çelik tüketimi yüzyılın sonunda 780 milyon ton oldu. 2013 yılında dünya ham çelik üretimi 1 milyar 607 milyon tona ulaştı. Dünyanın ilk 10 demir çelik üreticisi ülke; Çin (779 milyon ton), Japonya (110 milyon ton), ABD (87 milyon ton), Hindistan (81 milyon ton), Rusya (69 milyon ton), Güney Kore (66 milyon ton), Almanya (43 milyon ton), Türkiye (35 milyon ton), Brezilya (34 milyon ton) ve Ukrayna (33 milyon ton)'dır. İlk 10 ülke, dünya üretiminin yüzde 83'ünü üretmiştir.[4]

Yıllar	Dünya DÇ Üretimi
2013	1.607
2012	1.545
2011	1.537
2010	1.433
2009	1.237
2008	1.343
2007	1.344
2006	1.244
2005	1.142
2000	848
1995	756
1990	775
1985	721
1980	717
1975	644
1970	595

Ort.Büyüme Oranı	
Yıllık	%
Yıllar	Dünya
2012-13	4
2010-11	7
2008-09	-8
2006-07	8
2005-06	9
2000-05	6,1
1995-00	2,3
1990-95	-0,5
1975-80	2,2
1970-75	1,6

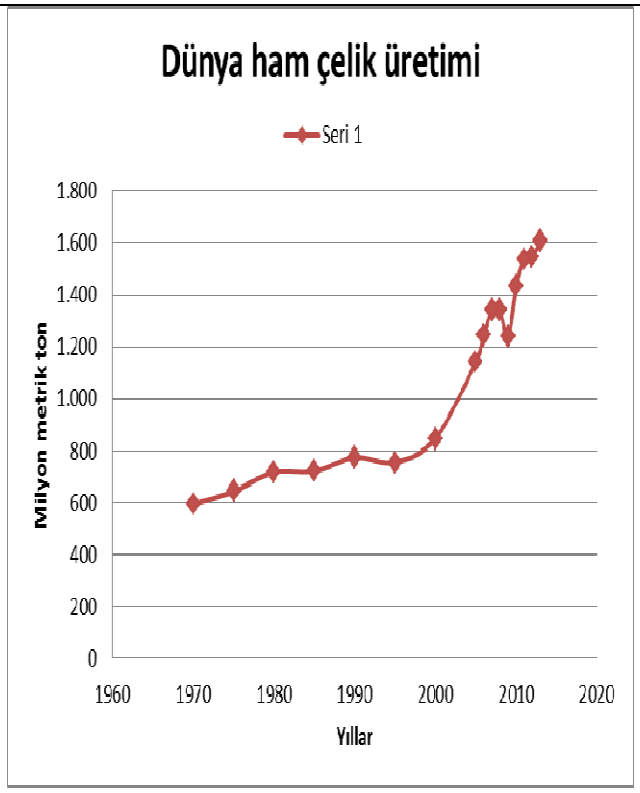

Şekil 1. 1970-2013 Dünya Ham Demir Çelik Üretimi

2013 yılında dünya ham çelik üretiminin yüzde 48'i Çin'de, yüzde 7'si Japonya'da, yüzde 5'i Amerika'da, yüzde 5'i Hindistan'da, üretilmiştir. Dünyada üretilen çeliğin yaklaşık yarısı Çin'de üretilmektedir. Demir çelik üretimiyle birlikte dünya üretimi coğrafya değiştirmiştir.

[3] NASA : http://climate.nasa.gov/evidence/
[4] Dünya Çelik Derneği, http://www.worldsteel.org

XIX yüzyılın başında, dünya nüfusunun az çok yüzde 3'ü kentlileşmişti; önümüzdeki beş yılın içinde insanlığın yarıdan fazlası kentlere yığılacak. 1950'de 1 milyon nüfuslu bir kent olan İstanbul, günümüzde 10 milyonu aşmıştır.[5]

3. DÜNYA DÖKÜM SANAYİ

2012 yılında, Dünya Döküm Sanayi için 37 ülkenin katıldığı 47. Sayım sonuçlarına göre; dünyada mevcut 50.909 dökümhanede 100,8 milyon ton döküm üretimi gerçekleştirilmiştir. Dünyada önemli 16 dökümcü ülkede üretilen dökümün parasal karşılığı yaklaşık 107,7 milyar dolardır ve döküm sektöründe istihdam edilen kişi sayısı yaklaşık 2 milyon civarındadır.[6]

Yıllar	Dünya Döküm Üretimi (Bin metrik ton)
2004	79.745
2007	94.900
2008	94.786
2009	80.343
2010	91.673
2011	98.593
2012	100.835

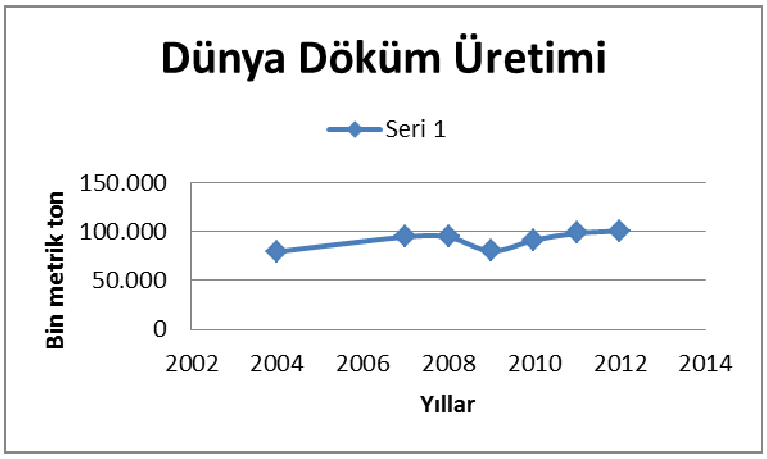

Şekil 2. Dünya Döküm Üretimi

Dünya döküm üretiminde ilk on sıradaki ülkeler; Çin (42,5 milyon ton), ABD (12,8 milyon ton), Hindistan (9,3 milyon ton), Japonya (5,3 milyon ton), Almanya (5,2 milyon ton), Rusya (4,3 milyon ton), Brezilya (2,9 milyon ton), G. Kore (2,4 milyon ton), İtalya (1,9 milyon ton) ve Fransa (1,8 milyon ton)'dur. 2012 yılında Çin ve ABD, dünya döküm üretiminin yüzde 56'sını, ilk 10 döküm üreticisi ülke yüzde 88'ini gerçekleştirmiştir. Dünya döküm üretiminin yüzde 46'sı pik döküm, dörtte biri sfero döküm, yüzde 11'i çelik döküm, yüzde 17'si demir dışı dökümlerden oluşmaktadır.

2012 yılında, Türkiye, 1.127 dökümhanesiyle dünyada 8. sıradadır. 1 milyon 445 bin tonluk döküm üretimi ve yaklaşık 4 milyar dolarlık katma değeriyle Avrupa'da 4. ve dünyada 13. sırada yer almıştır. Türkiye döküm üretiminin yüzde 42'si pik döküm, yüzde 35'i sfero döküm, yüzde 10'u çelik döküm, yüzde 11'i alüminyum döküm yüzde 2'si de diğer demir dışı dökümlerden oluşmuştur. Bu sektörümüzde 20.000 kişi çalışmaktadır.

4. DÜNYADA PASLANMAZ ÇELİK ÜRETİMİ

1950'li yılların başında 1 milyon ton civarında olan dünya paslanmaz çelik üretimi, 20. Yüzyılın sonunda 20 milyon ton oldu. Uluslararası Paslanmaz Çelik Forumu'nun verilerine göre 2013 yılında dünya paslanmaz ham çelik üretimi bir önceki yıla göre yüzde 8 oranında

[5] Server Tanilli, İnsanlığı Nasıl Bir Gelecek Bekliyor?, 2006, Sayfa 18
[6] Modern Casting /Aralık 2013, Dünya Döküm Sanayi 47. Sayımı

artarak 38 milyon 130 bin ton oldu. Dünya paslanmaz ve ısıya dayanıklı ham çelik üretiminin yarısı Çin de üretildi. [7]

Yıllar	Dünya Paslanmaz Çelik Üretimi (Bin metrik ton)
2008	26.218
2009	24.904
2010	31.094
2011	33.621
2012	35.363
2013	38.130

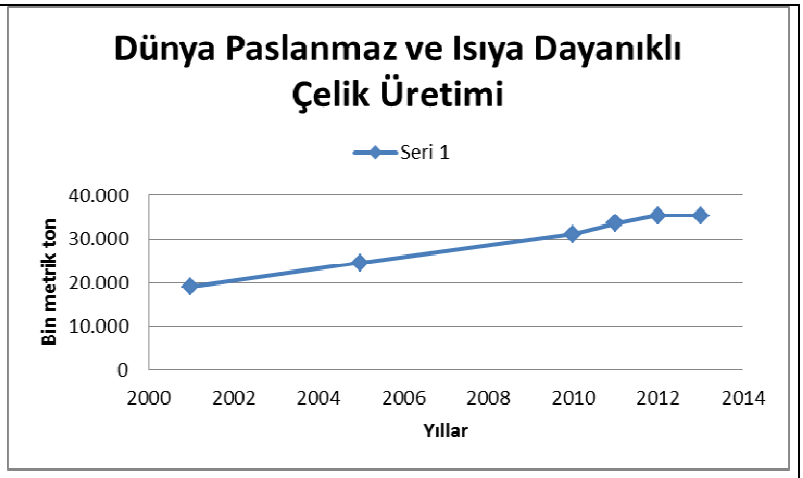

Şekil 3. Dünya Paslanmaz Çelik Üretimi

5. TÜRKİYE'DE DEMİR ÇELİK

Bugün Türkiye'de birisi Orta Karadeniz; Karabük ve Ereğli'nin bulunduğu yer, ikincisi Akdeniz; İskenderun ve Ekinciler'in bulunduğu yer, üçüncüsü Marmara Çolakoğlu'nun ve ark ocaklarının bulunduğu yer; dördüncüsü Aliağa İzmir; orası da ark ocaklarının bulunduğu yer olmak üzere dört tane demir-çelik ağır sanayi merkezi vardır. Demir çelik üretimi ülkemiz için stratejik sektördür.[8] Toplam yıllık çelik üretim kapasitesi 50 milyon tona ulaşan Türkiye, 2013 yılında 35 milyon tonluk ham çelik üretimiyle Avrupa'nın 2. ve dünyanın 8. büyük demir çelik üreticisi olmuştur. [9]

Türkiye dünyada krom cevheri üretiminde ilk 8 ülke içindedir. Krom cevherimiz yüksek kalitelidir. Yalnızca krom üreten Türkiye ve Arnavutluk'un paslanmaz çelik tesisi yoktur. Küba'da ihracat yapabilen 150.000 ton kapasiteli bir paslanmaz çelik tesisi bulunmaktadır. Ülkemiz demir ve çelik üretiminde birikim ve deneyim sahibidir. Türkiye için paslanmaz çelik üretimi kritik bir teknolojidir.

6. DÜNYA MOTORLU ARAÇ ÜRETİMİ [10]

LMC verilerine göre 2013 yılı dünya toplam motorlu araç üretimi 2012 yılına göre yüzde 2 oranında aratarak 86,7 milyon adet oldu. Çin 21,3 milyon adetle ilk sırada yer almıştır. Daha sonra 11 milyon adetle ABD, 9,5 milyon adetle Japonya gelmektedir. 2013 yılında Türkiye 1 milyon 126 bin adetlik üretimle dünya sıralamasında 15. Sırada yer almıştır. 1999 yılında dünya motorlu araç üretiminden yüzde 0,53 pay alan Türkiye'nin 2013 yılındaki payı 1,29'a yükselmiştir. Küresel gelişmelerle ilgili gelecek değerlendirmeleri dikkate alındığında gelecekte üretimin Güney Doğu Asya ile Brezilya, Çin, Hindistan ve Rusya'dan oluşan BRIC ülkelerinde yoğunlaşacağı bilinmektedir. Son 5 yıldır bu bölgelerde üretim ve talep artışı

[7] ISSF, Uluslararası Paslanmaz Çelik Forumu haber bülteni,04 Nisan 2008, www.wordstainless.org
[8] Paydossuz Bir Yaşam, Selahaddin ŞANBAŞOĞLU, Türk Demir Çelik Sektörünün Dünü ve Bugünü, TMMOB Metalurji Mühendisleri Odası, 1998, s.93.
[9] Türkiye Çelik Üreticileri Derneği, www.dcud.org.tr
[10] Otomotiv Sanayii Dermeği Otomotiv Sanayii 2013 Değerlendirme Raporu, sayfa 6-7

gözlenmektedir. Buna karşılık ABD, AB, Japonya ve G. Kore'den oluşan pazarlarda gelişmenin daha yatay seyredeceği beklenmektedir.

Sıra	Ülkeler	2013
1.	Çin	21.344
2.	ABD	11.054
3.	JAPONYA	9.499
4.	ALMANYA	5.528
5.	G.KORE	4.563
6.	HİNDİSTAN	3.930
7.	BREZİLYA	3.705
8.	MEKSİKA	3.080
9.	TAYLAND	2.508
10.	KANADA	2.339
11.	RUSYA	2.280
12.	İSPANYA	2.030
13.	FRANSA	1.690
14.	İNGİLTERE	1.559
15.	TÜRKİYE	1.126

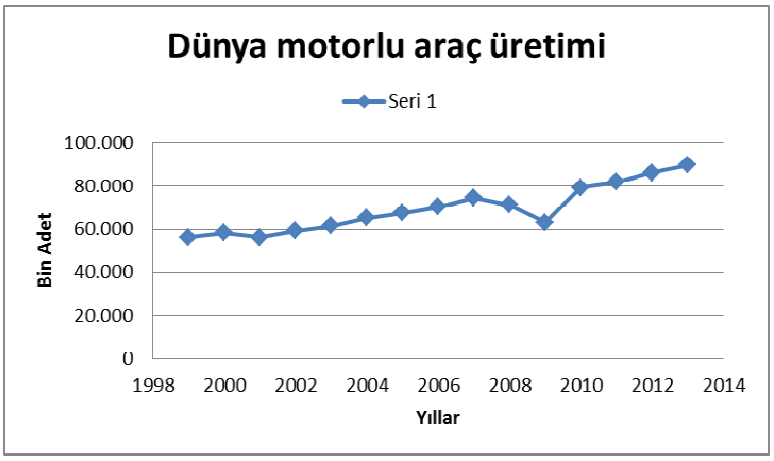

Şekil 4. Dünya Motorlu Araç Üretimi (Bin Adet)

Gelişmemiş toplumların ortak bir bilgisizlikleri var. Evrensel teknolojik gelişmenin evrensel bir ağ bağlantısı olduğunu, birbirlerinden ayrılması olanağı olmayan öğelerden oluştuğunu henüz öğrenemediler. Otomobile sahip olan, onun arkasındaki bilimsel, teknolojik, ekonomik bileşenleri bilmiyor. Satanlar ve onların sözcüsü olan politikacılar bu ilişkileri onlara anlatmıyor. Otomobil kullananın, üniversitedeki fizik dersinden enerjiden enerjinin geleceğinden haberi yok. Ama uyandırılması gerek çünkü her üretim sürecinin arkasında geleceğinizi tehlikeye sokabilecek bazı sorunlar var. Kaldı ki size de bırakılmış bir seçim de söz konusu değil.[11]

7. DÜNYA NÜFUSU

Dünyanın nüfuslanma süreci, insanın yerleşik hayata geçtiği Neolitik Dönemle başlar. Daha sonraki dönemlerde insanın meydana getirdiği teknolojik gelişmeler sayesinde hem insanın ortalama ömrü uzamış, hem de nüfus artışı hızlanmıştır. Günümüzden 10-12 bin yıl önce 80 milyon civarında olan dünya nüfusu 1650 lerde 500 milyona ulaşmıştır. Son 350 yılda ise, 500 milyondan 6 milyara yükselmiştir. Günümüzde dünya nüfusunun ortalama artış hızı yüzde 1,7 'dir.

Birleşmiş Milletler (BM) Nüfus fonu verilerine göre, 31 Ekim 2011 tarihinde dünya nüfusu 7 milyar kişiye ulaştı. Türkiye 18. sıradaki en kalabalık nüfusla 75 milyona ulaştı. Dünyanın 2050'lerde 10 milyara yaklaşacağı beklenmektedir. Gelişmekte olan ülkelerde halen nüfusun çoğunluğu kırsalda yaşamaktadır. Gelişmişlerde ise kentlerde yoğunlaşan bir nüfus sorunu yaşanmaktadır. Dünya nüfusunun yüzde 50'si günümüzde kentlerde yaşarken, önümüzdeki dönemde iklim değişikliğindeki hızlanma ve kaynakların tükenmesi ile kentlere göç hızlanacak. Bu da beraberinde toprak üzerindeki baskıyı daha da artıracaktır.[12]

[11] Doğan Kuban, Cumhuriyet Bilim ve Teknoloji (01.02.2014) " Çağa Uyumsuzluk Cehaletten mi,Tutuculuktan mı Temelleniyor?

[12] Prof. Dr. İbrahim Ortaş, Dünya Nüfus Artışı ve bunun Tarım ve iklim değişimleri üzerindeki etkileri, (01.02.2013) http://blog.milliyet.com.tr/dunya-nufus-artisi-ve-bunun-tarim-ve-iklim-degisimleri-uzerindeki-etkileri/Blog/?BlogNo=400449

Türkiye yaş ortalaması, şimdilik 30 yaş ki dünya için çok kıymetli bir yaş ortalamasıdır. Türkiye'de beklenenin aksine nüfus artışının binde 12,1 oranı ile azalma eğilimine girmiş olduğu görülüyor. Büyük kentlere olan göç oranının azaldığı ancak nüfusun üçte birinden fazlasının yaklaşık 27 milyonun 5 büyük kentte yaşadığı görülüyor. Alt yapı yetersizliği ve dengesiz gelişen büyük kentlerde yaşanan sosyal sorunlardan çok çevre üzerindeki olumsuz etkilerin tarım ve iklim bilimcilerince dikkatle izlenmesi gerekiyor. Dünya gelirlerinin önemli bir kısmını elinde tutan ülkeler dünya gıda hâkimiyeti ve enerji güvenliği konusunda dünden daha şahin davranarak diğer ülkeler üzerinde egemenliklerini artırmaktadırlar. Dünyada özellikle de Asya ve Afrika'da üretim ile tüketim arasındaki fark hızla azalmakta ve yoksul ülkelerin gıda yönünden dışa bağımlılıkları artmaktadır. Ortadoğu ülkelerinin tamamı (İran hariç) gıda temini yönünden dışa bağımlı durumdadır (Ortaş 2013).

Nüfusu hızla büyüyen dünyanın özellikle de gelişmekte olan ülkelerinde 2030 yılından itibaren nüfus artışı ve kaynak yetersizliğiyle ilgili farklı konulara çözüm arayışları daha da hızlanacaktır. BM'nin verilerine göre, 2050 yılında dünya nüfusu 10 milyar kişi olacak. Bu artışın da gıda güvenliği, su ve diğer doğal kaynakların sürdürülebilirliği açısından büyük tehdit oluşturması öngörülüyor. Bu nüfusun önemli kısmının şehirlerde yaşayacak olması da şehirler üzerinde dolaylı olarak tarım toprakları ve doğa üzerinden büyük bir baskı oluşturacaktır. İklim değişikliğinin sonucunda etkileri daha da artarak hissedilen hızlı ve ani yağışların sellere dönüşmesi, kuraklık, sıcak hava dalgaları ve deniz suyu seviyesindeki yükselmeler, nüfus artışı ile birlikte önümüzdeki yıllarda insanoğlu için daha ciddi barınma ve beslenme sorunlarını beraberinde getirecek. Yaşanabilir, sağlıklı, iklim değişikliğinin etkilerine dayanıklı şehirlerin ve yerleşim yerlerinin kurulması günümüzün en öncelikli konusu olacak.

Mevcut tahminlere göre 2050 yılında dünya nüfusunun yüzde 80-85'i yine az gelişmiş ve gelişmekte olan ülkelerde yaşayacak. Eğer dengeli bir gelir dağılımı hedefi ile düşük karbonlu kalkınma modeline geçiş sağlanmaz ise dünya kaynaklarının hızla artan dünya nüfusunu kaldırabilmesi mümkün olmayacak. Bunun en önemli sebebi özellikle Çin ve Hindistan olmak üzere, benzeri ülkelerde yükselen orta sınıf tüketiminin artması, doğal kaynakların beklenenden çok daha hızlı ve erken tüketilmesi olacak. Bu durum özellikle de şehirlerin bir an önce gerekli tedbirleri almasını ve eyleme geçmesini gerektiriyor. Hızla gelişmekte olan bir ülke olarak Türkiye'nin şehirleri de bu değişimin bir parçası olmak ve acilen önlem almak durumunda.

Ortadoğu bölgesi bu doğal etkilerden en fazla etkilenecek bölgelerin başında geliyor. Bölge bugün doğal enerji kaynakları nedeniyle tüketimini satın alarak gideriyor ancak eğitim, bilgi ve teknolojik dönüşümden yoksun olduğu her halinden belli oluyor. Çin, Hindistan gibi nüfusu milyarın üzerindeki ülkeler için gelecek çok daha düşündürücü. Bütün bu nüfus artışının anlamı, her şeyden önce daha fazla gıda talebi, daha fazla yerleşim yeri daha fazla enerji gereksinimi demektir. Artan talepler beraberinde doğa ve çevre üzerinde ciddi bir etki yapacaktır. Kentlerin büyümesi, tarım alanlarının amaç dışı kullanımı, artan su eksikliği bunu takiben çölleşme ve verimsizlik kaçınılmaz olacaktır.

Birleşmiş Milletler Nüfus Fonu'nun iklim değişikliği ve dünya nüfusuna ilişkin açıkladığı verilere göre, iklim değişikliği günümüzde tüm dünya nüfusunu ilgilendiren en önemli sorun oluşturmaktadır. İklim değişikliği sadece iklimlerde gözle görülen değişiklikler değil, dünyanın ekolojik sisteminin başta toprak yapısının hızla bozulması, doğal kaynakların tükenmesi, bazı canlı türleri evrimleşirken bazı türlerin tamamen yok olmasına neden olacağı

kaçınılmaz duruma gelmektedir. Türkiye iklim değişimleri ve topraklarının erozyona uğrama potansiyeli bakımından en sorunlu coğrafyada bulunmakta olup önlem alınmaması durumunda önümüzdeki yıllarda ciddi sorunlar yaşayacağı kaçınılmaz olacaktır.

8. İKLİM DEĞİŞİKLİĞİ

Tokyo'da 31 Mart 2014 tarihinde 38. kez toplanan Hükümetlerarası İklim Değişikliği Paneli'nin (IPCC) ardından küresel ısınmanın nedenleri, etkileri ve çözümler konusunda yeni bir rapor yayınlandı. Dünyada konuyla ilgili yayınlanan en kapsamlı araştırma olan bu rapora göre iklim değişikliği şimdiye kadar doğal sistemler üzerinde etkili oldu, bundan sonra insanlar üzerinde de kriz etkisi görülecek. Raporda, "Artan sıcaklıklar sağlığımızı, evlerimizi, gıdamızı ve güvenliğimizi tehdit ediyor" denildi. Kesin olarak biliyoruz ki iklim değişikliği dünyayı etkiliyor ve bunun temel nedeni de atmosfere saldığımız sera gazlarıdır. Karbondioksit (CO_2), metan (CH_4), ve diazotmonoksit (N_2O) gazlarının atmosferik birikimleri en az 650.000 yıllık dönemde hiç olmadığı kadar yüksek bir düzeye ulaşmıştır. CO_2 birikimleri, temel olarak fosil yakıt yanması ve ikincil olarak net arazi kullanımı değişikliğinden kaynaklanan salımlar nedeniyle, sanayi öncesi döneme göre arttı. Okyanuslar atmosfere salınan insan kaynaklı Karbondioksitin yaklaşık yüzde 30'unu emerek asitlendi.

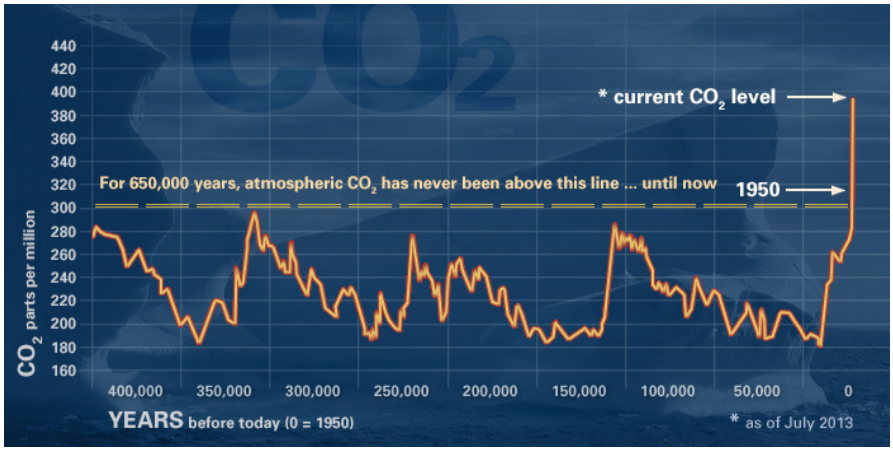

Şekil 5. Sanayi devriminden sonra atmosferik karbondioksit (CO_2) artışı

650.000 yıldır değişmeyen atmosferik karbondioksit (CO_2) 300 ppm düzeyindeydi, 1950 yılından itibaren hızla artarak 400 ppm'e yükseldi. [13]

IPCC Başkanı Rejandra Pachauri Yokohoma'da düzenlediği basın toplantısında " Bu gezegendeki hiç kimse iklim değişikliğinin etkilerinden muaf olmayacak " dedi. Dünya Meteoroloji Örgütü Başkanı Michel Jarraud daha önce insanların dünyanın iklimine bilgisizlik nedeniyle zarar vermiş olabileceklerini vurguladı ve "Artık bilmiyordum demek iyi bir bahane değil" diye konuştu. IPCC, dünyanın dört bir yanını etkileyecek doğal afetlerle ilgili bir liste hazırlıyor. Listede kentlerin sular altında kalacağı, çiftliklerin aşırı sıcak ve kuraktan ürün veremez hale geleceği, altyapıların aşırı hava koşullarından çökeceği, balık kaynaklarının tükeneceği, sıcak dalgalarının can alacağı, denize kıyısı olan yerleşim alanlarının sular altında kalacağı, yer altı sularının kuruyacağı yer alıyor.

[13] NASA: http://climate.nasa.gov/news/1050

9. HIZLI İKLİM DEĞİŞİKLİĞİNİN KANITLARI

Isınan okyanuslar : Artan ısının çoğu okyanusların en üst 700 metresinde tutulmaktadır. Bu da 1969'dan beri okyanusların 0,302°F ısınmasına neden olmuştur.

Fevkalade olaylar: 1950'den beri ABD'de sıcaklıkların en soğuk olduğu günler azalmakta, en sıcak günler artmaktadır. Yoğun yağışlı günlerin sayısının arttığına şahit olunmaktadır.

Okyanuslarda asitlenme: Sanayi devriminden beri okyanus suyunun asitliği yüzde 30 arttı. Bu yükselme insanların neden olduğu çok miktarda karbondioksit çıkışından kaynaklanmaktadır. Her yıl okyanusların üst katmanında tutulan karbondioksit bir milyar tonu aşmaktadır.

Maldiv Cumhuriyeti'nde deniz düzeyinin yükselmesi: Son yüzyılda, küresel deniz düzeyi 17 cm. yükseldi. Son on yıldaki yükselme hızı son yüzyılın iki katına çıktı.

Küresel sıcaklık artışı : Üç büyük küresel yüzey sıcaklığı araştırma merkezinin verilerine göre dünya 1880 yılından itibaren ısındı. Bu ısınmanın en çoğu 1970'den sonra oldu.

Şekil 6. İklim Değişikliğinin İşaretleri

Grönland buzullarında eriyen suyun akışı: Çatlayan buz levhaları : Grönland buzulları 2002-2006 yılları arasında 150-250 kilometre küp ve Antarktika buzulları, 2002-2005 yılları arasında 152 kilometre küp azaldı.

Kilimanjero dağında azalan kar örtüsünün uzaydan görünüşü

Kar ve buzullarda azalma **:** Alpler, Himalayalar, And dağlarında, Alaska ve Afrika dahil dünyanın her yerinde kar ve buzullar azalmaktadır.

Şekil 7. İklim Değişikliğinin Belirtileri

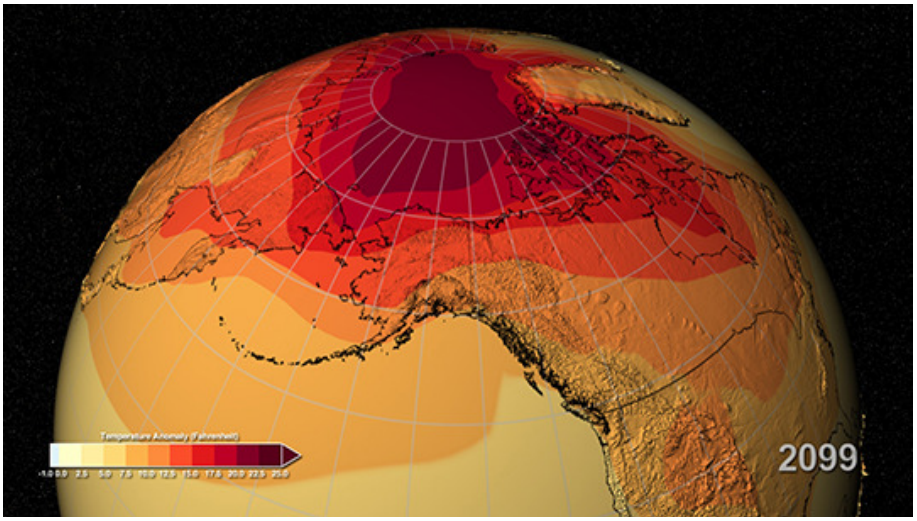

Şekil 8. 2099 yılında küresel ısınma

NASA İklim Similasyon Merkezi'ne göre 2099 yılında kuzey kutbunun sıcaklığı 25 Fahrennayt dereceye ulaşacak. [14]

10. İKLİM DEĞİŞİKLİĞİNE KARŞI ALINAN ÖNLEMLER [15]

İnsanların iklim değişikliğini nasıl karşıladığını araştıran Warner, Van Der Geest ve ekibi, Asya, Afrika ve Mikronezya'da 9 ülkeyi ziyaret etti. Buralarda 3269 aile ile görüştüler ve aldıkları önlemlerle ilgili bilgi aldılar. Van Der Geest, izlenimlerini şöyle aktarıyor: " Buralarda çeşitli iklim değişikliklerine maruz kalmış insanlarla görüştük. Bu insanlar kendi yaşam alanlarını korumak için çok şey yapmış. Riskleri minimize etmek için yalnızca bugünkü yaşam tarzlarını değiştirmekle kalmamışlar, geleneksel yaşam tarzlarını zor da olsa terk etmişler. Eğer Afrika'da bir çiftçinin iki hektar tarlası varsa, her birine değişik tohumlar ekerek kuraklıkta tüm ürünlerin yok olma riskini azaltabiliyor. Benzer şekilde Bangladeş'te çiftçiler deniz sularının yükselme tehlikesine karşı tuza dirençli pirinç ekimi yapıyor.

Butan'da çiftçiler muson yağmurlarındaki ani değişiklikten etkilenmemek için yeni yağmur rejimine ayak uyduracak yöntemler geliştirdiler. Bazı çiftçiler komşularıyla işbirliği yaparak suyun paylaşımında yepyeni bir düzen oluşturdular. Mozambik'te ise şiddetli sellerden sonra hükümet çiftçileri daha yüksek bölgelere taşıdı. Ancak bu bölgelerdeki toprak, tarıma elverişli olmadığı için halk dağlarda yaşamaya devam etmekle birlikte, ovalarda ekim yapmaya devam etti. Şu anda ova ile dağ arasında sürekli olarak mekik dokuyorlar. Geceleri güvenli bölgelerde bulundukları için yaşamları risk altında bulunmasa da sel durumunda tüm ekinlerini kaybetme riskiyle karşı karşıyalar.

Afrika ülkelerinde pek çok insan doğal afet durumunda dış yardımlar sayesinde hayatta kalabiliyor. Bazıları da hayvanlarını ve diğer mallarını satıp yiyecek satın alıyor. Siklonlar gibi aşırı doğa olayları ise hayatlarını zar zor sürdüren insanların tümüyle yer değiştirmesine yol açabiliyor. Van Der Geest, görüştükleri kişilerin yüzde 70'inin önlem almalarına karşın

[14] http://www.nasa.gov/press/2014/march/long-term-warming-likely-to-be-significant-despite-recent-slowdown/#.U14nC1V_vCt
[15] Reyhan Oksay, Kaynak New Scientist , 5 Nisan 2014

büyük kayıplar verdiğini belirtiyor. Bu da yüzde 30'u kadarının ya felaketlerden etkilenmediğini ya da buldukları çözümlerin daha başarılı olduğu anlamına geliyor.

11. TÜRKİYE ANAYASASINDA ÇEVRE VE ÇOK TARAFLI SÖZLEŞMELER

Anayasa`nın 56. Maddesi: Sağlık Hizmetleri ve Çevrenin Korunması; Herkes, sağlıklı ve dengeli bir çevrede yaşama hakkına sahiptir. Çevreyi geliştirmek, çevre sağlığını korumak ve çevre kirlenmesini önlemek Devletin ve vatandaşların ödevidir. Devlet, herkesin hayatını, beden ve ruh sağlığı içinde sürdürmesini sağlamak; insan ve madde gücünde tasarruf ve verimi artırarak, işbirliğini gerçekleştirmek amacıyla sağlık kuruluşlarını tek elden planlayıp hizmet vermesini düzenler. Devlet, bu görevini kamu ve özel kesimlerdeki sağlık ve sosyal kurumlarından yararlanarak, onları denetleyerek yerine getirir.[16]

Anayasanın 90/5. maddesinde "Usulüne göre yürürlüğe konulmuş milletlerarası antlaşmalar kanun hükmündedir. Bunlar hakkında Anayasaya aykırılık iddiası ile Anayasa Mahkemesine başvurulamaz" hükmüne yer verilmiş bulunmaktadır. Bunun yanında Türkiye 18.05.1954 tarihinde Avrupa İnsan Hakları Sözleşmesini imzalamış olup bu tarihten itibaren adı geçen sözleşme iç hukukumuzun bir parçası olmuştur.

12. SONUÇLAR

Dünyada demir çelik üreten ilk 7 ülke, dünyada en çok motorlu araç üreten ve döküm yapan ülkelerdir. Çelik, düşük karbon dünyası için taşıma, ulaşım, inşaat, iskan ve elektrik üretiminde zaruri olmakla birlikte; bu 7 ülke üretimlerinde en çok enerji kullanan ayni zamanda en çok karbondioksit çıkışına neden olan; diğer bir değişle iklim değişikliğine önemli katkısı olan ülkelerdir. İklim değişiminin sonuçlarından ilk etkilenen ülkeler, bu 7 ülkeden farklı ülkelerdir. Geçmişte çok demir çelik üreten bazı ülkeler iklim değişikliği riskini önceden öngörmüş, demir çelik üretimlerini düşürmüş veya bu sektörü terk etmişlerdir. Bu ülkeler demir çelik ihtiyaçlarını ithalatla karşılamayı sürdürmektedir.

Sera gazlarının sürmekte olan salımları, daha fazla ısınmaya ve iklim sisteminin tüm bileşenlerinde değişikliklere neden olacaktır. İklim değişikliğinin sınırlandırılması, sera gazı salımlarının önemli miktarda ve sürekli azaltılmasını gerektirecektir.

Hükümetlerarası İklim Değişikliği Paneli'nin üç rapordan oluşan 5. Değerlendirme Raporlarını koordine eden üç bilim insanından biri olan Mali'li Youba Sokona, ortaya çıkan raporlar için şu ifadeyi kullanıyor, "… biz haritayı hazırlıyoruz ama dümen onlarda… Yer yüzünün egemenleri; Davos'da toplanan klik, gücü elinde tutanlar gezegenin geleceğini bu raporlarda görüyor ve kaderini de ellerinde tutuyorlar. IPCC'nin ard arda çıkan son raporları, iklim değişikliğinin bugün gerçekleşmekte olduğunu, başta tarımsal üretimin gerilemesi olmak üzere insani ve ekonomik yıkımın şu anda yaşanmakta olduğunu kontrol altına alınamadığı takdirde olacaklara ve sonuçlara işaret ediyor. [17]

IPCC, Sanayi Devrimi sonrası küresel sıcaklık artışlarının 4 dereceyi bulmasının kabul edilemeyecek boyutta riskler ve tehlikeler taşıdığını belirtirken, artışları 2 derecede tutmak için ne yapılmasına dikkat çekiyor. 3. raporda bugün hala dünya enerji ihtiyacının (%80'den fazla) sağlayan fosil yakıt rezervlerinin, kömür, petrol ve doğalgazın, önümüzdeki onyıllardan

[16] http://www.tbmm.gov.tr/develop/owa/anayasa.uc?p1=56
[17] Baha Kuban, Cumhuriyet Bilim ve Teknoloji (25.04.2014) Teknoloji-Politik: Dünya Egemenlerine Gerçeği Söylemek

itibaren yeraltında kalmaları gerektiğine işaret ederken, 2050 yılına kadar yenilenebilir enerji kaynaklarından enerji tedariğinin 3 hatta 4 kat artması gerektiğini vurguluyor.

Çevre sorunlarının evrensel niteliği nedeniyle olumsuz sonuçlardan hiçbir kişi ya da devletin kaçamayacağı ve bu sorunlarda dereceleri farklı olmakla birlikte herkesin payı olması sorunun çözümü için ulusal, bölgesel ve evrensel adımların birlikte atılmasını zorunlu kılmıştır.[18] Bunun somut anlamı, bütün devletler ve toplumlar için "ortak bir ilgi ve menfaat alanı oluşturan bu konuda herkese yükümlülükler getirilmesinin ve herkesin bunlara uymasının kaçınılmazlığıdır. Ortak bir soruna getirilecek ortak çözümler yine kerkesin menfaatına olacaktır. Çevre korumayı amaçlayan çok taraflı sözleşmeler (kısaca ÇS) de Birleşmiş Milletler düzeyinde ve bölgesel düzeylerde hazırlanmak suretiyle önemli sayıda ülkeyi ortak sorumluluğa kattığından bu özgünlüğü yansıtmaktadır.

İklim değişikliğinin ekosistemlere olan etkisi nedeniyle her canlı yaşamı olumsuz etkilenme riski taşımaktadır. İnsanlık varoluşunu tehdit eden ve dünya tarihinin en önemli sorununa çözüm aramalıdır.

Einstein, çılgınlığı, "bir hareketi tekrar tekrar, her seferinde öncekilerden farklı sonuç almayı umarak, ısrarla yapmaya devam etmek" olarak tanımlamıştı. Günümüzde uygarlığı yönetmeye çalışanların akıl durumu bu tanıma çok uyuyor.

KAYNAKLAR

1) Selahaddin Şanbaşoğlu, Metalurji Yüksek Mühendisi, Standart Çeliklerin Uluslararası Eşdeğerleri, 1985, Sayfa 3
2) Prof. Dr. H. Çimenoğlu, Prof. Dr. E. Geçkinli, Y. Müh. S. Yıldırım, Y. Müh. M. Baydoğan, TMMOB Metalurji Mühendisleri Odası, Çelik ve Dökme Demirlerin Metalografisi ve Mekanik Muayenesi, 16-18.05.2001 Sayfa 1.1
3) NASA : http://climate.nasa.gov/evidence/
4) Dünya Çelik Derneği, http://www.worldsteel.org
5) Server Tanilli, İnsanlığı Nasıl Bir Gelecek Bekliyor?, 2006, Sayfa 18
6) Modern Casting /Aralık 2013, Dünya Döküm Sanayi 47. Sayımı
7) ISSF, Uluslararası Paslanmaz Çelik Forumu haber bülteni,04 Nisan 2008, www.wordstainless.org
8) Paydossuz Bir Yaşam, Selahaddin ŞANBAŞOĞLU, Türk Demir Çelik Sektörünün Dünü ve Bugünü, TMMOB Metalurji Mühendisleri Odası, 1998, s.93.
9) Türkiye Çelik Üreticileri Derneği, www.dcud.org.tr
10) Otomotiv Sanayii Dermeği Otomotiv Sanayii 2013 Değerlendirme Raporu, sayfa 6-7
11) Doğan Kuban, Cumhuriyet Bilim ve Teknoloji (01.02.2014) " Çağa Uyumsuzluk Cehaletten mi,Tutuculuktan mı Temelleniyor?
12) Prof. Dr. İbrahim Ortaş, Dünya Nüfus Artışı ve bunun Tarım ve iklim değişimleri üzerindeki etkileri, (01.02.2013) http://blog.milliyet.com.tr/dunya-nufus-artisi-ve-bunun-tarim-ve-iklim-degisimleri-uzerindeki-etkileri/Blog/?BlogNo=400449
13) NASA: http://climate.nasa.gov/news/1050
14) http://www.nasa.gov/press/2014/march/long-term-warming-likely-to-be-significant-despite-recent-slowdown/#.U14nC1V_vCt
15) Reyhan Oksay, Kaynak New Scientist , 5 Nisan 2014
16) http://www.tbmm.gov.tr/develop/owa/anayasa.uc?p1=56
17) Baha Kuban, Cumhuriyet Bilim ve Teknoloji (25.04.2014) Teknoloji-Politik: Dünya Egemenlerine Gerçeği Söylemek
18) Prof. Dr. Nükhet Yılmaz Turgut, Cumhuriyet Bilim ve Teknoloji (04.04.2014) " Çevreyi Koruyucu Çok Taraflı Uluslar arası Sözleşmelerin Özgünlüğü Ülkemizde de Dikkate Alınmalıdır."

[18] Prof. Dr. Nükhet Yılmaz Turgut, Cumhuriyet Bilim ve Teknoloji (04.04.2014) " Çevreyi Koruyucu Çok Taraflı Uluslar arası Sözleşmelerin Özgünlüğü Ülkemizde de Dikkate Alınmalıdır."

SICAK HADDEHANELERDE ENERJİ TASARRUFU İÇİN SICAK VE DİREKT ŞARJ UYGULAMASI

Nazmi SARIKAYA*, Özgür BİLGİN*

*İSDEMİR A.Ş. Üretim Planlama Müdürlüğü

ÖZET

Bu çalışmada, İskenderun Demir ve Çelik Fabrikaları'nda (İSDEMİR) Sıcak Haddehane tavlama fırınlarına şarj edilen slabların sıcaklığını kaybetmeden şarj edilmesinin yapılabilirliği araştırılmış ve yeni bir uygulama geliştirilmiştir. Bu sıcak şarj metodunda, sürekli döküm makinalarında üretilen yarı mamulün bekletilmeden sıcak haddehane tavlama fırınlarına şarjı amaçlanmaktadır. Standart bir metodun olmaması nedeniyle kolay bir uygulama olmamakla beraber, uygulamanın önünde birçok engel bulunmaktadır.

Çalışmanın amacı Çelikhane, Döküm Makinaları ve Sıcak Haddehane arasında senkronizasyonu, kurulan sistematikler yoluyla sağlamak ve slab stok sahası bekleme süresini yönetebilmektir. Geliştirilen metod ile sıcak şarj metodu direkt şarja dönüşebilmekte ve sürekli döküm makinalarıyla senkronize olarak vinçlerin yerine besleyici konveyörle slabları tavlama fırınına şarj edebilmektedir.

Sonuç olarak, 2013 yılında şarj edilen slabların %54 lük kısmı 586 °C sıcaklık ortalamasını yakalamış, ortalama şarj sıcaklığı 111 °C den 357 °C'ye çıkartılmıştır. Yakıt tüketiminde %22 civarında tasarruf sağlanmıştır.

Anahtar Kelimeler: Sıcak Şarj, Direkt Şarj, Enerji Tasarrufu, Planlama, Tavlama Fırını

HOT CHARGE AND DIRECT CHARGE APPLICATION FOR ENERGY SAVING AT HOT STRIP MILL

ABSTRACT

In this study, feasibility of charging of the slabs to the reheat furnace without losing heat was investigated and as a result a new application was developed in Iskenderun Iron and Steel Plants (İSDEMİR). In this Hot Charge method, the semi-product; which is produced at the slab casting machine is aimed to charge as early as possible to Hot Strip Mill reheat furnace. This application is not easy due to lack of a standard method and there are difficulties for application.

Purpose of this application is to provide a synchronization between Steel Plant, Casting Machines and Hot Strip Mill by using of developed systematics to manage the waiting time of the semi-product in slab stock area. The developed hot charge method can be converted to direct charge method so that the slabs can be charged to the furnace synchronously with continuous casting machine by feeder conveyor instead of cranes.

As a result, in 2013, 54 percent of the total amount of the slabs were charged to the reheat furnace with average 586° C and general average temperature reached up to 357 °C from 111 °C . Energy consumption was decreased 22 percent.

Key Words: Hot Charge, Direct Charge, Energy Saving , Planning , Reheat Furnace

GİRİŞ

Ülkemizin kuruluş tarihi itibari ile üçüncü, uzun ürün üretim kapasitesine göre en büyük entegre demir ve çelik fabrikası olan İSDEMİR, 2008 yılında devreye aldığı 3,5 milyon ton/yıl sıcak haddeleme kapasitesi ile Türkiye'nin uzun ve yassı ürün üreten tek entegre tesisidir. İSDEMİR'de 2003 yılı içerisinde planlanan ve 2004 yılı içerisinde başlayan Modernizasyon ve Dönüşüm Yatırımları tamamlanarak başlangıçta 2,2 milyon ton/yıl olan sıvı çelik kapasitesi 5,3 milyon ton/yıl seviyesine çıkarılmış olup, uzun ürünün yanı sıra ağırlıklı olarak yassı mamul üretimi yapılmaktadır.

İSDEMİR'de yassı mamül (sıcak rulo) üretimine yönelik olarak, 680-2050 mm arasındaki genişliklerde, twin ve/veya single, çift kanal döküm yapabilen ve hareketli kalıp sistemine sahip 5 milyon ton/yıl üretim kapasiteli 2 adet slab döküm tesisi bulunmaktadır.

İSDEMİR 2008 Ağustos ayında, 3,5milyon ton/yıl kapasiteli sıcak haddehane tesisini devreye alarak, yassı ürün üretmeye başlamıştır. İSDEMİR Sıcak Haddehanesinde her biri 400 ton/saat üretim kapasitesine sahip yürüyen tabanlı 2 adet slab tav fırını bulunmaktadır. Sıcak haddehane, kullanım alanlarına yönelik olarak çok farklı kalite yelpazesinde 1,39-22 mm kalınlık aralığında haddeleme yapabilmektedir.

İSDEMİR Sıcak Haddehane slab tavlama fırınları ve Slab Sürekli Döküm tesisleri yerleşim planları, sıcak ve direkt şarj yapılabilmesine uygun olarak tasarlanmıştır. 1 nolu slab makinasında üretilen slabların, slab stok sahasına indirilmeden doğrudan Sıcak haddehane tav fırınlarına şarj edilebilmesi amacıyla döküm tesisi ile tav fırınları arasında besleyici konveyörler yerleştirilmiştir. 2 nolu slab makinasında üretilen slablar ise, ferry car isimli aktarma arabaları ile 1 Nolu slab tesisi hat boyuna aktarılabilmekte ve bu hat üzerinden aynı besleyici konveyör ile sıcak haddehane tav fırınlarına slabların aktarılması sağlanmaktadır.

Yassı mamül üreten tesislerde yarımamül olarak tanımladığımız slablar, hat üzerinde işlenmeden önce sıcak haddehane tav fırınlarına şarj edilerek, belirli bir sıcaklığa (1150-1230 °C) ulaştıktan sonra hatta alınarak haddeleme işlemi gerçekleştirilmektedir. Slab döküm makinasında üretilen slabların hat çıkış sıcaklığı yaklaşık 800-1000°C civarındadır. Bu tesislerde üretilen slablar haddeleme sırasını beklemek amacı ile slab stok sahalarında belirli bir düzende istiflenirler. Bu bekleme süresine bağlı olarak slablar, ortam sıcaklığına kadar soğumakta ve haddeleme programına alındıklarında yeniden sıcak haddehane tav fırınlarına alınarak deşarj sıcaklığına ulaşıncaya kadar yeniden ısıtılırlar. Bu döngüde slabın mevcut sıcaklık değeri kaybedilmekte ve yeniden ısıtma için önemli bir enerji harcanmaktadır. Sıcak şarj ve direkt şarj uygulamaları, bu sıcaklık kaybını minimize ederek işletmelerde enerji verimliliği sağlanmasını amaçlamaktadır.

BULGULAR

İSDEMİR'de slab tav fırınlarına şarj edilen slablar, fırın giriş sıcaklıklarına göre soğuk şarj, ılık şarj, sıcak şarj ve direkt şarj olarak tanımlanmaktadır. Direkt şarj olarak tanımlanmış bir slab, slab stok sahasına vinç yardımı ile indirilmeden doğrudan besleyici konveyörler ile slab tav fırınlarına şarj ediliyor ise, bu özelliklerdeki slablar için "hat üzerinden direkt şarj" tanımlaması yapılmaktadır. Tablo1'de İSDEMİR'de kullanılan şarj tipleri ve bu şarj tipleri için kabul edilen slab tav fırın giriş sıcaklık aralıkları yer almaktadır.

Tablo 1. Şarj Tipleri ve Slab Tavlama Fırın Giriş Sıcaklık Aralıkları

Şarj Tipi	Slab Tavlama Fırın Giriş Sıcaklık Aralığı (°C)
Soğuk Şarj	0-100
Ilık Şarj	101-300
Sıcak Şarj	301-600
Direkt Şarj	601 ve üzeri
Hat Üzerinden Direkt Şarj	

Üretilen slabların sıcak ve direkt şarj yapılabilmesi amacıyla oluşturulan Sıcak haddehane üretim programları; merdane tüketimi ve haddehane verimliliği açısından birçok farklı kriterin sağlanması koşulu ile hazırlanabilmektedir. İSDEMİR'de slabın fiziksel özellikleri (genişlik, boy ve kalınlık), kalite grubu ve hat çıkış özelliklerine bağlı olarak 42 farklı haddeleme kriteri bulunmaktadır.

Sıcak haddehane tesisinde sıcak ve direkt şarj olarak haddelenmek üzere planlanan slabları içeren sürekli döküm tundiş planları, azami ölçüde sıcak haddehane kriterlerini karşılayacak şekilde oluşturulmaktadır. Genişlik dağılımları, sıcak haddehane çıkış kalınlık atlamaları, kalınlıklar arası kullanılması gereken kademe geçiş kalınlıkları ve kalite grupları, tandiş planlamasında dikkat edilen hususlar arasında yer almaktadır.

Sürekli dökümler tandiş programının hazırlanması ile, sıcak haddehane sıcak ve direkt şarj üretim programları hazırlanabilmektedir. Sıcak haddehane programları içerisinde, üretimden gelerek sıcak ve direkt şarj yapılması planlanan slablar (hayali slab) ile sıcak haddehane programı hazırlanması için gerekli temel ihtiyaçları karşılamak üzere, slab stoklarında yer alan diğer soğuk slablar da yer alabilmektedir.

Sıcak haddehane programlarında yer alan hayali slabların, slab döküm tesislerinde üretilmesi ile birlikte; İSDEMİR bilgi sistemleri, planlanan hayali slablar ile üretilmiş gerçek slabların programlar içerisindeki dönüşüm işlemlerini yapmaktadır. Hayali slab/gerçek slab dönüşüm işlemleri belirlenen kriterlere göre bilgi sistemleri tarafından otomatik olarak gerçekleştirilmektedir. Sıcak haddehane programları içerisinde yer alan slab üretimleri tamamlandığında, hayali slab/gerçek slab dönüşüm işlemleri de sonlandırılmakta ve sıcak slabları içeren üretim programları Sıcak haddehane tesisine bilgi sistemleri aracılığı ile yayınlanmaktadır.

Üretimi tamamlanan programların en kısa sürede sıcak haddehane tesisinde şarja alınabilmesi için, hangi programın hangi sırada şarj edilmesi gerektiği ile ilgili olarak Üretim Planlama Müdürlüğü tarafından "Program Sırası" hazırlanmakta ve sıcak haddehane işletme gruplarına dağıtımı yapılmaktadır. Programların sıcak haddehane fırınlarına planlanan sırada şarj edilmesinden sorumlu slab stok sahası görevlileri, dağıtımı yapılan "Program Sırası" na uygun olarak, slabların sahada stoklanmasını ve slab tav fırınlara şarjını organize etmektedir.

Sıcak şarj programları, döküm tamamlandıktan ve slablar stok sahasına indikten sonra sıcak haddehane tav fırınlarına şarj edildiği için, sıcak haddehane kriterlerine uygun olması koşulu ile çok farklı ebat ve miktarlarda planlanabilmektedir. Direkt şarj programlarında ise üretilen slablar, stok sahasına indirilmeden doğrudan besleyici konveyerler ile slab tav fırınlarına şarj edildiğinden, planlanan slabların sıcak haddehane kriterlerine uygunluğuna ilave olarak, aynı fiziksel/sipariş özelliklerinde ve en önemlisi slab üretim ve sıcak haddehane slab tüketim hızı dengeli olabilecek ebatlarda planlanması önem arz etmektedir. Şekil 1'de sıcak haddehane program yapısına uygun örnek sıcak ve direkt şarj program yapıları gösterilmektedir.

Şekil 1. Sıcak Şarj ve Direkt Şarj Örnek Program Yapıları

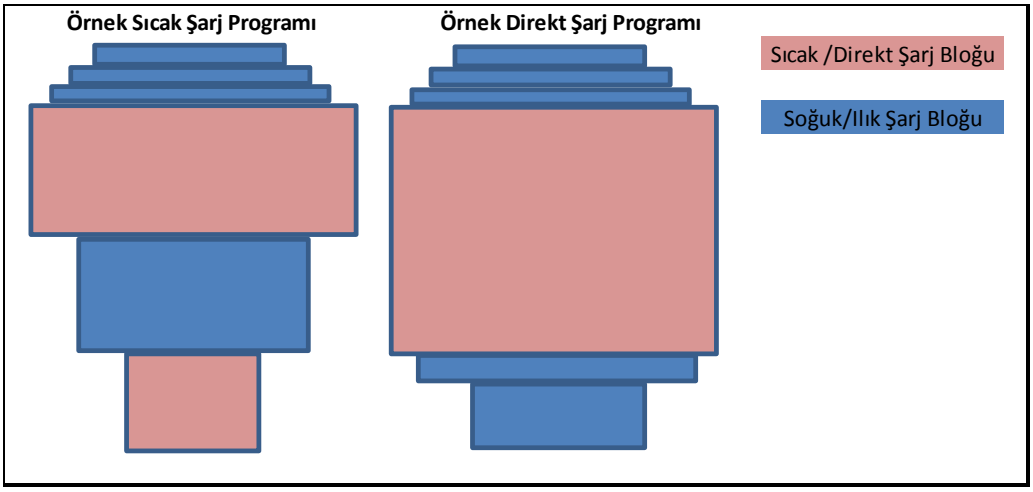

Kurulan sistemlerin izlenebilirliği ve farklı birimler tarafından sorunsuz yönetilebilmesi amacıyla, İSDEMİR'de bilgi ve otomasyon sistemlerinde birçok yapısal değişikliklere gidilmiştir. Bunlara ilave olarak Planlama, Kalite, Çelik Üretim, Slab stok sahası işletme ve Sıcak haddehane işletme gibi farklı birimlerin iş yapış şekillerinde de sıcak ve direkt şarj programlarının sağlıklı yönetilebilmesine yönelik revizyonlar yapılmıştır.

SONUÇLAR

Kurulan sistematiklerin 2012 yılı itibari ile devreye alınması ile birlikte sıcak şarj programlama yüzdesi belirgin bir şekilde artmış, bu durumun fırın enerji tüketimlerine olumlu katkısı gözlemlenmiştir. Şekil 2 ve Şekil 3'de 2010-2013 yılları arası slab tavlama fırınlarına şarj edilmiş slabların, sıcaklık değerlerine göre oluşturulmuş soğuk, ılık ve sıcak+direkt şarj oranları ve ortalama fırın şarj sıcaklıkları görülmektedir. Şekil 4'de ise aynı dönemlerdeki ton ürün başına fırın enerji tüketimlerindeki azalma eğilimi gözükmektedir.

Şekil 2. Yıllar İtibari İle Sıcak+Direkt Şarj Gerçekleşme Oranları

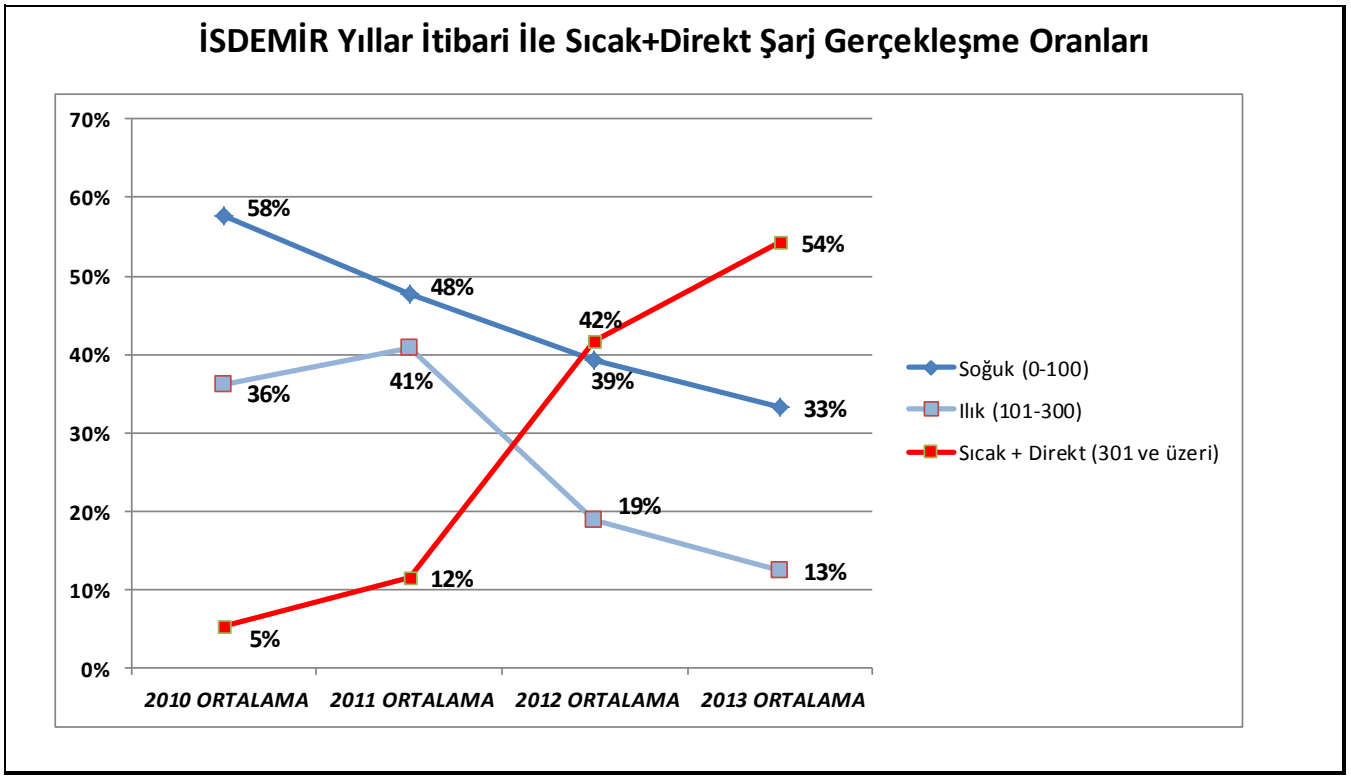

Şekil 3. Yıllar İtibari İle Sıcak+Direkt Şarj Sıcaklık Ortalamaları

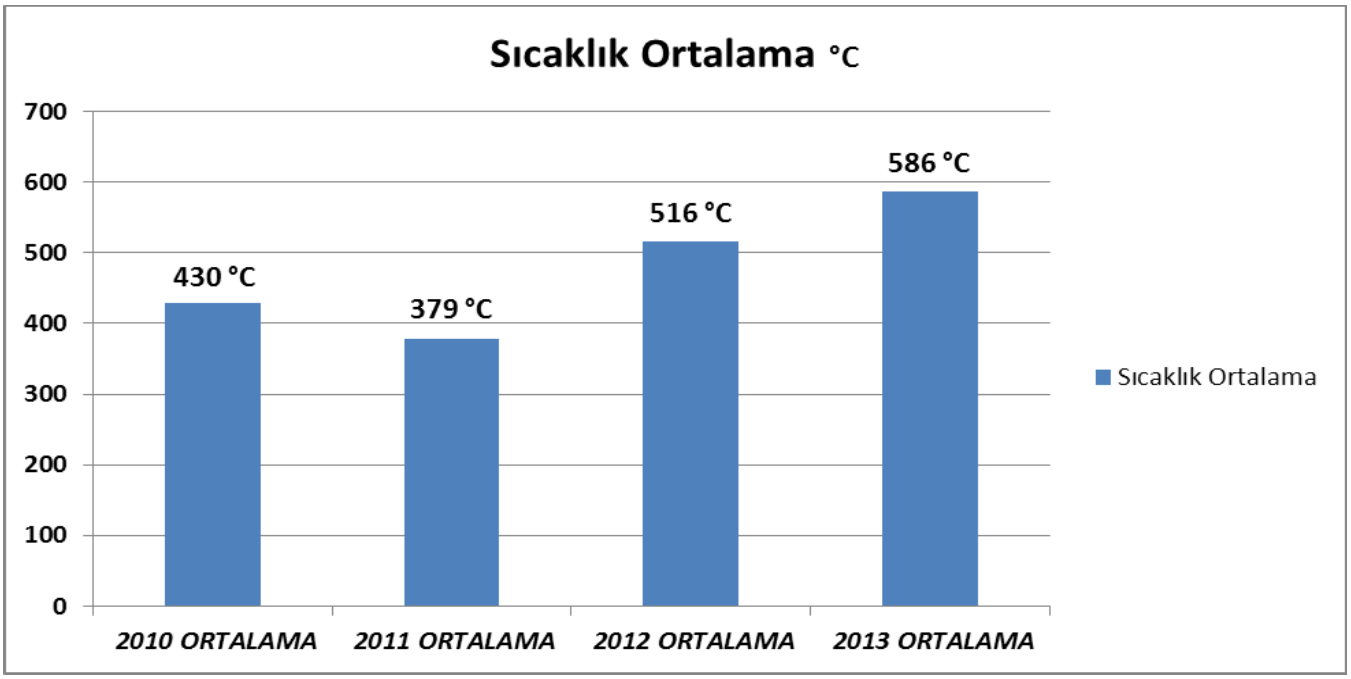

Şekil 4. Yıllar İtibari İle İSDEMİR Slab Tavlama Fırınları Tüketim Değerleri

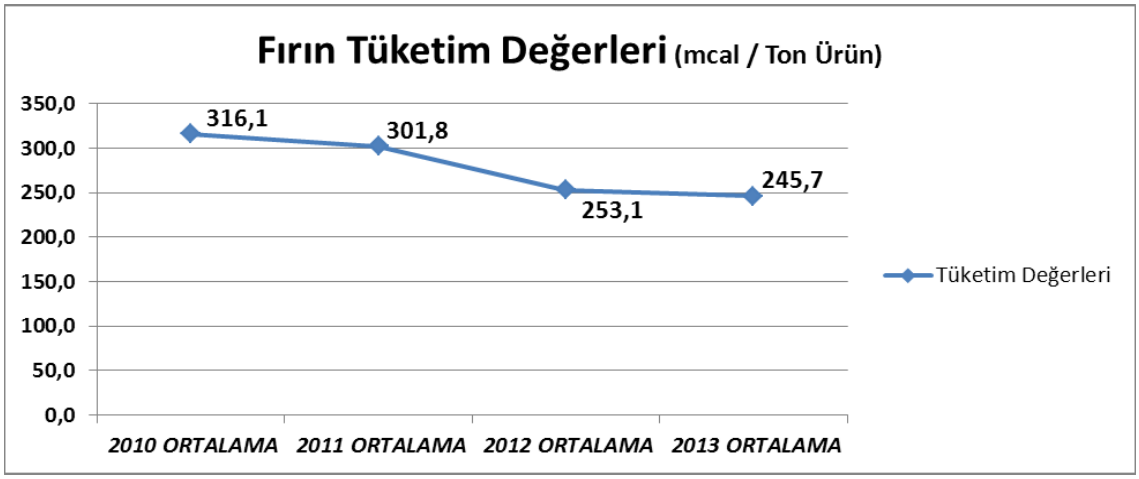

Sıcak ve direkt şarj uygulamasının fırın enerji tüketimlerine katkısına ilave olarak, slab stok sahalarındaki vinç maniplasyon sayılarının azalması kaynaklı enerji verimliliği ve sıcak şarj yapılan slablarda % 0,03'lük tufal kaybının önlenmesi gibi maliyet avantajları da yer almaktadır. Sıcak ve direkt şarj uygulamasına geçiş ile birlikte 2011-2013 yılları için, fırın enerji tüketimleri, vinç maniplasyon ve tufal kaybı miktarlarının önlenmesi kalemlerinden oluşan toplam maliyet kazancı yaklaşık olarak 12.762.374 $ olarak hesaplanmıştır.

Tesis yerleşimi, ürün çeşitliliği, hat verimliliklerini esas alan üretim programı hazırlama kriterleri, sipariş dağılımı ve terminin de üretim gibi kısıtlar, sıcak ve direkt şarj uygulamasını doğrudan etkileyen faktörlerdir. Çok farklı fiziksel özelliklerde ve düşük tonajlı sipariş dağılımı, sıcak haddehane edger ezme kabiliyeti ve buna bağlı sürekli döküm ebat sayısı fazlalığı gibi kısıtlar sıcak ve direkt şarj programlama yapılmasını olumsuz yönde etkilemektedir. İSDEMİR'de sıcak ve direkt şarj miktarlarının sürekli olarak artırılmasına yönelik olarak iyileştirme çalışmaları devam etmektedir.

THE USE OF ETİKROM CONCENTRATE THROUGH SHS PROCESS IN THE PRODUCTION OF LOW CARBON FERROCHROMIUM

Meryem Niş Güngör, Murat Alkan, Onuralp Yücel

nismer@itu.edu.tr, alkanmura@itu.edu.tr, yucel@itu.edu.tr

İstanbul Teknik Üniversitesi, Kimya-Metalurji Fakültesi, Metalurji ve Malzeme Mühendisliği Bölümü, Maslak, İstanbul, 34469, Türkiye

ABSTRACT

In today's world, 95% of the chromium, of which 90% of is, is used as an alloying element in stainless steels and heat-resistant steels, produced as ferrochromium. Although Turkey does not have large reserves of chromium ores which are named as chromite, due to the fact that these ores have high quality, they are preferred to be used in metallurgical sectors and have an increasing importance for ferrochromium production. In this study, having Etikrom concentrates as the raw material used, instead of producing ferrochromium with a high carbon level by a highly energy consuming process of approximately 10000 kWh /t power which has a low added value, it was aimed to synthesize a product with a low carbon level and a higher added value via self-propagating high temperature synthesis(SHS), calculate the total metal gain efficiency of production parameters and examine their effects on the final alloy composition.

Keywords: Ferrochromium, SHS, chromite ore

ÖZET

Günümüzde, metalurji sektöründe kullanılmakta olan Krom (Cr) metalinin % 95'i ferrokrom olarak üretilmekte ve üretilen ferrokromun yaklaşık % 90'ı paslanmaz ve ısıya dirençli çelik üretiminde alaşım ilavesi olarak kullanılmaktadır. Türkiye, krom cevheri olan kromit açısından çok geniş rezerve sahip olmamasına rağmen, sahip olduğu rezervlerin cevher kalitesinin yüksek olması sebebiyle metalurjik sektörlerde tercih edilmekte ve özellikle ferroalaşım üretiminde giderek önemini arttırmaktadır. Bu çalışmada, hammadde olarak Eti Krom konsantresi kullanılarak, yaklaşık 10000 kWh / t gibi enerji yoğun yöntemle katma değeri düşük yüksek karbonlu ferrokrom alaşımı eldesi yerine daha ekonomik ve yüksek hızda üretim olanağı sağlayan kendiliğinden ilerleyen yüksek sıcaklık sentezi (SHS)

yöntemiyle katma değeri nispeten daha çok olan düşük karbonlu ferroalaşımların üretilmesi ve üretim parametrelerinin toplam metal kazanım verimleri ve sonuç alaşım bileşimi üzerine olan etkilerinin incelenmesi amaçlanmıştır.

Anahtar kelimeler: Ferrokrom, SHS, Kromit cevheri

INTRODUCTION

Chrome , one of the natural components of the earth crusts, is one of the basic element of metallurgy, chemical and refractory industry. In metallurgical industry , the most important uses of chromium ore is ferrochromium production which use in making stainless steel. Ferrochromium is crucial ingredient of stainless steel, metal and also arms industry. Because of showing high resistance to atmosferic corrosion, chemical effects and abrassion ,besides all these hard structure ,it widely used coating of steel and other materials [1].

Chromium containing economically important mineral is named as chromite. In the world, chromite resources level is totally 7.6 billion tons but just 3.6 billion tones can be classified as reserve. Chrome ore deposits that can be economically operated mainly located in the world such as South Africa, Kazakhstan, Zimbabwe, Finland, India, Turkey, Iran, the Philippines, Cuba and Brazil [2].

Ferrochrome an alloy of iron and chromium ,chromium containing rate of 45-95%, usually use to rust and corrosion prevention and resistance increasing in the iron and steel industry . According to the amount of C contained, it is divided 3 groups, high carbon (4-10% C), medium carbon (0.5-4% C), low-carbon (0.01 to 0.5% C) ferrochromium. First time in 1820, it was produced by chromium and oxide mixture reducing by charcoal in a crucible. The use of electrothermal process at ferrochrome production was a turning point for development. In 1893, Moisson obtained ferrochrome, containing %60 Cr and %6 C, in an electric furnace. In 1907, low carbon ferrochrome production was carried out by F. M. Becket [3].

Self propagating high temperature synthesis (SHS), distinguished from the other production methods by characterized several features. Some of them are listed as easy applicability, high reaction rate, low power requirements and low cost [4,5].

In this study, it was aimed to produce low carbon ferrochromium with using Etikrom concentrate via the production method relatively easy than others with self propagating high temperature synthesis.

EXPERIMENTAL STUDY

Experimental studies of low carbon ferrochrome production having the composition indicated in Table 1 for Etikrom concentrate, %98 purity Al powder and minimum % 99.7 CrO3 containing chromic acid.

Table 1: Composition of Etikrom A.Ş. concentrate (%)

Cr_2O_3	47,16
Fe_2O_3	16,00
SiO_2	6,5
Al_2O_3	10,63
CaO	0,32
MgO	19,05

Before the experiments, chromic acid grinded by using cyclic grinder and concentrate was dried at 105^0C in an oven about 30 minutes. Ratio of concentrate and chromic acid fixed by using FactSage 6.2 Thermochemical Software datas also addittion of Al which used to reductant, calculated. According to calculation, mixture scale with using assay balance. Then base mixture prepared in turbula mixer.

After mixturing base mixture put into cupper crucible. To provide power supply connection tungsten resistance wire was placed on the top of the mixture. Cupper crucible was closed and trigger for starting reaction. After this crucible was allowed to cooling. Getting ready for chemical analysis metal and slag was seperated, eliminated from empurities in arc melting device.

Table 2. Experimental datas for mixture compound

Deney No	Cevher-CrO_3	Cevher	CrO_3	Al(%)
1	%50 - %50	50	50	100
2	%55 - %45	55	45	100
3	%60 - %40	60	40	100
4	%65 - %35	65	35	100
5	%70 - %30	70	30	100
6	%65 - %35	195	105	100
7	%65 - %35	65	35	90
8	%65 - %35	65	35	110
9	%65 - %35	65	35	120

RESULT AND DISCUSSION

By using SHS method, making use of the chemical analysis of metal yield, total metal recovery, the scattering ratio parameters calculated results are shown below in table form.

Besides concentrate and chromic acid ratio, the amount of Al changed. In the case where the high yields obtained, in the stoichiometric ratio was changed. Effects were observed by varying experimental parameters. Also parameters where high yield obtain increasing 3 times to observe the test result. Below in table 3 efficiency of Cr and in table 4 metal gain and scattering ratio is located.

Table 3: Efficiency of test parameter to Cr yield

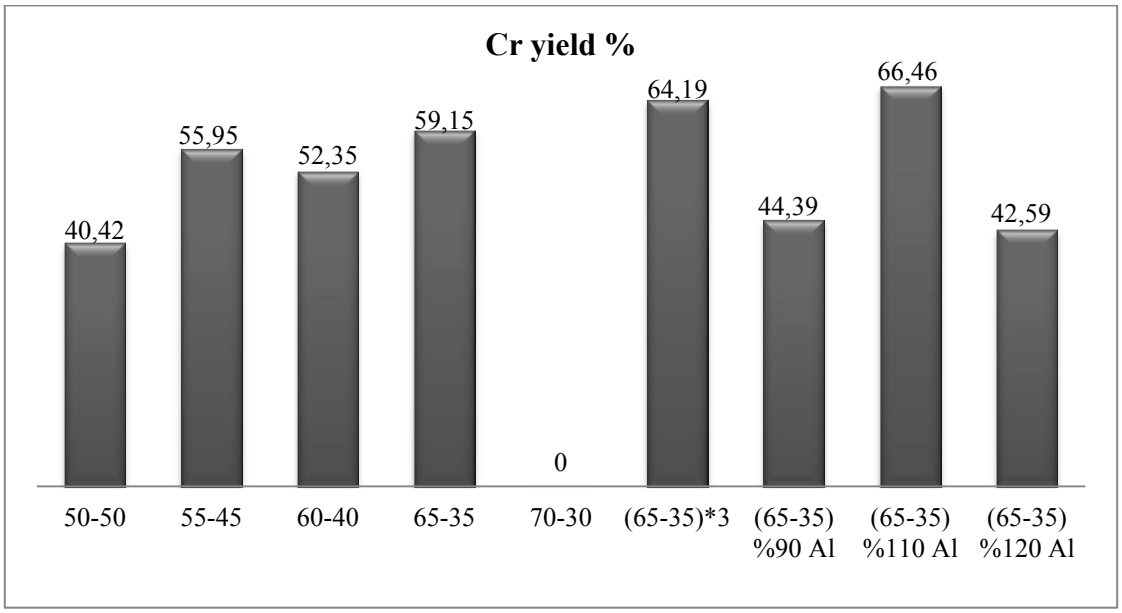

Table 4: Metal gain ratio and scaterring ratio according to test parameter

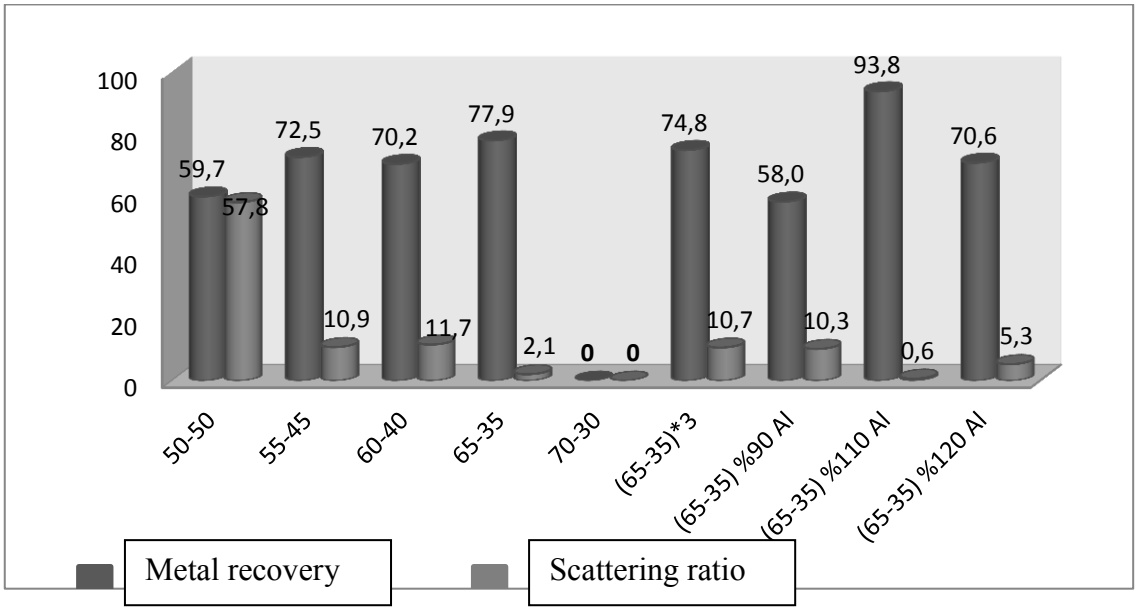

CONCLUSION

The study is not completed yet but the results is shown that to obtain low carbon ferrochromium is possible.

The highest yield occurs in additional %110 Al and 65-35 concentrate - CrO_3 . It is calculated approximately % 66,46. In our future study, additional Al and charge amount optimization will be attempted.

REFERENCES

[1] www.mta.gov.tr , Madenlerin Kullanım Alanları

[2] www.jmo.org.tr, TMMOB Jeoloji Mühendisleri Odası, Krom

[3] Fichte, R., Habashi, F., Hall, F. W., 1997. Ferroalloys, in Handbook of Extractive Metallurgy III, Ed. F. Habashi, Wiley VCH, Weinheim, Germany. pp. 438-453

[4] O. Yücel, F.C. Sahin, A. Tekin, High. Temp. Mater. Proc., 15 No.1-2 (1996) 103–106.

[5] Merzhanov, A.G., 2002. Self-propagating High-temperature Synthesis (SHS), ISMAN, Russia.

IRON ORE OF CONCENTRATE USED AT ISDEMIR SINTER PLANTS

[*]Ömer Saltuk BÖLÜKBAŞI, [**]Ali UÇAR, [**]Uğur DEMİR

[*]Mustafa Kemal Üniversitesi, Turkey
osbolukbasi@gmail.com
[**]İskenderun Demir ve Çelik A.Ş. İskenderun, Turkey
aucar@isdemir.com.tr
[**]İskenderun Demir ve Çelik A.Ş. İskenderun, Turkey
udemir@isdemir.com.tr

ABSTRACT

Integrated iron and steel industry in developing technology is directed to use of new iron ore that enriched in fine size (-75µm), because of rapidly decreasing quality iron ore reserves in all over the world. In this study, concentrate iron ore is used in İSDEMİR (İskenderun Iron and Steel Works Co.) Sinter Plants, was investigated the effects of the sinter quality, productivity and also on the blast furnace process. Iron ore of concentrate was used rates of 5-10-15 % in the sinter blends. According to the normal sinter blends, the content of Fe increased 2.81 % due to the concentrate ore has high Fe grade and low SiO_2 value. Return dusts inside the blend from Sinter and Blast Furnace by the regular sinter blend showed an increase of 2.36% during period with additive concentrate. Burnt lime used at ratio of 1.4% (25 kg/tss) and the productivity of machine was decreased about 11,41%. The values of sinter tromel haven't been occurred a significant reduction.

Keywords: Concentrate, sinter, blend, tromel, iron ore, productivity.

İSDEMİR SİNTER FABRİKALARINDA KONSANTRE DEMİR CEVHERİ KULLANIMI

ÖZET

Tüm dünyada hızla azalan kaliteli demir cevheri rezervleri nedeni ile demir ve çelik sektörü gelişen teknolojisi ile ince boyutta zenginleştirilen (-75µm) yeni demir cevherlerinin kullanımına yönelmiştir. Bu çalışmada İSDEMİR (İskenderun Demir ve Çelik İşletmeleri) Sinter fabrikasında konsantre cevher kullanımının sinter kalitesi ve verimliliği ile üretilen sinterin Yüksek Fırın proseslerine etkileri araştırılmıştır. Sinter harmanlarında konsantre demir cevheri % 5-10-15 oranlarında kullanılmıştır. Konsantre cevherin yüksek Fe tenör ve düşük SiO_2 değerine sahip olması nedeni ile normal sinter harmanlarına göre % 2,81'lik Fe artışı olmuştur. Harman içerisindeki Sinter ve Yüksek Fırınlardan geri dönen sinter tozu normal sinter harmanlarına göre, konsantre ilaveli dönemde % 2,36 artış göstermiştir. Testlerde yanmış kireç % 1,4 (25 kg/tss) oranında kullanılmış ve makine verimi yaklaşık % 11,41 azalmıştır. Sinter tromel değerlerinde önemli bir azalma meydana gelmemiştir.

Anahtar Kelime: Konsantre, sinter, harman, tromel, demir cevheri, verimlilik.

1. GİRİŞ

Entegre demir çelik tesislerinde demir cevheri kullanımındaki, önemli sorunlardan biri; yüksek tenörlü, doğrudan beslenmeye uygun üretilebilir demir cevheri rezervlerinin, sınırlı olmasıdır. Divriği'de üretilen konsantre ve pelet dışında ülke içerisinde üretilen cevherlerin Fe tenörleri genelde % 50-60 arasındadır. Bu cevherler, istenmeyen safsızlıklarıda bünyesinde bulundurduğu için entegre demir çelik tesislerinde sınırlı miktarlarda kullanılabilmektedir. Bu durumda yüksek tenörlü demir cevheri yataklarında, rezerv araştırma çalışmaları yapılmasının yanı sıra düşük tenörlü demir cevherlerinin zenginleştirilebileceği tesislerin kurulması önem arz etmektedir [2,6].

Türkiye'deki demir çelik fabrikalarının bugün ve gelecekteki üretiminde, en önemli hammadde gereksiniminin demir cevheri olduğu açıktır. Mevcut durumda; ülkemizde yeterli miktar ve kalitede üretilemeyen demir cevheri önemli miktarda ithal edilmektedir. Uygun kalite, miktar ve fiyat'a sahip demir cevherinin yurtiçi kaynaklardan karşılanması önemle üzerinde durulan konulardan bir tanesidir [9]. Bununla birlikte yerli cevher kullanılmasının, entegre demir çelik tesisleri tarafından üretilen özellikle yassı ve uç ürün kalitesi üzerinde olumsuz bir etkiye sahip olması en önemli sorunu oluşturmaktadır. Ancak işletilebilir demir cevheri rezervleri bakımından zengin olmayan ülkemizde yurt içi demir madenciliğine etüt ve arama bazında gereken yatırım yapılmadığı için hammadde gereksinimleri yerli kaynaklardan karşılanamayacak duruma gelmiştir [5]. Demir cevherinin rezervi, kalite, verimlilik ve maliyetleri konusunda iyileştirmeler yapılmadığı sürece de demir cevheri ithalatı yılara göre artarak devam edecektir. (8)

Bununla birlikte, giderek ağırlaşan rekabet koşullarına uyum sağlanması ve özellikle ithal cevher ve hurda ithalatının minimize edilmesine yönelik tesis yatırımlarının gerçekleştirilmesine paralel olarak artacak demir cevheri ihtiyaçlarının azami ölçüde yerli kaynaklardan karşılanmasının ülke ekonomisi açısından hayati önem taşıması bu konuda ciddi araştırmalar yapılmasını zorunlu hale getirmiştir.[2,7]

Bu araştırmaların yapılması hem ülkemizin atıl durumdaki yer altı doğal kaynaklarının değerlendirilerek ülke ekonomisine kazandırılmasının, hem de Türk demir çelik endüstrisinin içinde bulunduğu giderek ağırlaşan küresel rekabet ortamına hazırlıklı olmasının önünü açacaktır. Ayrıca ülkenin kalkınmasına yardımcı olmak, özellikle demir rezervlerinin büyük bir kısmını barındıran İç Anadolu ve Doğu Anadolu bölgelerinin ekonomik sorunlarına çözüm bulmak için bu bölgelerdeki demir cevherlerinin işletilmesi amacıyla gerekli yatırımların yapılmasının yanı sıra mevcut rezervlerin arttırılması ve yeni rezervlerin ortaya çıkarılması için arama çalışmalarının yapılması büyük önem taşımaktadır [1, 3].

İsdemir Sinter tesislerinde 2 adet sinter fabrikası bulunmaktadır. 2. Sinter fabrikası 2011 yılında yapılmış olup, bu fabrikanın faaliyete geçmesi ile toplam 6,3 milyon t/yıl üretim kapasitesine sahip olunmuştur. Sıvı ham demir üretim projeksiyonlarına göre; sinter fabrikası mevcut üretim kapasitesinin yaklaşık %60'ını kullanmakta olup, önemli bir kapasite fazlalığına sahip bulunmaktadır. Son yıllardaki entegre demir çelik tesislerinin istediği kalitede demir cevheri rezervlerinin dünyada ve ülkemizde hızla azalması, küresel rekabet koşullarından dolayı konsantre gibi atıl durumdaki demir cevherlerinin kullanılmasını ön plana çıkarmıştır. İsdemir sinter tesislerinin sahip olduğu fazla üretim kapasitesinden dolayı, konsantre demir cevherini sinter üretiminden kullanılmasında; konsantredeki ince tane yapısından kaynaklı sinter makine hızının ve üretim veriminin düşmesi nedeni ile oluşan üretim kayıpları üretim projeksiyonunu aksatmayacak şekilde hissedilmiştir. İsdemir sinter üretim kapasite fazlalığına sahip olması nedeni ile konsantre demir cevheri kullanım denemelerine başlanılabilmiştir.

2. İSDEMİR'DE SİNTER ÜRETİMİ

Demir cevherlerinden sıvı metal üretiminde kullanılan yüksek fırın, yüklenen malzemenin aşağıya, sıcak gazların ise yukarıya doğru hareket ettiği bir katı gaz reaktörüdür. Katılarla, indirgeyici gazlar arasında en iyi temas yüksek gaz geçirgenliğine sahip üniform gaz akımı ve aynı zamanda minimum kanallanma olan bir yatakta sağlanabilir [8]. Yüksek fırına yüklenecek demir cevheri belli bir tane iriliğinden daha ince ise (genellikle 1 cm), kimyasal özellikleri yeterli olsa da, yüksek fırın geçirgenliğini azaltacağı ve gaz kanallanmasını arttıracağı için yüksek fırına doğrudan doğruya şarj edilemez. Bu gibi hallerde aglomere (sinterleme) yapmak suretiyle şarj yapılabilinir [2,13].

Sinter üretiminde; sinterlik toz cevher, elek altı boyutta geri dönen sinter tozu, kok tozu ve flux yapıcı gibi zorunlu bileşenler yanında baca tozu, tufal gibi diğer demir içerikli atıklardan oluşan yaklaşık % 7 rutubete sahip sinterlik harman oluşturulmaktadır. Bu harman; demir cevherinin ergime sıcaklığı altında (1000-1350^{o}C) ısısal işlem ile yüksek fırın için uygun boyut, dayanım ve gaz geçirgenliğine sahip topak haline getirilmesi işlemidir. Sinterleme ile yüksek fırının ham demir üretim kapasitesinde artış, kok tüketiminde düşüş, cüruf ve baca tozlarında azalma sağlanmaktadır. Şekil 1'de sinter malzeme akış şeması görülmektedir.

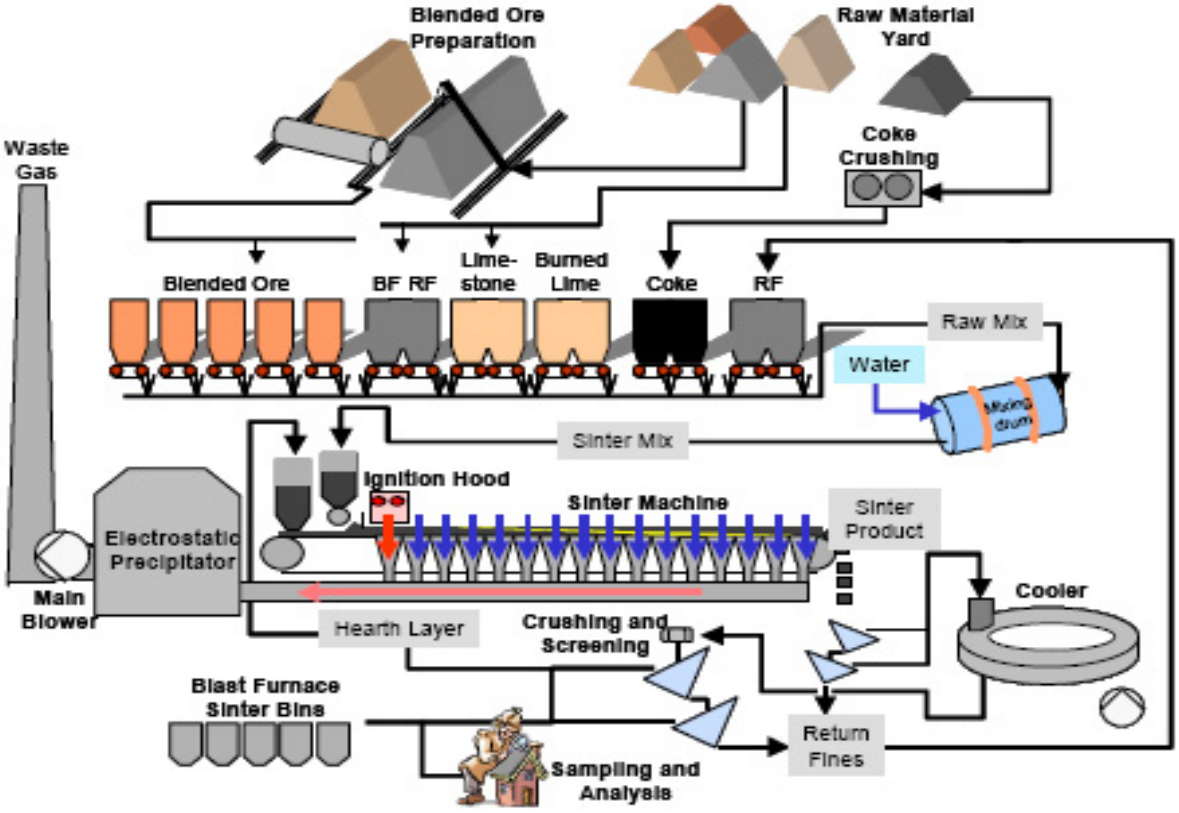

Şekil 1. Sinter fabrikası malzeme akış diyagramı [11].

3. KONSANTRE DEMİR CEVHERİ CEVHER KULLANIMI

Dünyada sinter tesislerinde konsantre cevher kullanan sinter fabrikaları yaklaşık % 65-%90 oranlarında sinter harmanlarında konsantre demir cevheri kullanabilmektedir. Konsantre cevherlerin Fe tenörleri genelde %18 ile %35 arasında değişmektedir [4]. Konsantre cevher genelde serbestleşme tane iriliği olan 75 μm'a kadar kırılıp magnetik separatör ile zenginleştirilerek % 62-68 Fe tenörüne çıkarılabilmektedir [12].

Dünyada konsantre cevher kullanan sinter tesisler genelde büyük sinter makinalarına (270 - 460 m^2) sahip olmalarına rağmen; düşük makine verimi, düşük üretim hızları ve düşük üretim miktarları ile çalışmaktadır [3]. Bu tesislerin öncelikli amaçlarının kendi ülkelerindeki konsantre demir cevherini değerlendirmek olduğu görülmektedir. Bu neden ile ürettikleri sinteri kendi çelik fabrikalarında kullanmaktadırlar [14].

Sinter üretiminde mevcut çalışma koşullarında; sinter harmanlarına gelen sinterlik yerli ve ithal demir cevherlerinin bünyesindeki -0,150 mm tane boyutu, yaklaşık %15-20 ağırlıksal oran gibi önemli bir miktarı oluşturmaktadır. Son dönemlerde İsdemir Sinter Fabrikasında kullanılan ithal toz cevherlerinde bulunan -0,150 mm tane boyut oranı artmış olup %20-%40 arasında değişiklik göstererek oldukça fazla bir hacim tutmaktadır.

Şekil 2. Konsantre demir cevheri resmi

Sinter fabrikalarının mevcut çalışma sistematiğinde –150 µm tane boyutunda toz cevher içeren sinterlik yerli ve ithal demir cevherleri sinter harmanlarında % 15–20 oranına kadar kullanılmaktadır. Cevherlerin -150 µm altında kalan dar tane boyut fraksiyonlarının miktarsal olarak bulunduğu tane aralıklarına bakılması daha doğru olacaktır.

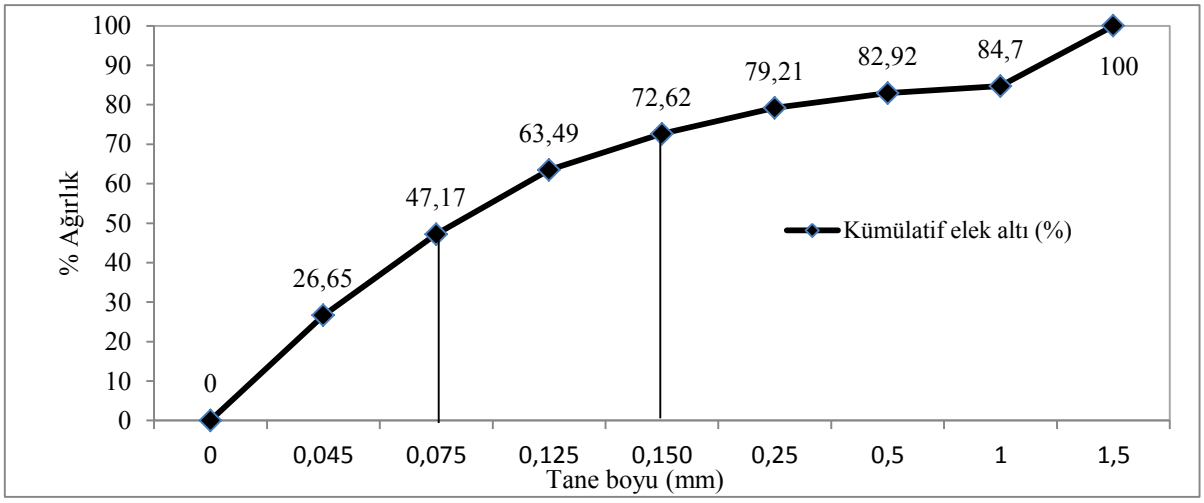

Şekil 3. Konsantre demir cevheri kümülatif elek altı tane dağılımı

Şekil 3 incelendiğinde +1mm konsantre cevher ağırlık oranı %15,30 iken, -0,150 mm tane boyut miktarı %72,62 olmuştur. -0,075 mm tane boyut dağılımı yaklaşık % 45-50 arasında olduğu görülmektedir. Sinter harmanlarında kullanılan demir cevherlerinde -0,150 mm tane boyut miktarının %15'i aşmaması istenmektedir. Sinter harmandaki ince boyut; sinter makinasındaki geçirgenliği azaltıp, sinterleşme süresini uzatıp yakıt sarfiyatını ve üretim verimini olumsuz yönde etkilemektedir.

4. DENEYSEL ÇALIŞMALAR VE KONSANTRENİN SİNTER KALİTESİNE ETKİLERİ

Bu çalışmada, konsantre demir cevherinin sinter prosesinde kullanımının sinter kalitesine etkileri ile üretilen sinterin Yüksek Fırın proseslerinde kullanım sırasındaki etkileri incelenmiştir. Konsantre demir cevherli sinter harmanı test çalışmaları, cevher harmanı içerisine sırasıyla %5, %10, ve %15 oranlarında konsantre demir cevheri ilave edilerek yapılmış olup, toplamda 3146 ton konsantre demir cevheri kullanılmıştır.

Sinter harmanında %5, %10 ve %15 oranlarında konsantre demir cevheri katkılı testler 10.000 ton'luk harmanlarda hazırlanıp İSDEMİR Sinter Fabrikasında üretim çalışmaları yapılmıştır. Konsansantre test çalışmaları; %60 ithal toz ve %10 siderit içeren sinter harmanlarında, %11 atık malzeme kullanılarak 1,60 küçük baziklik değerinde gerçekleştirilmiştir.

Karşılaştırma tablolarında farklı oranlarda konsantre kullanımlarından elde edilen sinter kalite parametreleri birbirleri ile karşılaştırılırken, ayrıca konsantre cevheri kullanılmayan dönemler ile de kıyaslama yapılmıştır.

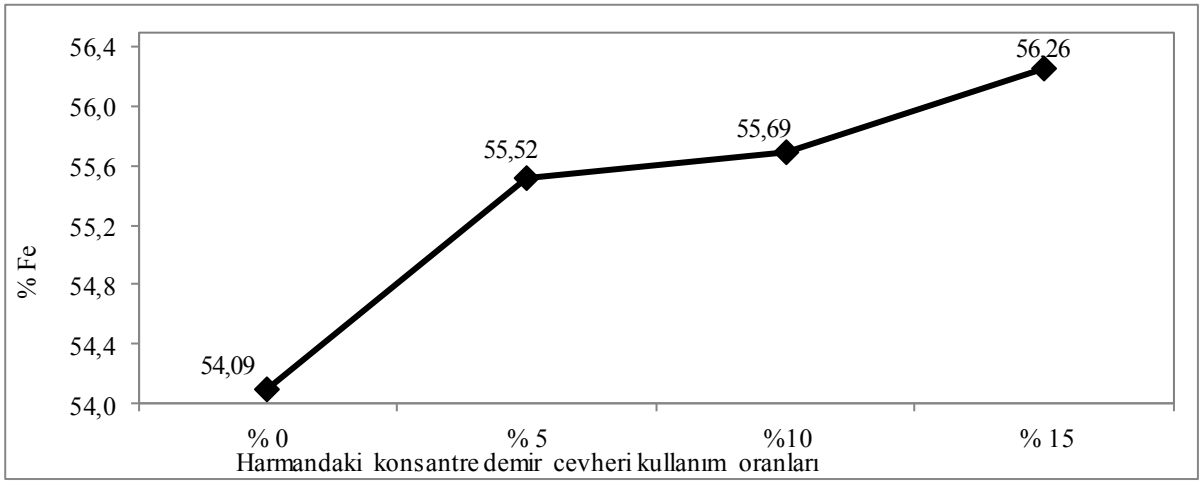

Şekil 4. Sinter harmanında konsantre demir cevheri kullanımı ile sinter üretiminde Fe tenörü değişimi

Şekil 4 incelendiğinde sinter harmanı içerisindeki konsantre demir cevheri kullanılmadığı dönemlerde Fe tenörü % 54,09 değerinde iken % 15 konsantre kullanılarak elde edilen ürün sinterde % 56,26 Fe değerine yükselmiştir. Bu Fe artışının nedeni konsantre demir cevherindeki yüksek Fe tenör ve düşük SiO_2 (%2,06) içeriğidir. Konsantre denemelerini kendi içinde kıyaslarsak, konsantre kullanım oranının artışına paralel olarak Fe tenörü de artmıştır.

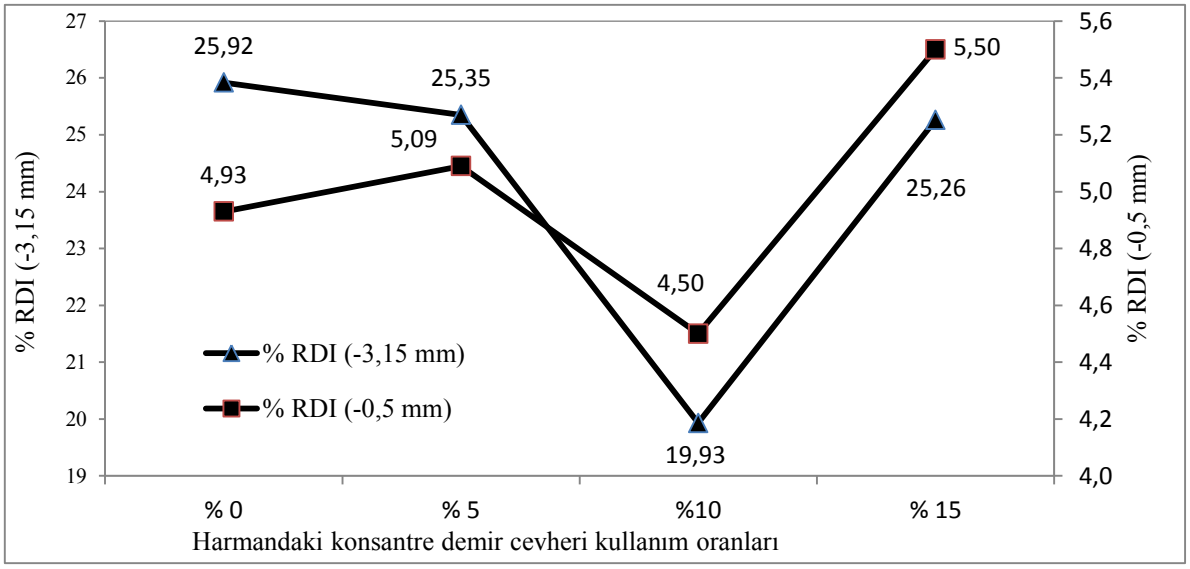

Şekil 5. Sinter harmanında konsantre cevheri kullanımına bağlı sinter RDI (+6,35mm) ve toz (-0,5mm) değişimi

Şekil 5'e bakıldığında sinter harmanı içerisindeki konsantre cevheri kullanılmadığı dönemlerde RDI (-3,15mm) değeri % 25,92 iken, % 5 konsantre kullanımında % 25,35, %10 konsantre kullanımında %19,93 değerine düşmüş olup, %15 konsantre kullanımında ise % 25,26 değerine ulaşmıştır. RDI (-0,5mm) değeri konsantre cevheri kullanılmadan hazırlanan sinter harmanında % 4,93 iken % 5 konsantre kullanımında % 5,09, %10 konsantre kullanımında 4,50, %15 konsantre kullanımında ise % 5,50 değerine yükselmiştir. Genel olarak, sinter harmanı içerisindeki konsantre kullanım oranına bağlı olarak RDI (-3,15mm) sinter sıcak mukavemet ve RDI (-0,5mm) tozlaşma indeks değerinde işletmeyi etkileyecek önemli bir olumsuzluk görülmemiştir.

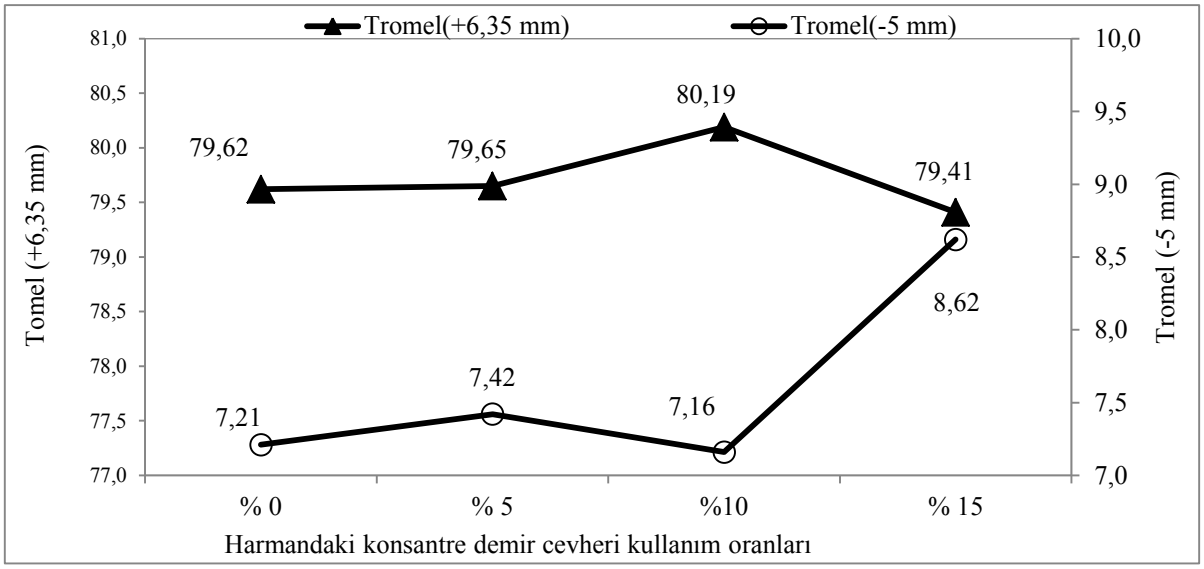

Şekil 6.Sinter harmanında konsantre demir cevheri kullanım oranına bağlı sinter tromel (+6,35mm) ve toz indeksi (-5mm) değişimi

Şekil 6'e incelendiğinde sinter harmanı içerisindeki konsantre cevheri kullanılmadığı dönemlerde Tromel (+6,35mm) değeri % 79,62 iken, % 5 konsantre kullanımında %79,65, %10 konsantre kullanımında 80,19, %15 konsantre kullanında ise %79,41 değerleri gerçekleşmiştir. Tromel (-5mm) değeri konsantre cevheri kullanılmadan hazırlanan sinter harmanında % 7,21 iken % 5 konsantre kullanımında % 7,42 değerine yükselmiş, %10 konsantre kullanımında 7,16 değerine düşmüş, %15 konsantre kullanımında ise % 8,62

değerine yükselmiştir. Sinter tromel (+6,35mm) soğuk mukavemet değerinde ve (-5mm) toz indeks değerinde işletmeyi olumsuz etkileyecek bir durum görülmemiştir.

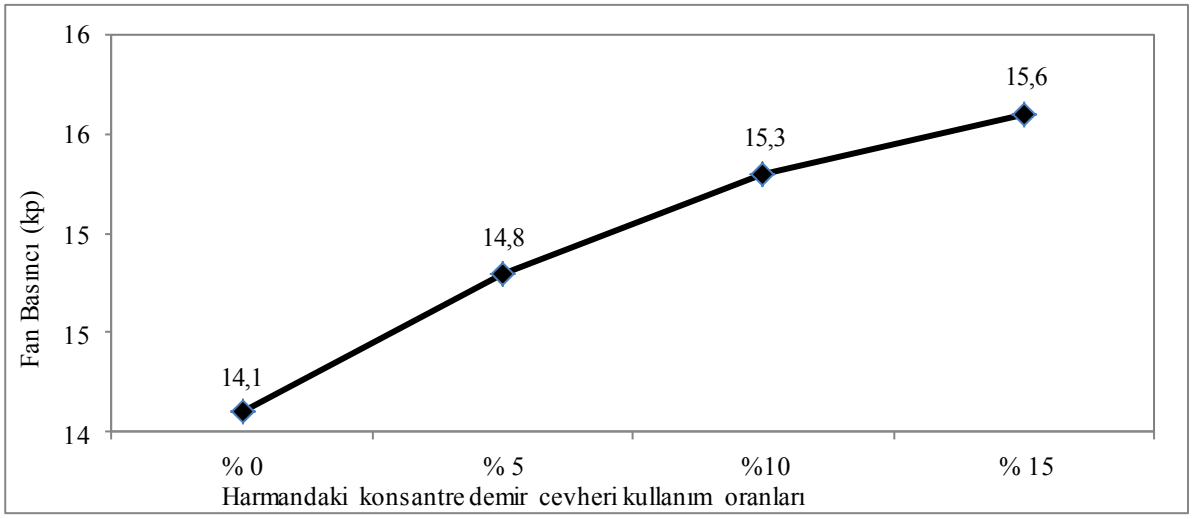

Şekil 7. Sinter harmanında konsantre cevheri kullanımına bağlı fan basıncı değişimi

Şekil 7'ya bakıldığında, sinter harmanında konsantre cevher kullanım miktarına bağlı olarak fan basıncı artmıştır. Basınç artışının sebebi konsantre cevherden gelen ince tane boyutundan kaynaklanan sinter kekindeki geçirgenliğin azalmasıdır.

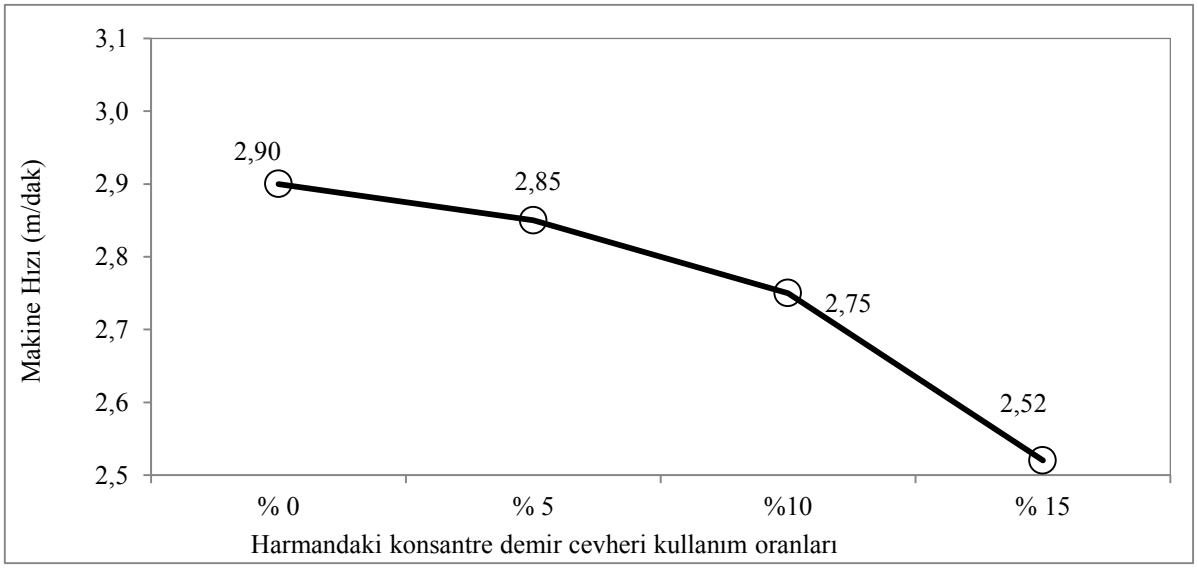

Şekil 8. Sinter harmanında konsantre cevheri kullanım oranına bağlı Sinter Makine hızı değişimi

Şekil 8 incelendiğinde sinter harmanı içerisindeki konsantre cevher kullanılmadığı dönemlerde 2,90 m/dak olan makina hızı % 5 konsantre kullanımında (2,85 m/dak.) fazla değişmemiş olup %15 konsantre kullanımında 2,52 m/dak.'ya düşmüştür. Sinter harmanı içerisindeki konsantre kullanım miktarının artışı ile birlikte sinter makine hızının azaldığı görülmektedir.

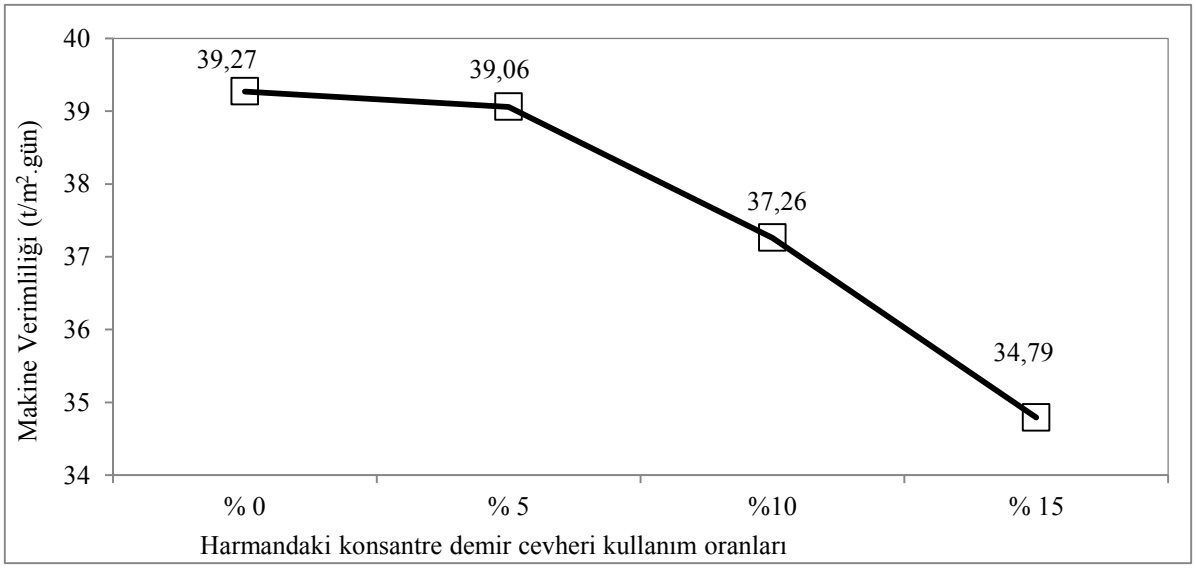

Şekil 9. Sinter harmanında konsantre cevheri kullanım oranına bağlı Sinter Makine verimliliği değişimi

Şekil 9'e bakıldığında, sinter harmanı içerisindeki konsantre cevheri kullanılmadığı dönemler ile % 5 oranlarında kullanıldığı dönemlerde sinter makina verimliliği yaklaşık 39 t/m^2.gün olduğu görülmektedir. Konsantre kullanım oranlarının %10 ve %15 olduğu sinter harmanlarında, makina verimliliği sırası ile 37,26 t/m^2.gün ve 34,79 t/m^2.gün değerlerine düşmüştür. Test çalışmalarında sinter harmanı içerisinde konsantre kullanımı arttıkça ince boyutun fazla olmasından dolayı makina verimliliğinin azaldığı görülmüştür.

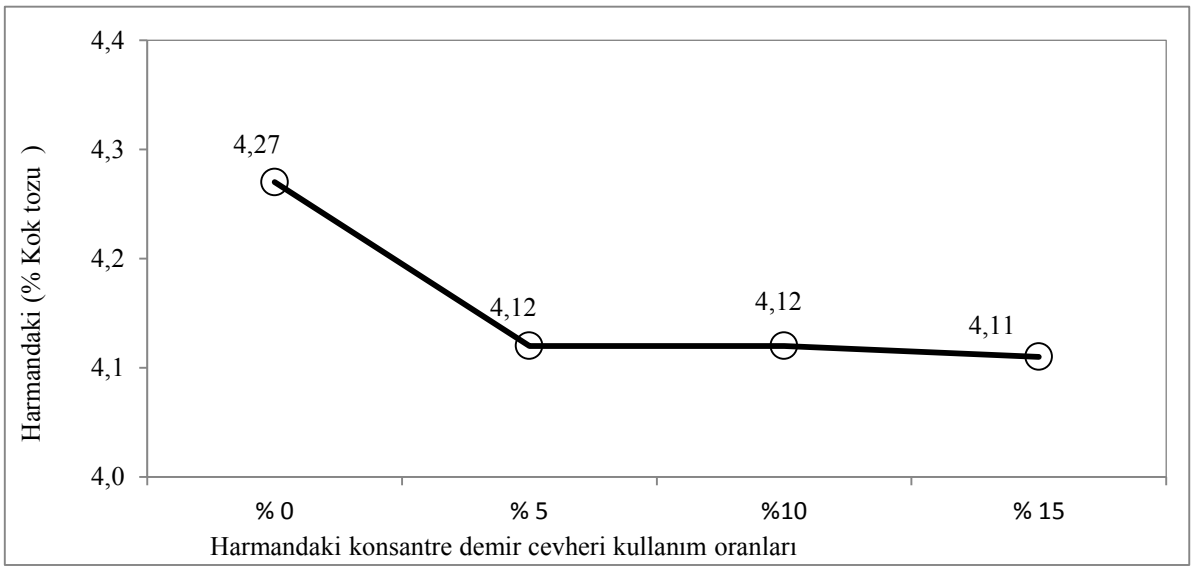

Şekil 10. Sinter harmanında konsantre cevheri kullanım oranına bağlı harman içerisinde kullanılan kok tozu oranı değişimi

Şekil 10 incelendiğinde sinter harmanı içerisindeki konsantre cevheri kullanılmadığı dönemlerde % 4,27 olan kok tozu kullanımı % 5 ve %10 konsantre kullanımı ile harman içerisindeki kok tozu oranı % 4,12'ye düşmüştür.%15 konsantre kullanımında kok tozu kullanım oranı % 4,11'e kadar düşer iken, konsantre ilaveli harman denemeleri sırasında, sinter fabrikasında 1,4% (25 kg/tss) oranında yanmış kireç kullanılmıştır. Kireç kullanıma bağlı olarak kok tozu tüketimi konsantresiz harman dönemlerine göre % 0,16 azalarak % 4,11 olarak gerçekleşmiştir. Konsantre denemelerinde yanmış kireç uygulanmasının, kok tozu kullanım oranının düşmesinde etkisinin olduğu görülmüştür.

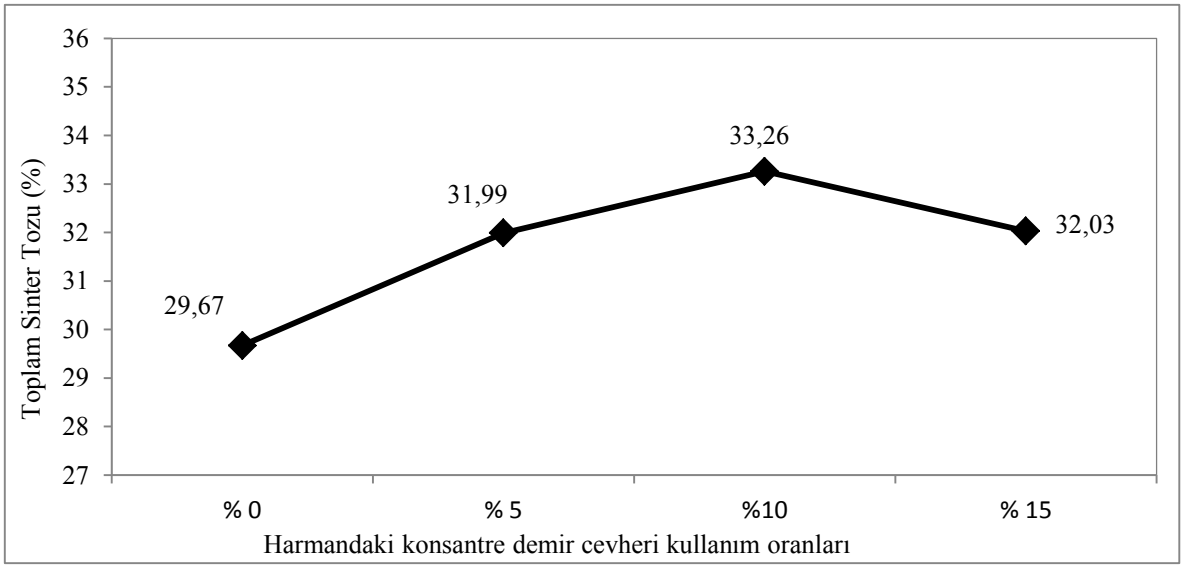

Şekil 11. Sinter harmanında konsantre cevher kullanım oranına bağlı olarak değişen toplam sinter dönüş tozu

Şekil 11'a bakıldığında sinter harmanı içerisindeki konsantre cevheri kullanılmadığı dönemlerde % 29,67 olan toplam sinter geri dönüş tozu oranı % 5 ve %10 konsantre kullanımında artış gösterip sırası ile %31,99 ve % 33,26 değerlerine yükselmiştir. %15 konsantre kullanımında sinter geri dönüş toz oranı %32,03 değerine düşmüştür. Sinter harmanında ilave edilen konsantre cevherinden gelen ince tane boyutundan dolayı, konsantre test çalışmalarında sinter geri dönüş tozlarında artış görülmektedir.

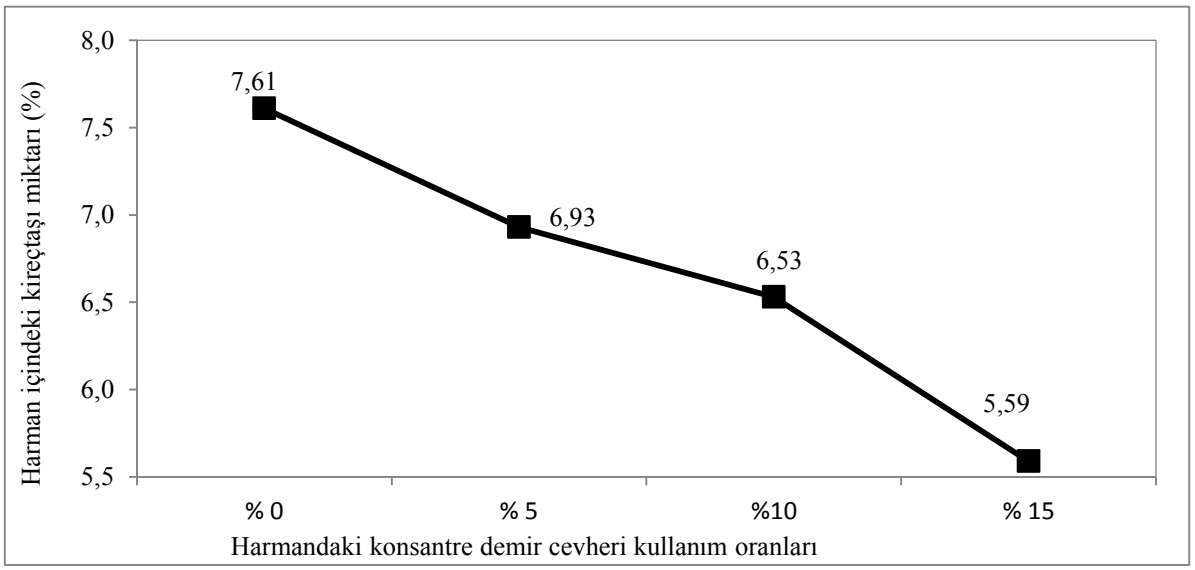

Şekil 12. Sinter harmanında konsantre cevheri kullanım oranına bağlı olarak değişen kireçtaşı miktarı

Şekil 12 incelendiğinde sinter harmanı içerisindeki konsantre cevheri kullanılmadığı dönemlerde %7,61 olan harman içerisindeki kireçtaşı kullanım oranı miktarı konsantre demir cevheri kullanımının %5 ve %10 olduğu testlerde düşüşe geçmiş sırası ile %6,93 ve %6,53 olmuştur. Konsantre cevherinin %15 oranında kullanıldığı dönemlerde %5,59'a kadar düşmüştür. Konsantre cevher denemelerinde kireçtaşı kullanımındaki azalmada yanmış kireç kullanımının etkisi olduğu görülmektedir.

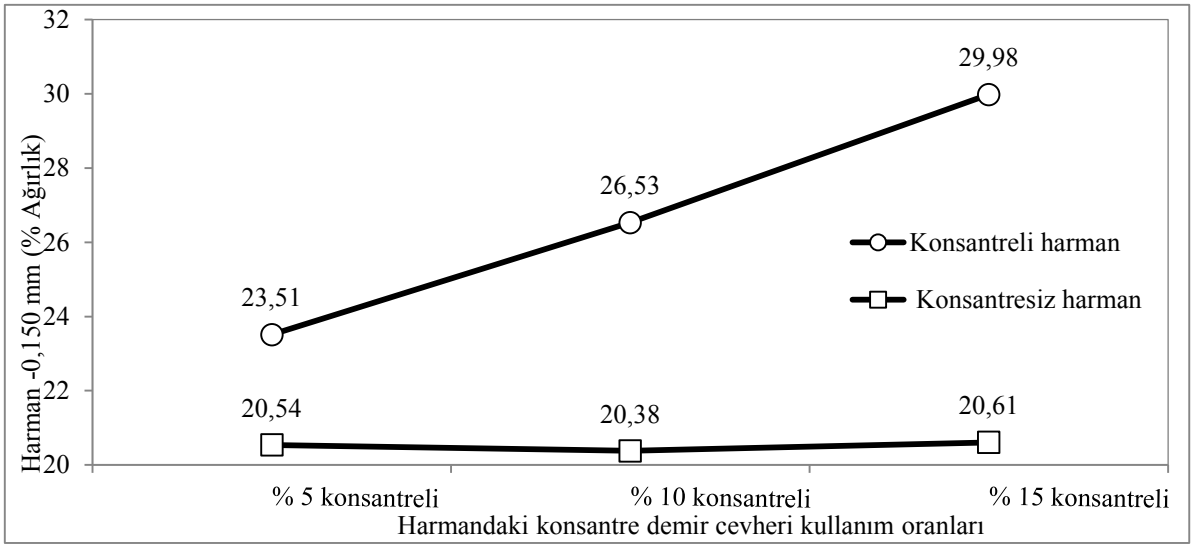

Şekil 13. Konsantre kullanılan ve kullanılmayan harmanlarda -0,150 mm tane boyut dağılımı

Şekil 13'de sinter harmanı içerisinde konsantre demir cevheri kullanılmadığı dönemlerde ağırlıksal olarak yaklaşık % 20 olan -0,150 mm tane boyut dağılımı %5 konsantre kullanımında % 23,51, %10 konsantre kullanımında % 26,53 ve %15 konsantre kullanımında %29,98 değere yükseldiği görülmüştür. Sinter harmanı içerisindeki konsantre demir cevheri kullanımına bağlı olarak -0,150 mm tane boyut oranının arttığı görülmektedir.

5. SONUÇLAR VE ÖNERİLER

1- Endüstriyel sinter fabrikasında yapılan test çalışmalarında; sinter harman içerisindeki geri dönen (iç sinter&Yüksek Fırın'dan gelen) sinter tozu, konsantre cevher kullanılmadan yapılan üretim döneminde % 29,67, % 5 konsantre ilaveli denemede %31,99 ,%10 ilaveli denemede % 33,26 ve %15 ilaveli denemede % 32,03 olarak gerçekleşmiştir. Konsantre ilaveli dönemde toplam sinter tozu % 2,36 oranında artış göstermiştir. Farklı oranlarda konsantre kullanılan dönemleri kendi içerisinde kıyasladığımızda toplam sinter geri dönüş tozu oranının konsantre cevher kullanım oranına bağlı olarak arttığı görülmektedir.

2- En dikkat çekici fark konsantre cevherindeki yüksek Fe tenör ve düşük SiO_2 empürite değeri nedeni ile ürün sinterin % Fe tenörlerinde artış olmasıdır. Konsantre ilavesiz harman kullanılan döneme göre % 15 konsantreli çalışmada Fe tenöründe ortalama % 2,81 artış meydana gelmiştir. Konsantre denemelerini kendi içinde kıyaslarsak, konsantre demir cevherinden gelen Fe içeriğinden dolayı (% 67,52) kullanım oranının artışına paralel olarak % Fe tenöründe artış göstermiştir.

3- Konsantre kullanılmadığı dönemde 39,27 t/m^2.gün olan makine verimi %15 konsantreli harman dönemde 34,79 t/m^2.gün değerine düşmüştür. Yaklaşık % 11,41 sinter üretiminde verim kaybı olmuştur. Sinter makine veriminin azalmasında en büyük etken konsantre cevher kullanım oranına bağlı olarak, sinter harmanında geçirgenliğin azalması ve makine hızının düşmesidir.

4- Konsantre demir cevheri kullanılmada yapılan sinter üretimlerinde % 0,9 oranına yanmış kireç kullanılırken konsantre ilaveli test çalışmalarında %1.4 (25 kg/tss) oranında yanmış kireç kullanılmıştır. %5 konsantre test uygulamasında konsantresiz çalışmaya göre sinter makine veriminde % 0,53 değerinde çok az azalma olmuştur. %10 ve %15 konsantre denemelerinde aynı oranda yanmış kireç kullanılmasına rağmen, konsantre artışına bağlı olarak sırası ile % 5,12 ve % 11,41 değerlerinde sinter makine verimliliği önemli oranda düşmüştür.

5- Konsantre kullanılmadan üretim dönemlerinde makine hızı 2,90 m/dak. olan makine hızı % 5 konsantre kullanımında 2,85 m/dak. olarak % 1,72 değerinde düşük bir azalma olmuştur. % 10 ve % 15 konsantre ilaveli test çalışmalarında 2,75 m/dak, 2,52 m/dak'ya düşerek sırası ile % 5,17, % 13,10 oranlarında azalma olmuştur. Sinter harmanında konsantre kullanım oranına bağlı olarak sinter makine hızlarının düştüğü görülmektedir.

6- Konsantresiz harman çalışma dönemlerinde sinter harmanı içerisindeki -0,150 mm tane iriliği ağırlıksal olarak yaklaşık %20 oranında iken, % 15 konsantre denemelerinde % 29,98 oranına yükselerek yaklaşık % 6 oranında artış olmuştur. Sinter harmanında -0,150 mm tane boyutu ağırlıksal olarak %15'i geçmemesi istenmektedir.

Konsantre katkılı üretilen sinterin Yüksek Fırın Prosesinde % 55 oranında kullanımında önemli bir olumsuzluk görülmemiştir. Konsantresiz çalışma ile % 15 konsantre kullanılarak üretilen sinterin Yüksek Fırınlar –5 mm elek geri dönüş değeri ile karşılaştırıldığında 3. Yüksek Fırın % 8,29 iken 10,64'e yükselmiştir. 4. Yüksek Fırın % 10,06 iken 13,74'e yükselmiştir. Harmanlara konsantre ilavesinin artışı ile birlikte sinter makine hızı ve üretim verimi düşmüştür. Denemeler esnasında Sinter tromel değerinde önemli bir azalma meydana gelmemiştir. İsdemir Sinter Tesislerinde sinter harmanı içerisine konsantre demir cevheri oranının artırılarak uygulama çalışmaları önümüzdeki dönemde artarak devam edecektir.

REFERANS

1. A. Akar ve J.W. Pressler, "Beneficiation Studies on the Hasançelebi Magnetite Deposit", Department of the Interior Geological Survey, Project Report, 25, 40, Turkey, November, 1971.
2. A. Coşkun, "Malatya-Hasançelebi Demir Projesi Fizibilite Etüdü", Maden Tetkik ve Arama Enstitüsü Genel Müdürlüğü Teknoloji Şubesi, 10, 12, 18, Ankara, Mayıs 1974.
3. A. Uçar, Ş. Kazokoğlu, M.E. Ertem, M.M. Akgün, H. Alsaç, K. Oktay, E. Şahin, Evraz Grup Vgok ve Kgok Tesisleri Konsantre Cevherin Sinterde Kullanımı İle İlgili Teknik Gezi Raporu, Rusya, Kasım, 2012.
4. A. Yılmaz, F. Torun, M. E. Ertem, M. M. Akgül, Chengde Steel ve Bai Steel Demir Çelik Tesislerinin Konsantre Cevheri Kullanımı ile İlgili Teknik Gezi Raporu, Çin, Mayıs, 2013.
5. A. Yörükoğlu "Türkiye Maden Potansiyeli ve Stratejik Madenler", Malatya ve Çevre İllerinin Maden Sempozyumu Bildiriler Kitabı, 180,181, Malatya, Nisan, 2013.
6. A.E. Yüce, A. Güney, B. Elevli, O. Kökkılıç, N. Acarkan, G. Ünal,A. Demirci,"Hasançelebi Demir Yatağı Revize Fizibilitesi", Türkiye Demir Yatakları Jeolojisi Madenciliği ve Mevcut Sorunları Sempozyumu, 308, 311, 314,İstanbul, 2005.
7. C. Şahintürk, E. Baş, B. Sönmez, "Ülkemizdeki Demirli Hammadde Kaynaklarının Belirlenmesi ve Değerlendirilmesi İmkanlarının Araştırılması Raporu", Ereğli Demir ve Çelik Fabrikaları T.A.Ş., 13, 14, 20, Zonguldak, Aralık 2013.
8. E. Oktay ve İ. Yusufoğlu, "Şarjdaki Empürite Elementlerin Yüksek Fırındaki Davranışları, Türkiye Demir Yatakları Jeolojisi Madenciliği ve Mevcut Sorunları Sempozyumu, 375, 380,İstanbul, 2005.
9. İ. Savaş, "Türkiye'de Ağır Sanayinin Kalkınmasında Merkezi Sünger Peletleme ve Sünger Demir Tesisinin Önemi, Sünger Demir Kullanılma İmkânları ve Bu Tesislerin Teknik Ekonomik Etütü". Tebliği Demir-Çelik Endüstrisi Semineri, Milli Prodüktivite Merkezi Yayınları, 77, 103, 154, Ankara 1970.
10. T.Ünlü, "Magmadan Cevhere" Türki ye'den bir örnek: Hasançelebi Demir Yatağı", Malatya ve Çevre İllerinin Maden Sempozyumu Bildiriler Kitabı, 180,181, Malatya, Nisan, 2013.
11. Voest Alpine, "VAI Automation for Iron & Steel. Product Description" ,Industrial Sinter Plant, 24, (2008).
12. W.Yuan, "The Industrial Practice of HPS Process in Japan", Sintering and Pelletizing, 36, Chine, 1992.
13. Y.Hong, Y. Zhang, H.Wang, Aplication and Efficiency of Pellet Sintering Tongsteel Sintering Plant, Sintering and Pelletizing, 34, Chine, 2009.
14. Z. Liu, R.Ma, Y. Xu, "Industrial Experimenton Double Pellet Sintering", Iron and Steel, 26, 1991.

Yeni Nesil Mikro Alaşımlı Çelik, AMÇ 1200®

Mehmet ÇAKICI*

*Asil Çelik Çelik San. ve Tic. A.Ş. , TURKİYE

mehmet.cakici@asilcelik.com.tr

AR-GE & Proses Kontrol Sorumlusu

ABSTRACT

The continuous wide spread use of microalloyed steel is related to their heigh strength properties than other heat treated alloying steel. The attractive mechanical properties are obtained due to the combination of an advanced metallurgical processing. Small additions of alloying elements like Nb, V and Ti result in the formation of carbides, nitrides and carbonitrides in the microstructure. These very fine precipitates are effective in preventing grain growth by the use of controlled cooling and increased tensile strength.

Keywords Microalloy steel, precipitation hardening, controlled cooling,

ÖZET

Mikro alaşımlı çelikler son dönemlerde geniş bir kullanım alanına sahiptir. Mikro alaşım özelliği kazandıran Nb, V ve Ti elementlerinin belirli oranlarda çeliğe katılmak suretiyle, dövme sonrası kontrollü soğutma uygulayarak çeliğin mekanik değerleri önemli oranda arttırılmaktadır. Buradaki mekanizma; ferit tane küçülmesi ve çökelme sertleşmesi oluşturarak mekanik değerlerin arttırılmasıdır.

YENİ NESİL MİKROALAŞIMLI ÇELİK, AMÇ 1200®

Bu çalışma, şu an mevcut kullanılmakta olan mikro alaşımlı çeliklerden daha yüksek bir mukavemete sahip ve EURO 6 motorlarda kullanılması plananlanan *Diesel Rail* parçası için ~ 2500 bar basınca dayanıklı çelik ihtiyacından doğmuştur. Geliştirilen yeni çelik, AMÇ1200 ® , ortalama olarak 1200 MPa 'lık bir çekme mukavemetine sahiptir. Kontrollü soğutma sonrası elde edilen bu mekanik değerin yanı sıra malzemenin içyapısı da beynitik yapıdadır.

Deneme çelik üretimi Asil Çelik'te gerçekleştirip, Ø 40 mm' ye haddelendikten sonra dövmeci firmada ***Diesel Rail*** parçası olarak dövülmüş ve çeşitli kontrollü soğutma işlemi uygulanmıştır.

Çalışmanın temeli, mikro alaşım çeliklerde (HSLA – High Strength Low Alloy) ısıl işlem (ıslah) uygulaması yapmadan, alaşımların (V, Nb ve Ti alaşımlarının) belirli miktarlarda kullanılmasıyla dövme operasyonu sonrası kontrollü soğutma ile malzemenin dayanımının arttırılmasıdır.

Burada temel mekanizma, dövme operasyonu sonrası kontrollü soğutma ile aşağıdaki metalurjik dengeyi sağlamaktır. Bunu gerçekleştirmenin en önemli şartı çeliğin içerisinde kullanılan mikro alaşım elementlerinin doğru miktarlarda kullanılmasıdır.

— Ferit tane küçülmesi

$$\sigma a(MPa) = \sigma o + k.d^{-1/2} \quad \text{(HALL – PETCH DENKLEMİ)} \qquad (1)$$

σo, k sabit d ise ferit tanelerinin çapıdır. Akma geriliminin (σa) attırılması için, ferrit tane çaplarının seçilecek olan mikro alaşım elementi ve miktarı ile küçültülmesi hedeflenmiştir.

— Çökelme sertleşmesi

$$\sigma a(MPa) = \frac{5{,}9*\sqrt{f}}{X} \quad \text{(GLADMAN DENKLEMİ)} \qquad (2)$$

Akma gerilimini etkileyen diğer mekanizma ise çökelme sertleşmesidir. Denklemde f ana yapıdaki çökelti yoğunluğu, X ise çökeltilerin ortalama çapıdır. Akma gerilimini (σa) attırmak için, ne kadar küçük ve yoğun dağılımlı çökelti oluşturulabilinirse o kadar yüksek dayanıma sahip çelik elde edilebilinir.

SONUÇ

Tablo1. Dövme sonrası kontrollü soğutma uygulanan parçaların mekanik değerleri ve mikro yapıları

					MEKANİK DEĞER SONUÇLARI										
KALİTE	Kesit	Y/K	Dövme işlemi sonrası *"Kontollü Soğutma"* şartları	SERTLİK (HB 10/3000)	Deneme No.	Do	Lo	EMod	Rt (EUL) 0,6	Rp 0,2	Rt (EUL) 0,5	Rm	A (m)	Z (alan)	CİHAZ
						mm	mm	N/mm²	N/mm²	N/mm²	N/mm²	N/mm²	%	%	
YENİ ÜRÜN	40	Y	*Konveyöre girmeden açık havada soğuyan parça	**367**	1	10.00	50	207422.74	783	759	726	1237	13.8	27.8	Z
YENİ ÜRÜN	40	Y	*Konveyörden geçen ve kasaya düşmeden alınan parça	**365**	2	10.00	50	213320.66	833	826	795	1265	14.4	27.8	Z
YENİ ÜRÜN	40	Y	Diğer parça ile bitişik olarak *konveyörden geçen ve kasaya	**334**	3	10.00	50	207955.04	733	700	684	1171	15	37.6	Z
YENİ ÜRÜN	40	Y	*Konveyörden geçen ve kasada soğuyan parça	**349**	4	10.03	50	213278.92	744	705	694	1227	16	33.2	Z
YENİ ÜRÜN	40	Y	*Konveyör girişinde hava üflenen parça	**363**	5	10.00	50	208081.53	791	772	738	1273	15	32.8	Z

Yeni ürün, AMÇ 1200®(Patent başvurunda bulunulmuş olup süreç devam etmektedir, o nedenle çeliğin sahip olduğu kimyasal analizler verilmemiştir)

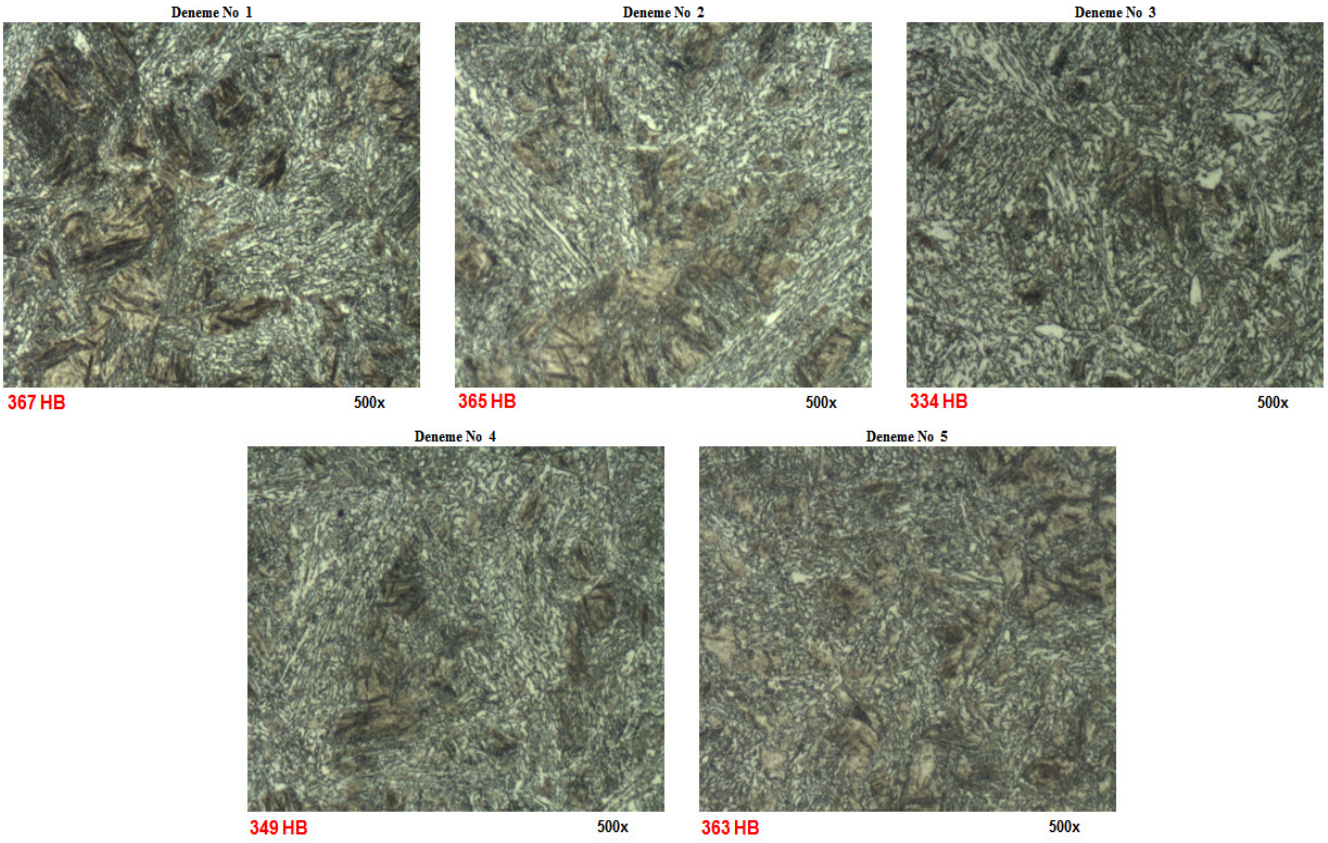

NOT: Sertlikler merkezden ölçülmüştür.

REFERANSLAR

Asil Çelik laboratuvar çalışmaları

İSKENDERUN DEMİR VE ÇELİK FABRİKALARI'NDA (İSDEMİR) KALİTE TASARIMI

[1]Muhammet BİLEN

[1]İSDEMİR A.Ş. Kalite Metalurji Müdürlüğü

İSDEMİR'de üretim ile ilgili 4 bilgi işlem ve otomasyon seviyesi bulunmaktadır: ilk 3 seviye makine, hat ya da bölüm bazında iken, seviye-4 ise tüm İSDEMİR genelinde üretim ve kontrol yapılmasını sağlayan, üretim emirlerini veren, gerçekleşen, kalite kontrol ve üretim takip fonksiyonlarını sağlayan sistemdir.

Seviye-4 sisteminin diğer bir adı Üretim Yönetim Sistemi (ÜYS)'dir. Kalite tasarımı, sipariş kabulü gibi işlemler ÜYS'de gerçekleştirilir. Her seviye, gerekli plan ve spesifikasyonları bir alt seviyeye gönderir ve bir alt seviyeden aldığı sonuç ve raporlamaları üst seviyeye aktarır.

İmalat Pratikleri Kodu (MPC - Manufacturing Practice Code) İSDEMİR'de üretilen yassı ve uzun mamûllere 13 parametrenin oluşturulmasıyla verilen anahtar numarasıdır. Mamul ile ilgili her türlü bilgi MPC altında toplanmıştır ve ürünlerin sipariş aşamasından itibaren müşteriye gönderilmesine kadar tüm safhalardaki üretimi ve kaliteyi etkileyen parametreler ile müşteri taleplerini içeren bir koddur.

MPC şu öğelerden oluşur: 'Ürün, çelik cinsi, kalınlık/çap, genişlik, boy, yerli/ihraç, ebat toleransı, boy toleransı, ambalaj tipi, iç-dış çap, test raporu, özel talimat, ağırlık. Bu kod altındaki bilgiler, malzemelerin takip edeceği üretim hatlarını, bu hatlardaki proses parametreleri ve toleransları belirler. Dolayısıyla üretimin yapılması ve etkin bir şekilde kontrolü sağlanmış olur. Müşteri taleplerinin tanımlamalarını karakterize eden MPC, ÜYS ile üretimin devamlığını ve sistematiğini sağlamaktadır.

Anahtar kelimeler: İSDEMİR, MPC, Üretim Yönetim Sistemi, Kalite Tasarım

QUALITY DESIGN IN ISKENDERUN IRON AND STEEL WORKS (İSDEMİR)

ISDEMIR has 4 levels of computing and automation system in the production process: The first three level is consist of machining, line or division basis whilst fourth level provides production and control, gives production orders, allows quality control and production monitoring functions generally in whole ISDEMIR.

The other name of Level-4 is Production Management System (PMS). Quality design and order acceptance processes are carried out in PMS. Each level transmits the necessary plans and specifications to a lower level and transfers the results and reports to upper level which received from lower level.

Manufacturing Practicing Code (MPC) is the key number created by 13 parameters and given to the flat and long products manufactured in ISDEMIR. All kind of information related with the product is gathered under MPC and this code contains customer demands which affect production and quality parameters in all phases from the stage of order placement until delivery to the customer.

MPC items are as follows: 'Product, steel grade, thickness/diameter, width, length, domestic/export, size tolerance, length tolerance, type of packaging, outside/inside diameter, test report, special instruction, weight. All information in this code determine the production line where the product has to be followed, processing parameters and tolerances in production lines.

Thus, production and effective control can be ensured accordingly. MPC which characterizes identification of customer demands provides continues production and systematic along with PMS.

Key words: ISDEMIR, MPC, Production Management System, Quality Design

1. İSDEMİR ÜRETİM YÖNETİM SİSTEMİ

Üretim Yönetim Sistemi, dört seviyeli bilgi işlem ve otomasyon sisteminin en üstünde yer alan ve alt seviyeden aldığı üretim sonuçlarını harmanlayan ve bir alt seviyeye gerekli bilgileri gönderen İsdemir'in tasarladığı bir sistemdir. İSDEMİR'de üretim ile ilgili 4 bilgi işlem ve otomasyon seviyesi bulunmaktadır:
Seviye-1 Sistemi, Seviye-2 Sisteminden aldığı komutları, işi yapan makinelere ileten, proses ölçüm değerlerini toplayan ve makinelerin üretimi yapmasını sağlayan sistemdir.
Seviye-2 Sistemi, Seviye-3 Sistemi tarafından gönderilen üretim emirlerini toplayan ve bu emirler için hatta çalışan makinelerin yönetimini sağlayan ve üretim sonuçlarını oluşturan sistemdir.
Seviye-3 Sistemi, Seviye-4 Sistemi tarafından gönderilen üretim emirlerinin gerçekleşmesini sağlayacak, alt sistemlerin ihtiyaç duyduğu bilgileri oluşturan ve üretim sonuçlarını da alt sistemlerden toplayan sistemdir.
Seviye-4 Sistemi (ÜYS – Üretim Yönetim Sistemi), tüm İSDEMİR genelinde üretim ve kontrol yapılmasını sağlayan, üretim emirlerini veren, gerçekleşen, kalite kontrol ve üretim takip fonksiyonlarını sağlayan sistemdir.

İsdemir Üretim Yönetim Sistemi (ÜYS) ürün ağacı oluşturulmasından, mamul etiketlerinin basılmasına kadar tüm üretim sürecinin entegre ve güvenli biçimde yönetilmesini sağlayan sistemdir. İsdemir'de 3 faz halinde tamamlanmıştır. Ağustos 2007 tarihinde Faz-1 devreye alınmış ve bu faz ile Çelikhane ve Sürekli Dökümler hatlarında ÜYS sistematiğine geçilmiştir. Ağustos 2008 tarihinde ise Faz-2 sistemi kapsamında Sıcak Haddehane hatlarının entegrasyonu tamamlanmıştır. Son olarak da Nisan 2009'da Faz-3 ile birlikte Kangal Haddehanesi ve Dilme/Makas Hatları ÜYS kapsamına alınmıştır.

ÜYS; Kalite Tasarım, Üretim Planlama, Kalite Kontrol ve Üretim Takip vs. alt sistemlerinden oluşmaktadır. ÜYS ile birlikte edinilen fayda ve kolaylıkları aşağıdaki şekilde özetleyebiliriz:

- İsdemir ürün ağacının tanımlanması
- Sipariş vadesi ve üretim spesifikasyonlarına uygun olarak imalat lotların oluşturulması
- Siparişten sevkiyata kadar üretimin izlenebilmesi ve müşteriye tam zamanında teslimatın yapılmasının kontrol altına alınması.
- Proses bilgisayarlarına gönderilecek mamul üretim spesifikasyonları ile hatalı mamul üretimi ve üretim maliyetleri azaltılması.
- Siparişe göre hatların birbirleriyle koordineli optimum şekilde yüklenmesi suretiyle ara stoklar ve nihai stoklar azaltılması.
- Kalite kontrolün etkin bir şekilde yapılarak test raporlarının hatasız alınması.
- İşlerin daha doğru, standartlara ve prosedürlere uygun olarak daha hızlı yapılmasının sağlanması.
- Etkin bir bilgi arşivi ile istatistiksel analiz yapma imkanına kavuşulması.
- Üretilen ürünlerin kalite ve döküm bilgileri uzun süreli saklanabilmesi neticesinde ürün geliştirme çalışmalarının hızlanması.
- Tüm hatlarda yarı/nihai mamul kalite kontrolünün yapılması, kalite uygulama ve numune işlemlerinin tamamlanması.
- Nihai mamulün barkodlu şekilde etiketlenip sevkiyata hazır hale getirilmesi.

2. KALİTE TASARIMI

İsdemir'de kalite tasarımı, müşteri istekleri ya da yeni ürün geliştirme süreci sonrasında hayata geçen ve ÜYS'de tüm akış ve detaylarının tanımlandığı bir faaliyettir. Ürün ağacının, üretim spesifikasyonlarının ve kısıtlarının belirtildiği, üretim aşamalarıyla ilgili tasarımın yapıldığı alt sistem olarak da tanımlanabilir.
Ana fonksiyonlar şu şekildedir;

- MPC order item (sipariş öğesi) tanımlamaları ;
- Döküm kalitesi spesifikasyonları ve malzeme tanımlamaları
- MPC işlemleri ve raporlama tanımlamaları

MPC Order Item Tanımlamaları
Ürün Kodu İşlemleri
Çelik Cinsi İşlemleri
Özel Talimat İşlemleri
Ambalaj Tanımlama İşlemleri
İç Çap Dış Çap Tanımlama İşlemleri
Ebat Toleransı Standardı İşlemleri
Ebat Tolerans (Yassı Mamul) Tanımlama İşlemleri
Ebat Tolerans (Uzun Mamul) Tanımlama İşlemleri
Boy Tolerans Tanımlama İşlemleri
Rapor Tipi Tanımlama İşlemleri
Ağırlık Tanımlama İşlemleri
Kalınlık Toleransı İşlemleri
Genişlik Toleransı İşlemleri
Sıcak Haddehane Kalite Uygulama İşlemleri
Sıcak Haddehane Crown Değeri İşlemleri
Sıcak Haddehane İki Kenar Farkı Değeri İşlemleri
Mekanik Değerler İşlemleri
Üretilebilirlik Limitleri İşlemleri
Üretilebilirlik Limitleri İşlemleri
MPC Skarf Kodları İşlemleri
Bobin Ağırlığı İşlemleri
Kangal Haddehanesi Kalite Uygulama İşlemleri
Skarf Yüzey Kodu İşlemleri
Erdemir Item Bilgileri İşlemleri
CE Standardı Kalite Kriter İşlemleri
TSE Standardı Açıklama İşlemleri
TSE Standartları Kalite Kriter İşlemleri
İsdemir Sertlik Grubu İşlemleri
İsdemir-Erdemir Sertlik Grubu İşlemleri

Döküm Kalitesi Spesifikasyonları ve Malzeme Tanımlamaları
Döküm Çelik Kalitesi İşlemleri
Döküm Çelik Kalitesi Kalınlık Uygulama İşlemleri
Sipariş Çelik Cinsi Bazında DÇK İşlemleri
Döküm Çelik Kalitesi Geniş Limit İşlemleri
Döküm Çelik Kalitesi Kompozisyon Revizyon Takibi İşlemleri
Alt Kalite Kayıt İşlemleri
Kalite Türü İşlemleri
Kullanım Alanı İşlemleri
Standart Analiz Karşılaştırma Tablosu İşlemleri
Döküm Çelik Kalitesi Geniş Limit Kompozisyon Raporu İşlemleri
Yan Ürün İşlemleri
Standart Dışı Ürün İşlemleri

MPC İşlemleri ve Raporlama Tanımlamaları
MPC Kayıt İşlemleri
MPC Onay İşlemleri
MPC Güncelleme İşlemleri
MPC Detayları İşlemleri
Ürün Koduna Hat Bağlama İşlemleri
Ürün Koduna Genel Hat Bağlama İşlemleri
Erdemir Ürün Kodu Dönüşüm İşlemleri
Erdemir Özel Talimat Dönüşüm İşlemleri
Erdemir Karşılığı Olmayan İsdemir MPC Bilgileri İşlemleri
Kalite Uygulama ve Proses Sıcaklıkları İşlemleri
Çelik Cinsi ve Kalınlık Aralığı Bazında Mekanik Değerler İşlemleri
Mekanik Numune Alma Standartları Raporu İşlemleri
Kalite Sayısı Raporu İşlemleri

Çizelge 1. Kalite Tasarım Fonksiyonları

3. MPC (MANUFACTURING PRACTICE CODE - ÜRETİM PRATİĞİ KODU)

3.1 MPC Oluşumu ve Tasarımı

MPC (Manufacturing Practice Code - Üretim Pratiği Kodu)'nin 13 adet karakteristik bileşeni vardır. Bu bileşenler ürünü ve müşteri isteklerini tanımlamaktadır. İsdemir Üretim Yönetim Sistemi, Üretim Kontrol Sistemi ve Uzun Mamul Satış Sistemi talep alımından sevkiyata kadar tamamen MPC üzerine kurulmuştur. MPC, ÜYS'de tasarlanmaktadır. Tasarım bilgileri alt seviyelere gönderilerek üretim ve kalite kontrolü yapılmasını sağlamaktadır. Üretim yönetim sisteminde ürün veya yarı-mamullerin bir sonraki hat veya prosese devam edebilmesi, müşteri siparişlerinin üretim planlamasının yapılabilmesi için olması zorunlu bir koddur. Bu nedenle MPC, sisteminin temel bileşeni olmaktadır. 9 karakter ile ifade edilen, ürün kodu ve sıralı numaradan oluşan nihai mamul özelliklerini yansıtan bir anahtardır. Örneğin RKK (Sıcak haddelenmiş kenarları kesilmemiş rulo) ürün kodu 0035 ile ifade edilmektedir. Bu ürün koduna ait 00256 sıra nolu MPC aşağıda belirtildiği gibi gösterilmektedir.

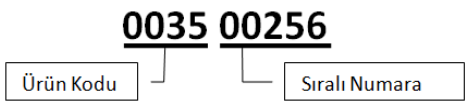

MPC'nin içerdiği sipariş öğeleri şunlardır: Ürün Kodu, Çelik Cinsi, Kalınlık, Genişlik, Boy, Ebat Toleransı, Boy Toleransı, Ambalaj/Paket Tipi, İç Çap-Dış Çap, Test Raporu, Özel Talimat, Ağırlık. Aşağıdaki şekilde sistem görüntüsü yer almaktadır.

Şekil 1. MPC sipariş öğeleri

Mamul ile ilgili her türlü bilgi MPC altında toplanmıştır. MPC tasarımı şu adımları içerir;

- MPC'nin hatlardaki üretim spesifikasyonlarını belirleme
- MPC'nin geçeceği hatları belirleme
- MPC'nin mekanik özelliklerini belirleme
- MPC oluşturma
- MPC onay

MPC oluşturulmadan önce MPC'nin 13 adet öğesi için gerekli olan tablolar ve spekler sisteme girilmektedir. Ayrıca mamulün üretim sırasında hangi hatlardan geçeceği ya da sapma durumunda nerelerden geçebileceği ifade edilmektedir. Genel hat bağlama ya da normal hat bağlama ile belirtilen bu alanlar vurgulandıktan sonra müşterinin talep ettiği kalitenin ait olduğu standardın gerektirdiği tüm analiz, mekanik (akma mukavemeti, çekme mukavemeti, akma/çekme değeri, % uzama, % kesit daralma, basma testi, darbe testi, DWT testi, katlama testi, sertlik vs.) testler ile numune alma sıklığı sisteme girilmektedir. Bu adımlar sonrası tüm spekleri, hatları ve yol haritası çizilmiş MPC, müşteri talebi doğrultusunda ya da diğer nedenlerle bağlantılı olarak meydana getirilerek kalite tasarım uzmanları tarafından onaylanmaktır.

Sipariş giriş kanallarından iletilen talep bilgileri önce Repeat Judgement denen bir işlemine tabi tutulur. 13 item'ın bileşiminden oluşan anahtar (MPC) ile daha önce bu tür mamulun

üretilip üretilmediği sistem tarafından kontrol edilir. Yani MPC‘ si olup olmadığı araştırılır. Eğer MPC ‘ si var ise sistem taleplere MPC kodu verir, MPC‘ si yok ise Kalite Tasarım bölümünün MPC ‘si olmayan talepler Listesi‘ nde yer alır. Kalite Tasarım bölümü MPC dizayn eder ya da otomatik oluşan MPC’yi onaylar. Kalite Tasarım bölümü MPC ‘si olmayan taleplere MPC verdiği gibi, ihtiyaç olduğunda siparişten bağımsız da MPC tasarlayabilir.

Sonuç olarak iki durumda MPC oluşumu söz konusudur:

- ✓ Siparişe Bağlı MPC Oluşumu: Sipariş kabulü ile ilgili uzmanlar tarafından – İSDEMİR sipariş kabul limitleri dahilinde - müşteri isteklerini üretim yönetim sistemine 13 değişken bilgi yoluyla tanıtması ile başlayan oluşum sürecidir.
- ✓ Siparişten Bağımsız MPC Oluşturma: Gerek görüldüğü zaman MPC tasarım uzmanı sisteme girerek de MPC kodu elde edilir. İki durumda buna gerek görülebilir:

• Yeni ürün geliştirme çalışmalarında ya da araştırma – deneme üretimlerde.
• Üretim sırasında talep edilen MPC’nin herhangi bir özelliklerinde sapma meydana gelmesi neticesinde o siparişe verilemeyecek ürünler için gerekebilir. Ürünün özelliklerine uygun başka bir sipariş olup olmadığı kontrol edilir. Eğer varsa o siparişe kaydırılır. Yok ise ürün veya yarı ürüne uygun MPC tasarlanması gerekmektedir.

3.2. MPC Sipariş Öğeleri ve Detay Tanımlamaları

Daha önce bahsedilen MPC’nin 13 adet öğesi ve detay bilgileri şunlardır:

1. Ürün Kodu: Üretilen her ürün cinsinin dört dijitli bir kodu vardır.

ÜRÜN KODU	ÜRÜN TİPİ	AÇIKLAMA
0035	RKK	Sıcak haddelenmiş kenarları kesilmemiş rulo
0010	KRKK	Sıcak haddelenmiş kenarları kesilmemiş kalın rulo
0055	HCKK	Sıcak haddelenmiş , soğuk haddelemeye uygun , kenarları kesilmemiş rulo
0032	LRKK	Sıcak Haddelenmiş , Kenarları Kesilmemiş Rulodan Kesilmiş Sac
0060	HRUKK	Sıcak Haddelenmiş , Kenarları Kesilmemiş Rulodan Kesilmiş Levha
0037	RD	Sıcak haddelenmiş kenarları kesilmemiş Dilinmiş rulo
0036	R	Sıcak haddelenmiş kenarları kesilmiş rulo

Çizelge 2. İsdemir ÜYS’de kayıtlı ürün kodları örnekleri

2. Çelik Cinsi : İSDEMİR çelik kalitesini belirten dokuz dijitli koddur.
Aşağıda İsdemir Çelik Cinsi örnekleri yer almaktadır.

İsdemir Sipariş Çelik Cinsi	Standart Karşılığı	Standart Kalitesi
1.3237_40	DIN EN 10025-2:2004	S235JR
1.3241_40	ASTM A36:2008	A36
1.4044_40	DIN EN 10025-2:2004	S275JRC
1.6222_40	DIN EN 10111:2008	DD11
1.4970_40	DIN EN 10149-2:1995	S700MC
1.9071_40	API 5L:2012 / EN ISO 3183:2012 PSL2	L485M / X70M
1.9080_40	API 5L:2012 / EN ISO 3183:2012 PSL2	L555M / X80M

1.9255_40	API 5CT:2005	J55
1.9415_40	EN ISO 3183:2012 PSL2 Annex M	L415ME
1.9460_40	DIN EN 10025-3:2004	S460N
1.9485_40	EN ISO 3183:2012 PSL2 Annex M	L485ME

Çizelge 3. İsdemir ÜYS'de kayıtlı sipariş çelik cinsi örnekleri

3. Sipariş Kalınlığı / Kesiti / Çapı; Kütük ürünler için kesit, kangal ürünler için çap ve yassı mamuller için kalınlık bilgileri esas alınmaktadır.

4. Sipariş Genişliği; Yassı ürünler için geçerlidir. Bu alanı etkileyen tolerans bilgilerinin ve standart tanımlamaların yer aldığı ekranlar bulunmaktadır.

5. Sipariş Uzunluğu; Levha, sac, slab ve kütük ürünleri için girilen bir sipariş öğesidir.

6. Boy Toleransı; İlgili standartlar çerçevesinde veya İsdemir pratiklerine göre üretilecek olan kütük, slab ya da makas malzemeleri (sac-levha) için tanımlanır. İlgili sipariş öğesinin tanımlama ekranı aşağıda belirtilmiştir.

Şekil 2. Boy toleransı tanımlanası

7. Ebat Toleransı; Öncelikle tüm ürünler için standart tanımlamalar yapılmakta ve daha sonra uzun ya da yassı mamul türüne göre tanımlamalar ve standarttaki kalite - ebat bazında tüm değerler sisteme girilerek MPC sipariş öğesi tanımlanmaktadır.

Şekil 3. Boy toleransı tanımlanması

Şekil 4. Ebat toleransı tanımlanması – yassı ürün

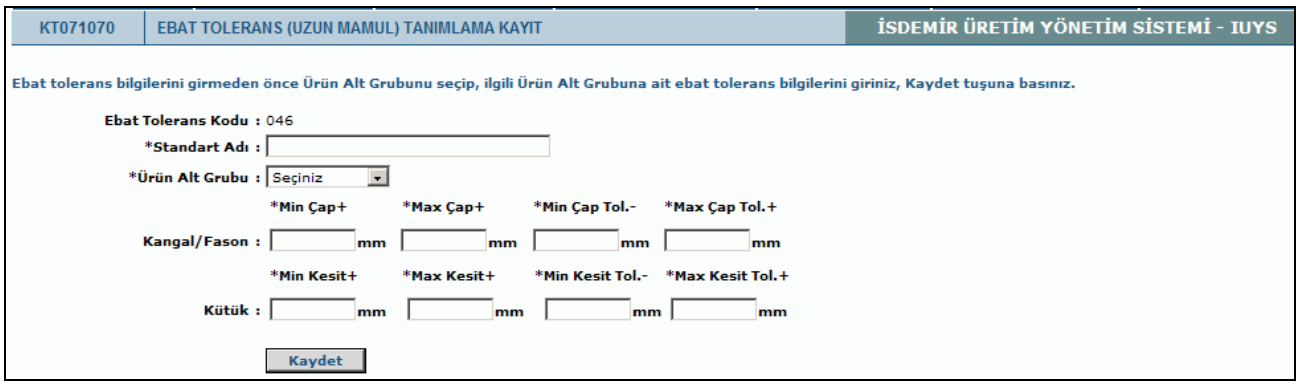

Şekil 5. Ebat toleransı tanımlanması – uzun ürün

8. Ambalaj/Paket Tipi; Malzemenin metal veya kağıt ambalajlı olarak ya da çemberlenerek sevk edilme talepleri çerçevesinde ilgili detaylar belirlenir.

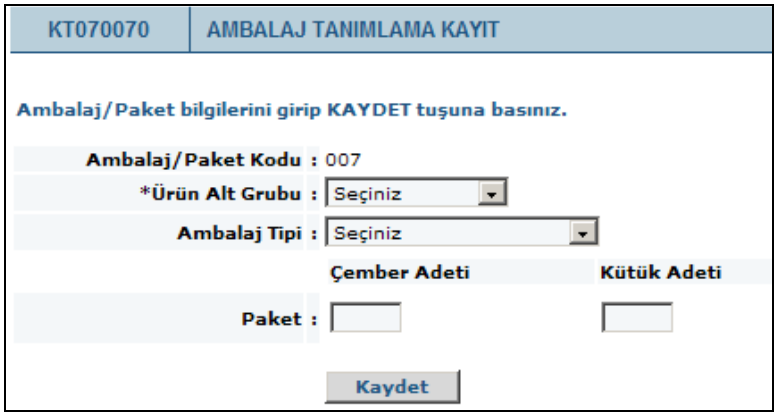

Şekil 6. Ambalaj bilgilerinin tanımlanması

9. İç Çap-Dış Çap; Sıcak haddehane sahası için veya dilme hatları için ihtiyaç duyulan iç çap ve dış çap ölçüleri bu alanda ifade edilir. Müşteri taleplerine göre yapılabilirlik durumu gözetilerek MPC kaydı için ön tablolar girilir.

Şekil 7. İç çap ve dış çap tanımlanması

10. Yerli / İhraç : Y ve I kodu ile belirtilir.

11. Ağırlık; Müşteri taleplerine göre bobin ağırları belirtilir.

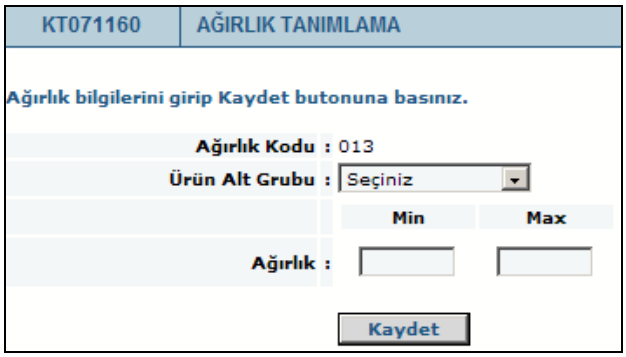

Şekil 8. Ağırlık kodu tanımlanması

Şekil 9. Ağırlık kaydı tanımlanması

12. Test Raporu; DIN EN 10204 standardı kapsamında verilecek olan 2.1 - 2.2 - 3.1 - 3.2 sertifikaları ya da ABS - Türk Loydu gibi sertifika türleri bu alanda belirtilir ve MPC kaydı esnasında seçilerek müşteri talepleri gerçekleştirilir.

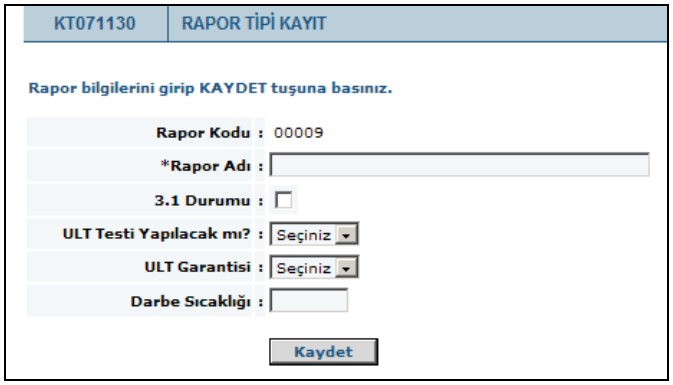

Şekil 10. Rapor tipi tanımlanması

13. Özel Talimat kodu; 12 adet diğer sipariş öğelerinde belirlenemeyen müşteri talepleri için kullanılan bir item olup, tabloda örnekleri görülmektedir.

Özel Talimat Kodu	Açıklama
005	Mukavemet Aralığı 960-1020 MPa olacaktır.
019	Akma Muk. 250-350MPa-Çekme Muk. 360-460MPa-% Uz. 35 min.-% K.D. 70 min.
044	Sarılma Sıcaklığı 600 max. olacaktır.
045	Sarılma Sıcaklığı 650 min. olacaktır.
053	-0,30mm / +0mm kalınlık toleransı ile üretim yapılacaktır.
055	ABS sertifikalı üretim yapılacaktır.
066	Açık Döküm Yapılacaktır.
067	Deneme Üretim için Oluşturulmuştur.
069	Erciyas Firması Siparişi İçin Oluşturulmuştur.
071	+20 derece sıcaklıkta darbe testi yapılacaktır.
072	Darbe değeri O (sıfır) derecede min. 60 J olacaktır.
074	-20 derece sıcaklıkta darbe testi yapılacaktır.
079	-0 mm / +0,20 mm kalınlık toleransı ile üretim yapılacaktır.
080	DIN EN 10160 standardına göre S0E0 seviyesinde ULT garanti edilmektedir.
081	Kapalı Döküm Yapılacaktır.
083	Katlama testi yapılacaktır.
087	ISO/TS 16949:2009 Otomotiv Müşterisi

Çizelge 4. Özel talimat kodu ve açıklama örnekleri

Bu bilgilerin üretim yönetim sistemine girilmesi sonrasında, belirli aralıklarla çalışan bir bilgi işlem programı daha önce bu bilgilerin aynısı olan özelliklerde MPC var olup olmadığını belirler. Eğer varsa, bu siparişi o MPC'ye bağlayarak Üretim Planlama departmanına ait sisteme gönderir ve MLN programı çalışarak uygun plana göre üretimine geçilir. Eğer yoksa sipariş özelliklerine göre yeni MPC tasarımı için tasarım uzmanına gönderir. MPC tasarım uzmanı kendisine gönderilen sipariş bilgilerini tasarım için kabul ettiği anda sistem tarafından o sipariş özelliklerine otomatik olarak sıralı numara yani MPC kodu verilir.

4. SONUÇ

İsdemir üretim yönetim sisteminde Nisan 2014 itibari ile yaklaşık 38.919 adet uzun ve yassı MPC mevcuttur ve sürekli artmaktadır. Yani, başka bir deyişle sistemde 38.919 farklı özellikte talebi hemen karşılayacak üretim reçetesi mevcuttur. Yani;

- İsdemir sürekli olarak müşterinin yeni taleplerini karşılayarak kalite tasarım faaliyetlerine devam etmektedir.
- Üretilen ürün cinslerine yenileri eklenmektedir.
- İsdemir'in geniş ürün yelpazesi ve müşteri sektörel çeşitliliği bulunmaktadır.

İsdemir üretim yönetim sisteminde yapılan MPC esnek ve dinamik yapıya sahiptir. MPC tasarımı ile aynı zamanda kalite tasarımı da yapılmış olmaktadır. Zira her talep ve siparişteki spesifik ayrım ve detaylar, MPC'yi farklılaştırmakta ve müşteriye özel bir üretim yapılmasını sağlamaktadır. Sonuç olarak MPC ile ürünlerde kalitenin ve ilgili standartların her defasında yerine getirilmesi güvence altına alınmaktadır.

KÜLÇE PİK AĞIRLĞINDAN KAYNAKLANAN PROBLEMLERİN ÇÖZÜMÜ

[1]Mehmet GÖKOĞLU, [2] Kamil EKEN

[1]İSDEMİR A.Ş. Yüksek Fırınlar Müdürlüğü
[2]İSDEMİR A.Ş. Yüksek Fırınlar Müdürlüğü

ÖZET

Bu çalışmada, İskenderun Demir ve Çelik A.Ş (İSDEMİR) Pik Döküm Tesisi'nde üretilen külçe piklerin mevcut dizaynından dolayı manüplasyon sırasında kırılma, elle taşıma ve yükleme sırasında İSG açısında taşıdığı risklerin azaltılmasına yönelik iyileştirme çalışması irdelenmektedir.

İSDEMİR Yüksek Fırınlara bağlı olarak faaliyet gösteren Pik Döküm Tesisinde 45-50 kg ağırlığındaki tek parçalar halinde farklı kalitelerde külçe pik üretimi yapılmaktadır. Külçe Piklerin büyük ve ağır olmasından dolayı; külçe pikin manipülasyonu sırasında kırılma, üretim ve müşteri kullanımı sırasında yapılan elle taşıma-yükleme işlemlerinin 2 kişi tarafından yapılsa bile İSG açısından (>40 kg) bel, diz vb. eklem rahatsızlığı meydana gelmesi risklerine yol açtığı şeklinde şikâyetler olmaktaydı.

Tüm bu problemlerin çözümü için mevcut kalıp ölçülerine sadık kalınarak kalıpların iç dizaynında yapılan revizyon ile yapılan deneme üretimlerinde 45-50 kg ağırlığındaki tek parça külçe pik yerine her kalıptan 10-12,5 kg ağırlığında 3 parça külçe pik üretimi yapılmıştır.

Deneme amaçlı 20 adet kalıpta yapılan ve 10-12,5 kg ağırlığındaki deneme üretimi sırasında; külçe piklerde manüplasyon sırasında oluşan kırılmaların hemen hemen yok denecek seviyelere geldiği, üretim sırasında ve tüketim sırasında el ile yapılan temizlik ve yükleme çalışmalarının tek personel tarafından kolay şekilde yapıldığı gözlenmiştir. Deneme üretimleri sonrası işletme personellerinden ve müşterilerden yeni dizayn külçe piklerle ilgili memnuniyet ifade eden geri bildirimler alınmıştır.

Anahtar kelimeler: Pik Döküm Tesisi, Külçe Pik, İSG

SUMMARY:

In this study, the evaluation of pig ingots produced in İskenderun Demir ve Çelik A.Ş (İSDEMİR) are examined for the breaking due to their design during the manipulation process, and also imporvement for the reduction of safety risks during the transportation of these ingot by hand and during loading are being carried out.

In the Pig Casting facilities of the Blast Furnace pig ingots of 45-50 kg each are being produced in different qualities. Because the pig ingots are big and heavy, complaints were made about the breaking of these ingots during manipulation and also there were safety issues due to transportation-loading by hand during production and customer usage. Even if transportaion-

loading is being made by 2 people, there is a safety risk (>40kg) for personel's waist, knees etc. joints.

To solve these problems without changing the existing molds dimensions we made changes in the inner design of the mold and instead of producing one 45-50 kg piece we produced 3 pieces each weighting 10-12,5 kg.

In the test production of these 10-12,5 kg ingots, 20 molds have been prepared and it has been seen that; breaking of the ingots due to maniplation was very low and that during production and consumption stage loading and cleaning of these ingots could be made very easily by one person. After the test production the working personnel and the customers expressed their positive opinions for this new ingot design.

Key Words: Pig Casting Facility, Pig ingot, Working Safety

1. GİRİŞ

Bu çalışmada, İskenderun Demir ve Çelik A.Ş (İSDEMİR) Pik Döküm Ünitesinde üretim yapılan külçe piklerin mevcut dizaynından dolayı kırılma, elle taşıma ve yükleme işlemleri sırasında İSG açısında karşılaşılan risklerin azaltılmasına yönelik yapılan iyileştirme çalışmaları araştırılmıştır.

İSDEMİR (İskenderun Demir ve Çelik A.Ş.) Yüksek Fırın'larına bağlı olarak faaliyet gösteren Pik Döküm Tesisinde 45-50 kg ağırlığında, tek parçalar halinde, farklı kalitelerde külçe pik üretimi yapılmaktadır.; Külçe pikin manipülasyonu sırasında kırılma, üretim ve müşteri kullanımı aşamalarında taşıma-yükleme işlemlerinin külçe Piklerin büyük ve ağır olmasından dolayı 2 kişi tarafından yapılsa bile İSG açısından (>40 kg) bel, diz vb. eklem rahatsızlıkları meydana gelmekteydi.

Tüm bu problemlerin çözümü için, mevcut kalıp ölçülerine bağlı kalınarak kalıpların iç dizaynında yapılan revizyon ile yapılan deneme üretimlerinde 45-50 kg ağırlığındaki tek parça külçe pik yerine her kalıptan 10-12,5 kg ağırlığında 3 parça külçe pik üretimi yapılmıştır.

Deneme amaçlı 20 adet kalıpta yapılan ve 10-12,5 kg ağırlığındaki deneme üretimi sırasında; külçe piklerde manüplasyon sırasında oluşan kırılmaların hemen hemen yok denecek seviyelere geldiği, üretim sırasında ve tüketim sırasında el ile yapılan temizlik ve yükleme çalışmalarının tek personel tarafından kolay bir şekilde yapılabildiği gözlenmiştir. Deneme üretimleri sonrası işletme personellerinden ve müşterilerden yeni dizayn külçe pikler hakkında olumlu geri bildirimler alınmıştır.

2. PROBLEM TESPİTİ

2.1. Külçe Pik Kırılması

Külçe pikin ağır olmasından dolayı özellikle külçe pikin vagonuna manipülsayonu sırasında aşırı kırılmalar meydana gelmektedir. Bu durum sonucuda; külçe pikler pik stok sahasında tekrar eleme işlemine tutularak sevkiyatı yapıldığı için üretim sevkiyat süreci artmaktadır. Bunun yanında kırık parça halinde külçe pikler müşteri tarafından istenmediği için, üretim maliyetini aşırı oranda artırmaktadır.

2.2. İSG Açısından Uygunsuzluk:

Külçe pik üretiminde yere düşen külçe piklerin perosnel tarafından temizliği sırasında;İSG açısından (>40 kg) bel, diz vb. eklem rahatsızlığı meydana gelmekteydi.

Bir çok perosnelin rahatsızlanması sonucu ise şu sorunlar olmuştur:

2.2.1. Vardiyada yeterli personel olamdığı için üretim kaybı yaşanmıştır.
2.2.2. Vardiyada eksik personel yerine fazla mesai ile çalışmak zorunda kalındığı için bu durum hem verimsiz çalışmaya hemde işiçilik maliyetlerinin artmasına neden olmuştur.
2.2.3. Uzun süre iş yerinden rahatsızlığı nedeniyle ayrı kalan personelde hem maddi hemde psikolojik sorunlar görülmüştür.

2.3. Müşteri Şikayetleri:

İSDEMİR'de üretilen külçe pik müşterileri küçük ve orta boyutlu işletmeler olduğu için, müşterilerden genelde sorunlar olmuştur:

2.3.1. Külçe pik boyutu büyük olduğu için; kendi endüksiyon ocaklarına şarj etme sırasında külçe pikleri ik üç parçaya kırmaları hem işgücü kaybına hemden kırma işlemi uzun sürdüğü için üretim kaybına neden oldupunu belirtmişlerdir.
2.3.2. Büyük boyutlu külçe piklerin elle maniplasyonü sırasında meydana gelen kırılmalardan dolayı oluşan küçük boyutlu paçaların endüksiyon ocağına şarj edilmesi ve erigitlmesinin üretim maliyetini artıırdığını belirtmişlerdir.

3. PROBLEM ÇÖZÜMÜ

3.1. Çözüm Araştırması ve Projelendirme

Külçe pik ağırlıkları ile ilgili yapılan araştırmada dünya genelinde üretilene külçe pik ağırlıklarının 7-18 kg arasında olduğu görülmüştür.

Külçe pik ağırlığından kaynaklanan problemlerin çözümü için mevcut külçe pik ölçülerine sadık kalınarak kalıp iç dizaynında değişiklik yapılarak yaklaşık 12 kg ağırlığında 3 parça şeklinde kalıp dizaynının projesi yapıldı.

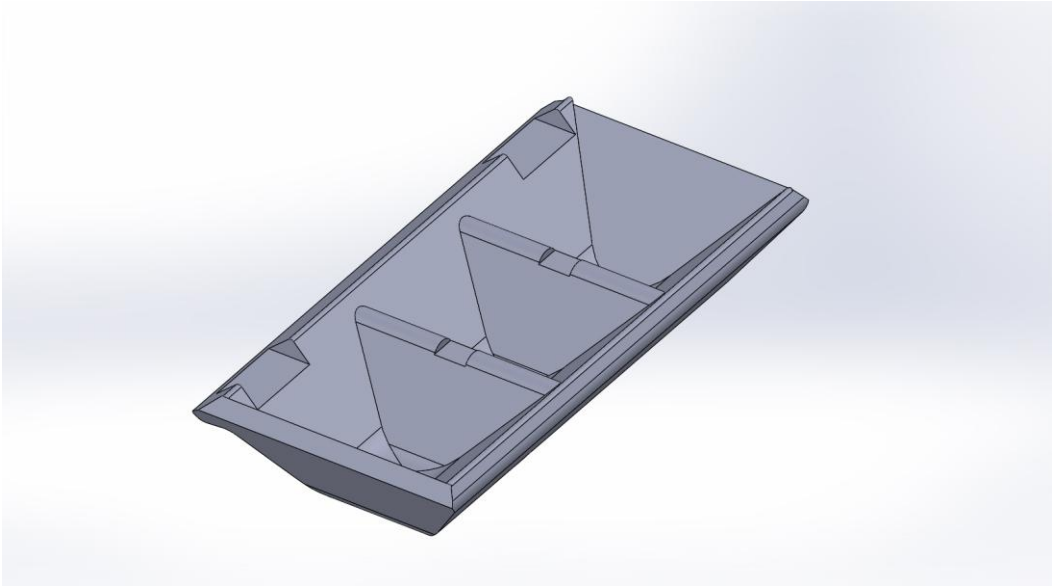

Resim 1:Yeni dizayn külçe pik kalıbının modeli

3.2. Yeni Dizayn Külçe Pik Kalıplarının İmalatı Ve Montajı

Yapılan kalıp dizaynına göre 10 adet logolu ve 10 adet logosuz olmak üzere toplam 20 adet külçe pik kalıp imalatı yapılmıştır.

Sağ ve sol döküm bandına 10 ar adet külçe pik kalıp montajı yapılmıştır. Yeni dizayn pik kalıplarının performansının iyi takip edebilmek için kalıplar üçerli ve rastgele montajı yapılmıştır.

Montaj sonrası bütün kalıplar normla dökümdeki gibi kireçleme işlemine tabi tutulmuş ve yeni dizayn külçe pik kalıplarının durumları incelenmiştir. Bu incelemede yeni dizayn külçe pik kalıplarının iç kısmına yeterince kirecin püskürtüldüğü görülmüştür.

Resim 2: Yeni dizayn külçe pik kalıplarının montajı

3.3. Yeni Dizayn Külçe Pik Kalıplarının Denenmesi ve Sonuçları

Külçe pik dökümü sırasında yeni dizayn külçe pik kalıpları ile ilgili elde edilen sonuçları şu şekildedir:

- ✓ Logolu kalıpların logosuz kalıplara göre daha zor kalıptan çıktığı görülmüştür
- ✓ Logolu kalıplardaki logolar fark edilmeyecek kadar küçük olduğu görülmüştür.

- ✓ Kalıplarda hiç yapışma olmadığı görülmüştür.
- ✓ Külçe pikler kalıptan üç ayrı parça halinde çıkmıştır.
- ✓ Yeni dizayn kalıplardan çıkan külçe piklerde nerdeyse hiç kırılma görülmemiştir. Mevcut kalıplarda kırılmalar devam etmektedir
- ✓ Özellikle yere düşen külçe piklerin temizliği sırasında personel hiçbir rahatsızlık çekmeden kolayca temizlediği görülmüştür.
- ✓ Yeni dizayn külçe pikler ile iğli müşterilerden başta İSG yönünden olmak üzere ve işletme açsından çok uygun olduğu şeklinde geri bildirimler alınmıştır.
- ✓ Külçe pik üretimi sırasında eski ve yeni dizayn kalıplarının tamamının dolduğu görülmüştür.

Resim 3: Külçe pik üretimi sırasında yeni ve eski dizayn külçe pik kalıplarının durumu

3.4. SONUÇ

Yüksek Fırınlar Müdürlüğü Pik Döküm Tesisi 1.Pik Makinesinde 10 adet logolu ve 10 adet logosuz yeni dizayn külçe pik kalıpların denemesi yapılmıştır. Deneme sonucuna göre personel tarafından yere düşen yeni dizayn külçe piklerin daha kolay ve bel rahatsızlığına neden olmadan

temizlendiği ve yeni dizayn külçe pik kalıplar ile üretilene külçe piklerin(Ç1,Ç2,ÇH3,H1 VE H2) üretiminde kırılma olmadığı görülmüştür. Bunun yanında birçok müşteriden başta İSG açsından olmak üzere, işletme açısından çok olumlu geri bildirimler alınmıştır.

Resim 4: Yeni ve eski dizayn külçe pikler

ÖSTENİTİK KROM-NİKELLİ PASLANMAZ ÇELİKLERİN KAYNAĞINDA KARŞILAŞILAN PROBLEMLER VE GİDERİLMESİ

Yüksel BİLİR

Yüksek Teknik Öğretmen, İSDEMİR A.Ş. ,HATAY

yubilir@isdemir.com.tr

ÖZET

Günümüzde teknolojisinde birçok paslanmaz çelik türü olmakla birlikte, bu paslanmaz çelikler çok değişik amaçlarda ve farklı kullanım alanlarında yaygın olarak kullanılmaktadır. Bu paslanmaz çelik türlerinden Östenitik krom-nikelli paslanmaz çelikler, gerek kaynak kabiliyeti, gerek yüksek korozyon direnci ve gerekse de iyi işlenebilirliği açısından paslanmaz çelikler içerisinde en yaygın olarak kullanılan türdür.

Östenitik krom-nikelli paslanmaz çeliklerin kaynağında "sıcak çatlak oluşumu, krom-karbür çökelmesi ve sigma fazı oluşumu" olmak üzere üç temel problem ile karşılaşılabilir. Bu problemler kaynak öncesi veya sonrası bir takım işlemlerle giderilebilir.

Anahtar Kelimeler: *Östenitik paslanmaz çelikler, kaynak, sıcak çatlak oluşumu, krom-karbür, sigma fazı*

PROBLEMS ENCOUNTERED DURING WELDING OF AUSTENITIC Cr-Ni STAINLESS STEELS AND POSSIBLE SOLUTIONS

SUMMARY

In today's technology, there are many different types of stainless steels available and they are used widely in various fields with different purposes. The austenitic Cr-Ni stainless steels, because of their high chromium and nickel content, are the most corrosion resistance of the stainless group .They are are selected for their high corrosion resistance with ease of forming and welding.

Three main problems encountered during welding of austenitic Cr-Ni stainless steels are as following; chrome carbide sensitisation, formation of sigma phase and high temperature cracking. These problems may be prevented before, during and after welding by taking appropriate actions.

Keywords: *Austenitic stainless steels, welding, high temperature cracking, chrome carbide, sigma phase*

1. GİRİŞ

Gelişmekte olan ülkemiz endüstrisinin paslanmaz çeliklere olan gereksinimi her geçen gün artmaktadır. Özellikle petro-kimya, kimya, gıda endüstrisinde kullanılan depolama tankları, basıncı kaplar, ısı değiştiricileri ve paslanmaz boruların üretimlerinde çok çeşitli türlerde paslanmaz çelik kullanılmaktadır.[1]

Östenitik paslanmaz çelikler, paslanmaz çelikler grubunda en yaygın kullanılan türdür. Östenitik krom-nikelli paslanmaz çelikler, bileşiminde %12-25 Cr ve %8-25 Ni içeren ve paslanmaz çelik ailesinin en yaygın kullanım alanına sahip olan çeliklerdir. Nikel kuvvetli östenit yapıcı olduğundan, bu çeliklerde katılaşma esnasında ortaya çıkan östenit oda sıcaklığının altındaki sıcaklık derecelerinde bile dönüşmeden kalır. Soğuma esnasında östenit-ferrit dönüşümü olmadığından bu tür paslanmaz çelikler su verme yoluyla sertleştirilemezler. [2]

TS 2535 Östenitik paslanmaz çelikleri "Bileşiminde korozyona karşı krom ve östenitik yapı sağlamak amacı ile de nikel bulunan, oda sıcaklığında manyetik olmayan, ısıl işlem ile sertleştirilemeyen soğuk biçimlendirilmeye elverişli paslanmaz çeliktir" diye tanımlar. [9]

2. ÖSTENİT OLUŞUMU VE KOROZYON DİRENCİNİ ARTTIRMAK İÇİN KATILAN ELEMENTLER

Antimanyetik olan östenitik paslanmazlar çeliklere östenit oluşumuna yardımcı olmak ve korozyon direnci arttırmak için katılan alaşım elementleri aşağıdaki şekilde sıralanabilir,[2, 3,9]

Karbon: Östenit oluşuma kuvvetli etkide bulunur. Krom ile birleşerek taneleraras korozyonda başrol oynayan karbürlerin oluşumuna etkide bulunur.

Nikel: Östenit oluşumuna etkide bulunur. Yüksek sıcaklıktaki direnci, korozyona karşı dayanımı ve sünekliği arttırır.

Azot: Östenit oluşumuna çok kuvvetli etkide bulunur. Bu konuda çoğu zaman nikel kadar etkilidir. Özellikle kriyojenik sıcaklıklardaki mukavemet değerini yükseltir.

Bakır: Paslanmaz çeliklere, bazı ortamlardaki dayanımlarını arttırmak amacıyla katılır. Gerilmeli korozyon çatlamasına karşı hassasiyeti azaltır ve yaşlanma yoluyla sertleşmeyi teşvik eder.

Molibden: Çukur ve çatlaklardaki korozyonu önlemek için kullanılır.

Niobyum, Titanyum: Kuvvetli karbür yapıcıdır. Östenitik paslanmaz çeliklerde krom-karbür çökelmesini önlemek için dengeleme elementi olarak konur.[9]

3. ÖSTENİTİK PASLANMAZ ÇELİKLERİN FİZİKSEL ÖZELLİKLERİ

Bu tür paslanmaz çeliklerin kaynak edilerek birleştirilmelerinde, kaynak kabiliyeti açısından fiziksel özelliklerini dikkate almak gerekir.[2] Tablo 3.1'de östenitik paslanmaz çeliklerin fiziksel özelliklerinin diğer tip çeliklerle karşılaştırılması verilmiştir. [9]

Tablo 3-1: Östenitik Paslanmaz Çeliklerin Fiziksel Özelliklerinin Diğer Tür Çeliklerle Karşılaştırılması [9]

Çelik Türü	α X10^{-6}	ƛ W/mC	Ώ nΏm	E kN/mm^2
Karbonlu Çelikler	13.0	47	150	205
Ferrit Çelikler	12.5	24	600	225
Ferritik-Östenitik Çelikler	13.5	20	850	225
Östenitik Çelikler	19.5	15	700	200
α: 20-800°C'da Isıl genleşme katsayısı λ : Isıl İletkenlik (20°C) Ώ: Elektrik Direnci (20°C) E: Elastiklik Modülü (20°C)				

Tabloda belirtilen fiziksel özellikleri aşağıdaki şekilde özetleyebiliriz,

- Isı iletme katsayıları oda sıcaklığında, karbonlu v az alaşımlı çeliklerin 1/3'ü kadardır.
- Isı genleşme katsayıları karbonlu ve az alaşımlı çeliklerin yaklaşık 1,5 katı yani %50 daha fazlasıdır.
- Bu çeliklerin elektrik iletme dirençleri, alaşımsız çeliklere nazaran 4-7 kat daha büyüktür.

4. BAŞLICA ÖSTENİTİK PASLANMAZ ÇELİK TÜRLERİ

Östenitik paslanmaz çelikler %16-26 Cr, %10-24 Ni+Mn, %0,40'a kadar C ve düşük miktarda Mo, Ti, Nb ve Ta gibi diğer alaşım elementleri içerir. Bu elementlerin değişik kompozisyonu ile elde edilen alaşımlar, geniş bir sıcaklık aralığında yüksek tokluk, dayanım ve korozyon direnci gösterirler. Tablo 4.2'de başlıca östenitik paslanmaz çelikler görülmektedir.[3]

Tablo-4.2: Başlıca Östenitik Paslanmaz Çeliklerin Nominal Kimyasal Analiz Değerleri,[3]

Türü	UNS No	Kimyasal Analiz Değerleri (%) *							Diğer
		C	Mn	Si	Cr	Ni	P	S	
302	S30200	0,15	2,00	1,00	17,0-19,0	8,0-10,0	0,045	0,03	
304	S30400	0,08	2,00	1,00	18,0-20,0	8,0-10,5	0,045	0,03	
308	S30800	0,08	2,00	1,00	19,0-21,0	10,0-12,0	0,045	0,03	
309	S30900	0,20	2,00	1,00	22,0-24,0	12,0-15,0	0,045	0,03	

310	S31000	0,25	2,00	1,00	24,0-26,0	19,0-22,0	0,045	0,03	
316	S31600	0,08	2,00	1,00	16,0-18,0	10,0-14,0	0,045	0,03	
321	S32100	0,08	2,00	1,00	17,0-19,0	9,0-12,0	0,045	0,03	Min 5x%C-Ti
347	S34700	0,08	2,00	1,00	17,0-19,0	9,0-13,0	0,045	0,03	Min 10x%C-Nb+Ta

***** Tek değerler maksimum değerlerdir.

5. ÖSTENİTİK KROM-NİKELLİ PASLANMAZ ÇELİKLERİN KAYNAĞINDA KARŞILAŞILAN BAŞLICA PROBLEMLER VE GİDERİLMESİ

Östenitik krom-nikelli paslanmaz çeliklerin kaynağında başlıca üç kaynak problemi ile karşılaşılır. Bunlar sırası ile şunlardır; [3]

- Krom karbür oluşumu,
- Sıcak çatlak oluşumu,
- Sigma fazı oluşumudur.

5.1. KROM KARBÜR OLUŞUMU

Isının tesiri altında kalan bölgenin (ITAB) 427-871 °C sıcaklığa kadar ısınan bölümde yer alan tane sınırlarında çökelen ve taneleraresı korozyonu hızlandıran krom karbürler burada "Hassas Yapı" oluşmasına neden olurlar. **(Şekil-5.1)** Bu oluşum sırasında bir miktar krom çözeltiden tane sınırlarına doğru yer değiştirir ve bunun sonucunda bu bölgesel alanlarda krom miktarında azalma olacağı için korozyon dayanımı düşer. **(Şekil-5.2)**. [3]

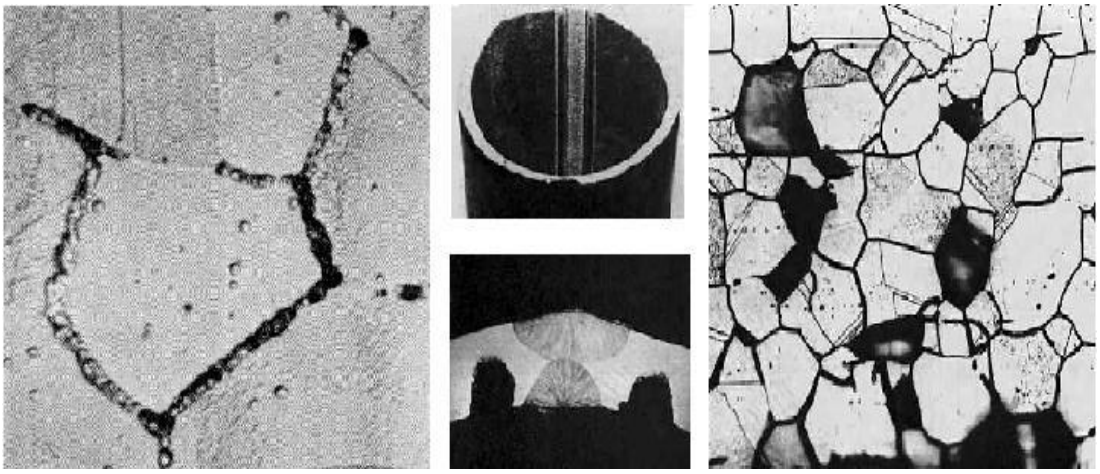

Şekil-5.1: 18 Cr / 8Ni (0,10)'lu Paslanmaz Çeliğin Tane Sınırlarında Oluşan Karbür Çökelmesi (x1200) [3]

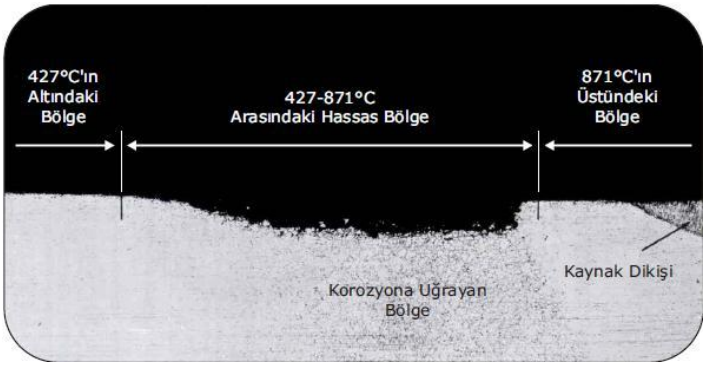

Şekil-5.2: Krom Karbür Çökelmesi Sonucu Hassas Bölgede Oluşan Korozyon [3]

Hassaslaşma, malzeme 500-900.°C sıcaklık aralığına ısıtıldığında meydana gelir. Bu sıcaklıklarda krom ve karbon, $Cr_{23}C_6$ tipi krom karbürler oluşturmak üzere tane sınırlarına yayınırlar. Karbürler oluşurken, ana metaldeki krom oranı azalmakta, tane sınırlarındaki oran ise ciddi miktarda artmaktadır. Krom seviyesi düşük olan alanlarda, krom içeriği alaşım bütününe kıyasla daha aşağıda kalmakta ve bu alanları korozyona hassas hale getirmektedir.[4,5,6]

Bu sorun, kromla birleşerek krom karbür oluşmasına neden olan karbonun yapıda düşük seviyelerde tutulduğu düşük karbonlu (L Tipi) ana metallerin ve dolgu metallerinin kullanılmasıyla önlenebilir. Bunun yanında kaynak işleminin öntav uygulanmadan yapılması, ısı girdisinin düşük seviyede tutulmasına özen gösterilmesi ve bakır altlık kullanılarak hızlı soğuma sağlanması hassas sıcaklık aralığında kalma süresinin kısa tutulması açısından oldukça yararlıdır. [3] Alaşımın veya dolgu telinin karbon miktarının % 0.08'den % 0.02'ye düşürülmesiyle, krom karbürün çökelme kinetiğinde 0.1'den 100 saate kadar bir artış görülmektedir. [5,6]

Diğer bir yöntem, sitabilize edilmiş olan paslanmaz çelik ana malzemelerin ve dolgu metallerinin kullanılmasıdır. Bu sayede stabilizatör görevi gören alaşım elementleri (Ti, Nb) karbon ile reaksiyona girecek ve krom miktarı azalmadan yapıda kalması sağlanacağından korozyon dayanımında herhangi bir düşüş olmayacaktır. [3,4]

ITAB (Isı Tesiri Altındaki Bölge) veya esas metalde krom karbür çökelmesinin oluştuğu hallerde, şayet parçanın boyutları ve konstrüksiyon uygun ise parça 1100 °C'ye kadar tavlanıp suda soğutulursa, yüksek sıcaklıkta östenit içerisinde çözünmüş karbürler hızlı bir soğutma esnasında tekrar oluşmazlar. [2]

Tek paso ile yapılan elektrik ark kaynağında 650 °C ile 750 °C arasındaki sıcaklığa kadar bir dakikadan daha az bir süre maruz kalır. Buna karşın, çok pasolu kaynak halinde bu süre üç dakikanın üzerine çıkar ve dolayısı ile karbür çökelme tehlikesi kendini gösterir.[2]

Çok pasolu kaynaklarda pasolar arası beklemek parçanın ve kaynak bölgesinin sıcaklığını düşürecek olması olumlu sonuçlar verecektir. Uygulama ile edinilen tecrübelere göre pasolar arası sıcaklığı 150-200 °C'da tutmak uygun olacaktır.

Östenitik paslanmaz çeliklerin klasik eritme yöntemlerine karşılık elektrik direnç nokta kaynağında krom karbür çökelmesi görülmez. Bu durum elektrik direnç kaynağındaki lokal olarak yüksek ısı yoğunluğu, düşük kaynak sıcaklığı, kısa kaynak süresi ve su ile soğutulan elektrodlar üzerinden gerçekleşen ısı transferi ile hızlı soğuma sonucu krom karbür çökelmesinin oluşmaması olarak açıklanmaktadır. [11]

5.2. SICAK ÇATLAK OLUŞUMU

Sıcak çatlamanın temel nedeni; kükürt (S) ve fosfor (P) gibi elementlerin oluşturduğu ve tane sınırlarında toplanma eğilimi yüksek olan düşük erime sıcaklığına sahip bileşimlerdir. Bu bileşimler, eğer kaynak dikişinde veya ısının tesiri altında kalan bölgede (ITAB) bulunuyorsa tane sınırlarına doğru yayılırlar ve kaynak dikişi soğurken ve çekme gerilmeleri oluştuğunda çatlamaya neden olurlar. [3]

Sıcak çatlak oluşumu, dolgu metalinin ve ana metalin kimyasal analizinin östenitik matriksde düşük miktarda ferrit içeren bir mikro yapı elde edilecek şekilde ayarlanmasıyla önlenebilir. Ferrit, kükürt ve fosfor bileşimlerini kontrol altında tutabilen ve ferritik-östenitik yapıya sahip olan tane sınırları oluşturarak sıcak çatlak oluşumunu engeller.[3]

Sıcak çatlama riskine karşı dayanım elde edebilmek için yapıdaki ferrit miktarının en az % 4 olması önerilmektedir. Ferrit varlığı AWS A4.2'ye göre kalibre edilen manyetik ölçüm aletleriyle sağlıklı bir şekilde belirlenebilir. Bunun dışında; dolgu malzemesinin ve ana metalin kimyasal analizi biliniyorsa, çeşitli diyagramlar kullanılarak da bir tahminde bulunmak mümkündür. Bu diyagramlardan en bilineni ve en eski olanı 1948 yılında SCHAEFFLER tarafından geliştirilen ve Şekil-5.3'de gösterilen "Schaeffler Diyagramı"dır. Bu diyagramda Cr eşdeğeri yatay eksende, Ni eşdeğeri ise dikey eksende yer almaktadır.

$Cr_{eş}$ = % Cr + % Mo +1.5 %Si + 0.5 %Nb

$Ni_{eş}$ = % Ni + 30 % C + 0.5 % Mn

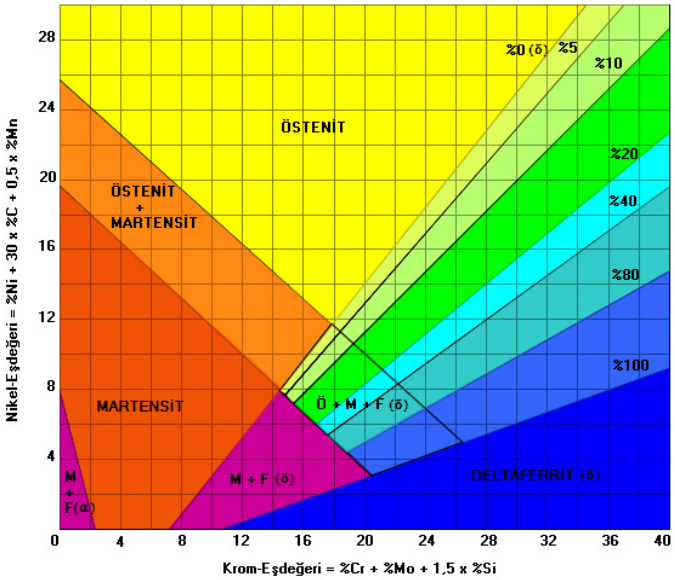

Şekil-5.3: Schaeffler Diyagramı

Schaeffler Diyagramı çok uzun yılladır kullanılmasına karşın, azotun (N) etkisini hesaba katmaması ve ayrıca konusunda uzman birkaç bilim adamının farklı ferrit yüzdeleri bulmalarından dolayı günümüzde etkinliğini yitirmiştir.

1973 WCR-De Long Diyagramı'nı Schaeffler diyagramından ayıran en önemli özellik nikel eşdeğeri hesaplanırken yapıdaki azot (N) miktarınında gözönüne alınması ve sonucun "FN-Ferrit Numarası" ile belirtilmesidir.

$Ni_{eş}$ = % Ni + 30 % C +30 %N + 0.5 % Mn

Günümüzde en sık kullanılan ve en sağlıklı sonucu veren diyagram Şekil-5.4'de belirtilen WCR-1992 diyagramıdır. Kabul edilen (ASME-1994,1995) en son diyagramda krom ve nikel eşdeğerleri aşağıdaki formüllerle hesaplanmaktadır.

$Cr_{eş}$ = % Cr + % Mo + 0.7 %Nb

$Ni_{eş}$ = % Ni + 35 % C + 0.5 % N + 0.25 Cu

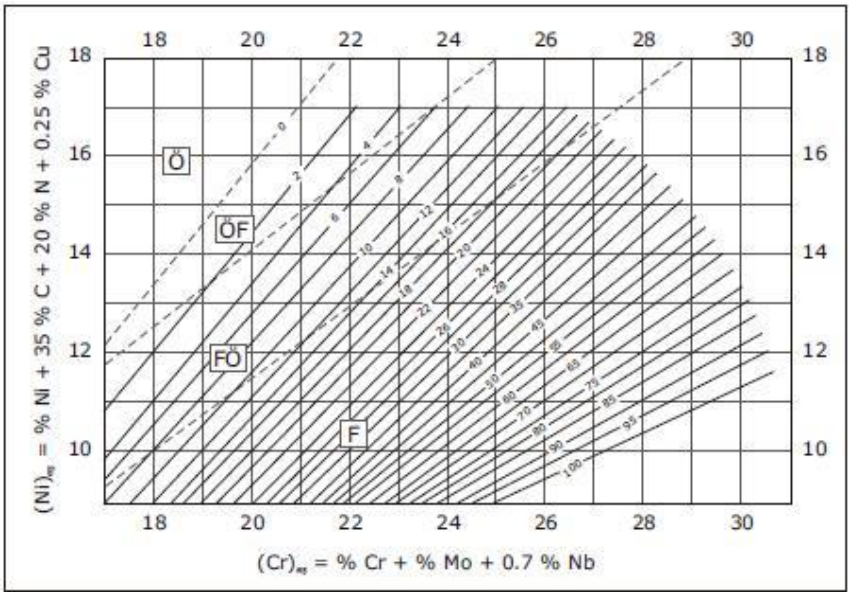

Şekil-5.4: Katılaşma Faz Sınırlarını da İçeren WRC-1992 Diyagramı

Ferrit miktarının sıcak çatlak oluşumundan korunmak için gereken orandan daha yüksek olmamasında ve belirli güvenlik sınırları içerisinde tutulmasında yarar vardır. Çünkü ferrit, bazı korozif ortamlarda, malzemelerin korozyon dayanımını düşürür ve yapıdaki aşırı ferrit süneklik ve tokluğu azaltır. [3]

5.3. SİGMA (σ) FAZI OLUŞUMU

"Sigma Fazı" çok sert (700-800 Vickers), manyetik olmayan ve gevrek yapıya sahip metallerarası bir bileşiktir. Röntgen ışını ile yapılan analizde bileşimin yaklaşık olarak %52 Krom ve %48 demirden oluştuğu ancak bunun yanında molibden gibi diğer alaşım elementlerini de içerebildiği görülmüştür. Sigma fazı, kromlu veya krom-nikelli paslanmaz ve ısıya dayanıklı çeliklerin kaynak bölgesinde oluşur. Saf östenitik bir yapıdaki sigma fazı oluşum hızı, östenitik kütle içerisinde ferrit içeren yapıdakine oranla daha düşüktür. [3,8]

Sigma fazı ile krom karbür çökelmesi birbirinden tamamen farklı iki oluşumdur. Sigma fazı kırılganlığı 650-850 °C sıcaklıklar arasında görülür ve bu sıcaklık arasında kalma süresi ile oluşan yapının yoğunluğu arasında yakın bir ilişki vardır. Faz dönüşüm hızının en yoğun olduğu sıcaklık 720 °C civarındadır. Yapıda bulunan ferrit miktarının %3-4 ile sınırlı tutulması durumunda, östenit tanelerinin etrafı ferrit ile çevrilmeyecek ve kırılganlık riski önlenecektir. Buna karşın ferrit miktarının %12'yi geçmesi ile birlikte esneklik kabiliyeti hızla azalacaktır. **(Şekil-5.5)** [3]

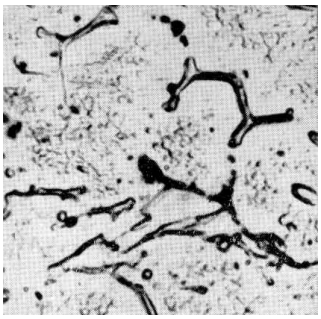

Şekil-5.5: 20 Cr / 10 Ni'li ve %3 Ferrit İçeren Paslanmaz Çelik (x1700)

Bir araştırmacı ferrit içerikleri %3 ile %12 arasında değişen 20 Cr / 10 Ni / 1 Nb'lu bir elektrodun kullanıldığı beş farklı deney parçası hazırlamıştır. Daha sonra bu deney parçaları 980-1100 °C arasındaki farklı sıcaklıklarda östenitleştirilmiş, 730 °C'da 300 saat boyunca tutulmuş ve sigma fazı oluşturularak kırılgan hale getirilmiştir. **(Şekil-5.6)** [3]

Buradan da anlaşılacağı üzere; ferrit miktarındaki artışa bağlı olarak esneklik azalmakta ve ferrit yüzdesi ne olursa olsun östenitleştirme sıcaklığında artış dikiş üzerinde olumlu bir etki yaratmaktadır.

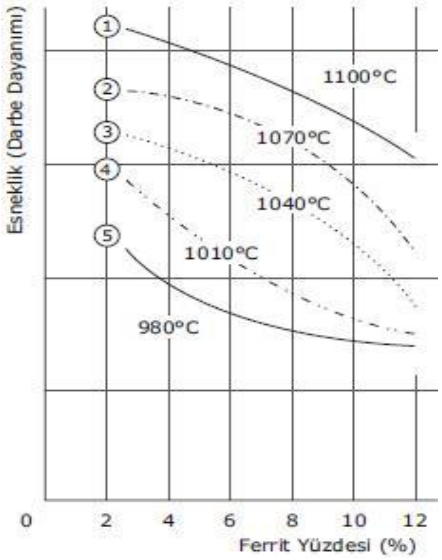

Şekil-5.6: Farklı sıcaklıklarda Isıl İşlem Uygulanan ve 780°C'da 300 Saat Tutulan, 20 Cr /10 Ni/ 1 Nb'lu Ostenitik Bir Yapıda Bulunan Ferrit Miktarının Gösterdiği Etki

Şekil-5.6 ve Şekil-7'de; 25 Cr / 20 Ni'li, ısıya dayanıklı bir elektrodla gerçekleştirilen farklı zaman dilimleri süresince dönüşüm sıcaklığında tutulan bağlantılara ait iç yapı fotoğrafları yer almaktadır. Görüldüğü gibi, parçanın 780°C'da 100 saat süre ile tutulması durumunda sigma fazı çizgileri oluşmaya başlamıştır **(Şekil-5.7)** ve yine aynı sıcaklıkta gerçekleştirilen 500 saatlik bir tutma işlemi sonucunda ise çökelen sigma fazı izlerinin çok daha yoğun olduğu görülmektedir.**(Şekil-5.8)**

Buradan anlaşılacağı gibi, kaynak işlemi sırasında banyonun çok hızlı soğuması ve katılaşması nedeni ile sigma fazı kolay oluşamaz. Bu sorun esas olarak ferrit içeriği çok yüksek olan kaynaklı bağlantının kaynak işleminden sonra uzun süre yüksek sıcaklık değerlerinde kalacak bir çalışma ortamında kullanılması durumunda karşımıza çıkar.[3]

Şekil-5.7: 25 Cr / 20 Ni (0.10 C)'lu Elektrod Kullanılarak 780°C'da 100 Saat Tutulan Malzemede Oluşan Sigma Fazı Görüntüsü (x1600)

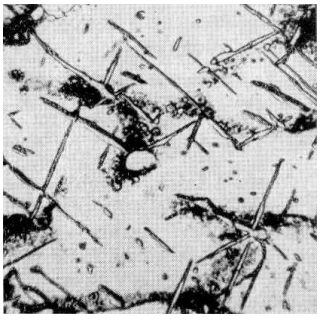

Şekil-5.8: 25 Cr / 20 Ni (0.10 C)'lu Elektrod Kullanılarak 780°C'da 500 Saat Tutulan Malzemede Oluşan Sigma Fazı Görüntüsü (x1600)

Çeşitli araştırmacıların yaptıkları araştırmalar neticesinde sigma fazı ile aşağıdaki sonuçlar belirlenmiştir; [3]

a) Sigma fazının oluşumu 750°C'da, 650°C'dakinden daha çabuk meydana gelir. 750°C'da 30 saat gibi bir zamana ihtiyaç varken bu süre 650°C'da 1 haftaya çıkar,

b) Sigma fazı oluşumu soğuk şekil değiştirme ile hızlanır,

c) Sigma fazı oluşumuna kuvvetli olarak etki eden elementler; molibden (Mo), krom (Cr), niobyum (Nb) ve silisyum (Si)'dur,

d) Sigma fazı oluşumunu kuvvetlendiren elementlerin miktarı yüksek ise, belirli şartlar altında, kaynağa bağlı olmadan ve ısıl işlem uygulamadan da sigma fazı meydana gelebilir,

e) Sigma fazı, 950-1100°C sıcaklıklar arasında belirli bir süre tavlandıktan sonra, suda hızlı soğutularak giderilebilir,

f) Sigma fazının giderilmesi için uygulanan ısıl işlemden sonra oluşan yapıdaki ferrit miktarı, ısıl işlem uygulanmamış yapıdakine oranla daha azdır,

g) Ferrit miktarı, parçaya 1150°C'da homojenleştirme tavlaması uygulanarak daha da düşürülebilir. Bu durumda ferrit mikro toplanmalar şeklinde oluşur,

6. DEĞERLENDİRME

6.1. Östenitik paslanmaz çeliklerde bulunan ferrit belirli bir yüzde değerine kadar kaynaklı bağlantının mukavemet değerlerine olumlu etki eder. Ancak ferrit oranı belirli bir oranı geçtikten sonra kaynaklı bağlantının özellikle sünekliğinde düşme olur,

6.2. Östenitik paslanmaz çeliklere, östenitleştirmeyi sağlamak ve korozyon direncini arttırmak için karbon, nikel, azot, bakır, molibden gibi alaşım elementleri katılır,

6.3. Östenitik paslanmaz çeliklerin kaynağında "Krom-karbür oluşumu, sıcak çatlak oluşumu ve sigma fazı oluşumu" olmak üzere 3 temel problem vardır,

6.4. Tek pasolu yapılan kaynaklarda ısı girdisi düşük olacağından sigma fazı oluşumu ve krom karbür çökelme riski yoktur.

6.5. Çok pasolu kaynaklarda pasolar arası beklemek krom-karbür oluşumunu önlemek açısından olumlu sonuçlar verir,

6.6. Parça boyutları uygun ise krom karbür oluşumu ve sigma fazı belirli sıcaklıkta ısıl işlem ve akabinde suda hızlı soğutma ile önlenebilir,

KAYNAKLAR

1. TÜLBENTÇİ, K., "Mig-Mag Gazaltı Kaynak Yöntemi", Artech Yayını, İstanbul, 1998

2. KALUÇ, E., "Östenitik Krom-Nikelli Paslanmaz Çeliklerin Kaynağı", Kaynak Dünyası, Nisan 1990, 15-21, (1990)

3. ODABAŞ, C., "Paslanmaz Çelikler, Temel Özellikleri, Kullanım Alanları, Kaynak Yöntemleri", Eczacıbaşı, Lincoln Electric, İstanbul, Şubat, 2004

4. http://www.euro-inox.org/, "Intergranular Corrosion" The European Stainless Steel Development Association

5. AYDOĞDU Gülgün H., AYDINOL M. Kadri, "AISI 316L Tipi Östenitik Paslanmaz Çeliklerin Tanelerarası Korozyona Duyarlılığının Elektrokimyasal Polarizasyon Yöntemiyle Belirlenmesi," Metalurji Dergisi, 2005

6. SAHLAOUI, H., K. MAKHLOUF, H. SIDHOM, and PHILIBERT, "Material Science and Engineering", 2004.

7. SOURMAIL, T., "Material Science and Technology", 2001

8. GÖZÜTOK, E. "Paslanmaz Çeliklerin Tıg Kaynağında Argon-Hidrojen Gaz Karışımının Birleştirmelerin Mekanik Ve Mikroyapı Özelliklerine Etkisi", Karabük, 2011

9. BİLİR, Y., "Ferritk Kromlu ve Östenitik Krom-Nikelli Paslanmaz Çeliklerin Kaynaklanabilirliği ve Isıl İşlemi", İstanbul, 2003

10. KARAMAN, N., GÜLENÇ B., AKÇA H., "Ark Kaynak Yöntemi ile Birleştirilen Östenitik Paslanmaz Çelik ile Düşük Karbonlu Çeliğin Mekanik Özelliklerinin İncelenmesi", Ankara, 2002

11. KALUÇ, E., "Elektrik direnç nokta kaynağı yapılmış Östenitik+Östentik, Ferritik+Ferritik ve Ferritik+Östenitik Çiftlerde Tanelerarası Korozyon", 1. Korozyon Sempozyumu, Ankara, 1988

YÜKSEK FIRIN HEAT EXCHANGER SİSTEMİ

[1]Ümit GEBENLİ, [2]Ahmet Serter KARABIYIK

[1]İSDEMİR A.Ş. Yüksek Fırınlar Müdürlüğü
[2]İSDEMİR A.Ş. Yüksek Fırınlar Müdürlüğü

ÖZET

Bu çalışmada, İskenderun Demir ve Çelik A.Ş'de (İSDEMİR) 2011 yılı Ağustos ayında devreye alınan 4 Nolu Yüksek Fırındaki Heat Exchanger sistemi incelenmektedir. Demir üretimi sürecinde kullanılan yüksek fırın sobalarının, ısıtılması işleminde açığa çıkan atık gaz sıcaklığı, heat exchanger sisteminde kullanılarak yakıt ve gaz tasarrufu yapılmasının temel avantajları irdelenmektedir.

İSDEMİR Yüksek Fırınlarında, yüksek fırın ve kok gazı, yakma havası ile sobaların yanma kamarası bölümünde yaklaşık 600 ^{0}C de karıştırılır. Gazın yanması sonucu açığa çıkan ısı ile sobaların içerisindeki çeker (checker) tuğlalar ısıtılır. Sobaların ısıtma işlemi sırasında açığa çıkan, sıcak atık gaz, heat exchanger sistemine gönderilir. Bu sistemde birbirlerine paralel 3 adet eşanjör bulunur. Bu eşanjörlerden baca atık gazı ana hattındaki eşanjör aldığı ısıyı içi su dolu borularla YF gazı hattındaki ve fan havası hattındaki eşanjörlere iletir. Bu eşanjörler yüksek fırın gazını ve fan havasın ısıtarak yanma öncesi ön ısıtma işlemini sağlar.

2500 m³'lük çalışma hacmiyle Türkiye'nin en büyük ve en yeni yüksek fırını olan İSDEMİR 4. Yüksek Fırın sobalarında yüksek fırın gazı ve fan havasını ısıtmak amacıyla heat exchanger sistemi kullanılmaktadır. Yüksek Fırın sobalarında heat exchanger sisteminin kullanılmasının; Sobaların daha az yüksek fırın gazı ve fan havası kullanımı, sobaların daha hızlı ısıtılması, sobaların daha verimli kullanılması sonucu yakıt tasarrufu sağlaması, düşük bakım maliyeti, enerji tasarrufu nedeniyle doğa dostu oluşu vb. birçok avantaja sahiptir.

Anahtar kelimeler: Demir-Çelik, İSDEMİR, Yüksek Fırın Gazı, Yüksek Fırın Sobası, Heat Exchanger, Yakma Havası,

SUMMARY:

In this paper, the HEAT EXCHANGER system is examined, this system was installed at BF No. 4, Iskenderun Iron & Steel Works Corp. (ISDEMIR) in August 2011.
Blast furnace stoves are used in the iron production process, while heating up the stoves proces the hot waste gas is released. The heat exchanger system uses this waste gas for raising the temperature of Blast Furnace gas and combustion air in order to reduce fuel and the amount of gas used to heat up the stoves. The main advantages of using the heat exchanger system are discussed.

BF gas, coke gas and fan air are mixed at a temperature of 600 ^{0}C in the combustion chamber of the stove. The checker bricks are heated up by this combustion and during the heating period of the stoves the released hot waste is sent to the heat exchanger system. There are a total of 3 heat exchangers which are located parallel to each other in this system. The heat exchanger which is located at the waste gas main, transports the heat with the help of water-filled pipes to the BF gas and combustion air heat exchanger system. The purpose of these heat exchangers is to provide preheating of blast furnace gas and combustion air before the actual combustion occurs.

With a total working volume of 2500 m³, ISDEMIR Blast Furnace #4 is Turkey's most newest and biggest Blast Furnace. The heat exchanger system is used in order to heat up the BF gas and combustion air of Blast Furnace #4 stoves. The main advantages of using the Heat exchanger system are as follows; low consumption of BF gas and Coke gas, shorter heating up period of stoves, low maintenance requirements, reduction of BF fuel, more efficient usage of gas and air in stoves, environmentally friendly, etc.

Key Words: Iron & Steel, ISDEMIR, Blast Furnace Blast Furnace Gas, BF Hot Stoves, Heat Exchanger, Combustin Air

1.GİRİŞ

Türkiye' nin en büyük ve en yeni yüksek fırını İSDEMİR A.Ş. de 17 Ağustos 2011 tarihinde devreye alınan 2500 m3 lük çalışma hacmi ile 4. Yüksek Fırın dır. 4. Yüksek fırında günlük sıvı ham demir üretim miktarı ortalama 6400ton/gün dür.

İSDEMİR 4. Yüksek Fırında sobalar, demir oksitlerin redüklenmesi için gerekli olan sıcak havayı elde etmek amacıyla kullanılmaktadır. Sobalardaki özel tuğlalar yüksek fırın gazı ve kok gazı belli bir (0,7-0,8) oranda hava ile karıştırıp yakılması sonucu ısıtılır. Atık gaz baca hattı üzerinde kullanılan heat exchanger sistemi, sobaların ısıtılması sonrası açığa çıkan atık gazın ısısını kullanmak amacıyla kullanılmaktadır.

Bu çalışmada Heat exchanger sistemi hakkında bilgilendirme ve temel avantajları irdelenmektedir.

2. 1. YÜKSEK FIRIN SOBALAR SİSTEMİ:

4. Yüksek Fırında dıştan yanmalı olarak adlandırılan, 4 adet yama kamarası ve bunlara kubbeden bağlı 4 adet checker bölümü olan, 4 adet soba bulunmaktadır.
Sobalarını ısıtmak için yakıt olarak;
Yüksek fırınların ve kok fabrikalarının yan ürünü olan yüksek fırın gazı ve kok gazı kullanılır.
Bu gazların özellikleri şöyledir:
Yüksek Fırın Gazı;
Yapısında yaklaşık olarak;
% 21-23 CO, %20-22 CO2, %2-4 H2, %0-1 CH4, %50-54 N2 gazı içermektedir.
Yandığında 800-900 Kcal/m3 enerji açığa çıkmaktadır.
Kok Gazı;
%7-8 CO, %2-3 CO2, % 60-65 H2, %20-22 CH4, %4-6 N2, %0-0,5 O2, %1-2 C2H6, %2-3 CnHm

Yandığında 4300 Kcal/m3 enerji açığa çıkmaktadır.

Yüksek fırın gazı kalorisinin düşük olması nedeniyle verimli bir yanma elde etmek için istenilen hava-sıcaklık değerine bağlı olarak bu gazın içerisine maksimum % 10 mertebesinde kok gazı karıştırılır. Elde edilen bu gaz "karışım gazı" olarak adlandırılır.

Bu gaz belirli bir oranda (0,7-0,8) fan havası ile sobaların yanma kamarası denilen bölgesinde yakılmaktadır. Sobalardaki karışım gazını yakmak için kullanılan hava, yani yakma havası 2 adet büyük fanlardan elde edilir.

Fotoğraf 1. İsdemir 4. Yüksek Fırın (Dilek) ve Sobaları

2.2. HEAT EXCHANGER SİSTEMİ

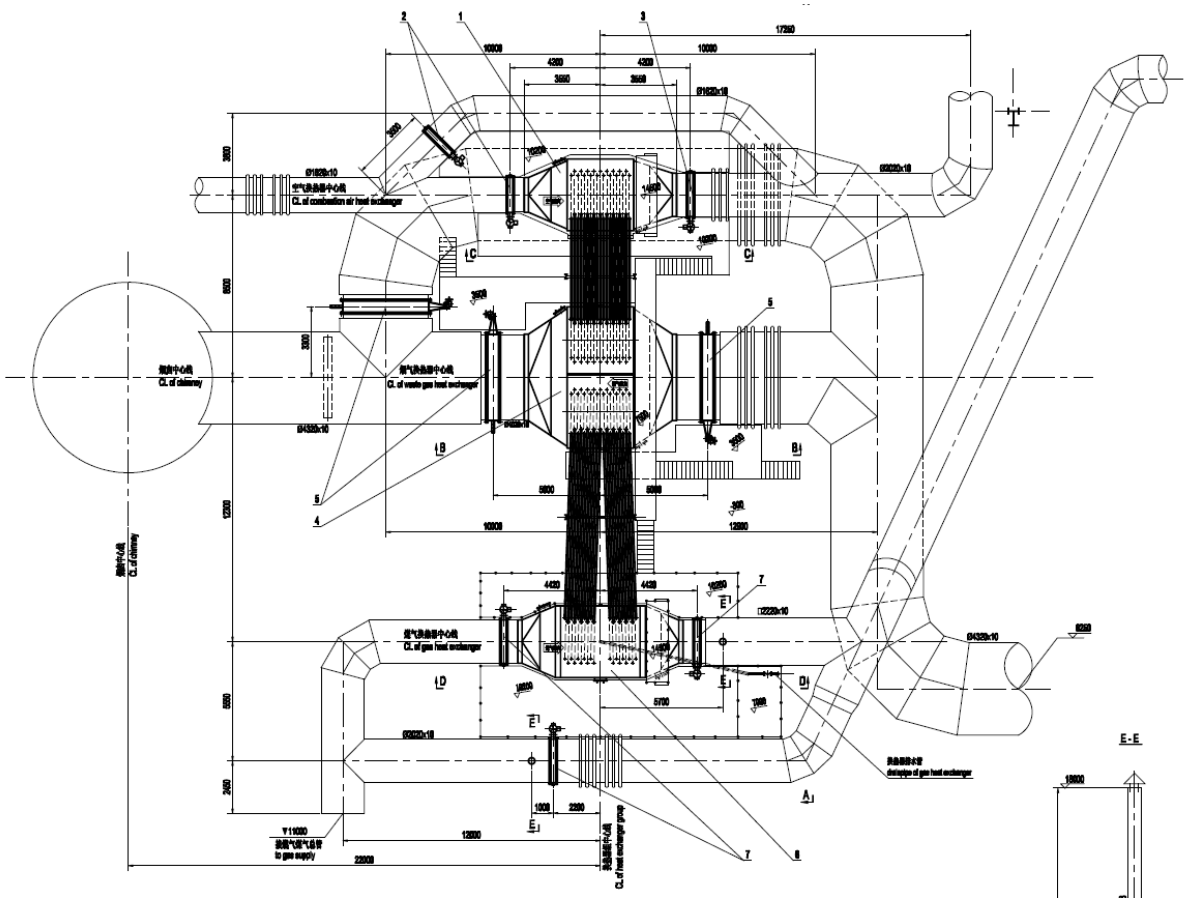

4. Yüksek Fırın sobalarında kullanılan heat exchanger sistemi 3 ana bölümden(eşanjör) oluşmaktadır.
1. Eşanjör, Sobalar atık gaz (baca gazı) hattı üzerinde bulunan ana eşanjör.
2. Eşanjör, Yüksek Fırın gazı ve kok gazı hattı üzerinde bulunan eşanjör
3. Eşanjör, Sobalar yakma havası hattı üzerinde bulunan eşanjör.

Eşanjörler birbirlerine borular ile bağlıdır. Bu boruların içerisinde yaklaşık 150 litre su bulunmaktadır. Eşanjöre giren atık gaz ısısını eşanjör içerisinde bulunan borların içerisindeki su-buhar karışımına bırakır. Eşanjörlerin birbirlerine ısı transferi su buharı ile sağlanmaktadır. Baca gazı eşanjöründe atık gazın ısı ile ısınan buhar borular ile gaz hattı eşanjörüne ve fan havası hattı eşanjörlerine geçer. Eşanjörler arasından geçen gaz karışımının ve fan havasısın sıcaklığı, içerisindeki bu boruların arasından geçerken yaklaşık 160 ℃ artar.

	Sıcak Akışkan	Soğuk Akışkan	
Ortam	Baca Gazı	Yüksek Fırın Gazı	Fan Havası
Tasarım Akışı Nm^3/h	315000	179500	160000
Giriş Sıcaklığı ℃	340	35	25
Çıkış Sıcaklığı ℃	145	175	200
Direnç Kaybı Pa	≤500	≤500	≤500
Toplam Isı Trasnferi kW	20070		

Heat exchanger sistemi eşanjörlerinde bypass hattı bulunası nedeniyle sobalar atık gazı istenildiği zaman devre dışı edilerek bacaya ya da pci (Pulvarize Kömür Enjeksiyon) tesisine gönderilebilmektedir.

2.2.1. BACAGAZI EŞANJÖRÜ

Sobalarda yanan yüksek fırın gazı ve kok gazı bacadan atılmak ya da pcı tesisine kurutma gazı olarak gönderilmek amacıyla atık gaz hattına gönderilir.
Bu hat üzerinde bulunan eşanjör, ilk ısıyı alan ana eşanjör olup baca gazı eşanjörü olarak adlandırılır. Eşanjörün içerisinde 19 adet yüksek fırın gazı eşanjörüne bağlı, 19 adet te fan havasını eşanjörüne bağlı olmak üzere toplam 38 adet boru bulunmaktadır. Bu boruların içerisi ort. 150 litre su ile doludur. Bu eşanjöre giren atık gazın sıcaklığı yaklaşık olarak 340 ℃ Derece olup eşanjörden çıkış sıcaklığı 140 ℃ dir.

2.2.2. GAZ HATTI EŞANJÖRÜ

Yüksek fırın ve kok gazı karışımının geçtiği hat üzerinde bulunan eşanjördür. Bu eşanjörün içerisinde de ana ejanjör ile bağlantılı olan 19 adet boru bulunmaktadır.
Baca gazı eşanjöründen buhar le taşınan ısı bu eşanjör içerisinden geçen gaz kırısımının sıcaklığını yaklaşık 140 ℃
arttırır. Gaz hattı eşanjörüne
giren gaz karışımı sıcaklığı
yaklaşık 35 ℃ olup borulardan aldığı ısı ile eşanjör çıkışında yaklaşık 175 ℃ ye ulaşmaktadır.

2.2.3. FAN HAVASI HATTI EŞANJÖRÜ

Yüksek fırın ve kok gazı karışımının sobalarda yakılması içiin gerekli olan yakma havasını sağlayan fanlar ürettiği havanın geçtiği hat üzerinde bulunan eşanjördür. Bu eşanjörün içerisinde de ana ejanjör ile bağlantılı olan 19 adet boru bulunmaktadır.
Baca gazı eşanjöründen buhar le taşınan ısı bu eşanjör içerisinden geçen fan havasını sıcaklığını yaklaşık 175 ℃ arttırır. Fan havası hattı eşanjörüne giren havanın sıcaklığı yaklaşık 25℃ olup borulardan aldığı ısı ile eşanjör çıkışında yaklaşık 200 ℃ye ulaşmaktadır.

3. HEAT EXCHANGER SİSTEMİNİN AVANTAJLARI

Yüksek Fırın sobalarında heat exchanger sisteminin kullanılmasının temel avantajları şu şekilde sıralanabilir;

- Yüksek Fırında yakıt tasarrufu sağlaması:

Yüksek Fırın çalışma parametrelerinin bilimsel çalışmalar sonucu, dünya literatürlerin de kabul edilen yakıt oranı(metalürjik kok) üzerindeki etkileri kullanılarak aşağıdaki tablolar hazırlanmıştır.
Tablolarda heat exchanger sistemi devrede iken ve devrede değilken İsdemir 4. Yüksek Fırınından (Dilek) alınan parametrelerin, yakıta etkisi hesaplanmış ve karşılaştırılmıştır.

Heat exchanger sistemi devrede iken yüksek fırın parametreleri aşağıdaki gibidir.

SOBALARIN ÜFLEME SÜRESİ	100	dak.
SOBALARIN GAZ ALMA SÜRESİ	110	dak.
SICAK HAVA MİKTARI	5000	Nm³/dak
SICAK HAVA SICAKLIĞI	1200	°C
SOĞUK HAVA SICAKLIĞI	210	°C
İLAVE NEM MİKTARI	30	Gr/Nm³
YAKMA HAVASI SIC.	200	°C
HAVA/GAZ ORANI set	1,26	
GAZ MİKTARI set	61.250	GCal/saat
GAZ MİKTARI	75.100	Nm³/saat
YAKMA HAVASI MİKTARI	54.906	Nm³/saat
KOK GAZI ZENGİNLEŞTİRME	2,70	%
BACA GAZINDA TEORİK O2	0,83	%
VERİM	85,69	%

Tablo1. Heat exchanger sistemi devrede iken

Heat exchanger sistemi devrede değil iken, mevcut gaz miktarlaında yüksek fırın parametreleri aşağıdaki gibidir.

SOBALARIN ÜFLEME SÜRESİ	100	dak.
SOBALARIN GAZ ALMA SÜRESİ	110	dak.
SICAK HAVA MİKTARI	5000	Nm³/dak
SICAK HAVA SICAKLIĞI	1167	°C
SOĞUK HAVA SICAKLIĞI	210	°C
İLAVE NEM MİKTARI	30	Gr/Nm³
YAKMA HAVASI SIC.	40	°C
HAVA/GAZ ORANI set	1,26	
GAZ MİKTARI set	61.250	GCal/saat
GAZ MİKTARI	75.100	Nm³/saat
YAKMA HAVASI MİKTARI	54.906	Nm³/saat
KOK GAZI ZENGİNLEŞTİRME	2,70	%
BACA GAZINDA TEORİK O2	0,83	%
VERİM	85,69	%

Tablo 2. Heat exchanger sistemi devrede değil iken

Tablo 1 ve Tablo 2 incelendiğinde heat exchanger sistemi devrede olduğunda aynı gaz miktarı ile sıcak hava sıcaklığı 33 derece artmaktadır. Bu durumda dünya literatürlerindeki kabullere göre yapılan hesaplamada;
(Sıcak hava sıcaklığının 100 derece düşmesi, 12kg met kok/ton sıvı ham demir artışına neden olur kabulü) **yaklaşık 3,96 kg metalürjik kok tasarrufu** sağlanmış olmaktadır.

- Yüksek Fırın sobalarında daha az gaz tüketimi sağlaması;

Tablolarda heat exchanger sistemi devrede iken ve devrede değilken İsdemir 4. Yüksek Fırınından (Dilek) alınan parametrelerin, yüksek fırın gazı ve kok gazı tüketimine etkisi hesaplanmış ve karşılaştırılmıştır.

Tablo 2. de aynı gaz miktarı ile heat exchanger sistemi devrede değilken sıcak hava sıcaklığı 1167 ℃ ulaşabilmektedir. Sıcak hava sıcaklığının 1200 ℃ sıcaklığa ulaşılabilmesi için kullanılması gereken gaz miktarı aşağıda Tablo 3. de hesaplanmıştır.

SOBALARIN ÜFLEME SÜRESİ	100	dak.
SOBALARIN GAZ ALMA SÜRESİ	110	dak.
SICAK HAVA MİKTARI	5000	Nm³/dak
SICAK HAVA SICAKLIĞI	1200	°C
SOĞUK HAVA SICAKLIĞI	210	°C
İLAVE NEM MİKTARI	30	Gr/Nm³
YAKMA HAVASI SIC.	40	°C
HAVA/GAZ ORANI set	1,17	
GAZ MİKTARI set	63.500	GCal/saat
GAZ MİKTARI	77.859	Nm³/saat
YAKMA HAVASI MİKTARI	52.857	Nm³/saat
KOK GAZI ZENGİNLEŞTİRME	2,70	%
BACA GAZINDA TEORİK O2	- 0,25	%
VERİM	85,58	%

Tablo 3. Sıcak hava sıcaklığının 1200 ℃ olması için gerekli gaz miktarının hesaplanması.

Tablo 2 incelendiğinde, heat exchanger sistemi devrede olduğu durumda sıcak hava sıcaklığının 1200 ℃ olması için 75100 Nm³ / saat yüksek fırın gazı ve kok gazı karışımı kullanılması gerekmektedir.
Tablo 3 incelendiğinde, heat exchanger sistemi devrede olmadı durumda sıcak hava sıcaklığının 1200 ℃ olması için 77857 Nm³ / saat yüksek fırın gazı ve kok gazı karışımı kullanılması gerekmektedir.
Bu durumda heat exchanger sisteminin sobalarda kullanılması **yaklaşık 2750 Nm³ / saat gaz karışımı tasarrufu** sağlamaktadır.

- Sistem Kurulum Esnekliği: Fabrika şartlarına göre uygun sistem yapılabilir.

- Düşük Bakım İhtiyaçları: Sistem her eşanjörde 3 er adet olmak üzere toplamda 9 adet elektrikli valf ile kontrol edilmektedir. Ekstrem bir durum olmadığı durumlarda, eşanjör içerisindeki borularda su kaçağı olması durumunda yüksek fırın duruşuna neden olmaz, bypass hattı kullanılabilir ve planlı bakım duruşlarında bakıma alına bilinir. Plansız bakım gerektirmez.

- Düşük Yatırım Maliyeti: Diğer sistemlerle kıyaslandığında kullanılan ekipman azlığı, otomasyonel olması nedeniyle kumanda odasından kontrol edilmektedir. Sistem ayrı bir personel kontrolüne ihtiyaç duyulmamaktadır.

- Düşük Bakım Maliyeti: Basit ve uzun ömürlü ekipman kullanımı

- PCI kömürünün kurutulmasında kullanılması: Soba atık gazı PCI tesisinde kömürün içerisindeki nemin uzaklaştırılması amacıyla PCI tesisine gönderilir.

- PCI tesisinde öğütücü teker ve tablalarının, pci filtrelerin ömrünün uzatılması ve öğütme tonajlarının düşmesini engellemesi: PCI tesisine gönderilen atık gazın sıcaklığının pcı kömürünün tutuşmaması için 140-160 ℃ olması gerekmektedir. Heat exchanger sistemi kullanılmadığı durumlarda soba atık gaz sıcaklığı yaklaşık 300 ℃ sıcaklıkta PCI tesisine gönderilmektedir. Bu atık gaz sıcaklığı pcı kömürü için tutuşma sıcaklığına yakın olduğu için kömür değirmene girmede ekstra nemlendirme işlemi gerekmektedir

Bu nemlendirme işlemi;

a) Öğütücü teker ve tablasına zarar vermektedir.
b) Filtrelerin asitleşme nedeniyle erken aşındırmaktadır.
c) Öğütme tonajını 7–10 ton/saat e düşürmektedir.

Heat Exchanger sistemi kullanılması ile atık gaz sıcaklığı yaklaşık 140 ^{0}C ye düşürmektedir. Bu durumda ekstra nemlendirme yapılmayıp kömürün neminin kolayca atılması sağlanmış olup yukarıda belirtilen kayıplarında önüne geçilmiş olur. Aynı zamanda PCI tesisinde öğütme kapasitesini artırıcı unsur da yaratmaktadır.

4. SONUÇ

2500 m³'lük çalışma hacmiyle Türkiye'nin en büyük ve en yeni yüksek fırını olan İSDEMİR 4. Yüksek Fırınında kullanılan heat exchanger sistemi; Yüksek fırın yakt tasarrufu, sistem kurulum esnekliği, düşük bakım ihtiyaçları, düşük yatırım maliyeti, pci kömürünün kurutulmasında kullanılması, pci tesisinde öğütücü teker ve tablalarının, pci filtrelerin ömrünün uzatılması ve öğütme tonajlarının düşmesini engellemesi avantajlarını sağlamaktadır.

KAYNAKLAR

1. İSDEMİR A.Ş. '4. Yüksek Fırın Heat Exchanger Projeleri' 2007
2. İSDEMİR A.Ş. '4. Yüksek Fırın Heat Exchanger Manuelleri' 2007
3. 4. Yüksek Fırın 2011 – 2013 dönemlerine ait parametreler
4. 'Yakıt tüketimine etki eden faktörler' Dünya literatürlerindeki Yüksek Fırın Parametre Kabulleri

SYNTHESIS OF BULK AMORPHOUS STEELS HAVING EXTREMELY HIGH HARDNESS

Bengi Yağmurlu, M. Vedat Akdeniz and Amdulla O. Mekhrabov

Novel Alloys Design and Development Laboratory (NOVALAB)
Department of Metallurgical and Materials Engineering, Middle East Technical University
06531-Ankara, Turkey

ABSTRACT

Bulk amorphous steels (BAS's) are one of the promising advanced materials with superior mechanical and physical properties compared with their crystalline counterparts. These unique properties make BAS's suitable candidates for various engineering applications.

In this study, the BAS's were synthesized by alloying cast iron scraps (3.5-4.5%C) with appropriate amount of alloying elements (Cr, Mo, B, Y), derived from theoretical calculations in order to enhance the glass forming ability of Fe-based metallic glasses, by arc melting under controlled atmosphere. Production of BAS samples in the form of cylinders was achieved by suction casting of molten alloy into a copper mold having a diameter of 3mm.

In this ongoing research, amorphous samples exhibit extremely high hardness values around 1200Hv in contrast to their crystalline counterparts (austenitic and martensitic stainless steels) whose hardness values were reported at most 500Hv. The effects of the alloying elements such as Mn, Al, V and Ti on hardness will be presented with the relation of structures and phases. Moreover the effect of nanocrystallization of amorphous samples on hardness will also be discussed by annealing the BAS's in the vicinity of T_g and T_x temperatures. Both amorphous and nanocrystallized samples will be compared in terms of their structures and associated mechanical properties.

Keywords: Fe-based metallic glasses, amorphous steels, hardness, cast iron, suction casting

ÖZET

İri hacimli camsı çelikler (İHCÇ), kristal yapıya sahip olan eşdeğerlerine göre bir çok üstün mekanik ve fiziksel özellik taşıyan geleceği parlak olan malzemelerdir. Bu eşsiz özellikler, İHCÇ'leri birçok farklı mühendislik uygulaması için uygun malzemeler kılmaktadırlar.

Bu çalışmada, İHCÇ'ler, simülasyon sonuçlarına gore cam oluşturma eğilimini geliştiren bir çok farklı alaşım elementi (Cr, Mo, B, Y) ile dökme demir hurdalarının (3.5-4.5% C) kontrollu bir atmosfer altında ark eritme yöntemi ile üretilmişlerdir. Ergimiş alaşımın emme döküm yöntemi ile bakır kalıba çekilmesiyle, 3mm çapında silindirler şeklinde İHCÇ'ler oluşturulmuştur.

Devam eden bu çalışmada, camsı yapıya sahip olan örnekler, maksimum 500Hv sertlik değerlerine sahip olan kristal eşdeğerlerinin tersine, 1200Hv yakınlarında aşırı yüksek sertlik değerleri göstermişlerdir. Alaşım elementlerinin bu sertliğe olan etkisi ise, numune de yer alan mikro yapılar ile açıklanmaya çalışılacaktır. Bunlara ek olarak, kritik sıcaklıklar olarak değerlendirilen T_g ve T_x sıcaklıkları arasında ısıl işlem yapılarak, nanokristalleşmenin sertliğe olan etkileri de tartışılacaktır. Camsı yapıya ve nanokristal yapıya sahip olan bu numunelerin mekanik değerleri kıyaslanacaktır.

Anahtar kelimeler: Fe bazlı camsı metaller, camsı çelikler, sertlik, dökme demir, emme döküm

1. INTRODUCTION

Metallic glasses are extensively studied during the last two decades due to their extreme properties and potential technological applications. When all types of metallic glasses are considered, Fe-based ones are become more significant owing to unique mechanical properties, extreme wear and corrosion resistance [1]. Among these, metallic glasses which are non-ferromagnetic and exhibit much higher strength than their counterparts, introduced as bulk amorphous steels. Because of their superior mechanical properties, they could be considered as a structural material.

Bulk amorphous steels offer significant advantages over crystalline counterparts and other metallic glasses such as; high strength, lower cost, excellent corrosion resistant, high thermal stability due to their high glass transition temperature and better glass forming ability[2,3]. Although there are diverse production techniques of these bulk amorphous steels from high purity constituent elements, however to our best knowledge, no research have been published about the synthesis of BAS's from scrap materials. In this study $M_{60}Cr_{13}Mo_{10}B_8Y_2Mn_7$, where M is scrap cast iron, was successfully produced and its thermal and magnetic properties were characterized and its hardness was compared with its crystalline counterparts.

2. EXPERIMENTAL PROCEDURE

Bulk amorphous steels were tried to produce by alloying cast iron scrap with some pure materials which are mainly Cr, Mo, B and Y. In this study, cast iron scraps were used to produce bulk amorphous steels. These cast iron scraps contained 3.5-4.5% C, 2% Si and 1% other elements. Cast iron scraps having mentioned composition named as M and all of the alloys were prepared in accordance with that. The alloys were prepared by using arc melting under argon gas and in order to homogenize the composition, alloy were re-melted 3 times. Then samples were prepared with suction casting into hollowed copper molds. The prepared samples are characterized by XRD, DSC, VSM and SEM. Using a Rigaku x-ray diffractometer and copper target, x-ray diffraction (XRD) was performed in order to determine the amorphicity of the prepared samples.

Thermal studies are performed in order to determine the glass transition temperature (T_g), crystallization temperature (T_x) and melting temperature (T_m) with a SETSYS-16/18 differential scanning calorimeter (DSC). The heating and cooling rate applied were both 40K/min and the temperature range was 40 to 1400°C. Samples are placed in Alumina crucibles for thermal measurements.

The metallographic inspections were carried by FEI Quanta 400F field emission electron microscope (FESEM). In addition to this, the compositions were analysed to be sure about the compositions of alloys by energy dispersive spectroscopy (EDS) by same electron microscope.

Preliminary measurements of non-ferromagnetic nature of the samples are done by a simply iron neodymium hard magnet. Then the detailed study was performed on specimens with ADE Magnetics EV9 vibrating sample magnetometer (VSM) to characterize and measure the crystalline parts of the produced samples. The magnetic field applied is in between 18000 to -18000 Oe. All of the magnetic measurements were applied at room temperature. Moreover, in order to obtain accurate results about the hardness of the samples, Vickers microhardness tester was used.

3. RESULTS

Cast iron scraps (M) were used as the constituent part of the alloys. These scraps are melted with 13%at Cr, 10%Mo, 8%at B, 7% at Mn and 2%at Y. The alloys were prepared with arc melting and then suction casting was applied to produce bulk amorphous steels with 3-mm diameter rods. After successfully production of $M_{60}Cr_{13}Mo_{10}B_8Y_2Mn_7$, X-Ray diffraction was applied to determine the structure of the alloy. Figure 1 shows the XRD patterns of as-cast samples and the samples subjected to rapid cooling rates. As it can be seen from the figure, the slowly cooled samples showed crystalline structures, however, when the same alloy subjected to rapid cooling rates these crystalline phases could not be formed which leads to the amorphous structure.

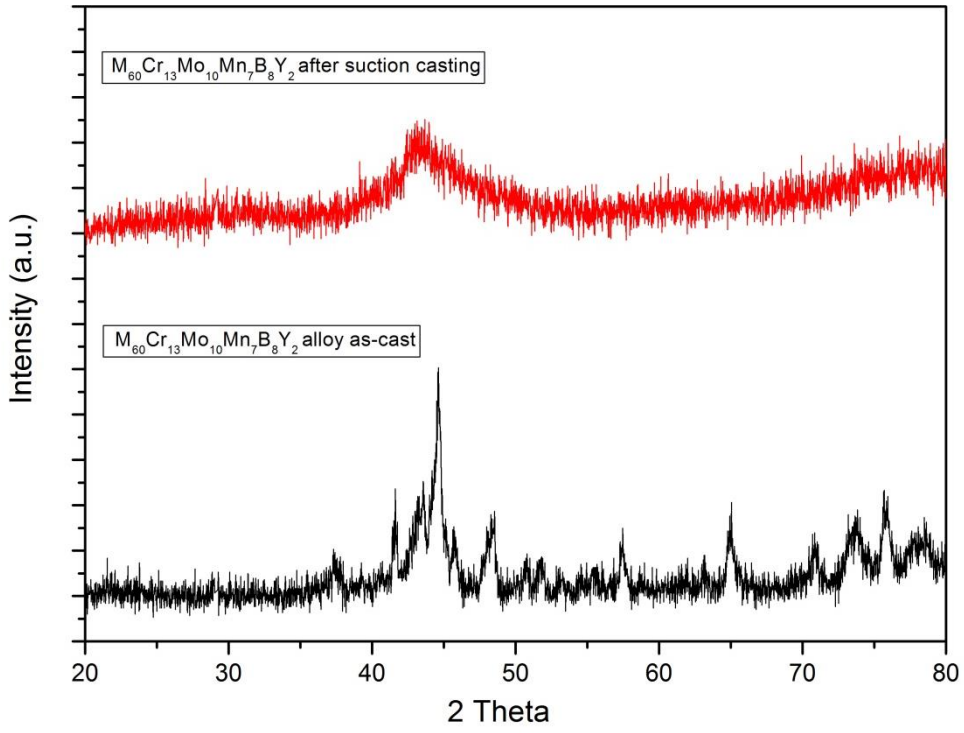

Figure 1: XRD patterns of $M_{60}Cr_{13}Mo_{10}B_8Y_2Mn_7$ samples before and after subjecting to rapid cooling

After the confirmation the amorphous nature of the samples, thermal analysis was applied to obtain the critical thermal parameters like glass transition temperature T_g, crystallization temperature T_x, melting temperature T_l and supercooled liquid region ΔT_x of the alloys. Samples were heated with 40K/min and then again cooled with 40K/min. In figure 2, the heating scans of the alloys can be seen. According to parameters, glass forming ability parameter T_{rg} was calculated, $T_{rg} = \frac{T_g}{T_l}$

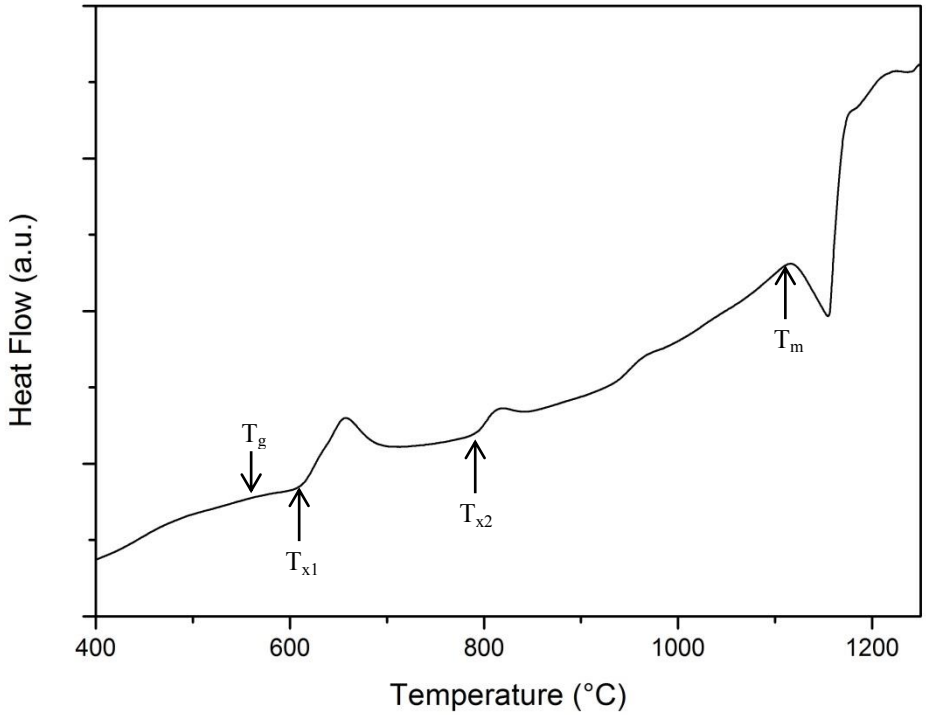

Figure 2: DSC scans of the $M_{60}Cr_{13}Mo_{10}B_8Y_2Mn_7$ samples

According to the DSC scans, alloys show a glass transition followed by two crystallization transformation. It shows glass transition at high temperatures which is another important parameter in order to popularize the BAS's usage in industry. The supercooled liquid region is around 25°C. The results of the DSC scans are summarized in table 1.

Table 1: The critical thermal properties of the alloys produced and the other BAS compositions according to the literature

Sample	T_g (°C)	T_x (°C)	T_m (°C)	ΔT_x (°C)	T_{rg}
$M_{60}Cr_{13}Mo_{10}B_8Y_2Mn_7$	589	614	1120	25	0.527
$Fe_{51}Mn_{10}Cr_4Mo_{14}C_{15}B_6$ [4]	530	600<	1130	40-50	0.469
$Fe_{50}Mn_{10}Cr_4Mo_{12}Er_3C_{15}B_6$ [4]	530	600<	1125	40-50	0.471
$Fe_{66}Mo_{10}P_{12}C_{10}B_2$ [5]	448	484	927	36	0.483
$Fe_{65}Cr_2Mo_9P_{10}C_8B_6$ [5]	483	547	959	64	0.503
$Fe_{50}Cr_{14}Mo_{14}C_{14}B_6Y_2$ [6]	567	619	1100	67	0.515

Table 1 shows the critical temperatures of some literature compositions and the alloys produced in this study. According to Table 1, $M_{60}Cr_{13}Mo_{10}B_8Y_2Mn_7$ shows one of the best results in terms of thermal properties. Among the compared compositions, it shows the highest glass transition and the crystallization temperature with a little sacrifice from supercooled liquid region. T_{rg} parameter is usually used for the representation of the glass forming ability. As it can be seen from the table, $M_{60}Cr_{13}Mo_{10}B_8Y_2Mn_7$ alloy showed the highest glass forming ability.

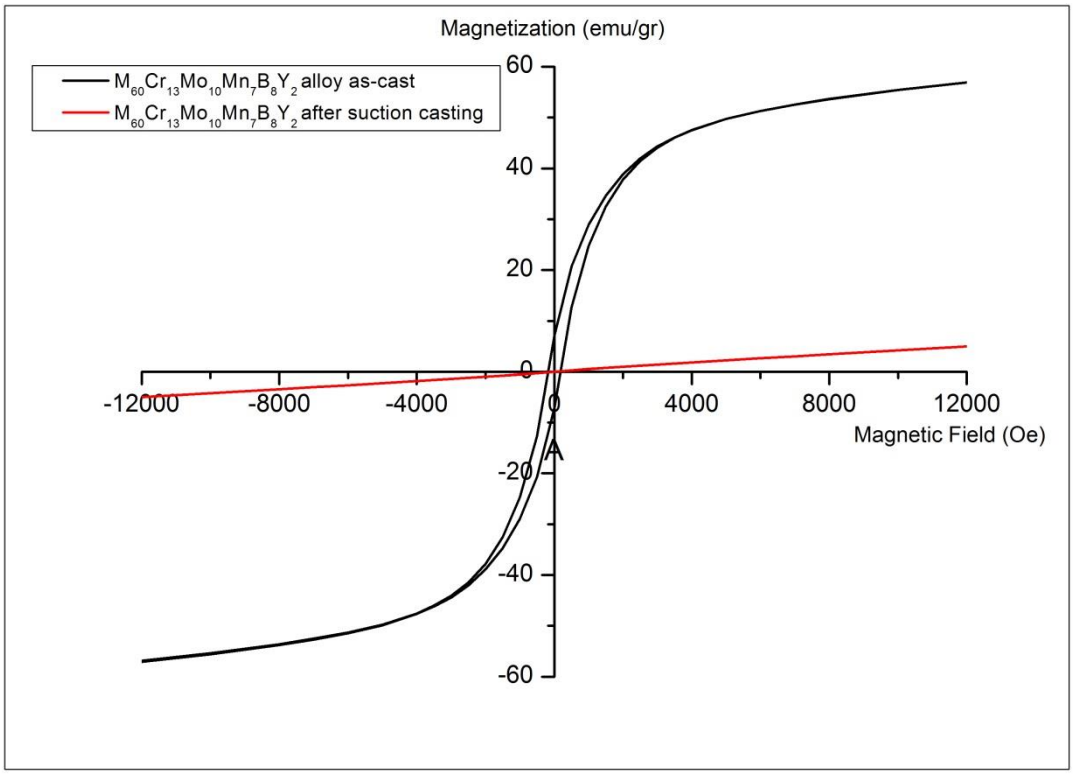

Figure 3: Magnetic measurements of rapid and slow cooled $M_{60}Cr_{13}Mo_{10}B_8Y_2Mn_7$

The magnetic measurements was applied to the samples in order to confirm the amorphous structure and to reveal the magnetic properties such as saturation magnetization M_s, remanent magnetization M_r, squareness $S = \frac{M_r}{M_s}$ and coercive field H_c of both slow and rapid cooled samples. Figure 3 shows the magnetic measurements of both rapidly cooled and slowly cooled samples of $M_{60}Cr_{13}Mo_{10}B_8Y_2Mn_7$ alloys. According to this figure, while the slowly cooled samples of $M_{60}Cr_{13}Mo_{10}B_8Y_2Mn_7$ showed a hysteresis curve, the rapidly cooled ones which had amorphous samples showed no hysteresis at all.

Table 2: Magnetic properties of slowly cooled and rapidly cooled samples of $M_{60}Cr_{13}Mo_{10}B_8Y_2Mn_7$

Sample	M_s (emu/gr)	M_r (emu/gr)	S	H_c (Oe)
$M_{60}Cr_{13}Mo_{10}B_8Y_2Mn_7$ (as-cast)	60.6	7.11	0.117	178.81
$M_{60}Cr_{13}Mo_{10}B_8Y_2Mn_7$ (after suction casting)	7.33	0.0255	0.0035	44.38

Hardness measurements of the $M_{60}Cr_{13}Mo_{10}B_8Y_2Mn_7$ alloy were done by Vickers micro hardness tester. In this test diamond tip was used with 9.807N load. To achieve accurate results, hardness measurements were taken from 10 different sites of the samples. According to the results, samples showed extreme high hardness values averagely, 1120 HV. In table 3 the comparison of the hardness values of $M_{60}Cr_{13}Mo_{10}B_8Y_2Mn_7$ BAS with some widespread industrial steels were given.

As it can be seen from table 3, when the samples of $M_{60}Cr_{13}Mo_{10}B_8Y_2Mn_7$ were compared with its crystalline counterpart and other commercially available steels, it had the highest hardness due to its amorphous structure.

Table 3: The hardness values of $M_{60}Cr_{13}Mo_{10}B_8Y_2Mn_7$ samples and commercially available steels

Sample	Hardness (HV)
$M_{60}Cr_{13}Mo_{10}B_8Y_2Mn_7$ (as-cast)	876
$M_{60}Cr_{13}Mo_{10}B_8Y_2Mn_7$ (after suction casting)	1120
Scrap Pig Iron (M)	182
AISI 304 Stainless Steel[7]	129
AISI 410S Stainless Steel[7]	446
AISI S1 Tool Steel[7]	661
AISI S5 Tool Steel[7]	602

$M_{60}Cr_{13}Mo_{10}B_8Y_2Mn_7$ samples were heat treated at 1000°C and left in the furnace for furnace cooling in order to obtain the homogeneous equilibrium structure. These samples then examined in SEM in order to observe the microstructures. The microstructures of $M_{60}Cr_{13}Mo_{10}B_8Y_2Mn_7$ samples can be seen from the Figure 5. As it can be seen from this figure the microstructure mainly constitute from dendrites and homogeneous matrix. The EDX scans were applied to ensure the composition of the samples and it was observed that there is no composition fluctuation caused by heat treatment. In order to see the change in composition from dendrites to matrix EDX line scan was applied. These results are shown in Figure 4. According to line scan obtained from different regions of microstructure, the dendrite arms contain Fe-rich zones.

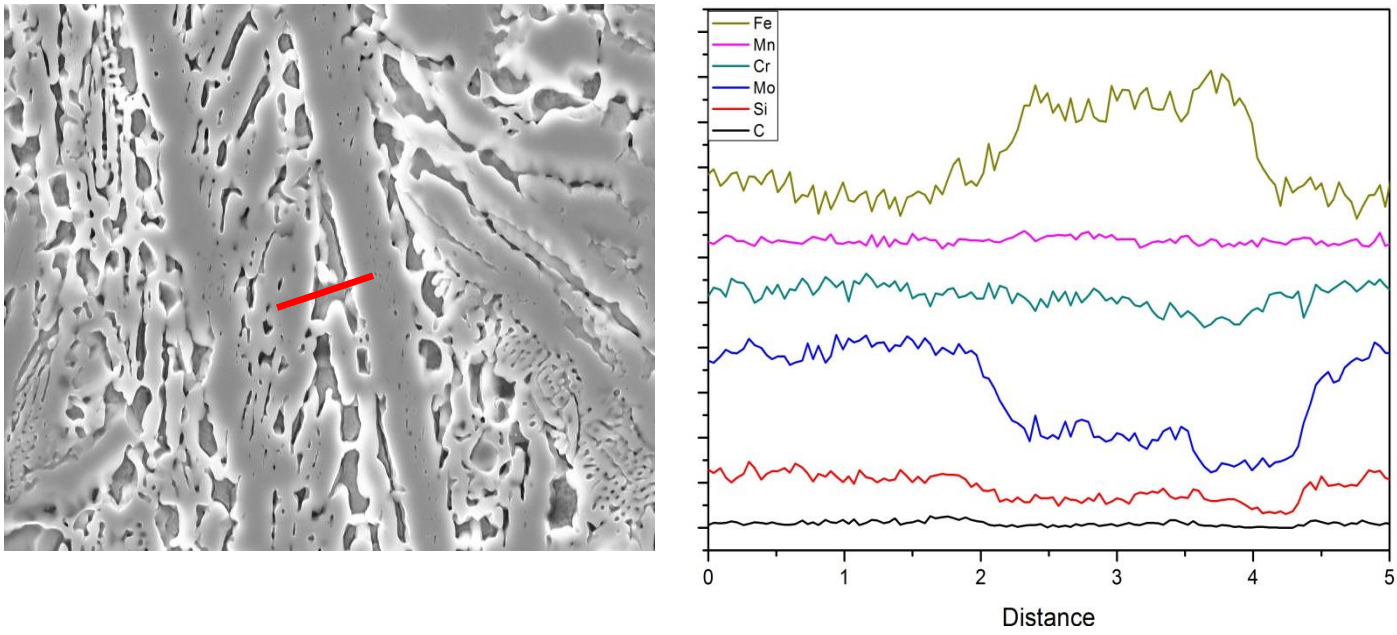

Figure 4: EDX line scan from heat treated $M_{60}Cr_{13}Mo_{10}Mn_7B_8Y_2$ samples

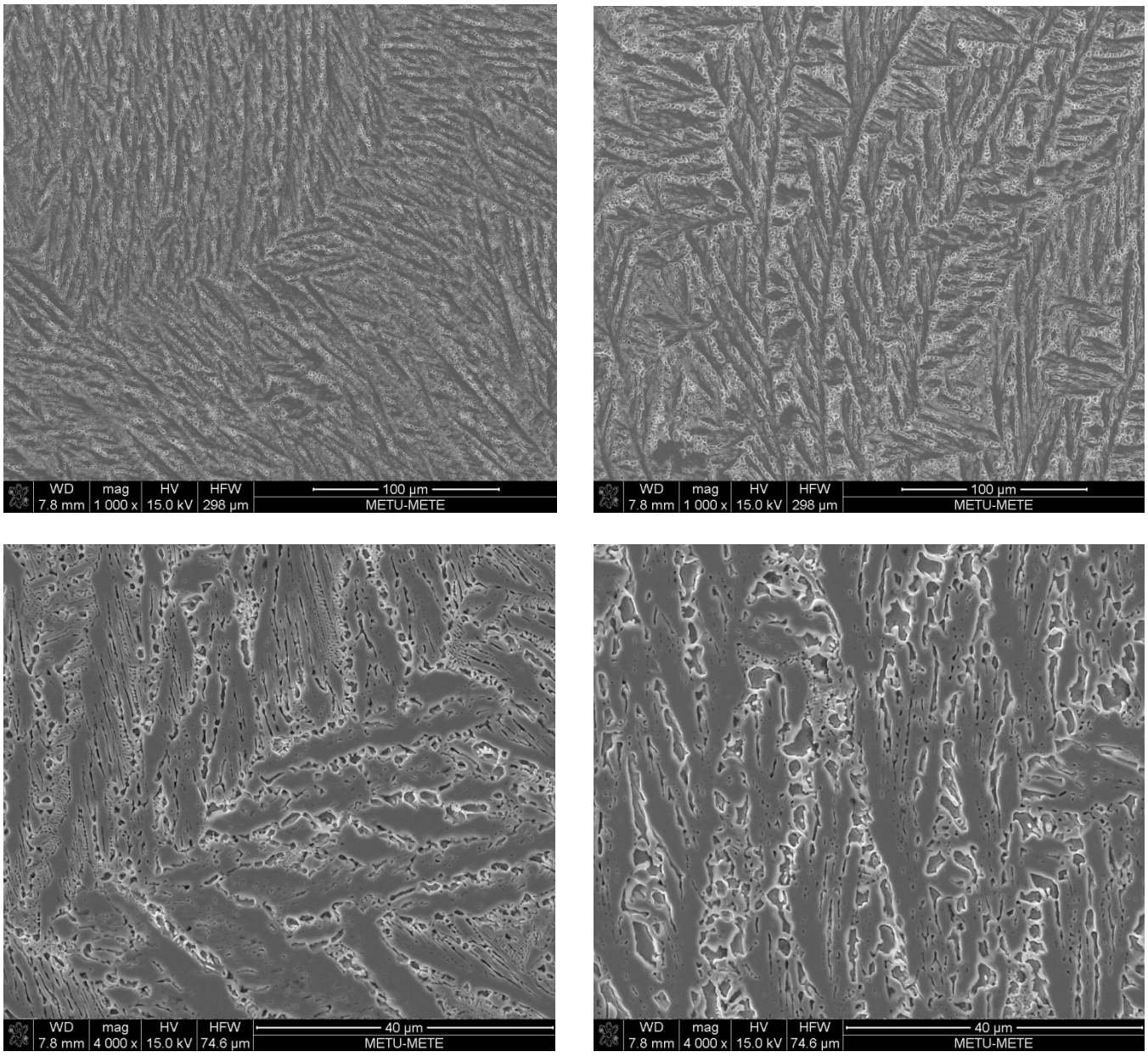

Figure 5: Microstructures of heat treated $M_{60}Cr_{13}Mo_{10}Mn_7B_8Y_2$ sample

4. SUMMARY

In this study, $M_{60}Cr_{13}Mo_{10}B_8Y_2Mn_7$ alloy samples were prepared by arc melting and then by suction casting, high cooling rates were applied to these prepared alloys. After obtaining the final structure of the alloys, samples were characterized.

According to the XRD analysis, the amorphous nature of the samples was confirmed. The analysis of the crystalline samples shows $Fe_{23}C_6$ phases as it was denoted in the literature before [4]. However with rapid cooling these phases were suppressed.

The thermal analysis results showed, samples showed glass transition which was followed by two crystallization transformation. When the critical parameters obtained by heating scans compared by the literature compositions, the $M_{60}Cr_{13}Mo_{10}B_8Y_2Mn_7$ samples showed one the highest glass transition and crystallization temperatures which will make the industrial adaptation of these kind of materials easier. Another important parameter T_{rg} which shows the glass forming ability, were again one of the highest values obtained when it

compared to mentioned literature alloys. This result showed that the BASs produced by scrap cast irons had a superior glass forming ability than the alloys made from completely pure elements.

Magnetic measurements were applied to ensure the non-ferromagnetic behavior of the BASs. The results showed that while the slowly cooled crystalline samples of $M_{60}Cr_{13}Mo_{10}B_8Y_2Mn_7$ showed a hysteresis curve, the suction casted ones showed no hysteresis.

Micro hardness tests and the comparisons of these values with the commercially available steels, proved BASs had extreme hardness values approximately 1120HV which is another important aspect for the adaptation for the industry.

SEM micrographs and EDX data showed that the heat treated samples contains generally dendritic structure and these dendrites include Fe-rich zones.

5. REFERENCES

[1] K.F. Yao, C.Q. Zhang, Appl. Phys. Lett. 90 (2007)
[2] P.A. Hess, S.J. Poon, G.J. Shiflet, R.H. Dauskardt, J. Mat. Res. 20 (2005) 783
[3] H. Chiriac, N. Lupu, Mater. Sci. Eng. A 375-377 (2004) 255.
[4] V. Ponnambalam, S. J. Poon, G. J. Shiflet, J. Mater. Res. 19(10) (2004) 3046-3052
[5] X.J. Gu, S.J. Poon, G. J. Shiflet, M. Widom, Acta Materiala 56 (2008) 88-94
[6] M. Iqbal, J. I. Akhter, H. F. Zhang, Z. Q. Hu, Journal of Non-Crystalline Solids, 354 (2008) 3284-3290
[7] Online Materials Information Resource – MatWeb (Retrieved on 2014)

CARBOTHERMIC REDUCTION OF LEAD-OXIDE AT LOW-TEMPERATURE

Bengisu YOLCU, Cevahir DURMAZ, Yasin KILIÇ, Güldem KARTAL ŞİRELİ, Servet TİMUR*

Istanbul Technical University, Metallurgical and Materials Eng. Dept., Istanbul- Turkey
*timur@itu.edu.tr

ABSTRACT
Waste lead-acid batteries are one of the most common recycled materials due to their hazardous components namely sulphuric acid and lead. Most parts of lead-acid batteries are recycled without using any reduction steps; however, waste battery paste needs further complex process stages because of its high sulphate content. The sulphate content of the battery pastes causes many problems during reduction periods, such as elevated furnace temperatures and high-energy consumption. Therefore, in many processes, sulphate content is removed through several desulphurization steps. During desulphurization, lead sulphate is transformed into lead-oxide. In theory, carbothermic reduction of desulphurized battery paste is possible to be conducted at 400-450°C. For this reason, carbothermic reduction of lead oxide is considered as a low-temperature reduction process compared to the conventional method in which the reduction temperature of sulphate is app. 1100°C. In this study, the lowest possible carbothermic reduction temperature of lead oxide was investigated by idealizing covering flux composition, reduction time as well as reductant ratio. Consequently, it was founded that electrochemically desulphurized lead paste was likely to be reduced carbothermically at 800^0C with the yield of 90%.

Keywords: Low-temperature carbothermic reduction, waste lead-acid batteries, desulphurized battery paste

KURŞUN OKSİTİN DÜŞÜK SICAKLIKTA KARBOTERMİK REDÜKSİYONU

ÖZET
Atık kurşun-asit aküler, içerdiği sülfürik asit ve kurşun gibi zararlı bileşenlerden dolayı en yüksek geri dönüşüm oranına sahip malzemelerden biridir. Geri dönüşüm prosesi sırasında, akünün büyük bir kısmı redüksiyon işlemi gerektirmeden dönüştürülebilirken, atık akü pastası, içerdiği yüksek sülfat bileşenleri sebebiyle daha karmaşık proses adımları gerektirmektedir. Atık akü pastalarının yüksek sülfat içeriği; redüksiyon işlemi sırasında yüksek enerji tüketimi ve yüksek fırın sıcaklıkları (1100^0C) gibi birçok sorunu ortaya çıkarmaktadır. Dolayısıyla, proseslerde çeşitli desülfürizasyon teknikleri kullanılarak akü pastasındaki sülfatın giderimi gerçekleştirilmektedir. Desülfürizasyon adımı sırasında, kurşun sülfat bileşiği kurşun oksit bileşiklerine dönüştürülmektedir. Teorik olarak; sülfatı giderilmiş atık akü pastasının karbotermikredüksiyonu 400-450°C civarında mümkün olmaktadır. Bu nedenle, kurşun oksitin karbotermik olarak redüksiyonu, konvensiyonel prosesin sıcaklığı olan 1100^0C ile karşılaştırıldığında düşük sıcaklık olarak tanımlanmaktadır. Bu çalışma kapsamında, idelize edilmiş örtücü flaks bileşimi yardımıyla, kurşun oksitin mümkün olan en düşük sıcaklıkta karbotermik olarak redüksiyon sıcaklığı, redüksiyon süresi ve redüktan oranı araştırılmıştır. Sonuç olarak; elektrokimyasal metodla desülfrize edilmiş akü pastası 800^0C'de karbotermik olarak redüklenmiş ve 90% 'ın üzerinde verim elde edilmiştir.

Anahtarkelimeler: Düşük sıcaklıkta karbotermik redüksiyon, atık kurşun-asit aküler, sülfatı giderilmiş akü pastası

1. INTRODUCTION

Lead-acid batteries constitute a considerable portion of world battery industry. They also hold the largest share of lead consumption as seen in Figure 1. Therefore, they are one of the materials with the largest recycling ratio and hence lead productions from secondary sources have been increasing day by day (Figure 2). So far, many lead recycling processes have been developed. These processes can be mainly categorized in two main groups: pyrometallurgical techniques, also known as conventional methods and electrometallurgical processes.

Pyrometallurgical processes have many disadvantages such as; high energy consumptions, elevated process temperatures as well as toxic lead and SO_2 emissions [1-3]. Although electrometallurgical methods have been established to overcome such issues experienced in the conventional method, several difficulties have arisen such as; low solubility of lead and its compounds. Especially some compounds in battery paste (PbO_2, $PbSO_4$) exhibit almost no solubility in solvents utilized in the electrochemical processes, and consequently low leach efficiencies are attained [1-4].

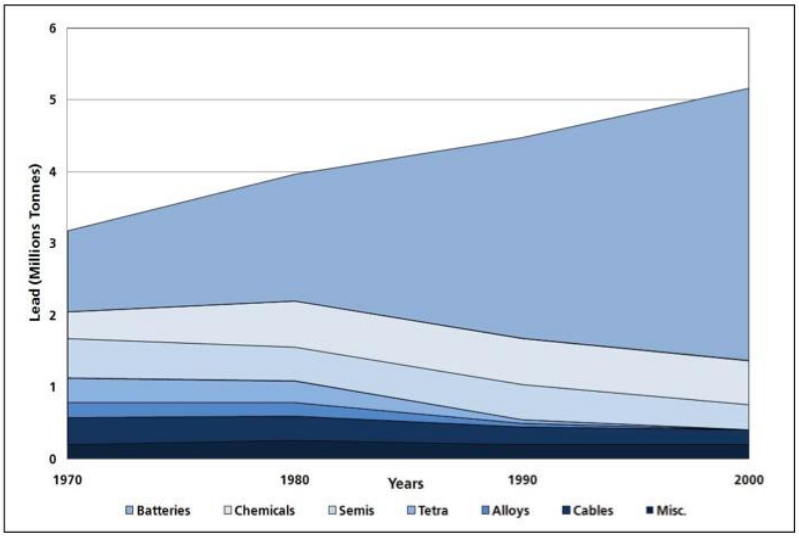

Figure 1. Lead consumption [4]

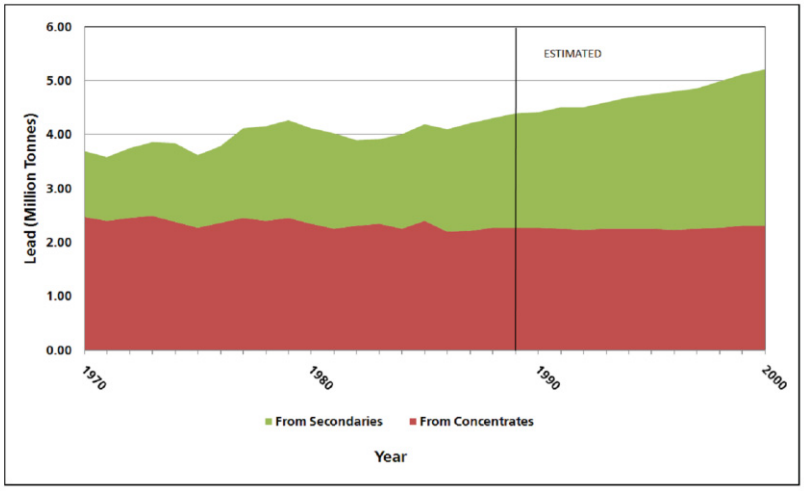

Figure 2. Lead production from primary and secondary sources [5]

The main trouble observed in both electro- and pyro-metallurgical methods was caused by the high sulphate content of the battery paste. Approximately, 56% of battery composes of paste and the major component of paste is lead sulphate with ~60% (Table.1) [6].

Table 1. Battery components [6]

Grid metal, poles, bridges	**44%**
Pb	96-98%
Sb	2-4%
(Ca)	<0.5%
Paste	**56%**
$PbSO_4$	60%
PbO (PbO_2)	19%
PB	21%
	100%

However, conventional recycling processes are inconvenient due to the low solubility of lead sulphate and hence the high temperature as high as 1100^0C was required for the decomposition of $PbSO_4$. The decomposition reactions are given in equations 1 to 4 [6].

$$PbSO_4 + 2C \rightarrow PbS + 2CO_2 \quad (1)$$

$$PbS + Fe \rightarrow Pb + FeS \quad (2)$$

$$PbS + 2PbO \rightarrow 3Pb + SO_2 \quad (3)$$

$$PbS + PbO_2 \rightarrow 2Pb + SO_2 \quad (4)$$

On the other hand, the reduction process could be carried out in a much simpler way by applying a pre-desulphurization step to the paste. The possible carbothermic reduction reactions of desulphurised paste which consists of basically lead oxide compounds are given in equations 5 and 6 [7].

$$2PbO + C \rightarrow 2Pb + CO_2 \quad (5)$$

$$PbO_2 + C \rightarrow Pb + CO_2 \quad (6)$$

As seen in Ellingham diagram (Fig. 3), the carbothermic reduction of lead oxide occurs at ~ 400°C. Therefore, if sulphate content is successfully eliminated, the pyrometallurgical process can be achieved at low temperatures due to the low melting point of lead (327°C).

The aim of this study is to offer an alternative lead-acid battery recycling process so as to minimize emissions and energy consumption. For this reason, the waste battery paste was initially desulphurized via electrochemical methods then carbothermically reduced. The lowest possible carbothermic reduction temperature of lead oxide was investigated by idealizing flux composition, reduction time as well as reductant ratio. Besides, the amount of covering salt flux was examined to prevent lead losses due to high volatilities of lead compounds.

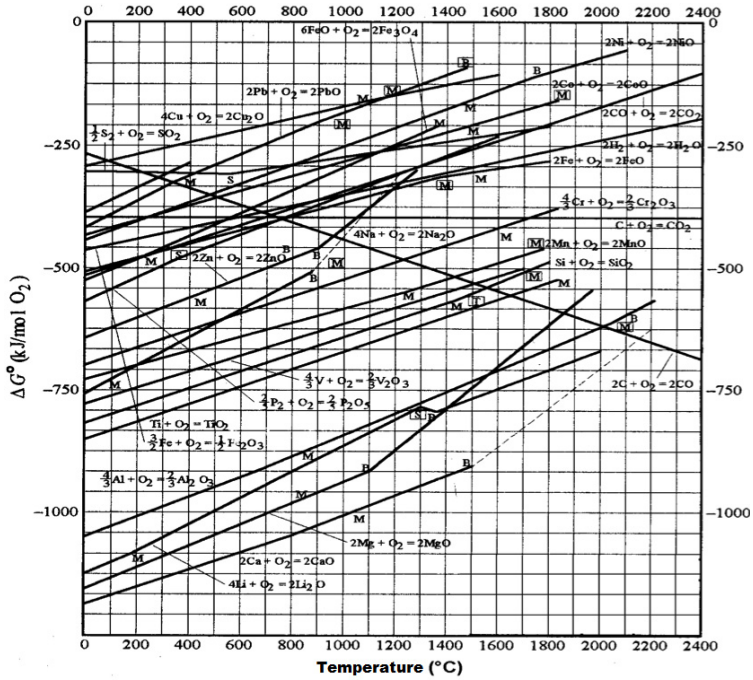

Figure 3. Ellingham Diagram

2. EXPERIMENTAL PROCEDURE

In carbothermic reduction experiments, electrochemically desulphurized paste containing app. 1 wt% $PbSO_4$ and mixed lead oxide compounds (PbO, PbO_2, PbO_x) as well as metallic lead was utilized as a raw material. The amount of lead in the desulphurized was determined as 86 wt% Pb via atomic absorption spectrometry (Perkin Elmer Analyst 800). The experiments were performed in a chamotte crucibles heated by an electrical resistance furnace. The main scheme of experiments was presented in Figure 4.

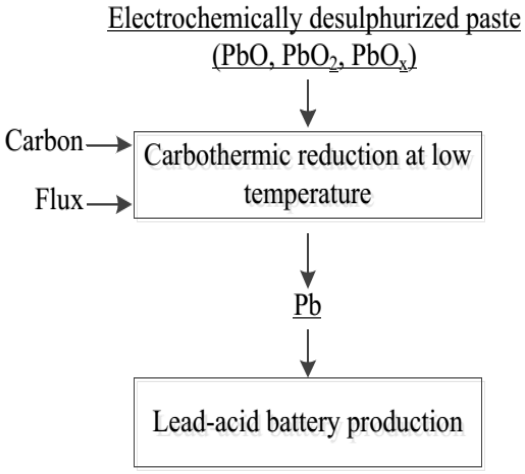

Figure 4. Process flow diagram

2.1. Reduction Temperature

In first part of experiments, the optimum temperature for reduction reactions (Eq. 5-6) was investigated. Initial test was conducted at the temperature ranging 350-800°C with a pure litarge due to its volatility at low temperatures.

2.2 Flux Composition

In the second part of the experiments, the ideal flux composition was investigated based on the optimum reduction temperature. Different types and composition of salts, namely NaCl, KCl, CaF_2 (0-3 wt%) and borax ($Na_2B_4O_7$) was used to develop a covering salt flux.

TG-DTA analysis was conducted to determine the melting characteristics of NaCl-KCl based fluxes. Two layered flux was tried to form by adding borax on to the NaCl-KCl salt flux to prevent flux loss (with a ratio of 1:2 borax:salt). Additionally, CaF_2 was added to inspect the effect on the viscosity of flux.

2.3. Reduction Parameters

In the third part of the study, optimum parameters for the reduction were invstigated by determining the ratio of reductant and process time. Electrochemically desulphurized battery paste containing metallic lead and lead oxide compounds was used as a raw material. Lead reduction yield was defined by the equation given below (Eq.7).

$$\% \text{ Reduction yield} = \frac{\text{Metallic lead obtained}}{\text{Raw material Pb content [g]}} * 100 \quad (7)$$

3. RESULTS

3.1. Reduction Temperature

The initial experiment conducted on litarge showed that the reduction of lead was possible at 450°C. However, metal and slag were not completely separated from each other at 450°C; due to the entrapping of lead bullions into the carbon structure (see Fig. 5). Metal/slag separation was occurred after 90 min. with 3.5 wt% carbon at 660°C.

Figure 5. Section of the crucible

[450°C, 90 min. reduction time, 3.5 wt% carbon, $ZnCl_2$ salt flux].

Based on the observation of the experiments, the optimum reduction temperature was chosen as a temperature ranging 660-700°C.

3.2 Flux Composition

The appropriate flux composition was examined at temperature of 650-760°C. NaCl-KCl based fluxes, widely used for aluminum smelting processes, were considered as a suitable flux at this temperature interval (see the binary phase diagram of NaCl-KCl in Fig. 6. TG-DTA analysis revealed that this flux melts around 650°C (Fig. 7). Additionally, a major weight drop was observed after 800°C due to the significant vaporization of NaCl-KCl system.

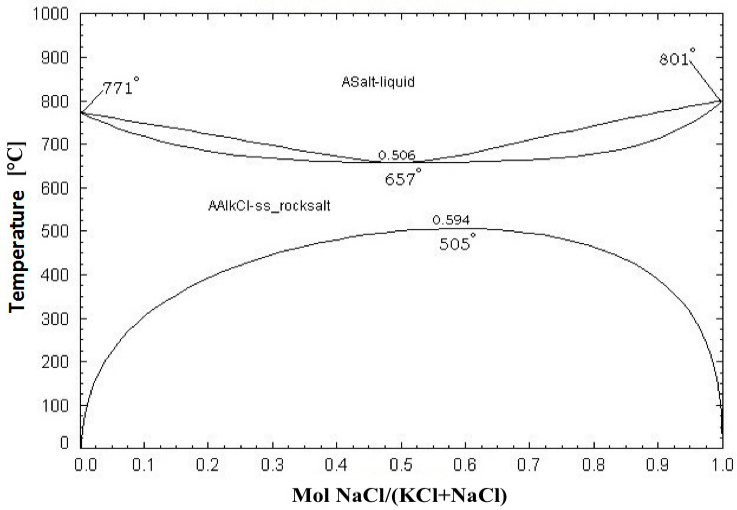

Figure 6. NaCl-KCl phase diagram [7].

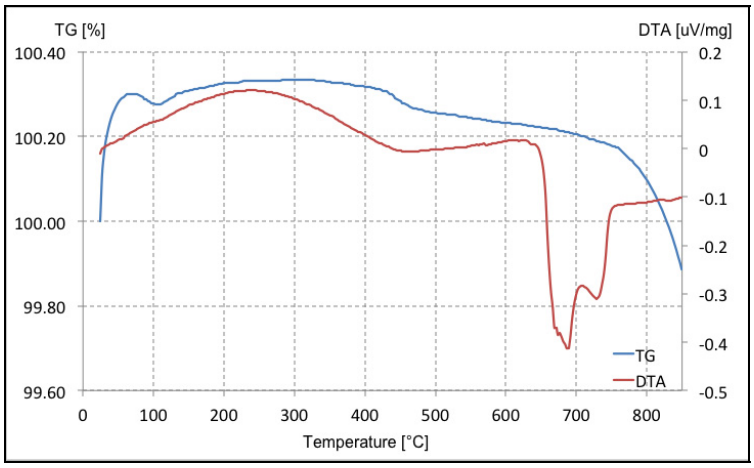

Figure 7. TG-DTA graph [50 wt% NaCl- 50% KCl +3% CaF_2]

Two layered flux was tried to form by adding borax on to the NaCl-KCl salt flux to prevent flux loss. Since borax has high melting point 744°C, the melting point of the NaCl-KCl flux rises with the addition of borax. For this reason, the reduction temperature was increased to 800°C for the subsequent experiments.

The viscosity of the flux system was adjusted with the addition of CaF_2. The effect of CaF_2 addition on lead loss was given Figure 8. Even though minimum material loss was occurred with 2.5 wt% CaF_2, the variations happened in the additions of 1-3% CaF_2 was negligible.

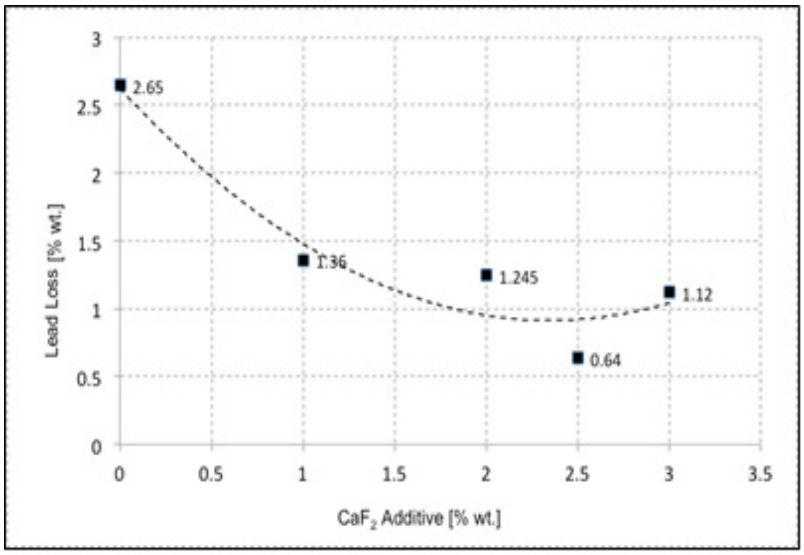

Figure 8. Variation of lead loss as a function of CaF_2 addition

3.2. Reduction Parameters

3.2.1. Reductant Ratio

In Theory, it was expected that reduction yield increases with increasing carbon content. However as seen lead reduction and reductant amount relation in Fig. 9, a sharp drop was observed on the reduction yield when carbon was used 10 wt%. The possible reason of this result detected in laboratory scale experiments was the occurrence of a strict structure formed carbon content which prevented the separation of reduced metal from slag. Therefore, 7 wt% carbon was determined as a sufficient amount for the carbothermic reduction.

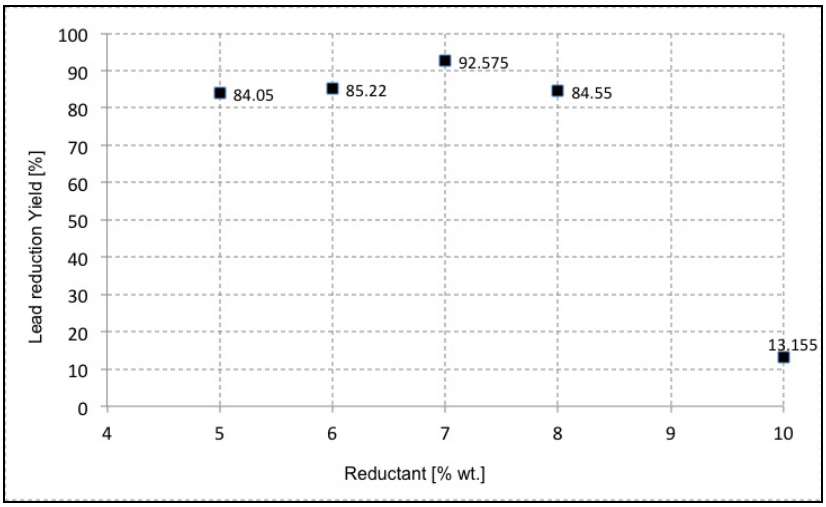

Figure 9. Lead reduction-reductant ratio

[800°C, 90 min. reduction time, 70% NaCl+ 30% KCl + 2% CaF_2flux, 1:2 borax:salt]

3.2.2. Reduction Time

In reduction time experiments, the yield calculated according to Eq.7 increased with time until a certain value. Beyond that value measured at 60 min, there was no significant rise taken in the value of yield (Figure 10). More than 90 % of lead reduction yield was achieved during laboratory scale experiments. Therefore, 60 minutes was chosen as the optimum process time.

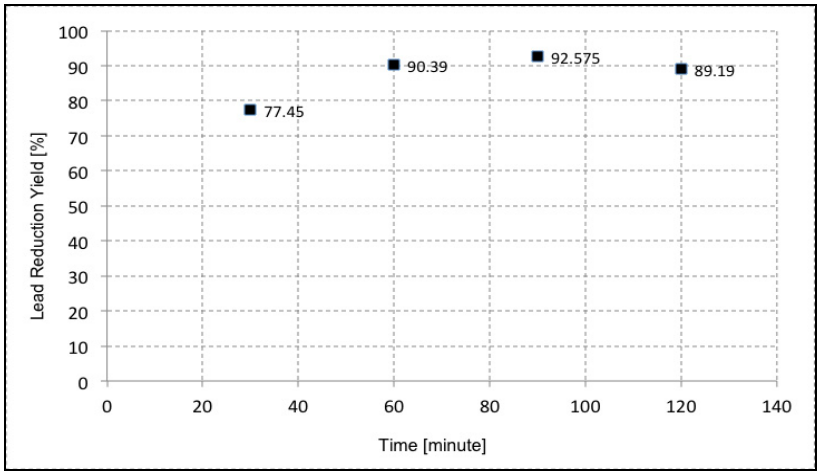

Figure 10. Lead reduction yield-Time

[800°C, 3.5 wt% C, 70% NaCl+ 30% KCl + 2% CaF2 flux, 1:2 borax:salt]

4. CONCLUSIONS

In this study, the lowest possible carbothermic reduction temperature of lead oxide was investigated by idealizing flux composition, reduction time as well as reductant ratio. Based on the reported results, the effect of process parameters could be concluded as following:

- Carbothermic reduction of lead oxide was achieved at the temperature ranging 660-700°C.
- The best covering flux was accomplished by a two-layered flux with the ratio borax to salt of 1:2. The salt composition was kept constant at 70 wt% NaCl - 30 wt% KCl and 2 wt % CaF_2 added as a viscosity modifying agent.
- The most efficient reductant ratio was determined as 7 wt% carbon for 60 min. of reduction time.
- Lead reduction yield was found as more than 90% under idealized conditions; 70 wt % NaCl- 30% KCl- 2% CaF_2, 1:2 borax:salt, 7 wt% carbon, 800°C, 1 hour reduction time.

According to obtained outcomes, the suggested alternative procedure provided promising solutions on many environmental and energy consumption issues experienced in currently available recycling processes developed for lead-acid battery.

Acknowledgements

"Republic of Turkey Ministry of Science, Industry and Technology" and "Inci Akü" are gratefully acknowledged for funding the project *Zero Waste Principled Recycling Process for Scrap Batteries* (STZ.00829-2011_1).

REFERENCES

1. C. Garcia, M. Diaz, G. Frias, "New clean technologies to improve lead-acid battery recycling", Lead-Zinc 2000, pp. 791-797, 2000.
2. D. Raychaudhuri, A. Frias, and C. Andrews., "Environmentally sound technologies for recycling secondary lead", Journal of Power Sources, no. 88, pp. 124-129, 2000.
3. M. Ş. Sönmez, and R. V Kumar,"Leaching of waste battery paste components. Part 1: Lead citrate synthesis from PbO and PbO_2", Hydrometallurgy, vol. 95, pp. 53-60, 2009.
4. B.M. Yolcu, "Atık akü pastalarından elektrolitik olarak kurşun geri kazanımı", Yüksek lisans tezi, İTÜ, İstanbul, 2013.
5. K. Hawkins, P. Ramus, "Lead/acid battery recycling and the new isasmelt process", Adress: http://www.isasmelt.com/EN/Publications/Technical%20Papers/LeadAcid%20Battery%20Recycling%20and%20the%20New%20Isasmelt%20Process.pdf, Downloaded date: 2013.
6. H. Vest, "Fundamentals of the recycling of lead-acid batteries", 2002.
7. FactSage-Center for Research in Computational Thermochemistry, Adress: http://www.crct.polymtl.ca/fact/phase_diagram.php?file=KCl-NaCl.jpg&dir=FTsalt, Downloaded date: 13.04.2013.

NEW GENERATION HIGH TEMPERATURE MATERIALS

Bo JÖNSSON, Thomas HELANDER, Erik STRÖM

Sandvik Heating Technology,
Box 502, SE 734-734 27 Hallstahammar, Sweden
bosse.jonsson@sandvik.com, thomas.helander@sandvik.com, erik.o.strom@sandvik.com

ABSTRACT

Three materials, two metallic and one ceramic, all with unique high temperature properties due to their alumina forming capability, have been developed and are recently introduced commercially. Some basic features and recent test results are presented on each of the materials.
Kanthal APMT™, a unique powder metallurgical alumina forming FeCrAlMo alloy which combines high temperature oxidation and corrosion resistance with mechanical properties sufficient for structural applications like retorts and muffles for high temperature PM sintering.
Nikrothal® PM 58 that is a recent development based on the success of Kanthal APMT. It is a new powder metallurgical Ni-base alloy, that in contrast to almost all other Ni-base alloys forms alumina protective oxide scales. It combines even higher creep strength than Kanthal APMT with high temperature corrosion and oxidation resistance. It has excellent properties for applications like mesh belts for sintering of powder metals.
Maxthal™ 211 (and Maxthal™ 312 not presented in this paper) are the only commercially available products based on MAX-phases, a new group of machinable and high toughness ternary carbides and nitrides that offer properties normally not found in ceramic materials. MAX-phase materials are perhaps one of the most interesting new material groups for the future and have found uses in components like burner nozzles and protective coatings.

Keywords: FeCrAl, NiCrAl, Ti2AlC, Alumina, oxidation, dispersion strengthened, high temperature, creep, oxidation

INTRODUCTION

Kanthal® materials and systems from Sandvik are since almost a century the standard solution when it comes to electrical resistance heating. The product range has expanded during the years from FeCrAl (and NiCr) metallic alloys to include a range of ceramic materials/heating elements, such as Kanthal Super™ ($MoSi_2$) and Kanthal Globar® (SiC) heating elements, as well as including more product forms (e.g. Kanthal APM™ extruded tubes) and also into components and systems for thermal processing and process heating.
This evolution is now taking another step by moving into a range of high temperature components that withstand heat and protect from heat rather than generating it, such as retorts for PM sintering, furnace rollers and furnace furniture. This is made possible by combining the mechanical, corrosion and oxidation properties of metals and ceramics, and by using the possibilities introduced by powder metallurgy.
This presentation will give a brief introduction to three developments/materials: one metallic FeCrAlMo alloy Kanthal APMT, one Ni-base alloy Nikrothal PM 58, and one machinable and tough ceramic material, Maxthal 211. Although coming from different material groups, they all help to bridge the gap between high temperature alloys and ceramics. They also share one of Kanthal products strongest features, i.e. the spontaneous formation of an Al_2O_3 surface

layer during operation, which provides a dense, adherent and self-healing protection against destructive corrosion and oxidation at very high temperatures.

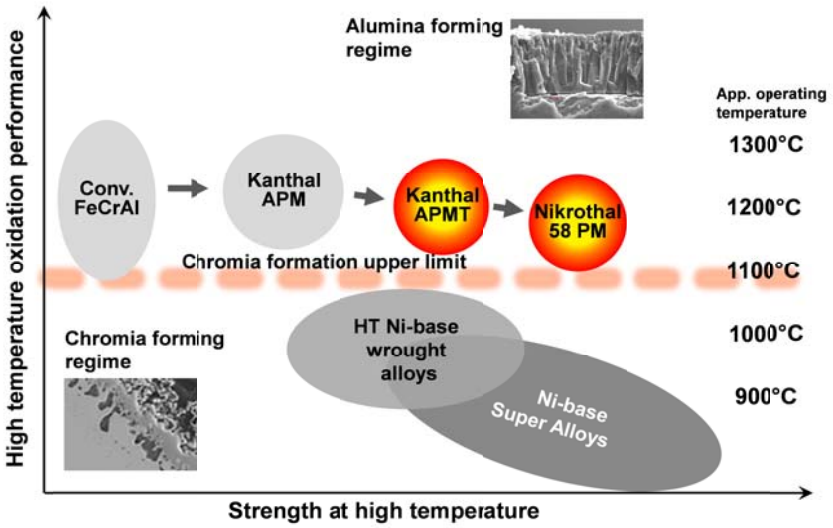

Fig. 1. Schematic relation between main groups of high temperature alloys in terms of creep strength and typical maximum application temperature in oxidizing environments. Ceramics may have very good oxidation and corrosion resistance, but are typically relatively brittle and are threfore not included in this schematic view.

KANTHAL APMT

Kanthal APMT is an FeCrAlMo alloy optimized for continuous service up to 1250°C(~2300°F) [1,2]. Rapid solidification powder metallurgy applied on this FeCrAlMo composition provides an ODS (Oxide Dispersion Strengthened) microstructure. The alloy exhibits a unique combination of resistance to oxidation and corrosion and excellent form stability. An adherent alumina layer on the alloy surface formed during service provides resistance to corrosion attacks in most industrial atmospheres and gives great advantages compared to chromia forming high temperature Ni-base alloys in terms of maximum operating temperature and life, see figure 1.
Traditionally, wrought or cast Ni-base alloys are commonly used for high temperature constructions, but the limited oxidation resistance above 1000 to 1100°C restricts the service temperature in oxidizing environments and carburizing may be a problem in many industrial high temperature processes. Conventional wrought FeCrAl high temperature alloys are on the other hand well known for their superior oxidation resistance up to 1300 or even 1400°C. This outstanding resistance to oxidation is based on their ability to form a very slow growing and protective alumina scale during service. The relatively low mechanical strength of these ferritic alloys at high temperatures strongly limits their application in mechanically stressed components. High temperature strength may however be increased by introducing powder metallurgy in the primary process. Rapid Solidification Powder metallurgy (RSP) was developed by Sandvik as a way to create a distribution of small refractory strengthening inclusions. Kanthal APM was introduced 1989 and was the first powder metallurgical FeCrAl alloy using this technology. The alloy is still state of the art for heating in high temperature industrial and semiconductor electric furnaces up to as much as 1400ºC material temperature and is used also for gas or electrically heated radiant tubes with material temperatures up to about 1250ºC. Kanthal APMT was introduced as the next step in terms of further improved

hot strength and retained alumina scale protection up to 1300ºC, which is a temperature range where Ni-base alloys degrade rapidly due to accelerated oxidation and grain boundary softening.

Table 1. Nominal chemical composition

	Cr	Al	Mo	RE	Fe
Kanthal APMT (RSPM)	22	5	3	Added	Balance
Kanthal APM (RSPM)	22	5.8	-	Added	Balance
Kanthal AF (Conventional)	22	5.3	-	Added	Balance

a) 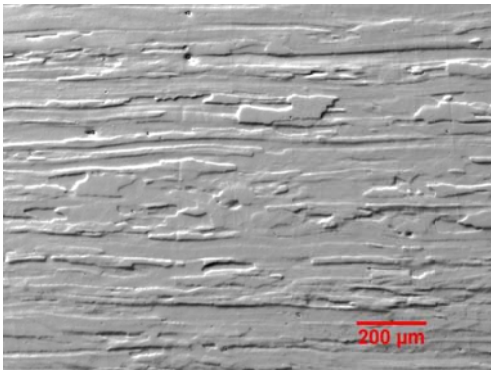

b) 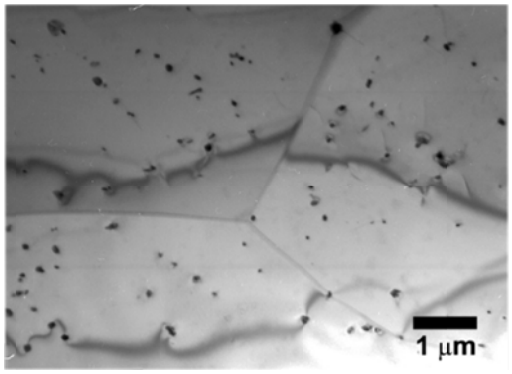

Figure 2. a) Polished and etched micrograph from 8 mm hot rolled plate, b) TEM section showing grain boundaries and strengthening particle dispersion

Oxidation resistance: The APMT is an alumina former. In contrast to the chromia scales that most Ni-base high temperature alloys depend on for heat resistance, alumina protection give several major advantages; slow growth rate, scale adherence, chemical stability towards water, carbon and sulphur. These advantages transform into a number of practical benefits in oxidizing and carburizing environments compared to the best Ni-based chromia formers such as longer lifetime, 100 to 200ºC (180 to 360°F) higher operating temperature, small spallation (particles flaking off) and negligible amounts of emissions to the gas phase. Although referred to as alumina former, Kanthal APMT actually forms a chromia scale at low temperatures, like all stainless steels. When temperature is raised, the composition of the protective scale gradually changes to a higher aluminum content, and recent investigations have shown that 700ºC (1292°F) may be sufficient to form a predominantly alumina scale [4]. There is also no critical temperature range where oxidation rates are accelerated, although isothermal exposures have shown that oxide growth, although very slow, is approximately the same at 800 and 900°C.

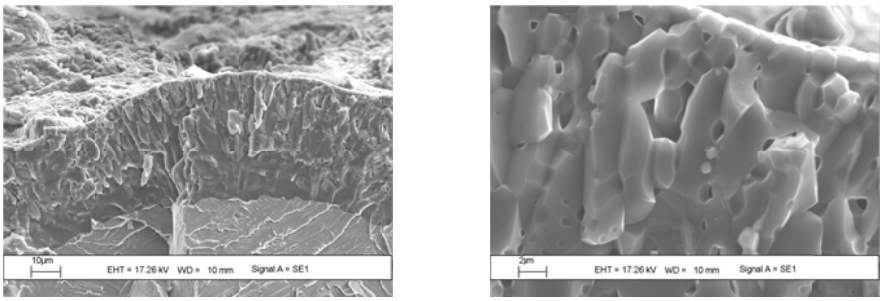

Fig. 3. SEM example from fractured section of APMT exposed to 1300ºC for 1100 hours using 20 hour thermal cycles. The dense and coherent oxide is evident even after this fairly tough exposure.

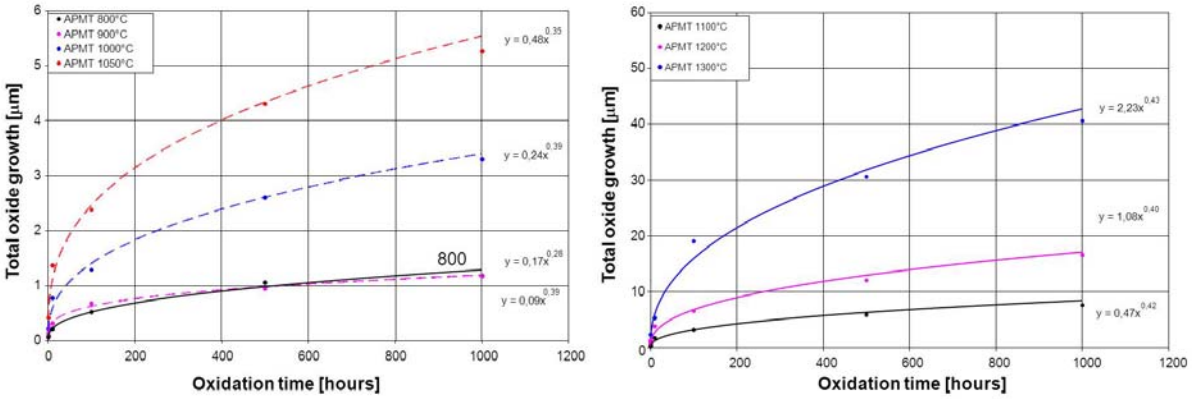

a) b)

Fig. 4. Gross oxide growth *vs*. time on isothermal exposure of APMT. Each measurement was made on a separate sample. Sample size 1 x 10 x 20 mm. Spallation was negligible under these conditions. a) 800 to 1050ºC b) 1100 to 1300ºC

Lifetime assessment: Lifetime is typically limited by creep deformation and/or by oxidation. Design of components for service at very high temperatures also makes it necessary to understand and control the combined action of simultaneous oxidation and mechanical stresses that may occur from external loads or from thermal gradients. At high temperature and below a certain critical load the failures are typically determined by the oxidation process. In the other corner, at higher loads and lower temperature, failure is often controlled by the mechanical properties.

During exposure, thermal cycling and also mechanical damage often cause micro cracks or even macro defects in the oxide scale. Al diffuse from the interior of the alloy to the scale interface and oxidation limited lifetime is reached when the aluminum level beneath the oxide layer is too low to support the continued alumina formation in those defects. It is found that the critical Al level is in a range from one to three wt.% Al remaining in the alloy. Comparative life testing, may be assessed by using electric current to heat the samples to a specified temperature as shown in figure 5.

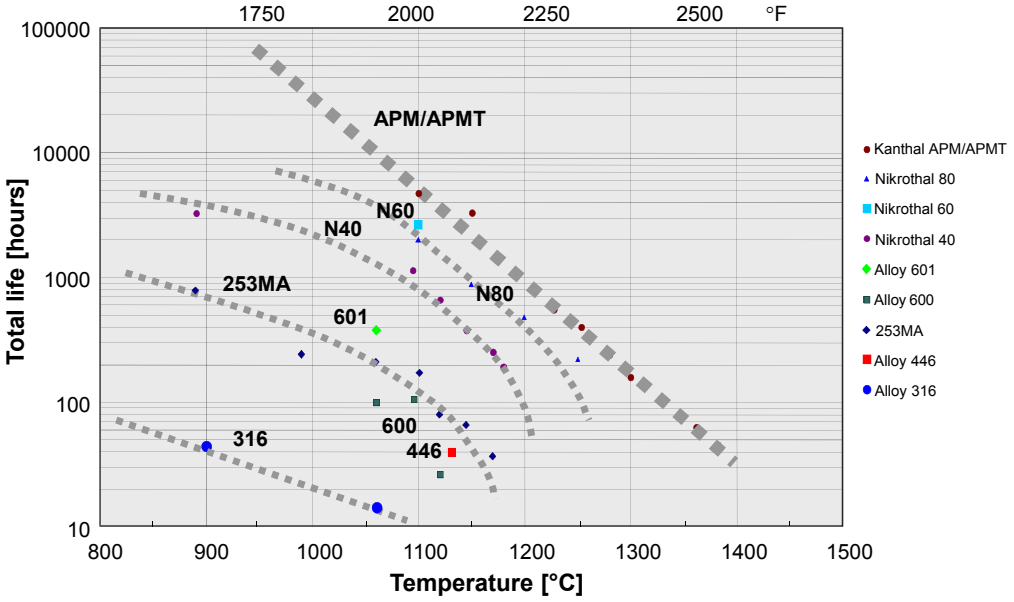

Fig. 5. Oxidation lifetime for various alloys as measured according to ASTM B78 – 81. Thermal cycling 2 minutes on/ 2 minutes off. Samples are Ø0,7 mm wire.

Carbon and sulphur resistance: Due to the extremely dense alumina scale formed and the low permeability of carbon containing species, the carburization properties of APMT are excellent in comparison to chromia forming materials. Further, APMT is almost entirely insensitive to metal dusting and is also very stable towards sulphur attack compared to Ni base alloys.

High Temperature Creep resistance: In general, the creep rupture strength for APMT is at similar levels as high temperature Ni base alloys above 900ºC, and the advantage towards Kanthal APMT becomes higher, the higher the temperature, see figure 6. Note is that well defined rupture and creep rate data exists for APMT in the temperature range 1100 to 1300ºC (2000 to 2400ºF) which is a range where Ni-base alloys suffer from severe oxidation and above 1200°C also loss of structural integrity due to initiating grain boundary sliding.

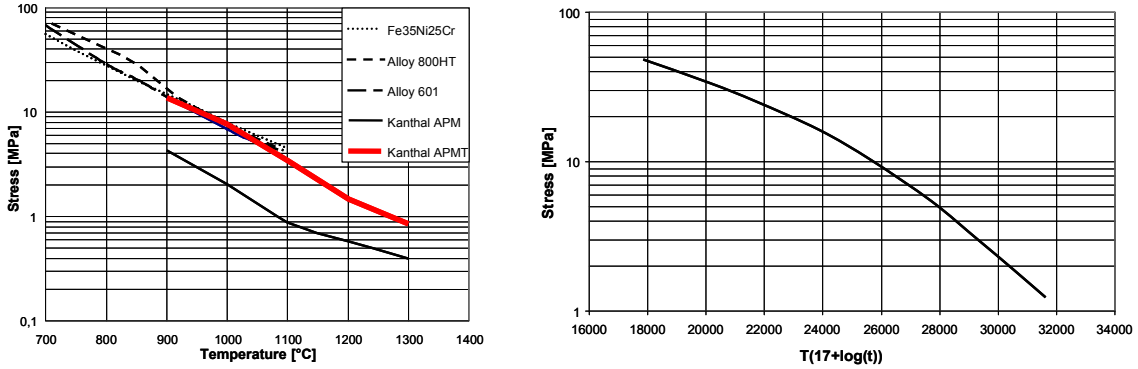

Fig. 6. a) 10 000 hour creep rupture life. The APMT line is representative for tube walls in the long direction. b) Larson-Miller plot of creep rupture data. Values are representative for extruded tubes in the long direction. LM constant assumed to 17.

Welding and joining: The APMT alloy is readily welded with TIG/GTAW which is the most commonly used joining method today. Preheating to approximately 250ºC and post-weld anneal to 850ºC is however necessary. Some creep strength is also lost in the weld, and this is normally handled by design so that welds are placed at positions where the stress level or the temperature are below their peak levels. Another possibility is of course to increase the section thickness at the position of the weld. In addition to TIG welding there are several welding techniques that can be used such as laser or MIG welding. Also brazing has been shown to give good results when it is possible to prepare the gap to adequate tolerance and to perform a heat cycle in vacuum.

Applications: Due to the combination of strength and oxidation resistance at temperatures >1250°C, the alloy is used as facilitator and problem solver in components such as furnace rollers at 1200°C, retorts for sintering at 1250°C, reformer tubing and thermocouple protection (resistance to metal dusting) and heat shields. A wide range of product forms including hot rolled plate and extruded tube is available.

NIKROTHAL PM 58

Nikrothal PM 58, is an alumina forming, NiFeCrAl-based alloy intended for use at high temperatures and in aggressive high temperature environments. Traditional wrought or cast Ni-base alloys uses additions of chromium and optional silicon in order to form a protective oxide scale. Nikrothal PM 58 uses instead an addition of aluminum sufficient for forming

alumina at elevated temperatures which results in a very good resistance to oxidation and corrosion in many controlled atmospheres at high temperatures.
Furthermore, dispersion strengthening by using RSP powder metallurgy is used in order to achieve very high levels of creep strength compared to most wrought nickel base alloys. Here, Nikrothal PM 58 is compared to some wrought nickel base alloys and stainless steels commonly used in high temperature applications listed in table 2 below.

Table 2. Nominal chemical composition of materials in study

Material	Ni	Fe	Cr	Al	Si	Mo	Mn	N	C	Nb	Trace
Nikrothal PM 58	Bal.	18-20	17-19	4-5							added
UNS S35315	35	Bal.	25	-	1.6		1.5	0.16	0.07		added
UNS N06009	Bal.		19-21		0.8-1.5					1.0	
UNS N06601	60	Bal.	23	1.3	0.3		0.6		0.03		

Table 3. Selected physical properties of materials in the study

	Nikrothal PM 58	Kanthal APMT	UNS S35315	UNS N06601	UNS N06009
Density (g/cm^3)	7.8	7.2	7.9	8.1	8.3
CTE [$\times 10^{-6}$ K^{-1}] (20-1000ºC)	18	15	18	17	17
Electrical resistivity [Ω·mm^2/m], 20 °C	1.33	1.40	1.00	1.18	1.09
Electrical resistivity [Ω·mm^2/m], 1000 °C	1.40	1.44	1.30	1.26	1.14
Thermal conductivity [W/m·K], 50°C	10	11	11	12	15

Oxidation performance: Oxidation testing at 1000ºC was performed using corrosion coupons with the dimensions 15 x 10 x 3mm. Comparative test was performed using samples of Nikrothal PM 58, Kanthal APMT and UNS S35315. The coupons were measured, ground to 600 mesh with a subsequent cleaning in ethanol and acetone. The weight was measured and the coupons were placed in alumina crucibles which were inserted in a pre-heated furnace. The furnace was sealed and synthetic air, 80%N_2-20%O_2 was flushed through the furnace at a 1000ml/minute rate. The net mass gain as a function of time is shown in the figure 7. The oxide formed on the samples after 2000 hours at 1000ºC was characterized using scanning FEG-SEM electron microscopy.

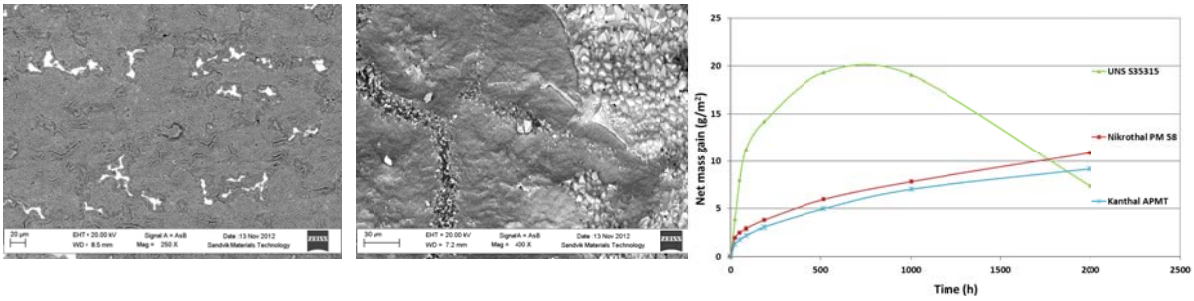

a) b) c)

Figure 7. Typical surfaces of a) Nikrothal PM 58 and b) UNS S35315 after 2000 hours of discontinuous oxidation testing at 1000ºC c) Net mass gains gain from discontinuous oxidation at 1000ºC

For Nikrothal PM 58 the oxide surface is relatively smooth with small areas where oxide spallation has occurred. A thin and protective alumina scale has formed which is consistent with the low mass gain shown in figure 7.
The oxide surface of UNS S35315, regarded as an alloy with excellent high temperature resistance, is coarser with regions of chromia and also regions with higher manganese content, possibly due to the formation of a manganese spinel. As can be seen in figure 7, the net mass

gain for UNS S35315 shows an initial increase followed by a loss due to repeated spallation and re-oxidation.

Carburization resistance: A pack carburization test was carried out in order to evaluate the resistance to carburization. Bar samples were turned, cleaned in ethanol and embedded in pure carbon powder. A container (actually made from pre-oxidized Kanthal APM) was used for the test. The entire assembly was heat treated for 100 hours at 1100ºC. Cross sections were prepared and studied by a Zeiss Ultra 55 FEG-SEM. Carbon concentration profiles were measured by turning the samples, collecting the chips and analyzing them in a LECO carbon analyzer.
As can be seen in figure 8, the sample of UNS S35315 increased its carbon content more than 10 times the original content whereas the alumina formers were virtually unaffected.

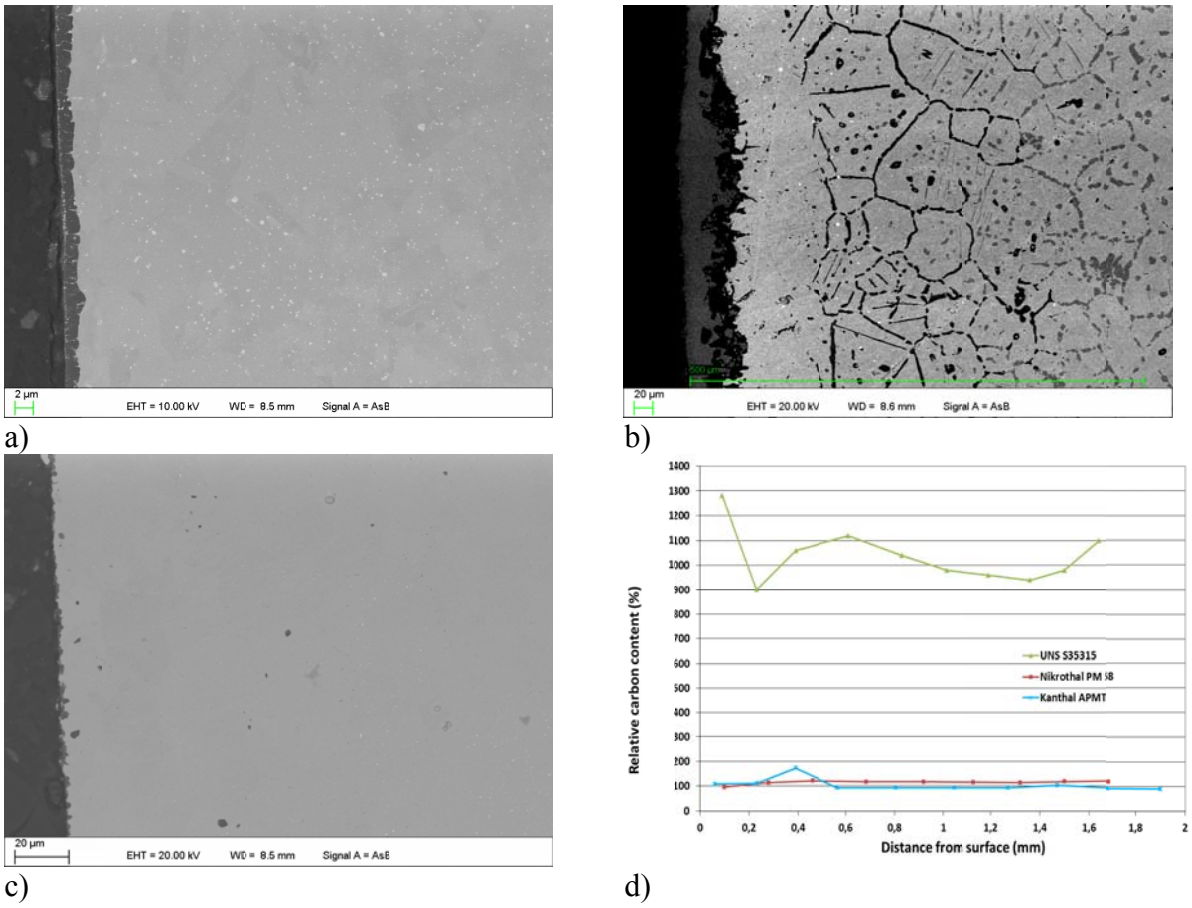

Figure 8. SEM-sections after carburizing experiments a) Nikrothal PM 58 b) UNS S35315 c) Kanthal APMT d) Concentration profile of carbon as a function of distance from the surface for samples exposed to pack carburizing for 100 hours at 1100ºC. The carbon content is given in % relative to the original carbon content.

Creep strength: A comparative test was performed to illustrate the creep strength. 4 mm wire samples made from Nikrothal PM 58, UNS N06601 and UNS N06009 were placed on a rig with a support distance of 200 mm. The entire assembly was placed in a furnace at 1200ºC. The assembly was removed from the furnace at regular intervals, cooled to room temperature and the gravitational deflection of the wire samples was measured using a fixture and micrometer. The test was performed for a total of 510 hours with measurements being performed after 0.25, 2, 4, 8, 16, 48, 180, 450 and 510 hours. The experimental setup and the

measured gravitational movement is seen from figure 9 below. The result is evident from the picture.

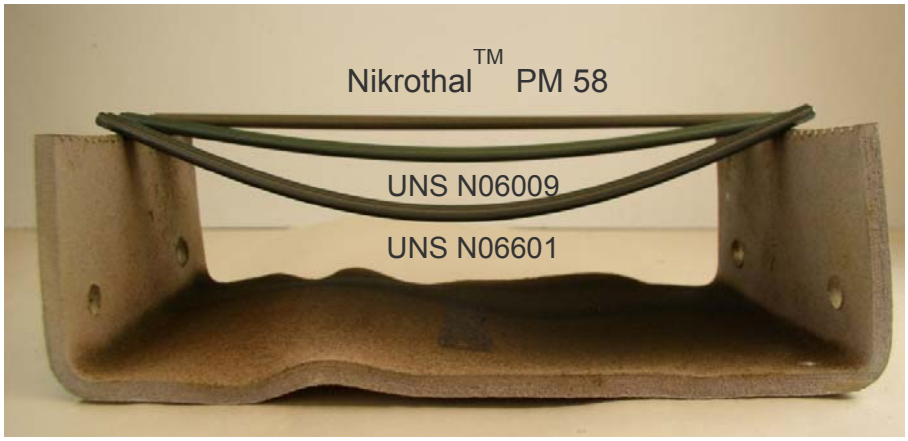

a)

b)

Figure 9. a) Experimental assembly after sag test at 1200ºC for 510 hours. b). Sample holder for creep testing after operating approximately 1200 hours at 1100ºC and 400 hours at 1200ºC. The threaded screw could still be loosened after this exposure.

Applications: Product forms currently being developed for Nikrothal PM 58 are tubes and wire but the range will expand. The alloy is mainly intended as a construction material for high temperature where high corrosion resistance and inert surfaces combined with very high creep strength is important. An example is wire mesh belts used for transport of goods through high temperature furnaces. These require a high strength to avoid deformation and fracture of the belt and novel processes require even higher processing temperature. Another example is fixtures, trays and other constructions found within heat treatment furnaces. An example of this is shown figure 9 b), a specimen holder for creep testing, entirely made from Nikrothal 58 PM.

MAXTHAL 211

MAX-phase is the commonly used name for a new class of ternary carbides or nitrides that offer properties normally found in ceramic materials. They are thermal shock resistant, damage tolerant and machinable apart from their high chemical stability. It is therefore also perhaps one of the most interesting new material groups explored in recent years. The ternary Al containing carbide Ti_2AlC is one member of a family of layered ternary carbides and nitrides with the general formula $M_{n+1}AX_n$ with n=1-3, and where M is an early transition metal, A is an A group element in the periodic table and where X is carbon or nitrogen [11, 12]. Maxthal 211 (and Maxthal 312, another Si-containing Maxthal alloy) are at present the only commercially available products based on this technology.

Physical and mechanical properties: Mechanically, Maxthal 211 is readily machinable, is a good thermal and electrical conductor, is relatively soft, thermal shock resistant, damage tolerant and has high stiffness. Grain size is about 100 μm in the commercial material. It has relatively low thermal expansion coefficient close to that of alumina, a fact that greatly helps scale adhesion as seen from the results below.

Table 4. A selection of physical properties of Maxthal 211 compared to Al_2O_3.

	Maxthal 211	**Al_2O_3**
Density [g/cm^3]	4.1	3.95
Thermal expansion coeff. CTE [×10^{-6} K^{-1}]	**8**	**7.5**
Electrical resistivity [Ω·mm^2/m], 20 °C	0.5	∞
Electrical resistivity [Ω·mm^2/m], 1500 °C	1.8	∞
Thermal conductivity [W/m·K]	40	30
Maximum use temperature [C°]	1450	<2000

Oxidation resistance: Maxthal 211 has been evaluated in terms of high temperature oxidation behaviour in various atmospheres including vacuum. All experimental work was performed on samples produced in the large scale production equipment in order to make sure that the results are valid also in real components and in real applications. A dense plate of 211 with dimensions 15×150×200 mm^3 was used to machine samples for testing of oxidation and to conduct thermal shock experiments.
Tests were performed using a Netzsch thermo gravimetric analyzer. Figure 10 a) shows the time dependence of the specific weight gain during oxidation at 1100, 1200 and 1300°C for 8 h at each temperature. The oxide growth rates were found to follow parabolic rate law (exponent n close to 2) for all temperatures tested.

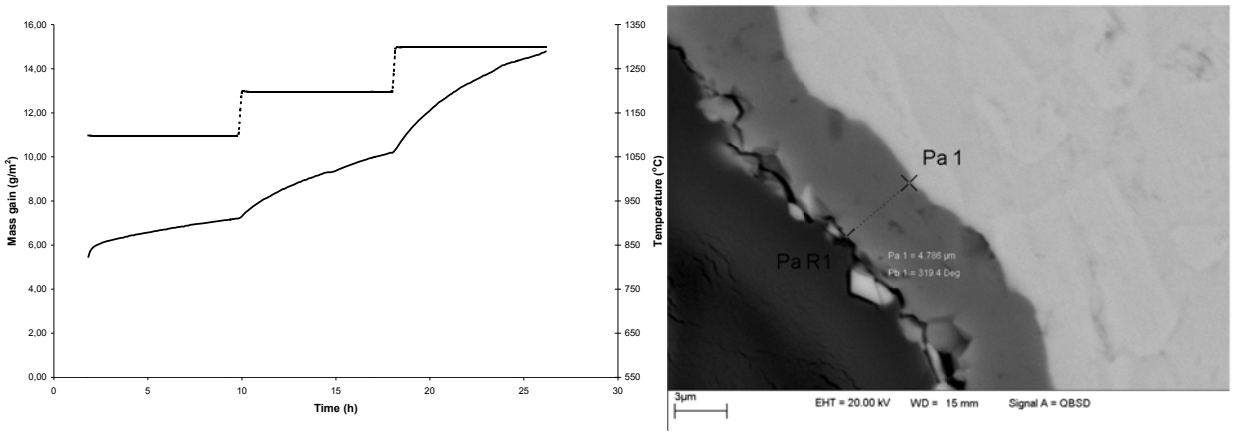

a) b)

Figure 10. a) Weight gain of Maxthal 211 at 1100, 1200 and 1300°C for 8 h at each temperature. b) SEM micrograph showing a 5 µm thick oxide after experiment. The oxide is dense and adheres to the base material.

To verify the stability of the oxide after longer time exposure, a sample was placed in an alumina tube furnace at 1200 ˚C in air for a total of 1000 hours and at 1400 °C for 500 hours showing continuous Al_2O_3 layers after completing the test. A preliminary test at 1500°C shows that this material may form protective alumina even at this high temperature.
Al_2O_3 formers typically exhibit at least some spalling of the oxide due to the thermal stresses that result from thermal expansion mismatch between the oxide and and the bulk. A sample was therefore cycled in air for 10 cycles between room temperature and 1200 °C. Each cycle consisted of heating the sample at 10°C/min to 1200 °C followed by a holding period of 4 h and a cool down at 10 °C/min to room temperature. The sample did not exhibit any weight loss at any stage which is a strong indication that the oxide layer is very adherent.
In conclusion, the material forms a stable and adherent protective alumina scale in air and also at low partial pressures of oxygen and shows a slow growing and adherent oxide growth up to

1400°C or perhaps even 1500°C in air. The kinetics of scale growth is parabolic temperature even under cyclic conditions up to these temperatures.

Applications: Maxthal 211 was tested as a resistance heating element with very good result. After about 8,000 on/off cycles from ambient temperature up to 1350 °C, the heater was still in operation. Sections of the element were investigated by SEM and confirmed that a dense 15 µm thick α-Al_2O_3 adhered to the base material.
Furnace burner nozzles working at ~1150°C in an 700°C furnace congaing air + SO_2 were tested for 8 months with very good results, as seen from figure 11 a). At Sandvik Heating Technology, single phase materials of Ti_3SiC_2 and Ti_2AlC (trade name Maxthal 211 and Maxthal 312 respectively) is manufactured in a variety of shapes and sizes using a powder metallurgy process.

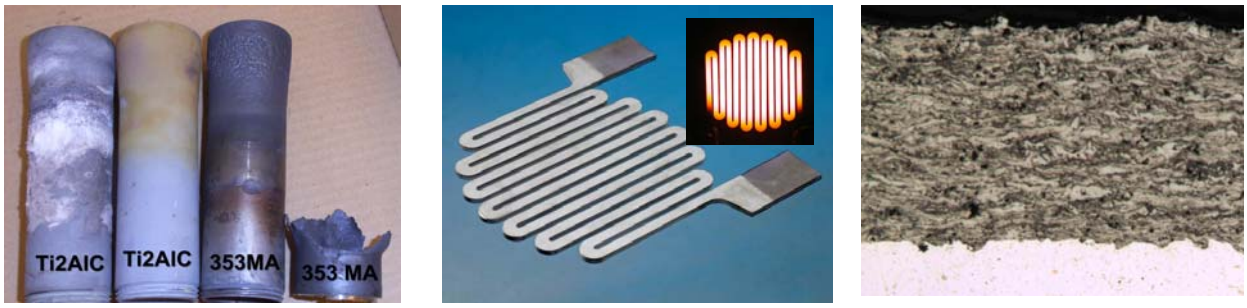

a) b) c)

Figure 11. a) Nozzles after 8 months in service.b) Flat heating element (small picture show element running at 1450°C) c) ~200 µm thick Maxthal 211 HVOF sprayed coating on a metallic substrate

CONCLUSIONS

Kanthal APMT is an advanced powder metallurgical FeCrAl alloy optimized for service as a construction material in the temperature range up to 1250°C (~2300°F). It combines excellent resistance to oxidation and hot corrosion with high creep resistance and excellent form stability.
Nikrothal PM 58 is a new powder metallurgical Ni-base alloy that in contrast to almost all other Ni-base alloys forms alumina protective oxide scales. It combines superior creep strength with high temperature corrosion and oxidation resistance. It has excellent properties for such applications like mesh belts for sintering of powder metals.
The aluminum containing MAX-phase material Maxthal 211 forms a stable, adherent and protective alumina protective scale up to >1400°C. This material shows promise for chemically inert components such as heating elements for various atmospheres as well as protective coatings and also replacing engineering high temperature ceramics when machinability and high toughness is a requirement.

REFERENCES

1. Bo Jönsson, Qin Lu, Dilip Chandrasekaran, Roger Berglund, Fernando Rave, Oxidation and Creep Limited Lifetime of Kanthal APMT®, a Dispersion Strengthened FeCrAlMo Alloy Designed for Strength and Oxidation Resistance at High Temperatures, Oxid. of Metals, 2012
2. B. Jönsson, R. Berglund et.al., High Temperature Properties of a New Powder Metallurgical FeCrAl Alloy, Materials Science Forum Vols. 461-464 (2004), pp. 455 – 462
3. S. Dryepondt, B. Pint and I. Wright, presentation at the Nov. 17 – 18, 2010, NETL ODS workshop in La Jolla, CA., http://www.netl.doe.gov/publications/proceedings/10/ods/index.html

4. H. Josefsson, F. Liu, J.-E. Svensson, M. Halvarsson and L.-G. Johansson, Oxidation of FeCrAl alloys at 500–900 °C in dry O_2, Materials and Corrosion 2005, 56, No. 11
5. J. Engkvist, S. Canovic, K. Hellström, et.al., Alumina Scale Formation on a Powder Metallurgical FeCrAl Alloy (Kanthal APMT) at 900-1100°C in Dry O_2 and in O_2 + H_2O, Oxid Met (2010) 73:233-253
6. B. Jönsson, A. Westerlund, G. Landor, Cyclic oxidation testing by resistance heating, in Cyclic Oxidation of High Temperature Materials: (EFC 27) Proceedings of an EFC Workshop, Frankfurt/Main, Edited by Schütze, M. and Quadakkers, W. J. (1999)
7. B. Jönsson and C. Svedberg, Limiting Factors for Fe-Cr-Al and NiCr in Controlled Industrial Atmospheres, Mater. Sci. Forum, 251–4 (1997) 551–8.
8. G. Grant, S. Weil, Friction Stir Welding of ODS Steels –Steps toward a Commercial Process, Workshop: Fe-Based ODS Alloys: Role and Future Applications, University of California San Diego La Jolla, CA, Nov 17^{th} –18^{th} 2010
9. H.C.M. Andersson, R. Sandström, D. Debord, Low cycle fatigue of four stainless steels in 20% CO–80% H_2, International Journal of Fatigue, Volume 29, Issue 1, January 2007, Pages 119–127
10. J. R. Davis (Ed.), Heat-Resistant Materials, ASM International, (1997) 67-85.
11. M. W. Barsoum, The $M_{N+1}AX_N$ phases: A new class of solids: Thermodynamically stable nanolaminates, Progress in Solid State Chemistry 28 (2000) 201-281.
12. M. W. Barsoum, T. El-Raghy, The MAX Phases: Unique Carbide and Nitride Materials, American Scientist 89 (2001) 334-343.
13. M. W. Barsoum, T. El-Raghy, Synthesis and Characterization of a remarkable Ceramic: Ti_3SiC_2, J. Amer. Cer. Soc. 79 (1996) 1953-1956.
14. M. W. Barsoum, T. El-Raghy, Oxidation Of Ti_3SiC_2 in Air, J. Electrochem. Soc. 144 (7) (1997) 2508-2516.
15. M. W. Barsoum, L. H. Ho-Duc, M. Radovic, and T. El-Raghy, Long Time Oxidation Study of Ti_3SiC_2, Ti_3SiC_2/SiC, and Ti_3SiC_2/TiC Composites in Air, J. Electrochem. Soc. 150 (4) (2003) B166-B175.
16. T. El-Raghy, M. Sundberg, Unpublished results.
17. M. W. Barsoum, N. Tzenov, A. Procopio, T. El-Raghy, M. Ali, Oxidation of Tin+1AlXn (n=1-3 and X=C,N) II. Experimental Results, J. Electrochem. Soc. 148 (8) (2001) C551-C562.
18. X. H. Wang and Y. C. Zhou, High-Temperature Oxidation Behavior of Ti_2AlC in Air, Oxidation of Metals, 59, 3-4, (2003), 303-320.

SERT BAKIR BERİLYUM ALAŞIMLARINA ALTERNATİF BİR CuNiSiCr-xFe ALAŞIMININ ISIL İŞLEMİ

Turhan Ürün Koçak*, Feriha Birol*

Sağlam Metal Industry and Trade Inc. Turkey
urun.kocak@saglammetal.com, feriha.birol@saglammetal.com

ÖZET

Bakır alaşımları içinde en sert ve en yüksek mukavemet değerlerine sahip olan alaşımlar bakır berilyum alaşımlarıdır. Üstün özelliklerine rağmen toksik etkileri nedeniyle çevreye, üretim ve işleme aşamalarında ise insan sağlığına tehdit oluşturan alaşımlardır. Bu nedenle sektörde berilyumlu bakır alaşımlarına alternatif malzeme arayışı önemini korumakta ve literatürde çeşitli alternatif alaşım geliştirme çalışmaları giderek artmaktadır. Yüksek nikel (% ağ.6-8) içeren ve henüz standartlara girmemiş CuNiSiCr-x tipi alaşım grubu bu alaşımlardandır. Bu çalışmada yüksek Ni (% ağ.7,2) içeren CuNiSiCr alaşımına düşük miktarlarda Fe ilavesinin alaşımın mukavemet ve elektrik iletkenliğine etkisi araştırılmıştır. Döküm numunelere dövme+çözeltiye alma işlemi uygulanmış ve en yüksek sertlik değerinin belirlenmesi için yaşlandırma çalışmaları yapılmıştır. Yaşlandırma sıcaklığı 375-600°C aralığında 25°C'lik değiştirilmiştir. Yaşlandırma sıcaklığına bağlı olarak iletkenlik ölçümleri yapılmış numunelerin mikroyapılarında değişimler incelenmiştir.

HEAT TREATMENT OF A CuNiSiCr-Fe ALLOY AS AN ALTERNATIVE OF HARD BERYLLIUM ALLOYS

ABSTRACT

Among copper alloys, copper beryllium alloys have the highest hardness and strength values. In spite of their superior properties, these alloys are hazardous for environment and worker health due do toxic effect of beryllium fumes. Recently EU directives forces to restrict usage of Be as an alloying element in copper alloys. Therefore, searching for alternative copper alloys to beryllium copper alloys have become important and studies on alternative alloy development has been increasing in the literature. The most favorite group of alternative alloys are of CuNiSiCr-x type alloys with high Ni content. In this study, the effect of low level of Fe addition on the strength and electrical conductivity of CuNiSiCr alloy with high Ni (6-8%w) was investigated. The cast samples were hot forged and solutionized. Aging temperature was scanned from 375^{o}C to 600^{o}C by using 25°C intervals to determine critical aging temperature for the peak hardness. Conductivity measurements were performed for all samples and microstructure studies as well.

Keywords: copper beryllium alloys, copper nickel alloys, high strength copper alloys

1. GİRİŞ:

Bakır berilyum alaşımları bakır alaşımları içerisinde en yüksek sertlik değerine sahip olan alaşımlardır. Berilyum içeriği arttıkça sertlik değerlerinde artış görülürken, iletkenlik değerlerinde düşüşler olur [1]. Üstün mekanik özelliklerine rağmen berilyum elementinin çevre ve işçi sağlığı açısından zehirli etkisi nedeniyle alternatif bir alaşım/alaşımlar arayışı önem taşımaktadır [2]. CuNiSi-x tipi alaşımlar daha yüksek iletkenlikleri ve nispeten yüksek mukavemet özellikleri nedeniyle CuBe alaşımlarına alternatif olarak en yaygın olarak kullanılan alaşım grubudur. Birçok uygulama için CuNiSi-x tipi alaşımlar CuBe alaşımlarına seçenek olmasına rağmen sertlik açısından CuBe alaşımlarının gerisinde kalmaktadır [4-5]. Bu nedenle, bu alaşım sisteminde iletkenlik düşürmeden mukavemet artışı sağlamak amacıyla çeşitli alaşım elementlerinin ilavesi ve ısıl işlem uygulamaları ile alaşım geliştirme çalışmaları önemini korumaktadır. Bu alaşım sisteminde belli Ni/Si oranları için Ni miktarı arttırılmasının [6], alaşıma çeşitli oranlarda Mg[7], Sn[8], Cr[9], P[9], Zn[10] ve Al[11] ilavelerinin etkileri literatürde incelenmiştir. Düşük nikel içerikli alaşımlara Fe ilavesinin etkisi de çalışılmış, sertlik ve iletkenliği arttırıcı yönde etki yaptığı görülmüştür [12].

CuNiSi sisteminde Ni içeriğinin %7-8 değerlerine çıkartılmasıyla alaşımın mukavemet özelliklerinde ciddi artışlar kaydedilmiştir [13]. Bu alaşımların hazırlanması sırasında zaman zaman prosesten gelen düşük miktarlarda Fe saptanmıştır. Ancak yüksek Ni içeren CuNiSiCr alaşımlarında düşük miktarlarda Fe ilavesinin etkisi ile ilgili bir çalışmaya rastlanmamıştır. Bu çalışmada, yüksek (% 7,2) CuNiSiCr tipi alaşımlara düşük oranlarda Fe ilavesinin mukavemet ve iletkenlik değerlerine etkisinin incelenmesi amaçlanmıştır. Bu amaçla iki farklı oranda Fe ilavesi yapılmış, dövme ve çözeltiye alma şartları ve yaşlandırma süresi sabit tutularak 375-600^{o}C sıcaklık aralığında yaşlandırma uygulanarak sertlik ve elektrik iletkenlik değerlerinin değişimi çalışılmıştır.

2. DENEYSEL:

Alaşım hazırlama 10 kg lab. ölçekli 5M marka orta frekans indüksiyon ergitme ocağında yapılmıştır. Demir içermeyen ve iki farklı oranda demir içeren , bileşimleri Tablo 1'de verilen 3 alaşım hazırlanmıştır. Alaşımın hazırlanmasında, yüksek saflıkta metalik Cu, Ni, Si ve Fe ile %10'luk Cu-Cr ön alaşımı kullanılmıştır. Hazırlanan alaşımların kimyasal bileşimleri optik emisyon spektrometresi (Spektrolab marka) kullanılarak belirlenmiştir. Çelik kokil kalıba dökülen alaşımlar oda sıcaklığında soğutulmuştur. Daha sonra ingottan kesilen dilimler 900°C'de dövme işlemine tabi tutularak çubuk şeklinde numuneler elde edilmiştir. Dövme işlemi sonrasında numunelere literatürde [3,10,11] belirlenen sıcaklık ve sürelerle çözeltiye alma işlemi uygulanmış, mikroyapı değerlendirmesi ile en iyi sonucun 970°C'de 4 saat şartlarında alındığı belirlenmiştir. Yaşlandırma çalışmalarında kullanılan tüm numunelere bu şartlar uygulanmıştır.

Tablo 1: Çalışmada kullanılan alaşımların kimyasal bileşimleri.

Alaşım	Ni	Si	Cr	Fe	Kalan Cu
1	7,12	1,88	0,92	-	90,08
2	7,25	2,16	1,05	0,1	89,44
3	7,28	2,25	1,05	0,28	89,14

Yaşlandırma işlemi için sabit süre (1 saat) ile 375°C-600°C aralığında 25°C'lik artışla sıcaklık taraması yapılmış, sertlik ölçümleri ile en yüksek sertliğin elde edildiği yaşlandırma sıcaklığı belirlenmiştir. Isıl işlemler Protherm marka PLF 120/12 model kutu fırın kullanılarak yapılmıştır. Sertlik ölçümleri BMS 200 – RB model sertlik cihazı ile, iletkenlik ölçümleri GE Inspection Tech marka, Autosigma 3000 model iletkenlik cihazı ile yapılmıştır. Elde edilen sonuçlar grafik haline getirilerek alaşımların yaşlandırma karakteristikleri çıkartılmıştır. Üretilen alaşımların farklı koşullarda mikroyapı karakterizasyonları Nikon Eplicase MA100 model ters metal mikroskobu ile çalışılmış, bazı örneklerde SEM çalışması gerçekleştirilmiştir.

3. DENEYSEL SONUÇLAR VE İRDELEME

3.1. Alaşımların Mikroyapısal Karakterizasyonu

Yüksek Ni (%7,2) içeren CuNiSiCr-xFe alaşımlarının mikroyapıları optik mikroskop ve SEM ile incelenmiştir. Döküm sonrasında oda sıcaklığında kendi haline soğumaya bırakılan ingotlarda dendiritik döküm yapısı elde edilmiştir. Döküm sonrası dendiritik yapı (dendirit boyutları ve dendiritlerarası mesafe açısından) Fe içeriğine göre dikkati çekecek bir değişiklik göstermemiştir (Şekil 1).

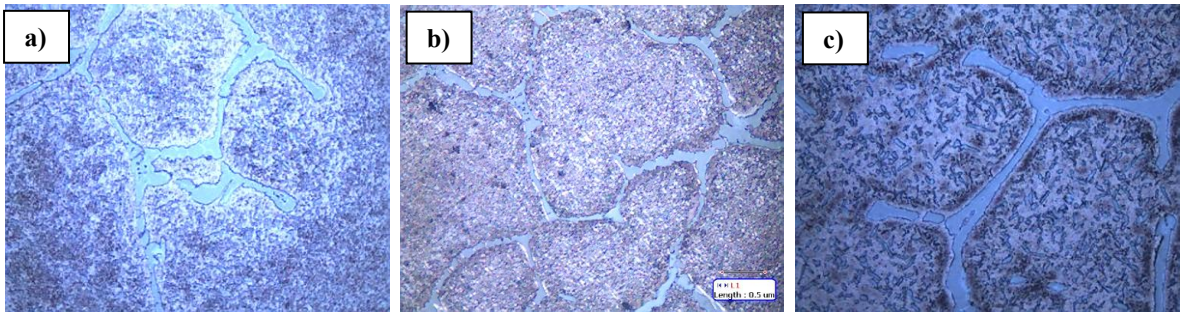

Şekil 1. %ağ. 7.2 Ni içeren CuNiSiCr-xFe ingotların kenarlarından alınan numunelerde dendiritik döküm yapısı a) 0 Fe; b) % 0,1 Fe; c) % 0.3 Fe.

SEM-EDS incelemesi dendiritlerarası oluşan fazın yüksek oranlarda Ni,Si ve Cr içerdiğini göstermiştir (Şekil 2). Dendiritlerarası yapıda 1-2 mikron boyutlarında çok sayıda partikül oluşumu gözlenmiştir (Şekil 2). Değişen Ni içerikli CuNiSi alaşımlarında döküm faz yapılarının incelendiği çalışmada [7], % 8,6 Ni ve % 1,38 Si içeren alaşımda dendiritik fazları XRD ve DTA ile β_1-Ni_3Si+αCu(Ni,Si) olarak tanımlanmıştır. Xiea ve arkadaşları dendiritlerarasında çökelen fazın alaşımın sertleşme kapasitesini oluşturan δ-Ni_2Si fazı olduğunu belirlemişlerdir. Ni ve Si yanında Cr da içeren bu çalışmadaki alaşımların SEM çalışmasında dendiritlerden alınan SEM-EDS analizlerinde Cr elementi de saptanmıştır. Cr da Ni gibi Si ile silisid yapıcı bir elementtir [13]. Bu alaşımlarda β_1-$(Ni,Cr)_3Si$+αCu(Ni,Si,Cr) ve δ-$(Ni,Cr)_2Si$ olarak yapıda yer aldığı tahmin edilmektedir. Daha ayrıntılı bir çalışma için alaşımların XRD çalışmaları gelecek çalışma olarak planlanmaktadır.

Döküm numuneleri 900°C'de dövme uygulanarak çubuk haline getirilmiş ve 970°C'de çözeltiye alınmıştır. % 0.1 Fe içeren alaşım için tipik döküm, dövme, çözeltiye alma ve pik sertlik yaşlandırma sıcaklığında oluşan mikroyapılar Şekil 4'de yer almaktadır.

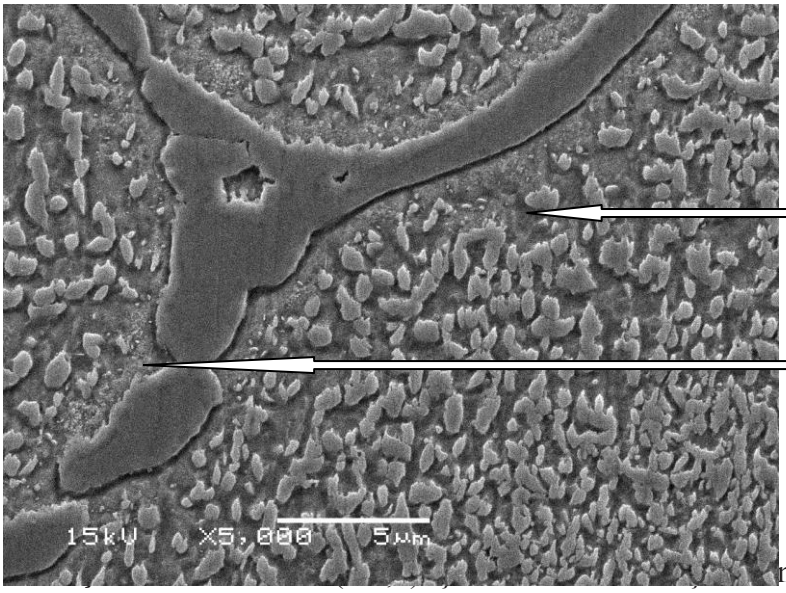

Element	Bileşim (% ağ.)
Si	**2,934**
Cr	**0,482**
Ni	**8,576**
Cu	**82,964**
Toplam	**94,956**

Element	Bileşim (% ağ.)
Si	**10,327**
Cr	**5,414**
Ni	**21,797**
Cu	**62.461**
Toplam	**100,000**

nın tipik döküm yapısı.

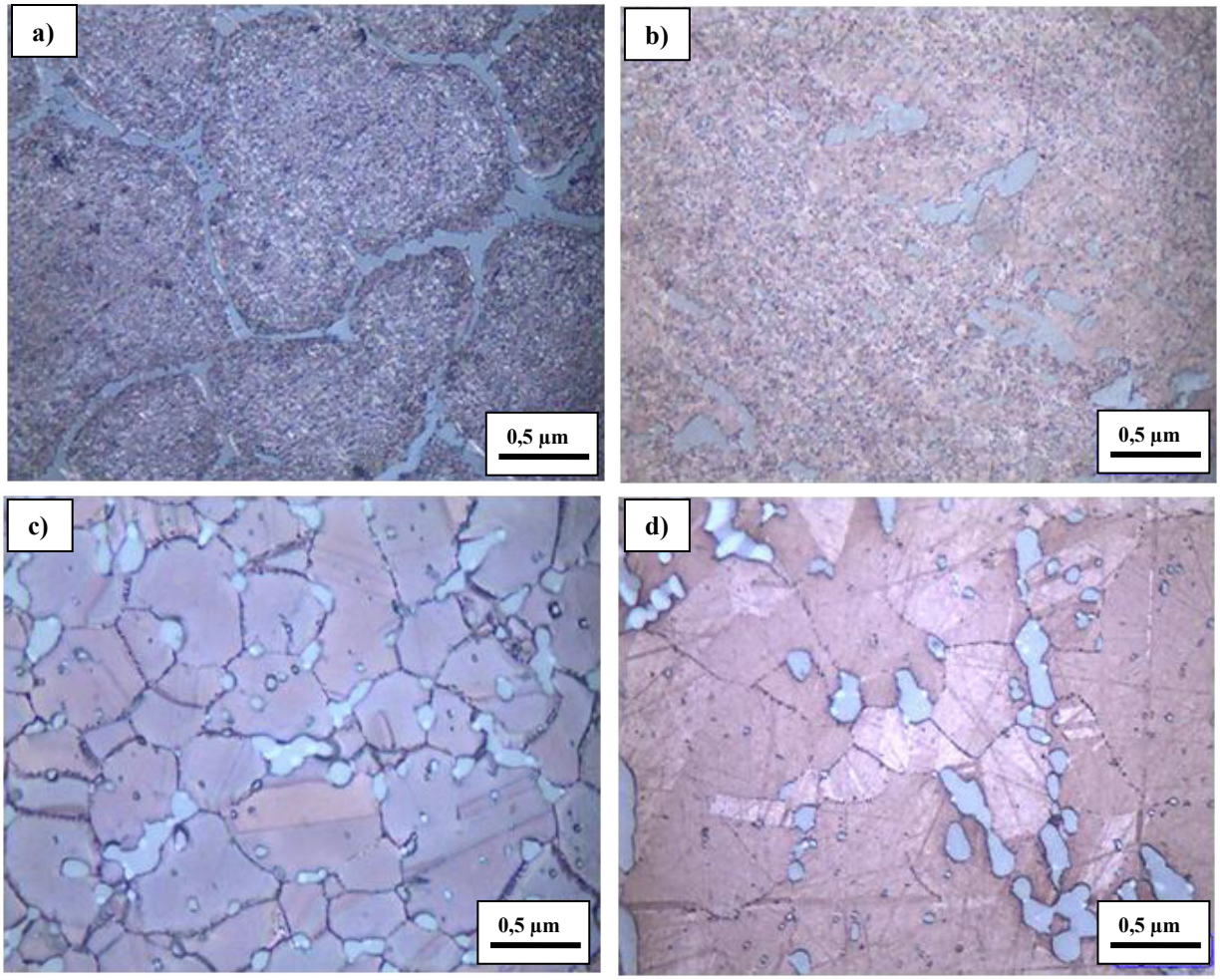

Şekil 4. %0,1 Fe içeren CuNiSiCr alaşımının a) Döküm, b) Dövme, c) Çözeltiye alma, d) 525C'de 1 saat yaşlandırma ile elde edilen tipik mikroyapıları (optik mikroskop)

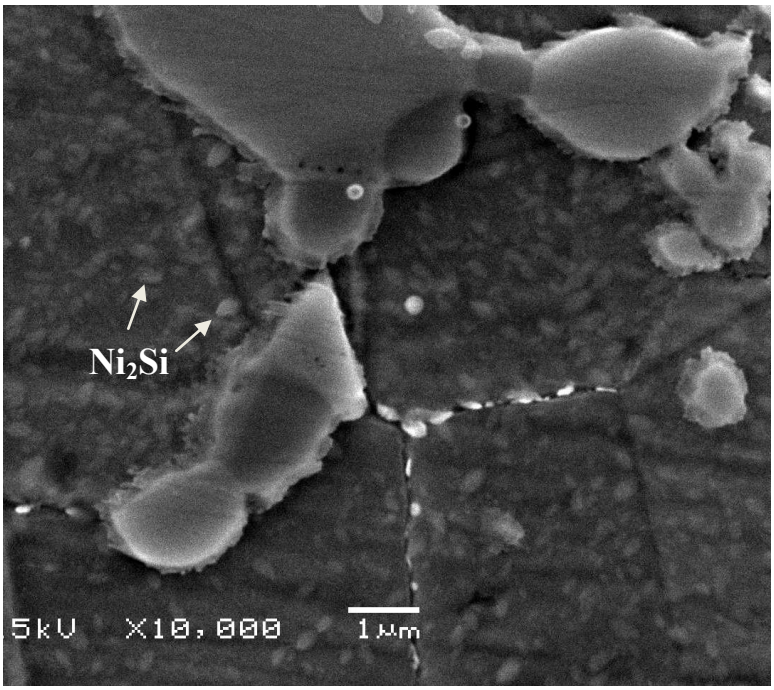

Şekil 5. %ağ. 7.2 Ni içeren CuNiSiCr-0.1Fe içeren alaşımda 525C'de 1 saat yaşlandırma sonrasında tane içlerinde çökelen disk şeklindeki partiküllerin SEM görüntüsü.

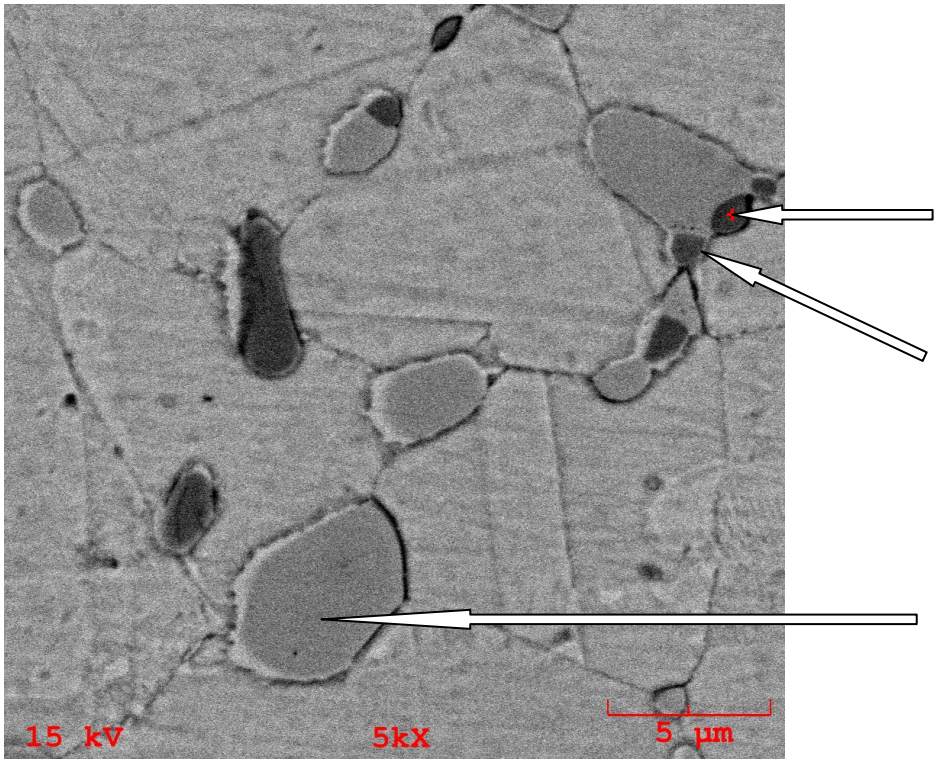

Element	Bileşim (%ağ)
O	**8,883**
Si	**17,566**
Cr	**56,769**
Ni	**3,200**
Cu	**13,582**
	100,000

Element	**B**ileşim (% ağ)
O	**5,195**
Si	**22,446**
Cr	**25,380**
Ni	**34,439**
Cu	**12,540**
	100,000

Element	Bileşim (%ağ)
Si	**23,872**
Cr	**3,789**
Ni	**72,339**
	100,000

Şekil 6. %ağ. 7.2 Ni içeren CuNiSiCr-0.1Fe içeren alaşımda 525C'de 1 saat yaşlandırma sonrasında mikroyapının BSE görüntüsü ve yapıdaki fazlar.

Dökümde oluşan dendiritik yapının dövme işlemi ile kırıldığı gözlenmiştir (Şekil 4b). Çözeltiye alma işlemi ile matrisde çökelmiş olan fazların önemli ölçüde çözündüğü ve tane içlerinde bir çökelti olmadığı dikkati çekmektedir (Şekil 4c). Bu da çözeltiye alma şartlarının başarıyla sağlandığını işaret etmektedir. Tepe noktası sertliğinin elde edildiği numunenin optik mikroskop görüntülerinde tane içlerinde bulutumsu bir yapı gözlenmiş (Şekil 4d), SEM çalışması ile bulutumsu yapıda çökelmiş partiküller ayırt edilmiştir (Şekil 5). Partiküllerin 0,1-0,2 boyutlarında disk şeklinde olduğu gözlenmiştir. Bu partiküllerin, bu alaşımların sertleşmesini sağlayan δ-$(Ni)_2Si$ partikülleri olduğu düşünülmektedir.

Yaşlandırılmış yapıların SEM-BSE görüntülerinde Ni'ce zengin (açık renk), Cr'ca zengin (açık griI, O içeren Ni ve Cr miktarı birbirine yakın (koyu gri) Si içeren fazlar saptanmıştır. Partikül boyut ve sayılarının alaşımın Fe içeriğine göre değişiminin belirlenmesi ve yapıdaki fazların tanımlanması için sistematik bir SEM ve XRD çalışmasına ihtiyaç vardır. Gelecek çalışmalar olarak planlamıştır.

3.2. Mekanik Özellikler ve Elektrik İletkenliği:

Çözeltiye alma işleminden sonra bu alaşımlarda 450-575°C aralığında 25°C'lik artışla yapılan 1'er saatlik yaşlandırma işlemi sonrasında sertlik değerlerinin ölçülmesi ile elde edilen Sıcaklık-Sertlik grafiği Şekil 7'de verilmiştir. Buna göre, Fe içermeyen CuNiSiCr alaşımı için en yüksek sertlik değeri 525°C'de yaşlandırma sonucunda 303 HV olarak elde edilmiştir. Bu alaşıma % 0,1 Fe ilavesi, en yüksek sertlik elde edilen sıcaklık değerini etkilemezken, ortalama sertlik değeri 5 HV artmış 307 HV olarak ölçülmüştür. Alaşımdaki Fe miktarı % 0,28'e arttırıldığında en yüksek sertlik elde edilen sıcaklık 500°C'ye kaymış, ortalama sertlikte hafif bir yükselme (310 HV) kaydedilmiştir (Şekil 7). Bu da alaşımda Fe miktarının % 0,28'e çıkartılmasıyla çökelme kinetiğinin değiştiği ve hızlandığı izlenimini vermiştir. Bu amaçla daha yüksek Fe oranları da çalışılacaktır.

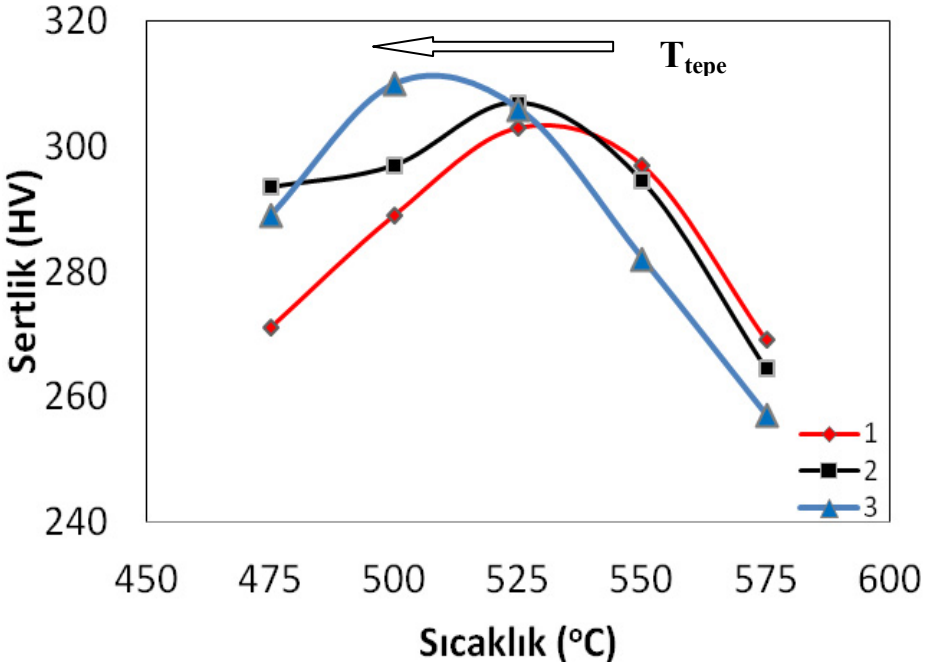

Şekil 7. 1 saat süre ile farklı sıcaklıklarda yaşlandırılan % ağ. 7.2 Ni içeren CuNiSiCr-xFe alaşımlarının sıcaklığa bağlı olarak sertlik grafiği 1: x=0; 2.x=0,1 ; x=0,28.

Fe içermeyen ve Fe içeren % 7,2 Ni içeren CunNiSiCr alaşımların 1 saat süreyle artan sıcaklıklarda yaşlandırılması sonrasında ölçülen elektrik iletkenliği değerlerinin sıcaklığa bağlı grafiği Şekil 8'de ve tepe nokta iletkenlik ve sertlik değerlerinin Fe içeriğine göre değerleri Tablo 2'de verilmiştir. Tüm alaşımların elektrik iletkenliği yaşlandırma sıcaklığı arttıkça artmıştır. Bu alaşımların yaşlandırma tepe sertlik sıcaklığındaki iletkenlik değerleri 1,2 ve 3 nolu alaşımlar için sırasıyla %26,72; %26,96 ve %27,58 IACS olarak ölçülmüştür. Fe içeriğinin artması ile elektrik iletkenliğinin az da olsa artması büyük bir olasılıkla çökelen partiküllerin matristeki çözünen element mikarını azaltması sonucunda matris safiyetinin artması sonucu olduğu düşünülmektedir.

Tablo 2 ve Şekil 8'de % 7.2 Ni içeren CuNiSiCr-xFe alaşımında değişen demir oranları ile yaşlandırma tepe noktalarında elde edilen sertlik ve iletkenlik değerlerinin değişimleri verilmiştir. Artan demir miktarına bağlı olarak tepe noktalarda elde edilen sertlik ve elektrik iletkenlik değerlerinde küçük artışlar gözlenmiştir.

Tablo 2: Alaşımların yaşlandırma sonrası tepe noktada, sertlik ve iletkenlik değerleri.

Alaşım	Fe	Cu	Sertlik (HV)	İletkenlik (%IACS)
1	0	90,08	303	26,72
2	0,1	89,44	307	26,96
3	0,28	89,14	310	27,58

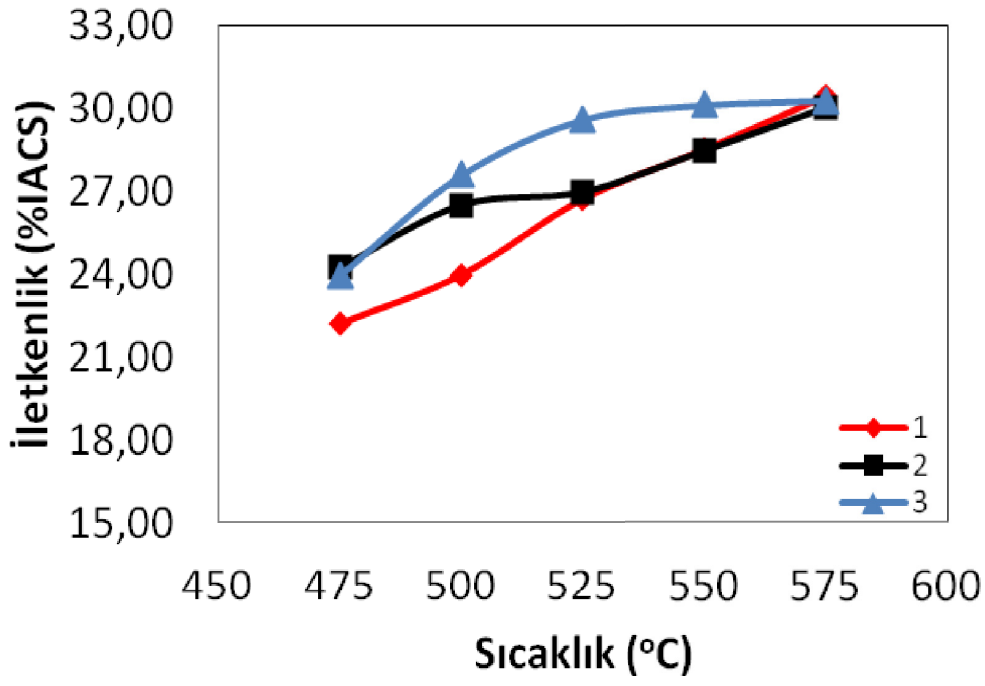

Şekil 8. Farklı sıcaklıklarda 1 saat yaşlandırılan % ağ. 7.2 Ni içeren CuNiSiCr-xFe alaşımının sıcaklığa bağlı olarak elektrik iletkenliği grafiği. 1: x=0; 2.x=0,1 ; x=0,28.

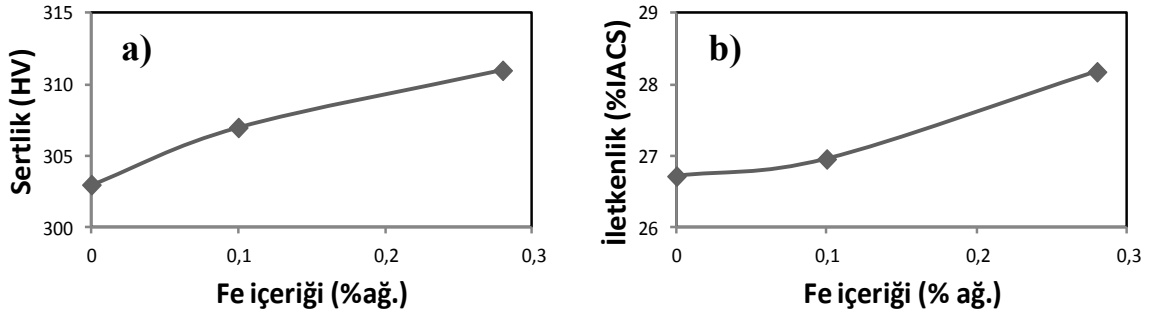

Şekil 9. Sabit 1 saat süre ile yaşlandırılan numunelerin demir içeriğine bağlı olarak (a) pik nokta sertlik değerleri grafiği ve (b) pik nokta iletkenlik grafiği.

Yüksek Ni içeren (% 7,2) CuNiSiCr alaşımına düşük seviyelerde Fe ilavesi alaşımın sertlik ve iletkenlik değerlerini olumsuz etkilememiş tam tersine az da olsa iyileşme yönünde katkıda bulunmuştur. Buna göre alaşım hazırlama ve döküm sırasında yapıya çeşitli kaynaklardan düşük miktarlarda Fe karışması halinde alaşımın sertlik ve iletkenlik değerlerinde kayıplar olmayacaktır.

4. SONUÇLAR

Yüksek Ni(%7,2) içeren CuNiSiCr alaşımına düşük miktarlarda Fe ilavesinin yaşlandırma, sertlik ve elektrik iletkenliğine etkisi çalışılmıştır.

Düşük miktarlarda (0,1 ve 0,28) Fe ilavesinin alaşımın döküm yapısını önemli ölçüde etkilemediği görülmüştür.

Artan Fe miktarı ile alaşımın sertlik ve iletkenlik değerleri az da olsa iyileşmiştir.

Bu çalışma ile % 7.2 Ni içeren CuNiSiCr alaşımına prosesten düşük miktarlarda Fe karışmasının alaşımın kritik özellikleri olan sertlik ve ieltekenlik değerini olumsuz yönde etkilemeyeceği, tam tersine olumlu bir katkısı olabileceği görülmüştür.

Daha yüksek Fe içerikleri ile çalışmanın % 7.2 Ni içeren CuNiSiCr alaşımlarına Fe'in etkisinin belirlenmesi açısından faydalı olacağı düşünülmektedir.

TEŞEKKÜR
SEM çalışmalarında desteği için Kocaeli Üniversitesi Metalurji Mühendisliği öğretim üyelerinden Sn. Yrd. Doç. Dr. Hakan Atapek'e teşekkür ederiz.

KAYNAKLAR

1. A. Woodcraft, R.V. Sudiwala, R.S Bhatia, ''The thermal conductivity of C17510 beryllium–copper alloy below 1 K'' Cryogenics 41 (2001) 603-606
2. A. Güven, O. Kahvecioglu, G. Kartal, S. Timur, ''Metallerin çevresel etkileri – III'' Metalurji Dergisi 138
3. L. Zhou, P. Z. Yong, Z. Yu-yuan, X. Zhu, W. Ming-pu,''Microstructure and properties of high conductivity, super high strength Cu-8.0Ni-1.8Si-0.6Sn-0.15Mg alloy'' Journal of Material Research, 2009, 24: 2123−2128.
4. L.Yong-qiang, L. Ping, L. Yong, Z. Wei-min, P. Jian-sheng, ''Simulation of recrystallization grain growth during re-aging process in the Cu-Ni-Si alloy based on phase field model'' Materials Letters, 2008, 62: 3039−3042.
5. L. Qian, L. Zhou, P. Zhi-yong, W. Ming-pu, X. Zhu, C. Chang, ''Dynamics of phase transformation of Cu-Ni-Si alloy with super-high strength and high conductivity during aging'' Trans. Nonferrous Met. Soc. Shina 20(2010) 1006-1011.
6. R. Monzen, C. Watanabe, ''Microstructure and mechanical properties of Cu–Ni–Si alloys''Materials Science and Engineering A 483-484 (2008) 117-119.
7. H. Xiea, L. Jiaa, Z. Lua, ''Microstructure and solidification behavior of Cu–Ni–Si alloys'' Materials Characterization 60 (2009) 114-118
8. S.S. Kim, J.C. Rhu, Y.C. Jung, S.Z. Han, C.J. Kim, ''Agıng characterıstıcs of thermomechanıcally processed Cu-9Ni-6Sn alloy'' Scripta Materialia 40 (1999) 1-6
9. C.Watanable, F.Nishijima, R.Monzen, ''Mechanical Properties of Cu-4.0wt%Ni-0.95wt%Si Alloys with and without P and Cr Addition''Materials Science Forum 561-565 (2007) 2321-2324
10. F. Huang, J.Ma, H.Ning, Y. Cao, Z. Geng, ''Precipitation in Cu–Ni–Si–Zn alloy for lead frame'' Materials Letters 57 (2003) 2135 - 2139
11. Q. Lei, Z.Li, C.Dai, J.Wang, X. Chen, J.M. Xie, W.W. Yang, D.L. Chen, ''Effect of aluminum on microstructure and property of Cu-Ni-Si alloys'' Materials Science & Engineering A 572 (2013) 65 - 74
12. S.Suzuki, Improvement in strength and electrical conductivity of Cu–Ni–Si alloys by aging and cold Rolling
13. Robert E. Kusner, John C. Kuli Jr. and Douglas B. Veitch, "A Copper-Nickel-Silicon-Chromium Alloy for Mold Tooling" Moldmaking Technology Magazine, www.materion..com 2008.

Cu, Cu-Mg ve Cu-Ag ALAŞIMLARININ HAVAİ HAT KATENER İLETKENİ OLARAK KULLANIMI VE KARAKTERİSTİK ÖZELLİKLERİ

A.Gamze ONUK, MSc.
Sarkuysan Elektrolitik Bakır Sanayi ve Ticaret A.Ş.

Özet

Son 20-30 yıldan bu yana gerek yurt içinde gerekse yurt dışında raylı sistemlerde elektrikli hareket gücü kullanımı yaygın hale gelmekte ve bu alandaki teknolojik gelişmeler her geçen gün artmaktadır. Gelişmelere paralel olarak, başta havai hat taşıma sistemleri olmak üzere toplu taşıma ve yüksek hız sistemleri, AC ve DC tipi uygulamalar, hafif raylı, tramvay ve hızlı tren sistemlerinde de gelişmeler sağlanmıştır. Bu sistemlerde hareket gücü sağlayan elektriğin üretim noktasından, besleme ve bileşen noktalarına kadar birçok iletken malzeme elektriğin dağıtımında önemlidir. Bu nedenle havai hat katener iletkenleri demiryolları projelerinin vazgeçilmez kilit parçalarından olmaktadır. Tüm hat boyunca sistem elektrifikasyonunda ise malzemelerin mekanik ve elektriksel karakteristikleri büyük önem taşır. Bu bağlamda başta bakır (Cu) olmak üzere bakır-gümüş (Cu-Ag), bakır-magnezyum (Cu-Mg), bakır-kadmiyum (Cu-Cd) ve bakır-kalay (Cu-Sn) alaşımları ise bugün bilinen en yaygın alaşım gruplarını oluşturmaktadır. Bu alaşım grupları başta seyir teli olmak üzere portör teli, pandül teli ve Y halatı gibi uygulamalarda gerek duyulan mekanik, fiziksel ve elektriksel özellikleri karşılayacak şekilde tercih edilmektedir.

Bu çalışmada demiryolu raylı sistemlerinin elektrifikasyonlarında kullanılan havai hat katener iletkenlerinden bakır ve bakır esaslı alaşımlar ele alınarak, günümüzde yaygın olarak kullanılan bakır, bakır-gümüş ve bakır-magnezyum alaşımları karakteristik davranışları ile detaylandırılmaktadır.

Anahtar kelimeler: Bakır, Bakır-Gümüş, Bakır-Kadmiyum, Bakır-Kalay, Bakır-Magnezyum, Havai Hat Katener Telleri, Raylı Sistem Elektrifikasyonu.

THE USE OF Cu, Cu-Mg AND Cu-Ag ALLOYS IN OVERHEAD CATENARY SYSTEMS AND INSPECTION OF CHARACTERISTIC PROPERTIES

Abstract

Nowadays, requirements of rail system technology are increasing day by day with human life quality. Since the last 20-30 years, using electricity power in rail systems has been widespread both in Turkey and other countries. Parallel to this situation, there are similar developments in overhead railway systems, both AC and DC applications, light rail, tram and trolley bus systems and overhead travelling cranes. In these systems, production of electricity, feeding and connection parts are important components for distribution of electric, so overhead catenary wires are a key product in electrification of overhead catenary systems. Copper (Cu), copper-silver (Cu-Ag), copper-magnesium (Cu-Mg), copper-cadmium (Cu-Cd) and copper-tin (Cu-Sn) alloys are commonly known material groups of this area. These specific materials are widely used and can meet good mechanical, physical and electrical properties for dropper, Y dropper, messenger wire and feeding cable.

Keywords: Copper, Copper-Cadmium, Copper-Magnesium, Copper-Silver, Copper-Tin, Electrification of Railway System, Overhead Catenary Wires.

1. GİRİŞ

Günümüzde raylı sistem teknolojisi ulaşım alanında bilinen en eski teknoloji olarak karşımıza çıkmaktadır. Dünyada raylı sistem ile ulaşım başta Rusya olmak üzere Almanya, Fransa, Polonya, İtalya ve İspanya'da yaygın olarak kullanılmaktadır. Ülkemizde ise 1923 yılı öncesinde 4.600 km ve 1923-2003 yılları arasında ise 6.400 km raylı hat yapılmıştır. Dünya geneli ile karşılaştırdığımızda Türkiye raylı sistem kullanımında 11.000 km raylı sistem hattı ile sekizinci sırada yer almaktadır. Mevcut hatlar her geçen gün artan teknolojik gelişmeler ile birlikte artış göstermekte, 2035 yılına kadar ise mevcut raylı sistem hatlarının yaklaşık 18.000 km ile %62 oranında artış göstereceği hedeflenmektedir. Şekil 1' de Türkiye'de raylı sistem kullanımının başlangıcındaki hat oranları ile 2035 yılına kadar hedeflenen hat oranları verilmiştir [1].

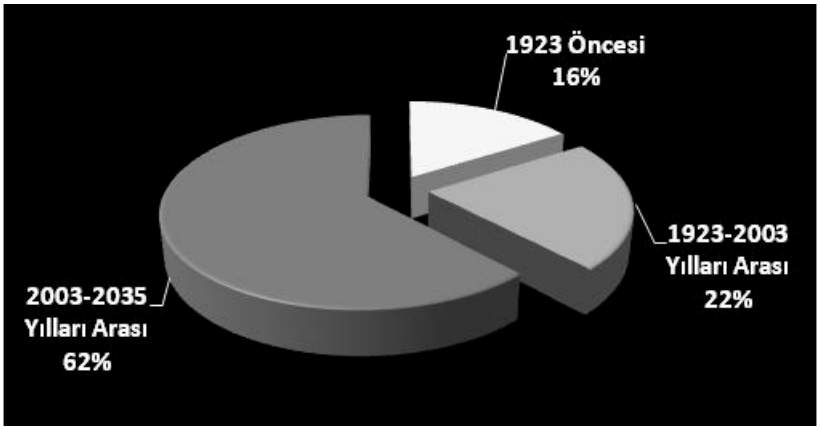

Şekil 1. 1923 öncesinden 2035 yılına kadar hedeflenen raylı sistem hat oranlarının yüzde dağılımı [1]

Türkiye ve dünyadaki bu gelişmeler göz önüne alındığında raylı sistem kullanımının artışı gerek sistem gereksinimlerinin gerekse bu alandaki teknolojilerin artışını beraberinde getirmektedir. Özellikle artan hız ve tasarım gereklilikleri sistem elektrifikasyonlarında mevcut malzemelerin iyileştirilmesine ve geliştirilmesine ayrıca yeni malzemelerin de keşfini hedeflemektedir. Bu bağlamda 1996 yılı verilerine göre yüksek hız trenlerindeki hızların 123 km/saat ile 300 km/saat arasında değişim gösterdiği, günümüzde bu değerler için maksimum hız 574 km/saat' e kadar ulaştığı bilinmektedir. Bu veriler ışığında özellikle havai hat katener sistemlerinde kullanılan bakır, bakır-magnezyum ve bakır-gümüş alaşımları da önemli rol oynamaktadır [2].

2. RAYLI SİSTEM ELEKTRİFİKASYONU

Raylı sistem projelendirmelerinde havai hat güç iletkenleri önemli yer almaktadır. Elektrik iletkenliğinin yanı sıra bu iletkenlerin yüzde uzama, çekme dayanımı ve kopma mukavemeti gibi mekanik karakteristikleri de kullanım etkinliğini belirlemektedir. Bu nedenle, havai hat güç iletkenlerinin dizaynlarında dizayn faktörü olarak malzeme karakteristiği olan birçok belirleyici faktör bulunmaktadır. Hat dizaynlarında kullanılmakta olan elektrik iletkenleri arasında çoğunlukla bakır ağırlıklı malzemeler olmakla birlikte çelik, çelik özlü alüminyum, bakır, bakır-magnezyum, bakır-gümüş, bakır-kalay, bakır-kadmiyum kullanılan temel metalik malzeme grupları da bulunmaktadır. Geniş bir ürün grubu oluşturan bu iletkenler arasında bakır ve bakır alaşımları yaygın olarak seyir teli, pandül teli, Y halatı ve portör teli gibi katener sistemi iletkenleri olarak tercih edilmektedir [3].

Özellikle yüksek hızlı tren hatlarının havai hat katener sistemleri için kontak teli anahtar bir üründür. Yüksek hızın beraberinde getirdiği titreşim ve yüksek genliğin önlenmesi için kontak teli spesifik yüksek gerilim altına konur. Bu nedenle yüksek mukavemet, yüksek termal kararlılık ve iyi elektrik iletkenliğine sahip özel bakır alaşımları geliştirilmiştir. Ek olarak, yüksek hız sistemlerindeki kontak tellerinin kink (kırılma) olmadan doğrusal bir yapıda olması ve bu doğrusallığının sabit bir yükseklikte fazla sapmalar olmadan sağlanması şarttır. Bu şekildeki yüksek kalite düzeyindeki sistemlerde kıvılcım atlamasından kaçınmak gereklidir. Çünkü pantograf kontak telinin atlama olmadan takip etmesini sağlar. Yüksek mukavemetli kontak telinin sabit yükseklikte mikro boyutta dalgalar olmaksızın yerleşimi saf bakıra göre daha karmaşıktır [4].

3. RAYLI SİSTEM ELEKTRİFİKASYONUNDA KULLANILAN ALAŞIM GRUPLARI

Raylı sistem bakır iletkenlerinde kullanılan temel alaşım elementleri arasında gümüş, magnezyum, kalay ve kadmiyum yer alır. Özellikle mukavemet arttırma, korozyon ve aşınma dayanımını geliştirme amaçlı kullanılan alaşım elementleri ile de bakırın mekanik ve fiziksel özellikleri geliştirilebilmektedir. Örneğin mukavemet arttırma amaçlı temel alaşım elementleri krom, alüminyum, fosfor, demir, silisyum, mangan, çinko, zirkonyum, kalay, nikel, berilyum, kobalttır. Korozyon dayanımı arttırıcı elementler ise nikel, alüminyum, kalay, mangan, arsenik, demir, silisyum. Aşınma dayanımını arttırmak amacıyla ise alüminyum, gümüş, silisyum, kadmiyum, kalay, berilyum ve kobalt bakıra ilave edilen temel alaşım elementlerindendir. Çinko, fosfor, silisyum, kalsiyum, berilyum, alüminyum, magnezyum gibi deoksidan elementleri olup, elektrik iletkenliğini düşürmektedir [5].

Standartlarda seyir teli iletkenleri olarak CuETP (Electrolytic Tough Pitch Copper), CuFRHC (Fire Refined Tough Pitch High Conductivity Copper), CuOF (Oxygen Free Copper), CuHCP (High Conductivity Phosphorous Copper), CuMg alaşımları, CuAg alaşımları, CuSn alaşımı ve CuCd alaşımı tanımlanmıştır. Standart ve yüksek dayanımlı bakır olarak CuETP, CuFRHC, CuOF, CuHCP malzemeler tercih edilmektedir. Birçok farklı alanlarda sahip oldukları mekanik ve elektriksel özelliklere göre kullanılan bu alaşımlar arasında CuCd alaşımları bazı ülkelerde insan sağlığını tehdit eden yan etkileri sebebiyle kullanımlarına kısıtlamalar getirilmiştir [6].

3.1. Bakır ve Bakır Alaşımları

Bakır bugün konvansiyonel hatlarda esas olarak iyi elektrik iletkenliği sağlaması açısından üstünlük sağlarken aşınması diğer bakır alaşımlarına göre daha kolaydır. Elektrik iletkenliğinin öne çıktığı uygulamalarda kullanılan birçok bakır alaşımı bulunmaktadır [7].

Bakır-magnezyum alaşımları; yüksek hızdaki tren hatlarında daha yüksek asılı gerilimler meydana gelmektedir. Bu sistemler bu nedenle daha iyi mekanik karakteristiklere ihtiyaç duyar. Bakırın magnezyum içinde çok zayıf eriyebilme kabiliyeti, bu ultra hafif alaşım tiplerinde iyi elektriksel ve ısıl iletkenliği öne çıkarmaktadır. Raylı sistem teknolojilerinde tercih edilen bakır-magnezyum alaşımları arasında CuMg0,2 ve CuMg0,5 yer almaktadır [5,8,9].

Bakır-gümüş alaşımları; gümüş esas malzemenin tavlamaya karşı olan direncini arttırmaktadır. Bu sayede malzemenin termal kararlılığı artar ve havai hat güç kablolarının mekanik veya elektriksel karakteristiğinden ödün vermeden kararlılığı artar. Bunun sonucu olarak da dayanıklılık artmış olur. Alaşım içerisinde gümüşün sağladığı termal kararlılık

sayesinde bu alaşımlardan CuAg0,1 çoğunlukla seyir telleri üretimlerinde sıklıkla tercih edilir [5,8].

Bakır-kalay alaşımları; bu alaşımlar yüksek asılı gerilimler karşısında oldukça iyi mekanik özellikler sağlar. Seyir teli üretimlerinde CuSn0,2 olarak kalaylı bakır alaşımı teller kullanılmaktadır. Yüksek hızlı tren sistemlerinde havai hat güç kablosundaki dalga yayılım hızlarında yeterli desteği sağlayan malzemelerdir [5,8].

Bakır-kadmiyum alaşımları; çekme dayanımları oldukça iyidir. CuCd0,7 ve CuCd1,0 bilinen raylı sistem iletkenlerindendir. Ancak raylı sistemlerde aşınma ile birlikte metalik tozların hava ile karışımı söz konusudur. Bakır-kadmiyum alaşımlarından kaynaklı bu metalik tozların akciğer kanseri gibi insan sağlığı üzerinde olumsuz etkileri tespit edilmiş ve bu nedenle bugün Avrupa ülkelerinin tamamına yakınında bu sebepten tercih edilmemektedir [5,8].

3.2. Cu, CuMg ve CuAg İletkenleri ve Kullanımları

Raylı sistem hatlarının temel yapıtaşlarını seyir telleri, portör telleri, pandül telleri, besleme iletkenleri oluşturmaktadır.

Seyir telleri; bir pantograf vasıtasıyla katener hatlarından sürtünme ile enerjiyi almayı sağlayan ana elemandır. Günümüzde bu teller DIN 43141, EN50149, EN 50149AC ve EN 50149BC uluslararası standartlarına göre kullanılmaktadır. Enerji iletiminin önemli olduğu bu yapılarda çoğunlukla Cu ve CuAg alaşımları tercih edilmektedir. Katener hatlarının bir diğer elemanı portör telleri ise; katener hatlarında seyir telini taşımayı sağlayarak seyir telinin de yükseklik ayarlarında etken olmasından dolayı 'taşıyıcı tel' olarak da adlandırılmaktadır. Portör tellerinden beklenen elektrik iletkenliğinden çok mekanik dayanımın yüksek olmasıdır. Uygulamada DIN48201 uluslararası standartlara göre değerlendirilen bu tellerde sert bakır ve sert CuMg alaşımları kullanılmaktadır. Pandül telleri ise; katener hatlarındaki üçüncü temel yapı elemanıdır. Kontak telinin taşıyıcı iletkene asılmasını sağlayan bu teller, seyir telinin flaş yapmasını engelleyerek yüksekliğin toleranslar içinde kalmasını ve portöre asılmasını sağlamaktır. DIN43138 uluslararası standardına göre değerlendirilen bu tellerde yaygın olarak sert CuMg alaşımları halat formunda kullanılmaktadır.

Ayrıca DIN43138 standardına uygun sert bakır halat formunda besleme teli, DIN48201 standardına uygun bakır direk topraklama teli ve DIN48201 standardına uygun sert CuMg0,4 Y.halatı olarak pratikte kullanılmaktadır. Tablo 1'de raylı sistemlerde kullanılan diğer bakır alaşımları örnekleri yer almaktadır [10,11,12].

Tablo 1. Raylı sistemlere göre katener iletkenleri ve kullanımı [10,11]

	Tramvay	**Tren (200km/saat)**	**Yüksek Hızlı Tren (> 200km/saat)**
Kontak&Seyir Teli	Cu, CuAg, CuCd (80-100-120 mm²)	Cu, CuAg, CuCd, CuMg, CuSn (100-107-120 mm²)	CuAg, CuCd, CuMg, CuSn (120-150 mm²)
Katener&Portör Teli	Cu, CuAg, CuCd (35-50-70 mm²)	Cu, CuAg, CuCd, CuMg (65-70-95-116 mm²)	CuAg, CuCd, CuMg (95-116 mm²)
Besleme Teli	CuAg (150 mm²)	AAAC/ACSR çeşitli bakır kablolar	AAAC/ACSR çeşitli bakır kablolar
Pandül Teli	CuCd (10 mm²)	CuCd, CuMg (10-12-16 mm²)	CuCd, CuMg (10-12-16 m²)

3.3. Cu, CuMg ve CuAg İletkenlerinin Özellikleri

Magnezyum bakırın elektrik iletkenliğini önemsiz derecede azaltan elementlerden biridir. Bununla birlikte kayda değer bir şekilde bakırın dayanıklılığını arttırıcıdır. CuMg alaşım ailesi içinde CuMg0,1 alaşımı en yüksek elektrik iletkenliğine sahiptir. Bu nedenle elektrik bağlantılarında özellikle askılı kablolarda kullanıma oldukça elverişlidir. CuMg alaşımı bakır için iletkenliğe göre nominal azalma ile yüksek mukavemet temin eden katı bir çözelti alaşımıdır. CuMg0,1 iyi mukavemet, mükemmel lehimlenebilme ve plaka haline getirilebilme kabiliyetine sahiptir. Kolayca geri kazanılabilmesi ise yeşil malzeme olarak adlandırılmasını sağlar. Temel kullanım alanları; terminal bağlantılar, kontak telleri, katener telleri, telekomünikasyon kablolarıdır [11].

Havai hat güç kablolarının dizaynlarında elektrik iletkenliği dizayn faktörü olarak belirleyici değildir. Bunun aksine mekanik karakteristikleri önemli rol oynar. Mekanik dayanım alaşım elementleri sayesinde konvansiyonel hatlarda geliştirilebilir Elektriksel özellikler incelendiğinde; özdirenç değerleri birim uzunluktaki direnç değerleri önemlidir. Şekil 2' de bakır, CuAg0.1, CuAg0.2 ve CuMg0.5 alaşımlarının azami özdirenç değerleri karşılaştırılmıştır. Elektriksel özellikleri için bu değerler 20˚C'deki ölçümler esas alınarak birim uzunluktan ölçülmektedir. Değerler esas alındığında elektrik akımına karşı en fazla dayanım gösteren malzeme bakır-magnezyum alaşımlarından CuMg0,5 olmaktadır [6,13].

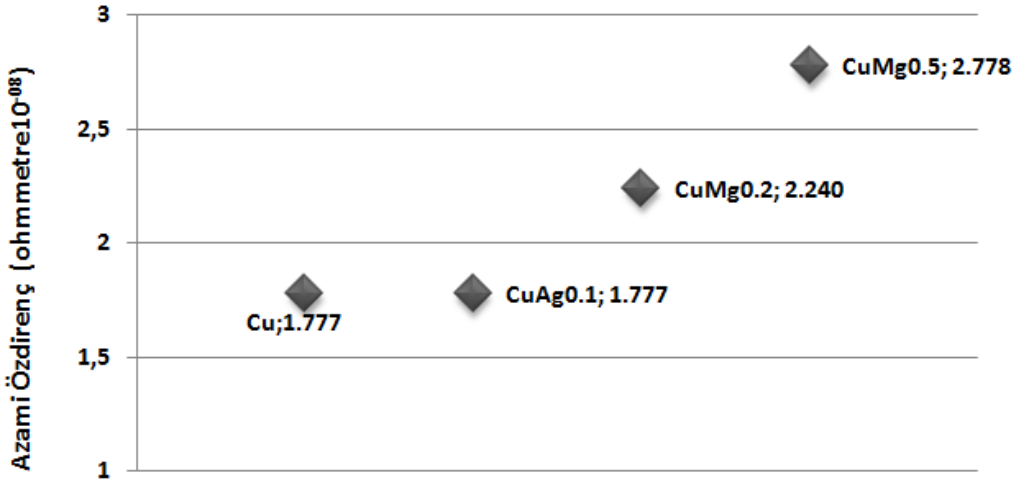

Şekil 2. Bakır, CuAg0.1, CuAg0.2 ve CuMg0.5 alaşımlarının azami özdirenç değerleri [6,13]

CuMg0,5 yüksek magnezyum içeren bakır-magnezyum ailesi alaşımıdır. Orta kuvvette bile yüksek şekillendirilebilme kabiliyetine sahiptir ve iyi iletkenliğe sahip bir alaşımdır. Elektrik iletkenliği yaklaşım %60 IACS değerlerinde muhafaza edildiğinde güçlü dayanımlara ulaşabilmektedir. Bu nedenle CuMg0,5 askılı kablolarda, uzun açıklık aralığı bulunan havai hat sistemleri gibi yerlerde kablo ve yüksek hızlı tren sistemlerinde katener teli olarak kullanıma uygundur. Ana uygulama alanları; otomotiv, elektrik-elektronik bağlantıları, röle, akım taşıyan temas yerlerinde, arabalarda kablo demetlerinde, telekomünikasyon kablolarında, katener tellerinde özellikle de yüksek hızlı trenlerde tercih edilirler. CuMg doğal ve endüstriyel (deniz havası ortamı gibi) atmosferlerde oldukça iyi dirence sahiptir. Endüstriyel ve içme suyu, sulu ve alkali çözeltilerde (oksitlenmemiş), su buharı, saf buhar, oksitleyici olmayan (çözelti içinde oksijen içermeyen) asitler ve bunların tuzlarında, nötr tuz çözeltilerinde kullanılabilirlerdir. Oksitleyici asitlere, siyanür, amonyak veya halojenler, sulu

amonyak halojen gazları, hidrojen sülfit ve deniz suyu içeren sistemlere karşı ise dayanıklı değildir [11].

CuMg0,2 bakır-magnezyum alaşımı bakırın düşük magnezyum içeren alaşımıdır. Oldukça iyi elektrik iletkenliği olduğu kadar mükemmel mekanik özellikleri ile de karakterize edilmektedir. Bakır ile karşılaştırıldığında CuMg0,2 soğuk şekillendirme şartlarında önemli yüksek dayanımlıdır. Esas olarak daha iyi yumuşatma performansı ve tersine bükme kuvvetinin altında olağanüstü dayanım ile de karakterize edilmektedir. CuMg0,2 iyi soğuk şekillendirme performansı ve ince çekilebilirlik özellikleri sunmaktadır. Bakırın elektrik iletkenliğini düşürmede etken olan magnezyum buna karşın dayanımı da belirgin ve önemli ölçüde olumlu etkilenmektedir. CuMg0,1 ve CuMg0,3 ile karşılaştırıldığında daha yüksek dayanım ile elektrik iletkenliğinde nispeten düşme görülebilmektedir. Bu nedenle de yüksek hız trenlerinde kontak teli ve katener teli olarak kullanıma uygundur [11].

Gümüş-bakır içine %0,12 altındaki düşük oranlarda bakır içine az miktarda eklenmesi elektrik iletkenliğinde bir değişiklik olmadan tavlama sıcaklığının artışını beraberinde getirir. Dolayısıyla da alaşım halindeki CuAg herhangi bir sertlik kaybı olmadan yumuşak lehim ile bağlanabilirdir. Yüksek performanslı motorların akım dönüştürücü bölümlerinde sık sık bu nedenle CuAg kullanılmaktadır. Yüksek oranda gümüş içeren (%2-8) bazı durumlarda %1,5 oranında kadmiyum (Cd) içermektedir ve kaynak yapılmadan transformatörlerin yük anahtarlarında kullanılmaktadır [11].

CuAg0,1 gümüş ana metalin tavlama direncini arttıran bir alaşım elementidir. Mekanik ya da elektriksel özelliklerden ödün vermeden daha yüksek ısı kararlılığı sağlar ve dolayısıyla da askılı kablolarda dayanıklılığı geliştirdiği için tercih edilir. Bakırın yüksek iletken türleri yükseltilmiş sıcaklıkta gelişmiş akış özellikleri ile karşılaştırıldığında önemli ölçüde geliştirilmiş özelliklere sahip tavlama ve çok yüksek elektrik iletkenliği sağlar. Saf bakıra gümüş ilavesi yumuşama sıcaklığını yükseltir ve elektrik iletkenliğine çok az etkide bulunur. Ayrıca gümüş mekanik özelliklere, özellikle de sünme direncini geliştirmektedir. %0,08-0,12 arası gümüş içeriğinde çok iyi sünme direnci sağlanmaktadır. Gümüş oranının artması sürünme dayanımı arttırır ve yüksek servis sıcaklıklarında da yumuşamaya olan direncini geliştirir. Örneğin 250°C' deki iyi sürünme direncine sahip olması elektrik motoru parçalarında, yarı iletken parçalarında ve aşınma plakalarında kullanılmalarını sağlamaktadır [11].

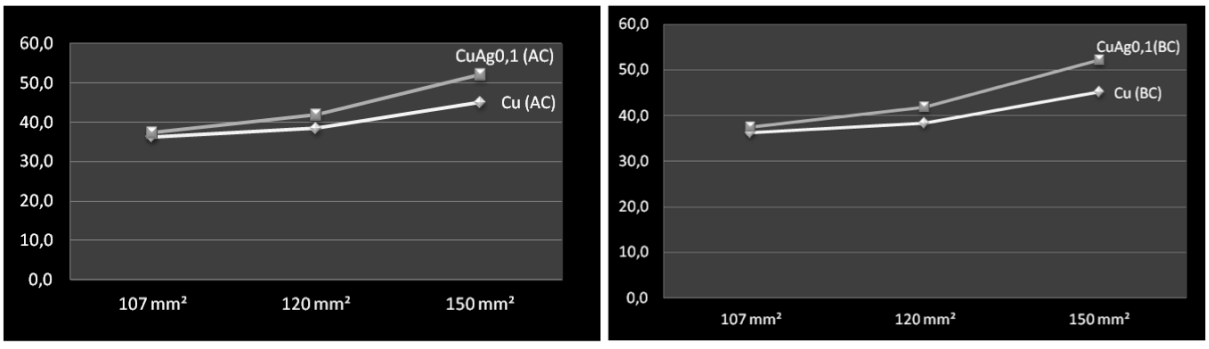

Şekil 3. AC ve BC tipi Cu ve CuAg0,1 nominal kopma kuvveti değerleri (kN)

CuAg0,1 alaşımı ile bakır seyir telinin AC ve BC tipi uygulamalarında her iki tip için de nominal kopma kuvvetleri karşılaştırıldığında bakır-gümüş alaşımının daha yüksek kopma kuvveti değerlerine sahip olduğu görülmektedir. Şekil 3'de AC ve BC tipi uygulamalarda CuAg0,1 alaşımı ve bakırın 107mm^2, 120mm^2 ve 150mm^2 kesitlerindeki nominal kopma kuvvetleri karşılaştırılmaktadır.

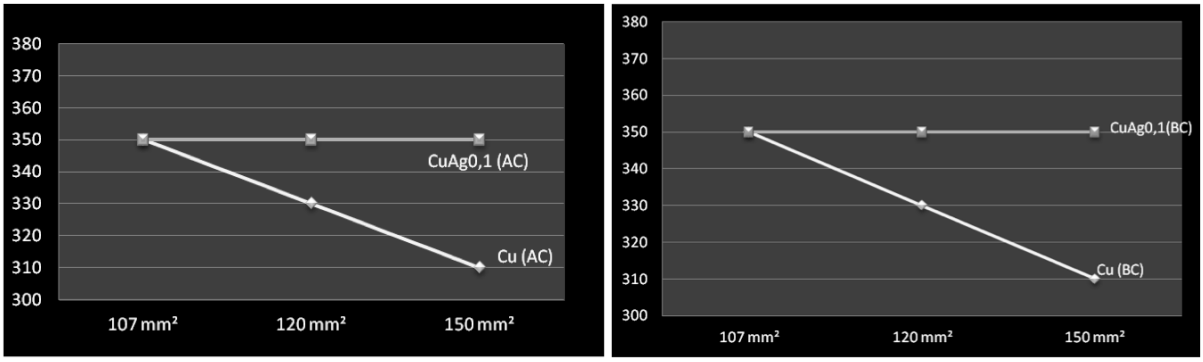

Şekil 4. AC ve BC tipi Cu ve CuAg0,1 çekme dayanımı değerleri (N/mm^2)

Bakır ve CuAg0,1 alaşımının farklı kesitlerdeki çekme dayanımları karşılaştırıldığında; CuAg0,1 alaşımının daha yüksek çekme dayanımı değerlerine sahip olduğu görülmüştür. Şekil 4' de 107mm^2, 120mm^2 ve 150mm^2 kesitleri için çekme dayanımı değerleri bakır ve CuAg0,1 alaşımı için karşılaştırılmaktadır.

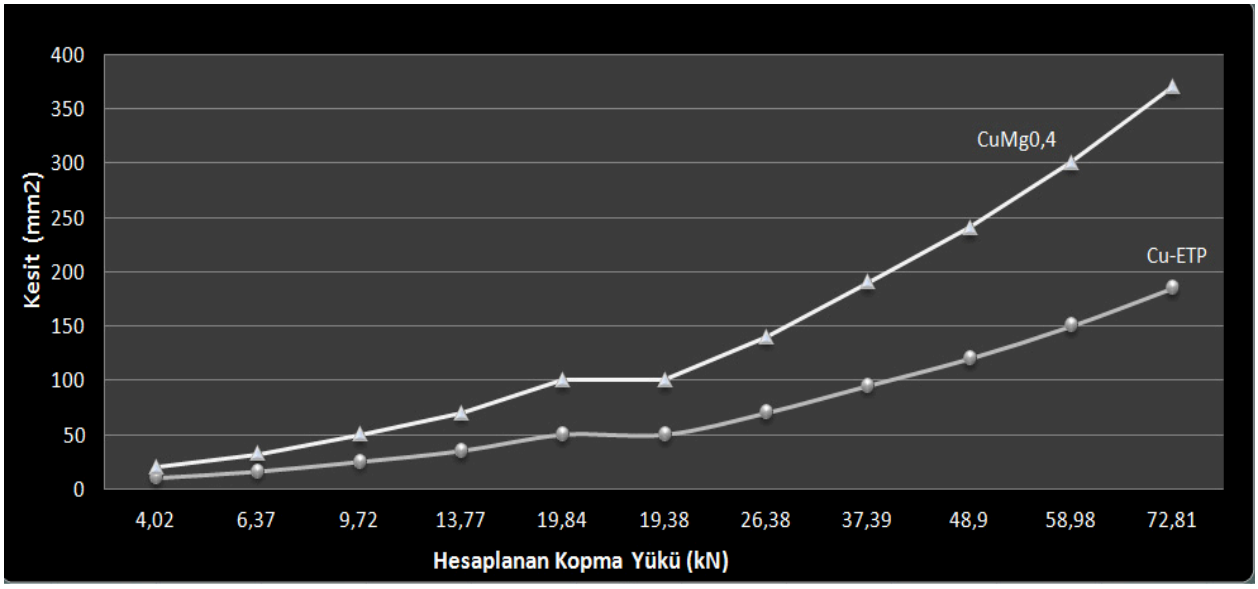

Şekil 5. Cu-ETP ve CuMg0,4 nominal kopma kuvveti değerleri (kN)

Farklı kesitlerdeki Cu-ETP ve CuMg0,4 alaşımı nominal kopma kuvvetleri karşılaştırılmıştır. Şekil 5' de kesite bağlı hesaplanan kopma yükü değerleri verilmiştir. Buna göre; Cu-ETP'nin ve CuMg0,4' ün artan kesite bağlı olarak nominal kopma yükü değerleri de arttığı görülmüştür. Artan kesitlere rağmen Cu-ETP daha düşük kopma yükü değerlerine sahiptir. Sonuç olarak; saf bakıra göre magnezyum ilavesi alaşımın yüke karşı kopma direncini geliştirdiği gözlemlenmektedir.

Çekme dayanımı açısından bakır, CuAg ve CuMg alaşımları karşılaştırıldığında, magnezyum alaşımlarının çekme dayanımımı diğer alaşımlara göre daha yüksek olduğu görülmektedir. Aynı kesitte CuMg0,5 alaşımın çekme dayanımı en yüksek olmakla birlikte en düşük çekme dayanımı saf bakırda görülmektedir. Kesit artışları ile birlikte çekme dayanımları arasındaki hiyerarşi aynı kalmaktadır. Şekil 6' da 80 mm², 100 mm², 107 mm², 120 mm² ve 150 mm² kesitleri için çekme dayanımı değerleri yer almaktadır.

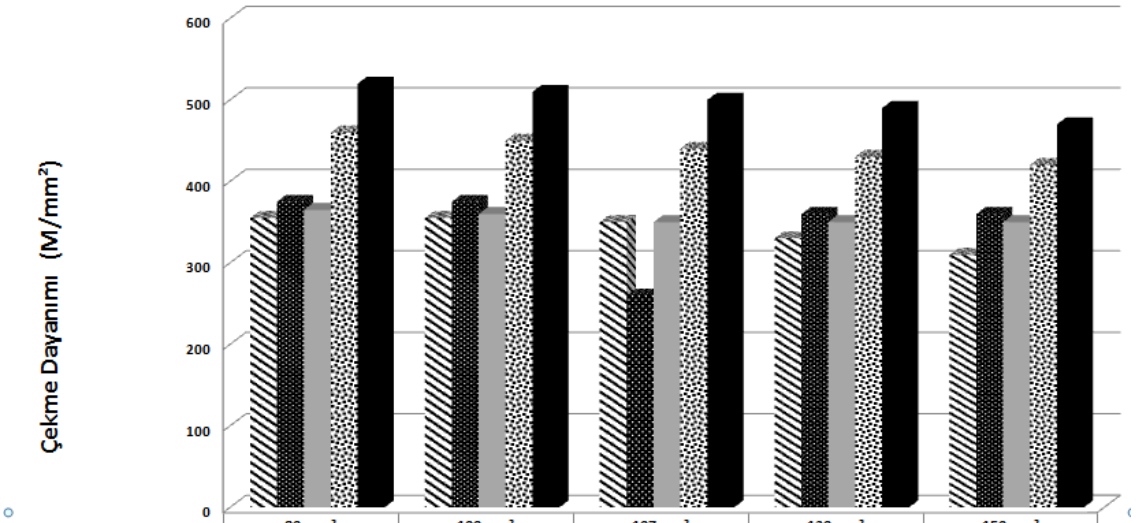

	80 mm²	100mm²	107mm²	120mm²	150mm²
Cu	355	355	350	330	310
Yüksek Daynımlı Cu ve Cu-Ag	375	375	260	360	360
CuAg0.1	365	360	350	350	350
CuMg0.2	460	450	440	430	420
CuMg0.5	520	510	500	490	470

Şekil 6. Bakır, CuAg0.1, CuAg0.2 ve CuMg0.5 alaşımlarının çekme dayanımı değerleri [6]

Mekanik ve elektriksel özelliklerin yanı sıra malzemelerin yüzey temizliği parlak, oksitli olmaması ve yabancı maddelerden arınmış olması gerekir. Ayrıca yüzey durumu açısından çapak, çukur oluşumu ve pürüzlülük de istenmemektedir.

4. DEĞERLENDİRME

Teknolojik beklentiler ışığında özellikle ülkemizde son 10 yıldır mevcut gelişimlerle birlikte gelişmekte olan demiryolu projelerinde bakır ve bakır alaşımları oldukça önemli rol oynamakta ve yaygın olarak kullanılmaktadır. Elektrik iletkenliğinin ön planda olduğu bu sistemlerde yeni nesil elektrik iletkenliği ve mekanik dayanımları açısından üstün özellikli alaşımlar ı geliştirme çalışmaları üzerinde çalışmalar devam etmektedir. Özellikle yüksek hızlı tren sistemleri açısından önemli olan bu alaşım grupları arasında bakıra magnezyum ve gümüş ilavesi ile elde edilen alaşımlar mekanik dayanımları geliştirmek için kullanılmaktadır. Bu çalışmada bakır, CuMg ve Cu Ag alaşımlarının özellikleri ve havai hat katener iletkenleri olarak kullanımları ve mekanik özellikleri incelenmiştir. Bu bağlamda özellikle bazı uygulamalarda magnezyum ve gümüş ilavesi ile elde edilen alaşımların saf bakıra göre üstün özellikler kazandırdığı tespit edilmiştir.

5. REFERANSLAR

1. UK Trade&Investment, May 2011
2. Yüksek Hızlı Tren Tübitak Raporu (http://kentvedemiryolu.com/icerik.php?id=180).
3. Bucca, g., Collina, A., "A Procedure for The Wear Prediction of Collector Strip and Contact Wire in Pantograph-Catenary System", Wear, 266, 46-59, 2009
4. Pupke, F., "Optimization and Development of Contact Wire for High Speed Lines", (www.uic.org/cdrom/2008/11.../PS.2.8.pdf).
5. Koçak, H., Bakır Alaşımları El Kitabı, İstanbul, Mayıs 2006

6. Turkish Standard, TS EN 50149, "Railway Applications - Fixed Installations - Electric Traction - Copper and Copper Alloy Grooved Contact Wires", Ankara, April 2006
7. Copper Development Association, "Copper in Electrical Contacts", Technical Note, 23, 1980
8. La Farga Technical Catalogue, Grooved Contact Wire, August 2013
9. Burhan, O., Demirdışı Metallerin Kaynağı, Oerlikon, 1990
10. http://www.copper.rs/trolley%20wire.html
11. http://conductivity-app.org/
12. Raylı Sistem Teknolojisi, "Sinyalizasyon Elektrifikasyon ve Haberleşme Tesisleri", T.C Milli Eğitim Bakanlığı, 521MMI508, Ankara, 2011
13. Nairn, M., "Continuous Casting of Copper Magnesium Conductor Alloys", WAI Technical Conference, April 2013

Recycling of Metals from Electronic Scrap – Finding the Optimum Between Pretreatment and Metallurgy

•

Elektronik Hurdadan Metallerin Geri Kazanımı-Önişlem Süreçleri ve Metalurji Arasında Optimumun Belirlenmesi

Bernd Friedrich

RWTH Aachen University - Germany

ABSTRACT

Many of the so-called critical or economic strategic metals are strongly dissipated in complex production residues from materials production and processing as well as in old products e.g. in the areas of IT, entertainment and communication electronics, high-tech materials and tools, batteries, and power generation systems. Today's processing routes of the relevant waste streams allow mainly for recovering major metals such as Copper, Gold and palladium , but show particularly low recovery rates for refractory metals such as tantalum, rhenium or tungsten, electronics metals such as indium, gallium or germanium or special metals such as antimony and rare earth elements. A few processes are being developed to specifically retrieve individual elements and singular and combined methods of mechanical processing, pyrometallurgy and hydrometallurgy are being used depending on the material flow. To determine the optimal connection points between the pretreatment and metallurgy and thus to achieve maximum yields taking in account all valuable metals, it is essential that coordination between all disciplines work perfectly. Today the impact of the separation degree and enrichment factor to the subsequent metal extraction remains in many cases unclear. In particular, for special technology metals which are not yet recovered to a large extent, suitable approaches are missing. A basic understanding to design an optimal combination of processes with variable input streams results must be created and such criteria for a decision to select the most effective processing modules for the potential process chains. For this purpose, the mechanical processing technology can contribute in the area of sensor-based sorting, another central point is the metallurgy slag design. Here an objective is to concentrate the technology metals by adding mineralization and crystallization affecting substances in the slag system and/or by controlled cooling of the slag, which in turn allow improved separation in a subsequent efficient mechanical treatment. The paper presented will focus on WEEE as a waste stream which is available in large economic quantities, but its complexity has made a recovery of the special metals hardly possible for technical reasons up to now.

Keywords: Recycling, electronic scrap, WEEE.

Bath Movement Effect on Agglomeration of Inclusions in Aluminium Melts

Mertol Gökelma[1], Bernd Friedrich[1]

mgoekelma@ime-aachen.de, bfriedrich@ime-aachen.de

[1]IME Process Metallurgy and Metal Recycling, RWTH Aachen University,

D-52056 Aachen, Germany

Abstract

Presence of non-metallic inclusions becomes more important with increasing quality demand of aluminium products. Understanding of inclusion behaviour for different conditions is necessary to develop better inclusion detection and removal techniques. Inclusion agglomeration is one of the main issues which can be often seen in aluminium alloys. Agglomerates behave differently from single particles which causes difficulties with estimating how inclusions move in melts. Effective bath movement is present in different steps of aluminium production such as launders, casting furnaces and gas purging units. Therefore, it is important to understand the influence of different melt flows on particles. Experiments were carried out in order to investigate behaviour of non-metallic particles in molten aluminium alloy under magnetic field. The influence of bath movement on particles was observed as agglomerates under optical microscope.

Keywords: inclusion behaviour, agglomeration, magnetic field effect, turbulent flow

1 Introduction

Molten systems are always influenced by any type of bath movement in ladle, launder or casting furnace. In all kind of movement areas, we have to consider agglomeration effect of bath movement. Turbulent heat and mass exchange including turbulent bath movement is a topic of great interest and knowledge about melt flow is the key of inclusion generation, transport and interactions. One of the factors which generate strong turbulence is induction heating technology.

The induction furnaces are widely used in industries for melting alloys. The main advantages of electromagnetic (EM) heating are, very fast melting and treating materials without direct contact which is important for high purity products. Beside these advantages, stirring effect of EM forces causes some unwanted phenomena. One of those phenomena is mixing of oxides by breakage of oxide layer on the melt which generates continuous oxidation in the case of oxidative atmosphere. Another possible unwanted phenomenon is agglomeration of non-metallic inclusions by turbulent flow which is the focus of this work.

Non-metallic inclusions in aluminium melt play critical role to reach required quality in final products. In order to develop better inclusion detection and removal techniques, it is necessary to have wide knowledge about behaviour of inclusions in molten aluminium and about how they are affected from different melting conditions. When the same material is melted in different furnace types, such as resistance, induction or gas injection, inclusions interact differently and the final product quality changes accordingly.

A fundamental research is carried out in this present work for validation of the experimental approach to investigate inclusion behaviour under turbulent flow, especially under the influence of electromagnetic forces.

2 Background

2.1 Agglomeration behaviour of inclusions

Particles collide with other particles and form dendritic structures due to their relative motions. This process is called agglomeration and results agglomerates and clusters. The relative motions can be Brownian motion, inhomogeneities in fluid and different forces such as electromagnetic, gravitational, shear or turbulence. Agglomeration can be simply described as natural tendency for minimization of energy by decreasing surface area.

If particles coalesce into each other due to collision, it is referred to as coagulation which is a special case of agglomeration. Coagulation and coalescence processes are also called for droplets which are commonly achieved by adding chemicals (coagulants) to destabilize the colloid dispersion.

Agglomeration of inclusions is a complex mechanism which is affected by different parameters such as inclusion type, size, stirring and temperature. This phenomenon was described by Levich mainly as four mechanisms which are not independent from

each other. These mechanisms are Brownian agglomeration, gradient agglomeration, turbulent agglomeration and agglomeration in polydisperse systems.

2.2 Influences on Agglomeration of Solid Particles in Melts

There are many different influences on agglomeration and cluster growth of inclusions in molten metal. It is known that stirring (turbulence) promotes inclusion clustering due to increasing collision frequency of particles. The collision between particles can also originate from Brownian motion and gravitational motion. However, collision mechanisms are not only factors influencing clustering. Attractive forces between particles have very strong influence and those forces vary for different types of inclusions.

2.2.1 Collision of Particles due to Different Mechanisms

Particles collide each other due to their relative motions and they form particle clusters. This clustering causes a reduction in the number of particles. The frequency of collision for spherical particles, N_{ij}, can be calculated per unit time by following equation.[2]

$$Nij = \beta vi, vj ninj \quad (1)$$

υi and υj are particles volumes and $\beta \upsilon i, \upsilon j$ is a function of collision frequency between two particles i and j. This function is defined by flow type and size of particles. Moreover, n_i and n_j are concentration of individual particles in i and j ($1/m^3$).

2.2.1.1 Brownian Motion

Brownian agglomeration is one of the mechanisms related to collision. It is defined as disorganized movement of small particles in fluids. This random movement of particles is caused by collisions with molecules of surrounding medium. Random motion of a particle can be seen in Figure 1. Brownian agglomeration can be described by following equation. [3]

$$\beta b \upsilon i, \upsilon j = 2kT3\mu 1\upsilon i 1/3 + 1\upsilon j 1/3 \upsilon i 1/3 + \upsilon j 1/3 \quad (2)$$

Here, k is Boltzmann constant (J/K), T is absolute temperature (K) and μ is viscosity of fluid (Pa.S).

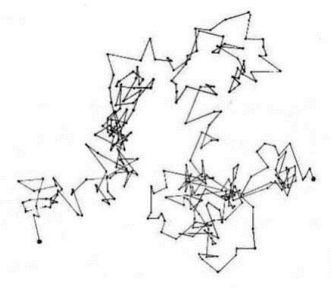

Figure 1: Brownian movemenent of a particle [4]

2.2.1.2 Turbulent Flow

Turbulent agglomeration can be understood by two processes which are turbulent inertial agglomeration and turbulent shear agglomeration (Saffman et al., 1956).

When the particles leave their flow streamlines due to inertia and promote collisions with the particles in the neighboring streamlines, this mechanism is called inertial agglomeration. In second type, turbulent shear, due to particle relative velocity gradients agglomeration, causes particles to collide with another particle in a different pathline because of their different traveling velocities. These two turbulent mechanisms can be described schematically as follows:

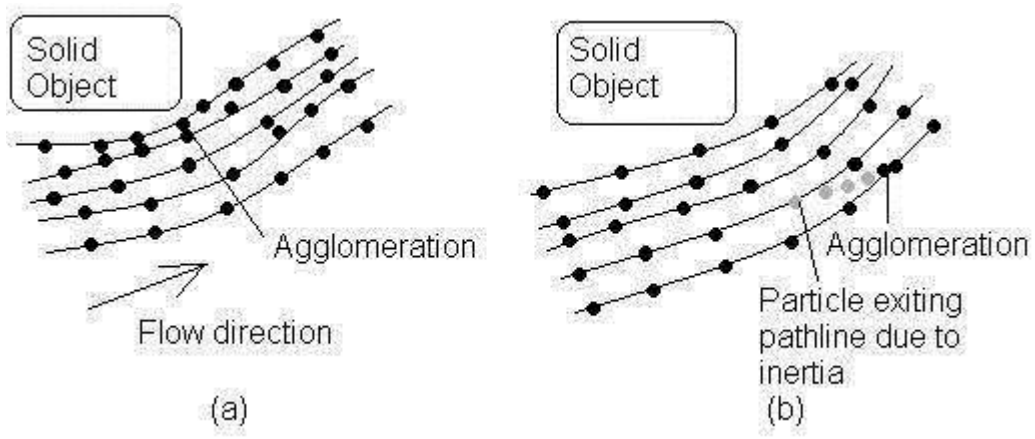

Figure 2: Turbulent agglomeration types (a) Shear Agglomeration, (b) Inertial Agglomeration [4]

These mechanisms must be well understood for further modellings and designs. Since turbulence flow has very complex and random behaviour, there are many difficulties to understand particle behaviour under these conditions. Function of collision frequency can be basically calculated by following equation. [6]

$$\beta t\upsilon i\,,\ \ \upsilon j = \alpha T1.3ai + aj3\varepsilon\upsilon 1/2 \qquad (3)$$

Here, α_T is coagulation coefficient, a_i and a_j are the radii of the spherical particles (m) and ε is the dissipation rate of turbulent kinetic energy.

Turbulent flow appears very often in induction heating furnaces. Therefore, understanding of particle movements in turbulent conditions plays an important role to be able to optimize the heating processes.

2.2.1.3 Gravitational Motion

Small particles settle slowly down in a fluid and the settling velocity increases with increasing size of particle due to higher gravitational forces (F_G). The function of collision frequency of particles due to different gravitational forces can be basically defined by following equation.[2]

$$\beta d_{ij}, \quad \upsilon_j = \pi a_i - a_j^2 v_i - v_j \qquad (4)$$

Here, vi and vj are the settling velocities of the particles (m/s).

During this settling process, the larger particles catch up and collide with smaller particles which cause agglomeration. This phenomenon is almost always present in all molten metal systems since there are always inclusions in different shapes and sizes. The mechanism can be seen in Figure 3.

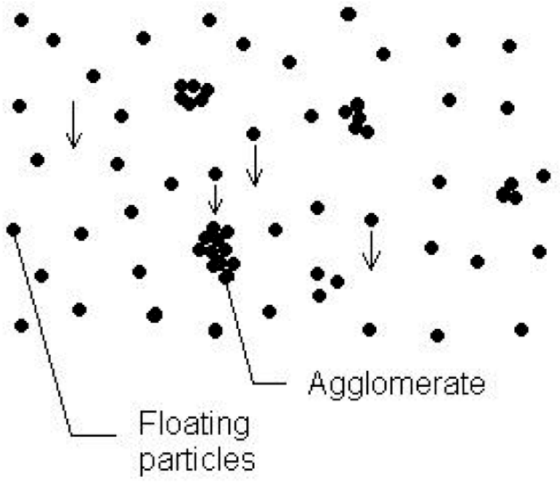

Figure 3: Agglomeration due to gravitational effect [4]

Velocity gradients between particles can be affected by particle shapes due to different drag coefficients (C_D). Drag forces (F_D) vary for each shape and it has strong influence on settling velocities. Another effect is caused by density of the melt which directly affects the buoyancy force (F_v). Main forces acting on a particle are shown in Figure 4.

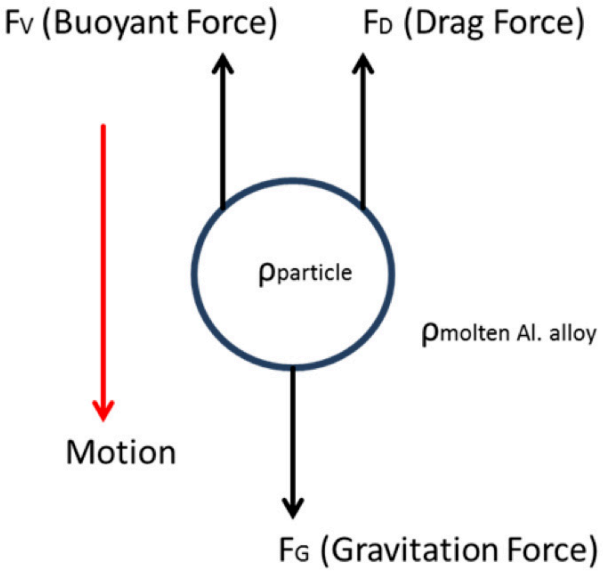

Figure 4: Forces acting on a particle in a melt while settling [7]

Each particle has its own nature such as, density, shape and size. Each particle in the system is influenced by melt flow differently according to its characteristics. In this case, the experimental researches must be performed with defined particle and size in order to understand the mechanism more specifically for different parameters.

2.2.2 Agglomeration due to Attractive Forces

Although it is known that melt flow has a strong effect on particle agglomeration, it is not the only crucial factor. Agglomeration tendency of some different particles such as alumina, calcium aluminate and spinel was investigated in the work of Kang et al. In this work, it has was reported that agglomeration tendency of each particle nature is different from each other and this difference is caused by attractive forces.

Every particle attracts other particle by a force which is proportional to masses and inversely proportional to square root of distance between those two particles. The force is called gravitation force (F_G) and can be described by Newton's law of universal gravitation:

$$\propto \mathbf{1\times 2\ 2} \qquad (5)$$

In some particular cases, the attractive forces can even dominate the bath movement. This mechanism has been investigated by Yin et al. and they reported that the attractive forces are a very dominating factor especially for alumina particles. Figure 5 presents an interesting explanation of attraction between particle A and B. Every step in the image presents 1/30 second interval and decreasing distance between two alumina particles can be clearly seen in each step. Distance between two particles decreases with an increasing rate and almost vertical to flow direction which shows how strong the attractive force is.

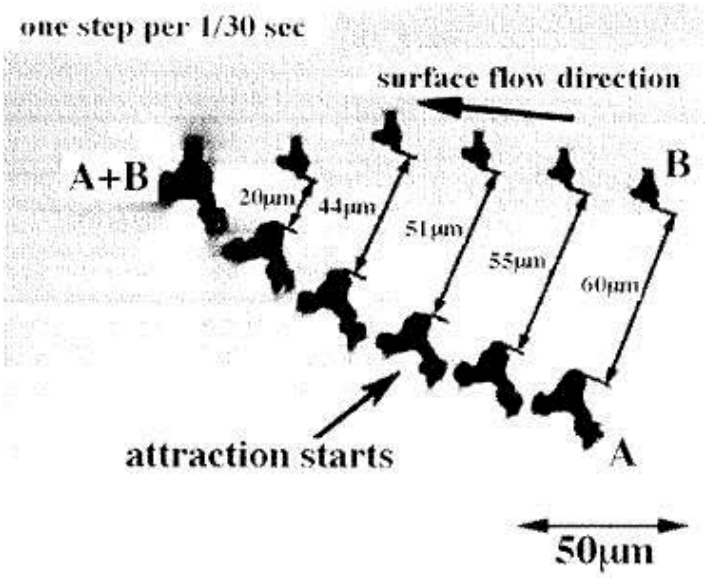

Figure 5: Sequence of agglomeration caused by strong attraction between alumina particles [9]

The distance between particles has also influence on attraction forces. Figure 6 presents the aggregates A and C, moving towards cluster B by surface flow. Aggregate reached the minimum distance of 30 μm to the cluster and it became a part of B due to attraction forces. On the other hand, the closest distance of aggregate C to the cluster B was 50 μm, and it was driven away by surface flow. In the second case melt flow was not able to dominate attractive forces due to longer distance between cluster and aggregate.[9]

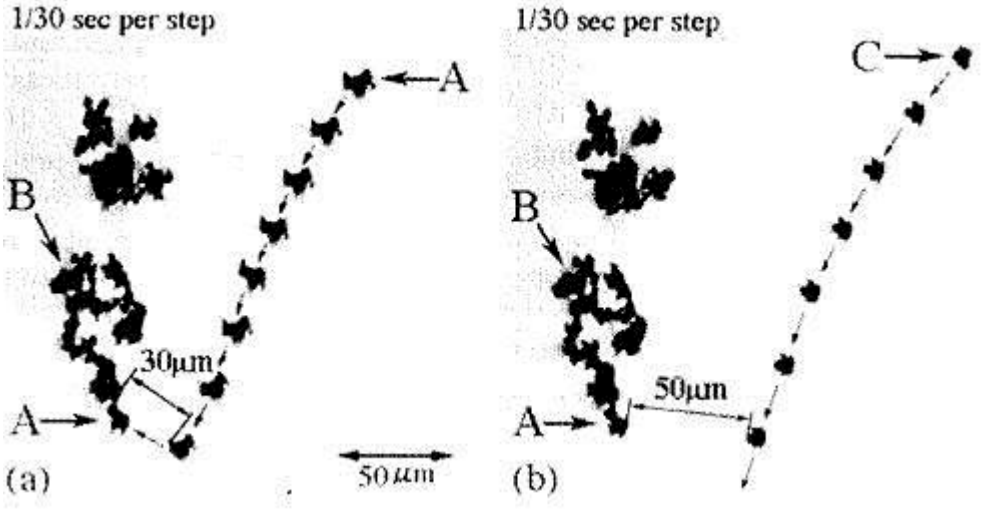

Figure 6: Two different cases of interaction between alumina cluster and particle a) attracted b) not attracted alumina particle by cluster [9]

2.3 Bath Movement with Special Focus on Induction Heating

Bath movement is generally present in most steps of aluminium production chain which is presented in Figure 7. Strong metal flow appears in launders, casting furnaces and gas purging units. Size of aggregates might change after these steps just because of the movement of molten metal. This size change due to clustering might have advantages and disadvantages but the key point is to understand the fundamental effects of different flow mechanisms on particles.

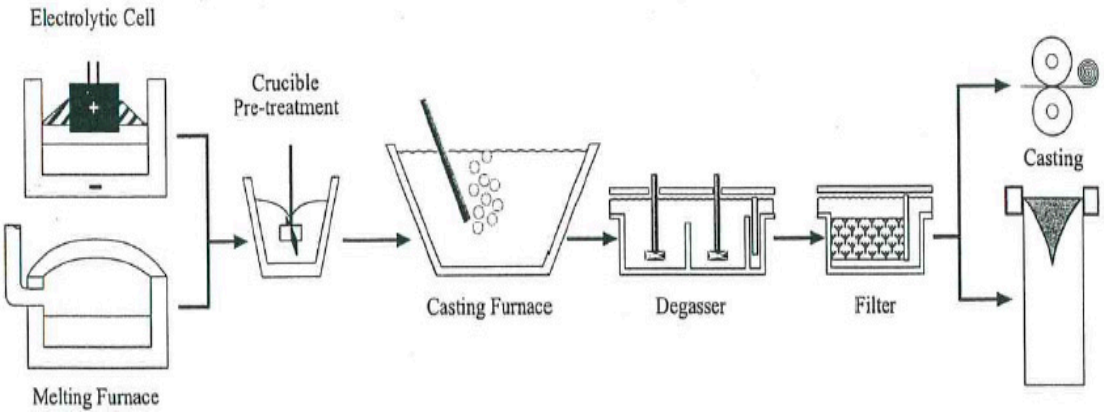

Figure 7: Molten aluminium processing steps [10]

Principle of Induction heating is based on the relationship between magnetism and electricity. Induction heating principle can be described with electromagnetic induction theorem and Joule-Lenz's law. An alternating voltage is applied to an induction coil, this voltage results an alternating current in the coil circuit which produces in its surroundings a time variable magnetic field and it has the same frequency as the coil current. The strength of magnetic field depends on the coil geometry, the current in the induction coil, and the distance from the coil. Alternating eddy currents produce heat by the Joule effect [11]:

$$Q= i^2.R \quad (6)$$

The heat produced by electromagnetic (EM) field, heats and melts a conducting material. The electromagnetic induction theorem can be described as following; when magnetic flux passes through the plane that is limited by each closed loop changes as time, the closed loop can produce motional electromotive force which is the magnetic force component of Lorentz force [12]:

$$F= q(E+VxB) \quad (7)$$

A conventional induction heating system that consists of a cylindrical load surrounded by a multiturn induction coil and flow cycle of melt is shown in Figure 8.

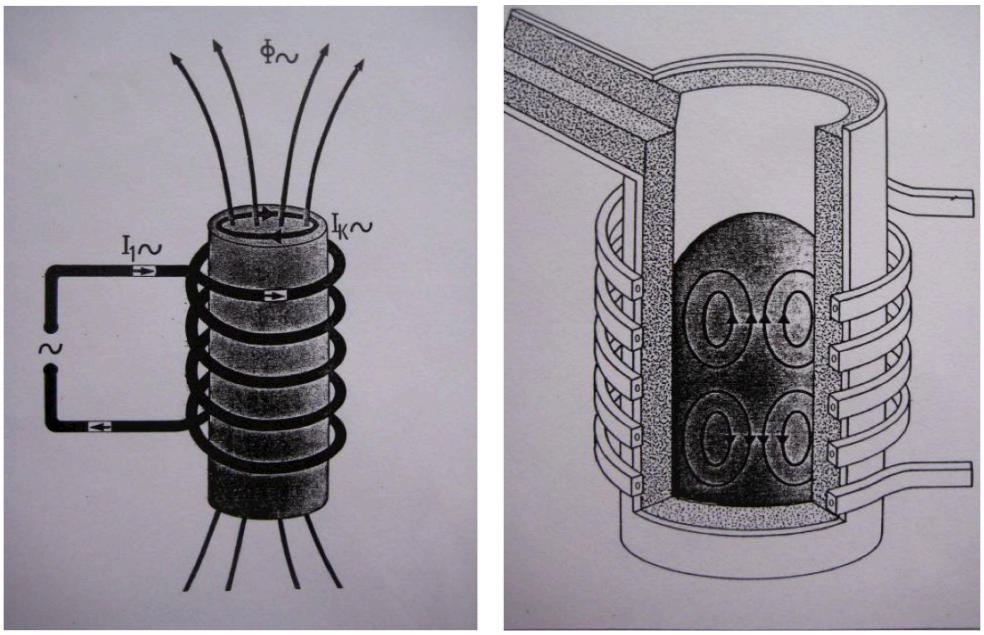

Figure 8: The principle of the heating system in an induction furnace (left) and the flow cycle in the crucible [13]

The molten metal behaves as moving conductor with velocity V and it flows perpendicular across magnetic field B of the magnet. This initiates the movement of liquid metal and results some characteristic phenomena which are bath cone and bath movement (see Figure 9). Magnetic field is proportional to the velocity of the flowing metal which corresponds to Reynolds numbers greater than 10^4 and this velocity is

influenced by; density and viscosity of the melt, type of crucible, frequency of induction system, and diameter of coil.[14] Melt velocity is defined by following equation:

$$vmelt = Icoil \times f \times \lambda\rho \times \mu \quad (8)$$

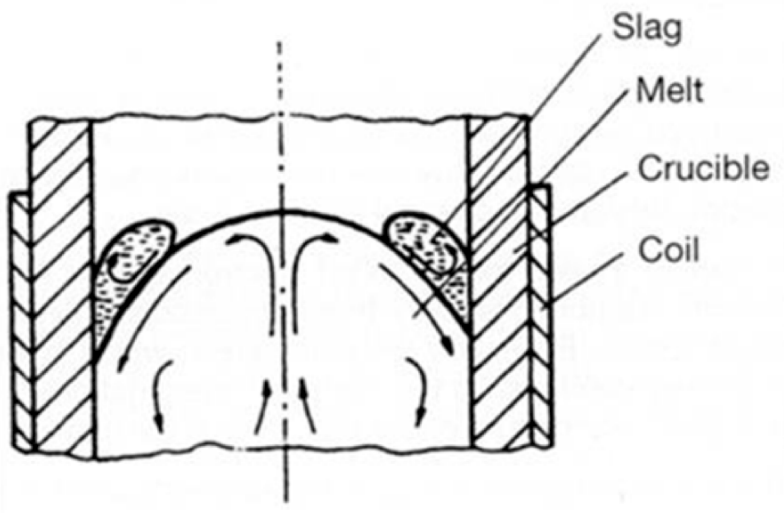

Figure 9: Bath cone and current melt and slags [15]

Turbulent flow is sometimes desired due to its positive effects such as improvement the quality of the final alloy with the effective melt mixing and homogenization of the melt. On the other hand, construction of melting equipment is more complicated and more expensive than a resistance furnace. Moreover, it is well known that inclusions is strongly influenced by melt flow. [14]

3

4 Experiments

4.1 Experimental Setup

A schematic view of the experimental setup is presented in Figure 10 which consists, an induction coil, a clay graphite crucible with diameter of 70mm^2 (0,2 l) and a thermocouple (type-k). The induction furnace with a maximum power of 50kW and the frequency of 10 kHz was used for remelting the inclusion containing aluminium alloys in order to generate turbulent stirring in melt.

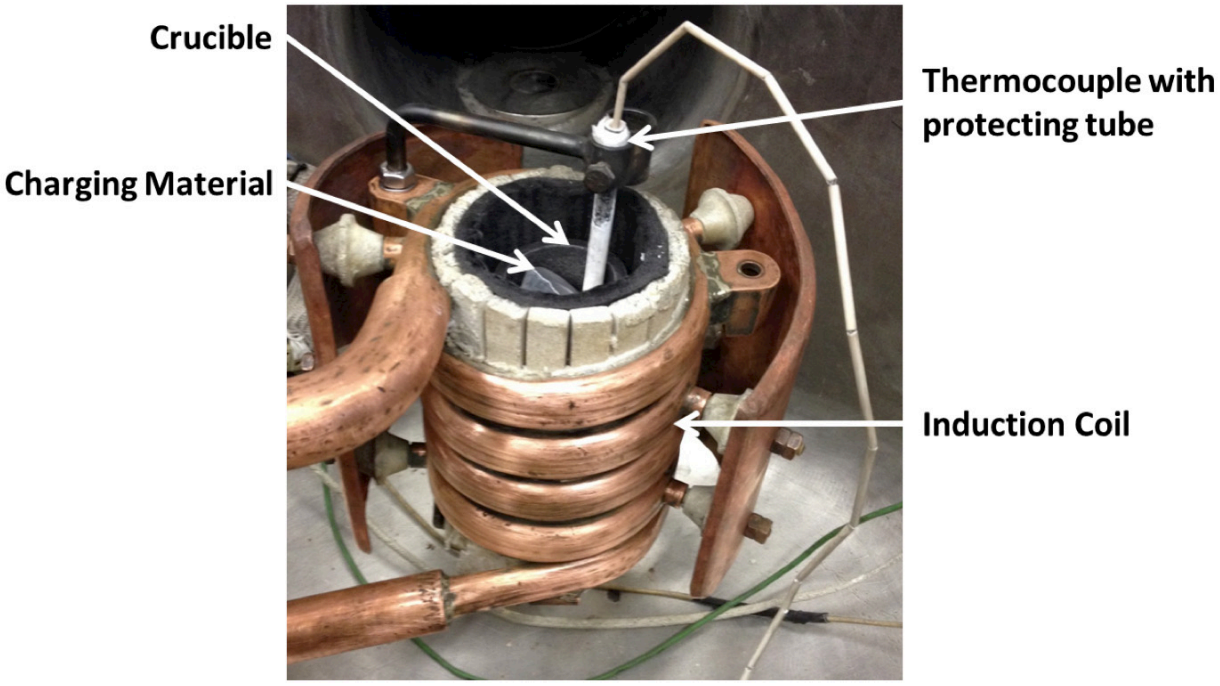

Figure 10: Experimental setup in an induction heating furnace

Temperature of molten metal was measured by an external thermocouple in order to reach desired temperature and to be able to manipulate the power of furnace in the range of 4.4 – 5.8 kW. A thick copper mould was used for casting of aluminium.

4.2 Experimental Procedure

Aluminium alloy with defined inclusion types were charged into induction furnace. The inclusion content of melt was targeted to 0.5wt% for different inclusion chemistries. Molten metal was hold under magnetic field which causes stirring by electromagnetic forces. The experiments were carried out for different durations to be able to observe turbulence duration influence on agglomeration. Bath movement caused by electromagnetic forces was clearly observed as bath cone during the experiments. Bath cone with a breakage of oxide layer is shown in Figure 11. Afterwards, molten aluminium was casted into a thick copper mould to accelerate the solidification.

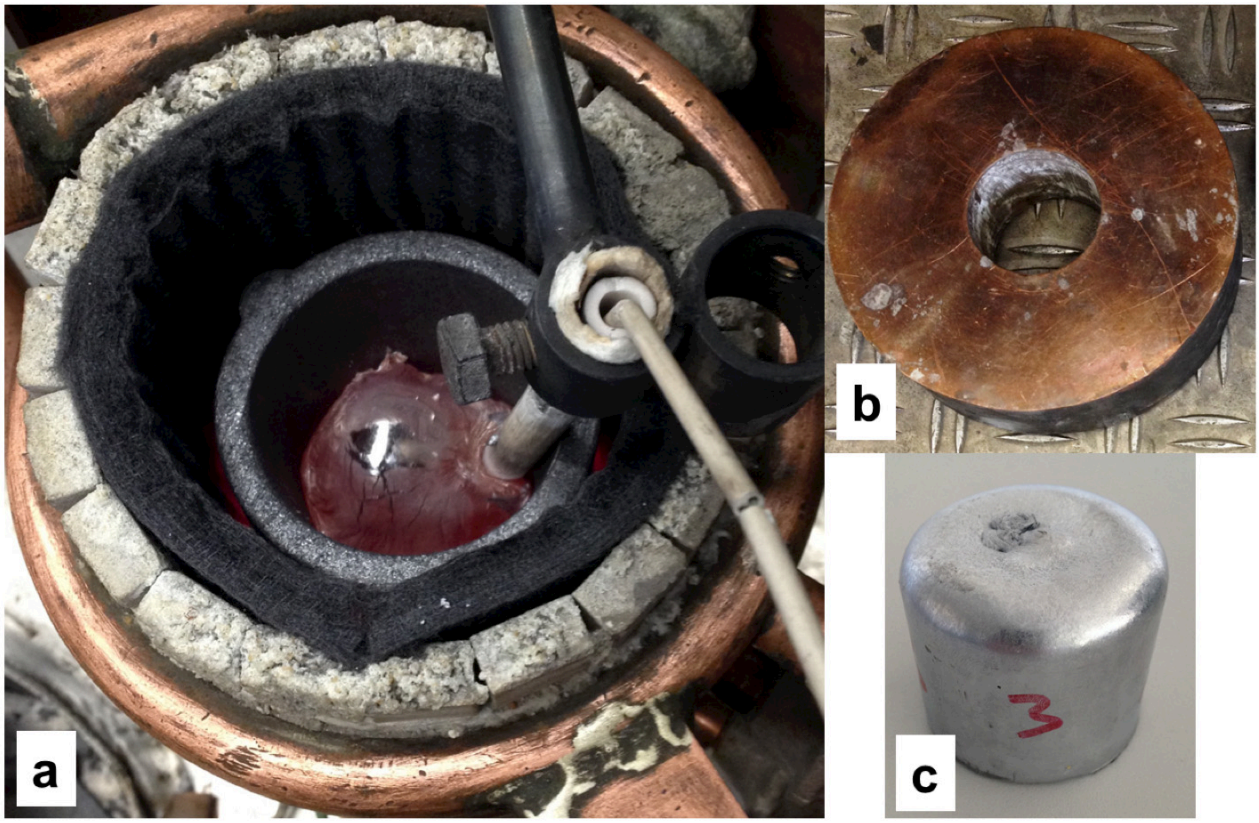

Figure 11: a) Experimental setup from top view and bath cone, b) copper mould, c) sample

Cross-section of each solid sample was firstly polished and then the whole area was scanned under light microscope. Images (50X magnification) were taken for each cluster and afterwards they were characterized by Image Analysis Software in order to define surface area, axis lengths, inclusion amount and form factor of clusters.

5 Validation of the Experimental Approach

Preliminary experiments have been performed in order to validate the experimental approach. First results showed that it is possible to observe the effect of bath movement on agglomeration behaviour of particles.

Two exemplary images are shown in Figure 12 and different growth tendencies of particles were observed. The experiments were carried out with approximately 0.5wt.% of inclusion amount and image analysis of following agglomerates showed that the agglomerates were quite high concentrated in comparison with starting concentration. The particle concentrations of following agglomerates are 19.37% (left) and 24.7% (right):

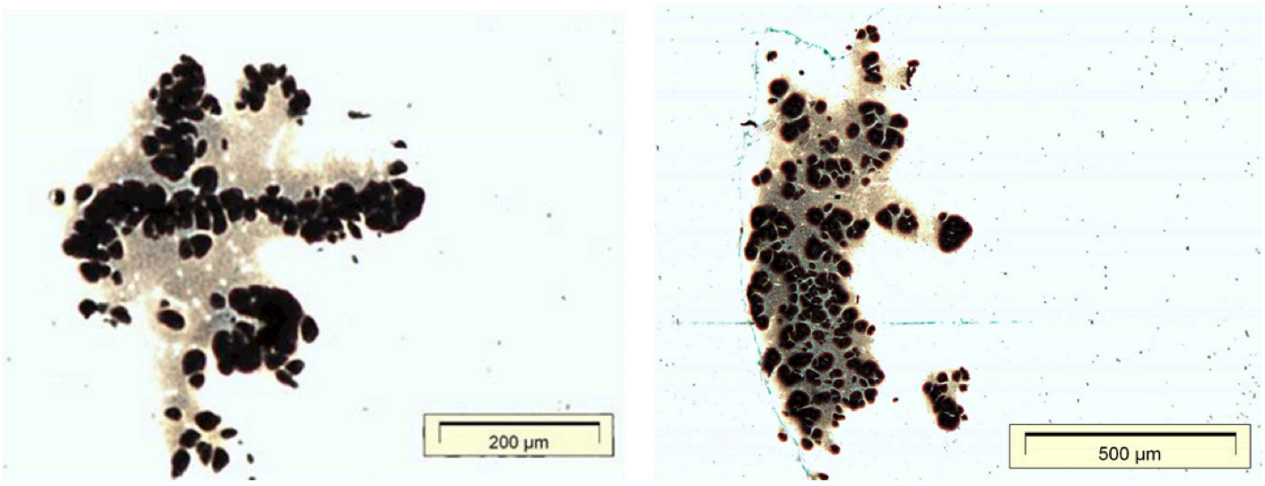

Figure 12: Exemplary images of different agglomeration behaviour of inclusions

Crucible shape, inclusion type and size, stirring duration and frequency of induction furnace will be deeper investigated by additional experiments and the full-paper will be published with more specific results in a peer review journal after this conference.

6 References

[1] V. G.Levich, Physicochemical Hydrodynamics. Englewood Cliffs, NJ: Prentice-Hall 1962

[2] S. Taniguchi and A. Kikuchi, Tetsu-to-Hagane 78, 1992, pp. 527

[3] M. Smoluchowski, Z. Phys. Chem. 92, 1917, pp. 129-168

[4] Srinivas Praveen Mokkapati, Simulation of Particle Agglomeration Using Dissipative Particle Dynamics, Master Thesis, Texas A&M University, 2006, pp. 3-10

[5] Saffman P. G. and Turner J. S. (1956): On the collision of drops in turbulent clouds. - J. Fluid Mech. vol.1, pp.16-30

[6] K. Higashitani, K. Yamaguchi, Y. Matuno and G. Hosokawa, J. Chem. Eng. Jpn. 16, 1983, pp. 299-304

[7] Mertol Gökelma, Agglomeration and Settling Behaviour of Non-metallic Inclusions in Aluminium Melts, Master Thesis, Institute IME, RWTH Aachen University, 2013

[8] Youngjo Kang, Bahman Sahebkar, Piotr R. Scheller, Kazuki Morita, Du Sichen, Observation on Physical Growth of Nonmetallic Inclusion in Liquid Steel During Ladle Treatment, Metallurgical and Materials Transactions B, June 2011, Volume 42, Issue 3, pp 522-534

[9] Hongbin Yin, Hiroyuki Shibata, Toshihiko Emi, Mikio Suzuki, "In-situ" Observation of Collision, Agglomeration and Cluster Formation of Alumina Inclusion Particles on Steel Melts, ISIJ International 37, 1997, pp. 936-945

[10] P. Weite, A Technical Perspective on Molten Aluminum Processing, Light Metals 2002, pp. 841-847

[11] Edgar Rapoport, Yulia Pleshivtseva, Optimal Control of Induction Heating Processes, by CRC Press, 2006, pp. 1-5

[12] Zhang Qingxin, Zhu Cuiyu, Tao Yong, Cui Zhanbo, The Research of Cylindrical Billets Induction Heating Based on Finite Difference Method, 2nd International Conference on Electronic & Mechanical Engineering and Information Technology, 2012, pp. 1642-1645

[13] Induktive Erwärmung; REW Energie Aktiengesellschaft; Essen; 1991; p.7-71

[14] Maksims Kirpo, Modeling of Turbulence Properties and Particle Transport in Recirculated Flows, Doctoral Thesis, University of Latvia Faculty of Physics and Mathematics Department of Physics, Riga, 2008

[15] Heinen, K.H.: Elektrostahlerzeugung (4th Edition); Verlag Stahleisen, Düsseldorf, 1997

THE BEHAVIOR OF CELESTITE IN OXALIC ACID SOLUTIONS

Mert ZORAGA, Cem KAHRUMAN, Ibrahim YUSUFOGLU

Department of Metallurgical and Materials Engineering,
Faculty of Engineering, Istanbul University, Avcilar, Istanbul, 34320, Turkey
mzoraga@istanbul.edu.tr

ABSTRACT
Celestite mineral ($SrSO_4$) is the main raw material used in strontium production. In this study the conversion of celestite to strontium oxalate in solutions containing oxalic acid ($H_2C_2O_4$) as reactant was studied at isothermal conditions under stirring. The effect of stirring speed, $H_2C_2O_4$ concentration, particle size and temperature on the conversion rate were investigated. During the conversion process, definite volumes of solutions were taken from the reactor at different times. The amounts of celestite converted were determined quantitatively by using Inductively Coupled Plasma-Optical Emission Spectrometer (ICP-OES). X-ray Powder Diffraction (XRD) technique was used for characterization. It was found that the conversion of celestite was increased by increasing the temperature, oxalic acid concentration and decreasing the particle size. The effect of stirring speed on the reaction rate was negligible.

Keywords: Celestite, Oxalic Acid, Conversion, Strontium Sulfate

SELESTİTİN OKZALİK ASİT ÇÖZELTİLERİNDEKİ DAVRANIŞI

ÖZET
Selestit minerali stronsiyum üretiminin ana hammaddesidir. Bu çalışmada reaktan olarak okzalik asit ($H_2C_2O_4$) içeren çözeltilerde sabit sıcaklıkta karıştırma yapılarak selestitin stronsiyum okzalata dönüşümü incelenmiştir. Karıştırma hızının, $H_2C_2O_4$ konsantrasyonunun, tane boyutunun ve sıcaklığın dönüştürme reaksiyonuna etkisi belirlenmiştir. Dönüştürme reaksiyonu sırasında belli sürelerde reaktörden alınan çözeltilerin kantitatif analizi ICP-OES cihazında gerçekleştirilmiş, Katı reaktanın karakterizasyonu X ışını toz difraksiyon analizi ile yapılmıştır. Selestit konsantresinin dönüşüm reaksiyon hızı üzerine karıştırma hızı, çözelti konsantrasyonu, tane boyutu ve sıcaklık parametrelerinin etkileri incelenmiştir. Sıcaklık ve $H_2C_2O_4$ konsantrasyonu arttıkça ve tane boyutu küçüldükçe dönüşümün arttığı; karıştırma hızı artışının fraksiyonel dönüşüm miktarını etkilemediği belirlenmiştir.

***Anahtar kelimeler*:** Selestit, Okzalik Asit, Dönüştürme, Stronsiyum Sülfat

1. INTRODUCTION

The celestite mineral contains strontium sulfate ($SrSO_4$) which is the main source for the production of strontium and other strontium chemicals such as strontium nitrate, strontium chloride, strontium hydroxide and strontium oxalate etc. The major use of strontium oxalate is in the synthesis of BiSCCO (bismuth strontium calcium copper oxide) high temperature superconductors. BiSCCO has been used to construct current leads for fusion applications and this material is available in industry and offers economic benefit, reducing losses at temperatures below 60 K when the magnetic background field is low [1].

The dissolution of celestite and SrS particles was found to proceed in sodium carbonate, ammonium carbonate and dissolved CO_2 solutions at low temperatures [2-14]. Also in the literature, no work was found on the behavior of celestite in oxalic acid solutions. Thermal analysis of solid compounds that was formed from strontium oxalate ions was investigated and thermally decomposed products were characterized [15-17].

The aim of this study is to determine the effects of stirring speed, oxalic acid concentration, particle size and temperature on the conversion rate.

2. MATERIALS AND METHOD

Crushed, ground and flotation-enriched celestite concentrate obtained from Barit Maden Turk A.S., Turkey was used in the conversion experiments. The celestite concentrate was wet sieved by Octagon 200 and the fraction of – 125 + 90 μm particle size was collected. Then it was dried at 378 K for 8 h. The phase characterization of celestite ($SrSO_4$) was performed using monochromatic Cu-Kα (λ=1.5406 Å) X-ray by XRD instrument (Rigaku D/Max2200). $H_2C_2O_4$ solutions prepared by dissolving of chemically pure anhydrous $H_2C_2O_4$ (Fluka) in deionized water were used in the conversion experiments.

Conversion experiments were carried out in water heated, jacketed borosilicate glass reactor (HWS DN 100) which has a volume of 1 L. The cover of the reactor included four necks. Polytetrafluoroethylene (PTFE) coated propeller was placed in the central joint. Mechanical stirrer (IKA, RW 20 DZM) was used. Cooler, temperature sensor and sampler were placed to the other joints. Solution temperature in the reactor was measured with PT100 sensor immersed into the solution. Water circulating thermostat (Julabo MV4) was used to heat the solution to reaction temperature and to maintain a constant temperature for the isothermal experimental conditions.

Conversion experiments were carried out to investigate the conversion behavior of celestite in $H_2C_2O_4$ solutions using 1 L of 0.2, 0.8 and 1.2 M of $H_2C_2O_4$ solutions, 301.5, 328 and 358 K temperatures and 8.33 rps stirring speed. When isothermal conditions were obtained 2 g of celestite concentrate was added to the reactor. Equal volume of fresh acid solution to the sample taken was added to the reactor after sampling at certain time intervals to maintain reactor volume and $H_2C_2O_4$ concentration approximately constant. Quantitative analyses of sulfate ions in the samples were carried out by ICP-OES instrument (Spectro Ciros Vision).

3. RESULTS AND DISCUSSION

Characterization of the celestite concentrate

The peaks in the XRD diagram of celestite (Fig. 1) were in good agreement with the peaks of $SrSO_4$ given in the ICDD 73–0529 card.

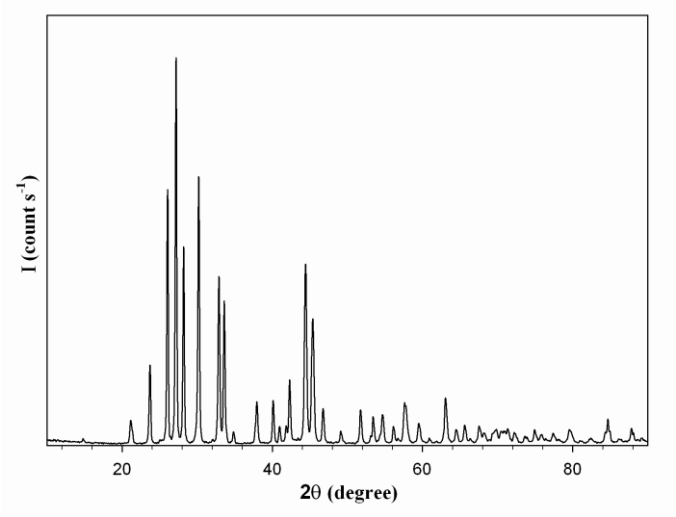

Figure 1. XRD diagram of celestite concentrate

The effects of stirring speed

The effect of stirring speed on the conversion reaction were determined using 2 g (– 125 + 90 μm particle size fraction) celestite concentrate, 1.2 M $H_2C_2O_4$ solution, 358 K temperature and 5, 6.66 and 8.33 rps stirring speeds. The fractional conversion of $SrSO_4$ (X) at any reaction time (t) was calculated according to the Eq. 1, where Wo is the initial weight of $SrSO_4$ fed to the solution, Wt is the weight of unreacted $SrSO_4$ at any reaction time.

$$X = \frac{W_0 - W_t}{W_0} \tag{1}$$

The fractional conversion of celestite (X) with respect to reaction time (t) at different stirring speeds was shown in Figure 2. It was found that the stirring speed has no significant effect on the reaction rate. Therefore in the experiments, the stirring speed was kept constant at 8.33 rps for the investigation of the effect of the other parameters on conversion.

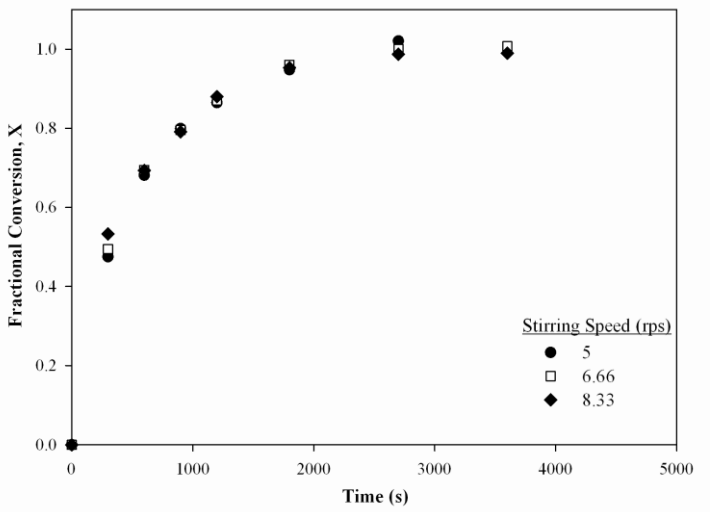

Figure 2. X vs t diagrams for different stirring speeds
(– 125 + 90 μm particle size fraction, 1.2 M $H_2C_2O_4$ concentration and 358 K temperature)

The effects of temperature and $H_2C_2O_4$ concentration

The X vs t diagrams obtained from the experiments carried out to investigate the effect of temperature at constant $H_2C_2O_4$ concentration on the conversion rate of celestite mineral were shown in Figures 3.

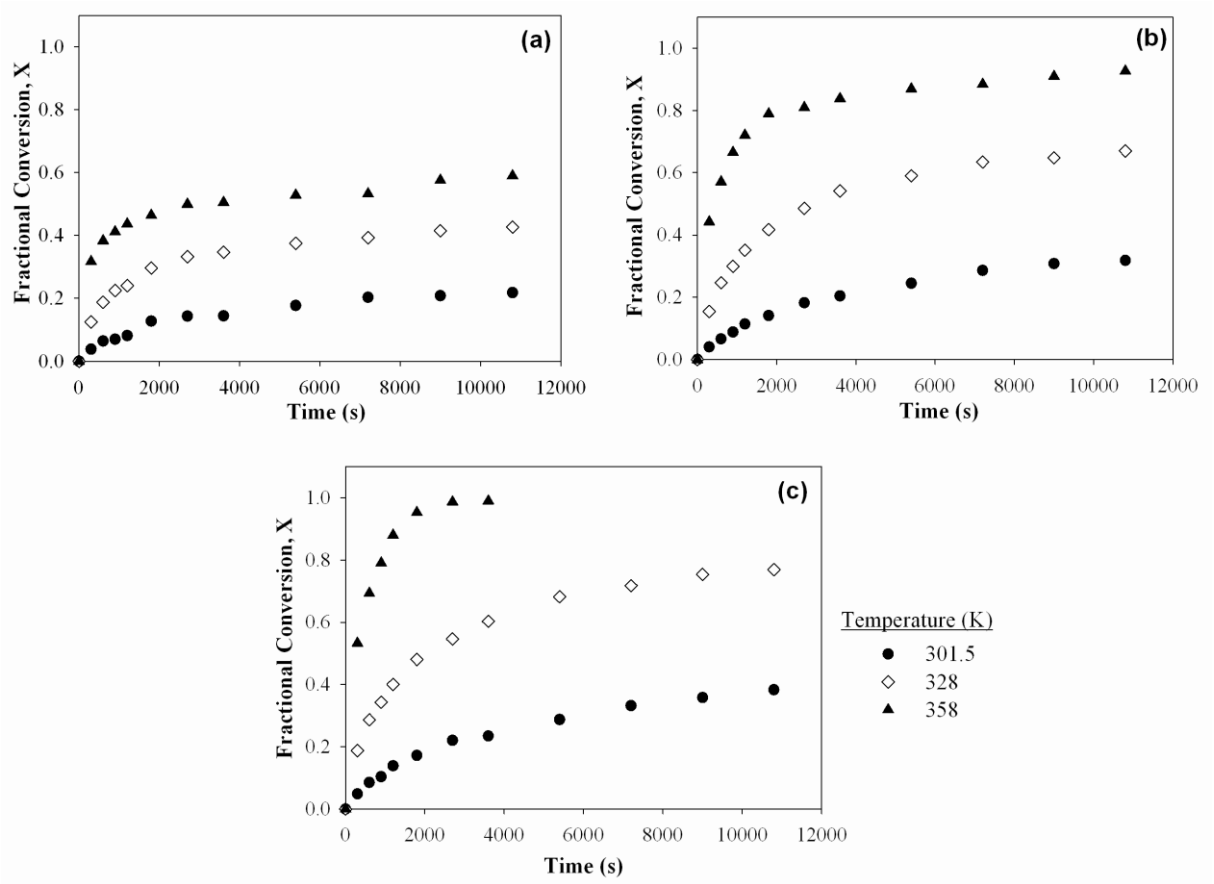

Figure 3. X vs t diagrams for different temperatures and constant $H_2C_2O_4$ concentrations; (a) 0.2 (b) 0.8 (c) 1.2 M $H_2C_2O_4$ solution
(– 125 + 90 μm particle size fraction and 8.33 rps stirring speed)

The diagrams given in Figure 3 were re-plotted at constant temperature for various $H_2C_2O_4$ concentrations in order to assist in observing the effect of $H_2C_2O_4$ concentration on the conversion rate (Fig. 4)

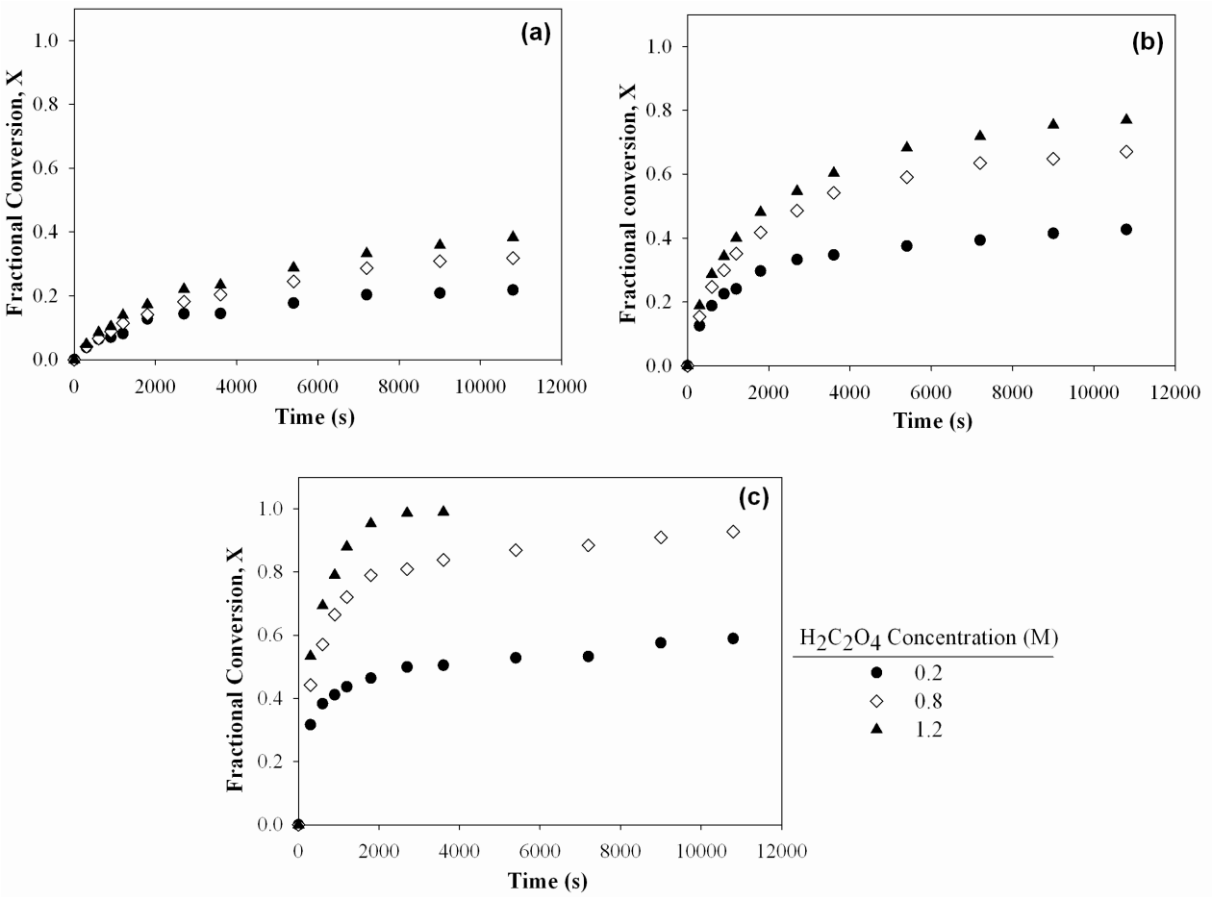

Figure 4. X vs t diagrams for different $H_2C_2O_4$ concentrations and constant temperatures; (a) 301.5 (b) 328 (c) 358 K
(– 125 + 90 μm particle size fraction and 8.33 rps stirring speed)

The effect of particle size

For the determination of particle size effect on the conversion of celestite, 2 g celestite concentrate, 1 L of 1.2 M $H_2C_2O_4$ solution, 358 K temperature and 8.33 rps stirring speed, – 38 + 45, – 125 + 90 and – 180 + 150μm particle size fractions were used. The X vs t diagrams were shown in Figure 5.

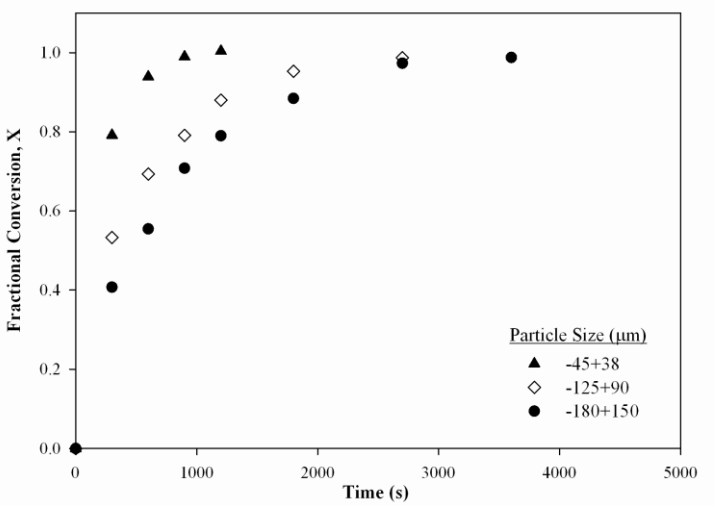

Figure 5. X vs t diagrams for different particle sizes
(1.2 M $H_2C_2O_4$ solution, 8.33 rps stirring speed and 358 K temperature)

Considering the experimental conditions given in Fig 2, stirring speed of 8.33 rps was seen to be enough to overcome the resistance of the liquid film that surrounds the celestite mineral particles. The reaction rate increases by increasing temperature (Fig. 3) and $H_2C_2O_4$ concentration (Fig. 4). The high temperature dependency of the reaction rate indicates that the chemical reaction is under chemical reaction control. In addition, decreasing the surface area of the celestite mineral particles increases the reaction rate (Fig. 5).

The conversion of the celestite mineral to strontium oxalate in $H_2C_2O_4$ solution takes place according to Eq. 2.

$$SrSO_4(s) + 1.5\ H_2C_2O_{4\ (aq)} - SrC_2O_4 0.5H_2C_2O_{4\ (s\ or\ aq)} + H_2SO_4\ (aq) \qquad (2)$$

The solubility of the acidic strontium oxalate plays an important role on the reaction rate. Therefore, the solubility of the acidic strontium oxalate should be determined. However, there are no studies in the literature on the solubility of the acidic strontium oxalate. In this work, it was found that complete dissolution of the acidic strontium oxalate formed during the reaction was achieved when 2 g of celestite concentrate was used. Therefore, 100 % conversion value was achieved in the experimental conditions studied in this work. In the experiments, where high amounts of celestite concentrate were used, while the solubility value was exceeded, a dense protective layer of acidic strontium oxalate forms on the surfaces of the celestite concentrate particles. The formation of a dense layer hindered the reaction rate and as a result the reaction could not be continued.

4. CONCLUSIONS

Celestite concentrate converts to acidic strontium oxalate in solutions containing oxalic acid as reactant. If the quantity of acidic strontium oxalate formed during the reaction is less than of its solubility value, a complete conversion of celestite was obtained. Otherwise, if the quantity of acidic strontium oxalate is more than of its solubility value, a dense protective layer forms around the particles, which hinders the chemical reaction.

REFERENCES

1. W.H. Fietz et al., Fusion Engineering and Design, 86, 1365, 2011
2. F. A. Al-Newaiser et al., Chemical Papers, 61 (5), 370, 2007
3. M. Erdemoglu and M. Canbazoglu, Hydrometallurgy, 49, 135, 1998
4. G. Owusu and J.E. Litz, Hydrometallurgy, 57, 23, 2000
5. M. Iwai and J.M. Toguri, Hydrometallurgy, 22, 87, 1989
6. A.H. Castillejos-Escobar, F.P. De La Cruz-Del Bosque and A. Uribe-Salas, Hydrometallurgy, 40, 207, 1996
7. F. De Buda, U.S Patent Office, no. 4,666,688, 1987
8. S. Kocakusak et al., World Intellectual Property Organization, no. WO 0177021, 2001
9. M. Erdemoglu, M. Sarikaya and M. Canbazoglu, Journal of Dispersion Science and Technology, 27, 439, 2006
10. S. Aydogan et al., Hydrometallurgy, 84 (3-4), 239, 2006
11. M. Erdemoglu, S. Aydogan and M. Canbazoglu, Hydrometallurgy, 86, 1, 2007
12. D. Bingol, S. Aydogan and S.S. Gultekin, Chemical Engineering Journal, 165 (2), 617, 2010
13. D. Bingol, S. Aydogan and S. K. Bozbas, Journal of Industrial and Engineering Chemistry, 18 (2), 834, 2012
14. D. Bingol, S. Aydogan and S. K. Bozbas, Metallurgical and Materials Transactions B, 43 (5), 1214, 2012
15. E.D. Bacce, A.M. Pires, M.R. Davalos and M. Jafelicci Jr, International Journal of Inorganic Materials, 3, 443, 2001
16. S.A. Selim and M. Abd-El-Khalik, Powder Technology, 20, 53, 1978
17. D. Dollimore, Thermochimica Acta, 117, 331, 1987

Eco Audit in Materials Selection

•

Malzeme Seçiminde Eko Denetim

Kazım Tur, Ozan Özkan
Atılım University - Türkiye

ABSTRACT

The focus of this paper is on the role of materials and processes among many human activities that have damaging effect on the environment and on how to incorporate eco-impact of materials in the early stages of design.

The intense competition among materials for products drives innovation in materials, cost reductions, and new designs both in terms of materials and in terms of the products and processes that compose world economic activity. A component or product can be made from a number of materials, with resulting differences in performance, cost, and other attributes. It is not sufficient to select the best material based on mechanical properties, cost, weight, etc. Environmental cost of the design should also be considered. Selecting a material is extremely complex and must satisfy the demands of consumers, corporations and politics. Therefore it involves balancing the usefulness, longevity, safety, cost, and style of a product, as well as its life-cycle energy and materials use, environmental discharges, recyclability, and depletion of scarce resources. One way to tackle this issue is using eco-indicators. However, they are determined from estimates, government policies and scientific estimates, and thus they are of arbitrary nature.

There are thousands of materials that a designer/engineer might choose, together with the millions of applications for materials. Different materials offer a huge range of properties: strength, stiffness, melting point, cost, and appearance. Finding the best material for each application is therefore an extremely challenging task, particularly because there are alternative product designs, each favoring a different material. Once a material has been selected for a product, dynamic factors work to impede the substitution of one material for another. Because engineers and workers become comfortable with a particular material, they are reluctant to pay the startup costs of substituting a new material, even when it offers superior characteristics in some respects such as decreased energy use, reduced risks to the environment and human health, and reduced consumption of scarce resources. The selection of design/materials is becoming more science and less art as computer modeling is able to encompass more of the dimensions of the selection process.

Life Cycle Assessment (LCA) techniques are generally used to deal with the environmental impact of a product. An LCA analysis examines the life cycle of a product and assesses the eco-impact it creates. It is a tool for the evaluation and comparison of existing products, rather than one that guides the new product designs. Therefore; LCA is considered as a product assessment tool, not a design tool and it is of no help for the decisions taken in the early stages of design. Moreover, a full LCA is time-consuming, expensive, and requires much detail, and it cannot cope with the problem that 80% of the environmental burden of a product is determined in the early stages of design during which many decisions are still changeable. Therefore; a design tool is also required that guides environmental awareness and exploits the information available early in the design process to minimize the materials damage on the environment. One important software tool for this purpose is CES Eco Selector and in an effort to increase the environmental awareness of prospective engineers, CES EduPack Eco Design Edition has been utilized since 2010 in Materials Selection in Design courses offered by the author at Atılım University. This paper introduces the problem, describes the method used in the software and illustrates the use of the system for selection with some examples incorporating embodied energy, CO_2 Footprint, NOX and SOX creation, effect of recycle content, material processing energy and CO_2, Turkey's energy mix and associated environmental footprint and end of life calculations.

Keywords: Materials selection in design, environmental cost,life-cycle energy, recyclability, eco-indicators, life cycle assessment, embodied energy, CO_2 footprint, NOX and SOX creation, environmental footprint.

RECOVERY OF GOLD FROM JEWELLERY BASED SLAGS BY FLOTATION

Cevahir DURMAZ, Yasin KILIÇ, Servet TİMUR

Istanbul Technical University, Metallurgical and Materials Eng. Dept., Istanbul- Turkey

ABSTRACT

Jewellery wastes, occurred at different stages with low gold content, can be generally recovered by hydrometallurgical and pyrometallurgical processes. Soda-borax based jewellery slags, generated during pyrometallurgical processes of refining, include gold grains defined as non-recoverable. In this study, recovery of these gold grains from these slags by flotation technique was researched. The effects of pH value and collector reagent type were investigated with the experiments performed by using the liberalization size of metallic grains in the slag structure,–38µm. As a result, the favorable impacts of natural pH value and dithiophosphate type collectors were determined on gold recovery by flotation.

Keywords: Recovery, Gold, Slag, Flotation.

KUYUMCULUK KÖKENLİ CURUFLARDAN FLOTASYONLA ALTIN GERİ KAZANIMI

ÖZET

Kuyumculuk işlemlerinin farklı aşamalarında ortaya çıkan altın içeriği düşük atıklarından, hidrometalurjik ve pirometalurjik prosesler yoluyla, altın geri kazanılabilmektedir. Pirometalurjik prosesler süresince ortaya çıkan soda-boraks esaslı curufların içerdiği altın tanecikleri geri kazanılamaz şeklinde tanımlanmaktadır. Bu çalışmada; curuflarda kalan altın taneciklerinin flotasyon yöntemiyle geri kazanımı araştırılmıştır. Deneylerde, metalik tane sebestleşmesinin -38 µm olduğu curuf kullanılarak pH değerinin ve toplayıcı reaktif türünün curufun flotasyonu üzerine etkisi incelenmiştir. Sonuç olarak; curuftan flotasyon ile altın geri kazanımında, doğal pH değerinin ve dithiyofosfat tipi toplayıcı reaktiflerin olumlu etkisi olduğu tespit edilmiştir.

Anahtar Kelimeler:Geri kazanım, Altın, Curuf, Flotasyon.

1. INTRODUCTION

Throughout history, gold was used for jewellery and money. At the present jewellery sector consumes 86% of gold production [1,2]. A considerable amount of noble metals are being lost in mechanical workings during jewellery manufacture. These valuable losses have a significant influence on not only the cost of the final gold product but also the competiveness of marketplace [3].

Jewellery wastes that are produced in manufacturing steps can be recovered with hydrometallurgical and pyrometallurgical processes. The slags, generated by pyrometallurgical processes, are entrapped substantially quantity of the gold grains in their structure.

The amount of entrapped gold depends on the melting temperature and time. In some cases, it can be up to 1200 g/t [4]. The aim of this research is to recover gold from jewellery based slag by flotation method.

2. MATERIAL AND METHODS

The slag is generated at the pyrometallurgical gold production was firstly recovered by the classical pyrometallurgical process and the remained tailing was used as a raw material in this study.

In experimental investigation; laboratory ball mill, test sieves, Humboldt Wedag mechanical flotation machine, flotation cells with different volume, pH meter, flotation reagents (collector and frother) were utilized.

Firstly, the size reduction of the raw material was performed by ball mill. After milling, it was sieved under -38 µm and separated as 500g samples. In flotation experiments; 500g samples, tap water, Aerofloat 208 and Aero 8761(dithiophosphate type), Aerophine 3418A (dialkaline dithiophosphate type), Aero Mx 980 (contains alcohols, eathers and mixture of aldehyde, carbamic acid, butylcarbamate and butanol) as collector reagents and Oreprep F- 523 (alcohol mixtures, heavy aldehydes, esters and polyglycols) as frother were used. The all experiments were performed as 5 steps rough and 2 steps cleaning flotation stages (see Figure. 1).

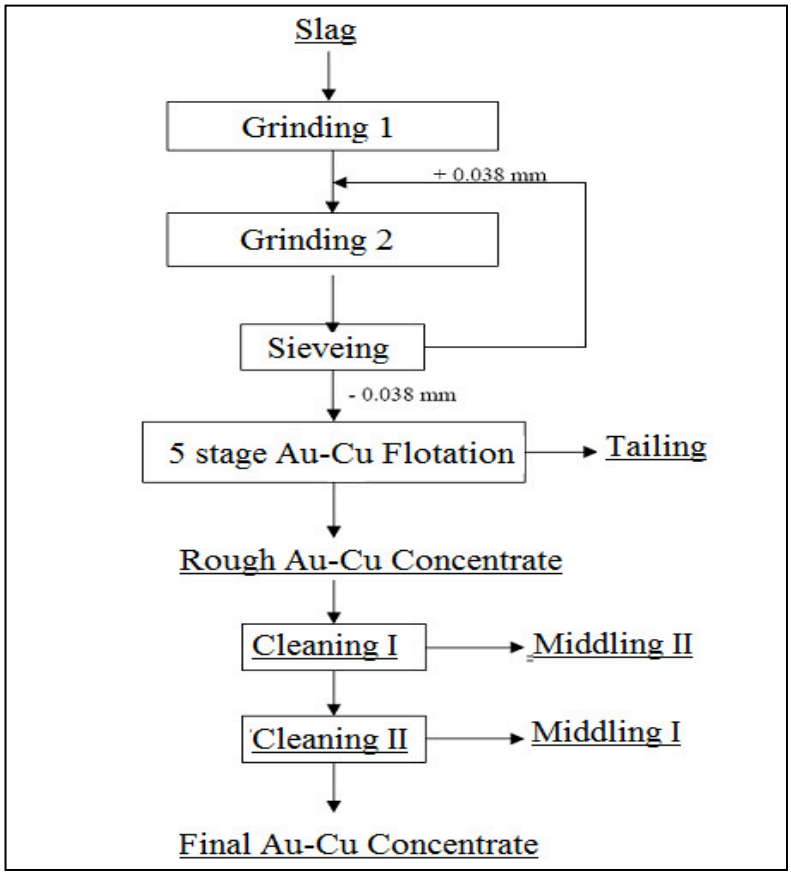

Figure 1: Experimental flowchart.

2.1. The effect of pH value

In flotation experiments to investigate the effect of pH value on gold recovery, Aerofloat 208 and Aerophine 3418A collector reagents (50 g/t) were used in acidic and alkaline conditions. Slag has an alkaline characteristic, thus; there wasn't any requirement of regulative chemical. On the other hand, H_2SO_4 was added into pulp to reach acidic pH value. The experimental conditions for alkaline and acidic pH values were summarized in Table 1 and 2.

Table 1: Experimental conditions at acidic pH value

Parameter	**Amount per step**
pH value of pulp	4.82-5.60
Aerofloat 208	50+50+50+50+50+50+50 g/t
Aerophine 3418A	50+50+50+50+50+50+50 g/t
Oreprep F-523	10+10+10+10+10+10+10 g/t
Condition time	5+3+3+3+3+3+3 min.
Flotation time	5+4+3+3+3+6+5 min.

Table 2: Experimental conditions at alkaline pH value

Parameter	**Amount per step**
pH value of pulp	10.28-10.71
Aerofloat 208	50+50+50+50+50+50+50 g/t
Aerophine 3418A	50+50+50+50+50+50+50 g/t
Oreprep F-523	10+10+10+10+10+10+10 g/t
Condition time	5+3+3+3+3+3+3 min.
Flotation time	5+3+3+3+3+6+5 min.

2.2. The effect of collector type

The experiments were performed with different type of collector reagents so as to determine the effect on gold recovery. The collector reagents; Aerofloat 208- Aerophine 3418A, Aero 8761- Aerophine 3418A, Aero Mx 980 and frother reagent; Oreprep F-523 was used in the experimental studies.5 rough and 2 cleaning steps were applied for flotation. In the rough and cleaning stages, the amount of used collector reagent was 50 g/t.The experimental conditions with different reagents were summarized in Table 3, 4 and 5.

Table 3: Experimental conditions with Aerofloat 208 - Aerophine 3418A collector reagents

Parameter	**Amount per step**
pH value of pulp	9.57-10.13
Aerofloat 208	50+50+50+50+50+50+50 g/t
Aerophine 3418A	50+50+50+50+50 g/t
Oreprep F-523	10+10+10+10+10+10+10 g/t
Condition time	5+3+3+3+3+3+3 min.
Flotation time	5+3+3+3+3+6+5 min.

Table 4: Experimental conditions with Aero 8761 - Aerophine 3418A collector reagents

Parameter	Amount per step
pH value of pulp	9.52-10.18
Aero 8761	50+50+50+50+50+50+50 g/t
Aerophine 3418A	50+50+50+50+50 g/t
Oreprep F-523	10+10+10+10+10+10+10 g/t
Condition time	5+3+3+3+3+3+3 min.
Flotation time	5+3+3+3+3+6+5 min.

Table 5: Experimental conditions with Aero Mx 980 collector reagent

Parameter	Amount per step
pH value of pulp	9.66-10.15
Aero Mx 980	50+50+50+50+50+50+50 g/t
Oreprep F-523	10+10+10+10+10+10+10 g/t
Condition time	5+3+3+3+3+3+3 min.
Flotation time	5+3+3+3+3+6+5 min.

3. RESULTS

3.1. The effect of pH value

The pH value changes in the range of 4.82-5.60 for the acidic pH conditions. Consequently, 322 g/t Au was recovered with the efficiency of 2.76 % (Table 6). In alkaline condition, pH value range changes between 10.28-10.71. This condition has demonstrated that the concentrate consists of 296 g/t recovered Au with the 30.06 % efficiency (Table 7). Taking into consideration both the results achieved in acidic and alkaline pH conditions and also the alkaline characteristics of slags, it is decided to study with natural pH value.

Table 6: Experimental result at acidic pH value [pH= 4.82-5.60].

PRODUCT	WEIGHT		Au [%]	DISTRIBUTION [Au]		Cu [%]
	[g]	[%]		[g]	[%]	
Concentrate	1,50	0,30	0,0322	0,0005	2,76	3,22
Middling	22,50	4,71	0,0096	0,0022	12,34	0,96
Tailing	478,00	95,22	0,0031	0,0148	84,67	0,31
Feed	502,00	100,00	0,0035	0,0175	99,78	0,35

Table 7: Experimental result at alkaline pH value [pH= 10.28-10.71].

PRODUCT	WEIGHT		Au [%]	DISTRIBUTION [Au]		Cu [%]
	[g]	[%]		[g]	[%]	
Concentrate	19,60	3,94	0,0296	0,0058	30,06	2,96
II. Middling	73,50	18,82	0,0032	0,0024	12,19	0,32
I. Middling	14,40	2,89	0,0041	0,0006	3,06	0,41
Tailing	390,50	78,41	0,0027	0,0105	54,63	0,27
Feed	498,00	100,00	0,0037±%5	0,0193	99,94	0,37±%5

3.2. The effect collector reagent type

The influences of collector reagent type on the gold recovery experimental results were shown in Table 8, 9 and 10. The concentrate comprises the amount of recovered gold with Aerofloat 208 - Aerophine 3418A reagent couple as 318 g/t with 27.06 % efficiency; with Aero 8761-Aerophine 3418A reagent couple as 293 g/t with 27.31 % efficiency and with Aero Mx 980 as 277 g/t with 31.28 % efficiency. According to grade of concentrates, the most effective result is determined as 50 g/t Aerofloat 208- Aerophine 3418A collector reagent couple with the amount of 318g/t recovered Au.

Table 8: Experimental results of Aerofloat 208 - Aerophine 3418A collector reagents

PRODUCT	WEIGHT		Au [%]	DISTRIBUTION [Au]		Cu [%]
	[g]	[%]		[g]	[%]	
Concentrate	15,1	3,04	0,0318	0,0048	27,60	3,18
II. Middling	63,5	15,82	0,0040	0,0025	14,60	0,40
I. Middling	15,8	3,19	0,0051	0,0008	4,63	0,51
Tailing	401,5	80,96	0,0023	0,0092	53,07	0,23
Feed	495,9	100,00	0,0035	0,0174	99,90	0,35

Table 9: Experimental results of Aero 8761 - Aerophine 3418A collector reagents

PRODUCT	WEIGHT		Au [%]	DISTRIBUTION [Au]		Cu [%]
	[g]	[%]		[g]	[%]	
Concentrate	16,5	3,31	0,0293	0,0048	27,31	2,93
II. Middling	41,5	9,65	0,0041	0,0017	9,61	0,41
I. Middling	9,8	1,97	0,0047	0,0005	2,60	0,47
Tailing	430	86,38	0,0025	0,0108	60,73	0,25
Feed	497,8	100,00	0,0036	0,0177	100,26	0,36

Table 10: Experimental results of Aero Mx 980 collector reagent

PRODUCT	WEIGHT		Au [%]	DISTRIBUTION [Au]		Cu [%]
	[g]	[%]		[g]	[%]	
Concentrate	20,1	4,02	0,0277	0,0056	31,28	2,77
II. Middling	89,8	24,26	0,0031	0,0028	15,64	0,31
I. Middling	20,3	4,06	0,0044	0,0009	5,02	0,44
Tailing	370,2	73,98	0,0023	0,0085	47,83	0,23
Feed	500,4	100,00	0,0035	0,0178	99,77	0,35

The comparison of collector reagent type with reference to efficiency has indicated that Aero Mx 980 has provided 31.28 % gold recovery in the concentrate. As a result, Aero Mx 980 can compete with other collector reagents even if it is used as separately (see Figure 2).

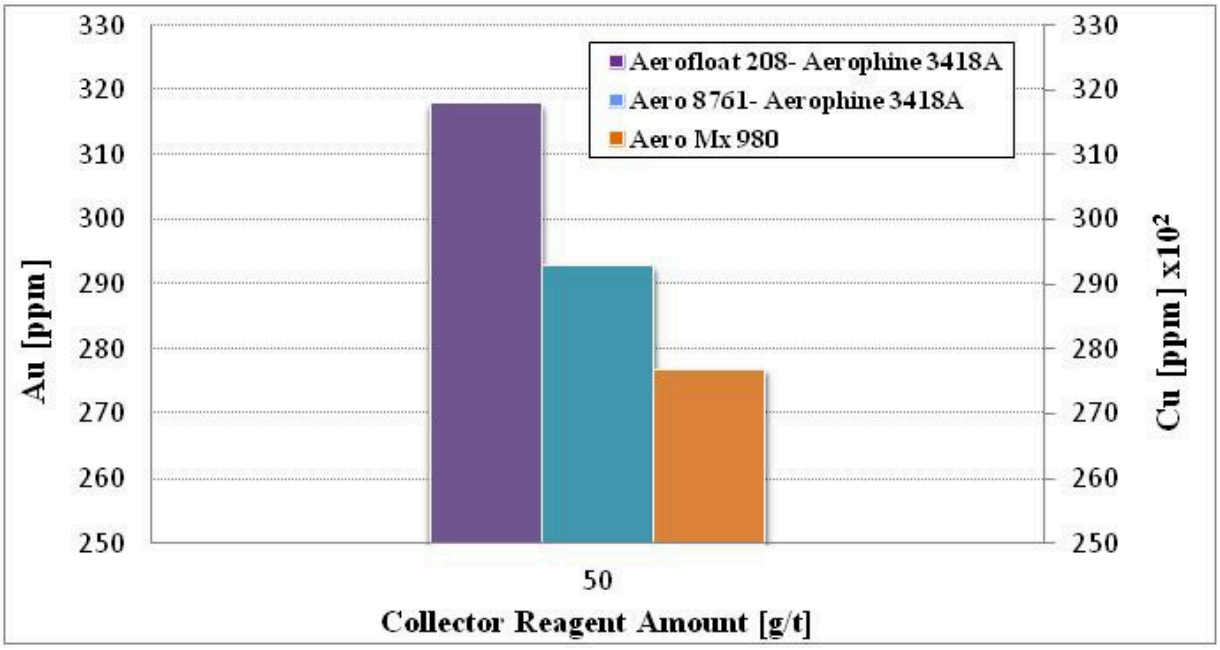

Figure 2: The effect of collector reagent type on concentrate grade [50g/t]

4. CONCLUSION

The flotation experiments in acidic pH conditions have given insufficient results compare with the alkaline pH. The natural pH value has favorable impact on flotation of gold. In natural Au-Cu flotation, Aerofloat 208- Aerophine 3418A was indicated as the most effective reagent couple. In this study, promising results are achieved within the scope of gold recovery from jewellery based slags by flotation.

Acknowledgement

Authors would like to thank ONSA RAFİNERİ for their valuable supports and their sample supply all along this research.

REFERENCES

1. V. Oygür and C. Zanbak, "Altın madenciliğinin türk ekonomisine katkısı", International Precious Stones and Metals Symposium, Yurt madenciliğini geliştirme vakfı yayınları, Istanbul, Türkiye, 2, Nisan 2005.
2. B. Gürdal, "Cila ramatlarından altın geri kazanımı", M.Sc. Thesis, Istanbul Technical University, Istanbul, 2008.
3. S. Kaspin, Z. M. Shaari, N. Mohamad, "An investigation on the effectiveness of traditional gold recovery process for jewellery scrap". Downloaded date: April 30th, 2012, adres:http://eprints.ptar.uitm.edu.my/3112/1/LP_SAADIAH_KASPIN_09_24.pdf.
4. Durmaz, C., "Kuyumculuk kökenli curuflardan fiziksel zenginleştirme yöntemleri ile altın geri kazanımı", M.Sc. Thesis, Istanbul Technical University, Istanbul, 2012.

PRETREATMENT OF JEWELRY WASTES BY PYROLYSIS TECHNOLOGY

Hasret AĞIRCAN, Levent KARTAL, Yasin KILIÇ, Servet TİMUR

Istanbul Technical University, Maslak, Turkey

ABSTRACT

Polishing dust waste that is combustible contains a wide array of impurities. To recovery precious metals from polishing dust waste, we used pyrolysis method and to prevent secondary reactions that decreases conversion yield, we preferred infrared heating. In this study, firstly effect of temperature on conversion yield was searched in electric resistance furnace. Yield increased from %29.65 to %36.86. The time was determined as 2.5 hours and reaction temperature was searched as 500°C. Effect of sweeping gas was investigated with 2.5 hours and 500°C temperature and it was found that yield was higher according to sweep gas when no in use. But increasing of gas flow rate has no effect on conversion yield. The time effect in the infrared furnace was searched at 500°C temperature. When time increased 1 hour to 2.5 hours, yield changed only about %1.15. The reaction time was confirmed shorter around 1.5 hour according to electric resistance furnace and it was observed that dusting was prevented.

Keywords: Polishing dust, Pyrolysis, Infrared heating

KUYUMCULUK ATIKLARININ PİROLİZ TEKNOLOJİSİ İLE İYİLEŞTİRİLMESİ

ÖZET

Cila ramatları, düşük kaliteli ikincil altın kaynaklarından olup, bünyesinde envai çeşit atık barındıran, yanabilir atıklardır. Tozlaşmayı önlemek için piroliz ön iyileştirme metodu olarak seçilmiştir. Piroliz daha küçük hacimli gaz oluşturması, bu gazlarla taşınan partikül sayısının oldukça düşük olması ve kanserojen olan NO_x ve PAH emisyon değerlerini azaltması avantajlarından dolayı oldukça popüler bir ileri termal teknolojidir. Pirolizde istenmeyen ikincil reaksiyonların oluşmasına neden olan klasik ısıtma sistemlerine alternatif olarak infrared ısıtma teknolojisi kullanılmıştır. Sıcaklığın piroliz üzerindeki etkisini incelemek için yapılan deneylerde verim %29.65'den, %36.86'ya yükseldiği görülmüştür. Sürekli tartım sisteminde kütlenin sabit tartıma ulaştığı süre 2.5 saat, verimin en yüksek olduğu sıcaklık ise 500°C olarak belirlenmiştir. Süpürücü gaz kullanımının dönüşüm oranı üzerindeki etkisi incelendiğinde ise; gaz kullanılmayan piroliz sistemi veriminin düşük olduğu, artan gaz hacmiyle verimin değişmediği görülmüştür. İnfrared fırında, sürenin incelendiği deneylerde verimin %1.15 oranında değiştiği görülmüştür. İnfrared fırındaki piroliz süresinin klasik fırındaki piroliz süresine göre 1 saat kısa olduğu belirlenmiştir. Fırın baca çıkışında yapılan analizde Ag'e rastlanmamış, tozlaşmanın önlendiği görülmüştür.

Anahtar kelimeler: Cila ramatları, Piroliz, İnfrared ısıtma

1. INTRODUCTION

Polishing dust that is formed when executed mechanical polishing treatment in jewelry manufacture, is low quality of secondary gold resources. From the jewelry surface, during the polishing process, precious metals particles are broken off by effect of abrasion and to reduce loss of material and vacuum motor captures them which are micrometric size. It that collected in vacuum bag, is named polishing dust waste which contains a wide array of wastes like as pumice stone, nails, parts of brushes, papers and bottles.

In conventional method, to recovery precious metals from polishing dust, combustion technology is used. This treatment method is becoming increasingly impracticable as concerns over environmental pollution and additional precious metals particles are carried out by the flames. In combustion method, due to using of air of above stoichiometric ratio, large volume gas of which NO_x emissions amount is too high, occurs. Unlike necessary oxygen amount is supplied to combustion chamber, amount of CO increases and the result of this unburned materials are seen. When the moisture content of waste is high, it decreases the yield of combustion [1],[2]. Thermal conversion methods are combustion, gasification and pyrolysis to transport waste to energy. In these three methods, combustion has a big part in the depletion of ozone layer due to large amounts of CO_2 that results global warming. The using of air in combustion thermal process, increases SO_x and NO_x emissions that causes the highest acidification impact [3]. The combustion can supply recovery of energy, but it also occurs dioxins (PCDD), polyaliphatic hydrocarbons (PAHs), VOCs and particles problem that affect on environment and human healthy, in the combustion of sophisticated masses [4]. The pyrolysis and gasification work on lower temperature and that assists to decrease NO_x and SO_x emissions and avoid formation of PCDD/F. The production of smaller gas volumes by pyrolysis and gasification, minimize the extents of gas cleanup systems so expenditure of them is reduced [5]. But some disadvantages of gasification as required high temperature according to pyrolysis, existence of tars and particulates, make it disfavor. But some researches evaluate pyrolysis as a part of gasification and it is explained that initially pyrolysis of mass accrues and then gasification of char that called Boudouard reaction between solid and steam occurs. If reactor reserves water, pyrolysis ought to be preferred, otherwise gasification ought to be preferred [6]. All of disadvantages of combustion show that, to prevent dusting and reduce to loss of precious small metal particles, the combustion method must be put off in jewelry manufacture so that pyrolysis has been chosen as a thermal conversion method to recovery precious metals from polishing dust.

Pyrolysis is one of thermal conversion method that consists of absence of oxygen around 500°C temperature. In fact, pyrolysis has been used for a long time, but it has been great value for last 4 decades, due to substantial productions [2], [7]. Pyrolysis is thermal decomposition of waste and an endothermic reaction [8], [9]. Productions of pyrolysis process are gas which is combusted to generate electric, liquid that is valuable just as petroleum [10] and solid, called char which can be used as an inert material due to pure carbon [11]. The major reactions of pyrolysis process occur in three stages; the first stage is loss of moisture of mass, the second stage is broken down of unreacted part of mass into volatile components (VOCs) and primary char and the third stage is an increase carbon content of char and in this stage the decomposition rate is quite low [12]. The pyrolysis of mass consists of endothermic and exothermic reactions. The endothermic reactions occur in second stage where VOCs and primary char are seen and after than secondary reactions create exothermic reactions. [13]. The secondary reactions which are undesirable likes as decomposition and polymerization,

happens because of reactions between pyrolysis vapor productions and char when mass is pyrolyzed [14], [15]. Pyrolysis is mentioned as a carbonization in earlier [16],[17], but nowadays perceived to product liquid which can be stored, easily transported and used to generate energy as needed [10],[18],[2]. Slow and fast pyrolysis processes are used for pyrolysis of mass. The slow pyrolysis is correlated to production of char for which slow heating rate, long char and gas residence time are required [19]. To product high liquid yield, fast pyrolysis of which parameters are particle size, temperature, vapour residence time, reactor design, heat transfer is preferred. At 500 °C temperature, the highest liquid yield is reached by the short residence time [18]. In the pyrolysis process, to increase the yield of char, low temperature and low heating rate; for the highest liquid yield, low temperature and short residence time; for the valuable gas product, high temperature, short heating time and long residence time must be chosen [20]. The changes which occurred during the thermal conversion is related to the heating rate [21],[22]. At high heating rate, the decomposition provides high yield of tar, although it increases yield of char and water amounts at low heating rate. The char is product of repolymerization that is the result of secondary reactions which occur in slow pyrolysis process. To prevent secondary reactions, size of mass particles must be made smaller or heating rate must be increased [22]. Low thermal conductivity materials also causes secondary reactions so that fast pyrolysis must be favored to increase the yield of liquid [18].

In the pyrolysis process, temperature, pressure and heating rate as well as qualification of mass is a substantial parameter. The heat transfer ability of mass and char is very low [23]. Pyrolysis reaction time of the low thermal conductivity materials like engine oil is more longer because of slow heat transfer. The traditional heating system that heats all of substances of furnaces until reaching the reaction temperature so that a large of energy is wasted and secondary reactions also occur due to heating of air in the furnace chamber. The secondary reactions also induce formation of PAHs and increasing yield of char [24]. Due to disadvantages of traditional heating methods, some researchers use new heating system like microwave, plasma heating on pyrolysis process [25]. Once microwave heating system is evaluated according to conventional heating, it is seen to have several advantages as energy-efficient, targeted mass to heat [26], controlled and rapid heating, no contact between heater and surface of sample [23], shorter reaction time, using of less inert gas and smaller furnaces [27]. The flow of volatiles pyrolysis production actualize from inner hot zone to outer cold zone so that secondary reactions and sediments on the surface of the refractor is prevented [23]. In this study due to advantages of electromagnetic radiation, we have applied infrared radiation which has similar operating principles with microwave to eliminate organic components of polishing dust waste by pyrolysis method.

2. EXPERIMENTS

2.1 Materials

Polishing dust waste that contained Ag was provided from Altınbaş Jewelry Manufacture Company. The sample structure was quite complex so it was impossible to implement a physical pre-treatment method. The experiments performed as samples were carried out from homogenous regions of the mass by qualitative basis.

2.2 Sample Analysis

The mass was dried in drying-oven to determine the moisture content. To find amount of ash, mass was burned until the mass reached the constant mass. Some of mass was placed

in receptacle that was having certain volume to measure bulk density. To have knowledge about weight loss, DSC-TGA analyses of polishing dust and polishing material that used during the abrasive blasting operation.

2.3 Conventional Pyrolysis Experiments

Pyrolysis experiments were performed in a nitrogen atmosphere at constant heating rate 10°C min^{-1}. Primarily electric resistance furnace was used for pyrolysis experiments. A retort which had 502.4 cm^3 volume, was done to use as sample vessel. To prevent heat loss, surrounding of retort was wrapped by fiberglass. Appropriate connections were done to install condenser to gas outlet pipe of retort and gas washing bottles were added to system. In this study, firstly the sample was heated up to different temperature (400,450, 500, 550, 600, 650 °C) to determine the pyrolysis temperature at constant time and sweeping gas flow rate.

Continuous Weighing System:

In pyrolysis experiments to investigate time that mass reached constant weighing, Sartorious brand CP 423S weight was integrated to system. The codes of Below Balance Weighing and Data Output features of weight were logged in to data transfer. The data were transferred to computer by RS Multi Weight program. In this system that does not require manual operation, the time when mass reached constant weight achieved at different temperatures (400, 450, 500 or 550°C). The furnace was heated up from 25 °C temperature to final temperature at constant heating rate 10 °C min^{-1}.

Sweeping Gas Experiments

Effect of sweeping gas flow was searched with helps of the obtained results. To investigate the effect of sweeping gas flow on conversion yield, 20, 40, 60 or 80 l/h flows were used.

2.4 Infrared Pyrolysis Experiments

In the infrared furnace, pyrolysis was realized at 500 °C temperature that was procured from pyrolysis experiments of electric resistance furnace and at different times (1, 1.5, 2, 2.5 hours). The time experiments were practiced at a constant sweeping gas rate 300 l/h. When the inlet temperature raised to 500 °C temperature, air was used as a sweeping gas. To define if Ag was carried out, glass pipe that was placed in flue outlet of the furnace, was compounded by HNO_3 and the solution was analyzed in ASS.

2.5 Production Analysis

With effect of increasing temperature, to examine the changes occurring in the solid production, analysis of solid production was performed by Perkin Elmer brand FTIR machine.

3. RESULTS AND DISCUSSION

3.1 Features of Sample

The features of polishing dust waste were given in Table 1. The Ag content of waste was specified around %10 by the hydrometallurgical processes.

DSC-TGA analysis of polishing dust was shown in Figure 1. According to results of analysis between 0 and 200 °C temperatures, weight of polishing dust showed a negligible change. Between 200 and 400 °C temperatures, the weight had decreased rapidly. The weight had indicated a low amount of change between 400 and 600 °C temperatures and then the mass had reached a constant weight.

Table 1 : The features of polishing dust

Moisture content	% 1.14
Volatile compounds	% 30-38
Bulk density	0.45 g cm^{-3}
Content of Ag	% 10

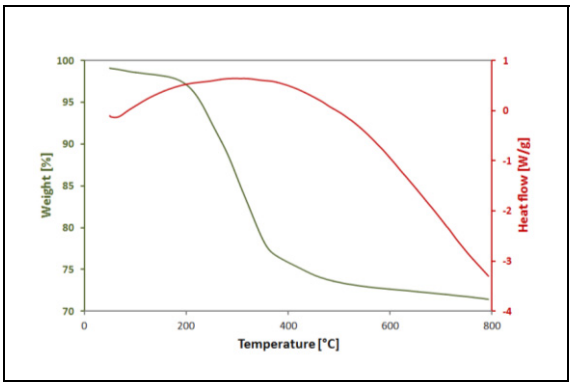

Figure 1: DSC-TGA analysis of polishing dust

3.2 Effects of temperature

Different temperatures were proved at constant time 1hour and sweeping gas rate 20 l/h N_2 to investigate yield of thermal conversion. The total thermal conversion yield change with temperature placed in Figure 2. The thermal conversion yield was searched from 400 °C temperature to 650 °C temperature.

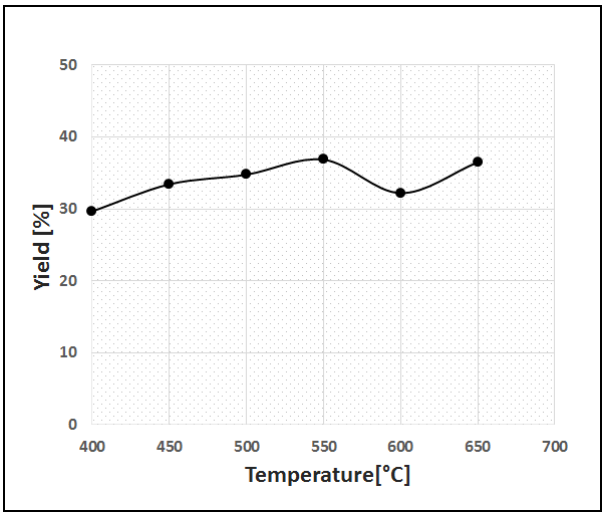

Figure 2: Effects of temperature on pyrolysis yield [1 h, 20 l/h]

The conversion yield increased from %29.65 to %36.86 between 400 and 550 °C temperatures. At 600 °C temperature the yield decreased to %32.21which of reason could be sampling error. The yield improved again to %36.5 at 650°C temperature that was nearly same with yield of 550°C.

Effect of time on weight

At different temperatures to define the time when the mass reached to a constant weight, data were taken at intervals of 7 seconds in continuous weight system. The experiments were achieved in the electric resistance furnace without using sweeping gas. The results of experiments were given in the Figure 3. At 400°C temperature the mass didn't come to a constant weight of which reason could be incomplete reactions. At 450°C temperature, the weight loss rate was very high between 30 and 60 minutes. Then weight loss continued descending rapidly between 60 and 120 minutes.

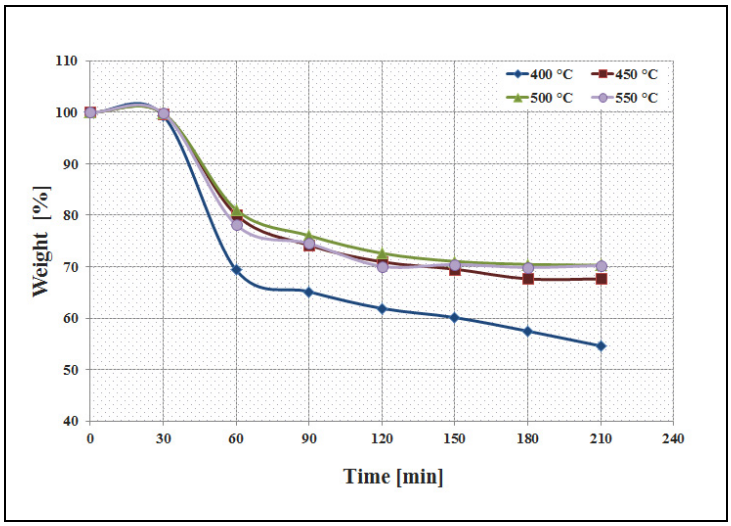

Figure 3: Definition of time that the mass reached to a constant weight at different temperatures

The weight loss changed in negligible amount between 150 and 180 minutes and finally it was seen that the mass reached to a constant weight 180 and 210 minutes. For 500°C and 550°C temperatures, the weight changes occurring in mass, were the same with 450 °C temperature between 30 and 150 minutes. The constant weight was obtained between 150 and 210 minutes for two temperatures, whereas it was seen between 180 and 210 minutes for 450°C temperature. The thermal conversion yield was the same for 500°C and 550°c temperatures, %29.7 and %29.65. The result showed us that both of temperatures could be preferred for pyrolysis reaction temperature and our choosing was 500°C that was compatible with the result of DSC-TGA analysis of polishing dust and the reaction was specified as 150 minutes (2.5 h) in the electric resistance furnace.

Effect of sweeping gas

The effect of sweeping gas was examined on pyrolysis yield at different flow rates 0, 20, 40, 60 and 80 l/h and results were given in Figure 4. The pyrolysis was actualized at 500°C temperature and 2.5 hour. Without using sweeping gas, the conversion yield was

%22.5. When 20, 40,60 l/h N_2 were attached to system as sweeping gas, the conversion yield was %25.5 . Once 80 l/h N_2 was used, the conversion yield raised to %27 of which reason could be that uncondensed vapors had carried out rapidly as mentioned literature [28]. Air was also used as sweeping gas with the same flow rates and results placed in Figure 4. When 20, 40, 60 l/h air was utilized, the yield of conversion was found %28.5. When the yield %28.5 was compared with amount of volatile compounds of the mass, it was disturbed that the amount of air used should be below stoichiometric ratio. When 80 l/h was issued to system, the conversion yield was defined as %25.3 which of reason might be caused by secondary reactions.

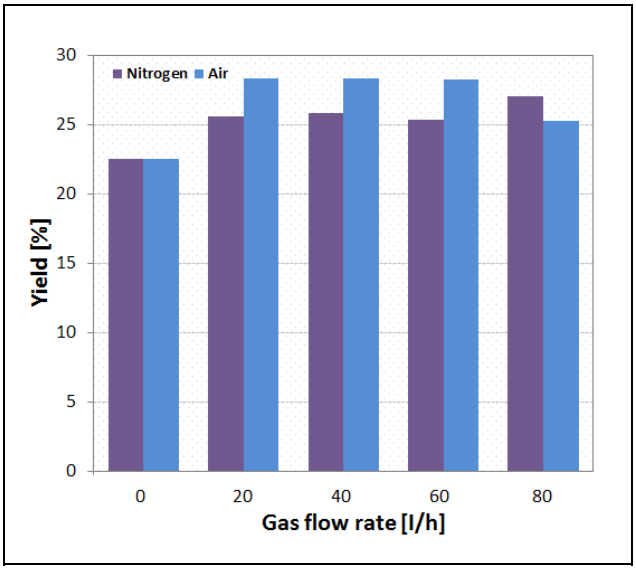

Figure 4: Effect of sweeping gas rate on the conversion yield

3.3 Infrared pyrolysis time

Infrared pyrolysis experiments were studied at 500°C temperature and a constant sweeping gas rate 300 l/h N_2 to indicate effect of time on thermal conversion yield. At different times (1, 1.5, 2 or 2.5 hours) results of the yield placed in Figure 5.

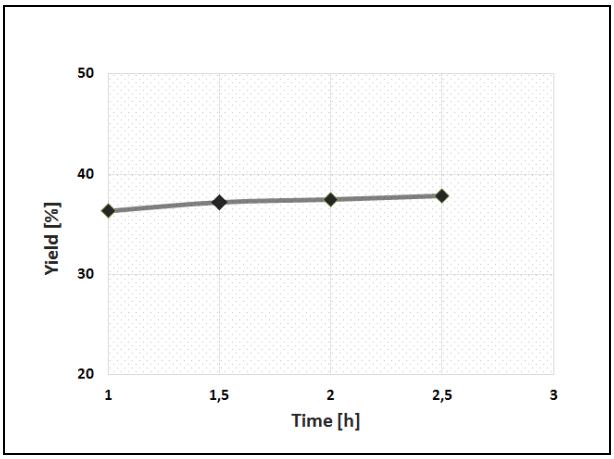

Figure 5: Effect of time on infrared pyrolysis [500°C, 300 l/h N_2]

75 minutes were required to reach of reaction temperature to 500°C in the electric resistance furnace, it was 40 minutes in the infrared furnace. The yield of thermal conversion increased from %36.33 to 37.85 by changes of the time. Duration with the rise of time from 1 hour to 2.5 hours, the thermal conversion yield improved %1.52. The pyrolysis reaction time was found 1 h.

3.4 FTIR Analysis

FTIR analysis of solid productions were performed to search changes occurring in the mass by increasing temperature and results place in Figure 6. In the original sample between the 2915.61 and 2848 cm^{-1}, C-H stretching vibrations were seen where could be noticed existence of alkene groups. The peaks of the absorbance demonstrated asymmetric stretching vibrations that could be presence of nitro compounds between 1550 and 1475 cm^{-1}. Between 1335 and 1250 cm^{-1} stretching of C-N was available that could be presence of aliphatic amines [29]. By the increasing of the temperature, stretching of C-H had disappeared and structure got through to steady state at all temperatures. The peaks between 1080 and 1090 cm^{-1} were seen for each temperature and presence of aromatics and amines could be mentioned on this spectra region. The results of FTIR analysis that performed to determine effect of time on solid productions of solid production were given in Figure 7. The peaks of absorbance were observed between 1080 and 1090 cm^{-1} spectra region where presence of aliphatic amines could be mentioned. By increasing of the time the intensity of peaks decreased.

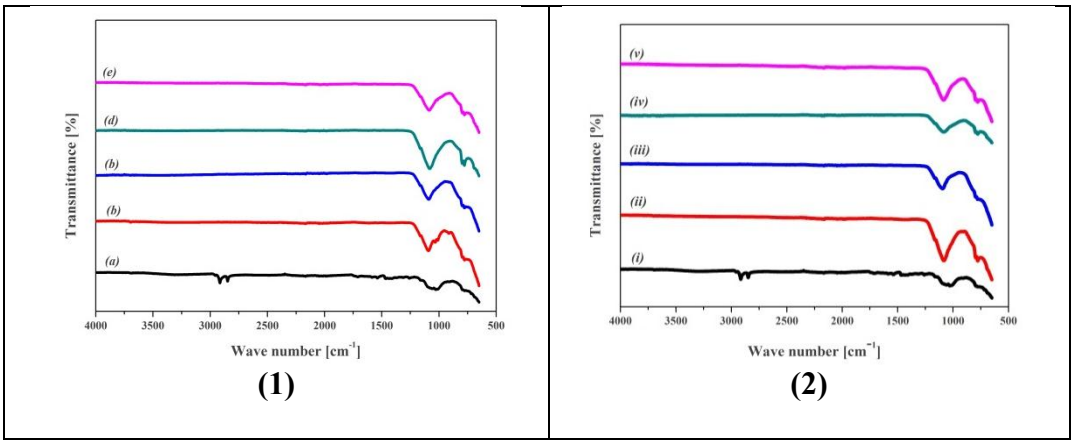

Figure 6: (1); Effect of temperature on solid productions; (a), original sample, (b), 400°C, (c), 450°C, (d), 500°C, (e), 550°C **(2);** Effect of time on solid productions; ;(i), original sample, (ii), 1 h, (iii), 1.5 h, (iv), 2 h, (v), 2.5 h

4. CONCLUSION

As a basic principle, increasing of temperature increased the thermal conversion yield in electric resistance furnace. In continuous weighing system, the highest yield was observed at 500°C temperature. The time that in thermal conversion ended, was defined as 2.5 hours. When effect of sweeping gas was evaluated, the yield of conversion increased according to sweeping gas when not in use. When the sweeping gas flow rate rises, there was no change in amount of conversion. When effect of heating system was searched on pyrolysis process, it

was seen that the reaction time was shorter about 1.5 hour in infrared furnace according to electric resistance furnace. Conversion yield increased amount %4 in infrared furnace according to conventional furnace. In the analysis performed in the infrared furnace gas outlet, Ag metal particles were not seen and it was seen that dusting was prevented. By the results, process flow chart was designed that placed in Figure 7.

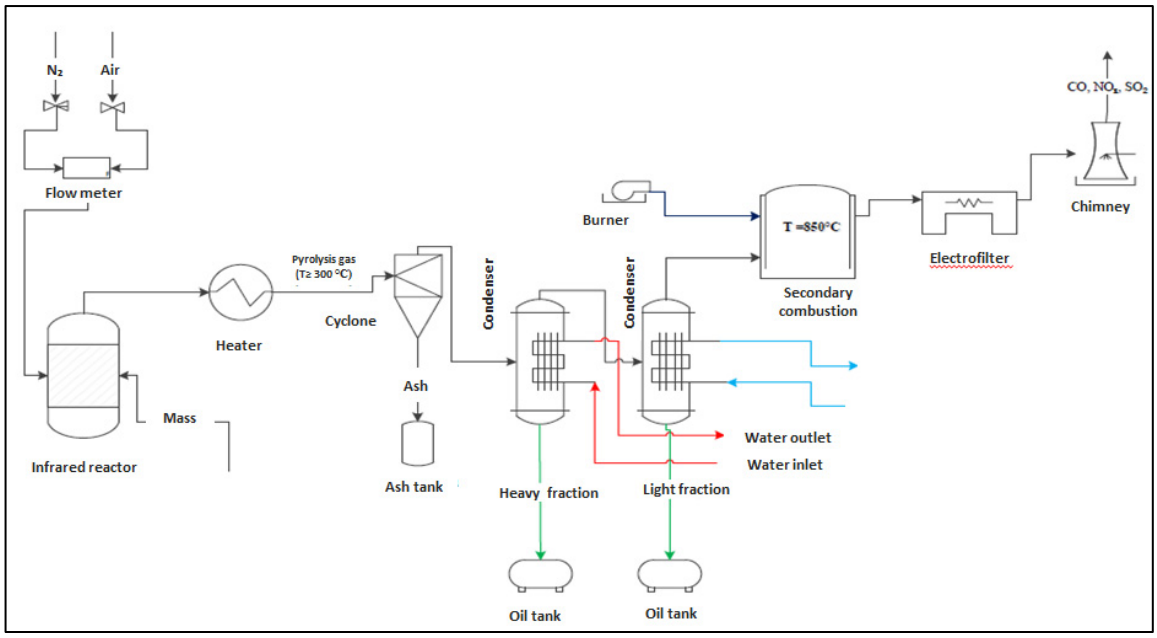

Figure 7: Pyrolysis process flow chart

ACKNOWLEDGEMENTS

We are grateful to ONSA Refinery, Director Hüseyin HAZIR and personnel for the supply of polishing dust waste.

REFERENCES

[1] F. Fiedler, "The state of the art of small-scale pellet-based heating systems and relevant regulations in Sweden, Austria and Germany," *Renew. Sustain. Energy Rev.*, vol. 8, no. 3, pp. 201–221, Jun. 2004.

[2] D. T. Chadwick, K. P. McDonnell, L. P. Brennan, C. C. Fagan, and C. D. Everard, "Evaluation of infrared techniques for the assessment of biomass and biofuel quality parameters and conversion technology processes: A review," *Renew. Sustain. Energy Rev.*, vol. 30, pp. 672–681, Feb. 2014.

[3] a. U. Zaman, "Comparative study of municipal solid waste treatment technologies using life cycle assessment method," *Int. J. Environ. Sci. Technol.*, vol. 7, no. 2, pp. 225–234, Mar. 2010.

[4] J. D. Martínez, N. Puy, R. Murillo, T. García, M. V. Navarro, and A. M. Mastral, "Waste tyre pyrolysis – A review," *Renew. Sustain. Energy Rev.*, vol. 23, pp. 179–213, Jul. 2013.

[5] T. Malkow, "Novel and innovative pyrolysis and gasification technologies for energy efficient and environmentally sound MSW disposal.," *Waste Manag.*, vol. 24, no. 1, pp. 53–79, Jan. 2004.

[6] P. Girods, A. Dufour, Y. Rogaume, C. Rogaume, and A. Zoulalian, "Comparison of gasification and pyrolysis of thermal pre-treated wood board waste," *J. Anal. Appl. Pyrolysis*, vol. 85, no. 1–2, pp. 171–183, May 2009.

[7] S. Bilgen, S. Keleş, and K. Kaygusuz, "Calculation of higher and lower heating values and chemical exergy values of liquid products obtained from pyrolysis of hazelnut cupulae," *Energy*, vol. 41, no. 1, pp. 380–385, May 2012.

[8] I. F. Fortuna, "and G.," vol. 39, no. 5, pp. 511–528, 1998.

[9] A. O. Oyedun, K. L. Lam, T. Gebreegziabher, and C. W. Hui, "Optimization of multi-stage pyrolysis," *Appl. Therm. Eng.*, vol. 61, no. 1, pp. 123–127, Oct. 2013.

[10] A. Bridgwater and G. Peacocke, "Fast pyrolysis processes for biomass," *Renew. Sustain. Energy*, vol. 4, 2000.

[11] V. Belgiorno, G. De Feo, C. Della Rocca, and R. M. a Napoli, "Energy from gasification of solid wastes.," *Waste Manag.*, vol. 23, no. 1, pp. 1–15, Jan. 2003.

[12] A. Demirbas, "Effects of temperature and particle size on bio-char yield from pyrolysis of agricultural residues," *J. Anal. Appl. Pyrolysis*, vol. 72, no. 2, pp. 243–248, Nov. 2004.

[13] K.-L. Lam, A. O. Oyedun, K.-Y. Cheung, K.-L. Lee, and C.-W. Hui, "Modelling pyrolysis with dynamic heating," *Chem. Eng. Sci.*, vol. 66, no. 24, pp. 6505–6514, Dec. 2011.

[14] T. S. Pather and W. a. Al-Masry, "The influence of bed depth on secondary reactions during slow pyrolysis of coal," *J. Anal. Appl. Pyrolysis*, vol. 37, no. 1, pp. 83–94, Aug. 1996.

[15] T. Pattanotai, H. Watanabe, and K. Okazaki, "Experimental investigation of intraparticle secondary reactions of tar during wood pyrolysis," *Fuel*, vol. 104, pp. 468–475, Feb. 2013.

[16] A. Demirbaş, "Hydrogen Production from Biomass by the Gasification Process," *Energy Sources*, vol. 24, no. 1, pp. 59–68, Jan. 2002.

[17] D. Mohan, C. U. Pittman,, and P. H. Steele, "Pyrolysis of Wood/Biomass for Bio-oil: A Critical Review," *Energy & Fuels*, vol. 20, no. 3, pp. 848–889, May 2006.

[18] a. V. Bridgwater, "Principles and practice of biomass fast pyrolysis processes for liquids," *J. Anal. Appl. Pyrolysis*, vol. 51, no. 1–2, pp. 3–22, Jul. 1999.

[19] E. W. Bruun, P. Ambus, H. Egsgaard, and H. Hauggaard-Nielsen, "Effects of slow and fast pyrolysis biochar on soil C and N turnover dynamics," *Soil Biol. Biochem.*, vol. 46, pp. 73–79, Mar. 2012.

[20] A. Demirbas and G. Arin, "An Overview of Biomass Pyrolysis," *Energy Sources*, vol. 24, no. 5, pp. 471–482, May 2002.

[21] H. Ben and A. J. Ragauskas, "Comparison for the compositions of fast and slow pyrolysis oils by NMR characterization.," *Bioresour. Technol.*, vol. 147, pp. 577–84, Nov. 2013.

[22] R. W. Court and M. a Sephton, "Quantitative flash pyrolysis Fourier transform infrared spectroscopy of organic materials.," *Anal. Chim. Acta*, vol. 639, no. 1–2, pp. 62–6, Apr. 2009.

[23] T. Ciacci, A. Galgano, and C. Di Blasi, "Numerical simulation of the electromagnetic field and the heat and mass transfer processes during microwave-induced pyrolysis of a wood block," *Chem. Eng. Sci.*, vol. 65, no. 14, pp. 4117–4133, Jul. 2010.

[24] S. S. Lam and H. a. Chase, "A Review on Waste to Energy Processes Using Microwave Pyrolysis," *Energies*, vol. 5, no. 12, pp. 4209–4232, Oct. 2012.

[25] X. Zhao, W. Wang, H. Liu, C. Ma, and Z. Song, "Microwave pyrolysis of wheat straw: Product distribution and generation mechanism.," *Bioresour. Technol.*, vol. 158C, pp. 278–285, Jan. 2014.

[26] S. S. Lam, A. D. Russell, C. L. Lee, S. K. Lam, and H. a. Chase, "Production of hydrogen and light hydrocarbons as a potential gaseous fuel from microwave-heated pyrolysis of waste automotive engine oil," *Int. J. Hydrogen Energy*, vol. 37, no. 6, pp. 5011–5021, Mar. 2012.

[27] E. M. Menendez, J. A. Menendez, M. J. Iglesias, and A. Garcıa, "Modification of the surface chemistry of active carbons by means of microwave-induced treatments," vol. 37, pp. 1115–1121, 1999.

[28] E. Pütün, B. B. Uzun, and A. E. Pütün, "Fixed-bed catalytic pyrolysis of cotton-seed cake: effects of pyrolysis temperature, natural zeolite content and sweeping gas flow rate.," *Bioresour. Technol.*, vol. 97, no. 5, pp. 701–10, Mar. 2006.

[29] S. S. Lam, A. D. Russell, C. L. Lee, and H. a. Chase, "Microwave-heated pyrolysis of waste automotive engine oil: Influence of operation parameters on the yield, composition, and fuel properties of pyrolysis oil," *Fuel*, vol. 92, no. 1, pp. 327–339, Feb. 2012.

BIOLEACHING OF METALS FROM PRINTED CIRCUIT BOARDS BY ACIDITHIOBACILLUS THIOOXIDANS

Cansu Demirel[1], Meryem Menekşe[1], Nurgul Balci[2] M. Seref Sonmez[3]

[1] ITU, Grad. School of Sci., Eng. & Tech., Geological Eng., Istanbul, Turkey
[2] ITU, Faculty of Mines, Dpt. of Geological Engineering, Istanbul, Turkey
[3] ITU, Faculty of Chemistry & Metallurgy, Dpt. of Met. & Mater. Eng., Istanbul, Turkey

ABSTRACT
Acidithiobacillus thiooxidans used to leach out metals from the waste printed circuit boards (PCBs) that is collected from production flaw samples. The experimental results demonstrate that different percentages of nickel, copper, zinc, silver and gold solubilized into the leaching solution from PCBs. The bioleaching was carried out in an incubator shaker (180 rpm) at 30°C. The change of both pH and Eh during the bioleaching of PCBs was monitored. pH of the system changed from 3.4 to 6.0 after 8 days and Ni and Zn was dissolved effectively, while the dissolution of Cu, Ag and Au was limited.

Keywords: printed circuit board, bioleaching, acidithiobacillus thiooxidans

BASKILI DEVRE KARTLARINDAN METALLERİN ACIDITHIOBACILLUS THIOOXIDANS YARDIMIYLA BİYOLİÇİ

ÖZET
Bu çalışmada, üretim hatası bulunan hurda baskılı devre kartlarında metallerin çözümlendirilmesi amacıyla Acidithiobacillus thiooxidans bakterileri kullanılmıştır. Deneysel çalışmalar baskılı devre kartlarından farklı oranlarda nikel, bakır, çinko, gümüş ve altın çözümlendirilebildiğini göstermiştir. Biyoliç deneyleri 30°C sıcaklıkta çalkalamalı inkübatörde (180 rpm) gerçekleştirilmiştir. Biyoliç sırasında çözelti pH değeri ile Eh değerindeki değişimler gözlemlenmiştir. Sistemin pH değeri 8 gün sonar 3.4'ten 6.0'ya çıkmış ve Ni ve Zn etkili olarak çözümlendirilirken Cu, Ag ve Au çözümlendirilmesi sınırlı seviyede kalmıştır.

Anahtar Kelimeler: baskılı devre kartları, biyoliç, acidithiobacillus thiooxidans

1. INTRODUCTION

Bioleaching is mostly described as the microbially mediated oxidation of metals and metal sulfides under oxic conditions at low pH environments (Schippers, 2004). In the scope of searching for a more environmental friendly solution for metal recovery, bioleaching was started to be used as an industrial method in 1950's with low-grade ore dump-leaching (Brierly and Brierly, 2001). Now, bioleaching is used not only for recovery of metals from ores, but also from other types of metal-rich solids as electronic wastes like PCB's (Lee and Pandley, 2012).

Great majority of bioleaching organisms are the acidophiles that are mainly isolated from acid mine drainage environments (Nordstrom and Stahl, 1997), which are generally highly acidic aquatic environments contaminated by oxidation of sulphur bearing ores and minerals (Schippers, 2004; Lottermoser, 2010). Most effective acidophiles in bioleaching are reported as Acidithiobacillus ferrooxidans , Leptospirillum ferrooxidans and Acidithiobacillus thiooxidans, respectively (Sand et al., 1992; Bigham and Nordstrom, 2000). Those acidophiles are also the most abundant types of bacteria isolated from leaching environments (Schippers, 2004).

Formerly known as Thiobacillus thiooxidans, Acidithiobacillus thiooxidans was isolated for the first time from soils with sulfur and phosphate content (Nordstrom and Southam, 1997) in 1922 (Waksman and Joffe, 1922). Acidithiobacillus thiooxidans is a type of Gram-negative sulfur-oxidizing bacteria (Nordstrom and Southam, 1997) that belong to genus Acidithiobacillus of the gamma subclass of Proteobacteria (Kelly and Wood, 2000). These rod shaped organisms are generally a micrometer long (Waksman and Joffe, 1922); chemlithotrophic (using inorganic compounds as a source of energy) (Nealson and Stahl, 1997) and mesophilic (living at moderate temperatures). Acidithiobacillus thiooxidans type bacteria are unable to oxidize inorganics other than elemental sulphur and reduced sulphur compounds (Bosecker, 1987; Schippers, 2004). Optimal living conditions are reported to be in the range of 28-30oC with pH values of 2.0-3.0 for this bacteria (Waksman and Joffe, 1922; Schippers, 2007; Schippers et al., 2013).

Bioleaching mechanisms and pathways of metal sulfides are studied for many years. Sand et al. (2001) reported that bacteria may either catalyse oxidation directly on the surface of the metal sulphide, or indirectly via oxidizing the free ferrous iron in the solution to form ferric iron, which is a very strong oxidizer. Along with the overall proposed mechanisms, numerous studies were made revealing the leaching characteristics of iron oxidizers like Leptospirillum ferrooxidans, iron and sulfur oxidizers like Acidithiobacillus ferrooxidans and sulphur oxidizers Acidithiobacillus thiooxidans (Stott et al., 2003; Balci et al., 2007, 2012; Penev and Karamanev, 2009; Thurston et al., 2010; He et al., 2012, Beviliqua et al., 2013; Dong et al., 2013; Feng et al., 2013; Zhao et al., 2013). Moreover, some comparative studies point out that mixed cultures containing both mesophilic iron oxidizers and sulfur oxidizers are more effective in metal recovery (Sand et al., 1992; Akçıl et al., 2007; Fu et al., 2008).

Metals doubtlessly have an irrevocable place in industry. With emerging technologies and progressively depleting reserves, need for metals is increasing along with the pile of electronic wastes day by day. This phenomena lead scientist to explore the ways for recycling and then, finding out more environmentally friendly solutions. In this scope, electronic wastes like PCB's were started to be exposed to bioleaching for metal recovery (Choi et al., 2004; Ilyas et al., 2007; Wang et al., 2009; Bas et al., 2013; Ilyas et al., 2014; Yang et al., 2014 Ilyas and Lee, 2014), mostly using Thiobacillus species (Krebs et al., 1997; Lee and Pandey, 2012). Along with the sulfur bearing minerals, there are also studies on bioleaching of PCB's with acidophilic iron and sulfur oxidizers, (Choi et al., 2004; Xiang et al., 2010; Liang et al., 2010; Lee and Pandey, 2012; Liang et al., 2013). Yet, limited work has been published on the role of Acidithiobacillus thiooxidans on bioleaching of PCB's.

This study aims to;
(i) Asses the ability of Acidithibacillus thiooxidans in leaching PCB's by itself, in the presence of sulphur,
(ii) Reveal factors that control recovery efficiency of metals (Ni, Cu, Zn, Ag, Au) with Acidithiobacillus thiooxidans and
(iii) Enlighten the next studies which are to elucidate the bacterial oxidation mechanisms of PCB's.

2. MATERIALS AND METHODS

2.1. Bacterial strain

The pure Acidithiobacillus thiooxidans strain used for leaching was obtained from an actively growing culture, previously purchased from the German Collection of Microorganisms and Cell Cultures (DSMZ).

2.2. Bacterial growth
A growth medium was prepared containing NH4Cl (0,1 g/l), KH2PO4 (3 g/l), MgCl2.6H2O (0,1 g/l) and CaCl2 (0,14 g/l) in 1000 ml of distilled water (DSMZ Medium 35) and dissolved with magnetic stirrer and pH was adjusted to 3 by using ultrapure HCI acid. The prepared liquid growth medium was autoclaved for 15 min at 121oC and powdered elemental sulfur sterilized under UV light with ethanol in a laminar flow chamber was added to the medium.

Prior to culture preparation, sterile conditions were provided via ethanol and UV light sterilized laminar flow for 20 min and the equipment (pipets, flasks, etc.) was sterilized with autoclave at ITU Geomicrobiology & Biogeohemistry Laboratory. The culture was inoculated with a 10% volume ratio to the growth medium in a sterile 250 ml flask, in sterile conditions. Sterilized elemental sulfur (of a weight that will provide 10 g/l concentration) was added into the medium and the opening of the flask was sealed. After inoculation, the culture was incubated for 30 days on a rotary shaker that was set to 180 rpm at 30oC.

2.3. Bacterial cell-counting
In order to make sure that an adequate number of bacterial cells was reached, bacterial cell-counting was performed. 100 µl of the grown culture was sampled in sterile conditions and investigated under microscope at ITU (Istanbul Technical University) / MOBGAM (Molecular Biology-Biotechnology & Genetics Research Center), using a Thoma Chamber. Results revealed that 1 ml of the sample contained 19 x 104 bacterial cells.

2.4. Bacterial culture preparation
50 ml of the incubated culture contained 9,5 x 106 number of cells was divided into 2 ml of aliquots to sterile tubes and centrifuged using a microcentrifuge at 14000 rpm for 10 minutes to precipitate the bacterial cells. The tubes were then discarded, while the last one was used to resuspend and combine the remaining pellets, in order to harvest the cells.

2.5. Bioleaching experiments
A biotic and an abiotic (bacteria free) experiment were setup in duplicates. Biotic experiments were used to take in account the chemical oxidation of PCB's, providing a chance to elucidate the role of bacteria in metal recovery. Duplicates were setup to eliminate the chance of missing out any contamination and losing samples.

Experiments were setup in 1000 ml sterile flasks under sterile conditions with a total volume of 500 ml each. Prior to usage, powdered elemental sulphur and PCB's that cut into small pieces (of averagely 4mm x 4mm in dimensions) were sterilized in laminar flow by rinsing with ethanol and leaving them to dry under UV light. For every experiment, 5 grams of sterilized PCB's were placed in the flasks and 5 grams of powdered elemental sulphur were added, following the growth medium. Concentrated pure cells of Acidithiobacillus thiooxidans were divided into two aliquots and inoculated to the flasks that will present the biotic experiments. No bacterial cells were inoculated to the chemical control experiments. Then the flasks were immediately sealed. All of four experimental media were placed on a rotary shaker operating at 180 rpm and 30oC. Along with the physicochemical properties, colour changes of the liquid media and PCB's during the experiments were monitored.

2.6. Sample preparation for analysis

2.6.1. Sampling liquid media: Starting with the first minute of all four experiments (t0), sampling of the liquid media was performed by a frequency of 2 hours in the first week, 2 days in the second week, 3 days in the third week and a sampling per week in the rest of the experiments. In sterile conditions, 10 ml of supernatants were withdrawn from the flask and the equal amounts of volumes

were replaced with a sterile growth medium (having the same composition as previously described). Samples were filtered through 0,2 μm syringe filters to remove bacterial cells and suspended particles. 7 ml of each sample was immediately acidified with research grade HNO3 (Merck), diluted by 1/10 with ultrapure water, and stored at 4oC for metal analysis. Remaining 3 ml of samples were used for pH and Eh measurements.

2.6.2. Obtaining solid residue: After 21 weeks of experiments, all four experimental media were centrifuged at 4500 rpm for 15 minutes. 50 ml of the supernatants of each experiment were sampled; pH and Eh measurements were made and stored for metal analysis as described previously. Remaining solid residues were dried in an oven at 30oC and collected for further analysis.

2.7. Analytical procedure

The solution pH and Eh were measured at ITU Geomicrobiology & Biogeochemistry Laboratory, with a desktop type pH meter (WTW, Multi 9310) using Sentix 940 and Sentix ORP 900 probes respectively. Calibrations were made prior to use at the beginning of every day that measurements will be made.

The concentrations of dissolved copper, nickel, zinc, silver and gold in leaching solutions were detected by ICP-MS (Inductively Coupled Plasma Mass Spectrometry) analysis,

3. RESULTS

Metal content of waste printed circuit boards used in experiments was determined as seen from Table 1. Main source of PCB was Cu and Zn while Ni, Au and Ag were also the components that has to be recovered.

Table 1: Metal content of waste printed circuit boards used in experiments.

Metal	Amount (%)
Au	0.0423
Ag	0.0085
Cu	61.46
Zn	31.72
Ni	1.72
Fe	0.0133

pH and potential change during the bioleaching of PCB for different durations was given by Figure 1. Slight increase of pH to 9.6 after about 690 hour bioleaching while potential of the system was calculated as 63.8 mV. After 1500 hours of bioleaching there were no significant changes in both pH and Eh.

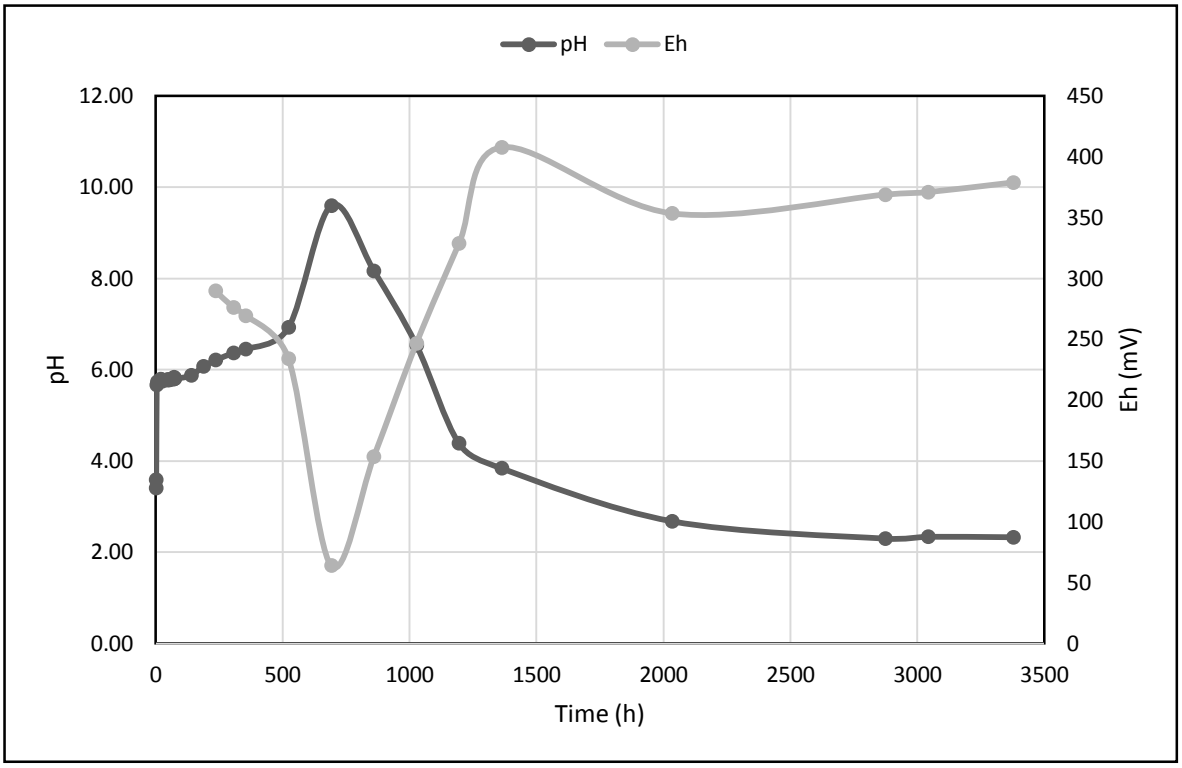

Figure 1: pH and potential change during the bioleaching of PCB for different durations.

During the very early of the bioleaching experiments it was analysed that Ni dissolution was obtained as about 100 ppm. On the other hand Ni concentration of the solution was decreased after about 1000 hours of bioleaching by Acidithiobacillus thiooxidans. Maximum recovery fo Ni was obtained as about 180 ppm after 1000 hours.

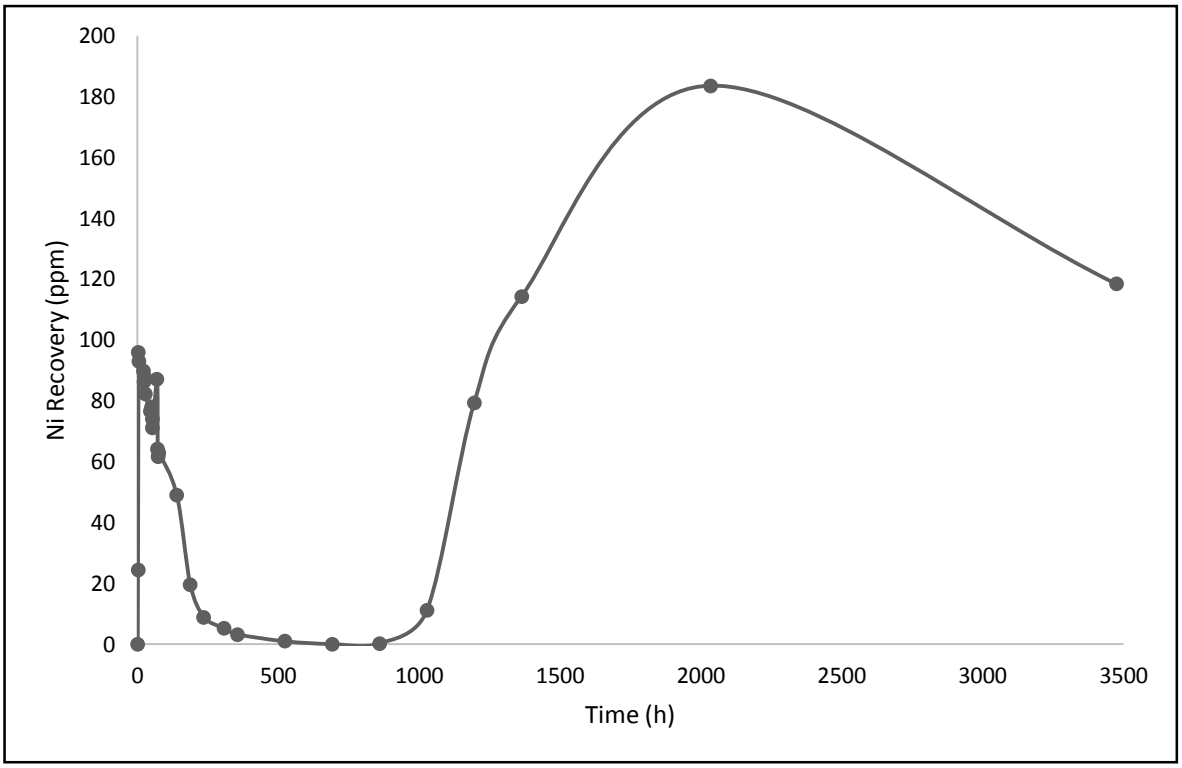

Figure 2: Ni recovery from PCB by bioleaching with Acidithiobacillus thiooxidans.

Cu dissolution was ineffective until about 2000 hours of leaching, while 700 ppm of Cu was analysed after 3500 hours.

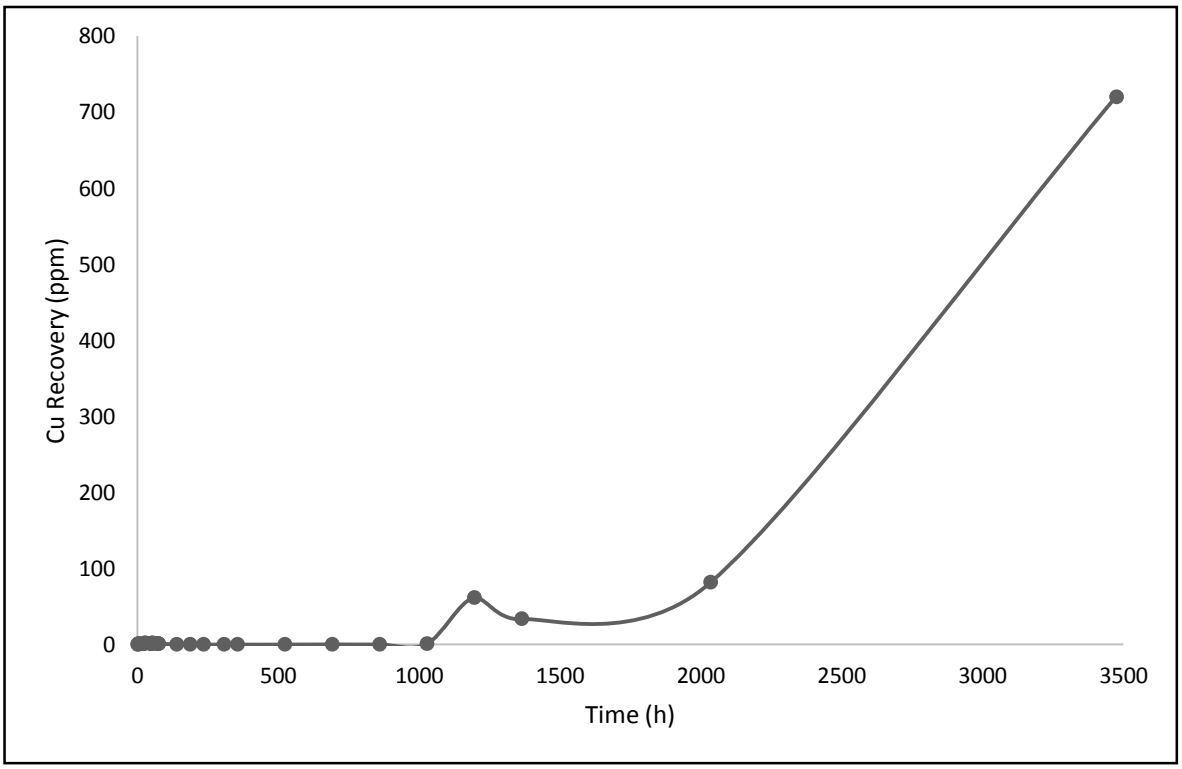

Figure 3: Cu recovery from PCB by bioleaching with Acidithiobacillus thiooxidans.

Optimum Zn recovery was determined after 2000 hours of leaching of PCB's by Acidithiobacillus thiooxidans as about 400 mg of zinc was dissolved.

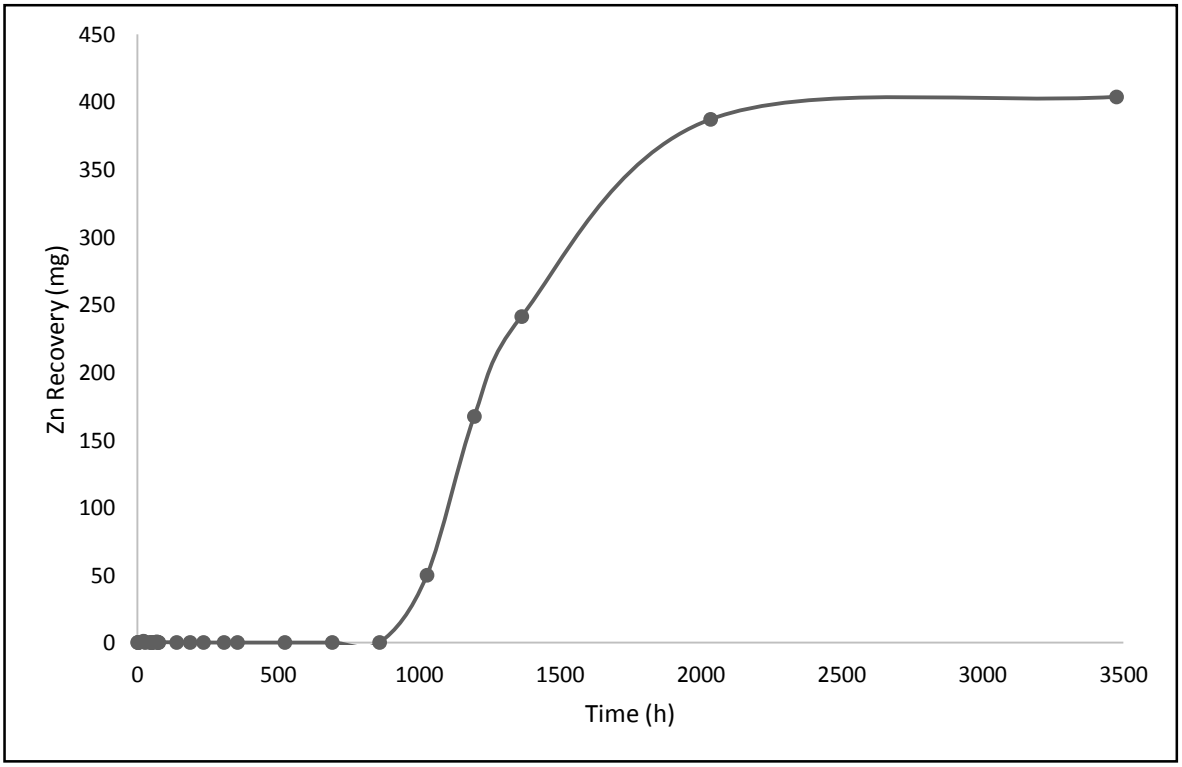

Figure 4: Zn recovery from PCB by bioleaching with Acidithiobacillus thiooxidans.

The dissolution of both Au and Ag was not effective by Acidithiobacillus thiooxidans as the concentration of ions in the solution changed uncontrolled. The change in concentration of both Au and Ag in the solution might be explained by the series of reactions between of the components in bioleaching medium.

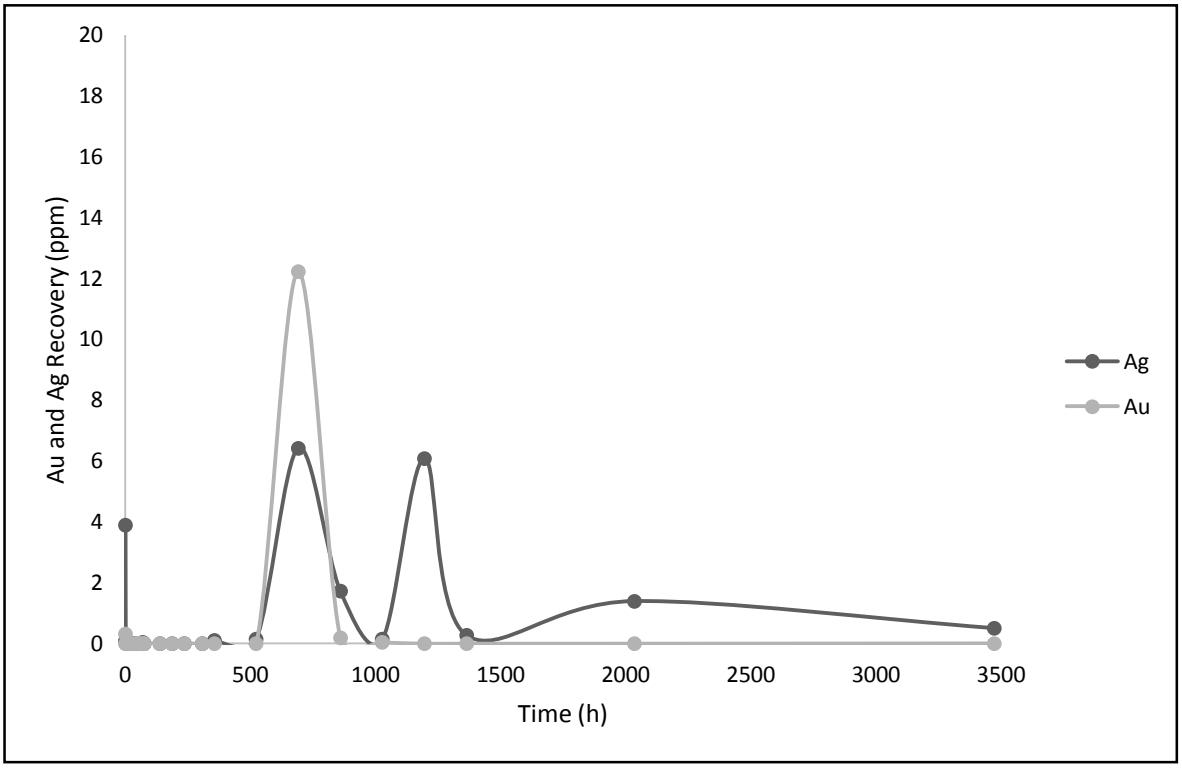

Figure 5: Au and Ag recovery from PCB by bioleaching with Acidithiobacillus thiooxidans.

4. CONCLUSION

Slightly lower pH values and slightly higher concentrations of heavy metals are detected in the presence of Acidithiobacillus thiooxidans. However, those results could be attributed to the lower initial pH values that inoculum caused. Our results point out that, Acidithiobacillus thiooxidans is not effective in PCB bioleaching and metal recovery, by itself.

REFERENCES

1. Akcil, A.,Ciftci, H., Deveci., H., 2007. Role and contribution of pure and mixed cultures of mesophiles in bioleaching of a pyritic chalcopyrite concentrate. Miner. Eng. 20, 310 –318. doi:10.1016/j.mineng.2006.10.016.
2. Balcı, N., Shanks, W.C., III, Mayer, B., Mandernack, K.W., 2007. Oxygen and sulfur isotope systematics of sulfate produced by bacterial and abiotic oxidation of pyrite. Geochimica et Cosmochimica Acta, 71 (15), 3796–3811.
3. Balcı, N., Mayer, B., Shanks, W.C., III, Mandernack, K.W., 2012. Oxygen and sulfur isotope systematics of sulfate produced during abiotic and bacterial oxidation of sphalerite and elemental sulfur. Geochimica et Cosmochimica Acta, 77, 335–351.
4. Bas, A. D., Deveci, H., Yazici, E.Y., 2013. Bioleaching of copper from low grade scrap TV circuit boards using mesophilic bacteria. Hydrometa. 138, 65 – 70.
5. Bevilaqua, D., Lahti,H., Suegama, P.H., Garcia, Jr., O., Benedetti, A.V., Puhakka, J.A., Tuovinen, O.H., 2013. Effect of Na-chloride on the bioleaching of a chalcopyrite concentrate in shake flasks and stirred tank bioreactors. Hydrometallurgy, 138, 1–13.

6. Bigham, J.M., Nordstrom, D.K., 2000. Iron and aluminum hydroxysulfates from acid sulfate waters. In: Alpers C.N., Jambor, J.L., Nordstrom, D.K. (eds.), Sulfate minerals: crystallography, geochemistry, and environmental significance. Rev. Mineral .Geochem., 40, 351–403.
7. Bosecker, K., 1987. Microbial leaching. In: Präve, P., Faust, U., Sittig, W., Sukatssch, D. A., (eds.), Fundamentals of Biotechnology, 661-683.
8. Brierley, J.A., and Brierley C.L., 2001. Present and future commercial applications of biohydro-metallurgy. Hydrometallurgy, 59(2-3), 233-239.
9. Choi, M.-s., Cho, K.-s., Kim, D.-s., 2004. Microbial recovery of copper from printed circuit boards of waste computer by Acidithiobacillus ferrooxidans. J. Environ. Sci. Health–Part A Toxic /Hazard. Subst. Control. A39 (11–12), 2973–2982.
10. Dong, Y.,Lin, H.,Xu, X., Zhou, S., 2013. Bioleaching of different copper sulfides by Acidithiobacillus ferrooxidans and its adsorption on minerals. Hydrometallurgy, 140, 42–47.
11. Feng, S.S., Yang, H.L., Xin, Y., Gao, K.., Yang, J.W., Liu, T., Zhang, L., Wang, W., 2013. A novel and highly efficient system for chalcopyrite bioleaching by mixed strains of Acidithiobacillus Bioresour. Technol., 129, 456–462.
12. Fu, B., Zhou, H., Zhang, R., Qiu, G., 2008. Bio-leaching of chalcopyrite by pure and mixed culturesof Acidithiobacillus spp. and Leptospirillum ferriphilum. Int. Biodeterior. Biodegradation, 62, 109-115. doi:10.1016/j.ibiod.2007.06.018.
13. He, H., Xia, J., Hong, F., Tao, X., Leng, Y., Zhao, Y., 2012. Analysis of sulfur speciation on chalcopyrite surface bioleached with Acidithiobacillus ferrooxidans, Miner. Eng. 27–28, 60–64.
14. Ilyas, S., Anwar, M., Niazi, S., Ghauri, M., 2007. Bioleaching of metals from electronic scrap by moderately thermophilic acidophilic bacteria. Hydrometallurgy, 88, 180–188.
15. Ilyas, S., Lee, J.-c., Kim, B.S., 2014. Bio-removal of heavy metals from electronic wastes; process development and optimization. J. Clean. Prod., 70, 194–202.
16. Ilyas, S., Lee, J-c., 2014. Bioleaching of metals from electronic scrap in a stirred tank reactor. Hydrometallurgy, 149, 50–62. DOI: 10.1016/j.hydromet.2014.07.004
17. Kelly, Donovan P. and Ann P. Wood (2000). "Reclassification of some species of Thiobacillus to the newly designated genera Acidithiobacillus gen. nov., Halothiobacillus gen. nov. andThermithiobacillus gen. nov." International Journal of Systematic and Evolutionary Microbiology, 50, 511-516.
18. Krebs, W., Brombacher, C., Bosshard, P.P., Bachfen, R., Brandl, H., 1997. Microbial recovery of metals from solids. FEMS Microbiol. Rev. 20, 605–617.
19. Lee, J and Pandey, B. D., 2012. "Bio-processing of solid wastes and secondary resources for metal extraction – A review," Waste Management, XXXII (1), 3–18.
20. Liang, G.B., Mo, Y.W., Zhou, Q.F., 2010. Novel strategies of bioleaching metals from printed circuit boards (PCBs) in mixed cultivation of two acidophiles, Enzyme Microb. Technol. 47, 322–326.
21. Liang, G., Tang, J., Liu, W., Zhou, Q., 2013. Optimizing mixed culture of two acidophiles to improve copper recovery from printed circuit boards (PCBs). J. Hazard. Mater. 250–251, 238–245.
22. Lottermoser, B.G., 2010. Mine Wastes: Characterization, Treatment and Environmental Impacts, Springer.
23. Nealson, K. H., and Stahl. D. A., 1997. Microorganisms and biogeochemical cycles: what can we learn from layered microbial communities?, 5-34. In: Nealson, K. H. and Banfield, J. F. (ed.), Geomicrobiology: interactions between microbes and minerals, vol. 35. Mineralogical Society of America, Washington, D.C.
24. Nordstrom, D.K., and Southam, G., 1997. Geomicrobiology of sulfide mineral oxidation, in, Banfield, J.F., and Nealson, K.H., eds., Geomicrobiology: Interactions between microbes and minerals, Reviews in Mineralogy, Volume 35: Washington D.C., Mineralogical Society of America, p. 361-390.

25. Penev, K. and Karamanev, D., 2009. Advanced Materials Research, 71-73, 255-258. DOI: 10.4028/www.scientific.net/AMR.71-73.255
26. Sand, W., Rohde, K., Sobotke, B. And Zenneck, C., 1992. Evaluation of Leptospirillum ferrooxidans for leaching. Appl. Environ. Microbiol. 58(1), 85-92.
27. Sand, W., Gehrke, T., Jozsa, P.-G., Schippers, A., 2001. (Bio)chemistry of bacterial leaching-direct vs. indirect bioleaching. Hydrometallurgy 59, 159–175.
28. Schippers, A., 2004, Biogeochemistry of metal sulfide oxidation in mining environments, sediments and soils. In: Amend, J.P., Edwards, K.J., Lyons, T.W. (Eds.), Sulfur Biogeochemistry — Past and Present. : Special Paper, 379. Geological Society of America, Boulder, Colorado, USA, pp. 49–62.
29. Schippers, A., 2007. Microorganisms involved in bioleaching and nucleic acid-based molecular methods for their identification and quantification. In: Donati, E.R., Sand, W. (Eds.), Microbial Processing of Metal Sulfides. Springer, 3–33.
30. Schippers, A, Hedrich, S., Vasters, J., Drobe, M., Sand, W., and Willsher, S., 2013. Biomining: Metal Recovery from Ores with Microorganisms. Adv. Biochem. Eng. Biotechnol. Springer, Berlin Heidelberg. ISSN: 0724-6145, DOI: 10.1007/10_2013_216.
31. Stott, M.B., Sutton, D.C., Watling, H.R., Franzmann, P.D., 2003. Comparative leaching of chalcopyrite by selected acidophilic Bacteria and Arachaea. Geomicrobiology Journal 20, 215–230.
32. Thurston, R.S., Mandernack, K.W., Shanks, W.C. III., 2010. Laboratory chalcopyrite oxidation by Acidithiobacillus ferrooxidans: oxygen and sulfur isotope fractionation. Chem. Geol. 269, 252–261.
33. Waksman, S.A., and Joffe, I.S., 1922. Micro-organisms concerned with the oxidation of sulphur insoil. II. Thiobacillus thiooxidans, a new sulphur oxidising organism isolated from the soil. Journal of Bacteriolology, 7, 239-256.
34. Wang, J., Bai, J., Xu, J., Liang, B., 2009. Bioleaching of metals from printed wire boards by Acidithiobacillus ferrooxidans and Acidithiobacillus thiooxidans and their mixture. J. Hazard. Mater. 172, 1100–1105.
35. Xiang, Y., Wu, P.X., Zhu, N.W., Zhang, T., Liu, W., Wu, J.H. and Li, P., 2010. Bioleaching of Copper from Waste Printed Circuit Boards by Bacterial Consortium Enriched from Acid Mine Drainage. J. Hazard. Mater., 184, 812–818.
36. Zhao, X., Wang, R., Lu, X., Lu, J., Li, C., Li, J., 2013. Bioleaching of chalcopyrite by Acidithiobacillus ferrooxidans. Minerals. Eng. 53, 184–192.

FABRICATION AND CHARACTERIZATION OF TiNi/SiC_p SHAPE MEMORY COMPOSITES

Kerim Emre ÖKSÜZ, Mehmet ŞİMŞİR, Hülya AKKAN

[1]Cumhuriyet University, Metallurgical & Materials Engineering Department, 58140, Sivas, Turkey.

Abstract : Nickel–Titanium alloy near the equi-atomic concentration is well known for its shape memory effect (SME), and also its unique mechanical and physical properties, such as good ductility at ambient temperature, good vibration damping properties, long fatigue life and corrosion properties in sea water. In the present study Ni and Ti elemental powders with purity of 99.5% were used as starting materials. Production of NiTi/SiCp alloy from elemental powders was conducted by powder metallurgy (PM). The mixtures were compacted under a uniaxial pressure of 350MPa for 1 min. The cylindrical samples sintered in an argon-protected atmosphere for 3 h at 1150˚C. The effects of SiCp additions, micro hardness, and porosity and corrosion behaviour on the characteristic of NiTi composites have been investigated. The samples were examined by scanning electron microscope (SEM), for microstructural studies and phase identification.

Keywords: NiTi Shape Memory Alloy, SiC, Powder Metallurgy, Corrosion.

1. INTRODUCTION

TiNi shape memory alloys (SMAs) have attracted significant interests due to their unique shape memory effect (SME), superelasticity and high damping performance [1−4]. These excellent physical and mechanical properties associated with the reversible martensitic transformation allow the commercial applications of TiNi SMAs in many fields, such as aerospace, biomedical and mechanical engineering [5, 6]. Generally, the most commonly used TiNi and TiNi-based alloys represent the major family of shape memory alloys [7]. On the other hand, continuous, short fiber, or particulate NiTi alloy reinforced metal matrix composites are attracting considerable interest due to their advanced mechanical properties. Usually, the shape recovery effect of NiTi reinforcements has been used to improve the mechanical properties of the composite materials. TiNi alloys have been fabricated using various methods like metal injection molding, hot izostatic pressing, combustion synthesis and spark plasma sintering. Solid state processes are generally used to obtain the best mechanical properties in titanium based composites. These processes exhibit excellent

finished performance due to the ability to obtain uniform distribution of reinforcement and near-net shape formability [8]. A significant contribution to NiTi fiber reinforced metal matrix composites have been made by Furuya et al. [9]. They reported improved tensile properties by creating compressive stress in the matrix caused by shape memory shrinkage of TiNi fibers. Later, Armstrong and Lorentz [10] and Armstrong et al. [11] reported that NiTi continuous fiber reinforced Al matrix composite combined high strength and high tensile toughness with unusual thermal mechanical behaviour. Dixit et al. [12] used friction-stir-process to prepare NiTi particle reinforced aluminium composite. They showed that improved mechanical properties could be achieved by using the shape memory effect of the NiTi particles to induce compressive and tensile stresses in the parent matrix. Porter et al. [13] investigated the fatigue and fracture behaviour of NiTi reinforced aluminium composite. They fabricated NiTi particle reinforced Al matrix composite using powder metallurgy and hot pressing and activated the shape memory effect by cold rolling. They reported significant improvement in the yield strength and ultimate strength compared with the monolithic Al samples, while the elongation was sharply reduced. A remarkable improvement on the fatigue life of the composite was observed particularly above the yield strength of the material. Xie et al. [14] and Xie et al. [15] developed short NiTi fiber reinforced Al6061 matrix composites prestraining the fibers at a temperature between martensite start temperature and austenite start temperature and investigated the relationship between the amount of prestrain and yield stress. They showed that the yield stress of the composite increase with increasing prestrain rates. However, a very limited study with reinforcement powders was used for manufacturing TiNi alloys. In recent study, the effects of SiC particle size on the microstructure and mechanical properties (hardness, porosity and corrosion) of pure Ti and TiNi/SiCp alloys with PM route have been investigated.

2. EXPERIMENTAL PROCEDURE

The test samples were prepared by powder metallurgy from Ni, Ti and SiC powders. Powders were produced by Alfa Aesar Company. In order to produce TiNi/SiCp based composites, Ti powders with an average particle size of 45 μm with 99.5% purity were chosen while SiC particles with 45 μm sizes were used as the reinforcements. The powders were weighed and put into a jar and then mixing was done with T_2-F turbula mixer. 1 wt. % and 5 wt. % SiCp were correspondingly mixed with TiNi powders. Then, the sufficiently blended powders were cold compacted into short-bar green samples (6 mm×10 mm, diameter × height) with a compact stress of 650 MPa for 1 min. The compacted green samples were

heated to 1100 °C and held for 3 h in an aluminium oxide tube furnace under the protective flowing argon gas (99.99% purity). Sintered specimens were cooled in the cold zone of the furnace at a rate of approximately 10-15 ◦C/min, sufficient to prevent formation of intermetallic other than TiNi due to possible oxidation problems that may occur during furnace cooling. Finally, all samples were produced using the same route. The theoretical-measured density, total porosity and water absorption were compared. The hardness of the composite and its alloy were measured by Vickers hardness (VHN) method and the mean of at least eight readings was taken. Corrosion tests were carried out in H_2SO_4 solution, pH-1.50 solution at RT and 45^{o}C. Samples were placed in H_2SO_4 of pH-1.50 for 3 hours. The surface microstructures of the samples were examined using a scanning electron microscope (SEM, Model JEOL-JSM 6060-LV, Japan).

3. RESULTS AND DISCUSSION

3.1 DENSITY MEASUREMENT AND POROSITY

The theoretical densities of each composite specimen were calculated from powder mixes. The density of the composites was obtained by weighing small pieces cut from the composites disc first in air and water, and calculating the density by Archimedean method. The vacuum method (EN 14411) is used in the laboratory to determine water absorption, porosity, bulk density with greater precision. The composition of intermetallic composites, theoretical-measured density, total porosity and water absorption were compared (Table 1).

Table 1. The composition of intermetallic composites, theoretical-measured density, total porosity and water absorption.

Material Types	Pure Ti	Ti_{50}+Ni_{50}	Ti50+Ni49+1SiCp	Ti_{50}+Ni_{45}+5SiCp
Theoretical	4,51	5,988	5,9175	5,6531
Measured	4,13	5,3	5,166	5,1375
Total Porosity (%)	2,05	4,068	5,03	6,12
Water Absorption (%)	0,99	0,373	1,95	5,62

3.2 HARDNESS TESTS

The variation of micro hardness of the composites is shown in Fig.1. This figure indicated that the hardness of the MMCs increased with increasing the content of particles up to 5wt. % and then decreased thereafter [16-17]. The hardness for pure Ti and its composite are about 404, 14 VHN, 459,42 VHN, 735,75 VHN and 756,4 VHN for the matrix, $Ti_{50+}Ni_{50}$ alloy, Ti_{50}+Ni_{49}+1SiCp composite, and Ti_{50}+Ni_{45}+5SiCp composites, respectively.

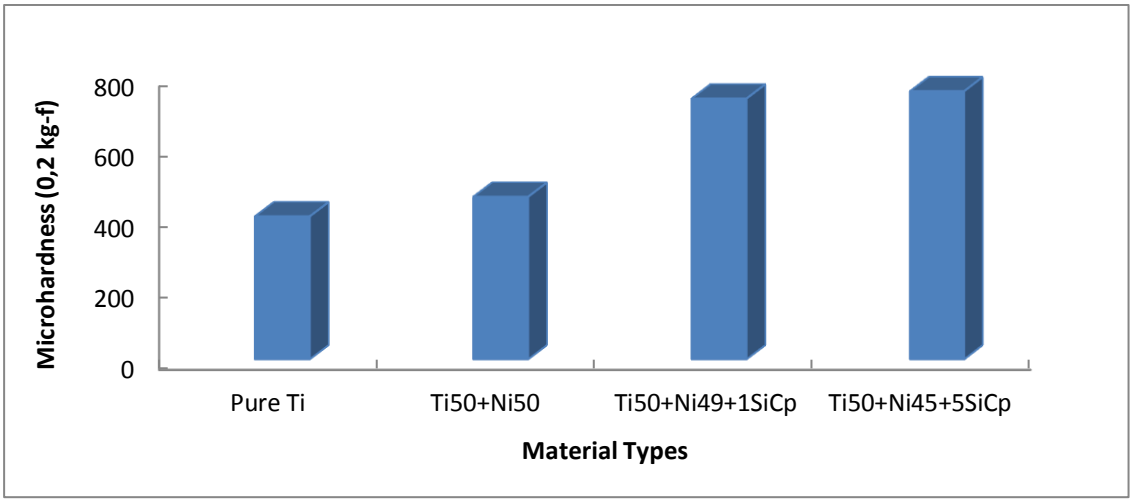

Fig.1. Micro hardness of TiNi alloy and it's composite.

3.3 MICROSTRUCTURE OF TiNi ALLOY AND ITS COMPOSITE

SEM ANALYSIS

Microstructure of the composite was examined using SEM. After grinding and polishing, the composite samples were etched with solution of Kroll's Reagent. Fig. 2 is an SEM image of the pure titanium and it's composite after sintering 1150ºC 3h. The majority of the area shown was of the medium gray phase forming a matrix surrounding several smaller light gray and dark gray: black areas. The dark phase is rich in Ti and the bright in Ni, SiC particles are black. Each area was assumed to be a distinct phase or mixture of phases resulting from various stages of the progression of diffusion.

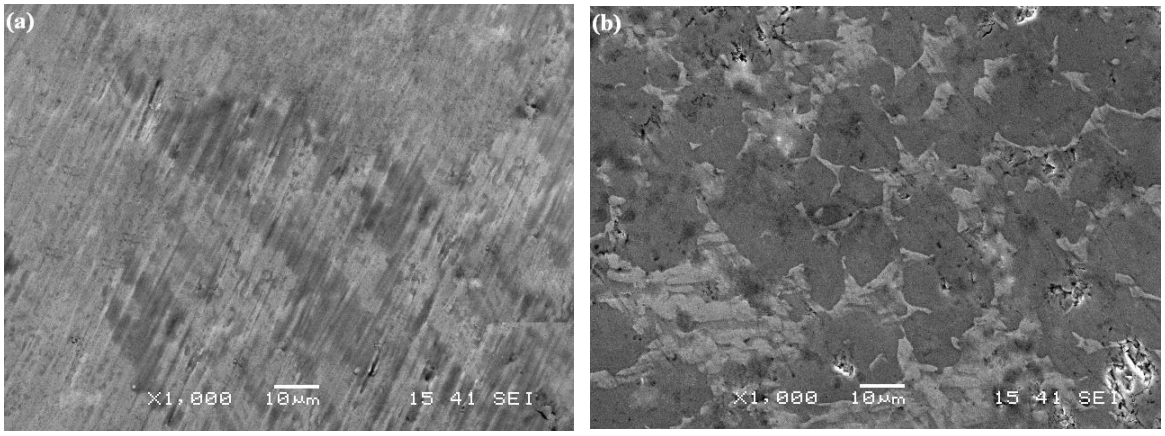

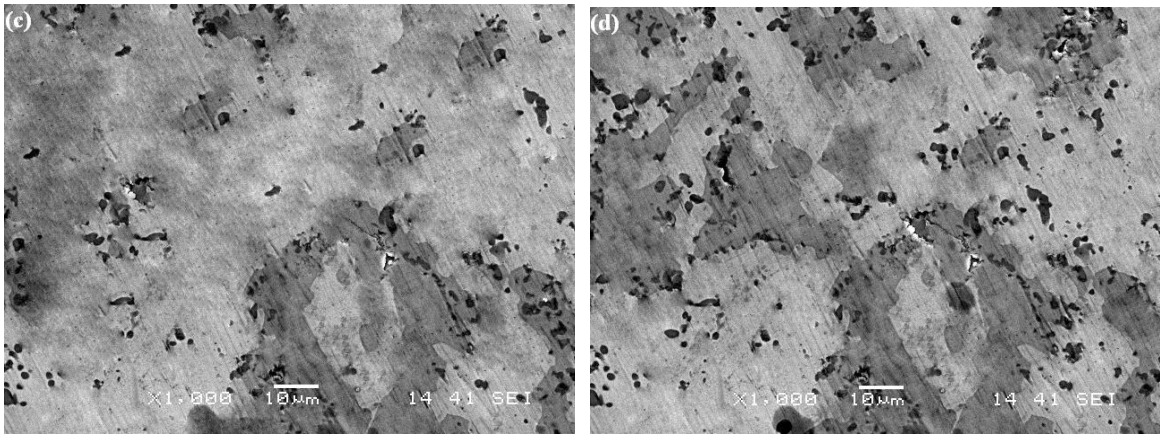

Figure 2. SEM images of the pure titanium and it's composite. (a) Pure titanium, (a) $Ti_{50+}Ni_{50}$ alloy. (c) $Ti_{50}+Ni_{49}+1SiCp$. (d) $Ti_{50}+Ni_{45}+5SiCp$.

Strong TiNi solid solutions presences were observed for the composite alloys (Fig.1b, c and d). It is attributed to the presence of content of Ni in these composite alloys. On the other hand, elemental dispersion of Ni and Ti is satisfactory, and SiC particles distributed into TiNi matrix, which confirms homogeneous structure formation (Fig. 2 c and d). At the beginning, it can be known that SiC particles are sharp-edged, having a particle size of ~40–45 μm. After sintering evaluation, the SiC particles were hanged on to the matrix and the surface of the composite specimens. Titanium nickel composite containing sub-micrometric SiC-particles and the dissolution of particle/metallic matrix composite in the interface between the titanium- nickel matrix and SiC particles. This microstructural features was responsible for the satisfactory values for the hardness and corrosion resistance for contents of SiC particles.

3.4 CORROSION TEST

Corrosion tests were carried out in H_2SO_4 with pH-1.50 solution at 3 hours. The test results are represented in Fig.3. It is clear from the result that pure Ti showed the best corrosion resistance, followed by silicon carbide reinforced based composites, but $Ti_{50}+Ni_{45}+5SiCp$ alloy indicated the highest corrosion rate due to strongly regarding to the porosity level.

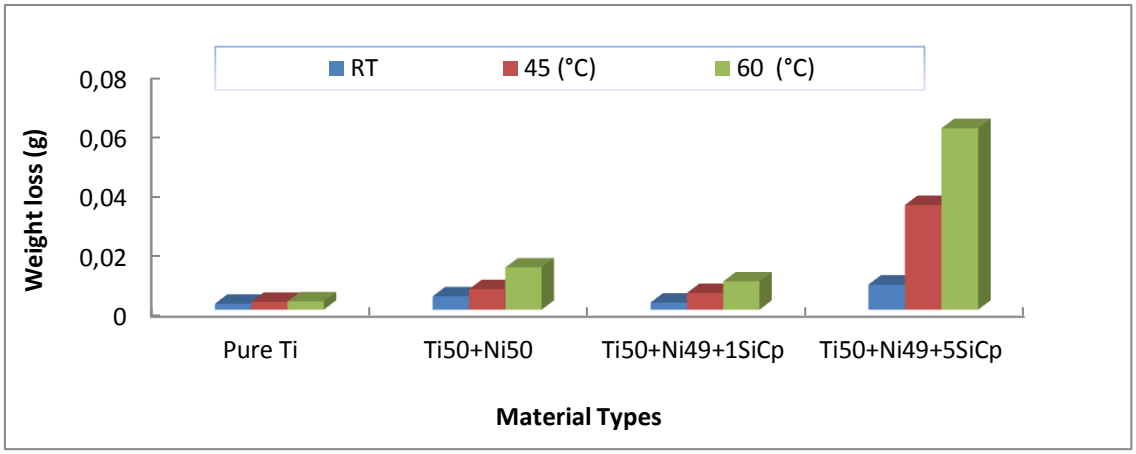

Figure 3. Corrosion test results on the composite samples.

4. CONCLUSIONS

In general, TiNi shape memory alloys were successfully fabricated by powder metallurgy process. The effect of SiC particles addition on microstructure and mechanical properties of TiNi alloy was investigated. In this exploratory work, the following results can be drawn:

• The fabrication procedure developed in this work did produce consolidated TiNi material with reasonably homogeneous microstructure.

• %5 SiC addition promoted an increase by 87.16% in hardness in the TiNi alloys;

• Among the tested samples, the best corrosion resistance was obtained for the Ti alloy because of lower porosity level.

REFERENCES

[1] Y.Liu, Van Humbeck, J. Stalmans, R, Delaey, "Some aspects of the properties of NiTi shape memory alloy". Journal of Alloys and Compounds, 247, 115−121, 1997.

[2] K. Otsuka, C Wayman, "Shape memory materials", Cambridge: Cambridge University Press, 49−96, 1998.

[3] S. Jiang, Y. Zhang, "Microstructure evolution and deformation behaviour of as-cast NiTi shape memory alloy under compression" Transactions of Nonferrous Metals Society of China, 90−96, 2012.

[4] S. Jiang, Y. Zhang, Y. Zhao, "Dynamic recovery and dynamic recrystallization of NiTi shape memory alloy under hot compression deformation", Transactions of Nonferrous Metals Society of China,140−147. 2013.

[5] M. Dolce, D. Cardone, "Mechanical behaviour of shape memory alloys for seismic applications, "International Journal of Mechanical Sciences, , 43, 2657−2677, 2001.

[6] S. Saadat, J. Salichs, M. Noori, Z. Hou, H Davoodi, I, Suzuki Y, Masuda, " An overview of vibration and seismic applications of NiTi shape memory alloy", Smart Materials and Structures,11, 218−229. 2002.

[7] K. Otsuka, X Ren, "Physical metallurgy of TiNi-based shape memory alloys. "Progress in Materials Science, 50, 511−678, 2005.

[8] M. Ninomi, "Mechanical properties of biomedical titanium alloys", Mater Sci and Eng A*;* 243, 231–36, 1998.

[9] Y Furuya, A Sasaki and M. Taya, "Enhanced Mechanical-Propertie of TiNi Shape Memory Fiber/Al Matrix Composite," Mater. Trans., JIM, **34**, pp. 224–227. 1993.

[10] W Armstrong, and D. Lorentzen, "Fiber Phase Transformation and Matrix Plastic Flow in a Room Temperature Tensile Strained NiTi Shape Memory Alloy Fiber Reinforced 6082 Aluminum Matrix Composite," Scr. Mater., **36**, pp. 1037–1043. 1997.

[11] W Armstrong, D. Lorentzen, T. Bréndsted and Larsen, P. H., "An Experimental and Modeling Investigation of the External Strain, Internal Stress, and Fiber Phase Transformation Behavior of a NiTi Actuated Aluminum Metal Matrix Composite," Acta Mater., **46**, pp. 3455–3466. 1998.

[12] M Dixit, J Newkirk and Mishra, "Properties of Friction Stir-Processes Al 1100-NiTi Composite," Scr. Mater., **56**, pp. 541–544. 2007.

[13] G. A Porter, P. K Liaw, T. N. Tiegs and K. H Wu, "Fatigue and Fracture Behavior of Nickel-Titanium Shape-Memory Alloy Reinforced Aluminum Composites," Mater. Sci. Eng., A, **314**, pp. 186–193. 2001.

[14] C. L, Xie, M. Hailat, Z. Abedin, X. Wu, G. Newaz, M. Taya and B. Raju,"Shape Memory Effect of TiNi Short Fiber on Mechanical Properties of TiNi/Al6061 Composite," SAE Paper No. 2005-01-1391. 2005.

[15] C. L, Xie, M. Hailat, Z. Abedin, X. Wu, G. Newaz, M. Taya and B. Raju, "Development of Short Fiber-Reinforced NiTi/Al6061Composite," ASME J. Eng. Mater. Technol., **129**, pp. 69–76. 2007.

[16] HZ. Ye, DY. Li, and RL, "Improvement in wear resistance of TiNi-based composite by hot isostatic pressing", *Mater. Sci. Eng.* A, 329–331, 750–55 (2002).

[17] DY Li, "The mechanism responsible for high **wear** resistance of pseudo-elastic TiNi alloy", *Wear,* 255, 617–28 (2003).

EFFECTS OF BORAX ON THE WEAR BEHAVIOR OF ORGANIC BRAKE LINING MATERIALS

İrem Burcu ALGAN *, Adem KURT*

*Gazi University,Turkey

irembalgan@gazi.edu.tr

ademkurt@gazi.edu.tr

ABSTRACT

Industrial brake lining materials are composites which consisting many different components. The expected properties of a brake lining material are high stable friction coefficient and good wear resistance. Borax ($Na_2B_4O_7.10\ H_2O$), the most common compound of boron, was used in the brake lining composition because it is oxidized easily at high temperatures and creates an oxide layer that modifies the surface characteristics**.** In this study borax was added 1%, 3% and 5% in organic and inorganic fiber based brake lining materials. The mixtures were initially stirred for three minutes, then hot pressed at pressure of 80 bar and finally sintered at 800 ºC in a conveyor type furnace. Produced samples were tested with Chase type friction test machine according to SAE-J661 test procedure. Test results indicate that, friction coefficient increases and the wear behavior improves with the increasing amount of borax addition.

Keywords: Borax, Brake lining material, Powder metallurgy, Wear resistance

ORGANİK FREN BALATA MALZEMELERİNİN AŞINMA DAVRANIŞINA BORAKSIN ETKİSİ

ÖZET

Endüstriyel fren balataları birbirinden farklı bileşenler içeren kompozit malzemelerdir. Yüksek ve kararlı sürtünme katsayısı ve iyi aşınma direnci, fren balatalarından beklenen özelliklerin başında gelmektedir. Bor elementinin en bilinen bileşiklerinden olan Boraks ($Na_2B_4O_7.10H_2O$), yüksek sıcaklıklarda kolayca oksitlenerek arayüzeylerde oksit tabakası oluşturmakta ve bu oksit tabakası yüzey özelliklerini değiştirmektedir. Bu çalışmada, organik ve inorganik fiber içeren ticari kullanımdaki fren balatası kompozisyona farklı oranlarda (% 1, %3 and % 5) boraks ilave edilmiştir. Karışımlar üçer dakika özel mikserde karıştırıldıktan sonra 80bar basınçla sıcak preslenmiştir ve ardından konveyör tipi fırında 800 ºC' de sinterlenmiştir. Üretilen numuneler Chase tipi sürtünme test cihazında SAE-J661 standartına göre test edilmiştir. Test sonuçları incelendiğinde, boraks miktarının artmasıyla birlikte balatanın sürtünme katsayısının artarak aşınma davranışında iyileşme olduğu görülmüştür.

Anahtar Kelimeler: Boraks, Fren Balata Malzemeleri, Toz Metalurjisi, Aşınma Direnci

1. INTRODUCTION

Friction materials are composed of many different components and these components are grouped according to their functions under four main headings: (I) reinforcements and binder materials, (II) friction modifiers, (III) fillers and (IV) abrasives. While the reinforcement and binder materials are dispersed on the each side of matrix and provide resistance, rigidity and integrity; friction modifiers change friction coefficient [1,2]. Usually metal, carbon, glass, and kevlar are used as reinforcement materials and are classified as organic or metallic pads according to type of reinforcement material. When examined of temperature, friction and wear relationships, organic-based brake linings are more advantage is observed. Nowadays, use of organic fiber increased since organic fibers are lighter than the other fibers, their raw materials are findable and specific strength are low [3].

Friction modifiers are two types: solid lubricants and abrasives. They largely affect the friction behavior of brake pad. While the powdered abrasive material such as alumina increases the friction coefficient, solid lubricant such as graphite decreases [4,5]. In recent studies, boron and boron compounds are added in brake lining composition to modify the friction coefficient. In metallurgy, boron compounds such as borax and boric acid are used as protective slag-forming substance due to the ability to create sticky, protective and burr-free liquid. For example, due to property of solvation in metal oxides and prevent surface oxidation, the iron surfaces are coated with borax [8]. As a result of studies, use of borax and boric acid is creating resistance against wear and provide to improvement of friction coefficient has been observed [6].

In the present study borax was added in different proportions (1%, 3% and 5%) in organic and inorganic fiber based brake lining materials. The samples were produced by powder metallurgy technique and afterward were sintered. The aim of this study is to show that the effect of borax in brake lining materials. Generally in friction materials, friction coefficient decreases with increasing temperature and this condition is defined as “fade” means elongation of the braking distance. This unwanted event reduces the safety of the brake system [7]. However, the present test results show that while the temperature is risen the friction coefficient increased with increasing borax addition and also wear rate increase partially.

2. EXPERIMENTAL PROCEDURE

2.1. Sample Preparation

Borax was added in Eren Brake Company’s commercial drum-organic-brake lining composition with different proportions (1%, 3% and 5%) and three different compositions were stirred in an industrial type mixer for three minutes. The ingredients of the composition are given in Table 1. All samples are hot pressed at pressure of 80 bar and finally sintered at 800 ºC in a conveyor type furnace.

Table 1. The ingredients in organic-based brake lining composition

Ingredients	Materials
Binder	phenolic resin
Fillers	barite, calcium carbonate
Reinforcements	glass fiber, steel fiber, PAN, aramid fiber
Abrasives	aluminum oxide, iron oxide
Friction Modifiers	metal oxide, metal sulfide, ceramic, borax
Lubricants	graphite

2.2. Friction Test and SEM Analysis

Samples were measured as 25mm x 25mm x 7mm then wear and friction tests were conducted with Chase type friction test machine (Model GM x 11.3 Pyramid Precision Engineering) according to SAE-J661 test procedure (Fig. 1).

Figure 1. Chase type friction machine

After friction and wear tests, the distribution of components on the wear surface was examined with EDS and mapping analysis using scanning electron microscopy (JEOL 6060 model).

3. RESULTS AND DISCUSSION

Fig. 2 shows the average friction coefficients for four samples with different contents. Accordingly Fig. 2, the sample was added 1% borax has the highest friction coefficient value at 93º C, 149 º C and 205 º C and friction coefficient increased with increasing temperature up to 205 º C for all samples.

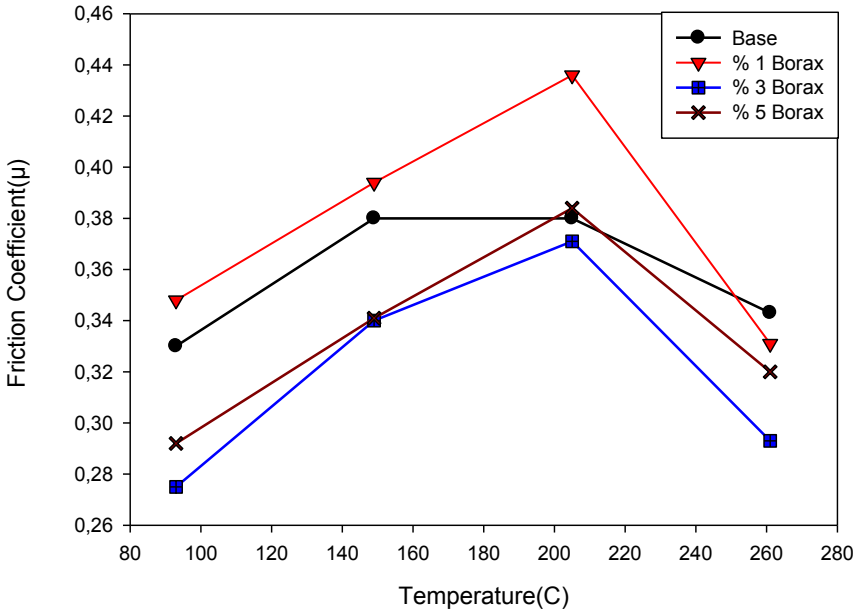

Figure 2. The average friction coefficients for different temperatures

The wear rates of the brake linings manufactured with different borax additions are given in Fig. 3. According the Fig. 3, the highest wear rate was measured in base brake lining composition and the lowest in 1% borax added sample. These wear results show that amount of wear decreased partially with the increasing borax rate.

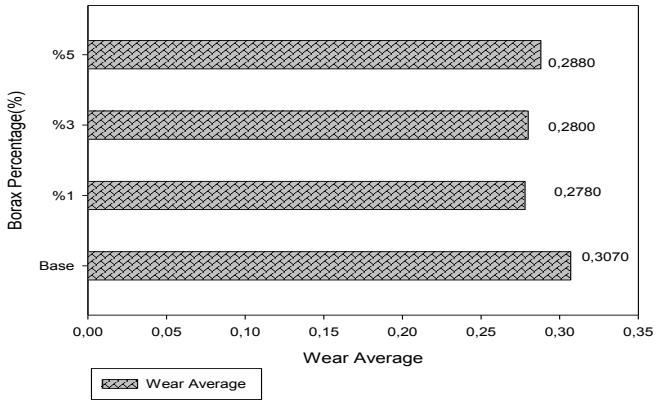

Figure 3. Wear average according to Borax percentage

Fig. 4 is SEM images comparison of samples at 100X magnification and four distinct areas are seen clearly in the each images. EDS analysis image of 3% borax added sample is given

exemplarily in Fig.5 and elementary analysis of four regions show that Table 2**.** According to EDS results, carbon and oxygen ratios in the first region; calcium, oxygen and iron ratios in the second region; iron, boron and oxygen ratios in the third region and oxygen, calcium and silicon ratios in the fourth region are higher than the other elements generally. The other elements are magnesium, titanium, sodium and sulfur in each region.

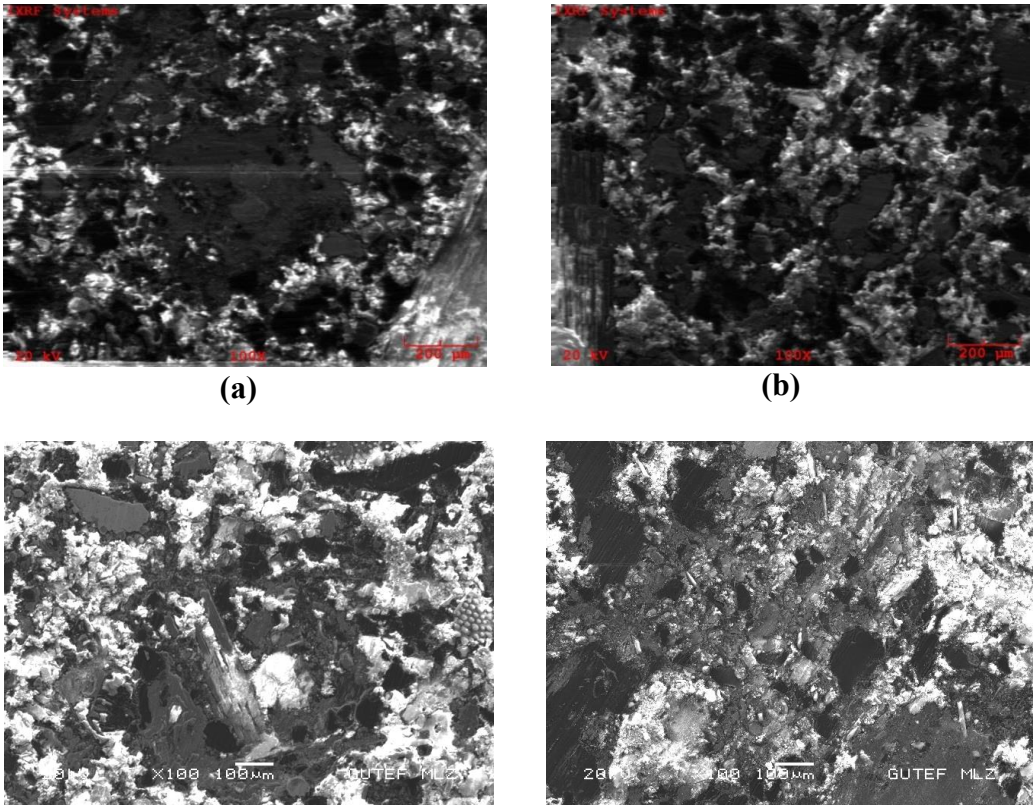

Figure 4. SEM images at 100 magnification of base specimen (a), 1% borax addition (b), 3% addition borax (c), 5% addition borax (d)

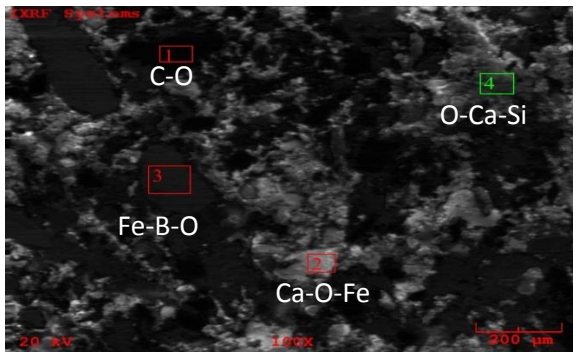

Figure 5. EDS image of 3% borax added sample

Table 2. The elementary analysis of four regions

Different Phases / Samples (%)	Region 1 % C- O	Region 2 % Ca-O-Fe	Region 3 % Fe-B-O	Region 4 % O-Ca-Si
Base	90-5,8	15,3-35,2-7,5	81,4-0-7,7	37,1-15,1-19,3
1 Borax	72,1-5,5	4,9-49,4-2,2	35,1-44-6,8	20-8,4-2,7
3 Borax	76,8-5,8	4,1-21,4-8,8	77,3-9-10,3	30,9-1,5-10,5
5 Borax	78,1-12,8	31,8-45-8,8	0,5-90-8	44,3-27-0,9

As a result of this study, wear rates of the borax containinig brake lining materials are approximately the same value with base material and the friction coefficient increases depending on the addition rate, were seen. Additionally, friction coefficient increases with increasing brake temperature was observed. This is an interesting situation because generally μ value reduces with increasing temperature in brake materials and this undesirable situation means prolongation of the braking distance in vehicles.

μ value of %1 borax addition sample is 0,34 at 93 ºC ; 0,39 at 149 ºC and 0,38 at 205 ºC. It shows that, even if 1% borax addition friction coefficient increases in hot work environments.

As the amount of borax increasing, the wear rate decreases and the μ value increases. This situation is borax easily oxidized at high temperatures and creates the interfacial oxide layer can be explained.

All of these results show that, borax can be used as friction modifiers in composition of brake lining materials.

REFERENCES

1. P.J.Blau "Compositions,Functions and Testing of Friction Brake Materials and Their Additivies", Metals and Ceramic Division,2001

2. Y.Lu "A Combinatorial Approach for automotive Friction Materials: Effects of Ingredients on Friction Performance",Beijing University, Beijing, China,2005

3. Y. Özdemir "Investigation of Mechanical Properties of Natural Fiber Reinforced Composites Materials Used in Automotive Industry by Finite Element Method", M.Sc. Thesis, Mersin University,2009

4. S.J. Kim,H.Jang "Friction and Wear of Friction Materials Containing Two Different Phenolic Resins Reinforced with Aramid Pulp", Tribology International

5. D.Chan,G.W.Stachowiak " Review of Automotive Brake Friction Materials", Proceedings The Institution of Mechanical Engineers,Part D-Journal of Automobile Engineering

6. İ.Mutlu,İ.Çevik,C.Öner "Experimental Investigating of Boric Acid and Borax Effect in Brake Lining

7. S. K. Rhee "Friction Coefficient of Automotive Friction Materials-It's Sensitivity to Load,Speed and Temperature" SAE Paper No 740415

8. Product Catalog of Eti Maden Management. Retrieved from, http://www.etimaden.gov.tr/d/file/boraks-dekahidrat.pdf

EFFECT OF NICKEL/COPPER RATIO ON THE MECHANICAL PROPERTIES FOR TUNGSTEN BASED HEAVY ALLOYS

N. Kaan ÇALIŞKAN*, Nuri DURLU**

*TÜBİTAK SAGE, Ankara, Turkey
**TOBB, University of Economics and Technology, Ankara, Turkey

ABSTRACT

In the present study, the effect of different Ni/Cu ratio on the mechanical properties of liquid phase sintered W90-Ni3-Cu7 and W90-Ni7-Cu3 alloys was investigated. In the processed alloys, amount of tungsten which forms the main phase was kept constant at 90 wt%, and the total amount of Ni-Cu binder phase was kept at 10 wt%, where Ni/Cu ratio was chosen as 3/7 and 7/3. Alloy samples were cold isostatically pressed at 300 MPa and sintered under hydrogen-argon atmosphere at 1430 °C for 30 minutes. As a result of the mechanical tests, tensile strength, % strain and microhardness (HV0.1) of W90-Ni3-Cu7 and W90-Ni7-Cu3 samples were measured as 713±6 MPa, % 6.06±1.8 and 314±31, and 743±13 MPa, 8.75±2.47 and 378±20 respectively. Microstructural analysis of the liquid phase sintered samples showed that average particle size of W increases and contiguity of W phase decreases with increase in the Ni/Cu ratio. Solubility of W particles increases with the increase in the Ni/Cu ratio and due to this solubility increase higher mechanical properties were achieved.

Keywords: Mechanical Properties, Tungsten Alloys, W-Ni-Cu Alloys

1. INTRODUCTION

Tungsten based alloys are two phase metal matrix composites which contain 80 to 97 wt.% brittle tungsten particles embedded in a tough, metallic binder phase composed of Ni, Cu, Fe or Co and dissolved W. The properties of high density and a unique combination of strength and ductility make these alloys useable for both civil and military applications such as nuclear, welding, radiation, counter weight and penetrator applications [1-3]. These alloys are mostly processed through conventional powder metallurgy techniques such as persistent liquid phase sintering, though for some specific applications mechanical alloying and infiltration processing techniques may also be conducted [3-5].

Price and his co-workers [6] were the first to introduce the new processing procedures of high density tungsten based alloys. They worked with tungsten based alloys containing nickel and copper. It was noted in their study that alloys with high tungsten content can be sintered to almost full density at the temperatures relatively well below the melting point of tungsten. Although W-Ni-Cu alloys are still used for some applications such as for non-magnetic applications, their mechanical properties were unsatisfactory compared to other high density tungsten based alloys especially for W-Ni-Fe alloys [7].

In liquid phase sintering processes, solid solubility in liquid phase is essential for the high degree and rapid densification [8] which led to satisfactory mechanical properties. It was cited

that, a range of tungsten solubility and dihedral angles can be obtained in the W-Ni-Cu alloy by varying the Ni:Cu ratio. An increase in nickel content in the matrix reduces the dihedral angle and increases the solubility of the tungsten in the matrix [9]. For the tungsten based alloys, it was also observed that, the rate of particle growth increases with the tungsten solubility which led to larger particle size and a lower contiguity which is the measure of the tungsten-tungsten interfaces in the final microstructure [10]. Contiguity is one of the critical microstructure parameter for the tungsten based alloy since tungsten-tungsten interfaces are the weakest points in the microstructure [11].

For alloys having lower ultimate tensile strength and ductility; large amounts of tungsten-binder phase interfacial separation is observed on the fracture surfaces. However, for alloys having high strength and ductility, a large amount of transgranular tungsten cleavage as well as ductile rupture of the matrix is observed [12]. Previous studies have also showed that tungsten-binder matrix phase interface properties dictated the ductility of the tungsten based alloys [11]. Strong interface due to high tungsten solubility induces the high ductility and the ultimate tensile strength [13-14].

The present work is performed to observe the effect of binder phase composition on the tensile strength and ductility properties of Ni-Cu based tungsten heavy alloys and aims to explain the correlation between the microstructural properties such as volume fraction of phases, contiguity, average particle size and mechanical properties.

2. EXPERIMENTAL

In the preparation of Ni-Cu based alloys, elemental Cu, Ni and W metal powders were used. Average particle size of the powders was measured by laser particle size analyzer (Mastersizer 2000, Malvern, USA). The shape of the particles (See Figure 1) was investigated with scanning electron microscopy (6400 JSM, Jeol, Japan). Appropriate amounts of Cu, Ni and W powders were prepared to give the alloy compositions W90-Ni7-Cu3 and W90-Ni3-Cu7. Mixing of the powders was carried out in a turbula mixer (T2F, Glenn Mills, Switzerland) at a speed of 67 rpm for 45 min in a sealed glass container. Tungsten carbide balls with a diameter of 4.76 mm were also charged with powders to reduce agglomeration and density gradients.

Powder mixes were cold isostatically pressed (CIP 42260, Flow Autoclave Engineers, USA) at 300 MPa for 15 s. After compaction, density of green parts was measured to be 55%-65% of theoretical density. The compacted samples were then sintered at 1430 ºC for 20 minutes under H_2 (with a dew point of -60 ºC) atmosphere and for 10 minutes under commercial purity argon in an atmosphere controlled furnace (Model: Linn HT-1800). The sintering cycle is; heating from room temperature to 1000 ºC at 9°C/min, holding at 1000 ºC for 30 minutes, heating to 1430 ºC at around 3°C/min, holding at 1430 ºC for 30 minutes and cooling to room temperature by furnace cooling under Ar.

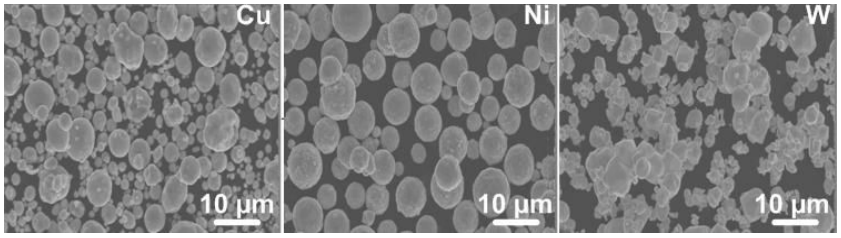

Figure 1 Shape and relative size distribution of elemental powders.

Sintered alloys were characterized by evaluating their mechanical properties such as tensile strength % elongation and microhardness. Density of the alloys was measured by Archimedes water immersion technique by using xylene with a density of 0.86 g/cm3. The tensile test specimens were prepared as per ASTM E8M [15] and were tested using a tensile testing machine (3369, Instron, USA) with a crosshead speed of 0.5 mm/min at room temperature. At least 3 specimens were tested and average value of the 3 specimens was reported. Micro hardness tester (Buehler, Illinois, USA) with a load of 100g was used to measure hardness of sintered alloys. Ten indentations were taken for each sample and the average value was reported.

The microstructure analysis of the alloys was performed by an optical microscope and a scanning electron microscope. Etching was done with Murakami's etchant. Analysis of volume fraction of phases were carried by according to ASTM E562 [16]. The contiguity of the samples was measured metallographically by using the equation below [17];

$$C_w = \frac{2N_{WW}}{2N_{WW}+N_{WB}} \quad (1)$$

N_{WW} = Number of W-W interfaces per unit length of test line
N_{WB} = Number of W-B (binder phase) interfaces per unit length of test line

In order to determine the liquidus temperatures of the alloys, thermal analysis experiments were conducted on liquid phase sintered alloys by using Differential Scanning Calorimeter (DSC) (DSC-TGA Setaram Setsys Evolution 16-18, Setaram Instrumentation, Caluire, France). Heating and cooling cycles were conducted under Ar atmosphere at a rate of 10 ºC/min.

3. RESULTS AND DISCUSSION

In order to select the optimum sintering process cycle which led to the acceptable physical and mechanical properties, green and sintered densities of the W90-3Ni-7Cu and W90-7Ni-3Cu alloys were measured. After the cold isostatic pressing process, the alloy samples had similar %relative densities values which are between %55 and %65. At the beginning of this study, argon was selected as sintering atmosphere which led to unsatisfactory results in terms of sintered densities which are around %96 which was similar to the density values cited in the literature. It was reported that non-reducing atmospheres such as argon led to incomplete densification and lower mechanical properties due to the rapid coarsening of tungsten particles when compared to the neck growth and incomplete reduction of metal oxides [18, 19, 20]. Hydrogen is generally preferred for the sintering atmosphere for the tungsten based alloys. However, sintering under pure hydrogen may also lead to the hydrogen brittleness due to the crystal structure of tungsten which is BCC. Hydrogen removal is necessary in order to achieve higher mechanical properties [21]; therefore, switching to an inert gas atmosphere

from hydrogen at the sintering cycle was applied at this study. After liquid phase sintering process under the mixture of hydrogen and argon, densities of the samples were measured to be above 98.5% theoretical density. The two phase microstructures of liquid phase sintered alloys are given in Figure 2. In the micrographs, relatively white regions are almost pure W particles which are surrounded by the black Ni-Cu binder matrix phase.

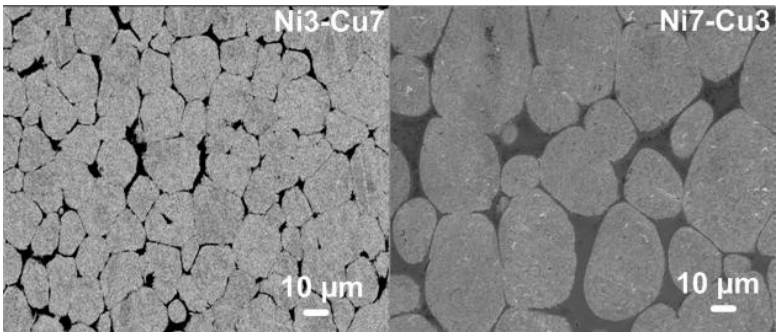

Figure 2 Backscattered scanning electron micrographs of liquid phase sintered alloys sintered at 1430°C for 30 minutes, 20 min H_2 + 10 min. Ar, W90-Cu7-Ni3(left) and W90-Ni7-Cu3(right).

Backscattered electron and optical micrographs were utilized to determine the microstructural characteristics such as the amount of binder matrix phase, average tungsten particle size, and contiguity of tungsten particles. The results of the microstructural characterization are summarized in Table 1.

Table 1 Microstructural properties of 90W-7Cu-3Ni and 90W-7Ni-3Cu alloys sintered at 1430°C for 30 minutes, 20 min H_2 + 10 min. Ar.

Alloy Composition	Binder Matrix Area (%)	Contiguity	Average Tungsten Particle Size (µm)
W90-Cu7-Ni3	11±0.06	0.51±0.08	16.44±4.62
W90-Ni7-Cu3	22±0.06	0.29±0.08	34.08±9.34

Increasing the nickel content in the alloy compositions has led to the significant changes in the microstructures as given in Table 1. In the alloys having nickel to copper ratio as 7/3, tungsten particles become more spherical and average particle size of tungsten were observed to be bigger (around 2 times) than the alloys having nickel to copper ratio as 3/7. It was also observed that amount of binder matrix phase increased and contiguity decreased with the increase in nickel content in the alloy compositions.

In the liquid phase sintering process, densification requires the high solid solubility in liquid and low liquid solubility in solid [8]. High solid solubility in the liquid also induces the low dihedral angle and faster solution re-precipitation step which led to the bigger average particle size in the final microstructure [22]. It was also reported that higher solubility of tungsten in the binder matrix results in the lower contiguity, higher binder matrix phase and higher ductility in the tungsten based alloys [10].

Solubility of tungsten in the binder matrix phase could also be varied by changing the Ni/Cu ratio in the alloy composition [23] for the tungsten based alloys. It is known that liquidus of binder matrix phase changes with the solubility of tungsten in the binder matrix phase since melting temperature of the binder phase increases with the increase in the solubility of tungsten. In order to determine the liquidus temperatures of the sintered alloys, DSC experiments were conducted. It was observed that liquidus of the W90-Ni7-Cu3 and W90-Cu7-Ni3 alloys were 1426 °C and 1262°C, respectively. After analyzing the Ni-Cu binary phase diagrams, it was observed that increase in the liquidus temperature of W90-Ni7-Cu3 alloy was 41°C and increase in the liquidus temperature of W90-Cu7-Ni3 alloy was determined as 17°C. Temperature differences and DSC experiments showed that W solubility increases as Ni content increases. This tungsten solubility increase in the binder matrix phase has led to increase in average particle size of tungsten and decrease in binder matrix phase and contiguity of the investigated alloys.

The microhardness, ductility and ultimate tensile strength of the alloys are given in Table 2. As given in Table 2, nickel content increase in the alloy composition has also resulted in the higher mechanical properties. The difference in the ultimate tensile strength and the hardness can also be attributed to the higher tungsten solubility which was caused by varying the Ni/Cu ratio in the binder matrix phase. This relation between the tungsten solubility and tensile strength and microhardness might be explained by the interactions between the tungsten atoms as solute atoms and dislocations that can be considered as solid solution strengthening of binder matrix phase. Tungsten atoms act as obstacles in the binder matrix phase to the dislocation motion which might increase the tensile strength and hardness of the alloys [24, 25]. It can be concluded that increase in Ni/Cu ratio which induced the higher tungsten solubility in the binder matrix phase has led to higher tensile strength and microhardness.

The ductility of W90-Ni7-Cu3 alloys is approximately 9% and considerably higher than the ductility of W90-Ni3-Cu7 which is around 6%. It is known that contiguity of the tungsten particles should be controlled or reduced by the subsequent sintering operations for the maximum elongation for the tungsten based alloys. A higher contiguity in the microstructure induces a lower ductility [26] since tungsten-tungsten interfaces are the weakest points in the microstructure [11]. This significant difference in the ductility of the alloys can be attributed to the higher amount of binder matrix phase present in the W90-Ni7-Cu3 alloys. The presence of higher amount of matrix phase led to lower contiguity values as seen in W90-Ni7-Cu3 alloys. For the alloys of W90-7Ni-3Cu, lower contiguity has led to higher ductility when compared to W90-Ni3-Cu7 alloys.

Table 2 Mechanical properties of 90W-7Cu-3Ni and 90W-7Ni-3Cu alloys sintered at 1430°C for 30 minutes, 20 min H_2 + 10 min. Ar.

Alloy Composition	Ultimate Tensile Strength (MPa)	%Elongation	Hardness (HV0.1)
W90-Cu7-Ni3	713±6	6.06±1.80	313.5±30.8
W90-Ni7-Cu3	743±12	8.75±2.47	378.4±20.8

In literature, there is not much work on the mechanical properties of W-Ni-Cu based alloys. Das et al. [7] reported the tensile strength and %strain of W-Ni-Cu alloys (W content ranging from 92.5% to 96.1% and Ni/Cu ratio ranging from 2.1% to 2.5%) as in the range of 655 - 681 MPa and %3-%6, respectively. These differences in the mechanical properties may be attributed to the differences in powder compositions, cooling cycles, and post-sintering operations. In this work, there was no need for post sintering operations such as vacuum annealing or heat treating under inert atmosphere after sintering due to selected compositions, since intermetallic phase precipitation are not expected for the Ni-Cu based tungsten alloys [27].

Tungsten solubility in the binder matrix phase has also affected the fracture characteristics of the alloys. Fracture surfaces of W90-Ni3-Cu7 and W90-Ni7-Cu3 are given in Figure 3. As seen in Figure 3, Ni3-Cu7 alloys were failed dominantly by the binder and/or interface (between tungsten particle and binder matrix phase) failure and there is almost no W cleavage in the fractured surfaces of Ni3-Cu7 alloys. However, in Ni7-Cu3 alloys, there is some cleavage fracture of tungsten particle and binder phase. Cleavage of W particles is signed by the black arrows in Figure 3 (Ni7-Cu3). In tungsten heavy alloys, poorer binder phase strength or interfacial strength are found to initiate the fracture by separation of tungsten particles either by binder phase failure or by interface failure [7]. Fracture images showed that Ni7-Cu3 alloys has a greater interfacial strength due to the higher tungsten solubility in the binder matrix phase.

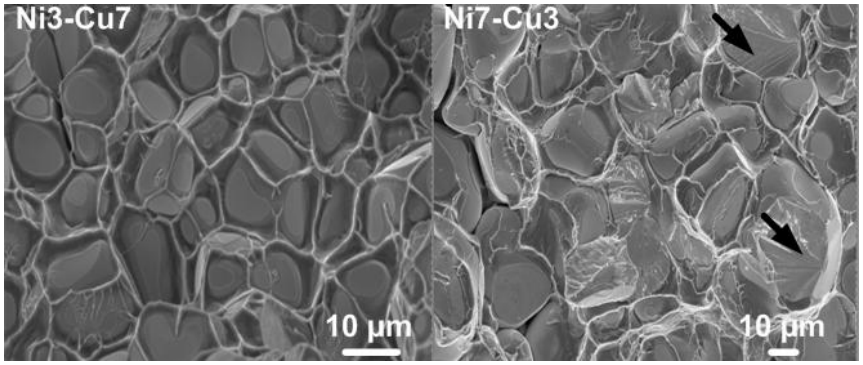

Figure 3 Fracture surfaces of the liquid phase sintered alloys sintered at 1430°C for 30 minutes, 20 min H_2 + 10 min. Ar, W90-Cu7-Ni3(left) and W90-Ni7-Cu3(right).

4. CONCLUSIONS

In this study, the effect of Ni/Cu ratio on the mechanical properties of W90-Ni3-Cu7 and W90-Ni7-Cu3 alloys has been investigated. The study showed that increase in the nickel of the alloys resulted in the increase in the average tungsten particle size as well as volume percent of binder phase and a reduction in the contiguity. Higher tensile strength and ductility of W90-Ni7-Cu3 alloys were observed due to the lower contiguity and tungsten solubility of tungsten in the binder matrix phase which led to transgranular cleavage of tungsten particles and ductile matrix failure. Lower mechanical properties observed in the W90-Ni3-Cu7 alloy were correlated to the higher contiguity of the tungsten particles and lower tungsten solubility in the binder matrix phase which led to the intergranular fracture of tungsten particles.

ACKNOWLEDGEMENTS

This study was supported by TÜBİTAK SAGE.

REFERENCES

1. R.M. German and L.L. Bourguignon and B.H. Rabin, J. Inst. Metals, 37(8), 36-39, 1985.
2. L.B. Ekbom, Scand J Metall, 20(3), 190-197, 1991.
3. A. Upadhyaya, Mater Chem Phys, 67, 101-110, 2001.
4. "Powder Metal Technologies and Applications", Metals Handbook, Volume 7, ASM International, Materials Park, Ohio, 1998.
5. E. Lassner E. and W.D. Schubert, "Tungsten Properties, Chemistry, Technology of the Element, Alloys and Chemical Compounds", Kluwer Academic/Plenum Publishers, New York, 1999.
6. G.H.S. Price, C.J. Smithells and S.V. Williams, Journal of the Institute of Metals, 62, 239-264, 1938.
7. J. Das, U. R. Kiran, A. Chakraborty and N. E. Prasad, International Journal of Refractory Metals and Hard Materials. 27, 577-583, 2009.
8. R.M. German, P. Suri and S.J. Park, Journal of Materials Science, 44, 1-39, 2009.
9. A. Upadhyaya and R.M. German, Metallurgical and Materials Transactions, 29A, 2631-2638, 1998.
10. A. Bose and R.M. German, Metallurgical and Materials Transactions, 21A, 1325-1327, 1990.
11. K.S. Churn, J.W. Nob, H.S. Song, E.P. Kim, S. Lee and W.H. Back, Proceedings of the First International Conference on Tungsten and Tungsten Alloys (Eds. A. Bose and R.J. Dowding), Metal Powder Industries Federation, 397-406, 1992.
12. B.H. Rabin "Microstructure and Tensile Properties of Liquid Phase Sintered Tungsten-Nickel-Iron Composites", Ph.D Thesis, Rensselaer Polytechnic Institute, 1986.
13. E.W. Kennedy, Proceedings of the Second International Conference on Tungsten and Refractory Metals (Eds. A. Bose and R.J. Dowding), Metal Powder Industries, 101-110, 1994.
14. S.G. Caldwell, Proceedings of the First International Conference on Tungsten and Tungsten Alloys (Eds. A. Bose and R.J. Dowding), Metal Powder Industries Federation, 89-96, 1992.
15. ASTM E8/E8M, Standard Test Methods for Tension Testing of Metallic Materials, 2009.
16. ASTM E562, Standard Test Method for Determining Volume Fraction by Systematic Manual Point Count, 2008.
17. J. Gurland, Trans AIME, 212, 452, 1958.
18. A. Bose and R.M. German, Metallurgical and Materials Transactions, 19A, 2467-2476, 1988.
19. I.H. Moon, J.H. Kim, M.J. Suk, K.M. Lee and J.K. Lee, International Journal of Refractory Metals and Hard Materials, 11, 309-315, 1992.
20. N.K. Çalışkan, N. Durlu N and Ş. Bor, International Journal of Refractory Metals and Hard Materials, 36, 260-264, 2013.
21. R.M. German and K.S. Churn, Metallurgical and Materials Transactions, 15A, 747-754, 1984.
22. R. M. German, Liquid Phase Sintering, Plenum Press, New York, 1985.
23. J. Liu and R.M. German, Metallurgical and Materials Transactions, 32A, 3125-3131, 2001.
24. G. E. Dieter, Mechanical Metallurgy, SI Metric edition, McGraw-Hill Book Company, 1988.
25. K.E. Knipling, G. Zeman, J.S. Marte, S.M. Kelly and S. L. Kampe, Metallurgical and Materials Transactions, 35A, 2821-2828, 2004.
26. K. S. Churn and R. M. German, Fracture Behavior of W-Ni-Fe Heavy Alloys, Metallurgical Transactions, 15A, 331-338, 1984.
27. D.V. Edmonds and P.N. Jones, Metallurgical and Materials Transactions, 10A, 289-295, 1979.

Selective Laser Sintering (SLS)/Selective Laser Melting (SLM) for Functional Applications

•

İşlevsel Uygulamalar için Seçmeli Lazer Sinterleme / Seçmeli Lazer Eritme

Cenk Aktaş

Leibniz Institute for New Materials - Germany

ABSTRACT

Selective Laser Sintering (SLS) was developed in the late 80's for Rapid Prototyping (RP). Nowadays, SLS - as well as its extended approach - Selective Laser Melting (SLM) - is used for prototyping, tooling and manufacturing purposes. Both SLS and SLM lead to processing of a large variety of materials. Especially for achieving more complex geometries, the SLS/SLM process seems to be the most promising way. Although the laser sintering process has been applied to a broad range of powders, several aspects such as sintering rate and the effects of processing parameters on the microstructural evolution during the layer manufacturing process have not been well understood yet. Laser sintering is a complex process and it is governed by several parameters such as powder material properties, processing parameters and the geometry of the 3D object to be printed. This work covers a brief introduction of the SLS/SLM method and the corresponding materials synthesis approaches. In addition a number of existing application areas of 3D SLS/SLM for instance the medical implant production will be presented as a case study.

Keywords: Selective laser sintering, selective laser melting, prototyping, 3D object.

THE EFFECT OF SINTERING TEMPERATURE AND TUNGSTEN CONTENT ON THE MICROSTRUCTURAL CHARACTERISTICS OF W-RICH W-NI-CO HEAVY ALLOYS

Onur DİNÇER[*], Ali KALKANLI[**], İshak KARAKAYA[**], M. Kaan PEHLİVANOĞLU[*]

*TÜBİTAK SAGE, Ankara, Turkey
**Middle East Technical University, Ankara, Turkey

ABSTRACT

In this study, the effect of sintering temperature and tungsten (W) content on the microstructural characteristics of selected W-rich W-Ni-Co alloys was investigated. The alloys studied were prepared with conventional powder metallurgy methods and have had 90, 92, 95 and 97 wt% W content balanced with 1/1 and 4/1 Ni/Co compositions. Alloy samples were sintered under pure hydrogen atmosphere at 1500, 1550 and 1600°C. All investigated alloys were found to reach nearly full density at all the sintering temperatures applied. The microstructures of the investigated alloys were observed to consist of rounded W grains embedded in a binder matrix phase, which is typical of liquid phase sintered tungsten heavy alloys. The binder matrix of all the investigated alloys with Ni/Co ratio 4/1 was found to be composed of a single phase. On the other hand, all Ni/Co ratio 1/1 alloys were observed to consist of a two-phase binder matrix. In these alloys, the ratio of the two phases of the binder matrix was found to vary with alloy W content and sintering temperature. The total amount of the binder matrix phase decreases with increasing alloy W content for both Ni/Co ratio 4/1 and 1/1 alloys, at all sintering temperatures. For these alloys, the average W grain size was found to increase with increasing sintering temperature and increasing alloy W content. However, the variation of W grain size with alloy W content was somehow unsystematic in Ni/Co ratio 1/1 alloys. This behavior was suggested to be related to the presence of a two-phase binder matrix in these alloys.

Keywords: Liquid phase sintering, Nickel, Cobalt, Tungsten Heavy Alloys, Microstructure

1. INTRODUCTION

Tungsten heavy alloys (WHAs) are composite materials with a typical microstructure consisting of W grains embedded in a ductile binder matrix phase. The binder matrix phase in these alloys can consist of Ni, Cu, Fe, Co, Mo, etc. and some dissolved W. WHAs are generally produced through powder metallurgy routes, especially by using solid state sintering (SSS) and liquid phase sintering (LPS) methods. WHAs can exhibit superior properties such as high tensile strength, high density, good wear and corrosion resistance. Owing to these beneficial properties, WHAs are used in both civil and military applications such as radiation shields, counter weight balances, kinetic energy penetrators, electrical contacts and damping devices [1- 4].

The most widely used tungsten heavy alloy system is W-Ni-Fe and LPS method has been preferred in the production of alloys in this system. In the manufacturing of high density WHAs, the amount of the binder phase used is usually between 2 to 10 wt%. The nickel/iron mass ratio for these alloys is commonly 2/1 and the W content of the alloys can range between 90-97 wt% W [5]. By the use of nickel-iron as the binder phase, W-Ni-Fe alloys with better mechanical properties in terms of strength and ductility were developed and these alloys were studied well in the literature [6]. So as to increase the mechanical properties of these alloys, 5 to 15% of nominal binder weight fraction of Co was generally added to the composition [7]. Furthermore, especially for superior mechanical properties which are commonly required in military penetrator applications, Fe was also replaced by Co in WHAs [8, 9]. The most commonly used W-Ni-Co alloy systems contain Ni/Co ratio ranging from 2 to 9. These alloys provide greater tensile strength, ductility and toughness as compared to W-Ni-Fe alloys after some post-sintering thermomechanical treatments [10-12]. W-Ni-Co is a newer ternary alloy system when compared to other WHAs and studies on microstructural and mechanical characterization of this alloy system are relatively scarce in the literature.

The main objective of this study is to investigate the effects of sintering temperature and tungsten content on the microstructural characteristics of selected W-Ni-Co alloys sintered under hydrogen atmosphere. The ternary alloys selected for the study have had Ni/Co mass ratios 1/1 and 4/1, and the tungsten content of the investigated alloys were selected as 90, 92, 95 and 97 wt%. W-rich W-Ni-Co alloys with Ni/Co ratio 4/1 are investigated in the study because, as mentioned previously, these alloy compositions lie within the most widely used Ni/Co range (i.e. Ni/Co range 2 to 9). Therefore, a deeper understanding of the microstructural characteristics of such alloys might be of valuable technological importance. On the other hand, the goal for choosing Ni/Co ratio 1/1 alloys is to investigate the effect of equal-mass-ratio binder addition on the characteristics of W-Ni-Co heavy alloys.

2. EXPERIMENTAL

The general properties of the elemental W, Ni and Co powders used in this study are given in Table 1. The elemental powders were of 99.9 % and above purity as indicated by the suppliers. The average particle size of the powders was measured by a laser particle size analyzer (Mastersizer 2000, Malvern, USA). Proper amounts of W, Ni and Co powders were weighted by a precision balance that has $\pm$ 0.01 g accuracy (CP3200S, Sartorius, Germany) in order to give the alloy compositions. In the alloy systems studied, the W content was chosen as 90, 92, 95 and 97 wt% and the Ni/Co mass ratio was varied as 1/1 and 4/1 for each W content. The composition of the alloys investigated in this study is given in Table 2. Powder mixing was performed in a turbula mixer (T2F, Glenn Mills, Switzerland) at a speed of 80 rpm for 40 minutes. Mixed powders were compacted by cold isostatic pressing (CIP 42260, Flow Autoclave Engineers, USA) at 310 MPa for 15 seconds. The compacted samples were then liquid phase sintered at 1500, 1550 and 1600ºC for 60 minutes according to the sintering cycle shown in Figure 1. Sintering process was conducted in a horizontal tube furnace (PTF105, Protherm Furnaces, Turkey) under flowing pure hydrogen with a gas flow rate of 0.5 l/min.

Densities of the alloys were measured by Archimedes immersion technique by using xylene (density: 0.86 gr/cm^3). The measured densities were divided by the theoretical densities and then multiplied by 100 in order to determine the percent relative densities (%RD) of the alloys. The theoretical densities were estimated by using the rule of mixtures method. For microstructural characterization, specimens were prepared with proper metallographic

Table 1. General properties of the elemental powders

Elemental Powder	Average Particle Size (µm)	Shape	Purity (wt%)	Source
W	4.8	Polygonal	99.9+	Eurotungstene AW2123
Ni	4.3	Polygonal	99.9	William Rowland Vale 123
Co	6.0	Polygonal	99.9+	Eurotungstene CO610A25

Table 2. Compositions of the investigated alloys

Alloy Code	W (wt%)	Ni (wt%)	Co (wt%)	Ni/Co Ratio
0W11	90	5.0	5.0	1/1
0W41	90	8.0	2.0	4/1
2W11	92	4.0	4.0	1/1
2W41	92	6.4	1.6	4/1
5W11	95	2.5	2.5	1/1
5W41	95	4.0	1.0	4/1
7W11	97	1.5	1.5	1/1
7W41	97	2.4	0.6	4/1

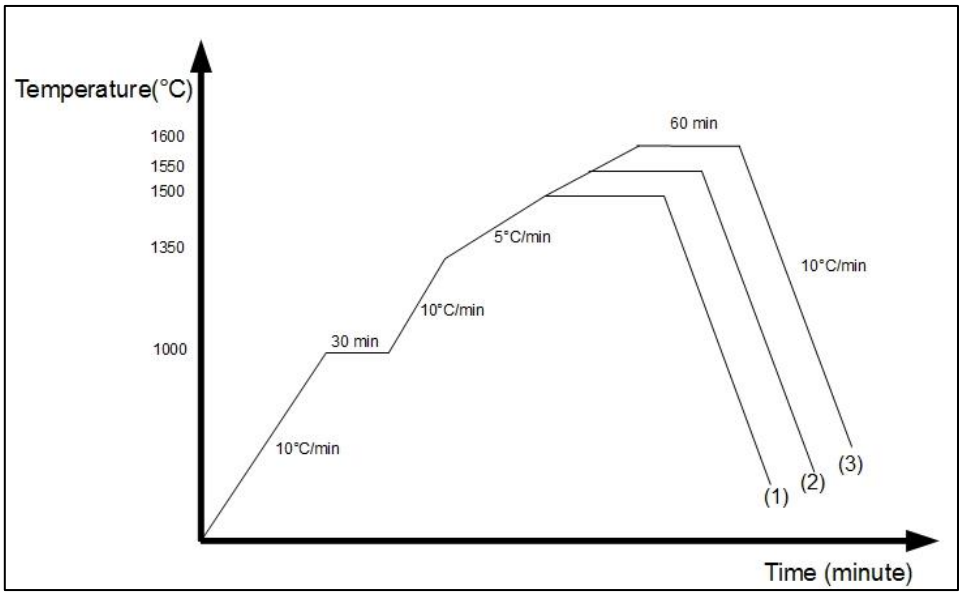

Figure 1. Temperature-time profile applied for the sintering experiments, (1) 1500ºC, (2) 1550ºC and (3) 1600ºC

techniques and etched by Murakami's etchant. The microstructure analysis of the alloys was performed by an optical microscope (Axioskop 2, Zeiss, Germany) and a scanning electron microscope (SEM) (6400 JSM, Jeol, Japan). The compositions of the constituent phases were identified in SEM by energy dispersive spectroscopy (EDS) (Northern Tracor EDS system equipped within 6400 JSM, Jeol, Japan). The average tungsten grain size (AGS) of the alloys was determined by using Planimetric method in accordance to ASTM E112 [13].

3. RESULTS and DISCUSSION

Archimedes immersion method was used to measure the densities of the alloy specimens. The %RDs of the alloys formed in this investigation are given Table 3. As can be seen in Table 3, it is found that all of the investigated alloys reached nearly full density at all the sintering temperatures applied. A very slight exception to this general trend was shown by 90 and 92 wt% W alloys with Ni/Co ratio 4/1 (alloys 0W41 and 2W41) sintered at 1500°C. As can be seen in Table 3, these alloys have shown a slightly limited densification at this sintering temperature, which was around 97-98 %RD.

Microstructural examination has shown that all alloy compositions were sintered with liquid phase sintering (LPS) at all applied sintering temperatures. That is, all of the investigated alloys have exhibited a microstructure consisting of rounded W grains embedded in a binder matrix phase, which is the typical microstructure of liquid phase sintered WHAs. Typical LPS sintered microstructures of the investigated alloys are given in Figures 2, 3 and 4. However, it was found that there is a major difference between the Ni/Co ratio 4/1 and 1/1 alloys in terms of the constitution of the binder matrix phase: Whereas the binder matrix of all the investigated alloys with Ni/Co ratio 4/1 was found to be comprised of a single phase, all Ni/Co ratio 1/1 alloys were observed to consist of a two-phase binder matrix. In SEM investigation of the Ni/Co ratio 1/1 alloys, the existence of the two phases in the binder matrix was more visible in the back scattered electron (BSE) imaging mode, which essentially generates compositional contrast. Representative BSE images showing the general appearance of the two-phase binder matrix observed in Ni/Co ratio 1/1 alloys can be seen in Figures 3 and 4. As can be seen in these figures, the two phases of the binder matrix generates darker and brighter contrast in BSE images. Based on this fact, these two constituent phases of the binder matrix will be termed as "dark" and "bright" phases, respectively, hereafter in the manuscript.

Table 3. Percent relative densities (%RD) of the investigated alloys

Alloy Code	Relative Density (%)		
	Sintering Temperature (°C)		
	1500	**1550**	**1600**
0W11	100	99.9	99.4
0W41	97.1	99.6	100
2W11	99.1	99.7	99.8
2W41	97.7	99.4	99.8
5W11	100	99.6	100
5W41	99.9	98.8	99.8
7W11	99.3	99.4	99.9
7W41	99.4	99.2	99.8

Although not determined quantitatively, it was found through microstructure examination studies that the amount of the binder matrix phase decreases with increasing alloy W content for both Ni/Co ratio 4/1 and 1/1 alloys, at all sintering temperatures. This phenomenon can be seen in Figure 2 for both Ni/Co ratio 4/1 and 1/1 alloys sintered at 1500°C, and the trend is similar for these alloys at all the other sintering temperatures. This phenomenon is expected based on phase diagram considerations and requires no further explanation.

For Ni/Co ratio 1/1 alloys, microstructural examination studies have shown that the relative amounts of the "dark" and "bright" phases in the two-phase binder matrix were changing both with alloy W content and sintering temperature. For these alloys, the typical variation of the ratio of the dark and bright phases with W content and sintering temperature is exemplified in Figures 3 and 4, respectively. As a general trend, microstructural examination studies have implied that the bright/dark phase proportion increases with increasing W content for a given sintering temperature, and decreases with increasing sintering temperature for a given W content. However, it should be mentioned here that the phase proportion variations observed in the study were obtained in a limited sintering time interval and therefore might not represent the equilibrium case. To determine the exact nature of the phase proportion variations with either alloy composition or sintering temperature, further detailed studies have to be conducted, which might involve extensive phase diagram construction experiments.

The compositions of the constituent phases were determined with EDS analysis for all of the investigated alloys. From the EDS results, it was found that W grains were almost pure in all investigated alloys. Therefore, the EDS analysis results for this W phase were not given in the manuscript. The compositions of the binder matrix phase are given in Table 4 and Table 5 for Ni/Co ratio 4/1 and 1/1 alloys, respectively. In Table 5, only the EDS results obtained for the sintering temperature of 1550°C were given for the Ni/Co ratio 1/1 alloys, but the results are similar for these alloys for the other sintering temperatures. Before going on further, it should be mentioned here that the EDS results given in Tables 4 and 5 may involve some error due to the semi-quantitative nature of the EDS analysis. Also, the results might be erroneous especially for alloys with relatively higher W content (i.e. W content at and above 95 wt%) due to the intricacy of the microstructure. Keeping these remarks in mind, it can be seen in Table 4 that the binder matrix phase of the investigated Ni/Co ratio 4/1 alloys dissolves up to nearly 42 - 43 wt% W in it. The EDS analysis results imply that the dissolution of W in the binder phase was completed up to the limits during the sintering process. There seems to be no significant variation in the dissolved W content with increasing W content of the alloys, for a given sintering temperature. For a given alloy W content, on the other hand, the dissolved W content in the binder phase seems to slightly increase with increasing sintering temperature, except occasional cases. These two phenomena are expected based on phase diagram considerations. Owing to the intricacy of the microstructures and the presence of a two-phase binder matrix, the EDS results for the Ni/Co ratio 1/1 alloys were more prone to be in error, especially for alloys with 95 wt% and above W content. However, the EDS analysis results have clearly shown for these alloys that the "dark" constituent phase of the binder matrix was similar in constitution to the binder matrix of the Ni/Co ratio 4/1 alloys. This dark phase was found to dissolve around 42 wt% W in it. However, the Ni/Co mass ratio in this dark binder matrix phase was different than the binder matrix of Ni/Co ratio 4/1 alloys. Based on ternary W-Ni-Co phase diagram information given in the literature [14] and EDS analysis results obtained in this study, the "bright" constituent phase of the binder matrix was interpreted to be Co_7W_6 intermetallic compound, with some Ni dissolved in it. Since Ni most probably substitutes Co in the structure, it is suggested that this bright phase might be represented as $(Co, Ni)_7W_6$. In this respect, please note that the EDS analysis results of the

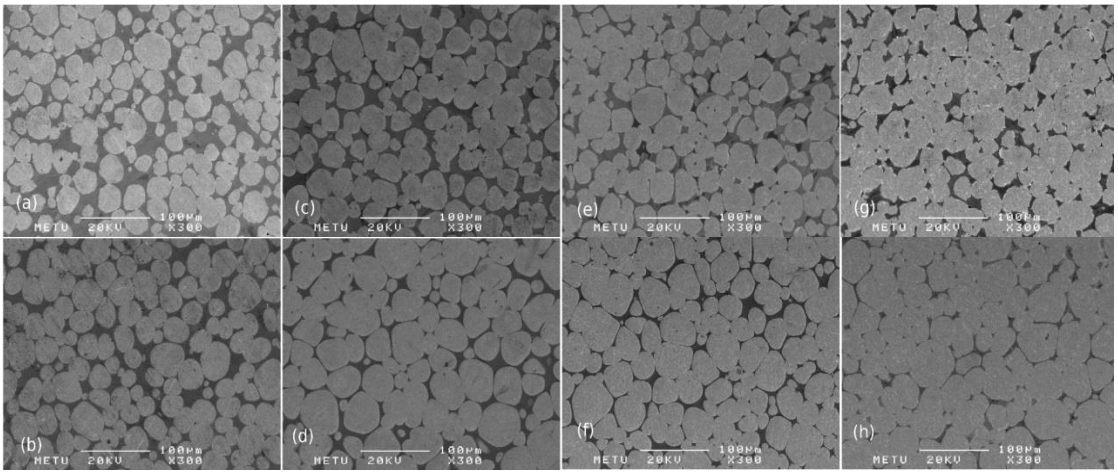

Figure 2. SEM secondary electron (SE) images showing the microstructures of (a) 0W11, (b) 0W41, (c) 2W11, (d) 2W41, (e) 5W11, (f) 5W41, (g) 7W11 and (h) 7W41 alloys sintered at 1500°C, (x300). It is seen in the figure that, at this sintering temperature, the volume percentage of the binder phase decreases with increasing alloy W content, for both Ni/Co ratio 4/1 and 1/1 alloys. This trend is similar at all the other sintering temperatures applied.

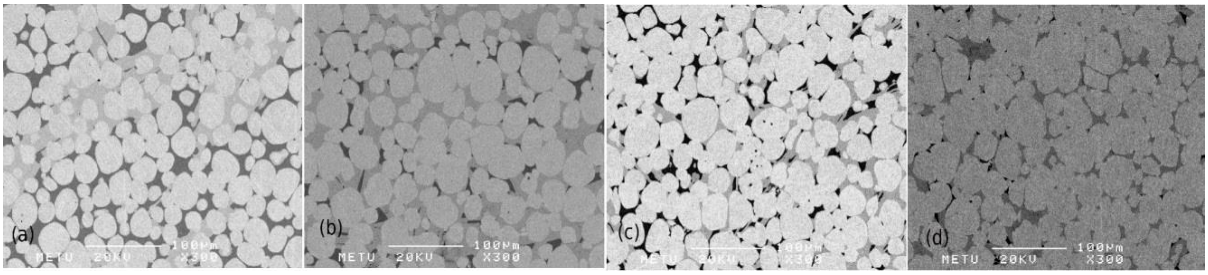

Figure 3. SEM back scattered electron (BSE) images showing the microstructures of (a) 0W11, (b) 2W11, (c) 5W11 and (d) 7W11 alloys sintered at 1500°C, (x300). The BSE images imply that, at this sintering temperature, the amount of the "dark" phase constituent of the two-phase binder matrix decreases with increasing alloy W content. This trend is generally similar at all the other sintering temperatures applied.

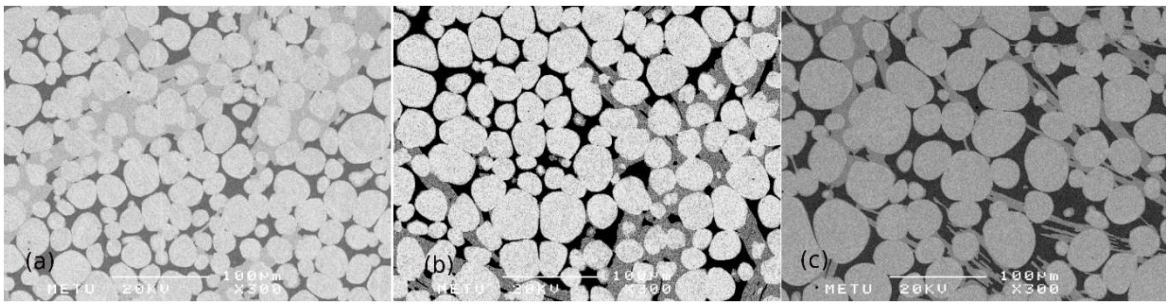

Figure 4. SEM back scattered electron (BSE) images showing the microstructure of 0W11 alloy sintered at (a) 1500°C, (b) 1550°C and (c) 1600°C, (x300). The BSE images show that, for this 90 wt% W alloy, the amount of the "dark" phase constituent of the two-phase binder matrix increases with increasing sintering temperature. This trend is generally similar for the other Ni/Co ratio 1/1 alloys with higher W content.

Table 4. Binder matrix phase composition of Ni/Co ratio 4/1 alloys

	Sintering Temperature (°C)								
	1500			1550			1600		
	Composition (wt%)								
Alloys	**W**	**Ni**	**Co**	**W**	**Ni**	**Co**	**W**	**Ni**	**Co**
0W41	39.6	48.4	12.1	39.6	48.0	12.4	42.1	46.1	11.8
2W41	37.4	49.5	13.1	41.5	46.6	11.9	38.4	48.8	12.9
5W41	38.9	49.1	12.0	42.1	46.4	11.5	42.8	45.5	11.7
7W41	36.7	49.9	13.3	39.5	48.4	12.1	40.3	47.8	11.9

Table 5. Binder matrix phase composition of Ni/Co ratio 1/1 alloys sintered at 1550°C

Alloys	**Constituent Binder Matrix Phase**	**Sintering Temperature (°C)**		
		1550		
		Composition (wt%)		
		W	**Ni**	**Co**
0W11	**Bright**	74.7	10.3	15.1
	Dark	41.8	32.8	25.4
2W11	**Bright**	74.9	10.7	14.4
	Dark	41.7	33.8	24.5
5W11	**Bright**	75.1	11.1	13.8
	Dark	35.8	45.4	18.8
7W11	**Bright**	75.0	10.3	14.7
	Dark	39.3	35.7	25.0

bright binder matrix phase also supports this suggestion, when evaluated in terms of atomic percentages (please refer to Table 5). In Ni/Co ratio 1/1 alloys, the effects of alloy W content and sintering temperature on the composition of the dark and bright phases could not be identified clearly.

Planimetric method in accordance to the ASTM E112 standard was used to determine the average W grain size (AGS) of the alloys. The AGS variation of the investigated alloys with increasing sintering temperature and increasing W content is shown in Figure 5 and Figure 6, respectively.

Generally, the AGS of the alloys studied were found to increase with increasing sintering temperature, as can be seen in Figure 5. This effect was expected, because sintering is a diffusion controlled process. On account of this diffusion control, the alloys sintered at higher temperatures have had higher sintering and coarsening rates when compared to those sintered at lower temperatures. Therefore, it is suggested that more grain growth and coarsening and, hence, higher AGS values were observed in those alloys.

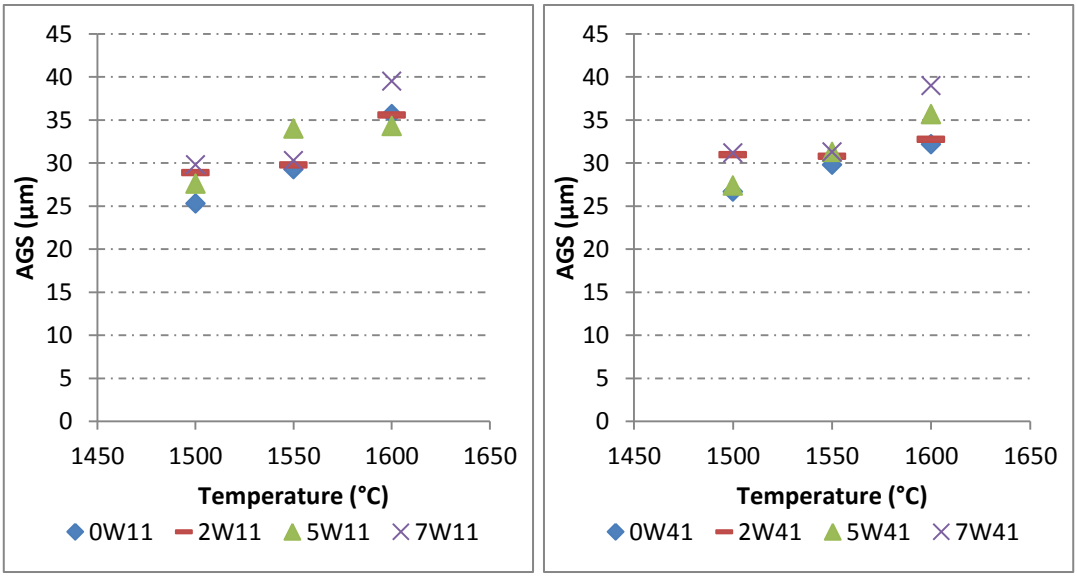

(a) (b)

Figure 5. The variation of average W grain size with sintering temperature for (a) Ni/Co ratio 1/1 alloys (b) Ni/Co ratio 4/1 alloys

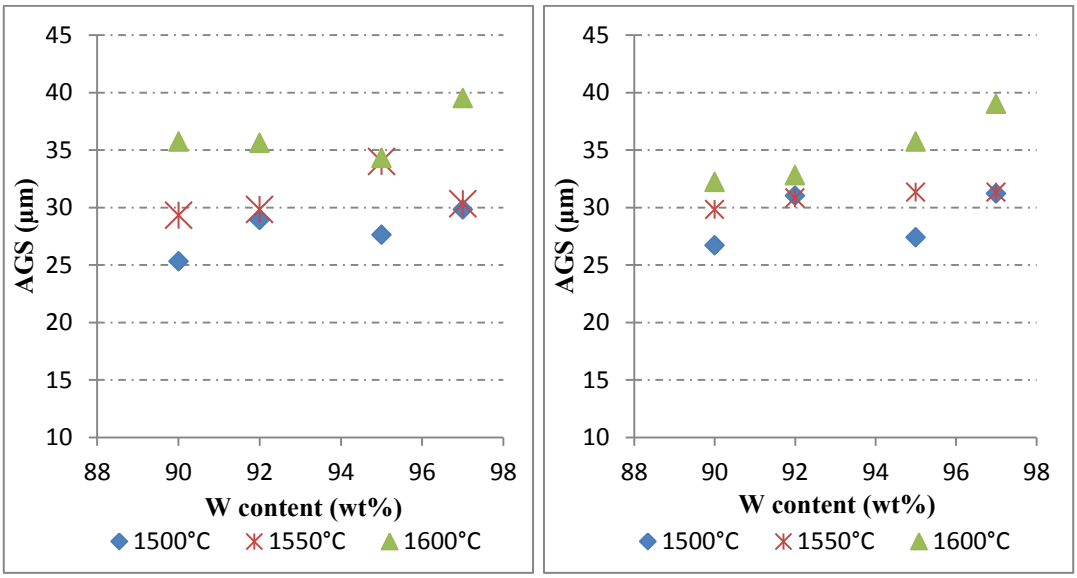

(a) (b)

Figure 6. Average W grain size variation with alloy W content for a) Ni/Co ratio 1/1 alloys, b) Ni/Co ratio 4/1 alloys sintered at 1500, 1550 and 1600°C

As can be seen in Figure 6 (b), the AGS of the Ni/Co ratio 4/1 alloys generally increase with increasing alloy W content, especially at and above 1550°C. However, the variation of the AGS with alloy W content seems to be somehow unsystematic in Ni/Co ratio 1/1 alloys, as seen in Figure 6 (a). The reason for this behavior is not known, but is suggested to be related to the presence of a two-phase binder matrix in these alloys. However, for Ni/Co ratio 1/1 alloys with widely separated alloy W content, i.e. for alloys with 90 and 97 wt% W, it is clear from Figure 6 (a) that AGS certainly increases with increasing W content, for all sintering temperatures. This implies that the effect of alloy W content on AGS becomes more dominant at higher alloy W contents for these alloys. The reason for the expectation of an increase in

AGS with alloy W content might be explained as follows: In alloys with higher W content, there will be much more W particles per unit volume, when compared to alloys with lower W content. Therefore, the volume percentage of the binder matrix will be smaller in these alloys. This implies that the diffusional path among the W particles will be smaller, and all diffusional processes within the binder matrix phase will take place over shorter distances in the alloys with higher W content. As a result, the densification and coarsening rate in these alloys might be higher, and therefore higher W content alloys might be expected to show larger AGS than the alloys having lower W content. However, it should be emphasized here that the sintering kinetics of WHAs is a complicated process which might be dependent on a number of interacting and counteracting variables. Therefore, it is possible that, under certain conditions dominated by counteracting variables, the expected AGS increase with alloy W content might not be realized in the sintering of these alloys.

4. CONCLUSIONS

The effects of sintering temperature and tungsten content on the microstructural characteristics of selected W-rich W-Ni-Co heavy alloys were investigated in this study. The following conclusions were drawn from the study:

1. All investigated alloys reached nearly full density at all sintering temperatures.
2. For the Ni/Co ratio 4/1 alloys, microstructural examination has revealed that the alloys investigated have a typical microstructure consisting of rounded, nearly pure W grains and a Ni-Co-W binder matrix phase. The binder matrix phase for Ni/Co ratio 4/1 alloys was found to dissolve up to 43 wt% W in it.
3. On the other hand, a microstructure consisting of nearly pure W grains and a two-phase binder matrix has been observed in all of the alloys with Ni/Co ratio 1/1 for all sintering temperatures. One constituent phase of this binder matrix was found to be similar to the binder matrix phase of Ni/Co ratio 4/1 alloys, with around 42 wt% W dissolved in it. However, the Ni/Co mass ratio in this binder matrix phase was different than that observed in the binder matrix of Ni/Co ratio 4/1 alloys. Based on EDS analysis results and phase diagram information given in the literature, the other constituent phase of the binder matrix was suggested to be Co_7W_6 intermetallic phase, with some Ni dissolved in it.
4. The ratio of the two phases in the binder matrix of Ni/Co ratio 1/1 alloys was found to vary with alloy W content and sintering temperature.
5. For both Ni/Co ratio 4/1 and 1/1 alloys, the total volume percentage of the binder matrix phase was found to decrease with increasing alloy W content, at a given sintering temperature.
6. The average W grain size (AGS) of Ni/Co ratio 4/1 alloys were found to increase both with increasing alloy W content and sintering temperature. This trend was similar in Ni/Co ratio 1/1 alloys, but the variation of the AGS with alloy W content was somehow unsystematic in these alloys.

Acknowledgements

This study was supported by TÜBİTAK-SAGE and Middle East Technical University. The authors acknowledge Mr. Fatih KOCA and Mr. Levent KUTLUCAN from TÜBİTAK-SAGE for their assistance in the metallographic preparations.

REFERENCES

1. R. M. German, Powder Metallurgy Science, New Jersey: Metal Powder Industries Federation, 1984.
2. R.M. German, P.Suri, S.J Park, "Review: Liquid Phase Sintering," Journal of Material Science, pp. 1-39, 2009
3. W. Yunxin, R.M. German, B. Marx, P. Suri, R. Bollina "Comparison of Densification and Distortion Behaviors of W-Ni-Cu and W-Ni-Fe Heavy Alloys in Liquid Phase Sintering," Journal of Materials Science, 2003,vol-10, pp. 2271-2281
4. A. Upadhyaya, "Processing Strategy for Consolidating Tungsten Based Alloys for Ordnance Applications," Materials Chemistry and Physics, no. 67, 2001
5. U. Ravi Kiran, A. Panchal, M. Sankaranarayana, T.K. Nandy, Tensile and Impact Behavior of Swaged Tungsten Heavy Alloys Processed by Liquid Phase Sintering, International Journal of Refractory Metals and Hard Materials, Volume 37, March 2013
6. S. G. Caldwell, "Variation of Ni/Fe Ratio in W-Ni-Fe Alloys: A Current Perspective," in Proceedings of the First International Conference on Tungsten and Tungsten Alloys, 1992
7. U.R. Kiran, A.S Rao, M. Sankaranarayana, T. K Nandy, "Swaging and Heat Treatment Studies on Sintered 90W-6Ni-2Fe-2Co Heavy Alloys," International Journal of Refractory Metals and Hard Materials, pp. 1-9, 2012.
8. N. Maitra, Development of a Tungsten-Nickel-Cobalt Heavy Alloy, Metal Powder Report, Volume 57, Issue 4, April 2002, Page 40
9. P. Ghosal, Electron Microscopy of Tungsten-Nickel-Cobalt Heavy Alloys, Metal Powder Report, Volume 57, Issue 9, September 2002, Page 37
10. ASM Handbook Vol.7, ASM International, 1998, pp. 2297-2310 and p. 667
11. B. Katavic, M. Nikacevic and Z. Odanovic, "Effect of Cold Swaging and Heat Treatment on Properties of the P/M 91W-6Ni-3Co Heavy Alloy," Science of Sintering, 2008, vol-40, pp. 319-331
12. E. W. Kennedy, "Influence of Microstructure on Fracture Characteristics and Tensile Properties of Two Tungsten Heavy Alloys," 2nd International Conference on Tungsten&Refractory Metals, Virginia, 1994.
13. ASTM E112-10; Standard Test Method for Determining Average Grain Size
14. K. P. Gupta, "The Co-Ni-W (Cobalt-Nickel-Tungsten) System," Journal of Phase Equilibria, 2000, Volume 21, Number 4, Page 396

SINTER-HARDENING OF FERROUS ASTALOY MO AND DISTALOY DH ALLOY POWDERS

Ahmet Murat ÖGE, Hakan HAFIZOĞLU, Nuri DURLU

TOBB University of Economics and Technology,
Department of Mechanical Engineering, 06560, Ankara, TURKEY

ABSTRACT

In this study, the effect of sinter-hardening operation and the secondary heat treatment on the mechanical properties of water atomized and prealloyed Distaloy DH (Fe-2Cu-1.5Mo) with 0.6C addition, prealloyed Astaloy Mo (Fe-1.5Mo) with 2Cu and 0.6C additions, Astaloy Mo (Fe-1.5Mo) with 2Cu and 0.7C additions, and prealloyed Astaloy 85 Mo (Fe-0.85Mo) with 2Cu and 0.8C additions was examined. The samples were pressed under 600 MPa and were sintered at 1120°C for 20 minutes in an industrial belt sintering furnace under endogas atmosphere. After the sintering process, 0.5°C/s, 1.5°C/s, 3°C/s cooling rates were applied to the samples. Heat treated samples were sintered at 1120°C for 45 minutes under 90%N_2-10%H_2 atmosphere. The samples were annealed at 1070°C for 20 minutes under nitrogen atmosphere. After annealing, the effect of normalizing, quenching and tempering on the microstructural and mechanical properties were studied. The study showed that sinter-hardening and secondary heat treatments led to an increase in the hardness due to formation of martensite and bainite in the samples. The increased hardness has led to an important decrease on the transverse rupture strength values in Astaloy Mo specimens due to the notch effect. Spherical and homogeneous pores of Distaloy DH specimens has weakened the affectivity of the notch effect and led to higher transverse rupture strength values.

Key Words: Sinter hardening, heat treatment, powder metallurgy, ferrous powder alloys, Astaloy Mo, Distaloy DH, notch effect

ÖZET

Bu çalışmada, su atomizasyon yöntemi ile üretilen ön alaşımlanmış Distaloy DH-0,6C, Astaloy Mo-0,6C-2Cu, Astaloy Mo-0,7C-2Cu ve Astaloy 0,85Mo-0,8C-2Cu alaşımlarında sinterleme ile sertleştirme işleminin mekanik özelliklere etkisi incelenmiştir. Numuneler, 600 MPa basınç altında preslendikten sonra 1120°C' de 20 dakika süre ile endüstriyel olarak kullanılan endogaz ortamında sinterlenmiş ve sinterleme sonrası 0,5°C/s, 1,5°C/s ve 3°C/s soğutma hızlarında soğutulmuştur. Sinterleme ile sertleştirme çalışmalarına ek olarak ikincil ısıl işlemin mekanik özelliklere etkisi de incelenmiştir. Toz alaşımları 600 MPa basınç altında preslendikten sonra, %90N2-%10H2 gaz ortamında 1120°C'de 45 dakika süre ile sinterlenmiştir. Sinterlenmiş numuneler, 1070°C'de 20 dakika süre ile azot ortamında tavlanmış ve tavlama işleminden sonra yapılan havada soğutma, su verme ve menevişleme işlemlerinin mikroyapı ve mekanik özelliklere etkisi incelenmiştir. Elde edilen yüksek sertlik değerleri nedeniyle bütün Astaloy Mo numunelerinde çentik etkisine bağlı olarak dayanımda önemli azalma gözlenmiştir. Ön alaşımlanmış Distaloy DH numunesi ise düzenli ve küçük gözenek dağılımı sayesinde en iyi mekanik özelliklere sahip numune olmuştur.

Anahtar Kelimeler: Sinterleme ile sertleştirme, ısıl işlem, toz metalürjisi, demir esaslı toz alaşımları, Astaloy Mo, Distaloy DH, çentik etkisi

1. INTRODUCTION

Sinter-hardening is a single step process used in the manufacturing of powder metallurgy (P/M) parts, which utilizes the formation of martensite (or bainite) upon rapid cooling from the sintering temperature [1]. In ferrous alloys the mechanical properties are related with the post sintering density and the morphology of the pores [2]. In the manufacturing of ferrous P/M parts, in order to obtain improvement in mechanical properties usually a secondary heat treatment after sintering is performed. The secondary heat treatment increases the cost in the manufacturing process of P/M parts [1]. Hence, the importance of the sinter hardening process rises up because it offers an important cost advantage over the traditional quench and temper processes [3].

In sinter hardening the cooling process takes place in the furnace itself. Therefore the sintering furnace must contain a cooling unit [4]. The rapid cooling in the unit is provided with fast air or gas circulation over P/M parts. The use of gas for the cooling process provides an important advantage over traditional oil quenching due to corrosion and distortion inhibition of the samples [3]. In traditional oil quenching of P/M parts the oil generally infiltrates and remains in the pores which cause corrosion along the sample. The cooling with air or gas eliminates this effect. In addition to this, due to lower cooling rates (0.5-10°C/s), sinter hardening leads to much lower residual stresses relative to quench and temper process. Hence, sinter hardening process provides a better dimensional control over P/M parts [3].

The alloying elements in steel powders powders would increase the hardenability high enough to avoid the formation of coarse pearlite and/or retained austenite [5,6]. The alloying elements shift the curve in continuous cooling transformation (CCT) diagrams of ferrous steels to the right side thus it eases the martensite formation in slower cooling rates [7]. The main alloying elements used to increase the hardenability of ferrous alloys are Mn, Cr, Mo, Cu and Ni [8]. Those elements are added to the alloy with various quantities in order to increase the hardenability without conceding the mechanical properties. The cooling rate of the furnaces must be high enough to generate the martensite phase. Depending on the chemical composition and the geometry of the P/M part, cooling rates of 1 to 10°C/s can be achieved [6].

Prealloyed Astaloy and Distaloy powders are widely used in sinter-hardening studies. Even if the prealloying process is known to decrease the compressibility of the powders, those powders are preferred in sinter-hardening because prealloyed powders are more homogenous than admixed powders [6,9]. Their high homogeneity provides higher hardenability, thus the studies are mainly focused on Mo, Cr, Cu and Ni prealloyed Astaloy and Distaloy powders.

In a study by Bocchini et al. the macro hardness of the Distaloy DH1 powder with 0.71%C addition was studied for a cooling rate of 7°C/s. The experiments were performed in a belt furnace, under endogas CH_4 atmosphere at 1120°C. The macro hardness of the specimen is measured 495HV5 [1]. In a study of James et al. the mechanical properties of oil quenched Distaloy DH steel [10] has been studied. The experiment was performed at 1120°C under a synthetic dissociated ammonia atmosphere for 30 minutes. After the sintering, the specimens were austenitized at 870°C for 30 minutes and oil quenched to 60°C. The tempering is done at 200°C for 1 hour under nitrogen atmosphere. The hardness value is noted as ~54HRA. In a study of Maroli et al. the macro hardness values of the Astaloy Mo with 2%Cu and 0.6-0.8%C addition specimens were stated for different cooling rates. The experiments were done in a laboratory scale furnace and under N_2 atmosphere. The macrohardness value for 1-1.5°C/s cooling rate was

noted 310HV10 for 0.6%C ratio and 340HV10 for 0.8%C ratio. For higher cooling rates (2-3°C/s and 5-6°C/s) the macrohardness values were measured 360HV10 and 430HV10 for 0.6%C and 375HV10 and 455HV10 for 0.8% [4].

The objective of this paper is to characterize the microstructure and the mechanical properties of sinter hardened and heat treated prealloyed Distaloy DH (Fe-2Cu-1.5Mo) with 0.6C addition, prealloyed Astaloy Mo (Fe-1.5Mo) with 2Cu and 0.6C additions, Astaloy Mo (Fe-1.5Mo) with 2Cu and 0.7C additions, and prealloyed Astaloy 85 Mo (Fe-0.85Mo) with 2Cu and 0.8C.

2. EXPERIMENTAL PROCEDURE

In this study, four water atomized prealloyed powder (Astaloy Mo 0.85-1.5 and Distaloy DH) manufactured by Höganas were used. The grain size of the powders is varying between 50-150 microns. The SEM images of the powders used in this study are given in Figure 1. The composition and the properties of the powders used are shown in the Table 1 [11].

The specimens were pressed under 600MPa to approach the industrial conditions. The green density of the specimens was ≥7.0 g/cm^3. A 60 tons Instron tension-compression testing machine was used during the pressing operation. In this study two different geometries were pressed. The first one is the standard transverse rupture strength bars (TS 4222 EN ISO 3325) and the second one is 18 mm diameter cylindrical specimens for microstructure studies.

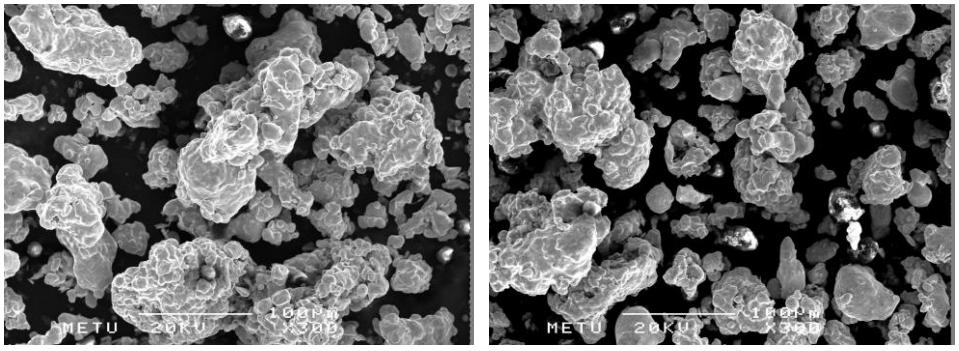

(a) (b)

Figure 1. SEM images of powders used in the study (a) Distaloy DH-0,6C (b) Astaloy Mo-0,6C-2Cu [11]

The specimens were sintered and sinter-hardened in an industrial continuous belt furnace at 1120°C, under endogas obtained from CH_4. Three different cooling rates were chosen for the study: 0.5°C/s, as sintering cooling rate, 1.5°C/s, as low sinter hardening cooling rate and 3.0°C/s, as high sinter-hardening cooling rate.

Table 1. Chemical composition and properties of studied powder mixes

Alloy	Graphite (%)	Cu (%)	Mo (%)	Fe (%)
Distaloy DH	0,6	2	1,5	Bal.
Astaloy Mo	0,6	2	1,5	Bal.
Astaloy Mo	0,7	2	1,5	Bal.
Astaloy 0,85Mo	0,8	2	0,85	Bal.

The specimens for secondary heat treatments were sintered in a laboratory sized tube furnace at 1120°C, under %90N_2-%10H_2 atmosphere for 45 minutes. Three different cooling conditions were used in the study: annealing, very slow cooling in the furnace; normalizing, slow cooling condition in air, at room temperature; quenching, rapid cooling in the water. The quenched and normalized specimens were austenitized in a laboratory box furnace at 1070°C for 20 minutes, under N_2 atmosphere. The heat treatment conditions were selected to be as close as it could be to the sintering conditions. Half of the quenched samples were tempered at 200°C for 1 hour under air atmosphere.
Microstructural characterization, macrohardness tests and microhardness tests were performed on the cross sections of the specimens. Specimens were grinded and polished, then etched with 4% picral solution. Macrohardness measurements were taken on Brinell scale using a Wilson-Wolpert universal hardness machine. Five measurements were made from each specimen. The microhardness measurements were taken on Vickers scale with a Buehler microhardness machine and 15 measurements were made for each specimen. The transverse rupture strength tests were performed according of standards (TS4222 EN ISO 3325) using a 5 tons Instron tension-compression machine. The compression speed was set to 1mm/min.

3. RESULTS AND DISCUSSION

3.1 Microstructural Properties

Polished optical micrographs of sinter-hardened alloys are given in Figure 2 [11]. It can be seen that the pores in Distaloy DH are much smaller and spherical than Astaloy Mo alloys.

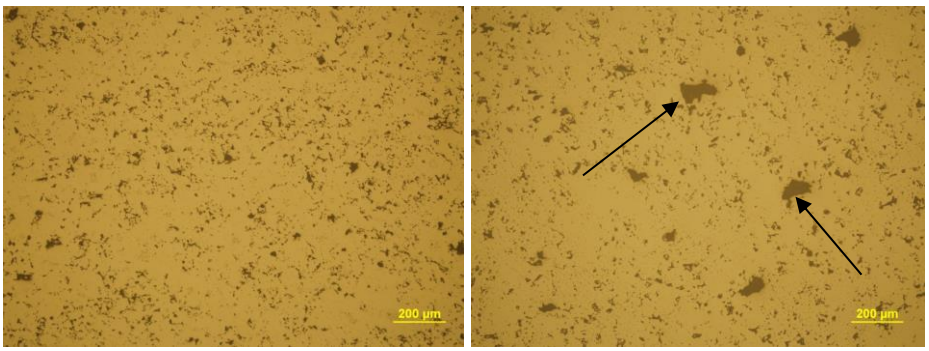

(a) (b)

Figure 2. Polished microstructure of sinter-hardened powder alloys at 1120°C under CH_4 atmosphere for 20 minutes (a) Distaloy DH-0,6C, 100X, (b) Astaloy Mo-0,6C-2Cu, 100X [11]

During sintering of Astaloy Mo alloys, admixed Cu particles melt and penetrate through iron particles and leave large pores behind as given in Figure 2.b. On the other hand, in Distaloy DH, Cu is prealloyed in the solid powder particles so, during the sintering process Cu does not melt and form large pores as in Astaloy Mo alloys. Since high hardness in porous components led to considerable decrease in strength [4,5], large pores in sinter hardened Astaloy Mo alloys led to a dramatic decrease in TRS value due to notch effect. However, the small, spherical and homogeneous pores in Distaloy DH alloy have led to higher TRS values.
In Figure 3.a the etched micrograph of Distaloy DH-0.6C alloy is given. In the figure the homogenous microstructure of this alloy can be seen. This is provided by the prealloying process and explains the high TRS values measured in the mechanical tests.

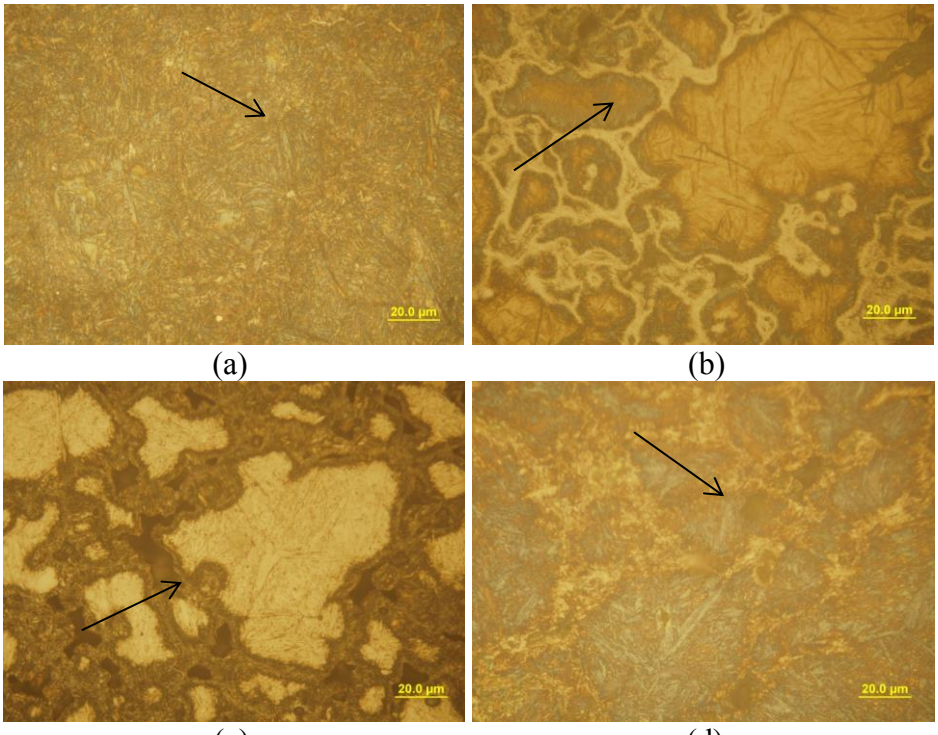

Figure 3. Etched microstructure of sinter-hardened powders alloys at 1120°C' under CH_4 atmosphere for 20 minutes cooled with 3°C/s (1000x). (a) Distaloy DH-0.6C (746HV0.1) (b) Astaloy Mo-0.6C-2Cu (799HV0.1), (c) Astaloy Mo-0.7C-2Cu (807HV0.1), (d) Astaloy 0.85Mo-0.8C-2Cu (753HV0.1) [11]

In Figure 3.b-d the microstructures of Astaloy Mo alloys are given. Comparing to the microstructure of Distaloy DH, the heterogeneous, two phased microstructure can be seen. It is known that in Astaloy Mo alloys, Cu is added with the admix mixing method. Thus, Cu forms a liquid phase, which can be seen around martensite isles in Figure 3.b-d. The arrows show indents obtained by macrohardness tests. In Figure 3.a the macrohardness of the phase is 746 HV0.1, in Figure 3.b it is 799 HV0.1, in Figure 3.c the hardness is 807 HV0.1 and in Figure 3.b the microhardness is 753 HV0.1. The microhardness values indicates the presence of martensite phase in all the specimens.

Optical micrographs of normalized and quenched Distaloy DH are given in Figure 4 [12]. The normalizing process provided coarse pearlite, fine pearlite and pro-eutectoid ferrite in the microstructure. The arrows on the micrographs are indicating the microhardness tests. In Figure 4.a the microhardness of the phase is 308 HV0.1, which indicates a composite of coarse-fine pearlite microstructure. On the other hand the quenching process leads to 100% martensitic microstructure. In Figure 4.b the microhardness of the phase is 799 HV0.1, which indicates the martensite phase.

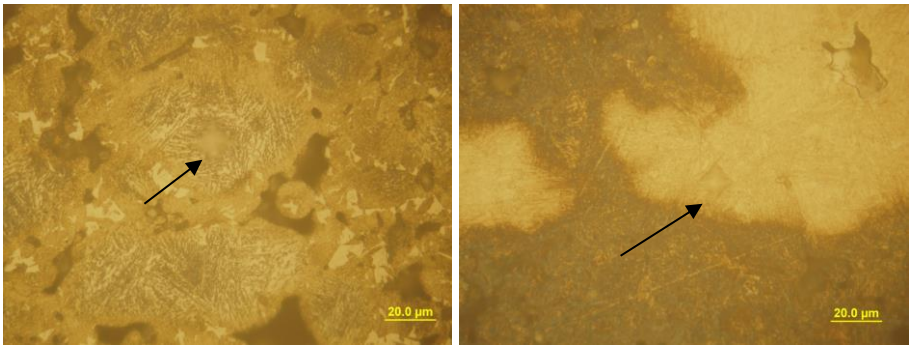

(a) (b)

Figure 4. Etched microstructure of heat treated Distaloy DH-0.6Cpowder alloy sintered at 1120°C under N_2-H_2 atmosphere for 45 minutes (1000x). (a) Normalizing (308HV0.1), (b) Quenching (799HV0.1) [12].

3.2. Mechanical Properties

The mechanical properties measured from different powders mixes are given in the following figures. In Figure 5, the macro hardness of sinter hardened alloys are given and in Figure 6 the transverse rupture strength (TRS) of those specimens are given.

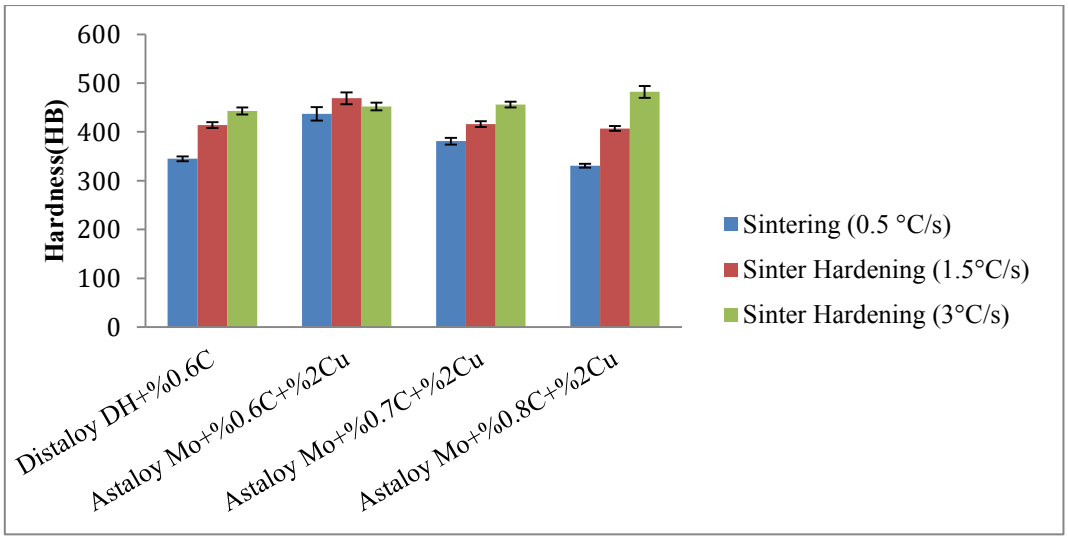

Figure 5. Macrohardness values of sinter-hardened powder alloys**.**

In sintered specimens of the Distaloy DH-0.6C alloy the macro hardness is measured 345HB. Meanwhile, in sinter hardened specimens, the macro hardness is measured 415HB for the low

cooling rate and 443HB for the high cooling rate. An increase of ~15% in macrohardness value with the sinter hardening process was observed. While the increase in hardness varies between 8% and 46% in Astaloy Mo alloys. The best macrohardness result is taken by the Astaloy 0.85Mo-2Cu-0.8C specimen. This is due to the high amount of C compared to the other alloys.

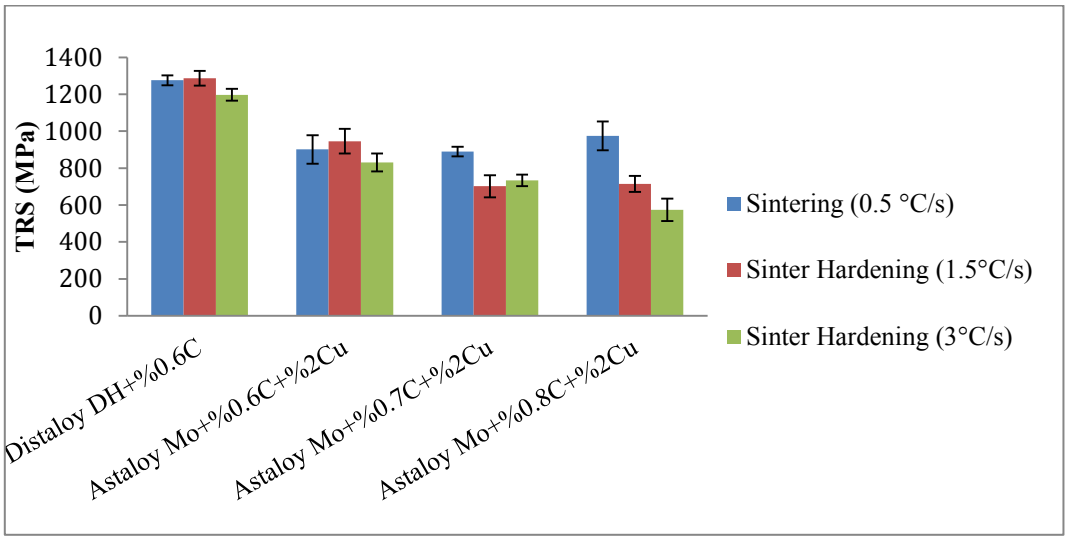

Figure 6. TRS values of sinter-hardened powder alloys.

In Figure 6, it can be seen that all the Astaloy Mo alloys shows a dramatic TRS decrease (up to 41% TRS loss) as the cooling rate increases. The raise of macrohardness in Astaloy Mo alloys has led to this decrease [13]. In a study Straffelini et al. this phenomenon is correlated to the notch effect. It is explained that P/M parts with high hardness values shows brittle behavior at sharp ends of irregular pores which causes unexpected failure at lower loads [14,15]. Meanwhile, Distaloy DH alloy preserve its TRS values (only ~6% TRS loss) as the macrohardness values increases with cooling rate. This is due to the prealloying effect. In a study of Hatami et al. it is stated that prealloyed powders gives better hardenability properties compared to admix or diffusion bonded powders [6]. As it can be seen in polished microstructures, Distaloy DH-0.6C alloy does not contain irregular pores. Thus, the notch effect which took place on Astaloy Mo specimens didn't occurred for Distaloy DH.

In Figure 7 the macrohardness and in Figure 8 the transverse rupture strength (TRS) of the secondary heat treated specimens are given. As expected, increase in cooling rates after sintering resulted much higher hardness values. Since the alloys used in this study were manufactured to obtain martensitic microstructure even at low cooling rates, water quenching after sintering led to the formation of a fully martensitic microstructure in all the specimens.

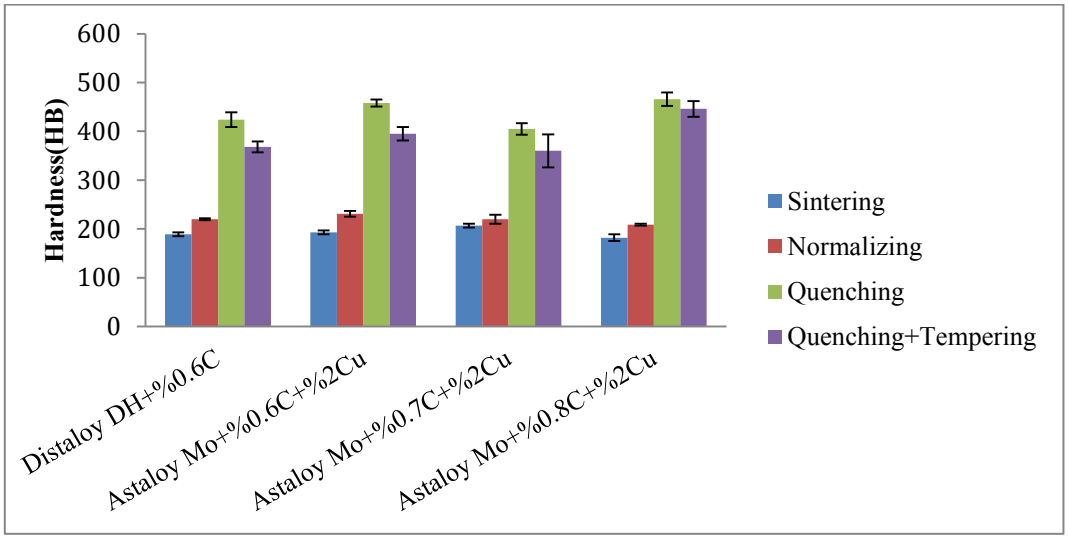

Figure 7. Macrohardness values of heat treated powder alloys**.**

As it can in Figure 8, very high cooling rates of the quenching has dramatically accentuated the notch effect which has been seen in sinter hardened specimens. Similar to sinter hardening the reduction in TRS with the formation of martensite is much less in Distaloy DH compared to Astaloy Mo alloys. After the water quenching, the TRS value of Distaloy DH-0.6C specimen is 980MPa while Astaloy Mo-2Cu-0.6C has a TRS value of 687MPa which is 30% lower than Distaloy DH. This difference is mainly caused by the prealloying effect which has been discussed previously.

The tempering process that has been applied to quenched specimens has boosted the TRS values of all the specimens. In Distaloy DH alloy, the tempering process has led to a 25% TRS increase, which gave the best results of the whole experiments with 1225MPa. The tempering process has stabilized the martensite phase of the specimens and eliminated the residual stresses. With more stabilized and more ductile tempered martensite phase the notch effect has lost its severity.

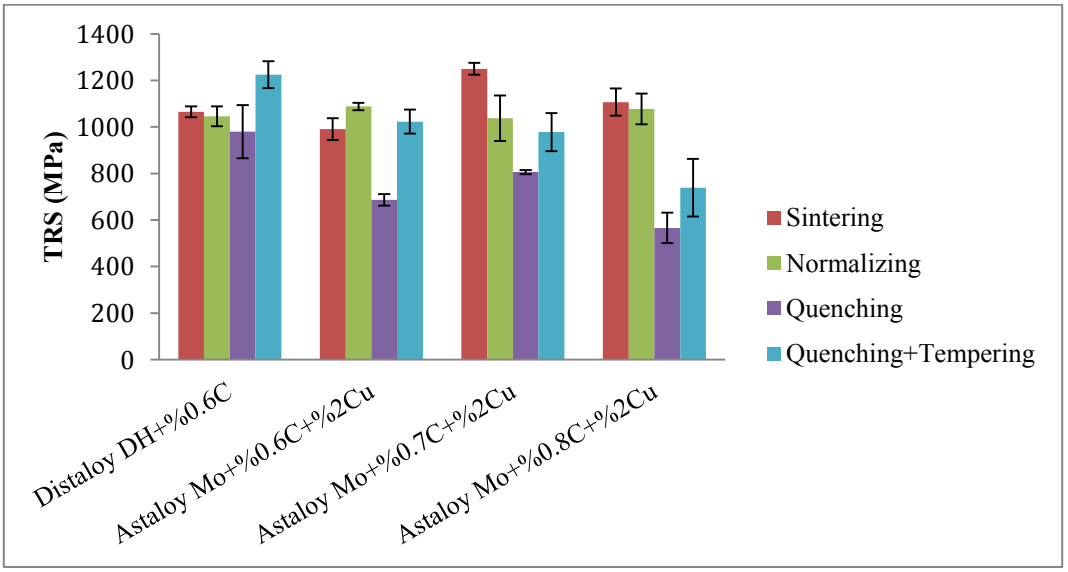

Figure 8. TRS values of heat treated powder alloys.

Vickers microhardness of the samples sintered at 1120°C and heat treated are given in Table 3. Similar to the macrohardness values obtained for those alloys, quenching has considerably increased the microhardness of the samples while the normalizing process does not have any important effect. The increase in microhardness is due to 100% martensite phase that has been obtained after the quenching process.

Table 3. Microhardness values of sinter-hardened and heat treated powder alloys.

Alloys	Sintering (0.5 °C/s)	Sinter Hardening (3°C/s)	Sintering	Normalizing	Quenching	Quenching + Tempering
Distaloy DH-0.6C	552±99	745±33	261±19	262±63	634±122	598±158
Astaloy Mo-0.6C-2Cu	593±121	676±146	276±40	315±84	677±154	568±200
Astaloy Mo-0.7C-2Cu	416±46	702±79	241±50	274±55	680±123	638±145
Astaloy 0.85Mo-0.8C-2Cu	490±130	704±21	253±37	291±45	802±59	659±164

4. CONCLUSIONS

In this study the effect of sinter-hardening and secondary heat treatment to various prealloyed Astaloy Mo and Distaloy DH powders has been investigated.

- The sinter-hardening process has successfully increased the macrohardness and microhardness values of all the alloys by the formation of martensite.
- In all alloys, the TRS values decreased due to notch effect, when the specimen has reached a critical hardness value.
- Between all the alloys, Distaloy DH has the least decrease of TRS value with the hardness increase due to its homogeneous microstructure and the spherical and small pores.
- In sinter-hardened specimens, the microstructures were constituted from bainite and martensite while in quenched specimens the microstructure is ~100% martensite.

ACKNOWLEDGEMENTS

This study was realized with the contributions of TOBB University of Economics and Technology. Cengiz Bozacı from TozMetal Ticaret ve Sanayi A.Ş. and Kaan Çalışkan from TUBİTAK SAGE is acknowledged for their help in sinter-hardening and heat treatment experiments.

REFERENCES

1. G.F. Bocchini, B. Rivolta, G. Silva, E. Poggio, M.R. Pinasco, M.G. Ienco, Microstructural and Mechanical Characterisation of some Sinter Hardening Alloys and Comparisons with Heat Treated PM Steels, Powder Metallurgy, Vol. 47 No. 4, 343-351, 2004
2. H. Khorsand, H Yoozbashizade., S.M. Habibi, K. Janghorban, A. Nangir, S.M.S. Reihani, Carbon, Porosity and Fatigue in Sintered Steel, Elsevier Science Ltd., 2002
3. H.G. Rutz, A.H. Graham, A.B. Davala, Sinter-Hardening P/M Steels, International Conference on Powder Metallurgy & Particulate Materials, June 29-July 2, 1997, Chicago, IL USA.
4. B. Maroli, S. Berg, M. Larsson, I. Hauer, Performance of Sinter-Hardened P/M Steels, EUROMAT ITALY, 2001
5. C. Blais, R.E.Jr. Serafini, G. L'Espérance, Effect of Hydrogen Concentration in Cooling Zone on Sinter Hardening, International Journal of Powder Metallurgy Volume 41, Issue 4, 33-41, 2005
6. S. Hatami, A. Malakizadi, L. Nyborg, D. Wallin, Critical Aspect of Sinter-Hardening of Prealloyed Cr-Mo Steel, Journal of Materials Processing Technology 2010 1180-1189.
7. G. Krauss, Steels: Processing, Structure, and Performance, ASM International, 316-317, 2005
8. Berg S., P/M Steel Suitable for Sinterhardening in Respect of Cost and Performance, PM²TEC 2001, in New Orleans, USA.
9. R.M. German, Powder Metallurgy&Particulate Materials Processing, Metal Powder Industries Federation, Princeton, NJ, 1994.
10. W.B. James, F.J. Semel, K.S. Narasimhan, 'The Development of Binder-Treated Alternatives to Diffusion Alloyed Powders', Högänas Corporation, Cinnaminson, NJ 08077, USA.
11. A.M. Öge, Demir Esaslı Astaloy Mo ve Distaloy DH Alaşımlarında Sinterleme İle Sertleştirme, M.Sc. Thesis, TOBB University of Economics and Technology, Ankara, 2013.
12. A.M. Öge, N. Durlu, The Effect of Heat Treatment on the Properties of Distaloy DH and Astaloy Mo Powder Alloys, Euro PM2013,Gothenburg, Sweden, 15-18 September 2013.
13. A.M. Öge, N. Durlu, C. Bozacı, P. Johansson, Mechanical Properties of Sinter Hardened Astaloy Mo and Distaloy DH Powder Alloys, 16th Int. Metallurgy & Materials Congress (IMMC 2012), Istanbul, Turkey, 13-15 September 2012.
14. G. Straffelini, C. Menapace, A. Molinari, Interpretation of effect of matrix hardening on tensile and impact strength of sintered steels, Powder Metallurgy, Volume 45, Issue 2, pp.167-172, 2002.
15. G. Straffelini, V. Fontanari, A. Hafez, M. Benedetti, Tensile and Fatigue Behavior of Sinter Hardened Fe-15Mo-0.6C Steels, Powder Metallurgy, Volume 41, Issue 4, 298-303, 2009.

MECHANICAL PROPERTIES OF SINTER-HARDENED AND HEAT TREATED ASTALOY CrA ALLOYS

Hakan HAFIZOĞLU, Ahmet Murat ÖGE, Nuri DURLU

TOBB University of Economics and Technology,

Department of Mechanical Engineering, 06560, Ankara, TURKEY

ABSTRACT

In this study, the effect of sinter-hardening and heat treatment processes on the mechanical and microstructural properties of water atomized Astaloy CrA-0.5C, Astaloy CrA-1Ni-0.5C, Astaloy CrA-1Cu-0.5C, Astaloy CrA-2Cu-0.5C powder alloys were investigated. In the first part of the study, the samples were pressed under 600 MPa and were sintered at 1120°C for 20 minutes in an industrial belt sintering furnace under endogas atmosphere. After sintering, samples were cooled with three different cooling rates (0.5°C/s, 1.5°C/s, 3°C/s). The study showed that sinter-hardening led to an increase in the hardness due to the formation of martensite and bainite. On the other hand, a decrease was observed in the transverse rupture strength and tensile strength values due to the irregular pores in the microstructure. In the second part of the study, the samples were pressed under 600 MPa and sintered at 1120°C for 45 minutes under 90%N_2-10%H_2 atmosphere. The sintered samples were austenitized at 1070°C for 20 minutes under nitrogen atmosphere, followed by cooling in air, quenching in water and tempering at 200°C for 60 minutes in air. Normalizing slightly improved hardness and TRS values due to formation of fine pearlite and proeutectoid ferrite, whereas quenching and tempering increased hardness and TRS values considerably due formation of martensite and tempered martensite.

Key Words: Powder metallurgy, Astaloy CrA, sinter hardening, heat treatment, mechanical properties, decarburization.

SİNTERLEME İLE SERTLEŞTİRİLMİŞ VE ISIL İŞLEM UYGULANMIŞ ASTALOY CrA ALAŞIMLARININ MEKANİK ÖZELLİKLERİ

ÖZET

Bu çalışmada, sinterleme ile sertleştirme ve ısıl işlemlerin su ile atomize edilmiş Astaloy CrA-0.5C, Astaloy CrA-1Ni-0.5C, Astaloy CrA-1Cu-0.5C, Astaloy CrA-2Cu-0.5C toz alaşımlarının mekanik özelliklerine ve mikroyapısına etkisi incelenmiştir. Çalışmanın ilk bölümünde, numuneler 600 MPa' da preslenmiş ve endüstriyel fırında endogaz atmosferi altında 1120°C' de 20 dakika süre ile sinterlenmiştir. Sinterleme sonrası numunelere üç farklı soğutma hızı (0.5°C/s, 1.5°C/s, 3°C/s) uygulanmıştır. Çalışma sonucunda; sinterleme ile

sertleştirme işleminin martensit ve beynit oluşumuna bağlı olarak sertlik artışı sağladığı, düzensiz gözeneklerin varlığından dolayı ise çapraz kırılma ve çekme dayanımı değerlerinde düşüşe neden olduğu görülmüştür. Çalışmanın ikinci bölümünde, 600 MPa altında preslenen numuneler %90N_2-%10H_2 atmosferi altında 1120°C' de 45 dakika sinterlenmiştir. Sinterlenen numuneler azot atmosferinde 1070°C' de 20 dakika sure ile östenitlendikten sonra havada soğutma, su verme ve hava ortamında 200°C' de 60 dakika menevişleme işlemlerine tabi tutulmuştur. Isıl işlem uygulanmış numunelerde, normalleme işleminin ince pörlit ve ötektoid öncesi ferrit oluşumuna bağlı olarak sertlik ve çapraz kırılma dayanımını arttırdığı gözlenmiştir. Suverme ve menevişleme işlemeleri ise, martensit ve menevişlenmiş martensit oluşumuna bağlı olarak sertlik ve çapraz kırılma dayanımında önemli artışlara yol açmıştır.

Anahtar Kelimeler: Toz metalurjisi, Astaloy CrA, sinterleme ile sertleştirme, ısıl işlem, mekanik özellikler, dekarbürizasyon.

1.INTRODUCTION

The superior mechanical properties of ferrous powder metallurgy (P/M) materials can be obtained with their high density and microstructural properties [1]. Therefore, many of the manufactured PM parts are heat treated after sintering in order to achieve martensite/tempered martensite in the parts. Sinter hardening plays an important role on avoiding the secondary heat treatment operations by obtaining martensitic/bainitic microstructures [2].

Some variables such as; alloying elements and cooling rates influence the sinter hardening by altering the hardenability of the parts [3, 4]. Alloying elements increase the cooling time for martensitic transformation so that fully martensitic microstructures can be manufactured [5]. The most frequently used alloying elements during sinter hardening are Mn, Cr, Mo, Ni, C, Cu. The other variable that alters the hardenability of PM parts is the cooling rate during the sinter hardening process. The required cooling rates for martensitic transformation are generally in the range of 1-10°C/s [4]. Part geometry, furnace design, porosity etc. are the parameters that change the cooling rates. Therefore, while determining the cooling rate during sinter hardening, these factors mentioned above must be considered.

Chromium is a cheap and recyclable alloying element that is used to increase the hardenability of the ferrous PM parts [6]. The most widely used Cr alloys for sinter hardening are Astaloy CrA with 1.8% wt. Cr, Astaloy CrL with 1.5% wt. Cr, and Astaloy CrM with 3% wt. Cr. The Cr alloys with low carbon contents are used for especially automotive and aerospace industries which require medium and high strength [7]. In a study by Engström et. al. [8], alloys 1.8Cr-0.6C and 1.8Cr-1Ni-0.6C were sintered at 1120°C for 30 minutes under 90N_2-10H_2 atmosphere and cooled with 0.5°C/s and 2°C/s cooling rates. The hardness values for the alloy 1.8Cr-0.6C are 165 HV10 for low cooling rate, 189 HV10 for high cooling rate and for the alloy 1.8Cr-1Ni-0.6C are 182 HV10 for slow cooling, 242 HV10 for high cooling rate. In another study by Larsson et. al. [9]., the effect of the sinter-hardening on the mechanical properties of Astaloy CrA-1Cu-0.65C was investigated. Prior to sintering, the samples were pressed under 700 MPa and then sintered at 1120°C for 20 minutes under 90N_2-10H_2 atmosphere. After sintering, the samples were cooled with 3°C/s and tempered at 200°C for 60 minutes. The mean tensile strength and hardness of the samples were 1060 MPa and 370 HV10. In a study by Frykholm et. al. [10]., the mechanical properties of Astaloy CrA-1Cu-0.6C and Astaloy CrA-1Ni-0.6C were determined after sintered at 1120°C for 30 min. and sinter hardened with a cooling rate of 3.5°C/s. The tensile strength and hardness of the

alloy with Cu were 1148 MPa and 337 HV10. The alloy with Ni had 845 MPa tensile strength and 242 HV10 hardness.

The objective of this study is to investigate the effect of sinter hardening and secondary heat treatments on the mechanical properties of four different Astaloy CrA alloys with Cu, Ni and graphite additions.

2.EXPERIMENTAL PROCEDURE

The investigated powder alloys are listed with their chemical compositions in Table 1. Powder mixtures were prepared by adding 1%Cu, 2%Cu, 1%Ni and 0.5% graphite to prealloyed Astaloy CrA (Fe-1.8%Cr). During the pressing of powders, Zinc stearate was used as lubricant.

Table 1. Chemical composition of the powder alloys.

Base Powder	Cr (%)	Cu (%)	Ni (%)	Graphite (%)	Fe (%)
Astaloy CrA	1.8	-	-	0.5	Bal.
Astaloy CrA	1.8	-	1	0.5	Bal.
Astaloy CrA	1.8	1	-	0.5	Bal.
Astaloy CrA	1.8	2	-	0.5	Bal.

All sinter hardened and secondary heat treated samples were pressed under 600 MPa. Sinter hardened samples were sintered at 1120 °C for 20 minutes in an industrial sintering furnace under endogas atmosphere. After sintering, the samples were cooled with a cooling rate of 0.5°C/s which corresponds to normal sintering cycle, and with higher cooling rates of 1.5°C/s and 3°C/s for sinter hardening process. In the second part of the study, samples were sintered at 1120°C in a laboratory scale furnace under 90%N_2-10%H_2 atmosphere for 45 minutes. After sintering, the annealing was applied to the samples at 1070°C under high purity nitrogen for about 20 minutes, followed by cooling in air, quenching in water, and tempering at 200°C for 60 minutes in air.

Microstructural characterization, macrohardness, microhardness, transverse rupture strength and tensile strength tests were performed to samples. Samples were grinded and polished and then etched with 4% picral solution. Macrohardness measurements were taken on Brinell scale using a Wilson-Wolpert macrohardness machine. The microhardness measurements were taken on Vickers scale (HV0.1) with a Buehler microhardness machine and 15 measurements were made from each sample. The transverse rupture strength tests of sinter hardened samples were performed according to standard TS4222 EN ISO 3325 with a speed of 1mm/min. Tensile strength tests were done according to the standard of ISO 2740 by using a 5 tons Instron machine with a speed of 0.5 mm/min.

3.RESULTS AND DISCUSSION

3.1. Mechanical Properties

The macrohardness values of the alloys were shown in the Figure 1. Sinter hardening process led to an increase in the macrohardness values of four Astaloy CrA alloys. The increase of the macrohardness after sinter hardening is in the range of ~13-25%. The minimum macrohardness values was obtained from Astaloy CrA-0.5C alloy as a result of absence of

alloying elements that increase hardenability, whereas the maximum macrohardness values was observed in Astaloy CrA-2Cu-0.5C alloy which has higher hardenability than other alloys due to excess alloying elements .

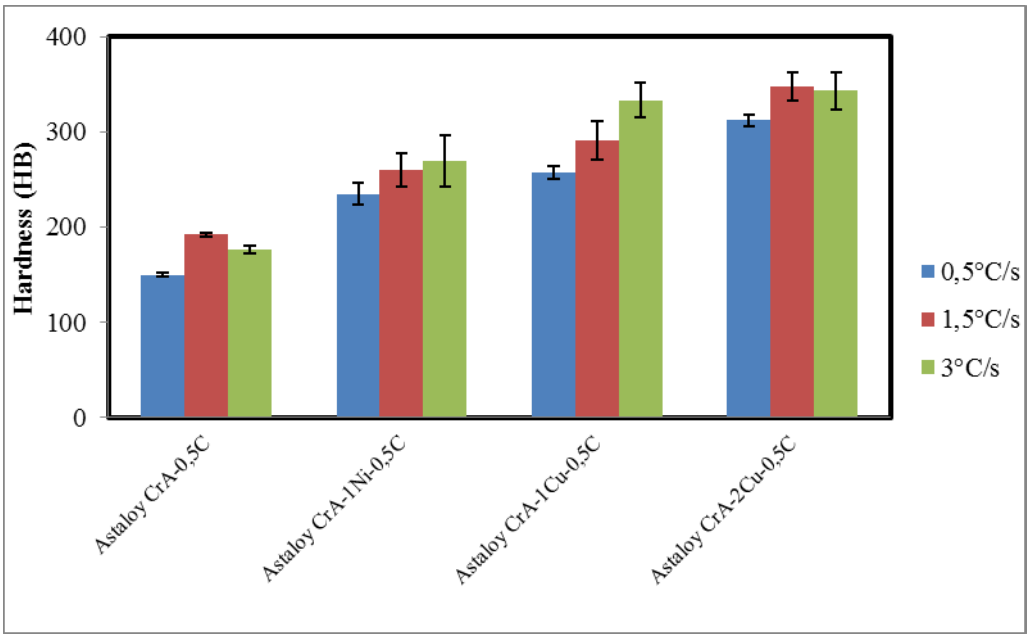

Figure 1. Macrohardness values of the alloys after sintering and sinter hardening processes.

The macrohardness value of Astaloy CrA after slow cooling (0.5°C/s) was obtained ~150 HB due to the formation of coarse pearlite in entire microstructure. In the alloys with 1%Cu and 1%Ni, fine pearlite and bainite were observed in the microstructure after slow cooling. The lower macrohardness value of the alloy with Ni is due to the lower hardenability effect of Ni compared to Cu [11]. The highest macrohardness value was measured from the sample with 2%Cu as a result of formation of bainite and some martensite. After a cooling rate of 3°C/s, the macrohardness values of all samples were increased about ~10-30%. In the microstructure of Astaloy CrA-0.5C, coarse pearlite and some fine pearlite were observed. In samples which involve additional alloying elements such as Cu and Ni, macrohardness increases due to the formation of bainite and martensite.

Macrohardness of the alloys Astaloy CrA-1Cu-0.5C and Astaloy CrA-2Cu-0.5C were higher than the other alloys due to the melting and penetrating of Cu during sintering. The higher density and better hardenability of these two samples provide higher macrohardness values.

The transverse rupture strength (TRS) values of Astaloy CrA alloys after sinter hardening were shown in Figure 2. The TRS values of the samples are in the range of 600-900 MPa. The experiments were realized in two parts. In the first part, the alloys Astaloy CrA-1Cu-0.5C and Astaloy CrA-1Ni-0.5C were sinter-hardened in the belt furnace. In the second part, the alloys Astaloy CrA-0.5C and Astaloy CrA-2Cu-0.5C were sinter-hardened in the same furnace.

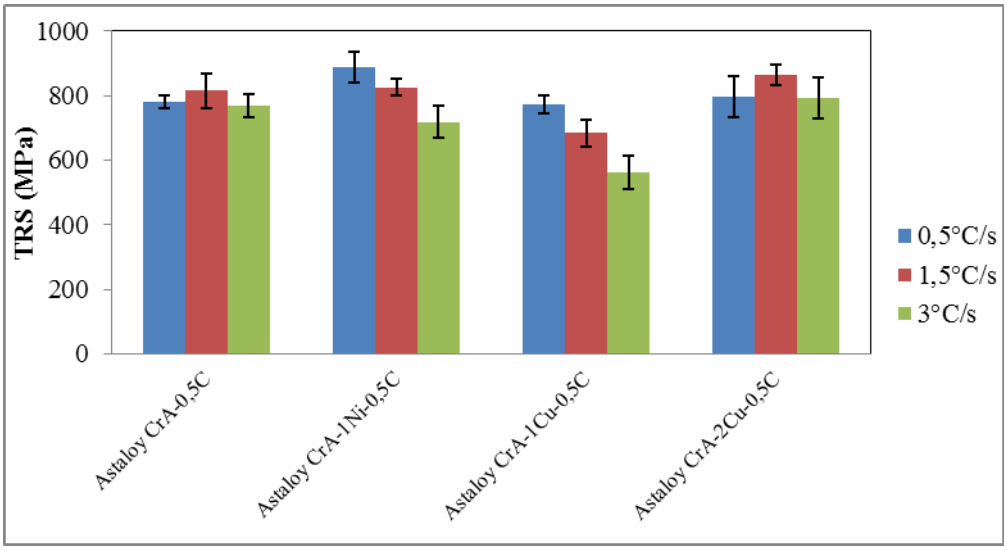

Figure 2. The transverse rupture strength values of four alloys after sintering and sinter hardening

Rapid cooling rates after sintering led to a decrease in TRS values for Astaloy CrA alloys with 1%Cu and 1%Ni due to the formation of bainite and martensite [12]. The decrease in TRS of the alloy which contained 1%Cu was about 27%, whereas less decrease which was about 19% was observed in the alloy with 1%Ni after the cooling of 3°C/s. The pores in the Astaloy CrA with the addition of 1%Cu are larger and more irregular than the sample of Astaloy CrA with 1Ni. This is a result of melting and penetrating of the Cu through the iron particules. In a study by Strafellini [13], it has been shown that the high matrix macrohardness (400-500 HV0.1) causes crack initiation and propagation at irregular pores. In our study, the formation of hard phases like bainite and martensite after sinter hardening led to crack initiation and failure of the samples even small loads were applied. The same trend was not observed for Astaloy CrA-0.5C and Astaloy CrA-2Cu-0.5C samples which were sinter hardened in the second part of the experiment because the cooling rate of 3°C/s could not be applied to the samples sufficiently for the formation of excess amount of bainite and martensite to cause crack initiation and failure of samples.

The tensile strength values of Astaloy CrA-1Cu-0.5C and Astaloy CrA-1Ni-0.5C were given in Figure 3. There is a decrease of tensile strength values with the increasing of cooling rate like transverse rupture strength. Tensile strength of Astaloy CrA with 1%Ni is in the range of about 575-350 MPa and a decrease of 40% with the increasing cooling rate was observed. There is a little change for the tensile strength of Astaloy CrA with 1%Cu compared to the sample with 1%Ni which is about 17% and the tensile strength of Astaloy CrA with 1%Cu decreases from about 410 to 340 MPa with increasing cooling rate.

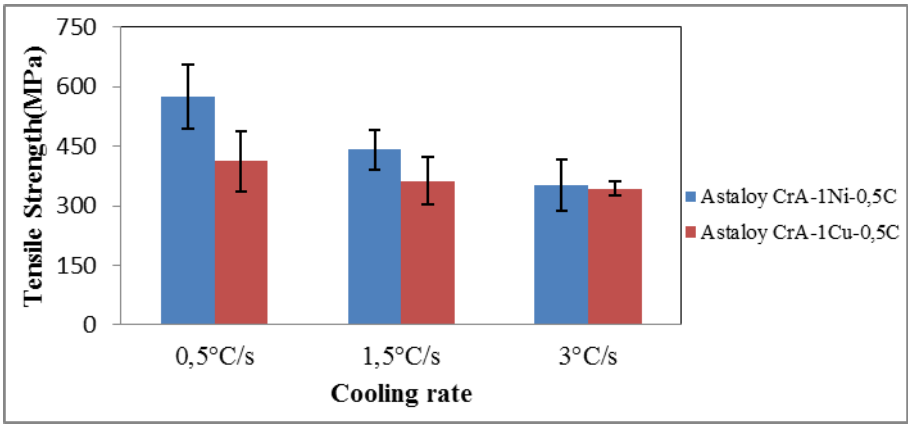

Figure 3. Tensile strength values of Astaloy CrA with the addition of 1Cu and 1Ni after sinter hardening.

Comparison of tensile strengths showed that the tensile strength values of Astaloy CrA with 1% Ni are higher than the values of Astaloy CrA with 1%Cu for all cooling rates. Melting of Cu and penetrating through the iron particles during solid state sintering generated irregular pores which were reasons for crack initiation and failure while loading. Therefore, higher tensile strength values were obtained with the absence of irregular pores in Astaloy CrA-1Ni-0.5C.

In the second part of the study, the effect of secondary heat treatments on the mechanical properties of the alloys was also investigated. The macrohardness values of the alloys after sintering, normalizing, quenching, quenching and tempering were shown in Figure 4. Normalizing provided little increase due to the formation of fine pearlite and proeutoctoid ferrite [14]. Quenching of the samples led to a fully martensitic microstructure which increased the hardness values around 230%. Tempering after quenching was used to obtain tempered martensite in the microstructure. Hence, in comparison to the quenching the macrohardness values slightly decreased after tempering.

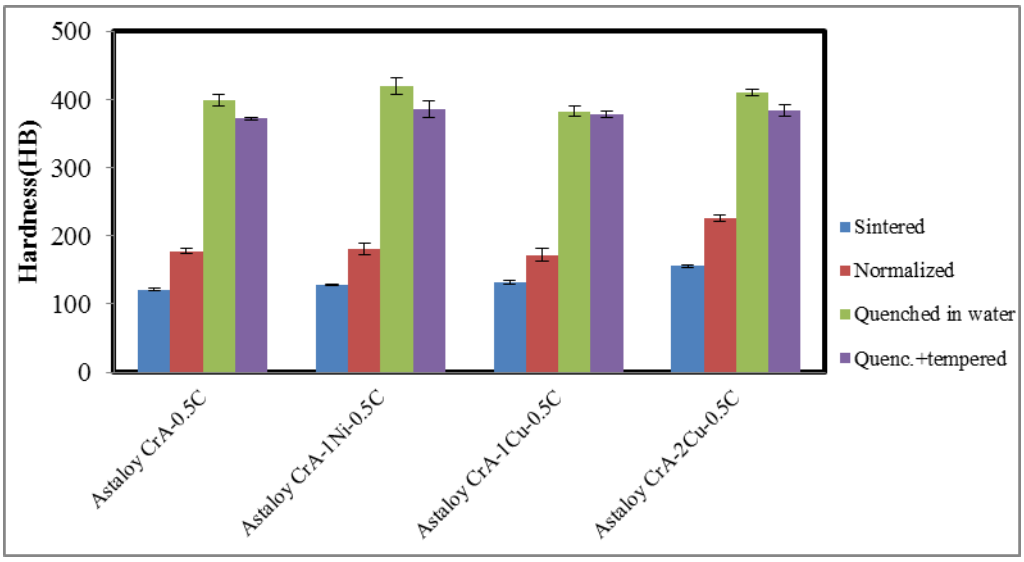

Figure 4. The macrohardness values of the samples after sintering, normalizing, quenching and tempering.

As shown in Figure 5, normalizing led to ~15% enhancement in TRS values compared with sintering. After quenching, the transverse rupture strengths significantly increased from about 800 MPa to 1250 MPa. The hard phases which were formed during secondary heat treatments did not cause any crack initiation around the irregular pores like sinter hardening due to the formation of decarburized ferrite surface layer during austenizing at 1070°C under nitrogen [14].

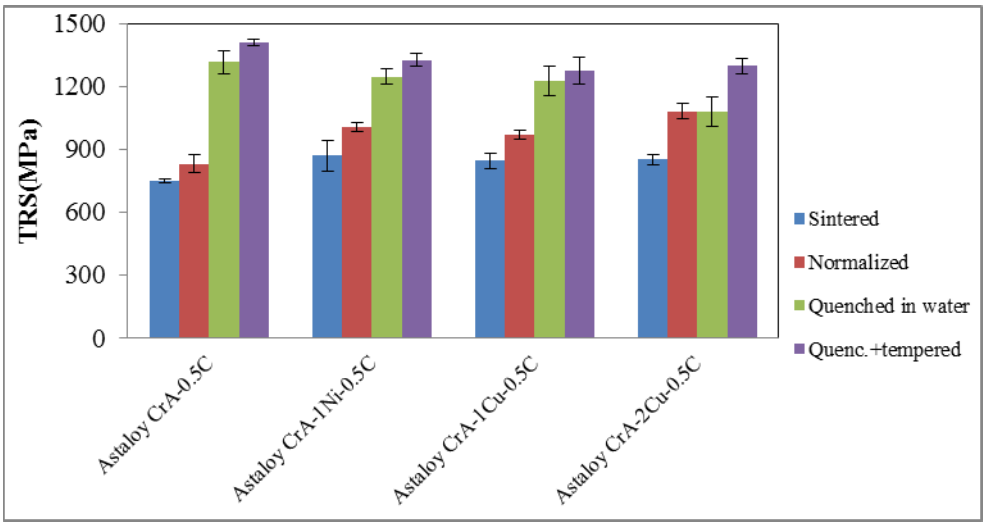

Figure 5. The change in transverse rupture strength of the sintered and heat treated Astaloy CrA powder alloys.

3.2. Microstructural Analysis

Astaloy CrA-0.5C and Astaloy CrA-1Ni-0.5C samples contain small and regular pores which are in the range of 5-20 microns, whereas the pores in Astaloy CrA-1Cu-0.5C and Astaloy-2Cu-0.5C samples are larger and more irregular with the size of 70-100 microns [15]. The porosity in four of the alloys is around 10%. However, the porosity in samples with 1Cu and 2Cu is higher (~12%) due to melting of Cu during solid state sintering and leaving much larger spaces relative to the other alloys. In a study about Astaloy CrM(Fe-3Cr-0,5Mo) by Puscas et. al. [16], the samples were pressed under 700 MPa and sintered at 1120°C under 90%N_2-10%H_2 for 30 minutes. The porosity of the samples was measured in the range of 9.4%-9.9%.

The optical micrographs of Astaloy CrA-2Cu-0.5C that was sinter hardened with cooling rates of 0.5 and 3°C/s and heat treated are given below in Figure 6 [15] In the alloy Astaloy CrA-0.5C, coarse pearlite has been observed after slow cooling due to lower hardenability. The addition of 1%Ni and 1%Cu increased the hardenability and fine pearlite and bainite occurred in the microstructures even slow cooling was applied. In the microstructure of Astaloy CrA-2Cu-0.5C, both bainite and martensite transformed after slow cooling. The sinter hardening with a cooling rate of 3°C/s increased the macro and microhardness values of the samples due to the transformation of fine and hard phases. After fast cooling, Astaloy CrA-0.5C had composite microstructure of coarse and fine pearlite. In the alloy with 1%Ni, the bainite was observed whereas in the alloy with 1%Cu martensite and bainite transformed due to the better hardenability of the alloy compared to the alloy with 1%Ni. The addition of 2%Cu provided more martensite and less bainite to be come across in the microstructure compared to the alloys with 1%Ni and 1%Cu.

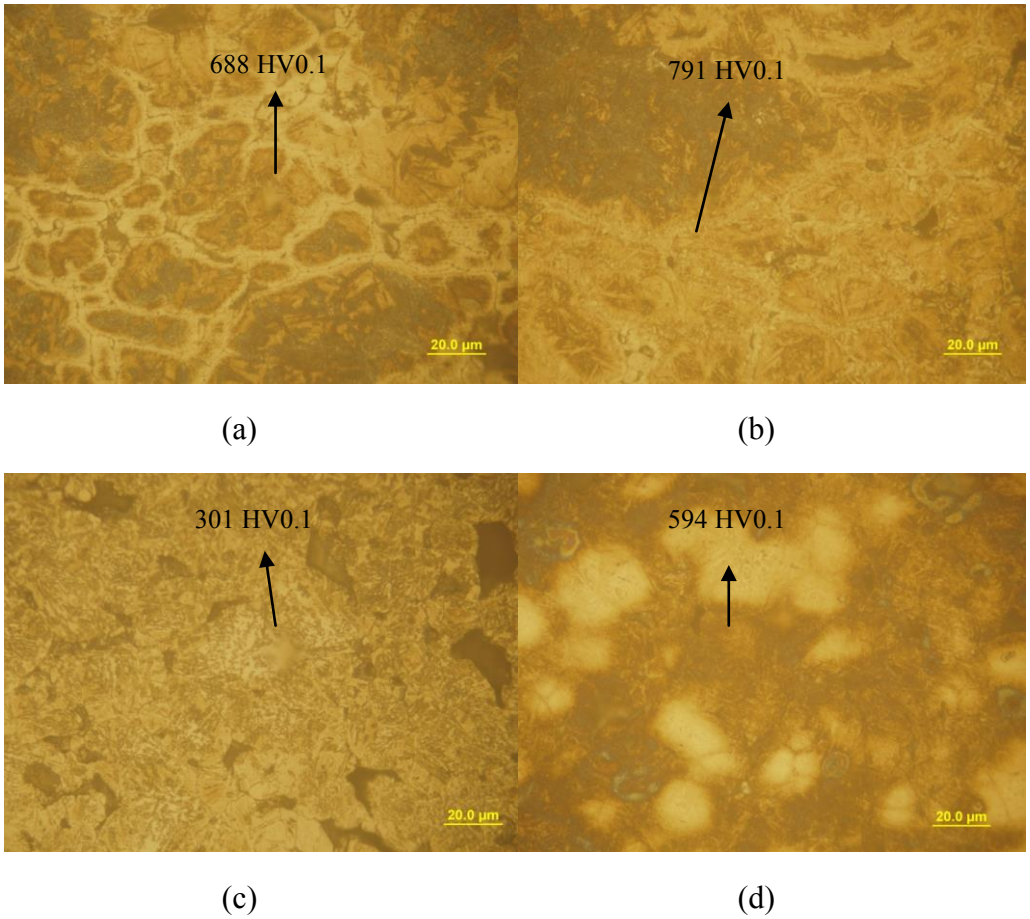

Figure 6. Optical micrographs of Astaloy CrA-2Cu-0.5C sinter hardened with cooling rates of 0.5 and 3 °C/s and heat treated. (1000x) (a) sintered (0.5°C/s) (b) sinter hardened (3°C/s) (c) normalized (d) quenched in water [15].

Normalizing led to fine pearlite formation in the microstructures of the alloys with alloying elements. However, the absence of alloying elements in Astaloy CrA-0.5C led to lower hardness due to the formation of coarse pearlite. The quenching in water increased the microhardness values at around ~600-700 HV0.1 due to 100% martensite formation in all alloys. In Figure 7, the micrographs of the ferrite layers of the alloys after secondary heat treatments from 1070°C are given [15]. After austenitizing at 1070°C, existence of decarburization layers (~200 microns to ~450 microns) was observed at the surface of the samples [14]. In Astaloy CrA-0.5C, the thickness of ferrite layer was determined to be higher than the alloys which comprise 1%Cu and 1%Ni. After heat treatment of the samples, the initial carbon content of the alloys was reduced to ~0.4%. Therefore, the existence of the ductile ferrite layers on heat treated Astaloy CrA alloys led to an increase in the TRS of the heat treated alloys even brittleness occurred through the samples with increasing hardness. Additionally, the C reduction due to decarburization during heat treatment, led to the formation of martensite that has lower hardness. The ductile ferrite layer formed at the surface of the samples and the martensite with lower hardness due to C loss prevented the crack initiation and propagation and this promotes to higher toughness and TRS values in quenched samples [14].

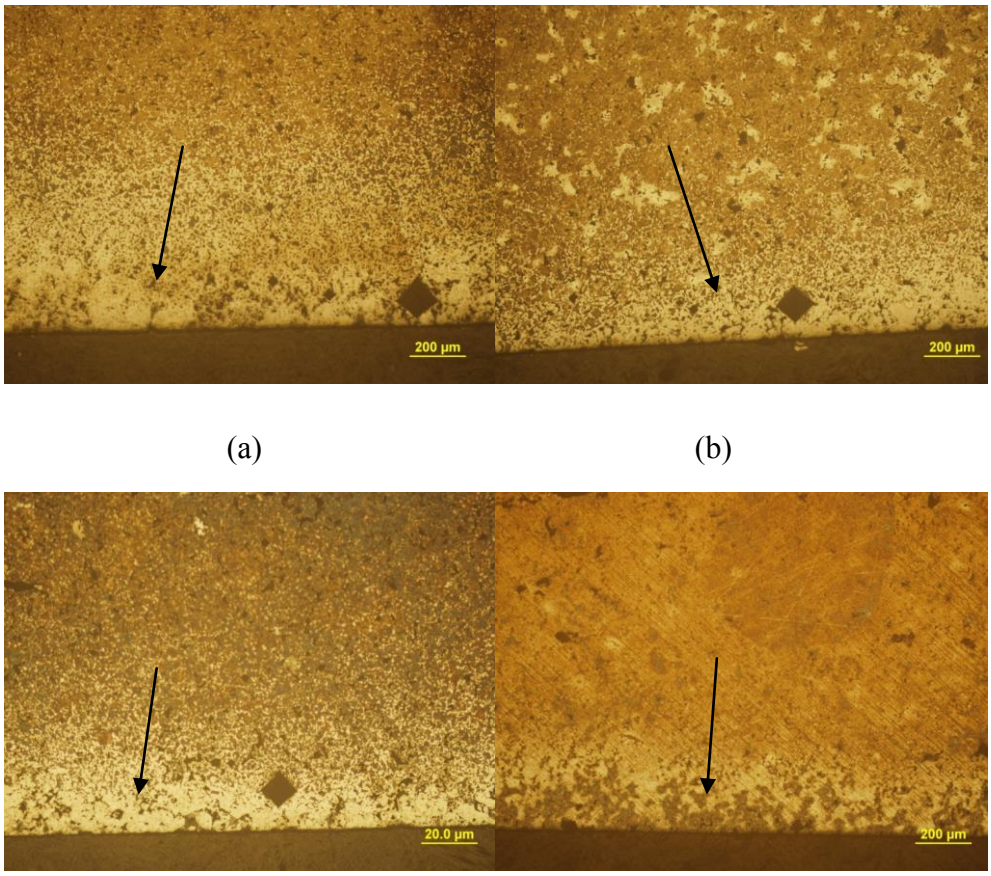

(a) (b)

(c) (d)

Figure 7. Optical micrographs of ferrite layers of alloys after secondary heat treatments from 1070°C (100x) (a) Astaloy CrA-0.5C (b) Astaloy CrA-1Ni-0.5C (c) Astaloy CrA-1Cu-0.5C (d) Astaloy CrA-2Cu-0.5C [15].

4.CONCLUSION

In this study, the effect of sinter hardening and various heat treatments on the properties of four different prealloyed Astaloy CrA with the addition of 0.5% graphite, 1%Ni, 1%Cu and 2%Cu has been investigated.

-Sinter-hardening led to an increase in hardness and a decrease in TRS values of the alloys due to formation of bainite and martensite after rapid cooling.

-Alloying elements (Cu and Ni) led to an increase in hardenability during both of sinter hardening and heat treatments. The lowest hardenability was observed in Astaloy CrA-0.5%C, whereas the highest hardenability was obtained in Astaloy CrA-2%Cu-0.5%C.

-Normalizing from 1070°C caused slight improvement on both of hardness and TRS values of the samples. This improvement is due to the formation of fine pearlite and proeutectoid ferrite. Hardness and TRS values were increased after quenching and tempering due to the formation of martensite and tempered martensite.

Acknowledgement

This study was supported by TOBB University of Economics and Technology. Aytac Atas from Tozmetal Company Istanbul/Turkey was acknowledged for his assistance in sinter-hardening experiments and N.Kaan Çalışkan from TUBITAK SAGE was acknowledged for his assistance in heat treatment experiments.

REFERENCES

1. G.F. Bocchini, G. Rivolta, G. Silva, E. Poggio, M.R. Pinasco, M.G. Ienco, 'Microstructural and Mechanical Characterisation of some Sinter Hardening Alloys and Comparisons with Heat Treated PM Steels', Powder Metallurgy, Vol:47, No:4, pp.343-351, 2004.
2. W. B. James, 'What is Sinter Hardening', International Conference on Powder Metallurgy&Particulate Materials, May 31-June 4, Las Vegas, Nevada, USA, 1998.
3. G. Straffelini, V. Fontanari, A. Hafez, M. Benedetti, 'Tensile and Fatigue Behaviour of Sinter Hardened Fe-1,5Mo-2Cu-0,6C Steels', Powder Metallurgy, Volume:52, No:4, pp.298-303, 2009.
4. S. Hatami, A. Malakizadi, L. Nyborg, D. Wallin, 'Critical aspect of sinter-hardening of prealloyed Cr-Mo steel', Journal of Materials Processing Technology, 1180-1189, 2010.
5. H.G. Rutz, A.H. Graham, A.B. Davala, 'Sinter-Hardening P/M Steels', International Conference on Powder Metallurgy & Particulate Materials, June 29-July 2, Chicago, IL USA, 1997.
6. B. Maroli, B. Sigurd, T. Peter, U. Engström, 'Sinter Hardening and Heat Treatment of Materials Based on Astaloy CrM', PM^2TEC, Las Vegas, USA, 2003.
7. S. Dizdar, 'High Performance Sintered Steel Gears for Use in Transmission and Machinery-A Critical Review', The International Conference on Gears, Germany, 2010.
8. U. Engström, S. Berg, R. Frykholm, 'High Performance Materials for Sinter Hardening Applications', World PM2010, Florence, Italy, 2010.
9. C. Larsson, U. Engström, S. Berg, 'Means to Lift Mechanical Properties to the Next Level, Enabling New Challenging Applications', Euro PM2012, Switzerland, 2012.
10. R. Frykholm, O. Litström, 'Influence of Composition and Processing Conditions on the Microstructure and Properties of Astaloy CrA', World PM2012, Japan, 2012.
11. S. Berg, B. Maroli, 'Properties Obtained by Chromium-Containing Materials', Powder Metallurgy and Particulate Materials, 2002.
12. H**.** Hafızoğlu, N. Durlu, A. Ataş, H. Özdural, 'Mechanical Properties of Sinter-Hardened Astaloy CrA Powder Alloys, 16th International Metallurgy and Materials Congress (IMMC 2012), Istanbul, Turkey, 112-119, 2012.
13. G. Straffelini, C. Menapace, A. Molinari, 'Interpretation of effect of matrix hardening on tensile and impact strength of sintered steels', Powder Metallurgy, Volume 45, Issue 2, pp. 167-172, 2002.
14. H. Hafızoğlu, N. Durlu, 'The Effect of Heat Treatment on the Properties of Astaloy CrA Powder Alloys ', EURO PM 2013 International Powder Metallurgy Congress & Exhibition, Gothenburg, Sweden, 2013
15. H. Hafızoğlu, 'Astaloy CrA Alaşımlarında Sinterleme ile Sertleştirme', M.Sc.Thesis, TOBB University of Economics and Technology, 2013.
16. T.M. Puscas, M. Signorini, A. Molinari, G. Straffelini, 'Image Analysis Investigation of the Effect of the Process Variables on the Porosity of Sintered Chromium Steels', Materials Characterization, 50, pp. 1-10, 2003.

SINTERING STUDIES ON W-RICH W-Ni-Co HEAVY ALLOYS WITH HIGH COBALT/NICKEL RATIO

Onur DİNÇER[*], Ali KALKANLI[**], İshak KARAKAYA[**], M. Kaan PEHLİVANOĞLU[*], N. Kaan ÇALIŞKAN[*]

*TÜBİTAK SAGE, Ankara, Turkey
**Middle East Technical University, Ankara, Turkey

ABSTRACT

In this study, the sintering behavior and microstructural characteristics of selected W-rich W-Ni-Co alloys with a relatively high Co/Ni ratio was investigated. 90W-8Co-2Ni and 95W-4Co-1Ni alloys with Co/Ni ratio 4/1 were investigated in the study, the compositions being expressed in weight percentages. Alloy samples prepared through conventional powder metallurgy routes were sintered at 1500, 1525, 1550 and 1600 °C under hydrogen atmosphere. It is found that the densification was limited at 1500°C for both 90 and 95 wt% W alloys. However, the relative density of the alloys increased with increasing sintering temperature and reached 100% at 1600°C. Microstructural examinations have implied that the sintering of the investigated alloys has most probably been realized in the solid state at all the sintering temperatures applied. Through energy dispersive spectroscopy (EDS) analyses, the binder phase in both of the alloys was suggested to be Co_7W_6 intermetallic phase with some Ni dissolved in it, Ni most likely substituting Co in the structure. The hardnesses of the alloys were both found to increase with increasing sintering temperature, in a manner similar to the density increase. This behavior was attributed to the enhancement of density and microstructure with increasing sintering temperature. In the fully dense condition, the hardness of the 90 wt% W alloy (alloy 90W-8Co-2Ni) was observed to be higher than that of the 95 wt% W alloy, most probably due to the higher volume percentage of the hard $(Co, Ni)_7W_6$ binder phase in the former alloy.

Keywords: Solid state sintering, High Cobalt content, Tungsten Heavy Alloys, Microstructure

1. INTRODUCTION

Liquid-phase sintered (LPS) tungsten heavy alloys (WHAs) show a typical microstructure where rounded BCC tungsten particles are surrounded in a FCC binder matrix containing Ni, Fe, Co etc. and some dissolved W. Generally, liquid-phase sintered WHAs are fabricated by blending raw powders and sintering at a temperature above 1460°C in a protective atmosphere. On the other hand, solid state sintering has been used to densify WHAs at relatively lower temperatures with respect to LPS method [1]. Due to their combination of high density, strength and ductility, WHAs are used as kinetic energy penetrators, counterweights, radiation shields, vibration damping devices and electrical contacts [2, 3].

Historically, the larger portion of WHA production has been consisted of W-Ni-Cu and W-Ni-Fe alloys and several efforts has been spent to understand these alloy systems [4, 5]. As a

newer ternary WHA system, W-Ni-Co alloys show higher mechanical properties than formers. W-Ni-Co heavy alloys are used mostly in military applications. Generally, W-rich W-Ni-Co heavy alloys with high Ni/Co ratio have been preferred in such uses due to their superior properties. The most commonly used W-Ni-Co alloy systems contain Ni/Co ratio ranging from 2 to 9. These alloys provide greater tensile strength, ductility and toughness as compared to W-Ni-Fe alloys [6-9].

Although there are some studies on the mechanical properties of W-Ni-Co heavy alloys, the effect of composition and sintering variables on the characteristics of these alloys has not been studied widely in the literature. In addition, most of the studies about the W-Ni-Co alloys have generally been focused on alloy systems with higher Ni/Co ratio.

Based on these facts, the sintering behavior and microstructural characteristics of W-rich W-Ni-Co alloys with a relatively high Co/Ni ratio was investigated in this study. The main aim of the study was to provide technical information on the subject. W-Ni-Co alloys with 90 and 95 wt% W and Co/Ni ratio 4/1 were investigated in the study. Conventional powder metallurgy routes were followed in order to produce the alloy specimens. The produced alloy samples were characterized by applying relevant physical and microstructural characterization methods.

2. EXPERIMENTAL

High purity elemental W, Ni and Co powders were used in the study. The general properties of these powders are given in Table 1. The average particle size of the powders was measured by a laser particle size analyzer (Mastersizer 2000, Malvern, USA) and the shape of the powders was determined by a scanning electron microscope (6400 JSM, Jeol, Japan). 90W-8Co-2Ni and 95W-4Co-1Ni alloys with 4/1 Co/Ni ratio were investigated in the study. Proper amounts of W, Ni and Co powders were weighted by a precision balance that has $\pm$ 0.01 g accuracy (CP3200S, Sartorius, Germany) in order to give the alloy compositions. Powder mixing was performed in a turbula mixer (T2F, Glenn Mills, Switzerland) at a speed of 80 rpm for 40 minutes. Mixed powders were compacted by cold isostatic pressing (CIP 42260, Flow Autoclave Engineers, USA) at 310 MPa for 15 seconds. The compacted samples were then sintered at 1500, 1525, 1550 and 1600ºC for 60 minutes, with 30 minute isothermal holding at 1000°C. Sintering was done in a horizontal tube furnace (PTF105, Protherm Furnaces, Turkey) under pure hydrogen gas flow at a rate of 0.5 l/min.

Sintered alloys were characterized by applying suitable techniques. The densities of the alloys were measured via Archimedes immersion technique by using xylene having a density of 0.86 g/cm^3. The measured densities were divided by the theoretical densities (estimated by the rule of mixtures method) and then multiplied by 100 in order to determine the percent relative densities (%RD) of the alloys. For microstructural characterization, specimens were prepared with suitable metallographic methods and etched by Murakami's etchant. The microstructure analysis of the alloys was performed both by an optical microscope (Axioskop 2, Zeiss, Germany) and a scanning electron microscope (SEM) (6400 JSM, Jeol, Japan). The compositions of the micro-constituent phases of the alloys were determined via Energy Dispersive Spectroscopy (EDS) analyses by using the Northern Tracor EDS system equipped within the SEM. Hardness measurements were done to sintered specimens by Vickers diamond indenter in HV0.5 scale (Duramin 500 Universal Hardness Tester, Struers, Denmark).

Table 1. General properties of the elemental powders

Elemental Powder	Average Particle Size (μm)	Shape	Purity (wt%)	Source
W	4.8	Polygonal	99.9+	Eurotungstene AW2123
Ni	4.3	Polygonal	99.9	William Rowland Vale 123
Co	6.0	Polygonal	99.9+	Eurotungstene CO610A25

3. RESULTS and DISCUSSION

Archimedes immersion method was used to measure the densities of the alloy specimens. The %RDs of the alloys formed in this investigation are given Table 2, and the variation of %RD with increasing sintering temperature for the investigated alloys is shown in Figure 1. As can be seen clearly in Table 2 and Figure 1, the densification of the investigated Co-rich alloys with Co/Ni ratio 4/1 is limited, when sintered at and below 1550°C. However, for both 90W-8Co-2Ni and 95W-4Co-1Ni alloys, the density was observed to increase with increasing sintering temperature and reach full density at 1600°C. In general, the sintering and densification of WHAs is a diffusion controlled process. It is known that temperature and composition have a strong influence in determining the kinetics of any diffusional process. In general, the temperature dependence of diffusional processes is exponential, meaning that increasing the temperature has a significant effect in enhancing the rate of such processes. Therefore, the densification rate in a sintering operation is expected to increase with increasing temperature, and this is the case observed in the study for the 90 and 95 % W Co-rich alloys.

On the other hand, it is seen from Table 2 and Figure 1 that %RD of the 95 wt% W alloy is greater than that of the 90 wt% W alloy for all sintering temperatures except 1600°C. Alloy 95W-4Co-1Ni has higher W content when compared to alloy 90W-8Co-2Ni. This means that there will be much more W powder particles per unit volume in alloy 95W-4Co-1Ni, both in the green condition and during the stages of sintering. Therefore, at any given sintering temperature, the mean free path among the W particles will be shorter, contact and neck formation among W and Ni or Co particles may be easier, and the amount of the binder phase may be smaller in alloy 95W-4Co-1Ni. As a result, all diffusional mass transport processes might take place over shorter distances in alloy 95W-4Co-1Ni, and this might enhance the rate of such processes. This may be the reason why alloy 95W-4Co-1Ni gets more densified when compared to alloy 90W-8Co-2Ni at a given sintering temperature.

Table 2. The percent relative density (%RD) of the investigated alloys

Alloy	Relative Density (%)			
	Sintering Temperature (°C)			
	1500	**1525**	**1550**	**1600**
90W-8Co-2Ni	82.0	87.3	92.3	100
95W-4Co-1Ni	86.0	89.2	92.9	100

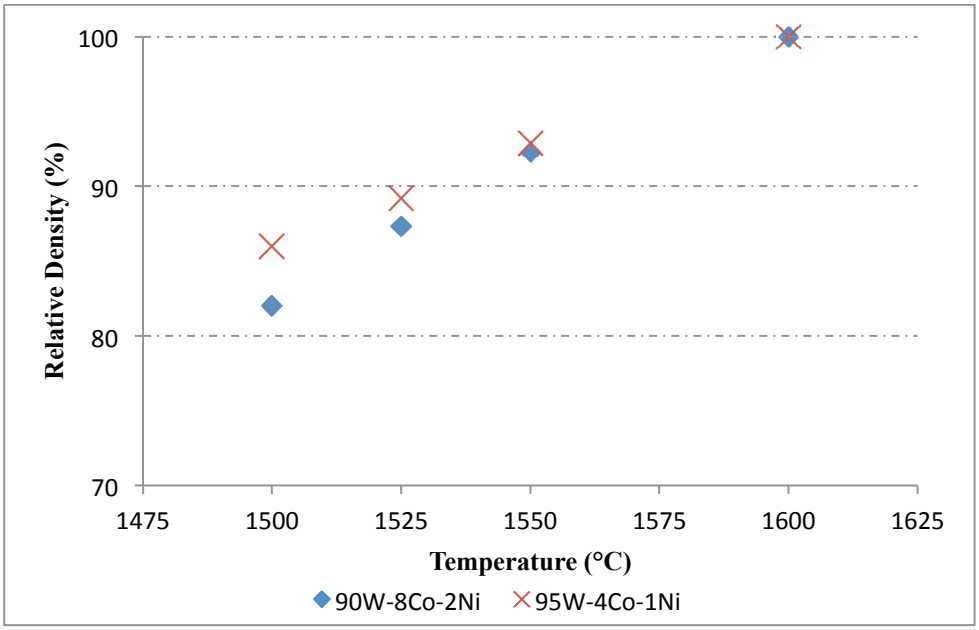

Figure 1. Variation of %RD with increasing sintering temperature for the investigated alloys

The microstructures of the investigated 90W-8Co-2Ni and 95W-4Co-1Ni alloys are shown in Figure 2 and Figure 3, respectively. The micrographs given in Figures 2 and 3 were taken in SEM. As seen in these figures, the microstructures of these Co-rich W-Ni-Co alloys are essentially different from those of liquid phase sintered Ni-rich alloys [8, 10]. The general appearance of the microstructures given in Figures 2 and 3 imply that both 90W-8Co-2Ni and 95W-4Co-1Ni alloys were probably sintered in the solid state at all the sintering temperatures applied in the study. In the microstructures given in these figures, the phase with brighter contrast is tungsten and the phase with darker contrast is the binder matrix. As can readily be seen in the figures, the amount of the binder matrix phase is higher in alloy 90W-8Co-2Ni when compared to alloy 95W-4Co-1Ni, at any given sintering temperature. This phenomenon is much more evident for sintering temperatures at and above 1550°C. In addition, the amount of the binder phase also seems to increase with increasing sintering temperature for both of the alloys. These two phenomena are expected based on phase diagram considerations and require no further explanation.

For both of the investigated alloys, the compositions of the constituent phases of the microstructure were tried to be determined by EDS analysis. This was a difficult task owing to the extreme fineness of the microstructures, and EDS analyses have provided more meaningful data for alloy samples sintered at higher temperatures. EDS analysis results have shown that the constituent phase of the microstructure which is seen in brighter contrast in Figures 2 and 3 was almost pure W for both of the alloys. The other constituent phase with darker contrast was forming the binder matrix in the microstructure of the investigated alloys. The composition of this binder matrix phase determined by EDS analysis is given in Table 3 both in weight (wt%) and atomic (at%) percentages. Owing to the fineness of the microstructure and semi-quantitative nature of the EDS analysis, the composition values given in Table 3 may involve a certain amount of error, especially for lower sintering temperatures. However, the EDS analysis results given in Table 3 certainly imply that the composition of the binder matrix phase is identical for both of the investigated alloys and does

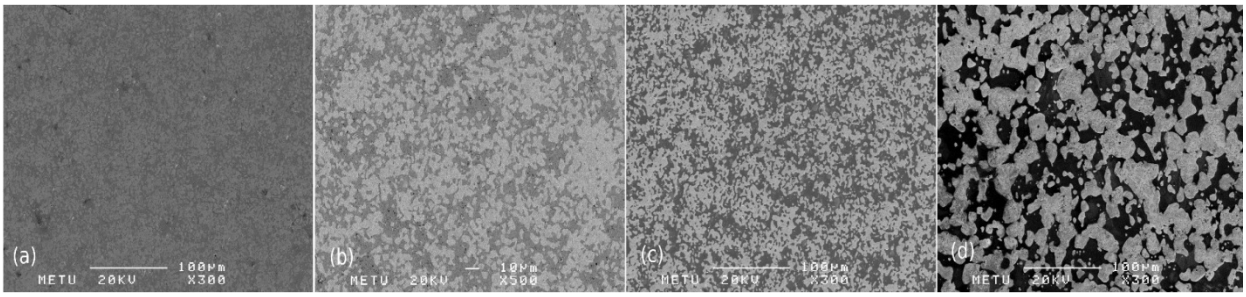

Figure 2. Microstructure of 90W-8Co-2Ni alloy sintered at: (a) 1500°C, secondary electron image (SEI), x300; (b) 1525°C, back scattered electron (BSE) image, x500; (c) 1550°C, SEI, x300 and (d) 1600°C, SEI, x300

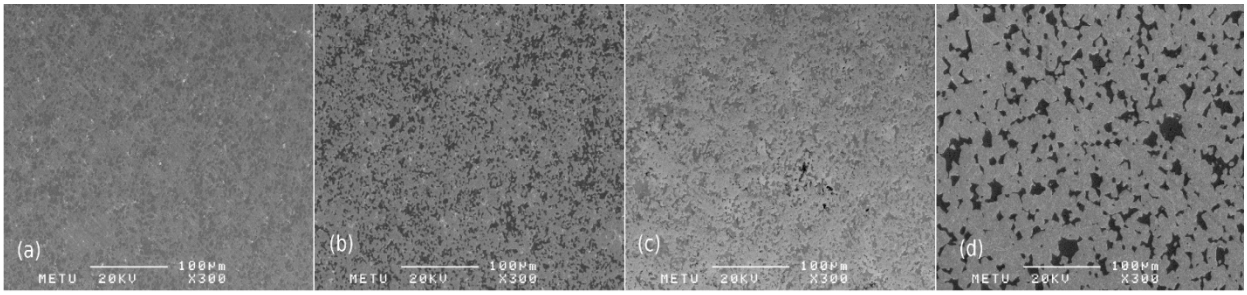

Figure 3. Microstructure of 95W-4Co-1Ni alloy sintered at: (a) 1500°C, (b) 1525°C, (c) 1550°C and (d) 1600°C, secondary electron images (SEI), x300

Table 3. Binder phase composition of the investigated alloys

	Binder Phase Composition (wt%)											
	Sintering Temperature (°C)											
	1500			**1525**			**1550**			**1600**		
Alloy	**W**	**Ni**	**Co**	**W**	**Ni**	**Co**	**W**	**Ni**	**Co**	**W**	**Ni**	**Co**
90W-8Co-2Ni	76.7	4.7	18.6	73.8	5.0	21.2	75.1	4.9	20.0	73.1	5.3	21.6
95W-4Co-1Ni	77.3	4.3	18.4	74.3	5.2	20.5	75.2	5.3	19.5	75.1	5.4	19.5
	Binder Phase Composition (at%)											
	Sintering Temperature (°C)											
	1500			**1525**			**1550**			**1600**		
Alloy	**W**	**Ni**	**Co**	**W**	**Ni**	**Co**	**W**	**Ni**	**Co**	**W**	**Ni**	**Co**
90W-8Co-2Ni	51.3	9.8	38.9	47.4	10.2	42.4	49.1	10.0	40.9	46.6	10.5	42.9
95W-4Co-1Ni	52.1	9.2	38.7	48.1	10.5	41.4	49.7	10.3	40.0	49.1	11.0	39.9

not vary significantly with sintering temperature. Based on these EDS analysis results and W-Ni-Co phase diagram information given in the literature [11], the binder matrix phase of the

investigated alloys was suggested to be Co_7W_6 intermetallic phase with some Ni dissolved in it. Both the available phase diagram data given in [11] and extensive EDS analyses carried out in a related study [10] imply that Ni most likely substitutes Co in the Co_7W_6 structure. Therefore, it is suggested that this intermetallic phase may be represented as $(Co, Ni)_7W_6$.

Vickers hardness tests were applied to sintered 90W-8Co-2Ni and 95W-4Co-1Ni alloy samples in HV0.5 scale. The variation of hardness with increasing sintering temperature is given in Figure 4 for both of the alloys. It is clearly seen in Figure 4 that the hardness of both alloys increase with increasing sintering temperature, in a manner similar to the density increase shown in Table 2 and Figure 2. At lower sintering temperatures, the densification of both 90W-8Co-2Ni and 95W-4Co-1Ni alloys is limited. It is believed that the higher porosity of these alloys at lower sintering temperatures, which can occasionally be seen in Figure 1, causes a decrease in the overall hardness of the alloys. Therefore, the increase in hardness with increasing sintering temperature is suggested to be due to the improvement of density and microstructure with increasing sintering temperature for both of the alloys. As seen in Figure 4, the hardness increase was steeper for 90W-8Co-2Ni alloy when compared to 95W-4Co-1Ni alloy. In the fully dense condition, the hardness of this alloy was also significantly higher than the latter alloy. As mentioned before and can be seen in Figures 2 and 3, the amount of the $(Co, Ni)_7W_6$ intermetallic binder matrix phase is higher in alloy 90W-8Co-2Ni for almost all sintering temperatures. Owing to its lower W content when compared to 95W-4Co-1Ni alloy, this phenomenon is expected based on phase diagram and "lever rule" considerations. As mentioned before, the other constituent phase of the composite microstructure was almost pure W in both of the alloys. Therefore, the steeper increase of

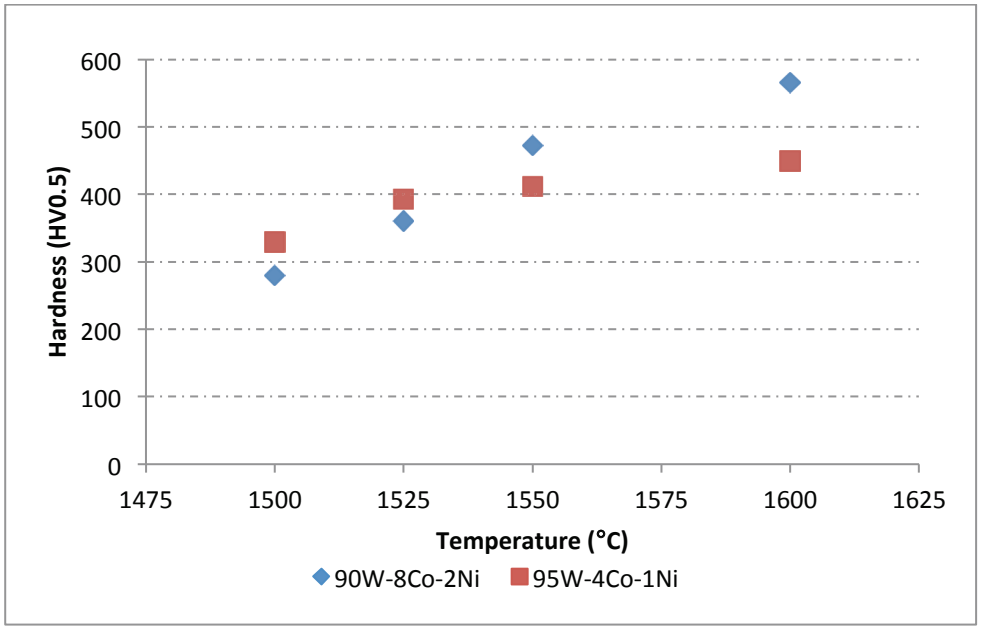

Figure 4. Hardness variation for 90W-8Co-2Ni and 95W-4Co-1Ni alloys with increasing sintering temperature

hardness with increasing sintering temperature and the higher full-density hardness observed in alloy 90W-8Co-2Ni is believed to result from the higher volume percentage of the hard $(Co, Ni)_7W_6$ intermetallic binder matrix phase in this alloy. As expected, the higher hardness

of the 90W-8Co-2Ni alloy when compared to alloy 95W-4Co-1Ni at full density also implies that the hardness of the intermetallic $(Co, Ni)_7W_6$ phase is relatively higher than the other constituent phase, i.e. pure W.

The "full-density" hardness of the investigated Co-rich W-Ni-Co alloys is significantly higher when compared to the conventionally exploited Ni-rich alloys, in the "as-sintered" condition. The "full-density" hardness of 90W-8Co-2Ni and 95W-4Co-1Ni alloys given in Figure 4 approximately corresponds to 54 and 45 HRC (Rockwell C) respectively, in the "as-sintered" condition. This implies that Co-rich W-Ni-Co alloys such as those investigated in this study might find technological use in civil or military applications where high values of hardness is of importance. It is also suggested that it is possible to influence and enhance the properties of such alloys through delicate control of alloy composition and sintering parameters.

4. CONCLUSIONS

The sintering behavior and microstructural characteristics of 90W-8Co-2Ni and 95W-4Co-1Ni alloys with Co/Ni ratio 4/1 were investigated in the study. The following conclusions were drawn:

1. Relative densities of the investigated alloys have both increased with increasing sintering temperature up to 1600°C and at 1600°C both alloys have reached full density.
2. Microstructural examinations have implied that both 90W-8Co-2Ni and 95W-4Co-1Ni alloys were most likely solid state sintered at all sintering temperatures.
3. Microstructural examination and EDS analysis results have shown that the binder matrix phase of both alloys were identical. This binder matrix phase of the alloys was determined to be hard $(Co, Ni)_7W_6$ intermetallic phase from EDS results.
4. The hardness of the investigated alloys was found to increase with increasing sintering temperature, in a manner similar to the density increase. This behavior is suggested to be due to the improvement of density and microstructure with increasing sintering temperature for both of the alloys.
5. When compared to alloy 95W-4Co-1Ni, the hardness of 90W-8Co-2Ni alloy was found to increase more steeply with increasing sintering temperature. The latter alloy was also observed to exhibit higher hardness at full density when compared to the former alloy. These two phenomena are suggested to occur as a result of the higher volume percentage of the hard $(Co, Ni)_7W_6$ intermetallic binder matrix phase in the 90W-8Co-2Ni alloy.

ACKNOWLEDGEMENTS

This study was supported by TÜBİTAK-SAGE and Middle East Technical University.

REFERENCES

1. Farid Akhtar, "An Investigation on the Solid State Sintering of Mechanically Alloyed Nano-structured 90W–Ni–Fe Tungsten Heavy Alloy, International Journal of Refractory Metals and Hard Materials, Volume 26, Issue 3, May 2008, Pages 145-151

2. Ho J. Ryu, Soon H. Hong, Woon H. Baek, "Microstructure And Mechanical Properties of Mechanically Alloyed and Solid-State Sintered Tungsten Heavy Alloys", Materials Science and Engineering: A, Volume 291, Issues 1–2, 31 October 2000, Pages 91-96

3. R. M. German, Powder Metallurgy Science, New Jersey: Metal Powder Industries Federation, 1984

4. W. Yunxin, R.M. German, B. Marx, P. Suri, R. Bollina "Comparison of Densification and Distortion Behaviors of W-Ni-Cu and W-Ni-Fe Heavy Alloys in Liquid Phase Sintering," Journal of Materials Science, 2003,vol-10, pp. 2271-2281

5. S. G. Caldwell, "Variation of Ni/Fe Ratio in W-Ni-Fe Alloys: A Current Perspective," in Proceedings of the First International Conference on Tungsten and Tungsten Alloys, 1992

6. N. Maitra, "Development of a Tungsten-Nickel-Cobalt Heavy Alloy", Metal Powder Report, Volume 57, Issue 4, April 2002, Page 40

7. P. Ghosal, Electron microscopy of tungsten-nickel-cobalt heavy alloys, Metal Powder Report, Volume 57, Issue 9, September 2002, Page 37

8. B. Katavic, M. Nikacevic and Z. Odanovic, "Effect of Cold Swaging and Heat Treatment on Properties of the P/M 91W-6Ni-3Co Heavy Alloy," Science of Sintering, 2008, vol-40, pp. 319-331

9. E. W. Kennedy, "Influence of Microstructure on Fracture Characteristics and Tensile Properties of Two Tungsten Heavy Alloys," 2nd International Conference on Tungsten&Refractory Metals, Virginia, 1994.

10. O. Dinçer, "Liquid Phase Sintering of Tungsten-Nickel-Cobalt Heavy Alloys", M.Sc. Thesis, Middle East Technical University, Ankara, 2014

11. K. P. Gupta, "The Co-Ni-W (Cobalt-Nickel- Tungsten) System," Journal of Phase Equilibria, 2000, Volume 21, Number 4, Page 396

VARIATION OF MICROSTRUCTURE AND HARDNESS WITH COMPOSITION IN W-RICH TERNARY W-Ni-Co ALLOYS

Onur DİNÇER[*], Ali KALKANLI[**], İshak KARAKAYA[**], M. Kaan PEHLİVANOĞLU[*]

*TÜBİTAK SAGE, Ankara, Turkey
**Middle East Technical University, Ankara, Turkey

ABSTRACT

In tungsten (W) heavy alloys (WHAs), minor additions of cobalt (Co) to the alloy composition is known to improve several mechanical properties, especially for use in military ordnance applications. Ternary W-rich W-Ni-Co alloys with relatively high Ni/Co ratios were also determined to have beneficial properties for ordnance applications, especially when subjected to post-sintering thermo-mechanical treatments. In this study, the effect of composition and sintering temperature on the microstructure and hardness of selected W-rich ternary W-Ni-Co alloys were investigated. Alloys with Ni/Co ratios 1/1, 3/1 and 6/1 balanced with 90 and 95 wt% W were examined in the study. The alloy samples were prepared by using conventional powder metallurgy methods such as mixing and compaction. Alloy samples were sintered under hydrogen atmosphere at 1475, 1500 and 1525 °C. Microstructural examinations have shown that Ni/Co ratio 1/1 alloys have consisted of a two-phase binder matrix. Ni/Co ratio 3/1 and 6/1 alloys, on the other hand, was found to exhibit a single matrix phase, which is the typical microstructure for the ordinary liquid phase sintered WHAs. Ni/Co ratio 1/1 alloys were determined to have substantially higher hardness than Ni-rich alloys, for all sintering temperatures.

Keywords: Hardness, Binder matrix, Cobalt, Nickel, Tungsten Heavy Alloys, Microstructure

1. INTRODUCTION

Tungsten based heavy alloys are produced mostly by solid state sintering (SSS) and liquid phase sintering (LPS) techniques with metallic additions like Ni, Cu, Co, Fe, etc. The resultant material is a metal matrix composite which contains tungsten grains and alloy binder matrix [1]. These alloys are mostly used in civil and military applications due to their higher strength, density and toughness. Generally, W-Ni-Cu and W-Ni-Fe alloys have been investigated and used in many applications. Due to higher mechanical property requirements, Fe has been replaced with Co in WHAs. By the aid of post sintering operations, it is reported that W-Ni-Co alloys reaches up to 1700 MPa tensile strength [2, 3].

In order to improve the mechanical properties of WHAs, it is very important to understand and describe the microstructural characteristics of such alloys. Bose [2] has showed that the change of matrix composition has affected the mechanical properties such as tensile strength and hardness for W-Ni-Fe alloys. In addition, sintering temperature has also affected the microstructure and mechanical properties of WHAs. Ryu [4] observed that increasing

sintering temperature from SSS to LPS region changes the microstructure and tensile strength of 93W-5.6Ni-1.4Fe alloys completely. Moreover, J. Das observed that compositional changes and minor additions to W-Ni-Cu and W-Ni-Fe alloys have altered the hardness of these alloys [5]. As can be seen from these studies, investigations on microstructural characteristics of WHAs are limited for only W-Ni-Cu and W-Ni-Fe heavy alloy systems. Besides, the studied W-Ni-Co systems are based only on the investigation of mechanical properties for such heavy alloys. The effects of composition and sintering variables on the microstructural characteristics of W-Ni-Co alloys have not been studied widely in the literature. By this reason, in this study, the effects of composition and sintering temperature on the microstructure and hardness of selected W-rich ternary W-Ni-Co alloys were investigated. Alloys with Ni/Co ratios 1/1, 3/1 and 6/1 balanced with 90 and 95 wt% W were selected to understand the effect of Ni/Co ratio and W content variations on microstructural and hardness characteristics. Typical powder metallurgy methods such as powder mixing and compaction were followed for alloy preparation. Alloys were sintered at 1475, 1500 and 1525°C under hydrogen atmosphere and characterized with suitable techniques.

2. EXPERIMENTAL

General properties of the elemental W, Ni and Co powders used in this study are given in Table 1. The elemental powders were 99.9 % and above purity as specified by the suppliers. The average particle size of the powders was measured by a laser particle size analyzer (Mastersizer 2000, Malvern, USA). The shape and morphology of the powder particles were investigated with scanning electron microscopy (SEM) (6400 JSM, Jeol, Japan). The general morphology of the powders is shown in Figure 1. A precision balance that has $\pm$ 0.01 g accuracy (CP3200S, Sartorius, Germany) was used to weigh appropriate amounts of W, Ni and Co powders to obtain the alloy compositions. In the alloy systems studied, the W content was chosen as 90 and 95 wt% and the Ni/Co mass ratio was varied as 1/1, 3/1 and 6/1. The composition of the alloys investigated in this study is given in Table 2. Mixing operation was performed in a turbula mixer (T2F, Glenn Mills, Switzerland) at a speed of 80 rpm for 40 minutes. Mixed powders were compacted by cold isostatic pressing (CIP 42260, Flow Autoclave Engineers, USA) at 310 MPa for 15 seconds. The compacted samples were then sintered at 1475, 1500, 1525ºC. Heating rate up to 1000 ºC is 10 ºC/min and at this temperature samples were hold for 30 minutes. Further heating was performed with 10 ºC/min ramp rate up to 1350 ºC and it was decreased to 5 ºC/min to final sintering temperature. Sintering was completed after holding at the determined sintering temperatures for 60 minutes and samples were then cooled down to room temperature with 10 ºC /min. Sintering process was conducted in a horizontal tube furnace (PTF105, Protherm Furnaces, Turkey) under pure hydrogen gas flow at a rate of 0.5 l/min.

Table 1. General Properties of the Elemental Powders

Elemental Powder	Average Particle Size (μm)	Shape	Purity (wt%)
W	4.8	Polygonal	99.9+
Co	6.0	Polygonal	99.9+
Ni	4.3	Polygonal	99.9

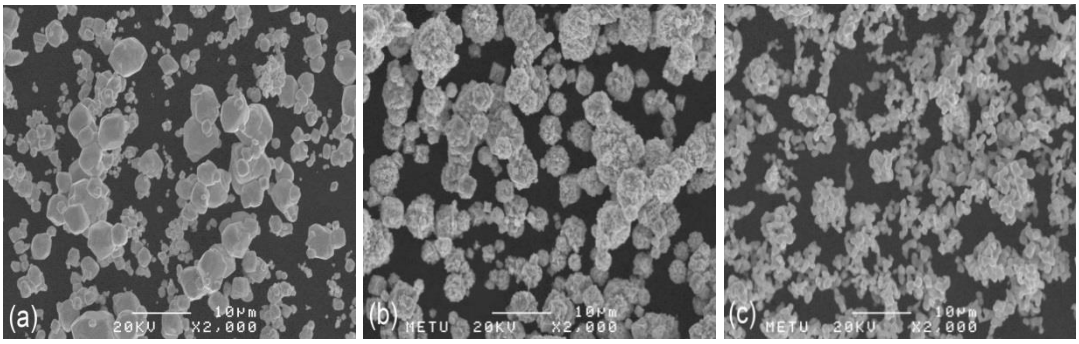

Figure 1. The general morphology of the elemental powders used in the study (a) W, (b) Ni and (c) Co (x2000), SEM images

Table 2. Compositions of the Alloys Investigated in This Study

Alloy Code	W (wt%)	Ni (wt%)	Co (wt%)	Ni/Co ratio
0W11	90	5.0	5.0	1/1
0W31	90	7.5	2.5	3/1
0W61	90	8.6	1.4	6/1
5W11	95	2.5	2.5	1/1
5W31	95	3.75	1.25	3/1
5W61	95	4.3	0.7	6/1

Sintered alloys were characterized by determining their microstructural properties. Densities of the alloys were measured by Archimedes water immersion technique by using xylene having a density of 0.86 g/cm^3. For microstructural characterization, specimens were prepared with proper metallographic techniques and etched by Murakami's etchant. The microstructure analysis of the alloys was performed by an optical microscope (Axioskop 2, Zeiss, Germany) and a scanning electron microscope (6400 JSM, Jeol, Japan). Hardness tests were applied to the sintered specimens with Vickers diamond indenter in HV10 scale (Duramin 500 Universal Hardness Tester, Struers, Denmark).

3. RESULTS and DISCUSSION

Archimedes immersion method was used to measure the densities of the alloy specimens. The percent relative density (%RD) of the alloys formed in this investigation are given Table 3. It is found that all the alloys reached nearly full density for all sintering temperatures.

Microstructural examination has shown that sintering temperature of 1475°C is not sufficient to obtain whole liquid phase sintering for 0W11 and 5W11 alloys, which can be seen Figure 2. It is suggested that these alloys exhibited mixed sintering type; i.e. both solid and liquid phase sintering. From the given microstructures, it is implied that all investigated alloys were in the presence of a liquid binder matrix phase at investigated sintering temperatures except 0W11 and 5W11 sintered at 1475°C. Also, it can be thought that LPS sintering enhances the densification behavior of examined alloys.

On the other hand, all Ni/Co ratio 1/1 alloys were found to have a two-phase binder matrix sintered at 1475, 1500 and 1525°C. From the back scattered electron images, it is observed

that binder matrix phase of these alloys consist of darker and brighter regions. Representative microstructures of 5W11 alloy showing this structure sintered at different sintering temperatures is given in Figure 3.

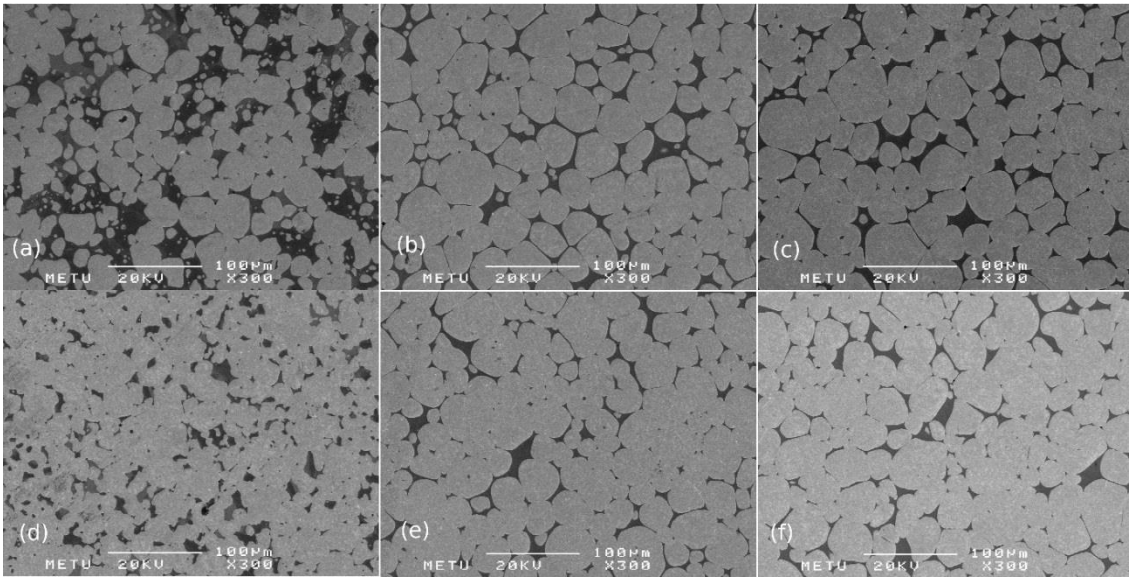

Figure 2. Microstructures of (a) 0W11, (b) 0W31, (c) 0W61, (d) 5W11, (e) 5W31 and (f) 5W61 alloys sintered at 1475°C, (x300), SEM secondary electron images

Table 3. The percent relative density (%RD) of the investigated alloys

Alloy Code	Relative Density (%)		
	Sintering Temperature (°C)		
	1475	1500	1525
0W11	100	100	98.5
0W31	99.5	99.3	100
0W61	99.7	99.2	99.9
5W11	99.3	100	99.3
5W31	99.4	99.2	100
5W61	99.5	99.4	99.9

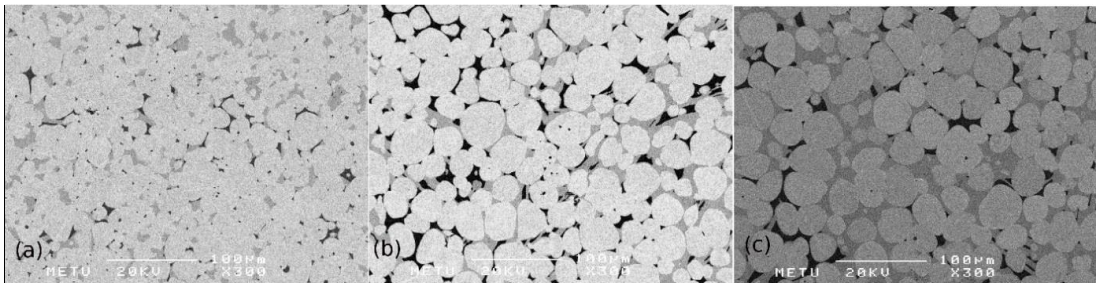

Figure 3. Microstructures showing 5W11 alloy sintered at (a) 1475°C, (b) 1500°C and (c) 1525°C, (x300), SEM back scattered images

Hardness measurements were done with Vickers diamond indenter in HV10 scale and the result are tabulated in Table 4. In Figure 4 and Figure 5 the hardness variation with increasing sintering temperature is given for both 90 and 95 wt% W alloys. From these figures, it is observed that no systematic changes can be found in hardness of alloys with increasing sintering temperature. On the other hand, the hardness values for Ni/Co ratio 3/1 and 6/1 with both 90 and 95 wt% W alloys are close to each other for all sintering temperatures, as seen in Table 4. The reason can be explained as that, as can be seen in Figure 2, these alloys have similar W grain size and matrix area. In addition, increasing the sintering temperature did not change the W content of the binder matrix phase dramatically for such alloys. Therefore, these comparably similar microstructures make hardness measurements very close to each other for 0W31, 0W61, 5W31 and 5W61 alloys.

On the contrary, the hardnesses of 0W11 and 5W11 alloys are higher than the remaining alloys for all sintering temperatures. The main microstructural difference of 0W11 and 5W11 alloys when compared to other alloys is the two-phase binder matrix (refer to Figure 3). The higher hardness obtained from 0W11 and 5W11 alloys is therefore attributed to this hard two-phase binder matrix. Also, this direct relationship between the hardness and the two-phase binder amount gives a strong indication that the hardness enhancement in the Ni/Co ratio 1/1 alloys is mainly determined by the two-phase binder matrix. In addition, it is expected that increasing W content in WHAs makes binder matrix area smaller. Comparing the microstructure in Figure 2 (a) and (d), one can realize that 0W11 has higher binder phase area than 5W11 sintered at 1475°C. Hence, larger binder matrix area makes 0W11 alloy harder than for 5W11 alloy for all sintering temperature. Consequently, the existence a two-phase binder matrix seems to be more beneficial for hardness enhancement in W-Ni-Co alloys, when compared to a single phase matrix.

Table 4. Hardness measurements for investigated alloys

Sintering Temperature (°C)	**Hardness (HV10)**					
	Alloy Code					
	90 wt% W			95 wt% W		
	0W11	**0W31**	**0W61**	**5W11**	**5W31**	**5W61**
1475	429±0.9	345±1.4	343±4.5	413±2.1	347±4.2	347±0.8
1500	433±8.3	338±2.9	343±1.6	402±0.5	353±0.5	346±4.3
1525	463±9.4	334±4.5	337±3.7	411±3.7	340±2.4	344±0.8

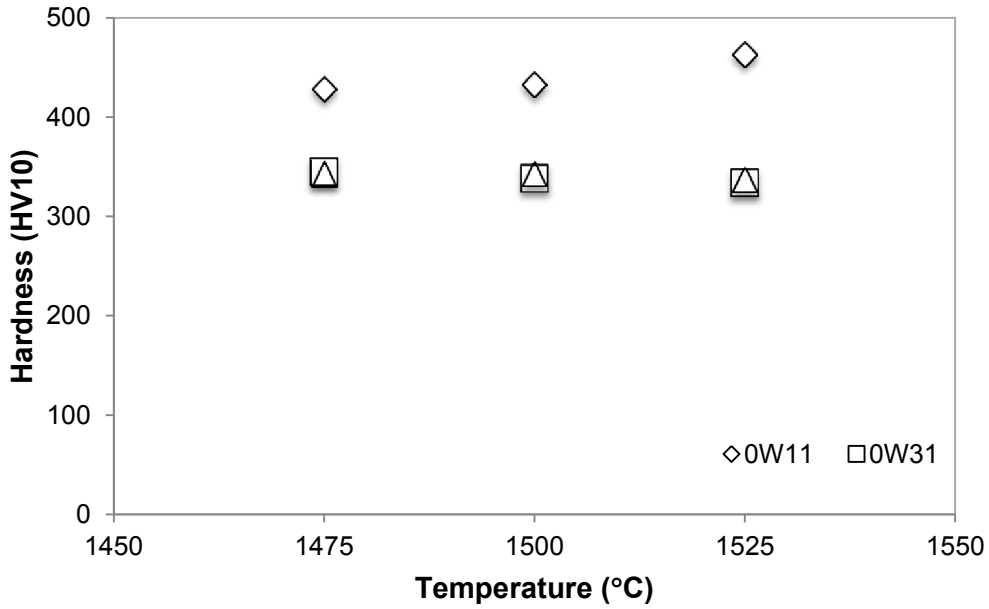

Figure 4. Hardness variation with increasing sintering temperature for alloys 0W11, 0W31 and 0W61

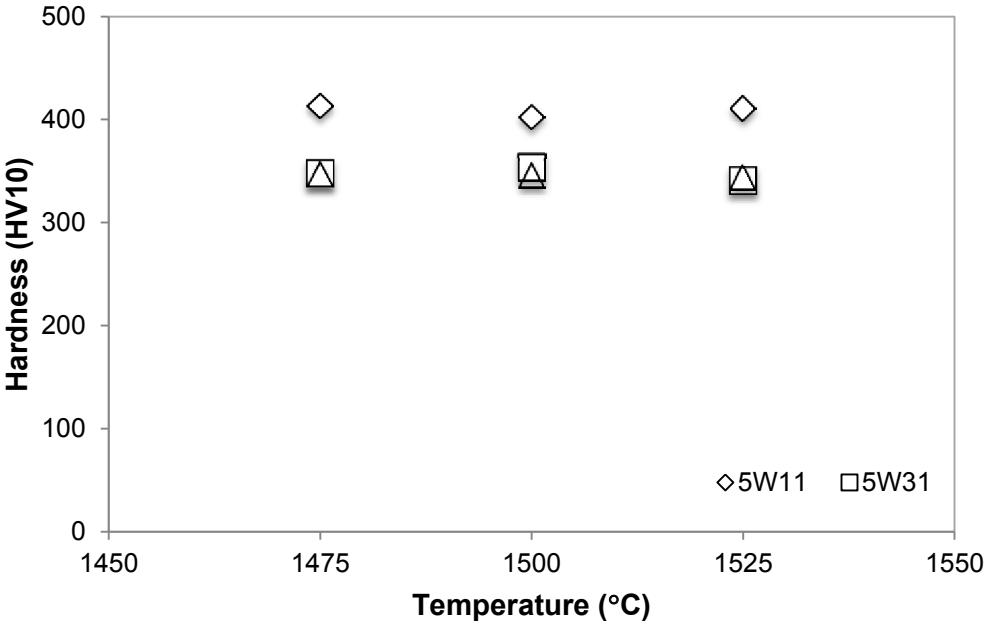

Figure 5. Hardness variation with increasing sintering temperature for alloys 5W11, 5W31 and 5W61

4. CONCLUSIONS

Variation of microstructure and hardness with composition for W-Ni-Co heavy alloys were investigated in this study. The following conclusions were drawn for this study:

1. All specimens reached nearly full density at all sintering temperatures.
2. The microstructure of all investigated alloys except 0W11 and 5W11 sintered at 1475°C is typical LPS microstructure, which consist of rounded W grains and a binder matrix. For 0W11 and 5W11 alloys sintered at 1475°C, it is thought that the sintering temperature and time are not sufficient to obtain ordinary microstructure. In contrast, all of the alloys with Ni/Co ratio 1/1 consist of nearly pure W grains and a two-phase binder matrix for all sintering temperatures.
3. Hardnesses of Ni/Co ratio 3/1 and 6/1 alloys for both 90 and 95 wt% W (alloys 0W31, 0W61, 5W31, 5W61) are close to each other for all sintering temperatures. On the other hand, 0W11 and 5W11 alloys have higher hardness than remaining alloys. This phenomenon has been attributed to the presence of a two-phase binder matrix in Ni/Co ratio 1/1 alloys.
4. 0W11 alloys have higher hardness compared to 5W11 alloys for all sintering temperatures. This may be explained with higher hard two phase binder matrix content of 0W11 alloys.

Acknowledgements

This study was supported by TÜBİTAK SAGE and Middle East Technical University.

REFERENCES

1. German, R. M., Bourguignon, L. L., & Rabin, B. H. (1985). Microstructure limitations of high tungsten content heavy alloys. JOM, 37(8), 36-39.
2. Bose, A., & German, R. M. (1990). Matrix composition effects on the tensile properties of tungsten-molybdenum heavy alloys. Metallurgical and Materials Transactions A, 21(5), 1325-1327.
3. Boris Katavik, Milutin Nikacevic, Properties of the cold swaged and strain aged P/M 91W–6Ni–3Co heavy alloy. Second International Conference on:Deformation Processing and Structure of Materials, May 26–28, 2005,Belgrade, Serbia and Montenegro. pp. 135–140.
4. Ryu, H. J., Hong, S. H., & Baek, W. H. (2000). Microstructure and mechanical properties of mechanically alloyed and solid-state sintered tungsten heavy alloys. Materials Science and Engineering: A, 291(1), 91-96.
5. Das, J., Kiran, U. R., Chakraborty, A., & Prasad, N. E. (2009). Hardness and tensile properties of tungsten based heavy alloys prepared by liquid phase sintering technique. International Journal of Refractory Metals and Hard Materials, 27(3), 577-583.

MACRO AND MICRO POROSITY CONTENTS OF LOW ALLOY STEEL FOAMS

Nuray BEKÖZ*, Enver OKTAY*

*Metallurgical and Materials Engineering Department, Istanbul University, Turkey
nbekoz@istanbul.edu.tr; oktay@istanbul.edu.tr

ABSTRACT

Low alloy steel (Fe-1.75 Ni-1.5 Cu-0.5 Mo-0.2 C) foams having total porosities in the range of 47.2-71.8%, produced by the space holder-water leaching technique in powder metallurgy. The foams produced using this technique were observed to contain mainly two types of pores: macropores formed as a result of the spacer, and micropores in the cell walls presumably resulting from the compaction and sintering during processing. The amount, size, shape and size distributions of the pores were determined using Clemex Vision PE commercial image-analyzer software. The densification of the green specimens was investigated as a function of spacer content. The results showed that the size and amount of macropores increased with increasing spacer content, but the size and amount of micropores decreased. Spacer fraction has a considerable effect on the densification during compaction of steel-spacer powder mixtures. The green densities increased with decreasing of spacer fraction, but the densification decreased.

Keywords: Steel foam, powder metallurgy, macro and micropore, mechanical property.

DÜŞÜK ALAŞIMLI ÇELİK KÖPÜKLERİN MAKRO VE MİKRO GÖZENEK ORANLARI

ÖZET

%47.2-71.8 gözenek oranlarında düşük alaşımlı çelik (Fe-1.75 Ni-1.5 Cu-0.5 Mo-0.2 C) köpükler toz metalurjisindeki boşluk yapıcı-suda çözündürme tekniği ile üretilmiştir. Bu teknikle üretilen köpüklerde temelde iki tür gözenek oluşur: boşluk yapıcıdan kaynaklanan makro gözenekler ve kompaktlama-sinterlemenin bir sonucu olarak gözenek duvarlarında oluşan mikro gözenekler. Gözeneklerin miktarı, boyutu, şekli ve dağılımları; Clemex Vision PE görüntü analiz programı kullanılarak belirlenmiştir. Ham numunelerdeki yoğunlaşma, boşluk yapıcı miktarının bir fonksiyonu olarak araştırılmıştır. Sonuçlar; artan boşluk yapıcı miktarıyla makro gözeneklerin boyut ve miktarının arttığını fakat mikro gözeneklerin boyut ve miktarının azaldığını göstermiştir. Çelik-boşluk yapıcı toz karışımlarının kompaktlanması boyunca; boşluk yapıcı oranı yoğunlaşma üzerine önemli etkiye sahiptir. Boşluk yapıcı oranının azalması ile ham yoğunluklar artmış ancak yoğunlaşma azalmıştır.

***Anahtar kelimeler*:** Çelik köpük, toz metalurjisi, makro ve mikro gözenek, mekanik özellikler.

1. INTRODUCTION

Metal foams have become the new trend materials due to their low densities, good mechanical properties and some specialized functions like high energy absorption, novel physical, mechanical, thermal, electrical and acoustic properties. Among these, steel foams can be used

as high-functional and lightweight materials in various fields of structural and functional applications due to their suitable properties [1-2]. In recent years, remarkable processing technologies have been developed for manufacturing steel foams. The space holder-water leaching technique in powder metallurgy has been studied by many researches, and is rather cost effective, flexible and leads to desired properties [3-4]. The foams produced using this technique were observed to contain mainly two types of pores: macropores obtained as a result of spacer, and micropores in cell walls presumably resulting from the compaction and sintering process during the production of the metal foam [3,5]. Markaki and Clyne [6] studied the effect of cell wall structure in influencing the mechanical behavior of aluminium foams, and found that it is clear that the nature of the structure within the cell walls can have a significant effect on the mechanical behavior of metallic foams. Park and Nutt [7] reported that the deformation mechanisms depend on steel foams structure (both micro and macro), which is controlled by the process parameters employed. The majority of research on processing of porous metal having macro and micropores has the special interest in steel foams with open or closed cells. The processing of steel foams has been the subject of numerous studies that mainly focus on the macropores structure of the foams and mechanical properties [3-4]. However, the mechanical behavior of the foams is not only affected by the macropore structure of the foam, i.e. porosity content, shape and size of the macropores, but also depends on the micropores formed in the pore wall [6-9]. The use of steel foams in a large scale and successful applications of them depend on detailed understanding of the effect of these factors on the properties. However, there is still uncertainly about the role of these factors in determining the properties.

There are some issues that must be considered on the green strength of powder–spacer compacts. Laptev et al. [10] investigated the green strength of titanium–ammonium bicarbonate compacts, and found that green strength mainly depends on the compaction pressure and the amount of spacer. A few researchers [10-12] indicated that the volume fraction of hard and soft particles has an important affect on the compressibility of powder mixtures. Tuncer et al. [11] reported that the fraction of soft carbamide and hard titanium powder affected compaction efficiency of the powder mixture. Bouvard [12] observed the negative influence of hard particles on densification during compaction of powder mixture. Sintering phenomenon in the porous structure containing both micro and macropores are considered. Laptev et al. [13] reported that the shrinkage during sintering occurs mainly due to reduction in size of micropores in the titanium framework, i.e. pore walls. On the other hand, the macropores generally retain their size or even tend to grow. Manonukul et al. [14] reported that the shrinkage of the cellular structure was a function of the spacer fraction. In all mentioned above reasons, it is important to describe the influence of the ratio of spacer to steel powder in the mixture on the densification of green compacts. In this study, Cu-Ni-Mo based low alloy steel foams having different porosities were produced by the space holder-water leaching technique in powder metallurgy. This study primarily concerns the role of macropores in the foam and micropores formed in the pore wall as a function of the spacer volume fraction which influences the densification of the compacts.

2. EXPERIMENTAL PROCEDURES

Low alloy steel foams were produced by the space holder-water leaching technique in powder metallurgy using water atomized Distaloy AB steel powder, which is a registered trademark of Höganäs Company, Sweden. The chemical composition of the Distaloy AB steel powder was Fe-1.5 Cu-1.75 Ni-0.5 Mo. The powder premix consisted of 0.8% Zn-stearate as lubricant and 0.2% carbon added as fine graphite (UF4). The steel powder had a size distribution in the

range 45-150 µm with an average particle size of 112 µm and a rounded but irregular shape. As a space holder material, carbamide was used for its very high solubility in water. Spacer particles were crushed and sieved to obtain the fraction of -1000+710 µm with irregular shape. The weight ratios of the steel powder to the carbamide were calculated to obtain defined porosities in the range of 50-80% in the specimens. The binder for green strength was polyvinyl alcohol (PVA), supplied by Merck, Germany. Initially, PVA solution, which consists of 2.5 wt% PVA and water, was added to the steel powder as a binder. The steel powder and 5 wt% PVA solution were mixed manually. Mixing of the steel and carbamide powders were performed in a Turbula mixer for 60 min. The mixture then compacted at 200 MPa into cylindrical specimens with a diameter of 20 mm and height of about 10 mm. The green specimens were immersed in distilled water at room temperature to leach the carbamide. The PVA in the green specimens was thermally removed as a part of sintering cycle. The specimens were sintered at 1200 ºC for 60 min under high purity hydrogen in a horizontal tube furnace (Lenton, UK).

The densities of the green specimens were calculated from measurements of the specimens' weights and dimensions. The density and the fraction of open and closed porosity content of the sintered foams were determined by Archimedes' principle in boiling paraffin at 150 ºC for 1 hour for impregnation of open pores using a Sartorius precision balance equipped with a density-determination kit. The pore morphology of the foam specimens were examined by the scanning electron microscope (SEM) and optical microscopy. The porous specimens were infiltrated in vacuum by a low viscosity resin (Epofix, supplied by Struers) for optical examination. Macro and micro porosity content, shape and size distributions of the pores were determined using Clemex Vision PE commercial image-analyzer software.

3. RESULTS AND DISCUSSION

The green densities increased with decreasing of carbamide fraction but the densification decreased. Densification of the compacts having high carbamide content was slightly higher than those of compacts having lower carbamide content. Volume fractions of soft carbamide and hard steel powder affected compaction efficiency of the powder mixture for carbamide particles have a greater compactibility and reduces friction between steel particles during compaction. This is because densification is mainly by the plastic deformation of soft particles [12]. Laptev et al. [10] found that compactibility of titanium-ammonium bicarbonate mixtures depended on the volume fraction of ammonium bicarbonate, and densification of mixtures increased with an increasing amount of spacer. Also, Laptev et al. [13] claimed that the existence of spacer particles disrupt pressure transfer between titanium particles during compaction. This leads to a decrease in titanium framework density with increasing amount of the spacers. Tuncer et al. [11] reported that the spacer–spacer and titanium–spacer contacts are easier to distort compared to titanium–titanium contacts. Similar effects were obtained in this study.

Steel foams with porosities in the range of 47.2-71.8% were produced after sintering. The foams have densities between 2.20 g cm^{-3} and 4.12 g cm^{-3} and the total porosity of the specimens consists of 32.8-64.5% open and 7.3-14.4% closed porosity. The final porosity content was directly concerned to the added fraction of carbamide. As the spacer content increased, the sintered density decreased and the total porosity increased in all compacts. Open porosity of the specimens also increased when the total porosity level of the sintered specimens increased. It is expected that connection possibility of the pores in the sintered

specimens will increase at high porosity levels. Figure 1 shows photograph of sintered steel foams.

Figure 1. Photograph of the sintered steel foams

Sintering caused 5.16% to 7.21% volumetric shrinkage in the specimens, and the shrinkage increased with increasing porosity. Substantial densification occurred during sintering, although carbamide was removed from the green specimens. Shrinkage increased as the volume fraction of macropores increased since the shrinkage during sintering varies inversely with green density. Bekoz and Oktay [3] and Manonukul et al. [14] studied the sintering shrinkage of steel foams, and also found that shrinkage was a function of the spacer volume fraction. It was observed that the densification of the foams increased with increasing spacer content, in agreement with the report of Laptev et al. [10]. Esen and Bor [15] reported that the titanium foam compacts shrink to some extent during sintering stage due to the combined effect of connection of pores and sintering shrinkage in the walls.

SEM image of the surfaces of the foams having 53.7% porosity is given in Figure 2(a). The specimens have a relatively uniform pore distribution. Cell walls separating each pore from its neighbors can be clearly seen. The morphology of the final pores was similar to that of the carbamide particles. No cracks were observed in the highly porous structures, however large numbers of micropores formed in the cell walls. A closer view of pore walls can be observed in Figure 2(b), which shows micropores apparent in the cell walls due to incomplete sintering of the steel powder.

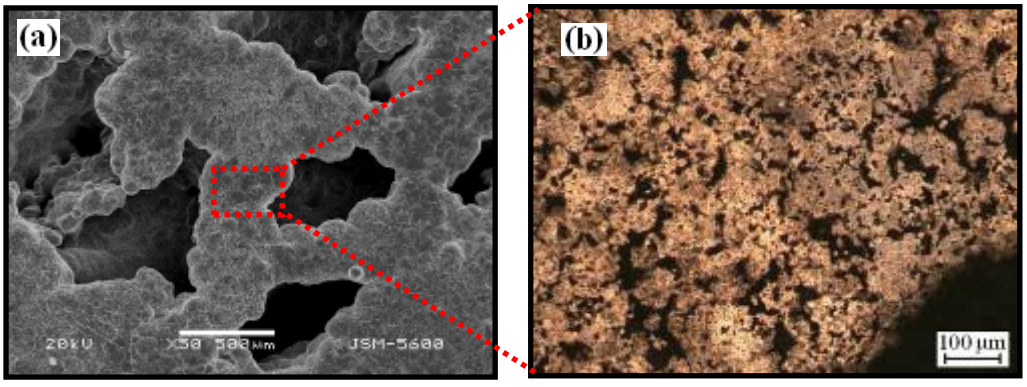

Figure 2. (a) SEM image of the structure of the foam and (b) optical microscope image of the micropores formed in the pore walls

Although the macropores in the specimens seem to be isolated from each other, they are in fact connected through the micropores in the cell walls. The interconnectivity of the foams also increases with porosity. When microstructure properties varying with porosity content were consider, the foams having high porosity were expected to reduce the micropore content

due to densification of the pore wall. Image analyzer software was used to determine the content, shape and size distributions of the pores from optical images of the sintered foams. Figure 3(a) and (b) show the morphology of the macropores at high magnification and the image analyzer results on the morphology for the foam having 47.2% porosity, respectively. Figure 4 shows the relationship between total, macro and micro porosity content of the foams as a function of spacer volume fraction.

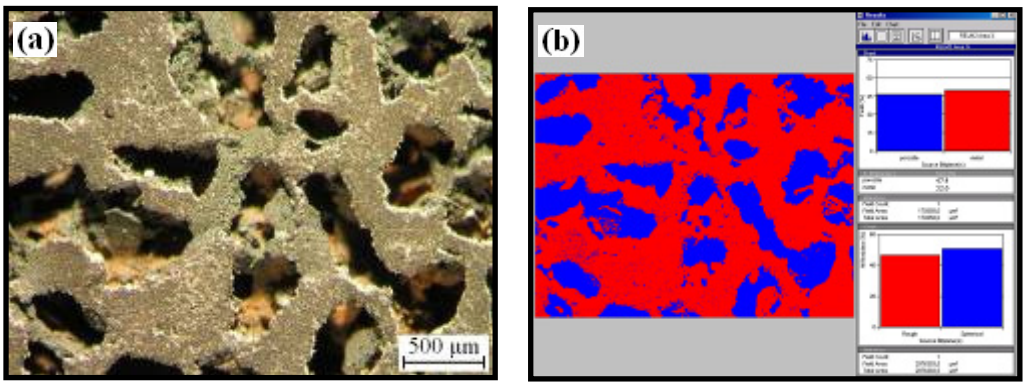

Figure 3. (a) Optical microscope image of the foam and, (b) Image analyzer illustration of macro morphology

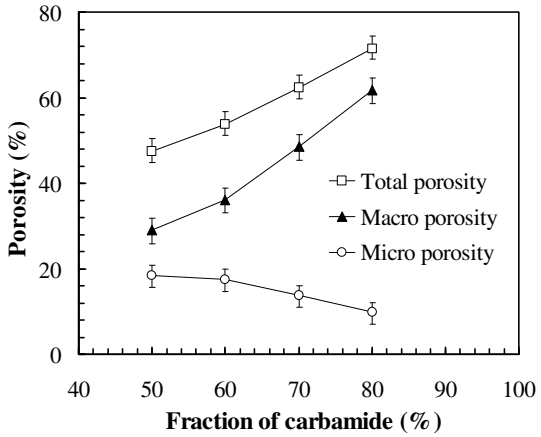

Figure 4. The change of total, macro and micro porosity contents of the foams with varied spacer amounts

The total amount of macro porosity increased with increasing carbamide content, whereas the micro porosity content decreased as the volume occupied by cell walls decreased with the macro porosity of specimens. These micropores in cell walls connect the macropores. While the interconnections in low porosity foams were achieved only by those micropores, macropores were connected directly as well as through micropores in high porosity foams. At a given porosity level, the enhanced number of contacts between steel particles in the case of using of high carbamide volume fraction leads to higher densification during sintering in the pore wall. The total porosity content of the low porosity foams is higher compared to initial spacer content of powder mixture mainly due to presence of partially sintered micro porous cell walls. Esen and Bor [15] reported that the total porosity content of foams does not match directly with the prior spacer content initially added to specimens mainly because of sintering shrinkage and partially sintered micro porous cell walls. The results in the present investigation showed that the relationship between micro and macropore contents of the steel foams varied depending on the spacer content due to the changes of contacts between steel

and spacer particles. Consequently, the densification of the mixture is higher when high fractions of spacer are used and, thus the content of micropore in the pore wall reduced. The relationship between the mean micropore and macropore size, and total porosity content of the foams is shown in Figure 5(a) and (b), respectively. The mean values of sphericity were between 0.54 and 0.62 for macropores and between 0.58 and 0.68 for micropores. The mean pore sizes were between 524.8 μm and 839.5 μm for macropores and between 121.6 μm and 148.2 μm for micropores.

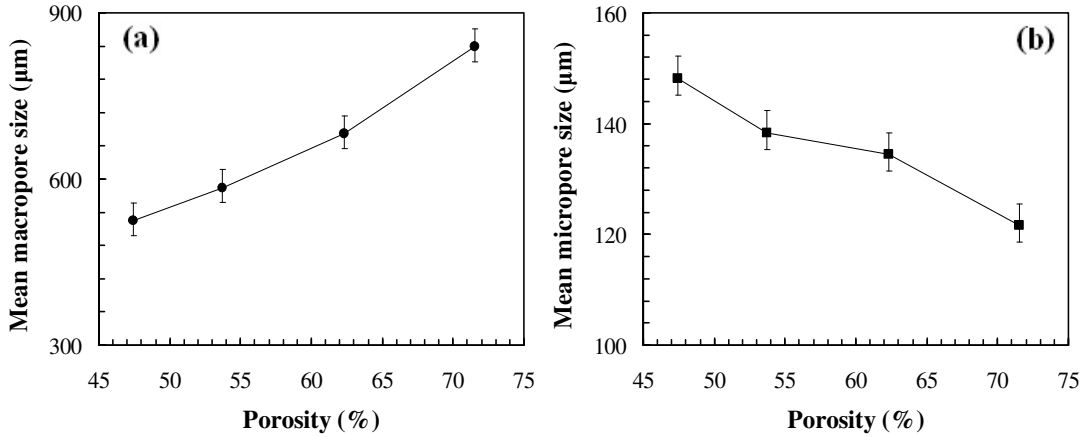

Figure 5. The change of (a) the mean macropore size and (b) the mean micropore size with varied porosities

As the total porosity content of the foams increased, the mean macropore size increased; however, mean sphericity values decreased as well mainly due to inter-connection of macropores at high porosity levels. As the total porosity content of the foams increased, mean micropore size value decreased. It was observed the positive influence of carbamide particles on densification during compaction of steel-carbamide mixture. This situation creates micropores within the pore walls, which decreased in number as a result of sintering with increasing amount of the spacer. Bafti and Habibolahzadeh [16] reported the resultant low compaction efficiency using low carbamide volume fraction leads to slightly higher microporosity content in the walls. The present results demonstrated that the mean spherical diameter and mean sphericity of macro and micropores changed as a function of the spacer volume fraction.

4. CONCLUSIONS

The role of the spacer fraction on the macropores in the foams and micropores in the pore walls investigated. The following conclusions can be drawn:

- Both the porosity content and size for the macro and micropores can be controlled by selecting the volume fraction of the carbamide particles; these have a considerable effect on the densification during compaction of steel-carbamide mixture.
- Two types of pores, macropore and micropore, were typically observed in the foams.
- The mean size and amount of macropore increased with increasing spacer content but the mean size and amount of micropores in the pore walls decreased.
- The micropore size and amount of the foams with high porosity are better than the foams with low porosity; however, the cell wall thickness is thinner.
- As a general conclusion, it is clear that the foam structure (macro and micro porosity) can have a significant effect on the properties of the steel foams.

Acknowledgements
This work was supported by Scientific Research Projects Coordination Unit of Istanbul University, Project number BYP-35272.

REFERENCES

1. B.H.Smith, S.Szyniszewski, J.F.Hajjar, B.W.Schafer and S.R.Arwade, J. Constr. Steel Res., 71, 1, 2012
2. A.Salimon, Y.Bréchet, M.F.Ashby and A.L.Greer, J. Mater. Sci., 40, 5793, 2005
3. N.Bekoz and E.Oktay, J. Mater. Process. Technol., 212, 2116, 2012
4. N.Bekoz and E.Oktay, Mater. Des., 51, 212, 2013
5. Z.Esen and Ş.Bor, Scr. Mater., 56, 341, 2007
6. A.E.Markaki and T.W.Clyne, Acta Mater., 49, 1677, 2001
7. C.Park and S.R.Nutt, Mater. Sci. Eng. A, 297, 62, 2001
8. N.Michailidis, F.Stergioudi, A.Tsouknidas and E.Pavlidou, Mater. Sci. Eng. A, 528, 1662, 2011
9. B.Jiang, N.Q.Zhao, C.S.Shi and J.J.Li, Scr. Mater., 53, 781, 2005
10. A.Laptev, O.Vyal, M.Bram, H.P.Buchkremer and D.Stöver, Powder Metall., 48, 358, 2005
11. N.Tuncer, G.Arslan, E.Maire and L.Salvo, Mater. Sci. Eng. A, 530, 633, 2011
12. D.Bouvard, Powder Technol., 111, 231, 2000
13. A.Laptev, M. Bram, H.P.Buchkremer and D.Stöver, Powder Metall., 47, 85, 2004
14. A.Manonukul, N.Muenya, F.Léaux and S.Amaranan, J. Mater. Process. Technol., 210, 529, 2010
15. Z.Esen and Ş.Bor, Mater. Sci. Eng. A, 528, 3200, 2011
16. H.Bafti and A. Habibolahzadeh, Mater. Des., 31, 4122, 2010

Ar-Ge - İnovasyon ve Teknoloji Yönetimi

•

R&D - Innovation and Technology Management

Tayfun Sığırtmaç

Coşkunöz Metal Form A.Ş. - Türkiye

ABSTRACT

Günümüzde toplumların gelişmişlik düzeylerini belirleyen önemli parametrelerden biri de teknoloji üretip değer yaratabilmektir.

Fakat teknoloji üretmek , bunu üretmeyi düşünmekle değil sistemli ve disiplinli bir çalışma, iyi bir temel bilimler bilgisi, derin araştırma ve geliştirme üzerine kurulu bir sistem, elde edilen araştırma sonuçlarının iyi analiz ve test edilmesi, labaratuar ortamlarında, Üniversite, Enstitü ya da ArGe merkezilerinde temelleri atılan bu araştırmaların sanayi ile ilişkilendirilmesi, çalışmaların pure ArGe'den toplum ve sanayiye değer yaratan bir forma dönüştürülme süreci ve tekrar teknolojik trendlerin ve toplum ihtiyaçlarının iyi analizi ile aynı döngünün tekrarı ile mümkündür. Aksi halde gelişmiş toplum ve ekonominin temelini oluşturan bu sarmalı iyi anlamaz isek, tüm zinciri sadece "bir fikrim var"' şeklindeki modelden öteye geçiremeyiz.

ArGe; çok özetle bilginin hem genişliğinin hem derinliğinin arttırıldığı, temel ve uygulamalı bilimlerin çokça kullanıldığı ve bir konuya/soruna odaklanarak yapılan, ciddi oranda kaynak (para, insan, ekipman, vb) gereksini olan araştırma ve geliştirme çalışmaları bütünüdür. Yani Para'nın bilgi'ye dönüşmesi sürecidir.

İnovasyon ise, sahip olduğunuz bilgi kaynaklarını kullanarak bu bilginin ekonomik değere dönüşmesi sürecidir. Altı sistematik ArGe faaliyetleri ve bilgi ile beslenmeyen inovasyon çalışmaları, büyük değerler ve önemli farklılıklar yaratamayan, küçük iyileştirmelerin ve o dönem için popüler bir kavram olmanın ötesine geçemez.

Teknoloji Yönetimi ise aslında size nasıl yapıldığını öğrendiğiniz bu ArGe ve İnovasyon süreçlerinde bir yol haritası oluşturmaktadır. Bugünün ilgili teknolojilerin gelişme süreçlerinin hangi evrelerinde, bu teknolojilerin alternatifleri neler ve ne zaman kullanılabilir hale gelecekler, Teknoloji yol Haritaları nasıl oluşturulur gibi soruların cevapları Teknoloji Yönetimi adı altında incelenmektedir. ArGe, İnovasyon ve Teknoloji Yönetimi süreçlerini gözardı eden Kodak gibi firmaları bekleyen kaçınılmaz son ile bu süreçleri iyi yöneten Samsung, Google gibi firmaların başarısı hepimiz için önemli birer örnektir.

Sizlerle, şirketlerdeki ArGe, İnovasyon ve Teknoloji Yönetim süreçlerini ne olduklarını, neden ve nasıl olması gerektiğini örneklerle paylaşmaya çalışacağım.

Keywords: Ar-Ge, inovasyon, teknoloji yönetimi, teknoloji yol haritası.

Endüstriyel Ar-Ge Çalışmalarında İşbirliği Mekanizmalarının Rolü

•

Role of Strategic Cooperations in Industrial Research and Development Activities

Altan Yıldırım

Farplas A.Ş. - Türkiye

ABSTRACT

Ülkemizde hızlı büyüme içerisinde olan endüstriyel firmalar kalite sistemleri dönüşümünü büyük oranda tamamlamış, üretim verimliliği, Ar-Ge ve inovasyona odaklanmaya başlamıştır. Yenilikçi çalışmaların en başında da malzeme geliştirme ve iyileştirme çalışmaları gelmektedir. Yenilikçi malzemelerin geliştirilmesi sürecinde karşılaşılan en önemli zorluk, tüm dünyadakine paralel olarak, bu çalışmalarda yer alacak yetkin personel ve teknik imkanların varlığı ve endüstrinin bu imkanlara ulaşımıdır. Firmada gerçekleştirilecek Ar-Ge çalışmasının başarıya ulaşabilmesi için, projenin teknik ve bilimsel derinliğine göre gereken bilgi ve tecrübenin yaratılması veya teknoloji transferi yapılarak firmada yerleştirilmesi gerekir. Radikal inovasyon seviyesindeki, önemli oranda ek katma değer yaratması amaçlanan çalışmalarda ise artık tüm dünyada işbirlikleri yapılmaktadır. Bu nedenle Üniversite-Sanayi, Sanayi-Sanayi ve Kamu-Üniversite-Sanayi işbirlikleri ciddi bir şekilde yönetilmesi gereken süreçlerdir. Bu seminerde işbirliği süreçlerinin dünyadaki örnekleri ve Türkiye'de uygulanabilirlikleri konusunda bilgiler verilecektir.

Keywords: Endüstriyel Ar-Ge, işbirliği mekanizmaları, radikal inovasyon.

Sanayi Kurumlarında Ar-Ge ve İnovasyon ile Katma Değerin Arttırılması

•

Increasing the Added Value by R&D and Innovation in Industry

Koray Mert Yılmaz

Cengiz Makine Sanayi - Türkiye

ABSTRACT

Inovasyon, bir işi, ürünü daha iyi yapabilmek, kullanıcıya kolaylık benzeri fayda sağlamak amacını güden, bunun için bulunan ve geliştirilen yeni bir yöntemdir. Bu yenilik ile pazarda var olan bir talep karşılanabilmektedir ve bu şekilde bilgi ticari bir materyale dönüşerek satılabilir hale gelmektedir. Araştırma ve Geliştirme ile oluşturulan orijinal ve doğal sonucu olarak da yeni bir fikrin pazara veya topluma bir ürün olarak tanınır hale gelmesi, diğer bir tabiriyle de pazara girmesidir. AR-GE toplumun ihtiyaçlarına veya üretilen bilgi veya ürünün ticari hayata faydasından ziyade bir problemin çözümüne odaklanırken, inovasyon bu bilginin toplum yararına, nasıl bir ürüne dönüştürülebileceğine odaklanır ve pazar ile AR-GE arasındaki köprüyü kurar. Her iki başlık da birbirlerinden bağımsız düşünülemez. Ortak noktaları orijinal olmaları ve yenilik getirebilmeleridir. Bugün inovasyon olarak nitelendirdiğimiz bir çok ticari başarının temelinde belki de çok uzun zaman öncesinde yapılmış bir çok AR-GE çalışması yatmaktadır.

Büyümenin ve istihdamın lokomotif sanayi dallarından olan İnşaat, Otomotiv ve Tekstil gibi sektörlerde Türkiye, 1950 li yıllarda başladığı sanayileşmesinde İnovasyon konularına bugüne kadar yeteri kadar yatırım yapmamış olmanın sıkıntılarını yaşamaktadır. İhracat rekorları kırılmasına rağmen ihraç edilen malın katma değerinin düşük olması, malzeme ve hammadde konusunda ithalata bağımlı olması ve gelişmiş ekonomilerdeki rakamların yarısından daha az olmasının en önemli nedenlerinden bir tanesi de inosvasyona yapılan yatırımın az olmasındandır.

Bu seminerde ülkemizde inovasyonun desteklenmesi için üniversite, devlet ve kurumlar üçgeninde yapılabilecek çalışmaları ve bunların örneklerini, gelişmiş ülkelerdeki uygulamalarla da karşılaştırarak paylaşmayı hedefliyorum.

Keywords: Katma değer, inovasyon, Ar-Ge.

Redefining Core Curriculum for Materials and Metallurgical Engineering

•

Malzeme ve Metalurji Mühendisliğinde Eğitim Programı Nasıl Olmalı?

Tayfur Öztürk

Middle East Technical University - Türkiye

ABSTRACT

Many of the engineering disciplines have grown out of basic sciences/natural philosophy in the end of 19 century and have turned into a well –defined disciplines in the 20th century. This is true for metallurgical engineering as in other engineering disciplines. Curriculum in the 60's and 70's were well defined and followed a sequence of courses on basic sciences, engineering sciences and specialized elective courses geared to particular industry in our field. Since then the curriculum has diversified enormously. Many of the programs today comprise courses on ceramic, polymeric materials, biomaterials, nanomaterials, etc. All these changes were implemented into the program by diversifying (mainly the fourth year) elective courses. However, the nature of changes is such that it is necessary to redefine the curriculum in such a manner that all these courses are not just additives but fully integrated into the program. This requires that a core curriculum should be redefined based on the existing needs and the future trends.

More space is needed in the core curriculum for basic sciences; biology has now a position similar to first year physics, chemistry and mathematics courses and would be useful to incorporate into the curriculum. It is necessary to redefine engineering sciences courses and some follow-up science courses on physics, chemistry and mathematics e.g. organic chemistry, solid state physics, numerical analysis etc. may be considered within this category. Luckily the use of computational software which is available in several main activity areas such as mechanics, thermodynamics etc. saves up valuable slots in the curriculum.

Elective courses may be built upon this core program where the aim is to illustrate the use of knowledge gained in the core program as well as to provide a framework to cover the multitude of materials, processes and applications.

Just as there is a need to re-question the curriculum, the same is also true for the mode of teaching. The ease of access to information has made the classical classroom teaching less exciting for students. Plus wealth of too much information has a disorienting effect on the students resulting in learn-and-erase attitude. Thus there is a need for guiding- perhaps passively - the students so that they will integrate what they learn in classroom environments. One mode of doing this would be to encourage students to pursue undergraduate research projects. In METU this has been implemented into the curriculum with material research courses which can be taken by students starting from second year onwards. This is particularly suitable for departments where they have well established research groups and infrastructure. The same may also be achieved with design projects which could be introduced quite early in the program. In short, the role of instructor is less to teach but more to stimulate the students to learn and be creative. This is particularly important because the role of university education is to "teach" students how to learn, an activity that bound to continue throughout their professional life and without the aid of an instructor nearby.

Keywords: Core curriculum, materials and metallurgical engineering, undergraduate reasearch projects.

Adoption of E-learning Tools in Metallurgical and Materials Engineering Education

•

Çevrimiçi Eğitim Araçlarının Metalurji ve Malzeme Mühendisliği Eğitimine Uyarlanması

Arda Çetin

Mühendishane - Türkiye

ABSTRACT

The higher education landscape have been dominated by the arise of MOOCs, a term that stands for Massive Online Open Courses, in the past few years and helped both universities and students to realize the potential of this new way of learning. Several universities have joined MOOCs, offering undergraduate level courses on almost every topic imaginable, and some of them have chosen to create their own open courseware, which lead to several different modes of online teaching, as well as different revenue models. In this talk, we will present an overview of different approaches to e-learning tools and discuss the obstacles to adoption of those tools by the university establishments, as well as the opportunities in this landscape. We will demonstrate a case study on how e-learning tools can be adapted to Metallurgical and Materials Engineering education, with the example of Muhendishane.org website.

Keywords: E-learning tools, massive online open courses, metallurgical and materials engineering.

Introducing Metallurgical and Materials Engineering to Prospective College Students

•

Lise Öğrencilerine Yönelik Metalurji ve Malzeme Mühendisliği Tanıtımları

Yunus Eren Kalay

Middle East Technical University - Türkiye

ABSTRACT

As compared to other engineering disciplines (i.e. electronics, mechanical and civil engineering), metallurgical and materials engineering is not sufficiently recognized between the high school students in Turkey. The traditional attempts towards to introducing the metallurgical and materials engineering i.e. annual short campus trips, everlasting university presentations seem to be incompetent. In order to increase the recognizability of the Metallurgy and Materials science, innovative approaches should be created particularly by university faculty and they should be effectively introduced to prospective college students. We have recently started an active program for bringing the notions of Metallurgy and Materials science together with the high school students. In this respect, several activities such as appearance in the social media, summer and winter schools; adapting electron microscopy into secondary education have been already established. Our current efforts, the future plans and possible collaborations within the respect of promoting Metallurgy and Materials science to prospective college students will be discussed in details.

Keywords: Metallurgical and materials engineering, high-school students, recognizability.

SEMI-SOLID FORMING AND PRESSURE DIE CASTING OF 7075-T6 ALUMINUM ALLOY WITH THERMAL ANALYSIS METHOD

Ahmet Umur GÜNGÖR , Ali KALKANLI***

* Middle East Technical University, Turkey
kalkanli@metu.edu.tr
** Middle East Technical University, Turkey
e155939@metu.edu.tr

ABSTRACT

7075 Aluminum alloy is widely used by aerospace and defense industries due to its low density and high strength. In this paper, the variation of surface hardness, mechanical properties and microstructure of 7075-T6 aluminum alloy production by semi-solid forming and pressure die casting methods are studied. In this study, target values are determined as 150HB hardness and 505MPa yield strength which are the properties of extrusion 7075-T6 alloy. Semi solid forming and pressure die casting methods are used as production methods. In this study, different temperature and pressure values are used.

Keywords: 7075-T6, semi-solid forming, pressure die casting

7075-T6 ALAŞIMININ TERMAL ANALİZ DESTEĞİ İLE YARI KATI ŞEKİLLENDİRME VE SIKIŞTIRMA DÖKÜM YÖNTEMLERİ İLE ÜRETİLMESİ

ÖZET

Bu çalışmada, 7075-T6 alaşımının yüzey sertliğinin, tane boyutlarının ve mekanik özelliklerinin, yarı katı şekillendirme ve sıkıştırma döküm yöntemleri ile nasıl değiştiği incelenmiştir. Bu alüminyum alaşımı düşük yoğunluk ve yüksek mukavemeti sebebi ile havacılık ve savunma sanayinde sıkça kullanılmaktadır. Bu çalışmada hedef 7075-T6 ekstrüzyon kütüğü değerleri olup 150HB sertlik ve 505MPa akma mukavemeti olarak belirlenmiştir. Deneylerde üretim yöntemi olarak sıkıştırma döküm ve yarı katı şekillendirme yöntemleri kullanılmıştır. Bu dene yöntemlerinde, çeşitli sıcaklık değerleri ve basınç değerleri denenmiştir.

***Anahtar kelimeler*:** 7075-T6, sıkıştırma döküm, yarı katı şekillendirme.

1. INTRODUCTION

Aluminum usage at industrial applications is getting increase day by day. Aluminum gets attention because of its low density values and adequate mechanical properties for industrial applications. 7075 is one of the aluminum alloys that have relatively higher mechanical properties than other aluminum alloys. Extruded 7075-T6 gives the highest mechanical properties than other production methods like casting or pressing etc.. In production of some complicate parts, extruded 7075-T6 is machined into final shape. If the complicate parts have hollow shape or need too much machining, production causes higher prices, loss of time and loss of raw material. That's why, other production methods are tried over years but none of them could have avoided failure.

In this paper, it is aimed to share knowledge and experience for this challenge. Semi-solid forming methods and pressure die casting method is used in experiments. Also, thermal analysis method is used to obtain optimum temperature values for semi-solid forming. As raw materials 7075 aluminum alloy and modified 7075 aluminum alloy are used. To obtain high mechanical properties T6 heat treatment is applied to the alloys.

2. EXPERIMENTAL PROCEDURES

2.1. Semi-Solid Forming with Vertical Pressure Die Casting

It is aimed to observe formability of 7075 at different temperatures and at different solid fractions. In this experiment, a vertical press with a die mold that have 90mm diameter is used (Figure 1.). 3 parts are cut from extruded 7075-T6 billet (40cm x 7.5cm x 2cm). 40cm is length, 2cm is thickness and 7.5 cm is width of the billet. Prepared specimens have dimensions as 7.5cm x 5cm x 2cm (Figure 2.). Then, specimens are put in a resistant furnace (Figure 3.) for heating up to desired temperatures. 3 different temperatures are used for this experiment; 580^{o}C, 595^{o}C and 605^{o}C. During preparations for pressing, die mold of vertical press is heated with a torch to 250^{o}C. After preparations, cut and heated specimens are placed in the pre-heated die mold with the 90mm diameter for pressing. Specimens are pressed with 150MPa pressure in the die mold. By this step, 3 semi-solid formed disks are produced.

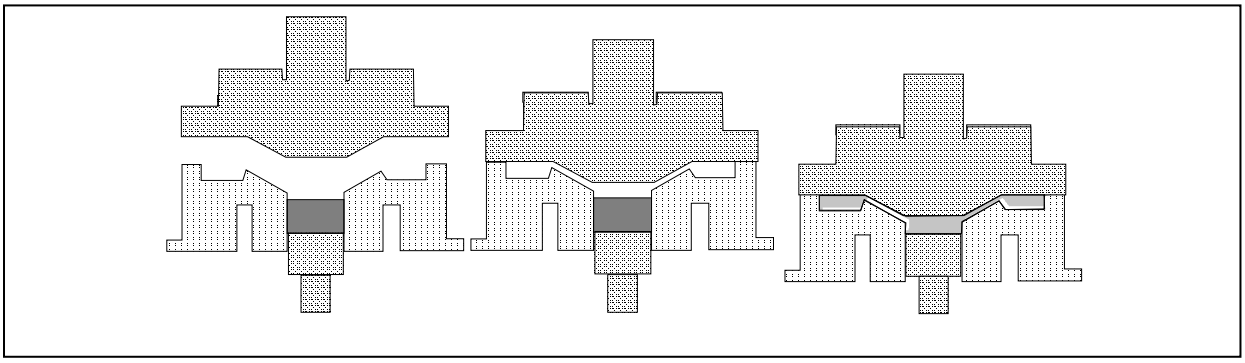

Figure 1. Die mold and working principle of vertical press.

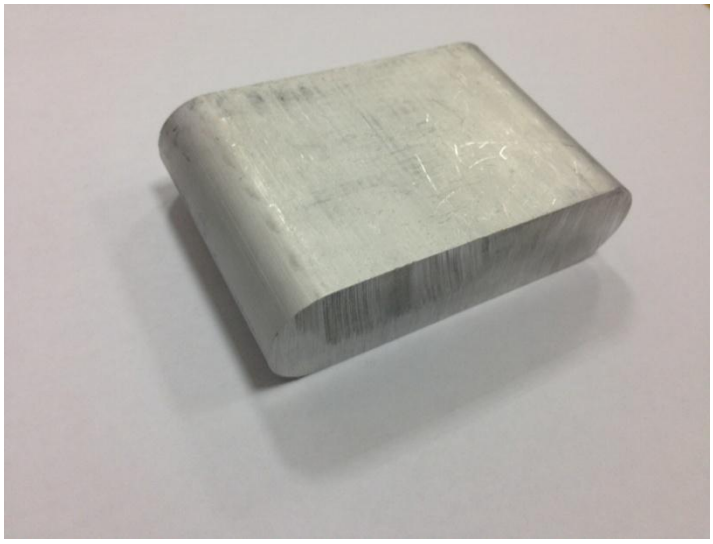

Figure 2. Cut specimen.

Figure 3. Resistant furnace that is used in experiments.

After production of disks, heat treatment is applied on the disks. T6 is chosen for heat treatment method due to its high mechanical properties. T6 heat treatment contains two types of treatment. First, parts are solutionized by heating up to solutionizing temperature and parts are kept at that temperature depending on its thickness, shape and production method. Afterwards, parts are quenched. Secondly, solutionized parts are artificially aged by again heating up to aging temperature. These temperatures for 7075 aluminum alloy are 480^{o}C for solutionizing temperature and 121^{o}C for artificial aging temperature.

Figure 4. Produced disks after T6 heat treatment.

2.2. Pressure Die Casting

In this experiment, aim is to observe mold filling properties of the 7075 alloy in a hollow shaped mold. The same vertical press with a die mold is used for this experiment. However, a different die mold is used in this experiment. This mold produces hollow shaped parts that have dimension as 31cm x 5cm x 3,5cm and a hollow part as in the figure 5. Extruded 7075-T6 billet is melted with an induction furnace. Then, melted 7075 aluminum alloy, which have 650^{o}C temperature is poured to the pre-heated die mold that have temperature less than 250^{o}C. 100 tones force is applied to the melted alloy in the die mold. By using this method 2 specimens are produced. After producing the specimens, specimens are heat treated with T6 as it is done on semi-solid forming with vertical pressure die casting specimens.

Figure 5. Produced hollow shaped parts after T6 heat treatment.

2.3. Semi-Solid Injection Molding

Aim for this experiment is to observe effects of solid fraction during pressing to mechanical properties of the 7075 alloy at an injection molding process. An injection molding machine is used in this experiment (Figure 6.). A die mold that can produce tensile test specimen and bending test specimen is used (Figure 7.). At the beginning, extruded 7075-T6 billet is melted with an induction molding. By the time, die mold is heated up to 200^{o}C. Before pouring the melted alloy, alloy is stirred with a thermocouple to cool the alloy down to desired temperatures. As alloy temperature reaches the below liquidus temperature, alloy is poured into shot sleeve and pressed. This part is press at 630^{o}C which is lower than the liquidus temperature of 7075. Liquidus temperature for 7075 is determined as 635^{o}C by ASM. However, this temperature depends on chemical composition of the alloy. Even the slightest changes in the composition can change liquidus temperature. Same procedure is repeated with a modified 7075 alloy. The chemical composition can be seen from Table 1. For this alloy, 5 different temperatures are used as pressing temperature. These temperatures are; 602^{o}C, 613^{o}C, 616^{o}C, 620^{o}C and 624^{o}C.

Figure 6. Injection molding machine that is used in experiment.

Figure 7. The die mold that can produce tensile test specimen and bending test specimen.

Table 1. Chemical compositions of extruded 7075 alloy and the modified 7075 alloy

	Zn (wt. %)	Mg (wt. %)	Cu (wt. %)	Mn (wt. %)	Ti (wt. %)	Al
Extruded 7075-T6	6,04	2,06	1,20	0,10	0,04	Bal.
Modified 7075	6,96	4,68	2,63	0,05	0,04	Bal.

2.4. Thermal Analysis and Solid Fraction Calculations

This experiment is aimed to obtain solid fractions amount of the alloys at a temperature. Different cooling rates are also used to obtain wider understanding of solid fraction. Calculation of solid fraction can be done by many methods. However, it is determined that using Newtonian thermal analysis method is best for this case. In Newtonian thermal analysis method, a cooling curve should be obtained from a cooling material. Then, first derivative of the cooling curve is obtained which should give phase transformation temperatures of the material. After that, a zero curve or baseline should be drawn onto the first derivative of the cooling curve. Zero curve is drawn as is assumed that there are no phase transformation through phase transformation temperatures since data are collected by one thermocouple. At the end, the area between the zero curve and the first derivative should be integrated to obtain the solid fraction data.

For thermal analysis experiment, a K-type thermocouple and a data collector is used. For faster cooling rate, melted alloy is placed in a graphite pot which is covered with thermal blankets from sides to avoid heat loss from sides (Figure 8). For slower cooling rate, graphite pot with solid alloy in it, is placed inside the resistant furnace. Then, resistant furnace is heated above the melting temperature of alloy to melt the alloy. After melting is completed, K-type thermocouple is placed in the graphite pot and furnace is turned down to let alloy cool down slowly.

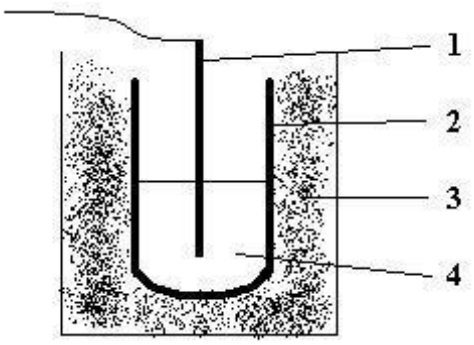

Figure 8. The graphite pot that is used in experiment (1. Thermocouple, 2. Graphite Pot, 3. Thermal Blanket, 4. Melted alloy).

As melted alloy is cooling, data is collected via thermocouple. This collected temperature vs. time data, computed in MATLAB program to obtain first derivative vs. time graph, zero curve and finally, solid fraction vs. temperature graph.

3. RESULTS AND DISCUSSION

Thermal Analysis and Solid Fraction Calculations Results

Thermal analysis and solid fraction calculation experiment is applied to modified 7075 aluminum alloys at 3 different cooling rate; 0.04^{o}C/s 0.25^{o}C/s and 0.38^{o}C/s. These cooling rates are obtained from experiments and they depend on environment and furnace conditions. According to the experimental data these graphs are found.

Modified 7075-1 aluminum alloy 0.04°C/s cooling rate results:

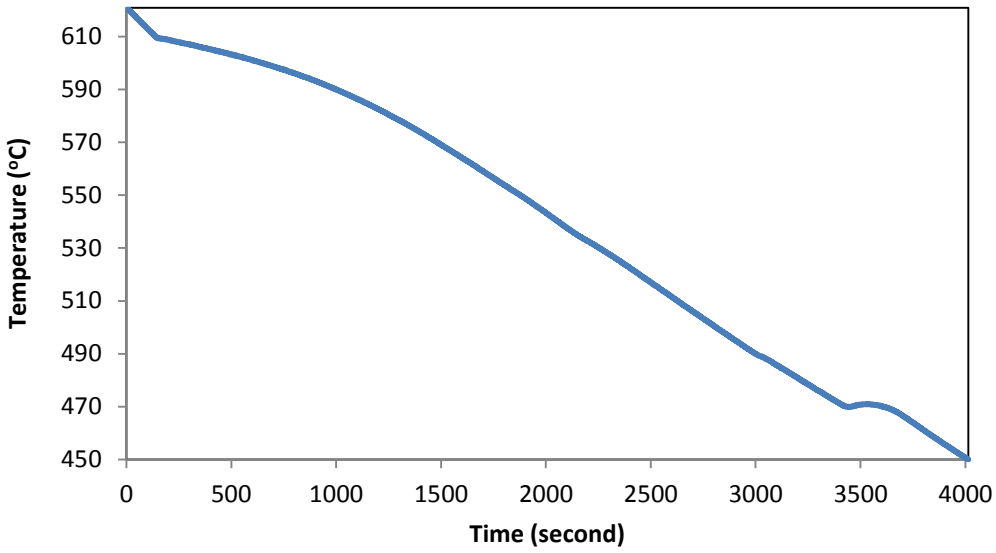

Figure 9. Temperature vs. time graph of modified 7075-1 aluminum alloy with 0.04°C/s cooling rate

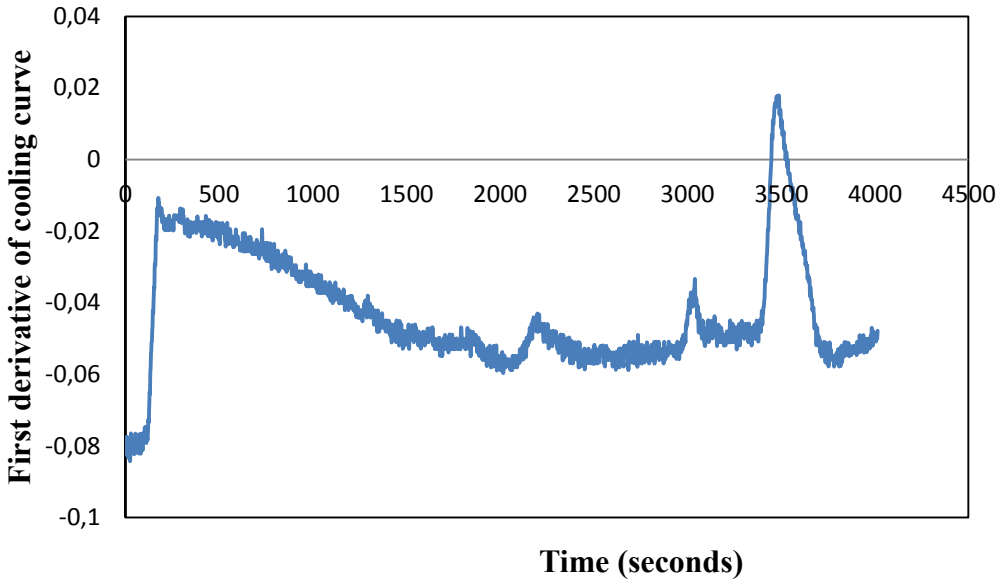

Figure 10. First derivative $\left(\frac{dT}{dt}\right)_{cc}$ vs. time graph of modified 7075-1 aluminum alloy with 0.04°C/s cooling rate

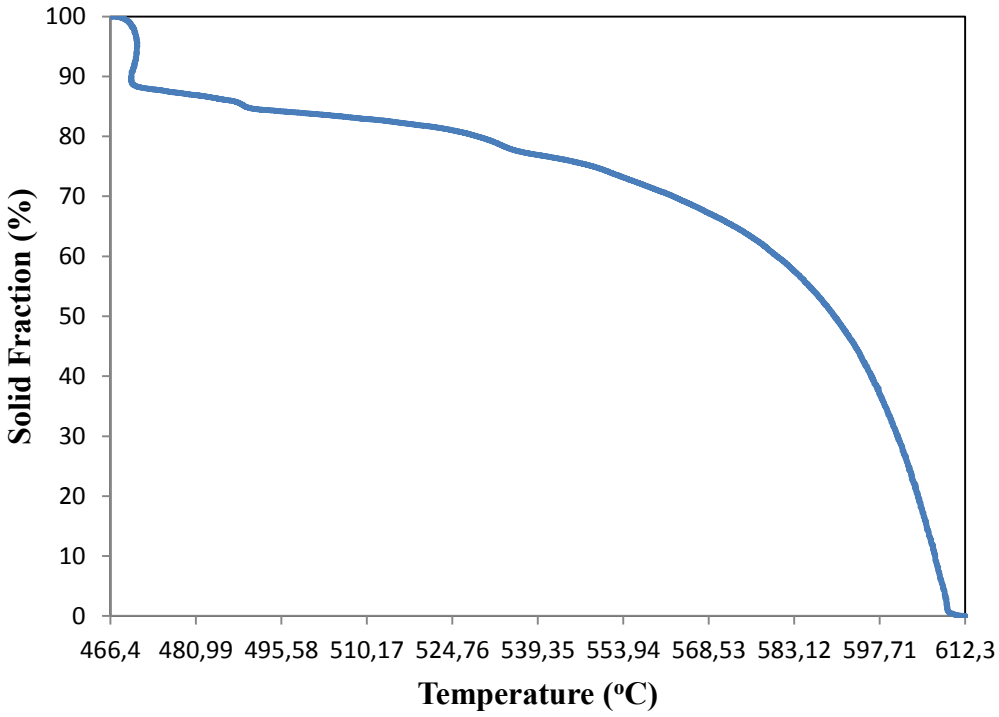

Figure 11. Solid fraction (%) vs. temperature graph of modified 7075-1 aluminum alloy with 0.04°C/s cooling rate

Modified 7075-1 aluminum alloy 0.25°C/s cooling rate results:

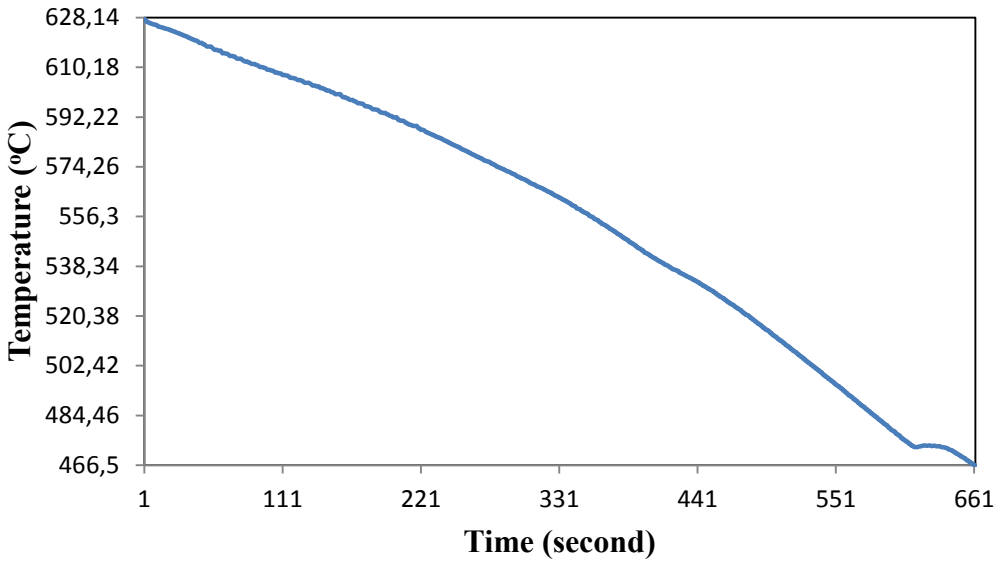

Figure 12. Temperature vs. time graph of modified 7075-1 aluminum alloy with 0.25°C/s cooling rate

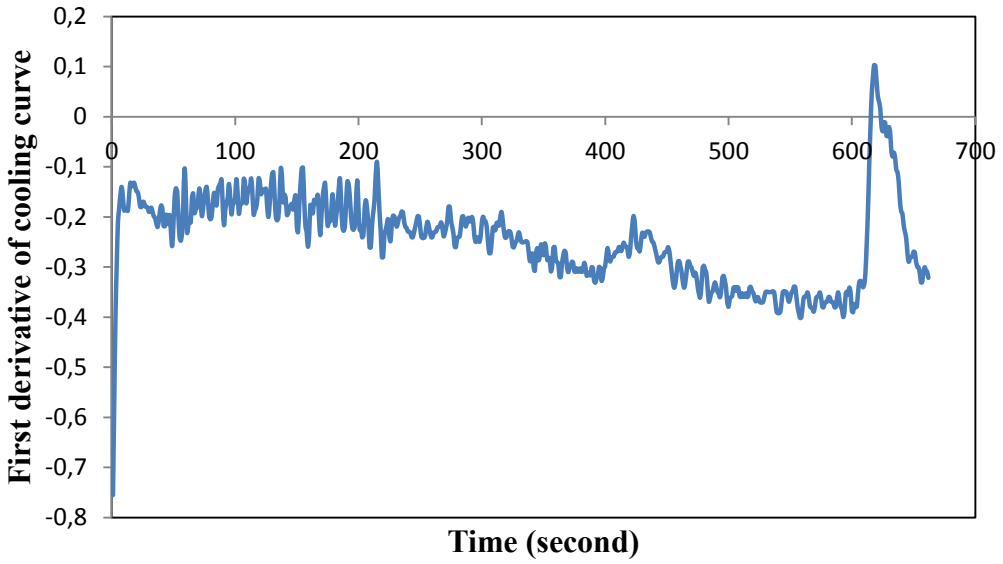

Figure 13. First derivative $\left(\frac{dT}{dt}\right)_{cc}$ vs. time graph of modified 7075-1 aluminum alloy with 0.25°C/s cooling rate

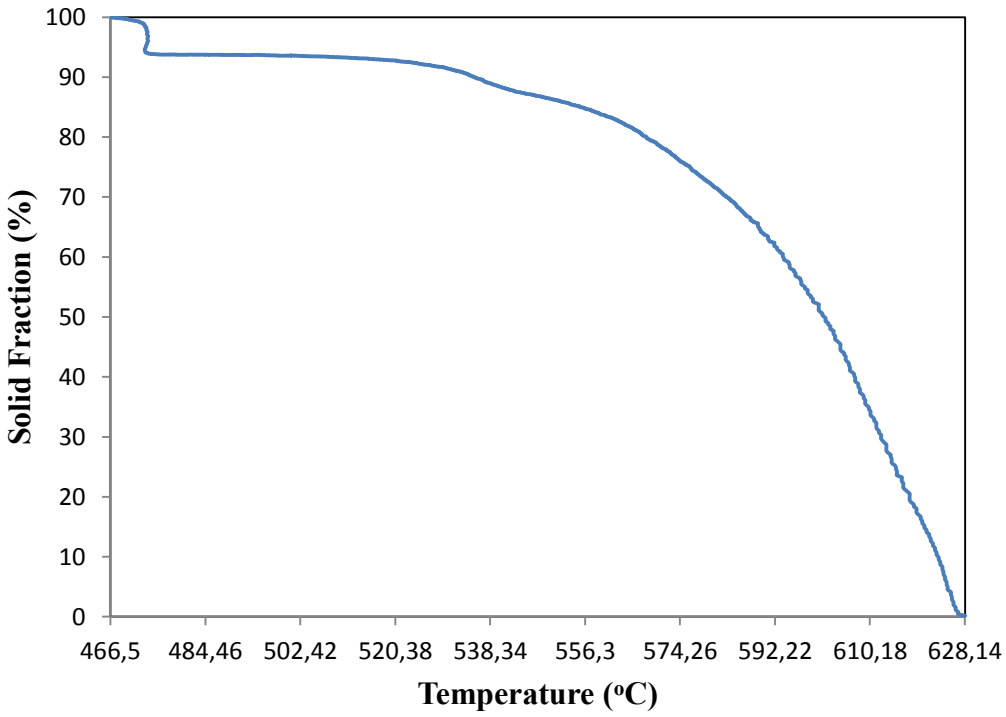

Figure 14. Solid fraction (%) vs. temperature graph of modified 7075-1 aluminum alloy with 0.25°C/s cooling rate

Modified 7075-2 aluminum alloy 0.38°C/s cooling rate results:

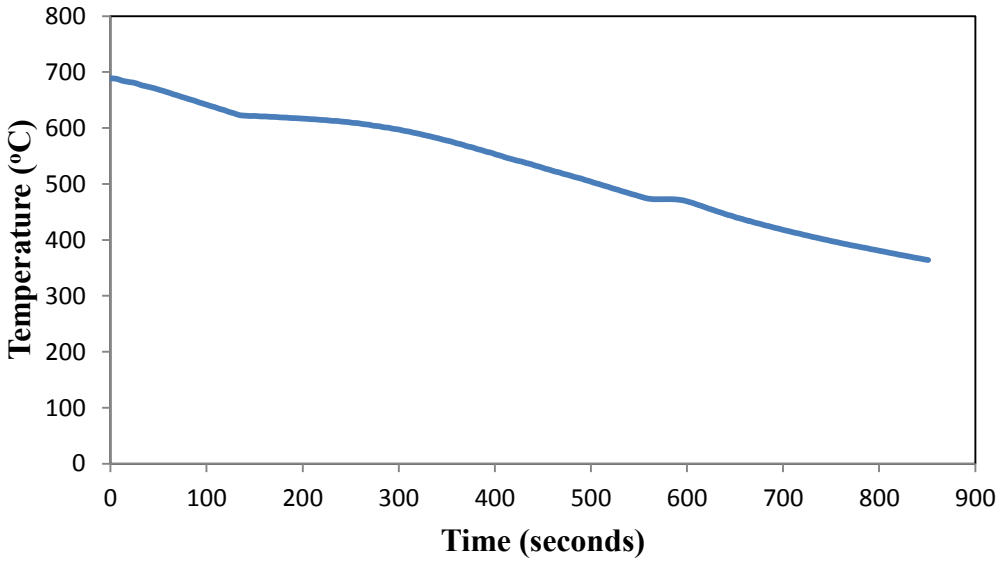

Figure 15. Temperature vs. time graph of modified 7075-2 aluminum alloy with 0.38°C/s cooling rate

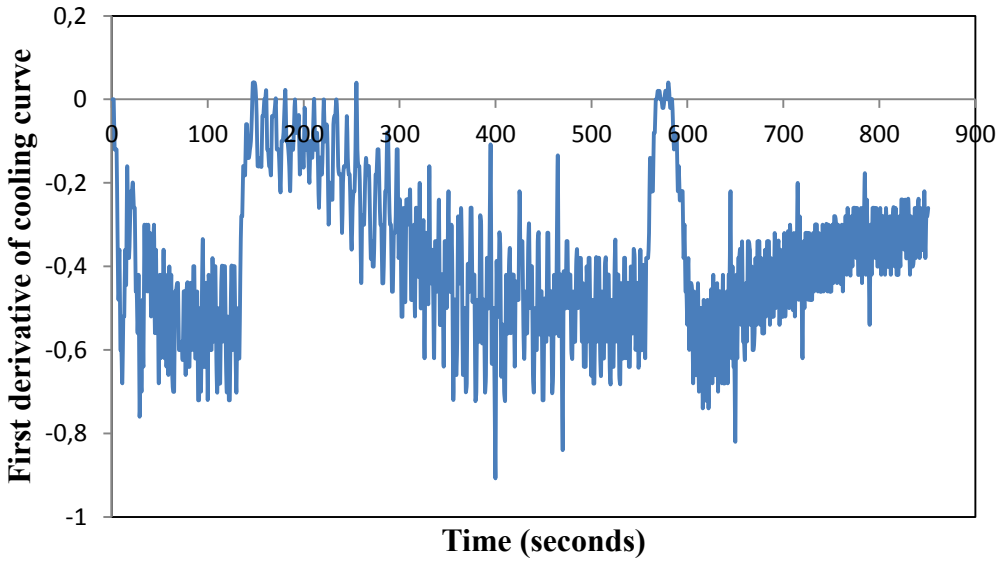

Figure 16. First derivative $\left(\frac{dT}{dt}\right)_{cc}$ vs. time graph of modified 7075-2 aluminum alloy with 0.38°C/s cooling rate.

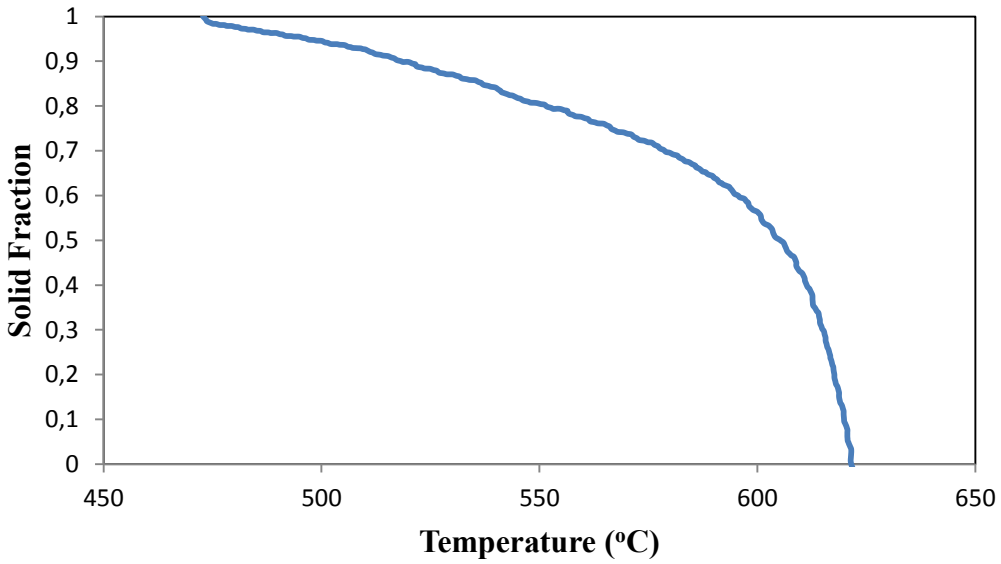

Figure 17. Solid fraction vs. temperature graph of modified 7075-2 aluminum alloy with 0.38°C/s cooling rate

Table 2 shows chemical composition differences between literature and this work. Table 3 also shows critical temperatures of these works. As comparing same cooling rates of different alloy, it can be said that liquidus temperature decreases with increasing amount of Mg added. It can be clearly seen that Zn and Cu addition to the alloy can only make liquidus decrease when modified 7075-1 and modified 7075-2 alloys compared. When these values are compared with the literature data, they show some differences due to chemical composition differences. These differences are caused because; alloys are supplied from different supplier. Even though Ahmad shows that solidus and eutectic temperatures are increasing with increasing cooling rate [1], in this work this trend cannot be obtained. This may be happened due to air flow and ambient temperature at the laboratory. Since, ambient temperature at the experiment area can affect cooling rates and solid fraction [4].

Table 2. Literature comparison of chemical compositions alloys used at thermal analysis experiment.

Source	Zn (wt. %)	Mg (wt. %)	Cu (wt. %)	Mn (wt. %)	Fe (wt. %)	Si (wt. %)	Ti (wt. %)	Al (wt. %)
Modified 7075-1	5,97	4,85	1,55	0,06	0,43	0,34	0,04	86,4
Modified 7075-2	6,96	4,68	2,63	0,05	0,23	0,21	0,04	84,9
Bäckerud[2]	-	2,49	1,36	-	0,28	0,11	-	Bal.
Ahmad[1]	6,04	2,38	2,02	0,12	0,24	0,14	0,09	88,5
ASM[3]	5,1-6,1	2,1-2,9	1,2-2,0	<0,3	<0,5	<0,4	<0,2	87,1-91,4

Table 3. Literature comparison of thermal data that are found in experiments.

Source	Cooling Rate (°C/s)	Liquidus Temperature(°C)	Eutectic Temperature(°C)	Solidus Temperature(°C)
7075	0,25	631,2	478,1	473,8
Modified 7075-1	0,04	623,1	476,2	471,1
Modified 7075-1	0,25	628,2	473,2	466,5
Modified 7075-2	0,38	621,5	485,3	472,8
Ahmad[1]	0,03	639,9	470,2	467,6
Ahmad[1]	0,21	638,0	474,7	470,2
Ahmad[1]	0,41	638,2	477,2	472,8
Bäckerud[2]	0,30	630,0	469,0	469,0
Bäckerud[2]	0,70	630,0	470,0	470,0
ASM[3]		635,0		477,0

As 7075 and modified 7075-1 are compared with the same cooling rate, it can be seen that liquidus temperature is almost the same. However, solidus and eutectic temperatures are different. It can be concluded from the results that Mg addition to the alloy decrease the eutectic and solidus temperatures.

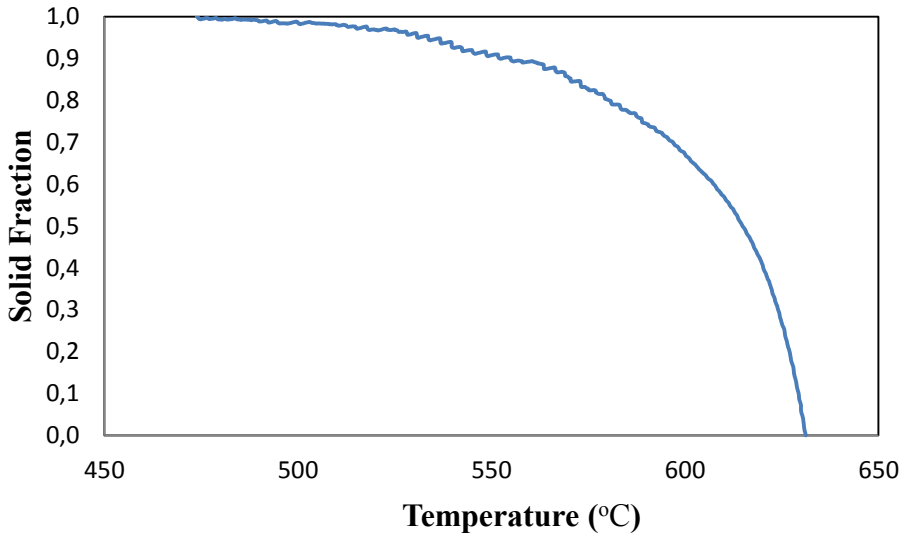

Figure 18. Solid fraction vs. temperature graph of 7075 extrusion billet.

Semi-Solid Forming with Vertical Pressure Die Casting Results

At semi-solid forming with vertical pressure die casting experiments, there are 3 parts that are produced and T6 heat treated. First part is formed at 580°C. This temperature corresponds to 0,8 solid fraction according to figure 18. Also thickness of this part is reduced from 20 mm to 13,9 mm. This part also has hardness value as 180HB. Second part is formed at 595°C which corresponds to 0,67 solid fraction. Thickness of this part is reduces from 20mm to 11,1 mm. This part has hardness value which is 173,4HB. Third part is formed at 605°C that matches with 0,62 solid fraction value. Third part has 158,7HB hardness value and also 10,8 mm thickness.

Table 4. Values of semi-solid forming with vertical pressure die casting experiments.

Part No.	Experimental Temperature (°C)	Solid Fraction	Thickness (mm)	Hardness (HB)	UTS (MPa)	Yield Strength (MPa)	Elongation (%)
1	580	0,8	13,9	180	246,6	212,5	2,6
2	595	0,67	11,1	173,4	583	526	4,6
3	605	0,62	10,8	158,7	302	292	0,9

It is seen from table 4 that as solid fraction increases, formability (thickness reduction) decreases. However, from a certain point of solid fraction formability do not change. Also, it can be observed that hardness values are decreasing as solid fraction decreases. It can be explained by precipitate densities of specimens. When parts are applied higher stress it becomes taking longer times to solitionize the parts, that's why there are differences between precipitate densities. Furthermore, UTS and elongation values can be seen as 2nd part has the highest UTS and elongation values. However, 1st and 3rd parts' tensile tests are resulted with a premature break due to cracks on the holding part of tensile specimen. Since, only 2nd part's tensile test is successfully resulted it cannot be possible to make a discussion about UTS change with respect to solid fraction change. On the other hand, it can be said that 0.67 solid fraction has reached the target value of 505MPa yield strength and 150HB hardness values. Table 5 illustrates a comparison between values of reduction rates and hardness values and precipitation densities. Precipitation density calculations are made by using Dewinter image analysis program. It calculates the precipitates' area over all area. Figures 19, 20 and 21 are the SEM photographs of parts. These pictures are given to give an opinion about precipitation size.

Table 5. Comparison between values of reduction rates, hardness values and second phase densities.

Part No.	Reduction Rate (%)	Hardness (HB)	Phase Densities (%)
1	30,5	180	2,096
2	44,5	173,4	1,534
3	46	159,7	1,058

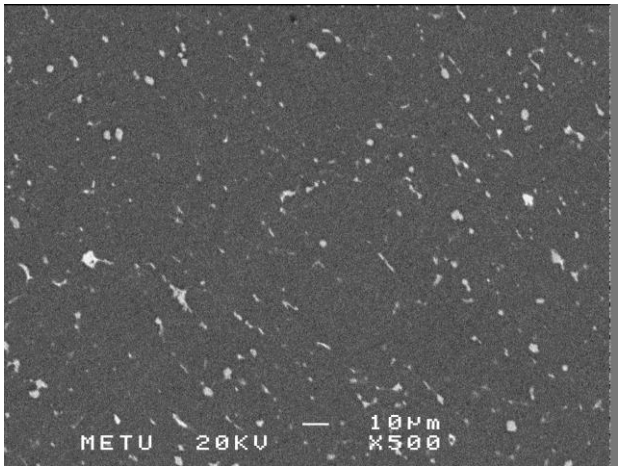

Figure 19. SEM picture of part 1.

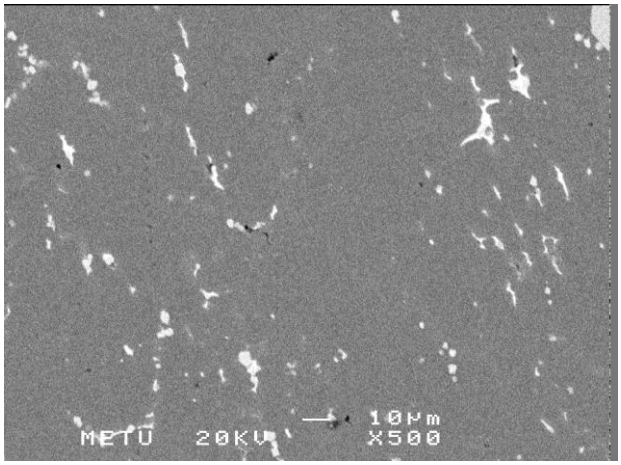

Figure 20. SEM picture of part 2.

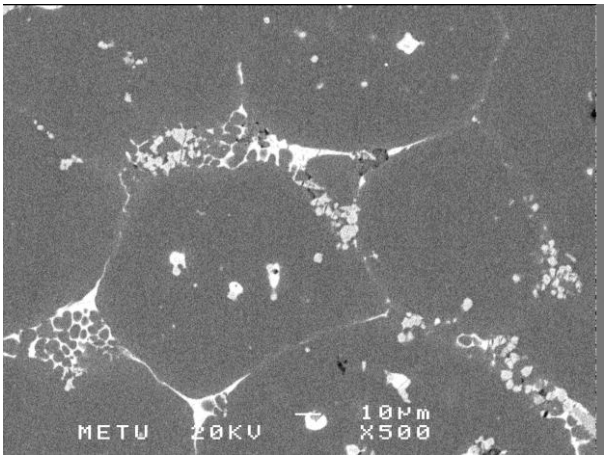

Figure 21. SEM picture of part 3.

Pressure Die Casting Results

Pressure die casting experiment is done at just above liquidus temperature of 7075 which is about 630^{o}C and then melted alloy is poured into the relatively cold die mold which is below 250^{o}C. It takes about 10-15 seconds to close the die mold and press the alloy. It is experienced that, 10 to 15 seconds cooling make great differences to alloys temperature. If it is considered as cooling in an isolated graphite pot, it would make its temperature just below liquidus. However, since there are more area to cool the melted alloy, cooling rate will be higher. From experience of modified 7075-2 with a cooling rate of 0,38^{o}C/s, it can be predicted that 1 or 2 ^{o}C cooling occurs during pressing which gives 4-8% solid phase amount. This small amount of solid causes some problems like hot tear [5] or liquid segregation [6] since it is assumed as thixoforming. 2 specimens are made by this method. One of them is made from 7075 extrusion billet and the other one is made from scrap 7075. Chemical composition differences between the two specimens are given at table 6. During macroscopic inspection of the specimens, it is seen that problems like surface cracks, shrinkage and bad surface quality are occurred. However, blister is not observed after T6 heat treatment to the specimens. Since, it not possible to make a tensile specimen due to the cracks, hardness values of specimens is investigated.

Table 6. Comparison of chemical compositions of alloys used at pressure die casting experiment.

Specimen	Zn (wt. %)	Mg (wt. %)	Cu (wt. %)	Fe (wt. %)	Si (wt. %)	Al (wt. %)
Extr. 7075	6,04	2,06	1,20	0,15	0,09	90,1
Scrap 7075	5,27	2,56	1,84	0,18	0,24	89,4

Table 7. Hardness values that are obtained from pressure die casting experiment

Specimen	Hardness (HB)
Extruded 7075	156
Scrap 7075	175

As can be seen from table 7 hardness values show some differences. This hardness difference is believed due to the chemical composition differences and heat distribution in the furnace during heat treatment because, harness values of extruded 7075 show gives hardness value distribution from 144HB to 173HB. Furthermore, T6 heat treatment may cause more precipitation to reveal like $MgZn_2$ which gives more hardness value [7].

Semi-Solid Injection Molding Results

In semi-solid injection molding experiment, 6 specimens from modified 7075-2 alloy and 2 specimens from extruded 7075 alloy are made. Specimens are pressed at 620°C, 616 °C, 602 °C, 624 °C, 613 °C and at liquid state by order from modified 7075-2 alloy. Also, 2 specimens from extruded 7075 alloy are pressed at 630°C. These temperatures correspond to 0.01, 0.265, 0.535, 0 and 0.351 solid fractions for modified 7075-2 and 0.04 to 0.075 solid fraction range for extruded 7075 respectively. Then, these specimens are heat treated with T6 heat treatment. 480°C for 17 hours to solutionize and 121°C for 34 hours to age artificially are used for modified 7075-2[8]. Previously used T6 times and temperatures are used for extruded 7075. After heat treatment, it is observed that large amount of oxidation occurred on the specimens (diameters of tensile specimens are enlarged from 19mm to approximately 20mm). Even though there are large oxidation on the surface, tensile test are made. At table 8, ultimate tensile strength, elongation at break, pouring temperature and solid fraction values can be seen.

Table 8. Ultimate tensile strength, elongation at fracture, pouring temperature and solid fraction values

Specimen	Pouring Temperature (°C)	Solid Fraction	UTS (MPa)	Elongation at fracture (%)
1st of mod. 7075-2	620	0,01	145,58	6,56
2nd of mod. 7075-2	616	0,265	115,36	7,69
3rd of mod. 7075-2	602	0,535	196,47	11,45
4th of mod. 7075-2	624	0	162,86	8,87
5th of mod. 7075-2	613	0,351	165,32	6,42
6th of mod. 7075-2	Above liquidus	0	207,58	5,91
1st of extr. 7075	630	0,04-0,075	268,03	4,16
2nd of extr. 7075	630	0,04-0,075	185,68	4,71

After tensile test, it is seen that porosities are present in the specimens that cause premature breaks. Moreover, 4th specimen of modified 7075-2 alloy has a hollow structure (Fig. 22). It is believed that happened due to small inlet mouth of tensile specimen mold at the die mold which causes atomization of alloy during filling the mold. Furthermore, this atomization lets air fill

porosities and cause blister problem. Since 630°C covers a range of solid fraction for extruded 7075 alloy, to make a conclusion is hard to do.

Figure 22. 4th specimen of modified7075-2 alloy after tensile test.

However, If UTS value of the 4th specimen is recalculated as area is replaced by the area at the break surface its UTS value becomes 405MPa. Form this point of view, porosities are calculated by weighting the specimens and calculating porosity content of 3rd specimen which has highest weight among other modified 7075-2 alloy specimens. Porosity calculation of 3rd specimen is done by Dewinter image analysis program. Porosity of other specimens assumed related to their weight with respect to 3rd specimen. Furthermore, according to recalculated 4th specimen's UTS value and porosity density other specimen's UTS values are recalculated as they have no porosity at all. Calculated porosities are given in table 9.

Table 9. Experimental and modified UTS values and porosities (underlined value is the base value of assumptions).

Specimen No.	Weight (g)	Porosity (%)	Modified UTS (MPa)	Solid Fraction
1st of mod. 7075-2	53,94	8,53	218,62	0,01
2nd of mod. 7075-2	53,43	9,39	179,07	0,265
3rd of mod. 7075-2	53,99	<u>8,45</u>	294,11	0,535
4th of mod. 7075-2	44,06	25,28	<u>405</u>	0
5th of mod. 7075-2	53,78	8,80	250,88	0,351

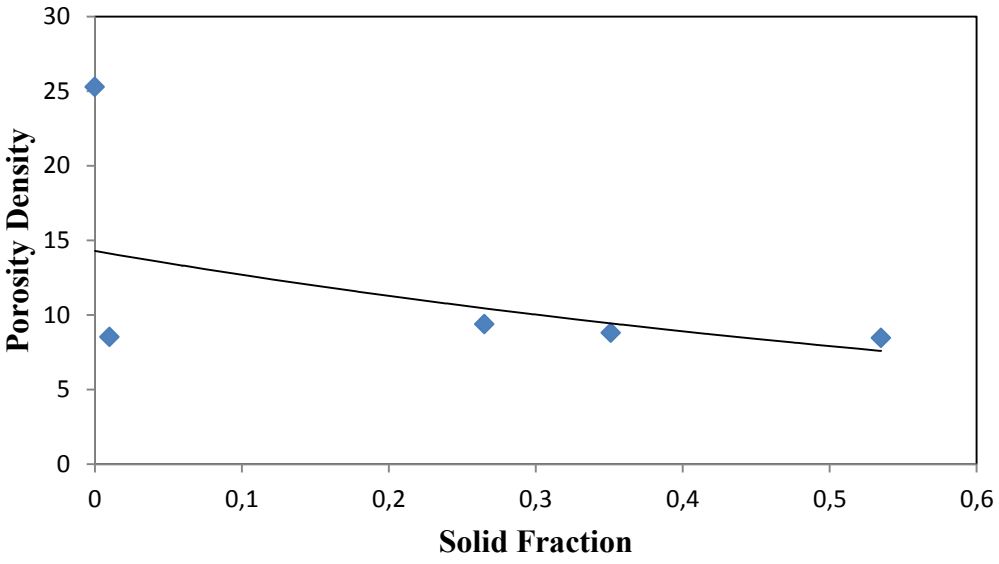

Figure 23. Porosity density vs. solid fraciton graph of modified 7075-2 alloy produced by injection molding.

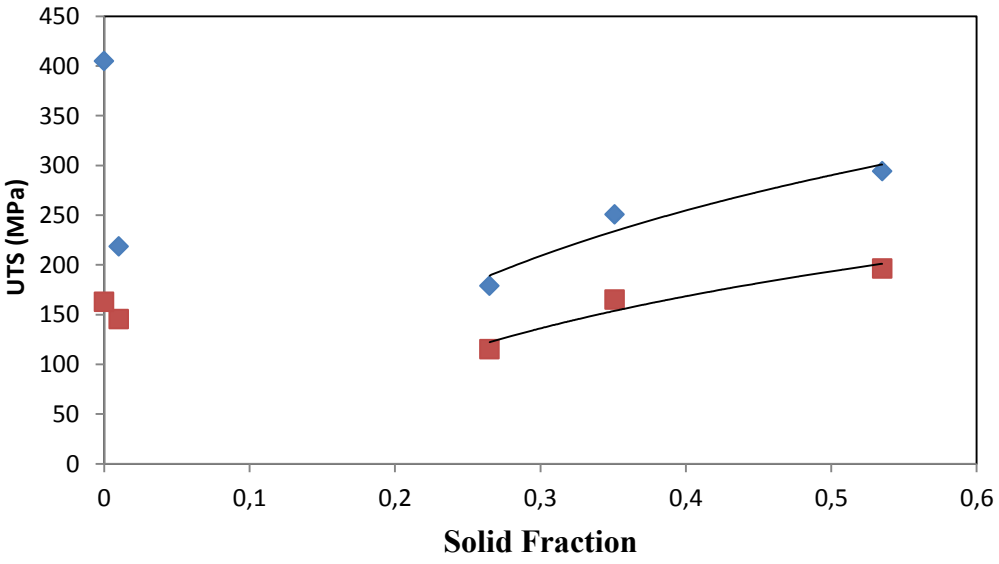

Figure 24. UTS vs. solid fraciton graph of modified 7075-2 alloy produced by injection molding (Red(square) dots are real values and blue(diamond) dots are recalculated values.)

It can be clearly seen from figure 23 that, total porosity content of specimens decrease as solid fraction increase. This can be explained by micro shrinkages decreases with decreasing liquid fraction. Furthermore, Figure 24 show that if low solid fraction values are not included, higher solid fraction gives higher UTS values. Since, increase in solid fraction cause castings with less porosity. Moreover, theoretical UTS values considering castings with no porosity also increase with increasing solid fraction. From figure 24, it can be concluded that it is possible to get 500MPa UTS value if technology is available making production at higher solid fraction.

Acknowledgment
Authors would like to thank to Seçkin Çardaklı for help in thermal analysis calculations and support in MATLAB. Also, authors would like to thank to Gülten Kılıç for SEM analysis. Finally, thanks to Özlem Sever for her help in SEM analysis, metallography and heat treatment of specimens.

REFERENCES

1. A.H.Ahmad, S.Naher, and D.Brabazon. "Thermal Profiles and Fraction Solid of Aluminium 7075 at Different Cooling Rate Conditions." Key Engineering Materials 554 (2013): 582-595.
2. L. Backerud, G. Chai, J. Tamminen, Solidification Characteristics of Aluminum Alloys. Volume 2: Foundry Alloys. University of Stockholm. 1991.
3. Metals Handbook, Vol.2 - Properties and Selection: Nonferrous Alloys and Special-Purpose Materials. ASM International: 1990.
4. J. W. Gibbs and P.F. Mendez "Solid Fraction Measurement Using Equation Based Cooling Curve Analysis", Scripta Materialia 58 (2008) 699–702.
5. D. Liu, H.V. Atkinson, P. Kapranos, W. Jirattiticharoean, H. Jones, Mater. Sci. Eng. A361 (2003) 213.
6. S. Chayong, H.V. Atkinson, P. Kapranos. "Thixoforming 7075 aluminium alloys" Materials Science and Engineering A 390 (2005) 3–12.
7. A.D. Isadare, B. Aremo, M. O. Adeoye, O. J. Olawale, M. D. Shittu.,"Effect of Heat Treatment on Some Mechanical Properties of 7075 Aluminium Alloy", Materials Research. 2013; 16(1): 190-194.
8. H. Atkinson, "Alloy Development for Thixoforming" Final Report for GR/M89096/01: 2003.

EFFECT OF GRAIN REFINING ON MICROSTRUCTURE OF A357 ALLOY

Muhammet ULUDAĞ*, Remzi ÇETİN*, Derya DIŞPINAR**

* Selcuk University, Faculty of Engineering–Metallurgical and Materials Eng. Dept., Konya-Turkey, uludag@selcuk.edu.tr, rcetin@selcuk.edu.tr
** Istanbul University, Faculty of Engineering, Metallurgical and Materials Eng. Dept., Istanbul-Turkey, deryad@istanbul.edu.tr

ABSTRACT
Aluminum alloys are preferred choice of materials due to their high-strength and low-density ratios. Although aluminum is a ductile material, by the addition of alloying elements, the strength is increased, but the alloys starts to suffer from ductility. In order to increase ductility, the grain size is aimed to be reduced by the addition of grain refiners. In industry, the typical grain refiner used is Al-Ti-B master alloy. One of the difficulties of the Ti grain refinement is the settlement of TiB_2 (i.e. fading effect). Thus, Al-B (without Ti) grain refiners has been investigated in the last decade. In this work, the aim was targeted to incorporate the effect of melt quality together with the grain refiners. The melts were prepared, grain refined and reduced pressure test was carried out to check melt quality by means of measuring bifilm index. A mould was prepared to produce six cylindrical bars. The hydrogen level of the melt measured by AlSPEK and grain size, porosity level and bifilm index were compared.

Keywords: A357 alloy, Casting, Grain refinement, Hydrogen content, Casting quality

A357 ALAŞIMINDA TANE İNCELTİCİLERİN MİKROYAPIYA ETKİSİ

ÖZET
Alüminyum alaşımlarında, yüksek mukavemet ve hafiflik malzemenin kalitesini ölçmede kullanılan önemli parametrelerden sadece ikisidir. Hafiflik, alüminyum alaşımlarının doğası gereği zaten mevcuttur. Mekanik özellikler ne kadar iyi olursa malzemenin kullanımı o kadar artmakta ve daha güvenli bir kullanım imkanı sağlamaktadır. Bu çalışmada, endüstriyel uygulamalarda en çok tercih edilen A357 alaşımının döküm kalitesini iyileştirme amaçlıyla tane inceltme uygulamaları yapılmıştır. Tane inceltme işlemleri 750 ^{0}C sıcaklıkta AlTi5B1 ve Al-3B master alaşımları kullanılarak yapılmıştır. Sıvı metalin hidrojen içeriği Alspek hidrojen ölçüm cihazı ile ölçülmüştür. Numunelerde, mikroyapısal incelemeler yapılmıştır, özellikle tane boyutu, ötektik faz oranı ve hacimsel porozite hesaplanmıştır. Elde edilen numunelerin tane inceltme işlemlerine ve döküm kalitesine bağlı olarak mikroyapısal değişimler araştırılmıştır. Sonuç olarak, döküm kalitesi, tane boyutu, faz dağılımları, hidrojen miktarı ile porozite arasındaki ilişki ortaya çıkartılmıştır.

Anahtar Kelimeler: A357 alaşımı, Döküm, Tane inceltme, Hidrojen içeriği, Döküm kalitesi

1. INTRODUCTION

Key characteristics of Al-Si alloys can be listed as high strength, high wear resistance and good castability. There properties make this alloy as preferred choice of material in many industrial applications. Many of this properties can be controlled by the microstructure which is typically determined by grain size (secondary dendrite arm spacing (SDAS)), eutectic phase ratio and silicon morphology [1]. In Al-Si alloys, Al-Ti master alloy is added in various ratios in order to refine the grain size. The mechanism suggests that the peritectic reaction of Al_3Ti acts as a heterogeneous site which helps the primary α-Al grains to be finer during solidification. On the other hand, Al-B grain refiners are also used. Dahle [2] had carried out several studies and show that more globular dendrites could be formed when B grain refiners are used in the absence of Ti. This process is defined by the eutectic reaction between Al-B which forms AlB_2. Due to the eutectic reaction, it is claimed that there is no fading effect of B grain refinement as it has been known for Ti.

Mohanty [3, 4] has studied the various ratios of Al-Ti-B grain refinement additions on Al-Si alloys in detail and proposes the mechanisms of grain refinement as follows: TiB_2 nucleates first and with Ti segregation, $TiAl_3$ forms which nucleates the primary α-Al grains. Spittle [5] and Sritharan [6] concluded that Ti-B type grain refiners work more efficiently in Al-Si alloys. Kori [7] studied the same ratios of Al-Ti and Al-B and found that Ti-free B addition castings had more homogeneous grain structures.

In this work, Al-5Ti-1B and Al-3B grain refiners were used to investigate the microstructural changes in A357 alloy with regard to the melt quality.

2. EXPERIMENTAL WORK

The chemical composition of A357 used in the experiments is given in Table 1.

Table 1. A357 alloy chemical composition

Si	Fe	Cu	Mn	Mg	Zn	Ti	Al
6,60-7,40	0,20	0,02	0,03	0,30-0,45	0,04	0,08-0,14	Rem

In the experiments, 20 kg capacity resistance furnace was used to melt A357. The alloy was provided as a primary charge and for each of the casting trials, Reduced Pressure Test (RPT) samples were collected where a sample was solidified under 80 mbar vacuum in a sand mould and the bifilm index was measured from the cross section of the samples. The castings were made into a 60-65 AFS sand mould where 13 mm diameter and 150 mm height of cylindrical bars were produced. Dimension of the mould cavity is given in Figure 1. Samples were collected and subjected to metallographical examination.

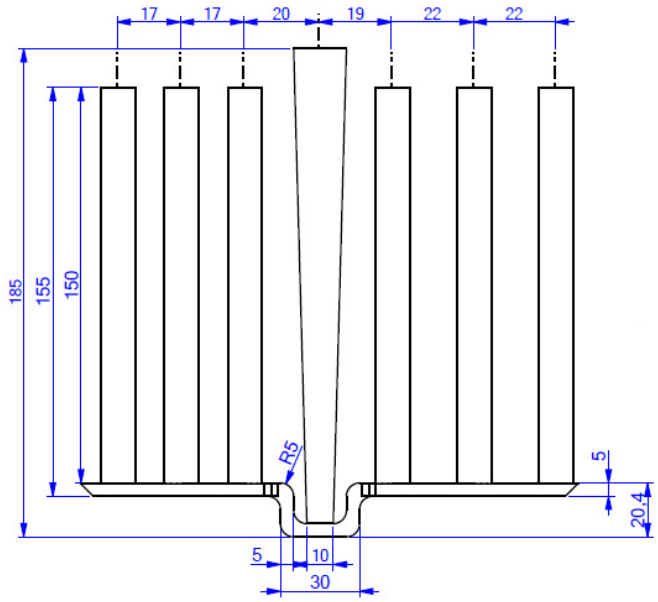

Figure 1. The dimension of the mould

Optical microscope was used together with an image analysis and several analysis results were used to investigate the micro and macro structural changes.

3. RESULTS and DISCUSSION

The cross section RPT samples showing the improvement of melt quality after degassing is given in Figure 2. As seen in figure, the size and number of pores were significantly lowered after degassing. This indicates that as the Ar bubbles were rising during degassing operation, the bifilms were being attached to these bubbles and thereby the number of bifilms were reduced in the melt which is clearly seen by the significant decrease of the number of pores (i.e. bifilms).

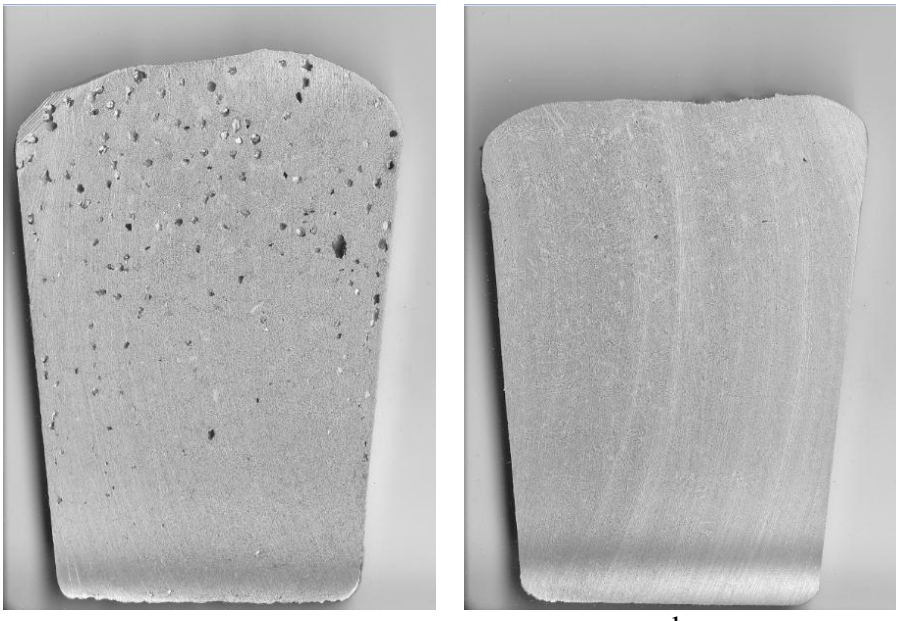

a b

Figure 2. Cross-section of RPT samples
a) before degassing, b) after degassing

The microstructures of the samples produced from the as-received charge, Ti grain refined and B grain refined are given in Figure 3. The as-received micrograph (Fig 3a) clearly stands out amongst the three conditions by having the most heterogeneous dendritic structure. On the other hand, by Ti (Fig 3b) and B (Fig 3c) addition, the longer primary arms were reduced and slightly better homogeneous structure was obtained. It is interesting to note that both as-received and Ti grain refined samples, there were few regions where porosity was observed. However, the total porosity was lowest in B grain refined castings.

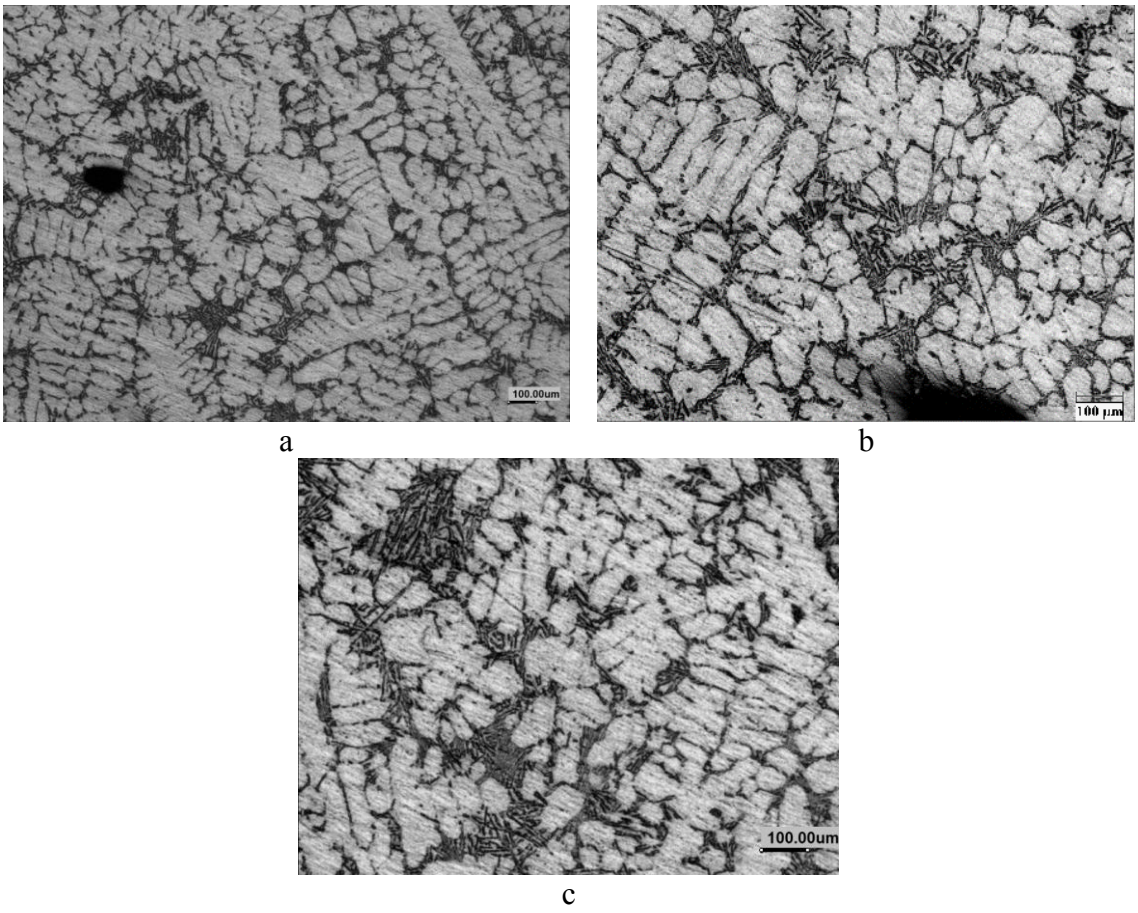

Figure 3. Presentation of the microstructures of samples:
a) as-received, b) Al-5Ti-1B added, c) Al-3B added

Secondary dendrite arm spacing (SDAS) of samples from each conditions (as received, Ti grain refined, B grain refined) before and after degassing operations is given in Figure 4. It can be seen that the highest SDAS was measured for Ti grain refined castings. It is interesting to note that the effect of degassing on the SDAS is only dominant in this casting as well. For as-received and B grain refined castings, the SDAS do not seem to be changing before and after degassing. The SDAS values are 41 μm and 38 μm for each conditions. However, these values dropped from 46 μm to 41 μm for Ti grain refined alloy. Yet, it needs to be pointed out that 4 μm change in the dendrite size is not that huge.

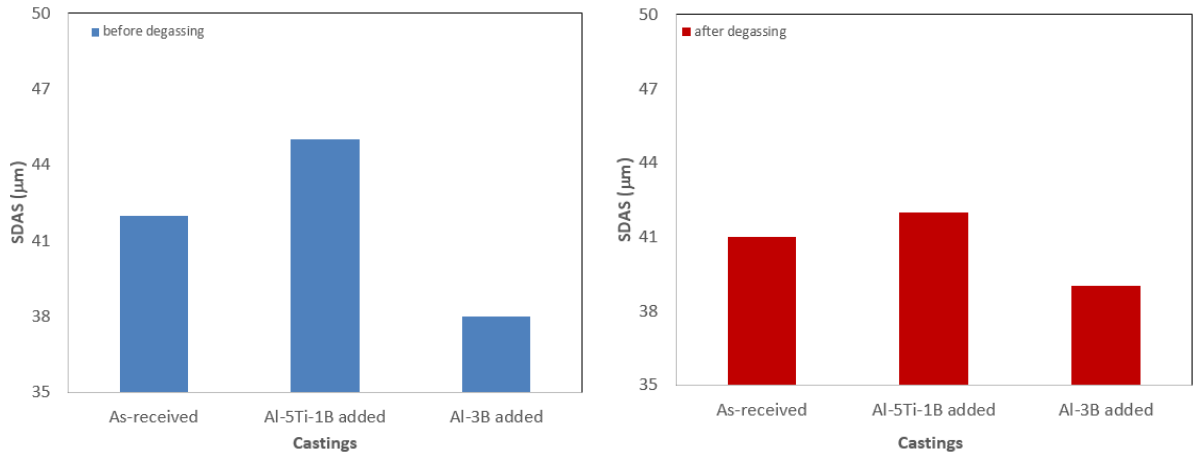

Figure 4. Casting conditions vs SDAS
a) before degassing, b) after degassing

Figure 5 shows the change in SDAS with bifilm index where Figure 6 is the eutectic phase ratio change with bifilm index before and after degassing. Theoretically, as the bifilm index increases, the population of defects in the melt increases and thus, they may readily act as heterogeneous nucleation sites and therefore, higher the bifilm index, lower the SDAS is expected. This correlation was not found in this work. As seen in Figure 5, there is almost no correlation between bifilm index and SDAS values. Similar conclusion can be found for the eutectic phase ratios. As seen in Figure 6, it is hard to define a relationship between bifilm index and eutectic phase ratio. In is a known fact that as the grain size is decreased, the liquid-solid ratio increases and thus more liquid is remained to solidify as late as possible which should increase the eutectic phase ratio. Actually, highest eutectic ratio was observed with B grain refined castings that had the lowest SDAS values.

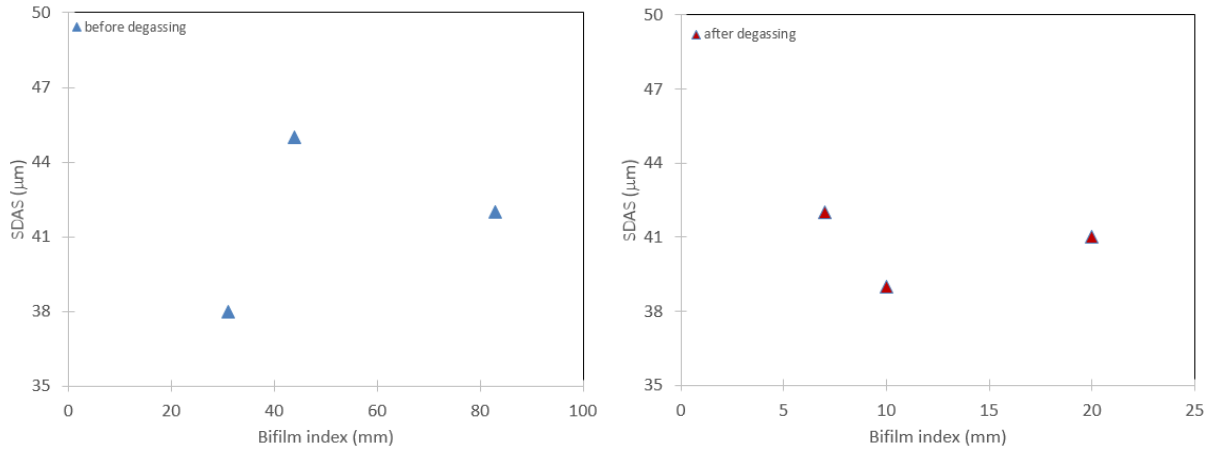

Figure 5. Bifilm index vs SDAS
a) Before degassing, b) After degassing

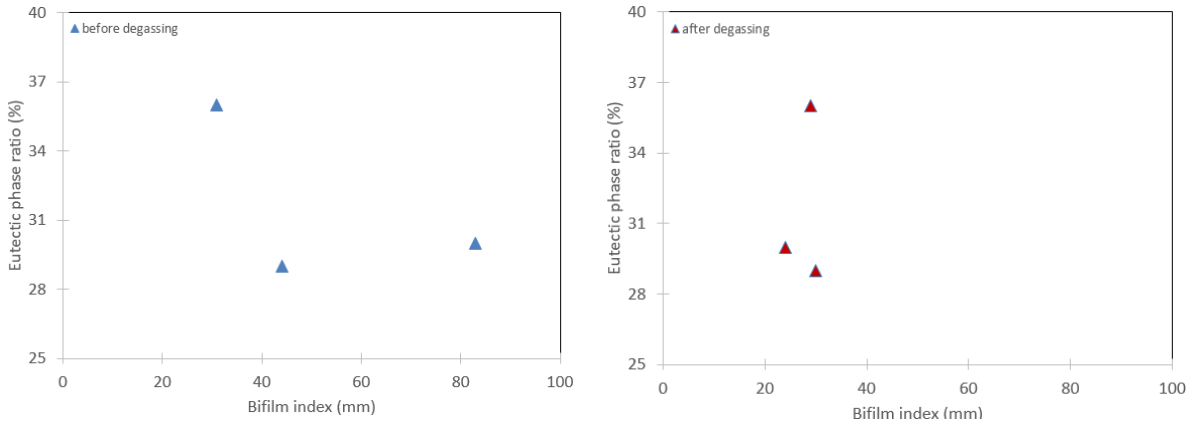

a b

Figure 6. Bifilm index vs eutectic phase ratio
a) Before degassing, b) after degassing

A comparison was made between the bifilm index calculations and hydrogen measurement of the melt. The result was given in Figure 7. As seen in figure, for the melt that was not degassed, there appears to be a correlation between hydrogen content and the bifilm index: as the hydrogen content was increased, bifilm index was increased (Fİg 7a). However, as seen in Figure 7b, this hypothesis fails when the melt was degassed. There is almost no relationship between hydrogen content and bifilm index. The bifilm index remained unchanged at low values regardless of the hydrogen content. This indicates that the amount of hydrogen do not have to be linearly equal to the amount of porosity that can be formed in castings. The main requirement for porosity formation is the presence of bifilm and when the conditions are met to open the bifilms, only then porosity can form. In the absence of bifilms, hydrogen cannot nucleate to form porosity.

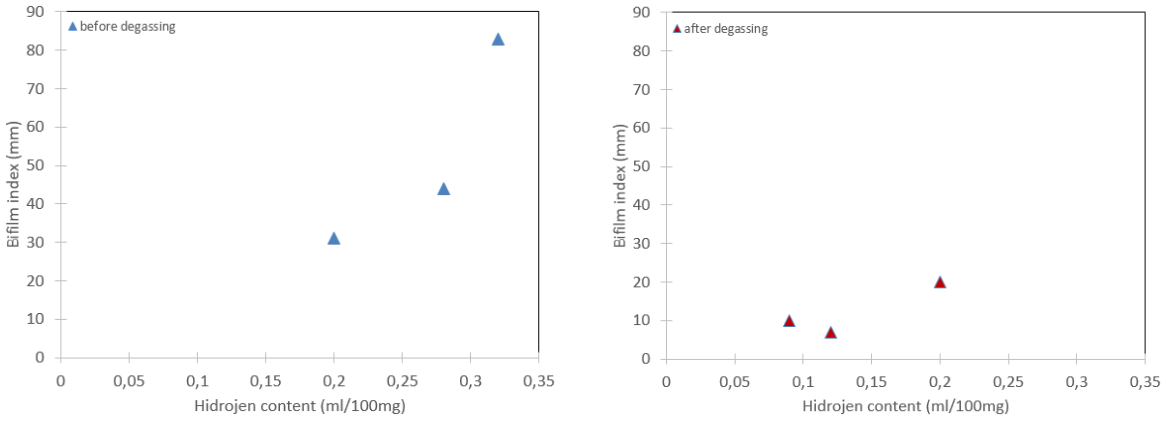

a b

Figure 7. hydrogen content vs bifilm index
a) Before degassing, b) after degassing

4. CONCLUSIONS

Degassing of a melt reduces the content of the bifilms which results in higher quality. This can be quantified and measured by bifilm index.

Higher hydrogen content of the melt do not necessarily indicate that porosity will be high. There is no relationship between porosity and hydrogen; and bifilm index and hydrogen.

It was assumed that bifilms in the melt would act as heterogeneous sites for nucleation; however there was no correlation between bifilm index and SDAS.

Lowest SDAS values were obtained when Ti-free B grain refinement was carried out. In addition, the eutectic phase ratio was also increased.

Acknowledgment

This work has been supported by the Scientific Research Projects Coordination Unit of Selcuk University (Project number: 13101026). The authors would like to acknowledge the support of ALTUN DÖKÜM sanayi A.Ş and FOSECO, Turkey for their help in the use of AlSPEK equipment for measuring hydrogen content of the melt.

REFERENCES

1. D.K., Y., TMS Light Metals, 1991: p. 1115.
2. Dahle, A.K., et al., *Eutectic modification and microstructure development in Al-Si Alloys.* Materials Science and Engineering A, 2005. **413-414**: p. 243-248.
3. Mohanty, P.S. and J.E. Gruzleski, *Grain refinement mechanisms of hypoeutectic Al-Si alloys.* Acta Materialia, **1996. 44(9): p. 3749-3760.**
4. Mohanty, P.S. and J.E. Gruzleski, *Mechanism of grain refinement in aluminium.* Acta Metallurgica et Materialia, 1995. **43**(5): p. 2001-2012.
5. Spittle, J.A., J.M. Keeble, and A.I. Meshhedani, TMS Light Metals, 1997: p. 795.
6. Sritharan, T. and H. Li, *Influence of titanium to boron ratio on the ability to grain refine aluminium-silicon alloys.* Journal of Materials Processing Technology, 1997. **63**(1–3): p. 585-589.
7. Kori, S.A., B.S. Murty, and M. Chakraborty, *Development of an efficient grain refiner for Al–7Si alloy and its modification with strontium.* Materials Science and Engineering: A, 2000. **283**(1–2): p. 94-104.

VERIFICATION OF THE FUNCTION OF FEEDERS BY CASTING SIMULATION

Haydar KAHRAMAN[*,**], Mithat Kemal TOZAN[***], Umit COCEN[*]

[*]Dokuz Eylul University Department of Metallurgical and Materials Engineering, Izmir, Turkey
haydar.kahraman@deu.edu.tr, umit.cocen@deu.edu.tr
[**]Dokuz Eylül University Graduate School of Natural and Applied Sciences Izmir, Turkey
[**]Cukurova Chemical Industry Company, Manisa, Turkey
k.tozan@cukurovakimya.com.tr

ABSTRACT

The aim of this study is to determine the functional behavior of feeder sleeve that are currently used in industry and test the accordance with casting simulation programme. Three different compositions of open cylindrical feeder sleeve were chosen to compare the exothermic properties of feeder sleeves such as high, mild and low exothermic. Experimental studies conducted with the samples of ductile iron in green sand molds. The distances between feeder sleeve and the outer surface of the mold and cross-sectional area of ingates are the same for all experimental studies. Reacting time, maximum temperature and cooling time are determined by taking temperature measurements from center of feeder sleeve. S type ceramic sleeved thermocouple is used for this purpose. Also the structural and composition change of sleeve before and after casting was determined by X-ray diffraction. The burning of sleeve in air was analyzed by DT-TG analyzer. Verification of all these data comprised with casting simulation programme and practical temperature measurements are discussed.

Keywords: Simulation, feeding, feeder sleeve, measuring temperature.

DÖKÜMLERDE BESLEYİCİ İŞLEVİNİN SÜREÇ BENZEŞİMİ İLE KONTROLÜ

ÖZET

Bu çalışmanın amacı sanayide sıkça kullanılmakta olan besleyici gömleklerinin döküm sırasındaki fonksiyonel davranışlarını belirleyerek bunların döküm süreç benzeşimi programları ile uyumunu incelemektir. Bu amaçla, deneysel ve benzeşim çalışmaları için yüksek, orta ve düşük olmak üzere üç farklı ekzotermik özelliğe sahip açık silindirik besleyici gömlekler seçilmiştir. Deneysel çalışmalar yaş kum kalıplarda küresel grafitli dökme demir dökümlerle gerçekleştirilmiştir. Besleyici gömleklerinin derece dış yüzeyine olan mesafeleri ve giriş yolluk kesitleri tüm deneysel çalışmalarda aynı tutulmuştur. Besleyici gömleklerinin merkezlerinden seramik kaplı S tipi termal çiftler kullanılarak yapılan sıcaklık ölçümleri ile soğuma eğrileri çıkarılmış ve reaksiyona girme süresi, en yüksek sıcaklık ve soğuma süreleri belirlenmiştir. Ayrıca besleyici gömleklerin döküm öncesi ve sonrası yapıları ile bileşim değişimleri X-ışınları kırınım cihazı kullanılarak kontrol edilmiştir. DT-TG analizleri ile de hava ortamında gömleklerin yanma davranışları incelenmiştir. Tüm bu verilerin döküm benzeşim programı ve uygulamalı sıcaklık ölçümleri ile uyumu irdelenmiştir.

Anahtar sözcükler: Süreç benzeşimi, besleme, besleyici gömlek, sıcaklık ölçümü

1. INTRODUCTION

The control of solidification enables accurate production at casting. Solidification can be effected by alloy, mold material and casting conditions. One of these variables changing will affect casting and also it will increase the diversity of castings. By the methods known, despite all the improvements at casting, at solidification of iron based alloy it is impossible to avoid shrinkage. Therefore, feeder usage at casting is inevitable [1,2,3].

The task of feeders starts with solidification. The feeder must be the last one solidify and delivered liquid metal to its radius until casting hardens within all the parts. Therefore, the shape, size of the feeder and connection portions of casting is meant to be designed to full fill the task [4,5]. Some additions also can be made to improve inefficiency. Feeder sleeves are commonly preferred and used especially by steel foundries. The liquid metal, in the exothermic and insulating based feeder sleeves, solidify later and also feeding distance is increased [6,7,8]. The different design, known modules in advance, can be pre-formed of feeder sleeve are the most important factors in the spread of the usage. But feeder sleeve manufacturers do not want to specify the properties of sleeves and from manufacturer to manufacturer composition changings is making hard to take precautions. Also there is very little information belonging to the feeder sleeves on the open literature. However, information can be gained from old literature. The feeder sleeves are incomprehensible despite ease of their applications [9,10]. Mathematical approaches for the calculations of the feeder are still current for years. Today, simulation programme are used which based on almost all of these theories and experimental studies [11].

One of the most improvement of casting technology is simulation programmes. By the usage of these programmes at mold design is more efficient (reduces craftsmanship, molding cost and less liquid metal) than ever. The most important advantage of simulating programme minimize the number of trial casting. In this way besides saving time, more efficient, economic and accurate casting is made. The casting defects can be predicted and can be taken precautions at the simulating process. With more data entered to simulations programmes, increased harmony with real life casting [7]. Such as density, specific heat and thermal conductivity of feeder sleeves which is defined at the simulation programme are remained unknown for the user [10].

In this study the harmony of simulating programme and real life casting applications were investigated. For this purpose, the experiments were designed to obtain the cooling curve of liquid metal at four different exothermic based and three different shape feeder

sleeves which are commonly preferred by foundries. Feeder sleeves characterizations were investigated before and after casting. This study is a preliminary study, at the same time study continuous.

2. Experimental Studies

There is no standard method for testing sleeves. Therefore, methods of this study were determined by temperature measurements of feeder sleeves in the mold and comparing the results with simulation programme and characterization of the exothermic materials. The details of this study are in the thesis master degree which is completed at 2013 [12].

Two different exothermic based feeder sleeves were molded to obtain the solidification curves at same casting. Temperature was measured from the last and longest solidified region (is determined by simulation programme) of casting.

The properties of feeder sleeves can be verified by different characterization method and experimental study. Burning temperature and time was determined by temperature measurement of thermocouple-radiation pyrometer and DT-TG analyzes and casting experimental.

At this experimental study all analysis and temperature measurements are presented as comparative graphs. Harmony of experimental results with data of feeder sleeves at simulation programme was analyzed.

Phases of feeder sleeves were also identified by X-Ray Diffraction before and after casting. Thus, the changing at exothermic reaction which generated processing principle of feeder sleeves is presented by this study. Weight loses and temperature ranges at feeder sleeves were determined by TGA.

2.1. Casting Experiments

The exothermic feeder sleeves which have different shape and casting module as shown in Table 2.1., were used in comparative casting studies (Fig 2.1.). Two different feeder sleeves were molded and meant to full fill at the same time and order. Thermocouples were placed at the center of feeder sleeves which solidified at last. More than 20 casting experiments were performed to have accurate temperature measurements. Reference measurements were tried to take from outer surface of feeder sleeves and region of mold sand that wasn't effected by temperature. But the space (occurred) between sleeve and

thermocouple after liquid metal solidified and feeder sleeves burned out, caused incoherence. Because of that these are not given at the result section.

The chemical composition EN-GJL 500 nodular cast iron are given at Table 2.2. Liquid metal was prepared by melting metal scrap in a high frequency induction furnace. Liquid metal furnace outlet temperature was measured as 1500-1550 ^{o}C.

% 10 of ruthenium doped ceramic coated platinum wire, S type, thermocouples were used at measuring temperatures.

One of the photo which was taken from the top of casting mold is shown at Figure 2.3. Temperature measurements were recorded in Datataker DT85 Series 2 S by four data per second.

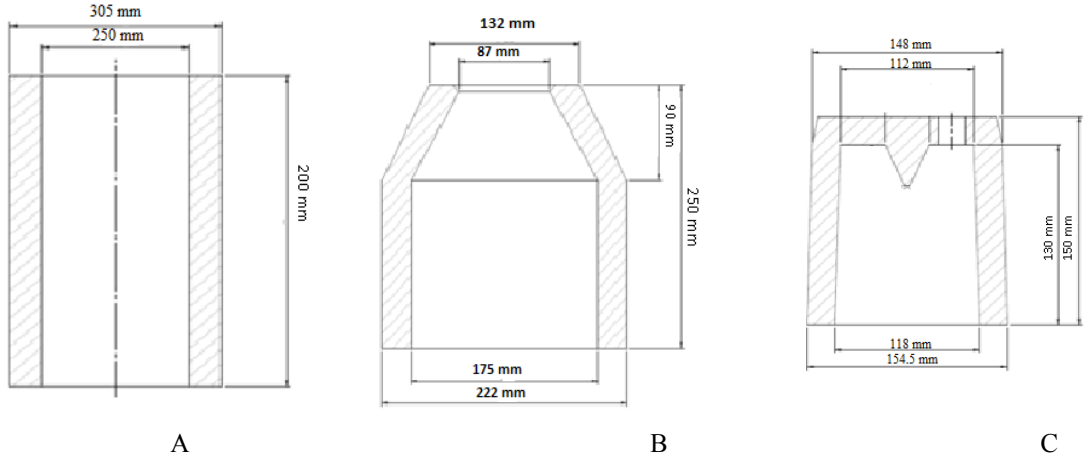

Figure 2.1. (a)open cylindrical, (b)conical and (c) closed cylindrical feeder sleeve

Table 2.1. Modules of feeder sleeves

Thermal modules(cm)	5,60	4,80	3,20
Geometrical modules(cm)	3,85	3,20	2,00

Table 2.2. Metal composition.(% weight)

C	Si	S	P	Mg	Mn	Cr	Ni	Mo	V	
>4.03	1,53	0,012	0,054	0,007	0,185	0,041	0,018	0,002	0,007	
>4.08	2,9	0,013	0,055	0,055	0,205	0,043	0,018	<0.001	0,011	
Cu	**Sn**	**Ce**	**Al**	**Ca**	**Co**	**Nb**	**Ti**	**B**	**Zn**	**Pb**
0,053	0,003	<0.001	0,005	<0.001	0,003	0,005	0,01	<0.0005	0,004	0,004
0,054	<0.001	<0.001	0,013	<0.001	0,004	0,006	0,012	<0.0005	0,003	0,003

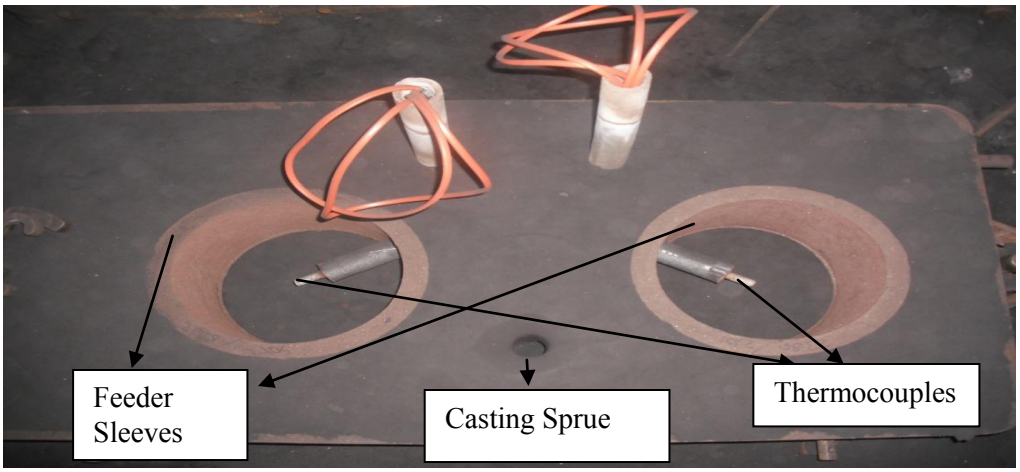

Figure 2.2. Casting mold

2.2. Simulation Studies

Nova Flow&Solid CV was used at simulation studies. Simulation studies are design considering the real life casting conditions. Approximately 50 simulation experiments were performed to get the closest results to the cooling curves obtained from experimental studies. Mold design was made by selecting high, medium and insulating based exothermic sleeves registered in the programme. Virtual temperature data was taken from this design (Fig 2.3) with using simulation programme. By making the flow and solidification, temperature measurements were taken.

After solidification, the latest status of the metals in the feeder sleeves was also investigated. Thus, metals at the latest and the earliest cooling conditions were compared.

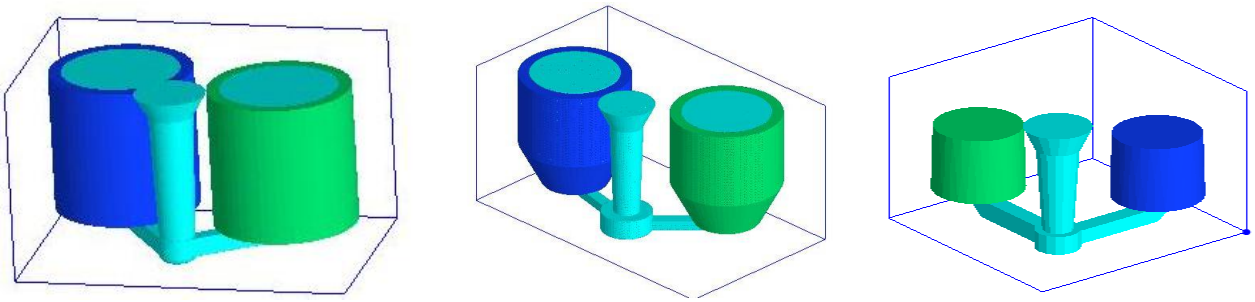

Figure 2.3. Mold design of (a) open Cylindrical, (b)conical and (c) closed cylindrical feeders sleeves

2.3. Phase Analysis of Feeder Sleeves Composition Before And After Casting

Samples, were extracted and grounded from feeder sleeves which were used in casting experiments, were analyzed by using Rigaku D Max 2200 XRD device. Phase differences were investigated on diffraction between before and after reaction.

2.4. Thermal Analysis of Feeder Sleeves

DT-TG analyzes were made on weight changing at starting temperature of exothermic reaction and time related. DT-TG analyses were made by using Shimadzu DTG-60H. Detection was made between room temperature to 1600^{o}C. Also burning experiments were applied on feeder sleeves. Temperature was measured by both radiation pyrometer and KER 610 ceramic coated S type thermocouple. Heating and cooling curves, which were obtained from burning test, were compared.

3. RESULT AND DISCUSSION

3.1. Simulation Results

After casting, metal status within feeder sleeves are similar to each other. High and mild exothermic feeder sleeves are compared and the results are given in Figure 3.1. The quantity of shrinkage is closed to each other. The amount of metal in the feeder sleeve is important to be efficient [9,10,17]. Measured temperature in the simulation programme and together with the results of experimental measurements are given at 'Casting Experiment Results Section'. Feeder sleeves parameters, which are taken from simulation programme, are

listed at Table 3.1. Examination of these parameters was compared with a result of DT-TG analysis.

Table 3.1. Parameters of feeder sleeves which are registered at the simulation programme [16].

Composition of Feeder Sleeve	Burning Duration (s)	Burning Temperature (^{o}C)	Burning Heat (kJ/kg)
High Exothermic	100	400	2000
Mild Exothermic	100	1000	1230
Low Exothermic	200	404	707
EXO	30	400	2200

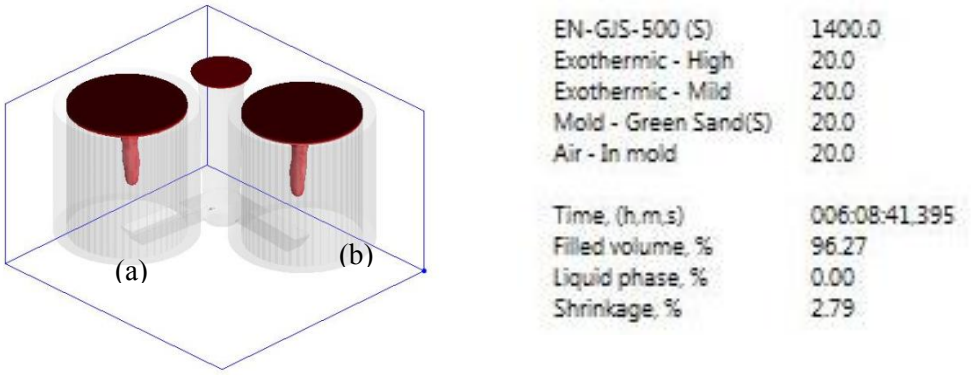

Figure 3.1. The last status of metal in High (a) and Mild (b) exothermic base open cylindrical feeder sleeve after solidification

3.2. Result of Casting Experiments

The slope of the curve which is obtained from the measurements during simulation programme and casting experiment, at a given temperature range approaching the horizontal position comes to zero. It is the typical cooling curve of eutectic alloy. The first point of the curve which starts to flatten is the point where cuts liquidus and solidus. Chemical compound can be identify by cooling curves of cast iron [15].

Graphical results were obtained from casting experiments and simulation study. Because of the similarities of cooling curves, one example is given in Figure 3.2. However cooling curves are similar to each other, there are differences at time and temperature. When all cooling curves are examined, the differences between the experimental results and simulation are observed. Start up cooling temperature, phase transition temperature, temperature reaching transition and cooling curves after completing the transition are given in Table 3.2.

First of all conical feeders are analyzed and examining the cooling of liquid metal near liquidus, it is seen that cooling curve of generated from simulation programme is cooling faster than experiment. As seen at Table 3.2., the cooling rate of liquid metal at simulation programme is av. 0.185^{o}C/s, while the average cooling rate of experimental measurement is 0.164^{o}C/s for conical feeder sleeves. The liquid metal in the EXO based conical feeder (EBCF) sleeves and high exothermic based conical feeder (HEBCF) sleeves starts to cool down from almost same temperatures. And it does show us that feeder sleeves have given the almost same amount of heat to the liquid metal. However, EBCF reaches to liquidus(where solidification starts), 115 second earlier than HEBCF. As a result of experimental studies, highest temperature of both feeder sleeves at casting experiment is less than simulation programme's which cool down faster.

The metal in the feeder sleeve, must have the highest temperature until solidification completed to have a sound casting. In this respect it is important that the metal must cool down slower than heating up. Especially the liquid metal (in the feeder) must have been slowly cooled down for allowing liquid metal movement at near solidus (where solidification ends). Softness should last as long as possible for preventing shrinkage which can be occurred right after solidus.

Table 3.2. Comparison of experimental and simulation results for all feeder sleeves

Feeder Sleeves		Maximum Temperature (^oC)	Cooling rate of liquid metal ($^oC/s$)	Time to reach liquidus (s)	Time to reach solidus (s)	Cooling rate of solid metal ($^oC/s$)
Conical	EXO (EBCF)	1291	0,186	953	2052	0,108
	EXO (Exp.)	1251	0,162	823	1739	0,086
	High Exothermic (HEBCF)	1290	0,184	1068	2254	0,109
	High Exothermic (Exp)	1255	0,166	782	1692	0,084
Close Cylindrical	EXO (ECCFS)	1396	0,168	1767	4048	0,094
	EXO (Exp.)	1360	0,225	1388	2592	0,103
	High Exothermic (HECCFS)	1393	0,180	1484	3677	0,092
	High Exothermic (Exp)	1353	0,217	1419	2654	0,114
Open Cylindrical	Mild Exothermic (OCMEBFS)	1311	0,127	1394	3520	0,045
	Mild Exothermic (Exp)	1313	0,157	1429	3029	0,119
	High Exothermic (OCHEBFS)	1310	0,181	1059	2245	0,077
	High Exothermic (Exp)	1307	0,180	1023	2205	0,085
Open Cylindrical	Low exothermic (OCLEBFS)	1270	0,260	728	2704	0,087
	Low exothermic (Exp)	1256	0,228	678	2034	0,088
	High Exothermic(OCHEBFS)	1271	0,232	747	2716	0,087
	High Exothermic (Exp)	1252	0,276	690	2124	0,069
Open Cylindrical	Low exothermic (OCLEBFS)	1311	0,316	641	2534	0,128
	Low exothermic (Exp)	1308	0,314	638	1789	0,161
	Mild Exothermic (OCMEBFS)	1313	0,200	972	3023	0,109
	Mild Exothermic (Exp.)	1319	0,252	778	1960	0,107

The liquid metal in the HEBCFS started to cool down at 1255^{o}C, but EBCFS started to cool down at a lower temperature which is 1251^{o}C. However comparison on cooling rates

between HEBCFS and EBCFS, HEBCFS has a faster cooling down which is rated 0.166^{o}C/s, and EBCFS is rated 0.162^{o}C/s.

HEBCFS reached to the solidus line 47 seconds later compare to EBCFS which is listed at Table 3.2. EBCFS reach solidus later than HEBCFS, after solidus HEBCFS has a lower cooling rate.

Exothermic composition of close cylindrical feeder sleeve (CCFS) is similar to the conical feeder sleeve (CFS) used in experimental studies. First of all analyzing the results of simulation programme, CCFS has reached a higher temperature and had slower cooling rate than CFS, and is shown at Table 3.2 but at real life casting conditions, it is vice versa, the cooling rate of CFS is bigger.

Unlike conical feeder sleeve, HECCFS cooled down faster compare to ECCFS by 0,012°C/s. In this context ECCFS reached liquidus 283 seconds later than HECCFS. After solidus, ECCFS cooled down 0,002°C/s faster than HECCFS.

Analyzing the results of experimental measurements of the two feeder sleeves cooling ranges are close to each other. Unlike the results of the simulation programme, ECCFS cooled down faster than HECCFS by 0,008°C/s. According to the experimental results, despite ECCFS started to cool down from a higher temperature such as 7°C than HECCFS, due to the difference cooling of liquid metal, ECCFS reached liquidus 31 seconds sooner. ECCFS continued to cool down as linear and reached solidus 62 seconds sooner than HECCFS.

Table 3.2 (ECCFS) is examined, simulation programme have the peak temperature is 36°C higher, cooling rate of liquid metal is 0,057^{o}C/s lower, reaching liquidus 379 seconds later, solidus 1456 seconds later and cooling rate of solid metal is 0,009 ^{o}C/s lower than experimental casting results. When results of HECCFS are examined, simulation programme have the peak temperature is 40°C higher, cooling rate of liquid metal is 0,037^{o}C/s lower, reaching liquidus 65 seconds later, solidus 1023 second later and cooling rate of solid metal is 0,012^{o}C/s lower than experimental casting results. According to these results, HECCFS's simulation results are closer to the experimental casting results than ECCFS. But the differences of both feeder sleeves are the obstacles to approach the experimental results.

For closed feeder sleeves, HECCFS cooling rate is lower at experimental, ECCFS cooling rate is lower at simulation programme. In this case, lower the cooling rate much the feeding time.

As a result of experimental casting studies, the effect of exothermic material at feeder sleeves on cooling of liquid metal was investigated. The liquid metal in open

cylindrical high exothermic based feeder sleeve (OCHEBFS) cooled down slower than the liquid metal at open cylindrical mild exothermic based feeder sleeve (OCMEBFS) at simulation programme unlike the results of other feeder sleeves temperature measurement at casting experiment.

The liquid metal in the OCHEBFS cooled down faster than OCMEBFS by 0,030°C/s despite of the both highest temperatures are very close. Due to difference of velocity, OCHEBFS reached liquidus 305 seconds earlier than OCMEBFS (Table 3.2). The liquid metal in OCMEBFS reached solidus 491 seconds later than OCHEBFS, therefore the metal remains liquid much longer in OCMEBFS.

Like the result of simulation programme, these two feeder sleeve's highest temperature is close to each other. Also according to the experimental measurements, the difference of cooling rate between OCMEBFS and OCHEBFS is 0,001°C/s. OCHEBFS reached solidus 36 seconds sooner than OCMEBFS. The liquid metal in the OCMEBFS stayed 40 seconds longer at solidus. After liquid metal in the OCHEBFS solidified, it cools down 0,008^{o}C/s faster than OCMEBFS.

Considering solidus and cooling rates, according to the data obtained from simulation programmes of the metal in the feeder sleeve is seen that the slow cooled above the experimental measurement values. Examining curves obtained from experiment, OCMEBFS obviously cooled down more slowly than OCHEBFS. (Table 3.3)

The cooling rates of OCHEBFS and OCLEBFS are similar to each other. The difference between the curve of simulation programme and the experiments measurement is seen at the peak point. This situation can be explained by in compatibility between casting temperature can change according to ambient temperature at experimental casting but at simulation casting temperature held constant. On the other hand, cooling rate of liquid metal until liquidus matched each other and continue same as. Kumruoglu and Ozer have similar conclusions in their studies with Menon [16,17].

Cooling rates between liquidus and solidus are seen to be closed to each other. After solidus, incompatibility can be observed between cooling curves obtained from simulation programme and experiment. That can be explained by the changes at the thermal conductivity after exothermic reactions were completed. That changing can not be determined at simulation programme so it can cause inharmony. But analyzing cooling of liquid metal at OCHEBFS and open cylindrical low exothermic based feeder sleeve (OCLEBFS), a compliance with simulation programme can be observed.

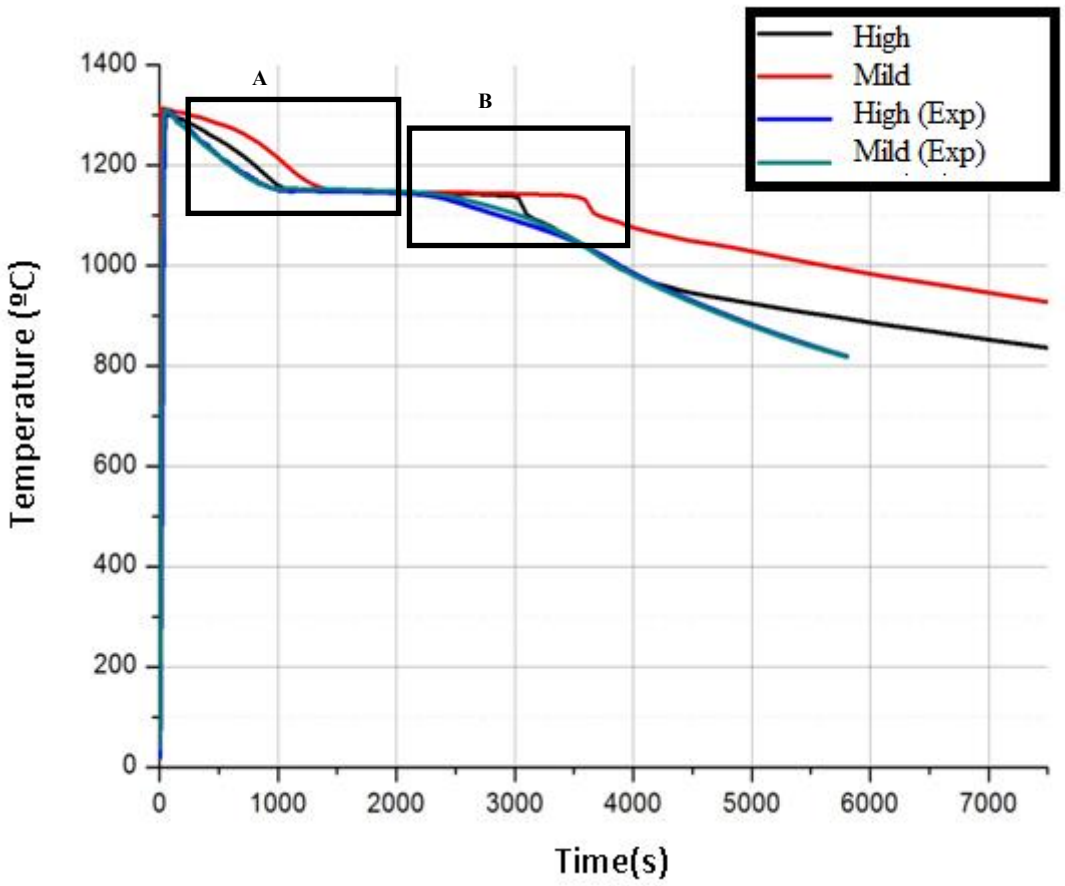

Figure 3.2. Cooling curves of mild and high exothermic base feeder sleeves taken from simulation and experimental

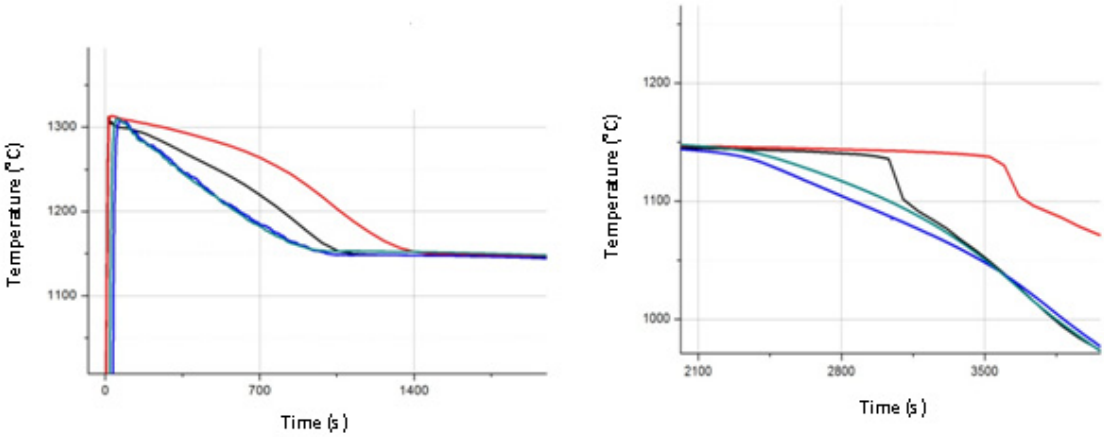

Figure 3.3. A and B region on Figure 3.2.

As a result of simulation OCLEBFS cools faster than OCHEBFS, it is vice verse at experimental study. The difference of result between simulation and experimental study is

decreased to 0,001°C/s after solidus. According to simulation results, 12 seconds difference can be observed between two feeder sleeves to at solidus.

They almost reached solidus at the same time. But at the experiment the difference between OCLEBFS and OCHEBFS is measured 90 seconds.

Analyzing the temperature changing between OCMEBFS and OCLEBFS at simulation programme and experimental measurement, similar results were obtained.

Analyzing the cooling rate obtained from simulation programme and experimental measurement, there is a 0,002^{o}C/s difference in OCLEBFS, 0,052^{o}C/s difference in OCMEBFS. The liquid metal in OCLEBFS cooled down faster at simulation programme compare to experimental results.

OCLEBFS reached solidus 1000 seconds sooner from OCMEBFS at both simulation programme and experimental measurement.(Table 3.2)

At literature, to verify the performance of feeder sleeves, similar methods are preferred. Temperature is verified by using thermocouples which are placed closed together so the thermal properties of feeder sleeves can be related to temperatures [6,9,10,13]. However, contrary to the use of thermocouples for verification, in this study current measurements were not obtained as a conformation, is a flaw.

3.3. Results of Phase Analysis

The phase analyze of bulk samples, were extracted from sleeves before casting is illustrated in Fig. 3.4. It is known that the composition of all feeder sleeves are consisted of aluminum and metal oxide as exothermic compound, polymeric binder and alumina and alumina silicate base with some filling agent as insulation compound [18.19]. Peaks of metallic aluminum and alumina on different phase are observed on XRD results (Fig. 3.4). Alumina base filling agent are preferred as insulation compound, so it is seen that peak of alumina is intense.

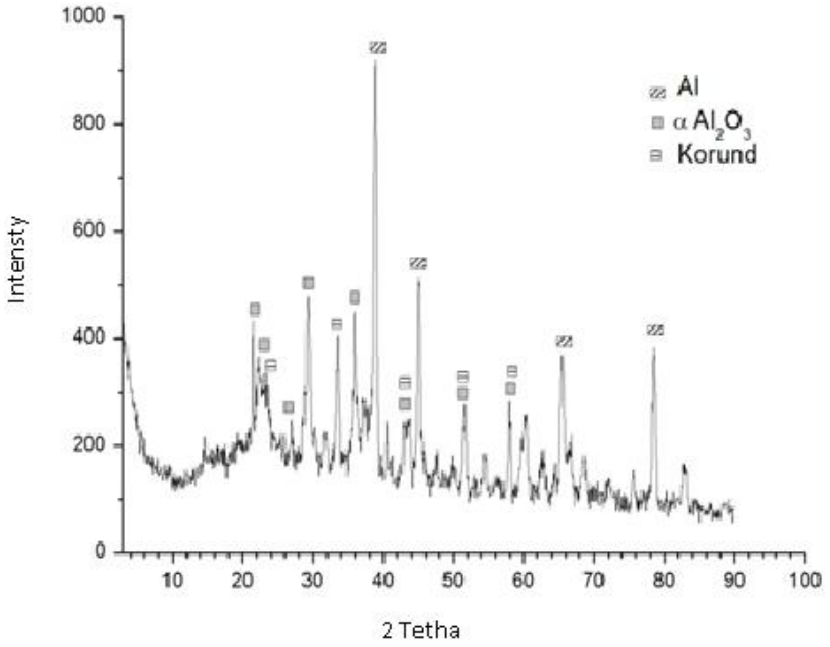

Figure 3.4. XRD result of feeder sleeves before casting.

In some cases complete combustion is not occurred after casting as shown in Fig. 3.5. Different phase aluminum oxide can be occurred depend on burning condition except alumina. Besides no matter how small metallic aluminum is shown in phase analyze. The difference of the reaction formation effects temperature of the liquid metal in feeder sleeve [19].

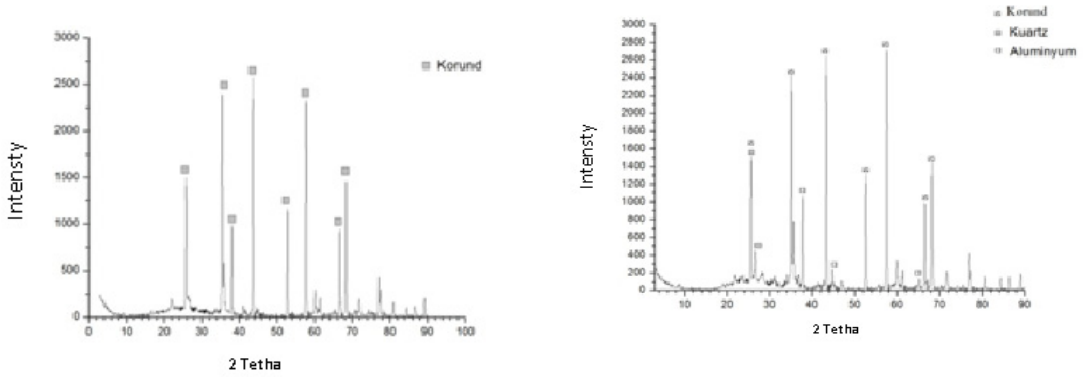

(a) (b)

Figure 3.5. XRD result of feeder sleeves after cating a) complete burning, b) incomplete burning

3.4. Results of Thermal Analayzis of Feeder Sleeves

When DT-TG analyzes under air atmosphere are observed, the exothermic reactions are seen between 400°C and 1400°C. Also the most energetic peaks are seen between 1000°C and 1400°C, the first exothermic reaction start temperature is 400°C. The data, taken from simulation programme is given Table 3.1 except mild exothermic reaction of all feeder sleeves are started at nearly 400°C. Due to rate of 10°C/min is too slower than real life casting, it is seen that reaction start and total reaction time are more different from data taken from simulation programme. The feeder sleeves must have low burning temperature such as 70-80 seconds at real life casting,

Compound with fluorine, is used as igniter is the part of feeder sleeve's composition. When the DT-TG curves, are shown in Fig 3.6, 3.7 and 3.8 are considered, DTA curve is getting higher as an indication of exothermic reaction starts, fluorine base igniter does its duty [20].

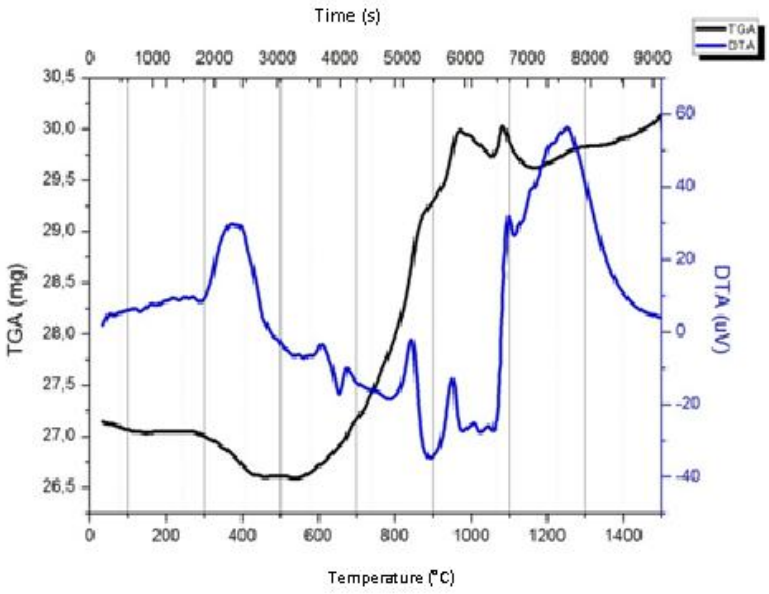

Figure 3.6. DTA-TGA curves of high exothermic based feeder sleeves

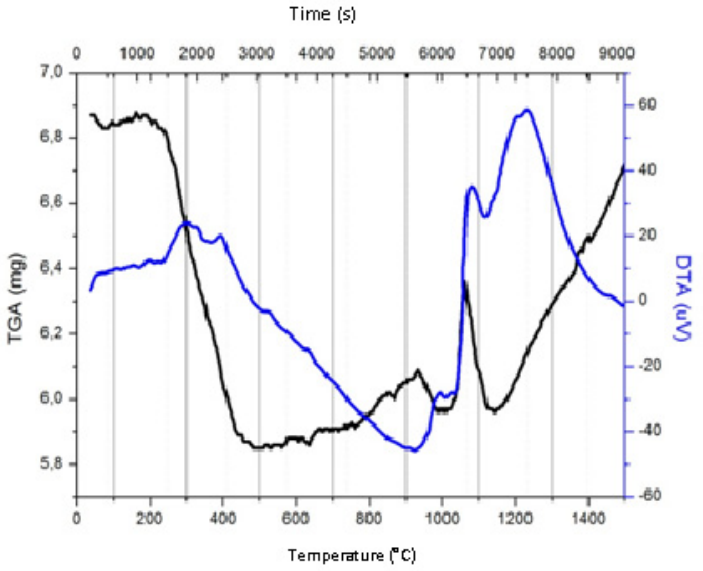

Figure 3.7. DTA-TGA curves of mild exothermic based feeder sleeves

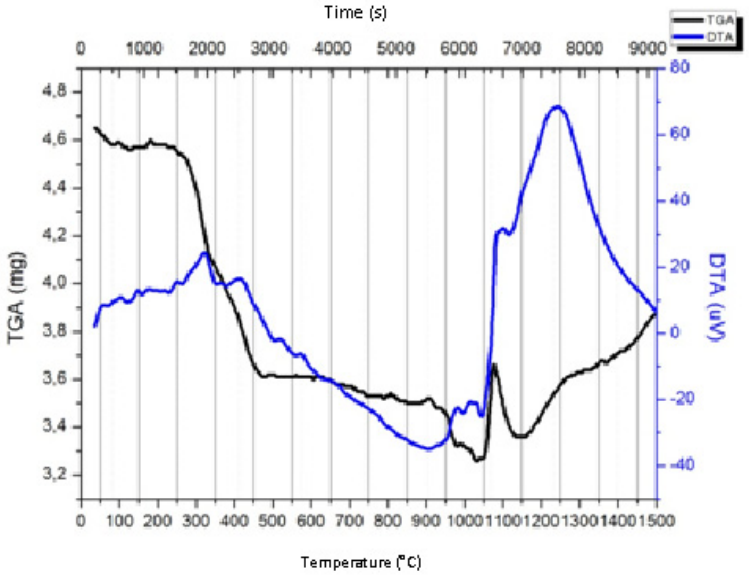

Figure 3.8. DTA-TGA curves of low exothermic based feeder sleeves.

The graphic, is observed in Fig. 3.9, is taken from result of consecutive burning operation under air atmosphere. It can be obviously observed that the maximum temperature of this graphic is different from burning in casting mold. Even as the value of maximum temperature can reach nearly 1300^{o}C in mold, it can reach 1600^{o}C under air atmosphere. It is thought that because of oxygen at open air atmosphere the energy, is generated as result of complete burning reaction is more than inner mould [10,20]. The reaction of feeder sleeves is started nearly 30 seconds in furnace at 900^{o}C. Total reaction time is 70-75 second too. During burning operations there is a difference between measured time of simulation programme and thermocouple measured time such as 30-35 seconds [Table 3.1].

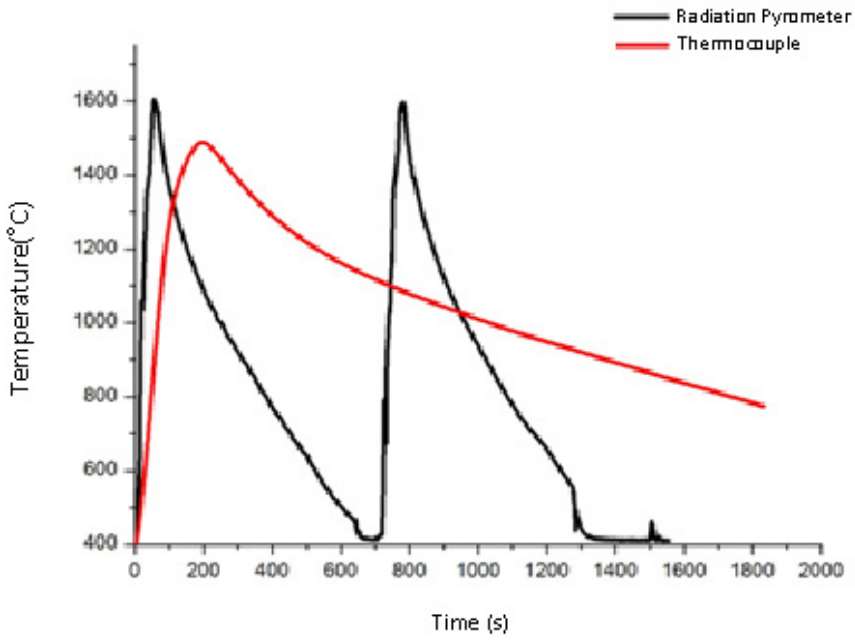

Figure 3.9. Temperature curves of burning high exothermic based feeder sleeve

4. CONLUSİONS

Commonly preferred feeder sleeves were used in this, it was researched the compatibility between NovaCast Flow&Solid casting simulation programme and real casting conditions were investigated. For this purpose, the properties of the feeder sleeve were determined and compared among themselves. The harmony between simulation programme and experimental casting conditions were analyzed by the cooling rate of the metal in the feeder sleeves.

Analyzing the high, mild and low exothermic based feeder sleeves which are registered to simulation programme, mild and low feeder sleeve's cooling curves are similar among the simulation programme and casting experimental. Besides, the molding of the feeder sleeves with basic shapes such as cube and plate instead of the molding without conjunction would be more accurate in terms of determining the performance of feeders. Despite all these deficiencies, the curves, obtained by comparing the simulation and experimental conditions, showed consistency.

It was detected that EXO and high exothermic based conic feeder sleeves registered to the simulation programme cooled faster in experimental application when compared to simulation programme.

It is expected that the metal in feeder cool down faster than conic feeder sleeve due to the thermal and geometric module of EXO and high exothermic based closed feeder sleeves registered to simulation programme. However the metal in conic feeder sleeves casted under the same conditions cooled faster according to the simulation. At the same time, there was a inharmony between the results obtained from the simulation programme and experimental casting conditions. Closed feeder sleeves cooled faster according to the module under experimental casting conditions.

As a result of the phase analyses of feeder sleeves contents, it was not detected much difference. The products cause exothermic reaction were determined. Especially increasing the amount of aluminum oxide in Corundum phase and the changing the aluminum oxide in other phases were detected.

In this study, it couldn't be identified all values given from simulation programme and the characterization of the thermal properties. It was similar to the exothermic reaction characteristic used aluminum according to the DT-TG analysis. The exothermic reaction starting temperature of the sleeves were in compability with real measurement, but the reaction times and maximum temperatures were not in compability with each other.

ACKNOWLEDGE

Experimental studies were performed with the support of Dokuz Eylul University Scientific Research Project (software and experiment equipment) In this study, special thanks to MSc. Metallurgy Engineer Yalcın Cay and other staff of MEDOKSAN Foundry Company who provides casting experiment available.

5. REFERENCES

1. American Society of Materials, (1998). Metal Handbook (10). *Casting,* Ohio

2. Beely, P. (2001). *Foundry technology,* Oxford:Butterworth-Heinemann

3. Campbell, J. (2003). *Casting.* Birmingham:Butterworth-Heinemann

4. Saturia, M., Gada, V. H., Sharma, A. and Ravi, B. (2012). Computation of feed-paths for casting solidification using level-set-method. *Journal of Materials Processing Technology* , 1236-1249.

5. Rio Tinto Iron and Titanium Inc. (2000). *Ductile iron the essentials of gating and risering system design.* Montreal: Sorelmetal.

6. Oliveira, M. J., Malherios, L. F. and Riberio, C. A. (1999). Evaluation of the heat of solidificaiton of cast irons from continuous cooling curves. *Journal of Materials Processing Technology* , 25-30.

7. Ravi, B. (2008). Casting simulation and optimisation: benefits, bottlenecks, and best practices. *Technical Paper for Indian Foundry Journal January* , 1-12.

8. Twardowska, H. and Aufderheide, R. C. (2002). *Patent No. US 006360808B1.* Dublin Ohio.

9. Hardin R. A.; Williams T. J. and Beckermann C. (2013) Riser sleeve properties for steel casting and the effect of sleeve type on casting yield, *Proceeding of The 67th SFSA Technical and Operating Conference*, Chicago

10. Lipowska B., Witek J., Stec K. (2010), Aluminium dross-based insulating and exothermic materials for metalurgical industry, Archives of Foundry Engineering, 115-118

11. Tavakoli, R. and Davami, P. (2008). Automatic optimal feeder design in steel casting process. *Computer Methods in Applied Mechanics and Engineering* , 921-932.

12. Kahraman H., (2013)"Dökümlerde besleyici işlevinin süreç benzeşimi ile kontrolü" Yüksek Lisans Tezi, İzmir

13. Foseco Foundry, C. (2000). *Foundry practice.* 24 Mayıs 2013. http://www.foseco.com.tr/tr/downloads/FoundryPractice/23001_Simulation_with_thermal_true_data.pdf.

14. NovaCast (2013), *Nova Flow&Solid Gravity CV User Guide 4.6.* Ronneby:Novacast System AB

15. Hardin, R., Ou, S. and Carlson, K. (2001). *Feeding and risering guidelines for steel casting.* Steel Founders Society of America

16. Kumruoğlu, L. C. and Özer, A. (2008). Investigation of critical liguid fraction factor in nodular iron casting by computer simulation. *Journal of Materials Processing Technology* , 182-188.

17. Menon, P. R. (1997). *Patent No. US 006133340A.* Sa Paulo, Brazil.

18. Neu, M. G. and Gough, M. J. (1993). *Patent No. US 005180759A.* Birmingham, England.

19. Hahma, A., Gany, A. and Palovuori, K. (2006). Combustion of activated aluminum. *Combustion and Flame* , 464-480.

20. Duraes, L., Costa, B. F., Santos, R., Correia, A., Campos, J. and Portugal, A. (2007). Fe_2O_3/aluminyum thermite reaction intermediate and final products characterization. *Materials Science and Engineering A* , 199-210.

Yeni Dünya, Yeni Eğilimler, Teknolojiler ve Türk Döküm Sektörü

New World, New Trends, Technologies and the Turkish Foundry Industry

Yaylalı Günay*

*Günay Danışmanlık

ÖZET:

Gelişmekte olan ülkelerdeki orta sınıfın sayı ve oranları yükseldikçe, bu ülkelerde gerek pazarın talebi, gerek ülke yönetimlerinin talebi ve gerekse rekabet koşulları nedeni ile araç, makine ve benzeri tüketim ürünlerinin üretimi bu ülkelere kaymaktadır.
Bunun yanında enerji, hava kirliliği, şehirleşme ve maliyet nedenleri ile araçlarda ve makinalarda ağırlık azaltma gündemin ana maddelerinden biri halindedir. Metalurji bilimi bu hafifleme sürecinde yeni malzemelerin ve üretim teknolojilerinin yaratılmasında ön plandadır.

Metalurji ve özellikle döküm sektörünün dünyada ve Türkiye'de rekabet gücünü koruyabilmesi, daralan pazarlarda payını koruyabilmesi için, bu yeni teknolojilere uyum sağlaması, yer yer öncülük etmesi gerekmektedir.
Tebliğde, yeni teknolojiler, malzemeler, üretim metodları değerlendirilmekte ve sektörün bu yeni dünyada rekabetçiliğinin devam ettirilebilmesi için yapılması gerekenler değerlendirilmektedir.

Anahtar sözcükler: Döküm, araçlarda hafifleme, üretim süreçleri, nano teknoloji, gelecekteki fabrikalar

ABSTRACT

With the increase in the number and percentage of the middle class in developing countries additionally süpported with the demand of the market and the changing competitive conditions, as well as the governmental regulations, the production facilities for the automotive, machinery and similar products are being transferred to these regions.
Due to the energy usage, air pollution, urbanization and cost factors, lightening of the transportation vehicles and machinery is another main issue on the agenda. In the design of technologies and development of new materials and alloys, metallurgical science and technology is on the front arena.
In order to protect their existing competitive power and to increase the market shares in these countries, metallurgical and mainly foundry industry of the World and Turkish foundry industry have to adopt their existing systems to these new technological trends and also be development leaders in certain cases. Present paper analyses the new technologies, trends, materials, production methods and brings forward some of the action plans the foundry sector has to apply in order to strengthen the competitive power in this new world.

Key Words: Casting, lightening in automotive industry, production processes, nano technology, future factories

GİRİŞ:
Yeni Dünya'ya Bir Bakış

Yeni oluşan, sürekli değişen ve birbiri ardından gelen yapısal, finansal krizlerin olduğu, bir bölgede olan gelişmenin diğer bölgeleri ve sektörleri kısa sürede etkilediği bir dünyada, iş yapış şekilleri de değişmektedir.
Her yapılanın satılabildiği, yeni fikir ve üretim şekillerinin devreye girmediği bir yapının, bu yeni ve çalkantılı bir dünyada yerini koruyabilmesi çok zor gözükmektedir.

Yeni dünya artık bir VUCA dünyasıdır.

VUCA kısaltması, İngilizce;
V:Volatile (Değişken);
U:Uncertain (Kesin değil);
C: Complex (Karmaşık ve kaotik)
A: Ambiguous (Çok yönlü) sözcüklerinin ilk harflerinden oluşmuştur.

VUCA dünyasında ana tema atılganlık, herkesin beklemediğini, beklemediği zamanda sunmak, karmaşıklıkta bile atılım yapmak, hafifte olsa bile işiniz ile ilgili bir ayak izi bırakmak ön plandadır.

Dünya ekonomisi ve yaşamını etkileyen başka bir kısaltılmış söz ise "4P"'dir.
Bu da İngilizce
People (İnsanlar),
Planet (Dünya),
Prosperity (Zenginlik)
Profit (Kar)
sözcüklerinin baş harflerinden oluşmuş bir kısaltmadır.
Bu kısaltmanın ana felsefesi kar ve zenginlik, insanlara ve dünyamıza rağmen elde edilmemeli, bu 4 vazgeçilmez faktör beraberce yeni dünyada var olabilmelidir.
Yeni dünya bu dengeler ve karmaşıklıkların akıllıca yönetilmesinin yanında, sistemin canlılığını sağlayacak bir teknoloji ve hızlı değişim dünyası olacak ve olmaktadır. Tüm üretim, hizmet ve geliştirme sistemleri eğer ayakta kalmak istiyorlarsa, bu teknolojiler ile yaşayıp varlıklarını değerlendirmek durumundadırlar. (Şekil 1)

Şekil 1 : 2014 ve sonrası Dünya'yı çalkalayacak teknolojiler (1)

Türkiye ve Türk metalurji sanayinin bu yeni dünya gerçeği karşısında yeri ve geleceğinin ne olabileceği tartışmaya açıktır. Bu yeni dünyada yer alabilmek için; Türk sanayicisi, "yaratıcı, yenilikçi ve maliyet kavramlı" oyuncular olmak zorundadır.

İNCELEME

1)2014 Yılı ve Sonrasında Dünya Döküm Sanayinin Genel Görüntüsü:

-Döküm fabrikası sayısının hem dünyada, hem Türkiye'de azalması, verimsiz ve karsız fabrikaların kapanması, birleşmeler, iki-üç tesisten oluşan üretim tesislerinin birleştirilmesi,
-Verimsiz ve kar etmeyen fabrikaların gelecek dönemlerde de tasfiyesinin devam etmesi,
-Mühendislik katkısı olmayan ürünleri üretmeyen fabrikalarda gerileyen kar marjları ve azalan talep,
- Gelişmekte olan ekonomiler hariç, gelişmiş ekonomilerde sıfırdan yeni döküm tesisi yatırım sayısı azalması. Genelde revizyon, kısmi yenileme, rekabet gücünü arttırıcı öne ve geriye doğru entegrasyon yatırımları tercih edilmesi. Özellikle Almanya'da yüksek işçilik ücretini dengeleyecek prodüktivite ve otomasyon yatırımları yapılmaktadır.
-Döküm sektöründe, 10000 yıldır önemli değişim göstermeye üretim süreci, son 50-60 yılda önemli yapısal değişime girmiştir. Son 10 yıldır ise, bir çok yaratıcı teknoloji, genelde tutucu döküm teknolojisini değiştirmektedir.
-İlk sürecinden son sürecine kadar sayısal teknoloji ile donanmış döküm tesisleri artık gündemdedir.
-Yeni malzemeler ve yeni üretim metotlarının uygulanması ile, dökümün vazgeçilmezliği tehlikeye girmektedir (Al, Mg, karbon fiber, komposit malzemeler, hibrit motorlar, elektrikli araçlar, plastik sistemler)
-Yeni dönemde, bu yeni teknolojiler ve metotlarla, döküm ürünleri diğer üretim rakiplerine göre yerlerini korumak ve güçlendirmek için önemli atılımlar yapmak zorundadır.
- Süreçlerinde ve çalışma şekillerinde yeni düzene uymakta zorlanan ve en önemlisi müşteriye güven vermede başarılı olamayan döküm fabrikalarının devre dışı

kalması kaçınılmaz olmaktadır. Uzun vadede, sadece dayanıklı olanlar ayakta kalabilmekte, bu nedenle dünyada döküm fabrikası sayısı her yıl %4-5 arasında azalmakta, fakat toplam üretim gelişmekte olan ülkelerin katkılarıyla artmaktadır. Çin'de döküm fabrikası sayısı 2020'ye kadar 30 000'den 10 000'e düşürülerek, verimliliğin 12 t/adam-yıl'dan 29 ton/adam-yıla yükseltilmesi hedeflenmektedir. (2) Benzer verimlilik iyileşmesi tüm dünyada da gözlenmektedir.

Otomasyon, verimlilik, çevre kurallarının sıkılığı, kalite beklentilerinin artması, süreçlerde yenilikler döküm yatırımlarını daha pahalı hale getirmekte, bu nedenle yeni yatırımlarda önemli büyüme beklenilmemektedir.
Üretilen ürünlerin kullanıldığı yerler, en azından bugün için alternatifsiz bir üretim şekli olması ve birçok dizayn problemine çözüm olmasına rağmen dökümün dünya milli gelirine katkısı %0.3'ü aşmamakta, dünyadaki tüm metal üretiminin ise %5'inin oluşturabilmektedir.(Şekil 2)

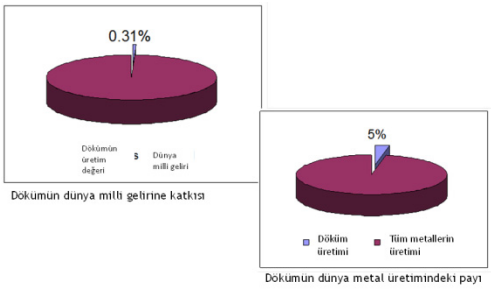

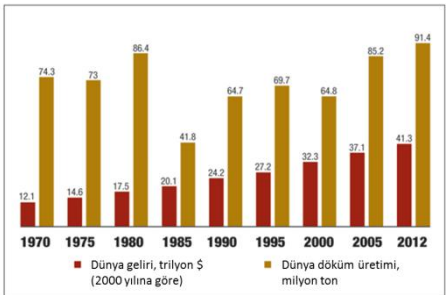

Şekil 2 : Döküm üretim değerinin dünya milli gelirine ve üretimini dünya metal üretimine oranı (üst) Dünya gayri safi gelirine göre dünya döküm üretim miktarının değişimi (alt) (3)

Dünya milli gelir artışı ile karşılaştırıldığında, döküm üretimi yılda % 1.5-1.8 arasında artmasına rağmen, dünya milli geliri % 3.5-3.7 arasında artmaktadır. Döküm sektöründe büyümede metaller arasında önemli farklılıklar olup, öncülüğü alüminyum almaktadır. Son 50 yılda alüminyum kullanımı 12.7 (yıllık %5), çelik kullanımı 4 katı artmıştır (Şekil 3)

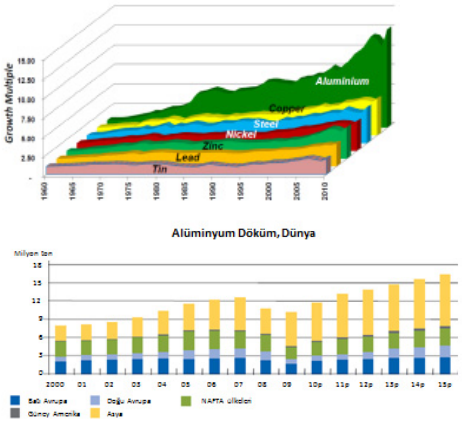

Şekil 3 :Yıllara göre alüminyum ve çelik kullanımının büyümesi

Döküm üretimi ve kullanımının, dünyadaki değişik ülkelerin ekonomilerinde farklı etkileri olmaktadır. En büyük etki Çin'de görülmekte, Türkiye alt sıralarda yer almaktadır (Şekil 4)

Ülke	Döküm üretimi (kişi başı kg)	Döküm üretimi (1.000$ bazında milli gelire göre kg)
Çin	26.4	9.52
Rusya	30.0	3.11
Hindistan	6.4	6.01
Brezilya	11.6	1.57
Kore	44.0	2.04
Japonya	34.5	0.90
Almanya	47.4	1.17
Türkiye	13.4	1.44
Dünya ort.	19.1	0.71
A.B.D	24.1	0.51
Meksika	13.4	1.34
İngiltere	6.4	0.14

Şekil 4 : Kişi başına ve 1000$'lık gayrisafi miili gelir başına düşen döküm üretimi (3)

Döküm ürünlerinin kişi başı kullanımı ve ekonomiye katkısı ise AB ve Nafta ülkelerinde yüksek (10 kg döküm 1000 € katma değer yaratıyor), gelişmekte olan ülkelerde ise alt seviyededir. (30 kg döküm 1000€ katma değer yaratabiliyor) (Şekil 5)

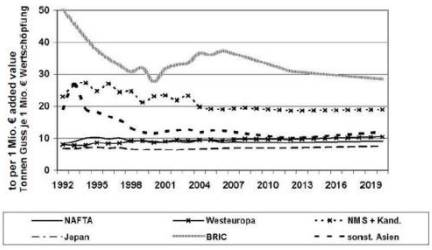

Şekil 5 : Döküm ürünlerinin kişi başına kullanımı (4)

2000'li yıllardan itibaren, döküm üretimi ve kullanımı gelişmekte olan ülkelerde artmaktadır. 2020 yılında BRİC ülkelerinin döküm üretiminin %60'ının yapacağı tahmin edilmektedir. (5)

Yıllar itibari ile sağlıklı bir gelişme gösteren Türk Döküm sektörü, dünya döküm üretiminde 13.cü, AB'de 4.cü, çelik dökümde 2.ci, lamel ve küresel grafitli dökme demir'de 3.cü, alüminyum dökümde 6.cı durumdadır.(Şekil 6)

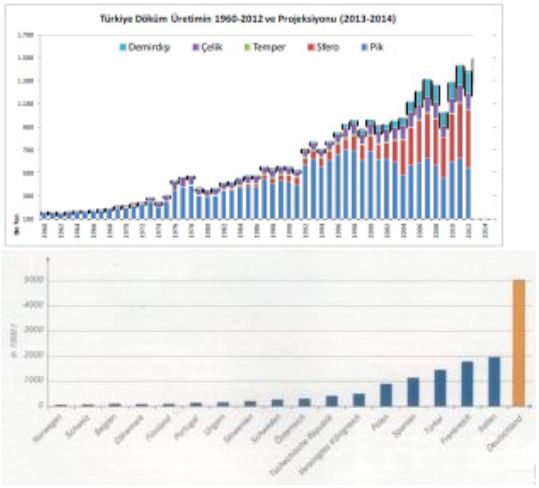

Şekil 6 : Türk döküm üretimi ve AB'deki yeri(6)

Üretilen ürünlerin karmaşıklığı, malzeme bilimi ve zorluk dereceleri göz önüne alındığında sıralama önceliği AB ve ABD'ye geçmektedir.
Türkiye'deki diğer sektörler göz önüne alındığında başarı gibi görünen bu sıralamanın gelecek yıllarda korunabilmesi için Türk döküm sektörü, teknoloji, müşteriye hizmet anlayışı, ileriye ve yerine göre geriye doğru entegrasyon, enerji ve ekoloji, üretim verimliliği ve ürün karmaşıklık seviyesi konularında yapısal değişikliklere girmek zorundadır.
Dökümün ilk Anadolu'da yapıldığı ve buradan Avrupa'ya dağıldığı çeşitli kaynaklar ve araştırmalarda belirtilmiştir. (Şekil7)

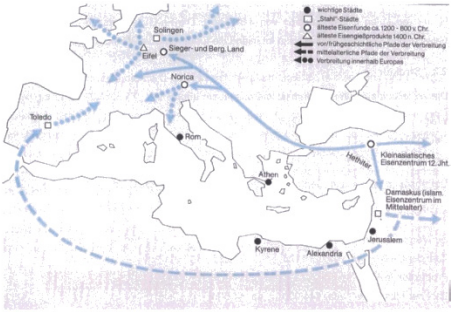

Şekil 7: Dökümün Anadolu'dan Avrupa'ya yayılması

Anadolu tarih boyunca insanların kullandığı araçlar ve malzemeler üretiminde öncü olmuştur. (ilk metal-Çatalhöyük 11000 yıl önce, ilk tapınak-Göbeklitepe 12000 yıl önce, ilk döküm-Nevari-Çöri, Kültepe-Kaniş 8000 yıl önce)

Dünyadaki bu yeni eğilimler karşısında, Türk döküm ve metalürji sektörü olarak kendi kendimize sormamız gereken bazı sorular:

-Döküm ve metalürji sektöründe ne kadar öncüyüz?
-Dünya nerede biz neredeyiz?
-Her şey yıllık üretim tonajı mı? Yoksa rekabet gücü ve inovasyon mu?
-Bu tonajlar ve sıralama gelecek yıllarda tutulabilecek mi?

Dünya'da her alanda, bir hiper rekabet dönemi olduğu, ülkelerin, şirketlerin uluslararası alanda pazar kapmak için her türlü yeni yaklaşımı değerlendirdiği bir ortamda, Türk sanayicisinin de teknoloji, prodüktivite, pazarlama, inovasyon yönünden atılımlar yapma zorunluluğu vardır. Türkiye BRİC ve AB ülkeleri ile karşılaştırıldığında rekabet gücü açısından geride kalmaktadır (Şekil 8)

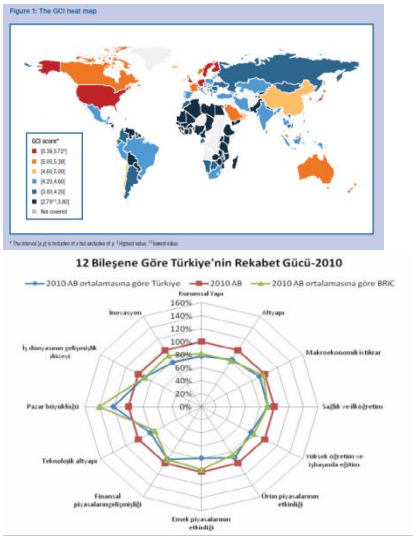

Şekil 8 : Türkiye'nin hiper rekabet döneminde dünya (üst) ve BRIC ülkelerine göre (alt) rekabet gücü

Teknolojik ürün fiyatları, basit ve klasik üretim teknolojileri ile yapılan üretimlere göre 10-20 kat daha yüksek fiyatlarla satılabilmektedir. Standart bir lamel grafitli dökme demir döküm parça 1.25 $/kg fiyata satılırken, bu dökümün kullanıldığı bir " Premium" otomobilin kg fiyatı 55 $'dır. Bunun yanında Türkiye'nin ürettiği, teknoloji ürünleri alt kategorilerde olup, 12.2 $/kg, ABD ve Japonya'nın sattığı teknolojik ürünler ise 53-68$/kg mertebesindedir.

2)Döküm Ürünlerinin Pazarı

Döküm ürünlerinin dünya pazar dağılımında, ana müşteri grubu otomotiv olup, üretimin %50'si otomotiv ve bağlı sektörlere, %30'u makine sektörüne satılmaktadır. Türkiye dağılımı da benzer yapıdadır.
Türkiye'nin döküm üretiminin %65'i AB ülkelerine ihraç edilmektedir. Bu nedenle AB ülkelerindeki ve özellikle araç ve makine sanayindeki ekonomik gelişmeler Türk döküm üretimini yakından ilgilendirmektedir. Türk döküm ihracatı ile AB'nin GSYH'sı ve sanayi üretimi birbirine paralellik göstermektedir. (Şekil 9)

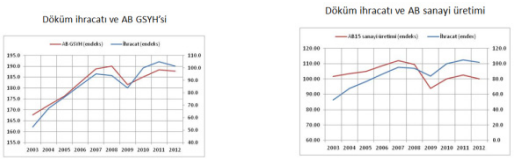

Şekil 9 : Türk döküm endüstrisinin AB ekonomisine bağlılığı (7)

3)Türk Döküm Sektörü Pazarının Değerlendirilmesi

Döküm sektörünün ana iki müşterisi olan taşıt araçları sanayii (%50) ve makine imalat sanayilerinin (%30) gelecek 10 yılda büyüyeceği ve satışlarını arttıracağı öngörülmektedir.

A)Makine İmalat ve Mühendislik Pazarı

2020 yılına kadar tüm dünyada ve en yakın pazarımız olan AB'de yıllık %3-10 arasında büyüme beklenilmektedir. Türk döküm sektörü, mühendislik ve makine ürünleri içeren bu pazara gerek yurt içi ve gerekse yurt dışında önemli hizmetler vermektedir.

B)Taşıt Araçları Pazarı

Türk döküm sektörünün ana müşterisi olan Türkiyede'ki ve AB'deki araç üreticilerinin gelecek yıllarda yıllık üretim adetleri önemli miktarda artmayacaktır.(Şekil 10) (8)(10)

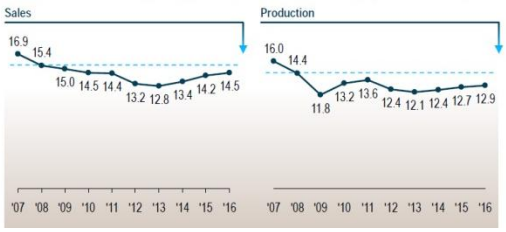

Şekil 10 :AB otomobil + hafif ticari araç üretiminin gelecek tahminleri (9)

Türk döküm sektörünün ana pazarı olan, AB'deki otomobil üreticilerinin ürettiği araçlar gittikçe lüks araç türüne doğru kaydığından (Şekil 11)), Türk komponent üreticileri ve bunlara döküm parça veren döküm sektörü, yüksek hizmet ve kalite bekleyen bu premium sınıf araç üreticileri

için kalite, müşteri, hizmet ve teknoloji anlayış ve yeteneklerini geliştirmek zorundadırlar. Döküm sektörünün üretimini arttırabilmek için genişleyen A/B sınıfı küçük araçlara ürün verme çalışmasına girmeleri gerekmektedir.

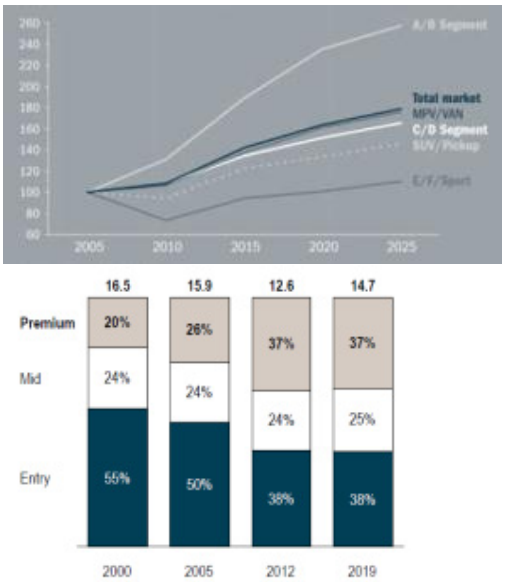

Şekil 11 AB 'de lüks araç üretimi artmasına rağmen (alt), dünyada ise küçük araç üretimi artmaktadır (üst).(11)

DEĞERLENDİRME

1)2014 Sonrası Döküm Pazarını Etkileyecek Faktörler

21.ci yüzyılda önemli değişimler yaşamakta olan dünya sanayii ve pazarları döküm sektörünün pazarlarını da önemli şekilde etkilemektedirler.

A) Düşük karbon teknolojileri:
   a) Araçlarda hafifleme
   b) Dökümlerde artan ölçüsel hassasiyet
   c) Değişen ve gelişen kalite yaklaşımı
   d) Yeni malzeme bilimi
B) Dijitalleşme (Sayısallaşma)
   a) Her yerde, her işlemde simülasyon
   b) Bilginin toplanması, paylaşılması, kullanılması
   c) Süreçlerin on-line takibi
C) Globalleşme
   a) Ürünlerin satıldığı yerde üretilmesi
   b) Yan sanayicilerin ana sanayinin yakınında üretim yapma zorunluluğu
   c) Ekolojik, geri dönüşümlü, etik ve toplum kurallarına uyumlu üretim

Bu yeni beklentilere karşı döküm fabrikaları ne yapabilirler:

A) Hiçbir şey:
   Zaman içinde küçülüp, niş pazarlara yöneliyorlar
B) Kapatma:
   Bir çok tesis zarar edip, gelecek görmediği için kapanıyor . Çalışan döküm tesis sayısı her yıl azalıyor
C) Satış:
   Büyüme ve yeni anlayışlarla çalışma heves ve gücü kendilerinde bulamayan döküm fabrikaları, tesis veya şirketlerini fonlara, rakiplere veya bu işi daha iyi yapacağına inananlara satıyorlar.
D) Yeni beklentilere uyum ve işe devam:
   Süreçler, müşteriye yaklaşım, ürün portföyü, insan kaynakları, teknolojik yatırımlar, yenilikçi sistemler ve en önemlisi "işi yönetmeye" başlayarak yeni pazarda yer almak

2)Otomotiv Sektöründeki Hafifleme ve Düşük CO2 Salınımı Hedefinin Döküm Sektörüne Etkisi;

Gerek AB, gerekse ABD'nin öncülük ettiği araç emisyon değerleri (gr CO2/km), bir çok otomobil, kamyon, traktör üreticisi firmanın cezalar nedeni ile ana hedefi haline gelmiştir. Bilinçli müşterilerin %60'ı düşük yakıt sarfiyatı ve emisyon değerine bakarak araç almaktadırlar. Aracın hafiflemesinin enerji kullanımı ile çevre kirliliğine direkt etkisi bulunmaktadır. (Şekil 12)

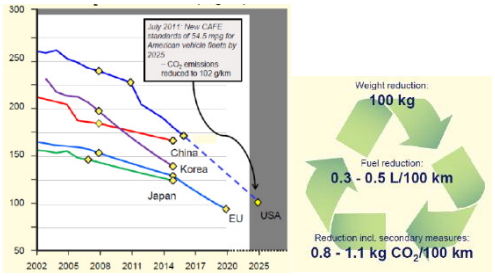

Şekil 12 : Araçlarda emisyon limit değerlerinin (gr CO2/km) yıllara göre değişimi

Araç hafifletmede görev "Metalurji Bilimi"'ne düşmektedir.

Araç üreticileri bu değerleri tutturmak için:

a) Araçların ölçü ve ağırlıklarını düşürmektedirler
b) Motor ve güç aktarma gruplarının ağırlıklarını indirmektedirler
c) Toplam araçta çeşitli aksesuarlar eklenmesine rağmen, ağırlık azalması sağlamaktadırlar.

Tüm bu tedbirler, aracın ağırlığının önemli bir kısmını oluşturan metalik malzemeler için hem bir tehdit, hem de bir fırsat ve meydan okuma olanağıdır.
Metalurji Bilimi yeni malzemeler geliştirmekte, araç dizayn edenler gereksiz şartnamelerini yeniden düzenlemekte, metal üreticileri ise bu yeni malzemeleri en ekonomik üretme süreçlerini oluşturmaktadırlar.

Araç hafiflemesinin döküm sektörüne etkisi iki alanda olacaktır:

a) Elektrikli araçlara geçişte azalacak döküm talebi, 2020'de dünya çapında üretilmesi planlanan takr. 10 milyon elektrikli araç için 650-700.000 tondur.
b) Araç hafifleme çalışmalarında azalacak döküm tonajı ise, motor, şasi, transmisyon, dingiller, et payı incelmeleri, Al/Mg'a dönüşüm, kompozitlere geçiş nedenleri ile 2-2.5 milyon tondur.

3)Araç hafiflemesinin döküm ve metalürji bilimine katkıları

A)Genel Bilgi:

Araçların emisyon limitlerini tutturabilmek ve yakıt tasarrufu sağlamak için hafifletilmesi döküm sektörünün yıllık üretim miktarını azaltmasına rağmen, yapısal değişiklik getireceği ve metalürji bilimini geliştireceği için sektör açısından artı bir kazanç olacaktır.
Araçta hafifleme denince ilk akla gelen, araçlarda çok miktarda kullanılan özgül ağırlığı yüksek olan dökme demir ve çelik malzemelerin yerlerine daha hafif olan Al ve Mg'un kullanılması olmuştur. Zaman içinde, bu ağırlık hafiflemesi emisyon limitlerine ulaşmaya yetmediğinden kompozitler, karbon fiber ve plastik ürünlere yönelinmiştir. (Şekil 13)

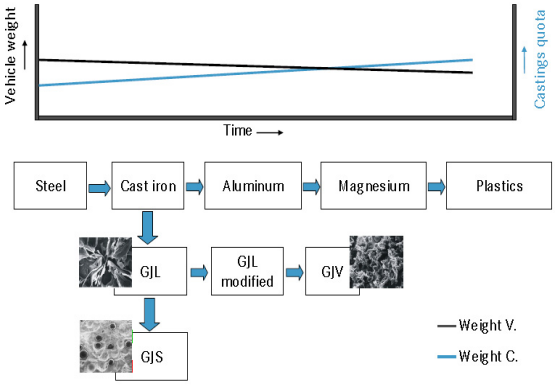

Şekil 13 : Araç üretiminde kullanılan malzemelerin zamana göre değişimi ve alüminyum ve kompozitlerin yıllara göre artışı

Araç hafiflemesi süresinde kullanılan malzemelerin özellikleri Şekil 14 'de verilmektedir.

	Çelikler	Alüminyum alaşımları	Magnezyum alaşımları	Polimerler	Polimer Kompozitler
Mevcut ürün şekilleri	Sac, çubuk, boru, döküm, dövme	Plaka, çubuk, ekstrüzyon, döküm, dövme	Döküm	Plaka, kalıplanmış şekil, ekstrüzyon	Plaka, kalıplanmış şekil, haddelenmiş şekil
Yoğunluk (g/mm3)x10-2	0.72 - 0.80	0.26 - 0.27	0.18	0.11 - 0.22	0.17 - 0.19
Elastik Modül (GPa)	207	69 - 73	45	0.69 - 3.3	3.4 - 34
Akma dayanımı (MPa)	172 - 900	68 - 590	206	41 - 90	97 - 145
Kopma dayanımı (MPa)	365 - 1200	310 - 620	310	55 - 1124	110 - 172
Uzama %(mm/mm)	10 - 55	6 - 20	15	-	-
Poisson Oranı	0.3	0.33	-	-	-
Termal genleşme (mm/mm/°C)	10.8 - 19.4	19.4 - 24.5	25	81 - 216	16.7 - 90
Termal iletkenlik (W/(m.°K))	36 - 52	159 - 216	100	0.2 - 0.5	0.2 - 0.5
Korozyon direnci	Orta	Yüksek	Düşük	Yüksek	Düşük
Kullanılabilir Sıcaklık Aralığı (°C)	315	150	120	120	150
Birleştirme teknigi	Ark, punta kaynağı, bükme, mekanik	Ark, punta kaynağı, bükme, mekanik	Bükme, mekanik	Bükme, mekanik	Bükme, mekanik
Şekillendirme özelliği	İyi	Orta - İyi	-	Düşük	Düşük
Göreceli fiyat	Düşük	Orta	Orta	Düşük	Orta

Şekil 14 : Araçların hafifletilmesinde kullanılan malzemelerin özellikleri

Malzemelerin mekanik özellikleri ve özgül ağırlıklarına göre yapılan hafifletme seçimine maliyetlerin eklenmesi ile, hafifletme sürecinde en fazla kullanılan alüminyum beher N/mm2 kopma dayanımı için en pahalı malzeme olmasına rağmen, emisyon değerleri nedeni ile gene alüminyum tercih edilmektedir. (Şekil 15)

Mekanik özelliklere göre maliyet		
Lamel grafitli DD	$\frac{1500\$/t}{250\ N/mm\oplus}$	= 6$/N/mm⊕
Çelik döküm	$\frac{3000\$/t}{500\ N/mm\oplus}$	= 6$/N/mm⊕
Temper döküm	$\frac{2000\$/t}{400\ N/mm\oplus}$	= 5$/N/mm⊕
Küresel grafitli DD	$\frac{1700\$/t}{500\ N/mm\oplus}$	= 3,4$/N/mm⊕
Ostemperlenmiş DD	$\frac{2500\$/t}{1000\ N/mm\oplus}$	= 2,5$/N/mm⊕
Alüminyum döküm	$\frac{8000\$/t}{200\ N/mm\oplus}$	= 40$/N/mm⊕

Şeki l15 : Çekme dayanımı ve ürün fiyatlarıyla, alternatif malzemelerin birim maliyeti

2 lt'lik motoru olan 1360 kg ağırlığındaki bir sedan araçta, hafifleme ve enerji tasarrufu nedenleri ile, alüminyum ve plastik kullanımı artmakta, dökme demir azalmaktadır. Araç üretiminde kullanılan döküm, dövme, hadde mamulü alüminyum miktarının 2030 yılı itibari ile ağırlıkça %67'ye ulaşması beklenilmektedir. (Şekil 16)

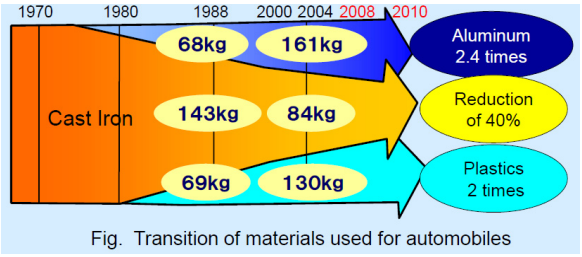

Fig. Transition of materials used for automobiles

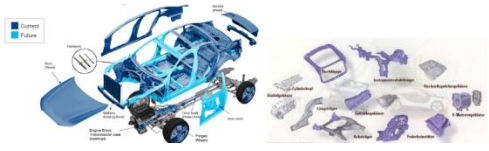

Şekil 16 : Araçlarda bugünkü ve gelecekteki alüminyum kullanım yerleri ve miktarları

B) Hafiflemenin döküm teknolojisindeki uygulamaları;

a) Tuz maça kullanılarak "closed deck" motor gövdesi dökümü

Araçlardaki esas ağırlık tasarrufu ve verim artışı, motor ve şanzıman gruplarında yapılan iyileştirmelerdir.

Bu ürünler genelde lamel grafitli dökme demir olarak üretilmelerine rağmen, yakıt verimi beklentilerinin artması ve döküm teknolojisinin ilerlemesi ile alüminyum döküm olarak imal edilmeye başlanılmıştır. İlk başlarda yüksek basınçlı alüminyum döküm metodu ile 'open deck' şeklinde üretilen motorlar, 2010 yılında geliştirilen 'tuz maça' sistemi ile 'closed deck' olarak üretimi yapılarak, toplam motor maliyeti azaltılmaktadır. (Şekil 17)

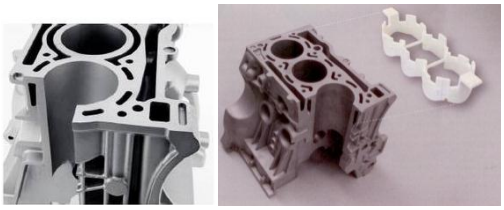

Şekil 17 : Tuz maça kullanılarak 'open deck' motor blokları, dökme demir gibi 'closed deck' olarak dökülebilmektedir.

b)Hibrit motor gövdesi

Bazı araç üreticileri alüminyum motorların ağırlığını daha da düşürebilmek için gövdeyi Mg yüksek basınçlı döküm, darbe ve ısıya maruz silindirler ve kep bölgesini alüminyum yüksek basınç olarak hibrit şekilde üretmektedirler. (Şekil 18)

Şekil 18 : Al-Mg hibrit motor

c)Aluminyum motorlara karşı demir dökümcülerin hamlesi:

Al ve Mg'un motor üretiminde kullanılması ile pazar kaybeden dökme demir üreticileri, teknolojilerini geliştirerek, döküm et paylarınıı inceltip, malzeme dayanımını yeni tip motorlarda artan yanma odası basıncına dayanacak yumru grafitli dökme

demir kullanarak arttırmayla cevap vermişlerdir. Döküm teknolojileri ve süreçlerindeki ilerleme, dökme demir motorlarda alışılagelmiş olan 4.5+/-1 mm olan et paylarını, dikey döküm yaparak 3.0 +/-0.5 mm'ye indirilmesini ve blok ağırlığını 38.5 kg'dan 28.5Kg'a inmesini sağlamıştır. (Şekil 19)

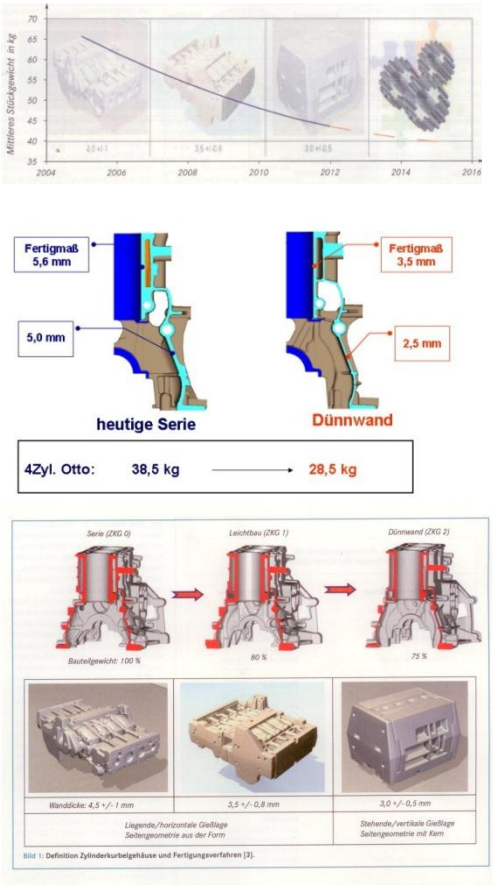

Şekil 19 . Dökme demir motor bloklarında teknoloji ve süreç iyileştirmeleri ile azalan blok ağırlığı ve et payı inceltilmesi (12)

Araçlarda hafifleme sadece otomobillerde kalmayıp, CO2 salınımı sınırlamasının kamyon ve kamyonetlerde de uygulanmaya başlaması ile ticari ve sokak aralarındaki çatışmalarda manevra yeteneği arayan askeri araçlarda da alüminyum ve kompozit kullanımı arttırılmaktadır. (Şekil 20)

Şekil 20 : Kamyonet ve askeri araçlarda alüminyum ve komposit kullanılan araçlar (13)

Araç şasi, platform ve karoserisinde kompozit malzemelere karşı Bi, B,Cr; Mn ve Ti katkılı alüminyum alaşımlar üretilerek, hafifletmede Pazar yarışı devam etmektedir. (Şekil 21)

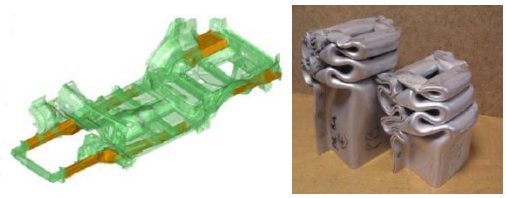

Şekil 21 : Al 6000 serisi malzemelerle araçta 6 kg ağırlık ve %9 maliyet tasarrufu sağlanılmaktadır (14)

d)Komposit malzemeler ve karbon fiber kullanımı,

Bu malzemelerin kullanımı hafifleme talebinin yükselmesi ile artmaya başlamıştır. Saç veya alüminyumdan üretilmiş gövde (Body in White), karbon fiber kullanılması ile (Body in Black) adını almaktadır. (Şekil 22)

Şekil 22 : Araçlarda artan 'karbon fiber' kullanışının artışı karoserinin adını 'beyaz gövde'den 'siyah gövde'ye çevirmektedir.(15)

e)Hafifleme hamlesinde çelik üreticilerinin tepkileri:

Aluminyum ve kompozitin araçlarda önemli bir pazarlarını ele geçirmeye başlaması üzerine, çelik üreticileri de yeni mikro alaşımlı ve nano katkılı çelikler üreterek dış saç, şasi ve platformda hafifleme sağlayarak, pazar savaşına girmişlerdir.(Şekil 23)

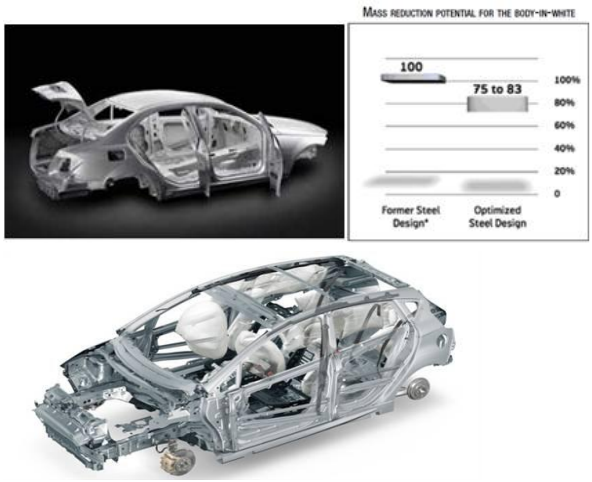

Şekil 23 : Nano katkılı ve mikro alaşımlı çeliklerle araç hafiflemeye çelik sektörü katkıda bulunmaktadır (16)(17)

Hafifleme yarışı, karada yürüyen araçlardan havada uçan araçlarda da devam etmekte, metalürji bilimi yeniliklerle uçak gövdelerini Al-Li alaşımlarından üreterek, %5-7 hafifleme ve %7 dayanım artışı sağlamaktadır.
Hafifleme çalışmaları uç noktalarda da denenmekte ve polystrene takviyeli kumaş kaplı araçlar denenmektedir.

f)Akü yükünün azaltılması

Elektrikli araçlarda aracın karoserisi içine akü plakaları yerleştirilerek, hafifleme ve yer kazanma çalışmaları yapılmaktadır. (Şekil 24)

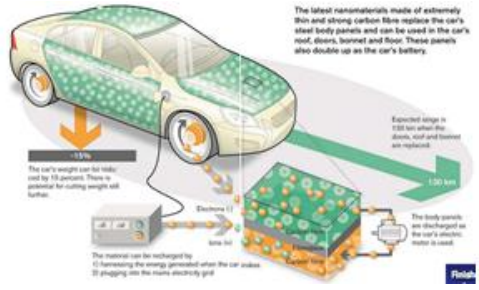

Şekil 24 : Elektrikli araçlarda akünün karesöri içine gömülmesi

C)Araçlarda kullanılan diğer döküm parçalarda hafifletme çalışmaları:

Döküm ve metalürji sektöründe rekabetçilik için yapılan yeni atılımlarda ilerleme ve fark yaratma inovasyon sınırlarını aşıp, deneme-seri üretim alanına girmiştir. Sonuçta kazanan rekabetçilik yaratabilen kuruluş ve sektörler olmaktadır.

a) Krank Millerinin içinin boşaltılması ve ostemperlenmiş inceltilmiş krank mili
b) İçi boş kam mili veya borudan yapılmış kam mili
c) Aluminyum göbekli veya yaylı fren diskleri. Dışı küresel grafitli dökme demir, fren yüzeyleri lamel grafitli dökme demir kampana
d) Saç veya alüminyum jant yerine, karbon fiber jant veya nano katkılı alüminyum jant
e) Aluminyum ve çinko alaşımlarında akışkanlığı arttırıp, baskı basıncı yükselterek 2 mm et payı kalınlığında Al ürünler, 0.3 mm kalınlığında Zn ürünler üretilmesi.
f) Diferansiyel kutularında dişli ve gövdenin yekpare ostemperlenmiş dökme demirden üretilmesi.
g) Artan eksoz gaz sıcaklıklarına dayanan Si_Mo eksoz manifoldları
h) Doğa en iyi ve en ekonomik dizaynıcıdır. Doğanın bu özel-liklerinden yararlanılarak "Bio-Design" metodolojisi çeşitli ürünlerin geliştirilmesinde kulla-nılmaya başlanılmıştır.(Şekil 25) Bio-Design anlayışı ile hafifletme çalışmaları %40'a yakın iyileşme sağlamaktadır.

Bio dizayn ile hafifleştirilmiş tezgah gövdesi

Şekil 25 : Bio-Design ile parça ağırlığının azaltılması (18)(19)(20)

4) Malzemelerde İnovasyon

Döküm tarihinin 9.000 yıllık süreci içinde metal bilimi önemli atılımlar geçirmiştir. 20-25 metalden oluşan periyodik tablo bugün 118 elemana büyümüş, sonuna gelinmediği için daha da büyüyecektir. Uzay çağı malzemeleri önce hayallerde, sonra kitaplarda, daha sonra filmlerde, daha sonra laboratuarda, kısa süre sonra ise seri üretimde üretilmektedirler.(Şekil 26)

Şekil 26 : Foranium, Carbonium gibi hayali malzemeler metalürji biliminin ufkunu açtı

Dökme demirde 150 N/mm2 çekme dayanımını başarıydı. Bugün ostemperlenmiş küresel grafitli dökme demirde 1000 N/mm2 ve % 5 uzama elde ediliyor.
Daha temiz metallerle (%99.9 yoğunluk) mevcut mekanik ve fiziksel özelikler en az iki misli artacaktır.
Tarih boyunca malzemelerin önemi bir uçtan bir uca gitmiştir. Medeniyetlerin ilerlemesi, seramik, metal ve polimerlerin gelişmesi ve bu malzemelerin üretim şekillerinin oluşturulması ile mümkün olmuştur. (Şekil 27)

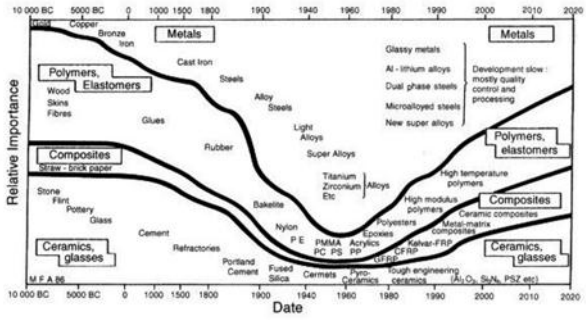

Şekil 27 : Malzemelerin tarih boyunca değişimi (21)

5) Nano katkılarla döküm ürünlerinin mekanik ve fiziksel özelliklerinin arttırılması:

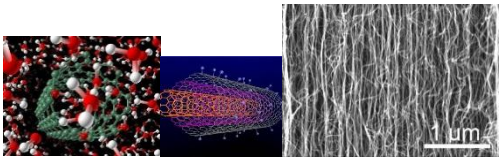

Şekil 28 : Nano katkı malzemeleri

Mevcut malzemelerle araçların hafifletilmesi, ancak süreç ve metodolijilerdeki sınırlı olanaklarla mümkün olmaktadır. (Et payı inceltme, döküm konikliklerinin azaltılması, hassas ve dar analiz kontrolü, empuritelerin azaltılması, çekinti ve gaz boşluklarının sıfırlanması, gibi)
Malzemelerin özelliklerini iyileştirebilecek atılımcı bir çözüm ise, bu malzemelere eriyik halde iken az miktarlarda SiC, karbon fiber, alümina gibi nano ölçekte tüp şeklinde katkılar yapmaktır. (Şekil 28)
Bu katkılarla üretilmiş alüminyum jant gibi parçalar araçlarda kullanılmaktadır.
Nano tüp katkılarla, malzeme özelliklerindeki %100'e varan artış sağlanan alüminyum, ferritik küresel grafitli dökme demir ve yüksek silisli küresel grafitli dökme demir malzemelerin özellikleri Şekil 29 a,b,'de verilmektedir

Nano ilavesi, gram		20	30	40	50	60	70
Malzeme Özellikleri							
Malzeme	Ferritik Küresel Grafitli DD	Yeni	Yeni	Yeni	Yeni	Yeni	Yeni
Kopma dayanımı	400	460	554	647	1020	1398	2144
Uzama	%18	%18	%18	%18	%18	%18	%18
Sertlik	130	143	157	173	190	209	230
Max. Çalışma Sıcaklığı	400	484	673	863	1054	1317	1687
Elastik Modül, GPa	60	1.E+02	3.E+02	2.E+03	9.E+03	7.E+04	6.E+05
Termal geçirgenlik	33	134	165	174	185	195	206
Erime Noktası	1150	1154	1296	1438	1582	1798	2121

Nano ilavesi, gram		20	30	40	50	60	70
Malzeme Özellikleri							
Malzeme	Alüminyum Döküm, 306	Yeni	Yeni	Yeni	Yeni	Yeni	Yeni
Kopma dayanımı	250	420	491	561	842	1128	1690
Uzama	%7	%7	%7	%7	%7	%7	%7
Sertlik	130	143	157	173	190	209	230
Max. Çalışma Sıcaklığı	200	270	426	582	739	953	1255
Elastik Modül, GPa	60	1.E+02	3.E+02	1.E+03	5.E+03	3.E+04	2.E+05
Termal geçirgenlik	170	413	443	494	516	544	568
Erime Noktası	1150	1155	1267	1382	1497	1671	1931

Şekil 29 a, b: Ferritik küresel grafitli dökme demir (sol) ve alüminyum (sağ) dökümde nano katkılarla özelliklerin değişimi

Gene nano teknoloji kullanarak üretilen kalıp ve parça boyaları, dayanım

ömürlerini %50 arttırarak, süreçlerde verimliliği arttırmaktadır. (Şekil 30)

Şekil 30 : Nano katkılı kalıp boyaları ile, kalıp ömür ve baskı sayıları arttırılmaktadır(22)

Metallere nano katkılar yaparak, fiziksel ve mekanik özelliklerin arttırılması kategorisine giren inovatif malzeme biliminin başka bir çalışması ise "bio-mimicry" adı verilen " Kendi kendini tedavi eden" malzemelerdir. (Şekil 31)

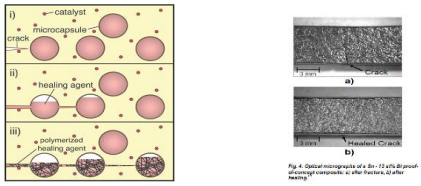

Şekil 31 : Kendi kendini tamir edebilen nano katkılı malzemeler. Sağda çatlağın kendi kendine tamir edildiği Sn-%13 Bi komposit malzeme

6) Additive Manufacturing- 3D Eklemeli Üretim

Özellikle kısa serili döküm üretimini etkilecek ve son yılların oyunun kurallarını değiştirebilecek teknolojik gelişmesi 3D-Baskı veya additive manufacturing (eklemeli üretim) teknolojisidir.(23)
Yeni yeni günlük hayatın içine giren bu teknoloji yetenekleri ve gelişme potansiyeli ile klasik üretim tekniklerine önemli bir rakip olmaktadır. (Şekil 32)

Şekil 32 : 3D Eklemeli üretim yolu ile üretilen paslanmaz çelik Airbus A380 parçası, İmplant ve protezler (24)

3D sistemini döküm sektöründe etkileyebileceği alanlar

a) Kısa serili ürünler
b) Prototipler ve hızlı ürün geliştirme (11 hafta yerine 5 hafta)
c) Çalışma ve dizayn için hızlı örnekler
d) Hızlı kalıp üretimi
e) Klasik modelciliğe büyük darbe
f) Kısa serili maça üretimi
g) Kalıp masraflarının düşmesi veya sıfırlaması ile bir çok döküm parçanın tekrar rekabetçi hale gelmesi (25)
h) Döküm süreçleri ile üretilmesi çok zor olan parçaların ekonomik olarak üretilebilmesi,
i) 3D'nin en büyük etkisi, müşterinin döküm teslimatçısını, yeni model yaptırma masrafından kaçınması nedeni ile bırakamaması olgusunu ortadan kaldırmasıdır. Bu şekilde mevcut işlere ortak olmak isteyecek yeni ucuz rakipler devreye girecektir.

Halen çelik bazlı bir toz ile 3D üretim yapılması 450€/kg'a mal olmasına rağmen, 10 yıl içerisinde bu rakamın 3'de bire ineceği hesaplanmaktadır. 3D metoduyla, bir tarayıcı vasıtası ile her hangi bir objenin 3D datası tarama yolu ile çıkartıldıktan sonra, bu data ile uygun malzemeden 3D baskı yolu ile aynısı yapılabilmektedir.(Şekil 33)

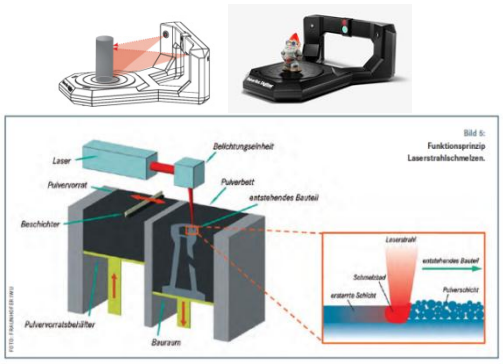

Şekil 33 : Tarayıcı ile 3D baskı için numuneden 3 boyutlu data çıkarılması (üst) ve 3D baskı sisteminin çalışma şekli (alt) (27)

Sistemde belirli ve ayarlanabilen bir kalınlıkta akan metalik toz lazer ışını ile kat kat sinterlenerek istenilen şekil oluşturulmaktadır.
Aynı şekilde, reçine bağlı kum kullanarak 3D data ile kat kat maça ve kalıplar yapılıp, istenilen numune veya kısa serili döküm parça üretilebilmektedir. (Şekil) 34)

Şekil 34 : 3D baskı tekniği ile maça yapılması

Sistemin maça yapma hızının artması ile, maça makinaları, maça bölümleri, maça sandıkları ve maça bekleme gibi konular geride kalacaktır.

Bunların yanında, döküm veya dövme teknolojisinde gerekli olan sıyırma açılarının sıfırlanması, daha yüksek hassasiyet nedeni ile işleme paylarının azaltılması, gaz-çekinti boşluğunun olmaması, yolluk ve besleyiciye gerek olmaması 3D baskı ile üretilen parçaların daha hafif olmasına katkıda bulunmaktadır.

Bugün için hayal gibi görülebilen, otomobil gövdesi kum kalıbının 3D ile oluşturulması, alüminyum veya benzer bir alaşımla kalıp dökülerek, yekpare gövde üretilmesidir. Bu hayal gerçekleşirse, şase kaynak olayı ortadan kalkacak, otomobil fabrika alanları çok küçülecektir. (Şekil 35)

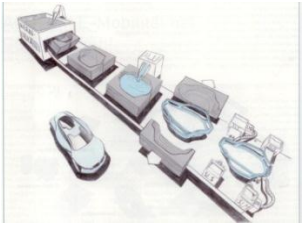

Şekil 35 : 3D eklemeli üretim ile araç gövdesinin dökümü

7)Döküm Fabrikalarının Gelecekte Kurulum ve Yerleşimlerinin yeni anlayışa göre yapılanması

Dünyada gelişmekte olan rekabetçilikteki yeni anlayışlar, maliyetlerin indirilmesi, döküm fabrikalarının yerleşimleri ve iç yapılarında da yenilikler getirmiştir. Geleceğin döküm fabrikaları, çalışanları, üretim yönetimi, süreçleri, verimliliği ürünleri ve teknolojiyi içeren akıllı fabrikalar olacaktır.(Şekil 36)

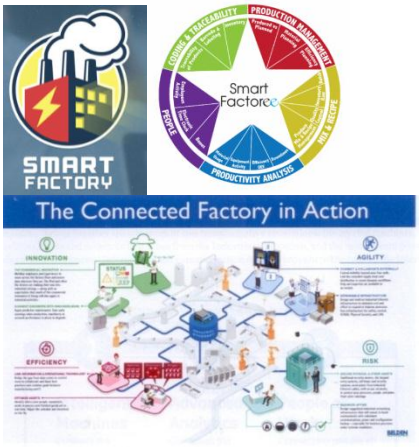

Şekil 36 : Geleceğin fabrikaları akıllı kendi içinde haberleşen, bilgi veren ve karar verebilen fabrikalar olacaktır. (28)

Tüm süreçler, üretim planlanması, yönetimi, müşteri ile bağlantılar gibi bir çok husus birbiri ile bağlı olarak çalışan sistemler halinde olacaktır.
Geleceğin döküm fabrikasına örnek bir görüntü Şekil 37 'de verilmektedir.

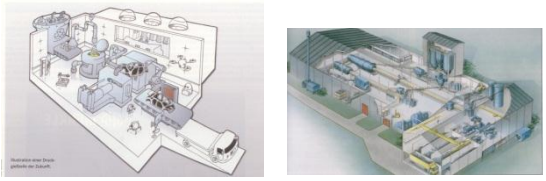

Şekil 37 : Geleceğin alüminyum döküm fabrikası (sol) ve doğru ve etkin yerleşimli bir dökme demir fabrikası (sağ)

Döküm sektörünün ana müşterisi taşıt üreticileri de, hem araçlarını modüler, hem tesislerini modüler hale getirmektedirler. (Şekil 38)

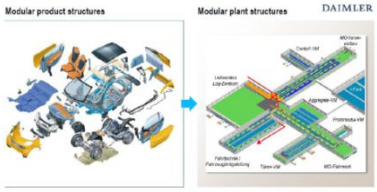

Şekil 38 : Moduler fabrika yapısı (Mercedes)

1-15 tona kadar küresel grafitli dökme demir döküm parçalar imal etmek üzere 2012 yılında devreye giren Heger Ferrit-Almanya döküm fabrikasında kalıplanan ve dökülen dereceler dairesel bir ray sistemi üzerinde hareket ediyor. Yan modüller maça, temizleme ve sevkiyat için kullanılıyor. Tesisteki otomasyon ve parçanın indir-bindir işlemlerinin olmaması nedeni ile kapıdan çıkan beher ton ürün için 200 kws enerji tasarrufu sağlanılmaktadır. (Şekil 39 sol)

Şekil 39 : İş akışını düzenleyen ve ara stokları sıfırlayan bir döküm fabrikası (sol) ve modüler bir hassas döküm fabrikası (sağ) (29)

Yenilikçi ve modüler bir hassas döküm fabrikasına örnek, ABD'de bulunan Signicast fabrikasıdır.. Her modül, ayrı ağırlıklarda ve analizde parça imal etmek üzere oluşturulmuştur. Modül 5: İşleme. Support (destek) modülü: Model imali, bakım, ambarlar ver sevkiyat için kullanılmaktadır. (Şekil 39 sağ)

Blok ve silindir kafası üreten modern bir alüminyum kokil döküm fabrikası- (Nemak-Dillingen, Almanya.) tam otomasyonla çalışan ve oksitlenmeye çok eğilimli sıvı alüminyumun manyetik olarak gaz tretman cihazına ve sonra döküm ocaklarına aktarma sistemi ile kurulmuştur. (Şekil 40)

Şekil 40 : Metalin aktarılmadığı modern bir alüminyum silindir kafası döküm fabrikası
İş akışı optimizasyonu ve elektronik data toplamanın yoğun uygulandığı kağıtsız bir fabrika. (Şekil 41)

Şekil 41 : Bilgi akışının elektronik ortamda yapıldığı kağıtsız bir fabrika ile iş akışı düzenli bir alüminyum döküm fabrikası

8)Enerji

Döküm sektörü birim ürün başına yüksek enerji kullanan ve atıkları çok olan bir sektördür. Bu nedenle toplum ve toplumun hassasiyetini takip eden ilgili kuruluşlar tarafından yakın mercekle izlenmektedir. Kullandığımız etkin enerjinin ve atık enerjinin termodinamik ve ekstraktif metalürjide tanımları "Entalpi" ve "Entropi"'dir.

Toplam Enerji= Entalpi + Entropi
Entalpi= Kullandığımız ve işe yarayan enerji
Entropi= Atık, kullanılmayan, fakat geri kazanılabilen enerji

Not: Her sürecin entropisi, başka bir sürecin veya başka kişilerin entalpisi olduğu unutulmayarak, atıkların tamamından yaralanılması şirket ana etik kurallarından biri olmalıdır.
.Bunlara ek olarak, bir çok akıllı döküm fabrikası gibi, güneş ve rüzgar gibi bedava ve yatırım fizibilitesi yüksek enerjilerden faydalanmak da, döküm tesislerinin rekabet gücünü arttırabilecektir.(Şekil 42) (30)

Şekil 42 : Güneş enerjisi ve rüzgar enerjilerinden yararlanan döküm fabrikaları

Dünyada atık döküm kumu için bir çok kullanım alanı bulunmuş ve uygulanmakta olup, döküm sisteminin entropisi, başka bir ihtiyaç sahibinin entalpisi olmaktadır. Türkiye'de de bir çok hammadde fiyatı yükselmeye başladığından, atık döküm kumu da başka endüstriler tarafından girdi (entalpi) olarak kullanamaya başlanılmıştır. (31)
Asfalt, yol yapımı, çimento, dolgu malzemesi, briket yapımı vs gibi her yerde uygulanan atık kum kullanım alanlarına, son yıllarda eklenen bir alan ise, atık kumun tarım toprağı olarak kullanılmasıdır. (Şekil 43)) (32)

Şekil 43 : %10 atık döküm kumu karıştırılan tarım toprağında yetiştirilen lahana ve ıspanak

Yeni ekoloji ve sanayici anayasası
" dairesel düşünce" anlayışı olmaktadır. "Atık" anlayışının yerini "Geri Kazanım" almaktadır. Artık "Al, Üret ve At" anlayışı yeni dönemde unutulacaktır. (Şekil 44)

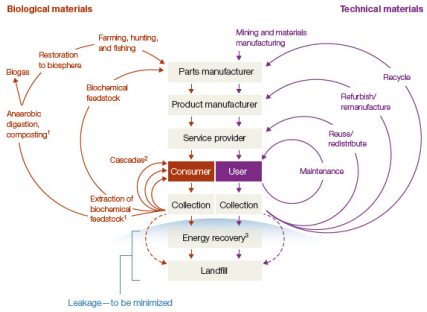

Şekil 44 : Hammadde, girdiler, ürün ve atıkların sürekli kullanılabileceği yeni anlayış: "Dairesel Düşünce" (33)

9)Sayısallaşma

21.yy sayısallaşma anlayışı, günlük hayatımızdan başlayarak, kullandığımız ürünlere, bu ürünlerin üretilmesine, yaratılmasına, hayal edilmesine ve en önemlisi maliyetlerinin düşürülerek, herkesin sahip olabilmesine olanak verecek yönde gelişmiştir.
Döküm sektörünün de bu gelişmelerin dışında kalması söz konusu olmadığından, döküm ürününün kavramdan - mezara kadar olan yolculuğu artık sayısallaşmıştır.(Şekil 45-46)

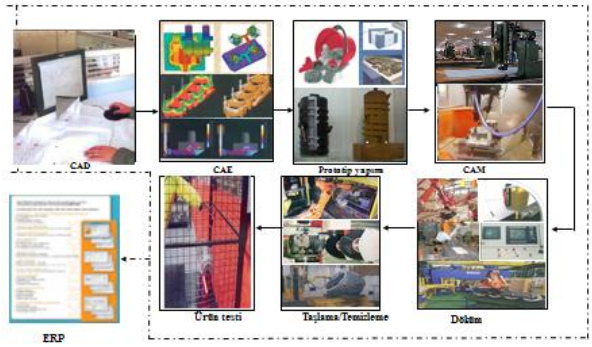

Şekil 45 : Tüm döküm süreçlerindeki sayısallaşma

Şekil 46 : Isıl işlem süresi , çatlak simülasyonu, sıcak kırılma, maçadaki iç gerilim
maçada emme, maça sandığı doldurma simülasyon örnekleri

Simulasyon sadece döküm işinde değil, araçların yol tutuşu, değişik malzemelerle yapılan karoseri ve platformların çarpışmasında ne şekil alacağının incelenmesinde de kullanılmaktadır.. (Şekil 47)

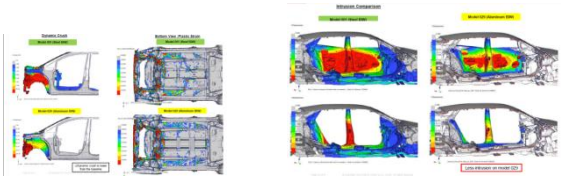

Şekil 47 : Araçlarda alüminyum veya özel çelik malzeme kullanılmasının çarpışma simülasyonu ile kontrolu

Dijital teknoloji kullanılarak, "Bilgisayarlı Tomografi" tekniği ile metalik ürünlerde çekinti, çatlak, et payı, ölçü kontrol, maça emmeleri vs gibi bir çok kontrol süratli ve güvenilir bir şekilde yapılabilmektedir. (Şekil 48)

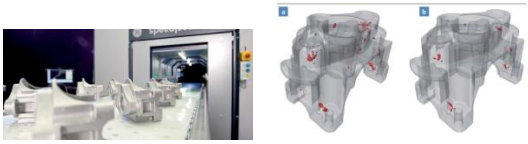

Şekil 48 : Bilgisayarlı tomografi cihazı (34)

SONUÇLAR ve İRDELEME

1) Sektörün Geleceği

Sektörün ve Türkiye sanayinin geleceğini planlarken cevaplanması gereken hususlar aşağıda verilmektedir.

a) Pazar hangi yönde gelişiyor?
b) Pazar nerelerde büyüyor?
c) Üretim teknolojileri gelişmesi ne yönde?
d) İnsan ve mali kaynaklarımız bu beklentilere cevap verebilecek kapasitede mi?
e) Dünya sınıfı üretim merkezleri haline nasıl gelebiliriz?

Ana tema: "En antremanlının ayakta kalacağıdır" (35)

Buna göre, döküm sanayinin rekabetçiliğini koruması için 5 yıl içinde geliştirmesi gereken eylem planları ise:

a) Müşteri odaklı sistemin kurulması
b) Konsept'ten son ürüne kadar hizmet
c) Piyasa rayicinde finansal sonuçlar ve yeterli kapital
d) Doğru teknolojik yatırımlar,
e) İşletme ve süreç verimliliğinin arttırılması,
f) Hafif ve dayanıklı yeni ürün ve malzemeler geliştirilmesi,
g) Paydaş haklarının korunması
h) Malzeme ve kalite yeteneklerinin arttırılması,
i) Enerji verimliliği
j) Ürün kalite ve güvenilirliğinin arttırılması
k) Çevre koruma, atıkların azaltılması, değerlendirilmesi, geri kazanılması ve çalışma koşullarının iyileştirilmesi

Dünya döküm talebinin 100 +/- 10 milyon ton ile tepe noktasında kalacağı, dökümün kullanımının başka malzemeler ile karşılanması, ağırlıkların azalması, dünyada genç ve yaşlı nüfusta otomobil satın almaya talebin azalması gibi faktörlerle, dünya döküm üretimi miktar yerine, teknoloji yönü ile ilerleyip, önem kazanacaktır.
Dünya döküm talebi ve nakliye, müşteriye hemen hizmet verme, maliyetler nedeni ile Asya ile Orta ve Güney Amerika'ya kaymaktadır. Bu ülkelerde Türk dökümcüsünün hem yatırımı yoktur, hem de ihracatı bulunmamaktadır.

Türk döküm sektöründe işçi ücretleri AB ülkelerine göre nispeten düşük olmasına rağmen, verimlilik açısından bu ülkelerin gerisinde kalmaktadır. Aluminyum döküm üretiminde Türkiye'de 14.1 ton/kişi yıl verim alınırken, Almanya'da bu rakam 22 ton/kişi-yıl'dır. Demir bazlı metallerin dökümünde Türkiye değeri 62 ton/adam-yıl iken, Almanya'da ortalama değer 90 ton/adam-yıldır. Gene, sektörde direkt olarak çalışan kişiler göz önüne alınarak, Türkiye'de kişi başı yıllık çiro 80.000 € olmasına rağmen, Almanya'da bu değer 170.000 €, ABD'de ise 100.000 €'dur.

Türk döküm sektöründe yıllık üretimin 1.5 milyon ton olarak yeni giren ve çıkacak olan pazar ile sabitleneceği öngörülmeli, bu üretimin katma değerli ve rekabet gücü yüksek ürünlerle değerlendirilmesi düşünülmelidir.
Mevcut takr. 2 milyon tonluk kapasitedeki eski ve hantal yapı teknoloji, verim ve ekoloji yönünden yenilenmeli ve Türk döküm sektörü uluslararası rekabet gücünü arttırıcı caba içinde olmalıdır.

Yeni araçlar, makinalar ve teçhizatta kullanılan yeni döküm parçaların hepsinde, gerek enerji tasarrufu, gerekse maliyet ve sosyal baskı nedeni ile hafifleme ve malzeme değişimi söz konusu olduğundan klasik "dökümcü-müşteri" yapısına göre oluşmuş Türk döküm sektörü ve benzer sanayilere talep azalacak, ihtiyaçlar yakın, daha etkin çalışan ve verimli yeni teknolojilere uygun yatırımlar yapmış, insan kaynakları eğitimli kaynaklardan temin yoluna gidilecektir.
Kendi bilimini, teknolojisine ve tasarımına dayanan ürünler üretmeyen, müşterinin verdiği resme göre ilk kademe olan döküm parçayı üreten firmalar artık 21.yy'da varlıklarını eskisi gibi sürdüremeyecektir.

Teknolojinin ilerlemesi, pazarın yapısal değişimi, rakiplerin hızlı atakları, Türk döküm sektörünün hikayesini azaltmıştır.

2)Sektöre eleman yetiştirilmesi ve bilgi dağarcığı

Bir çok ülkede döküm işinde çalışmak isteyen mühendis, ara kademe ve operatör seviyesinde eleman bulmak zorlaşmaktadır.
Gelişmekte olan ülkelerde gelir barajının aşılması etkin çalışan mühendis ve bilim adamı sayısına bağlıdır

30-35 sene evvel bu sektöre girmiş elemanların bilgileri ile beraber ayrılmaları sektörde tüm dünyada bilgi ve tecrübe eksikliği yaşanmasına neden olmaktadır. Bir çok ülke bu konuyu önceden görerek, mühendis ve ara kademe elemanları döküm sektörüne cezbetmek üzere tanıtım programları yapmakta burslar vermektedir. (ABD: Foundry Education Foundation, Japonya: Smart. İngiltere: EAL) (37)

Almanya'da döküm mühendisi olarak 10 yıl evvel 20-25 kişi mezun olurken, yapılan tanıtım çalışmaları sonucu bu rakam 100 mezun/yıla ulaşmıştır.(Şekil 49) Özellikle Almanya'da ara kademe elemanları sektöre cezbedebilmek için, gençlerin iyi Almanca bilmeyen ebeveynlerine hitaben Türkçe broşürler dağıtılmaktadır.
ABD'de 2012'de toplam 105 metalurji mühendisi mezun olmuş, bu mezunları döküm sektörüne cezbetmek için mezun olmadan adaylarla görüşmeler yapılmıştır.

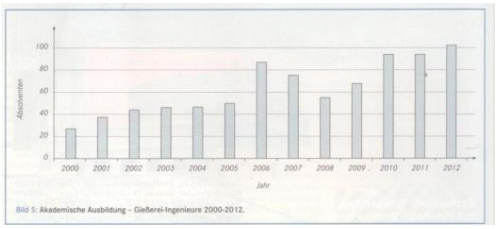

Şekil 49 : Almanya'da yıllar itibari ile yetişen döküm mühendisi sayıları (38)

Türkiye'de diğer tüm dallarda olduğu gibi metalürji mühendisi yetiştirmede de bir enflasyon vardır. Takr. 45 Metalurji Bölümünden her yıl 750 civarında mühendis mezun olmaktadır. Biraz İngilizce, biraz bilgisayar ve biraz da karbon, kükürt bilen ortalama seviyede mühendis diplomalı orta seviyede elemanlar yetiştiriyoruz. Bu arkadaşların tecrübe ve bilgileri en alt düzeyde olup, en fazla 50'sinde öğrenme, çalışma ve başarı hevesi bulunmaktadır. Her yıl metalürji sektöründe çalışmayacak işsiz mühendisler mezun edilmektedir.
Metalurji sektörünün bol miktarda ihtiyacı olan temel metalürji kavramlarına haiz, çalışmaya ve öğrenmeye hevesli mühendis ve operatörler arasında görev yapacak ara kademe elemanıdır. Bunları yetiştirecek yerler ise, yurt dışındaki sanayileşmiş ülkelerde olduğu gibi üniversite destekli enstitülerdir.
Tecrübenin satın alınması bazan çok pahalı, bazan da mümkün değildir. Elemanların tecrübe kazanana kadar beklenilmesi ve hataların maliyetine katlanılması gerekmektedir.. Maalesef, döküm fabrikalarında çalışanların tecrübeleri ve hatadan öğrenme olanakları, döküm pazarı artış hızının altında kalmaktadır.

Bir çok gelişmiş ülkede inovasyon ve yenilikçilik maddi ve manevi olarak desteklenmektedir. (Şekil 50)

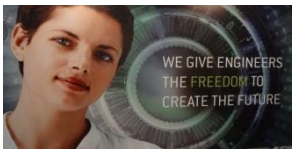

Şekil 50: Mühendisliği öne çıkaran çeşitli ilanlar

3)Türk döküm sektörünün problemleri:

Sektörün ilerlemesi ve kapasitesini etkileyen bir çok idari ve teknik problemleri bulunmaktadır:

a) Yerli araç ve makine üretiminde belirli bir yerli oran tutturma zorunluluğu olmaması,
b) Döviz/TL değerinin genelde, TL'nin değerli tutulma politikaları nedeni ile yurt dışından döküm alımı kullanıcılar için daha cazip,
c) Teknoloji nedeni ile yurt dışından alım,
d) Ana araç üretim fabrikalarının bitmiş montajlı komponent olarak yurt dışından alımları,
e) Türkiye'de işleme ve montaj tesis ve kapasitesi olmadığı için yurt dışından alım,
f) Ana şirket politikası nedeni ile ana ülkeden alma kararı,
g) Türkiye'de özel teknolojilere göre (1.5-2 mm et payı) döküm üretecek tesis olmaması,
h) Bir çok üretim sisteminin patentli olması ve ana şirketlerin buralardan mal alma zorunluluğu
i) Sektörde onaylı Arge merkezi sayısının sadece 1 adet olması (Tüm Türk sanayinde onaylı 122 Arge merkezi mevcut)
j) Sektörün her gelen işi yapma yapısı ve bu nedenle yetersiz ihtisaslaşma,

Bitmiş ürün olarak yurt dışından alınan içinde döküm ürünleri bulunan komponentler Türk döküm sektörünün yıllık 350.000 ton üretim kaybına neden olmaktadır. İşlenmiş ve montajlı bu ürünler ort. 10$/kg hesabı ile Türkiye'ye ithal edildikleri için 3.5 milyar dolarlık bir döviz kaybı söz konusu olup, bu bedelle bu ürünleri üretecek en az 5 döküm, işleme ve montaj tesisi kurulabilecektir.

Bütün bunlara göre,Türk dökümsektörünün gelecek stratejileri neler olmalıdır?

a) Tonaj mı?
b) Kar mı?
c) Pazar payı mı?
d) Belirli müşteri gruplarına liderlik mi?
e) Belirli teknolojilerde liderlik mi?
f) Belirli pazarlarda üstünlük mü?
g) İhracat mı, yerli Pazar mı?
h) Maliyetlerin kontrolü ile ürün rekabeti mi?

Sonuçta;

A) Döküm sektörü bölgesel (Kuzey Amerika, Günay Amerika, Uzak Doğu, Avrupa -Rusya, K.Afrika ve Türkiye dahil bölgesel pazarlarda büyüyecek. Bölgeler arasında döküm ticareti özel anlaşmalar veya bitmiş ürün bazında olacak.
B) Döküm ürünleri kullanıldığı yerlere yakın üretilmek zorunda kalacak. Otomotiv (2020'de 5 milyon araç üretimi) ve makine sanayinde önemli şekilde büyüyen ve yerli yatırımlara destek veren Rusya, Türk döküm sektörü için gerek ortaklık, gerek satınalma, gerekse yeni tesis kurarak pay alınabilecek bir pazar görüntüsündedir. Bir başka yurt dışı yatırım olanağı, Hindistan olup, şartlar değerlendirilmelidir.
C) Ürün fiyatı: Ucuz olmak pazar payı için her zaman yeterli değildir.(Şekil 51) Ucuz satılacak kategorideki bir ürün, satınalmacının fiyat indirimi için sürekli baskı yapacağı bir üründür.

Her ürün için, sizin tesisinizin yetenekleri, yeri, performansı, mali

durumu, vazgeçilmezliği gibi birçok faktöre dayanan "iyi" bir satınalmacının kafasında oluşmuş bir "algılanan değer" vardır. Fiyatınız bunun üstünde ise, işi almak zor, altında ise beraber çalışma olanağı oluşacaktır.

Şekil 51) : Satın alınan ürünün toplam maliyeti

D) Dökme demir üretiminde yerli katkı %60, çelik dökümde %70, alüminyum dökümde %45 olduğundan, tüm süreçlerde verimlilik arttırılması, Türk döküm sektörünün rekabet avantajını belirginleştirecektir. Teknoloji, maliyet, dijitalleşme, ekoloji, enerji, eğitimli/yetenekli insan kaynağı, müşteri ilişkileri rekabette önemli faktörler olacaktır.

SON SÖZ

Bütün bu a) teknolojiler, b) bilgi, c) yatırımlar d) elemanlar, e) yönetim teknikleri, f) dijitalleşme, g) otomasyonunuz var ise ve bunları yeterince uygulayabilirsek, artık ideal hedefleri hayal etmeye hakkımız olmalıdır.

a) Kalıp verimi = %100
b) İş kazaları = %0
c) Sakat/Fire = %0
d) Pota yok
e) Maça makinası yok
f) Model/kalıp yok,
g) +/- 0.8 mm gibi geniş toleranslar yok
h) En iyi ve verimli döküm metoduna çok yakınız
i) Müşteriler ile uyuşmazlığın unutulduğu ve bu döküm tecrübesinin hem döküm üreticisi, hem de kullanıcının hizmetinde olduğu bir dünya

Türk döküm üreticileri oyunda kalmak istiyorlarsa; az işçilik, az enerji, en az fire ile en hafif, en sağlam, en teknolojik, en ucuz, en rekabetçi ürünü üretmenin ve bunu pazarlamanın yolunu bulup, uygulamak zorundadır.

KAYNAKLAR:

1)J.Manyika, Distruptive Technologies, Mc.Kinse, Mayıs 2013
2)Fan Gi, Status and Outlook of China Foundry Industry, IFF, Sept 2012
3)M.Schwartzlander, Metalcasting Growth Strageties, Foundry M+T,Feb 2013
4)G.Wolf, Global Trends in Foundry Technology and Casting Production, VDG, 2012
5)EU Foundry and Automotive Industry Forecasts, CAEF, November 2013
6)TÜDOKSAD Raporları, 2012,2013
7)F.Özatay, Türkiye Ekonomisi; Nerede? Nereye?,Tüdoksad, Kasım 2013
8)S.Udvardy, State of the Industry, NADCA, Ekim 2013
9)Future Automotive Industry Structure, 2025, Oliver Wyman, 2012
10)W.Diez, Competing in the Global Truck Industry, KPMG, Eylül 2011
11)Rightsizing Europe, Roland Berger Report, Mart 2013
12)H.Wolff, Energy Efficiency in Foundries, Metal Casting Conference,S.Africa, 2013
13)A.Weber, New Materials Allow Soldiers to Shed Weight, Assembly, Kasım 2013
14)H.Koch, Innovative Lösungen in Aluminium durch Werkstoffentwicklung, Trimet, 2013
15)Future Developments in the Automotive Industry and its Markets, Management Engineers Report,IFF, 2010
16)Advanced High-Strength Steel Family Car, World Steel Organisation, www.worldsteel.org,2008
17)Nano Steels, Arcelor-Mittai, 2013
18)J.Beckmann, Evolutionaere Strategien zur Gestaltung moderner Gussbauteile, Giesserei, 05/2007
19)Guss-Abdeckung im Wabendesign, Birco Baustoffwerk GmbH,
20)L.Kniewallner, Bionik und Guss-eine gute Kombination, Giesserei-Rundschau, 2009
21)D.Weiss, Foundries: The Final Frontier-the Next Thousand Years of Casting Technology, AFS Transactions, 2009
22)Modern Casting, AFS, Mart 2010
23)T.Wohlers, Worlwide Trends in Additive Manufacturing, RapidTech Conference Proceedings, 2009

24)B.Stucker, İmproving Implants Using Laser-based Metal Deposition Technologies, BoneZone, 2010

25)J.Danko,Use of Additive Manufacturing in Foundry Patternmaking, 2013 Annual Additive Manufacturing Users Group Conference, 2013
26)Additive Manufacturing, Roland Berger Study, Kasım 2013
27)N.Gerth, Prozessoptimierung in Druckgiessverfahren, Giesserei, 04/2013
28)T.Hessmann, Dawn of the Smart Factory, Industry Week, Şubat 2013
29)W.Lutz, In Pursuit of Manufacturing Excellence, www.terrylutz.net, 2013
30)Y.Günay, Döküm Fabrikaları da Bir Enerji Şirketi Olmak Zorundadır, 6..Döküm Kongresi, İstanbul, Eylül 2012
31)Y.Günay, Döküm Fabrikaları, Ekoloji ve Enerji, Ortak Yaşam Mümkün mü?, 3.Döküm ve Çevre Konferansı, İstanbul, 2009
32)R.Dungan, Solutions for Waste in the Foundry Sector, Agricultural Research Service, 2012
33)M.Zils, Moving Toward a Circular Economy, McKinsey Report, Şubat 2014
34)E.Amboss, High Speed Computer Tomography Employed in Pressure Die Casting, Casting Plant and Technology, 03/2012
35)Y.Günay, What Do We Do Next; To Survive, Grow and Be Distinquished, Proceedings of the 69th World Foundry Congress, Ekim 2010
36)Y.Günay, Türk Döküm Sanayinin Rekabet Gücü, 5.Döküm Kongresi, İstanbul, Kasım 2010
37)P.A.Murrell, Developing the Future Workforce, WFC, Bilbao, 2014
38)G.Landerl, Gussanwendungen Gestern, Heute und Morgen, Giesserei, 01/2014

MICROSTRUCTURAL CHARACTERIZATION OF RAPIDLY SOLIDIFIED 8% CHROMIUM COLD WORK TOOL STEEL

Seçkin ÇARDAKLI*, Ali KALKANLI**

*** Middle East Technical University, Turkey**

cardakli@metu.edu.tr

**** Middle East Technical University, Turkey**

kalkanli@metu.edu.tr

ABSTRACT

Cold work tool steels forms the most important type of alloy steels for all cold work applications where resistance to abrasive wear is of prime importance. Cold work tool steels are employed for the manufacture of tools for applications involving surface temperatures of not more than 200 ^{0}C . In this temperature range, they must possess high hardness, high wear resistance and toughness and high dimensional stability during hardening and tempering. The typical as-cast microstructure of these alloys consists of coarse primary carbides in a metastable austenitic and martensitic matrix. The hard and coarse primary carbides are mainly responsible for the good abrasion resistance but they are also stress concentration points and cause failure during loading. Once solidified, carbide morphology is relatively immune to a subsequent modification by heat treatment. Such a phenomenon brings attention to the importance of the solidification to be studied to refine these coarse primary carbides for homogeneous and fine distribution in matrix. In this study, coarse carbide structure of 8% chromium cold work tool steel are refined by rapid solidification and fast cooling techniques and carbide characterization is done after solidification by optical microscopy, X–ray diffraction, SEM analysis techniques. Scrap cold work tool steels was melted and poured into copper mould with vacuum assisted suction casting and 8 mm thick slabs were obtained and than examined by optical microscopy and SEM techniques to reveal soldification structures. The carbide extraction was performed by leaching tool steel in HCl to reveal carbide type. X-Ray diffraction results of the samples showed that when %0,5 FeSi containing %2 Al alloy added for deoxidation yielded Cr_7C_3 on contrary without FeSi addition $(CrMo)_2$ (C,N) formation was observed.

Keywords: cold work tool steel, carbide characterization, rapid solidification, carbide extraction

Hızlı Katılaşmış %8 Kromlu Soğuk İş Takım Çeliğinin Mikroyapısal Karakterizasyonu

ÖZET

Soğuk iş takım çelikleri aşınma direncinin büyük önem arz ettiği soğuk iş uygulamaları için alaşımlı çeliklerin en önemli tipini oluşturur. Soğuk iş takım çelikleri en fazla 200 ^{o}C arasında yüzey sıcaklıkları içeren uygulamalar için araçların üretimi için kullanılır. Bu sıcaklık aralığında sertleştirme ve tavlama sırasındaki yüksek sertlik, yüksek aşınma direnci ve tokluk ve yüksek boyutsal stabilite özelliklerini korumaları gerekir. Bu alaşımların tipik döküm mikroyapıları kararlı bir ostenitik ve martensitik matris içinde kaba birincil karbürlerden oluşur. Sert ve kaba birincil karbürler iyi aşınma direnci ile sorumludur fakat onlar da stres konsantrasyon noktaları ve yükleme sırasında kırılmaya neden olurlar. Katılaştıktan sonra karbür morfolojisi ısıl işlem ile daha sonraki bir değişiklik nispeten bağışıktır. Bu olgu, bu kaba birincil karbürlerin matris içinde homojen ve iyi bir dağılımı için katılaşmanın önemine dikkat getirir. Bu çalışmada , % 8 krom içeren soğuk iş takım çeliğinin kaba karbür yapısı hızlı katılaşma ve hızlı soğutma teknikleri rafine edilmektedir ve katılaşma sonrası karbür karakterizasyonu optik mikroskop , X - ışını kırınımı , SEM teknikleri ile yapıldı. Hurda soğuk iş takım çelikleri eritildi ve vakum destekli emme döküm yöntemi ile bakır kalıplara döküldü ve 8 mm kalınlığında plakalar elde edildi ve katılaşma yapılar ortaya çıkarmak için optik mikroskopi ve SEM teknikleri ile incelendi. Karbür türünü ve ortaya çıkarmak için takım çeliği hidroklorik asitte liç edilerek karbür çıkarma yapıldı. Numunelerin X -ışını kırınım sonuçları gösterdi ki oksidasyonu önlemek için %2 aluminyum içeren %0.5 ferrosilikon ilavesi Cr_7C_3 meydana getirirken ferrosilikon ilavesi yapılmadığında $(CrMo)_2$ (C,N) oluşumu gözlemlendi.

Anahtar Kelimeler: soğuk iş takım çeliği, karbür karakterizasyonu, hızlı katılaşma, karbür çıkarma

INTRODUCTION

High C-high Cr alloy steels are widely used around the world as a material for many dies and tools in cold press forming and cold forging of parts for automobiles, electronics and electrical appliances. In the case of cold working process, these tools, punches and dies subject to repeated usage require material quality featuring wear resistance, compressive strength, toughness and fatigue strength. The hard and coarse primary carbides are mainly responsible for the good abrasion resistance but they are also stress concentration points and debonding at the carbide-matrix interface can initiate fatigue, acting similarly to cracked inclusions. [1] During the solidification of this steel, γ dendrites are nucleated firstly. The volume fraction of γ phase is increased with decreasing temperature At the final stage of solidification because of segregation, grain boundaries saturated by carbon and chromium. transformed a skeletal morphology of chromium carbide, Cr_7C_3 [2] Large eutectic carbides, existing in tool steel ingots from casting, are changed into small carbides and uniformly distributed in the steel matrix by forging processes [3,4]. However, the conventional routes (casting and forging) consume a lot of energy and time. Consequently, an innovative route that involves less energy consumption and shorter processing time and can substitute the

conventional manufacturing routes is desired. Therefore, a strong need exists to develop low-cost tool steels with high strength and toughness as well as high resistance to fatigue.[5]

In this study, coarse carbide structure of 8% chromium cold work tool steel are refined by rapid solidification with vacuum assisted suction casting and 8 mm thick slabs and carbide and microstructural characterization is done after solidification by optical microscopy, X–ray diffraction, SEM techniques. Moreover, the effect of the addition of FeSi for deoxidation purposes on carbide type were also investigated.

EXPERIMENTAL PROCEDURE

The chemical compositions of the specimens are indicated in table 1 The melt of designed steel was prepared using an air atmosphere induction furnace. Firstly The melt was poured at 1550 ^{o}C in sand mould with the dimensions of casting sample 300mm * 60 mm * 40 mm with 0.5% FeSi addition to melt. And secondly the melt was poured at 1550 ^{o}C in and vacuum assisted suction copper moulds with 0,5% FeSi addition and without FeSi addition as listed table 2. To control segregation during solidification, copper the mould temperature was held at about 200 ^{o}C temperature. The dimensions of casting samples were 300 mm * 60 mm * 8 mm. Microstructural examinations were done by optical microscope and scanning electron microscope and X-ray diffraction. Etchant reagent was Picral for the as-cast samples. The carbide extraction was performed by leaching tool steel in HCl to reveal carbide type.

Table 1. Chemical compositions of the steels used (mass%).

	C	Cr	Mn	Si	Mo	V	Fe
Steel	0.9	7.8	0.5	0.9	2.5	0.5	Bal.

Table 2. Specimens, solidification rates and information of their cast moulds.

Sample	Solidification rate	Mould	Initial temperture of mould	FeSi addition
1	Slow	Sand	25 ^{o}C	Yes
2	Rapid	Copper	200 ^{o}C	No
3	Rapid	Copper	200 ^{o}C	Yes

RESULTS AND DISCUSSION

Figure 1, Figure 2 and Figure 3 shows the X-ray diffraction pattern of sample 1, sample 2 and sample 3 respectively.

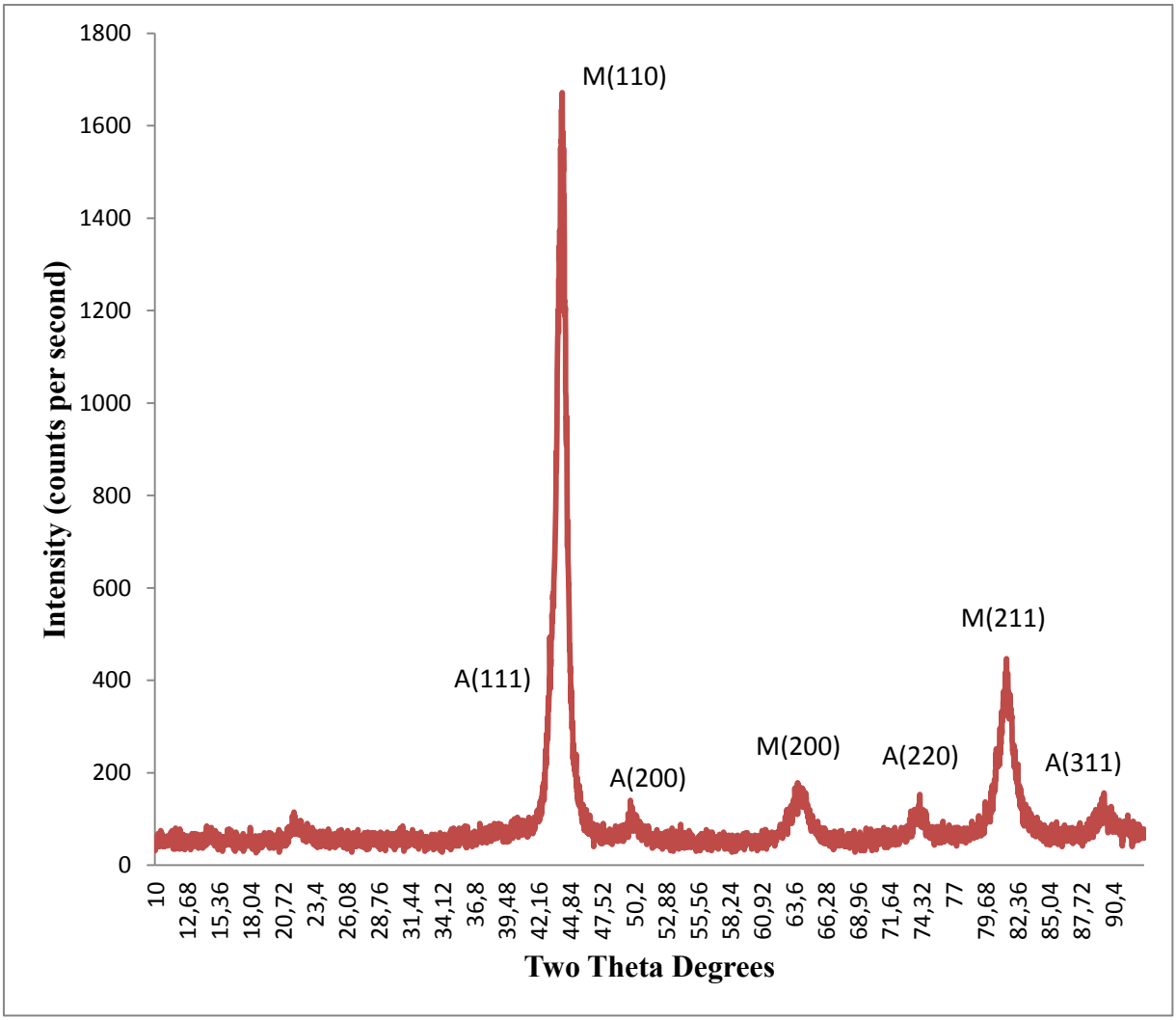

Figure 1. The X-ray diffraction pattern of sample 1

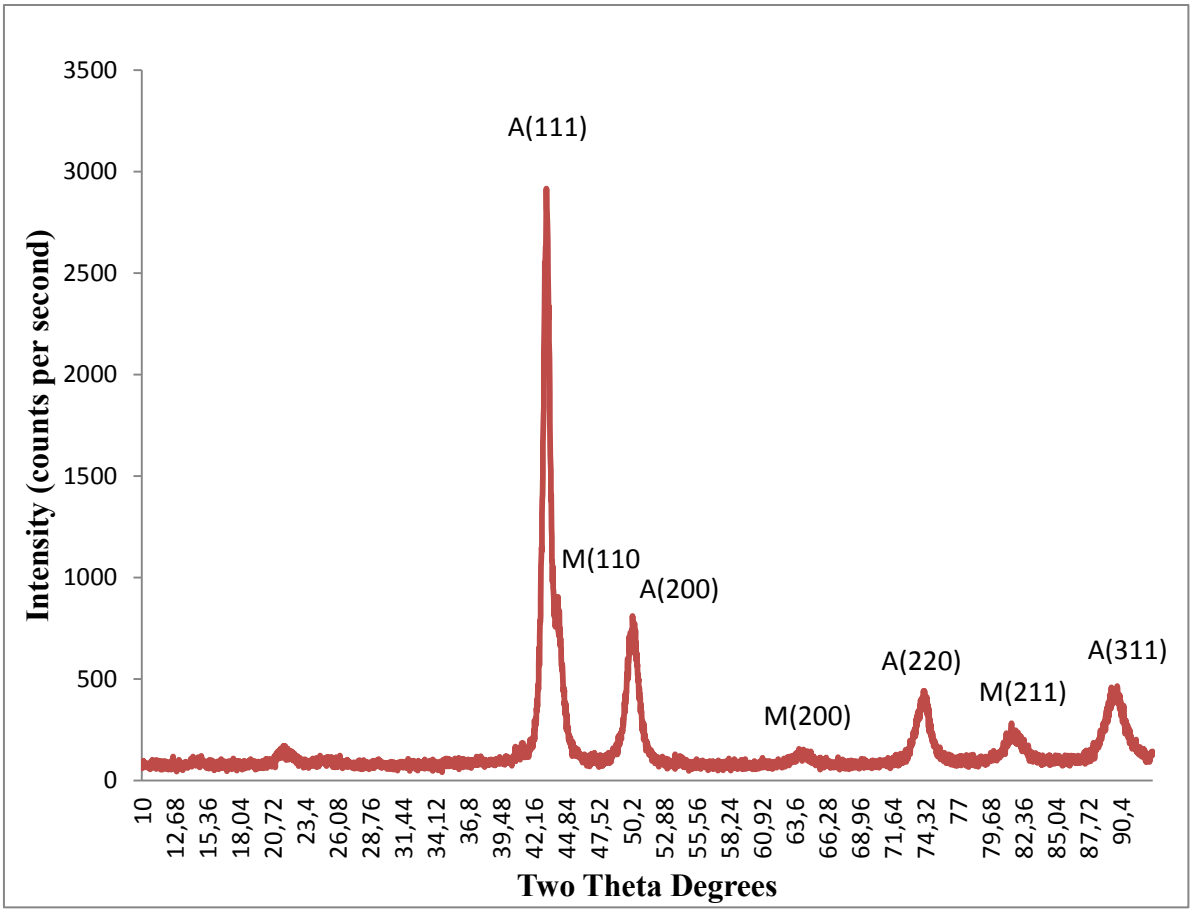

Figure 2. The X-ray diffraction pattern of sample 2

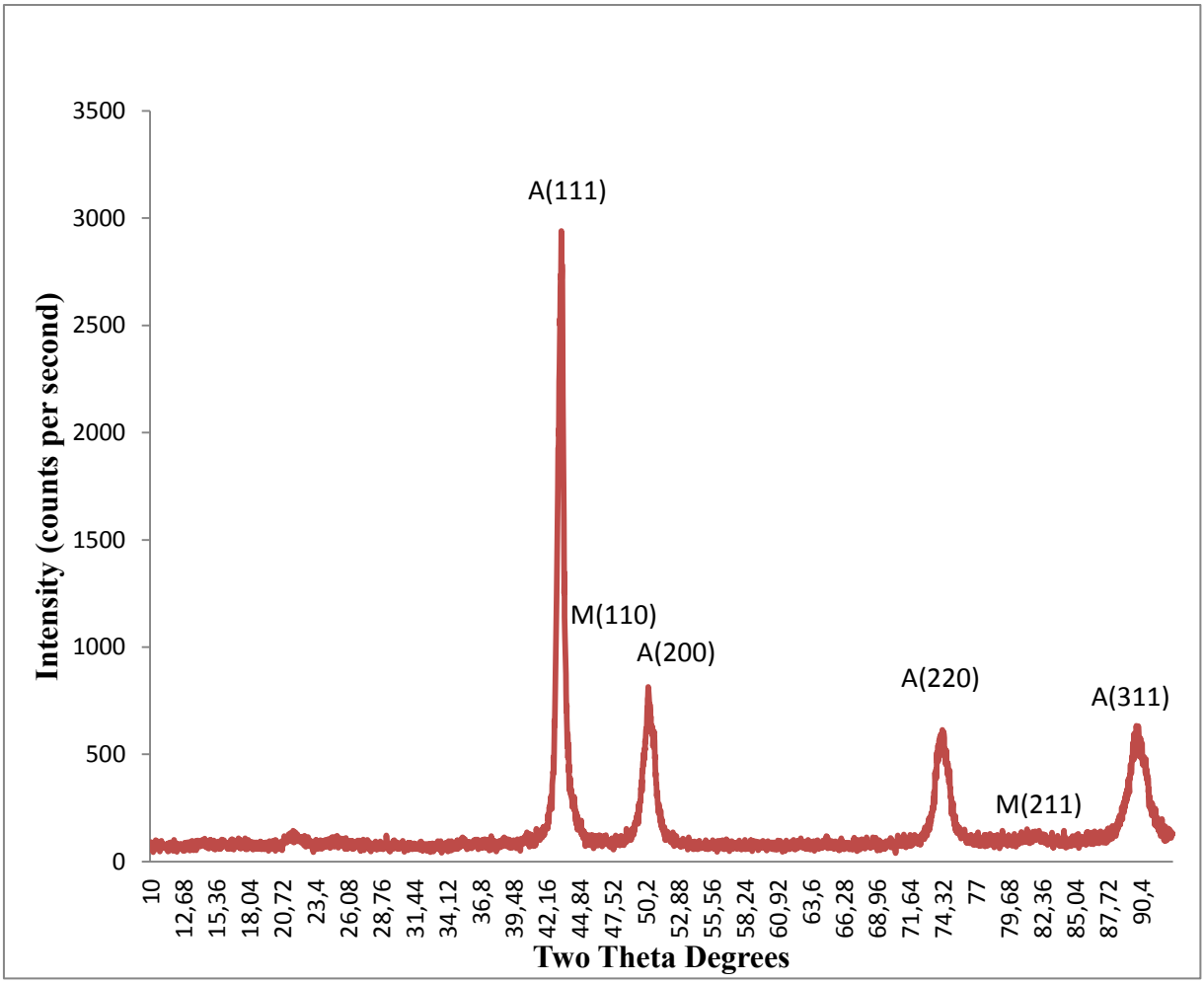

Figure 3. The X-ray diffraction pattern of sample 3

It is found retained austenite and martensite phases exist in each sample. The amounts of retained austenite are measured by XRD [6]. The volume of retained austenite is 30% at sample 1 and increases to 51% at sample 2, and then reaches approximately 55% at sample 3. Therefore it can be understood that retained austenite amount increases with increasing solidification rates. The main reason of that is that more segregation occurs during slow cooling and skeletal primary carbides precipitate in grain boundaries as shown in figure 4. This causes passing of carbon atoms and alloying elements from matrix to carbides. Low carbon concentration in matrix stabilize the martensite phase and decrease volume percent of retained austenite.

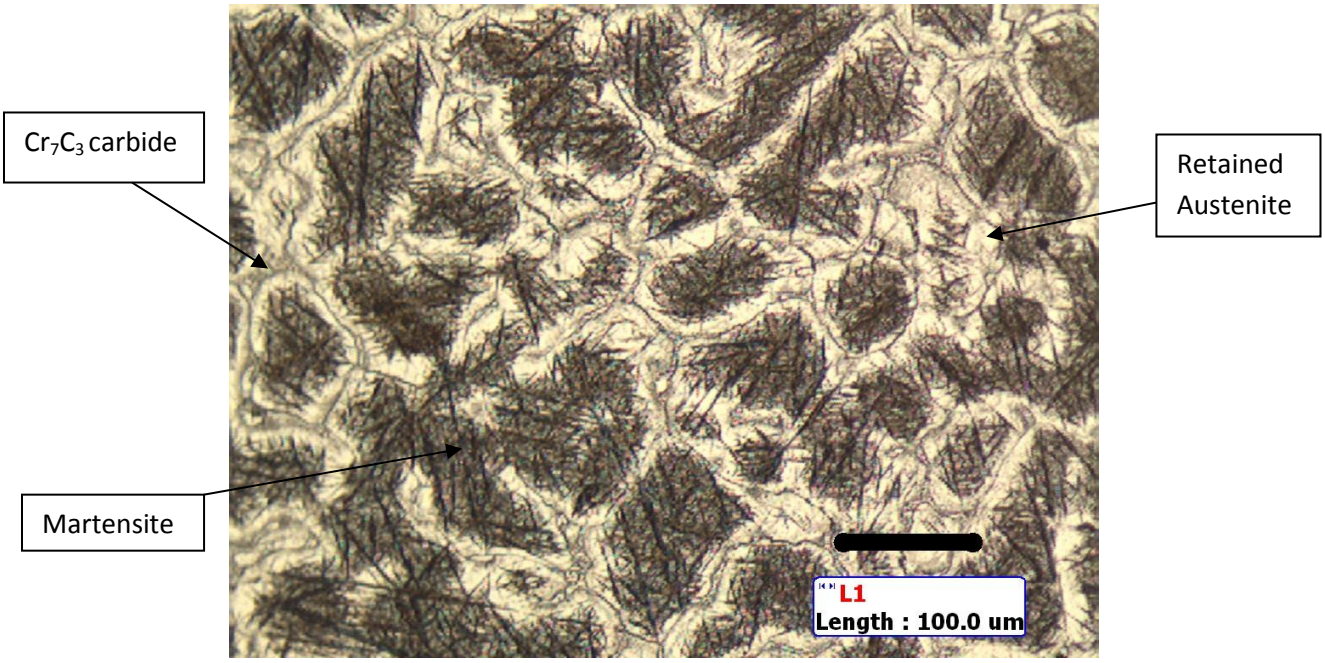

Figure 4. Optical micrograph of sample 1

At fast cooling rates, segregation is low which is observed in microstructures as shown in figure 5 and figure 6. More carbon atoms remaining and alloying elements like Cr, Mo and V at the matrix with fast cooling rates favor more retained austenite and refined primary carbides in matrix.

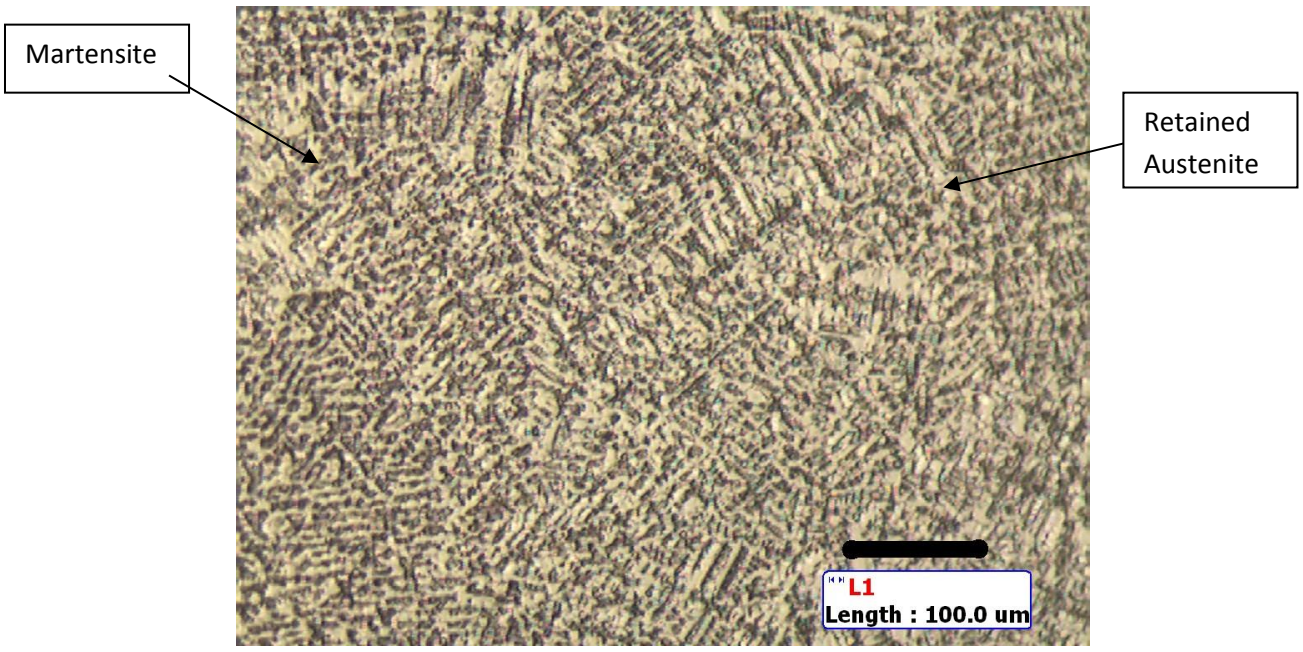

Figure 5. Optical micrograph of sample 2

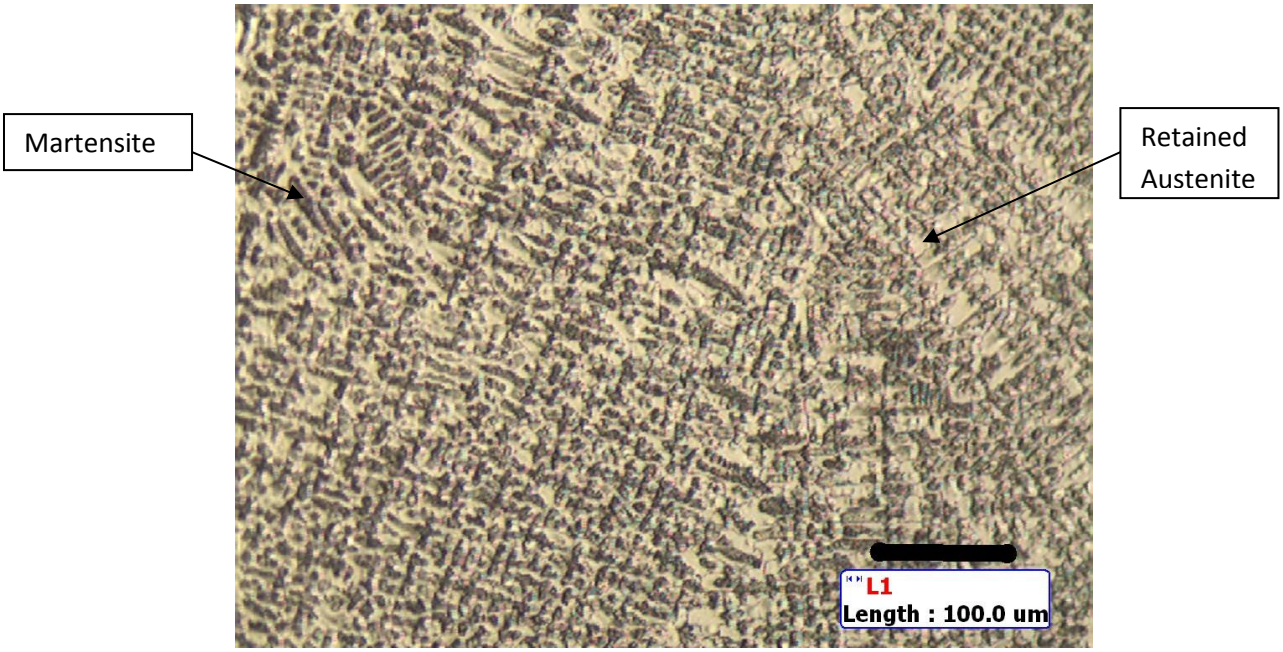

Figure 6. Optical micrograph of sample 3

Figure 7 , figure 8 and figure 9 shows the SEM morphologies of the primary carbides in each specimen.

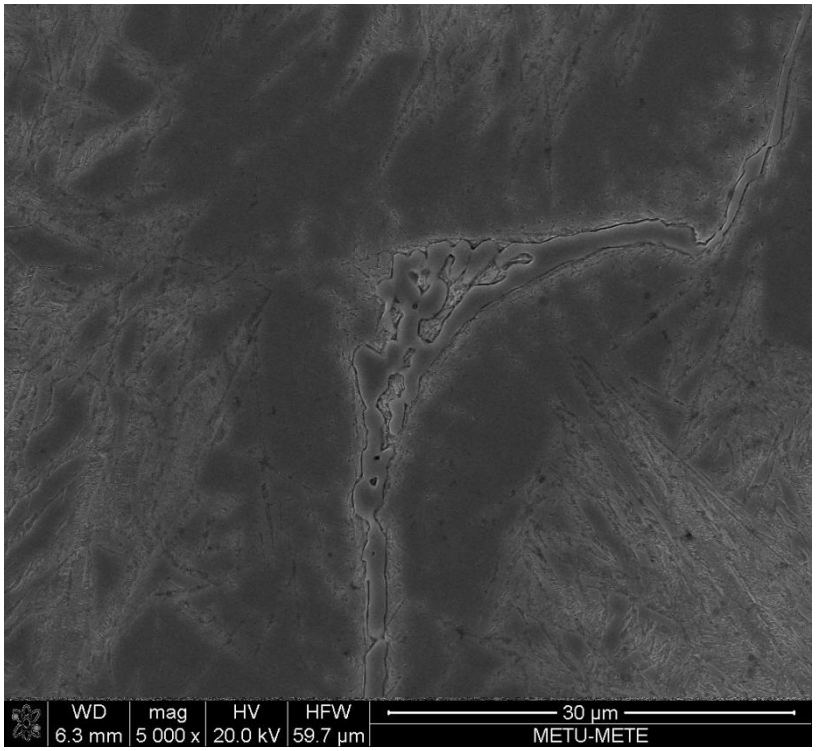

Figure 7. Sem micrograph of primary carbide of sample 1

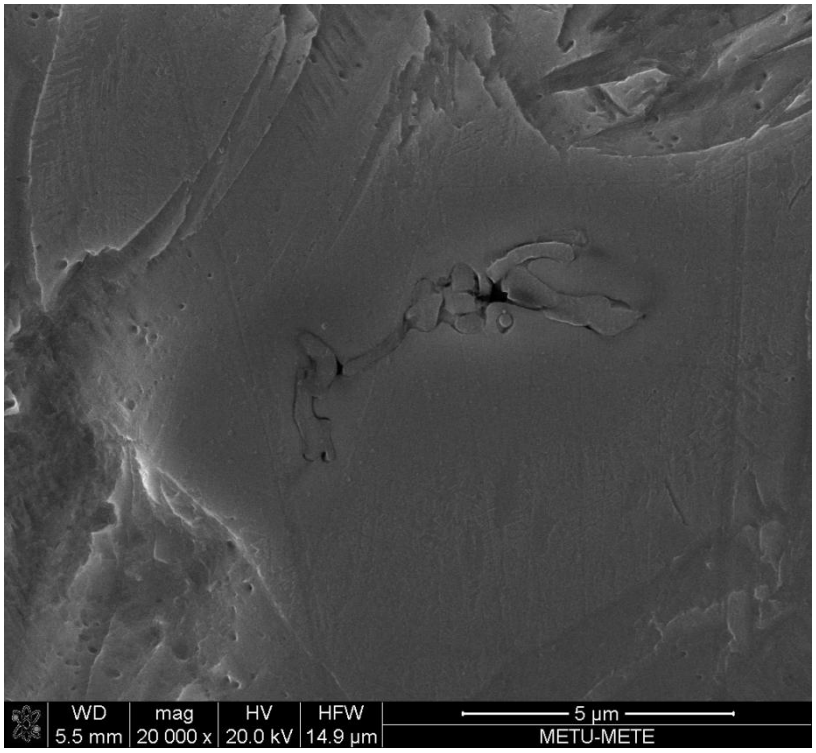

Figure 8. Sem micrograph of primary carbide of sample 2

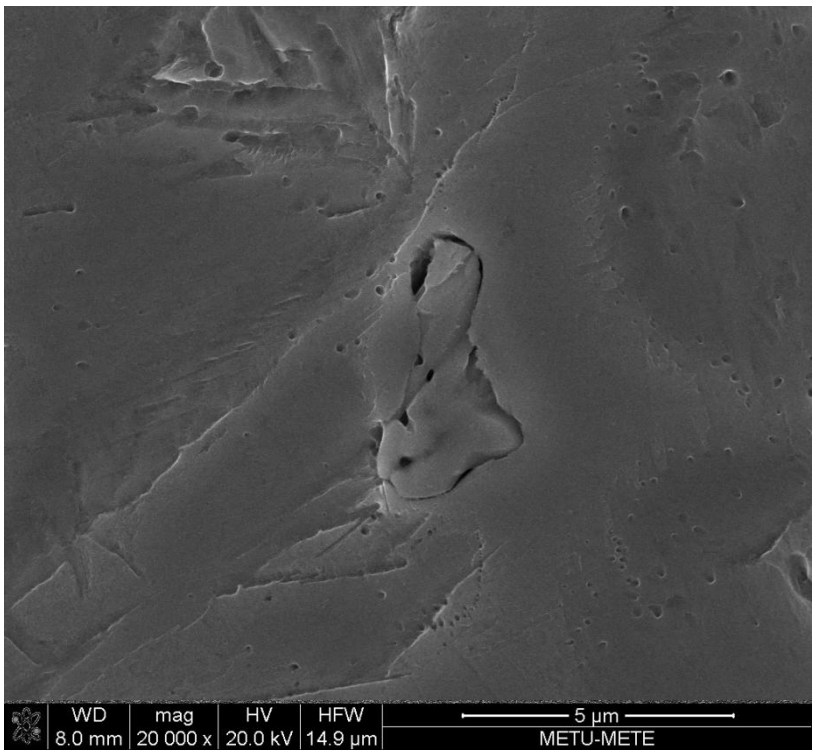

Figure 9. Sem micrograph of primary carbide of sample 3

The X-ray diffraction pattern of residues obtained from acid leaching of samples show that that $(Cr,Mo)_2$ (C,N) exist in sample 2 and Cr_7C_3 exist in sample 1 and sample 3. The addition of FeSi causes that silicon in FeSi reacts with nitrogen in liquid steel and forming silicon nitrides (Si_3N_4) goes to slag and reduces nitrogen content in steel. It is found that 5%

FeSi addition reduces nitrogen content from 450 ppm to 250 ppm. Reduced nitrogen content favours Cr_7C_3 formation with respect to $(Cr,Mo)_2$ (C,N) formation as primary carbide in matrix [7].

CONCLUSION

Sand and iron molds with different initial temperatures have been employed to produce cast tool steels having different solidification rates. The morphology and distribution of the carbides formed under these solidification rates have been studied with optical microscopy and scanning electron microscopy. The following conclusions have been reached:

(1) When the solidification rate is low, the primary carbides nucleating beside the existent solid phases have enough time to grow and become large and distribute along the grain boundaries network.

(2) When the solidification rate is high, the rate of the formation of the nuclei increases and primary carbides are refined

(3) FeSi addition to liquid steel decreases nitrogen content in steel. Reduced nitrogen content favours Cr_7C_3 formation with respect to $(Cr,Mo)_2$ (C,N) formation as primary carbidein matrix.

REFERENCES

1- K. Fukaura, Y. Yokoyama, D. Yokoi, N. Tsujii, K. Ono, Metall. Mater. Trans. A, 35 (2004), pp. 1289–1300

2- Sh. Kheirandish , H. Saghafian, J. Hedjazi, M. Momeni, Journal of Iron and Steel Research International, 17, (2010), 40-45.

3- H. X. Chi, D. S. Ma, Q. L. Yong, L. Z. Wu, Z. P. Zhang and Y. W. Wang, J. of Iron and Steel Research Vol. 17(6), (2010)

4- P. S. Babu, P. Rajendran and K. N. RAO, Int. J. Mater. Sci., Vol. 210, (2010)

5- M. N. Mohammed, M. Z. Omar, J. Syarif, Z. Sajuri, M. S. Salleh, and K. S. Alhawari, The Scientific World Journal, Volume 2013 (2013), Article ID 828926

6- Standard Practice for X-Ray Determination of Retained Austenite in Steel with Near Random Crystallographic Orientation , ASTM International, E975 – 13

7- Joseph Ki Leuk Lai, Chan Hung Shek, Kin Ho Lo, "Stainless Steels: An Introduction and Their Recent Developments, Bentham Books, 2012

THE INVESTIGATION OF THE RELATIONSHIP BETWEEN GRAIN REFINERS AND HOT TEARING IN A357 ALLOY

Muhammet ULUDAĞ*, Remzi ÇETİN*, Derya DIŞPINAR**

* Selcuk University, Faculty of Engineering–Metallurgical and Materials Eng. Dept., Konya-Turkey, uludag@selcuk.edu.tr, rcetin@selcuk.edu.tr
** Istanbul University, Faculty of Engineering, Metallurgical and Materials Eng. Dept., Istanbul-Turkey, deryad@istanbul.edu.tr

ABSTRACT
Hot tearing is one of the serious problems that may occur during casting of aluminum alloys. There are numerous number of works in the literature about the hot tearing susceptibility of cast aluminium alloys. Yet, the exact mechanism of formation of hot tear has not been clarified. None of the studies had considered the contribution of surface entrained defects known as bifilms. In this work, two different grain refiners (Ti and B) were used and CRC (constrained rod casting) method was used to check the hot tearing susceptibility. The samples were cast in various forms: (i) prior to and after grain refinement addition; (ii) prior to and after degassing. In each of the tests, reduced pressure test sample was collected and bifilm index was measured. The correlation between melt quality, grain refinement and hot tearing susceptibility was evaluated.

Keywords: Hot tearing, Bifilm index, Grain refinement, Hydrogen content, Degassing

A357 ALAŞIMINDA TANE İNCELTME VE SICAK YIRTILMA ARASI İLİŞKİ

ÖZET:
Sıcak yırtılma hatası alüminyum döküm alaşımlarında sık rastlanan ve önemli bir problemdir. Bu problemin çözümü için pek çok araştırmacı çeşitli çalışmalar yapmışlardır. Yapılan çalışmalarla çözüm henüz net olarak ortaya çıkmamıştır. Çünkü sıcak yırtılma hatasının oluşumunda en büyük kaynağın ne olduğu halen belirsizdir. Bu çalışmada, A357 alüminyum alaşımlarında farklı tane incelticilerinin sıcak yırtılma oluşumuna etkisi incelenmiştir. Bu incelemeleri yapmak için sınırlanmış çubuk döküm (CRC- constrained-rod casting) test modelinin hem kum hem de kokil kalıplarına dökümler yapılmıştır. Dökümler, tane incelticisiz ve AlTi10B1 ve Al-3B alaşımları ile tane inceltme işlemine tabi tutulmuş şekilde yapılmıştır. Aynı zamanda gaz gidermenin etkisini görebilmek adına dökümler gaz gidermeli ve gidermesiz olarak çalışılmıştır. Sınırlandırılmış çubuk döküm kalıbından elde edilen sıcak yırtılma test numuneleri hem makro hem mikro boyutlarda incelenerek tane boyutu ve porozite ile sıcak yırtılma arası ilişki araştırılmıştır. Her bir dökümden önce azaltılmış basınç testi numunesi alınarak bifilm indeks hesaplanmıştır ve döküm kalitesi ile sıcak yırtılma arasındaki ilişki de ortaya çıkartılmıştır.

Anahtar Kelimeler: Sıcak yırtılma, Bifilm indeks, Tane inceltme, Hidrojen içeriği, Gaz giderme

1. INTRODUCTION

The term "castability" has yet being described properly. In some cases, it is defined as the determination of chemical composition of a part that has been solidified to contain no defects. When the casting is carried out under gravity, the definition becomes the fluidity of a melt that can fill the mould cavity without forming any hot tear or shrinkage porosity [1].

Hot tear is defined as the tear that occurs at a hot spot of a cast part during solidification at the mushy zone even though the solid fraction is high [2]. Therefore, the width of the mushy zone is one of the key parameters of an alloy. The defect is usually associated with the degree of segregation that takes place in a macroscopic scale [3]. The liquid film perfectly wets the solid grains and acts as a lubricant to aid hydrostatic pressure to decrease [4]. It is well known that grain refinement and chill application lowers the hot tear formation [5-7]; and thus, by preventing the formation of this defect, many technical and economic advantages can be established.

In this work, the effect of Ti and B grain refinements on the hot tear susceptibility of Al-7Si alloy was investigated.

2. EXPERIMENTAL WORK

Commercially available primary A357 alloy was provided from Eti Aluminium, Turkey and used in the casting trials. Al-5Ti-1B master alloy was used for Ti grain refinement and Al-3B master alloy was used as the Ti-free B grain refinement. The experiments were conducted in CRC (constrained rod casting) moulds in both sand and dies. The dimension is given in Figure 1.

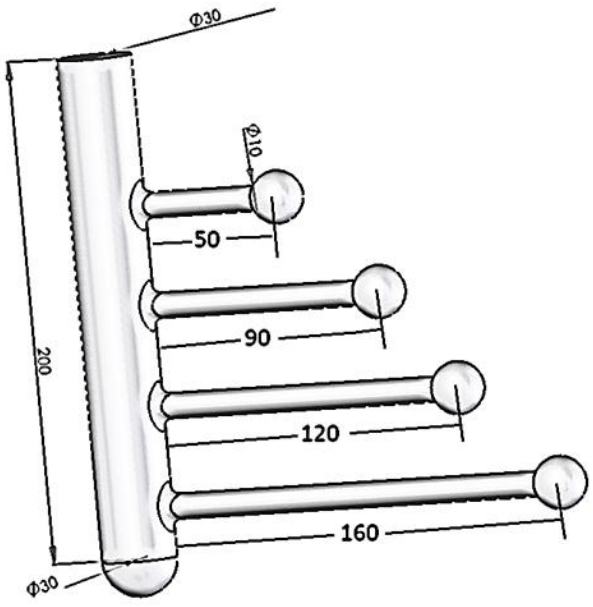

Figure 1. Dimension of CRC mould

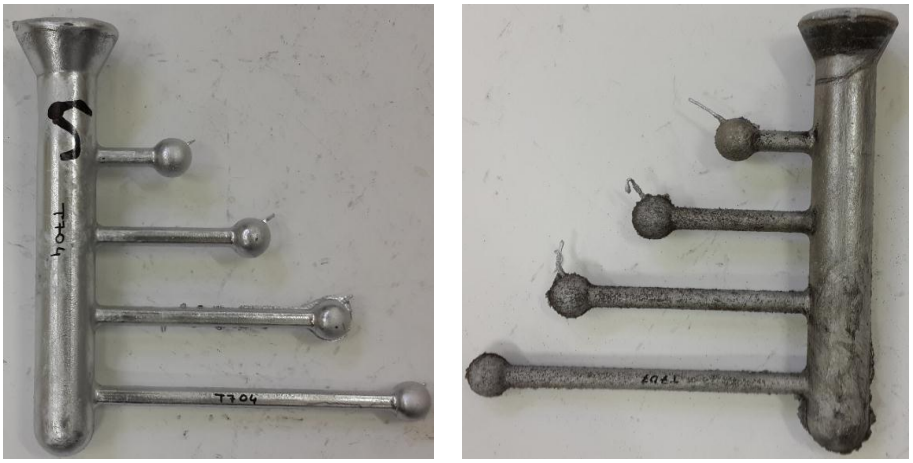

a b

Figure 2. Samples cast in a) die and b) sand moulds

Once the castings were completed, the first examination by done visually. The crack formation along the cast part was checked. Then, the samples were marked and each sphere at the edge of the rods were cut and sectioned to the half thickness. Macroscopic examinations were carried out by using image analysis software and pore size, shape and area were measured. In addition, secondary dendrite arm spacing (SDAS) was also calculated.

In order to see the effect of melt quality on the hot tearing susceptibility, reduced pressure test samples were collected by using sand mould and solidification under 80 mbar (Figure 3).

Figure 3. Reduced pressure test machine

3. RESULTS and DISCUSSION

The bifilm index change of the melts before and after degassing is given in Figure 4. As can be seen the melt quality was significantly increased after degassing in all the cases. For the unmodified charge, this decrease of bifilm index is from 80 mm to 20 mm. For Ti grain refinement from 50 to 10 and for B grain refinement 30 to 10 mm. It is interesting to note that

the bifilm index was decreased (i.e. melt quality was increased) when both of the grain refiners were added.

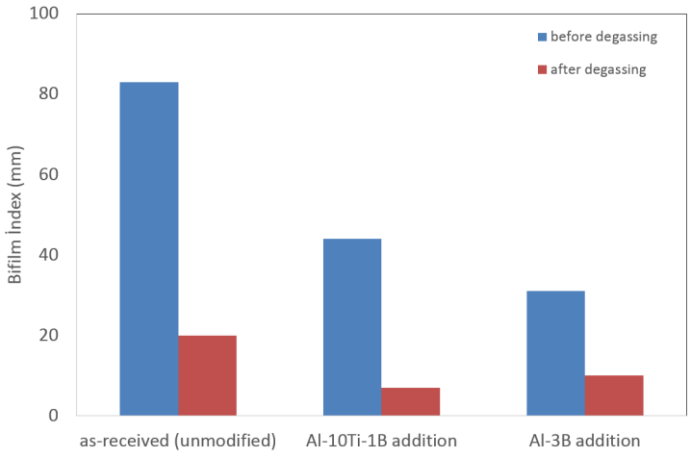

Figure 4. Bifilm index change of the melts before and after degassing

The visual inspection results show that there were no hot tears on the CRC rods of both die and sand mould castings. Therefore, porosity inside the spheres of the cast parts were investigated. Figure 5 shows the average pore area measurements taken from different melts before and after degassing.

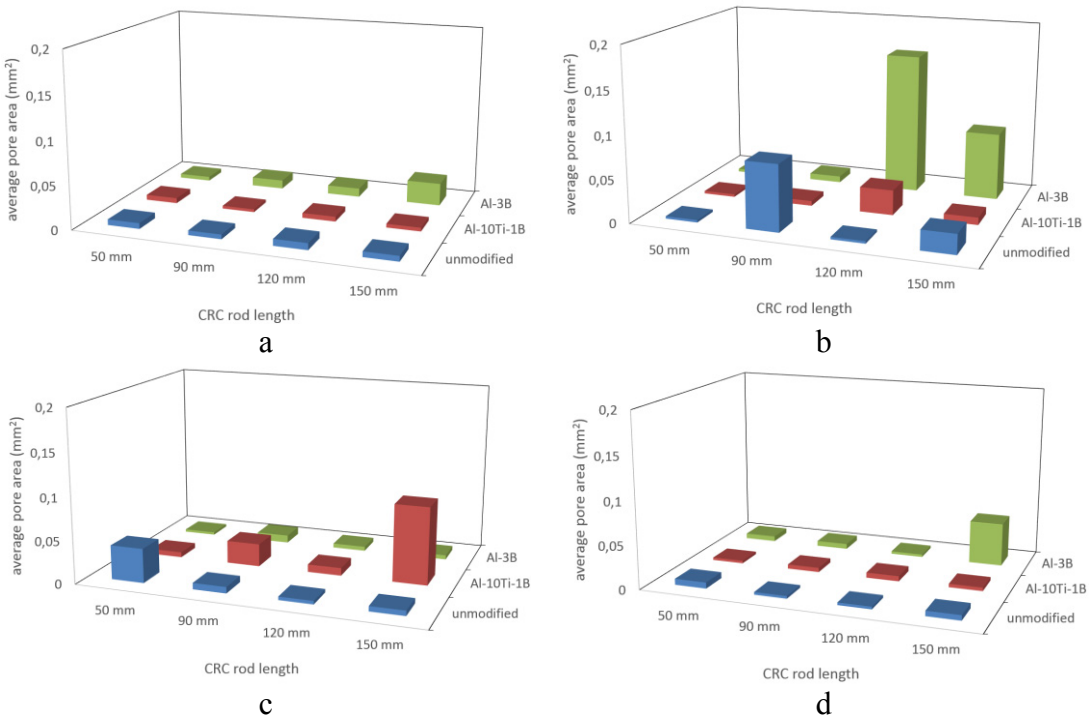

Figure 5. Average pore area with regard to the CRC rod length for sand moulds (a) before, (b) after degassing; for die (c) before and (d) after degassing

It is interesting to note that in sand mould, the porosity was increased after degassing whereas in die mould, average pore area was decreased after degassing. Arnberg and Dispinar had reported that with B grain refinement, more globular dendrites were formed. Therefore, in comparison to the elongated and heterogeneous dendritic structure, the pores that can be formed would be more localised and thus led to larger areas. And since solidification is slower in sand mould, the pore area is highest in Fig 5a and b. In the die mould, similarly, B grain refined alloy has the highest porosity but the values are smaller than the san mould (Fig 5c-d).

These findings were also confirmed by the image analysis results found on the measurement of length of pores. As seen in Figure 6, bigger pores were observed for the sand mould casting, as the heat transfer is decreased from permanent to sand mould, the slower cooling lets the bifilms to open more easily.

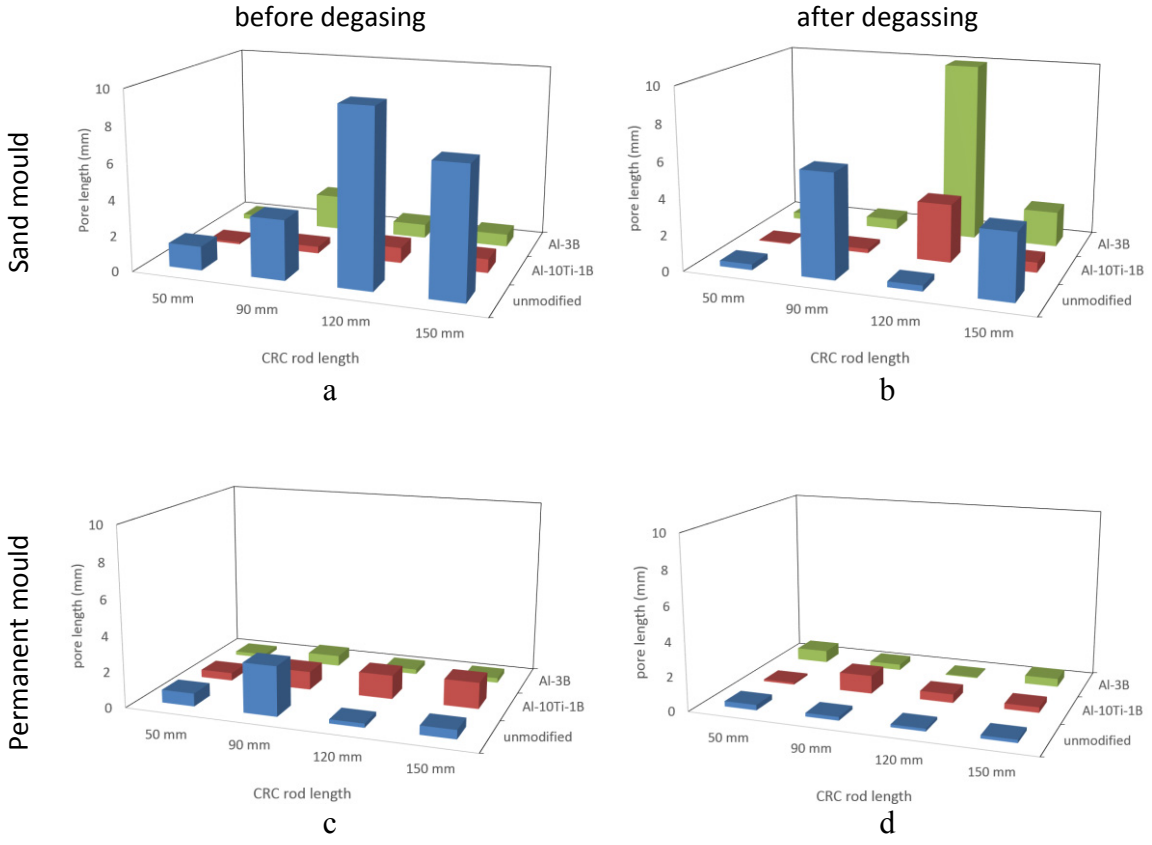

Figure 6. Average pore length with regard to the CRC rod length for sand moulds (a) before, (b) after degassing; for permanent mould (c) before and (d) after degassing

Figure 7 shows the number of pores measured on the sectioned surface of spheres on each of the CRC rods for sand and permanent mould. The highest number of pores were found in the unmodified charge before degassing. However, the number of pores were reduced in both sand and permanent mould castings after degassing.

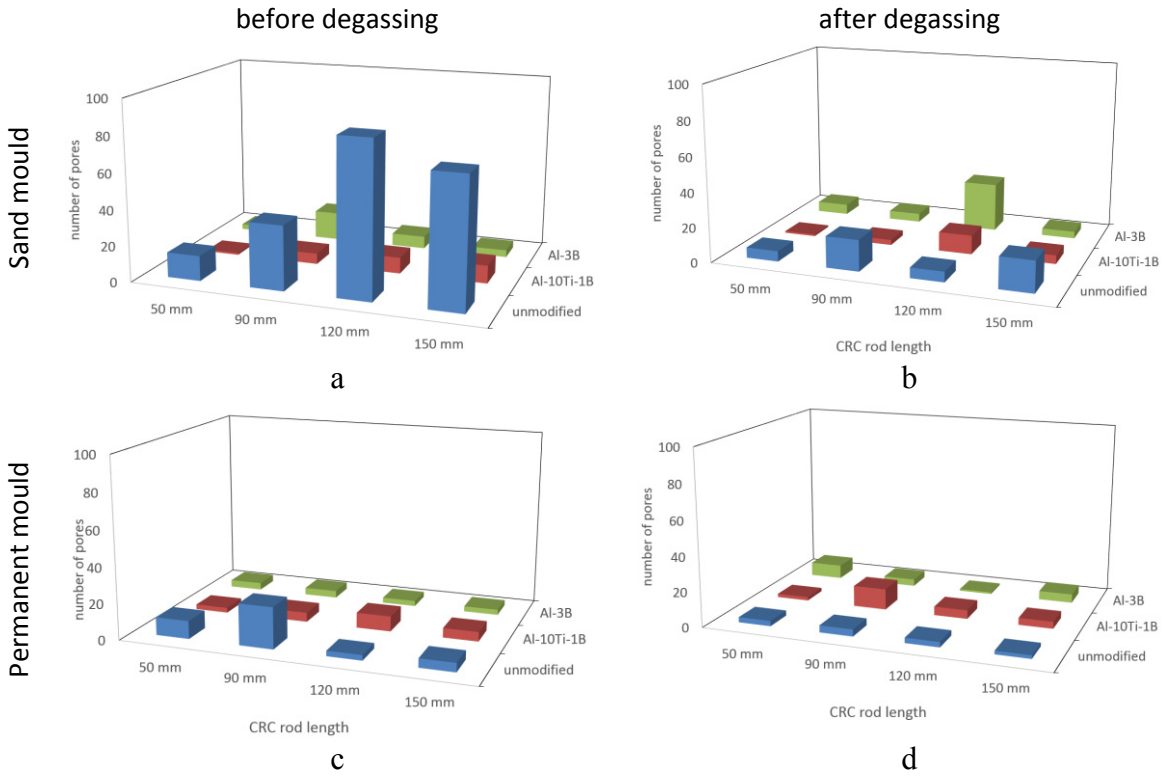

Figure 7. Number of pores with regard to the CRC rod length for sand moulds (a) before, (b) after degassing; for permanent mould (c) before and (d) after degassing

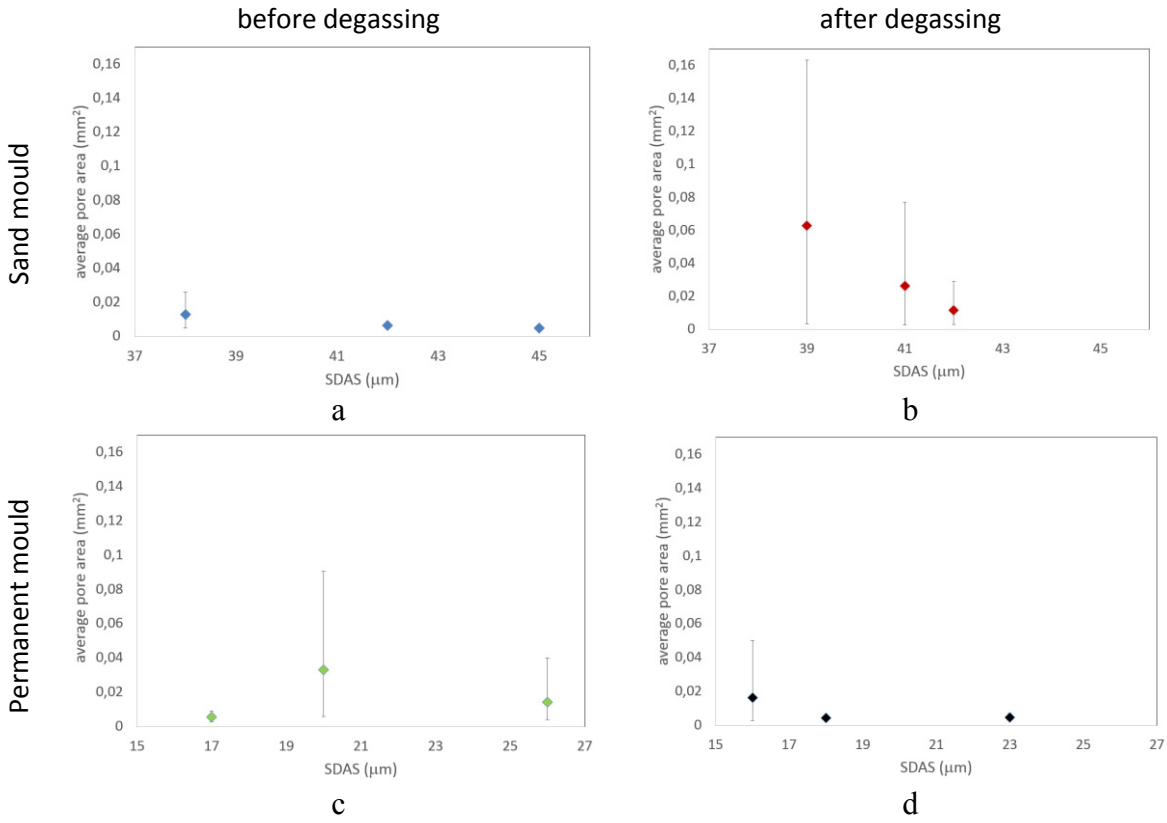

Figure 8. Average pore area and SDAS for sand moulds (a) before, (b) after degassing; for permanent mould (c) before and (d) after degassing

Secondary dendrite arm spacings (SDAS) were measured from all the spheres at the edge of each rod on the CRC mould. The results were compared with the average pore area and given in Figure 8. The most clear and expected result is the higher SDAS values (i.e. coarser grains) in sand moulds compare to permanent mould. The other observation was the decrease in SDAS after the melts were degassed. The interesting finding was the high average pore area and the scatter of results when B grain refiners were used (Fig 8a-b). Dispinar had done some studies with Ti-free B grain refiners and had found similar results. It was concluded that with B grain refinement, more localised and higher areas of pore formation was observed compared to the finer and evenly distributed pores in Ti grain refinement.

It appears that the hot tearing tendency was over-compensated by the pore formation in each of the spheres at the edge of the CRC rods. If there were no pore formation, then the remaining liquid inside the sphere that had to solidify last (i.e. hot spot) would contract and cause a crack at the joints of the rods and spheres. Thus, hot tearing would be observed.

4. CONCLUSIONS

Average pore area in a hot spot increases with B grain refinement and decreases with Ti grain refinement. Correspondingly, number of pores increases with Ti grain refinement and it decreases with B grain refinement.

Ti-free B grain refinement causes localised and large pores compare to the homogeneously distributed fine pores in Ti grain refinement.

Hot tearing tendency of a hot spot can be compensated by the pore formation.

Acknowledgment

This work has been supported by the Scientific Research Projects Coordination Unit of Selcuk University (Project number: 13101026). The authors would like to thank ALTUN DÖKÜM sanayi A.Ş. for their support in this study.

REFERENCES

1. Kaufman, J.G., E.L. Rooy, and A.F. Society, *Aluminum Alloy Castings: Properties, Processes, and Applications*. 2004: ASM International.
2. Campbell, J., *Castings : [the new metallurgy of cast metals]*. 2003, Butterworth Heinemann.
3. Larouche, D., et al., *A constitutive model for the tensile deformation of a binary aluminum alloy at high fractions of solid.* Metallurgical and Materials Transactions B: Process Metallurgy and Materials Processing Science, 2006. **37**(3): p. 431-443.
4. Rappaz, M., J.M. Drezet, and M. Gremaud, *A new hot-tearing criterion.* Metallurgical and Materials Transactions A: Physical Metallurgy and Materials Science, 1999. **30**(2): p. 449-455.
5. Apelian, D., G.K. Sigworth, and K.R. Whaler, *Assessment of Grain Refinement and Modification of Al-Si Foundry Alloys by Thermal Analysis.* American Foundrymen's Society Inc., 1984: p. 99297-99307.
6. Chalmers, B., *The structure of ingots.* Journal of Australian Institute Metallurgy, 1963. **8**: p. 255-263.
7. Metz, S.A. and M.C. Flemings, *A fundamental study of hot tearing.* The Merton C. Flemings Symposium on Solidification and Materials Processing, 2001: p. 181-188.
8. McCartney, D.G., *Grain refining of aluminium and its alloys using inoculants.* International Materials Reviews, 1989. **34**(5): p. 247-260.

THE EFFECT OF DENDRITE ARM COARSENING ON MICROSEGREGATION WITHOUT BACK-DIFFUSION IN SOLID

Altan TÜRKELİ

Marmara University, Turkey
altan.turkeli@marmara.edu.tr

ABSTRACT

In literature, several attempts have been done in order to analyze solute distribution during solidification of a binary alloy. The first and simplest analytical model for a binary alloy came from Gulliver-Scheil, considering a constant partition coefficient at the interface during solidification without back diffusion in solid. Later, Brody-Flemings proposed an approximate analytical model, taking into account one dimensional diffusion of solute in solid during solidification in plate-like dendrite arms. Kirkwood modified the Brody-Flemings model for the dendrite arm coarsening situation. This Kirkwood microsegregation equation has been solved analytically by Mortenson for 1D, 2D, and 3D constant cooling rate cases without back diffusion in solid. However, it has not been solved analytically for 1D, 2D, and 3D exponential growth rates without back diffusion in solid. In this paper, the exact analytical solutions for these cases are presented. It is also showed that if growth rate is exponential, the composition becomes infinite at the end of solidification as in the case of Gulliver-Scheil equation.

Keywords: Casting, Solidification, Modelling

KATIDA DİFÜZYON OLMAKSIZIN İKİNCİ DENDRİT KOLLARI KABALAŞMASININ MİKROSEGREGASYONA ETKİSİ

ÖZET

Bir ikili sistemde, çözelti elementinin dağılımını analiz eden bir kaç temel model önerilmiştir. Katı-sıvı ara yüzeyinde denge dağılım katsayısını sabit kabul eden Gulliver-Scheil, en basit ve ilk mikrosegregasyon denklemini önermişlerdir. Daha sonra, Brody-Flemings, düzlemsel katılaşan bir sıvı-katı arayüzeyinde geri difüzyonu da dikkate alan yeni bir mikrosegregasyon modeli geliştirmişlerdir. Kirkwood ise bu modele dendrit kollarının kabalaşması etkisini de ilave ederek modifiye etmiştir. Katıda difüzyon olamaksızın, Mortenson, Kirkwood mirosegregasyon denklemini 1D, 2D ve 3D durumları için sabit soğuma şartlarında çözmüştür. Ancak, bu denklem, üstel büyümeli katılaşma (liner veya parabolik büyüme gibi) şartları için çözülmemiştir. Bu çalışmada bu şartlar için genel mikrosegregasyon denkleminin çözümü sunulacaktır. Ayrıca, Gulliver-Scheil denkleminde olduğu gibi, bu denklemlerde katılaşmanın sonunda bileşim sonsuza gittiği gösterilmiştir.

***Anahtar kelimeler*:** Döküm, Katılaşma, Modelleme.

1. INTRODUCTION

At the solid–liquid interface three different morphologies can occur during solidification of

alloys. These are planar, cellular, and dendritic structures. In the case of planar solidification, no solute redistribution occur, i.e. no microsegregation exist in solid. However, in other two morhological structures solute elements are non-homogenously distributed in unit elements during solidification, so-called microsegregation. Representative unit element for cellular morphology is primary arm spacing which can be taken as a constant during solidification, However, in the case of dendritic solidification, secondary arms grow from the primary stalks and these secondary arms are dinamic and coarsen during solidification, therefore secondary arm spacing increases and should be taken as a variable parameter in microsegregation models[1-6].

This dendrite arm coarsening is a surface tension driven phenomenon and mainly occurs in the two different form of coarsening mechanisms, coalescence and ripening. In the case of coalescence process, two adjacent secondary arms can agglomerate starting from tips of secondary arms or from roots of two adjacent secondary arms. For ripening, four different mechnisms are suggested. In the first one, it is assumed that secondary arms can only remelt radially from both sides of thin arm, i.e. the remelting rate of the hot and cold side of thin arm is equal to each other. However, under infuence of temperature gradient zone melting at high temperature gradients asymmetrical radial remelting can occur while secondary arms migrate. In the third model, it is assumed that thin secondary arms can remelt from tip to root whereas in the fourth model, remelting can occur from roots of secondary arms. The difference between two coarsening mechanisms is that ripening mechanism is diluted the liquid composition whereas coalesence mechnism is not, therefore this dilution can affect significantly microsegregation [4-8].

Kirkwood microsegregation equation without back-diffusion in solid has been solved analytically by Mortenson for 1D, 2D, and 3D constant cooling rate cases. Voller-Beckerman solved this Kirkwood microsegregation equation only for parabolic growth rate. However, it has not been solved analytically for 1D, 2D, and 3D any exponential growth rates without back diffusion in solid[5-8].

2. SOLUTION OF KIRKWOOD'S MICROSEGREGATION EQUATION

The Kirkwood microsegregation equation can be written as follows[6]:

$$C_L(1-k)\frac{dx_i}{dt} = D_s\left(\frac{dC_s}{dx}\right) + (L_C - X_i)\frac{dC_L}{dt} + (C_L - C_O)\frac{dL_c}{dt} \quad (1)$$

where C_L liquid composition (wt %)
C_O average composition (wt %)
k partition coefficient at the solid-liquid interface
D_S diffusibility of solute element in solid (m^2/s)
X_i the length of solid (m)
L_C the half length of representative unit element (m), is equal to $L_C=At^n$
n coarsening exponent
t time(s)
A pre-exponent constant (m/s^n)
$\left(\frac{dC_S}{dx}\right)$ concentration gradient of solid at the solid-liquid interface (wt %/m)
$\frac{dx_i}{dt}$ velocity of solid-liquid interface (m/s)

For Ds=0 (without back diffusion in solid), the equation-1 becomes :

$$C_L(1-k)\frac{dx_i}{dt} = (L_C - X_i)\frac{dC_L}{dt} + (C_L - C_O)\frac{dL_c}{dt} \quad (2)$$

Mortenson solved the equation-2 for constant colling rate[7].

$$C_L = Co + W*t/ml \quad (3)$$

where ml liquidus slope (K/wt %)
W cooling rate (-) (K/s)
t time (s)
k partition coefficient at the solid-liquid interface, $k=Cs/C_L$

$$f = \frac{1+n}{1-k}\frac{C_L^{(1/k-1)}}{(C_L - C_O)^n}\int_{C_O}^{C_L} \emptyset^{[k/(1-k)]}(\emptyset - C_O)^n d\emptyset \quad (4)$$

Where

$$f_1 = \frac{X_i}{L_c}$$

He also solved this equation for 2D (cylinderical solidification of secondary arms) and 3D (spherical solidification) as follows [7]:

$$f = \frac{1+2n}{1-k}\frac{C_L^{(1/k-1)}}{(C_L - C_O)^{2n}}\int_{C_O}^{C_L} \emptyset^{[k/(1-k)]}(\emptyset - C_O)^{2n} d\emptyset \quad (5)$$

Where

$$f = \frac{X_i^2}{L_C^2}$$

$$f = \frac{1+3n}{1-k}\frac{C_L^{(1/k-1)}}{(C_L - C_O)^{3n}}\int_{C_O}^{C_L} \emptyset^{[k/(1-k)]}(\emptyset - C_O)^{3n} d\emptyset \quad (6)$$

Where

$$f = \frac{X_i^3}{L_C^3}$$

These equations can be re-written as follows:

$$f_i = \frac{1+in}{1-k}\frac{C_L^{(1/k-1)}}{(C_L - C_O)^{in}}\int_{C_O}^{C_L} \emptyset^{[k/(1-k)]}(\emptyset - C_O)^{in} d\emptyset \quad (7)$$

Where i the dimension of solidification.

i=1 for planar solidification
i=2 for cylindrical solidification

i=3 for spherical solidification

Voller-Beckermann[8] solved the equation-2 only for parabolic growth rate as follows.

$$f_S = \left(\frac{t}{t_f}\right)^{0.5}$$

where tf solidification time (s)

$$\frac{C_L}{C_O} = \frac{(2n)(1-f_S)^{(1+2n)k-1}}{f_S^{(2n)}} \int_0^{f_S} \emptyset^{(2n-1)} (1-\emptyset)^{-(1+2n)k} d\emptyset \tag{8}$$

In this study, the equation 2 has been solved for planar solidification and any exponential growth rate conditions as follows. Relationship between time and fraction of solid is defined as given below:

$$f_S = \left(\frac{X_i}{L_C}\right) = \left(\frac{t}{t_f}\right)^m \tag{9}$$

$$L_C = At^n \tag{10}$$

Where m is constant.
m=1 for linear growth rate
m=0.5 for parabolic growth rate.

Using equations 9 and 10, the equation 2 can be re-written as follows:

.

$$C_L(1-k)\frac{(L_C)(n+m)}{f_S^{\left(\frac{1-m}{m}\right)} t_f} = (L_C)(1-f_S)\frac{dC_L}{\left(\frac{1}{m}\right) f_S^{\left(\frac{1-m}{m}\right)} t_f df_s} + (C_L - C_O)\frac{(n)(L_C)}{f_S^{\left(\frac{1}{m}\right)} t_f} \tag{11}$$

After some arrangment, it becomes:

$$\frac{dC_L}{df_S} = \frac{C_L(1-k)\left(\frac{n+m}{m}\right) f_S - (C_L - C_O)\left(\frac{n}{m}\right)}{(1-f_S)f_S} \tag{12}$$

or

$$\frac{dC_L}{df_S} + C_L\left[\frac{\left[\left(1+\frac{n}{m}\right)k-1\right]}{(1-f_S)} + \frac{\left(\frac{n}{m}\right)}{f}\right] = C_O\frac{\left(\frac{n}{m}\right)}{(1-f_S)f_S} \tag{13}$$

The solution of this differential equation is :

$$\frac{C_L}{C_O} = \frac{\left(\frac{n}{m}\right)(1-f_S)^{\left(1+\frac{n}{m}\right)k-1}}{f_S^{\left(\frac{n}{m}\right)}} \int_0^{f_S} \emptyset^{\left(\frac{n}{m}-1\right)} (1-\emptyset)^{-\left(1+\frac{n}{m}\right)k} d\emptyset \tag{14}$$

The Kirkwood microsegregation equation for 2D and 3D can be written as follows:

$$C_L(1-k)\frac{dV_i}{dt} = (V_C - V_i)\frac{dC_L}{dt} + (C_L - C_O)\frac{dV_c}{dt} \tag{15}$$

The analytical solution of this equation 15 for cylindrical secondary arms and for any exponential growth rate is :

$$\frac{C_L}{C_O} = \frac{\left(\frac{2n}{m}\right)(1-f_S)^{\left(1+\frac{2n}{m}\right)k-1}}{f_S^{\left(\frac{2n}{m}\right)}} \int_0^{f_S} \emptyset^{\left(\frac{2n}{m}-1\right)} (1-\emptyset)^{-\left(1+\frac{2n}{m}\right)k} d\emptyset \tag{16}$$

The analytical solution of this equation 15 for spherical particles and for any exponential growth rate is :

$$\frac{C_L}{C_O} = \frac{\left(\frac{3n}{m}\right)(1-f_S)^{\left(1+\frac{3n}{m}\right)k-1}}{f_S^{\left(\frac{3n}{m}\right)}} \int_0^{f_S} \emptyset^{\left(\frac{3n}{m}-1\right)} (1-\emptyset)^{-\left(1+\frac{3n}{m}\right)k} d\emptyset \tag{17}$$

These equations 14,16, and 17 can be re-written as follows:

$$\frac{C_L}{C_O} = \frac{\left(\frac{in}{m}\right)(1-f_i)^{\left(1+\frac{in}{m}\right)k-1}}{f_i^{\left(\frac{in}{m}\right)}} \int_0^{f_i} \emptyset^{\left(\frac{in}{m}-1\right)} (1-\emptyset)^{-\left(1+\frac{in}{m}\right)k} d\emptyset \tag{18}$$

Where i the dimension of solidification.

i=1 for planar solidification
i=2 for cylindrical solidification
i=3 for spherical solidification

3. RESULTS AND DISCUSSION

It may be easily recognized that there are some simple solutions of the equation-18 for some values. For example, if for i=3 m=3n and k=0.5, or
i=2 m=2n and k=0.5, or
i=1 m=n and k=0.5, are taken,
the equation 18 becomes:

$$C_S = \frac{kC_O ln\left[\frac{1}{(1-f_i)}\right]}{f_i} \tag{19}$$

It is clear that when fi becomes one i.e. at the end of solidification, Cs goes to infinite as in the case of Gulliver-Scheil equation.

Eutectic composition and average composition are chosen as 5 and 1, repectively in order to demonstrate variables in the equation 18. The figure-1 shows the effect of exponential growth rate on the volume fraction of eutectic structure. It is clear that the volume fraction of eutectic structure increases with increasing, m, growth rate expoenential coefficient for constant coarsening exponent.

The figure-2 shows the effect of coarsening exponent on the volume fraction of eutectic structure. It is clear that the volume fraction of eutectic structure decreases with increasing, n, coarsening exponent for parabolic growth rate (m=0.5, constant expoenetial growth rate).

The figure-3 shows the effect of solidification mode (i.e. planar, cylindrical, spherical solidification) on the volume fraction of eutectic structure. It is clear that the volume fraction of eutectic structure decreases with increasing the dimension of solidification mode.

The figure-4 shows the effect of coarsening exponent on concentration profiles. It is clear that concentratşon profile shifts down with increasing coarsening exponent.

3. CONCLUSION

In this paper, the exact analytical solutions of Kirkwood's microsegregation equation are presented for 1D, 2D, and 3D and for any exponential growth rates. It is also showed that if growth rate is exponential, the composition becomes infinite at the end of solidification as in the case of Gulliver-Scheil equation.

REFERENCES

1. G.H. Gulliver, "Metallic Alloys", Griffin, London, 1922
2. T.E. Scheil, Zeitschrift für Metallkunde, 34, 70, 1942
3 H.D. Brody, M.C. Flemings, Trans. Of Metal. Society, of AIME, 236, 615, 1966
4. M.C. Flemings "Solidification Processing",McGraw-Hill, New York, 1974
5. K.P. Young, D.H. Kirkwood, Metal. Trans. 6A, 197, 1975
6. Ogilvy, A. J. W. and Kirkwood, D. H., Appl Sci. Res. 44, 43, 1987
7. A. Mortenson, Metall. Trans. 20A, 247, 1989
8. V.R. Voller, C. Beckermann, Metall. Trans. 30A, 2183, 1999

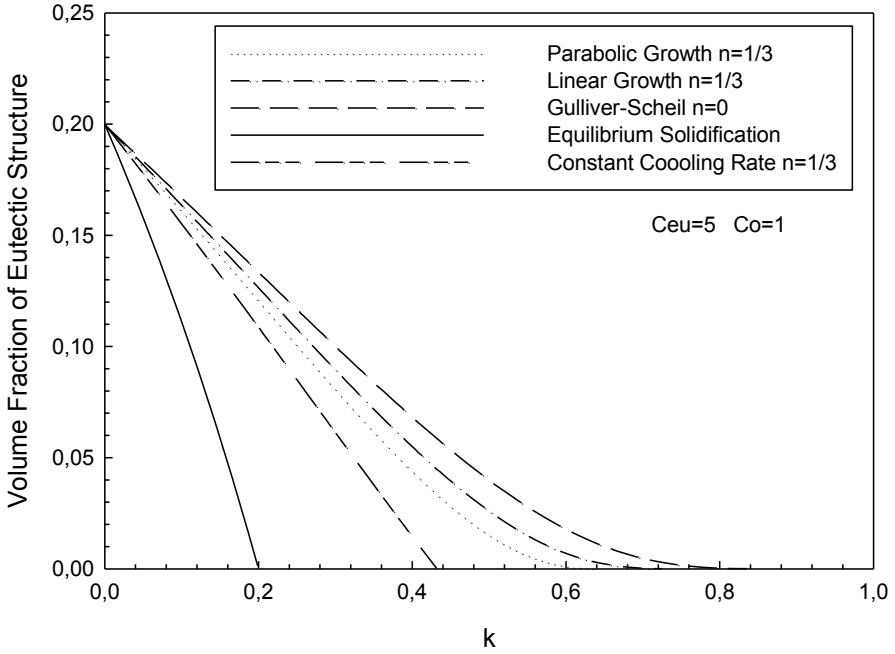

Figure-1 The effect of growth rate on volume fraction of eutectic structure as a function of partition coefficient for constant coarsening exponent and comparison with other solidification conditions.

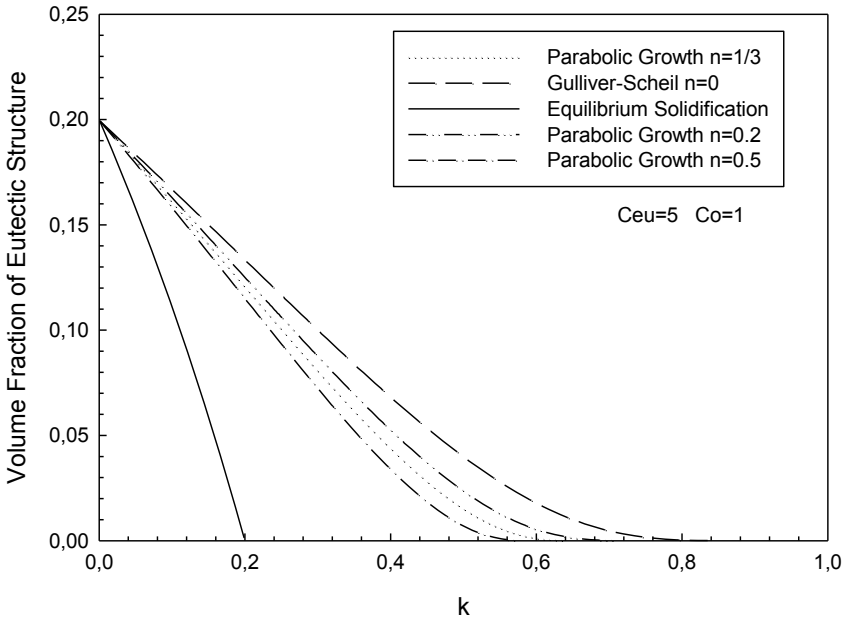

Figure-2 The effect of coarsening exponent on volume fraction of eutectic structure as a function of partition coefficient for parabolic growth rate and comparison with other solidification conditions.

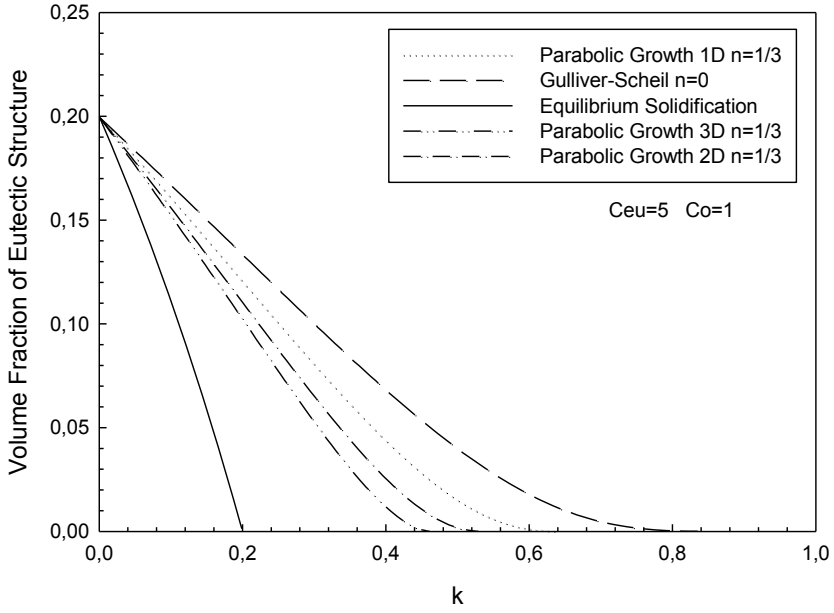

Figure-3 The effect of solidification mode on volume fraction of eutectic structure as a function of partition coefficient for parabolic growth rate and for constant coarsening exponent, and comparison with other solidification conditions.

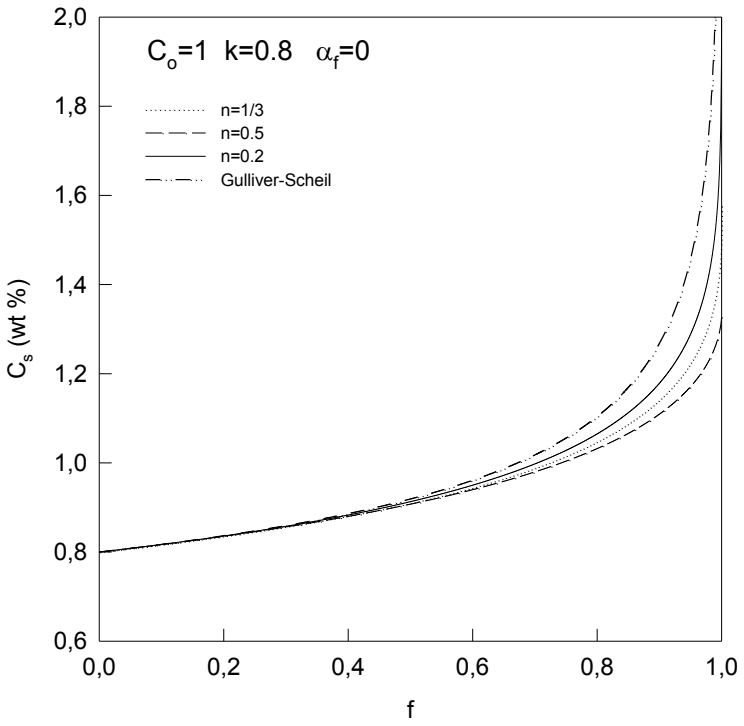

Figure-4 The effect of coarsening exponent on concentration profiles as a function of solid fraction.

SOLIDIFICATION MODELING OF AN AXIAL STEEL CAST IMPELLER BY USING FINITE VOLUME METHOD

Murat ÇOPUR*,, Ahmet TURAN*,***, Mehmet Niyazi ERUSLU*,****

* Metallurgical and Materials Engineering Department, Faculty of Chemical and Metallurgical Engineering, Istanbul Technical University, 34469, Maslak, Istanbul, Turkey
** Alarko Carrier Sanayi ve Ticaret A.Ş., Gebze OSB, 41480, Gebze, Kocaeli, Turkey
murat.copur@alarko-carrier.com.tr
*** Yalova Community College, Yalova University, 77100, Yalova, Turkey
turanah@itu.edu.tr
**** Chemical and Process Engineering Department, Faculty of Engineering, Yalova University, 77100, Yalova, Turkey
eruslu@itu.edu.tr

ABSTRACT
Determination of the solidification contours in cast geometries is extremely important in the foundry industry. Thus, it provides a prediction of the last location(s) to solidify in order to define the correct feeding path and the number of risers. This study presents a three-dimensional simulation of transient conduction heat transfer within an axial impeller, made of AISI 1016 steel, poured and solidified in chemically bonded mold and core medium, by using Finite Volume Method (FVM) and ANSYS CFX. Specific heat, density and thermal conductivity of AISI 1016 steel, mold and core materials were considered as functions of temperatures. In this transient thermal analysis, the convection heat transfer phenomenon was also considered at the outer surfaces of the mold. In order to shorten the run-time, the nonlinear transient analysis was made for 60°/360° segment of the impeller, core and mold. The solidification contours of the impeller as well as isothermal lines in core and mold were obtained in 3-D. The cooling curves of different points were also given.

Keywords: *ANSYS, Finite Volume Modeling, Heat Transfer of Casting, Solidification, Steel Impeller*

SONLU HACİMLER YÖNTEMİNİ KULLANARAK TEK EKSENLİ ÇELİK DÖKÜM PARÇALARIN KATILAŞMASININ MODELLENMESİ

ÖZET
Döküm endüstrisinde, dökülecek parça geometrilerinde katılaşma şekillerinin belirlenmesi çok önemlidir. Böylelikle, döküm parçasındaki son katılaşacak bölgeler belirlenerek besleme yolu ve besleyiciler sayesinde ön görüde bulunabilmektedir. Bu çalışmada, Sonlu Hacimler Yöntemi'nden (SHY) yararlanan ANSYS CFX yazılımı ile kimyasal bağlı kalıp ve maça sistemi içerisine dökülmüş AISI 1016 kalite çeliğin katılaşmasında ısı akışının 3-boyutlu modellemesi araştırılmıştır. AISI 1016 çeliğin, kalıp ve maça malzemelerinin spesifik ısı, yoğunluk ve ısıl iletkenlik değerleri sıcaklığın bir fonksiyonu olarak hesaplanmıştır. Ayrıca, kalıp dış yüzeylerindeki ısı konveksiyonu da modellemelerde hesaba katılmıştır. Hesaplamaların kolaylaştırılması için modellemeler 60°/360°'lik alanlara indirgenen katılaşan metal, kalıp ve maça sistemleri üzerinden gerçekleştirilmiştir. Katılaşan parçaların, kalıp ve maçaların soğuma esnasındaki ısıl gradyanları da 3-boyutlu bir biçimde gösterilmiştir.

***Anahtar kelimeler*:** ANSYS, Sonlu Hacimler Yöntemi, Dökümde Isı Transferi, Katılaşma, Çelik Parça.

1. INTRODUCTION

Solidification sequence is very important for designing risers and their connections for foundry industry. Besides, knowing the solidification sequence and contours helps to the foundry engineer to improve the manufacturability by modifying the original casting designs which are created by the design engineers who are often not familiar with the solidification and how the design parameters affect the solidification pattern. Chvorinov's rule and Chvorinov's concept of relative solidification time of the riser and casting were utilized on the development of the first risering equations [1-10].

In fact, modulus method works best for the casting geometries in which none of the mold materials become saturated with heat such as internal corners, internal cores and concave mold surfaces. Nevertheless, almost all casting parts have such geometric features. Thus, foundry engineers faced with a choice: simple but rough modulus method versus complex but more sophisticated numerical methods. Later, the emphasis has shifted to the use of numerical methods such as Finite Difference Method/Finite Element Method (FDM/FEM). In the first studies, FDM technique was used to simulate solidifications of simple geometries and then applied this technique to designing and risering castings [11-13]. Numerical methods provided more sophistication than simple relation derived by Chvorinov. However, these techniques require knowledge of thermo-physical properties of metal and mold materials such as specific heat, density and thermal conductivity. These properties are functions of temperature, composition of metal and the solidification rate.

The uses of numerical techniques have been increased as the thermo-physical properties of metals and mold materials at elevated temperatures were studied by several researchers [14-21]. All thermo-physical properties are temperature dependent and vary with compositions. Thus, today, the most challenging and time consuming parts of the simulations are determination of the thermo-physical properties of the materials which will be used in analysis. Special algorithm was developed to calculate the solidification-related thermo-physical properties for plain carbon and stainless steels. The calculated figures were compared with the experimental results, and good correlation was obtained especially for plain carbon steel [16].

The high cost of foundry experiments and trials under daily production conditions makes it appropriate to use all available methods to simulate and to improve the casting design by small modifications. These methods must provide quick results with reasonable accuracy.

Impellers which are the most critical parts of the centrifugal pumps have great impacts on the pump characteristics: Pressure head and flow. Today's pump design engineers use computational fluid dynamic programs in order to design efficient impellers for the targeted pressure heads and flows. Computational Fluid Dynamics programs provide impeller geometries in order to balance the pressures of the fluids that flow over two sides of the blades of impellers. Thus, outcomes are often designs for the targeted pressure heads and flows, but far from cases of easy and economic casting process. In the successive works, design engineers and the foundry engineers try to modify the impeller geometries for economic casting without losing the pump characteristics. So, it is extremely important to know how a modification affects on the solidification happens during casting to determine the number of risers and their volumes in order to reach better casting yields, and at the end low cost casting.

It is known that several commercial codes are available in the foundry industry to obtain the solidification pattern. However, these commercial codes are used in the foundry industry by foundry engineers, not by engineers in the R&D departments of the pump manufacturers. Once a 3D model of an impeller is created for CFX modeling, the same model can be used as the preliminary approach to estimate the solidification pattern. In this study, it was shown that the same model can be used to run analyzes for fluid flow and heat transfer together. This gives the possibility to reduce the model setup time and also reduces the first investment cost that is very important for mid-sized pump manufacturers.

The object of this article is to simulate the solidification of an axial impeller made of AISI 1016 steel, widely used steel in pump industry, poured into chemically bonded urethane molding sand (coarse) and chemically bonded furan core sand (fine) by using a finite volume package. Even though typically pouring temperature is 1,923 K, sometime extra high pouring temperatures are used in order to ensure the proper flow through thin blades. Thus, in this study, high pouring temperatures such as 1,973 K and 2,023 K are also studied in order to understand the effect of superheat on solidification time of different parts of the impeller, especially in the thin blades. The density, specific heat, thermal conductivity of AISI 1016 steel, mold and core sand were considered as temperature dependent. The natural convection properties of the outer surfaces of the mold were considered as constant.

2. EXPERIMENTAL STUDIES

2.1. Thermal Governing Equation

The analytical solutions for the heat conduction equations were derived for infinite and semi-infinite solid bodies at certain boundary conditions. And, the accurate solutions can be obtained for simple geometries. However, the analytical solutions cannot be used for complex geometries having single or multiple cores and concave/convex contours. It is identical to the transient energy equation given in the following formula [22].

$$\nabla \cdot (k \nabla T) = \rho \cdot \frac{\partial (c_p T)}{\partial t} \quad (1)$$

Where ρ is the density, k is conductivity, and Cp is specific heat including latent heat of solidification. All properties are temperature dependant.

2.2. Thermophysical Properties of AISI 1016 Steel, Mold and Core Materials

Thermo-physical data of AISI 1016 steel are presented in Figure 1 [16]. In this study, chemically bonded urethane sand (coarse) for mold and chemically bonded furan sand (fine) for core have been used. The related thermo-physical data for mold and core materials are presented in Figure 1 as well [23].

2.3. Experimental Methodology

In this study, geometries of impeller and core were designed including the mold medium by using a commercial design program, seen in Figure 2 (Outer radius, height and riser diameter are 300 mm, 172 mm and 150 mm respectively).

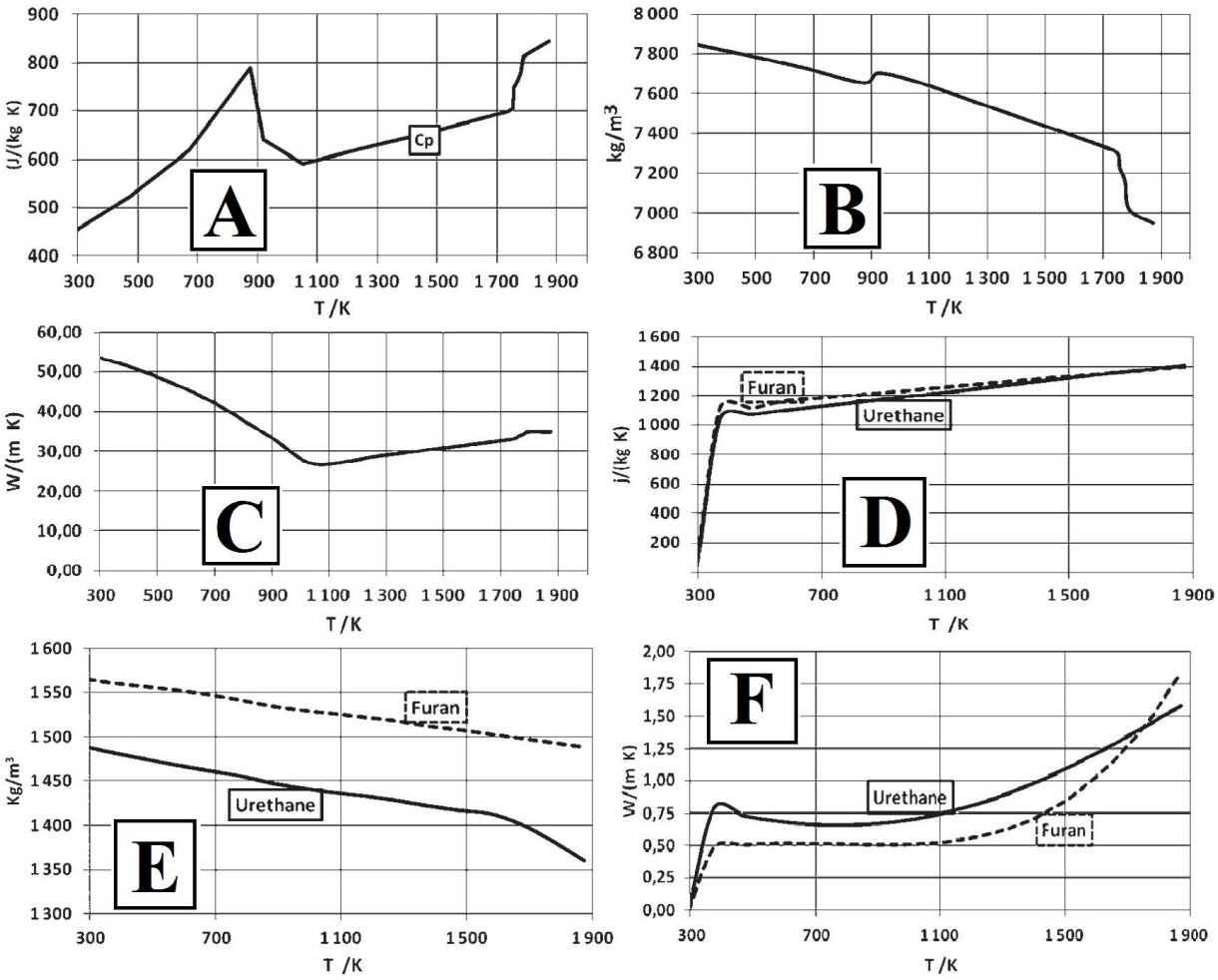

Figure 1. Thermo-physical data of AISI 1016 steel, mold (urethane bonded, coarse) and core (furan bonded, fine) materials (A: Specific heat of AISI 1016, B: Density of AISI 1016, C: Thermal conductivity of AISI 1016, D: Specific heat of urethane and furan bonded sand, E: Density of urethane and furan bonded sand, F: Thermal conductivity of urethane and furan bonded sand) [16, 23]

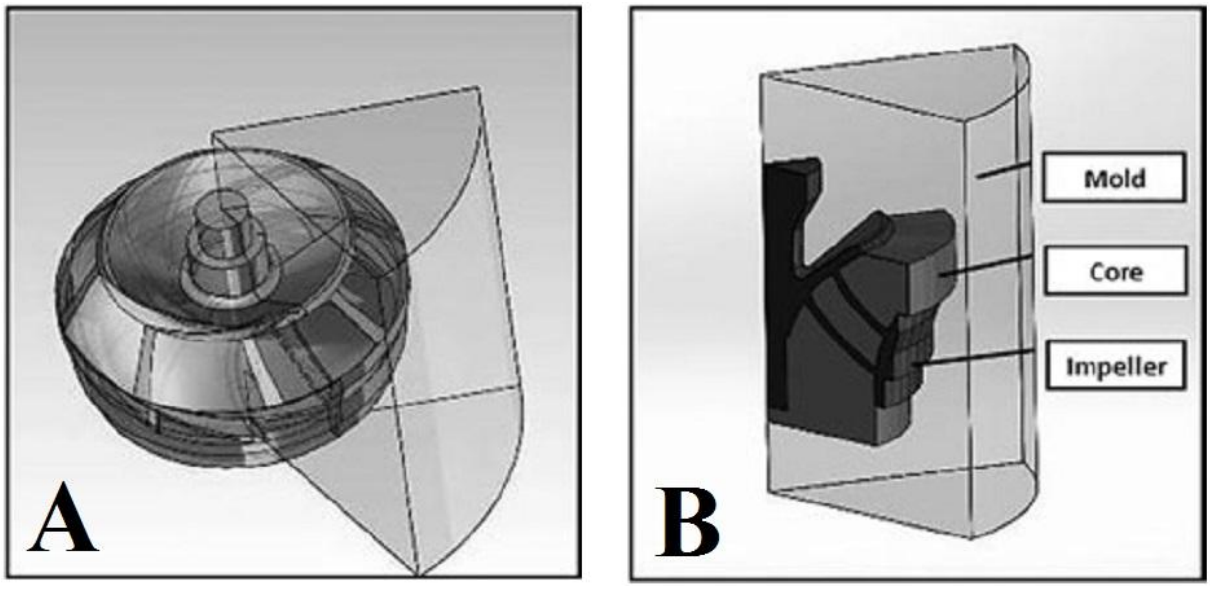

Figure 2. 3D drawing of impeller geometry (A) and 3D model as segmented 60° (B)

The geometry was segmented as 60° symmetric parts in Figure as seen in Figure 2. The model impeller geometry has perfect symmetry so it was segmented in order to reduce the number of grids and the run time accordingly. By employing 60° segment model, the number of nodes of the segment has been reduced almost 6 times. After obtaining a solution, 6 segments can be combined to form a complete impeller when analyzing the results by 3-D appearance.

When the geometry is segmented, the initial boundary conditions must be specified that the symmetry is rotational and the symmetry areas are adiabatic. A CFX program was used to simulate the solidification of AISI 1016 steel in urethane mold and furan core by using a computer of i5 2.9 GHz and 16 GB of ram.

2.4. Meshing

After the model design was imported into CFX software, an automatic mesh was generated throughout the volume of each domain. In spite of the fact that the automatic mesh provides accurate results for many geometries, because of very complex geometry of the model and high temperature difference between metal/core and metal/mold interfaces, some specific features of software had to be employed to modify the mesh. The options of medium mesh size, Proximity/Curvature and inflation as advanced size functions of mesh were used to generate proper mesh for the model [24-27]. Proximity size function was used to specify a minimum number of element layers created in the regions that constitute gaps in the model such as impeller blades. The proximity was assigned as 3 so that at least 3 layers in cross-sectional dimension of each blade were created. Curvature size feature examines curvature on the edges and faces, and computes element sizes on these entities such that size will not violate the maximum size or the curvature normal angle, which are either computed by the mesher automatically or user-defined. Here in this study, the curvature default was assigned as 0.18 which will enable to simulate a 180^0 semi-circle curvature as a semi-decagon. Additionally, single body inflation feature was employed in 3-D of impeller body (metal). The inflation feature provides high quality mesh generation close to the wall boundaries to resolve the drastic changes in physical properties. In this study, because of the very high temperature difference at two adjacent grids on the interfaces of metal/mold and metal/core at initial time (t = 0 s), inflation feature was used to reduce the size of mesh elements on the skin of impeller in 3-D. Maximum layer thickness was assigned as 0.4 mm.

After employing these special features of CFX software, the final mesh was generated. After modification of the mesh by employing mesh size features, mesh statistics was given as 146,962 nodes and 639,981 elements in 60° model segment of impeller, mold and core.

2.5. Materials and Boundary Conditions

Specific heat, thermal conductivity and density properties, described in Section 2.2. as functions of temperature, were inserted as the thermophysical properties of the impeller (AISI 1016 steel), the mold (Chemically bonded urethane molding sand – coarse) and the core (Chemically bonded furan core sand – fine).

As the initial conditions, at t = 0 s, 1,923 K, 1,973 K and 2,023 K were assigned to impeller (metal) for three different solutions. It was 298 K for the mold and the core in all simulations.

The boundary condition is the natural convection generated by the natural aerated environment. For the mold top/bottom surfaces [27] and outer vertical surface [28], 5.75 W/(m^2K) and 11.45 W/(m^2K) film coefficient values were assigned as the ambient temperature was 298 K.

2.6. Transient Analysis

Transient type of analysis which employs solution of second order backward Euler equation was used. The convergence of solutions in transient analyzes are the factor that has to be controlled. The CFX software uses a special algorithm to control and to achieve desired convergence criterion. For this, the incremental form of the system equations is solved, the nodal temperature is updated, internal nodal heat flow rates are calculated, the convergence norm (Residual Root-Mean-Square=RMS) is calculated and compared against the criterion. If the norm is equal or smaller than the criterion, no further iteration is needed, and the next time step is performed.

In this study, the convergence criterion (Residual RMS) is assigned as 10^{-4}. In order to reach such Residual RMS, the number of iteration, called coefficient loop, in each time step is assigned as 1 for minimum and 15 for maximum.

In this study, 0.5 s for the time step and 7,200 s for the total time were used and, Residual RMS as convergence criterion (10^{-4}) was achieved. The run time for the complete solution was approximately 12 hours.

3. RESULTS AND DISCUSSION

The results of this study are mainly the temperature distribution versus time, temperature gradients and cooling curves of points located different place of impeller, core and mold.

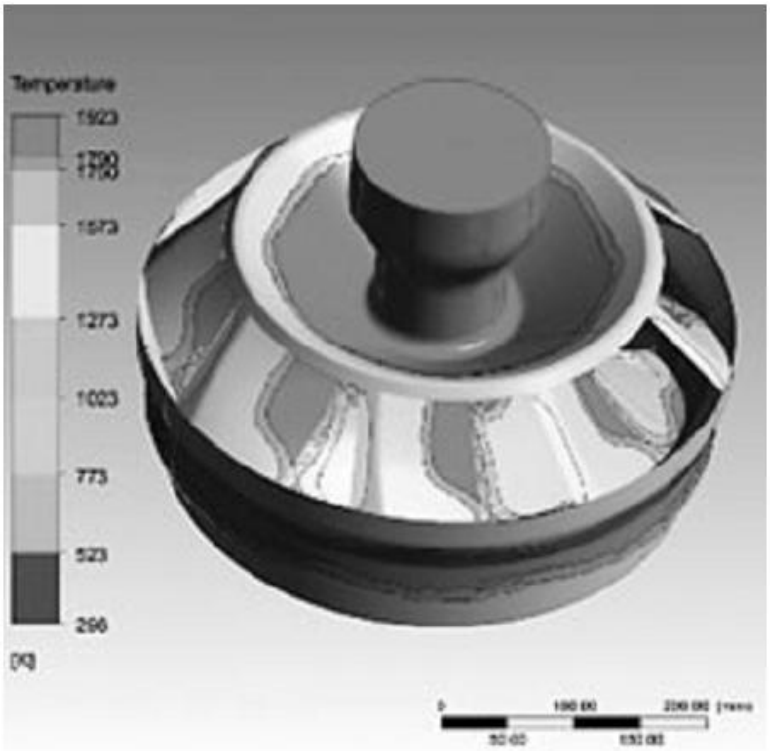

Figure 3. 3D impeller at t: 45 s ($T_{pouring}$: 1,923 K)

After the model is created and simulation is run, it is easy to review the temperature distribution of the impeller as a 60° segment, multiple of segments or in full 3-D appearance, shown in Figure 3.

Additionally, each domain alone or combination of domains may also be easily reviewed. Since the program calculates temperature at all nodes in all domains for all time steps, the review can be done in each incremental time step which had to be defined in the model set-up. In this study, 2.5 s of incremental step was used. It means that the program restores data for the temperature distribution in all domains in every 2.5 s.

The movement of the mushy zone at which hot tear may occur can be reviewed for any time step of solidification.

After the user enters liquidus and solidus temperatures, 1,750 K and 1,790 K respectively, and the time step ($t = t_1$) to the model, the contours of solidus and liquidus temperature are displayed at $t = t_1$.

Figures 4 shows the temperature distributions in the impeller and the core at t = 25 s, t = 45 s and t = 60 s respectively for $T_{pouring}$: 1,923 K.

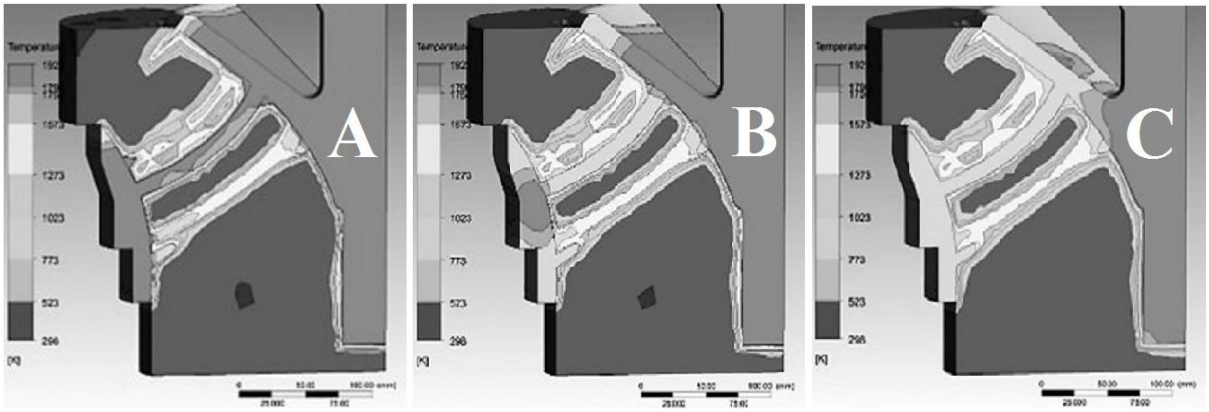

Figure 4. Temperature contours in 60° segment of the impeller and the core at t: 25 s (A), t: 45 s (B) and t: 60 s (C) ($T_{pouring}$: 1,923 K)

As it is seen from the Figure 4, the liquid portion becomes smaller as the time passes. At the end of 55 s, metal becomes solid. In the meantime, the movement of the mushy zone versus time can also be seen in the Figures. Similar temperature contours are seen at the outer shell for $T_{pouring}$: 1,923 K and $T_{pouring}$: 2,023 K with 45 s time difference. It is shown in Figure 5.

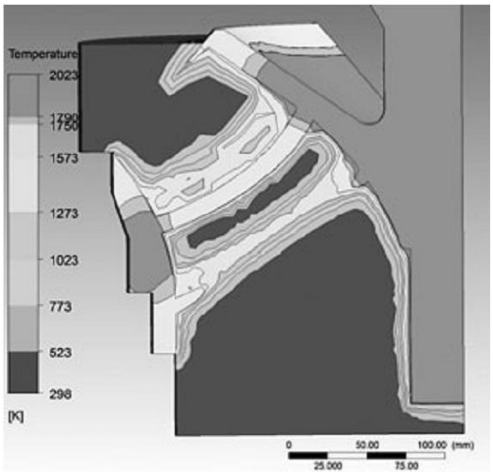

Figure 5. Temperature contours in 60° segment of the impeller and the core at t: 90 s ($T_{pouring}$: 2,023 K)

Depending on the pouring temperature, the complete solidification times of the outer shell and hub of impeller is shown in Figure 6.

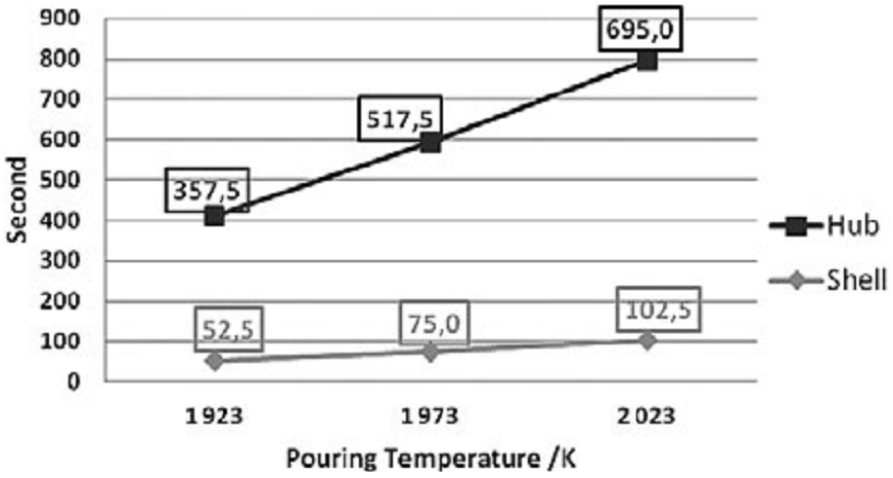

Figure 6. Solidification time calculated at the outer shell and the hub

After a time period of 7,200 s, the simulation is completed. As it is seen in Figure 7 for $T_{pouring}$: 2,023 K, even after such a long time, the outer surface of the mold stays approximately at the room temperature. However, after 7 200 s, the inside of the mold including impeller and core have the temperature range between 1,273 K and 1,023 K as the outside of this part have temperature range of 773 K and 523 K. The temperature of the inner parts of the core at early stages of the solidification approaches to the melting temperature of AISI 1016 steel.

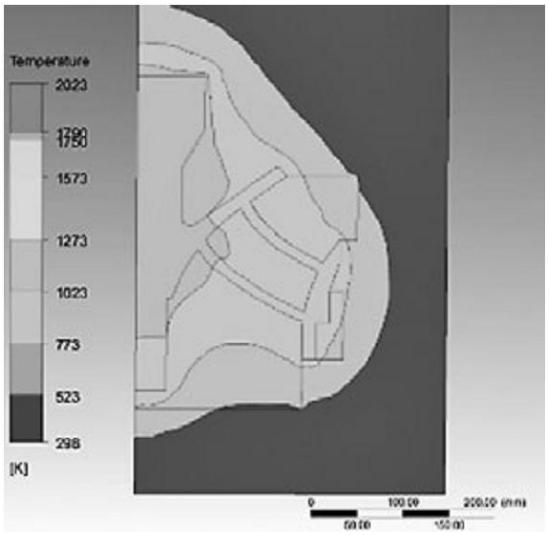

Figure 7. Temperature contours in 60° segment of the impeller, the core and the mold at t: 7,200 s ($T_{pouring}$: 2,023 K)

4. CONCLUSION

In this study, transient heat transfer equations were solved to estimate the solidification sequence of an axial centrifugal pump impeller for different initial conditions by using a Finite Volume Program, Ansys CFX.

The superheat of metal is studied in order to review its effects on the solidification time which changes linearly with superheat. At the lowest pouring temperature (1,923 K) the exterior shell of

the impeller solidifies in 35 s. As the superheat goes up to 2,023 K, the solidification time becomes 70 s.

REFERENCES

1. N. Chvorinov, Giesserei, 27, 177-186.
2. J. B. Caine, Foundry, 87 (1963), 120-125.
3. C. M. Adams, Jr. and H. F . Taylor, AFS Transactions, 61 (1953), 686-693.
4. C. M. Adams, Jr. and H. F . Taylor, AFS Transactions, 65 (1957), 170-176.
5. R. W. Heine, AFS Transactions, 76 (1968), 463-469.
6. R. Roberts, C. R. Loper, Jr. and R. W. Heine, AFS Transactions, 77 (1969), 373-377.
7. R. M. Kotschi and C. R. Loper , Jr., AFS Transactions, 82 (1974), 535-542.
8. C. R. Loper, Jr., AFS Transactions, 83 (1975), 173-184.
9. R. M. Kotschi and C. R. Loper , Jr., AFS Transactions, 84 (1976), 631-640.
10. R. M. Kotschi and C. R. Loper, Jr and M. Copur, AFS Conference, 1986.
11. A. Jeyarajan and R. D. Pehlke, AFS Transactions, 83 (1975), 405-412.
12. A. Jeyarajan and R. D. Pehlke, AFS Monograph, 1976.
13. A. Jeyarajan and R. D. Pehlke, AFS Transactions, 86 (1978), 457-463.
14. K. Harste: PhD Dissertation Thesis, 1989, Technical University of Clausthal.
15. R. D. Pehlke, A. Jeyarajan and H. Wada: Michigan Univ., Report No. NSFMEA82028, 1982.
16. J. Miettinen, Metall. Trans. B, 28B (1997), 281-297.
17. Y. Meng and B. G. Thomas, Metal. Trans. B, 34B (2003), 685-705.
18. A. C. Midea ans M. Burns, International Foundry Research, 59 (2007), 34-43.
19. A. A. Santos, J. M. V. Quaresma and A. Garcia, Journal Alloys and Compounds, 319 (2001) 174-186.
20. M. J. Peet, H. S. Hassan and K. D. H. Bhadeshia, International Journal of Heat and Mass Transfer, 54 (2011), 2602-2608.
21. S. I. Bakhtiyarov, R. A. Overfelt and D. Wang, International Journal of Thermophysics, 26 (2005), 141-149.
22. R. W. Lewis, K. Morgan, H. R. Thomas and K. N. Seethe-ramu, The Finite Element Method in Heat Transfer Analysis, Wiley, Wiley, New York, 1996.
23. M. J. Keil, j. Rodriguez and S. N. Ramrattan: AFS Transactions, 107 (1999), 71-74.
24. ANSYS Handbook, Chapter 6, Ansys Inc., Canonsbyrg, USA. 2011.
25. ANSYS Handbook, Fundamental FEA Concepts and Applications, Ansys Inc., Canonsbyrg, USA, 2011.
26. ANSYS Workbench Tutorial, Ansys Inc., Canonsbyrg, USA, 2010.
27. ANSYS Thermal Analysis Guide, Ansys Inc., Canonsbyrg, 2010, USA.
28. M. M. Pariona and A. C. Mossi: J. Ofrge Braz. Soc. of Mech. Sci. and Eng., 27 (2005), 399-406.

A MODIFICATION FOR THE OHNAKA BACK DIFFUSION EQUATION

Altan TÜRKELİ

Marmara University, Turkey
altan.turkeli@marmara.edu.tr

ABSTRACT
The first and simplest analytical model for a binary alloy came from Gulliver-Scheil, considering a constant partition coefficient at the interface during solidification without back diffusion in solid. Later, Brody-Flemings proposed an approximate analytical model, taking into account one dimensional diffusion of solute in solid during solidification in plate-like dendrite arms for parabolic growth. However, this model does not work well at high back diffusion values. Ohnaka modified this back diffusion parameter. The Ohnaka model works well at the low and high back diffusion values but it underestimates between them. In this paper, Voller-Ohnaka back diffusion model is modified further to predict concentration profile more accurately than all others analytical models for the parabolic growth rate.

Keywords: Casting, Solidification, Microsegregation, Modelling

OHNAKA GERI DİFÜZYON DEKNLEMİ İÇİN BİR MODİFİKASYON

ÖZET
Katı-sıvı ara yüzeyinde denge dağılım katsayısını sabit kabul eden Gulliver-Scheil, en basit ve ilk mikrosegregasyon denklemini önermişlerdir. Daha sonra, Brody-Flemings, düzlemsel katılaşan bir sıvı-katı arayüzeyinde geri difüzyonu da dikkate alan yeni bir mikrosegregasyon modeli geliştirmişlerdir. Fakat bu model yüksek back difüzyon değerlerinde iyi çalışmamakatdır. Ohnaka geri diffuzyon parametresini modifiye etmiştir. Ohnaka'nın modeli düşük ve yüksek geri difüzyon değerlerinde iyi çalışmasına karşın ara değerlerde iyi sonuç vermemektedir. Bu makalede Ohnaka-Voller geri difüzyon parametresi modifiye edilerek parabolik büyüme için diğer analitik modellerden daha hasas konsantrasyon profileri hesaplamak mümkün olmuştur.

***Anahtar kelimeler*:** Döküm, Katılaşma, Mikrosegregasyon, Modelleme.

1. INTRODUCTION

During the solidification of an alloy, the solute rejected at the solid-liquid interface is redistributed in the dendritic structure, which is known as microsegregation. This controls the amount of interdendritic eutectic, the amount of inclusions, solidification temperature range, and hot tear, and also decreases mechanical and corrosion properties of final product.

The first attempts to predict microsegregation quantitatively were derived by Gulliver and Scheil and the equation is known as Gulliver-Scheil equation. It is assumed that there is complete mixing of solute in the liquid but no diffusion of solute in the solid can occur and local thermodynamic equilibrium exists at the solid-liquid intrerface, described by a constant

equilibrium disribution coefficient (k) and negligible undercooling occurs at the tip. This equition is [1-2]:

$$C_s = kC_o(1-f)^{k-1} \quad \textbf{(1)}$$

where C_s the solid composition (wt%),
C_o the average composition of an alloy (wt%),
f the fraction of solid,

It predicts the worst segregation values.

Since the introduction of the probe microanalysis technique in the late 1950s, it is shown that the assumption of no solid state diffusion is unjustified. Brody and Flemings recogniced this and presented an analysis which quantifies the effect of solid state diffusion occuring between the Gulliver-Scheil and the lever rule cases. Their analytical solution for parabolic growth rate is[3-4]:

$$C_s = C_o k(1-(1-2\alpha k)f)^{\left(\frac{k-1}{1-2\alpha k}\right)} \quad \textbf{(2)}$$

where $\alpha=(D_s t_f)/L^2$ back diffusion parameter at the solid-liquid interface,
Ds the diffusion coeffient in solid (m^2/s)
t_f the solidification time (s),
L the half of the solidifed distance (m),

In this equation the dimensionless parameter, α, determines the extent of diffusion in the solid. However, this treatment does not conseve solute, especially for fast diffusion elements, i.e. the applicability of this equation is limited to $k\alpha < 0.1$.

Since Brody-Flemings introduced this back diffusion parameter into the microsegregation equation, several researchers have attempted to modify back difffusion parameter to predict concentration profile more accuraletely than Brody-Flemings model. They may be summurized briefly as follows.

Clyne and Kurz examined the influence of rapid solid state diffusion in solidification. They derived a relationship involving a modified function in a heuristic way rather than by mathematical procedure. The Ω replaced by α is[5]:

$$\Omega = \alpha\left(1-exp\left(-\frac{1}{\alpha}\right)\right) - 0.5exp\left(-\frac{1}{2\alpha}\right) \quad \textbf{(3)}$$

This equation works well at low and high α values but not between them.

Ohnaka has criticised this method and solved back diffusion equation approximately for the planar solidification[6]. He assumed that the solute profile in the solid can be expressed with a quadratic equation, then he obtained the following back diffusion equation.

$$\Gamma = \frac{2\alpha}{1+2\alpha} \quad \textbf{(4)}$$

Comparing with the Kurz-Fisher equation he replaced 2Ω with Γ. His results showed that his equation can estimate the concentration better than the Brody-Flemings's solution but it gives similar results to the Clyne-Kurz solution.

Later, using infinite series expansion approach, Kobayashi derived an exact analytical solution for solidification with parabolic growth rate. His model for the solid-liquid interface is[7]:

$$C_s = kC_o \sum_{n=0}^{\infty} \zeta_n f^n \tag{5}$$

$$\zeta_n = \prod_{m=0}^{n-1} \left[1 - k \frac{F\left(-\frac{m}{2}, \frac{3}{2}; -\frac{1}{4\alpha}\right)}{F\left(-\frac{m}{2}, \frac{1}{2}; -\frac{1}{4\alpha}\right)} \right] \tag{6}$$

$$F(p,q;z) = \sum_{r=0}^{\infty} \frac{(p)_r \, z^r}{(q)_r \; r!} \tag{7}$$

where $(p)_r$ and $(q)_r$ are the Pochhammer symbols which are defined by:

$(p)_r = p(p+1)\ldots\ldots\ldots\ldots(p+r-1)$

$(p)_o = 1$

However, the number of terms needed to generate an accurate solution can be excessively large for small values of α and k. Thus, it is diffucult to use this technique for practical purposes.

Ganesan and Poirier wrote a numerical programs for the planar dendritic solidification with the parabolic growth rate. Then comparing this numerical model with Brody-Flemings analytical model for large number of α and k values and using a statistical package they developed an alternative back diffusion equation for parabolic growth rate. In their model the μ replaced by α is [8]:

$$\mu = \frac{exp\left(-\frac{Af}{(\alpha k)^B}\right)}{2 + \frac{Cf}{\alpha^D}} \tag{8}$$

where A, B, C, and D are constant and

A=0.1523, B=0.4331, C=1.1093, and D=0.9367.

They results showed that back diffusion is not constant during solidification but is a function of α, k, and f.

Wang and Beckermann criticised the assumption of dc/dt=0 in the Ohnaka's model. They developed a different analytical equation for microsegregation as follows[9]:

$$\frac{C_L}{C_o} = \frac{6\alpha(1-f)^{(1+6\alpha)k-1}}{f^{6\alpha}} \int_0^f \varepsilon^{6\alpha-1}(1-\varepsilon)^{-(1+6\alpha)k} d\varepsilon \tag{9}$$

The main difference of this model from other microsegregation models is that requires an

evaluation of the integral in the equation 9.

When this equation is rewritten (the equation 10), it can be easily recognised the weak point of this model that the composition becomes infinite at f=1 as in the case of Gulliver-Scheil equation, therefore it cannot predict the maximum concentration at the end of solidification.

$$\frac{C_L}{C_o} = \frac{6\alpha(1-f)^{(1+6\alpha)k}}{(1-f)f^{6\alpha}} \int_0^f \varepsilon^{6\alpha-1}(1-\varepsilon)^{-(1+6\alpha)k} d\varepsilon \quad \textbf{(10)}$$

On the other hand Voller suggested two different approaches for the back diffusion at the solid-liquid interface which are called as the profile model and the parameter model. In the parameter model he replaced β with Γ in the Ohnaka's model. His model for parabolic growth rate is[10]:

$$\beta = \frac{2\gamma\alpha}{2\alpha+\gamma} \quad \textbf{(11)}$$

where γ an integration factor

$$\gamma = \frac{A\alpha k}{A\alpha k+1} \quad \textbf{(12)}$$

He calculated A=4 in this parameter by comparing Kobayashi's exact results with his suggested equation. These two equations can simplified as follows.

$$\beta = \frac{2\alpha}{1+2\alpha+cor} \quad \textbf{(13)}$$

Comparing to Ohnaka's back diffusion model he only added cor (cor=(1/2k)) to the denominator part of the Ohnaka's equation.

On the other hand Nastac and Stefanescu proposed an analytical microsegregation model for Fickian diffusion with time-independent diffusion coefficients and zero-flux boundry condition in the system solidifying with equiaxed morphology. Their model can be used for planar or equiaxed dendrites. Their model takes into account solute transport in the solid and liquid phases. Their planar microsegregation equation for the complete diffusion in the liquid phase can be rewritten as follows:

$$\frac{C_L}{C_o} = \left[1 - \frac{(1-k)f}{1-kI}\right]^{-1} \quad \textbf{(14)}$$

where

$$I = \frac{2f}{\pi^2}\sum_{n=1}^{\infty}\frac{1}{(n-0.5)^2}\exp\left[-\left((n-0.5)\pi\right)^2\alpha\right] \quad \textbf{(15)}$$

It is intesting to note that in this microsegregation model no any growth rate is dictated.

As you see above short review, several alternative analytical microsegregation models have been developed after Brody-Flemings. However non of them can predict amount of eutectic stucture and maximum concentration very closely to the Kobayashi's model as shown in this study. The aim of this paper is to improve the back diffusion model of Voller.

2. RESULTS AND DISCUSSION

The prediction of amount of eutectic structure of several analytical models are compared to each other in figures 1-3 for Ceu/Co=3 , 6.5 and 12 values, respectively. As you can see in the figure 1, the prediction of amount of eutectic of present numerical model is very close to the Kobayashi's results, only slightly less than them whereas the prediction of Ohnaka's model underestimates at the low value of the eutectic structure and the prediction of Voller model overestimates at the high value of the eutectic stucture. The performance of Wang-Beckermann and Ganesan-Poirier models are also very close to the exact solution.

For Ceu/Co=6.5, all analytical models are compared with the exact analytical model and numerical model in the figure 2a and 2b. The behaviour of all analytical models are almost same as in the previous figure. Kurz-Fisher and Ohnaka models underestimates values whereas Voller model overestimates. The prediction of Wang-Beckermann model at low partition coefficients are very close to the exact model, however, increasing k values it overpredicts the amount of eutectic because this model becomes infinite when the fraction of solid approaches to one. Ganesan-Poirier model and the present numerical model estimates very closely to the exact model of Kobayashi. The prediction of Nastac-Stefanescu model has its own unique profile because no any growth rate is dictated in the assumption of this model.
Some models are compared to each other for Ceu/Co=12. As shwon in the figure 3, the prediction of present numerical and Ganesan-Poirier models are very close to the the prediction of exact solution of Kobayashi whearas the Wang-Beckermann model overestimates it with increasing k values.

Voller already developed a simple back diffusion model for parabolic growth rate. He showed that his model can predict very closely the maximum concentration of Kobayashi's model. However, the prediction of this model for amount of eutectic and therfore concentration profile is not very close to the exact model. In order to improve his back diffusion model, the preciction of concentration profile of present numerical model (Cn) is compared with that of Voller and Ohanka's models (Ci) as ratio of (Cn-Ci)/Cn. It is shown that Voller model overestimates concentration profile whereas Ohnaka model underestimates numerical model. After trying several fitting functions, for examples f^{30} and $f^{(10+20f12)}$, it is found that when

$$cor = \frac{f^{10+20f^{12}}}{2k}$$

is chosen the prediction of Voller model is significantly improved. His back diffusion equation becomes

$$\beta = \frac{2\alpha}{1 + 2\alpha + \frac{f^{10+20f^{12}}}{2k}}$$

As you can see in this equation cor is not constant but is a function of k, α, and f. It is not anymore a intetegration factor but is a correction factor for back difffusion model. It can be easily seen in this equation that cor factor decreases gradually from Ohnaka back diffusion equation to the Voller back difffusion model after f=0.6 and it is equal to the Voller back diffusion model at f=1, therefore it does not affect its prediction of maximum concentration.

3. CONCLUSION

In this paper, Voller-Ohnaka back diffusion model is modified further to predict concentration profile more accurately than all others analytical models for the parabolic growth rate.

REFERENCES

1. G.H. Gulliver, "Metallic Alloys", Griffin, London, 1922
2. T.E. Scheil, Zeitschrift für Metallkunde, 34, 70, 1942
3 H.D. Brody, M.C. Flemings, Trans. Of Metal. Society, of AIME, 236, 615, 1966
4. M.C. Flemings "Solidification Processing",McGraw-Hill, New York, 1974
5. T.W. Clyne and W. Kurz, Metall. Trans. 12A, 965, 1981
6. I. Ohnaka, Trans. ISI of Japan, 26, 1045, 1986
7. S. Kobayashi, Trans. ISI of Japan, 28, 728, 1988
8. S. Ganesan, D.R. Poirier, J. of Crystal Growth, 97, 851, 1989
9. C. Y. Wang , C. Beckermann, Materials Science and Eng, A171 199, 1993
10. V.R. Voller, J. of Crystal Growth, 226, 562, 2001
11. L. Nastac , D.M. Stefanescu, Metall. Trans., 24A, 2107, 1993

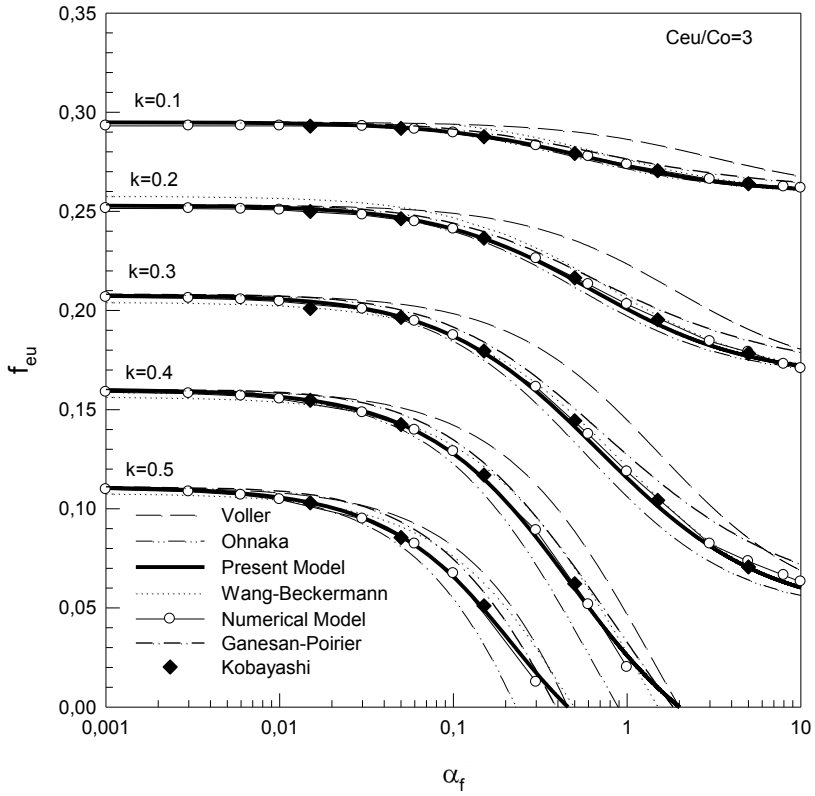

Figure-1 Prediction of eutectic structure as a function of back diffusion parameter

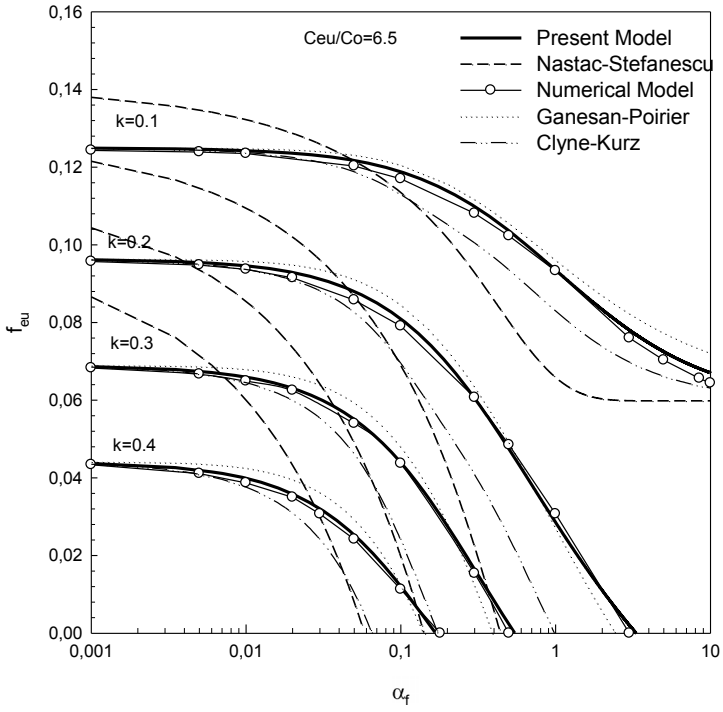

Figure-2-a

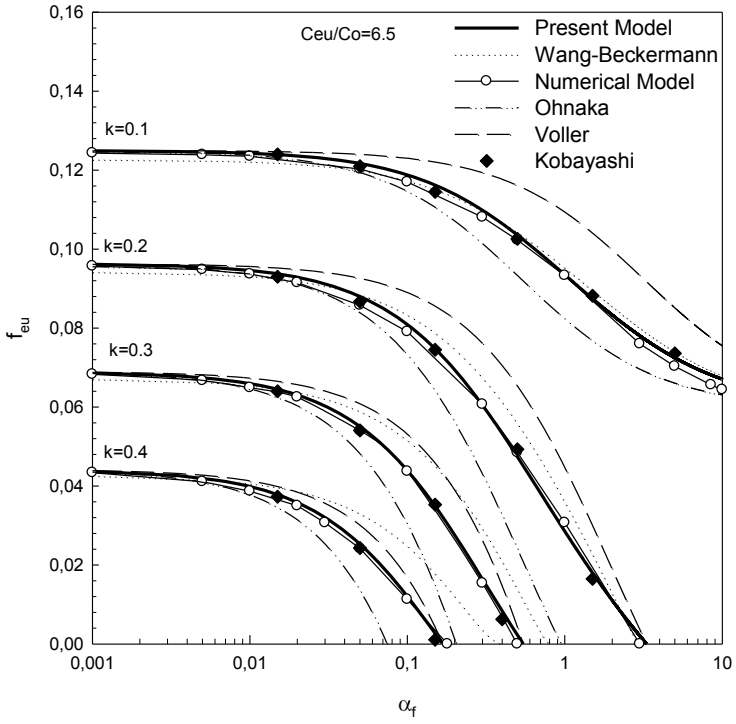

Figure-2b Prediction of eutectic structure as a function of back diffusion parameter

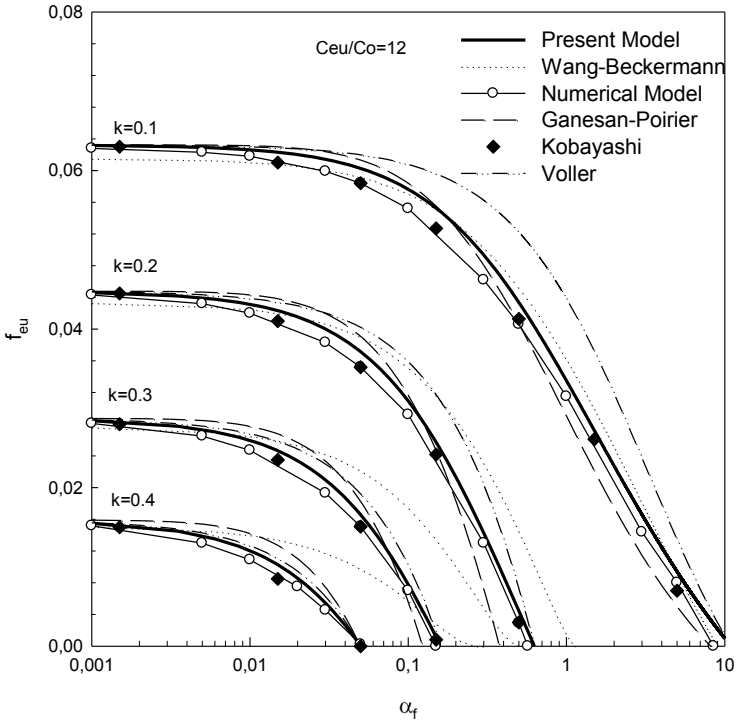

Figure-3 Prediction of eutectic structure as a function of back diffusion parameter

THE EFFECT OF HOLDING TIME ON POROSITY OF A357

Muhammet ULUDAĞ[*], Remzi ÇETİN[*], Lokman GEMİ[**], Osman AYDOĞUŞ[*], Kerim ÇAM[*], Derya DIŞPINAR[***]

* Selcuk University, Faculty of Engineering–Metallurgical and Materials Eng. Dept., Konya-Turkey, uludag@selcuk.edu.tr, rcetin@selcuk.edu.tr, o_aydogus@hotmail.com, kerimcam91@gmail.com
** Selcuk University, Institute of Science, Konya-Turkey, lgemi@selcuk.edu.tr
*** Istanbul University, Faculty of Engineering, Metallurgical and Materials Eng. Dept., Istanbul-Turkey, deryad@istanbul.edu.tr

ABSTRACT
During casting of aluminum alloys, the final microstructure and mechanical properties are strongly affected by the ambient atmosphere. The liquid aluminum reacts with water vapour to form aluminum oxide on the surface and hydrogen is dissolved in the melt. The intrusion of these defects into the cast part will result in decreasing of the properties. Excess hydrogen is typically removed by degassing with inert gasses. Considering the density difference of liquid and oxide, holding of the liquid for a certain period of time is assumed to be the solution for the removal of oxides. However, the possible change in the morphology of the oxide structure (thin or thick film) has been disregarded. Therefore, in this work, two different charges of A357 alloy was melt at 750ºC in a resistance furnace and held for 4 hours. One of the melts were left untreated, and the other was degassed. At certain time intervals (30, 60, 120 and 240 minute), samples were collected for reduced pressure tests. A mould that consisted of various thickness steps was used to cast parts in order to check the porosity distribution. Both die and sand moulds were used.

Keywords: Casting, Al alloys, Degassing, Holding time, Porosity, Bifilm index

A357 ALAŞIMINDA TUTMA SÜRESİNİN POROZİTE ÜZERİNE ETKİSİ

ÖZET
Alüminyum döküm alaşımları, hem mikro yapı hem de mekanik özellikleri açısından üretim sürecinde dış ortamdan etkilenirler. Sıvı alüminyumun ortamdaki rutubet ile reaksiyonu sonrasında hidrojenin çözünmesi ve oksit tabakasının oluşması gözlemlenir. Bu hataların sıvı metal içerisine karışması ile döküm kalitesi ve mekanik özellikler önemli derecede azalır. Sıvıdaki hidrojen içeriği çeşitli gaz giderme işlemleri ile azaltılabilir. Diğer yandan, oksitlerin uzaklaştırılmasında geleneksel olarak bekletme süresi üzerine çalışmalar yapılmıştır. Böylelikle sıvı alüminyum ve oksit arasındaki yoğunluk farkından yararlanarak çöktürme ile uzaklaştırılması pratik olarak uygulanan bir yöntemdir. Ancak; bu yöntemlerde göz ardı edilen önemli hususlardan birisi de bekletme süresi ile oksit tabakasının yapısında olabilecek değişimlerdir. Bu amaçla, bu çalışmada, tutma süresinin etkisi detaylı olarak irdelenecektir. Farklı kesit kalınlıklarına sahip basamak tipli kum kalıplara döküm yapılmıştır. A357 alaşımı 750 ^{0}C'ye ulaştığında 30, 60, 120 ve 240 dk. sürelerle sıvı halde bekletilmiştir. Döküm kalitesini belirlemek için azaltılmış basınç test numuneleri alınarak bifilm indeks

hesaplanmıştır. Sonuç olarak, soğuma hızı ve bekletme süresinin sıvı metal kalitesi ve porozite ile arasındaki ilişki araştırılmıştır.

Anahtar Kelimeler: Döküm, Alüminyum alaşımları, Gaz giderme, Sıvı halde bekletme, Porozite, Bifilm indeks

1. INTRODUCTION

Al-Si alloys exhibit good corrosion resistance, castability, high thermal and electrical conductivity. In addition, aluminum alloys are famous for having high strength and low density ratios. Therefore, typical application areas are found to be in automotive and aerospace industries [1-5]. Due to this critical uses, it is important that high quality castings are produced.

Hydrogen is known to be the only soluble gas in liquid aluminum [6]. The source of hydrogen is the moisture which can be present in the ambient atmosphere in the cast floor, crucibles, charges and refractories. As the temperature of the melt is decreased (i.e. solidification), the solubility of hydrogen decreases. And thus, it is believed to form porosity since the dissolved hydrogen has the tendency to produce hydrogen gas [7-8]. On the other hand, the turbulence of the liquid metal during transfer or uncontrolled filling may generate a defect known as bifilms [9]. These folded oxide skins act as a crack which can easily open up to form porosity during solidification contraction [10]. These defects can deteriorate the mechanical properties significantly [7].

Since the formation of porosity causes the properties to be lowered, it is important that it should be kept to the mininum and if possible, there should be no pores in the final product [6]. One of the simplest way to reduce porosity is to increase the solidification rate. Faster cooling leads to better properties, not just due to the lowered porosity, but also, the grain size gets smaller and finer and thus, mechanical properties increase [11].

In this work, a step mould design was used to obtain different cooling rates and A357 alloy was cast to investigate the correlation between dendrite size and porosity. In addition, bifilm index was measured and the effect of melt quality was also incorporated for the porosity formation phenomena.

2. EXPERIMENTAL WORK

The chemical composition of the A357 alloy used in the experiments is given in Table 1.

Table 1. A357 composition

Si	Fe	Cu	Mn	Mg	Zn	Ti	Al
6,60-7,40	0,20	0,02	0,03	0,30-0,45	0,04	0,08-0,14	Rem.

The melting procedure was carried out in a resistance furnace at 750 °C. Once the charge was completely melted, the liquid melt was led to settle for 30, 60, 120 and 240 minutes and samples were collected at these time intervals. Reduced Pressure Test (RPT) was used to quantify the melt quality by using bifilm index. The step mould was designed have the thinnest section at the bottom and the thickest section at the top. The mould cavity was filled from a high sprue followed by a upward (counter gravity) casting so that no turbulence would occur during filling. A sample of one of the cast parts is given in Figure 1.

a b

Figure 1. a) front, and b) side view of the cast part

Each thickness was cut and microstructural analysis was carried out. Archimedes principle was used to measure density of each sections. Secondary dendrite arms spacing (SDAS), porosity size, shape and distribution were measured using an image analysis software.

3. RESULTS and DISCUSSION

There were four steps in the design and four different holding times and at each duration, at least three castings were made. Overall, there were 48 samples produced and analysed. For simplicity, few selected micrographs were given here as seen in Fig 2.

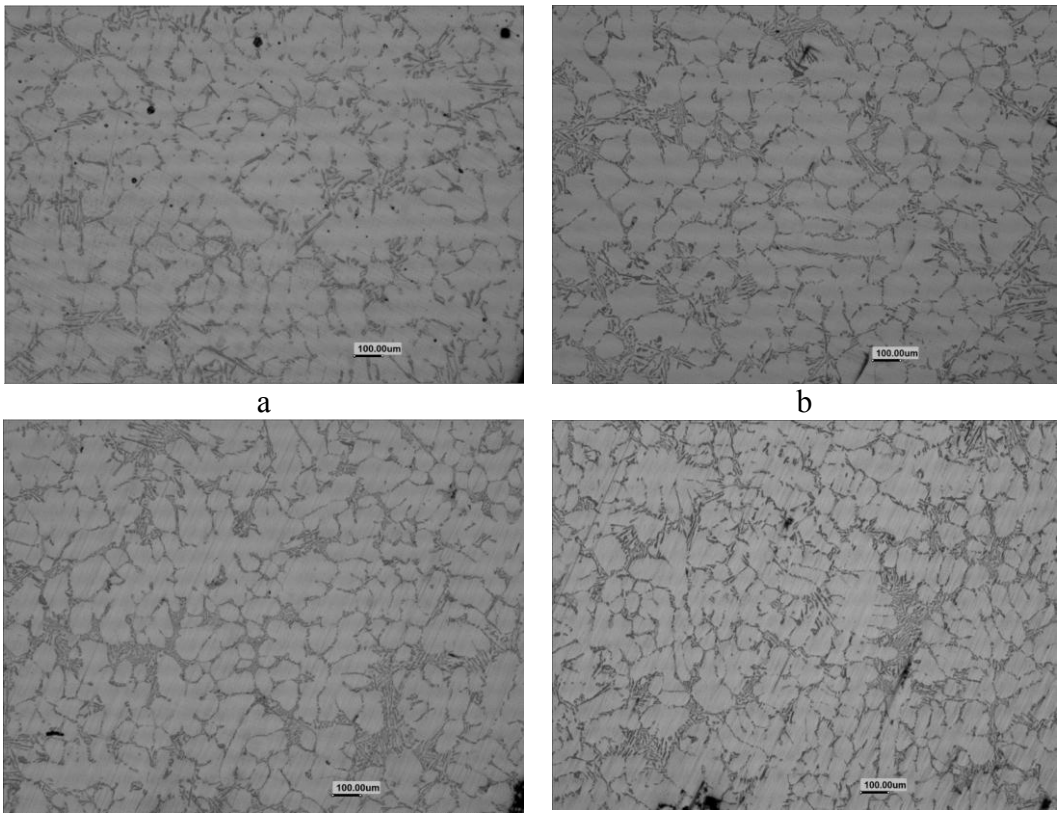

a b

c d

Figure 2. Microstructure of various sections a) 30 mm, b) 20 mm, c) 15 mm, d) 10 mm

cast at 60 minutes of holding

Figure 3 shows the SDAS measurements taken from the different thicknesses cast at various holding times. It can be seen that as the section thickness decreases, SDAS decreased. Although it may not be so straight forward to conclude that as the holding time of the liquid is increased, the grain size decreased. Yet, the general trend seems to be in good agreement with the previous proposal.

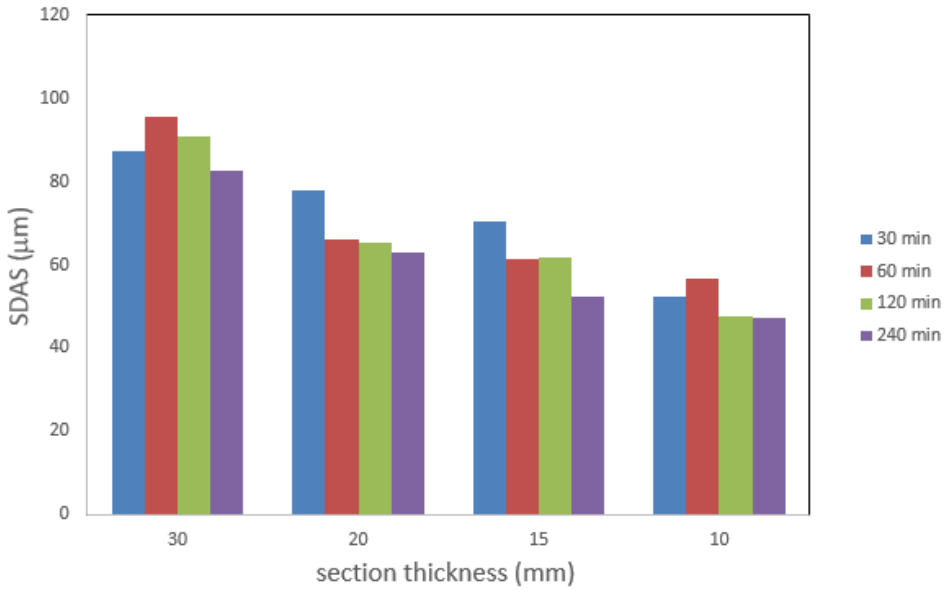

Figure 3. SDAS change with section thickness and holding times

Figure 4 is the density measurements of each sections with regard to the holding times.

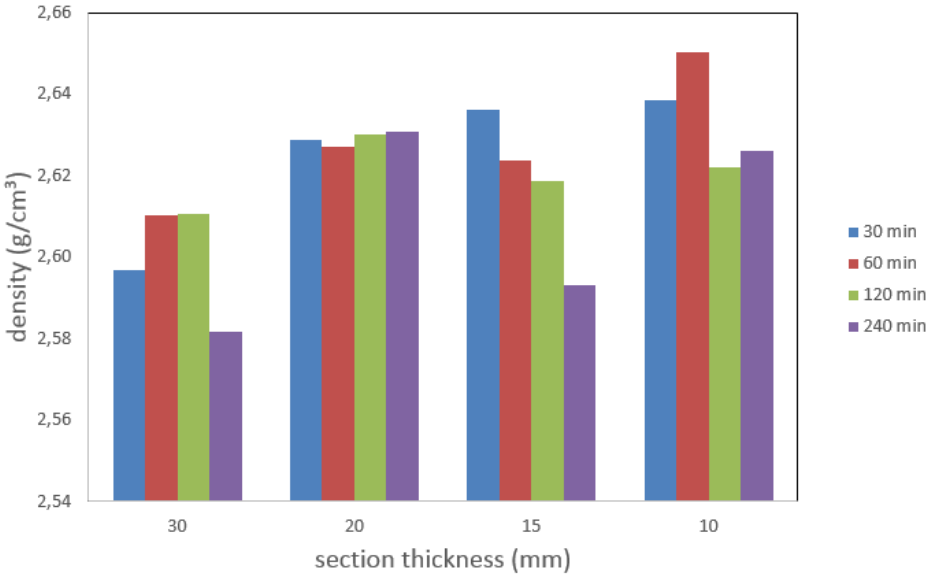

Figure 4. Density change with section thickness at various holding times

As seen in Figure 4, it is very difficult to correlate the change in the density with holding time, although as the section thickness decreased, density increased. For example, for 20 mm

section thickness, there appears to be no effect of holding time on the porosity amount. For all of the holding times, the density remained unchanged around 2630 kg/m^3. For the samples analysed at 15 mm section thickness, the density was decreased (i.e. porosity was increased) as the holding time was increased. For 30 mm section thickness, the density increases and then decreases from 30 to 240 minutes of holding times. 10 mm section thickness seems to have the highest density which indicates that the porosity was lowest amongst the cast part.

It is understandable and explainable that 30 mm section must have the lowest density, since there was no feeders used, this region of the cast part would act as the feeder and therefore have the highest level of porosity. This effect can also explain the fact that the density of the 20 mm sectioned samples were constant and unchanged with the holding time. The 30 mm section that was above the 20 mm section had acted as a feeder and thus, 20 mm section had the best feeder effect. Similarly, the thinnest section (10 mm), was located at the bottom of the cast part which had the highest metallostatic pressure acting on it. Therefore, highest density (i.e. lowest porosity) was found at this section of the cast part. As a result, all the troubles were occurring between 10 and 15 mm sections, since the solidification shrinkage, feeding, fluidity and permeability of the liquid above would have the most dominant effect in these regions. Therefore, 15 mm section has the most scattered results.

Figure 5 shows the correlation between average pore area and number of pores. It can be seen that there are no certain relationship between the number of pores and pore area. There are big and few pores and sometimes there are a lot of small pores. The distribution suggests that the size and distribution of pores are not homogeneous throughout the section of the cast part.

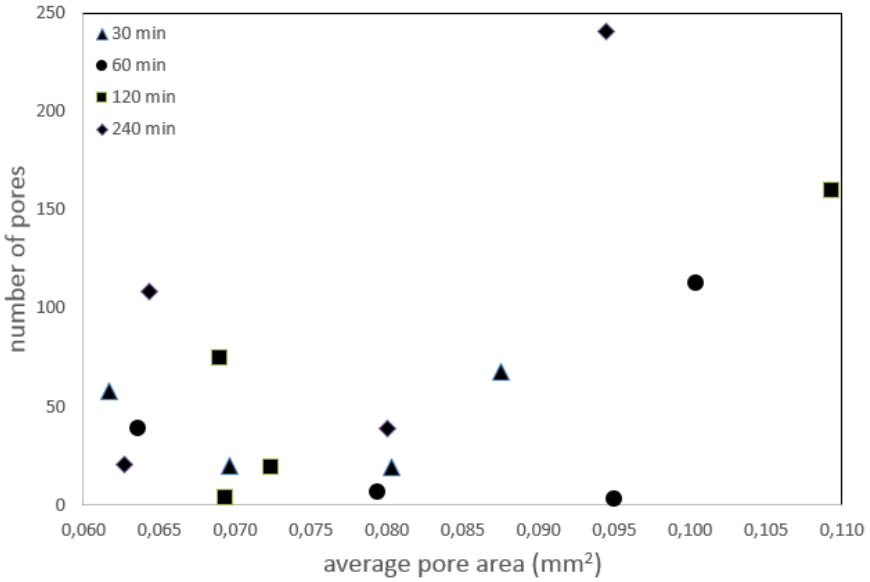

Figure 5. The correlation between average pore area and number of pores

Figure 6 shows the relationship between section thickness and total pore area at different holding times of the melt. It can be clearly seen that as the section thickness increases and holding time increases, total pore area increases.

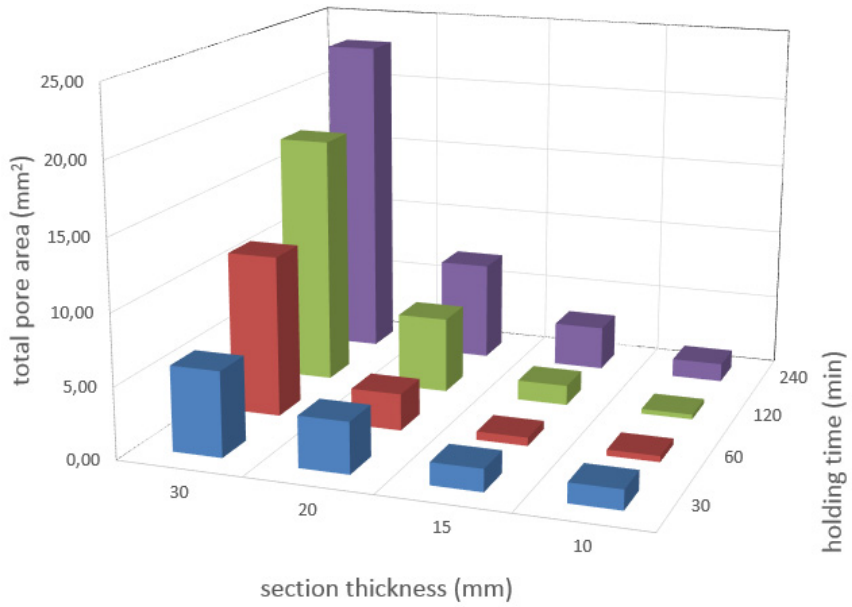

Figure 6. Total pore area change with section thickness at different holding times

Bifilm index measurements were made for each of the melt that were held at different holding times. The results were calculated to be 81, 105, 109 and 243 mm for 30, 60, 120 and 240 minutes of holding. This increase in bifilm index with increased holding time is attributed to the fact that oxidation rate was increased with increased holding at 750 °C for long times. The comparison of pore length with bifilm index and section thickness is given in Figure 7. It can be seen that in general, as the bifilm index was increased, the length of pores were increased.

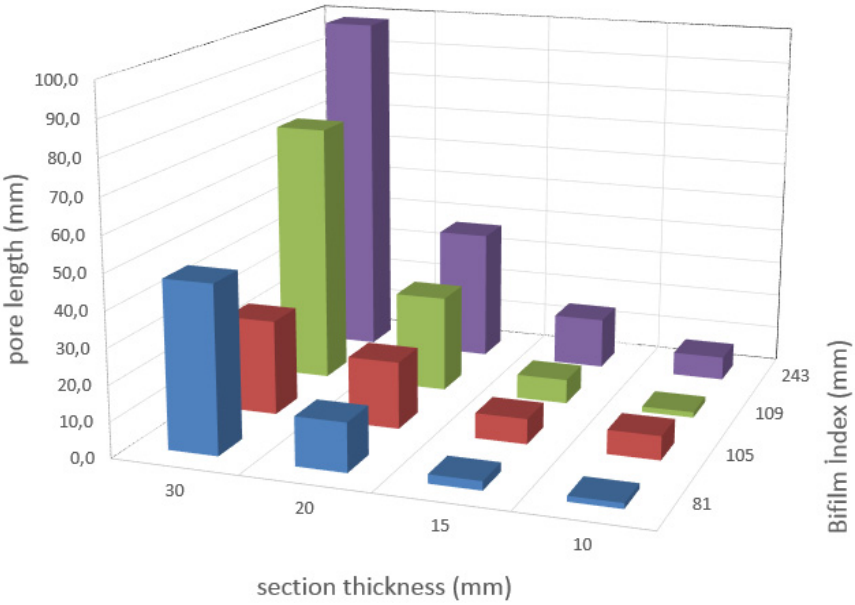

Figure 7. Pore length change with bifilm index and section thickness

Similar findings were found for the number of pores. As bifilm index was increased, the number of pores were increased (Fig 8). The reason for low number of pores at the thinnest section is based on the fact that as the solidification rate increases, bifilms do not find the time to unravel and form porosity. Therefore, bifilms may still be present but they are not observed as pores since they were not opened.

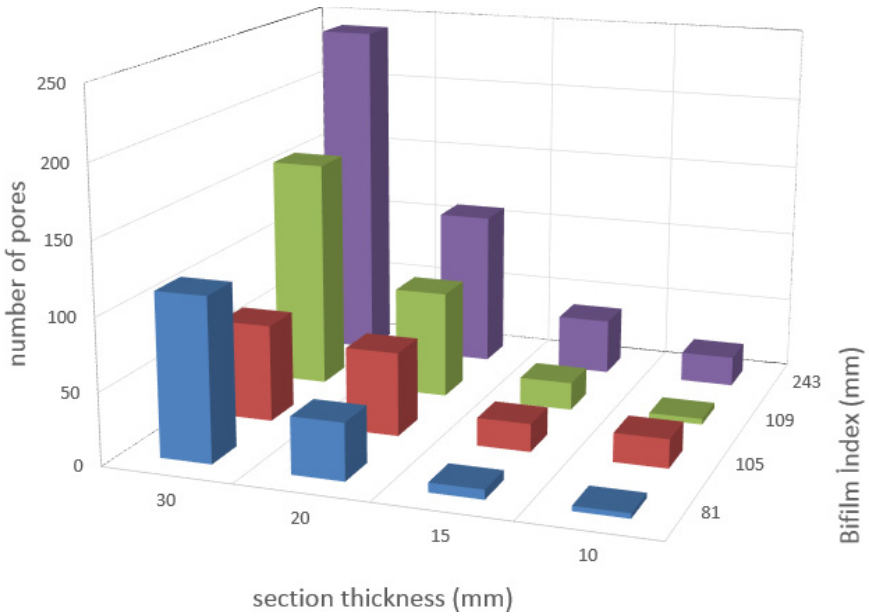

Figure 8. Number of pores change with bifilm index and section thickness

4. CONCLUSIONS

As the holding of the melt is increased, the quality of the melt decreased significantly resulting in higher porosity.

Cooling rate has effect over the pore size and distribution, but not due to hydrogen evolution, simply due to the unravelling mechanism of bifilms.

There is good correlation between number of pores and bifilm index. The size of the pores (i.e. pore area) is only related with the opening mechanism of bifilms. If enough time is given, the pores can grow to larger sizes. On the other hand, faster cooling will hinder unravelling of bifilm and lead to less pore formation.

Acknowledgment

This work has been supported by the Scientific Research Projects Coordination Unit of Selcuk University (Project number: 13401012). The authors would like to thank Metal Market Metalurji San.Tic.Ltd.Şti for their support in this study.

REFERENCES

1. Alexopoulos, N.D. and M. Tiryakioğlu, *On the uniform elongation of cast Al–7%Si–0.6%Mg (A357) alloys.* Materials Science and Engineering: A, 2009. **507**(1–2): p. 236-240.
2. Campbell, J., *Castings : [the new metallurgy of cast metals]*. 2003, Butterworth Heinemann.
3. García-García, G., J. Espinoza-Cuadra, and H. Mancha-Molinar, *Copper content and cooling rate effects over second phase particles behavior in industrial aluminum–silicon alloy 319.* Materials & Design, 2007. **28**(2): p. 428-433.
4. Tsai, Y.-C., et al., *Effect of trace La addition on the microstructures and mechanical properties of A356 (Al–7Si–0.35Mg) aluminum alloys.* Journal of Alloys and Compounds, 2009. **487**(1–2): p. 157-162.

5. Hsu, F.-Y. and Y.-M. Yang, *Confluence weld in an aluminum gravity casting.* Journal of Materials Processing Technology, 2012. **212**(4): p. 825-840.

6. Haghayeghi, R., H. Bahai, and P. Kapranos, *Effect of ultrasonic argon degassing on dissolved hydrogen in aluminium alloy.* Materials Letters, 2012. **82**(0): p. 230-232.

7. Dispinar, D., et al., *Degassing, hydrogen and porosity phenomena in A356.* Materials Science and Engineering: A, 2010. **527**(16–17): p. 3719-3725.

8. Tan, E., et al., *Reproducibility of Reduced Pressure Test Results in Testing of Liquid Aluminum Gas Levels* in *International Advanced Technologies Symposium*. 2011. p. 321-324.

9. Dispinar, D. and J. Campbell, *Porosity, hydrogen and bifilm content in Al alloy castings.* Materials Science and Engineering: A, 2011. **528**(10–11): p. 3860-3865.

10. Dışpınar, D. and J. Campbell, *DETERMINATION OF ALUMINIUM CASTING QUALITY USING BIFILM INDEX*, in *Metallurgical and Materials Congress*. 2004.

11. Hosseini, V.A., S.G. Shabestari, and R. Gholizadeh, *Study on the effect of cooling rate on the solidification parameters, microstructure, and mechanical properties of LM13 alloy using cooling curve thermal analysis technique.* Materials & Design, 2013. **50**(0): p. 7-14.

EFFECT OF HOLDING TIME ON THE EFFICIENCY OF Sr MODIFICATION IN Al-Si ALLOYS

Muhammet ULUDAĞ[*], Remzi ÇETİN[*], Lokman GEMİ[**], Merve BİNGÖL[*], Özgür ORTAÇ[*], Ahmet İrbey ARSLAN[*], Derya DIŞPINAR[***]

* Selcuk University, Faculty of Engineering–Metallurgical and Materials Eng. Dept., Konya-Turkey, uludag@selcuk.edu.tr, rcetin@selcuk.edu.tr, mervebingol91@hotmail.com, ozgurortac@windowslive.com, ahmet.irbey.arslan@gmail.com
** Selcuk University, Institute of Science, Konya-Turkey, lgemi@selcuk.edu.tr
*** Istanbul University, Faculty of Engineering, Metallurgical and Materials Eng. Dept., Istanbul-Turkey, deryad@istanbul.edu.tr

ABSTRACT
In order to obtain finer and fibrous silicon eutectic, Al-Si alloys are typically modified by Sr. The treatment is known to increase the mechanical properties, however there is a long going debate is to whether the porosity increases or decreases by Sr modification. In this work, the change in the microstructure of A357 alloy was investigated over a period of holding time. 300 ppm Sr was added to the melt and the melt was let to settle for 2 hours. Every 20 minutes, samples were collected from the melt to produce plates (120 X 50 mm) with various thicknesses (10, 15, 20 and 30 mm). Sand moulds were used so that different secondary dendrite arm spacing could be achieved. The centre of each section of the cast parts were subjected to metallographical examination. The level of hydrogen in the melt was continuously measured and recorded by AlSPEK.

Keywords: Al-Si alloys, Modification, Holding time, Cooling rate, Porosity

Al-Si ALAŞIMLARINDA Sr MODİFİKASYONU SONRASINDA TUTMA SÜRESİNİN MİKROYAPIYA ETKİSİ

ÖZET
Alüminyum silisyum alaşımlarında kaba yapıda çökelen silis yapısını ince ve homojen dağıtmak üzere (modifiye etmek için) çok az oranlarda (< % 0,08) Sodyum (Na), Potasyum (K) veya Stronsiyum (Sr) ilave edilir. Sodyum ve potasyumun çevre dostu olmaması ve modifiye edici olarak zamanla özelliğini yitirmesinden dolayısı birçok araştırmacı Sr ile modifikasyona yönelmiştir. Mekanik özellikler açısından üstün özellikler sergilemesi de bu elementi tipik bir modifikatör olarak tercih edilme sebebi yapmıştır. Bu çalışmada, A357 alaşımında Sr modifikasyonunun süreye bağlı etkisi incelenmiştir. 300 ppm Sr ilavesi ile 20, 40, 60 ve 120 dakika bekleme sürelerinden sonra dökümler yapılmıştır. Döküm parçası olarak, soğuma hızı farkının incelenmesi amacıyla kesit kalınlıkları farklı, basamak tipli kum kalıplar kullanılmıştır. Her bir kesitte, mikroyapı ve porozite analizleri yapılmıştır. Böylelikle, modifikasyon etkisi, süreye ve katılaşma hızına bağlı olarak mikroyapının yanında porozite ile de ilişkilendirilmiştir.

Anahtar Kelimeler: Al-Si alaşımları, Modifikasyon, Bekleme süresi, Soğuma hızı, Porozite

1. INTRODUCTION

Aluminium alloys exhibit light weight, improvable mechanical properties, high corrosion resistance, and high electrical and heat conduction. Therefore these alloy groups have been preferred choice of transport industry and the application areas have been growing and growing every day [1-2].

For Al-Si type of alloys, Sr addition has been known to be an effective way of improving mechanical properties, simply by modifying the Si into finer fibrous morphology. This modification not only increases mechanical properties but also lowers porosity and improves feedability leading to better castability of the alloy [3].

Before the modifying effect of Sr was discovered, Na and Sb was used which were volatile and non-environmental friendly. In recent years, it has been shown that only 300 ppm of Sr is good enough to modify the structure [4]. There are several works that describes the mechanism of Sr modification [5,6] which are typically based on the fact that Sr presence retards the Si growth and thus refines the structure.

There are also contradicting approaches to porosity formation in Al-Si alloys in the presence of Sr [7]. Some works suggest that hydrogen dissolution is increased and thus porosity is increased when Sr is added. Some concluded that Sr decreases eutectic temperature (i.e. depression) and thus results in better feeding and lowered porosity.

In this work, Al-7Si-0.3Mg alloy was used to cast into a sand mould that had various section thicknesses; and the efficiency of Sr modification was investigated.

2. EXPERIMENTAL WORK

The chemical composition of the primary alloy used in the experiments is given in Table 1.

Table 1. Chemical analysis of primary Al-7Si-0.3Mg

Si	Fe	Cu	Mn	Mg	Zn	Ti	Al
6,60-7,40	0,20	0,20	0,03	0,30-0,45	0,04	0,08-0,14	Rem.

The casting trials were carried out by changing the holding time the melt after Sr was added. The holding times were selected to be 20, 40, 60 and 120 minutes. The sand mould had the cavities varying from 10 to 30 mm and at least, three castings were made for each of the conditions. Metallographical examinations were carried out at each step of the cast part. Correlation between cooling rate, holding time and efficiency of Sr modification was investigated. Macro and micro porosity measurements were made from each thicknesses. SDAS was also measured by Clemex Image Analysis software.

3. RESULTS and DISCUSSION

The microstructures of different thicknesses after 20 minutes and 120 minutes of holding are given in Figure 1 and Figure 2, respectively.

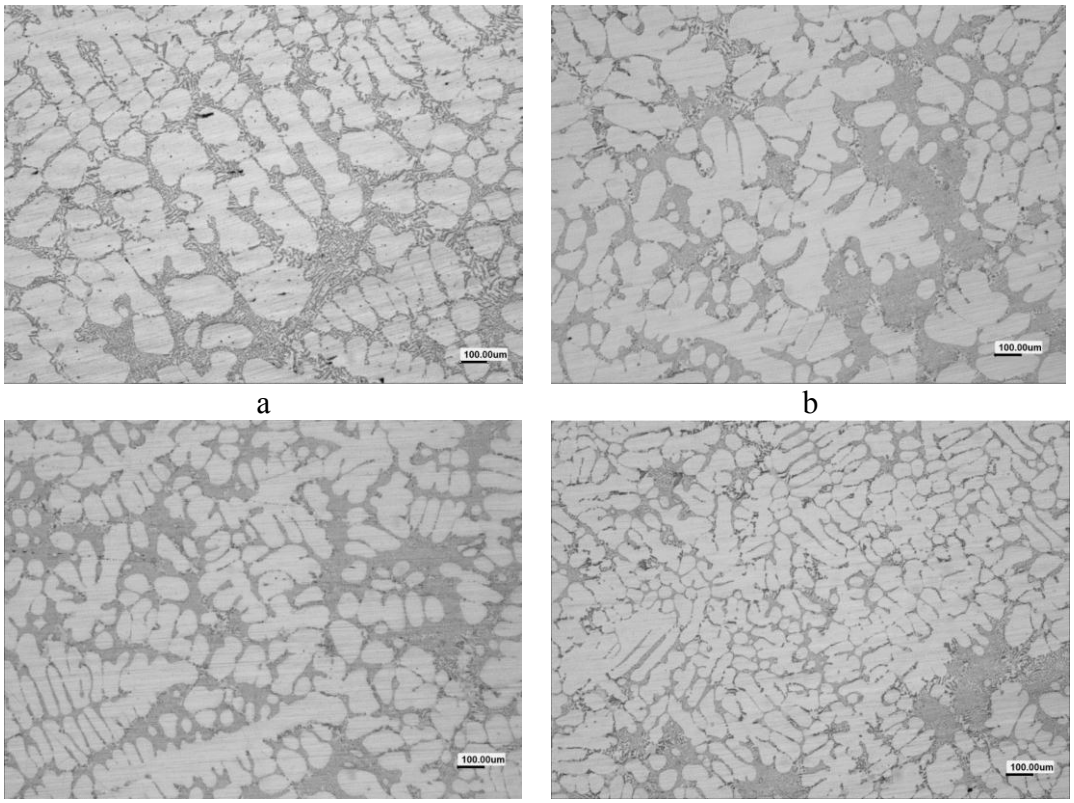

Figure 1. Microstructures of samples after 20 minutes of holing time at different cross sections: a) 30mm, b) 20mm, c) 15mm, and d) 10mm.

As seen in Figure 1, as the section thickness was decreased, i.e. faster cooling, the efficiency of Sr modification was increased. It can be seen that the size of Si particles in the eutectic region is heterogeneous in the thick section (30 mm: Fig 1a). It is important to note that the images in Fig 1 was taken at same magnification, thus, it can be clearly seen that as the section thickness was decreased, SDAS was decreased.

When the holding time was increased to 120 minutes, it can be seen that the modification ratio was decreased. As seen in Figure 2, even at 10 mm section thickness (i.e. lowest section and highest cooling rate: Fig 2d), there were still remnants of coarse Si in between the dendrites.

It is also interesting to note that the eutectic phases were more in discontinues type of distribution at the samples cast after 20 minutes of holding (Fig 1). On the other hand, after 120 minutes of holding, the eutectic phase was becoming more localised and less homogeneous along the microstructure (Fig 2). In other words, the dendritic network was increased as the holding time was increased.

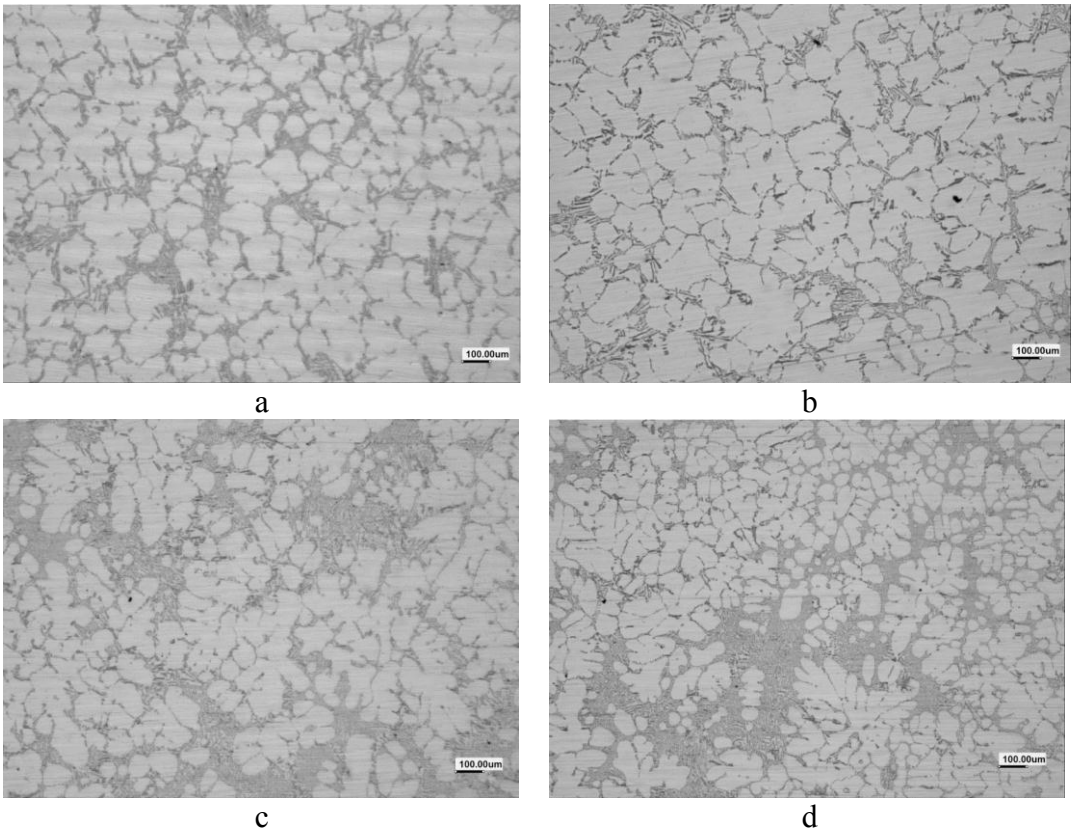

Figure 2. Microstructures of samples after 120 minutes of holing time at different cross sections: a) 30mm, b) 20mm, c) 15mm, and d) 10mm.

Figure 3 summarises the image analysis results: SDAS change with different section thickness and holding times. It can be seen that as section thickness is decreased, SDAS was decreased in all the holding time durations. Thus, as the cooling rate was increased, finer microstructure was obtained. On the other hand, when the SDAS values were compared for different holding times, a general trend appears that as the holding time of liquid metal was increased, SDAS was increased; indicating that more coarser structure was achieved with increased holding time. To put it in numbers; average SDAS is around 20 μm for 20 minutes of holding, but it increases up to 50 μm for 40 minutes of holding and 60 μm for 60 and 70 μm for 120 minutes of holing. As the grain size gets larger, there are two concurrent events take place. First, this indicates that the cooling is slower which results in coarser Si formation; second, the remaining liquid ratio is decreased which results in lowered eutectic phase ratio. The increase in SDAS can be described by the fading of grain refinement where Ti is typically sedimented after 1 hours of holding as was concluded by Shaffer. In this work, the fading of Sr was also observed which was also known as the poisoning effect.

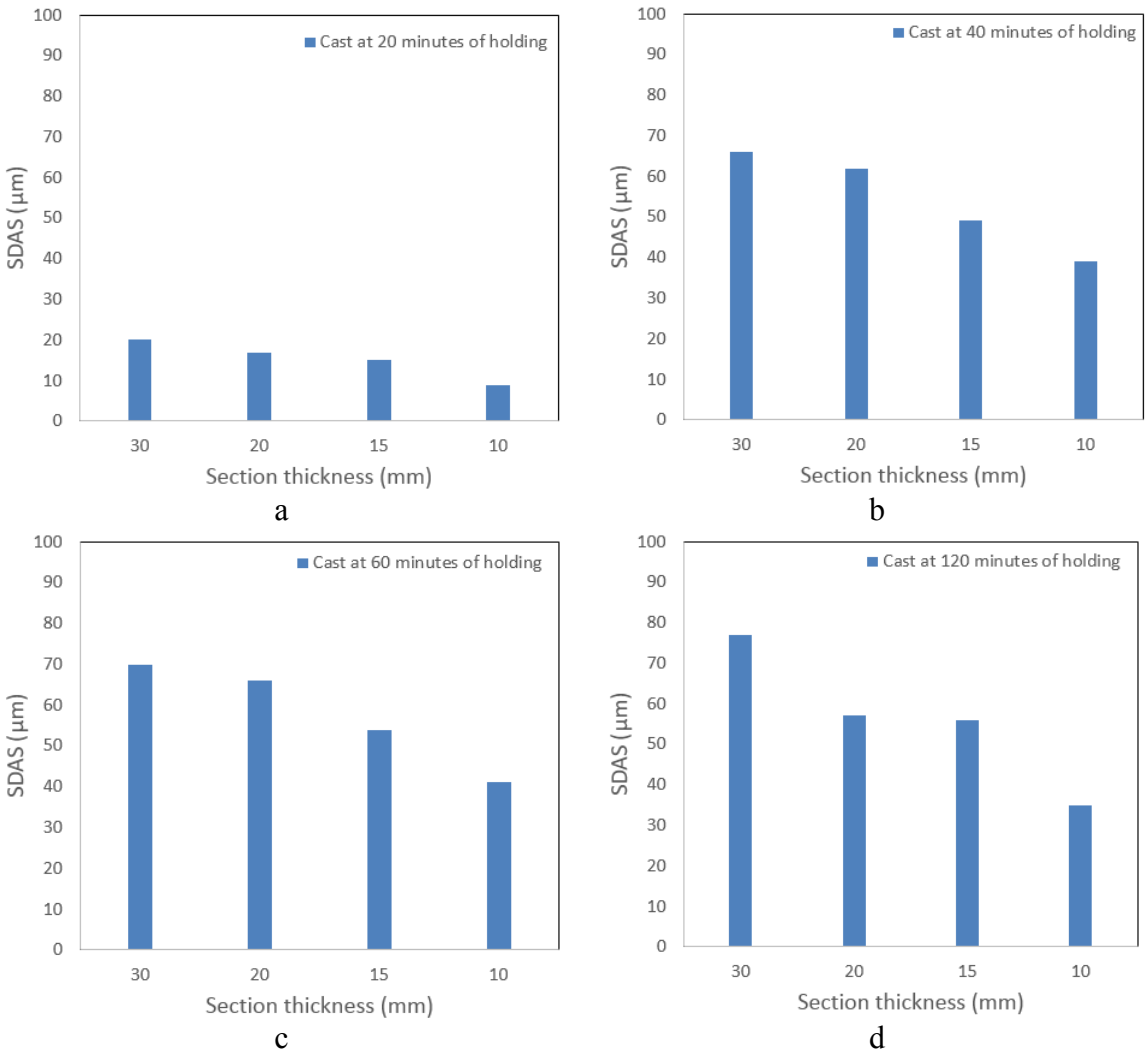

Figure 3. SDAS change with section thickness and holding time

As seen in Figure 4, the average Si length revealed the same findings observed in Figure 1 and 2. The numerical calculations made from the microstructures by the image analysis show that Si size was increasing with increased holding time. The most interesting observation was the constant Si length at each section thickness in the castings made after 40 minutes of holding times (Figure 4 b, c and d). For the casting made after 20 minutes of holding, the Si size was decreased with increasing cooling rate (i.e. from thicker to thinner sections) from 30 to 20 µm gradually. However, for the rest of the castings, the average Si length was around 33 µm.

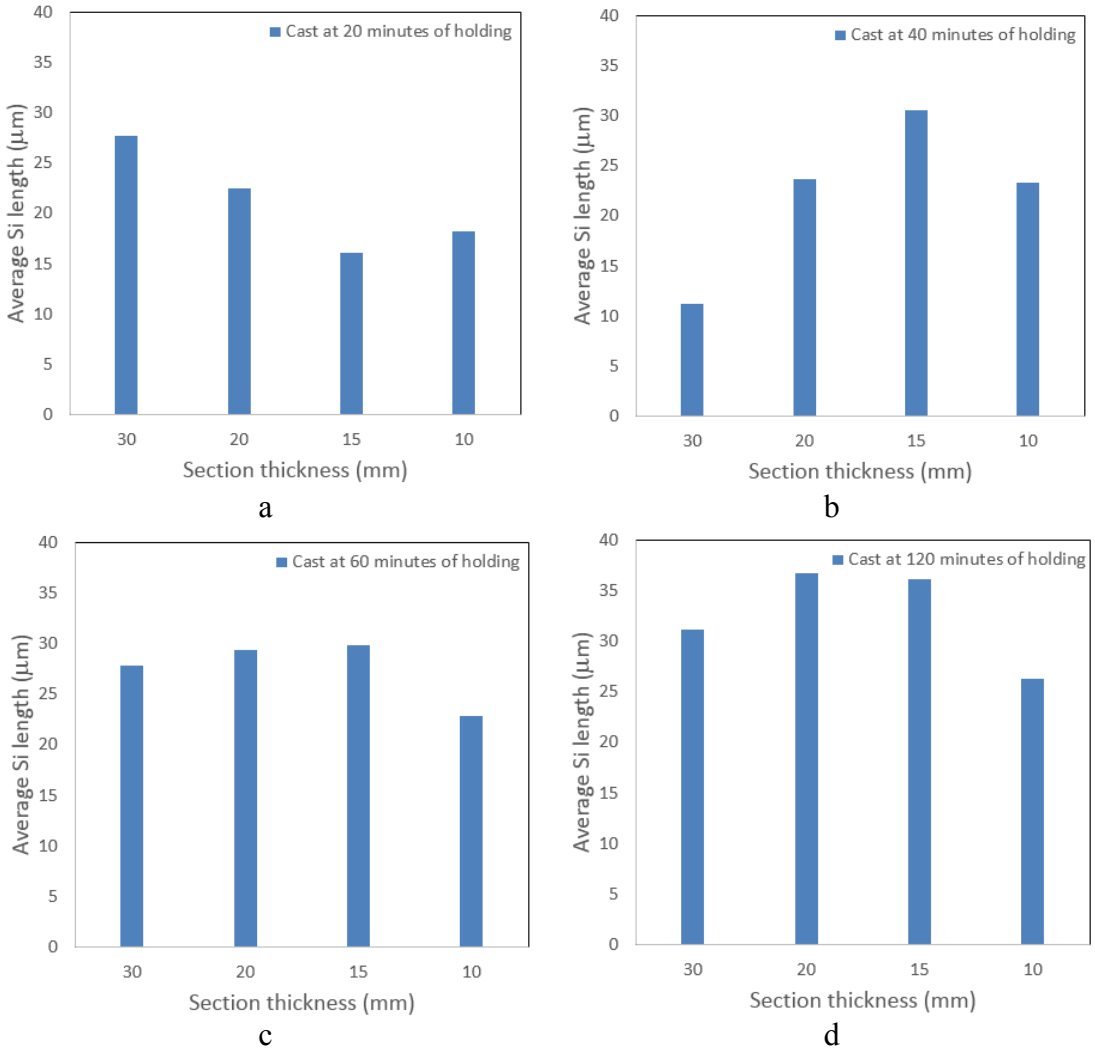

Figure 4. Si size change with section thickness and holding time

Figure 5 shows the porosity measurements on the cross section of each thicknesses. It can be seen that the distribution of porosity is so complex there is no easy correlation between the effect of cooling rate (section thickness) or the holding time. It is expected that typically, as the section thickness decreases, the cooling rate increases which leads to lowered porosity. Likewise, in all of the castings, 30 mm thickness (the highest one with slowest cooling) had the highest porosity level. However, it is interesting to note that in general, the average porosity seems to be decreasing with increasing holding time up to 120 minutes. Similarly, as seen in Figure 6, the average number of pores decreases with increasing holding time up to 120 minutes of holding.

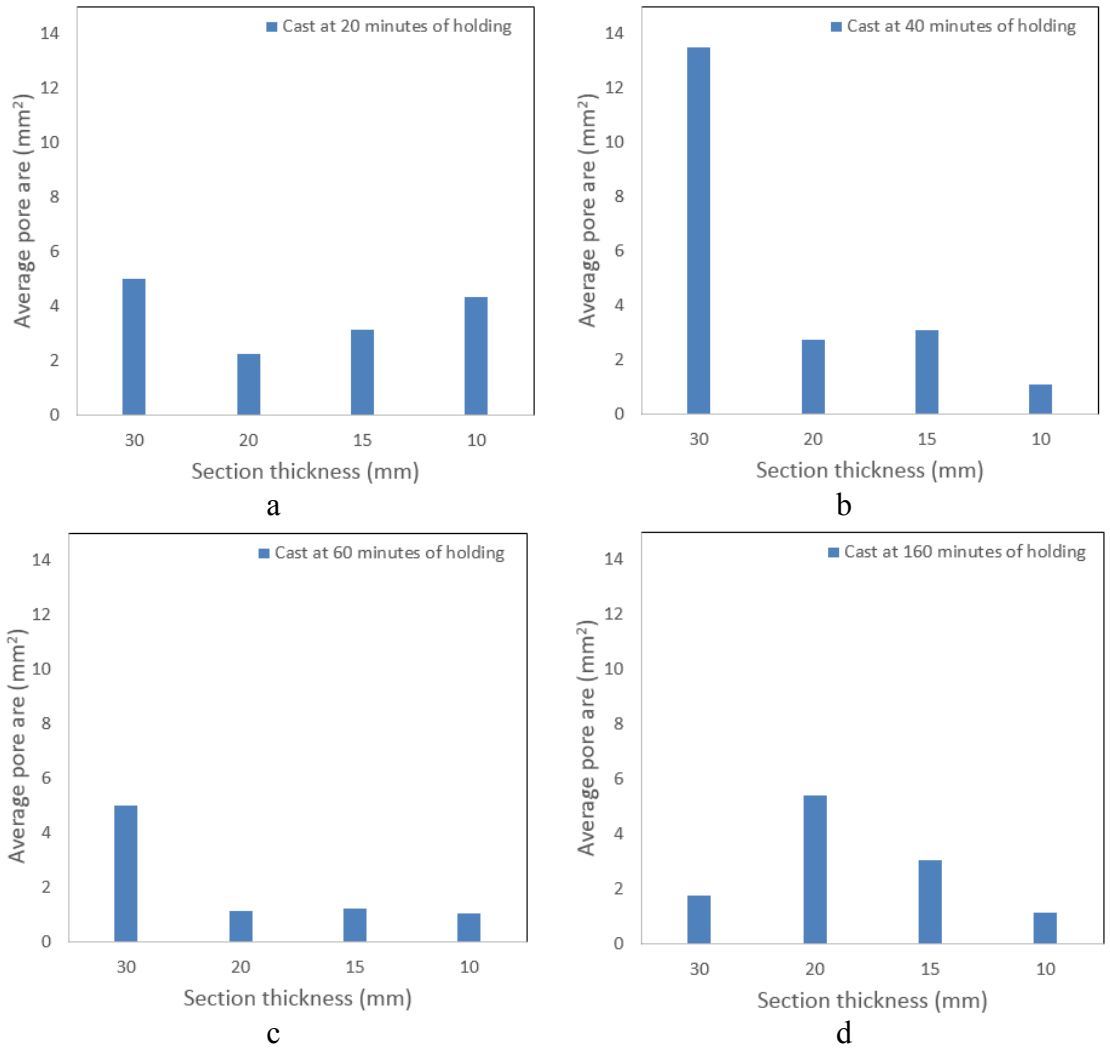

Figure 5. Change in average pore area with section thickness and holding time

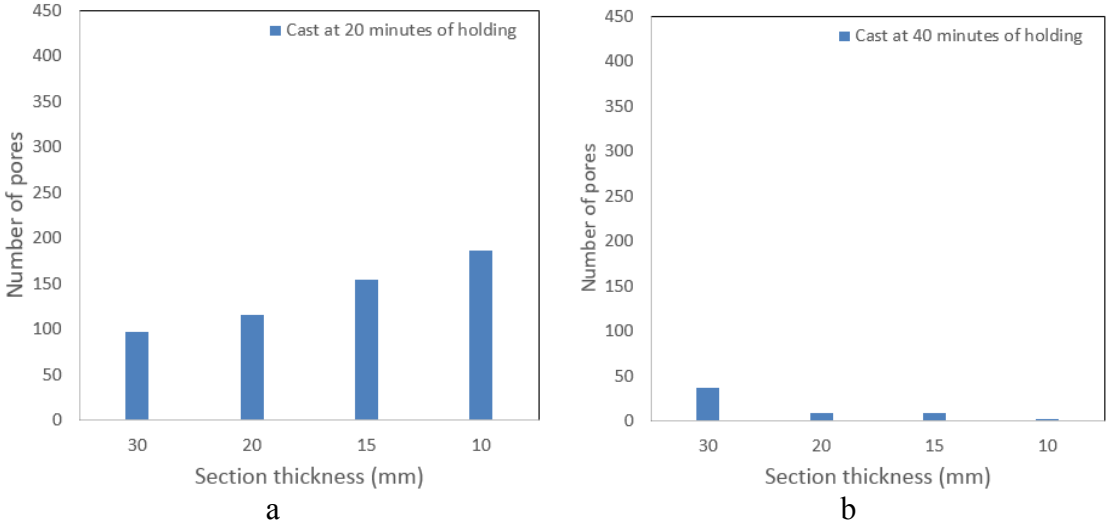

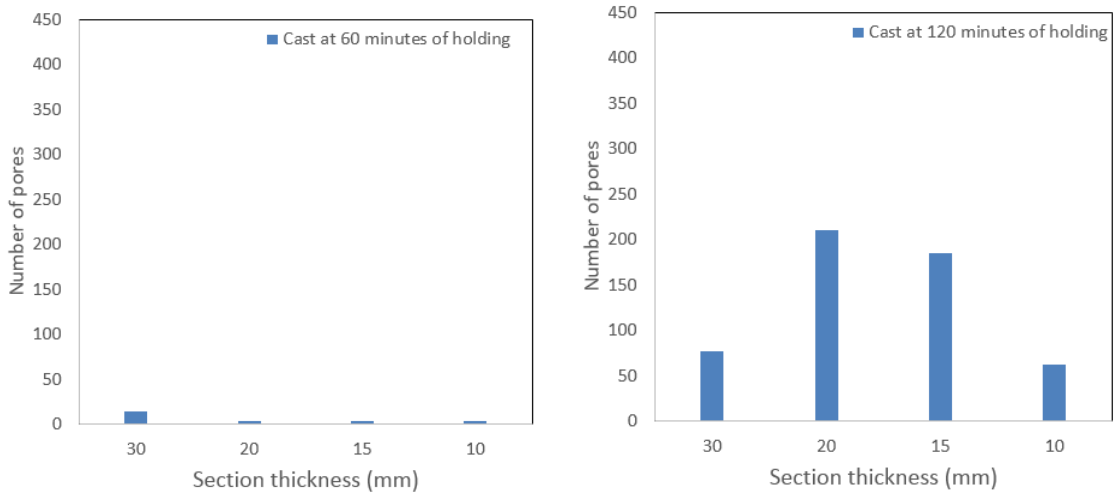

c d

Figure 6. Change in number of pores with section thickness and holding time

CONCLUSIONS

The efficiency of Sr modification is ceased after 20 minutes of holding the metal in the liquid state.

The size of Si particles in the eutectic phase increases with increased holding time. The sizes are affected by the cooling rate only when the melt is held less than 20 minutes. Prolonged holding times lead to constant Si size distribution regardless of the cooling rate.

Secondary dendrite arm spacing increases with increasing holding time.

As the holding time of the melt is increased, the number and size of pores decreases.

ACKNOWLEDGMENT

This work has been supported by the Scientific Research Projects Coordination Unit of Selcuk University (Project number: 13401013). The authors would like to thank ÖREN DÖKÜM for their support in this study.

REFERENCES

1. Dey, A.K., et al., *Mechanical and wear properties of rheocast and conventional gravity die cast A356 alloy.* Materials Science and Engineering: A, 2006. **435–436**(0): p. 521-529.
2. Campbell, J., *Castings : [the new metallurgy of cast metals]*. 2003, Butterworth Heinemann.
3. Ejiofor, J.U. and R.G. Reddy, *Developments in the processing and properties of particulate Al-Si composites.* JOM, 1997. **49**(11): p. 31-37.
4. Cho, Y.H., et al., *Effect of Strontium and Phosphorus on Eutectic Al-Si Nucleation and Formation of β-Al5FeSi in Hypoeutectic Al-Si Foundry Alloys.* Metallurgical and Materials Transactions A, 2008. **39**(10): p. 2435-2448.
5. Dahle, A.K., et al., *Eutectic modification and microstructure development in Al–Si Alloys.* Materials Science and Engineering: A, 2005. **413–414**(0): p. 243-248.
6. Espinoza-Cuadra, J., et al., *Effect of Sr and solidification conditions on characteristics of intermetallic in Al–Si 319 industrial alloys.* Materials & Design, 2010. **31**(1): p. 343-356.
7. Stefanescu, D.M. and A.V. Catalina, *Physics of microporosity formation in casting alloys - sensitivity analysis for Al-Si alloys.* International Journal of Cast Metals Research, 2011. **24**(3/4): p. 144-150.

THE MICROSTRUCTURAL CHANGE OF HYPEREUTECTIC Al-Si ALLOY BY ADDITION OF Sr and B

Muhammet ULUDAĞ[*], Lokman GEMİ[**], Zafer YAVAŞ[*], Ümmühan ÖZTÜRK[*], Nesibe Sevde ÜLVAN[*], Derya DIŞPINAR[***]

*Selcuk University, Faculty of Engineering, Metallurgical and Materials Eng. Dept., Konya-Turkey, uludag@selcuk.edu.tr, zfryvs@gmail.com, ummuhan.ozturk2@hotmail.com, nesibesevde@hotmail.com
** Selcuk University, Institute of Science, Konya-Turkey, lgemi@selcuk.edu.tr
*** Istanbul University, Faculty of Engineering, Metallurgical and Materials Eng. Dept., Istanbul-Turkey, derya.dispinar@gmail.com

ABSTRACT
Hypereutectic Al-Si is widely used in applications where the combination of light weight and high wear resistance is required. When it is not controlled, the nucleation of primary Si in these alloys is known to cause several problems such as reduced fluidity. Strontium has been commonly used for the modification of Si. In addition, Ca and P are sufficient to refine primary Si. In this work, the microstructural change has been investigated by the addition of Sr and B to Etial 195 (Al-18Si). Step mould design was used to produce cast parts where the castings were carried out both vertically and horizontally. The mechanism of both primary Si nucleation and porosity formation was investigated.

Keywords: Hypereutectic, Al-Si alloy, Grain refinement, Modification, Morphology of Si

ÖTEKTİK ÜSTÜ Al-Si ALAŞIMLARINDA B VE Sr MODİFİKASYONUNUN MİKROYAPISAL DÖNÜŞÜM MEKANİZMASI

ÖZET
Ötektik üstü Al-Si alaşımlarında, primer silislerin tercihli olarak heterojen kaynaklarda çekirdekleştiği bilinmektedir. Bu çalışmada, Etial 195 primer alaşımının dökümünde AlB_3 master alaşımı ve Sr modifikasyonunun mikroyapıya etkisi incelenmiştir. Dökümler, 750 ^{0}C sıcaklıkta ve farklı kesit kalınlıklarına sahip basamak tipli kum kalıplara yatay ve dikey olarak yapılmıştır. Tüm dökümlerde, B ve Sr ilavesi gaz giderme işlemi sonrasında yapılmıştır. Bütün kesitler için soğuma hızları ile hem Si morfolojisi hem de mikroyapısal dönüşümler incelenmiştir. Aynı zamanda porozite oluşum mekanizmaları da araştırılmıştır. Her kesitten numuneler üretilerek mikroyapı ve porozite arasında ki ilişki ortaya çıkartılmıştır.

Anahtar Kelimeler: Ötektik üstü, Al-Si alaşımı, Tane inceltici, Modifikasyon, Si morfolojisi

1. INTRODUCTION

Hypereutectic Al-Si alloys have high temperature stability, good wear resistance and low thermal expansion coefficients. Therefore these alloy are preferably used in engine blocks, pistons etc [1, 2]. The microstructure consists of primary Si which improves wear resistance. Therefore, there were several works that studied the effects of alloying elements on the

morphology of Si. The known mechanism is called twin plane re-entrant edge. The addition of other elements either restrict the growth and thus Si may have one single hexagonal type morphology or grows towards a selected oriented direction to have more finer and fibrous shape [3-4].

In addition to the primary Si morphology change by alloying element additions, grain refinement by Ti or B causes α-Al dendrites to be finer which may also result in change of the morphology of primary Si simply because cooling rate and thus growth rate is changed. Grain refinement is also important in terms of the dendrite coherency, feedability and porosity distribution [5-7].

The addition of grain refiners to the melts such as Ti and B forms TiB_2 and $TiAl_3$ intermetallics which nucleates α-Al. In this way, segregation is minimised and distribution of secondary phases are altered and thus the microstructure is changed. With Ti addition, although the dendrites becomes finer, yet, the homogeneity and the size of the dendrites may not be typically achieved. In recent years, studies have shown that Ti-free B grain refinement results in more globular and homogeneous grain distribution [3,6]. Therefore better mechanical properties can be obtained.

The studies have shown that when grain refiners were added, the size of TiB_2 intermetallic was 1-2 μm and this value was 30-40 μm for $TiAl_3$ [8-9]. These values depend on the Ti/B ratios in the master alloy.

In this work, Etial 195 alloy was used to investigate the effects of grain refiners and modification on the morphology of Si. In addition, the size and distribution of porosity was also analysed.

2. EXPERIMENTAL WORK

For the casting trials, 20 kg capacity electrical furnace was used and the charge was a primary alloy and melted in a SiC crucible at 750ºC. For modification, Al-Sr and Al-B master alloys were used. The composition of Etial 195 is given in Table 1.

Table 1. *Chemical composition of Etial 195*

Si	Fe	Cu	Mn	Mg	Zn	Ti	Ni	Al
17,0-19,0	0,60	0,80	0,20	0,80	0,20	0,10	0,80-1,3	Rem

After the melting was complete, degassing of the melt was done with Ar for 25 minutes. The castings were made into sand mould that had various section thickness in the form of a step: 10, 15, 20 and 30 mm. As seen in Fig 1, two types of castings were made: vertical and horizontal.

The cast parts were all sectioned according to their thicknesses and subjected to microstructural analysis. Image analysis software was used to measure, dendrite arm spacing, Si phase size, length, shape factor and distribution. In addition, porosity was also analysed.

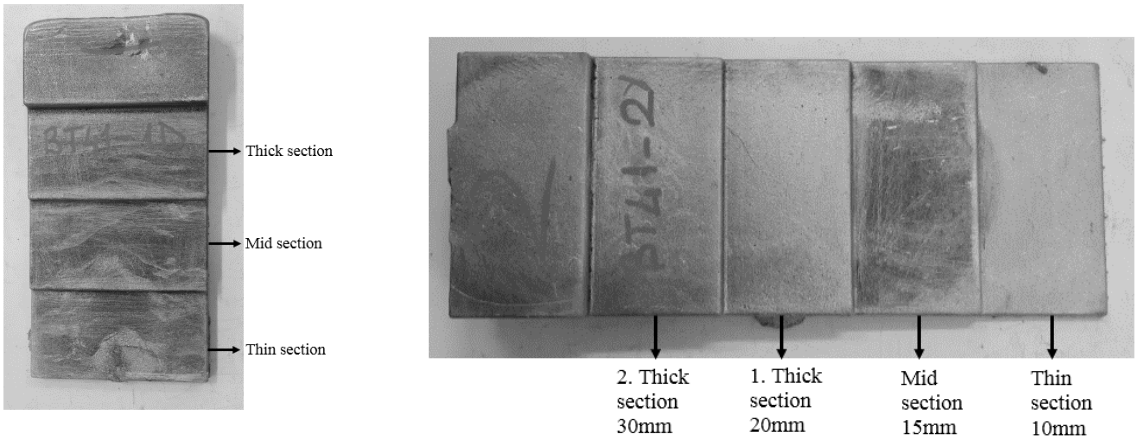

Figure 1. The cast parts produced in the experiments; (a) vertical, (b) horizontal steps

3. RESULTS and DISCUSSION

In order to correlate the change of Si morphology by Sr and B additions, unmodified alloy was cast first in the as-received form. The microstructures of these castings made in both vertical and horizontal steps at various section thicknesses is given in Figure 3. Due to the high number of samples, it was difficult to prove all the microstructural images in this manuscript. For simplicity, 15 section thickness was selected and the images are given in Fig 3 and 4 for Si and B modifications respectively.

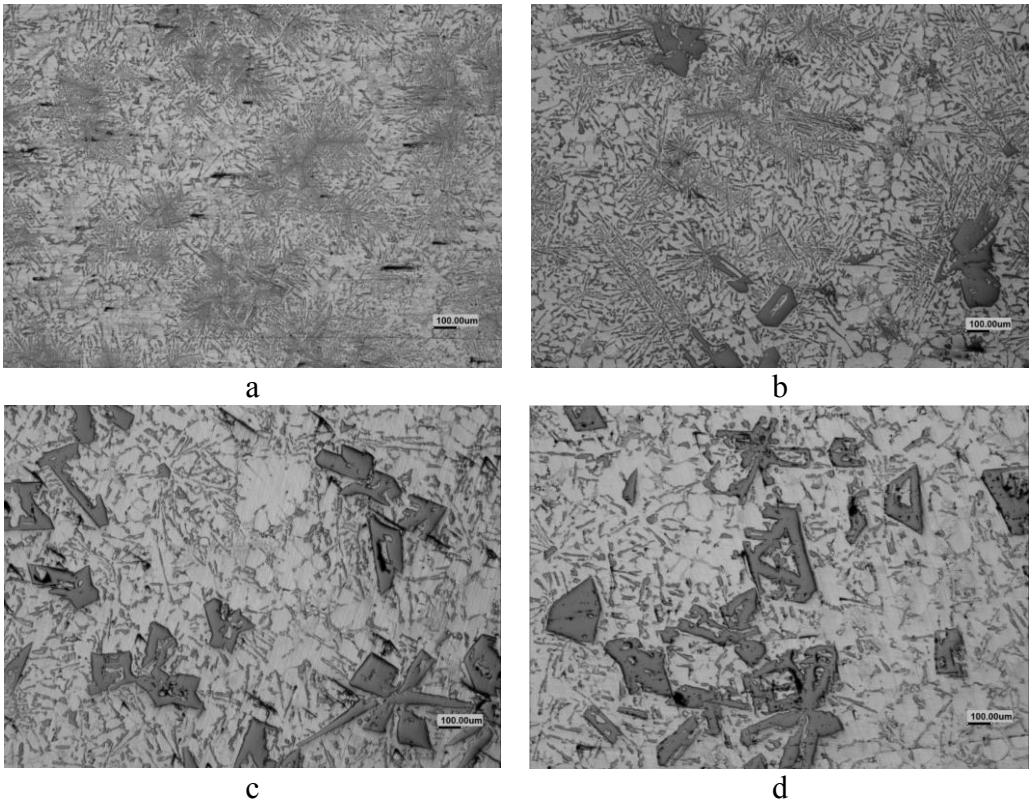

Figure 2. Horizontal step casting of the as-received alloy for various section thickness: a) 10 mm, b) 15 mm, c) 20 mm, d) 30 mm

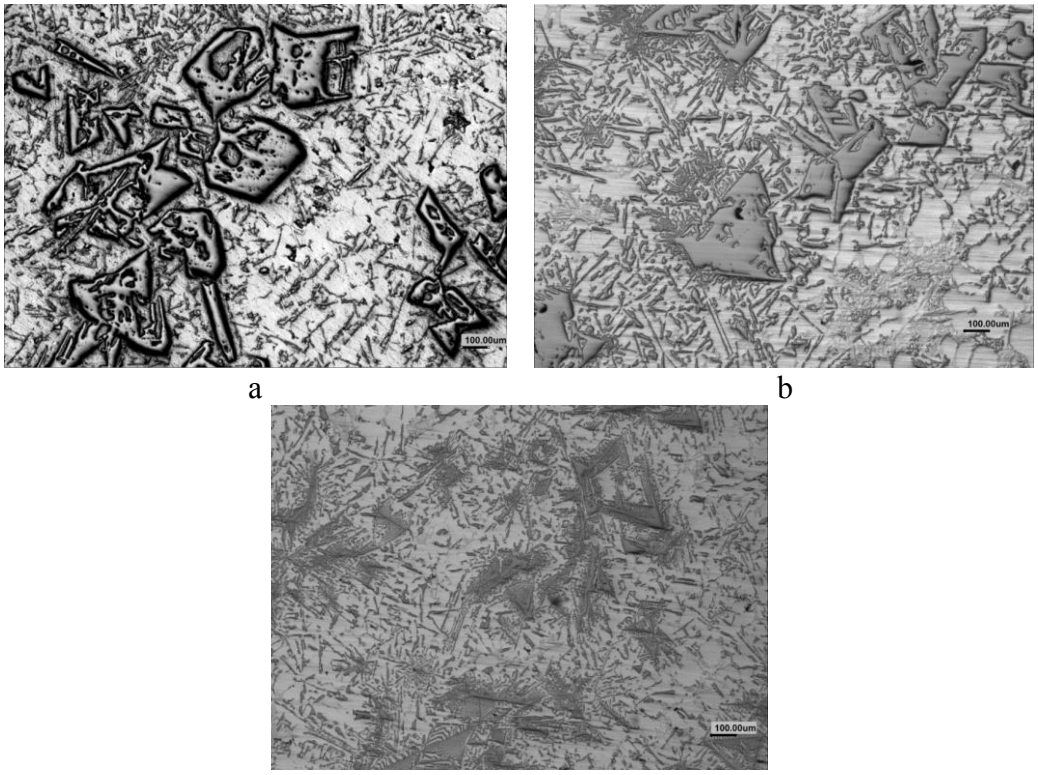

a b

c

Figure 3. Vertical step mould castings, 15 mm section,
a) as-received, b) Sr modified, c) B added

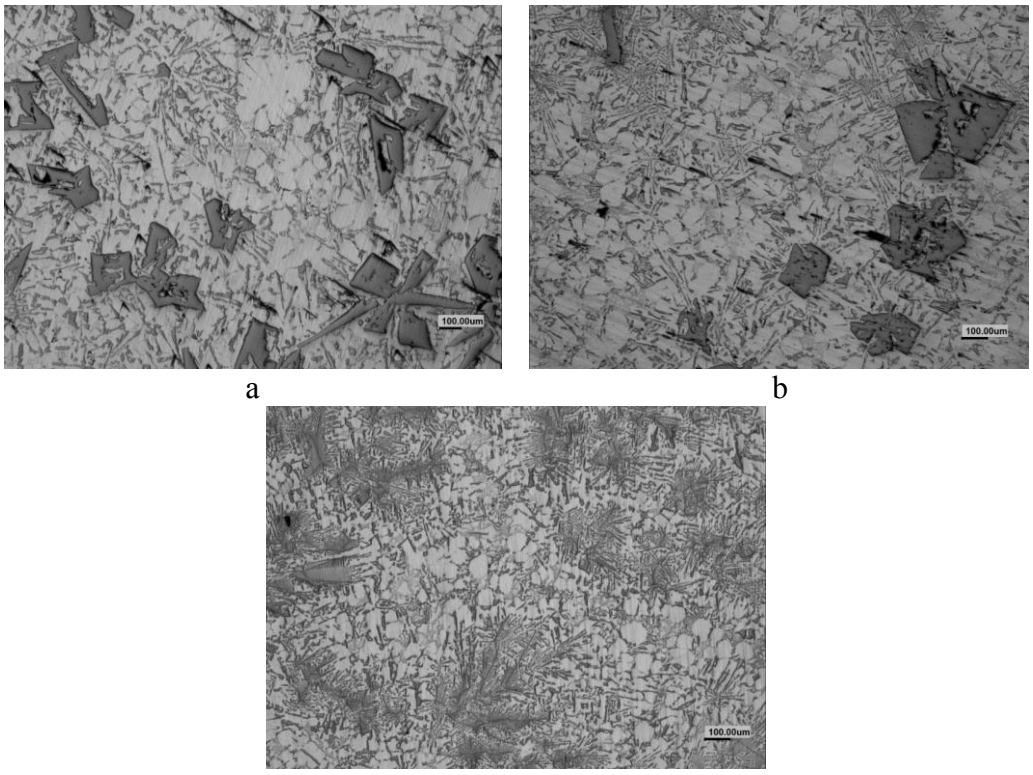

a b

c

Figure 4. Horizontal step mould casting, 15 section thickness
a) as-received, b) Sr modified, c) B added

Figure 5 shows the pore area change at different section thickness according to the modification of the alloy.

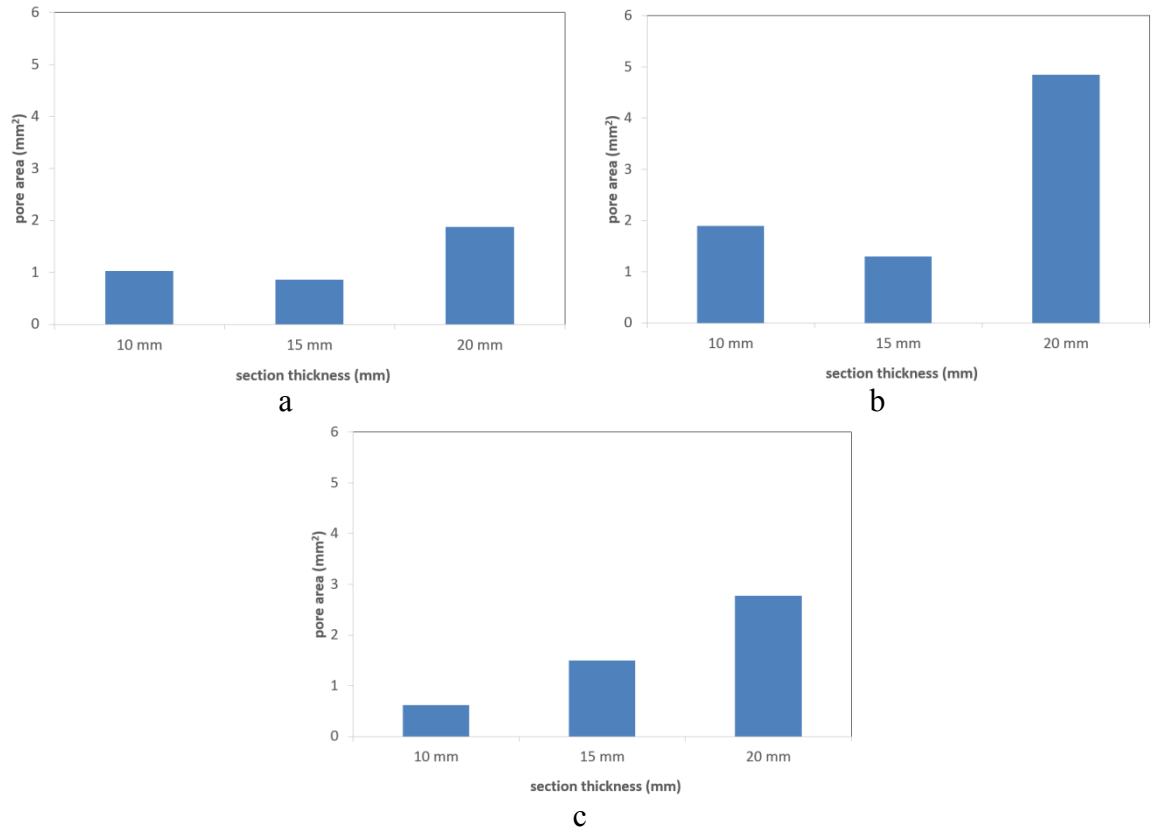

Figure 5. Pore area according to the section thickness and modification
a) unmodified (as-received), b) Sr modified, c) B added

Figure 6 shows the correlation between the number of pores and pore area.

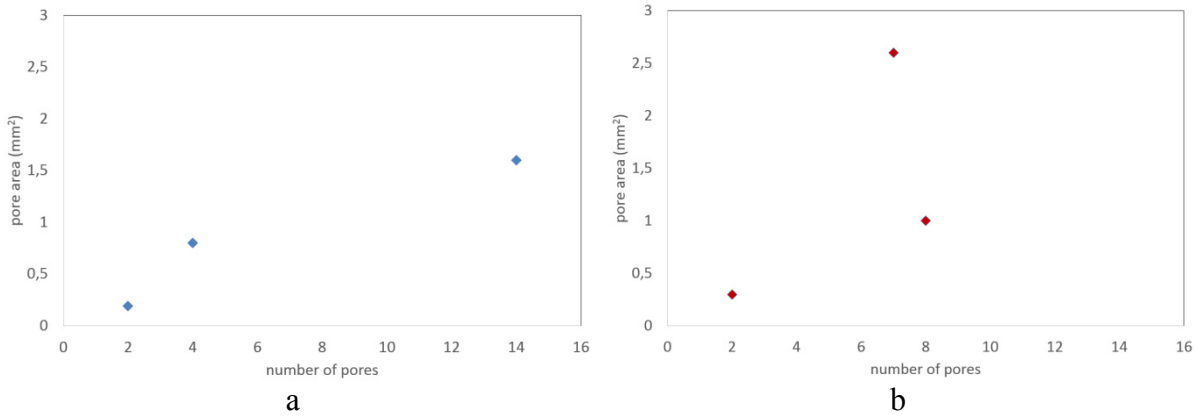

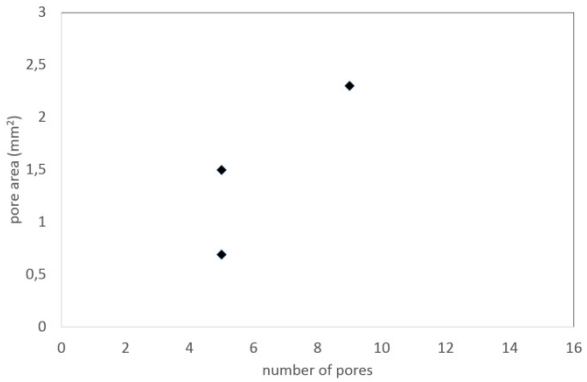

c

Figure 6. Pore area and pore number correlation in horizontal step mould casting
a) unmodified, b) Sr modified, c) B added

As seen in Figure 2, as the section thickness was increased, the size and number of primary silicon was increased. At the same time, the eutectic phase ratio and size was decreased. Fig 2a, the microstructure consists of finely distributed almost complete eutectic in the absence of primary Si. As the section thickness was increased, with the formation of primary Si, the matrix was depleted from Si, and thus resulted in coarser eutectic phase distribution and larger surface area of α-Al dendrites were observed (Fig 2d). It appears that even in low thermal conductivity mould material such as sand, at the thinnest section, due to the relatively faster cooling, finer microstructure was obtained.

With the addition of Sr, the coarse eutectic phase was modified into finer eutectic. However, as seen in Fig 3, this modification was not active all throughout the microstructure. The effective zone for eutectic modification was only near the primary Si phases (Fig 3b). With the addition of B, this change in the microstructure was even more dominant. This time, even the size of the primary Si was decreased and finer eutectic phase ratio was increased around these primary Si (Fig 3c).

Same scenario was valid for horizontal step mould castings as seen in Figure 4. What was the most surprising finding was that with the addition of B, the size of primary Si was decreased significantly and a branchy looking fine eutectic phase was seem to be growing around through these primary Si phases.

The average pore area was not affected by the section thickness in the unmodified primary Etial-195 alloy. As seen in Figure 5, these values are around 1 mm^2. When B was added, porosity seems to be increasing with increased section thickness (i.e. slower cooling and coarser grains size). On the other hand, Sr modification has the highest porosity amongst the casting trials. As seen in Fig 6, with the Sr modification, the number of huge pores increases whereas small and few pores exist in unmodified and B added alloy.

4. CONCLUSIONS

1. The morphology of primary Si in hypoeutectic Al-Si alloy decreases as the cooling rate increases and finer eutectics form.

2. By the addition of Sr, the size of both primary and secondary Si increases.

3. B addition is more effective than Sr in terms of refining of both primary and secondary Si in hypoeutectic Al-Si.

4. Porosity distribution linearly increases with decreased the cooling rate in B addition, however, more and larger pores are formed regardless of the cooling rate with Sr modifications.

Acknowledgment

The authors would like to thank MODEL 91 Makina ve Kalıp Sanayi Ticaret Ltd. Şti. for their support in this study.

REFERENCES

1. Campbell, J., *Discussion of ''Effect of Strontium and Phosphorus on Eutectic Al-Si Nucleation and Formation of b-Al5FeSi in Hypoeutectic Al-Si Foundry Alloys".* Metallurgical and Materials Transactions A, 2009. **40A**: p. 1009-1010.
2. Kim, H.J., *Effect of calcium on primary silicon particle size in hypereutectic Al-Si alloys.* Materials Science and Technology, 2003. **19**(7): p. 915-918.
3. Atasoy, O.A., F. Yilmaz, and R. Elliott, *Growth structures in aluminium-silicon alloys I. The coupled zone.* Journal of Crystal Growth, 1984. **66**(1): p. 137-146.
4. Dispinar, D. and J. Campbell, *Use of bifilm index as an assessment of liquid metal quality.* International Journal of Cast Metals Research, 2006. **19**(1): p. 5-17.
5. Bryant, M. and P. Fisher, *Grain Refining and the Aluminium Industry (Past, Present and Future).* Aluminium Casthouse Technology, 1993.
6. Çolak, M. and R. Kayıkcı, *AITİB MASTIR ALAŞIMI İLAVESİNİN ETİAL160 DÖKÜM ALAŞIMI ÜZERİNDE TANE İNCELTME ETKİSİNİN İNCELENMESİ*, in *5. Uluslararası İleri Teknolojiler Sempozyumu (IATS'09)*. 2009.
7. Quested, T.E., *Understanding mechanisms of grain refinement of aluminium alloys by inoculation.* Materials Science and Technology, 2004. **20**: p. 1357-1371.
8. Cooper, P., et al., *Characterisation of new genaration of grain refiners fort he foundry industry*, in *132. Annual Meeting & Exhibition*. 2003.
9. Cooper, P., A. Jacob, and A. Detomi, *Additive developments in the Aluminium Industry*, in *1. International Congress of the Aluminium Industry*.
10. Budic, I., D. Novoselovic, and J. Gros, *SOLVABILITY OF HYDROGEN IN ALUMINUM.* Annals of DAAAM & Proceedings, 2009: p. 1805-1806.

THE EFFECT OF Sr MODIFICATION AND HOLDING TIME ON MICROSTRUCTURE IN HYPEREUTECTIC Al-Si ALLOYS

Muhammet ULUDAĞ[*], Lokman GEMİ[**], Muhammed Raşit ERYILMAZ[*], Derya DIŞPINAR[***]

* Selcuk University, Faculty of Engineering–Metallurgical and Materials Eng. Dept., Konya-Turkey, uludag@selcuk.edu.tr, rasit.eryilmaz@gmail.com
** Selcuk University, Institute of Science, Konya-Turkey, lgemi@selcuk.edu.tr
*** Istanbul University, Faculty of Engineering, Metallurgical and Materials Eng. Dept., Istanbul-Turkey, deryad@istanbul.edu.tr

ABSTRACT
Melt treatment of aluminum alloys are typically carried out in transfer furnaces prior to casting. Depending on the size of the crucible and the volume of the castings, the melt may be led to remain in the liquid state up to two hours. It is well known that as the holding period is increased, the effect of modifiers fade away. In this work, the mechanism of this fading effect has been investigated for the first time by means of melt cleanliness. Reduced pressure test was used to measure bifilm index of the melt. Al-19Si was used and two temperatures were selected: 725ºC and 800ºC. Hydrogen content of the melt was measured by AlSPEK and excess amount of Al-15Sr modifier was added once the desired temperature was reached. Samples were collected castings that were achieved in two different holding time (0 and 2 hours) and the microstructural results (i.e. efficiency of modification) was correlated with bifilm index (melt quality).

Keywords: Hypereutectic Al-Si alloy, Modification, Morphology of Si, Hydrogen content, Bifilm index

ÖTEKTİK ÜSTÜ Al-Si ALAŞIMLARINDA MODİFİKASYON VE BEKLETME SÜRELERİNİN MİKROYAPI ÜZERİNE ETKİSİ

ÖZET
Bu çalışmada ötektik üstü Al-Si alaşımlarının modifikasyonu ve sıvı halde bekletilmesi üzerine bir araştırma yapılmıştır. Ötektik üstü alaşımlarda, farklı soğuma hızlarında silisyumun katılaşma morfolojisi önemli değişikliler göstermektedir. Bu silisyum morfolojisini inceleme amaçlı farklı kesit kalınlıklarına sahip basamak tipli kum kalıplara döküm yapılmıştır. Dökümlerde Al15Sr master alaşımı modifikatör olarak kullanılmıştır. Döküm kalitesini ve modifikasyon oluşumunu incelemek için farklı sıcaklıklarda (725 ^{0}C ve 800 ^{0}C) dökümler yapılmıştır. Her dökümden önce sıvı metalin hidrojen içeriği AlSPEK cihazı ile ölçülmüştür. Modifikasyon işleminin etkinliği, tutma süresi değiştirilerek (0 ve 2 saat) araştırılmıştır. Böylelikle, silisyum morfolojisinin değişimi incelenmiştir. Bununla beraber farklı sıcaklıklarda ve bekleme sürelerinde modifikasyonun ne derece etkili olduğu ortaya çıkartılmıştır.

Anahtar Kelimeler: Ötektik üstü Al-Si alaşımı, Modifikasyon, Silisyum morfolojisi, Hidrojen içeriği, Bifilm indeks

1. INTRODUCTION

Hypoeutectic Al-Si alloys are typically used in applications where high wear resistance is required. In addition, these alloys exhibit good corrosion resistance [1,2]. The microstructure of such alloys consists of nucleation of primary Si, followed by the eutectic (α-Al dendrites and secondary Si) phase formation. The size, shape and distribution of primary Si plays a significant role on the mechanical properties [3].

The primary Si usually had coarse pentagonal shape compare to the Si in hypereutectic Al-Si alloys. This geometry gives a huge advantage for improved wear resistance and thus these alloys can be found in pistons and etc [4]. However, although high wear resistance is obtained by primary Si, the ductility is significantly reduced [5]. Therefore, there are several studies in literature on the modification of Si [6].

The methods to modify primary Si can be listed as addition of alloying elements, heat treatment, ultrasonic vibration and rapid cooling [5-8]. Modification of primary Si also results in modification of the remaining eutectic.

Many of the modification studied earlier have been found to be unstable and non-environmental friendly. The loss of additives, burning and pollution made phosphorus not a good choice of modifier [5, 7]. Therefore, Sr has been studied in the last decade as the primary Si modifier [9].

In this work, the effect of pouring temperature, holding time, cooling rate and Sr modification on the morphology of primary Si have been investigated.

2. EXPERIMENTAL WORK

Primary Al-17Si alloy was used in the experiments which was provided form Eti Aluminum, Turkey. The chemical composition is given in Table 1. The charge was melted in 20 kg capacity resistance furnace. The castings were made at 725^{o}C and 800^{o}C in the following order: as melted, 1 hour and 2 hours later. In the final casting, at 800^{o}C, Sr was added.

Table 1. Chemical composition of the alloy used in the experiments

Si	Fe	Cu	Mn	Mg	Zn	Ti	Ni	Al
17,0-19,0	0,60	0,80	0,20	0,80	0,20	0,10	0,80-1,3	rem

In order to investigate the effect of cooling rate, a step mould geometry was used (10, 15, 20 and 30 mm). A picture representing a casting has been given in Figure 1.

Figure 1. Top and side view of a cast part

Each thickness of the cast part was sectioned and subjected to metallographical examination. Image analysis was used to evaluate primary Si size, shape and dimension.

Reduced Pressure Test (RPT) samples were collected from each melt in order to check the melt quality by measuring bifilm index and the results were correlated with bifilm content.

3. RESULTS and DISCUSSION

Figure 2 shows a selected microstructural representation of 30 mm thickness obtained from 725 °C, 800 °C and 800 °C+Sr additions. As seen in this figure, there are group of blocky primary Si phases grown in various directions. There is a quite homogeneous distribution of eutectic phase around the primary Si. As the section thickness was lowered from 30 to 20, 15 and 10 mm, the primary Si size was getting smaller and finer and evenly distributed along the sectioned surface. Furthermore, the eutectic phase was also getting finer and α-Al size was getting larger in terms of fraction of area. What was interesting was the ratio of primary Si getting lower around the α-Al dendritic structure. In general, it can be concluded that when the alloy is cast at 725^{o}C, the primary Si size decreases with decreased section thickness and the shape becomes more smoother.

When the casting was carried out at 800^{o}C, the microstructural evaluation was almost similar to the ones cast at 725^{o}C. The main difference was the size of primary Si was slightly higher.

When Sr was added to the melt, it was observed that the size and ratio of primary Si was significantly reduced and the eutectic phase ratio was increased. More regular α-Al phase formation was observed and secondary Si was segregated along the microstructure.

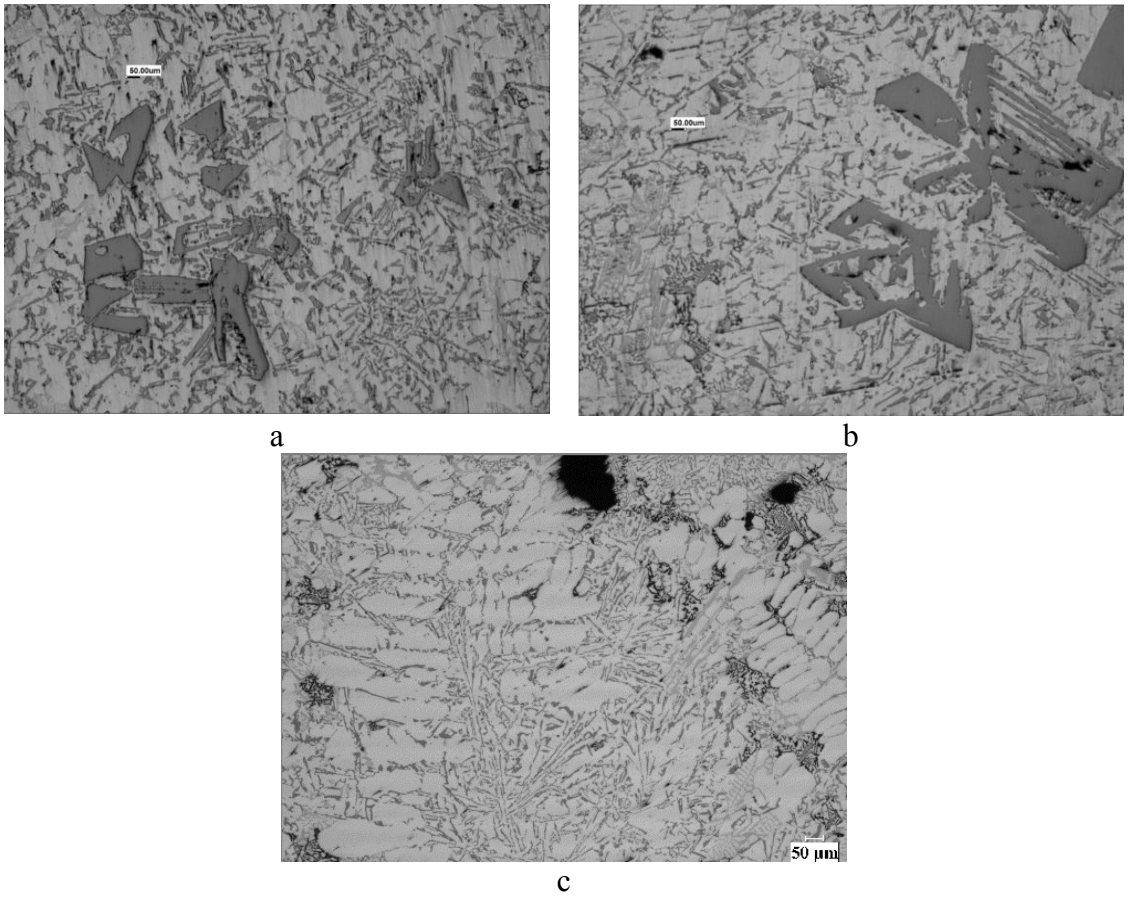

Figure 2. Microstructural change with casting parameters
a) 725 °C, b) 800 °C, c) 800 °C+Sr

Bifilm index measurement were made from RPT samples' cross section and the results are reported in Figure 3.

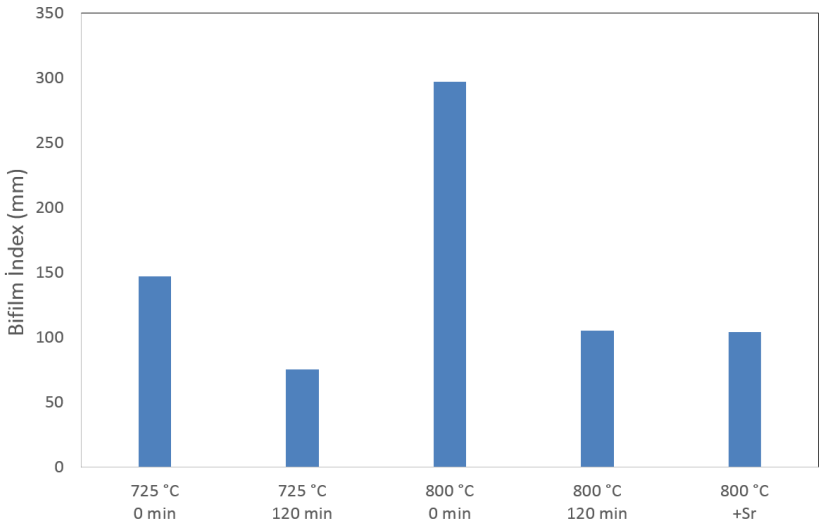

Figure 3. Bifilm index results of the casting experiments

One interesting observation in the melt quality measurements in Figure 3 was that was the melt was kept at the liquid state for 120 minutes, bifilm index was decreased almost three folds from

150 to 50 mm for 725°C, and 300 to 100 mm for 800°C castings. The change in the primary Si morphology was carried out by image analysis software and the results are given in Figures 4-7.

As seen in Figure 4, in the thinnest section of the mould (10 mm), the primary Si length was decreased from 10 to 15 µm when pouring temperature was increased from 725°C to 800°C. However, on 30 mm section, there is not much change in Si length. The significant change in primary Si was achieved by the addition Sr. On both cases, lowest primary Si length was obtained by Sr modification. Figure 4b shows the change in the shape factor of primary Si. Shape factor is given by the ratio of square of perimeter and area. Thus, 1 indicates a perfect sphere and 0 indicates a line. The more the shape factor is closer to zero, the more the complex the shape of the measured phase. Here, it can be seen that as the pouring temperature was increased, the more the complex primary Si was. This was more clear when the alloy was Sr modified.

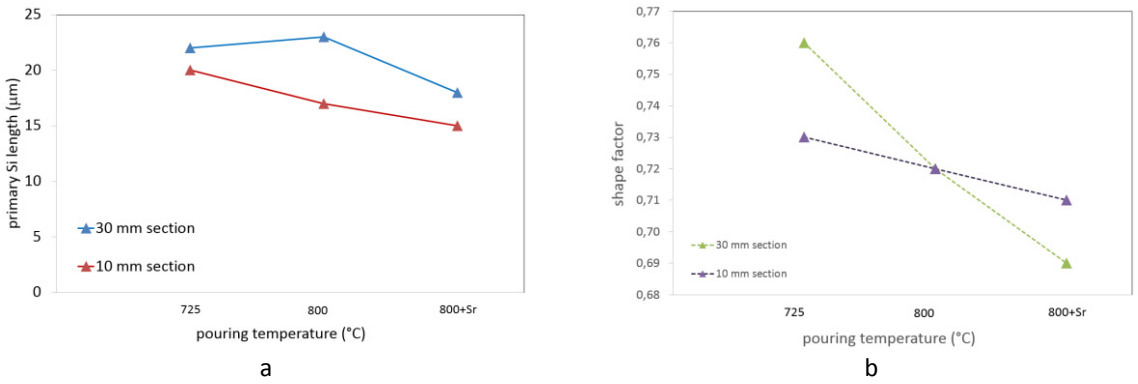

Figure 4. Pouring temperature *vs* (a) primary Si length and (b) shape factor at 0 min

The same parameters were used to plot the change of primary Si and shape factor with changing pouring temperature, but this time, the melts were kept at pouring temperature for 120 minutes; and the results are given in Figure 5. As seen in Fig 5a, the change of primary Si length with increasing pouring temperature from 725 to 800 is more significant when the melt was held for 120 minutes. In Fig 4a, this change was quite low. However, in Fig 5a, the length of primary Si is increased from 18 to 23 µm for 30 mm section thickness and it decreased from 16 to 9 µm at 10 mm section. On the other hand, the shape factor remained unchanged at 30 mm section when the pouring temperature increased to 800°C. Furthermore, it was increased at 10 mm section.

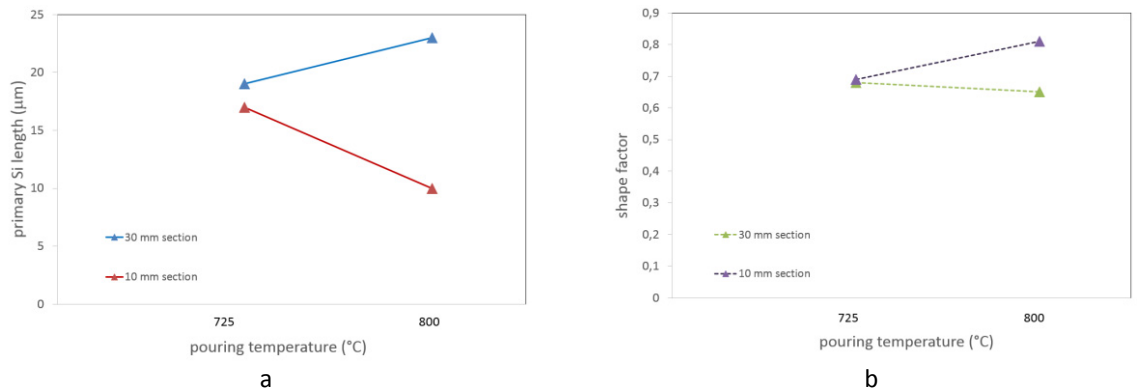

Figure 5. Pouring temperature *vs* (a) primary Si length and (b) shape factor after 120 min

These findings indicate that when the casting of hypoeutectic Al-Si alloys are carried out at low temperatures such as 725°C, the shape and size and distribution of primary Si and secondary eutectic phase is not effect by the cooling rate. As seen in Figure 4 and 5, all the findings of 725°C casting lies almost on top of each other. However, when the pouring temperature is increased to 800°C, the effect of cooling rate, i.e. section thickness, was more dominant. At sections that were thicker than 30 mm, the size and shape of primary Si was increased and at 10 mm sections, these values were decreased significantly.

The change of primary Si size and shape factor with bifilm index after 0 and 120 minutes of holding was given in Figure 6 and 7 respectively.

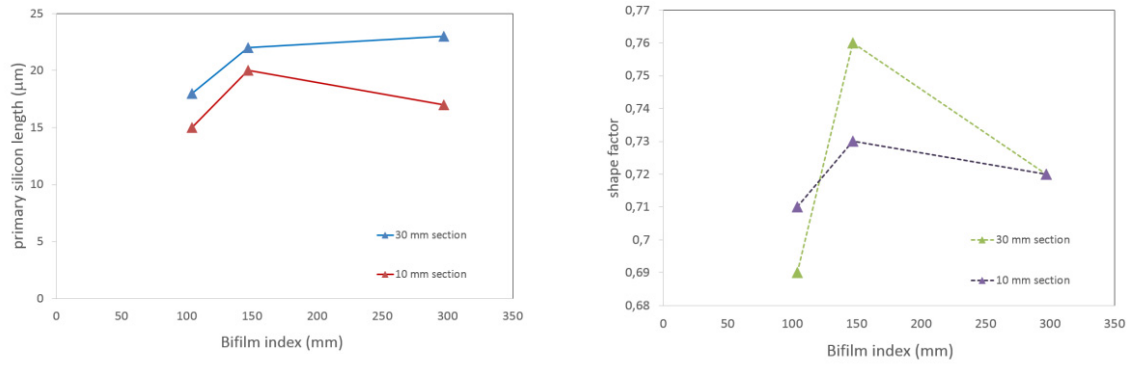

a b

Figure 6. Bifilm index and (a) primary Si size and (b) shape factor relationship, cast after 0 min of holding

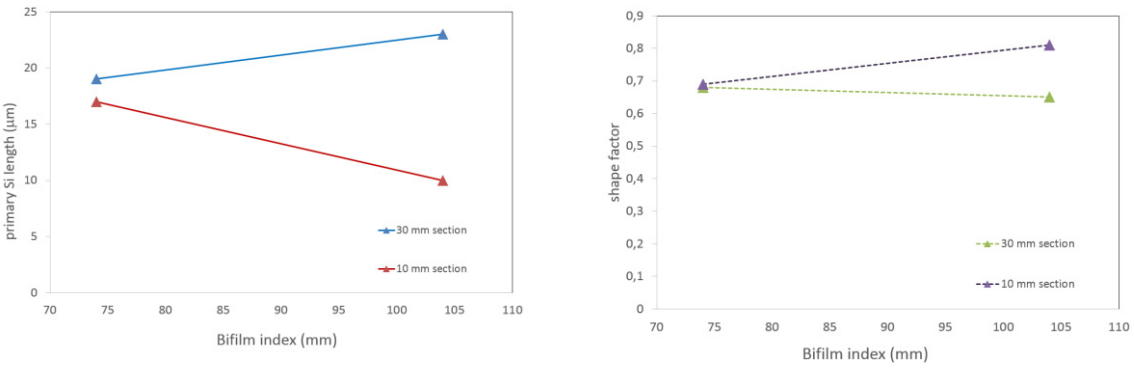

a b

Figure 7. Bifilm index and (a) primary Si size and (b) shape factor relationship, cast after 120 min of holding

Bifilm are folded oxide skin defects that are introduced into the melt by turbulence. Therefore, they can act as nucleation sites for many of the defects as well as intermetallic phases. Here, in this work, such effect of bifilms can be clearly seen. As the bifilm index is increased, coarser primary Si phase is formed. On the other hand, when the cooling rate is increased (from 30 mm section thickness to 10 mm), the diffusion rate decreases and primary Si cannot find the time to nucleate on bifilms, and freeze on their own to form more finer and homogeneously distributed primary and secondary eutectic phases.

4. CONCLUSIONS

Pouring temperature affects the primary Si morphology only when the section thickness is smaller than 30 mm.

As the pouring temperature is increased, coarser primary Si can be obtained. As the cooling rate is increased, finer primary Si can be produced.

By Sr modification of hypoeutectic Al-Si alloys, both primary and secondary Si size decreases and more ordered, regular growth can be achieved.

As the melt was held for longer times in the liquid state, bifilm index was decreased. There was not much clear correlation between bifilm index and morphology of primary Si.

Acknowledgment

The authors would like to thank AN-MET METALURJİ MAKİNE for their support in this study.

REFERENCES

1. Matsuura, K., et al., *Precipitation of Si particles in a super-rapidly solidified Al–Si hypereutectic alloy.* Materials Chemistry and Physics, 2003. **81**(2–3): p. 393-395.
2. Xu, C.L. and Q.C. Jiang, *Morphologies of primary silicon in hypereutectic Al–Si alloys with melt overheating temperature and cooling rate.* Materials Science and Engineering A, 2006. **437**: p. 451-455.
3. Li, Q., et al., *Effect of rare earth cerium addition on the microstructure and tensile properties of hypereutectic Al–20%Si alloy.* Journal of Alloys and Compounds, 2013. **562**(0): p. 25-32.
4. Chien, C.W., et al., *Effects of Sip size and volume fraction on properties of Al/Sip composites.* Materials Letters, 2002. **52**(4–5): p. 334-341.
5. Shi, W.X., et al., *Effect of Nd on microstructure and wear resistance of hypereutectic Al–20%Si alloy.* Journal of Alloys and Compounds, 2010. **508**(2): p. 480-485.
6. Zhao, L.Z., et al., *Ultra-fine Al–Si hypereutectic alloy fabricated by direct metal deposition.* Materials & Design, 2014. **56**(0): p. 542-548.
7. Hu, X., et al., *Effects of rare earth Er additions on microstructure development and mechanical properties of die-cast ADC12 aluminum alloy.* Journal of Alloys and Compounds, 2012. **538**(0): p. 21-27.
8. Ward, P.J., et al., *Semi-solid processing of novel MMCs based on hypereutectic aluminium-silicon alloys.* Acta Materialia, 1996. **44**(5): p. 1717-1727.
9. Kang, H.S., et al., *Microstructure selections in the undercooled hypereutectic Al–Si alloys.* Materials Science and Engineering: A, 2005. **404**(1–2): p. 117-123.

ASSESSMENT OF MECHANISM OF PORE FORMATION IN DIRECTIONALLY SOLIDIFIED Al-Si ALLOY

Muhammet ULUDAĞ*, Derya DIŞPINAR**

* Selcuk University, Faculty of Engineering–Metallurgical and Materials Eng. Dept., Konya-Turkey, uludag@selcuk.edu.tr
** Istanbul University, Faculty of Engineering, Metallurgical and Materials Eng. Dept., Istanbul-Turkey, deryad@istanbul.edu.tr

ABSTRACT
It is well-known that the better the control of the liquid aluminum, better the properties. One of the most important defects that is held responsible for lower properties has been the formation of porosity. Porosity has always been associated with the amount of dissolved hydrogen in the liquid. However, it was shown that hydrogen was not the major source but only a contributor the porosity. In this work, a cylindrical mould was designed (Ø30 x 300) from die. Water cooled copper chill was places at the bottom of the mould. After the melt was prepared, reduced pressure test sample was taken to measure the melt quality (i.e. bifilm index). The cast parts were then sectioned into regions and longitudinal and transverse areas were investigated metallographically. The formation of porosity was evaluated by means of bifilm content, size and distribution in A357 alloy.

Keywords: Directional solidification, Porosity, Bifilm index, Grain refinement, Casting

YÖNLENDİREREK KATILAŞTIRILAN Al-Si ALAŞIMLARINDA POROZİTE OLUŞUM MEKANİZMASININ İNCELENMESİ

ÖZET
Otomotiv endüstrisi başta olmak üzere çok sayıda endüstriyel alanda kullanılan A357 alaşımının, üretim süreci ne kadar iyi kontrol edilirse malzeme özelliklerinin de o kadar yüksek olacağı birçok araştırmacı tarafından dile getirilmiştir. Bu alaşımların üretiminde karşılaşılan en büyük problemlerden birisi porozite oluşumudur. Sıvı metalde hidrojen çözünürlüğü ne kadar yüksek olursa döküm parçasında porozite miktarı o kadar fazla olduğu ileri sürülmektedir. Bu çalışmada, Ø30x300mm boyutlarında silindirik modelin kokil kalıplarına dökümler yapılmıştır. Katılaşmayı yönlendirmek amacıyla kalıbın alt tarafına yerleştirilen bakır çil içerisinden sürekli olarak oda sıcaklığında olan su geçirilmiştir. Dökümler, gaz gidermeli-gidermesiz, tane inceltme işlemi uygulanarak yapılmıştır. Her parametre için RPT (azaltılmış basınç testi) numuneleri alınmıştır. Yönlenmiş katılaşma numuneleri belli aralıklarla bölünmüş her kesim bölgesinde hem dikey hem de yatay olarak makro incelemeler yapılmıştır. Elde edilen verilerle, soğuma hızına bağlı olarak tane incelticilerin etkisi ve porozite oluşum mekanizmaları ortaya çıkartılmıştır. Kokil kalıp dökümünde oluşacak soğuma hızlarının katılaşmanın yönlenmesi üzerine etkisi incelenerek, porozite oluşumları ile bifilm indeksi arasında ilişki araştırılmıştır.

Anahtar Kelimeler: Yönlenmiş katılaşma, Porozite, Bifilm indeks, Tane inceltme, Döküm

1. INTRODUCTION

Al-7Si alloys are used in many parts of automobiles such as wheels. The properties of this alloys depend on the microstructure during solidification and chemical composition [1]. The microstructure is a function of rate of advancement of solid/liquid interface (i.e. cooling rate) and its direction is opposite the heat flow [2]. Therefore, typical parameters that are studied can be listed as heat flow and mass flow. In this way, the amount of shrinkage can be minimised by means of analysing the defects in a directional solidification apparatus. Large risers, a casting thickness gradient, insulating sleeves and chills can be used to achieve such conditions [3].

Typically, it has been aimed to obtain finer grain structure by addition of grain refiners. It has been shown that the level of impurity decrease with increased area of grain boundary and decreased grain size [4]. For Al-Si alloys, Al-Ti-B grain refiners can be added to alter the coarse α-Al to finer dendrites without changing the morphology of eutectic Si [5].

As an alternative to Ti grain refinement, Al-3B alloy can also be used. This master alloy contains B, AlB_2 and AlB_{12} particulates. AlB_{12} can be unstable depending on the B content of the melt; and reacts with Al to form AlB_2 which is a peritectic reaction [6, 7].

Dispinar [8] has carried out an extensive study with reduced pressure test (RPT) and showed that hydrogen was not the major source of porosity. He proposed an index that could be used to quantify aluminium melt quality by measuring the sum of maximum length of pores and called it bifilm index [9].

In this work, Al-7Si-0.3Mg alloy was used to investigate the porosity distribution in directional solidification. Grain refiners were added and the effect of melt quality over the size and distribution of porosity was also studied.

2. EXPERIMENTAL WORK

The composition of the alloy used in the experiments is given in Table 1. The alloy was a primary alloy obtained from a plant.

Table 1. Chemical composition of A357 alloy

Si	Fe	Cu	Mn	Mg	Zn	Ti	Al
6,60-7,40	0,20	0,02	0,03	0,30-0,45	0,04	0,08-0,14	Rem.

Copper chill with a water cooling channels was used in the experiments in order to create a directional solidification was shown in Figure 1. As seen in figure, two simultaneous castings were made where the dimension was Ø30 by 300 mm.

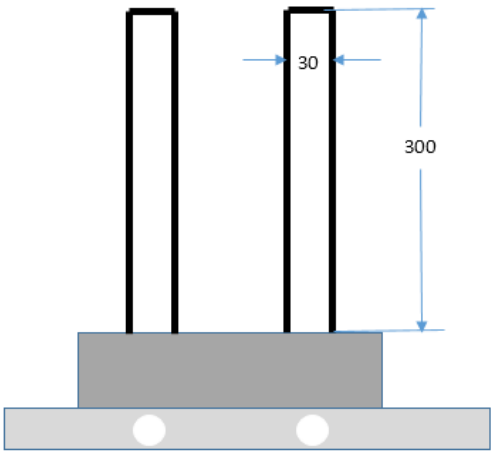

Figure 1. Directional solidification apparatus used in the experiments

After the castings were complete, sample collection was carried out from various heights and directions as shown in Figure 2. Five samples were horizontally cut which had 6 mm height. And each of these cylinders were sectioned into top and bottom; and left and right, in order to investigate the porosity vertically and horizontally.

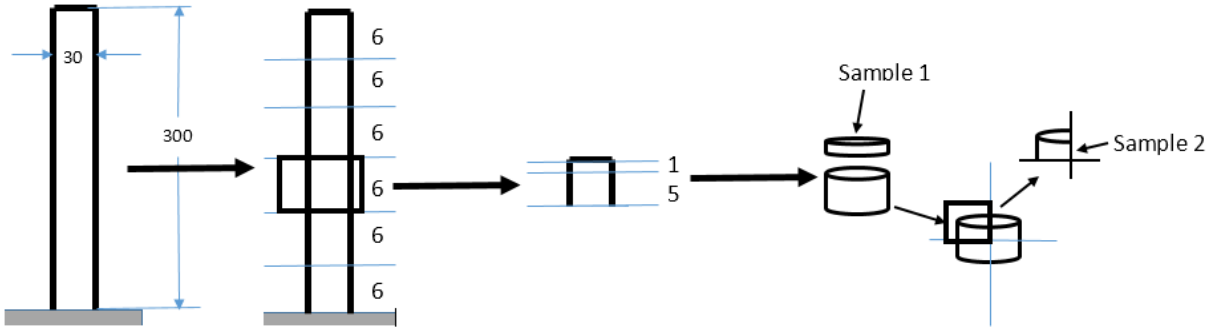

Figure 2. Preparation of sectioned surfaces of the cast part for examining

Two melts were prepared; one of them was modified with Ti grain refinement and other was modified with Ti-free B grain refiners. Degassing was carried out for 20 minutes with Ar and macrostructural investigations were made for each of the melts before and after degassing. Image analysis software (Clemex) was used to measure pore size and distribution.

Reduced Pressure Test (RPT) samples were collected at 80 mbar in a sand mould; and thereby, bifilm index measurements were made to correlate melt quality with the porosity distribution.

3. RESULTS and DISCUSSION

Bifilm index measurement results of both castings before and after degassing is given in Figure 3.

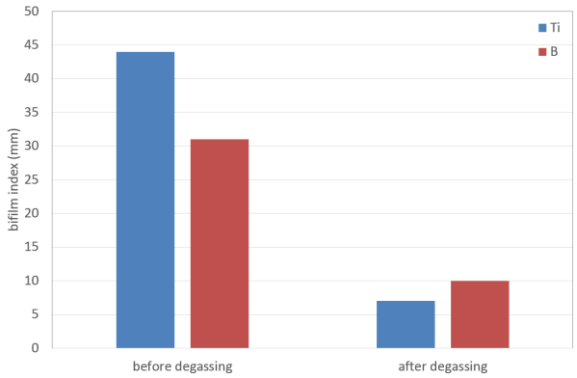

Figure 3. Bifilm index measurements

The macro images of the vertical sections of castings are given in Figure 4. In this figure, U1-U4 stands for the position of the sample, 1 being the top and 4 being the bottom.

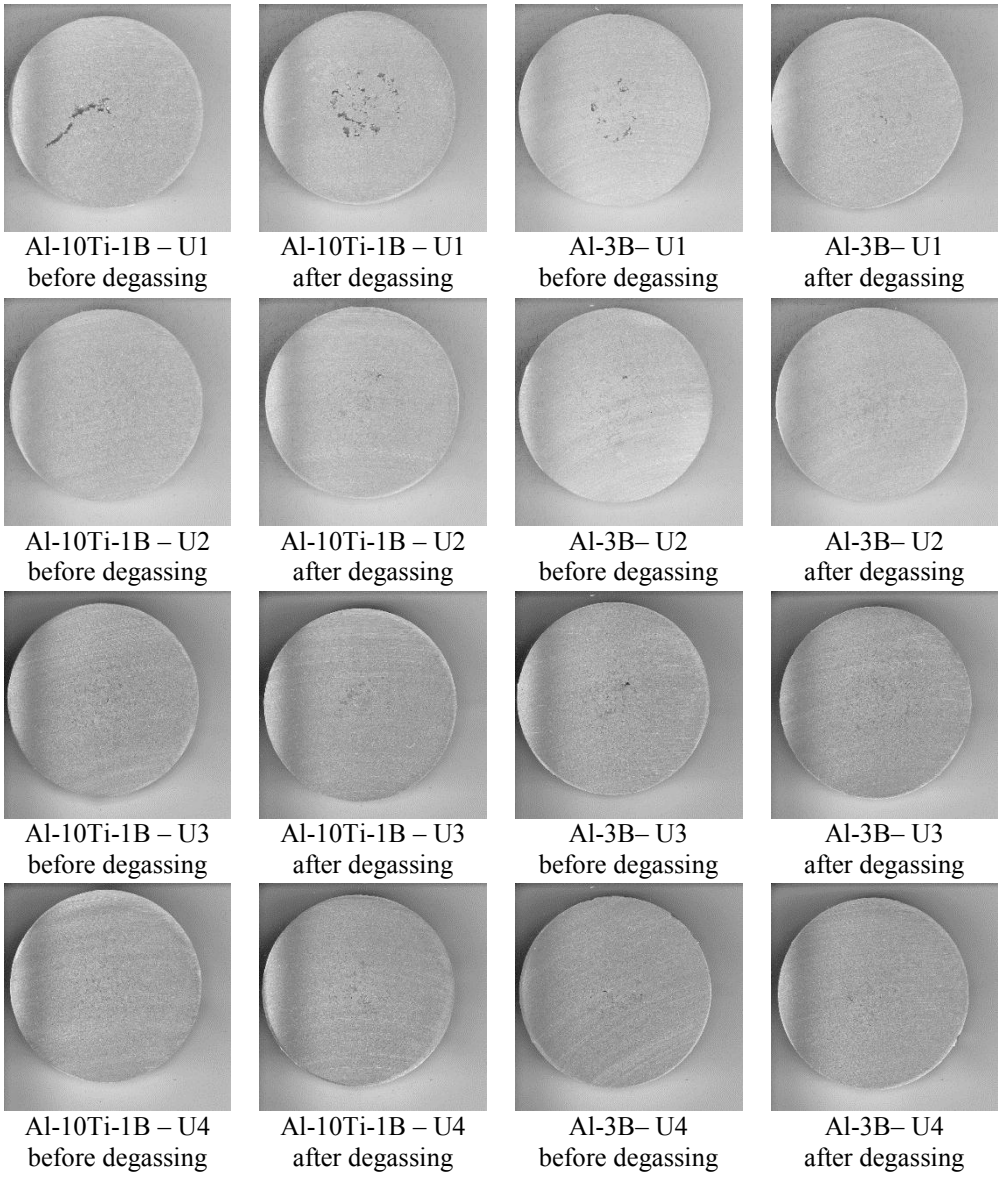

Figure 4. Top view (vertical) of directionally solidified samples at various heights

Pore size, number, area and distribution results obtained from Figure 4 is reported in Figure 5.

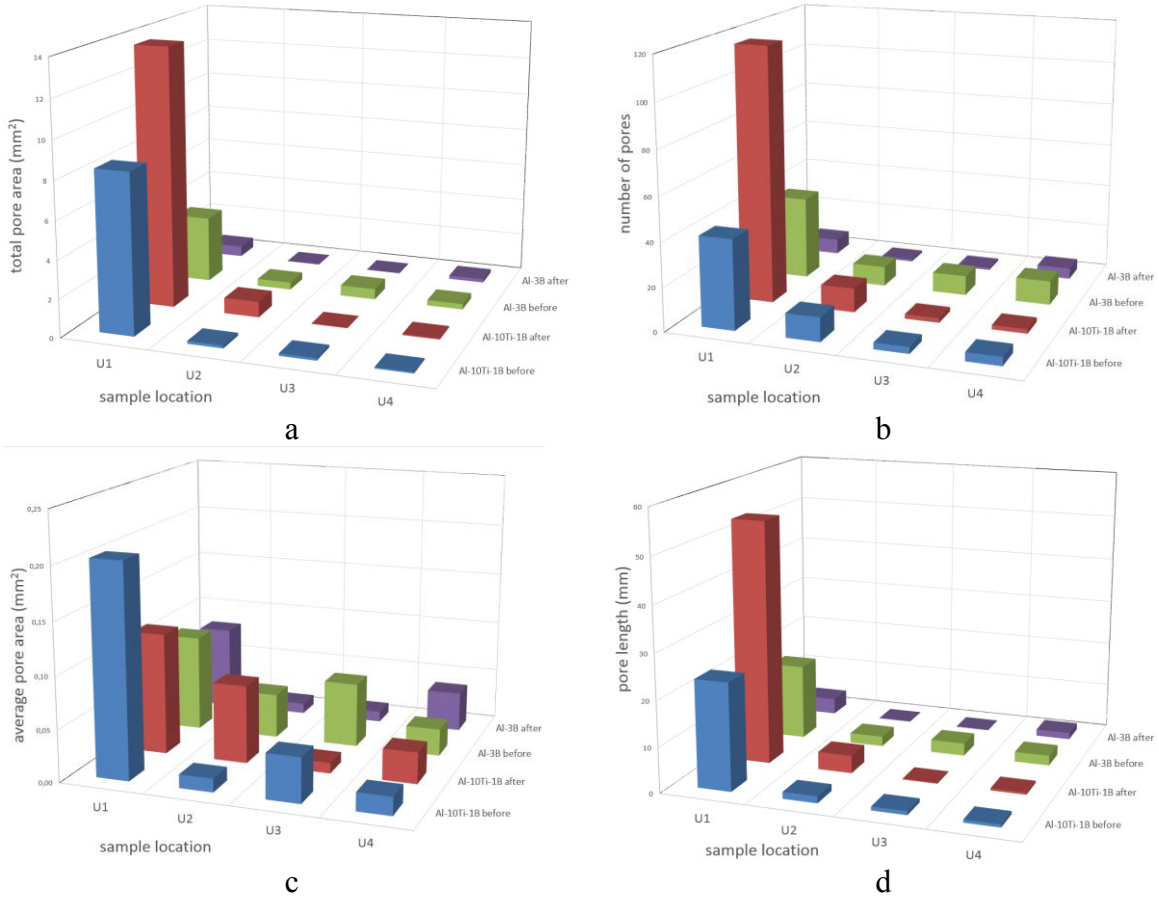

Figure 5. Porosity results of samples taken from the vertical sections.
a) total pore area, b) number of pores, c) average pore area,
d) pore length (Before and after donates to "degassing")

The examinatıon of pore distribution on the vertical plane with regard to the position (height) of the sample was summarised in Fig 4 and 5. It can be seen that as the height from the bottom is increased (i.e. counter gravity direction), the size and distribution of porosity increased. This is expected since the action of gravity and metallostatic head pressure should be the highest at the bottom of the cast part and thus even if there any porosity, it would be diminished under these effects. It can also be seen that highest number of pores, total pore area, average pore area and pore length were achieved by Ti grain refined castings. When the same alloy was modified with Ti-free B, these values were dropped. It is interesting to note that as seen in Fig 3, Ti grain refined melt had the highest bifilm index indicating that the melt quality level lower than B grain refined melt. Thus, the conclusion that Ti grain refinement causes higher porosity than B grain refinement may not be a solid result.

The macro images of the horizontal sections of castings are given in Figure 6. In this figure, U1-U4 stands for the position of the sample, 1 being the top and 4 being the bottom.

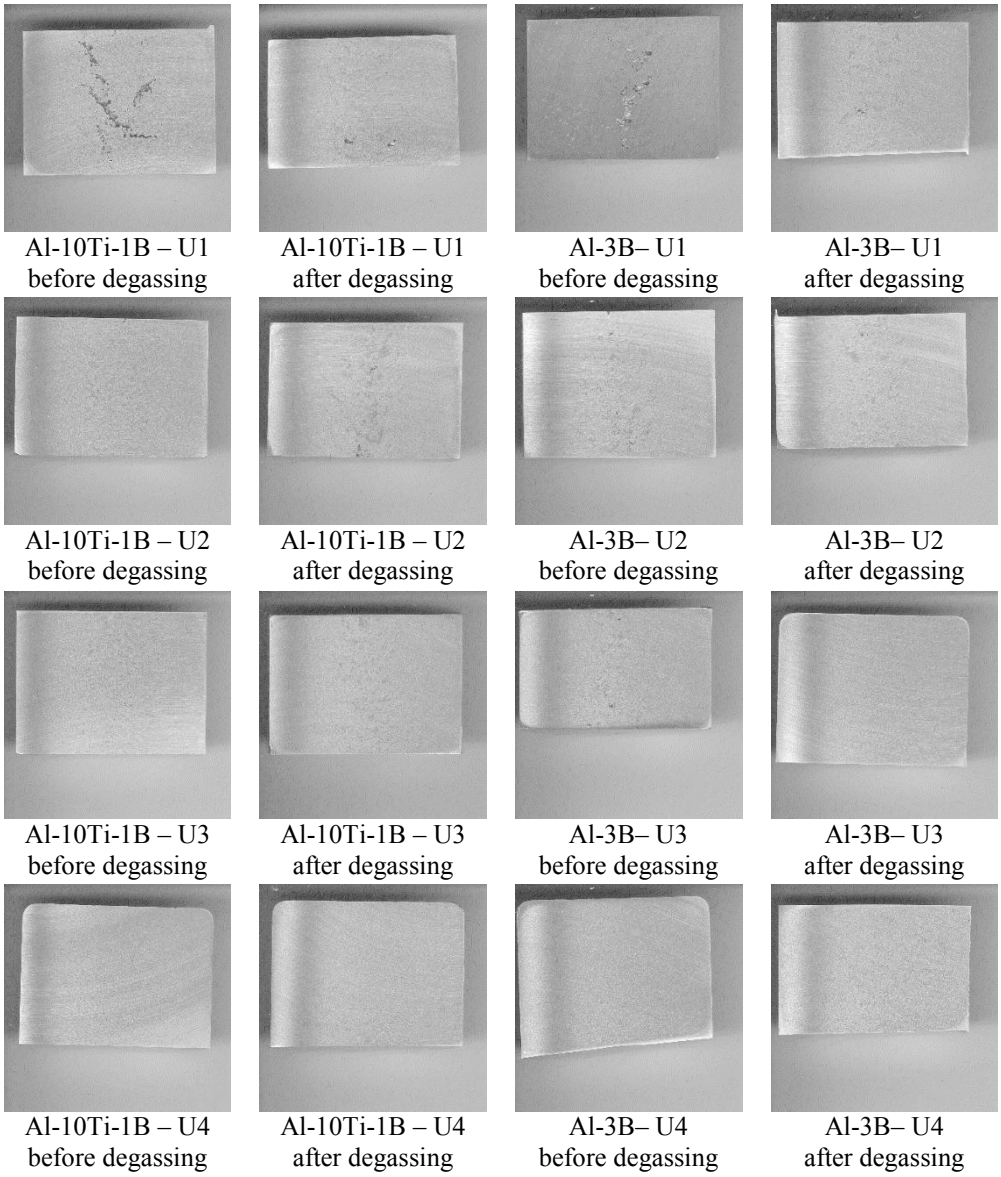

Figure 6. Side view (horizontal) of directionally solidified samples at various heights

Pore size, number, area and distribution results obtained from Figure 6 is reported in Figure 7.

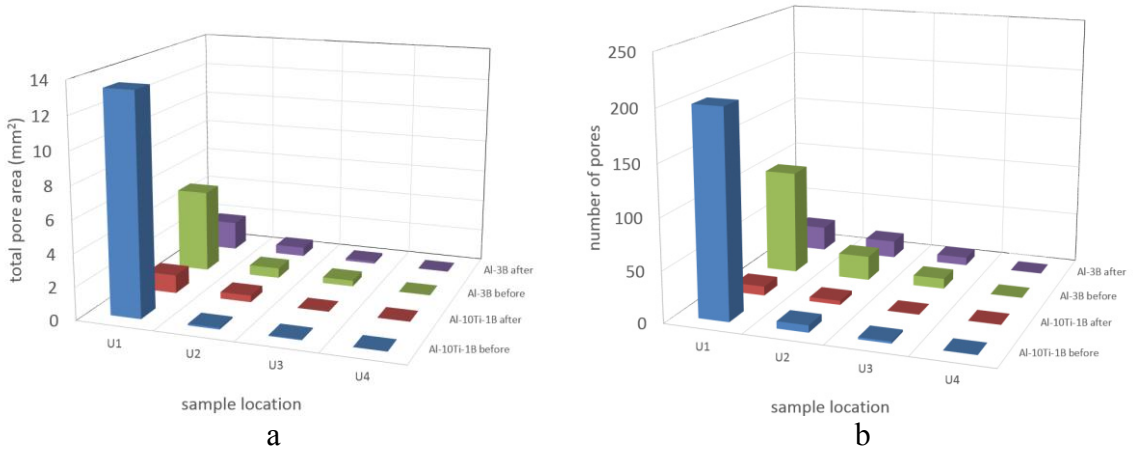

a b

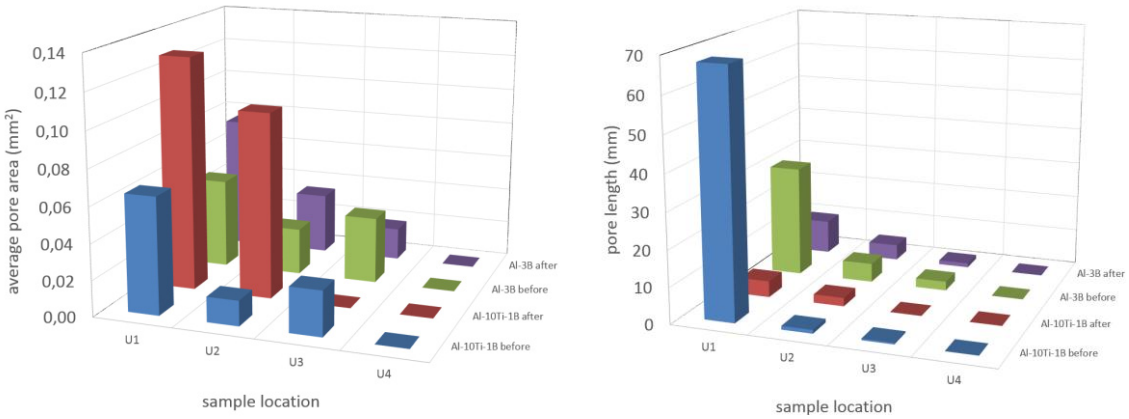

c d

Figure 7. Porosity results of samples taken from the horizontal sections.
a) total pore area, b) number of pores, c) average pore area,
d) pore length (Before and after donates to "degassing")

The size and distribution of pores along the Z axis (horizontal examination) is far more linear than the X-Y axis (vertical examination) results. In Fig 4 and 5, there is not much clear relationship between the height (position) of the sample and the pore parameters. However, in Fİg 6 and 7, the trend is linear. The pore parameters are linearly decreasing as the height is changed from top to the bottom of the cast part. This is true for both of the melts: Ti grain refined and B-grain refined.

This suggested that the pores that are forming along the solidification path (i.e. reserve direction to the heat flow), are more homogeneous and easy to predict. However, the size, shape and distribution of pores that are normal to the solidification path can have heterogeneous and unpredicted size and shapes. It is important to note that the most significant correlation was achieved between the bifilm index of the melt and porosity.

4. CONCLUSIONS

There is a good correlation between bifilm index and porosity formation in the directionally solidified Al-7Si-0.3Mg alloy. As the bifilm index increases, the number, size and area of porosity increases.

With the degassing of the melt, bifilm index was decreased because bifilms were removed from the melt and thus porosity was decreased.

Ti-free B grain refinement leads to lowered porosity in Al-Si alloys.

Acknowledgment

The authors would like to thank Metal Market Metalurji San.Tic.Ltd.Şti for their support in this study.

REFERENCES

1. Zimmermann, G., et al., *Effect of melt flow on dendritic growth in AlSi7-based alloys during directional solidification.* International Journal of Cast Metals Research, 2009. **22**(1-4): p. 335-338.

2. Dold, P. and K.W. Benz, *Rotating magnetic fields: Fluid flow and crystal growth applications.* Progress in Crystal Growth and Characterization of Materials, 1999. **38**(1): p. 7-38.

3. Goto, I., S. Horiuchi, and K. Anzai, *Defect formation mechanism in directional solidification method using chills and high temperature mould.* International Journal of Cast Metals Research, 2011. **24**(3-4): p. 243-246.

4. Campbell, J., *Castings : [the new metallurgy of cast metals]*. 2003, Butterworth Heinemann.

5. Kori, S.A., B.S. Murty, and M. Chakraborty, *Development of an efficient grain refiner for Al–7Si alloy and its modification with strontium.* Materials Science and Engineering: A, 2000. **283**(1–2): p. 94-104.

6. SIGWORTH, G. and G. MM, *Grain refinement of hypoeutectic Al-Si alloy [J]*. AFS Transaction, 1985. **93**: p. 907-912.

7. WANG, X., *The formation of AlB2 in an Al-B master alloy [J]*. Journal of Alloys and Compounds, 2005. **403**: p. 283-287.

8. Dispinar, D. and J. Campbell, *Use of bifilm index as an assessment of liquid metal quality.* International Journal of Cast Metals Research, 2006. **19**(1): p. 5-17.

9. Dispinar, D., et al., *Degassing, hydrogen and porosity phenomena in A356.* Materials Science and Engineering A, 2010. **527**(16-17): p. 3719-3725.

CORROSION RESISTANCE OF HYBRID SILICA SOL GEL COATINGS ON MILD STEEL

Sebahattin KIRTAY

Istanbul University, Turkey
kirtay@istanbul.edu.tr

ABSTRACT

Dip coating technique was used to produce hybrid silica sol gel coatings on mild steel substrate which were heat treated at 200 °C. The coating sols were synthesised using Glycidoxypropyltrimethoxysilane (glymo) and Aminopropylethoxysilane (ameo) as precursor materials. Electrochemical Impedance Spectroscopy technique (EIS) was applied to 3.5 wt% NaCl solution. The surface and cross-section morphology of coated specimens were characterized by scanning electron microscopy (SEM). Fourier transformed infrared (FTIR) analysis was used to identify the functional groups in the coating solutions. The measurements showed that the corrosion resistance of the coated mild steel was improved. The EIS data showed a noticeable increase in R_{cor} value and a low value of CPE_{dl} implied a better corrosion protective ability of the ameo coating as compared to mild steel. The measured values of the electrochemical parameters indicated that the coating film increased the resistance of mild steel against corrosion. The coating film was noted to be smooth and its thickness varied between 1.8-2 µm.

Keywords: Corrosion, Hybrid coating, Ormosil, Mild steel, Sol gel.

DÜŞÜK KARBONLU ÇELİĞE YAPILAN HİBRİD SİLİKA SOL JEL KAPLAMALARIN KOROZYON DİRENCİ

ÖZET

Bu çalışmada, düşük karbonlu çeliğe dip coating yöntemiyle hibrid silika sol jel kaplamalar yapılmış ve kaplanan numunelere 200 °C'de ısıl işlem uygulanmıştır. Kaplama çözeltilerinin hazırlanmasında Glycidoxypropyltrimethoxysilane (glymo) and Aminopropylethoxysilane (ameo) kullanılmıştır. Kaplanmış ve kaplanmamış numunelere ağırlıkça % 3.5 NaCl içeren çözeltide Elektrokimyasal Empedans Spektroskopisi (EIS) analizleri yapılmıştır. Kaplanmış numunelerin yüzey ve kesit görünümleri taramalı elektron mikroskobunda (SEM) incelenmiştir. Kaplama çözeltisinin jelleştirilip kurutulup ve öğütülmesiyle elde edilen tozlar kullanılarak kaplama çözeltisindeki fonksiyonel grupların tanımlanması Fourier transformed infrared (FTIR) analizi ile gerçekleştirilmiştir. Yapılan ölçümler ile kaplanmış numunelerin korozyon dirençlerinin arttığı gösterilmiştir. EIS sonuçları incelendiğinde ameo ile yapılan kaplamanın artan R_{cor} ve düşük CPE_{dl} değere sahip olduğu, bunun da kaplanmamış numuneye göre daha iyi korozyon direnci sağladığı belirlenmiştir. Ayrıca kaplama kalınlığının da 1.8-2 µm arasında değiştiği tespit edilmiştir.

Anahtar kelimeler: Korozyon, Hibrid kaplama, Ormosil, Düşük karbonlu çelik, Sol jel.

1. INTRODUCTION

One of the most common problems in the industry is the damage in materials due to corrosion which occurs as a result of decomposition of metal by chemical or electrochemical reactions. Corrosion cannot be avoided but delayed by applying various techniques such as the heat and rate reduction, removal of oxygen or oxidizing materials and changing the concentration of the working environment. There are also inhibitors that can be added in small amounts into the corrosion environment to reduce the corrosion rate. Furthermore, anodic and cathodic protection methods can be applied to improve corrosion resistance [1].

In recent years, surface coating methods have been widely used to protect materials from corrosion. Ceramic materials are preferred choice of coating materials because they exhibit protection from high temperature oxidation, corrosion and wear [2].

Today, different technologies are used for coating of metallic materials. Sol-gel based coatings are used to produce amorphous or crystalline oxide coatings that gelify by using chemical reactions, followed by the conversion of these materials into oxides by heat treatment. Sol-gel coatings provide enhanced protection for the substrate surface. In addition, the incorporation of organic groups made the coating to be flexible and these can be cured at low temperatures which reduces the micro-cracks [3-5]. Silicon alkoxides such as $Si(OR')_4$ and $R_nSi(OR')_{4-n}$ are typically used as source of the monomers due to their rapid hydrolysis features. Organosilanes with phenyl, amino, carboxyl, are commonly used as organically modified silicate (ormosil) materials [6]. The sol-gel method is a relatively simple process that allows the deposition of vitreous, ceramic and organic inorganic hybrid dense layer on different substrates below 500 °C [7]. It has been reported that sol gel coatings have been successfully applied to improve corrosion and wear resistance in metals [2, 8]. Coating material such as zirconium oxide [9], borosilicate [10], alumina silicate [11], cerium [12], TiO_2 [13] and SiO_2 [14] have been reported to offer corrosion protection.

In the presented study, steel specimens were coated with two different ormosil based solution by applying sol-gel dip coating method. This was followed by heat treatment at 200 °C, in order to study their performance and behaviour as a barrier against wet corrosion in 3.5 wt% NaCl solution. Corrosion characteristics were assessed through the use of EIS impedance analysis of electrochemical parameters. The remaining sols were allowed to gelify at room temperature and ground to obtain suitable samples for the FTIR analysis.

2. EXPERIMENTAL PROCEDURE

A AISI 1005 steel having a 0.8 mm thickness was coated with two different ormosil based solutions. Samples were withdrawn at different speeds from the coating solutions. Thus, different coating thicknesses were obtained. Table 1 shows the result of spectral analysis of mild steel used in the experiments.

Table 1. Spectral analysis of mild steel (wt %)

C	Si	Mn	P	S	Cu	Al
0,0257	0,0107	0,1709	0,01	0,0052	0,0437	0,0512

In this study, two different ormosil based coating solutions that included SiO_2 were prepared. The chemical compositions of these sols are given in Table 2.

Table 2. Chemical composition of sols (mole)

Glycidoxytrimethoxysilane ($C_9H_{20}O_5Si$)	**H_2O**	**C_2H_5OH**
0,1	0,2	3
Aminoproplyethoxysilane ($C_9H_{23}NO_3Si$)	**H_2O**	**C_2H_5OH**
0,2	0,4	2

In the preparation of the solutions the first step was the mixing of ethanol and distilled water for 30 minutes at room temperature using magnetic stirrer in a beaker. Glycidoxypropyltrimethoxysilane (glymo) (Merck 841807) was slowly added to one of the two solutions. Aminopropylethoxysilane (ameo) (Merck 821619) was slowly added to the second solution. Solutions were then stirred for 1 h. The degree of hydrolysis which is defined as water / alkoxide ratio (R) was taken to be 2 for each solution (see Table 2). After 12 hours of dwell time, samples were coated with the prepared coating sols.

Reactions comprising hydrolysis and polymerization in the solution and the steel / coating bond structure at the interface were investigated.

Gelation process was carried out at room temperature. Gels were ground and heat treated at 100, 200, 300 and 400 °C temperatures. The presence of functional groups in the gel was analysed using FTIR (Perkin Elmer Spectrum 100) in a frequency of 4000 - 400 cm^{-1}.

The samples were sectioned to the dimensions of 10 x 40 mm. Prior to the coating process, in order to clean surfaces, samples were placed in a beaker at 80°C that contained 1:1 mixture of HCl and distilled water; and held for 30 minutes. After this period, the samples were cleaned with distilled water and preserved in acetone to protect oxide formation.

The coating process was carried out by a computer-controlled KSV type dip coating apparatus with 100, 500 and 1000 mm / min withdrawn speeds. The samples were immersed in the solution in an upright position with a standby time of 200 seconds to ensure that both sides were coated. The samples were then subjected to pre-drying at 60 °C incubator for 15 minutes, followed by heat treatment at 200 ° C for 1 h in Protherm PID controlled furnace. The samples were taken out from the furnace to cool to room temperature. In order to determine the corrosion properties of the coated specimens, corrosion tests of uncoated samples were also carried out for comparison.

Thickness measurements of the coatings were characterized by Jeol JSM 5600 Scanning Electron Microscope (SEM).

The electrochemical measurements of both coated and uncoated specimens were investigated by means of open circuit potential (E_{ocp}) variation with time, Electrochemical Impedance Spectroscopy (EIS) in a 3.5 wt% NaCl solution using Gamry PCI4G750 potentiostat. The analysis was carried out at room temperature in a standard electrochemical cell equipped with a frequency response analyzer module. A three-electrode cell including a saturated calomel electrode as a reference electrode, graphite bar as a counter electrode and the specimens as a working electrode were used in the experiments. EIS measurements were carried out from open circuit potential with an AC voltage amplitude of 10 mV and a frequency range of 100.000 to 0.01 Hz (ten points were measured for each decade of frequency). Free corrosion potential measurements were made approximately 2 hours and then polarization resistance

was measured. Different parameters related to impedance measurements were derived from a curve fitting method using Gamry Echem. analyst software.

3. RESULTS AND DISCUSSION

Hydrolysis and polymerization reactions occurred simultaneously during the preparation of coating solutions. Si-OR groups were reacted with water in the environment during the hydrolysis reaction to form Si-OH. Meanwhile, polymerization reactions began in the solution. Si-OH, OH-Si or Si-OR, OH-Si groups in the solution were merged by creating Si-O-Si bonds. ROH or H_2O was released from these reactions (polymerization). H_2O was again used for hydrolysis. During the coating process, the silanol groups of hydrolyzed silane interact both with themselves and with the hydroxyl groups (Fe-OH) on metal substrate (inter- condensation) through temporary weak hydrogen bonding. The formation of strong covalent bonds takes place during sintering [13, 15, 16]. This is schematically shown in Fig. 1. The initial bonding of the coating was established by Fe-OH and Si-OH (Fig 1a). After heat treatment, as seen in Fig 1b, Fe-O-Si bonds were formed. Fig 1c shows the bonding of amine group to the Fe substrate.

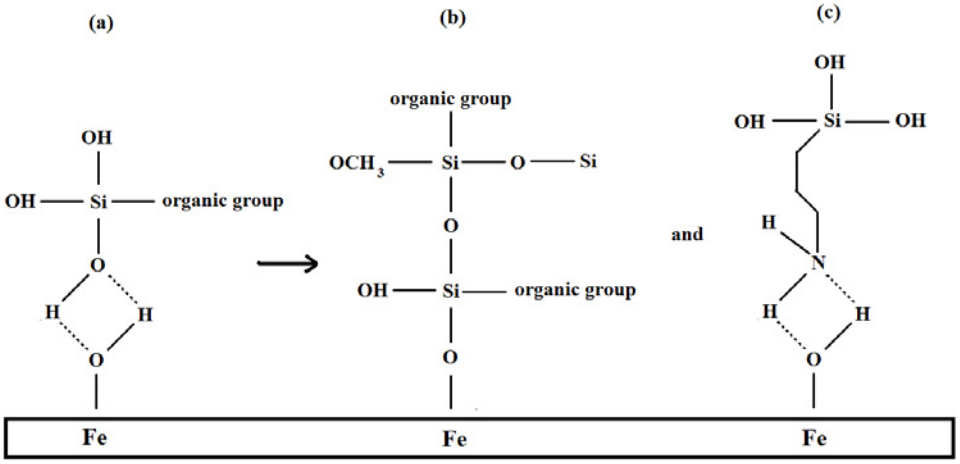

Figure 1. Schematical representation of chemical bond formed between metal and coating interface

Fig. 2 illustrates the FTIR spectra of ameo gel heat treated at 100 °C, 200 °C, 300 °C and 400°C temperatures. The absorption peaks at 3400-3600 cm^{-1} belong to H_2O and hydroxyl group vibrations. These were identified as O-H asymmetric stretching of ethanol. The small peak located at about 3300 cm^{-1} is due to the N-H stretching of ameo. The 3000-2800 cm^{-1} region shows the absorption bands of the CH_2 stretching from both ameo and ethanol. There is a band at 1600 cm^{-1} which belongs to NH_2 bending of ameo. Bands at 1400 cm^{-1} correspond to C-H vibrations. The broad bands between 1200-1000 cm^{-1} belong to Si–O (Si-O-Si and Si-O-C) stretching [13, 17]. With an increasing sintering temperature, the intensity of some peaks reduced significantly and they almost disappeared after sintering at 400°C. This indicates the removal of organic groups from the gels when heat treated at 300 and 400°C. On the other hand, gels still had the organic groups after sintering at 100 and 200 °C. The elasticity of the coating can be improved by the presence of organic groups in the coating which reduces stress and crack formation during sintering [18].

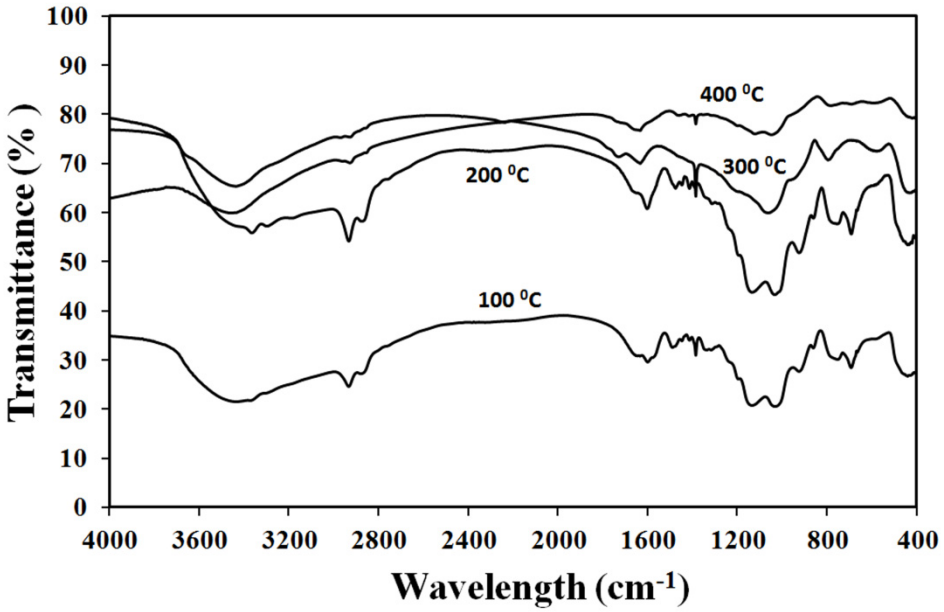

Figure 2. FTIR analysis of ameo gel heat treated at different temperatures

Fig.3 shows the SEM micrograph of the ameo coated specimen (1000 mm/min) heat treated at 200 °C. The coating thickness was measured to be around 1.8-2 µm.

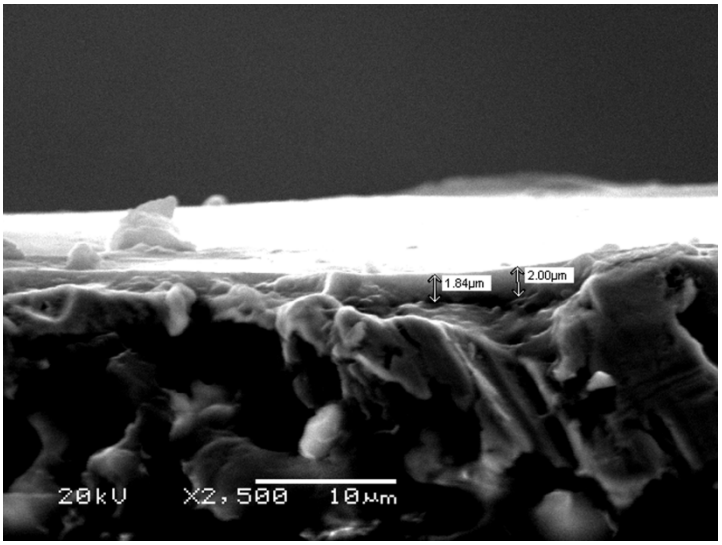

Figure 3. SEM micrographs of ameo coatings on the mild steel by the sol gel technique heat treated at 200 °C

The corrosion potential was calculated from intersection of cathodic and anodic Tafel curves (not given in this study)using Tafel extrapolation method and the corrosion rates of specimens were determined by Stern-Geary equation from the polarization measurements [19].

The corrosion currents, i_{corr}, corrosion potentials, E_{corr}, and corrosion rate values of both coated and uncoated specimens show that the i_{corr} values of the coating specimens were 3 to 33 times smaller than those of uncoated specimen.

To determine the mechanism of corrosion behaviour of mild steel and ormosil silica coatings, the electrochemical impedance spectroscopy was applied. Impedance measurement of the specimens was carried out at open circuit potential (E_{ocp}) where the samples were immersed in NaCl 3.5 wt% solution at room temperature. The results were analysed in Nyquist plots and Bode plots which are given in Figs. 4, 5a and b, respectively. Fig. 4 shows the capacitive-like depressed semicircle. The diameter of semicircle is associated with the corrosion resistance and, thus, the corrosion rate. A larger diameter leads to a higher corrosion resistance, i.e. a lower corrosion rate [20]. In Fig. 4, it can be seen that the largest diameter was obtained for the specimen coated with ameo.

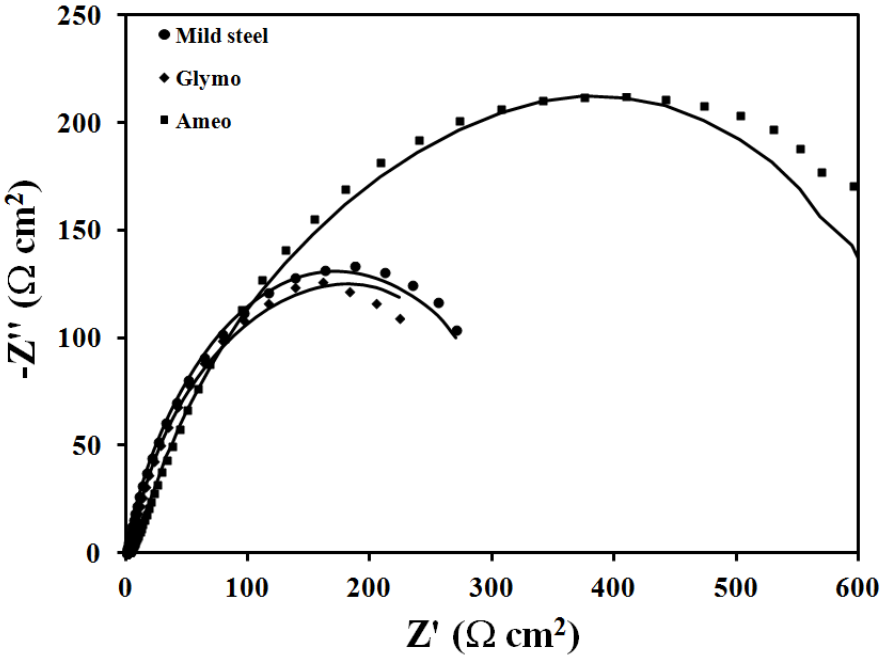

Figure 4. Nyquist plots for the mild steel and sol gel coated specimens

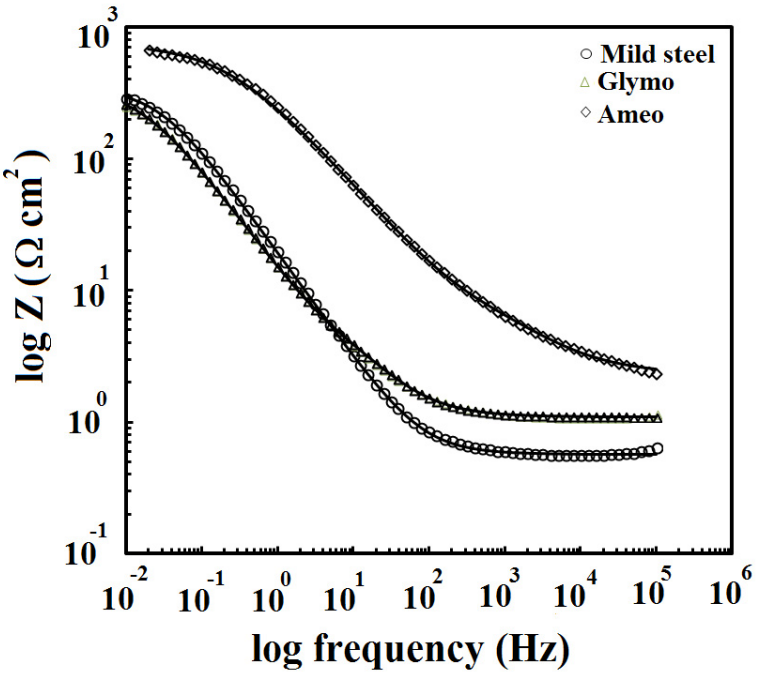

(a)

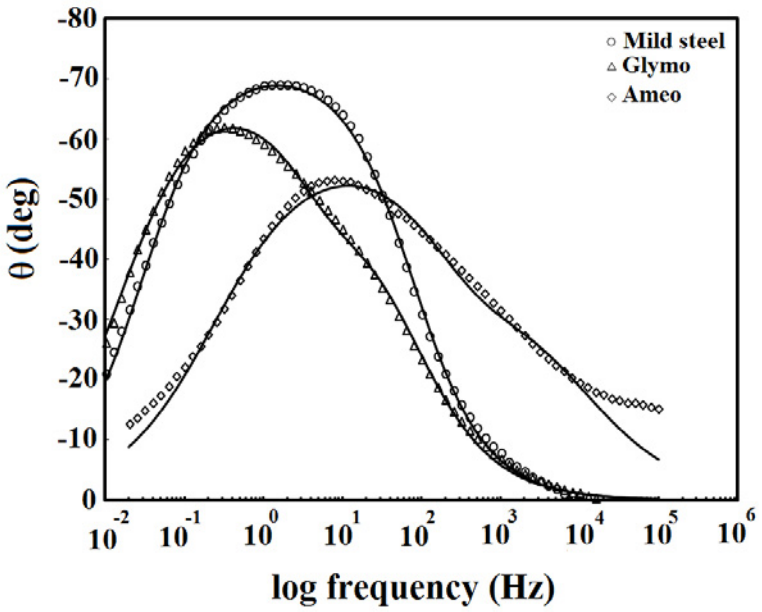

(b)

Figure 5. Bode impedance plots for mild steel and the sol gel coated specimens, (a) Bode modulus diagrams, (b) Bode phase diagrams

In comparison to the Nyquist plot, the Bode plot is more informative due to the simultaneous measurement of total impedance and phase angle with respect to the frequency. Bode plots are presented in Figs. 5a and b. Mild steel shows one time constant. However, after coating the mild steel with ameo and glymo, the spectrum shows a different Bode plot (Theta vs. freq.). This suggests that the system's response can be composed of two time constants: the one at higher frequencies can be associated with the coating's response resulting from the penetration of the electrolyte through pores or cracks; the second one at low frequencies can be attributed to the corrosion process. Only one time constant was observed for the mild steel and thus it was concluded that only one mechanism was valid for the corrosion process. This occurrence can be related to the electrolyte / steel surface interaction. It could also indicate that the corrosion of the specimens in NaCl solution is mostly controlled by a charge transfer process. Generally, the higher Z modulus at lower frequency indicates a better corrosion resistance [15]. In this study, the highest Z modulus was obtained from ameo coating as shown in Fig. 5a. When the phase angle is near 90°, the current predominantly passes through capacitor. In such a case, the electrochemical behaviour of metal / electrolyte interface can be considered as capacitive. It can be observed that the coated and uncoated samples show wide capacitive behaviour with phase angle values of -50°, -60° and -70° (Figs. 5a and b). In the case of capacitance, smaller value was observed for the coated samples compared to the mild steel (Table 3). The capacitive behaviour is related to the extent of water uptake. In the absence of the coating, the corrosion product layer formed on mild steel surface allows a continuous contact between the electrolyte and the substrate. This can be the main reason for the observance of a higher capacitance, i.e. lower corrosion resistance for mild steel sample. In low frequency region, phase angle gradually decreases and finally reaches to -10°, -25° and -20° for coated and uncoated mild steel surfaces. It can be seen in Fig 5b that the ameo coating has the lowest phase angle. This can ultimately be attributed to the decrease of corrosion phenomena at coating / solution interface [2].

An equivalent circuit can be used to describe the electrochemical behaviour which is given in Figs. 6a and b as EIS fit results. Different parameters related to impedance measurement were derived by curve fitting method and these are given in Table 3. An equivalent circuit consisting of a resistor connected in series to a parallel connected resistor and capacitor for mild steel is shown in Fig. 6a. The simplistic circuit was applied to extract the impedance data due to the observation of one time constant in Bode plot (Fig. 5). In Fig. 6b, a circuit of a resistor connected in series to a parallel connected resistors and capacitors for coated samples is shown. In these equivalent circuits, R_s is the solution resistance. The corrosion resistance (R_{cor}) is the charge transfer process and CPE_{dl} is the non-ideal double layer capacitance occurring at steel or coating / electrolyte interfaces. Also, in Fig. 6b, the pore resistance (R_{po}) is the resistance of ion conducting paths such as pores and cracks developed in the coating. A coating capacitance (CPE_{coat}) describes the behaviour of the coating. A constant phase element (CPE) was used instead of capacitance due to the non-pure capacitance in the real electrochemical process. The CPE impedance is described by the following equation:

$$Z_{CPE} = 1/ Y_0(J\omega)^n \quad (1)$$

Where, ω is the frequency and Y_0 is the capacitance of the system. For a constant phase element, the exponent n is less than one [21]. Typically, n is close to 1, representing a capacitive characteristic of the interfaces. The solution resistances are very low around 0.5-2 Ω due to the highly conductive NaCl solution (Table 3).

CPE_{coat} is also related to the dielectric properties of coating. CPE_{coat} can be defined by equation 2.

$$CPE_{coat} = r.\varepsilon.\varepsilon_0.A /d \quad (2)$$

Where, ε_0 is the electrical permittivity, ε is the dielectric constant of the surface film, d is the film thickness, r is a roughness factor and A is the exposed area [22]. The dielectric constant of the surface film can vary depending on the chemical and physical nature of the film such as density of the film and type of bond formed with substrate [23]. The water uptake in coatings can be monitored by the increase of CPE_{coat} due to the increase of ε because the dielectric constant of water is around 80, higher than those of organic and inorganic coatings (in the range of 5–10) [24].

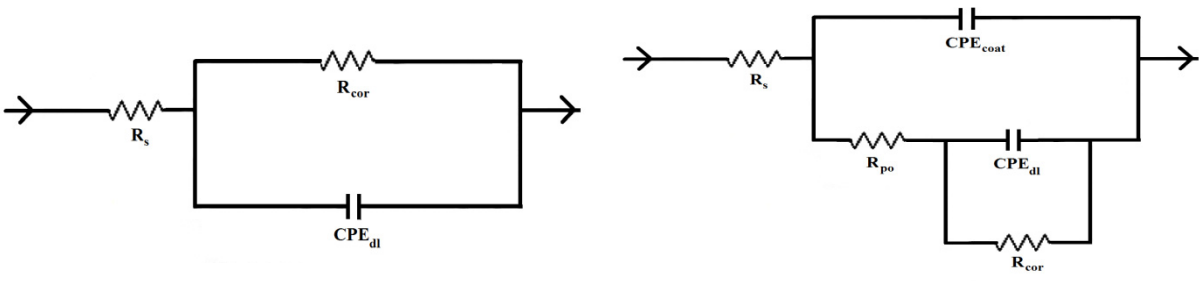

(a) (b)

Figure 6. Fitted and equivalent circuit on experimental data obtained from impedance, (a) mild steel, (b) ormosil silica coatings

Table 3. Different electrochemical parameters obtained by impedance analysis

Electrode	R_s (Ωcm^2)	R_{cor} (Ωcm^2)	R_{po} (Ωcm^2)	CPE_{dl}		CPE_{coat}	
				$Y_0(S.s^{-n})$ $x10^{-3}$	n	$Y_0(S.s^{-m})$	m
Mild steel	0.57	352	---	11.36	0.81	---	---
Glymo	1.09	351	9.6	5.58	0.83	0.01	0.75
Ameo	2.29	748	12.4	0.31	0.73	0.0007	0.62

R_{po} can be correlated with the compactness of the coating. Occurrence of lower R_{po} and high capacitance indicates the presence of a defective layer of corrosion products on the coating surface which may be attributed to the continuous diffusion of chloride ion at the metal/coating interface. In this work, R_{po} values of both coatings were low and close to each other. This may be due to the low sintering temperature or insufficient sintering time. Therefore, the decrease in the i_{corr} values of both coatings was limited to 3 to 33 times of the uncoated sample in this work.

Charge transfer processes took place on the substrate, which was covered with a sol-gel coating. The R_{cor} is affected by cracks or pores in the coating. Therefore, this is the most important parameter in the equivalent circuit as far as the corrosion protection is concerned. In this work, R_{cor} values of glymo and mild steel were calculated to be similar. This may be due to the presence of porosity and crack formation on the glymo coating surface which allows a continuous contact between the electrolyte and the substrate. R_{cor} value of ameo coating is about two times higher than those of mild steel and glymo coatings. The high values of R_{cor} and low values of CPE_{dl} imply a better corrosion protective ability of the ameo coating. The corrosion resistance of sol gel coated specimens appears to be improved appreciably.

The electrochemical studies (i. e. Tafel and EIS experiments) show that the coated samples have better corrosion behaviour compared to the uncoated sample. However, samples coated with ameo exhibit the highest corrosion resistance in NaCl solution. This may simply be related to the difference in specific characteristic of organic groups. Trabelsi et al. [25] reported that the metal surface conditions and organofunctional groups (e. g. amino groups) play an important role for the bonding between silane and metal surface. Balgude et al. [16] pointed out that the functional silanes like gamma-aminopropyltrimethoxysilane have better binding ability compared to non-functional silanes, such as propyltrimethoxysilane.

4. CONCLUSIONS

Aqueous organic-inorganic hybrid silica coatings on mild steel were prepared by sol-gel dip coating method by using glycidoxypropyltrimethoxysilane and aminopropyltriethoxysilane sols. It was observed that the thickness of the coating increased with increasing withdrawal speed. The coating film was found to be a maximum thickness of 1.8-2 μm was achieved.

The results showed that the specimens coated with ormosil sols possessed higher corrosion resistance than that of uncoated specimen. The i_{corr} values of the coated specimens were 3 to 33 times smaller than those of uncoated specimen. The ameo coated specimen heat treated at 200 °C exhibited the maximum R_{corr} (748 Ωcm^2). It was shown that the organic groups could

be removed from the sols by heat treatment above 300 °C. Furthermore, the elasticity of the coating was improved by the presence of organic groups in the coating which reduced stress and crack formation during the sintering.

ACKNOWLEDGMENT

This work was supported by Scientific Research Projects Coordination Unit of Istanbul University. Project number 3004.

REFERENCES

1. R.Z. Zand, K. Verbeken, A. Adriaens, Int. J. Electrochem. Sci., 8, 548, 2013
2. G. Ruhi, O.P. Modi, A.S.K. Sinha, I.B. Singh, Corr. Sci., 50, 639, 2008
3. M.A. Dominguez-Crespo, A. Garcia-Murillo, A.M. Torres-Huerta, F.J. Carrillo-Romo, E. Onfore-Bustamante, C. Yanez-Zamora, Electrochim. Acta., 54, 2932, 2009
4. L. Jianguo, G. Gaoping, Y. Chuanwei, Surf. Coat. Technol., 200, 4967, 2006
5. H. Wang, R. Akid, Corr. Sci., 49, 4491, 2007
6. M. Pagliaro, R. Ciriminna, M.W.C. Man, S. Campestrini, J. Phys. Chem. B, 110, 1976, 2006
7. A. Pepe, P. Galliano, S. Cere, M. Aparicio, A. Duran, Mater. Lett., 59, 2219, 2005
8. M. Fallet, H. Mahdjoub, B. Gautier, J.P. Bauer, J. Non-Cryst. Solids, 293-295, 527, 2001
9. K. Izumi, M. Murakami, A. Morita, J. Am. Ceram. Soc., 72, 1465, 1989
10. M. Guglielmi, D. Festa, P.C. Innocenzi, P. Colombo, M. Gobbin, J. Non-Cryst. Solids, 147-148, 474, 1992
11. S.I. Seok, J.H. Kim, K.H. Choi, Y.Y. Hwang, Surf. Coat. Technol., 200, 3468, 2006
12. M. Garcia-Heras, A. Jimenez-Morales, B. Casal, J.C. Galvan, S. Radzki, M.A. Villegas, J. Alloys Comp., 380, 219, 2004
13. T.K. Rout, N. Bandyopadhyay, R. Narayan, N. Rani, D.K. Sengupta, Script. Mater., 58, 473, 2008
14. Y.H. Koh, O.S. Kwon, S.H. Hong, H.E. Kim, S.K. Lee, J. Euro. Ceram. Soc., 21, 2407, 2011
15. Y. Mingming, H.Yedong, Z. Ying, Y. Qiuxia, J. Rare Earths., 24, 587, 2006
16. D. Balgude, A. Sabnis, J. Sol-Gel Sci. Technol., 64, 124, 2012
17. R. Pena-Alonso, F. Rubio, J. Rubio, J.L. Oteo, J. Mater. Sci., 42, 595, 2007
18. J. Gallardo, A. Duran, J.J. De Danberenea, Corr. Sci., 46, 795, 2004
19. M. Stern, A.L. Geary, J. Elecrochem. Soc., 104, 56, 1957
20. E. Samiento-Bustos, J.G. Gonzalez-Rodriguez, J. Uruchurtu, G. Dominguez-Patino, V.M. Salinas-Bravo, Corr. Sci., 50, 2296, 2008
21. A. Pepe, P. Galliano, M. Aparicio, A. Duran, S. Cere, Surf. Coat. Technol., 200, 3486, 2006
22. H. Hassannejad, T. Shahrabi, F. Malekmohammadi, A. Shanagi, M. Aliofkhazraei, A. Oskuie, Cur. Appl. Phys., 10, 1022, 2010
23. A.G. Kannan, N.R. Choudhury, N.K. Dutta, J. Electroanal. Chem., 641, 28, 2010
24. D.A. Lopez, N.C. Rosero-Navarro, J. Ballarre, A. Duran, M. Aparicio, S. Cere, Surf. Coat. Technol., 202, 2194, 2008
25. W. Trabelsi, L. Dhouibi, E. Triki, M.G.S. Ferreira, M.F. Montemor, Surf. Coat. Technol., 192, 284, 2005

PREPARATION AND ELECTROCHEMICAL EVALUATION OF HYBRID SiO_2-TiO_2 SOL GEL THIN FILM

Sebahattin KIRTAY

Istanbul University, Turkey
kirtay@istanbul.edu.tr

ABSTRACT

Organic-inorganic SiO_2-TiO_2 sol gel coatings were prepared and applied to mild steel substrate using dip coating technique and subsequently heat treated at 200 and 300 °C in order to improve the corrosion resistance. The coating sol were synthesized using Glycidoxypropyltrimethoxysilane and titaniumtetraisopropoxide. The corrosion resistance of both coated and uncoated samples were evaluated by the Tafel polarization in 3.5 wt% NaCl solution. The microstructures of coated specimens were characterized by scanning electron microscopy (SEM). Fourier transformed infrared (FTIR) analyses was used to identify the presence of various functional groups in the coating solution. The results showed that the corrosion potential (E_{corr}) was increased and corrosion current density (i_{corr}) was decreased. i_{corr} values of the coated specimens heat treated at 200 °C were between 6.9 and 9.2 times, similarly, i_{corr} values of the coated specimens heat treated at 300 °C were 4.4-5 times smaller than those measured for uncoated specimen. The results showed that the coating film increased the resistance of mild steel against corrosion. The thickness of the coating film was noted to be smooth and between 7.2-7.5 μm.

Keywords: Corrosion resistance, Hybrid coating, Mild steel, Sol gel, Tafel.

HİBRİD SiO_2-TiO_2 SOL JEL İNCE FİLM HAZIRLANMASI VE ELEKTROKİMYASAL ÖLÇÜMÜ

ÖZET

Korozyon direncinin arttırılması için organik-inorganik SiO_2-TiO_2 içeren sol jel kaplama çözeltisi hazırlanarak daldırma yöntemiyle düşük karbonlu çeliğe kaplanmıştır. Kaplanan numunelere 200 ve 300 °C 'de ısıl işlem yapılmıştır. Kaplama çözeltisinin hazırlanmasında Glycidoxypropyltrimethoxysilane ve titaniumtetraisopropoxide kullanılmıştır. Hem kaplanmış hem de kaplanmamış numunelerin korozyon dirençleri ağırlıkça % 3.5 NaCl çözeltisinde Tafel eğrileri ile incelenmiştir. Kaplanmış numunelerin mikroyapıları taramalı elektron mikroskobunda (SEM) incelenmiştir. Kaplama çözeltisindeki fonksiyonel gurupların tanımlanması Fourier transformed infrared (FTIR) analizi ile gerçekleştirilmiştir. Yapılan ölçümler sonucunda korozyon potansiyelinin (E_{corr}) arttığı ve korozyon akım yoğunluğunun (i_{corr}) düştüğü gösterilmiştir. Kaplanmış ve 200 °C'de ısıl işlem yapılmış numunelerin (i_{corr}) değerlerinin kaplanmamış numuneye göre 6.9 ile 9.2 kat, benzer şekilde kaplanmış ve 300 °C'de ısıl işlem görmüş numunelerin (i_{corr}) değerleri ise kaplanmamış numuneye göre 4.4-5 kat daha düşük olduğu bulunmuştur. Bu sonuçlar kaplamanın düşük karbonlu çeliğin korozyona karşı direncini arttırdığını göstermiştir. Yapılan kaplamaların kalınlıklarının maksimum 7.2-7.5 μm arasında olduğu belirlenmiştir.

Anahtar kelimeler: Korozyon direnci, Hibrid kaplama, Düşük karbonlu çelik, Sol jel, Tafel.

1. INTRODUCTION

Dagradation of materials due to corrosion is a big problem in the industrial applications. Corrosion is delayed by some techinques such as inhibitors that can be added in small amounts into the corrosion environment to reduce the corrosion rate, anodic and cathodic protection methods and removal of oxidizing materials of the working environment [1]. Coatings on metals and alloys have various properties such as wear resistance, high temperature stability and corrosion protection. By this time, different technologies are used for coating of metallic materials as physical vapour deposition, chemical vapour deposition and sol-gel etc.[2] . The sol-gel method is one of the most used techniques to produce amorphous or crystalline oxide coatings because of the homogeneous film obtained at low temperature, more feasible economically and wide compositions have been produced to expand some properties. Sol-gel coatings could provide enhanced protection for the substrate surface [3]. Also, the sol-gel coatings have been found in wide applications as optics, electronics and for the purpose of protection as well [2]. Recently, organic-inorganic hybrid coated materials produced by using sol-gel method have improved for corrosion protection.

Carbon steels are widely used as engineering materials. Although its good machinability, high thermal conductivity and superior mechanical strength, it has a poor corrosion resistance in aggressive solutions and atmospheres. Therefore, its service life is qualified. In recent years, surface coating methods have been widely used to protect materials from corrosion. Ceramic coating materials exhibited high temperature oxidation, corrosion and wear resistance which are higher than those associated with metals are preferred [4]. Zirconium oxide [5], borosilicate [6], alumina silicate [7], cerium [8], TiO_2 [9], Fe_2B [10], Al_2O_3 [11] and SiO_2 [12] have been studied as barriers against oxidation on metal substrates in literature.

Corrosion on metals occurs as chemical reactions between the metal surface and the environment. The presence of cracks on coating cause corrosion because of the penetration of corrosive materials that exist in the environment into the material. To prevent of crack formation on the coating, the thermal expansion coefficients of the coating material and the material to be coated need to be close. In addition, a dense oxide layer needs to be formed at low temperatures. Organic-inorganic hybrid coatings (ormosil) are widely used for such purposes [7,13,14].

In this paper, SiO_2-TiO_2(organic-inorganic) alcohol based coatings on mild steel were prepared by sol-gel processing. The specimens were coated by dip coating technique. The coated specimens were followed by heat treated at 200 and 300 °C, in order to study their performance and corrosion behaviour in 3.5 wt % NaCl solution. The corrosion characteristics have been utilized through the potentiodynamic polarization curves (Tafel plots). The microstructure and adherence of both coated and uncoated specimens were then investigated. The remaining sols were kept to gelify at room temperature and ground. Its heat treated at different temperatures such as 100, 200, 250, 300 and 350 °C for the Fourier transformed infrared (FTIR) technique analyses.

2. EXPERIMENTAL PROCEDURE

Mild steel (AISI 1005) having a thickness of 0.8 mm were coated with SiO_2-TiO_2 alcohol based ormosil solution. Samples were withdrawn at different speeds from the coating solution to obtain different coating thicknesses. Glicidoxytrimethoxysilane (Glymo)(Merck 841807), $Ti(OC_3H_7)_4$ (titanium tetraisopropoxide) (Merck 821895) were used sources for SiO_2 and TiO_2 respectively.

The chemical composition of the sol are given in Table 1. The preparation of the solutions was carried out as follows: first, 100 g GLYMO + 100 g C_2H_5OH + 8 g H_2O + 0.3 g HNO_3 were stirred for 8 minutes at room temperature using magnetic stirrer in a beaker. Then, 40 g $Ti(OC_3H_7)_4$ was slowly added to the mixture. After this stage, all the solutions were stirred for 10 minutes. Then, mixtures of 20 g H_2O and 60 g C_2H_5OH were added and all the solution stirred for 60 minutes. After 24 hours of dwell time, samples were coated with the prepared coating sols.

Table 1. Chemical composition of SiO_2-TiO_2 sol (wt %)

GLYMO ($C_9H_{20}O_5Si$)	**C_2H_5OH**	**H_2O**	**HNO_3**	**$Ti(OC_3H_7)_4$**
30.45	48.73	8.53	0.09	12.18

Samples were sectioned to the dimensions of 10 x 40 mm. Prior to the coating process, in order to clean surfaces, samples were placed in a beaker at 80°C that contained 1:1 mixture of HCl and water and held for 30 minutes. After this period, the samples were cleaned with distilled water and preserved in acetone to protect oxide formation.

Coating process was carried out by a computer-controlled KSV type dip coating apparatus with 100, 250, 500 and 1000 mm / min withdrawn speeds. Samples were immersed in the solution in an upright position with a standby time of 200 seconds. In this way, both sides of the samples were coated. The samples were then subjected to pre-drying at 60 ° C incubator for 15 minutes, followed by heat treatment at 200 and 300° C for 1 h in Protherm PID controlled furnace. The samples were taken out from the furnace to cool to room temperature. In order to compare the corrosion properties of the steel specimens were named as "original" in the figures.

The electrochemical measurements of the both coated and uncoated specimens were investigated by means of open circuit potential (E_{ocp}) variation with time, Tafel plots in a 3.5 wt% NaCl solution using Gamry PCI4G750 potentiostat. The analyses was carried out at room temperature in a standard electrochemical cell equipped with a frequency response analyzer module. A three-electrode cell including a saturated calomel electrode as a reference electrode, graphite bar as a counter electrode and the specimens as a working electrode were used in the experiments. The Tafel polarization curves were obtained from potentiodynamic polarisation at a constant scan rate of 1 mV/sec by sweeping the potential between +250 mV and -250 mV from open circuit potential. Free corrosion potential measurements were made about 2 hours and then polarization resistance was measured. The different parameters related to potantiodynamic polarization were derived from a curve fitting method using Gamry Echem. analyst software.

For thickness measurements, surfaces of the coatings and EDS analyses were characterized by Jeol JSM 5600 Scanning Electron Microscope (SEM).

Gelation process was carried out at room temperature. Gels were ground and heat treated at 100, 200, 250, 300 and 350 °C temperatures. The presence of functional groups in the gel was analysed using FTIR (Perkin Elmer Spectrum 100) in a frequency of 4000 - 400 cm^{-1}.

3. RESULTS AND DISCUSSION

Figs. 1 and 2 present the polarization curves for the ormosil SiO_2-TiO_2 coated and uncoated specimens heat treated at 200 and 300°C for 1 h, respectively. The open circuit potential (OCP) of the uncoated specimen was measured as -685.9 mV, the corresponding values for the coated specimens were among the -561.4 mV and -582.1 mV as shown in Fig. 1, E_{corr} values of coated specimens were -644.1 mV, -658.8 mV and -637.2 mV in Fig. 2. OCP decreased gradually with time up to 2 hours of immersion and then attained a steady state value. The higher the positive values, better the corrosion resistance in the OCP conditions [15,16]. In this work, it was found that E_{corr} values were in the range 27-124 mV high for the coated specimens (Figs. 1 and 2).

The corrosion potential was calculated from intersection of cathodic and anodic Tafel curves using Tafel extrapolation method and the corrosion rates of specimens were determined by Stern-Geary equation from the polarization measurements [17].

Different electrochemical parameters obtained by Tafel extrapolation are given in Table 2. Table 2 shows that the i_{corr} values of the coating specimens heat treated at 200 °C were between 6.9 and 9.2 times, 4.4 and 5 times heat treated at 300 °C smaller than those of uncoated specimen. This is simply due to the different thicknesses obtained by the different withdrawal speed in the Sol-gel dip coating method. The thickness of the coating increase with increasing withdrawal speed.

It was observed that all the values of the corrosion currents of the coated specimens were close. This shows that the critical coating thickness for protection was achieved. It is important to note that for heat treated at 200 °C coatings, the lowest corrosion current was obtained at 1000 mm/min withdrawal speeds among the coated samples. The i_{corr} values obtained at the sample that was heat treated at 300°C more twice as much for the sample heat treated at 200 °C. This is attributed to the crack formation on the surface of 300°C heat treated sample which is simply due to the removal of organic groups at this temperature. The increase in corrosion resistance of the specimens heat treated at 200 °C might be attributable to the thickness of the coatings and a denser microstructure formation from the ormosil sols. Similar polarization tests have been used for the SiO_2 and böhmite sols on the galvanized steel [7], ormosil based silica on the austempered ductile iron [13], yttria-stabilized zirconia on carbon steel sheets [15]. The corrosion behaviour of the specimens examined during the course of this study is in good agreement with the literature.

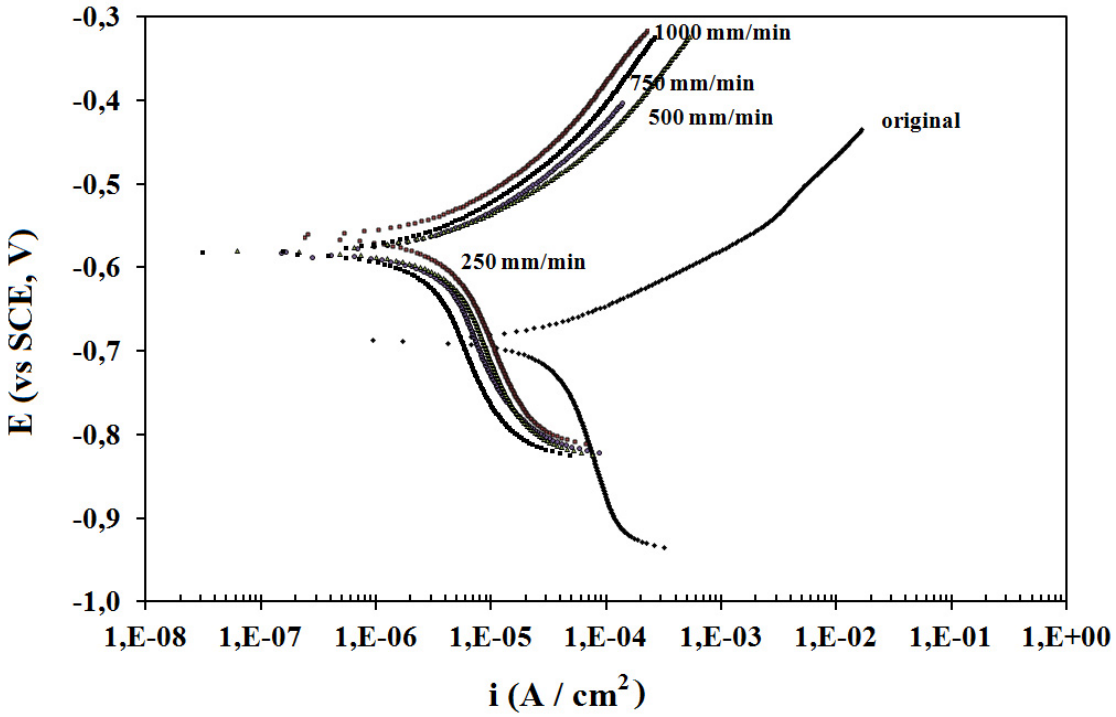

Figure 1. Polarization curves for the ormosil SiO_2-TiO_2 coated and uncoated specimens heat treated at 200 °C for 1 h.

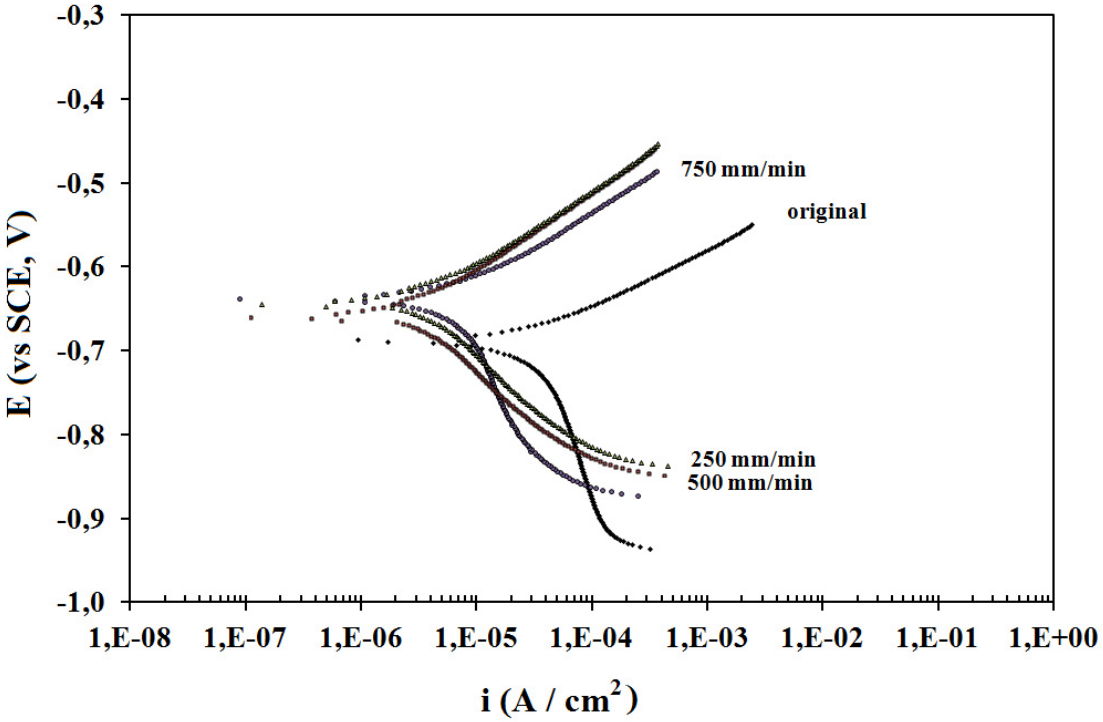

Figure 2. Polarization curves for the ormosil SiO_2-TiO_2 coated and uncoated specimens heat treated at 300°C for 1 h.

Table 2. Different electrochemical parameters obtained by Tafel extrapolation

Electrode	E_{corr} (mV)		i_{corr} (Acm^{-2})		Corr. rate (mm/year)	
Mild steel	-685.9		11.78×10^{-6}		0.1241	
	200 °C heat treated	**300 °C heat treated**	**200 °C heat treated**	**300 °C heat treated**	**200 °C heat treated**	**300 °C heat treated**
SiO_2-TiO_2 coated (250 mm/min)	-561.4	-644.1	1.382×10^{-6}	2.27×10^{-6}	0.0145	0.0240
SiO_2-TiO_2 coated (500 mm/min)	-578.7	-658.8	1.701×10^{-6}	2.539×10^{-6}	0.0179	0.0267
SiO_2-TiO_2 coated (750 mm/min)	-582.1	-637.2	1.479×10^{-6}	2.67×10^{-6}	0.0155	0.0281
SiO_2-TiO_2 coated (1000 mm/min)	-581.6	--	1.279×10^{-6}	--	0.0134	--

Fig. 3 illustrates the FTIR spectra of SiO_2-TiO_2 gel heat treated at 100, 200, 250, 300 and 350°C temperatures. The absorption bands in Fig. 3 due to the OH, CH_2, H-OH (free water), C-H and Si-CH_3 bonds are 3200-3600, 2800-3000, 1600-1800, 1390, 1210 cm^{-1}, respectively [18,19]. The absorption bands at 1000-1200 cm^{-1} and 950 cm^{-1} correspond to Si-O-Si and Si-O-Ti (and Si-OH) vibrations respectively. The characteristic peak for Si-O-Si bond is given as 1000-1200 cm^{-1} and for the Si-OH bond is given as 940-950 cm^{-1} [20]. In this study, the peak due to Si-O-Ti bonds stays unchanged up to 350°C heat treatment temperature. This indicates that the peak at 950 cm^{-1} is due to the Si-O-Ti bond. The FTIR spectra clearly revealed that the organic groups, Si-O-Ti and Si-O-Si bonds form in the gels heat treated at 200°C.

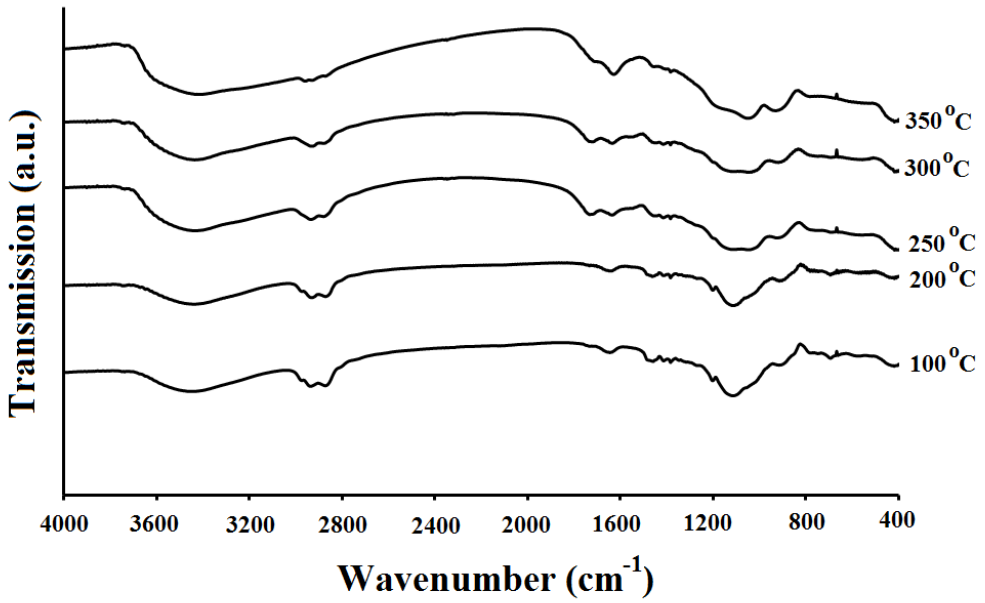

Figure 3. FTIR analyses of SiO_2-TiO_2 gel heat treated at different temperatures

Fig. 4 shows the SEM micrograph of the SiO_2-TiO_2 coated specimens surface heat treated at 200 °C (Fig 4a and b). The coating thickness was measured to be around 7.2-7.5 µm (1000 mm/min). As shown in the SEM images and FTIR analyses, organic groups are still present on the surface substrate after sintering at 200 °C. This is the evidence of presence of both organic and inorganic compounds on the coatings. It was seen that cracks formation on surface of coating heat treated at 300°C. This indicates the removal of organic groups from the coatings when heat treated at 300°C and above. The elasticity of the coating can be improved by the presence of organic groups in the coating which reduces stress and crack formation during sintering [21].

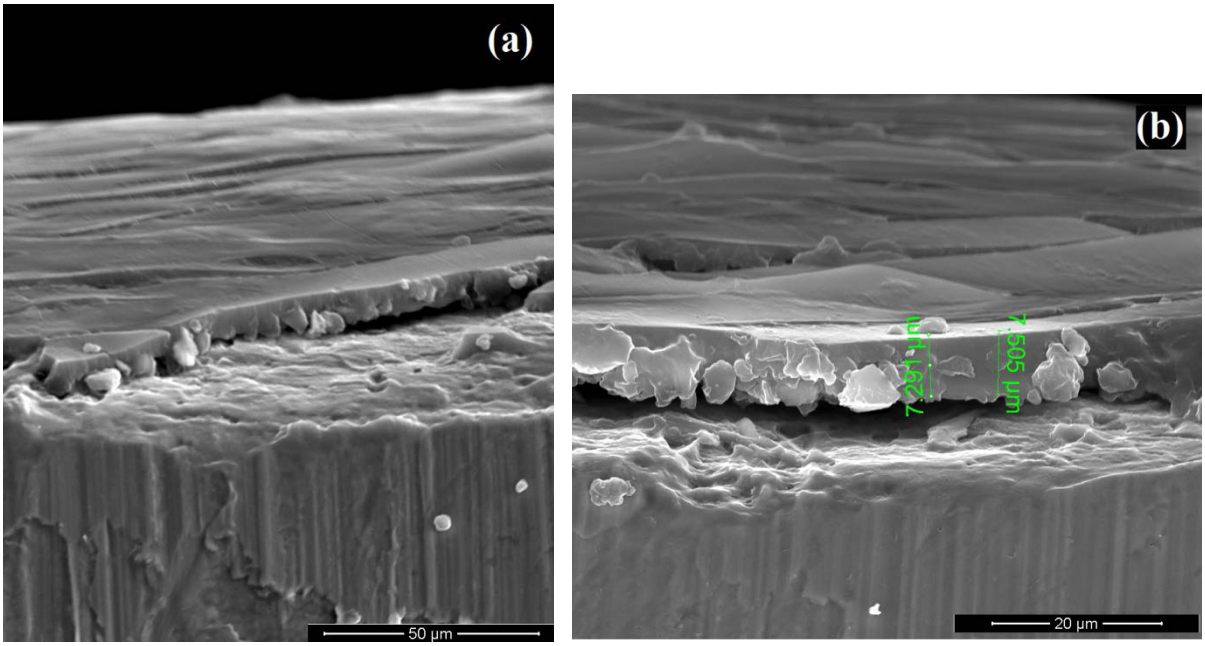

Figure 4. SEM micrographs, (a) and (b) SiO_2-TiO_2 coated specimens surface heat treated at 200 °C.

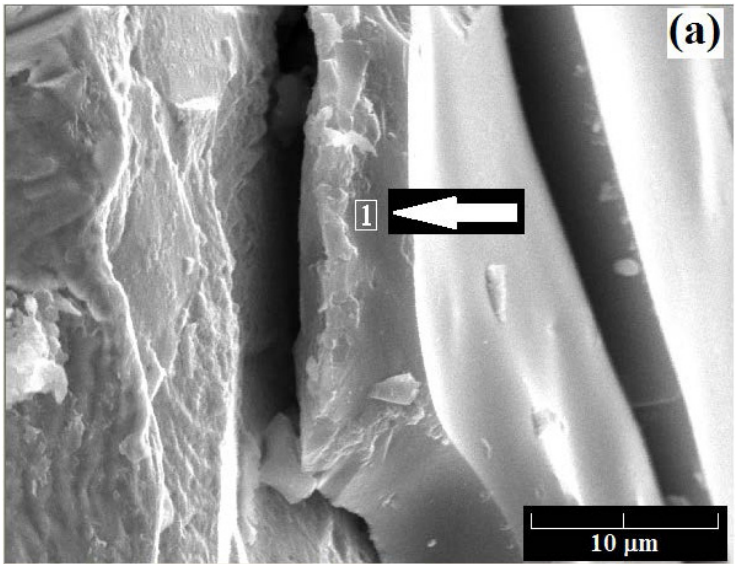

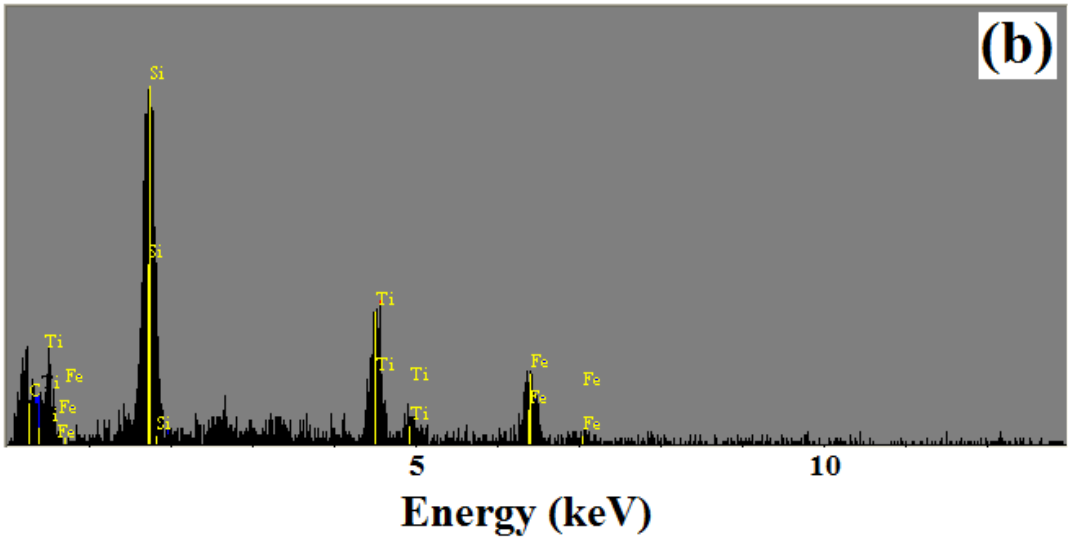

Figure 5. (a) SEM image of SiO_2-TiO_2 coated sample that was heat treated at 200 °C, (b) EDS analyses of that sample

Fig. 5a shows the SEM image of SiO_2-TiO_2 coated sample that was heat treated at 200 °C. Fig. 5b shows the EDS analyses of the area indicated in Fig. 5a, where the presence of SiO_2 and TiO_2 are seen. It can be clearly that the intensity of Si peaks are higher than Ti peaks. It is important to note that Fe peaks are coming from the substrate. Considering the solutions that are used for sources of Si and Ti, the theoretical calculations suggest that the solid ratio of SiO_2 / TiO_2 prepared as 70 / 30 wt %. This is confirmed by the low intensity peaks of Ti compare to Si in Fig 5b.

4. CONCLUSIONS

Alcohol based organic-inorganic hybrid SiO_2-TiO_2 coatings on mild steel were prepared by sol-gel dip coating method. The thickness of the coating increases with increasing withdrawal speed. The coating film was noted to be smooth and maximum between 7.2-7.5 µm thick. Results of this study showed that the specimens coated with ormosil sols possess higher corrosion resistance than that of uncoated specimen. i_{corr} values of the coating specimens heat treated at 200 °C were between 6.9 and 9.2 times, 4.4 and 5 times heat treated at 300 °C smaller than those of uncoated specimen. It was showed that cracks formation on surface of coating heat treated at 300°C. The organic groups were removed from the sols heat treated above 300 °C. The FTIR spectra clearly revealed that the organic groups, Si-O-Ti and Si-O-Si bonds form in the gels heat treated at 200 °C. The elasticity of the coating can be improved by the presence of organic groups in the coating which reduces stress and crack formation during sintering.

ACKNOWLEDGMENT

This work was supported by Scientific Research Projects Coordination Unit of Istanbul University. Project number 3004.

REFERENCES

1. R. Z. Zand, K. Verbeken, A. Adriaens, Int. J. Electrochem. Sci., 8, 548, 2013
2. Y. Mingming, H.Yedong, Z. Ying, Y. Qiuxia, J. Rare Earths, 24, 587, 2006
3. M. Fallet, H. Mahdjoub, B. Gautier, J.P. Bauer, J. Non-Cryst. Solids, 293-295, 527, 2001
4. G. Ruhi, O. P. Modi, A. S. K. Sinha, I. B. Singh, Corros. Sci., 50, 639, 2008
5. K. Izumi, M. Murakami, A. Morita, J. Am. Ceram. Soc., 72, 1465, 1989
6. M. Guglielmi, D. Festa, P.C. Innocenzi, P. Colombo, M. Gobbin, J. Non-Cryst. Solids, 147-148, 474, 1992
7. S.I.Seok, J.H. Kim, K. H. Choi, Y. Y. Hwang, Surf. Coat. Technol., 200, 3468, 2006
8. M. Garcia-Heras, A. Jimenez-Morales, B. Casal, J. C. Galvan, S. Radzki, M. A. Villegas, J. Alloys Comp., 380, 219, 2004
9. T. K. Rout, N. Bandyopadhyay, R. Narayan, N. Rani, D. K. Sengupta, Script. Mater., 58, 473, 2008
10. J. Jiang, Y. Wang, Q. Zhong, Q. Zhou, L. Zhang, Surf. Coat. Technol., 206, 473, 2011
11. S. K. Tiwari, R. K. Sahu, A. K. Pramanick, R. Singh, Surf. Coat. Technol., 205, 4960, 2011
12. Y. H. Koh, O. S. Kwon, S. H. Hong, H. E. Kim, S. K. Lee, J. Euro. Ceram. Soc., 21, 2407, 2011
13. A. Pepe, P. Galliano, S. Cere, M. Aparicio, A. Duran, Mater. Lett., 59, 2219, 2005
14. M. Qian, A. M. Soutar, X. H. Tan, X. T. Zeng, S. L. Wijestinghe, Thin Solid Films, 517, 5237, 2009
15. M. A. Dominguez-Crespo, A. Garcia-Murillo, A. M. Torres-Huerta, C. Yanez-Zamora, F. De. J. Carrillo-Romo, J. Alloys Comp., 483, 437, 2009

16. H.M. Hawthorne, A. Neville, T. Troczynski, X. Hu, M. Thammachart, Y. Xie, J. Fu, Q. Yang, Surf. Coat. Technol., 176, 243, 2004
17. M. Stern, A. L. Geary, J. Elecrochem. Soc., 104, 56, 1957
18. M.W.Barsoum, "Fundamentals of Ceramics", McGraw Hill Companies, International Editions, ISBN : 0-07-005521-1, Singapore, 1997
19. V. Verganalakis, P.D. Nicolaou, G. Kardas, Glass Tech., 41, 22, 2000
20. Y. M. Chiang, D. P. Birnie, W. D. Kingery, "Physical Ceramics", John Wiley & Sons, Canada, ISBN : 0-471-59873-9, 1997
21. J. Gallardo, A. Duran, J. J. De Danberenea, Corros. Sci., 46, 795, 2004

EVALUATION OF THE EFFECTIVENESS OF COATINGS ON REINFORCEMENT CORROSION APPLIED TO THE EXTERNAL SURFACE OF REINFORCEMENT STEEL

Özlem AYDIN *, Zeki ÇİZMECİOĞLU **

* Gedik University, Turkey
oaydin@gedik.edu.tr
** Istanbul Commerce University, Turkey
zcizmecioglu@ticaret.edu.tr

ABSTRACT
Studies have been carried out to investigate the performance of two steel coatings.First one is epoxy resin based epoxy coating with two components and solvent. Second one is a cementitious, silica fume and corrosion inhibitor containing, polymer modified, one-component coating material. The coated and uncoated concrete specimens were subjected to accelerated corrosion to determine the time-to-corrosion initiation. The accelerated corrosion test results clearly showed that the specimens coated with both coating materials performed very well against reinforcement corrosion and better than uncoated specimens.

Keywords: Reinforcement, inhibitor, corrosion, concrete, chloride.

BETONARME ÇELİĞİNİN DIŞ YÜZEYİNE UYGULANAN KAPLAMALARIN BETONARME KOROZYONU ÜZERİNE ETKİNLİĞİNİN DEĞERLENDİRİLMESİ

ÖZET
Çalışmalar iki adet çelik kaplamasının performansını değerlendirmek için gerçekleştirilmiştir.Birincisi iki bileşenli ve solventli epoksi reçine esaslı epoksi kaplamadır.İkincisi çimentolu, silis dumanı ve korozyon inhibitörü içeren, polimer modifiyeli, tek bileşenli kaplama malzemesidir.Kaplamalı ve kaplamasız beton numuneler korozyon başlangıç zamanına karar vermek için hızlandırılmış korozyona tabi tutulmuştur.Hızlandırılmış korozyon test sonuçları, her iki kaplama malzemesi ile de kaplanan numunelerin betonarme korozyonuna karşı çok iyi performans gösterdiğini ve kaplamasız numunelerden daha iyi durumda olduklarını açıkça göstermiştir.

***Anahtar kelimeler*:** Betonarme,inhibitör,korozyon,beton,klor.

1. INTRODUCTION

Durability is the global problem prevailing in the reinforced concrete structures. Normally, the design life of a reinforced concrete structure is about 60 years. In recent days, the instances of failures indicate that failures occur within 10–20 years. Thus, the durability of concrete structures is adversely affected, i.e., the actual trouble free life of structures in aggressive environment is only about one-fifth of the design life. The main reason for lack of durability of concrete structures is corrosion damage to the rebar embedded in concrete. The

two most common causes of reinforcement corrosion are (a) localized breakdown of passive film on the steel by chloride ions and (b) general breakdown of passivity by neutralization of the concrete, predominantly by reaction with atmospheric carbon dioxide. [1].

It is very much essential to adopt all possible methods to control corrosion in concrete structures. Use of good construction design and procedures, adequate concrete cover depth, corrosion inhibiting admixtures and low permeability concrete alone will not abate the corrosion problem, because concrete has a tendency to crack inordinately.This situation essentially leaves the reinforcing steel itself as the line of defense against corrosion. For this reason, use of a coating system on the reinforcing steel is critical in abating this corrosion problem. [1].

Epoxy resins are thermosetting plastics that have good long-term durability in concrete and are resistant to solvents, chemicals and water. Tests have shown that the diffusion rates of oxygen and chloride ions through a quality coating of adequate thickness (177 μm, 7 mils) are extremely low, even in severe exposure conditions. However, epoxy based coatings are not impermeable to water. Epoxy coatings function in two ways, first by acting as a barrier, keeping oxygen and chloride ions from reaching the surface of the steel, and second by increasing the electrical resistance between adjacent steel locations. Epoxy coatings reduce the magnitude of macrocell currents, which are responsible for extensive deterioration. [2].

In this study, the formation of corrosion in concrete structures and the results of a study concerning with the corrosion behavior of reinforced concrete in presence of epoxy resin based epoxy coating and cementitious, silica fume and corrosion inhibitor containing, polymer modified, one-component coating material in chlorinated environment have been described.

2. EXPERIMENTAL PROGRAMME

The reinforced concrete specimens were used to evaluate the effectiveness of coating materials were 70x140 mm concrete cylinders in which a 10 mm diameter steel bar was centrally embedded.

The selected reinforcing steel was a 10 mm-diameter ribbed bar and complied with TS 708. TS EN 197-1 CEM I 42.5 R Portland cement, manufactured by Aslan (OYAK) Cement Manufacturing Co., was used in all reinforced concrete specimens.

Compressive and tensile strength at 28 days were measured by 150 mm-cubic samples (Table 1).

Table 1. Compressive and tensile strength at 28 days (MPa)

Compressive strength	28,5
Tensile strength	2,9

After 24 h of setting, the samples were removed from the molds and air cured under laboratory conditions at 23 ± 2 º C temperature for 28 days.

In this study, the following coating materials were examined.

Epoxy resin based epoxy coating with two components and solvent (ER) : ER is solvent containing, high performance, pigmented, epoxy coating with two components which is strong enough to work in heavy conditions and resistant to chemicals.

ER was applied on the reinforcement steel according to the suppliers' recommendations by brush.

Cementitious, silica fume and corrosion inhibitor containing, polymer modified, one-component coating material.(SPI): SPI has excellent bond to steel and concrete highly impermeable to water and chlorides substrates and high mechanical strengths.

SPI was applied on the reinforcement steel according to the suppliers' recommendations by brush.

Three groups of concrete specimens as shown in Figure 1 were prepared. First group consists of uncoated control concrete specimens and the other two groups represent concrete specimens coated with the selected two coating materials described above after air cured for 28 days.

Figure 1. Cube and Lollipop Cylindrical Samples

At the end of the curing period, each concrete test specimen was partially immersed in NaCl solution and subjected to accelerated corrosion in a sodium chloride solution for 3 months.

The goal of concrete samples partially immersed is to provide needed moisture for reinforcement steel corrosion.The purpose of accelerated corrosion test to determine the effectiveness of selected coating materials protecting steel against the entry of harmful ions.

Half-cell potential measurements and corrosion current density measurements were made regularly for three months.

Half-cell potential measurement method, reinforcement potential was measured by a high impedance voltmeter $Cu/CuSO_4$ (copper / copper sulphate) (CSE) according to the reference electrode.

The corrosion rate(Ikor = $\mu A/cm^2$) of steel reinforcement embedded in concrete was measured according to linear polarization method.

3. RESULTS

If the half cell potential between saturated $Cu/CuSO_4$ reference electrode and steel bar was more positive than -200 mV, it is considered a non corrosion (passive) state for steel, while if the value was more negative than -350 mV this indicates active corrosion. Between -200 and -350 mV, the steel surface may be active or passive.[3]

The half-cell potential values measured as shown in Figure 2 for samples ER coated and control.

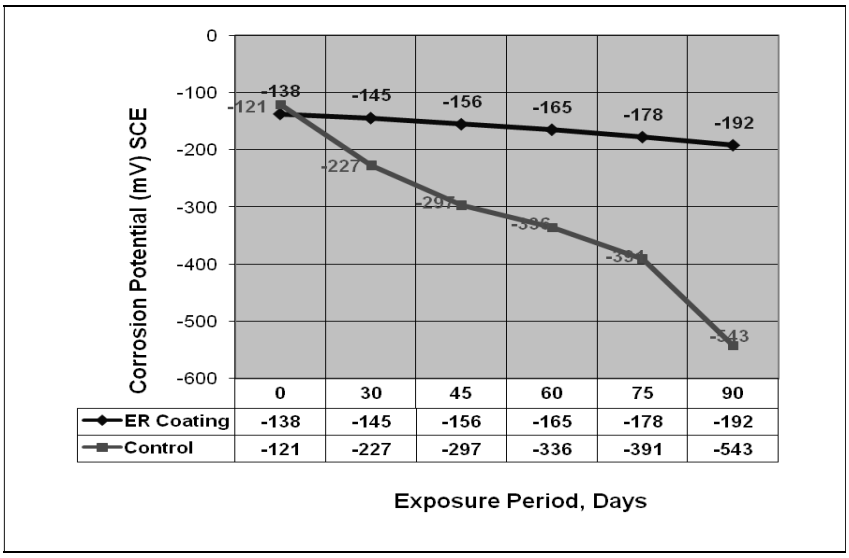

Figure 2. ER coated samples and control samples half cell potential-time curves

Half-cell potential average values measured for concrete specimens coated with ER as -192 mV at the end of ninetieth day.This average value remains in the region considered a non corrosion (passive) state for steel.Besides this potential value is not only affected by dissolved ions concentration of reinforcement, it is also affected by many factors like oxygen depletion. In addition this opinion is supported by similar results obtained Elsener's study and noted comments.
Elsener is indicated that the potential of passive rebars in concrete is governed (according to the Nernst equation) by the oxygen content at the rebars.With lack in oxygen (e.g. in very wet ,dense or epoxy modified mortars and concrete) shifts the potentials to more negative values.[4]. Due to ER coating's strong water-repellent effects, it is considered that ER is prevents enough oxygen diffusion to occur corrosion around reinforcement.After ER application lack of oxygen around the reinforcement directs the values of the potential in the negative direction is believed.

The half-cell potential values measured as shown in Figure 3 for SPI coated samples and control samples. This average value remains in the region showing the presence of reinforcement corrosion but as it mentioned before this potential value is not only affected by dissolved ions concentration of reinforcement, it is also affected by many factors like oxygen lack.

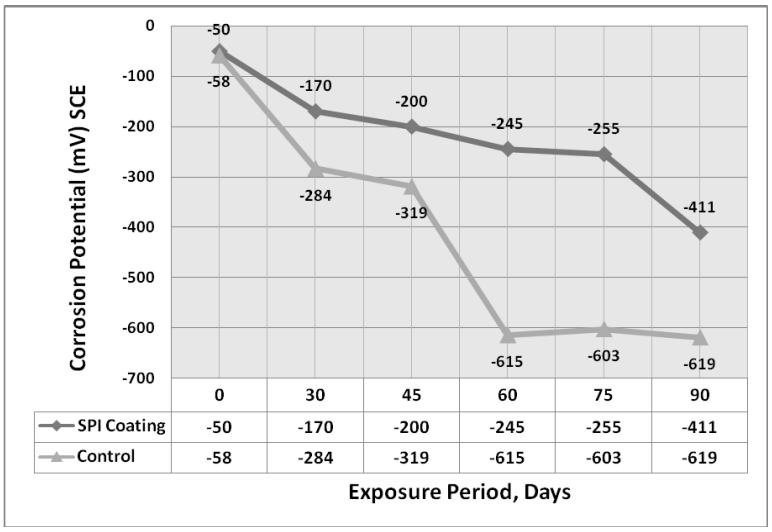

Figure 3. SPI coated samples and control samples half cell potential-time curves

Due to this uncertainties, half-cell potential measurements cannot be used as single technique to assess the effectiveness and durability of an inhibitor treatment on-site. [4].

Corrosion rates (Icorr = $\mu A/cm^2$) of steel reinforcement embedded in the concrete measured according to the ASTM G59 (1991) standard.Interpretation criteria of the LPR measurements are given in Table 2.

Table 2. Interpretation Criteria of the LPR Measurements

Corrosion Current Density	**Corrosion Level**
Icor <0,1 $\mu A/cm^2$	Negligible
0,1 $\mu A/cm^2$<Icor< 0,5 $\mu A/cm^2$	Low to moderate corrosion
0,5 $\mu A/cm^2$<Icor< 1,0 $\mu A/cm^2$	Moderate to high corrosion
Icor> 1 $\mu A/cm^2$	High corrosion rate

Average corrosion current density values measured as shown in Figure 4 for samples ER coated and control. Corrosion current density average values measured for concrete specimens coated with ER as 0.19 $\mu A/cm^2$ at the end of ninetieth day.

Several researchers have considered values of current density greater than 0.3 $\mu A/cm^2$ to be indicative of active.[5]

According to this result it couldn't detected a danger in terms of durability of ER coated reinforced concrete even if 90 days exposure to aggressive conditions.So this condition shows that ER coating can protect the reinforced concrete against aggressive chloride ions and oxygen which penetrates the pores of the concrete and that is absolutely necessary for the formation of corrosion and water which acts as the electrolyte.Consequently this situation shows that ER coating can protect the reinforced concrete structure long term compared to control samples.

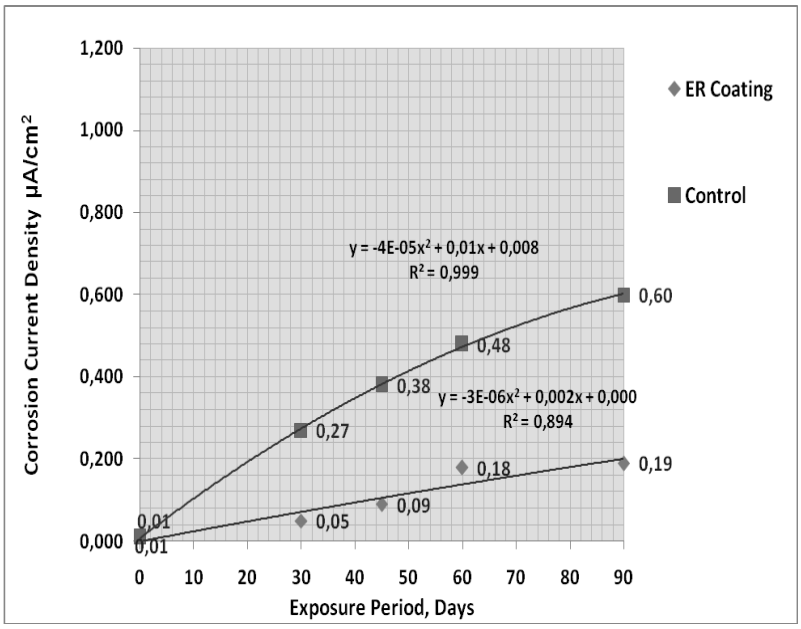

Figure 4. ER coated samples and control samples corrosion current density- time curves

Average corrosion current density values measured as shown in Figure 5 for samples SPI coated and control. Corrosion current density average values measured for concrete specimens coated with SPI as 0.14 µA/cm^2 at the end of ninetieth day.

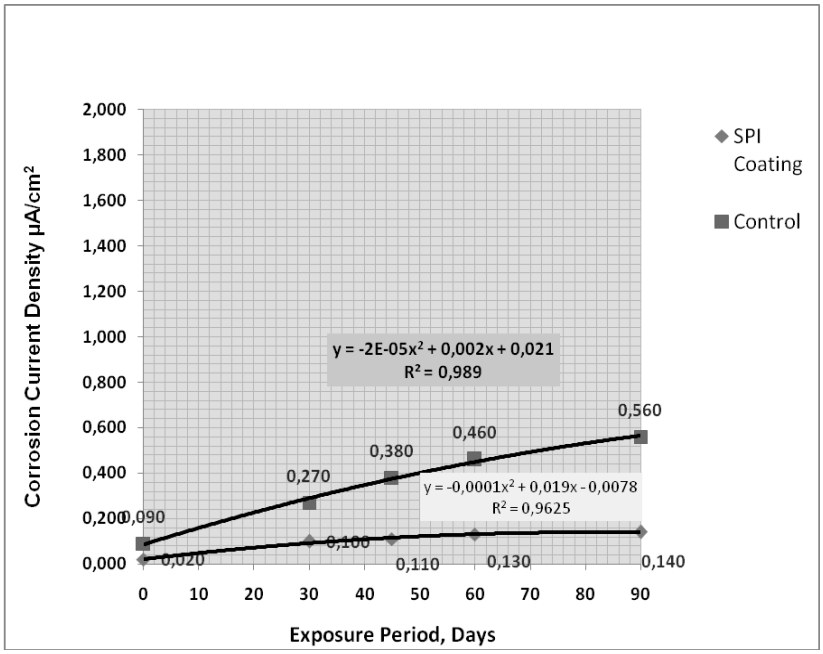

Figure 5. SPI coated samples and control samples corrosion current density -time curves

According to this result it couldn't detected a danger in terms of durability of SPI coated reinforced concrete even if 90 days exposure to aggressive conditions.

4. CONCLUSIONS

This investigation was conducted to assess the effectiveness of reinforcement steel exterior surface coatings in mitigating reinforcement corrosion in the concrete specimens. Based on the

results obtained within the time frame of this study, the following conclusions can be drawn:

(1) Half-cell potential values is not enough to determine whether corrosion of steel embedded in concrete. Because these values are effected the presence of oxygen, inhibitors, etc.Therefore to make a reliable interpretation the other corrosion detection method known as corrosion current density measurement were also used.

(2) Although both two reinforcement steel exterior surface coatings investigated were effective in delaying the initiation of reinforcement corrosion, SPI coating was slightly more efficient in the concrete specimens.

(3) Corrosion current density average values measured for control specimens remains in the region showing the presence of moderate reinforcement corrosion at the end of ninetieth day.If this situation is taken into account, ER and SPI are fairly well preserved of reinforcement steel against aggressive chloride ions compared to control samples.

REFERENCES

1. K. Saravanan, S. Sathiyanarayanan, S. Muralidharan, S. Syed Azim and G. Venkatachari," Performance evaluation of polyaniline pigmented epoxy coating for corrosion protection of steel in concrete environment", Progress in Organic Coatings, (59), 2: 160-167, 2007.
2. J. Kepler, "Evaluation of Corrosion Protection Methods for Reinforced Concrete Highway Structures", http://www.iri.ku.edu/publications/SM58.PDF, 01.04.2010.
3. R.K. Dhir and M.D.Newlands,"Controlling Concrete Degradation", Thomas Telford, London, 1999.
4. B. Elsener, "Half-cell potential mapping to assess repair work on RC Structures", Construction and Building Materials, 15(2-3): 133-139, 2001.
5. O. Kayali and B. Zhu,"Corrosion performance of medium-strength and silica fume high-strength reinforced concrete in a chloride solution", Cement and Concrete Composites, (27), 1: 117-124, 2005.

PRODUCTION OF METALLIC PARTS BY ADDITIVE MANUFACTURING

Fevzi YILMAZ*, Ebubekir KOÇ, Mustafa Tekkeşin*****

*Fatih Sultan Mehmet Vakıf University (FSMVU), İstanbul/Turkey
f.yilmaz@fsm.edu.tr
**FSMVU Aluminium Test, Training and Research Center (ALUTEAM), İstanbul/Turkey
ekoc@fsm.edu.tr
***Medistate Kavacık Hospital, İstanbul/Turkey
mustafa.tekkesin@medistate.com.tr

ABSTRACT

The additive manufacturing technology has been introduced early in 1980s, since then it became one of the key technologies to manufacture everything from prosthetic limbs to aircraft parts in many industries.

In this paper, the advantages of forming of metal-based materials by additive manufacturing technologies are investigated. Several different metal powders for additive manufacturing and their properties and applications for biomedical field are introduced. Additive manufacturing is compared with standard manufacturing technologies and their mechanical and physical properties of manufactured products are also described.

Keywords: Additive Manufacturing, Direct Metal Laser Sintering, DMLS, 3D printing, Biomedical

METALİK PARÇALARIN EKLEMELİ İMLATLA ÜRETİMİ

ÖZET

Eklemeli üretim teknolojisi 1980'lerin başlarından itibaren gelişmeye başladı, bugün takma bacaktan uçak parçalarına kadar her şeyin üretmesini olanaklı kılan bir teknoloji halini almıştır.

Bu çalışmada, metal esaslı malzemelerin eklemeli-kat kat üretim yöntemiyle şekillendirilmesinin avantajlarına değinilmiştir. Eklemeli üretimde kullanılan metal tozlar, özellikleri ve kullanım alanları biyomedikal alan ekseninde tanıtılmıştır. 3D Baskı ürünler, standart üretim metotlarıyla şekillendirilmiş ürünlerle karşılaştırılmış, mekanik ve fiziksel özellikleri de açıklanmıştır.

***Anahtar kelimeler*:** Eklemeli Üretim, Direkt Metal Lazer Sinterleme, DMLS, 3D Baskı, Biyomedikal

1. ADDITIVE MANUFACTURING

Fine metal powders are used to produce metal parts in additive manufacturing. Roughly to explain, layer by layer melting and solidification processes turns this fine metal powder into a

3D geometrical parts which can be deployed in many different industries. The structure and properties of engineering parts produced by this method is different compare to conventional production methods such as casting, plastic deformation, machining, welding etc. As experienced in all production methods, the properties of product depends on charge material (powder), production technology and process parameters. Laser sintering or electron beam sintering in additive manufacturing results in satisfactory and reliable material property. The aim of this study is to establish a relationship between material, process and metallurgical property for laser based additive manufacturing of metallic components.

Additive manufacturing of metal-based materials deploys very fine metal powders. These powders passing solidification process in layers are produced gradually to a desired (predesigned) geometry. Additive manufacturing is completed within a few hours by turning three-dimensional CAD data into real parts. Manufactured parts are either prototypes (models) or final products. 3D Printing is also referred as e-manufacturing in general and direct metal laser sintering (DMLS) for metals only manufacturing. With this process a thin layer of metal powder is melted and rapidly solidified layer by layer using laser beam. Electron beam sintering (EBS) is another technological achievement in additive metal manufacturing.

In Figure 1, additive manufacturing process is explained briefly in three steps. Many consumer goods, machinery parts, shoes - architectural models, body parts and complicated shapes can be produced by 3D printing as a first step. Any changes on products can be corrected in considerable shorter times. Today, many personalized goods, millions of dentures and teeth are manufactured using 3D printing technologies. In near future, 3D printers will make not only prototypes but many finished goods too, from aircraft parts to customized kitchen gadgets, medical implants and personalized jewelry. In this way, very complex three-dimensional geometries, and deep holes with details such as cooling channels, in general and personalized medical applications (in the form of implants) is produced [1-7].

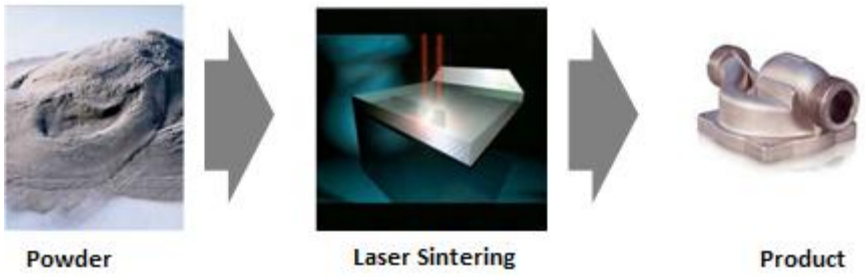

Figure 1 Direct metal laser sintering (DMLS) production method from powder to product [1].

Additive manufacturing creates layered structure with anisotropic properties. Anisotropic structure cannot be completely homogenized by heat treatment. This fact gives importance in terms of design and makes it necessary to take the worst state. Parts produced by additive manufacturing carry the risk of cracks and the risk is reduced by heat treatment. Surface roughness is a function of geometry. Stress points and crack propagation can generally occur in inland areas. This situation makes specifications complex, requires a good surface polishing. The risk of deformation, especially in the lower plate can be seen and additive support is used at the point of production. Obviously, stress–relieving heat treatment solutions and other precautions naturally increases the cost and production time will be longer. When the surface area of powder increases, the oxygen content is raised and negative structural effects are expected. Lower than 10 ppm oxygen induced powder is preferred and control oxygen atmosphere must be provided during production. Flat – plate

structured porosity (5-50 micro meters) can be seen in final product.

Additive manufacturing is very suitable for medical applications since fields' need on personalized parts opens many new horizons for this ever-rising technology. Especially, Cobalt-Chromium alloys and titanium alloys are increasing their market share and they are exploited in many more promising applications. In this study, the medical applications of additive manufacturing, shortly DMLS of indicated alloys are explained in details.

2. COBALT – CHROMIUM (CoCrMo) ALLOYS

Cobalt–Chromium (CoCrMo) alloys are in use as prototypes and series of final product. Key characteristics of Cobalt-Chromium alloys are high strength, high temperature and corrosion resistance and biocompatibility. 3D Printing of this alloy fits in to chemical and mechanical specifications of ISO 5832-4 and ASTM F75 (cast CoCrMo implant alloys), and most of ISO 5832-12, ASTM F1537 (wrought CoCrMo implants) and medical device directive 93/42/EEC (for dentistry).

CoCrMo alloys have typical applications as medical implants. This alloy, by satisfying high–temperature engineering applications (turbine blades) has an important share. Alloys include high cobalt (62%), chromium (28%) and molybdenum (16%). Nickel in the alloy is not desirable and should be very low (<0,10%) (Table 1).

Table 1 Cobalt – chromium alloys [1].

Element	Content (by weight)
Cobalt	60 – 65 %
Chromium	26 - 30 %
Molybdenum	5 - 7 %
Silicon	≤ 1.0 %
Manganese	≤ 1.0 %
Iron	≤ 0.75 %
Carbon	≤ 0.16 %
Nickel	≤ 0.10 %

CoCrMo alloy has advanced mechanical and physical properties as shown in Tables 2-4.

Table 2 The mechanical properties of Cobalt – Chromium alloy 20°C [1].

Property	As built	Heat treated (1)
Tensile strength		
- horizontal (XY)	1350 ± 100 MPa	1100 ± 100 MPa
- vertical (Z)	1200 ± 150 MPa	1100 ± 100 MPa
Yield strength (Rp 0.2 %)		
- horizontal (XY)	1060 ± 100 MPa	600 ± 50 MPa
- vertical (Z)	800 ± 100 MPa	600 ± 50 MPa
Elongation at break		
- horizontal (XY)	(11 ± 3) %	min. 20 %
- vertical (Z)	(24 ± 4) %	min. 20 %

(1) 6 hours at 1150°C

Table 3 CoCrMo alloys physical and thermal properties [1].

Property	Value
Relative density	approx. 100 %
Density	8.29 g/cm³
Thermal conductivity	
- at 20 °C:	13 W/m°C
- at 300 °C:	18 W/m°C
- at 500 °C:	22 W/m°C
- at 1000 °C:	33 W/m°C
Coefficient of thermal expansion	
- 20 – 500 °C	13.6 x10^{-6} m/m°C
- 500 – 1000 °C	15.1 x10^{-6} m/m°C

Table 4 CoCrMo alloys used in dentistry for a sample of certified (Commercial name: EOS Cobalt–Chromium SP2: EOS system, the EOS M 270 INT certified material for crowns and bridges for) [2].

Element Content (wt %)	Features	
Co:63,8	The relative density	Approx. 100%
Cr:24,7	Density	8,5 g/cm^3
Mo:5,1	Yield (Rp0,2%)	850MPa
W:5,4	Ultimate tensile strength	1350MPa
Si:1,0	% Elongation	3%
Fe: max. 0,50	Young module	Approx. 200 GPa
Mn: max. 0,10	HV10	420HV
Prohibited elements. Ni, Be, and Cd acc. to EN ISO 22674	Thermal expansion coefficient (25-500°C)	14,3x10E-6m/m°C
	Thermal expansion coefficient (20-600°C)	14,5x10E-6m/m°C
	Melting range	1410-1450°C

CoCrMo based super alloys used for the production of crowns and bridges are given in Table 4. This, in comparison with other metal alloys, suitable for dental sector, biocompatible (CE 0537), certified and is very inexpensive.

The microstructural characteristics of CoCrMo alloys are given in Figure 2. Layered structures, micro and macro features are remarkable and facinating.

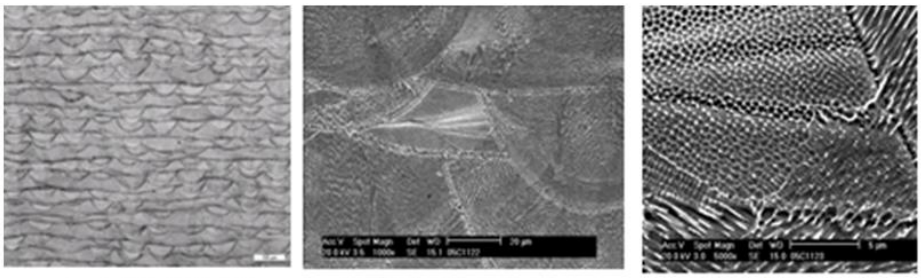

a) 10X OPTIC b) 1000X SEM c) 5000X SEM

Figure 2 CoCrMo alloy microstructure a) obtained by completely melting appears dense layered structure, b) Grain shape, c) Details (very fine 0,3 to 0,6 micrometer size beads) [1,2].

3. TITANIUM ALLOYS

Standard titanium alloys are used in implants and various industrial applications. Table 5 gives the important properties of titanium alloys.

Table 5 Summary of the most important Ti alloys [1, 2].

Material name	Composition	Typical applications	Tensile strength (*) [MPa]	Elongation at break (*) [%]
Ti CP grade 1	Ti; O <0.18%; N <0.03%	Medical and dental	240	24
Ti CP grade 2	Ti; O <0.25%, N <0.03%	Medical and dental, chemical industry	345	20
Ti CP grade 3	Ti; O <0.35%, N < 0.05%	Medical and dental	450	18
Ti CP grade 4	Ti; O < 0.40%, N < 0.05%	Medical and dental	550	15
Ti6Al4V (grade 5)	Ti; Al 6%; V 4%; O <0.20%, N < 0.05%	Aerospace, medical, dental etc.	895	10
Ti6Al4V ELI	Ti; Al 6%; V 4%; O <0.15%, N < 0.05%	Medical and dental		

CP = commercially pure, ELI = extra-low interstitials
(*) Source: Euro-Titan Handels AG, Solingen, Germany

Key characteristics: Light weight with high specific strength (strength per weight), corrosion resistance and biocompatibility. Typical applications are aerospace, engineering applications and biomedical implants.

3D Printing product carries superior properties and production standards are better than conventional types. Table 6 gives mechanical properties of the alloy of Ti 64 and Table 7 gives the compositions.

Table 6 Ti64 mechanical properties [1, 2].

Property	As built	Heat treated [1]
Tensile strength		min. 930 MPa
- horizontal (XY)	1230 ± 40 MPa	typ. 1050 ± 20 MPa
- vertical (Z)	1200 ± 40 MPa	typ. 1060 ± 20 MPa
Yield strength (Rp 0.2 %)		min. 860 MPa
- horizontal (XY)	1060 ± 40 MPa	typ. 1000 ± 20 MPa
- vertical (Z)	1070 ± 40 MPa	typ. 1000 ± 20 MPa
Elongation at break		min. 10 %
- horizontal (XY)	(10 ± 2) %	typ. (14 ± 1) %
- vertical (Z)	(11 ± 3) %	typ. (15 ± 1) %
Hardness	320 ± 12 HV5	

Chemical composition corresponds to ISO 5832-3, ASTM F1472 and ASTM B348. Chemical properties parts fulfil requirements of ASTM F1472 (for Ti6Al4V) and ASTM F136 (for Ti6Al4V ELI) regarding maximum concentration of impurities.

Table 7 Ti64 alloy chemical composition [1, 2].

Element	Content (by weight)
Titanium	balance
Aluminium	5.5 – 6.75 %
Vanadium	3.5 – 4.5 %
Oxygen	< 2000 ppm
Nitrogen	< 500 ppm
Carbon	< 800 ppm
Hydrogen	< 150 ppm
Iron	< 3000 ppm

Ti64 alloy with superior physical and metallographic properties are presented in Table 8 and Figure 3.

Table 8 Ti64 alloys physical and thermal properties [1, 2].

Property	
Relative density	approx. 100 %
Density	4.41 g/cm³
Maximum long-term operating temperature	approx. 350 °C

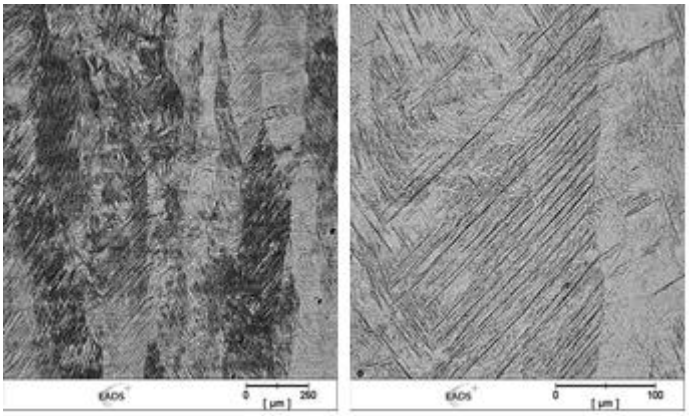

Figure 3 Ti64 alloy Widmanstatten martensitic structure [1, 2].

4. APPLICATION EXAMPLES

Biomedical applications of 3D print CoCrMo and titanium alloys are given in Figure 4-11.

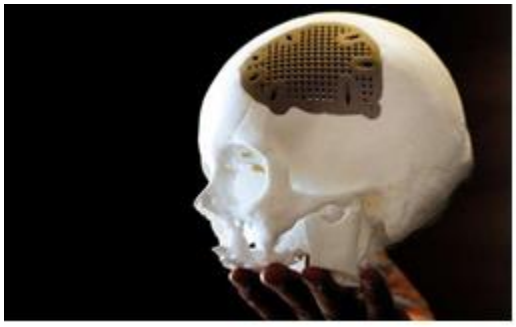

Figure 4 Head injury and solution by 3D print PEEK material or titanium plate (general usage). PEEK enabling bone in growth [2].

(a) (b)

Figure 5 Medical applications. (a) Spinal (waist) implants, (b) Finger implants Ti64 [2].

Figure 6 Direct Metal Laser Sintering (DMLS) CoCrMo alloy for dental applications [2].

Figure 7 Batch of finger implants in EOS CobaltChrome MP1[2].

(a) (b)

Figure 8 Medical applications. (a) Humeral mount EOS Titanium Tİ64 for a fully integrated arm, (b) Medical parts in EOS Stainless Steel GP1 [2].

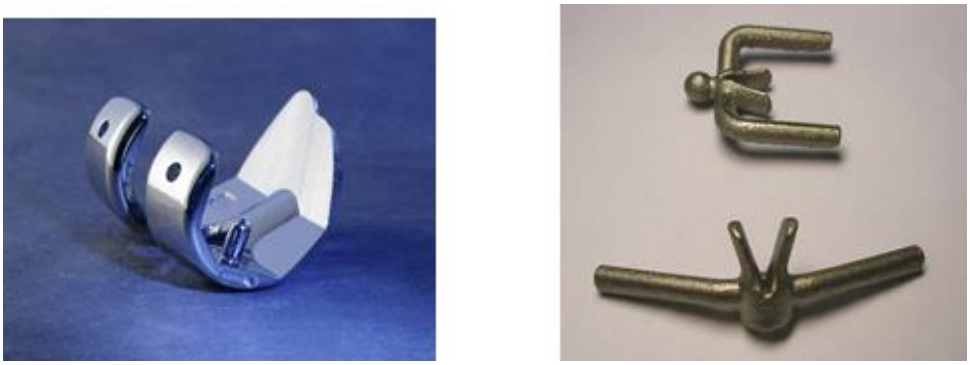

(a) (b)

Figure 9 Medical applications. (a) Replacement knee joint in EOS CoCr MP1, (b) Spinal implants in EOS Titanium Ti64 [2].

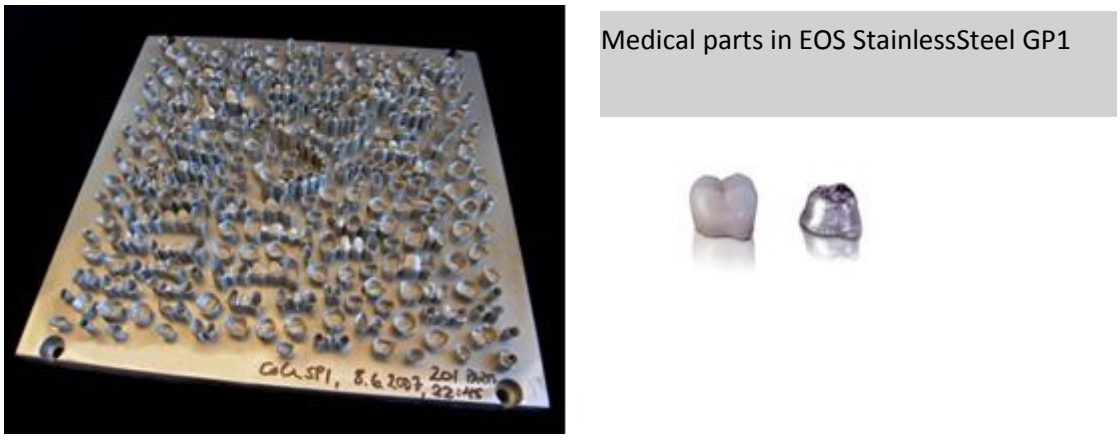

Figure 10 Dental applications [2].

(a) (b)

Figure 11 Dental applications. (a) Aligner in EOS CoCr MP1, (b) Dental device in EOS Titanium Ti64 [2].

5. RESULTS

The additive manufacturing or 3D printers, now used to manufacture everything from architectural prototyping to aircraft turbocharge turbines. Many researchers prefer the term "additive manufacturing" rather than "3D printing" to stress out the "manufacturing" aspect of the technology. One reason is that printing is not quite the right term for some of the technologies given under this subject. Whereas hobbyist-scale 3D printers typically build a product from filaments of plastic, selective laser melting zaps successive layers of powders with a laser or ion beam hardening only certain bits. The term, 3D printing gives a sense of small scale office work.

3D printers are in use for either prototyping or final product. Today, 28% of 3D printing outcomes are focusing on the final production. In 2016, it is reckoned that this ratio will exceed 50% and will go up to 80% by 2020. It will never expand to 100% since other technologies will always be still in use.3D printing presenting an ever-growing trend on medical field.

Building body parts and living tissue with a 3D printing or additive manufacturing is a novel area of research and becoming a growing business. This technology has two promising material centred in medical field, namely; cobalt – chromium alloys and titanium alloys.

The field of 3D bio-printing is promising even bigger: to create human tissues-layer by layer-for research, drug development and testing, and ultimately as replacement organs, such as a kidney or pancreas for patients desperately in need of a transplant. Various bioprinted organs and miniature body parts like kidney could also be manufactured on demand.

6. REFERENCES

1. C. Brancher: Materials Solutions 3D Printing/DMLS Expectation to Enlightenment, EOS IUM 2013
2. ……EOS Catalog Sources 7, Additive Manufacturing in Dentistry, EOS Catalog, 2011
3. J. Goebner: A Peek into the EOS Lab: Micro Laser Sintering, EOS, International User Meetings 22/04/2013 – 24/04/2013
4. J. Greses: Area Sales Manager South Europe and South America, EOS innovation for e-manufacturing Presentation, 2011
5. …….Applications of Direct Metal Laser Sintering (DMLS) with EOSINT M, EOS Catalog, 2011
6. E.Ateş: Seminar, 3D Printers and Application, Fatih Sultan Mehmet Foundation University Aluminum Test, Education and Research Center (ALUTEAM), İstanbul, 2013
7. ……..:Additive Manufacturing Heavy Metal, The Economist, p:56-57, May 3rd 2014

Artificial neural network approach for the prediction of coating thickness in Fe-Al coatings fabricated by mechanical milling

Aykut Canakci[a*], Fatih Erdemir[a], Temel Varol[a], Sukru Ozsahin[b], Serdar Ozkaya[a]

[a]Department of Metallurgical and Materials Engineering, Engineering Faculty,
[b]Department of Industry Engineering, Engineering Faculty
Karadeniz Technical University, Trabzon, Turkey.
aykut@ktu.edu.tr

Abstract
The aim of this study was to investigate the effect of milling time, milling speed and particle size of initial powders on the coating thickness of Fe-Al intermetallic coating produced by mechanical milling using an artificial neural network (ANN). The formation of intermetallics was confirmed by X-ray diffraction analysis. Coating morphology and cross-section microstructures were evaluated using a scanning electron microscope. As a result of this study the ANN was found to be successful for predicting the coating thickness of Fe-Al intermetallic coatings. The mean absolute percentage error (MAPE) for the predicted values didn't exceed 7.46%. The ANN model can be used for predicting of coating thickness of Fe-Al intermetallic coating produced with the different milling time, milling speed and particle size.

Keywords: Artificial neural network; Fe-Al coating; mechanical milling

Mekanik Öğütme ile üretilen Fe-Al kaplamalarında kaplama kalınlığı için yapay sinir ağı yaklaşımı

[a]Metalurji ve Malzeme Mühendisliği Bölümü, Mühendislik Fakültesi,
[b]Endüstri Mühendisliği Bölümü, Mühendislik Fakültesi,
Karadeniz Teknik Üniversitesi, Trabzon, Türkiye
aykut@ktu.edu.tr

Özet
Bu çalışmanın amacı bir yapay sinir ağı modeli kullanılarak mekanik öğütme ile üretilen Fe-Al intermetalik kaplamalarının kaplama kalınlığı üzerine öğütme zamanı, öğütme hızı ve başlangıç tozlarının partikül boyutunun etkisini araştırmaktır. İntermetalik oluşumu X ışını analizi ile araştırıldı. Kaplama morfolojisi ve mikroyapı incelemeleri taramalı elektron mikroskobu ile gerçekleştirildi. Bu çalışmanın bir sonucu olarak oluşturulan tahmin modelinin Fe-Al intermetalik kaplama kalınlığının tahmininde oldukça olduğu görüldü. Tahmin değerleri için ortalama mutlak yüzde hata (MAPE) % 7.46 değerini aşmadı. Geliştirilen tahmin modeli farklı öğütme zamanı, öğütme hızı ve başlangıç toz boyutu şartlarında üretilen Fe-Al intermetalik kaplamaların kalınlıklarının tahmini için kullanılabilir.

Anahtar Kelimeler: Yapay sinir ağı, Fe-Al kaplama, mekanik öğütme

1. INTRODUCTION

Mechanical milling is a new research area with potential industrial applications for coating on steel. Mechanical milling is a practical processing route for synthesis of phases or phase mixtures. When a powder mixture is processed by mechanical milling, some part of the milled powder forms a coating film over the milling balls and on the inside wall of the container. It was recognized recently that this phenomenon could be utilized as a flexible method to coat the surface of a steel substrate. The impacts of the milling balls activate and harden the surface. They also deliver and attach the powder particles and also can initiate chemical interactions between target object and coating powder [1].

Artificial neural networks (ANNs) which possess massive parallel computing capability can map the input-output relationships. This modeling frameworks has been recently used by many authors in various fields, for example, such as modeling of powder characteristics [2], coating process [3] wear behavior of coatings [4], and oxidation behavior of coatings [5]. Though ANN models have been developed to study the modeling of various coating process, very limited efforts have been reported to predict for coating thickness in Fe-Al coatings fabricated by mechanical milling. Thus, the primary aim of this paper was to reveal the relationship among the, microstructure, coating thickness and the process parameters during Fe-Al intermetallics formation on the steel substrate obtained by mechanical milling method. The second aim of this paper was to develop a multilayered feed-forward neural network trained with the back-propagation algorithm to model the relationship between coating thickness and process parameters (i.e. milling time, milling speed and particle size of as-received powders).

2. EXPERIMENTAL

Specimens of the low-carbon steel were used as the substrate material. The steel substrate (12 mm x12 mm x3 mm) and Al 2024 powders (d_{50}: 23 μm, d_{50}: 60 μm and d_{50}: 155 μm) were charged into the vial that made of tungsten carbide of 80 ml volume. Mechanical milling was performed in a Fritsch Pulverisette 7 planetary ball mill in an Argon atmosphere using balls (10 mm in diameter) at room temperature. The rotation rates were selected as 200, 300 and 400 rpm while the ball to powder weight ratio of 10:1 was kept constant in all the experiments. The milling times of 1, 2, 4, 6, 8 and 10 h were selected, respectively. The specimens were cut from steel substrate using a cutting machine and prepared by standard metallographic procedures for characterization. The measurement of coating thickness and morphological investigation of coated steel substrates were performed by a Zeiss Evo LS10 scanning electron microscope (SEM). The phase analysis of coated samples was evaluated by X-ray diffraction (Rigaku Corporation, Japan) using CuKα radiation (1.5405^{o}A) operating at 30 mA and 40 kV. The XRD patterns were recorded in the 2Θ range of 20-100 ^{o}C (step size 0.02^{o} and time per step 1s).

Fig. 1 shows the ANN models containing one input layer, two hidden layers and one output layer.

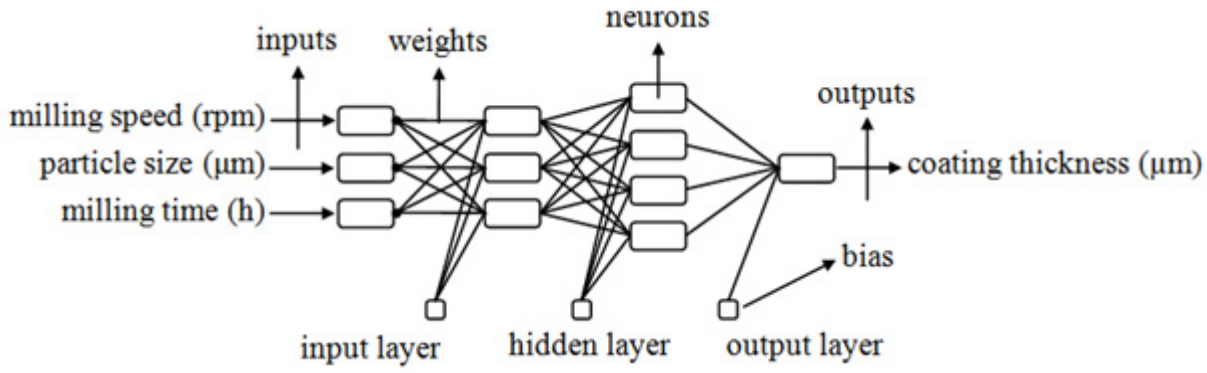

Figure 1. The ANN architecture selected as the prediction model for the coating thickness

The input layer is the first layer and is responsible for receiving the in-coming data for the ANN and for delivering the data to the intermediate layer. The hidden layer processes the information that comes from the input layer and sends it to the output layer. The neurons in the hidden layer do not have any connection to the external environment. The output layer processes the information coming from the intermediate layer and produces output data for the input layer of the network, which sends this to the outside world. Inputs (x_i) are data, obtained from the external environment or the other artificial neurons. The quantities (w_{ij}) demonstrate the effect of a data point arrives at an artificial neural cell. The addition function (threshold function, Eq.1) (net_j) calculates the net input on a neural cell. The sigmoid function (Eq.2) is the most common activation function in the ANN because it combines nearly linear behavior, curvilinear behavior, and nearly constant behavior. All of these components depend on the value of the input [6-8]. In the cell model, a bias with +1 value may increase the net input or polarization threshold input (θ_j) by a value of, -1, thereby decreasing the net input according to:

$$net_j = \sum_{i=1}^{n} x_i w_{ij} - \theta_i \quad (1)$$

where x_i indicates the i. input, w_{ij} is the connection weight from j. element to i. element, θ_j is the polarization value (negative of the threshold value), and n indicates the sent input signal of the artificial neuron number in the previous layer. The artificial neuron output value, which depends on the selected activation function, employs a sigmoid function as the activation function [9] and is calculated using Eq. 2. The produced output is sent via network connections between different cells, as explained by:

$$y_j = f(net_j) = \frac{1}{1 + e^{-net_j}} \quad (2)$$

The processing element numbers (neurons) of the hidden layers were 3 and 4 for the model in Fig. 1. The total data are divided into two sets (67% for training data and 33% for testing data). Training and testing data was selected randomly from the experimental data set. The MATLAB software package was used for training the ANN models. The training data were used in the forecast model, as shown in Table 1.

Table 1. Experimental data and predicted output from the ANN network for training

Sample ID	Milling Speed (rpm)	Particle Size (μm)	Milling Time (h)	Coating Thickness (μm)		
				Measured	Predicted	% Error
1	200	155	1	13	13.76	-5.86
2	200	155	2	28	28.11	-0.38
4	200	155	6	50	48.90	2.21
5	200	155	8	61	62.36	-2.24
7	200	60	1	9	8.22	8.65
9	200	60	4	25	25.51	-2.03
10	200	60	6	42	39.94	4.92
12	200	60	10	66	66.61	-0.92
14	200	23	2	13	12.49	3.95
15	200	23	4	17	18.75	-10.28
17	200	23	8	40	38.97	2.58
18	200	23	10	53	53.72	-1.36
20	300	155	2	30	30.06	-0.19
21	300	155	4	36	36.33	-0.92
23	300	155	8	145	146.58	-1.09
24	300	155	10	188	186.12	1.00
25	300	60	1	15	12.13	19.14
26	300	60	2	21	20.63	1.78
28	300	60	6	90	88.58	1.57
29	300	60	8	130	133.98	-3.06
31	300	23	1	9	11.05	-22.82
33	300	23	4	21	19.82	5.60
34	300	23	6	75	76.20	-1.60
36	300	23	10	157	155.08	1.22
37	400	155	1	30	30.46	-1.55
39	400	155	4	110	109.35	0.59
40	400	155	6	184	185.12	-0.61
42	400	155	10	267	267.35	-0.13
44	400	60	2	31	29.43	5.05
45	400	60	4	60	60.97	-1.61
47	400	60	8	189	183.13	3.10
48	400	60	10	215	217.88	-1.34
49	400	23	1	17	16.16	4.91
50	400	23	2	21	24.42	-16.28
52	400	23	6	107	107.75	-0.70
53	400	23	8	156	157.76	-1.13
MAPE				**3.955**		
RMSE				**1.835**		

3. RESULTS AND DISCUSSION

3.1. The mechanism of intermetallics formation

During ball milling, a sudden (10^{-8} s.) increase in the temperature (up to 800 ^{o}C) and pressure (10^{10} -10^{11} dyn/cm^2) occurs in local areas (10^{-6} cm) which results in the formation of intermetallics. As the starting points of FeAl, $FeAl_3$ and Fe_2Al_5 formation are close to 520 ^{o}C, 580 ^{o}C and 650 ^{o}C, respectively. In addition, rise in increasing in the local temperature (up to 800 ^{o}C) can also allow formation of Fe-Al intermetallic compounds of Fe_3Al, Fe_2Al_5, $FeAl_2$ and FeAl [10]. The reaction between the low carbon steel substrate and the Al 2024 powder

can be examined by XRD. Fig. 2 shows the XRD spectra of coating surface, after heat treatment at 600 °C. The XRD patterns confirm the presence of both elemental Fe and Al components with amounts of Fe_3Al, Fe_2Al_5, $FeAl_2$ and FeAl.

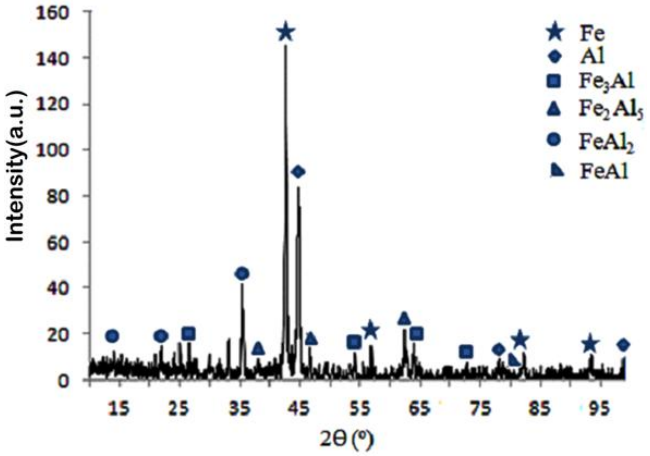

Figure 2. XRD patterns of steel substrates coated with Al2024 powders in a planetary ball mill

Fig. 3 shows the cross-section microstructures and main element distributions of the steel substrates with Fe-Al coatings produced under different milling times of 2h (Fig. 3a), 6h (Fig. 3b), and 10h (Fig. 3c). The EDX line scans were performed along the arrow lines marked in Fig. 3 from the inner substrate to the top coating surface. As shown in Fig 3a, the discontinuous and thin diffusion layers were formed on the steel surface at the beginning of the formation of Fe-Al coating. Mechanical milling process made the substrate surface to be more activated. Therefore, the steel surface was easier to be diffused and deposited by Al atoms. The initial diffusion layer of Fe-Al deposited a foundation for the following deposition of coating. The thickening mechanisms of depositing coating were substantiated with highly activated surfaces. Thicker Fe-Al coating was deposited on the surface of steel substrate (Fig. 3b). A flaking phenomenon occurred on the coating surface due to the repeated affects of ball milling during mechanical milling process. After a milling time of 10h, highest coating thickness was finally obtained on the surface of steel substrate (Fig. 3c). Moreover, the diffusion layer generally showed a gradual change of Al element concentrations. When the milling time was 10h, approximately 200 µm thickness of Fe-Al coating was deposited on the steel substrate through the mechanical milling process (Fig. 3c).

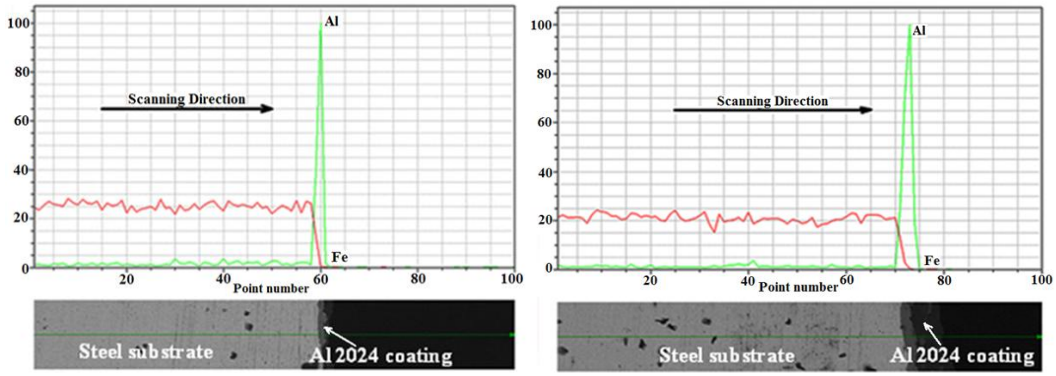

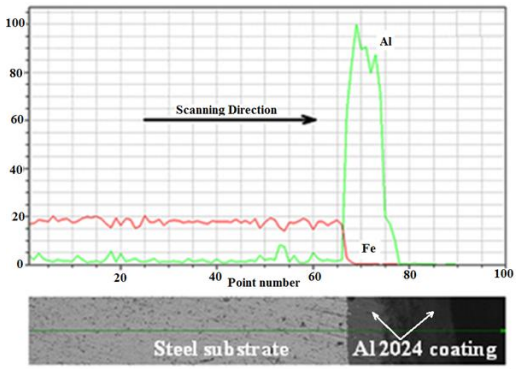

(c)

Figure 3. Cross-section images by SEM and EDX element line scan on Fe-Al coatings prepared using the same rotation speed (400 rpm) and the different milling times of 2h (a), 6h (b), and 10h (c)

3.2. Morphological evaluations

Fig. 4 shows the surface morphologies of the Fe-Al coating at 300 rpm. In the initial stage of milling, ductile Al 2024 powders are subjected to ball-powder-ball and ball-steel substrate-ball collisions. As can be seen in Fig. 4a, dark fields show deposition region of Al 2024 powders while light fields show the steel surface. In the second stage of milling, powders coated on the steel substrate are subjected to ball-steel substrate-ball collisions. Uncovered powders on the substrate tend to deposit on coating layer of the first stage due to ductile coating layer in this stage (Fig. 4b). Furthermore, cold welding process between ductile Al2024 particles is very important for coating process in the second stage (Fig 4b and Fig. 4c). In the final stage of milling, more homogeneous surface coating was obtained for Al 2024 particles (Fig. 4d).

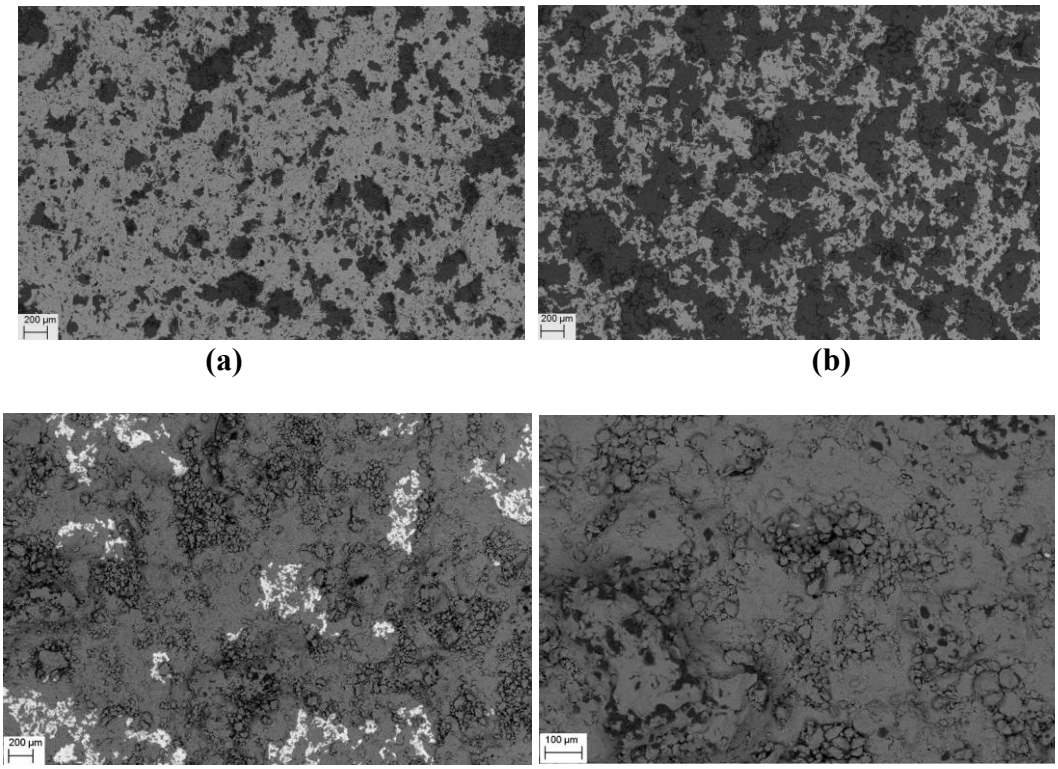

(a) **(b)**

(c) **(d)**

Fig. 4. SEM images showing the characteristic morphologies of the top surfaces of the deposited coatings milling times at 300rpm: (a) 1h, (b) 4h, (c) 8h and (d) 10h

3.3. ANN modeling results

From the well known and widespread identification tools, the root mean squared error (RMSE) and the mean absolute percentage error (MAPE) values were calculated from Eqs.6 and 7 [11]. Models that produce the best estimated values were selected as the forecasting models.

$$RMSE = \sqrt{\frac{1}{N}\sum_{i=1}^{N}(t_i - td_i)^2} \quad (6)$$

$$\mathrm{MAPE} = \frac{1}{\mathrm{N}}\left(\sum_{\mathrm{i}=1}^{\mathrm{N}}\left[\left|\frac{\mathrm{t_i} - \mathrm{td_i}}{\mathrm{t_i}}\right|\right]\right)\times 100 \quad (7)$$

where t_i is the real value, td_i is the model prediction value and N is the number of testing data. Table 1 shows the actual values, degrees of deviation, percentage error rates, RMSE and MAPE calculated using the estimated models. The normalization (scaling) operations were carried out using Eq. 8:

$$\mathrm{X_{norm}} = 2\times\frac{\mathrm{X} - \mathrm{X_{min}}}{\mathrm{X_{max}} - \mathrm{X_{min}}} - 1 \quad (8)$$

where X_{norm} is the normalized value, X is the true value of the variable, X_{min} is minimum value of the data set and X_{max} is the maximum value of the data set.

The predicted values, deviation and % error for the coating thickness on the steel substrate are provided in Tables 1 and 2.

Table 2. Experiment data and predicted output from the ANN network for testing

Sample ID	Milling Speed (rpm)	Particle Size (μm)	Milling Time (h)	Coating Thickness (μm)		
				Measured	Predicted	% Error
3	200	155	4	34	32.71	3.81
6	200	155	10	86	76.51	11.04
8	200	60	2	17	15.97	6.06
11	200	60	8	55	52.74	4.12
13	200	23	1	4	4.16	-4.12
16	200	23	6	34	29.50	13.22
19	300	155	1	20	19.07	4.63
22	300	155	6	105	98.72	5.98
27	300	60	4	27	26.74	0.96
30	300	60	10	174	172.34	0.95
32	300	23	2	16	17.92	-12.00
35	300	23	8	100	118.11	-18.11
38	400	155	2	47	43.72	6.99
41	400	155	8	203	238.24	-17.36
43	400	60	1	22	19.75	10.23
46	400	60	6	135	130.83	3.09
51	400	23	4	38	41.62	-9.51
54	400	23	10	198	193.65	2.20
MAPE				**7.466**		
RMSE				**10.001**		

However, several values were not as close as others, which was due to the errors caused by the material, the measurements and process parameters. These errors could be neglected given

that the learning level of the artificial neural network is 92.5 %. This study revealed that the predictions made using the ANN produced more accurate results. Fig. 5 shows the regression analysis of the ANN model for the volume loss, specific wear rate and surface roughness. The correlation coefficient was obtained to be 0.99, indicating good agreement between the experimental results and the model prediction (for training data set: $R_{\text{coating thickness}}$=0.99964 and for testing data set: $R_{\text{coating thickness}}$=0.99055).

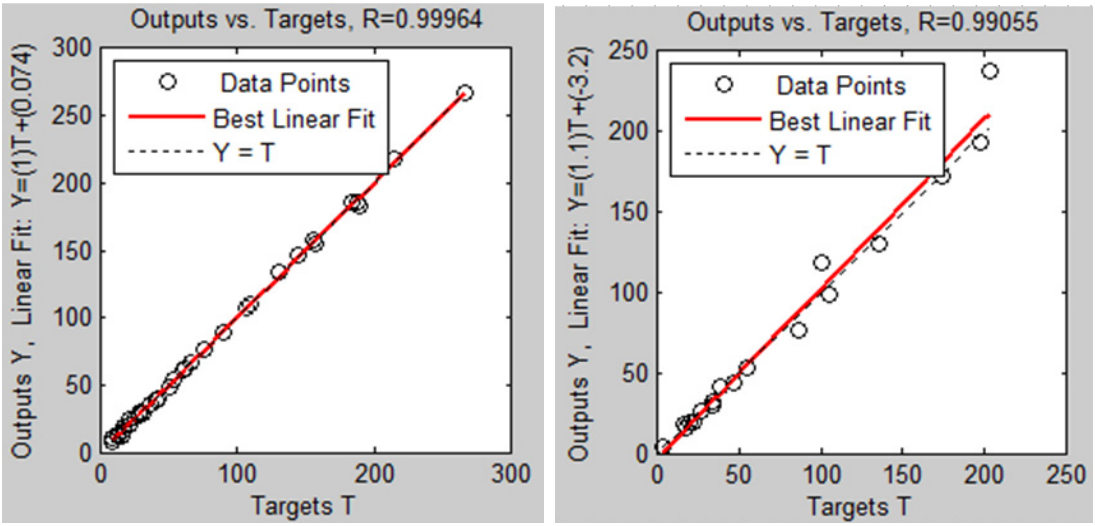

(a) (b)

Figure 5. Regression analysis for the neural network responses and the target for the training data set (a) and the testing data set (b)

A comparative plot of these values was provided in Fig. 6. A comparison between the measured and predicted composite powder properties at the testing stage indicates a high correlation.

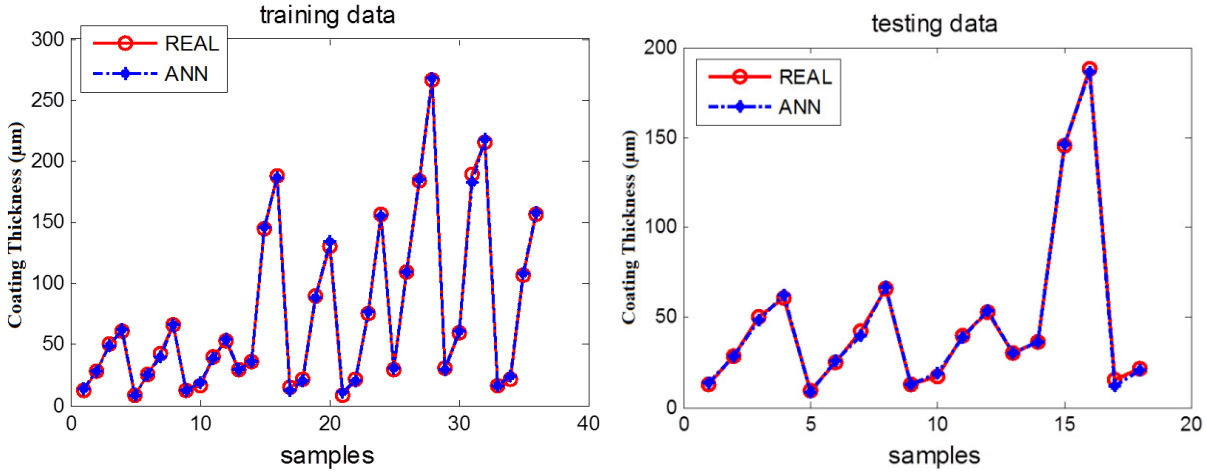

Figure 6. The comparison of measured values and ANN values for the (a) training data set (b) testing data set

4. CONCLUSIONS

The Fe-Al coatings were fabricated on the low carbon steel by mechanical alloying method. It was found that an increase in the applied milling time, the milling speed and size of milled powders affect the coating thickness. The deposition of a uniform coating by mechanical milling is possible, but it requires optimization of milling parameters and properties of as-

received powders so that the uniform distribution of ball-substrate-ball collisions over the processed surface is efficient. The coating thickness on the steel substrate increased with increasing milling time. The coating thickness increased to its maximum value after 10h of milling. The ANN model generated satisfactory results with high correlation coefficients. The mean absolute percentage error (MAPE) for predicted values did not exceed 7.466%. Therefore, using ANN model, results can be estimated satisfactorily which thereby reduces the testing time and cost.

Acknowledgements
The authors are grateful to the Karadeniz Technical University Research Fund for financially supporting this research (No: BTAP-9582). The researchers would also like to thank the Gundogdu Exotherm Service for providing the Al 2024 powders.

REFERENCES

1. Zhan Z, He Y, Wang D, Gao W (2006) Low-temperature processing of Fe-Al intermetallic coatings assisted by ball milling. Intermetallics 14:75-81.
2. Canakci A, Ozsahin S, Varol T (2012) Modeling the influence of a process control agent on the properties of metal matrix composite powders using artificial neural networks. Powder Technol 228:26-35.
3. Guessasma S, Montavon G, Gougeon Patrick, Coddet C (2003) Designing expert system using neural computation in view of the control of plasma spray processes. Mater Des 24: 497-502.
4. Çetinel H, Öztürk H, Çelik E, Karlık B (2006) Artificial neural network-based prediction technique for wear loss quantities in Mo coatings. Wear 261:1064-1068.
5. Rashidi AM, Hayati M, Rezaei A (2012) Application of artificial neural network for prediction of the oxidation behavior of aluminized nano-crystalline nickel. Mater Des 42: 308-316.
[6] Guessasma S, Coddet C (2004) Microstructure of APS alumina-titania coatings analysed using artificial neural network. Acta Mater 52:5157-5164.
[7 Pham DT, Liu X (1995) Neural Network for Identification, Prediction and Control. 2nd printing, Springer-Verlag, London.

[8] Zhang C, Kanta AF, Li CX, Li CJ, Planche MP, Liao H, Coddet C. (2009) Effect of in-flight particle characteristics on the coating properties of atmospheric plasma-sprayed 8 mol% Y_2O_3–ZrO_2 electrolyte coating studying by artificial neural Networks. Surf Coat Int 204:463-469.
[9] Hayajneh M, Hassan AM, Alrashdan A, Mayyas AT (2009) Prediction of tribological behavior of aluminum-copper based composite using artificial neural network. J Alloys Compd 470:584-588.
[10] Urakaev FK, Boldyrev VV (2000) Mechanism and kinetics of mechanochemical processes in comminuting devices: 2. Applications of the theory. Experiment. Powder Technol 107:197-206.
[11] Canakci A, Varol T, Ozsahin S (2013) Analysis of the effect of a new process control agent technique on the mechanical milling process using a neural network model: Measurement and Modeling, Measurement 46:1818-1827.

LONGER RANGE CORRELATIONS IN LIQUID AND AMORPHOUS $Al_{91}Tb_9$ ALLOY

Mert Ovun* Tuba Demirtas, Matthew J. Kramer***, Yunus Eren Kalay******

* Middle East Technical University, Turkey

ovun@metu.edu.tr

**Middle East Technical University, Turkey

demirtas.t@gmail.com

*** Ames Laboratory US DOE, USA

mjkramer@ameslab.gov

****Middle East Technical University, Turkey

ekalay@metu.edu.tr

ABSTRACT

The structural correlations within the $Al_{91}Tb_9$ marginal glass forming alloy was investigated through high-energy synchrotron X-ray diffraction (HEXRD) and ab-initio constrained reverse Monte Carlo simulations (RMC). The diffraction patterns corresponding to solid and liquid phases show a distinct pre-peak formation at relatively low scattering angles. Short-range structural order of Al- and Tb-centered clusters was investigated using ab-initio implemented RMC simulations based on the HEXRD patterns. The Voronoi polyhedral analyses of these clusters indicated high population of Al around Tb atoms for the first shell neighborhood. Some of these clusters show structural similarities with the pseudo-crystalline structure of binary Al-Tb system.

Keywords: *Marginal glass forming alloys, RMC simulations, ab-initio Molecular Dynamics, HEXRD*

AMORF VE SIVI $Al_{91}Tb_9$ ALAŞIMINDA UZUN ERİM ATOMİK KORELASYONLARIN İNCELENMESİ

ÖZ

$Al_{91}Tb_9$ marjinal cam oluşturucu alaşımında varolan yapısal ilişkiler yüksek enerjili X-ışını kırınımı (HEXRD) ve ab-initio ile sınırlandırılmış ters Monte Carlo simülasyonları (RMC) kullanılarak incelenmiştir. Katı ve sıvı fazlara ait kırınım motifleri düşük dağılım açılarında belirgin bir ön-tepe oluşumuna işaret etmektedir. Al- ve Tb-merkezli atom kümelerindeki düşük-menzilli yapısal düzen, HEXRD deneylerine bağlı ab-initio ile sınırlandırılmış RMC simülasyonlarıyla incelenmiştir. Bu atom kümelerinin Voronoi çokyüzlü analizleri, terbiyum atomlarının birinci-sıra komşuları içerisinde yüksek miktarlarda alüminyum atomu olduğuna işaret etmektedir. Bu atom kümelerinden bazıları, Al-Tb sistemine ait kristalimsi yapılarla yapısal benzerlik göstermektedir.

Anahtar Kelimeler: *Marjinal cam oluşturucu alaşımlar, RMC simülasyonları, ab-initio Moleküler Dinamik, Yüksek Enerjili XRD*

1. INTRODUCTION

As compared to conventional bulk metallic glass; marginal glass forming alloys require high solidification rate which is on the order of 10^5K/s. These alloys are promising materials to produce nanocrystals for several critical applications due to their ability of forming high number density of nuclei upon crystallization [1-5]. Lightweight high-strength Al-RE based alloys [1] and magnetically soft and hard Fe-RE (RE: rare-earth element) based alloys [3] are two well-known classes of marginal glass formers. Unlike the bulk metallic glasses, the devitrification process of marginally amorphous metals quite often results in the formation of very high number densities of primary crystals (10^{21}-10^{24} m^{-3}) with sizes of less than 50 nm. Despite the volume of the research [1-5], an exact explanation for the mechanism underlying the formation of highly populated nanocrystals is still missing.

The previous studies on Al-RE and Al-RE-TM amorphous alloys have been resulted in two main hypothesizes with respect to the formation of highly populated nanocrystals after low-temperature annealing process. The first one relies on the fact that small fractions of crystallite nuclei already exist in the as-quenched solid [6]. This hypothesis was tested by using melt-spun and cold-rolled Al-Sm amorphous specimens [6]. The existence of highly populated Al-nanocrystals, as observed for melt-spun specimens, was not detected in the cold rolled specimens upon similar heat treatment processes. Moreover, fluctuation electron microscopy signals [7] indicating an fcc-like medium-range order (MRO) for Al atoms in melt-spun alloy were absent for cold-rolled specimen. The other approach is based on phase separation [5, 8] in amorphous matrix. The origin of the phase-separation was explained through a time independent homogeneous nucleation theory called as coupled-flux nucleation [8-9]. Both approaches were questioned on different aspects [10-12]. For instance, a phase separation was reported for $Al_{88}Gd_6La_2Ni_4$ [8] alloy but not observed for $Al_{88}Gd_6ErNi_4$ [13] or a two-stage fcc nanocrystallization was indicated for several Al-TM-RE amorphous which contradicts with "quenched-in" nuclei hypothesis [14]. It has also been stated that the phase separation in Al may even actually present at nanoscales in the as-quenched state [5, 8-12, 15]. APT results collected from the specimens annealed to temperatures just before the crystallization temperature, point out coalescence of pure Al regions which reduce the population of pure Al clusters [11]. Fluctuation electron microscopy (FEM) studies [7-11] from both as-quenched and annealed specimens clearly reveal some medium range order. Therefore, the phase-separated Al and RE rich regions may possess their own atomic structure at a first place in the as-quenched state.

In this study, short to medium range correlations in amorphous and liquid $Al_{91}Tb_9$ alloy was investigated in details by using high energy X-ray diffraction (HEXRD) and ab-initio Molecular Dynamics (AIMD) simulations. Relatively large 3D configurations were constructed by using reverse Monte Carlo (RMC) simulations to investigate higher order correlation in the medium range order scale. The consistency of RMC was improved by constraining the simulations with ab-initio MD results. The chemical and topological orders in the simulated cells were investigated in details with Voronoi polyhedral analyses.

2. EXPERIMENTAL PROCEDURE

The $Al_{91}Tb_9$ ingots were produced by electric arc melting under Ar atmosphere by using highly pure Al (99.99 wt%) and Tb (99.9 wt%) elements. Amorphous ribbons with widths of 2.0 - 3.0 mm and thicknesses of 30 - 50 μm were produced from $Al_{91}Tb_9$ ingots by Cu-block single melt-spinner under Ar atmosphere at a tangential speed of 30 m/s. The final compositions were verified by microprobe analysis.

The high energy X-ray diffraction studies were performed by using the high-energy transmission synchrotron X-ray diffraction (HEXRD) at the Advanced Photon Source at Argonne National Laboratory. Specimens for liquid phase analysis were cast into 2 mm diameter rods, inserted into quartz capillaries and sealed under Ar atmosphere. Capillaries were lined with carbon to reduce the interaction between the quartz and the molten alloy at elevated temperatures. The sealed carbon-lined quartz capillaries were heated up to 1323 K and exposed to 100 keV of X-rays corresponding to a wavelength of 0.0124 nm. The diffraction data from molten alloy were collected in transmission (Debye-Scherrer) geometry by a MAR charge coupled device (CCD) with 60 seconds of exposure time. Similar diffraction patterns were collected from the blank holder and empty carbon-lined quartz capillary for background corrections. The diffraction data for amorphous state were collected from free-standing melt-spun ribbons at room temperature. The raw HEXRD data collected for amorphous and liquid were corrected for polarization, absorption, multiple, Compton scattering and converted to the total structure factor function, S(Q) by a procedure described in [15].

The ab-initio Molecular Dynamics (MD) simulations were performed by using Vienna Ab-initio Simulation Package (VASP). Periodic boundary conditions were applied with constant number of particles, volume and temperature (NVT) by using Nosé-Hoover thermostat to control the temperature [16-19]. 200 atoms were distributed randomly in a box cell with correct stoichiometry of the produced alloys. Initially, system was heated up to 2500 K to erase the memory effects for preparing the liquid Al-Tb alloy then subsequently cooled down to. 1900 K, 1700 K, 1309 K, 1247 K, 1208 K and to room temperature (300 K) respectively.

RMC simulations were conducted by using RMC++ simulation package [20] in order to construct 3D configuration with large number of atoms for studying longer range correlations within amorphous and liquid states. 20,000 atoms with the proper stoichiometry, density and nearest neighbor distances were distributed randomly in a cubic box with periodic boundary conditions. In order to overcome the fundamental weaknesses of RMC [20, 21], simulations were constrained with experimentally measured S(Q) and AI MD simulated partial pair-correlation function. It is widely accepted that, AIMD is effective to describe the short range topological and chemical order in amorphous and liquid structures. Therefore, the density of the alloy and the first shell neighborhood of Al and Tb atoms were constrained under MD simulations. The cut-off distances for the partial pairs for the first shell distances in the RMC calculations were chosen from direct Fourier transforms of experimental S(Q) and ab-initio MD calculations.

3. RESULTS AND DISCUSSION

AIMD is an effective technique to study the topological and chemical correlations at short-range order (SRO). However because of its slow-moving dynamic nature, it is elusive to extend its capabilities beyond the first nearest-neighbor shell. In that sense, reverse Monte Carlo (RMC)

calculations were conducted using 20,000 atoms via experimentally collected synchrotron HEXRD S(Q)-Q data as the input data. In order to overcome the well-known entropy problems of RMC [20-21], the density, cut-off distances and first shell neighborhood (SRO) were constrained with ab-initio MD calculations. The structure factor S(Q) measured by HEXRD and calculated by RMC are shown in Figure 1. A reasonably good agreement was achieved in the overall Q regions (including the pre-peak) with the applied constraints at all temperatures. The PCFs of amorphous and two different liquids of $Al_{91}Tb_9$ alloy were also calculated using RMC analysis and the results have been compared with ab-initio analysis. A remarkably good fit was observed especially in Al-Al and Al-Tb curves as indicated in Figure 2.

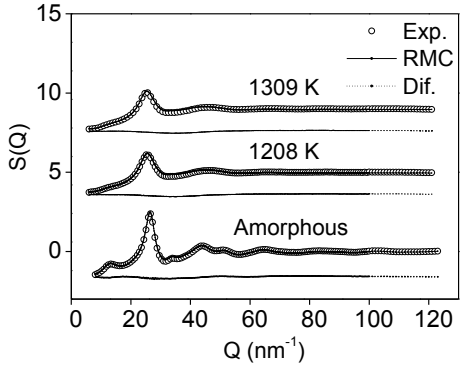

Figure 1. Total structure function data measured (circles) and calculated using RMC (solid line) for amorphous and two different liquids (at 1208 K and 1309 K) $Al_{91}Tb_9$. The bottom lines show the difference between experimental and calculated S(Q) data.

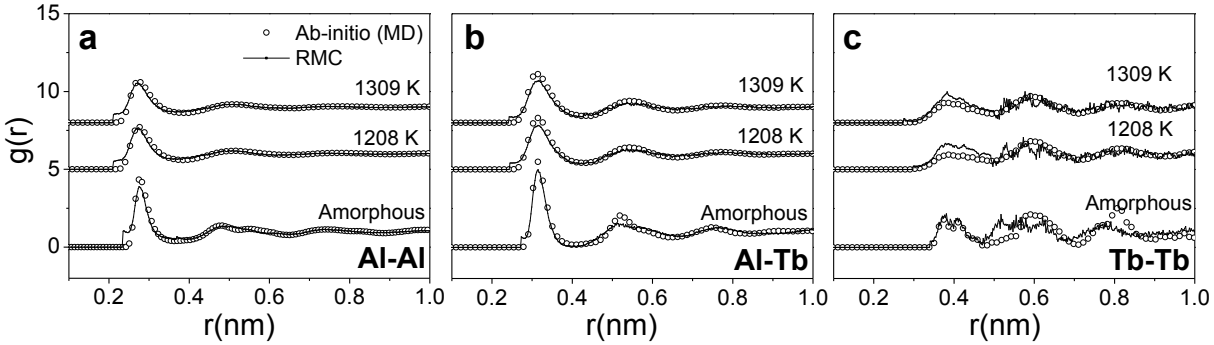

Figure 2. Partial pair distribution function (PDFs) data calculated using ab-initio (circles) and RMC (solid line) for amorphous and two different liquids of $Al_{91}Tb_9$ alloy for (a) Al-Al, (b) Al-Tb and (c) Tb-Tb respectively.

In order to get the insights into the presence of any longer range correlations; 3D configuration created by RMC was further investigated with several polyhedral analyses. Figure 3 displays the

predominant types Voronoi polyehdra (VP) in amorphous and liquid configurations. These indices were constructed according to the type of the center atom. Although the perfect icosahedral structure with a VP index of <0,0,12,0,0> is not on the top list several icosahedral like VPs like <0,2,8,2,0>, <0,1,10,2,0>, <0,3,6,4,0> were detected particularly around Al atoms. On the other hand Tb atoms prefer to host bcc-like clusters such as <0,2,8,6,0>, <0,1,10,5,0> and <0,2,8,5,0>. According to Voronoi Tessellation analysis, each atom in the space can be represented by a Voronoi polyhedron while number of faces forming a polyhedron corresponds to the coordination number of the given atom. Every single face of the polyhedron determines the border between the central atom and one of its neighboring atoms, and the number of edges forming the face gives the number of common neighbors of the corresponding atom pair. Thus, the method provides a powerful set of information about local atomic inclination of the system in different conditions. From higher temperatures in liquid to frozen amorphous phase, the diversity of Voronoi indices were decreased from 2746 to 1475 species implying an increase in order. Moreover, particular types of polyhedrons have been noticed to become dominant (Fig. 3). According to the classification made before [24], among Al-centered clusters, icosahedral-like group such as <0, 0, 12, 0, 0>, <0, 1, 10, 2, 0> and <0, 2, 8, x, 0> (with low x values) are highly increased in number in glass state. Existence of crystal-like groups (e.g. <0, 4, 4, x, 0> where x=4, 5, 6) is also a bit more developed in glass while still present in liquid. An increase in icosahedral-like Tb-centered clusters in liquid state is also seen clearly. The complete short-range topological evolution highly resembles to the previous study on Al-Sm marginal glass former system [10].

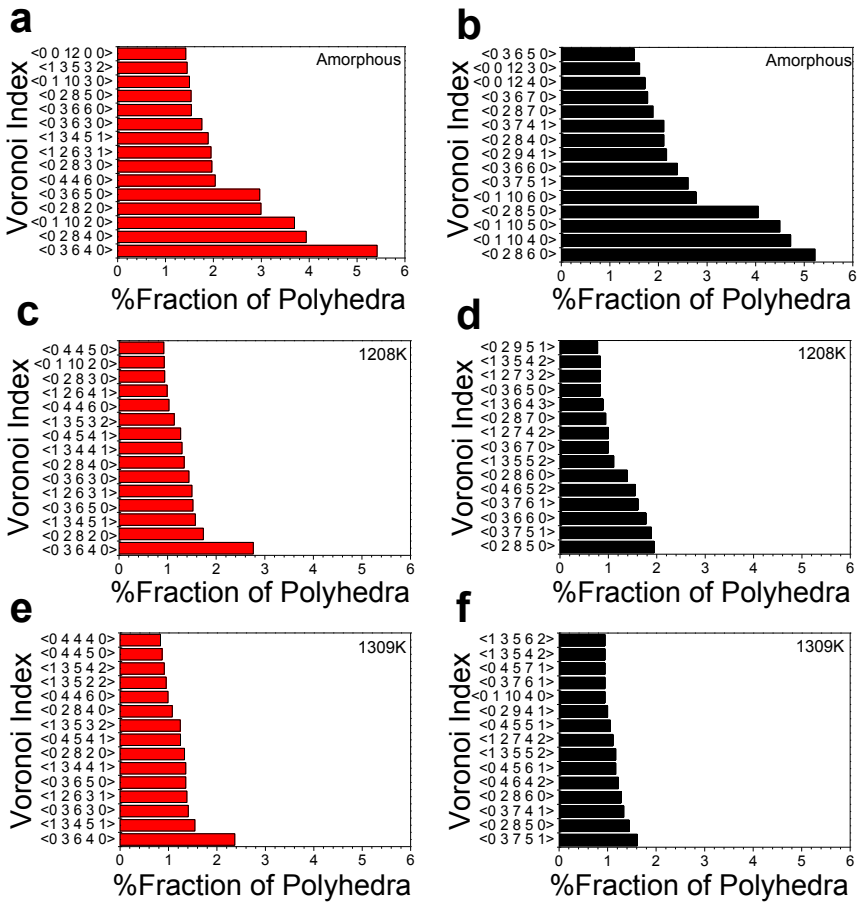

Figure 3. Most populated VP histograms of (a, c, e) Al and (b, d, f) Tb centered structure models for amorphous (a, b), 1208K (c, d) and 1309K (e, f) $Al_{91}Tb_9$ alloy.

The pre-peak observed on amorphous diffraction patterns, also called as first sharp diffraction peak, has been discussed extensively in the literature. Several works on metallic, network glasses and liquids have reported the existence of pre-peak in X-ray or neutron diffraction patterns. The structural origin of the pre-peak has often related to quasi-periodic crystal, chemical short-range order, structural medium-range order (MRO),and ordered interstitial void formation within the disordered structure. In our previous studies with $Al_{90}Sm_{10}$ marginal glass forming alloys, some MRO structure corresponding to a high-temperature metastable pseudo-tetragonal $Al_{11}Sm_3$ (SG: I4/mmm) were detected by HEXRD and RMC studies [15]. Similarly, using fluctuation electron microscopy (FEM), MRO of pseudo-trigonal Al_3Tb was highlighted for as-quenched $Al_{90}Tb_{10}$ alloy [11]. When the current HEXRD and ab-initio constrained RMC results are considered, there are some common structural insights with the tetragonal $Al_{11}Tb_3$ (SG: I4/mmm), trigonal Al_3Tb(SG:R-3m) and metastable hexagonal $Al_{17}Tb_2$ (SG:$P6_3$/mmc). A tetragonal $Al_{11}Tb_3$ (SG: I4/mmm) structure has not been yet reported for Al-Tb system. But, it should be noted that Al-Tb is not a well-studied binary alloy system. Therefore, further thermodynamic and/or high-temperature XRD studies may reveal the existence of such structure. In this study, a hypothetical t-$Al_{11}Tb_3$ with I4/mmm space group symmetry is adapted by correcting the lattice parameters using atomic radii. Structural features of the hypothetical tetragonal $Al_{11}Tb_3$, trigonal Al_3Tb and metastable hexagonal $Al_{17}Tb_2$ are given in Figure 4. Both of these structures have strong Bragg reflections in close vicinity of 12.8 nm^{-1} which matches with the observed position of the pre-peak in amorphous Al-Tb system. Other than the position of the pre-peak, the atomic configurations calculated by ab-initio constrained RMC simulations have similarities with these two intermetallic structures. Here it should be noted that, the efforts are not towards to match up the extra peaks in HEXRD pattern with the possible known crystal structures of Al-Tb, but instead to take attention to the specific distribution of the atoms within these crystal structures which give rise to high coordination of RE atoms and Bragg reflections at pre-peak position. When these crystal structures are considered, it is clearly seen that they consists of repetition of SRO clusters of Tb centered atoms surrounded by a definite number of Al atoms. Particularly, in h- $Al_{17}Tb_2$ and t-$Al_{11}Sm_3$ clusters of Tb with 18 or 20 Al atoms and 16 Al atoms are self-repeating respectively. The repetition of Al surrounded Tb clusters naturally causes the high-coordination number around RE atoms, and gives specific Al-Al, Al-RE and RE-RE distances in the first shell neighborhood. Therefore, instead of directly relating the disordered structure to well-defined crystal structures of Al-Tb, it is more logical to correlate to MRO clusters of Tb centered Al atoms. The correlation length calculated from HEXRD is on the order of 2.4 nm for the solid amorphous state which corresponds to 5 or 6 repeating layers of corresponding planes for pseudo crystal structure.

In that sense, the clusters of Tb centered Al atoms are thought to exist in the as-quenched state by forming a network of MRO structure. The formation of a network was previously shown by atom probe tomography experiments in Al-Tb amorphous system [11]. The results of this previous study indicated regions of interconnected Tb rich network separating pure Al islands with an average size of 1 nm.

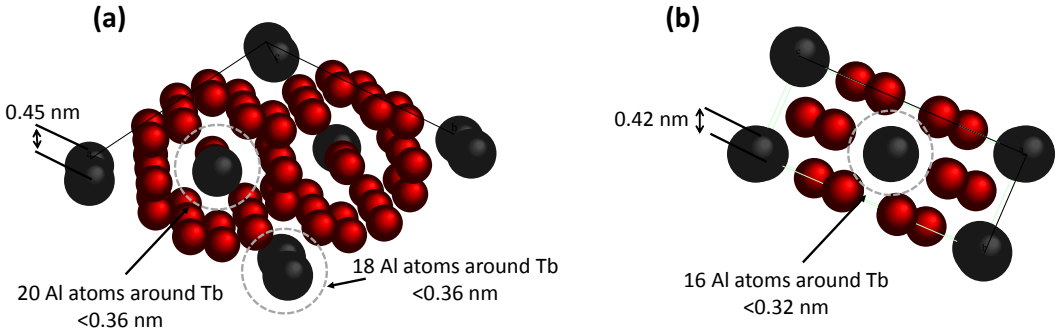

Figure 4. 3D representation of (a) h- $Al_{17}Tb_2$ (SG: $P6_3/mmc$) and (b) hypothetical t-$Al_{11}Tb_3$ (SG: I4/mmm) compounds. The lattice parameters for hypothetical t-$Al_{11}Tb_3$ were estimated using atomic radii.

Al-RE marginal glass former alloys exhibit an appealing phenomenon of fcc-Al nanocrystallization during the first stages of devitrification with an extreme nucleation density emphasizing the limitations of the classical nucleation theory. According to our previous APT and current ab-initio constrained HEXRD results, we believe that some regions may possess MRO structure having some pseudo-crystal periodicity in the as-solidified structure with large correlation lengths as calculated from HEXRD. These regions may be responsible of potential nucleation sites for stable and metastable intermetallic nanocrystals and rare-earth concentrated network with high fraction of icosahedral-like groups enveloping Al-rich regions and acting as a diffusion barrier due to its low atomic mobility. The obstruction of rare-earth rich barrier results in limited growth of fcc-Al nanocrystals.

ACKNOWLEDGEMENT

The work at METU was supported by METU-BAP (Project code: BAP-08-11-2011-106). The high-energy X-ray work at the MUCAT sector of the APS was supported by the US Department of Energy, Office of Science, and Basic Energy Sciences under Contract No. DE-AC02-06CH11357.

REFERENCES

1. A. Inoue, Amorphous, nanoquasicrystalline and nanocrystalline alloys in Al-based systems, Prog. Mater. Sci. 43 (1998) 365-520
2. J.H. Perepezko, R.J. Hebert, R.I. Wu Wilde, Primary crystallization in amorphous Al-based alloys, J. Non-Cryst. Solids 317 (2003) 52-61
3. T. Kulik, Nanocrystallization of metallic glasses, J. Non-Cryst. Solids 287 (2001) 145-161
4. L. Battezzati, S. Pozzovivo, P. Rizzi, Nanocrystalline aluminum alloys, ENN 6 (2004) 341-364

5. K.F. Kelton, M.K. Miller, K.K. Sahu, N. A. Mauro, L. Longsreth-Spoor, D. Saha, Z. Nussinov, Phase separation mediated devitrification of $Al_{88}Y_7Fe_5$ glasses, Acta Mater. 58 (2010) 4199-4206

6. G. Wilde, H. Sieber, JH. Perepezko, Glass formation versus nanocrystallization in an $Al_{92}Sm_8$ alloy, Scripta Mater. 40 (1999) 779-783

7. W.G. Stratton, J. Hamann, J.H. Perepezko, P.M. Voyles, Aluminum nanoscale order in amorphous $Al_{92}Sm_8$ measured by fluctuation electron microcopy, Appl. Phys. Lett. 86 (2005) 141910-1-3

8. A.K. Gangopadhyay, T.K. Croat, K.F. Kelton, The effect of phase separation on subsequent crystallization in $Al_{88}Gd_6La_2Ni_4$, Acta Mater. 48 (2000) 4035-4043

9. K.F. Kelton, Time-dependent nucleation in partitioning transformations, Acta Mater. 48 (2000) 1967-1980

10. Y.E. Kalay, C. Yeager, L.S. Chumbley, M.J. Kramer, I.E. Anderson, Initial crystallization in a nanostructured Al-Sm rare earth alloy, J. Non-Cryst. Solids 356 (2010) 1416-1424

11. Y.E. Kalay, I. Kalay, J. Hwang, P.M. Voyles, M.J. Kramer, Local chemical and topological order in Al-Tb and its role in controlling nanocrystal formation, Acta Mater. 60 (2012) 994-1003

12. Y.E. Kalay, L.S. Chumbley, I.E. Anderson, Characterization of a marginal glass former alloy solidified in gas atomized powders, Mater. Sci. Eng. A 490 (2008) 72-80.

13. N. Tian, M. Ohnuma, T. Ohkubo, K. Hono, Primary crystallization of an Al88Gd6Er2Ni4 metallic glass, Mater. Trans. JIM 46 (2005) 2880-2885

14. Q. Li, E. Johnson, A. Johansen, L. Sharlot-Kristensen, On glass formation in rapidly solidified aluminum-based alloys, J. Mater. Res. 7, (1992) 2756-2764

15. Y. E. Kalay, L. S. Chumbley, M. J. Kramer, I. E. Anderson, Local structure in marginal glass forming Al-Sm alloy, Intermetallics 18 (2010) 1676-1682

16. G. Kresse, D, Joubert, From ultrasoft pseudopotentials to the projector augmented-wave method, Phys. Rev. B 59 (1999) 1758-1775

17. G. Kresse, J. Hafner, Abinitio molecular-dynamics for liquid-metals, Phys. Rev. B 47 (1993) 558-561

18. G. Kresse, J. Furthmüller, Efficient iterative schemes for ab initio total-energy calculations using a plane-wave basis set, Phys. Rev. B 54 (1996) 11169-11186

19. G. Kresse, J. Furthmüller, Efficiency of ab-initio total energy calculations for metals and semiconductors using a plane-wave basis set, Comput. Mater. Sci. 6 (1996) 15-50

20. R.L. McGreevy, Reverse monte carlo modelling, J. Phys–Condens Matter 13 (2001) 877-913

21. Y.Q. Cheng, E. Ma, Atomic–level structure and structure–property relationship in metallic glasses, Prog. Mater. Sci. 56 (2011) 379-473

22. B.E. Warren, X-ray diffraction, Dover Publications Inc., New York 1990

23. J.M. Cowley, X-Ray measurement of order in single crystals of Cu_3Au, J Appl Phys 21 (1950) 24-29.

24. J. Hwang, Z.H. Malgarejo, Y.E. Kalay, I. Kalay, M. J. Kramer, D. S. Stone, P. M. Voyles, Nanoscale structure and structural relaxation in $Zr_{50}Cu_{45}Al_5$ bulk metallic glass, Phys. Rev. Lett. 108 (2012) 195505_1-5

25. Y.Q. Cheng, H.W. Sheng, E. Ma, Relationship between structure, dynamics and mechanical properties in metalic glass-forming alloys, Phys. Rev. B 78 (2008) 014207_1-7

DETERMINING GRAPHENE LAYERS NUMBER AND N-LAYER REGION COVERAGE BY XRD DATA DISTRIBUTION MODEL

Beti ANDONOVIC, Anita GROZDANOV, Perica PAUNOVIĆ, Aleksandar DIMITROV Abdulakim ADEMI

Faculty of Technology and Metallurgy, SS Cyril and Methodius University, Skopje, Macedonia
beti@tmf.ukim.edu.mk

ABSTRACT

A model consisting of an equation which includes graphene thickness distribution is used to calculate theoretical 002 XRD peak intensities. An analysis was performed upon graphene samples produced by two different electrochemical procedures: electrolysis in aqueous electrolyte and electrolysis in molten salts, both using reverse change of the applied potential. The model applied to the corresponding 2θ interval enables obtaining theoretical curves that exhibit fitting with a sufficient accuracy to the XRD intensities curves of the studied graphene samples. The employed equation parameters make it possible to calculate the n-layer graphene regions coverage of the graphene samples, and the average value for number of graphene layers. Results of the analysis are in agreement with the calculated number of graphene layers from Raman spectra C-peak position values, and indicate that graphene samples are few-layered.

Key words: Graphene, electrochemical production, XRD analysis, layers.

1. INTRODUCTION

Graphene is 2D building unit of all wide-variety carbon allotropes, having unique and exotic properties largely due to its structure. Graphene can be produced by many ways such as mechanical exfoliation of graphite, chemical vapor deposition (CVD) of carbon bearing gases on the surface of copper films [3], cutting open nanotubes [4]. Electrochemical approach is a proven low-cost method for a high-yield production of graphene.

Depending on the production procedure, graphene can be produced as a mixture of monolayers, bi-layers and multilayers (3–10 monolayers) in form of flakes or flat sheets [5].

Herein, an XRD pattern around a graphene 002 peak was used for layer number non-uniform distribution determination for graphene samples obtained by two different electrochemical procedures: electrolysis in aqueous electrolyte and electrolysis in molten salts, both using reverse potential.

2. MODEL THAT PROVIDES CALCULATION OF GRAPHENE THICKNESS DISTRIBUTION BY XRD DATA

The XRD pattern was analyzed by using the following Equation 1 that uses Laue functions which includes graphene thickness distribution and certain parameters, hence XRD intensities of the curves were calculated thereof: [6]

$$|F|^2 \sim |f(\theta)|^2 \left| \sum_{j=0}^{N} \beta_j e^{jka_j i} \right|^2 \quad (1)$$

where F is a structure factor, N is the number of graphene layer, $|f(\theta)|$ is an atomic scattering factor which varies from 6.00 to 6.15 e/atom with incident radiation ranging from 2 to 433 KeV, $ka_j = (4\pi d_j \sin\theta)/\lambda$, where d_j is a lattice spacing between jth and (j-1)th layer, θ is an angle between the incident ray and the scattering planes, λ is a wavelength of X-ray, and β_j is an occupancy of jth graphene layer. The value of β_j is between 0 and 1. The employed equation parameters β_j make it possible to calculate the n-layer graphene regions coverage of the graphene samples produced by the two electrochemical procedures.

2.1. Graphene produced by electrolysis in molten salts and model (1)

Two graphene samples produced by electrolysis in molten salts are considered and discussed herein: graphene sample 2G and graphene sample x.

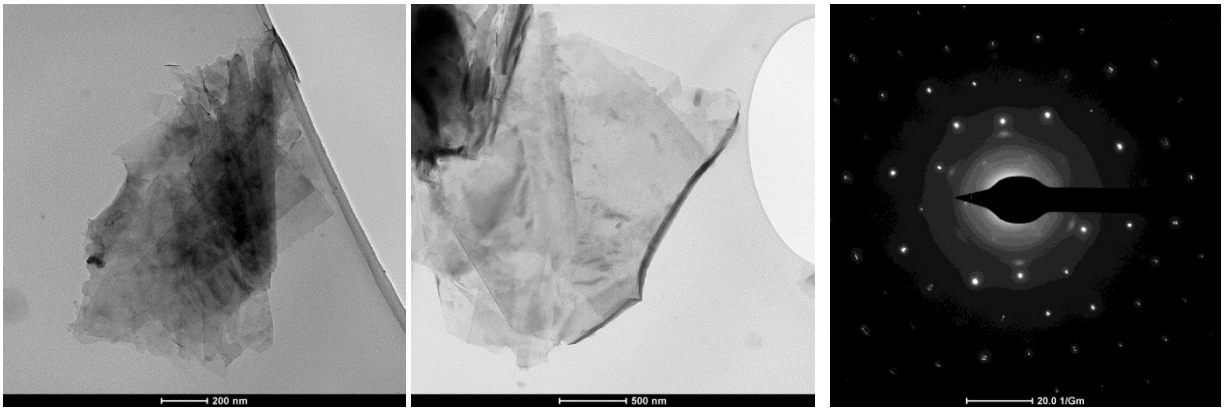

Figure 1. a) TEM images of 2G graphene sheets; b) Diffraction pattern of image

Using Eq. (1), XRD intensities of the curves in Fig. 2 are calculated as further discussed. The three red lines are calculated curves from the Eq. 1 for $\beta_j \neq 1$, which suggests that the number of graphene layers has a distribution.

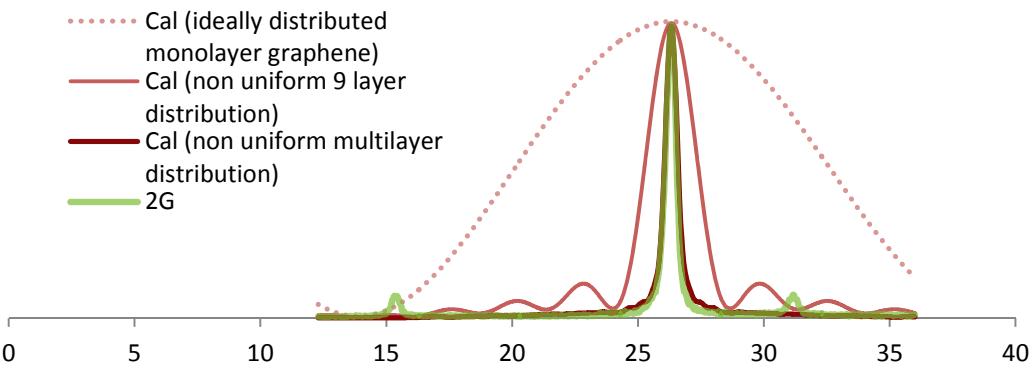

Figure 2. Non uniform multilayer distribution curve for Sample 2G calculated from Eq.(1)

The broadest red dotted line in Fig. 2 is calculated curve for ideally distributed monolayer graphene, the light red line which is narrower than the monolayer graphene line, but broader than the green experimental curve, is calculated curve for a non uniform distribution of graphene layers number for a 9-layered graphene. The dark red line is calculated curve for a non uniform distribution of graphene layers number for a multi-layered graphene, which exhibits a good fitting to the experimental curve, as it is symmetrical and the correlation coefficient is $\rho = 0.986$. According to its β_j parameters, the coverages of n-layer graphene regions are calculated as in Table 1 a).

Apparently, the dominant structure is few-layered, and the average value for number of graphene 2G layers is calculated as N_{GL}=2.87 for the dominant structure and N_{GL}=5.16 for the overall structure.

In Fig.3 a), there are calculated theoretical curves from Eq. 1 presented in red, for graphene sample x, and the experimental curve x in green. In Fig 3 b), there is part of the Raman spectrum for sample x, showing off its C-peak. Its position $\mathrm{Pos}(C)_N$ is directly connected to the graphene layers number N, and it varies with N as in the formula: [7]

$$\mathrm{Pos}(C)_N = \sqrt{\frac{2\alpha}{\mu}}\sqrt{1+\cos\left(\frac{\pi}{N}\right)}$$

where $\alpha = 12.8\times10^{18}\,\mathrm{Nm}^{-3}$ is the interlayer coupling, and $\mu = 7.6\times10^{-27}\,\mathrm{kg\,\mathring{A}}^{-2}$ is the graphene mass per unit area.

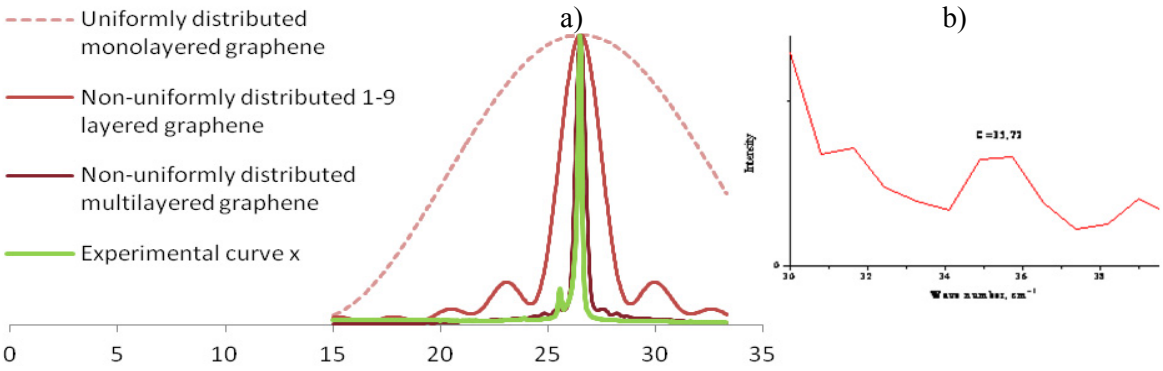

Figure 3. a) Non uniform multilayer distribution curve for Sample x calculated from Eq.1; b) C-peak position in Raman spectrum for graphene sample x

According to the analysis of the XRD 002 peak, the n layer region coverages are as in Table 1 b).

Table 1. a) Coverages of n-layer 2G graphene regions
b) Coverages of n-layer x graphene regions

a)			b)		
	Monolayer region coverage	~ 35%		Monolayer region coverage	~ 18.75%
	2-3 layers region coverage	~ 5-10%		2 layers region coverage	~ 21.25%
	5-6 layers region coverage	~ 5%		3 layers region coverage	~ 3.75%
	7-8 layers region coverage	~ 5%		4-6 layers region coverage	~ 2.5%
	9-10 layers region coverage	~ 5%		7-8 layers region coverage	~ 2.5%
	> 10 layers region coverage	< 20%		9-10 layers region coverage	~ 1.25%
				> 10 layers region coverage	< 25%

The average value for number of graphene x layers is calculated as N_{GL}=2.4 for the dominant structure and N_{GL}=7.43 for the overall structure.
According to the C-peak position, the number of graphene x layers for sample x is N=2.54.

2.2. Graphene produced by electrolysis in aqueous electrolyte and model (1)
Graphene samples 4 and 10 produced by electrolysis in aqueous solution, using reverse potential, are considered herein and analyzed.

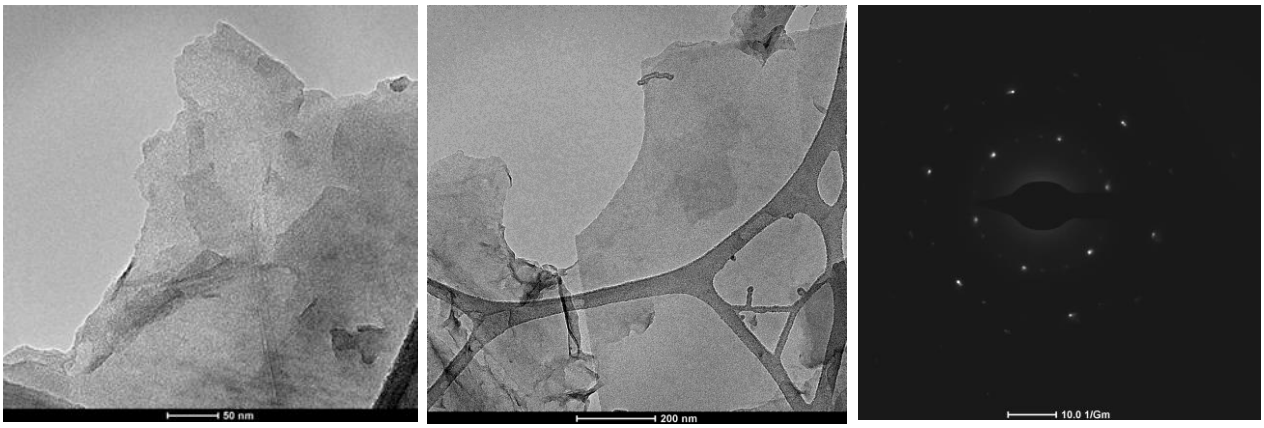

Figure 4. a) TEM images of Sample 4 graphene sheets; b) Diffraction pattern of image

The three blue lines in Fig. 5 are calculated curves from the Eq. 1 for $\beta_j \neq 1$, which suggests that the number of graphene layers has a distribution.

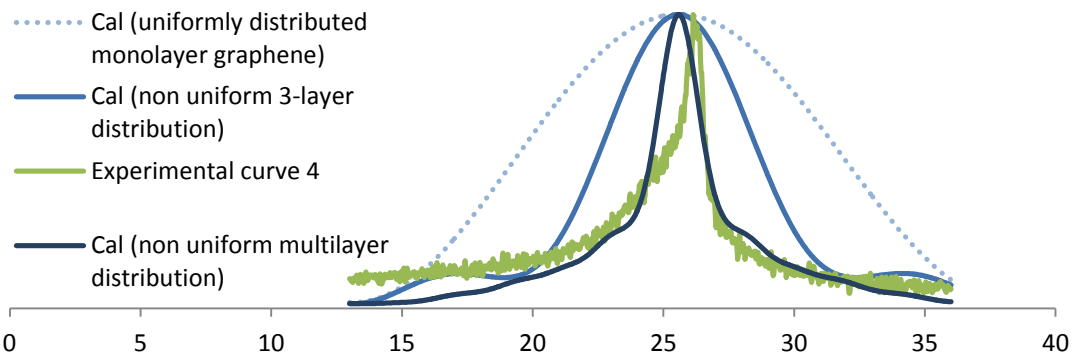

Figure 5. Non uniform multilayer distribution curve for Sample 4 calculated from Eq.1

The broadest blue dotted line in Fig. 5 is calculated curve for uniformly distributed monolayer graphene, the light blue line which is narrower than the monolayer graphene line, but broader than the green experimental curve 4, is calculated curve for a non uniform distribution of graphene layers number for a 3-layered graphene. The dark blue line is calculated curve for a non uniform distribution of graphene layers number for a multi-layered graphene. There is a noticeable discrepancy with the experimental curve due to its asymmetry. However, as the correlation coefficient is $\rho = 0.92$, it provides an additional insight into n-layer graphene regions share, and the results are in agreement with the results obtained by other methods. According to its β_j parameters, the coverages of n-layer graphene regions are calculated as in Table 2 a).

According to these calculations, the dominant structure is few-layered, and the average value for number of sample 4 graphene layers is calculated as N_{GL}=2.57 for the dominant graphene structure and N_{GL}=4.25 for the overall graphene structure.

In Fig. 6 the three blue lines are calculated curves from the Eq. 1 for $\beta_j \neq 1$, which again suggests that the number of graphene layers has a distribution.

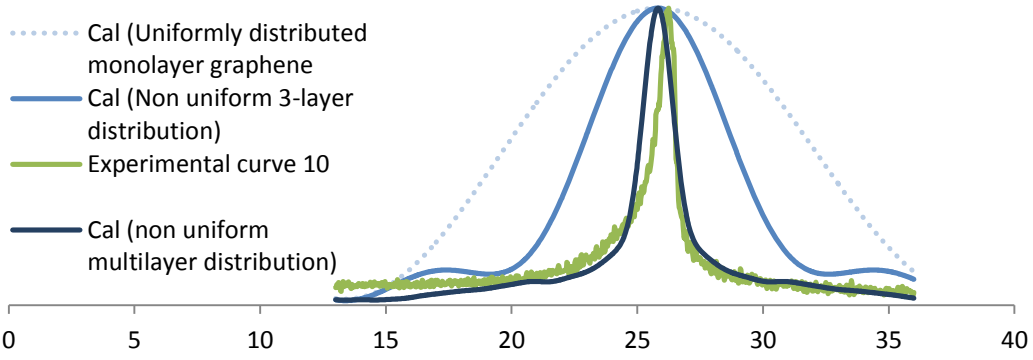

Figure 6. Non uniform multilayer distribution curve for Sample 4 calculated from Eq.1

The broadest blue dotted line is calculated curve for uniformly distributed monolayer graphene, the light blue line which is narrower than the monolayer graphene line, but broader than the green experimental curve 10, is calculated curve for a non uniform distribution of graphene layers number for a 3-layered graphene. The dark blue line is calculated curve for a non uniform

distribution of graphene layers number for a multi-layered graphene with a correlation coefficient $\rho = 0.93$, and according to its β_j parameters, the coverages of n-layer graphene regions are calculated as in Table 2 b).

Table 2. a) Coverages of n-layer graphene sample 4 regions
b) Coverages of n-layer graphene sample 10 regions

a)			b)		
	Monolayer region coverage	~ 40%		Monolayer region coverage	~ 30-35%
	2 layers region coverage	~ 10%		3-4 layers region coverage	~ 5-10%
	3-6 layers region coverage	~ 15%		5-6 layers region coverage	~ 5-10%
	7-10 layers region coverage	~ 5%		7-10 layers region coverage	~ 5-10%
	> 10 layers region coverage	< 10%		> 10 layers region coverage	< 10%

The dominant structure is few-layered, and the average value for number of sample 10 graphene layers is calculated as N_{GL}=3.53 for the dominant graphene structure and N_{GL}=5.6 for the overall graphene structure.

3. CONCLUSIONS

There are several clear conclusions to be drawn from the preceding analysis. The model that is used provides an additional insight into graphene samples n-layer occupancies and therefore coverages with a sufficient accuracy. However, a limitation to this model that should not be disregarded is the fact that in general case graphene sheets which are subject of research may have layer structure that varies across the studied sample and hence an asymmetrical 002 XRD peak. Experimental 002 XRD peaks which are highly asymmetrical are inconvenient to be analyzed by this model, and therefore adequate alterations to the model should be considered and researched. The results relevant to graphene samples produced by electrolysis in aqueous electrolyte and by electrolysis in molten salts, both using reverse change of the applied potential, which were studied and analyzed herein using this model, are in accordance with other methods results, and have shown that these graphene samples are few-layered.

Acknowledgment: This study was done within the FP7 Project "Cost-effective sensors, interoperable with international existing ocean observing systems, to meet eu policies requirements" (Project reference 614155) and the Project “Research and development of new nanostructured sensors aimed for protection and development of environment and nature” financed by Ministry of environment physical planning of R. Macedonia.

REFERENCES

[1] K. S. Novoselov, et al., “Two-dimensional atomic crystals”, Proc. Natl Acad. Sci. USA **102**, 10451-10453, 2005

[2] C. T. J. Low, F. C. Walsh, M. H. Chakrabarti, M. A. Hashim, M. A. Hussain, “Electrochemical approaches to the production of graphene flakes and their potential applications”, Carbon, 54, 1-21, 2013

[3] A. Ismach, C. Druzgalski, S. Penwell, A. Schwartzberg, M. Zheng, A. Javey, J. Bokor, Y. Zhang, “Direct chemical vapor deposition of graphene on dielectric surfaces”, Nano Letters 10, 1542, 2010

[4] L. Jiao, L. Zhang, X. Wang, G. Diankov, H. Dai, “Narrow graphene nanoribbons from carbon nanotubes”, Nature 458, 877, 2009

[5] Yan L, Zheng YB, Zhao F, Li S, Gao X, Xu B, et al., "Chemistry and physics of a single atomic layer: strategies and challenges for functionalization of graphene and graphene based materials", Chem Soc Rev, 41:97–114, 2012

[6] A. Ruammaitree, H. Nakahara, K. Akimoto, K. Soda, Y. Saito, "Determination of non-uniform graphene thickness on SiC (0 0 0 1) by X-ray diffraction", Applied Surface Science 282, 297– 301, 2013

[7] A. C. Ferrari, D. M. Basko, "Raman spectroscopy as a versatile tool for studying the properties of graphene", Nature Nanotechnology 8, 235, 2013